

Structures in Fire

SiF'2018

**10TH INTERNATIONAL CONFERENCE ON STRUCTURES IN
FIRE**

**BELFAST, UNITED KINGDOM
6-8 JUNE 2018**

EDITORS

**Ali Nadjai
Faris Ali
Jean-Marc Franssen
Olivier Vassart**

ORGANISED BY

**Ulster University
Faculty of Computing Engineering and Built Environment
Fire Safety Engineering Technology & Research Institute (FireSERT)**



STRUCTURES IN FIRE

First published in United Kingdom in 2018 by Ulster University.

All rights reserved. No part of this book may be reproduced or transmitted in any form or by any means, electronic, mechanical, photocopying, recording, or otherwise, without the prior written permission of the publisher.

© Ulster University, Shore Road, Newtownabbey, Co. Antrim, BT37 0QB

Tel: +44 (0)28 7012 3456

ISBN: 978-1-85923-274-3

Conference Proceedings of the 10th International Conference on Structures in Fire 2018.

Distribution:

Ulster University

Editors;

Ali Nadjai, Faris Ali, Jean-Marc Franssen, Olivier Vassart

ORGANISING COMMITTEE

Chairman

Prof Ali Nadjai – United Kingdom

Members

Prof Faris Ali – United Kingdom

Dr Karen Boyce – United Kingdom

Dr Jianping Zhang – United Kingdom

Dr Nigel McConnell – United Kingdom

Dr Talal Fateh – United Kingdom

Dr Eleni Asimakopoulou – United Kingdom

Mr Maurice McKee – United Kingdom

Mrs Heather Griffiths – United Kingdom

Mrs Sadie Magee – United Kingdom

Mr Naveed Alam – United Kingdom

STEERING COMMITTEE

Prof Jean-Marc Franssen - Belgium

Prof Kang Hai Tan - Singapore

Prof Kodur Venkatesh - USA

Prof Paulo Vila Real - Portugal

SCIENTIFIC COMMITTEE

Chairman

Prof Jean-Marc Franssen - Belgium

Members

Track 1: Applications of Structural Fire Safety Engineering

Kang Hai Tan – Singapore (Track Leader)

Daniel Joyeux - France

Florian Block - UK

Olivier Vassart - Luxembourg

Susan Lamont - UAE

Tom Lenon - UK

Frantisek Wald - Czech Republic

Yong Wang - UK

Timothy Liu - UK

LinHai Han - China

Charles Clifton - New Zealand

Track 2: Concrete Structures

Venkatesh Kodur – USA (Track Leader)

Faris Ali - UK

Bhargava Pradeep - India

Luke Bisby - UK

Mario Fontana - Switzerland

Gambarova Pietro - Italy

Mark Green - Canada

Vasant Matsagar - India

Priyan Mendis - Australia

Mohannad Z. Naser - USA

Ananth Raman - India

Luc Taerwe - Belgium

Bo Wu - China

Haiyan Zhang - China

Rami Haweeleh - UAE

Anil Agarwal - India

Track 3: Timber Structures and Fire

Protection Materials

Andrea Frangi - Switzerland (Track Leader)

Alar Just - Estonia

Andy Buchanan - New Zealand

Birgit Östman - Sweden

Christian Dagenais - Canada

Daniel Brandon - Sweden

Joachim Schmid - Switzerland

Marc Janssens - USA

Massimo Fragiaco - Italy

Michael Klippel - Switzerland

Norman Werther - Germany

Pedro Palma - Switzerland

Rory Hadden - UK

Steve Craft - Canada

Track 4: Numerical Modelling

Asif Usmani - Hong Kong (Track Leader)

Angus Law - UK

Anne Jeffers - USA

Bin Zhao - France

Chao Zhang - USA

CS Manohar - India

Hamid Ronagh - Australia

Jean-Marc Franssen - Belgium

Martin Gillie - UK

Suwen Chen - China

Kazunori Harada - Japan

Liming Jiang - Hong Kong

Cristian Maluk Zedan - Australia

Track 5: Composite Structures

Guo Qiang Li - China (Track Leader)

Ali Nadjai - UK

Colin Bailey - UK

David LANGE - Sweden

Dionis Dhima - France

Jian Jiang - USA

João Paulo Rodrigues - Portugal

Manuel Romero - Spain

Martin Mensinger - Germany

Peijun Wang - China

Peter Schaumann - Germany

Weiyong Wang - China

Yong Du – China

Track 6: Steel Structures

Paulo Vila Real - Portugal (Track Leader)

Carlos Couto - Portugal

Christophe Renaud - France

Ian Burgess - UK

Jyri Outinen - Finland

Leroy Gardner - UK

Mahen Mahendran - Australia

Maria Garlok - USA

Markus Knobloch - Switzerland

Michael D. Engelhardt - USA

Nuno Lopes - Portugal

Raul Zaharia – Romania

Track 7: Experimental Research and any Other

Ali Nadjai - UK (Track Leader)

Aldina Santiago - Portugal

Danny Hopkin - UK
Emidio Nigro - Italy
Francois Hanus - Luxembourg
Gisèle BIHINA - France
Konstantinos Daniel Tsavdaridis - UK
Muhammad Masood Rafi - Pakistan
OZAKI Fuminobu - Japan
Piergiacomo Cancelliere - Italy
Thomas Gernay - Belgium
Jochen Zehfuss - Germany
Richard Emberley - USA
Jose Terero - USA
Amar Khennane - Australia
Ricardo Fakury - Brazil
Talal Fetah - UK

SPONSORS



Fire Engineering Consultants



PREFACE

Structural fire safety is a key consideration in the design of buildings and infrastructure. Until the 1990's, there were very few forums for structural fire engineers to exchange ideas and share the research findings. The "Structures in Fire" (SiF) specialized workshop series was conceived in the late 1990's and bore fruit in 2000 when the "First International SiF workshop" was held in Copenhagen, Denmark. This was followed by International SiF workshops which were held in New Zealand (2002), in Canada (2004) and in Portugal (2006). The title was then changed from workshop to International conference, with the SiF'08 International Conference being held in Singapore (2008). Later SiF'10 was held in Michigan State University, USA (2010), SiF'12 in ETH Zurich, Switzerland (2012), SiF'14 in Shanghai, China (2014) and the latest one, SiF'16, in Princeton University, USA (2016). FireSERT at Ulster University, United Kingdom, was honoured to host the 2018 Structures in Fire International Conference (SiF'2018) from June 6 to June 8.

The main mission of the SiF conferences is to provide an opportunity for researchers, practitioners and engineers to share their "structures in fire" research, technology and expertise with their peers in an international forum. Allowing papers to be submitted only a few months before the conference provided the researchers an opportunity to present their most relevant recent work. In addition to high quality state-of-the-art presentations, the SiF 2018 conference will place significant value on discussions both formally, following presentations and informally through receptions, meals and breaks at Belfast's Titanic centre and City Hall.

SiF'2018 received over 250 abstracts for consideration. The Scientific Committee made three reviews of each abstract with blind authors and institutions. Based on the recommendation of the reviews, 138 papers were invited for publication, from which 125 accepted the invitation. These proceedings represent those 125 papers and collectively they represent state of the art in fundamental knowledge and practical application of structures in fire. Thirty countries from the globe have contributed to the knowledge contained in this book which is presented in two volumes.

In these proceedings, the papers are grouped into the following categories:

- Applications of Structural Fire Safety Engineering
- Concrete Structures
- Timber Structures and Fire Protection Materials
- Numerical Modelling
- Composite Structures
- Steel Structures
- Experimental Research and Any Other

We hope that the work presented in these proceedings will lead to safer, more economical and more relevant fire designs for structures.

We extend a sincere 'Thank You' to the Steering Committee for their guidance in making important decisions regarding the program format and proceedings. Our appreciation also goes to the members of the Scientific Committee for dedicating their time reviewing the abstracts. We are grateful to the Organising Committee who were instrumental in developing the conference program and website. A huge 'Thank You' to Ulster University IT services "Mark Kennedy and James Roger". A big thank you to FireSERT staff in particular to Heather Griffiths for managing registrations, finances, reservations, catering, purchasing and what not. A huge Thank You to Naveed Alam for supporting abstract and paper submissions, preparing invitation letters, attending

to emails and a huge ‘Thank You’ to Karen Boyce for her coordination with Interscience Communications Ltd, the conference book supplier.

Our sincere thanks to all authors for their contribution to the proceedings and to participants for making SIF’ 18 a successful conference.

Ali Nadjai
Chair, organizing Committee
FireSERT, Ulster University, UK

Jean Marc Franssen
Chair, Scientific Committee
Liege University, Belgium

TABLE OF CONTENTS

Committees	i
Sponsors	v
Preface	vi

APPLICATIONS OF STRUCTURAL FIRE SAFETY ENGINEERING

Design Fires for Performance-Based Engineering of Bridges <i>Jiayu Hu, Xu Dai, Ricky Carvel, The University of Edinburgh, Edinburgh, UK, Asif Usmani, The Hong Kong Polytechnic University, Kowloon, China</i>	3
Structural Design of Tall Steel Framed Buildings Under Multi-Storey Fires <i>Graeme Flint, Panagiotis Kotsovinos, Yavor Panev and Peter Woodburn Arup, UK</i>	11
Calculating Fire-Induced Heat Flux Contours on Concrete Tunnel Liners to Evaluate Structural Consequences <i>Kyle Root, Qi Guo, Spencer Quiel, Clay Naito, Lehigh University, USA</i>	17
Case Study of Travelling Fire Scenarios for Performance-Based Structural Fire Engineering <i>Erica Fischer, Oregon State University, USA and Amit Varma, Purdue University, USA</i>	25
Fire-Induced Progressive Collapse of the Plasco Building in Tehran <i>Amir Saedi Daryan, Hesam Ketabdari, Shahid Beheshti University, Iran, Mahmood Yahyai Toosi University of Technology, Tehran, Mohammed Morovat and Michael Engelhardt, University of Texas at Austin, USA</i>	33
Collapse Analysis of the Plasco Tower using Opensees <i>Hamzeh Hajiloo, Mark Green, Queen's University, Canada, Liming Jiang, Tejeswar Yarlagadda, Asif Usmani, Hong Kong Polytechnic University, China</i>	41

CONCRETE STRUCTURES

Experimental Studies on Shear Behaviour of Deep Prestressed Concrete Hollow Core Slabs Under Fire Conditions <i>Hang Nguyen and Kang-Hai Tan, Nanyang Technological University, Singapore</i>	51
Experimental Study and Numerical Simulation of Fire Resistance of Two-Way Restrained Precast Concrete Composite Slabs <i>Qingfeng Xu, Lingzhu Chen, Xiangmin Li, Shanghai Research Institute of Building Sciences, China, Chongqing Han, Southeast University, China, Yang Zhang, CIFI Group, Yong Wang, University of Manchester, UK and Weichen Xue, Tongji University, China</i>	61
Behavior of CFRP-Concrete Bond System at Elevated Temperatures <i>Thiago Carlo and João Paulo Rodrigues, University of Coimbra, Portugal</i>	69

The Effect of Explosive Spalling on Punching Shear Strength of Concrete Slabs Exposed to Fire <i>Fangxia Lu, ETH Zurich, Institute of Structural Engineering (IBK)/ Baertschi Partner Bauingenieure AG, Switzerland, Johann Eduard van der Merwe, Mario Fontana, ETH Zurich, Institute of Structural Engineering (IBK), Switzerland and Roland Baertschi, Baertschi Partner Bauingenieure AG, Switzerland</i>	77
Role of Polymer Fibres in Prevention of Explosive Spalling in Ultra-High Performance Concrete <i>Dong Zhang, Kang Hai Tan, Aravind Dasari, Nanyang Technological University, Singapore</i>	85
Role of Load Eccentricity and Transverse Reinforcement in Fire Resistance of Reinforced Concrete Columns <i>Shujaat Hussain and Umesh Kumar Sharma, IIT Roorkee, India</i>	93
Verification of a Tabulated Method of Eurocode for Concrete Columns Using a Response Surface and Advanced Methods <i>Marcus Achenbach, LGA KdöR, Germany, Thomas Gernay, Johns Hopkins University, USA and Guido Morgenthal, Bauhaus University, Germany</i>	101
Numerical Model for Fire Resistance Evaluation of Steel Reinforced Polymer Strengthened Concrete Beams <i>Pratik Bhatt, Venkatesh Kodur, Michigan State University, USA, Rami Haweeleh, Jamal Abdalla, American University of Sharjah, UAE and Nasser Al-Nuaimi, Qatar University, Qatar</i>	107
Fibre Reinforced Shotcrete – Presence of Synthetic Macro Fibres after Fire <i>Cristian Maluk, The University of Queensland, Australia, Todd Clark and Andrew Ridout, Elasto Plastic Concrete, Australia</i>	117
Fire Performance of Concrete Flat Slabs <i>Pasindu Weerasinghe, Priyan Mendis, Kate Nguyen and Tuan Ngo, The University of Melbourne, Australia</i>	125
Relationships Between Destructive and Non-Destructive Methods for Normal Strength Limestone Concrete After Exposure to High Temperatures <i>Urška Dolinar, Tomaž Hozjan, University of Ljubljana, Slovenia and Gregor Trtnik, Building Materials Institute (IGMAT), Slovenia</i>	133
Structural Behaviour of R/C Beams Exposed to Natural Fires <i>Nataša Kalaba, Patrick Bamonte, Politecnico di Milano, Italy, Venkatesh Kodu and Ankit Agrawal, Michigan State University, USA</i>	139
Residual Strength of Ultra-High Performance Fibre Reinforced Concrete <i>Charles Kahanji, Stellenbosch University, South Africa, Faris Ali and Ali Nadjai, Ulster University, UK</i>	147
Study of Fire Resistance of RC Columns with Varying Shear Reinforcement <i>Hemanth Kumar Chinthapalli and Anil Agarwal, Indian Institute of Technology Hyderabad, India</i> ...	157
On the Pull-Out Capacity of Post-Installed Bonded Anchors and Rebars During Fire <i>Hitesh Lakhani and Jan Hofmann, University of Stuttgart, Germany</i>	165
Design of Post Tensioned Concrete Structures Exposed to Travelling Fires <i>Chloe Jeanneret, Imperial College, UK/ York University, Canada, John Gales, York University, Canada, Panagiotis Kotsovinos Arup UK and Guillermo Rein, Imperial College, UK</i>	173

TIMBER STRUCTURES AND FIRE PROTECTION MATERIALS

Parametric Studies on the Fire Resistance of Steel-To-Timber Dowelled Connections Loaded Perpendicularly to the Grain <i>Pedro Palma, Empa – Materials Science and Technology, Switzerland and Andrea Frangi, ETH Zurich – Institute of Structural Engineering (IBK), Switzerland</i>	183
Thermal Characterisation and Fire Performance of Phase Change Material Incorporated Plasterboards <i>Sayilacksha Gnanachelvam, Mahen Mahendran, Anthony Ariyanayagam and Poologanathan Keerthan, Queensland University of Technology, Australia</i>	193
Fire-Retardant Coatings for Concrete Substrate: A Comparison Between One-Dimensional and Two-Dimensional Heat Transfer <i>Yan Hao Ng, Aravind Dasari and Kang Hai Tan, Nanyang Technological University, Singapore</i>	201
Fire Tests to ASTM E119 on Full-Size Glulam Beam to Column Connections <i>David Barber, Arup, USA</i>	209
A Methodology for Quantifying Fire Resistance of Exposed Structural Mass Timber Elements <i>David Barber, Arup, USA, Lizzie Sieverts, Robert Dixon and Jarrod Alston, Arup, Australia</i>	217
Numerical Model for the Fire Protection Performance of Intumescent Coatings Exposed to Natural Fires <i>Waldemar Weisheim, Peter Schaumann, Leibniz Universität Hannover, Germany, Lisa Sander and Jochen Zehfuß, Technische Universität Braunschweig, Germany</i>	225
Fire Resistance of Timber Frame Assemblies with Cavities Partially Filled by Insulation Materials <i>Mattia Tiso, Tallinn University of Technology, Estonia and Alar Just, Tallinn University of Technology, Estonia/ RISE Research Institutes of Sweden</i>	233
The Use of Furnace Tests to Describe Real Fires of Timber Structures <i>Joachim Schmid, Michael Klippel, Andrea Frangi, ETH Zürich, Switzerland, David Lange, University of Queensland, Australia, Johan Sjöström and Daniel Brandon, RISE Research Institutes of Sweden</i>	241
Fire Safety Challenges of Tall Wood Buildings: Large-Scale Cross Laminated Timber Compartment Fire Tests <i>Matthew Hoehler, Matthew Bundy, NIST, USA, Joseph Su, Pier-Simon Lafrance, NRCC, Canada, Amanda Kimball, Fire Protection Research Foundation, USA, Daniel Brandon, RISE Research Institutes of Sweden and Birgit Östman, Linneaus University, Sweden</i>	249
Investigation of Different Temperature Measurement Designs and Installations in Timber Members as Low Conductive Material <i>Reto Fahrni, Joachim Schmid, Michael Klippel and Andrea Frangi, ETH Zurich, Switzerland</i>	257
Comparison of Fire Resistance of Damaged Fireproofed Steel Beams Under Hydrocarbon Pool Fire and ASTM E119 Fire Exposure <i>Mustafa Mahamid, Ataollah Taghipour Anvari and Ines Torra-Bilal, University of Illinois at Chicago, USA</i>	265
Modelling Non-Metallic Timber Connections in Fire <i>Ranim Dahli, John Gales, York University, Canada and Martin Gillie, University of Warwick, UK</i>	275

Improvements to the Component Additive Method <i>Katrin Nele Mäger, Tallinn University of Technology, Estonia, Alar Just, Tallinn University of Technology, Estonia/Rise Research Institutes of Sweden and Andrea Frangi, ETH Zürich, Switzerland</i>	283
Influence of Gas Temperature During Cooling Phase on Load-Bearing Period of Structural Glued Laminated Timber Beams Exposed to Fire <i>T. Hirashima, Y. Katakura, M. Ichikawa, S. Ishii, Chiba University, Japan</i>	291
Experimental Fire-Simulator for Post-Flashover Compartment Fires <i>Daniel Brandon, RISE Research Institutes of Sweden, Joachim Schmid, ETH Zürich, Switzerland, Joseph Su, NRCC, Canada, Matthew Hoehler, NIST, USA, Birgit Östman, Linneaus University, Sweden and Amanda Kimball, Fire Protection Research Foundation, USA</i>	299

NUMERICAL MODELLING

A Storey-Based Stability Analysis Approach for Predicting of the Worst-Case Fire Scenario of Unbraced Steel Frames <i>Terence Ma and Lei Xu, University of Waterloo, Canada</i>	309
Discussion on a Systematic Approach to Validation of Software for Structures in Fire <i>João Daniel Romeiro Ferreira, Jean-Marc Franssen, Liege University, Belgium and Thomas Gernay, Johns Hopkins University, USA</i>	317
Branch-Switching Procedure for Buckling Problems of Steel Elements in Fire <i>Luca Possidente, Nicola Tondini, University of Trento, Italy, Jean-Marc Battini, KTH, Sweden</i>	325
Two-Dimensional Modelling of Thermal Responses of GFRP Profiles Exposed to ISO-834 Fire <i>Lu Wang, Weiqing Liu, Nanjing Tech University, China and Lingfeng Zhang, Southeast University, China</i>	333
CFD Analyses used to Evaluate the Influence of Compartment Geometry on the Possibility of Development of a Travelling Fire <i>Marion Charlier, Olivier Vassart, ArcelorMittal Global R&D, Luxembourg, Antonio Gamba, Jean-Marc Franssen, Liege University, Belgium, Xu Dai, Stephen Welch, The University of Edinburgh, UK</i>	341
Numerical Modelling of the Fire Behaviour of Restrained Cellular Beams using a Hybrid Simulation Approach <i>Mustesin Ali Khan, Katherine Cashell, Brunel University London, UK, Liming Jiang and Asif Usmani, The Hong Kong Polytechnic University, Hong Kong</i>	349
Fracture Simulation for Steel Shear Tab Connections at Elevated Temperature <i>Wenyu Cai, Hefei University of Technology, China, Mohammed Morovat and Michael Engelhardt, University of Texas at Austin, USA</i>	359
Numerical Modeling of Thermal Behaviour of CFRP Reinforced Concrete Structure Exposed to Elevated Temperature <i>Phi Long Nguyen, Xuan Hong Vu and Emmanuel Ferrier, University of Lyon, France</i>	367
Contribution to the Numerical Modelling of the Thermo-Mechanical Behavior of Structural Elements “Beam” Reinforced with TRC <i>Najib Douk, Amir Si Larbi, Xuan Hong Vu and Maxime Audebert, University of Lyon, France</i>	375

A Numerical Methodology to Predict the Gas/Solid Interaction in Fire Resistance Tests <i>Rene Prieler, Markus Mayrhofer, Markus Eichhorn-Gruber, Günther Schwabegger and Christoph Hochenauer, Graz University of Technology, Austria</i>	383
Virtual Test of Fire-Resistance of a Timber Beam <i>Kamila Cábová, Filip Zeman, Lukáš Blesák, Martin Benýšek and František Wald, Czech Technical University in Prague, Czechoslovakia</i>	391
Reduced-Order Thermal Analysis of Fire Effects on Composite Slabs <i>Jian Jiang, Joseph Main, Jonathan Weigand and Fahim Sadek, NIST, USA</i>	399
Numerical Investigation of Fire and Post-Fire Performance of CFT Columns in an Open Car Park Fire <i>Wojciech Szymkuć, Adam Glema, Michał Malendowski, Poznan University of Technology, Poland, Aleksandra Mielcarek, Piotr Smardz and Adrian Poteralski, INBEPO Sp. z o.o., Poland</i>	407
Analysis of The Influence of Ventilation in the Structural Response of a Cut-And-Cover Tunnel Under Fire <i>Juan Pagán-Martínez, Jeremy Gardner Associates, Ireland, Ignacio Payá-Zaforteza, Antonio Hospitaler and Toni Hospitaler, Universitat Politècnica de València, Spain</i>	415
Reverse Engineering of Standard Temperature Curves to Obtain the HRR of the Fire in Various Enclosure Configurations - What Can We Learn From That? <i>Piotr Tofiło, Main School of Fire Service (SGSP), Poland, Wojciech Węgrzyński, Building Research Institute (ITB), Poland and Michał Malendowski, Poznan University of Technology, Poland</i>	423
Fragility of Reinforced Concrete Structure Subjected to Elevated Temperature <i>Ranjit Kumar Chaudhary, Tathagata Roy and Vasant Matsagar, Indian Institute of Technology Delhi, India</i>	431
Advance Heat Transfer Analysis and Capacity Curves Accounting for the Effect of Spalling <i>Hitesh Lakhani and Jan Hofmann, University of Stuttgart, Germany</i>	439
Fire Resistance of Concrete Slabs Acting in Compressive Membrane Action with Various Edge Conditions <i>Tom Molkens, Sweco Belgium</i>	447
Structural Implications Due to an Extended Travelling Fire Methodology (ETFM) Framework Using SIFbuilder <i>Xu Dai, Stephen Welch, The University of Edinburgh, UK and Asif Usmani, Hong Kong Polytechnic University, Hong Kong</i>	455
Elevated-Temperature Tension Stiffening Model for Reinforced Concrete Structures Under Fire <i>Jason Martinez and Ann Jeffers, University of Michigan, USA</i>	463

COMPOSITE STRUCTURES

Experimental and Analytical Investigations on Thermal Performance of Slim Floor Beams With Web Openings in Fire <i>Naveed Alam, Ali Nadjai, Faris Ali, Ulster University, UK, Olivier Vassart, ArcelorMittal Global R&D Long Carbon and Francois Hanus, ArcelorMittal Long Products, Luxembourg</i>	473
--	-----

Fire Performance of Steel Reinforced Ultra High Toughness Cementitious Composites Beam <i>Chao-Jie Sun, Qing-Hua Li, Shi-Lang Xu, Zhejiang University, China and Jun-Feng Lu, China Southwest Architecture Design and Research Institute Corp.Ltd, China</i>	481
Numerical and Experimental Investigation of the Structural Behavior of Perforated Beams Exposed to Hydrocarbon Fires in Offshore Platforms <i>Hooman Atefi, Mott MacDonald, UK, Ali Nadjai and Faris Ali, Ulster University, UK</i>	489
Experimental Study of a Steel-Concrete Composite Bridge Under Fire <i>Jose Alos-Moya, Ignacio Paya-Zaforteza and Antonio Hospitaller, Universitat Politècnica de València, Spain</i>	497
Experimental Investigation of Post-Tensioned Concrete Bridge Beams Exposed to Hydrocarbon Fire <i>Xi Qiang Wu, Francis Tat Kwong Au, The University of Hong Kong, China and Jing Li, South China University of Technology, China</i>	505
Fire Behaviour of Steel Reinforced Concrete Filled Stainless Steel Tubular (SRCFSST) Columns with Square Hollow Section <i>Qinghua Tan, Bin Chen, National University of Defense Technology, China, Leroy Gardner, Yaoyuan Zhang, Imperial College London, UK and Linhai Han, Tsinghua University, China</i>	513
Behavior of Circular Concrete-Filled Double-Skin, Double-Tube and Inner Concrete Ring Tubular Columns Subjected to Fire <i>Aline Camargo, Ricardo Fakury, Federal University of Minas Gerais, Brazil, João Paulo Rodrigues, University of Coimbra, Portugal and Tiago Pires, Federal University of Pernambuco, Brazil</i>	521
Numerical and Experimental Tests on Concrete Filled Square and Rectangular Hollow Columns Subjected to Fire <i>Luís Laím, João Paulo Rodrigues, University of Coimbra, Portugal and Venkatesh Kodur, Michigan State University, USA</i>	529
Investigation of Partial Connection Theory on Composite Beams Under Fire Exposure <i>Sven Brunkhorst, Jochen Zehfuß, Technische Universität Braunschweig, Germany, Samuel Pfenning and Martin Mensinger, Technical University of Munich, Germany</i>	537
Key Governing Factors that Define the Fire Performance of Structural Insulated Panels Used in Floor Systems <i>Aaron Bolanos, Cristian Maluk, The University of Queensland, Australia and Jose Torero, The University of Maryland, USA</i>	545
Experimental and Numerical Investigations on the Load-Bearing Behaviour of an Innovative Prestressed Composite Slab System Under a Natural Fire Scenario <i>P. Schaumann, P. Meyer, Leibniz Universität Hannover, Germany, M. Mensinger and S. K. Koh, Technische Universität München, Germany</i>	553
Load-Bearing Fire Tests of Unprotected Composite Beams Pinned with Steel Girders <i>R. Dwiputra, Nihon Sekkei Inc., Japan, N. Yotsumoto, General Building Research Corporation of Japan, T. Hirashima, Chiba University, Japan, F. Ozaki, Nagoya University, Japan, Y. Murakami, JFE Steel Corporation, Japan, K. Kimura, Nippon Steel & Sumitomo Metal Corporation, Japan</i>	561
Fire Behaviour of Slender Concrete-Filled Steel Tubular Columns Under Biaxial Bending <i>Ana Espinós, Vicente Alberó, Manuel L. Romero, Universitat Politècnica de València, Spain, Maximilian Mund, Patrick Meyer, Peter Schaumann, Leibniz Universität Hannover, Germany and Inka Kleiboemer, Hagen Ingenieurgesellschaft für Brandschutz, Germany</i>	569

Numerical Analysis of the Thermal Behaviour of Steel-Timber Hybrid Beams in Fire Situation
Antoine Bérezyiat, Maxime Audebert, University of Lyon, France, Abdelhamid Bouchaïr and Sébastien Durif, Université Clermont Auvergne, France577

Study on the Use of Ultra-Lightweight Cement Composite for Enhancing Fire Performance of Concrete-Filled Tubular Columns
Wojciech Szymkuc, Piotr Tokłowicz, Adam Glema, Poznan University of Technology, Poland and Helder Craveiro, University of Coimbra, Portugal585

Methods to Assess the Bearing Capacity of Concrete-Filled Hollow Section Columns in Fire
Alberto Compagnone, Antonio Bilotta and Emidio Nigro, University of Naples Federico II, Italy.....593

Fire Performance of Long-Span Composite Beams with Gravity Connections
Lisa Choe, Selvarajah Ramesh, Mina Seif, Matthew Hoehler, William Grosshandler, John Gross and Matthew Bundy, NIST, USA.....601

STEEL STRUCTURES

Performance of Beam-Column Subassemblages with Continuous H Shaped Columns in Severe Fires
Chia Mohammadjani, Charles Clifton, University of Auckland, New Zealand and Anthony Abu, University of Canterbury, New Zealand.....611

Experimental Analysis of the Influence of Creep on Fire-Exposed Steel and Aluminium Columns
Neno Torić, Ivica Boko, Vladimir Divić, Marko Goreta, University of Split, Croatia and Ian Burgess, University of Sheffield, UK.....619

Influence of Fire on the Shear Capacity of Steel-Sheathed Cold-Formed Steel Framed Shear Walls
Matthew Hoehler, NIST, USA and Blanca Andres, Danish Institute of Fire and Security Technology, Denmark.....625

Behaviour of Steel Frame Structures Under Localised Fire Including Progressive Collapse During Cooling
Thomas Gernay, Johns Hopkins University, USA and Antonio Gamba, University of Liège, Belgium.....633

Fire Tests of Load Bearing Double Stud LSF Walls
Harikrishnan Magarabooshanam, Anthony Deloge Ariyanayagam, Mahen Mahendran, Queensland University of Technology, Australia.....641

Performance of Intumescent Fire Protection Coatings on Steel Tension Rod Systems
Mai Häßler, Dustin Häßler, Sascha Hothan and Simone Krüger, BAM, Germany649

Preliminary Study on Quantitative Determination of Collapse Process of Steel Portal Frames in Fire
Guobiao Lou, Chenghao Wang, Jian Jiang and Guo-Qiang Li, Tongji University, China.....655

Steady-State and Transient-State Tests on S355 to S500 Steel Grades
François Hanus, Nicolas Caillet, Olivier Vassart, ArcelorMittal Global R&D, Luxembourg and Sylvain Gaillard, Luxembourg Institute of Science and Technology (LIST), Luxembourg.....663

Estimation of Charpy Impact Values for Steel Welded Connections at High Temperature and After Heating and Cooling Processes
Kai Ye and Fuminobu Ozaki, Nagoya University, Japan.....671

Study on Temperature Distribution of Welded Tubular Square Joints <i>Jolanta Bączkiewicz, Mikko Malaska, Sami Pajunen and Markku Heinisuo, Tampere University of Technology, Finland</i>	679
Progressive Collapse of Braced Steel Framed Structures Exposed to Fire <i>Jian Jiang and Guo-Qiang Li, Tongji University, China</i>	687
Numerical Parametric Study of Cold-Formed Steel C-Shaped Columns Exposed to Fire <i>Luís Laím, João Paulo Rodrigues, University of Coimbra, Portugal and Leroy Gardner, Imperial College London, UK</i>	695
An Equivalent Stress Method for Considering Local Buckling in Beam Finite Elements in the Fire Situation <i>Chrysanthos Maraveas, Jean-Marc Franssen, Liège University, Belgium and Thomas Gernay, Johns Hopkins University, USA</i>	703
Behavior of Bolted Connections Component Under Elevated Temperatures <i>Ioan Both, Florea Dinu, Calin Neagu, Ioan Marginean and Raul Zaharia, Politehnica University of Timisoara, Romania</i>	711
Behaviour of Full High Strength Steel Extended Endplate Connections After Fire <i>Xuhong Qiang, Xu Jiang, Tongji University, China/Delft University of Technology, The Netherlands, Huan Chen, Tongji University, China and Frans Bijlaard, Delft University of Technology, The Netherlands</i>	717
Direct Method for Critical Temperature of a Steel Member Susceptible to Stability Loss <i>Teemu Tiainen, Jolanta Bączkiewicz, Tampere University of Technology, Finland. Timo Jokinen, Markku Kauriala Ltd, Finland and Mikko Salminen, Finnish Constructional Steelwork Association, Finland</i>	725
Analytical Determination of Temperature Distribution in Steel Cables Considering Cavity Radiation Effect <i>Yong Du, Liang Li, Nanjing Tech University, China, Jian Jiang, NIST, USA and Guo-Qiang Li, State Key Laboratory for Disaster Reduction in Civil Engineering, China</i>	733
Research on Post-Fire Load-Bearing Capacity Assessment of Axial Restrained High-Strength Steel Columns <i>Guo-Qiang Li and Jia-Rong Miao, Tongji University, China</i>	741
Effects of Topcoat on Insulation of Intumescent Coating for Fire Protection of Steel Structures <i>Qing Xu, Guo-Qiang Li, Xiao Zhao, Xing-Yuan Zhao, Tongji University, China</i>	747
Development of An Analytical Method for the Fire Resistance Calculation of Angelina Beams <i>Jérôme Randaxhe, François Hanus and Olivier Vassart, ArcelorMittal Global R&D, Luxembourg</i> ..	755
Tests on Creep Buckling of High Strength Steel Columns at Elevated Temperatures <i>Weiyong Wang, Linbo Zhang, Hongyang Zhou, Chongqing University, China and Venkatesh Kodur, Michigan State University, USA</i>	763
Developing Fragility Curves and Estimating Failure Probabilities for Protected Steel Structural Elements Subject to Fully Developed Fires <i>Danny Hopkin, Olsson Fire and Risk/University of Sheffield, UK, Ruben Van Coile, University of Ghent, Belgium and Ian Fu, Olsson Fire and Risk, UK</i>	771

Stability Check of Tapered Steel Beams in Fire <i>Carlos Couto, Elio Maia, Paulo Vila Real and Nuno Lopes, University of Aveiro, Portugal</i>	779
Shear Analysis of Clipped Webs in Fire and Ambient Conditions <i>Veronica Boyce and Maria Moreyra Garlock, Princeton University, USA</i>	787
Effectiveness of Stiffeners on the Shear Capacity of Steel Web Plates at Ambient and Elevated Temperatures <i>Veronica Boyce, Maria Moreyra Garlock, Princeton University, USA and Jonathan Glassman, Exponent, Inc., USA</i>	795
Failure Mechanism of Steel Frames Subjected to Post-Earthquake Fires <i>Gabriel-Victor Risco, Trenton Fire Ltd, Luisa Giuliani and Varvara Zania, Technical University of Denmark</i>	803
Characterising the Thermomechanical Response of Steel Columns Subject to Localised Fires <i>Yavor Panev, Panos Kotsovinos, Graeme Flint, Arup, UK, Teodor Sofroniev, Cundall, UK and Luke Bisby, University of Edinburgh, UK</i>	811
Cross-Section Resistance of Slender Stainless Steel I Profiles in Case of Fire <i>Nuno Lopes, Carlos Couto, Jorge Azevedo and Paulo Vila Real, University of Aveiro, Portugal</i>	819
Implication of the End Connection Type of Steel Beams on the Critical/Limiting Temperature Equations <i>Jashnav Pancheti and Arul Jayachandran, Indian Institute of Technology Madras, India</i>	827
Direct Strength Method for Calculating Distortional Buckling Resistance of Cold-Formed Thin-Walled Steel Beams with Non-Uniform Elevated Temperatures <i>Mutiu Adeoye Alabi-Bello and Yong Chang Wang, University of Manchester, UK</i>	835
Thermo-Mechanical Behaviour of Structural Stainless Steel Frames in Fire <i>Mian Zhou, Rui Cardoso, Hamid Bahai, Brunel University, UK and Aisf Usmani, Hong Kong Polytechnic University, China</i>	843
 EXPERIMENTAL RESEARCH AND ANY OTHER	
Performance Assessment of a Structure Subjected to Fire Through Hybrid (Numerical-Experimental) Simulation <i>Xuguang Wang, Oh-Sung Kwon, University of Toronto, Canada, Robin Kim, Inwhan Yeo and Jaekwon Ahn, Korea Institute of Civil Engineering and Building Technology</i>	853
A Pi-Controller for Hybrid Fire Testing in a Non-Linear Environment <i>Elke Mergny, Guillaume Drion, Jean-Marc Franssen, Liège University, Belgium and Thomas Gernay, Johns Hopkins University, USA</i>	861
Effect of Combined Polypropylene and Steel Fibres on Pore-Pressure Development in Ultra-High-Performance Concrete in Fire <i>Ye Li, Kang Hai Tan, Nanyang Technological University, Singapore, Pierre Pimienta and Nicolas Pinoteau, CSTB, France</i>	869
Scaling Approach for Studying Fire Response of Steel Beams <i>Mahmood Yahyai, Toosi University of Technology, Iran, Abbas Rezaeian, Shahid Chamran University of Ahvaz, Iran and Peter Chang, University of Maryland, USA</i>	877

Radiative Flux Affecting Vertical Steel Member Away From the Fire – Simplified Method LOCAFI <i>Camille Sautot, Christophe Thauvoye, CTICM, France, François Hanus, ArcelorMittal Global R&D, Luxembourg, Giacomo Erez and Aurélien Thiry, Central Police Laboratory, France</i>	885
Evaluating Uncertainty in Steel-Composite Structure Response Under Fire – Application of the ME-MDRM <i>Ruben Van Coile, Ghent University, Belgium, Thomas Gernay, Johns Hopkins University, USA, Negar Elhami Khorasani, University at Buffalo, USA, Danny Hopkin, University of Sheffield, UK</i> ...	893
Experimental Investigation of Liquid Pool Fires and Externally Venting Flames in Corridor-Like Enclosures <i>Kostantinos Chotzoglou, Ulster University, UK/Effectis, UK/Ireland, Eleni Asimakopoulou, Jianping Zhang, Ulster University, UK and Michael Delichatsios, Northeastern University, USA University of Science and Technology of China</i>	901
Seismic Performance of Reinforced Concrete Frames After Fire <i>Ling-Zhi Li, Xin Liu, Zhou-Dao Lu and Kai Wei, Tongji University, China</i>	909
Monitoring Spalling of Heated Concrete Using Laser Distance Metre <i>Jin-Cheng Liu and Kang Hai Tan, Nanyang Technological University, Singapore</i>	917
Experimental Studies on Early Warning Approaches of the Collapse of Steel Portal Frame Structures in Fire <i>Ya-Qiang Jiang, Bo Zhong, Jun-Jun Liu, Guo-Jian Lu, Jian-Zhong Rong, Sichuan Fire Research Institute of Ministry of Public Security, China, Guo-Biao Lou, Tongji University, China</i>	925
Instantaneous Stiffness Correction for Hybrid Fire Testing <i>Ramla Qureshi and Negar Elhami-Khorasani, University at Buffalo, USA</i>	933
Experimental Investigation of Thermomechanical Behaviour of the Carbon Textile Reinforced Concrete Composite: Efficiency Coefficient of Carbon Textile at Elevated Temperature <i>Manh Tien Tran, Xuan Hong Vu and Emmanuel Ferrier, University of LYON, France</i>	941
An Experimental Approach for Evaluating Residual Capacity of Fire Damaged Concrete Members <i>Ankit Agrawal and Venkatesh Kodur, Michigan State University, USA</i>	949
Evaluation Method of Thermal Elongation of Steel Beams During Fire Based on Actual Scale Tests <i>Tomohito Okazaki, Takenaka Corporation, Japan and Mamoru Kohno, Tokyo University of Science, Japan</i>	959
Experimental Investigation of Stainless Steel Bolts A2-70 During and After Fire <i>Sheng Lin Tang, Ying Hu and George Adomako Kumi, Chongqing University, China</i>	967
Experimental Study on Thermal and Structural Responses of a Full-Scale Steel Structure Under Natural Fire <i>Bo Zhong, Ya-Qiang Jiang, Sichuan Fire Research Institute of Ministry of Public Security, China and Guo-Biao Lou, Tongji University, China</i>	975
Fire Resistant GFRP Façade System <i>Kate Nguyen, Tuan Ngo and Priyan Mendis, University of Melbourne, Australia</i>	981
Timber and the Fire Resistance Furnace – A Comparative Study of the Conditions in a Fire Resistance Furnace When Testing Combustible and Non-Combustible Construction <i>David Lange, University of Queensland, Australia, Johan Sjöström, Daniel Brandon. RISE Research Institutes of Sweden and Joachim Schmid, ETH Zurich, Switzerland</i>	989

Hybrid Fire Testing of a Single Degree-of-Freedom Linear System <i>Ana Sauca, Chao Zhang, Artur Chernovsky and Mina Seif, NIST, USA</i>	997
Experimental and Analysis of Localized Pool Fire Tests on Steel Columns with Compartment Open Ceiling <i>Ali Nadjai, Sanghoon Han, Ulster University, UK, Olivier Vassart, ArcelorMittal Global R&D, Luxembourg and Francois Hanus, ArcelorMittal Long Product, Luxembourg</i>	1005
Author Index	1013

APPLICATIONS OF STRUCTURAL FIRE SAFETY ENGINEERING

Applications of Structural Fire Safety Engineering

DESIGN FIRES FOR PERFORMANCE-BASED ENGINEERING OF BRIDGES

Jiayu Hu¹, Xu Dai², Asif Usmani³, Ricky Carvel⁴

ABSTRACT

This paper presents a series of 2D localised fires for various vehicle fire scenarios under bridges, which have been developed using CFD models based on estimated HRR and considering different types and locations of vehicles. This method provides a varying heat flux which decays with distance from the fire origin to produce a more realistic scenario than previous code-based prescriptive fires. The design fire curves were then fitted as exponential functions and embedded in OpenSees enabling users to predict the structural response of a bridge in the selected design fire scenario. This aims at enabling OpenSees to be used for identifying the range of accepted fire loads to ensure that bridge structures have adequate fire resistance. In the final section, a heat transfer analysis is presented, comparing the proposed design fires with the standard hydrocarbon fire.

Keywords: Bridges in fires, CFD models, OpenSees, heat transfer

1 INTRODUCTION

In most previous studies of bridge performance under fire heating, a uniform temperature along the entire bridge span is commonly assumed, generally using a prescriptive fire curve [1,2]. The most serious bridge fire incidents usually involve fuel tanker fires, which has led researchers to the use of the hydrocarbon fire to characterise fire hazard for bridges. While this may be a reasonably conservative assumption in the context of an extreme load, it is not consistent with reality or the principles of performance based engineering (PBE), where different magnitudes of hazard intensity are linked to correspondingly different levels of performance (see *Table 1*). In order to develop a more realistic representation of vehicle fires for highway bridges, this paper introduces the concept of idealized vehicle fire scenarios. It is expected that a bridge can be subjected to a variety of fires depending upon the location and size of the vehicle involved in an incident. Further uncertainties arise from the unknown magnitude of liquid fuels and/or other combustibles present in the burning vehicle and the resulting heat release rate (HRR), which determines the fire size and enables the quantification of the likely fire behaviour and its interaction with adjacent structures [3].

¹ PhD Candidate. Institute for infrastructure and Environment, School of Engineering, The University of Edinburgh, Edinburgh, UK.
e-mail: Jiayu.Hu@ed.ac.uk

² Post-Doctoral Research Associate. Institute for infrastructure and Environment, School of Engineering, The University of Edinburgh, Edinburgh, UK.
e-mail: x.dai@ed.ac.uk

³ Professor and Head of the Department. Department of Building Services Engineering, Faculty of Construction and Environment, The Hong Kong Polytechnic University, Kowloon, Hong Kong.
e-mail: asif.usmani@polyu.edu.hk

⁴ Lecturer. Institute for infrastructure and Environment, School of Engineering, The University of Edinburgh, Edinburgh, UK.
e-mail: Ricky.Carvel@ed.ac.uk

Table 1 Correlation of hazard intensity and damage level in the context of expected performance levels

Damage level/ Hazard Intensity (HRR in MW)	None or Superficial Damage	Minor Damage	Major Damage	Collapse
Low to Moderate (<5)	Expected performance	Bad	Poor	Catastrophic
Moderate to High (5-20)	Conservative design	Expected performance	Bad	Poor
High to Very High (20-50)	Overdesigned	Conservative design	Expected performance	Bad
Exceptional (>50)	Massively overdesigned	Overdesigned	Conservative design	Expected performance

A series of fire scenarios have been developed and quantified using computational fluid dynamics (CFD) models constructed using the public domain software Fire Dynamics Simulator 6.5.3 (FDS) developed by NIST (USA). The models produce a spatially varying heat flux that is used to provide the thermal boundary conditions for the bridge superstructure.

The vehicle fire models were then simplified to exponential functions and have been implemented into OpenSees. Envelopes of suitable design fires can be used by engineers to ensure that a bridge structure has adequate level of performance for all possible fire scenarios. Acceptable threshold performance measures such as deflections, rotations and horizontal displacements can be specified for all fire scenarios (including collapse for the most severe fires). The proposed approach aims at providing a powerful quantitative decision tool for bridge managers.

To demonstrate the approach above, a heat transfer model of a composite section is presented. The model compares the temperature distribution results using hydrocarbon fire and a new design fire. In this paper, only one case will be presented. The functions for all the fire scenarios will be published elsewhere and are not described here.

2 DESIGNED CFD LOCALISED VEHICLE FIRES

2.1 Parameters in the designed fires

The possible fire scenarios depend predominantly on the fire accident location and the fire intensity, which will vary with vehicle type. Therefore, the design fires have been categorized into four types of vehicles corresponding to different magnitude of hazards: low to moderate (cars), moderate to high (light goods vehicles, LGVs), high to very high (heavy goods vehicles, HGVs) and exceptional (fuel tankers). For each category a different magnitude range of HRR is assumed to represent different levels of fire intensity, and is estimated based on the available literature for vehicles, goods trailers and liquid pool fire experiments. Table 2 shows the defined HRR ranges with the corresponding vehicle types and vehicle dimensions.

Table 2 Parameters used in each category

	HRR (MW)	L (m)	W (m)	H (m)
Low – Moderate (Cars)	2-5	3.2	1.6	1, 1.6
Moderate – High (LGVs)	5-20	5.2	2	1.6, 2.6
High - v. High (HGVs)	20-50	12	2.4	2, 3, 4
Exceptional (Fuel tanker)	50-100	14.8	2.4	2, 4.6

As shown in Figure 1, the fuel bed is assumed to be a fixed rectangular region which is positioned above the ground based on the fact that most of the burning material would be at some height above

ground level. In order to have a general value, the dimensions of the fuel bed are assumed to be the footprint of the vehicles.

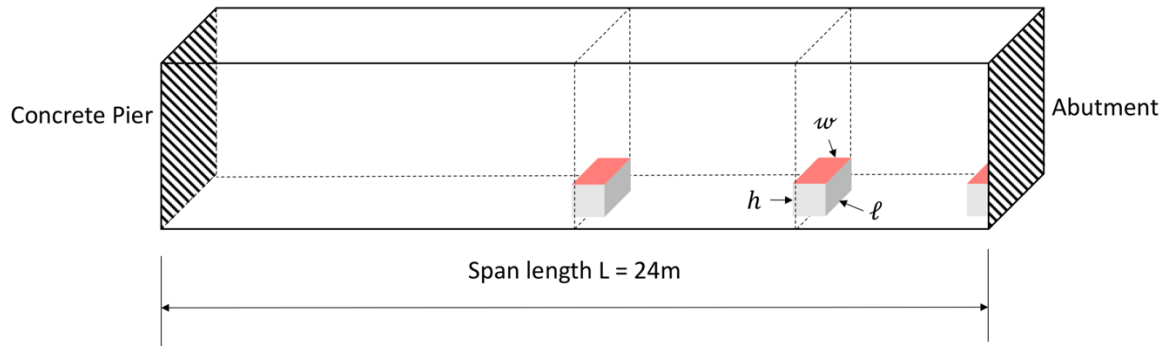


Figure 1 Schematic representation of the fire model under bridge span

Three accident locations under the span have been investigated: near the abutment, at midpoints and quarter points of the span. Fire location has been situated at the mid-span to quantify the heat flux due to the fire exposure resulting from an accident below the centre of span as this is the most critical location in terms of potential damage level. The fire location adjacent to the abutment is expected to generate the largest heat flux because of the abutment boundary effect and will also test the reduced shear capacity of the bridge superstructure. The quarter span location is investigated as an intermediate case.

2.2 An example of CFD model

This section presents one of the bridge fire cases investigated using FDS as an example. As shown in Figure 2, a fuel bed with dimensions $3.2\text{ m} \times 1.6\text{ m} \times 1.6\text{ m}$ of HRR 5MW located below the centre of the span is used to represent low to moderate (e.g. car) fires.

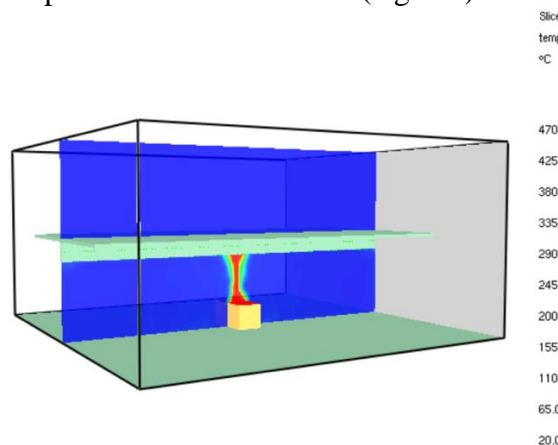


Figure 2 A case of CFD vehicle fire model (Low to Moderate, 5MW, $3.2\text{ m} \times 1.6\text{ m} \times 1.0\text{ m}$, flat slab)

For all the models, the computational domain is set to 24m in length, 24m in width and 12m in depth to generate sufficient space for the fire and smoke spread. The top, foreground and background side boundaries were left open to ambient conditions while the left and right surfaces of domain were defined as adiabatic surfaces to represent the concrete pier and abutment respectively. The bottom surface was modelled as concrete to represent the roadway.

In the CFD models, the fire intensity is defined by a time dependent HRRPUA (Heat Release Rate Per Unit Area) curve. Considering the FDS results are inherently transient, a sufficient run time is necessary to eliminate the influence of the initial conditions and averaging out the time-dependent

outputs. In this research, fires were modelled for 30 minutes allowing 60 seconds of growth and flow stabilization, with no decay period considered. HRRPUA curve was linearly increased from zero to a capped value $HRRPUA_{max}$, which varied for each category. The HRRPUA curves remain constant for the rest of the run time where the average values of $HRRPUA_{max}$ can be obtained at steady state. This assumption gives a conservative result since a variable heat release rate would normally occur in reality.

2.3 Heat flux results

The heat flux imposed on the bridge structure is dependent on the fire size, the bridge geometry and the thermal properties of the boundaries. This research compares the predicted heat fluxes to study the influence of parameters in two directions: along the slab at distances away from the fire centreline (x-axis); and at three positions along the height of the beam (y-axis) at the centreline of the domain width. The results at different positions along the beam depth will not be discussed in this paper. All the results shown in *Figure 3* have been processed from the raw data to determine the heat flux envelope along the beam depth.

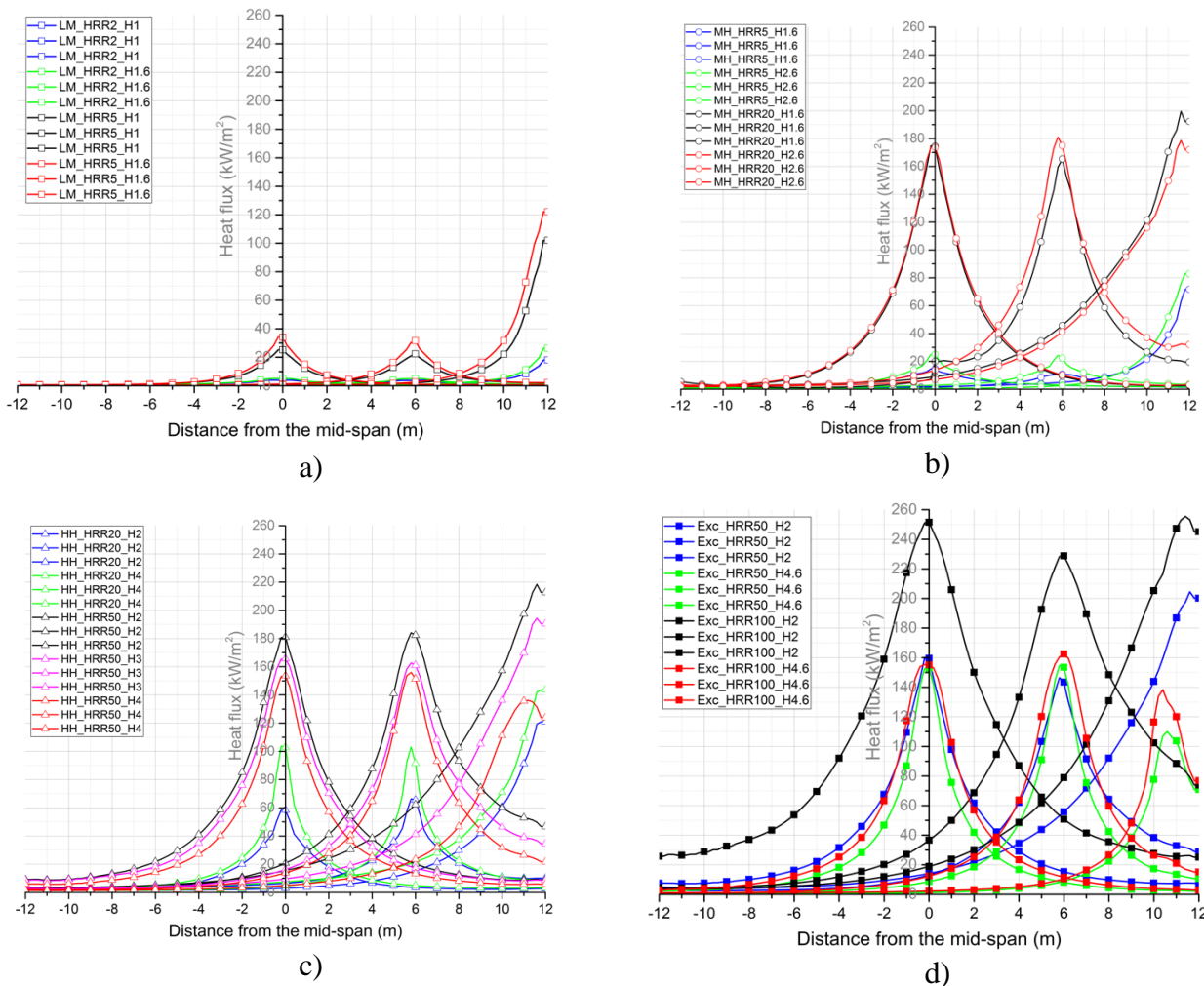


Figure 3 Heat flux variation with the distance from the mid-span for a) Low – Moderate b) Moderate – High c) High – very High d) Exceptional models

Figure 3 shows the estimated heat flux along the span for each of the four categories. It shows that the received flux is maximum above the fire source and decays with increasing distance from fire origin as expected. As fires become larger in size, the maximum value of heat flux to the structural surfaces increases due to the radiation feedback between the fire and the structure. This also happens

when the fuel bed is located at an elevated location and is therefore closer to the bridge deck. In addition, moving the fuel bed away from the abutment decreases the heat fluxes to the bridge boundaries as expected. The incident heat flux at the bridge deck near the abutment is higher than the other two locations, especially for low to moderate fires (*Figure 3a*). This considered reasonable due to the feedback effect.

However, for the very large fires with HRR magnitude larger than 50MW, the models are counter-intuitive, showing that greater height or being close to the abutment does not produce greater heat flux. In some cases, the heat flux received at the location near the abutment is even lower than the other two locations (*Figure 3c and Figure 3d*). This may be caused by the fact that when the height of fuel bed is above 2m (under a bridge deck of 6m), the released fuel has to travel away from the vehicle before it encounters sufficient air to allow burning, so the flames (and hence the higher temperatures) happen away from the vehicle location. This is effectively a ventilation controlled fire. This phenomenon suggests that the open environment may not always be fuel controlled when the fire is large. The environment may change from ‘open air’ to ‘partially enclosed’ when a large lorry is burning only a short distance below the bridge deck.

2.4 Fitting functions

The correlations for the heat flux along the bridge span have been developed using exponential functions. This aims to represent the heat flux based on the user-input variables such as HRR, location, and dimensions of the fuel bed. *Figure 4* shows the fitting results and data points of the models for a low to moderate fire. It shows the fitting curves provide a reasonable estimate of incident heat flux from the CFD calculated data.

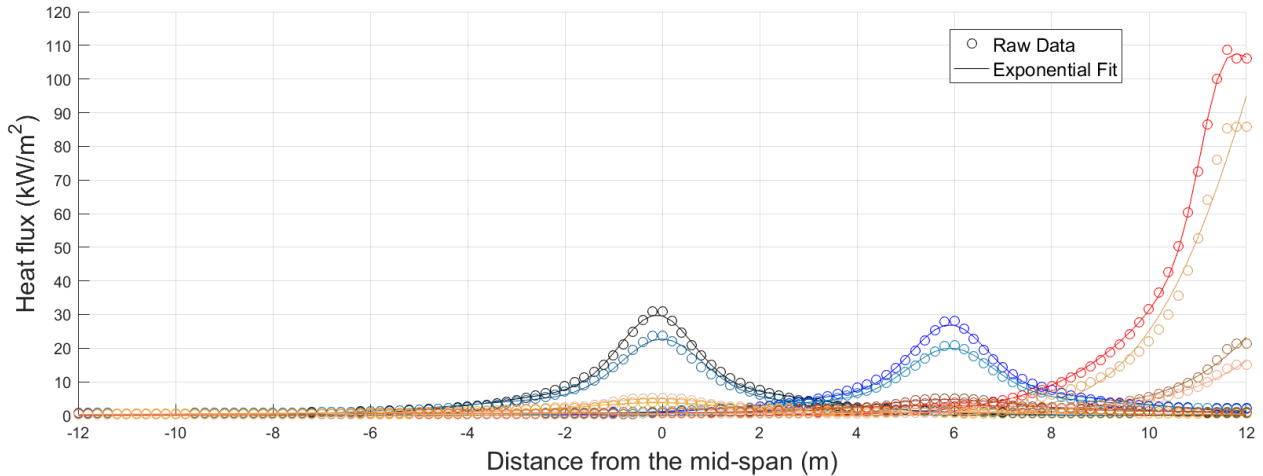


Figure 4 Results of the low to moderate fires and the exponential fit

The heat flux to structural surfaces is represented as a function of the radial distance from the fire origin. The heat flux functions are expressed as follows.

$$\dot{q}'' = \text{fn}(Q, L, l, w, h, \text{loc}, x) \quad (1)$$

Where Q is the heat release rate (MW)
 L is the span length (m)
 l is the length (m) of the fuel bed
 w is the width (m) of the fuel bed

h is the height (m) of the fuel bed

loc is the location (-) of the fuel bed under span, represented by 0 (centre), 0.25 (quarter), 0.5 (near abutment)

The finalized functions for all the models and categories will be presented at the conference. An example of a fitted function is shown in *Eq.(2)* representing a car fire under the centre of span. In this case, HRR is 5MW and the burning surface is assumed to be located above the ground at 1.6m. Each coefficient in *Eq.(2)* is: C1 = 9.3, C2 = 1, C3 = 2.39, C4 = 20.81, C5 = -0.11, C6 = 1.04.

$$\dot{q}'' = C1 \cdot \frac{Q}{l \cdot w} \cdot e^{-\left(\frac{x-C2 \cdot loc \cdot L}{C3 \cdot h}\right)^2} + C4 \cdot e^{-\left(\frac{x-C5}{C6}\right)^2} \quad (2)$$

3 OPENSEES FRAMEWORK

3.1 Introduction

The fitted functions from CFD fire models have been programmed into the open source software OpenSees. OpenSees is an object-oriented, open-source, finite element software, which was originally developed at UC Berkeley for earthquake engineering. OpenSees is implemented primarily in C++ but uses considerable legacy Fortran code [4]. Being open source, OpenSees allows new algorithms to be coded by other developers, thereby extending OpenSees capabilities. Commercial GUIs are now available [4] from a few software companies, including nvStructural, from Novel CAE Solutions, and CDS Win, from Software Tecnico Scientifico.

Until this project, only idealized building fires have been embedded in OpenSees, including the standard fire, parametric fire, EC1 localised fire and a travelling fire [5]. OpenSees users can choose the embedded material types or fire curves interpreted by Tcl to automatically generate a heat transfer and thermal response analysis. The temperature output from heat transfer analysis is automatically applied to the structural mesh. The spatially non-uniform design heat fluxes imposed at the exposed surfaces of the bridge structural components should provide more realistic design scenarios than possible with currently available models.

3.2 Applications to a heat transfer model

In order to analyse the post-fire behaviour of bridges, the heat transfer from the flames to the surfaces needs to be determined. This section presents a modelling study for a composite section, where embedded functions have been used to define the thermal environment.

In order to perform the OpenSees heat transfer model, a comparison with an ABAQUS model [6] was carried out using the hydrocarbon fire curve for a verification. *Figure 5* shows the heat transfer analysis of a composite section by using ABAQUS. *Figure 6* shows the comparison of the temperature distribution along the cross section between ABAQUS and OpenSees. It shows a good agreement of the predicted temperature between the two software packages. As expected, the temperature in the concrete is significantly lower than that in the steel section due to its lower thermal conductivity. Also, the steel web heats up at a much higher rate compared to the lower flange due to its smaller thickness. However, because of the high thermal conductivity of steel, the temperatures at different positions in the steel section tend to approach the same value after about 30 minutes of exposure.

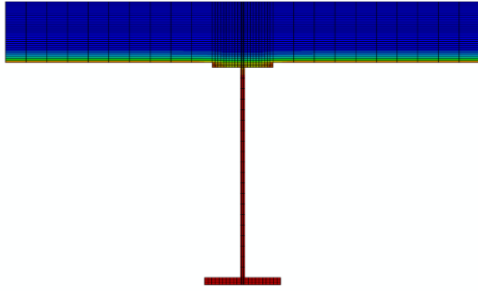


Figure 5 A heat transfer model performed using ABAQUS

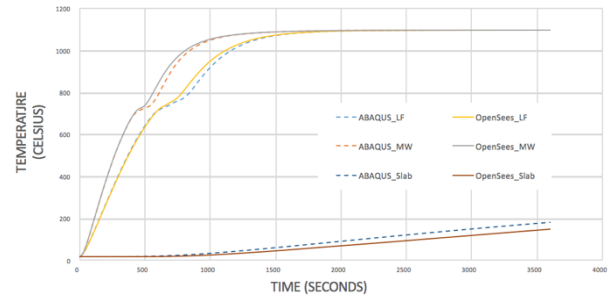


Figure 6 Comparison of heat transfer results under hydrocarbon fire between OpenSees and ABAQUS

Figure 7 shows the heat transfer results performed by OpenSees when using the new design fires with Eq.(2) (low to moderate, 5MW, $2.1\text{ m} \times 1.2\text{ m} \times 1.6\text{ m}$). It also compares the temperature differences obtained with hydrocarbon fire. In this model, the convection coefficient was set to $35\text{ W}/(\text{m}^2\text{K})$ for the fire-exposed surfaces and $4\text{ W}/(\text{m}^2\text{K})$ for the top surface of concrete [7]. An effective emissivity factor of 0.7 was used for fire-exposed surface and 0.8 for the unexposed surfaces. It shows that there are no large differences between the two fire models for temperatures in the slab. However, for both the steel lower flange and the web, the bridge fire model has predictably lower temperatures, around $200\sim 250\text{ }^\circ\text{C}$ lower when compared to the model with hydrocarbon fire.

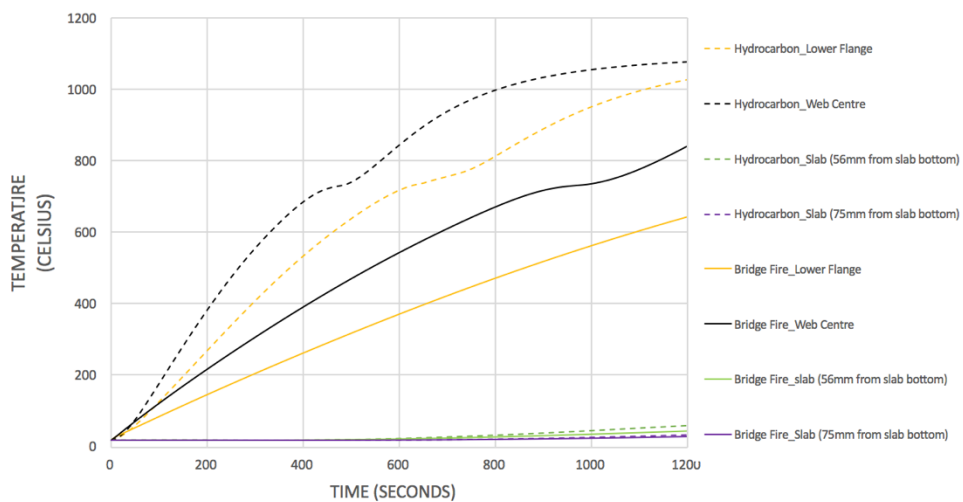


Figure 7 Comparison of the heat transfer results between hydrocarbon and the designed bridge fire (OpenSees)

4 CONCLUSIONS

When comparing against the commonly used hydrocarbon fire for bridges, we can see that the highest temperature in the CFD models are much lower (around 500°C), resulting in $200\sim 250\text{ }^\circ\text{C}$ lower temperatures in the heated steel section. The differences may cause the estimated resistance of bridge under fire to be greater, but this needs to be confirmed by future studies of thermo-mechanical response. However, only the example of car fires has been presented in this paper. The thermal results of fuel tanker design fire will be presented to compare with hydrocarbon fire at the conference. Besides, the decay along the bridge span also produces a more realistic fire model which will have a significant influence on the thermal and thermo-mechanical response of structure. However, the new design fires have limitations, especially there is a need for studies where the fire growth rates need to be established. Currently only the steady-state fire distribution is considered in the design fires. In

future work, the temperature evolution with time will be extracted to provide structural model inputs to determine the thermal and thermo-mechanical responses induced by the new non-uniform fires.

REFERENCES

- [1] M. Garlock, I. Paya-Zaforteza, V. Kodur, L. Gu, Fire hazard in bridges: Review, assessment and repair strategies, *Eng. Struct.* 35 (2012) 89–98. doi:10.1016/j.engstruct.2011.11.002.
- [2] V. Kodur, E. Aziz, M. Dwaikat, Evaluating fire resistance of steel girders in bridges, *J. Bridg. Eng.* 18 (2013) 633–643. doi:10.1061/(ASCE)BE.1943-5592.0000412.
- [3] D. Drysdale, *An introduction to fire dynamics*, John Wiley & Sons, 2011.
- [4] F. McKenna, *OpenSees: A framework for earthquake engineering simulation*, *Comput. Sci. Eng.* 13 (2011) 58–66. doi:10.1109/MCSE.2011.66.
- [5] X. Dai, S. Welch, A. Usmani, A critical review of “travelling fire” scenarios for performance-based structural engineering, *Fire Saf. J.* (2017) 1–11. doi:10.1016/j.firesaf.2017.04.001.
- [6] J. Hu, A. Sanad, A. Usmani, Structure response analysis of a highway bridge when subjected to accidental vehicle fires, in: A. Usmani, Y. Lu, P. Das (Eds.), *First Int. Conf. Struct. Saf. under Fire Blast*, 2015: pp. 465–474.
- [7] J.-M. Franssen, V. Kodur, R. Zaharia, *Designing Steel Structures for Fire Safety*, CRC Press/Balkema, 2009.
- [8] BS EN 1992-1-2:2004, *Eurocode 2: Design of concrete structures - Part 1-2: General rules - Structural fire design*, (2004).
- [9] BS EN 1993-1-2:2005, *Eurocode 3: Design of Steel Structures - Part 1.2: General Rules - Structural Fire Design*, (2005).

STRUCTURAL DESIGN OF TALL STEEL FRAMED BUILDINGS UNDER MULTI-STOREY FIRES

Graeme Flint, Panagiotis Kotsovinos, Yavor Panev & Peter Woodburn
Arup, United Kingdom

1 INTRODUCTION/KNOWLEDGE GAP

Fire induced progressive collapse of tall buildings represents a high consequence event due to their occupant profile and importance for the surrounding community. The fire induced collapse of a number of tall buildings such as the WTC towers, Windsor Tower, the Plasco Building and the Delft University Building among others have identified that the stability of columns exposed to multi-storey fires in tall buildings may have a significant impact on the overall stability of the building.

For tall buildings, fire safety design guidance in the UK and elsewhere relies on the provision of compartment floors to restrict fire and smoke spread to restrict the occurrence of a multi-storey fire within a building. However, for modern building arrangements incorporating atria, open stairs or other open voids, designers need to consider the risk of fire spread between storeys, noting that the design guidance for structural fire resistance of buildings typically requires sprinkler failure to be considered.

The potential effects of restrained thermal expansion acting on a column from a multi-storey fire are ignored when isolated elements are tested in accordance with prescriptive guidance or when single element based structural fire engineering methods have been adopted.

Additionally, even when compartment floors are provided, previous experience has shown that fires can travel vertically and therefore a multi-floor fire assessment may be desired to be considered when investigating the overall robustness of a building design, or where specific property protection criteria are to be addressed in a building design.

An overview of the structural design of steel framed tall buildings under multi-storey fires will be presented in this paper based on the authors' experience of research and application on a number of commercial projects

2 FAILURE MECHANISMS UNDER MULTI-STOREY FIRES

A number of previous studies have studied the structural response of tall buildings under multi-storey fires. The collapse mechanisms of composite structures similar to the WTC Towers with long-span perimeter truss floor or universal beams were considered by [1,2] and subsequently a closed form equation was proposed by [3] as an assessment method of structural failure under multi-storey fires. The potential for vertical travelling fires with an inter-storey time delay were considered by [4,5] that highlighted that they could introduce different structural responses. The aforementioned research on composite steel-concrete buildings with concrete cores and perimeter steel columns has identified two potential collapse mechanisms; 'strong floor' and 'weak floor'. In the former, bending failure is initiated the perimeter columns due to the thermal expansion of the floorplate while in the latter a plastic hinge is formed in the composite beam.

Others such as [6] studied the effect of multi-floor and travelling fires on the structural response of a steel moment resisting frame. Depending on the number of storeys on fire and the type of fire, the failure mechanism was dominated by either strength degradation or thermal expansion and collapse was initiated either through the pull-in of external columns or swaying of the frame to the side of fire origin.

3 CONCEPTUAL MODELS

A widely verified analytical methodology does not exist for the assessment of the structural response of tall buildings under multi-floor fires. Therefore, to understand the response of a given structure to a multi-floor fire, numerical assessment using non-linear finite element analysis are required.

As a result, future research should consider the verification and limitations of the methodology by Lange et al. [3] for structural forms different to those studied by the authors and the development of appropriate closed form equations.

Different conceptual finite element models of different complexity (global vs local) can be developed depending on the objectives of the analysis and the structural form of the building. When localised areas are considered, appropriate boundary conditions need to be used [7].

Figure 1 illustrates the adopted model for a commercial project by Arup (Heron Tower) with explicit representation of all structural members of the floorplates that are involved in the multi-storey fire and appropriate boundary conditions to include the structure below and above.

The model illustrated in Figure 2, based on a different commercial project by Arup (52 Lime Street) where compartment floors were provided in the building, aimed to capture the impact that a two storey fire might have on the overall stability of the building. The structural response of specific components within the building were considered such as the perimeter columns and a perimeter two-storey truss structure. The lateral (push-out) expansions at the perimeter of the full floorplate were extracted from the single storey full floor model and applied across two storeys to replicate the impact of a two-storey fire acting on the column.

Based on our experience finite element analysis can be supplemented by the use of section interaction diagrams [8] to assess in detail the axial-moment interaction within the structural sections, in particular for columns, and establish appropriate mitigation measures.

From the research undertaken and the range of building forms analysed by Arup in the past, typical mitigation measures to the structural and fire protection design that can be evaluated numerically include:

- limiting the maximum steel temperature of key structural members by increasing fire protection thickness
- increasing section capacities of structural members (typically columns due to p-delta effects)
- allowing the capacity of connections to accommodate the thermally induced forces.

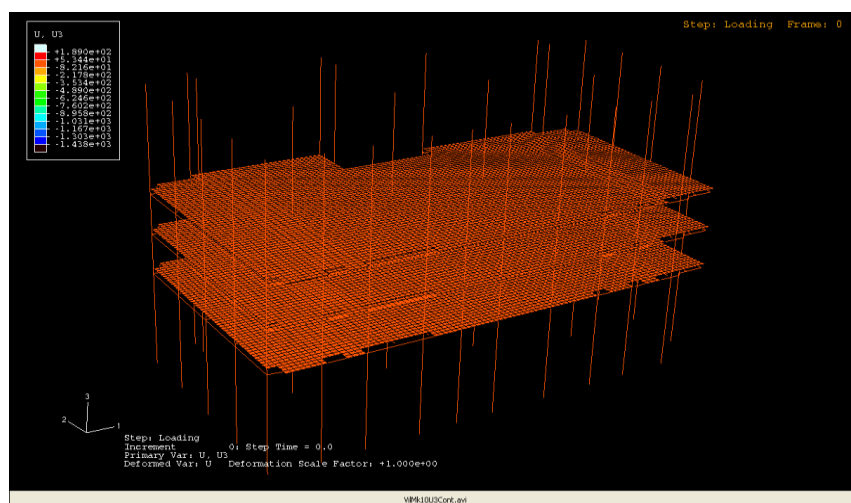


Figure 1 Indicative model that includes all structural members within the fire affects storeys

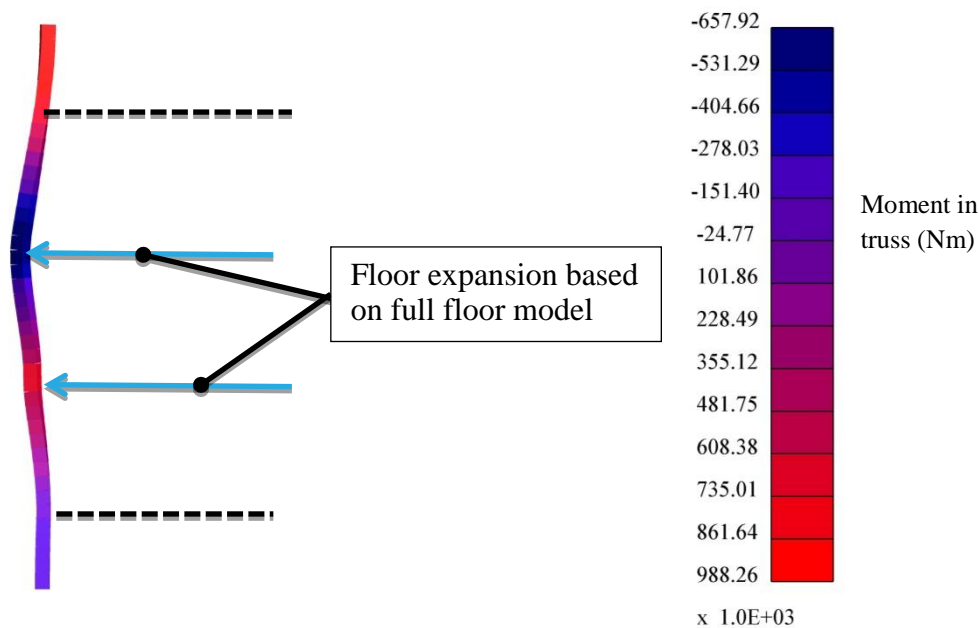


Figure 2 Indicative localised model

4 CASE STUDY OF OFFICE BUILDING WITH OPEN STAIR ARRANGEMENT

The presented case study is based on a commercial project undertaken by Arup involving the refurbishment and renovation of an office building. The selected case study highlights the importance of structural form and fire definition on the structural response of tall steel frame buildings under multiple floor fires.

The building is of office use and there is an architectural desire to connect multiple storeys through an open stair. Therefore, the building structure was assessed to demonstrate whether additional fire safety measures, such as fire resistant construction around the stair (e.g. fire rated glazing) or the presence of appropriate active smoke control systems that could inhibit vertical fire spread, would be required. A potential fire on multiple storeys was considered as part of the structural fire assessment.

The building structure steps back at each level as seen in Figure 3. Therefore the location of the perimeter columns changes at different levels. Previous research has not considered the effect of multi-storey fires on buildings where step back occurs. A representation of the conceptual model as well as the boundary conditions adopted for the purposes of the analysis are illustrated in Figure 3.

The majority of the steel frame was protected with 60 minutes loadbearing fire resistance following a probabilistic time equivalence assessment. The transfer beams in the locations where the columns step back (to transfer the loads vertically) were protected to 120 minutes.

An aspiration to connect 3 storeys together into a single compartment was considered. Therefore, the following fire scenarios were assessed:

1. Single storey fire;
2. Two-storey simultaneous fire;
3. Three-storey simultaneous fire; and
4. A vertically travelling fire with an inter-storey time delay of 8.8 minutes.

The parametric fire model in accordance with EN1991-1-2 was adopted to define the fire conditions. The selected fires were based on probabilistic basis (Monte Carlo analysis) to correspond to the structural reliability of the building and were equivalent to a fire severity of 60 minutes to the standard fire. This is the fire resistance rating determined to be appropriate for the

Structural design of tall steel framed buildings under multi-storey fires

building by a separate fire engineered assessment. The travelling fire inter-storey delay of 8.8 minutes was based on the temperature time characteristics of the parametric fire adopted and was selected such that when an upper storey is heated it coincides with the stage where the structures on the storey below experiences cooling. This was to maximise the push-pull effect of the columns due to differential thermal expansion.

For each of the different fire scenarios, the analysis investigated the influence of the applied loading on the columns, the critical temperature of the columns and the applied fire protection on the beams. The LS Dyna general purpose finite element modelling software was used. Validation and verification of this software for use in structural fire engineering assessments was carried out by Arup (and others) and is available on request.

Details of the model used are not included in this paper, but is intended to be presented in a future journal publication.

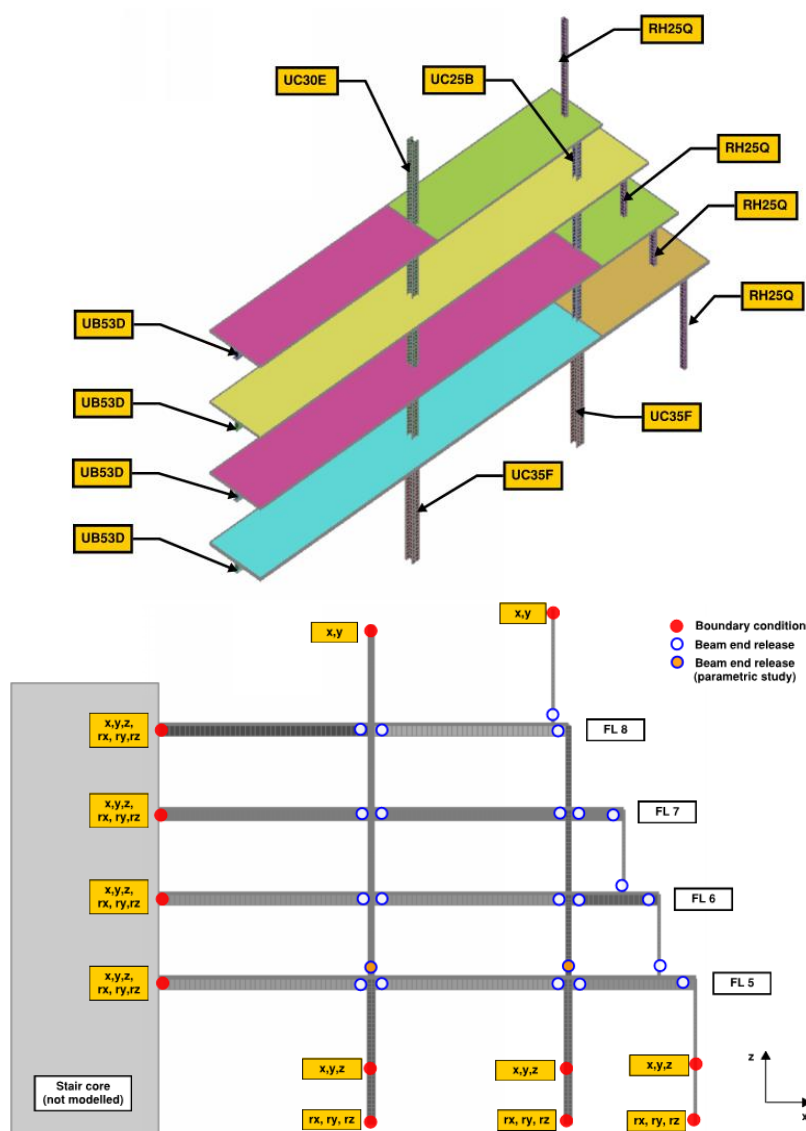


Figure 3 Conceptual model adopted for the case study

For the case study examined, failure occurs in the columns after a plastic hinge formation due to combination of moment action and axial force following the thermal expansion of the floorplate as per [1,2,4]. Based on the parametric study undertaken, it was determined that:

- The maximum lateral thermal expansion of the floorplate on the perimeter of the structure, recorded in any of the finite element models, is 140mm (see Figure 4). This is consistent with the results of analytical hand calculations.
- The sectional capacity of the columns is critical with regards to the stability of the frame. An increase in column sectional capacity would there provide additional robustness;
- The thermally induced moments on the perimeter columns were primarily due to the lateral expansion of the floorplate. Second order p-delta effects contributed less than 10% of the applied load to the columns;
- Adequate performance of the columns in all multi-storey fire scenarios could be demonstrated by increasing protection beyond the code compliant recommendations.;
- Increasing the level of fire protection to the beams (from 60 minutes to 90 or 120 minutes) did not avoid failure in many of the cases since the thermal elongation of the beams was still significant. This is consistent with the analysis by Law et al. [9] on geometrically bi-linear columns where similar failure mechanisms were observed;
- Fire on two floors was the most severe case followed by fire on three floors, traveling fire and fire on a single floor. This is because the bending moment distribution in a two-floor fire is uniform between the two expanding floorplates which makes the columns more susceptible to buckling;

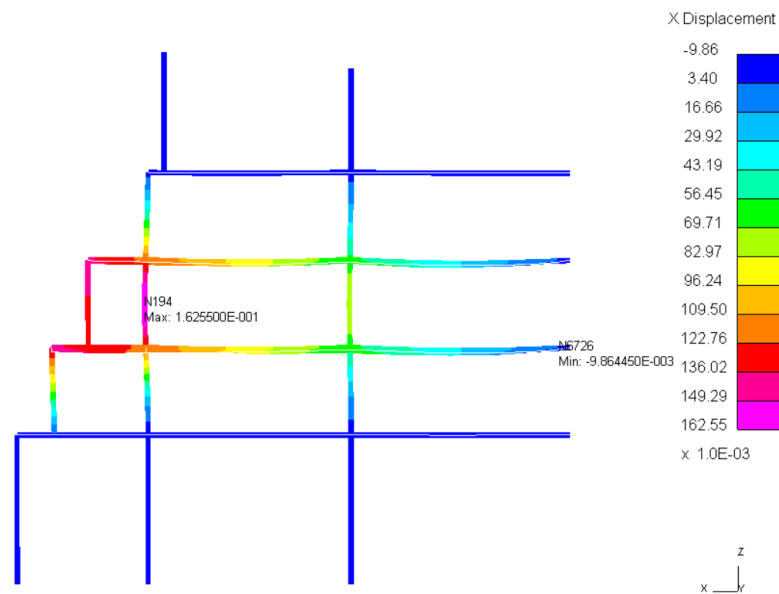


Figure 3 Indicative thermal expansion of the floorplate (two-storey fire)

5 CONCLUSIONS AND NEXT STEPS

This paper presents an overview of the structural design of tall buildings under multi-storey fires. The potential failure mechanisms based on the available research and the information that needs to be provided in conceptual models for design purposes is discussed.

An indicative case study is presented that illustrates the key phenomena that steel frame structures experience when subjected to fire and the mitigation measures that can be provided in the structural and fire protection design. For the frame examined, a two storey fire was found to be more severe than a three storey fire due to the applied moments profile on the perimeter columns which made

them more susceptible to buckling. For the case study, maintaining lower temperatures in the columns by increasing the thickness of the column protection to the columns was found to be an adequate strategy while limiting the thermal expansion of the beams through additional fire protection was not always successful.

Future research should be undertaken to develop a holistic methodology for the structural design of tall buildings under multi-storey fires for a range of structural forms and fire scenarios. There is also a need for appropriate analytical tools to be developed to be used as part of feasibility studies to reduce initial reliance on finite element analysis.

REFERENCES

- [1] G. Flint, A. Usmani, S. Lamont, B. Lane, J. Torero, Structural response of tall buildings to multiple floor fires, *J. Struct. Eng.* 133 (2007) 1719–1732.
- [2] P. Kotsovinos, A. Usmani, The World Trade Center 9/11 disaster and progressive collapse of tall buildings, *Fire Technol.* 49 (2013) 741–765.
- [3] D. Lange, C. Röben, A. Usmani, Tall building collapse mechanisms initiated by fire: mechanisms and design methodology, *Eng. Struct.* 36 (2012) 90–103.
- [4] P. Kotsovinos, Analysis of the Structural Response of Tall Buildings Under Multifloor and Travelling Fires (PhD Thesis), The University of Edinburgh, 2013
- [5] C. Röben, M. Gillie, J.L. Torero, Structural behaviour during a vertically travelling fire, *J. Constr. Steel Res.* 66 (2010) 191–197.
- [6] E. Rackauskaite, P. Kotsovinos, G. Rein, Structural response of a steel-frame building to horizontal and vertical travelling fires in multiple floors, *Fire Safety Journal* 91 (2017) 542-552.
- [7] A. Law, Perimeter column boundary conditions in structural fire modelling, *Fire Technology* 52, 6 (2016) 1845-1861
- [8] S. E. Quiel, M. E. M. M. Garlock, A closed-form analysis of perimeter member behaviour in a steel building frame subject to fire, *Eng. Struct.*, 30, 11, (2008) pp. 3276–3284.
- [9] A. Law, P. Kotsovinos, N. Butterworth, Engineering geometrically bi-linear columns to deliver fire resistance: standard heating, *Eng. Struct.*, 100, (2015) pp. 590-598.

CALCULATING FIRE-INDUCED HEAT FLUX CONTOURS ON CONCRETE TUNNEL LINERS TO EVALUATE STRUCTURAL CONSEQUENCES

Kyle Root¹, Qi Guo², Spencer Quiel³, Clay Naito⁴

ABSTRACT

Road tunnels are susceptible to severe fire-induced heat flux due to the constant presence of vehicular traffic combined with the likelihood of accidents and subsequent combustion. Rapid assessment of thermal demands is a necessity to calculate appropriate design limit states and to better understand risk potential in a multitude of underground environments. A proposed approach is developed which allows for rapid assessment of thermal demands using models that are validated and informed through computationally intensive numerical assessment, experimental data, and semi-empirical relationships based on first principles. Utilizing this approach, thermal demands for numerous fire scenarios can be generated efficiently and investigated stochastically. Potential for cracking, spalling, breach, and other adverse structural consequences can be evaluated based on contour maps of total heat flux over the tunnel liner.

1. INTRODUCTION

Recent tunnel fires have highlighted the need for enhanced understanding of the structural response of the reinforced concrete liner to fire events. For example, the St. Gotthard Tunnel fire of 2001 claimed the lives of 11 people and resulted in over 250 m of collapsed concrete lining within the tunnel [1]. Also, the 1999 Mont Blanc Tunnel fire resulted in 39 casualties and over 900 m of damaged tunnel lining, with the blaze continuing for over 50 hours [1]. As space above ground becomes limited, there is a concerted effort to move transportation infrastructure underground. A major example of this momentum is the 2016 establishment of the Boring Company in California, which aims to significantly increase the presence of underground transportation [2].

Accurate and rapid assessment methods for tunnel systems would facilitate risk evaluation, retrofit design, suppression system deployment, and the potential development of new tunnel configurations. To enable engineering practitioners to assess structural damage from fire in a tunnel, thermal demands must first be considered in a manner which is conservatively accurate but also as computationally efficient as possible.

Though high-fidelity computational fluid dynamics (CFD) packages can provide high-quality analysis of fire demands, these models require extensive computing time and a large amount of

¹ Graduate student, ATLSS Research Center, Lehigh University, 117 ATLSS Dr., Bethlehem, PA, 18015, Email: kjr216@lehigh.edu.

² Graduate student, ATLSS Research Center, Lehigh University, 117 ATLSS Dr., Bethlehem, PA, 18015, Email: qig317@lehigh.edu.

³ Assistant Professor, ATLSS Research Center, Lehigh University, 117 ATLSS Dr., Bethlehem, PA, 18015, Email: squiel@lehigh.edu. *Corresponding Author

⁴ Professor, ATLSS Research Center, Lehigh University, 117 ATLSS Dr., Bethlehem, PA, 18015, Ph: 610-758-6229, Email: cjn3@lehigh.edu.

input, much of which must be assumed if experimental data or design guidance are not available. Such an approach is not feasible for rapid assessment of numerous tunnel networks, nor is it practical in the case of a stochastic assessment to determine structural resilience. Zone modelling packages (such as Ozone [3]) and empirical relationships (like those presented in SFPE Handbook [4]) have been developed for compartment fires and can conservatively account for corner and wall effects inside a room. However, similar approaches specifically for tunnel applications are far less common.

The array and inherent variability of inputs for a fire event calculation can be incorporated into a modified discretized solid flame (MDSF) model, which represents the flames and smoke as discretized solid objects with varying radiative power. The MDSF model was previously proposed by Quiel et al. [5] for bridges exposed to open-air hydrocarbon fires - this method requires an “intermediate” level of computational effort between analytical calculations, semi-empirical models, and high-fidelity CFD solutions. This paper proposes a hybridized MDSF approach - the H-MDSF is adapted from the MDSF and additionally accounts for convective smoke effects in the tunnel. The H-MDSF is validated and further refined via comparison with experimental data and CFD analyses.

2. FIRE DYNAMICS SIMULATOR (FDS) MODEL

In order to determine realistic levels of thermal demand in a tunnel, high fidelity modelling is first employed and validated against experimental data. The Fire Dynamics Simulator (FDS), a CFD package developed by NIST [6], is used as the high fidelity modelling package in this study. The FDS model is validated against experimental data from a full-scale tunnel fire test program in the Memorial Tunnel in West Virginia, which considered a range of fire sizes and ventilation systems [7].

One representative test (Test No.502) without a forced ventilation system was selected as the basis for developing a validated FDS model. Diesel was used as the fuel in the test with a heat release rate (HRR) of 50MW, equivalent to the HRR of a heavy goods vehicle (HGV) [8]. The fire source was modelled as a rectangular pool in FDS - the area and heat release rate per unit area (HRRPUA) are set to achieve the same HRR as in the experiment. Considering that diesel is a mixture of hydrocarbons, its average chemical formula, $C_{12}H_{24}$, is used for the fuel definition. Besides the reactant, products should also be defined for combustion. Soot yield, which is the fraction of fuel mass converted into smoke particulate, is taken to be 0.1 for diesel fuel per the SFPE Handbook [4]. Radiative fraction, which is the fraction of energy emitted from the fire as thermal radiation, is defined as 0.27 according to the relationship between radiative fraction and equivalent diameter of pool fires [9]. Radiation in FDS is calculated by solving the radiation transport equation in a finite number of solid angles with a grey gas assumption. This analysis used the default value of 100 solid angles for calculation. A wide band model is also available for radiation transport calculation with significantly greater computation time; however, as will be shown in the results, the grey gas model provided adequate levels of accuracy versus the experimental data in this case while enabling computational savings.

The Memorial Tunnel is a horseshoe shaped tunnel with a total length of 853 m and a north-to-south slope of 3.2%. Approximately one-third of the total tunnel length centered about the fire is modelled, as thermal demand significantly reduces with increased standoff. Multiple meshes in

FDS are adopted for efficiency. As shown in *Figure 1*, 5 parallel zones with a total length of 50 m centred at the fire location were modelled with “fine” mesh at 25-cm volumetric discretization. Beyond the 50 m length, a “coarse” mesh with 50-cm discretization was utilized. Use of multiple meshes not only enables various mesh size definitions, but also allows for the use of parallel analysis to improve computational efficiency.

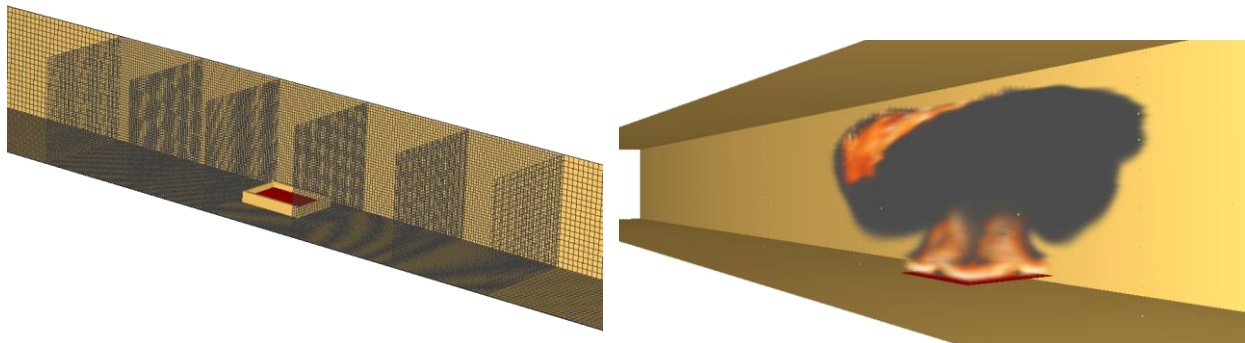


Figure 1: Mesh system in FDS (left) and combustion snapshot in Smokeview (right)

Three types of surfaces were used in the model: concrete, burner, and inert. A concrete surface with thickness of 0.3 m was applied on the tunnel liner, and material properties were defined using default settings from NIST library resources [6]. The concrete wall thickness is consistent with that reported in the test documentation [7]. To model the diesel pool fire, a burner surface with an assigned HRRPUA was utilized. The fuel container and road surfaces were defined as inert.

The numerical analysis was performed on a personal computer with quad-core i7 processor and 16 GB of RAM with an SSD hard drive. Computation required 13 hours to analyze a fire duration of 200 seconds for the 50MW fire.

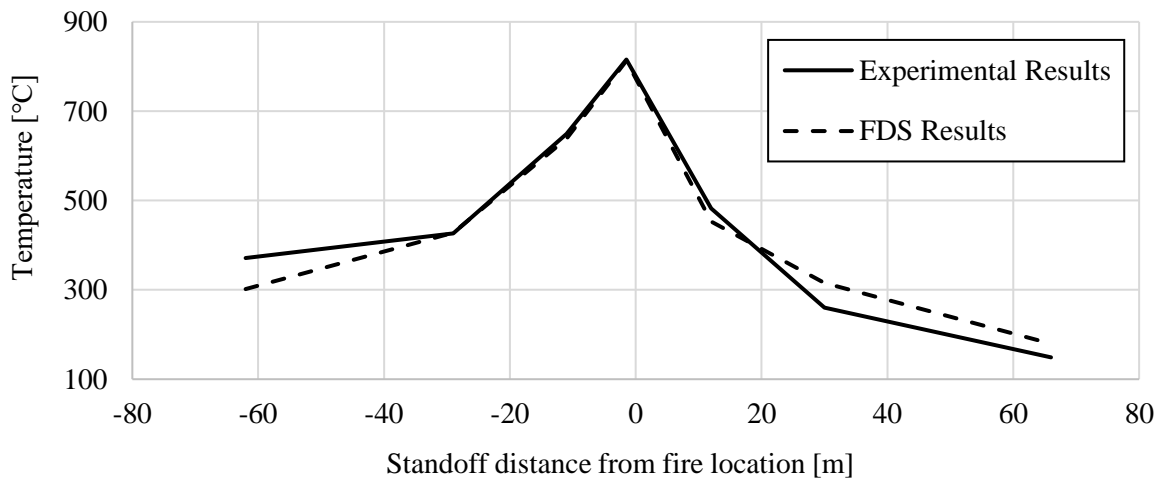


Figure 2: Ceiling temperature along tunnel with fuel tanker fire (50MW)

Figure 2 above shows the comparison of numerical analysis and experimental results for ceiling temperatures measured along the tunnel centerline after 3 minutes. Experimental results were extrapolated from temperature profile plots given in the test report [7]. The FDS model provides strong agreement with test results along the length of the tunnel.

3. HYBRIDIZED MODIFIED DISCRETIZED SOLID FLAME (H-MDSF) MODEL

The MDSF is a radiation-driven model, which segments the fire into a two zones (luminous flame and smoke) with different emissive powers. The radiative contribution from each emitting surface, i , is summed at each target surface, j . Incident heat flux at each discretized surface, q''_j is calculated as a function of the emissive power and view factor, $F_{i \rightarrow j}$ between receiving and emitting surfaces as shown below in Eq. (1).

$$q''_j = \sum_{i=1}^n E_i F_{i \rightarrow j} = \sum_{i=1}^n E_i \frac{A_i \cos \theta_i \cos \theta_j}{\pi r_{i \rightarrow j}^2} \quad (1)$$

Previous versions of the MDSF have treated the flame as cylindrical or as a rectangular cube. More recent developments have modelled the flame as a cylinder and top cone as suggested by Zhou [10], where the cone and cylinder are proportioned from the total flame height as $0.4H_f$ and $0.6H_f$, respectively. The conical shape mimics the flaring shape of an actual fire and can better predict the heat fluxes experienced by an engulfed surface. The MDSF has been previously deployed in Matlab [11] and utilized by the authors in the case of open air, bridge fires [5].

For this study, the MDSF model is adopted into a 3D parametric CAD environment for further modification in order to also account for smoke effects. The hybridized MDSF, or H-MDSF, calculates summed radiative energy from the flame's emitting surfaces and incorporates convective heat flux driven by the entrapment and movement of smoke and hot gas in the tunnel. Radiative energy is accounted for as shown above in Eq. (1). Emissive power of the flame is taken as 80 kW/m^2 as recommended by Muñoz et al. [12]. Targets engulfed by the flame receive a heat flux of 190 kW/m^2 , representative of the values recommended by Lattimer [4]. Convective heat flux is conservatively modeled as an additional flux of 50 kW/m^2 at the fire source, linearly decaying with distance to a minimum, computationally-informed value at the end of the model length. The maximum smoke flux is consistent with previous work by Muñoz et al., who calculated a maximum emissive power from the soot filled region of open air fires as 40 kW/m^2 [12]. This value has been slightly increased to account for the entrapment of hot gases in the tunnel under the ceiling. Convective heat transfer is imparted only to target surfaces above the height of the lower luminous flame region (i.e. at $H > 0.4H_f$). In this way, the original intent of the MDSF where luminous and smoke layers occur at varied heights of the flame is preserved.

In Figure 3, the Memorial Tunnel is modelled and discretized in the Rhinoceros/Grasshopper environment to compare the H-MDSF to FDS validation results.

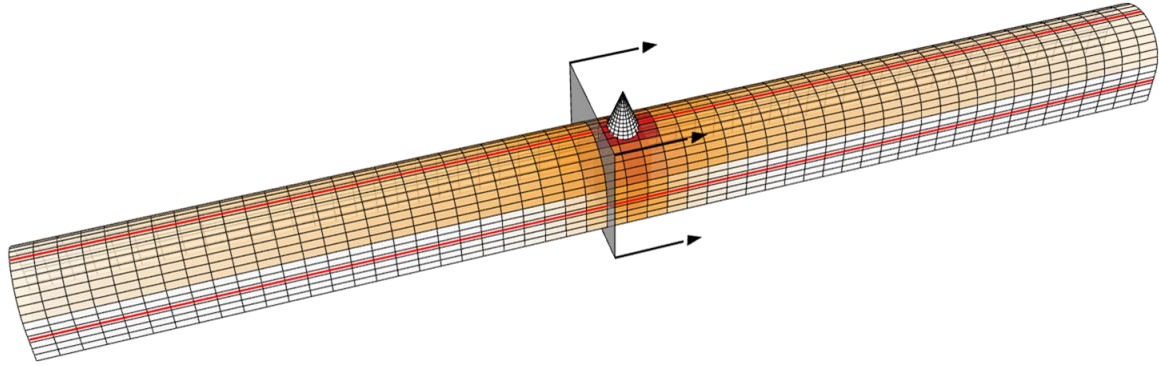


Figure 3: Tunnel analysis mesh

The 50 MW fire is first geometrically translated to a flame size through Heskestad's correlation [4], where the height of the flame, H_f is computed as a function of the peak heat release rate, $\dot{Q}_{f,max}$ and the effective diameter of the fire, $D_{f,eff}$ in Eq. (2).

$$H_f = 0.235\dot{Q}_{f,max}^{0.4} - 1.02D_{f,eff} \quad (2)$$

Because the Memorial Tunnel test utilized a rectangular fuel pan, the effective diameter of the fire must be determined using an equivalent area as noted in Eq. (3). This equivalence has been used in the past for hydrocarbon pool fires [5] and is applicable for a footprint aspect ratio less than 2.

$$D_{f,eff} = \sqrt{\frac{4L_fW_f}{\pi}} \quad (3)$$

A critical mesh size was determined for tunnel and flame discretization. A comparison has been performed to investigate the effect of flame shape on calculated thermal demands, where the flame is modelled with both a rectangular and equivalent cylindrical cross section. The resulting spatial distribution of incident heat flux on the inside face of the tunnel liner is shown below in Figure 4. The section cut shown is clearly noted above in Figure 3.

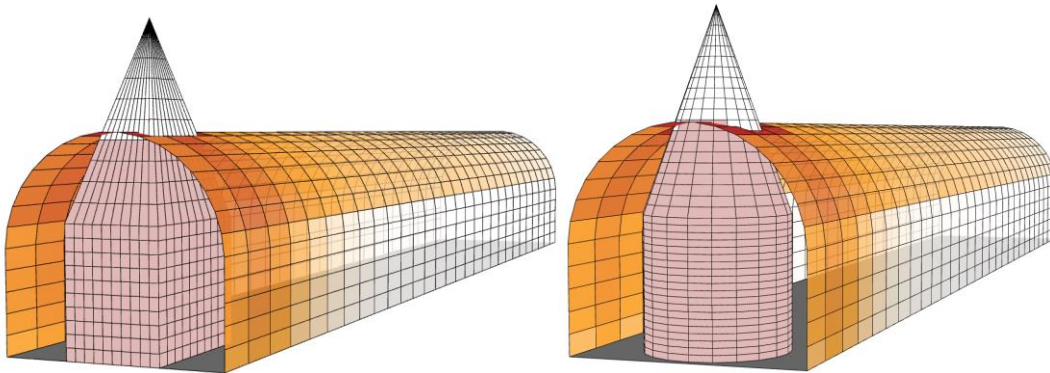


Figure 4: Resulting tunnel flux at section cut near mid-length

Rhino, a 3D modelling software, and Grasshopper, a graphical algorithm editor tightly integrated with Rhino, are used for all modelling and calculations [13-14]. Rhino and Grasshopper have been recently embraced by several leading, multinational structural engineering firms to visualize and solve complex geometric problems. The powerful, 3D parametric environment readily allows for tunnel geometry creation and manipulation, as well as instant visualization of calculation processes and results for fire exposure. While becoming a utilized tool in industry, the authors have yet to see Rhino and Grasshopper used for this application.

4. COMPARISON AND DISCUSSION

A numeric comparison of incident heat flux on the tunnel ceiling along its centreline for FDS and the H-MDSF can be seen below in *Figure 5*. Fluxes along the side wall of the tunnel at 3 m above the road surface are also compared below in *Figure 6*. These two locations are marked with longitudinal lines in *Figure 3*. Results along the ceiling show good agreement between the H-MDSF and the numerical evaluation. Peak values are within 2% agreement, with general decay of flux along the tunnel length in close proximity. The H-MDSF model remains robust when calculating thermal demands on the ceiling via either flame geometry. Flux values from rectangular and circular flame representations are nearly indistinguishable in *Figure 5*. Slight asymmetry can also be observed in the FDS solution below. This is due to the inherent variability in the large eddy simulation (LES) and natural ventilation in the FDS solution.

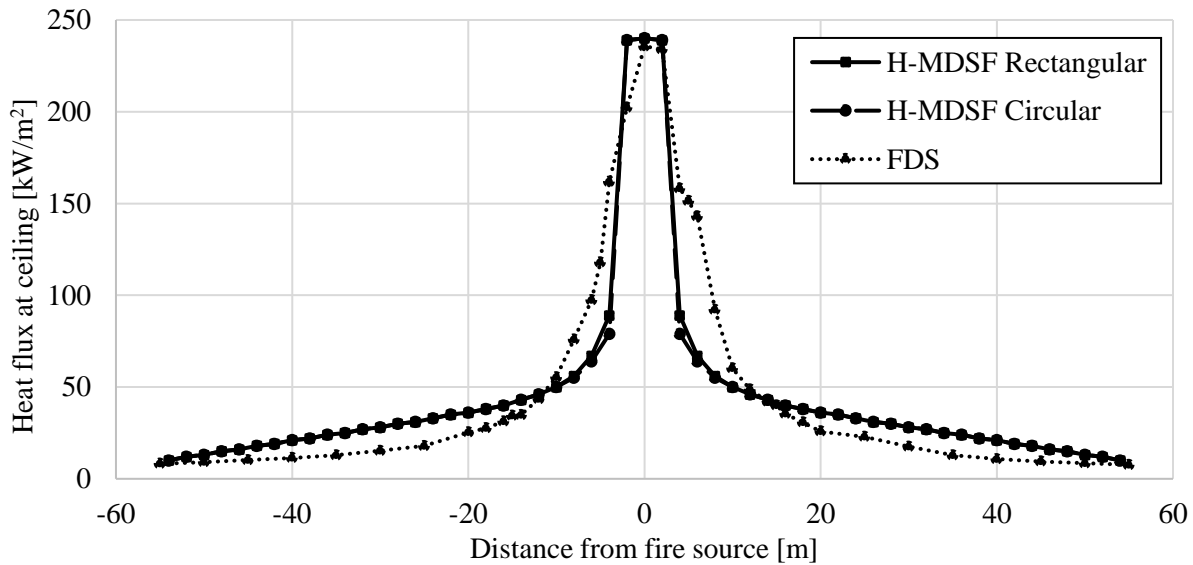


Figure 5: Incident heat flux comparison at ceiling

Flux profiles along the side wall of the tunnel show conservative agreement, though the H-MDSF solution remains highly conservative at close proximity to the fire source. Adoption of the circular flame geometry reduces the radiation-driven flux values along the side wall. Upcoming phases of

this project will develop improved accuracy of the side-wall heat flux calculation and examine the spatial contour of the total heat flux on the tunnel liner.

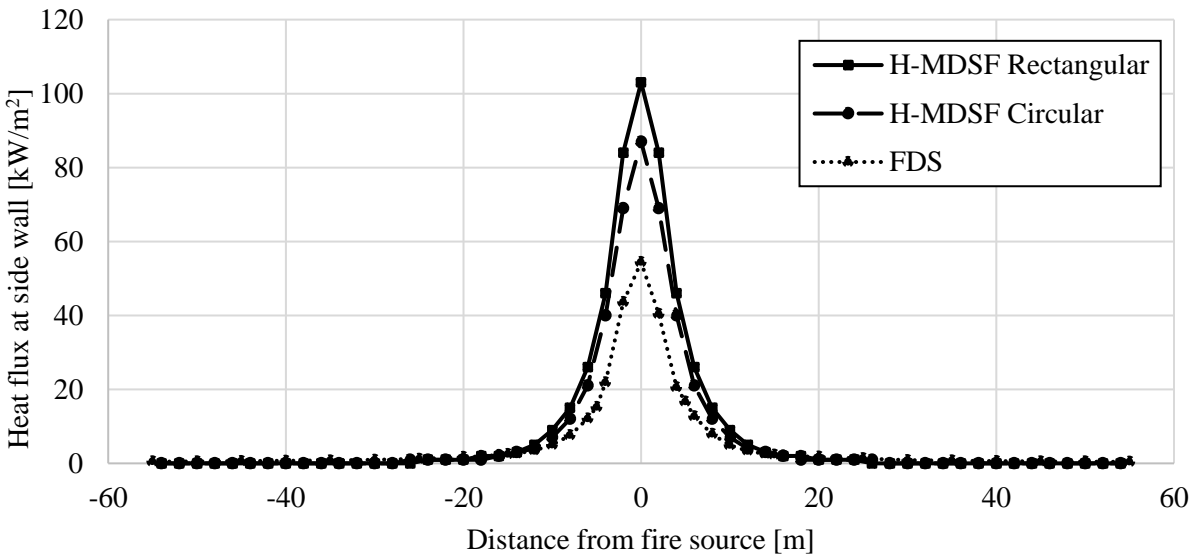


Figure 6: Incident heat flux comparison at side wall

5. SUMMARY AND CONCLUSION

To address an increasing need for evaluating tunnel structures under fire, the authors have proposed a new modelling approach which accounts for flame radiation as well as convective heat transfer from the smoke layer formed at the tunnel ceiling during a fire event. This approach has “intermediate” computational complexity and hybridizes an MDSF model that was previously developed by the authors to evaluate bridges under fire. The H-MDSF has been adopted into a powerful, parametric CAD environment similar to those used by leading structural design firms for other applications. CFD analyses utilizing NIST’s FDS software have been validated against full scale experimental results from a previous experimental program by others. Preliminary comparison shows good agreement between validated FDS results and the proposed approach. The H-MDSF model has been shown to conservatively predict the expected total incident heat flux on the tunnel lining.

Going forward, planned research efforts will focus on model development to more accurately predict incident heat flux at numerous locations throughout the tunnel. With the framework for the model well established in the user-friendly Rhino/Grasshopper environment, parameters can be efficiently modified and instantly visualized. Different flame geometries and realistic smoke movement will be investigated in future work.

Future work will also aim to incorporate correlations between spatial thermal demands and expected damage levels. Leveraging existing experimental data such as the work performed by Maluk et al. [15], as well as experimental work performed by the authors, an efficient damage mapping tool for tunnel linings will be developed. These developments will provide tunnel owners and operators with an efficient, visual tool to assess both new designs and existing infrastructure.

REFERENCES

- [1] R. Carvel, *Fire Size in Tunnels*, Heriot-Watt University, 2004.
- [2] “The Boring Company.” [Online]. Available: <https://www.boringcompany.com/>. [Accessed: 20-Dec-2017].
- [3] J. Cadorin, D. Pintea, and J. Franssen, “The Design Fire Tool OZone V2.0 - Theoretical Description and Validation On Experimental Fire Tests,” 2001.
- [4] National Fire Protection Association, *SFPE Handbook on Fire Protection Engineering*, 5th ed. Quincy, MA, 2016.
- [5] S. E. Quiel, T. Yokoyama, L. S. Bregman, K. A. Mueller, and S. M. Marjanishvili, “A streamlined framework for calculating the response of steel-supported bridges to open-air tanker truck fires,” *Fire Saf. J.*, 2015.
- [6] R. McDermott, K. McGrattan, J. Floyd, and S. Hostikka, *NIST Special Publication 1019-5: Fire Dynamics Simulator (version 5), User’s Guide*. National Institute of Standards and Technology, Gaithersburg, MD, 2010.
- [7] Bechtel and Parsons Brinckerhoff, *Memorial Tunnel Fire Ventilation Test Program*, 1995.
- [8] M. K. Cheong, M. J. Spearpoint, and C. M. Fleischmann, “Design Fire for Vehicles in Road Tunnels,” *Perform. Based Codes Fire Saf. Des. Methods, Auckland, New Zeal.*, January, pp. 229–240, 2008.
- [9] K. B. McGrattan, H. R. Baum, and A. Hamins, *Thermal Radiation from Large Pool Fires*, National Institute of Standards and Technology, Gaithersburg, MD, 2000.
- [10] K. Zhou, N. Liu, L. Zhang, and K. Satoh, “Thermal Radiation from Fire Whirls :,” *Fire Technol.*, vol. 50, no. 6, pp. 1573–1587, 2014.
- [11] Mathworks Inc., *MATLAB. Version R2016a*. 2016.
- [12] M. Muñoz, E. Planas, F. Ferrero, and J. Casal, “Predicting the emissive power of hydrocarbon pool fires,” *J. Hazard. Mater.*, vol. 144, no. 3, pp. 725–729, 2007.
- [13] Robert McNeel & Associates, “Rhinoceros.” 2017.
- [14] Robert McNeel & Associates, “Grasshopper.” 2014.
- [15] C. Maluk, L. Bisby, and G. P. Terrasi, “Effects of polypropylene fibre type and dose on the propensity for heat-induced concrete spalling,” *Eng. Struct.*, vol. 141, pp. 584–595, 2017.

CASE STUDY OF TRAVELLING FIRE SCENARIOS FOR PERFORMANCE-BASED STRUCTURAL FIRE ENGINEERING

Erica C. Fischer¹ and Amit H. Varma²

ABSTRACT

Many studies and observations of large building fires show that in large compartments, fires do not burn uniformly. Rather, fires will burn locally and move across a floor plate as fuel is consumed. Currently fire engineering practice assumes uniformly burning fires within a compartment and the fire design methodologies are based upon small compartment fire scenarios. Travelling fire modeling that accounts for fire dynamics is necessary for performance-based fire engineering. This paper reviews two travelling fire models presented in literature and implements both models in a case study. The case study consists of a ten-storey office building designed with perimeter moment resisting frames designed to be located in Chicago, IL.

Keywords: Structures, finite element modelling, travelling fires

1 INTRODUCTION

Structural engineers are moving towards performance-based design approaches for extreme loads. Performance-based fire engineering design is especially useful for landmark buildings that do not fit the mold of conventional building architecture. However, structural engineers face a challenge in how to characterize the fire potential used during the design phase. Modern buildings use atriums, exposed structure, open office floor plans, and high ceilings. All of these parameters are outside of the scope of conventional fire engineering design. These parameters also highly influence the potential fire that could occur within the space.

The current method for characterizing a fire is the standard fire curve through ASTM E119 [1]. This fire curve is represented through a logarithmic increase in gas temperature over time. The standard fire curve was intended to represent a worst case fire in an enclosure to determine if the structure could withstand a full burnout of the fire. However, this fire curve was developed before modern day fire dynamics was developed. It is independent of the parameters of the compartment that could influence the severity and intensity of the fire such as ventilation, materials, and size. The ASTM E119 standard fire curve also does not include a cooling portion of the curve due to fire decay [2].

Performance-based design approaches for structural fire engineering must include advanced analyses of the building exposed to various fire scenarios. *AISC Specification* [3] Appendix 4 provides little guidance for the designer to follow for advanced analyses. Eurocode [4] parametric $T-t$ curve is widely used in the structural fire engineering practice today. However, this particular curve is valid for small fire compartments ($< 500 \text{ m}^2$) only with a maximum compartment length of 4 m (13 ft). Modern day architecture typically provides open floor plans, which would fall outside of the scope of applicability for this particular $T-t$ curve.

¹ Assistant Professor. School of Civil and Construction Engineering, Oregon State University, Oregon, USA.
e-mail: erica.fischer@oregonstate.edu

² Professor. School of Civil and Environmental Engineering Purdue University, West Lafayette, Indiana, USA.
e-mail: ahvarma@purdue.edu

Current performance-based design approaches for structural fire engineering do not provide guidance to engineers on travelling fire models. Modern-day architecture consists of complex structures that fall outside of the limits of traditional prescriptive fire engineering approaches. Structural fire engineering requires simulation of the mechanical response of structural elements to design for the imposed forces and thermal restraints that result from fire scenarios, including travelling fires. This paper presents two methods for characterizing travelling fires. One method considers fire dynamics and elevated smoke temperatures and the other applies the same fire time-temperature ($T-t$) curve independently and sequentially along the floor plate of a building. The authors perform a case study where these methods are applied to a ten-storey office building. The structural response of the building to these travelling fires is presented within this paper along with a discussion of the two travelling fire methods.

Large building fires have led to structural failure and collapse. Stern-Gottfried and Rein [5] summarized a number of examples of accidental fires that demonstrated non-uniform burning of compartments. These fires moved horizontally across the floor plate and vertically throughout the building. In addition, the duration of the fires was well in excess of the time associated with the FRR on each of the structural members. Previous experimental tests of large building fires such as the Cardington Tests [6] and the Dalmarnock Fire Tests [7] demonstrated the travelling nature of fires. These experiments provided the foundation for the travelling fire methodology developed at the University of Edinburgh.

2 FIRE SCENARIOS

The goal of this research study is to compare two different travelling fire models in a typical 10-storey office building. This comparison includes quantifying the effects of the fires on the structure through displacement histories of the gravity columns. Each of the models are also compared with a full-storey fire. The two travelling fire models used in this study are: (1) Bailey et al. [8], and (2) Travelling Fire Methodology (TFM) [5, 9]. In each case, the fire took place on the fifth floor of the building. The fifth floor is representative of a typical storey within the building. The gravity column utilization ratio is about 0.46, which is approximately the same as the gravity column utilization ratios on the other floors of the building.

The full storey fire $T-t$ was generated using the Eurocode parametric $T-t$ curves [4]. This fire curve simulates both the heating and cooling portions of the fire. The heating portion of the $T-t$ fire curve was generated using parameters typical to a commercial office building. The opening factor (O) and design fuel load density ($q_{f,d}$) are $0.032 \text{ m}^{1/2}$ and 570 MJ/m^2 , respectively. The fuel load density corresponds to the 80th percentile fuel load density provided by Eurocode [4] in Annex E.

2.1 Fire scenario #1

Fire scenario #1 is represented by the travelling fire model presented by Bailey et al. [8]. The fire was defined by a $T-t$ curve that represented a “natural” fire. When the $T-t$ curve in the first bay reached its peak, the fire in the subsequent bay began, and so on down the length of the building. A large compartment is divided into smaller design areas and each area is subjected to a $T-t$ curve individually and sequentially. Each area has the same $T-t$ curve applied with the start point offset by the time of the travelling fire. This model uses the Eurocode [4] parametric $T-t$ curves. For this study, the fire $T-t$ curve developed for the full storey fire was used for fire scenario #1 as shown in Fig. 1. The fire begins in Bay 1 and moves horizontally to Bay 5. The bay designations are shown in Fig. 3. As the fire moves along the floor plate of the building, the fires start sequentially and independently of one another. The fire in one bay does not influence the gas temperature in the neighbouring bays, therefore, not including the effects of fire dynamics or elevated smoke temperatures into the fire model.

The same design parameters were used (opening factor and fuel load density) as the full-storey fire to generate the fire curves shown in Fig. 1. The spread rate (m/s) of the fire was calculated per [9] and assumed to be constant throughout the entire duration of the fires. The spread rate (s) is the

length the fire (L_f) divided by the time of the burning of the fire (t_b). In order for the models to be compared to one another directly, the spread rate for the two fire scenarios are the same.

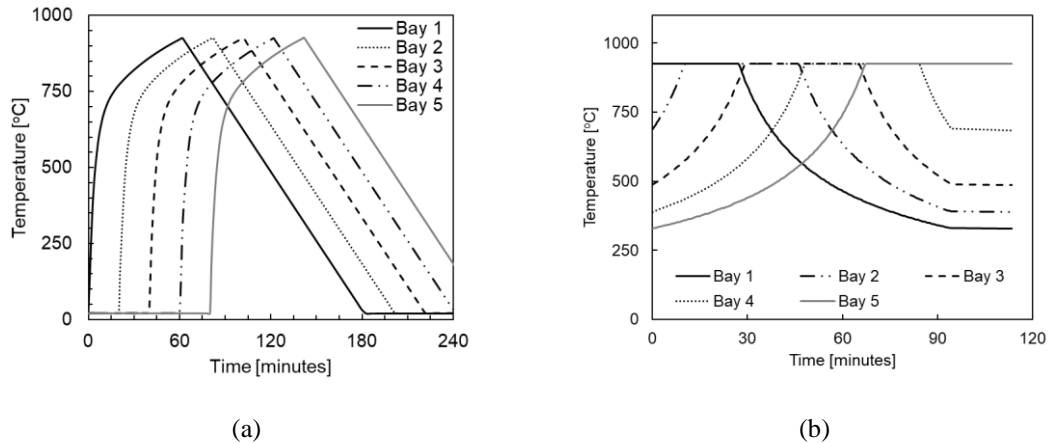


Fig. 1. Gas temperatures of the bays for each fire scenario (a) fire scenario #1, and (b) fire scenario #2

2.2 Fire scenario #2

The Travelling Fire Methodology (TFM) calculates the thermal field accounting for fire dynamics that is specific to the building under evaluation. In order to implement this, the fire model must account for the spatial and temporal evolution of the temperature field [5, 9]. The thermal field is divided into two regions: (1) near field, and (2) far field. The near field is when the elements are directly heated by the fire itself, and the far field is when the elements are heated due to hot combustion gases rather than the flames.

The TFM assumes a uniform fuel load along the path of the fire and that the fire burns at a constant heat release rate. When the fire is in the near field, the gas temperatures surrounding the elements will be the maximum temperature of the fire. When the fire is in the far field, gas temperatures are calculated using traditional heat transfer and fire dynamic methods.

For the TFM model used within this study, the heat release rate of the fire per unit area was 500 kW/m^2 . This is a typical heat release rate per unit area for densely furnished spaces. The local burning time of the fire (t_b) over area (A_f) is calculated as the fuel load density ($q_{f,d}$) divided by the heat release rate per unit area. The fuel load density for this calculation is the same fuel load density used for fire scenario #1 model calculations (570 MJ/m^2). Therefore, t_b is 19 minutes.

Typically, for TFM, the far field temperature is 1200°C [5, 9]. For this particular study, the authors set the maximum fire temperature of the TFM model to the maximum temperature of the parametric $T-t$ fire curves developed for the fire scenario #1 and full-storey model. The far field temperatures are calculated using typical engineering tools that provide temperature distributions away from the fire. This study used the Albert [10] model that was developed for ceiling jet correlation. The far field moves with the fire in a quasi-state form. As the fire consumes the available fuel and ignites new material in its path, the fire will move across the floor plate. The gas temperature next to any of the structural members will change as the fire travels both closer and further away from the member.

To implement the far field model, the floor is discretized into nodes with a fixed width of Δx . Each node has a single far field temperature at a given time. The more nodes that are used, the more refined the far field temperature is. Fig. 1(b) shows the $T-t$ curves for the gas temperatures in each of the bays. These curves look quite different from the curves shown in Fig. 1 for the fire scenario #1. At time of 0 minutes, in the TFM fire, the gas temperature is in the near field in Bay 1 and the gas temperature equals the maximum temperature of the fire (926°C). At this time, due to fire dynamics and elevated smoke temperature, the gas temperature in Bay 5 is 355°C . In contrast, at time of 0 minutes for fire scenario #1, the temperature in all of the bays is ambient temperature (20°C) and Bay 5 remains at this temperature until about 80 minutes after the fire ignites in Bay 1.

3 BUILDING DESIGN OF A TEN-STOREY OFFICE BUILDING

3.1 Structural design

A ten-storey office steel-frame office building located in Chicago, IL was designed using U.S. building codes and standards [3, 11-13]. The building uses perimeter moment-resisting frames (MRF) to resist lateral demands and composite steel beams for the gravity floor framing. The floor systems consist of 75 mm (3 in) metal deck with 65 mm (2.5 in) lightweight concrete on top. This decking system was chosen because it did not need to be shored during construction. In addition, 65 mm (2.5 in) of concrete on metal deck provides a 1 hr FRR, therefore eliminating the need for additional fire proofing on the metal deck. The steel beams are composite with the deck through 12.7 mm (0.5 in) diameter shear studs. The concrete is reinforced with welded wire reinforcement 152 mm x 152 mm MW10.

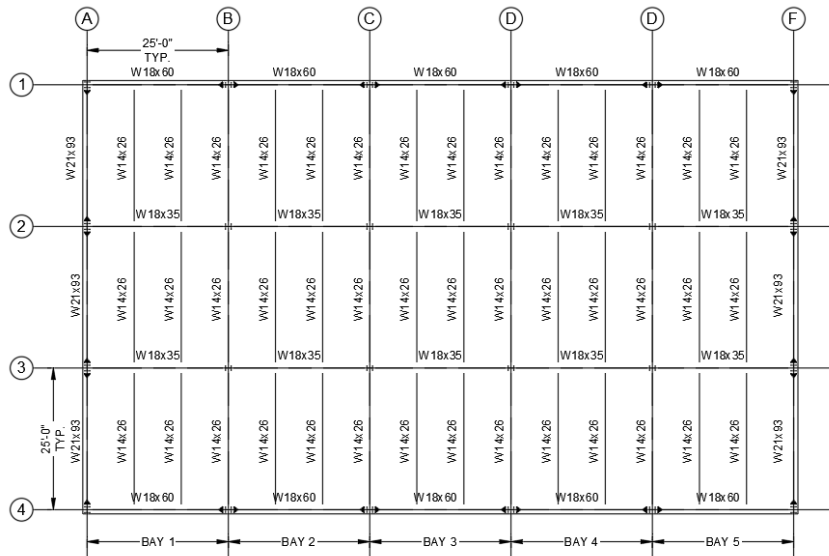


Fig. 2. Fifth floor framing with beam sizes

The building is designed using the recommended dead, live, wind, and earthquake loads from [12]. The dead and live loads for a typical office building are 3.1kN/m^2 (65psf) and 2.4kN/m^2 (50psf), respectively. The perimeter MRFs are designed to resist flexural demands without composite action. All of the gravity connections within the building are shear-tab connections and all of the MRF connections are moment connections. At the corner columns, the beams of the MRFs in the east-west direction use pinned connections to eliminate biaxial bending imposed on the corner MRF column. Gravity columns are designed with pinned base conditions. Fig. 2 shows the floor framing plan for the fifth storey of the building and Fig. 3 shows the elevation of the gravity framing on Grid Lines B, C, D, and E. More detailed information regarding the design of the building and lateral system is provided in [14].

3.2 Fire protection design

Buildings with businesses are categorized as occupancy (B) and must meet the requirements of Type IB buildings [11]. These requirements correspond to 2 hr FRR on all framing members. However, when a building's sprinkler system has control valves equipped with supervisory initiating devices and water-flow initiating devices for each floor, a reduction in FRR of building elements is allowed. The building reduces from a Type IB to Type IIA building and therefore framing members are required to have 1 hr FRR. The building discussed within this paper uses 1 hr FRR on all structural framing members. The fire protection was Isolatek Type-D C/F Spray-Applied Fire Resistive Material (SFRM). Using the UL Directory, 1hr FRR for the W14x26 floor beams, 15mm (9/16in) is required; for W18x35 floor beams, 13mm (1/2in) is required; and for W12x58 columns, 15mm (9/16in) is required.

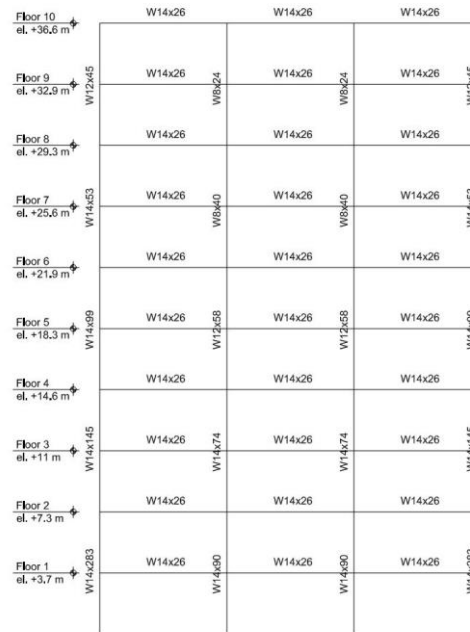


Fig. 3. Elevation of gravity framing members on Grid Lines B, C, D, and E

4 BUILDING MODELING AND ANALYSIS TECHNIQUES

Each building model simulation contains two parts: (1) heat transfer analysis to obtain nodal temperature distributions through the cross-section, and (2) structural analysis (or stress-based analysis) to model the stability and failure of the structure when subjected to thermal loads. The heat transfer step uses (1) temperature-dependent material properties, (2) $T-t$ fire curves for the gas temperatures surrounding the structural elements as boundary conditions, and (3) models heat transfer in the form of convection, conduction, and radiation. The structural analysis step: (1) utilizes nodal temperatures from the heat transfer analysis step as thermal load effects, (2) incorporates temperature-dependent material properties, (3) incorporates concrete material models that account for concrete crushing in compression and concrete cracking in tension, (4) incorporates steel material models that account for plasticity, (5) utilizes connection constitutive models that account for nonlinear failure behavior of shear tab connections, and (6) simulates the structural response of a building after initial failure. ABAQUS [15] is a commercially available finite element modeling (FEM) software that can successfully implement these two sequential steps. The analysis steps are described more in detail in [14]. This method of heat transfer analysis has been validated by [14, 16]. The validation of this study is not presented within this paper for brevity.

4.1 Material modelling

Eurocode [17] is used for the temperature-dependent steel material model. This includes temperature-dependent $\sigma-\epsilon$ relationships for the mechanical and thermal behaviour of structural steel. These relationships are used to model the beams, columns, and connections within the building. Eurocode [18] is used for the temperature-dependent lightweight concrete material and thermal properties. The thermal conductivity, mass density, and specific heat of SFRM from AISC Design Guide 19 [13].

4.2 Structural modelling

The beams and columns in the building are modelled using beam elements (B31) within ABAQUS. The composite deck is modelled using shell (S4R) elements. Wire mesh was embedded as reinforcement within the concrete deck. The shear tab connections were modelled using wire

connector elements that simulated the axial force (P) – axial displacement (δ) – moment (M) – rotation (θ) – temperature (T) relationship of the specific geometry of the connection. This relationship is based off of the spring model developed by Sarraj [19] and further refined by Agarwal [13]. The component model considers failure mechanisms within the connection: bolt shear fracture, bolt bearing on beam web and shear-tab. This model was benchmarked against experimental bolt shear and plate bearing tests [19, 20]. A nonlinear gap element spring considers the behaviour between the beam bottom flange and the connecting element closing and the potential for beam bottom flange local buckling. Details of this particular constitutive model are presented [14].

4.3 Load combinations

Equation 1 shows the load combination provided by ASCE 7 and AISC *Specification* Appendix 4 for extreme loading conditions. To account for potential imperfections in the structural members, AISC *Specification* Appendix 4 requires a 0.2% notional load. Each of the floors in the model were assigned the gravity load combination shown in Equation 1 and each storey was offset 0.2% from the storey below to account for the imperfections. This load combination also accounts for the imposed loads and effects due to the thermal loading (A_T). These effects are inherently considered within the model by simulating the entire building framing system.

$$(0.9 \text{ or } 1.2)D + A_T + 0.5L + 0.2S \quad (1)$$

5 ANALYSIS RESULTS

The results of the analysis presented in this section are for three different fire scenarios discussed in Section 2. In all of the fire scenarios, the gravity columns were the first structural framing member to fail; however, the time and temperature at which the failure occurred differed based on the fire scenario. This section will summarize the behaviour of the gravity columns and the simple connections.

5.1 Behaviour of gravity columns

Table 1 summarizes the failure time and mechanisms. When the fifth floor is subjected to a full storey design fire, all of the gravity columns buckle at 87.5 minutes. Since all of the gravity columns fail at the same time, load redistribution to the surrounding MRF columns is not possible and the building collapses. The gravity column temperature at failure is 564°C. Fig. 5a shows the axial force ($P-t$) and temperature histories ($T-t$) of the gravity columns. This plot shows that the gravity columns lose their load carrying capacity at approximately 87.5 minutes.

5.1.1 Fire scenario #1

When the fifth floor is subjected to a travelling fire using fire scenario #1 travelling fire model, the gravity columns on Grid Line B fail followed by the gravity columns on Grid Line C. Fig. 5b shows the axial force histories of the each of the gravity columns and the MRF columns heated by the fire. The gravity columns on Grid Line B (Bay 1) fail first at approximately 85 minutes (568°C). When these columns buckle, load is redistributed to the gravity columns on Grid Line C (Bay 2) and the MRF columns on Grid Lines A and 4. This is shown in Fig. 5b as an increase in axial force in the columns at the time of failure of the gravity columns on Grid Line B. Similarly, when the gravity columns on Grid Line C (Bay 2) fail at approximately 111 minutes, load is redistributed to the MRF columns on Grid Lines A and 4. The gravity columns failed in sequential order from Grid Line B to E as the fire moved sequentially from Bay 1 to Bay 5. As the gravity columns failed, load was redistributed to the MRF columns and the gravity columns in the next bay until the building collapsed.

Table 1. Summary of failure time and temperature of gravity columns for different fire scenarios

Fire Scenario	Failure time of gravity columns	Failure temperature of gravity columns
Full-storey fire	All Bays – 87.5 minutes	All bays – 564°C
Fire scenario #1	Bay 1 (Grid Line B) – 85 minutes Bay 2 (Grid Line C) – 111 minutes	Bay 1 (Grid Line B) – 568°C Bay 2 (Grid Line C) – 572°C
Fire scenario #2	Bay 3 (Grid Line D) – 75 minutes Bay 4 (Grid Line E) – 86 minutes Bay 2 (Grid Line C) – 105 minutes	Bay 3 (Grid Line D) – 581°C Bay 4 (Grid Line E) – 574°C Bay 2 (Grid Line C) – 523°C

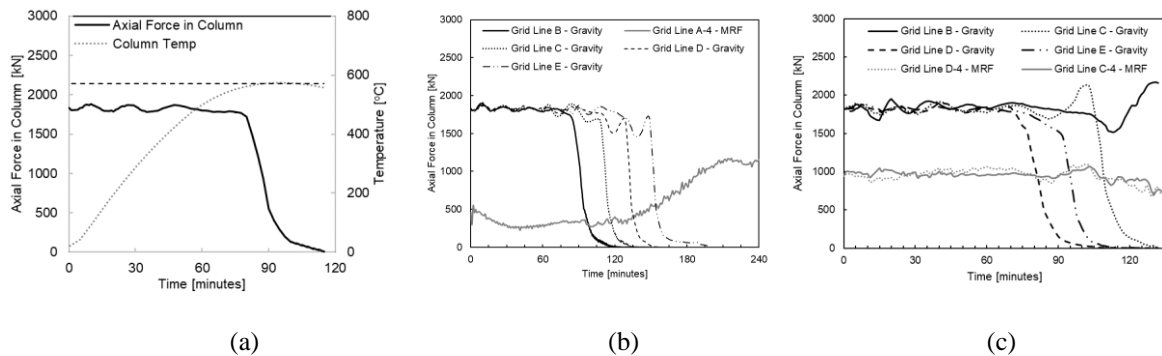


Fig. 4. Axial force (P) and temperature (T) history of gravity columns for (a) full-storey fire, (b) fire scenario #1, and (c) fire scenario #2

5.1.2 Fire scenario #2

When the fifth floor is subjected to a travelling fire using the TFM model, the gravity columns in Bay 3 (Grid Line D) buckle first, followed by the gravity columns in Bay 4 (Grid Line E), and then Bay 2 (Grid Line C), which ultimately causes the collapse of the building. Fig. 4c shows the axial force histories of each of the gravity columns heated by the fire. The gravity columns on Grid Line D (Bay 3) buckle at time 75 minutes (581°C). Failure of the gravity columns on Grid Line E occur shortly after at 86 minutes (574°C). At this time, the load in the MRF columns at Grid Lines C-1, C-4, D-1, and D-4 and gravity columns on Grid Line C increase. The gravity columns on Grid Line C fail at a time of about 105 minutes (523°C). At this time, the building is unstable and collapse begins. The gravity columns further away from the source of the fire failed before the gravity columns near the source of the fire. The temperature histories of the gravity columns shown in Fig. 4c demonstrates that the temperatures of the columns further away from the source were heated more intensely due to the far field heating.

6 CONCLUSIONS

The results of the study demonstrate that consideration of far field heating is necessary to simulate the time-dependent performance of the building. Buckling of gravity columns occurs about 12 minutes earlier when considering the TFM model versus a full storey fire and 10 minutes earlier than fire scenario #1. In addition, the order in which the failure occurs differs between the two travelling fire models. When fire dynamics is considered, the source of the fire will cause the gas temperatures in the compartments further away to increase in temperature therefore heating the structural elements. Travelling fire research is still in development. There is a lack of realistic large-scale test measurements available to researchers and engineers that can benchmark and validate the models. This data is necessary in order to codify methodologies for performance-based structural engineering design approaches.

REFERENCES

1. ASTM. (2016). "Standard Test Method for Fire Tests of Building Construction and Materials." ASTM E119-16a, West Conshohocken, PA.
2. Buchanan, A. (2002). Structural Design for Fire Safety, John Wiley & Sons.
3. AISC. (2016). "Specification for Structural Steel Buildings", ANSI/AISC 360-16, Chicago, IL.
4. Eurocode 1: Actions on structures – Part 1-2: General actions – Actions on structures exposed to fire, European standard EN 1991-1-1, 2002. CEN, Brussels.
5. Stern-Gottfried, J. and Rein, G. (2012). "Travelling Fires for Structural Design. Part I: Literature Review," Fire Safety Journal, vol. 54, pp. 74-85.
6. Kirby, B.R. et al. (1994). "Natural Fires in Large Scale Compartments," British Steel Technical, Fire Research Station Collaborative Project Report, Rotherham, U.K.
7. Rein, G. et al. (2007). "Multi-storey fire analysis for high-rise buildings," *Proc. 11th Int. Interflam Conf.* London, UK, pp. 605-616.
8. Bailey, C.G., Burgess, I.W., and Plank, R.J. (1996). "Analyses of the Effects of Cooling and Fire Spread on Steel-framed Buildings," Fire Safety Journal, vol. 26, pp. 273-293.
9. Stern-Gottfried, J. and Rein, G. (2012). "Travelling Fires for Structural Design. Part II: Design Methodology," Fire Safety Journal, vol. 54, pp. 96-112.
10. Albert, R.L. (1972). "Calculation of Response Time of Ceiling-Mounted Fire Detectors," Fire Technology, vol. 8, pp. 181-195.
11. IBC. (2012). "International Building Code." IBC 2012, Falls Church, VA.
12. ASCE. (2010). "Min. Design Loads for Buildings and Other Structures." ASCE 7-10, Reston, VA.
13. Ruddy, J. L. et al. (2003). "Design Guide 19: Fire Resistance of Structural Steel Framing," AISC.
14. Agarwal, A. (2011). Stability Behavior of Steel Building Structures in Fire Conditions, West Lafayette, IN: Purdue University.
15. Abaqus/Standard. (2014). Version 6.13 User's Manual, Providence, RI.
16. Fischer, E.C. and Varma, A.H. (2015). "Fire behavior of composite beams with simple connections: benchmarking of numerical models," Journal of Constructional Steel Research, 111, 112-125.
17. Eurocode 3: Design of steel structures – Part 1-2: General rules – Structural fire design, European standard EN 1993-1-2, 2005. CEN, Brussels.
18. Eurocode 4: Design of composite steel and concrete structures – Part 1-2: General rules – Structural Fire Design, European standard EN 1994-1-1, 2005. CEN, Brussels.
19. Sarraj, M. (2007). The Behaviour of Steel Fin Plate Connections in Fire, Sheffield, UK: The University of Sheffield.
20. Fischer, E.C., Varma, A.H., and Zhu, Q. (2017). "Experimental evaluation of single-bolted lap joints at elevated temperatures," Journal of Structural Engineering, vol. 144(1).

FIRE-INDUCED PROGRESSIVE COLLAPSE OF THE PLASCO BUILDING IN TEHRAN

Amir Saedi Daryan¹, Hesam Ketabdari², Mahmood Yahyai³, Mohammed A. Morovat⁴, Michael D. Engelhardt⁵

ABSTRACT

Fire is one of the most significant loads that a building structure may see throughout its service life, with potentially major consequences such as partial or total collapse. Considering the high potential consequence of structurally-significant fires, it is important to understand and quantify the effects of fire on structures, especially with reference to the progressive collapse of tall buildings. An unfortunate event of a building collapse due a structurally significant fire provides a unique opportunity to study the fire-induced collapse phenomenon of tall buildings, and to help develop appropriate measures to prevent such collapses in the future. The Plasco building tragedy in Iran was one of the most significant examples of progressive collapse of a high-rise building in fire. Therefore, a comprehensive study was conducted by the authors to reconstruct the fire performance of the Plasco building through the development of a detailed finite element model of the building structural system. This paper first describes the development of the finite element model of the Plasco building, and highlights some of its unique features. The paper further outlines the main causes of the collapse of Plasco building, and discusses the major findings on the progressive collapse study of the structure. Finally, considerations for designing against fire-induced progressive collapse are proposed.

Keywords: Plasco Building, finite element modelling, connection failure, collapse modelling

1 INTRODUCTION

With the increase in demand for high-rise buildings and with the increase in the complexity of structural systems of tall buildings, concerns have been raised regarding the impact of fire incidents on the integrity of these structures. These concerns have been intensified due to recent fire events in high-rise buildings around the world resulting in minor damage or even collapse in some cases. As a result, the study of the behavior of high-rise buildings in fire and the performance of their structural members is of great importance.

The Plasco building tragedy in Iran was one of the most significant examples of progressive collapse of a high-rise building in fire. Therefore, a comprehensive study was conducted by the authors to reconstruct the fire performance of the Plasco building through the development of a detailed finite element model of the building structural system. This paper highlights some of the results from this extensive computational study. The focus of the study reported here was to

¹ Assistant Professor, Civil Engineering Department, Shahid Beheshti University, Tehran, Iran.
e-mail: amir_saedi_d@yahoo.com

² Ph.D. Student, Civil Engineering Department, Shahid Beheshti University, Tehran, Iran.
e-mail: H_Ketabdari@sbu.ac.ir

³ Professor, Civil Engineering Department, K.N. Toosi University of Technology, Tehran, Iran.
e-mail: yahyai@kntu.ac.ir

⁴ Research Scientist Associate. Department of Civil, Architectural and Environmental Engineering, University of Texas at Austin, Austin, USA.

e-mail: morovatma@utexas.edu

⁵ Professor. Department of Civil, Architectural and Environmental Engineering, University of Texas at Austin, Austin, USA.
e-mail: mde@mail.utexas.edu

examine the effect of fire on the structural elements at the tenth floor and the cause of the first failure event. The motivation was that photographic evidences as well as results of an official investigation indicated that the progressive collapse of the Plasco building was started by an initial local failure at the tenth floor. Further, due to the complexity of the structural system, only the northwestern part of the tenth floor was been studied.

2 THE PLASCO BUILDING AND THE FIRE INCIDENT

The Plasco building was located in downtown Tehran, the capital city of Iran. Construction of the building, consisting of the two North and South Towers, began in 1960 and was completed in 1962. The South Tower had 16 floors, consisting of a basement, a ground floor, and 14 floors above the ground. The building had commercial use and most of its units belonged to clothing businesses. On January 19, 2017, just before 8 am, a fire started at one of the 10th floor units. Although firefighting operations began shortly after 8am, the fire gradually spread vertically and horizontally throughout the building and eventually engulfed several floors. Unfortunately, at around 11:33 am, a progressive collapse led to the destruction of a major portion of the South Tower. Pictures of the Plasco building before and after collapse in fire are shown in *Fig. 1*.

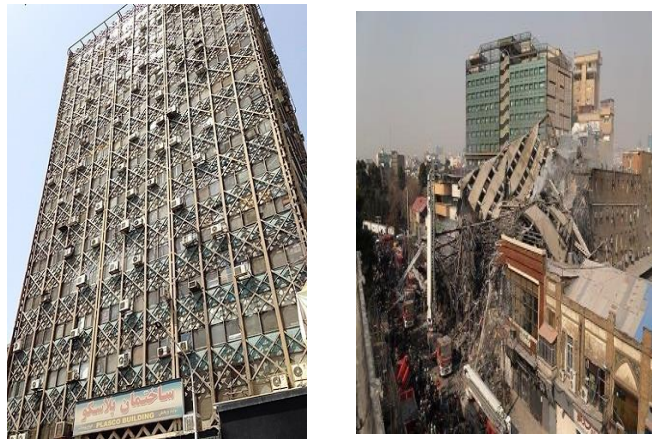


Figure 1. The Plasco building before and after collapse in fire

The structural system of the Plasco building was similar to a tube system. In this structure, most of the columns were located at the perimeter of the building, and only 4 central columns were responsible for carrying a significant portion of gravity loads. The main components of the structural system of the Plasco building were: concrete slabs, joists, Vierendeel trusses, main load-carrying trusses, central columns, corner columns, main skin columns, subsidiary skin columns, skin trusses, and connections.

3 MODELING THE FAILURE OF PLASCO BUILDING

The Abaqus finite element software [4] was used to model the complex structural system of the Plasco building and to model and analyze the effect of fire. In addition, as indicated before, the focus of the study reported here was to examine the effect of fire on the structural elements at the tenth floor and the cause of the first failure event. Therefore, the tenth floor was modeled and analyzed. In the following, more details about the modelling are provided.

3.1 Structural elements

Shell elements of type S4RT were used to model steel and thermal solid elements of type C3D8T are used for modelling the concrete members of the structure. Quad-dominated meshing technique for steel elements and structural meshing technique for concrete elements are used [4, 5].

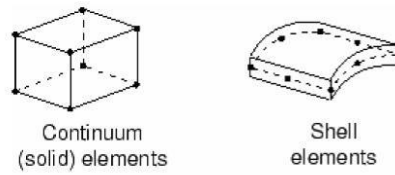


Figure 2. Solid and Shell elements used in the finite element models of the Plasco building

Further details of the structural model of the tenth floor of the Plasco building is shown in Fig. 3.

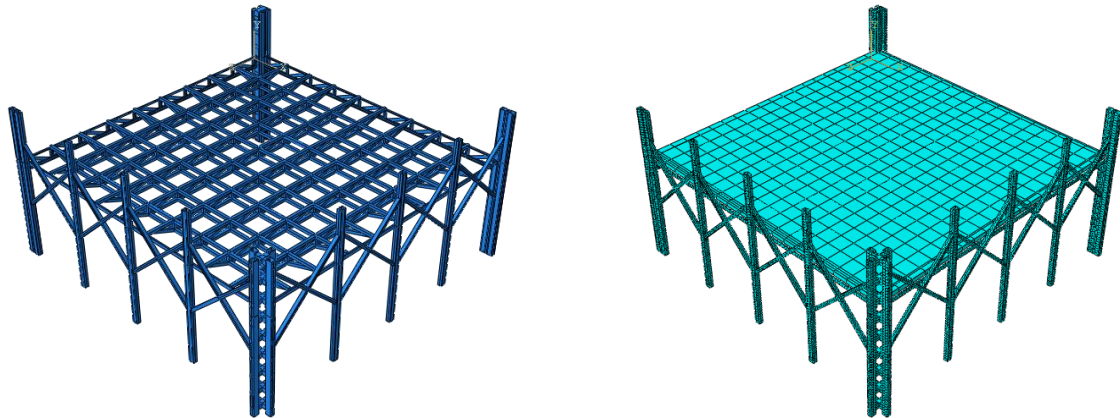


Figure 3. Modelling the tenth floor of the western part of the Plasco building

3.2 Material properties and constitutive models

Examination of the samples recovered from the Plasco building following the collapse incident, indicated that ST44 and ST33 steel materials were mostly used in the construction of the Plasco building. The mean and standard deviation of the samples taken from the concrete further showed the compressive strength of the concrete was in the range of about 25 to 30 MPa. According to the results of the tests, material properties used in the modelling, were the steel grade 44 and the concrete with a compressive strength of 28 MPa [3, 6].

A strain hardening bilinear model was used to simulate steel behavior while damaged plasticity was employed for modelling concrete in the software.

In order to capture the change of the mechanical properties of the materials with increasing temperature, the reduction factors given in Section 8 of Eurocode 3 [7] is used for steel, while the factors reported by Saedi Daryan [8] was assumed for concrete material. These reduction factors are presented in Tables 2 and 3.

Table 2: Reduction Factors of steel properties with increasing temperature [7]

Steel temperature (°C)	Normalized Modulus Elasticity	Normalized yield stress	Normalized Thermal expansion	Normalized specific heat	Normalized Thermal conductivity
20	1	1	1	1	1
100	1	1	1.035	1.1	0.95
200	0.9	1	1.067	1.2	0.89
300	0.8	1	1.097	1.28	0.825
400	0.7	1	1.128	1.38	0.76
500	0.6	0.78	1.159	1.5	0.695
600	0.31	0.47	1.19	1.7	0.64
700	0.13	0.23	1.221	2.1	0.575
800	0.09	0.11	1.2	1.8	0.51
900	0.0675	0.06	1.05	1.5	0.51

Table 3: Reduction Factors of concrete properties with increasing temperature [8]

concrete temperature (°C)	Thermal conductivity coefficient	Normalized Density variation	Normalized Compressive Strength	Normalized Modulus Elasticity
20	1.951408	1	1	1
100	1.7656	1	1	0.9
200	1.5526	0.98	0.93	0.8
300	1.361	0.965	0.9	0.65
400	1.1908	0.95	0.85	0.5
500	1.042	0.94125	0.7	0.45
600	0.9146	0.9325	0.35	0.43
700	0.8086	0.92375	0.25	0.35
800	0.724	0.915	0.2	0.3
900	0.6608	0.90625	-	-

3.3 MODEL VERIFICATION

The finite element model of the tenth floor was created in Abaqus software. All structural elements including columns, girders, joists and connections were accurately modelled using shell and solid elements, explained in section 3.1. The results obtained for 10th floor under gravity loads are compared with the corresponding values reported by the Special Investigating Board (SIB) through modelling the entire structure using SAP software [3, 6]. Table 4 depicts the results of the FEM model with those reported by SIB.

Table 4: Different response predictions from the national report and from the present study

Items	SIB results	FEM results
The deformation of the main north-south beam in the examined span (mm)	45.3	43.9
Maximum shear in the north-south main beam in the examined span (ton)	21.75	21.55
The deformation of the main east-west beam in the examined span (mm)	48	49.7
Maximum shear in the east-west main beam in the examined span (ton)	20.26	20.07

As the results show, the finite element model provides satisfactory results of the structural modelling and performance. In order to ensure the accuracy of the finite element method in heat modelling, a widely three-story reference experiments for natural fire incidents has been selected to be modelled by FEM.

3.3.1 Three story steel frame under uniform fire

This frame is adopted by Bailey et al. (1996) [9], and Liew et al. (1998) [10] for numerical simulation of the effects of the spread of fire. The geometry and material specifications of members are shown in Fig. 4. In this frame, all internal beam sections were UB 610×229×1.1 and all column sections were UC 254×254×132. Connections are considered to be rigid.

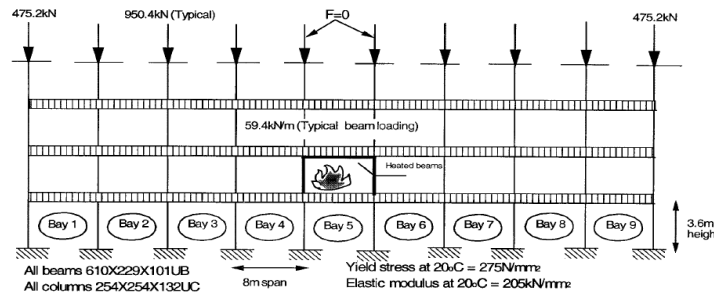


Figure 4. The three-story, 9 span frame exposed to fire used for verification of the modelling technique

The steel members including the beams and columns marked with thick lines in Fig. 4 are uniformly heated and then cooled to room temperature.

It should be noted that due to the possibility of an early failure, the members which are directly exposed to fire and may experience large axial loads are eliminated. In this example, the axial load of the columns in bay 5 were eliminated. The results of this fire analysis using Abaqus software and the results of Bailey [9] research are shown in Fig. 5.

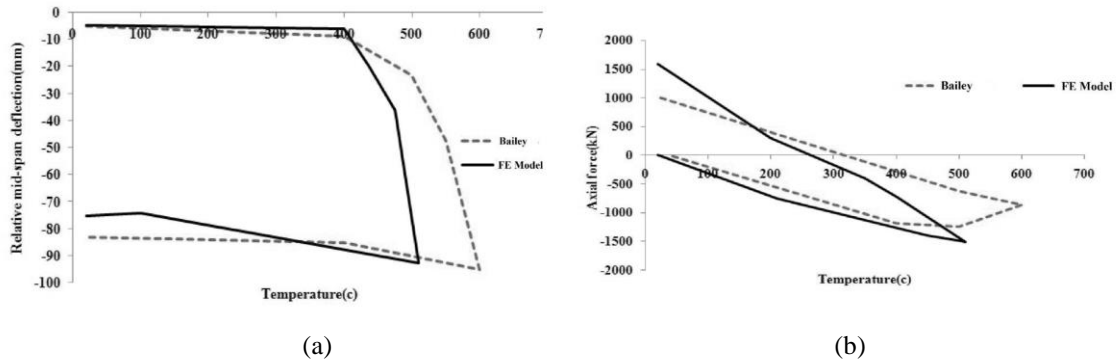


Figure 5. a) Temperature – Displacement of steel frame; b) Axial forces in bay 5

As shown in Fig. 5, modelling and analysis of fire exposed steel frames present acceptable results.

4 DISCUSSION

Thorough examination of hours of incident footage, and the provision of reports from eyewitnesses and firefighters, as well as an investigation of the location of the incident, the authors tried to reconstruct and investigate the fire collapse incident of the Plasco building. The process of initiation of the first local failure at the tenth floor and its subsequent progressive collapse is depicted in Figs. 6 and 7. As seen in Fig. 7, the tenth floor ceiling collapsed in both the northwest and southeast parts of the building. The destruction of the northwestern region was only limited to one unit. However, the destruction of the southeastern region had been developed and led to the collapse of a major part of the structure

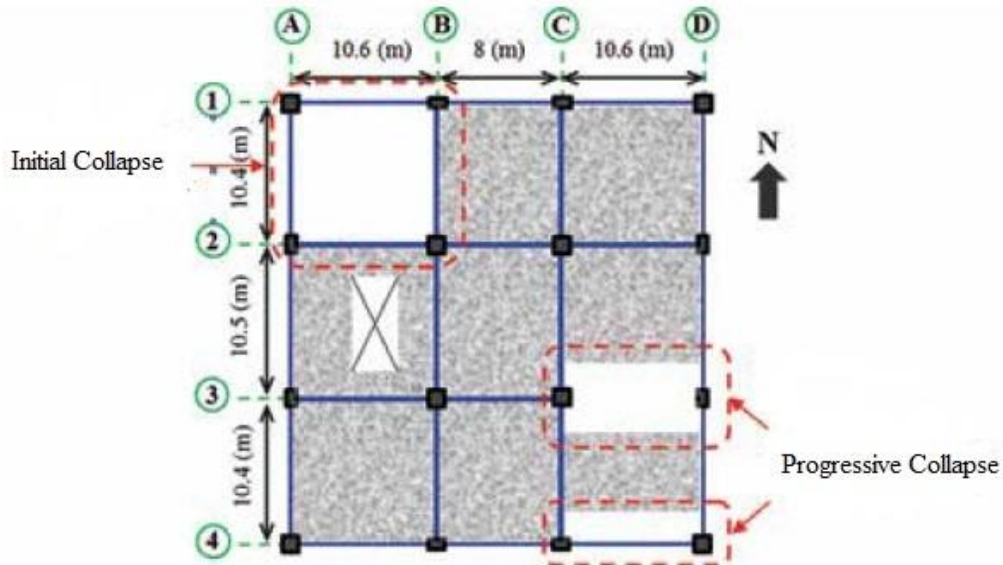


Figure 6. Plan view of the failure initiation and progression in the tenth floor of the Plasco building

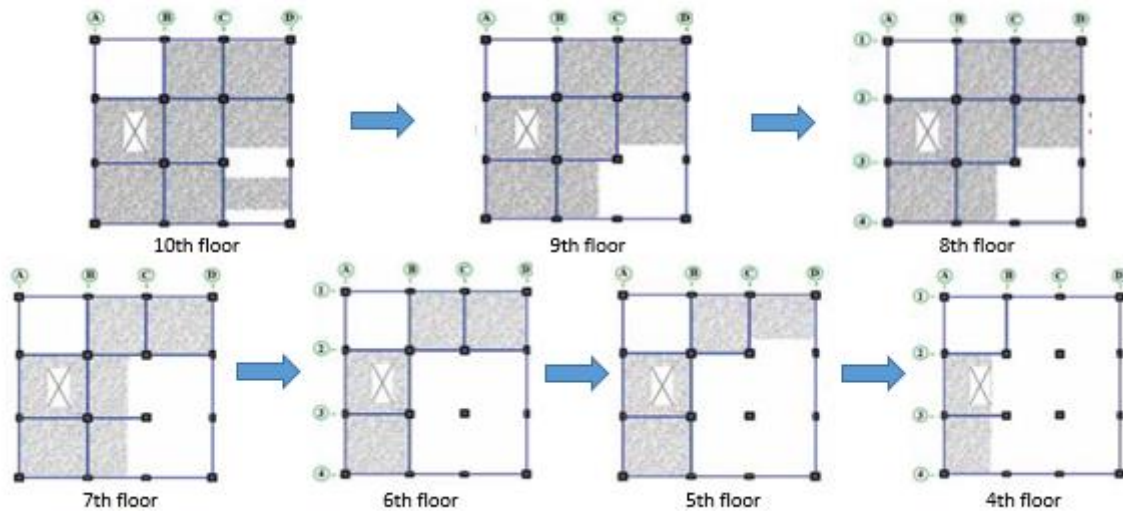


Figure 7. The failure event in the tenth floor and its progression to the collapse of the building

Since the progressive collapse of the structure was started by an initial local failure, the main objective of this research was to study the effect of fire on the structural elements at the tenth floor and the cause of the first failure event. Due to the complexity of the structural system, only the northwestern part of the tenth floor was been studied. As introduced in previous sections, the general-purpose finite element software Abaqus was utilized to model the structure and the progression of failure. The results from this comprehensive finite element analysis show that, after about 3 hours into the fire and loss of fire protection for several structural elements, the temperature rise of steel members in this section resulted in large deformations of the joists (Figs. 8 and 9). As a result of large deformations, excessive rotations and significant tensile forces were induced to the beam-to-column connections. More specifically, the connections initially failed at the location of high gravity loads and eventually failed at other locations as well due to stress redistributions. The connection failure resulted in collapse of the ceiling of the tenth floor. The occurrence of this failure event initiated and caused the progressive failure of the building.

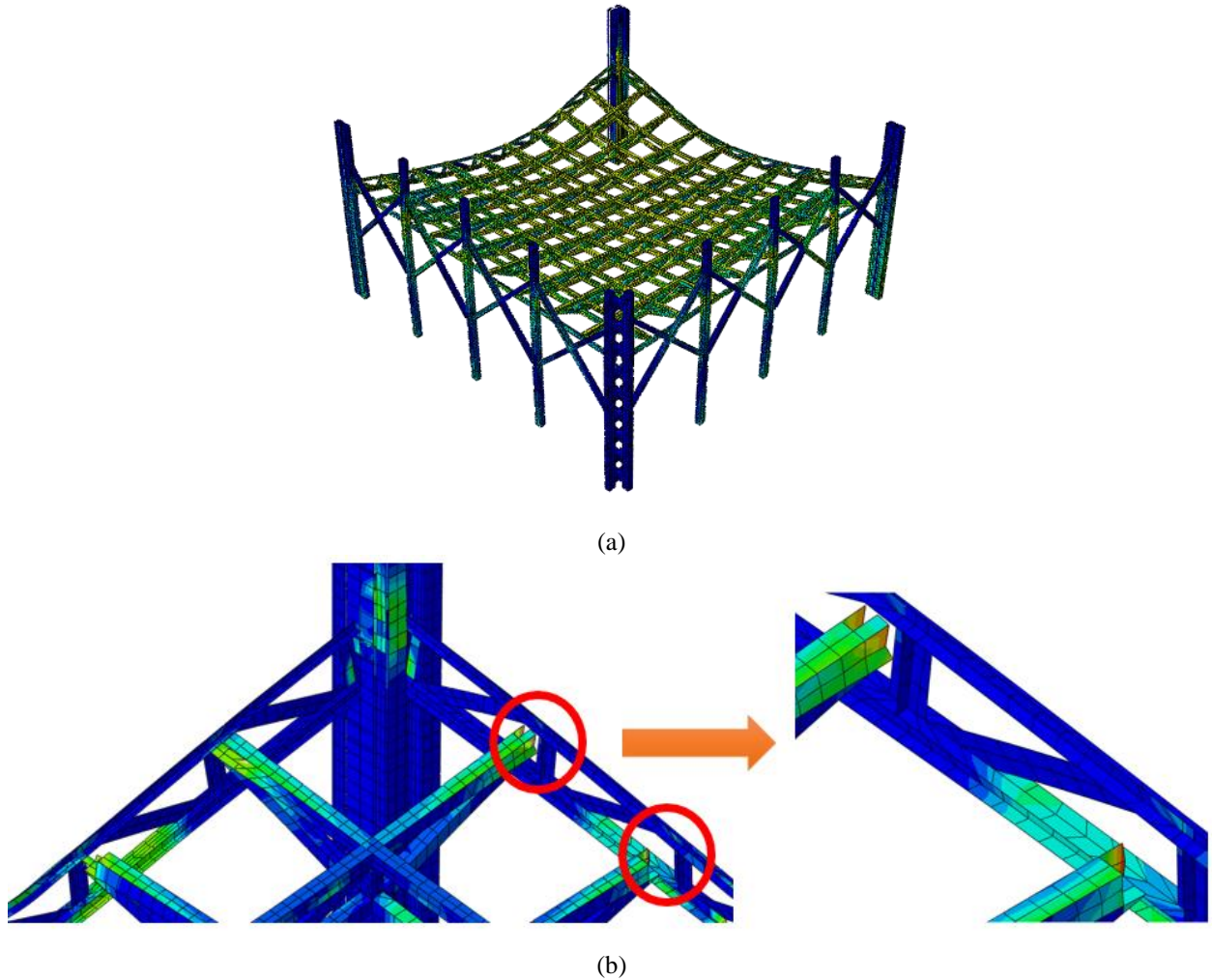


Figure 8. Secondary beams connections and their failure mode. a) Before failure; b) After failure.

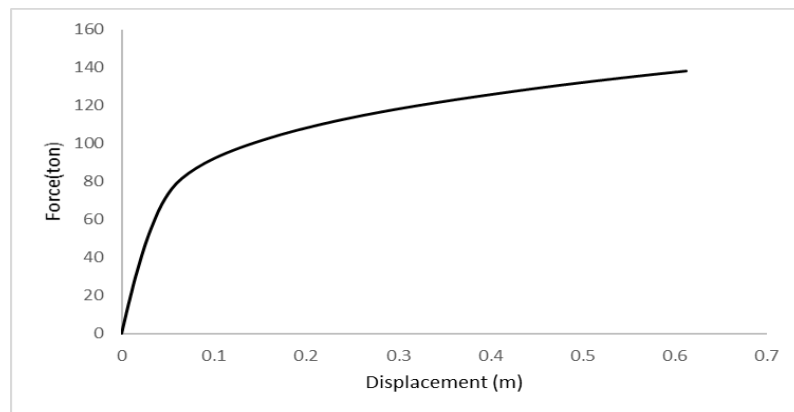


Figure 9. Load – deflection relations of secondary beams

5 CONCLUSIONS

The study reported in this paper is part of an on-going comprehensive research being conducted by the authors on the structural performance of the Plasco building during a fire incident that resulted in the total collapse of the building. The general-purpose finite element software Abaqus was utilized to model the structure and the progression of failure. The results from this comprehensive finite element analysis show that, after about 3 hours into the fire and loss of fire protection for several structural elements, the temperature rise of steel members in this section resulted in large

deformations of the joists. As a result of large deformations, excessive rotations and significant tensile forces were induced to the beam-to-column connections. More specifically, the connections initially failed at the location of high gravity loads and eventually failed at other locations as well due to stress redistributions. The connection failure resulted in collapse of the ceiling of the tenth floor. The occurrence of this failure event initiated and caused the progressive failure of the building.

More detailed results and discussions from the comprehensive study on the fire collapse of the Plasco building is beyond the scope of this paper and will be published and summarized in future publications.

REFERENCES

1. S. Lamont, Barbara Lane, Graeme Flint, Asif Usmani, *Behavior of Structures in Fire and Real Design – A Case Study*, *Journal of Fire Protection Engineering*, Vol. 16, February 2006
2. Ian Burgess, *Fire Resistance of Framed Buildings*, *Physics Education*, September 2002
3. Special Investigating Board (SIB), *National Report on the Fire Collapse of Plasco Building*, Islamic Republic of Iran President Office, April 2017.
4. *Abaqus Version 6.14-2*, SIMULIA. Inc., Providence, RI. 2015.
5. Saedi Daryan, A. Bahrampour, H. Arabzadeh, H. "ABAQUS Software Guideline", 2011.
6. *Technical and Emergency Management Investigation of Fire Collapse of Plasco Building*, Tehran Urban Research and Planning Center, May 2017
7. Eurocode 3: *Design of steel Structures-Part 1-1: General rules and rules for buildings*, European Committee for Standardization, Brussels.2005
8. Saedi Daryan, A. *Investigating behavior of concrete structures in Iran expose to fire*, Municipality and City Council of Tehran, June 2016.
9. Bailey, C. G., Burgess, I. W., and Plank, R. J. *Computer simulation of a full-scale structural fire test*, *Structural Engineer*, 1996, 74, 93-100.
10. Liew, J. R., Tang, L. K., Holmaas, T., & Choo, Y. S. *Advanced analysis for the assessment of steel frames in fire*, *Journal of Constructional Steel Research*, 1998, 47(1-2), 19-45.

COLLAPSE ANALYSIS OF THE PLASCO TOWER USING OPENSEES

Hamzeh Hajiloo¹, Liming Jiang², Tejeswar Yarlagadda³, Asif Usmani⁴, and Mark F. Green⁵

ABSTRACT

The progressive collapse of structures, such as the tragic collapse of the World Trade Centre (WTC) towers, are rare events that cause catastrophic losses especially if the collapse occurs during rescue operations. In a recent tragic fire incident, the Plasco Tower collapsed after an intense outburst of fire lasting for three and a half hours and claiming the lives of 16 firefighters and 6 civilians. The tower was a 16-storey commercial building built in 1962 and served as a major centre in the garment industry. This paper presents the current progress on a collaborative research project on simulating the collapse of the tower with respect to the travelling fire phenomenon as observed during the fire disaster. The simulation work is based on structural details, material properties and loading conditions obtained from published reports from the official investigation in Iran (in Persian). Photographic and video evidence provides insight for establishing the fire loading sequences and scenarios that caused the ultimate collapse. The simulation uses the open source software framework OpenSees. This paper presents the preliminary work for developing the full model in OpenSees and establishing the base level structural response of the Plasco Tower structure to the fire.

Keywords: Progressive collapse; structures in fire; Plasco Tower; OpenSees simulation

1 INTRODUCTION

Constructed in 1962, the Plasco building consisted of a 16-storey tower and a 5-storey podium (Fig. 1). Although the tower was the tallest structure ever built in Iran at the time, it was constructed incorporating some advanced construction methods and elements such as post-tensioned floor trusses, a lateral-load bracing system, and composite concrete floors. Fig. 2 (a) shows the flooring trusses in the tower during construction and Fig. 2 (b) shows the cross bracing system on the sides of the Plasco tower. Initially, the low-rise podium part of the building and the lower floors of the tower were used as a shopping centre while the upper floors of the tower were occupied as offices. At the time that the fire occurred, however, most of the units in the tower were used as garment manufacturing units. Fire safety measures were not adopted in the building regardless of the extreme vulnerability of the structural steel components to heat. Neither passive nor active fire safety measures were implemented in the building. There was an ongoing attempt to improve the fire safety of the building, but it was postponed because of financial constraints and the resistance of the tenants to pause their activities during the proposed retrofitting work. Hajiloo et al. [1] studied various aspects of the Plasco fire including the condition of the tower before the fire, initiation of the fire, the evacuation process, and the progressive collapse of the building. It was shown that the fire could have been extinguished earlier and the catastrophic loss of the firefighters could have been prevented if an expert knowledge of the performance of steel structures was used. The authors have not conducted an independent site investigation, and the work presented in this paper was developed based on the information in the available reports [1-3], photographs, and videos of the fire event.

1. Postdoctoral fellow, Department of Civil Engineering, Queen's University, Canada. Email: hajiloo.h@queensu.ca

2. Postdoctoral fellow, Department of Building Services Engineering, Hong Kong Polytechnic University, HKSAR, China. Email: liming.jiang@polyu.edu.hk

3. PhD Student, Department of Building Services Engineering, Hong Kong Polytechnic University, HKSAR, China. Email: tejeswar.yarlagadda@connect.polyu.hk

4. Professor, Department of Building Services Engineering, Hong Kong Polytechnic University, HKSAR, China. Email: asif.usmani@polyu.edu.hk

5. Professor, Department of Civil Engineering, Queen's University, Canada. Email: greenm@queensu.ca

Collapse Analysis of the Plasco Tower Using OpenSees



Fig. 1. Steel frame and bracing system around all sides of the Plasco tower; (b) the attached 5-storey shopping centre; (all images courtesy of IRNA)

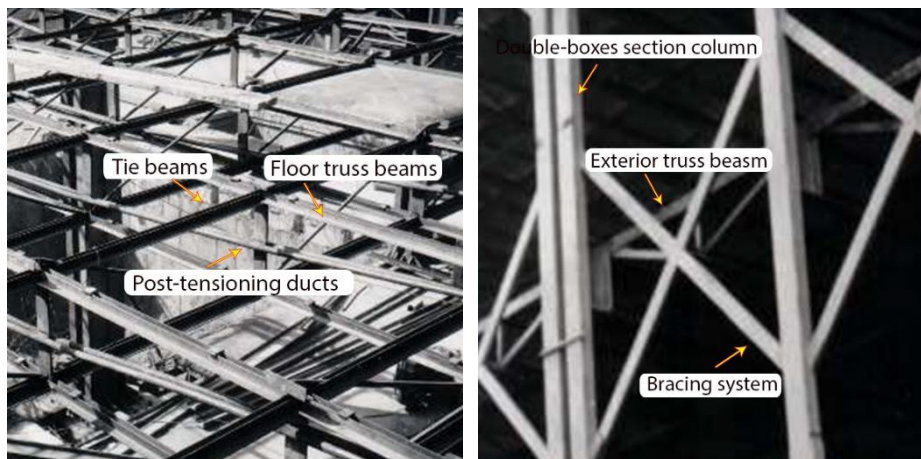


Fig. 2. The Plasco tower under construction: (a) the flooring system; (b) the bracing system on the sides of the tower (adapted from [3])

The Open System for Earthquake Engineering Simulation (OpenSees) was developed at the University of California, Berkeley [4]. It was initially designed to simulate non-linear response of structural frames under seismic excitations. OpenSees is written in C++ and has an object-oriented architecture, which enables structural engineers to focus on specific objects comprising structural models that have their own attributes and functions rather than just data. Major attributes such as elements, materials, analysis procedures, and solution algorithms are designed as individual objects and they can be added into the framework freely by anyone anywhere. In 2009, OpenSees was adopted at the University of Edinburgh to further develop it to perform structural fire analysis [5]. Significant contributions in terms of heat transfer and thermo-mechanical classes have been made to the framework in developing the Thermal version of OpenSees, where a loose coupling method is adopted in order to separate the heat transfer analysis from the thermo-mechanical analysis. For the latter, temperature dependent formulations have been incorporated for frame element and shell elements to account for the thermal effects [6; 7], while new temperature dependent material models for steel and concrete based on Eurocodes [8; 9] are also added to the material library.

2 ENGINEERING DETAILS OF THE PLASCO TOWER

2.1 Preliminary analysis

A preliminary analysis of the performance of the Plasco tower was conducted by Tehran's city council technical committee [3] that was formed to investigate the Plasco fire incident. The committee's analysis was performed with the commercial program SAP2000. First, the tower was evaluated against the gravity load and seismic loads. The tower was adequate for gravity load but failed to meet the requirements of the current seismic demands in Tehran's seismic zone. Then, progressive collapse of the tower was analysed using the "Staged Construction" feature of SAP2000. The procedure proposed by the US Department of Defence to simulate the progressive collapse of structures [10] was adopted. This guideline allowed a linear static analysis because of the regular plan of the tower. The assessment of the collapse process using the visual evidence [3] showed that the most probable cause of the progressive failure was the collapse of one beam on the 12th floor.

When linear static analysis was used, the actions in the structure were classified as deformation-controlled or force-controlled [10; 11]. The gravity load was applied to the structure using the relevant load cases for deformation-controlled and force-controlled actions. Concurrently, the gravity load on the areas affected by the removed elements was increased by a load increase factor of 2 for force-controlled actions. The procedure assigned each structural component an m factor that was determined from ASCE 41 [11]. Then, the primary elements were checked against the acceptance criteria for force-controlled and deformation-controlled actions.

According to the material tests that were conducted on the coupons taken from the various structural elements, the average tensile yield strength of the steel was 290 MPa. As such, the steel was considered equivalent to ASTM A992. In the analysis, the temperature of the steel structural elements was roughly assumed to be above 600 °C and thus the steel was assumed to have lost half of its strength and stiffness. Although it was an unrealistic assumption that the temperatures at all structural elements above the 11th floor would all be the same, the authors [3] claimed it did not influence the results. Their analysis [3] showed little dependence of the progressive collapse on the temperature of the elements. According to the report [3], the impact of the collapsing floor on its lower floor was the most destructive factor. Although the analysis was performed using linear static analysis, the effects of dynamic impacts were taken into account by the load increase factors. The accumulating weight of the upper collapsing floors on the lower floor caused the progressive collapse.

2.2 Gravity (dead and live) loading details

The gravity dead load consists of the weight of the composite concrete floor (4.30 kN/m²) and the partitioning walls (1.0 kN/m²) which are distributed uniformly on the floors. The external walls were heavier, and their weight is applied on the external perimeter beams. The weight of the external walls on the east and west sides was 6.8 kN/m, and 4.5 kN/m on the north and south sides.

Because most of the commercial units in the upper floors were wholesale stores with some manufacturing purposes, it is assumed that they contained a considerable amount of materials. According to ASCE-7 [12], the storage live load of typical wholesale stores is 6.0 kN/m². Although it is typically assumed that only a portion of the live load (e.g., 25%) is present in a building during a fire incident, the whole live load is considered to be present in the Plasco tower in this analysis because the building was heavily used for storage.

2.3 The fire

Few people were in the Plasco tower when the fire broke out at 7:50 AM local time on the 10th floor in the northwest corner of the tower. There were no fire extinguishers nor sprinklers in the tower, and by the time that the firefighters arrived at the location, the 10th floor was already filled with smoke. Fig. 3 (a) shows that the flames were put out at the end of the first attempt at firefighting, but the fire again erupted and spread to the upper floors as shown in Fig. 3 (b and c).

The fire load was estimated by the Special Investigation Committee [2] to be 452 MJ/m^2 which is comparable to a typical fire load in a shopping centre category in Eurocode-1 [13]. This fire load is equivalent to around 22 kg/m^2 of clothes with a net calorific value of 20 MJ/kg . Some unauthorized alterations were made in areas of the Plasco tower by the tenant that likely increased the fire load. For instance, mezzanines were added in some units to store more clothes and fabrics, and in some cases, dropped ceilings were also used as storage space.

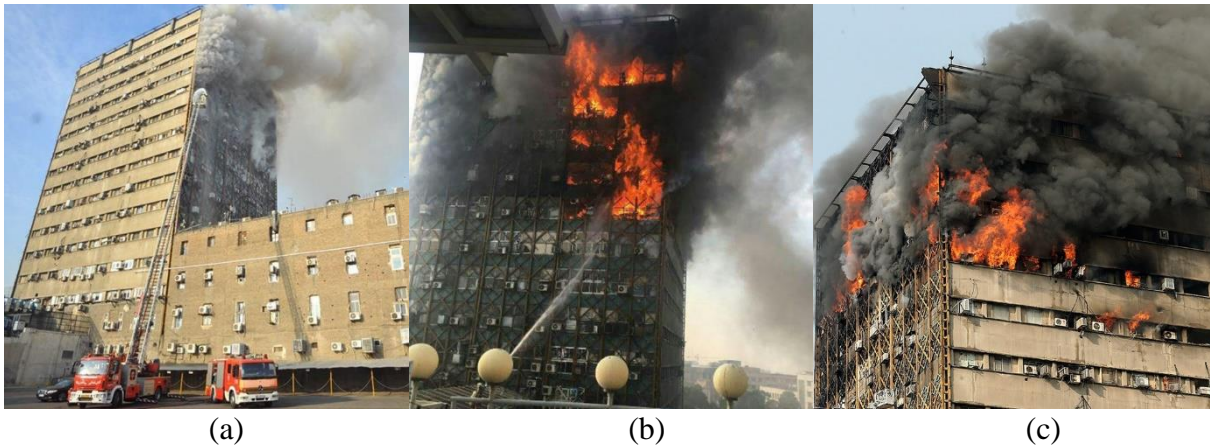


Fig. 3. The extent of fire: (a) at early stages; (b) spreading in the northwest side; (c) extending throughout the entire floor levels; (all images courtesy of ISNA NEWS Agency)

3 OPENSEES MODELLING

3.1 General modelling philosophy and aims and scope of the simulation

The aim of this work is to understand the reasons for the total collapse of the Plasco Tower through subjecting a reasonably comprehensive 3D finite element model of the building to the type of fire loading it experienced during the incident that caused its collapse. The long-term aim is to simulate the progressive collapse of the tower with respect to the travelling fire phenomenon as observed during the fire disaster. The fire started on the 10th floor and was observed to have travelled along the floor horizontally and through the staircase and windows vertically. By comprehensively studying the photos taken from different sides of the building during the fire, various potential trajectories of fire were identified, and will eventually be implemented in the analysis enabled by OpenSees-SiFBuilder [7]. The advanced travelling fire models available in the fire library of OpenSees-SiFBuilder will be used to model the fire evolution in the Plasco tower. The horizontal travelling fire behaviour will be adopted based on the model proposed by Dai et al. [14] and the vertical travel will be represented by time-delays as assumed by Kotsovinos et al. [15]. The SiFBuilder tool will orchestrate the analysis sequence, from the fire models which provide heat flux boundary conditions to the structural members. Information from interviews with the fire crew and the residents will be combined with the observations of the extent of the fire in the photos to generate the fire models. This will be followed by a heat transfer analysis that will produce the temperature evolution history for each structural member. The temperature history will then be applied as a load in the thermo-mechanical analysis to simulate the nonlinear structural response to the fire. For the preliminary stage of this work, the team has focused on understanding the structural system of the Plasco Building and its capacity for fire resistance. This paper presents the progress of the work achieved so far.

3.2 Structural details of the building

The plan of the Plasco tower is shown in Fig. 4. Four internal columns carried the loads transferred by the primary beams and box columns were constructed along the perimeter of the building. All the steel sections were fabricated by welding standard European channel or angle profiles and no fire protection was applied. OpenSees fibre-based sections and displacement-based beam-column elements are used to model the frames, while shell elements are used for concrete slabs. The material properties of the steel at room temperature were taken from experiments performed on the coupons gained from the crumbled structural elements [3].

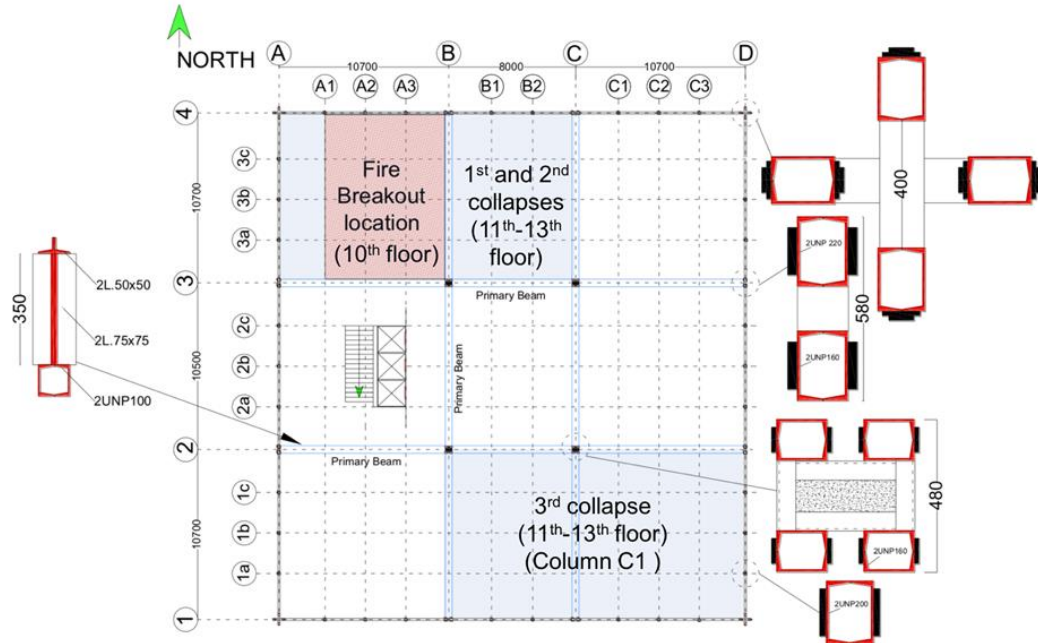


Fig. 4. The plan view of Plasco tower and collapse locations [1]

3.3 Structural model of the floor system (preliminary assumption)

In the first attempt to model the Plasco tower, a grillage floor system was assumed at which the primary trusses and the secondary floor beams were assumed continuous over the middle columns. The information on the conditions and the structural configuration of the Plasco tower is not quite adequate for modelling the Plasco tower with absolute certainty [1]. Limited information is available on the connections of the trusses to the columns. The beam-column connections are recommended to be considered semi-rigid in the report [2], and as a start, the beams were considered continuous. Fig. 5(a) shows the OpenSees floor model based on a preliminary interpretation of photos from the construction phase of the building (e.g., Fig. 2). The floor system is essentially a grillage structure. The East-West direction in the plan (Fig. 4) is spanned by a system of primary trusses (Fig. 5-c) and the North-West direction is spanned by a system of Vierendeel trusses (Fig. 5-d), which are also post-tensioned. Both truss systems are 350 mm deep topped by a composite reinforced concrete slab, the depth of which is assumed to be 100 mm (because the information is currently unavailable). The post-tensioning force for the Vierendeel trusses is also unknown at this stage. The reinforced concrete slab is not explicitly modelled; however, an equivalent area of steel is added to the top chord members of the trusses to represent the slab strength and stiffness.

3.4 Fire load modelling

For the preliminary modelling in this paper, the fire is assumed to be a uniform increment of temperature of up to 800 °C, which is applied uniformly to all the grillage members excluding the concrete slab (which is not explicitly modelled). The temperature increment is applied to the whole floor to understand the response of the floor under heating and the potential failure temperature for

the grillage system. A 10-storey multiple floor model is then be constructed from the 5th to the 14th floor and subjected to single, double, and triple floor simultaneous fires (incrementing all grillage member temperatures to 800 °C). This analysis provides the upper bound for potential failure of the whole structure with the collapse of columns as indicated in Lange et al. [16]. Subsequent investigations will consider realistic fire scenarios based on forensic evidence as mentioned earlier.

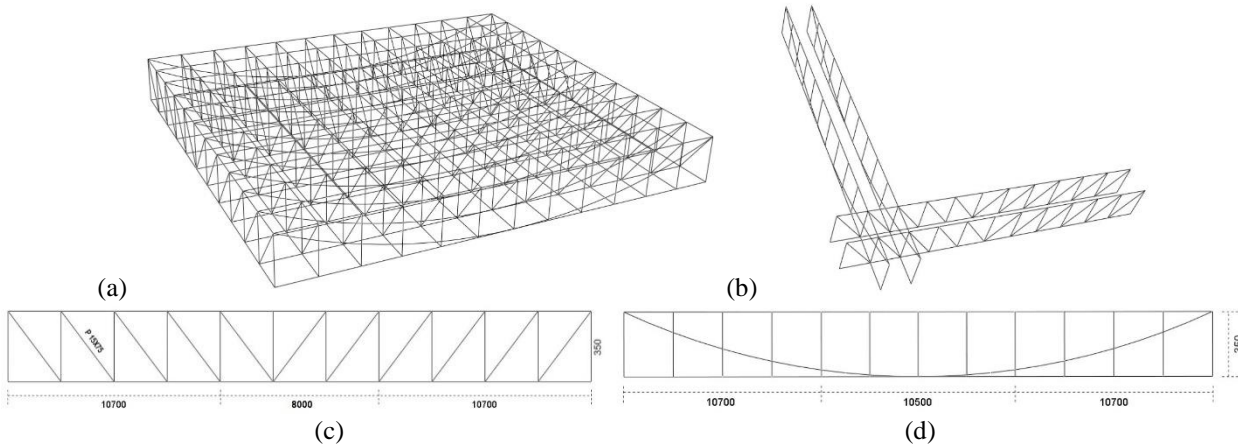


Fig. 5. (a) Whole floor model; (b) Primary EW truss and NS Vierendeel truss; (c) EW truss; (d) NS truss

3.5 Individual truss system behaviour under loading and fire

Fig. 6 shows the deformed shapes of the primary (EW) truss after loading (Fig. 6-a) and after heating to 600 °C (Fig. 6-b) as obtained from a 2D analysis of the truss over the full building length along lines 2 and 3 in the plan as shown in Fig. 4. The truss is supported at the ends and two points in the middle where the greatest deformations can be observed (Fig. 6-b). These deformations are primarily caused by restrained thermal expansion and the compression caused by hogging moments over the middle supports. The deformations from a 2D analysis of the NS Vierendeel trusses along lines B and C are shown in Fig. 6(c) due to the gravity load and post-tensioning. Fig. 6(d) shows the deformation of the NS Vierendeel at 600 °C. The greatest deformation is again at the two middle supports for the same reasons as for the EW trusses. Fig. 7 shows the deflections of the EW and NS trusses at 600 °C. The deflection pattern is as expected with the greatest deflections in both set of trusses being in the free spanning regions on the sides.

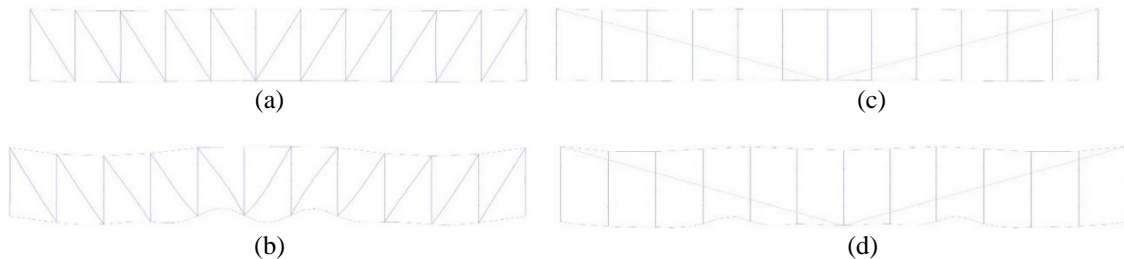


Fig. 6. (a) EW truss after gravity loading; (b) EW truss at 600°C; (c) NS truss after post-tensioning and gravity loading; (d) NS truss at 600 °C

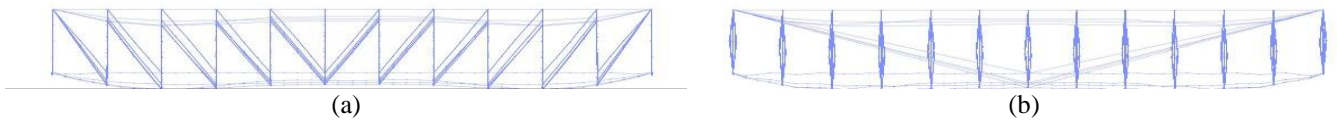


Fig. 7. Whole floor model: (a) EW trusses at 600 °C; (b) NS truss at 600 °C

3.6 Behaviour of the building under multiple floor fires

Fig. 8 shows the deformed shape (magnified 10 times) of the EW and NS frames (10-storey model of the Plasco Building) at 654 °C. Both EW and NS trusses are pushing the columns out. This behaviour is usually expected in the early stages when thermally induced expansion is dominant. However, the persistence of this behaviour in this model to high temperatures is due to the absence of a composite concrete floor slab in this model, which would lead to significant thermal bowing. To mimic the slab, an equivalent volume of steel is included in the top chord and it is not subjected to heating. However, it appears that this approach does not reproduce the high thermal gradient that should be expected and the higher thermal bowing induced deflections and a resultant “pulling-in” of the columns has not started. Because of this limitation, shell elements will be introduced in the model to simulate the effect of the concrete slab composite with the trusses.

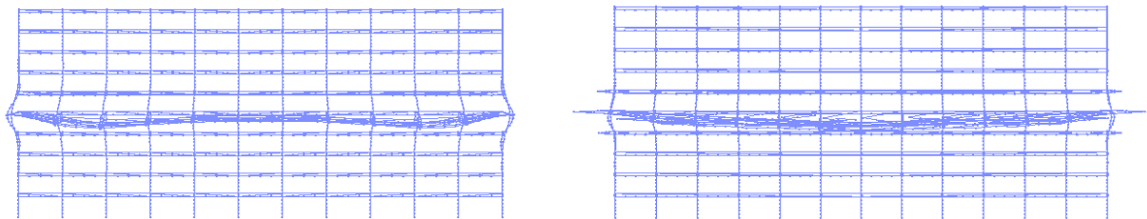


Fig. 8. 10-storey model with middle floor heated: (a) EW trusses at 654 °C; (b) NS truss at 654 °C

3.7 Continuing work

Based on more careful interpretation of the report by Shakib et al. [3] (in Persian), a new floor model was created with a considerably denser floor system as shown in Fig. 9. The floor configuration and the layout of the beams in Fig. 9 is more representative of reasonable construction practice than the assumed continuous truss beams in section 3.3. This model will be the basis for further simulations. Analyses are continuing with this model and progress will be reported at the SiF conference in June 2018.

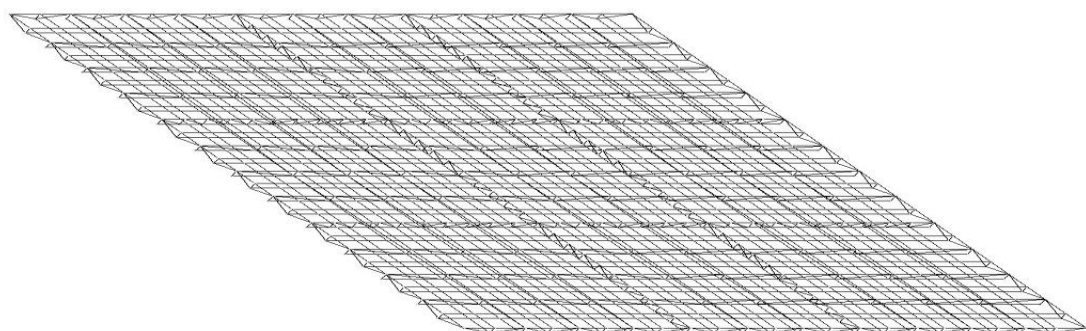


Fig. 9. Reinterpreted floor model with 12 primary trusses, continuous N-S post-tensioned Vierendeel trusses, E-W tie trusses and top and bottom tie beams between the Vierendeel and the tie trusses.

4 CONCLUSIONS

The authors believe that it is extremely important for structural engineers to analyse major failures with great care and dedication, such as is routine in the aerospace industry. This will help the profession learn from these failures and help improve the robustness and resilience of buildings and urban infrastructure that may be similarly vulnerable through appropriate strengthening and retrofit. While this particular analysis is not conclusive at this initial stage of investigation, the authors feel that the structural system of the Plasco Tower has considerable similarity to that of the WTC towers, specifically the floor system. As such, one of the collapse mechanisms described by Lange et al. [16] was likely responsible for the collapse.

ACKNOWLEDGMENT

The authors in Hong Kong would like to acknowledge funding provided by the Hong Kong Polytechnic University for this work to through research grant 1-ZVJG to Asif Usmani and Liming Jiang and PhD scholarship to Tejeswar Yarlagadda.

REFERENCES

- [1] Hajiloo, H., Adelzadeh, M., and Green, M. F. (2017). "*Collapse of the Plasco Tower in Fire.*" Proc., The Second International Conference on Structural Safety under Fire & Blast, London, UK.
- [2] Plasco Investigation committee (2017). "*Plasco Fire's National Report.*" Tehran, Iran.
- [3] Shakib, H., Dardaie, S., and Zaker Salehi, M. (2017). "*Final Report on the Technical, Management, and Legal Aspects of the Plasco Fire.*" Commissioned by Tehran's City Council, Tehran.
- [4] Mckenna, F. T. (1999). "*Object-oriented finite element programming: Frameworks for analysis, algorithms and parallel computing.*"
- [5] Usmani, A., Zhang, J., Jiang, J., and May, I. (2012). "*Using OpenSees for structures in fire.*" Journal of Structural Fire Engineering, 3(1), 57-70.
- [6] Jiang, J., and Usmani, A. (2013). "*Modeling of steel frame structures in fire using OpenSees.*" Computers & Structures, 118, 90-99.
- [7] Jiang, J., Jiang, L., Kotsovinos, P., Zhang, J., Usmani, A., McKenna, F., and Li, G.-Q. (2013). "*OpenSees software architecture for the analysis of structures in fire.*" Journal of Computing in Civil Engineering, 29(1), 04014030.
- [8] CEN (European committee for standardization). (2004). "*Eurocode 2: Design of concrete structures - Part 1-2: General rules- Structural fire design.*" EN 1992-1-2, Brussels, Belgium.
- [9] CEN (European committee for standardization) (1993). "*3: Design of steel structures—Part 1.2: General rules—Structural fire design.*" Brussels: European Committee for Standardization. DD ENV, 1-2.
- [10] US Department of Defence (2016). "*Design of buildings to resist progressive collapse.*" Unified Facilities Criteria.
- [11] American Society of Civil Engineers. (2007). "*Seismic rehabilitation of existing buildings*" (ASCE/SEI 41-06),
- [12] American Society of Civil Engineers. (2005). "*Minimum design loads for buildings and other structures.*" ASCE/SEI-7, Reston, Virginia.
- [13] CEN (European committee for standardization). (2002). "*Eurocode 1: Actions on Structures - Part 1-2: General actions—Actions on structures exposed to fire.*" EN 1991-1-2, Brussels, Belgium.
- [14] Dai, X., Welch, S., and Usmani, A. (2017). "*A critical review of "travelling fire" scenarios for performance-based structural engineering.*" Fire Safety Journal, 91, 568-578.
- [15] Kotsovinos, P., Jiang, Y., and Usmani, A. (2013). "*Effect of vertically travelling fires on the collapse of tall buildings.*"
- [16] Lange, D., Röben, C., and Usmani, A. (2012). "*Tall building collapse mechanisms initiated by fire: Mechanisms and design methodology.*" Engineering Structures, 36, 90-103.

CONCRETE STRUCTURES

Concrete Structures

EXPERIMENTAL STUDIES ON SHEAR BEHAVIOUR OF DEEP PRESTRESSED CONCRETE HOLLOW CORE SLABS UNDER FIRE CONDITIONS

Hang T.N Nguyen¹ and Kang-Hai Tan²

ABSTRACT

This paper presents an experimental programme, test results, and failure modes of two precast/prestressed concrete hollow core (PCHC) slabs tested under elevated temperatures. The objectives of this study were to investigate shear failure mechanisms of deep PCHC slabs under fire conditions, and to verify the shear strength formula in EN 1168: 2005+A3:2011. Two slabs with depths of 320 mm and 400 mm, namely, HC-320 and HC-400, respectively, were tested. The hollow-core units were 4.15 m long, 1.2 m wide, characterised by non-circular voids, placed on top of an electric furnace, and simply supported at their two ends. Shear span was selected to be 800 mm to ensure that both specimens fail in shear instead of flexure. The specimens were first loaded to 40% of their ambient capacities which were already defined by ambient tests, and subsequently heated up to failure. The fire tests followed a heating curve which increased linearly from ambient to 1000°C at 60 min and remained at this temperature until the end. Four types of cracks, i.e., longitudinal cracks, splitting cracks, thermal cracks, and shear cracks, were identified in the tests. It was also observed that while HC-400 finally failed due to diagonal tensile cracking in concrete webs, the so-called web-shear failure, HC-320 failed due to a combination of web-shear and anchorage failures. No temperature-induced spalling was observed during the fire tests. Shear strength results obtained from the tests were compared to those predicted by EN 1168:2005+A3:2011. It is shown that the code provides conservative predictions for shear strengths of PCHC slabs compared to the ones tested.

Keywords: Prestressed concrete, hollow core slabs, shear resistance, web-shear failure, fire conditions

1 INTRODUCTION

Although PCHC slabs have been widely used since the early 1970s, there are still some concerns regarding their performance in fire conditions, in particular, their shear capacity. PCHC slabs produced by extrusion method do not contain any stirrups. Therefore, the shear capacity of such units solely depends on tensile strength of concrete webs. With a reduction in the cross section due to longitudinal voids and relatively low tensile strength of concrete, PCHC slabs are naturally susceptible to shear and anchorage failures. This aspect is even more critical for deep PCHC slabs, which are characterised by non-circular voids with depths exceeding 300 mm. Previous studies have shown that deep PCHC slabs failed in web-shear mode at loads less than those predicted by design codes [1-3]. Under fire conditions, the web-shear capacity of PCHC slabs substantially decreases due to degradation of material properties and temperature-induced tensile stress at concrete webs caused by thermal gradient, which is more pronounced for deeper units. However, there are limited shear tests of PCHC slabs under fire conditions found in the literature. Moreover, most of the available relevant tests were conducted on shallow PCHC slabs (150 mm to 265 mm in depth) with

¹ PhD candidate. School of Civil and Environmental Engineering, Nanyang Technological University, Singapore.

e-mail: NGUYENTH002@e.ntu.edu.sg

² Professor. School of Civil and Environmental Engineering, Nanyang Technological University, Singapore.

e-mail: CKHTAN@ntu.edu.sg

circular voids. As a result, the shear behaviour of fire-exposed, deep PCHC slabs has not been well established.

Despite the fact that shear and anchorage failures govern the fire behaviour of deep PCHC slabs (rather than flexure), an empirical formula to predict shear strengths of fire-exposed PCHC slabs was only introduced in a design code in 2011, i.e. EN 1168:2005+A3:2011 Annex G [4]. Nonetheless, two out of four fire tests on deep PCHC slabs from Jansze *et al.* [5] showed that EN 1168:2005+A3:2011 overestimated the shear capacity of the tested specimens under fire conditions. Therefore, a rational revision is needed for more conservative predictions of shear capacity of deep PCHC slabs exposed to fire.

To investigate shear failure mechanisms of deep PCHC slabs and to validate the shear-strength formula in EN 1168: 2005+A3:2011, fire shear tests on deep PCHC slabs with depths ranging from 320 mm to 500 mm are being conducted in Nanyang Technological University (NTU), Singapore. This paper presents the experimental programme, test results, and failure modes of two deep PCHC slabs tested under elevated temperatures.

2 TESTING PROGRAMME

2.1 Specimen properties

To study shear behaviour of deep PCHC slabs under fire conditions, full-scaled fire tests were conducted on two hollow-core specimens named as HC-320 and HC-400 with depths of 320 mm and 400 mm, respectively. The specimens were 4.15 m long, 1.2 m wide, consisting of 4 non-circular voids and fabricated using extrusion process. *Table 1* presents the material properties while *Fig.1* shows cross-sectional configurations of HC-320 and HC-400. It should be noted that concrete strengths shown in *Table 1* were defined at concrete ages of 460 and 400 days for HC-320 and HC-400, respectively, while the fire tests were performed about 7 months later.

Table 1. Material properties

Slab ID.	Concrete			Prestressing steel (seven-wire, low-relaxation type)			
	Compressive strength (MPa)	Tensile strength (MPa)	Elastic modulus (GPa)	Nominal diameter (mm)	Nominal area (mm ²)	f_{pu} (MPa)	E_{ps} (GPa)
HC-320	54	3.6	34.9	9.6	54.8	1860	200
HC-400	57	4.2	35.2	9.6/12.9*	54.8/98.7*	1860	200

*Two types of strands were used in HC-400 as shown in *Fig. 1*

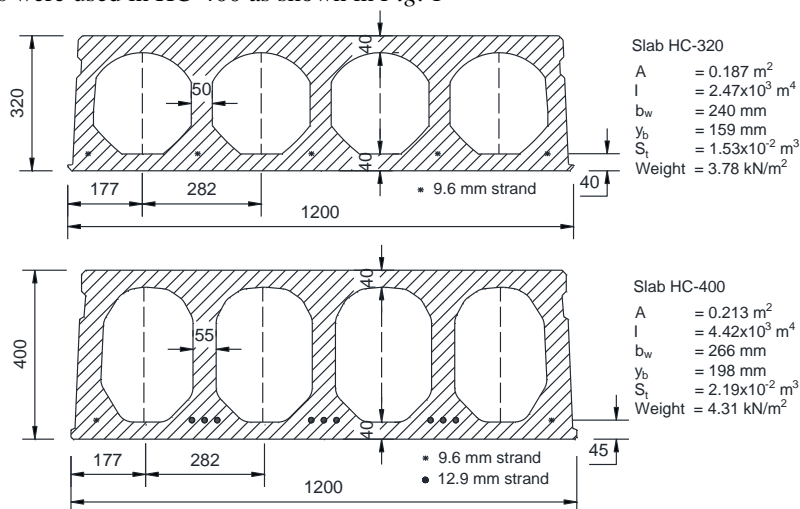


Fig. 1. Specimen cross-sectional properties and configurations

2.2 Test setup

Fig.2 shows an overall test setup for the fire tests. The specimens were placed on top of an electric furnace of 3 m long, 3 m wide, and 0.75 m deep (interior dimensions) and simply supported at two ends by two A-frames. They were loaded by two line loads placed symmetrically with respect to the slab centre. The distance from the centre line of the support to the edge of the specimens was 75 mm. Shear span was selected to be 800 mm for both specimens to ensure that they would fail in shear instead of flexure. Opening parts of the top of the furnace were covered with thermal wool to prevent heat loss.

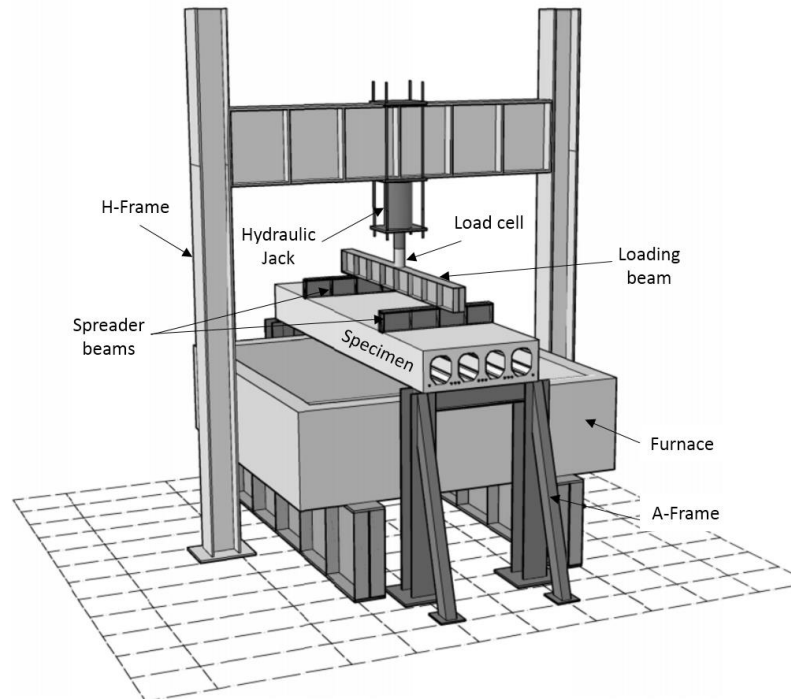


Fig. 2. 3-D view of fire shear tests

2.3 Instrumentation

Instrumentation in the fire tests included load cells (LC), linear variable displacement transducers (LVDT) and thermocouples (T). Three load cells (LC1 to LC3) placed on top of the loading beam and the spreader beams were arranged to monitor transferred loads from a 100-ton hydraulic jack to the specimens (*Fig 3*). Eight LVDTs were placed on top of each specimen to measure vertical displacements during fire exposure at mid-span, applied load, and support locations. Thermocouples were placed at different depths by drilling holes at two different sections along the specimen length, namely, Section A and Section B. While Section A was at the centre line of the slab, Section B was 1100 mm from one end of the specimen (*Fig. 3*). Once the thermocouples had been embedded, the holes were filled by cement paste. *Fig. 3* shows the arrangement of load cells and LVDTs while *Fig. 4* shows the locations of thermocouples.

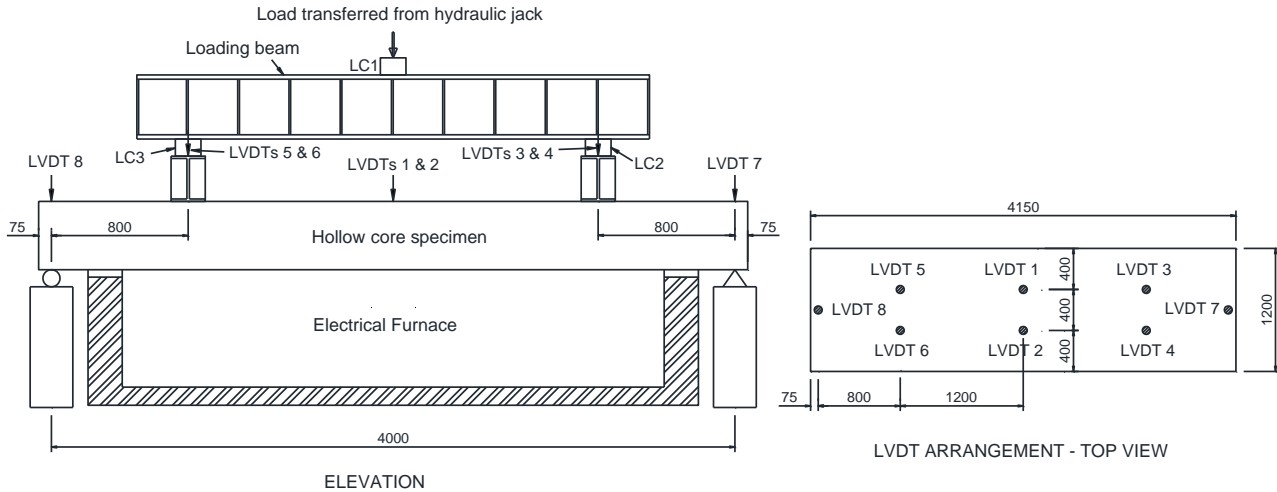


Fig. 3. Arrangement of load cells and LVDTs

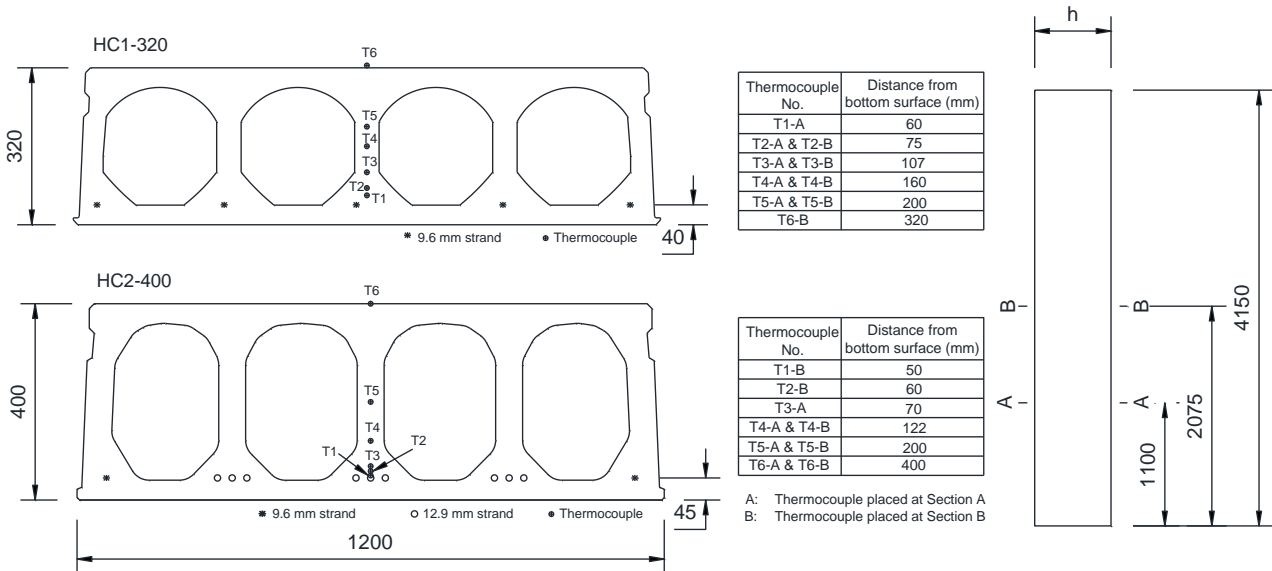


Fig. 4. Thermocouple arrangement

2.4 Testing procedure and heating curve

Slabs HC-320 and HC-400 were first loaded to 74 kN and 204 kN, respectively, which corresponded to 40 % of their capacities defined by ambient tests, and subsequently heated up to failure. The applied loads were maintained during the heating stage. The fire tests were programmed to follow a heating curve which increased linearly from ambient to 1000°C at 60 min (heating rate of 17°C/min) and remained at this temperature until the end (Fig. 5). It is noteworthy that in the standard fire tests, specimens are heated using the standard fire curve ISO-834 (or ASTM E119), in which temperature rises rapidly during the initial heating phase (achieving 600°C after 5 min and 1000°C after 90 min of heating). However, due to the limitation of power supply in NTU Annex Lab (only 500 Amps), the furnace could not simulate the standard fire curve. Therefore, the fire tests in this study were to investigate the structural behaviour of deep PCHC slabs rather than obtaining their fire resistance under a standard fire curve. Fig. 5 shows measured furnace temperatures in the two tests, together with the programmed heating curve. It should be noted that the fire test was first conducted for HC-400 and due to a problem of the control panel of the electric furnace, the furnace temperature for the test only achieved 849°C at 65 min (about 150°C lower than the expected peak temperature). The problem was soon fixed after the test. Therefore, no such incident occurred in the second test.

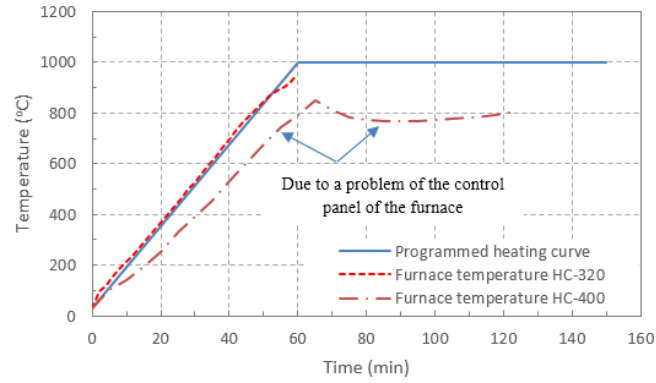


Fig. 5. Furnace temperatures

3 TEST RESULTS AND DISCUSSIONS

No fire-induced spalling was observed in any of the two tests during their heating time. Test results are summarised in *Table 2*. Data and observations from the fire tests will then be presented and discussed regarding thermal response, structural response, damage and failure modes.

Table 2. Test results

Slab ID.	Shear span (mm)	Applied load (LC1) (kN)	Test day RH* (%)	Maximum furnace temperature (°C)	Failure time (min)	Failure mode
HC-320	800	74	74	944	57	Web-shear & Anchorage
HC-400	800	204	78	849	118	Web-shear

* RH = Relative humidity

3.1 Thermal response

Temperature profiles recorded by installed thermocouples are plotted in *Fig. 6*, in which x denotes the distance from fire exposed surface (bottom slab) to the sections in mm. For each section that had more than one thermocouple, the average value was taken. Data from thermocouples showed reasonable results since cross-sectional temperatures in the concrete decreased as the distance from the fire exposure surface increased. It is because of low thermal conductivity and high specific heat capacity of concrete that resulted in a delay in heat transmission over the cross section of the specimen.

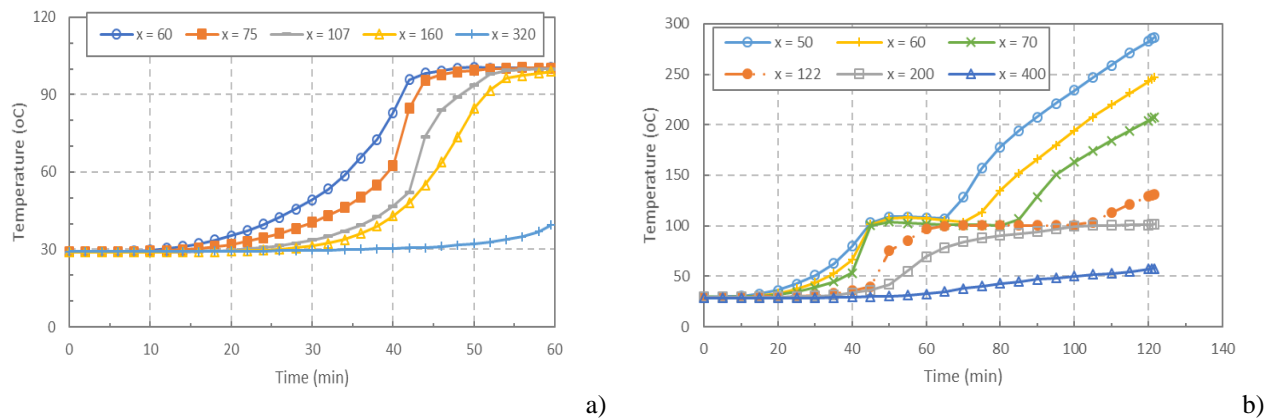


Fig. 6. Development of temperature over the cross section. a) Slab HC-320; b) Slab HC-400

The temperature profiles from thermocouples also indicate that concrete temperature gradually increased from ambient to 100°C. Thereafter, there was a temperature plateau observed from 45 min of fire exposure. This plateau was due to migration of water inside the concrete from outer layers (close to the exposed surface) to inner layers. As temperature reached 100°C, water was transformed from liquid to gas phase, resulting in a moisture clog that prevented temperature to increase until the layers dried out.

3.2 Structural response

As fire shear tests were conducted, failure was defined at the time when there was a significant drop in the resistance caused by the formation of shear cracks. At this stage, specimens were not able to maintain the imposed load. *Fig. 7* presents time histories of the applied load and the mid-span deflection. As shown in the figure, HC-320 started losing its bearing capacity at 57 min of fire exposure, while it took 118 min for HC-400 to fail. Deflection suddenly increased due to the formation of web-shear cracks.

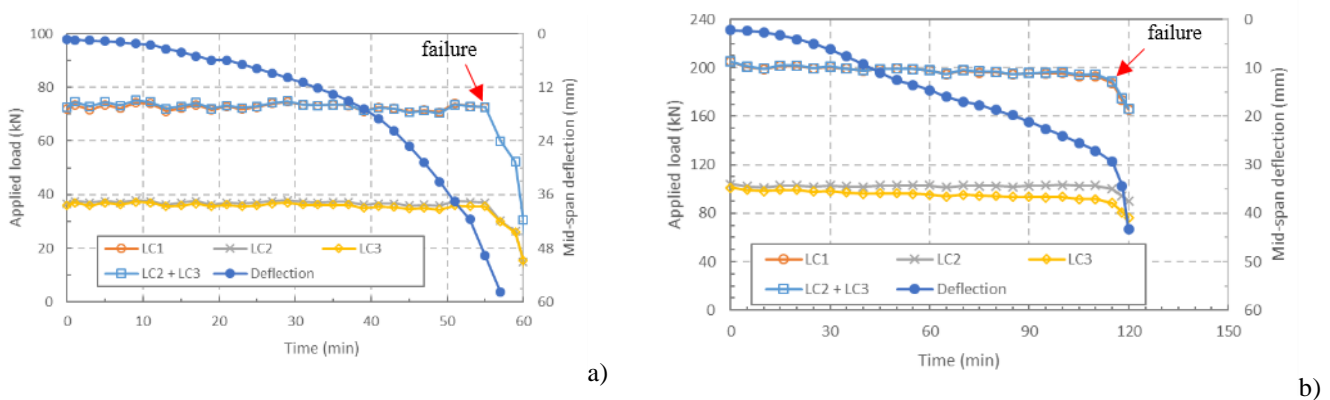


Fig. 7. Applied load and mid-span deflection vs. time a) HC-320; b) HC-400

3.3 Damages and failure modes

Damages and failure modes of HC-320 and HC-400 are illustrated in *Fig. 8* and *Fig. 9*, respectively. HC-400 failed due to diagonal tensile cracks in concrete webs, the so-called web-shear failure, whereas HC-320 failed due to a combination of web-shear and anchorage failures. Four types of cracks were identified, i.e., thermal cracks, longitudinal cracks, splitting cracks, and shear cracks. Thermal cracks occurred in concrete webs due to non-uniform temperature distribution over the cross-sections of tested slabs. The thermal gradient produced tensile stress in concrete webs, resulting in vertical thermal cracks. On the other hand, longitudinal cracks occurred due to thermal expansion of concrete exposed to fire. These cracks first occurred at the top and the bottom of longitudinal voids at the two slab ends at 45 to 50 min of fire exposure. Subsequently, they propagated towards the slab centre. These longitudinal cracks were also observed and explained in PCHC slabs tests by Fellingner [6], Aguado *et al.* [7], and Shakya and Kodur [8], as a result of a transverse bending moment caused by incompatible thermal expansion. Due to a lack of transverse reinforcement in both the top and bottom flanges, the transverse bending moment caused longitudinal cracks at the weakest cross section, where the flange thickness had minimum values (*Fig. 8*). Splitting cracks occurred due to a partial loss of contact between the strands and the concrete caused by high-temperature gradient at the lower part of the section and different thermal conductivity of strand and concrete [7]. The splitting cracks were more pronounced in HC-400 in which a larger strand diameter was used. Finally, web-shear cracks occurred as a combination of principal tensile stress at concrete webs (due to prestressing force and applied load) and thermal stress caused by thermal gradient exceeded tensile strength of concrete. While the formation of thermal cracks, longitudinal cracks, and splitting cracks had little effect on fire resistance of the

hollow core specimens, the sudden formation of web-shear cracks resulted in a significant drop in load-carrying capacity, leading to brittle failure.

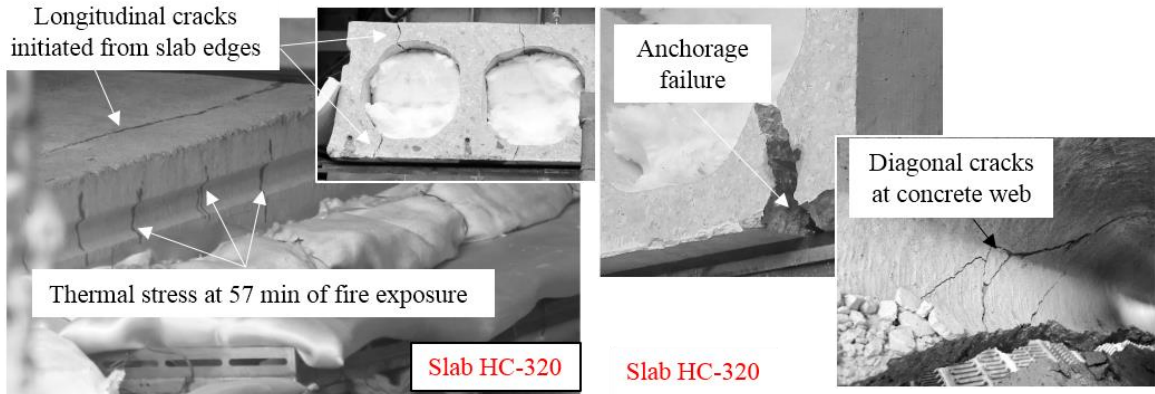


Fig. 8. Damages and failure modes – HC-320

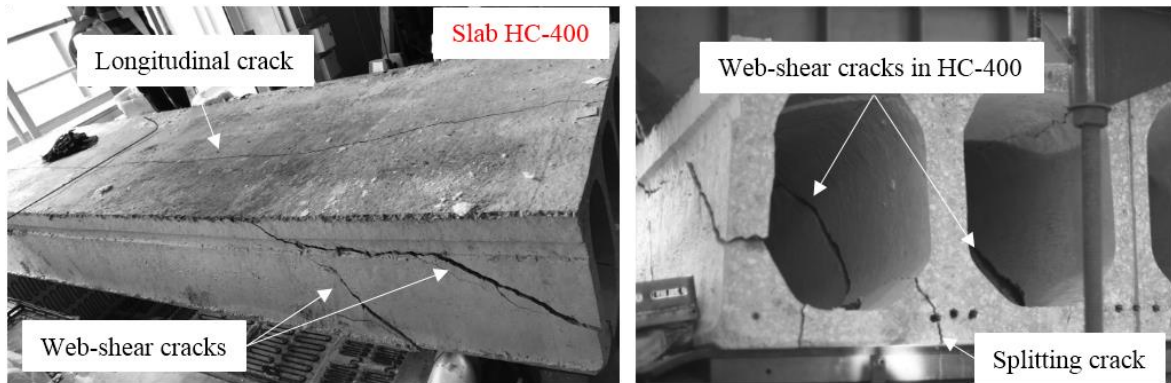


Fig. 9. Damages and failure modes – HC-400

4 SHEAR RESISTANCE ACCORDING TO EN 1168:2005+A3:2011 [4]

EN 1168 shear capacity of PCHC slabs under fire conditions is given as follows

$$V_{Rd,c,fi} = [C_{\theta,1} + \alpha_k C_{\theta,2}] b_w d$$

where

$$C_{\theta,1} = 0.15 \min(k_p(\theta_p) \sigma_{cp,20^\circ C}; \frac{F_{R,a,fi,p}}{A_c})$$

$$\alpha_k = 1 + \sqrt{\frac{200}{d}} \leq 2$$

$$C_{\theta,2} = \sqrt[3]{0.58 \frac{F_{R,a,fi}}{f_{yk} b_w d} f_{c,fi,m}}$$

$V_{Rd,c,fi}$ is fire shear strength in regions cracked in bending in N,

$C_{\theta,1}$ is Coefficient accounting for concrete stress under fire conditions,

$k_p(\theta_p)$ is strength reduction factor for the prestressing steel in Eurocode 2 Part 1-2

$\sigma_{cp,20^\circ C}$ is average concrete stress due to prestressing at room temperature

A_c is concrete area in mm²,

$F_{R,a,fi,p}$ is force capacity of prestressing steel anchored in considered cross section,

- $C_{\theta,2}$ is coefficient accounting for anchored longitudinal reinforcement,
- $F_{R,s,f,i,p}$ is force capacity of prestressing steel anchored in considered cross section,
- f_{yk} is characteristic yield strength of the reinforcement,
- $f_{c,f,i,m}$ is average strength of concrete at elevated temperature,
- b_w is total web thickness of hollow core slab,
- d is effective depth of hollow core slab at ambient temperature.

To predict shear capacity of PCHC slabs subjected to fire using EN 1168, strand temperatures must be defined. However, such data were not available in the tests as the thermocouples were placed into the specimens by drilling holes. During the installation, drill bits were not allowed to touch strands to prevent potential damages on them. Therefore, strand temperatures were defined using a finite element (FE) based numerical approach. An FE heat transfer model was proposed and validated. Thermal properties of concrete including conductivity, specific heat were taken following Eurocode 2 Part 1-2 [9]. Fig 10 shows temperature comparisons between the tests and FE models, together with predictions of strand temperatures from the FE model. The figure shows a good correlation between the two sets of temperature, illustrating that the developed FE model was capable of tracing temperature development in the tested PCHC slabs.

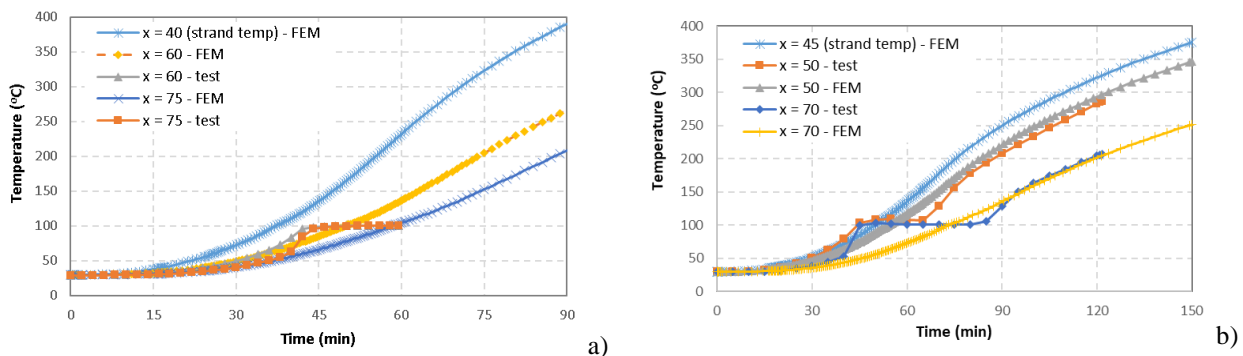


Fig. 10. Temperature comparison between the test and the FE model a) Slab HC-320; b) Slab HC-400

Temperature results from the tests (at mid-web level) and FE models (for strand temperatures) were used to calculate shear capacity of the PCHC slabs in the experimental programme. Strength properties of concrete and strands at such temperatures were calculated following Eurocode 2 Part 1-2 [9]. In the calculations, mean strengths of concrete obtained from the material tests were used. In addition, no safety factors for both concrete and prestressing steel were considered. Shear strengths predicted by EN 1168 were compared with the test results, presented in Table 3. The comparison shows that the code provides conservative predictions for shear strengths of the tested hollow core units.

Table 3. Comparison between the experimental results and predictions from EN 1168

Slab ID.	Exp. Failure load (kN)*	Time at failure (min)	Strand temp. (FEM)	Mid web temp. (°C)	EN 1168 failure load (kN)	$V_{test}/V_{predict}$
HC-320	103.5	57	212	100	74.4	1.40
HC-400	245	118	320	99	125.0	1.96

* Including weight of slab and the loading system

5 CONCLUSIONS

Two fire tests on deep PCHC slabs were conducted under fire conditions resulting in web-shear failure. Four types of cracks were identified during the tests, i.e., thermal cracks, longitudinal cracks, splitting cracks, and web-shear cracks. While the formation of the first three had little effects on structural resistance of the specimens, the formation of the last one significantly reduced load bearing capacity, leading to brittle failure. Data from the tests and the developed FM models were used to validate the shear-strength formula in EN 1168:2005+A3:2011. It is shown that the shear design formula given in EN 1168 provides conservative predictions of deep PCHC slabs compared to the ones tested in the experimental programme.

ACKNOWLEDGMENT

This material is based on research/work supported by the Singapore Ministry of National Development and National Research Foundation under L2 NIC Award No. L2NICCFP1-2013-4. Any opinions, findings, and conclusions expressed in this material are those of the authors and do not necessarily reflect the views of L2 NIC.

REFERENCES

1. Walraven, J.C. and W.P.M. Mercx, *The bearing capacity of prestressed hollow core slabs*. Heron, 1983. **Vol. 28** (No. 3).
2. Hawkins, N.M. and S. Ghosh, *Shear strength of hollow-core slabs*. PCI journal, 2006. **51**(1): p. 110-114.
3. Rahman, M.K., et al., *Flexural and Shear Strength of Prestressed Precast Hollow-Core Slabs*. Arabian Journal for Science and Engineering, 2012. **37**(2): p. 443-455.
4. CEN, *EN 1168:2005+A3:2011: Precast concrete products - Hollow core slabs*.
5. Jansze, W., A.V. Acker, and R. Klein-Holte, *Fire resistance of hollow core floors regarding shear and anchorage capacity*, in *Structures in Fire*. 2012: Zurich, Switzerland. p. 709-718.
6. Fellingner, J., *Shear and anchorage behaviour of fire exposed hollow core slabs*. 2004: TU Delft, Delft University of Technology.
7. Aguado, J.V., et al., *Influence of reinforcement arrangement in flexural fire behavior of hollow core slabs*. Fire safety journal, 2012. **53**: p. 72-84.
8. Shakya, A. and V. Kodur, *Response of precast prestressed concrete hollowcore slabs under fire conditions*. Engineering Structures, 2015. **87**: p. 126-138.
9. EN-1992-1-2, *Eurocode 2: Design of concrete structures, in Part 1-2: General rules - Structural fire design*. 2004: Brussels.

Concrete Structures

EXPERIMENTAL STUDY AND NUMERICAL SIMULATION OF FIRE RESISTANCE OF TWO-WAY RESTRAINED PRECAST CONCRETE COMPOSITE SLABS

Qingfeng Xu¹, Lingzhu Chen², Xiangmin Li³, Chongqing Han⁴, Yang Zhang⁵, Yong C. Wang⁶,
Weichen Xue⁷

ABSTRACT

This paper presents experimental test and numerical simulation results of fire performance of two-way precast concrete (PC) composite slabs under the standard ISO 834 condition. The fire tests include three specimens with two different load levels and with/without in-plane restraint. The in-plane restraint was applied on two specimens by casting four edge beams together with the PC composite slabs. An ambient temperature test was also conducted on one restrained slab. Tensile membrane action was observed in all specimens. No debonding was observed at the interface between the bottom of the precast slab and the top of the cast-in-situ composite layer for the restrained slabs, while cracks were observed in the un-restrained slab. The fire resistance of the restrained specimens (S2 and S3) subjected to load ratios of 0.3 and 0.5 were 195 min and 131 min respectively, according to the deflection criterion, and that of the unrestrained specimen (S4) with the same load as specimen S2 was 130 min. These results show that the fire resistance of restrained PC composite slabs decrease with increasing load ratio, and the in-plane restraint greatly increases the fire resistance of PC composite slabs. A numerical model was developed to predict the fire resistance of PC composite slabs. Good agreement was achieved between the predicted and test results, for temperatures and load-deflection relationships.

Keywords: Precast concrete composite slabs, restraint, fire resistance, numerical simulation

1 INTRODUCTION

Prefabricated buildings are widely used now in China because of their advantages including green credential, energy saving, environment friendly and cost effectiveness. Precast concrete (PC)

¹ Professor senior engineer. Shanghai Key Laboratory of Engineering Structure Safety, Shanghai Research Institute of Building Sciences, Shanghai, China.

e-mail: xuqingfeng73@163.com

² Senior engineer. Shanghai Key Laboratory of Engineering Structure Safety, Shanghai Research Institute of Building Sciences, Shanghai, China.

e-mail: 20040392chen@163.com

³ Professor senior engineer and head of Shanghai Key Laboratory of Engineering Structure Safety, Shanghai Research Institute of Building Sciences, Shanghai, China.

e-mail: lixiangmin@sribs.com.cn

⁴ Professor senior engineer. Architects & Engineers Co., LTD of Southeast University, Nanjing, China.

e-mail: chq_han@seu.edu.cn

⁵ Engineer. CIFI GROUP CO.,LTD, Nanjing, China.

e-mail: zhangyang-1990@foxmail.com

⁶ Professor. School of Mechanical, Aerospace and Civil Engineering, The University of Manchester, UK.

e-mail: yong.wang@manchester.ac.uk

⁷ Professor. School of Civil Engineering, Tongji University, Shanghai 200092, China.

e-mail: xuewc@tongji.edu.cn

composite slabs, consisting of precast slabs with a layer of cast-in-situ concrete slab at the top, are commonly used in precast concrete structures. The fire performance of two-way cast-in-situ concrete slabs has been carefully studied by many researchers through full-scale and small-scale furnace tests and theoretical analysis after the Cardington fire tests[1-5]. In particular, the beneficial effects of tensile membrane action in improving the load bearing capacity of concrete slabs were observed and investigated; and simplified calculation methods have been developed to take advantage of tensile membrane action in fire resistance design of structures (Bailey[1], Zhang et al[5] and Dong et al[6]). In contrast, there is a lack of study on fire performance of two-way PC composite slabs. Since the fire performance of PC composite slabs may be different from that of cast-in-situ slabs due to the existence of an interface between the precast slab and the cast-in-situ concrete layer, it is necessary to investigate how two-way PC composite slabs behave in fire. This paper represents the results of such a study, based on experimental tests and numerical simulations.

2 EXPERIMENTAL PROGRAMME

2.1 Test specimens

Four PC composite slabs (to be referred as S1~S4) were prepared and tested at ambient temperature and in fire. All the slabs were designed with the same geometry according to Chinese Code *GB/T 51231-2016 Technical Code for Precast Concrete Buildings*[7], as illustrated in Figure 1. These slabs were 2640 mm wide and 4000 mm long, and the thickness of both the precast slab and top cast-in-situ concrete layer was 60 mm. The cast-in-situ layer was cast after the precast layer reached its design strength. Two layers of steel rebars with a diameter of 8 mm at a spacing of 200mm were placed in the cast-in-situ layer in two directions. A steel rebar truss was placed along the short span at a spacing of 600 mm to ensure composite action between the precast slab and cast-in-situ concrete layer. Specimens S1~S3 were restrained with four edge beams that were cast together with the slabs to simulate the restraint condition from adjacent beams, while specimen S4 had no restraint and was used for comparison. The edge beams, with a cross-section width of 200 mm and a depth of 400 mm, were composite beams commonly used in precast concrete structures. Specimen S1 was tested at ambient temperature to obtain the load carrying capacity at room temperature, and specimens S2 and S3 were exposed to the ISO 834 standard fire curve under load ratios of 0.3 and 0.5 respectively. Specimen S4 was also tested in fire and subjected to the same load value a specimen S2, but it had no restraint.

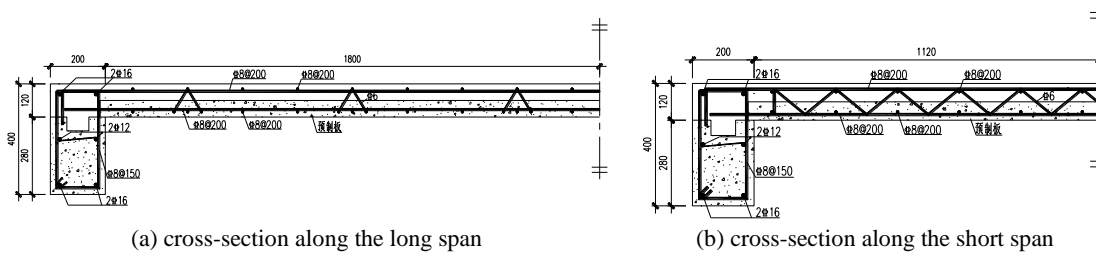


Fig.1. Geometry of PC composite slabs S1~S3

2.2 Material properties

All samples were cast with commercial concrete. The measured cube compressive strengths of the precast layer and the cast-in-situ layer at ambient temperature at 28 days were 26.4 MPa and 24.8 MPa respectively. Table 1 gives the measured mechanical properties of reinforcing steel.

Table 1. Measured mechanical properties of reinforcing steel

Grade	Diameter/mm	$f_{yk}/(N/mm^2)$	$f_{stk}/(N/mm^2)$
HRB400	8mm	419.6	599.1
HRB400	12mm	427.4	604.6
HRB400	16mm	456.2	604.1

2.3 Instrumentation

The experiments were carried out in the horizontal furnace at Southeast University, Nanjing, China. Figure 2 shows the test setup. In the fire test, loads were applied at twelve points to pre-defined values using a load distribution system and kept constant through the fire test. The steel load distribution system comprises twelve square plates, four triangle plates, two short I-shape beams and an I-shape long beam. These components were laid below the loading jack in such a way so that the load was spread evenly on the concrete slab even when the slab experienced large deflections. For specimens S1~S3, the four edges beams were directly supported by the furnace walls. Specimen S4, which does not have restraint beams, was simply supported on the furnace walls through angle steel beams and circular steel tubes. The furnace temperature followed the ISO-834 standard fire curve. The fire exposure was on the bottom side of the slab and sides of the edge beams if using.

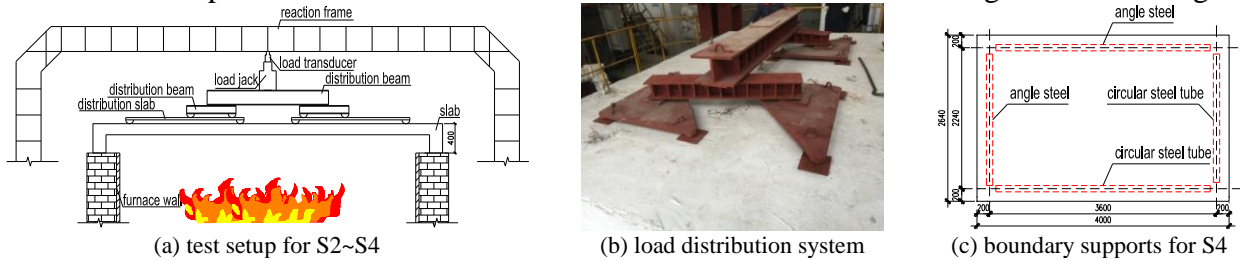


Fig.2. Test setup

Displacement transducers were attached at different points to monitor the vertical displacements of the slab and the horizontal and vertical displacements at the restraint edge beams. Figure 3 shows the locations of the displacement transducers.

2.4 Temperature measurement arrangement

Before casting concrete, thermocouples were installed for monitoring temperature distributions in the concrete slab and steel reinforcement. Figure 4 shows the locations of thermocouples in the concrete slab. Nickel chromium alloy thermocouples, with a temperature range from -200 °C to 1100 °C, were used.

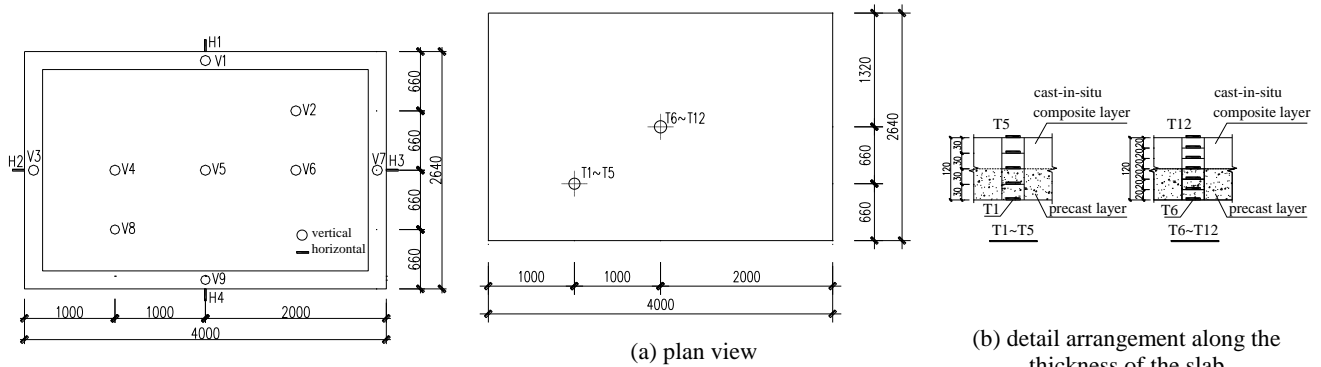


Fig. 3. Layout of displacement transducers

Fig. 4. Locations of thermocouples

3 TEST OBSERVATIONS

3.1 Specimen S1

At the initial stage of loading, all deflections increased linearly with the applied load and no cracks were observed. Cracks of about 0.1mm wide began to appear at the top of the slab along the long span at a distance of 180 mm from the slab edge when the applied load was about 210 kN. When the load was increased to 230kN, cracks of about 0.1mm wide were observed at the top of the slab along the short span at a distance of 180 mm from the slab edge. These cracks may be caused by the negative moments over the edge beams. With further increase of the applied load, these cracks gradually extended to the corners and their width increased. When the applied load reached 300kN,

arc-shaped cracks formed at the corners, and they connected with the straight cracks along edge beams. When the load was increased to around 650 kN, the maximum width of the cracks reached 1.5 mm. At a load of 800 kN, the maximum width of the cracks reached 2.5 mm and the concrete at the corners of the restraint beams began to peel off the specimen. The applied load was stopped at 950 kN due to limitation of the load jack, but neither concrete crushing nor steel rebar fracture was observed. Figure 5 shows the distribution of cracks after the test. Elliptical cracks developed around the edges of the slab, indicating formation of tensile membrane action. The crack pattern at the bottom of the slab was generally identical to the pattern assumed by classical yield line theory. According to yield line theory, the load carrying capacity was calculated to be 650kN.

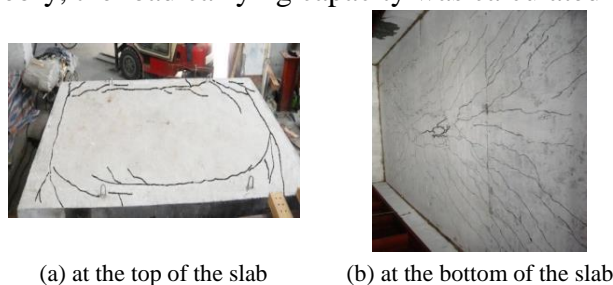


Fig. 5. Distribution of cracks in specimen S1

3.2 Specimens S2 and S3

The applied loads for specimens S2 and S3 were 195 kN and 325 kN respectively, based on the assumption that the ambient temperature load carrying capacity of the slab was 650 kN. The ambient temperature observations of specimens S2 and S3 were comparable with specimen S1. The observations during the heating process for both specimens S2 and S3 were similar. At about 20 mins, water vapour began to evaporate from the slab close to the load distribution boards, accompanied by small temperature cracks at the corners and close to the edge beams. The amount of water vapour increased with the fire exposure time. The maximum amount of water vapour was observed at around 60 mins, and it was drained at about 115 mins. The deflection rates increased rapidly when the slabs were close to failure, and fire tests were stopped.

Figure 6 shows the distribution of cracks at the top and bottom of the slabs for specimens S2 and S3. Elliptical cracks were also observed at the boundary of the slabs, indicating tensile membrane action. Spalling of concrete can be clearly observed at the bottom of both slabs and part of the bottom steel rebars were exposed in specimen S2.

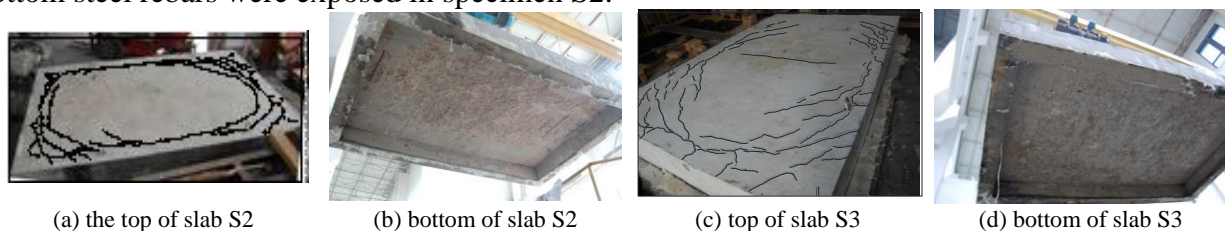


Fig. 6. Distributions of cracks of specimens S2 and S3

3.3 Specimens S4

Before fire testing, no crack was observed at the top of the slab, and only one vertical crack was observed at the side slab close to the corner. The maximum vertical deflection of the slab was about 21.1 mm. As with specimens S2 and S3, water vapour was first observed at about 20 mins and drained at about 115 mins. Because this specimen had no edge beams, the corners of the slab began to warp at about 44 mins. In addition, horizontal cracks at the interface between the precast layer and the cast-in-situ layer formed at about 62 mins and their width increased with the fire exposure time. At 130~135 mins, the warp displacement at the corners and the width of the horizontal cracks at the interface were very clear to the naked eye.

Figure 7 shows the distribution of cracks at the slab top and bottom. Elliptical cracks were also observed at the boundary of the slab, indicating the development of tensile membrane action,

although the shape of the elliptical cracks was slightly different from those of specimens S2 and S3,.The colour of concrete at the bottom of the slab became grey and many fissures were observed.

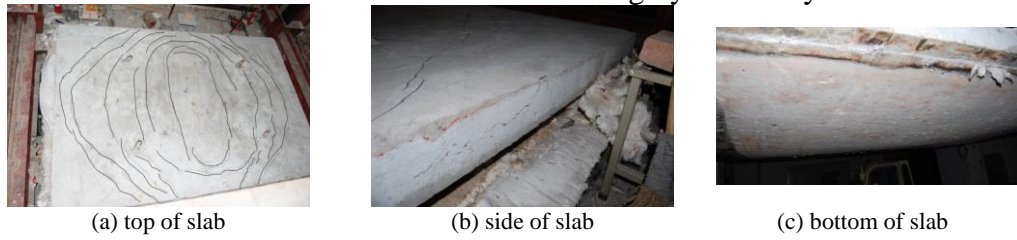


Fig. 7. Distribution of cracks of specimen S4

4 TEST RESULTS AND ANALYSIS

4.1 Load-displacement curves for specimen S1

Figure 8 presents the load - mid-span deflection relationship for specimen S1 and the distribution of displacements along the long span. Non-linear slab behaviour started at about 400 kN.

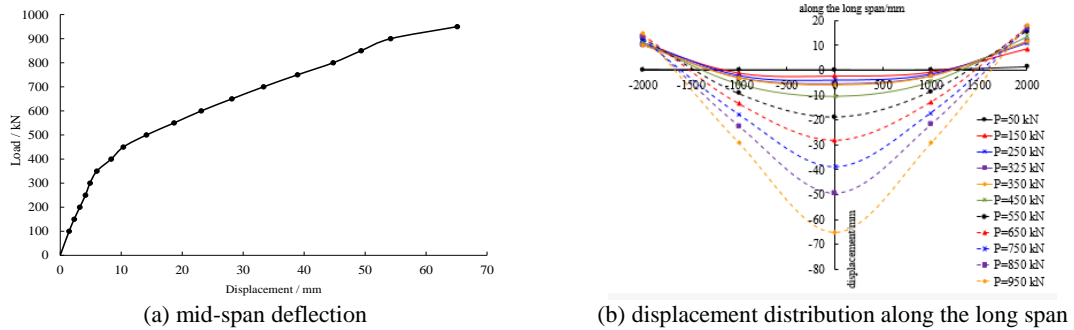


Fig. 8. Development of displacements for specimen S1

4.2 Temperature distribution

Figure 9 shows typical temperature distributions for specimens S2 and S4. A small plateau was observed close to 100 °C, as a result of water evaporation.

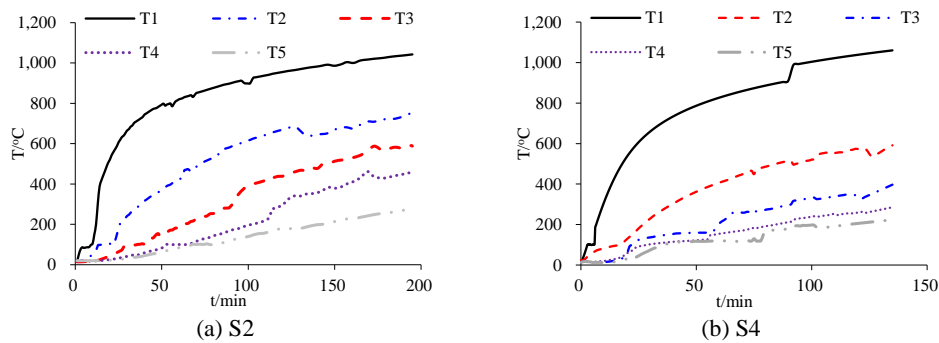


Fig. 9. Typical temperature developments for specimens S2 and S4

4.3 Fire resistance

According to the fire resistance testing recommendation in *GB/T 9978—2008 Fire-resistance tests-Elements of building construction-Part 1: General requirements*, flexural members can be considered to have reached their fire resistance when the maximum mid-span deflection reaches $L^2/(400d)$ or the rate of maximum deflection is $L^2/(9000d)$, where L is the span of the flexural member and d is the depth of the cross-section. For the test specimens of this paper, these values are 105 mm and 4.6 mm/min respectively. Table 2 gives the fire resistance times in terms of the above limits. The deflection criterion were reached earlier than the deflection rate criterion in all tests. The fire resistance of restrained PC composite slabs decreased with increasing load ratio, and the edge restraints greatly increased the fire resistance of PC composite slabs.

Table 2. Fire resistance times of the test specimens

Specimen number	Load ratio /%	Load /kN	fire resistance /min	
			deflection criterion	deflection rate criterion
S2	30	195	195	203
S3	50	325	131	133
S4	/	195	130	142

Figures 10 and 11 present the developments of mid-span deflections and rates of mid-span deflections as functions of time.

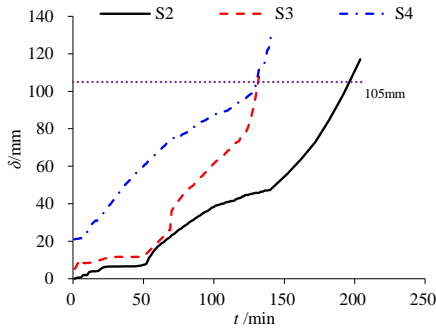


Fig.10. Development of mid-span deflections with time

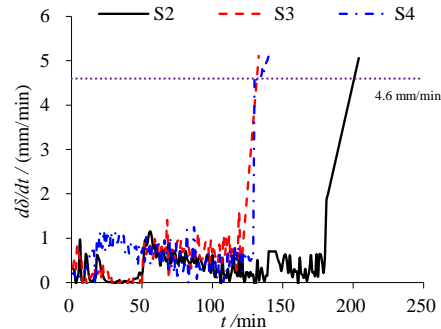


Fig.11. Development of rates of mid-span deflections with time

5 NUMERICAL SIMULATION

A three-dimensional finite element model was developed using the commercial software ABAQUS to predict the mechanical behaviour of the composite slabs exposed to fire. To consider the influence of the fire exposure on the material property of concrete and steel rebar, heat transfer analysis was conducted first to evaluate the temperature distributions within the sample when subjected to fire. A mechanical analysis was then implemented with ABAQUS Standard to simulate the structural response of the slab.

In the heat transfer analysis, the concrete slab, edge beams were simulated with 8-node linear heat transfer brick elements (DC3D8), while the steel rebar was represented with a 2-node linear heat transfer line elements (DC1D2). The finite element model is illustrated in Figure 12. The temperature-dependent thermal properties of both concrete and steel materials recommended in EC4 were used in the analysis. Convection and radiation boundary conditions were applied through the interaction module embedded in ABAQUS. The convective heat transfer coefficient on the exposed surface was taken as $25 W/(m^2 \cdot ^\circ C)$, and the resultant emissivity was 0.5. The top surface of the slab and outside of the edge beams were not exposed to fire so the total heat transfer coefficient was taken as $9 W/(m^2 \cdot ^\circ C)$. The influence of the interface between the precast slab and cast-in-situ concrete layer was not considered because they were assumed to be completely bonded. As the temperature developments were similar for specimens SB2~SB4, only the simulated temperatures for specimen S2 are shown in Figure 13, which experienced the longest fire time. The simulated temperature developments compare well with test results.

The same model for heat transfer analysis as shown in Figure 12 was adopted in the mechanical analysis. The concrete slab, edge beams were simulated using C3D8R elements, and the steel rebars were simulated with T3D2 elements. A bi-linear stress-strain curve was adopted for the reinforcing steel. Concrete was modelled using the Concrete Damage Plasticity model with an initial linear-elastic response until 40% of the compressive strength. The non-linear stress-strain curves at elevated temperatures suggested in EC4 were adopted under the uni-axial loading condition. As no debonding was observed at the interface between the precast slab and cast-in-situ concrete layer, its influence was not considered in this current study. Figure 14 compares the simulation and experimental results, indicating good agreement.

The numerical model was then used to conduct a parametric study on the influence of load ratio on the fire resistance of restrained PC composite slabs and the results are presented in Table 3. The fire resistance decreased with increasing load ratio. In all cases, the two fire resistance test criteria give similar results. More extensive numerical simulation results will be reported in the future to investigate the effects of various design parameters.

Table 3. Effects of load ratio on fire resistance time

Load ratio	Load /kN	fire resistance /min	
		deflection criterion	deflection rate criterion
0.2	130	332	346
0.3	195	201 (195)	208 (203)
0.4	260	166	171
0.5	325	134 (131)	136 (133)
0.6	390	119	123
0.7	455	101	105
0.8	520	88	89
0.9	585	76	74

Note: Test results in brackets.



Fig.12. Finite element model

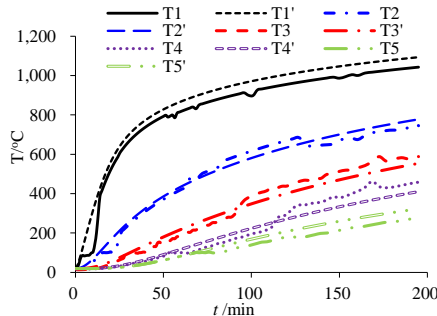


Fig.13. Comparison between simulated temperature-time developments

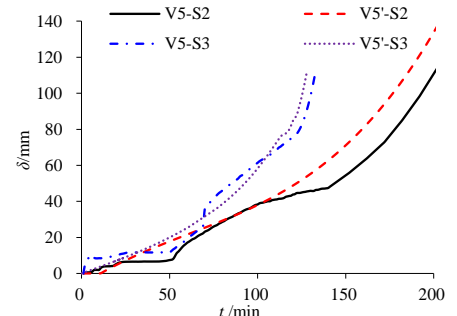


Fig.14. Comparison between simulated mid-span deflection – time curves

6 CONCLUSIONS

This paper has presented the results of an experimental and numerical study to investigate the fire resistance performance of precast concrete (PC) composite slabs. In total, four tests were carried out including one test at room temperature to determine the ultimate capacity of the slabs and three pre-loaded slabs exposed to the ISO 834 standard fire. Among these tests, three PC composite slabs were restrained with four edge beams and the other had no restraint. A numerical simulation model, built using ABAQUS for both heat transfer and mechanical analysis, was developed. The validated numerical simulation model was used to conduct a parametric study to extend the scope of the experimental results, in particular to examine the effects of different load ratios. The following conclusions have been drawn:

- 1) Tensile membrane action was observed in all specimens, tested at ambient temperature and in fire. No debonding was observed at the interface between the bottom precast slab and the top cast-in-situ concrete layer for the restrained PC composite slabs. But cracks formed at the interface for the un-restrained PC composite slab.
- 2) The fire resistance of restrained specimens S2 and S3 subjected to load ratios of 0.3 and 0.5 were 195 min and 131 min, respectively, while the fire resistance of the unrestrained specimen S4 with same load as specimen S2 was 130 min.
- 3) The predicted temperature and deflection developments using the numerical model were in good agreement with the experimental results.

ACKNOWLEDGMENT

This work was financially supported by the Shanghai Science and Technology Commission Program (No. 17DZ2202600) and the Program of Shanghai Subject Chief Scientist (B type) (No.15XD1522600).

REFERENCES

1. Colin G. Bailey (2004). *Membrane action of slab/beam composite floor systems in fire*. Engineering Structures, 26(12). pp 1691-1703.
2. Guo Qiang Li, Nasi Zhang, and Jian Jiang(2017). *Experimental investigation on thermal and mechanical behaviour of composite floors exposed to standard fire*. Fire Safety Journal, 89. pp 63-76.
3. T. T. Nguyen, K.H. Tan (2017). *Behaviour of composite floors with different sizes of edge beams in fire*. Journal of Constructional Steel Research, 129. pp 28-41.
4. Yong Wang, Guanglin Yuan, Zhaohui Huang, Junli Lyv, Zhiqi Li, Tengyan Wang (2016). *Experimental study on the fire behaviour of reinforced concrete slabs under combined uni-axial in-plane and out-of-plane loads*. Engineering Structures, 128. pp 316-332.
5. Nasi Zhang, Guoqiang Li (2009). *A New Method to Analyze the Membrane Action of Composite Floor Slabs in Fire Condition*. Fire Technology, 46(1). pp 3-18.
6. Y. L. Dong, Y.Y. Fang (2010). *Determination of tensile membrane effects by segment equilibrium*. Magazine of Concrete Research, 62(1): pp 17-23.
7. GB/T 51231-2016(2016). *Technical Code for Precast Concrete Buildings*. China Architecture & Building Press, Beijing.

BEHAVIOR OF CFRP-CONCRETE BOND SYSTEM AT ELEVATED TEMPERATURES

Thiago B. Carlos¹, João Paulo C. Rodrigues²

ABSTRACT

This paper presents results of an experimental research on the behaviour of the concrete and carbon fibre reinforced polymer (CFRP) laminate interface at elevated temperatures. The experimental program consisted on fire resistance (FR) tests on RC beams strengthened with CFRP laminates and single lap shear (SLS) tests on concrete blocks with a CFRP laminate bonded. The laminate was in both assembled using the externally bonded reinforcement (EBR) technique. The FR tests (transient state conditions) have been performed following the ISO 834 standard fire curve with the specimens being subjected to a serviceability loading. The SLS tests were conducted under steady state conditions, the specimen was first heated to temperatures of 40 °C, 65 °C, 90 °C, 115 °C, 140 °C, 165 °C and subsequently loaded up to failure. Reference tests at ambient temperature have also been carried out. According to the results, approximately 40% of the bond strength was lost at temperatures near to the glass transition temperature (T_g) of the adhesive. However, despite the loss of bond strength with the increasing temperatures a significant residual strength retention was still noticed for temperatures higher than T_g . Similar tendency was noticed on the CFRP-strengthened RC beams, where the debonding of the strengthening system occurred for temperatures above T_g of the adhesive.

Keywords: CFRP strengthening, concrete, bond strength, EBR technique, elevated temperatures

1 INTRODUCTION

The knowledge of the mechanical behaviour of the bond between the carbon fibre reinforced polymer (CFRP) strengthening system and the concrete at elevated temperatures is a key factor on the fire design of concrete structures. This fact becomes important in view of the increasing use of these materials over the years on strengthening and rehabilitation of concrete structures. The CFRP-concrete bond interface is a critical zone where should be maintained the effectiveness of the externally bonded reinforced (EBR) system, very vulnerable to elevated temperatures as the ones developed in fire case. Usually, failure of bond occurs at temperatures near or above to glass transition temperature (T_g) of the adhesive resin matrix. However, in some cases, this happens for temperatures below T_g . The T_g is typically between 65 and 120 °C [1].

A limited number of studies were reported in the literature [2-10] regarding the behaviour of CFRP-concrete interface at elevated temperatures. Blontrock [2] performed double lap shear (DLS) tests on CFRP strengthened concrete blocks. The specimens were strengthened using the EBR technique and the T_g of the epoxy adhesive used to bond the CFRP laminates to the concrete members was quoted as 62 °C (the test and estimation method used to obtain the T_g was not specified). The specimens were tested at ambient temperature, 40 °C, 55 °C and 70 °C. The bond strength of the CFRP-concrete at 40 °C, 55 °C and 70 °C were 141%, 124% and 82% of the value at ambient temperature, respectively. A rapid loss of bond strength for temperatures above T_g was observed. Despite this, a significant residual strength retention was verified even at temperatures exceeding T_g . The authors attributed the thermal stresses induced by the different thermal expansion coefficient of the materials, CFRP and concrete,

¹ PhD Candidate. LAETA. Department of Civil Engineering, University of Coimbra, Portugal.
e-mail: thiago.carlos@student.dec.uc.pt

² Professor. LAETA. Department of Civil Engineering, University of Coimbra, Portugal.
e-mail: jpaulocr@dec.uc.pt

to justify the strength increase to temperatures below and decrease to temperatures above T_g (around 70 °C).

The DLS tests carried out by Klamer et al. [3] presented similarity with the ones performed by Blontrock [2]. The specimens were bonded according the EBR technique and subjected to temperatures of 10 °C, 50 °C and 70 °C. The T_g was in this case around 62 °C and the test and estimation method used to obtain this temperature was not specified. A moderate low increase of the bond strength for temperatures above the T_g (about 110% of bond strength retention at 50 °C) and a moderate loss of the bond strength for temperatures above the T_g (about 63% of residual strength retention at 70 °C) was verified. Similar tendencies were reported by Klamer [4] in an experimental investigation that included DLS tests at temperatures ranging from 20 °C to 90 °C. The results also revealed an increase on the strength retention at temperatures below T_g and a loss at temperatures above T_g .

Firmo et al. [5] conducted also DLS tests on concrete blocks strengthened with CFRP laminates externally bonded. The specimens were subjected to temperatures of 20 °C, 55 °C, 90 °C and 120 °C. The T_g of the adhesive, determined by Dynamic Mechanical Analyses (DMA) and based on the storage modulus curve, was estimated as 47 °C. The heating for temperatures of 55 °C (above T_g) induced a low loss of bond strength, around 90% when compared to ambient temperature. In addition, a residual bond strength retention at temperatures much higher than T_g (32% at 90 °C and 23% at 120 °C) could be noticed.

Ferrier [6] has also carried out DLS tests on CFRP-concrete blocks externally strengthened. The blocks were heated up to different levels of temperatures between 40 and 120 °C. Test results demonstrate an increase on the bond strength retention for temperatures below T_g (40 °C) and a decrease for temperatures above T_g .

Another work was the one of Leone et al. [7] that has carried out DLS tests on concrete blocks externally strengthened with CFRP laminates. The specimens were tested at ambient temperature and for temperatures of 50 °C, 65 °C and 80 °C. The T_g of the adhesive (55 °C) was determined by Differential Scanning Calorimetry (DSC) tests and the estimation method to obtain was not specified. The results of these authors presented some differences to the ones of Blontrock [2], Klamer et al. [3], Klamer [4], Firmo et al. [5] and Ferrier [6]. A slight decrease of the bond strength was observed for temperatures lower than T_g (85% of strength retention at 50 °C) and a slight increase to temperatures higher than T_g (109% of strength retention at 80 °C).

Other important investigations were the ones of Wang et al. [8], Chowdhury et al. [9] and Gamage et al. [10]. The works of these authors presented similar tendencies to the ones of Leone et al. [7] concerning the behaviour at elevated temperatures of the bond between the CFRP laminate and the concrete element.

Despite the aforementioned investigations most of the previous studies have been performed for temperatures below, near or slightly exceeding the T_g of the adhesive. The thermal and mechanical response of the CFRP-concrete bond in temperature higher or much higher than T_g needs to be analysed and the research presented in this paper tried to address these issues. The present paper includes the results of a large experimental program on the behaviour of the bond between the concrete member and CFRP laminate at elevated temperatures. SLS tests at elevated temperatures on concrete blocks strengthened with CFRP laminates and FR tests [11] on RC beams strengthened with CFRP laminates have been carried out.

2 EXPERIMENTAL TESTS

2.1 Test set-up

The experimental system for the FR tests and the SLS tests at elevated temperatures are illustrated in *Figs. 1a and 1b*, respectively. The test set-ups consisted for both type of tests on a two-dimensional (2D) reaction steel frame (no. 1 in *Fig. 1*). The loading was applied in the specimens by a hydraulic actuator (no. 2 in *Fig. 1*) hanged on this reaction frame. In the FR tests the load was in compression applied by a static hydraulic actuator with a maximum load capacity of 200 kN and a maximum stroke of 200 mm that was servo-controlled by a W+B central unit. In the SLS tests the load was in tension applied by a dynamic hydraulic actuator with a maximum load capacity of 295 kN and a maximum stroke of 360 mm that was in this case servo-controlled by a Dartec (Instron) central unit.

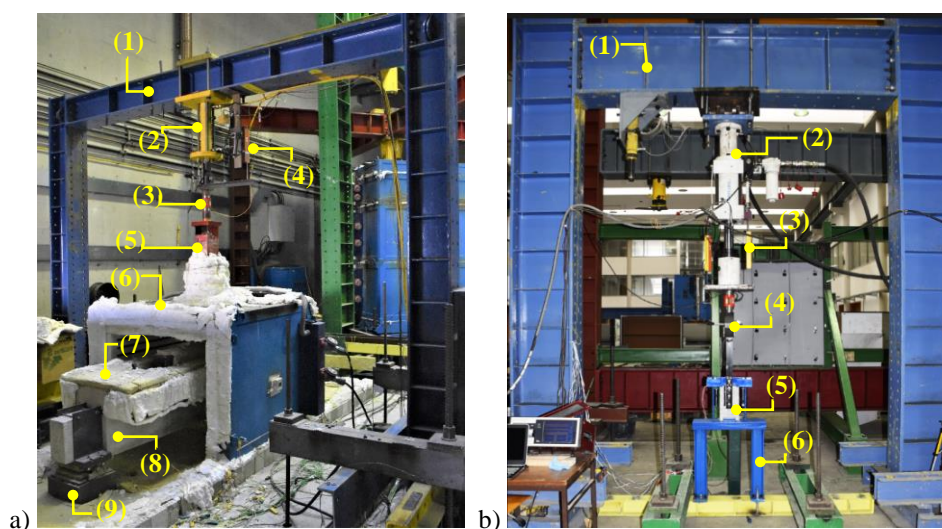


Fig. 1. Test set-up for the a) FR tests and b) SLS tests at high temperatures (without furnace)

In the FR tests the specimens (no. 8 in *Fig. 1a*) were loaded at two points 1.0 m apart the beam's supports in such a way to provide a four-point bending test in order that between the two loading points the beam presented a pure bending state. The load applied during the FR tests was monitored by a load cell (no. 3 in *Fig. 1a*). This loading was transferred from the hydraulic jack to the specimen by a HEA160 stub column and applied at the loading points by means of a HEB140 beam (no. 5 in *Fig. 1a*). As it can be seen in *Fig. 1a* (no. 9), the tested beams were simply supported over a roller and pinned support, simulating a static determinate beam. The span between the beam's axis supports was 3000 mm long, even they are completely inside the furnace and directly exposed to heating (see *Fig. 2b*). The thermal action was applied by a horizontal electric furnace (no. 6 in *Fig. 1a*), capable to heat up to 1200°C and followed the ISO 834 fire curve. In these tests three sides of the beams were exposed to fire, corresponding to the bottom and lateral ones, therefore, only the upper side was not subjected to heating. The unexposed face of the testing beams was protected by ceramic wool and a concrete slab (no. 7 in *Fig. 1a*). This system intended to reproduce, as faithful as possible, a RC beam in contact with a slab as in a real building structure and thus constituting a more or less thermal adiabatic surface for these tests. The vertical displacements at different sections of the beams were measured with linear variable displacement transducers (LVDTs), indicated as no. 4 in *Fig. 1a*. Type K probe thermocouples were used for temperature measurements inside the furnace and type K cable thermocouples were used for temperature measurements at different points of the specimen's cross-sections. The thermocouple distribution is presented in *Fig. 2a*.

In the SLS tests the specimen (no. 5 in *Fig. 1b*) was at the bottom built in a small steel frame (no. 6 in *Fig. 1b*). The CFRP laminate was pulled by a clamping system (no. 4 in *Fig. 1b*). The specimen was first heated by an electric furnace, capable to reach temperatures up to 1200 °C, at a heating rate

of 1°C/min. In these tests have been used similar type K thermocouples. In these tests the thermocouple distribution allowed the assessment of the temperatures along the cross-section of the concrete blocks, in the CFRP laminate exposed surface and at three different points of the interface between the laminate and the concrete block. TML strain gauges were mounted along the bonded and free length of the CFRP laminate for axial strain measurements. The displacements of the specimens were measured with LVDTs (no. 3 in *Fig. 1b*) positioned in the cross-head of the system and by the internal transducer of the hydraulic actuator.

A TML data logger TDS 630 was used for data acquisition in both test set-ups.

2.2 Specimens

The specimens for the FR tests consisted on RC beams of rectangular cross-section with 150 mm wide and 300 mm height and 3400 mm length. The CFRP laminate was bonded along the bottom side of the RC beams using the EBR technique. The beams were then protected with three types of fire protection systems composed by the following sprayed materials: vermiculite-perlite (VP), expanded clay (EC) and ordinary Portland (OP) cement based mortars. The fire protection material was applied on the bottom and lateral side of the beams by dry spraying technique. *Fig. 2b* shows the geometric configuration and other details of the test specimens.

The SLS tests consisted on concrete blocks externally bonded with CFRP laminates. The concrete blocks were prismatic with dimensions of 150 mm wide, 150 mm height and 290 mm length. The laminate was bonded along 190mm of the concrete blocks surface using also the EBR technique. The geometry and other details of the specimens are illustrated in *Fig. 2c*.

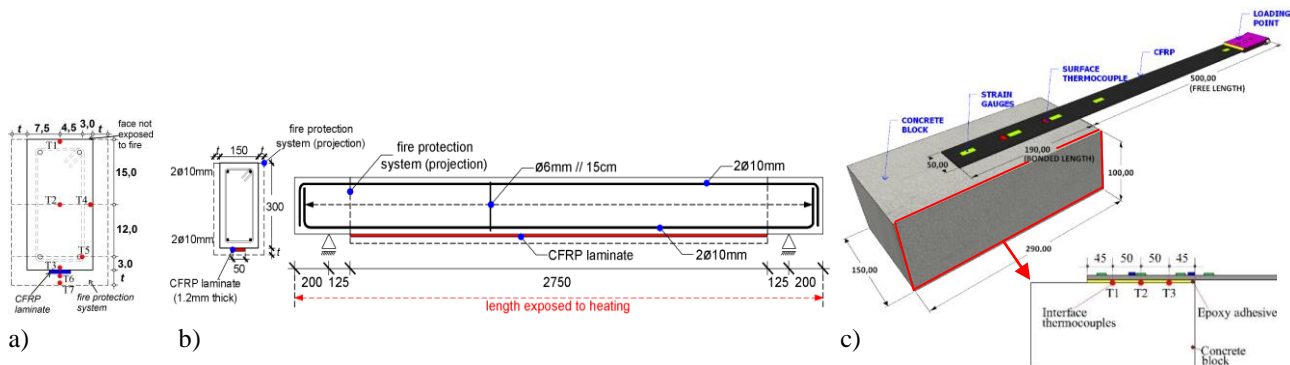


Fig. 2. Schemes of the specimens: a) location of thermocouples on the CFRP-strengthened RC beams; b) geometry and details of the specimens for the FR tests; c) geometry and details of the specimens for the SLS tests (dimensions in mm)

The mean cube compressive strength (f_{cm}) of the concrete used in all tested specimens (at 28 days) was $f_{cm} = 30.1$ MPa.

The mechanical properties of the rebars on the RC beams were: yield stress of 500 MPa, modulus of elasticity of 210 GPa and ultimate tensile strength of 550 MPa.

The CFRP used on all specimens have a cross-section of 50 mm x 1.2 mm and was commercially designated as S&P Laminates 150/2000. This type of laminate has an average tensile strength of 2800 MPa, modulus of elasticity of 170 GPa and ultimate strain of 16.0‰ (at ambient temperature), according to the manufacturer [13].

A two-component epoxy resin (commercially designated *S&P Resin 220*) was used to bond the CFRP laminate to the surface of the concrete specimens. This adhesive has a tensile strength of 17.3 MPa and a modulus of elasticity of 8.8 GPa (at ambient temperature). The T_g of the adhesive was quoted as 75 °C and was determined by DMA tests. In addition, the T_g was defined based on the peak value of the *Tan δ curve* (loss factor).

The VP mortar presents a relation water/compounds of 0.67-0.80 l/kg, a dry density of 450-500 kg/m³ and a thermal conductivity of 0.0581 W/m.K [14]. The OP mortar had a dry density of 1500-1800 kg/m³, thermal conductivity of 0.67 W/m.K and a ratio water/compounds of 0.13-0.15 l/kg [15]. The EC mortar had a dry density of 468–633 kg/m³, a thermal conductivity of 0.13 W/m.K and ratio water/compounds of 0.35–0.40 l/kg [16].

2.3 Test program and procedure

In this research they were carried out 21 SLS tests on CFRP-strengthened concrete blocks at elevated temperatures and 10 FR tests on CFRP-strengthened RC beams protected with VP, EC and VP mortars. The test program is summarised in *Table 1*.

Table 1. Test program

Test reference	Temperature	Loading	Type of test
TA-1, TA-2, TA-3	Ambient	After reaching the desired temperature level the load has been increased in displacement control at 0.005mm/min until specimen's rupture	Single Lap Shear (SLS)
T40-1, T40-2, T40-3	40 °C		
T65-1, T65-2, T65-3	65 °C		
T90-1, T90-2, T90-3	90 °C		
T115-1, T115-2, T115-3	115 °C		
T140-1, T140-2, T140-3	140 °C		
T165-1, T165-2, T165-3	165 °C		
RC	Standard fire curve ISO 834	Subjected to a service load of 70% of the design value of the loadbearing capacity of the beam at ambient temperature	Fire Resistance (FR)
EC-20, EC-35, EC-50			
VP-20, VP-35, VP-50			
OP-20, OP-35, OP-50			

Among the FR tests, 9 tests were performed on CFRP-strengthened RC beams protected with three different fire protection materials of three possible thicknesses (t) and one test on a normal RC beam (reference test). The CFRP-strengthened RC beams were divided in three batches, according to the type of fire protection system. They were carried out 3 tests per each batch, one for each thickness of the fire protection material. Therefore, according to the thickness applied, the specimens protected with EC mortar for example were designated as EC-20, EC-35 and EC-50 (20, 35 and 50mm thick, respectively). The same type of reference was used for the specimens protected with OP and VP mortars. The reference test was only designated as RC.

Regarding the SLS tests, 18 tests were performed under heating conditions and 3 tests at ambient temperature. The test specimens were divided in seven batches, according to the respective temperature level. Thus, they were carried out 3 tests for each temperature series, in order to obtain a better correlation of the results. Therefore, the test specimens subjected to temperatures of 40 °C, 65 °C, 90 °C, 115 °C, 140 °C and 165 °C were respectively designated by T40, T65, T90, T115, T140 and T165. Specimens tested at ambient temperature (reference tests) were designated in the experimental plan as TA.

In terms of test procedure in the FR tests the specimens were first loaded with serviceability load and then heated up following the standard fire curve ISO 834 [12] until failure. The failure criteria adopted was the one of EN 1363-1 [17].

In the SLS tests the specimens were first heated to the desired temperature level and in a second stage (after stabilization of the temperature) loaded in tension up to failure. The specimens were completely inside the furnace and subjected to the heating. After the heating stage the loading was applied under displacement control at a rate of 0.005 mm/min until failure of the CFRP-concrete bond.

3 BOND BEHAVIOUR AT ELEVATED TEMPERATURES

3.1 SLS tests

The bond strength as function of temperature for the specimens in the SLS tests are presented in Fig. 3. The relative load bearing capacity of the CFRP-concrete interface is determined by the ratio between the ultimate load for the different temperatures and the one at ambient temperature.

These results reveal a reduction of bond strength of the CFRP-concrete interface with the increasing temperature. For moderate temperature (40 °C) a low decrease (5%) in the bonding strength is observed. The bond strength is most affected when the temperatures approach the T_g of the adhesive (75 °C). In this case about 40% reduction at 65 °C is noticed compared to the ambient temperature. For the higher temperatures (90 °C, 115 °C and 140 °C) this reduction is also higher, more than 66%. However, an unexpected residual bond strength was observed for temperatures higher than the T_g . For the temperature series of 90 °C, 115 °C and 140 °C a bond strength retention of 34%, 21% and 11% was registered, respectively. The bond strength was only completely lost for temperatures of around 165 °C. The presence of friction forces and chemical adhesion at the concrete–adhesive interface may have promoted this important residual bond strength at so elevated temperatures.

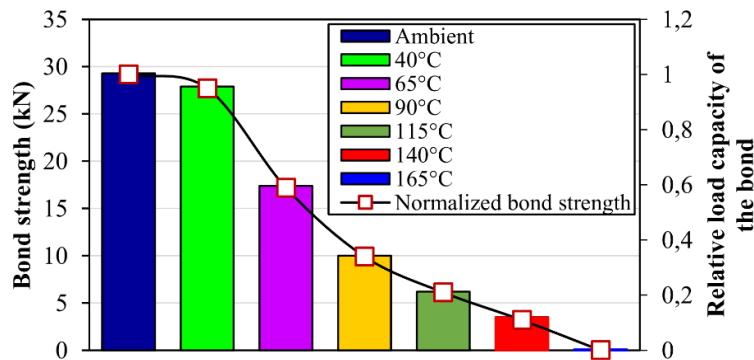
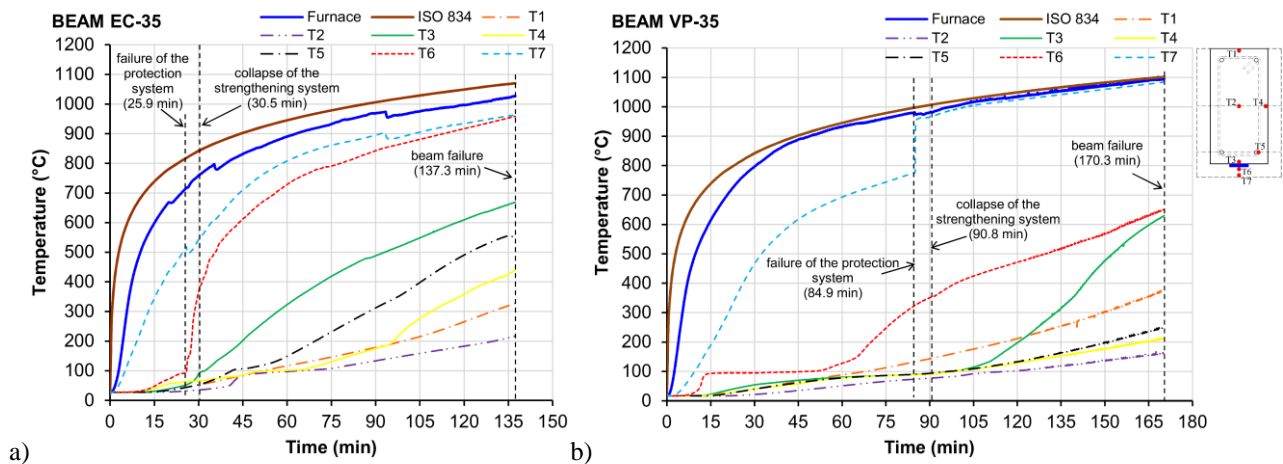


Fig. 3. Bond strength and relative bond capacity for the different temperature testing series

3.2 FR tests

The temperatures recorded at different points of mid-span cross-section of beams EC-35, VP-35 and OP-35, in the furnace and the standard fire curve ISO 834 [12] temperatures, as a function of time, are shown in Fig. 4.



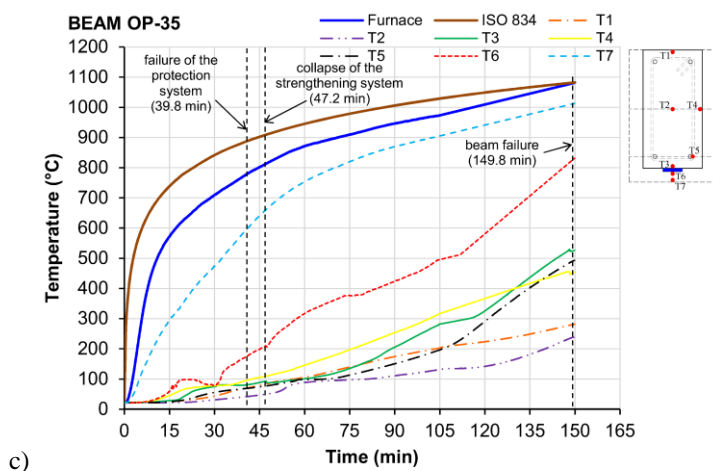


Fig 4. Temperatures at cross-section S1 of the beams: (a) EC-35, (b) VP-35 and c) OP-35

The origin of the time scale in *Fig. 4* corresponds to the beginning of the heating. The instant corresponding to the debonding of the CFRP strengthening system was also indicated in *Figs. 4a-c*. The results reveal that the temperature at the CFRP-concrete interface, when the strengthening system collapsed, ($T_{f_{CFRP}}$) was about 93 ± 1 °C for all specimens. Therefore, the debonding of the strengthening system occurred for temperatures above T_g of the adhesive, which in turn was 75 °C.

The presence of a residual bond strength observed in the SLS tests (*section 3.1*) can be explain the effectiveness of the strengthening system for temperatures higher than the T_g . Moreover, it is possible that the $T_{f_{CFRP}}$ recorded on the strengthened specimens has been lower in some regions, especially close to the supports (extremities of the CFRP laminates). These colder zones have suffered thermal influence from the support's elements and the surrounding structure. The collapse of the fire protection system in different parts also contributed to this phenomenon. Consequently, non-uniform temperature profiles might have generated along the length of the beams.

4 CONCLUSIONS

In this research the following conclusions may be drawn:

- In the SLS tests a continuous reduction in the bond strength was observed with the increasing temperatures. However, a significant residual bond strength was observed for temperatures of the adhesive higher than T_g . These results confirmed that an important residual bond strength was retained for temperatures above the glass transition process on the epoxy adhesive.
- This was also observed in the FR tests on CFRP-strengthened RC beams, since the debonding of the strengthening system occurred for temperatures of the adhesive above T_g . This fact led the RC beams to withstand the serviceability loading for longer time periods.
- Therefore, analysing the results of the FR and SLS tests it can be concluded that the T_g cannot mean a critical temperature of the CFRP-concrete interface.
- The failure modes on the SLS test specimens at ambient temperature and 40 °C occurred in concrete along bonded region and at higher temperatures in adhesive of the CFRP-concrete interface.
- The failure modes on the FR test specimens was by bending and in some cases, for later stages of the tests, some rebars have also collapsed.

ACKNOWLEDGMENTS

The authors grateful acknowledge CNPq – National Council of Scientific and Technological Development, Brazil, for the PhD scholarship give to the first author and the S&P Clever Reinforcement Ibérica, Lda. (<http://www.sp-reinforcement.pt>) for supplying the CFRP laminates.

REFERENCES

1. ACI Committee 440. *Guide for the design and construction of externally bonded FRP systems for strengthening concrete structures*, ACI 440.2R-08. Farmington Hills, MI, USA: American Concrete Institute; 2008.
2. Blontrock H. *Analysis and modelling of the fire resistance of concrete elements with externally bonded FRP reinforcement*. PhD thesis, Ghent University, Ghent, Belgium; 2003.
3. Klamer EL, Hordijk DA, Janssen HJM. The influence of temperature on the debonding of externally bonded CFRP. *7th international symposium on fibre reinforced polymer reinforcement for reinforced concrete structures (FRPRCS-7)*; 2005. 1551–70.
4. Klamer EL. *Influence of temperature on concrete beams strengthened in flexure with CFRP*. PhD thesis, Eindhoven, Eindhoven University of Technology, Netherlands; 2009.
5. Firmo JP, Pitta D, Correia JR, Tiago C, Arruda MRT. *Experimental characterization of the bond between externally bonded reinforcement (EBR) CFRP strips and concrete at elevated temperatures*. *Cement and Concrete Composites*; 2015. 60: 44-54.
6. Ferrier E, Agbossou A. *Temperature effects on the shear capacity of external bonded fibre reinforced polymer on concrete*. *Construction and Building Materials*; 2017. 152: 333-344.
7. Leone M, Matthys S, Aiello MA. *Effect of elevated service temperature on bond between FRP EBR systems and concrete*. *Composites Part B*; 2009. 40(1): 85–93.
8. Wang K, Young B, Smith ST. *Mechanical properties of pultruded carbon fibre reinforced polymer (CFRP) plates at elevated temperatures*. *Engineering Structures*; 2011. 33(7): 2154-61.
9. Chowdhury EU, Eedson R, Bisby LA, Green MF, Benichou N. *Mechanical characterization of fibre reinforced polymers materials at high temperature*. *Fire Technol*; 2011. 47(4): 1063-80.
10. Gamage JCPH, Al-Mahaidi R, Wong MB. *Bond characteristics of CFRP plated concrete members under elevated temperatures*. *Composite Structures*; 2006. 75(1–4): 199–205.
11. Carlos TB, Rodrigues JPC, de Lima, RCA, Dhima, D. *Experimental analysis on flexural behaviour of RC beams strengthened with CFRP laminates and under fire conditions*. *Composite Structures*; 2018. 189: 516-528.
12. ISO 834-1. *Fire resistance tests – elements of building construction, Part 1: general requirements*. Geneva, Switzerland: International Organization for Standardization (ISO); 1999.
13. S&P C-Laminate. Carbon fibre polymer plates for structural reinforcement: *product technical specifications*. Seewen, Switzerland; 2008.
14. Perlita Y, Vermiculita SL. *Biofire: product technical specifications*. Barcelona, Spain; 2008.
15. Secil Martingança SA. RHP manual interior: *product technical specifications*. Leiria, Portugal; 2013.
16. Argex – Argila Expandida, S.A. ARGEX® 0-2: *product technical specifications*. Aveiro, Portugal; 2008.
17. EN 1363-1. *Fire resistance tests – Part 1: general requirements*. Brussels, Belgium: European Committee for Standardization (CEN); 1999.

THE EFFECT OF EXPLOSIVE SPALLING ON PUNCHING SHEAR STRENGTH OF CONCRETE SLABS EXPOSED TO FIRE

Fangxia Lu^{1,2}, Roland Baertschi², Johann Eduard van der Merwe¹, Mario Fontana¹

ABSTRACT

Explosive spalling of concrete exposed to fire is known to depend not only on material properties, but also on geometry and loading conditions. Experimental observations typically indicate an increased susceptibility to spalling when compressive stress is applied [7]. In addition to axial loads, hogging bending moments in flat reinforced concrete slabs can be expected to result in such compressive stresses at concrete surfaces potentially exposed to fire. A case study of explosive spalling at the soffit of a reinforced concrete flat slab around a supporting column during a fire is presented. Based on a previously developed spalling model at ETH Zurich [3, 4], the effect of compressive stress in the lower concrete slab section surrounding the column is shown to increase the risk of explosive spalling. Moreover, the influence of explosive spalling on reduced punching shear resistance after critical shear crack theory is investigated. It is shown that explosive spalling of slab soffits in the vicinity of supporting columns can reduce punching shear resistance by up to 50%. The spalling model is finally used to propose fire safety measures to avoid punching shear failure induced by explosive spalling. This preliminary model needs further research and verification against fire test.

Keywords: Explosive spalling, punching shear, spalling model, fire safety, performance-based approach

1 INTRODUCTION

The often violent occurrence of explosive spalling typically leads to a loss of cover concrete, resulting in a reduced concrete cross section and exposure of reinforcement to fire [1, 2]. In severe cases this can lead to a loss of structural integrity. Although structural effects such as compressive loading have been shown to increase the susceptibility of concrete to spall in fire (e.g. [7]), most design codes consider explosive spalling as a material related phenomenon. Following a parameter study at ETH Zurich, a spalling model has been developed which accounts for the contribution of mechanical loading on the risk of explosive spalling [3, 4].

The development of modern, dense, high performance concrete (HPC) has seen the increased occurrence of explosive spalling in fire [1, 2]. However, under compressive loading, even ordinary Portland concrete (OPC) can be prone to explosive spalling. This has been observed in a recent fire in the basement parking area of a building in Switzerland. Figure 1 shows spalling of the slab soffit exposed to the fire. The extent of spalling agrees well with the zone of hogging moment over the column support, where the slab soffit is in compression.

¹ ETH Zurich, Institute of Structural Engineering (IBK), Switzerland

² Baertschi Partner Bauingenieure AG, Switzerland



Fig. 1. Explosive spalling damage to a reinforced concrete flat slab in the region of hogging bending moments near a column support following fire exposure in an underground parking structure in Switzerland (2016).

Explosive spalling in regions of hogging bending moment can be expected to extend over an area where punching shear resistance should be considered. Although the actual shear crack area is not influenced, the reduced concrete depth over this area increases slab rotations and thus decreases punching shear resistance. This brittle form of failure should therefore carefully be considered in the case of fire exposure.

Observations from tests have shown that the depth of explosive spalling can reach up to 10 cm within 30 minutes [5]. Such spalling can be expected to have a significant influence on a slab similar to the case study slab, with a depth of 25 to 35 cm prior to spalling. The spalling model is used to investigate possible protective measures to avoid spalling in regions of hogging bending moments near column supports.

2 EXPLOSIVE SPALLING RISK UNDER COMPRESSIVE STRESS

2.1 Spalling model

The spalling model [3] is based on the energy method proposed by Zhukov [6] which accounts for the total strain resulting from pore pressure, thermal stresses and external loads. This allows for both thermo-hydro and thermo-mechanical effects to be combined in order to predict the occurrence of explosive spalling. Spalling is identified when the strain energy density, w_p as shown in Equation (1), exceeds the critical spalling energy, $w_{spalling}$ as shown in Equation (2). Here, the strain ε_p is determined by the pore pressure and thermal stresses.

$$w_p = \frac{1}{2} \alpha \sigma_p \varepsilon_p \quad (1)$$

$$w_{spalling} = \frac{1}{2} f_{t,T} \frac{f_{t,T}}{E} \quad (2)$$

$$\varepsilon_p = \frac{1}{E} [\alpha \sigma_p - \nu (\sigma_{thermal,vert} + \sigma_{thermal,hor} + 2\alpha \sigma_p + \sigma_{load})] \quad (3)$$

In the above, $f_{t,T}$ is the tensile strength of concrete at temperature T , σ_p is the pore pressure, α is Biot's coefficient for spalling defining the fraction of pore pressure transferred to the total stress in the concrete matrix, $\sigma_{thermal}$ is the thermal stress perpendicular to the spalling direction, ν is Poisson's Ratio for concrete, σ_{load} is stress induced by the mechanical loading and E is Young's modulus. The thermal stresses are self-equilibrating and calculated based on a linear coefficient of thermal expansion.

Equations (1) to (3) can be used to relate the strain energy densities to equivalent stresses and, given that spalling is identified when $w_p \geq w_{spalling}$, a spalling stress limit is defined in Equation (4). Spalling is identified when the combined internal stress exceeds the temperature dependent tensile strength of the concrete matrix.

$$\sigma_{spalling} = \sqrt{(1 - 2\nu)\alpha^2\sigma_p^2 - \nu(\sigma_{thermal,vert} + \sigma_{thermal,hor} + \sigma_{load})\alpha\sigma_p} \geq f_{t,T} \quad (4)$$

Predictions from the spalling model have compared well with test results [3]. It should be noted that mechanical compressive stress will increase the spalling stress limit in Equation (4). The risk of explosive spalling can subsequently be expected to increase under the influence of external compressive load, even for OPC, as experimental observations have shown [7]. The model therefore proposes the mechanism by which compressive stress increases the risk of explosive spalling and allows a means of quantifying its contribution.

2.2 Explosive spalling risk in regions of hogging bending moment

To illustrate the potential problem with respect to spalling and punching shear strength, a concrete slab in a parking garage has been studied. In addition to the widely known high spalling risk of HPC, a garage slab made of OPC has been selected to show that in a more general situation OPC under compressive stress is prone to explosive spalling in fire cases.

The case study slab was designed in the 1980's. Design details for this 30 cm thick slab specified the use of OPC concrete of class B35/25. Due to conservative construction quality control and long-term hydration, the concrete class at the time of fire exposure was approximately C45/55. Considering the moisture content in the concrete, an intrinsic permeability was determined from the permeability model [4, 8] to be $1 \cdot 10^{-17} \text{ m}^2$. With these parameters, the thermos-hydro process in the slab exposed to ISO fire has been simulated by the spalling model. Without mechanical loading, no spalling of the OPC slab is predicted within the first 60 minutes of ISO fire exposure. As shown in Fig. 2, the spalling stress was lower than the tensile strength during this period of ISO fire exposure and is therefore not expected to lead to explosive spalling.

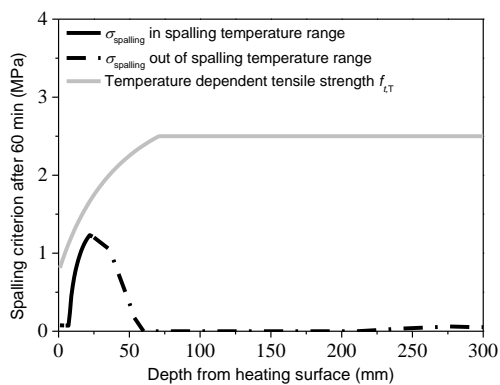


Fig. 2. Without mechanical loading, no explosive spalling is predicted in 60 minutes.

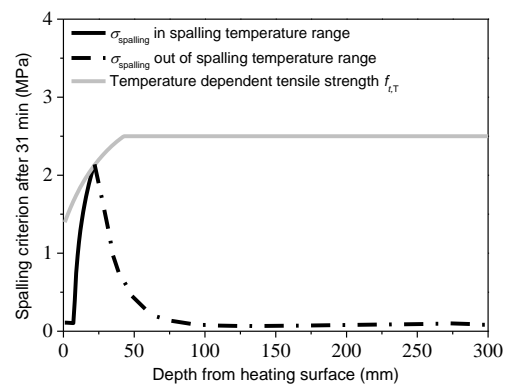


Fig. 3. With mechanical loading, explosive spalling is predicted after 31 minutes of ISO fire exposure.

When the fire exposed OPC slab surface is under compressive stress, e.g. resulting from thermal restraint or from bending moments, the spalling stress, as described in Equation (4), is increased. During a fire scenario, the compressive stress in the soffit concrete of this parking garage slab near the supporting column, is calculated to be approximately 10 MPa. Accounting for this compressive stress, the spalling stress is predicted to reach the tensile strength after 31 minutes of ISO fire exposure, as shown in Figure 3., resulting in an estimated initial spalling depth of 2.3 cm.

The analysis clearly indicates the increase in explosive spalling risk of slab soffit concrete in regions of hogging bending moments – i.e. in regions surrounding column supports. It is in these regions where brittle punching shear failure of flat slabs is an important design consideration. The influence of reduced slab depth on the punching shear resistance during a fire should therefore be carefully considered.

3 EFFECT OF EXPLOSIVE SPALLING ON PUNCHING SHEAR STRENGTH

3.1 Critical shear crack theory

The punching shear failure criterion considered in this investigation is based on the critical shear crack theory as recommended in the Swiss code SIA 262 [9] and fib model code 2010 [10], as this theory has been reported to agree well with experimental punching shear test results [11]. Accordingly, the punching shear capacity is obtained from the intersection of a failure criterion and a load-rotation relationship obtained from a nonlinear flexural analysis.

Punching shear resistance following explosive spalling is determined based on a reduced concrete depth according to the predicted depth of spalling. High-temperature material properties are not taken into account for this assessment as the relatively low temperature associated with the occurrence of spalling (approximately 250 °C – 400 °C) is deemed to be of lesser significance to the material properties compared to the effect of a reduced concrete section depth.

3.2 Reduced punching shear resistance due to explosive spalling

Punching shear resistance was investigated following explosive spalling to various depths. The case study slab is required to achieve a 60 minute fire resistance (R60). Since the first occurrence of spalling is predicted after only 30 minutes of ISO fire exposure, continuous spalling should be considered beyond the first occurrence and up to 60 minutes of exposure. The maximum depth of explosive spalling is assumed to be 10 cm, based on previous experimental observations at ETH Zurich [5].

A local fire case close to column C1 of the parking structure slab shown in Figure 4 was investigated. Bending moment redistribution following various depths of explosive spalling was accounted for from nonlinear analysis using the commercial software package CUBUS [13]. Punching shear resistance around column C1 is calculated prior to spalling and compared to that following spalling depths of 2.5 cm, 5 cm and 10 cm.

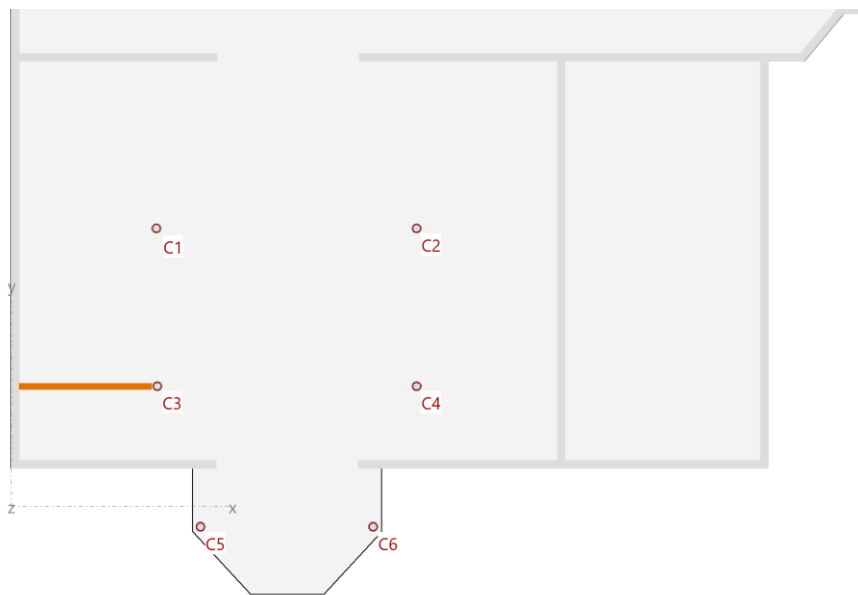


Fig. 4. Plan of the parking structure. Explosive spalling is investigated around column C1.

Figure 5 shows the intersection of the failure criterion and the load-rotation relationship for the slab prior to explosive spalling, indicating a punching shear resistance of 1164 kN. Following an initial

spalling depth of 2.5 cm, the failure criterion curve reduces, resulting in punching shear failure at a smaller slab rotation. Figure 6 shows this reduced failure criterion, indicating a punching shear resistance of 1044 kN (a 10% reduction in punching shear resistance). Punching shear resistance reduces further as the spalling depth increases. Figure 7 and Figure 8 indicate a punching shear resistance of 915 kN (21% reduction) and 614 kN (47% reduction) following a spalling depth of 5 cm and 10 cm respectively.

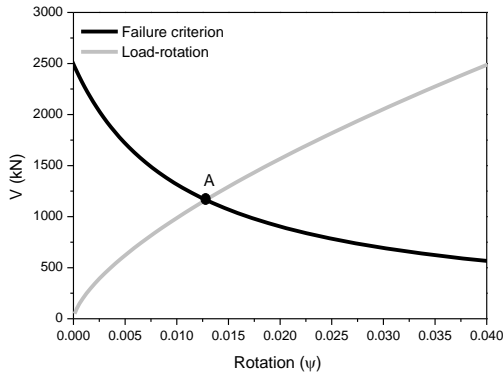


Fig. 5. Punching strength according to SIA 262, prior to explosive spalling; A = 1164 kN.

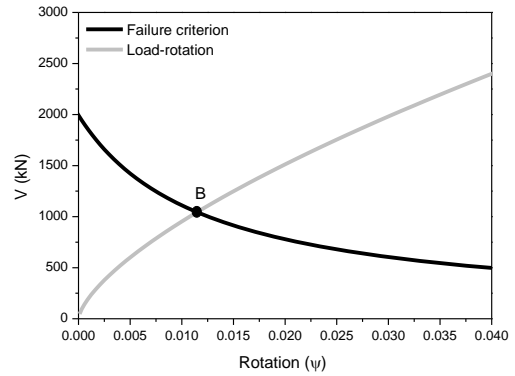


Fig. 6. Punching strength according to SIA 262, with 2.5 cm spalling depth; B = 1044 kN (-10%).

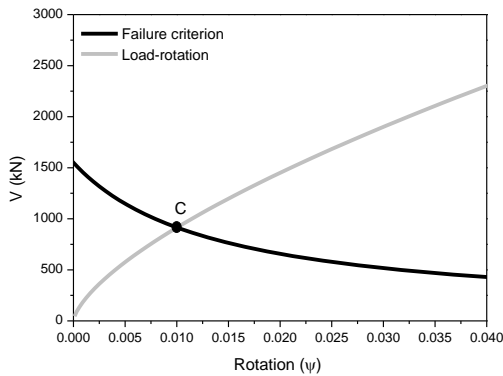


Fig. 7. Punching strength according to SIA 262, with 5 cm spalling depth; C = 915 kN (-21%).

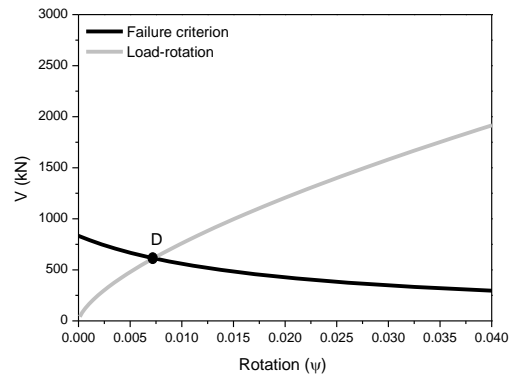


Fig. 8. Punching strength according to SIA 262, with 10 cm spalling depth; D = 614 kN (-47%).

Figure 9 shows how the relative punching shear resistance reduces as the explosive spalling depth increases. When the section loses a third of its depth (i.e. 10 cm spalling depth), the punching shear resistance is approximately halved.

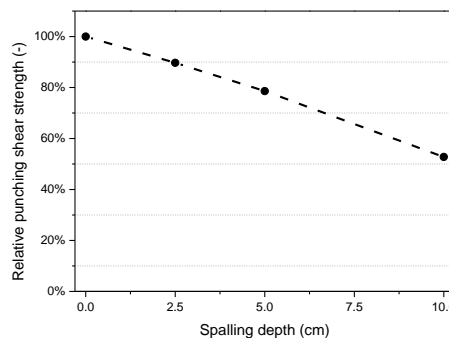


Fig. 9. Decrease in relative punching shear resistance with increased spalling depth.

For an estimated depth of explosive spalling of 10 cm within the first 60 minutes of fire exposure, sufficient punching shear resistance to achieve an R60 fire rating would most likely not be possible. The influence of compressive stresses resulting from hogging bending moments is therefore shown to have a significant impact on the explosive spalling risk of even lower concrete strength classes. Moreover, it indicates the significant increase in the risk of brittle structural failure within the first 60 minutes of fire exposure. Amongst other possible reasons, reduced punching shear resistance induced by explosive spalling could have contributed to structural collapse in practice, e.g. Gretzenbach, Switzerland, in November 2004 [12].

For many types of concrete elements, the local loss of cross section following explosive spalling does not result in structural failure. However, for flat slabs close to a supporting column, explosive spalling can be continuous due to the contribution from compressive stress, resulting in a significant spalling depth. Therefore, to maintain sufficient punching shear resistance in these areas, it is proposed that the occurrence of explosive spalling should be prevented.

4 METHODS TO PREVENT EXPLOSIVE SPALLING

The spalling model enables the investigation of the effectiveness of methods to prevent explosive spalling. By using the model to determine and design the most appropriate protective method to achieve a desired fire rating, a performance based design approach to fire safety is followed. The influence of protective methods such as fire protective boards, fire resistant mortars and intumescent coatings, on the occurrence of explosive spalling have been studied with the model and results have compared well with experimental observations [3, 4]. In this study, an intumescent coating is chosen as a representative protective method due to its light weight which would not induce additional loading on the slab.

Following a series of simulations of the parking structure slab, and accounting for the compressive stress from hogging bending moments, the required intumescent coating to prevent explosive spalling was determined. Figure 10 shows that, for a 1.5 mm intumescent coating thickness, the spalling stress does not exceed 1.5 MPa for at least 60 minutes of ISO fire exposure and is therefore considered to be below the expected tensile strength of the concrete. As such, application of this protective method is expected to ensure a fire safety resistance of R60 according to the Swiss code SIA 262 [9].

Application of the intumescent coating would be required over the region of hogging bending moment; in this case an area of 3 x 3 m² around the investigated column support. This relates to 25% of the tributary area to the column support and is therefore considered as a cost-effective method of achieving the desired fire rating.

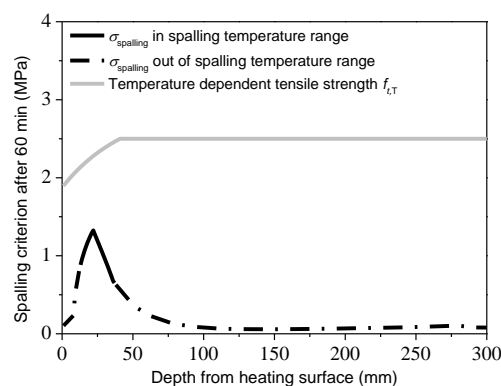


Fig. 10. Spalling model simulation with 1.5 mm intumescent coating thickness. No explosive spalling is predicted within 60 minutes of ISO fire exposure.

5 CONCLUSION AND OUTLOOK

Based on the results from simulations of the case study reinforced concrete slab, the following conclusions are made:

- The soffit of suspended reinforced concrete flat slabs has been observed to be more prone to explosive spalling in the region of column supports than in mid-span regions. According to the spalling model, compressive stress in soffit concrete layers in regions of hogging bending moment is confirmed as the mechanism for the observed increased spalling risk.
- Although HPC is known to be susceptible to explosive spalling, the contribution of mechanical compressive stress increases the explosive spalling risk of even OPC. Since such compressive stress is typically present, either from external loads or as a result of thermal restraint, the explosive spalling risk of OPC should not be neglected.
- Explosive spalling of flat slab soffit concrete around column supports significantly reduces its punching shear resistance. According to critical shear crack theory, the punching shear resistance of the case study slab can be expected to reduce by up to 50% for an assumed 10 cm spalling depth. Considering the degradation of concrete and reinforcement, and the additional compressive stress during fire exposure, this resistance reduction could be more severe.
- Cost effective protective methods are available to avoid explosive spalling and ensure sufficient punching shear resistance for a desired fire rating. The spalling model enables a performance based method of identifying the most appropriate protective method.

The current investigation focussed on the potential increase in punching shear failure risk following explosive spalling. Only compressive stress due to hogging bending moments were considered. A subsequent study will include additional compressive stress due to thermal expansion of the heated concrete slab, and the critical shear crack theory should be validated in fire case considering explosive spalling.

REFERENCES

1. Kodur V.K.R., Fire Performance of High-Strength Concrete Structural Members. Construction Technology Update No. 31. Dec. 1999.
2. Koury, G.A., Effect of fire on concrete structures. Progress in Structural Engineering and Materials, Vol. 2, No. 4, pp. 429-447, 2000.
3. Lu F. and Fontana M., A thermo-hydro model for predicting spalling and evaluating the protective methods, 4th International RILEM Workshop on Concrete spalling due to fire exposure (IWCS), Leipzig, Germany, 2015.
4. Lu F., Baertschi R. and Fontana M., A method to inspect the risk of fire spalling of existing concrete members, Fourth Conference on Smart Monitoring, Assessment and Rehabilitation of Civil Structures (SMAR), Zürich, Switzerland, 2017
5. Klingsch E., Frangi A. and Fontana M., Explosive spalling of concrete in fire, Test report. IBK Tests report No. 352. 2013: Institute of Structural Engineering (IBK), ETH Zurich, Switzerland.
6. Zhukov, V.V., 'Explosive failure of concrete during a fire (in Russian) '. Translation No. DT 2124, Joint Fire Research Organization, Borchamwood.
7. Miah J., Lo Monte F., Felicetti R., Pimienta P., Carré H. and la Borderie C., Experimental Investigation on Fire Spalling Behavior of Concrete: Effect of Biaxial Compressive Loading and Cement Type, 5th International Workshop on Concrete Spalling due to Fire Exposure, Borås, Sweden, 2017.
8. Lu F. and Fontana M., Concrete Permeability and Explosive Spalling in Fire, The 8th International Conference on Concrete Under Severe Conditions-Environment & Loading, Lecco, Italy, 2016.
9. Code SIA 262:2003 Civil Engineering Zürich: The Swiss Standards Association.

10. Fib Model Code for Concrete Structures 2010, October 2013, International Federation for Structural Concrete (fib), Lausanne, Switzerland.
11. Muttoni A., Punching Shear Strength of Reinforced Concrete Slabs without Transverse Reinforcement, ACI Structural Journal, July-August 2008, Title no. 105-S42.
12. Muttoni, A. (E.), Fernández Ruiz, M., Fürst, A., Guanali, S., Hunkeler, F., Moser, K., Seiler, H.: Tragsicherheit von Einstellhallen, Dokumentation D 0226 SIA, Schweizerischer Ingenieur- und Architektenverein, Zürich, Schweiz, 105 Seiten, 2008.
13. Cubus Engineering Software, Version 8, Cubus AG, Statik-7

ROLE OF POLYMER FIBRES IN PREVENTION OF EXPLOSIVE SPALLING IN ULTRA-HIGH PERFORMANCE CONCRETE

Dong Zhang¹, Kang Hai Tan², Aravind Dasari³

ABSTRACT

Polymer fibres are widely applied to prevent explosive spalling in ultra-high performance concrete (UHPC). However, the role of polymer fibres in the reduction of explosive spalling is still not fully understood. In this work, different types of polymer fibres are used in UHPC to assess and understand the mechanisms thoroughly. Spalling tests and permeability tests at different temperatures are conducted for this purpose. It is found that melting of polymer fibres does not affect permeability of UHPC significantly, while the thermal mismatch between embedded fibres and matrix is essential for preventing spalling. The expansion of polymer fibres creates microcracks before the melting of fibres begins and results in an obvious increase in permeability, thereby improving the spalling resistance of UHPC.

Keywords: ultra-high performance concrete; fibres; gas permeability; thermal mismatch, spalling.

1 INTRODUCTION

Ultra-high performance concrete (UHPC) is a relatively new generation of concrete with superior strength and excellent durability. In the last two decades, it has been widely used in structures like high rise buildings, bridges and tunnels [1]. However, the dense microstructure of UHPC makes it vulnerable to explosive spalling under fire conditions. Explosive spalling reduces the cross-section of a structure member rapidly and subjects deeper layers of concrete to fire, resulting in a rapid loss of load capacity of s members [2]. It is believed that the main factors of spalling is due to accumulation of vapour pressure at high temperatures arising from the dense microstructure of UHPC [3-6]. Hence, one of the most widely accepted methods to prevent spalling is the addition of polymer fibres to concrete that could relieve vapour pressure by creating pathways at high temperature [7, 8]. Polymer fibres, including polypropylene (PP), polyamide and polyethylene, are commonly used for this purpose.

It is stated that adding polymer fibres can create a transport system that is beneficial for increasing permeability of concrete and releasing trapped vapour pressure. PP fibres are commonly believed to be partially or totally absorbed by the porous network of the cement matrix after melting at about 170°C, leaving channels in concrete[8]. However, Khoury [9] holds the view that the high viscosity and large molecular size of PP make penetration of PP fibres into cement matrix impossible. Recent studies also argue that the permeability of concrete starts to increase significantly before melting of PP fibres [1, 10, 11], which cannot be explained clearly by the above statements. Khoury [9]

¹ Research associate and PhD student. School of Civil and Environmental Engineering and School of Materials Science and Engineering, Nanyang Technological University, Singapore.

e-mail: zhangdong@ntu.edu.sg

² Professor. School of Civil and Environmental Engineering, Nanyang Technological University, Singapore.

e-mail: CKHTAN@ntu.edu.sg

³ Associate Professor. School of Materials Science and Engineering, Nanyang Technological University, Singapore.

e-mail: aravind@ntu.edu.sg

proposes that pressure-induced tangential space (PITS) between the interface of fibre and concrete paste can increase the permeability of concrete above 100°C. The theory is also supported by other researchers[3, 11], but it has not yet been proven by experiment. In view of the above controversy, how fibres function in concrete is still not fully understood.

Thus, to investigate the role of polymer fibres in preventing spalling of UHPC, different types of polymer fibres, including PP, linear low-density polyethylene (LLDPE) and ultra-high molecular weight polyethylene (UHMWPE) fibres, were added to in the UHPC mix. Spalling test and gas permeability tests were conducted to show the effectiveness of different polymer fibres on spalling prevention of UHPC. The behaviour of polymer fibres in UHPC at high temperature was studied by a scanning electron microscope (SEM).

2 MATERIAL AND EXPERIMENTS

2.1 Mix proportion and sample preparation

The mix proportions of UHPC in this study are given in Table 1. Portland cement (ASIA@ CEM II 52.5 R) was used in the mix. Silica sand used in this study had a mean size of 110µm. Silica fume was Grade 940 and bought from Elkem Micro silica®. Fine aggregate was natural river sand sieved by using a sieve with 0.6mm mesh. Sika ViscoCrete-2044, which is a third generation polycarboxylic type, was applied as superplasticizer. PP, LLDPE and UHMWPE fibres were used in the mix and the samples were denoted as UHPC-PP, UHPC-LLDPE and UHPC-UHMWPE, respectively. UHPC-C represented the control UHPC samples without any fibres.

A Hobart® planetary mixer was used for mixing. The specimens were poured into moulds on a vibration table. Discs of 45 mm thick and 150mm in diameter were cast for permeability test. Cylinders (50mm in diameter and 100mm in height) were prepared for spalling tests. Cubic samples with the size of 50mm were cast for compressive strength tests.

All the specimens were demoulded after they were cast for 1 day and stored in lime-saturated water at ambient temperature for another 27 days. The compressive strength of each mix was the mean value of three samples (as shown in Table 1). After curing, the discs for permeability tests were grinded from both sides to get a smooth surface. The thickness of the discs was around 40mm after grinding.

Table 1. Mixture compositions of UHPC (unit in kg/m³).

Mix design	W/B	C	SF	SS	SP	FA	W	Fibre	f_c (MPa)
UHPC-C	0.2	830	208	208	33	913	208	0	148.6
UHPC-PP	0.2	830	208	208	33	913	208	3	159.9
UHPC-LLDPE	0.2	830	208	208	33	913	208	3	140.6
UHPC-UHMWPE	0.2	830	208	208	33	913	208	3	137.8

W/B: water binder ratio	SS: Silica sand
C: cement	SP: superplasticizer
SF: silica fume	FA: fine aggregate.
f_c : compressive strength at 28 days	

2.2 Spalling test

Cylinders with a diameter of 50mm and a height of 100mm were adopted for spalling tests. Two cylinders were tested for each mix design. Spalling tests were conducted in an electrical furnace, which was heated according to the standard heating curve of ISO 834 for 1 h. The extent of spalling on the cylinders was visually observed after they were naturally cooled down for 24h.

2.3 Permeability measurement

The details of experimental setup for permeability test can be found in [1, 12]. As explosive spalling occurs typically at temperature between 200°C to 300°C [4, 13], permeability test was

conducted under 300°C. Additionally, moisture in the UHPC may block the dense microstructure of UHPC, making it difficult to obtain gas permeability of UHPC at ambient temperature. As a result, permeability was measured at 105°C, 150°C, 200°C and 300°C. The samples were initially oven-dried at 105°C to equilibrium and then placed into the test set-up. A heating rate of 0.5°C/min was adopted during the test. For each mix, at least two specimens were tested.

3 RESULTS AND DISCUSSION

3.1 Spalling test and permeability

Results of the spalling test are shown in Fig.1. UHPC-C experienced severe spalling under high temperature and only some small pieces could be found after the test. As expected, UHPC-PP remained intact after being heated, indicating that PP fibres were beneficial for preventing spalling of UHPC. UHPC-LLDPE also showed good integrity after the test. However, it was interesting to find that UHPC-UHMWPE also broke into small pieces, similar to UHPC-C. Adding UHMWPE fibres was not effective in preventing spalling of UHPC. In fact, some other studies also showed that even a dosage of 12.5kg/m³ of UHMWPE did not prevent spalling of concrete [14].

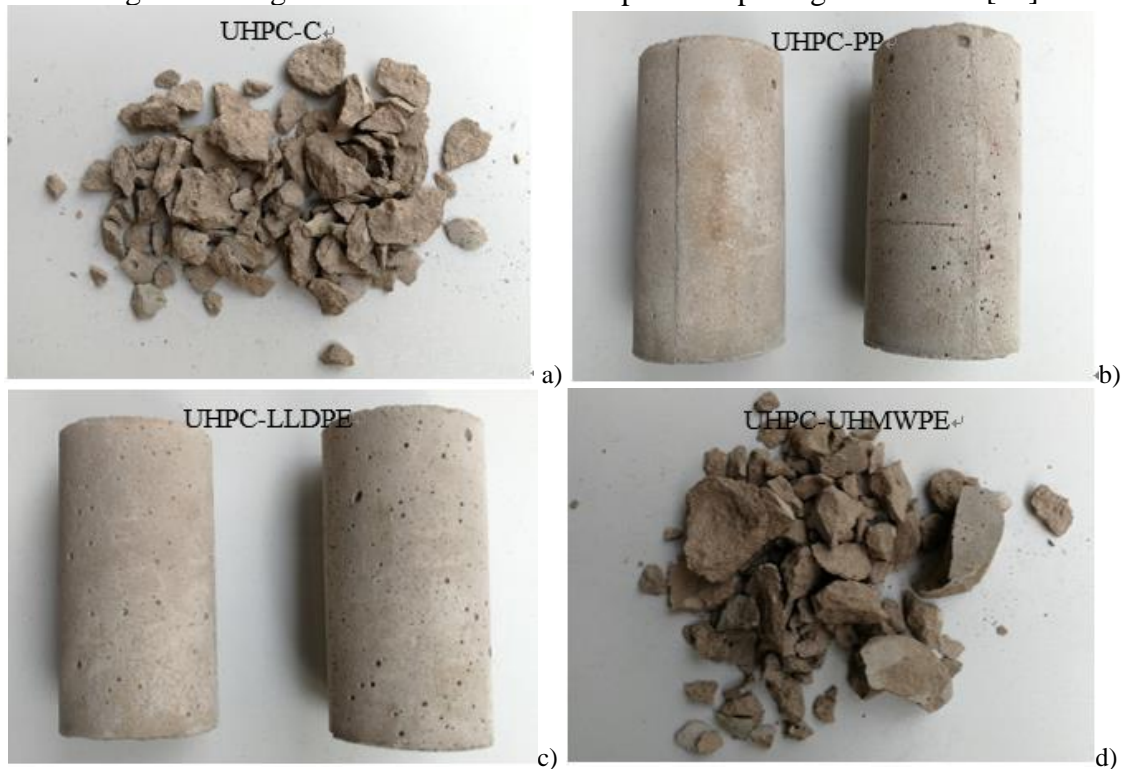


Fig. 1. Results of spalling test for a) UHPC -C, b) UHPC-PP, c) UHPC-LLDPE and d) UHPC-UHMWPE.

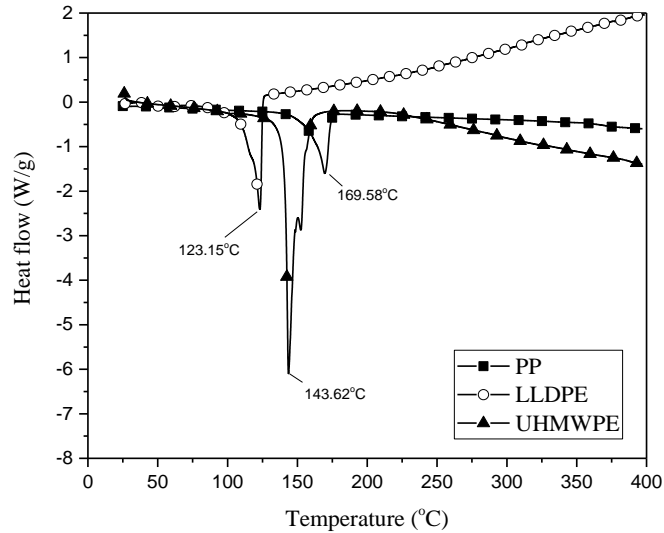


Fig. 2. DSC results of polymer fibres used in the current study.

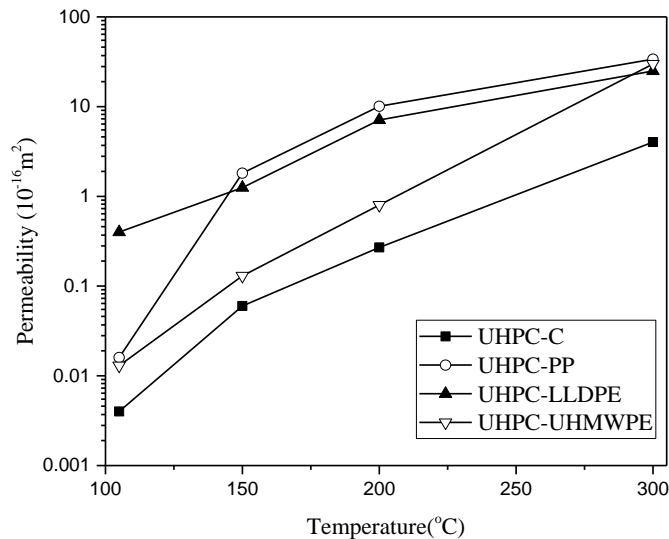


Fig. 3. Hot gas permeability of UHPC with increasing temperature.

DSC results of polymer fibres used in this study (Fig.2) showed that the melting points of PP, LLDPE and UHMWPE fibres were 169.58°C, 143.62°C and 123.15°C, respectively. In previous studies, it was usually considered that the melting of polymer fibres would create empty channels in concrete and lead to relief of vapour pressure[8]. Melting point of fibres was usually considered as an important parameter for spalling protection [7, 8]. However, the results presented here clearly showed that melting point of polymer fibres was not a dominant parameter in preventing spalling. UHMWPE fibres with a lower melting point than PP fibres did not prevent spalling of UHPC.

Permeability represents the capacity of vapour relief in concrete at high temperature. Permeability of each mix design was measured at hot state and the results are plotted in Fig.3. As can be seen, permeability of UHPC-C was the lowest at high temperature. It kept increasing during heating. This was due to formation of microcracks during heating, caused by the shrinkage of cement matrix and expansion of aggregates.

It was interesting to find that the permeability of UHPC-LLDPE was around two-order of magnitude greater than that of UHPC-C at 105°C, which was before the melting point of LLDPE (123.15°C). In contrast, permeability values of UHPC-PP and UHPC-UHMWPE were only slightly greater than that of UHPC-C at this temperature. With increasing temperature, permeability of

UHPC-PP showed a significant increase of two-order of magnitude at 150°C, while permeability of other specimens only increased slightly at this stage. Clearly, the melting of polymer fibres did not provide obvious effect on permeability in UHPC-LLDPE and UHPC-UHMWPE. At 200°C, permeability of all specimens only increased slightly. It was also found that PP fibres did not increase permeability significantly after melting. It is interesting to find that the significant increase on permeability of UHPC-LLDPE and UHPC-PP samples happened before the melting point of the corresponding polymer fibres. In fact, an increase of permeability in concrete before melting of PP fibres has also been reported in [1, 10, 11] and it was attributed to the PITS caused by the weak interface of fibres and cement matrix. However, the results of UHPC-UHMWPE showed that the PITS might not lead to the increase of permeability, as permeability of UHPC-UHMWPE did not increase before melting. The study clearly showed that melting of polymer fibres was not required for increasing permeability of UHPC at high temperature.

It was also found that all the specimens showed high permeability at 300°C. The permeability values of UHPC-C and UHPC-UHMWPE showed a significant increase at 300°C. This can be attributed to the formation of cracks in the samples at 300°C during testing. However, it was reported that spalling usually occurs between 200°C and 300°C [9]. The high permeability at 300°C may have little influence on the spalling resistance of UHPC. Due to the low permeability under 200°C, all the specimens of UHPC-C and UHPC-UHMWPE showed severe spalling (Fig.1 a and d).

3.2 Microscopic investigation

To understand the behaviour of polymer fibres at high temperature, SEM investigations were conducted on the UHPC samples with different polymer fibres before and after being heated to high temperature. Small samples were cut from cubic samples of each mix by using diamond saw and were polished using silico carbide papers to get a flat surface. A SEM (JSM 6360) was applied for microscopic observation. An accelerating voltage of 5 kV was used for observation. The SEM images of UHPC with different polymer fibres are presented in Fig. 4. It can be seen that PP fibres did not show any obvious change after being heated to 150°C. However, there were some microcracks formed around PP fibres (Fig.4 a). The coefficient of thermal expansion (CTE) of PP fibres is around 100 times greater than that of cement paste [15]. When exposed to high temperature, this thermal mismatch could create microcracks at the interface of fibres and cement paste. The width of these microcracks was around 0.5µm, large enough for the escape of vapour. As a result, permeability of UHPC-PP showed a significant increase at 150°C. A similar result could be observed in UHPC with LLDPE fibres. As shown in Fig. 4c, microcracks were formed around LLDPE fibres before melting of fibres. In contrast, no obvious microcrack was found around UHMWPE fibres after being heating to 105°C (Fig. 4e). As UHMWPE has a very high packing density, its CTE is relatively low compared with LLDPE. The expansion of UHMWPE may not be sufficient to cause microcracks in the concrete. This could explain why UHPC-UHMWPE showed low permeability at 105°C.

After exposure to 200°C, PP fibres disappeared in the initial channel (Fig.4b). In the UHPC-LLDPE and UHPC-UHMWPE samples, both LLDPE and UHMWPE also disappeared in their initial channels (Fig.4 d and f). However, it should be noted that permeability did not increase significantly after melting of fibres in all the samples.

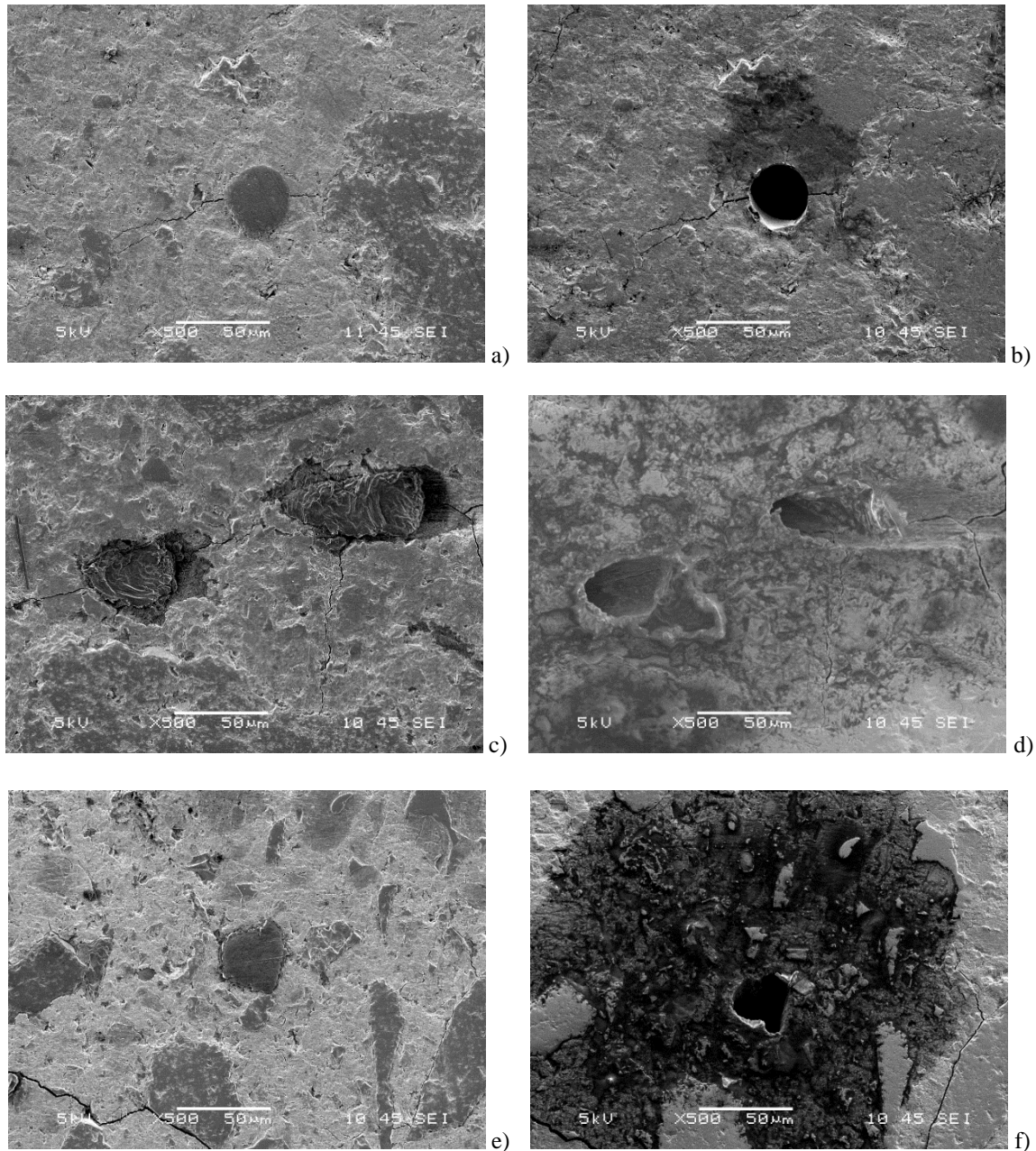


Fig. 4. SEM images of UHPC with polymer fibres: a) UHPC-PP after exposure to 150°C, b) UHPC-PP after exposure to 200°C, c) UHPC-LLDPE after exposure to 105°C, d) UHPC-PP after exposure to 150°C, e) UHPC-UHMWPE after exposure to 105°C, f) UHPC-UHMWPE after exposure to 150°C.

4 CONCLUSIONS

This paper presents the spalling behaviours of UHPC with different types of polymer fibres, including PP, LLDPE and UHMWPE fibres. It was found that only PP and LLDPE fibres could prevent spalling of UHPC. Although UHMWPE has a lower melting point than PP, UHMWPE fibres did not help in enhancing spalling resistance. Permeability of UHPC-PP and UHPC-LLDPE showed a sudden increase before the melting of polymer fibres, while permeability of UHPC-UHMWPE was similar to that of UHPC-C. SEM results showed that microcracks were created around PP and LLDPE fibres before melting, which contributed to an increase of permeability. However, there was no microcracks around UHMWPE. The melting of polymer fibres did not increase permeability of UHPC significantly.

ACKNOWLEDGMENT

This research is supported by Singapore's Ministry of National Development – National Research Foundation (MND-NRF) through Land and Livability National Innovation Challenge (L2NIC), Award No. L2NICCFP1-2013-4.

REFERENCES

1. Li, Y. and K.H. Tan, *Effects of Polypropylene and Steel Fibers on Permeability of Ultra-high Performance Concrete at Hot State*, in *Structures in Fire (Proceedings of the Ninth International Conference)*, M.E.M. Garlock and V.K.R. Kodur, Editors. 2016, DEStech Publications: Princeton University. p. 145-152.
2. Kodur, V.K.R. and L. Phan, *Critical factors governing the fire performance of high strength concrete systems*. Fire Safety Journal, 2007. **42**(6-7): p. 482-488.
3. Ozawa, M. and H. Morimoto, *Effects of various fibres on high-temperature spalling in high-performance concrete*. Construction and Building Materials, 2014. **71**: p. 83-92.
4. Khoury, G.A., *Effect of fire on concrete and concrete structures*. Progress in Structural Engineering and Materials, 2000. **2**(4): p. 429-447.
5. Ma, Q., et al., *Mechanical properties of concrete at high temperature—A review*. Construction and Building Materials, 2015. **93**: p. 371-383.
6. Liu, J.-C. and K.H. Tan, *Fire resistance of strain hardening cementitious composite with hybrid PVA and steel fibers*. Construction and Building Materials, 2017. **135**: p. 600-611.
7. Lee, G., et al., *Combining polypropylene and nylon fibers to optimize fiber addition for spalling protection of high-strength concrete*. Construction and Building Materials, 2012. **34**: p. 313-320.
8. Kalifa, P., G. Chene, and C. Galle, *High-temperature behaviour of HPC with polypropylene fibres: From spalling to microstructure*. Cement and concrete research, 2001. **31**(10): p. 1487-1499.
9. Khoury, G.A., *Polypropylene fibres in heated concrete. Part 2: Pressure relief mechanisms and modelling criteria*. Magazine of Concrete Research, 2008. **60**(3): p. 189-204.
10. Hager, I. and T. Tracz, *The impact of the amount and length of fibrillated polypropylene fibres on the properties of HPC exposed to high temperature*. Archives of Civil Engineering, 2010. **56**(1): p. 57-68.
11. Bošnjak, J., J. Ožbolt, and R. Hahn, *Permeability measurement on high strength concrete without and with polypropylene fibers at elevated temperatures using a new test setup*. Cement and Concrete Research, 2013. **53**: p. 104-111.
12. Klingsch, E.W., et al., *Tests on the hot and residual permeability of concrete at high temperatures*, in *4th International Workshop on Concrete Spalling due to Fire Exposure*, F. Dehn, Editor. 2015, MFPA Leipzig: Leipzig, Germany. p. 65-75.
13. Tan, K.H., J.-C. Liu, and J. Liu. *Fire Performance Of Fiber-Reinforced Concrete: Research Needs*. in *4th International Workshop on Concrete Spalling due to Fire Exposure*. 2015. Kassel, Germany.
14. Liu, J.-C. and K.H. Tan, *Fire resistance of ultra-high performance strain hardening cementitious composite: Residual mechanical properties and spalling resistance*. Cement and Concrete Composites.
15. Khoury, G.A. and B. Willoughby, *Polypropylene fibres in heated concrete. Part 1: Molecular structure and materials behaviour*. Magazine of Concrete Research, 2008. **60**(2): p. 125-136.

Concrete Structures

ROLE OF LOAD ECCENTRICITY AND TRANSVERSE REINFORCEMENT IN FIRE RESISTANCE OF REINFORCED CONCRETE COLUMNS

Shujaat Hussain¹, Umesh Kumar Sharma²

ABSTRACT

In this study, experimental tests were conducted on full-scale Reinforced Concrete (RC) columns to determine the role of load eccentricity and transverse reinforcement spacing on fire resistance of RC columns. The aim was also to determine the effective confinement under fire for reduced spacing's of transverse reinforcement, considering the variable amount and nature of spalling. Experimentally spalling was found to significantly determine the buckling and failure mode of RC columns. In high strength concrete columns, uniform exposure of longitudinal bars occurs. Thereby an increase in load eccentricity leads to global buckling of RC columns for reduced transverse reinforcement spacing's ensuring better internal confinement. Whereas lesser load eccentricity led to localized exposure of longitudinal bars even at reduced spacing of transverse reinforcement. Thereby, premature local buckling of exposed longitudinal bars occurred. Numerical 3D modelling in ABAQUS software was used to determine Moment-curvature relations for various transverse reinforcement spacings. Various spalling scenarios under different load eccentricities were considered. It was concluded that the lateral confinement of RC columns under fire increases with decrease in transverse reinforcement spacing.

Keywords: Column, concrete, eccentricity, fire resistance, spalling

1 INTRODUCTION

Tests were conducted on nine full scale RC columns of 3.15m unsupported length constructed with two concrete grades of 30MPa and 60MPa. The load eccentricity and transverse reinforcement spacing were taken as variable parameters to be studied. The aim was to study the role of transverse reinforcement spacing on fire resistance of RC column. The impact of spalling occurring under variable load eccentricity for two different grades of concrete was also observed. The relative influence of these parameters on fire resistance was co-related from experimental data. Finally numerical models were used to determine the moment-curvature relations. The same was done by developing sequential 3D models for heat and mechanical stress. The validation of these models was done for temperature profiles for 2D section models and for deformations obtained after considering various spalling scenarios under different load eccentricities.

2 RESEARCH SIGNIFICANCE

Most of the methods of determining fire resistance for Reinforced Concrete (RC) structures are prescriptive formulations that do not take into account the time of survivability of the structure. The survivability is defined by compartment burnout or failure of structural element. But if the structural element is a column, the criticality of this element cannot be governed by prescriptive formulations

¹ Research Scholar of Civil Engineering Department, IIT Roorkee, Roorkee, India.

e-mail: shujaatbuch@gmail.com

² Associate Professor. Department of Civil Engineering, IIT Roorkee, India.

e-mail: umuksh@rediffmail.com

as that would encourage the structural failure before whole compartment burnout. This is not recognised to be good practice as fire scenarios throughout the world lead to billions of dollars of loss to infrastructure, most of which is beyond repair and also to number of deaths [1]. Accordingly giving due importance to the fire resistance of the RC column, the parameters influencing [2-3] also need to be consistent with the existing construction codes [4-6] as well as relating to importance of parameters not given adequate consideration. For example, load eccentricity considerably decreases the fire resistance of RC columns [7]. Studies however do not focus on nature of spalling under varying load eccentricities, while as spalling is considered to be an essential condition for limiting fire resistance.

Similarly, transverse reinforcement spacing is also seen to influence the fire resistance of the RC columns [8-9]. The nature and extent of lateral confinement provided by transverse reinforcement during fire would change due to spalling. It has been seen that spalling occurs at either corners, or on surface of the column specimen [10]. Another criteria would be the rate of spalling which has been seen to be high in explosively spalled high strength concrete [11]. The idea in succeeding sections would be to relate the role of transverse reinforcement spacing on fire resistance of RC columns, primarily considering the role of spalling under different load eccentricities.

3 EXPERIMENTAL PROGRAM

3.1 Test Columns

Nine full scale RC columns were tested under ISO-834 fire curve after pre-loading at 33% of ultimate design load determined as per ACI [12]. Two grades of concrete (normal and high strength) made from carbonaceous aggregates were considered. Silica fume was used by proportion of 10% of cement in 60MPa grade concrete. The w/c ratio was maintained below 32% for high grade concrete while as Relative Humidity for test day columns varied from 65% to 80% from 30mm to 100mm depth. The working slump of 100-110mm was used in casting of columns. The area of longitudinal reinforcement was maintained at 2.29% in all the columns. Key details of tested columns and test set up are shown in *Fig. 1*. The end conditions maintained were bottom fixed and top pinned. Thermocouples were placed at three key locations along the length to capture thermal profiles as given in *Fig. 1* and LVDTs were used for determining lateral and vertical deformations during the test. The details of key parameters tested are given in *Table 1*. The load was maintained during the whole period of fire heating. The test was terminated once the state of column reached was that either the column could not take any further load or the rate of deflection or amount of deflection exceeded the limits set in as per BS-476 [13]. Key observations with regard to spalling were recorded during the tests.

3.2 Results

The key outcomes of this testing were that fire resistance of RC columns increased by 53.7% with decrease in spacing of transverse reinforcement spacing from $15\phi_1$ to $7.5\phi_1$ for normal strength concrete columns (N3E40, N4E35) and by 35.6% with decrease in spacing from $7.5\phi_1$ to $3.75\phi_1$ for high strength concrete columns (H3E35 and H4E35). In above ' ϕ_1 ' indicates longitudinal reinforcement diameter. There was no appreciable change in fire resistance for change in transverse reinforcement spacing from $7.5\phi_1$ to $3.75\phi_1$ in case of normal strength RC columns (N4E35 and N5E35). It was seen that increase in thermal gradients occurred which could be considered to have influence on restricting the influence of decreasing spacing of transverse reinforcement. The increase in fire resistance of high strength concrete columns was also restricted by localized failure of longitudinal bars. However, decrease in spacing of transverse reinforcement in high strength concrete column 'H4E35' (*Fig. 1b*) at higher load eccentricity led to global mode of buckling failure with deformations increasing by 371% as compared to high strength concrete column 'H2E20' (*Fig. 1c*). Spalling was also seen to progressively decrease for normal strength concrete

columns N3E40 (35.4%) to N4E35 (13.4%) to N5E35 (3.9%) and in high strength concrete columns H3E35 (52.6%) to H4E35 (47.7%) with decrease in spacing of transverse reinforcement. Another important result is that the fire resistance decreases with increase in load eccentricity in both normal strength concrete columns and high strength concrete columns. Fire resistance decreased for column ‘N3E40’ with 40mm eccentricity by 42% as compared to column ‘N2E20’ with 20mm eccentricity. There was considerable increase in amount of spalling area with increase in load eccentricity in both normal and high strength concrete columns. Column ‘N3E40’ with 40mm eccentricity had 436% increase in amount of spalling as compared to column ‘N1E0’ with no eccentricity. Likewise, column ‘H2E20’ with 20mm eccentricity had a 26.7% increase in amount of spalling area as compared to column ‘H1E0’ with no eccentricity. A 4-directional plot depicting the role of spalling on fire resistance is given in Fig. 2. This plot also states the role of transverse reinforcement spacing and load eccentricity on both spalling and fire resistance of RC column.

Table 1. Experimental parameters and results

S.No.	Column specimen	Concrete strength ‘f _c ’ (MPa)	Eccentricity ‘e _x ’-(mm)	Transverse reinforcement spacing ‘S _w ’ (mm)	Spalling amount ‘S _a ’ (% Area)	Fire resistance ‘t _f ’ (min’s)
1	N1E0	25	0	300	6.6	236
2	N2E20	28	20	300	0	231
3	N3E40	27	40	300	35.4	134
4	H1E0	65	0	300	78.9	69
5	H2E20	56	20	300	100	37
6	N4E35	27	35	150	13.4	206
7	N5E35	26	35	75	3.9	193
8	H3E35	66	35	150	52.6	59
9	H4E35	65	35	75	47.7	80

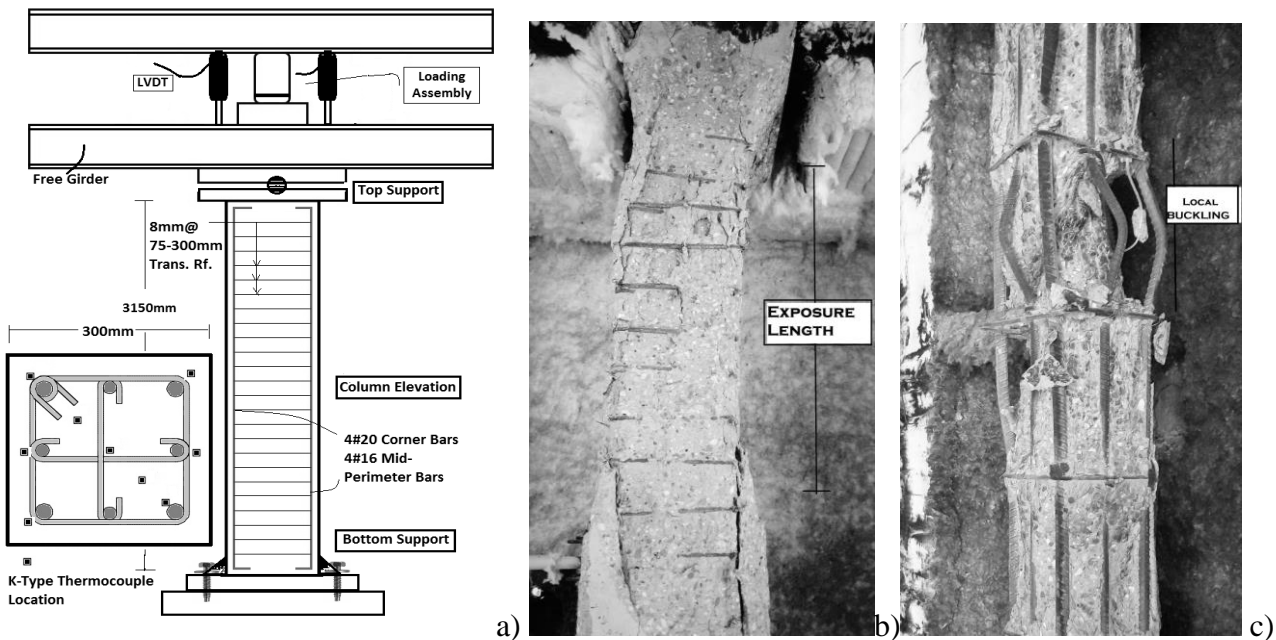


Fig. 1. a) Column Specifications b) Column H4E35 global buckling c) Column H2E20

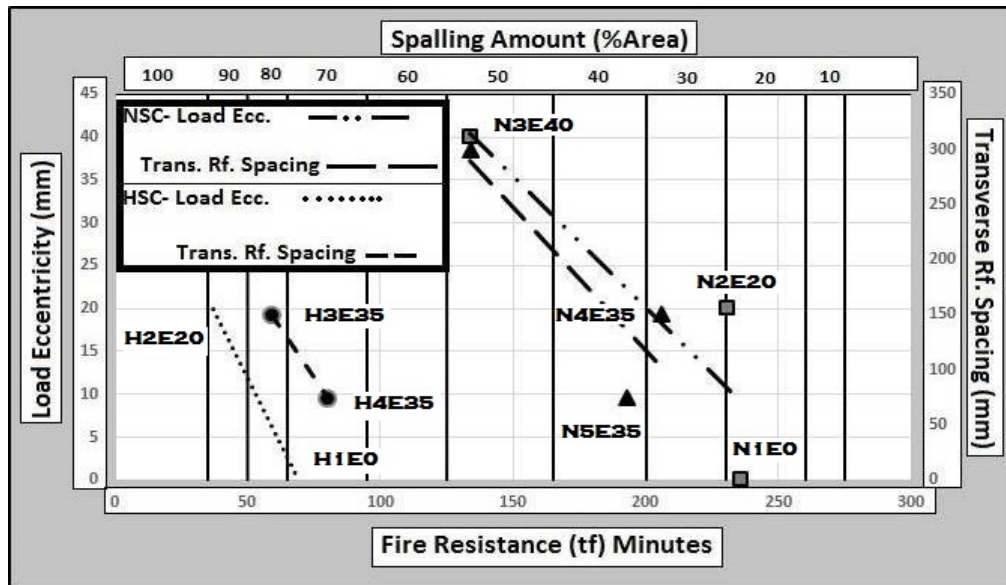


Fig. 2. Results from experimentation

4 NUMERICAL STUDIES

The aim of this study was to determine the role of spacing of transverse reinforcement in fire resistance determination for normal and high strength concrete columns. As spalling plays vital role in determination of fire resistance of RC columns, it was imperative to model spalling. Spalling scenarios were considered to be primarily dependant on the concrete permeability. Existing models for predicting spalling were seen to be unreliable with predicting the nature of spalling along the length of the RC column due to influence of reinforcement detailing. The present models were also seen to be inconsequential for determining the specific location of spalling along the surface of the column. Many reasons including the nature of moisture flow migration around the reinforcement is not clear. Thereby, spalling scenarios were developed which were consistent with the experimental results. The sequential procedure of numerical analysis was done. ABAQUS software was used for modelling and analysis. The RC column was modelled as 8-noded linear brick element. The mesh size selected was 15mm and the analysis was done primarily in two stages. First stage consisted of heat transfer analysis and second stage consisted of static stress analysis. 2D and 3D models were developed sequentially for validation and convergence studies. 2D section models were primarily developed for heat transfer studies. The heat transfer patterns were based on conduction flow through solid homogenous concrete media with tie as a heat transfer constraint for linking steel reinforcement. The spalling scenarios were developed for 2D models and heat transfer patterns compared for experimental and numerical models for validation. 3D column models were subsequently developed. Solid homogenous damage plastic model for concrete elements with embedded condition of plastic steel reinforcement was used for model development. Column model had a fixed base and pinned top condition. The spalling scenarios were pre-determined based on 2D heat transfer spalling models. The fire zone of the column model was analysed for heat transfer study. The sequential analysis for static load with transient restraint condition under heat induced deformations was performed for these 3D column models. Each of the 3D column model was analysed at different loading and eccentric conditions. Axial and lateral deformations were obtained and used for validation of the present experimental work. The Moment-curvature (M-K) relationships were thereafter obtained in order to co-relate confinement characteristics of RC columns during fire. The flow-chart depicting this detailed process is given in Fig. 3.

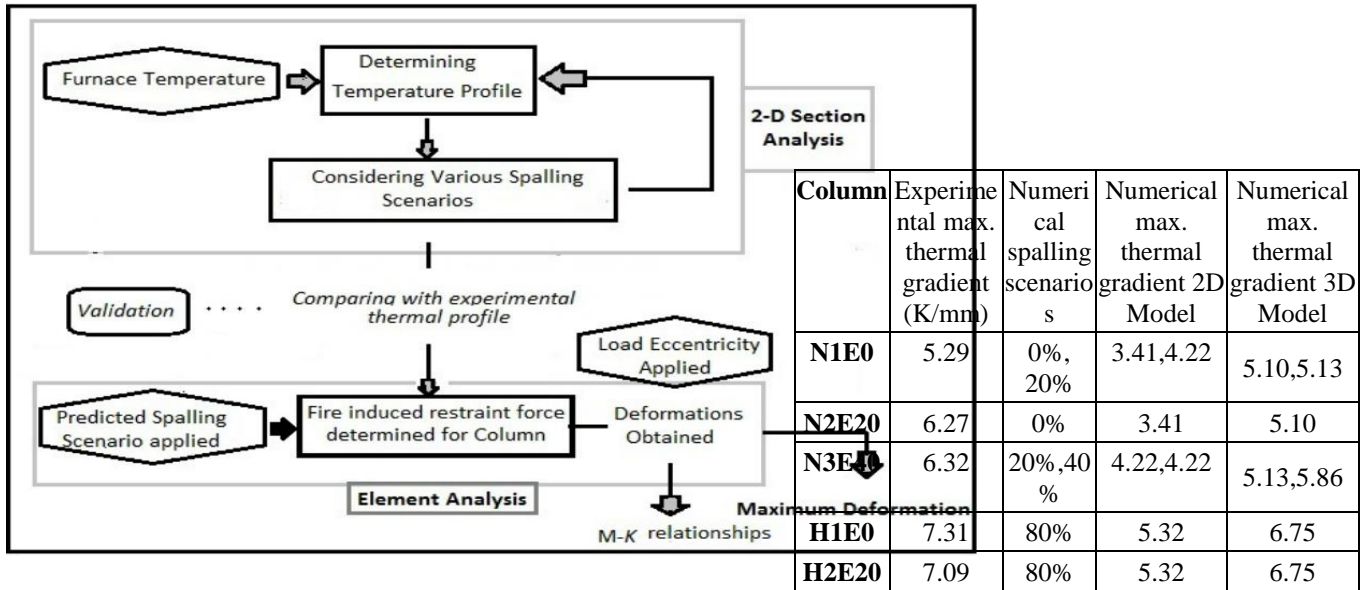


Fig. 3. Procedure for numerical modelling

4.1 Spalling scenarios

The time-temperature curves for each column show that spalling initiates 10-15 minutes into start of fire and continues upto 50-60 minutes. Thereby, a sequential progressive spalling damage was initiated from 15-30 minutes for normal strength RC columns and from 10 minutes-50 minutes for high strength RC columns. The time step of damage progression was 5 minutes. Every 3D column model started at 0% spalling damage and achieved required spalling damage scenario with damage progression analysis at every 5 minutes time step. Damage was considered to progress only along length of column with time, starting from mid-column section as observed from experiments. The reason for this behaviour is that maximum moment curvatures are at mid-section of column and moment-curvatures at other sections increase proportionately compared to mid-section of column. For 2D section models and 3D column models, the various spalling scenarios that were considered for study are 0%, 20%, 40%, 60% and 80% of the total area of the fire zone. The spalling width to depth ratios were taken as 2:1 for corner spalling and along whole width for explosive surface spalling. It was assumed that 20% and 40% spalling area scenarios were corner spalling while as 60% and 80% spalling area scenarios were whole section face spalling's. The reason for such a model was the nature of explosive spalling to be surface spalling and normal spalling to be more corner spalling [14].

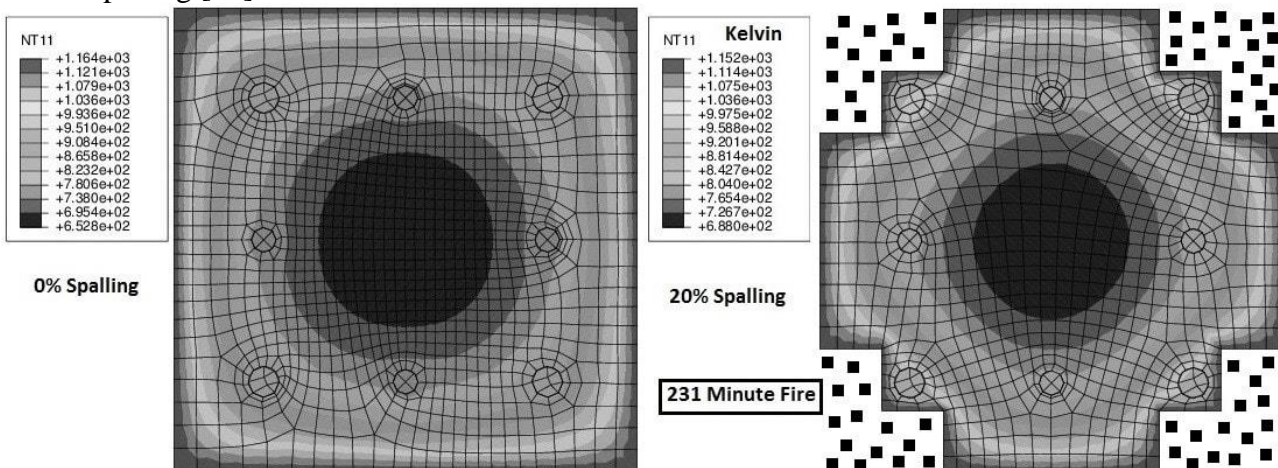


Fig. 4. 2D section model for Spalling prediction and thermal equivalency for a 231minute fire

Table. 2. Spalling Scenarios

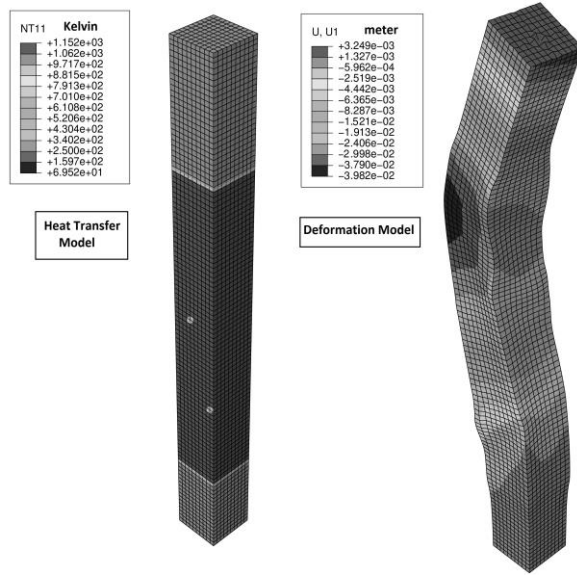


Fig. 5. Numerical 231 minute fire simulation of ‘N2E20’ RC Column

Table 3. Numerical Validation

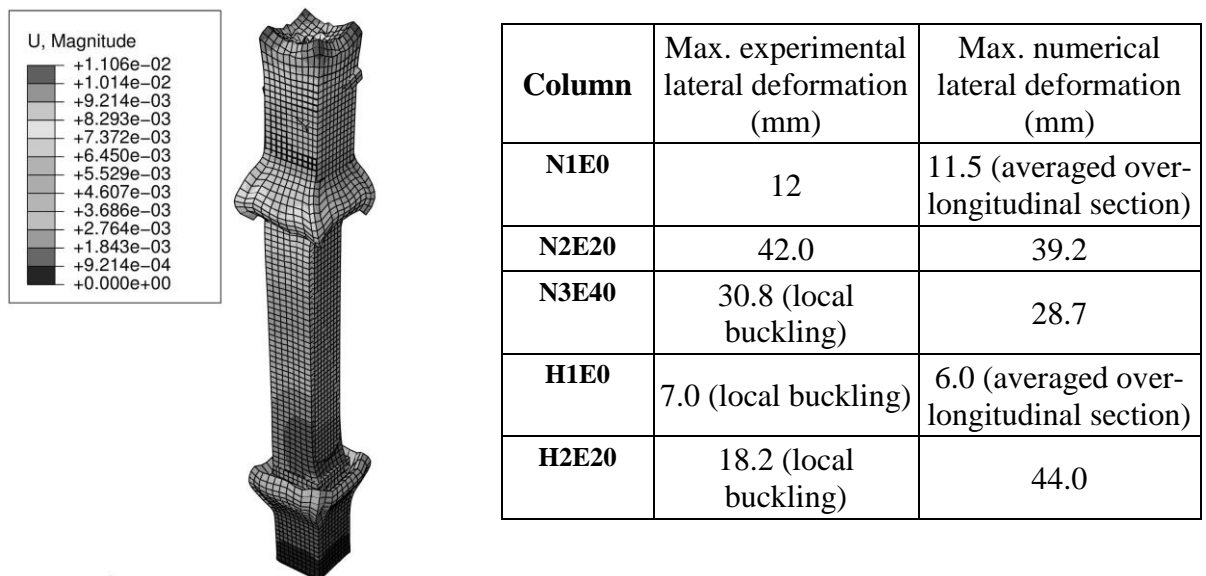


Fig. 6. Deformation and Spalling in Column Model simulating ‘H1E0’ for 69 minute fire

In case of 3D models, (for sake of simplicity) the spalling length was considered to be at mid-section of column face and proportionately on all the faces of column. The depth of spalling was fixed at 40mm for all 2D section and 3D column models. Fig. 4 illustrates the analysis for heat transfer of various spalling scenarios of 2D section models.

4.2 Deformation behaviour

The aim of studying deformations was to co-relate the predicted spalling scenarios as well as deformations in numerical models with the spalling scenarios and deformations determined experimentally. The procedure consisted of developing various numerical spalling scenarios for 3D column models. Next the deformations were compared for equivalent spalling scenarios and loading conditions as in case of experiments. The maximum deformations were determined for time step that characterises the fire resistance for RC columns tested experimentally. The comparable maximum deformations for experimental and numerical results for RC columns are given in Table

3. The spalling scenarios are as given in Table 2. It was seen that lateral deformations increase with increase in load eccentricity as in the case of columns 'N1E0 and 'N2E20' while as local buckling occurred in case of high strength concrete columns, thereby restricting lateral deformations. The variation of present numerical modelling from experimental deformation was less in case of normal strength RC columns. In case of high strength concrete columns, embedded conditions for steel reinforcement were used even after spalling had occurred. Thereafter, prediction of local buckling was not accurately co-relating with the experimental results for columns with load eccentricity. However, co-relations were perfect for all models with no local reinforcement buckling. The deformation and spalling behaviour of 3D numerical column models is given in *Fig. 5* and *Fig. 6*.

4.3 Moment-curvature relationships

Numerical models developed and validated for spalling area scenarios and deformation behaviour were used to determine the M-K relations for experimentally tested RC columns. The M-K relations are plotted in *Fig. 7* for two spacing's of transverse reinforcement, 300mm and 75mm. While as numerical models predict brittle failure for concrete in high strength concrete columns, the failure is more plastic in case of normal strength concrete columns. It was seen that with decrease in spacing of transverse reinforcement in normal and high strength concrete columns, there is an increase in curvature ductility due to confinement of bars. The increase in ductility is more in case of high strength concrete columns 'H4E35' than in case of normal strength concrete column 'N4E35' for 75mm spacing of transverse reinforcement.

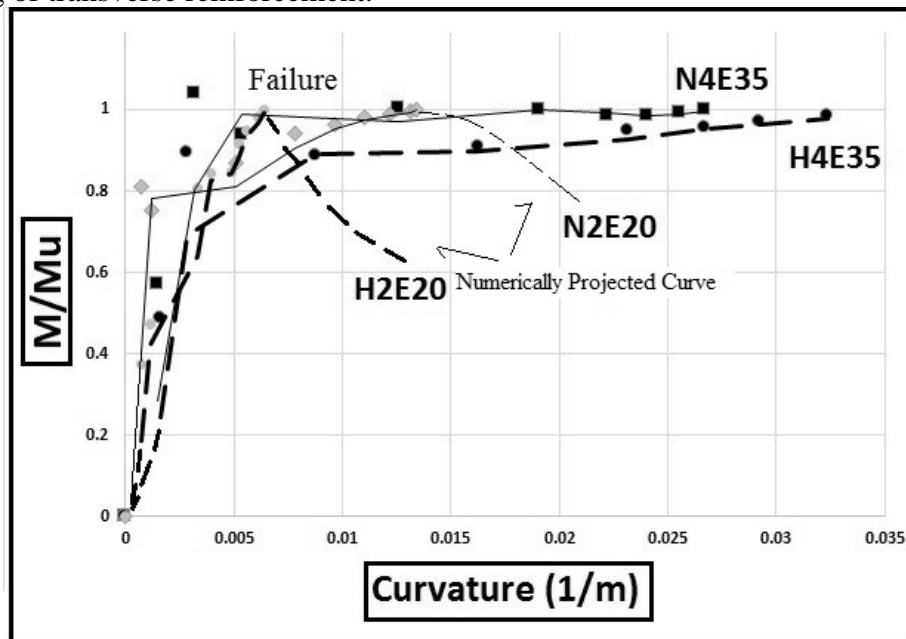


Fig. 7. Numerical Moment-Curvature relations for different RC columns under fire

5 CONCLUSIONS

Following conclusions can be drawn from this study:

1. Fire resistance of RC columns increases with decrease in spacing of transverse reinforcement. The increase in fire resistance was 53.7% for decrease in spacing from $15\phi_1$ to $7.5\phi_1$ for normal strength columns. The increase in fire resistance was 35.6% for decrease in spacing from $7.5\phi_1$ to $3.75\phi_1$ for high strength concrete columns.
2. There was no appreciable change in fire resistance for decrease in spacing of transverse reinforcement from $7.5\phi_1$ to $3.75\phi_1$ for normal strength concrete columns.
3. Fire resistance of RC columns considerably decreased for increase in load eccentricity. The decrease in fire resistance was 42% for increase in load eccentricity from 20mm to 40mm in

normal strength concrete columns. The decrease in fire resistance was 46.4% for increase in load eccentricity from 20mm to 40mm in case of high strength concrete columns.

4. Spalling considerably reduced fire resistance for all cases of increase in load eccentricity and far spacing of transverse reinforcement spacing. Spalling area decreased by 10.2% for decrease in spacing from $7.5\phi_1$ to $3.75\phi_1$. Local buckling in high strength concrete columns led to pre-mature failure. Various spalling scenarios were modelled and found to be consistent with experimental tests.
5. Curvature ductility of high strength RC columns increased by 176% for decrease in transverse reinforcement spacing from $15\phi_1$ to $3.75\phi_1$ and increase in load eccentricity from 20mm to 35mm.

REFERENCES

1. Residential Building Fire Trends (2017). *National Estimates Methodology for Building Fires and Losses*. National Fire Data Center, FEMA, Emmetsburg, MD, U.S.A.
2. Shujaat Buch, Umesh Kumar Sharma (2017). Fire resistance of reinforced concrete columns-a systematic review. *Applications of Fire Engineering*, Manchester United Kingdom, September 7-8, 2017. pp 141-150
3. J.-C. Dotreppe, J.-M. Franssen, A. Bruls, R. Baus, P. Vandeveld, R.Minne, D.van Nieuwenburg, H.Lambotte. *Experimental research on the determination of the main parameters affecting the behaviour of reinforced concrete columns under fire conditions*. Magazine of Concrete Research, 179. pp 117-127.
<https://doi.org/10.1680/mac.1997.49.179.117>
4. BS EN 1992-1-2 (2004). *Eurocode 2: Design of concrete structures - Part 1-2: general rules-structural fire design*. British Standards Institution, London, UK.
5. ACI 216 (2010). *Code Requirements for Determining Fire Resistance of Concrete and Masonry*. American Standards, MI, USA.
6. AS 3600 (2009). *Australian Standard-Concrete Structures*. Standards Australian Committee, Sydney, USA.
7. Venkatesh Kodur, Nikhil Raut (2011). *Response of reinforced concrete columns under fire induced biaxial bending*. Structural Journal, 108. pp 610–619
8. Szymon Serega (2015). *Effect of transverse reinforcement spacing on fire resistance of high strength concrete columns*. Fire Safety Journal, 71. pp 150–161
9. Asif Hussain Shah, Umesh Sharma (2017). *Fire resistance and spalling performance of confined concrete columns*. Construction and Building Materials, 156. pp 161 – 174
10. P Doherty, F. Ali, A. Nadjai, S. Choi (2012). *Explosive Spalling of Concrete Columns with Steel and Polypropylene Fibres Subjected To Severe Fire*. Journal of Structural Fire Engineering, 3. pp 95-104
<https://doi.org/10.1260/2040-2317.3.1.95>
11. Faris Ali, Ali Nadjai, S Choi (2010). *Numerical and experimental investigation of the behaviour of high strength concrete columns in fire*. Engineering Structures, 32. pp 1236-1243
12. ACI 318 (2014). *Building code requirements for structural concrete and commentary*. American Standards, MI, USA.
13. BS-476-20 (1987). *Fire test on building materials and structures-Method of determination of the fire resistance of elements of construction*. British Standard, London, UK.
14. K.D. Hertz (2003). *Limits of spalling of fire-exposed concrete*. Fire Safety Journal, 38. pp. 103-116

VERIFICATION OF A TABULATED METHOD OF EUROCODE FOR CONCRETE COLUMNS USING A RESPONSE SURFACE AND ADVANCED METHODS

Marcus Achenbach¹, Thomas Gernay², Guido Morgenthal³

ABSTRACT

Tabulated values for the check of the fire resistance of concrete columns are widely used by professional engineers because of their ease of use. Especially the tables given in Annex C of Eurocode 2 cover a wide range of applications for buildings. Yet the accuracy of the predicted fire resistance in the latter tables has been recently questioned. Hence there is a need for verification of these tables. In this paper, a verification is carried out on ten reinforced concrete columns designed using Annex C. The columns are recalculated using different methods: an empirical equation given in Eurocode 2; a linear response surface interpolating between published results of the recalculation of laboratory tests; and a non-linear finite element analysis with the software SAFIR. The results indicate that the fire rating predicted by Annex C exceeds the fire resistance predicted by other methods in many cases; thus the use of Annex C tabulated data might be unconservative.

Keywords: Concrete, Columns, Fire, Tabulated values, Response surface, Advanced method

1 INTRODUCTION

Fire resistance design of concrete columns using tabulated values is a simple and well accepted method for civil engineers in design offices. In EN 1992-1-2 [1] two methods for the application of tabulated values are given in section 5.3 for braced structures. Method A, which is based on the corresponding empirical *Eq. (5.7)*, and method B, which is based on tabulated values for minimum concrete cover and dimensions as a function of the desired fire rating R , the load level n , the mechanical reinforcement ratio ω , the eccentricity e_0 and the slenderness λ_{fi} .

Method A is well accepted and backed by many publications, whereas some doubts have been raised concerning method B [2]. Therefore, there is a need for the cross check and validation of method B, especially the tables given in Annex C. This validation is carried out using *Eq. (5.7)* from method A of EN 1992-1-2; the Advanced Method using FEM and different constitutive material laws; and a response surface, which allows the interpolation between published results.

2 APPLIED METHODS

2.1 Tabulated values from EN 1992-1-2, method B

In method B, the fire resistance R30, R60 ... R240 of braced concrete columns is given as a function of the slenderness under fire condition λ_{fi} , the eccentricity e_0 , the load level n and the mechanical reinforcement ratio ω .

¹ Dipl.-Ing. Bereich Prüfstatik, LGA KdöR, Nürnberg, Germany.

e-mail: marcus.achenbach@lga.de

² Assistant Professor. Department of Civil Engineering, Johns Hopkins University, Baltimore, USA.

e-mail: tgernay@jhu.edu

³ Full Professor. Department of Civil Engineering, Bauhaus University, Weimar, Germany.

e-mail: guido.morgenthal@uni-weimar.de

The slenderness under fire condition is given by

$$\lambda_{fi} = l_{0,fi} / i \quad (1)$$

where $l_{0,fi}$ is the buckling length under fire condition and i is the minimum radius of inertia. The eccentricity

$$e_0 = M_{0,fi} / N_{fi} \quad (2)$$

is calculated using the first order moments $M_{0,fi}$ and the axial load N_{fi} . The load level at ambient temperature is defined by

$$n = |N_{fi}| / (0.7(A_c f_{cd} + A_s f_{yd})) \quad (3)$$

with $A_c f_{cd} + A_s f_{yd}$ = axial resistance of the concrete cross section at ambient temperature. The mechanical reinforcement ratio is:

$$\omega = A_s f_{yd} / A_c f_{cd} \quad (4)$$

Tabulated values for a slenderness $\lambda_{fi} \leq 30$ are given in Table 5.2b of EN 1992-1-2, where values up to $\lambda_{fi} \leq 80$ are provided in Annex C. Hence, method B covers a wide range of applications for rectangular columns in braced buildings and is easy to use for structural engineers because of the limited number of input parameters.

2.2 Tabulated values from EN 1992-1-2, method A

Method A is based on the empirical Eq. (5.7) of EN 1992-1-2

$$R = 120((R_{\eta fi} + R_a + R_l + R_b + R_n)/120)^{1.8} \quad (5)$$

where $R_{\eta fi}$ is a function of the reinforcement ratio ω and the degree of utilisation $\mu_{fi} = N_{fi} / N_{Rd}$. Second order effects are included in the calculation of the design resistance N_{Rd} of the column at room temperature. Therefore a “cold” design of the considered column is necessary for the calculation of the degree of utilisation. The parameter R_a describes the influence of the axis distance of the longitudinal reinforcement whereas R_l represents the buckling length under fire condition. The effect of the width of the cross section is covered by R_b . R_n includes the influence of the layout of the reinforcement on the fire resistance. Tabulated values obtained from Eq. (5.7) of Eurocode are given for a buckling length $l_{0,fi} \leq 3$ m in Table 5.2a of EN 1992-1-2.

2.3 Advanced Methods

The finite element software SAFIR [3] is used for the calculation of the time to failure with advanced methods. The thermal analysis of the considered columns is carried out using the material properties of EN 1992-1-2. The temperature dependent behaviour of reinforcing steel is considered by the stress-strain curves given in EN 1992-1-2. For the simulation of the behaviour of concrete at elevated temperatures, two different material models are implemented: the model from EN 1992-1-2 and the ETC model [4]. The EN 1992-1-2 model is referred as “SAFIR Eurocode” in this paper, whereas the ETC model is referred as “SAFIR ETC”. The considered models differ in the treatment of transient creep strains: in EN 1992-1-2 these strains are included implicitly in the given stress-strain curves, whereas in ETC they are treated explicitly through a separate term. The more sophisticated formulation of ETC allows the calculation of unloading paths, heating-cooling sequences, and restraint forces in case of hindered thermal expansions, but requires the calculation of strain-temperature history for each fibre of the considered cross section [4].

2.4 Response Surface

Achenbach [5] has performed the recalculation of 56 laboratory tests on concrete columns subjected to a standard fire using the advanced method given in EN 1992-1-2. The data base consisted of 51

columns in a pin ended condition (Euler case 2 [6]) and 5 columns fixed at the bottom (Euler case 3). Only square and rectangular columns with a symmetric layout of reinforcement were selected. The measured concrete strength $\beta_{w,t}$ at the age of test using 200 mm cubes and the yield strength f_y were available for every specimen. For the recalculation of these tests, the concrete strength $f_c = 0.77\beta_{w,t}$ was considered according to Schnell and Loch [7]. The time to failure t_f was calculated for each column using the thermal and mechanical properties of EN 1992-1-2.

These results are used as data base for interpolation using a response surface method. The documented input parameters as indicated in *Fig. 1* are: width b , height h , number of rebars n , total area of reinforcement A_s , axis distance a , concrete strength f_c , yield strength of reinforcement f_y , buckling length l_{col} , load eccentricity e_0 and acting load N_{fi} . In order to consider the utilisation of the cross section, the ultimate load according to Rankine [6] and the bending resistance are evaluated. With the nomenclature given in *Fig. 1* the axial resistance is

$$N_R = bhf_c + A_s f_y \quad (6)$$

and the buckling load of the concrete cross section is determined by

$$N_{Ec} = \pi^2 E_c b h^3 / (12 l_{col}^2) \quad (7)$$

with $E_c = 22000 ((f_{ck} [\text{MPa}] + 8) / 10)^{0.3}$. The buckling load of the reinforcement is

$$N_{Es} = \pi^2 (h/2 - a)^2 A_s E_s / l_{col}^2 \quad (8)$$

and the buckling load of the reinforced concrete cross section is

$$N_E = N_{Ec} + N_{Es}. \quad (9)$$

The ultimate load according to Rankine can be estimated by:

$$1/N_U = 1/N_R + 1/N_E. \quad (10)$$

The estimated bending resistance is given by

$$M_R = f_y A_s (h - 2a) / 2 \quad (11)$$

and allows the calculation of the utilization U according to

$$U = |N_{fi}| / N_U + |e_0 N_{fi}| / M_R. \quad (12)$$

For the interpolation of the fire resistance, the input parameters b , n , a , l_{col} and U are considered. This interpolation is carried out using a linear response surface [8]: the "exact" fire resistance t_f by recalculation is approximated by:

$$\hat{t}_f(b, n, a, l_{col}, U) = c_0 + c_1 b + c_2 n + \dots + c_5 U. \quad (13)$$

The coefficients c_0, c_1, \dots, c_5 are obtained by multiple linear regression [9]. The quality of this approximation can be judged by the coefficient of determination:

$$COD = 1 - \sum_{i=1}^N (t_{f,i} - \hat{t}_{f,i})^2 / \sum_{i=1}^N (t_{f,i} - \bar{t}_f)^2 \quad (14)$$

where \bar{t}_f is the mean value of the fire resistance. A COD of one indicates a perfect fit between the approximated time failure \hat{t}_f and the exact time t_f .

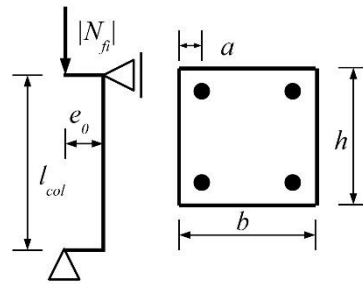


Fig. 1. Structural system of columns

2.5 Considered Examples from Annex C (Method B)

The examples are chosen in order to stay within the boundaries of well documented laboratory tests. Hence a slenderness $\lambda \approx 60$ and square cross sections with $b = h = 20$ cm and 30 cm are considered as governing input parameters. A set of 10 columns is selected from Annex C of EN 1992-1-2 and the corresponding parameters are given in *Table 1* with the nomenclature of *Fig. 1*. A concrete strength $f_{ck} = 25$ MPa, a yield strength $f_{yk} = 500$ MPa are assumed and the design values at room temperature are taken as $f_{cd} = 0.85 f_{ck} / 1.5$ and $f_{yd} = f_{yk} / 1.15$. The corresponding total area of reinforcement $A_{s,tot}$ can be derived by *Eq. (4)*. The acting axial force N_{fi} is given by *Eq. (3)*.

The design of the columns at room temperature is a necessary step for application of method A, as described in Section 2.2. It is assumed, that $Q/G = 0.5$ and $\psi_2 = 0.5$ leading to $N_{fi} = G_k + 0.5 Q_k = G_k + 0.25 G_k$. The characteristic loads G_k and Q_k can be derived easily. The design at room temperature is performed using the simplified method based on nominal stiffness. The total area of reinforcement is increased where necessary and considered in the applied methods for validation given in Sections 2.2 to 2.4.

The thermal conductivity λ_c with its lower limit, a moisture content $u = 1.5$ %, hot rolled reinforcement and siliceous aggregates are considered for the SAFIR thermal analysis. The characteristic strengths ($f_{ck} = 25$ MPa, $f_{yk} = 500$ MPa) are used for the SAFIR mechanical analysis. A mean concrete strength $f_{cm} = 8$ MPa + f_{ck} is considered as input parameter for the response surface, because the data base is valid for measured mean values and not the fractile f_{ck} .

 Table 1. Input parameters of considered columns (¹concrete cover controls, ²cold design decisive)

#	R [min]	n [-]	ω [-]	$b=h$ [cm]	a [cm]	l_{col} [cm]	e_0 [cm]	$ N_{fi} $ [kN]	$A_{s,tot}$ [cm ²]
1	30	0.5	0.1	20	2.5 ¹	350	1.0	216	1.3
2	60	0.5	0.1	30	2.5 ¹	520	1.0	485	2.9
3	90	0.3	0.1	30	2.5 ¹	520	1.0	291	2.9
4	30	0.7	0.5	20	3.0	350	1.0	412	9.9 ²
5	60	0.3	0.5	20	3.0	350	1.0	176	6.4
6	90	0.5	0.5	30	4.5	520	1.0	662	14.5
7	30	0.3	0.1	30	2.5 ¹	520	7.5	291	4.1 ²
8	90	0.15	0.1	30	5.0	520	7.5	146	2.9
9	30	0.5	0.5	30	2.5 ¹	520	7.5	662	22.6 ²
10	90	0.15	0.5	20	5.0	350	5.0	88	6.4

3 RESULTS

The design of the columns at room temperature reveals that the minimum concrete cover is not met for every column. The minimum axis distance $a = 2.5$ cm prescribed by Annex C for the examples indicated by the footmark 1 in *Table 1* would not be sufficient to guarantee the nominal concrete cover c_{nom} at room temperature. Nevertheless here, the axis distance of Annex C has been considered in the recalculations, because the objective is to assess the accuracy of Annex C. It is acknowledged that, for the examples marked by the footmark 1, the columns would not be built in practice with such a reduced cover since it would not comply with ambient design requirements.

Also, cold design can control over the needs of fire resistance regarding reinforcement area. In *Table 1*, $A_{s,tot}$ is the maximum between the reinforcement required by cold design and by Annex C. For columns 4, 7 and 9 the required area of reinforcement at ambient temperature exceeds the area of reinforcement for the desired fire resistance. Thus for these columns, the recalculations are done considering the required area of reinforcement at ambient temperature.

Fig. 2 plots the results of the recalculations. The fire rating in accordance to Annex C (*Table 1*) is displayed on the vertical axis. The fire resistance calculated using the other models is shown on the horizontal axis: method A of EN 1992-1-2 (Eq. 5.7); linear response surface (RS lin.); advanced analysis with the Eurocode stress-strain curves (SAFIR EC2) and with the ETC model (SAFIR ETC). Results below the diagonal are considered to be conservative and safe, because the fire rating of Annex C is exceeded by the recalculation method. The number of unsafe results according to each recalculation method is given in *Table 2*. The empirical Eq. (5.7) of EN 1992-1-2 leads to 3 columns for which the fire rating of Annex C is not met. This method shows a very significant scatter for fire ratings of R90. Using the linear response surface to predict the fire resistance leads to 7 unsafe results. There is a big scatter of results for all fire resistance ratings, probably due to the moderate quality of the response surface. The calculated COD according to Eq. (14) is 0.65, which indicates differences between model and approximation. For both advanced methods, the scatter of results is increasing with the fire resistance, as indicated in *Fig. 2*. The application of SAFIR with the Eurocode material model detects 9 unsafe results, whereas 7 results are detected with the ETC model.

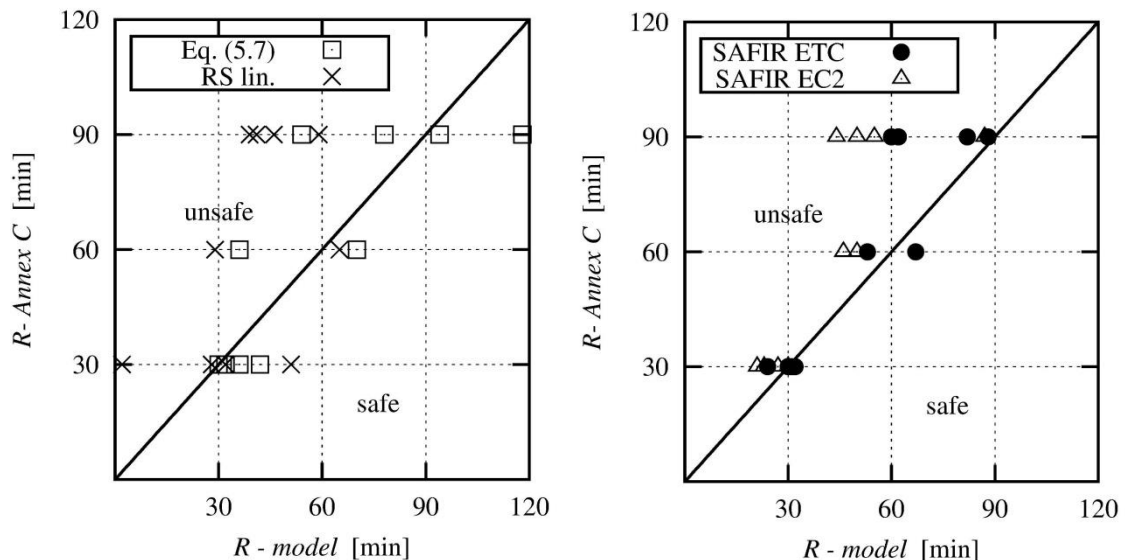


Fig. 2. Vertical axis: expected fire resistance according to EN 1992-1-2, Annex C – horizontal axis: calculated fire resistance using different verification methods: Method A of EN 1992-1-2 (Eq. 5.7); a linear response surface (RS lin.), SAFIR with material models given in EN 1992-1-2 (SAFIR EC2) and with ETC (SAFIR ETC).

Table 2. Number n_{unsafe} of columns with fire rating other model < fire rating Annex C, over a total of 10 recalculated columns

model	n_{unsafe}
Eq. (5.7)	3
linear response surface	7
SAFIR Eurocode	9
SAFIR ETC	6

4 CONCLUSIONS

For concrete columns, tabulated values for minimum dimensions and axis distances of the reinforcement are an easy method for the check of the fire resistance. However analyses performed in this paper to recalculate the fire resistance of columns designed with tabulated data of Annex C of Eurocode EN1992-1-2 raise two significant concerns:

- Design values obtained from Annex C for axis distances and minimum reinforcement ratio are not always compatible with ambient design provisions. In particular for a fire rating R30, a revision of the tabulated values regarding practical applications seems to be reasonable.
- The different methods applied for recalculation of the columns fire resistance all predicted shorter fire resistance than the tabulated data of Annex C in several cases. This suggests that the use of Annex C is not consistently on the safe side.

REFERENCES

1. EN 1992-1-2 (2004). *Eurocode 2: Design of concrete structures – Part 1-2: General rules – Structural fire design*.
2. D. Hosser, E. Richter (2006). *Überführung von EN 1992-1-2 in EN-Norm und Bestimmung der national festzulegenden Parameter (NDP) im Nationalen Anhang zu EN 1992-1-2*. Schlussbericht, TU Braunschweig.
3. J.-M. Franssen, T. Gernay (2017). *Modeling structures in fire with SAFIR®: Theoretical background and capabilities*. Journal of Structural Fire Engineering, 8(3). pp 300-323. doi: 10.1108/JSFE-07-2016-0010.
4. T. Gernay, J.-M. Franssen (2012). *A formulation of the Eurocode 2 concrete model at elevated temperature that includes an explicit term for transient creep*. Fire Safety Journal, 51. pp 1-9.
5. M. Achenbach (2018). *Weiterentwicklung der Zonenmethode für den Nachweis der Feuerwiderstandsdauer von rechteckigen Stahlbetondruckgliedern*. Ph.D. thesis, Bauhaus University Weimar. – Submitted.
6. C. Petersen (1982). *Statik und Stabilität der Baukonstruktionen*. Vieweg, Wiesbaden.
7. J. Schnell, M. Loch (2009). *Umrechnung historischer Baustoffkennwerte auf charakteristische Werte*. Der Prüferingenieur, 34, pp. 50-61.
8. C. Bucher (2009). *Computational Analysis of Randomness in Structural Mechanics*. CRC Press, Leiden.
9. H. Rinne (2008). *Taschenbuch der Statistik*. Harri Deutsch, Frankfurt.

NUMERICAL MODEL FOR FIRE RESISTANCE EVALUATION OF STEEL REINFORCED POLYMER STRENGTHENED CONCRETE BEAMS

Pratik Bhatt¹, Venkatesh Kodur², Rami Haweeleh³, Nasser Al-Nuaimi⁴, Jamal Abdalla⁵

ABSTRACT

A macroscopic finite element based numerical approach is applied to trace the fire response of steel reinforced polymer (SRP) strengthened reinforced concrete (RC) beams from pre-fire exposure stage to collapse under fire conditions. The model utilizes a member level approach wherein, temperature dependent sectional moment curvature ($M-\kappa$) relations are utilized to trace the response of a fire exposed SRP-strengthened RC beam. In the analysis high-temperature material properties of constituent materials as well as temperature induced degradation of bond between concrete and SRP is accounted for. A case study illustrating the application of the model for evaluating comparative fire performance of fiber reinforced polymer (FRP), and SRP-strengthened RC beams is presented. Results from the analysis indicate that fire performance of a SRP-strengthened beam is similar to that of an FRP-strengthened RC beam.

Keywords: Fiber reinforced polymer, FRP, fire resistance, EBR, reinforced concrete beams, steel reinforced polymer, SRP

1. INTRODUCTION

In recent years there is a growing demand for strengthening and rehabilitation of concrete structures for enhancing the load carrying capacity or for retrofitting of damaged structures. Till 1990's, flexural strengthening of reinforced concrete (RC) beams used to be carried out by attaching steel plates to the tension face of the beam. However, in recent years, steel plates have given way to fiber reinforced polymer (FRP) strips, typically made of carbon fiber reinforced polymer (CFRP), wherein, CFRP is attached to the bottom face for flexural strengthening or to the sides of the beam for shear strengthening. FRP offers several advantages including, corrosion resistance and ease of application, over steel plates. However, addition of FRP has few disadvantages such as, brittleness, poor bond, and lower fire resistance properties, as well as higher costs.

To overcome some of these issues, a new composite material, consisting of unidirectional steel fabric/reinforcing mesh impregnated with polymeric resins, and referred to as steel reinforced polymers (SRP), have been introduced for strengthening of RC structures. The reinforcing mesh is made of Ultra High Tensile Strength Steel (UHTSS) cords, which are assembled parallel to each other and fixed to a net of plastic or glass fibers, thereby forming a unidirectional fabric. The cords in the

1 PhD Student. Department of Civil and Environmental Engineering, Michigan State University, East Lansing, MI, USA.

e-mail: bhattpr1@egr.msu.edu

2 University Distinguished Professor and Chairperson. Department of Civil and Environmental Engineering, Michigan State University, East Lansing, MI, USA.

e-mail: kodur@egr.msu.edu

3 Professor. Department of Civil Engineering, American University of Sharjah, Sharjah, UAE.

e-mail: rhaweeleh@aus.edu

4 Assistant Professor and Director of the Center of Advanced Material (CAM). Department of Civil and Architectural Engineering, Qatar University, Doha, Qatar.

e-mail: anasser@qu.edu.qa

5 Professor. Department of Civil Engineering, American University of Sharjah, Sharjah, UAE.

e-mail: jabdalla@aus.edu

fabric/reinforcing mesh are made by twisting 5-12 UHTSS micro-wires, having a cross-section area of 0.04-0.12 mm². The cords formed from the UHTSS microwires are identical to the cords used for reinforcement of automotive tires and have a tensile strength ranging from 2800-3200 MPa and elastic modulus ranging from 180-210 GPa. Depending on the area of each wire, number of wires in the cord, and the cord spacing, the equivalent thickness of the steel fabric ranges between 0.0075 mm and 0.439 mm and the surface mass density varies from 600-3300 g/m² (GSM).

Use of SRP sheets as a structural strengthening material for RC beams was first proposed by Barton et al. [1]. Since then a number of studies have been carried out on performance of SRP-strengthened RC beams at room temperature. These studies indicate that the strength properties of SRP, as well as capacity improvement provided by SRP-strengthening system, is analogous or in certain cases even better than CFRP. Further, these studies indicate that SRP-strengthening system has better bond performance, higher deformation capability, as well as higher compatibility with existing structural member, compared to CFRP strengthening system [2]. Additionally, design equations developed for FRP-strengthened members can be extended to SRP-strengthened members for evaluating enhanced capacity of the member. Moreover, installation procedure of SRP to concrete beam is similar to the procedure used for applying FRP strips/sheets on beam. Like FRPs, SRP can be externally bonded to concrete surface via wet lay-up using epoxy or other polymeric resins. Thus, use of SRP-strengthening system can provide a viable, cost-effective alternative to CFRP strengthening system for structural members in indoor applications.

When used in buildings, structural members are required to satisfy fire resistance ratings as prescribed in building codes. Fire performance of FRP-strengthened RC beams has been extensively studied both experimentally and numerically [3, 4, 5, 6, 7]. To enhance fire resistance of FRP-strengthened beams, researchers have recommended adding external fire insulation on the strengthened beam. However, there are no studies in the literature, on fire performance of SRP-strengthened RC beams. To address some of these knowledge gaps, experimental and numerical studies for evaluating fire performance of SRP-strengthened RC beams is currently in progress at Michigan State University. As a part of this research, a macroscopic finite element based approach is being applied to evaluate fire performance of SRP-strengthened RC beams and the development of this numerical model is presented in this paper. In addition, a comparison is made between fire performance of an FRP and an SRP-strengthened RC beam.

2. NUMERICAL MODEL

Kodur and Ahmed [5] proposed a macroscopic finite element based approach for evaluating fire response of FRP-strengthened RC beams. The model accounts for temperature induced degradation of material properties including bond, and different failure limit states in tracing fire response of FRP-strengthened RC beam over the entire range of loading till collapse of the beam. As part of current study, this numerical model is extended to trace the fire response of SRP-strengthened RC beams. The updated model utilizes a member level approach wherein, temperature dependent sectional moment curvature ($M-\kappa$) relations are utilized to trace the response of an SRP-strengthened RC beam under combined effects of fire exposure and structural loading. The detailed steps involved in the analysis are illustrated through a flowchart shown in *Fig. 1.* and briefly described in following sections.

2.1. Discretization of beam

An SRP-strengthened RC beam typically comprises of a RC beam with SRP-strengthening system applied at the bottom surface and with optional fire insulation provided at the bottom and two side surfaces. Fire resistance analysis starts by discretizing the given beam into 20-30 segments along its length [as shown in *Fig. 2(c)*], and discretizing the cross-section of each segment into a mesh of rectangular elements [as shown in *Fig. 2(d)*]. The cross-section at the middle of each segment is assumed to represent the overall behavior of the segment. As insulation and SRP layers are in close proximity of the fire source, a finer mesh size (about 1-2 mm in both width and depth) is adopted for

discretizing the insulation and SRP, to achieve better accuracy in numerical analysis. Whereas, for concrete a coarser mesh size of (5-10 mm in width and depth) is adopted.

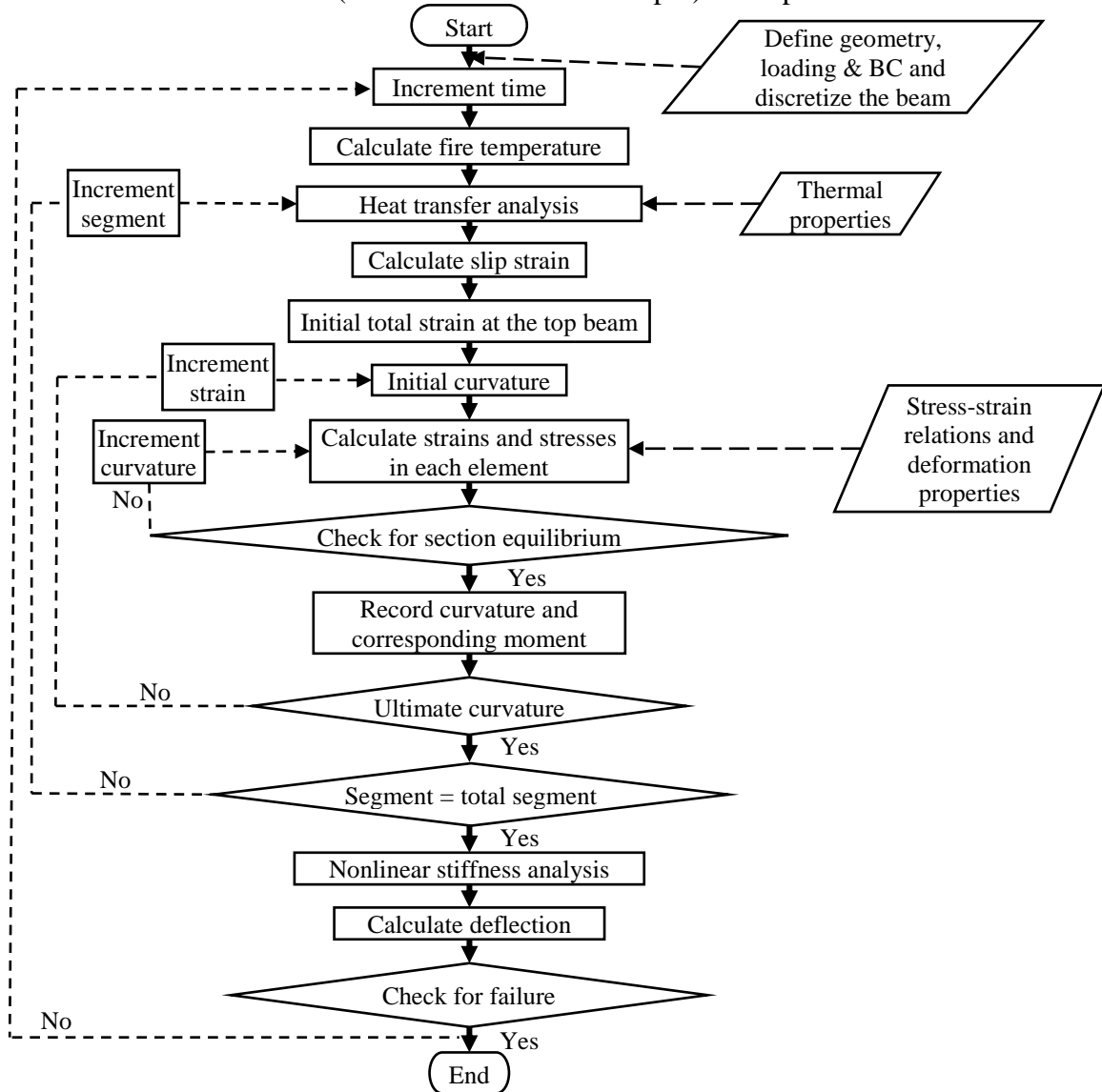


Fig. 1. Flowchart illustrating numerical procedure for fire resistance evaluation of an SRP-strengthened RC beam

2.2. Numerical Procedure

Fire resistance of an SRP-strengthened RC beam is evaluated through a sequential thermo-mechanical analysis in various time increments. Following the discretization of the beam, fire is applied on the bottom and two sides of the beam, through time-temperature relation, as per standard fire curve or any given design fire scenario. In the analysis, the fire exposure time is incremented in smaller time steps of 30 seconds each. At each time step, a thermal analysis, followed by structural analysis, is carried out.

In thermal analysis, temperature from fire is computed using the specified time-temperature relations. Following this, a heat transfer analysis is carried out to evaluate the temperature distribution within the cross-section of the segment. The heat transfer analysis takes into account the high-temperature thermal properties of constituent materials. In the analysis, temperature distribution in the cross-section is assumed to be uniform along the entire length of the segment, and therefore, the calculations are carried out for a unit length of the segment. Further, the temperature at the center of the element is computed by taking the mean of temperatures at the nodes of rectangular elements, which is then provided as an input to the structural analysis.

The structural analysis starts by computing strains, at each segment, resulting from relative slip between SRP and concrete, due to degradation of the interfacial bond. Following this, the $M-\kappa$ relationships for each segment are generated taking into account temperature dependent degradation in mechanical properties of constituent materials. These $M-\kappa$ relations for each segment are generated through an iterative procedure, wherein the curvature corresponding to the strain in the topmost fiber of concrete is iterated until force equilibrium and strain compatibility conditions in each segment are satisfied, within a specified numerical (convergence) tolerance. The maximum value of the moment in the $M-\kappa$ relations, determines the moment capacity of the beam. Following the generation of $M-\kappa$ relations for each segment, the secant stiffness matrix of each segment is evaluated depending on the load level reached in the segment. These secant stiffness matrices of each segment are then utilized in a stiffness analysis, to evaluate structural response of the beam.

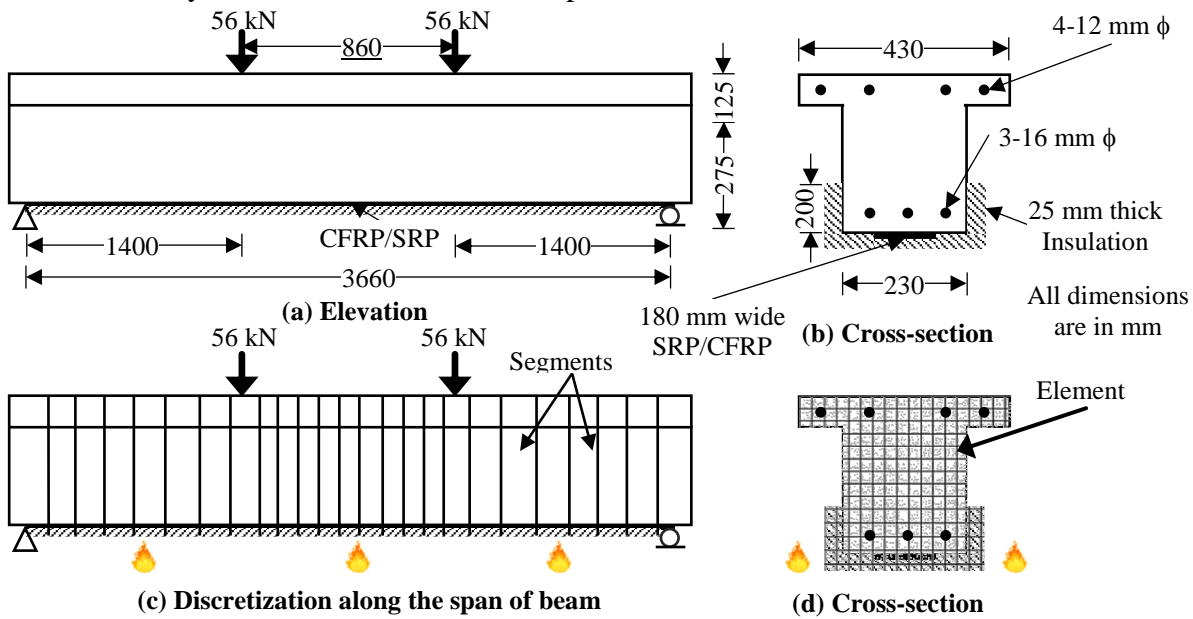


Fig 2. Typical beam layout and discretization of beam into segments and elements

2.3. Material Properties

Evaluation of fire performance of SRP and FRP-strengthened RC beams essentially requires temperature dependent thermal and mechanical properties of the constituent materials. For concrete and reinforcing steel, variation of thermal conductivity and specific heat with temperature, as well as the degradation in strength and elastic modulus along with the stress-strain response at elevated temperatures are incorporated in the model using the relations specified in ASCE Manual [8] and Eurocode 2 [9]. Further, temperature dependent values of coefficient of thermal expansion of concrete and reinforcing steel rebars, as specified in Eurocode 2 [9], are also incorporated in the model.

Since the cross-sectional area of SRP (or FRP) is very small, compared to the overall concrete area, its effect on temperature rise in the beam is negligible. Therefore, thermal properties of SRP and FRP are not specifically considered in the model. In case of FRP, degradation of strength and elastic modulus with temperature is defined using the semi-empirical relationships proposed by Bisby et al. [10]. The stress-strain relations for FRP are considered as linear elastic at both ambient and elevated temperatures and are computed using the reduction factors for strength and stiffness. Further, since the fibers in FRP are considered to be oriented along the longitudinal axis of the beam and the thermal expansion coefficient in fiber direction is very small ($-0.09 \times 10^{-6}/^{\circ}\text{C}$), the thermal strain in FRP is assumed to be negligible.

The SRP-strengthening system consists of steel fabric mesh impregnated with polymeric resin. The steel fabric mesh consists of cords of UHTSS microwires which are 6 to 7 times stronger than reinforcing steel rebars. Few studies reporting the tensile properties of SRP at ambient temperature, indicate that the tensile response of SRP at room temperature is linear elastic up to 60-70% of peak

stress, followed by a non-linear behaviour with a slight reduction in stiffness. The non-linear pre-peak behaviour is due to inherent ductility of steel cords and twisting of micro-wires. These studies further indicate that the tensile behaviour of SRP in terms of maximum stress, ultimate strain, and stress-strain response is mainly governed by the steel fabric mesh, whereas, the contribution of polymer resin is negligible.

Currently, no information is available regarding the temperature dependent thermal and mechanical properties of SRP. Therefore, for the purpose of this paper, strength and stiffness reduction factors for SRP are assumed to lie between strength and stiffness reduction factors of steel rebars and FRP, as shown in *Fig. 3 (a) and (b)*. These reduction factors are computed as the sum of 70% reduction factors of steel rebar and 30% reduction factor of FRP. The higher weight is assigned to the reduction factor of steel because the behaviour of SRP is governed by steel fabric. Although, tensile stress-strain response of SRP at room temperature consist a non-linear branch, for the purpose of analysis in this paper, the temperature dependent stress-strain relations of SRP are assumed to be linear elastic. For fire insulation, the high-temperature thermal properties are incorporated in the numerical model based on thermal properties generated through material property tests. In the numerical study presented in this paper, Tyfo ® AFP insulation is used for which properties reported by Kodur and Shakya [11] is used.

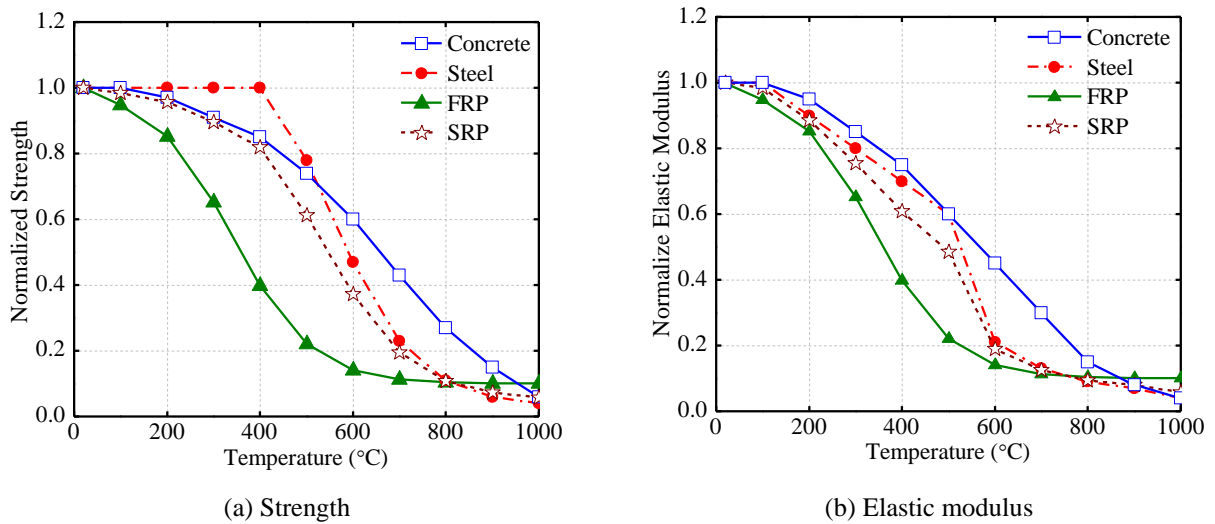


Fig. 3. Normalized variation of strength and elastic modulus of concrete, steel, FRP, and SRP with temperature (a) strength (b) elastic modulus

Like FRP, SRP-strengthening system is applied to the concrete surface using polymer-based bonding adhesive which provides a load path for transfer of stresses from concrete to SRP. Polymers such as epoxy, being thermosetting material, softens even at moderately elevated temperature (around 80°C), resulting in degradation of bond between concrete and SRP, which in turn leads to relative slip between SRP and concrete, thereby reducing the effectiveness of SRP. Hence, it is necessary to consider the effect bond degradation in evaluating fire resistance of SRP-strengthened RC beams. However, there are no studies in the literature on bond characteristics between SRP-concrete at elevated temperatures. Research on bond between SRP-concrete surface at room temperature indicate that the bond behaviour of SRP-concrete is analogous to bond behaviour of CFRP-concrete, and therefore, bond-slip laws available for CFRP-concrete can be used for evaluating the slip at SRP-concrete interface [2]. Therefore, in the current analysis, the elevated temperature bond-slip relations available for CFRP-concrete bond interface, proposed by Dai et al. [12], are used to compute the slip strain at SRP-concrete interface at elevated temperatures. These relations are based on the interfacial fracture energy and interfacial brittleness index and take into account the effect of glass transition temperature (T_g) of bonding adhesive, width of SRP and concrete, as well as tensile and compressive strength of concrete.

2.4. Failure Criteria

At each time step, the numerical model generates various output parameters such as cross-sectional temperatures, stresses and strains in rebars, concrete, and SRP, mid-span deflection, and moment capacity of the beam. These output parameters are compared with relevant applicable limit states to evaluate the failure of the beam. The beam is considered to have failed when one of following limit states [13] is reached:

- The moment capacity of the beam drops below the applied moment due to external loading present during fire exposure.
- Mid-span deflection exceeds $L^2/400d$, and the rate of deflection exceed $L^2/9000d$ (mm/min) limit between subsequent time steps; where, L = span length of the beam (mm), and d = effective depth of the beam (mm).

The time at which any of the applicable failure limit state is exceeded, is taken as fire resistance of the beam.

3. NUMERICAL STUDIES

To illustrate the applicability of the proposed model in evaluating fire resistance of strengthened concrete beams, a concrete T-beam was selected for analysis. This beam was strengthened with one of the two types of strengthening systems, i.e., SRP and CFRP, to enhance flexural capacity by about 50%. These strengthened beams were then analyzed using the above developed macroscopic finite element model to evaluate response during fire exposure.

3.1. Geometrical Configuration and Parameters for Numerical Study

The elevation and cross-section details of the RC beam selected for the analysis of the beam is shown in *Fig. 1. (a)* and *(b)*, respectively. The beam is 3.96 m long with a clear span of 3.66 m. The flange of the beam is 430 mm wide, and 125 mm thick, and the web of the beam is 230 mm wide and 275 mm deep. The main tensile reinforcement at the bottom of the beams comprises of 3-16 mm ϕ steel rebars, whereas the compressive reinforcement at the top of the beam comprises of 4-12 mm ϕ steel rebars. The shear reinforcement in the beam consists of the 6 mm stirrups spaced at 150 mm *c/c*, whereas the transverse reinforcement in the top flange comprises of 12 mm ϕ steel rebars spaced at 150 mm *c/c*. The clear concrete cover to reinforcement is 51 mm. The room temperature ultimate capacity of this un-strengthened RC beam is computed to be 105 kNm, as per ACI 318 [14]. This beam was strengthened with a 180 mm wide SRP or CFRP sheet to increase the flexural capacity of the beam to 158 kNm, computed using ACI 440.2R [15], based on the strength properties of constituent materials summarized in *Table 1*.

For the numerical study, four configurations of above T-beam, designated as B1, B2, B3, and B4 were analyzed for relative performance comparison. Beams B1 and B3 represent case of beams strengthened with a 1 mm thick CFRP sheet. Whereas, beams B2 and B4 represent case of beam strengthened with a 0.4 mm thick SRP sheet. Beams B1 and B2 were not provided with any fire insulation, whereas beams B3 and B4 were provided with 25 mm thick Tyfo[®] AFP fire insulation at the bottom and two sides, to see the level of fire performance. The insulation on the sides was extended up to 200 mm along the depth of the web. The beams were subjected to two-point loads each of 56 kN and had simply supported end conditions [as shown in *Fig. 2 (a)*]. The fire resistance analysis was carried out for 240 minutes, wherein the two sides and bottom surface of the beam were subjected to ASTM E119 standard fire exposure.

Table 1. Details of parameters considered in the numerical study

Property/Material	Name of Beam			
	B1	B2	B3	B4
Concrete compressive strength (f'_c , MPa)	42			
Steel yield strength (f_y , MPa)	460			
Strengthening material	FRP	SRP	FRP	SRP
Width×thickness of strengthening sheet (mm)	180×1	180×0.4	180×1	180×0.4
Modulus of elasticity of SRP/FRP (E_f , GPa)	73.770	190	73.770	190
Ultimate tensile strength of SRP/FRP (f_u , MPa)	1034	2800	1034	2800
Rupture strain of SRP/FRP (ε_{su} , %)	1.4	1.5	1.4	1.5
Insulation	Un-insulated	Un-insulated	25 mm Tyfo® AFP	25 mm Tyfo® AFP
Moment due to applied loading (kNm)	78			
Deflection (δ , mm) at failure or end of analysis	128	147	59	69
Moment capacity (kNm) at failure and end of analysis	77	77	93	94
Fire resistance (minutes)	150	150	>240	>240
Failure limit state reached	Deflection	Deflection	No failure	No Failure

3.2. Results and Discussion

The above developed numerical model was applied to evaluate fire resistance of four beams. Results generated from fire resistance analysis (summarized in *Table 1*) are utilized to evaluate the comparative fire performance of beams under FRP and SRP strengthening. The thermal response of beams B1 and B3 is illustrated in *Fig. 4* by plotting the temperatures at the interface of concrete and CFRP or SRP sheet, as well as at the corner and mid-rebar as a function of fire exposure time. Since, beams B1 and B2, and beams B3 and B4, have same geometrical configuration, made of same constituent materials, and are subjected to similar thermal loading, temperature rise in beams B1 and B2 is identical, and same is the case in beams B3 and B4. Therefore, for the purpose of comparison, only temperature rise in beams B1 and B3 are plotted in *Fig. 4*. It can be seen from the figure that temperatures in the insulated beam B3 are significantly lower than the temperatures in un-insulated beam B1, throughout the fire exposure duration. The temperature at CFRP-concrete interface in beams B3 exceeds glass transition temperature T_g of epoxy, which is 82°C, after 20 minutes of fire exposure, as compared to 5 minutes in beam B1. Moreover, temperature rise in the corner rebars in both beams is slightly higher than the temperature rise in mid-rebar. This is attributed to the fact that concrete surrounding the corner rebar is heated from bottom as well as two sides (due to three side fire exposure), thereby increasing heat transmission to corner rebar. However, the mid-rebar predominantly gets heated only from the bottom surface. Further, it can be seen from the figure that the temperature in all the rebars is below the critical rebar temperature of 593°C for entire fire exposure duration, indicating no imminent thermal failure.

The structural response in all four beams (B1 to B4), as monitored through deflection and moment capacity degradation is plotted as a function of fire exposure time, in *Fig. 5 (a)* and *(b)*, respectively. It can be seen from the *Fig. 5 (a)* that the un-insulated beams B1 and B2 experience increased deflections from the start of the fire exposure time. This is attributed to the fact that sectional temperatures at the CFRP-concrete and SRP-concrete interface increase rapidly and exceed T_g of the epoxy at about 5 minutes into fire exposure. At about 30 minutes, the temperature at the interface exceeds 500°C, which leads to significant reduction in the strength and modulus of CFRP and SRP, approximately 25% and 40% of room temperature value, respectively. Although reduction in strength and modulus of SRP is less than that in CFRP, the effective stress transfer in both the beams gets reduced significantly due to temperature induced degradation in interfacial bond. As a result, beams B1 and B2 undergo deflection at an accelerated rate. With further increase in fire exposure time,

temperature in the steel rebars exceed 400°C at about 125 minutes, due to which strength and modulus of rebars start degrading. As a result, deflection in these beams increase rapidly and exceed deflection limit state, at 150 minutes, and attains failure. Similar trends are observed in moment capacity degradation of beams B1 and B2 [Fig. 5 (b)]. The moment capacity of beams B1 and B2, decreases drastically in the first 30 minutes of fire exposure due to rapid deterioration in bond, followed by a gradual decrease until 60 minutes. After 60 minutes, the strengthened beams behave as a conventional RC beam, without much contribution from FRP or SRP. As a result, the moment capacity of beams degrade gradually and drops below the applied moment level at 165 minutes, indicating attainment of strength failure.

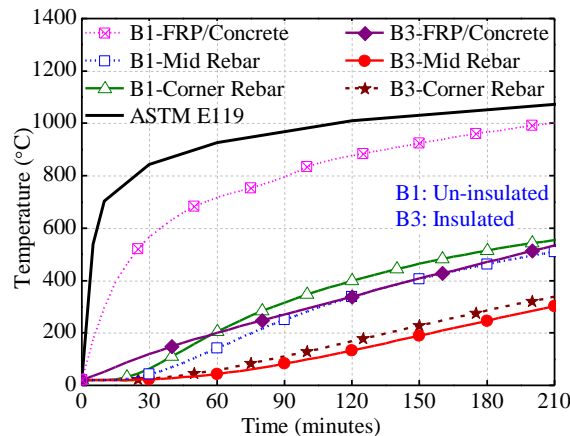


Fig. 4 Comparison of temperature progression at the concrete and CFRP/SRP interface and at corner and mid-rebar of insulated and un-insulated strengthened T-beams

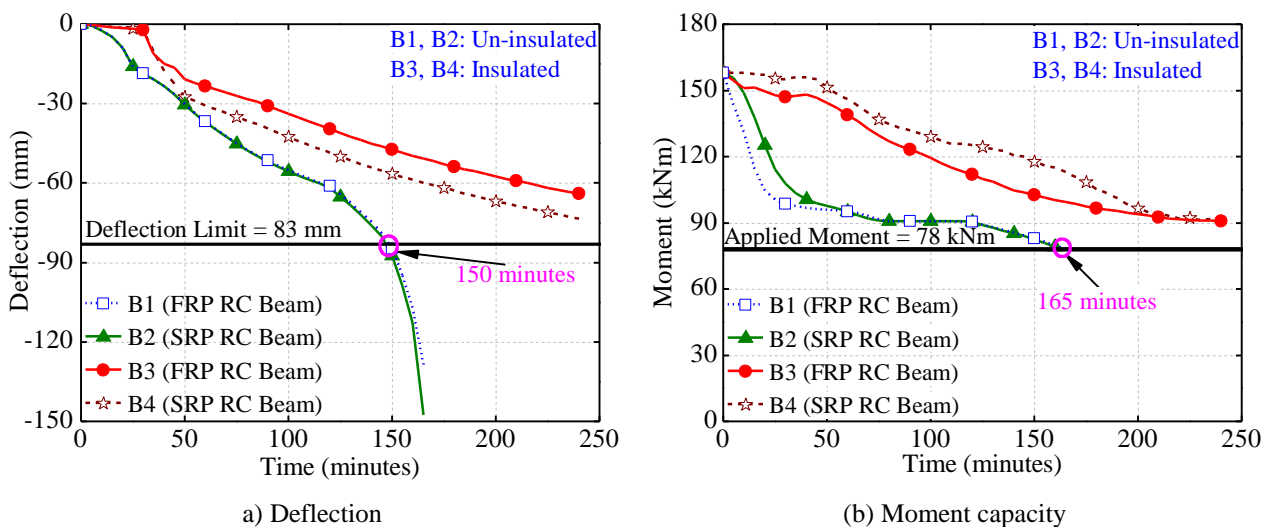


Fig. 5 Comparison of deflection and moment capacity degradation in insulated and un-insulated FRP and SRP-strengthened RC T-beams exposed to fire

The presence of fire insulation in beams B3 and B4 slows down temperature progression within the cross-section, which in turn enhances structural performance, as can be seen in Fig. 5 (a) and (b). Both beams (B3 with CFRP-strengthening and B4 with SRP-strengthening) experience similar, but relatively low increase in deflection in initial stages, until 35 minutes of fire exposure. However, after 35 minutes, beam B4 undergoes higher deflections than beam B2. This is due to lower stiffness of strengthening material SRP, as compared to that of CFRP at elevated temperatures. After this sudden increase in deflection in beam B4, both beams B3 and B4 undergo increased deflection at similar rate and reach 64 mm and 73 mm, respectively. Similar trends are observed in the degradation of moment capacity with fire exposure time in beams B3 and B4 [as shown in Fig. 5 (b)]. The moment capacity

of beams B3 and B4 degrade slowly in the initial stages of fire exposure. The moment capacity of both these beams remain almost constant up to about 35 minutes of fire exposure. After this, the moment capacity in these two beams degrade gradually at a similar rate for the entire duration of fire exposure and remains above the moment due to applied loading, indicating no strength failure, till 240 minutes of fire exposure.

The deflection and moment capacity of four beams at the time of failure, as well as resulting fire resistance, are summarized in *Table 2*. The un-insulated CFRP and SRP-strengthened RC T-beams, B1 and B2, had attained same fire resistance (of 150 minutes), and failed through attaining deflection limit state i.e., when the mid-span deflection in the beam exceeded the deflection limit as per ASTM E119 (2016) criterion. Whereas, insulated CFRP and SRP-strengthened RC T-beams, B3 and B4, continued to sustain the applied loading, for the entire duration of fire exposure of 240 minutes without attaining failure. The similar fire response observed in SRP and FRP-strengthened beams can be attributed to the fact that the strengthened beams had similar moment capacity and also polymer (which is similar) in the SRP and FRP control the performance at elevated temperatures. Thus, from the aforementioned analysis it is clear that the fire response of SRP-strengthened RC beams is similar to that of FRP-strengthened RC beams. Overall, SRP-strengthened RC beam (as in the case of CFRP strengthened beam) with the above configuration, can provide 2 hours of fire resistance without any external fire insulation. However, to increase the fire resistance beyond 2 hours, a layer of fire insulation is required.

4. FUTURE STUDIES

A macroscopic finite element based numerical model is applied to evaluate the fire resistance of a new strengthening system for RC flexural members, namely, steel fiber reinforced polymer (SRP). This strengthening system has numerous advantages over fiber reinforced polymer (FRP) strengthening system, such as, low-cost, high deformation capability, and better compatibility with existing structural members. Currently, the analyses is carried out based on certain assumption related to SRP properties at elevated temperatures. Material property tests at elevated temperature are being carried out at Michigan State University, to evaluate high temperature properties of SRP. In addition, fire tests are also currently under progress at Michigan State University, to generate test data. This test data will be used to validate the numerical approach further. Upon validation, the model would be further applied to undertake a series of parametric studies, results of which will be utilized to develop guidelines for use of SRP in strengthening applications.

5. CONCLUSIONS

Based on the information presented in the paper, the following conclusions can be drawn on fire performance of steel reinforced polymer (SRP) reinforced concrete (RC) beams:

1. The proposed macroscopic finite element based numerical approach can be applied to evaluate fire response of steel reinforced polymer (SRP)-strengthened RC beams, over the entire range of behaviour from pre-fire exposure to failure stage.
2. The behaviour of SRP-strengthened beams is similar to that of carbon fiber reinforced polymer (CFRP) strengthened beams at elevated temperatures, provided all the design parameters are equivalent.
3. SRP-strengthened RC beam, without any fire insulation, can achieve two hours of fire resistance, as in the case of CFRP-strengthened RC beam. To attain more than two hours of fire resistance SRP-strengthened beams need to be provided with a layer of fire insulation as detailed in this paper.

ACKNOWLEDGEMENT

The authors wish to acknowledge the support of Qatar National Research Fund (QNRF) through grant NPRP8-418-2-175 and Michigan State University for undertaking this research. Any opinions, findings, conclusions, or recommendations expressed in this paper are those of the author and do not necessarily reflect the views of the sponsoring institutions.

REFERENCES

1. Barton, B., Wobbe, E., Dharani, L. R., Silva, P., Birman, V., and Nanni, A., Alkhrdaji, T., Thomas, J., and Tunis, G. (2005). "Characterization of Reinforced Concrete Beams Strengthened by Steel Reinforced Polymer and Grout (SRP and SRG) Composites." *Materials Science and Engineering A*, 412,129-136.
2. Santis, De S., de Felice, G., Napoli, A., and Realfonzo, R. (2016). "Strengthening of structures with Steel Reinforced Polymers: A state-of-the-art review." *Composites Part B: Engineering*, 104, 87-110.
3. Blontrock, H., Taerwe, L., and Vandeveld, P. (2000). "Fire Tests on Concrete Beams Strengthened with Fiber Composite Laminates." *In Proceedings of the International PhD Symposium in Civil Engineering, Vienna (Austria), October 5th-7th*, ed. Konrad Bergmeister, 2, 151-161.
4. Williams, B., Kodur, V. K. R., Green, M. F., and Bisby, L. A. (2008). "Fire Endurance of Fiber-Reinforced Polymer Strengthened Concrete T-Beams." *ACI Structural Journal*, 105(1), 60-67.
5. Kodur, V. K. R., and Ahmed, A. (2010). "Numerical Model for Tracing the Response of FRP-Strengthened RC Beams Exposed to Fire." *Journal of Composites for Construction*, 14(6), 730-742.
6. Ahmed, A., and Kodur, V. (2011). "The Experimental Behavior of FRP-Strengthened RC Beams Subjected to Design Fire Exposure." *Engineering Structures*, 33(7), 2201-2211.
7. Dai, J., Gao, W., and Teng, J. (2014). "Finite Element Modeling of Insulated FRP-Strengthened RC Beams Exposed to Fire." *Journal of Composite for Construction* 19(2), 1-15.
8. Lie, T. T. (1992) "Structural Fire Protection." *ASCE Manuals and Reports of Engineering Practice* 78, ASCE, New York, NY, USA.
9. Eurocode 2 (2004). "EN 1992-1-2 Design of Concrete Structures, Part 1-2: General Rules-Structural Fire Design." *European Committee for Standardization*, Brussels, Belgium.
10. Bisby, L. A., Green, M. F., and Kodur, V. K. (2005). "Response to Fire of Concrete Structures that Incorporate FRP." *Progress in Structural Engineering and Materials*, 7(3), 136-149.
11. Kodur, V. K. R., and Shakya, A. (2013). "Effect of Temperature on Thermal Properties of Spray Applied Fire Resistive Materials." *Fire Safety Journal*, 61,314-323.
12. Dai, J. G., Gao, W. Y., and Teng, J. G. (2013). "Bond-Slip Model for FRP Laminates Externally Bonded to Concrete at Elevated Temperature." *Journal of Composite Construction*, 17(2), 217- 228.
13. ASTM E119. (2016). "Standard Test Methods for Fire Tests of Building Construction and Materials." *American Society for Testing and Materials*, West Conshohocken, PA, USA.
14. ACI 318 (2014). "Building Code Requirements for Structural Concrete and Commentary." *American Concrete Institute (ACI)*, Farmington Hills, MI, USA.
15. ACI 440.2R-17 (2017). "Guide for the Design and Construction of Externally Bonded FRP Systems for Strengthening Concrete Structures." *American Concrete Institute (ACI)*, Farmington Hills, MI, USA.

FIBRE REINFORCED SHOTCRETE – PRESENCE OF SYNTHETIC MACRO FIBRES AFTER FIRE

Cristian Maluk¹, Todd Clarke², Andrew Ridout³

ABSTRACT

The performance of concrete tunnel linings during and after fire is a key component in the fire safe design of a tunnel. Recent innovations in the concrete tunnel industry have resulted in the inclusion of macro synthetic fibres in shotcrete. The fire performance of shotcrete, during and after a fire event, incorporating macro synthetic fibres must be understood before these can be used with confidence in tunnel situations where rapid growing, long-duration fires can occur. Within the scope of this study, a Heat-Transfer Rate Inducing System (H-TRIS) test method was used for controlling the thermal boundary conditions at the exposed surface of tested concrete samples. The heating conditions imposed using H-TRIS were equivalent to those experienced, under idealised conditions, during a standard furnace test controlled with the Hydrocarbon curve. A comprehensive experimental study was performed to investigate (1) the occurrence of fire-induced concrete spalling, (2) the presence of macro fibres after heating, and (3) residual compressive and splitting tensile strength of concrete after heating. Test results evidenced the capacity of macro fibres to remain intact for depths at which temperature remain lower than 300°C; for these specific test samples under tested under these specific thermal conditions.

Keywords: Shotcrete, tunnel linings, synthetic fibres, fire performance, residual strength, H-TRIS.

1 INTRODUCTION AND BACKGROUND

Tunnel structures, or any other underground construction for that matter, cannot be fully utilized until stakeholders (e.g. public, owners, regulators) are satisfied that the tunnel is safe. It is the part of the social-technical commitment that infrastructure is perceived to be, and are, safe. Numerous systems exist which are used by tunnel and fire safety engineers for mitigating the effects and challenges of fires in tunnels. Nevertheless, there are few comprehensive tools that cover the fire safety strategy in tunnels as a whole to tackle the relevant challenges described above.

From a life safety perspective, adequate structural fire performance becomes key for assuring safety of users in the tunnel during fire. Additional to life safety considerations, assurance of an appropriate structural fire performance allows for reducing the risk of disruption in tunnels operation; which can have, specifically in a high transit urban environment, innumerable economic and social effects [1]. Although, not often, fire-induced structural failure and collapse in tunnels can have devastating consequences. In 1999 a fire in the Mont Blanc tunnel (11.6 km long) connecting the cities of Courmayeur, Italy and Chamonix, France, killed 39 people. The fire, initiated in a Volvo truck

¹ Lecturer in Civil Engineering, The University of Queensland, Australia
e-mail: c.maluk@uq.edu.au

² Lead Engineer, Elasto Plastic Concrete, Australia
e-mail: tclarke@elastoplastic.com

³ Chief Operating Officer, Elasto Plastic Concrete, Australia
e-mail: aridout@elastoplastic.com

carrying margarine and flour, lasted for 53 hours [2]. Fire investigations concluded that there was a major occurrence of fire-induced concrete spalling which yielded partial structural collapse of the tunnel roof over a length of 900 m. Restoration of the tunnel lasted for three years and had a direct cost over 400 million euros in direct costs. Therefore, assuring structural fire performance becomes key in support of a fire safety strategy in a tunnel; more specifically assuring safe egress of users, guaranteeing firefighter accessibility, minimize economic impact, and mitigate structural damage.

In order to limit the potential for progressive structural collapse, numerous tunnel fire safety design standards (and regulatory authorities) specify that a tunnel's structural fire performance assessment must include an analysis of the effects of progressive fire-induced concrete spalling (e.g. [4]). The concrete tunnel design industry (precast linings or shotcrete) has traditionally, and to a large extent justifiably, relied on the perceived 'inherent' fire safety features of concrete (e.g. non-combustible, non-flammable, high thermal inertia) to assure the design and construction of fire safe tunnel structures [5]. While modern concretes used in precast and shotcrete applications outperform more traditional concrete (of normal strength) in nearly all performance criteria, it has a high propensity for spalling which has a detrimental effect on its structural fire performance during and after fire [6].

More than a century of research studies into the occurrence of fire-induced concrete spalling have led to the conclusion that spalling is a sudden and stochastic phenomenon characterized by its dependency upon multiple influencing parameters (e.g. [7]). For instance, spalling is known to be influenced by (at least): concrete strength, moisture condition, age, aggregate type and grading, certain admixtures, mechanical loads, mechanical restraint, heated area, element thickness, severity of thermal exposure, and the inclusion of steel and/or polypropylene fibres. Understanding fire-induced spalling of modern concrete mixes presents a serious challenge in the context of the historically deterministic approach to structural fire safety whereby standard fire resistance tests (furnace tests) are done on isolated structural elements [6]. The number of factors known to influence spalling make its prediction difficult, if not impossible, in practice. It is currently difficult to state with confidence which phenomena or mechanisms primarily influence the occurrence of spalling [7].

2 MOTIVATION

Traditionally, Australian regulatory authorities require compliance to the standard fire resistance test controlling the furnace with the Hydrocarbon time-temperature curve. Within the scope of this study, the occurrence of spalling was assessed for (1) plain concrete, (2) concrete incorporating macro fibres, and (3) concrete incorporating both macro and micro fibres. The dimensions of the cast concrete samples were 600 x 500 mm², with a depth of 300 mm. A comprehensive experimental study was performed to investigate (1) the occurrence of fire-induced concrete spalling, (2) the presence of fibres after heating, and (3) residual compressive strength of concrete after heating.

3 EXPERIMENTAL METHODOLOGIES

In order to investigate the fire behaviour of plain concrete and fibre reinforced concrete mixes, a Heat-Transfer Rate Inducing System (H-TRIS) fire test method was used. Described herein, the test method carefully quantifies and controls the thermal boundary conditions imposed on the target surface of test samples [8]. This is possible by controlling the relative position between the exposed surface of the test sample and an array of high performance radiant heaters coupled with a mechanical linear motion system (see Fig. 1). Moreover, using this test method enables the visual inspection of the test samples during fire testing, which is technically very challenging during a furnace test. The test setup allows for the direct and independent control of the thermal boundary conditions imposed on test samples by controlling a specified time-history of incident radiant heat flux at its exposed surface [8].



Fig. 1. Heat-Transfer Rate Inducing System testing concrete samples (the photograph on the right shows the sample protected prior to initiation of the test).

Sixteen high-performance radiant heaters are mounted on a frame, creating a 600 x 800 mm² radiant source of heat (refer to Fig. 1). This configuration enables a heating system with a high and stable operational temperature and outstanding thermal homogeneity at the emitting surface. The linear motion system is used to control the relative position between the array of radiant panels and the exposed surface of the test sample. The computer-controlled linear motion system is programmed to impose potentially any time-history of incident radiant heat flux, limited by the maximum proximity to the test sample. The maximum possible incident radiant heat flux that could be achieved using the H-TRIS at The University of Queensland is >250 kW/m². A desired time-history of incident radiant heat flux (refer to Fig. 3) can be actively controlled. Because the research objective of the study described herein is to examine the fire behaviour (including the potential occurrence of progressive spalling), tests with H-TRIS were continued for a duration of 2 hours.

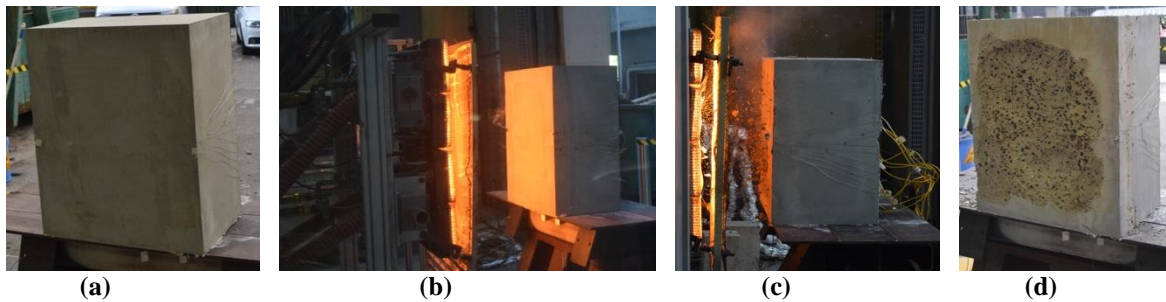


Fig. 2. Typical sequence of events for a spalling test; (a) exposed surface of the sample prior to testing, (b) initiation of the heating conditions, (c) snapshot of a single spalling event, and (d) spalled exposed surface after testing.

3.1 Heating regimes

To understand the need for the novel fire testing approach described herein, a brief review of heat transfer theory is required in this section. Regardless of the design fire selected, the heat transferred from the fire to the exposed surface of a concrete structure (e.g. concrete lining) is normally expressed in terms of a net heat flux, \bar{q}_{net}'' [9]:

$$\bar{q}_{net}'' = -k_s \left. \frac{\partial T}{\partial x} \right|_{x=0} \quad (1)$$

Where \bar{k}_s is the thermal conductivity of the solid, and $\left. \frac{\partial T}{\partial x} \right|_{x=0}$ represents the in-depth time dependent temperature distribution at the exposed surface. For simplicity, in the current analysis heat conduction through the surface is taken only in the direction of the principal heat flow.

Within the scope of this study, H-TRIS was programmed to impose a thermal boundary condition equivalent to that experienced by a concrete sample of equivalent depth under ideal conditions during

a standard furnace test (i.e. standard fire resistance tests) controlled with the Hydrocarbon time-temperature curve (see Fig. 3). Fig. 3 shows the time-history of incident radiant heat flux yielding an equivalent time-history of net heat flux, and hence equivalent in-depth temperature distributions as experienced during the fire resistance tests. It is worth highlighting that within the work described herein, incident radiant heat flux refers to the rate of thermal energy imposed (per unit of exposed surface and per unit of time) at the exposed surface of test specimens during testing. All parameters used in the model (e.g. convective heat transfer coefficient) are in accordance for those in the design and test standard using the Hydrocarbon time-temperature curve and European concrete design guidelines.

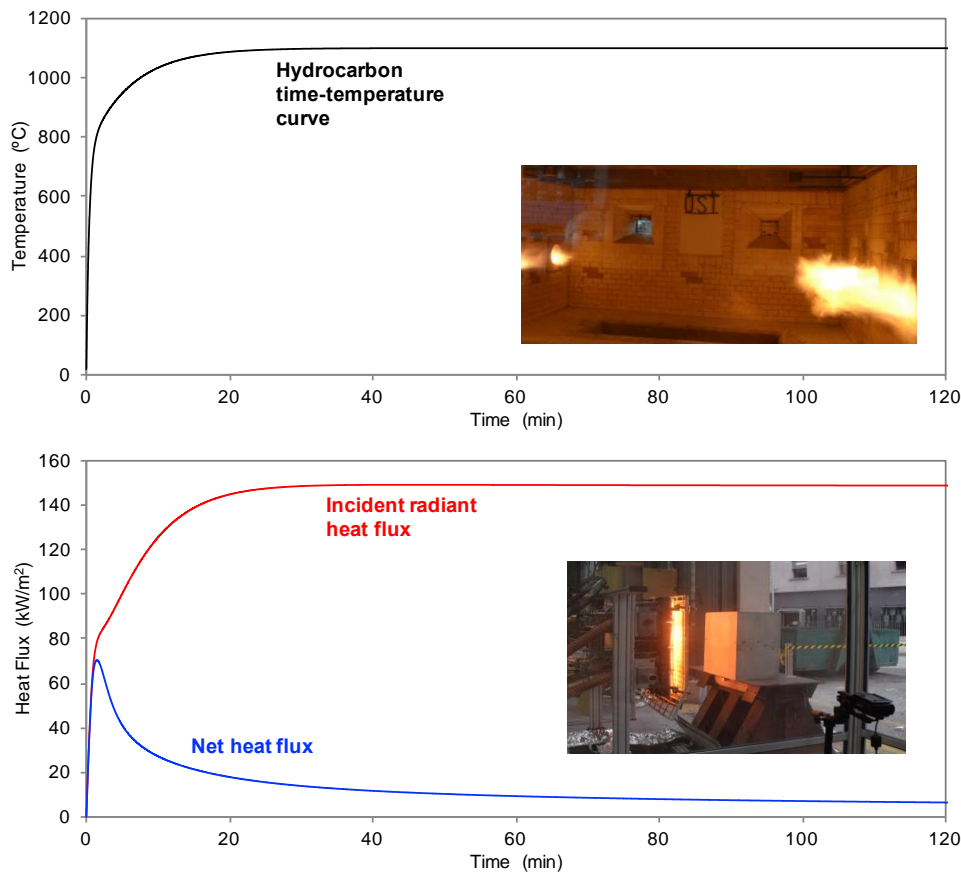


Fig. 3. Hydrocarbon time-temperature curve (above) and time-history of incident radiant and net heat flux imposed using H-TRIS; replicating the thermal boundary conditions during the standard furnace test (i.e. standard fire resistance tests) controlled with the Hydrocarbon curve.

4 CONCRETE MIXES AND TEST SAMPLES

For practical considerations, the concrete mixes were chosen to reflect a nominal shotcrete mix used in the Australian civil underground market generally in accordance with current practice. Although not detailed herein, the concrete mix included general purpose cement, fly ash, silica fume, 10 mm basalt aggregates, normal and fine sand, and a commercially available water reducer. The curing conditions remained constant for all test samples (and for samples used for compressive strength and moisture content measurements); (1) kept in the casting moulds for 36 hours, (2) demoulded, (3) placed under water for 7 days, and then (4) kept in a control environment at 20C and 50% RH.

Casting moulds of internal dimensions 500×600×300 mm³ were manufactured (two per concrete mix). Moulds incorporated temperature gauges, precisely placed at thirteen depths from the target exposed surface (1, 5, 10, 15, 20, 25, 50, 75, 100, 150, 200, 250, and 300 mm). Additionally, standard

cylindrical moulds were cast for monitoring compressive strength and moisture content prior to testing. After testing, cores were taken from the spalled test samples for investigating compressive strength, splitting tensile strength, and presence of fibres after testing (after heating and cooling). All samples were cast from the same concrete batch and fibres were incorporated and mixed as required for each of the mixes. Three concrete mixes were investigated within the scope of this study:

- Plain concrete (no fibres);
- Concrete incorporating macro fibres (7.0 kg per m³ of concrete); and
- Concrete incorporating macro (7.0 kg per m³) and micro (1.0 kg per m³) fibres.

The fibre doses were chosen to reflect amounts generally used in mix designs in the Australian civil underground market. Both types of fibres conform to European standards on fibres for concrete [10]; the macro fibre is Class I and the micro fibre is Class II under this standard. Table 1 shows the fresh and hardened properties of the concrete mixes. The synthetic fibres used were both manufactured from polypropylene with the following dimensions:

- Macro fibres – 840 micron (0.84 mm) equiv. diameter cross section, 60 mm long (Class II); and
- Micro fibres – 32 micron diameter cross section, 6 mm long (Class Ib).

Table 1. Fresh and hardened properties of the concrete mixes.

Concrete Mix	Properties of fresh concrete		Properties of hardened concrete		
	Slump (mm)	Air Content (%)	Compressive strength at 28 days (MPa)	Compressive strength at 284 days* (MPa)	Moisture content at 284 days* (mass/mass)
Plain concrete	220	3.0	54.1	79.5	4.9%
Concrete incorporating macro fibre	170	3.2	51.4	59.3	4.4%
Concrete incorporating macro and micro fibre	100	3.1	52.5	60.5	4.6%

* These compressive strength tests were performed at the same time as the spalling tests.

5 RESULTS AND DISCUSSION

Six precisely controlled and repeatable spalling tests were performed at one test per day which in itself demonstrated the low cost and relative ease of using the H-TRIS method. It is noteworthy that contrary to expectations based on prior heat-induced concrete spalling experimental studies [9], when spalling occurred for a given mix it occurred for both repeat tests and at similar times from the start of the test.

5.1 Occurrence of concrete spalling

Table 2 shows the time-to-first and -last spalling event. All samples suffered from progressive spalling that started between one and two minutes from the start of the test and lasted for as long as 18 minutes after which no spalling occurred for the remainder of the test (approx. 105 mins). When comparing the plain concrete with the fibre reinforced concrete, the time-to-first spalling event occurred earlier into the test for samples incorporating macro or macro + micro fibres. There is not enough data to derive any conclusions regarding the governing factors that define the time-to-last spalling event.

Table 2. Occurrence of spalling during testing.

Concrete Mix	Sample #	Type of spalling events	Time-to-first spalling event (mm:ss)	Time-to-last spalling event (mm:ss)
Plain concrete	Sample #1	Progressive spalling	2:19	9:00
	Sample #2		2:30	16:00
Concrete incorporating macro fibres	Sample #1		1:15	17:30
	Sample #2		1:48	10:26
Concrete incorporating macro and micro fibres	Sample #1		1:05	9:30
	Sample #2		1:20	8:50

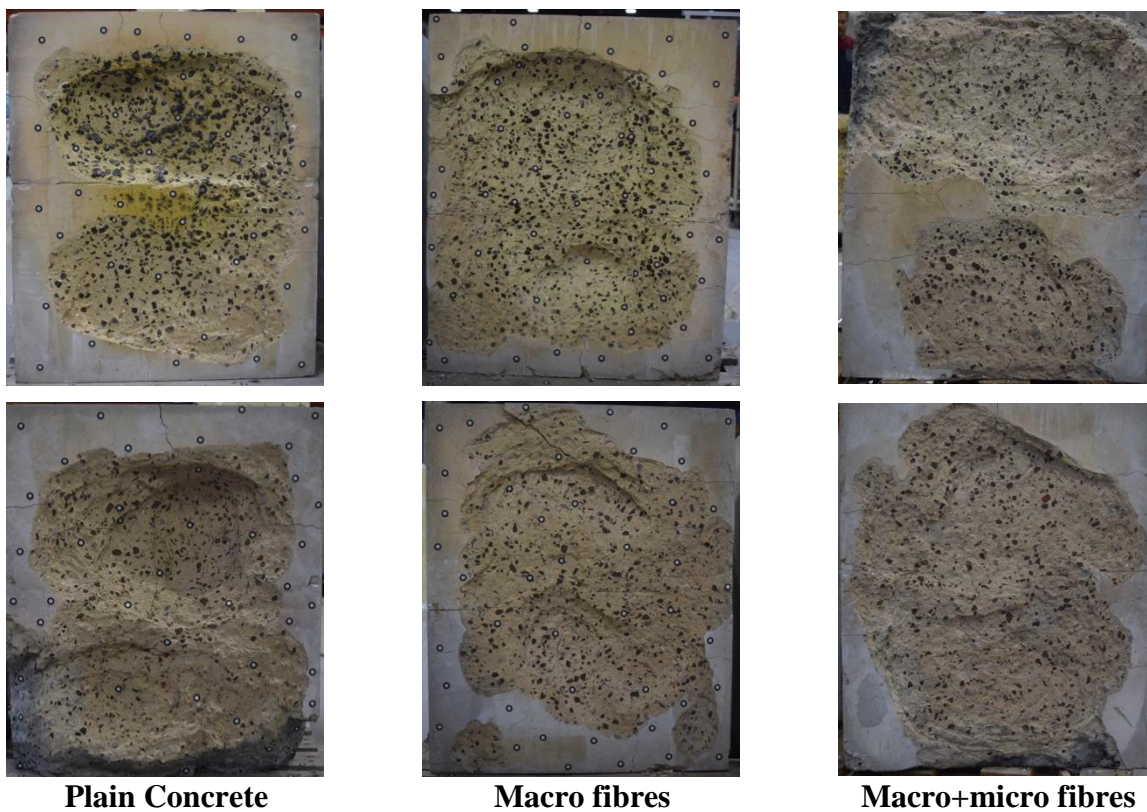


Fig. 4. Spalled surface of concrete test samples after testing.

5.2 Presence of fibres after fire testing

Cylinders cored (diameter 95 mm approx.) from the spalled samples were inspected to investigate the presence of macro and/or micro fibres after testing (heating and cooling). Up to five cores were taken from each tested sample. Outcomes of this investigation showed that for concrete mixes incorporating macro fibres the presence of macro fibres was visible for depths at which temperature remain lower than 300°C (details of this experimental data is presented elsewhere) The presence of micro fibres could not be visually assessed with this technique.

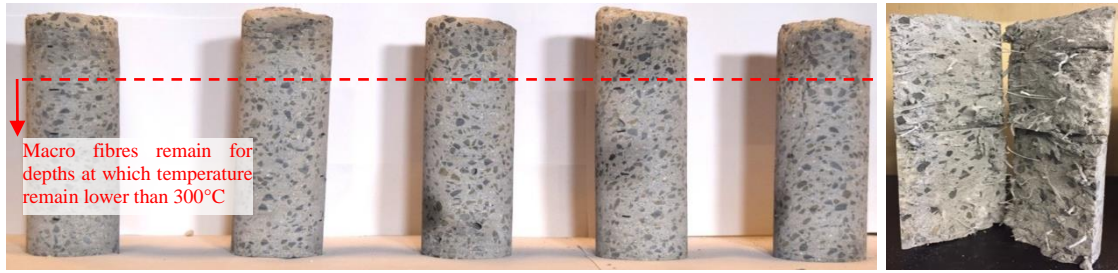


Fig. 5. Cylinders cored from a spalled sample (left) and a split sample (right) in order to inspect fibres' presence (this photograph only shows the Middle and Back section of the sample; refer to the following section for explanation).

5.3 Residual compressive strength fire testing

Cylinders cored from the spalled samples were sliced in order to assess their residual compressive and splitting tensile strength at different depths after testing (heating and cooling). For each of the cylinders cored, slices were cut in order to obtain a Front, Middle and Back sample. The length of the Middle and Back cylinders was 100mm while the length of the front cylinder was determined by to the amount of spalling. The Front sample was not tested. Fig. 6 shows the test results from the residual compressive and splitting tensile strength test. These results show that the concrete incorporating macro fibres (with and without micro fibres) experienced a comparative lesser strength reduction after testing (heating and cooling) than plain concrete. The compressive strength reduction for each concrete mix was:

- Plain concrete – 41% and 50% reduction at the Back and Middle, respectively;
- Macro fibre concrete – 27% and 36% reduction at the Back and Middle, respectively; and
- Macro+micro fibre concrete – 31% and 42% reduction at the Back and Middle, respectively.

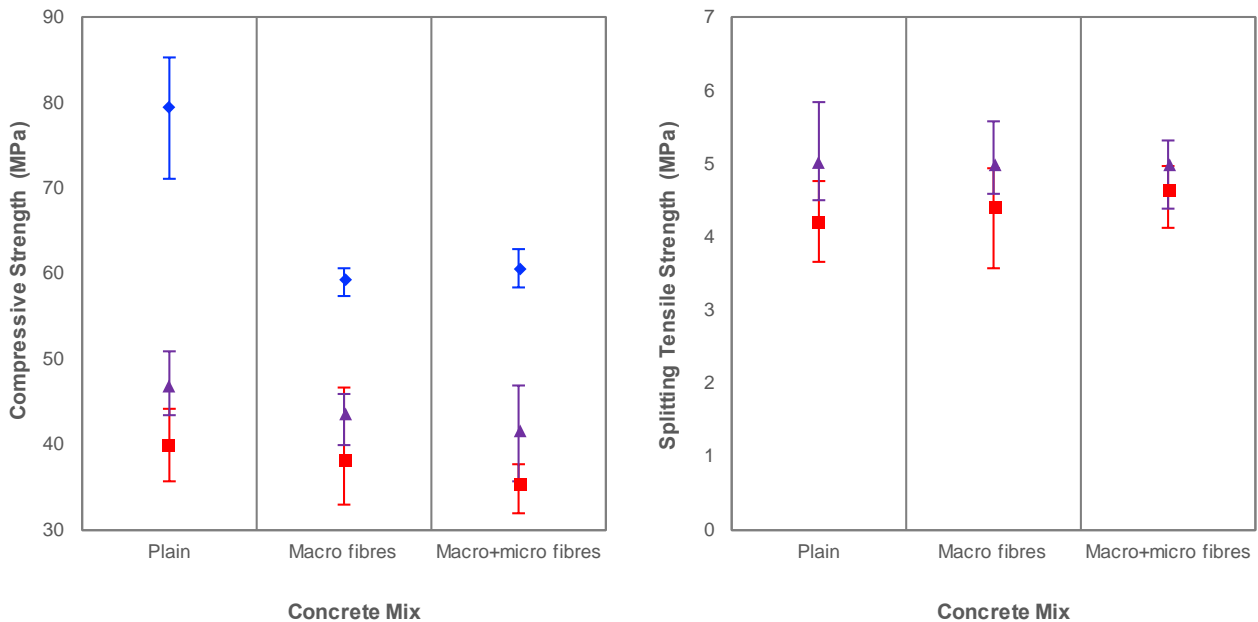


Fig. 6. Compressive and splitting tensile strength prior to testing (blue), at Middle (mid-depth) of the tested concrete (red) and at the Back (unexposed) end of the tested concrete (purple). No splitting tensile strength test were done prior to testing.

6 CONCLUDING REMARKS

This paper has presented the outcomes of an experimental study focused on the fire behaviour of (1) plain concrete, (2) concrete incorporating macro fibres, and (3) concrete incorporating both macro and micro fibres. A comprehensive experimental study was performed to investigate (1) the occurrence of fire-induced concrete spalling, (2) the presence of macro fibres after heating, and (3) residual compressive and splitting tensile strength of concrete after heating. More specifically, this study concluded the following:

- **Occurrence of fire-induced concrete spalling** – time-to-first spalling event occurred earlier into the test for samples incorporating macro or macro + micro fibres.
- **Presence of macro fibres after heating** – macro fibres to remain intact for depths at which temperature remain lower than 300°C; evidencing the capacity of macro fibres to remain intact after severe heating conditions.
- **Residual compressive and splitting tensile strength of concrete after heating** – concrete incorporating macro fibres (with and without micro fibres) experienced a comparative lesser strength reduction after testing (heating and cooling) than plain concrete.
- ***In-depth temperature distribution in concrete** – the concrete mix has only a minor influence in the temperature profile for depths higher than 150 mm.

ACKNOWLEDGMENT

The authors would like to thank Elasto Plastic Concrete Pty Ltd and The University of Queensland, and in particular to Craig Wright, Jason Tignard, Marta Tena, Andrea Lucherini, Fransiska Bektı, Janis Chan, Jessica Barton, Tristan Goode, Moin Mushfiqur, Cameron Wallace, Mateo Gutierrez, Jeronimo Carrascal, and Jurij Karlovsek.

REFERENCES

1. Maraveas C. and Vrakas A.A. (2014). Design of concrete tunnel linings for fire safety, *Structural Engineering International*, 24(3), pp. 319-329.
2. Vuilleumier F., Weatherill A., and Crausaz B. (2002). Safety aspects of railway and road tunnel: example of the Lötschberg railway tunnel and Mont-Blanc road tunnel, *Tunnelling and Underground Space Technology*, 17(2), pp. 153-158.
3. Casalé E., Haak A., Ingason H., Malhotra H.L., and Richter E. (1995). *Fires in Transport Tunnels: Report on full-scale tests, EUREKA-Project EU 499: FIRETUN*, Shipping & Sales, ISBN 3-930621-44-4.
4. AS (2011). Tunnel fire safety (AS 4825-2011), *Standards Australia*, NSW, Australia, 80 pp.
5. Bilow DN and Kamara ME. (2008). Fire and Concrete Structures, *ASCE Structures Congress 2008: Crossing Borders*, 10 pp.
6. Maluk C, Terrasi GP, Bisby L, Stutz A, and Hugi E. (2015). Fire resistance tests on thin CFRP prestressed concrete slabs, *Construction and Building Materials*, 101(1), pp. 558-571.
7. Maluk C, Bisby L., and Terrasi GP. (2017). Effects of polypropylene fibre type and dose on the propensity for heat-induced concrete spalling. *Engineering Structures*, 131, pp. 584-595.
8. Maluk C, Bisby L, Krajcovic M, and Torero JL. (2017). The Heat-Transfer Rate Inducing System (H-TRIS) Test Method. *Fire Safety Journal*. (corrected proof)
9. Maluk C. (2014). *Development and Application of a Novel Test Method for Studying the Fire Behaviour of CFRP Prestressed Concrete Structural Elements*. PhD Thesis, The University of Edinburgh, UK, 473 pp.
10. EN (2016). Fibres for concrete. Steel fibres. Definitions, specifications and conformity (EN 14889-1:2006), BSI, 30 pp.

FIRE PERFORMANCE OF CONCRETE FLAT SLABS

Pasindu Weerasinghe¹, Priyan Mendis², Kate Nguyen³, Tuan Ngo⁴

ABSTRACT

With the increasing use of concrete flat slabs especially in multi-storey buildings, fire resistance requirements tend to be critical in the design. Current design guidelines are conservative as they are based on isolated member tests which does not consider the continuous action of flat slabs in actual structures. Issues experienced in the industry due to such design guidelines are discussed and the need for more representative experimental and analytical models are highlighted. General purpose FE program ABAQUS is used to model the thermo-mechanical behaviour of flat slabs in elevated temperatures. Improvisations that can be used to avoid convergence issues and methods to reduce the computational cost are presented. Thermal and mechanical response of the model is validated with experimental results from a fire test on restrained concrete flat slabs. Further enhancements that can be used to improve the accuracy and reliability of such models are discussed. The expected outcome is to provide a reliable research base to improve the current building code and design guidelines regarding fire design of concrete flat slabs and provide more accurate rational guidelines for designers leading to significant cost savings. Preliminary findings from this project are presented in the paper.

Keywords: Flat slabs, finite element modelling, thermo-mechanical analysis

1 INTRODUCTION

The use of flat slabs is becoming very popular in modern buildings because of their speed of construction and use of cost-effective formwork. In the absence of beams, lower story heights can be achieved which saves cost in vertical cladding, partition walls, mechanical systems and plumbing especially in multi-story buildings. However, building code regulations regarding fire design of flat slabs are based on research carried out a few decades ago. They are incomplete or over conservative causing extra thick slabs in buildings.

With the increasing number of fire related disasters occurring around the world, more emphasis was placed on the fire resistive design of structures. Compared to other materials, reinforced concrete structures have comparatively performed better under fire because it is non-combustible and have a low thermal conductivity. This could mean that the occupants will have more time to evacuate the building before a total collapse. However, exposure to high temperatures can alter the thermal and mechanical properties of concrete and steel which would reduce the capacity of the structural elements. Ultimately it could damage the structure permanently causing harm to occupants and resulting in a significant financial loss. In the context of flat slabs, the limited number of

¹ PhD Candidate. Department of Infrastructure Engineering, The University of Melbourne, Melbourne, Australia.
e-mail: pthalpe@student.unimelb.edu.au

² Professor. Department of Infrastructure Engineering, The University of Melbourne, Melbourne, Australia.
e-mail: pamendis@unimelb.edu.au * Corresponding Author

³ Reserach Fellow. Department of Infrastructure Engineering, The University of Melbourne, Melbourne, Australia.
e-mail: kate.nguyen@unimelb.edu.au

⁴ Professor. Department of Infrastructure Engineering, The University of Melbourne, Melbourne, Australia.
e-mail: dtngo@unimelb.edu.au

experimental studies have shown that punching shear failure could be critical when exposed to fire [1-5]. Interpretation of such experimental results and how well they represent the actual condition of a flat slab in a building will be further discussed in this paper.

Fire design of structural elements is carried out in accordance with the guidance given in the concrete design code of the respective country. Many of the modern day codes follow a performance-based approach for fire design. Three main performance criteria considered are stability, insulation and integrity. Fire design of flat slabs in Australian Concrete structures code AS 3600 [6] and other major codes is based on the European guidelines (EN 1992-1-2) [7] which specify a minimum thickness and cover to reinforcement in order to satisfy the aforementioned performance criteria. For fire ratings of 90 min and above it specifies a constant thickness (200mm). This is a major problem for designers. For example, the National Construction Code of Australia (NCC) [8] requires a minimum fire rating level (FRL) of 90 min for class A construction (Buildings over 4 stories). Therefore, the flat slab thickness should be always higher than 200mm for multi-storey buildings.

Another critical issue that has been raised due to this 200mm thickness limit is when there is a requirement for a set down in slabs. Set downs are placed on slabs in bathroom areas to have a proper drainage of water. Typical set down can be 30mm. However, even a 30mm set down in a 200mm thick flat slab would violate the concrete code and NCC requirement to achieve a 90 min FRL [8]. Increasing the total slab thickness by 30mm would prove to be uneconomical when costs accumulate for many floors throughout the height of a multi-storey building. Rather than having a uniform 200mm minimum thickness throughout out the floor, it is more rational to propose certain limits i.e. A minimum distance from columns where set downs are permitted, because only certain areas of the floor slab will be critical under fire conditions. To make such decisions a comprehensive research base is needed.

The main aim of the research conducted at the University of Melbourne by the authors is to conduct a comprehensive study of the performance of concrete flat slabs under fire taking into account the different boundary conditions and load cases. Limited studies conducted up to now are reviewed and preliminary findings from this project related to modelling the behaviour of concrete flat slabs under fire are presented in the paper.

2 EXPERIMENTAL STUDIES ON FIRE PERFORMANCE OF CONCRETE FLAT SLABS

Only a limited number of experimental studies were conducted on flat slabs exposed to fire. Some important tests will be discussed highlighting their significance and limitations.

Minimum thickness specification for fire design of concrete flat slabs in BS EN 1992-1-2 and AS 3600 is based on the tests conducted by Kordina [1]. The tests involved a simply supported slab panel connected to single central column, heated from bottom surface with loading applied via a ring to the slab panel to simulate uniformly distributed load (see *Fig. 1*). This setup would not allow for any catenary actions to be considered between columns. 10 slabs with thickness 200mm and 4 slabs with thickness 150mm were tested and failure mechanism observed for all the cases was punching shear failure. Time to failure ranged from 17 to 120mins for 200mm thick slabs and 8 to 180mins for 150mm thick slabs. With such a loading arrangement for a slab supported from a single column it is clear that failure mechanism can only be punching shear after top reinforcement has yielded. Membrane action of the slab which is there in an actual slab of a building would not be taken into account as the slab is simply supported during the test.

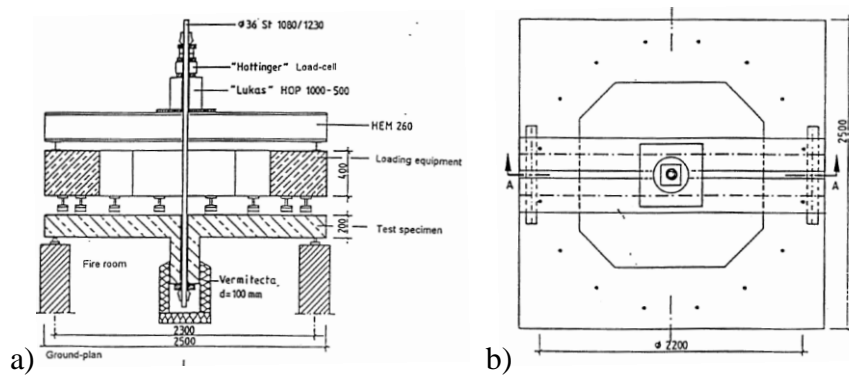


Fig. 1. Test set-up used by Kordina [1] a) Sectional view; b) Plan view

However the normal failure mode for a one-way or two-way slab, subjected to fire from below, is yielding of the bottom reinforcement due to heat that leads to moment redistribution to the support and top reinforcement. In such a scenario a hinge will be formed at the support and slab will act like a cantilever which tends to be a more ductile failure than punching shear failure.

Annerel et al. [2], Salem et al. [3] and Ghoreishi et al. [4] have conducted similar fire tests on isolated flat slabs. Test set-up used by Annerel et al. [2] is similar to that of Kordina and they have tested four 250mm thick slabs (with added stirrups near the column face) under fire. Two slabs did not fail at the total duration of 120 min and two slabs failed after 20 mins due to punching shear failure. Salem et al. [3] have used an inverted specimen (see Fig. 2(b)) and heated from the tension surface. Twelve specimens of 100mm thickness were tested and more attention was given to the load deflection behaviour and failure load rather than fire resistance period. Ghoreishi et al. [4] have used a similar inverted test arrangement and 6 slabs of 120 mm thickness (3 at ambient temperature and 3 heated) were tested. However, the main difference of this test is that first the slabs were heated up to a constant temperature and then load was applied until failure to find the punching shear capacity. All the above tests have used a simply supported boundary condition along the perimeter of the sample.

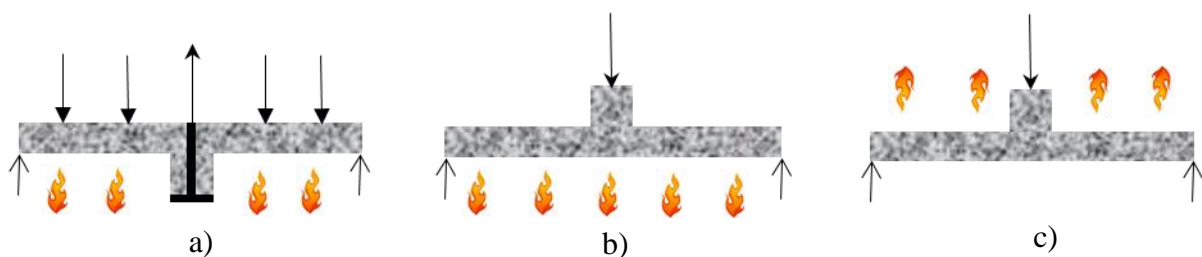


Fig. 2. Support conditions, loading and heated surfaces of experiments by a) Annerel et al.[2] ;b) Salem et al. [3] and c) Ghoreishi et al. [4]

A recent study conducted by Smith et al. [5, 9] has used a specially built steel frame to restrain the slabs against lateral displacement and rotation as an attempt to represent the actual boundary conditions of a continuous flat slab in a building. Results show that fire resistance of restrained slabs is considerably higher than that of unrestrained slabs. An analytical study conducted using the software SAFIR [10] has also shown that the fire resistance of flat slabs is significantly improved due to restraint conditions provided by adjacent slab panels and membrane action. Therefore, Smith et al. test results [5, 9] were chosen to model and validate the behaviour of flat slabs when exposed to fire.

3 MODELLING OF BEHAVIOUR OF CONCRETE FLAT SLABS SUBJECTED TO FIRE

3.1 General details

The tests conducted by Smith et al. which involved restrained support conditions were used to develop the finite element model of the flat slab. The study consisted of a total of 15 slab specimens (50, 75 and 100mm thick) which were tested at ambient temperature and elevated temperature under restrained and unrestrained support conditions. Details of the experiment can be found in Smith et al. [5, 9]. *Fig. 3* shows the specimen size, loading arrangement, fire exposure and support conditions along with the reinforcement arrangement of flat slab specimens used in the test. 100mm thick, 0.8% reinforced, restrained slab specimen was selected to illustrate the modelling technique.

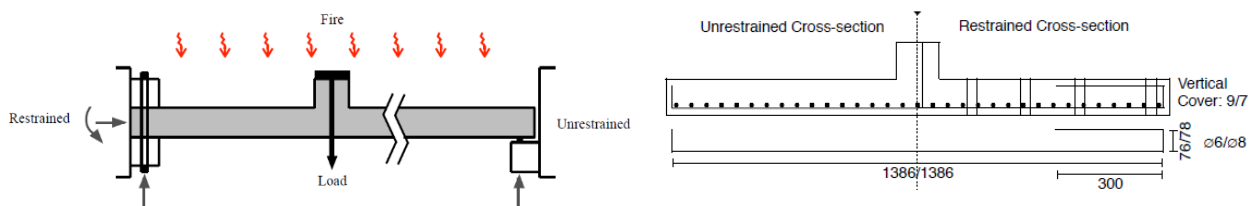


Fig. 3. Test set up used by Smith et al. [5, 9] a) Support conditions, loading and fire exposure; b) Reinforcement arrangement (Specimen size – 1.4m x 1.4m x 0.1m, 0.25m x 0.25m x 0.1m column at the middle)

3.2 Finite element modelling of behaviour under fire

The widely used finite element program ABAQUS was chosen to model the fire behaviour of slabs. The concrete damage plasticity model was selected to represent concrete as previous studies have validated the use of this model for flat slabs in ambient conditions and other concrete elements subjected to elevated temperatures. Convergence was reported as a common issue related to modelling behaviour under fire as it contains both material nonlinearities and geometric nonlinearities [11]. Temperature dependency of material properties make it even more difficult to converge on a solution. As a remedy in standard implicit modelling, the time increment of an iteration can be made very small. However, the computational costs of such models are very high as the usual duration of the applied fire in an analysis can be 1 to 4 hours. Therefore, an explicit dynamic solver was used in this analysis to simulate the quasi-static behaviour with some improvisations. The techniques used will be discussed in detail in the following sections.

Concrete damage plasticity (CDP) model in ABAQUS uses concepts of isotropic damaged elasticity in combination with isotropic tensile and compressive plasticity to represent the inelastic behaviour of concrete [12]. The main two failure mechanisms assumed are tensile cracking and compressive crushing in concrete. More details can be found in [13]. General parameters considered for the CDP model are the dilation angle (ψ) 30° , the eccentricity 0.1, the stress ratio (f_{bo}/f_{co}) 1.16, the shape factor (K_c) 0.667 and the viscosity parameter 0.005 which have been used in other similar studies as well [11, 13, 14].

3.3 Material data and other parameters used in FE model

Stress-strain behaviour of concrete in compression and tension at elevated temperatures were calculated in accordance with the guidelines given in Table 3.1 of EN 1992-1-2 [7]. Concrete compressive strength (f_{cu}) and tensile strength ($f_{ct,t}$) were determined experimentally as 51 MPa and 4MPa respectively [9]. Based on that a linear elastic behaviour was assumed up to $0.4f_{cu}$ for compressive stress strain behaviour of concrete. It was followed by a parabolic variation until it reaches the ultimate strength according to the relationship given in [7]. The softening behaviour of concrete is represented through a linear descending branch.

For the stress-strain response of concrete in tension, a linear elastic behaviour was assumed up to its tensile strength followed by a bilinear softening response. The area under the softening branch was determined based on the fracture energy (G_f) which is assumed to be 0.25 N/mm for this model. More details of this method can be found in [13, 15].

The stress-strain relationship for reinforcing steel at elevated temperatures was determined according to Table 3.2b of EN 1992-1-2 [7] having a yield strength of 549MPa and an elastic modulus of 200GPa [9].

Thermal properties of concrete (specific heat and conductivity) were also derived from relationships given in EN 1992-1-2 [7] for siliceous concrete [9]. Lower limit of thermal conductivity was selected as it gives more realistic temperatures for concrete structures than the upper limit [7]. Thermal elongation for siliceous concrete was determined in accordance with section 3.3.1 [7]. Thermal properties of steel were not taken into account as the element types used in the FE model for reinforcing steel did not participate in the heat transfer analysis. Wang [16] has showed that the temperature across the depth with and without reinforcing bars was very similar and therefore the effect from steel for the heat transfer can be negligible. However, the temperature of the reinforcement can be indirectly found by relating to the temperature of the concrete at the same depth.

Based on the symmetricity of loading and boundary conditions, only a quarter of the slab (0.7 m x 0.7m x 0.1m) was modelled to save the computational time. C3D8RT (An 8-node thermally coupled brick) elements were used to model concrete whereas reinforcement was modelled using T3D2 (A 2-node linear 3-D truss.) elements. Truss elements representing reinforcement were embedded using the embedded region constraint assuming a perfect bond between concrete and reinforcement. This assumption is made in several other studies [13, 17] as well and it has given accurate results. Slab specimen in the experiment was restrained along the perimeter against both translation and rotation. (See Fig. 3). In the model the bottom edge was restrained, and axial spring elements were used along the side surfaces to represent the lateral restrained (see Fig. 4). A similar approach was used by Genikomsou et al. [18] to investigate the compressive membrane action in flat slabs. The advantage of using spring supports in this particular case is further explained under the results section.

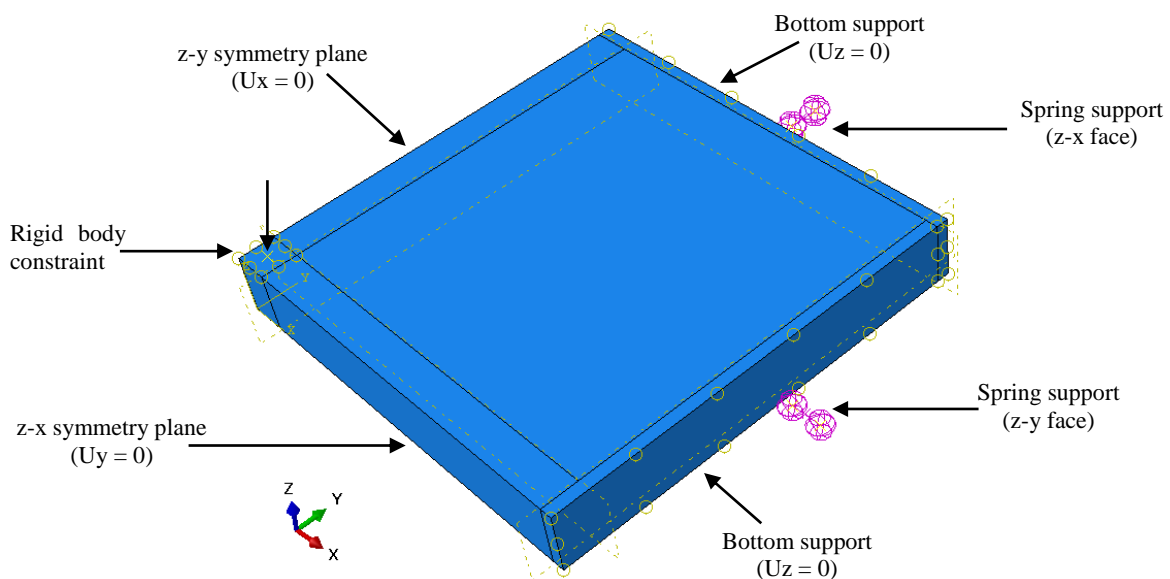


Fig. 4. Boundary conditions, loading and constraints used in the FE model

3.4 Analysis steps

Analysis is carried out in two different steps. First, loading was applied using a dynamic explicit step. Although ABAQUS/Explicit uses a dynamic solution procedure it can be used for quasi-static analysis with a low rate of loading [13]. In the experiment, the slab was casted along with a short column where the loading was applied through a hydraulic jack to the column. However, in the analysis only the slab was modelled and to simulate the effect of the column, a rigid body constraint was applied to the location of loading. (See *Fig. 4*). Then, dynamic explicit coupled temperature displacement step in ABAQUS was used to carry out the thermo-mechanical analysis. In this step, the load (P) applied in the first step was kept constant while the temperature measured in the experiment was applied to the top surface of the slab. The use of an explicit solver avoids the convergence issues encountered in a standard static implicit analysis.

Total duration of the test is 4 hours; 2 hours of heating followed by 2 hours of cooling. For the heating step the convective coefficients were taken as $25 \text{ W/m}^2\text{K}$ and $9 \text{ W/m}^2\text{K}$ for exposed surface and unexposed surface respectively [7]. In the cooling step a convective coefficient of $9 \text{ W/m}^2\text{K}$ was assigned for all the surfaces. Concrete emissivity was taken as 0.7 to simulate the radiative heat flux in both steps.

Generally an explicit step is particularly well-suited to simulate brief transient dynamic events [12]. However, it can be used for an analysis consisting of a long duration with some improvisations. Explicit time integration algorithm uses a very small time increment. It can be increased by either artificially increasing the mass of the structure (mass scaling) or by artificially increasing the loading speed (load factoring) [14]. Mass scaling can cause large inertia forces which can deviate the solution from quasi-static state to dynamic state. Therefore, load factoring method is applied in this model. It should be noted that load factoring in this study refers to the thermal load. Although the duration of heating is 2 hours, it has been scaled down to 2 seconds in the coupled temperature displacement step with modifications to the units involving time. i.e. conductivity, specific heat, coefficient of convection and Stefan-Boltzmann constant for radiation.

4 RESULTS AND DISCUSSION

4.1 Thermal Response

Thermocouples (TCs) in the experiment were placed 200 mm away from the column surface across the depth (at 10, 33, 65, 82 and 101mm). TC which was used to measure the exposed surface temperature was located 10mm inside the slab depth [9]. Therefore, measured temperatures were extrapolated to calculate the applied temperature to the exposed surface. Nodal temperature results from 200 mm away from the column surface across the depth were compared with the measured temperature values. It should be noted that temperatures at 20mm intervals across the depth were determined using the temperature profiles at 10min intervals from Smith [9]. *Fig. 5*. shows the temperature variation across the slab depth during heating and cooling phases of the experiment and model. Modelled temperatures are in good agreement with the measured data.

4.2 Structural Response

Deflection criteria were considered to validate the structural response of the FE model. Downward displacement was determined using two methods in the experiment, by employing a displacement transducer (LP) connected to the loading rod which goes through the column and using digital image correlation (DIC). However, it was concluded that the DIC measurements were more accurate than LP as localised crushing of the concrete around the column stub and extension of the loading rod due to the elevated temperature can artificially increase the LP measurements [9].

Therefore, DIC measurements were taken to compare the modelled displacements with experimental displacements.

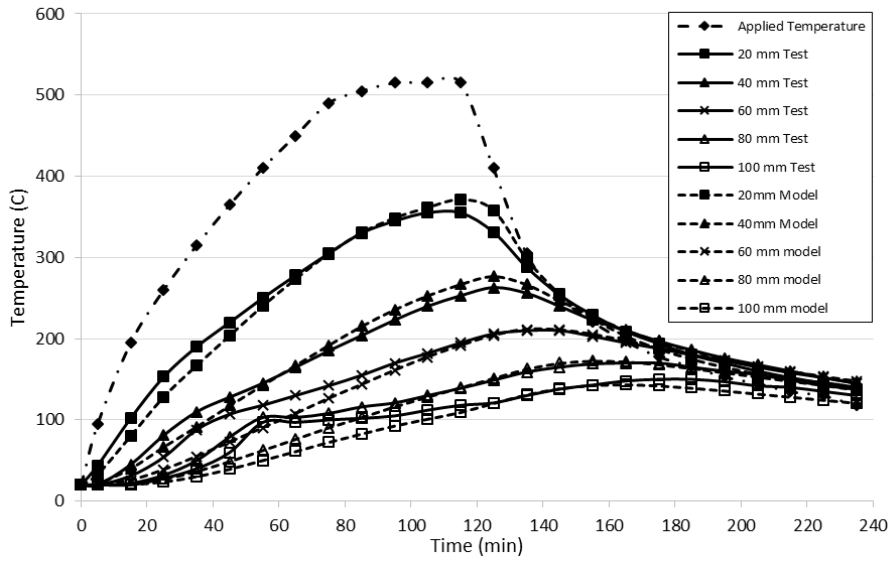


Fig. 5. Experimental and modelled temperature variation across the slab depth

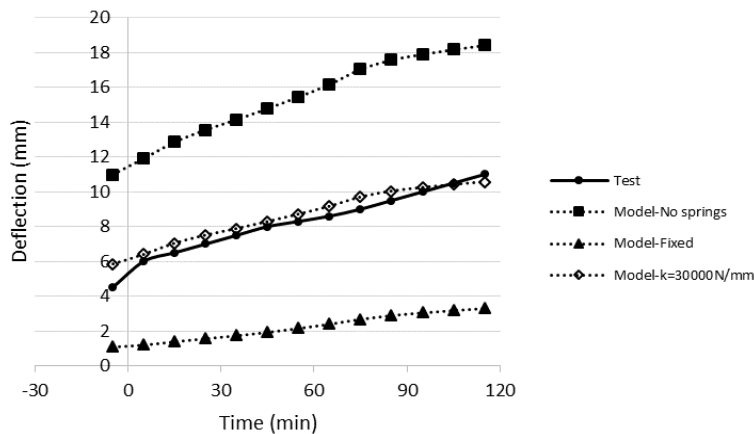


Fig. 6. Experimental and modelled deflection of the slab during heating phase

Deflections only during the heating phase was considered at this stage as material properties during the cooling phase undergoes changes after experiencing elevated temperatures. The incorporation of residual material properties is being further studied by the authors at present. The results are presented in Fig. 6. It should be highlighted that when the perimeter is fully fixed the modelled deflections are much lower than the measured deflections. Releasing the restraints increase the deflection, but makes the model too relaxed. Therefore, spring supports were used as discussed before and a spring stiffness of 30,000 N/mm used in the model as suggested by [18] to represent the membrane action due to lateral restraints. With the use of spring supports a close match between measured and modelled deflections have been achieved. Further studies are underway to evaluate and validate the damage and failure criteria predicted by the model.

5 CONCLUDING REMARKS

- Current design guidelines regarding fire design of concrete flat slabs are based on isolated member tests which do not consider the continuous action and thus neglects effects such as membrane action which could improve the fire resistance.

- General purpose FE program ABAQUS was successfully used to simulate the thermal and mechanical response of concrete flat slabs exposed to fire.
- The use of ABAQUS/Explicit solver with coupled-temperature displacement analysis procedure is beneficial in eliminating the convergence issues arising as a result of added nonlinearities due to temperature dependant material properties.
- Computational cost for the explicit analysis can be significantly reduced by reducing the step time with modifications to time dependant thermal properties of materials.
- Modelled thermo-mechanical behaviour and the experimental results are in good agreement, which endorses the accuracy of the model.
- Such FE models can be used to study the effect of different support conditions, load combinations, changes in the slab thickness etc. to fire resistance level.

REFERENCES

1. Kordina, K., *Flat slabs under fire—Redistribution of the internal forces and punching tests*. Institut für Baustoffe, Massivbau und Brandschutz, Technische Universität Braunschweig, Germany, CEN/TC, 1993. **250**: p. 1-2.
2. Annerel, E., L. Lu, and L. Taerwe, *Punching shear tests on flat concrete slabs exposed to fire*. Fire Safety Journal, 2013. **57**: p. 83-95.
3. Salem, H., et al., *Punching shear strength of reinforced concrete flat slabs subjected to fire on their tension sides*. HBRC Journal, 2012. **8**(1): p. 36-46.
4. Ghoreishi, M., A. Bagchi, and M.A. Sultan, *Punching shear behavior of concrete flat slabs in elevated temperature and fire*. Advances in Structural Engineering, 2015. **18**(5): p. 659-674.
5. Smith, H.K., T.J. Stratford, and L.A. Bisby. *Punching shear of restrained reinforced concrete slabs under fire conditions*. in *8th International Conference on Structures in Fire*. 2014.
6. Standards Australia, *AS 3600 - Concrete structures*. 2009.
7. European committee for standardization, *Eurocode 2: Design of concrete structures - Part 1-2: General rules -Structural fire design*. 2004.
8. The Australian Building Codes Board, *National Construction Code: Volume 1*. 2016.
9. Smith, H.K.M., *Punching shear of flat reinforced-concrete slabs under fire conditions*. 2016, The University of Edinburgh.
10. Moss, P.J., et al., *The fire behaviour of multi-bay, two-way reinforced concrete slabs*. Engineering Structures, 2008. **30**(12): p. 3566-3573.
11. George, S.J. and Y. Tian, *Structural performance of reinforced concrete flat plate buildings subjected to fire*. International Journal of Concrete Structures and Materials, 2012. **6**(2): p. 111-121.
12. Dassault Systèmes, *ABAQUS version 6.14 documentation*. 2014.
13. Genikomsou, A.S. and M.A. Polak, *Finite element analysis of punching shear of concrete slabs using damaged plasticity model in ABAQUS*. Engineering Structures, 2015. **98**: p. 38-48.
14. Albrifkani, S. and Y.C. Wang, *Explicit modelling of large deflection behaviour of restrained reinforced concrete beams in fire*. Engineering Structures, 2016. **121**: p. 97-119.
15. Ellobody, E. and C.G. Bailey, *Modelling of unbonded post-tensioned concrete slabs under fire conditions*. Fire Safety Journal, 2009. **44**(2): p. 159-167.
16. Wang, G., *Performance of Reinforced Concrete Flat Slabs Exposed to Fire*. 2006: Department of Civil Engineering, University of Canterbury.
17. Kodur, V. and A. Agrawal, *An approach for evaluating residual capacity of reinforced concrete beams exposed to fire*. Engineering Structures, 2016. **110**: p. 293-306.
18. Genikomsou, A.S. and M.A. Polak, *3D finite element investigation of the compressive membrane action effect in reinforced concrete flat slabs*. Engineering Structures, 2017. **136**: p. 233-244.

RELATIONSHIPS BETWEEN DESTRUCTIVE AND NON-DESTRUCTIVE METHODS FOR NORMAL STRENGTH LIMESTONE CONCRETE AFTER EXPOSURE TO HIGH TEMPERATURES

Urška Dolinar¹, Gregor Trtnik², Tomaž Hozjan³

ABSTRACT

This paper introduces experimental study on mechanical properties of a normal strength limestone concrete after exposure to high temperatures up to 800 °C. Compressive strength, tensile strength, surface hardness, dynamic elastic, and shear modulus are investigated. The aforementioned mechanical properties are obtained on 15 cubic and 15 prismatic samples using destructive and non-destructive methods. The experimental results are used to determine correlations between: (i) ultrasonic (US) pulse velocity and compressive strength, (ii) US pulse velocity and surface hardness, (iii) surface hardness and compressive strength, and (iv) torsional resonant frequency and tensile strength. It is found out, that the best fit between the compressive strength and the US pulse velocity is a linear trend line, while for the tensile strength and the torsional resonant frequency it is a power trend line. The presented results are a part of the comprehensive ongoing research aimed to develop a numerical method based on artificial neural network approach to estimate mechanical properties of concrete after exposure to high temperatures based on non-destructive methods.

Keywords: Concrete, high temperatures, compressive strength, non-destructive methods

1 INTRODUCTION

Concrete is the most popular structural material for various reasons, e.g. high compressive strength, durability, ease of fabrication, plasticity, non-combustible behaviour [1] and low cost. However, when exposed to high temperatures different chemical, physical, and mechanical changes occur which significantly fasten degradation of the material's mechanical properties [2]. Assessment of bearing capacity of concrete structures after fire depends on adequate knowledge of the maximum temperatures reached during fire, its duration, heating rate, and material properties after fire. Based on this information the decision on reconstruction or demolition of the structure can be made. In general, the bearing capacity of structures after fire is often assessed with simplified calculation procedures and experimental investigations. These mainly cover visual inspection of the damaged structure and the execution of some standard, mostly destructive tests [3]. Such tests are precise, but often difficult to implement, time-consuming, limited to certain pre-selected locations, expensive, and can weaken the individual structural element to some extent. Recently, a lot of experimental work has been done on concrete after exposure to high temperatures with destructive [4, 5, 6] and non-destructive tests [7, 8, 9]. However, mechanical properties of concrete after exposure to high temperatures are usually determined with destructive methods. On the other hand, results from non-destructive methods are used in regression analysis where relationships between destructive and

¹ PhD Candidate. Chair of Mechanics, Faculty of Civil and Geodetic Engineering (FGG), University of Ljubljana, Slovenia.
e-mail: urska.dolinar@fgg.uni-lj.si

² Head of Structural Department, Building Materials Institute (IGMAT), Ljubljana, Slovenia.
e-mail: grega.trtnik@igmat.eu

³ Associated Professor. Chair of Mechanics, Faculty of Civil and Geodetic Engineering (FGG), University of Ljubljana, Slovenia.
e-mail: tomaz.hozjan@fgg.uni-lj.si

non-destructive test results are given at ambient temperature [7] or after exposure to high temperatures [8]. Different US methods have been widely used for non-destructive evaluation of concrete mechanical properties [10] and monitoring of internal damage progression [11] at ambient temperatures. Among others, an effective method for estimating compressive strength of concrete at ambient temperature using artificial neural networks was developed based on US pulse velocity measurements [12].

This paper presents first part of the ongoing research and is focused on the experimental evaluation of mechanical properties of the limestone concrete specimens initially exposed to various levels of high temperatures. The compressive and tensile strengths were determined with standard destructive tests and the US pulse velocity, surface hardness, and basic frequencies of vibration were determined using the US test, rebound hammer, and resonant frequency method, respectively. A regression analysis was made in order to determine relationships between the material's mechanical properties measured with the destructive and non-destructive methods.

2 EXPERIMENTAL PROGRAMME

2.1 Material and specimen preparation

A concrete mixture was prepared with the high initial strength Portland cement (CEM I 52.5 R), water, plasticizer, and limestone aggregate with maximum nominal size of 16 mm. The concrete mix proportions are summarized in *Table 1*.

Table 1. Concrete mix proportions

material	type	amount [kg]
cement	cem I 52.5 R	15.65
water	tap	7.36
hyper plasticizer		0.09
limestone aggregate	0-4 mm	40.50
limestone aggregate	4-8 mm	12.15
limestone aggregate	8-16 mm	28.35

Small prismatic specimens of 40 x 40 x 160 mm and big prismatic specimens of 100 x 100 x 400 mm were casted and cured in water for 28 days. Afterwards, they were air dried under standard laboratory conditions for 5 days. Before experimental testing, the bigger prisms were divided into four cubes of 100 x 100 x 100 mm. One of the cubes had two embedded temperature resistant thermocouples for monitoring temperature development in the specimen. One thermocouple was installed 5 millimetres below the surface and the other one in the centre of the cube. In total 15 cubes and 15 small prisms were tested.

2.2 Heating regime

Three cubes and three small prisms were tested immediately after curing period to obtain initial mechanical properties of concrete, while the remaining 12 cubes and 12 prisms were divided into four sub-groups heated in an electric furnace up to 200 °C, 400 °C, 600 °C or 800 °C. Average heating rate in the middle of the cube was 0.78 °C/min and 1.61 °C/min for heating up to the maximum temperature of 200 °C and 800 °C, respectively. During the heating, temperatures within one concrete cube were continuously recorded with thermocouples to obtain isothermal conditions. For example, such conditions were reached after 4.3 hours and 8.3 hours when exposed to 200 °C and 800 °C, respectively. The maximum temperature of the particular specimen was maintained for a short time. Then, the specimens were slowly cooled down to the room temperature and afterwards experimentally investigated. The temperature-time curves obtained from the thermocouple inside the cube are shown in *Fig. 1*.

Concrete Structures

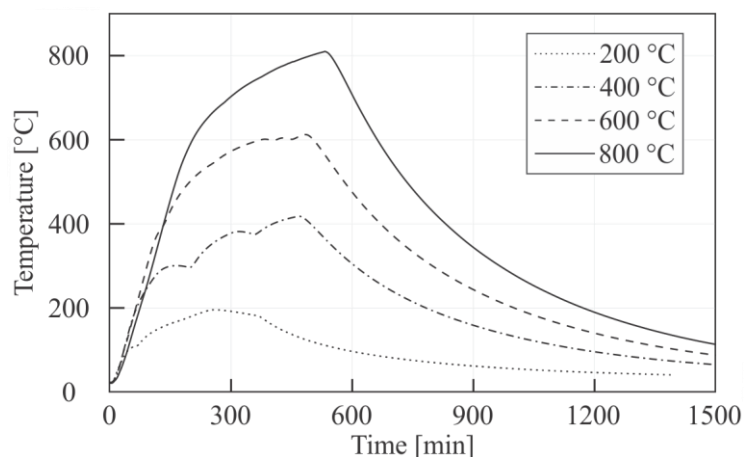


Fig. 1. Heating regime inside the concrete cube

2.3 Testing protocol

The cubes were tested using the US method where time of the US pulse traveling through the specimen was measured. Based on these measurements the US pulse velocity was calculated according to the standard EN 12504 [13]. The US tests were carried out with Proceq Pundit PL-200 instrument shown in Fig. 2 a). The next measurements were made with the resonant frequency method using GrindoSonic MK5 instrument shown in Fig. 2 b). Wave initiation in prisms was caused by a mechanical impulse. The obtained results were dynamic elastic and shear modulus determined according to the ASTM standard [14]. Schmidt rebound hammer was used on cubes to determine surface hardness of concrete according to the standard EN 12504 [15]. The standard compressive and bending tests were carried out on the cubes and small prisms, respectively, where the compressive and tensile strengths were determined according to the EN 12390 standards [16, 17].

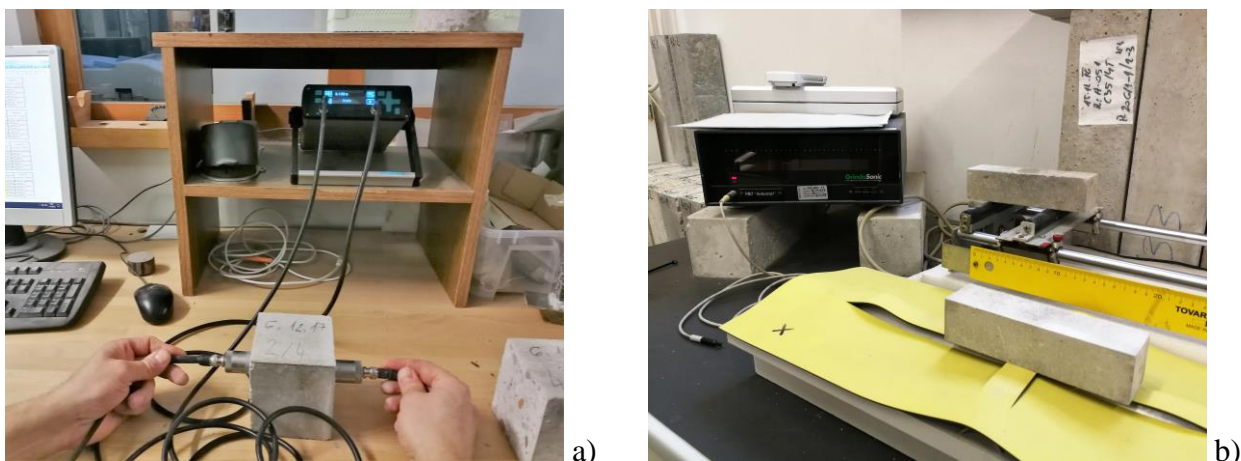


Fig. 2. a) US testing; b) Resonant frequency method

3 EXPERIMENTAL RESULTS

In Fig. 3, the influence of elevated temperatures on compressive strength, surface hardness, tensile strength, dynamic elastic modulus, and shear modulus is shown. The marks on the figure present average values of three tested specimens. As it can be seen in Fig. 3, the surface hardness is 95.2 %, 56.4 % and 39.7 % of the initial ones after exposure to 400 °C, 600 °C and 800 °C, respectively. Interestingly, the surface hardness for specimens exposed to 200 °C increased by 12.8 % when compared to the initial hardness. The compressive strength retained 77.0 % of the initial strength after exposure to 200 °C this is further reduced to 57.8 %, 39.3 % and 14.0 % after exposure to 400

°C, 600 °C and 800 °C, respectively. As seen in Fig. 3, the tensile strength, dynamic elastic modulus and shear modulus have similar decrease with increasing temperature. These mechanical properties are around 80 %, 30 %, 15 % and 5 % of the initial ones after exposure to 200 °C, 400 °C, 600 °C and 800 °C, respectively.

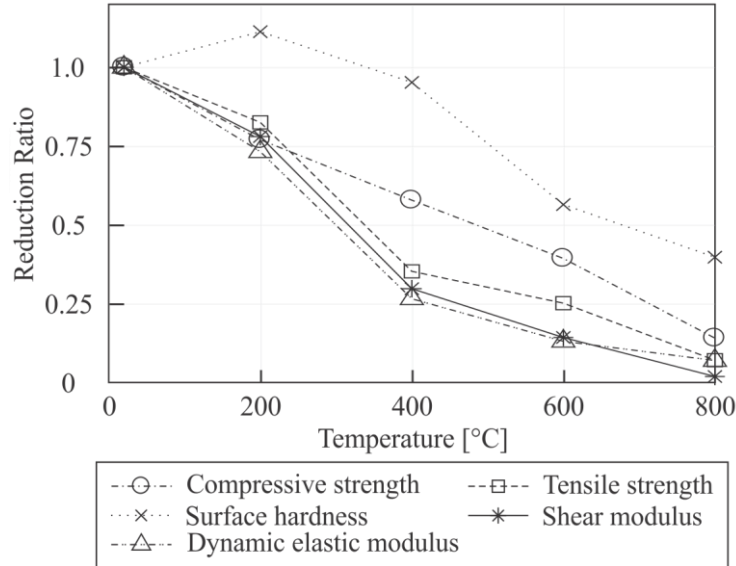


Fig. 3. Residual mechanical properties of limestone concrete after exposure to high temperatures

As observed in Fig. 3, the compressive strength of concrete decreases almost linearly with increasing temperature. The greatest influence of high temperatures is observed for the tensile strength, dynamic elastic modulus, and shear modulus between 200 °C and 400 °C, since these are reduced around 50 %.

4 RELATIONSHIPS BETWEEN DESTRUCTIVE AND NON-DESTRUCTIVE TESTS

Fig. 4 shows relationships between destructive and non-destructive methods for various mechanical properties of concrete initially exposed to high temperatures. The best fit-curve between the compressive strength S and the US pulse velocity V_p is given with a linear relationship by Eq. (1).

$$S = 18.927 V_p - 3.6221 \quad (1)$$

Coefficient of correlation between these two quantities, based on the proposed regression model, is $R^2 = 0.7953$. Similarly, the best fit between the surface hardness S_{surf} and the US pulse velocity V_p is also obtained by the linear relationship given in Eq. (2) with the coefficient of correlation $R^2 = 0.6436$.

$$S_{\text{surf}} = 11.4 V_p + 12.15 \quad (2)$$

For the compressive strength S and the surface hardness S_{surf} , the best correlation is described with the power law function given in Eq. (3) where the corresponding coefficient of correlation is $R^2 = 0.8376$.

$$S = 0.2389 S_{\text{surf}}^{1.3859} \quad (3)$$

The power law function gives a good fit also for the relationship between the tensile strength f_{ctm} and the torsional resonant frequency R_t given in Eq. (4). In this case, a high coefficient of correlation is obtained, i.e., $R^2 = 0.9774$.

$$f_{\text{ctm}} = 15821 R_t^{-1.399} \quad (4)$$

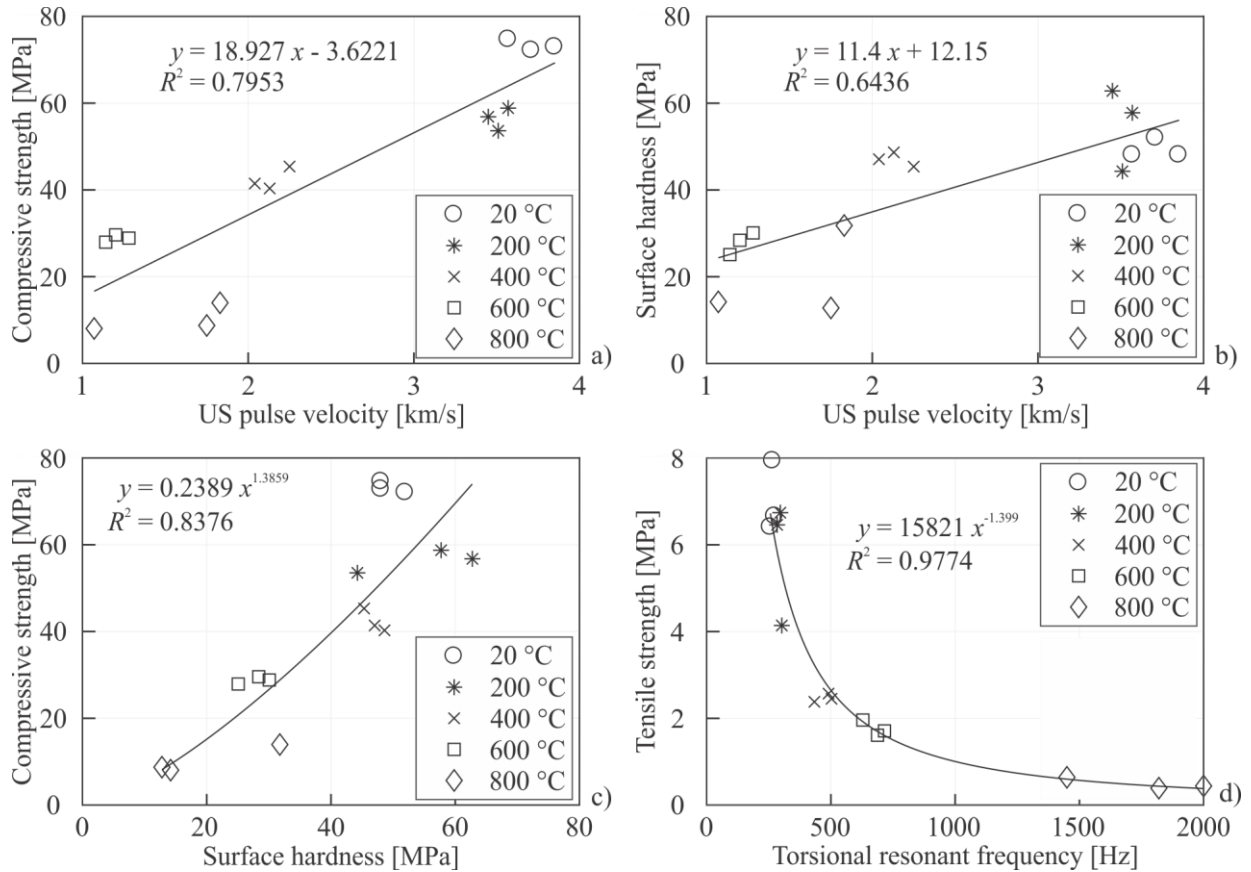


Fig. 4. Relationships between destructive and non-destructive methods for: a) US and compressive test; b) US and rebound hammer; c) Rebound hammer and compressive test; d) Resonant frequency method and bending test

5 CONCLUSIONS

The limestone concrete specimens initially exposed to high temperatures, were experimentally studied. The specimens were exposed to maximum temperatures of 200 °C, 400 °C, 600 °C or 800 °C. After cooling down to ambient temperature, the compressive strength, tensile strength, surface hardness, US pulse velocity, dynamic elastic modulus, and shear modulus of concrete were determined with destructive and non-destructive methods. The biggest influence of high temperatures was noticed for the tensile strength, dynamic elastic and shear modulus. The correlations between the different experimentally determined mechanical properties were proposed. The best correlation described by the power function was found between the tensile strength and the torsional resonant frequency. Interestingly, the relationship between the compressive strength and the US pulse velocity is linear. The performed experimental research indicates relatively good correlation between the results of the destructive and non-destructive methods. In the future, this could be used for the development of a numerical model for estimating various mechanical properties of concrete after fire, based on non-destructive measurements.

ACKNOWLEDGMENT

The work of U. Dolinar was financially supported by the Slovenian Research Agency with decision No. 802-7/2016-215. The work of G. Trtnik and T. Hozjan was also supported by the Slovenian Research Agency through the research core funding No. P2-0260. The support is gratefully acknowledged.

REFERENCES

1. Byeong-Chan Kim, Jin-Yeon Kim (2009). *Characterization of ultrasonic properties of concrete*. Mechanics Research Communications 36. pp 207-214.
<https://doi.org/10.1016/j.mechrescom.2008.07.003>
2. Omer Arioiz (2007). Effects of elevated temperatures on properties of concrete. Fire Safety Journal 42. pp 516-522. <https://doi.org/10.1016/j.firesaf.2007.01.003>
3. Musa Hakan Arslan, Özgür Erdoğan, Ali Köken, İbrahim Hakkı Erkan, Gamze Doğan (2017). *Evaluation of fire performance of prefabricated concrete buildings in Turkey*. Magazine of Concrete Research 69(8). pp 389-401. <https://doi.org/10.1680/jmacr.15.00306>
4. Kristian Dahl Hertz (2005). *Concrete strength for fire safety design*. Magazine of Concrete Research 57(8). pp. 445-453. <https://doi.org/10.1680/macr.2005.57.8.445>
5. Cristina Calmeiro dos Santos, João Paulo C. Rodrigues (2016). *Calcareous and granite aggregate concretes after fire*. Journal of Building Engineering 8. pp. 231-242.
<https://doi.org/10.1016/j.jobe.2016.09.009>
6. Izabela Hager, Tomasz Tracz, Jacek Śliwiński, Katarzyna Krzemień (2015). *The influence of aggregate type on the physical and mechanical properties of high-performance concrete subjected to high temperature*. Fire and Materials 40(5). pp. 668-682. <https://doi.org/10.1002/fam.2318>
7. Athina Savva, P. Manita, Kosmas K. Sideris (2005). *Influence of elevated temperatures on the mechanical properties of blended cement concretes prepared with limestone and siliceous aggregates*. Cement & Concrete Composites 27. pp. 239-248.
<https://doi.org/10.1016/j.cemconcomp.2004.02.013>
8. Muhammad Yaqub, Colin G. Bailey (2016). *Non-destructive evaluation of residual compressive strength of post-heated reinforced concrete columns*. Construction and Building Materials 120. pp. 482-493. <http://dx.doi.org/10.1016/j.conbuildmat.2016.05.022>
9. Gang-Kyu Park, Hong Jae Yim (2017). *Evaluation of fire-damaged concrete: An experimental analysis based on destructive and nondestructive methods*. International Journal of Concrete Structures and Materials 11(3). pp. 447-457. <https://doi.org/10.1007/s40069-017-0211-x>
10. Sandor Popovics, Joseph L. Rose, John S. Popovics (1990). The behavior of ultrasonic pulses in concrete. Cement and Concrete Research 20. pp. 259-270.
[https://doi.org/10.1016/0008-8846\(90\)90079-D](https://doi.org/10.1016/0008-8846(90)90079-D)
11. S. F. Selleck, E. N. Landis, M. L. Peterson, S. P. Shah, J. D. Achenbach (1998). *Ultrasonic investigation of concrete with distributed damage*. ACI Materials Journal 95(1). pp. 27-36.
12. Gregor Trtnik, Franci Kavčič, Goran Turk (2009). *Prediction of concrete strength using ultrasonic pulse velocity and artificial neural networks*. Ultrasonics 49. pp. 53-60.
<https://doi.org/10.1016/j.ultras.2008.05.001>
13. SIST EN 12504-4 (2004). *Testing concrete – Part 4: Determination of ultrasonic pulse velocity*. European Committee for Standardization, Brussels. 14 pp.
14. ASTM E1876-99 (2001). *Standard test method for dynamic Young's modulus, shear modulus, and Poisson's ratio by impulse excitation of vibration*. ASTM International, West Conshohocken, PA. www.astm.org.
15. SIST EN 12504-2 (2002). *Testing concrete in structures – Part 2: Non-destructive testing – Determination of rebound number*. European Committee for Standardization, Brussels. 5 pp.
16. SIST EN 12390-3 (2009). *Testing hardened concrete – Part 3: Compressive strength of test specimens*. European Committee for Standardization, Brussels. 19 pp.
17. SIST EN 12390-5 (2009). *Testing hardened concrete – Part 5: Flexural strength of test specimens*. European Committee for Standardization, Brussels. 11 pp.

STRUCTURAL BEHAVIOUR OF R/C BEAMS EXPOSED TO NATURAL FIRES

Nataša Kalaba¹, Venkatesh Kodur², Ankit Agrawal³, Patrick Bamonte⁴

ABSTRACT

The inherent fire resistance of concrete makes a complete collapse of R/C structures in fire a rare event. In recent years, however, some cases were reported where failure took place after the maximum ambient temperature had been reached, i.e. during the cooling phase. The present work is aimed at the investigation of the structural behaviour of reinforced concrete beams under the effect of natural fires, which are characterized by heating and cooling down phase. To this aim, the present constitutive models proposed in Eurocode 2 are suitably modified, in order to account for the intrinsic issues regarding the materials' behaviour during the cooling phase. A 3D finite element model of a fire exposed R/C beam was developed in ABAQUS software, taking into account as many realistic parameters as possible. The model was validated against the available experimental results and the agreement between the numerical and experimental results is very good. A parametric study is carried out, in order to identify the critical parameters governing the R/C beam fire response. Results show that parameters such as duration of heating and cooling phase, beam size, as well as concrete cover depth play a crucial role in the magnitude of the residual displacements and the amount of recovery upon cooling.

Keywords: reinforced concrete members, fire, cooling, residual behaviour.

1 INTRODUCTION

Most of the current knowledge about the behaviour of reinforced concrete members comes from standard fire testing or relatively simplified calculations and numerical models. In view of achieving fire safety through effective and cost-effective solutions, there is a tendency to move from prescriptive to performance based design. Moreover, the most recent version of EC1-Fire Design [1] paves the way for performance-based design, as the fire curve can be worked out taking as many significant parameters as possible into consideration, so as to eventually yield a more accurate representation of the fire scenario. Switching to performance-based design calls for a more realistic representation of the fire, and thus for the use of fire scenarios that include not only a heating phase, where the gas temperature is monotonically increasing (such as the standard fire), but also a cooling down phase. The use of natural fires implies that the behaviour of the members has to be studied not only in the heating phase, but also during or after the cooling phase. Delayed failure,

¹ PhD Candidate. Department of Civil and Environmental Engineering, Politecnico di Milano, Milan, Italy.
e-mail: natasa.kalaba@polimi.it

² Professor. Department of Civil and Environmental Engineering, Michigan State University, East Lansing, USA.
e-mail: kodur@egr.msu.edu

³ PhD Candidate. Department of Civil and Environmental Engineering, Michigan State University, East Lansing, USA.
e-mail: ank.agr@gmail.com

⁴ Assistant Professor. Department of Civil and Environmental Engineering, Politecnico di Milano, Milan, Italy.
e-mail: patrick.bamonte@polimi.it

residual displacements just after the cooling phase or residual capacity after the complete cooling down of the member can be investigated.

Given that most of the current knowledge on the fire behaviour of R/C beams comes from standard fire resistance testing or simplified numerical models, many parameters such as specimen size, aggregate type, concrete strength, load level, but also realistic description of fire scenario and realistic restraint conditions (presence of axial and rotational restraints) are not included.

Studies dealing with the possibility of failure in the cooling phase are very few to this date. Gernay and Dimia [2] investigated the structural behaviour of concrete columns subjected to a natural fire, with special focus on the cooling phase and the possibility of collapse during or after the cooling phase. The main mechanism leading to this type of failure is found to be the delayed increase of temperature in the central zones of the element and the ensuing additional loss of concrete strength during the cooling phase. A parametric study showed that the most critical situations with respect to delayed failure arise for short fires and for columns with low slenderness (short length and/or massive sections). Studies on the possibility of failure in the cooling phase for R/C beams are not available, to the Authors' knowledge.

Studies investigating the residual behaviour through either destructive testing in the laboratory or numerical approaches are certainly more numerous. Kumar and Kumar [3] tested five R/C beams, exposed to ISO834 fires of varying fire duration, without any loads applied. The aim was to measure the residual load capacity; unfortunately, the temperature and displacement measurements during the cooling phase have not been reported. Kodur et al. [4] tested a set of three reinforced concrete beams by subjecting them to fire curves with heating and cooling phase. Then, the beams were tested for measuring their residual bearing capacity. Two beams, B1 and B3, were tested with axial restraints at the extremities, while B2 was simply supported. Two beams were made of high-strength concrete and the third beam was of normal-strength concrete. Results from the experimental tests indicate that R/C beams retain most of their room-temperature flexural capacity after exposure to fire. Data from fire tests and numerical studies are utilised to develop a simplified approach for evaluating the post-fire residual strength of R/C beams. The approach has been validated against the measured values of the residual strength obtained from the tests and the proposed approach shows sufficient accuracy for practical applications.

Available numerical studies utilized two approaches so far. First approach is simplified cross-sectional analysis, as, for example, in [4]-[6]. Simplified cross-sectional approaches are based mainly on empirical equations to predict the residual and post-fire load capacity R/C beams and columns. Maximum temperature in the rebar is identified as a key parameter. The behaviour of a fire-exposed R/C beam depends on the internal temperatures in the beam, the load level during the fire event, the cooling method and rate, as well as the strength recovery time following the cooling period. In most of the studies, temperature-induced degradation of materials' mechanical properties is based on the heating phase alone, not accounting for the irrecoverable material damage that takes place during cooling. Through the current simplified approaches, it is not possible to accurately predict post-fire residual deformations. Second used approach is detailed FEM analysis [7]-[8], where the latter model does not use distinct material properties during heating, cooling and residual phases.

The objective of this paper is to investigate the structural behaviour of simply supported R/C members exposed to natural fires, in order to highlight the residual behaviour (i.e. after the cooling phase of the fire), and to clarify the role played by duration of the heating phase, concrete cover and cooling rate. To this end, a 3D finite element model of a fire exposed R/C beam was developed in ABAQUS 6.16, taking into account as many realistic parameters as possible. Contribution of this research is in the refinement of the constitutive models of concrete and steel, to properly take into account the different irreversible phenomena that take place in a full heating-cooling cycle. The modelling approach is validated against an experimental test showing satisfying agreement. The role of the different parameters coming into play is then investigated by means of parametric analyses carried out on two beams.

2 NUMERICAL MODEL

Sequentially coupled thermo-mechanical analysis is performed by means of the commercial finite element software ABAQUS 6.16. Two sub-models are built: a model for thermal analysis and a model for mechanical analysis. The temperatures in the member obtained from the thermal analysis act as thermal body-loads in the structural model, being the initial condition for the subsequent mechanical analysis. Longitudinal reinforcing bars and stirrups are present in both thermal and mechanical model. The objective of the mechanical analysis is to obtain the displacements of the beam member.

2.1 Thermal analysis

Eight-noded linear brick elements (DC3D8) are used for concrete while reinforcing bars are discretized using two-noded link or truss elements (DC1D2). These elements have the nodal temperature as the only active degree of freedom. Heat transfer within the element is assumed to be governed by conduction. At the boundaries of the heat exposed surfaces, convection with convective coefficient of $25 \text{ W/m}^2\text{K}$ is assumed, while for the unexposed surfaces, convective coefficient is set to $9 \text{ W/m}^2\text{K}$, accounting for the radiation. Radiation with $\varepsilon = 0.7$ is assumed for all the heat-exposed concrete surfaces. At the concrete-rebar interface, a tie constraint is present, to enforce the unique temperature at the nodes shared between steel and concrete.

Thermal properties of concrete and steel are assumed as per Eurocode 2 [1]. Conductivity and specific heat of concrete are considered irreversible upon cooling, as some of the most recent studies are suggesting [2].

2.2 Mechanical analysis

Concrete is discretized using 8-node continuum elements (C3D8), with translations in three directions as active degrees of freedom at each node. For steel, 2-noded truss elements (T3D2), which deform by axial elongation only, are used. Concrete-rebar interface is modelled with embedded region constraint, i.e. no slip is allowed. Material mechanical properties for both concrete and reinforcing steel are taken as per Eurocode 2 [1], but in the cooling phase, they are considered as irrecoverable.

3 MATERIAL PROPERTIES

3.1 Concrete

To accurately model the behaviour of concrete in tension and compression at elevated temperatures, Concrete Damage Plasticity model [9] has been used. This model allows capturing the strong nonlinearity of concrete and different failure mechanisms in tension (by cracking) and compression (by crushing), and is primarily intended for modelling reinforced concrete structures. The model assumes that the uniaxial tensile and compressive responses of concrete are characterized by a plastic behaviour, whereas the irreversible phenomena that characterize the unloading phase (if any) are treated by means of a damage mechanics approach. The contribution of the tensile stiffness of uncracked concrete after to the reinforcement stiffness (tension stiffening [10]), which is caused by bond properties of the reinforcement, is modelled through a trilinear descending branch of the constitutive model in tension [11].

The temperature-induced decay of the mechanical properties of concrete is taken as per Eurocode 2 [1]. Still, these properties are considered as irrecoverable during cooling, to account for the damage in the material. This has been done by implementing a FORTRAN user subroutine – UFIELD [10], which updates the mechanical properties only in the heating phase, when the temperature in the current time increment has increased with respect to the previous one.

Moreover, unloading is allowed to take place along the branch defined by the unloading stiffness, that is somewhat higher than the initial stiffness. In this way, the irrecoverable strain components (i.e. transient creep strain) are implicitly accounted for.

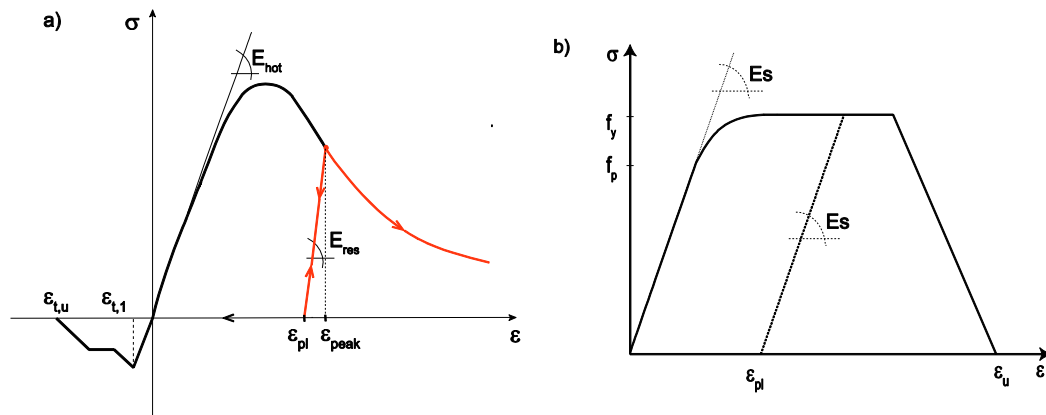


Fig. 1 Constitutive model for: a) concrete; b) steel

3.2 Steel

Plasticity model that uses Mises yield surface with associated plastic flow and isotropic hardening was used to model the steel in tension and compression [10]. Eurocode-proposed model with distinct elastic and yield strength was used. Variation of the mechanical properties, namely strength and elastic modulus, is taken as per Eurocode. If the maximum temperature in the rebars exceeded 500°C , mechanical properties of steel are not recovered upon cooling. Otherwise, influence of irrecoverable creep can be neglected and steel recovers its strength and elastic modulus upon cooling down [12].

4 VALIDATION

Validation was carried out against measured data on one of the beams tested in the experimental campaign by Dwaikat and Kodur [13]. The beam, designated as B2, was axially restrained. Details of the beam geometry and cross section can be found in [13]. Rebars had a yield strength of 420 MPa and beam was made of NSC having average compressive strength of 55 MPa. Beam is tested under two point loads of 50 kN, applied 30 minutes before the start of the fire and maintained constant throughout the fire exposure, which produced a bending moment equal to 55% of the flexural capacity of the beam. In the test, the beam was subjected to short design fire (SF). There was no spalling during the test. Rate of temperature rise at the beginning is rather high, due to steeper temperature rise of SF fire. Maximum temperature both in the rebar and concrete core is reached during the cooling phase of the fire. After reaching the maximum temperature, decrease in temperature takes place due to decay phase of fire exposure, as it can be seen in Fig. 2a. Given that the behaviour of R/C members in flexure is governed primarily by the temperature in the rebars, midspan deflections are increasing as long as the rebar temperature is increasing. As the rebars start to cool down, the trend of the deflection response reverses, leading to a certain recovery and a residual deflection smaller than the maximum one [Fig. 2b]. Overall, the agreement between the numerical and experimental values is good, both for the temperatures and the midspan deflection.

5 PARAMETRIC ANALYSIS

Parametric analyses were performed on two R/C beams, with span $L=5\text{m}$. Central portion of the span was exposed to fire. Beam geometry and cross-section details can be seen in Fig. 3. Reinforcement ratio for both beams was 1.2%. Section BX2 is more massive than BX1; in this way, the role of the section size in the overall structural response can be highlighted.

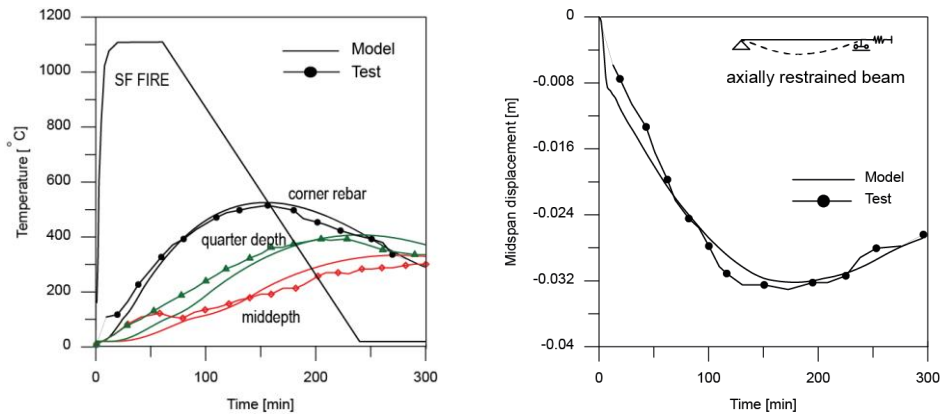
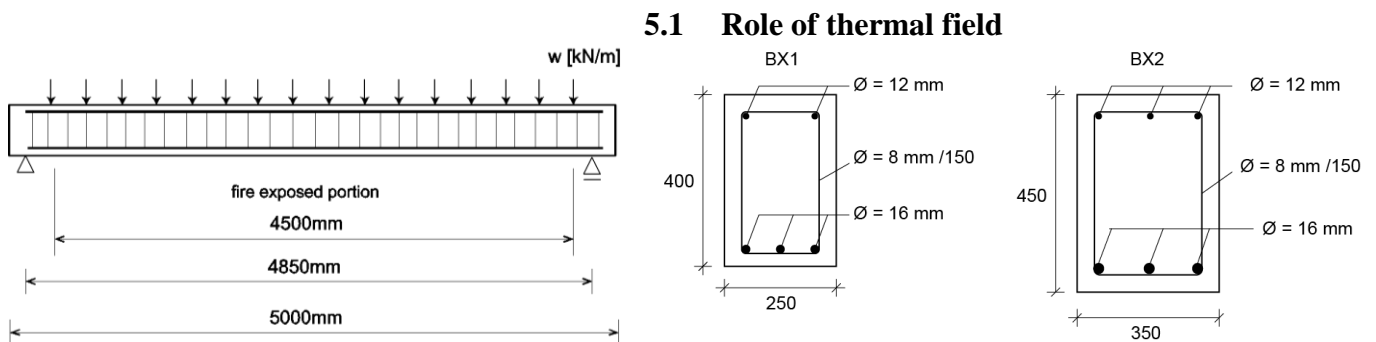


Fig. 2 Comparison between experimental results and numerical simulations: (a) temperature in the rebars and concrete core; (b) deflection at midspan.

Concrete compressive strength is $f_c=50$ MPa while the steel yield strength is $f_y=450$ MPa. Bending capacity of the two beams at ambient temperature is $M_{rd}=126$ kNm for BX1 and $M_{rd}=191$ kNm for BX2. Uniformly distributed load acting on both beams causes maximum bending moments equal to 50% of the capacity at ambient temperature.

Parameters such as duration of the heating phase, cooling rate and concrete cover were varied. All the fire scenarios correspond to the parametric fire of Eurocode 1. The amount of fuel load varied (from 250 to 750 MJ/m²), resulting in the heating phase duration of 1h for fire scenario PF1, 2h for fire scenario PF2 and 3h for fire scenario PF3. Cooling took place along a linear branch, with cooling rate computed according to Eurocode - faster cooling [1] and Buchanan - slower cooling [14]. The initiation of the cooling phase of fire is also indicated in the figures. Concrete cover varied from 20 to 40 mm. Reference parameters are PF1 fire scenario with Eurocode cooling rate and concrete cover of 4 cm.

Fig. 3 Beam geometry and cross-section details



5.1 Role of thermal field

Given that almost the full moment capacity of the R/C beam is provided by the reinforcing steel, it is more than clear that a sizable loss of stiffness and strength has to be prevented in order to minimize the residual deflections and eventually avoid failure. However, since the reference concrete cover depth is 4 cm, very high temperatures are likely to be attained in most cases. In Fig. 4a, the average temperature in the corner rebars is plotted as a function of the fire duration. It is worth noting that the temperature continues to increase for some time after the onset of the cooling phase: as a matter of fact, the maximum temperature is reached at approximately 120, 180 and 270 minutes for heating phase durations of 60, 120 and 180 minutes, respectively. Maximum temperature varies significantly with the duration of the heating phase, from 484°C for 1h fire duration to 791°C for 3h fire duration. As previously mentioned, this can be attributed to the low conductivity and high thermal capacity of concrete, which delay the heat transfer towards the inner layers of the section. Note that failing to account for the cooling phase can lead to a significant

underestimation of the maximum temperature (from -20 to -50%). Similar trends are followed also for beam BX2, but given that it is more massive, the temperatures are somewhat lower [Fig. 4b]. In Fig. 5a, the average temperature in the strands is plotted as a function of the cooling rate, for the reference duration of the heating phase (= 120 minutes). Cooling rate has a significant influence on the temperature in both the concrete core and the rebars, with slower cooling leading to higher temperatures. Moreover, better protected steel rebars experience lower temperatures [Fig. 5b].

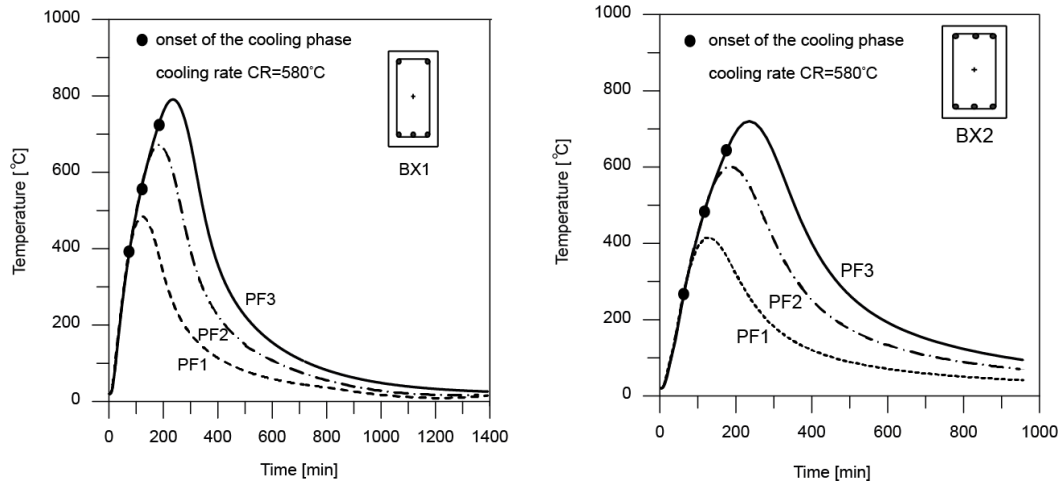


Fig. 4 Temperature in the corner rebar for different fire duration for: a) BX1; b) BX2

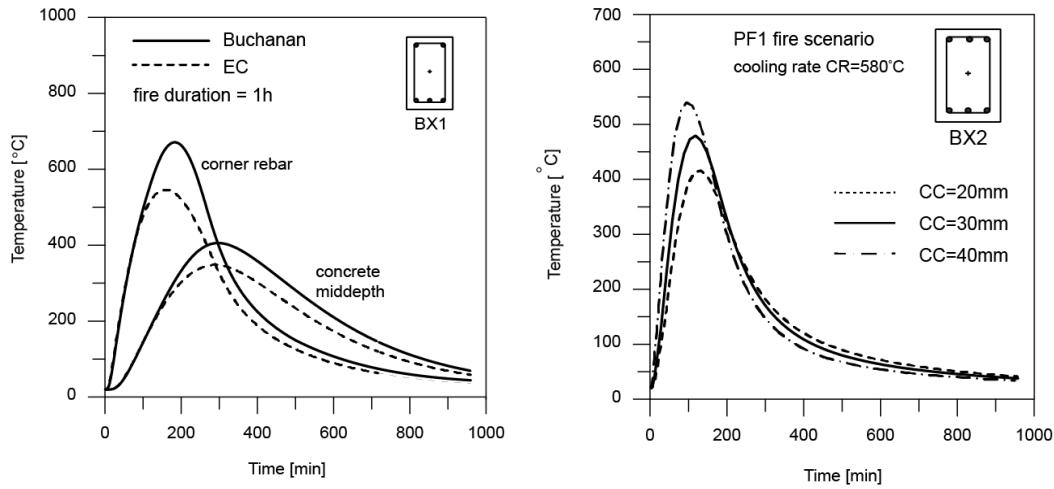


Fig. 5 Temperature in the: a) corner rebar/middepth for different cooling rate (beam BX1); b) corner rebar for different concrete cover (beam BX2)

5.2 Structural response

In Fig. 6a and Fig. 6b, the evolution of the deflection at midspan is shown for fire durations of 1, 2 and 3 hours. Increasing the fire duration increases the temperature in the rebars which then leads to higher peak deflections and also higher residual deflections. The deflections continue to increase also in the cooling phase of the fire; therefore neglecting the cooling phase of fire can lead to a significant underestimation of the maximum deflection (up to 40%). Upon cooling, the deflection trend reverses, leading to a limited recovery. In Fig. 6c the effect of the cooling rate on the evolution of the midspan deflection can be noticed. Slower cooling leads to higher maximum deflection, due to prolonged increase of the temperatures inside the member. The recovery of the deflection, however, is more pronounced than in the case of faster cooling, with the residual

deflection being around 75% of the maximum value. Nevertheless, faster cooling is more beneficial, given that it leads to lower both peak and residual deflections.

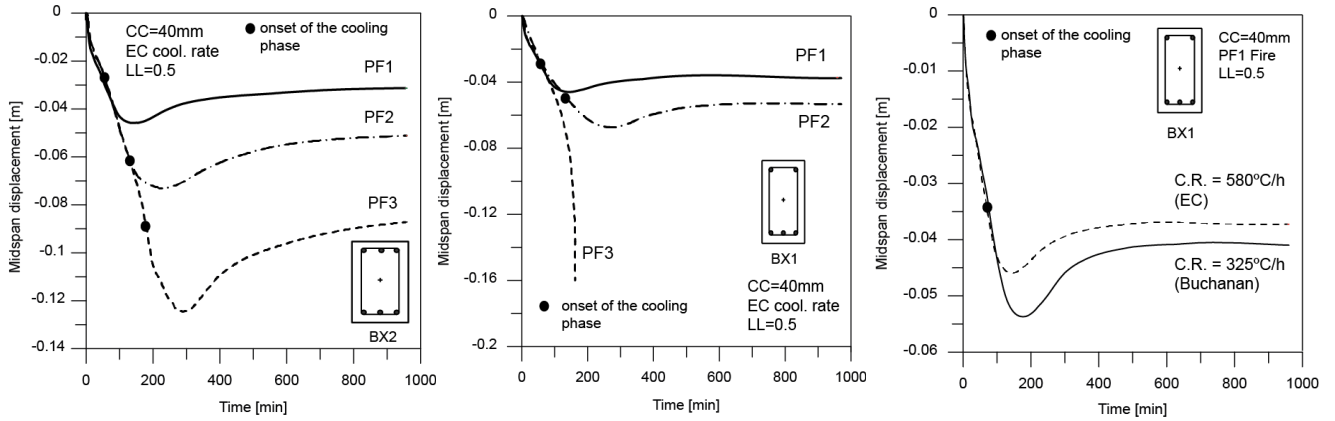


Fig. 6 Midspan deflection in time for: a) varying fire scenario for BX2; b) varying fire scenario for BX1; c) varying cooling rate for BX1

Effect of the concrete cover can be seen in Fig. 7a. Poorly protected rebars experience higher temperatures which then lead to higher maximum deflection at midspan and almost no recovery after cooling down. As for the effect of the dimension of the section, in the Fig. 7b and Fig. 7c it can be seen that more massive beam (BX2), for the fire duration of 2h, experiences more recovery in the deflections during the cooling down phase, eventually leading to lower residual deflections than in beam BX1. Moreover, for the fire duration of 3h, more massive beam did not fail while beam BX1 failed in the heating phase.

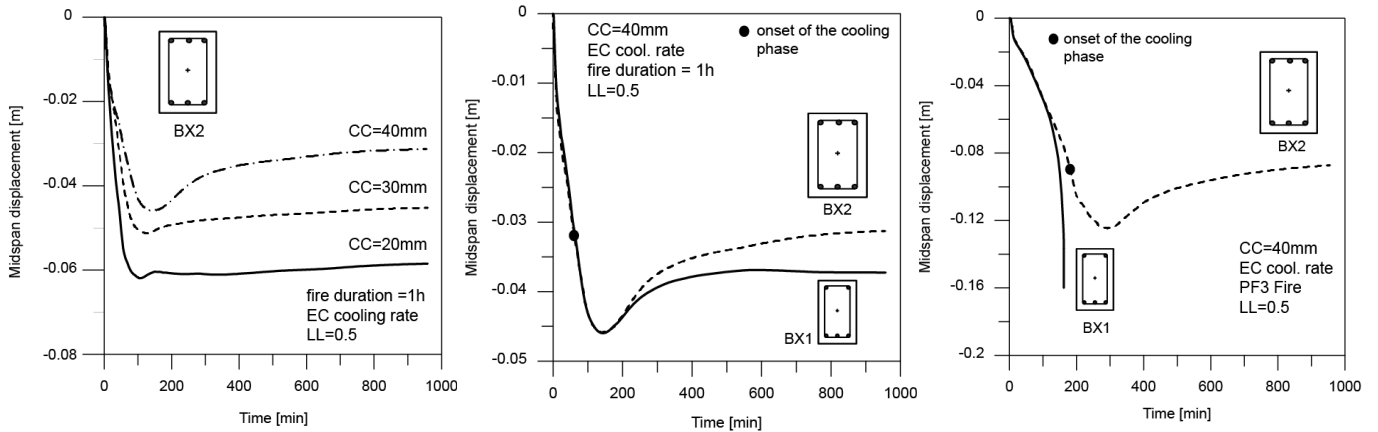


Fig. 7 Midspan deflection in time for: a) different concrete cover; b) different cross-sections for PF1 fire scenario; c) different cross-sections for PF3 fire scenario

6 CONCLUSIONS

The numerical investigations carried out allow to draw some general conclusions on the structural behaviour of reinforced concrete members exposed to natural fires:

- Evolution of the deflections is primarily governed by the maximum temperature in the steel rebars. Temperature continues to increase sometime after the onset of cooling.
- Influence of the beam geometry is determined mainly by the concrete cover depth and available “thermal mass”. More massive beam exhibited better performance in terms of magnitude of peak and residual deflection.

- Upon cooling, trend of the deflections reverses and the magnitude of the residual deflections and the amount of recovery upon cooling will strongly depend on the fire duration and cooling rate and on how well the steel bars are protected.

REFERENCES

1. Eurocode 2 – EN 1992-1-2: Design of Structures, Part 1-2: General Rules- Structural Fire Design, 2004, European Committee for Standardization, Brussels, Belgium.
2. Thomas Gernay, Mohamed Salah Dimia, (2013) *Structural behaviour of concrete columns under natural fires*. Engineering Computations 30(6), pp. 854-872, <https://doi.org/10.1108/EC-05-2012-0103>
3. Kumar Awadhesh, Kumar Vivek Anuj, (2003). *Behaviour of RCC beams after exposure to elevated temperatures*. Journal of the Institution of Engineers (India): Civil Engineering Division, 84. pp. 165-170
4. Kodur Venkatesh, Dwaikat Monther B., Fike RS, (2010). *An approach for evaluating the residual strength of fire-exposed RC beams*. Magazine of Concrete Research. 62. pp. 479-488
5. Kodur Venkatesh K, Raut Nikhil R, Mao Xiaoyong and Khaliq Wasim, (2013). *Simplified approach for evaluating residual strength of fire-exposed reinforced concrete columns*. Materials and Structures. 46. pp. 2059-2075
6. Kodur Venkatesh, Dwaikat Monther B., (2008). *A numerical model for predicting the fire resistance of reinforced concrete beams*. Cement and Concrete Composites. 30(5). pp. 431-443
7. Kodur Venkatesh, Agrawal Ankit, (2016). *Critical factors governing the residual response of reinforced concrete beams exposed to fire*. Fire Technology. 52(4). pp. 967-993.
8. Ozbolt Josko, Bosnjak Josipa, Periskic Goran, Sharma Akanshu. (2014). *3D numerical analysis of reinforced concrete beams exposed to elevated temperatures*. Engineering Structures. 58. pp.166-174
9. Lo Monte Francesco, Kalaba Nataša and Bamonte Patrick. (2017). *On the extension of a plastic-damage model to high temperature and fire*. Proceedings of IFireSS, Ed. Nigro E. and Bilotta A.-- 2nd International Fire Safety Symposium, Naples, Italy. pp. 703-710
10. ABAQUS (2016) Version 6.16 Documentation. Dassault Systems Simulia Corp., Providence (RI, USA).
11. Feenstra Peter, de Borst Rene. (1995). *Constitutive model for Reinforced Concrete*. Journal of Engineering Mechanics. 121(5). pp. 587-595.
12. Neves Ildefonso Cabrita, Rodrigues Joao Paulo Correia and Loureiro Antonio De Padua. (1996). *Mechanical Properties of Reinforcing and Prestressing Steel After Heating*. Journal of Materials in Civil Engineering, 8(4), pp. 189-194.
13. Dwaikat Monther B, Kodur Venkatesh (2009). *Response of restrained concrete beams under design fire exposure*. Journal of Structural Fire Engineering. 135(11). pp. 1408-1417. DOI: 10.1061/_ASCE_ST.1943-541X.0000058
14. Feasey Roger, Buchanan Andrew (2002). *Post-Flashover fires for structural design*. Fire Safety Journal. 37(1). pp. 83-105

RESIDUAL STRENGTH OF ULTRA-HIGH PERFORMANCE FIBRE REINFORCED CONCRETE

Charles Kahanji¹, Faris Ali², Ali Nadjai³

ABSTRACT

This paper presents the residual strength of ultra-high performance fibre reinforced concrete (UHPFRC) containing both steel and polypropylene fibres. Previous results have shown that UHPFRC cured at different temperatures differ in mechanical properties. This experimental investigation compares the influence of the cold and the hot curing temperatures on the residual strength. This study focusses on UHPFRC that is spalling-resistant, hence, in addition to steel fibres, polypropylene fibres were added to eliminate the phenomenon. The test elements were heated at 8 different temperatures ranging between 200°C and 900°C. The test results showed that UHPFRC have a higher strength retention up to 600°C in stark contrast to commonly used concrete which lose considerable strength when exposed to temperatures as low as 300°C. The results further showed that elements cured in cold water had higher strength gains of up to 30% compared to 14% for hot cured. Overall, the cold cured specimens had a higher relative residual strength at almost all temperatures.

Keywords: Residual strength, high performance concrete, polypropylene fibres, steel fibres

1 INTRODUCTION

The mechanical strength of both normal strength concrete (NSC) and high strength concrete (HSC) is widely reported to deteriorate when exposed to elevated temperatures. In their investigations, Chan et al. [1] exposed both NSC and HSC elements to temperatures of up to 1200 °C. The specimens retained their ambient strength between 0 to 400 °C. Severe strength deterioration was observed between 400 °C and 800 °C. Beyond 800°C, only a tiny fraction of their original strength was retained. Chen and Liu [2] also observed similar trends in the residual strength of HSC reinforced with steel, carbon and polypropylene (PP) fibres. The residual strength investigations carried out by Xiao and Falkner [3] on high performance concrete (HPC) also recorded drastic strength degradation at temperatures greater than 400°C. Below 400°C, the residual strength did not change significantly from the ambient compressive strength. There appears to be insufficient research information relating to the residual strength of ultra-high performance fibre reinforced concrete (UHPFRC). Burke [4] performed residual strength tests of UHPC commercial formula Ductal FM (steel fibres only) and Ductal AF (steel fibres and PP) at 200 °C, 300 °C, 400 °C 500 °C and 600 °C. The specimens made from Ductal FM spalled at higher temperatures and residual strength at higher temperatures was only analysed for the specimens obtained from Ductal AF. The residual strength was measured at different exposure durations ranging from 1 hour to 6 hours. 1 hour was lower than the ambient temperature strength for all temperatures. The results showed that the change in residual compressive strength of

¹ Post-Doctoral Research Associate, Department of Civil Engineering, Fire Research Unit, Stellenbosch University, South Africa
e-mail: ckahanji@sun.ac.za

² Professor. Belfast School of Architecture and the Built Environment, Ulster University, Belfast, UK.
e-mail: f.ali@ulster.ac.uk

³ Professor and Director of Fire Safety Engineering Research Technology Centre, Ulster University, Belfast, UK.
e-mail: a.nadjai@ulster.ac.uk

UHPC closely follow that of other types of concrete (NSC, HSC) with respect to an increase in exposure temperature.

Because of their inherent spalling behaviour, UHPFRC specimens usually explode when heated. Research has shown that adding polypropylene fibres to high performance concrete eliminates spalling [2,4,5]. Polypropylene fibres have a melting temperature of about 160°C. The concrete surface in direct contact may attain temperatures beyond the melting point of polypropylene fibres. Once the concrete attains the temperature higher than 160°C, polypropylene fibres in the vicinity would melt and vaporise thereby creating a series of connected paths or channels from the inner concrete core to the concrete surface. These channels thus act as passage routes for gases under high pressure, created inside the concrete to escape through the free surface [6]. The pressure inside the concrete is therefore relieved which eventually prevents any explosions [7]. Thus, adding polypropylene fibres to the mix at casting stage is one viable ways of effectively determining the residual strength of UHPFRC. The test specimens may not explode and would remain intact on exposure to elevated temperatures, thereby enabling the determination of their residual strength.

1.1 Significance of the study

In this paper, the residual strength of spalling resistant UHPFRC with a dosage of 2 vol. % of steel fibres and 4kg/m³ of polypropylene fibre was determined at 8 different temperatures ranging between 200°C and 900°C. Owing to the fact that the mechanical properties of concrete are influenced by the curing temperature, this paper studies the influence of the two curing temperatures on the residual strength behaviour. Heat treatment of concrete elements leads to accelerated strength development of concrete. UHPFRC contains vast amounts of silica fumes. The latter reacts with calcium hydroxide to form additional binders called calcium hydrate silicate (C-S-H) which are triggered at elevated temperature. Studies have shown that concrete cured at elevated temperatures has a denser and more compact matrix due to enhanced pozzolanic activities [8]. In addition to investigating the compressive strength of elements heated at several temperatures, this study compares the influence of cold water curing and heat treatment of UHPFRC on the residual strength. This paper presents findings that would help in understanding the strength degradation of UHPFRC when exposed to elevated temperatures. The obtained results of residual strength of concrete heated at elevated temperatures can be useful in the post-fire analysis.

2 EXPERIMENTAL PROGRAMME

2.1 Materials and the casting process

The residual strength tests were performed on the 100 mm cube specimens. The materials used in the casting of the cube specimens were; fine sand ($\leq 0.6\text{mm}$), cement (CEM I 52.5N) with 0.2 water-cement ratio, steel fibres (13 mm long and 0.2 mm diameter), polypropylene fibres (4 kg/m³), silica fume and superplasticiser. A detailed casting procedure and material proportions used can be found in the authors' other publication [9]. In total, 54 cube elements were analysed. These were all made from the same batch. The elements were divided into two different streams based on their curing regime. The first stream contained 27 cubes which were all cured in ambient water for 28 days. The second stream had an identical number but was cured in hot water (90 °C). The curing period for the latter was 7 days.

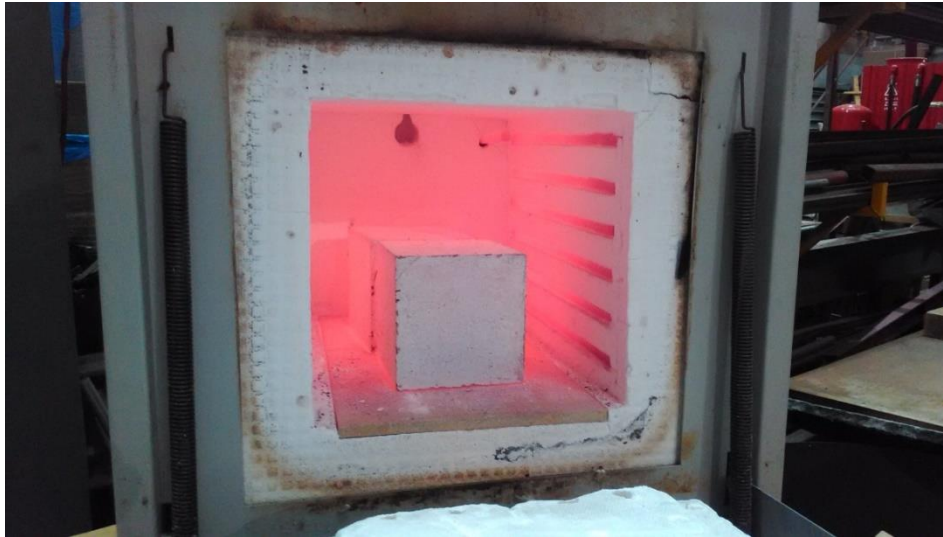


Figure 1: Test elements inside the EFF Carbolite Furnace

2.2 Heating

Test specimens were heated in the ELF Carbolite Furnace, shown in Figure 1. The furnace had an internal chamber measuring 200 mm high, 220 mm wide and 315 mm in depth (14 litres). The furnace chamber was well insulated with ceramic fibre boards which had exceptionally low heat of conductivity. The furnace could accommodate a maximum of three 100 mm cubes. The maximum heating temperature of the furnace was 1100 °C. The specimens from each curing streams were analysed at nine different temperatures i.e. room temperature (20°C), 200, 300, 400, 500, 600, 700, 800 and 900°C. For both curing conditions, three specimens were investigated at each of the nine temperatures. The specimens were placed in the furnace chamber and heated to the target temperature with a heating rate of about 10 °C/minute. Once the target temperature was attained, it was maintained for 1 hour for purposes of achieving thermal stability. After being heated for 1 hour, the cubes were removed and placed outside to cool in natural air. Some of the cube specimens are shown in Figure 2 after undergoing natural cooling. The test cubes were then tested in a standard compression machine to determine the residual compressive strength. The residual strength tests were performed within 24 hours of heating the cubes.



Figure 2. 100 mm cube specimens after being heated at various temperatures

3 RESULTS AND DISCUSSIONS

The ambient compressive strength of the cold-cured specimen was 100 MPa. On the other hand, the compressive strength of the hot-cured samples at ambient temperature was 150 MPa. The residual strength results of all the specimens for temperatures between 200 °C and 900 °C are shown in Both

sets of results show that the highest gain in strength was recorded at 400 °C. The cold-cured specimens generally had a higher relative residual strength at all temperatures. Overall, all the tested UHPFRC elements recorded higher residual compressive strength than the ambient temperature compressive strength up to the temperature of 600°C. This is in contrast to the documented behaviour of NSC and HSC which normally record losses in strength at elevated temperatures even at temperatures as low as 200°C.

Table 1. The residual strength for both the cold and hot-cured specimens is plotted in Figure 3. The reported residual strength was higher than the corresponding ambient temperature strength up to 500 °C for the hot-cured and 600 °C for the elements cured in cold water. The results show that the rate of increase in residual strength between 200 and 400 °C was much greater in the cold-cured specimens.. The results further indicate that from 500 °C, the rate of strength degradation was higher in hot-cured specimens. Both sets of results show that the highest gain in strength was recorded at 400 °C. The cold-cured specimens generally had a higher relative residual strength at all temperatures. Overall, all the tested UHPFRC elements recorded higher residual compressive strength than the ambient temperature compressive strength up to the temperature of 600°C. This is in contrast to the documented behaviour of NSC and HSC which normally record losses in strength at elevated temperatures even at temperatures as low as 200°C.

Table 1: Residual strength and relative residual strength of test specimens

Temperature [°C]	Compressive strength [MPa]		Relative residual strength $\left[\frac{f_{ck-T}}{f_{ck-20}} \right]$	
	Cold-cured	Hot-cured	Cold-cured	Hot-cured
Room Temp	100.0	150.6	1.0	1.0
200	111.2	152.8	1.11	1.01
300	120.6	161.5	1.21	1.07
400	130.7	171.6	1.31	1.14
500	104.8	163.6	1.05	1.09
600	101.5	136.2	1.02	0.90
700	87.9	110.7	0.88	0.74
800	52.5	65.9	0.53	0.44
900	28.8	20.1	0.29	0.13

3.1 Relative Residual strength

The residual strength results have been expressed in form of relative residual for purposes of analysing and comparing changes in strength. The relative residual strength at a given temperature (T) is the ratio of the residual strength (fck-T) to the ambient temperature compressive strength (fck-20). The relative residual strengths are expressed in graphical form in Figure 4. The relative residual strength for cold-cured specimens was higher than in hot-cured up to 400 °C. The peak residual strength (at 400°C) was higher than the corresponding ambient strength by 31 % and 14 % for the cold-cured and hot-cured elements respectively. At 500 °C the residual strength was still higher than the ambient strength by 5 % and 9 % for the cold-cured and the hot-cured respectively. The results have shown how UHPFRC have a higher strength retention capacity after being exposed to higher temperatures such that even at 600 °C the elements (cold-cured) still had a marginal 2 % strength gain although the hot-cured lost 10 % of their ambient strength. At 700 °C, it can be seen that the strength of both sets of specimens was lower than their ambient strength; 12 % and 26 % losses for the cold and hot cured, respectively. These losses are still significantly lower compared to what obtains in the case of NSC and HSC. The cold-cured elements continued to record lower strength losses for the remaining temperatures i.e. 47 % at 800 °C and 71 % at 900 °C compared to 56 % loss at 800 and 87 % loss at 900 °C for the hot-cured.

3.1.1 Influence curing of temperature

There is a clear difference in the residual strength patterns for the cold and the hot cured elements. The disparities can be explained in terms of the hydration process. In hot-cured specimens, there is a near complete hydration process due to the activation of pozzolanic reactions. For the concrete cured in ambient temperature water, the hydration process at 28 days is normally not fully complete; the bulk of silica fume added at mixing stage is usually present in its raw form as a filler. The cold-cured elements were left to cure in cold water for 28 days and were straightway heated in the oven. They thus potentially contained relatively higher levels of moisture content than hot-cured elements. Exposing the cube elements having higher moisture content and chemically bound water to elevated temperatures resulted in a resumption of the hydration process. The unreacted silica fume and the cement paste in the element went on to react when heated, forming new C-S-H binders. This process would result in concrete having stronger bonds and higher compressive strength between 200 and 400 °C. The C-S-H also led to concrete having a denser matrix. The strength loss recorded beyond 600 °C could be attributed to the decomposition of the C-S-H bonds due to excessive heat.

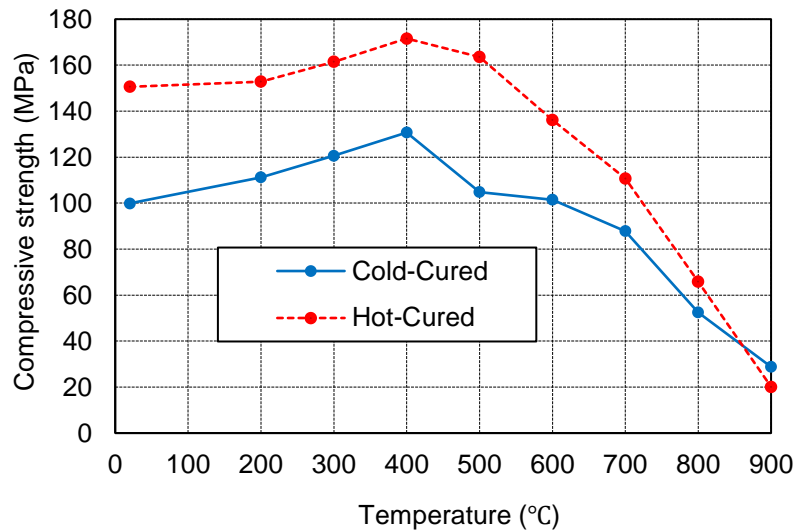


Figure 3: Graphical representation of the residual strength from both curing streams

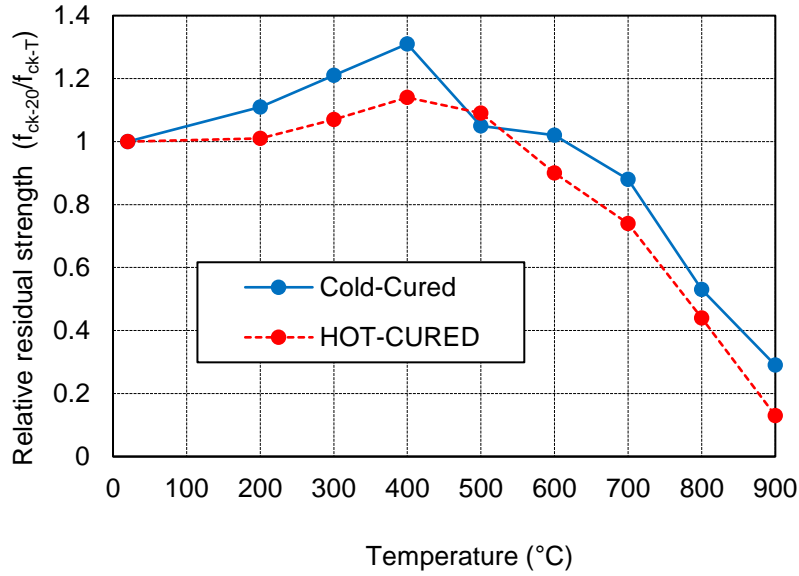


Figure 4: Graphical representation of relative residual strength from both curing streams

3.2 Regression analysis

Using the relative residual strength results, the regression curves were derived for both the hot and the cold cured specimens. These are presented in Figure 5. They were derived from the best fitting curves which were obtained from the 3rd order polynomials and expressed in terms of the relative residual strength.

3.2.1 The model for cold-cured elements

Equation (1) shows the regression curve for the cold-cured specimens. The curve was obtained from the best fitting curve of the relative residual strength curve shown in Figure 4.

$$\frac{f_{ck-T}}{f_{ck-20}} = -0.000702 \left(\frac{T}{100}\right)^3 - 0.018326 \left(\frac{T}{100}\right)^2 + 0.145 \left(\frac{T}{100}\right) + 0.95609 \quad (1)$$

Adjusted R-square = 0.94545

where T Exposure temperature of test specimen [°C]

f_{ck-T} Residual compressive strength at temperature T

f_{ck-20} Compressive strength of specimen at 20 °C

From Both sets of results show that the highest gain in strength was recorded at 400 °C. The cold-cured specimens generally had a higher relative residual strength at all temperatures. Overall, all the tested UHPFRC elements recorded higher residual compressive strength than the ambient temperature compressive strength up to the temperature of 600°C. This is in contrast to the documented behaviour of NSC and HSC which normally record losses in strength at elevated temperatures even at temperatures as low as 200°C.

Table 1, it can be observed that the residual strength pattern shows a gradual increase in strength reaching a peak at 400 °C. From 400 °C, the strength can be seen to decrease gradually from 400 °C to 900 °C. From these two distinct regions, simplified linear relationships can be developed. The first

one relates to temperatures between 20 °C - 400 °C and the second for 400 °C- 900 °C. The two expressions are presented in Equations (2) and (3).

$$\frac{f_{ck-T}}{f_{ck-20}} = 0.081345 + \left(\frac{T}{100}\right) + 0.97041; \leq 400^{\circ}\text{C} \quad (2)$$

$$\frac{f_{ck-T}}{f_{ck-20}} = -0.194 + \left(\frac{T}{100}\right) + 2.10952; > 400^{\circ}\text{C} \quad (3)$$

3.2.2 Model for hot-cured elements

Similarly, the regression curve for the hot-cured elements is derived from the best fitting curve of Figure 4. The resulting third-order polynomial is expressed in Equation (4). The resulting polynomial function is shown graphically in Figure 5.

$$\frac{f_{ck-T}}{f_{ck-20}} = -0.00242 \left(\frac{T}{100}\right)^3 + 0.00638 \left(\frac{T}{100}\right)^2 + 0.0423 \left(\frac{T}{100}\right) + 0.97147 \quad (4)$$

Adjusted R-square = 0.97942

It can equally be deduced from the graph that the residual strength increased gradually and reached its peak at 400 °C before reducing drastically up to 900 °C. Two distinct regions of the curve can be observed from the graph, i.e. positive and negative gradients regions. The third order polynomial equation can be transformed into two linear equations. Equation (5) can be used to approximate the relative residual strength between 0 and 400 °C while Equation (6) is more suited for temperatures above 400 °C.

$$\frac{f_{ck-T}}{f_{ck-20}} = 0.03604 + \left(\frac{T}{100}\right) + 0.97211; \leq 400^{\circ}\text{C} \quad (5)$$

$$\frac{f_{ck-T}}{f_{ck-20}} = -0.238 + \left(\frac{T}{100}\right) + 2.326; > 400^{\circ}\text{C} \quad (6)$$

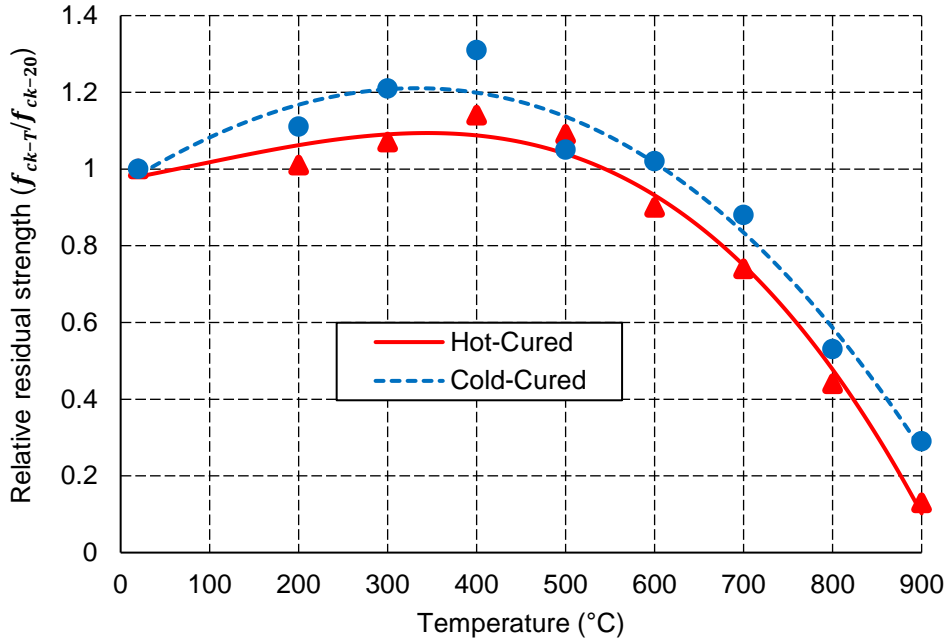


Figure 5. The relative residual strength derived from regression analysis

4 CONCLUSIONS

The residual strength tests were performed on 54 UHPFRC cubes containing both steel and polypropylene fibres. The elements were heated at 8 different target temperatures and tested for residual strength and then compared with the ambient compressive strength. The study further compared the influence of the two curing temperatures on the residual strength of elements. Below are some of the main points from the study.

- UHPFRC elements recorded higher residual compressive strength than the corresponding ambient temperature compressive strength up to the temperature of 500 °C (for hot cured) and 600 (for cold-cured).
- The gains in compressive strength peaked at 400 °C in both sets of specimens: 31 % and 14 % higher than the ambient strength for the cold-cured and the hot-cured elements respectively.
- The cold-cured specimens reported higher strength retention than the hot-cured specimens. This could be due to the resumption of the hydration process when exposed to higher temperatures in the furnace.
- Even on exposure to a temperature as high as 800°C, the elements still retained at least 50 % (cold-cured) and 40 % (hot-cured) of their original strength.
- Overall, the results have shown that UHPFRC have a higher strength retention capacity. This is in contrast to the NSC and HSC which normally record losses in strength at elevated temperatures.

ACKNOWLEDGMENT

The authors would like to acknowledge the funding support from Ulster University through the Vice Chancellor’s Research Scholarship.

REFERENCES

[1] Y.N. Chan, G.F. Peng, M. Anson, Residual strength and pore structure of high-strength concrete and

- normal strength concrete after exposure to high temperatures, *Cem. Concr. Compos.* 21 (1999) 23–27. doi:[http://dx.doi.org/10.1016/S0958-9465\(98\)00034-1](http://dx.doi.org/10.1016/S0958-9465(98)00034-1).
- [2] B. Chen, J. Liu, Residual strength of hybrid-fiber-reinforced high-strength concrete after exposure to high temperatures, *Cem. Concr. Res.* 34 (2004) 1065–1069. doi:10.1016/j.cemconres.2003.11.010.
- [3] J. Xiao, H. Falkner, On residual strength of high-performance concrete with and without polypropylene fibres at elevated temperatures, *Fire Saf. J.* 41 (2006) 115–121. doi:<http://dx.doi.org/10.1016/j.firesaf.2005.11.004>.
- [4] B.T. Burke, *Residual Strength of Ultra-High Performance Concrete After Exposure to Elevated Temperatures*, University of Connecticut, 2011.
- [5] C. Kahanji, F. Ali, A. Nadjai, Explosive spalling of ultra-high performance fibre reinforced concrete beams under fire, *J. Struct. Fire Eng.* 7 (2016) 328–348. doi:10.1108/JSFE-12-2016-023.
- [6] G.A. Khoury, B. Willoughby, Polypropylene fibres in heated concrete. Part 1: Molecular structure and materials behaviour, *Mag. Concr. Res.* 60 (2008) 125–136. doi:10.1680/mac.2008.60.2.125.
- [7] G.A. Khoury, Polypropylene fibres in heated concrete. Part 2: Pressure relief mechanisms and modelling criteria, *Mag. Concr. Res.* 60 (2008) 189–204. doi:10.1680/mac.2007.00042.
- [8] H. Zanni, M. Cheyrezy, V. Maret, S. Philippet, P. Nieto, Investigation of hydration and pozzolanic reaction in Reactive Powder Concrete (RPC) using ²⁹Si NMR, *Cem. Concr. Res.* 26 (1996) 93–100. doi:[http://dx.doi.org/10.1016/0008-8846\(95\)00197-2](http://dx.doi.org/10.1016/0008-8846(95)00197-2).
- [9] C. Kahanji, F. Ali, A. Nadjai, Structural performance of ultra-high-performance fiber-reinforced concrete beams, *Struct. Concr.* 18 (2017) 249–258. doi:10.1002/suco.201600006.

Concrete Structures

STUDY OF FIRE RESISTANCE OF RC COLUMNS WITH VARYING SHEAR REINFORCEMENT

Hemanth Kumar Chinthapalli¹, Anil Agarwal²

ABSTRACT

Lateral ties or transverse reinforcement provides the confinement effect to RC columns and helps enhance the compressive and shear strength of concrete. During fire conditions, the outer periphery of the column is at elevated temperatures. As a result, the stirrup temperature rises more rapidly than the core of concrete column. The confinement offered by the stirrups should decrease significantly at elevated temperatures. There are several full-scale concrete columns tested at ambient temperature under pure axial load with different confinement ratios. However, the effect of shear reinforcement on the compression behavior of RC columns at elevated temperatures has not been studied in detail. This paper presents an experimental and numerical study to investigate the effect of the shear reinforcement on the compressive behavior of RC columns in fire conditions. The initial results from the experimental study are presented. Numerical models are also developed using Abaqus. RC columns tested by Kodur et al. [5] and Lie and Woollerton [7] in fire conditions are simulated using Abaqus for validation of the proposed methodology. A sequential coupled analysis is conducted to simulate the behavior of RC columns under fire. The effects of radiation and convection between the fire and the column surface are included in the heat transfer analysis. The stress analysis is conducted in two steps. First, the axial load is applied to the column models. Then, the time-temperature field obtained from the heat-transfer analysis is applied directly while the explicit dynamic analysis is carried out. A parametric study is conducted by varying the shear and longitudinal reinforcement ratios. The fire resistance increased by thirty minutes when shear reinforcement increases from 0.56% to 2.26%.

Keywords: Fire tests, Shear reinforcement, Finite element modeling.

1 INTRODUCTION

The behavior of reinforced concrete (RC) columns under fire conditions is different from the ambient condition due to the loss of concrete strength with temperature, built-up of pore pressure, and high thermal gradients. These result in thermal stresses and spalling of the concrete. To explore the behavior of RC column under high thermal conditions, several researchers have tested columns at high temperatures. Lie and Woollerton [7, 6] tested 41 full-scale concrete columns designed as per national building code of Canada. Dotreppe et.al.[2] tested 26 full-scale concrete columns designed as per the euro code. Wu and Lie [10] tested seven columns designed as per the Chinese standards. Kodur et al., tested 15 columns to compare normal strength and high strength concrete columns with and without steel and polypropylene fibers. Asif et al., [8, 9] studied the full-scale fire behavior of RC frames under post-earthquake fire conditions and observed that the frame with ductile detailing performs better in the post-earthquake fire.

¹ Research Scholar, Department of civil engineering, Indian Institute of Technology Hyderabad, Hyderabad, Telangana.
e-mail: ce15resch11006@iith.ac.in

² Assistant Professor, Department of civil engineering, Indian Institute of Technology Hyderabad, Hyderabad, Telangana..
e-mail: anil@iith.ac.in

2 NUMERICAL MODEL

2.1 Abaqus Modelling Procedure

The general procedure for transient thermal-stress analysis of an RC structure in Abaqus [1] consists of the following steps:

1. Build a three-dimensional model of the column. The model incorporates the geometry (Concrete, and Steel bars as Reinforcement), appropriate material properties, and boundary conditions.
2. Applying the thermal loads to the desired surface of the structure resulting from the furnace transient fire (in the form of temperatures versus time curves) using “Standard Time-Temperature” curve applied according to the ISO 834 or ASTM E119.
3. Apply mechanical load on the suitable surfaces (axial load for the column) to simulate the dead and live gravity service loads during fire exposure.
4. Apply the thermal loads in the form of nodal-temperature at several time points obtained in step 2 and compute the deflection and strains in the structure.

2.2 Heat Transfer Analysis

In the heat transfer analysis, temperature dependent thermal properties are considered as per the EU code [3]. Wherever possible, symmetric boundary conditions were used to reduce the analysis time. The concrete was modeled using DC3D8 elements. It is an 8-noded brick element for heat transfer analyses. It has a single degree of freedom, i.e., temperature, at each node. The reinforcement bars are modeled using DC1D2 truss element with the ability to conduct heat between its two nodes for heat transfer analyses. This element also has a single degree of freedom, temperature, at each node. Temperature compatibility is assumed between the rebars and the concrete. This is achieved by using “tie” constraint option available in Abaqus which ties the degrees of freedom at the node of the slave elements (rebars) to that of the master element (here concrete). The entire beam model is subjected to an ambient room temperature of 20°C in the form of the predefined initial condition. The beam is subjected to fire in the form of the standard time-temperature curve as per ISO 834 at four faces of the columns.

2.3 Stress Analysis

In the second step, stress analysis of columns is carried out by first applying the desired compressive load to the FE model and then subjecting the structure to the temperature history obtained from the heat transfer analysis. The FE model used for the stress analysis had the mesh and other geometric configurations same as the heat transfer analysis FE model. However, 8-noded brick element C3D8 and 2-noded B31 beam elements were used for 3D stress analysis. The stress-strain curve for concrete is defined as per EN code [3] in compression. The damaged plasticity model of concrete modeling is used to incorporate the non-linear behavior of the concrete. The temperature variation of various mechanical properties incorporated as per EN Code. The reinforcing steel is considered to behave as elasto-plastic hardening material (i.e., bilinear stress-strain curve) both in tension and compression, using Von-Mises plasticity yielding criterion applied using classical metal plasticity model available in Abaqus. Moreover, the interaction between steel rebars and concrete is achieved using “embedded” constraint option available in Abaqus. This option constrains all the degree of freedom of the slave region to the nodes of the master region. Geometric nonlinearity is considered in the analysis using “nlgeom” option in Abaqus.

3 VALIDATION

3.1 Validation of Model at Ambient Temperature

For the validation of the model at ambient conditions, the specimens tested by Jain et al. [4] are simulated and the results are compared.

Jain et.al.[4] tested four 230 X 230 columns in which two reinforced cement concrete (RCC), and two are plain cement concrete (PCC) columns of height 450 mm. The cross section details and load versus deformation curves presented in Fig 1.

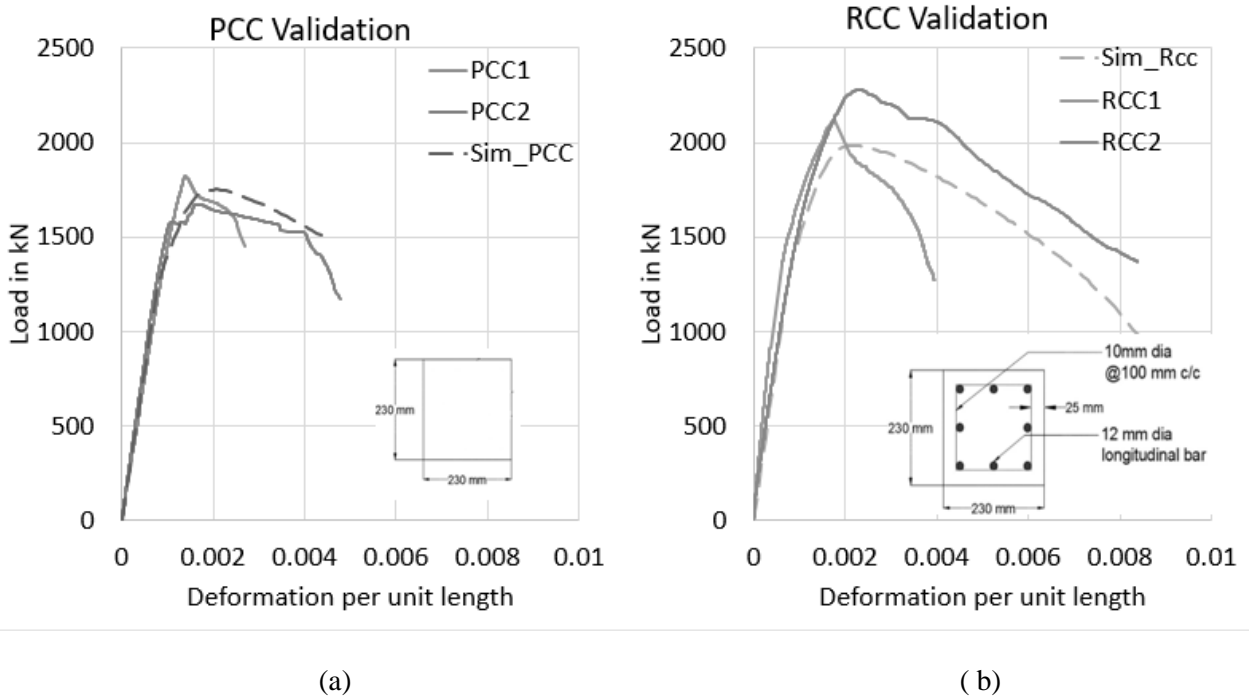


Fig 1: Validation of Model with (a) PCC Columns (b) RCC Columns

The dotted line is the simulated results using Abaqus whereas continuous lines indicate the experimental results presented in the literature. The simulation results are in good agreement with experimental data, approximately the average of the experimentally tested two specimens.

3.2 Validation of the Model at Elevated Temperatures

To check the applicability of the model at elevated temperatures, the model is validated against the elevated temperature tests available in the literature and listed in the table below.

Table 1. Specimens from literature for validation of the model

S.No	f_c (MPa)	Long. $\phi - f_y$	R.H (%)	Ecc. (mm)	Supp. Cond.	Stirrup $\phi - (f_y)$	Test Load (kN)	Stirrup Spacing (in mm)	Fire Resistance (in min)	Tested by and Sample
1	40.2	25 ϕ -420	90	0	F-F	10 ϕ -280	930	75mm at ends 145mm at mid	278	Kodur_S1
2	34.8	25 ϕ -444	74	0	F-F	10 ϕ -427	1778	305 mm through out the section	146	Lie_S8
3	40.2	25 ϕ -420	51	0	F-F	10 ϕ -280	1500	75mm at ends 145mm at mid	204	Kodur_S2
4	40.2	25 ϕ -420	92	25.4	P-P	10 ϕ -280	1000	75mm at ends 145mm at mid	90	Kodur_S3

The heat transfer analysis results for specimen 1 and 2 of the four columns listed in Table 1 are presented in Fig 2 and Fig 3, respectively. They also compare the heat transfer analysis results with the experimental results. Axial deformation versus time curves for the four specimens listed in Table 1

are presented in *Fig 4*. The simulation results of heat transfer and load versus deformation curves are in good agreement with experimental data.

4 EXPERIMENTAL SET-UP AND SPECIMENS

4.1 Specimens

To study the effect of confinement on the fire behavior of RC columns under fire conditions, a set of 10 specimens were planned to be tested. The test matrix is presented in *Table 3*. The concrete mix proportion designed as per IS 10262:2009 [11] for M30 and M50 concrete is presented in *Table 2*.

Table 2. Concrete mix proportions

Mix	W/c ratio	Cement	Sand	Course Aggregate	Admixture
M30	0.4	362	696	1307	0.3% of Cement
M50	0.33	440	646	1291	0.5% of Cement

The thermocouples are placed at two locations, one cross-section is at 150 mm from one end and the other cross-section at the mid-length location. There are eight thermocouples at each cross-section. The position of thermocouples is shown in *Fig 5*.

4.2 Furnace and Loading Frame

A cylindrical split electrical furnace of internal diameter 350mm is used to heat the specimen to the desired time-temperature curve. The furnace has three zones of controls along the length of the furnace. The length of the furnace is 600mm. Each zone of 200mm length can be controlled individually to maintain a uniform temperature in the furnace. The displacement control loading frame is capable of applying up to 2000kN load. The loading frame and furnace are shown in the *Fig 6*.

5 PARAMETRIC STUDY

A set of twenty-four columns were analyzed to understand the behavior of shear reinforcement on the fire resistance performance of RC columns. The length, cross-section dimensions, axial load acting on the column are kept same for all the twenty-four columns, longitudinal reinforcement is kept same for twelve columns (4 no-16 mm Dia., 12 specimens and 4-25 Dia., 12 specimens), and the amount of shear reinforcement is varied from 0.25% to 2.26%. The details of the shear reinforcement and the failure time for each specimen are given in *Table 4*. *Fig 7* shows fire resistance against the percentage of shear reinforcement for the 24 columns. The fire resistance capacity of the column increases by 10 to 15% when shear reinforcement increases from 0.25 to 2.26%.

Concrete Structures

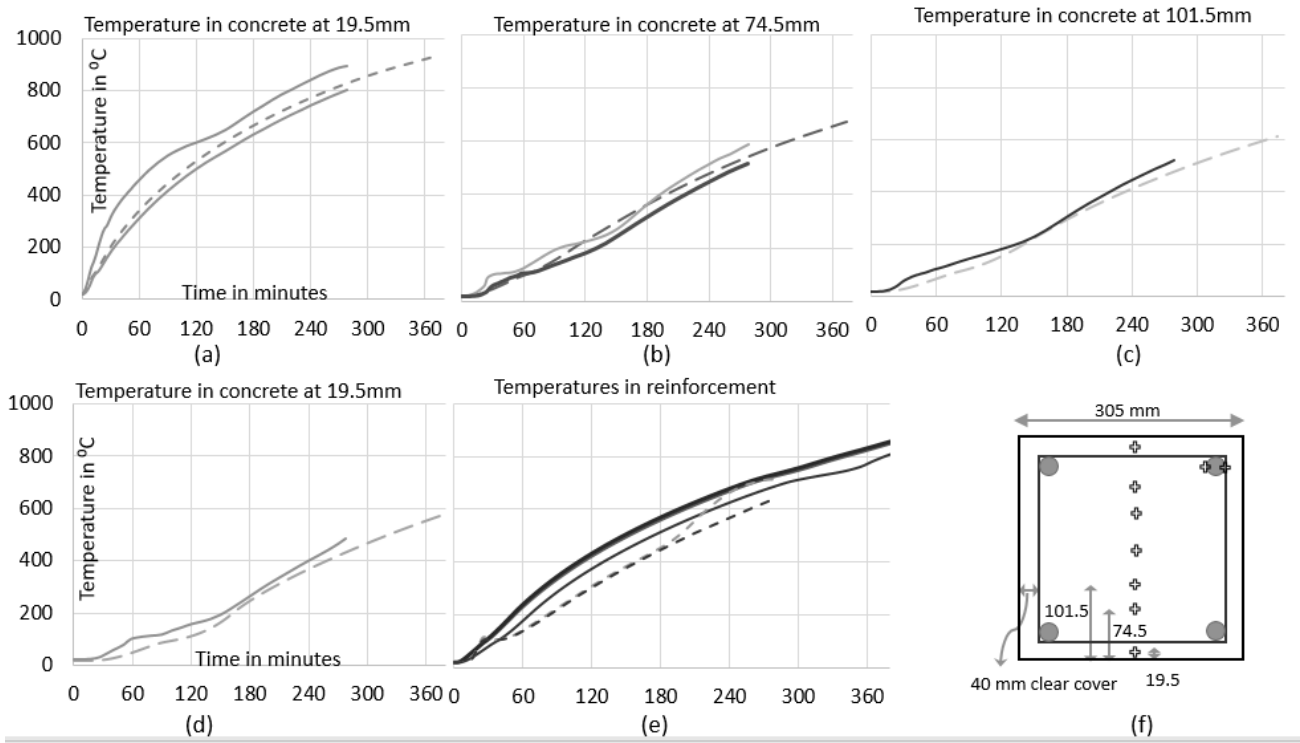


Fig 2: (a), (b), (c), (d) temperature profiles in concrete, (e) in reinforcement and (f) cross section details of specimen 1

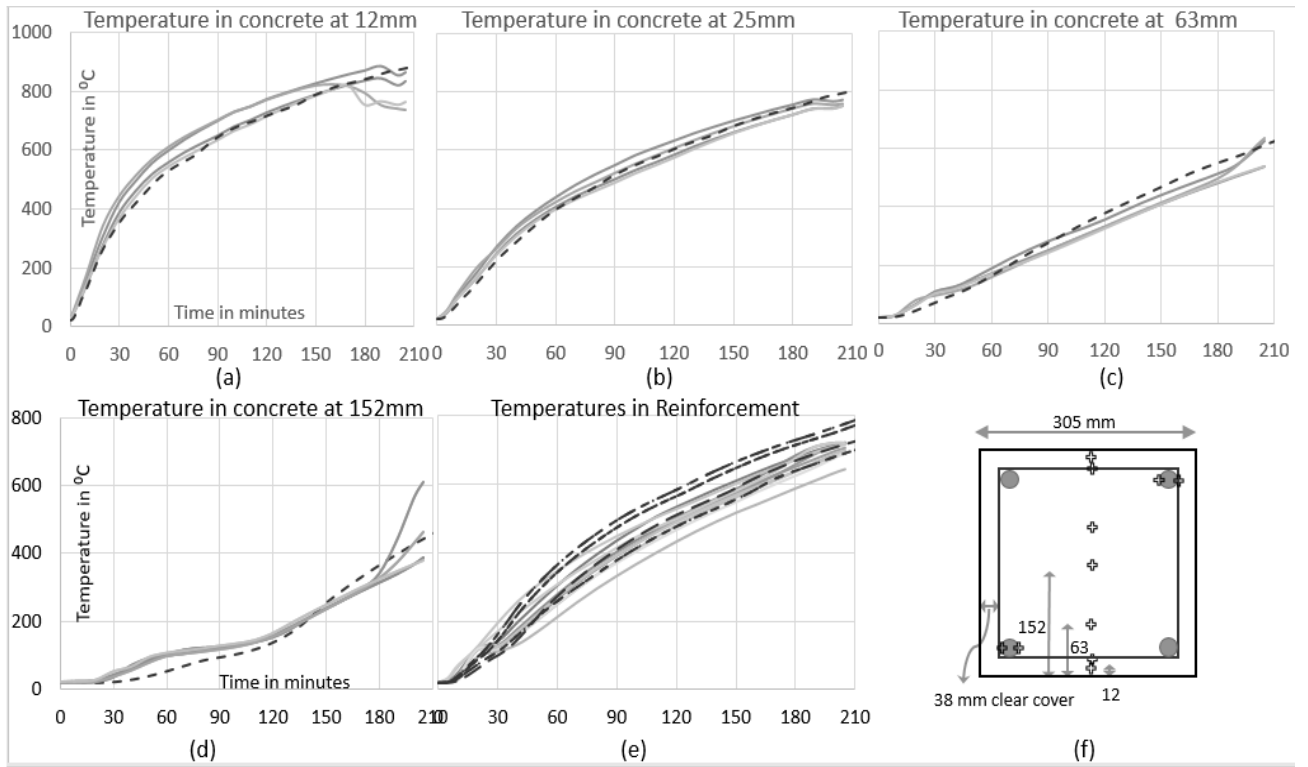


Fig 3: (a), (b), (c), (d) temperature profiles in concrete, (e) in reinforcement and (f) cross section details of specimen 2

Study of fire resistance of RC columns with varying shear reinforcement

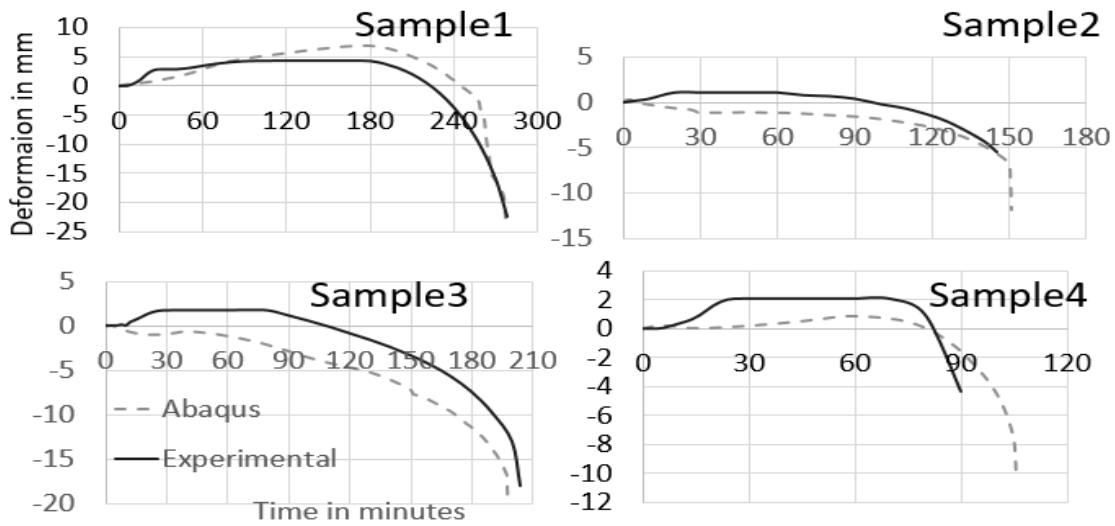


Fig 4: Deformation versus time graphs specimens listed in Table1, simulated versus experimental

Table 3. Specimens cast to understand the confinement effect at elevated temperatures

S. No	Reinforcement			Heating Duration in hours	Section Dimensions (in mm)	f'_c (N/mm ²)
	Long.	Spacing of Stirrups (in mm)	Dia. of Stirrup (in mm)			
1.	16dia-4Nos	50mm	10	2	230x230x860	30
2.	16dia-4Nos	50mm	10	3	230x230x860	
3.	16dia-4Nos	150mm	6	2	230x230x860	
4.	16dia-4Nos	150mm	6	3	230x230x860	
5.	16dia-4Nos	150mm	6	0	230x230x860	
6.	16dia-4Nos	50mm	10	2	230x230x860	50
7.	16dia-4Nos	50mm	10	3	230x230x860	
8.	16dia-4Nos	150mm	6	2	230x230x860	
9.	16dia-4Nos	150mm	6	3	230x230x860	
10.	16dia-4Nos	50mm	10	0	230x230x860	

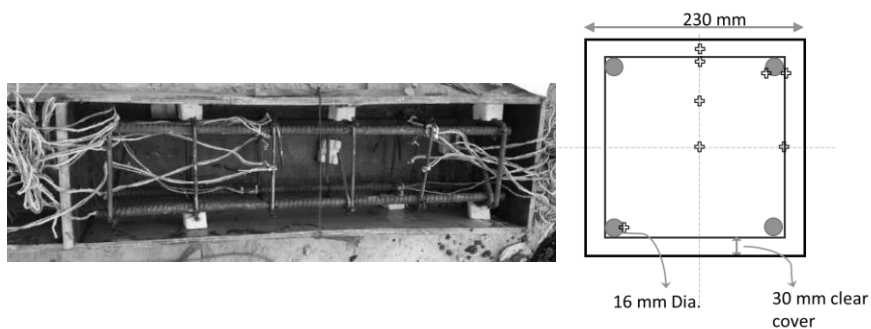


Fig 5: Location of thermocouples along the length and in the cross-section during the casting process



Fig 6: Furnace top-view, loading frame and furnace during testing, Specimen when the split furnace opened after the test

6 RESULTS

The testing is being carried out for specimens listed in *Table 3*. The test for specimen 1 in *Table 3* has been completed. It failed at a load of 1800kN, whereas the capacity of this column at ambient temperature is 2570kN. A 30% degradation of capacity was observed when the column was heated for 2 hrs. The more detailed experimental results will be presented in the conference. The fire resistance of specimens tabulated in *Table 4* shows an increase in fire resistance capacity by increasing amount of shear reinforcement.

Table 4. Details of shear reinforcement for numerical analysis

Sample	Failure Time	% of Shear Reinf.	Sample	Failure Time	% of Shear Reinf.	Sample	Failure Time	% of Shear Reinf.
SA-16dL-50mm-8Dia	289	1.01	SA-16dL-50mm-10Dia	281	1.57	SA-16dL-50mm-12Dia	286	2.26
SA-16dL-100mm-8Dia	273	0.50	SA-16dL-100mm-10Dia	273	0.79	SA-16dL-100mm-12Dia	283	1.13
SA-16dL-150mm-8Dia	276	0.34	SA-16dL-150mm-10Dia	267	0.52	SA-16dL-150mm-12Dia	267	0.75
SA-16dL-200mm-8Dia	256	0.25	SA-16dL-200mm-10Dia	258	0.39	SA-16dL-200mm-12Dia	261	0.57
SA-25dL-50mm-8Dia	284	1.01	SA-25dL-50mm-10Dia	283	1.57	SA-25dL-50mm-12Dia	286	2.26
SA-25dL-100mm-8Dia	265	0.50	SA-25dL-100mm-10Dia	276	0.79	SA-25dL-100mm-12Dia	284	1.13
SA-25dL-150mm-8Dia	247	0.34	SA-25dL-150mm-10Dia	259	0.52	SA-25dL-150mm-12Dia	273	0.75
SA-25dL-200mm-8Dia	246	0.25	SA-25dL-200mm-10Dia	258	0.39	SA-25dL-200mm-12Dia	267	0.57

7 CONCLUSIONS

The shear reinforcement not only increases the capacity of the column at ambient temperature but also the fire resistance of the column increases. The amount of load acting on the column during fire conditions will also influence the fire resistance rating. A detailed experimental and numerical study with a wide range of shear reinforcement is being conducted to develop a better understanding of the effect of shear reinforcement at elevated temperatures.

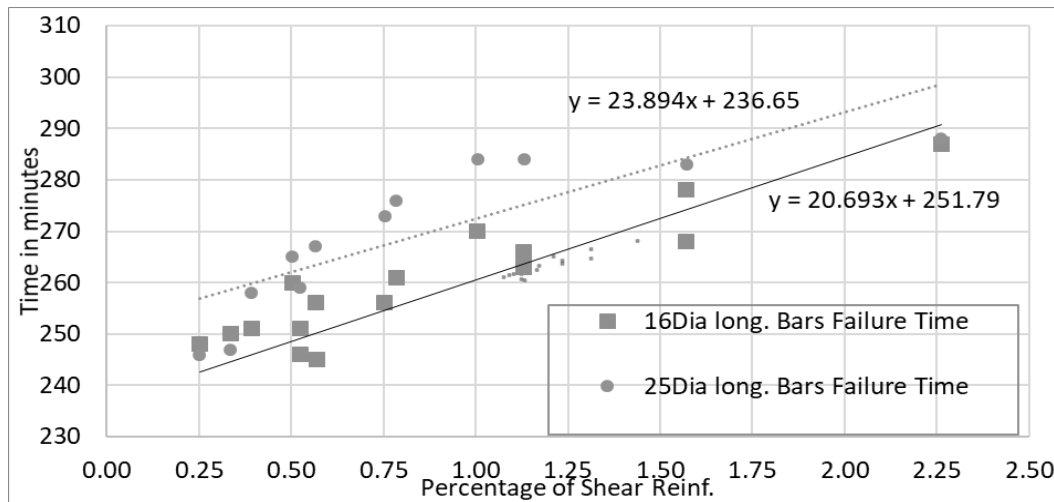


Fig 7: Fire resistance obtained from numerical analysis

REFERENCES

1. Abaqus. (2010). *Abaqus Analysis User's Manual*. Materials. Other plasticity models. Concrete, 113.
2. J-C Dotreppe, J-M Franssen, Alois Bruls, Raymond Baus, Paul Vandeveld, Roland Minne, D Van Nieuwenburg, and Hendrik Lambotte. (1997). *Experimental Research on the Determination of the Main Parameters Affecting the Behaviour of Reinforced Concrete Columns Under Fire Conditions*. Magazine of Concrete Research, 49(179), 117-127.
3. EN:1992-1-2; *Eurocode2: Design of concrete structures-Part 1-2: General rules-Structural fire design*. 2004.
4. Saumitra Jain, M Chellapandian, and S Suriya Prakash. (2017). *Emergency Repair of Severely Damaged Reinforced Concrete Column Elements Under Axial Compression: An Experimental Study*. Construction and Building Materials, 155, 751-761.
5. VKR Kodur, FP Cheng, TC Wang, JC Latour, and P Leroux. (2001). *Fire resistance of high-performance concrete columns*. NRC Publications Record(IR C - I R - 8 3 4).
6. Tiam Tjoan Lie. (1989). *Fire Resistance of Reinforced Concrete Columns: A Parametric Study*. Journal of Fire Protection Engineering, 1(4), 121-129.
7. TT Lie and JL Woollerton. (1988). *Fire Resistance of Reinforced Concrete Columns: Test Results, National Research Council of Canada*. Institute for Research in Construction, Internal Report(569).
8. Asif H Shah, UK Sharma, Praveen Kamath, Pradeep Bhargava, GR Reddy, and Tarvinder Singh. (2016). *Fire Performance of Earthquake-Damaged Reinforced-Concrete Structures*. Materials and Structures, 49(7), 2971-2989.
9. Asif H Shah, UK Sharma, Praveen Kamath, Pradeep Bhargava, GR Reddy, and Tarvinder Singh. (2016). *Effect of Ductile Detailing on the Performance of a Reinforced Concrete Building Frame Subjected to Earthquake and Fire*. Journal of Performance of Constructed Facilities, 30(5), 04016035.
10. HJ Wu and Tiam Tjoan Lie. (1992). *Fire resistance of reinforced concrete columns: experimental studies*. NRC Publications Record(No.632).
11. BIS 10262:(2009). *Concrete Mix Proportioning-Guidelines*. Bureau of Indian Standards.

ON THE PULL-OUT CAPACITY OF POST-INSTALLED BONDED ANCHORS AND REBARS DURING FIRE

Hitesh Lakhani¹, Jan Hofmann²

ABSTRACT

The paper presents a numerical model to determine the pull-out capacity of post-installed bonded fastening systems viz., bonded anchors and Post Installed Rebars (PIR) during fire. The model consists of carrying out a transient heat transfer analysis to obtain the temporal and spatial distribution of temperature, as the first step. Once, the temperature variation along the anchor/rebar depth/length is obtained, the pull-out capacity of the anchor is computed by integrating the temperature dependent bond-strength over the depth/length of the anchor/rebar. The presented model has been implemented in an inhouse code, capable of conducting transient heat transfer analysis for different thermal boundary conditions and also considers the temperature dependency of various material properties of concrete and steel. The application of the model has been discussed separately for bonded anchors and the PIRs, due to the inherent differences in the two applications. The validation of the model with the experiments available in literature has been presented, which shows a good comparison between the numerical and the corresponding experimental pull-out strengths.

Keywords: Bonded anchors, Post installed rebars, transient heat transfer analysis, pull-out capacity

1 INTRODUCTION

There is an increased used of post-installed bonded fastening systems viz., bonded anchors and Post Installed Rebars (PIR), for various applications in the field of structural engineering. The bonded anchor system consists of a bonding material, threaded rod/ inserts/proprietary anchor element and reinforcing bars. There are a lot of such systems readily available in the market with technical approvals. At ambient conditions these post installed bonded systems have been demonstrated to have strengths similar to the classic cast-in systems. In general, the load carrying capacity of any anchor system reduces when exposed to fire due to the degradation of material properties with rising temperatures. But, the pull-out capacity of bonded systems shows a rapid degradation when exposed to fire. This drastic reduction in pull-out capacity is because of the polymeric adhesive material whose properties changes significantly over a short temperature range. Hence, can cause safety related issues [1].

Possible failure modes for anchor loaded in tension are steel failure, pull-out failure and concrete cone failure. At present EOTA TR 020 (2004) [2] can be used for evaluating only steel failure under fire for bonded anchors. Due to this fact, that the bond-strength degradation with temperature is highly product dependend, as it depends on the composition of the adhesive material (inorganic/organic/vinylester/epoxy) [3,4] and pull-out failure of bonded anchors (during fire) may

¹ Scientific Associate, Department of Fastening and Strengthening Methods, Institute of Construction Materials, University of Stuttgart, Stuttgart, Germany.

e-mail: hitesh_lakhani06@rediffmail.com

² Professor. Department of Fastening and Strengthening Methods, Institute of Construction Materials, University of Stuttgart, Stuttgart, Germany.

e-mail: jan.hofmann@iw.uni-stuttgart.de

be decisive in majority of its application. It is recommended to evaluate behaviour of bonded anchors under fire by performing tests.

2 NUMERICAL MODEL

The model consists of carrying out a transient heat transfer analysis to obtain the temporal and spatial distribution of temperature, as the first step. For carrying out the analysis the domain which consists of concrete & steel is divided into segments. Using lumped system concept, each segment is considered to have a uniform temperature and properties, lumped at the center of the segment. Temperature dependent thermal properties (conductivity and specific heat) of concrete and steel as shown in *Fig. 1* were used. The presented model has been numerically implemented in a standalone inhouse code.

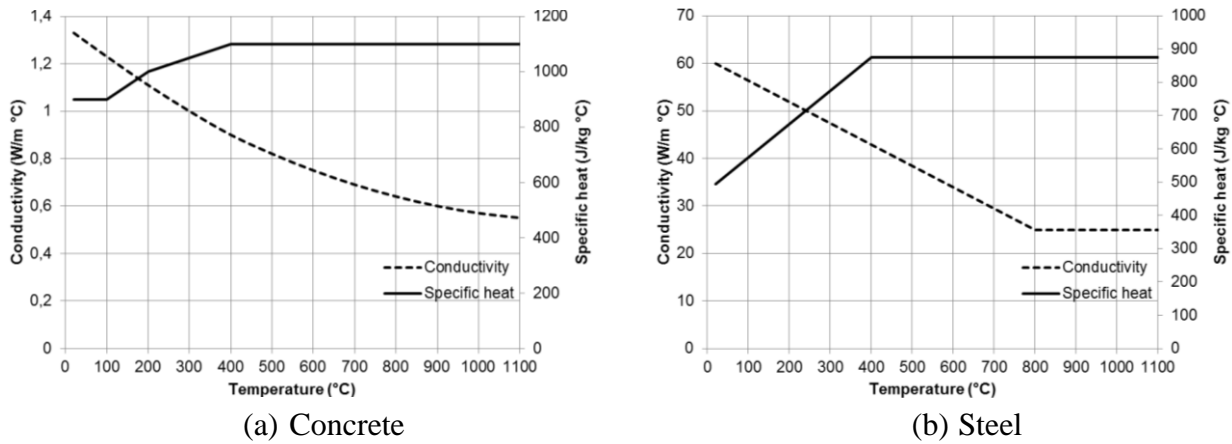


Fig. 1. Thermal properties for concrete and steel

The numerical model is based on the following assumptions:

1. Thermal spalling does not occur.
2. A 2D heat transfer analysis is carried out assuming a constant temperature field along the length of the structural member in which the anchor is installed.
3. Variation of bond stress along the anchor/rebar depth/length is ignored. Hence, might not be applicable for large embedment depths.

2.1 Thermal analysis

The first and most crucial step in the field of structural fire engineering is to estimate the temperature distribution in a structural member. The governing differential equation for 2D transient heat conduction problem is given by *Eq. (1)*. The governing equation is solved using implicit Central Difference Scheme and iterative solver to obtain the spatial and temporal distribution of temperature, $T(x,t)$. *Eq. (2)* states the (radiative and convective) boundary condition that needs to be satisfied.

$$\rho c \frac{\partial T}{\partial t} = k \left[\frac{\partial^2 T}{\partial x^2} + \frac{\partial^2 T}{\partial y^2} \right] \quad (1)$$

$$-k \frac{\partial T}{\partial n} = h[T_g - T_s] + \varepsilon \sigma [(T_g + 273)^4 - (T_s + 273)^4] \quad (2)$$

Where:

- k is the thermal conductivity (W/m °C),
- ρ is the mass density (kg/m³),
- c is the specific heat of solid (J/kg. °C),

- h is convective heat transfer coefficient ($25 \text{ W/m}^2 \text{ }^\circ\text{C}$),
 ϵ is Stephen Boltzmann constant ($5.667 \times 10^{-8} \text{ W/m}^2 \text{ }^\circ\text{K}^4$),
 σ is surface emissivity (0.8),
 T_g is gas temperature ($^\circ\text{C}$),
 T_s is surface temperature ($^\circ\text{C}$).

In the presented heat transfer analysis the steel anchor/rebar has been modelled explicitly in contrast to some of the previous studies [5]. It is a general practice and widely accepted assumption that the temperature of reinforcement is assumed to be equal to that of concrete at the rebar centroidal location but such assumptions can lead to unconservative results in case of PIR. This point is further elaborated in sections 3.2.

2.2 Pull out capacity

Based on the transient heat transfer analysis carried out in the first step, the temperature variation along the anchor/rebar depth is known. The second input required for this step is the variation of bond strength with increasing temperatures. This variation can be obtained for each product according to the European Technical Document [6]. Using the above stated inputs (temperature along anchor depth & temperature dependent bond strength) the variation of bond strength along the anchor depth is known. The pull out capacity of the bonded anchor is computed by integrating the temperature dependent bond strength over the anchor length.

2.3 Demand on PIRs

In case of bonded anchor one can assume the applied forces to constant during fire as it's due to an externally applied load. Whereas, the forces/loads acting on the rebar, (in case of PIRs) varies during the fire, due to the internal stress redistribution (shifting of neutral axis). This redistribution of stress at the section takes place due to the changes in the mechanical properties of concrete and reinforcing steel with temperature. This means for real life applications, to estimate the failure time for PIRs one also need to consider the change in demand imposed on PIRs. Hence, for predicting the failure time for PIR systems, the numerical model was coupled with the sectional analysis subroutine to compute the forces acting on the PIR during fire. This coupling makes the presented model more realistic and advance, as compared to some recently proposed models [7]. Sectional analysis procedure for RC flexural members is well established [8]. Hence, is not discussed in detail but the salient assumptions and constitutive laws used are mentioned below:

1. Plain section remains plain after bending.
2. Tensile strength of concrete is negligible.
3. A perfect bond is assumed between reinforcing steel and concrete.
4. Temperature of the reinforcement is equal to the corresponding concrete temperature at rebar centroidal location.
5. The temperature dependent constitutive law for concrete and reinforcing steel were taken from Eurocode2 [9].

3 APPLICATION

3.1 Bonded anchors

Muciaccia et al (2016) [10] performed an experimental study to investigate the post installed connections using vinylester polymer under high temperatures. They performed 6 tests at steady state and 14 tests under transient conditions. Tests performed under transient conditions were picked for validation. The specimen consists of a 12mm ribbed bar post installed (using vinylester polymer mortar) in a steel cased C20/25 uncracked concrete cylinder with diameter 150mm and 200mm height, as shown in *Fig. 2*. The bar was loaded with different sustained loads before heating the specimen at a rate of approximately $10^\circ\text{C}/\text{min}$ until failure. The load was maintained constant

during the heating period. The specimen was exposed to fire from all sides except the side on which anchor was installed.

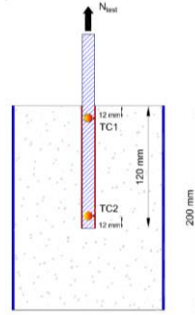


Fig. 2. Specimen used by Muciaccia et al (2016)

Fig. 3 shows a good comparison between the numerical predicted interface temperature & pull-out capacity with the corresponding experimental observations.

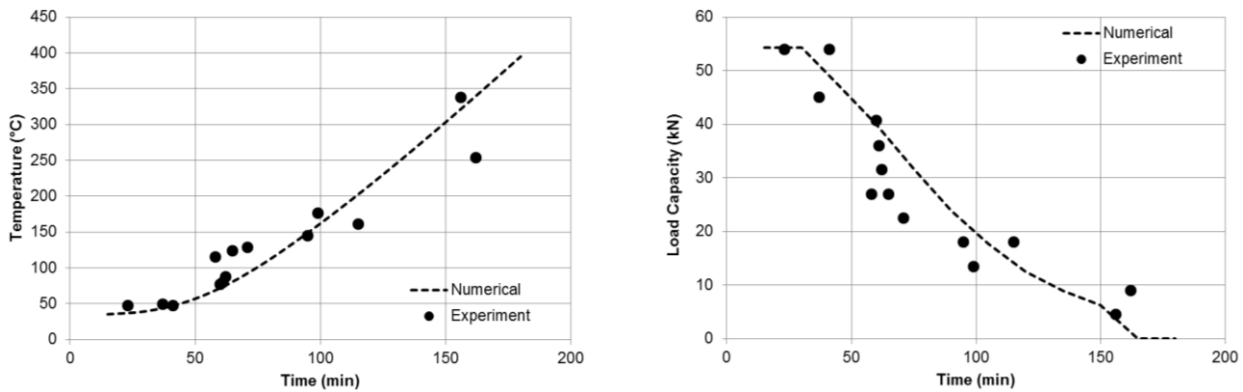


Fig. 3. Comparison of predicted (temperature and pullout capacities) for bonded anchors [11]

3.2 Post installed rebar

Full scale experiment on slab-wall connection using PIRs subjected to standard fire (ISO834-1 [Error! Reference source not found.]), conducted by Lahouar et al (2017) [7] is picked from literature to demonstrate the application of the presented model to PIR systems. The cantilever slab was $2.94 \times 2 \times 0.15$ m large, with an imposed dead load of 325 kg at 2.2 m from the wall-connection end. The cantilever wall was made of C20/25 grade concrete. The slab was connected to the wall using 8 nos of 135mm long (embedment length of PIRs in the wall) 16Ø rebar and epoxy based resin. The total applied moment (self weight + imposed dead load) at the slab-wall connection was ≈ 32.5 kN. The experimental set-up along with location of thermocouple locations is shown in Fig. 4. The variation of bond strength with temperature was also measured by Lahouar et al (2017), as mentioned below.

$$f_{bm}(\theta) = f_{bm} (a \cdot e^{-b \cdot \theta}) \quad \theta_{min} \leq \theta \leq \theta_{max}$$

Where,

θ = temperature ($^{\circ}\text{C}$)

$f_{bm}(\theta)$ = mean bond resistance at temperature θ (MPa)

f_{bm} = mean bond resistance at ambient conditions (27 MPa)

a, b = exponential fitting curve constants ($a = 58.853$; $b = 0.025$)

θ_{min} = minimum temperature required to initiate the degradation in bond strength (31°C)

θ_{max} = temperature above which the bond resistance is zero (115°C)

Concrete Structures

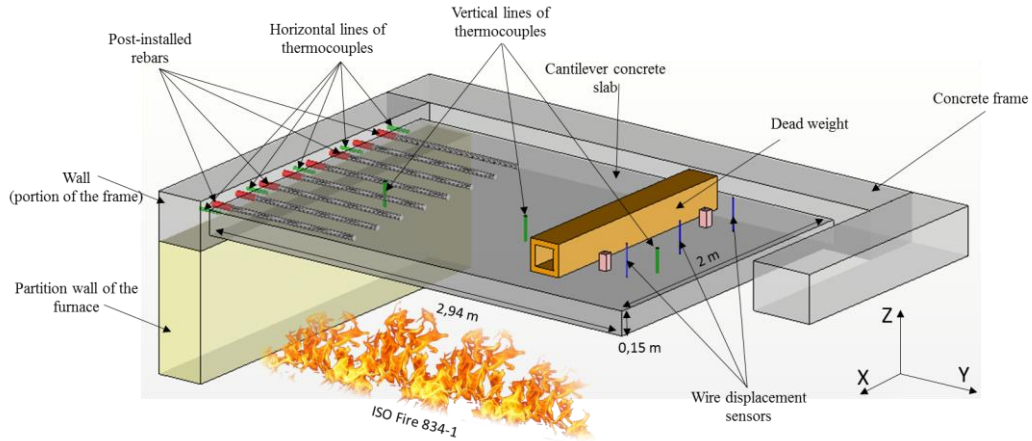


Fig. 4. Fire test configuration for slab-wall connection with PIR [7]

Heat transfer analysis was performed with and without modelling reinforcing bar and the results are shown in *Fig. 5*. It can be observed that the predicted temperature variation along the rebar depth is drastically different. This can be attributed to the explicit modelled rebar which acts as a heat sink and carries more heat into the joint region. *Fig. 6* shows the predicted temperature gradients across the wall at various exposure time, which are in good agreement with the experimental values.

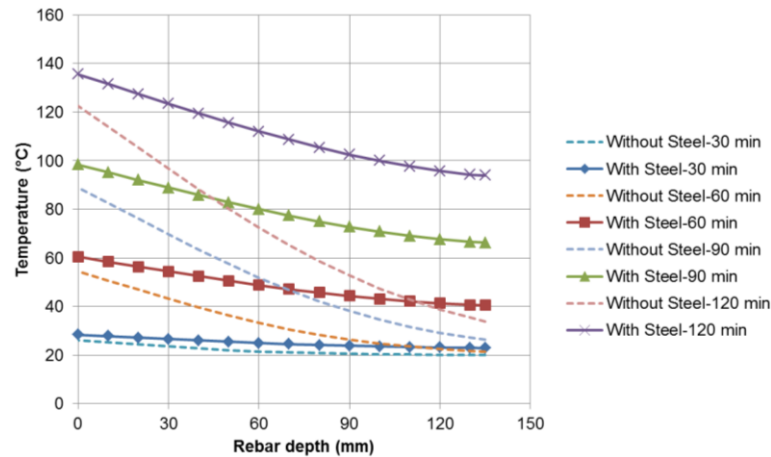


Fig. 5. Predicted temperature at centroidal axis location along the rebar embedment depth (Location 0 corresponds to the fire exposed face of the wall)

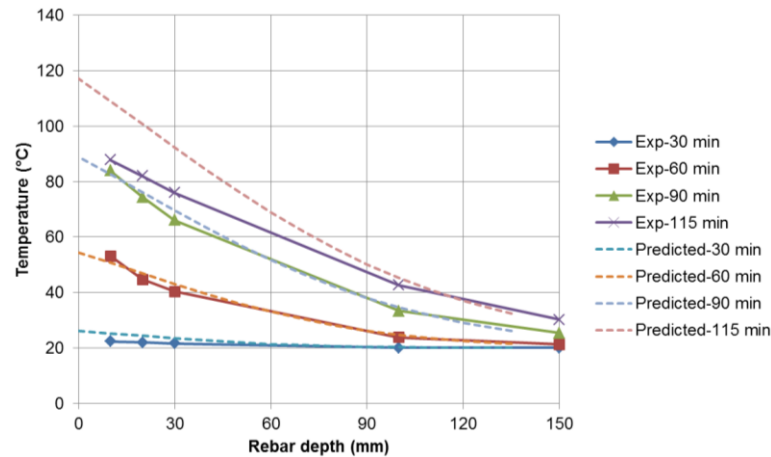


Fig. 6. Predicted temperature gradients across the wall

To be able to predict the failure time for the post installed cantilever floor, sectional analysis was conducted and the load demand (stress*rebar area) was computed per rebar. For the sectional analysis siliceous aggregates ($f_c=23$ MPa) and cold rolled reinforcing steel ($f_y = 460$ MPa) was assumed. From Fig. 7 it can be observed that the pull-out capacity of rebars reduces rapidly with increase in exposure duration. The predicted pullout capacity for the case when steel is modelled during heat transfer is significantly lower than those where heat transfer through rebar is ignored. It should also be noted that the demand imposed on rebar increases with the exposure duration. The predicted failure time for cantilever floor, as computed from Fig. 7 is ≈ 80 minutes (considering heat transfer through rebar) as compared to experimentally obtained failure time of 117 minutes. The difference between predicted failure times can be attributed to several factors like the assumed perfect thermal contact & bond between steel and concrete, ignored effect of moisture content/moisture migration etc.

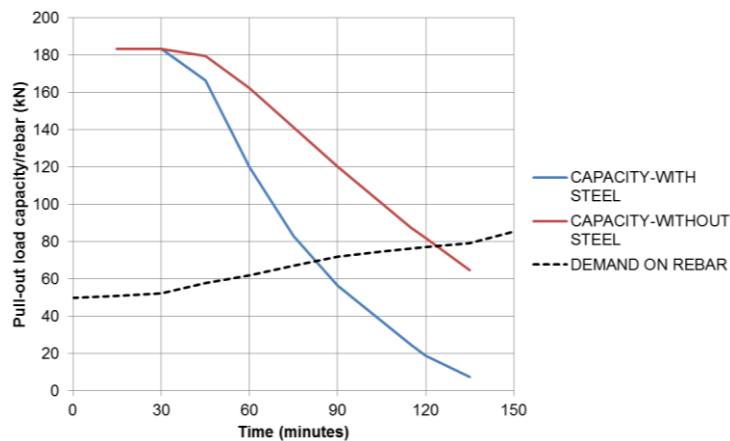


Fig. 7. Variation of load/demand on each rebar

4 CONCLUSIONS

- A numerical model for computing the pull-out capacity of post installed bonded anchor and rebars in reinforced concrete exposed to fire has been presented. The only product dependent parameter in the proposed model is the variation of bond strength with temperature which can be obtained by conducting experiments on relatively small specimens.
- The application of the proposed model has been demonstrated separately for bonded anchors and PIRs. A reasonably good comparison is obtained between experimentally obtained and numerically calculated values of the pull-out capacity.
- The results also indicate that the common modelling assumption of not considering the reinforcing steel during heat transfer analysis may not be realistic while dealing with PIR systems.
- For realistic prediction of fire rating of PIR systems the changing demand should also be considered.
- More experiments on bonded anchors and PIR system are required for further validating the proposed numerical model.

REFERENCES

1. Fuchs, W., & Silva, J. (2012). EOTA approach to qualification and design of post installed adhesive anchors for fire exposure. *Understanding Adhesive Anchors: Behavior, Materials, Installation, ACI SP 283*.

2. EOTA TR 020. (2004). *Evaluation of anchorages in concrete concerning resistance to fire*. Brussels: European Organisation for Technical Approvals.
3. Pinoteau, N., Pimienta, P., Guillet, T., Rivillon, R., & Remond, S. (2012). Effect of heat on the adhesion between post-installed bars and concrete using polymeric mortars. In J. Cairns, G. Metelli, & G. Plizzari (Ed.), *Bond in Concrete 2012 - Bond in New Materials and under Severe Conditions*, (pp. 573-580). Brescia. Italy.
4. Zhang, Y., Lou, G.-b., & Li, H.-q. (2016). Residual strength of organic anchorage adhesive for post installed rebar at elevated temperatures and after cooling. *Fire Technology*, 52, 877-895.
5. Pinoteau, N., Heck, J., Rivillon, P., Avenel, R., Pimienta, P., Guillet, T., & Remond, S. (2013). Prediction of failure of a cantilever-wall connection using post-installed rebar under thermal loading. *Engineering Structures*, 56, 1607-1619.
6. EAD-330087-00-0601. (2015). *System for post installed rebar connections with mortar*.
7. Lahouar, A., Pinoteau, N., Caron, J., Foret, G., Guillet, T., & Mege, R. (2017). Chemically bonded post installed steel rebars in a full scale slab-wall connection subjected to standard fire (ISO834-1). *3rd International symposium on Connections between Steel and Concrete*, (S. 1119-1130). Stuttgart.
8. Park, R., & Paulay, T. (1975). *Reinforced Concrete Structures*. John Wiley & Sons.
9. Eurocode2. (2004). *Design of concrete structures - Part 1-2: General rules - Structural fire design*. Brussels: European Committee For Standardization.
10. Muciaccia, G., Consiglio, A., & Rosati, G. (2016). Behavior and design of post installed rebar connections under temperature. *Key Engineering Materials*, 711, 783-790.
11. Lakhani, H., & Hofmann, J. (2017). A numerical method to evaluate the pull-out strength of bonded anchors under fire. *3rd International Symposium on Connections between Steel and Concrete*. Stuttgart.
12. ISO 834-1. (1999). *Fire resistance tests-elements of building construction*.

Concrete Structures

DESIGN OF POST TENSIONED CONCRETE STRUCTURES EXPOSED TO TRAVELLING FIRES

Chloe Jeanneret ¹, John Gales ², Panagiotis Kotsovinos ³, and Guillermo Rein ⁴

ABSTRACT

Modern architecture is driven by the desire to have large open plan spaces. As a result, the travelling fires methodology, which is valid for large open spaces where flashover would not occur, has been developed and various buildings have used this methodology as part of their fire resistance design. The on-going research focus in this area is on improvements in the methodology based upon real fire dynamics and novel uses for non-traditional and advanced material construction. This research studies travelling fires inside a flat-plate post-tensioned concrete buildings. This structural system is used to ensure architecturally desired long flooring spans which often result in large compartments. This research study undertakes modelled structural validation of high temperature prestressing tendon relaxation and rupture (unbonded) compared with results of previous fire experiments (based on thermal response). This validated structural model is then used to analyse the floor plan of a real case study building in the United Kingdom to build novel fire design guidance. The focus is on the localised nature of a travelling fire and the unique deformation mechanisms present when prestressing steel has been heated locally. Results indicate acceptable validation of prestressing tendon relaxation models (when slab deflection is negligible), and allows for a unique discussion on how travelling fires may impact the design of this type of concrete construction. Results suggest that slow moving fires are a more erroneous in structural terms than fast moving or uniform fires. These slow moving fires are essential design fires that should be considered for this structure type as they can result in responses not necessarily observed through the adoption of uniform fires and therefore critical behaviours may be missed. Additional research needs are discussed herein which include the development of structural deformation acceptance criterion.

Keywords: Travelling fires, post-tensioned, prestressing steel, concrete, fire

1 INTRODUCTION AND BACKGROUND

Contemporary architecture of concrete structures demands structural engineering systems which can permit large open spaces (airports, theatres, stadia, condos, offices, etc). A number of real fire events have shown that that fires in large open spaces will not result in uniform thermal exposure to the structure as it is conventionally assumed. In reality, fires can exhibit characteristics that demonstrate a “travelling” behaviour. In the transition towards objective- and performance-based design in many jurisdictions, it is becoming more important to model and understand structures to a range of likely and expected design fire exposures. This is typically done by selecting realistic design fires (based on engineering judgement, local practice or probabilistic studies) to ensure a robust design. The fire resistance design of structures is predominantly based on the adoption of the

¹ Research Assistant. Department of Mechanical Engineering, Imperial College, London, UK/ York University, Canada.

^{2*} Professor. Civil Engineering, York University, Toronto, Canada. e-mail: jgales@yorku.ca

³ Arup, Manchester, UK.

⁴ Professor. Department of Mechanical Engineering, Imperial College, London, UK.

ISO 834 standard fire test (or ASTM equivalent) that has its origins more than 100 years ago. The adoption of the standard fire makes it possible to establish a qualification-based fire resistance metric for classification purposes, and the comparative performance of structures and other building components (doors, fire stops etc); therefore, it does have its place for design purposes. It has been recognised that it does not necessarily resemble the behaviour that structures experience in a real fire. When considering the real behaviour of structures in fire, a range of responses can be expected depending on the fire conditions which can differ to those determined when using the standard fire. Research studies on composite steel concrete structures have shown that “short hot” and “long cool” uniform fires can lead to different responses [1]. Rackauskaite et al [2, 3] compared the influence of travelling fires and uniform fires in a steel multi-storey building, and determined that travelling fires can introduce a range of responses. Thermally travelling fires are more severe, and structurally it depends on the specific heating scenario. The travelling fire methodology is based on a moving localised fire with a leading edge due to the flame spread and a trailing edge that gradually burns out. Law et al [4] also reached similar conclusions for a reinforced concrete structure subjected to uniform and travelling fires. For post-tensioned concrete structures, Gales has shown experimentally that a localised fire can be more onerous in comparison with a uniform fire (that is the assumption of the standard fire test) due to stiffer restraint from the unheated areas [5]. Multiple buildings have now been designed and built with the travelling fire design methodology. Its use in design is global from Europe, Asia, and now includes preliminary demonstration consideration in North America. To date, the structures that have used it are open plan offices of largely steel composite or traditional reinforced concrete configuration – mostly because the structural fire model validation exists for these structure types. However, other structural systems, which also enable large compartmentation, have seen limited application of the travelling fires design methodology in practice. Post-tensioned concrete, which uses highly stressed prestressing steel tendons to achieve long spans, is such an example that has received limited research attention. This application of travelling fires could be in particular critical as previous experimental research has indicated that PT concrete has specific vulnerabilities to localised heating that can cause its steel reinforcing to rupture – specifically if the steel is left unbonded to the concrete and rather than bonded [5] with corresponding reductions in stress relaxation which hampers the structures ability to balance applied loading over long spans. By including travelling fires within a family of fires and identifying the most critical heating scenarios, it becomes possible to design these structures so that such failure mechanisms are mitigated. This study holistically aims to develop the capabilities in modelling post-tensioned concrete for reinforcing tendon (steel) relaxation and rupture, rationally identify the critical design fires necessary to ensure this type of structure’s fire resilience, and to conclude with a priority listing of research needs for this structure type for industry.

2 RESEARCH INTO POST-TENSIONED CONCRETE IN FIRE

One of the most comprehensive structural fire testing programmes that permits the study towards rational design of post-tensioned concrete in fire are the tests performed at the University of Edinburgh between 2011 to 2013 [5]. These tests included multiple bay (realistically-restrained) concrete slabs heated locally with radiant heaters. Those tests did not show tendon failure, but they did show significant stress relaxation which has an effect on the load balancing capabilities of the concrete slab. Those tests (A and C) can be found in detail accompanied with a state of the art review of prestressed concrete in fire literature [5]. The reader is referred to that work for details on the test procedure and its results. For brevity sake, it is beyond the scope of this current study to provide specific test details of that research programme as these have been presented before in previous *Structures in Fire* Conferences [6-8]. It should be noted that a third bonded tendon configuration slab can be considered (Test B), but this is beyond the scope of this current research. Recent industry reports, such as NIST 1188 and ASCE Manual of Practice (MOP), have both called for additional research into the performance of post-tensioned concrete in fire as well as a more

complete understanding of the realistic thermal boundary these structures are expected to encounter in fire [9, 10]. The research needs from the ASCE MOP are highlighted in Table 1 and are largely adapted from NIST 1188. This study focuses on moving towards addressing these critical research needs, whereby a valid acceptance criterion for post-tensioned concrete in fire may begin to be established against a range of more realistic fires. The emphasis on this current study is not to investigate spalling or related mechanisms. Instead, the focus is on research needs 2 and 3 as identified in the document and Table 1: local and global behaviour; and analytical tools and analysis to lead to novel design tools. It is expected that research will follow these endeavours and indeed various other organisations are currently studying these phenomena – RILEM [10]. Post-tensioned concrete fire research is an important and needed area of investigation which has received little contemporary attention, in part due to its difficult to study nature. If prestressing steel tendons do fail, they have the potential for significant damage and life safety concerns.

Table 1. Research Needs from ACSE MOP (Manual of Practice), 2018

Topic	Milestone
1. Concrete Cover Spalling	a. Determine acceptable limits (e.g., temperature) for spalling
	b. Quantify the beneficial effects of specific mitigation techniques (e.g., incorporating polypropylene fibers into the concrete mix design)
	c. Develop appropriate acceptance criteria for concrete cover spalling
	d. Develop new spalling mitigation recommendations
2. Local and Global Behavior	a. Define acceptable limits for out-of-plumb concrete column behavior and slab deflection, particularly when related to realistic restraining mechanisms in actual buildings
	b. Develop appropriate local and global behavior acceptance criteria which considers the structural system performance of reinforced and prestressed concrete structures
3. Analytical Tools and Analysis	a. Develop acceptance criteria for reinforced and prestressed concrete structures under fire exposure that consider realistic fire scenarios

3 VALIDATION OF TENDON DEFORMATION MODEL IN POST-TENSIONED CONCRETE IN FIRE

This study begins with a thermal and tendon rupture computational model validation against a previously experimental data set of a two span PT concrete flooring system exposed to localised heating, available in the public domain [5]. This finite difference based analysis assumed a thermal boundary condition representative of heating conditions experienced during testing (see [5]). There was some minor variation in heating along the slabs, therefore a representative thermal boundary equation was developed which adequately describes the temperature-time exposure to the slab induced in all tests. The boundary represents a best fit least squares approximation of the average of eight thermocouples used on the exposed soffit in these tests. The thermal boundary was defined on the first two and a half hours of heating and extrapolated beyond this point. Using this initial heating curve and a heat transfer analysis, temperature profiles can be determined. Through thickness slab temperatures were estimated and used to determine tendon temperatures based on the experimental heating. The input thermal model parameters considered a 95 mm thick slab with 4% moisture content. Utilising the tendon stress relaxation and rupture modelling found in Gales et al. [11], the expected stress relaxation was computed for BS 5896 prestressing steel. The stress relaxation observed was then compared to the tendon stress observed in the test. The results are illustrated in Figure 1.

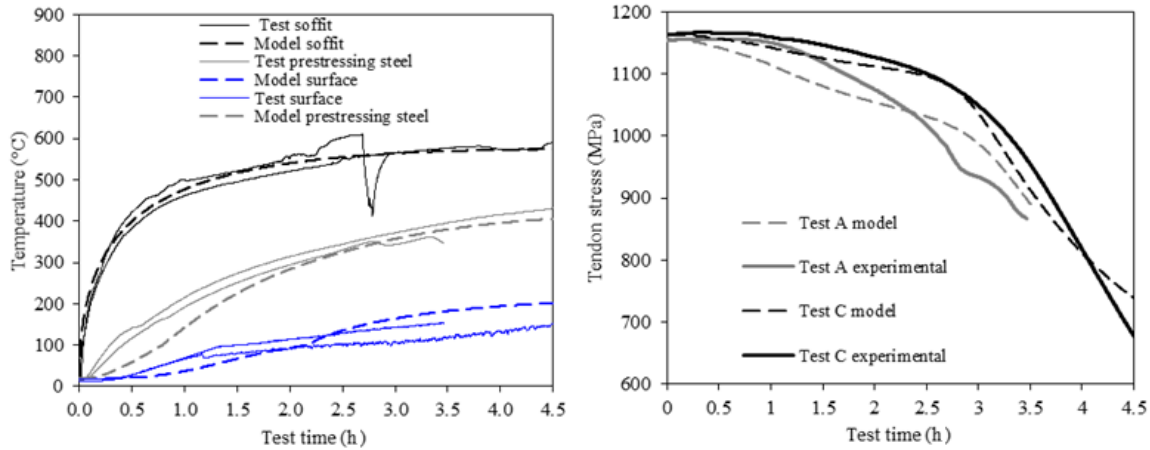


Fig. 1. (a) Thermal response and (b) Prestressing tendon response of UPT multi span tests A and C (see [5])

Test A showed a maximum difference of 47 MPa (5% error), while Test C showed a maximum difference of 27 MPa (3% error) during the first three hours of testing. The observed accuracy of the structural model is in line with that shown in Gales [11] (i.e. less than 6% error). The experimental data from Tests A and C show little stress relaxation at the start of the tests, whereas the structural modelling predicts clear relaxation during this period of the tests. This could be due to tendon elongation caused by thermal bowing at the start of the test, which would counteract stress relaxation induced by heating and is not accounted for in the current structural modelling that does not consider structural response. As shown in [5], deflection (12 mm maximum) was relatively small considering the spanning length (4140 mm mid span length), and therefore the resulting elongation from deflection alone of the tendon would be small. The comparison between Tests A and C however supports the utilised creep parameters from [11] and the overall stress relaxation modelling approach suggested herein for the below case study.

4 POST TENSIONED CONCRETE BUILDING CASE STUDY

The structural layout of a realistic a PT concrete building, based on a commercial project designed by Arup, is considered herein (see Figures 2 and 3). The structure has 8.15m spans, 6 to 32m tendon lengths, 250mm depth and 35mm tendon axis distance at supports and mid span. The structure has over 100 tendons, though for simplicity, symmetry is assumed in the author's analysis. There are limitations that need to be considered prior to the presentation of the case study's results. First, the authors are making limited attempt to investigate the thermal-mechanical response of the concrete slab. Very limited progress has been made in literature in this subject owing to a dearth in available experimental programme to allow that validation. It is encouraged that practitioners attempt these validations using the tests as aforementioned in [5]. Transient thermal straining has received some attention by researchers in recent literature. This straining mechanism appears to govern the deformation response of these slabs which thereby make performance criteria difficult to establish [9, 10]. Tendon rupture and stress relaxation is the current focus of this investigation, and the below case study explicitly considers this aspect herein. Future research could consider other performance criteria and what criteria govern the design depending on the structural layout. The case study structure presented herein was thermally evaluated for a range of design fires, including fully involved (standard), parametric and travelling fires, to determine the concrete's thermal response as a function of time. All fires were selected qualitatively based on experience from previous studies by the authors to reflect a typical design process. The heat transfer analysis of structural members was calculated using nonlinear finite difference calculation. It was assumed that explosive spalling is unlikely to occur, as the XC1 class is considered with moisture content less than 3% and the concrete strength is below 55 MPa, in accordance with EC2-1-2. The most critical fires that may

provoke tendon rupture, based upon region specific material usage, are identified using the validated region-specific tendon rupture models from [11]. To simplify presentation herein, this manuscript considers fires moving across grid “4” with a 32m long parabolic draped tendon running lines N to C (East to West) as seen in Figures 2 and 3. The analysis presented in this paper is one out of 100 possible tendons, a more complete statistical study will follow by the authors where all tendons are considered.

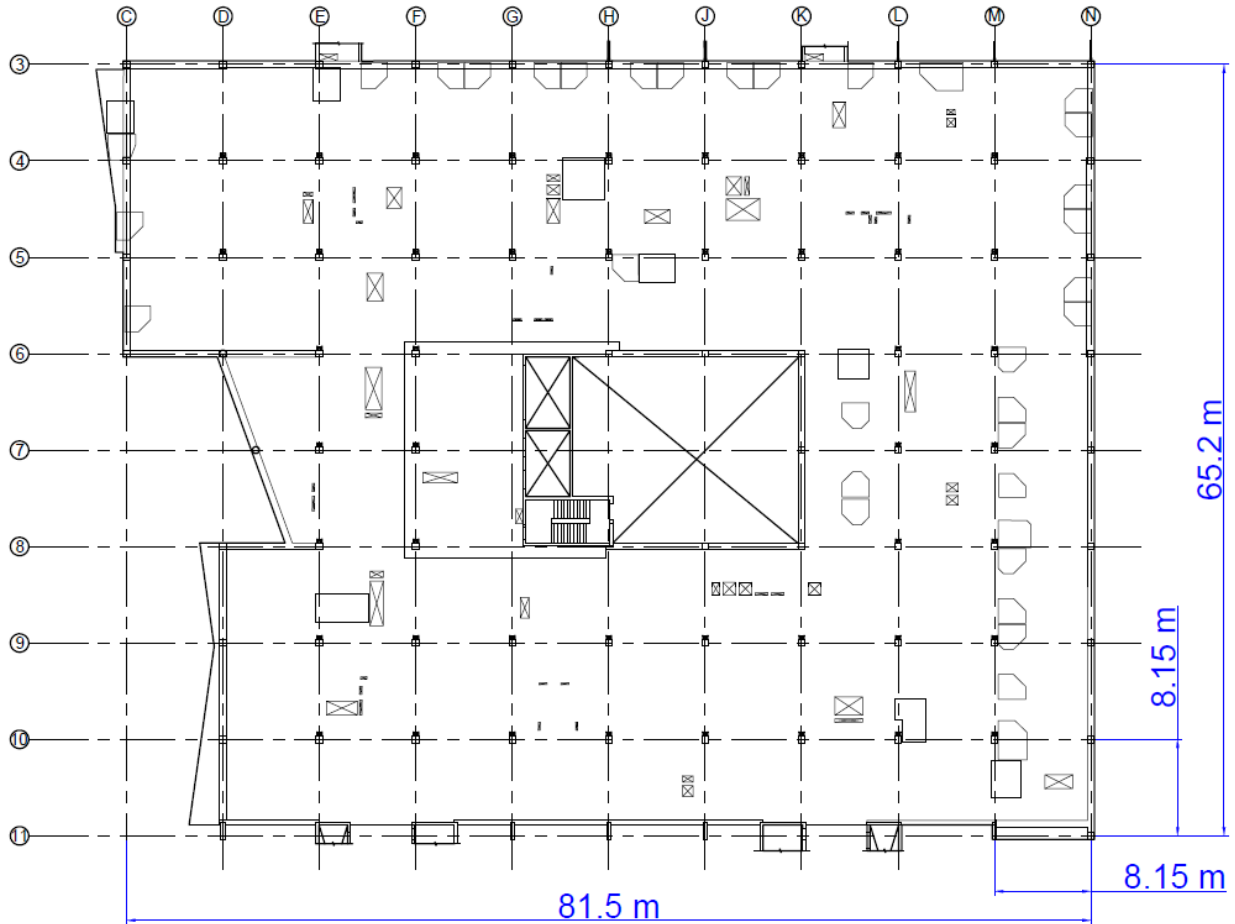


Fig. 2. Structural layout for the case study building showing column grid spacing

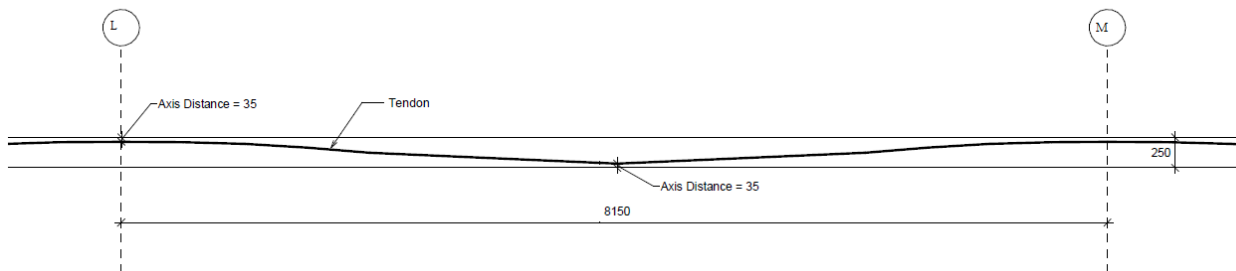


Fig. 3. Cross section of slab Grid M-L showing concrete cover and parabolic tendon (dim in mm)

The improved Travelling Fire methodology (iTFM) [3] has been adopted for characterising the design fires in the compartment. The methodology divides the thermal environment into two regions, the “near field” and the “far field” which generates spatially non-uniform and transient temperatures in the compartment. The near field represents the burning region of the fire while the far field represents the region remote from the burning area where the structure is heated by hot smoke moving away from the fire source. It assumes that the fire travels in a one-dimensional direction and at a constant speed. Fire load density and heat release rate per unit area were taken for office type accommodation in accordance with EN1991-1-2. A flapping angle of 6.5 degrees was

adopted. As Rackauskaite et al [2] have shown, travelling fires of different speeds can lead to different thermal and structural responses. As a result, for the purposes of this study, three representative travelling fire scenarios were qualitatively considered of a slow, medium and fast travelling fire (5%, 20% and 40% fire sizes with respect to the compartment size respectively) to ensure a range of responses. Figure 4 briefly highlights utilised time temperature curves for the medium sized travelling fire across the entire structures floor (10 curves are shown for simplicity).

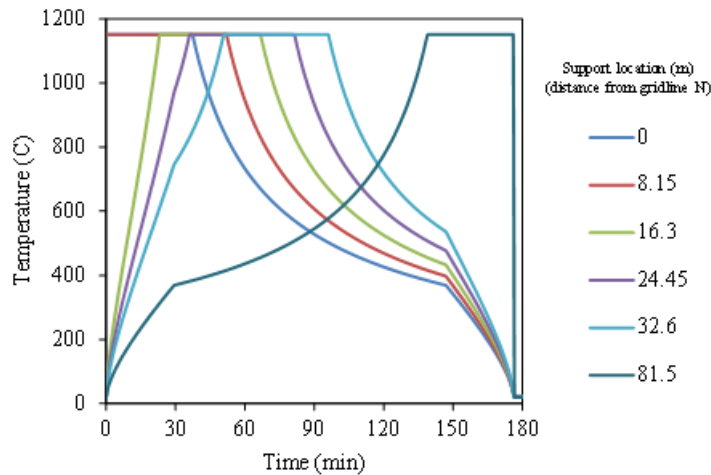


Fig. 4. Medium sized travelling fire thermal exposure across gridline N-C (see Fig. 2 for gridline location)

After the thermal boundaries and concrete temperatures were calculated, the corresponding tendon temperature was extracted from the thermal analysis. This temperature was then inputted into a stress relaxation subroutine developed and described in reference [11]. Two types of steel were analyzed; the first being BS (fabricated accordingly to BS 5896), and the second being NZ (fabricated accordingly to AS/NZ 4672). The prestressing stress and strength analysis considered both these steel types to assess whether region specific influences in manufacture may control the response of the unbonded prestressing steel. Once the prestressing steel stress relaxation was calculated using thermal properties from [11], significant differences in behaviour emerged with respect to relaxation and the introduction of the travelling fire as the design thermal boundary. Figure 5 briefly illustrates the response of one 32m long prestressing steel exposed to the array of these design fires

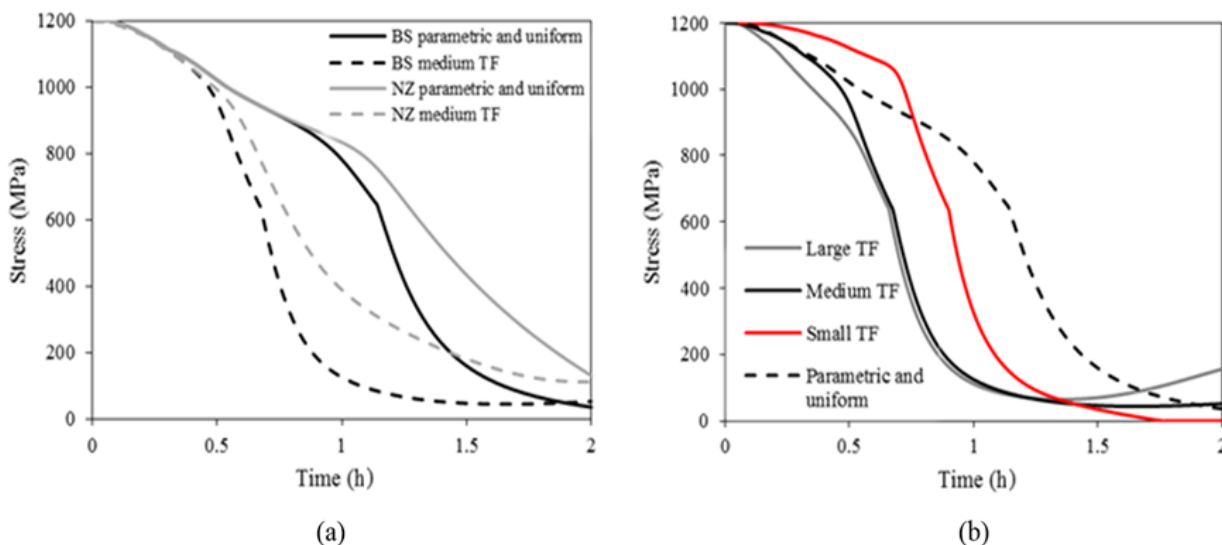


Fig. 5. Tendon stress relaxation modelled from (strength failures not shown) (a) medium travelling fire both NZ and BS steel (b) BS all design fires considered

The stress relaxation results first imply that NZ prestressing steel in all cases has less stress relaxation than its BS counterpart. When various travelling fires are considered, all seem to

converge by two hours to a below acceptable stress state regardless of the make of steel. It appears though that for most cases, the stress relaxation calculated in travelling fires is actually more significant than a uniform fire exposure (parametric and standard) for the prestressing steel tendon. This is likely as the travelling fire leads to longer heating durations and therefore higher steel temperatures, but further studies are required to assess the influence of travelling fires. When strength reduction is considered (where tertiary creep is simplified in the calculation, and rupture is implied to occur during secondary creep when tendon stress exceeds time dependent strength), the more erroneous fire emerges as the small travelling fire with respect to tendon rupture. Rupture is predicted between 345C and 362C for both steels. Strength reduction utilised the Eurocode recommended reduction factors and are considered overly conservative with respect to available literature [11]. The preliminary evaluation is tabulated within Table 2. Table 2 also implies that a large and medium travelling fire is nearly convergent in respect to stress relaxation and lack of observed tendon rupture.

Table 2. Peak temperature (C) at 50% tendon stress relaxation / Peak temperature (C) tendon rupture using EC2 strength reduction stress relaxation intercept

Steel type	Parametric	Small	Medium	Large
BS	454 / -	478 / 362	389 / -	386 / -
NZ	508 / 394	501 / 345	438 / -	433 / -

5 FUTURE RESEARCH AND PRELIMINARY CONCLUSIONS

The results of the paper establish the first steps towards the definition of the critical design thermal boundaries for post tensioned concrete flat-plate slabs. For the case study and design fires examined, a slow travelling fire (5%) is the critical case. The result is expected as the fire leads to longer durations that the concrete will be exposed to heat. Additional research is required, which will then require additional tendon modelling to confirm. These include but are not limited to various grid orientations of the travelling fire will have to be considered as the tendons span multi-directional (east west, and north south); tendons of different length; multi-banded; bond type; various tendon profiles, and sensitivity of concrete properties, will also need consideration. The impending research will inform practitioners how to structurally design these assemblies to prevent tendon rupture and improve upon probabilistic design approaches for this structure type. The research can lead to needed acceptance criterion. The research will inform suitable performance criteria for adoption in design guidance manuals for post-tensioned concrete. Large scale test validation of fire dynamics in large compartments, will also need to follow with further probabilistic investigations. Those efforts are underway by multiple researchers. Further research is also necessary to consider other fire sizes and speeds of the travelling fire for a more complete analysis which is underway by the authorship team.

It was found that by simulating a range of traditional and travelling fires, there was limited risk of tendon ruptures when the NZ steel was utilised. Lessons in the Christchurch earthquake taught the fire community that the quality of steel is very imperative. It could easily be deduced that stress relaxation of NZ is less than BS, and therefore all steel should be sourced there – however, that is not necessarily true. The reason NZ performs with less relaxation is because the stock considered in reference [11] had a sizably larger concentration of chromium than the stock of BS. Chromium addition can improve creep properties [11]. There is no guarantee that this addition is intentional and consistent; it may not be nothing more than a consequence of the manufacturing of prestressing steel using recycled components. The quality and make of the stock of prestressing steel is critical. Hence, the authors are confident only in using the Eurocode strength reductions specified currently in literature, rather than the tabulated reductions found in various literature. Furthermore, Robertson

et al. [12] indicated very significant strength reductions as a function of heating time (even when specimens had no load during heating). It is prudent that if a long travelling fire is considered, the corresponding strength reduction should also be considered more carefully. This is because as prestressing steel is heated for a longer period at the same elevated temperature, it can lose additional strength. That research has only been completed at residual condition, not in fire. All of these research advancements are beyond the scope of the current study but necessary to consider when formulating generalized design considerations for highly complex prestressing steel.

The undertaken structural modelling does not consider the thermal-mechanical relations of load induced thermal strains, and thermal gradients which invoke complicated deflection mechanisms or load shedding from tendon failure. These will need to be considered in the future.

ACKNOWLEDGEMENTS

The researchers thank the previous contributions of L. Bisby and M. Heidari. NSERC Canada is acknowledged for their financial support of C. Jeanneret through the USRA programme and J. Gales through the Discovery programme.

REFERENCES

1. Lamont, L., Usmani, A., Drysdale, D. (2001) Heat transfer analysis of the composite slab in the Cardington frame fire tests *Fire Saf J*, 36 (8), 815-839.
2. Rackauskaite, E., Kotsovinos, P., Jeffers, A., & Rein, G. (2017). Structural analysis of multi-storey steel frames exposed to travelling fires and traditional design fires. *Engineering Structures*, 150, 271-287.
3. Rackauskaite, E., Hamel, C., Law, A. and Rein, G. (2015) Improved Formulation of Travelling Fires and Application to Concrete and Steel Structures, *Structures* 3:250–260,
4. Law, A., Stern-Gottfried, J., Gillie, M. and Rein, G. (2011) The influence of travelling fires on a concrete frame, *Engineering Structures* 33:1635–1642,
5. Gales, J., Hartin, K., and Bisby, L. (2016) Structural Fire Performance of Contemporary Post-tensioned Concrete Construction. *SpringerBriefs in Fire*. 91 pp
6. Gales, J., and Bisby L. (2016) Insights into the complexity of structural fire response from repeated heating tests on post-tensioned concrete. *Proceedings of the 9th International Conference on Structures in Fire*. New Jersey, USA. 53-61.
7. Gales, J., and Bisby, L. (2014) Deformation and response of continuous and restrained post-tensioned concrete slabs at high temperatures. *Proceedings of the 8th International Conference on Structures in Fire*. Shanghai, China. 305-312.
8. Gales, J., Bisby, L., and Stratford, T. (2012) High temperature creep deformation and failure behaviour of prestressing steel. *Proceedings of the 7th International Conference on Structures in Fire*. Zurich, Switzerland. 659-668.
9. NIST (2015). International R&D roadmap for fire resistance of structures: summary of NIST/CIB workshop. NIST Special Publication 1188.
10. LaMalva, K., Jeffers, A., Quiel, S., Gales, J., et al. (2017) Structural fire engineering: guide to SEI ASCE 16-7 Appendix E. 235 pp. Accepted.
11. Gales, J., Robertson, L., and Bisby, L. (2016) Creep of Prestressing Steels in Fire. *Fire and Materials*. 40, 875–895
12. Roberston, L., and Gales, J. (2016) Post-fire Guidance for the Critical Temperature of Prestressing Steel. *Interflam 2016: 14th International Conference and Exhibition on Fire Science and Engineering*. Royal Holloway College, Windsor, UK. 1027- 1037.

TIMBER STRUCTURES AND FIRE PROTECTION MATERIALS

PARAMETRIC STUDIES ON THE FIRE RESISTANCE OF STEEL-TO-TIMBER DOWELLED CONNECTIONS LOADED PERPENDICULARLY TO THE GRAIN

Pedro Palma¹, Andrea Frangi²

ABSTRACT

A framework to model timber connections at normal temperature and in fire, based on combined finite-element (FE) heat-transfer analyses and temperature-dependent Johansen-type load-carrying models, was developed and applied in a parametric study of previously tested beam-to-column steel-to-timber dowelled connections. Comparison with experimental results shows that the FE heat transfer models provide good estimates of measured temperatures and the load-carrying model gives good approximations of the load-carrying capacity at normal temperature and under standard fire exposure. For the degrees of utilisation expected in fire $E_{fi} / R_{20} \approx 0.3$, the models are able to predict the failure mode of each dowel and the expected load-carrying capacity. Simulation results showed a clear influence of the thickness of the side members on the fire resistance of the analysed connections. The influence of dowel spacing is not so clear, as it also depends on the dowel diameter. A smaller dowel diameter seems to slightly improve the fire resistance, namely for smaller degrees of utilisation or thinner side members, but compromises the load carrying capacity at normal temperature.

Keywords: timber connections, fire resistance, FE models

1 INTRODUCTION

1.1 Background

Due to the strong anisotropic nature of wood, the different possible failure modes, the high localized stresses close to the fasteners, and the transient nature of the behaviour of timber exposed to fire, the development of models for dowelled timber connections in fire can become very complex, even for simple situations. A commonly used approach to develop numerical models for timber connections in fire is to combine thermal finite element (FE) models with numerical load-carrying models of a single fastener. In this approach, an heat transfer FE analysis is performed to assess the temperature fields in the connection and an appropriate load-carrying model (such as Johansen's yield models [1–5] or beam-on-elastic-foundation models [6] is then used to estimate the load-carrying capacity at each time step. Uncoupled heat transfer FE analyses require temperature-dependent thermal and physical properties of connections components (timber and steel) and the load-carrying models only require temperature-dependent embedment properties of wood. An advantage of this approach is that, since the analytical models are usually based on a single fastener, the thermal model can be simplified due to symmetry and, therefore, the heat-transfer analysis will be much faster. In addition, since no FE stress analysis is performed, there is no need to define temperature-dependent mechanical properties and mechanical and thermal contact

¹ Project Leader. Empa – Materials Science and Technology, Dübendorf, Switzerland.
e-mail: pedro.palma@empa.ch

² Professor. ETH Zurich – Institute of Structural Engineering (IBK), Switzerland.
e-mail: frangi@ibk.baug.ethz.ch

interactions between the different components of the connection (fasteners, steel plates, and timber members). Therefore, a simpler single-part model that takes into account symmetry simplifications can be used. The main shortcoming of this modelling approach is that aspects related to the behaviour of the connection as a whole (e.g. load distribution between fasteners) are usually not considered, because of the single-fastener nature of the load-carrying models.

1.2 Scope and objectives

The fire resistance tests on beam-to-column steel-to-timber dowelled connections conducted by the authors [7, 8] comprised various geometries of the beam side of the connection, with different cross sections, dowel diameters, number of dowels, and position of the group of dowels. Overview of some of the tested configurations is presented in Figure 1 and Table 1. The test results showed mostly embedment failures but dowel bending failures were also observed and allowed to identify the main geometric parameters influencing the fire resistance of timber connections. However, further parametric analyses were deemed necessary to assess the relative influence of some of these parameters, namely the thickness of the timber side members and the dowel spacing, in the fire resistance.

In this paper, the development of a framework to model timber connections exposed to fire and its application to this parametric study are presented and discussed. An overview of the numerical simulations is presented in Table 2.

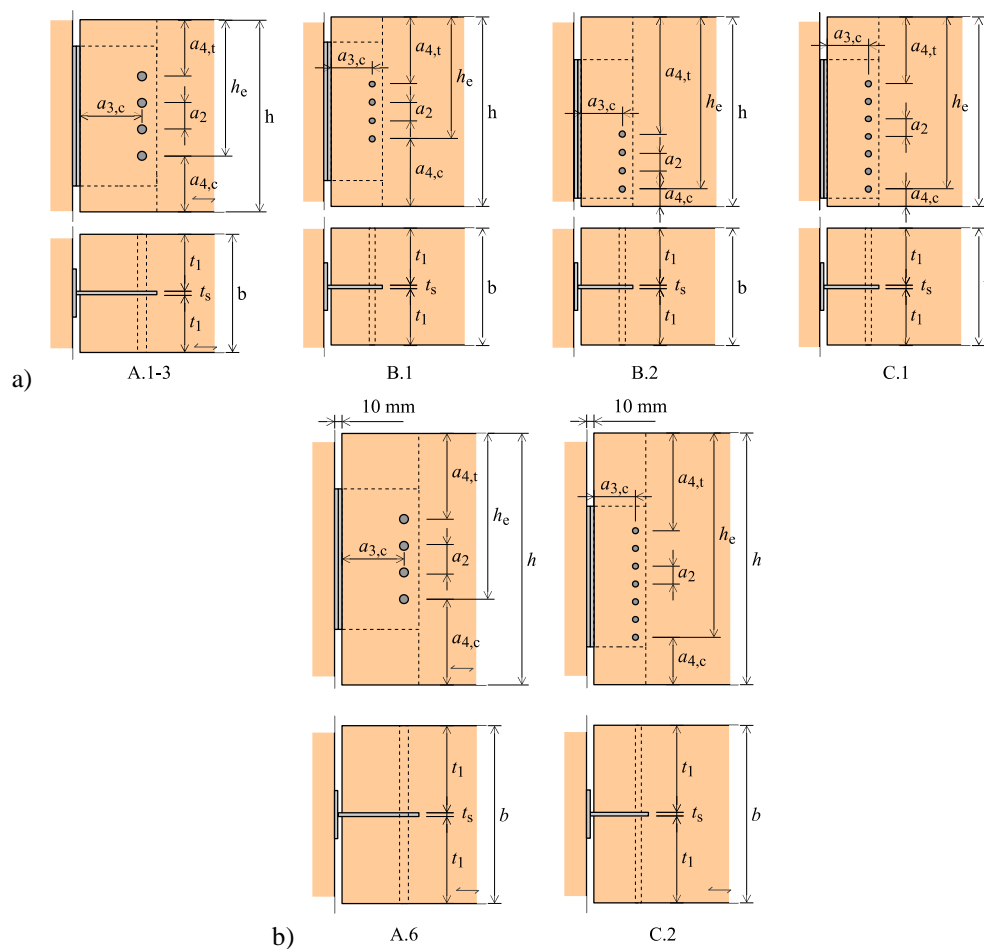


Fig. 1. Geometries of the beam side of connections: a) A.1–3, B.1, B.2, and C.1; b) A.6 and C.2.

Table 1. Geometries of the beam side of the connections tested by the authors [7, 8].

Connection typology	$b \times h$ [mm ²]	t_1 [mm]	t_s [mm]	d [mm]	n_{dowels} []	$h_e=h$ []	a_2 [mm]	a_3 [mm]	a_{4t} [mm]	a_{4c} [mm]
A.1	160×260	77	5	12	4	0.71	36	84	76	76
A.6	240×340	117	5	12	4	0.66	36	84	116	116
B.1	160×260	77	5	8	4	0.64	24	56	94	94
B.2	160×260	77	5	8	4	0.91	24	56	164	24
C.1	160×260	77	5	8	7	0.91	24	56	92	24
C.2	240×340	117	5	8	7	0.81	24	56	132	64

2 MODELLING FRAMEWORK

2.1 Overview

The modelling framework was developed using the *Python* programming language [9] and *Abaqus Unified FEA* software suite for finite element analysis [10]. The finite element heat transfer models of dowelled steel-to-timber connections with a slotted-in steel plate were generated using Abaqus' Python scripting interface, based on specified number and layout of fasteners, member geometry, material properties, and thermal interactions. The analyses were then submitted to the Abaqus solver in the meanwhile decommissioned high-performance cluster *Brutus* of ETH Zurich, which allowed running multiple simulations simultaneously and also faster, due to the possibility of using multiple processors. Afterwards, the generated output databases were analysed, again using Abaqus' Python scripting interface, to sample temperatures at specified locations and time steps. Finally, the load-carrying capacity of the connections at the specified time steps was calculated, based on the previously sampled temperatures, using a temperature-dependent Johansen-type load-carrying model.

2.2 Heat transfer models

Only the beam side of the connection was modelled, comprising the end part of the timber beam, the steel dowels, and a steel plate. The models take into account orthotropic thermal properties. They are composed by multiple parts, between which thermal (or mechanical) interactions are defined. Mesh generation considers the most relevant geometric features and its refinement is adjusted accordingly. A geometric symmetry simplification was considered in the form of a vertical adiabatic surface in the middle of the timber member. Convective and radiative thermal interactions were defined for the outer timber surfaces, for the exposed end-surfaces of the dowels, and for the edges of the steel plate. No heat coming from the end surface facing the column was considered, as well as no additional heat from the burning timber column, in the tests the columns were protected with thermal insulation [7, 8]. Since thermal FE analyses were performed and, therefore, regarding material properties, only thermal properties (thermal conductivity and specific heat) and density were needed. The used temperature-dependent physical and thermal properties for timber were those prescribed in Annex B of EN 1995-1-2:2004 for thermal conductivity in the direction perpendicular to the grain (in the direction parallel to the grain the temperature-conductivity curve of EN 1995-1-2:2004 was multiplied by approximately 4 to account for the higher conductivity in this direction [11]), specific heat capacity, and density to dry density ratio. The physical and thermal properties assigned to the steel components were those prescribed by EN 1993-1-2:2005.

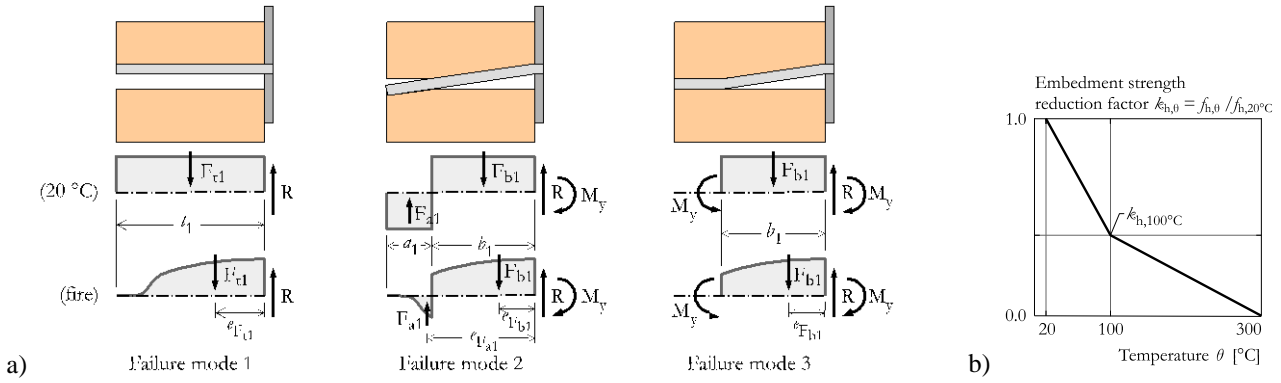


Fig. 2. Johansen-type load-carrying models: a) failure modes and load-carrying capacities R at 20 °C and in fire (with reduced embedment strength); b) bi-linear temperature-dependent embedment strength.

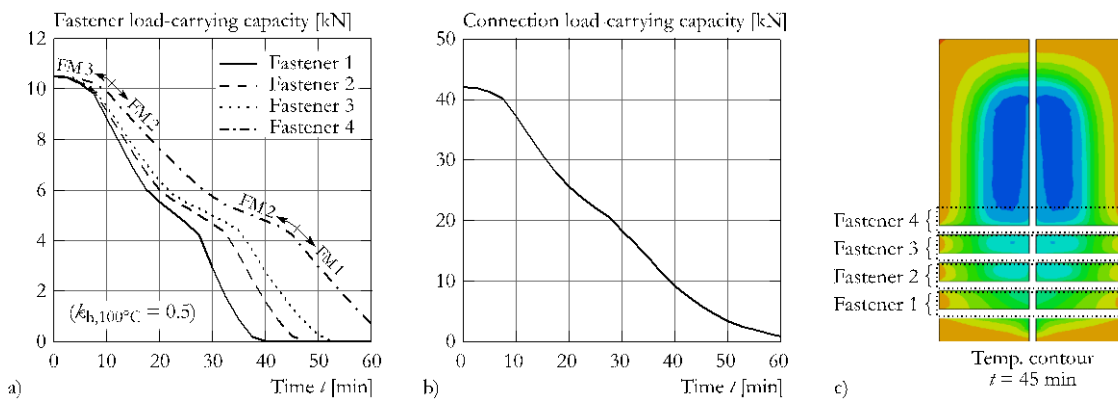


Fig. 3. Load-carrying capacity as a function of time of fire exposure for connection B.2 (Fig. 1), with $k_{h,100^{\circ}\text{C}} = 0.5$: a) fastener load-carrying capacity (failure modes of fastener 4); b) connections load-carrying capacity; c) temperature contours and temperature sampling areas for each fastener, at $t = 45$ min..

2.3 Load-carrying models

An adaptation of Johansen's [12] model to account for temperature-dependent embedment properties was used to estimate the load-carrying capacity of the modelled connections (Figure 2a). Johansen's approach was developed for a single fastener and assumes that its load-carrying capacity depends on the resistance of timber to the embedding of the fastener and on the resistance of the fastener to bending, both assumed to exhibit ideal rigid-plastic behaviour. Of these two properties, embedment strength shows a much more pronounced temperature-dependency and the simulations were fitted to test results using the reduction factor for embedment strength $k_{h,100^{\circ}\text{C}}$ as a calibration parameter (Figure 2b). The load-carrying capacity of the connection as a function of time of fire exposure is taken as the sum of the load-carrying capacity of each fastener (Figure 3).

3 PARAMETRIC ANALYSES

The programme of numerical simulations comprised parametric studies on the thickness of side members and the spacing between fasteners of the beam side of tested connection typologies (Table 2). The simulations were conducted using the reduction factors $k_{h,100^{\circ}\text{C}}$ that best fitted the experimental data of each connections typology, as discussed in the previous section.

Table 2. Overview of the numerical simulations.

Connection typology	Experimental research		Numerical simulations	
	Side member thickness t_1	Dowel spacing a_2	Side member thickness $t_{1,sim}$	Dowel spacing $a_{2,sim}$
A.1, A.3	77 mm	$3 \cdot d$	$t_1 - 40$ mm	$3 \cdot d$
			$t_1 - 20$ mm	
			t_1	
			$t_1 + 20$ mm	
			$t_1 + 40$ mm	
A.6 (R60)	77 + 40 mm	$3 \cdot d$	t_1	$4 \cdot d$
				$5 \cdot d$
				$3 \cdot d$
B.1	77 mm	$3 \cdot d$	$t_1 - 40$ mm	$3 \cdot d$
			$t_1 - 20$ mm	
			t_1	
			$t_1 + 20$ mm	
			$t_1 + 40$ mm	
B.2	77 mm	$3 \cdot d$		$4 \cdot d$
				$5 \cdot d$
				$6 \cdot d$
				$7 \cdot d$
B.2	77 mm	$3 \cdot d$	$t_1 - 40$ mm	$3 \cdot d$
			$t_1 - 20$ mm	
			t_1	
			$t_1 + 20$ mm	
			$t_1 + 40$ mm	
C.2 (R60)	77 + 40 mm	$3 \cdot d$	t_1	$4 \cdot d$
				$3 \cdot d$

3.1 Influence of side member thickness

As observed by the authors in another study [13], the side member thickness and the degree of utilisation are the most important parameters influencing the fire resistance of timber connections loaded in the direction parallel to the grain. Four thicknesses were selected: $t_1 - 40$ mm, $t_1 - 20$ mm, $t_1 + 20$ mm, and $t_1 + 40$ mm, where $t_1 = 77$ mm is the side member thickness of the tested R 30 connections. The 20 mm levels represent approximately 30 min of fire resistance for a wide cross section and $t_1 + 40$ mm = 117 mm is the side member thickness of the tested R 60 connections.

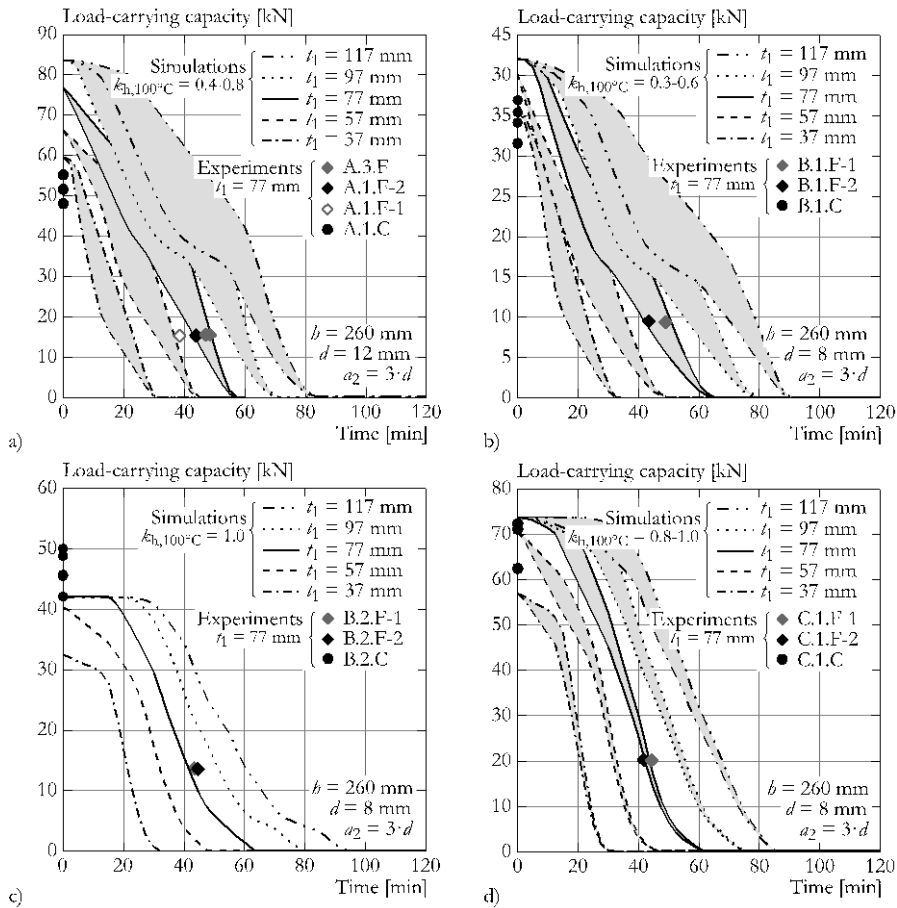


Fig. 4. Estimated and experimental load-carrying capacities for varying side member thickness: a) A.1 and A.3; b) B.1; c) B.2; d) C.1.

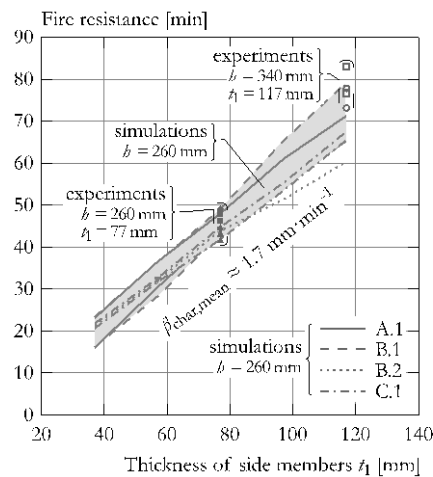


Fig. 5. Simulated and experimental fire resistances as a function of the thickness of the side members (for a degree of utilisation $\eta = E_{\text{fr}}/R_{20^\circ\text{C}} = 0.3$).

The results of these simulations show a significant influence of the side member thickness on the load-carrying capacity in fire (Fig. 4). According to the simulations and the experiments, there is a linear dependency between the fire resistance and the thickness of the side members, with a corresponding average charring rate $\beta_{\text{char}} = 1.7 \text{ mm} \cdot \text{min}^{-1}$ (Fig. 5).

3.2 Influence of dowel spacing

A parametric study was conducted to assess the influence of fastener spacing in the direction perpendicular to the grain on the fire resistance of the tested connections. For every R 30 typology (A.1, B.1, B.2, and C.1), simulations were performed assuming the same cross section of the side members, but increasing the fastener spacing until the minimum loaded edge distance $a_{4,t,min}$ was reached. This meant that some typologies could accommodate higher fastener spacings than others, from only $a_{2,max} = 4 \cdot d$ in typology C.1 up to $a_{2,max} = 7 \cdot d$ in typology B.1. In the connections A.1 and B.1 the group of fasteners remained centred in the cross section, and in connections B.2 and C.1 the group of dowels remained at the minimum distance from the unloaded edge.

The results of the parametric study are presented in Fig. 6 and show that dowel spacing is not such a relevant parameter as the thickness of the side members, at least for the analysed cross sections ($160 \times 240 \text{ mm}^2$) and times of fire exposure (up to 60 min). This limited influence of the dowel spacing is due to the exposure to fire of the upper and lower surfaces, which severely affects the outer fasteners and limits their load-carrying capacity. This effect could not have been captured with the previous simplified model. One exception to the mostly negligible influence of dowel spacing on the fire resistance is typology B.2 (Fig. 6c), in which increasing the spacing from $a_2 = 3 \cdot d$ to $6 \cdot d$ increases the fire resistance from 42-44 min to 55 min. However, further increasing the spacing to $a_2 = 7 \cdot d$ reduces the fire resistance to 50 min, because the uppermost dowel is more affected by the heating from above. The results of this parametric study do not rule out the influence of fastener spacing on the fire resistance, but for the analysed cross sectional dimensions and four-sided exposure, its influence seems limited.

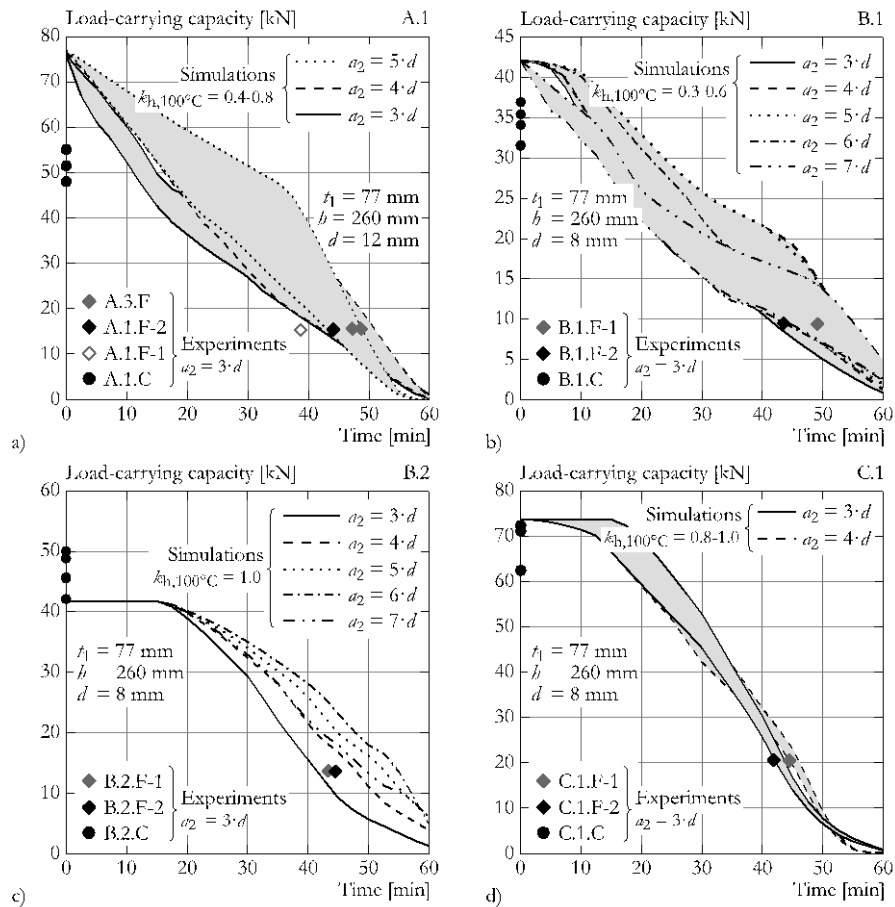


Fig. 6. Estimated load-carrying capacities for varying fastener spacing a_2 : a) A.1; b) B.1; c) B.2; d) C.1.

3.3 Influence of dowel diameter

The influence of the dowel diameter can be analysed comparing the experimental results and simulations of connection typology A.1 ($d = 12$ mm, and $a_2 = 3 \cdot d = 36$ mm) with the simulations of connection typology B.1 with increased fastener spacing ($d = 8$ mm, and $a_2 = 4.5 \cdot d = 36$ mm). Both connections have the group of dowels centred in the cross section and the dowels in the same locations. Since both connections have different load-carrying capacities at normal temperature, the comparison is presented in Fig. 6a with each load-carrying capacity normalised to its value at normal temperature. For degrees of utilisation below 0.3, reducing the dowel diameter seems to improve the fire resistance – for a degree of utilisation $\eta = 0.1$ the fire resistance increases from approximately 52 to 60 min. For higher degrees of utilisation this effect cannot be inferred, as the models only account for Johansen failure modes and not for the splitting failures observed at normal temperature in typology A.1. However, even though it could improve fire resistance, reducing the fastener diameter will compromise the absolute load-carrying capacity (Fig. 6a). A connection with smaller dowels but higher load-carrying capacity than A.1 ($d = 12$ mm, $a_2 = 3 \cdot d$, $n_{\text{fasteners}} = 4$, $R_{20^\circ\text{C,mean}} = 52$ kN) is connection C.1 ($d = 8$ mm, $a_2 = 3 \cdot d$, $n_{\text{fasteners}} = 7$, $R_{20^\circ\text{C,mean}} = 69$ kN). Comparing the behaviour of these connections (Fig. 6b) there is no significant improvement in fire resistance in the connection with smaller dowels.

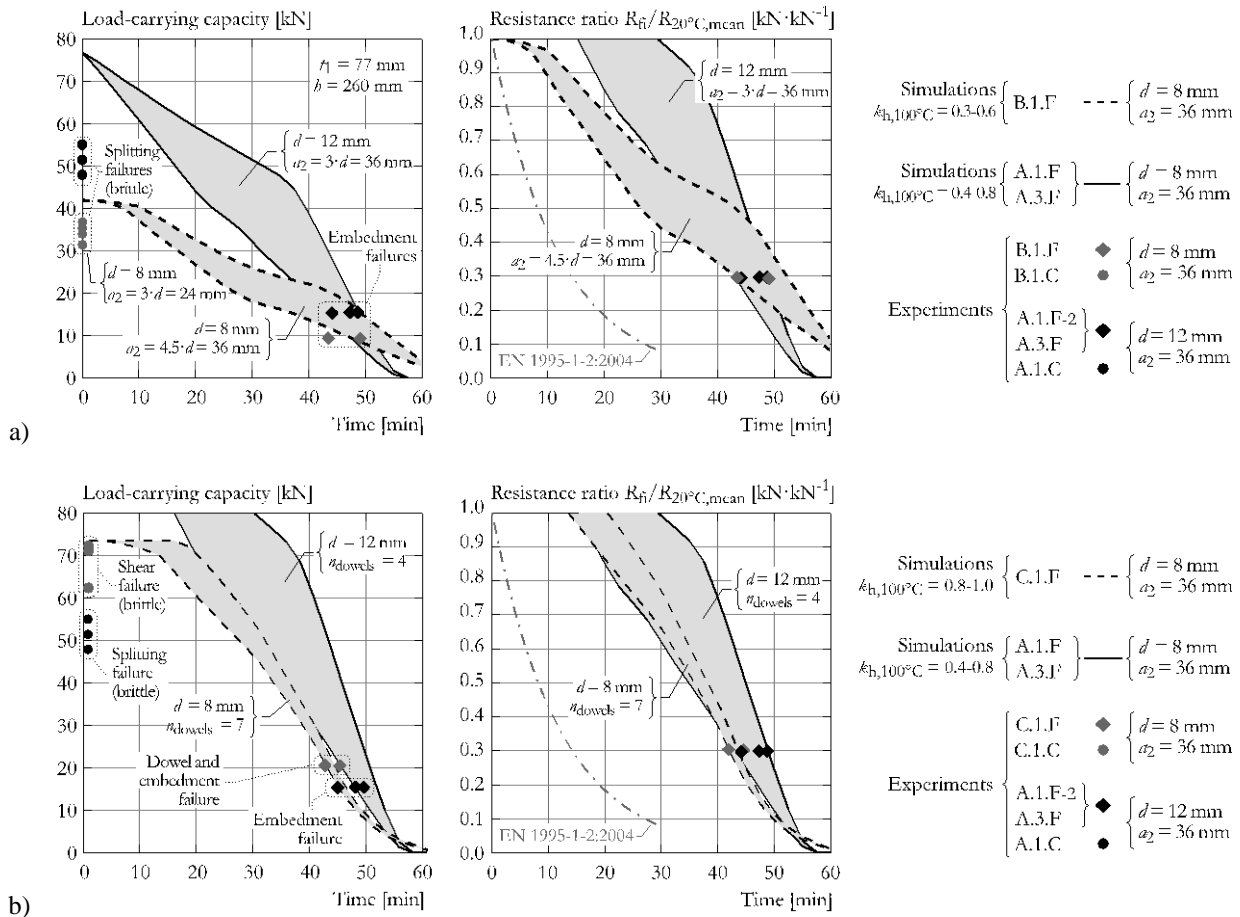


Fig. 6. Influence of dowel diameter: connections: a) A.1 ($d = 12$ mm, $a_2 = 3 \cdot d = 36$ mm) and B.1 ($d = 8$ mm, $a_2 = 4.5 \cdot d = 36$ mm); b) A.1 ($d = 12$ mm, $a_2 = 3 \cdot d = 36$ mm, $n_{\text{fasteners}} = 4$, $R_{20^\circ\text{C,mean}} = 52$ kN) and C.1 ($d = 8$ mm, $a_2 = 3 \cdot d = 24$ mm, $n_{\text{fasteners}} = 7$, $R_{20^\circ\text{C,mean}} = 69$ kN).

4 CONCLUSIONS

The results of performed simulations showed a clear influence of the thickness of the side members on the fire resistance of the analysed connections (Fig. 4). A side member thickness $t_1 = 116$ mm would suffice for reaching 60 min of fire resistance, which is approximately the requirement (cross section width $b = 240$ mm) set by Lignum's Dokumentation Brandschutz [14]. The influence of the dowel spacing is not so clear (Fig. 5), as increasing spacing did reduce the average temperature between the dowels but is also moved the outermost dowels closer to the exposed edges (Fig. 29). A smaller dowel diameter, for the same fastener spacing, seems to have slightly improved the fire resistance, namely for smaller degrees of utilisation and/or thinner side members, but compromised the load carrying capacity at normal temperature (Fig. 6).

These results are valid for connections exposed on all four sides. In beams supporting a ceiling and exposed only from three sides, keeping the group of fasteners centred in the cross section and increasing fastener spacing might provide higher fire resistances than in the simulated configuration.

REFERENCES

1. Scheer C, Povel D (2002) Stabförmige Verbindungsmittel im Brandfall – Grundlagenuntersuchungen (Dowel-type fasteners in fire – Fundamental research). Technische Universität Berlin, Berlin, Germany
2. Erchinger C (2009) Zum Verhalten von mehrschnittigen Stahl-Holz-Stabdübelverbindungen im Brandfall (On the behavior of multiple shear steel-to-timber dowel connections in fire). Doctoral thesis, ETH Zürich
3. Moss P, Buchanan A, Fragiaco M, Austruy C (2010) Experimental testing and analytical prediction of the behaviour of timber bolted connections subjected to fire. *Fire Technol* 46:129–148 . doi: 10.1007/s10694-009-0096-6
4. Peng L, Hadjisophocleous G, Mehaffey J, Mohammad M (2012) Fire performance of timber connections, Part 2: Thermal and structural modelling. *J Struct Fire Eng* 3:133–154 . doi: 10.1260/2040-2317.3.2.133
5. Palma P, Frangi A (2017) Modelling the fire resistance of steel-to-timber dowelled connections loaded perpendicularly to the grain. *Fire Saf J*. doi: 10.1016/j.firesaf.2017.12.001
6. Cachim P, Franssen J-M (2009) Numerical modelling of timber connections under fire loading using a component model. *Fire Saf J* 44:840–853 . doi: 10.1016/j.firesaf.2009.03.013
7. Palma P (2016) Fire behaviour of timber connections. Doctoral thesis, ETH Zürich
8. Palma P, Frangi A, Hugli E, et al (2016) Fire resistance tests on timber beam-to-column shear connections. *J Struct Fire Eng* 7:41–57 . doi: 10.1108/JSFE-03-2016-004
9. Python Software Foundation (2015) Python (version 2.7.11) [programming language]. Python Software Foundation
10. Dassault Systemes (2013) Abaqus FEA (version 6.13-2) [computer program]. Dassault Systemes
11. Cachim P, Franssen J-M (2009) Comparison between the charring rate model and the conductive model of Eurocode 5. *Fire Mater* 33:129–143 . doi: 10.1002/fam.985
12. Johansen KW (1949) Theory of timber connections. *IABSE Publ* 9:249–262 . doi: http://dx.doi.org/10.5169/seals-9703
13. Palma P, Frangi A (2016) Fire design of timber connections – assessment of current design rules and improvement proposals. In: International Network on Timber Engineering Research (INTER) – Meeting Forty-Nine. Timber Scientific Publishing, Graz, Austria, pp 299–313
14. Frangi A, Brühwiler I, Studhalter J, Wiederkehr R (2011) Lignum-Dokumentation Brandschutz. 3.1 Feuerwiderstandsbemessung – Bauteile und Verbindungen. Lignum Holzwirtschaft Schweiz, Zurich

THERMAL CHARACTERISATION AND FIRE PERFORMANCE OF PHASE CHANGE MATERIAL INCORPORATED PLASTERBOARDS

Sayilacksha Gnanachelvam¹, Mahen Mahendran², Anthony D. Ariyanayagam³, Poologanathan Keerthan⁴

ABSTRACT

Phase Change Material (PCM) incorporated plasterboards (referred to as PCM-plasterboards in this paper) have been introduced to the lightweight wall construction industry due to their high thermal storage capacity, which improves the thermal performance. However, the fire performance of these wall systems must be investigated to ensure the safety of building structures in fire. The fire performance of lightweight wall systems mainly depends on the wall lining. Hence, the fire performance of PCM-plasterboard has been investigated using thermal characterisation, small-scale fire tests and Finite Element (FE) analyses in this research. This paper describes the details of this research and presents the results of PCM-plasterboards in comparison with commonly used, standard gypsum plasterboards. The thermal characteristics of PCM-plasterboard and standard gypsum plasterboard at elevated temperatures were determined based on thermal property tests whereas small-scale standard fire tests of the boards were conducted to evaluate the fire performance based on time-temperature profiles. FE models were then developed and analysed to simulate the performance of these boards exposed to standard fire conditions. Results from both experimental and FE studies show that lower Fire Resistance Levels (FRL) were obtained for PCM-plasterboards compared to gypsum plasterboards while importantly, PCM-plasterboard provided additional fuel to the fire.

Keywords: Phase Change Material (PCM)-plasterboard, Fire Resistance Level, Thermal storage, Finite Element Modelling, Small-scale fire test

1 INTRODUCTION

Scarcity and limitation in energy have led to sustainable construction through the development of innovative building materials. Light gauge steel framed (LSF) wall systems made of cold-formed steel (CFS) studs lined with wallboards are being used in many countries but without a full understanding of their fire and energy performance. The thermal mass of LSF wall systems is not adequate compared to conventional wall systems, which leads to poor thermal performance. The indoor thermal comfort level of buildings is greatly affected by this performance, which has to be maintained without fluctuations regardless of seasonal variations. High levels of energy usage are common to maintain the indoor thermal comfort, for example, 40% of the total energy in South Australian homes is used for heating and cooling purposes [1]. Thermal energy storage techniques

¹ PhD Researcher. Science and Engineering Faculty, Queensland University of Technology (QUT), Brisbane, Australia.
e-mail: sayilacksha.gnanachelvam@hdr.qut.edu.au

² Professor. Science and Engineering Faculty, Queensland University of Technology (QUT), Brisbane, Australia.
e-mail: m.mahendran@qut.edu.au

³ Research Fellow. Science and Engineering Faculty, Queensland University of Technology (QUT), Brisbane, Australia.
e-mail: a.ariyanayagam@qut.edu.au

⁴ Lecturer. Science and Engineering Faculty, Queensland University of Technology (QUT), Brisbane, Australia.
e-mail: keeds123@qut.edu.au

can be used to avoid indoor temperature fluctuations by increasing the thermal mass of wall systems. Phase change materials (PCMs) with high latent heat storage capacities can be used as thermal energy storage materials in buildings [2]. PCM absorbs or loses considerable energy and undergoes a phase transition from solid to liquid or liquid to solid, respectively. PCM melts during daytime and solidifies at night times, and thus helps to maintain the indoor thermal comfort level.

PCM enhanced dry wallboards are currently used for their high thermal storage capacity in drywall systems [3]. They are primarily made of organic paraffin PCM added to plasterboards and are aimed at improving indoor thermal comfort level by having a phase change temperature of 23-26 °C. Leakage of PCM is one of the major issues in packaging of PCM for building applications. Mostly, microencapsulation technique is widely used in packaging PCM, where a small droplet (less than 1 mm) of PCM is coated by a protective shell. Usually, the PCM loading is 70-85% in microencapsulation [4]. However, the organic paraffin PCM being a flammable material increases the flammability of PCM-plasterboards [5] and directly affects the fire performance [6].

Researchers have focused on developing LSF wall systems with adequate fire performance as required by the National Construction Code (NCC) of Australia [7, 8]. Fire performance of load-bearing elements is measured as Fire Resistance Level (FRL) in minutes for three failure criteria, structural adequacy, integrity and insulation as given in AS 1530.4 [9]. However, fire performance studies of PCM-plasterboards are limited. Therefore, this research investigated the fire performance of available PCM-plasterboards under standard fire conditions using small-scale fire tests and FE analyses and compares with standard gypsum plasterboard results. It also included thermal characterisation of PCM-plasterboards and gypsum plasterboards based on a series of thermal property tests. This paper presents the details of this research and the results.

2 THERMAL CHARACTERISATION OF PCM-PLASTERBOARD

Standard gypsum plasterboard is comprised of calcium sulphate di-hydrate ($\text{CaSO}_4 \cdot 2\text{H}_2\text{O}$), which contains 21% of chemically bound water [10]. This chemically bound water is released in the form of vapour during the dehydration process due to heat absorption. Further, fly ash-high quartz, cellulose, vermiculite, starch and glass fibre are mixed in small quantities to delay the shrinkage cracks, board fall-off and ablation. PCM-plasterboards are made of a gypsum core with small quantities of starch, microencapsulated paraffin, etc. However, the exact material composition of PCM-plasterboard is not known as manufacturers use different proportions of raw material.

Thermal properties of construction materials at ambient and elevated temperatures are critical factors that affect the thermal and fire performance of the buildings, respectively. Manufacturers provide ambient temperature thermal properties of materials. However, limited results are available for elevated temperature thermal properties. Therefore, it is necessary to determine accurate temperature dependent thermal properties at elevated temperatures in order to have a clear understanding of the fire performance of individual materials used in wall systems. A series of thermal property tests of PCM-plasterboard and standard plasterboard were conducted at elevated temperatures to determine their specific heat capacity at constant pressure (C_p), thermal conductivity (λ) and mass loss variations.

The specific heat capacity of materials varies with temperature due to the mass loss at elevated temperatures that can affect the thermal performance of LSF wall systems at elevated temperatures. The simultaneous thermal analyser (STA) was used to measure the specific heat capacity at constant pressure (C_p) and mass loss variation. Powdered board samples (three samples per board) were tested from 30-1200 °C with a heating rate of 20 K/min. *Fig. 1 a)* shows the average C_p of PCM-plasterboard and standard gypsum plasterboard with increasing temperature. The C_p variation of gypsum plasterboard shows the highest peak value of 10672 J/kgK at 160 °C while PCM-plasterboard shows the highest peak value of 13882 J/kgK at 172 °C. This implies that the heat absorption capacity of PCM-plasterboard is higher than standard gypsum plasterboard. However,

PCM-plasterboard has a very high mass loss due to the evaporation of PCM and dehydration from the board at elevated temperatures. This is about 40% compared to 20% in standard gypsum plasterboard (see Fig. 1 b)), which is due to dehydration. The highest mass loss may create cracks on the board surface that can increase the likelihood of integrity failures. Rusthi et al. [11] explains how the high mass loss of a wallboard affects the integrity failure. Some Magnesium Oxide boards with about 40% mass loss led to premature integrity failures when used as lining materials in LSF walls in fire.

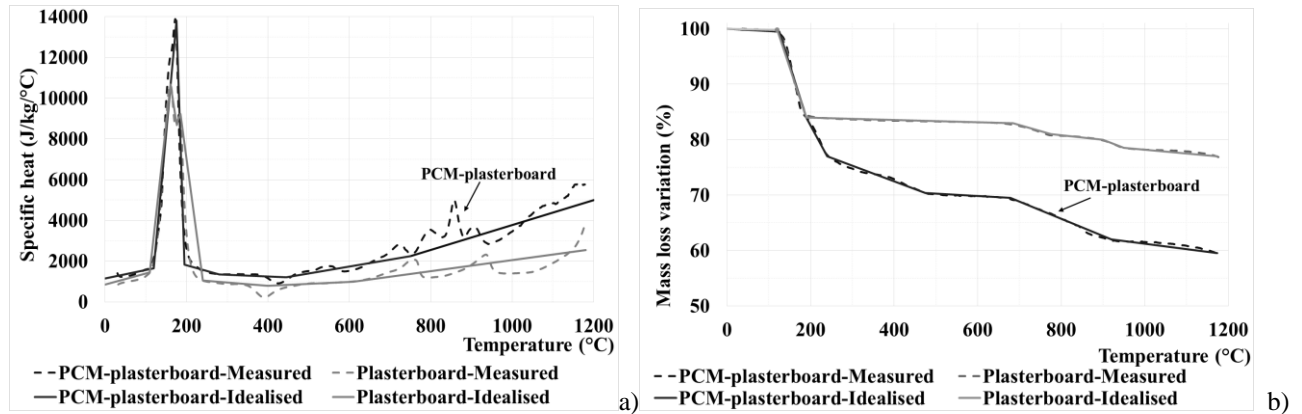


Fig. 1. Thermal properties of PCM-plasterboard and standard gypsum plasterboard a) Specific heat capacity; b) Mass loss

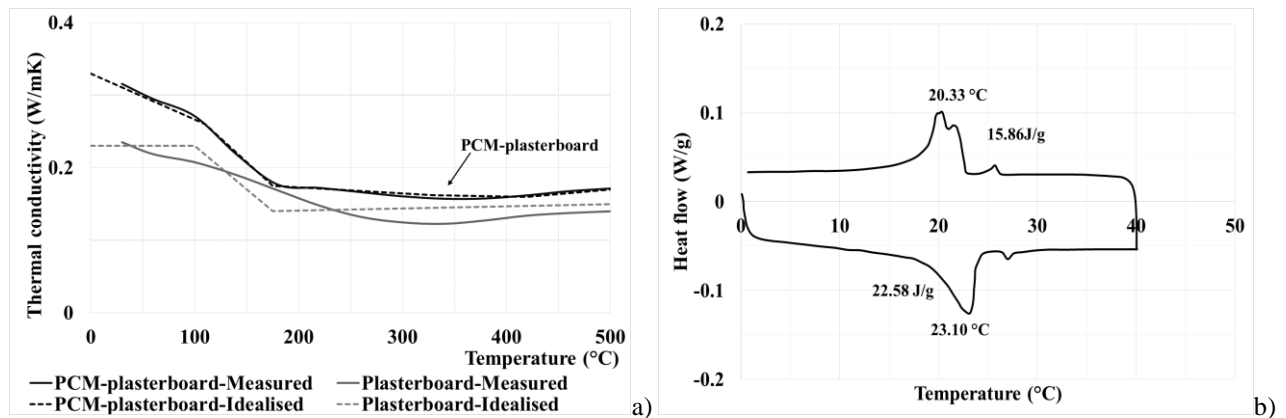


Fig. 2. Thermal Properties a) Thermal conductivity of both boards; b) Latent heat capacity of PCM-plasterboard

Thermal conductivity (λ) is one of the prime factors that affects the heat transfer rate. Laser flash apparatus (LFA) was used to measure the thermal diffusivity of 10×10×2 mm solid square samples (three samples per board) from 30-500 °C, which was then used to determine the thermal conductivity. Fig.2. a) shows the average thermal conductivity variation of PCM-plasterboard and standard gypsum plasterboard with temperature. A higher thermal conductivity value was obtained for PCM-plasterboard compared with standard gypsum plasterboard, ie. 0.33 W/mK versus 0.23 W/mK at 30 °C and 0.17 W/mK versus 0.14 W/mK at 500 °C. Reduction in thermal conductivity values were obtained from 100-200 °C for both PCM-plasterboard and standard gypsum plasterboard, when peak values of specific heat capacity and a sudden mass loss were observed. Heat transfer through the wallboards increases with higher thermal conductivity, which is likely in PCM-plasterboards.

Latent heat capacity (L), melting, and freezing points of powdered PCM-plasterboard samples were also determined using differential scanning calorimetry (DSC) within 0-40 °C. The latent heat capacity of 22.58 J/g was obtained during melting at 23 °C and 15.86 J/g was obtained during

freezing at 20 °C as shown in *Fig.2. b)*, which will increase the thermal storage capacity of lightweight wall systems. Although the PCM with latent heat capacity increases the heat absorption of PCM-plasterboard at lower temperatures, it is flammable [5]. Hence thermal property tests alone are inadequate to study the fire performance of PCM-plasterboards. Small-scale fire tests were conducted while heat transfer finite element (FE) models were developed to simulate the fire performance of these wall boards under standard fire conditions. The measured thermal property variations will be used to develop Abaqus heat transfer FE models.

3 EXPERIMENTAL STUDIES

Small-scale fire tests were conducted in a gas furnace as shown in *Fig. 3. a)*, with 1×1 m fire exposed area to study the fire performance of standard gypsum plasterboard and PCM-plasterboard according to AS 1530.4 [9]. Standard fire tests of 1.2×1.2 m, 16 mm gypsum plasterboard and 12.5 mm PCM-plasterboard were conducted with two samples from each type of board. Ten thermocouples were attached to both fire side and ambient side of each board at various locations (top, centre and bottom) and were connected to a data logger to record the test data. The external gas supply of the furnace was terminated when one of the ambient side thermocouples reached around 200 °C. However, temperature data was continuously recorded to study the behaviour of both standard gypsum plasterboard and PCM-plasterboard during the cooling period.

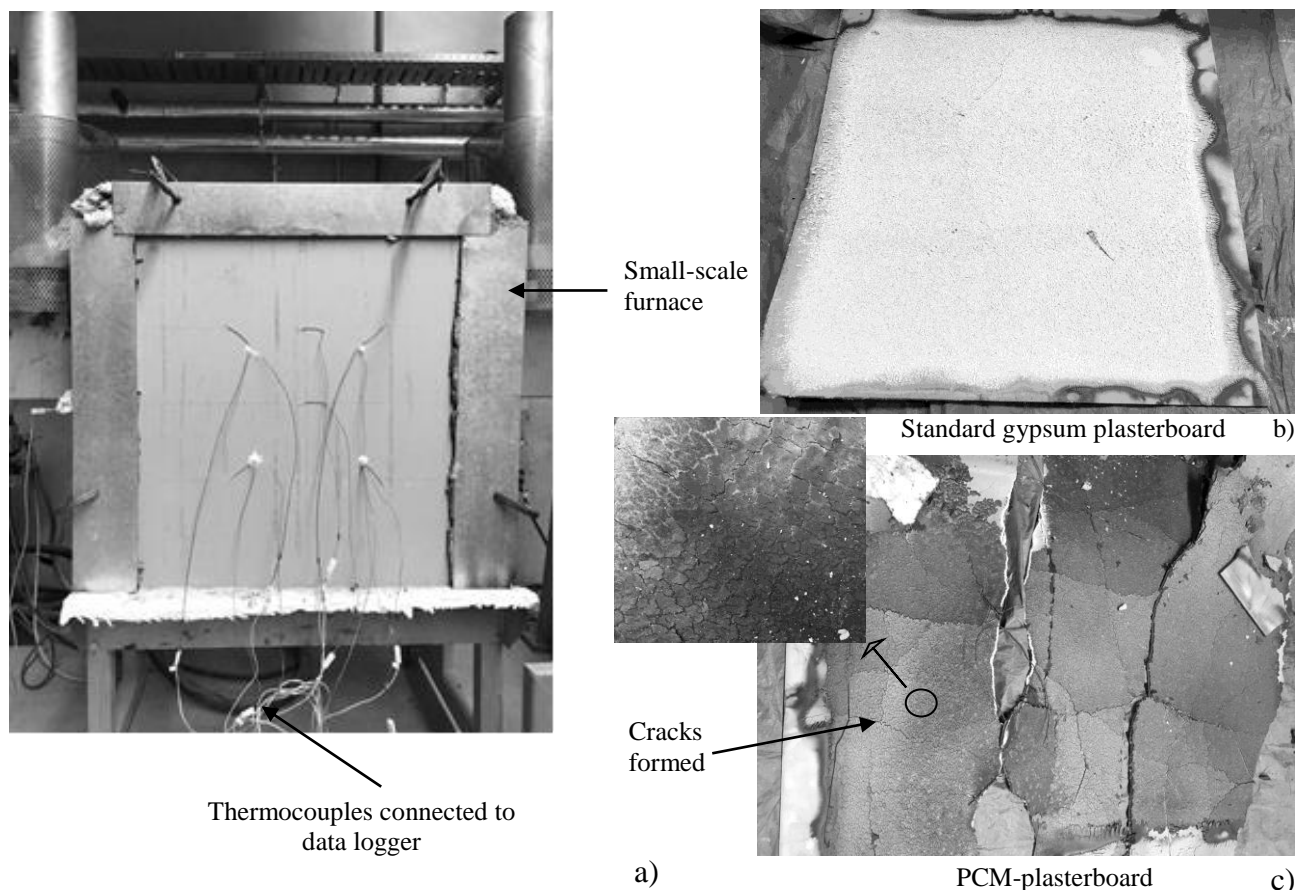


Fig. 3. Small-scale fire tests a) Test set up; b) Plasterboard and c) PCM-plasterboard after tests

During plasterboard fire tests, smoke was visible after 30 s due to the burning of paper and water drops were seen after 12 min at the bottom of the furnace. The colour of the ambient side plasterboard started to turn to brown after 24 min, which continued after the gas supply was stopped. During PCM-plasterboard tests, smoke was visible after 30 s and continued throughout the tests. Grey smoke was visible from 8 min to 15 min of the test. The flame was observed from about

8 min through the gas exhausts of the furnace until a few minutes after the test was stopped. Ambient side colour of the PCM-plasterboard started to turn dark after the gas supply was stopped and cracks appeared on the surface. PCM-plasterboard and standard gypsum plasterboard were removed from the furnace after they have cooled down for the observation of the fire side. *Fig. 3. b) & c)* show the fire exposed surfaces of standard gypsum plasterboard and PCM-Plasterboard after the fire tests. The paper surface of the plasterboard had burnt and discoloured into grey, whereas the PCM-plasterboard burnt and turned to black. The plasterboard retained its geometry without any cracking or spalling as seen in *Fig. 3. b)*. However, the PCM-plasterboard lost its structural integrity with severe cracking as seen in *Fig. 3. c)*.

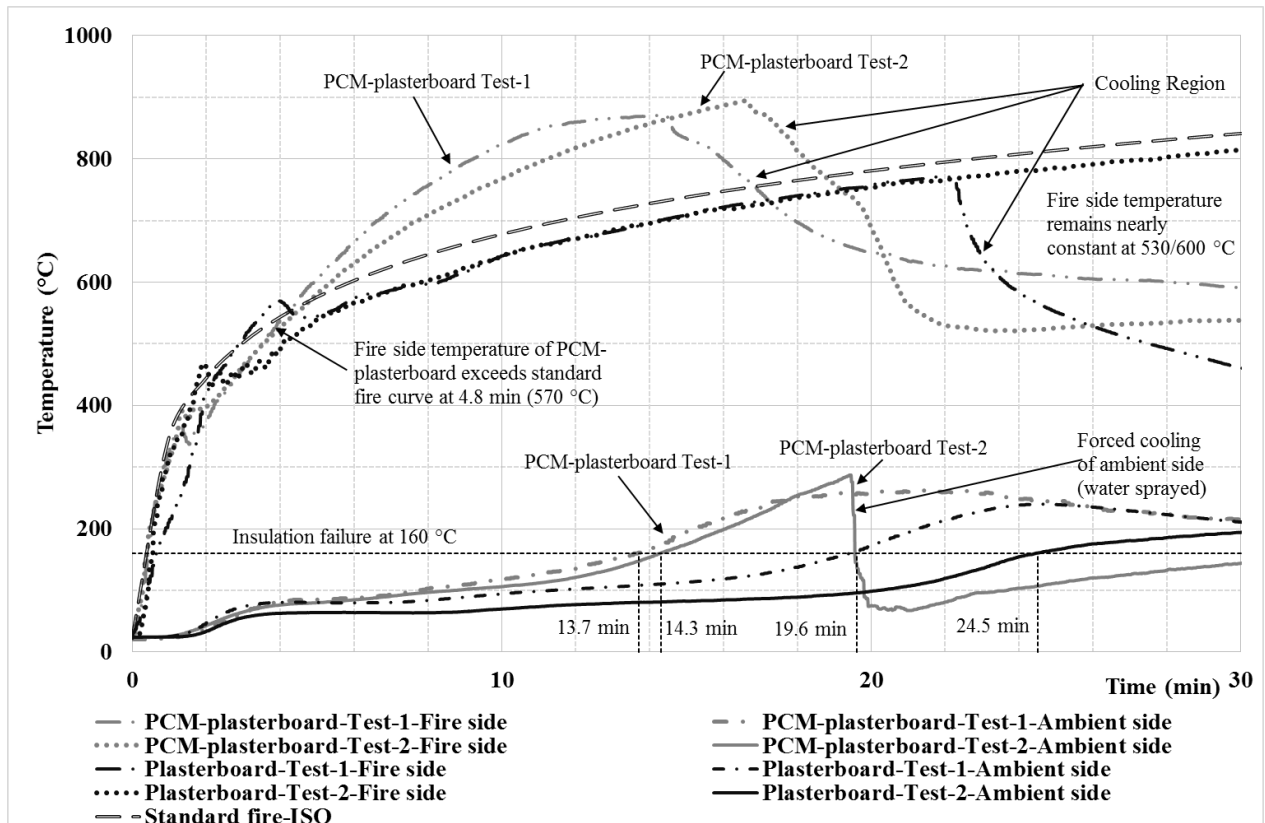


Fig. 4. Standard fire test results

Fig. 4 shows the average of all the thermocouple readings for both standard gypsum plasterboard and PCM-plasterboard obtained from the standard fire tests. The insulation based failure time (FRL) was obtained based on the average insulation criterion. Fire side temperatures obtained for standard gypsum plasterboards show good agreement with the standard fire curve. FRL of 20 min and 24 min were obtained for the two gypsum plasterboard samples. Other researchers also reported the insulation based FRL for gypsum plasterboard to be between 20 and 24 min. However, insulation based FRL of both PCM-plasterboard samples was 14 min. As seen in *Fig. 4*, fire side temperature variation of these boards did not agree with the in-input standard fire curve, which exceeded the standard fire curve after 4.8 min when the temperature reached 570 °C. PCM mixed with plasterboard evaporated at a certain temperature and provided additional fuel to the fire, which increased the fire side temperature of the PCM-plasterboard. This contrasting behaviour in the case of PCM-plasterboards can affect the fire performance of PCM-plasterboard, as reflected by the reduced FRL based on ambient side temperatures.

Fire side temperature of standard gypsum plasterboard dropped immediately when the gas supply was stopped. The ambient side temperature remained constant for a few minutes and then started to drop. In the case of PCM-plasterboards, fire side temperature was higher than the standard fire

curve, but started to drop gradually to 530 °C and remained constant for a certain time period when the gas supply was stopped. However, the ambient side temperature kept on rising to 300 °C in about 6 min. Hence, water was sprayed to the ambient side of the board to minimise the risk during the test, which then reduced the ambient side temperature immediately. However, it continued to increase again when water spraying was stopped. Continuous burning was observed inside the furnace for both PCM-plasterboard samples during the cooling periods at 530 °C and 600 °C. This unique fire behaviour might have been by the evaporated paraffin PCM acting as an additional fuel [12]. Also, the fire side temperature started to drop only after the complete burning of the PCM inside the furnace.

4 FINITE ELEMENT THERMAL MODELLING

Finite element (FE) analysis was used to study the fire performance, as experimental analyses are expensive and time-consuming. FE method is commonly used for the numerical simulations and the models are validated using experimental results. 3-D heat transfer FE models were developed to simulate the standard fire tests in Abaqus/CAE and were validated using Kolarkar and Mahendran's [8] results. FE models of 1.2×1.2 m were developed for PCM-plasterboard and gypsum plasterboard. 8-node linear heat transfer brick elements (DC3D8) of 20×20×4 mm were used in the mesh development. The measured thermal properties in Section 2 of this paper were used in modelling. An emissivity value of 0.9 was used for both fire and ambient sides of the plasterboard while a convective coefficient of 25 W/m²K for the fire side and 10 W/m²K for the ambient side were used for both boards to take the convection and radiation effects, respectively. Further parameters used in the FE analysis are discussed in Rusthi et al. [10] in more detail.

Fig. 5 shows the time-temperature profiles obtained from FE modelling for single layer PCM-plasterboard and gypsum plasterboard exposed to standard fire conditions. Insulation based Fire resistance level (FRL) of 12 min was obtained for 12.5 mm thick PCM-plasterboard, which is two min lower than the fire test results. FRL of 21 min was obtained for 16 mm thick standard gypsum plasterboard, which agrees with the fire test results. FRL of commercially available 12.5 mm thick PCM-plasterboard and 16 mm thick standard gypsum plasterboard were determined experimentally and used to simulate the 3-D heat transfer FE models. To investigate the FRL variation with respect to board thickness, FE models were reanalysed for 16 mm thick PCM-plasterboard. This gave an insulation based FRL of 17 min (see *Fig. 5*), which is less than that of standard gypsum plasterboard. FRL/thickness is 1.24 times higher for gypsum plasterboard, which is 1.31 min/mm compared to 1.06 min/mm of PCM-plasterboard.

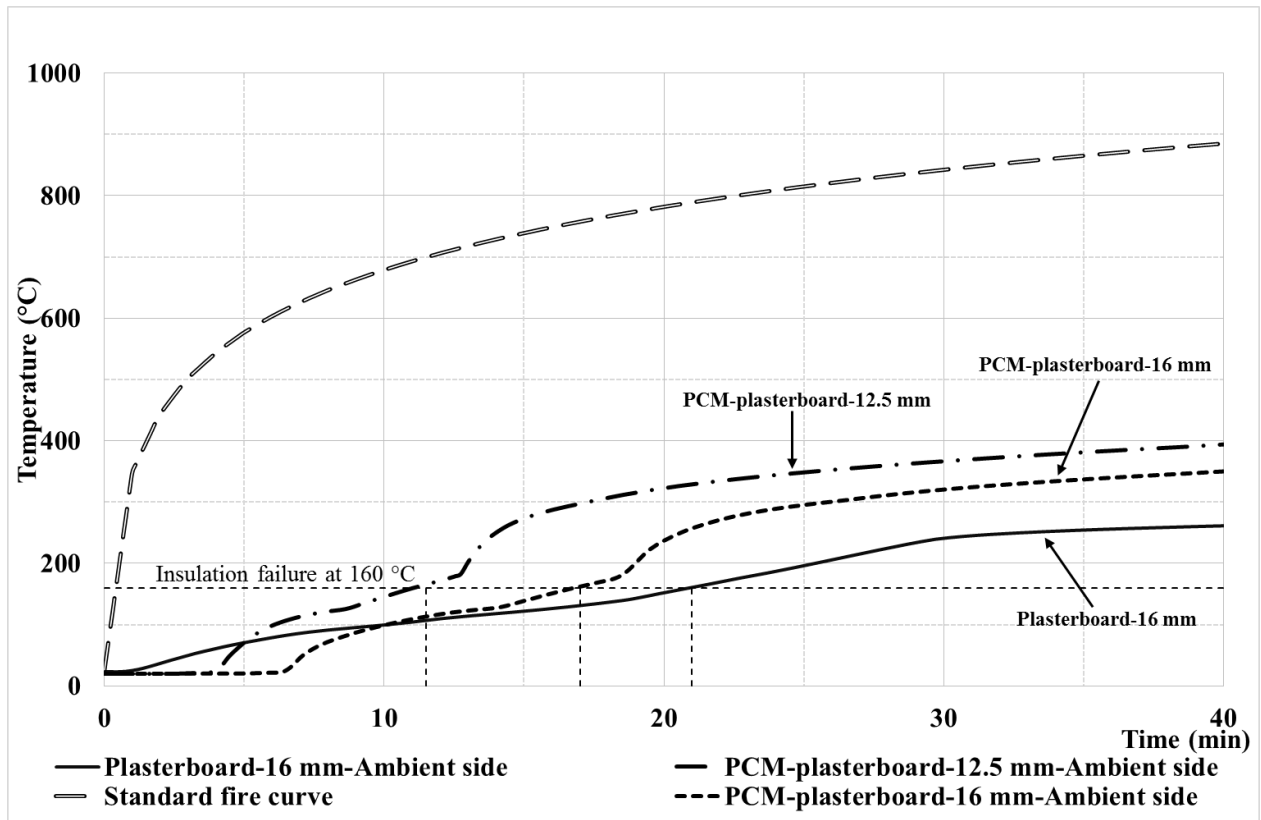


Fig. 5. FE modelling results for standard fire curves

5 CONCLUSIONS

This paper has presented the details of research on the fire performance of PCM-plasterboards in comparison with standard gypsum plasterboard using thermal property tests, small scale fire tests of boards and finite element thermal analyses. Although higher heat absorption capacity was expected for PCM-plasterboards compared to standard gypsum plasterboards due to their higher specific heat capacity with temperature and the latent heat capacity, PCM-plasterboards exhibited higher mass loss (twice) and higher thermal conductivity than standard gypsum plasterboard. PCM-plasterboards reached the insulation failure in 14 min in comparison with 20-24 min for standard gypsum plasterboards during the small-scale standard fire tests. Further, PCM mixed with plasterboard evaporated and provided considerable, additional fuel to the fire, which significantly increased the fire side temperature of the PCM-plasterboard after about 4.8 min of standard fire at 570 °C. FE analyses support the small-scale fire test results and further indicate that the insulation based FRL/thickness of standard gypsum plasterboard is 1.24 times higher than that of PCM-plasterboard. Overall, a lower FRL was obtained for PCM-plasterboards compared to gypsum plasterboards from small-scale standard fire tests and finite element modelling. Further studies have to be carried out to increase the FRL of PCM-plasterboards and delay the effect of evaporated PCM during fire by increasing the number of wallboard layers and changing the location of PCM-plasterboard within the lightweight wall systems.

ACKNOWLEDGEMENT

The authors wish to thank Australian Research Council (ARC) for the financial support to this project and QUT for providing testing facilities.

REFERENCES

1. *Home energy use*. Accessed on 05 March 2018; Available from: <http://www.sa.gov.au/topics/energy-and-environment/using-saving-energy/home-energy-use>.
2. Soares, N., *THERMAL ENERGY STORAGE WITH PHASE CHANGE MATERIALS (PCMs) FOR THE IMPROVEMENT OF THE ENERGY PERFORMANCE OF BUILDINGS*, in *Department of Mechanical Engineering, Faculty of Sciences and Technology of the University of Coimbra*. 2015, University of Coimbra: Coimbra. pp. 216.
3. Sharma, A., V.V. Tyagi, C.R. Chen, and D. Buddhi, *Review on thermal energy storage with phase change materials and applications*. *Renewable and Sustainable Energy Reviews*, 2009. **13**(2): pp. 318-345.
4. Kosny, J., *PCM-Enhanced Building Components*. 2015, Cham, SWITZERLAND: Springer International Publishing.
5. McLaggan, M.S., R.M. Hadden, and M. Gillie, *Flammability assessment of phase change material wall lining and insulation materials with different weight fractions*. *Energy and Buildings*, 2017. **153**(Supplement C): pp. 439-447.
6. Asimakopoulou, E.K., D.I. Kolaitis, and M.A. Founti, *Fire safety aspects of PCM-enhanced gypsum plasterboards: An experimental and numerical investigation*. *Fire Safety Journal*, 2015. **72**: pp. 50-58.
7. Ariyanayagam, A.D. and M. Mahendran, *Fire tests of non-load bearing light gauge steel frame walls lined with calcium silicate boards and gypsum plasterboards*. *Thin-Walled Structures*, 2017. **115**: pp. 86-99.
8. Kolarkar, P. and M. Mahendran, *Experimental studies of non-load bearing steel wall systems under fire conditions*. *Fire Safety Journal*, 2012. **53**: pp. 85-104.
9. Standards Australia (AS) AS 1530.4: 2014, *Method for fire test on building materials, components and structures, Part-4: Fire-resistance test of elements of construction*, Sydney, Australia, 2014.
10. Rusthi, M., P. Keerthan, M. Mahendran, and A.D. Ariyanayagam, *Thermal Performance of Magnesium Oxide Wall Board Using Numerical Modelling*, in *Fire Science and Technology 2015: The Proceedings of 10th Asia-Oceania Symposium on Fire Science and Technology*, K. Harada, et al., Editors. 2015, Springer Singapore: Singapore. pp. 667-676.
11. Rusthi, M., A. Ariyanayagam, M. Mahendran, and P. Keerthan, *Fire tests of Magnesium Oxide board lined light gauge steel frame wall systems*. *Fire Safety Journal*, 2017. **90**: pp. 15-27.
12. McLaggan, M.S., R.M. Hadden, and M. Gillie, *Fire Performance of Phase Change Material Enhanced Plasterboard*. *Fire Technology*, 2018. **54**(1): pp. 117-134.

FIRE-RETARDANT COATINGS FOR CONCRETE SUBSTRATE: A COMPARISON BETWEEN ONE-DIMENSIONAL AND TWO- DIMENSIONAL HEAT TRANSFER

Yan Hao Ng¹, Aravind Dasari², Kang Hai Tan³

ABSTRACT

Intumescent coatings were extensively used to protect steel structures from fire and the mechanism of typical intumescent system has been studied and is well-reported in literature. Research in intumescent systems for the past two decades has largely involved the optimisation of traditional formulation, i.e. a system that consists of an inorganic or organic acid, a carbonising agent, and a blowing agent. This paper discusses a non-halogenated polymer-based fire-retardant coating for concrete structures using expandable graphite as a blowing agent. The preliminary thermal performance of the developed coatings on concrete substrate was assessed using the ISO834 heating curve. The flame-retardant mechanism behind improved thermal performance will be discussed. Based on the heat transfer results, numerical simulation using ABAQUS was performed to assess the potential of this type of coating on structural members.

Keywords: Flame-retardant coatings, expandable graphite, concrete

1 INTRODUCTION

Intumescent systems were initially introduced as coatings to protect steel structures from fire and subsequently applied to flame-retarded polymers [1]. Due to a drastic reduction in yield strength at high temperatures (500 to 700 °C), it is essential to provide fire protection to ensure structural integrity in a fire. According to design guides in the UK, unprotected steel members typically have a fire resistance rating of only 15 min [2]. The use of intumescent coatings became prevalent in 2001 and started to dominate the steel fire protection in 2005. Research work improved the performance of such coatings and off-site application allowed them to continue its dominance in the passive fire protection market. [3].

Apart from protecting steel structures from fire, there may be a need to provide passive fire protection on concrete members. This is due to increasing trend of adopting high strength concrete, which is susceptible to fire-induced explosive spalling. Embedding polypropylene fibres have shown to mitigate spalling by reducing pore pressure but research work is still ongoing to elucidate the mechanism of spalling and the role of polypropylene fibres. Thermal barrier is deemed as an effective way to mitigate spalling as it reduces thermal ingress and alleviates pore pressure and thermal stress spalling [4].

¹ PhD Candidate. School of Civil and Environmental Engineering & School of Materials Science and Engineering, Nanyang Technological University, Singapore

e-mail: yhng@ntu.edu.sg

² Associate Professor. School of Materials Science and Engineering, Nanyang Technological University, Singapore

e-mail: aravind@ntu.edu.sg

³ Professor. School of Civil and Environmental Engineering, Nanyang Technological University, Singapore

e-mail: ckhtan@ntu.edu.sg

Cementitious-based and geopolymer-based thermal barriers are commonly explored to meet the stringent demands of tunnel fire curves (e.g. RABT, RWS fire curve). These barriers rely on its low thermal conductivity to reduce heat transfer to the substrate and due to their passive nature, there will be an increase in concrete cover (up to 50mm). Polymer-based coatings (e.g. intumescent coatings) will not reduce cross section of tunnel or increase weight of structural elements, and has the potential to replace conventional passive fire protection materials [5]. Moreover, polymer-based coatings can easily be applied to existing buildings should there be a change in the type of occupancy, and consequentially, an increase in fire-resistance rating.

This paper presents the performance of a non-halogenated polymer-based fire-retardant coating that uses expandable graphite as one of the key fire-retardant additives. According to a comprehensive review of intumescence materials [6], expandable graphite has been highlighted as one of the novel flame-retardant additives. It was also mentioned that expandable graphite follows a different flame-retardant mechanism, compared to traditional intumescent systems that are based on acid source, carbonising and blowing agents. Although it has been demonstrated that expandable graphite does improve the flame retardancy of certain polymers such as polyethylene and epoxy, it is difficult to relate these results to fire resistance rating of a structural member. Methods (LOI, UL94 tests, or cone calorimeter) used to assess flame retardancy of these formulations are conducted using small-scale samples. The behaviour is largely different from structural fire tests used to assess fire resistance of a structural element (loaded large-scale element subjected to a thermo-oxidative environment with ISO834/ASTM E119 heating profile). In this paper, the developed coatings are assessed with 1- and 2- dimensional heat transfer tests. Numerical simulations using ABAQUS will be performed to demonstrate the potential of using developed coatings on structural members.

2 EXPERIMENTAL WORK

2.1 Materials

This paper emphasizes the performance of expandable graphite as a fire-retardant additive. Moreover, due to the confidentiality of the coating, the complete composition of the developed coating will not be disclosed in this paper on in the presentation. Expandable graphite is a pseudo-2D solid-like layered compound where carbon atoms within the layered nano-sheets form hexagonal cells through covalent bonds, and the carbon layers are joined to each other by weak van der Waals forces. It is intercalated with oxidants such as sulphuric acid, hydrogen peroxide and/or potassium permanganate. SEM micrograph of expandable graphite platelets is shown in *Fig. 1b* and *c* and the compacted layered nano-sheets can be seen in *Fig. 1c*. The particle size of the expandable graphite is measured using Mastersizer 2000. The particle size of the expandable graphite used in the coatings ranges from 103 to 593 μm , with a mean particle size of 282 μm .

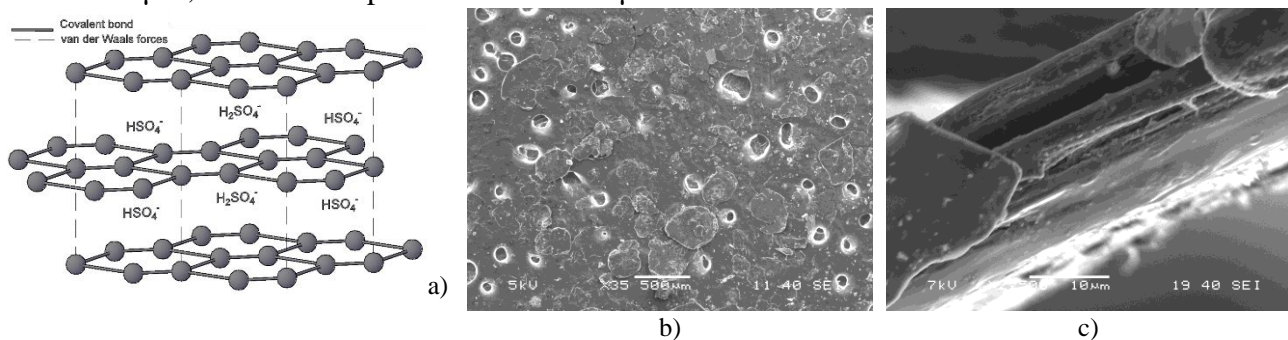


Fig. 1. a) Structure of expandable graphite; b) Top view SEM micrograph of expandable graphite; c) Sectional view SEM micrograph of expandable graphite

2.2 Experimental setup

The coatings are evaluated using a one- and two-dimensional heat transfer experimental setup. The coatings are spray-applied over the concrete substrates. For a one-dimensional heat transfer test, a 150 x 150 x 50 mm (length by width by thickness) concrete panel was used (*Fig. 2a*). For the two-dimensional heat transfer test, a triangular prism was used. The prism is essentially a 150 mm concrete cube, cut diagonally along its edges (*Fig. 2b*). As the objective of this test is to assess the performance of the developed coatings, thermocouples are placed at the concrete-coating interface. This can also provide an indication of the adhesion of coating onto the surface of the substrate. To ensure the required heat transfer conditions were met, a gypsum board fixture was designed and placed at the opening of a rapid heating electrical furnace. Small openings around the gypsum board fixture were covered using thermal wool to prevent excessive heat loss to the surrounding.

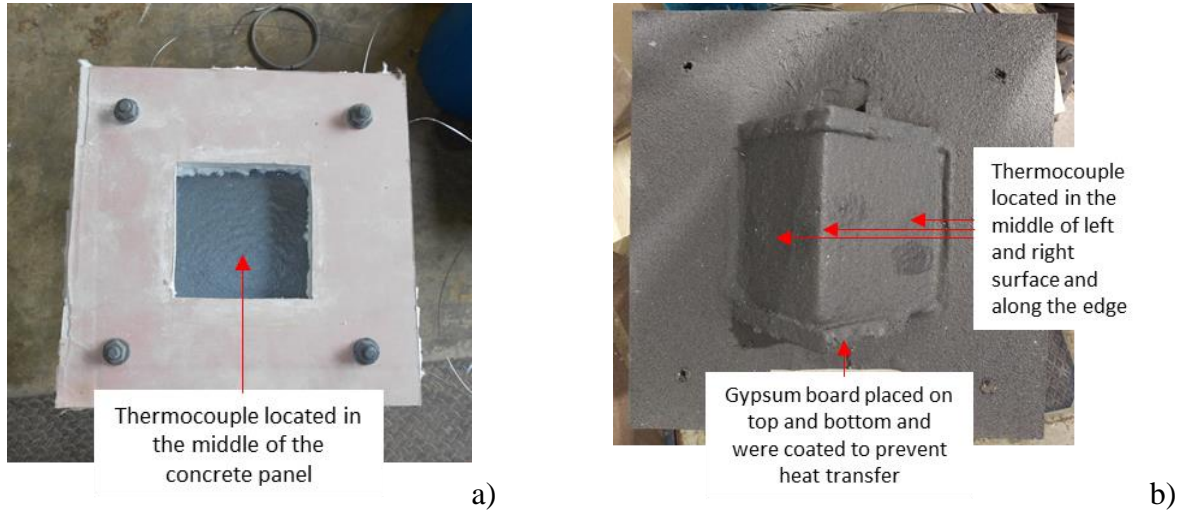


Fig. 2. a) One-dimensional heat transfer setup; b) two-dimensional heat transfer setup

This paper discusses the experimental results of 4 heat transfer tests. A one-dimensional and two two-dimensional heat transfer tests with coated samples were performed. The composition of the coatings and the thickness (5 – 6 mm) was kept the same for all 3 tests. For test T4-FR-N-2D, coating was sprayed till 2.5 mm before a nylon net was placed above. A second layer of 2.5mm coating was then applied over the net until a total thickness of 5 – 6mm is achieved. The nylon net was included to improve the adhesion of char.

Table 1. Summary of test specimens

Test number	T1-C-1D	T2-FR-1D	T3-FR-2D	T4-FR-N-2D
Substrate	Concrete panel	Concrete panel	Concrete prism	Concrete prism
Composition	-	FR1	FR1	FR1
Application	Uncoated	Spray	Spray	Spray
Thickness	-	5 to 6 mm	5 to 6 mm	5 to 6 mm
Net	-	-	-	Nylon net at 2.5 mm coating thickness

3 RESULTS AND DISCUSSION

3.1 One-dimensional (1D) heat transfer test

Temperature measurements of the concrete surface and gas temperature in the furnace are presented in *Fig. 3a*. The temperature of the gas in the furnace is recorded in each test and a typical gas temperature is shown in *Fig. 3a*. It can be seen that the typical gas temperature in the furnace corresponds well to the ISO834 standard fire curve.

Fire-retardant coatings for concrete substrate: A comparison between one-dimensional and two-dimensional heat transfer

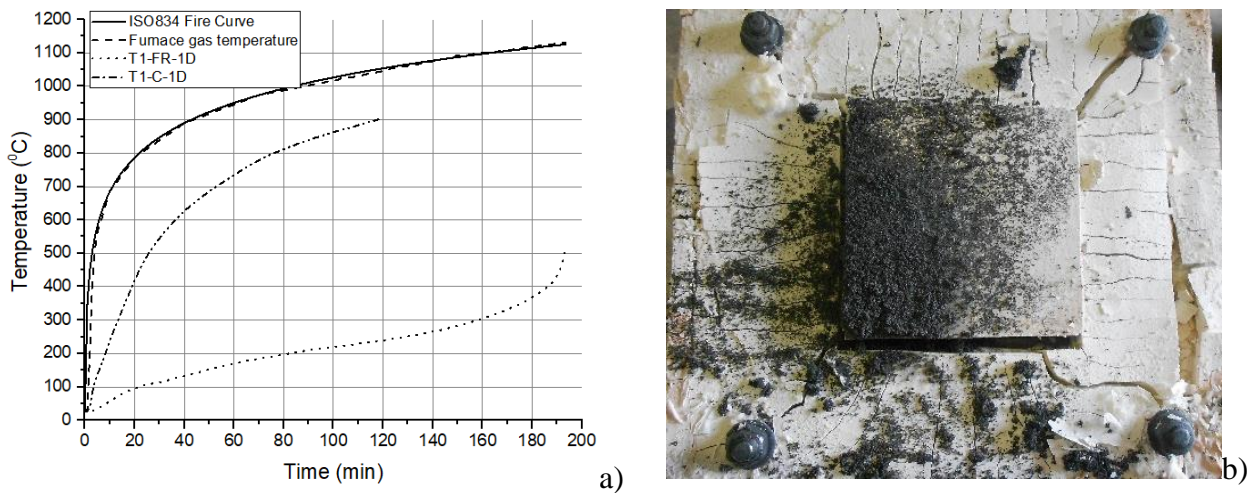


Fig. 3. a) Time-temperature profile of 1D heat transfer tests; b) Digital photo of residual char after the sample is removed from the furnace

The coating performed well as a thermal barrier in the 1D test when compared to the control sample (Test T1-C). The temperature of the uncoated concrete surface reached 500 °C at 26 min and continue to increase to 900 °C at the end of the test (120 min). As for the coated sample, it requires approximately 193 min for the interface temperature to reach 500 °C. However, it is also apparent that there is a sudden increase in temperature at 183 min, which suggests that the coating failed to adhere to the substrate. It is worth noting that the residue of the coating remained on the surface of the concrete after the setup was removed the next day (Fig. 3b). The concrete specimen remained intact, except for minor cracks on the surface.

3.2 Two-dimensional (2D) heat transfer test

The time-temperature profiles of concrete-coating interface for the specimens used in the two-dimensional heat transfer tests are shown in Fig. 4a. A reduction in fire-protective performance of the coatings can be observed in the two-dimensional heat transfer test. The time taken for one of the thermocouple in T3-FR-2D to reach 500 °C is approximately 74 min, which is a reduction of 119 min compared to the one-dimensional heating test for T2-FR-1D. The rate at which the centre of T3-FR-2D (450 °C at 70 min) increases is also faster compared to that at T2-FR-1D (185 °C at 70 min).

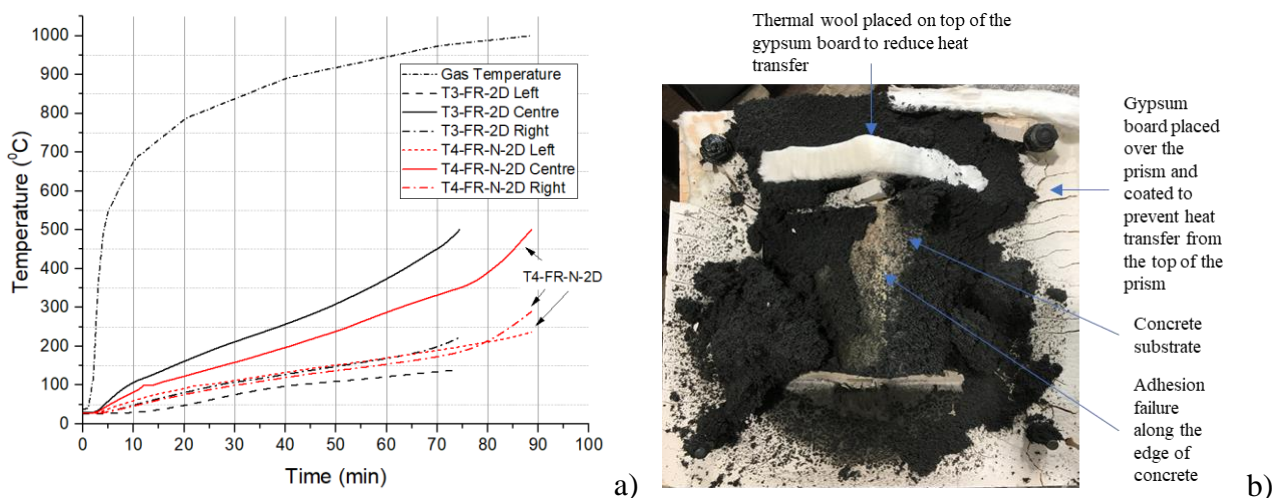


Fig. 4. a) Time-temperature profile of 2D heat transfer tests; b) Digital photo of residual char for T2-FR

As shown in *Fig. 4b*, the coating failed to adhere to the edge of concrete and resulted in a much higher increase in temperature at the edge compared to the left and right surface. Char was found to adhere to both surfaces of the concrete after the specimens were removed. The temperature measurement at left and right of T3-FR-2D at the end of the test (74 min) are 140 and 223 °C, respectively. These measurements are close to the recorded temperature T1-FR-1D (190 °C) at 74 min, which further suggests that failure occurred at to the edge of the prism section.

The addition of nylon net increased the time for any thermocouple to reach 500 °C to 88 min. Moreover, the rate at which the temperature increases at the centre of T4-FR-N-2D is slower compared to the centre of T3-FR-2D. This can be attributed to an increase in cohesion of char along the edge of the concrete sample due to the presence of the net. However, the improvement to char adhesion on concrete substrate does not seem significant as the change in the temperature gradient of at the centre of T4-FR-N-2D after 75 min also indicates adhesion failure. In fact, temperature measurement at the left of T4-FR-N-2D also demonstrates adhesion failure after 75 min with a change in its temperature gradient. This adhesion failure could have initiated from the centre and delamination of the coating propagated to both sides.

3.3 Discussion

The coating demonstrated excellent performance as a thermal barrier in the 1D heat transfer test (T1-FR-1D). Apart from char formation in the coating, expansion of the expandable graphite plays an important role in its performance. Upon exposure to heat, redox reaction occurs resulting in exfoliation of the graphite. The reaction, represented as *Eq. (1)*, starts at 200 °C and continues all the way up to 300 °C.



The exfoliation occurs along the c-axis of the crystal structure, forming a puffed-up material of low density with a worm-like structure (*Fig. 5a*). This layer in fact, shields the substrate underneath from the heat, insulating the virgin material in a fire or in the degradation conditions from the action of the heat source. The graphite layers become clearly visible under a scanning electron microscope. In large quantities, the expanded graphite forms a network over the surface of the carbonaceous materials. Since the graphite is dispersed within the polymer matrix and the orientation of the expanded graphite layers are random in nature, the network formed by the expandable graphite is likely to be filled with voids. This network acts as a protective barrier (*Fig. 5b*) and shields the heat source from the substrate.

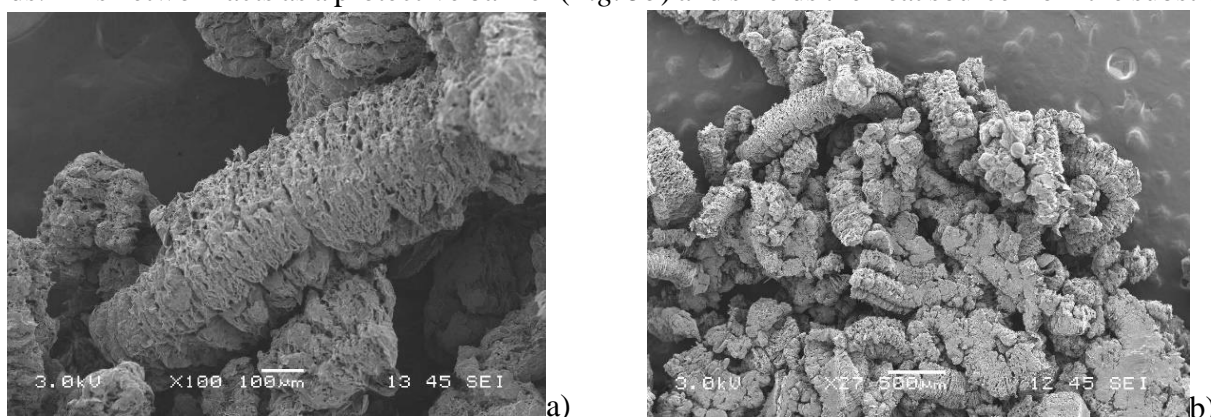


Fig. 5. SEM micrograph a) of expanded graphite layers after a furnace test; and b) a network of expanded graphite

The extensive expansion of graphite layers can also contribute to the lack of adhesion observed in the 2D tests. At the microscopic level, it is clear that the expansion of graphite layers is random in nature. However, the expansion of the graphite seems perpendicular to the surface of the sample, which is in a different direction compared to the expansion of graphite along the edge (*Fig. 6*). This results in an

area that is covered with a network of graphite network and allows heat to penetrate to the underlying layer much faster. Therefore, the coating degrades at a much faster rate along the edge and eventually fails to adhere to the substrate. It seems that the nylon net has managed to mitigate this effect by slightly compressing the char structure and reducing the area exposed to heat (Fig. 6b).

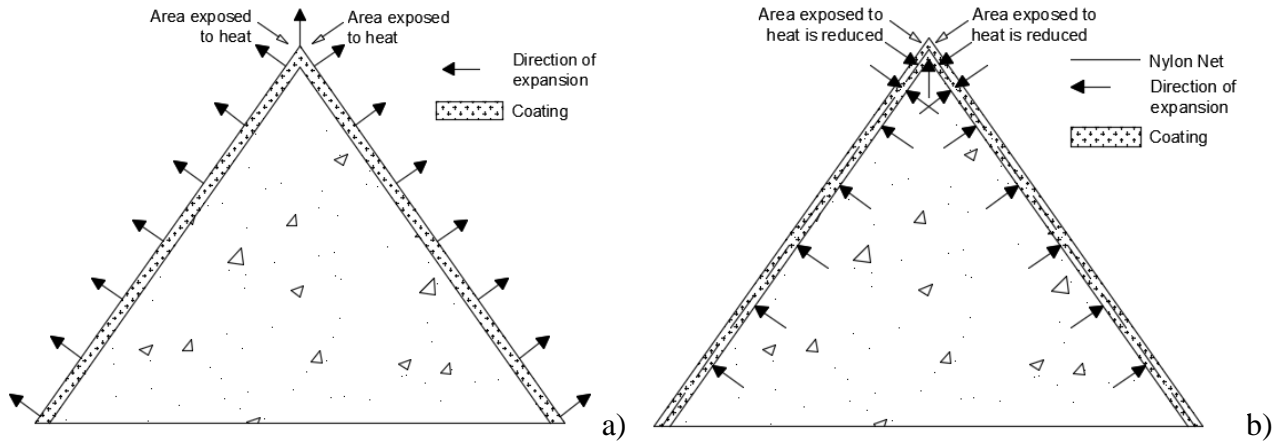


Fig. 6. Idealised drawing of expansion of graphite layer a) with; and b) without nylon net.

Another possible explanation for the reduction in fire-protective performance can be attributed to the radiant heating elements in the furnace. The edge of the concrete prism would be exposed to a higher radiation compared to the sample in 1D heat transfer test. The heat flux (W/m^2) transferred to the edge of the concrete prism can also be larger as it is closer to the heating element, and consequently, exposed to a higher radiation energy. At this moment, there is not enough data to conclude the reason behind the reduction in fire protection performance. However, this series of tests demonstrates that a 2D heat transfer test may provide a better understanding of fire protective coatings at the development stages.

4 NUMERICAL STUDY

The potential of adopting the fire-protective coating on a structural member can be assessed through numerical studies. A model was created to validate heat transfer using ABAQUS simulation software. The model assumes that the column is heated on all four surfaces in the form of convection and radiation based on ISO 834 time-temperature curve, as illustrated in Fig. 7a. Heat conducted across the section of the column was computed based on specific heat capacity and thermal conductivity of concrete. The input parameters (i.e. specific heat capacity, thermal conductivity, emissivity of concrete, coefficient of heat transfer by convection) for the simulation model were obtained from Eurocode, EN1992-1-2.

The square column has a dimension of 300 mm by 300 mm and the results obtained from the heat transfer analysis were validated using the R120 temperature profile in Figure A.14 of Eurocode 2 (EC2). Fig. 7b presents a comparison of temperature profile obtained from the model with the temperature profile depicted in EC2. Results from the model demonstrated good agreement with the temperature profile in EC2.

Four numerical models with the same dimensions (150 mm by 150 mm) were used as case studies to assess the effectiveness of coatings. Heat transfer analysis for the first model (Model 1) was performed using convection and radiation based on ISO 834 heating curve for a duration of 74 min, depicting a concrete section that was not protected with the coating. Similar to the model used for validation, thermal conductivity and specific heat capacity were used to compute the heat conducted

across the concrete column. Since there is insufficient data to incorporate coatings in a numerical model at the time of this study, the time-temperature profile of the concrete-coating interface (*Fig. 3a & Fig. 4a*) was used to analyse heat transfer across a concrete column.

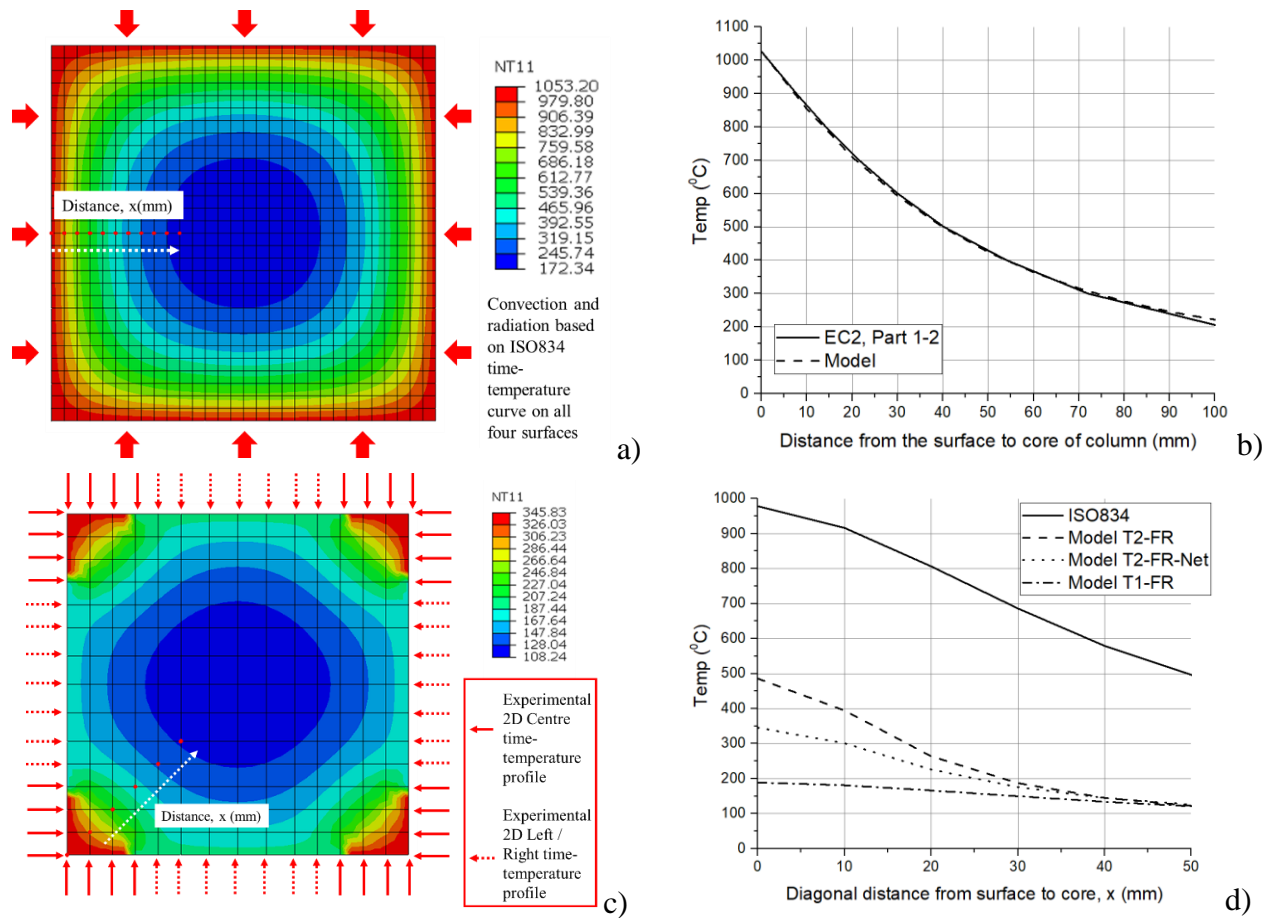


Fig. 7. a) Illustration of heat transfer model used for validation; b) Comparison of temperature profile given in EC2 (as Figure A.14, Curve R120) with results from the model; c) Illustration of heat transfer model based on experimental results, T2-FR-N; d) Time-distance profile from edge to the core based on different test results at 74 min.

In Model A, the 1D time-temperature profile was used to analyse heat transfer and to demonstrate the effectiveness if the coating did not exhibit any adhesion failure. In Model B and C, the 2D time-temperature profiles were used. The temperature profiles of the edge of the concrete prism (T3-FR-2D Centre and T4-FR-N-2D Centre in *Fig. 4a*) were applied at the edges of the column, while the remaining temperature profiles (T3-FR-2D Left / Right & T4-FR-N-2D Left / Right) were applied at the surface of the column. This is illustrated in *Fig. 7c*.

As shown in *Fig. 7d*, heat transfer has been drastically reduced due to the presence of coatings, especially in Model A, where the coating did show adhesion failure before 74 min. The differences in temperature reduce as the distance from the edge to the core increases due to the low thermal conductivity and high specific heat capacity of concrete. The addition of a nylon net has delayed the adhesive failure and improve the performance of the coating slightly. The differences in temperature between Model C and Model D at 10 mm and 20 mm are 93 °C and 37 °C, respectively.

5 CONCLUSIONS

This paper demonstrated the problems associated with adopting expandable graphite as an additive to fire protective coatings for structural members. Though the mechanism differs from conventional intumescent coatings, there are still significant problems associated with two- and three- dimensional heat transfer tests. Further, there is also a need to address the adhesion of such coatings under temperature to utilise the coating effectively.

ACKNOWLEDGEMENT

This material is based on research/work supported by the Singapore Ministry of National Development and National Research Foundation under L2 NIC Award No. L2NICCFP1-2013-4. Any opinions, findings, and conclusions or recommendations expressed in this material are those of the author(s) and do not necessarily reflect the views of L2 NIC. The authors acknowledge Mr Wesley Yeo Kah Yen and Mr Tan Jian Ming Clement for their assistance in this research work.

REFERENCES

1. Duquesne, S. and T. Fütterer, *Intumescent Systems*, in *Non-Halogenated Flame Retardant Handbook*. 2014, John Wiley & Sons, Inc. p. 293-346.
2. Bailey, C.G., G.M. Newman, and W.I. Simms, *Design of Steel Framed Buildings without Applied Fire Protection*. SCI Publication P186, 1999.
3. Mariappan, T., *Recent developments of intumescent fire protection coatings for structural steel: A review*. *Journal of Fire Sciences*, 2016. **34**(2): p. 120-163.
4. Khoury, G.A., *Passive fire protection of concrete structures*. *Proceedings of the ICE - Structures and Buildings*, 2008. **161**(3): p. 135-145.
5. Ng, Y.H., et al., *Thermal decomposition and fire response of non-halogenated polymer-based thermal coatings for concrete structures*. *Surface and Coatings Technology*, 2016.
6. Alongi, J., Z. Han, and S. Bourbigot, *Intumescence: Tradition versus novelty. A comprehensive review*. *Progress in Polymer Science*, 2015. **51**: p. 28-73.

FIRE TESTS TO ASTM E119 ON FULL-SIZE GLULAM BEAM TO COLUMN CONNECTIONS

David Barber¹

ABSTRACT

Mass timber buildings constructed with cross laminated timber and glulam are being completed globally. When glulam is utilized as part of the primary structure, the preferred connectors between beams and columns are either a concealed steel plate with dowels; or a concealed proprietary screw-in sleeve type connector. Where the beam to column connection requires a fire resistance rating and the timber is not clad with fire protective plasterboard, there are few methodologies to assess capacity under fire for periods of exposure exceeding 60 minutes. The lack of simple design correlations for glulam beam to column connections significantly limits the use of glulam in mid and high-rise building applications, where a fire rating is needed. To provide data and test results for architects, engineers and building officials, a program of fire tests on full-size glulam beam to column connections has been completed in the US. The loaded specimens replicated medium and high-rise building situations and were tested to ASTM E119. Fire resistance ratings have been successfully achieved for fully concealed connectors to 60, 90 and 120 minutes, using four differing connection typologies. The fire tests have shown that detailing and timber cover to the connector has an influence on the fire rating. The test data is being utilised to assist with finite element model validation and developing a simple design method for connection fire resistance.

Keywords: Mass timber, Glulam connections, Fire resistance ratings, Fire testing

1 INTRODUCTION

Mass timber construction is growing in popularity globally due to the availability of innovative materials such as cross-laminated timber (CLT). High-rise mass timber buildings are being planned and constructed in the US, with buildings using a combination of glulam as the primary structural gravity frame, with CLT floors and walls. For large timber structures, where the connectors are carrying significant gravity or lateral forces, mechanical fasteners are used that may consist of steel plates with dowels or bolts, or a proprietary sleeve connector with screws or nails.

Connectors in engineered timber, such as glulam, are an unresolved fire safety design issue, as there is limited information to assess their capacity under fire, where the architect, building owner or developer wants to have some of the timber exposed. Connectors must be designed to have a fire resistance rating (FRR) equal to that of the connecting members and of 60 to 120 minutes, depending on the height of the building. There are very few full-size fire tests on glulam-beam to column connections that have been completed, with most research on small-scale members, loaded in tension, not loaded in shear. Without the proven fire rating, building approval can be difficult. Thus, completion of fire tests on full-size glulam members are important for future construction.

¹ Arup, 1120 Connecticut Avenue, Suite 1110, Washington, D.C. 20036, USA. email: david.barber@arup.com

1.1 Motivation for Fire Testing

In 2015 the United States Department of Agriculture (USDA) and Softwood Lumber Board (SLB) sponsored a Tall Wood Building Competition [1]. A twelve-floor mixed-use office and residential building in Portland (Framework [2]), utilising a combination of glulam as the primary structural gravity frame, with CLT floors was awarded funding. To achieve a building approval, a 120min FRR was required for the structure, which included exposed glulam beam to column and column to column connections. A proven 120min FRR beam to column connection was required. It was also recognised by SLB that there was a lack of an “off-the-shelf” fire rated solution for glulam beam to column connectors achieving a 60min FRR for medium-rise mass timber construction (4 to 8 stories, below 25.9m). To assist the construction industry, a program of glulam beam to column connections were fire tested at an approved fire testing facility.

The most widely accepted method for proving a building element achieves a FRR is through a fire test, to meet the requirements of Chapter 7 of the International Building Code (IBC) [3]. The completed fire tests and supporting reports allow engineers and architects to specify these tested connection assemblies and satisfy the requirements of the IBC. Approval by an authority having jurisdiction (AHJ) will therefore be easier for future building projects.

2 COMPLIANCE BACKGROUND

2.1 Code Requirements

Within the US, each state and some cities adopt one or more model building codes. All 50 states adopt the IBC, with some states also adopting NFPA 101 ‘Life Safety Code’ [4]. Each State adapts and amends the model codes to provide the basis for construction compliance. The load-bearing structure (i.e., columns, beams, floors and any load-bearing walls) for mid-rise and high-rise buildings are required to have a FRR. Buildings that are four floors or more in height are required to have a 60 minute FRR and once the building is a high-rise structure, being more than 22.9m in height, the building requires a 120 to 180 minute FRR. A high-rise building is required to have load-bearing elements that survive full burn out of a fire, where the sprinklers have failed and the fire department has limited intervention.

2.2 Guidance on Fire Rated Connections in Glulam

For design engineers, there is a lack of fire testing to utilise for 60 and 120 minute FRR glulam beam-to-column, or column-to-column connections [5]. This leaves engineers having to extrapolate from tension tests, small scale tests and methodologies validated to 30 mins FRR. Engineering guidance is also limited. Within the US, the IBC references the American Wood Council’s (AWC) “National Design Specification for Wood Construction” (NDS) [6]. The NDS details the methods for determining an FRR for mass timber construction, including CLT, up to 120 minutes. The NDS references “Calculating the Fire Resistance of Exposed Wood Members, Technical Report No. 10” (TR-10) [7], which provides significant detail on how an FRR can be determined for mass timber products. TR-10 provides some information on connections in mass timber. TR-10 has an approach of limited validity up to 60 minutes, using the reduced cross-section method. Also available to an engineer are the methods from EN 1995-1-2 Eurocode 5 (EC5) [8]. EC5 has methods validated up to 30 minutes, using simplified rules or a reduced load method. Both TR-10 and EC5 methods are based on determining a char layer for the timber that surrounds the connection and this char layer provides the “cover” to protect the concealed connector from the heat of the fire.

Using the TR-10 method, the depth of char to a bolt or dowel or steel connector is determined through assessing a char rate of 1.5 in/hr (0.64mm/min), for 60 minutes FRR. The minimum timber cover required is calculated as 38.1mm. The distance from the bottom of the member to the

connection is also required to be at least 38.1mm. Using the “simplified method” within EC5 for a doweled connection behind timber plugs to achieve a 60 min FRR, the cover depth is required to be 49mm. It is noted that using the simplified method to calculate a 60 min rating is beyond its stated limitations. The other option provided is the “reduced load method”, which requires knowledge of the cold capacity of the connector, but is also limited to 30 mins.

The two approaches produce different results, with the cover to the connector, bolts or dowels being 38.1mm from TR-10 and 49mm using EC5. The approaches from TR-10 and EC 5 are based on several assumptions. Firstly, the assumed char rate for the timber member can be used to determine a thickness of char that provides insulation at the connection. The next assumption is that the timber directly behind the char has zero strength, for a set depth (zero-strength layer). The third assumption is that the timber directly behind the zero-strength layer has the strength and stiffness of ambient timber. These assumptions are considered to be non-conservative, especially for connections exposed to standard fires for 60 mins or longer. Accounting for the reduced strength and stiffness of the timber directly behind the char layer is considered an important factor [5].

3 METHOD FOR ACHIEVING AN FRR IN EXCESS OF 60 MINUTES

3.1 Why do Connectors Fail at Elevated Temperatures?

When timber is exposed to fire it loses strength in the char layer at 280°C to 300°C [9, 10]. The char acts as an insulating barrier to the unheated timber beneath. The mechanical properties of timber under heating have been well researched [11]. The key factor in the failure of timber connections under fire is the reduction in compressive strength of the timber as it heats up, given the need for the connection to resist shear forces, which are transferred through the steel knife-plate or sleeve connection, via screws, bolts or dowels. With fire exposure and increased heating of the timber surrounding the connection results in an embedment failure at the dowels, bolts or screws. Embedment strength in timber is the ability to resist a shear force, induced by a connector and hence an important factor in determining connector failure [11 - 18]. Embedment failure is first seen through increased ovalisation that occurs around the dowels or bolts, due to the wood strength weakening as the dowels or bolts heat up [19, 20]. For timber heated to 150°C, the embedment strength is reduced by 40% to 60% in comparison to the 20°C value. Strength loss continues with increasing temperatures.

From the review of the fire test data and research, it is evident that there is no simple method for determining an FRR. To design a connection to resist a standard time-temperature curve of 60 minutes or more requires several factors to be addressed and engineered, which are primarily the rate of char, heat transfer into the connection over time and accounting for the timber strength and stiffness directly behind the zero-strength layer. The basis of connection design to resist fire is that the timber cover will provide adequate resistance to the heat from the fire exposure, such that the connector components are within timber that retains 50% of its embedment strength [5].

4 FIRE TESTING METHODOLOGY AND SET-UP

To prove a glulam beam to column could achieve an FRR of 60 or 120 minutes, the most appropriate test method is to construct a full-size connection with identical glulam timber, apply the worst case structural loads and expose this to a standard fire curve, such as ASTM E119-16a [21]. From the research carried out on mass timber connection fire testing, there had been few tests of this type carried out, with only the tests by Palma [16] using a similar approach. The challenges in undertaking this type of fire testing were numerous, including the testing methodology, fire testing standard, test specimen and funding. With the Framework project requiring a 120 min fire test to

support building approval and funding available from the USDA, via the Tall Wood Building Competition, a methodology was developed.

4.1 Fire Testing Standard

The fire tests were carried out to meet the time-temperature requirements of ASTM E119, which does not provide a testing methodology for load-bearing connections, for any type of construction materials. Using the work by Palma [16], a sketch plan of a potential fire test set-up was discussed with a testing facility. After a number of iterations, a vertical test method meeting with ASTM E119 was developed. By meeting ASTM E119, compliance with the IBC is achieved.

4.2 Test Method

The test method is shown below in *Fig 1*. The fire tests were carried out in an upright furnace, with the glulam beam to column connection located within a specialized loading frame. The loading frame sits within the upright furnace that is programmed to deliver a standard time-temperature curve to meet ASTM E119. The test specimen is made up of a glulam beam, connected directly to a glulam column, with a concealed end-grain connector. A CLT floor is screw-fixed to the glulam beam. A jack on the frame applies the load direct to the CLT floor, located over the beam end connection. The CLT floor also acts as the lid of the furnace.

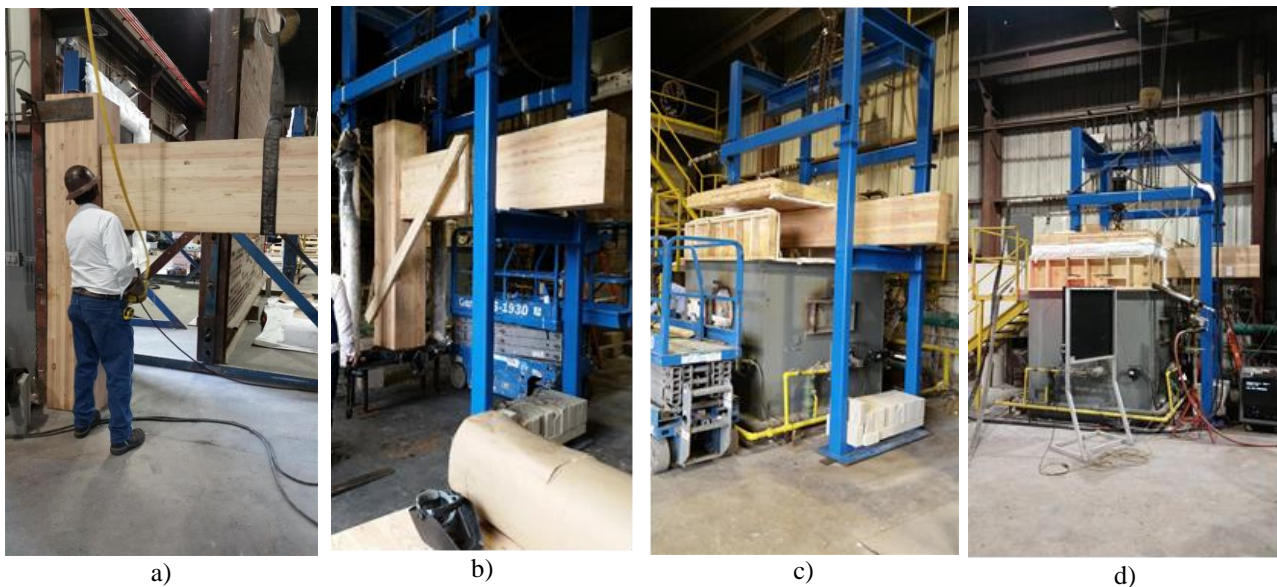


Fig 1 – a) Test 2 specimen being assembled; b) before CLT floor is installed; c) specimen in loading frame with CLT floor attached to beam; c) within upright furnace

4.3 Fire Tests Undertaken

Table 1 summarises the five tests carried out and the components used. The applied load is also provided. The applied load was determined from calculations carried out by Arup, based on an assumed structural grid for a typical office building. Tests 1 to 3 were carried out on “off the shelf” connectors (see *Fig 2*). Tests 4 and 5 were on a project specific connector (see *Fig. 3*). A brief description of each test is below:

- Test 1 was based on the beam acting as a secondary member and hence a relative lighter applied load, with the aim of achieving a 60 min fire rating.
- Tests 2 and 3 were based on the beam acting as a primary beam and hence a higher applied load, with the aim of achieving a 60 to 90 min fire rating

- Tests 4 and 5 were based on the beam acting as a primary beam and hence a higher applied load, with the aim of achieving a 120 min fire rating.

The connectors tested were all concealed and located centrally within the beam.

4.4 Timber Used

Tests 1, 2, 3 and 5 were carried out with North American Douglas Fir glulam, grade 24F-V4. Test 4 was carried out with European Spruce-Fir glulam, GL24h grade. All glulam timber dimensions were chosen based on commodity glulam stock, so that the timber was economical to source. The CLT was Douglas Fir 5 ply “V1” grade for all tests. Dimensions are detailed within *Table 1*.

Table 1. Fire test data for members used

Element	Test 1	Test 2	Test 3	Test 4	Test 5
CLT floor	5 ply Douglas Fir (5 plys each of 35mm)	As for Test 1	As for Test 1	As for Test 1	As for Test 1
Column	Douglas Fir 419mm x 362mm, beam located on 362mm side	Douglas Fir 419mm x 362mm, beam located on 362mm side	Douglas Fir 419mm x 362mm, beam located on 362mm side	European Spruce glulam 400mm x 360mm, beam located on the 360mm side	Douglas Fir 419mm x 362mm, beam located on 362mm side
Beam	Douglas Fir 222mm x 457mm (w x ht)	Douglas Fir 273mm x 610mm (w x ht)	Douglas Fir 273mm x 610mm (w x ht)	European Spruce glulam 360mm x 600mm (w x ht)	Douglas Fir 312mm x 610mm (w x ht)
Applied load at connector	17.4kN (not at capacity)	73.9kN	73.9kN	108kN	108kN
Connector type	Single Ricon S VS 290x80	Staggered double Ricon S VS 200x80	1 Knapp Megant 430 x 150	Project specific connector	Project specific connector
Base cover distance	100mm	100mm	100mm	115mm	115mm
Beam edge cover distance	71mm	56mm	61mm	110mm	86mm

Fire Tests to ASTM E119 on Full-Size Glulam Beam to Column Connections

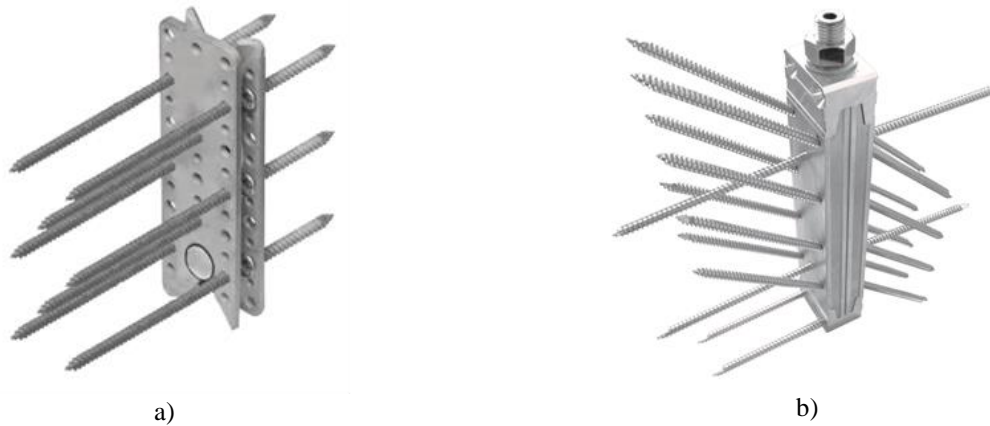


Figure 2 – a) Ricon VS 200 x 80 connector; b) Megant 430 x 150 connector (images from MyTiCon)

The project specific connector was a welded steel “L” plate, with a stiffening web. The connector was 140mm in width and 295mm in depth. The steel plate used was 6mm thick. See Fig 3.



Figure 3 – Project specific connector on column, with routed beam about to be lowered onto the connector. Wooden block at the base provides solid timber seal to the base of the beam. Fire rated sealant yet to be installed.

4.4.1 Fire Stop Sealant

Fire stop sealant (also called fire caulk) was applied at the beam to column interface for all tests and for the project specific test, also at the wooden block filler. For the beam to column interface, a 10 to 15mm bead of fire stop sealant was applied on the column face, such that it was located 30 to 35mm from the beam edge. The sealant was applied prior to connection of the beam. Excess sealant was then cleaned away once the beam was fitted. This was to ensure the gap between beam and column was effectively fire sealed.

4.5 Failure Criteria

The failure criteria was based on deflection at the connection, measured through displacement at the CLT panel and glulam beam. A maximum vertical displacement at the connection of 50mm was considered failure. Load resistance was also measured and a load-carrying drop-off of more than 25% was considered failure.

5 FIRE TEST RESULTS

The results from the fire tests are shown in *Table 2* and images of the testing are shown in *Fig 4*:

Table 2. Fire test results

Test	Connector(s)	FRR Achieved
1	Ricon S VS 290x80	60 mins
2	Staggered double Ricon S VS 200x80	90 mins
3	Megant 430 x 150	90 mins
4	Project specific connector	120 mins
5	Project specific connector	120 mins

The deflections recorded for Tests 1, 3 and 5 were all less than 5mm by the test end. Test 2 and Test 4 deflections were at 10mm and 12mm respectively. Tests were not continued past the goal FRR, where that was achieved.

5.1 Test Failures

As part of the fire test program, two fire tests were undertaken that failed to reach the expected fire duration of 120mins, with failures at 88mins and 113mins. These failures informed improvements to the detailing to improve test outcomes. An observation from the series of tests was the need for a wider bead of fire rated sealant at the beam to column interface, to assist with prevention of heat intrusion as the char contracts, especially for the longer duration fire testing. The 120 min tests that passed had two rows of fire caulk, each 10mm to 15mm wide, located at approximately 30mm from the beam edge and 60mm from the beam edge.

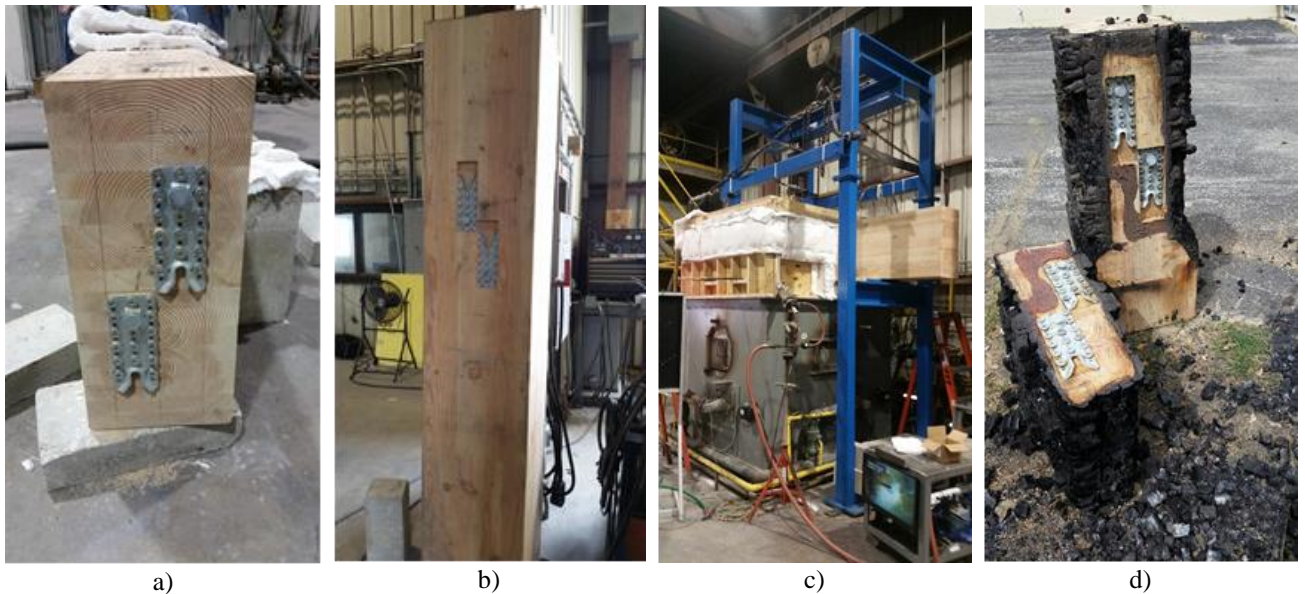


Fig 4 – a) Test 2 beam prior to assembly; b) Test 2 column prior to assembly; c) Test 2 during fire test; d) Test 2 post-test (beam and columns cut for inspection)

6 CONCLUSIONS

The full-scale fire testing of the glulam beam to column connections has proven that a standardized testing methodology can be used to successfully test glulam beam to column connections. The tests have provided data to assist with validation of numerical models and importantly, shown that concealed connections that are loaded to represent actual building conditions can achieve an FRR of 60, 90 and 120 minutes. A simplistic approach to the required timber cover to achieve an FRR is also being developed from the fire test results.

ACKNOWLEDGMENTS

The fire testing has been supported by funding and supply contributions from the USDA, Softwood Lumber Board, Lever Architecture, Arup, MyTiCon and DR Johnson.

REFERENCES

1. USDA Tall Wood Building Competition, <https://tallwoodbuildingcompetition.org>
2. Framework, Portland <http://www.frameworkportland.com/>
3. International Code Council “International Building Code”, 2015
4. National Fire Protection Association, 2015, “Life Safety Code” NFPA 101
5. Barber, D., 2017, “Determination of Fire Resistance Ratings for Glulam Connectors Within US High rise Timber Buildings”, *Fire Safety Journal* 91 (2017), pp 579-585
6. American Wood Council 2015, ‘National Design Specification for Wood Construction’ Virginia
7. American Wood Council, 2015, “Calculating the Fire Resistance of Exposed Wood Members”, Technical Report No. 10, Virginia
8. British Standards Institute “Eurocode 5: Design of Timber Structures – Part 1-2: General – Structural Fire Design”, BS EN 1995-1-2, 2009
9. White R., 2015 “Analytical Methods for Determining Fire Resistance of Wood Members: Society of Fire Protection Engineers Handbook of Fire Protection Engineering”, 5th Edition, SFPE Gaithersburg
10. Buchanan, A. 2001 “Structural Design for Fire Safety”, John Wiley and Sons
11. Maraveas, C., Miamis, K., Mathew, C., 2013, “Performance of Timber Connections Exposed to Fire: A Review” *Fire Technology*, Published online November, 2013
12. Buchanan, A., Barber, D., 1996, “Fire Resistance of Epoxied Steel Rods in Glulam Timber”, *New Zealand Timber Design Journal*, Issue 2, Volume 5
13. Peng, L., 2010, “Performance of Heavy Timber Connections in Fire” Thesis, Department of Civil and Environmental Engineering, Carleton University
14. Erchinger, C., Frangi, A., Fontana, M., 2010, “Fire Design of Steel-to-Timber Dowelled Connections”, *Engineering Structures* 32, pp580-589
15. Chuo, C.B., 2007, *Fire Performance of Connections in Laminated Veneer Lumber*”, thesis, University of Canterbury, Christchurch, New Zealand
16. Palma, P., Frangi, A., Hugi E., Cachim, P., Cruz, H., 2014, “Fire Resistance tests on beam-column shear connections” 8th International Conference on Structures in Fire, Shanghai, China, June 11-13
17. Boadi, S., 2015, “Full Scale Tests on the Performance of Hybrid Timber Connections in Real Fires”, Thesis, Department of Civil and Environmental Engineering, Carleton University, Ottawa, Ontario
18. Audebert, M., Dhima D., Taazount, M., Bouchaïr, A., 2011, “Numerical Investigations On The Thermo-Mechanical Behavior Of Steel To Timber Joints Exposed To Fire” *Engineering Structures* 33, 3257-3268
19. Noren, J. 1996, “Load-bearing capacity of nailed joints exposed to fire. *Fire and Materials*” 1996-20: p. 133-143
20. Moss, P., Buchanan, A., Fragiacomio, M., Austruy, C. 2010, “Experimental Testing and Analytical Prediction of the Behaviour of Timber Bolted Connections Subjected to Fire”, *Fire Technology* 46(1): p. 129-148
21. American Society for Testing and Materials, 2016, “ASTM E119: Standard Test Methods for Fire Tests of Building Construction and Materials”

A METHODOLOGY FOR QUANTIFYING FIRE RESISTANCE OF EXPOSED STRUCTURAL MASS TIMBER ELEMENTS

David Barber¹, Lizzie Sieverts², Robert Dixon³, Jarrod Alston⁴

ABSTRACT

With new timber technologies, architects and owners are requesting high-rise timber buildings are constructed with more of the structural timber exposed. Addressing how exposed mass timber and in particular cross laminated timber, influences fire development from ignition to a fully developed fire through to fire extinguishment is a current and complex fire safety issue. This paper summarises a methodology that focuses on the contribution of exposed mass timber within a fire compartment to determine the fire resistance rating as a function of char depth. The methodology takes into account variations in heat flux, heat release rate and additional fire load due to exposed timber. The method has been validated against the results from five full-size compartment fire tests, with exposed cross laminated timber. The methodology has been shown to provide a conservative approximation of resultant char depth, thus allowing for verification of structural fire resistance ratings. Limitations of the methodology and further work required have been highlighted and discussed.

Keywords: Mass timber, cross laminated timber, fire dynamics, FDS, exposed mass timber

1 INTRODUCTION

Construction of multi-story buildings using a primary structure of mass timber with glulam and cross laminated timber (CLT) are being developed globally, with interest in the timber structure being exposed. To date, the design of high-rise and multi-storey timber buildings has been predominantly based on timber elements being encapsulated (protected) within fire rated gypsum plasterboard products, such that the plasterboard provides a non-combustible finish. The plasterboard may also improve the required fire resistance rating (FRR). Examples of this approach include the Stadthaus [1] in London, Forte [2] in Melbourne and Brock Commons in British Columbia [3]. An exposed mass timber structure represents a challenge for fire safety engineers, as the structure is a source of additional fire fuel. This is a significant departure from traditional non-combustible structures. A key factor for the determination of the FRR for the structure is how the combustible structure will impact on the compartment fire dynamics.

2 BACKGROUND

2.1 Building Fire Resistance and Building Height

Mass timber construction is based on using engineered timber for the load-bearing structure. Within most building codes [6 - 9], buildings are typically split into low, medium and high-rise. For high-rise buildings, normally defined by building height or number of stories, higher fire resistance ratings are required to allow for longer evacuation times, support fire department intervention via the fire protected

¹ Arup, 1120 Connecticut Avenue, Suite 1110, Washington, D.C. 20036, USA. david.barber@arup.com

² Arup, Level 17, 1 Nicholson Street, Melbourne, VIC 3000, Australia

³ Arup, Level 17, 1 Nicholson Street, Melbourne, VIC 3000, Australia

⁴ Arup, Level 17, 1 Nicholson Street, Melbourne, VIC 3000, Australia

stairwells and also provide for structural stability in the highly unlikely situation of the sprinkler protection failing to control a fire. A high-rise building is to remain structurally intact, such that the fire decays (“burns out”), before the structure succumbs to the heat energy released by the fire. The approach of addressing structural fire ratings based on the full burn out of a fire for high-rise buildings is consistent in codes internationally [10, 11].

2.2 Exposed Mass Timber in Buildings – Defining the Problem

Architects designing mass timber buildings are requesting more timber is exposed. There is concern and debate in the design and approval community as to the extent of fire hazard posed when mass timber is exposed. The issue to be addressed though is the requirement for a high-rise building to have a structure that can withstand the full burn-out of a fully developed fire, where the sprinklers have failed and the fire department has limited intervention. If too much timber is exposed, then the total fuel within the space (furniture, fixtures and exposed timber) can result in a fire that releases more energy than the installed fire resistance ratings are constructed to resist. This may result in localized and subsequently global structural failure. The areas of concern are the fire resistance of the mass timber members and the fire dynamics of the compartment, which are influenced by the mass timber as additional fuel.

2.3 Traditional Approaches Challenged by Fire Testing Results

Behaviour of structural timber elements exposed to fire is very much influenced by the amount of strong timber that remains within the char layer as a function of time. This is a widely accepted and adopted design philosophy, known as the ‘Reduced Cross Section Method’. The outcomes of this methodology inform fundamental aspects of the structural design. Traditionally, simple char rate calculations have been used to underpin calculations of residual cross sections. Various global design standards [12 – 14] offer char rate calculations. However, these calculations are either not applicable to for specific mass timber elements (such as CLT) or are generalised, and do not consider specific aspects of buildings, such as location and configuration of structural elements, proximity to re-radiating surfaces, compartment fire dynamics, heat release rate and fire intensity (particularly taking into account increases due to exposed timber), delamination, time and heat flux dependence of charring rates. Each factor can have a significant impact on the char rate of structural elements and therefore FRR of the building, and may be overlooked by contemporary timber design methodologies for fire resistance. It is considered that determination of the residual cross section should incorporate consideration of the factors discussed.

The intent of this work is to facilitate development of a methodology which considers relevant factors which may influence the char rate of timber (hence FRR), to provide confidence in the outputs (residual cross sections) on which fundamental structural design is based. The work documented in this paper is primarily validation of the simulations that form the basis of the input to structural design of exposed timber buildings.

There are a limited number of studies that investigate the fire contribution of combustible structures in real fires. Studies by ETH, VTT, TU Delft, SP Norway, Carleton University, University of Edinburgh, University of Queensland and the Fire Protection Research Foundation (FPRF) [15 – 24] have shown that if large areas of timber are exposed within a compartment, there will be an impact on the heat release rate (HRR) and fire duration. Also, if the non-combustible timber protection fails during the fire, such that uncharred timber is exposed, then the impact on HRR is significant and can result in a ‘run-away’ fire. CLT performance in fire can also impact the compartment HRR with the process of CLT char fall-off potentially resulting in fire re-growth. Given the link between compartment HRR and char rates, traditional methods of calculating FRR should be approached with caution, where the mass timber structure is exposed.

3 EXPLANATION OF METHODOLOGY

3.1 Methodology to Assess Exposed Timber

If a fire grows within a furnished, exposed timber compartment and is not controlled by sprinkler protection, the fire consumes the furnishings, fixtures and the exposed timber. The influence of the exposed mass timber on the energy released from the fire is key. Predicting how the compartment fire is impacted by the location and area of exposed timber has had limited investigation by the research community to date. Thus, to meet the needs of building owners and architects, Arup have invested in developing a robust, conservative and transparent methodology. The approach focuses on the contribution of exposed mass timber to determine the structure FRR as a function of char depth, taking into account local and global variations in heat flux, HRR, and additional fire load due to the exposed mass timber. The compartment fire model utilizes the pyrolysis functionality within Fire Dynamics Simulator (FDS), a widely used CFD package [25].

3.2 Fire Validation

The heat release calibration was carried out by building a model that replicated the experimental set-up documented in the CLT compartment fire tests by McGregor [19] and FPRF [24] and compared the measured data with the FDS results. This was carried out for the case of no CLT exposure and CLT exposed as per the experimental set up to understand the contribution to heat release rate calculated by FDS. The ‘no CLT exposure’ tests were used to create the baseline design fires from the furniture in the compartments. The McGregor test represented a bedroom and the fire was represented by a single HRR curve located centrally to the compartment. The FPRF tests represented a typical residential studio apartment, and for those simulations the impact of a moving fire was captured by grouping the furniture into discrete fuel packages (see Fig. 1).

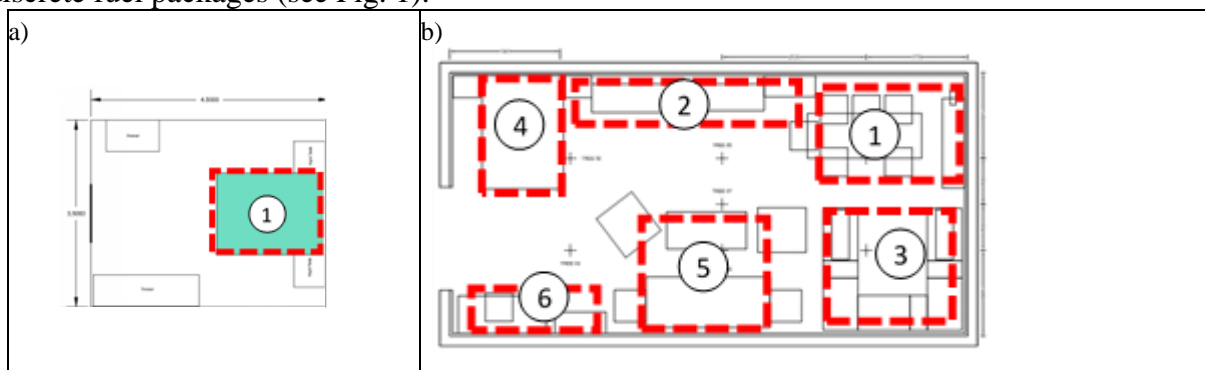


Fig. 1. FDS defined fire location/s overlaid on the fire test furniture layouts - a) McGregor tests - single HRR curve, b) FPRF tests - six HRR curves with predefined ignition times

Specifying the furniture fires allowed variations between simulation and measured predictions to be attributed to the simulated pyrolysis function and subsequent energy release from the exposed CLT. The exposed CLT models consisted of an accurate geometrical representation of the test compartment and included the reproduction of the materials and fixings present (i.e. plasterboard walls, flooring details, CLT to ceiling etc). Prior to building the test compartment models, pyrolysis functionality was calibrated against measured data from cone calibration tests for the type of timber being used in the CLT. McGregor’s fire tests used CLT of 105mm thick 3 ply panel. The FPRF fire tests used 175mm thick 5 ply panels. Work carried out by Wang et al. [26] was used as the basis of the inputs for the pyrolysis modelling. In the FDS models, thermocouple devices are embedded within the CLT surface and used to monitor the char front. Charring was assumed to have occurred when the temperature devices exceed 300°C [11, 27].

3.3 McGregor Tests

The FDS simulations of the McGregor Tests included the base case with no exposed CLT and exposed CLT on the ceiling only. The CLT validation results shows good initial agreement with McGregor’s experimental results with respect to HRR contribution from the CLT up to around 1,200 seconds (see Fig. 2). The FDS results also display some sustained burning of the CLT thereafter, following consumption of the furniture fuel load.

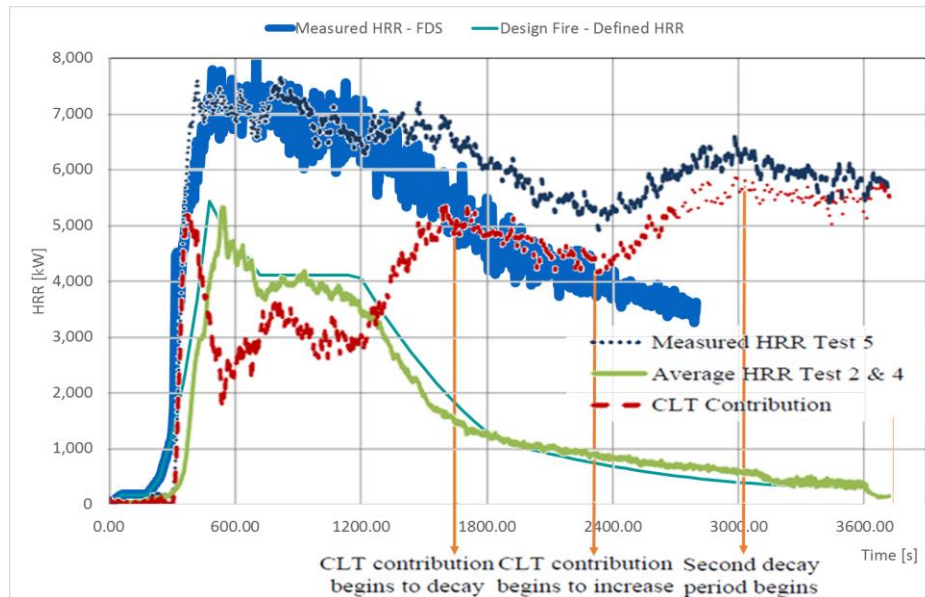


Fig. 2. FDS Model HRR compared to Experimental HRR ref: McGregor, 2013

3.3.1 Discussion of Modelling Results

A key difference between McGregor’s experimental results and the FDS simulations occurs up to 1,800 seconds, where the simulated HRR begins to reduce, whereas the experimental HRR increases slightly for around 300 seconds before starting to reduce at around 1500 seconds. The total energy released during sustained burning of CLT is somewhat captured within the FDS simulation. This is evident as the rate of decrease of total HRR is not as steep as the rate of decrease in the base design fire, across the 1,200 to 1,800 seconds range, where the contribution of the furniture fire load diminishes. While this suggests the CLT continues to burn, FDS appears to under predict the magnitude of HRR. Another difference occurs at around 2,400 seconds, where char fall off occurs and exposes the second layer of CLT was observed. This is not captured in the FDS modelling to date. The presented methodology calculates heat transfer through a char layer that remains in place throughout the simulation. Char fall off suddenly exposes ‘fresh’ timber, which increases HRR and fire intensity [28]. McGregor recorded char depths of between 50 - 70 mm based on a 60 minute burn time. Char depth was slightly under predicted by the FDS simulation, which returned char depths of between 40 - 70 mm, when extrapolated. Though small, the under-estimation is non-conservative and needs consideration when reviewing results.

3.4 FPRF Tests

The FPRF recently completed a series of six fire tests on a full size residential compartment, with exposed CLT walls or ceiling. The experiments ran in the order of 3.5 hours (12,600 seconds). Results from four FPRF tests have been used to further validate the FDS modelling, focussing on the experiments that represented different configurations of exposed CLT surfaces, under similar ventilation conditions. The tests modelled within FDS consisted of a compartment 9.1m x 4.6m x 2.7m high with an opening of 1.8m wide x 2.0m high. Test 1-1 had no exposed CLT; Test 1-4 had an exposed CLT ceiling; Test 1-5

had an exposed CLT wall and Test 1-6 had an exposed CLT wall and ceiling. Further details are provided within the test report [24].

3.4.1 Discussion of HRR Results

The FDS models were run through to 3,600 seconds (60 minutes). This period within the model captures the early, more complex stages of fire development, with the transition between ambient conditions through flashover to the fully developed phase of the fire. The simulations predicted the heat release rate reasonable well compared with the experiments, through the initial stages of the fire, including the flashover process. The implication being that ignition of the CLT and the onset of pyrolysis of the timber was well captured within the simulations (see Fig 3).

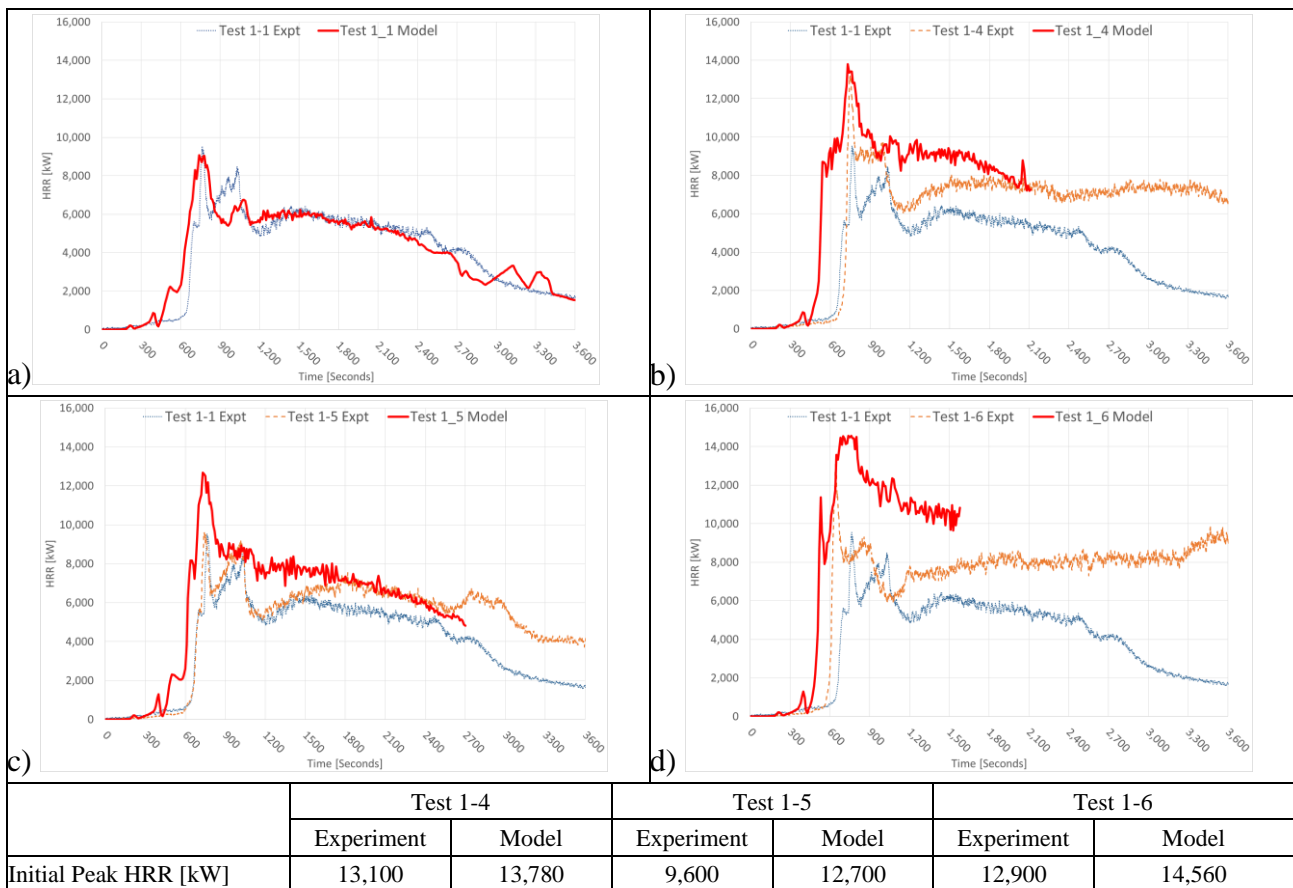


Fig. 3. HRR FDS simulation compared to experimental results. a) Test 1-1: No exposed CLT, b) Test 1-4: Exposed CLT ceiling, c) Test 1-5: Exposed CLT wall, d) Test 1-6: Exposed CLT wall and ceiling

The differences in contribution from the exposed CLT located at the wall or ceiling are conservative and satisfactorily captured in the FDS modelling. The duration, time to and magnitude of the initial peak HRR in the simulations are reasonably consistent with the experimental results (see Fig. 4). The results show the total heat release is over predicted. Furthermore, the relative over prediction appears to increase with more onerous exposure conditions, with Test 1-6 model yielding the largest relative over estimation. This will need to be investigated in further work (see Fig. 4).

Test 1-4 provides the most accurate correlation with respect to peak HRR in the initial stage, with a peak HRR closely aligned to the experimental peak HRR, followed by a period of consistent contribution by the CLT ceiling. The simulation of Test 1-4 over predicted the HRR until 2,100 seconds (35 minutes) but like the McGregor validation tests, the duration of the fully developed phase reduced more rapidly than the experimental results. This indicates that in the early stages of the fire a larger proportion of the CLT

ceiling is involved and exhibiting burning compared to the experiment and that the burning rate of the CLT is more efficient than the experiment. As the fire progresses in the FDS simulations, there continues to be a significant contribution to the HRR from the CLT, however the pyrolysis model does not appear to simulate the self-sustained burning of CLT without the influence of the external heat flux from the furnishings). Due to the initial over prediction of the HRR, there appears be reasonable correlation of the total heat released and the contribution of the CLT up to at least 60 minutes or until the degree of char fall off noticeably increases the burning rate of the timber below the char front. In the experiments there is a rapid increase in the burning rate when char fall off occurs, leading to a second peak HRR at around 160 minutes, which is not captured in the FDS simulations as char fall off has not been modelled. This is an important consideration for further work.

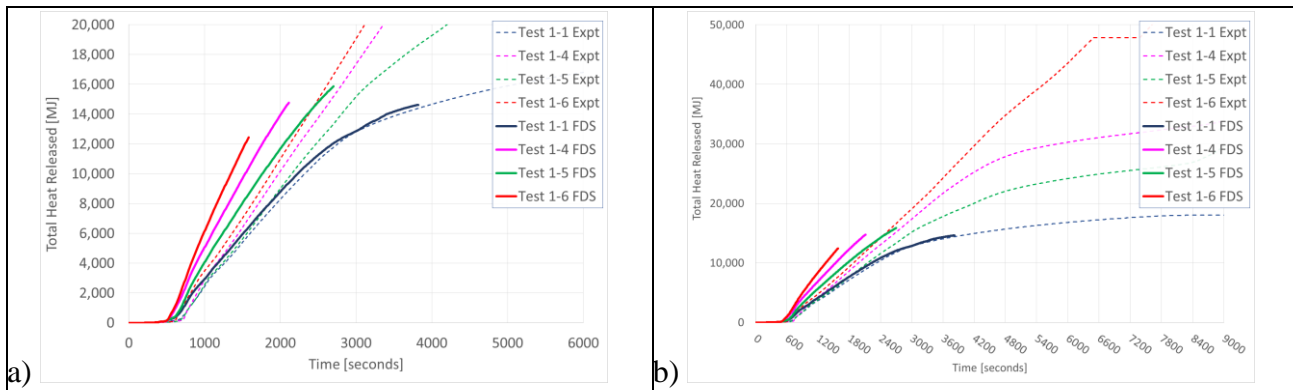


Fig. 4. Total Heat Released - FDS simulation compared to experimental results - a) Over the first 3,600 seconds (60 minutes), b) Over the duration of the test ~9,000 seconds (150 minutes)

The FDS models of Test 1-5 and Test 1-6 resulted in similar outcomes compared to the experimental results. The modelling results over-predict the peak HRR by 5% in Test 1-4 and 13% in Test 1-6. For Test 1-5, the initial peak HRR was over predicted in the order of 30%, though the duration of this peak was short (120 seconds). This suggests that during flashover the simulation predicted involvement from a greater proportion of the CLT wall, compared with the experiment. In the fully developed phase the HRR curve reflects the experimental results more closely, indicating the incident heat flux on the CLT wall was not sufficient to maintain pyrolysis across the whole surface simultaneously. The contribution of the CLT wall and the burning behaviour of the vertical surface was more difficult to simulate, as shown in the greater over prediction of peak HRR. However, it is noted that in terms of total heat released, Test 1-5 which had the exposed CLT wall, had a better correlation than those experiments with the exposed CLT ceiling.

3.4.2 Discussion of Temperature Results

The over prediction was also reflected in the temperatures recorded in the embedded thermocouples. Initially the temperature rise is in advance of the experimental results with the temperatures plateauing and intercepting the experimental temperatures later in the test. This is shown below with a comparison of the thermocouples encompassed within the CLT at the 20mm, 35mm, 50mm depths (see Fig. 5). There is a significant variability in the measured and predicted temperatures, particularly in terms of time dependence. The experimental results show a gradual increase in temperature and then a sharp rise, compared to the simulated results where the internal temperature increases at a steady rate. This difference can be attributed to the residual moisture being driven off the CLT in the experiments, which is not included in the definition of the CLT in the FDS simulations. The modelling results are conservative and will remain so until such a time where the experiment's thermocouple temperatures exceed the simulation temperatures. With respect to char depth, the result is conservative as long as the 300°C

isotherm is achieved in the model prior to the experiment. As stated previously, embedded temperatures within the models become non-conservative where char fall off occurs in the experiment.

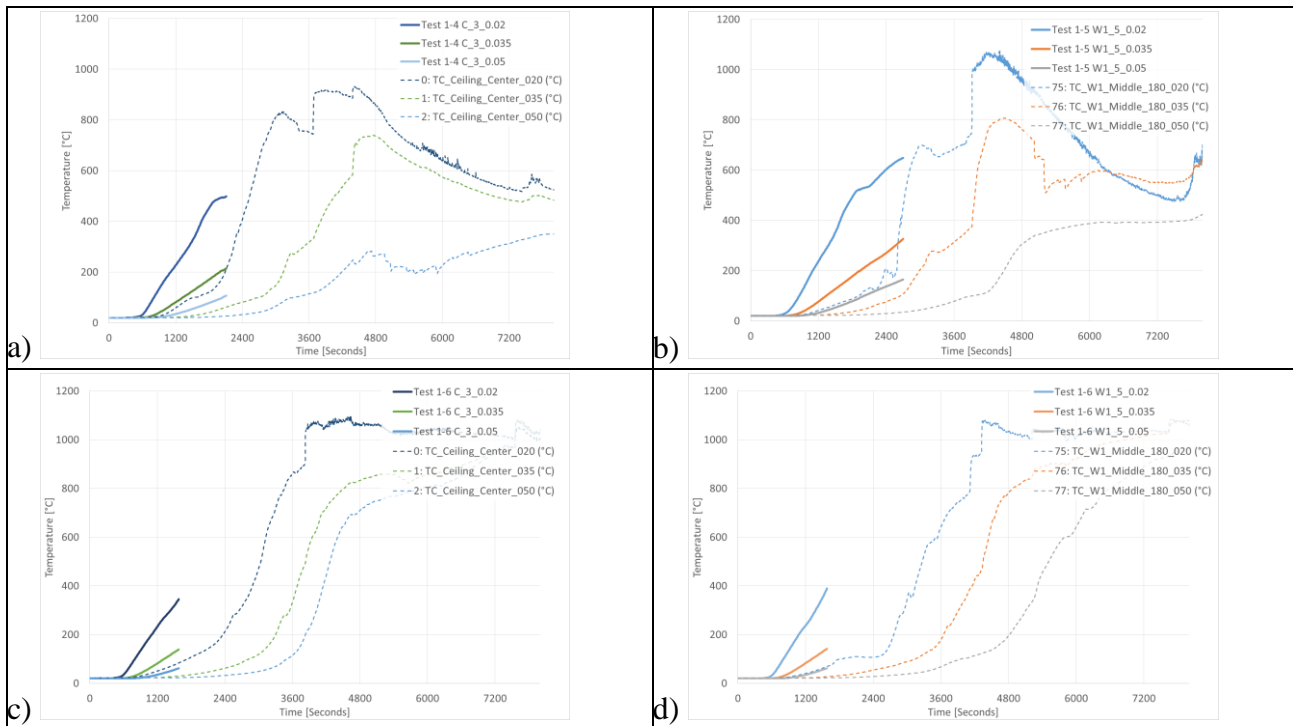


Fig. 5. Embedded thermocouples - FDS simulation compared to experimental results - a) Test 1-4: Exposed CLT ceiling, b) Test 1-5: Exposed CLT wall, c) Test 1-6: Exposed CLT ceiling, d) Test 1-6: Exposed CLT wall

3.5 Limitations

The variance between the simulations and the experiments can be attributed to a number of limitations identified in modelling the compartment fire and the exposed CLT. These include the definition of the material properties of the CLT within the FDS models; the source of the fire was fully defined, not reflecting the experiment HRR; phenomena not accounting for inconsistent pyrolysis of the CLT within FDS models; char fall off; gypsum board fall off and charring of CLT behind the gypsum board. The computational time to undertake pyrolysis modelling is extensive, the simulation run times may be considered too long to be used as a viable design tool.

4 CONCLUSIONS

This paper presents a methodology by which FDS is utilised to determine the response of an exposed mass timber structure within a fire compartment. The modelling predicts char depths resulting from fully developed fire conditions, which is directly related to the FRR of an exposed mass timber structure. Validation based on actual compartment fire tests has shown the modelling can predict char depths within 20%, based on a fully developed fire. A number of observed phenomena during fire tests with exposed timber have not been fully captured, such as CLT char fall-off. Further work is required to accurately represent this within the model, to correlate modelling results to those observed during experiments.

REFERENCES

1. <http://www.waughthistleton.com/project/murray-grove/>
2. <https://www.woodsolutions.com.au/Inspiration-Case-Study/forte-living>
3. <http://www.naturallywood.com/emerging-trends/tall-wood-buildings/ubc-brock-commons>

4. Barber, D., Gerard, R., 2015 “Summary of the Fire Protection Foundation Report - Fire Safety Challenges of Tall Wood Buildings” *Fire Science Reviews*, 4:5, DOI 10.1186/s40038-015-0009-3
5. White R., 2016 “Analytical Methods for Determining Fire Resistance of Timber Members”, *SFPE Handbook of Fire Protection Engineering*, 5th Edition, Gaithersburg
6. International Code Council “International Building Code”, 2015
7. National Research Council, Canada, 2010 “National Building Code of Canada”
8. Australian Building Codes Board, 2015, “Building Code of Australia”, Canberra
9. Department for Communities and Local Government, 2010 “Fire Safety: Approved Document B”
10. Department of Commerce, 1942 “Building Materials and Structures, Report BMS92, Fire Resistance Classification of Structures”, National Bureau of Standards, Report of Sub-committee on Fire Resistance Classifications of Central Housing Committee on Research, Design and Construction.
11. Buchanan, A. 2001 “Structural Design for Fire Safety”, John Wiley and Sons
12. Australian Standard 1720 Part 4-2006 “Fire resistance for structural adequacy of timber members”
13. BS EN 1995-1-2, 2009, “Eurocode 5: Design of Timber Structures – Part 1-2: General – Structural Fire Design”
14. American Wood Council, 2015 “Calculating the Fire Resistance of Exposed Wood Members: Technical Report No. 10”, Leesburg
15. Frangi, A., and Fontana, M., 2005, “Fire Performance of Timber Structures Under Natural Fire Conditions” *Fire Safety Science – Proceedings of the Eighth International Symposium*, pp. 279-290
16. Hakkarainen, T., 2002, “Post-Flashover Fires in Light and Heavy Timber Construction Compartments” *Journal of Fire Sciences* 20: 133-175. DOI: 10.1177/0734904102020002074
17. Crielaard, R., 2015, “Self-Extinguishment of Cross-Laminated Timber”, Thesis, Delft University of Technology, Netherlands
18. Hox, K., 2015, “Branntest av massivtre” SP Fire Research, Report A15101 (in Norwegian, translated by Arup)
19. McGregor, C., 2013, “Contribution of Cross Laminated Timber Panels to Room Fires”, Thesis, Carleton University, Ottawa, Canada
20. Medina, A., 2014 “Fire Resistance of Partially Protected CLT Rooms”, Thesis, Carleton University, Ottawa, Canada
21. Li, X., 2015, “Modelling of Barrier Failure and Fire Spread in CURisk”, Thesis, Carleton University, Ottawa, Canada
22. Hadden, R., Bartlett, A., Hidalgo, J., Santamaria, S., Wiesner, F., Bisby, L., Deeny S., Lane, B., 2017, “Effects of Exposed Engineered Timber on Compartment Fire Dynamics”, *Proceedings of the 12th International Association of Fire Safety Science Symposium*, Lund, June 10 to 16 2017
23. Emberley, R., Gorska C., Bolanosa, A., Lucherinia, A., Solartea, A., Soriguera, D., Gutierrez, M., Humphreys, K., Hidalgo, J., Maluka, C., Law, A., Torero, J., 2017, “Description of Small and Large-scale Cross Laminated Timber Fire Tests”, *Fire Safety Journal* 91, pp 327–335
24. Su, J., Lafrance, P., Hoehler, M., Bundy, M., 2018, “Fire Safety Challenges of Tall Wood Buildings Phase 2: Tasks 2 & 3 – Development and Implementation of Cross Laminated Timber (CLT) Compartment Fire Tests” *Fire Protection Research Foundation*
25. Fire Dynamic Simulator, developed and maintained by the Building and Fire Research Laboratory (BFRL) at National Institute for Standards and Technology (NIST), Gaithersburg
26. Wang, X., Fleischmann, C., Spearpoint, M., and Huang, X., 2015, “The Application of Different Component Schemes to Predict Wood Pyrolysis and Fire Behaviour”, *Proceedings IFireSS – International Fire Safety Symposium*
27. Drysdale, D., 2011 “An Introduction to Fire Dynamics, Third Edition”, Wiley
28. Klippel, M., Schmid, J., Frangi, A., 2016 “Fire Design of CLT”, paper submitted for joint event of COST Actions FP1402 and FP1404, KTH Stockholm

NUMERICAL MODEL FOR THE FIRE PROTECTION PERFORMANCE OF INTUMESCENT COATINGS EXPOSED TO NATURAL FIRES

Waldemar Weisheim¹, Peter Schaumann², Lisa Sander³, Jochen Zehfuß⁴

ABSTRACT

This paper presents a numerical model to simulate the fire protection performance of a water-based intumescent coating in case of a natural fire scenario. Based on own experimental investigations the insulation efficiency of the coating is expressed by temperature and heating rate dependent material properties within the numerical model, such as expansion factors, thermal conductivities and heat capacities. Within the paper two-dimensional numerical models of a coated I-profile in case of a natural fire scenario are presented taking into account the temperature and heating rate dependent expansion process of the coating explicitly. Moreover, a modelling technique is presented to introduce the material properties of the intumescent coating for both the heating and cooling phase. The results of the numerical models are compared to results of a fire test of an unloaded I-section beam and column. The main objective of the paper is to provide a generic numerical model describing the fire protection performance of the investigated intumescent coating in case of arbitrary natural fire scenarios.

Keywords: Intumescent coating, natural fire, numerical model, expansion

1 INTRODUCTION

In European Technical Assessments (ETAs) the insulating efficiency of intumescent coatings (ICs) is verified by small-scale fire tests according to ETAG 018 part 2 [1]. Within these fire tests coated steel panels with a nominal thickness of 5 mm are exposed to the standard time-temperature curve in accordance with EN 1363-1 [2]. To assess the insulation efficiency of the ICs the temperature of the coated panel is measured during the fire exposure. The time at which the panel temperature reaches a mean value of 500 °C is recorded and used for evaluation purposes.

Beside the small-scale fire tests on coated panels, additional fire tests on loaded and unloaded beams and columns are prescribed in ETAG 018 part 2 [1]. These tests are performed according to EN 13381-8 [3] to give guidelines to design the dry film thickness (DFT) of ICs as a function of section factor and intended steel profile temperature. Based on the desired fire resistance class the values for the DFT are given for fire resistance times of 30, 60, 90 or 120 minutes.

Except the smouldering fire according to EN 1363-2 [4] all fire tests described in ETAG 018 part 2 [1] are based on the standard time-temperature curve. Therefore, the assessment of the thermal performance of ICs is solely related to this fire scenario.

¹ Doctoral Student. Institute for Steel Construction, Leibniz Universität Hannover, GERMANY.
e-mail: weisheim@stahl.uni-hannover.de

² Professor. Institute for Steel Construction, Leibniz Universität Hannover, GERMANY.
e-mail: schaumann@stahl.uni-hannover.de

³ Doctoral Student. Institute of Building Materials, Concrete Construction and Fire Safety, Technische Universität Braunschweig, GERMANY. e-mail: l.sander@ibnm.tu-bs.de

⁴ Professor. Institute of Building Materials, Concrete Construction and Fire Safety, Technische Universität Braunschweig, GERMANY. e-mail: j.zehfuss@ibnm.tu-bs.de

According to the harmonised European rules for the fire design of structural members in fire (EN 1993-1-2), steel structures with ICs can be also designed for natural fire scenarios. The evolution and propagation of natural fires are essentially based on the fire load and the ventilation conditions inside a building. Natural fire scenarios can show arbitrary regimes as well as heating and cooling rates. Facing this fact, it is of great importance to know the thermal performance of ICs when being exposed to heating rates deviating from the standard fire condition.

Recent experimental studies of Lucherini et al. [5] and Schaumann et al. [6] revealed a clear dependency of the thermal behaviour of ICs on heating rates. The research groups found out independently that the investigated water-based and solvent-borne ICs showed a better insulating performance when being exposed to higher heating rates. Lower heating rates resulted in a lower expansion of the char. Therefore, the coatings provided a mitigated insulation to the steel members. Based on these findings the fire protection performance of ICs and therefore the heating behaviour of coated steel members cannot be evaluated for natural fire scenarios by the test methods given in ETAG 018 part 2 [1].

As fire tests are cost and time-intensive, numerical simulations are favourable to predict the heating behaviour of coated steel members when being exposed to natural fires. Therefore, in this paper two-dimensional, coupled thermo-mechanical analyses are presented to simulate the fire protection performance of a water-based IC applied on I-profiles.

2 EXPERIMENTAL INVESTIGATIONS

2.1 Test specimens and test procedure

In order to investigate the influence of a natural fire scenario on the fire protection performance of ICs, a fire test was conducted at the testing facility of the Institute of Building Materials, Concrete Construction and Fire Safety (iBMB) in Braunschweig (Germany) in November 2017. As test specimens an unloaded I-section beam and column (HEA 240) with a length of 1000 mm were used (see Fig. 1 and 2). Both test specimens were coated by a water-based IC with a DFT of 350 and 360 μm for the beam and the column respectively. To ensure a three-sided fire exposure, the beam was disposed under the furnace ceiling, which consisted of cover panels made from aerated concrete. The column was placed on the bottom of the furnace, thus ensuring a four-sided fire exposure. The free ends of the test specimens were covered by 50 mm thick insulation boards made from vermiculite. The temperature of the test specimens was measured by thermocouples (TCs) type K, which were applied on the flanges and webs by welding. The locations of the TC are given in Fig. 1 and 2 for each test specimen respectively.

To control the temperature inside the furnace, plate thermometers were placed near the test specimens. Thus, the natural fire scenario shown in Fig. 2 could be realized using gas burners. The chosen natural fire scenario is based on a CFAST calculation for a room with a floor area of 500 m^2 and a fire load of 300 MJ/m^2 .

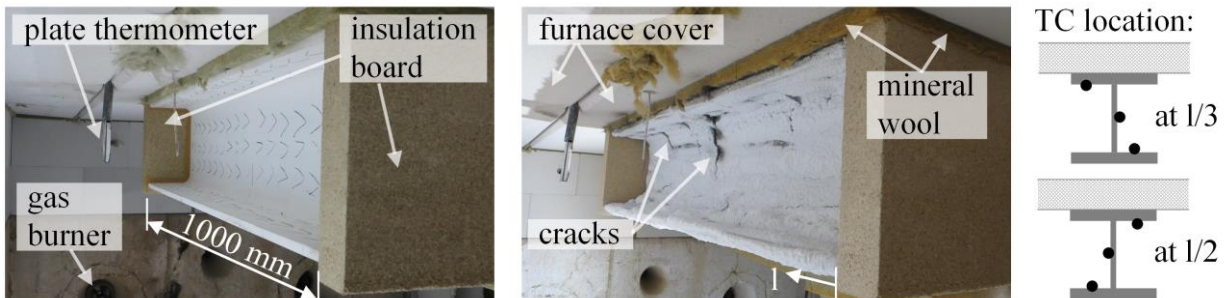


Fig. 1. I-section beam (HEA 240) with a water-based intumescent coating (DFT = 350 μm) before (left) and after (right) a three-sided fire exposure

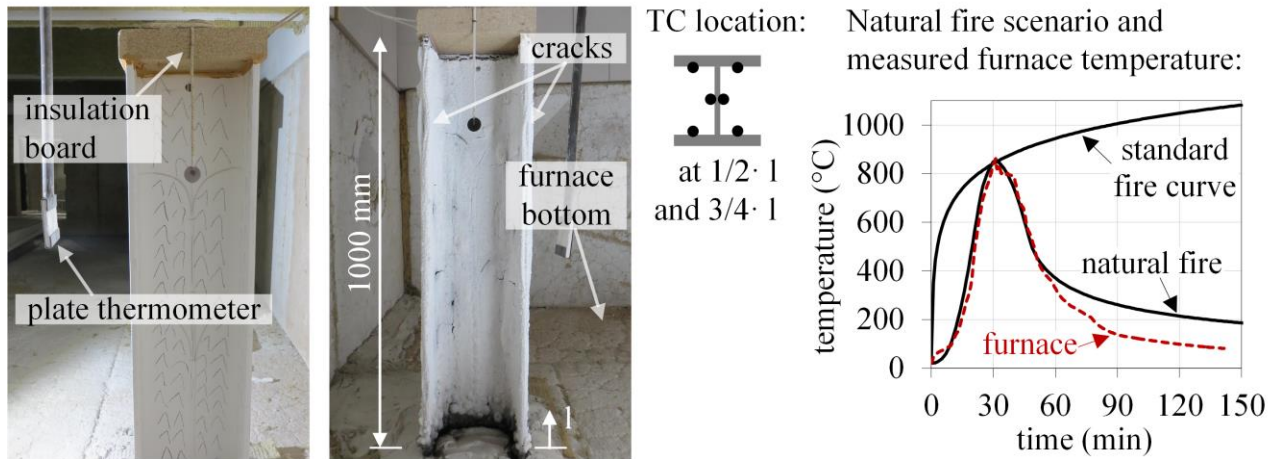


Fig. 2. I-section column (HEA 240) with a water-based intumescent coating (DFT = 360 µm) before and after a four-sided fire exposure (left), natural fire scenario and measured furnace temperature (right)

The natural fire scenario is characterized by a non-linear heating phase that reaches its maximum temperature (852 °C) after 31 minutes. At this point the temperature exceeds the standard time-temperature curve (see Fig. 2). The cooling phase of the natural fire scenario shows approximately a bilinear behaviour with a change in cooling rate after 50 minutes.

2.2 Results

The furnace temperature was well controlled by the plate thermometers during the fire test up to 50 minutes (see Fig. 2). Therefore, the heating phase and the first part of the cooling phase were in great accordance with the natural fire scenario. A deviation between the furnace temperature and the fire scenario occurred in the second part of the cooling phase (after 50 minutes). This was due to the gas burners, which were switched off to realise the change in the cooling rate.

The start of the expansion process due to the natural fire scenario occurred after 21 minutes for both test specimens resulting in averaged char thicknesses of approximately 9 mm for the flanges and 12 mm for the webs. Due to the char formation the measured temperature of the test specimens changed when reaching the value of 220 °C (see Fig. 7). This effect is less pronounced for the upper flange of the beam since its heating behaviour was additionally affected by the insulation of the cover panels. This is also the reason why the temperature of the upper flange reached only the maximum of 470 °C after 51 minutes. The web of the beam was subjected to a higher heating since the maximum temperature of 570 °C occurred after 45 minutes (see top diagrams in Fig. 7).

The temperature development inside the column is more homogeneous compared to the beam. For both the flange and the web the maximum temperature (flange: 595 °C, web: 585 °C) occurred after 45 minutes (see bottom diagrams in Fig. 7).

In the cooling phase both test specimens showed lower cooling rates compared to the furnace temperature resulting in a temperature difference of 110 °C to 200 °C. This temperature difference between the test specimens and the gas temperature was due to the inverted insulation effect of the IC and the thermal inertia of the steel profiles.

3 MATERIAL PROPERTIES OF THE INTUMESCENT COATING

3.1 Expansion and mass loss behaviour

Material properties of the investigated IC are required to be understood and to simulate the thermal behaviour of the coating. Therefore, small-scale tests and thermal analyses were performed by the authors obtaining the data given in Fig. 3 and 4. In Fig. 3 the expansion behaviour is described by an expansion factor α , given as a ratio between the measured char thickness and the DFT. The test specimens (coated steel plates 25 x 25 x 0.7 mm with a DFT of 250 µm) were exposed to different

heating rates. Therefore, the expansion factors show a dependency on the heating conditions resulting in higher expansion values and higher char temperatures for increasing heating rates.

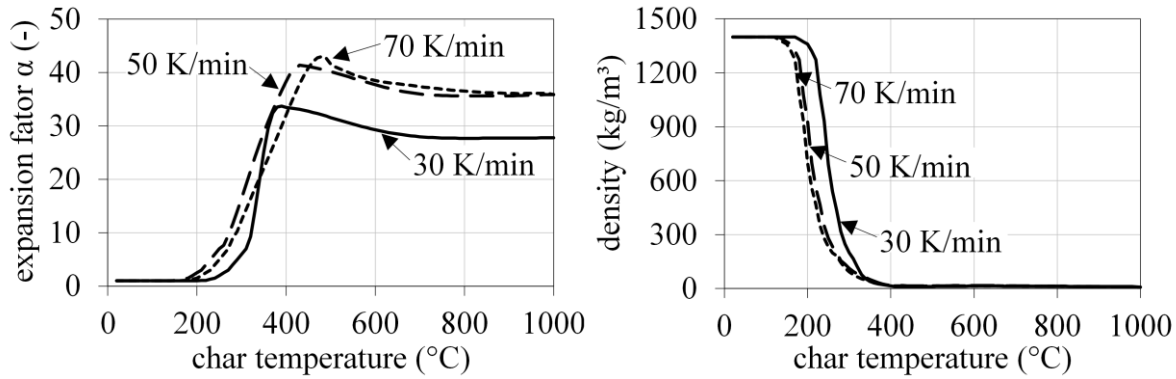


Fig. 3. Temperature and heating rate dependent expansion factor (left) and density (right) of a water-based IC

As the initial density (1400 kg/m³) of the IC is changing due to mass loss and expansion, the curves given in Fig. 3 show also a dependency on the heating rates. To calculate the temperature dependent density, in addition to the expansion analyses, thermogravimetric analyses (TGA) were performed in a temperature range of 20 up to 1000 °C for samples of 7 to 8 mg using a NETZSCH STA 409 PC/PG DSC-TGA analyser. The analyses were carried out under synthetic air for 5, 10 and 20 K/min.

3.2 Thermal conductivity and heat capacity

Due to the transient expansion behaviour and the different reaction stages which the IC passes through, the thermal conductivity cannot be measured directly. Therefore, the equivalent conductivity (λ_{eq}) of the investigated water-based IC was calculated by the mixture rule given by equation (1) and Schaumann et al. [7].

$$\lambda_{eq}(\theta) = \psi \cdot (\lambda_p + 4 \cdot \sigma \cdot \theta_M^3 \cdot d_p) + (1 - \psi) \cdot \lambda_{IC} \quad (1)$$

Herein, the conductivity of the air inside the pores (λ_p) and the conductivity of the coating at room temperature (λ_{IC}) are weighted by the porosity (ψ). The porosity describes the fraction of pores inside the char and therefore can be calculated from the expansion factor as follows: $\psi = (\alpha - 1)/\alpha$. The approach for the equivalent conductivity considers also the radiation inside the pores by the Stefan-Boltzmann constant (σ), the temperature (θ_M) and the diameter of the pores (d_p). Based on microscopic analyses a non-linear growth of the pore diameter is considered as a function of char temperature.

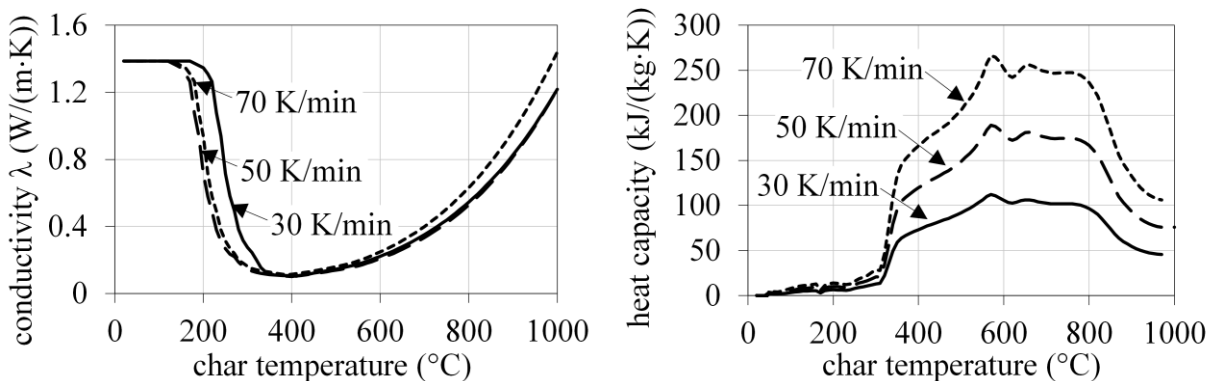


Fig. 4. Temperature and heating rate dependent conductivity (left) and heat capacity (right) of a water-based IC

Using the approach for the calculation of the equivalent thermal conductivity of the water-based IC leads to the curves given in Fig. 4. As the conductivity is a function of porosity, the calculated

values show a dependency on the heating rates. Therefore, the measured initial value of 1.40 (W/m·K) decreases at lower char temperatures when the heating rate increases. Nevertheless, the minimum value of 0.11 (W/m·K) at 390 °C remains the same for all heating rates.

To measure the heat capacity of the investigated IC, differential scanning calorimetry (DSC) analyses were performed simultaneously to the thermogravimetric analyses. As the analyses were carried out for heating rates of 5, 10 and 20 K/min, the heat capacities for the heating rates of 30, 50 and 70 K/min were calculated using the model free kinetics approach of Vyazovkin [8]. The heating rate dependent heat capacities are shown in Fig. 4. A high increase in heat capacity occurs at 310 °C resulting in maximum values of 110, 184 and 258 kJ/(kg·K) at 560 °C for 30, 50 and 70 K/min respectively. With further reaction progress and pyrolysis of organic components the heat capacity decreases after 800 °C reaching different final values.

4 NUMERICAL INVESTIGATIONS

4.1 Two-dimensional models of the test specimens

To investigate the influence of the natural fire scenario on the fire protection performance of the water-based IC numerically, two-dimensional models of the test specimens were set up in Abaqus using CPE4T shell elements. As the setup is equal for the beam and the column except the modelling of the furnace cover, only the beam model will be presented in the following

The three-sided fire exposed beam (HEA 240) was modelled with a 600 mm wide and 150 mm thick furnace cover on the top of the upper flange (see Fig. 5). The IC was modelled circumferentially on the remaining surface of the I-section with a DFT of 350 µm. Between the profile and the furnace cover as well as between the profile and the IC a perfect heat transfer was assumed. The fire exposure was applied circumferentially on the IC and the bottom of the furnace cover within a coupled thermo-mechanical analysis. For this purpose, the measured furnace temperature was implemented using an emissivity value of $\varepsilon = 0.8$ for the IC and $\varepsilon = 0.7$ for the furnace cover. Following the recommendations of EN 1991-1-2 [9] the coefficient for the convection was set to $\alpha_c = 35$ W/(m²·K). The thermal behaviour of the steel profile was modelled using the material properties given in EN 1993-1-2 [10].

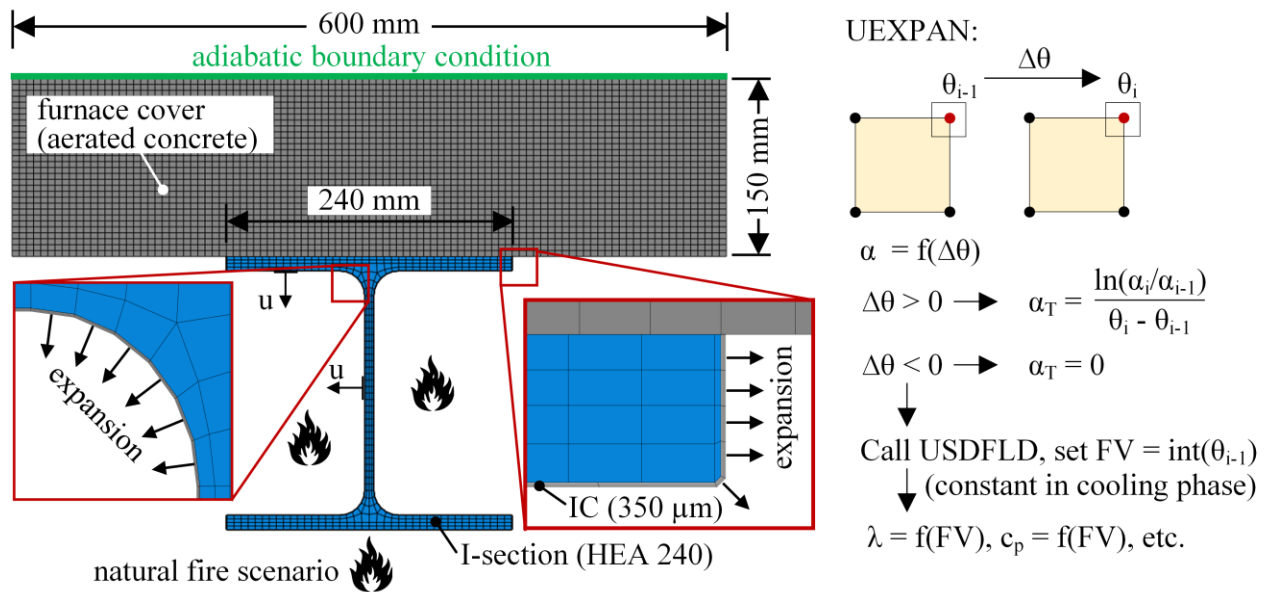


Fig. 5. Finite element model (2D) of a coated I-section beam exposed to a three-sided natural fire scenario (left) and schematic description of the implementation of the user subroutines for the intumescent coating (right)

The thermal material properties of the furnace cover were set to $\rho = 550$ kg/m³, $c_p = 1100$ J/(kg·K) and $\lambda = 0.12$ W/(m·K) according to the data provided by the manufacturer. To simulate a heating

rate dependent behaviour of the IC, the material properties presented in *Fig. 3* and *4* were introduced. The values for the density, the thermal conductivity and the heat capacity were implemented as tabulated data as a function of temperature. For the cooling phase additional field variables (FV) were introduced to ensure constant thermal material properties for the coating (see *Fig. 5*). In this way, the thermal material properties were set constant to the last value that corresponded to the element temperature before the temperature decrease ($\Delta\theta < 0$) occurred using the user subroutine USDFLD. Additionally, the user subroutine UEXPAN was used to implement the heating rate dependent expansion curves of the coating to ensure the strict orthogonal expansion behaviour as described in *Fig. 5*. Based on the incremental change in heating rate ($\Delta\theta = \theta_i - \theta_{i-1}$) the expansion of the coating is calculated by the thermal expansion coefficient (α_T) using the expansion factors ($\alpha = f(\Delta\theta)$). In this way, the coating thickness changes with temperature or remains unchanged when the expansion coefficient is set to $\alpha_T = 0$ during the cooling phase (see *Fig. 5*).

4.2 Results

To illustrate the temperature development inside the coated H-section profile and the expanded coating, the simulated temperature fields of the four-sided fire exposed column are shown in *Fig. 6*. In order to save space, only the half of the simulated model is depicted.

The start of expansion occurs in the simulation after 20 minutes on the web and the edges of the flanges. At this point in time the steel profile reaches a temperature of 250 °C, whereas the outer layer of the coating exhibits a surface temperature of 430 °C. With further progress of the simulation the coating is exposed to higher surface temperatures reaching a maximum value of 822 °C after 30 minutes. At that time the char thickness expands maximally resulting in a high temperature gradient inside the char. Due to this insulation effect the temperature inside the steel profile is only 353 °C. Although the DFT of the coating is only 360 µm, the expanded coating is able to prevent the column from a faster heating. When the cooling phase of the natural fire scenario occurs, the expanded coating thickness remains unchanged. This is due to the implemented behaviour in the user subroutine UEXPAN. As the coating has still low conductivity values, the expanded coating prevents the steel profile from a faster cooling. This effect can be seen from the inverted temperature gradient inside the expanded coating after 90 minutes (see *Fig. 6*). With 347 °C the steel profile has a 138 °C higher temperature than the outer surface of the coating.

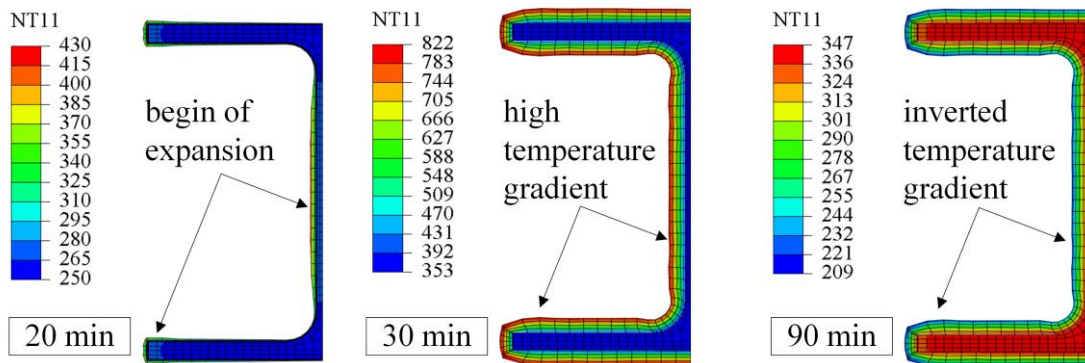


Fig. 6. Simulated temperature fields of the coated column (HEA 240, DFT = 360 µm) at different points in time

In order to evaluate the accuracy of the numerical simulations, the simulated results of the beam and column are compared to the test data. In *Fig. 7* for both models the simulated and measured flange and web temperatures as well as the simulated and measured char thicknesses are compared to each other. Both the temperatures in the heating phase and in the cooling phase are in great accordance with the test data. Only the maximum flange temperature of the column is underestimated by 35 °C in the simulation. The change in temperature during the expansion process of the coating is more distinctive in the simulation than in the test. Nevertheless, the point in time at which the expansion of the coating occurs coincides very well with the temperature development inside the steel profile.

This can be seen from the blue dashed curves in *Fig. 7* which represent the expanded char thickness obtained from the simulations.

As the temperature development inside the column is nearly homogeneous, the simulated char thicknesses at the flange and the web develop equally (see bottom diagrams in *Fig. 7*). At the end of the simulation the char thicknesses reach a value of 10 mm and thus overestimate the measured thickness at the flange by 1 mm. However, the measured thickness of the web is underestimated since the char thickness was determined after the fire test to 12 mm (see data point in *Fig. 7*).

A comparable accuracy regarding the development of the char thickness was also achieved for the beam model. Nevertheless, the simulated char thickness at the flange and the web differ from each other due to the uneven temperature distribution inside the steel profile.

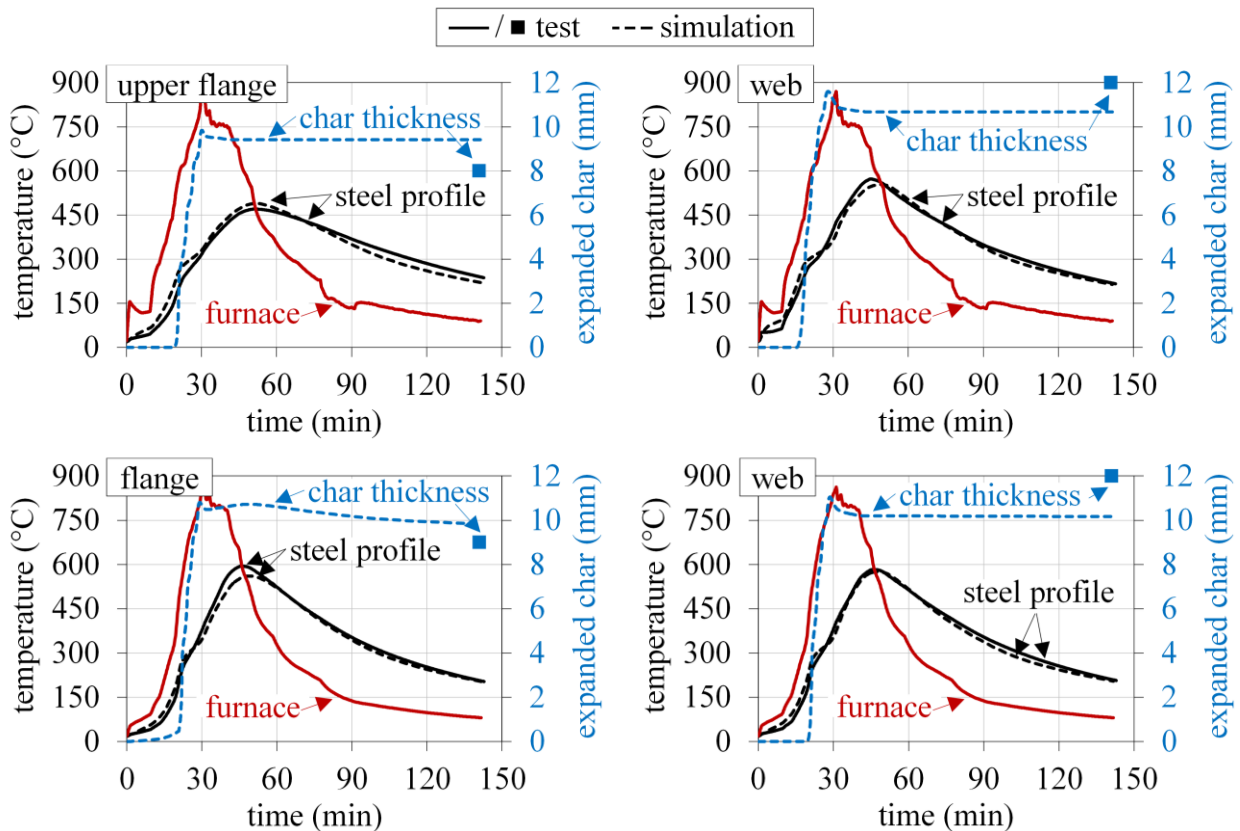


Fig. 7. Comparison between the test data and numerical simulations of the steel temperature and char thickness for the flange (left) and web (right) of the beam (top) and the column (bottom)

The good agreement between the simulated and measured data reveals that the developed numerical model is suitable to simulate the fire protection performance of the investigated water-based IC in case of a natural fire scenario. Based on the temperature and heating rate dependent material properties of the coating and the differentiation between the heating and cooling phase, the temperature distribution inside the beam and column can be simulated close to reality.

5 CONCLUSIONS

The main objective of the paper is to provide a numerical model for the simulation of the fire protection performance of a water-based intumescent coating in case of a natural fire scenario. This is achieved by implementing the temperature and heating rate dependent material properties of the coating in two-dimensional finite element models using user subroutines in Abaqus. The material properties of the coating, such as expansion factors, thermal conductivities and heat capacities, were determined experimentally and used as input data for the simulations. In accordance with recent

publications, the investigated intumescent coating reveals a clear dependency on heating rates. A better insulation performance can be observed when the coating is exposed to higher heating conditions. This is due to the fact that the fire protection performance of intumescent coatings is solely assessed for a fire exposure according to the standard time-temperature curve within the European Technical Assessments.

As the temperature regime of a natural fire scenario can deviate significantly from the standard time-temperature curve, it is highly recommended to assess the influence of varying heating conditions on the thermal behaviour of the coatings. Otherwise a reliable design of steel members protected by intumescent coatings cannot be ensured. As fire tests are time- and cost-intensive, the numerical simulations presented in this paper offer a good alternative for the assessment of the fire protection performance of intumescent coatings. Nevertheless, it is worth to mention that the material properties provided in this paper were determined for a water-based intumescent coating. Due to the huge variability of the coatings, the modelling technique presented in this paper can only be applied, when the required material properties of the investigated coating are available.

ACKNOWLEDGMENT

The work presented in this paper is part of the German research project ‘Test procedures for thermal material properties of fire protection claddings and intumescent coatings for the design of steel structures exposed to natural fires (in German: ‘*Prüfverfahren für thermische Materialkennwerte von Brandschutzbekleidungen und reaktiven Brandschutzsystemen für die Bemessung von Stahltragwerken bei Naturbränden*’) (AiF 19176 N). The authors express their deep gratitude for the financial support received from the Federal Ministry for Economic Affairs and Energy.

Supported by:



on the basis of a decision
by the German Bundestag

REFERENCES

1. European Organization for Technical Approvals (2006): *ETAG 018, Guideline for European Technical Approval of fire protective products, Part 2: Reactive coatings for fire protection of steel elements*.
2. EN 1363-1 (2012): *Fire resistance tests – Part 1: General Requirements*, European Standard, CEN, European Committee for Standardization, Brussels.
3. EN 13381-8 (2013): *Test methods for determining the contribution to the fire resistance of structural members – Part 8: Applied reactive protection to steel members*, European Standard, CEN, European Committee for Standardization, Brussels.
4. EN 1363-2 (1999): *Fire resistance tests – Part 2: Alternative and additional procedures*, European Standard, CEN, European Committee for Standardization, Brussels.
5. Lucherini, A.; Giuliani, L.; Jomaas, G. (2018): *Experimental study of the performance of intumescent coatings exposed to standard and non-standard fire conditions*, Fire Safety Journal, 95, pp. 42-50.
6. Schaumann, P.; Weisheim, W. (2017): *Effect of heating rates in natural fires on the thermal performance of a solvent-borne intumescent coating*, 2nd International Fire Safety Symposium, Naples, Italy, 7th-9th June 2017, pp. 373-380.
7. Schaumann, P.; Tabeling, F.; Weisheim, W. (2016): *Numerical simulation of the heating behaviour of steel profiles with intumescent coating adjacent to trapezoidal steel sheets in fire*, Journal of Structural Fire Engineering, 7 (2), pp. 158-167.
8. Vyazovkin, S. (2015): *Isoconversional Kinetics of Thermally Stimulated Processes*, Springer International Publishing, Switzerland, DOI: 10.1007/978-3-319-14175-6.
9. EN 1991-1-2 (2010): *Eurocode 1: Actions on structures – Part 1-2: General actions – Actions on structures exposed to fire*, European Standard, CEN, European Committee for Standardization, Brussels.
10. EN 1993-1-2 (2010): *Eurocode 3: Design of steel structures – Part 1-2: General rules – Structural fire design*, European Standard, CEN, European Committee for Standardization, Brussels.

FIRE RESISTANCE OF TIMBER FRAME ASSEMBLIES WITH CAVITIES PARTIALLY FILLED BY INSULATION MATERIALS

Mattia Tiso¹, Alar Just²

ABSTRACT

The load-bearing capacity of timber frame assemblies (TFA) exposed to fire is influenced by the protective properties of cladding and cavity insulation. Current Eurocode 5 Part 1-2 includes an analytical design model for TFA exposed to standard fire exposure according to EN 1363-1, however it takes into account only the fire protection provided by stone wool products after that the cladding has fallen-off. An improved design approach which has the potential to consider the fire protection provided by a wider range of insulation products was recently presented. This improved design approach is composed of a methodology to evaluate the fire protection provided by a specific insulation product and an improved design model. Design model included in the Eurocode 5 Part 1-2 and improved design model are valid if cavities are completely filled with insulation. A design model for TFA with void cavities exists. In literature, information on the fire behaviour of TFA with cavities partially filled are still missing. In this paper, rules that allow the application of the improved design model for TFA with cavities partially filled by insulation materials are presented.

Keywords: timber frame assemblies; cavity insulation; insulation materials; fire resistance

1 INTRODUCTION

Timber frame assemblies (TFA) are composed of load-bearing timber members (beams or studs) covered by claddings or decking (*Fig. 1*). The space between two consecutive timber members might be filled with an insulation material, i.e. cavity insulation. In general, the fire resistance of TFA can be evaluated by means of (i) fire tests (ii) simplified design models and (iii) advanced calculations. Simplified design models are usually preferred by structural engineers because are easy-to-use tools. The behaviour of TFA in fire is influenced by both the protective properties of the cladding and the cavity insulation. The primary protection for a timber member is given by the cladding. The period in which charring of the timber member occurs while the cladding is still in place is considered as the protection phase, indicated as Phase 2. After the fall-off (failure) of the cladding, the secondary protection of the timber member might be provided by the cavity insulation. The period after the fall-off of the cladding is considered as the post-protection phase, indicated as Phase 3.

When the cavities of TFA are completely filled with insulation materials in addition to the protective effect of the cladding, the charring of a timber member is strongly dependent on the type of insulation used. Today, there are two design models available for the fire design of TFA with cavities completely filled. Annex C of the current Eurocode 5 Part 1-2 [1] presents a design model that considers the fire protection provided by stone wool products during protection and post-protection phases, while the

¹ PhD Student. Department of Civil Engineering and Architecture: Structural Engineering Research Group, Tallinn University of Technology, Estonia.

e-mail: tisomatt@gmail.com

² Professor. Department of Civil Engineering and Architecture: Structural Engineering Research Group, Tallinn University of Technology, Estonia.

Researcher, Safety, Fire Research, RISE Research Institutes of Sweden.

e-mail: alar.just@ttu.ee

fire protection provided by glass wool products is limited only to the protection phase. The European guideline Fire Safety in Timber Buildings (FSITB) [2] includes a design model that considers the contribution of glass wool insulation to the fire resistance also during the post-protection phase. All other types of insulation materials available on the market are excluded in the models described above.

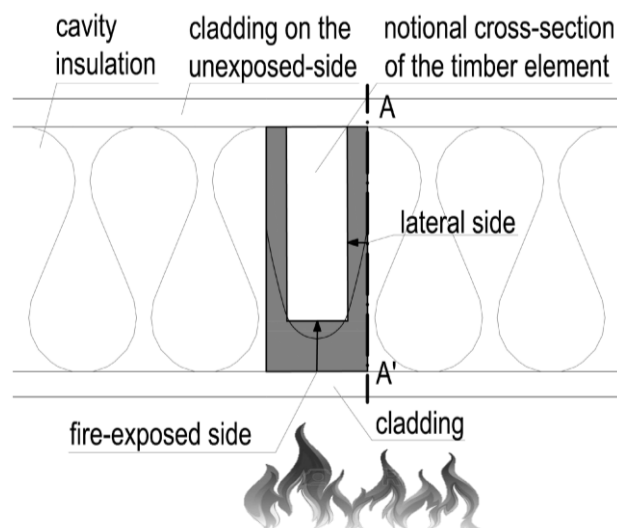


Fig 1. Cross-section of a timber frame assembly used as a floor.

A design model capable to evaluated the charring of TFA with void cavities also exists [3]. An improved design approach capable to take into account the fire protection provided a wider range of insulation products was presented by the authors of this paper [4,5]. This design approach is valid only if the cavities are completely filled by an insulation material. In this study, an extension of the improved design approach for timber frame assemblies with cavity partially filled by insulation material is presented.

2 IMPROVED DESIGN APPROACH FOR TIMBER FRAME ASSEMBLIES

The improved design approach is composed of a methodology to evaluate the fire protection provided by a specific insulation product and an improved design model.

2.1 Qualification methodology for cavity insulations

A methodology to evaluate the protection against the charring of timber elements provided by the cavity insulation was presented by the authors [4]. The main assumption was that the protection against charring provided by insulation materials can be viewed as a decrease in the heat flux affecting the sides of the beam. It was assumed that the protection against the heat flux coming from the sides ceases where charring occurs on the sides. Thus, the position of the 300°C isotherm on the interface between wood and insulation ($d_{300,s}$) was defined as an indicator of charring on the sides of the beam (line A-A' on Fig. 1), i.e. as an indicator of the loss of protection against charring given by an insulation material.

A criterion to distinguish the protection provided by different insulations based whether the 300°C isotherm on the interface between wood and insulation ($d_{300,s}$) exceed 100 mm or not was proposed [4]. The position of $d_{300,s}$ is evaluated using a specimen of floor to be tested in a cubic meter furnace. The specimen set-up includes a timber beam 45 mm wide and 145 mm depth, gypsum plasterboard Type F 15 mm thick as cladding on the fire side where its fall-off is imposed at 45 minutes. This methodology is meant to compare different insulation materials in a pre-defined test set-up. Differences in terms of charring of the timber elements that might occurred with different set-up (for example, a different cladding) are taken into account by the design model following explained.

Three different protection levels were proposed (from stronger to weaker):

- Protection Level 1 (PL1): insulation materials which allow less than 100 mm of charring depth on the sides ($d_{300,s} < 100$ mm) at 60 minutes of fire test.
- Protection Level 2 (PL2): insulation materials which allow 100 mm of charring depth on the sides during post-protection phase and before 60 minutes of fire test (line A on Fig. 2),
- Protection Level 3 (PL3): insulation materials which allow 100 mm of charring depth on the sides during the protection phase (line A on Fig. 2).

Insulation products as stone wool (SW) and high temperature mineral wool (HTE) are qualified as PL1. Glass wool (GF) and cellulose fibre (CF) insulation products are qualified as PL2, while extruded polystyrene (EPS) is qualified as PL3 [4].

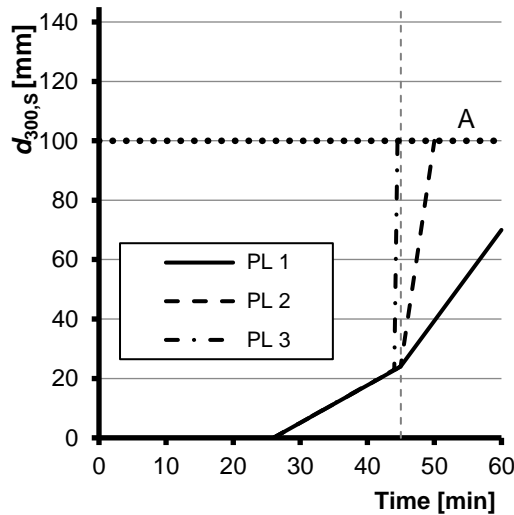


Fig. 2. Determination of protection level according to Ref. [4].

2.2 Design model for the load-bearing function

The improved design model for TFA [4,5] considers three possible charring scenarios:

1. If the cavities are completely filled with cavity insulation qualified as PL1 [4], charring occurs mainly on the fire-exposed side of the timber member, while the lateral sides are protected by the cavity insulation (Fig. 3a). Fire exposed side and lateral sides of the timber cross-section are defined in Fig 1.

2. If the cavities are completely filled with cavity insulation qualified as PL2 [4], charring is regarded from one side during the protection phase (Fig. 3b) and from three sides of the timber cross-section during the post-protection phase (Fig. 3c).

3. If the cavities are completely filled with cavity insulation qualified as PL3 [4], charring is regarded from three sides of the cross-section already during the protection phase.

The improved design model assumes that cavity insulations stay in place after the fall-off of the cladding. Provisions to ensure this assumption are currently under investigation.

The charring depth from the fire exposed side ($d_{char,1,n}$) can be calculated as follows:

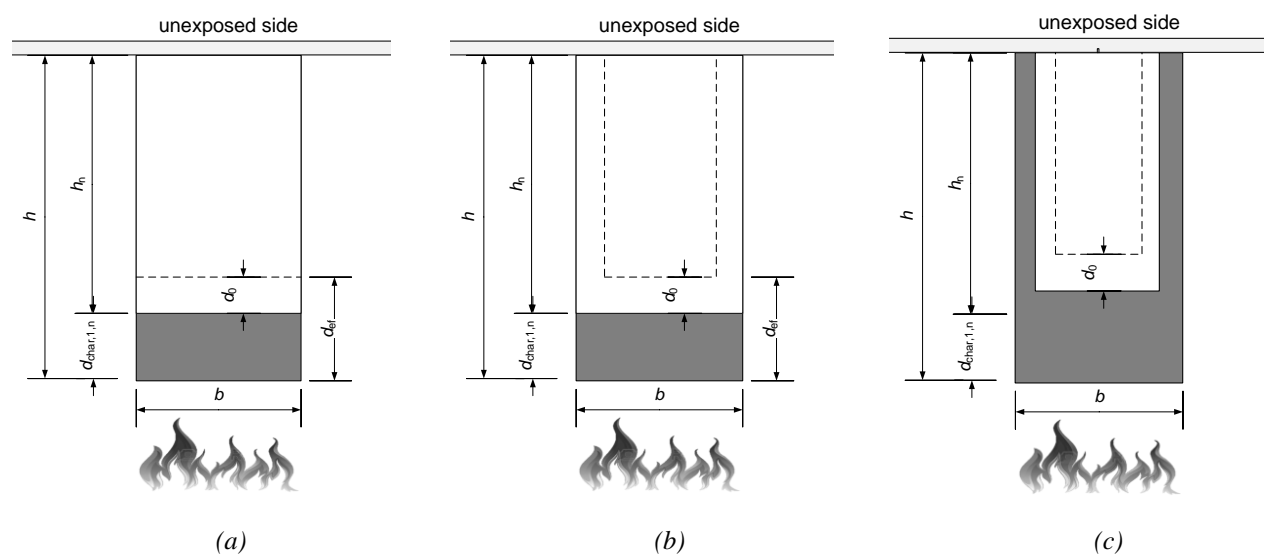
$$d_{char,1,n} = \beta_0 k_{s,n} k_2 (t_f - t_{ch}) + \beta_0 k_{s,n} k_{3,1} (t - t_f) \quad (1)$$

where β_0 is the basic design charring rate [6], $k_{s,n}$ is a cross-section factor used to consider the influence of cross-section width and depth on the charring rate, k_2 and $k_{3,1}$ describe different charring rates in the protection and post-protection phase, t_{ch} is the start time of charring from the fire-exposed side, t_f is the fall-off time of the cladding and t is the fire exposure time.

After the start of lateral charring, the charring depth on the lateral sides ($d_{char,2,n}$) can be evaluated as:

$$d_{char,2,n} = \beta_0 k_{s,n} k_{3,2} (t - t_{ch,2}) \quad (2)$$

where $k_{3,2}$ is the factor that considers the influence of the cavity insulation on the fire protection on the lateral sides, $t_{ch,2}$ is the start time of charring from lateral sides. The start time of charring of the lateral sides is assumed when $d_{300,s}$ has reached two third of the timber member depth [4,5].



KEY: h - initial depth of the beam, b - initial width of the beam, h_n - notional depth of the beam, $d_{char,1,n}$ - charring from the fire-exposed side, d_0 - zero-strength layer.

Fig. 2. Improved design model for TFA with (a) PL1 cavity insulation; with PL2 cavity insulation (b) before and (c) after that start time of charring from lateral sides has occurred.

To evaluate the load-bearing capacity of a timber member exposed to fire, one subtracts the notional charring depth, a reduction of strength and stiffness properties of the uncharred wood has to be taken into account. In the effective cross-section method (ECSM), the reduction of mechanical properties is taken into account by an additional fictive layer called “zero-strength layer”. An effective charring depth (d_{ef}) can be calculated by increasing the notional charring depth by a zero-strength layer (d_0):

$$d_{ef} = d_{char,n} + d_0 \quad (3)$$

The cross-section reduced by the notional char layer and the zero-strength layer is defined as the effective cross-section, in which the strength and stiffness properties of the timber are considered as at ambient temperature.

In the case of TFA with cavity insulations qualified as PL1, notional charring of the timber member and zero-strength layer depth are considered only from the fire-exposed side (see Fig. 2a) during the total time of fire exposure. For TFA with PL2, zero-strength layers have to be subtracted from three sides (as shown in Fig. 2b and Fig. 3c) during the total time of fire exposure.

Values of the post-protection factors ($k_{3,1}$ and $k_{3,2}$) to be used in the improved design model for timber frame assemblies with cavity completely filled by GW, HTE and CF products have been published [5]. Expressions to evaluate the depths of the zero-strength layer for timber frame assemblies with SW and HTE cavity insulations and for different load conditions were also proposed by the authors [7].

3 TIMBER FRAME ASSEMBLIES WITH CAVITIES PARTIALLY FILLED

Often, timber frame assemblies are constructed with cavities partially filled by insulations. In this study, TFA with cavities partially filled are investigated by means of heat-transfer simulations. The position of the 300°C isotherm on the interface between wood and insulation ($d_{300,s}$) for different configurations are evaluated and compared with the configuration of cavities completely filled. Design rules for different configurations of TFA with cavity partially filled are investigated.

3.1 Heat-transfer analysis

Two-dimensional (2D) models were implemented in the SAFIR software package [8]. Different configurations of the cavity insulation were investigated: Configuration 1 where the cavity is completely filled (*Fig 4a*), Configuration 2 where 2/3 of the cavity depth is filled with insulation toward the fire-exposed side (*Fig 4b*) and Configuration 3 (*Fig 4c*) where a strip of insulation is placed against the lateral side of the timber member. For the Configuration 3, the insulation strip had the same depth of the cavity, while four different width were investigated: 50 mm, 100 mm, 120 mm and 150 mm. Configuration 1 is representative of the fire test conditions necessary to evaluate the protection level of an insulation material according to Ref. [4]. In all the heat-transfer analysis, HTE as insulation was considered. This insulation product is qualified as PL1 [4].

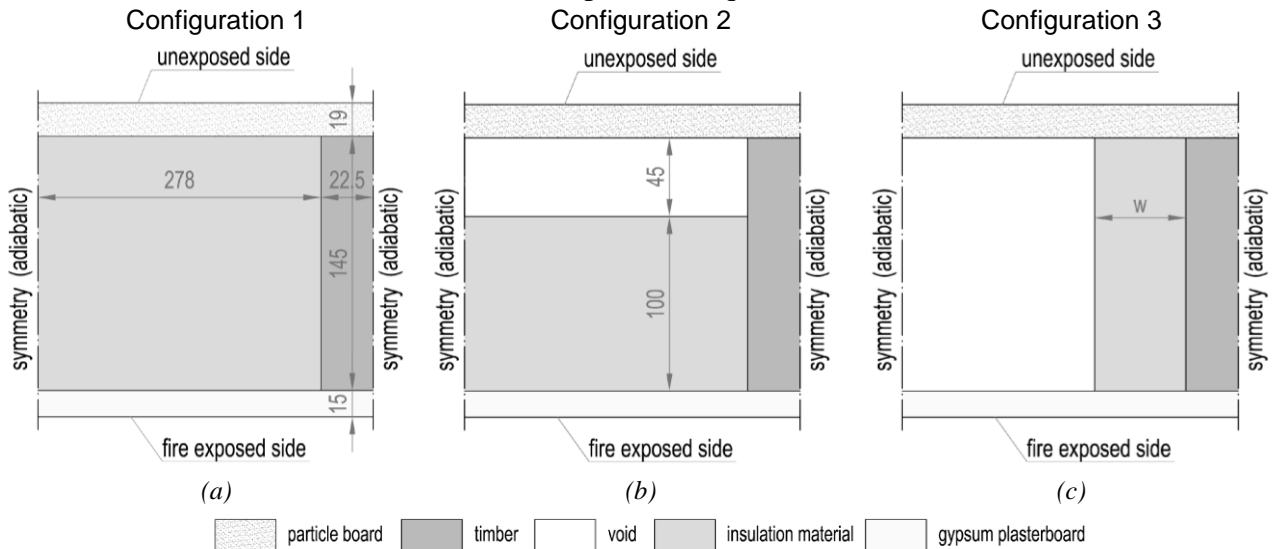


Fig. 4. Schematization of the heat-transfer analysis with (a) cavity completely filled; with (b) 2/3 of the cavity depth filled and with (c) insulation strip applied on the lateral side of the timber member.

The thermal exposure was described by means of the ISO 834 standard fire time-temperature curve [9]. The heat transfer by convection and radiation to the fire-exposed side of the model was considered using a convection coefficient of 25 W/m²K and an emissivity of 0.8, as prescribed in Eurocode 1 Part 1-2 [10]. The heat-transfer through the timber member was modelled using the effective thermal properties of timber given in Eurocode 5 Part 1-2 [1]. Effective thermal properties of HTE insulations were calibrated for this study. Gypsum plasterboards and particle board were described using the effective thermal properties given in FSITB [2]. The heat-transfer calculations considered 60 minutes of fire exposure.

3.2 Results

The position of the 300°C isotherm on the interface between wood and insulation ($d_{300,s}$) as function of the time was evaluated for all the heat-transfer analysis performed. Results are shown in *Fig. 5*. In the Configuration 1, the position of $d_{300,s}$ was less than 100 mm at 60 minutes. Also in the Configuration 2 and Configuration 3 with a strip of insulation 150 mm wide the position of $d_{300,s}$ was less than 100 mm at 60 minutes. While in the Configuration 3, when the insulation strips are 50, 100 and 120 mm wide, the 300°C isotherm on the interface between wood and insulation has reached a depth of 100 mm between 45 and 60 minutes.

By applying the criteria to evaluate the protection level of an insulation to the Configuration 2, it is possible to observe that a cavity insulated by 2/3 of the depth with the insulation toward the fire-exposed side guarantee the same protection level of the cavity fully insulated.

Regarding the Configuration 3, to guarantee the same protection level of a fully insulated cavity, the insulation strip should be at least 150 mm wide.

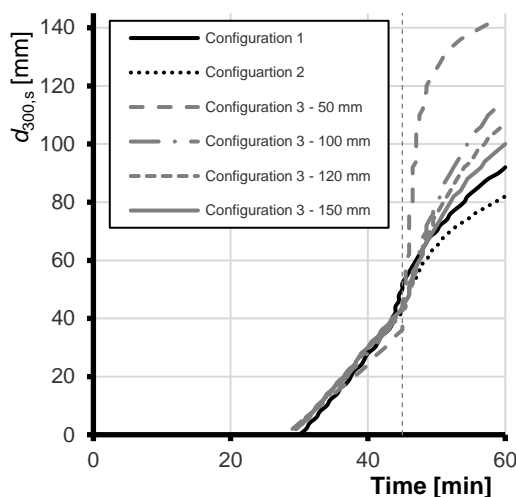


Fig. 5. Position of the 300°C isotherm on the interface between wood and insulation ($d_{300,s}$) as function of the time evaluated by means of heat-transfer analysis.

3.3 Design prescriptions for timber frame assemblies with cavity partially filled

The improved design model is valid if cavities of TFA are completely filled with an insulation material. Based on the results of the heat-transfer analyses carried out in this study, different strategies can be adopted to use the improved design model for TFA when cavity are partially filled.

Design rules for TFA insulated with PL1 cavity insulations can be used when:

- strips of an insulation material qualified as PL1 with the same depth of the timber members and at least 150 mm wide are applied on the sides of the timber members,
- the cavities are filled with an insulation material qualified as PL1 by 2/3 of the cavity depth and the insulation is placed against the cladding exposed to fire.

Design rules for TFA insulated with PL2 cavity insulations can be used when:

- strips of an insulation material qualified as PL1 with the same depth of the timber members and width comprised between 50 and 150 mm are applied on the sides of the timber members.

Once applied strips on the sides of timber element, the rest of the cavity might be not filled, partially filled or completely filled with a different insulation product.

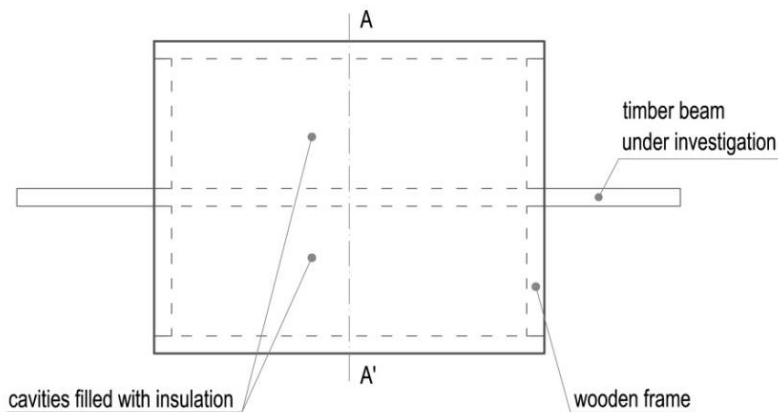
The improved design model assumes that the insulation remains in the cavity after the fall-off of the cladding. To ensure the validity of the improved design model, insulations strips have to be fixed on the sides of the timber members. Prescriptions to prevent the fall-off of the cavity insulation after the fall-off of the cladding are currently under investigation.

4 REFERENCES FIRE TESTS

Two cubic-meter furnace tests were performed as a benchmark for the heat-transfer analysis. The two tests presented the same configuration. Specimens were composed of a wooden frame (dimensions 800×1000 mm) with a massive timber beam (cross-section dimensions 45×145 mm) present in the middle of the frame, as shown in Fig. 6. The two cavities adjacent to the beam measuring 333×910 mm, were completely filled with the HTE insulation. The two insulation batts were 5 mm larger than the cavity in both directions (final dimensions 338×915 mm). The exposed side of the assembly was protected by a 15-mm thick gypsum plasterboard (Type F) held by a metal fastening system. On the unexposed side, a particle board with the thickness of 19 mm was placed.

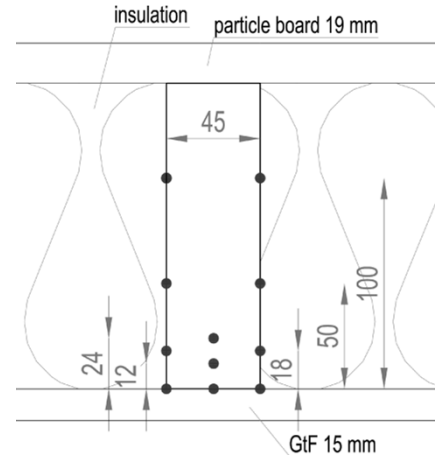
The specimens were subjected to standard fire exposure conditions in accordance with EN 1363-1 [11]. Thermal action was controlled by means of two plate thermometers installed in the cubic meter furnace. In both tests, the fall-off of the gypsum plasterboard was imposed at 45 minutes from the beginning of the test. The tests were interrupted at 60 minutes.

TOP VIEW



(a)

SECTION A-A'



(b)

Fig. 6. Test specimen for the cubic-meter furnace: (a) top view; (b) position of thermocouples on the timber beam cross-section.

In both tests, the position of the 300°C isotherm on the interface between wood and insulation ($d_{300,s}$) was evaluated by means of thermocouple measurements. The position of $d_{300,s}$ as function of the time evaluated in the fire tests are compared with results obtained from the heat-transfer analysis of Configuration 1 (see Fig. 7).

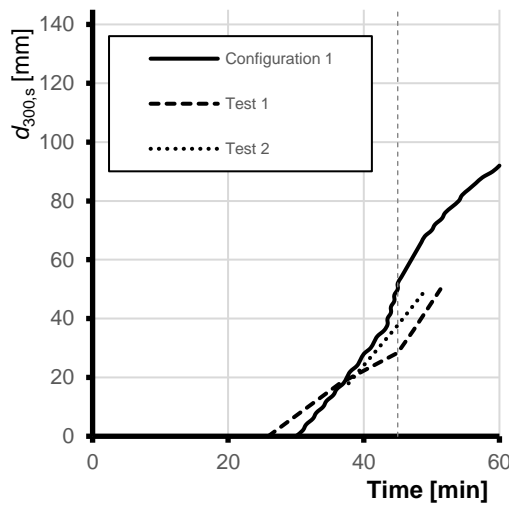


Fig. 7. Position of the 300°C isotherm on the interface between wood and insulation ($d_{300,s}$) as function of the time evaluated in the heat-transfer analysis of Configuration 1 compared with cubic-meter furnace tests results.

After 60 minutes of fire exposure, the position of $d_{300,s}$ did not reach 100 mm in both tests. The results of $d_{300,s}$ as function of the time evaluated by means of heat-transfer analysis show good agreement with fire test results.

5 CONCLUSIONS

The purpose of this study was to extend the application of the improved design model also to TFA where the cavities are partially filled with insulation materials. Heat-transfer analyses of different configurations of TFA with partially filled cavities were performed. For each configuration the position of the 300°C isotherm on the interface between wood and insulation ($d_{300,s}$) was evaluated as function of the time.. By this parameter, it was possible to verify if it is possible to evaluate the

charring on the timber member for the TFA with partially filled cavities by using the improved design model [4].

Furthermore, design prescriptions that allow the use of the improved design model also to predict the fire resistance of TFA with cavities partially filled have been provided. These rules are valid if the insulation material which protect the timber members against the charring is qualified as PL1 according to Ref. [4].

To validate the results of the heat-transfer analysis, two cubic-meter fire tests have been performed. Further studies will be focused on the definition of design requirements to prevent the fall-off of the cavities insulations after the fall-off of the cladding. This research will serve as a basis for future studies on behaviour of timber frame assemblies with cavities partially filled exposed to fire.

ACKNOWLEDGMENT

The authors acknowledge the network of COST Action FP1404 for the contribution of the Task Group 5 within the Working Group 2 “Structural Elements made of bio-based building materials and detailing”. This work was supported by the Estonian Research Council grant PUT 794.

REFERENCES

- 1 CEN, European Committee for Standardization (2004). *EN 1995-1-2:2004. Eurocode 5 - Design of timber structures - Part 1-2 - General: Structural fire design.*
- 2 Birgit Östman, Esko Mikkola, René Stein, Andrea Frangi, Jürgen König, Dhionis Dhima, Tuula Hakkarainen, Julie Bregulla (2010). *Fire safety in timber buildings: technical guideline for Europe*, SP Technical Research Institute of Sweden, Borås, Sweden.
- 3 Andrea Frangi, Carsten Erchinger, Mario Fontana (2008). *Charring model for timber frame floor assemblies with void cavities*, Fire Saf. J. 43 551–564. doi:10.1016/j.firesaf.2007.12.009.
- 4 Mattia Tiso, Alar Just (2017). *Fire Protection Provided by Insulation Materials—A New Design Approach for Timber Frame Assemblies*, Struct. Eng. Int. 27 231–237. doi:10.2749/101686617X14881932435899.
- 5 Mattia Tiso, Alar Just (2017). *Design criteria for insulation materials applied in timber frame assemblies*, J. Struct. Fire Eng. doi:10.1108/JSFE-01-2017-0015.
- 6 Michael Klippel, Joachim Schmid (2017). *Design of Cross-Laminated Timber in Fire*, Struct. Eng. Int. 27 224–230. doi:10.2749/101686617X14881932436096.
- 7 Mattia Tiso, Alar Just, Michael Klippel, Joachim Schmid, Daniel Brandon (2017). *Zero-Strength Layers for Timber Frame Assemblies in a Standard Fire*, in: Proc. 4th INTER Meet., Kyoto, Japan.
- 8 Jean-Marc Franssen (2005). *SAFIR: A thermal/structural program for modeling structures under fire*, Eng. J.-Am. Inst. Steel Constr. Inc. 42 143–158.
- 9 ISO International Organization for Standardization (1999). *ISO 834-1:1999: Fire Resistance Tests – Elements of Building Construction – Part 1: General Requirements.*
- 10 CEN, European Committee for Standardization (2003). *EN 1991-1-2:2003. Eurocode 1 General Actions – Part 1-2 - Actions on structures exposed to fire.*
- 11 CEN, European Committee for Standardization (2012). *EN 1363-1:2012. Fire resistance tests - Part 1: General Requirements.*

THE USE OF FURNACE TESTS TO DESCRIBE REAL FIRES OF TIMBER STRUCTURES

Joachim Schmid¹, David Lange², Johan Sjöström³, Daniel Brandon⁴, Michael Klippel⁵, Andrea Frangi⁶

ABSTRACT

Fire resistance is an important characteristic for all building structures regardless the building materials used. Methodologies for fire resistance testing were developed already before 1900 to measure the response of the structure in fire and compare different products. In the last decade, the increased popularity of timber buildings has led to a renewed interest in the performance of timber structures in fire and timber products were frequently tested in furnaces. Recently, fire resistance testing in furnaces for timber products was questioned in general and in particular the *thermal exposure* which might be different for combustibles and incombustibles in furnaces and combustibles in furnaces and real fires. Other critics mentioned that burn-out cannot be tested in furnaces which are the basis in the current fire resistance framework. This paper investigates the validity of furnace resistance testing for combustible products and its limitations. It is shown that, firstly, the thermal exposure in fire resistance tests of incombustibles and combustibles are similar. Secondly, in addition to *thermal exposure*, the term *fire exposure* should be introduced where the oxygen content is described in addition, as the oxygen content significantly influences the behaviour of combustible material in fires. Thirdly, the furnace and compartment environment in flash-over fires is similar with respect to this *fire exposure*. Finally, it is not possible to directly use furnace test results to predict a compartment response in real fires including the cooling phase but recent investigations indicate that results from fire resistance tests can be used to predict burn-out.

Keywords: Structures, compartment fires, fire resistance tests, timber, combustibility

1 INTRODUCTION

The framework for fire resistance design based on testing was developed between 1900 and 1946 [1, 2, 3, 4]. Recently, results of fire resistance tests for combustibles came into question [5]; it was mentioned that thermal exposure in real fires is different from fire resistance tests. Recent discussions claim that burn-out (cooling phase without re-ignition towards the ambient conditions; without intervention) is a requirement of fire safety design using the standard fire tests as the basis for fire resistance design. In discussions at the world conference on timber engineering (WCTE

¹ Research assistant, PhD Candidate, ETH Zürich, Switzerland.

e-mail: schmid@ibk.baug.ethz.ch

² Senior Lecturer, School of Civil Engineering, Faculty of Engineering, Architecture and Information Technology, University of Queensland, Brisbane, Australia.

e-mail: d.lange@uq.edu.au

³ Senior researcher, RISE, Research Institutes of Sweden, Risk and Safety, Borås, Sweden.

e-mail: johan.sjostrom@ri.se

⁴ Senior researcher, RISE, Research Institutes of Sweden, Risk and Safety, Stockholm, Sweden.

e-mail: daniel.brandon@ri.se

⁵ Senior researcher, ETH Zürich, Switzerland.

e-mail: klippel@ibk.baug.ethz.ch

⁶ Professor, ETH Zürich, Switzerland.

e-mail: frangi@ibk.baug.ethz.ch

2016, Vienna), it was stated that fire resistance tests were intended for incombustible products only as combustibles provide a contribution to the fire during the tests – thus, the applicability of furnace test results is limited to incombustibles only.

In early codes, there was no knowledge that fire temperatures may deviate in different fires [6]. In 1903, one of the first codes with respect to fire design specified six different categories of protection level depending on how much the building owner would like to afford for it [8]. In the beginning of fire resistance testing, temporary furnace compartments were erected for testing and mean temperatures (e.g. 926°C [7]) were specified [8]. Most likely after the introduction of industrial burners, a time-temperature curve was introduced.

In 1916, the ASTM standard fire temperature-time curve, originally indicated as *Columbian Curve*, was presented [8], see Figure 1. Aiming for a measure of comparison, Ingberg [2] performed burn-out tests in non-combustible buildings which lasted up to 28h. The authors of this paper expect that the long testing times are a result of a limited combustion rate of the fire load (stacked paper files) used. Subsequently, fire durations corresponding to the fire load equivalent fire durations of 1 to 4.5 h (incombustible furniture) and 7.5 h (combustible furniture) were proposed for office buildings. Based on these findings, fire-resistance classifications were proposed [3]. For *Fireproof Construction*, a fire resistance rating of 1 h was requested based on the available fire load (approx. 770 MJ/m² floor surface), which corresponds to the mean value for residential buildings required in Eurocode [18]. Only this type is acknowledged to withstand burn-out (complete combustion of the interior); an upper limit of 4 h for higher loads was seen more reasonable for this type based on UK tests [4]. Further, [3] introduces the term of *fire severity* in *fireproof construction* simply as result of the available fire load and the comparison of the standard temperature-time curve and Ingberg's curves including the cooling phase; it is a value between 0.5 h and 7.5 h [3]. The standard [3] refers to a large range of data sources, among others, fire resistance tests with timber columns.

In Europe, the first building regulation referring to the concept of *fire severity* was published in 1946 [4]. The code introduces three grades of occupancies with respect to the available fire load, i.e. (I) low, (II) moderate and (III) high fire load and inherits the concept of the *fire severity*. As simplification, with respect to the three grades (I), (II) and (III), the requirement for the fire resistance is set to one, two and four hours respectively. Further, the measures of firefighting services are acknowledged. It should be highlighted that -historically- the fire resistance testing was introduced for buildings typically not rated as *fireproof structures*, this means, for buildings which are not required to survive a burn-out [3].

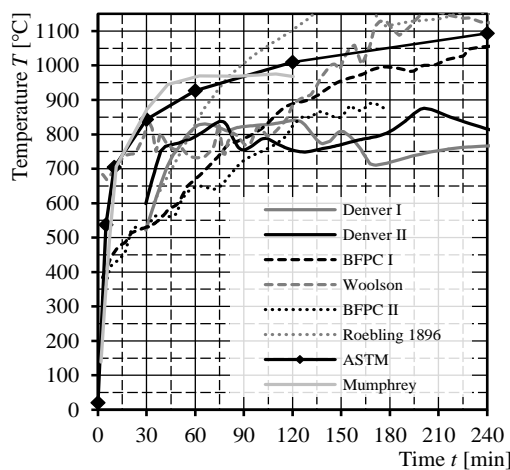


Fig. 1. Standard fire curve from 1916 (ASTM) and earlier test curves. Reproduced from [6].

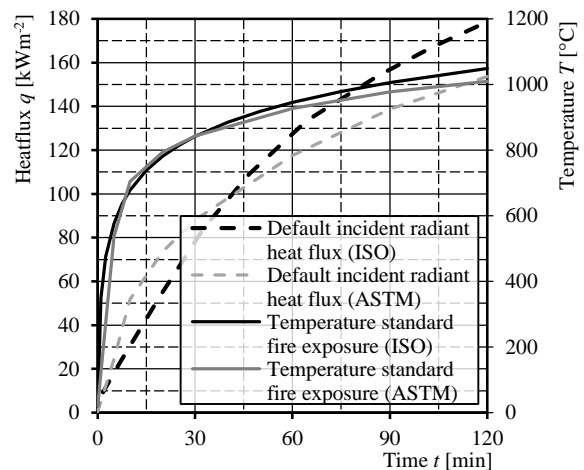


Fig. 2. Standard fire and default heat flux measurements during standard fire tests acc. to ISO 834 [1] and ASTM E119 [7].

Currently available standard fire temperature-times according to EN/ISO and ASTM and corresponding default incident radiant heat fluxes ($\dot{q}'' = \sigma \cdot T^4$) are shown in Figure 2. Differences for the EN/ISO and ASTM time temperature curve are very limited which is also valid for default incident radiant heat fluxes. However, it should be noted that direct measurements of the latter with water cooled heat flux sensors may include uncertainties as the sensor's surface temperature may differ from the test specimen's surface [9]. Summarizing the critics, an attempt to create a common understanding is made based to the following questions.

- I. How is thermal exposure defined?
- II. Why is the burner fuel load different for tests with combustibles and incombustibles?
- III. Are combustible products changing the thermal exposure in standard furnace tests?
- IV. To what extent can standard furnace tests describe real fires?

2 AVAILABLE DATA AND COMPLEMENTARY DATA AQUISATION

The literature was consulted with respect to a general but basic definition of the thermal exposure, e.g. [10]. It was decided to perform tests in different scales with instrumentation exceeding standard tests (additional gas analyser, heat flux sensor, mass, fuel flow, internal specimen temperatures) and to test combustible (C) and incombustible (IC) products, represented by solid timber panels (STPs, C), cross-laminated timber panels (CLTs, C) and concrete (IC). With the exception of the compartment tests, all tests performed followed the EN/ISO standard fire [1]:

- *Ten model scale tests (~1 m²) following the standard fire with CLT and STPs. Tests covered combustible and incombustible surfaces. Results were compared to a database of tests with concrete slabs;*
- *Two large scale tests (~15 m²) one with STP and one with a concrete slab;*
- *Two compartment fire tests with partially protected CLT elements.*

3 FIRE TESTS

3.1 Model scale fire resistance tests

Test data of more than 30 fire resistance tests performed in the same furnace was analysed in order to investigate the burner fuel consumption of tests done with IC and C. To extend data from the literature [8], ten model scale tests (specimen size approximately 1 m²) were conducted [9]. Except one STP, all specimens were tested without any protection, i.e. with combustible surface. Test results were heat flux sensor measurements (see *Fig. 3*), temperature measurements in the furnace compartment (plate thermometers and wire thermocouples $A=0.4 \text{ mm}^2$) and in the specimen. For CLT, internal thermocouples were installed during production to avoid dispositioning of the measurement point due to drilling errors and to keep the thermocouples parallel to the isotherms which is needed when highly conductive thermocouple elements are inserted in low conductive material such as wood [11]. Heat flux sensor measurements flush with the specimen' surface are plotted in *Fig. 3* together with data from the literature [8]. In addition, measurements below the control devices of the furnace were taken, results agreed well with the data presented in *Fig. 3*. The oxygen content was analysed in different positions, while it was about 5% in the furnace compartment, at the surface it was about zero throughout the test, see *Fig. 4*. Additionally, the mean gas velocity was estimated to exceed 3m /sec. The burner oil consumption of the tests of this study were compared to data obtained in the same furnace. Trend lines are significantly different of IC and C, which are about 50% of the IC specimen, see *Fig. 5*. One test with STP was performed with an incombustible surface (applied protection using a mineral bound lining) which is indicated as IC-C. Fall-off of the protection was initiated manually at about 100 min to observe the change of

burner fuel flow. The mass loss of the C specimens was considered as wood fuel and is plotted in Fig. 6 in addition to the particular fuel consumption. It can be seen that about 20% (in tests presented here) can be assigned to the typically reduced thermal inertia of Cs.

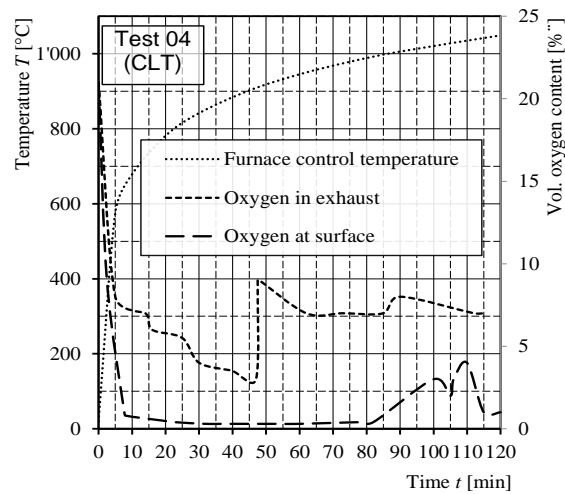
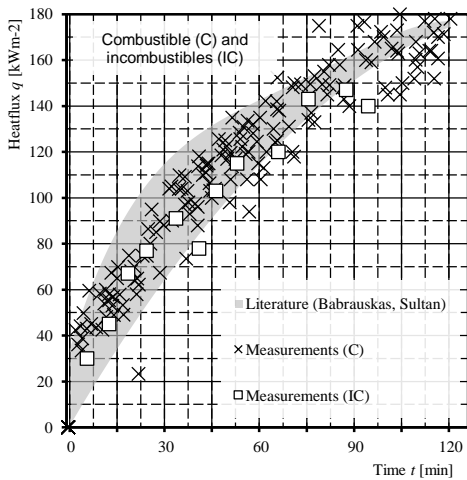


Fig. 3. Heat flux sensor measurements for all tests. Fig. 4. Oxygen content measurements during a furnace test with a Combustibles (C) and incombustibles (I) of the tests performed for this study [9] and marked area for measurements found in literature [8].

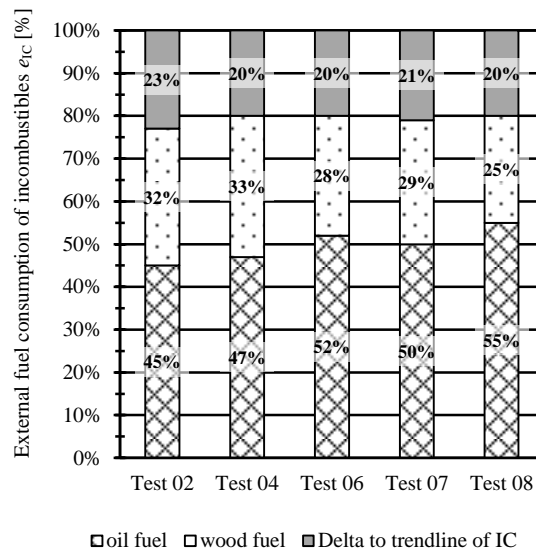
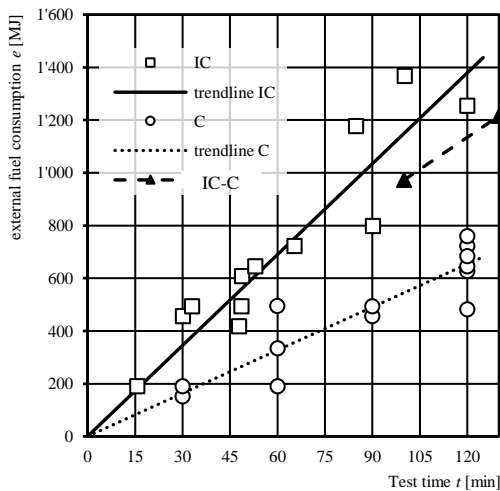


Fig. 5. Burner oil fuel consumption of incombustibles (IC) and combustibles (C) with trend lines [9].

Fig. 6. Percent of burner oil and wood fuel of 120 min fire resistance tests with solid wood panels (C) and difference to the estimated value for a concrete specimens (IC) [9].

3.2 Large scale fire resistance tests

Two large-scale fire tests (specimen size 5m x 3m) were performed on a full-scale furnace with a concrete slab (IC) and a Solid Timber Deck Plate (STP, C) [11]. Both tests lasted 90 min and were equipped with a large number of temperature measurement devices (standard plate thermometers (PT) and sheathed thermocouples) and oxygen measurement probes. The temperatures of PTs were more uniform in the test C compared to test IC, see Fig. 7, while the oxygen content was around 5% in the test IC, the average was about 2% in the test C. For the test C, the measurements closer to the surface were generally lower than in the centre of the surface and in the exhaust duct, see Fig. 8. Additionally, the gas velocity was estimated on average to about 1 m/sec. PTs installed at the IC specimen's surface showed not higher temperatures than the control PTs.

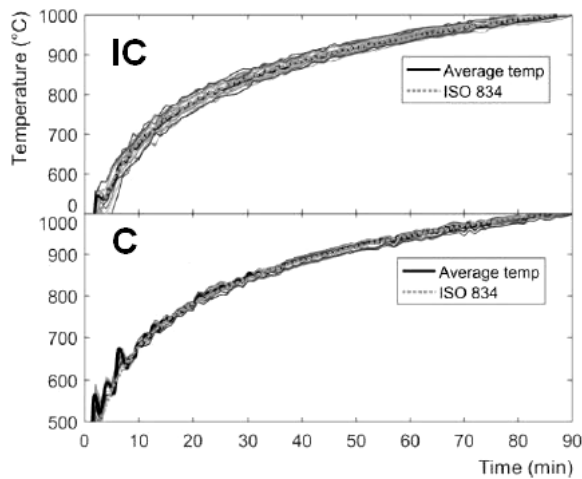


Fig. 7. Temperature development in the full-scale furnaces of the tests with IC (concrete) and C (STP) slabs.

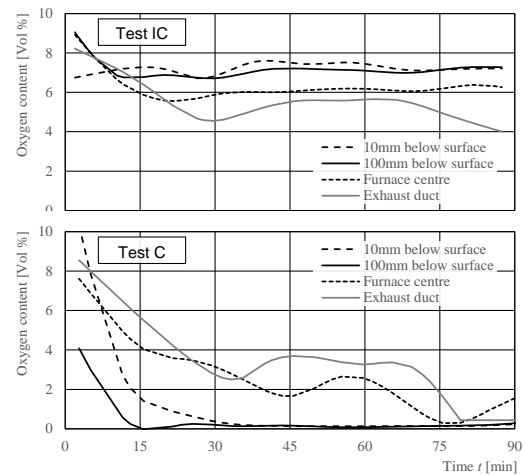


Fig. 8. Oxygen content development in the full-scale furnaces of the tests with IC (concrete) and C (STP) slabs.

3.3 Compartment fire test

Compartment (or room) fire tests have been performed in the past at various research institutes. While many test (series) aimed for convincing the fire brigades that extinguishing the fire in buildings made from combustible materials is not more complicated than for those made from incombustibles, e.g. [12], tests that are more recent aim for testing of other characteristics such as the burn-out and behaviour of glued timber products such as CLT in more realistic fires.

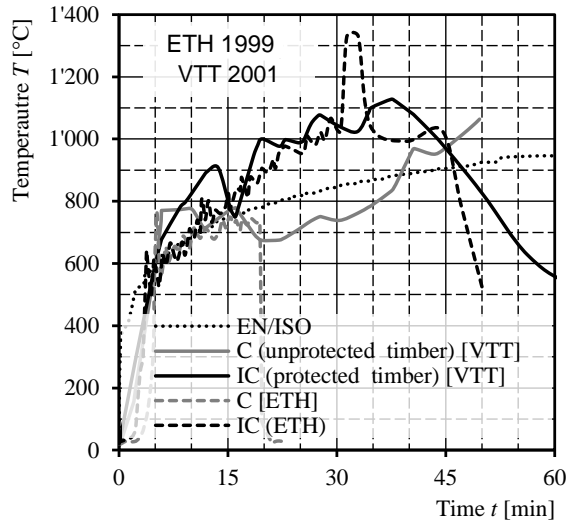


Fig 9. Temperature development in 60min compartment tests with surfaces C (combustible) and IC (incombustible) in timber compartments; CLT and TF (timber frame). Data [16].

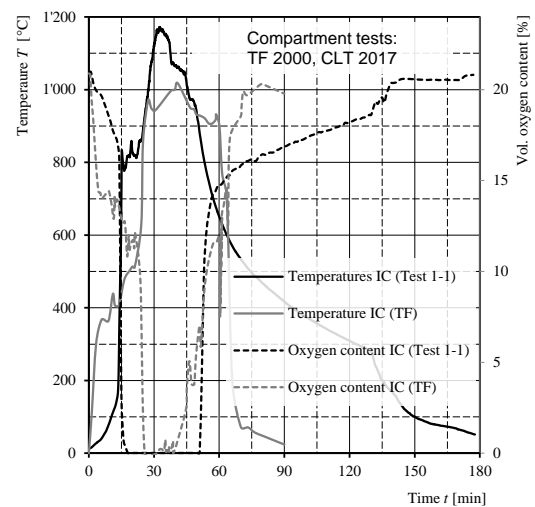


Fig 10. Temperature and oxygen content during a fire test tests with surfaces C (combustible) and IC (incombustible) in timber compartments; CLT and TF (timber frame). Data from [12,14].

With respect to the temperature development, the thermal inertia of the compartment's surfaces is obviously influencing the compartment temperature. The combustibility has no significant influence on the compartment temperature which is shown in Fig 9. In general, the essentials for combustion are (i) an energy source (ii) the available of fuel and (iii) the availability of sufficient oxygen; thus, the need for oxygen measurements especially for combustible products in fire tests is obvious [15] but rarely never measured. Fig 10 gives an example of the oxygen content in the compartment; it is close to zero during the fully developed fire. During this phase, the *fire exposure* is similar to the test environments in furnace tests, see Section 3.1 and 3.2. Thus, in this phase no flames occur at the surface of the timber elements, which would require an oxygen content significantly higher than

10% [9]. More recent compartment tests [14] investigated the oxygen content and the temperatures of CLT compartments without any intervention of fire brigades. The development of the oxygen content is similar to furnace tests; at flash-over, corresponding to the sudden temperature increase, the oxygen content drops and rises not before the compartment temperature decreases again.

4 RESULTS AND DISCUSSION

The thermal exposure can be defined as the combination of gas and radiation temperature, alternatively the gas temperature and the incident radiant heat flux. They are to be combined with an appropriate thermal boundary condition (BC). BCs prescribing the surface temperature (Dirichlet BC) or prescribing the surface heat flux (Neumann BC) are of limited use in fire safety design as other factors (re-radiation at the surface, convection) influence the heat transfer to any solid. The most general BC, the natural BC is applicable for fire safety design but contains depending variables difficult to measure or estimate (surface temperature, convective heat transfer coefficient) which may be difficult to solve. In fire conditions (furnaces and compartment fires) the gas- and surface temperature might be close to each other reducing the effect of the convection which is not the case in ad-hoc tests with radiant heat sources or cone heater tests where typically the gas temperature remains low.

In heat flux sensor measurements presented in Section 3.1, it is shown that there is no difference for specimens with different combustibility, which is obvious as the PT is a proxy for the incident radiant heat flux; all data is in line with the literature [3,4]. Thus it can be concluded, considering the uncertainty of the typically water cooled heat flux sensors, IC and C elements are exposed in furnace tests to the same thermal exposure measured with and at the control devices (PTs) if C specimens don't burn undetected behind the PTs. Heat flux sensor measurements at different positions below the specimens C in the model scale tests (Section 3.1) -flush, behind and in front of the control PT- did not show higher measurements when placed flush with the surface of the C specimens. In the large-scale test (Section 3.2), additional PTs were installed without distance to the test specimen. PT measurements close to the specimen's surface did not measure more than the control PTs. It can be concluded, that there is no flaming combustion at the surface which would add radiation energy to the specimen without being detected by the PTs. It is reported that flaming combustion would require an oxygen content of 14% [16], a value which can't be measured near the surface of the combustible specimen or in the furnace. However, at the moment it is not clear if the low oxygen content at the surface can be used as a proof for no flaming combustion.

That the burner fuel is reduced when Cs are tested is obvious as they contribute to the heating of the (furnace) compartment. However, a certain share (ca. 20% in tests presented here) can be assigned to the typically reduced thermal inertia of Cs.

The authors conclude that besides the description of the thermal load by the *thermal exposure*, the oxygen content is of significant importance for the fire safety engineering and propose to introduce the term *fire exposure* in addition where the oxygen reaction between the surface and the compartment are described. The oxygen content during *fire exposure* is the key measure for the link between furnace tests and compartment fires. Thus, as long as the *fire exposure* is similar, i.e. during the fully developed phase, furnace tests provide a similar test environment regardless the combustibility of the products. The fuel provided by the C elements in the furnace tests would also deliver fuel in compartment fires. However, as the oxygen inflow is limited, no higher burning rate is expected rather than more combustion outside of the compartment [16].

Regardless the combustibility, a standard fire test cannot estimate the behaviour of a construction in the cooling phase. Generally, the fall-off of charred lamellae of glued engineered products (which can happen in case of CLT) counteract the capability of a burn-out but might be required by authorities for certain buildings. Recently, it was shown that mass-loss measurements of non-glued solid timber plates (about 15kg/m²h without fall-off of charred parts) in standard fire resistance tests

could be used as benchmark to verify the behaviour of CLT with regard to fall-off of charred parts; research is currently performed and results will be presented at WCTE 2018 [17].

5 CONCLUSIONS

Based on the results presented in this paper, using the literature and additional fire tests, we conclude that the fire resistance furnace is a suitable tool for studying the response of incombustible and combustible construction as long as the fire exposure (thermal exposure and oxygen content) is similar. In particular, with respect to the above introduced research questions, the following can be stated:

I. How is thermal exposure defined?

Thermal exposure is defined as the combination of the gas and radiation temperature (alternatively the combined gas temperature and the incident radiant heat flux). In fire resistance tests, the control devices ensure the same thermal exposure regardless the combustibility of the specimen. Obviously, specimens made from different materials may absorb different heat fluxes (absorbed heat flux) as this is depending on the material characteristics (thermal inertia; surface temperature) but not due to surface flaming which can't be observed in fire resistance furnace tests.

II. Why is the burner fuel load different for tests with combustibles and incombustibles?

Burner fuel load in fire resistance furnace tests varies quite considerably when testing C and IC. Shares are depending on the particular test equipment (e.g. furnace lining) but were estimated in study. For combustibles, only 50% of the burner fuel was needed which is a result of the additional fuel provided by the specimen, ca. 30%, and differences in the thermal inertia which account for about 20% of the burner fuel difference.

III. Are combustible products changing the thermal exposure in standard fire resistance furnace tests?

Based on the definition of thermal exposure presented above, the combustible products do not change the thermal exposure in a fire resistance furnace tests. No undetected surface flaming behind the furnace control devices is possible due to the limited oxygen content.

IV. To what extend can fire resistance furnace tests describe real fires?

Generally, it can be stated that fires in different and exactly the same compartments show a large natural scatter, thus, aiming for an exact replication of a fire development seems to be unreasonable. Thus, it should be aimed for quantitative description– or simulation- of a fire. Besides the *thermal exposure* it seems to be reasonable to define the *fire exposure* where in addition the oxygen content is described. Given the similar *fire exposure* in fire resistance furnace tests and compartment fires, it is reasonable to use fire resistance furnace tests to simulate compartment fires and the structural response of the elements in this environment. However, as the oxygen content has an impact on the behaviour of (combustible) elements, furnace tests cannot simulate the cooling phase. Thus, the validity of furnace test (results) seem to be limited to the phase of the fully developed fire. For some building types, burn-out (cooling phase without re-ignition towards the ambient conditions; without intervention) may be required. To ensure this, additional means should be taken. At the moment, it does not seem reasonable that burn-out can be guaranteed when tested in compartment test as these tests are not well controlled and ventilation conditions in tests may deviate considerably from real compartments. To solve this interaction of the specimen with the compartment further research is needed.

ACKNOWLEDGMENT

The authors would like to acknowledge the framework COST FP1404 that helped defining and discussing the research question. Further, all colleagues who helped obtaining and/or analysing the data; these are M. Tiso, R. Fahrni, V. Cullen, N. Werther and P. Morf.

REFERENCES

1. ISO 834-1, Fire resistance tests, Geneva, Switzerland, 1999.
2. Ingberg SH. Tests of the severity of building fires. *NFPA Quarterly*. 1928 Jul;22(1):43-61.
3. Dunham, J. W., O'Connor, W. J., Ingberg, S. H., Thorud, B. M., Diener, Ch. N., Fire-Resistance Classification of Building Materials. In *Building Materials and Structures*, Report BMS92, Report of the Subcommittee on Fire-Resistance Classifications of the Central Housing Committee, National Bureau of Standards, 1942.
4. Fire Grading of Buildings. Part 1, General Principles and structural Precautions. Post-war building studies no. 20. Ministry of works. London, Great Britain, 1946.
5. Law, A., Hadden R., (2017). Burnout means Burnout, *SFPE Europe*, Q1, 2017, Issue 5.
6. Babrauskas, V., Williamson, R. B., The historical basis of fire resistance testing—Part II. *Fire Technology* 14.4 (1978): 304-316.
7. Standard test methods for fire tests of building construction and materials (ASTM E 119). West Conshohocken, PA: ASTM.
8. Babrauskas, V. (2005). Charring rate of wood as a tool for fire investigations. *Fire Safety Journal*, 40(6), 528-554.
9. Schmid, J., Brandon, D., Werther, N., Klippel, M., Thermal Exposure of Wood in standard fire resistance tests. *Fire Safety Journal (FISJ2690)*, 2017.
10. Hurley MJ, Gottuk DT, Hall Jr JR, Harada K, Kuligowski ED, Puchovsky M, Watts Jr JM, Wiecek CJ, editors. *SFPE handbook of fire protection engineering*. Springer; 2015 Oct 7.
11. Fahrni, R., Schmid, J., Klippel, M, Frangi, A., Investigation of different designs and installations of temperature measurements in wood as low conductive materials, Conference Structures in Fire SIF'18, Belfast, 2018.
12. Lange, D., Sjöström, J., Schmid, J., Daniel, B., Timber and the fire resistance furnace – A comparative Study of the conditions in a fire Resistance furnace when testing combustible and non-combustible construction, Conference Structures in Fire SIF'18, Belfast, 2018.
13. Lennon, T., Bullock M.J., Enjivy, V., The fire resistance of medium-rise timber frame buildings, 2000.
14. Matthew S. Hoehler , Joseph Su , Pier-Simon Lafrance , Matthew F. Bundy , Amanda Kimball , Daniel Brandon , Birgit Östman. Fire Safety Challenges of Tall Wood Buildings: Large-Scale Cross Laminated Timber Compartment Fire Tests. Conference Structures in Fire SIF'18, Belfast, 2018.
15. Schmid, Joachim, Schmid, Joachim, Alessandro Santomaso, Daniel Brandon, Ulf Wickström, and Andrea Frangi. Timber under real fire conditions—the influence of oxygen content and gas velocity on the charring behavior. *Journal of Structural Fire Engineering*, 2017.
16. Joachim Schmid, Michael Klippel, Daniel Brandon, Norman Werther, David Lange, Andrea Frangi. Thermal Exposure in Standard Fire Tests and Post-Flash over fires. *Fire and Materials*, 2018.
17. Michael Klippel, Joachim Schmid, Reto Fahrni, Andrea Frangi, David Lange, Assessing the adhesive performance in CLT exposed to fire, WCTE 2018, Seoul, South Korea.
18. EN 1991-1-2, Eurocode 1, Eurocode 1. Actions on structures. General actions. Actions on structures exposed to fire. 2002.

FIRE SAFETY CHALLENGES OF TALL WOOD BUILDINGS: LARGE-SCALE CROSS LAMINATED TIMBER COMPARTMENT FIRE TESTS

Matthew S. Hoehler¹, Joseph Su², Pier-Simon Lafrance³, Matthew F. Bundy⁴, Amanda Kimball⁵, Daniel Brandon⁶, Birgit Östman⁷

ABSTRACT

This study investigates the contribution of cross laminated timber (CLT) building elements to compartment fires. Six compartments (9.1 m long × 4.6 m wide × 2.7 m high) were constructed using 175 mm thick 5-ply CLT structural panels and fire tested using residential contents and furnishings to provide a fuel load density of 550 MJ/m². The results show that gypsum board can delay or prevent the involvement of the CLT in the fire, and that the ventilation conditions and exposed surface area of the CLT play a decisive role in the outcome of the test. The results highlight the need to use heat-resistant adhesives in cross laminated timber to minimize delamination.

Keywords: cross laminated timber, compartment fires, fire tests, delamination, ventilation

1 INTRODUCTION

Recent architectural trends include the design and construction of increasingly tall buildings with structural components comprised of mass timber including cross laminated timber (CLT). These buildings are cited for their advantages for sustainability resulting from the use of wood as a renewable construction material.

This research aimed to quantify the contribution of CLT building elements to compartment fires, and to characterize the fire protection of the CLT using gypsum board for delaying or preventing its involvement in the fire. Six large-scale CLT compartment fire tests were planned in consultation with the Project Technical Panel [1–3] and in consideration of gaps identified by a literature review [4]. Modelling was also conducted to support the choice of test parameters [5].

¹ Research Structural Engineer, National Institute of Standards and Technology, Gaithersburg, USA.
e-mail: matthew.hoehler@nist.gov

² Principal Research Officer, National Research Council of Canada, Ottawa, Canada.
e-mail: joseph.su@nrc-cnrc.gc.ca

³ Technical Officer, National Research Council of Canada, Ottawa, Canada.
e-mail: pier-simon.lafrance@nrc-cnrc.gc.ca

⁴ Director National Fire Research Laboratory, National Institute of Standards and Technology, Gaithersburg, USA.
e-mail: matthew.bundy@nist.gov

⁵ Research Director, Fire Protection Research Foundation, Quincy, MA, USA.
e-mail: akimball@nfpa.org

⁶ Researcher, Research Institutes of Sweden, Borås, Sweden.
e-mail: daniel.brandon@ri.se

⁷ Senior Advisor, Linneaus University, Växjö, Sweden.
e-mail: birgit.ostman@lnu.se

North American codes require that all tall buildings be fully sprinklered in accordance with National Fire Protection Association (NFPA) standard NFPA 13 [6] and that fire services are required to respond to fire incidents in accordance with NFPA 1710 and 1720 [7,8]. However, to achieve the project objective to quantify the contribution of CLT building elements, the CLT compartment fire tests were conducted without sprinklers and without firefighting intervention.

2 TEST SETUP AND PROCEDURE

2.1 Test structure

Six compartments (9.1 m long \times 4.6 m wide \times 2.7 m high) were constructed using 175 mm thick 5-ply CLT structural panels manufactured using 2 \times 4 spruce-pine-fir lumber glued with a polyurethane adhesive for all wall and ceiling assemblies. All CLT panels conformed to American National Standard ANSI/APA PRG-320 [9]. The ceiling assembly spanned in the 4.6 m direction parallel to walls W2 and W4 (*Fig. 1a*). The wall panels were connected using lap joints and the adjacent walls were connected using butt joints with screws. The ceiling panels were connected to the walls using butt joints with screws (*Fig. 1b*). The inside of the compartments was fully or partially lined using multiple layers of 15.9 mm thick Type X gypsum board.

The compartment had a rough opening in Wall W2 (front) of 1.8 m wide \times 2.0 m high in four tests and 3.6 m wide \times 2.0 m high in two tests. The ventilation factor was 0.03 m^{1/2} with the 1.8 m \times 2.0 m opening, and 0.06 m^{1/2} with the 3.6 m \times 2.0 m opening, respectively. Additionally, two small openings of 150 mm diameter were created in wall W4 at 0.3 m and 1.8 m heights to provide an equivalent leakage of 0.035 m² without actually having a door located in the rear wall. Additional details and drawings for the compartments can be found in the final report [10].

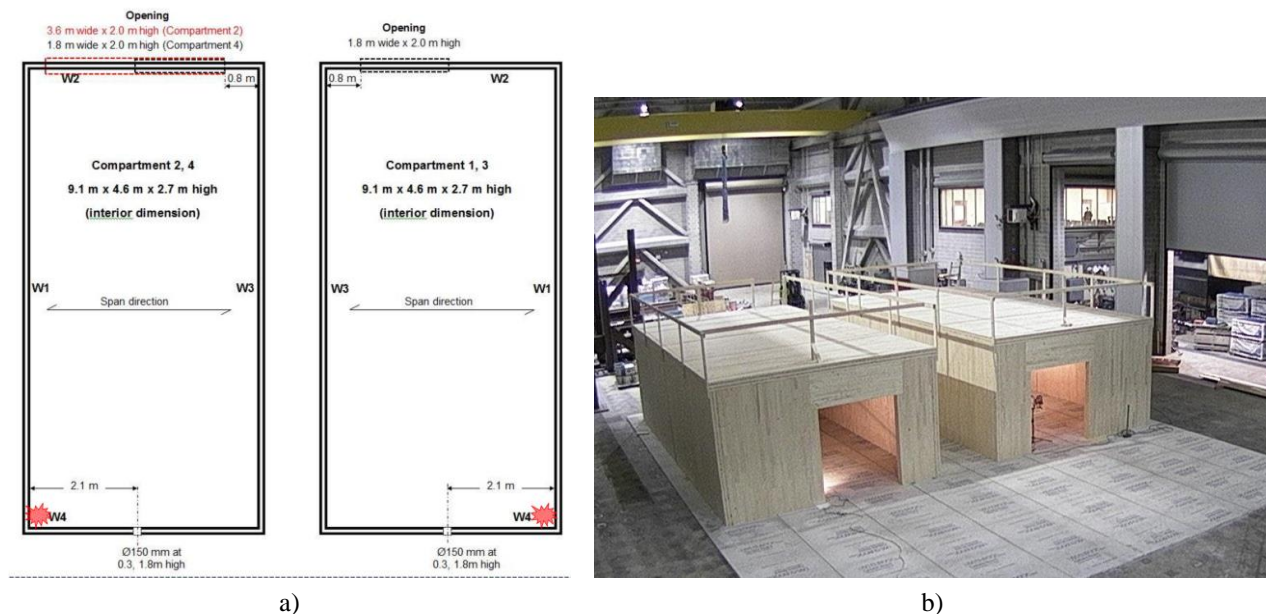


Fig. 1. a) Plan view schematic of test compartments; b) Photograph of test compartments (bare structure)

2.2 Test program

Table 1 provides the test matrix. Test 1-1 served as a baseline for the tests with the 1.8 m \times 2.0 m opening. Three layers of the gypsum board were used to cover the CLT walls and ceiling in Test 1-1 so that the CLT would neither contribute to the fire nor develop char during the test. Test 1-2 served as a baseline for the tests with the 3.6 m \times 2.0 m opening. An exposed wall (W1) was tested in both ventilation configurations (Test 1-3 and Test 1-5). Test 1-4 and Test 1-6 involved an exposed ceiling and a combination of exposed ceiling and wall, respectively, with the 1.8 m \times 2.0 m

opening. In all tests, a structural load of 0.95 kN/m^2 , which is one half of the design live load for a residential occupancy, was superimposed on top of the ceiling using eight cylindrical water tanks.

Table 1. Test matrix

Rough Opening in Wall W2	Compartment Surface					Test	CLT Compartment
	W1 9.1m x 2.7m	W2 4.6m x 2.7m	W3 9.1m x 2.7m	W4 4.6m x 2.7m	Ceiling 9.1m x 4.6m		
1.8m wide x 2.0m high	3GB	3GB	3GB	3GB	3GB	1-1	1
	3GB	3GB	3GB	3GB	exposed	1-4*	1*
	exposed	3GB	3GB	3GB	3GB	1-5	4
	exposed	3GB	3GB	3GB	exposed	1-6	3
3.6m wide x 2.0m high	2GB	2GB	2GB	2GB	2GB	1-2	2
	exposed	2GB	2GB	2GB	3GB	1-3*	2*

GB: 15.9 mm (5/8 in.) thick Type X gypsum board; 2GB: 2 layers of GB; 3GB: 3 layers of GB

* Reused CLT structure.

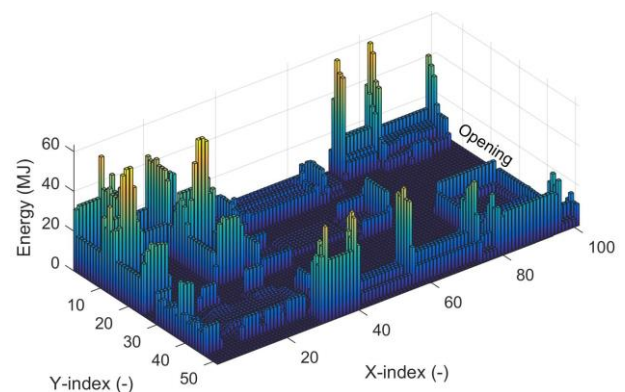
2.3 Ignition scenario and fuel load

Since the primary objective of the experiments was to evaluate the effect of the CLT structural elements on the fire growth and fire dynamics, the contents fire load and ignition scenario were designed to produce a medium fire growth rate. The movable fuel⁸ represented residential contents in a studio apartment with sleeping, living and kitchen areas (Fig. 2a) and had target a fire load density of 550 MJ/m^2 . The mass, dimensions and position of all combustible material were measured prior to placement in the compartment. These measurements along with assumed calorific values for each material were used to create a 3D model of the fuel energy distribution in the compartment (Fig. 2b). The highest fuel density was in the kitchenette at the rear of the compartment, however, the rest of the fuel density was roughly evenly distributed throughout the compartment.

The ignition source was a natural gas burner (200 mm × 400 mm) placed in the corner adjacent to walls W1 and W4 partially under a sideboard. A heat release rate of 50 kW (similar to a burning waste basket) from the burner was maintained until the total measured heat release rate from the compartment exceeded 1000 kW (due to ignited contents), at which time the burner was shut off.



a)



b)

Fig. 2. a) Photograph of movable fuel as installed; b) Model of fuel energy distribution in the compartment

⁸ Movable fuel refers to all combustible material inside of the compartment (including the laminated flooring) that is not a CLT structural element.

2.4 Measurement systems and instrumentation

Data was collected from multiple systems during the experiments. These systems can be grouped into four categories related to: (1) the calorimeter – dedicated to measuring fuel flow to the small ignition burner and performing oxygen depletion calorimetry, (2) gas sampling in the compartment, (3) the constituent measurements for the test specimens, and (4) imaging and video. 185 specimen-related data channels were recorded. A detailed description of the instrumentation and the estimated uncertainty of the measurements are provided in the final report [10].

3 RESULTS

A large amount of technical data was produced, including measurements of the heat release rate, temperatures inside and outside the compartment, as well as through the encapsulation material and structural assemblies, simulated sprinkler response time, gas species concentrations (O_2 , CO_2 , CO), pressure and flow conditions, interior and exterior heat fluxes, smoke density, and char depth. In this paper, we limit our discussion to the fire development, select temperature measurements, and comparisons of heat release rates. All of the measured data, as well as videos can be downloaded at [11].

Although the tests were conducted without sprinklers, simulated thermal elements (STEs) were placed at typical sprinkler heights to replicate the time temperature response of a quick-response sprinkler. The time from ignition for each STE to reach the temperature of $68\text{ }^\circ\text{C}$ (a typical temperature rating for residential sprinklers) was always less than 5.8 minutes. At these times, the fires were still limited to the first item ignited. Had sprinklers been installed, flashover would not have occurred with effective sprinkler operations.

3.1 Fire development for the baseline ventilation conditions

Fig. 3 shows the typical pre-flashover condition of the compartment and a subsequent view of the compartment when most of the movable fuel has been consumed by the fire. In this example (Test 1-2), all CLT surfaces on the walls and ceiling were protected using two layers of gypsum board and the opening was $3.6\text{ m} \times 2.0\text{ m}$ (wide opening). Test 1-2 served as a baseline to define the contribution of the movable fire loads and to quantify CLT contribution to the fire in a subsequent test with the same ventilation conditions (Test 1-3).

The test started with the ignition of a sideboard in the room corner and progressed through the dining area. The smoke layer descended to the mid height in the compartment and stayed at this height until flashover. After flashover, an intense burning of room contents lasted for approximately 24 min. The fire started to decay at 37 min and the fire plume ceased to issue from the opening at 40 min. The test lasted for 104 min and was terminated after the heat release rate fell below 500 kW. A hose was used to lightly mist the debris on the floor with water to terminate the test.

The fire development described above was similar for both tests in which the CLT was fully protected by the gypsum and did not contribute to the heat release rate; i.e., Test 1-1 and Test 1-2. *Fig. 4* shows comparisons of the heat release rates during these tests. Test 1-2 with the larger ventilation opening had a higher heat release rate but earlier fire decay than Test 1-1. The two tests released virtually the same amount of total heat of 18 000 MJ, which is equivalent to the total energy of the movable fuel with 80 % combustion efficiency. However, the heat exposure conditions inside the compartment were more severe in Test 1-1 than in Test 1-2, because more intense burning occur outside the fire compartment in Test 1-2 [10]. The fire development for Test 1-3 to Test 1-6, which were affected to varying degrees by contributions from the burning CLT, is illustrated by the heat release rate comparisons in Section 3.3.



Fig. 3. Photographs of the CLT compartment during Test 1-2 (wide opening)

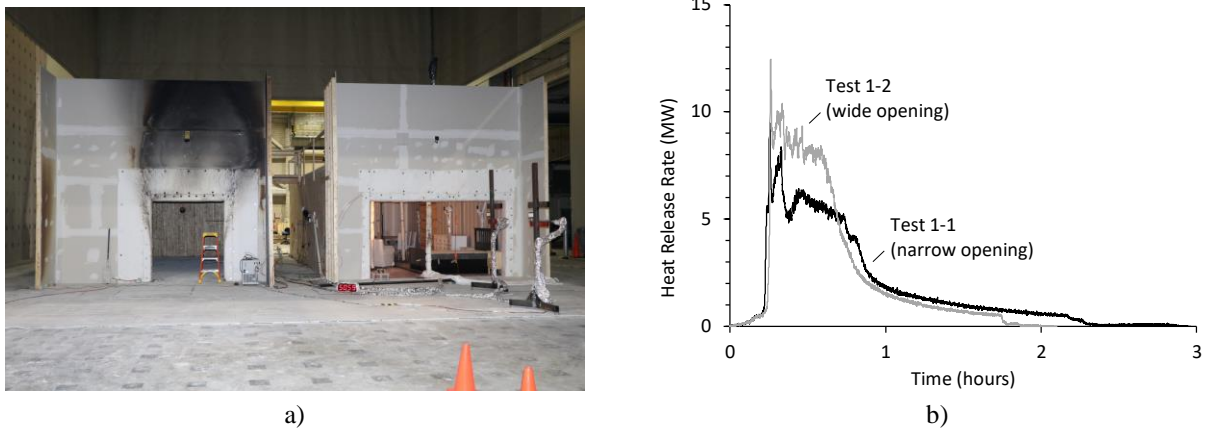


Fig. 4. Influence of opening size on the measured heat release rate for the same movable fuel load of 550 MJ/m² and no participation of CLT: a) Test 1-1 with narrow opening; b) Test 1-2 with wide opening

3.2 Encapsulation material and structural assembly temperatures

In this section we show temperature time-histories for a wall assembly that successfully prevented participation of the CLT in the fire for the compartment with a wide opening, as well as an unprotected wall assembly under the same compartment ventilation conditions.

Fig. 5 shows the temperatures measured at the interfaces between the adjacent gypsum board layers, and between the CLT interior surface and the gypsum board base layer, as well as inside the CLT panels at various depths for Wall W1 in Test 1-2 (wide opening) with two layers of gypsum. The heat transfer through the gypsum board followed the typical three-stage pattern as indicated by the temperature profiles at the interfaces: an initial temperature rise up to 100 °C, a period of gypsum calcinations at the constant temperature of 100 °C, then temperature increasing again after the calcination. Although the temperatures at the interface between the face and base layers of gypsum board increased significantly (up to 800 °C) at various locations in the wall, the face layer gypsum board stayed intact until the end of the test (Fig. 3b). The maximum temperature measured at the CLT interface with gypsum board was 263 °C on wall W1 at the 1.8 m height; at other measurement locations, the CLT wall interface temperatures were 100 °C to 170 °C. The CLT wall panels were at the ambient temperature on the exterior surface. For Test 1-1, which provided a baseline for the compartments with a narrow opening, three layers gypsum board were necessary to successfully protect the CLT structure, preventing the ignition and involvement of CLT structural elements in the fire.

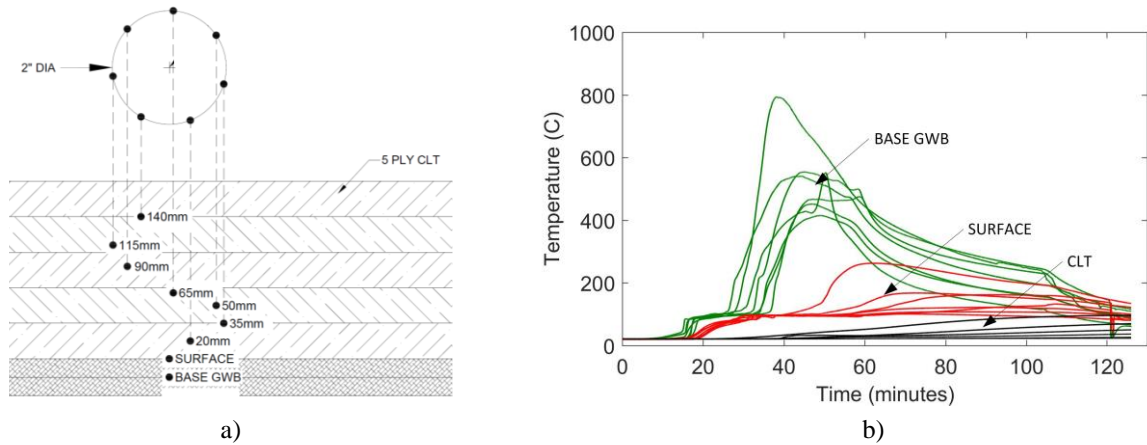


Fig. 5. Temperatures in a wall assembly with two layers of 15.9 mm thick Type X gypsum protection in Test 1-2 (wide opening): a) Details of embedded thermocouples in Wall W1 with the drilled holes in a circular pattern and sealed from the outside; b) Temperatures in Wall W1 at various depths from the fire exposed surface (1 inch = 25.4 mm)

Fig. 6 shows temperatures measured on the surface of and inside the CLT panels for Wall W1 in Test 1-3 (wide opening) which had no gypsum protection. The temperature profiles show that before the flashover, the upper portion of the exposed W1 wall was already ignited. Based on the timing when the embedded thermocouples in Wall W1 (mid-length at 1.8 m height) measured 300 °C, the char front reached 20 mm, 35 mm, 50 mm and 65 mm deep at 32 min, 83 min, 172 min, and 213 min, respectively. The embedded thermocouple in 35 mm depth of the W1 wall shows a sharp temperature rise at around 80 min. The starting point of this temperature rise, 220 °C, is below the wood charring temperature. The end point of this temperature rise, 500 °C, is the prevailing compartment temperature. Given that 35 mm inside CLT corresponds with a glue line and that the char front should be at around 300 °C, this temperature rise indicates that the delamination of the first ply of the CLT occurred prior to the char front reaching the first glue line. The embedded thermocouple in 65 mm depth of the W1 wall shows a similar temperature rise at around 210 min, indicating the delamination of the second ply of the CLT prior to the char front reaching the second glue line. At the end of the test (242 min), the temperatures at the 90 mm, 115 mm and 140 mm depths in the CLT panel were 132 °C, 80 °C, and 40 °C, respectively.

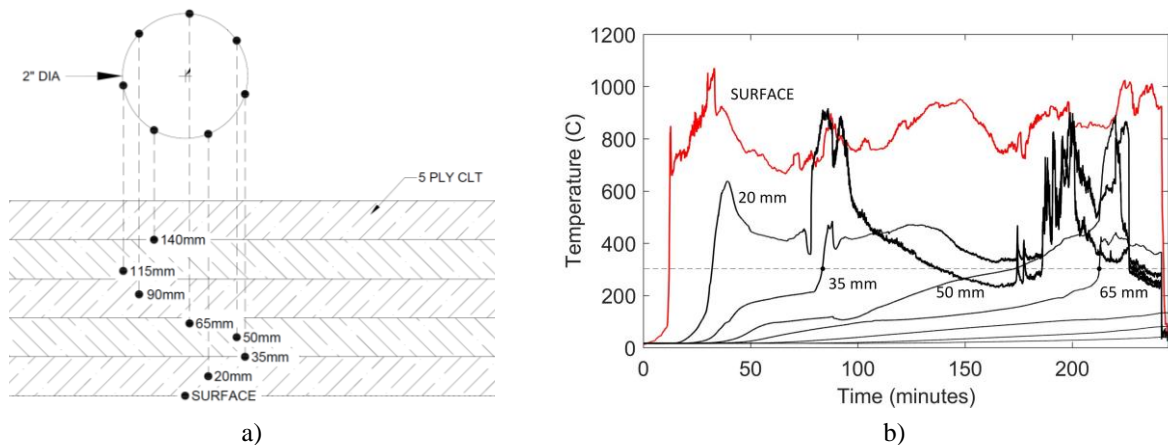


Fig. 6. Temperatures in a wall assembly without gypsum protection in Test 1-3 (wide opening): a) Details of embedded thermocouples in Wall W1 with the drilled holes in a circular pattern and sealed from the outside; b) Temperatures in Wall W1 at various depths from the fire exposed surface (1 inch = 25.4 mm)

3.3 Heat release rate

The influence of exposing CLT under the investigated fuel load density and ventilation conditions is illustrated by comparing the measured heat release rates.

Fig. 7a compares the baseline case for the wide opening and no CLT participation (Test 1-2) with the case where one wall of the compartment is exposed (Test 1-3). With the exposed W1 wall in Test 1-3, flashover occurred 3 min earlier and the heat release rate was approximately 2 MW higher than the baseline (Test 1-2) in the growth and fully developed fire stages. The CLT contribution is most prominent, however, during the decay phase of the fire when flaming in the compartment reoccurred as the first and second plies in Wall W1 delaminated. Based on the volume (depth \times area) of the CLT charred, which was measured after the test, the CLT panels were estimated to contribute approximately 1100 kg of timber to the fire (mainly by the W1 wall panels), which translated to 540 MJ/m² fuel load density to the floor area in addition to the movable fuel load. This brought the effective fuel load density to 1090 MJ/m² in Test 1-3.

Fig. 7b compares the baseline case for the narrow opening and no CLT participation (Test 1-1) with various combinations of ceiling and wall CLT exposure (Test 1-4 to Test 1-6). In the three investigated cases (one wall exposed, ceiling exposed, and one wall and ceiling exposed), exposure of the CLT with the narrow opening resulted in a decreased time to flashover (3.4 min to 5.1 min sooner) and ultimately to runaway fire growth that required manual fire suppression. The exposed CLT panels translated to more fuel loads in addition to the movable fuel load (room contents) in the compartment. Due to the intensity and duration of the thermal exposure in the compartment, the CLT surfaces protected by three layers of 15.9-mm thick Type X gypsum also contributed to the fire in the later part of the tests. The estimated contributions of the CLT to the total fuel load for these tests depended on the time at which the fire was suppressed and can be found in [10].

Comparing the heat release rates for Tests 1-3 (*Fig. 7a*) and Test 1-5 (*Fig. 7b*) in which both tests had one exposed CLT wall, illustrates the importance of the ventilation conditions on the outcome of the test. In Test 1-3 with a wide opening (ventilation factor = 0.06 m^{1/2}), the delamination in the exposed wall does not prevent the fire from continuing to decay, whereas in Test 1-5 with a narrow opening (ventilation factor = 0.03 m^{1/2}), the delamination of the plies led to runaway growth of the fire.

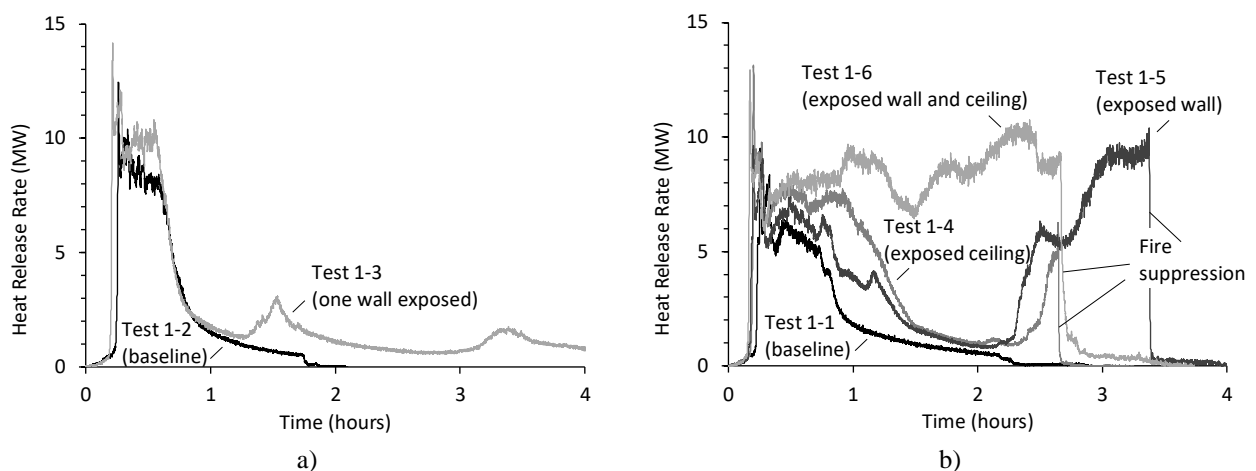


Fig. 7. Comparison of CLT compartment heat release rates: a) compartments with wide openings. b) compartments with narrow openings

4 CONCLUSIONS

The following conclusions are made based on the results:

- *Ventilation conditions had significant impacts on the fire development in the compartments;*
- *The larger opening (ventilation factor = 0.06 m^2) increased the peak heat release rate, but reduced the fire challenges to the CLT compartment structure inside;*
- *The CLT contribution to the fire increased with increasing exposed surface area of the CLT; and,*
- *There is a need to use better heat-resistant adhesives in CLT for exposed CLT applications to minimize delamination.*

ACKNOWLEDGMENT

The authors gratefully acknowledge the project management provided by the Fire Protection Research Foundation and the technical oversight of its Project Technical Panel. Financial support from the Fire Protection Research Foundation, Property Insurance Research Group, U.S. Department of Agriculture, U.S. Forest Service, American Wood Council, and National Research Council Canada is gratefully acknowledged. Donations of STE devices from FM Global and gypsum board from USG Corporation are also gratefully acknowledged.

REFERENCES

- [1] J. Su, G. Lougheed, Fire Safety Challenges of Tall Wood Buildings – Phase 2, Test Options for Task 2 – A Discussion Paper, Ottawa, Ontario, 2016.
- [2] J. Su, G. Lougheed, Fire Safety Challenges of Tall Wood Buildings – Phase 2, Test Options for Task 2 – Second Discussion Paper, Ottawa, Ontario, 2016.
- [3] J. Su, G. Lougheed, Test Plan for Fire Safety Challenges of Tall Wood Buildings - Phase 2, Ottawa, Ontario, 2016.
- [4] D. Brandon, B. Östman, FPRF Project Fire Safety Challenges of Tall Wood Buildings – Phase 2, Task 1 – Literature review: The contribution of CLT to compartment fires, 2015.
- [5] D. Brandon, B. Östman, FPRF Project Fire Safety Challenges of Tall Wood Buildings – Phase 2, Task 2 – Test plan, modeling: The contribution of CLT to compartment fires, 2016.
- [6] National Fire Protection Association (NFPA), NFPA 13. Standard for the Installation of Sprinkler Systems, Quincy, MA, 2016.
- [7] National Fire Protection Association (NFPA), NFPA 1710. Standard for the Organization and Deployment of Fire Suppression Operations, Emergency Medical Operations, and Special Operations to the Public by Career Fire Departments, Quincy, MA, 2016.
- [8] National Fire Protection Association (NFPA), NFPA 1720. Standard for the Organization and Deployment of Fire Suppression Operations, Emergency Medical Operations and Special Operations to the Public by Volunteer Fire Departments, Quincy, MA, 2014.
- [9] ANSI/APA PRG 320-2012. Standard for Performance-Rated Cross-Laminated Timber, 2012.
- [10] J. Su, P. Lafrance, M. Hoehler, M. Bundy, Fire Safety Challenges of Tall Wood Buildings – Phase 2: Task 2 & 3 – Cross Laminated Timber Compartment Fire Tests, Fire Protection Research Foundation, Quincy, MA, 2018.
- [11] M.S. Hoehler, M.F. Bundy, J. Su, Dataset from Fire Safety Challenges of Tall Wood Buildings – Phase 2: Task 3 - Cross Laminated Timber Compartment Fire Tests, (2018). doi:<https://doi.org/10.18434/T4/1422512>.

INVESTIGATION OF DIFFERENT TEMPERATURE MEASUREMENT DESIGNS AND INSTALLATIONS IN TIMBER MEMBERS AS LOW CONDUCTIVE MATERIAL

Reto Fahrni¹, Joachim Schmid², Michael Klippel³, Andrea Frangi⁴

ABSTRACT

An accurate measurement of the temperature during fire tests is of utmost importance. The measuring device used therefore (1) shall indicate the exact temperatures in the specimen and (2) shall not disturb its temperature field. For timber as a low conductive material this is particularly difficult.

The paper presents five standard fire tests (four cross laminated timber panels and one solid timber panel), in which eight different thermocouple designs and installations were investigated. The tests showed that any thermocouple design installed in boreholes perpendicular to the isotherms leads to considerably lower measurements than wire thermocouples placed parallel to the isotherms. Referring to the time when the measurement indicates 300°C the difference is between 10 and 35 min.

An installation parallel to the isotherms is found to be accurate, while perpendicular to them suffers from significant heat loss through conduction in the thermocouple. Additionally, missing contact pressure between the thermocouple and the sample increases the temperature discrepancy. Convection in the tight gaps between the thermocouple and the borehole does not happen in usual configuration and hence has no effect on the measured temperature. For proper temperature measurements in timber, it is thus recommended to install thermocouples parallel to the isotherms, to use thermocouples with fewest possible conductive material and a high contact pressure.

Keywords: timber, fire exposure, temperature measurement, thermocouples, measurement error

1 INTRODUCTION

Information about the temperature development in a structural member is of major importance for the interpretation of experimental results and for conclusions about the member's response in fire. For low conductive materials such as timber exposed to a post-flashover or ISO 834 fire [1], steep temperature gradients appear in the structural member. Steep temperature gradients make the measurement more prone to measurement errors, as for example a small change in the measurement position has a considerable impact. Additionally, the heat loss due to conduction in the particular measurement device leads to a lower measured temperature and may cool down the surrounding material.

In order to limit temperature measurement errors in low conductive materials, old literature and guidance documents recommend to install the thermocouples (TCs) parallel to isotherms [2,3,4]. It

¹ Research assistant and PhD Candidate. Institute of Structural Engineering, ETH Zurich, Switzerland.
e-mail: fahrni@ibk.baug.ethz.ch

² Research assistant and PhD Candidate. Institute of Structural Engineering, ETH Zurich, Switzerland.
e-mail: schmid@ibk.baug.ethz.ch

³ Senior Scientist. Institute of Structural Engineering, ETH Zurich, Switzerland.
e-mail: klippel@ibk.baug.ethz.ch

⁴ Professor. Institute of Structural Engineering, ETH Zurich, Switzerland.
e-mail: frangi@ibk.baug.ethz.ch

was observed that in recently published standard fire tests, ad-hoc tests and experiments, the well-known procedures were not followed and thus the measured temperatures may not be accurate. Thus, if the depth of the char layer over time is determined with temperature measurements (in combination with a defined temperature at the char layer), significant errors are expected when the temperature is not measured correctly. The accuracy of the temperature measurement readings of TCs is in general in the range of one degree Celsius, however, the error caused by improper installation and/or choice of TC design can be in the range of several hundred degrees Celsius. Such errors result in an inaccurate estimation and late detection of any char temperature and char layer depth, leading to wrong charring rates, incorrect models and finally to inappropriate design.

This paper presents an experimental series of tests performed in solid timber elements exposed to ISO 834 standard fire corresponding to default incident radiant heat fluxes between 0 and 180 kW/m² [5]. Measurements with wire and sheathed TCs were investigated and compared. The installation alternative was varied to follow existing rules [3,4].

2 TEST SETUPS

Different alternatives to measure temperatures were investigated during five model-scale fire tests with four cross laminated timber (CLT) panels and one solid timber panel (STP), see *Figure 1*. *Table 1* shows an overview of the performed tests.

Table 1: Overview of performed tests

Test specimen	Adhesive*	Layup [mm]	Total height [mm]	Time of fire exposure [min]	Borehole sealing
CLT 1	PUR	7x25	175	120	Only sheathed TCs
CLT 2	PUR	7x20	140	90	Yes
CLT 3	MUF	7x25	175	120	No
CLT 4	PUR	5x35	175	120	No
STP	-	-	160	120	No

* PUR: One-component polyurethane; passes compartment test according to PRG-320:2018 [6]
MUF: Melamine-urea-formaldehyde; certified according to EN 301:2017 [7] for the use in structural timber

For analysing the influence of different TC designs and installation alternatives on the temperature measurement in timber specimens, a STP panel is favourable compared to CLT, since no falling-off of charred or charring layers is expected. In case of STP, (1) the charring direction is parallel to the vertical bond lines. Thus, the charring corresponds to solid timber and (2) it is possible to install wire TCs parallel to the isotherms at any specimen depth and not only at each interlayer of lamellae as with CLT specimens.

All specimens were made of spruce (specimen density between 438 and 472 kg/m³). During the test, the specimens were unloaded and exposed to standard ISO fire [1] in the horizontal model-scale furnace at the VKF fire lab in Dübendorf (Switzerland), which is controlled by plate thermometers. The specimens were 800 mm x 960 mm in size and had varying height and thicknesses of the lamellas, see *Table 1*. The tests lasted 90 and 120 minutes. The CLT specimens were glued with either MUF or PUR type adhesive.



Figure 1: STP (left) and CLT (right) specimens, fire exposure on bottom surface, with indicated positions of the measurement stations (stars)

Two ways of TC installations were investigated: (1) Drilled in from the fire unexposed surface of the specimen and (2) inlaid during the production of the specimen (*Figure 2*). Wire TCs were installed in both ways, whereas sheathed TCs were only installed in the boreholes. Each specimen had three identically equipped so-called temperature measurement stations along the centreline in length (black filled stars in *Figure 1*). Thereby, every measurement alternative was installed three times per specimen. The STP test had two additional measurement stations, where only wire-TCs were installed (white filled stars in *Figure 1* left). The idea of the ‘measurement stations’ was that the TCs are allocated as close as reasonably possible inside a station to reduce the influence of the inhomogeneous material properties, but still do not influence each other. Individual measurement points had a minimum horizontal distance of 20 mm to minimize an influence between the TCs.

For the CLT specimens, the inlaid wire-TCs were simply placed on the timber boards (*Figure 3* right). The wires then followed the bond line to the side of the specimens and thus along the isotherms (*Figure 2* right). In the STP specimen, the inlaid wire-TCs were installed in holes drilled (vertical drill press) from the face of the board to its half depth (25 mm). The wires then followed at least 50 mm along the isotherms and then turned towards the fire unexposed side of the specimen in slightly milled channels (*Figure 2* left and *Figure 3* left).

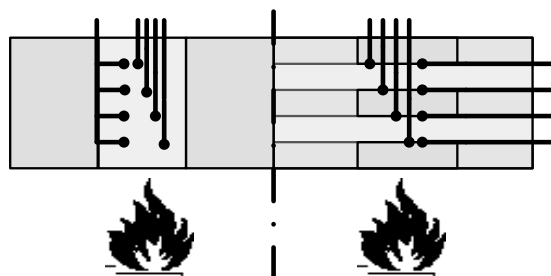


Figure 2: Instrumentation of STP (left) and CLT (right) with conductor direction and ply orientation.

Investigation of different temperature measurement designs and installations in timber members as low conductive material

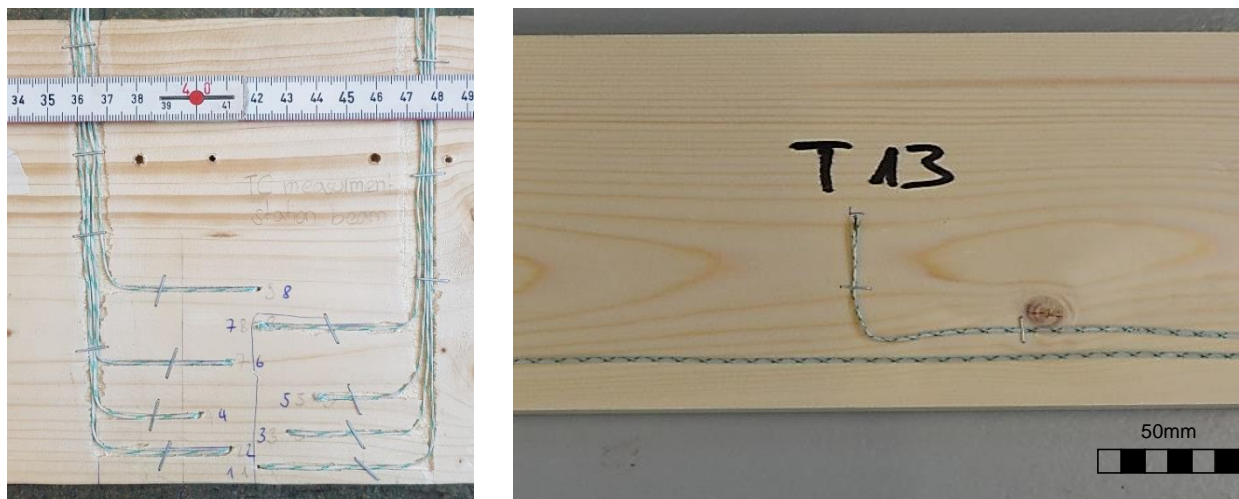


Figure 3: Inlaid wire-TC installation in STP (left) and CLT (right)

Drilling from the fire unexposed side was done manually with cordless drills (*Figure 4* centre and right). The holes were drilled perpendicular to the surface, which was controlled by visual judgement. The resulting error due to a wrong angle was estimated and is insignificant for boreholes perpendicular to the isotherms (5° axial error (conservative) at 150 mm depth (maximum) would lead to a perpendicular depth of 149.43 mm, a mispositioning of 0.57 mm). When the TCs were inserted (until the tip reached the end of the borehole), the depth was checked once more by measuring the inserted length.



Figure 4: Drilling procedure: grid marking (left), measuring the depth (centre), drilling with depth-marker (right)

Eight different alternatives of temperature measurements (measurement devices and installation; see legend in *Figure 6*) were investigated, but only CLT 3 and CLT 4 had all different alternatives installed. All TCs were of type K. The wire TCs had a conductor diameter of 0.5 mm and the hot junction was welded. The sheathed TCs had an outer diameter of 1.5 mm or 3.0 mm and each diameter was investigated with three different alternatives of hot-junction designs: (1) grounded with the sheath, (2) insulated from the sheath or (3) exposed outside the sheath, see *Figure 5*. The boreholes for the wire TCs had a diameter of 2.5 mm, whereas the diameter of the boreholes of the sheathed TCs was 2.0 mm and 4.0 mm, respectively.

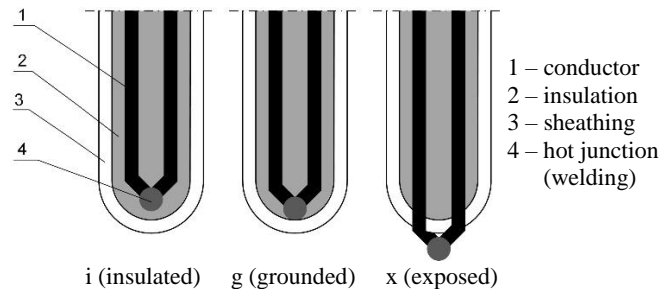


Figure 5: Hot junction design, i, g, x of sheathed TCs (s) [8].

After removal of the char coal, the residual height of the specimen was measured manually every 50 mm in a grid and then averaged. Edge effects were excluded. In the evaluation, the char depth was assumed to be represented by the 300 °C isotherm [9].

3 RESULTS

3.1 General observations

Figure 6 presents the time-temperature plot for particular tests, showing the average measured temperature over all three measurement stations per measurement alternative and the mean furnace temperature over all five furnace control plate thermometers. The measurement depths (distance to the fire exposed surface) of the particular measurements are indicated.

The plots show a significant temperature difference between the measurements of the inlaid wire TCs and all other measurement alternatives for the same depth. The different hot junction designs of the sheathed TCs (i, g, x) had no significant effect on the result. However, all measurements installed in boreholes (wire and sheathed TCs) showed significantly lower temperatures than the inlaid wire TCs at the exact same time.

With respect to the char line, which is assumed to be at 300 °C, the difference of the time, when the char line is detected in a certain depth is between 10 minutes (CLT 2 at 20 mm) and 35 minutes (CLT 1 at 75 mm) for the inlaid wire TCs compared to the other measurement alternatives. Table 2 exemplarily shows the times for the STP specimen (no falling off of charred layer) when the mean temperature per TC alternative reached 300°C and the therewith calculated charring rate. The resulting charring rates with the inlaid wire TCs are 0.82 mm/min and 0.62 mm/min for 6 mm and 30 mm depth, respectively, and thus in the range as expected. The charring rates derived from the other measurements are significantly too low being between 0.21 and 0.30 mm for 6 mm depth and between 0.44 and 0.50 mm for 30 mm depth. For 6 mm depth, it is also clearly visible that the 3.0 mm sheathed TCs show lower temperatures and charring rates than the other drilled in TCs.

Table 2: Time t when TCs reach 300°C (charring temperature) and the respective charring rates β for the STP test

Distance to fire exposed surface [min] / [mm/min]	6 mm		30 mm	
	t	β	t	β
wire inlaid	7.4	0.82	48.5	0.62
wire drilled	19.9	0.30	62.3	0.48
Sheathed, grounded (g) 1.5 mm	20.2	0.30	67.8	0.44
Sheathed, grounded (g) 3.0 mm	28.9	0.21	62.5	0.48
Sheathed, exposed (x) 1.5 mm	21.3	0.28	59.5	0.50
Sheathed, exposed (x) 3.0 mm	28.7	0.21	60.1	0.50
Sheathed insulated (i) 1.5 mm	23.8	0.25	63.8	0.47

With the general assumption that the indicated measured temperature accurately delivers the temperature of the TC at its tip, several causes for differences between measurement alternatives

exist: (1) steep temperature gradients in the highly conductive metallic TCs, (2) heat transfer between the specimen and the TC and, when applicable, (3) convection in the gap of the borehole. These causes are explained in detail in the following.

3.2 Steep temperature gradients in conductive TCs

This effect is caused mainly by the perpendicular-to-isotherms installation of the drilled in TCs. As the TCs record very high temperatures at its measuring tip and are at ambient temperature outside the specimen, the TCs are subjected to a steep temperature gradient as the timber specimen itself. However, due to the markedly higher thermal diffusivity of the metallic parts of the TCs compared to the timber, heat is transmitted away from the measuring tip and thus (1) cools the measuring tip and leads to recording of too low temperatures and (2) cools the surrounding timber material leading additionally to an underestimation of the true undisturbed timber temperature.

The influence of heat conductance in the TCs can be seen in *Figure 6* by the difference between the various measuring alternatives: the more metal they contain, the lower the temperatures they indicate. As the colour of the plotted lines distinguishes the diameter of two otherwise identical sheathed TC alternatives (black=1.5 mm, grey=3.0 mm), comparing curves with the same line style proofs this. Naturally this does not hold for every comparison at all the time, since despite the averaging between the three identically built measurement stations, the scattering effect shall still be bore in mind when analysing the results.

3.3 Heat transfer between TC and specimen

The heat transfer between the timber and the TC is generally not perfect in a sense that the TC tip does not have the exact same temperature as the surrounding timber, as a result of the surface roughness and the contact pressure [10]. The heat transfer, expressed by the heat transfer coefficient, increases with increasing contact pressure. Thus, the inlaid wire TCs of the CLT specimens that get pressed into the timber during the production of the specimens, are expected to have a high heat transfer coefficient. The loosely installed TCs in the borehole (0.5 mm to 1 mm larger than the TC diameter) in contrast have a significantly lower heat transfer coefficient. Comparing the inlaid wire measurements of the CLT specimens with those of the STP specimen (where the inlaid wire TCs had no contact pressure as they are installed in parallel-to-the-isotherms drilled holes), shows a difference of the slope in the time-temperature-plot. The measurements with more contact pressure (CLT) and thus a higher heat transfer coefficient show a higher gradient than without contact pressure (STP). However, it is important to note that falling off of charring layers, which happens only with CLT, also pronounces that difference in the slopes. If it was possible to insert a sheathed TC in a borehole of the same diameter as the TC itself, this effect could be minimized and the resulting time-temperature curve would be closer to the one of inlaid wire TCs.

3.4 Convection

Natural convection in the empty space between the borehole and the TC could additionally increase the temperature loss. However, this requires the air to flow in and out in the same open volume, which is only possible when the size of the gap is in the same order as the depth of the borehole. This is not the case for the here presented measurements and thus it is not surprising that a convection effect could not be determined. If the effect was present in the tests, then the measurements in the tests CLT1 and CLT2, in which the boreholes were (partially) sealed, would look clearly different than in the other tests.

Timber Structures and Fire Protection Materials

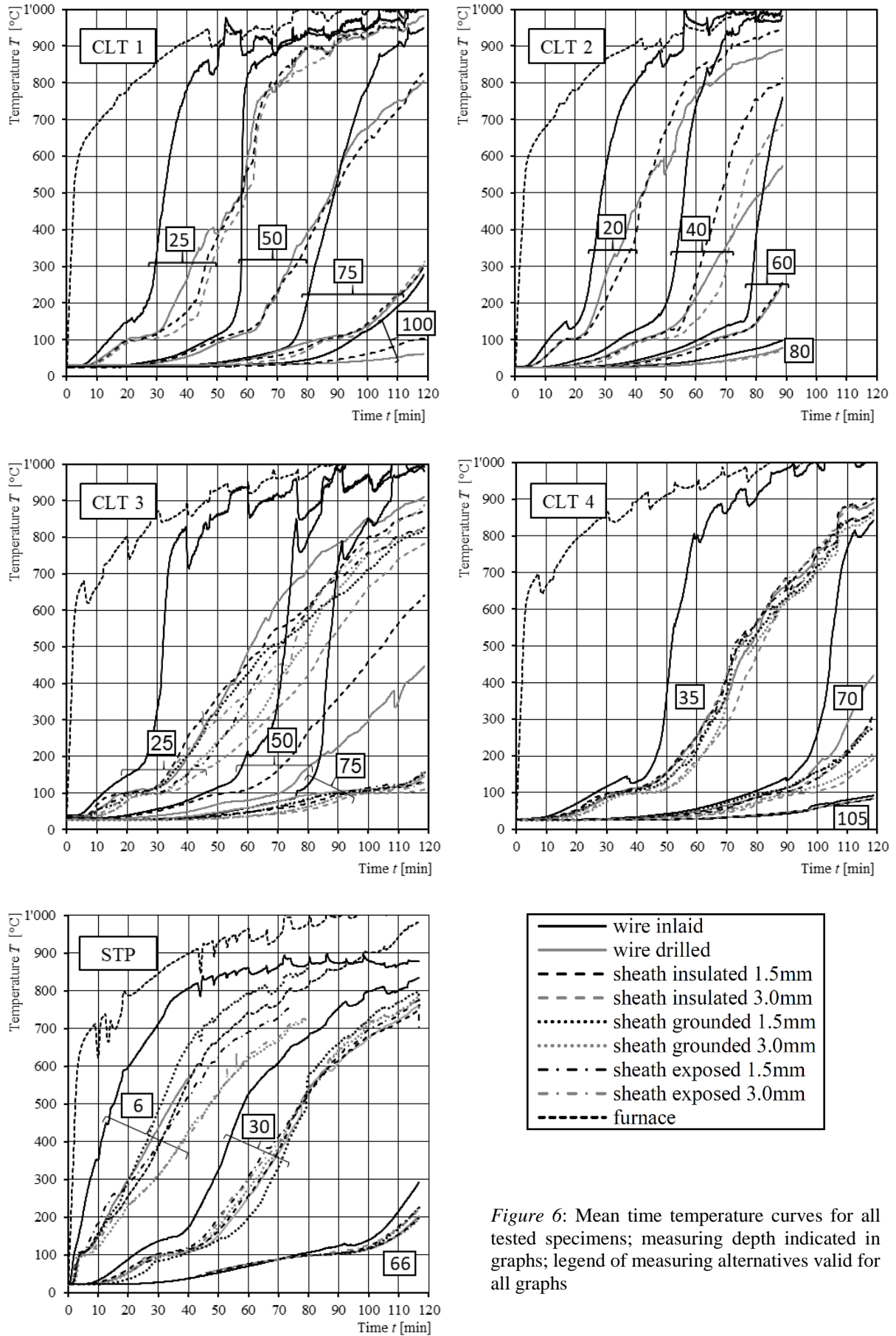


Figure 6: Mean time temperature curves for all tested specimens; measuring depth indicated in graphs; legend of measuring alternatives valid for all graphs

4 CONCLUSION

Based on the physical considerations and the results shown in this paper, the already existing recommendations [2,3,4] on how to install TCs in standard fire tests, ad-hoc tests and heating experiments are confirmed. To replicate undisturbed temperature measurements, the TCs shall be installed along the isotherms at least for a certain length. This length is heavily dependent on the heat transfer capacity of the TC. Whereas for wired TCs 50 mm might be reasonable as specified in [11], for sheathed TCs with much higher heat conductance this length is significantly longer. However, as the heat transfer in the TC should be minimized anyway, the use of sheathed TCs cannot be recommended for absolute temperature measurements within low conductive materials as timber, when exposed to high temperatures resulting in steep temperature gradients in the solid. Wire TCs seem to be the better option if they can be applied. The hot junction design of sheathed TCs does not change the measurements measurably.

Additional to the choice of the TC design, the arrangement of multiple TCs is of high importance. It shall be bore in mind that multiple TCs placed in a small area might lead to an increased underestimation of the measured temperature due to the superposition of the cooling effects of neighbouring TCs. Moreover, this can remove such a significant amount of heat that the charring process is measurably slowed down. Lastly, knowing the exact position of the measurement by appropriate drilling is as important as the heat transfer considerations illustrated in this paper.

Convection was seen to have no effect (respectively not to happen) in usual setups with drilling depths significantly larger than the open volume between the borehole surface and the TC.

The measurement error of TCs installed in boreholes perpendicular to isotherms reaches several hundred degrees Celsius. Referring to the time delay to reach 300 °C at the TC tip, the error was between 10 and 35 minutes for the analysed configurations.

REFERENCES

1. ISO 834-1:1999, *Fire - Resistance Tests - Elements of Building Construction - Part 1: General Requirements*. International Organization for Standardization, Geneva, 1999.
2. William D. Brewer (1967), *Effect of thermocouple wire size and configuration on internal temperature measurements in a charring Ablator*. National Aeronautics and space Administration, Washington DC.
3. VDI/VDE 3511-5 (1994), *Temperature measurement in Industry – Installation of Thermometers*. Verein Deutscher Ingenieure. Düsseldorf, Germany.
4. James V. Beck (1962), *Thermocouple Temperature Disturbances in Low Conductivity Materials*. Journal of heat transfer.
5. Joachim Schmid, Daniel Brandon, Norman Werther, Michael Klippel (2018), *Technical note - Thermal exposure of wood in standard fire resistance tests*. Fire Safety Journal. <https://doi.org/10.1016/j.firesaf.2018.02.002>
6. ANSI/APA PRG 320-2018, *Standard for Performance-Rated Cross-Laminated Timber*. American national standard. ANSI / ARPA 2018.
7. EN 301:2017, *Adhesives, phenolic and aminoplastic, for load-bearing timber structures – Classification and performance requirements*. Brussels, 2017.
8. EN 1995-1-2, Eurocode 5, *Design of timber structures. General. Structural fire design*. Brussels, 2004.
9. Reto Fahrni, Joachim Schmid, Michael Klippel, Andrea Frangi. *Temperature measurements in timber members for experimental fire testing*. Fire and Materials, submitted.
10. Yunus A. Cengel (2007), *Introduction to Thermodynamics and Heat Transfer. 2nd ed.* McGraw-Hill Science/Engineering/Math.
11. EN 1363-1:2012. *Fire resistance tests – Part 1: General requirements*. Brussels, 2012.

COMPARISON OF FIRE RESISTANCE OF DAMAGED FIREPROOFED STEEL BEAMS UNDER HYDROCARBON POOL FIRE AND ASTM E119 FIRE EXPOSURE

Mustafa Mahamid¹, Ataollah Taghipour Anvari², Ines Torra-Bilal³

ABSTRACT

One of the main disadvantages of structural steel is its low fire resistance. Fire incidents and elevated temperatures significantly reduce the strength of structural steel members. Concrete encasement is a common passive fireproofing method used to protect steel structures against fire. However, during their service life of a structure, the fireproofing material may be damaged. Characterized by high thermal conductivity, high temperatures spread quickly throughout the structure. This study focuses on investigating and comparing the effects of two different types of fire, Hydrocarbon Pool Fire and ASTM E119 standard fire on the response of structural steel members with damaged concrete fireproofing. Thermal and structural nonlinear Finite Element (FE) models were developed and analysed for several beam sections under different fire scenarios. A structural response comparison was carried out between the damaged fireproofed beams and fully protected beams exposed to ASTM E119 fire and Hydrocarbon Pool Fire temperatures. The deflection and strength failure limit states were investigated for each fire scenario and fire resistance of the analysed beams was determined

Keywords: Damaged fireproofing, Finite Element Analysis, Thermal-structural analysis, ASTM standard fire, Hydrocarbon pool fire.

1 INTRODUCTION

Structural steel is one of the most widely used materials in structural engineering and construction and it possesses many advantages such as high strength, high ductility, high stiffness, good durability, versatility and cost effectivity. However, when steel structures are exposed to high temperatures during fire events, strength and stiffness degrades significantly [1]. Additionally, due to high thermal conductivity, structural steel allows for a fast spread of high temperature throughout the member. Passive fireproofing is a common protection type used to protect steel members against fire in order to maintain their load-carrying capacity for a specific period of time during a fire event. One of the widely used passive fireproofing methods is concrete encasement, which provides insulation by covering structural steel members with concrete. Due to its low thermal conductivity, concrete is used to reduce the heat transfer rate during exposure to elevated fire temperatures to allow for a safe evacuation of building occupants. Fire resistance is defined as the property of a structure to withstand fire or give protection from it in order to maintain its structural integrity and stability [2]. However, during the service life of a structure, the concrete encasement is susceptible to spalling and damages. Damages in fire protection material may occur during the service life of structures due to impact, inappropriate application of fire protection material, environmental effects, removal of fire protection at connections and spalling after rapid rise of temperature [3,4].

¹ Clinical Associate Professor, University of Illinois at Chicago, Illinois, USA..

e-mail: mmahamid@uic.edu

² PhD Candidate, University of Illinois at Chicago, Illinois, USA..

e-mail: ataghi4@uic.edu

³ PhD Candidate, University of Illinois at Chicago, Illinois, USA..

e-mail: itorra2@uic.edu

Based on a specified time-temperature curve such as ASTM E119 fire [5], structural elements were exposed to elevated temperatures of a furnace. In 1980s, multiple failures of fireproofed steel members exposed to petroleum spill fires occurred in the petroleum industry [2]. This created a need to develop a new test curve to account for the severity of such incidents. The new implemented time-temperature curve was proposed to intensively expose the steel structures to significantly high temperatures, greater than that of ASTM E119 fire. This forms the basis of Hydrocarbon Pool Fire.

It is important to note that little research has been conducted on comparing the effects of different applied fires on the fire resistance of steel beams with damaged fire protection material. Kang et al. [6] performed a parametric study on steel beams with partial loss of spray-on fire protection exposed to ASTM E119 fire. It was concluded that damages in the web closer to the flanges cause more fire resistance reduction and lighter sections experience more reduction in their fire resistance than the heavier section. Gu and Kodur [7] performed a study on the response of the beams with partial damaged concrete encasement fire protection and it was concluded that fire resistance is highly dependent on the extent of insulation damage. Paya-Zaforteza et al. [8] studied the structural response of a simply supported bridge consisting of five steel girders supporting a reinforced concrete slab exposed to fire caused by the crash of a gasoline tanker. Numerical analyses were performed based on the Hydrocarbon fire curve. Dotreppe et al. [9] performed numerical simulations of Vivegnis bridge collapse in Belgium due to fire event based on the Hydrocarbon fire curve.

The aim of this study is to compare the fire resistance of damaged fireproofed steel beams under two different applied fires, the Hydrocarbon pool fire and ASTM E119 Standard fire. This study considers the effect of two parameters on various steel beam sections: fireproofing damage scenarios and type of fire scenario. Three-dimensional (3D) non-linear FE models were developed to investigate the thermal and the structural response of steel beams with damage vs. undamaged fire protection under two different types of fires. The fire resistances of various steel beams with damage scenarios were compared to the fire resistance of the fully protected beams at different load levels exposed to ASTM E119 and the Hydrocarbon fire.

2 FINITE ELEMENT ANALYSIS

Thermal and nonlinear structural finite element models were created using ANSYS [10]. In order to validate the models, the finite element analysis results were compared against previously published experimental results from large scale tests [11]. It was assumed that the structural and thermal analyses loads were independently applied and that no concrete spalling occurs due to high temperatures. Load transfer method was utilized to transfer the transient thermal results to structural analysis [12]. Similar mesh size in thermal and structural FE models was used to enable accurate mapping of the thermal results to the structural analysis.

The thermal load was applied in several time steps in the form of convection and radiation to the exposed parts to fire. Simply supported boundary conditions were applied to all studied beams. A pin support was simulated by applying zero translation in X, Y and Z axes to a row of nodes at one end and a roller support was simulated by applying zero translation in X and Y axes to a row of nodes at the other end. *Fig. 1.* shows the applied boundary conditions and loads. Lateral bracing at distances less than the maximum unbraced length for the limit state of yielding (L_p) based on *Eq. (1)* from AISC 360-16 [13] was provided to avoid any lateral-torsional buckling for all investigated cases. This was achieved by applying lateral restraint at the top and bottom flanges.

SOLID70, SHELL131 and SURF152 element types were used to create thermal FE models to simulate the concrete slab, steel sections and exposed part of the beam, respectively. Surface to surface contact pairs with bonded contact behaviour (CONTA174 and TARGE170) were used to simulate the heat transfer between parts in thermal analysis. The convection was defined as $25 \text{ W/m}^2\text{°C}$ for ASTM E119 Standard fire curve and $50 \text{ W/m}^2\text{°C}$ for the Hydrocarbon pool fire curve [5,14]. Stephan-Boltzmann coefficient of $5.67 \times 10^{-8} \text{ W/m}^2\text{°C}$ was applied per Eurocode 1 [14].

Thermal conductivity, specific heat, thermal expansion of steel and concrete at elevated temperatures were input in FE models per the proposed equations by Eurocodes 2 and 3 [15,16].

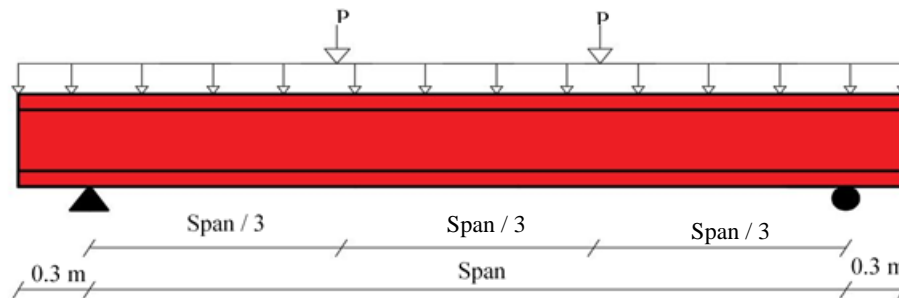


Fig. 1. Boundary conditions and applied loads configuration

$$L_p = 1.76 r_y \sqrt{\frac{E}{F_y}} \quad (\text{mm}) \quad (1)$$

Where: L_p : Maximum unbraced length for yielding limit state (mm)
 r_y : Radius of gyration about y-axis (mm)
 E : Modulus of elasticity (MPa)
 F_y : Steel yielding stress (MPa)

SOLID 185, two-layered SHELL181 and LINK180 element types were used to create structural FE models to simulate the concrete slab, steel beams and the reinforcing bars in the concrete slab, respectively. Paired surface to surface contact elements (CONTA174 and TARGE170) with bonded contact behaviour with penalty method were applied in order to simulate the interface and to allow load transfer between the concrete slab and steel beams in the FE structural analysis model. Fig. 2. shows the developed finite element model for W12x50 section.

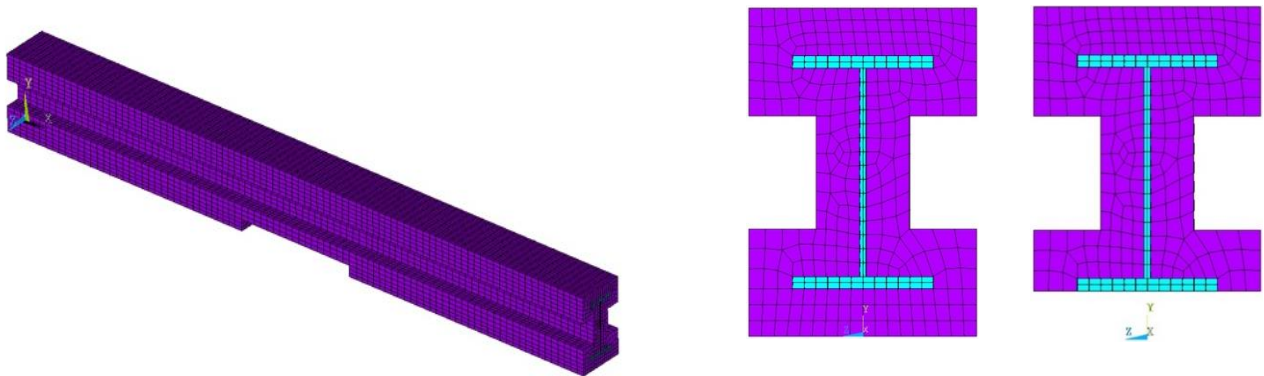


Fig. 2. The developed FE model for W12x50 with partial damaged fire protection

Material properties were inputted at various temperatures per Eurocodes 2 and 3 [15,16]. A reduction factor of yield strength and modulus of elasticity of steel was applied at elevated temperatures. The stress-strain relation of steel at high temperatures was applied per Eurocode 3 using the kinematic material model [16]. The modelling of concrete was only necessary for verification purposes since the slab is part of the structure in the analysis. Concrete simulation was not needed for the parametric study due to having no effect on the capacity of beams. Nonlinear behaviour of concrete was simulated using Drucker-Prager material model [17].

3 MODEL VALIDATION

To validate the thermal and structural finite element models, a steel girder was simulated, and the thermal and structural response of the girder was compared to the experimental results from ASTM E119 fire tests [11]. The girder includes a hot-rolled W24×62 with a 3.66 m span, a total length of 4.17 m and supported a concrete slab with 140 mm thickness and 813 mm width. Based on the coupon tests' result, 480 MPa yield stress and 240,000 MPa elastic modulus of the steel were used in the analyses along with a compressive strength of 66 MPa for the concrete, at room temperature. A concentrated load was applied at girder's mid-span. *Table 2* shows the cross-sectional properties and the applied loads of the analysed girder. *Fig. 3* shows the finite element model of the girder developed for validation purposes

Table 1. Dimensions and applied load of girder

Properties	Girder
Steel beam	W24×62
Flanges	177.8×12.7
Web	577.9×11.1
Concrete slab	813×140
Supports stiffeners	76.2×9.5
Mid-span stiffeners	76.2×12.7
Intermediate stiffeners	-
Applied load (KN)	691
Applied load/ Flexural capacity	40%
Applied load/ Shear capacity	27%
Applied load/ Shear web buckling	27%

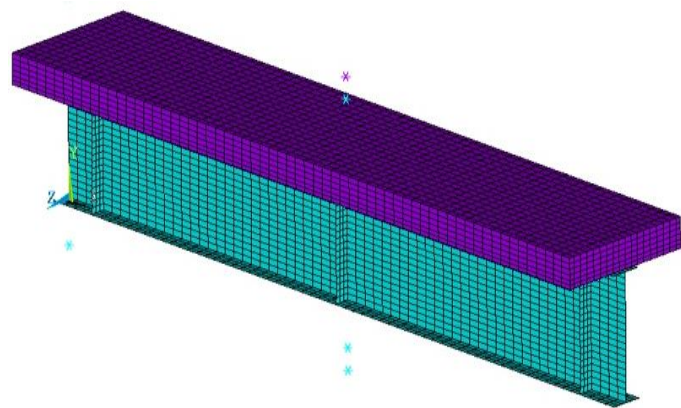


Fig. 3. FEA model of girder

The comparison of the temperatures at the flanges, web mid-depth and concrete slab mid-depth of the steel girders under ASTM E119 standard fire curve is illustrated in *Fig. 4*. As this figure illustrates, the thermal analysis results and the temperatures measured in the fire tests were in good agreement. The minor divergences between FE analysis-predicted temperatures and the ones measured during fire tests may have been caused by the small differences between actual and thermal analysis's coefficients.

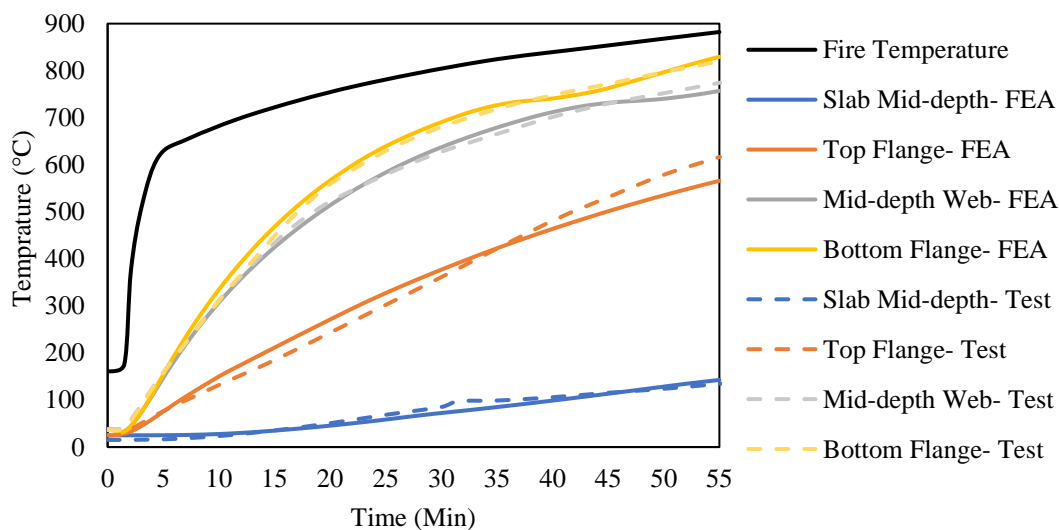


Fig. 4. Comparison of the thermal response of the tests and FEA thermal results

To validate the structural FE analysis, the measured and predicted mid-span deflections of the fire tests and FE analyses were compared over time as shown in *Fig.5*. As this figure illustrates, the structural analysis results and the mid-span deflections measured in the fire tests were in good agreement. As presented in *Fig. 4* and *Fig. 5*, the nonlinear thermal and structural finite element models were validated against previously performed test data, which proves the effectiveness of the models.

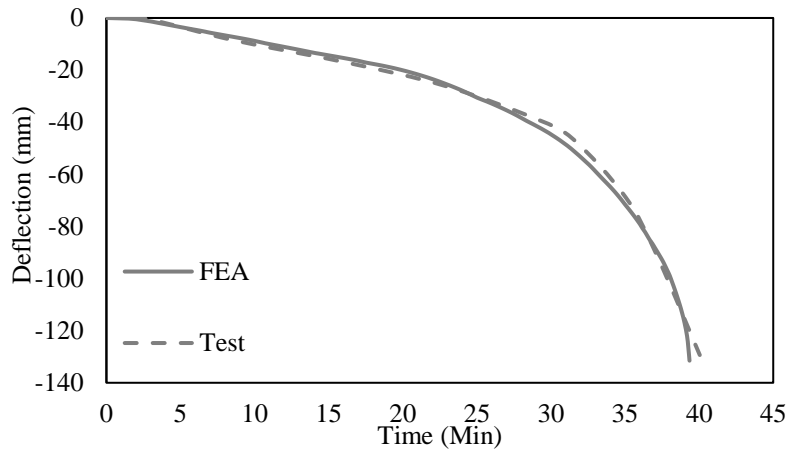


Fig. 5 Comparison of the mid-span deflection of the FEA and test results

4 PARAMETRIC STUDY

The heat propagation within the steel members has a major effect on the structural behavior of members. Thermal and structural FE models were developed to investigate the influence of the partial damages at the fire protection of the beams on the behavior of the beams. The thermal and structural FE models were validated through the comparison of the cross-section’s temperatures and mid-span deflections with experiments [11]. Damages were applied to the fire protection material (concrete encasement) on the bottom flange at the middle of the span. The behavior of four steel beams with various load levels and damage types were studied under two fire scenarios. In *Table 2*, the four beams sizes with their properties are presented.

In thermal FE analysis the temperatures of the various parts of the beam sections as well as the mid-span deflection were traced during the fire exposure. In *Fig.6*, the temperatures of various parts of W14×30 at the mid-span are compared exposed to ASTM E119 and Hydrocarbon fire. In the designation of the curves, the first part represents the applied fire scenario. The second part of the curves’ designation represents the part of the section where the temperature is measured (TF: Top Flange, W: Web, BF: Bottom Flange).

Table 2. The properties of steel beams selected for the parametric study

Section Size	Span	Area	Depth	Web	Flanges	
					Width	Thickness
in×lbs/ft	mm	cm ²	mm	t _w	b _f	t _f
				mm	mm	mm
W 14x30	488	57.10	351.5	6.9	170.9	9.8
W 14x74	488	140.64	359.9	11.4	255.8	19.9
W 18x40	823	76.13	454.7	8.0	152.8	13.3
W 18x86	823	163.23	467.1	12.2	281.7	19.6

The steel beams were exposed to fire from three sides and room temperature was applied at the top of the beam. Therefore, due to the heat dissipation from the top side, the temperature of the top flange increased at a lower rate than the bottom flange and the mid-depth of web. As it is illustrated in Fig.6 the temperatures of the bottom flanges in the damaged studied cases increased rapidly and they were close to the temperatures of the applied fire scenario's temperatures at the later stages of fire exposure. However, the temperatures in the bottom flanges and the web experienced small increase in fully protected beams. Considering that the Hydrocarbon fire is more severe than ASTM E119 fire temperature, at all cases the temperature of the different parts of beams exposed to Hydrocarbon fire were higher than the cases exposed to ASTM E119 fire temperature. The temperature of the other studied cases followed the similar trend as is presented in Fig. 6.

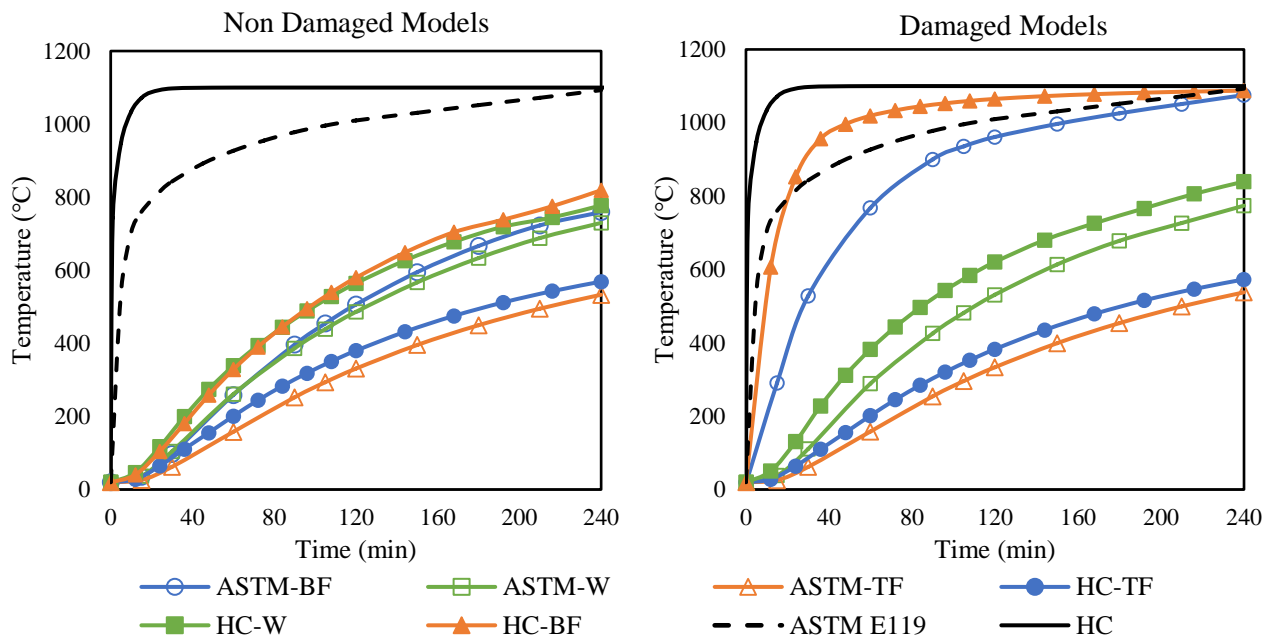


Fig. 6. Temperature of various parts of damaged and undamaged W14x30

Constant point loads were applied at one-third of the span from both ends to all studied cases to produce a bending moment at the mid-span equivalent to 50%, 70% and 90 % of the plastic moment capacity of the beams at room temperature based on AISC 360 [13]. The mid-span deflections of W14x30 under different fire scenarios exposure and load levels are shown in Fig. 7. Similar to the designation of the thermal results' curves the first part of the designation shows the applied fire scenario and the ratio of the applied load is defined in the second part of the designation.

The rapid rise of the temperature at the damaged region led to reduction of the strength of the section at mid-span. Plastic hinge was formed at the damaged area due to spread of the plasticity at mid-span that caused high deflection and failure of the beams. Similar deflections at early stages of the fire exposure can be associated with the effect of thermal gradient that the load level does not have any contribution. At later stages, the stress at the bottom flange of the cross-section reached the yielding stress at elevated temperatures. Due to the degradation of the capacity of the cross under fire exposure, the rate of deflection rise at later stages increases, which is more critical in cases with higher load levels. Additionally, at later stages, due to the spread of plasticity within the bottom flange and web of the sections at damaged region, the mid-span deflection increased rapidly, and beam could not sustain the applied load.

In Table. 3. the fire resistance of the four W shape sections under various load and fire scenarios are presented. Also, the ratio of the fire resistance of each section under Hydrocarbon fire exposure to fire resistance of the member exposed to ASTM E119 is shown. The comparison of the fire resistance ratio of the members without any damage, shows that due to exposure to a more severe

fire scenario (Hydrocarbon fire), the fire resistance of the beams is reduced for similar percentage at different load levels. However, the reduction of fire resistance of the damaged beams is more critical. Comparing the fire resistance ratio of damaged sections with similar depth, shows that the heavier beams experience higher reduction in their fire resistance. As an example, the fire resistance ratio for W14x30 is 71% for 50% load level, while that ratio is about 45% for W14x74 under the same load level which shows 29% and 55% reduction in fire resistance, respectively. The critical reduction in the fire resistance of heavier sections can be associated with the wider flanges size of the heavier sections. The larger width of the heavier sections leads to a larger exposure area to fire and rapid propagation of the high temperature within the sections. Similar pattern was also observed in the W18s' fire resistance as shown in *Table 3*.

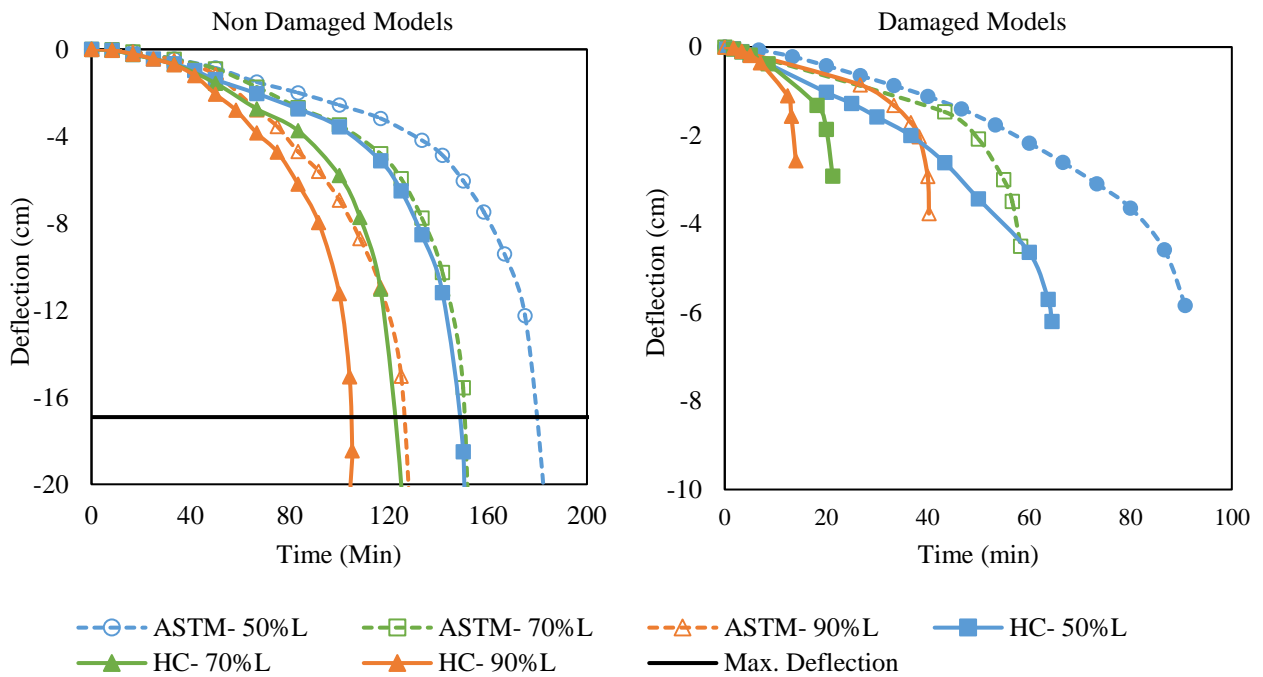


Fig. 7. Temperature of various parts of damaged and undamaged W14×30

Furthermore, the comparison of the fire resistance of the members at different load levels shows that by increasing the load level, the fire resistance of the damaged beams was reduced. Because of the existing stresses and forces within the sections at high loads, the stresses within the section reaches to elevated temperatures' yield stress rapidly during the fire exposure.

Table 3. Fire resistance of the undamaged and damaged members and the associated ratio

	Beam Sections	Fire resistance (min)						Ratio (%)		
		ASTM E119			Hydrocarbon Fire			50%L	70%L	90%L
		50%L	70%L	90%L	50%L	70%L	90%L			
No Damage (ND)	W14x30	180	151	127	142	124	105	79	82	83
	W14x74	198	165	138	167	138	113	84	84	82
	W18x40	197	164	139	150	137	116	76	84	83
	W18x86	206	172	145	175	144	120	85	84	83
Damaged (t)	W14x30	91	58	40	65	21	14	71	36	35
	W14x74	77	59	48	35	24	18	45	41	38
	W18x40	119	81	54	91	48	20	68	59	37
	W18x86	92	65	52	53	28	20	58	43	38

5 CONCLUSIONS

The following conclusions can be drawn according to the results presented in this study:

1. Deterioration of the concrete fireproofing material at the bottom flange of the steel beams may lead to a significant reduction in fire resistance of the steel members. The degradation of the strength and stiffness of the section results in increase in the mid-span deflection of the beams and ultimately causes early failure of beams.
2. At cases with the similar damage extension in the fire protection at the bottom flange, the fire resistance reduction of heavier steel beam is more critical. The larger dimension of the width of the heavier beams' leads to larger exposed area to fire and rapid increase of temperature at the cross section.
3. The application of different fire scenarios in FE thermal analyses of studied cases shows that high temperature spreads at a higher rate within the section when exposed to Hydrocarbon fire. Exposure to Hydrocarbon fire temperature curve resulted in failure of beams at earlier time compared to beams exposed to ASTM E119 standard fire temperature.

REFERENCES

1. V. Kodur, M. Dwaikat, R. Fike, (2010). *High temperature properties of steel for fire resistance modeling of structures*, J. Mater. Civ. Eng. 22 423–434. doi:10.1061/(ASCE)MT.1943-5533.0000041
2. J. Milke, V. Kodur, C. Marrion. *A overview of fire protection in buildings*, World Trade Center Building Performance Study
3. M.M.S. Dwaikat, V.K.R. Kodur, (2012). *A Simplified Approach for Predicting Temperature Profile in Steel Members With Locally Damaged Fire Protection*, Fire Technol. 48 493–512. doi:10.1007/s10694-011-0241-x.
4. W.Y. Wang, G.Q. Li, *Behavior of steel columns in a fire with partial damage to fire protection*, J. Constr. Steel Res. 65 (2009) 1392–1400.
5. ASTM E119-16a Standard Test Methods for Fire Tests of Building Construction and Materials, ASTM International, West Conshohocken, PA, 2016, <https://doi.org/10.1520/E0119-16A>, (n.d.). doi:10.1520/E0119-15.
6. Kang, Y., G. V. Hadjisophocleous, and H. A. Khoo. "Effect of Partial loss of Spray-on Protection on the Load Capacity of Steel Beams during a Standard Fire." *Journal of Fire Protection Engineering* 18, no. 1 (2008): 5-27.
7. L. Gu, V. Kodur, (2012). *Role of Insulation Effectiveness on Fire Resistance of Steel Structures under Extreme Loading Events*, J. Perform. Constr. Facil. 25 277–286. doi:10.1061/(ASCE)CF.1943-5509.0000172.
8. Payá-Zaforteza I, Garlock, MEM. (2010). *A 3D numerical analysis of a typical steel highway overpass bridge under a Hydrocarbon fire*, Fifth international conference for structures in fire. East Lansing, p. 11–8.
9. Dotreppe JC, Majkut S, Franssen JM. (2006). *Failure of a tied-arch bridge submitted to a severe localized fire, structures and extreme events*. IABSE Symposium;. p. 272–273.
10. ANSYS® Academic Research, Release 17.1, (n.d.).
11. E.M. Aziz, V.K. Kodur, J.D. Glassman, M.E. Moreyra Garlock, (2015). *Behavior of steel bridge girders under fire conditions*, J. Constr. Steel Res. doi:10.1016/j.jcsr.2014.12.001.
12. ANSYS® Academic Research, Release 17.1, Help System, Coupled Field Analysis Guide, ANSYS, Inc.
13. Specification for Structural Steel Buildings, Specification for Structural Steel Buildings, 2016.

14. EN 1991-1-2 (English): Eurocode 1: Actions on structures - Part 1-2: General actions - Actions on structures exposed to fire, 2002.
15. EN 1992-1-2 (English): Eurocode 2: Design of concrete structures -Part 1-2: General rules -Structural fire design, 2004.
16. EN 1993-1-2 (English): Eurocode 3: Design of steel structures -Part 1-2: General rules -Structural fire design, 2005.
17. ANSYS® Academic Research, Release 17.1, Help System, Material Reference, ANSYS, Inc.

Timber Structures and Fire Protection Materials

MODELLING NON-METALLIC TIMBER CONNECTIONS IN FIRE

Ranim Dahli ¹, Martin Gillie ², John Gales ³

ABSTRACT

With growing interest in using timber in high-rise construction, the fire safety of such structures has been questioned, especially given that timber is a combustible material. Connections are a key element in structural design, with increasing importance in the design of timber structures because they can influence the fire resistance of timber assemblies. Since metallic connections conduct heat rapidly, they cause internal charring of timber members resulting in decreased fire performance. Non-metallic timber connections have been considered as a solution to this problem, and their fire performance has been tested to confirm their lower heat conductivity and better fire resistance. This paper presents a sequential thermal-stress analysis using FEM in order to develop a better understanding of non-metallic timber connections at elevated temperatures. A heat-transfer model allows the study of the temperature profiles through thickness, and the influence of metallic dowels is also examined. This permits a better understanding of the behaviour of connections at elevated temperatures, as the residual strength of timber could be studied using a sequential-coupled stress model. The results of this elastic model show that, despite the simplicity of the input material properties based on ‘reduced properties method’, the behaviour of connections is still captured. Thus, the results of this investigation encourage further development of 3D FEM modelling of timber behaviour in fire. Lastly, this research shows FEM to be a potentially powerful tool that will enable advanced understanding of the behaviour of timber components in elevated temperatures.

Keywords: Timber structures, finite element modelling, connections.

1 INTRODUCTION

The combustible nature of timber has led to questions about its fire-safety as a structural material, especially for mid- and high-rise buildings. Previous literature covered a range of key fire safety issues and the application of timber in modern construction [1], [2]. The charring rate of timber has been substantially investigated, as it’s currently the predominant approach in quantifying fire resistance. A recent investigation [3] of the charring rates of Cross Laminated Timber (CLT) samples exposed to simulated standard fire curve showed close agreement with existing literature, however, cases of more and even less severe fires demonstrate conflicting values. The authors suggest that it is necessary to look beyond charring as it is just one part of the pyrolysis process, and in order to develop a better understanding of the strength of timber in fire, temperature profiles through the thickness must be determined. Therefore, work is needed to develop tools that enable the predication of the temperature profiles in cross-sections, and then to link these to reductions in mechanical properties.

Another key fire safety concern in timber construction is understanding the fire behavior of connections between members. Connections can determine the load carrying capacity of timber structures at both normal and elevated temperatures, and they are a key element in structural design

¹ Postgraduate Student, Department of Civil Engineering, York University, Toronto, Canada.
e-mail: rdahli@yorku.ca

² Professor of Civil Engineering, School of Engineering, University of Warwick, Warwick, UK.
e-mail: m.gillie@warwick.ac.uk

³ Assistant Professor, Department of Civil Engineering, York University, Toronto, Canada.
e-mail: jgales@yorku.ca

[4]. The fire resistance of exposed timber connections containing metal usually does not exceed 20 minutes [5]. This can be explained by metal's high thermal conductivity, At high temperatures, connections conduct heat from the surface to the interior fast, leading to wood charring within timber members and thus the loss of the strength [6]. To try and ensure the fire performance of steel connections in timber structures, encapsulation with fire barriers has been the common design approach. However, the solution has proven to be neither aesthetically appealing, nor cost effective [7]. Gypsum plasterboards are often used for encapsulation, and fall-off times are not monitored appropriately in full scale tests [8]. In addition, fall-off times may not reflect the behaviour of real fire exposure, as they are based on a standard fire exposure [9]. Given these problems with metal connections, alternative non-metallic connections have been investigated to enhance the fire resistance of timber structures.

Thomson showed the viability of an alternative non-metallic connection that consists of glass-fibre-reinforced-polymers (GFRPs) shear dowels, combined with a densified veneer wood (DVW) flitch plate [10]. Reducing the amount of metal within timber structures has advantages that include; corrosion resistance, reduced weight of connection, improved fire resistance and reduced thermal bridging potential. The connections have been investigated experimentally and new analysis methods were proposed by Thomson [10] in order to predict the connection's behaviour - based on the works of Shanks and Walker [11]. Following the works of Thomson, new analytical predictions of interlaminar shear failure of composite dowels were presented in Brandon's thesis [12]. Brandon also conducted an experimental study [13] investigated the fire performance of the connection using a standard cone calorimeter apparatus and a novel heat transfer rate inducing system (H-TRIS) [14]. An environmental chamber of temperatures up to 610°C was used to study the mechanical behaviour of the connections during severe heating. The temperature was increased at a rate of 15°C /min until it reached 610°C where it was kept for the remaining duration of the test.

Thus, for the research of timber connections, experimental approaches have dominated to date, with the development of numerical modelling techniques seeing a dearth of attention. With high costs associated with full scale fire experiments and limited to no available facilities in some countries, the development of experimentally validated numerical models would reduce the number of future tests needed, which will be of great benefit in advancing knowledge on timber structures in fire. This is especially true since the variability of wood currently requires a variety of specimens to be tested, an expense which could be overcome by a validated modelling approach. Moreover, numerical modelling techniques enable the study of a specific parameter or failure criterion, unlike experimental approaches where the isolation of the influence of a specific parameter is often not possible. Hence, numerical models of timber structures could become a powerful tool to fire-engineers if well-validated methods were developed. They would allow understanding of structural behaviour, and provide sound optimised designs. Currently however there is a need to develop such models based on pre-existing data sets. To address this research need, this study presents a novel approach to 3-D finite element modelling of timber that enables the study of non-metallic dowel-flitch plate connections in fire.

2 NUMERICAL STUDY

2.1 Heat Transfer Modelling

In the first modelling step, the evolution of temperature profiles across timber cross-sections is predicted, a process which is uncommon in timber research. However, a large portion of Brandon et al.'s work [13] was aimed at investigating the temperature evolution of non-metallic timber connections. This was driven by the need to determine the influence of the GFRP dowel on the heat-transfer within the connection. Consequently, a better understanding of mechanical properties of

timber could be achieved by determining the temperature profile through thickness and resulting strength.

The parameters used to create the model are described to allow future adaptation of this model, by incorporating the parameters in the same software or another more accessible software. In this case the Abaqus finite element modelling software was used for computational analysis. A heat-transfer model was set up in order to examine temperature profiles at the connection. The dowels were included, and Fig. 1 shows the dimensions of the model built in Solid Works.

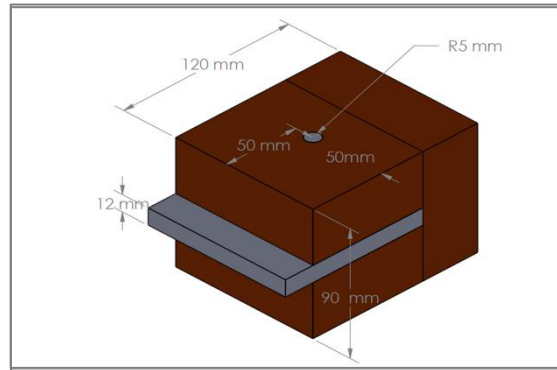


Fig. 1. Non-metallic connection dimensions in SolidWorks

To predict the temperatures in the connection, timber thermal properties were taken from data in Annex B in Eurocode 5 [15]. This data is intended for softwood, while the connections are actually made of DVW and LVL. However, previous literature, including [12] and [16], indicates that the use of these properties leads to acceptable modelling results.

To simplify the numerical model, heat transfer by conduction is modelled, which is achieved by defining the surface temperature of the connection block as a boundary condition. The initial temperature of the material was set to 20°C in accordance with Eurocode 5, and the temperature curve implemented represents that in the environmental chamber.

Fig. 2 shows experimentally and numerically determined temperatures of test series FA by [12]. Thermocouples were placed at the surface of the specimens in order to capture the surface temperature denoted as Node A. The internal temperatures, at Nodes B, C and D, are averaged values of four thermocouples in an unloaded test, where nodes are placed 15 mm apart. The ABAQUS FEM results show close agreement with the experimental and numerical results presented in Figure 2. despite the thermal properties used strictly being for standard fire exposure, and for softwood.

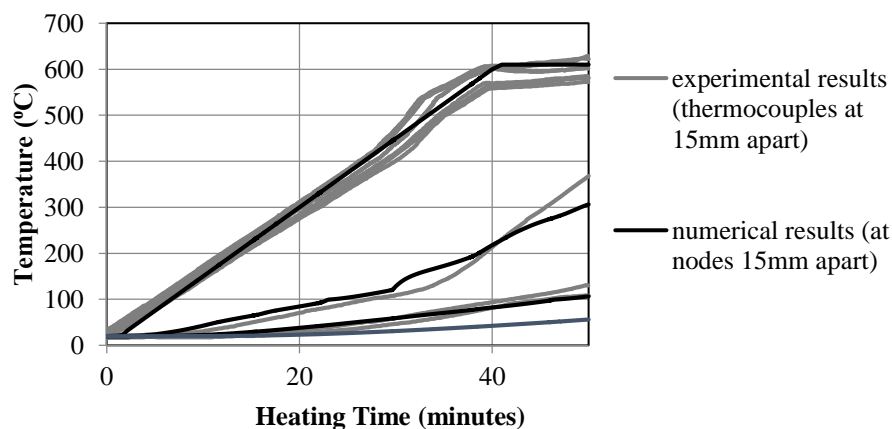


Fig. 2. Validation of FEM temperature profiles against experimental and numerical predications

2.2 Structural Modelling

Abaqus was again used to model the stresses in the connection. The model was set up to study the behaviour of the GFRP dowels only and not the metallic ones. The geometry used in this stage of the analysis is the same as the one used in the heat transfer model. The number of elements of the model, and their assembly is consistent with previous heat-transfer model created.

In order to model the resultant stresses at elevated temperatures, mechanical properties varying with temperature are required. The properties of timber have been defined based on the relative modulus of elasticity in tension from Eurocode 5. The effect of temperature on the modulus of elasticity parallel to the grain is shown below. Poisson's ratio was taken as 0.27. Moreover, the properties of GFRP have been defined based on Brandon's experimental determination of the behaviour of GFRP with exposure to increasing temperature [12] and on that basis, Young's Modulus was defined in the model. The Young's Modulus at temperatures above 200 °C was assumed not to change. Poisson's ratio taken as 0.29.

3 RESULTS AND ANALYSIS

3.1 Heat Transfer Model

Using Finite Element as a modelling tool provides very refined data that can be generated for specific points of interest. In experimental investigations, thermocouples are placed at specific points where data would be collected, and in some cases they might drop-off and the repetition of the experiment is required. FEM has another additive advantage of providing visuals that convey the results more effectively. In this investigation, the 3-dimensional modelling enabled a better understanding of the temperature profiles in the direction of the heat flow and perpendicular to it. It also allows focusing on specific parts of different members, which in other approaches could be difficult.

3.1.1 Temperature Profiles within dowels

A comparison between the use of metallic and non-metallic timber connections is achieved by changing the material properties of the dowels. The temperature profiles in dowels are examined first and the results are presented in the below figures.

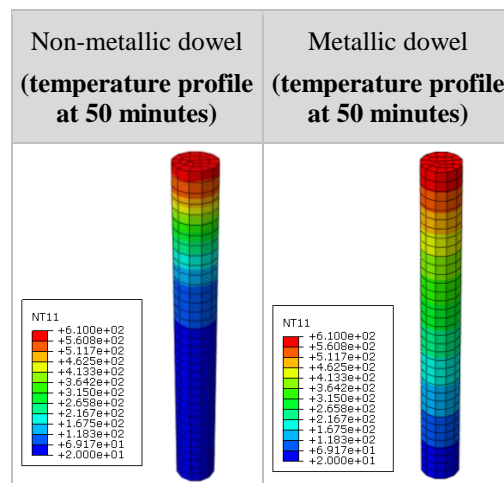


Fig. 3. Temperatures of metallic and non-metallic dowels

The results confirm our existing knowledge of thermal properties of both timber and steel; with steel being a high heat conductor, unlike timber. Nevertheless, at first instance from looking at Fig. 3 above, it can be noted that significant temperature changes occur at about one-third of non-metallic dowels, and almost fully throughout the metallic dowels. Particular degrees of temperatures associated with

the start of pyrolysis and charring are the most relevant to this discussion. The timber is known to char at approximately 300 °C and the pyrolysis process starts at around 200 °C. Bearing in mind the temperature range of 200-300 °C, the proportion of timber prone to undergoing pyrolysis and forming char could be determined. Approximately, 57% of the metal dowel’s length represents temperatures that lead to pyrolysis or timber charring. In contrast, only 22% of the length of non-metallic connection corresponds to those temperatures. Furthermore, the change in temperature is plotted along the length of the dowels and presented in Fig. 4.

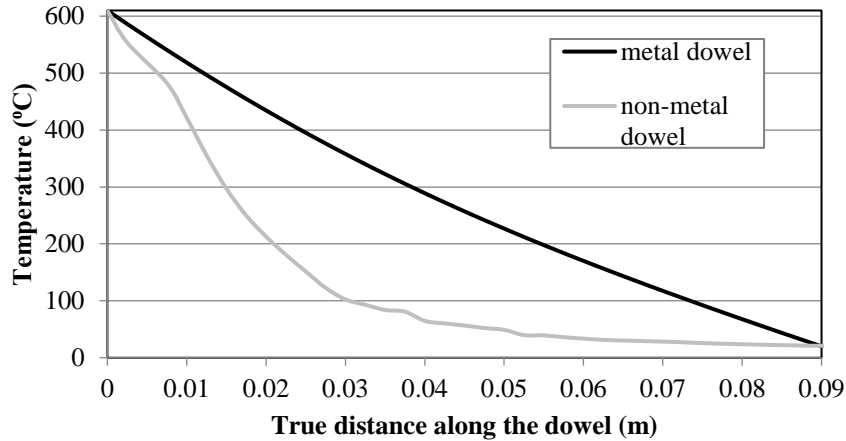


Fig. 4. FEM Results of Temperature against the distance along the dowel

3.1.2 Temperature profiles in the direction of heat flow

In order to investigate the temperature profiles in the direction of the heat flow a longitudinal section has been made in the Abaqus model at mid-point of the connection. The results below (Figure 5 – Fig. 5) represent the assumption made at the start of modelling, where the timber governs the heat transfer across the whole section. It is evident that the top half section above the flitch plate is heated, while the remaining section is exposed to very little heat that is almost negligible. In comparison, the model sections of the metallic connections are presented in Fig. 5.

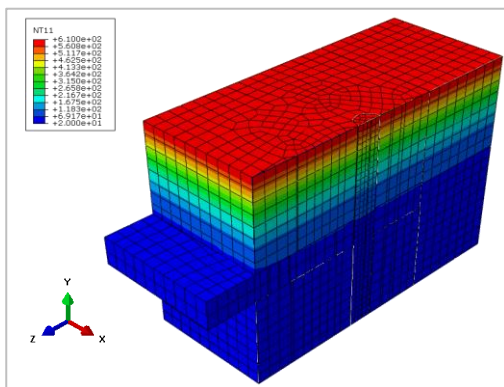


Fig. 5. Temperature profile of non-metallic connection in the direction of heat flow, at 50 minutes of heating (longitudinal 3D section)

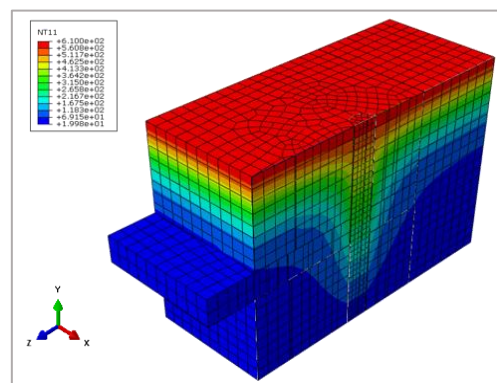


Fig. 5. Temperature profile of metallic connection in the direction of heat flow, at 50 minutes of heating (longitudinal 3D section)

In the section above, the influence of the metallic connection in the direction of heat flow is clear. The temperature contours extend beyond the flitch plate, unlike in the non-metallic connection. Temperature profiles associated with charring and pyrolysis (between 200-300 °C) also increase,

meaning a greater proportion of timber is likely to char. The temperature contours have been adjusted to illustrate the depth of the char and the sections undergoing pyrolysis. Light grey area represents the area undergoing pyrolysis in Figure 7, where the maximum limit was set as 200 °C. In Figure 8, the maximum limit was set as 300 °C representing the charred layer.

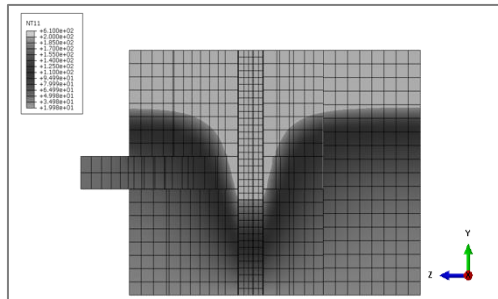


Fig. 7. Section illustrating pyrolysis (at 200 °C) through connection (at 50 minutes)

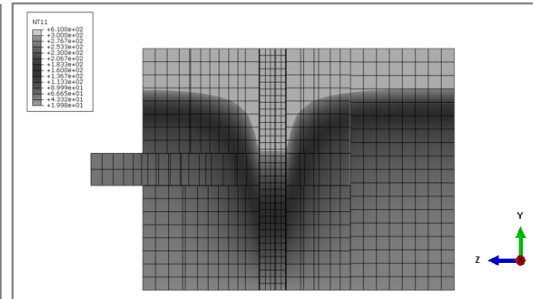


Fig. 8. Section illustrating charring (at 300 °C) through connection (at 50 minutes)

The layer of timber undergoing pyrolysis in Figure 7 has approximately a thickness of 40mm from the edge, and increases to about 55mm in the area adjacent to the dowel. The proportion of char out of the layer undergoing pyrolysis is around 15mm at the edge and 38mm close to the dowel as shown in Figure 8. In comparison, the figure illustrating the metallic connection shows that the timber char formed deeper in the section. The area surrounding the dowel also fully charred, which is known to be the location where the highest stress are formed. This resulted in an embedment failure of the specimen when the specimen was mechanically loaded [13].

3.2 Structural Model

The findings of Brandon et al.’s investigation [13] suggest that flitch plate failure and shear plug failure could be prevented by the intumescent layer, hence other failure modes are likely to occur at later points in time. The failure-modes of the connection after the application of the protective layer haven’t been studied yet. The numerical model presented here enables the investigation of the behaviour of the non-metallic connection beyond the points experimentally investigated.

As previously mentioned in the heat-transfer section, the model was created by only exposing one side of the connection to heat (in Figure 1, heat exposure was applied to the top side of the connection). Thus, the influence of having one side of the connection char on the remaining section of the connection could be explored. Eurocode 5 provides expressions to determine the strength of mechanically fastened metallic connections. These expressions were adapted from the European Yield Model (EYM) which was originally proposed by Johansen. Figure 9 presents EC5 failure modes for connections made out of central plates and dowels.

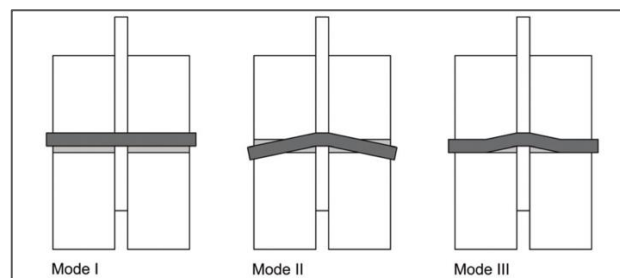


Fig. 9. European Yield Model failure modes of flitch plate connections

The results of the numerical model below, presented a failure mode similar to Mode III of the European Yield Model for the behaviour of the connections at ambient temperatures (Figure 10). At elevated temperatures, a new failure mode was predicted at one sided exposure, of a combined shear plug failure and an embedment failure (Figure 11). The behaviour of the connection did not change with increasing load, this is due to the use of elastic parameters in this model.

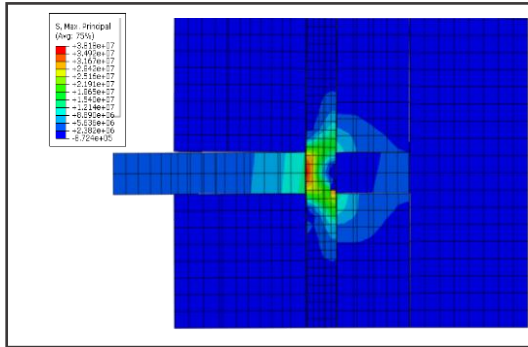


Fig. 10. FEM results of stresses at ambient temperature of the non-metallic connection (maximum principle stresses at 40% load case)

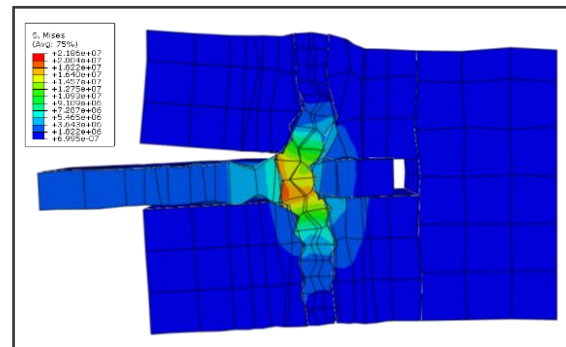


Fig. 11. Deflected shape of Abaqus stress model (at 20% load case and 200 deflection factor)

Further improvements to this model would include the study of the plastic behaviour of the connection, and inclusion of inter-laminar shear behaviour of the dowel. Finally, as there are no current experimental investigations of the behaviour of the connection after the use of an intumescent layer, a new project could be set up to determine failure modes at elevated temperatures experimentally and modelled numerically. The results could be used to confirm time-to failure predicted by FEM.

4 CONCLUSIONS

This study has presented a 3-D finite element model used to examine non-metallic timber connection in fire. The model was created as a sequential thermal-stress analysis using the Abaqus software. The heat-transfer model was created using softwood properties available in Eurocode 5 Appendix B. The results of the model were validated against analytical and numerical results confirming that the heat transfer in the connection is governed by timber. Validation results also confirm that EC5's thermal properties yield good results, without the need for a complicated timber material property model. A comparison between metallic and non-metallic dowels indicated that the heat flow in metallic connections is controlled by the metal dowels where a larger proportion of timber charred deeper in the section.

Key conclusions from this study are:

- Numerical heat-transfer modelling of timber connections in fire offers insights into temperature distributions not available from experimental or analytical methods. Given the close link between connection (and by extension structural) strength, temperature, in timber structures in fire, the ability to predict temperatures in this way is valuable.
- Stress and failure analysis of timber connections in fire using a numerical approach has also been shown to be practical. This is believed to be the first study able to predict connection failures in this way. Given the complexity and novel materials increasingly being used connections, this ability is also of value.
- It has been shown that the FE model, despite its relative simplicity, was quite capable of modelling the elastic behaviour of the connection at elevated temperature. Thus, the results of

this investigation encourage more effort to develop 3D FEM in order to address the limited number of numerical models available of connections at elevated temperatures.

REFERENCES

- [1] C. Jeanneret, M. Smith, and J. Gales, "Fire Safety Research Towards Enabling Timber Structures in Canada," in *Applications of Fire Engineering*, 2017, pp. 263–273.
- [2] B. Östman, D. Brandon, and H. Frantzich, "Fire safety engineering in timber buildings," *Fire Saf. J.*, vol. 91, no. April, pp. 11–20, 2017.
- [3] A. I. Bartlett, R. M. Hadden, L. A. Bisby, and A. Law, "Analysis of Cross-Laminated Timber Charring Rates Upon Exposure To Non- Standard Heating Conditions," *14th Int. Conf. Fire Mater. 2015*, 2015.
- [4] B. Östman *et al.*, "Fire Safety in Timber Buildings : Technical Guideline for Europe," 2010.
- [5] O. Carling, *Fire Resistance of Joint Details in Loadbearing Timber Construction: A Literature Survey*. Building Research Association of New Zealand, 1990.
- [6] A. H. Buchanan, *Structural design for fire safety*. John Wiley & Sons, 2002.
- [7] R. Gerard, D. Barber, and A. Wolski, "Fire Safety Challenges of Green Buildings," *Arup North Am.*, no. November, p. 45, 2012.
- [8] A Just, J Schmid, J. König, "Gypsum plasterboards used as fire protection-analysis of a database." 2010.
- [9] A. Frangi, M. Fontana, and M. Knobloch, "Fire design concepts for tall timber buildings," *Struct. Eng. Int. J. Int. Assoc. Bridg. Struct. Eng.*, vol. 18, no. 2, pp. 148–155, 2008.
- [10] A. Thomson, "The structural performance of non-metallic timber connections," University of Bath, 2010.
- [11] J. Shanks and P. Walker, "Strength and Stiffness of All-Timber Pegged Connections," *J. Mater. Civ. Eng.*, vol. 21, no. 1, pp. 10–18, 2009.
- [12] D. Brandon, "Fire and structural performance of non-metallic timber connections," University of Bath, 2015.
- [13] D. Brandon *et al.*, "Fire performance of metal-free timber connections," *Proc. Inst. Civ. Eng. - Constr. Mater.*, vol. 168, no. 4, pp. 173–186, Aug. 2015.
- [14] L. Maluk, C & Bisby, "A NOVEL TEST METHOD FOR MATERIALS AND STRUCTURES," in *8th International Conference on Structures in Fire*, 2014.
- [15] EN1995-1-2, "Eurocode 5: Design of timber structures - Part 1-2: General -structural fire design." 2004.
- [16] P. B. Cachim and J.-M. Franssen, "Numerical modelling of timber connections under fire loading using a component model," *Fire Saf. J.*, vol. 44, no. 6, pp. 840–853, 2009.

IMPROVEMENTS TO THE COMPONENT ADDITIVE METHOD

Katrin Nele Mäger¹, Alar Just², Andrea Frangi³

ABSTRACT

Different component additive methods (CAM) for the calculation of the separating function of timber structures have been established. Currently the most versatile method was developed by Schleifer [1] (also presented in [2]) as an improvement to the method detailed in Annex E of EN 1995-1-2:2004 [3]. The method developed by Schleifer is included in the Swiss and Austrian national annexes of EN 1995-1-2.

Within this paper some important clarifications, recommendations, improvements and ties to other normative references will be detailed. The new approach to the contribution of fire rated claddings presented in [4] will be summarised. Additionally, the connections between CAM and the testing standard EN 13381-7 [5] will be explained. Recommendations for detailing and some simplifications for the use of the method are presented as a guidance for the practicing engineer. A comparison of CAM and the method in Annex E of the current EN 1995-1-2 is given.

The study is based on a large collection of full-scale and model-scale fire tests and thermal simulations and aims to further improve the calculation methods in the revised EN 1995-1-2 where CAM will be included in the main part.

Keywords: Timber structures, Component Additive Method, separating function, finite element modelling

1 COMPONENT ADDITIVE METHOD

The Component Additive Method is based on the contributions of each layer to the fire resistance of the whole assembly considering different heat transfer paths. This method is applicable to timber assemblies consisting of unlimited number of layers of inorganic claddings, wood-based materials, insulations and their combinations. Extended use of the method for verification of the separating function of other light frame structures may be possible in the future.

The fire resistance of the assembly to fulfil the insulation criterion is the time between the start of the fire exposure and the time when the temperature on the unexposed side of the structure reaches a temperature rise of 140 K on average over the whole surface or 180 K in a single point [7]. Generally, the starting (ambient) temperature is 20°C, therefore the temperature criteria become 160°C and 200°C, respectively. Only the average temperature rise can be assessed by calculations. As the assembly usually consists of multiple layers that fulfil different functions, different names and symbols are used according to *Fig. 1*. The layer on the fire unexposed side is a layer with

¹ Project Specialist. Department of Civil Engineering and Architecture, Tallinn University of Technology, Tallinn, Estonia.
e-mail: katrin.mager@ttu.ee

² Professor. Department of Civil Engineering and Architecture, Tallinn University of Technology, Tallinn, Estonia.
Researcher. Safety, RISE Research Institutes of Sweden, Stockholm, Sweden.
e-mail: alar.just@ttu.ee

³ Professor. Institute of Structural Engineering, ETH Zürich, Zürich, Switzerland.
e-mail: frangi@ibk.baug.ethz.ch

insulating function. For this layer the insulation time is determined. All the other layers have a protecting function and the protection time is determined.

In analogy to the classification of fire protective claddings (coverings) according to EN 13501-2 [7], the protection time is the time until the temperature rise behind the considered layer is 250 K on average or 270 K at any point. Ambient conditions are usually 20°C, hence the temperature criteria become 270°C and 290°C, respectively. These criteria are approximations to account for the failure (or fall-off) of thermally degraded material layers. They are also close to the charring temperature of timber (300°C). Therefore, the sum of protection times of the layers preceding the timber elements may be used as a slightly conservative starting time of charring.

The insulation time of the last material layer is the time during which the temperature rise on the unexposed side is equal to 140 K on average over the whole area and 180 K at any point. The same temperature criteria are used for the fire resistance (insulation time) of the whole assembly.

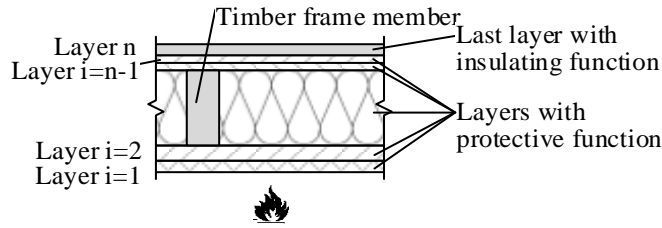


Fig. 1. Numbering and function of the layers in a timber frame structure

The time of fire resistance for insulation criterion of the whole assembly is calculated as shown in Eq. (1).

$$t_{ins} = \sum_{i=1}^{i=n-1} t_{prot,i} + t_{ins,n} \quad (1)$$

where t_{ins} is the total insulation time of the assembly [min];

$t_{prot,i}$ is the protection time of each layer in the direction of the heat flux [min];

$t_{ins,n}$ is the insulation time of the last layer of the assembly on the unexposed side [min].

The protection times of layers before the last layer can be calculated taking into account the basic values of the layers, the position coefficients and joint coefficients by Eq. (2).

$$t_{prot,i} = (t_{prot,0,i} \cdot k_{pos,exp,i} \cdot k_{pos,unexp,i} + \Delta t_i) \cdot k_{j,i} \quad (2)$$

where $t_{prot,i}$ is the protection time of the considered layer i [min];

$t_{prot,0,i}$ is the basic protection value of the considered layer i [min];

$k_{pos,exp,i}$ is the position coefficient that takes into account the influence of layers preceding the layer considered;

$k_{pos,unexp,i}$ is the position coefficient that takes into account the influence of layers backing the layer considered;

Δt_i is the correction time for considered layer i protected by fire rated cladding [min];

$k_{j,i}$ is the joint coefficient for layer i .

Insulation time of the last layer is calculated similarly to protection time, taking into account the basic insulation time of the layer, the position coefficients and joint coefficients.

The coefficients and basic values are dependent on the material of the considered layer and the preceding and backing layers. Generic values of the basic protection times, basic insulation times and coefficients for timber, gypsum boards and mineral wool insulations are presented in the European technical guideline Fire Safety in Timber Buildings (FSITB) [2] based on the work of Schleifer [1]. The necessary parameters for other materials and products should be determined according to [6].

2 NORMATIVE CONNECTIONS

Although CAM is used for the calculation of separating function of timber assemblies, it is closely tied to other calculation methods and linked to testing standards. Such links mean that less information is needed by the designers of timber structures to make a comprehensive evaluation of the assembly. These connections with other European standards are explained in the following.

2.1 Ties with EN 13381-7

The European testing standard for the performance of applied fire protection to timber members EN 13381-7 [5] gives rules for experimental assessment of the start of charring, charring rate and failure time of fire protection system. These characteristics are determined from temperature measurements taken using thermocouples placed at different locations within the specimen.

The new approach regarding correction times (presented in the next chapter) includes the protection coefficient k_2 and fall-off time t_f of claddings determined according to the standard. The protection coefficient k_2 is the ratio of the measured charring rate of the substrate while protected by a cladding and unprotected charring rate. Both parameters are also used to calculate the load-bearing capacity of initially protected timber members using the Effective Cross-Section Method (ECSM).

The start time of charring measured by thermocouples on the interface of protective material and timber substrate according to this standard can be used as input in the method as the protection time of the fire protection system if the tested system is applied on the fire exposed side of the assembly in exactly the tested configuration.

2.2 Ties with EN 13501-2

The European standard EN 13501-2 [7] defines, among other things, the resistance to fire performance characteristics. These include the Thermal insulation criteria – I – and the Fire protection ability – K. Both these characteristics are given as a time of standard temperature/time fire exposure during which the performance criteria are fulfilled.

Thermal insulation criteria according to EN 13501-2 are the same as set as the insulation time criteria in CAM: the mean temperature rise on the unexposed surface of the assembly shall not exceed 140°C and the maximum temperature rise at any point is limited to 180°C.

If the protection material or system (covering) is classified as K₁ or K₂ it is assigned a time (10, 30 or 60 minutes) during which the criteria are fulfilled. This time value can be used as a conservative basic protection time for the tested material. The temperature criteria (mean temperature rise of 250°C and maximum 270°C at any one point) are in correlation with the criteria of the method. The test of the protective material is simple, the substrate used behind the investigated material shall be one that is commonly protected by the tested material and often the substrate is a chipboard (similar to the wood fibreboard used as the substrate for CAM). The implied conservativeness is due to a second criterion set in the standard which states that no visible burnt, charred, melted or shrunk material can be present on the substrate.

If the K-class is used as the basic protection time, other coefficients necessary for the method shall be taken from relevant literature (e.g. FSITB [2]) or determined according to the procedure for implementing new materials [6].

3 FIRE RATED CLADDINGS (FRC)

The layer, usually cladding, on the fire exposed side of the separating structure has the greatest influence on the fire resistance of the whole structure. Where higher fire resistances are required, this cladding material is usually a gypsum plasterboard type F or gypsum fibreboard which are both currently the only material types considered as fire rated claddings in the method.

A new approach to more realistically account for the better performance of fire rated claddings or cladding systems has been presented [4]. The calculations include the fall-off time (t_f) and the

protection coefficient (k_2) of the cladding or cladding system. This approach is summarised and extended/clarified in the following.

The calculation of correction time starts with the determination of the fall-off time of the fire rated cladding ($t_{f,p}$). The protection time of the FRC ($t_{prot,p}$) should also be calculated. Then, the maximum protection time of the layer i when the cladding stays in place is determined according to Eq. 3:

$$t_{prot,max,i} = \frac{t_{prot,0,i}}{k_2} \quad (3)$$

where k_2 is protection coefficient of the protective cladding or cladding system.

For gypsum plasterboards the coefficient is taken according to Eq (C.3) from EN 1995-1-2:2004:

$$k_2 = 1,05 - 0,0073 \cdot h_p \quad (4)$$

where h_p is thickness of gypsum plasterboard(s) in millimetres.

The determination of correction time to be added to the investigated layer follows the limits shown in Fig. 2. and described by Eq. 5-9.

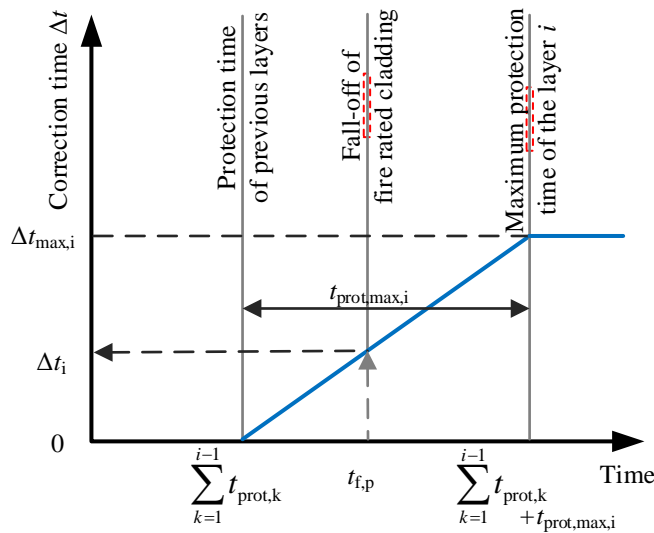


Fig. 2. Limits of the correction time

The indices used in Fig. 2. and in the following equations:

i investigated layer (may be the first or any next layer after the FRC);

p fire rated cladding (FRC) or cladding system.

The limits for the correction times are defined as follows (see Fig. 2):

- When the fall-off time of the cladding $t_{f,p}$ is less than or equal to the sum of protection times of the preceding layers (including the protection time of the fire rated cladding $t_{prot,p}$), then no correction time is applied.

$$t_{f,p} \leq \sum_{k=1}^{i-1} t_{prot,k}, \Delta t_i = 0 \quad (5)$$

- When the fall-off time of the cladding $t_{f,p}$ is greater than the sum of protection times of the preceding layers (including the protection time of the fire rated cladding $t_{prot,p}$) and the maximum protection time of the investigated layer i , then the maximum correction time for layer i is applied.

$$t_{f,p} \geq \sum_{k=1}^{i-1} t_{prot,k} + t_{prot,max,i}, \Delta t_i = \Delta t_{max,i} \quad (6)$$

The maximum correction time that can be considered is expressed as

$$\Delta t_{max,i} = t_{prot,max,i} - t_{p,i} \quad (7)$$

where $t_{p,i}$ is the protection time of the investigated layer without correction time (Eq. 8).

$$t_{p,i} = t_{prot,0,i} \cdot k_{pos,exp,i} \cdot k_{pos,unexp,i} \cdot k_{j,i} \quad (8)$$

- When the fall-off time of the cladding is greater than the sum of protection times of the preceding layers but less than the sum of protection times of the preceding layers and the maximum possible protection time of the layer i , then linear interpolation is possible.

$$\sum_{k=1}^{i-1} t_{prot,k} \leq t_{f,p} \leq \sum_{k=1}^{i-1} t_{prot,k} + t_{prot,max,i}, \Delta t_i = \frac{\left(t_{f,p} - \sum_{k=1}^{i-1} t_{prot,k} \right) \cdot \Delta t_{max,i}}{t_{prot,max,i}} \quad (9)$$

where $t_{f,p}$ is the fall-off time of the cladding (system).

Correction time Δt can be applied for the next layer(s) after the fire rated cladding system which can consist of single or multiple layers. The correction time is added to all layers after the fire rated cladding where the sum of the protection times of the preceding layers is less than the fall-off time of the fire rated cladding.

In the following, a schematic example calculation is shown in Fig.3. The continuous line in the figure shows the sum of protection times after each layer of the assembly. The dashed lines show the resulting protection times if no correction times are added (or if correction time is added only to layer 3 which is directly protected by the FRC).

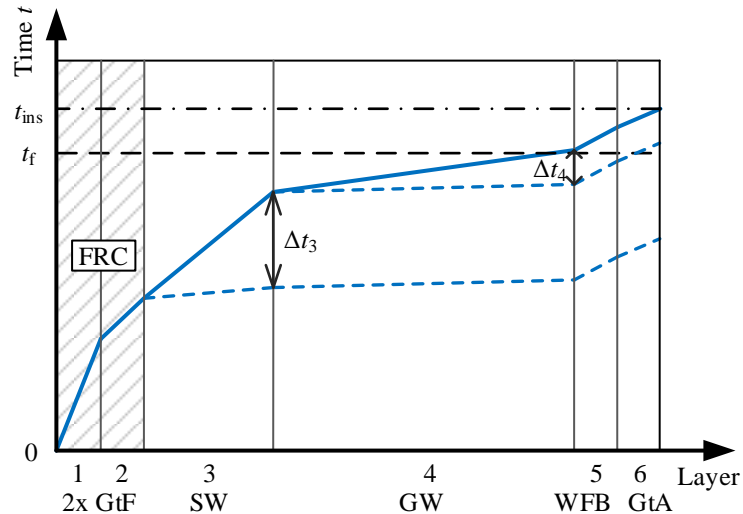


Fig. 3. Example calculation of insulation time for a 6-layer structure

4 DETAILING

The calculated structures must be shown to have the designed performance. To ensure that, some important detailing of fixations and air-tightness must be specified.

The greatest influence on the fire separating function lies on the performance of the FRC (e.g. gypsum plasterboard type F or X). The fixation of such boards should be made with screws of adequate length (penetration in uncharred wood at least 10 mm). Distance between the screws should be kept small to postpone the fall-off time. Ideally, the boards should be mounted horizontally on walls which extends the fall-off and helps to limit the opening of gaps between boards.

The fixation of insulation material is extremely important to be able to consider their contribution. Many fixation methods are used, the simplest of which are timber laths, which allow the calculation of their charring time as the end time of the adequate fixation of the insulation. Steel nets and lightweight steel resilient channels are also often used, the latter of which is also advantageous for sound insulation of the structure. Thirdly, the insulation can be fixed to the substrate or the timber members adjacent to the cavity by long screws or special staples or clamps. The unexposed side of the insulation batt may be glued to the substrate.

Another factor which inadvertently influences the fire resistance of assemblies is the air-tightness of the structure and, more generally speaking, of the compartment. This means that with the introduction of proper measures to ensure the air-tightness of the building, the risk of fire spread can be mitigated. It is recommended from the fire safety aspect to keep the air-tightness membranes, tapes, etc on the fire unexposed side of the structure. Intumescent gap fillers or tapes should be used in joints where the passage of hot gasses cannot be avoided otherwise.

5 CALCULATION TIPS

The use of the method should be simple. Therefore, clarifications and principles of use will be detailed in the paper, for example regarding multiple layers of insulation.

The basic protection times of wood-based claddings should be compared with the corrected charring rates (acc. to EN 1995-1-2), based on the material, density and thickness of the wood-based boards.

The protection times of cross-laminated timber (CLT) layers should be compared to the relevant charring scenario, whereas the protection time must be less than or equal to the time it takes for the CLT layer to char completely.

As described in chapter 3, the claddings have the greatest influence on the fire resistance of assemblies. The contribution of insulation materials is relatively smaller while being heavily influenced by many factors the designer must consider.

Fixation of insulation layers must be carefully designed, otherwise, the insulation is considered to fall off when the previous layer on the fire side of the assembly falls off. In calculations, the protection time of the insulation must always be less than or equal to the fall-off time of the insulation layer.

Density is necessary to calculate the basic protection time and position coefficients for insulation materials. However, the density of insulation is not a parameter the producer is required to declare according to the product standard for mineral wool insulations EN 13162 [8]. The designer should calculate the insulation time of the planned structure with the minimum density covered by the method (26 kg/m³ for stone wool and 15 kg/m³ for glass wool) or specify a suitable minimum density which fulfils the required fire resistance. Based on this information a product of the specified type and density can be chosen in the later phases of the project.

When calculating multiple layers of the same heat-resistant insulation (e.g. the insulation thickness necessary for the energy efficiency is greater than any products on the market) these layers shall be calculated separately unless the insulation layer on the fire side is adequately fixed. The method considers a layer to fall off when the temperature rise behind it reaches 250°C. Therefore, if it cannot be proven that the first layer of insulation stays in place for the whole duration of the fire, it must be calculated as a separate layer from the insulation behind it. If fixation is guaranteed and the insulation can withstand high temperatures, then the layers of the same insulation can be calculated as one thick layer.

Insulation materials should not be used as the primary contributing layer to the fire separating function, especially if the insulation experiences the post-protection phase (after the fall-off of cladding). In the post-protection phase glass wool melts almost immediately and normal stone wool (density 26...50 kg/m³) will also slightly degrade. All mineral wool insulation materials allow the passage of hot gasses and therefore do not protect the underlying structure completely during the post-protection phase. If the insulation layer is protected by a FRC then no limit is set for the protection time of this layer.

Based on an analysis of the database of full-scale standard fire tests held at RISE [9], the length of post-protection phase t_3 sustained by stone and glass wool insulation materials was compared with the real fall-off times of claddings. In the protection phase stone and glass wool behave quite similarly, but in the post-protection phase large differences can be seen.

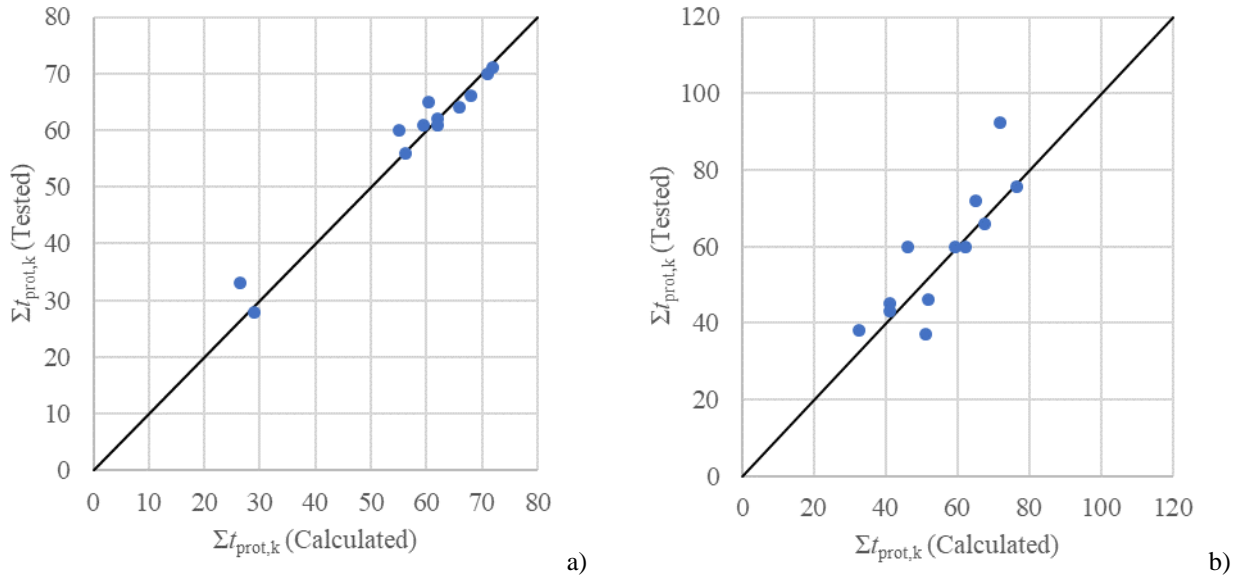


Fig. 4. Comparison of test results and calculations with a) Glass wool; b) Stone wool.

The limits of contribution of insulation depend on the protection level of the insulation material (according to [10]).

For insulation materials qualified as protection level 1 [10], the sum of the protection times of the layers preceding the insulation layer and the insulation layer is limited as shown by Eq.10.

For insulation materials qualified as protection level 2 [10], the sum of the protection times of the layers preceding the insulation layer and the insulation layer is limited as shown by Eq.11.

$$\sum_{k=1}^{i-1} t_{\text{prot},k} \leq \frac{h_i}{0,11 \cdot t_f + 1,3} + t_f \quad (10)$$

$$\sum_{k=1}^{i-1} t_{\text{prot},k} \leq \frac{h_i}{v_{\text{rec}}} + t_f \quad (11)$$

where $t_{\text{prot},k}$ is the sum of protection times including the insulation layer;
 h_i is the thickness of the insulation layer;
 t_f is the fall-off time of the FRC;
 v_{rec} is the recession speed of the insulation material.

The component additive method can also be used to calculate the start time of charring of load-bearing timber members in an assembly. The temperature criterion for the protection time (270°C) is close to the charring temperature of timber (300°C), therefore the sum of protection times of the layers preceding the timber member from the fire side is the slightly conservative start time of charring.

6 COMPARISON WITH THE CURRENT METHOD

For practical information a comparison with the component additive method currently detailed in Annex E of EN 1995-1-2:2004 is briefly explained in the following.

Annex E is an informative annex detailing the recommended method for calculation of fire separating function of timber frame assemblies. The basic idea of the method is similar to the method described in FSITB, however some aspects are too simplified. Additionally, the Annex E method is very limited in its applications, it describes the basic insulation times, position and joint coefficients for single and double claddings, single layer stone and glass wool insulations and voids. In the case of double claddings, the structures which can be analysed must be symmetrical and no information is given about the performance of structures insulated with glass wool.

The method detailed in Annex E is too optimistic with regards to the performance of non-combustible claddings, especially Type A gypsum plasterboards. The contribution of timber and wood-based materials is underestimated. Therefore, it is not recommended to use this method.

7 CONCLUSIONS

Within this article some important clarifications for the use of CAM for the calculation of separating function of assemblies have been presented. The method is shown to be versatile and to have strong links with existing norms and other calculation methods. Compared with the current methods the additions presented in this article have greatly improved the capabilities of CAM and brought it closer to the reality of the performance of the structures seen in fire tests.

ACKNOWLEDGEMENTS

This work was supported by the start-up research grant PUT794 “Effect of protective materials on the fire performance of timber structures” (2015-2018) financed by the Estonian Research Council. The authors acknowledge the network of COST Action FP1404 for the contribution of the Task Group 5 within the Working Group 2 “Structural Elements made of bio-based building materials and detailing”.

REFERENCES

1. V. Schleifer, "Zum Verhalten von raubabschliessenden mehrschichtigen Holzbauteilen im Brandfall," ETH Zürich, 2009.
2. B. Östman, E. Mikkola, R. Stein, A. Frangi, J. König, D. Dhima, T. Hakkarainen and J. Bregulla, “Fire safety in timber buildings,” Stockholm: SP Technical Research Institute of Sweden, 2010.
3. CEN, "EN 1995-1-2:2004 Eurocode 5: Design of timber structures - Part 1-2: General - Structural fire design," 2004.
4. K. N. Mäger, A. Just, A. Frangi and D. Brandon, "Protection by Fire Rated Claddings in the Component Additive Method," in Proceedings of 50th INTER meeting, Kyoto, 2017.
5. CEN, "EN 13381-7:2002 Test methods for determining the contribution to the fire resistance of structural members - Part 7: Applied protection to timber members," 2002.
6. K. N. Mäger, A. Just, J. Schmid, N. Werther, M. Klippel, D. Brandon, A. Frangi, “Procedure for implementing new materials to the component additive method,” Fire Safety Journal (2017), <https://doi.org/10.1016/j.firesaf.2017.09.006>
7. CEN, “EN 13501-2:2016 Fire classification of construction products and building elements. Classification using data from fire resistance tests, excluding ventilation services.” 2002.
8. CEN, “EN 13162:2012 Thermal insulation products for buildings – Factory made mineral wool (MW) products – Specification,” 2012.
9. Just, A, Schmid, J, König, J, “Gypsum plasterboards used as fire protection – Analysis of a database,” SP Report 2010:28, Stockholm, 2010.
10. M. Tiso, A. Just, “Fire Protection Provided by Insulation Materials – A New Design Approach for Timber Frame Assemblies,” Structural Engineering International (2017), 27:2, 231-237, <https://doi.org/10.2749/101686617X14881932435899>

INFLUENCE OF GAS TEMPERATURE DURING COOLING PHASE ON LOAD-BEARING PERIOD OF STRUCTURAL GLUED LAMINATED TIMBER BEAMS EXPOSED TO FIRE

T. Hirashima¹, Y. Katakura¹, M. Ichikawa¹, S. Ishii¹

ABSTRACT

Timber elements, unlike other structural elements, have a characteristic problem in that the load-bearing capacity decreases due to self-burning in the case of a fire, and self-burning may continue even after all other fuel in the room has been consumed. It is important to understand the sectional temperature, the structural performance and the failure behaviour not only during the heating phase but also during the cooling down phase. Previous test research which focused this problem was conducted on structural glued laminated timber beams exposed to 1 hour standard fire heating. The test results indicated that the deflection of the beam increases gradually during the cooling phase because temperature in the cross section increases after the end of heating, and then the beam fails. This paper shows that finite element numerical analysis results on the basis of the material properties in accordance with Eurocode 5 approximately agreed with the previous test results of the behaviour of the timber beam during not only heating phase but also cooling down phase, and discusses the influence of gas temperature during cooling down phase on failure time of the timber beam.

Keywords: Glulam timber beam, Fire resistance, Deflection behaviour, Finite element analysis

1 INTRODUCTION

In recent years, owing to environmental considerations related to soundness of forests and forest resources and carbon offset, using timber structural elements meeting the requirements of fire-resistance of structures (below, fire-resistance of timber structures), advanced large-scale fire-resistant timber buildings have been increasing in number [1]. However, timber elements, unlike other structural elements, have a characteristic problem in that the load-bearing capacity decreases due to self-burning in the case of a fire, and self-burning may continue even after all other fuel in the room has been consumed. In order to make possible more wide spread use of timber structures using large cross-section columns and beams of structural, glued, laminated timber by demonstrating fire resistance potential, it is important to understand the sectional temperature, the structural performance and the failure behaviour not only during the heating phase but also during the cooling down phase. However, standard fire resistance evaluation tests to confirm the structural performance (i.e. the deformation amount and deformation rate do not exceed the limit value) for a predetermined time unless the structural failure of the specimen has occurred, the data regarding fire performance is not available including the cooling down phase (i.e., strength corresponding to the time the failure occurred). Although there were some experimental reports on fire resistance of timber structural elements, few experimental reports had discussed the structural fire behaviour

¹ Graduate School of Engineering, Chiba University, Chiba, Japan
e-mail: hirashima@faculty.chiba-u.jp

during the cooling down phase after the end of fire heating. Therefore, loading tests after heating and load-bearing fire tests were conducted in order to clarify the behaviour during the cooling down phase of a structural, glued, laminated timber beam (glulam beam) exposed to standard fire heating. And their results, which included the charring properties, the cross-sectional temperature distribution, the deflection behaviour, the fire resistance and the failure mode during the cooling down phase, were reported [2, 3].

In this paper, it is indicated that numerical analysis result on the basis of the material properties in accordance with Eurocode 5 [4] approximately agreed with the previous test results [3] of the temperature in the cross section and the deflection behaviour of the glulam beam during not only heating phase but also cooling down phase. And then, the influence of gas temperature during cooling down phase on load-bearing period of the glulam beam is discussed by the finite element (FE) analysis.

2 FINITE ELEMENT ANALYSIS OF THE PREVIOUS BEAM TESTS

2.1 Outlines of the previous beam test

The tree species selected for the previous tests was Japanese larch. Each glulam beam was 210 mm wide, 420 mm height, and 6000 mm long. The distance between supports was 5,400 mm. The thickness of each lamina was 30 mm, and 14 laminas were bonded using resorcinol-phenol resin. The strength grade of the glulam utilized fully complied with the standards of same-grade composition structural members stipulated in the Japan Agricultural Standard (JAS) E95-F315 standard. The average density of the specimens was 0.53 g/cm^3 , and moisture content was 10.7 %. The temperature in the furnace was controlled to follow the ISO834 standard fire for 1 hour. The following behaviours were observed from the test results [2, 3].

- (1) Charring behaviour: The charring rate during the heating phase, which was obtained from the charring depth of the separated specimens after heating for 1 hour, was 0.61 to 0.68 mm/min. During the cooling down phase, specifically after 2 hours, flame did not be found and the charring rate was approximately zero, although a dark area had spread around the heating boundary. The charring area of the glulam beam with Japanese larch did not increase during the cooling down phase so much.
- (2) Cross section temperature: The temperature at the centroid reached approximately 30°C after 1 hour and then increased gradually during the cooling down phase. The mean temperature of the un-charred section reached approximately 150°C between the fourth and fifth hour, yet remained at 100°C and above after seven hours of natural cooling. The cross section temperature of the un-charred section increased rather during the cooling phase than during the heating phase.
- (3) Deflection behaviour: The deflection rate did not decrease after the end of heating or the deflection rather increased during the cooling down phase. Meanwhile, the glulam beam maintained a load bearing capacity of less than 40% of the allowable design load for the permanent action after the one hour heating period, except in the case of the specimen that suffered a shear failure.

2.2 Thermal analysis

For discussion on the behaviour during the cooling down phase, it is important to predict correctly the temperature of the non-charring area of the glulam beam. Finite element numerical analysis of heat transfer and heat conduction was carried out in order to obtain the temperature in the cross section of the beam exposed to 1 hour standard fire heating. The thermal properties (thermal conductivity, specific heat and density) of soften wood were given in accordance with Eurocode 5. At first, the accuracy of numerical analysis was checked by comparison between the numerical results and the previous test results on the glulam beam. In this thermal analysis, gas temperature during heating phase was given in accordance with ISO 834-1. Gas temperature during cooling down phase was given by 2 kinds of temperature as shown in *Fig. 1*.

Case A: The temperature was given by the previous test results on the charred or disappeared cross section temperature near the heating surface. Purpose of the analysis Case A was to make the input data of cross sectional temperatures for the structural analysis and to confirm the validity of the structural analysis. Therefore, the cross sectional temperatures from the analysis result should be agreeable with them from the test result.

Case B: This case was assumed that gas temperature does not decrease rapidly in case of a real compartment fire. This is to investigate the influence of gas temperature during cooling down phase on the cross sectional temperature and the deflection behaviour.

Fig. 2 shows the half figure (left side) of the cross section for two dimensional FE analysis model. The glulam beams were heated at bottom surface and both side surfaces and the analysis was taken into account with the symmetrical behaviour. Table 1 shows the initial thermal properties of the glulam beam at ambient temperature.

2.3 Structural analysis

The structural analysis program used originates in a report by Becker and Bresler at the University of California, Berkeley [5], and had been amended at Chiba University. This is an FE analysis using Bernoulli-Euler beam elements, which is capable of modelling the deflection behaviour of steel and concrete frames subjected to fire, and includes geometrical and material non-linearities. In this study, the stress-strain relationship of the timber at elevated temperatures was added in the FE analysis program.

The properties of the timber were given on the basis of reduction factor for strength and modulus of elasticity parallel to grain of softwood in accordance with EN 1995-1-2:2004 Annex B [4]. The strength of the timber at ambient temperature was given by the glulam beam test result at ambient temperature. Stress-strain relationships for use in calculation of the load-bearing fire test of the glulam beams were represented by Eq. 1 [6]. Table 2 shows the values of Eq. 1.

$$\sigma = \frac{(E - E_t) \cdot \varepsilon}{\left\{ 1 + (\varepsilon / \varepsilon_0)^n \right\}^{\frac{1}{n}}} \quad (1)$$

Where σ is the stress,
 E is the Young's modulus,
 E_t is the plastic modulus,
 ε is the strain,
 ε_0 is the yield strain,
 n is the shape factor of the stress-strain curve.

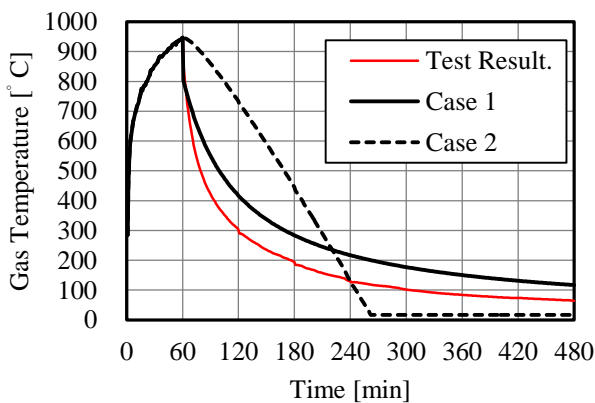


Fig. 1. Input gas temperatures for thermal analysis

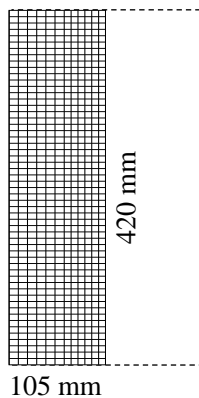


Fig. 2. Analytical model of the cross section

Table 1. Thermal properties at ambient temperature

thermal conductivity	0.127	W/(m·K)
specific heat	1.25	kJ/(kg·K)
density	0.53	g/cm ³
water content	11.0	%
emissivity	0.90	
heat transfer coefficient	23	W/(m ² ·K)

In this equation, the yield strain relates to the strength of the timber. Fig. 3 shows the stress-strain relationships. Timber is a brittle material. The failure tensile strain was $4,000 \times 10^{-6}$. This value was determined by the test result of extreme fibre stress value from strain gages when the glulam beam collapsed at ambient temperature. The mechanical properties of the timber elements were not reversible in case of fire situation and were given from the values of maximum temperature at each slice in the section of the beam. Fig. 4 shows the analytical beam model for the structural FE analysis. This model was considered with the symmetry of the beam tests. The beam was divided longitudinally into 9 elements. These elements were further divided into small slices within the cross section as shown in Fig. 2. The minimum width and depth of the slices were 7.5 mm. The input data on cross section temperatures for structural FE analysis was based on the thermal analysis results.

Table 2. The values of Eq. 1.

Temperature	Compression				Tension			
	E N/mm ²	E_t N/mm ²	ϵ_0 $\times 10^{-6}$	n	E N/mm ²	E_t N/mm ²	ϵ_0 $\times 10^{-6}$	n
20°C	969	0.969	2730	4.0	969	0.969	2380	4.0
50°C	733	0.733	2600	3.2	788	0.788	2550	3.2
100°C	339	0.339	1960	2.0	485	0.485	3110	2.0
150°C	255	0.255	1960	2.0	363	0.363	3110	2.0
200°C	170	0.170	1950	2.0	242	0.242	3100	2.0
250°C	85	0.085	1950	2.0	121	0.121	3100	2.0

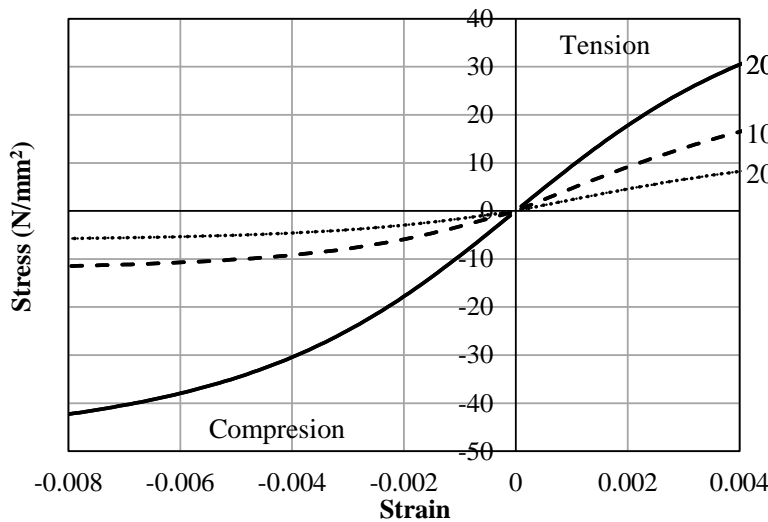


Fig. 3. Stress-strain relationships.

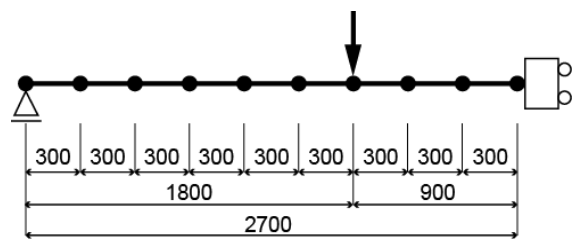


Fig. 4. Model for the structural FE analysis.

3 ANALYSIS RESULTS AND DISCUSSIONS

3.1 Cross sectional temperatures

Fig. 5 shows results on cross sectional temperatures of the glulam beam exposed to 1 hour standard fire heating from the test and numerical thermal analysis. “d” denotes the depth from the heating surface in the initial condition. The temperature at $d=30$ mm, which was near heating surface and in charring area, reached about 650 °C after 60 min from the ignition, and then it decreased gradually due to decrease of the gas temperature in the furnace. Meanwhile, the cross sectional temperature of

the un-charred area ($d=65$ mm and Centre) increased rather during the cooling down phase after 60 min from the ignition than during the heating phase and reached approximately 150°C between the fourth and fifth hour, yet remained at 100°C and above after seven hours of natural cooling.

The analysis results on Case A approximately agreed with the test results. It was indicated that the thermal properties (thermal conductivity, specific heat and density) of soft wood of Eurocode 5 are reasonable for the thermal analysis of the timber beams made with Japanese larch. And it is important that the gas temperature around the beam surfaces is given adequately. Fig. 6 shows the comparison between the test and the analysis results of the cross sectional temperatures. Their gaps were approximately within 20%. The thermal analysis result on Case A may enable to confirm the validity of the following structural analysis on the deflection behaviour of the glulam beams.

In the analysis result on Case B, the maximum cross sectional temperatures were considerably larger than them from the test result of all measurement points as shown in Fig. 5. Meanwhile, the temperatures of Case B decreased earlier than them of Case A and test result because of the difference of their gas temperatures during the cooling down phase. It was indicated that the gas temperature during the cooling phase influences the cross sectional temperature of timber beams considerably.

Fig. 7 shows the temperature distribution from the analysis results. The charring area developed during 1 hour heating and then the temperature of the un-charred section gradually increased during the cooling down phase. The boundary line at temperature 300°C of Case A approximately agreed with the charring depth line from the test results and the change was not found after 120 min. Fig. 7 also showed that the un-charred area was smaller for Case B than for Case A.

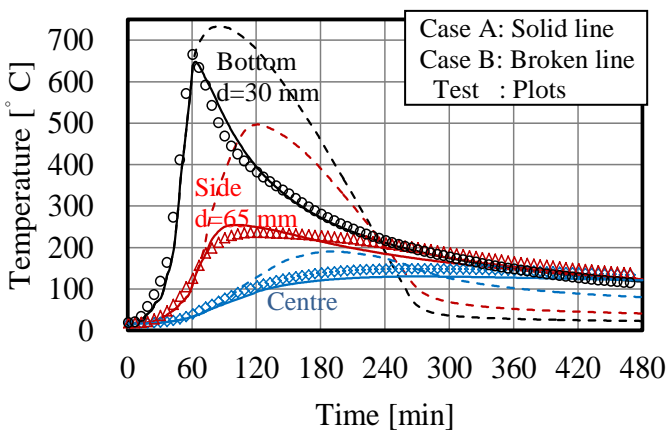


Fig. 5. Cross sectional temperatures of the timber beam.

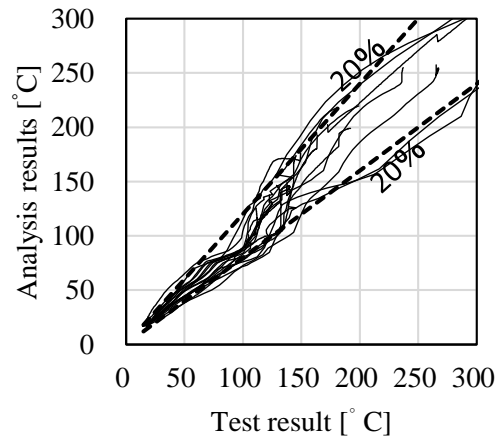


Fig. 6. Comparison between analysis and test results (Analysis: Case A)

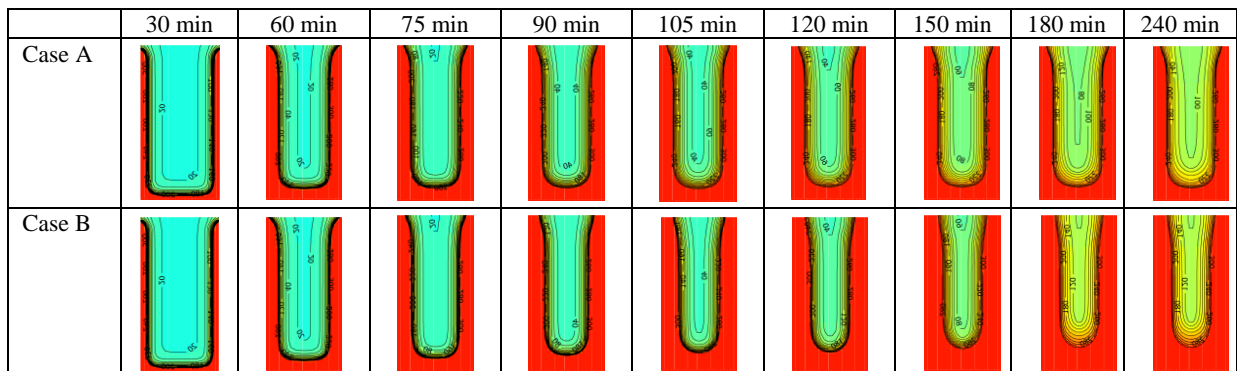


Fig. 7. Temperature distribution in the cross section of the timber beams

Deflection behaviour

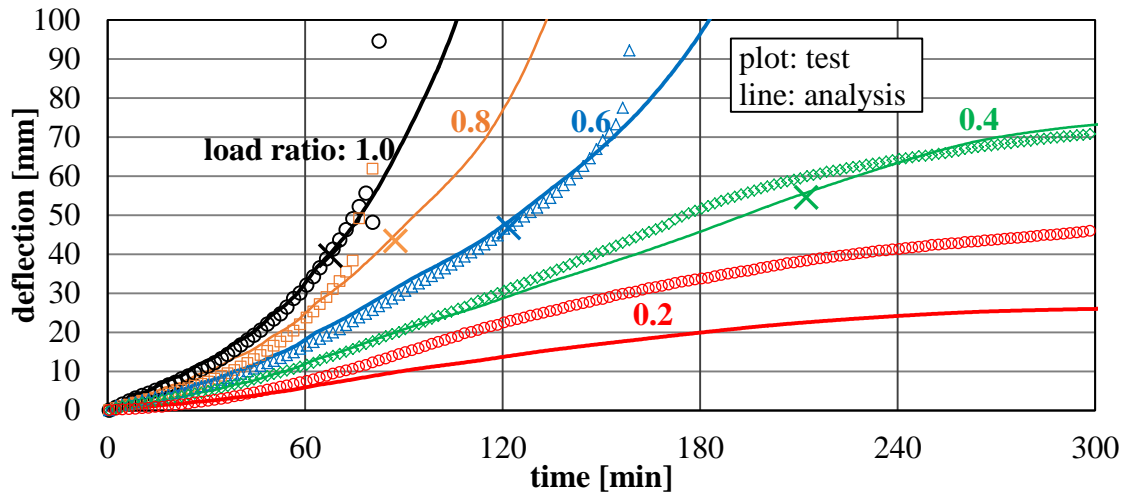
Fig. 8 (a) and (b) show the deflection behaviour of the glulam beam under constant load exposed to 1 hour of standard fire heating and also shows the comparison between the structural analysis results and the test results. Five load bearing fire tests were carried out. The constant load ratios were based on the permanent allowable design load of the beam specimen at ambient temperature. Legend “load ratio: 1.0” means that the applied constant load was same as the allowable design load [7] of the specimen at ambient temperature. Legend “0.4” means that the applied constant load was 0.4 times the allowable design load. In analytical results, symbol “×” means the point that the extreme fibre stress in tension reached $4,000 \times 10^{-6}$ and the failure time was determined by this point. In case of the lower load conditions (load ratio: 0.2), the specimens did not fail in the test and the extreme fibre stress did not reach $4,000 \times 10^{-6}$ in the analysis of Case A.

As shown in *Fig. 8 (a)*, the analysis results of the deflection behaviour approximately agreed with the experimental results. It was indicated that the reduction factor for strength and relative modulus of elasticity of Eurocode 5 are reasonable for the structural analysis of the timber beams made with Japanese larch. However, in case of the load ratio 0.2, as the time passed during the cooling down phase, the difference of the deflection between the analysis value and the experimental value gradually increased, and finally the analysis values were considerably lower than the experimental values. The deflection behaviour of the glulam beam may be influenced with the transient creep due to drying of the timber. It is a future subject how to model the creep behaviour under high temperature and evaporative condition for the numerical analysis.

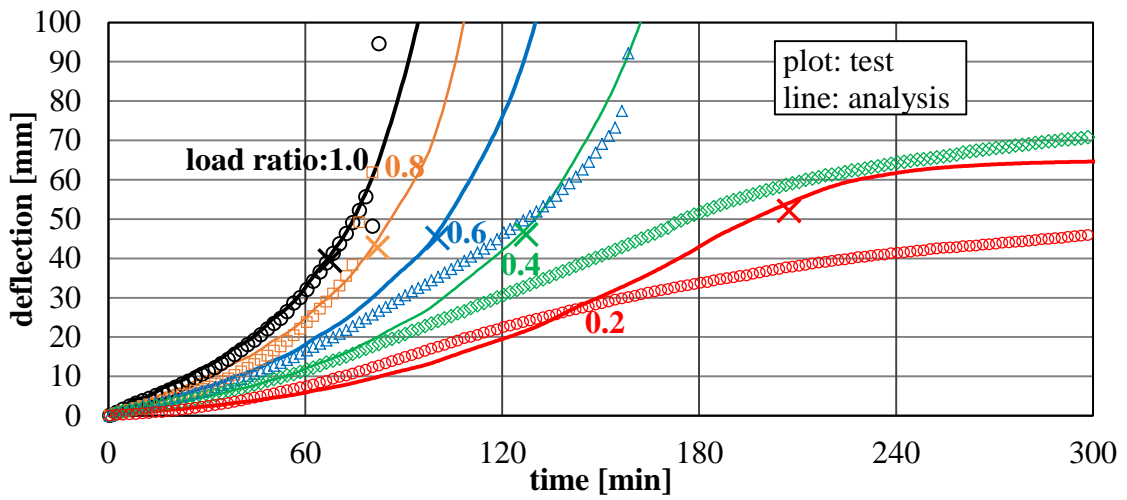
As shown in *Fig. 8 (a) and (b)*, the deflection behaviour was considerably influenced by gas temperature during cooling down phase. This phenomenon was found, especially when the load ratio was lower. The analysis predicted that the timber beam may be fail in case the load ratio is 0.2 and the beam is exposed fire heating of Case B. So the failure time was also very different between Case A and Case B.

3.2 Failure time

Fig. 9 shows relationships between the failure time (or load-bearing period) and load ratio from the numerical analysis of the glulam beam (210 mm wide x 420 mm height). The failure time was determined by the aforesaid criteria of the extreme fibre stress. As same as the deflection behaviour, the failure time was influenced by gas temperature during the cooling down phase and the difference of failure time between Case A and Case B was larger in case of the lower load. Therefore, the gas temperature should be carefully determined in case of structural fire engineering design for timber buildings during not only heating phase but also cooling down phase. And, discussion on the criteria of the failure time will be needed continually. In addition, this scope on the structural fire behaviour of the timber beams was limited. The behaviour depends on tree species, cross sectional size, length, boundary condition, heating time etc. More research will be needed in this behaviour.



(a) Case A



(b) Case B

Fig. 8. Deflection at the mid-span of the beam

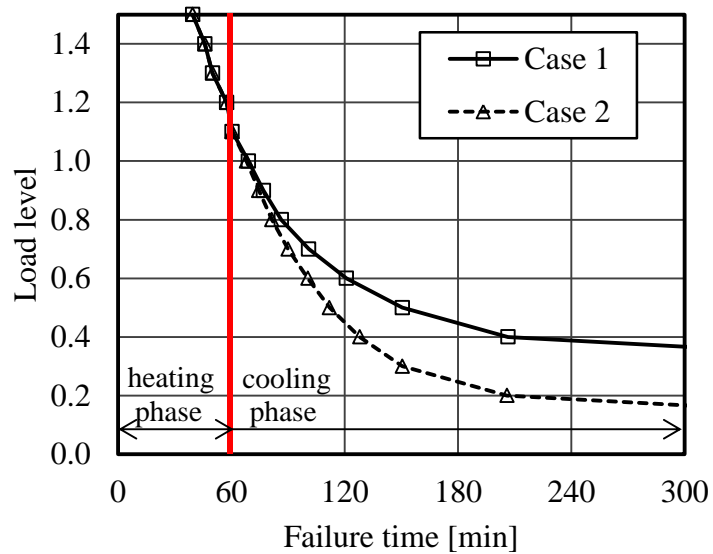


Fig. 9. Failure time

4 CONCLUSIONS

This paper has presented the comparison of experimental results and the analysis results on the cross sectional temperature and the deflection behaviour of a structural glued laminated timber beam exposed to 1 hour of standard fire heating including the cooling down phase. The main conclusions of this study were as follows:

- 1) Thermal properties (thermal conductivity, specific heat and density) of softwood in Eurocode 5 were reasonable for the thermal analysis of the timber beams made with Japanese larch.
- 2) The gas temperature during the cooling down phase influenced the cross sectional temperature and charring area of timber beams considerably.
- 3) Mechanical properties (the reduction factor for strength and relative modulus of elasticity) of parallel to grain of softwood in Eurocode 5 were also reasonable for the structural analysis of the glulam beams made with Japanese larch.
- 4) The deflection behaviour and the failure time of the glulam beams were also influenced by gas temperature during the cooling down phase and the difference due to the gas temperature was larger in case of the lower load.
- 5) Therefore, the gas temperature should be carefully determined in case of structural fire engineering design for timber buildings during not only heating phase but also cooling down phase.

ACKNOWLEDGMENT

This work was supported by Center for Better Living and Saito Wood Industry Co. Ltd. The authors would like to thank the participants.

REFERENCES

1. Andrew Buchanan (2015). Fire resistance of multi-storey timber buildings. *Proceedings of 10th Asia-Oceania Symposium on Fire Science and Technology*, pp 9-16.
https://doi.org/10.1007/978-981-10-0376-9_2
2. Hitoshi Kinjo, Takeo Hirashima, Shuitsu Yusa, Kiyoshi Saito (2016). Fire Performance, Including the Cooling Phase, of Structural Glued Laminated Timber Beams, *Journal of Structural Fire Engineering*, Vol. 7, Issue 4, pp 349-364. <https://doi.org/10.1108/JSFE-12-2016-024>
3. Yusuke Katakura, Hitoshi Kinjo, Takeo Hirashima, Shuitsu Yusa, Kiyoshi Saito (2016). Deflection Behavior and Load-Bearing-Period of Structural Glued Laminated Timber Beams in Fire Including Cooling Phase. *Proc. of 9th international Conference on Structures in fire*, pp 667-674.
4. EN 1995-1-2 (2004). Eurocode 5: Design of timber structures, Part 1-2: General-Structural fire design.
5. James Becker, Boris Bresler (1974). FIRES-RC, A Computer Program for the Fire Response of Structure, Reinforced Concrete Frames, Report No. UCB FRG 74-3, University of California Berkeley.
6. Richard, R.M and Abbott, B.J. (1975). Versatile Elastic-Plastic Stress-Strain Formula, *EM4 Technical Note*, pp 511-515.
7. Architectural Institute of Japan (2006). Standard for Structural Design of Timber Structures (in Japanese)

EXPERIMENTAL FIRE-SIMULATOR FOR POST-FLASHOVER COMPARTMENT FIRES

Daniel Brandon¹, Joachim Schmid², Joseph Su³, Matthew S. Hoehler⁴, Birgit Östman⁵,
Amanda Kimball⁶

ABSTRACT

The number of tall timber buildings around the world is rapidly increasing as a result of changes in regulations and the development of new engineered timber products. However, due to the combustibility of timber, the fire safety of tall timber buildings has been questioned. Building regulations for structural elements are based on fixed periods for which specimens shall resist standard fire exposure in a fire resistance furnace. Because no distinction is made between the exposure in fire resistance tests of combustible and non-combustible specimens, less conventional testing methods have been used for research of timber structures. This study aims to identify aspects that are important to simulate realistic fire conditions relevant to assess the structural performance of timber in post-flashover fires. A test method is developed aiming to replicate conditions in compartment fire tests using an experimental fire simulator that results in similar damage types and rates of damage in the timber specimen. Based on observations from these tests and results obtained using other testing methods, the applicability of standard fire resistance tests and other non-conventional tests for investigating the fire performance of timber are discussed.

Keywords: Cross laminated timber, compartment fires, fire resistance tests, simulation

1 INTRODUCTION

The number of tall timber buildings around the world is rapidly increasing as a result of changes in regulations and the development of new engineered , often glued, timber products; such as Cross Laminated Timber (CLT). This increase in building height creates new challenges for fire safety. Various methods have been used to study the performance of timber products in post flashover fires; such as standard fire resistance tests [1] and tests with a radiant heat source in an open environment (e.g. [2]). Differences in results from these tests have led to various hypotheses regarding the important aspects to achieve realistic fire exposures relevant for timber structures [3,4].

This paper focusses on key parameters that must be controlled to produce results relevant for the structural assessment of timber in post-flashover compartment fires. While full scale compartment

¹ Researcher, Fire Research, RISE Safety, Sweden.

e-mail: daniel.brandon@ri.se

² Research assistant, PhD Candidate, IBK, ETH Zürich, Switzerland.

e-mail: schmid@ibk.baug.ethz.ch

³ Principal Research Officer, National Research Council of Canada, Ottawa, Canada.

e-mail: joseph.su@nrc-cnrc.gc.ca

⁴ Research Structural Engineer, National Institute of Standards and Technology, Gaithersburg, USA.

e-mail: matthew.hoehler@nist.gov

⁵ Senior Advisor, Linneaus University, Växjö, Sweden.

e-mail: birgit.ostman@lnu.se

⁶ Research Director, Fire Protection Research Foundation, Quincy, MA, USA.

e-mail: akimball@nfpa.org

fire tests can be used to represent real building fires, these tests can be time consuming and costly. Therefore, we present an intermediate scale method to replicate relevant conditions of a specific compartment fire test [5]. Successful replication of the compartment fire should result in similar damage to that observed in a comparable full scale test.

2 REFERENCE COMPARTMENT FIRE TEST

An extensive study led by the Fire Protection Research Foundation involved six full scale compartment fire experiments, performed by the National Research Council Canada and the National Institute of Standards and Technology to study the contribution of exposed Cross Laminated Timber (CLT) to the fuel load of the fire [5]. The study involved compartment tests with various configurations of exposed CLT surfaces and ventilation. Due to weakening of the CLT adhesive in the fire, fire induced delamination (hereafter *delamination*) occurred during the compartment fire tests with exposed CLT. In the compartment tests, delamination led to increased combustion and subsequent fire growth or continuation of the fully-developed fire [5]. Delamination depends on the adhesive used to produce CLT. To study whether delamination would have occurred had other adhesives been used, an intermediate scale fire testing method was developed as discussed herein. For this, compartment Test 1-4 described by Su et al. [5] was chosen for reference. A short summary of the test setup is discussed below.

The compartment was made of 175 mm thick 5-ply CLT walls and ceiling. The interior of the compartment was 9.1 m × 4.6 m × 2.7 m (depth × width × height) and there was an opening of 1.8 m × 2.0 m in one of the 4.6 m × 2.7 m walls. Three layers of 15.9 mm type X gypsum boards were applied on the CLT walls and the CLT ceiling was left exposed. Typical residential furniture with a fuel load density of 550 MJ/m² was used as fuel.

After ignition, flashover occurred after approximately 11 min and the exposed ceiling became fully involved in the fire. A significant fire plume was observed during the fully-developed stage of the fire. Two layers of the exposed CLT delaminated. Delamination of the second layer occurred during the decay phase of the fire, leading to a secondary flashover. The results from Test 1-4 are used in Section 3 to benchmark the fire conditions in the intermediate scale tests.

3 EXPERIMENTAL FIRE SIMULATOR FOR POST-FLASHOVER FIRES

An experimental method to replicate fire conditions was needed to study whether other adhesives would have performed better under the conditions of Test 1-4 (discussed above). For the purpose of this study, a successful replication of the fire conditions of the compartment fire test in a furnace should lead to similar damage in both tests if the same product is tested. Recent studies have indicated that the oxygen concentration of ambient gasses has a significant influence on the rate of damage of timber exposed to fire. Timber tested in fire conditions involving oxygen concentrations over 10 % had significant char oxidation leading to the gasification of protective char layers and more thermal damage of the timber [6]. Therefore, oxygen concentrations, in addition to plate thermometer temperatures, measured in Test 1-4 were used to replicate the conditions of a flashover compartment fire in a furnace. This setup is referred to here as the ‘experimental fire simulator’.

To study whether delamination would occur for an arbitrary adhesive, the delamination induced temperature increase and the reduction of oxygen concentration after 120 min in Test 1-4 were ignored (Figure 1). The target oxygen content and temperature in the final stage of the test (from 120 min to 180 min) were extrapolated based on a similar compartment test without exposed CLT (Test 1-1 in [5]).

Two replicates (denoted A and B) of CLT panels constructed using five different adhesives were tested. In this paper, the results of two polyurethane adhesives (referred to as PU1 and PU2) are discussed. PU1 is the same adhesive as used in Test 1-4. The other polyurethane adhesive (PU2) was enhanced to avoid delamination.

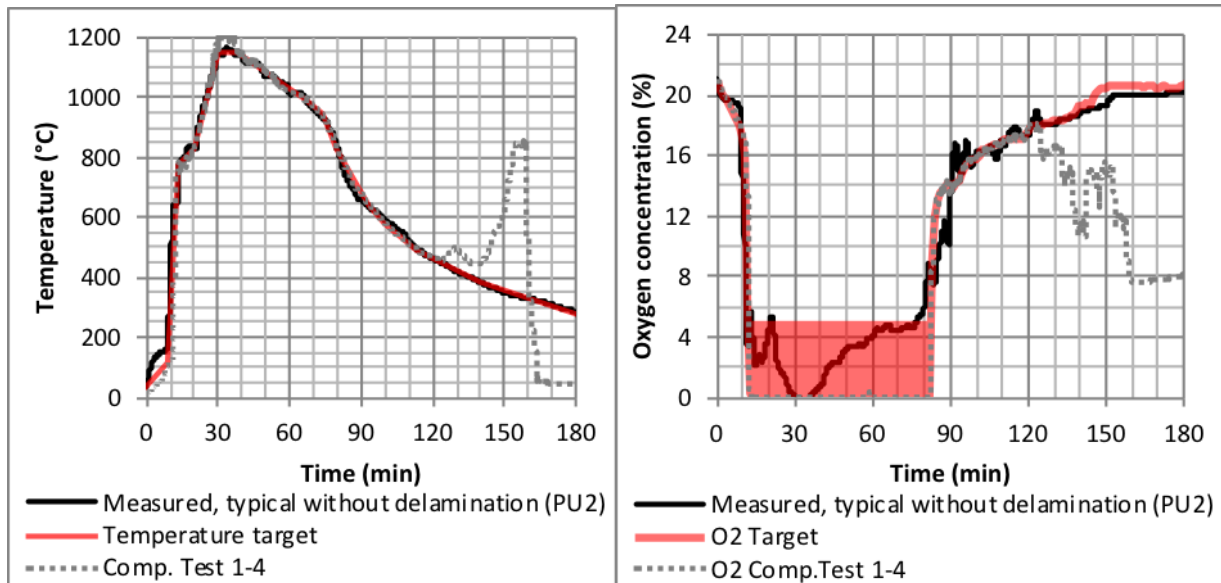


Figure 1: Target and typical temperature and oxygen concentration in fire simulator tests

The experimental fire-simulator had interior dimensions of 1.0 m × 1.0 m × 1.0 m (Figure 2). The CLT floor specimen was 1400 mm × 600 mm, of which 1000 mm × 600 mm was exposed. One of plate thermometers was positioned at 100 mm distance from the CLT surface directed away from the surface (similar to the plate thermometer in Test 1-4) and an additional plate thermometer was positioned 150 mm from the surface. The oxygen concentration was measured in the exhaust of the furnace. There was an inlet for air and nitrogen to control the oxygen concentration and the temperature during the cooling phase. Temperatures were measured in the adhesive bond line of the CLT in a similar fashion as was measured in the compartment fire tests discussed above. The incident radiant heat flux was determined in two different ways:

1. From the plate thermometer temperature and the gas temperature measured by a thermocouple near the plate thermometer.
2. From a water cooled heat flux gauge flush with the surface of the CLT specimen. The temperature of the cooled sensor was measured using a thermocouple. The heat flux was estimated for corresponding to different convection coefficients.

Delamination was indicated using: (1) temperature measurements in the lamellae and in at the bond line of the CLT, (2) video recordings of the specimen surface during the test, (3) charring rates determined from temperature measurements, (4) final charring depth measured after the test, and (5) measurements of the mass loss.

An experimental fire-simulator of post-flashover compartment fires

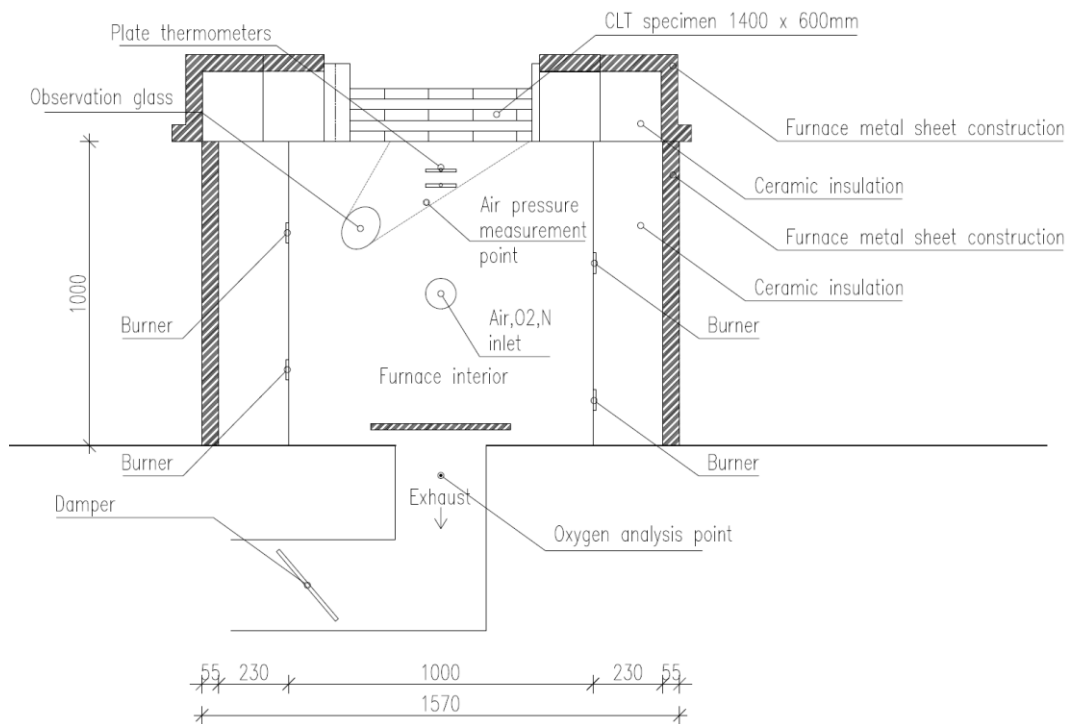


Figure 2: Cross section of the test setup

3.1 Results and evaluation of the furnace tests

In this section, the damage and temperatures for compartment Test 1-4 and the intermediate scale tests are compared. A successful replication of the fire conditions of a compartment test should lead to a similar rate of charring for the same CLT product.

Figure 3 shows the average char depth measured after Test 1-4 and the estimated average char depth from the intermediate scale furnace tests after the same time (160 min). Because the furnace test was 20 min longer, the corresponding average char depth was estimated using linear interpolation of measurements of the char depth at the end of the test and the depth at the time at which the thermocouples read 300 °C. A distinct difference can be seen between the charring depth of CLT with non-delaminating adhesives and CLT with a delaminating adhesive (PU1). The average char depth determined after Test 1-4 only deviates a few millimeters from the average charring depth determined from the furnace tests. Based on a study of the uncertainty of thermocouple locations and temperature measurements, the expanded total uncertainty for the interpolated char depth is estimated to be ± 0.9 mm (95 % confidence). It should be noted that there was significant spatial (24 mm) variation in char depth across the ceiling, as measured after Test 1-4. For both intermediate scale tests of the same CLT product (PU1), the spatial variation of char depth measured was 9 mm. The spatial variation of charring depth measured in tests with non-delaminating polyurethane adhesives (PU2-A and PU2-B) was significantly less (2 mm).

Figure 4 shows the temperatures measured in the CLT of the compartment fire test together with the furnace tests. For the comparisons, only temperature measurements of the furnace tests with the same CLT product as the compartment test are shown (PU1). It can be seen that the temperature increased in the decay phase of PU1-A, despite the reducing furnace temperature. Due to delamination and the high oxygen content, the temperature could not be controlled in this phase. The temperature increase is, however, similar to that of the compartment fire. Test replicate PU1-B had the same specimen, but only had small parts of lamellae falling during the decay phase. At the end of the test, however, most of the second lamella fell-off.

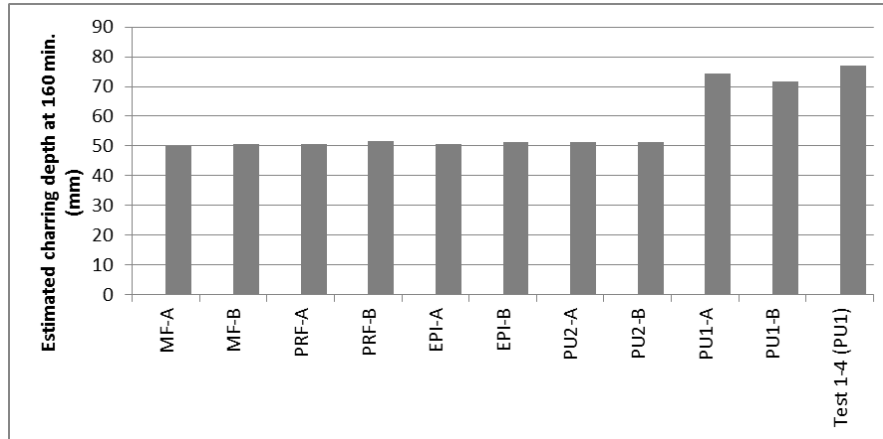


Figure 3: Estimated average charring depth at 160 min using linear interpolation

The temperature jumps measured by the thermocouple indicate delamination, which is confirmed by video recordings of the surface. The times at which delamination occurs is determined from temperature measurements in the adhesive bond line and in the falling lamellae. Times at which temperature increases of 100 °C within 1 minute were measured in the fully-developed phase and times at which temperature increases of 100 °C within 5 min were measured in the decay phase, were found to correspond well with the times of delamination determined from video recordings. Box plots of the times at which this temperature increase was observed in all thermocouples are shown in Figure 5. It can be seen that the time at which delamination of the second layer was observed in Test 1-4 is within the range of delamination times observed in the furnace tests.

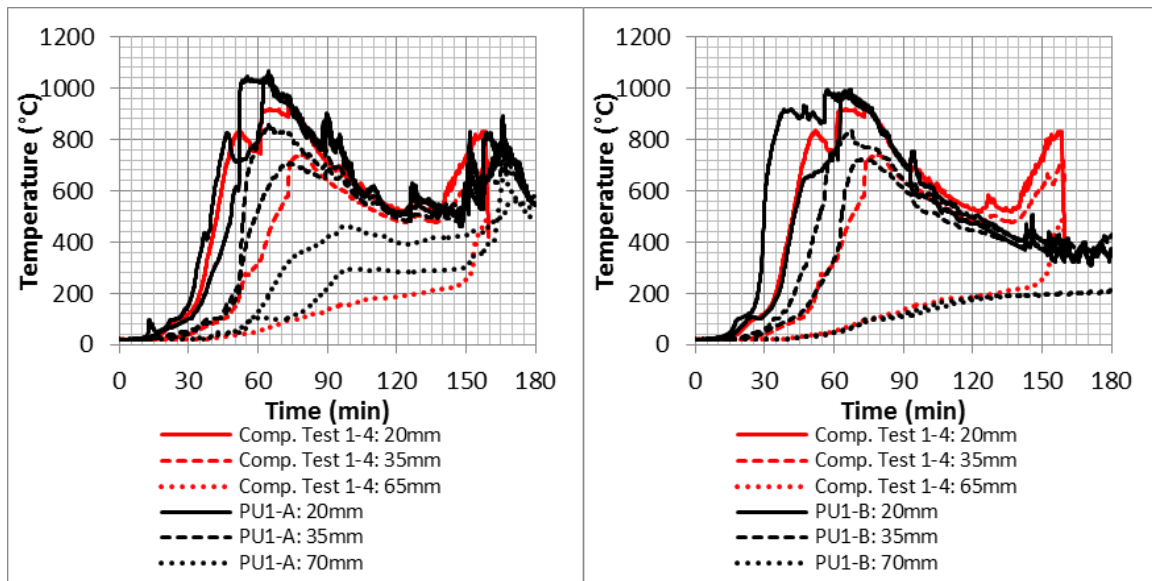


Figure 4: Temperature measurements at specified depths of PU1-A, PU1-B and compartment Test 1-4. In PU1-B thermocouples were installed at 50 mm instead of 70 mm depth

The incident radiant heat flux determined of the compartment and the replicating tests are shown in Figure 6. The incident heat flux was calculated using the following equation, assuming different convection coefficients of 0 W/m²K and 25 W/m²K (see Figure 6, “PT and TC h_c=0” or “h_c=25”):

$$\dot{q}_{inc} = \sigma T_{PT}^4 - \frac{h_c}{\epsilon_{PT}} (T_g - T_{PT}) \quad (1)$$

Where: σ is the Stefan Boltzmann constant; T_{PT} is the temperature measured by the plate thermometer; T_g is the gas temperature approximated by a thermocouple; h_c is the convection coefficient; ε_{PT} is the emissivity. The thermocouple probes measuring the plate thermometer temperatures were compliant with IEC 60584-2 requirements for class 1 K-type thermocouples, having a tolerance of 0.4 % of the measured temperature for temperatures exceeding 375 °C and ± 1.5 °C for lower temperatures. The similarity between the incident heat flux of the compartment tests and the furnace tests, suggest that the incident heat flux can also be used to control the furnace test instead of the plate thermometer temperature.

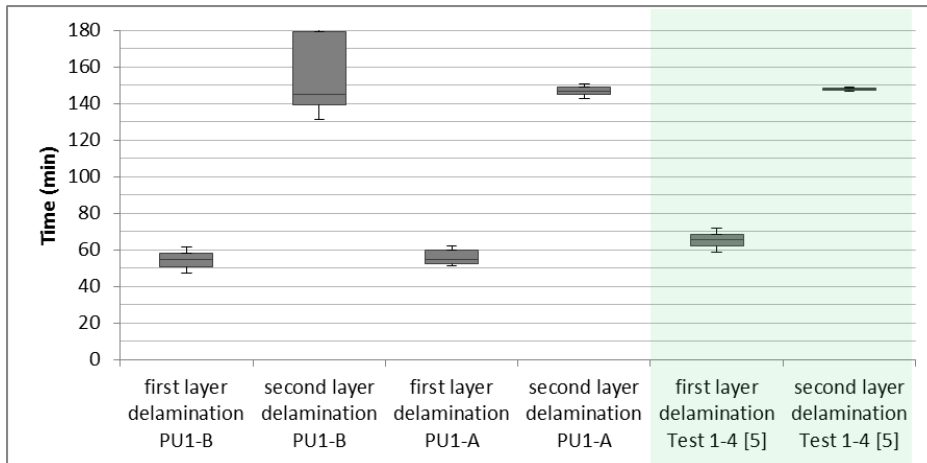


Figure 5: Time of delamination determined from thermocouple measurements

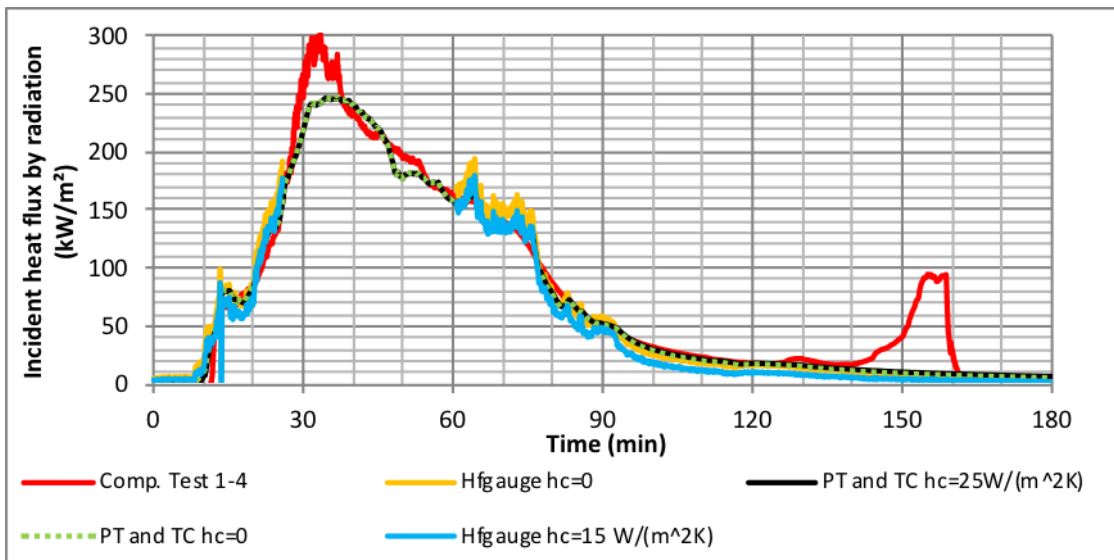


Figure 6: Incident heat flux by radiation corresponding to non-delaminating CLT with PU2 adhesive

4 DISCUSSION OF OTHER TESTING METHODS

Results of Section 3 suggest that certain relevant fire conditions of compartment fire Test 1-4 can be replicated in a furnace in which the oxygen concentration is controlled. The results of this paper indicate that this can be done by replicating the plate thermometer temperature or the incident radiant heat flux as well as the oxygen concentration of the compartment test in the furnace. In this section, the relevance of test methods in which the oxygen concentration is not similar to that of post-flashover compartment fires is discussed.

4.1 Test setups in open environments

Recently, new test setups have been introduced in which the thermal exposure is controlled by a radiant heat source in open environments with atmospheric oxygen concentration. A test published in [3] involved a testing method developed in [8] and had significantly lower incident radiant heat fluxes than those measured during Test 1-4. If the incident heat flux alone would be enough to describe reasonable fire exposure, the test with a significantly lower incident heat flux should show lower charring rates (less damage). However, despite that the incident heat flux was more than twice as high in the compartment for approximately most of the first 30 min, it was found that the charring rates corresponding to this period of both tests were similar. Due to the high oxygen concentration, the char oxidizes significantly in the radiant panel test. Additionally, surface flaming occurs which causes additional radiation and convection to the timber, which does not occur in the fully developed phase of a compartment fire due to the low oxygen content. Therefore, results of tests in which the oxygen concentration does not correspond to a post-flashover fire condition, should be considered with care for the assessment of timber in post-flashover fires.

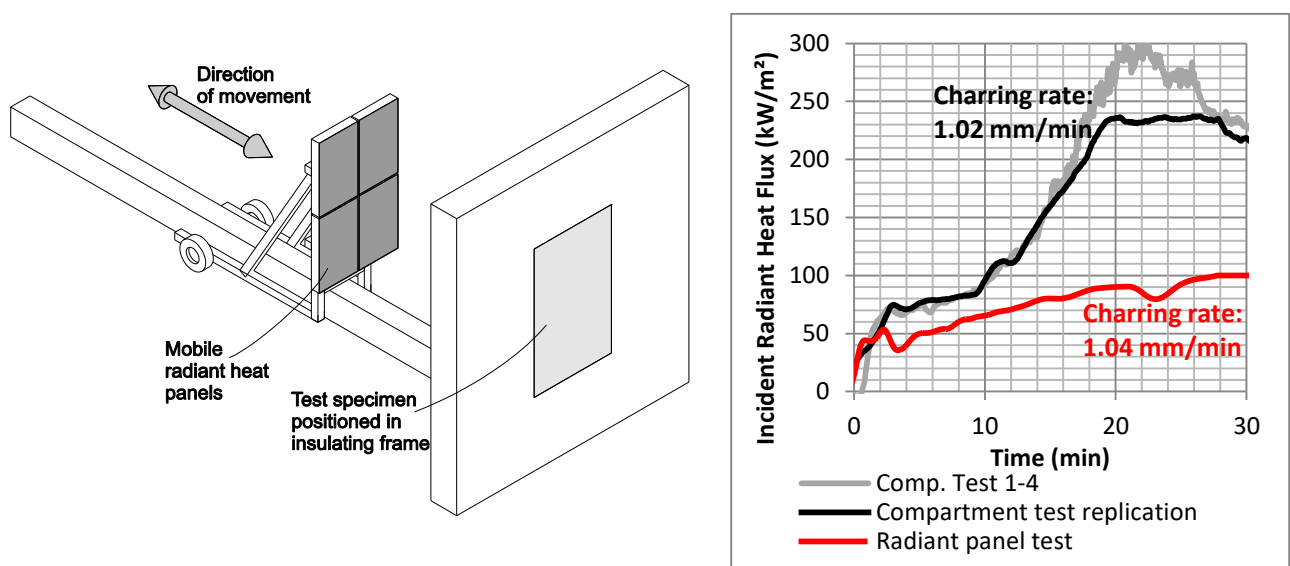


Figure 7: Setup of the position controlled radiant panel test [3] (left) & incident rad. heat flux of a radiant panel test, compartment test and replicating furnace test and corresponding charring rates

4.2 Standard Fire Resistance Tests

Standard fire resistance tests are performed in furnaces typically with low oxygen concentrations. This corresponds to the fully developed phase of compartment fire tests, which is often the most damaging phase of a fire for structures [10]. However, the decay phase with increasing oxygen concentration and increasing char oxidation of a compartment fire is, commonly, not represented in standard fire resistance tests. The validity of fire resistance tests is generally limited to a fully developed fire according to a recent publication [10], as the cooling phase cannot be described with standard fire resistance tests. It should be noted, that the temperatures of the ISO 834 time-temperature curve are significantly lower than temperatures measured during the fully developed phase of recent compartment tests [5]. Whether timber elements would allow for a cooling phase (including burn-out) is dependent on the interaction of the element with the fire compartment. It may be needed to require withstanding burn-out for tall buildings and buildings which the fire service cannot easily reach. If withstanding burn-out is required, it can be stated that the comparison of different materials in standard fire resistance tests can only be fair if the fire exposure (fire temperature to be measured by plate thermometer in front of the exposed surface or incident radiant heat flux, and oxygen concentration) of post-flashover fires of compartments, with these materials exposed, would be similar. Recent studies indicate that this is the case if (1) a limited amount of

timber is exposed and (2) delamination of exposed engineered timber and fall-off of the base layer of gypsum boards are avoided [e.g. 5]. If that is not achieved using prescriptive regulations, performance-based methods such as proposed in [11] are needed.

5 CONCLUSIONS

This paper shows that relevant fire conditions of a post-flashover fire can be successfully replicated in fire testing furnaces. Hereby, a successful replication of a compartment fire in a furnace, should lead to the same rate of damage as was observed in the replicated compartment fire test. It was shown that controlling (1) the plate thermometer temperature or the incident heat flux and (2) the oxygen concentration, so that it resembles the conditions measured in the compartment test, leads to a successful replication. Fire tests of timber elements performed in an open environment with unlimited oxygen can lead to significantly higher charring rates than observed in compartment tests due to oxidation and surface flaming.

ACKNOWLEDGMENT

This paper includes work funded and managed by the Fire Protection Research Foundation which is acknowledged by the authors. Additionally, the framework COST Action FP1404 is acknowledged for highlighting the need of the discussions of the validity of test methods.

REFERENCES

1. ISO 834-1 (1999), Fire resistance tests, Geneva, Switzerland.
2. Lineham S, Thomson D, Bartlett A, Bisby L, Hadden R (2016) Structural response of fire-exposed cross-laminated timber beams under sustained loads. *Fire Safety Journal* 85: 23-34.
3. Brandon D, Maluk C, Ansell MP, Harris R, Walker P, Bisby L, Bregulla J (2015) Fire performance of metal-free timber connections. *Proceedings of the Institution of Civil Engineers: Construction Materials* 168(4): 173-186.
4. Schmid, J., Daniel, B, Werther, N., Klippel, M., Thermal exposure of wood in standard fire resistance tests, *Fire Safety Journal*, 2017.
5. Su J, Lafrance PS, Hoehler M, Bundy M (2018) Cross Laminated Timber compartment fire tests for research on fire safety challenges of Tall Wood Buildings – Phase 2. FPRF/NFPA.
6. Schmid J, Santomaso A, Brandon D, Wickström U, Frangi A (2017) Timber under real fire conditions – the influence of oxygen content and gas velocity on the charring behaviour. *Journal of Structural Fire Engineering*.
7. Wickström (2016) *Temperature Calculation in Fire Safety Engineering*. Springer Switzerland
8. Maluk C, Bisby L, Krajcovic M, Torero J (2016) A Heat-Transfer Rate Inducing System (H-TRIS) Test Method. *Fire Safety Journal* (In press).
9. Brandon and Just (2018) Analysis of fire damages and limitation of fire spread. SP Report, Borås, Sweden.
10. Schmid J, Lange D, Sjöström J, Brandon D, Klippel M, Frangi A. The Use of Furnace tests to describe real fires of timber structures, SIF 2018.
11. Brandon D (2018) Engineering methods for performance-based design -Fire safety challenges of Tall Wood Buildings – Phase 2 report. FPRF/NFPA.

NUMERICAL MODELLING

Numerical Modelling

A STOREY-BASED STABILITY ANALYSIS APPROACH FOR PREDICTING OF THE WORST-CASE FIRE SCENARIO OF UNBRACED STEEL FRAMES

Terence Ma¹, Lei Xu²

ABSTRACT

A computational method is presented for determining the worst-case fire scenario resulting in the instability of an unbraced steel storey frame. Although there are many different fire scenarios that can result in the instability of such a frame, the proposed method identifies the most critical scenario by minimizing the objective function that quantify the severity of each scenario. Based on the results of the presented numerical example, it is apparent that the frame is most vulnerable when the members contributing most to the frame stability are heated most severely. Moreover, the worst-case fire scenario may often coincide with the most concentrated heating scenario. By using the proposed method, designers can assess the relative importance of compartments and members toward the stability of the frame, and alter the configuration of the frame to achieve the desired fire safety performance.

Keywords: Steel frames, stability, analysis, compartment fires, fire scenarios, minimization

1 INTRODUCTION

It is well known that the mechanical properties of steel degrade at elevated temperatures, resulting in the need for thermal protection of structural steel members. Traditionally, the design of fire-protected steel members has been based on the results of standard fire tests on individual components. However, designs based on these tests exhibit shortcomings in that they cannot consider the response of the structural system as a whole, and do not consider realistic fires [11]. Thus, the fire response of a structure cannot adequately be predicted from the results of standard fire tests. For these reasons, the design of structures for fire safety has been transitioning from prescriptive- to performance-based approaches over the past few decades.

Presented in this paper is a new method for determining the overall stability of unbraced steel frames subjected to variable fire scenarios. It predicts the stability condition of an unbraced steel frame based on any combination of its member temperatures. Moreover, through minimization of the objective function it identifies critical fire scenarios, such as the worst case combination of temperatures that would cause lateral instability. A numerical example is presented to demonstrate the efficiency of this method. In this way, the proposed formulation can serve as an invaluable tool for designers in meeting future performance requirements.

2 BACKGROUND

In 1996, the British Research Establishment [1] conducted a series of fire tests on full-scale, multi-storey steel structures. The tests demonstrated that an overall structure performs better in fire than

¹ MASC Candidate. Department of Civil and Environmental Engineering, University of Waterloo, Canada.

e-mail: tc2ma@uwaterloo.ca

² Professor. Department of Civil and Environmental Engineering, University of Waterloo, Canada.

e-mail: lxu@uwaterloo.ca

that predicted when considering the members individually [14]. Ever since, researchers have developed a number of calculation procedures to model the fire resistance and structural response of steel frames subjected elevated temperatures [2, 3, 8, 13]. One issue that has not yet been addressed is there are many different fire scenarios which equally result in the collapse of a structure, and there needs to be a way to determine the worst case scenario. For example, a fire scenario where a given frame collapses at low member temperatures should warrant more attention than a different scenario where the same frame collapses at high member temperatures, and there exists a worst case scenario where the minimum member temperatures will cause collapse. In address to this issue, a new method which was recently developed by Xu et al. [7] is presented in this paper. It is unique in that it is consists of a minimization problem with stability constraints that identifies the most important temperature loading scenario that will result in the instability of an unbraced storey frame. In this way, all possible combinations of member temperatures causing instability are considered within a single minimization problem. The proposed method is similar to the minimization problem proposed by Xu [5], which was then only used for non-proportional applied loading in ambient temperature. In addition to the presentation of the method, this paper offers a modification by also considering approximate relationships between the temperatures of the beams and the temperatures of the columns not addressed by Xu et al. [7].

3 PROPOSED METHOD

Consider the general two-dimensional storey frame with n bays in *Fig. 1*.

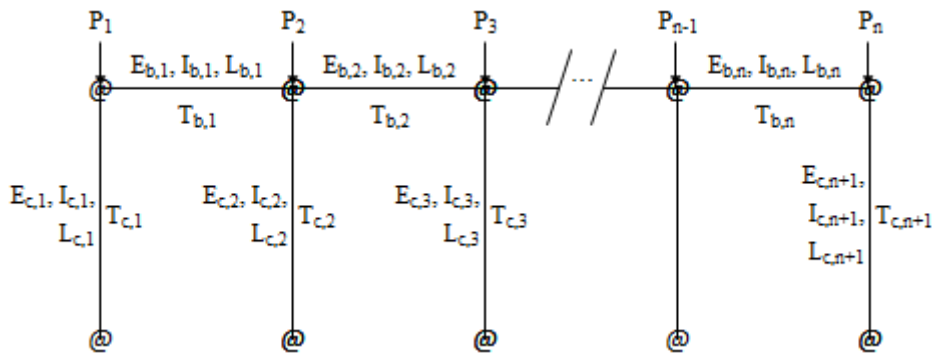


Fig. 1. General storey frame configuration

Each column in the frame is axially loaded by P . E , I , L , and T refers to the modulus of elasticity, moment of inertia, length and temperature, respectively. The subscripts b and c denote beams and columns, respectively. The end connections for all of the members are generalized as semi-rigidly connected with rotational springs, and each column base is restrained from translation.

The proposed formulation contains several assumptions. First, the temperature of each member is assumed to be uniform throughout its length and section. Also, the assumptions of the Euler-Bernoulli beam theory are required as they were used in the derivation. The frame is assumed to be unbraced. The degradation of the members is represented by a reduction in the Young's modulus of elasticity according to *Eq. (1)* [12].

$$E_T = \lambda_T E_{20}; \quad \lambda_T = \begin{cases} 1.0 + \frac{T}{2000 \ln(T/1100)}, & 0^\circ\text{C} \leq T \leq 600^\circ\text{C} \\ \frac{690 - 0.69T}{T - 53.5}, & 600^\circ\text{C} \leq 1000^\circ\text{C} \end{cases} \quad (1)$$

Finally, to more closely represent the effects of fire on members in the same compartment, there is assumed to be a constant ratio, k , between temperatures of the columns to the average temperature of the connecting beams. Since columns usually have more stringent fire protection requirements

than that of beams, it is appropriate to assume $0 \leq k \leq 1$ unless the effects of thermal lag during the cooling phase of a parametric fire need to be accounted for. Although this ratio depends on many factors such as duration of fire, fire curve, and the relative amount of insulation applied to the members, a parametric analysis using a simplified method for predicting member temperatures proposed by Dwaikat and Kodur [10] suggested that $k < 0.9$ for standard fires. Finally, the time-temperature relationships for the members are not considered. Instead, the temperatures of the members in the critical scenario are reported.

Given all of the aforementioned assumptions, an objective function for the minimization problem can be presented in Eq. (2):

$$\min : T_{b,avg} = \frac{1}{n} \sum_{j=1}^n T_{b,j} \quad (2)$$

where $T_{b,avg}$ is the average beam temperature. Minimizing Eq. (2) produces the worst case scenario as it represents the least degradation required to cause instability.

The objective function is subjected to several constraints. The first constraint is that the overall lateral stability of the frame, S_T , is set to zero in Eq. (3). Note that a frame is stable if $S_T > 0$ based on the concept of storey-based buckling. The equality constraint presented here represents the condition where lateral instability has occurred due to the applied axial loads and material degradation as a result of elevated temperature.

$$S_T = \sum_{i=1}^{n+1} S_{c,i} = \sum_{i=1}^{n+1} \left(\frac{12E_{c,i}I_{c,i}}{L_{c,i}^3} \beta_{c,i} \right) = 0 \quad (3)$$

where $S_{c,i}$ is the lateral stiffness of the i^{th} column, $E_{c,i}$ is the elastic modulus of that column at elevated temperature given in Eq. (1), and $\beta_{c,i}$ is a modification factor given by Eq. (4) [5]. For $\beta_{c,i} < 0$ (and thus, $S_{c,i} < 0$), the column has lost its lateral stiffness and “relies on the lateral restraint of the other columns in the same storey in order to sustain the axial load” [5].

$$\beta_{c,i} = \frac{\phi_{c,i}^3}{12} \left(\frac{a_1 \phi_{c,i} \cos \phi_{c,i} + a_2 \sin \phi_{c,i}}{18r_{l,c,i}r_{u,c,i} - a_3 \cos \phi_{c,i} + (a_1 - a_2)\phi_{c,i} \sin \phi_{c,i}} \right) \quad (4)$$

$$a_1 = 3[r_{l,c,i}(1 - r_{u,c,i}) + r_{u,c,i}(1 - r_l)]$$

$$a_2 = 9r_{l,c,i}r_{u,c,i} - (1 - r_{l,c,i})(1 - r_{u,c,i})\phi_{c,i}^2$$

$$a_3 = 18r_{l,c,i}r_{u,c,i} + a_1\phi_{c,i}^2$$

where $\phi_{c,i}$ is the load parameter and $r_{u,c,i}$ and $r_{l,c,i}$ are the upper and lower end fixity factors defined in Eq. (5). The end fixity factor was first derived in [4] and is a measure of the rotational stiffness of a general rotational spring at the end of a member. An end fixity factor of zero represents an ideal pin connection, whereas a value of unity represents a fixed connection.

$$\phi_{c,i} = \sqrt{\frac{P_{c,i}}{E_{c,i}I_{c,i}}} L_{c,i}$$

$$r_{u,c,i} = \frac{1}{1 + 3E_{c,i}I_{c,i} / R_{u,c,i}L_{c,i}}; \quad R_{u,c,i} = \sum_{j_u=1}^{m_u} R_{i,j_u} \quad (5)$$

$$r_{l,c,i} = \frac{1}{1 + 3E_{c,i}I_{c,i} / R_{l,c,i}L_{c,i}}; \quad R_{l,c,i} = \sum_{j_l=1}^{m_l} R_{i,j_l}$$

where $P_{c,i}$ is the axial load, and m_u and m_l are the number of beams connected to the column at the upper and lower ends, respectively. $R_{u,i,j}$ and $R_{l,i,j}$ are the rotational stiffnesses of the connections between the upper or lower end of column i and the j^{th} or j_l^{th} beam that is connected to the that end of column i , expressed in Eq. (6).

$$R_{i,j} = \frac{6E_{b,j}I_{b,j}r_{b,j,N}}{L_{b,j}} \left[\frac{2 + \nu r_{b,j,F}}{4 - r_{b,j,N}r_{b,j,F}} \right] \quad (6)$$

where $r_{b,j,N}$ and $r_{b,j,F}$ are the near- and far-side end fixity factors of the j^{th} beam that is connected to column i at the appropriate end, respectively. $E_{b,j}$ is the elastic modulus of the beam at elevated temperature, $I_{b,j}$ is the moment of inertia, $L_{b,j}$ is the length, and ν is the ratio of the near- and far-end rotations. When asymmetric buckling is assumed, ν equals unity [5].

The second constraint requires that the axial load for each column does not exceed its rotational buckling load, $P_{u,c,i}$, and is not less than $P_{l,c,i}$, which can be taken as either zero or the axial load associated with the service dead load. This inequality constraint is given in Eq. (7).

$$P_{l,c,i} \leq P_{c,i} \leq P_{u,c,i} = \frac{\pi^2 E_{c,i} I_{c,i}}{(K_{c,i} L_{c,i})^2}; \quad i = \{1, 2, \dots, n+1\} \quad (7)$$

where $K_{c,i}$ is the effective length factor, which can be expressed as a function of the end fixity factors in Eq. (8) [6].

$$K_{c,i} = \sqrt{\frac{(\pi^2 + (6 - \pi^2)r_{u,c,i}) \times (\pi^2 + (6 - \pi^2)r_{l,c,i})}{(\pi^2 + (12 - \pi^2)r_{u,c,i}) \times (\pi^2 + (12 - \pi^2)r_{l,c,i})}} \quad (8)$$

Based on the applicable range for Eq. (1), the temperatures of the beams and columns are bounded in Eq. (9). The column temperatures are taken as averages of the connecting beams multiplied by k .

$$T_0 \leq T_{b,j} \leq 1000^\circ\text{C}; \quad j = \{1, 2, \dots, n\}$$

$$T_{c,i} = \frac{k}{m_u + m_l} \left(\sum_{j_u=1}^{m_u} T_{b,j_u} + \sum_{j_l=1}^{m_l} T_{b,j_l} \right) \geq T_0; \quad k \in [0, 1] \quad (9)$$

The lower bound temperature is the ambient temperature, T_0 , typically 20°C . Finally, to eliminate unrealistic scenarios, an optional ‘‘single-fire’’ constraint is presented in the form of Eq. (10).

$$T_{b,j} - \text{median}\{T_{b,r}, T_{b,j}, T_{b,s}\} \geq 0; \quad 1 \leq r < j < s \leq n \quad \forall 2 \leq j \leq n-1 \quad (10)$$

The ‘‘single-fire’’ constraint eliminates scenarios where any internal beam has a local minimum temperature, which can only result from multiple separately originating fires on either side of the compartment unless a fire skips over or around the compartment and ignites the next compartment. Since the exception may need to be considered, this constraint is left as optional.

By solving the minimization problem given in Eqs. (2) through (10), the minimum temperature scenario causing instability of the frame can be determined. Alternatively, the worst-case scenario may be defined differently by replacing Eq. (2) with any other objective function. For example, one might define the worst-case scenario as the most locally concentrated fire causing instability. Then the objective function in Eq. (2) can then be replaced by a locality-based objective function shown in Eq. (11).

$$\text{min or max: } \psi = \frac{T_{b,\max}}{T_{b,\text{avg}}} \quad (11)$$

where ψ is called the locality factor, $T_{b,max}$ is the maximum beam temperature of the frame, and $T_{b,avg}$ is the average beam temperature of the frame. Maximizing ψ results in the most locally concentrated heating case that would result in lateral instability, usually coinciding with the minimum temperature case from Eq. (2). Conversely, minimizing ψ to unity gives the uniform beam temperature that would cause instability, which might represent a full-storey post-flashover fire scenario.

4 NUMERICAL EXAMPLE

In this section, the use of the proposed minimization problem is demonstrated by the example depicted in Fig. 2.

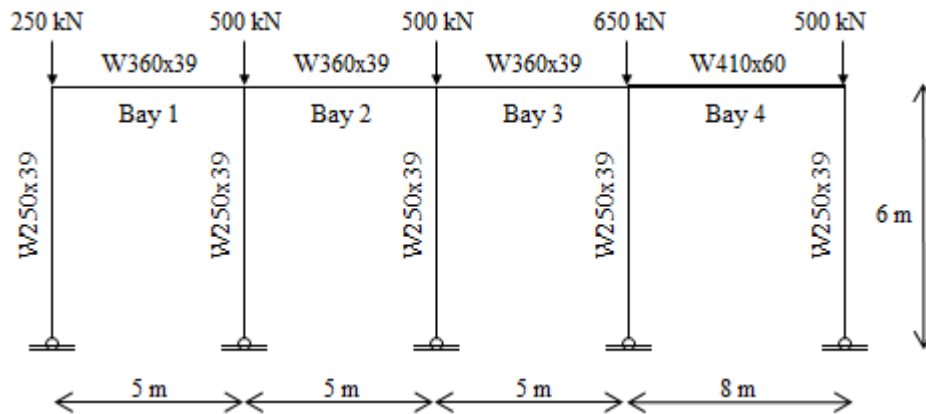


Fig. 2. Frame configuration for numerical example

The four-bay frame is located on the ground floor of a generic building. The three bays on the left-hand side are identical, while the exterior bay on the right-hand side is wider and requires a larger beam section. The axial loads on each column are given in proportion to their tributary widths. All ground connections are considered pinned ($r_{l,c,i} = 0$). The W250x39 columns have $I = 6.01 \times 10^{-5} \text{ m}^4$, the W360x39 beams have $I = 1.77 \times 10^{-4} \text{ m}^4$ and the W410x60 beams have $I = 2.16 \times 10^{-4} \text{ m}^4$. $E_0 = 200 \text{ GPa}$ for all members, and $T_0 = 20^\circ\text{C}$. For all beams, it is assumed that $r_{b,j,N} = r_{b,j,F} = 1.0$, and $\nu = 1$. It is further assumed that $k = 0.8$ when computing column temperatures.

The solution to the minimization problem was computed using the GRG Nonlinear solver algorithm [9] built in Microsoft Excel. Minimizing the temperature-based objective function in Eq. (2) with all of the constraints (including the single-fire constraint) yields the worst-case combination of member temperatures shown in Table 1.

Table 1. Worst-case temperature scenario beam temperatures for numerical example

Beam 1	Beam 2	Beam 3	Beam 4	Average
1000°C	947°C	20°C	20°C	497°C

Based on Table 1, the critical temperature case is one where a severe fire originating from the left bay of the frame and spreads into Bay 2, while the rest of the frame remains unaffected. Note that if the temperatures of the members are flipped so that Beams 4 and 3 were 1000°C and 947°C, respectively, and Beams 1 and 2 were maintained at ambient temperature, the frame would be stable ($S_T = +7.4 \text{ kN/m}$). The reason for the values in Table 1 representing the worst-case is best explained

by comparing the lateral stiffness, $S_{c,i}$, of the columns under ambient temperature conditions and during the worst-case instability scenario, shown in *Table 2*.

Table 2. Loss of lateral stiffness to columns for numerical example

Temperature Condition	Column 1	Column 2	Column 3	Column 4	Column 5	Total
Ambient	113 kN/m	63.8 kN/m	58.4 kN/m	25.9 kN/m	63.8 kN/m	327 kN/m
Elevated and Worst Case	-41.4 kN/m	-72.8 kN/m	24.7 kN/m	25.9 kN/m	63.8 kN/m	0.00 kN/m
Lateral Stiffness Change	-154 kN/m	-137 kN/m	-33.7 kN/m	0.00 kN/m	0.00 kN/m	-327 kN/m

According to *Table 2*, under ambient temperature conditions the bay containing Columns 1 and 2 contributed the greatest portion to the total lateral stiffness of the frame (113 kN/m plus 63.8 kN/m). Therefore, when Bay 1 was heated most severely, the strongest portion of the frame was compromised and the structure collapsed at the minimum possible combination of temperatures. Thus, the example supports the conclusion that heating the strongest members causes the most severe decrease in the lateral stiffness of the frame, and a structure is most vulnerable when a fire originates at the location with the strongest columns to maintain frame stability.

The locality factor in *Eq. (11)* was also maximized and minimized to determine the most localized and uniform temperature cases causing lateral instability, respectively. The results of the analysis are shown in *Table 4*.

Table 4. Most localized and uniform cases based on the locality factor

	Beam 1	Beam 2	Beam 3	Beam 4	ψ
Maximize ψ (most localized)	1000°C	947°C	20°C	20°C	2.01
Minimize ψ (uniform temperature)	668°C	668°C	668°C	668°C	1.00

The most localized fire was found to coincide with the minimum temperature case from *Table 1*. The case where the temperature of all the beams is 668°C may be representative of an entire storey undergoing post-flashover fire, which is not uncommon in historical studies of fires occurring in multi-storey buildings. It may therefore be useful for designers to assess whether or not the uniform temperature case is sufficiently high to prevent instability in the event of post-flashover fire, and to modify the design accordingly if it is inadequate.

5 PARAMETRIC STUDY

A brief parametric study on the sensitivity of the solution obtained from the minimization problem to the column-to-beam temperature ratio, k , in *Eq. (9)* is presented in this section. The frame in *Fig. 2* was repeatedly analysed for the worst-case temperatures scenario in *Eq. (2)* while varying k from 0 to 1. The beam temperatures, as well as the value of T_{avg} , in the critical case are plotted as a function k in *Fig. 3*.

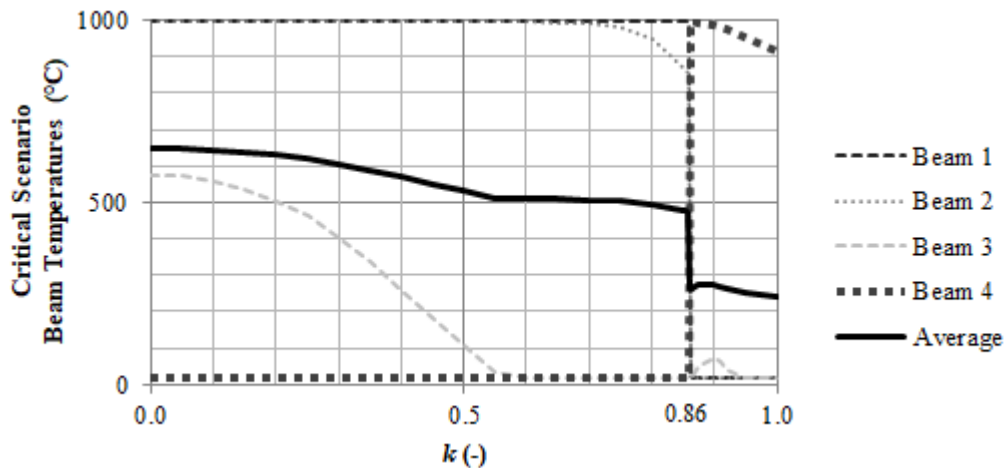


Fig. 3. Effects of varying k on the member temperatures in the critical case

From Figure 3, it is apparent that T_{avg} in the critical case generally decreases as k increases, which is expected since k elevates the relative amount of degradation to column stiffness. For k below 0.86, the critical case always requires Beam 1 at 1000°C, Beam 4 at 20°C, and Beams 2 and 3 at intermediate temperatures. At $k \geq 0.86$, the critical case switches to only Beam 4 experiencing the elevated temperatures. The reason for the change in failure mode for $k \geq 0.86$ is that k is large enough to cause $T_{c,5} = 860^\circ\text{C}$, at which point the internal axial force, P_5 , reaches the rotational buckling capacity, P_{u5} in Eq. (7), causing severe loss of frame lateral stiffness as Column 5 is relatively strong at ambient temperature. Thus, the buckling of Column 5 governs the solution for $k \geq 0.86$. It is worth mentioning that the abrupt change at $k = 0.90$ for Beam 3 occurs because the buckling of Column 5 reduces the maximum allowable temperature of Beam 4, which actually helps to strengthen Column 4, so the temperature of Beam 3 must increase to maintain similar degrees of degradation to Column 4.

For this example, it can be seen that the failure mode in the critical case remains consistent between $0 \leq k \leq 0.86$, and $0.86 \leq k \leq 1.0$. Thus, the solution to the minimization problem is able to provide useful information about potential failure modes, in addition to identifying the critical compartments. Moreover, the failure mode and critical compartment can be changed by adjusting the amount of insulation (thereby changing the value of k) for the beams and the columns.

6 CONCLUSIONS

A minimization problem with stability constraints was presented in this paper for determining the critical member temperature scenarios for any unbraced steel frame subjected to variable fire loading. Although many different combinations of member temperatures can equally cause the instability of a frame, the proposed method is able to identify the most critical of such cases by use of any objective function, such as the average temperature of the beams. The minimization problem is subjected to several constraints, which define the condition of lateral instability and the limits for the temperature of the members, etc.

The proposed minimization problem was demonstrated via a numerical example, and it was concluded that the critical case of minimum member temperatures causing instability occurs when the strongest areas of the frame are heated the most. It is also apparent that the most local combination of temperatures causing instability coincides with the minimum temperature case. The minimization problem can further be used to determine the uniform temperature of the beams that would cause instability. Finally, it is shown that by varying the amount of insulation on the columns

relative to that of the beams, the failure mode of the critical case can be changed. Overall, the proposed formulation was found to provide useful information about the relative importance of the compartments and structural members in a steel frame towards fire safety.

ACKNOWLEDGMENT

The authors wish to thank the National Science and Engineering Research Council of Canada for the financial support of this work.

REFERENCES

1. British Research Establishment. (1996). Fire, static, dynamic tests at the large building test facility. Proceedings of the 2nd Cardington Conference.
2. Carlos Couto, Paulo Vila Real, Nuno Lopes, Joao Paulo Rodrigues (2013). *Buckling analysis of braced and unbraced steel frames exposed to fire*. Engineering Structures, 49(2013). pp 541-559.
3. Egle Rackauskaite, Panagiotis Kotsovinos, Ann Jeffers, Guillermo Rein (2017). *Structural analysis of multi-storey steel frames exposed to travelling fires and traditional design fires*. Engineering Structures, 150(2017). pp 271-287.
4. G.R. Monforton, Tien Hsing Wu (1963). Matrix analysis of semi-rigidly connected frames. Journal of the Structural Division, 89(6). pp 13-42.
5. Lei Xu (2001). *The buckling loads of unbraced PR frames under non-proportional loading*. Journal of Constructional Steel Research, 58(2002). pp 443-465.
6. Lei Xu (2003). *A NLP approach for evaluating storey-buckling strengths of steel frames under variable loading*. Structural and Multidisciplinary Optimization, 25(2). pp. 141-150.
7. Lei Xu, Terence Ma, Yi Zhuang (2017). *Storey-based stability of unbraced structural steel frames subjected to variable fire loading*. Manuscript submitted for publication, Journal of Constructional Steel Research.
8. Lei Xu, Yi Zhuang (2014). *Storey stability of unbraced steel frames subjected to non-uniform elevated temperature distribution*. Engineering Structures, 62-63(2014). pp 164-173.
9. Léon S. Lasdon, Richard L. Fox, Margery W. Ratner (1974). *Nonlinear optimization using the generalized reduced gradient method*. RAIOR – Operations Research - Recherche Opérationnelle, 8.V3(1974). pp 73-103.
10. Mahmud M.S. Dwaikat, Venkatesh K.R. Kodur (2013). A simplified approach for predicting temperatures in fire exposed steel members. Fire Safety Journal, 56(2013). pp 87-96.
11. Sangdo Hong, Amit H. Varma, Anil Agarwal, Kuldeep Prasad (2008). Behaviour of steel building structures under realistic fire loading. *Structures Congress 2008*, Vancouver, British Columbia, Canada, ASCE, April 24-26, 2008.
12. T.T. Lie (1992). Structural Fire Protection. American Society of Civil Engineers, New York.
13. W.S. Toh, T.C. Fung, K.H. Tan (2001). *Fire resistance of steel frames using classical and numerical methods*. Journal of Structural Engineering, 127(7). pp 829-838.
14. Yong C. Wang, Venkatesh K.R. Kodur (2000). Research toward the use of unprotected steel structures. Journal of Structural Engineering, 126(12). pp. 1442-1450.

DISCUSSION ON A SYSTEMATIC APPROACH TO VALIDATION OF SOFTWARE FOR STRUCTURES IN FIRE

João Daniel Romeiro Ferreira¹, Thomas Gernay², Jean-Marc Franssen³

ABSTRACT

A validation exercise has been performed for the thermo-mechanical software SAFIR[®] based on a dual approach. First, the examples proposed in the German National Annex of EN 1992-1-2 have been calculated with SAFIR and, second, the references to SAFIR found in scientific publications have been analysed with respect to the level of accuracy estimated by the authors for the results of SAFIR. The aim of this paper is not to present the detailed results of this validation exercise (which are published in open access reports). The focus is more on a critical analysis of the examples presented in the German National Annex which indeed paved the way to a systematic approach to validation of SiF software but could be improved, namely by including sensitivity analyses on the discretisation, a better description of some input data particularly in the material models, a presentation of the means used to obtain some reference results and a clear definition of the failure criteria to be used for determining fire resistance times. Furthermore, extensive analysis of the literature showed that the wide field of application of a typical SiF software requires an extension of the domain covered by the standard on concrete structures.

Keywords: Structures, finite element modelling, benchmarking, validation, fire tests

1 INTRODUCTION

Numerical models are used more and more in structural fire engineering. This trend is supported by extensive research efforts toward the development of computational models. However, it has to be recognised that, compared to CFD software, the validation of advanced tools for the thermo-mechanical analysis of structures in fire has received little attention, which may be partly due to a lack of clear guidelines and standards. Some efforts have been undertaken ([2], [12]), but systematic validations of software used in the field remain the exception rather than the norm. Validation of structural fire analysis codes can rely on benchmarking examples such as those provided in the German National Annex of EN 1992-1-2 [1], which has attracted the attention of the authors and will be commented in this paper. On the other hand, confidence in numerical models may rely on their validation against experimental tests, but to infer validity from such comparisons, a statistically relevant database of tests should be considered, which is rarely the case.

This paper describes a systematic approach for software validation based on a combination of standard benchmarking examples and literature tests review. The work, applied to the particular software SAFIR[®] [3] but valid in general, aims to:

1. Critically discuss the numerical modelling of the DIN benchmarking examples, while proposing relevant sensitivity analyses;

¹ Research Engineer. Department of Architecture, Geology, Environment & Constructions (ArGEnCo), Liege University, Belgium.
e-mail: jdferreira@uliege.be

² Assistant Professor. Department of Civil Engineering, Johns Hopkins University, Baltimore, USA.
e-mail: tgernay@jhu.edu

³ Professor. Department of Architecture, Geology, Environment & Constructions (ArGEnCo), Liege University, Belgium.
e-mail: jm.franssen@uliege.be

2. Present a meta-analysis review of published tests modelled with a well-established software. This review also allows identifying gaps between the DIN benchmarking examples and common numerical modelling applications.

2 VALIDATION THROUGH BECHMARKING CASES

2.1 German National Annex to the Eurocode

Annex CC of DIN EN 1992-1-2 NA (here referred as “DIN”) [1] presents a series of cases that allow benchmarking software tools aimed at the design of concrete structures in a fire situation. The validation typically consists in a comparison between the value of a result (e.g. temperature, or displacement) obtained by the tool under validation and the value given as a reference and supposed to be the *true* result. The value obtained must fall within an interval stipulated by the document.

The eleven examples present in DIN are based on a research project conducted by Hosser et al [4]. The seven first cases aim at checking specific calculations, for which results are expected to be matched with a great accuracy by the tool being tested. Some of these tests are simple “Unity tests”. That means a specific test built up to verify good coding of a specific function. This is the case, for example, of Example 4 about thermal expansion of a simple unloaded bar. Ideally, code developers should develop their own unity tests for every function involved in the code. The four last cases aim at checking the entire calculation process, for which results are expected to be close to the ones obtained from specific software (namely Ansys and STABA-F) that are described in [5] as “*approved programs*”.

All the examples in the DIN were modelled using SAFIR. A detailed description of these analyses can be found in [6]. Table 1 shows a short description of the examples and the results of the comparison between the values obtained by SAFIR and the reference values prescribed in DIN.

Table 1. Summary of results obtained with SAFIR for the collection of examples in DIN.

Example	Test criterion	Check on	Limits respected
1	Heat transfer (cooling)	Specific function	Yes
2	Heat transfer (heating)	Specific function	Yes
3	Heat transfer through several layers	Specific function	Yes
4	Thermal expansion	Specific function	Yes
5	Temperature-dependent stress-strain curves of concrete and steel	Specific function	Yes
6	Temperature-dependent limit-load-bearing capacity of concrete and steel	Specific function	Yes
7	Development of restraint stresses	Specific function	Yes
8	Weakly reinforced concrete beam	Full calculation process	Yes
9	Heavily reinforced concrete beam	Full calculation process	Yes*
10	Reinforced concrete column	Full calculation process	Yes*
11	Composite column with concrete cores	Full calculation process	Not all

* values are within limits depending on the assumptions considered

2.2 Sensitivity analyses

DIN gives reference values to be obtained by the simulation, with some tolerance, but it does not address at all the questions of discretization in time or in space, which can significantly affect the accuracy and quality of the results. A tool that can meet the requirements only with an extremely fine mesh and an extremely short time step may yield unrealistic results with more practical meshes and time steps. It is of uttermost importance to know how the quality of the results is affected when the discretisation is degraded. Only by testing different refinements and configurations of the mesh, different time steps and other parameters, is it possible to learn how a tool responds and to prove

that results are consistent when enough detail is used in the models. Therefore, extensive sensitivity analyses have been conducted in the validation process of SAFIR through the DIN benchmarking cases [6]. As an example, Fig. 1 shows part of a sensitivity analysis made for Example 1.

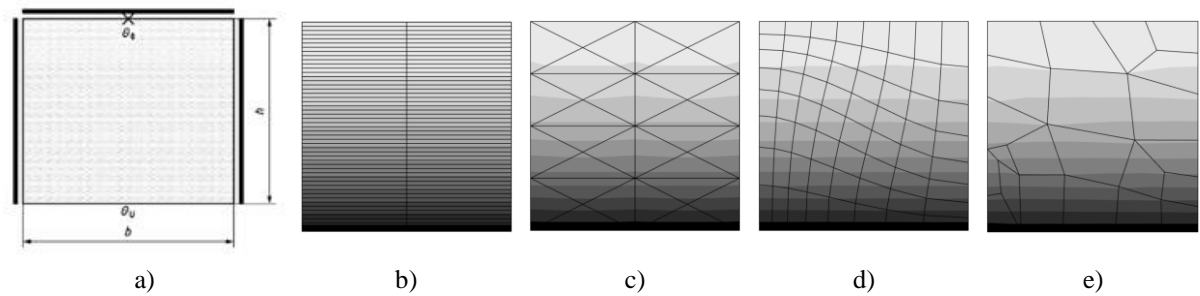


Fig. 1. Part of a sensitivity analysis performed with SAFIR® for Example 1 in DIN (temperatures plotted): a) section tested; b) mesh with rectangles; c) mesh with triangles; d) distorted mesh; e) unstructured mesh

The analysis allowed quantifying how the solution converges to the theoretical solution when the density of the mesh is increased and the value of the time step is reduced. Additional conclusions drawn in [6] state that, when refining the mesh:

- Rectangular elements converge slightly faster than triangular elements.
- Structured meshes are more efficient.
- Slight differences are observed in distorted structured meshes but those are still efficient;
- Unstructured meshes are less efficient but still lie in the acceptable range of the standard.

2.3 Sources of discrepancies in results

The results of SAFIR for the last three examples present issues with regards to the limits stipulated by the DIN. For Example 9, the goal is to determine the area of steel A_s that makes the beam resist exactly 90min under standard ISO fire. If one considers the last converged time step of the simulation as the time of failure, the determined A_s will fall outside the boundaries establish by the DIN. However, if the failure criteria described in EN1363-1 [7] is applied, the time of failure is shorter than the last converged time step (see Fig. 2) and the results fall within the limits. Even in a prescriptive framework, ambiguities in the definition of the failure criteria can influence the fire resistance rating as shown in [13]. Therefore, a clear definition of failure, and the criteria used to determine the failure time, should be specified in the DIN as being on the basis of the results.

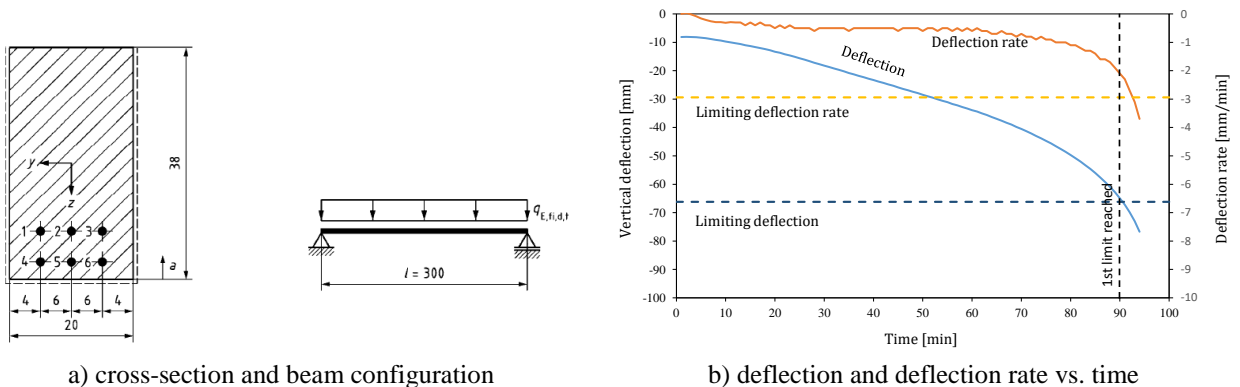


Fig. 2. Geometry and configuration of the beam and deflection and deflection rate vs. time, with $A_s = 8.84\text{cm}^2$ for Example 9 in DIN, with limits for the load bearing capacity according to the criteria in EN1363-1 [7]

Another question that can be raised is that, despite being referred to as “*approved tools*” in [5], there is no unquestionable proof of the accuracy of these tools that have been granted some sort of

grandfather's right. There is also no indication on the assumptions made in the analyses that produced the reference results. For instance, it is not explicitly mentioned in this Annex CC of DIN what should be the values used for the thermal conductivity or the moisture content in concrete. Additionally, it is noted that 3 other tools developed independently, namely InfoGraph [8], FRILO [9] and mbAEC [10], yield identical results to those obtained with SAFIR for the considered DIN examples. This fact is certainly something that should not be neglected and that contributes to the uncertainty on how the results taken as reference in DIN were determined and on their accuracy.

3 META-ANALYSIS OF PUBLISHED TEST MODELS

3.1 Research methodology

The goal of this meta-analysis is to assess the suitability of SAFIR to model practical and full-scale problems of engineering, based on the accuracy of predictions of the temperature distributions in real structures subjected to fire and fire resistance times as well as a correct prediction of the structural behaviour. The approach consisted in reviewing the scientific documents that have cited SAFIR throughout the years, and extracting from these documents any published comparisons between SAFIR results and results from experimental tests and/or results obtained with other software. Results were then compiled in a list that has been made available online [11].

Only documents written in English were considered. These constitute the major part of the documents found during this research, with only a very minor part being written in other languages.

3.2 Documents

As of March 2018, 551 documents with a reference to SAFIR have been found. From these, 411 have calculations performed by SAFIR, 108 have only a reference to SAFIR, and it was not possible to check the content of the remaining 32 documents, because they are not available online and could not be obtained by any of the methods used.

Most of the documents found (about 90 %) are either journal articles or conference papers. Only these were further considered. This is justified by the fact that usually the results of the same calculations made in PhD thesis or books are also published in articles and papers, and that MSc thesis and technical reports do not necessarily have a sufficiently reliable cross checking of results that justify their inclusion in such an analysis.

Fig. 3 shows the 134 documents containing comparisons between SAFIR and the two types of sources of results: experimental tests and other advanced calculation models.

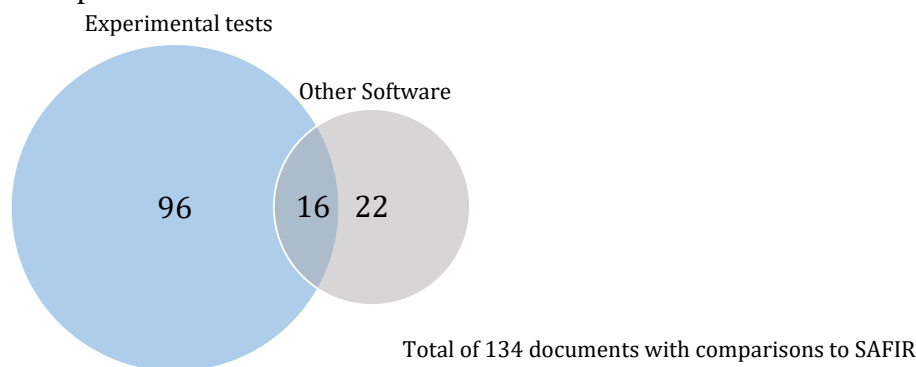


Fig. 3. Number of journal articles and conference papers with comparisons of SAFIR to experimental tests, to other software, and to both.

3.3 Classification

A classification was made by quantifying the number of documents for the different structural elements and materials used, the kinds of phenomenon, property or behaviour analysed, the types of finite elements used in the model, and the fire curves applied. The results are depicted in Fig. 4.

Numerical Modelling

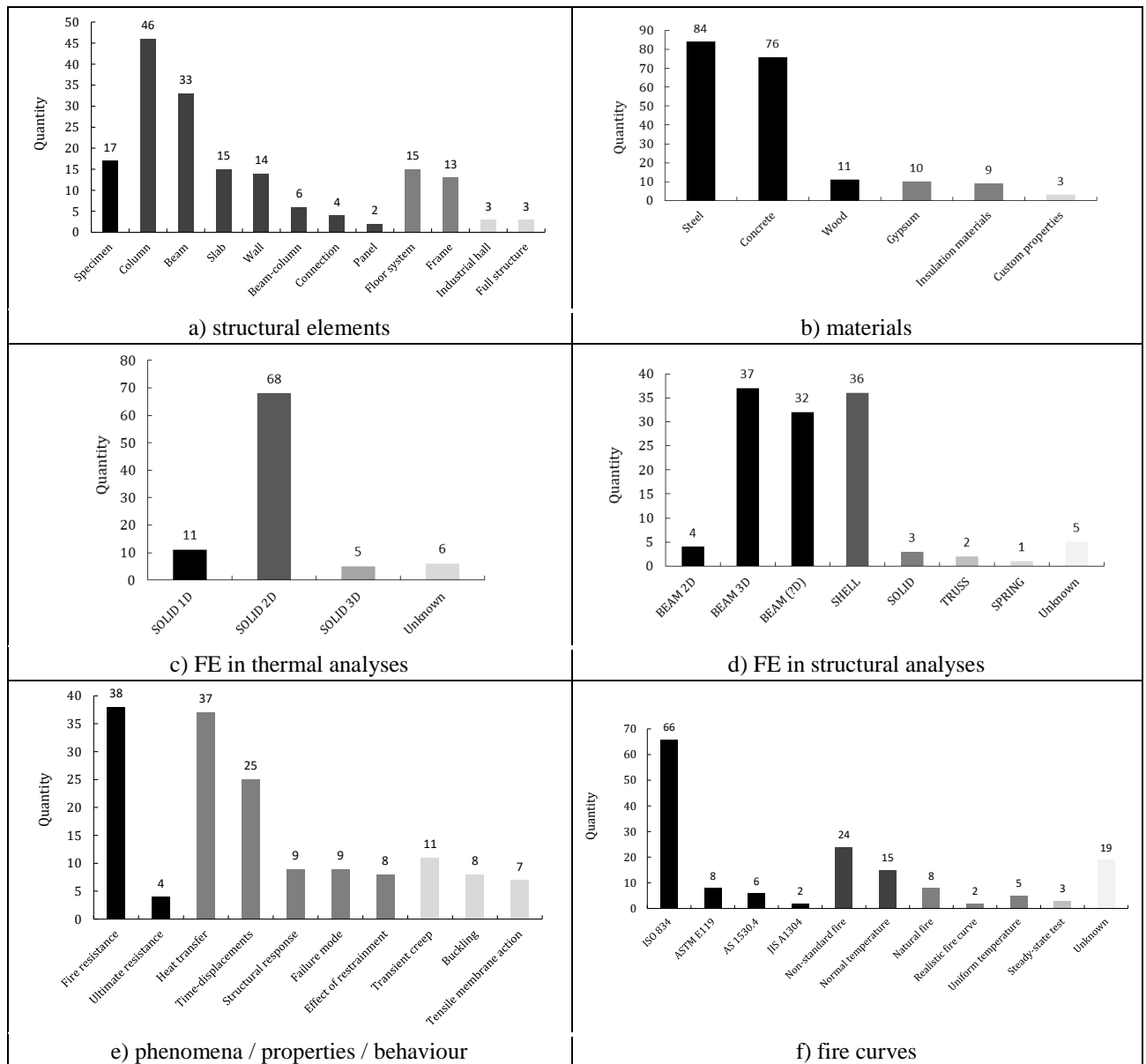


Fig. 4. Classification of journal articles and conference papers presenting comparisons between SAFIR and experimental tests or other software, according to different aspects

Based on Fig. 4, the following conclusions are drawn:

- Most analyses are done for isolated members, especially columns, beams, slabs and walls.
- Steel and concrete are by far the two materials most used in the comparisons.
- SOLID 2D, in thermal analyses, and BEAM (2D and 3D) are clearly the FE most extensively covered, while SHELL are also commonly used.
- Fire resistance, time-displacements and heat-transfer are the most studied subjects.
- A large part of the analyses use the Standard ISO834 fire curve, whereas an also significant amount of analyses are done with non-standard fires and at normal temperature.

3.4 Comparisons

An attempt at a qualitative analysis that may easily provide an overall picture of the results was made, and the comments done by the authors of the analyses were reviewed, so that they may provide some insights on the results of the comparisons.

3.4.1 Level of agreement

The level of agreement between results from SAFIR and other sources of results was qualitatively classified according to a scale that went from ‘very poor’ to ‘very good’. As with any other qualitative evaluation, the interpretation of the published results and comments involved some level of subjectivity. Nevertheless, the objective was to match the typical keywords used by the authors of the analyses, such as “very good” and “quite satisfactory”, with the scale previously mentioned. Fig. 5 shows the distribution of the documents according to the different levels of agreement:

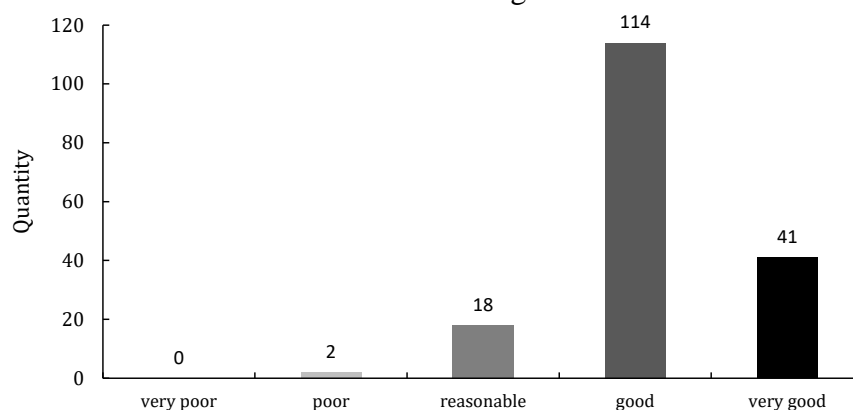


Fig. 5. Classification of scientific publications presenting comparisons between SAFIR and experimental tests or other software, as a function of the level of agreement.

3.4.2 Review of comments

Based on the comments extracted from the considered 134 publications, the main conclusions indicated by authors on their comparisons to SAFIR are, as regards the capabilities of SAFIR:

- Temperature distributions throughout time are generally well predicted.
- Good agreement is generally obtained for fire resistance times, ultimate loads and time-displacements.
- Forces generated by loads and resulting from restrained thermal expansion are well predicted.
- Failure modes and buckling shapes are well captured in steel structures. Residual stresses, when considered, are correctly taken in account.

However, the following limitations of SAFIR are noted:

- Water movement within concrete is not simulated, which may result in slight over-predictions of temperature.
- Spalling is not accounted for, which can result in over-predictions of the resistance of RC structures.
- BEAM elements do not capture shear deformation and can lead to over-estimations of resistance whenever shear is the main failure mode.

4 DISCUSSION

4.1 Benchmarking

Benchmarking examples should include sensitivity analyses that can provide proof that results converge as more refined models and shorter time steps are considered. Other analyses may include the study of the influence of the different types of analysis or solvers (static, dynamic, implicit, explicit, etc.). Detailed description of the inputs of the models is required, as well as an explicit definition of the “failure” criteria used to define the fire resistance time.

As such information is missing in some of the examples of the DIN, the authors consider that the excessive deviation observed for some of the Examples does not invalidate the ability of SAFIR to model the behaviour of concrete beams subjected to fire.

Although the DIN document was a major step in the good direction, it is clear that the comprehensive benchmarking of an advanced SiF software with a wide field of application requires addressing a broader range. Benchmark examples should be developed namely in:

- timber structures;
- structures with shell elements, such as concrete walls and slabs or slender steel structures where local buckling may develop;
- full structures or substructures with load redistribution.

The amplitude of the task is such that it cannot be undertaken at a national level.

4.2 Meta-analysis

The meta-analysis on the typology and quality of the comparisons that have been made in the literature between SAFIR and tests or other advanced tools offers valuable information.

Most of the comparisons have been done on single structural members. This is justified by the fact that it is harder to have access to tests on complete structures. However, it is important that at least some comparisons of results for these full structures are done with the software being tested (if not against experimental tests at least against other advanced tools), as this will be the main use for the software in practice.

Another conclusion from the analysis is that, despite the fact that SAFIR offers the use of solid 3D FE for thermal and structural analysis, these have been scarcely subject to validation by users. This can be both a consequence of the fact that these elements have been included only recently in the software, but may also indicate that these still represent big computational efforts that most users do not want to cope with considering that, even at room temperature, building structures are typically modelled with oriented elements such as trusses, beams and shells.

The qualitative analysis of the results yields a clear visualization of the level of accuracy of the software, by an easily interpreted graph that sums up the results of the comparisons made by the users. The review of the comments made by the users allow to clearly identify the types of analyses for which the program returns accurate results and what are the main constraints when using the software.

5 CONCLUSIONS

The analyses presented in the paper allow drawing the following main conclusions:

- Benchmarking examples should include sensitivity analyses. Indeed, the results of a code should be proven not to be disproportionately sensitive to input parameters such as the size of the elements or the time step. Also, if any software would require extremely small elements and/or extremely short time steps to achieve satisfactory results, this should be put to the attention of the users.
- The results given for the DIN for some of the examples are determined by “approved software”. Some of the reference values are not matched by other software which, on the other hand, yield similar results between them. The assumptions made in calculating the reference solutions should be mentioned to allow determining the reasons of eventual deviations between the tests and the simulations.
- The benchmarking examples currently available for structural fire analysis codes do not cover sufficiently the range of applications commonly found in the literature. It is notably urgent to add new benchmarking examples with steel and concrete shell finite elements and with timber structures, preferably at an international level.

- Failure criteria should be clearly mentioned when a mechanical calculation must be compared with the results of an experimental test of other software, if the ultimate resistance or fire resistance are being considered.
- Meta-analyses of comparisons of results with real-world structures offer a great way to provide additional validation to a software, by delivering insight about the quality of the results obtained and the typology of the comparisons made.

REFERENCES

1. DIN EN 1991-1-2/NA (2010), *National Annex - National determined parameter – Eurocode 1: Actions on structures – Part 1-2: General actions – Actions on structures exposed to fire*, Deutsche Norm.
2. Rackauskaite E, Kotsovinos P, Rein G (2017). *Model parameter sensitivity and benchmarking of the explicit dynamic solver of LS-DYNA for structural analysis in case of fire*. Fire Safety J 90:123-138.
3. Franssen J-M, Gernay T (2017). *Modeling structures in fire with SAFIR®: Theoretical background and capabilities*, J. Str. Fire Engng, Vol. 8, No 3, pp 300-323. <https://doi.org/10.1108/JSFE-07-2016-0010>
4. Hosser D, Richter E, Zehfuß J (1999). *Erarbeitung von Nationalen Anwendungsrichtlinien fürrechnerische Nachweise nach den Brandschutzteilen der Eurocodes 2 – 5*, Abschlussbericht (Az. RS III 4 – 67 41 – 97.120), IBMB, Braunschweig (in German).
5. COST report (2014), *Benchmark studies - Verification of numerical models in fire engineering*, ISBN: 978-80-01-05442-0, Czech Technical University in Prague, pp 23-29.
6. Ferreira J, Franssen J-M, Gernay T, Gamba A (2017). *Validation of SAFIR through the DIN EN 1992-1-2 NA*, Liege University, Belgium. <http://hdl.handle.net/2268/208197>, Available at http://www.uee.uliege.be/cms/c_2673990/fr/safir-free-downloads
7. CEN (2012), *EN 1363-1 Fire resistance tests – Part 1: General requirements*, European Committee for Standardisation, Brussels.
8. InfoGraph (2015), *Prüfung und validierung von rechenprogrammen für brandschutznachweise mittels allgemeiner rechenverfahren*, Germany. http://download.infograph.de/de/validierung_brand.pdf (url last consulted on 25/09/2017)
9. FRILO (2017), *Analyses on reinforced concrete sections*, Germany. http://www.frilo.eu/tl_files/frilo/pdf/en/pdf_doku/Analyses%20on%20Reinforced%20Concrete%20Cross%20Sections.pdf (url last consulted on 25/09/2017)
10. mbAEC (2014), *Validierung gemäß DIN EN 1991-1-2 / NA:2015-09*, Germany. https://www.mbaec.de/fileadmin/Datenblaetter/U412de_Validierung.pdf (url last consulted on 25/09/2017)
11. Ferreira J, Franssen J-M, Gernay T (2017). *List of SAFIR citations and comparisons with tests and other software*, University of Liège, Belgium. http://www.uee.uliege.be/cms/c_2673990/fr/safir-free-downloads
12. Franssen J-M, Schleich J-B, Cajot L-G, Zhao B, Twilt L, Both K (1994). A comparison between five structural fire codes applied to steel elements. Proc. 4th IAFSS Symposium (pp. 1125-1136).
13. Dumont F, Wellens E, Gernay T, Franssen J-M (2016). Loadbearing capacity criteria in fire resistance testing. *Materials and Structures*, 49(11), pp. 4565-4581.f

BRANCH-SWITCHING PROCEDURE FOR BUCKLING PROBLEMS OF STEEL ELEMENTS IN FIRE

Luca Possidente¹, Nicola Tondini², Jean-Marc Battini³

ABSTRACT

In numerical shell-based simulations employed to capture both local and global buckling of steel members, the definition of a consistent initial geometrical imperfection plays a primary role. However, the choice of an appropriate amplitude and the introduction of such an imperfection is not straightforward, above all if the behaviour at elevated temperatures is being investigated. In fact, when the temperature of a steel member increases due to a fire, the material properties degrade and redistribution of the load may also occur. In order to tackle the outlined problem, an investigation was performed to analyse the effect of the imperfections on compression steel plates by means of an advanced approach based on a triangular thermomechanical co-rotational shell element that incorporates a branch-switching procedure. This procedure allows for a complete description of the physical behaviour of a structure by checking the existence of possible critical points along the fundamental path at each time step and then switching to the secondary path. Analyses were performed on perfect and imperfect plates representative of web panels. The study confirmed that the introduction of imperfections is not trivial and that the branch-switching procedure may represent an appealing preliminary tool to understand the structural behaviour.

1 INTRODUCTION

An increasing interest is arising in the investigation of buckling phenomena for slender and thin-walled steel members subjected to fire. Numerical simulations employed to capture both local and global buckling of steel elements are usually based on shell models with applied initial imperfections or perturbative forces. Although for 2D beam models the application of a single perturbative force usually suffices to obtain satisfactory results, this may not be the case in shell analysis; in particular for complex members composed of several plate elements. Hence, the definition of consistent geometrical imperfections plays a primary role. However, in fire analyses the choice of an appropriate amplitude and the introduction of such an imperfection may not be trivial in shell models owing to material degradation. In fact, the buckling modes may vary over time and may be significantly different from the ones at ambient temperature. Therefore, the practice of defining the shape of imperfections according to the buckling modes at ambient temperature may introduce inconsistencies in a fire analysis. In this respect, recent works [1, 2] showed that the number of half waves that are introduced to characterise the imperfections is one of the parameters that strongly affects the plate behaviour at high temperature. In order to tackle the problem, an advanced approach based on a triangular thermomechanical co-rotational shell element that incorporates a branch-switching procedure is proposed. The shell element, specifically developed for steel elements, is well suited for analyses in which small strains and large

¹ PhD Candidate. Department of Civil, Environmental and Mechanical Engineering, University of Trento, Italy.
e-mail: luca.possidente@unitn.it

² Assistant Professor. Department of Civil, Environmental and Mechanical Engineering, University of Trento, Italy.
e-mail: nicola.tondini@unitn.it

³ Professor., Division of Structural Engineering and Bridges, KTH, Stockholm, Sweden
e-mail: jean-marc.battini@byv.kth.se

displacements occur. The branch-switching procedure differs from the classical procedure implemented in commercial codes, allowing for a complete description of the physical behaviour of a structure analysed without initial imperfections. The paper is organised as follows: in Section 2 a brief description of the corotational shell element is given. Section 3 provides insight into the branch-switching procedure. In Section 4 the results of the numerical analysis on four Case studies are discussed. Conclusions are drawn in Section 5.

2 COROTATIONAL SHELL ELEMENT

2.1 Corotational framework

The co-rotational approach relies on the idea that the motion of an element can be decomposed into rigid body and pure deformational parts. The latter is captured at the level of a local reference frame, which continuously translates and rotates with the element. The transformation matrices relating local and global systems allow for accounting the geometric nonlinearity induced by the large rigid-body motion. Thus, a simple linear element can be chosen as local element. However, material nonlinearity needs to be introduced at the level of the local formulation. In this chapter, the corotational framework for 3-node flat shell elements is briefly described (*Figure 1-a*). For a more comprehensive presentation the interested reader may refer to [3].

The motion of the shell element from the initial to the final deformed configuration can be split into two stages, consisting in a rigid body motion and a pure deformation. The rigid translation is defined by the displacement of point C, denoted by \mathbf{u}_c . The global rotation at the node i is defined by the matrix \mathbf{R}_i . $\bar{\mathbf{R}}_i$ describes the local small rotation acting on the nodes due to the pure deformation. The global displacement vector consists of displacements \mathbf{u}_i^g and rotations $\boldsymbol{\Psi}_i^g$ expressed in global coordinates:

$$\mathbf{p}_g = [\mathbf{u}_1^{gT} \quad \boldsymbol{\Psi}_1^{gT} \quad \mathbf{u}_2^{gT} \quad \boldsymbol{\Psi}_2^{gT} \quad \mathbf{u}_3^{gT} \quad \boldsymbol{\Psi}_3^{gT}]^T \quad (2.1)$$

$$\mathbf{R}_i = \exp(\boldsymbol{\Psi}_i^g) \quad (2.2)$$

The local displacement vector \mathbf{p}_l expressed in the local frame is composed by three displacements $\bar{\mathbf{u}}_i$ and three rotations $\bar{\boldsymbol{\vartheta}}_i$

$$\mathbf{p}_l = [\bar{\mathbf{u}}_1^T \quad \bar{\boldsymbol{\vartheta}}_1^T \quad \bar{\mathbf{u}}_2^T \quad \bar{\boldsymbol{\vartheta}}_2^T \quad \bar{\mathbf{u}}_3^T \quad \bar{\boldsymbol{\vartheta}}_3^T]^T \quad (2.3)$$

$$\bar{\boldsymbol{\vartheta}}_i = \log(\bar{\mathbf{R}}_i) \quad i = 1,2,3 \quad (2.4)$$

The global internal force vector \mathbf{f}_g and global tangent stiffness matrix \mathbf{K}_g associated with the global displacement vector \mathbf{p}_g are obtained from the corresponding local quantities \mathbf{f}_l and \mathbf{K}_l associated to \mathbf{p}_l through three successive changes of variables. The local triangular shell element consists in the superposition of a membrane and a plate element. In detail, according to an assessment of different elements presented in [4], an optimal ANDES membrane element and a DKT (Discrete Kirchhoff Triangle) plate element were employed in the definition of the shell local element. The element accounts for elasto-plastic deformations and the local quantities \mathbf{f}_l and \mathbf{K}_l are computed using three interior Gauss points and 7 Gauss points across the thickness of the element.

The plane stress behaviour was defined by a von Mises yield surface and both the thermal strain and the nonlinear constitutive law for carbon steel at elevated temperature defined in accordance with Eurocode 3 Part 1-2 [5] were implemented. To account for the material nonlinearities and the effects of temperature, the unloading procedure showed in [6] was adopted.

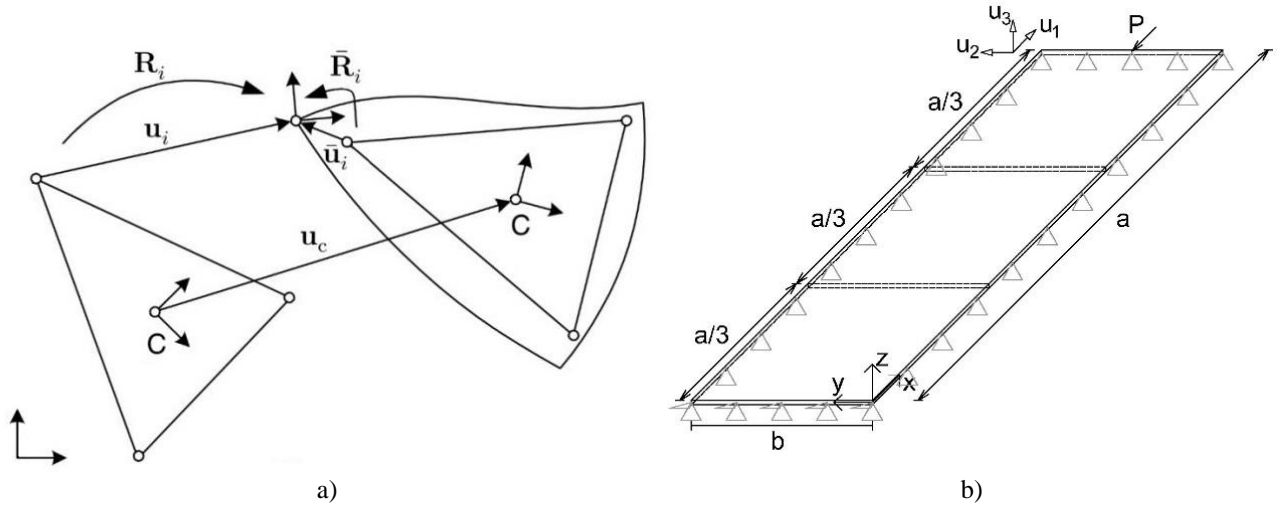


Fig. 1 a) Corotational framework 1; b) Investigated plates

3 BRANCH-SWITCHING PROCEDURE

In order to study instability problems of steel members exposed to fire, the so-called “Branch-switching” procedure is implemented in the finite element code. The branch-switching method was presented in [7] for elastoplastic instability problems. The procedure allows for the complete description of the physical behaviour of a structure by detecting critical points along the fundamental equilibrium path and by switching to the secondary path without the introduction of initial imperfections. In more detail, the implemented algorithm is based on the minimisation procedure developed by Petryk [8] and on the fact that along a stable deformational path, the displacement vector \mathbf{d} corresponds to an absolute minimum of the functional J , where

$$J = \frac{1}{2} \mathbf{d}^T \mathbf{K}_g \mathbf{d} - \mathbf{d}^T \mathbf{f}_{ex} \quad (3.1)$$

\mathbf{K}_g is the global stiffness matrix and \mathbf{f}_{ex} is the vector of external loads. Based on this property, the branch-switching procedure is performed by finding an incremental solution which minimises J . For this purpose, first the critical point needs to be detected, by analysing the lowest eigenvalues w of the stiffness matrix \mathbf{K}_g calculated at each converged solution. Thus, at the end of each step these eigenvalues are checked and if at least one eigenvalue is negative it means that the last converged point is unstable and a bifurcation point has been passed.

Once the critical point is detected, in the new step n the first equilibrium point on the secondary path is searched by minimising J . A new predictor is introduced by adding a small perturbation vector to the usual predictor, in order to ensure that the minimisation procedure will not terminate on the fundamental path. The minimisation procedure consists then in solving at each iteration k the following nonlinear system

$$\left(\mathbf{K}_g^{(k)} + \beta \mathbf{I} \right) \Delta \mathbf{d} = -\mathbf{r}^{(k)} \quad (3.2)$$

$\mathbf{r}^{(k)}$ is the residual vector at iteration k , \mathbf{I} is the identity matrix and β is a coefficient that can be set equal to 0 if \mathbf{K}_g is definite positive (classical nonlinear system) or to $1.1 \min(w)$ otherwise.

4 NUMERICAL ANALYSIS OF PERFECT AND IMPERFECT PLATES

Simply supported plates on four sides representative of web panels were analysed by means of the branch-switching procedure and results were then compared with those obtained introducing geometrical imperfections, as mechanical imperfections (residual stresses) at elevated temperature

were deemed negligible (*Figure 1-b*). The amplitude of the geometrical imperfections varied from very small, in the order of 10^{-3} mm, to magnitudes that were in accordance with design provisions [9]. An S355 steel grade was used and the plates were free to expand. A compressive load was applied to one side and a uniform axial displacement for this side was guaranteed by master-slave constraints. The opposite side was restrained in the loading direction. The length of the plates was $a = 2250$ mm and the width $b = 450$ mm, so that the length-to-width ratio was $a/b = 5$. The mesh discretization consisted of 4000 triangular shell elements, which corresponded to a mesh grid 20×100 elements. Temperature was considered uniform through the thickness of the plate. In order to analyse the occurrence of buckling both in the elastic and in the plastic range as well as the effect of the imperfections, four case studies with different plate slenderness λ_p defined as

$$\lambda_p = \frac{b/t}{28.4\epsilon\sqrt{k_\sigma}} \quad (4.1)$$

were investigated; where b is the plate width, t is the thickness, $\epsilon = (235/f_y)^{1/2}$ and k_σ is the buckling factor, which for internal compression elements and uniform compression is equal to 4.

- Case study 1: perfect and imperfect plate, uniform constant temperature in the whole plate, displacement control, buckling in elasticity;
- Case study 2: perfect and imperfect plate, uniform constant temperature in the whole plate, displacement control, buckling in plasticity;
- Case study 3: perfect and imperfect plate, only one third of the plate heated with increasing temperature, constant applied load, buckling in elasticity;
- Case study 4: perfect and imperfect plate, only one third of the plate heated with increasing temperature, constant applied load, buckling in plasticity.

With finite elements, buckling analyses are usually performed by introducing imperfections. In practice this is fulfilled by performing an elastic buckling analysis at ambient temperature and the lowest buckling mode shape is then included into the model with amplitude given by the relevant Standard. In this respect, according to the theory of buckling of perfect plates in elasticity, for a simply supported plate on four sides with $a/b=5$ the shape of the lowest buckling mode at ambient temperature reads

$$w(x, y) = w_0 \sin\left(\frac{m\pi x}{a}\right) \sin\left(\frac{n\pi y}{b}\right) \quad (4.2)$$

in which $n = 1$, $m = 5$ and w_0 is the amplitude. This is what was also done in the present work when dealing with the imperfect plates. However, it will be shown in the following that $m = 5$ does not always give the lowest maximum load nor the lowest temperature at failure of the analysed plates.

4.1 Case study 1

In the first example a plate with a thickness $t = 8.5$ mm, corresponding to a slenderness at ambient temperature of $\lambda_p = 1.15$, was investigated. The analysis was performed at a temperature of 200°C implying that both the elastic modulus and the proportional limit were degraded. Buckling occurred in elasticity and, as expected, a buckling mode described by 5 half waves was detected by the branch-switching analysis of the perfect plate (*Figure 2-a*). In *Figure 2-b* the maximum load P_{max} obtained introducing different initial imperfections was compared. The results are presented for four different imperfection amplitudes (w_0) and a number of half waves (m) from 1 to 8. It is interesting to note that the amplitude of the imperfections influences the number of half waves that gives the lowest P_{max} . In particular, for imperfection amplitudes typically selected in the design practice for steel plated elements, i.e. $w_0 = 0.1t$ and $w_0 = b/200$, the number of half waves that gives the lowest P_{max} is not $m = 5$, as suggested by elastic buckling analysis, but $m = 6$ and $m = 7$, respectively (see *Figure 2-b*). As expected, the lowest value of P_{max} obtained from branch-switching analysis of the perfect plate is higher than the P_{max} of imperfect plates. *Figure 3-a* and *Figure 3-b* show the applied

load vs. the out-of-plane displacement for an imperfection amplitude of $w_o=0.1t$ with m varying from 5 to 7 as well as for the branch-switching analysis. In the latter, the post-buckling branch was initially stable and then becomes unstable.

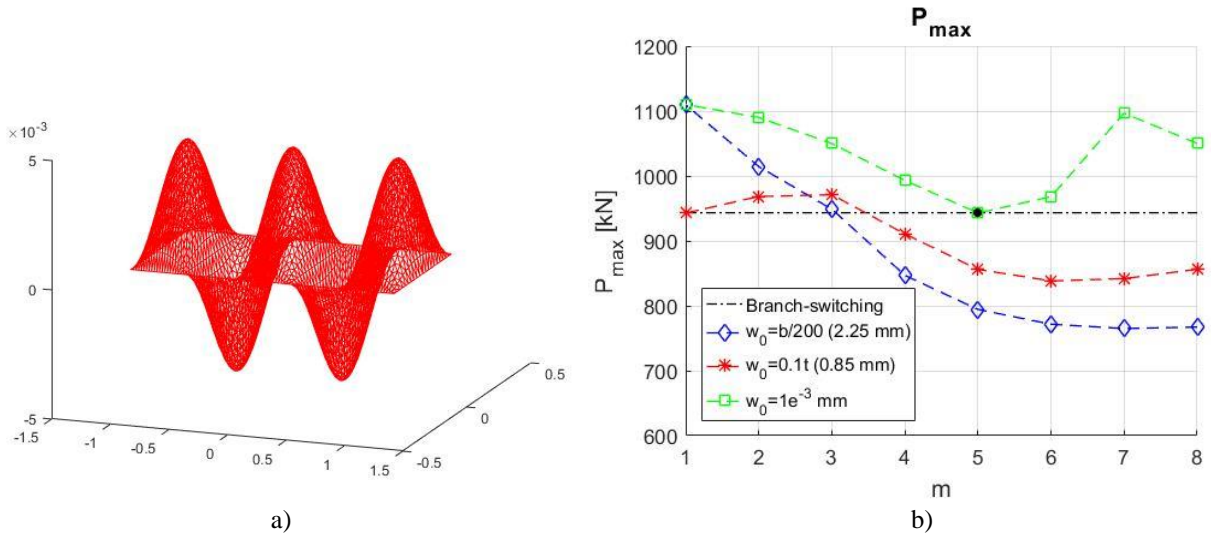


Fig. 2. Case study 1: a) buckling mode of perfect plate; b) P_{max} vs. m . Values of imperfections in mm.

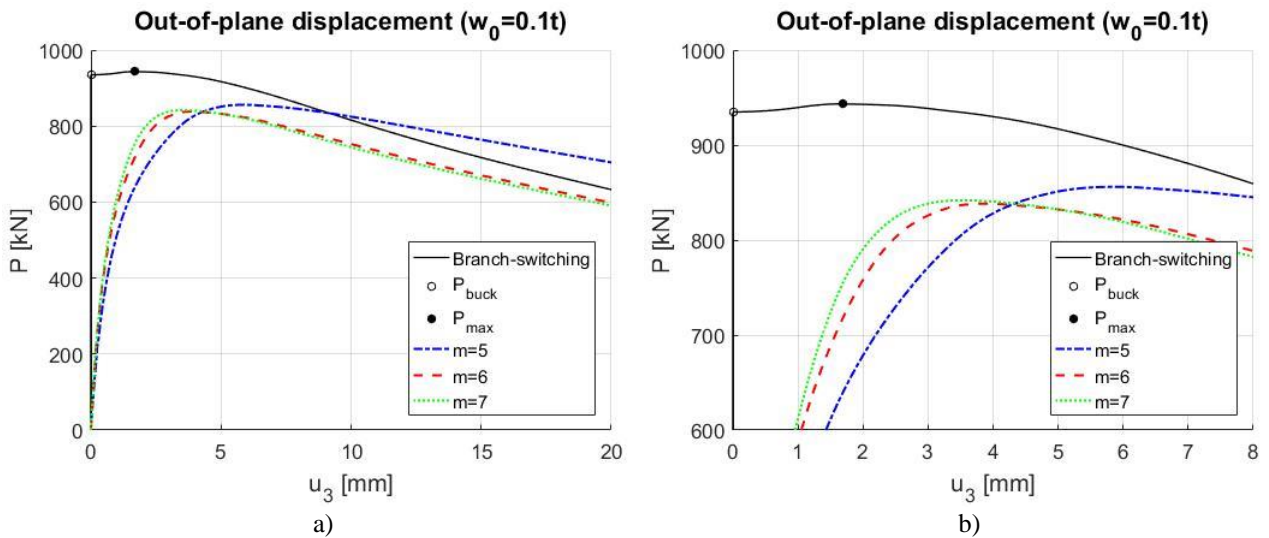


Fig. 3. Case study 1: a) Load vs. out-of-plane displacement; b) enlargement

4.2 Case study 2

In this case study a plate with thickness $t = 11$ mm ($\lambda_p = 0.89$) and at uniform temperature of 500 °C was studied. Contrary to Case study 1, the branch-switching analysis of the perfect plate detected a buckling mode described by 7 half waves (*Figure 4-a*) and bifurcation occurred in the plastic range. As reported in *Figure 4-b*, the imperfection amplitudes did not affect the estimate of the number of half-waves that provided the lowest P_{max} , i.e. $m = 7$. However, the introduction of small imperfections ($w_o = 10^{-3}$ mm) led to a more significant reduction of the P_{max} than in Case study 1, i.e. up to -6.95% . The load vs. out-of-plane displacement relationship for $w_o = 0.1t$ is presented in *Figure 5-a* and *Figure 5-b* respectively. For the analysis without imperfections, the secondary path presents a shorter stable part compared to Case study 1.

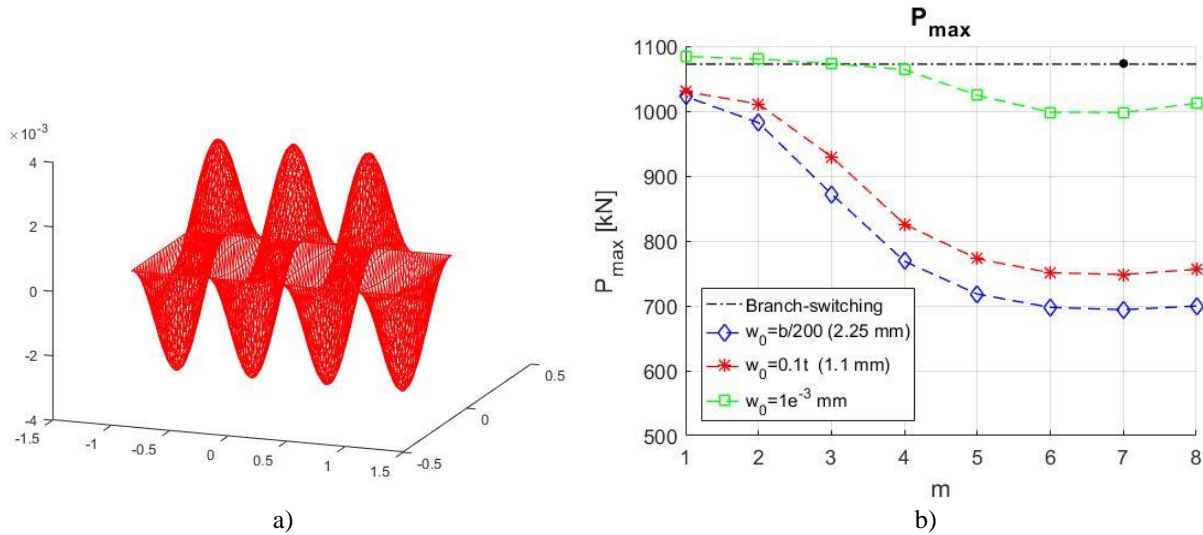


Fig. 4. Case study 2: a) buckling mode of perfect plate; b) P_{max} vs. m . Values of imperfections in mm.

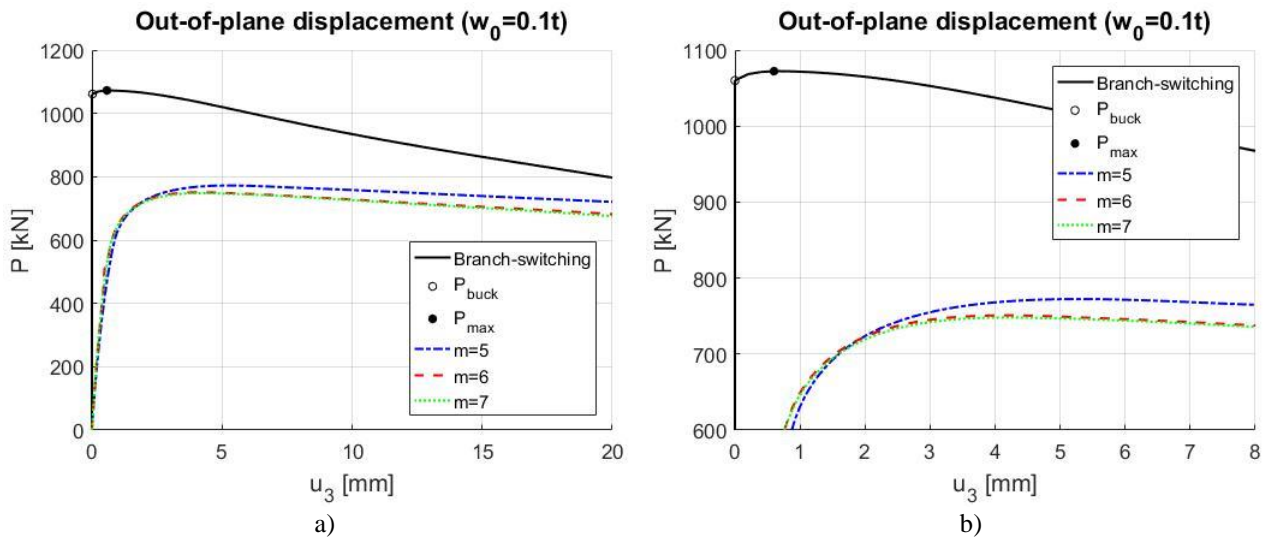


Fig. 5. Case study 2: a) Load vs. out-of-plane displacement; b) enlargement

4.3 Case study 3

A constant axial load $P = 250$ kN was applied to a plate with thickness $t = 7$ mm ($\lambda_p = 1.39$). Only the middle third of the plate was heated uniformly with linear heating rate 2 °C/min, whereas the rest of the plate remained at ambient temperature. In this way, it was investigated the effect of possible non-uniform heating, that could happen, for instance, in localised fires, on the buckling behaviour. According to the branch-switching procedure, buckling occurred in elasticity at $T_{buck} = 363$ °C and was characterised by the buckling mode illustrated in Figure 6-a. Thus, the imperfection shape with $m = 5$ is not representative of the plate buckling behaviour at elevated temperature. The temperature at failure was $T_{fail} = 557$ °C. In Figure 6-b the maximum out-of-plane displacement of the perfect plate is compared with the one obtained for different imperfection amplitudes. In addition to the classical sinusoidal imperfections, a further imperfection is defined by scaling the buckling mode in Figure 6-a to the amplitude $w_0 = 0.1t$. It is possible to observe that once buckling has occurred, the post-buckling path presents a large stable part.

4.4 Case study 4

The last simulation was performed on a plate with $t = 10$ mm ($\lambda_p = 0.97$) heated as in Case study 3. A constant load $P = 700$ kN was applied and buckling occurred when the heated part experienced plastic behaviour. T_{buck} and T_{fail} recorded in the branch-switching analysis were 479 °C and 563 °C,

respectively. The buckling mode showed two peaks in the heated part (*Figure 7-a*). The maximum out-of-plane displacement of the plate with and without imperfections is shown in *Figure 7-b*. The buckling mode in *Figure 7-a* is scaled to define a further initial imperfection. In all cases when buckling occurred in plasticity, the plates reached collapse soon after. Also in this case the imperfection $m = 5$ did not provide the lowest temperature at failure.

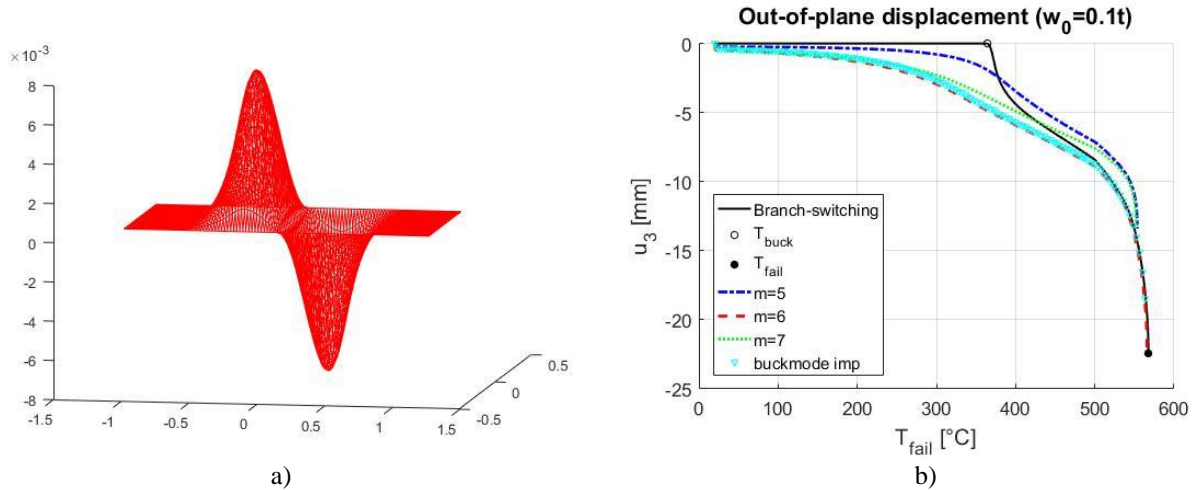


Fig. 6. Case study 3: a) Buckling mode of perfect plate; b) Maximum out-of-plane displacement vs. Temperature

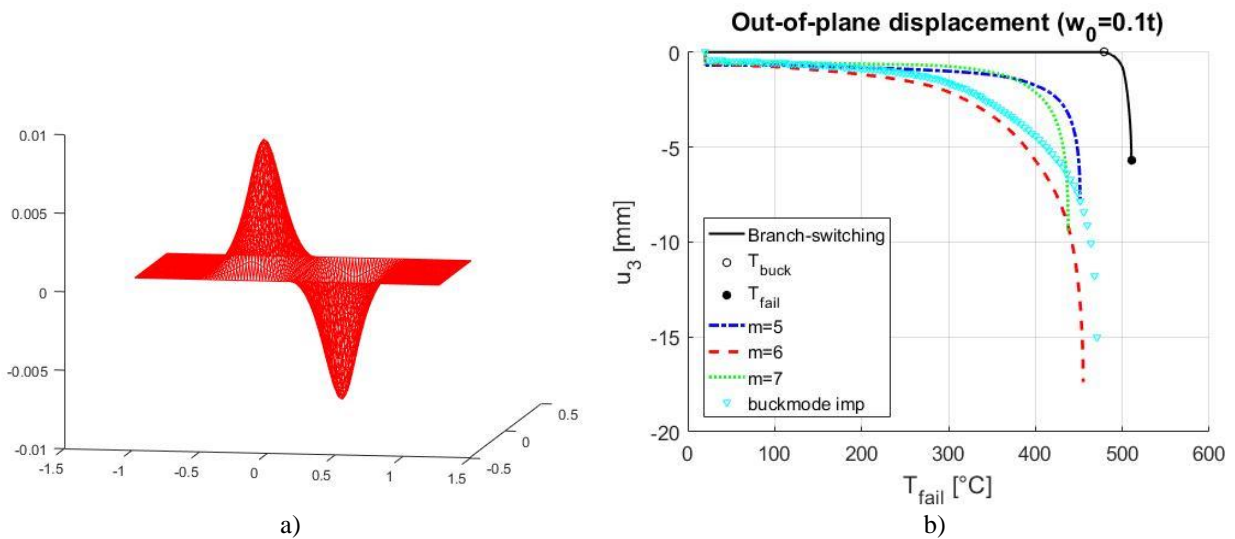


Fig. 7. Case study 4: a) Buckling mode of perfect plate; b) Maximum out-of-plane displacement vs. Temperature

5 CONCLUSIONS

- The collected results show that buckling mode cannot be determined by a linear elastic buckling analysis at ambient temperature. This is obviously the case when only one part of the structure is heated (Case study 3-4), but also when plastic deformations occur before buckling (Case study 2).
- The choice of the number of half waves for the initial imperfection affected the results in terms of both the evaluation of the maximum load P_{max} and of the overall behaviour of the plate. The lowest maximum load P_{max} was not always obtained with imperfections corresponding to the lowest buckling mode determined by linear elastic buckling analysis. In addition, the shape of the imperfections (number of half waves) that provides the lowest

P_{max} may depend also on the amplitudes of the imperfections, as in Case study 1. Thus, the choice of an appropriate imperfection is a challenging task and the definition of a pattern for the imperfections is not trivial.

- The branch-switching procedure provides an appealing preliminary alternative to study the physical instability behaviour without considering the nature and the amplitudes of the imperfections. The perfect structure (i.e. without imperfections) is studied and once a critical point has been detected, a branch switching is performed. This procedure does not always give an accurate estimate of the maximum load or the failure temperature, but it allows the exact determination of the buckling load and the associated eigenmode. Moreover, it provides insight into the post-buckling behaviour by showing if the structure has still some load capacity after buckling as in Case study 3 and not in Case study 4.

REFERENCES

1. Chrysanthos Maraveas, Thomas Gernay, Jean-Marc Franssen (2017). *Buckling of steel plates at elevated temperatures: theory of perfect plates vs finite element analysis*. CONFAB 2017, 10-12 September; London, UK.
2. Chrysanthos Maraveas, Thomas Gernay, Jean-Marc Franssen (2017). *Sensitivity of elevated temperature load carrying capacity of thin-walled steel members to local imperfections*. Proceedings of ASFE 2017 Conference, 7 September; Manchester, UK.
3. Costine Pacoste (1998). *Co-rotational flat facet triangular elements for shell instability analysis*, Computer Methods in Applied Mechanics and Engineering 156. pp.75–110.
4. Jean-Marc Battini, Costine Pacoste (2006). *On the choice of linear element frame for corotational triangular shell elements*. Computer Methods in Applied Mechanics and Engineering 195(44-47). pp 6362-6377.
5. European Comitee for Standardisation (2005). *Eurocode 3 Design of steel structures - Part 1-2: General rules - Structural fire design*
6. Jean-Marc Franssen (1990). *The unloading of building materials submitted to fire*. Fire Safety Journal 16(3). pp 213-227.
7. Jean-Marc Battini, Costine Pacoste (2002). *Plastic instability of beam structures using co-rotational elements*. Computer Methods in Applied Mechanics and Engineering 191(51-52). pp 5811-5831.
8. Henryk Petryk, Klaus Thermann (1992). *On discretized plasticity problems with bifurcations*. International Journal of Solid and Structures 29(6). pp 745-765.
9. European Comitee for Standardisation (2006). *Eurocode 3 Design of steel structures - Part 1-5: General rules - Plated structural elements*

TWO-DIMENSIONAL MODELLING OF THERMAL RESPONSES OF GFRP PROFILES EXPOSED TO ISO-834 FIRE

Lu Wang¹, Lingfeng Zhang², Weiqing Liu³

ABSTRACT

In the past three decades, one-dimensional (1-D) thermal model was usually used to estimate the thermal responses of glass fiber-reinforced polymer (GFRP) materials and structures. However, the temperature gradient and mechanical degradation of whole cross sections cannot be accurately evaluated. To address this issue, a two-dimensional (2-D) thermo-mechanical model was developed predict the thermal and mechanical responses of rectangular GFRP tubes subjected to one-side ISO-834 fire exposure in this paper. The 2-D governing heat transfer equations with thermal boundary conditions, discretized by alternating direction implicit (ADI) method, were solved by Gauss-Seidel iterative approach. Then the temperature-dependent mechanical responses were obtained by considering the elastic modulus degradation from glass transition and decomposition of resin. The temperatures of available experimental results can be reasonably predicted. This model can also be extended to simulate the thermo-mechanical responses of beams and columns subjected to multi-side fire loading, which may occur in real fire scenarios.

Keywords: Polymer-matrix composites, thermal properties, thermo-mechanical properties, computational modelling, two-dimensional modeling

1 INTRODUCTION

In the past two decades, a large number of experimental studies have been conducted to evaluate the thermal and thermo-mechanical performances of FRP materials. In 1999, the fire resistance of GFRP sprinkler pipes with empty cavity, stagnant water and flowing water were investigated by Davies and Dewhurst [1]. The failure time of the pipes with empty cavity and stagnant water were 1.5 min and 8.5 min, respectively, while the flowing water-cooled pipe remained structural integrity subjected to 120 min fire exposure. Inspired by the water-cooling concept of filament wound GFRP pipe used in [1], this concept, developed by Keller, was applied in the fire endurance of pultruded GFRP multi-cellular panels [2-3]. The fire performance of GFRP panels were investigated in three different experimental parts: charring of GFRP laminates, fire endurance of liquid cooling moderately-sized GFRP panels and fire resistance of structural liquid cooling full-scale GFRP panels, respectively. In the first part, the pultruded GFRP laminates started burning at roughly 6 min, and the temperature of cold face reached the T_g at approximately 10 min [4]. In the second part, the temperature profiles through the thickness of lower face sheet were much lower than those of charring experiments[2]. In the third part, for the non-cooled specimens, the cold face of lower face sheet reached T_g and T_d in 10 min and 57 min, respectively. The test results demonstrated that

¹ Associate Professor. College of Civil Engineering, Nanjing Tech University, Nanjing, China.
e-mail: kevinlwang@njtech.edu.cn

² PhD Candidate. School of Civil Engineering, Southeast University, Nanjing, China.
e-mail: lfzhang@seu.edu.cn

³ Professor. College of Civil Engineering, Nanjing Tech University, Nanjing, China.
e-mail: wqliu@njtech.edu.cn

liquid-cooling was an effective way to improve the fire resistance of pultruded GFRP components. The non-cooled column failed at 49 min due to global buckling, while structural function of the water cooled columns could be maintained for two hours. In 2010, the fire resistances of non-cooled and water-cooled pultruded GFRP beams with square hollow section were investigated by Correia et al [5]. The bottom flange of the GFRP beams were subjected to ISO-834 fire. The fire resistance was over 120 min by using the water-cooled approach with a 72 mm/s flowing rate. But the non-cooled specimen failed abruptly after about 38 min due to the kinking and buckling of top flange.

The mathematical modeling of the thermal response of FRP composite under elevated and high temperatures has been proposed. In 2006, the apparent specific capacity, developed by Lattimer [6], was input into a heat transfer model to predict the temperature profile through E-glass/vinyl ester composite laminates. Gibson et al. [7,8] investigated the post-fire mechanical properties of polymer composites by combing the thermal model with Mouritz's two-layer mechanical model [9]. In 2012, the thermal responses of FRP laminates subjected to three-point bending and one-side heat flux were experimental and numerical investigated by Gibson et al. [10]. Feih et al. [11,12] presented the thermo-mechanical model to predict the tension and compression properties of FRP laminates in fire. A 1-D model was further developed to simulate the thermo-mechanical responses of sandwich composites [13]. This model also validated and applied by Anjiang et al. [14,15] to investigate the in-fire and post-fire mechanical properties of FRP sandwich composite structures with balsa wood core. In 2006, a thermo-chemical and thermo mechanical models were introduced by Keller [16]. The models were used to predict the structural response of water-cooled multi-cellular GFRP slabs. In 2007, Bai and Keller [17] proposed the chemical kinetics-based thermo-physical model by considering the decomposition of matrix resin. Based on the temperature-dependent thermo-physical model, an 1-D thermal model with the effective specific capacity was developed [18]. More recently, a 3-D FE model was developed by Shi et al. [19] to investigate the coupled temperature-diffusion-deformation problem of silica/phenolic composite materials. The accuracy of this model was validated by comparing the measured temperatures and displacements with numerical results.

Among the various existing thermal models, the 1-D finite difference method was most frequently used to predict the thermal response of FRP composites. However, the FRP structural components applied in building construction were subjected to multi-dimensional fire exposures. The temperature profile of heated zone of FRP composites cannot be predicted by the use of 1-D model. Hence, to address this issue, a 2-D thermal model was proposed in this study. The accuracy of the proposed model was validated by the existing experimental data of pultruded E-glass/polyester rectangular tube under fire from one side. The comparison indicated that the developed two-dimensional thermal model can be reasonable to predict the thermal responses of GFRP composites.

2 MATHEMATICAL MODEL

2.1 Modeling assumptions

When subjected to fire, FRP composites undergo many complex thermal, physical, chemical and structural failure processes. The challenge to accurately modeling the temperature responses is to consider complex interaction of degradation processes. Previous studies [4,18] showed that the thermal and mechanical processes were dominated by glass transition and thermal decomposition. The convective heat transfer of volatiles flow up through the decomposition front to the surface may have a small effect on the temperature profile in the FRP material[7]. Hence, in this study, the 2-D thermo-mechanical model was simplified by considering heat conduction, physical process (glass transition), chemical (decomposition) and mechanical degradations.

2.2 Thermo-physical properties model

During fire processes, thermo-physical properties include density, specific capacity and thermal conductivity of virgin (non-char) and char material.

A lot of works were made to investigate these properties. The temperature-dependent density can be described by using an Arrhenius equation based on chemical kinetics [19]:

$$\frac{\partial \rho}{\partial t} = -A\rho \exp\left(\frac{-E_A}{RT}\right) \quad (1)$$

where ρ is the density; A represents the pre-exponential factor; E_A is the activation energy; R is the universal gas constant; and T is temperature.

The change of density can be described by Eq. (1). But in the existing literatures, specific capacity and thermal conductivity of virgin and char were usually expressed by polynomial fitting instead of analytical form. Hence, the parameters used in fitting have no clear physical meaning. Bai et al. [19] developed a model for predicting temperature-dependent thermo-physical properties. In this model, a conversion degree of decomposition was introduced to characterize the pyrolysis process of polymer resin, as indicated in Eq. (2).

$$\frac{d\alpha_d}{dt} = A_d \exp\left(\frac{-E_{A,d}}{RT}\right) (1-\alpha_d)^{nr_d} \quad (2)$$

where α_d denotes the decomposition degree, A_d , $E_{A,d}$, nr_d are kinetic parameters, which can be derived from thermo-gravimetric analysis.

Based on decomposition degree α_d , the temperature-dependent density can be obtained,

$$\rho = (1-\alpha_d)\rho_b + \alpha_d\rho_a \quad (3)$$

where ρ_b is the density of virgin composite, and ρ_a is the density of char material.

The apparent specific capacity can be given as [19]

$$C_p = f_b C_{p,b} + (1-f_b)C_{p,a} + \frac{d\alpha_d}{dT} C_d \quad (4)$$

where C_p is the apparent specific capacity, which increases due to endothermic phenomenon during decomposition process [20]; $C_{p,b}$ and $C_{p,a}$ are apparent specific capacity before and after decomposition respectively; C_d is decomposition heat; and f_b is mass fraction of un-decomposed FRP materials, which can be calculated by Eq. (5) [28].

$$f_b = \frac{M_{a,v}(1-\alpha_d)}{M_{a,v}(1-\alpha_d) + M_{a,e}\alpha_d} \quad (5)$$

where $M_{a,v}$ ($M_{a,e}$) is the initial(final) mass of FRP material.

In this paper the main research object is the cross section of rectangular GFRP tubes, only the cross sectional properties should be considered. Previous study showed that thermal conductivity parallel to the axis of fiber (0°) was much higher than in the transverse (90°) and through thickness direction, while the thermal conductivity of transverse and through thickness direction were similar for glass fiber/polyester composites. Hence, the transverse thermal conductivity can be simplified by using the through thickness thermal conductivity. The thermal conductivity through the thickness of FRP composites can be expressed as [19]

$$\frac{1}{k_\perp} = \frac{(1-\alpha_d)}{k_{\perp,b}} + \frac{\alpha_d}{k_{\perp,a}} \quad (6)$$

where k_\perp denotes the through thickness thermal conductivity; the subscripts b and a represents the thermal conductivity before and after decomposition, respectively; and $k_{\perp,b}$ and $k_{\perp,a}$ can be obtained by using the inverse rule of mixtures.

$$\frac{1}{k_{\perp b}} = \frac{V_f}{k_f} + \frac{V_m}{k_m}$$

$$\frac{1}{k_{\perp a}} = \frac{V_f}{k_f} + \frac{V_{ga}}{k_{ga}} \quad (7)$$

where k_f , k_m and k_{ga} are the thermal conductivities of fiber, matrix and volatile gas, respectively; V_f , V_m and V_{ga} are the volume fractions of fiber, matrix and volatile gas, respectively.

2.3. 2-D Heat transfer model

2-D transient heat transfer equation can be expressed as

$$\rho C_p \frac{\partial T}{\partial t} = \frac{\partial}{\partial x} \left(k_x \frac{\partial T}{\partial x} \right) + \frac{\partial}{\partial y} \left(k_y \frac{\partial T}{\partial y} \right) \quad (8)$$

where k_x and k_y are the thermal conductivity in x and y directions, respectively. The term on the left side of Eq. (9) refers to the rate of change of internal energy, and the other two terms on the right side denote the net heat flux.

The boundary conditions applied in thermal analysis can be divided into three types. The first one is the Dirichlet boundary condition, which can be expressed as

$$T(x, y, t)|_{bd} = T(t) \quad (9)$$

where x and y represent the 2-D spatial Descartes coordinates; Subscript bd denotes the boundaries of rectangular tube; and $T(t)$ is the time-dependent specific temperature on the boundary. The second one is the prescribed heat flux, which can be expressed as

$$-k_x \frac{\partial T(x, y, t)}{\partial x} |_{bd} = q(t) \quad (10)$$

$$-k_y \frac{\partial T(x, y, t)}{\partial y} |_{bd} = q(t) \quad (11)$$

where $q(t)$ is the time-dependent heat flux at the boundaries. The last one is the convection between the boundary and external environment, which can be expressed as

$$-k_x \frac{\partial T(x, y, t)}{\partial x} |_{bd} = h(T_{\infty}(t) - T(x, y, t)|_{bd}) \quad (12)$$

$$-k_y \frac{\partial T(x, y, t)}{\partial y} |_{bd} = h(T_{\infty}(t) - T(x, y, t)|_{bd}) \quad (13)$$

where h denotes the convective coefficients, and $T_{\infty}(t)$ represents the time-dependent temperature of external environment.

In this study, convection and radiation between the boundaries and external/internal environment can be obtained from

$$q(t) = h_x [T_{\infty}(t) - T(x, y, t)|_{bd}] + \varepsilon_{x,r} \sigma_{x,r} [T_{\infty}(t)^4 - T(x, y, t)^4 |_{bd}] \quad (14)$$

$$q(t) = h_y [T_{\infty}(t) - T(x, y, t)|_{bd}] + \varepsilon_{y,r} \sigma_{y,r} [T_{\infty}(t)^4 - T(x, y, t)^4 |_{bd}] \quad (15)$$

3 VALIDATION

3.1 Basic model

As described in Section 1, Correia et al. [5] conducted the fire structural experiment of pultruded E-glass/polyester composite square beam subjected to ISO-834 fire, and a 37 min fire resistance was reached. In this paper, this experiment is used to validate the proposed 2-D numerical model. The heat convective coefficients at the cold face of bottom flange were estimated as 2 W/m² K by fitting the temperature profiles at the cold face of the bottom flange [21].

Numerical Modelling

3.2 Validation and comparison

Fig. 2 shows the 2-D modelling and experimental temperatures through the thickness of GFRP bottom flange. Reasonable agreement was found, especially in the first 5 min and last 20min. some fluctuations can be seen after 5 min fire exposure due to the jump of the oven temperature. The 2- D temperature gradients at 5 min, 10 min, 20 min and 40 min were presented in Fig. 2. A large temperature gradient through the thickness of bottom flange was found at 5 min and 10 min, however, the gradient decreased from 10 min to 40 min. This indicated that a more even temperature distribution was found through the thickness of bottom flange, and the temperatures of hot face and inner face were approximately 750 °C and 900 °C at 40 min..

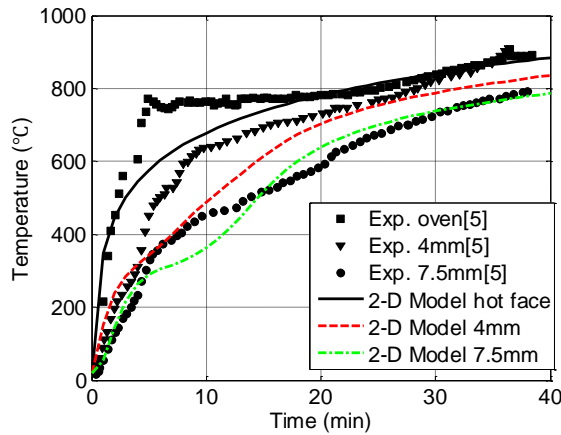


Fig. 1 Model validation by temperature comparison

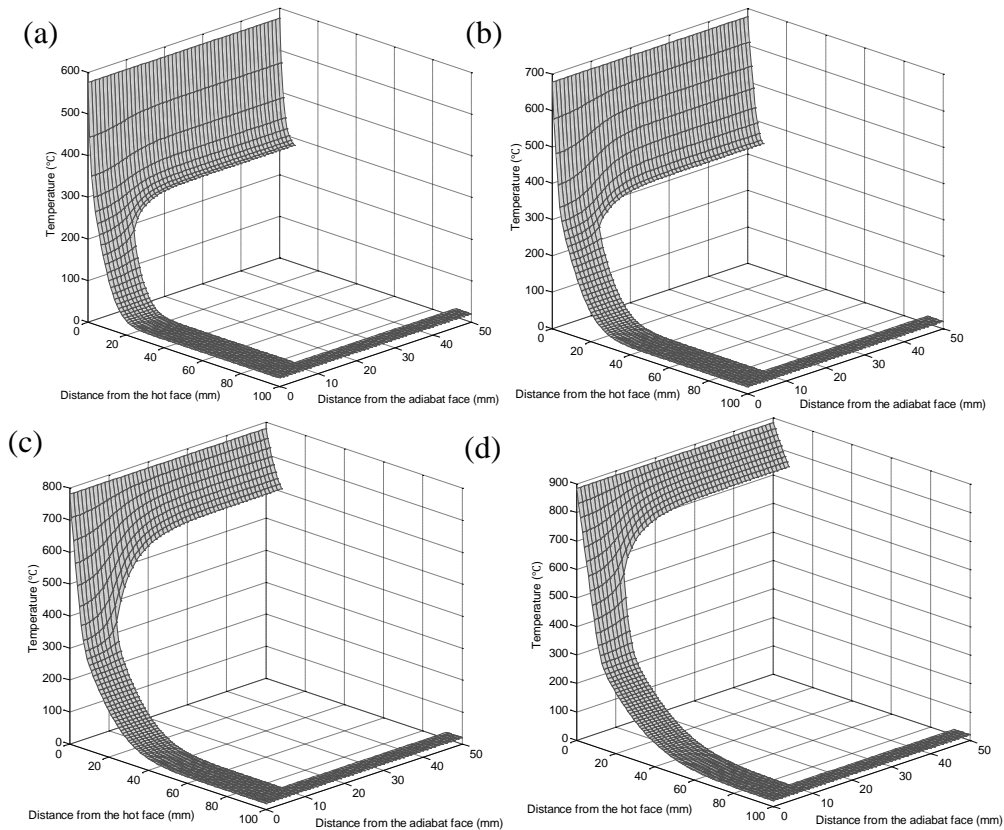


Fig. 2 Temperature distribution of GFRP tube: (a) 5 min, (b) 10 min, (c) 20 min, (d) 40 min.

4 CONCLUSIONS

In this study, a 2-D model to predict the thermal responses of rectangular GFRP tubes were developed and solved by ADI finite difference scheme. The modeling results were compared with the temperature from experiment on GFRP rectangular beam under one-side fire exposure. The main conclusion remarks were drawn:

- (1) A 2-D thermo-mechanical model based on finite difference method was developed and solved by Gauss-Seidel iterative approach. The detailed ADI schemes considering complex boundary conditions were also presented, and the numerical results were stable due to the stability of this difference format.
- (2) The proposed 2-D thermal model can reasonably predict the temperatures of GFRP rectangular tube. Based on the calculated temperature, the temperature-dependent conversion degree of glass transition and decomposition as well as thermo-physical properties of the whole cross-section can also be obtained.

ACKNOWLEDGEMENT

The work described here was supported by the National key research and development program of China (Grant No. 2017YFC0703001) and the National Natural Science Foundation of China (Grant No. 51678297).

REFERENCES

1. Davies JM, Dewhurst DW (1999). The fire performance of GRP pipes in empty and dry, stagnant water filled and flowing water filled conditions. *Composites in Fire. Proceedings of the International Conference on the Response of Composite Materials*. Newcastle upon Tyne, 1999. pp. 69-84.
2. Keller Thomas, Zhou Aixi, Tracy Craig, Hugi Erich, Schnewlin Peter (2005). *Experimental study on the concept of liquid cooling for improving fire resistance of FRP structures for construction*. Composites Part A, 36(11). pp 1569-1580.
3. Keller Thomas, Tracy Craig, Hugi Erich (2006). *Fire endurance of loaded and liquid-cooled GFRP slabs for construction*. Composites Part A, 37(7).pp 1055-1067.
4. Tracy Craig(2005). *Fire endurance of multicellular panels in an FRP building system*. Ph.D. Thesis No. 3235, EPFL-CCLab.
5. Correia JR, Branco FA, Ferreira JG, Bai Yu, Keller Thomas (2010). *Fire protection systems for building floors made of pultruded GFRP profiles: Part 1: Experimental investigations*. Composites Part B, 41(8). pp 617-629.
6. Bai Yu, Hugi Erich, Ludwig Carsten, Keller Thomas (2011). *Fire performance of water-cooled GFRP columns. I: fire endurance investigation*. Journal of Composites for Construction, 15(3). pp 404-412.
7. Henderson JB, Wiebelt JA, Tant MR (1985). *A model for the thermal response of polymer composite materials with experimental verification*. Journal of composite materials, 19(6). pp 579-595.
8. Lattimer B Y, Ouellette J (2006). *Properties of composite materials for thermal analysis involving fires*. Composites Part A, 37(7). pp 1068-1081.
9. Gibson AG, Wright PNH, Wu Y, Mouritz AP, Mathys Z, Gardiner CP (2003). *Modelling residual mechanical properties of polymer composites after fire*. Plastics, Rubber and Composites, 32(2). pp 81-90.
10. Gibson A G, Wright P N H, Wu Y S, Mouritz AP, Mathys Z, Gardiner CP (2004). *The integrity of polymer composites during and after fire*. Journal of composite materials, 38(15). pp 1283-1307.

Numerical Modelling

11. Mouritz AP, Mathys Z(1999). *Post-fire mechanical properties of marine polymer composites*. Composite Structures, 47(1). pp 643-653.
12. Gibson AG, Browne TNA, Feih S, Mouritz AP (2012). *Modeling composite high temperature behavior and fire response under load*. Journal of composite materials, 46(16). pp 2005-2022.
13. Feih S, Mathys Z, Gibson AG, Mouritz AP (2007). *Modelling the compression strength of polymer laminates in fire*. Composites Part A, 38(11). pp 2354-2365.
14. Feih S, Mathys Z, Gibson AG, Mouritz AP (2007). *Modelling the tension and compression strengths of polymer laminates in fire*. Composites Science and Technology, 67(3). pp 551-564.
15. Feih S, Mathys Z, Gibson A G, Mouritz AP (2008). *Modeling compressive skin failure of sandwich composites in fire*. Journal of Sandwich Structures & Materials, 10(3). pp 217-245.
16. Anjang A, Chevali VS, Kandare E, Mouritz AP, Feih S(2014;). *Tension modelling and testing of sandwich composites in fire*. Composite Structures, 113. pp 437-445.
17. Anjang A, Chevali VS, Lattimer BY, Case SW, Feih S, Mouritz AP(2015;). *Post-fire mechanical properties of sandwich composite structures*. Composite Structures, 132. pp 1019-1028.
18. Keller Thomas, Tracy Craig, Zhou Aixi (2006).*Structural response of liquid-cooled GFRP slabs subjected to fire–Part II: Thermo-chemical and thermo-mechanical modeling*. Composites Part A, 37(9). pp 1296-1308.
19. Bai Yu, Vallée Till, Keller Thomas (2007). *Modeling of thermo-physical properties for FRP composites under elevated and high temperature*. Composite Science and Technology, 67(15). pp 3098-3109.
20. Bai Yu, Vallée Till, Keller Thomas(2008). *Modeling of thermal responses for FRP composites under elevated and high temperatures*. Composite Science and Technology, 68(1). pp 47-56.
21. Bai Yu, Keller Thomas, Correia JR, Branco FA, Ferreira JG(2010). *Fire protection systems for building floors made of pultruded GFRP profiles–Part 2: Modeling of thermomechanical responses*. Composite Part B, 41(8). pp 630-636.

Numerical Modelling

CFD ANALYSES USED TO EVALUATE THE INFLUENCE OF COMPARTMENT GEOMETRY ON THE POSSIBILITY OF DEVELOPMENT OF A TRAVELLING FIRE

Marion Charlier¹, Antonio Gamba², Xu Dai³, Stephen Welch³, Olivier Vassart¹, Jean-Marc Franssen²

ABSTRACT

The response of structures exposed to fire is highly dependent on the type of fire that occurs, which is in turn very dependent on the compartment geometry. In the frame of the European RFCS TRAFIR project, CFD simulations using FDS software were carried out to analyse the influence of compartment geometry and the interaction with representative fuel loads to explore the conditions leading to the development of a travelling fire. The influence observed of ceiling height, crib spacing, and opening geometry in controlling spread rates tend to confirm the possibility to predict the occurrence or not of travelling fire. In a subsequent step, the radiative intensities and gas temperatures calculated by FDS have been used by SAFIR[®] to calculate the temperatures in steel structural elements located in the compartment and the structural behavior of a frame made of these elements.

Keywords: CFD, Fire scenario, Travelling fire, Coupling FDS-SAFIR[®]

1 INTRODUCTION

Small compartment fires behave in a relatively well understood manner, usually defined as post-flashover fires, where the temperatures within the compartment are considered to be uniform. Yet, fires in large compartments do not always reach a post-flashover fire state and there is instead a more localised fire that may travel within the compartment. More recently, the “travelling fire” terminology has been used to define fires burning locally and moving across entire floor plates over a period of time [1]. Several studies have been presented about the behaviour of a structure when it is subjected to a travelling fire ([2], [3], [4]). These experimental campaigns provide first insights regarding the parameters influencing fire spread, such as heat release rate density and wood moisture content. Furthermore, in 2005, Thomas [5] set an experimental program in a deep enclosure and the main conclusion was that fires in deep compartments are strongly affected by the ventilation. Nevertheless, no proper information or scientific knowledge has been established yet on the configurations that can lead to the development of travelling fires [6]. In the frame of TRAFIR project, several CFD numerical simulations were made to identify and attempt to quantify the parameters that may lead to a travelling fire. This paper presents some of these simulations and explains how the CFD results can be used to perform a numerical analysis of the temperature development and resulting mechanical behaviour of a steel structure that considers comprehensively the travelling nature of the fire.

¹ ArcelorMittal Global R&D, Luxembourg.

e-mails: marion.charlier@arcelormittal.com and olivier.vassart@arcelormittal.com

² Department of Architecture, Geology, Environment & Constructions (ArGEnCo), Liege University, Belgium.

e-mails: antonio.gamba@uliege.be and jm.franssen@ulg.ac.be

³ School of Engineering, BRE Centre for Fire Safety, The University of Edinburgh, United Kingdom.

e-mails: x.dai@ed.ac.uk and s.welch@ed.ac.uk

2 THE SETUP OF FDS SIMULATIONS AND ITS CORRESPONDING ASSUMPTIONS

The Fire Dynamics Simulator (FDS) [7] is adopted as numerical simulation tool. The conditions examined in this work are confined to the initial localised and spreading phase of the fire. In the simplified hypothesis of a well-stirred reactor leading to a uniform situation in the compartment, under-ventilated conditions do not prevail. In the hereafter described analyses, the use of CFD allows to consider in detail the different aspects of fluid mechanics and highlight that the fire may be under-ventilated at certain moments in some regions of the compartment.

2.1 Grid size

The cell size used in the FDS models depends highly on the situation that is modelled and on the purpose of the simulation. For simulations involving buoyant plumes, FDS User's Guide [7] defines a non-dimensional parameter to assess the quality of the mesh: $D^*/\delta x$. In all the hereafter described simulations, cell size of 0.25m x 0.25m x 0.25m was considered. These values were not based on a sensitivity analysis but on existing analyses representing fire dynamics in large enclosures. Indeed, the FDS Validation Guide contains a table of the values of $D^*/\delta x$ used in the simulation of the validation experiments and were used as guidance. Furthermore, for all the FDS models presented hereafter, the cell size is smaller than the suggested fine cell size recommended by the "Mesh Size Calculator" [8] tool developed by Kristopher Overholt. Extra cells have been defined outside the compartment boundaries in order to consider the coupling to the external environment.

2.2 Representation of fuel

The fire load is supposed to be made of discrete wood cribs. No detailed representation of a wood crib (i.e. involving alternation of sticks and air gap) was used but a simpler approach was adopted, using 1m³ solid cubes. This approach is based on the work done by Degler & Eliasson [9]. The overall heat release rate was used as input to VENTs with each VENT representing a wood crib burning surface. The wood constituting the cubes is red oak type with the following chemical composition: C_{3.4}H_{5.78}O_{2.448}N_{0.0034} and a soot yield of 0.0015 [g/g]. These values are adopted from the SFPE Handbook [10]. The properties of the modelled wood are: conductivity 0.1 W/m/K, specific heat 1.3 kJ/kg/K, emissivity 0.9 and density 400 kg/m³. The predefined HRR curve considered come from Degler & Eliasson's work [9]: it was first obtained numerically using complex pyrolysis model in FDS then validated by comparison with pallet HRR curves obtained experimentally. The HRR curve has a peak at 480 [kW/m²] and lasts for 33 minutes.

2.3 Fire spread

Planar devices were placed on each faces of the cribs (except on the face in contact with the floor) to measure the temperatures on the solid surfaces. If the surface temperature reaches 300°C on at least one face of the volume, then the five surfaces start burning following the prescribed HRR curve. This temperature of ignition was arbitrarily set equal to 300°C, which is a reasonable approximation of ignition temperature for certain cellulosic materials [10].

2.4 Openings and boundary walls

The openings represented in the models are present from the beginning of the fire. Walls and ceiling are made of 25 cm thick concrete (conductivity 2.4 W/m/K, specific heat 1 kJ/kg/K, density 2400 kg/m³). In all the compartments presented in this paper, openings are present on both walls along the X axis, and centred. For the sake of clarity, X and Y axis mentioned hereafter correspond respectively to the horizontal and the vertical axis of plan views of the compartments.

3 RESULTS OF FDS SIMULATIONS

Different typologies of large compartments were modelled: the conditions supporting travelling fire development are explored by varying some of the fundamental inputs to the model, i.e. ceiling height, opening size, fuel load density and compartment layout. Two series of configurations are

investigated, in which series 1 relates to a deep rectangular compartment and series 2 relates to a large square compartment.

Table 1. Different configurations of large compartments

Configuration	Compartment dimensions x,y,z	Opening size	Opening factor [11]	Separation between the solid cubes (cribs)
1.a	50m x 10m x 4m	45m x 3.5m	0,20 m ^{1/2}	1m
1.b	50m x 10m x 4m	20m x 3.25m	0,08 m ^{1/2}	1m
2.a	20m x 20m x 8m	16m x 6.75m	0,26 m ^{1/2}	2m
2.b	20m x 20m x 3.5m	16m x 2.25m	0,05 m ^{1/2}	2m

3.1 Deep rectangular compartment – 1D spread

In configuration 1, a 50m x 10m x 4m compartment is defined in a model domain of 60m x 12m x 5m. The openings extend vertically from 0.25m above floor level. In both configurations (1.a and 1.b) the fire starts by the ignition of the wood crib placed at the left-end of the compartment, at mid-width (see *Fig. 1*). According to *Fig. 2*, in configuration 1.a the fire spreads slowly at the beginning (0m – 15m), then faster (15m – 50m) when the effects of pre-heating by radiation from the hot layer become more significant. Specifically, at beginning of the fire (0 – 20 minutes), the pattern of the burning area indicates a t^2 development, but the acceleration is soon damped with the remaining spread being closer to a steady rate of increase along the length of the compartment. Steady spread can be expected when the process is being driven primarily by local crib-to-crib spread and where the effects of preheating from the hot layer to cribs ahead of the front is relatively minor, and does not significantly increase with time. Also, the fire spread front edge has a clear time lag when it is in the area near the openings, as depicted on *Fig. 2* around $y=0m$ and $y=10m$. This may be due to the fact that in those areas the pyrolysis is moderated by exposure to the adjacent cold ambient air and the main combustion zone at the diffusion interface in the gas phase is not moving ahead of the pyrolysis zone. As shown in *Fig. 2* and *Fig. 3*, the fire spreads much faster overall under configuration 1.b compared with configuration 1.a. Indeed, configuration 1.b requires 52 minutes to spread over the whole compartment compared to 90 minutes for configuration 1.a. This can be explained by more energy leaving the compartment through the larger openings of configuration 1.a. Compared with configuration 1.a, the compartment of configuration 1.b is more likely to increase the fire spread rate, due to greater retained heat but also due to the burning zone seeking oxygen towards the openings (0m – 10m).

Some interesting differences are also apparent in the instantaneous fire spread rate evolution. The speed at the horizontal centreline, versus X location, is directly represented in *Fig. 4*. The values are determined from the straight-line distance between two ignited wood crib centres (mm) divided by the time for the second wood crib being ignited (s) and for each of these values, the depicted relative X location corresponds to the mid-distance between two ignited wood cribs. Thus, higher velocity regions of the chart represent rapid transitions between cribs, but are of relatively short duration. In configuration 1.b when the fire has passed the opening (10m – 20m), more oxygen is available to sustain more vigorous combustion, and compensating to some extent for the reduction in retained heat. This may be part of the reason that the fire spread rate is higher in this region, compared with the region from 0m – 10m. Then the fire spread rate decreases from 30m – 35m as access to oxygen diminishes towards end of opening. In configuration 1.b, at the region of 35m – 50m, the fire spread rate increases again, due to heat retention in the more enclosed region, though much of the gas-phase combustion may still be located near the opening at around 35m. Moreover, as shown in *Fig. 4*, the fire spread rate in configuration 1.b is at times significantly higher than the one in configuration 1.a. Overall, compared to the more open configuration 1.a, the fire travel

CFD analyses used to evaluate the influence of compartment geometry on the possibility of development of a travelling fire

format in configuration 1.b is less steady, being strongly influenced by phenomena associated with the smaller openings.

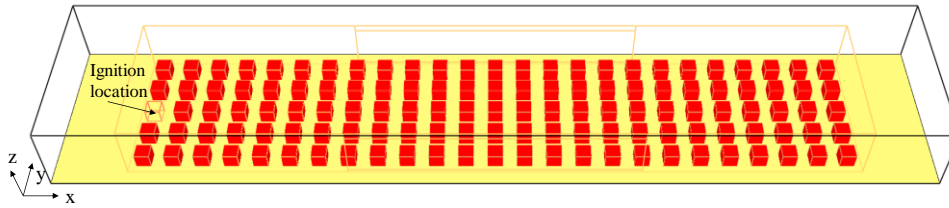


Fig. 1: Model of configuration 1.b

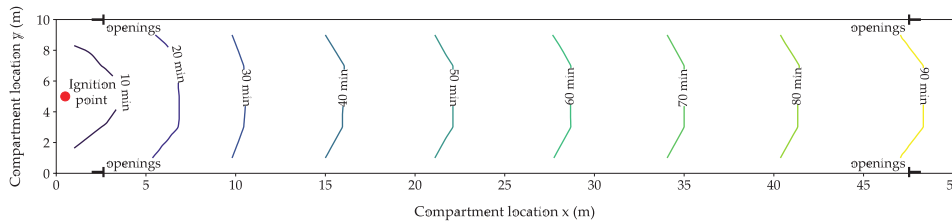


Fig. 2: Fire spread time vs. compartment location, under configuration 1.a

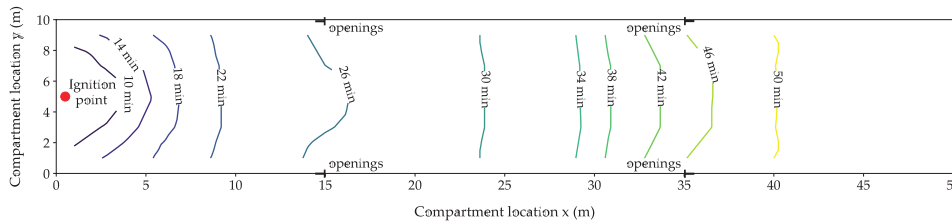


Fig. 3: Fire spread time vs. compartment location, under configuration 1.b

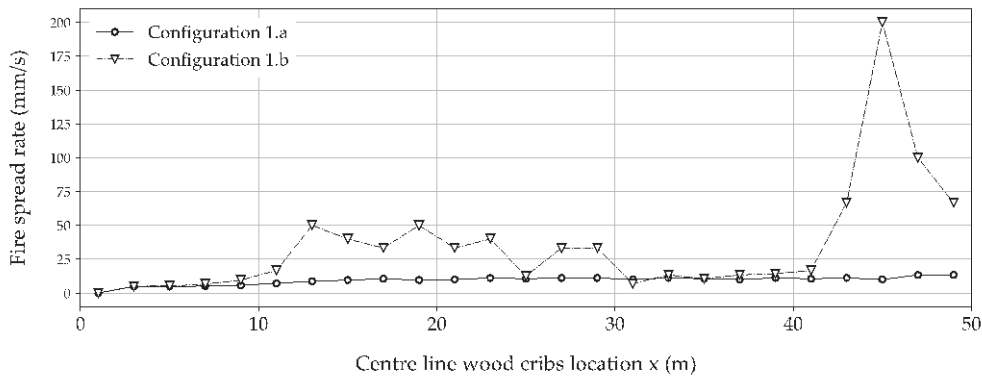


Fig. 4: Fire spread rate vs. compartment location, under configurations 1.a and 1.b

3.2 Square compartment – 2D spread

In configurations 2.a and 2.b, the compartment dimensions are respectively 20m x 20m x 8m and 20m x 20m x 3.5m and the model domains respectively 21m x 21m x 9m and 24m x 24m x 4m. The openings are placed 0.25m above floor level. The fire starts by the ignition of the wood crib placed at the centre of the compartment and the fire load consists of 1m³ wood cribs spaced 2m away from each other. This fuel density was chosen to represent the rate of heat release density of an office building prescribed by EN1991-1-2 Annex E [11], which is 250 kW/m². When compared with configurations 1, the results indicate generally slower spread rates, which is consistent with the greater crib spacing. Also, a 2D spread is observed in both cases, but with a slightly slower spread

at the openings side for configuration 2.a where less heat is retained, as depicted in *Fig. 5.a*. In configuration 2.b the fire spread accelerates more rapidly, taking 28 minutes to spread over the entire floor versus 45 minutes in configuration 2.a. This difference is suggested to result mainly from lowering the ceiling height, due to the stronger coupling between the hot gases and the pyrolyzing cubes. The change of opening factor also impacts on the ventilation airflows at the openings, and the more regular spread depicted on *Fig. 5.b* is a net result of the enhanced heat transfer with the lower ceiling together with changes in burning behaviour related to ventilation differences and the reduced overall duration of spread.

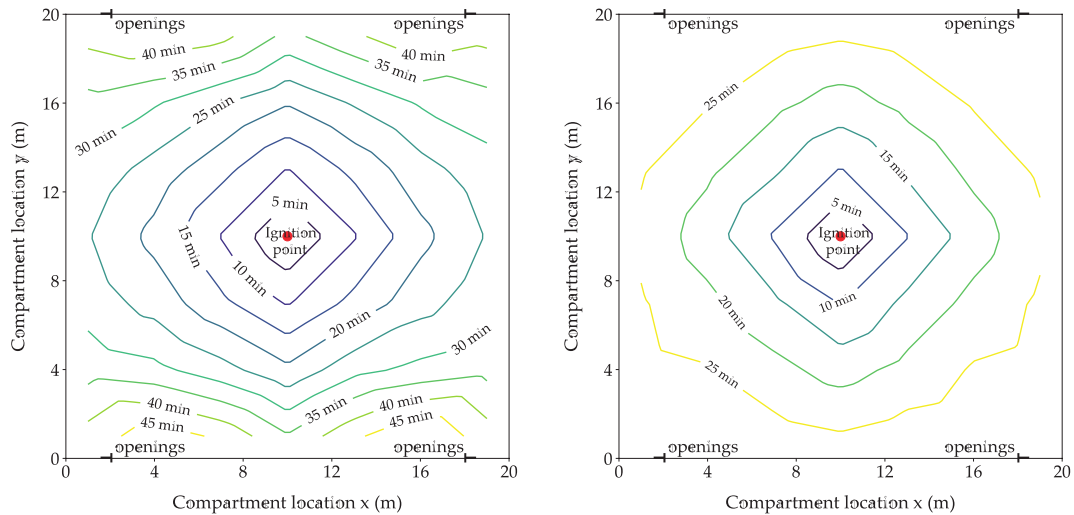


Fig. 5: Fire spread time vs. compartment location under a) configuration 2.a; b) configuration 2.b

4 LINKING CFD AND FEM WHILE COUPLING FDS AND SAFIR SOFTWARES

The CFD analyses are performed with a model of the compartment that does not necessarily contain the structural elements [12]. Structural elements must be present in the CFD model if they form a boundary of the fire compartment (walls and ceiling slab) or if they significantly influence the mass flow or the radiative flow in the compartment (deep concrete beams, wide columns, shear walls...). If the structure is made of linear steel members, it is likely that the characteristic size in the transverse direction of the steel elements is small with respect to the characteristic length of the compartment, which can justify the absence of these elements in the CFD domain. A dedicated version of FDS 6 has been written where the sole modification is the creation by FDS of a new file in which particular results are written to be used by the subsequent structural analysis by SAFIR [13]. The results are:

- *gas temperature*, used for the convective heat transfer to the structural elements;
- *coefficient of convection*, depends on the gas velocity. NB – SAFIR does not currently use this coefficient; it uses a constant value, for example 35 W/m²K, for simplicity;
- *Radiation intensity in several directions*. These intensities have been preferred to the impinging flux or the adiabatic surface temperature for different orientations, because these latter quantities both result from an integral on a surface and the information about the direction of the impinging intensities considered in these integrals is lost, with the consequence that concave sections cannot be considered appropriately.

In order to reduce the size of this transfer file, the time steps, the spatial steps in the 3 directions, as well as the limits of the domain covered in the file, do not necessarily coincide with the respective values of the CFD analysis. Linear interpolations are used by FDS between its internal results to write the file, and linear interpolations are performed by SAFIR when reading the file to compute the relevant values at the requested positions in time and in space. Based on the data found in the transfer file, a series of 2D transient thermal analyses are performed along the structural members and the results are stored in appropriate files. As these 2D temperature distributions will be used

subsequently to represent the temperature in beam finite elements, a temperature distribution is calculated for each longitudinal point of integration of each beam finite element; SAFIR uses 2 or 3 points of Gauss along the beam elements. In these 2D thermal analyses, the impinging flux is computed for each boundary (in the sense of finite element discretisation) of the section, depending on its orientation. As an approximation, the position of the boundaries of the section in the fire compartment is the same for all boundaries of a section (at the position of the node line of the beam finite element, based on the assumption that half of the characteristic length of the section is small with respect to the size of the compartment). For the boundaries on concave parts of the section, impinging radiative intensities from certain direction are discarded if there is an obstruction by other parts of the section. Mutual radiation between different boundaries of the section in the concave regions is not considered.

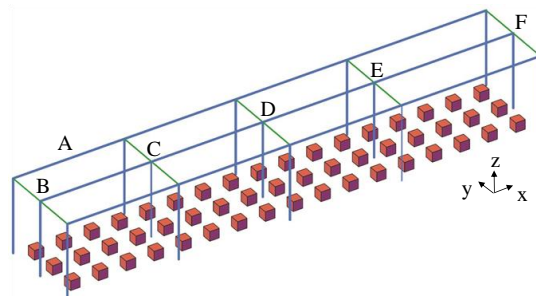


Fig. 6: Steel structure in the compartment and solid cribs

In order to illustrate the capabilities of the CFD-FEM coupling, the steel structure shown on Fig. 6 is supposed to be present in a compartment similar to the one depicted in Fig. 1, i.e. a 51m x 9m x 4m compartment with 20m x 3.25m opening size. The solid cribs are spaced 2m away from each other to represent the rate of heat release density of an office building, which is 250 kW/m² [11]. Fig. 7.a shows the isotherms after 41 minutes in the IPE400 beam in the middle of the first span (point A in Fig. 6). A clear difference is observed between the lower flange and the upper flange, the latter being exposed to fire only on 3 sides. A gradient can also be observed in the flanges from right (toward the centre of the compartment) to left (toward the wall). Also, the lower part of the web is somehow protected by the lower flange from the radiation intensities that come mainly from the bottom right direction (i.e. the ground in the compartment). Fig. 7.b shows the evolution of the temperature in the centre of the section in the central beam (from B to F) after 67 and 92 minutes. The offset between the plots reflects the spread of the fire in the compartment.

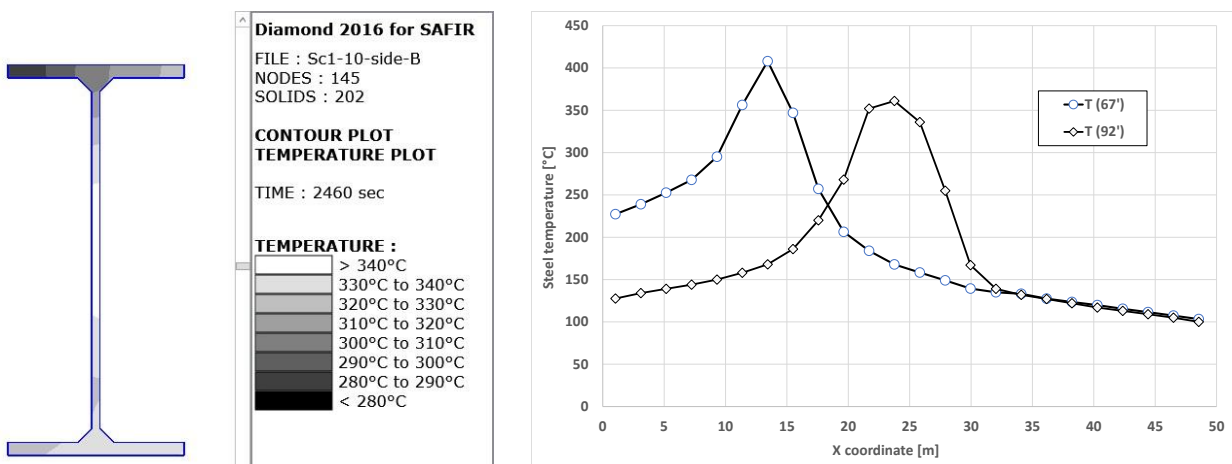


Fig. 7: Steel temperatures in beams. a) Isotherms after 41 minutes at A; b) Evolution along central beam B-F

The temperatures computed in the sections of the 3D beam finite elements that form the structure are taken into account in a geometrically transient and materially nonlinear structural analysis performed with SAFIR. Many different results can be obtained from this type of analysis, such as the evolution of axial forces and bending moments in the elements, the stresses in the elements, the displacements of the nodes and finally, the fire resistance time and the failure mode (or the absence of failure). The evolution of the vertical displacement at the top of the five columns from the central frame is represented on *Fig. 8*. As the structure does not collapse, the vertical displacement is essentially elastic and is therefore a result of thermal elongation. The travelling nature of the fire is highlighted by the time shift of the thermal elongation in the columns B to F.

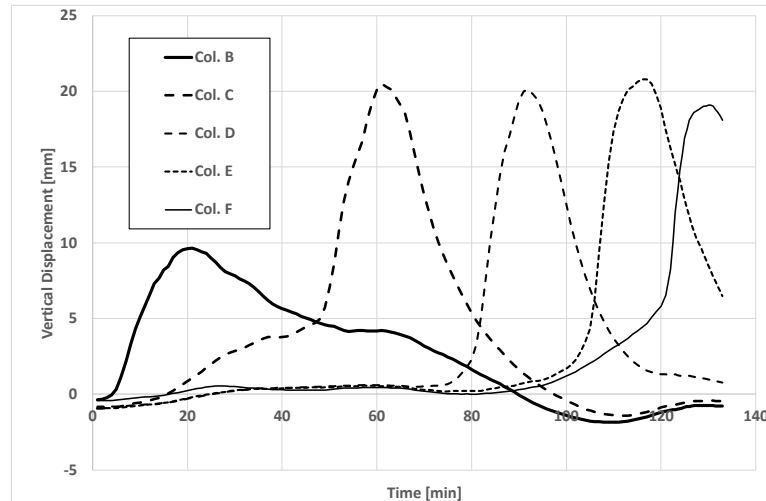


Fig. 8: Evolution of the elongation of the columns in the central frame as a function of time

5 DISCUSSIONS AND FURTHER IMPROVEMENTS

The sample cases presented illustrate the potential value of CFD for generating and analysing fire dynamic conditions which influence the likelihood of fire spread. It is important to note that these are numerical examples and not validation studies. Thus there are important provisos on the interpretation of the results. Further work would be required to quantify any deviations arising due to numerical effects. Also, concerning the methodology used for the representation of burning fuel, Degler & Eliasson [14] highlight that it presents some drawbacks. Before a cell reaches the ignition temperature, its heating is computed while considering heat exchanges with the environment. But as soon as the ignition temperature is met, FDS represents the fire by releasing volatile combustibles which, if all are burnt, results in the prescribed HRR curve. This is done without considering the evolution of heat exchange with the environment. Moreover, the uniform cubic shape of the obstruction prevents air flow through the object. Nevertheless, it was concluded that this approach can yield a good representation of a burning wood crib in comparison with hand calculations of the upper and mean value of the mass loss rate [13]. In next steps, different ignition locations will be considered and FDS results will be analysed to highlight the spread of cribs extinction. Furthermore, the details of glazing failure have been ignored at this stage, and more realistic compartment geometries and boundary materials should also be considered. Moreover, having demonstrated the value of the methodology, further systematic use of numerical simulations will be undertaken to perform more comprehensive parametrical analyses. The calibration of these simulations will also benefit from experimental tests from the literature or to be performed in the frame of the TRAFIR project. It will then be possible to determine the conditions in which a travelling fire may develop, or not, and therefore inform on appropriate fire scenarios to be considered. In the analysis performed to calculate the temperature in the structure, it would be possible to consider the real position of each boundary of the sections instead of approximating this position to the centre of the section. Parallelisation of the code, which is currently under way, will

reduce the CPU time requested for the large number of 2D thermal analyses performed in the sections.

6 CONCLUSIONS

Using Fire Dynamics Simulator, different geometrical arrangements were modelled in terms of compartment layout, opening size and ceiling height. A fire load composed of wood cribs has been considered using discrete volumes arranged on regular grids and a temperature criterion on the volume surfaces was used to trigger the start of a predefined heat release curve. It has proved possible to extract from CFD results quantitative measures of fire behaviour, in particular the fire spread rates. It was possible to interpret all the observed trends in terms of fundamental principles of fire dynamics. Such method is built on several explicit assumptions but permits a first assessment of the conditions required for fire spread and provides an indication of some of the influential parameters and likely sensitivities. Further, by considering the detailed results of the CFD analysis in a nonlinear thermomechanical analysis of a structure located in the fire compartment, the coupling of the structural response to the travelling fire characteristics has been demonstrated.

ACKNOWLEDGMENT

This work was carried out in the frame of the TRAFIR project with funding from the Research Fund for Coal and Steel (grant N°754198). Partners are ArcelorMittal Belval & Differdange, Liège Univ., the Univ. of Edinburgh, RISE Research Inst. of Sweden and the Univ. of Ulster.

REFERENCES

1. J. Stern-Gottfried, G. Rein (2012). *Travelling fires for structural design – Part I: Literature review*. Fire Safety Journal 54. pp 74-85.
2. K. Horová, T. Jána, F. Wald (2013). *Temperature heterogeneity during travelling fire on experimental building*. Advances in Engineering Software 62-63. pp 119-130.
3. J.P. Hidalgo, A. Cowlard, C. Abecassis-Empis, C. Maluk, A.H. Majdalani, S. Kahrmann, R. Hilditch, M. Krajcovic, J.L. Torero (2017). *An experimental study of full-scale open floor plan enclosure fires*. Fire Safety Journal 89. pp 22-40.
4. D. Rush, D. Lange, J. Maclean, E. Rackauskaite (2015). *Effects of a Travelling Fire on a Concrete Column – Tisova Fire Test*. Proceedings of the 2015 ASFE Conference.
5. I. Thomas, K. Moinuddin, I. Bennetts (2005). *Fire development in deep enclosure*. Proceedings of the Eighth IAFSS Symposium. pp 1277-1288.
6. X. Dai, S. Welch, A. Usmani (2017). *A critical review of ‘travelling fire’ scenarios for performance-based structural engineering*. Fire Safety Journal 91. pp 568–578.
7. K. McGrattan, S. Hostikka, R. McDermott, J. Floyd, C. Weinschenk, K. Overholt (2017). *Fire Dynamics Simulator User’s Guide*. Sixth Edit. National Institute of Standards and Technology (NIST).
8. K. Overholt (2018). FDS Mesh Size Calculator [Online]. <http://www.koverholt.com/fds-mesh-size-calc/>.
9. J. Degler, A. Eliasson, A. Anderson, D. Lange, D. Rush (2015). *A-priori modelling of the Tisova fire test as input to the experimental work*. Proc. 1st Int. Conf. on Struct. Safety under Fire & Blast, Glasgow, UK.
10. SFPE Handbook of Fire Protection Engineering (2002). Third Edition. NFPA.
11. EN1991-1-2 (2002). Eurocode 1: Actions on structures – Part 1-2: General actions-Actions on structures exposed to fire. CEN, Brussels.
12. N. Tondini, A. Morbioli, O. Vassart, S. Lechêne, J.-M. Franssen (2016). *An integrated modelling strategy between a CFD and an FE software: Methodology and application to compartment fires*. Journal of Structural Fire Engineering 7 Issue 3, pp 217-233.
13. J.M. Franssen, T. Gernay (2017). *Modeling structures in fire with SAFIR®: theoretical background and capabilities*. Journal of Structural Fire Engineering 8. pp 300-323.
14. J. Degler, A. Eliasson (2015), *A Priori Modeling of the Tisova Fire Test in FDS*, Bachelor’s Thesis, Luleå University of Technology.

NUMERICAL MODELLING OF THE FIRE BEHAVIOUR OF RESTRAINED CELLULAR BEAMS USING A HYBRID SIMULATION APPROACH

Mustesin Ali Khan¹, Liming Jiang², Katherine A Cashell³, Asif Usmani⁴

ABSTRACT

Cellular composite beams are an increasingly popular choice in the construction of buildings as they can provide a structurally and materially efficient design solution as well as allowing the passage of services. The behaviour of restrained composite cellular beams with a profiled slab exposed to fire has not been considered in great detail to date and is the focus of the current study. A finite element model is developed using OpenSees and OpenFresco utilising a hybrid simulation technique, and the accuracy of the model is validated using available fire test data. Temperatures obtained from test results are directly applied to various locations, i.e., the top flange, bottom flange, web, profiled deck, and slab. The effect of axial and rotational restraints due to the connection type between the beams and columns is also investigated. Furthermore, the hybrid simulation model is employed to study a number of salient parameters, including the effect of the position of the openings and the boundary conditions on the overall beam behaviour. The stress pattern at various locations was also examined for different cases during the fire. It is shown that position of the opening along the span and boundary conditions has a considerable effect on time-displacement behaviour and the fire performance of the beam.

Keywords: Structures, cellular beams, OpenSees, OpenFresco, hybrid simulation.

1 INTRODUCTION

In practice, most of the composite cellular beams are axially and rotationally restrained, and their behaviour is very much dependent on the presence of restraints. Various experiments and numerical investigations have been performed to analyse framed steel structures exposed to fire [1–4], but there are very few studies in the literature on fire restrained cellular beams exposed to fire [5,6].

In the majority studies in the literature, the behaviour of cellular beams exposed to fire was investigated by performing isolated fire tests or numerical modelling on single elements. Various researchers [7–10] have conducted analytical studies and performed fire tests on simply supported cellular beams. For example, Najafi and Wang [11,12] have conducted studies on steel cellular beams with different level of axial restraint, but this study does not

¹ PhD Candidate. Department of Civil and Environmental Engineering, Brunel University London, London, UK.
e-mail: mustesin.khan@brunel.ac.uk

² Post Doctoral Candidate. Department of Building Services Engineering, The Hong Kong Polytechnic University, Hong Kong.
e-mail: liming.jiang@polyu.edu.hk

³ Senior Lecturer. Department of Civil and Environmental Engineering, Brunel University London, London, UK.
e-mail: katherine.cashell@brunel.ac.uk

⁴ Professor. Department of Building Services Engineering, The Hong Kong Polytechnic University, Hong Kong.
e-mail: asif.usmani@polyu.edu.hk

focus on the behaviour of composite action and the actual restraint developed when the beam is a part of an real structure.

Limited tests have been performed on framed cellular beams exposed to fire [5] [13]. A simplified analysis was also performed by Abu [14] on framed cellular beams exposed to fire by validating the Mokrsko fire tests on an administrative building [5]. The effect of the openings was incorporated by calculating the equivalent web thickness. There is a lack of numerical data for framed composite cellular beams exposed to fire. The study reported in this paper bridges this gap and explains the behaviour of restrained composite cellular beams exposed to fire.

In the literature [15], two finite element (FE) codes (both models in 2D) have been coupled to analyse the behaviour of buildings exposed to seismic loads. In this study, a hybrid simulation approach is utilised to investigate the behaviour of restrained cellular beams exposed to high temperature, as occurs in a fire. Typically, the phrase ‘hybrid simulation’ refers to modelling a structure using different sub-assemblies, some of which may be represented using standard FE elements (such as beam-column elements) while the areas requiring more focused attention are modelled using more complex (and hence computationally expensive) elements (such as 3D shell elements). This results in master and slave assemblies, respectively. Both the master and the slave assemblies are modelled in OpenSees in the current study. A middleware software is required to connect the master and slave assemblies using super and adapter elements. Such software solves potential issues such as data storage, communication methods, system control, optimisation and data transformations. The middleware used in this work is OpenFresco.

2 NUMERICAL MODELLING

The modelling approach is validated using the fire tests which were completed on an administrative building in Mokrsko, Poland, which included a composite cellular beam subjected to fire [5]. The beam was made using an IPE270 profile with an overall depth of 395 mm and a steel grade of S235. The composite profiled deck slab was made with an effective depth of 130 mm. The compressive strength of concrete used in slab and ribs was 32.5 MPa with a mass density of 2400 kg/m³. The nominal reinforcement in the concrete slab is modelled at mid-depth with 5 mm diameter bar at a spacing of 100 mm in both directions.

In the model, the part of the structure exposed to the fire (i.e. the AS2 composite cellular beam and connected slab) is represented using more complex 3D elements in a slave assembly whilst less detailed elements are employed for the rest of the structure in a master assembly. The steel portion of the AS2 cellular beam is modelled using the ShellMITC4Thermal 3D shell elements, available in Opensees. The composite deck slab above the cellular beam is modelled using 3D beam-column elements for the ribs, and 3D shell elements for the flat parts of the slab. The reinforcement in the deck slab is modelled using a smeared layer approach. The cellular beam is connected to the slab decking using link elements called rigid link in Opensees. SteelECThermal and ConcreteDamagedPlasticity material classes present in OpenSees are utilised to model the material in the ribs and slab respectively. The newly developed J2plasticity material model [16] is assigned to the steel beam. In the fire test, the openings were sinusoidal in shape. However, in order to simplify the model, the openings are idealised herein as rectangles with equivalent opening areas to the test specimens, in accordance with the guidelines given in SCI P355 design manual [17]. In the model, each rectangular opening has dimensions of 625 × 250 mm. The remainder of the frame is modelled in a master assembly using 3D beam-column elements. The analysis was also performed in two stages, just as the test was performed. In the first stage, a static load of 5.6kN/m² with a load ratio of 0.26 is

applied uniformly on the beam. In the second stage, the time-temperature curves obtained from the test are applied at various locations along the beam, in accordance with the available information (see Fig. 1) [5].

The analysis is performed using a hybrid simulation approach. The frame in the master assembly and the composite cellular beam in the slave assembly are connected using a middleware software OpenFresco. Both the substructures are connected at interface nodes. A 26 noded super element is defined in the master assembly and a 26 noded adapter element is defined in the slave assembly to connect the two FE codes. The communication between the two codes takes place according to a sequence of steps. The sequence of steps in exchanging the data between the master and slave assemblies to perform the hybrid simulation is shown in Fig. 2.

Step 1. Run the analysis for the master program and, as a result, the super element receives a displacement vector of global trial displacements (u_{super}) for all of its degrees of freedom from the master integration program

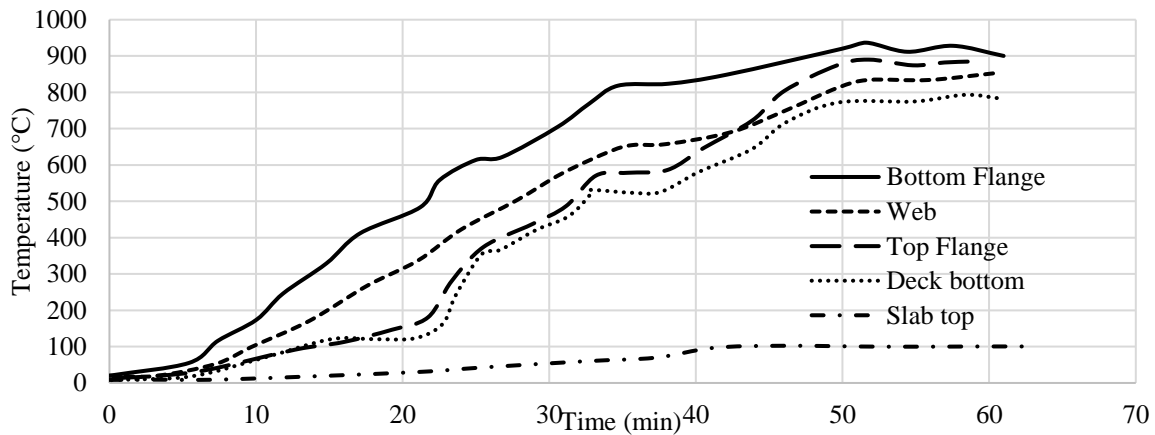


Fig. 1 Temperature profile at the various location [5]

Step 2. The displacement vector obtained in the previous step is sent to OpenFresco using a TCP/IP socket (where TCP/IP means a Transmission Control Protocol/Internet Protocol which is the basic communication language or protocol of the Internet) as can be seen in Fig. 2. Here the ‘SimAppSiteServer’ class is used to start the simulation server process.

Step 3. The storage and transformation tasks for the displacement vector are performed by the ‘LocalExpSite’ and ‘ExperimentalSetup’ objects (see Fig. 2). Transformation of the data is not required in this instance because no physical specimen (i.e. laboratory test specimen) is involved. So, the ‘NoTransformation’ object as ‘ExpSetup’ is utilised.

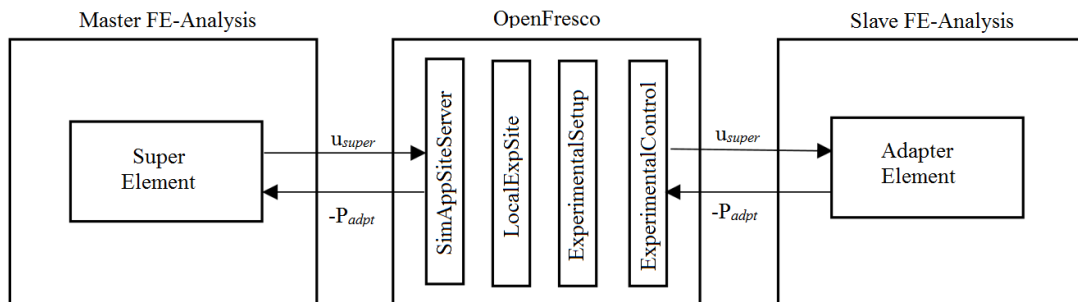


Fig. 2 Sequence of operations and data exchange

Step 4. The trial displacement vector is then transferred to the ‘ExperimentalControl’ object which feeds the trial displacement vector to the adapter element in the slave assembly, using a TCP/IP socket. The adapter element then forms a resultant displacement vector by combining the trial displacements (u_{super}) with its own elemental displacements. Subsequently, the element force vector (P_{adpt}) for the adapter element is updated and returned to the slave assembly.

Step 5. After the solution convergence from the slave program, the negative resultant force vector ($-P_{adpt}$) is sent to the ‘ExperimentalControl’ object through the TCP/IP socket. Again, the storage and transformation of the force vector are carried out by the ‘LocalExpSite’ and ‘ExperimentalSetup’ objects (see Fig. 2).

Step 6. The ‘SimAppSiteServer’ then sends the force vector to the super element in the master program through the TCP/IP socket.

Step 7. The super element saves these values as element forces and returns them to the master integration method for the next step. The master program then determines the new trial displacements and Step 1 to Step 7 are repeated until the analysis is complete.

3 VALIDATION AND PARAMETRIC STUDY

Midspan vertical deflection of the restrained composite cellular beam (AS2) is plotted against time and compared with the test results. A reasonable agreement (see Fig. 3) has been obtained between the test result and the result of the analysis.

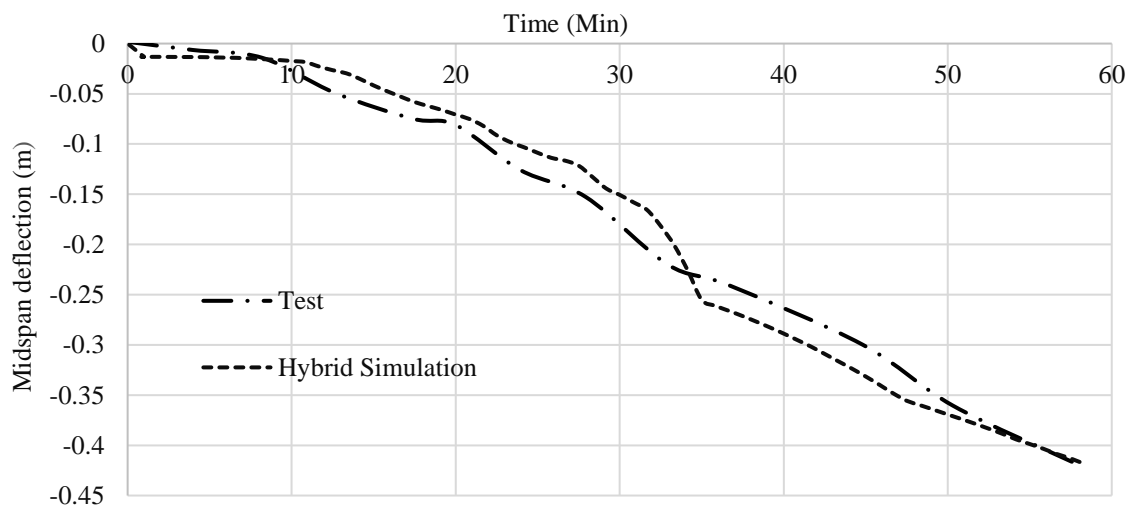


Fig. 3 Vertical deflection comparison at mid-span

Once validated, the model is employed to study the effect of the opening position and support conditions on the behaviour of restrained composite cellular beams. The FE model prepared for the AS2 beam is used to perform the study and connected to columns in the master assembly at the location of the AS4 beam. Various cases are investigated with openings in the bending zone and the shear zone. To study the effect of real boundary conditions, both opening cases are analysed using the hybrid simulation (HS) technique and simply supported (SS) boundary conditions. In hybrid simulation, the composite cellular beam is modelled as a slave assembly. The steel portion of the AS2 cellular beam is modelled using the ShellMITC4Thermal 3D shell elements, available in OpenSees. The composite slab above the cellular beam is modelled using 3D beam-column elements for the ribs, and 3D shell elements for the flat parts of the slab. The

rest of the frame is modelled in master assembly using 3D beam-column elements. Both the assemblies are connected using the middleware OpenFresco. On the other hand, in simply supported simulations, an isolated simply supported beam is modelled without including the rest of the structure. The four cases which are investigated in this study are as follows.

Case 1 Openings in the centre of the beam (Bending Zone) HS

Case 2 Openings at 500 mm from the one end (One Shear Zone) HS

Case 3 Openings in the centre of the beam (Bending Zone) SS

Case 4 Openings at 500 mm from the one end (One Shear Zone) SS

Fig.4 shows the size and position of the openings used for this study, where all dimensions are in mm. All the cases are analysed in two phases, i.e., phase 1 as the application of mechanical load and phase 2 is the application of thermal load. The beam in each case is exposed to the same thermal loading as experienced by AS2 test beam.

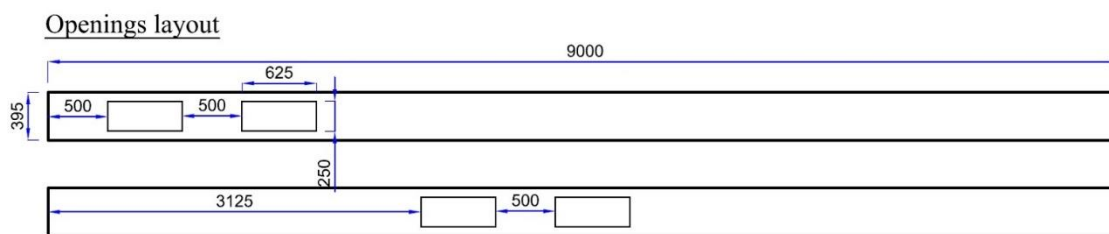


Fig. 4 Opening layout for both opening positions (all dimensions are in mm)

4 RESULTS AND DISCUSSION

4.1 Effect of position of the openings

It is observed that for Case 1, initially, the beam deflects in an upward direction which can be seen in Fig. 5. The thermal profiles across the depth of the beam show that the temperature in the bottom flange increases at a rapid rate compared to the temperature of the web and the top flange.

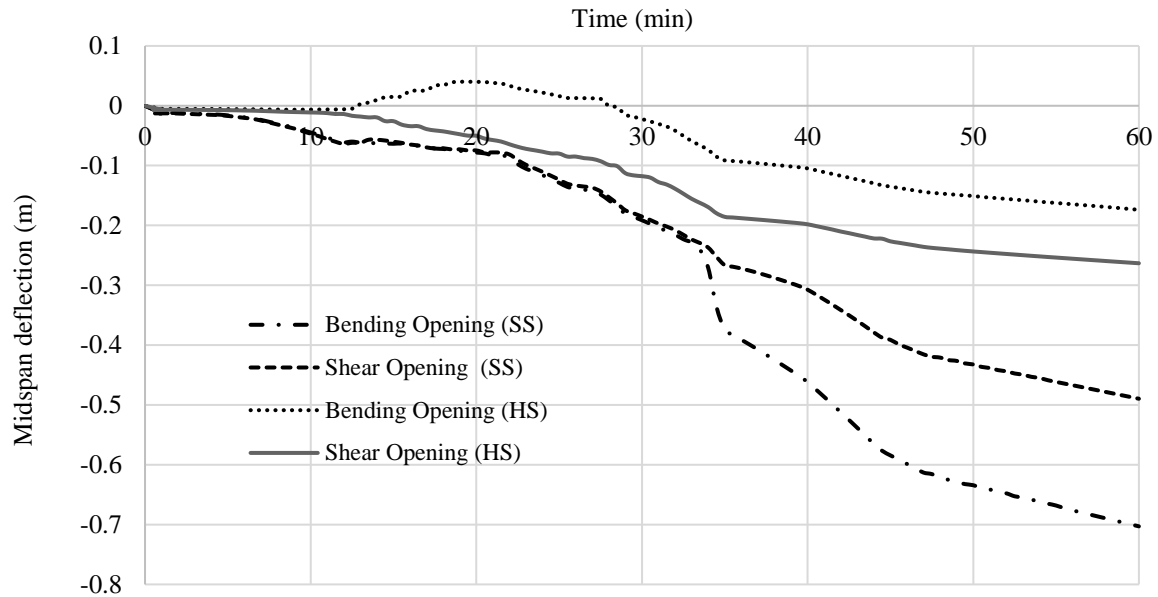


Fig. 5 Time-deflection behaviour of various cases

As a result of this, for the initial 20 minutes, the compressive force developed in the bottom flange due to the restrained thermal expansion exceeds the combined compressive force developed in the top flange and slab, as shown in Fig. 6. This unbalanced compressive force generates a hogging moment in the beam. The effect of the hogging moment is that the beam tends to deflect in the upward direction however, at the onset of yielding of the bottom flange under compressive forces, it starts to deflect in the downward direction.

On the other hand in Case 2, the opening is present near one end of the beam so axial and rotational restraint develop partially. This behaviour can be verified by low compressive and tensile forces during the first phase of the analysis, and can be seen in Fig.7. In addition, Fig.7 shows that for most of the duration of the fire, the combined compressive force in the slab and the top flange is greater than the compressive force developed in the bottom flange. The distribution of forces makes the beam deflect in a downward direction for the whole of the duration of the fire. Fig.8 displays the horizontal end displacement for Case 1 and Case 2. As the development of restraint forces is partial in Case 2 (shown in Fig.7), therefore this Case allows less horizontal end displacement than Case 1 as displayed in Fig.8.

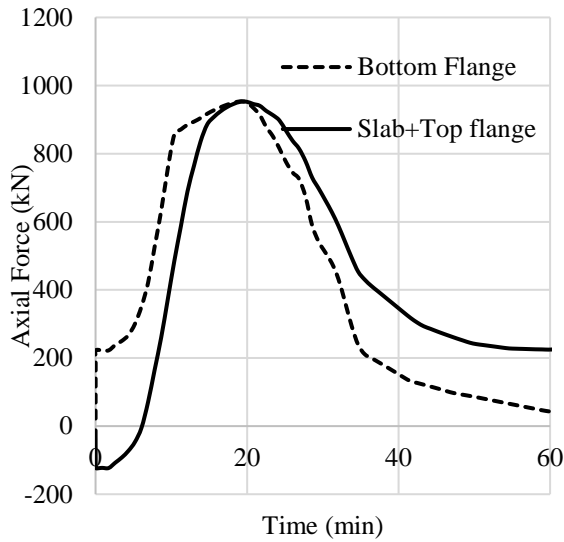


Fig. 6 Axial forces for Case 1

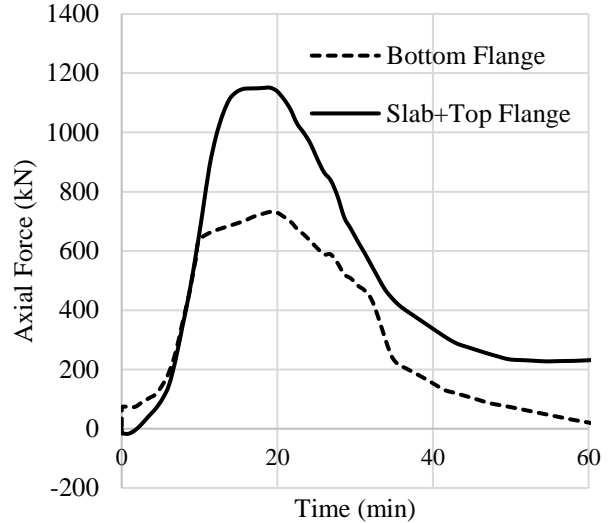


Fig. 7 Axial forces for Case 2

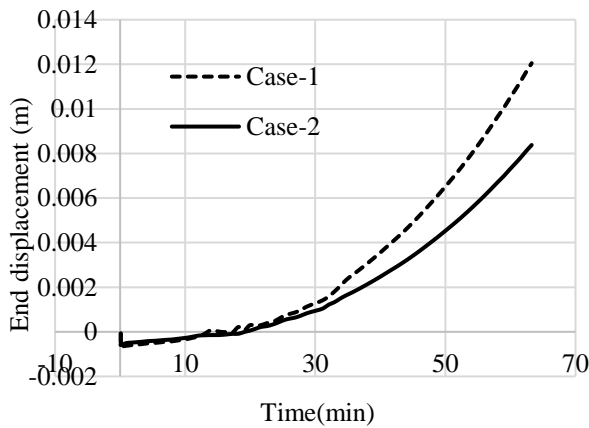


Fig. 8 Beam end displacement for HS

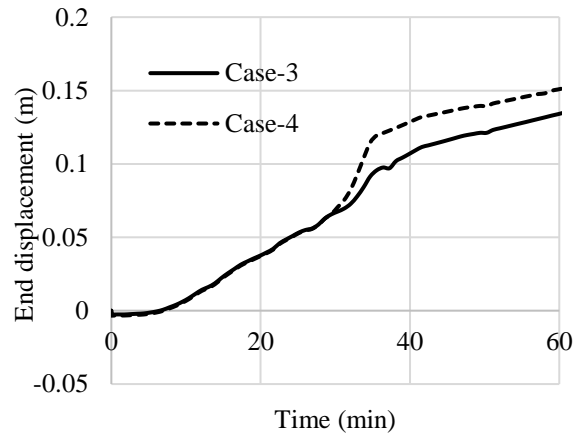


Fig. 9 Beam end displacement for SS

When openings are present in the bending zone, buckling of the top flange due to the presence of high axial forces is observed as the main failure mode. When the openings are present in the shear zone, a Viernedeel mechanism is observed as the main failure mode. In this mechanism, transverse shear is transferred across the opening which leads to the formation of plastic hinges at the corners of the opening.

If the openings are present in the shear zone, it has to resist the maximum hogging moment, vertical shear force, axial forces and the Vierendeel bending, whereas if the openings are present in the bending zone, the shear force is at its minimum value and no Vierendeel mechanism is observed, which makes this zone a favourable place to have openings in restrained cellular beams. However, the openings area for Case 1 and Case 2 are the same but due to the facts mentioned above, Case 1 shows less mid-span deflections and improved performance in fire. So, it can be concluded that for restrained beams, openings are preferred in the bending zone rather than the shear zone.

4.2 Effect of support condition

Case 3 and 4 are simulated by applying simply supported boundary conditions. Here, the behaviour of beams with simply supported boundary conditions is completely different than the beams analysed by using a hybrid simulation technique. In hybrid simulation, Case 2 (opening in the shear zone) was shown to be critical with higher mid-span deflections and less fire resistance than Case 1. However, in the simply supported simulation, Case 3 (opening in the bending zone) shows more mid-span deflection and less fire resistance than Case 4 (openings in the shear zone). The absence of axial and rotational restraint does not allow the development of hogging moment in simply supported beams. So, no initial upward movement is observed in Case 3. Due to the presence of opening at the mid-span in Case 3, the section becomes weak and the increased value of the sagging moment at the weak section results in higher vertical deflections and less horizontal end displacements (see Fig. 9) compared with Case 4. Therefore, it can be concluded that Case 3 shows more mid-span deflection and less fire resistance than Case 4.

5 CONCLUSIONS

This paper presents the behaviour of cellular beams exposed to fire using a hybrid simulation technique and simply supported boundary conditions. For beams simulated using a hybrid simulation technique, the compressive forces are developed initially in the whole section and on gradual degradation of materials the distribution of forces comes to its original state, which is compression at the top and tension at the bottom surface for mid-section. The combined effect of bending moment, shear force, axial force and Vierendeel bending moments makes Case 2 as the critical in hybrid simulations with Vierendeel mechanism as the main failure mode. While for beams simulated with simply supported boundary conditions, the nature of forces developed in the beam remains same throughout the duration of fire, which is compression at the top and tension at the bottom surface for mid-section. In simply supported beams, Case 3 experiences higher mid-span deflection and less fire resistance than Case 4.

REFERENCES

- [1] British Steel (BS) plc. The behaviour of multi-storey steel framed buildings in fire. Swinden Technology Centre, Rotherham: 1999.
- [2] Dwaikat MMS, Kodur VKR. A performance based methodology for fire design of restrained steel beams. *J Constr Steel Res* 2011. doi:10.1016/j.jcsr.2010.09.004.
- [3] Li GQ, Guo SX. Experiment on restrained steel beams subjected to heating and cooling. *J Constr Steel Res* 2008. doi:10.1016/j.jcsr.2007.07.007.
- [4] Liu TCH, Fahad MK, Davies JM. Experimental investigation of behaviour of axially restrained steel beams in fire. *J Constr Steel Res* 2002. doi:10.1016/S0143-974X(01)00062-1.
- [5] Kallerová P, Wald F, Chlouba P, Sokol Z. Fire Test on Administrative Building. Mokrsko: 2011.
- [6] Nadjai A, Han S, Ali F, Alam N, Allam A. Fire resistance of axial restraint composite floor steel cellular beams. *J Constr Steel Res* 2017. doi:10.1016/j.jcsr.2017.05.016.
- [7] Nadjai A, Vassart O, Ali F, Talamona D, Allam A, Hawes M. Performance of cellular composite floor beams at elevated temperatures. *Fire Saf J* 2007;42:489–97. doi:10.1016/j.firesaf.2007.05.001.
- [8] Engineering S. Behaviour of Composite Cellular Steel - Concrete Beams at Elevated Temperatures 2009;9:29–37.

Numerical Modelling

- [9] Ellobody E, Young B. Nonlinear analysis of composite castellated beams with profiled steel sheeting exposed to different fire conditions. *J Constr Steel Res* 2015;113:247–60. doi:10.1016/j.jcsr.2015.02.012.
- [10] Nadjai A, Petrou K, Han S, Ali F. Performance of unprotected and protected cellular beams in fire conditions. *Constr Build Mater* 2016;105:579–88. doi:10.1016/j.conbuildmat.2015.12.150.
- [11] Najafi M, Wang YC. Axially restrained steel beams with web openings at elevated temperatures, part 1: Behaviour and numerical simulation results. *J Constr Steel Res* 2017;128:745–61. doi:10.1016/j.jcsr.2016.10.002.
- [12] Najafi M, Wang YC. Axially restrained steel beams with web openings at elevated temperatures, part 2: Development of an analytical method. *J Constr Steel Res* 2017. doi:10.1016/j.jcsr.2016.10.003.
- [13] Nadjai A, Bailey CG, Vassart O, Han S, Zhao B, Hawes M, et al. Full-scale fire test on a composite floor slab incorporating long span cellular steel beams. *Struct Eng* 2011.
- [14] Abu A, Block F, Butterworth N, Burgess I. Structural fire engineering assessments of the Fracof and Moksko fire tests: An Engineering prediction. *Appl. Struct. Fire Eng.*, Prague, Czech Republic: 2009.
- [15] A. S, Huang Y, Mahin SA. Structural FE-Software Coupling through the Experimental Software Framework, OpenFresco. 14th World Conf. Earthq. Eng., Beijing: 2008.
- [16] Khan M, Jiang L, Cashell K, Usmani A. Analysis Of Composite Beams Exposed To Fire Using Hybrid Simulation Approach. 2nd Int. Conf. Struct. Saf. under Fire Blast Load., London: 2017.
- [17] Lawson RM, Hicks SJ. Design of beams with large web openings. Berkshire: 1998.

Numerical Modelling

FRACTURE SIMULATION FOR STEEL SHEAR TAB CONNECTIONS AT ELEVATED TEMPERATURE

Wenyu Cai¹, Mohammed A. Morovat², Michael D. Engelhardt^{3*}

ABSTRACT

Steel shear tab connections (also known as single-plate connections or fin-plate connections) are widely used for beam-to-column connections in steel building structures. To accurately simulate the complete response of steel shear tab connections in fire requires the ability to simulate fracture of connection components. In this study, to simulate fracture in steel connection components, the Hooputra shear fracture model parameters are calibrated at both ambient and elevated temperatures by using results from tests and numerical simulations in Abaqus. At ambient temperature, data from notched bar tests on structural steel are used to determine the stress and strain state at the fracture initiation point and further to compute the shear fracture model parameters. At elevated temperature, model parameters are calibrated by a trial and error process from steel connection tests due to lack of test data from notched bar tests at elevated temperatures. Various sets of parameters for the shear fracture model are input into Abaqus to simulate the tests until the simulated load-deformation results and fracture failure modes reasonably match those observed in the tests. The calibrated model parameters are mainly validated by simulating steel connection tests which were not used for parameters calibration and comparing the load-deformation performance between test and simulation.

Keywords: Steel shear tab connection, shear fracture, elevated temperature, fracture simulation

1 INTRODUCTION

The ultimate failure of connections in steel buildings, either at ambient temperature or at elevated temperatures, often involves fracture. Steel shear tab connections (also known as single-plate connections or fin-plate connections) are widely used for beam-to-column and beam-to-girder connections in steel building structures. The strength and deformation capacity of these connections, either at room temperature or at elevated temperatures, is typically controlled by ductile fracture of connection components. This can include fracture of bolts and welds, bearing tear-out fracture of bolt holes in the beam web or shear tab, block shear fracture in the beam web or shear tab, etc. To accurately simulate the complete response of steel shear tab connections under fire conditions therefore requires the ability to simulate ductile fracture of connection components. Computationally simulating fracture of steel shear tab connections requires an appropriate fracture model together with accurate model parameters. From elevated-temperature experiments on steel shear tab connections, it is observed that shear fracture is a dominant fracture mode in the connection elements. Therefore, the shear fracture model derived by Hooputra et al. [1] may be

¹ Assistant Professor of School of Civil Engineering, Hefei University of Technology, Hefei, China.

e-mail: wenyucai@utexas.edu

² Research Scientist Associate. Department of Civil, Architectural and Environmental Engineering, University of Texas at Austin, USA.

e-mail: morovatma@utexas.edu

³ Professor. Department of Civil, Architectural and Environmental Engineering, University of Texas at Austin, USA.

e-mail: mde@mail.utexas.edu

suitable to perform fracture simulations for steel shear tab connections. However, parameters for the Hooputra shear fracture model have not been reported in the literature on the fracture simulation for structural steel at either ambient or elevated temperatures. Thus, in this study, to simulate fracture in steel connection components, the Hooputra shear fracture model parameters are calibrated at both ambient and elevated temperatures by using results from tests and numerical simulations in Abaqus.

2 OVERVIEW OF HOOPUTRA'S SHEAR FRACTURE MODEL

Hooputra's shear fracture model [1], given by Eq. (1), predicts the equivalent plastic strain at the initiation of ductile fracture ($\varepsilon_{p,critical}$) as a function of the state of stress at the location of ductile fracture initiation. In this model, θ^+ and θ^- are the shear stress ratios in equibiaxial tensile loading and equibiaxial compressive loading respectively. Correspondingly, ε_s^+ and ε_s^- represent the equivalent plastic strain at fracture in an equibiaxial tensile test and an equibiaxial compressive test respectively. The parameter f is an orientation dependent parameter which depends on the angle between the direction of loading and the direction of the first principal strain ε_1 [1]. According to Hooputra's investigations, if the material is isotropic, the parameter f can be taken as constant.

$$\varepsilon_{p,critical} = \frac{\varepsilon_s^+ \sinh[f(\theta - \theta^-)] + \varepsilon_s^- \sinh[f(\theta^+ - \theta)]}{\sinh[f(\theta^+ - \theta^-)]} \quad (1)$$

The shear stress ratio θ is given by Eq. (2) and is a function of the mean stress σ_m , von Mises stress σ_e , maximum shear stress τ_{max} as well as a material dependent parameter k_s .

$$\theta = \frac{1 - k_s \frac{3\sigma_m}{\sigma_e}}{\frac{\tau_{max}}{\sigma_e}} \quad (2)$$

Hooputra et al. [1] calibrated the fracture model parameters based on a series of tests on aluminum alloy EN AW-7108 T6. Based on a review of the literature, there appears to be no test data or recommendations for the shear fracture model parameters for structural steel, either at room temperature or at elevated temperatures. Thus, for this research, some parameters will be estimated from previous work on the aluminum alloy and some parameters will be derived from finite element analysis of elevated temperature tests on structural steel connections. According to Hooputra's investigations, θ^+ and θ^- can be estimated using Eqs. (3) and (4) and the material parameters k_s and f can be estimated as 0.1 and 4 for metals. Therefore, to use the shear fracture model for structural steel, the unknown parameters ε_s^+ and ε_s^- must be determined by calibration to test data.

$$\theta^+ = 2 - 4k_s \quad (3)$$

$$\theta^- = 2 + 4k_s \quad (4)$$

3 CALIBRATION OF SHEAR FRACTURE MODELS AT AMBIENT AND ELEVATED TEMPERATURE

To use Hooputra's shear fracture model to computationally predict fracture of steel shear tab connection requires the parameters ε_s^+ and ε_s^- in Eq. (1). This section describes the calibration process used to determine these parameters. Two different approaches were applied to estimate these two parameters at ambient and at elevated temperature. For ambient temperature, test data on notched specimens reported by Kanvinde [2] together with finite element simulation of the tested specimens was used for calibration. Based on investigations of notched bar tests, triaxiality driven ductile fracture dominates the failure mode at the centre of the notched zone, while shear fracture

dominates the failure mode around the outer surface of the notched area. Using stress and strain values obtained from simulated results for elements close to the outer surface, the shear fracture parameters can be calibrated. The procedure for estimating ε_s^+ and ε_s^- is described below. The first step is to obtain the state of stress and strain from simulation of notched bar tests (*Fig. 1*) at the initiation of shear fracture for the outer elements of the notch region. In this step, the outer region elements are examined to obtain the shear stress ratio and equivalent plastic strain. The shear stress ratio is derived from *Eq. (2)*. Shear fracture initiation is estimated to occur at one step after ductile fracture initiation which is taken as the point of rapid reduction in load. The equivalent plastic strain can be output directly from the Abaqus simulation results. Then, the calculated shear stress ratio and equivalent plastic strain are input in *Eq. (1)*. Since results from two notched bar tests with two different radii of 3.175 mm and 1.524 mm are used to calibrate the parameters, therefore, finally two equations with unknown variables ε_s^+ and ε_s^- are established. By solving these two equations, the calibrated shear fracture model for structural steel at ambient temperature can be expressed in *Eq. (5)* as follow:

$$\varepsilon_{p,critical} = \frac{0.4 \sinh[4(\theta - 2.4)] + 9 \sinh[4(1.6 - \theta)]}{\sinh[-3.2]} \quad (5)$$

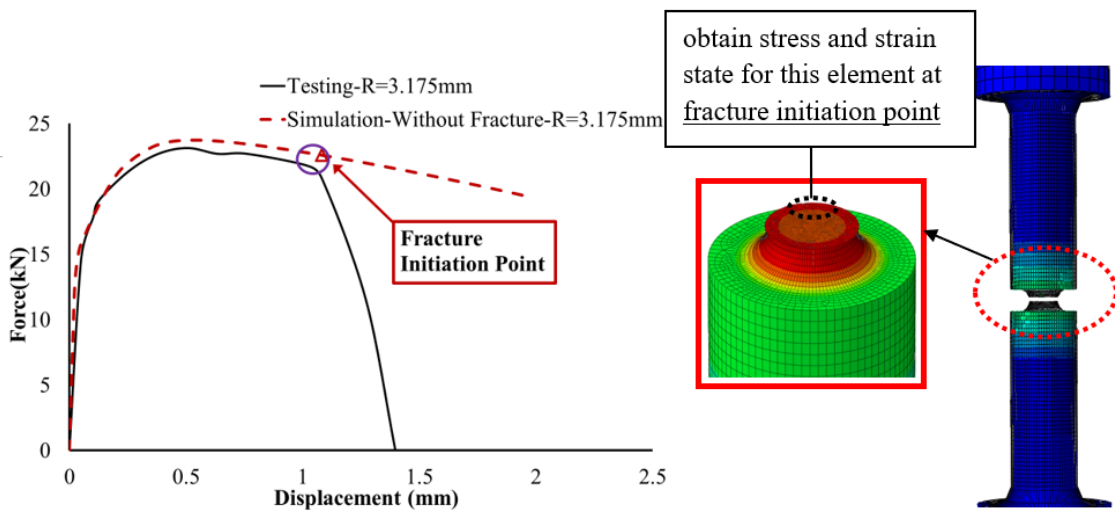


Fig. 1. Stress Strain State Calculation at Fracture Point

For elevated temperature, based on a review of the literature, very few data are reported on notched bar tests on structural steel at elevated temperatures that can be used to calibrate the shear fracture model parameters. Therefore, in this study, shear fracture model parameters will be estimated using a trial and error process based on simulations of available elevated temperature tests on bolted steel connection subassemblies. Simulations of connection tests will be conducted using different fracture parameters until the simulation reasonably agrees with test measurements and observations.

One of the available connection tests at elevated temperature reported by Hu [3] is used to estimate shear fracture parameters at temperatures of 400°C, 500°C, and 700°C. Hu performed a series of shear tab connection tests under axial tension and inclined tension (combined tension, shear and rotation) at both room and elevated temperatures. The axial tension test (*Fig. 2(a)*) is used to calibrate the fracture parameters at each temperature case; then at the same temperature case, the inclined tension test (*Fig. 2(b)*) is used to validate the accuracy of the calibrated fracture parameters.

Two-bolt connection tension tests reported by Yu (2006) (*Fig. 3*) were used to estimate fracture parameters at 300°C and 600°C. Yu also performed two-bolt connection tension tests at 400°C, 500°C, and 700°C which were used to verify the derived parameters from Hu's tests.

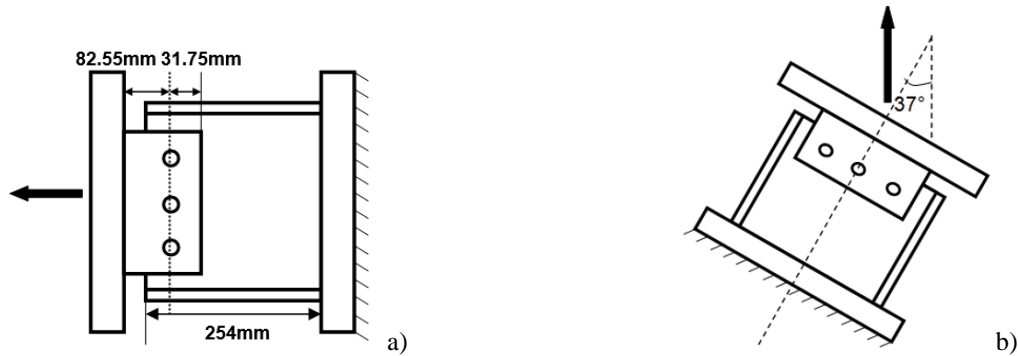


Fig. 2. a) Hu's connection test in axial tension; b) Hu's connection test in inclined tension

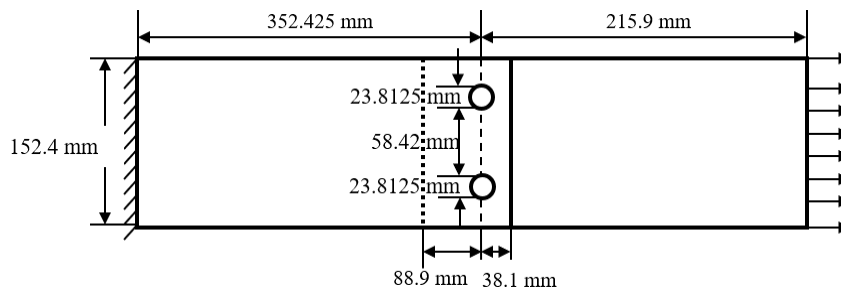


Fig. 3. Yu's two-bolt connection test at elevated temperature

4 FRACTURE SIMULATION FOR STEEL SHEAR TAB CONNECTIONS AT AMBIENT AND ELEVATED TEMPERATURE

The tested specimen recorded by Hu were simulated in the finite element program Abaqus together with the calibrated shear fracture model. The beam portion of the connection assembly was made from ASTM A992 steel, for which the true stress strain properties at both ambient and elevated temperatures can be derived from the results reported by Cai et al. [5]. Material properties of the ASTM A325 bolts were derived from the results reported by Kodur et al. [6]. The shear tab was made from ASTM A36 steel and the true stress strain curve was developed from the engineering stress strain curves obtained from Harmathy and Stanzak [7]. The shear fracture parameters ε_s^+ and ε_s^- in *Eq. (1)* were calibrated from Hu's connection tests in axial tension as 0.4 and 9 for ambient temperature, as 0.2 and 4 for 400°C and as 1 and 9 for both 500°C and 700°C. The scattered data of shear stress ratio θ and corresponding $\varepsilon_{p,critical}$ from *Eq. (1)* were calibrated from derived ε_s^+ and ε_s^- and then input into material properties in Abaqus to describe the shear fracture behaviour of beam, shear tab, and bolts. The solid element C3D8R in Abaqus was used with a minimum mesh size of 0.762 mm based on mesh sensitivity studies. For the boundary conditions, one end of the specimen was fixed for all degrees of freedom while the other end was assigned a target displacement of 76.2 mm.

At room temperature, *Fig. 4* shows the test specimen and the simulated specimen after failure. Failure in the test specimen occurred by bearing tear-out at the bolt holes in the beam. The three bolt holes did not tear-out simultaneously. Rather, the tear-out failures occurred at different times as result of the inclined loading. The simulated test specimen also captured this observed behaviour. *Fig. 5* illustrates the load versus displacement and load versus rotation behaviour, both from the test and from the simulation. In the experimental curves, there are three peak loads in these plots, and

the peak loads are reduced gradually. The three peak loads indicate the sequential failure from the three beam holes. The first peak load is estimated with reasonable accuracy from the simulation, but for the second and third peak loads the simulation results are overestimated. Although the load displacement and rotation plots differ somewhat between the test and simulation, the correct failure mode, peak load, and overall deformation capacity were captured reasonably well in the simulation.

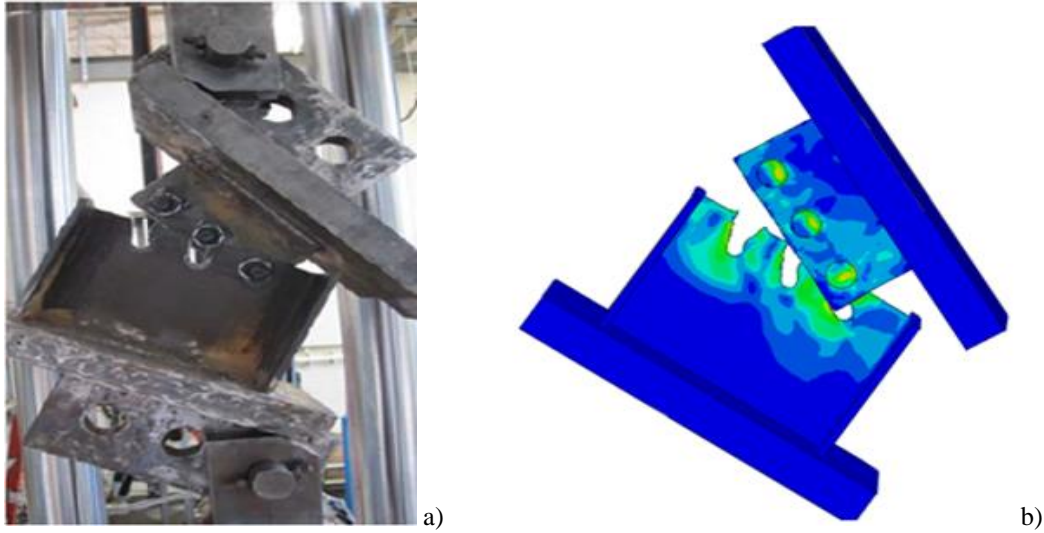


Fig. 4. a) Connection failure after test at ambient temperature [3]; b) Connection failure from simulation results at ambient temperature

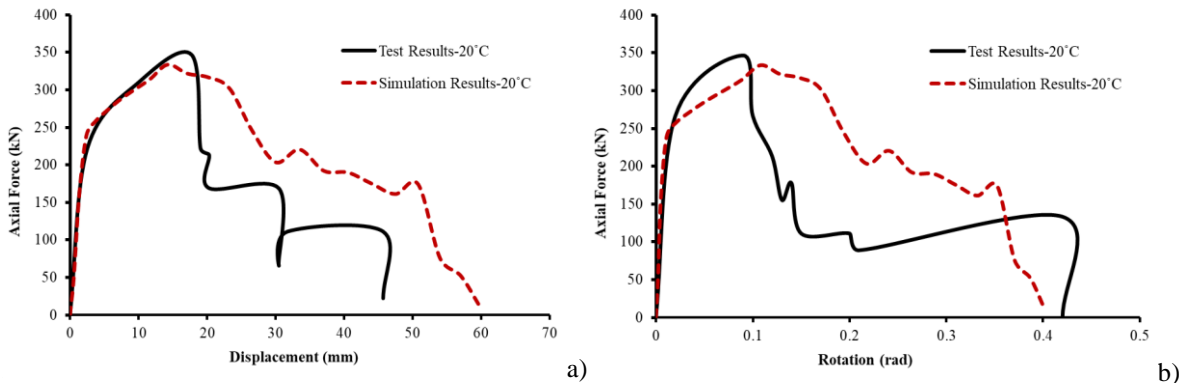


Fig. 5. a) Comparison of results of load versus displacement at ambient temperature; b) Comparison of results of load versus rotation at ambient temperature

At elevated temperature, *Fig. 6* shows the actual and simulated specimens after failure. Taking 500°C temperature case as an example, failure occurred by bolt shear fracture, both in the test specimens and in the simulation. *Fig. 7* demonstrates plots of load versus displacement and load versus rotation for the inclined loading test and simulation at 500°C. It is seen that both tests and simulations captured three different peak loads. However, the first loading peak obtained from the simulations are somewhat below the test values; the second and third peak load are overestimated by the simulations; the displacement capacity from simulations are quite close to that from the tests. In general, the failure mode and prediction of connection capacity are captured reasonably well in the simulations. However, improvement is still required in further research.

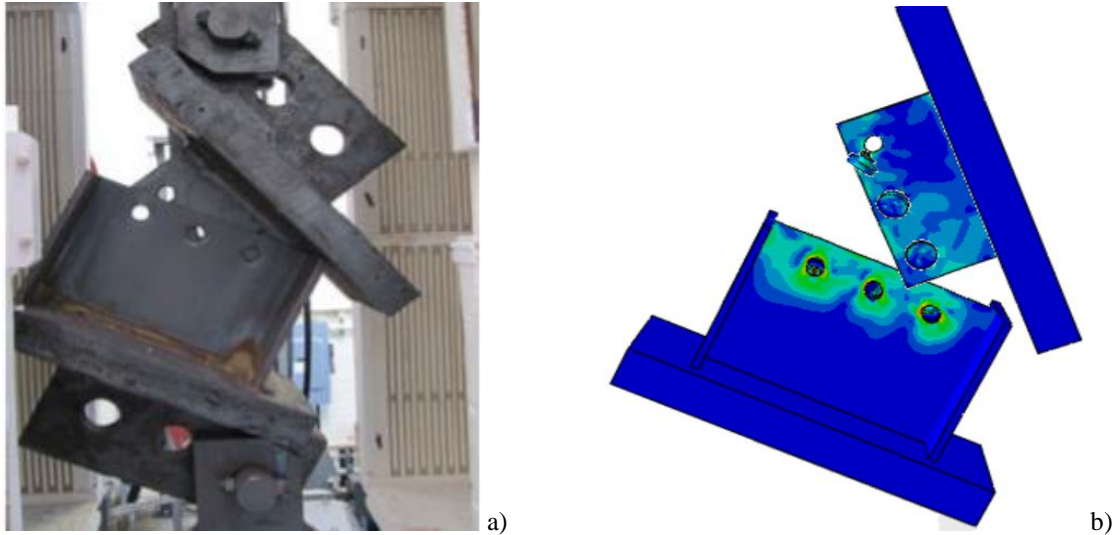


Fig. 6. a) Connection failure after test at 500°C [3]; b) Connection failure from simulation results at 500°C

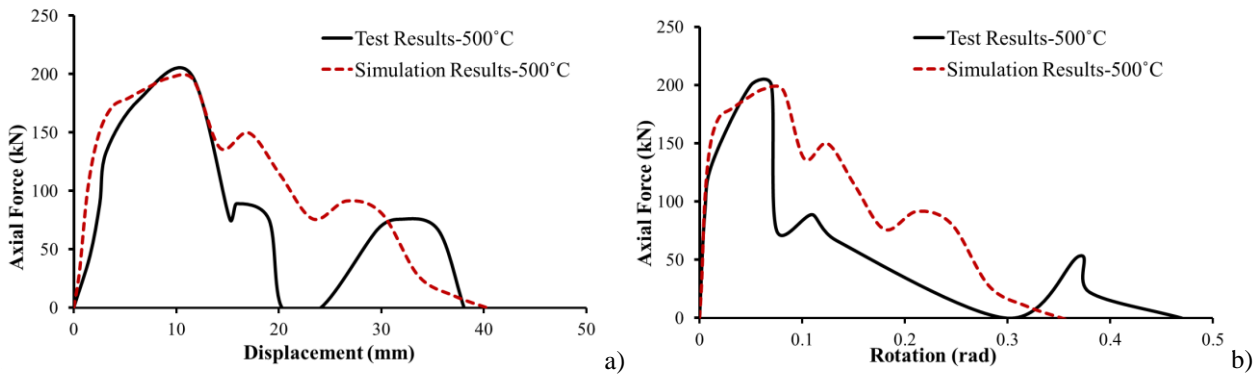


Fig. 7. a) Comparison of results of load versus displacement from Hu's test and simulation at 500°C; b) Comparison of results of load versus rotation from Hu's test and simulation at 500°C

Two-bolt connection tests by Yu were used to calibrate shear fracture parameters at 300°C and 600°C. However, due to very limited data of connection tests recorded at these two temperatures, the accuracy of the derived fracture parameters can only be examined by comparing the fracture failure mode and load-displacement behaviour from simulations with those from these tests. The connection plates are ASTM A572 Grade 50 steel and the bolts are ASTM A490. The parameters that were derived by trial and error are 0.2 and 4 for ϵ_s^+ and ϵ_s^- at 300°C, and 1.0 and 9.0 at 600°C. The calibrated shear fracture model at each temperature were used for both plates and bolts. Yu also performed the tests on two-bolt connections at 400°C, 500°C and 700°C which can be used to verify fracture parameters derived from Hu's tests.

Fig. 8 shows the comparison of the specimens after testing and the corresponding simulation results at 600°C. The block shear fracture failures predicted by simulations are quite close to those observed in the tests. Overall, the simulations predicted the peak load capacity and the deformation capacities measured in the tests reasonably well.

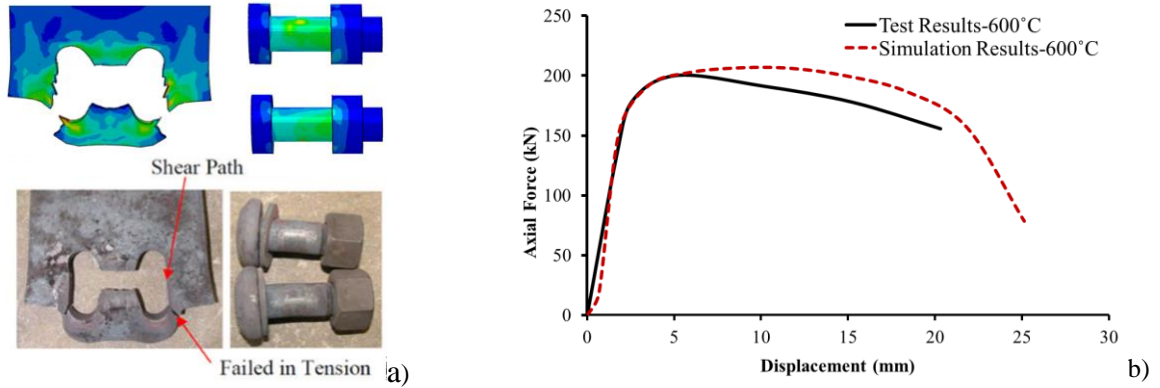


Fig. 8. a) Comparison of results of failure mode from Yu's test and simulation at 600°C; b) Comparison of results of load versus displacement from Yu's test and simulation at 600°C

The derived shear fracture model parameters from tests reported by Hu [3] and by Yu [4] are summarized in *Table 1*. It is shown that the parameters can be divided into three groups. The first group is for ambient temperatures close to 20°C, for which the derived parameters are 0.4 and 9 for ϵ_s^+ and ϵ_s^- respectively. The second group is for the cases at 300°C and 400°C, for which the derived parameters are 0.2 and 4 for ϵ_s^+ and ϵ_s^- respectively. The third group consists of temperature cases at 500°C, 600°C and 700°C and the derived parameters of shear fracture model are 1 and 9 for ϵ_s^+ and ϵ_s^- respectively. It is also important to note that the same parameters are used for different grades of steel and for high strength bolts represented in the tests used for calibration. Based on these limited studies, the shear fracture model parameters worked well over this wide range of steel types and strengths.

Table 1. Derived shear fracture model at ambient and elevated temperature

Shear Fracture Parameters	Temperature					
	20°C	300°C	400°C	500°C	600°C	700°C
ϵ_s^+	0.4	0.2	0.2	1	1	1
ϵ_s^-	9	4	4	9	9	9

5 CONCLUSIONS AND FUTURE RESEARCH NEEDS

Results of this research showed that the calibrated shear fracture model can predict the observed fracture behaviour of a range of bolted connection tests with reasonable accuracy. Interestingly, at any given temperature, the same model parameters were able to reasonably predict the fracture of a variety of steel grades as well as high strength bolts. This suggests that the fracture model parameters may not be highly sensitive to changes in steel strength. The numerous comparisons between simulations and experiments provided in this study offer the hope that fracture behaviour of steel connections and members at elevated temperatures can ultimately be simulated with confidence.

The attempts at fracture simulations in this study are based on limited experimental data and should be considered preliminary in nature. Far more work is needed to further develop these capabilities. All the tests used to calibrate fracture models in this study were conducted at a constant temperature. In actual fires, both the temperature and load change with time. Thus, work is needed to study predicting fracture of connections under conditions of simultaneously changing temperature and load levels. In addition, work is needed to understand and quantify the influence of time dependent behaviour on fracture at elevated temperature. Advancing capabilities in fracture

prediction at elevated temperatures can ultimately lead to powerful new tools for designers and researchers in the field of structural-fire engineering.

REFERENCES

1. Hooputra, H., Gese, H., Dell, H. and Werner, G. (2004). *A comprehensive failure model for crashworthiness simulation of aluminum extrusions*. International Journal of Crashworthiness, 9:5, 449-464, DOI: 10.1533/ijcr.2004.0289.
2. Kanvinde A. M. (2004). *Micromechanical simulation of earthquake-induced fracture in steel structures*. Stanford University, 65-04,272(2004).
3. Hu, G. (2011). *Behavior of Beam Shear Connections in Steel Buildings Subject to Fire*. Ph.D. dissertation. The University of Texas at Austin.
4. Yu, L. (2006). *Behavior of Bolted Connections During and After a Fire*. Ph.D. Dissertation, Department of Civil, Architectural and Environmental Engineering, University of Texas at Austin.
5. Cai, W., Morovat, M. A., & Engelhardt, M. D. (2017). *True stress-strain curves for ASTM A992 steel for fracture simulation at elevated temperatures*. Journal of Constructional Steel Research, 139, 272-279.
6. Kodur, V., Kand, S., and Khaliq, W. (2012). *Effect of Temperature on Thermal and Mechanical Properties of Steel Bolts*. J. Mater. Civ. Eng., 24(6), 765–774.
7. Harmathy, T. Z., Stanzak, W. W. (1970). *Elevated-Temperature Tensile and Creep Properties of Some Structural and Prestressing Steels*. Fire Test Performance, ASTM STP 464, American Society for Testing and Materials, pp 186-208.

NUMERICAL MODELING OF THERMAL BEHAVIOUR OF CFRP REINFORCED CONCRETE STRUCTURE EXPOSED TO ELEVATED TEMPERATURE

Phi Long NGUYEN¹, Xuan Hong VU², Emmanuel FERRIER³

ABSTRACT

In recent decades, Carbon Fiber Reinforced Polymer (CFRP) has been commonly used in civil engineering to reinforce concrete structure such as beams, columns and slabs for its good points in properties as well as simply installation process. There are two basic methods to apply the CFRP to concrete structure: externally bonding reinforcement method (EBR) and near surface mounted method (NSM). When a CFRP reinforced concrete structure is subjected to fire, all elements including substrate, CFRP, adhesive are simultaneously affected by elevated temperature and mechanical load. Recent numerical investigations indicated that the NSM seemed to be better than EBR for delaying the debonding at elevated temperature and thus allowing CFRP to be exploited more efficient regarding to severe thermal effects. This paper presents numerical investigations on thermal behaviour of concrete structure strengthened with pultruded CFRP using NSM and using high temperature adhesive. In this research, a double shear CFRP NSM reinforced concrete specimen has been prepared and tested with thermo-mechanical testing condition. A 3D finite element model has been then developed using ANSYS MECHANICAL APDL software to analyze the heat transfer solution to compare with the experimental results. The numerical results, which show good response in comparison with the obtained experiment, are then developed to apply for predicting the thermo-mechanical performance of CFRP reinforced concrete specimen under elevated temperature and fire-temperature with reliability.

Keywords: Polymer Reinforced by Carbon Fibres (CFRP); CFRP reinforced concrete structure; Near Surface Mounted reinforcement (NSM); Externally Bonding Reinforcement (EBR); adhesive; elevated temperature; numerical modelling.

1 INTRODUCTION

Among the Fiber Reinforced Polymer (FRP) reinforcement solutions, CFRP reinforcement is still a good and traditional option for concrete structures such as beams, slabs, columns...It is because of its advantages for instance: high strength/weight ratio, good properties in corrosion resistance, high fatigue durability as well as rapid installation procedure. To apply the CFRP on to concrete structure, the CFRP can be directly bonded to concrete surface (Externally Bonding Reinforcement method - EBR) or via dipping CFRP in to trenches on concrete surface with epoxy adhesive (Near Surface Mounted reinforcement - NSM). The selection of method depends on the structure type and particular condition. Since its initial applications, fire performance of CFRP reinforced structure is always a significant concern for involving both the temperature and mechanical loadings. Up to now, the issues seem to be an inadequately answered question. According to a literature review by Firmo et al. [1], there are several experimental studies focusing on the performance of concrete, steel, FRP, epoxy at elevated temperature and fire conditions. In Eurocode, the properties of steel

¹ PhD Candidate, Université de LYON, Université Claude Bernard LYON 1; Laboratoire des Matériaux Composites pour la Construction LMC2; e-mail: phi-long.nguyen@etu.univ-lyon1.fr; Lecturer, Ho Chi Minh City University of Transport, Faculty of Construction Engineering, Campus 1: Number 2, D3 Street, Ward 25, Binh Thanh District, Ho Chi Minh City, Vietnam. e-mail: long.nguyen@ut.edu.vn

² Associated Professor, Université de LYON, Université Claude Bernard LYON 1; Laboratoire des Matériaux Composites pour la Construction LMC2, France. e-mail: xuan-hong.vu@univ-lyon1.fr

³ Professor and Director, Université de LYON, Université Claude Bernard LYON 1; Laboratoire des Matériaux Composites pour la Construction LMC2, France. e-mail: emmanuel.ferrier@univ-lyon1.fr

and concrete are described to be reduced as temperature increases [2]. Since then, several studies have been conducted on material and structural scales. According to these results, CFRP properties including Young's modulus and ultimate strength were reported to be reduced as the rise of temperature with the reduction rate that is depended on particular elevated temperature condition. Nguyen et al. studied two CFRPs: pultruded CFRP and manually fabricated CFRP at various thermal and mechanical combined conditions including two thermo-mechanical conditions and also residual condition [3,4]. In structure scale, regarding fire concerns, several observations have been conducted to identify the performance of CFRP reinforced concrete structure with two common reinforcement methods: EBR and NSM. With EBR method, Bisby et al. investigated the residual performance of CFRP EBR reinforced concrete beams and columns subjected to fire [5]. Firmo et al. experimentally studied the thermo-mechanical bond performance of the EBR reinforced concrete structures between 20°C and 120°C [6]. There is also the investigation regarding the fire performance of EBR CFRP reinforced concrete beams under various load levels [7]. For NSM method, Al-Abdwais et al. observed the NSM CFRP reinforced concrete structures using cement-based adhesive at elevated temperature condition [8]. Jadooe et al. investigated the performance of NSM CFRP repaired heated-and-cooled-concrete via single lap test using cement-based and epoxy adhesives (concrete prisms were preheated for 2 hour at temperatures of 200°C, 400°C and 600°C) [9]. Firmo et al. [10] compared two reinforcement methods at room temperature and then used these results with numerical models to explain the fire performance of CFRP reinforced concrete structure. These authors concluded that at the room temperature, the NSM reinforced beam has 21%-35% better performance in comparison with EBR reinforced one depending on the bond configuration [10]. With experiment on the performance of CFRP reinforced concrete structure using NSM and EBR methods at room temperature condition, Kotynia et al. indicated that NSM method allowed concrete beam higher failure strain, compare to EBR method [11]. There are also other available studies for shear strengthening, compression strengthening of concrete structures or even CFRP pretensioned slabs at various temperature-mechanic testing conditions. Tan et al. investigated the residual performance of shear strengthening of glass FRP wrapped beams after exposing to temperature-time history [12]. Kim et al. studied the residual shear performance of CFRP strengthened short beams after exposing to temperature up to 200°C [13]. Considering temperature-mechanical loadings, Cree et al. observed the shear performance of hand laid lap-splice test in two cases of loads with elevated temperature up to 200 °C [14]. Regarding fire-concerned issues, few numerical simulations were conducted: on bond performance of NSM CFRP repaired concrete prism [9], or insulated EBR CFRP strengthened T-beam subjected to mechanical loading [15]. For that reason, this research aims to study the thermo-mechanical performance of CFRP reinforced concrete structure using both experimental and numerical approaches. The numerical solution is then expected to be applied in estimating the fire performance of CFRP reinforced concrete structures which are under service load.

2 EXPERIMENTAL APPROACH

In this study, the thermo-mechanical system was used to experimentally study the performance of CFRP reinforced concrete specimen at different temperature-mechanical conditions [4]. The details of the specimen and testing procedure are presented in the following subsections.

2.1 Materials and specimens

This section presents specimen design and materials used for this study.

1. Specimen design

This study aims to investigate the bonding behaviour between the CFRP-concrete interface at thermo-mechanical condition. Several methods can be found in the literature to determine shear capacity of the joint such as single lap, double lap [16,17] or even beam test [18]. In this study, an improvement from standard double shear method [19] has been used to conduct the experiment. The double lap testing specimen includes two concrete blocks connected by two laminate CFRP

strips using near surface mounted reinforcement method (NSM) (Fig. 1). The sample dimensions have been reduced to meet the limit heating space of the furnace. A steel system in the middle was designed to connect the specimen with two loading heads and also to reduce tensile effects on concrete and to better exploit compressive strength of concrete. The CFRP-concrete bonded areas were designed to be equal on both sides (10mm x 70mm and 10mm x 90mm on two parts) and were totally 2800 mm² for both strips.

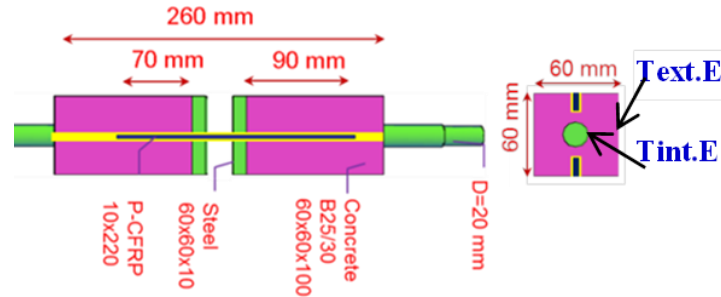


Fig. 1. Design of the experimental sample; Text.E and Tint.E: positions of the thermocouples measuring the exterior temperature (Text.E) and the interior one (Tint.E).

2. Materials

The gravels have been sieved and their maximum dimensions are 6mm. This choice of gravels met requirement for the maximum size of the CFRP/concrete specimen tested in the furnace. The concrete was designed to obtain the resistance class C25/30 after 28 days with the mixing ratio as described in Table 1. The used CFRP is uni-directional prefabricated laminate with produced cross-section 1.2mm x 50mm. According to supplier's datasheet, this CFRP contains 68% fibers in volume and its Young modulus is 165 GPa and its ultimate strength is 2800 MPa. To bond this CFRP to concrete block, a two-component high-temperature-performance adhesive, filled with Al₂O₃ + metal, has been used. As material specifications, its tensile strength at 20°C is about 81.4 MPa with the performance is up to 350°C for short term and 320°C for long term application.

Table 1: Concrete mixing ratio (for 1m³ of concrete)

Cement, 32.5 (kg)	Water (kg)	Gravel (grain size d≤6mm) (kg)	Sand (grain size d≤2mm) (kg)
336	180	1262	622

2.2 Test procedures

In this experiment, the specimen was tested following a thermo-mechanical regime with constant load condition [3]. Firstly, the specimen was imposed with a load called applied force (F_w). Afterwards, the temperature surrounding sample increases with the ramp rate of 30°C/min from ambient temperature until its rupture temperature (maximum 1100°C for safety reason of the furnace). The temperature, at which the specimen collapses, is identified as the failure temperature (T_r) under the load level F_w . The duration, from when temperature starts increasing until when specimen collapses, is identified as the exposure duration under applied load level F_w . During the heating stage, the inside and outside temperatures of the tested concrete block (Text.E and Tint.E, Fig. 1) were measured via four thermocouples: one at the concrete-steel interface and three along the sides of specimen. These results were then used to calibrate the heat-transfer finite element (FE) model. In this study, three tests have been conducted at $F_w = 840$ N. Its results are presented and discussed in the following sections.

3 NUMERICAL INVESTIGATION

The finite element model has been generated to study the heat transfer problem within the CFRP reinforced concrete specimen that was presented in the experiment at different temperature conditions. The developed heat transfer model, which is able to predict temperature evolution in the 3D specimen, is based on the partial differential equation of heat:

$$\rho c \frac{\partial T}{\partial t} = \nabla \cdot (k \nabla T) = \frac{\partial}{\partial x} \left(k_x \frac{\partial T}{\partial x} \right) + \frac{\partial}{\partial y} \left(k_y \frac{\partial T}{\partial y} \right) + \frac{\partial}{\partial z} \left(k_z \frac{\partial T}{\partial z} \right)$$

In which: T is temperature, t is time, k is thermal conductivity, ρ is density and c is heat capacity

In this study, the numerical model focuses on the thermal effects on the tested specimens and expects that this can contribute an answer to the elevated-temperature performance of CFRP reinforced concrete structure.

3.1 Numerical model

Due to the symmetry of loading, boundary condition, material and temperature loading, a fourth model was generated and analyzed using ANSYS APDL (Fig. 2a). The simplified model can accelerate the computation by reducing elements while maintain its reliability. The element type for the heat transfer analysis is SOLID70 (3D 8-nodes thermal solid). It is because the failure mode of three experiments shows that CFRP, concrete and steel are little affected in comparison with the used adhesive. With small adhesive thickness, thus has small influence to the thermal result, the direct CFRP-concrete bond is assumed in FE model. The meshed is finer at the contacts between CFRP and concrete, steel and concrete and coarser in concrete material (Fig. 2b).

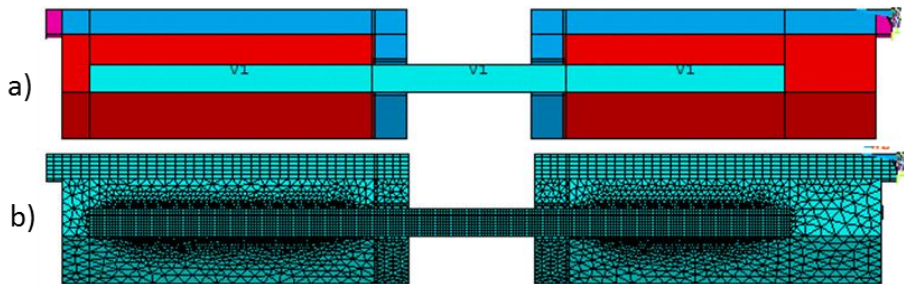


Fig. 2. FE model for heat transfer and result of temperature distribution in sample; a) 3D model; b) Meshed elements;

3.2 Material properties

In the literature as well as design standards, there is available data for thermal properties of concrete, steel and laminate CFRP. The material properties at ambient and elevated temperatures in this FE model are adopted from Eurocode and Hawileh et al. [15] (Table 2 and Fig. 3). The thermal boundary condition of FE model is based on the exterior temperature evolution followed by three thermocouples along the side of specimens during the experiment.

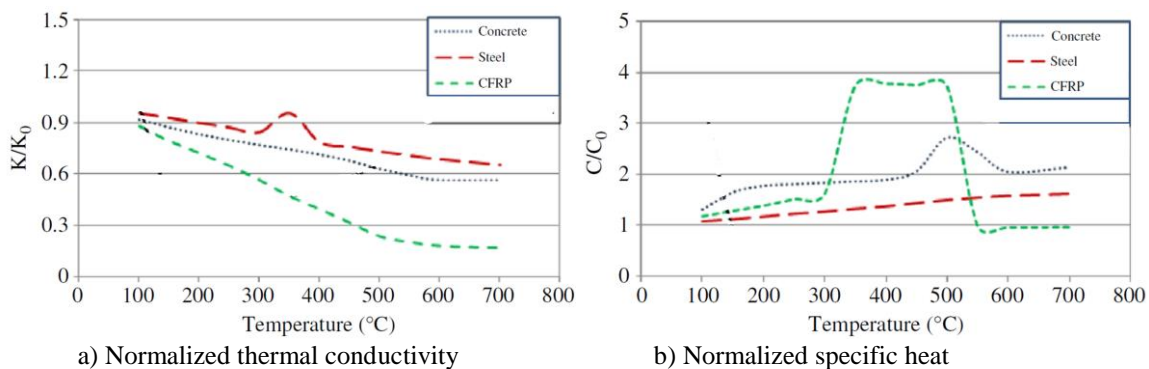


Fig. 3. Normalized thermal properties with temperature [15].

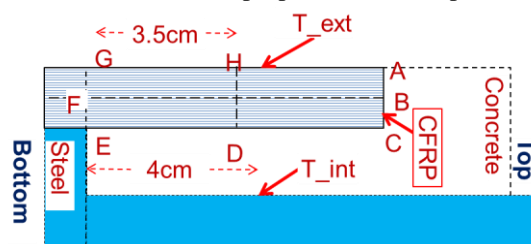


Fig. 4. Bonded region between concrete and CFRP

Table 2: Thermal properties of material at room temperature [15]

Material	K_{20} , W/mm.K	C_{20} , J/kg.K	ρ_{20} , kg/mm ³
Concrete	2.70E-03	722.8	2.40E-06
Steel	5.20E-03	452.2	7.86E-06
CFRP	1.30E-03	1210	1.60E-06

[K_{20} : thermal conductivity (W/mm.K); C_{20} : specific heat(J/kg.K); ρ_{20} : density(kg/mm³) at ambient temperature]

4 RESULTS AND DISCUSSION

This section presents experimental and numerical results and then the discussion. The numerical model was then developed to estimate the performance of specimens in fire-temperature condition.

4.1 Experimental results

Table 3 summarizes the details of three conducted tests with the exterior and interior temperatures at failure and the actual heating rates during the experiments. According to this table, the actual heating rate of three tests varies between 24.34°C/min to 25.44°C/min (25.02°C/min on average). These results show that the temperature conditions among these tests are similar. As these results, the exterior temperature, at which the specimen collapses, widely varies among 441°C to 655°C (544°C on average). However, the interior temperature at failure of three experiments slightly varies between 236°C to 251°C (243°C on average). This means that the specimen failure concerns the interior temperature status more than its exterior temperature. Fig. 5 displays the failure mode obtained in three tests. It is shown that at the failure, the exterior of CFRP and adhesive are partly influenced by temperature while concrete and steel are little affected. There is a slipping at interface between CFRP and adhesive which results in the specimen collapse.

Table 3: Summary of experimental results

Test No	Mechanical load, N		Temperature at failure, °C		Actual heating rate °C/min
	Programmed	Actual	Exterior, T_ext	Interior, T_int	
1	840	841	655	251	25.27
2	840	847	441	236	25.44
3	840	842	535	243	24.34
Average			544	243	25.02

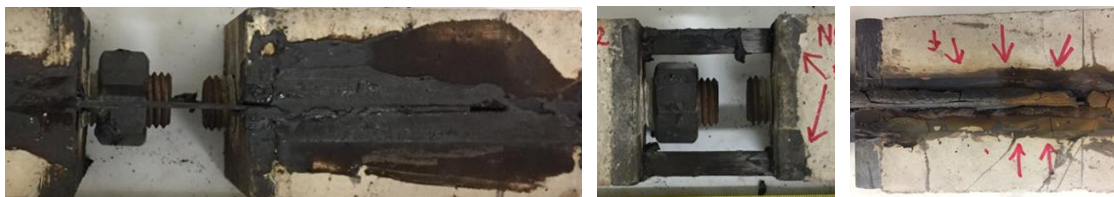


Fig. 5. Failure mode of the tested CFRP-concrete specimen

4.2 Numerical results and discussions

Fig. 6 shows the temperature distribution inside specimen after being applied with the temperature evolution reaching up to 500°C.

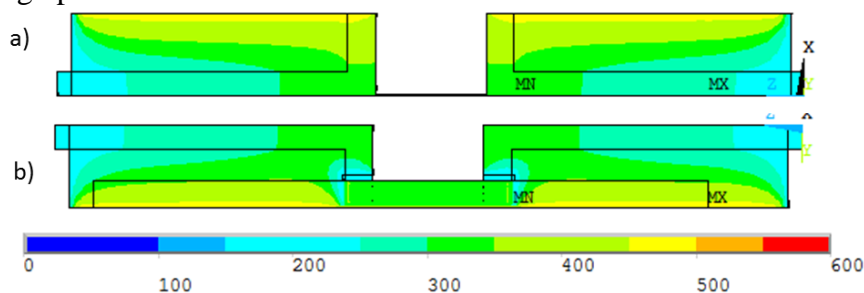


Fig. 6. Numerical result of temperature distribution in sample along two symmetric planes

Fig. 7 displays the temperature evolution at two observed points outside and inside specimen ($T_{ext.*}$ and $T_{int.*}$) obtained in experiments and numerical solutions. The numerical exterior-temperature evolution ($T_{ext.N}$, Fig. 7) confirms that the temperature condition is well applied on FE model. The numerical interior temperature result ($T_{int.N}$, Fig. 8) displays the good response to that obtained from the experimental test 2 and similar trend with those obtained from the test 1 and the test 3.

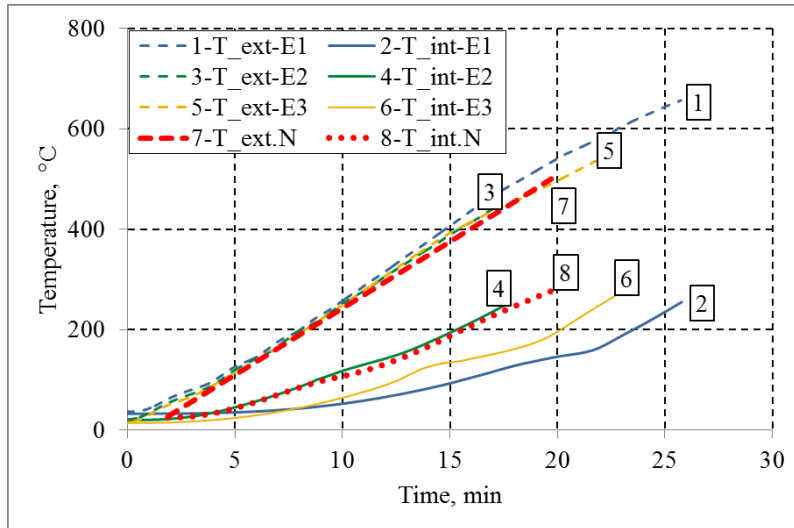


Fig. 7. Evolution of exterior temperature ($T_{ext.N}$ or $T_{ext.Ei}$) and interior temperature ($T_{int.N}$ or $T_{int.Ei}$) in sample obtained by numerical modelling (*.N) and experiment (*.Ei); i: experiment number.

Based on the experimental results, the specimen collapses when the temperature at concrete-steel interface (T_{int} , Table 3) reaches 243°C on average despite of the difference between temperature evolutions (Fig. 7). Figure 8 shows the numerical temperature distribution along four paths on the CFRP-concrete interface at the failure: two along the specimen axis (BF and CE, Fig. 8a) and two across specimen axis (AC and HD, Fig. 8) (see Fig. 4 for the positions of four paths).

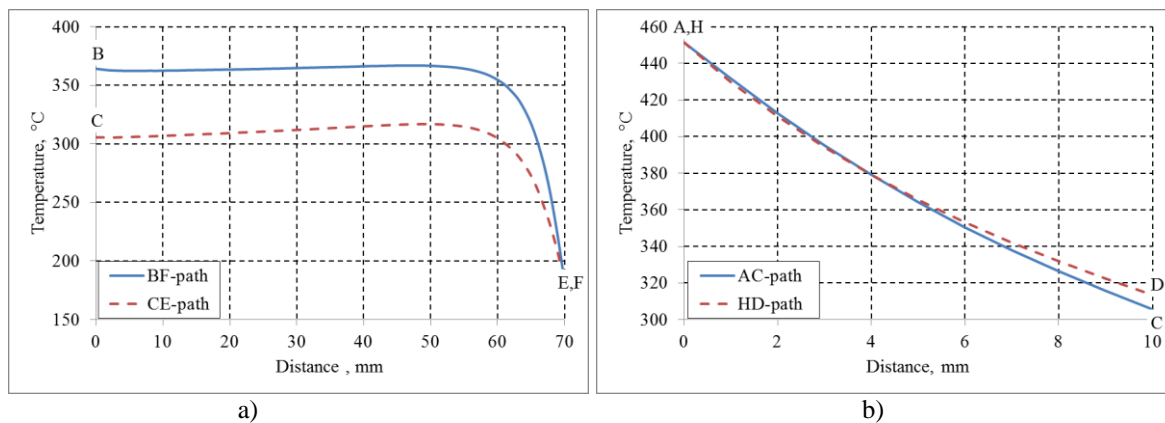


Fig. 8. Temperature distribution along four paths on the CFRP-concrete interface at the moment of specimen failure (see the paths on the CFRP-concrete interface (BF; CE; AC; HD in Figure 4)

The temperature distributions along BF and CE display the small difference between beginning points B and C to distance about 55mm (Fig. 8a). The temperature ranges of two paths are about 363°C and 310°C respectively. At the end of two paths, the temperature turns smaller and is about 200°C at the points F and E. It is because that in the design, it is expected that the CFRP and steel plate are not contacted together so that the CFRP-concrete bond can be thoroughly investigated. However, in the preparation step, it is difficult to maintain the adhesive in the slots according to the design. A small amount of adhesive flows into spaces between CFRP and steel plate and it is

difficult to be quantified. Therefore, this corner is modelled in the numerical solution according to the design, and the temperature in this corner is assumed to be equal to steel plate temperature. The temperature distribution along the paths AC and HD widely vary from 451°C at the exterior (points A and H, Fig. 4) to about 310°C at the interior (points C and D, Fig. 4).

4.3 Thermal response of specimen under standard fire temperature

As far as the author's acknowledgement, the elevated temperature performance of the CFRP reinforced concrete structure mainly depends on CFRP-concrete bond which is significantly influenced by the used adhesive [1]. According to FE result, due to small temperature variation along path CE, the temperature at the middle point D of CE path is proposed as a referenced failure criterion for the specimen under the service load and elevated temperature condition. Therefore, under mechanical load $F_w = 840\text{N}$, the specimen is assumed to fail as the temperature at the point D exceeds 310°C. Fig. 9a presents the temperature evolution at three points obtained from FE model: side of specimen ($T_{\text{ext.N}}$), concrete-steel interface ($T_{\text{int.N}}$) and at CFRP-concrete interface ($T_{\text{point D.N}}$). Based on the proposed failure criteria for the imposed mechanical load ($F_w = 840\text{N}$), the numerical result can estimate the performance of the specimen that can be maintained for the duration up to 16.08 minutes (Fig. 9a). Fig. 9b shows the result of the developed model in which the temperature evolution surrounding the specimen is adopted from standard fire case, ISO-834 curve. The temperature evolutions at the top and the bottom of the specimen are interpolated from the experiments. With the proposed failure criterion (with $F_w = 840\text{N}$), the service duration of the specimen is up to 6.67 minutes under ISO-834 fire-temperature condition.

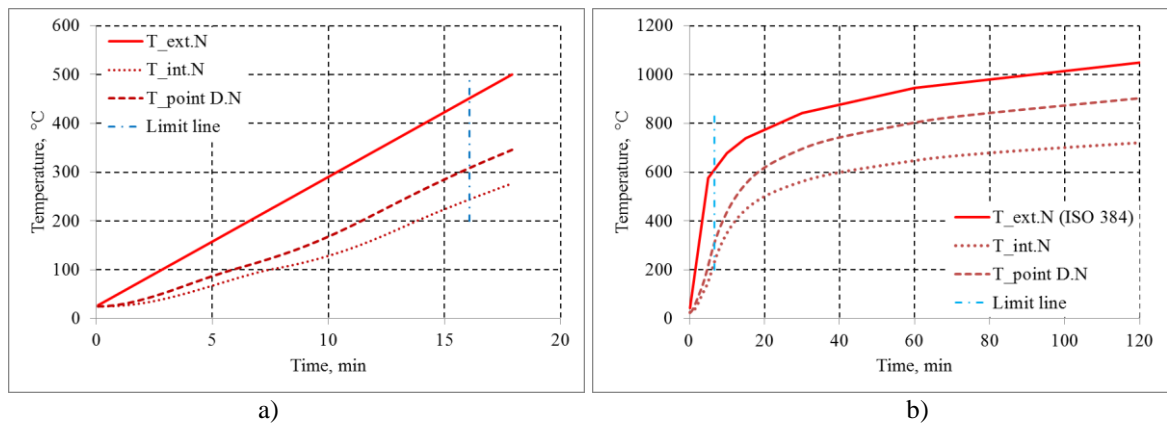


Fig. 9: Numerical temperature evolution of three points obtained: a) based on experiment; b) based on ISO 384 curve

5 CONCLUSION

This study has successfully investigated the performance of CFRP reinforced concrete specimen, which is under service load and elevated temperature condition, with the combined experiment and numerical solutions. The actual temperature evolution on the experiment has been considered and then reproduced in FE models. The appropriateness of simulation to experiment shows that with adopted material data, the FE model is able to estimate the thermal distribution inside the specimen under elevated temperature condition. With NSM reinforcement method, the result shows that the temperature in the adhesive is lower than the temperature surrounding specimen and varies along the bonded interface. Combined with the conclusions in the literature, a thermal-based failure criterion has been proposed to predict the service duration of the mechanically loaded specimen at elevated temperature condition. This FE model can be developed to evaluate the service duration of CFRP reinforced concrete structures under fire-temperature condition regarding heat transfer solution.

ACKNOWLEDGMENT

This research is performed with the financial support of the LMC2 (thanks to industrial projects) and from doctoral scholarship by the Ministry of Education and Training of Vietnam for the first author. We would like to thank the technicians (Mr. E. JANIN and Mr. N. COTTET) from the civil engineering department of the IUT Lyon 1 and the LMC2, University LYON 1 (France) for technical supports.

REFERENCES

1. J.P. Firmo, J.R. Correia, L.A. Bisby. Fire behaviour of FRP-strengthened reinforced concrete structural elements: A state-of-the-art review. *Compos Part B Eng.* 2015 Oct;80:198–216.
2. EN 1992-1-2. EN 1992-1-2: Eurocode 2: Design of concrete structures - Part 1-2: General rules - Structural fire design. CEN;
3. Phi Long NGUYEN, Xuan Hong VU, Emmanuel FERRIER. Experimental study on the thermo-mechanical behavior of Hand-made CFRP simultaneously subjected to elevated temperature and mechanical loading. In: *Proceedings of CIGOS2017*. HCMC, Vietnam: Springer; 2017. p. 484–496.
4. Phi Long NGUYEN, Xuan Hong VU, Emmanuel FERRIER. Characterization of pultruded carbon fibre reinforced polymer (P-CFRP) under two elevated temperature-mechanical load cases: Residual and thermo-mechanical regimes. *Constr Build Mater.* 2018 Mar;165:395–412.
5. L.A. Bisby, M.F. Green, V.K.R Kodur. Response to fire of concrete structures that incorporate FRP. *Prog Struct Eng Mater.* 2005 Jul;7(3):136–49.
6. J.P. Firmo, J.R. Correia, D. Pitta, C. Tiago, M.R.T. Arruda. Experimental characterization of the bond between externally bonded reinforcement (EBR) CFRP strips and concrete at elevated temperatures. *Cem Concr Compos.* 2015 Jul;60:44–54.
7. P. Turkowski, M. Łukomski, P. Sulik, P. Roszkowski. Fire Resistance of CFRP-strengthened Reinforced Concrete Beams under Various Load Levels. *Procedia Eng.* 2017;172:1176–83.
8. A. Al-Abdwais, R. Al-Mahaidi, A. Al-Tamimi. Performance of NSM CFRP strengthened concrete using modified cement-based adhesive at elevated temperature. *Constr Build Mater.* 2017 Feb;132:296–302.
9. A. Jadooe, R. Al-Mahaidi, K. Abdouka. Modelling of NSM CFRP strips embedded in concrete after exposure to elevated temperature using epoxy adhesives. *Constr Build Mater.* 2017 Sep;148:155–66.
10. J.P. Firmo, M.R.T. Arruda, J.R. Correia. Contribution to the understanding of the mechanical behaviour of CFRP-strengthened RC beams subjected to fire: Experimental and numerical assessment. *Compos Part B Eng.* 2014 Nov;66:15–24.
11. R. Kotynia. Bond between FRP and concrete in reinforced concrete beams strengthened with near surface mounted and externally bonded reinforcement. *Constr Build Mater.* 2012 Jul;32:41–54.
12. Kiang Hwee Tan., Yuqian Zhou. Performance of FRP-Strengthened Beams Subjected to Elevated Temperatures. *J Compos Constr.* 2011 Jun 1;15(3):304–11.
13. A.R. Namrou, Y.J. Kim. Residual performance of concrete–adhesive interface at elevated temperatures. *Constr Build Mater.* 2016 Feb;105:113–22.
14. D. Cree, T. Gamanjouk, M.L. Loong, M.F. Green. Tensile and Lap-Splice Shear Strength Properties of CFRP Composites at High Temperatures. *J Compos Constr.* 2015 Apr;19(2):04014043.
15. R.A. Hawileh, M. Naser, W. Zaidan, H.A. Rasheed. Modeling of insulated CFRP-strengthened reinforced concrete T-beam exposed to fire. *Eng Struct.* 2009 Dec;31(12):3072–9.
16. U.S. Camli, B. Binici. Strength of carbon fiber reinforced polymers bonded to concrete and masonry. *Constr Build Mater.* 2007 Jul;21(7):1431–46.
17. C. Mazzotti, M. Savoia, B. Ferracuti. An experimental study on delamination of FRP plates bonded to concrete. *Constr Build Mater.* 2008 Jul;22(7):1409–21.
18. J.F. Chen, J.G. Teng. *Proceedings of International Symposium on Bond Behaviour of FRP in Structures (BBFS 2005)*. International Institute for FRP in Construction; 2005.
19. E. Ferrier, M. Quiertant, K. Benzarti, P. Hamelin. Influence of the properties of EB CFRP on the shear behavior of concrete/composite adhesive joints. *Compos Part B Eng.* 2010 Jul;41(5):354–62.

CONTRIBUTION TO THE NUMERICAL MODELLING OF THE THERMO-MECHANICAL BEHAVIOR OF STRUCTURAL ELEMENTS “BEAM” REINFORCED WITH TRC

Najib DOUK¹, Amir SI LARBI², Xuan Hong VU³, Maxime AUDEBERT⁴

ABSTRACT

This paper deals with the development of a new reinforcement procedure for horizontal structural elements in case of fire. During the last decades, Carbon Fiber Reinforced Polymer (CFRP) has been used to strengthen steel reinforced concrete (RC) structural elements; however, the performance of polymer within CFRP against fire is poor, hence the development of new reinforcement procedures with new recyclable material as textile reinforced concrete (TRC) has an important potentiality in the field of fire safety. The bibliographic review presented herein shows that many authors have worked on the general aspects of TRC in structural uses, but, very few of them worked on the high temperature behavior and the uses of TRC in fire safety. A comparative study between performances of TRC and CFRP has been established. This comparison puts forward their similarities and differences in order to understand more clearly the efficiency of TRC when it is used for the strengthening of structures subjected to fire.

Keywords : Textile reinforced concrete (TRC), Carbon fiber reinforced polymer (CFRP), structures on fire, ISO-834, numerical modelling, concrete structure

1. INTRODUCTION

Authors have started to study concrete on fire since the 70's. After the tragic incidents of the tunnel under the Mont-blanc in 1999 and the Eurotunnel in 1996, more and more authors have gotten interested in concrete on fire. All these studies have been focused on concrete behaviour under fire exposure [1]. When a fire takes place, different aspects of concrete are affected due to physicochemical changes that happen inside the material (deterioration of thermal and mechanical properties). Consequently, structural elements exposed to fire long enough would hardly keep supporting the mechanical loads they were designed for. Among the solutions that have been proposed for mechanical resistance drop of concrete under fire is the reinforcement of structure by Carbon Fiber Reinforced Polymer (CFRP) [2]. CFRP has been used for decades for reinforcement of concrete structures at ambient temperatures. A recent study [2] has shown that the use of CFRP on concrete under fire is efficient at the first minutes of the fire exposure, as long as the temperature remains below 200 °C on the CFRP/concrete interface, which is the critical temperature for the adhesive used to attach the CFRP composite strips. Beyond this critical temperature the reinforced structural element acts like a non-reinforced one since the bond between concrete and CFRP is reduced to zero. In addition to that, CFRP releases toxic fumes when exposed to high temperatures, which makes it hazardous for people living in the fired building [3]. For this purpose, a new method for reinforcing structural elements at high temperature (fire exposure) is developed in this paper. Textile Reinforced Concrete TRC has proved its efficiency on the reinforcement of structures in normal conditions of temperature [3]. And since it is attached to structures with a cementitious

¹ PhD Candidate, University of Lyon, ENISE, LTDS (UMR 5513 CNRS), 58 rue Jean Parot, 42023 Saint-Etienne Cedex 2, France. e-mail: najib.douk@gmail.com

² Professor, University of Lyon, ENISE, LTDS (UMR 5513 CNRS), 58 rue Jean Parot, 42023 Saint-Etienne Cedex 2, France. e-mail: amir.si-larbi@enise.fr

³ Associated Professor, Université de LYON, Université Claude Bernard LYON 1; Laboratoire des Matériaux Composites pour la Construction LMC2, France. e-mail: Xuan-Hong.Vu@univ-lyon1.fr

⁴ Associated Professor, University of Lyon, ENISE, LTDS (UMR 5513 CNRS), 58 rue Jean Parot, 42023 Saint-Etienne Cedex 2, France. e-mail: maxime.audebert@enise.fr

bond, its potential in fire reinforcing is worth exploring. In this paper, a numerico-experimental validation of the standard reinforced concrete beams (reference structure) will be established in order to verify the reliability of the concrete elasto-plastic model. Numerical models of TRC reinforced concrete beams will be then established and comparisons between CFRP and TRC fire-efficiency will be done.

2. NUMERICAL METHODS

In order to get to the objectives drawn in the introduction part, finite element method has been used via the MSC Software MARC Mentat [4].

2.1. Numerical approach

Approaching the thermal aspect of concrete is a complex procedure. A quick state of art review has shown two different approaches. The Thermo-Hydro-Mechanical (THM) approach [5] is the complex one since it considers the concrete as a three phase entity that contains solid concrete, liquid and gas water. But the most used approach for structural elements is the Thermo-Mechanical (TM) approach in which the concrete is considered as a homogenous entity. The mechanical part is influenced by the thermal part by material properties degradation and thermal dilatation. Since we are seeking to explore the TRC reinforced elements behaviour on a structural scale, a THM approach is far refined for this scale; in fact, it would take a tremendous amount of time so we chose the Thermo-Mechanical approach.

The thermal numerical calculation in the TM approach is established by implementing intrinsic thermal properties depending on temperature of the modeled materials. Concrete’s and steel’s thermal characteristics are taken equal to those of the Eurocode 2. The structural specimen modelled is subjected to a thermal flux corresponding to ISO-834. The two classical heat transfer modes are taken into account: convection at the surfaces exposed to the thermal flux and conduction within the materials. Once the thermal calculations are done, a map of the temperature fields of the specimens is extracted from the calculations. This map is implemented later on the mechanical calculations as a thermal boundary condition via thermal dilation (Eurocode 2) and degradation of mechanical properties of the constitutive materials (Eurocode 2) (steel and concrete). It worth noting, that during the thermal calculations, the thermal dilation is not taken into consideration. Steel and concrete are considered as elasto-plastic materials. Steel’s behavior is implemented by a Von-Mises plastic criterion and the hardening law is shown on Figure 1.

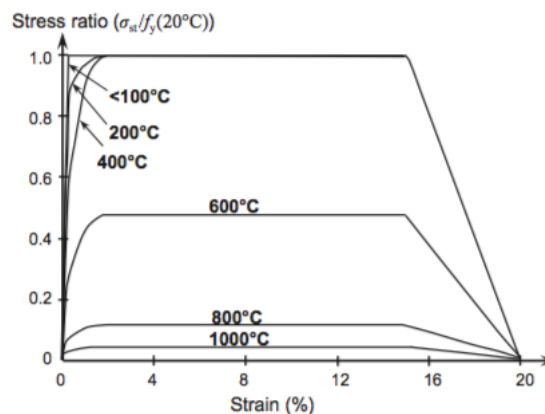


Figure 1: Hardening law of steel for different temperatures [1]

Concrete’s plastic law is implemented using a Buyukozturk criterion [6], it is a criterion with a plasticity surface equal to (1) which is very similar to the often used Drucker-Prager’s criterion in concrete’s calculations. The softening law of concrete is shown in Figure 2.

$$f = \beta \sqrt{3} \bar{\sigma} J_1 + \gamma J_1^2 + 3J_2 - \bar{\sigma}^2 \quad (1)$$

2.2. Test specimens

Two studies of structural elements under fire have been selected [2,7]. On one hand, a numerico-experimental confrontation was done in order to validate the concrete's and steel's thermo-mechanical models; on the other hand and once the latter step was done, numerical models of the specimens were implemented with a TRC composite reinforcement in order to witness the effect of the composite on the overall behaviour of the concrete structural element in case of fire. Table 1, Figures 4 and 5 summarize chosen test specimens. Figure 3 shows the mechanical behaviour of a TRC composite for different temperatures, this curves were obtained by the help of the LMC2 laboratory [8]. Thermal characteristics of TRC are taken equal to those of concrete.

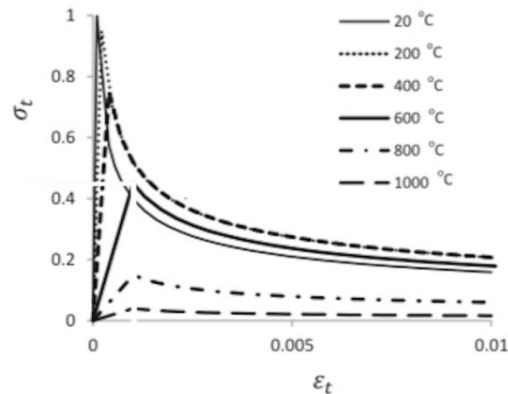


Figure 2: Hardening law of concrete for different temperatures [9]

Table 1: Specific information about test specimens

	Test specimen 1	Test specimen 2
Concrete strength	30,1 MPa	32 MPa
Steel strength	500 MPa	542 MPa
Thermal load	ISO-834 (Lateral and bottom faces)	ISO-834 (Lateral and bottom faces)
Mechanical load	24 KN (4 point bending test)	10,2 KN (4 Point bending test)

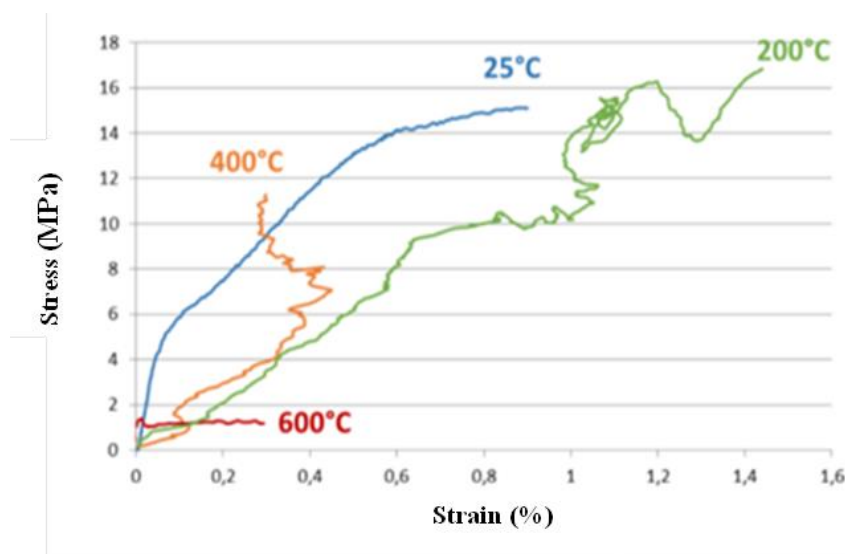


Figure 3: Thermo-mechanical behaviour of TRC for different temperatures [8]

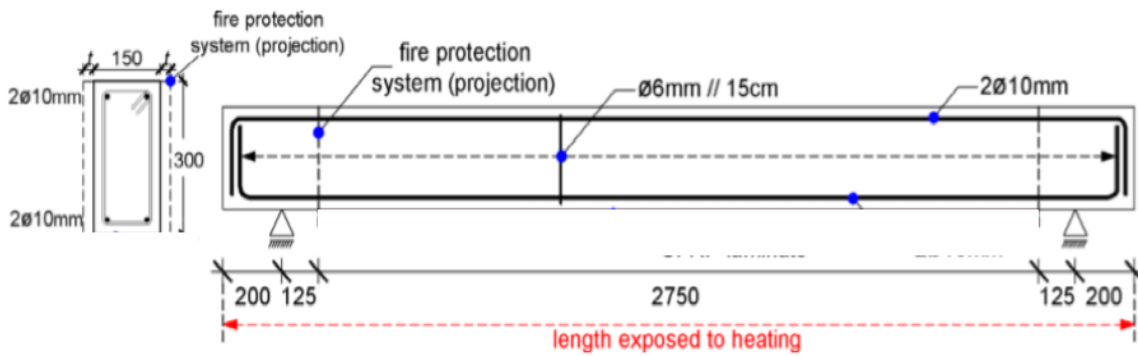


Figure 4: Geometry of the tested beam 1 “test specimen 1” [7]

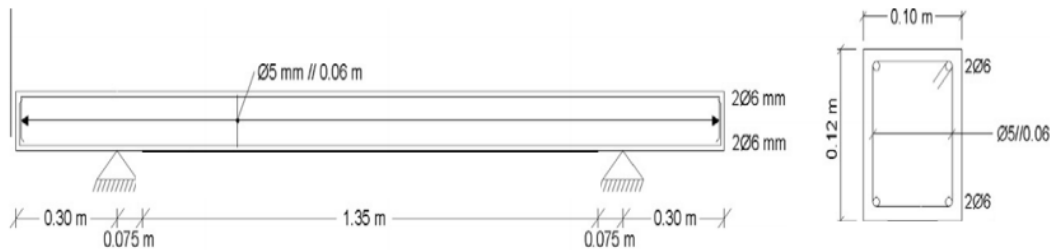


Figure 5: Geometry of the tested beam 2 “test specimen 2” [2]

2.3. Numerical models

As it was explained above, the finite element software MSC Marc Mentat has been used to implement the numerical models (Figures 6 and 7). A cubic mesh is adopted for the models with 4 integration points each, both of the models are loaded mechanically then thermally. The mechanical load consists of a 4 points bending load with a total load of 10.4 KN and 24 KN for specimen 1 and 2 respectively. Once the mechanical loads are applied fully, a thermal flux is applied on the models’ faces as described in Table 1. The thermal flux is applied as an external temperature of the ambient air surrounding the models, this external temperature follows an ISO-834 temperature curve which is conform to the evolution of the air’s temperature in case of fire.

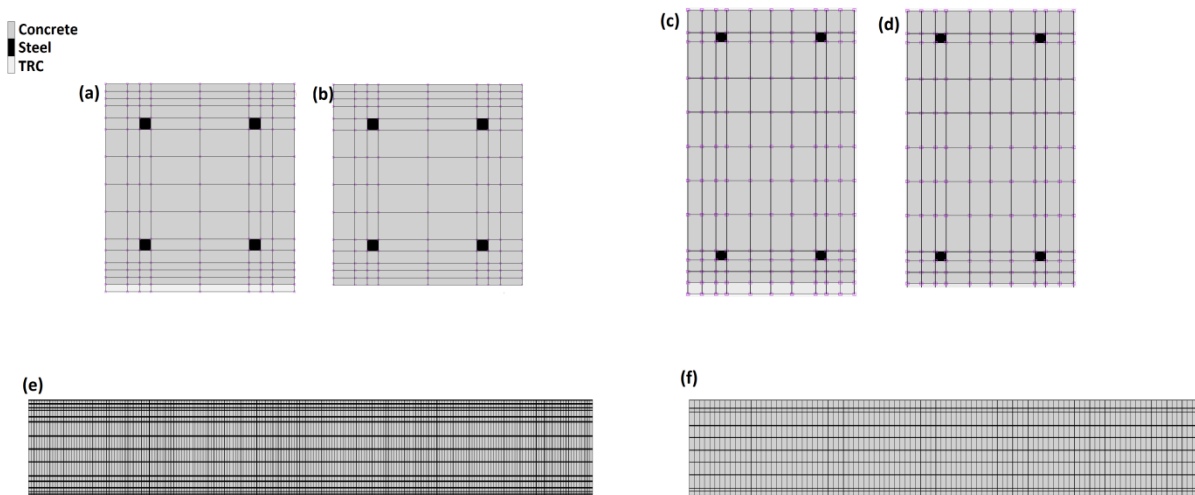


Figure 6: Numerical models of the modeled specimens: (a) specimen 1 with TRC; (b) specimen 1 without TRC; (c) specimen 2 with TRC; (d) specimen 2 without TRC; (e) lateral view of the specimen 1 model; (f) lateral view of the specimen 2 model

3. RESULTS

This section presents thermal results and mechanical results obtained by the element finite modelling shown in previous sections.

3.1. Thermal results

The first step of the thermo-mechanical analysis is the thermal calculation, and since the temperature's evolution is the driving factor of all the thermo-mechanical phenomenon, a verification of the validity of the thermal fields with the experimental results should be done.

Figures 7 and **8** show a confrontation between numerical and experimental temperatures measured at different locations inside the specimens 1 and 2. Numerical thermal results showed a good agreement with the experimental measurements. This proves that using intrinsic thermal characteristics of concrete and steel for a thermal analysis ensures accurate thermal predictions.

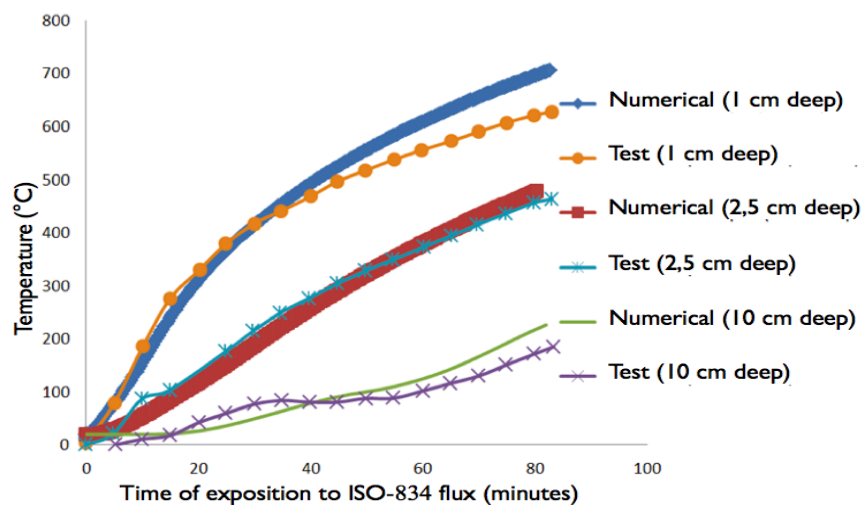


Figure 7: Numerico-experimental confrontation of temperature fields of the specimen 1

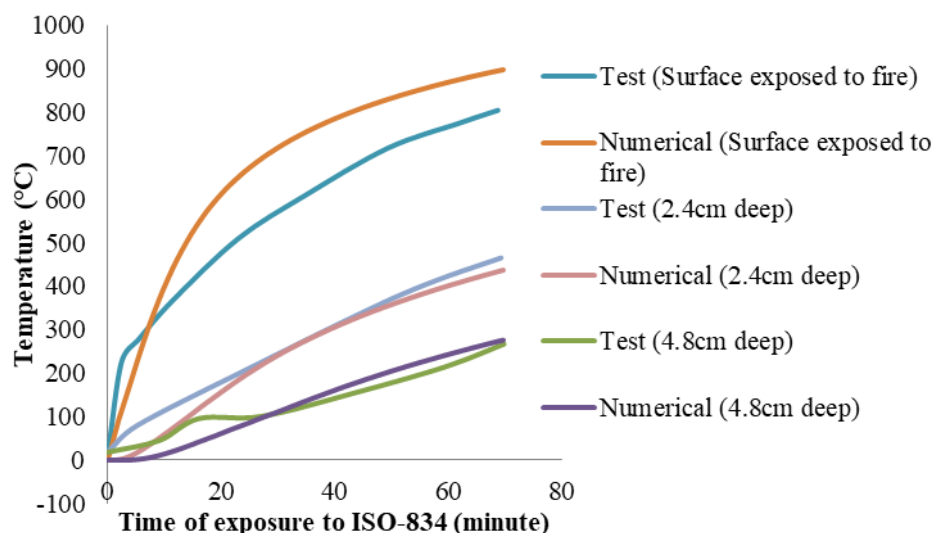


Figure 8: Numerico-experimental confrontation of temperature fields of the specimen 2

3.2. Mechanical results

Now that it is safe to say that the thermal study is validated, a mechanical analysis based on the latter thermal study was established. Mid-span deflections of the two specimens are shown in **Figures 9** and **10** respectively. The numerico-experimental confrontation of mid-span deflection has shown that the predictions of thermo-mechanical models implemented are in good agreement with the experimental tests. Now, it is certain that numerical

model’s prediction of the specimen reinforced with TRC shall be correct. It should be noted that the latter assumption is undoubtedly correct but only under the hypothesis of a perfect contact law between TRC and concrete. In fact, the TRC reinforcement consolidates the stretched lower part of the beam when the concrete starts losing its bearing capacity due to the evolution of temperature.

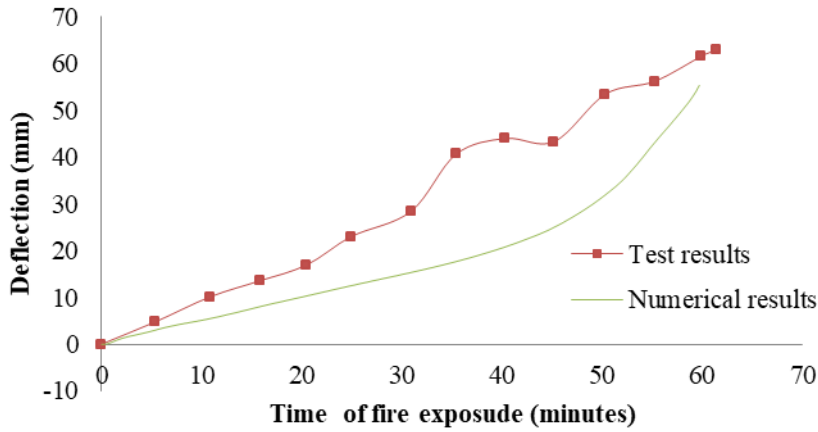


Figure 9: Numerico-experimental confrontation of the mid-span deflection of the specimen 1

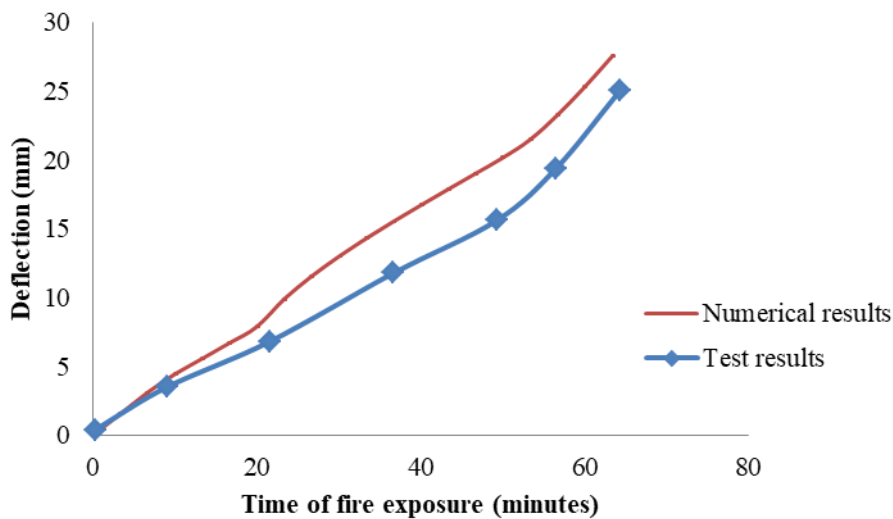


Figure 10: Numerico-experimental confrontation of the deflection of specimen 2

Figure 11 and 12 show a confrontation between numerical results of the deflection versus the time of exposure to fire for the specimens 1 and 2 respectively with and without TRC. One can conclude the effect of the TRC on the overall behavior is absent at first, that is to say, that on the first minutes the behavior of the beams with and without TRC is practically the same but, once the concrete starts damaging, the reinforced and non reinforced specimens start having different overall behaviors.. Even if the behavior of the specimen 2 Figure 12 with and without TRC is practically the same, it is worth saying that the TRC reinforced configurations (specimen 1) show less deflection for the same time of fire exposure, this aspect can't be noticed in specimen 2 probably because the calculations has stopped before concrete's damaging.

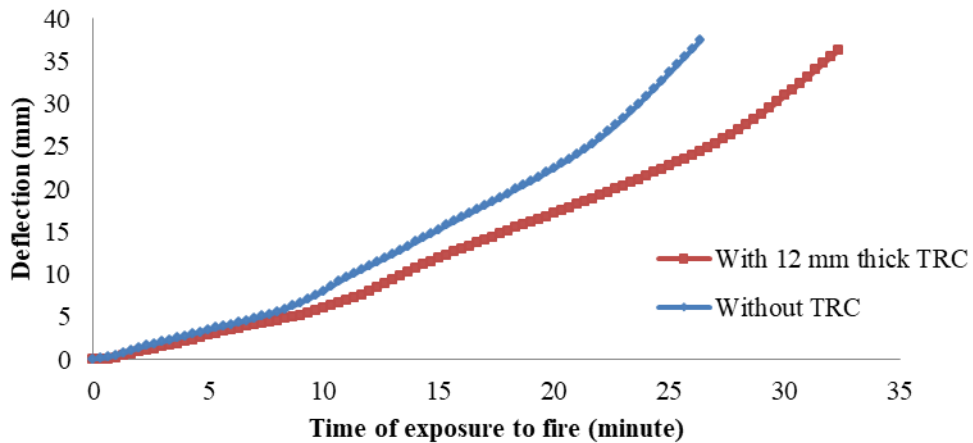


Figure 11: Numerical results of specimen 1 with and without TRC

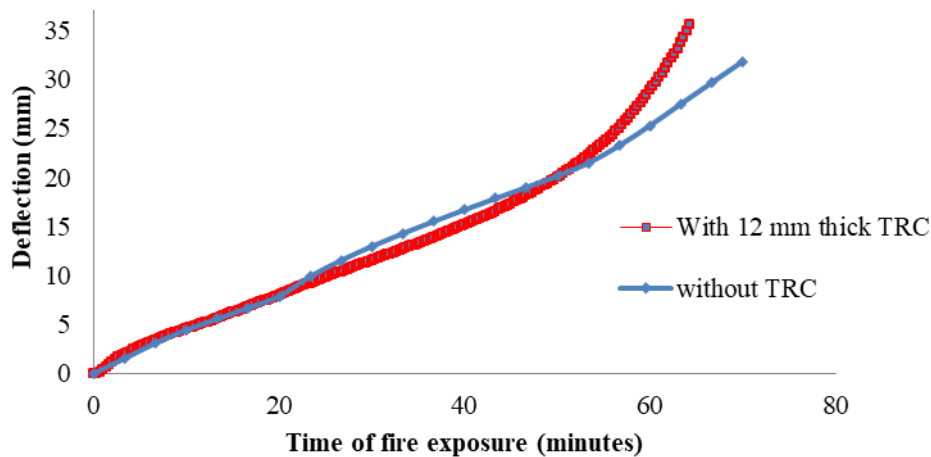


Figure 12: Numerical results of the specimen 2 with and without TRC

4. CONCLUSION

This paper showed the numerical element finite modelling of the thermo-mechanical behavior of structural elements “beam” reinforced with TRC. The findings of this study are shown below:

- The use of the intrinsic thermal characteristics of concrete and steel featured in the Eurocode 2 ensures to obtain properly accurate thermal fields for a reinforced concrete configuration under an ISO-834 curve.
- The strengthening of a reinforced concrete beam with TRC changes its overall behaviour in case of fire.
- The behaviour of a reinforced concrete beam strengthened with TRC is practically the same for the first minutes.
- The change in the behaviour of specimen reinforced with a TRC is seen when the concrete starts damaging.
- The addition of TRC to a reinforced concrete beam increases its life span in a fire case.

Through this study, TRC has proven to be a good reinforcement solution in case of fire. This solution will be further developed to stand well against heat by protecting the

reinforcement with thermal insulation materials and will also be developed to avoid adherence problems by setting up the TRC reinforcement with an anchorage system.

REFERENCES

- [1] *Eurocode 2 – Calcul des structures en béton armé* [in French].
- [2] João P. Firmo, Joao R. Correia, P. França. «*Fire behavior of reinforced concrete beams strengthened with CFRP laminates: Protection systems with insulation of the anchorage zones*» *Composites Part B*: 43 (2012) 1545-1556.
- [3] Raphael Contamine «*Contribution à l'étude du comportement mécanique de composites textile-mortier. Application à la réparation et/ou renforcement de poutres en béton armé vis-à-vis de l'effort tranchant*» PHd thesis, 7 august. [in french]
- [4] MSC Software MARC Mentat Volume A: theory and user information
- [5] Marcus V. G. de Morais, Benoit Bary, Guillaume Ranc, Sabine Durand, Alexis Courtois. «*Simulation of the thermo-hydro-mechanical behavior of an annular reinforced concrete structure heated up to 200 °C*». *Engineering structures* 36 (2012) 302-315.
- [6] MSC Software Marc Mentat Volume C: Program Input
- [7] Thiago B. Carlos, Joao P.C Rodrigues, Rogério C.A de lima, Dhionis Dhima«*Experimental investigation on the flexural behavior of RC beams strengthened with CFRP laminate strips subjected to fire*» IFiress2017-2nd International Fire Safety Symposium 2017.
- [8] Tala TLAIJI, Xuan Hong VU, Emmanuel FERRIER. Lois de comportement du composite RC-M100 en fonction de la température [in French]. Research report number 10 of the UCBL/LMC2 for the project PRORETEX II. April 2017.
- [9] Feiyu Liao, Zhaohui Huang. «*An extended finite element model for modelling localized fracture of reinforced concrete beams in fire*». *Computers and structures* 152 (2015) 11-26.

ACKNOWLEDGMENT

This research was performed with the financial subvention of the public investment bank of France (BPI France) for the lot 6 “Design method & normative aspects” of the PRORETEX II research project. This project is the collaborative research project between four industrial partners (SULITEC - project leader; FOTIA; ER2I; CIMEO) and two academic partners (ENISE/LTDS, UCBL/LMC2).

A NUMERICAL METHODOLOGY TO PREDICT THE GAS/SOLID INTERACTION IN FIRE RESISTANCE TESTS

Rene Prieler¹, Markus Mayrhofer², Markus Eichhorn-Gruber³, Günther Schwabegger⁴, Christoph Hochenauer⁵

ABSTRACT

The present study investigates different simulation approaches to predict the temperature of fire exposed structures and building materials with the main emphasis on fire resistance tests. In many cases (e.g. steel structures) the consideration of the heat transfer between the gas phase combustion (fire) and the solid test specimen in the numerical model is sufficient. However, chemical reactions can occur in the solid test specimen, leading to the release of volatile gaseous components into the gas phase. These components can affect the gas phase and heat transfer in a significant way by increasing (combustibles from wood parts) or decreasing (water vapour from gypsum) the gas temperature. To test the simulation models a fire resistance test of gypsum blocks was used and predicted temperatures were compared to measured data. It was found that the simulation approaches, neglecting the release of water vapour by the gypsum clearly over-predict the gas temperature as well as the temperature of the gypsum. Using the concept of the “Adiabatic Surface Temperature” the temperatures were 167 K (gas) and 19.8 K (gypsum) higher than observed in the experiment. A numerical model was also proposed, which considers the “two-way” coupling (heat transfer and release of water vapour). The prediction of the temperature was significantly improved and showed a deviation of 3.3 K for the gypsum. Thus, the release of volatile components is a crucial part in fire modelling and heat transfer.

Keywords: Combustion modelling, computational fluid dynamics, fire resistance test, gypsum dehydration

1 INTRODUCTION

The response of building materials and constructions on the high temperatures from fire sources has to be tested before they can be used, or classified as fire protective according to a certain standard. Their assessment on fire safety is determined in fire resistance tests, where the test specimen is exposed to the hot flue gases and flames from the burner(s) installed. The fire resistance tests are carried out according to a pre-defined procedure, which is given by the standard EN 1363-1:2012-07 [1]. In order to avoid expensive test runs, computational methods considering furnaces for high

¹ Senior Researcher. Institute of Thermal Engineering, Graz University of Technology, Inffeldgasse 25/B, A-8010 Graz, Austria.
e-mail: rene.prieler@tugraz.at

² Master Student. Institute of Thermal Engineering, Graz University of Technology, Inffeldgasse 25/B, A-8010 Graz, Austria.
e-mail: markus.mayrhofer@gmx.at

³ Head of Test Centre. Institute of Thermal Engineering, Graz University of Technology, Inffeldgasse 25/B, A-8010 Graz, Austria.
e-mail: m.eichhorn-gruber@ibs-austria.at

⁴ Head R&D. Institute of Thermal Engineering, Graz University of Technology, Inffeldgasse 25/B, A-8010 Graz, Austria.
e-mail: g.schwabegger@bvs-ooe.at

⁵ Professor and Head of the Institute of Thermal Engineering, Graz University of Technology, Inffeldgasse 25/B, A-8010 Graz, Austria.
e-mail: christoph.hochenauer@tugraz.at

temperature applications (e.g. the steel industry) are already in use, including the heat transfer to the furnace load (e.g. [2]). However, the accurate prediction of a fire resistance test is still a complicated task due to the close interaction between fluid flow, gas phase combustion, heat transfer and other transport phenomena as well as the deformation of the tested material/construction. Tondini et al. [3] and Welch et al. [4] already examined the interactions between the gas phase combustion in the furnace, the heat conduction in the solid and the deformation of the test specimen, which have to be covered by a numerical approach (see *Fig. 1a*). The consideration of all processes is a demanding task, which was not reported so far in fire research. Nevertheless, the literature research revealed many numerical studies using Computational Fluid Dynamics (CFD), Finite Element Method (FEM), as well as applying both methods in coupled simulations. The present study will focus on the numerical investigation of the gas/solid interaction between the gas phase combustion and the solid test specimen made of gypsum and their effect on the heat transfer. Besides the heat transfer to the test specimen, water vapour is released into the gas phase due to the dehydration of the calcium sulphate di-hydrate ($\text{CaSO}_4 \cdot 2\text{H}_2\text{O}$), when gypsum blocks are used (see *Fig. 1b*).

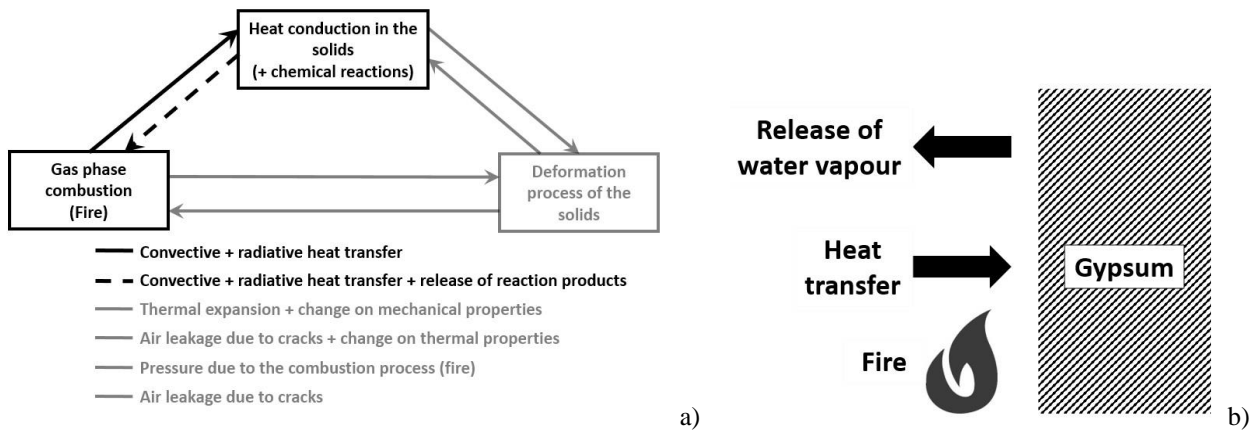


Fig. 1. a) Transport phenomena and their interaction in fire resistance tests; b) Gas/solid interaction in fire resistance tests of gypsum.

1.1 Simulation approaches to predict the thermal heat conduction in the test specimen

As already mentioned, numerical simulations of combustion processes in furnaces are well established and can provide detailed information of the heat transfer. Welch and Rubini [5] carried out a CFD study of a fire resistance test furnace and predicted the heat fluxes to the test specimen. However, the thermal heat conduction in the solid was not reported. To investigate the thermal heat conduction in the solid test specimen several methods were published:

- i. Consideration of the thermal heat conduction in the solid: The pre-defined temperature trend, according to the standard, is used as boundary condition for the thermal analysis (no gas phase combustion). The effect of gaseous components released from the solid and their effect on the temperature is not observed (e.g. steel door frames [6], [7] or gypsum [8]).
- ii. Coupled CFD/FEM simulation – Gas phase combustion and thermal analysis of the solid (without interaction): The gas phase combustion, commonly calculated by CFD (e.g. Fire Dynamic Simulator), and the thermal heat conduction, using FEM (e.g. ANSYS) are solved separately. The resulting heat transfer to the test specimen, which can be calculated for example by the concept of the “Adiabatic Surface Temperature” (AST) [9], is transported from the CFD to the FEM simulation by an interface. Such studies were carried out in [10]–[15], without gas/solid interaction, which can be referred as “one-way” coupling.
- iii. CFD simulation of the gas phase combustion and thermal analysis of the solid (with interaction): One study was found in literature, proposed by Kolaitis and Founti [16], where the dehydration of gypsum and release of water vapour was considered by a solid reaction kinetic model. They investigated gypsum plasterboard assemblies using CFD simulations.

Unfortunately, no temperatures in the gas phase, where the combustion occurs, are reported. The same model was also used by Kolaitis et al. [17] to simulate a residential building.

1.2 Objectives – CFD Simulations

In the following investigation different simulation approaches are used to predict the thermal heat conduction in the solid test specimen, when exposed to the standard fire condition. The results will reveal the effect on the heat transfer with and without gas/solid interaction. For this purpose, a fire resistance test with gypsum blocks was used to generate experimental data making the validation of the simulation methods possible. Several numerical simulations were carried out:

1. CFD simulation of the solid using the standard fire condition (similar to (i)).
2. CFD simulation of the gas phase without the solid to predict the heat fluxes. Using the heat fluxes as boundary condition for the thermal analysis (AST) (similar to (ii)).
3. Simultaneous simulation of the gas phase combustion and the heat transfer in the solid test specimen **without** gas/solid interaction.
4. Simultaneous simulation of the gas phase combustion and the heat transfer in the solid test specimen **with** gas/solid interaction (similar to (iii)).

2 EXPERIMENTAL SETUP

The fire resistance test furnace with the wall made of gypsum blocks is displayed in *Fig. 2a*. The size of the furnace was 9 x 4 x 1.25 m (height, width and depth), which represents the main combustion chamber. It was surrounded by a multi-layer insulation made of bricks and fibre insulation panels with a total thickness of 0.345 (bottom and side walls) and 0.23 m (ceiling). To simplify the CFD model the furnace walls were considered as homogenous instead of the multi-layer construction with the following constant material properties: 450 kg/m³ for density, 733 J/(kg·K) for the specific heat capacity and 0.2 W/(m·K) for the thermal conductivity. The test specimen was a wall made of gypsum blocks with a height of 6 m. It was placed on a wall of bricks. Both were fixed at the front of the fire resistance test furnace. The gypsum blocks have a thickness of 0.1 m.

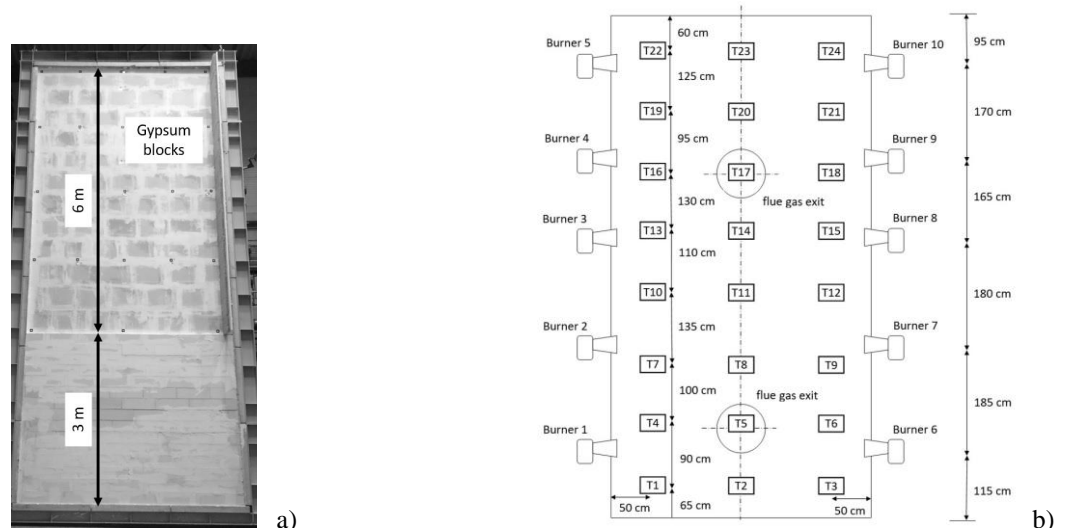


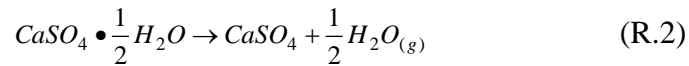
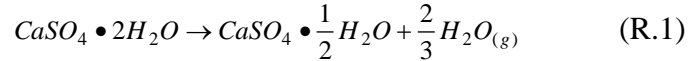
Fig. 2. a) Experimental setup with the wall made of gypsum blocks; b) Position of the thermocouples and burners in the testing furnace.

The temperature in the furnace is observed by 24 plate thermocouples (T1-T24), which are arranged in a distance of 10 cm from the test specimen. The average temperature measured at the thermocouples has to achieve the pre-defined temperature trend according to the standard. At the side walls of the furnace 10 natural gas burners were placed (5 on each side) with a total fuel input of 1.2 MW. The natural gas was equally distributed on the burners, which were operated with an

equivalence ratio to maintain an oxygen concentration in the flue gas of 7% per volume. The position of the thermocouples as well as the burners are displayed in *Fig. 2b*. The duration of the fire resistance test was 120 minutes.

2.1 Gypsum

During the heating process of the gypsum in the fire resistance test furnace chemical reactions occur in the solid material (calcium sulphate di-hydrate). In two steps water is separated from the calcium sulphate according to the reactions *R.1* and *R.2*. Thus, the thermal properties of the gypsum are very sensitive to the temperature. Therefore, the consideration of the temperature-dependent material properties is inevitable for accurate simulations.



In this work the material properties proposed by Kolaitis and Founti [16] for gypsum were integrated in the CFD simulation via user-defined functions. The trend for the specific heat is displayed in *Fig. 3*, which was derived from the “effective” specific heat model from Kontogeorgos et al. [18].

3 NUMERICAL APPROACH

In this study a pressure-based solver was used to predict the fluid flow and heat transfer (fluid and solid) solving the Reynolds-averaged Navier-Stokes equations in conjunction with the energy equation. The flue gas in the furnace was treated as incompressible with an operating pressure of 1013.25 mbar. Density fluctuations due to the temperature gradients in the flue gas were calculated by the ideal gas law. For the spatial discretization the second order upwind scheme was used and the pressure-velocity coupling was considered by the SIMPLE algorithm. The realizable k-epsilon model [19], representing a two-equation turbulence model, was applied.

The combustion process in the furnace was simulated with the steady laminar flamelet approach (SFM). In contrast to species transport models, where a transport equation for each species has to be solved, the SFM assumes that the turbulent flame can be seen as a number of small laminar counter-flow diffusion flamelets [20]. The thermochemical state of the fluid (species concentrations, temperature and density) is completely defined by the mixture fraction in *Eq. (1)*. In this equation Z_i denotes the elemental mass fraction of the element i and the subscripts *fuel* and *ox* stand for the fuel and oxidant. The advantage of this approach is that the integration of the chemistry in the diffusion flamelet can be done before the CFD simulation and the results are stored in look-up tables. In the present study a reaction kinetic involving 17 species and 25 reversible reactions [21] was used to simulate the laminar diffusion flamelet.

$$f = \frac{Z_i - Z_{i,ox}}{Z_{i,fuel} - Z_{i,ox}} \quad (1)$$

The radiative transfer equation (RTE) was solved using the discrete ordinates model (DOM) [22], [23], considering 128 discrete angles for the radiative heat transfer. The radiative properties of the flue gas were calculated by the weighted sum of grey gases model (WSGGM) with coefficients from Smith et al. [24]. Scattering was neglected in this study and the refractive index was 1.

3.1 Numerical grid and boundary conditions

The numerical grid of the entire domain consists of 1,765,919 cells (walls, gas phase and test specimen). To model the gypsum wall 42,640 hexahedron cells were used. For the walls and the gas phase polyhedron cells were applied with a very small cells in the vicinity of the burner, because of the high temperature gradients in this region.

In the following part the boundary conditions for the simulations are explained according to the listing in *section 1*:

1. In this simulation a mixed boundary condition was defined at the fire exposed and unexposed side of the test specimen (see *Table 1*).

Table 1. Boundary conditions at the fire exposed and unexposed side.

	Emissivity	Temperature [K]	Heat transfer coefficient [W/(m ² ·K)]
Fire exposed side	0.7	Pre-defined temperature according to the standard	25
Fire unexposed side	0.5	298.15	10

2. Simulation of the gas phase combustion in the furnace with an adiabatic wall at the test specimen (no solid cells of the gypsum involved). The temperature trend (AST) at this wall was reported. In the following simulation of the gypsum, the heat conduction was calculated with the same boundary conditions as presented in *Table 1*. At the fire exposed side the reported AST was applied.
3. Simultaneous simulation of the gas phase combustion and the heat transfer in the test specimen without gas solid interaction due to the release of water vapour. The boundary condition at the fire unexposed side is given in *Table 1*.
4. The interaction due to the release of water vapour was modelled by an additional source term in the energy equation. This source was only defined in the first cell layer next to the test specimen's wall and was calculated according to *Eq. (2)*. In this equation m_{H_2O} is the mass-flow rate of water vapour into the gas phase, c_p is the specific heat of the water, T_{gas} is the flue gas temperature at the outlet, T_{H_2O} is the temperature of the water vapour and V_{cell} is the volume of the considered cells. The mass-flow-rate was assumed to be constant during the experiment, where 380 kg of water vapour was released in 120 minutes. Furthermore, the temperature of the water vapour was defined with 200°C because the second dehydration step is finished at approximately this temperature level.

$$q = \frac{m_{H_2O} * c_p * (T_{gas} - T_{H_2O})}{V_{cell}} \quad (2)$$

4 RESULTS

4.1 Simulation approaches without gas/solid interaction

In *Fig. 3a* the average gas temperature in the furnace, measured at T1-T24, is displayed for all simulations where no release of water vapour was considered. The simulations are numbered in the legend according to their listing in the *sections 1.2* and *3.1*. A close accordance between the measured and the pre-defined temperature trend (1) was observed, which leads to the conclusion that the experiment was carried out according to the standard. In contrast, the CFD simulation using the AST approach (2) highly over-predicted the gas temperature at the measurement positions during the entire experiment. After 120 minutes the temperature with the AST was 167 K higher than the average measured temperature of 1041°C. A better agreement with the measurement was found when the heat transfer in the solid test specimen was included in the simulation (3). Although the release of water vapour was not taken into account, the predicted gas temperature is significantly lower than in the simulation with the AST approach. The comparison with the measured average temperature showed a deviation of 52 K.

A numerical methodology to predict the gas/solid interaction in fire resistance tests

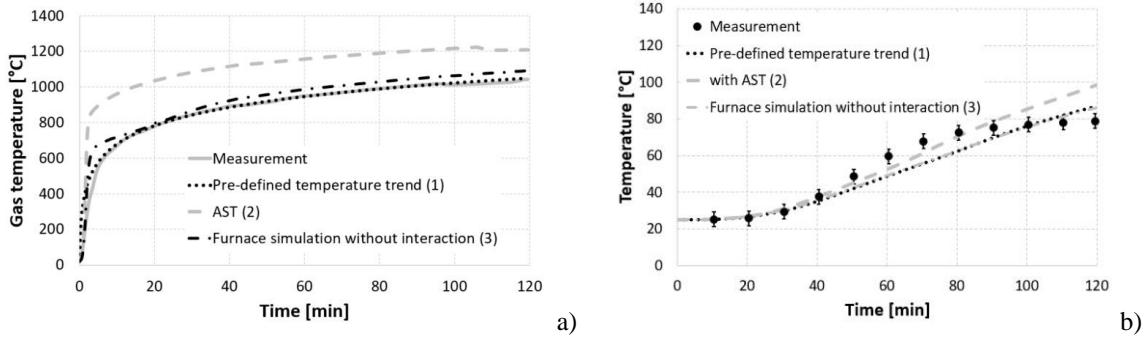


Fig.3. a) Average gas temperature in the furnace measured at T1-T24 and the pre-defined gas temperature trend according to the standard; b) Temperatures at the fire unexposed side of the gypsum wall (position in the middle of the outer surface).

The observed temperatures at the fire unexposed side of the test specimen is presented in Fig. 3b. Since the same material properties for the gypsum were used in all simulations, the calculated data show the same temperature trend at the solid. However, heating rate was higher when the AST (2) was used as boundary condition for the solid test specimen. As a consequence, the predicted surface temperature at the end of the experiment was 98.5°C compared to 78.7°C in the measurement. Furthermore, the simulation without gas/solid interaction (3) and the analysis of the thermal heat conduction using the pre-defined temperature (1) predicted the same temperature at the gypsum surface (89.1 and 89.9°C). Although the gas temperature in (3) was 52 K higher than the measured/pre-defined temperature the temperature at the test specimen’s surface is similar. This can be explained by the fact that the gas temperature in (3) was observed in a distance of 10 cm from the fire exposed surface of the test specimen, whereas the pre-defined temperature is directly related to this surface in simulation (1). Thus, it can be concluded that the temperature difference between the measurement positions and the fire exposed surface is approximately 50 K without consideration of the release of water vapour.

4.2 Simulation approaches with gas/solid interaction

Additionally, a CFD simulation of the gas phase combustion and the thermal heat conduction in the gypsum was carried out, including the release of water vapour. In Fig. 4a the average gas temperature at the end of the experiment is shown for the simulations without interaction (1-3) as well as with interaction between the gas and solid (4). This simulation showed the best agreement with the measured data with a deviation of 21 K for the average temperature, compared to 52 K (3) when no interaction was considered. This means that the heat transfer to the fire exposed side of the gypsum is more realistic than without interaction between the gas phase and solid.

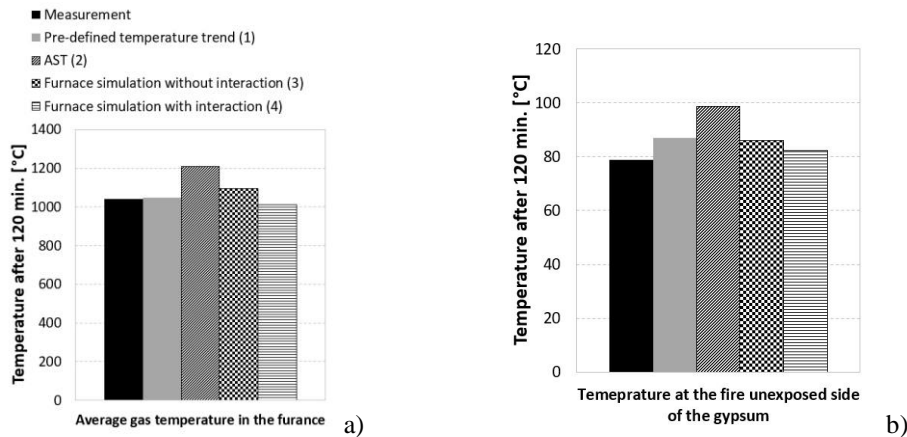


Fig.4. a) Average gas temperatures in the furnace at the end of the experiment; b) Temperature in the middle of the fire unexposed side of the test specimen.

Improving the heat transfer to the test specimen will affect the thermal heat conduction in the solid, which is highlighted in *Fig. 4b*. The figure shows the temperatures in the middle of the fire unexposed surface at the end of the experiment. As already mentioned above the AST approach (2) totally fails to predict the heat transfer in the solid, leading to higher temperature at the surface. The same was found when the pre-defined temperature was used as boundary condition (1) and no release of water vapour was considered (3). In contrast, using a gas/solid interaction model as proposed in this work the predicted surface temperature at the test specimen is more accurate. This is determined by the results of simulation (4), which calculated a temperature of 82°C compared to 78.7°C in the measurement. Although the gas temperature is very similar with and without gas/solid interaction, as presented in *Fig. 4a* for the simulation (1) and (4), the effect on the heat transfer is obvious. The reason is that the pre-defined temperature is fixed on the fire exposed surface, whereas the gas temperature from (4) was determined in a distance of 10 cm from this surface. In this gap between the measurement positions and the surface the water vapour released by the gypsum cools down the gas phase significantly, and, subsequently reduces the heat transfer.

5 CONCLUSION

In the past several attempts to numerically predict fire resistance tests as well as conventional fire cases for a better understanding of the gas phase combustion and/or the thermal heat conduction in the solids. The methods found in scientific literature commonly considers only a one-way coupling between the gas phase combustion and the solid test specimen. Thus, no release of volatile components such as H₂O or combustible gases released from wood parts are considered, which, obviously affect the heat transfer and the temperature in the gas phase. In this study several methods were tested to predict the temperature of gypsum during a fire resistance test with the following remarks:

- The concept of the AST is not suitable for fire cases where volatile components are released in the gas phase. Also an appropriate interface between the gas and solid, which considers this interaction was not found so far in literature. The AST approach over-predicts the temperature of the gas and gypsum of 167 K and 19.8 K, respectively.
- The simulation of the solid gypsum using the pre-defined temperature trend showed better agreement with the measurement due to the more realistic temperature at the fire exposed side. However, the temperature at the gypsum was over-predicted with a value of 10.4 K
- The simultaneous CFD simulation of the gas phase combustion and the heat transfer in the gypsum (without release of water vapour) showed also a higher temperature at the solid of 11.2 K
- The proposed model to consider the release of the water vapour, which was implemented in the CFD simulation, showed an improvement of the heat transfer from the hot flue gases to the gypsum wall. Thus, the predicted gypsum temperature was only 3.3K higher than the measurement.

This study showed that it is inevitable to consider the release of components from the solid test specimen in order to predict the heat transfer in the gas phase and to the walls as well as the temperature with high accuracy.

ACKNOWLEDGMENT

This work was financially supported by the Austrian Research Promotion Agency (FFG), “Virtuelle Bauteilprüfung mittels gekoppelter CFD/FEM-Brandsimulation” (project 857075, eCall 6846234).

REFERENCES

- [1] European Committee for Standardization CEN, *European standard EN 1363-1, Fire resistance test - Part 1: General requirements*. Brussels, Belgium, 2012.
- [2] R. Prieler, B. Mayr, M. Demuth, B. Holleis, and C. Hochenauer, “Prediction of the heating

- characteristic of billets in a walking hearth type reheating furnace using CFD,” *Int. J. Heat Mass Transf.*, vol. 92, 2016.
- [3] N. Tondini, O. Vassart, and J. Franssen, “Development of an Interface Between Cfd and Fe Software,” in *7th International Conference on Structures in Fire*, 2012, no. June, pp. 459–468.
- [4] S. Welch, S. Miles, S. Kumar, T. Lemaire, and A. Chan, “FIRESTRUC - Integrating advanced three-dimensional modelling methodologies for predicting thermo-mechanical behaviour of steel and composite structures subjected to natural fires,” in *Fire Safety Science*, 2008, pp. 1315–1326.
- [5] S. Welch and P. Rubini, “Three-dimensional Simulation of a Fire-Resistance Furnace,” in *Fire Safety Science - Proceedings of the fifth International Symposium*, 1997, pp. 1009–1020.
- [6] E. Hugi, K. Ghazi Wakili, and L. Wullschleger, “Measured and calculated temperature evolution on the room side of a butted steel door frame subjected to the standard fire of ISO 834,” *Fire Saf. J.*, vol. 44, no. 5, pp. 808–812, 2009.
- [7] K. Ghazi Wakili, L. Wullschleger, and E. Hugi, “Thermal behaviour of a steel door frame subjected to the standard fire of ISO 834: Measurements, numerical simulation and parameter study,” *Fire Saf. J.*, vol. 43, no. 5, pp. 325–333, 2008.
- [8] D. Lazaro, E. Puente, M. Lazaro, P. Lazaro, and J. Pena, “Thermal modelling of gypsum plasterboard assemblies exposed to standard fire tests,” *Fire Mater.*, vol. 40, pp. 568–585, 2016.
- [9] U. Wickström, “Methods for Predicting Temperatures in Fire-Exposed Structures,” in *SFPE Handbook of Fire Protection Engineering*, New York, USA: Springer-Verlag, 2016.
- [10] J. Sandström, U. Wickström, and M. Veljkovic, “Adiabatic surface temperature - A sufficient input data for a thermal model,” in *Application of Structural Fire Engineering*, 2009, pp. 1–7.
- [11] K. Cábová, N. Lišková, M. Benýšek, F. Zeman, and F. Wald, “Numerical simulation of fire-resistance test of steel beam,” in *Ce/Papers*, 2017, vol. 1, no. 2–3, pp. 2518–2525.
- [12] U. Wickström, A. Robbins, and G. Baker, “The Use of Adiabatic Surface Temperature to Design Structures For Fire Exposure,” *J. Struct. Fire Eng.*, vol. 2, no. 1, pp. 21–28, 2011.
- [13] U. Wickström, D. Duthinh, and K. McGrattan, “Adiabatic surface temperature for calculating heat transfer to fire exposed structures,” in *Interflam 2007 11th International Interflam Conference*, 2007, vol. 2.
- [14] K. Prasad and H. R. Baum, “Coupled fire dynamics and thermal response of complex building structures,” *Proc. Combust. Inst.*, vol. 30, no. 2, pp. 2255–2262, 2005.
- [15] X. Yu and A. E. Jeffers, “A comparison of subcycling algorithms for bridging disparities in temporal scale between the fire and solid domains,” *Fire Saf. J.*, vol. 59, pp. 55–61, 2013.
- [16] D. I. Kolaitis and M. A. Founti, “Development of a solid reaction kinetics gypsum dehydration model appropriate for CFD simulation of gypsum plasterboard wall assemblies exposed to fire,” *Fire Saf. J.*, vol. 58, pp. 151–159, 2013.
- [17] D. I. Kolaitis, E. K. Asimakopoulou, and M. A. Founti, “Fire behaviour of gypsum plasterboard wall assemblies: CFD simulation of a full-scale residential building,” *Case Stud. Fire Saf.*, vol. 7, pp. 23–35, 2017.
- [18] D. Kontogeorgos, K. Ghazi Wakili, E. Hugi, and M. Founti, “Heat and moisture transfer through a steel stud gypsum board assembly exposed to fire,” *Constr. Build. Mater.*, vol. 26, no. 1, pp. 746–754, 2012.
- [19] T.-H. Shih, W. W. Liou, A. Shabbir, Z. Yang, and J. Zhu, “A new $k-\epsilon$ eddy viscosity model for high Reynolds number turbulent flows,” *Computers Fluids*, vol. 24, no. 3, pp. 227–238, 1995.
- [20] N. Peters, “Laminar diffusion flamelet models in non-premixed turbulent combustion,” *Prog. Energy Combust. Sci.*, vol. 10, pp. 319–339, 1984.
- [21] T. Peeters, “Numerical modeling of turbulent natural-gas diffusion flames,” Delft Technical University, 1995.
- [22] G. D. Raithby and E. H. Chui, “A Finite-Volume Method for Predicting a Radiant Heat Transfer in Enclosures With Participating Media,” *J. Heat Transfer*, vol. 112, pp. 415–423, 1990.
- [23] E. Chui and G. Raithby, “Computation of radiant heat transfer on a nonorthogonal mesh using the finite-volume method,” *Numer. Heat Transf. Part B Fundam. An Int. Comput. Methodol.*, vol. 23, pp. 269–288, 1993.
- [24] T. F. Smith, Z. F. Shen, and J. N. Friedman, “Evaluation of Coefficients for the Weighted Sum of Gray Gases Model,” *J. Heat Transfer*, vol. 104, no. 4, p. 602, 1982.

VIRTUAL TEST OF FIRE-RESISTANCE OF A TIMBER BEAM

Kamila Cábová¹, Filip Zeman², Lukáš Blesák³, Martin Benýšek⁴, František Wald⁵

ABSTRACT

The paper presents a part of coupled numerical model for prediction the fire resistance of elements in a horizontal furnace. The presented part lies in a virtual furnace which simulates temperature environment around tested elements in the furnace. The virtual furnace takes advantage of great possibilities of computational fluid dynamics code Fire Dynamics Simulator. The model is based on an accurate representation of a real fire furnace of fire laboratory PAVUS a.s. located in the Czech Republic. It includes geometry of the real furnace, material properties of the furnace linings, burners, ventilation conditions and also tested elements – in this case three timber beams. Gas temperature calculated in the virtual furnace is validated to temperatures measured during a fire test. Comparison of results show good agreement in the case when burning of timber is included in the numerical model. A contribution of burning of timber beams to temperature increase inside the furnace is graphically demonstrated. The temperature fields calculated in the virtual furnace are then passed to finite element model created in software Atena Science. In this model heat transfer into the timber beam is solved. Temperatures calculated inside the timber beam are compared to measured values from the fire test.

1 INTRODUCTION

Testing by standard fire test is the common method of obtaining fire-resistance rating of structural elements, see [1]. Despite fire-resistance tests are very common, they can be time consuming. The cost of the test is also very high. Because of these drawbacks a numerical model of a horizontal furnace which can save both time and money, is developed. The model solves a problem including fluid dynamics. Heat transfer into a tested element and mechanical behaviour of the element can be then solved in FE model.

In this paper the temperature of environment in the horizontal furnace which is solved by computational fluid dynamics (CFD) method creates boundary conditions for the thermal model. The fluid dynamics part is solved by Fire Dynamics Simulator (FDS) [2] and the thermal part is computed by software Atena Science [3]. The accuracy of calculated temperature environment in FDS as well as accuracy of calculated temperature inside the timber beam from the FE model is validated to measured values from a fire tests executed in horizontal furnace of fire laboratory PAVUS a.s., Czech Republic.

¹ Assistant Professor. Faculty of Civil Engineering, Czech Technical University in Prague, Prague, CZ.
e-mail: kamila.cabova@fsv.cvut.cz

² Researcher. Faculty of Civil Engineering, Czech Technical University in Prague, Prague, CZ.
e-mail: filip.zeman@fsv.cvut.cz

³ Assistant Professor. Faculty of Civil Engineering, Czech Technical University in Prague, Prague, CZ.
e-mail: lukas.blesak@fsv.cvut.cz

⁴ PhD Candidate. Faculty of Civil Engineering, Czech Technical University in Prague, Prague, CZ.
e-mail: martin.benysek1@fsv.cvut.cz

⁵ Professor. Faculty of Civil Engineering, Czech Technical University in Prague, Prague, CZ.
e-mail: wald@fsv.cvut.cz

2 GAS TEMPERATURE ANALYSIS

2.1 Model of temperature environment in the furnace

Temperature environment inside the furnace is simulated by the aid of the computational fluid dynamics code FDS version 6.4.0. Geometry of the furnace, material properties of furnace linings, burners and ventilation conditions corresponds to the horizontal furnace of fire laboratory PAVUS a.s. Inside the furnace three timber beams of dimensions 100 mm x 250 mm x 3000 mm are located below the ceiling. The location of the beams is shown in *Fig. 1* and *Fig. 2*.

Considering dimensions of the real furnace, time needed for numerical solution and sufficient level of accuracy of results, size of the general mesh of 100 mm x 100 mm x 100 mm is selected. In the region of timber beams the mesh is finer, 50 mm x 50 mm x 50 mm, see *Fig. 2*. Material properties of the furnace linings are taken from data sheets of manufacturers. These include: density, specific heat capacity and thermal conductivity of high alumina bricks, thermally insulating bricks, calcium silicate boards, blocks of refractory ceramic fibers, steel and insulating refractory concrete. Material properties of the tested beams corresponds to GL24h timber.

In the model burners are simulated as eight square surfaces of type VENT of dimension 200 mm x 200 mm, which are located 0.5 m above the floor. In *Fig. 1* and *Fig. 2* the burners are illustrated as red squares. The fuel in the real furnace is composed of the mixture of natural gas and air, just as the case of the virtual furnace with the prescribed reaction of burning of this mixture. Power of the burners in the model is gradually increased in dependence on time according to the power of burners measured during the fire test. In the model it is defined by a ramp function of heat release rate per unit area (HRRPUA).

In the model burning of timber is simulated by specified RAMP_Q function. After reaching the ignition temperature of the timber, the energy from the timber beams is released according to the function of heat release rate per unit area (HRRPUA). Detailed description is presented in [4].

In the bottom part of the model the mesh is enlarged to simulate the conduit of the gas exhaust system. The hole leading into the conduit is protected with welded steel structures. A niche of the door (0.5 m x 1.75 m) and four visors are also simulated.

In the model gas temperature is calculated by device type THERMOCOUPLE. Properties of the device are modified in the model to correspond to properties of coated thermocouple used in the validation fire test. Then, device type ADIABATIC SURFACE TEMPERATURE is used in the model to simulate a weighted average value of the radiation temperature and the gas temperature. The adiabatic surface temperature also allows later calculation of temperature inside the timber beam.

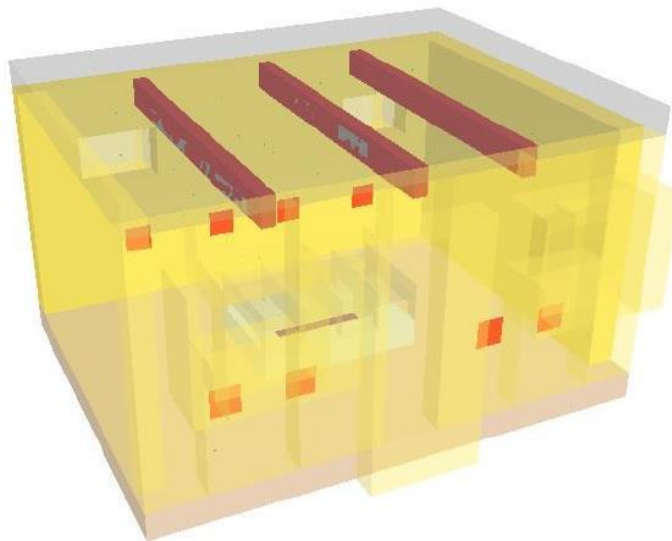


Fig. 1 FDS model of the furnace with timber beams

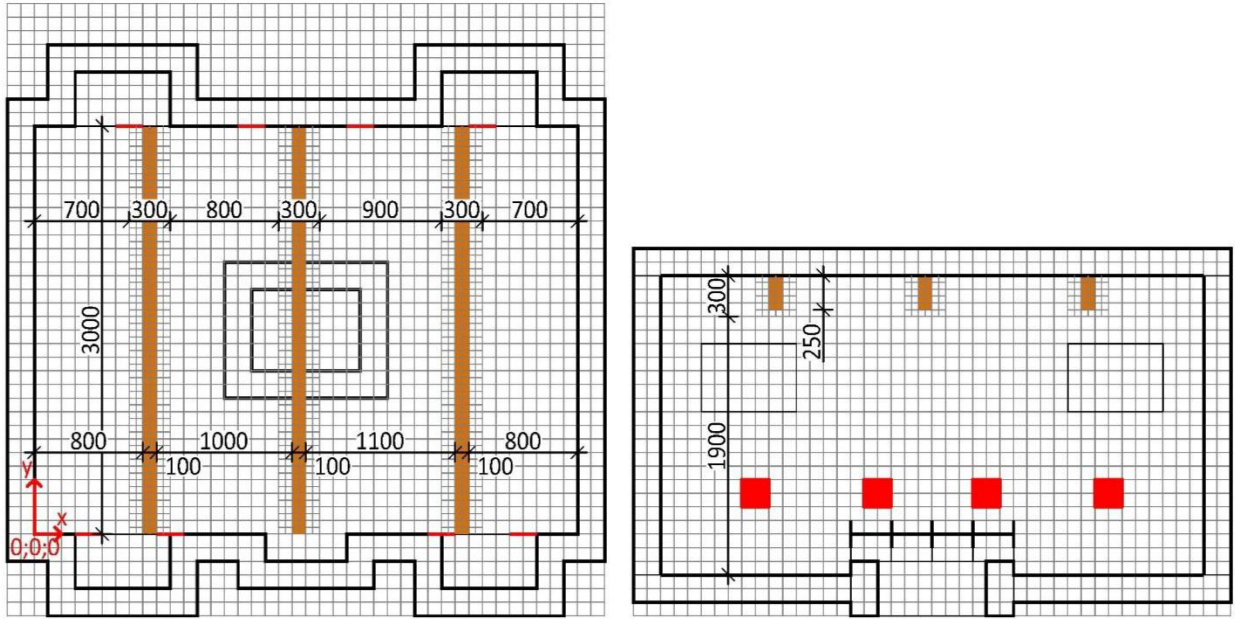


Fig. 2 Location of timber beams and meshing in the FDS model

2.2 Validation of the temperature environment

For standard fire testing it is important to meet requirements of European standard EN 1363-1: 2013, which defines the conditions of fire resistance tests. The average temperature in the furnace is monitored and controlled to follow the standard temperature-time curve. According to EN 1363-1 there are specified tolerances for the temperature distribution in the furnace, where it is allowed to vary by $\pm 100^\circ\text{C}$. Development of the adiabatic surface temperature (AST) below the ceiling of the furnace calculated in FDS model is shown in Fig. 3. The development of gas temperature from the model is compared with the standard temperature-time curve and with the curve measured during the fire test. In the figure there are also two curves showing the upper and the lower tolerance according to EN 1363 – 1. Based on the diagram it may be stated that after 5 min the gas temperature is within the acceptable tolerance given in EN 1363 – 1.

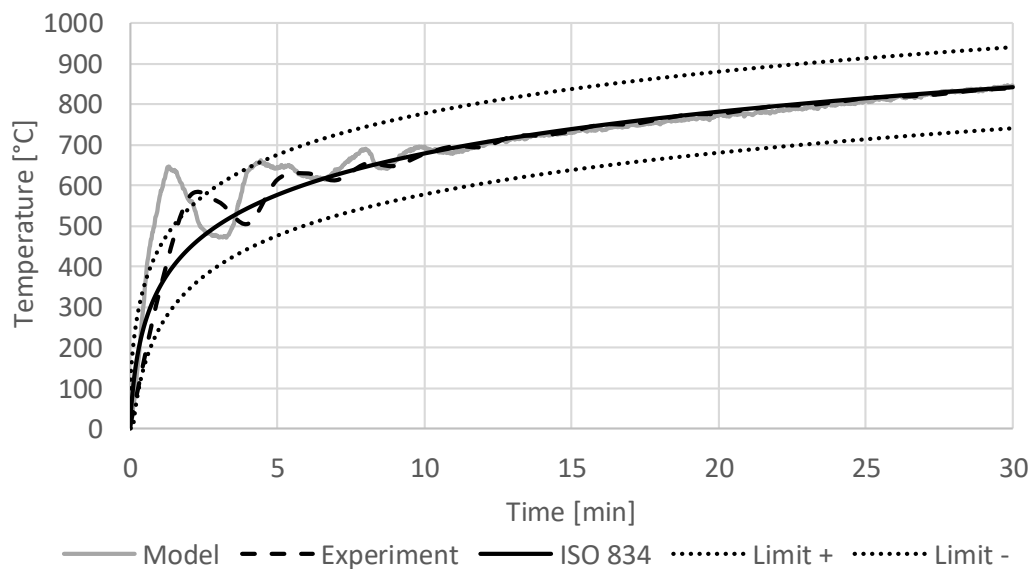


Fig. 3 Comparison of gas temperature

2.3 Contribution of burning of timber beams

During the fire test gas burners in the furnace reduced their function after 5 min and the overall energy inside the furnace was supported by heat which was generated from the burning of timber beams. Burning of the beams during the fire test is shown in *Fig. 4*. The decrease of power of burners measured during the fire test with timber beams is shown in *Fig. 5*. In *Fig. 5* the power of burners from the fire test with timber beams is compared to the power measured during a fire test of empty furnace (no structural element present). The difference of both curves in a later time of the simulation is about 500 kW/m² [5].



Fig. 4 Burning of timber beams during the fire test

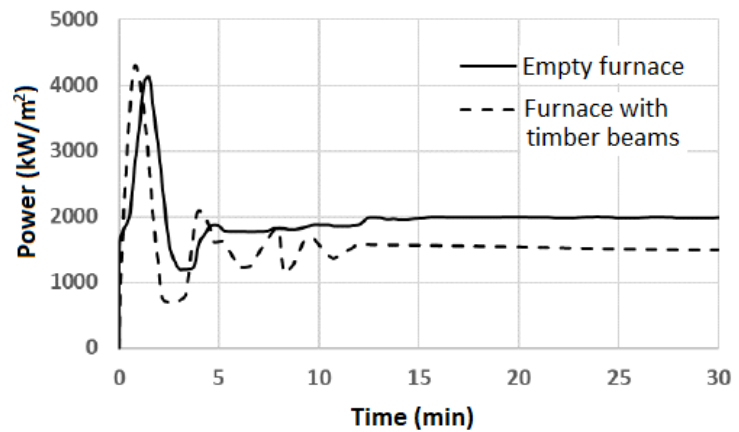


Fig. 5 Power of burners measured during fire tests

With the purpose of showing the contribution of burning of timber beams, FDS model with no timber burning (energy from timber is not released, the beams serve as obstacles only) was prepared. In *Fig. 6* results of gas temperatures calculated in both FDS models (including burning of timber and with no burning of timber) are presented. Full grey curve refers to FDS model which reflects burning of timber. Dashed grey curve is the temperature calculated in FDS model where is no timber burning. The two curves of gas temperature calculated in FDS are compared to the standard temperature-time curve. In the same diagram there is also development of temperature measured during the fire test. The comparison of all results in *Fig. 6* shows that burning of timber has to be included in FDS model.

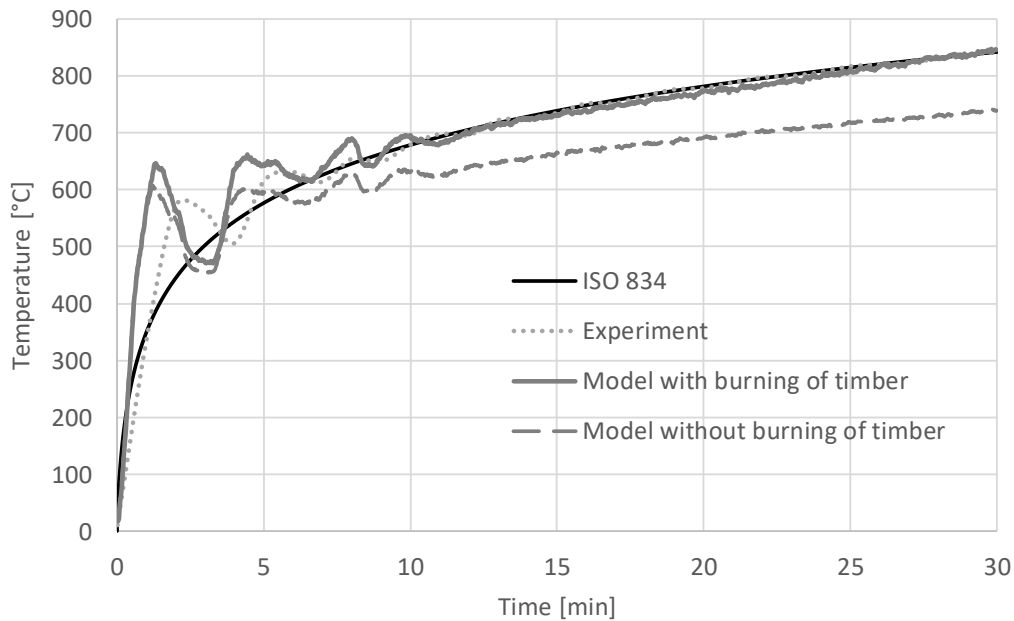


Fig. 6 Comparison of gas temperature for different FDS models

3 TEMPERATURE OF TIMBER BEAM

3.1 Description of FE model

After validation of the FDS model, temperature environment in means of AST values could be used as boundary conditions in FE model of the timber beam. To solve the heat transfer into the timber beam software Atena Science V.513 is used. Input values of the model are set by the aid of pre-processor GiD 12.0.8.

In the FE model properties of timber follows [6]. Initial moisture contain of the timber is 12%. Its density equals to 530 kg/m^3 . In the model decrease of the moisture contain and decrease of the density with increasing temperature of timber is included. Specific heat capacity and coefficient of thermal conductivity are set as temperature dependant properties. The dependence also follows [6]. For the thermal analysis a material model CCTransportMaterial is chosen. Gas temperatures originated from the FDS model are applied to three boundary lines of the timber cross-section. Fig. 7 shows dimensions of the timber beam cross-section. The beam is 100 mm width and 240 mm high. Fig. 7 also informs about a size of 2D mesh elements of the model. Two sizes of the mesh are used – 2 mm and 5 mm. Calculation time step is set to 6 s.

In order to compare results from the model with temperatures measured during the fire test, temperature is calculated at the same positions as it was during the fire test – control point A, B and C. As it is illustrated in Fig. 7 all points are located in depth of 30 mm. Each of them lies in different height of the beam – 10 mm, 45 mm and 120 mm from the lower edge of the beam.

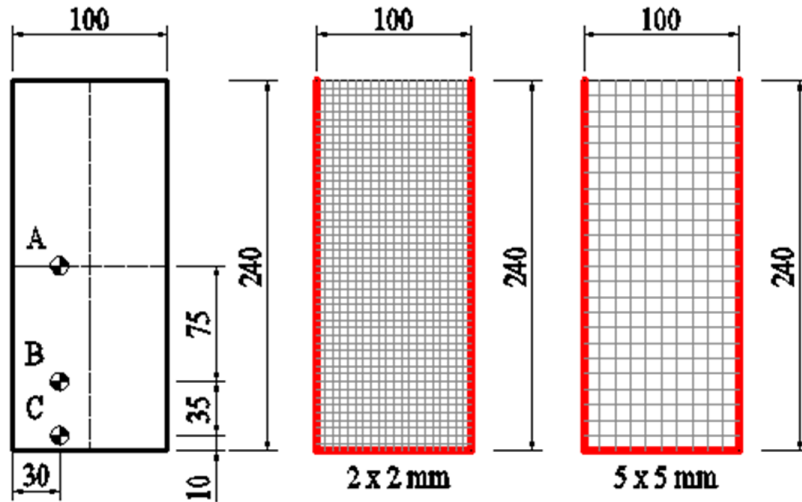


Fig. 7 Timber beam cross-section with locations of control points and meshing of the model

3.2 Results and comparison

Fig. 8 shows distribution of temperature inside the timber beam in 30 min. Temperature difference is negligible when comparing the model with 5 mm mesh and 2 mm mesh. Therefore, in later comparison only results coming from the model with 2 mm mesh is presented.

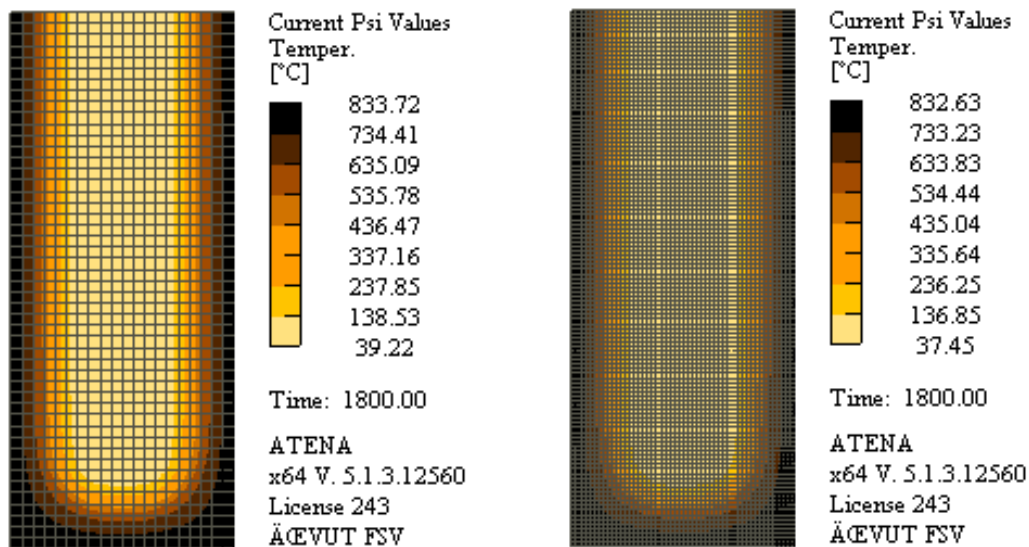


Fig. 8 Distribution of temperature across the timber beam in 30 min – 5 mm mesh and 2 mm mesh

Developments of temperatures at highlighted control points A, B and C are presented in Fig. 9. The results come from the model with mesh of 2 mm. The highest temperature is reached in point C which was the closest point to the lower edge of the beam. The depth of the point C was too small to be protected by a char layer. From Fig. 9 it is clear that points A and B are protected by a char layer. The temperature is noticeably lower in these point. Fig. 9 also shows temperatures measured during the fire test. Results of the comparison show the best agreement in point C which was located in height of 10 mm from the lower edge of the beam. In points A and B difference between

calculated and measured temperatures is about 100°C. These two points are more complicated for numerical solution as they lie below the char layer.

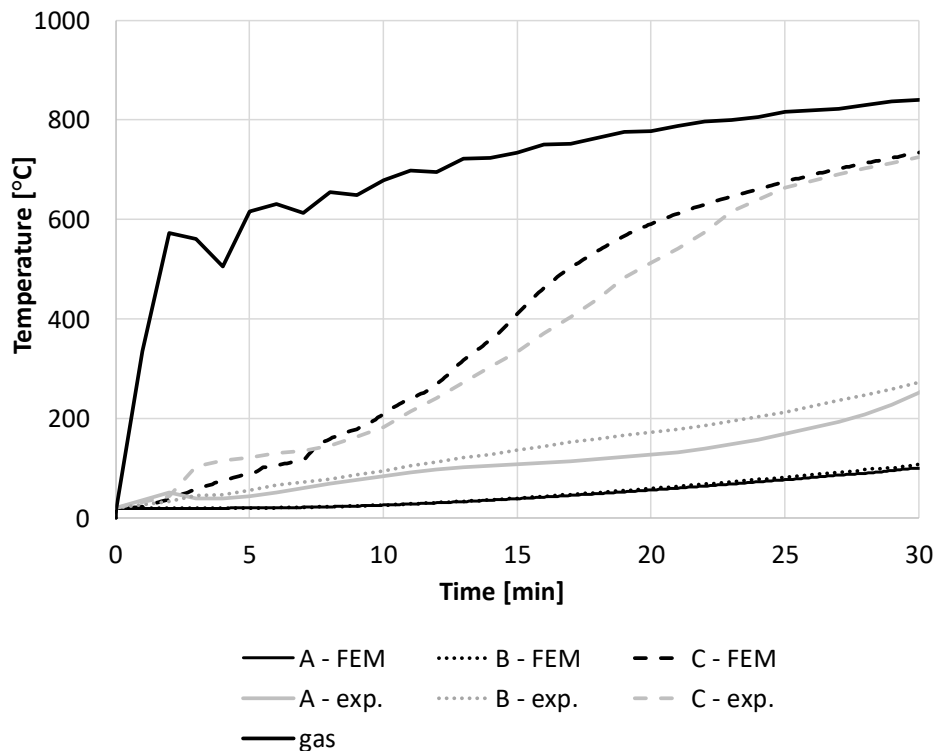


Fig. 9 Comparison of calculated temperatures and measured temperatures in control points A, B and C

4 CONCLUSIONS

The virtual furnace presented in this paper allows to calculate temperature environment around three timber beams. After validation of the FDS model, the temperature conditions are passed to the FE model which solves heat transfer to the tested element. Temperatures inside the timber beam which are solved in software Atena Science are compared to measured temperatures from the fire test. The comparison of temperatures in three control points shows good accuracy of the calculation in the point closer to the heated edge. An inaccuracy is shown in points located deeper in the beam cross-section - below the char layer.

In conclusion, the virtual furnace has a great potential for investigating the thermal behaviour of fire-resistance tests. A huge advantage inheres in the evaluation of the thermal effect throughout the volume of the furnace, which allows an accurate prediction of fire-resistance tests and evaluation of large number of technical alternatives and boundary conditions. However, passing the temperature field from the FDS model into FE model may decrease the level of accuracy. The solution lies in a coupled CFD-FE model. A weakly-coupled model including fluid dynamics, heat transfer and mechanical behaviour is under development at Faculty of Civil Engineering, Czech Technical University in Prague. The fluid dynamics part which is presented in this paper is solved by Fire Dynamics Simulator (FDS) and the thermo-mechanical part is computed by Object Oriented Finite Element Model (OOFEM) [7]. The interconnection of both software is made thanks to MuPIF python library.

ACKNOWLEDGMENT

Research presented in this paper was supported by project n. 16-18448S in the frame of the Czech science foundation (GA CR) and project n. VI20162019034 of Ministry of Interior of the Czech

Republic.

REFERENCES

1. Andy H. Buchanan (2001). *Structural Design for Fire Safety*. University of Canterbury, New Zealand.
2. Kevin McGrattan, et al. (2014). *Fire Dynamics Simulator (Version 6) - User's Guide*. Gaithersburg, Maryland, USA: National Institute for Standards and Technology, Special Publication 1019 - Sixth Edition.
3. V. Červenka, J. Červenka, Z. Janda, D. Pryl (2014). *ATENA program documentation. Part 8. User's manual for ATENA-GiD. Interface*, Červenka Consulting Ltd, 115 pp.
4. Kamila Horova (2015). *Modelling of fire spread in structural fire engineering*. PhD thesis. Czech Technical University in Prague.
5. Filip Zeman (2018). *Virtual furnace for fire resistance test of structures*. Diploma thesis. Czech Technical University in Prague.
6. ČSN EN 1995-1-2, 2006: *Design of timber structures – Part 1-2: General – Structural fire design*.
7. Borek Patzák (2012). *OOFEM - an object-oriented simulation tool for advanced modeling of materials and structures*. *Acta Polytechnica*, 52(6): pp. 59–66.

REDUCED-ORDER THERMAL ANALYSIS OF FIRE EFFECTS ON COMPOSITE SLABS

Jian Jiang¹, Joseph A. Main², Jonathan Weigand³, Fahim Sadek⁴

ABSTRACT

This paper describes a reduced-order modeling approach for thermal analyses of composite slabs with profiled decking. The reduced-order modeling approach consists of alternating strips of layered shell elements, representing the thick and thin portions of slab. Layered shell elements representing the thick portion of the slab adopt a linear reduction in the density of concrete within the rib to account for the tapered profile of the ribs. A “dummy material” with low specific heat and high through-thickness thermal conductivity is used to represent the voids between the ribs. The specific heat of concrete in the rib is also modified to indirectly consider the heat input through the web of the decking. The optimal ratio of modified to actual specific heat of concrete in the rib is determined, depending on the ratio of the height of the upper continuous portion to the height of the rib. The reduced-order modeling approach is validated against experimental results.

Keywords: thermal analysis; composite slab; reduced-order model; shell element; validation.

1 INTRODUCTION

Composite slabs consisting of concrete topping on profiled steel decking are widely used as floor systems in modern steel-framed buildings. Analyzing the response of composite slabs to fire-induced thermal loading requires both heat transfer analysis and structural analysis. Both thermal and structural analyses of composite slabs present their own unique challenges, and different types of models are typically used, which introduces an additional challenge of transferring analysis results between models with different element types and potentially different mesh resolutions. A key objective of this study is to develop a reduced-order modeling approach for thermal analysis that is also suitable for structural analysis. This would allow the same model to be used for both types of analysis, facilitating the analysis of structural response under various fire scenarios, with realistic thermal loading applied from computational simulations of fire dynamics.

Numerical analysis of heat transfer in composite slabs typically uses a high-fidelity finite element modeling approach, with solid elements for the concrete slab and shell elements for the steel decking [1-4]. This approach can realistically simulate the orthotropic behavior of composite slabs, but requires significant computing time. Thus, structural analysis of fire effects on composite slabs commonly uses grillage-type beam element models [5,6] or shell element formulations [7,8]. In considering the suitability of the reduced-order structural analysis approaches for heat transfer analysis, the grillage approach with beam elements [5,6] is unsuitable because of the inadequacy of

¹ PhD. National Institute of Standards and Technology, 100 Bureau Drive, Stop 8611, Gaithersburg, MD, USA, 20899
e-mail: jian.jiang@nist.gov

² PhD. National Institute of Standards and Technology, 100 Bureau Drive, Stop 8611, Gaithersburg, MD, USA, 20899
e-mail: joseph.main@nist.gov

³ PhD. National Institute of Standards and Technology, 100 Bureau Drive, Stop 8611, Gaithersburg, MD, USA, 20899
e-mail: jonathan.weigand@nist.gov

⁴ PhD. National Institute of Standards and Technology, 100 Bureau Drive, Stop 8611, Gaithersburg, MD, USA, 20899
e-mail: fahim.sadek@nist.gov

the 1D elements to represent in-plane and through-thickness heat transfer in the slab. Modeling approaches that use a constant shell thickness [7,8] are unsuitable because they fail to capture the shielding effect of the ribs, which results in curved isotherms in the floor slab, significantly affecting both the structural response and the thermal insulation provided by the slab. Kwasniewski [9] and Main [10] proposed approaches in which alternating strips of layered shell elements were used to represent the thick and thin parts of a composite slab. This modeling approach has the potential to capture both in-plane and through-thickness heat transfer in composite slabs, including the shielding effect of the ribs, and this approach is pursued in this study.

This paper reports on a reduced-order modeling approach consisting of alternating strips of layered shell elements to represent the thick and thin portions of the composite slab. A “dummy material” with high through-thickness thermal conductivity and low specific heat is used to represent the voids between the ribs, and a linear reduction in the density of concrete in the ribs is used to represent the tapered profile of the ribs. Modifications in the specific heat of concrete in the rib are incorporated to indirectly account for heat input through the web of the decking, since thermal loading can only be directly applied to the upper and lower flanges of the decking in the reduced-order modeling approach. Comparisons with temperature histories from detailed finite-element models are used to determine the optimal modification of the specific heat as a function of the slab dimensions. Finally, the reduced-order modeling approach is validated through comparisons with experimental measurements.

2 DEVELOPMENT OF REDUCED-ORDER MODELING APPROACH

The proposed reduced-order modeling approach uses a layered composite shell formulation, in which a distinct structural material, thermal material, and thickness are specified for each layer (*PART_COMPOSITE in LS-DYNA [11]). This allows individual layers to be specified for the steel decking and the reinforcement, with multiple layers representing concrete through the thickness of the slab. The proposed approach uses alternating strips of shell elements to represent the thick and thin portions of composite slabs, with the width of the thick and thin portions each being spanned by a single shell element. For the simple half-slab configuration shown in *Fig. 1*, only two shell elements were needed, i.e., Shell A for the thick portion of the slab and Shell B for the thin portion as shown in the figure. A thick thermal shell formulation is used, which allows for both in-plane and through-thickness heat conduction, with thermal gradients through the thickness of each layer.

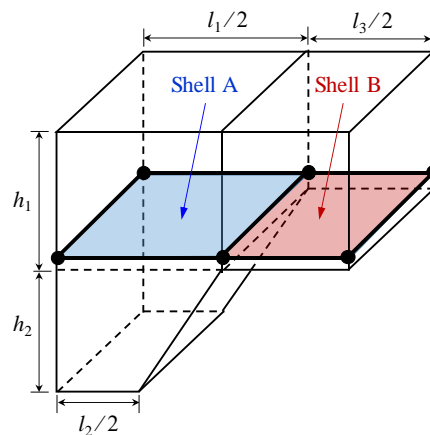


Fig. 1. Schematic of the reduced-order model of composite slabs with dimensions described in the text

Fig. 2 illustrates the layers used to represent the thick part of the slab (shell A) and the thin part of the slab (shell B) in the composite shell formulation. Based on mesh sensitivity analyses reported by Jiang et al. [12], it was found that sufficient accuracy could be achieved by using four layers in the composite shell representing the upper portion of the concrete slab and using an additional four layers to represent the concrete in the rib (see Fig. 2). An additional layer in shells A and B was used to represent the lower and upper flange of the steel decking, respectively. Fig. 2 illustrates the following two aspects of the reduced-order modeling approach: (1) reduction of the concrete density in the ribs to represent the tapered profile. The reduced concrete density for the i th layer of the rib, ρ_i , is calculated based on the ratio of the average rib width for that layer, w_i , to the total width at the top of the rib, l_1 , as $\rho_i = \rho_0 \times (w_i / l_1)$, where ρ_0 is the concrete density; (2) use of a “dummy material” to represent the voids between the ribs. This is done to allow shell A and shell B to have the same thickness, which is required for proper modeling of in-plane heat conduction between corresponding layers of adjoining shell elements. Radiation and convection boundary conditions are applied at the fictitious lower surface of shell B. A high through-thickness thermal conductivity for the dummy material, along with low specific heat (values of 100 W/(m·K) and 1 J/(kg·K), respectively, were used in this study), ensure an essentially equivalent temperature at the top of the dummy material, thus providing appropriate thermal boundary conditions for the upper flange of the steel decking.

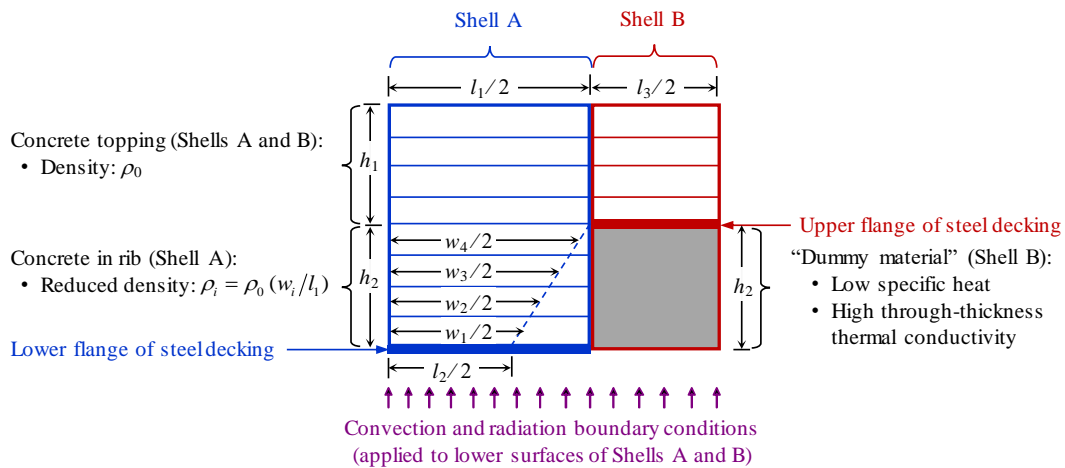


Fig. 2. Layered-shell representation of thick and thin portions of composite slab.

Fig. 3 shows a comparison of temperature histories computed using the reduced-order modeling approach with corresponding temperature histories computed using a validated, detailed modeling approach described by Jiang et al. [12], in which the concrete slab was modeled using solid elements and the steel decking was modeled using shell elements. The comparison corresponds to a commonly used composite slab with a Vulcraft 3VLI decking. The temperature histories presented in Fig. 3 correspond to layer-averaged temperatures. Shell-element temperatures at the lower, middle, and upper surfaces were presented from the reduced-order model, and layer-averaged temperatures from the detailed model were calculated at consistent elevations. The high through-thickness thermal conductivity of the dummy material ensured that the temperature at the fictitious lower surface of shell B was virtually equivalent to the temperature in the upper flange of the steel decking. For this reason, the upper flange of the steel decking is labeled as the lower surface in Fig. 3b. The temperature differences between the reduced-order and detailed models in Fig. 3 resulted from approximations inherent in the layered composite shell formulation, which underestimated the heat input through the web of the decking. This resulted in delayed heating just above the rib (middle surface in Fig. 3a), where the reduced-order model underestimated the temperature by about 16 % at the end of the analysis. To reduce this error, it is necessary to more accurately capture

the heat input through the web of the decking. This can be achieved by modifying the specific heat for concrete in the ribs, as presented in the next section.

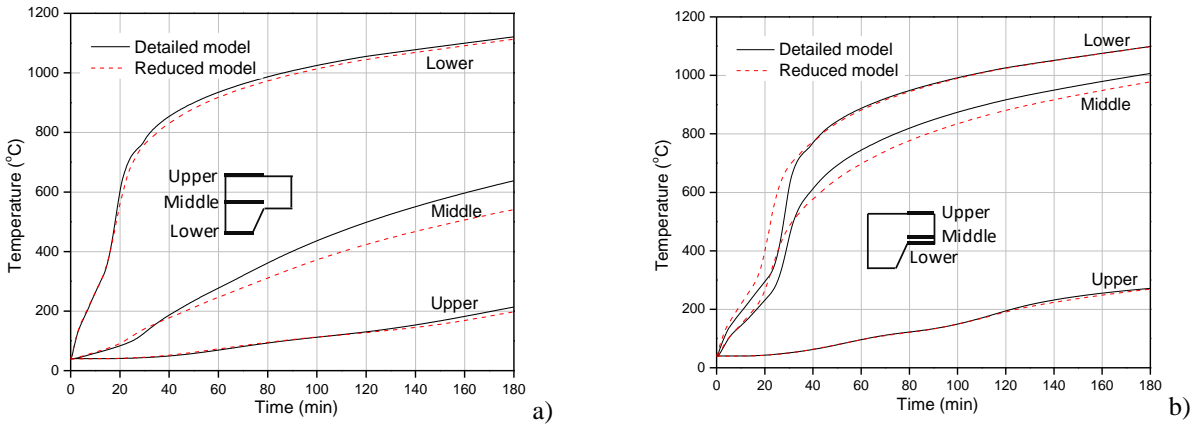


Fig. 3. Comparison of layer-averaged temperature histories from detailed model and reduced-order model: a) thick portion of slab; b) thin portion of slab

3 MODIFICATION OF SPECIFIC HEAT FOR CONCRETE IN THE RIBS

The most effective approach to account for the influence of heat input through the web of the decking was found to be through modification of the specific heat of the concrete in the rib. In this approach, an artificial specific heat, c'_p , was used for the concrete in the rib, while the actual specific heat, c_p , was used for the rest of the concrete in the slab. A reduction in the specific heat indirectly accounts for additional heat input through the web, since the reduced specific heat increases the thermal diffusivity, thus increasing the rate of heat flow through the rib. This approach allowed for improved accuracy in the temperature above the rib, with minimal effect on the temperatures at other locations in the slab.

The optimal value of c'_p / c_p was determined by minimizing the root-mean-square (RMS) difference between the temperature histories from the reduced-order and detailed models, defined as follows:

$$T_{\text{RMSD}} = \sqrt{\frac{\sum_{i=1}^n (T_R(t_i) - T_D(t_i))^2}{n}} \quad (1)$$

where T_D and T_R are the temperatures obtained from the detailed and reduced-order models, respectively, t_i is the i th time sample, and n is the total number of time samples over the heating period. The RMS temperature deviation was evaluated for temperature histories from the middle surface of the thick part of the slab, where the largest discrepancy was observed in Fig. 3.

Parametric studies were conducted to evaluate the optimal value based on a set of slab geometries [12], as shown in Fig. 4. The recommended optimal specific heat ratio c'_p / c_p was expressed as a function of h_1 / h_2 , where h_1 is the thickness of the continuous upper portion of the slab and h_2 is the thickness of the rib. The ratio c'_p / c_p was reduced linearly from a value of 1.0 for $h_1 / h_2 = 1$ to a value of 0.5 for $h_1 / h_2 = 1.2$. An upper limit of $c'_p / c_p = 1.0$ is recommended for $h_1 / h_2 < 1$, because values of c'_p / c_p exceeding 1.0 can result in underestimation of temperatures in the later stages of heating, which is not conservative. Similarly, a lower limit of $c'_p / c_p = 0.5$ is recommended for $h_1 / h_2 > 1.2$, because reducing c'_p / c_p below 0.5 produced only marginal reductions in the RMS temperature deviation.

Numerical Modelling

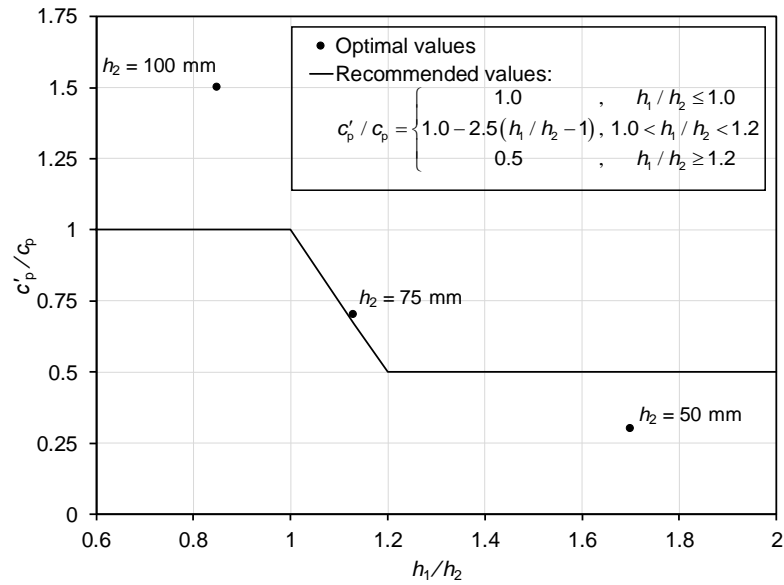


Fig. 4. Recommended specific heat of concrete in the rib as a function of h_1 / h_2

4 VALIDATION OF REDUCED-ORDER MODELING APPROACH

A standard fire test per ISO 834 [13] on a simply supported one-way concrete slab (Test 2 from Hamerlinck et al. [1]) was selected to validate the proposed reduced-order modeling approach. Fig. 5 shows the configuration of the tested slab. The slab had six ribs and used Prins PSV73 steel decking and normal-weight concrete with a measured moisture content of 3.4 %. Heat transfer parameters reported by Hamerlinck et al. [1] were used in the modeling, as summarized in the following. The convective heat transfer coefficient for the lower flange of the steel decking was taken as $25 \text{ W}/(\text{m}^2 \cdot \text{K})$, and a lower value of $15 \text{ W}/(\text{m}^2 \cdot \text{K})$ was used for the web and upper flange of the decking to account for the shielding effect of the ribs. A convective heat transfer coefficient of $8 \text{ W}/(\text{m}^2 \cdot \text{K})$ and an emissivity of 0.78 were used for the unexposed top surface of the concrete. View factors for the upper flange and the web of the steel decking were 0.3 and 0.6, respectively, and a view factor of 1.0 was used for the lower flange of the steel decking and the unexposed top concrete surface.

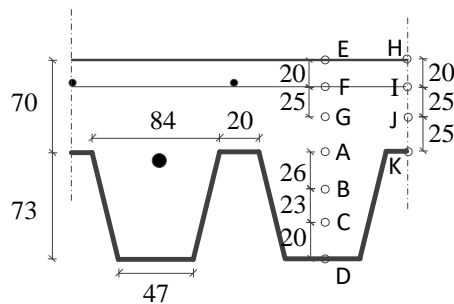


Fig. 5. Geometry of TNO tested slab (Hamerlinck et al. 1990) (dimensions in mm)

Fig. 6 presents a comparison of the measured temperature histories from the slab test with the computed temperatures from the detailed and reduced-order models. For consistency with the experimental measurements, point temperatures rather than layer-averaged temperatures are presented from the numerical models (i.e., nodal temperatures, rather than element temperatures, are presented from the reduced-order model). The tested slab had a height ratio of $h_1 / h_2 = 0.96$, for which Fig. 4 recommends a specific heat ratio of $c'_p / c_p = 1.0$, and therefore, no modification of the specific heat of concrete in the rib was used. For comparison with the computed results, the measured temperature at point M (mid-height of the thick portion of the slab) was obtained by

interpolation of measured temperatures at adjacent points (points A and G in Fig. 5). The largest discrepancies were at point K, where the RMS temperature differences were 42 °C and 73 °C for the detailed and reduced-order models, respectively. At all other locations, the RMS temperature differences were less than 30 °C. The largest percent differences at the end of the test were +14 % and +17 % for the detailed and reduced-order models, at points H and E, respectively.

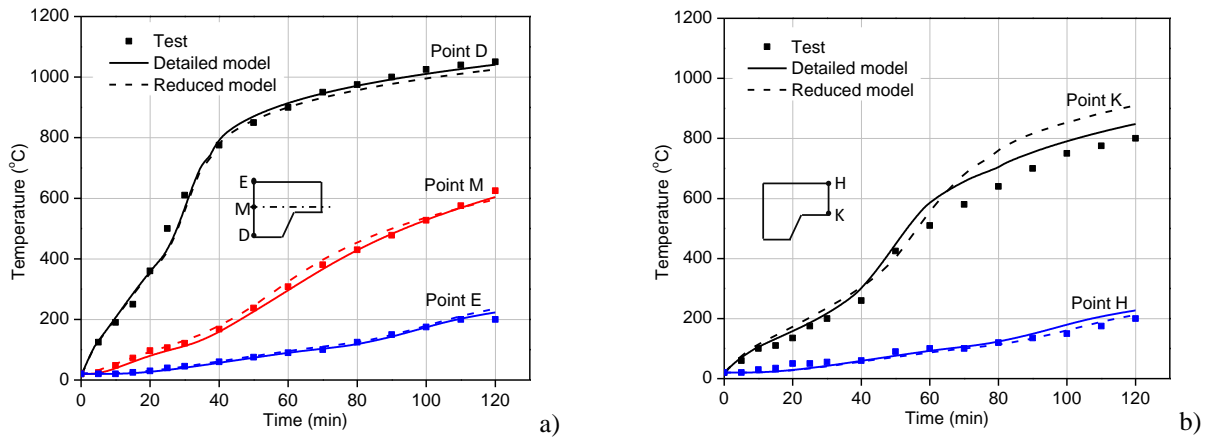


Fig. 6. Comparison of measured temperatures from TNO test [1] with computed temperatures from detailed and reduced-order models: a) thick portion of slab; b) thin portion of slab

5 CONCLUSIONS

This paper presented a reduced-order modeling approach that used a layered composite shell formulation for heat transfer analysis of composite slabs. This modeling approach can be readily extended to structural analysis, allowing thermal and structural analysis to be performed using the same model. The geometry of composite slabs was captured by using alternating strips of shell elements to represent the thick and thin portions of the slab. The density of concrete was reduced linearly with depth in the rib to account for the tapered profile of the ribs. Shell elements representing the thin portions of the slab incorporated a “dummy material” with low specific heat and high through-thickness thermal conductivity to represent the voids between the ribs. This approach allows the thick and thin portions of the slab to be modeled using shell elements with the same thickness. Adequately accounting for heat input through the web of the decking was the greatest challenge in the reduced-order modeling approach, and modifying the specific heat of concrete in the rib was found to be an effective method to achieve this. The modification factor for the specific heat in the rib, c'_p / c_p , was recommended as 0.5 for slabs with $h_1 / h_2 > 1.2$ and as 1.0 for slabs with $h_1 / h_2 < 1.0$, with a linear interpolation between these values for h_1/h_2 between 1.0 and 1.2. The reduced-order modeling approach was calibrated against detailed models of composite slabs and validated against experimental results.

DISCLAIMER

Certain commercial entities, equipment, products, or materials are identified in this document in order to describe a procedure or concept adequately. Such identification is not intended to imply recommendation, endorsement, or implication that the entities, products, materials, or equipment are necessarily the best available for the purpose. The policy of the National Institute of Standards and Technology is to include statements of uncertainty with all NIST measurements. In this document, however, measurements of authors outside of NIST are presented, for which uncertainties were not reported and are unknown.

REFERENCES

1. R. Hamerlinck, L. Twilt, J. Stark (1990). *A numerical model for fire-exposed composite steel/concrete slabs*. Proceedings of tenth International Specialty Conference on Cold-formed Steel Structures, USA, 115-130.
2. S. Lamont, A.S. Usmani, M. Gillie (2004). *Behaviour of a small composite steel frame structure in a “long-cool” and a “short-hot” fire*. Fire Safety Journal 39. pp 327-357.
3. S. Guo (2012). *Experimental and numerical study on restrained composite slab during heating and cooling*. Journal of Constructional Steel Research 69. pp 95-105.
4. D. Pantousa, E. Mistakidis (2013). *Advanced modelling of composite slabs with thin-walled steel sheeting submitted to fire*. Fire Technology 49. pp 293-327.
5. A.Y. Elghazouli, B.A. Izzuddin, A.J. Richardson (2000). *Numerical modelling of the structural fire behaviour of composite buildings*. Fire Safety Journal 35. pp 279-297.
6. A.M. Sanad, S. Lamont, A.S. Usmani, J.M. Rotter (2000). *Structural behaviour in a fire compartment under different heating regimes—part 1 (slab thermal gradients)*. Fire Safety Journal 35. pp 99-116.
7. Z. Huang, I.W. Burgess, R.J. Plank (2000). *Effective stiffness modelling of composite concrete slabs in fire*. Engineering Structures 22(9). pp 1133-1144.
8. B.A. Izzuddin, X.Y. Tao, A.Y. Elghazouli (2004). *Realistic modelling of composite and R/C floor slabs under extreme loading-Part I: Analytical method*. Journal of Structural Engineering 130(12). pp 1972-1984.
9. L. Kwasniewski (2010). *Nonlinear dynamic simulations of progressive collapse for a multistory building*. Engineering Structures 30. pp 1308-1318.
10. J.A. Main (2014). *Composite floor systems under column loss: Collapse resistance and tie force requirements*. Journal of Structural Engineering 140(8). A4014003.
11. Livermore Software Technology Corporation (LSTC). (2014). *LS-DYNA Keyword User’s Manual, R7.1*, LSTC, Livermore, California.
12. J. Jiang, J.A. Main, F. Sadek, J.M. Weigand (2017). *Numerical Modeling and Analysis of Heat Transfer in Composite Slabs with Profiled Steel Decking*. NIST Technical Note 1958, National Institute of Standards and Technology, Gaithersburg, MD.
13. International Organization for Standardization (ISO). 2014. *Fire-resistance tests – Elements of building construction*, ISO 834-11, Geneva, Switzerland.

Numerical Modelling

NUMERICAL INVESTIGATION OF FIRE AND POST-FIRE PERFORMANCE OF CFT COLUMNS IN AN OPEN CAR PARK FIRE

Wojciech Szymkuć¹, Adam Glema², Michał Malendowski³, Aleksandra Mielcarek⁴, Piotr Smardz⁵,
Adrian Poteralski⁶

ABSTRACT

This paper investigates a performance-based approach for assessment of performance of Concrete Filled Tubular (CFT) column in an open car park fire. The selected fire scenario involves 4 cars around the column on the lowest deck of a multi-storey car park. A full-scale car fire simulation is performed in FDS software. Coupling between CFD and FEM is developed to provide temperature data around column during heating and cooling stage. FE package Abaqus is used to calculate temperatures inside column, taking into account material properties that are non-reversible after heating. Afterwards, the performance of column is studied during ISO and localised fire. The localised fire includes fire decay stage, where mechanical properties of concrete are assumed as a function of highest temperature reached during analysis. It is shown, that selected fire scenario gives relatively low temperatures that do not affect column's performance during and after the fire.

Keywords: Structures, finite element modelling, localised fires, open car parks, CFT columns

1 INTRODUCTION

Three approaches are commonly employed when the effect of fire on structures is considered, i.e. heating conditions according to the standard temperature-time curve, parametric curves or localised fires [1]. Localised fires can be applied for large compartments, where a fully developed fire is rather unlikely to occur. This motivated to a study concerning fire performance of concrete-filled tubular (CFT) columns exposed to high temperatures due to a car fire. The investigation is based on the thermo-mechanical analyses of structures in fire, where the thermal exposure is obtained from the CFD analyses of fire. Most of the existing analyses regarding car park fires focus either heavily on a fire simulation, while analysing structural performance in a simplified manner. On the other hand, fire is often simplified and then structure is calculated in an advanced way. This contribution combines these two approaches by providing a fire simulation (CFD) and using a full 3D FE numerical model with material properties for both heating and cooling.

¹ Research assistant. Institute of Structural Engineering, Poznan University of Technology, Piotrowo 5, 60-965 Poznań, Poland.
e-mail: wojciech.szymkuc@put.poznan.pl

² Professor. Deputy Director of Institute of Structural Engineering, Poznan University of Technology, Piotrowo 5, 60-965 Poznań, Poland.

e-mail: adam.glema@put.poznan.pl

³ Research assistant. Institute of Structural Engineering, Poznan University of Technology, Piotrowo 5, 60-965 Poznań, Poland.

e-mail: michal.malendowski@put.poznan.pl

⁴ Fire Safety Engineer at INBEPO Sp. z o.o., Ignacego Domeyki 9a, 53-209 Wrocław, Poland.

e-mail: aleksandra@inbepo.pl

⁵ Fire Safety Engineer at INBEPO Sp. z o.o., Ignacego Domeyki 9a, 53-209 Wrocław, Poland.

e-mail: piotr@inbepo.pl

⁶ Fire Safety Engineer at INBEPO Sp. z o.o., Ignacego Domeyki 9a, 53-209 Wrocław, Poland.

e-mail: adrian@inbepo.pl

2 CFD ANALYSIS

2.1 Case study - open car park

AA flat-deck multi-storey open car park is considered. The structure consists of 4 levels. Each floor is 32.0 m wide and 55.0 m long. The minimum clearance height is 2.4 m and the car park storey height is 3.0 m. CFT columns are positioned at all four corners of 16.0 m x 5.0 m parking module. The composite floor structure is formed by 16.0 m long beams positioned at 5.0 m c/c and concrete slabs. The parking levels are accessible by a ramp that is located lengthwise and by two staircases for internal communication and means of escape. The parking spot size is 2.5 m x 5.0 m. Spandrels are used to prevent the external/vertical fire spread.

2.2 Fire scenario

Fire scenarios, commonly used for this type of a building, assume localised fire of one burning car below the beam or next to the column and also a progressive spread of a fire to cars in a row or surrounding the column [1, 2, 3]. In this paper, the fire scenario involves 4 cars around the column on the lowest deck. The fire starts in a car no.1 and, after 12 min, spreads simultaneously to cars 2 and 3. After another 10 min, the fire propagates to car 4 (Fig. 1a). The spread of the fire to the nearby car occurs before the first ignited car is burned-out. In this type of a car park, it is assumed that the fire travels only horizontally and cannot travel to another level. The heat release rate curve of one burning car is based on the reference curve obtained from [2] (Fig. 1b). This HRR curve includes both the fire growth and decay phases. Hence, both heating and cooling of structural elements are considered.

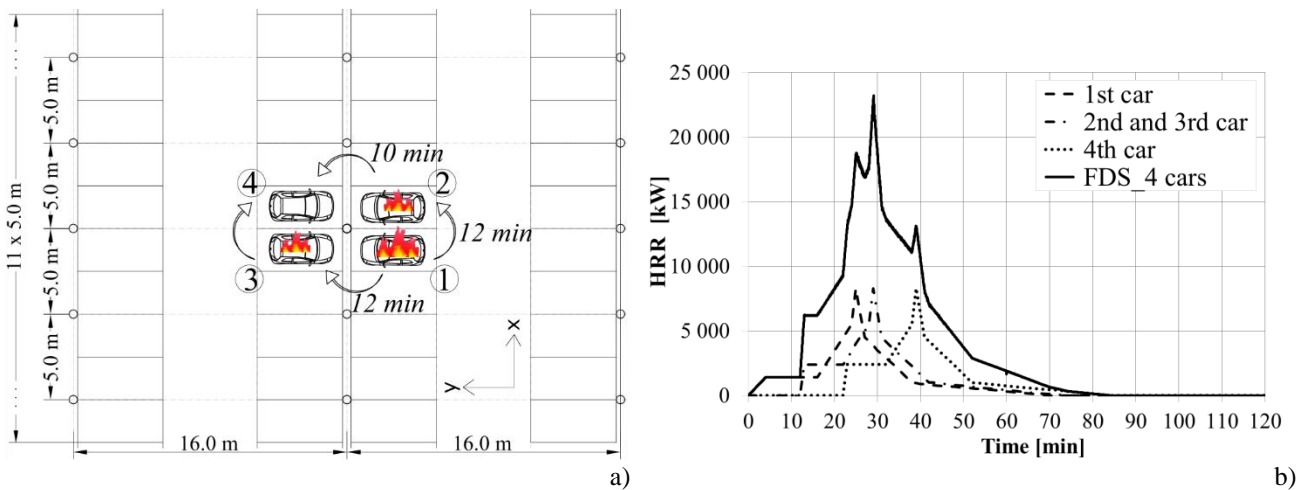


Fig. 1. a) Fire scenario; b) Reference curves of HRR for each car [2] and the total HRR from CFD analysis

2.3 Numerical model

A full-scale car fire simulation is performed in FDS 6.6.0 software. A computational domain is limited to the space where the impact of the fire is the most severe. The dimensions of the computational domain are: 40.5 m x 10.8 m x 3.6 m (Fig. 2). A sensitivity study has been performed for the grid resolutions of 0.075 m, 0.100 m, 0.125 m, 0.150 m, 0.200 m and 0.300 m with the cell aspect ratio equal to 1.0. In terms of obtained results, their convergence and run times, the grid size 0.15 m x 0.15 m x 0.15 m is chosen. A single car is implemented as a cuboid platform with a burning top surface, burning tires and a roof. Simple pyrolysis model is used by specifying the Heat Release Rate Per Unit Area to the surfaces [4]. Most of the heat release rate is prescribed to the top of the cuboid platform – rectangular surface 4.5 m x 1.8 m at height 0.6 m, which gives $HRR_{PUA} = 975 \text{ kW/m}^2$. The influence of external weather conditions is not considered. The

boundaries of the computational domain are set as OPEN, allowing the free heat and smoke outflow, as well as the fresh air inflow. The parameters such as fuel species ($C_{1.0}H_{1.8}O_{0.17}N_{0.17}$), soot yield (0.1 kg/kg), radiative fraction (0.2), the distances between the cars (0.75-0.90 m), temperature-dependent materials properties are taken from the available literature [4, 5, 6, 7].

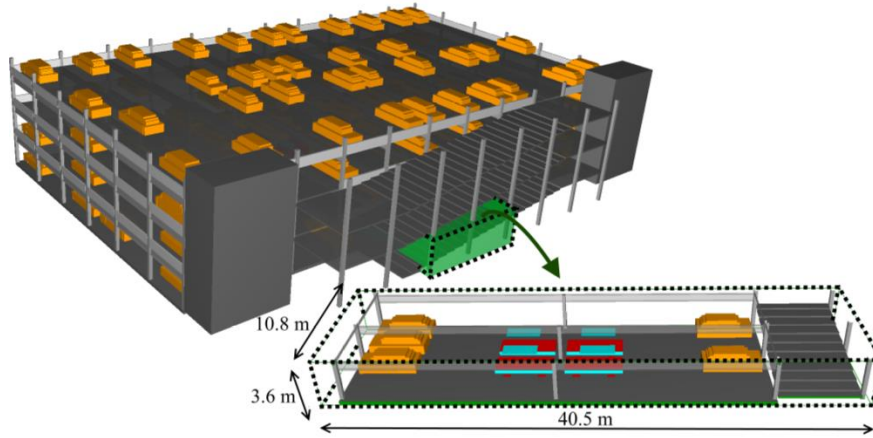


Fig. 2. Model in FDS and boundaries of the computational domain

3 CFD – FEM COUPLING

3.1 FDS and Abaqus coupling

The coupling between FDS and Abaqus is done in a sequential way. This means, the simulation of fire is carried out a priori and the results of it are transferred into the thermo-mechanical analyses in the form of boundary conditions. A concept of the Adiabatic Surface Temperature (AST) is used to provide a complementary amount of information about the heat exposure of the structure. It is a single quantity which can be used to describe the actual convection and radiation influences [8], according to a relationship given in [9]. Heat flux between surrounding fire environment and a surface of the CFT column is described by the equation:

$$\dot{q}_{tot} = \varepsilon\sigma(T_{AST}^4 - T_{CFT,surface}^4) + h_c(T_{AST} - T_{CFT,surface}) \quad (1)$$

where ε is a steel emissivity equal to 0.7, σ is a Stefan–Boltzmann constant, h_c is a convective heat transfer coefficient and T_{AST} and $T_{CFT,surface}$ are AST of an adjacent ‘dummy’ surface and temperature of a CFT column surface, respectively.

Two approaches are used to perform the CFD-FEM coupling. First uses the AST history stored by FDS in boundary files (BNDF approach) as boundary conditions in the FE analysis. Second approach (AST GAS approach) uses the virtual devices that measure the AST at particular points of the space in particular direction.

In the first approach data needed for the solid phase heat transfer analysis is transferred to the FE model directly from the corresponding surfaces of the FDS model. Boundary conditions are in the form of prescribed nodal temperature histories of dummy surface adjacent to the analysed column (dummy square surface in Fig. 3). The dummy surface complies with rectangular FDS grid. Since the grid size 0.15 m x 0.15 m x 0.15 m is chosen in this analysis and the diameter of the column is 0.219 m, each of these dummy surfaces is 0.30 x 3.00 m and four of them make a square tube, so that column fits inside. This dummy surface is reflected in FDS model as a physical obstacle in the centre of four cars around it (Fig. 2). The details regarding the BNDF approach are given in [10].

Since FDS 6.5.2 has been released, it is possible to calculate 'ADIABATIC SURFACE TEMPERATURE GAS' (AST GAS) and get the AST away from a solid wall. This approach allows to collect data from more than 4 basic directions, contrary to the BNDF approach, where surfaces

could face only North, East, South or West direction. In this paper, 8 such measuring points are used along the circumference on each selected height (arrows in Fig. 3), at 20 different, equally distributed levels – resulting in 160 measurement points. The AST GAS is calculated, assuming emissivity equal to 1.0 (the surface is adiabatic) and $h_c=10 \text{ W}/(\text{m}^2\cdot\text{K})$. It is found in the BNDF approach, that h_c is between 6 and $10 \text{ W}/(\text{m}^2\cdot\text{K})$ during a fire action. Since the AST GAS approach requires setting the heat transfer coefficient apriori, it is assumed as $10 \text{ W}/(\text{m}^2\cdot\text{K})$ for all devices during analysis. AST GAS is used in conjunction with another ‘dummy’ surface – circular (Fig. 3). Each node on the surface is assumed to follow temperature of the closest AST GAS device. Regardless the BNDF approach or the AST GAS approach, heat fluxes at solid surfaces are calculated according to equation (1). However, in the BNDF approach it is between dummy square surface and steel tube, while in the AST GAS approach it is calculated between dummy circular surface and steel tube. Solid phase heat transfer analyses are carried out in FE software Abaqus, taking into account thermal contact conductance (gap conductance) between steel and concrete equal to $100 \text{ W}/(\text{m}^2\cdot\text{K})$ and material properties described in Section 4.

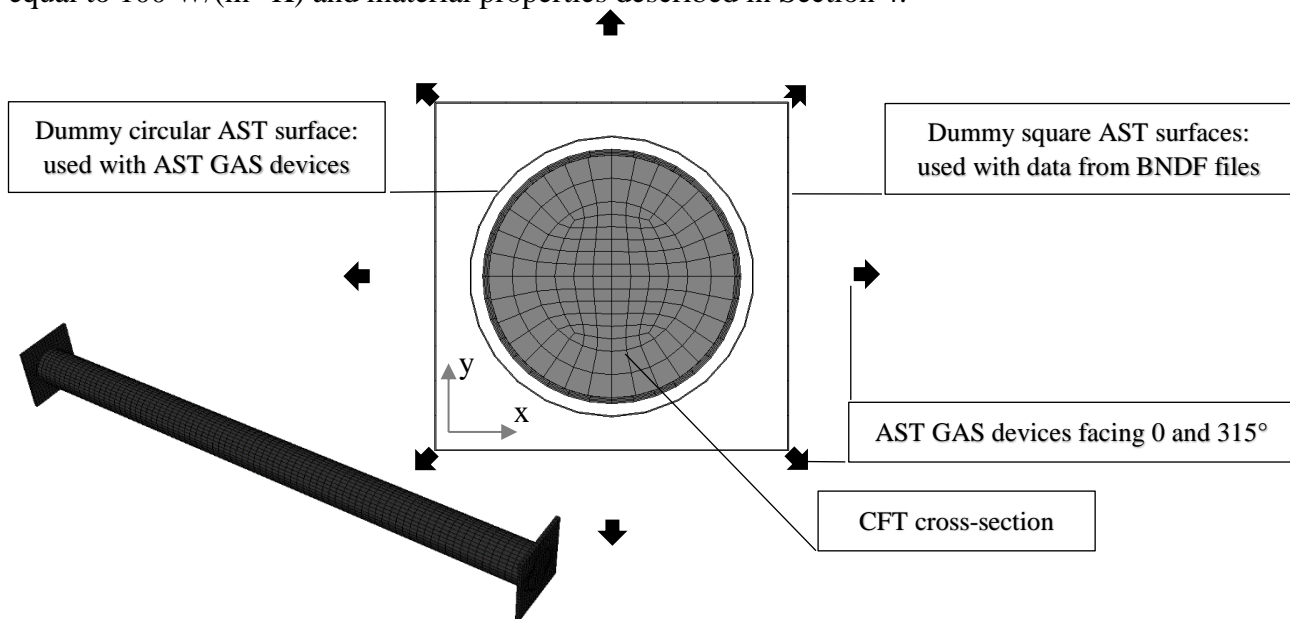


Fig. 3. Schematic view of approaches for data transfer between FDS and Abaqus. CFT cross-section inside two surfaces used for the AST: circular ($d=0.22 \text{ m}$, $h=3.0 \text{ m}$) and square ($a=0.30 \text{ m}$, $h=3.0 \text{ m}$). 8 FDS devices around recording AST GAS. Schematic view of the full 3D FE model in the left corner (dummy surfaces are not shown).

Dummy surfaces described above are present only in heat transfer analyses. They do not contribute to the mechanical analyses, which are performed to assess the structural behaviour of CFT column during and after fire. Details of mechanical analysis are given in Section 4.

4 FE ANALYSIS

4.1 Material properties

Material properties during heating are taken from Eurocodes. Mises and Drucker-Prager yield criterions are used for steel and concrete, respectively. The properties of steel during and after cooling are considered to be fully-reversible. While this is not true for yield strength after heating to temperatures higher than 550°C [11], the temperatures obtained from CFD and FE analyses allowed us to neglect this phenomenon, since steel temperature does not exceed 400°C .

Temperature-dependent properties of concrete are considered to be mostly non-reversible. This concerns properties affecting temperature inside the column: specific heat, thermal conductivity and density, as well as properties influencing its structural behaviour: Young’s modulus and stress-

strain relationships of concrete. Peak of specific heat is modelled at 150°C, according to Eurocode 4, and corresponds to free water content of 3% (2020 J/kg·K). Since this peak represents mainly evaporation of free water, it is not present during cooling. Initial density of concrete is assumed as 2300 kg/m³, and its change during heating is non-reversible (after heating to 1200°C and cooling density loss would be 12%). Thermal conductivity change is also considered to be non-reversible, what is inline with results presented by [12]. According to [13], there is a small conductivity rise after cooling below 100°C, due to presence of water. Since the core of CFT column is not directly exposed to atmospheric air, this change is not investigated.

For concrete, both Young's modulus and stress-strain relationship are a function of current and maximum temperature. Additional compressive strength loss during or after cooling is not studied in this paper. Thermal expansion of concrete is considered to be fully reversible in our model, however the influence of residual thermal expansion [13] should be studied as well, since temperature causes aggregate to grow and cement paste to shrink [14]. At this stage, Load Induced Transient Strain is not included.

4.2 Thermal analysis

Approaches used for calculation of temperature field inside the column's cross-section are described in Section 3. It is found, that introducing in the given FE element non-reversible thermal properties that are functions of maximum temperatures, does not have a major effect on results. In this paper a tubular cross-section (219.1 x 5 mm) filled with concrete is studied. For reference, temperatures along its diameter are presented in Fig. 4 after 60 minutes of ISO fire exposure, followed by linear decay during next 60 minutes. Additionally, the relationship between the distance from the centre and time at which maximum temperature is reached, is given for the same heating conditions. As expected – highest temperature of steel tube is reached at the end of fire exposure. However, the highest temperature in the centre is reached after almost 140 minutes. This means that the lowest load bearing capacity is likely to occur not within 60 minutes of ISO fire but later, during cooling. A general approach to take that into account has been proposed in [15].

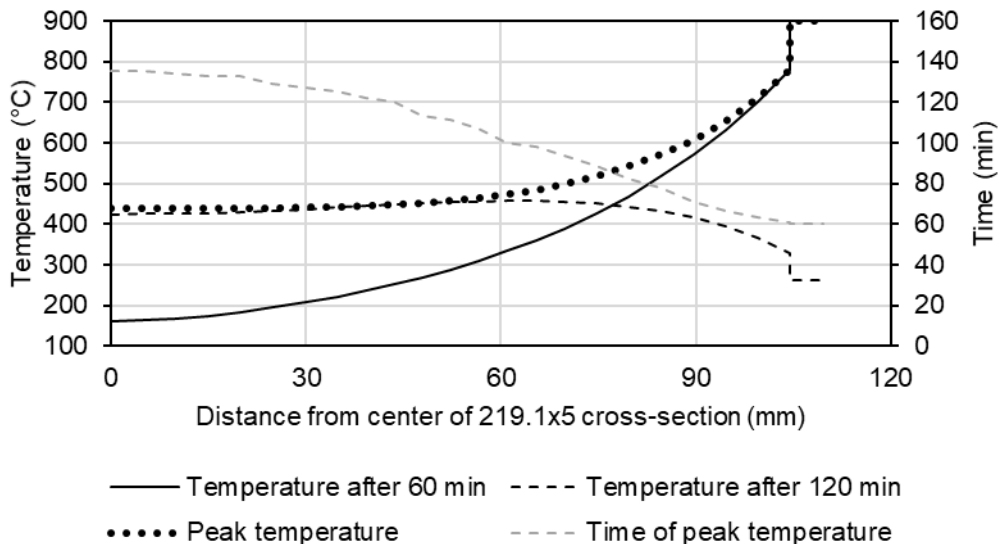


Fig. 4. Temperatures inside 219.1x5 mm tubular cross section filled with concrete, exposed to the ISO fire for 60 minutes followed by linear cooling in the next 60 minutes. Maximum temperature is obtained using non-reversible thermal properties described in Section 4.1 – it is recorded during cooling until steady-state at room temperature is reached.

In the CFD model, car fire in FDS is simulated for 120 minutes, after that time temperatures of dummy surfaces are assumed to be 20°C. Heat transfer analysis is further carried out in Abaqus for additional 18 hours, until the steady state at room temperature is reached (22±2°C in the entire solid

model). To model material properties that are a function of maximum temperature reached during heat transfer analysis, two subroutines are written in Fortran: USDFLD and UVARM.

Two previously described approaches are compared in terms of resulting temperatures. Selected results are presented in Fig. 5. It can be seen that the AST GAS approach yielded higher steel temperatures when compared to the BNDF approach.

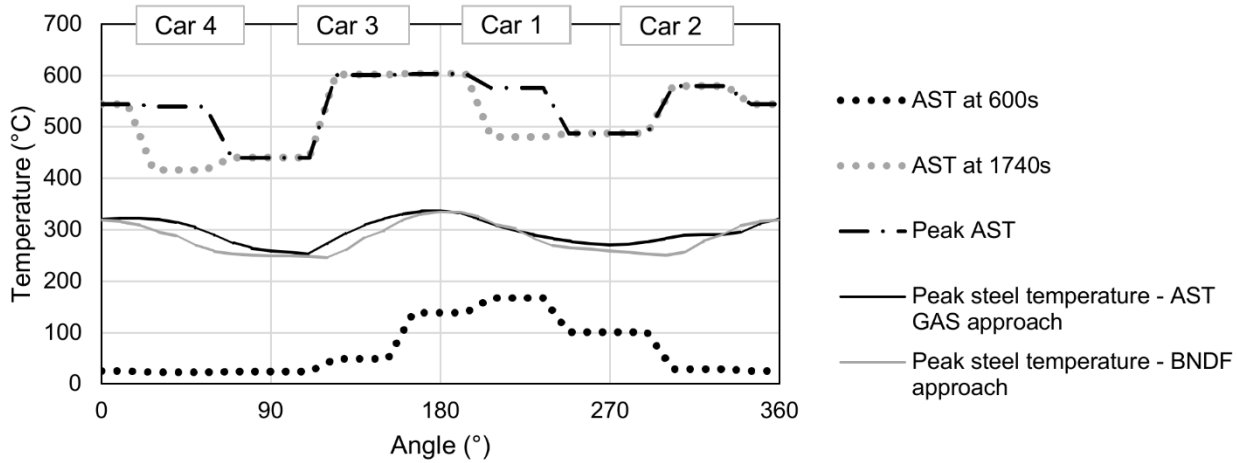


Fig. 5. The AST and steel surface temperatures at column's mid-height ($z=1600$ mm) along its circumference. The AST is presented 3 times: 600 s (only car 1 is in fire), 1740 s (all cars are burning, peak of HRR, Fig. 1) and maximum AST during whole analysis. AST is given only for the AST GAS approach, where dummy surface is circular. Solid lines represent peak steel temperatures during analysis.

4.3 FE model validation in fire

Results of a detailed study of performance of CFT columns in fire are presented in [16]. To validate FE model, calculated fire resistance times of 41 full-scale specimens are compared to data from tests in furnaces. Specimens included in the validation process were taken from research conducted in the recent years (1992-2013). Utilisation ratio of the analysed columns varied from 20 to 77 %, while the length varied from 3180 to 3810 mm. In terms of normalised resistance, the mean ratio between calculated and experimental fire resistance time is 1.00 with standard deviation equal to 0.26. Detailed validation results and model description is given in [16]. The above-mentioned model served as a base for study presented in this paper.

4.4 Mechanical analysis during and after fire

The typical response presented in terms of evolution of vertical displacement in time is shown in Fig. 6. The response can be divided into three separate stages, the first one is the thermally induced expansion of steel tube. During this stage tube separates from the concrete core and all loads are carried by the tube. While steel and concrete have similar thermal expansion coefficients, due to temperature differences, concrete core and steel tube act independently – load is carried only by steel tube. After that, loss of tube stability and a noticeable shortening of the column occurs. Since loading plate comes in contact with the concrete core, both steel tube and concrete core serve their load-bearing role. Failure occurs after a certain time due to further degradation of mechanical properties of both materials.

CFT columns are positioned at all four corners of 16.0 m x 5.0 m parking module, as presented in Fig. 1. Permanent load is assumed as 2.8 kN/m² and variable load (category F) as 2.5 kN/m². Hence, according to Eurocode 1, axial force applied on a column before fire analysis is 1100 kN. In the next step of mechanical analysis, results of previous heat transfer analyses are imported to the model, and temperature is changing according to the previously calculated conditions. After

20 hours of simulation time (see Section 4.2), column is loaded until failure using displacement control of top node. This way, its residual load-bearing capacity is estimated. Unfortunately, due to relatively non-harsh conditions, residual strength of steel remains unaffected (temperatures below 400°C), while the temperatures of concrete core do not exceed 200°C (Fig. 5). This means residual load-bearing capacity of CFT column is affected mainly by degradation of Young's modulus of concrete, which is less than 50% of its original value when compared to value at room temperature according to EN 1992-1-2. The highest temperature at concrete face is about 190°C, at depth of 20 mm it is 163°C, and at 40 mm it is 133°C. Neglecting the parts of the column that are close to supports, lowest temperature inside concrete core is slightly above 100°C. Although at this temperature there is no strength loss, Young modulus at this temperature is about 40% lower than its initial value. Difference between the BNDF approach and the AST GAS approach is found to be negligible in this analysis, however it might be worth to study performance of structures in more severe fires to draw general conclusions.

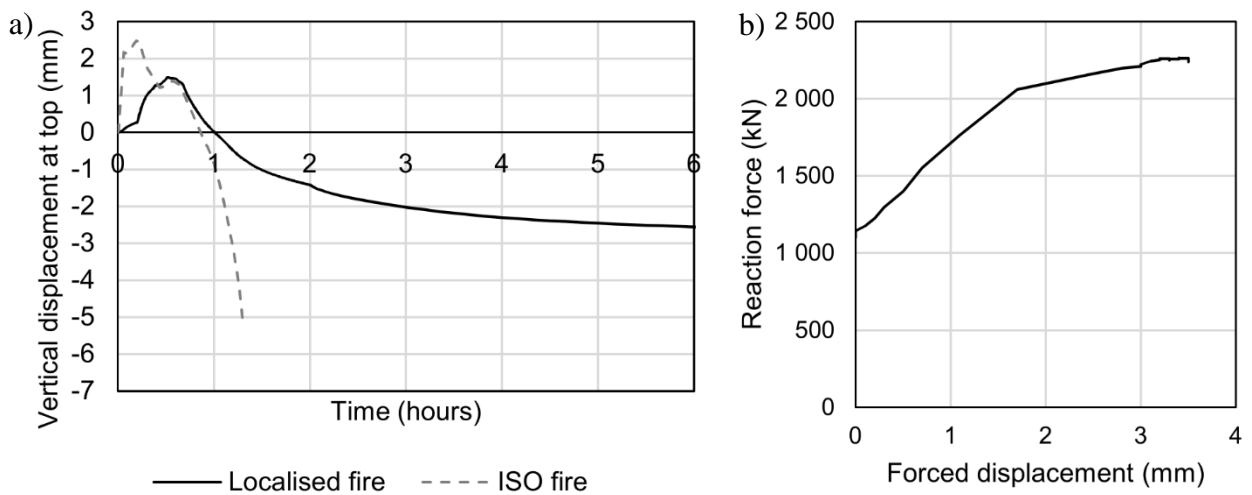


Fig. 6. a) column vertical displacements during localised fire (with CFD-FEM coupling) and ISO fire. Axial load: 1100 kN; b) Change of reaction force during displacement-controlled simulation of residual load-bearing capacity.

After reaching steady state close to room temperature, column previously exposed to localised fire is loaded until failure using displacement control of top node. The ultimate residual load-bearing capacity is 2 240 kN (Fig. 6 b).

5 CONCLUSIONS

This paper investigates a performance-based approach for assessment of performance of CFT column in an open car park fire. The selected fire scenario involves 4 cars around the column on the lowest deck of a multi-storey car park. A full-scale car fire simulation is performed in FDS software. Coupling between CFD and FEM is presented to provide temperature data around column during both heating and cooling stage. FE package Abaqus is used to calculate temperatures inside column, taking into account non-reversible material properties of concrete. Additionally, two approaches for data transfer between FDS and Abaqus are studied (using BNDF and Adiabatic Surface Temperature GAS), however the difference is found to be negligible. Afterwards, the performance of column is studied during the ISO and localised fire. The localised fire includes fire decay stage, where mechanical properties of concrete are assumed to be function of highest temperature reached during analysis. It is shown, that selected fire scenario gives relatively low temperatures that do not affect column's performance during and after fire. The maximum temperatures are about 650°C for the AST, below 400°C for steel tube surface and between 100 and 200°C for concrete core. Nevertheless, it is shown that general framework for performance-based

approach for assessment of performance can be established and CFT columns have a good performance in case of fire.

REFERENCES

1. Haremza, C., Santiago, A., da Silva, L.S. (2013). *Design of open steel and composite car parks under fire*, Advanced Steel Construction Vol. 9, No. 4, pp. 321-339.
2. Schleich, J.P., Cajot, L.G, Pierre, M., Brasseur, M., Franssen, J.M., Kruppa, J., Joyeux, D., Twilt, L., Van Oerle, J., Aurtenetxe, G. (1999). *Development of design rules for steel structures subjected to natural fires in closed car parks*, External report, pp. 49-59.
3. Charlier, M., Hanus, F, Vassart, O. (2017). *Parametric analyses of fire resistance of steel columns subjected to car park fire scenarios*. 2nd International Fire Safety Symposium, Naples, Italy, June 7-9, IFireSS, 2017.
4. McGrattan, K., Hostikka, S., McDermott, R., Floyd, J., Vanella, M., Weinschenk, C., Overholt, K., (2017) *Fire Dynamics Simulator User's Guide*, NIST Special Publication 1019 Sixth Edition, Baltimore, Maryland, USA, November 1.
5. Society of Fire Protection Engineers, *SFPE handbook of Fire Protection Engineering*, 3rd Edition, 2003.
6. Eurocode 2: Design of concrete structures - Part 1-2: General rules - Structural fire design, European Committee for Standardization, December 2004.
7. Eurocode 3: Design of steel structures - Part 1-2: General rules - Structural fire design, European Committee for Standardization, April 2005.
8. Wickström, U., Duthinh, D., McGrattan, K. (2007). *Adiabatic surface temperature for calculating heat transfer to fire exposed structures*, Interflam 2007: Vol. 2, Proceedings of the 11th International Interflam Conference, London, England, Vol. 2, pp. 943-953.
9. Malendowski, M. (2017). *Analytical Solution for Adiabatic Surface Temperature (AST)*, Fire Technology, Vol. 53, Issue 1, pp. 413-420.
10. Szymkuć, W., Glema, A., Malendowski, M. (2016). *Fire performance of composite concrete filled tubular columns exposed to localized fire*, Advances in Mechanics: Theoretical, Computational and Interdisciplinary Issues: Proceedings of the 3rd Polish Congress of Mechanics (PCM) and 21st International Conference of Computer Methods in Mechanics (CMM), CRC Press, pp. 573-576.
11. Tao, Z., Wang, X-Q, Uy, B. (2013). *Stress-Strain Curves of Structural and Reinforcing Steels after Exposure to Elevated Temperatures*, Journal of Materials in Civil Engineering, 25 (2013), pp. 1306-1316.
12. Jansson R., (2004). *Measurement of Concrete Thermal Properties at High Temperature*. Proceedings from the fib Task Group 4.3 workshop "Fire Design of Concrete Structures: What now? What next?", Milan, Italy, December 2-3, 2004.
13. Khoury, G.A., Anderberg, Y., Both, K., Fellingner, J, Høj, N.P., Majorana, C. (2007). *fib Bulletin No. 38: Fire design of concrete structures - materials, structures and modelling*, International Federation for Structural Concrete (fib).
14. Hager, I., (2013). *Behaviour of cement concrete at high temperature*, Bulletin of the Polish Academy of Sciences. Technical Sciences, Vol. 61, No. 1, 2013, pp. 145-154.
15. Gernay, T., Franssen, J.-M. (2015). *A performance indicator for structures under natural fire*, Engineering Structures 100 (2015), pp. 94-103.
16. Szymkuć, W., Glema, A., Malendowski, M. (2015). *Fire performance of steel tubular columns filled with normal strength concrete*, Proceedings of 5th International Workshop on Performance, Protection & Strengthening of Structures under Extreme Loading (PROTECT 2015), Michigan State University, East Lansing, USA, DEStech Publications Inc., pp. 865-872.

ANALYSIS OF THE INFLUENCE OF VENTILATION IN THE STRUCTURAL RESPONSE OF A CUT-AND-COVER TUNNEL UNDER FIRE

Juan Pagán-Martínez¹, Ignacio Payá-Zaforteza², Antonio Hospitaler³, Toni Hospitaler⁴

ABSTRACT

This paper analyses the influence of tunnel ventilation on the structural response of a 500 m long cut-and-cover tunnel submitted to the combustion of a truck carrying dangerous goods inside. The tunnel has a rectangular cross section, which is an important difference with previous studies which focused on other types of section (e.g. circular or ovoidal).

The analysis uses a performance approach with three basic components: a model of the fire event, a heat transfer analysis to obtain the temperatures within the structure and a simplified model to obtain the tunnel structural response.

The fire model is built using Computational Fluid Dynamics (CFD). It uses the tunnel geometry, materials, traffic and ventilation as the main input parameters. Nine different fire scenarios considering different truck positions have been studied and two different possibilities were considered regarding ventilation for the worst fire scenario.

If the designed ventilation systems fail to work properly during the fire, then tunnel will collapse after 30 minutes of fire exposure. However, if they work properly, the maximum temperature reached in the central section of the tunnel decreases by an amount of 37% and then, the tunnel will not collapse even after two hours of fire exposure. Therefore, ventilation is crucial for the appropriate response of the tunnel during the fire.

Keywords: Tunnel Ventilation, Computational Fluid Dynamics, Thermo-structural Analysis.

1 INTRODUCTION

Tunnel fires have specific features (e.g. oven effect, poor visibility and increased toxic gas concentrations) that make them have consequences much more severe than open air fires. In addition, from the point of view of structural analysis, the sharp rise of the ceiling gas temperature, often in excess of 1000°C within a few minutes and induces abrupt reductions of the structural capacity of the tunnel structural elements. Therefore, tunnel fires deserve special attention as also proved by previous incidents.

Within this context, the goal of this paper is to apply a performance based approach methodology to evaluate the influence of the ventilation in the tunnel structural response.

¹ Fire Engineer. Jeremy Gardner Associates. Dublin, Ireland.

e-mail: jpmartinez@jgafire.com

² Associate Professor. ICITECH. Universitat Politècnica de València, Valencia, Spain.

e-mail: igpaza@upvnet.upv.es

³ Professor. ICITECH. Universitat Politècnica de València, Valencia, Spain.

e-mail: ahospitaler@cst.upv.es

⁴ Fire Engineer. ICITECH. Universitat Politècnica de València, Valencia, Spain.

e-mail: toni.hospitaler@gmail.com

A cut-and-cover tunnel with rectangular cross section, reinforced concrete retaining walls and a top reinforced concrete slab has been analysed. The tunnel is 477m long and has a rectangular cross section with an average width of 16m and an average height of 6m.

2 FIRE MODEL

2.1 Fire Scenarios

In order to model the fire scenario and obtain the temperature field within the tunnel domain, a performance based (in lieu a prescriptive analysis) by using the FDS software (Fire Dynamics Simulation) has been used. FDS is a Computational Fluid Dynamic software orientated to fire dynamics. The analysis is developed within a computational domain created by rectangular cells generating a rectilinear Cartesian grid. FDS provides numerical solution for the low-speed thermal flow Navier-Stokes equations, emphasizing the smoke and heat transport from the fire.

Different fire scenarios considering nine fire load positions have been studied (i.e. fire load located at the beginning of the tunnel, at the end and centered). Additionally, fire loads placed adjacent to the lateral retaining walls and centered on the road have been considered respectively in each longitudinal position.

2.2 Control Volume

In order to assess the adequate control volume, a number of fire models have been carried out considering different variables (i.e. taking into consideration the influence of the road geometry, fire load, external conditions, tunnel ventilation and grid sensibility).

A 500 m long cut-and-cover tunnel with rectangular cross section, reinforced concrete retaining walls and a top reinforced concrete slab have been included in the FDS model using a three-dimensional CAD model as a basis.

External areas at the beginning and at the end of the tunnel have been included in the simulation domain to provide a transition between the internal fire scenario and the fixed ambient conditions on the mesh boundary. This design improves the smoke movement coming out from the tunnel developing a more reliable simulation and avoiding numerical instabilities in the analysis.

The control volume is comprised by 17 parallelepiped meshes (15 meshes of 30x30x5.7m in average for the tunnel geometry and 2 meshes of 15x30x20m for the tunnel external). On this basis, the model has been formed by 846,000 cells approximately.

The cell size (dx) for a given simulation can be related to the characteristic fire diameter (D^*), i.e., the smaller the characteristic fire diameter, the smaller the cell size should be in order to adequately resolve the fluid flow and fire dynamics. The characteristic fire diameter (D^*) is given by the following relationship:

$$D^* = \left(\frac{\dot{Q}}{\rho C_p T \sqrt{g}} \right)^{\frac{2}{5}} \quad (1)$$

Where \dot{Q} is the heat release rate (kW), ρ is the air density (kg / m^3), C_p is the specific heat (kJ/KgK), T is the ambient temperature (K) and g the gravity (m/s^2).

On this basis, according to our model variables, a fire diameter of 7.89 has been obtained. Therefore, following the U.S. Nuclear Regulatory Commission (NRC) recommendations (i.e. D^*/dx ratio should be between 4 and 16), a cubic cell size (dx) of 0.5m has been implemented as a result of the sensibility analysis.

In addition, a numerical efficiency criterion has been carried out so that the number of divisions (number of cells) in each direction (within each mesh) are factorable by 2, 3 and 5.

2.3 Tunnel Ventilation Hypotheses

Two different hypotheses have been considered regarding the ventilation during the fire event:

- Situation 1. Emergency ventilation systems are affected by the fire exposure and therefore cannot work during the fire event. The worst scenario in terms of structural damage has been developed via this hypothesis.
- Situation 2. The tunnel longitudinal ventilation works during the fire. This ventilation has been introduced in the CFD model.

2.4 Tunnel Ventilation design

2.4.1 Critical Velocity

The tunnel ventilation design has been carried out considering the ventilation needs of the tunnel according to its geometric characteristics and the fire load with the aim of preventing backlayering. Critical velocity parameter has been analysed to study this phenomenon which can be defined as the minimum steady-state velocity of the ventilation airflow moving toward the fire, that is required to prevent backlayering at the fire site.

Once the critical speed velocity of a tunnel has been calculated, it is possible to proceed designing the emergency ventilation system in case of fire by calculating the necessary thrust so that the ventilation system is able to avoid the backpropagation of smoke and hot gases.

In order to calculate the critical velocity, Kennedy [1] provided two equations, *Eq. (2)* and *Eq. (4)*, that can be solved simultaneously by iteration or via using the expression provided by Tarada [2], *Eq. (5)*, solving a cubic equation of critical velocity with real coefficients.

$$V_c = \left(\frac{gH\dot{Q}_c}{\rho C_p A T_f Fr_m} \right)^{\frac{1}{3}} \quad (2)$$

$$Fr_m = 4.5(1 + 0.0374 |\min(\text{grade}, 0)|^{0.8})^{-3} \quad (3)$$

$$T_f = \frac{\dot{Q}_c}{\rho C_p A V_c} + T \quad (4)$$

$$(Fr_m A C_p T \rho) \cdot V_c^3 + (Fr_m \dot{Q}_c) \cdot V_c^2 - gH\dot{Q}_c = 0 \quad (5)$$

Where V_c is the critical velocity (m/sec), Fr_m is the critical Froude number factor, g is gravitational acceleration (m/sec^2), H is the height of the tunnel (m), \dot{Q}_c is the convective fire heat release rate (W), ρ is the density of the upstream air (kg/m^3), C_p is the specific heat of air at constant pressure (J/kgK), A is the tunnel area (m^2), T_f is the average temperature of the fire site gases ($^{\circ}\text{K}$), and T is the temperature of the approach air ($^{\circ}\text{K}$).

The convective fire heat release rate has been considered as 80% of the maximum heat release rate, as per Ingason [3] recommendations. A rectangular cross-section tunnel of 477m in length, 5.77m in height and 16.2m in width has been analysed, considering a maximum heat release rate of 200MW as assessed in Section (2.6). On this basis, a critical velocity of 2.81 m/s has been obtained.

2.4.2 Emergency ventilation design

Longitudinal ventilation design has been considered via by using jet fans that, through an exchange of momentum between jet fans and mass of air in the tunnel, are able to induce a large fresh air flow into the tunnel. During fire scenario they avoid smoke back layering and keep under control the smoke propagation maintaining clear zones occupied by users. In addition, a significant temperature reduction has been achieved, which is vital for the structural load bearing capacity.

The main characteristic of a jet fan is the thrust, that has been defined by the following expression: -

$$T_m = \frac{\rho q_{vF}^2}{A_f} \quad (6)$$

Where T_m is the jet fan thrust (N), ρ is the density of the jet fan upstream air (kg/m^3), A_f is the jet fan cross-section area (m^2) and q_{vF} is the impulsion flow provided by the jet fan (m^3/s).

Based on the critical velocity, the thrust force, number and location of required jet fans have been calculated so that the smoke backlayering is prevented, considering the pressure losses (p_t) due to different factors in the fire scenario. Therefore, the total thrust (T_t) to be installed within the tunnel ventilation has been estimated as follows:

$$T_t = p_t \cdot A \quad (7)$$

$$p_t = p_{en-ex} + p_{drag} + p_L + p_{fire} + p_{chim} \quad (8)$$

Where p_{en-ex} are the pressure losses provoked by the entrance and exit tunnel sections. These losses are related to the tunnel shape and the dynamic pressure within the tunnel during the fire, which itself is related to the critical velocity; p_{drag} are the pressure losses due to the traffic in the tunnel, where a stopped heavy vehicle has been considered during the fire; p_L are the pressure losses due to the tunnel surface friction; p_{fire} are the pressure losses due to the fire and p_{chim} are the pressure losses due to the chimney effect based on the tunnel grade.

All factors have been evaluated, obtaining 127 Pa of total pressure losses within the tunnel and therefore, 11875 N of total thrust force has been implemented considering Eq. (7).

On this basis, six groups of 2 parallel Jet Fans were provided in the actual tunnel. Each Jet Fan therefore, provides a thrust force of 990N with a cross-section area of 0.37m^2 .

2.4.3 Jet Fans disposition

To prevent that jet fans are affected by the influence of each other in longitudinal and transversal disposition, the recommendations given by Cory [4] have been implemented as follows:

- Two parallel Jet Fans should be separated a distance similar to the tunnel hydraulic diameter. Additionally, this distance should be greater than the Jet Fan dynamic pressure measured in mmHg.
- Two Jet Fans should be separated a distance greater than 10 times the tunnel hydraulic diameter lengthwise. Additionally, a separation equal to one tenth of the jet fan dynamic pressure measured in Pa can be considered as empiric recommendation.

The hydraulic diameter of the tunnel has been evaluated as 8.5m and Jet Fan dynamic pressure has been calculated as 990Pa (7.4 mmHg).

On this basis, each couple of parallel jet fans has been placed 10m separated crosswise and 85m lengthwise. In addition, each fan has been implemented 1m from the tunnel concrete upper slab and 2m from the adjacent lateral retaining wall.

2.4.4 FDS ventilation model

Each Jet Fan has been modelled in FDS via the HVAC tool implemented in the software. In FDS, an HVAC system is described as a network of duct segments and nodes. Nodes can either connect two or more ducts or be an endpoint where an HVAC duct connects to the FDS computational domain. Therefore, it is only necessary to draw the true geometry at vents where the HVAC system connects to the FDS domain. To model a jet fan, connection between the inlet flow to the outlet while preserving the fuel, air, and product mixture has been carried out.

For the HVAC model, a standard HVAC duct of 1m with vents and both downstream and upstream square hollow shrouds of 2m in length and have been implemented. The reason to add a shroud is to make sure the outlet flow is in the axial direction, ensuring that the one dimensional axial velocity is preserved at the fan outlet.

A quadratic relation between pressure (Pa) and volume flow rate (m³/s) has been implemented defining two working situations (i.e. maximum flow rate and maximum pressure).

2.5 Load. Justification

The heat release rate peak value for heavy goods vehicles greater than 3.5m in height proposed by Ingason [5] as a variation of presented in the French regulations [6] has been implemented. In addition, the exponential curve proposed by Ingason for fuel-controlled fires has been chosen to represent the fire behaviour as it gives a realistic model of fire in tunnels and being a single expression, it is more robust and easier to implement.

2.6 Fire Model Results

Fire model results (temperatures in the gas surrounding the tunnel structure) considering that ventilation system has been damage due to the fire show that maximum temperatures (i.e. 1300°C approximately) are achieved in the central section of the tunnel (specifically within the concrete slab area) when the fire load is centered lengthwise and crosswise.

Fig. 1 shows temperatures measured by the FDS thermocouple located above the fire load and attached to the top concrete slab during the fire. Fire model results show a decrease of the maximum temperature reached in the central section of the tunnel of 37% (i.e. from 1300°C to 820°C) when longitudinal ventilation is provided within the tunnel.

3 HEAT TRANSFER MODEL

Fire models usually predict the heat flux to geometrically simple solid surfaces which are thermally defined by one-dimensional heat transfer model, while thermal/structural finite element models typically assume a global gas temperature surrounding a detailed two or even three dimensional model of a structural element.

In order to transfer gas phase data from numerical fire simulations (CFD calculations) in the form of single temperatures as boundary input to finite element codes (for calculating temperatures in fire exposed structures), the concept of adiabatic surface temperature (T_{AST}) proposed by Wickström [7] has been used.

On this basis, the equation that governs the total heat flux per unit area as the sum of the heat flow per unit area due to convection and radiation, is as follows:

$$q_{tot} = q_{rad} + q_{conv} \quad (10)$$

$$q_{tot} = \varepsilon_m \sigma (T_{AST}^4 - T_S^4) + h(T_{AST} - T_S) \quad (11)$$

Where q_{tot} is the total heat flow per unit area (W/m²), q_{rad} and q_{conv} the radiation and convection heat flow respectively per unit area (W/m²), ε_m the material emissivity, h the convection heat transfer coefficient (W/m²K), T_S the surface temperature (K) and σ the Stefan-Boltzman constant = $5.67 \cdot 10^{-8}$ (W/m²K⁴).

Eq. (11) shows the T_{AST} as a fluid phase temperature which can be used for calculating both the radiation and convection heat transfer. Therefore T_{AST} is interpreted by the FEM as the radiation temperature analysing the heat transfer by radiation and, in addition, the gas temperature surrounding the surface analysing the heat transfer by convection.

The influence of temperature results from the fire model on the developed temperatures within the most unfavourable tunnel section has been evaluated through a heat transfer transient finite element analysis done with the Abaqus software.

Two-dimensional heat transfer elements (four-node linear elements with a nodal temperature degree of freedom) have been used for estimating the thermal response of the tunnel section. Thermal properties of materials are indicated in *Table 1*: -

The heat transfer model has been calibrated with the results obtained by Wickström [8] and the Eurocode recommendations [9] and results show that the top slab is the critical element of the structure. This slab reached maximum temperatures of 1100°C in the absence of ventilation.

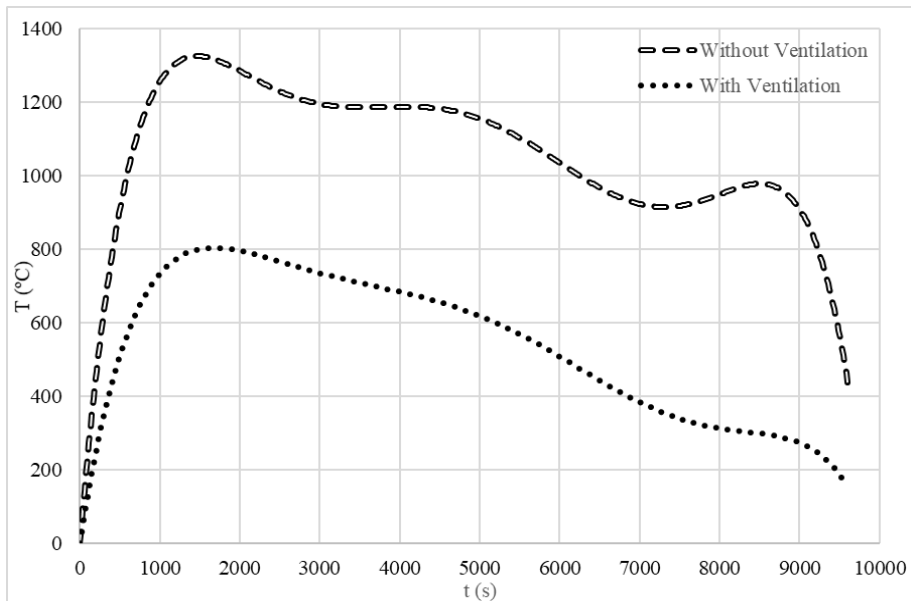


Fig 1. Gas temperature comparison between the ventilated and non-ventilated tunnel. Temperatures measured by the FDS thermocouple centered longitudinally and transversally on the tunnel top slab.

Table 1. Thermal Properties of materials

Material	Specific Heat (Cp) [J/KgK]	Density (ρ) [Kg/m ³]	Thermal Conductivity (λ) [WmK]
Reinforced concrete	Variation with temperature proposed by [8] assuming a moisture content of 3%	Variation with temperature proposed by [8]. ρ (20°C) = 2500kg/m ³	Variation with temperature proposed by [8] considering the top limit
Neoprene	2140	1240	0.23
Asphalt	1000	2100	0.7
Graded aggregates	Linear variation with temperature: 910-1180	Linear variation with temperature: 1700-2200	2

4 STRUCTURAL ANALYSIS

4.1 Simplified Method of Isotherm 500°C

The 500°C Isotherm method provides a process to evaluate the resistance of a reinforced concrete structural element exposed to fire through a sectional analysis.

This method, recommended by the Eurocode 2 [10], assumes a reduction of the reinforced concrete cross section when the temperature achieves 500°C within the concrete element.

On this basis, it is considered that concrete areas with a temperature higher than 500°C have their properties so depleted that the resistant contribution to the structural element can be neglected.

The steel bars located outside of the reduced section keep their full strength, whereas the bars whose temperature is higher than 500 °C have their strength reduced as a consequence of their temperature.

4.2 Geometrical and mechanical properties

As outlined in Section 3, the top concrete slab is the most unfavourable structural element within the tunnel section exposed to the fire. Additionally, the central section of this concrete slab has reached the highest temperatures and therefore, this section has been evaluated in the present article. A 1500-mm high and 1750-mm wide I-shape cross-section reinforced with three layers of steel bars (i.e. fifteen 25-mm steel bars with a cover depth of 47,5 mm, eight 25-mm steel bars with a cover depth of 87,5 mm and fifteen 16-mm steel bars with a cover depth of 1432 mm) are considered.

The mechanical material behaviour for reinforced concrete (30 MPa of characteristic strength at ambient temperature and calcareous aggregates) as a function of temperature has been implemented based on the model recommended by EC 2 Part 1-2 [10].

The stress diagrams caused by external loadings applied on each structural element of the tunnel have been obtained developing a geotechnical model using the finite element software Plaxis.

In this model, the construction process, geotechnical and hydrogeological properties of the soil and traffic loads have been considered.

4.3 Interaction Diagrams

The interaction diagrams M-N (bending moment –axial force) for the analysed concrete slab section in fire situation have been developed based on the reduced section properties and the mechanical behaviour of materials as a function of temperature. On this basis, *Fig. 2* shows the interaction diagrams of the mid-span cross section of the top slab without ventilation system and when the designed longitudinal ventilation system is provided.

Without ventilation, the increment of temperatures within the section reduces the strength gradually from the beginning of the fire. This reduction becomes especially sharp up to 30 minutes of fire exposure so that the ultimate bending moment capacity is reduced to 68% of the actual value at ambient conditions. After 30 minutes of fire exposure, the concrete cover is reduced more than 40mm as temperature within this region reaches 560°C and its strength is neglected. After 30 minutes of fire exposure, the temperature in the first rebar layer (closest to the fire) achieves 260°C, and therefore, the yield strength of reinforcement is reduced to 69% of the actual value at ambient conditions (i.e. from 500MPa to 345Mpa). As a result, 30 minutes after the beginning of the fire, stresses induced by the external loads are greater than the capacity of the structural element and therefore, structural failure is predicted.

When the designed longitudinal ventilation system is provided, the strength reduction within the structural element can be neglected showing that the ultimate bending moment capacity is reduced to 94% of the actual value at ambient conditions after 1hour of fire exposure. As a result, the capacity of the structural element is greater than the stresses induced by the external loads and therefore, structural failure will not be produced during the fire exposure.

5 CONCLUSIONS

A structural analysis of the fire response of a cut and cover tunnel has been presented.

The analysis has been carried out using a performance approach, obtaining the temperatures field during the fire (higher than 1200°C) from a detailed fire model in lieu of using a prescriptive approach based on the fire curves proposed in the literature. Using this fire model information as input parameter, a transient heat transfer finite element analysis has been performed providing field temperatures information within the tunnel section. A longitudinal ventilation system design via Jet Fans has been developed and included in the fire model so that the ventilation influence has been analysed in the gas temperatures achieved during the fire and the structural tunnel behaviour.

Results from the structural analysis based on the isotherm 500°C method show that the tunnel top slab is the critical element and that it would collapse 30 minutes after the beginning of the fire if the emergency ventilation system fails. However, if ventilation systems work properly during the fire, the structural collapse will not occur. Therefore, ventilation systems are of major importance for both, the objective of life safety and the objective of structural safety, and should be properly protected and maintained.

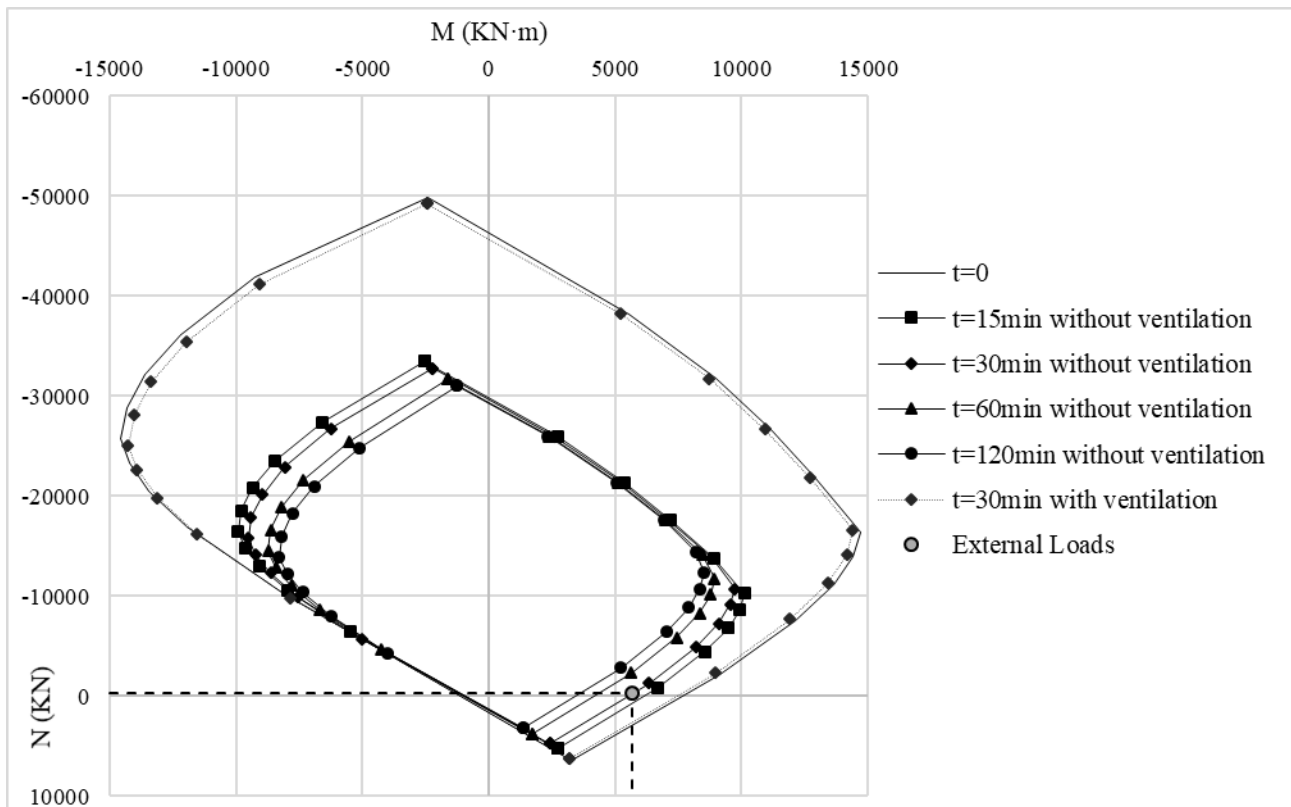


Fig 2. Interaction diagrams for the central section of the top concrete slab without emergency ventilation. Emergency ventilation system influence after 30 minutes of fire exposure.

REFERENCES

1. Kennedy W.D. (2011). *Critical Velocity: Past, Present and Future*. One Day Seminar on Smoke and Critical Velocity in Tunnels.
2. Tarada F, (2010). *New Perspectives on the Critical Velocity for Smoke Control*. 4th International Symposium on Tunnel Safety and Security.
3. Ingason H, Li Y. Z., Lönnemark A, *Tunnel Fire Dynamics*.
4. Cory W. (2005). *Fans & Ventilation A Practical Guide: ELSEVIER*.
5. Ingason H. (2005). *Fire Development in Large Tunnel Fires*. 8th Fire Safety Science Proceedings, pp. 1497–1508.
6. Lacroix, D. (1997). *New French Recommendations for Fire Ventilation in Road Tunnels*. 9th International Conference on Aerodynamics and Ventilation of Vehicle Tunnels, Aosta. Valley, Italy, 6-8 October.
7. Wickstrom, D, et al. (2007). *Adiabatic Surface Temperature for Calculating Heat Transfer to Fire Exposed Structures*.
8. Wickström, Ulf (1986). *A very simple method for estimating temperature in fire exposed concrete structures*, reprinted from “New Technology to Reduce fire Losses & Cost”. Swedish National Testing Institute.
9. European Committee for Standardization (CEN) (2004). *Eurocode 2: Design of concrete structures – Part 1–2: General rules – Structural fire design. ENV 1992-1-2*.

REVERSE ENGINEERING OF STANDARD TEMPERATURE CURVES TO OBTAIN THE HRR OF THE FIRE IN VARIOUS ENCLOSURE CONFIGURATIONS - WHAT CAN WE LEARN FROM THAT?

Piotr Tofiło¹, Wojciech Węgrzyński², Michał Malendowski³

ABSTRACT

As fire engineers we sometimes ask ourselves a question: what kind of a fire would need to occur for an ISO-curve temperature to develop in a given compartment? How would it be affected by various sizes of the compartment, openings or materials? This information could potentially provide us some guidance when trying to quickly assess the fire safety of the structure by comparing the HRR curve of a particular design fire with such a reverse engineered HRR curve.

Keywords: standard temperature curve, heat release rate, equivalent time of fire exposure

1 INTRODUCTION

As fire engineers we sometimes ask ourselves a question: what kind of a fire would need to occur for an ISO-curve temperature to develop in a given compartment? How would it be affected by various sizes of the compartment, openings or materials? This information could potentially provide us some guidance when trying to quickly assess the fire safety of the structure by comparing the HRR curve of a particular design fire with such a reverse engineered HRR curve.

2 THE ALGORITHM FOR REVERSE ENGINEERING OF THE TEMPERATURE CURVE TO OBTAIN THE HRR CURVE OF THE FIRE

There is no single formula that could answer the question of how big the fire should be to cause an ISO-curve temperature of the upper gas layer, however some solutions exist to correlate the gas phase temperature with the size of fire like the MQH equation which can be reorganized to become a formula for HRR.

$$Q = \sqrt{\left(\frac{\Delta T}{6.85}\right)^3 h_R A_T A_o \sqrt{H_o}} \quad (1)$$

This approach however has some important limitations i.e. steady state HRR, single construction material and single timestep analysis. Another option is the commonly known formula for the maximum heat release in the compartment based on the size of opening. This approach does not

¹ Main School of Fire Service (SGSP), ul. Słowackiego 52/54, Warsaw, 01-629, Poland

e-mail: ptofilo@sgsp.edu.pl

² Building Research Institute Institute (ITB), ul. Filtrowa 1, 00-611, Poland

e-mail: w.wegrzynski@itb.pl

³ Institute of Structural Engineering, Poznan University of Technology, Piotrowo 5, 60-965 Poznań, Poland.

e-mail: michal.malendowski@put.poznan.pl

include any information on enclosure size or materials used, so at this stage we can assume it may be less accurate, but admittedly easy to use.

$$Q_{MAX} = 1500A_o\sqrt{H_o} \quad (2)$$

To solve the problem with a discrete temporal domain authors have developed a computer program which runs multiple CFAST simulations in a given compartment to implicitly solve for target gas layer temperature by varying the HRR within each discrete time step. Each time step is solved iteratively until the desired value of the upper layer temperature (ISO) is reached within specified tolerance and then the solution is passed to the next time step until 240th minute of calculation is solved. The algorithm starts with a guess or previous HRR value and continues towards the temperature curve using steps that are doubled until it crosses the temperature curve and from there every next step is a half of previous one. This is iterated until we reach a desired tolerance. This iterative procedure is explained below visually.

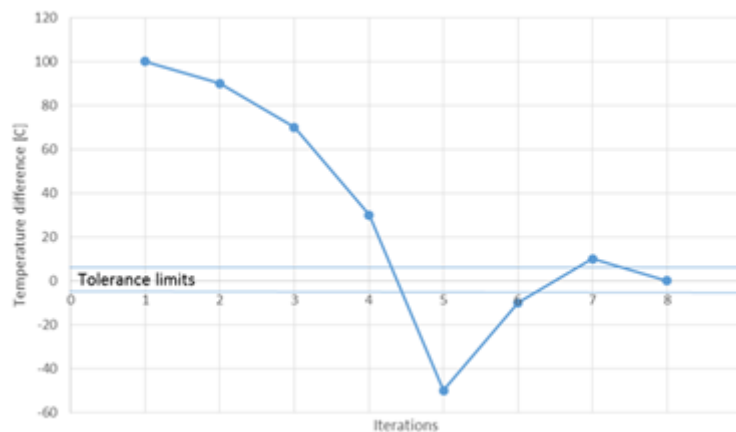


Fig. 1. Iterative procedure to achieve a desired tolerance for the prediction of HRR

3 INITIAL OBSERVATIONS

From the experiments performed so far (Fig. 2) the opening size seems to have the strongest effect on HRR curve, stronger than the opening factor $O = A_o\sqrt{H_o}/A_T$. This means that the larger the opening, the more HRR we need to maintain the desired temperature because a lot of heat we lose through the opening. The HRR curve may be considered as “steady state” for small values of opening factor (0.02), while it is growing with time for larger values. The height of the compartment has a small effect on HRR if the opening is at the bottom. Reverse HRR curves seem to correspond to 30-50% of the maximum theoretical HRR (Eq.2). This suggests that the “standard” fires are not yet underventilated. Definitely more insight is possible here. For example other temperature curves can be studied in a similar way e.g. Eurocode parametric fire. In general we would like to see how parametric fire compares with zone models.

Numerical Modelling

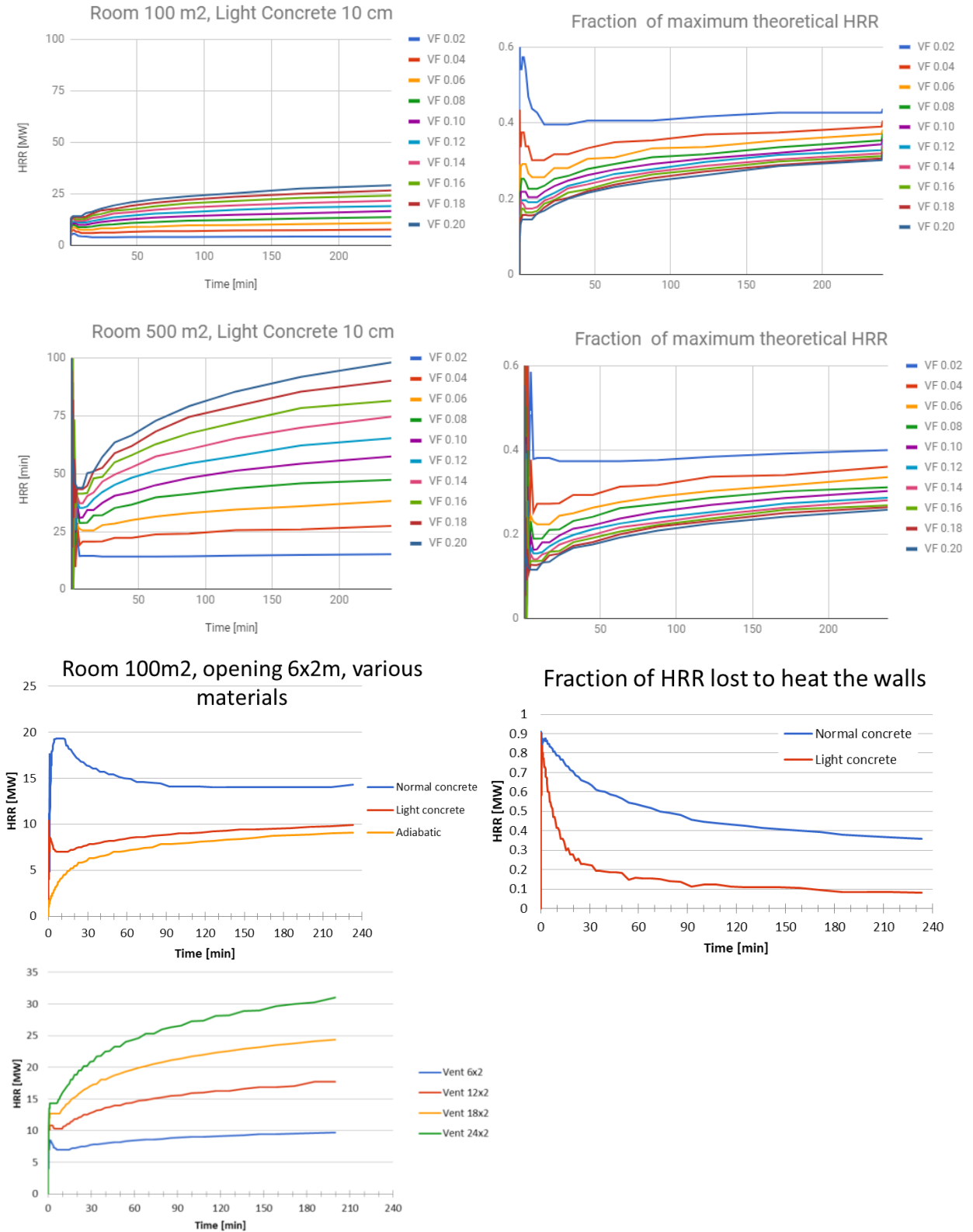


Fig.2. Initial studies of: a-d) fraction of theoretical HRR e-f) effect of boundary materials on HRR g) effect of vent size

4 COMPARISON BETWEEN THE REVERSE ENGINEERING HRR AND T2 FIRES.

Two compartments are compared, with floor areas equal to 100m² and 500m². In both cases, analyses are done for two extreme values of opening factors: 0.02 and 0.2 (Eurocode 1991-1-2). Hence, 4 geometrically different configurations are considered. In all the analyses, α -t² fires, with slow, medium, and fast growing rates are taken into account. The fire load density is assumed equal to 750MJ/m², whereas two values of the maximum rate of heat release per unit area are considered: 250 kW/m² and 500 kW/m². The fire load is assumed to be uniformly distributed over the compartment's floor. Decay phase starts when 70% of fuel is burnt. The condition for the maximum heat release rate due to ventilation conditions (eq.2) is taken into account.

Figs. 3-4 show the comparisons between HRR curves obtained from the reverse engineering algorithm and the α -t² HRR curves evaluated according to Eurocode 1991-1-2. Fig.3 refers to 100 m² compartment, whereas Fig.4 refers to 500 m² compartment. It can be seen, the initial, parabolic, heat release rate is slower than the HRR needed to obtain ISO-curve conditions, but only to some extent. The maximum HRR can easily exceed the reverse engineering HRR curve. It happens between 15 and 60 minute of fire, depending on the assumed HRRmax and the fire growth rate. It happens especially fast for weak ventilation conditions (opening factor 0.02).

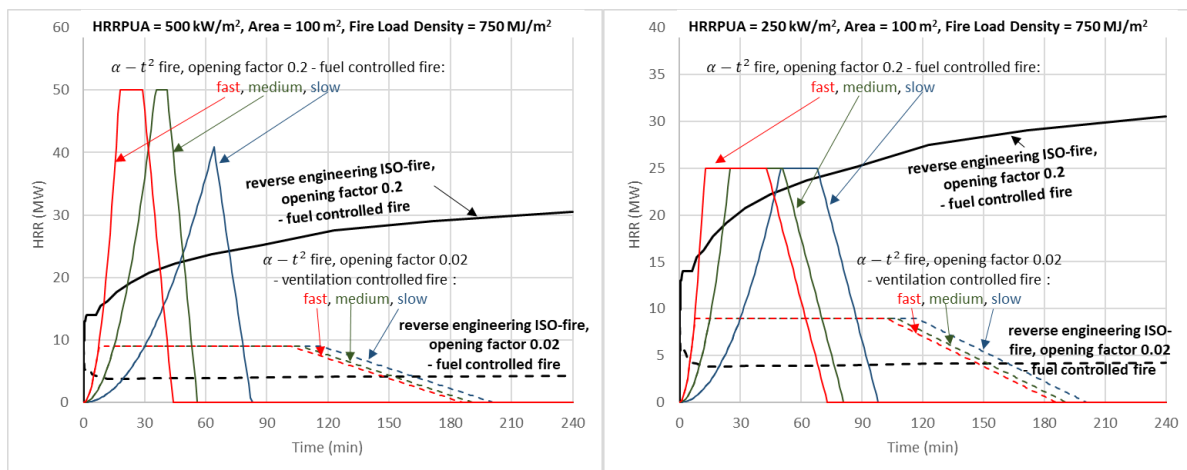


Fig. 3. Comparisons between reverse engineering HRR and α -t² fires for 100 m² compartment:
 a) HRRPUA = 500 kW/m²; b) HRRPUA = 250 kW/m²

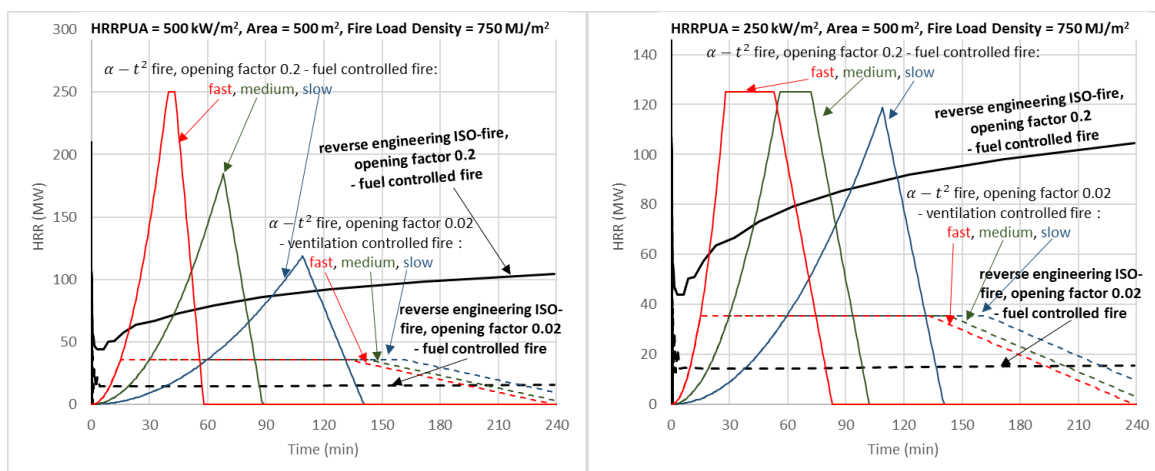


Fig. 4. Comparisons between reverse engineering HRR and α -t² fires for 500 m² compartment:
 a) HRRPUA = 500 kW/m²; b) HRRPUA = 250 kW/m²

5 ESTIMATION OF AN EQUIVALENT TIME OF FIRE EXPOSURE

Estimation of an equivalent time of fire exposure is one of the main questions structural fire engineers ask when dealing with natural fires. All the fire resistance testing is carried out for an ISO-fire exposure. Here the energy-based procedure of an equivalent time of fire exposure is proposed. Assume, the known relationship between the rate of heat released and time that results in ISO-curve conditions in the upper layer of fire in a compartment, as well as the known HRR relationship for a designed fire. Then, an integral of a HRR-curve is the cumulative energy released. The graphs of a total energy released versus time for a ISO-fire and designed fire are then compared, as shown in Fig. 5.

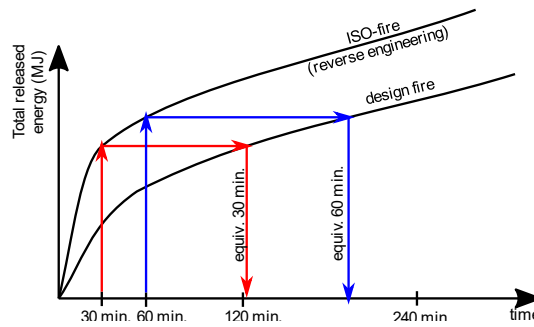


Fig. 5. Idea of an estimation of an equivalent time of fire exposure

The equivalent time of fire exposure is then estimated based on the comparison of total energies released by the ISO-fire and the design fire. This is shown in Fig. by two exemplary estimations for 30 min and 60 min.

This approach is essentially simpler than material-based approaches already existed in literature [2-6]. In the previous approaches, the estimation of the equivalent time of fire exposure based on the comparison between the total energy stored by the structural elements in the ISO-fire exposure and the design fire (often referred to a parametric fire curves). Here, the parameters of materials that creates the physical obstacles are inherently included in the zone-model used to evaluate the HRR-curves. As long as the heating rate of structural elements lies between 2-50 K/min, the fire-induced structural response should not differs between the ISO-curve exposure and design fire of an equivalent time.

Figs. 6-9 show the cumulative energy graphs for reverse engineering ISO-fires and $\alpha-t^2$ fires. The energy necessary to be released in order to obtain ISO-curve conditions is smaller than the energy released from $\alpha-t^2$ fires for small values of opening factors. On the other hand, when the opening factor is equal to 0.2, this is not so obvious anymore. When max. HRRPUA is equal to 500 kW/m², and fast growing rate is considered, conditions equivalent to 30 min of an ISO-fire are obtained before 30 min of $\alpha-t^2$ fire. Similarly, 60 min ISO-fire conditions are achieved before 60 min. of $\alpha-t^2$ fire exposure. However, for max. HRRPUA equal to 250 kW/m², an opening factor equal to 0.2, and fast growth rate, the equivalent times of fire exposure for R30 and R60 is more less equal to 30 and 60 min., respectively, whereas for medium and slow growth rates, the equivalent time of fire exposures is exceeds the values from ISO-fire exposures. Moreover, for higher values of opening factors, conditions equivalent to R120 and R240 cannot be even obtained, because of the lack of combustible materials.

Reverse engineering of standard temperature curves to obtain the hrr of the fire in various enclosure configurations - what can we learn from that?

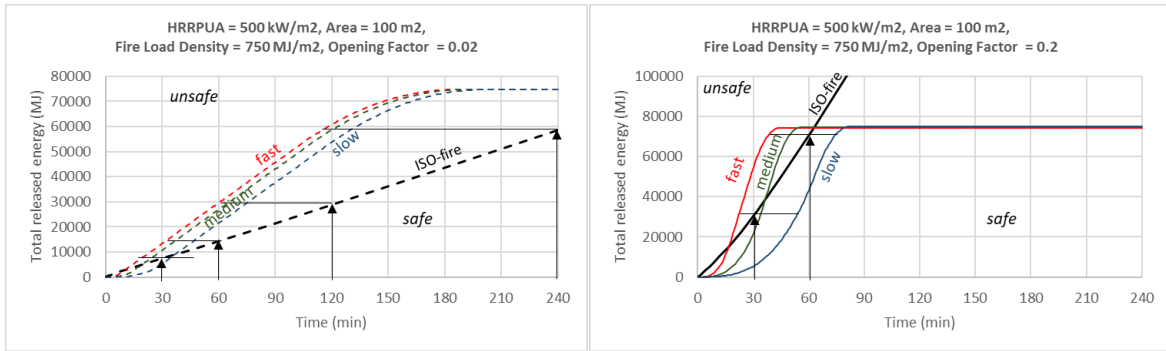


Fig. 6. Comparisons between total energies released in reverse engineering HRR and α - t^2 fires for 100 m² compartment and HRRPUA = 500 kW/m²: a) opening factor = 0.02; b) opening factor = 0.2

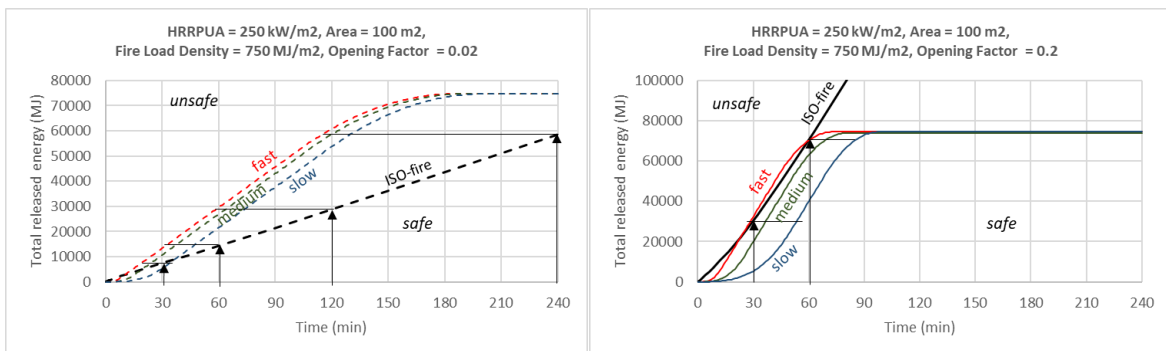


Fig. 7. Comparisons between total energies released in reverse engineering HRR and α - t^2 fires for 100 m² compartment and HRRPUA = 250 kW/m²: a) opening factor = 0.02; b) opening factor = 0.2

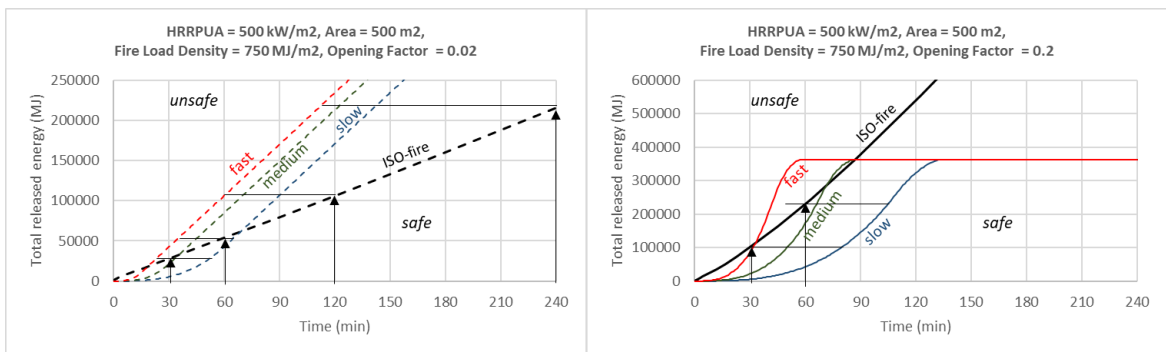


Fig. 8. Comparisons between total energies released in reverse engineering HRR and α - t^2 fires for 500 m² compartment and HRRPUA = 500 kW/m²: a) opening factor = 0.02; b) opening factor = 0.2

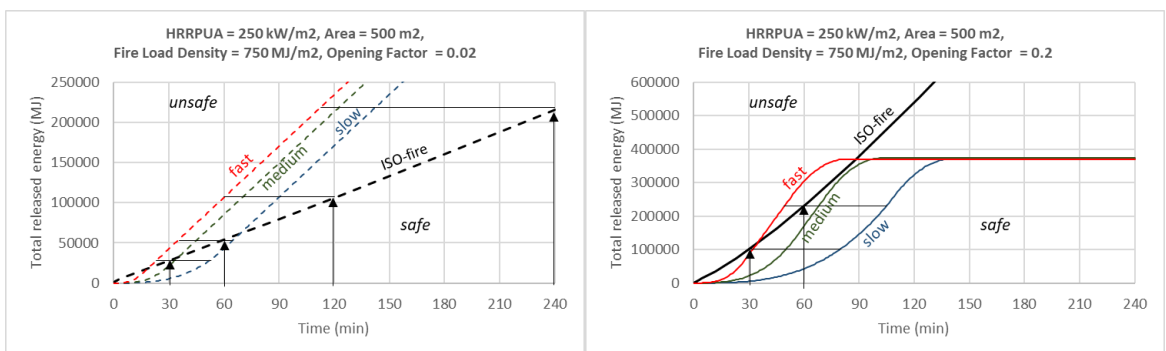


Fig. 9. Comparisons between total energies released in reverse engineering HRR and α - t^2 fires for 500 m² compartment and HRRPUA = 250 kW/m²: a) opening factor = 0.02; b) opening factor = 0.2

6 CONCLUSIONS

The work presented here may be considered as an uncommon application of numerical modelling to quantify the “standard fire curve” in terms of the heat release rate. It may allow for a better understanding of the level of safety provided by the traditional fire testing and gives a reference point for the use of PBD in structural fire engineering. Such approach can also provide some new insight into well-known Eurocode solutions and parametric fires. The results presented so far are still very much work in progress and further work is needed to better utilize this approach.

REFERENCES

1. *Eurocode 1991-1-2*
2. Kodur, V. K. R., Pakala, P., & Dwaikat, M. B. (2010). *Energy based time equivalent approach for evaluating fire resistance of reinforced concrete beams*. Fire Safety Journal, 45(4), 211-220. Harmathy: 10.1002/fam.810110206
3. Law, M. (1997). *A review of formulae for T-equivalent*. Fire Safety Science, 5, 985-996.
4. Franssen: Franssen, J. M., Cadorin, J. F., Cajot, L. G., Schleich, J. B., Schweppe, H., & Kindmann, R. (1996). *Connection between parametric temperature-time curves and Equivalent time of fire exposure (Annexes B and E of ENV 1991-2-2)*. IABSE report Vol. 74, 407-417.
5. Thomas, G. C., Buchanan, A. H., & Fleischmann, C. M. (1997). *Structural fire design: the role of time equivalence*. Fire Safety Science, 5, 607-618.
6. Harmathy, T. Z. (1987), *On the equivalent fire exposure*. Fire Mater., 11: 95–104. doi:10.1002/fam.810110206

Numerical Modelling

FRAGILITY OF REINFORCED CONCRETE STRUCTURE SUBJECTED TO ELEVATED TEMPERATURE

Ranjit Kumar Chaudhary¹, Tathagata Roy², Vasant Matsagar³

ABSTRACT

Fragility assessment of a reinforced concrete (RC) portal frame subjected to elevated temperature is carried out. A three-dimensional (3-D) nonlinear finite element (FE) model of the RC portal frame subjected to elevated temperature is developed. The model duly incorporates mechanical and thermal behavior of concrete and steel reinforcing bars at elevated temperature. The response of the RC portal frame is obtained in terms of deformation and temperature distribution in the structure. The probabilistic study is carried out in order to quantify failure probability of the structure and assess structural vulnerability considering uncertainty of fire loading. Parametric studies are carried out by varying the mechanical properties of concrete and reinforcing bars. The proposed stochastic analysis framework provides an approach to improve the performance-based fire design of the RC structures at member and structure levels by identifying the parameters affecting the structural fire resistance.

Keywords: RC portal frame, Fire hazard, Probabilistic approach, Fragility curves

1 INTRODUCTION

Several incidents of fire outbreak have been reported since ancient times that have led to the catastrophic consequences of structures and infrastructure systems. Thus, it becomes necessary to understand the risk imposed to the structure under fire hazard. Concrete structures have exhibited satisfactory fire performance; hence, this construction material is widely used for fire-resistant design. The structural fire resistance of typical reinforced concrete (RC) structure is achieved by a prescribed nominal cover to the reinforcing bars for given member size, fire category, and aggregate type [1-2]. The other fire mitigation strategies include use of escape routes, installation of active and passive fire protection units, etc. to limit the severity caused by fire hazard. However, the damage due to fire hazards depends mainly on duration of fire, amount of fuel loading, maximum temperature of fire, thermal capacity of materials, etc. Hence, the effect of variabilities on the performance of the RC structures is noticeable, which requires probabilistic approach to investigate the influence of uncertainties on the behavior of structures under fire. The probabilistic approach has been gaining much importance as the system incorporates the variabilities associated in parameters of fire loading for improved structural resistance [3].

Initially, the probabilistic aspects of fire safety were used for determining load and resistance factors. Thereafter, reliability methods and Monte Carlo simulations were used to investigate structural fire resistance based on structural capacity and uncertainty in fire loading. Some of the research works were also conducted on probabilistic aspect of fire hazard on steel structures using several reliability-based tools and techniques [4]. The recent research works on

¹ Graduate Student. Department of Civil Engineering, Indian Institute of Technology Delhi , Hauz Khas, New Delhi, India.
e-mail: ces162172@civil.iitd.ac.in

² PhD Research Scholar. Department of Civil Engineering, Indian Institute of Technology Delhi , Hauz Khas, New Delhi, India.
e-mail: tathagata.roy@civil.iitd.ac.in

³ Associate Professor. Department of Civil Engineering, Indian Institute of Technology Delhi , Hauz Khas, New Delhi, India.
e-mail: matsagar@civil.iitd.ac.in

probabilistic aspects of fire engineering have shown that uncertain parameters have significant effect on vulnerability and reliability index of structure [5]. The research conducted so far deals with the probabilistic aspects of the RC structure at member level (beams and columns). The behavior of portal frame under thermal and mechanical loads might not be obtained clearly based on the studies carried out at member level. Hence, probability-based study considering parameter uncertainties to evaluate the performance of the structural systems exposed to fire is necessary, which would facilitate more reliable performance-based fire design methodology.

Herein, the effect of various uncertainties in fire loading on the RC structure subjected to elevated temperature is investigated. The major objectives of the current study are: (i) to study the behavior of 3-D non-linear FE model under thermo-mechanical loading, (ii) to study the variation of response due to the uncertainties considered in thermal loading, and (iii) to carry out the fragility assessment of RC structure by obtaining probability density function and fragility curves under the effect of elevated temperature.

2 FRAGILITY ASSESSMENT

The conventional design approaches and codal recommendations emphasize mainly on deterministic approaches. To quantify the performance of the structure due to the effect of uncertainty, fragility assessment is carried out. The structural vulnerability due to a particular hazard may be quantified more appropriately using probabilistic approaches. The probabilistic approach in the present study helps to assess the performance of the structure by developing fragility curves under fire hazard. In this approach, the performance of the structure is based on capacity of structure and hazard gives the required criteria for demand at a specific site,

$$F(DV) = \iiint p(DV | DM)p(DM | EDP)p(EDP | IM)p(IM)d(IM)d(EDP)d(DM) \quad (1)$$

For fire fragility case, the vulnerability of structure can be calculated by,

$$F(DM) = \iint p(DM | EDP)p(EDP | IM)p(IM)d(IM)d(EDP) \quad (2)$$

where, DV stands for decision variable; DM stands for damage measure; EDP stands for engineering demand parameter; and IM stands for intensity measure. Here, $p(DM|EDP)$ represents the vulnerability of the structure to a given limiting EDP value, $p(EDP|IM)$ represents the probability of uncertain structural response for a given site specific IM. For developing fragility functions, a probabilistic study needs to be carried out to assess the capacity of structure based on relative damage states or demand of the structure.

The capacity of the structure needs to be assessed in order to develop fragility function for a structure. The capacity of the structure can be defined in terms of limiting deformation, stresses, and strains in the structure. The limit state adopted in the current study is limiting deformation in beam, which is $L/66$ [6], with L representing the length of beam. The demand estimation is done subjected to some chosen IM parameter. The IM parameters in case of the fire hazard are thermal inertia, fuel load, heat release rate, opening factor, duration of fire exposure, maximum temperature developed etc. However, the IM parameters considered for the present study are fire load density (q), thermal inertia (b), maximum fire temperature (T), and fire duration (t).

3 NUMERICAL STUDY

A 3-D nonlinear RC portal frame subjected to elevated temperature is analyzed on probabilistic scale in order to quantify the probability of failure of structure. A single bay RC portal frame, which is a part of a typical office building, is considered for the study. The RC portal frame consists of two columns of height 3000 mm with cross-section 300 mm × 300 mm and a beam of 2700 mm (clear span) with cross-section 300 mm × 230 mm. The columns consist of 8 rebar of 25φ with shear stirrups of 10φ spaced at 150 mm centers. Similarly, the beam consists of 6 rebar of 16φ as main reinforcement and shear stirrups of 6φ with spacing 100 mm centers as secondary

reinforcement. As shear force is not a governing criterion during thermal analysis, shear reinforcement is not modeled. The loadings on the structure are calculated for the business and office buildings as per Indian standard (IS) 875 (1987). The design of the portal frame is carried out for the seismic load for building located at New Delhi. However, the RC portal frame has not been designed for resisting accidental loads such as fire loading.

3.1 STRUCTURAL MODELING

The analysis of the RC portal frame is carried out using commercially available software ABAQUS to predict its behavior under mechanical and thermal loading. The concrete is modeled using concrete damaged plasticity (CDP) model, which can depict the nonlinear behavior in both tension and compression. The CDP model is a smeared crack approach, which takes into account degradation of elasticity modulus induced by plastic strains in both compression and tension. The steel reinforcement is modeled using the classical theory of plasticity. The steel is modeled using bilinear stress-strain curves in both compression and tension with von-Mises yielding criterion. The concrete is modeled using C3D8RT elements, capable of both mechanical and thermal analysis. The size of the element used for modelling concrete is 100 mm based on the mesh convergence studies. The steel bars are modeled using lumped truss element T3D2T with temperature degree of freedom necessary for thermo-mechanical analysis. The reinforcing bars are tied to concrete elements through TIE constraint option available in ABAQUS for coupled thermo-mechanical analysis.

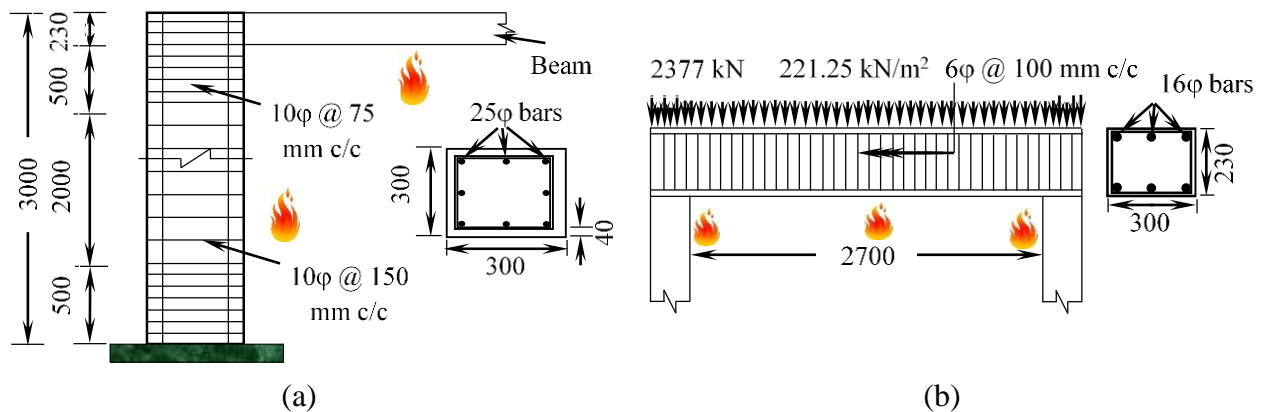


Fig. 1. Details of reinforcement in (a) column and (b) beam of RC portal frame

3.2 MATERIAL MODELING

The properties of RC material at elevated temperature need to be known explicitly in order to predict the behavior of the RC portal frame subjected to fire. The thermal properties required for obtaining the temperature distribution inside the RC material are thermal conductivity (λ), specific heat (c), coefficient of thermal expansion (α), and mass/density (ρ) of concrete and reinforcing bars for thermal analysis. The thermal conductivity and mass loss for normal strength concrete are obtained from the studies conducted earlier [7]. The specific heat and coefficient of thermal expansion are obtained from the equations proposed earlier [8]. From the comparative studies conducted previously [9], the thermal conductivity, coefficient of thermal expansion, and specific heat capacity of reinforcing bars are obtained.

The mechanical properties of RC material for thermo-mechanical analysis are temperature dependent compressive and tensile stress-strain curves and modulus of elasticity of concrete and reinforcing bars. The compressive and tensile strengths of concrete at elevated temperature are obtained from the expressions proposed previously [10]. The stress-strain curve of steel reinforcing bars is assumed bi-linear. The coefficient of degradation of strength and modulus of elasticity of reinforcing bars are obtained from the Eurocodes [11].

Table 1. Mechanical and thermal properties of concrete at ambient temperature

	Parameters	M20	M30	M40
Material properties	Strength of concrete, f_{ck} (MPa)	20	30	40
	Elastic modulus of concrete, E_c (MPa)	22360.68	27386.12	31622.77
Thermal properties	Density, ρ (kg/m ³)	2400		
	Conductivity, λ (W/m°C)	1.52		
	Specific heat, c (J/(kg°C))	1069.17		
	Coefficient of expansion, α (/°C)	9.0×10^{-6}		

Table 2. Mechanical and thermal properties of steel reinforcing bars at ambient temperature

	Parameters	Fe415	Fe500
Material properties	Yield strength of steel, f_y (MPa)	415	500
	Ultimate strength of steel, f_u (MPa)	621	750
	Elastic modulus of steel, E_y (MPa)	2×10^5	
Thermal properties	Density, ρ (kg/m ³)	7850	
	Conductivity, λ (W/m°C)	53.34	
	Specific heat, c (J/kg°C)	436.09	
	Coefficient of expansion, α (/°C)	1.15×10^{-5}	

3.3 THERMO-MECHANICAL LOADING

The mechanical loading is applied in the form of pressure loading at the upper surface of beam and column. In the current study, a mechanical loading of 221.25 kN/m² and 2377 kN is applied on the upper surface of beam and column, respectively. The thermal loading is applied to the desired surface (soffit of the beam and interior sides of both the column) of the RC portal frame in the form of convection and radiation for thermo-mechanical analysis. The fire loading is applied in the form of time-temperature curve in order to simulate structure-fire interface. The fire curve used in the current study is natural fire curve obtained as per the recommendation of Eurocodes [12]. The coefficient of convection used for thermal analysis is 35 W/m²K and emissivity for radiation considered is 0.8.

4 RESULTS AND DISCUSSION

The probabilistic analysis of RC portal frame under thermo-mechanical loading is carried out considering all the types of material and geometrical nonlinearities associated with the structure. A parametric study is carried out considering different characteristic strength of concrete and yield strength of reinforcing bars. *Fig. 2* shows the deflection time history of beam and columns of the RC portal frame for various grades of concrete. The central deflection for M20 grade of concrete is higher in comparison to the other grades and is highly vulnerable to fire hazard. Steep gradient in temperature is observed within the concrete section due to the higher thermal inertia of concrete, which relatively lowers the maximum temperature reached in section reducing to 650°C. Initially, the effect of thermal loading is very high causing higher thermal expansion on the exposed face of beam. Due to the joint rotation at the ends, thermal bowing of beam takes place. With the degradation in mechanical properties of concrete and reinforcing bars, the downward deflection overcomes the effect of thermal bowing, leading to the downward deflection.

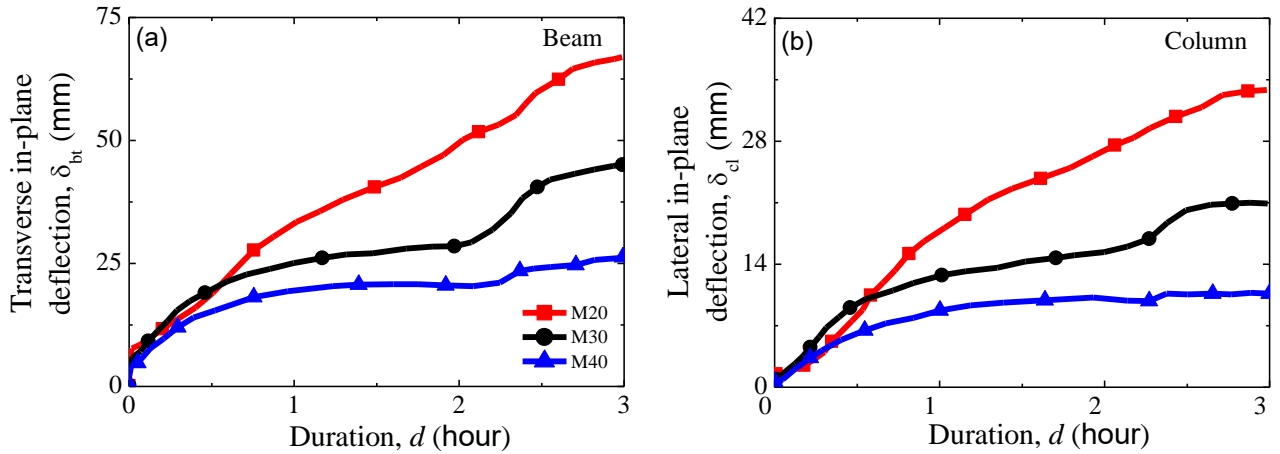


Fig. 2. Maximum deflection time history of (a) beam and (b) column for different concrete grades

Fig. 3 shows time-temperature history at various positions inside beam and column sections. The maximum temperature of the exposed face of the beam and column is 800°C whereas the maximum temperature on the unexposed face is lesser than 50°C. This huge temperature difference between exposed and unexposed face of the RC portal frame is due to the higher thermal inertia of concrete. The maximum temperature attained by steel reinforcing bars is around 420°C. The steel reinforcing bars is degraded to half of its strength for the temperature of around 540°C.

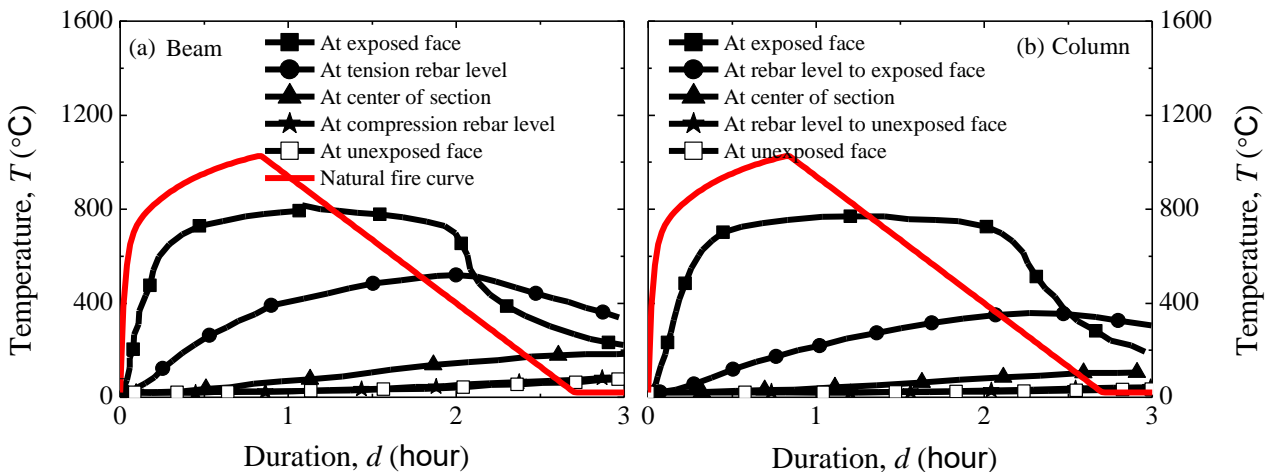


Fig. 3. Time-temperature history across (a) beam; (b) column sections

The RC portal frame is further investigated for the uncertainties in thermal loading. Although, the input variables for the thermo-mechanical analysis are assumed normal distribution, the distribution of the responses followed lognormal distribution. The deflection response shows a wide variation in fire load density whereas the distribution of responses for uncertainty in thermal inertia is closely ranged. For performance-based design for a hazard, distribution of responses is one of the most important factors for decision making regarding the extreme threats due to uncertain factors. The mean of the distribution of responses is also higher for the uncertainty in thermal inertia. Thus, uncertainties in parameters have significant effect on the thermo-mechanical analysis and needs to be taken in consideration for performance-based fire safety design.

Fig. 4 and Fig. 5 represent the probability of failure (p_f) of the RC portal frame under fire hazard with the uncertainties in fire load density (q), thermal inertia (b), maximum fire temperature (T), and duration of fire loading (d). Fig. 4 shows the probability of failure of the portal frame due to the uncertainty in fire load density and thermal inertia.

Table 3. Stochastic parameters used for thermo-mechanical analysis

	Parameters	Distribution	Mean Values	COV
Material properties (concrete and steel)	Strength of concrete/ steel (f_{ck}/f_y)	Deterministic	Table 1	-
	Elastic modulus of concrete/ steel (E_c/E_s)			
Thermal properties (concrete and steel)	Density (ρ)	Deterministic	Tables 1 and 2	-
	Conductivity (λ)			
	Specific heat (c)			
	Coefficient of expansion (α)			
Fire loading	Thermal inertia (b)	Normal	2000	0.2
	Fire load density (q)		420	0.2
	Maximum temperature (T)		800	0.2
	Duration of fire loading (d)		3	0.2
	Opening factor (O)	Deterministic	0.1	-
	Fire growth (t_{lim})	Deterministic	Slow (25)	-
Heat transfer	Stefan-Boltzmann constant	-	5.67×10^{-8}	-
	Convection	Deterministic	25	-
	Radiation/ emissivity		0.8	-

The probability of failure is the highest for the lowest grade of concrete for same strength of steel bars. The strength of reinforcing bars has insignificant influence over the probability of failure for the higher grade of concrete. Therefore, increasing the strength of steel does not necessarily reduce the failure probability. The steepness of the fragility curve observed is higher for lower grade of concrete strength, M20 and M30. In conventional design method, the major importance is given to the size of cross-section of member rather than strength for fire safety. Based on the observation above, it can be concluded that thermal inertia plays important role for fire safety design of structures. The uncertainty in fire load density also has significant effect in determining probability of failure of the RC portal frame with varying structural capacity. A fire load density of above 600 MJ/m^2 is highly vulnerable to the structure designed with conventional codal recommendations. The structures such as dwelling houses, shopping centers, libraries etc. thus need to be designed with utmost care for fire hazard. The probability of failure decreases with the increasing structural strength and there is negligible failure for highest considered material strength at mean value of fire load density. Most of the structural fire design is based on the standard fire curve which does not consider the aspect of fire load density. This has no effect on temperature growth of fire curve due to the fuel loading. This factor may also lead to the overestimation of design parameters required for fire safety. Thus, the study of the effect of uncertainty in fire load is crucial in the performance-based approach of design of structures in fire.

Fig. 5 illustrates the probability of failure for uncertainty in maximum temperature of fire curve and duration of loading. The failure probability for deterministic scenario with mean temperature of 800°C is negligible. This is because of the ventilation factor being high due to which heating phase is reduced and there is less severity. The scenario may be different when the opening factor is reduced. The severity of fire thus influences the risk of failure of the structure. Thereby, the failure probability of structure is more for the maximum temperature of fire curve. At opening factor of about 0.1, the failure in portal frame starts at temperature of about 1000°C of the fire. In the similar manner, the randomness in the duration of fire loading also have significant role in determining probability of failure of the structure. However, the uncertainty has negligible effect on the failure probability for higher material strengths. For the deterministic scenario with fire duration of 3 hours, the duration of fire loading has minimal effect due to higher material strength. However, the scenario becomes worst for the lower material strength.

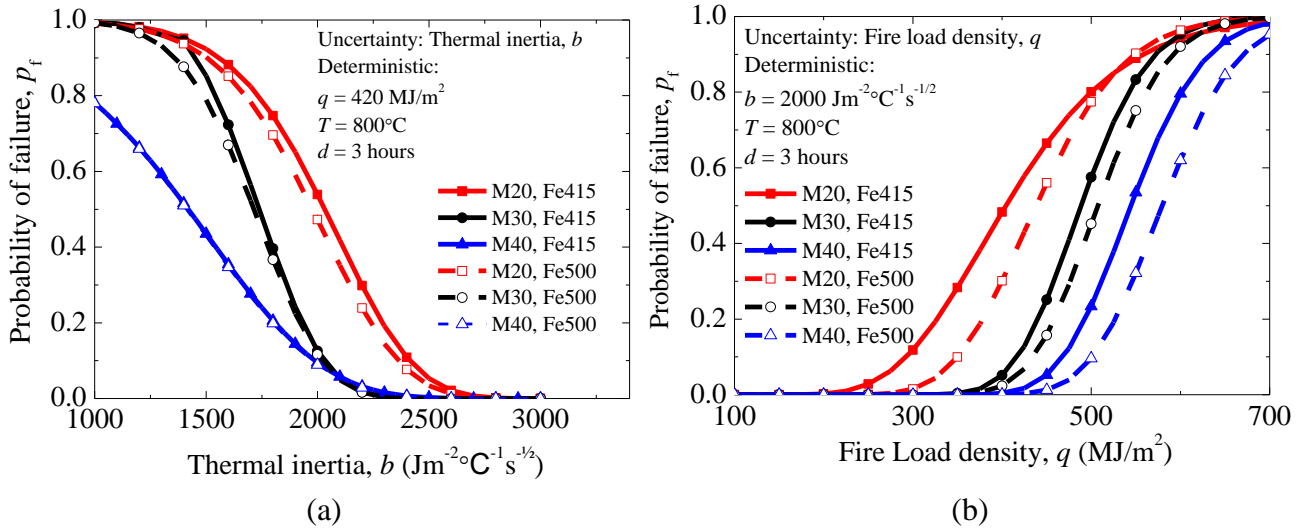


Fig. 4. Fragility curves for the RC portal frame due to uncertainty in (a) thermal inertia; (b) fire load density

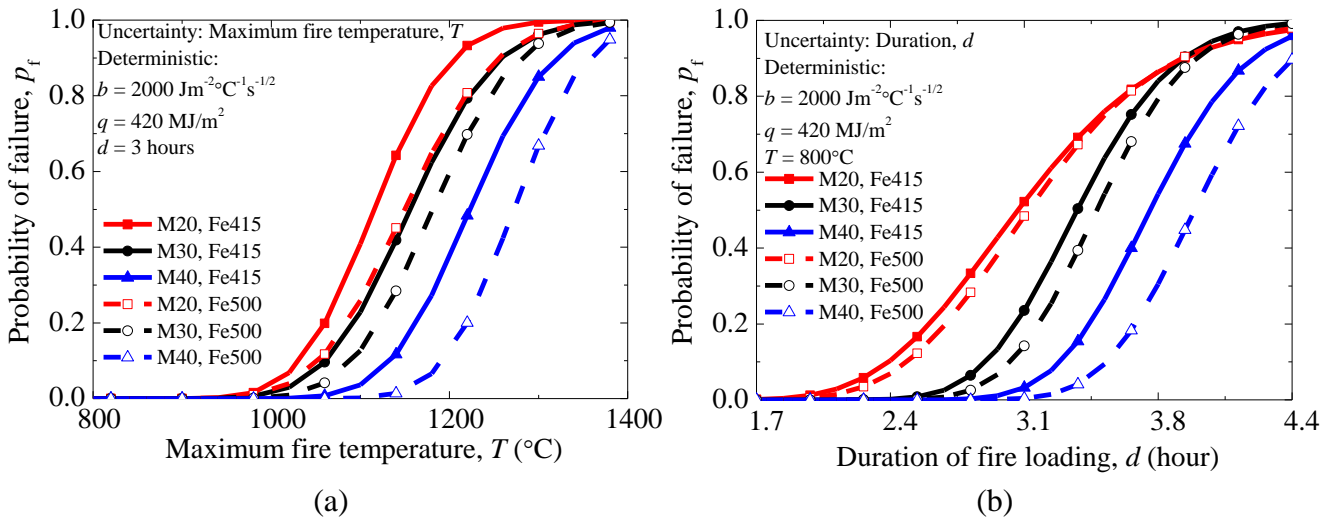


Fig. 5. Fragility curves for the RC portal frame due to uncertainty in (a) maximum fire temperature; (b) duration of fire loading

It is also common practice to measure the resistance of structure to fire in terms of duration of fire loading termed as fire rating. Thus, the influence of duration of fire loading may form a basis for estimating fire rating of a structure taking into account the effect of material properties. The fragility curves developed under the different uncertain conditions is helpful in assessing the structural damage and may pave path towards performance-based design for fire hazard posed to a structure.

5 CONCLUSION

In the current study, the influence of uncertainties on the performance of a RC portal frame is investigated through nonlinear FE thermo-mechanical analysis. This study provides a methodology for constructing structural fragility based on a suitable limit state to assess the performance of the structure under fire hazard. As per prescriptive methodology, the fire resistant design is mainly based on the size of cross-section of member rather than strength of material. However, the strength of the materials used in the structure also has significant influence on failure probability of a structure. Hence, the fire resistance of the structure needs to be based on strength of the materials.

The fire load density is one of the most crucial factors in the fire safety design of the structure and needs to be assessed properly for a particular structure. The buildings with the higher fire load density such as dwelling houses, libraries, shopping centers, etc. need to be given utmost importance for fire safety design. The fragility curves are helpful in predicting the structural damage due to the effect of uncertainty for improved performance of the structure. This methodology can be utilized for constructing fragility functions for RC framed structures.

REFERENCES

1. IS: 456-2000. Indian standard code of practice for plain and reinforced concrete. 4th revision, Bureau of Indian Standards, New Delhi; 2000.
2. ASTM. Designation: E119-00a — Standard test methods for fire tests of building construction and materials. West Conshohocken, (PA): ASTM International; 2000.
3. Kho, T.-S., Block, F.M. and Lowry, T.G. (2017). *Determining the fire rating of concrete structures: case study of using a probabilistic approach and travelling fires*. Applications of Structural Fire Engineering, Dubrovnik, Croatia.
4. Balogh, T. and Vigh, L.G. (2016). *Complex and comprehensive method for reliability calculation of structures under fire exposure*. Fire Safety Journal, 86, 41-52.
5. Van Coile, R., Caspeepe, R. and Taerwe, L. (2014). *Reliability-based evaluation of the inherent safety presumptions in common fire safety design*. Engineering Structures, 77, 181-192.
6. Moss, P., Abu, A. and Dhakal, R. (2016). Intensity measures for probabilistic structural fire engineering. *Structures in Fire (SiF)*, Princeton, New Jersey (NJ), USA.
7. Kodur, V. (2014). *Properties of concrete at elevated temperatures*. ISRN Civil Engineering, 2014, Article number 468510.
8. Ruan, Z., Chen, L. and Fang, Q. (2015). *Numerical investigation into dynamic responses of RC columns subjected for fire and blast*. Journal of Loss Prevention in the Process Industries, 34, 10-21
9. Gardner, L.; Bu, Y.; Francis, P.; Baddoo, N.R.; Cashell, K.A.; and McCann, F. (2016). *Elevated temperature material properties of stainless steel reinforcing bar*. Construction and Building Materials, 114, 977-997.
10. Aslani, F.; and Bastami, M. (2011). *Constitutive relationships for normal-and high-strength concrete at elevated temperatures*. Materials Journal, 108(4), 355-364.
11. EN 1992-1-2 (2004) Eurocode 2: *Design of concrete structures* - Part 1-2: General rules - Structural fire design.
12. EN 1991-1-2 (2002) Eurocode 1: *Actions on structures* - Part 1-2: General actions - Actions on structures exposed to fire.

ADVANCE HEAT TRANSFER ANALYSIS AND CAPACITY CURVES ACCOUNTING FOR THE EFFECT OF SPALLING

Hitesh Lakhani¹, Jan Hofmann²

ABSTRACT

The paper presents a numerical model for transient heat transfer analysis capable of accounting for the effect of spalling i.e, changing domain boundaries and moving thermal Boundary Conditions (BC). It should be acknowledged that the model does not predict spalling rather is developed as a tool to study the effect of thermal spalling. Hence, information regarding the location, amount and time of spalling act as an input to the model. Although, there exist in the literature some complex hygrothermo mechanical models to predict spalling but the effect of extent of spalling on fire rating of structural members have not being addressed/studied. The proposed numerical model has been implemented in an inhouse code and its validation is presented. As expected, significant differences were observed in the predicted temperatures with and without spalling. The predicted temperatures, considering spalling were in good agreements with the experimentally measured temperatures reported in literature. The presented results also emphasis the importance of considering the time of spalling.

The thermal subroutine was later sequentially coupled with the mechanical subroutine (sectional-analysis) to compute the variation of member capacity with exposure time. The present paper deals only with the effect of spalling on Reinforced Concrete (RC) beams.

Keywords: transient heat-transfer analysis, flexural members, spalling, moving BC's

1 INTRODUCTION

Concrete due to its incombustible nature, high specific heat & low conductivity, is known to have good fire resistance as compared to other commonly used building materials. It is the degrading effects of high temperature viz., degradation of material properties of concrete & reinforcing steel, thermal cracking, spalling, interaction between hot & cold structural members (load/moments/force redistribution), that can leads to structural failure.

The current prescriptive design provisions [1,2] for Fire Rating (FR) of Reinforced Concrete (RC) structural members relies on the insulation provided by the concrete cover to main reinforcement. Hence, a reduction in the concrete cover due to thermal spalling may affect the FR of the member. Depending on the amount of spalling the reinforcement may be directly exposed to fire, and adversely affect the load carrying capacity of the RC members. The effect of spalling is two fold: i) it reduces the cross-section of the member and ii) leads to higher temperature ingress into the member (leads to higher temperature of the reinforcement and the member core region). Both of these effects have negative impact on the member's capacity during fire. Hence, to compute

¹ Scientific Associate, Department of Fastening and Strengthening Methods, Institute of Construction Materials, University of Stuttgart, Stuttgart, Germany.

e-mail: hitesh_lakhani06@rediffmail.com

² Professor. Department of Fastening and Strengthening Methods, Institute of Construction Materials, University of Stuttgart, Stuttgart, Germany.

e-mail: jan.hofmann@iw.uni-stuttgart.de

realistic capacity of RC beams during fire, especially those made of High Strength Concrete (HSC), it is important to consider the effect of spalling.

The modelling of the complex moisture migration process through concrete at elevated temperature itself forms a separate domain of study. The phenomenon responsible for the thermal spalling which takes place when RC member/structure is exposed to fire is not completely understood and is widely debated across various research forums. Although, some numerical models which couple the hygrothermal analysis to stress analysis with some simplified spalling criteria [3,4] can be found in literature but the effect of thermal spalling on FR of RC beams have not being addressed explicitly.

2 NUMERICAL MODEL

In order to carryout the thermal analysis and to evaluate the flexural capacity of the RC beams the cross-section of the beam is divided into $m \times n$ segments along its width and depth. Based on the assumption of lumped system (which is a common approximation for transient conduction problems [5]), each segment is considered to have a uniform temperature and properties (thermal and mechanical) lumped at the centre of the segment.

2.1 Thermal analysis

Equation (1) gives the governing differential equation for 2D transient heat conduction problem. This equation is solved using Finite Difference Method. The Eq (1) is formulated using implicit central difference scheme and solved using iterative solver to obtain the spatial and temporal distribution of temperature, $T(x,y,t)$. Equation (2) stated the radiative and convective boundary conditions which are used for modelling the heat transfer from the gas to the member surface. Fig. 2 shows a representative discretization along with the computational points.

$$\rho c \frac{\partial T}{\partial t} = k \left[\frac{\partial^2 T}{\partial x^2} + \frac{\partial^2 T}{\partial y^2} \right] \quad (1)$$

$$-k \frac{\partial T}{\partial n} = h[T_g - T_s] + \varepsilon \sigma [(T_g + 273)^4 - (T_s + 273)^4] \quad (2)$$

Where:

- k is the thermal conductivity (W/m °C),
- ρ is the mass density (kg/m³),
- c is the specific heat of solid (J/kg. °C),
- h is convective heat transfer coefficient (25 W/m² °C),
- ε is Stephen Boltzmann constant (5.667×10^{-8} W/m² °K⁴),
- σ is surface emissivity (0.8),
- T_g is gas temperature (°C),
- T_s is surface temperature (°C).

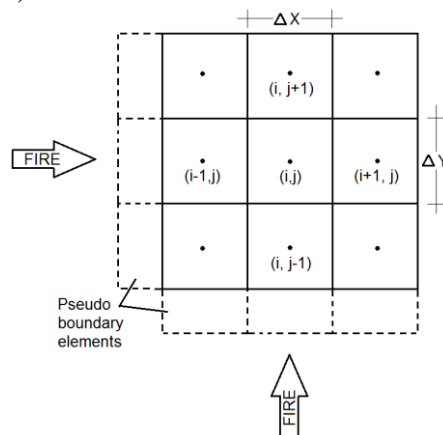


Fig. 1 Segment nomenclature for the section discretization

Reinforcing steel has not been considered / modelled explicitly during the heat transfer analysis. The thermal properties (specific heat and conductivity) for concrete as function of temperature were taken from Eurocode2 [2] based on the parametric study and validation done by Lakhani et al (2013) [6]. The sequence of spalling in terms of element number and the time are read from a user input file. The model checks for any spalling input before starting the iteration for the k^{th} time increment. If spalling input is found the spalled elements are excluded/deleted from the analysis. It also checks if the element being deleted had any boundary conditions, if yes, these boundary conditions are transferred to the surrounding element which will be now directly exposed to fire.

2.2 Sectional analysis

Sectional analysis procedure for RC flexural members is well established [7]. Numerous numerical models & guidelines/proposals for evaluating RC structural members under fire [8,9,10,11], are based on sectional analysis. Hence, it is not discussed in detail but the salient points are mentioned below:

Sectional analysis is based on the following assumptions:

1. Plain section remains plain after bending.
2. Tensile strength of concrete is negligible.
3. A perfect bond is assumed between reinforcing steel and concrete.
4. Temperature of the reinforcement is equal to the corresponding concrete temperature at rebar centroidal location.

The temperature dependent constitutive law for concrete and reinforcing steel were taken from Eurocode2 [2]. This implies that the transient strain component (Load Induced Thermal Strain-LITS) is accounted implicitly. Hence, the mechanical strain is computed by simply subtracting the free thermal strain component from total strain. Stress for each segment is computed using the computed mechanical strain and corresponding constitutive law based on the segment temperature. Finally, the flexural capacity is computed by integrating the stress over the beam cross-section. It should be noted that the above mentioned steps are to be executed in an iterative manner.

3 VALIDATION

The numerical model for the transient heat transfer analysis & sectional analysis, as discussed above has been implemented in an inhouse code. This section presents the validation of the inhouse code against the experiment from Choi & Shin (2011) [13].

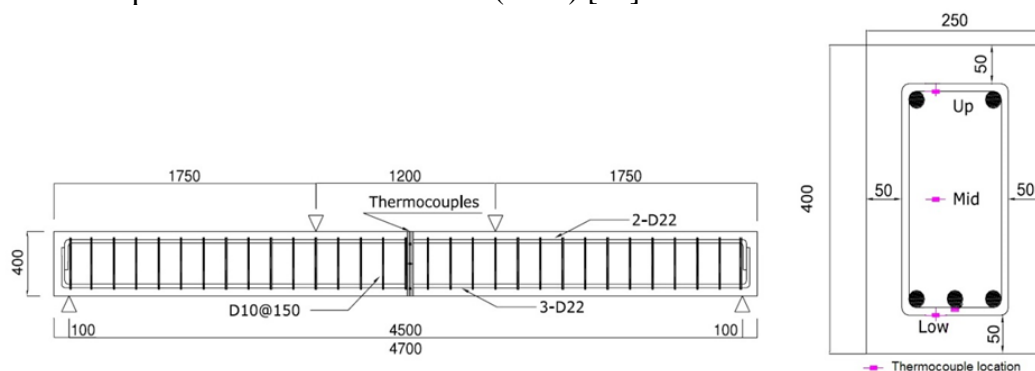


Fig. 2. Geometric and loading details of beam H5 [13] (All dimenions are in mm)

Choi & Shin (2011) [13] tested full scale beams under standard fire (as per ISO 834 [14]). The experimental study was aimed to investigate the effect of concrete strength and cover on the behaviour of reinforced concrete beams during fire. The test matrix consisted of four beams, two each of normal strength concrete (21MPa) and high strength concrete (55 MPa). The concrete was made of siliceous aggregates. The beams had a total length of 4700 mm and a cross section of 250 x 400 mm. All beams had 3-22Ø as tension reinforcement and 2-22Ø as compression reinforcement. For stirrup 10 Ø deformed bars with 150 mm spacing were used. The geometric and reinforcement

details along with the location of thermocouples are shown in Fig. 2. The beams were loaded with a load equivalent to 55% of its ambient load carrying capacity. Beam H5 was chosen for validation, as it was the only beam for which the spalling profile was reported in detail (Shown in Fig. 3).

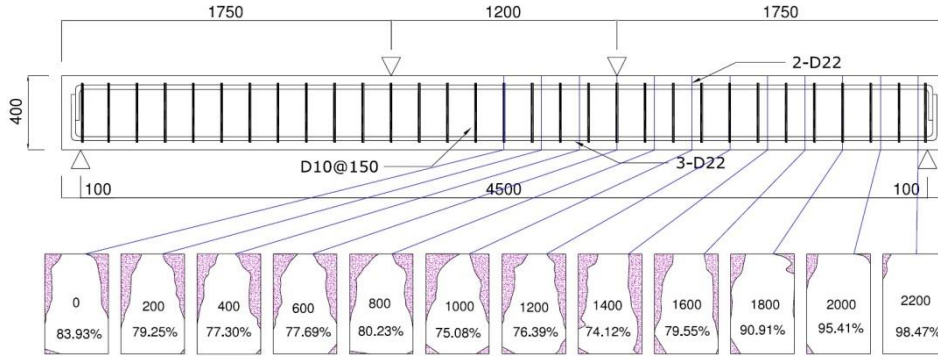


Fig. 3. Cross-section of beam H5 after spalling [13] (All dimensions are in mm)

3.1 Thermal analysis: Beam H5

The beam cross-section was discretized with a mesh size of 10mm. The top face of the beam had insulated boundary condition. Convective & radiative boundary conditions were applied on the remaining three faces of the beam with a convective coefficient of $25 \text{ W/m}^2 \text{ K}$ (as per Eurocode1 [12]) and emissivity equal to 0.8. Lower bound conductivity and specific heat modified for 3% moisture content, as per Eurocode2 were used. It was reported by Choi & Shin that the explosive spalling was observed after 10-15 minutes and continued till 60 minutes but the active spalling was observed only until 45 minutes. Fig. 4 shows the changing beam cross-section due to spalling which were assumed based on the information from Fig. 3. Thermal analysis was performed for three different cases viz., C0 corresponding to no spalling, C1 corresponding to $t_1 = 15$ minutes & $t_2 = 40$ minutes and C2 corresponding to a simplified case where the spalled section (observed after fire test) is considered as the initial section for heat transfer analysis. The time (t_1) corresponding to the beam section changing to cross-section:2 and time (t_2) corresponding to the beam section further changing to cross-section:3 were taken as the start and the end time for active spalling.

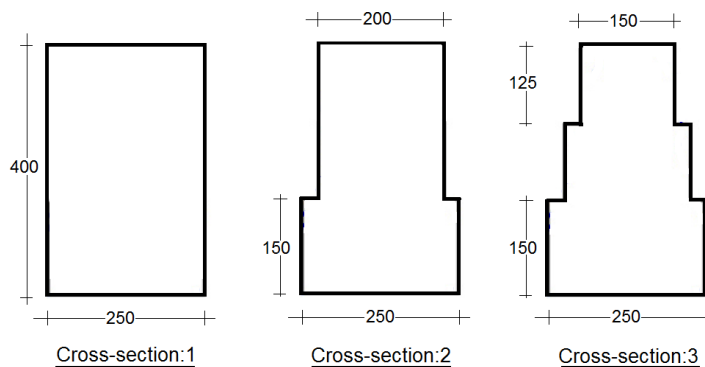


Fig. 4. Spalling configuration (All dimensions are in mm)

The temperature contours and comparison between the computed temperatures at various thermocouples for case C1 are shown in Fig. 5 and Fig. 6 respectively. The comparison between all the cases is discussed briefly in section 4 “Results and discussion”. It can be observed from Fig. 6 that the predicted temperatures are in good agreement with the experimental values.

Numerical Modelling

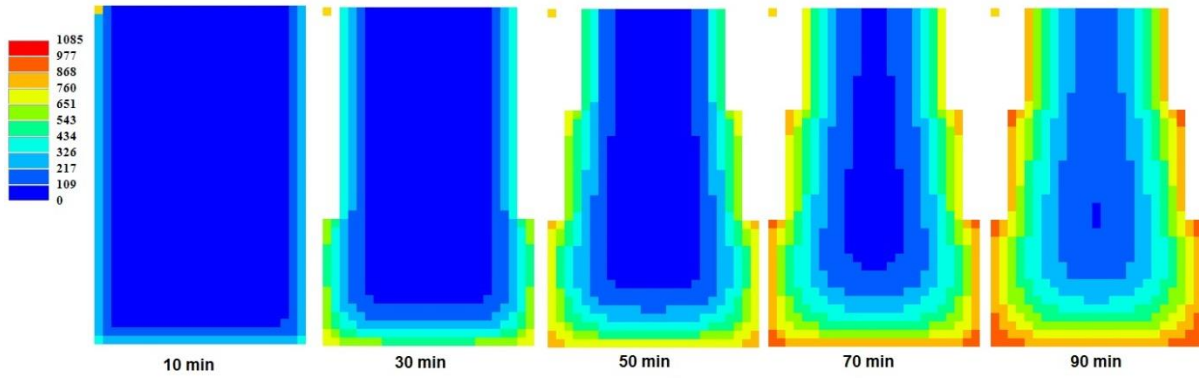


Fig. 5. Predicted temperature contours for beam H5

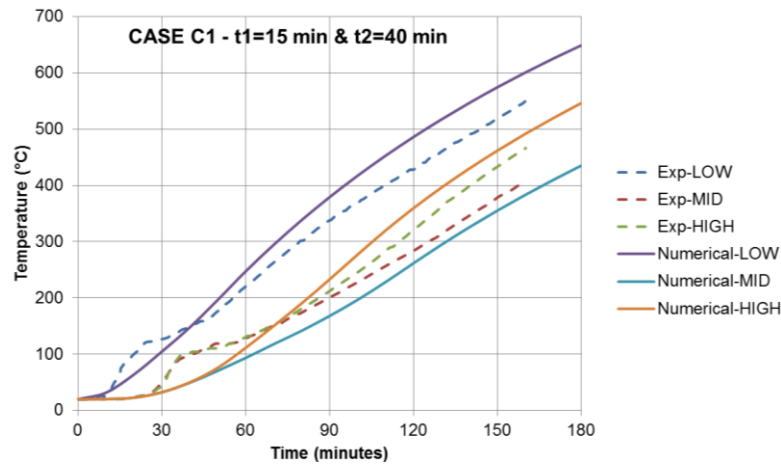


Fig. 6. Comparison between computed and measured temperatures (Case: C1)

(Refer Fig. 2 for the thermocouple locations corresponding to LOW, MID & HIGH; Exp-Experimental)

3.2 Sectional analysis: Beam H5

The sectional analysis was carried out with the assumptions and constitutive laws discussed in section 2.2. Since the compressive strength of HSC was 55 MPa, it was classified as Class-I high strength concrete as per Eurocode2. Hence, the compressive strength degradation as suggested by Eurocode2 for Class-I HSC was used. The yield strength for 22Ø and 10Ø reinforcing bar were 439 MPa and 390 MPa respectively. The degradation of mechanical properties (Modulus of elasticity, yield strength, proportional limit and ultimate strength) of reinforcing steel was assumed as per Eurocode2, for hot rolled steel. The computed moment capacity normalized to the ambient moment capacity is shown in Fig. 9 for all the three cases studied in this paper. The comparison between all the cases is briefly discussed in section 4 “Results and discussion”.

Since the beam was simply supported its fire rating based on the limit state of strength can be directly obtained from Fig. 9 by superimposing the applied moment (demand) curve on the graph. As the beam was loaded with a load equivalent to 55% of its ambient load capacity, fire rating of \approx 160 minutes (corresponding to case C1) is obtained using the presented model which is in good agreement with the experimentally obtained fire rating of 161 minutes.

4 RESULTS AND DISCUSSION

As stated in section 3.1, three different cases (C0, C1 & C2) were studied, which correspond to no spalling (Case-C0), considering spalling and corresponding time of spalling (Case-C1) (beam section changing to cross-section:2 at time t_1 and then to cross-section:3 at time t_2 as shown in Fig. 4) and simplified case where cross-section:3 is assumed as initial beam section (Case-C2). The three cases were chosen with an objective to highlight the importance of considering spalling (along with spalling time) on the predicted temperatures and fire rating of RC beams. Case C2 was included to

emphasis on the fact that such simplified assumptions for design purposes may be very conservative depending on the spalling configurations. *Fig. 7* and *Fig. 8*, shows the comparison of predicted temperatures for case C0 and C2 respectively. It is observed that the temperatures are under predicted for case C0 (no spalling) and are over predicted for case C2 (complete spalling considered from the beginning of fire i.e, ignoring the time of spalling). Hence, case C0 is un-conservative and case C2 is over-conservative. Most reasonable results are obtained for case C1 (refer *Fig. 6*) where the spalling has been considered in steps along with the time of spalling.

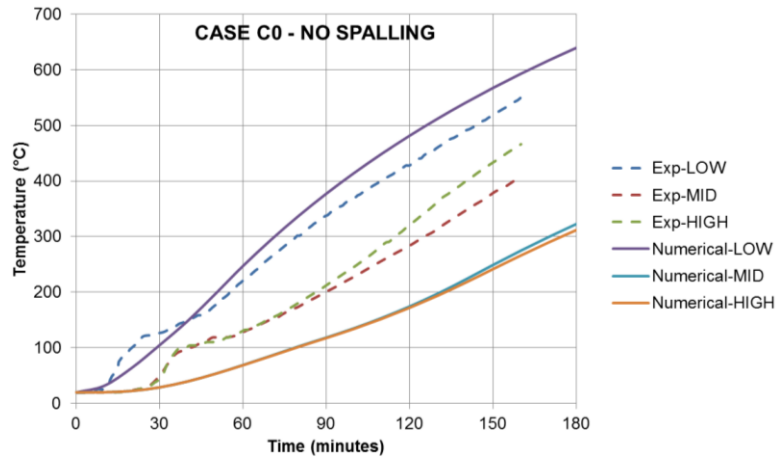


Fig. 7. Temperature comparison for Case: C0

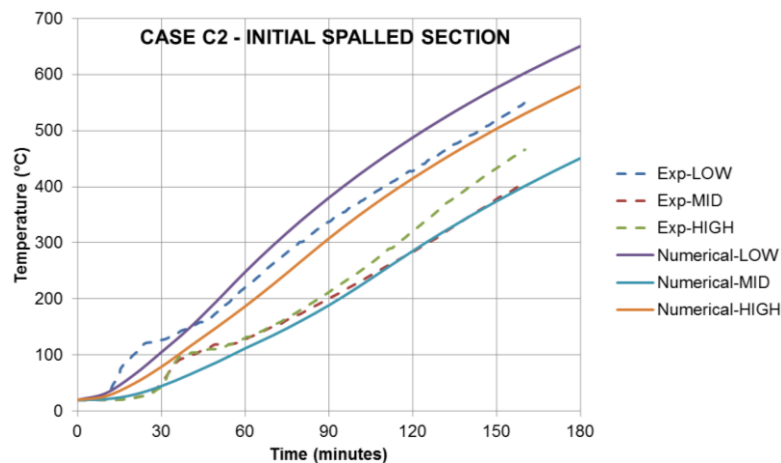


Fig. 8. Temperature comparison for Case: C2

Fig. 9 shows the computed moment capacity degradation for beam H5 for all three cases considered. Once gain it can be observed that (as expected) case C0 gives un-conservative fire rating (>180 minutes) as compared to case C1, due to the ignored spalling. Case C2 predicts a rather drastic fall in the moment capacity, especially during the initial 30 minutes. This is due to the fact that the time of spalling was ignored and the complete spalling was assumed at the beginning of the fire. Moment capacity degradation curves for case C1 and C2 are very similar (almost overlapping) after 60 minutes. But this observed similarity between C1 and C2 is valid/applicable only for the present case of beam H5 or for beams where the spalling is confined to the compression zone of the beam and the cover to the tension reinforcement remains fully intact. For cases where the cover to tension reinforcement is lost due to spalling the capacity curve for case C2 may be expected to deviate from C1 with high degradation rate.

Numerical Modelling

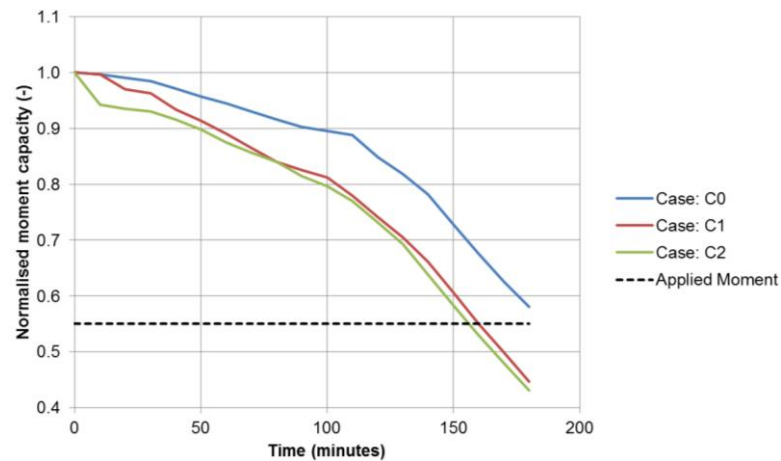


Fig. 9. Variation of moment capacity with time for different cases

5 CONCLUSIONS

The paper presented a numerical model for heat transfer capable of accounting the effect of spalling both in terms of extent of spalling and the time of spalling. The presented numerical model does not predict spalling but provides a handy tool to study the effect of spalling on the fire rating of RC beams. The heat transfer between the concrete surface and hot gases is modelled using radiative & convective BC's, which are updated at every time step to the new boundaries generated due to spalling (moving BC). The model has been successfully implemented in an inhouse code and its validation has been presented.

A comparative case study comprising of three different modelling possibilities have been presented to highlight the importance of considering spalling and the corresponding spalling time. It has been shown that the predicted temperatures and the moment capacity are on the un-conservative side when spalling is ignored. It has also been shown that the simplified approach of ignoring the spalling time and considering complete spalling at the beginning of the fire may be applicable only for cases where the spalling is confined to compression zone of the beam.

It can be concluded that in order to predict the fire rating of simply supported reinforced concrete beams and to accurately predict the temperatures across the cross-section it is important to also consider the time of spalling.

REFERENCES

1. ACI/TMS216.1-14. (2014). *Code requirements for determining fire resistance of concrete and masonry construction assemblies*. Detroit: American Concrete Society.
2. Eurocode2. (2004). *Design of concrete structures - Part 1-2: General rules - Structural fire design*. Brussels: European Committee For Standardization.
3. Kodur, V., Dwaikat, M., & Raut, N. (2009). Mesoscopic FE model for tracing the fire response of reinforced concrete structures. *Engineering Structures*, 31, 2368-2379.
4. Srivastava, G., & Prakash, P. (2017). An integrated framework for nonlinear analysis of plane frames exposed to fire using the direct stiffness method. *Comput. Struct.*, 190, 173-185.
5. Lienhard IV, J., & Lienhard V, J. (2015). *A heat transfer textbook* (Fourth Edition). Cambridge, Massachusetts: Phlogiston Press.
6. Lakhani, H., Kamath, P., Bhargava, P., Sharma, U., & Reddy, G. (2013). Thermal analysis of reinforced concrete structural elements. *Journal of Structural Fire Engineering*, 4(4), 227-243.
7. Park, R., & Paulay, T. (1975). *Reinforced Concrete Structures*. John Wiley & Sons.

8. Ellingwood, B., & Shaver, J. R. (1979). *Analysis of reinforced concrete beams subjected to fire*. National Bureau of Standard, US Department of Commerce.
9. Fib Bulletin 46, (2008). Fire design of concrete structures - Structural behaviour and assessment. *Federation Internationale du beton (fib)*.
10. Kodur, V., & Dwaikat, M. (2008). A numerical model for predicting the fire resistance of reinforced concrete beams. *Cement & Concrete Composites*, 30, 431-443.
11. Fitiany, S., & Youssef, M. (2017). Fire performance of reinforced concrete frames using sectional analysis. *Engineering Structures*, 142, 165-181.
12. Eurocode1. (2002). *Actions on structures-Part 1-2: General actions - Actions on structures exposed to fire*. Brussels: European Committee For Standardization.
13. Choi, E., & Shin, Y. (2011). The structural behaviour and simplified thermal analysis of normal strength and high strength concrete beams under fire. *Engineering Structures*, 33, 1123 - 1132.
14. ISO 834-1. (1999). *Fire resistance tests-elements of building construction*.

FIRE RESISTANCE OF CONCRETE SLABS ACTING IN COMPRESSIVE MEMBRANE ACTION WITH VARIOUS EDGE CONDITIONS

Tom Molkens¹

ABSTRACT

The use of the compressive membrane action (CMA) mechanism to explain the behaviour of slabs during fire is just starting and experiences are built up. Just till now fire tests doesn't consider this kind of effects due to the leak of lateral restraints above a furnace. This is the main reason why this investigation stays rather theoretical in case of fire, however at ambient conditions loading test of an existing building are available. It was already mentioned that by the aid of a plastic damage constitutive model with an explicit transient creep formulation the concrete behaviour at elevated temperatures can be simulated. This previously theoretical investigation was based on shell elements with perfect rigid boundaries. In the present article an extension is made to semi-rigid boundaries, where the rigidity is obtained by a weak coupling from a macro-model made by a commercial (Buildsoft) 3D finite element model of an existing building to the well-known SAFIR® finite element software for the verification of a part of the slab with various edge conditions.

Keywords: Compressive membrane action (CMA), horizontal stiffness, boundary and edge conditions

1 INTRODUCTION

In the design of slabs at ambient temperature the horizontal stiffness of the adjacent structure will be neglected. Due to thermal expansion in case of fire these horizontal boundary conditions can cause serious compressive stresses, where the favourable or unfavourable impact is not clear. These restraints are the reason why CMA can develop in between rigid cores or cold parts of the structures which are linked to each other by (cold) peripheral beams. Mostly CMA can be seen as an alternative load path which increases the bearing capacity of a slab.

Question rises which influence realistic boundary conditions in terms of horizontal stiffness will mean for the development of this alternative load path, if the development of CMA is anyway possible under such extreme loading.

2 HISTORY AND APPROACH

2.1 History

In previous work [1] it was stated out that a combination of shell elements and a plastic damage model [2] for concrete incorporating an explicit term for transient creep [3] in the finite element-based software SAFIR® [4] can simulate CMA. For modelling the temperature dependent behaviour, the shell of 1 m width was built up by several layers where each layer follows a time dependant temperature profile following EC2-1-2 [5]. Some layers do have the properties of unreinforced concrete but those at the position of the reinforcement include the contribution of this

¹ Senior project expert at Sweco Belgium nv, Hasselt, Belgium.
e-mail: tom.molkens@swecobelgium.be

reinforcement in a smeared way. In between the layers there is a mechanical, but no thermal coupling so heat transfer between the layers is not regarded.

However, in this previous study a case study was illustrating the mechanical behaviour with completely fixed end conditions *Fig 1 a)*, which is off course out of reality. In addition, in case of fire some uplifting of the slab from the beam could be seen probably due to the leak of stirrups in the presented model. In the actual model *Fig. 1 a & b)*, which is presented here, also stirrups are included and in contradiction with previous work [1] the beam is subjected to a thermal load coming from the fire. All these modifications must lead to a higher accuracy level.

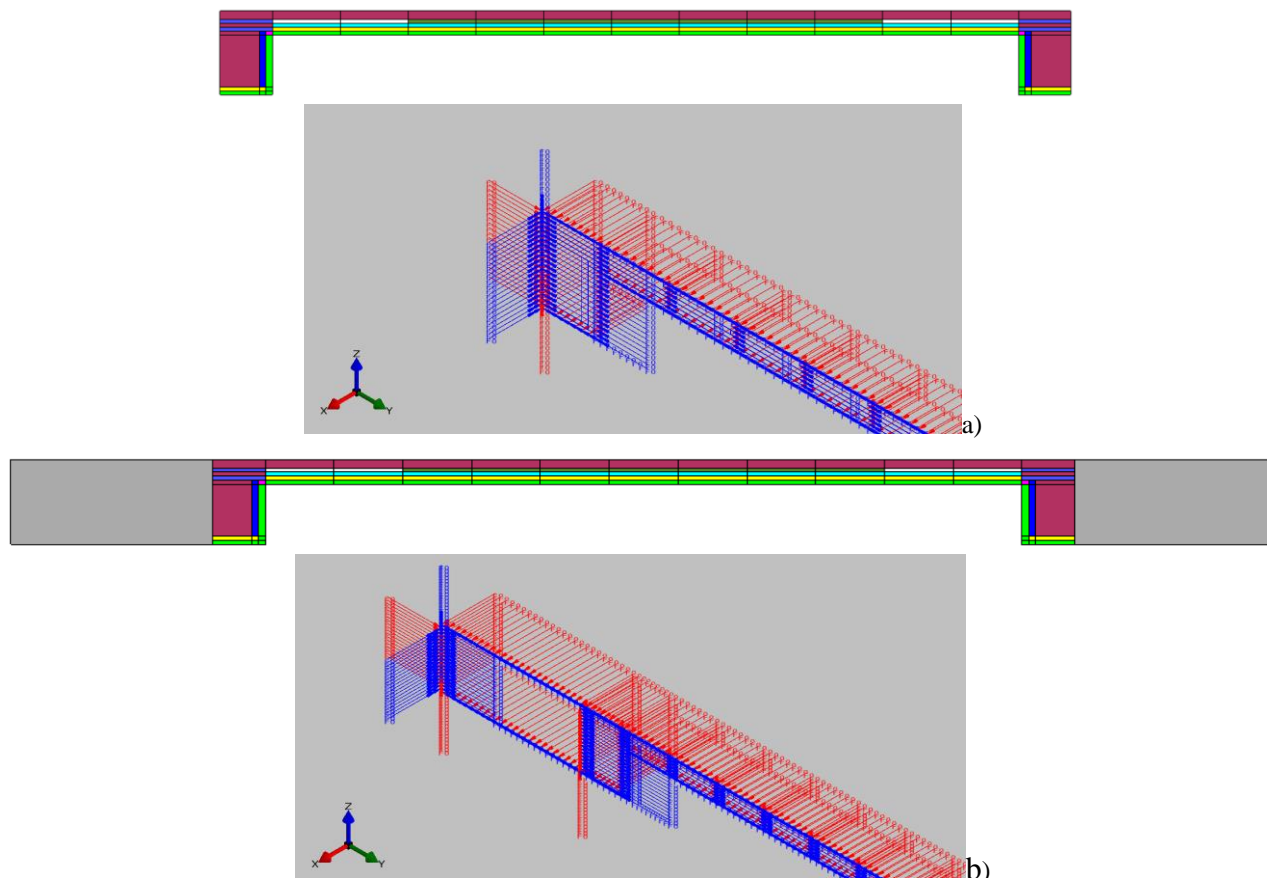


Fig. 1. Geometry of the model a) With fixed ends; b) With elastic body ends

More information about the building in the case study, his slab properties (like for example span 5.04 m, thickness 0.14 m, beam 0.62 by 0.59 m², concrete C30/37, reinforcement BE400, ratios of 335 mm²/m and load in case of fire equal to 6.96 kN/m²), CMA in general and the modelling of it like presented here can be found in [1].

2.2 Boundary conditions

Besides enhancing the modelling of the concrete and reinforcement an extension of the model is made by the aid of an elastic body *Fig 1 b)*. The Young modulus of this massive part is adapted on such a way that the horizontal rigidity of the building can be simulated. At mid width of the beam all displacements are blocked except the horizontal ones which are only blocked at the end of the so called elastic body. For intermediate lines displacements out of plane and rotation around the axis parallel with the bearing direction are blocked.

3 GLOBAL ANALYSIS

3.1 Case study

The slab is a part of an existing building nearby Brussels which is turned over from an office building to dwellings *Fig 2*. The building has a very stiff central core and at the ends secondary shafts and staircases are present which could be presumed as stiff cores, however those cores are much more flexible due to their dimensions. By the aid of a 3D model of the structure (made by ordinary elastic FEM Diamonds software of Buildsoft) *Fig 2 a)*, the horizontal displacements are verified obtained by a horizontal load of 100 kN/m applied at 1st, 9th and 18th floor level. This model is called the macro model.

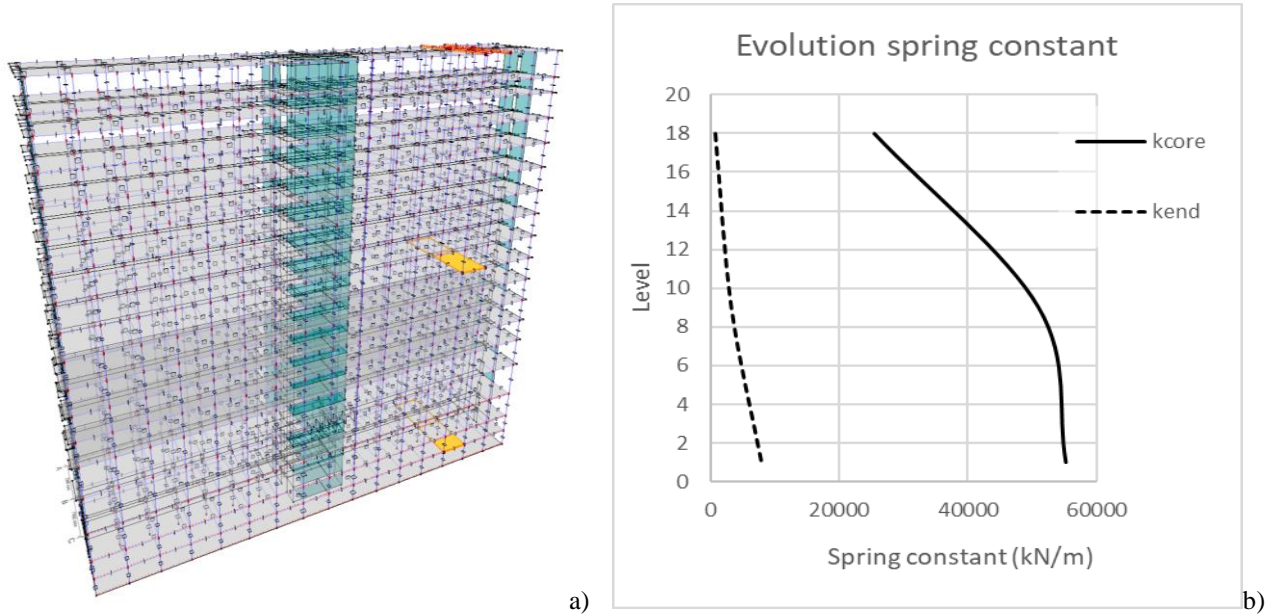


Fig. 2. a) Macro model of the structure; b) Evolution of spring constant for different levels

Three separate runs from the model are needed where each time the slab was erased where the load was applied (yellow surfaces in *Fig 2*). Dividing the 100 kN/m by the horizontal displacements delivers a spring constant which can be found in *Table 1*, as numerical values and in *Fig 2 b)* on a graphical way. A difference in stiffness of about factor 7 to almost 40 can be found.

Table 1. Values of spring constants obtained out of macro model

Level	Spring to the core k_{core} (kN/m)	Spring to the end k_{end} (kN/m)
18	25445	641
9	51020	3125
1	55249	7806

In the next part analysis are extended to complete fixed boundary conditions and once with the same spring constant (1000 kN/m) on both sides to obtain an idea of the influence of various and extreme boundary conditions.

3.2 Behaviour at ambient temperature

To illustrate the importance of the boundary conditions and the effect of CMA we present in *Fig. 3* the result of two simulations at ambient conditions till the ultimate load level. This is done by the FLOAD command in SAFIR® [4] which means that the load is increased in 20 steps to obtain at 20 s the total load. At the moment that the iterations stop before this time no equilibrium could be found. In a first simulation all reinforcement was incorporated in the model with at both edges a spring constant of 1000 kN/m (amb_4). This slab would fail after 6.2 s or a load level of only 3.57

kN/m² where 11.58 kN/m² in ULS is required. The second simulation (am_5) is done without any reinforcement in the slab (stirrups in the beam are kept avoiding splitting), and at that moment we reach the needed load level of 11.58 kN/m². By presenting the principal forces in the slab in *Fig 3 a) and b)* respectively for amb_4 and amb_5 the CMA of the unreinforced slab is shown. Deformations are enlarged by a scale factor of 10, this factor is kept constant for all next figures.

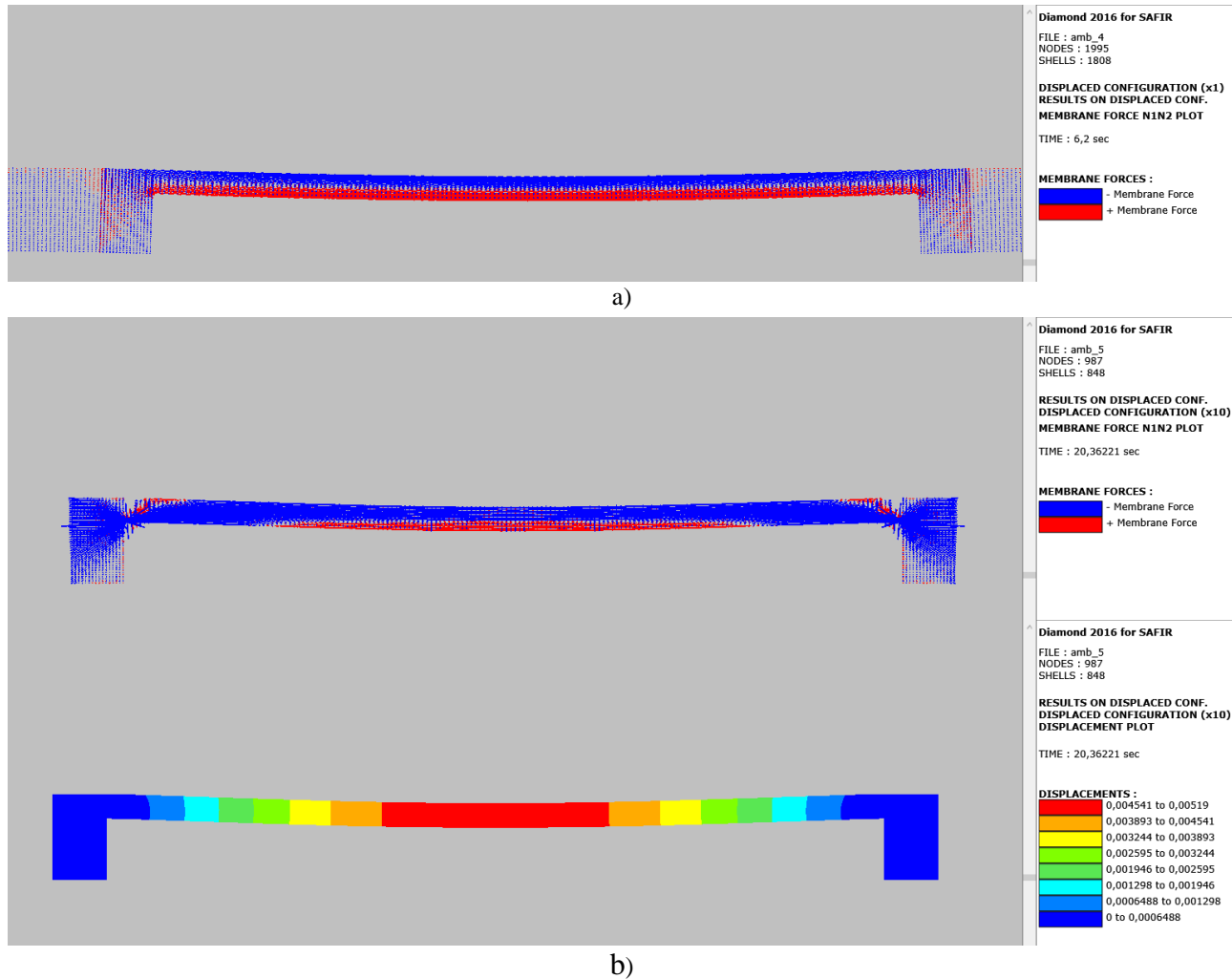


Fig. 3. Principal forces a) With reinforcement; b) Without reinforcement (developing CMA)

It seems that the presence of reinforcement is in some way disturbing the development of CMA and lower reinforcement would fail. At that moment the model of *Fig 3 b)* will develop and assure stability. This is also reported in a real scale test; a deflection of 5 mm could be measured (after 30 minutes, stable after 10 minutes) which is in very good agreement with the 5.2 mm out of *Fig 3 b)*.

4 SLAB ANALYSIS AT ELEVATED TEMPERATURE

4.1 Results with reinforcement

Analysis were executed for the 3 kind of spring constant out of *Table 1* together with the so called extreme values as described at the end of previous article 3.1. A summary of results is given in *Table 2.*, a ranking was made from more flexible to infinity rigid. The following can be found:

- i) Difference between more flexible supports and infinity rigid results in a benefit of factor 2 but in absolute values for this case study this means only lesser as 4 minutes which is not significant for this kind of advanced analysis.

Numerical Modelling

- ii) The failure time is varying depending the level and the most rigid structure (above ground floor) doesn't result in the highest failure time as could be expected.
- iii) Even in the worst case the resistance passes in the beginning the load level at the fire condition which is equal to 6.96 kN/m² which is more as was find before in article 3.2.

Table 2. Failure time depending of spring constant at different levels + extreme values

Level	Spring constant (kN/m)	Failure time in s
	1000/1000	221
18	25445/641	349
9	51020/3125	257
1	55249/7806	311
0	∞/∞	447

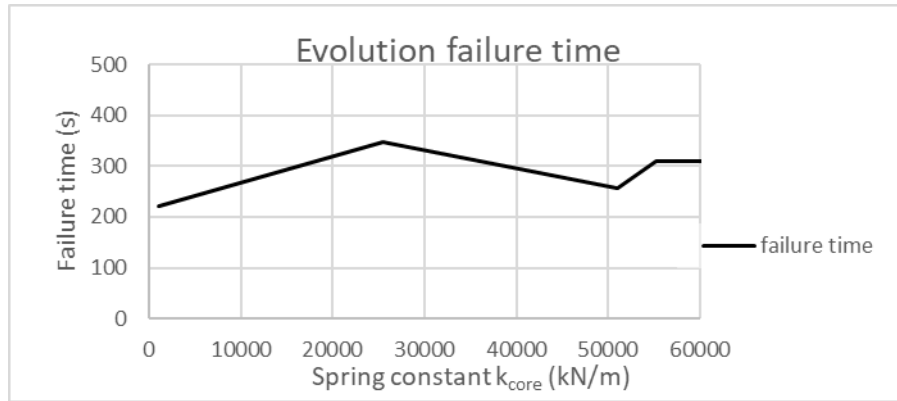
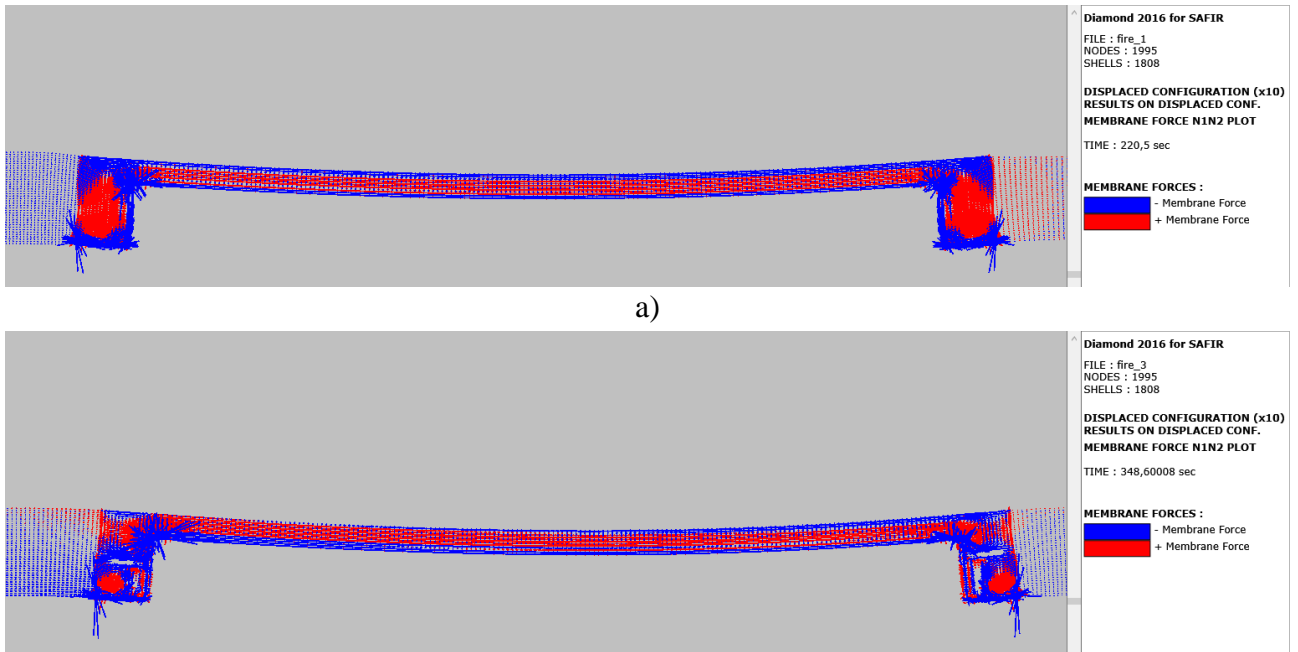


Fig. 4. Failure time depending of spring constant at different levels + extreme values

To understand the failure mechanism an overview of the principal forces is given in Fig 5, at the side of the stiffest boundary condition more tensile forces are developed. Remark that at the upper mostly tensile forces are developed and that only in the case of fixed ends Fig 5 e) the biggest part of the slab is working in compression without developing CMA as it did in the cold situation (Fig 3 b)), out of the deformation it can however be presumed that some CMA is developed before failure.



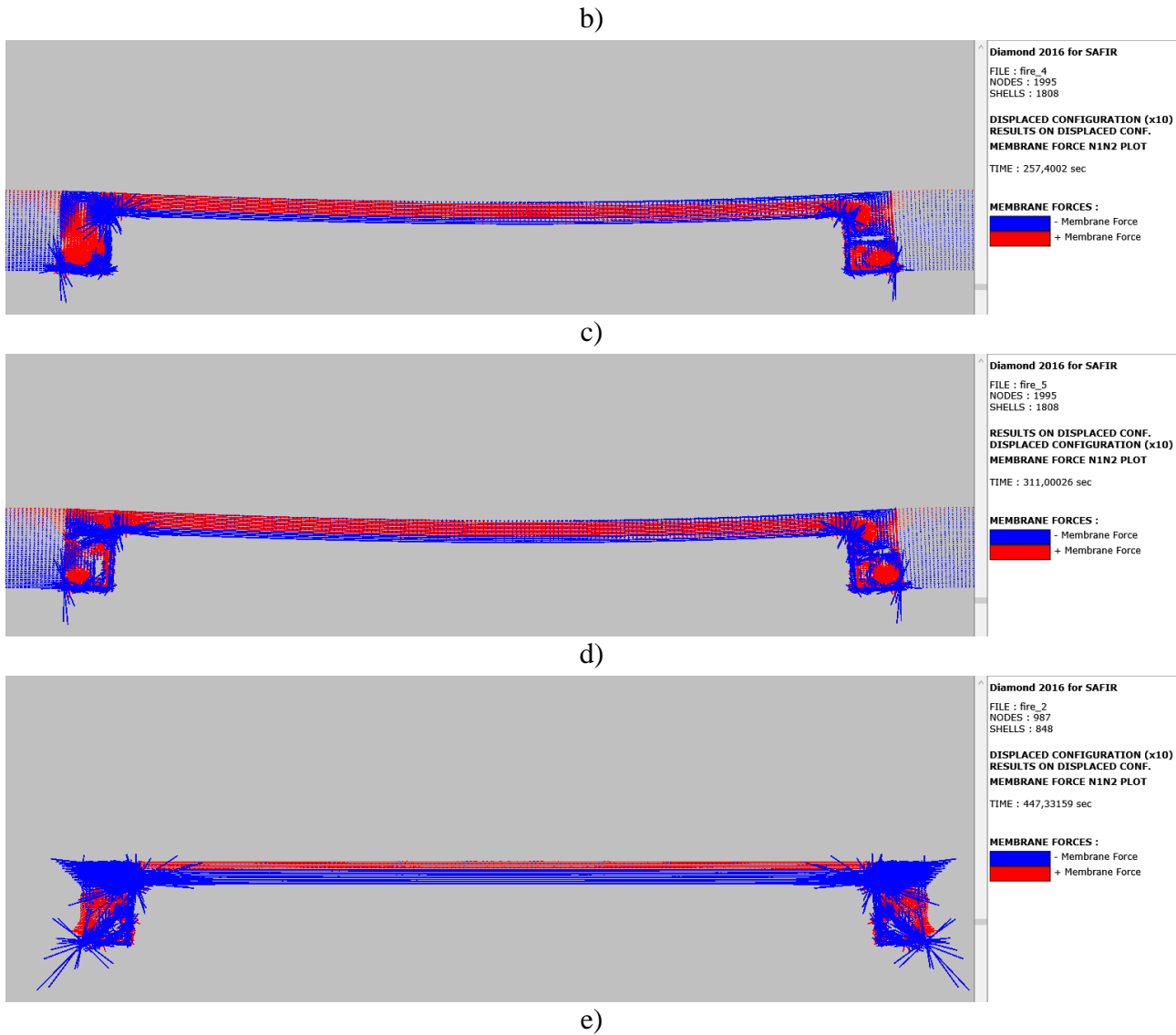


Fig. 5. Principal forces at failure time a) = 2 x 1000 kN/m, b) = 18th, c) = 9th, d) = 1st and e) = ∞

4.2 Results without reinforcement

Figure 3 before showed out that the presence of reinforcement might disturb the development of CMA in the slab. For this reason, the for failure time almost weakest simulation, level 9, was repeated after erasing all reinforcement and replacing it by ordinary concrete. The failure time finally arrived at 235 s or slightly bellow the result with reinforcement. Out of the principal forces it can be seen that the slab tries to develop tensile membrane action.

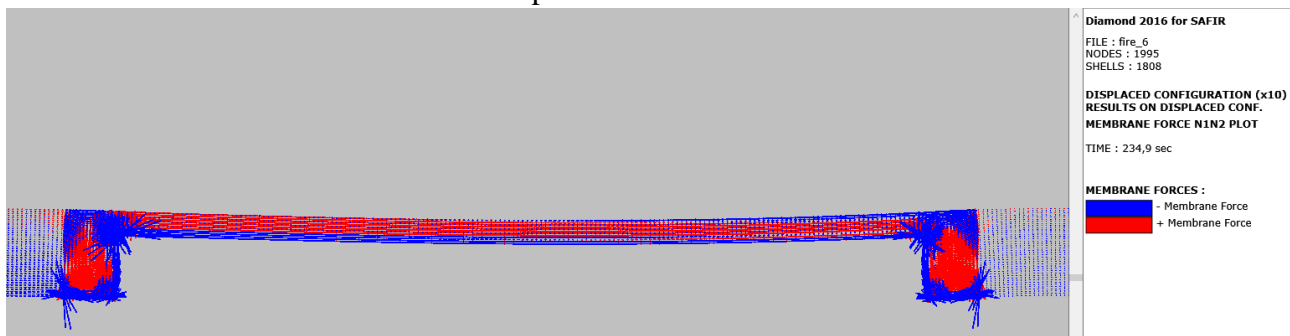


Fig. 6. Principal forces at failure time for level 9

5 CONCLUSIONS

Where at ambient conditions and with fixed ends in case of fire, compressive membrane action seems to be promising, it is stated out that with more realistic boundary conditions the positive effect seems to disappear. An advanced and more enhanced model was proposed regarding to previous work done in this field, but it underlines only the leak of CMA at elevated temperature. Slabs which work on CMA in ambient condition have the tendency to fail in case of fire even after a limited time of about 4 minutes. Depending of the stiffness of the adjacent structure an extra benefit of 4 minutes can be obtained, which is not enough to justify this kind of design. More classic tools as concrete cover for bending or tensile membrane action are more appropriate. Further research can only be encouraged at the moment that test results at elevated temperature shows the presence of this effect, which is out of this study doubtful.

ACKNOWLEDGMENT

The support of Sweco company to invest in research is greatly appreciated.

REFERENCES

1. Tom Molken, Thomas Gernay, Robby Caspeepele (2017). Fire resistance of concrete slabs acting in compressive membrane action. *2nd International Fire Safety Symposium*, Naples Italy, June 7–9, IFireSS, 2017. pp 661-668
2. Gernay T., Millard A., Franssen J.M. (2013). *A multiaxial constitutive model for concrete in the fire situation: Theoretical formulation*. International Journal of Solids and Structures 50(22-23): 3659-3673.
3. Gernay T., Franssen J.-M. (2012). *A formulation of the Eurocode 2 concrete model at elevated temperature that includes an explicit term for transient creep*. Fire Safety Journal 51: 1-9.
4. Franssen J.M. (2005). *SAFIR A Thermal/Structural Program for Modelling structures under Fire*, Engineering Journal A.I.S.C. 42(3): 143-158.
5. EN 1992-1-2 (2004+AC2008). *Eurocode 2: Design of concrete structures – Part 1-2: General rules – Structural fire design (+AC2008)*. CEN, Brussels, Belgium, December 2004.

Numerical Modelling

STRUCTURAL IMPLICATIONS DUE TO AN EXTENDED TRAVELLING FIRE METHODOLOGY (ETFM) FRAMEWORK USING SIFBUILDER

Xu Dai¹, Stephen Welch², Asif Usmani³

ABSTRACT

Modern architectures often contain large and/or complex space where traditional concepts of compartment fire behaviour are undermined and consideration of “travelling fires” is required. The structural fire behaviour under such conditions has been little explored. Here, the cross-sectional time-temperature evolution of a steel beam supporting a concrete slab is examined in simplified example scenarios implemented in the integrated software framework SIFBuilder. The fire boundary conditions are represented using the extended travelling fire methodology (ETFM) framework, which considers the essential energy and mass conservations, and encompass sensitivity studies on fire spread rate and fire load. The results highlight the phenomenon of ‘thermal gradient reversal’ due to the near-field fire plume approaching and leaving the design structural member, thereby reversing the thermally-induced bending moment from hogging to sagging. Within the assumed ranges of parameter variation, the maximum thermal gradient due to smoke-preheating is proportional to the fire spread rate and less sensitive to the fuel load density. By contrast, the peak thermal gradients due to approach and departure of the fire “near-field” are more sensitive to the fuel load density, with larger peak values at lower fuel load densities.

Keywords: Performance-based design, travelling fires, FEM modelling, OpenSees/SIFBuilder.

1 INTRODUCTION

There are three representations of travelling fires which can be found in the literature [1]: Clifton’s model [2], Rein’s model [3–5], and an extended travelling fire methodology (ETFM) framework developed by the authors [6,7]. The ETFM framework is developed by ‘mobilising’ Hasemi’s localized fire model [8] for the fire plume near the structure (i.e. near-field), and combined with a simple smoke layer calculation by utilising the FIRM zone model [9] for the areas of the compartment away from the fire (i.e. far-field). The heat fluxes generated by the ETFM framework will enable both a heating phase and a cooling phase for each structural member in the large compartment. This combined fire model enables the analysis to comprehensively capture both spatial and temporal changes of the thermal field, thus addressing more of the fire dynamics. Fire temperatures are variable for the near field in the ETFM framework, contrasting the uniform 800°C-1200°C assumption in Rein’s model, while all elements in one firecell share the same fire exposure history in Clifton’s model. Furthermore, the FIRM zone model also enables the ETFM to consider smoke accumulation under the ceiling, which is ignored in both previous models. More importantly, utilising the FIRM zone model into the ETFM framework, means that the energy conservation and the mass conservation are both satisfied at a global level for the design compartment. Previously proposed dedicated travelling fire methodologies simply force other existing models to ‘travel’ (i.e.

¹ Post-Doctoral Research Associate, BRE Centre for Fire Safety Engineering, the University of Edinburgh, UK.

e-mail: x.dai@ed.ac.uk

² Senior Lecturer and Discipline Programme Manager, BRE Centre for Fire Safety Engineering, the University of Edinburgh, UK.

e-mail: s.welch@ed.ac.uk

³ Professor and Head of the Department of Building Services Engineering, Hong Kong Polytechnic University, Hong Kong.

e-mail: asif.usmani@polyu.edu.hk

modified parametric fire curves in Clifton's model, 800°C-1200°C temperature block and the Alpert's ceiling jet model in Rein's model), and have not attempted to explicitly account for the mass and energy balance in the compartment. The work presented in this paper is on this basis, to improve the understanding of the structural implications due to travelling fires, through a more fire science-bounded travelling fire model, i.e. the ETFM framework.

Although axial force histories due to the progress of travelling fires have been quantitatively investigated using Rein's model [10,11], the development of thermal gradient-induced bending moment is not investigated by the previous researchers, even qualitatively. This is because lumped capacitance is assumed in their heat transfer analysis [10,11]. This is an acceptable assumption for 'thermally thin' structural members, such as a steel beam with four-sided fire exposure conditions. But in real buildings, a concrete slab is normally on top of these steel beams generating a heat sink effect, hence neglecting the through-depth thermal gradient under this situation is not appropriate. Jiang *et al.* [12] investigated the maximum thermal gradient of a steel-composite structure using Rein's model, concluding that higher through-depth thermal gradient in the beam would be generated with larger travelling fire sizes. However, the thermal gradient histories as the travelling progresses in the timeline were not studied. Further, maximum or peak thermal gradients due to different heating and cooling regimes were not investigated.

Some of the initial ETFM applications were presented in Dai *et al.* (2017) [1]. It is worth noting that those parametric studies were performed by running the 'travelling Hasemi' component and FIRM zone model component separately, to investigate the individual rather than combined thermal impacts. The full version of ETFM is demonstrated in this paper with a case study, to investigate the thermal impact due to the combined thermal inputs. The thermal response implications on the subsequent structural responses (e.g. the axial force induced by thermal expansion with uniform temperature increase and axial restraints, the change of thermal bowing bending moment induced by reversal of the thermal gradient through the depth, with rotational restraints) are discussed. Furthermore, as opposed to investigating the thermal impact due to the various ratios of the fire size to the compartment size (e.g. 5%, 10%, 25%, 75%, etc.), as in Rein's model, this paper explicitly investigates the impact of the ETFM parameters (i.e. fire spread rate, fuel load density), through quantifying the cross-sectional time-temperature evolution of the investigated steel beam in the case study. The thermal gradients through the depth arising from different travelling fire scenarios are extensively explored, especially with regards to the 'thermal gradient reversal' due to the near-field fire plume approaching and leaving the design structural member, as this 'thermal gradient reversal' fundamentally reverses the thermally-induced bending moment from hogging to sagging. All these analyses are performed using SIFBuilder [7,13], which is an OpenSees-based [14] open-source software framework with features of facilitating analysis of fire, heat transfer and thermo-mechanical response in one single software package. Its 'thermal' modelling robustness has been verified and validated by Jiang [15].

2 FUNDAMENTAL PRINCIPLES OF A BEAM MEMBER UNDER FIRE

The fundamentals of thermal effects on structural behaviour were discussed by Usmani *et al.* in 2001 [16]. According to this work, if temperature in the longitudinal direction of a beam is assumed to be 'uniformly' distributed, then its structural behaviour would be dominated by the temperature distributions over its cross-sectional depth, and boundary conditions. *Fig. 1.* a) schematically presents the thermal effects over the beam depth with 'a simplified equation': a realistic temperature distribution over the depth of a beam is decomposed into uniform temperature increase (ΔT) causing thermal expansion, and thermal gradient (T_y) causing the thermal bowing effect. If the heated beam is restrained by a certain level of boundary conditions (i.e. finite rotational restraints and horizontal restraints), internal forces would be induced. As shown in *Fig. 1.* b), the thermal

expansion due to ΔT would be constrained by the horizontal restraints, hence an internal compressive axial force would be generated during the heating stage. Meanwhile, thermal bowing due to T_y would be constrained by rotational restraints, hence a hogging bending moment would be generated during the heating stage.

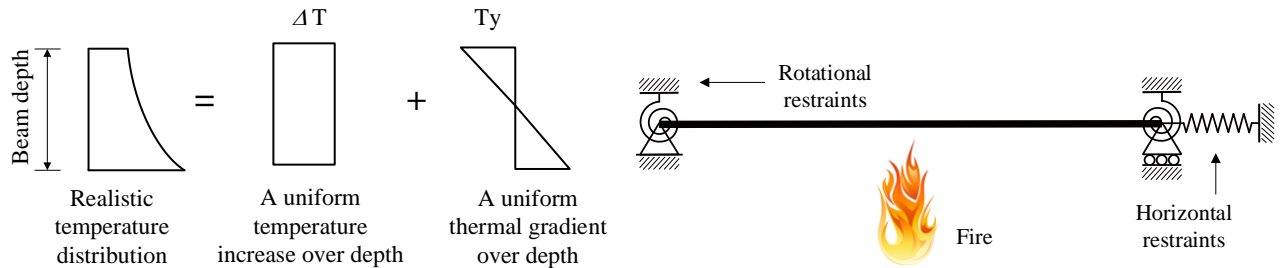


Fig. 1. a) Decomposition of temperature effects over the depth of a beam section; b) A beam member with finite boundary conditions under fire

However, once the design fire severity upgrades from a simple model (e.g. ISO-834 standard fire curve with a single heating regime) to a more realistic fire model (e.g. ETFM framework with ‘cyclic’ heating and cooling regimes), the interpretation of the corresponding structural behaviour becomes more complicated. The subsequent sections investigate these types of complexities under ETFM framework with a case study.

3 THE STRUCTURE FOR CASE STUDY

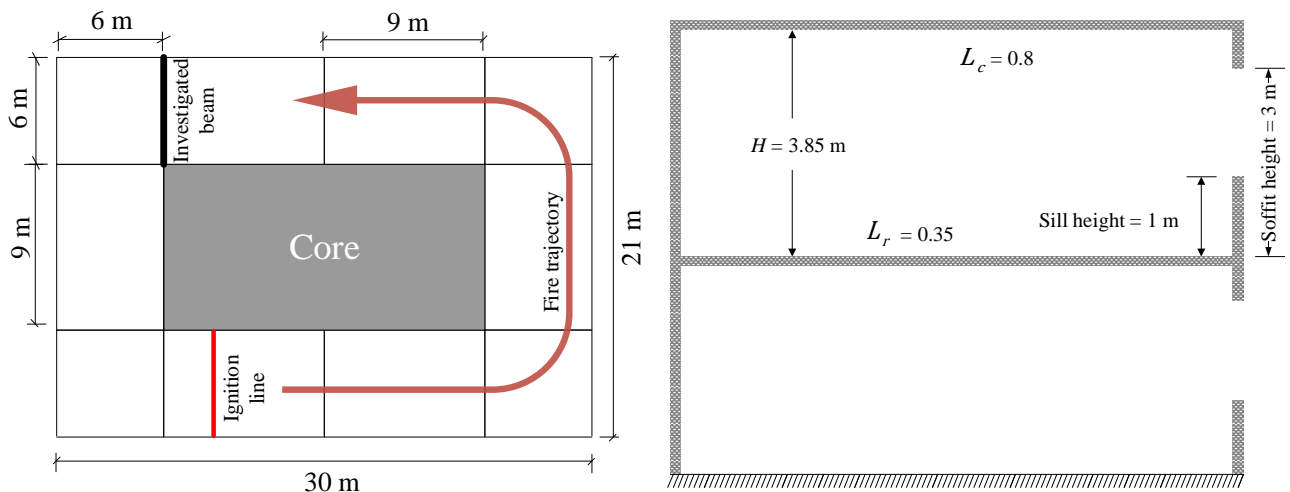


Fig. 2. a) Case study structural plan view with predefined travelling fire trajectory; b) Case study structural elevation view (fire applied on first floor using the ETFM framework, L_c is the heat loss fraction ratio through the compartment boundaries assumed to be 0.8 (0.6 ~ 0.9 as recommended in [9]), and L_r is the radiative loss fraction of the fire plume assumed to be 0.35 (as recommended in [9]))

Fig. 2. a) shows the plan view of an idealised structural layout for the case study (630 m² floor area), which is a generic representation of modern tall buildings with a core (162 m² area) in the middle. A steel beam is investigated, with size UB 305×127×42, located at the top left of the floor plan. Concrete slabs are assumed to be carried on top of the steel beams. The ignition line of the travelling fire is also shown in Fig. 2. a). The travelling fire trajectory is predefined to be under the mid-span of the main beams, which would normally represent the worst case for the structural response. Fig. 2. b) shows a schematic of the elevation of the investigated case study. The fire is ignited on the first floor of the building. The clear compartment height, H , is 3.85 m. The total vent widths of this large compartment are 28 m. The soffit height and sill height are 3 m and 1 m, respectively.

4 TRAVELLING FIRE SCENARIOS AND HEAT TRANSFER SETUP

The ETFM framework involves a certain number of input parameters, such as the fuel load densities, ventilation dimensions, heat release rates, etc [6,7]. To minimise the uncertainties and complexities, with more interpretable results, only two key design parameters are investigated: the constant fire spread rate, ν (mm/s), and the characteristic fuel load density, $q_{f,k}$ (MJ/m²). The range of these two values are 1.6-15 mm/s [5] and 100-780 MJ/m² [17], respectively. A 'base line scenario' of the travelling fires is assumed, with fire spread rate of 10.0 mm/s, fuel load density of 570 MJ/m², and the heat release rate per unit area 500 kW/m². The travelling fire scenarios applied in the case study structure (as mentioned in the previous section) are summarized in *Table 1*, where each black dot stands for a design fire scenario using the ETFM framework. The total number of sampling data points is 29, which is the total number of travelling fire scenarios investigated.

Table 1. Travelling fire scenarios adopted to perform parametric studies for the ETFM framework.

Fire Spread rate ν (mm/s) \n Fuel load density $q_{f,k}$ (MJ/m ²)	1.6	2.0	5.0	8.0	10.0	15.0
100 (Transport)	•	•	•	•	•	•
230 (Hospital)	•	•	•		•	
300 (Theatre)	•	•	•		•	
420 (Office)	•			•	•	
570	•	•	•	•	•	•
600 (Shopping centre)	•				•	•
780 (Dwelling)	•				•	•

In the heat transfer modelling, only three sides of the investigated steel beam are exposed to the thermal impact using the ETFM framework, since a concrete slab is assumed to be at the top, generating a heat sink effect, as shown in *Fig. 3*. Two-dimensional heat transfer analysis is carried out for the cross-section at the mid-span of the beam, using 35 W/m²K as the convection coefficient for fire-exposed surfaces and 0.7 as the emissivity of the steel (two coefficients recommended in [17]). *Fig. 3* is a schematic of the cross-section of the investigated steel beam, in which temperatures are recorded at three locations: the top flange, the mid-web, and the bottom flange.

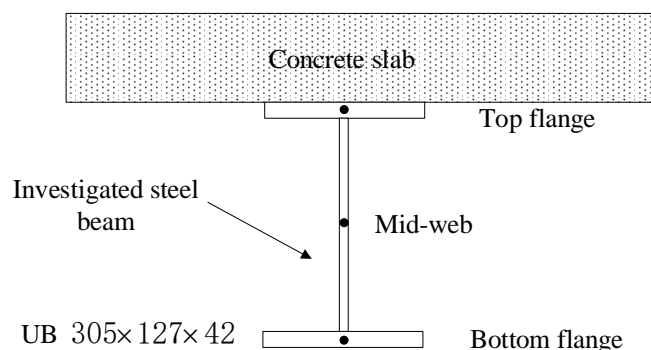


Fig. 3. Schematic of the investigated steel beam cross-section for heat transfer

5 THERMAL RESPONSE AND CORRESPONDING STRUCTURAL IMPLICATIONS

Fig. 4 shows the cross-sectional temperature histories of the investigated steel beam in the case study, under the ‘slow’ but ‘dense’ fire scenario with $v = 1.6 \text{ mm/s}$, $q_{f,k} = 780 \text{ MJ/m}^2$, $RHR_f = 500 \text{ kW/m}^2$. It is assumed that the investigated beam is constrained with both rotational and horizontal restraints. A compressive force would have been first induced by the far-field smoke preheating. After a certain duration of the stabilized smoke heating, larger compressive forces would be generated when the near-field fire plume approaches the investigated beam (assuming the beam is not yielded, and no catenary action happens at this stage). Following this, a contraction force due to cooling would be generated, as the near-field fire plume travels away from the beam. Finally, more cooling-induced contraction forces would be generated, during the decay stage of the far-field smoke.

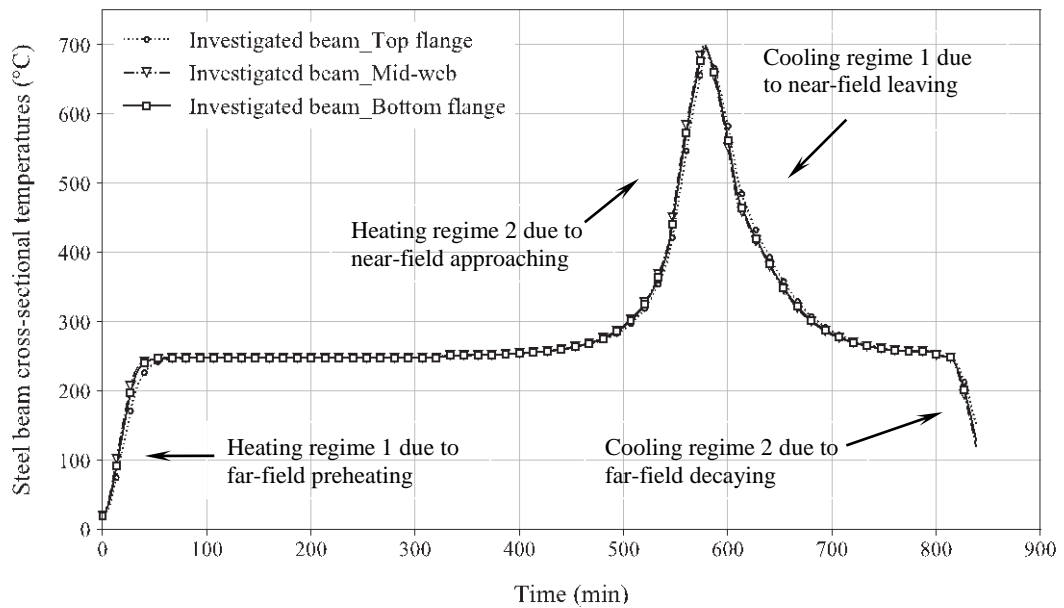


Fig. 4. Temperature histories of the investigated beam, under travelling fire scenario with $v = 1.6 \text{ mm/s}$, $q_{f,k} = 780 \text{ MJ/m}^2$, $RHR_f = 500 \text{ kW/m}^2$.

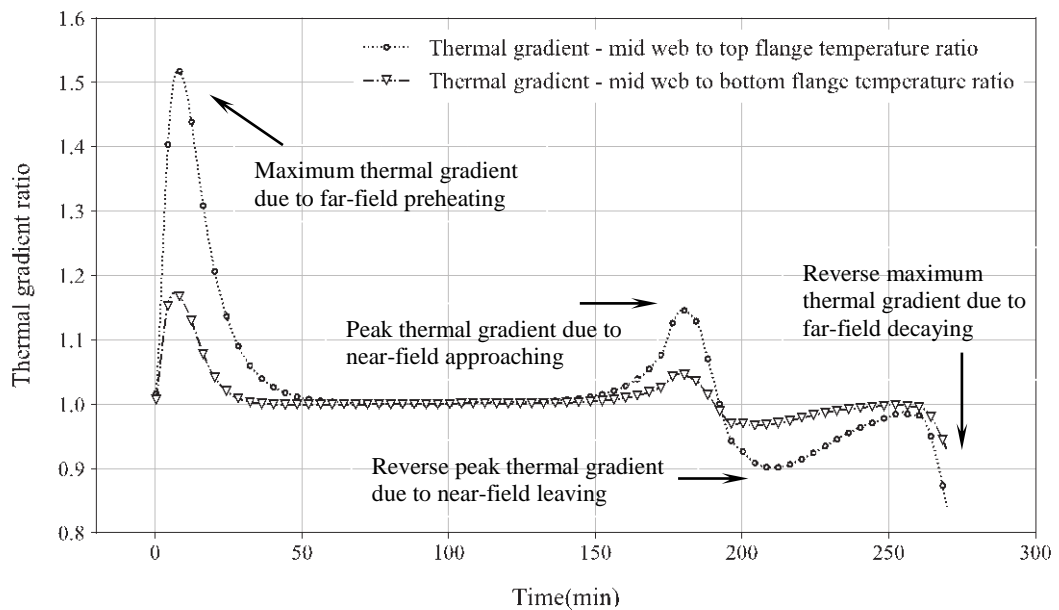


Fig. 5. Thermal gradient histories of the investigated beam, under travelling fire scenario with $v = 5.0 \text{ mm/s}$, $q_{f,k} = 300 \text{ MJ/m}^2$, $RHR_f = 500 \text{ kW/m}^2$.

Fig. 5 demonstrates the cross-sectional thermal gradient histories of the investigated steel beam, under a travelling fire scenario with $v = 5.0$ mm/s, $q_{f,k} = 300$ MJ/m², $RHR_f = 500$ kW/m². Assuming the investigated beam is constrained with both rotational and horizontal restraints, a clear thermal gradient is first captured due to the far-field smoke preheating. This thermal gradient would generate hogging bending moment as the beam is rotationally constrained. This bending moment would then gradually disappear along with the smoke-induced thermal gradient reducing to 1.0, caused by a stabilized heating duration from far-field smoke. After this, hogging bending moment would be generated again, since the corresponding thermal gradient is induced when the near-field fire plume is approaching the investigated beam. More interestingly, when the near-field fire plume is travelling away from the beam, this thermal gradient would be reversed to 0.9 rather than reduced to 1.0. This ‘thermal gradient reversal’ means the bending moment would be reversed from hogging type to sagging type. Finally, this thermal gradient again gradually turns to 1.0 until the smoke temperature steps into its decay stage, where another thermal gradient which is below 1.0 shows up.

Fig. 5 presents the thermal gradient histories under one single travelling fire scenario. It is worth to analyse the thermal gradient histories with more travelling fire scenarios, especially for the ‘thermal gradient reversal’ phenomena due to the period when the near-field fire plume approaches and leaves the investigated beam, as the entire thermal gradient histories are directly related to the corresponding hogging or sagging bending moments. Fig. 6 demonstrates the comparison of thermal gradient histories of the investigated steel beam, with various fuel load densities ranging from $q_{f,k} = 100$ MJ/m² to $q_{f,k} = 780$ MJ/m², and constant $v = 10$ mm/s, $RHR_f = 500$ kW/m². This thermal gradient is the ratio of mid-web temperature to top flange temperature. It can be seen that both the maximum thermal gradient due to smoke pre-heating (1.6 approximately), and reverse maximum thermal gradient due to smoke decaying (0.8 approximately), are not sensitive to various fuel load densities. However, both the peak thermal gradient due to near-field approaching and the reverse peak thermal gradient due to near-field leaving the investigated beam, change dramatically with various fuel load densities. In general, these peak and reverse peak thermal gradients decrease with increasing fuel load densities.

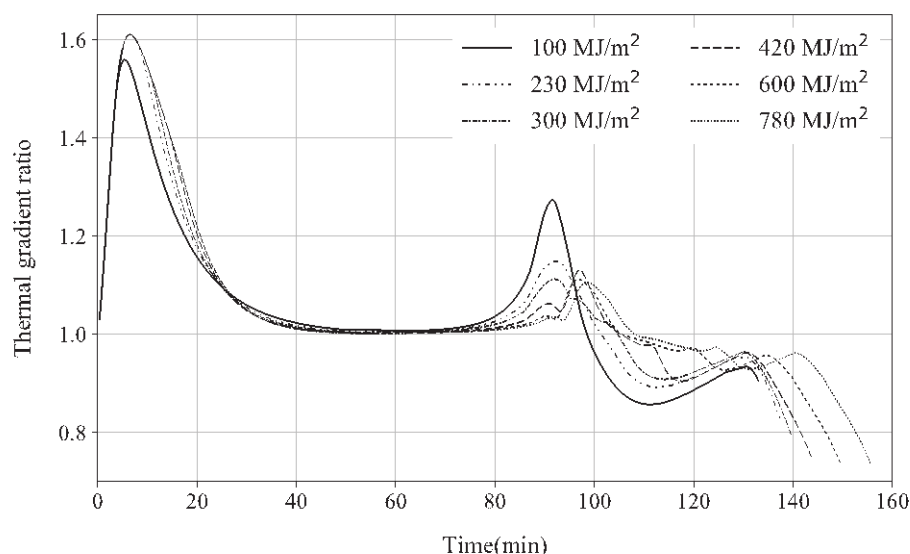


Fig. 6. Thermal gradient histories of the investigated steel beam, with various fuel load densities ranging from $q_{f,k} = 100$ MJ/m² to $q_{f,k} = 780$ MJ/m², and constant $v = 10$ mm/s, $RHR_f = 500$ kW/m².

Fig. 7 demonstrates the comparison of thermal gradient histories of the investigated steel beam, with various fire spread rates ranging from $v = 1.6$ mm/s to $v = 15$ mm/s, and constant $q_{f,k} = 570$ MJ/m², $RHR_f = 500$ kW/m². It can be seen that both the peak thermal gradient due to near-field approaching (1.1 approximately), and reverse peak thermal gradient due to near-field leaving (0.9

approximately), are not sensitive to various fire spread rates. However, both the maximum thermal gradient due to smoke pre-heating and the reverse maximum thermal gradient due to smoke decaying are sensitive to various fire spread rates. In general, these maximum and reverse maximum thermal gradients increase with higher fire spread rates.

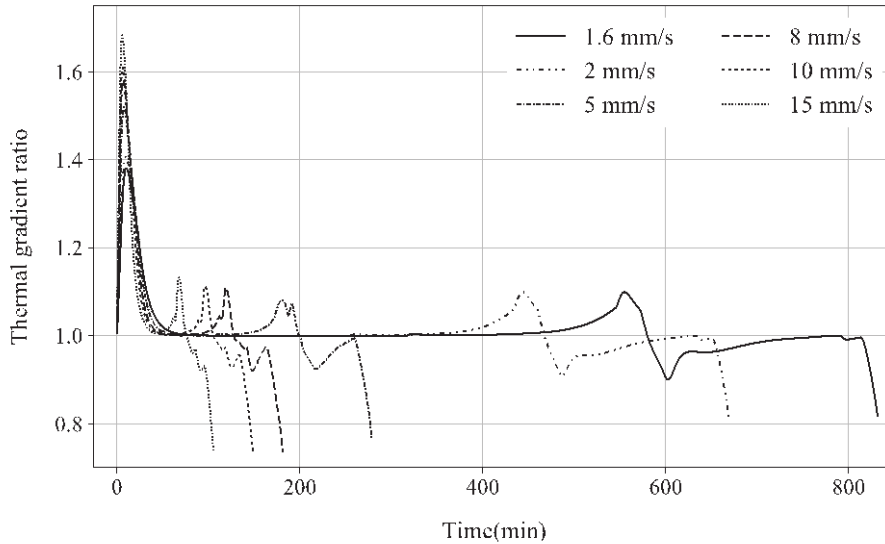


Fig. 7. Thermal gradient histories of the investigated steel beam, with various fire spread rates ranging from $v = 1.6$ mm/s to $v = 15$ mm/s, and constant $q_{f,k} = 570$ MJ/m², $RHR_f = 500$ kW/m².

Fig. 8 shows the ratio of the difference between the peak thermal gradient and reverse peak thermal gradient under all 29 travelling fire scenarios, to further investigate this thermal gradient reversal 'phenomena'. It implies this thermal gradient is more sensitive to the fuel load density rather than fire spread rate, where markedly larger difference values are captured with lower fuel load densities.

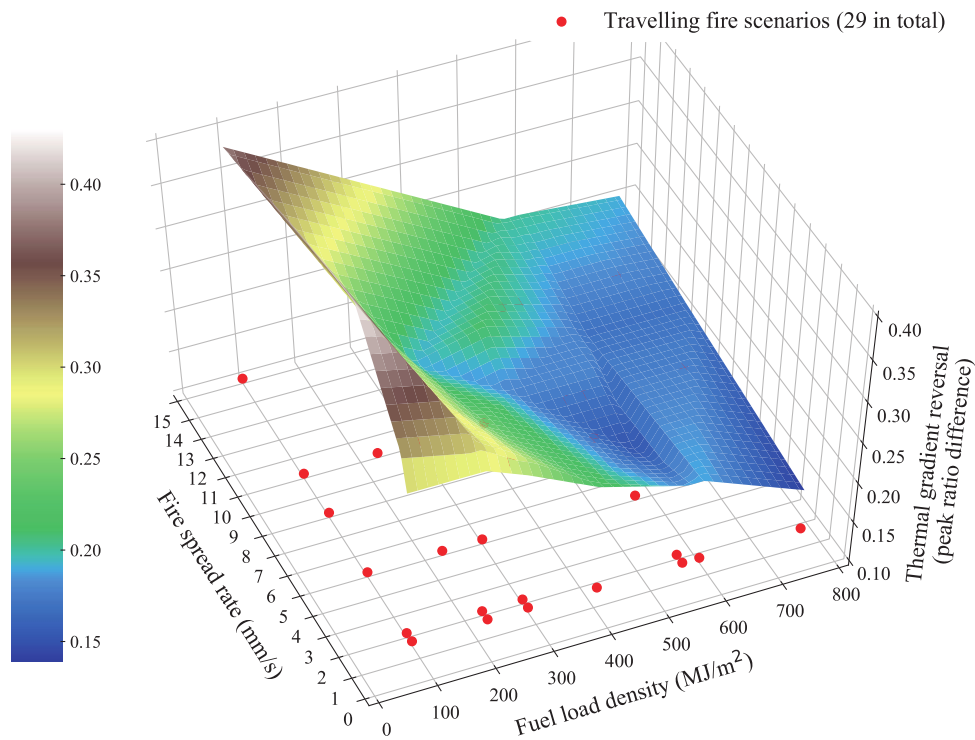


Fig. 8. Peak and reverse peak thermal gradient difference, due to near-field approaching and leaving the investigated beam, under all the 29 travelling fire scenarios.

6 CONCLUSIONS

Structural response of a loaded I-beam to a range of travelling fire scenarios (spread rates and fire loads) has been investigated. Within the assumed ranges of parameter variation the results suggest that the maximum thermal gradient due to smoke-preheating is proportional to the fire spread rate and less sensitive to the fuel load density. The peak and reverse peak thermal gradients, due to approach and departure of the fire near-field, respectively, are both more sensitive to the fuel load density, where larger peak values are captured with lower fuel load densities. These results demonstrate the potential for this type of methodology to provide insights into the fire-structural coupling in more realistic scenarios relevant to design.

REFERENCES

1. X. Dai, S. Welch, and A. Usmani (2017) "A critical review of 'travelling fire' scenarios for performance-based structural engineering," *Fire Safety Journal*, vol. 91, pp. 568–578.
2. C.G. Clifton (1996) "Fire Models for Large Firecells. HERA Report R4-83".
3. G. Rein, X. Zhang, P. Williams, B. Hume, A. Heise, A. Jowsey, B. Lane, & J.L. Torero (2007) "Multi-storey fire analysis for high-rise buildings," in *Proceedings of the 11th International Interflam Conference, London, UK*, pp. 605–616.
4. J. Stern-Gottfried & G. Rein (2012) "Travelling fires for structural design-Part II: Design methodology," *Fire Safety Journal*, vol. 54, pp. 96–112.
5. E. Rackauskaite, C. Hamel, A. Law & G. Rein (2015) "Improved formulation of travelling fires and application to concrete and steel structures," *Structures*, vol. 3, pp. 250–260.
6. X. Dai, L. Jiang, J. Maclean, S. Welch & A. Usmani (2016) "A conceptual framework for a design travelling fire for large compartments with fire resistant islands," in *Proceedings of the 14th International Interflam Conference*, pp. 1039–1050.
7. X. Dai, L. Jiang, J. Maclean, S. Welch & A. Usmani (2016) "Implementation of a new design travelling fire model for global structural analysis," in *the 9th International Conference on Structures in Fire*, pp. 959–966.
8. Y. Hasemi, Y. Yokobayashi, T. Wakamatsu & A.V. Pchelintsev (1996) "Modelling of heating mechanism and thermal response of structural components exposed to localised fires," *Thirteenth meeting of the UJNR panel on fire research and safety*. pp. 237–247.
9. M.L. Janssens (2000) *An Introduction to Mathematical Fire Modeling*, 2nd ed. CRC Press,.
10. E. Rackauskaite, P. Kotsovinos & G. Rein (2017) "Structural response of a steel-frame building to horizontal and vertical travelling fires in multiple floors," *Fire Safety Journal*, vol. 91, pp. 542–552.
11. F.H. Rezvani & H.R. Ronagh (2015) "Structural response of a MRF exposed to travelling fire," *Proc. of the Institution of Civil Engineers - Structures and Buildings*, vol. 168, no. 9, pp. 619–635.
12. Y. Jiang, P. Kotsovinos, A. Usmani, G. Rein & J. Stern-Gottfried (2013) "Numerical investigation of thermal responses of a composite structure in horizontally travelling fires using OpenSees," *Procedia Engineering*, vol. 62, pp. 736–744.
13. L. Jiang, X. Dai, A. Usmani & P. Kamath (2015) "OpenSees-based integrated tool for modelling structures in fire," in *The First International Conference on Structural Safety under Fire & Blast, Glasgow, Scotland, UK*, pp. 461–468.
14. F.T. McKenna (1997) "Object-Oriented Finite Element Programming: Frameworks for Analysis, Algorithms and Parallel Computing," PhD Thesis, the University of California.
15. Y. Jiang (2012) "Development and Application of a Thermal Analysis Framework in OpenSees for Structures in fire," PhD Thesis, the University of Edinburgh.
16. A.S. Usmani, J.M. Rotter, S. Lamont, A.M. Sanad & M. Gillie (2001) "Fundamental principles of structural behaviour under thermal effects," *Fire Safety Journal*, vol. 36, no. 8, pp. 721–744.
17. Eurocode1: Actions on Structures - Part 1-2: General Actions - Actions on Structures Exposed to Fire. European Standard EN 1991-1-2, CEN, Brussels, 2002.

ELEVATED-TEMPERATURE TENSION STIFFENING MODEL FOR REINFORCED CONCRETE STRUCTURES UNDER FIRE

Jason Martinez¹, Ann E. Jeffers²

ABSTRACT

In this study, a tension stiffening approach for modelling concrete-rebar interactions at elevated temperature condition is proposed for the numerical analysis of composite floor systems under fire. Tension stiffening is an approach that allows concrete-rebar interactions in reinforced concrete (RC) to be implicitly simulated. In finite element models where a perfect bond between the elements representing concrete and reinforcing bars is made, such as in a layered-shell element representation of a composite slab, an indirect tension stiffening model is required as input to account for the interactions between cracked concrete and the reinforcement. However, for elevated temperature analysis of RC members, an established tension stiffening model does not exist in the current literature. Thus, a tension stiffening model for analysing RC member under fire is presented, based on the modifications of the fracture theory of plain concrete at ambient temperature. The adequacy of this approach is validated against the Cardington Fire Test 3. Comparisons of numerical results against experimental results show that the approach is adequate and leads to convergence of the static analysis solver past the first instance of localized cracking, which is a major problem when existing ambient-temperature tension stiffening approaches are utilized.

Keywords: Tension stiffening, fracture energy, composite floor system, finite element modelling.

1 INTRODUCTION

In finite element (FE) modelling of reinforced concrete (RC), steel and concrete materials are typically modelled using separate elements. The assumption that the individual constitutive material model of bare steel and concrete can be used to describe the composite behaviour of RC rests entirely on the proper modelling of the bond behavior at the concrete-rebar interface. An accurate solution requires the bond interaction between nodes of finite elements representing the steel rebar and the surrounding concrete to be made via special dimensionless contact and/or spring elements. These special elements define explicitly the bond-slip relation between individual nodes of discrete elements representing steel and concrete and allows bond-action between cracked concrete and embedded steel rebar to be directly modelled.

However, such a micro-level representation of RC requires a level of sophistication that is often associated with prohibitively large model assembly time and simulation time. Moreover, there are circumstances when a smeared representation of reinforcement is preferred, such as in the modelling of RC composite floor slabs. In these cases, it is impractical to define an explicit bond-slip relation between steel and concrete. For this reason, it is efficient to assume a perfect bond between steel and concrete elements, and implicitly account for the bond interaction through appropriate modification of the individual constitutive material models of bare steel and/or plain concrete. In this macro-level representation of RC, utilizing the constituent models of bare steel and

¹ Ph.D. Candidate, Department of Civil and Environmental Engineering, University of Michigan, USA.
e-mail: marjason@umich.edu

² Associate Professor, Department of Civil and Environmental Engineering, University of Michigan, USA.
e-mail: jffrs@umich.edu

plain concrete does not provide a realistic behaviour. The realistic behavior of RC is an integrated outcome of the individual constitutive material models and their interaction with one another.

The focus of this paper lies in the indirect tension stiffening approach for modelling concrete-rebar interactions in RC composite floor slabs under fire. In a macro-model representation of a floor slab, a layered shell element is utilized, and the steel reinforcement is expressed as a uniformly distributed smeared steel layer. Because a perfect rigid bond exists between the steel and concrete layers, effects associated with concrete-rebar interactions must be simulated approximately using an indirect tension stiffening approach. This requires a modification to the constituent material models of bare steel and/or plain concrete to be made. Unfortunately, the majority of existing tension stiffening models were developed for the ambient-temperature condition. Research on tension stiffening of RC at elevated temperature is very limited, and tension stiffening models for RC at elevated temperatures do not exist in the current literature. The purpose of this paper is to address this knowledge gap and propose a rational method to define the post-cracking tension stiffening stress-strain curve of RC at elevated temperatures. The appropriateness of the approach is validated against the Cardington Test 3 [1].

2 BACKGROUND

2.1 Fracture Theory of Plain Concrete at Ambient-Temperature

The uniaxial stress-strain relation of plain concrete in tension can be described using the fracture theory of concrete proposed by Bažant and Oh [2]. When a plain concrete specimen is subjected to direct tension past the peak tensile strength f_{to} , a band of densely distributed micro-cracks occurs in part of the specimen, causing strain to be localized within this region. Progressive micro-cracking in this region (known as the crack band region) under increasing strain causes a strain-softening response once the tensile strength f_{to} has been reached. As this occurs, elastic strain energy stored in the concrete from elastic deformation is slowly released in the form of fracture energy.

Assuming that the fracture of concrete can be described by a fictitious band of densely distributed cracks of width w_c allows a strain-displacement relation for plain concrete in tension to be made. The significance of this is that it allows the tensile stress-strain relation of concrete to be constructed for use in numerical FE application, for example, using a concrete tensile stress-displacement relation, or, moreover, the area under this curve. Stress-displacement is a fundamental tensile property of concrete, as it is independent of the specimen size, whereas the tensile stress-strain relation of concrete, which is not a fundamental tensile property of concrete, depends on the coupon specimen size [3].

Often, a simple linear descending post-peak response is assumed for the strain-softening regime of the tensile stress-displacement and stress-strain diagram (see *Fig. 1*). This simple form is suitable for FE analysis due to its simplicity, and it also fits reasonably well with test data on the actual post-peak tensile response of plain concrete [4]. Crack band fracture theory [2] states the cracking displacement w_{ck} , (i.e., the displacement occurring after the post-peak tensile strength f_{to} has been reached) is related to the cracking strain ε_{ck} by the width of the crack band region w_c :

$$\varepsilon_{ck} = \frac{w_{ck}}{w_c} \quad (1)$$

This is justified by the fact that when the peak tensile strength f_{to} is reached, micro-cracking occurs within the crack band region, and simultaneously the portion of the concrete coupon specimen outside of the crack band region unloads elastically. Thus, a progressive increase of strain past the peak tensile strength of the specimen (i.e., the cracking strain ε_{ck}) is localized within the width of the crack band region w_c . Using the strain-displacement relation given in *Eq. (1)*, it can be shown that the fracture energy of plain concrete G_f (defined as the area under the post-cracking

stress-displacement curve in Fig. 1(a) is related to the fracture energy density g_f (defined as the area under the stress-cracking strain diagram in Fig. 1(c)) by the following expression:

$$G_f = w_c g_f \quad (2)$$

Cracking strain ε_{ck} is defined as the total strain ε_t minus the elastic strain corresponding to the undamaged material, i.e., $\varepsilon_{ck} = \varepsilon_t - f_t/E_t$. Using this expression, we see that $\varepsilon_{ck,u} = \varepsilon_{tu}$, where ε_{tu} is the peak tensile strain of the stress-strain diagram in Fig. 1(b). Both $\varepsilon_{ck,u}$ and ε_{tu} correspond to the peak tensile strain corresponding to the end of the strain-softening regime, where the micro-cracks located within the crack band region coalesce into a single continuous macro-crack. Additionally, since $\varepsilon_{ck,u} = \varepsilon_{tu}$, the area under the total stress-strain diagram in Fig. 1(b), W_f , is equivalent to the area under the stress-cracking strain diagram in Fig. 1(c), g_f . Thus, using Eq. (2), the fracture energy G_f can be related to the area under the total stress-strain diagram W_f , by the width of the crack band zone, i.e., $G_f = w_c W_f$. This relation is used to generate the complete tensile $f_t - \varepsilon_t$ curve of concrete.

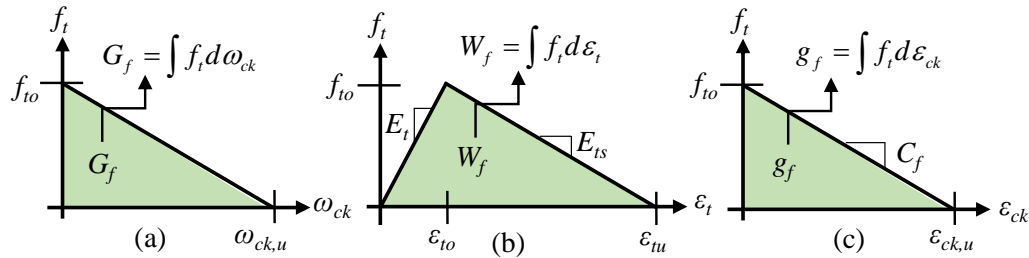


Figure 1. Tensile response of plain concrete: (a) stress-cracking displacement diagram; (b) stress-strain diagram, (c) stress-cracking strain diagram.

For FE applications, the width of the crack band w_c is taken as a characteristic length of the finite element l_n , which is generally defined as a factor of the element mesh size, i.e., $l_n = \alpha_f h$, where h is the size of an element. Thus, the tensile stress-strain curve of concrete is dependent on the size of the element. This is an essential aspect of numerical modelling of concrete, where to obtain objectivity in any numerical modelling results, the tensile stress-strain curve of concrete must be dependent on the mesh size (or the width of the crack band region), to preserve the correct fracture energy released during micro-cracking [2]. For a given concrete material with known tensile properties G_f , f_{io} , and E_t , the complete uniaxial stress-strain diagram can be derived for a particular finite element mesh size h using the expression $G_f = w_c W_f$, where w_c is now taken as $\alpha_f h$. Assuming a linear loss of strength after the peak tensile strength has been reached (as is shown in Fig. 1(b)), the peak tensile strain ε_{tu} can be defined as:

$$\varepsilon_{tu} = \frac{2G_f}{f_{io} \alpha_f h} \quad (3)$$

The tensile fracture theory of plain concrete at ambient temperature can be extended to elevated temperature using appropriate temperature-dependent reduction factors for the peak tensile strength f_{io} , the elastic modulus in tension E_t , and the fracture energy G_f . However, before such an extension can be made, the effects of concrete-rebar interaction must be included in the stress-strain relation of concrete utilized in numerical FE models of RC. This discussion is given in § 2.2.

2.2 Tension stiffening of RC at Ambient-Temperature

Tension stiffening arises from the interaction between un-cracked concrete and the surrounding reinforcement. To describe tension stiffening, take a RC member subjected to a uniaxial tensile force P as shown in *Fig. 2*. The complete tensile axial response of this RC member is shown in *Fig. 2(b)*, along with the tensile axial response of a bare steel bar. As the applied load on the RC member is increased, the concrete stress f_t reaches its peak tensile strength f_{t0} and primary cracks develop along the length of the member at a load P_o (*Fig. 2(b)*). At this stage, the applied load is transferred across the primary cracks by the reinforcement. However, the intact concrete situated between the primary cracks can still carry tensile stress due to the existing bond with the steel reinforcement bar. This is evident by the concrete stress distribution shown in *Fig. 2(a)*, which shows that intact concrete between primary cracks still carries tension. The net result is that the load-strain response of the RC member is stiffer than the load-strain response of the bare steel rebar as shown in *Fig. 2(b)*. As the load P is further increased, secondary cracks form between primary cracks and the concrete stress carried by the intact concrete slowly diminishes under increasing strain. Secondary cracks soften the response of the RC member until the yielding of the steel reinforcement occurs at the primary cracks. After yielding of steel at the primary cracks, the tensile axial response of the composite member follows that of the bare steel member.

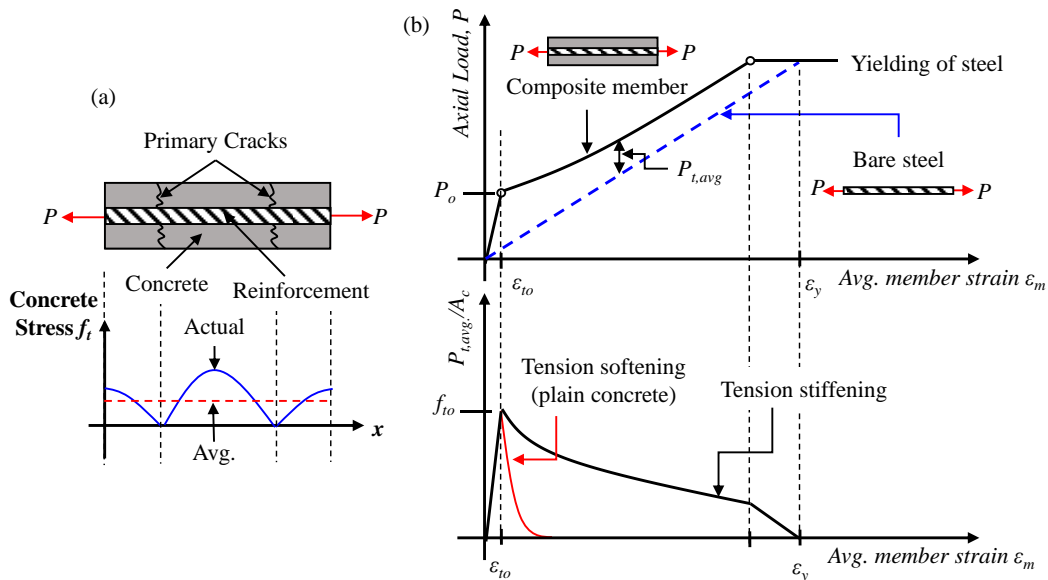


Figure 2. (a) Concrete stress distribution in a cracked RC member subjected to an axial tensile load, (b) Tensile response of the RC member compared to that of a bare steel rebar.

The strength contribution of the intact concrete still bonded to reinforcement between primary cracks, acts to stiffen the RC member in tension. This net stiffening phenomena is called tension stiffening. Moreover, the difference between the tensile axial response of the RC member and bare steel member represents tension stiffening.

In FE models where bond interaction between the steel rebar and surrounding concrete is not explicitly modelled, the average concrete stress $f_{t,avg}$ as a function of the total strain of the RC member ϵ_m , is required as input for plain concrete to account for tension stiffening effects. The average concrete stress $f_{t,avg}$ can be obtained by dividing the average load carried by the cracked concrete $P_{t,avg}$, which is found by subtracting the bare steel response from the measured RC member response in *Fig. 2(b)*, by the area of the concrete, A_c . The average concrete stress-strain curve $f_{t,avg} - \epsilon_m$ defines the constitutive stress-strain law of cracked concrete in RC (with associated tension stiffening effects), and differ significantly from the constitutive stress-strain law of plain concrete in tension as shown in *Fig. 2(b)*.

To account for the effects associated with tension stiffening, the ultimate tensile strain ε_{tu} of the tensile-softening curve of plain concrete (Fig. 1(b)) must be artificially increased. Here, the peak tensile strain cracked concrete in RC, defined here as ε_{tu}^* , is taken as the product of the peak tensile strain of plain concrete ε_{tu} and a tension stiffening factor TS , i.e., $\varepsilon_{tu}^* = \varepsilon_{tu} \times TS$. A proper tension stiffening model should include the influence of many factors such as the reinforcement ratio $\rho = A_s/A_c$, the modular ratio $n = E_s/E_c$, and bond properties at the steel-concrete interface [5]. Because these parameters are not explicitly accounted for in the factor TS , the approach calls for a sensitivity analysis to be carried out to calibrate TS against experimentally-recorded data. Suitability of the TS factor is accessed by its ability to allow: (1) numerical results, which compare reasonably well against experimental results, to be obtained, and (2) improved numerical convergence of a static analysis to be achieved.

3 TENSION STIFFENING MODEL OF RC AT ELEVATED TEMPERATURE

The final form of the average tensile stress-strain curve of cracked concrete at elevated temperature (with associated tension stiffening effects) is shown in Fig. 3(a). To avoid numerical issues, an ultimate tensile stress of $f_{tu} = 0$ cannot be used input. Instead, the ultimate tensile stress f_{tu} is defined as a factor of the peak tensile strength f_{io} , i.e., $f_{tu} = f_{io}/K_{res}$ where K_{res} is the residual stiffness factor. As will be shown later, this factor must also be calibrated against experimental data.

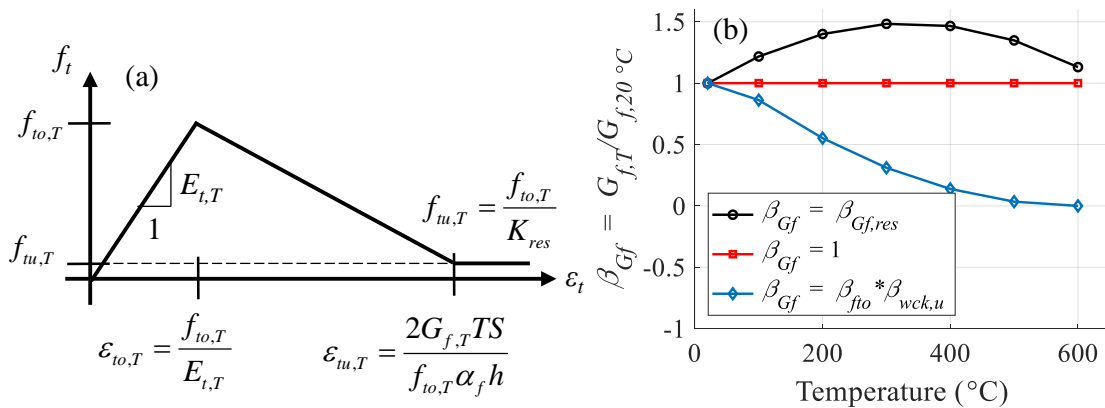


Figure 3. (a) Average tensile stress-strain curve of cracked concrete in RC at elevated temperature, (b) Three models defining the temperature-dependence of the fracture energy of concrete G_f .

The main tensile material properties required for the model are the temperature-dependent tensile strength $f_{io,T}$, the temperature-dependent elastic modulus in tension $E_{t,T}$, and the temperature-dependent fracture energy of plain concrete, $G_{f,T}$. Appropriate reduction factors for the tensile strength f_{io} and the elastic modulus in tension E_t , that is $\beta_{f_{to}} = f_{io,T}/f_{io,20^\circ C}$ and $\beta_{E_t} = E_{t,T}/E_{t,20^\circ C}$, can be found in the literature (see for e.g., [6]). However, there are very limited test results on the elevated temperature effects on the tensile fracture energy of plain concrete G_f . The majority of the available test data in the literature are associated with the residual tensile fracture energy of concrete after the specimen has cooled down to ambient-room temperature [7-12]. To the authors' knowledge only one test has been performed at elevated temperature conditions [13]. However, a reliable dependency of fracture energy with elevated temperature cannot be made for structural fire applications since it does not surpass $T = 200^\circ C$.

Based on the limited test data available and the assumptions made in prior numerical studies, three general models can be assumed for defining the temperature dependence of the fracture energy of plain concrete β_{Gf} (i.e., $\beta_{Gf} = G_{f,T}/G_{f,20^\circ C}$), as shown in Fig. 3(b). The most common assumption is to take the fracture energy of concrete to be temperature-independent (i.e., $\beta_{Gf} = 1$). This is conservative and justified given the lack of experimental data in the literature. The second assumption is to take the temperature-dependence of the fracture energy of plain concrete to be

equal the temperature-dependence of the residual fracture energy of plain concrete (i.e., $\beta_{Gf} = \beta_{Gf,res}$). Using existing data on the temperature-dependence of the residual tensile fracture energy for normal strength concrete (NSC) [7-12], least squares regression was used to obtain a general expression for this relation as shown in Eq. (4). For brevity, a plot of the data from ref.'s [7-12], with the associated quadratic curve is not shown in the paper.

$$\beta_{Gf,res} = -5.01 \times 10^{-6} T^2 + 3.33 \times 10^{-3} T + 0.934 \quad (4)$$

A more general approach to obtain the temperature-dependency of the fracture energy of plain concrete with temperature can be obtained by examining its general definition. The fracture energy of concrete is defined as the area under the post-cracking stress-displacement curve as shown in Fig. 1(a). Assuming a linear loss of strength after cracking, the fracture energy is defined as $G_f = \frac{1}{2} f_{io} \omega_{ck,u}$. Extending this definition to elevated temperature yields $G_{f,T} = \frac{1}{2} f_{io,T} \omega_{ck,u}^T$. Utilizing appropriate temperature-dependent reduction factors and re-arranging yields $G_{f,T} = (\frac{1}{2} \cdot f_{io,20^\circ C} \cdot \omega_{ck,u}^{20^\circ C}) (\beta_{fto} \beta_{wck,u})$. It is evident that the expression in the first parentheses is the ambient-temperature fracture energy $G_{f,20^\circ C}$ while the expression in the second parentheses represents the temperature-dependent reduction factor β_{Gf} . Thus, $\beta_{Gf} = \beta_{fto} \beta_{wck,u}$, and the temperature dependency of the fracture energy depends on the temperature-dependency of the peak tensile strength f_{io} and the ultimate cracking displacement $\omega_{ck,u}$. Because limited test data exist on the temperature-dependency of $\omega_{ck,u}$, it is conservative to assume that $\omega_{ck,u}$ decreases linearly from $T = 20^\circ C$ up until the temperature at which the tensile strength f_{io} diminishes to zero. Using the temperature-dependent reduction factor of f_{io} from Eurocode 4 Part 1-2 [6] and the assumption made for the temperature-dependency of $\omega_{ck,u}$, the curve shown in Fig. 3(b) for $\beta_{Gf} = \beta_{fto} \beta_{wck,u}$ is constructed.

4 VALIDATION OF TENSION STIFFENING MODEL

The Cardington Test 3 was used to examine the appropriateness of the elevated-temperature tension stiffening model proposed in this paper. The three temperature-dependent models for the fracture energy shown in Fig. 3(b) were examined, along with varying *TS* factors of 1, 5, 10, 20, 30, 40, and 50. The residual stiffness factor K_{res} was also varied from 100, 10, and 5, where 100 represents the default value recommended by ABAQUS [14]. A series of average tensile stress-strain-temperature curves for cracked concrete were generated using the model shown in Fig. 3(a) and a sensitivity analysis was carried out to determine the appropriateness of the tension stiffening model.

A macro-modelling approach was utilized to construct the Cardington floor plan in commercial software ABAQUS. The composite floor system was modelled as an assembly of beam and shell elements, using two-node linear beam elements (type *B31*) and four-node linear quadrilateral shell elements (type *S4R*). Full composite action was assumed by imposing a rigid coupling constraint on aligning nodes between the shell and beam elements. Both geometric and material nonlinearities were included in the analyses, with the classical metal plasticity model used to define the plasticity response of steel, while the damaged plasticity model was used to define the inelastic response of concrete in both tension and compression. Temperature dependence of both steel and concrete were defined by utilizing the constitutive σ - ϵ - T models available in Eurocode 4 1-2 [6]. Thermal expansion was also included in the model by utilizing the temperature-dependent thermal elongation models available in Eurocode 4 1-2 [6] for both steel and concrete. For simplicity, beam-end connections were assumed to be perfectly pinned, which was justifiable for the purpose of the study. The model employed a mesh size of 500 mm for both the shell and beam elements, which corresponds to an appropriate spacing to ensure proper compatibility between the shell and beam element during flexural bending. Experimentally-recorded temperature-time histories from the Cardington test 3 were used as predefined nodal temperatures to define the temperature field of the structural members. The solution to all analyses were obtained by employing a static analysis procedure available in ABAQUS/Standard.

The results of the sensitivity analyses revealed several important findings. First, a TS of 1 was found to be insufficient to allow convergence of the static analysis past the gravity loading step. Thus, ignoring the effects of tension stiffening is not recommended when modelling RC floor slabs. Increasing the TS factor was found to stiffen the overall response of the composite floor slab and produced smaller displacements. Reducing K_{res} was found to improve the convergence of the static analysis solver. *Fig. 4* shows the mid-span displacement of the interior floor beam (labelled pt. *D11* in the Cardington Test series) for $\beta_{Gf} = 1$ under different TS and K_{res} values. As K_{res} is reduced, the ability of the static analyses to converge to completion is improved as demonstrated in *Fig. 4(a)* through *Fig. 4(c)*. A value of $K_{res} = 5$ allows the analysis to converge to completion irrespective of the TS utilized. Finally, a TS of 10 was found to be appropriate since it produced numerical results which matched reasonably well against experimental results as shown in *Fig. 4(c)*. Similar findings were obtained irrespective of the tensile fracture energy model utilized (i.e., $\beta_{Gf} = \beta_{Gf,res}$ and $\beta_{Gf} = \beta_{fto}\beta_{wck,u}$). For this reason, these results are not included in the paper.

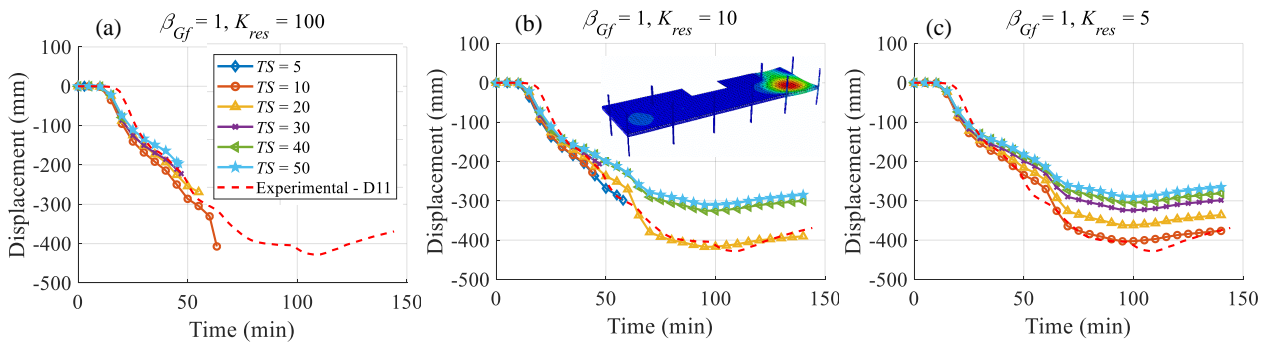


Figure 4. The influence of TS on the displacement-time history of Cardington Test 3 using $\beta_{Gf} = 1$: (a) $K_{res} = 100$, (b) $K_{res} = 10$, and (c) $K_{res} = 5$.

The sensitivity analysis also revealed that the temperature-dependency of the fracture energy did not play a significant role in the response obtained when utilizing the proposed tension stiffening model. As shown in *Fig. 5*, the three temperature-dependent fracture energy models produced nearly identical displacements for $TS = 10$ and $K_{res} = 5$. Overall, the $\beta_{Gf} = \beta_{Gf,res}$ model allowed for better convergence, although very marginally.

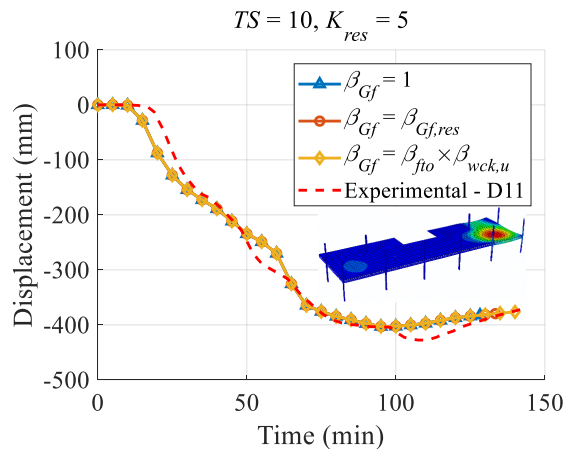


Figure 5. The influence of β_{Gf} on the displacement-time history of Cardington Test 3 using $TS = 10$ and $K_{res} = 5$.

5 CONCLUSIONS

An elevated-temperature tension stiffening model was developed based on the tensile fracture theory of plain concrete. The appropriateness of the model was examined against the Cardington Test 3. It was determined that increasing the tension stiffening factor TS stiffens the response, while reducing the residual stiffness factor K_{res} improves the convergence rate of the static analysis solver utilized. A sensitivity analysis is recommended to calibrate these two parameters for a given test case. For the Cardington Test 3, a tension stiffening factor of $TS = 10$ and a residual stiffness factor of $K_{res} = 5$ was found to be appropriate. The influence of the temperature dependency of the fracture energy was found to be insignificant. Thus, a fracture energy model which is independent of temperature can be used as input when utilizing the tension stiffening model proposed in this paper.

ACKNOWLEDGEMENT

The work presented was supported in part by the University of Michigan Rackham Engineering Award and the U.S.A. National Science Foundation through Grant No. DGE 1256260.

REFERENCES

1. British Steel. (1999). "The Behaviour of Multi-Storey Steel Framed Buildings in Fire." British Steel plc, Swinden Technology Centre, Rotherham.
2. Bažant, Z.P., and Oh, B.H. (1983). *Crack band theory for fracture of concrete*. *Matériaux et Constructions*, 16(3). pp 155–177.
3. Hofstetter, H.A., and Mang, H.A. (1996). *Computational plasticity of reinforced and prestressed concrete structures*. *Comp. Mech.*, 17. pp 243 – 254.
4. Hillerborg, A., et al. (1976). *Analysis and Crack Formation and Crack Growth in Concrete by Means of Fracture Mechanics and Finite Elements*. *Cem. and Conc. Res.*, 6. pp 773–782.
5. Fields, K., and Bischoff, P.H. (2004). *Tension stiffening and cracking of high-strength reinforced concrete tension members*. *ACI Struct. Journal*, 101(4). pp 447–456.
6. European Committee for Standardization (CEN). (2005). "Eurocode 4: Design of composite steel and concrete structures-Part 1-2: General rules - Structural fire design." EN 1994-1-2, Brussels, Belgium.
7. Baker, G. (1996). *The effect of exposure to elevated temperatures on the fracture energy of plain concrete*. *Mat. and Struct.*, 29(6). pp 383–388.
8. Zhang, B., et al. (2000). *Residual fracture properties of normal- and high-strength concrete subject to elevated temperatures*. *Mag. of Conc. Res.*, 52(2). pp 123–136.
9. Nielsen, C.V., and Biéanić, N. (2003). *Residual fracture energy of high-performance and normal concrete subject to high temperatures*. *Mat. and Struct.*, 36(8). pp 515–521.
10. Tang, W.C., and Lo, T.Y. (2009). *Mechanical and fracture properties of normal- and high-strength concretes with fly ash after exposure to high temperatures*. *Mag. of Conc. Res.*, 61(5). pp 323–330.
11. Menou, A., et al. (2006). *Residual fracture energy of cement paste, mortar and concrete subject to high temperature*. *Theor. and Appl. Fract. Mech.*, 45(1). pp 64–71.
12. Yu, J., Yu, K., and Lu, Z. (2012). *Residual fracture properties of concrete subjected to elevated temperatures*. *Mat. and Struct.*, 45(8). pp 1155–1165.
13. Bažant, Z.P., and Prat, P.C. (1988). *Effect of temperature and humidity on fracture energy of concrete*. *ACI Mat. Journal*, (85). pp 262–271.
14. Dassault Systemes Simulia Corp. (DSS). (2014). "ABAQUS 6.14 Online Documentation." DSS, Providence, RI, USA.

COMPOSITE STRUCTURES

EXPERIMENTAL AND ANALYTICAL INVESTIGATIONS ON THERMAL PERFORMANCE OF SLIM FLOOR BEAMS WITH WEB OPENINGS IN FIRE

Naveed Alam¹, Ali Nadjai², Faris Ali³, Olivier Vassart⁴, Francois Hanus⁵

ABSTRACT

Steel beams with web openings are widely used in constructions to reduce the weight of steelwork, especially in structures comprising of traditional composite beams with down-stand steel sections. In recent times, the use of steel sections with web openings has become common as slim floor beams since they offer a reduction in weight of the steelwork, accommodate services within the floor depth and provide the plug composite action. Though these web openings offer several benefits in slim floor beams, however, they induce the material discontinuity in the web affecting their shear capacity and thermal behaviour. During the pouring of concrete, the steel in the web openings is replaced by the concrete with a low thermal conductivity. This research presents findings from experimental and analytical investigations conducted to study the thermal behaviour of slim floor beams with web openings in fire. For this purpose, an experimental investigation was conducted to study the thermal response of slim floor beams in fire. Data obtained from the fire test shows that the presence of web openings has a significant influence on temperature development across the steel section as well as along the span of these beams. The temperatures on the web below the openings are higher in comparison to those on the adjacent web-posts. It is also observed that temperatures on the web above the openings are significantly lesser than those on the adjacent web-posts. Parametric studies conducted using the finite element modelling show that smaller opening spacings and larger opening sizes have a severe influence on the thermal behaviour of these beams in fire. The findings of this research will help in selecting appropriate opening sizes and spacings in slim floor beams to avoid any severe temperature distributions in fire and to ensure their suitable utility.

Keywords: Slim floor beams, web openings, thermal response, fire tests, finite element modelling.

1 INTRODUCTION

Though the use of composite beams offers longer floor spans, however, the depth of these beams being higher in comparison to the reinforced concrete beams, is a major disadvantage especially in tall buildings. On the other hand, the use of slim floor beams in high-rise buildings is advantageous due to their shallower depth resulting from their partial encasement within the floor [1]. This partial

¹ PhD Candidate. Belfast School of Architecture and the Built Environment, , Ulster University, Belfast, UK.
e-mail: alam.n1@ulster.ac.uk

² Professor and Director of Fire Safety Engineering Research Technology Centre, Ulster University, Belfast, UK..
e-mail: a.nadjai@ulster.ac.uk

³ Professor, Fire Safety Engineering and Technology (FireSERT), Ulster University:
e-mail: f.ali@email.ulster.ac.uk

⁴ Head of ArcelorMittal Global R&D Long Carbon
e-mail: olivier.vassart@arcelormittal.com

⁵ Senior Research Engineer ArcelorMittal Long Products:
e-mail: francois.hanus@arcelormittal.com

encasement also improves their fire resistance and their stiffness. The increase in stiffness enhances the bending resistance of these beams by reducing deflections and vibrations in service conditions. Use of the slim floor beams aids in reducing the construction cost as they consume lesser building materials. The combination of these beams with the metal decking reduces the construction time and eliminates any requirements of formwork and scaffolding [2] [3]. Slim floor beams also help in assimilating the services within the floor depth through the web openings. Though the web openings offer numerous advantages, however, they also reduce the shear resistance of these beams. Previous experimental and analytical investigations have shown that the concrete between the flanges of the steel section in these beams contributes towards their shear capacity compensating for the loss of the steel web. In some cases, this concrete increases their shear capacity significantly, twice as compared to that offered by the bare steel beam [4] [5]. Further, experimental investigations are also conducted to study the longitudinal shear resistance offered by these beams in terms of the plug composite action. These investigations have shown that the plug composite action improves the longitudinal shear transfer mechanism in these beams [6].

1.1 Aims and objectives

The work presented herein is an experimental and analytical investigation conducted to study the effect of web openings on the thermal response of slim floor beams in fire. This investigation addresses the effect of material discontinuities and resulting influences on the thermal behaviour of slim floor beams in fire. The data acquired from this test is one of its kind and will help to understand the behaviour of these beams at elevated temperatures. Analytical investigations on the spacings and sizes of web openings will highlight the influence of these parameters on the thermal behaviour of these beams in fire.

1.2 The scope of research

The scope of this study is limited to thermal behaviour only and no investigations are conducted to analyse the influence of the web openings on the structural response of slim floor beams in fire.

2 EXPERIMENTAL PROGRAMME

2.1 Test specimen and heating conditions

A fire test was conducted on a slim floor beam assembly to analyse any influence of the presence of web openings on their thermal behaviour in fire. As mentioned before, the scope of this study is limited to investigations on thermal behaviour only, hence, no external loads are applied during the test. The tested slim floor beam assembly is 1000 mm wide and 2000 mm long, corresponding to the size of the furnace which is 2000 mm x 2000 mm in the plan. The slim floor beam consisted of a steel section, HEA-220 and a steel plate 400 mm wide and 15 mm thick made from grade S355 steel and welded to the bottom flange along its length. The overall depth of the steel section is 225 mm including the welded plate, *Fig 1(c)*. The composite floor consisted of a steel decking and normal weight concrete with a target strength of 30 MPa at 28 days. The steel decking used for the floor construction is MD 50, a high performance, profiled, galvanised steel floor decking used for the construction of composite floor slabs. Total depth of the test assembly is 280 mm including a 55 mm layer of concrete above the top flange and the 15 mm thick welded steel plate, *Fig 1*. Concrete above the top flange is reinforced using A-142 steel mesh with flying ends and with minimum laps of 400 mm. This reinforcing mesh is placed using 15 mm deep spacers to maintain its position above the top flange. The sides of the slim floor beam assembly are designed using steel sheets which serve as a permanent formwork during concreting, *Fig 1(b)*.

The steel section of the slim floor beam is fabricated with 100 mm diameter web openings spaced at 200 mm centres throughout its length as shown in *Fig 1(a)*. In total, 10 openings are fabricated in the web in such a way that their centres coincide with the centreline of the web, 94 mm from the top and the bottom flange. In between these web openings, a solid web with a minimum width of 100 mm is produced. This solid web is referred to as the web-post in this paper. The first openings at

both ends of the steel section are centred at 100 mm from the edges. The depth of the solid web above and below the edge of openings is 44 mm.

Keeping in view the scope of this research, only thermal data is recorded while no arrangements are made to record any deformations during the test. Temperatures within the furnace and on the slim floor beam assembly are acquired using K-type thermocouples. The furnace temperatures are monitored via five thermocouples to ensure the heating conditions are in accordance with the standard fire, while the temperatures on the slim floor beam assembly are monitored through thermocouples positioned on the steel beam at two locations, section AA' and section BB'. The temperatures at section AA' are monitored using two thermocouples, one on the middle of the welded steel plate and the other on the web-post at 40 mm from the inner edge of the bottom flange, Fig 1(d). On the other hand, temperatures at the opening are monitored at section BB' using three thermocouples. Two of these thermocouples are positioned in the middle of flanges, one each on the top and the bottom flange, while the third thermocouple is positioned on the web at 40 mm from the inner edge of the bottom flange, adjacent to the thermocouple on the web-post at section AA', Fig 1(e). Thermocouples 3 and 4 are at same distances from the bottom flange Fig 1(d) & Fig 1(e).

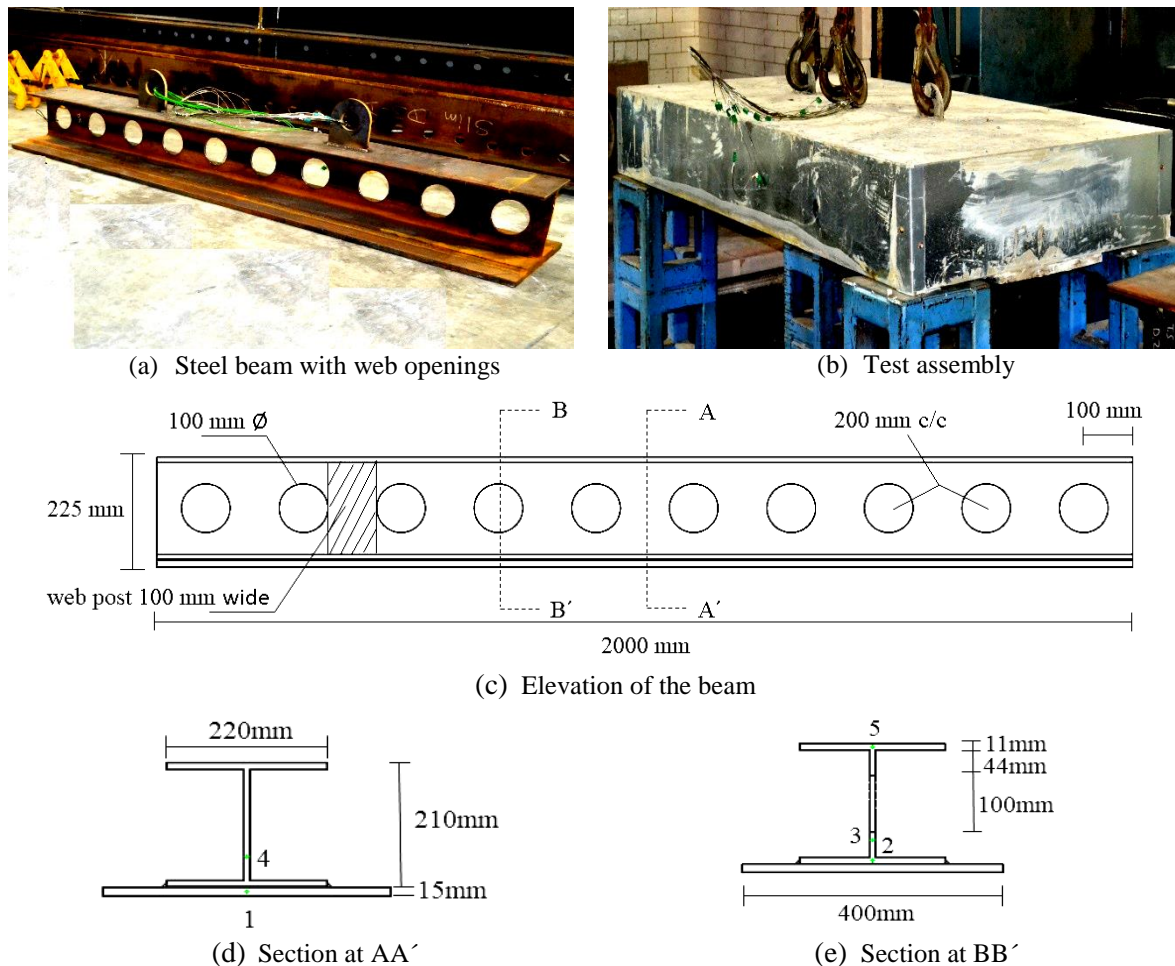


Fig 1: Details of the test assembly

2.2 Test procedure and results

The fire test on the slim floor beam assembly with web openings was conducted at Fire Safety Engineering Research and Technology (FireSERT), Ulster University on the 18th of January 2018. The test conducted using a gas-fired furnace lasted for 90 minutes during which thermal data was recorded for the furnace and for the slim floor beam. The test assembly was placed on top of the furnace while the remaining part of the furnace top was covered using concrete slabs. The interface

between the test assembly and the concrete slabs as well as any openings were filled using ceramic fibre blanket to control the heat and smoke and to allow any deformations resulting at higher temperatures. Hence, the ceramic fibre blanket not only served as an insulator but also served as a flexible filler to accommodate the beam deflections. The beam assembly was put on top of the furnace walls directly and no special support conditions were provided. To accommodate any expansion resulting at higher temperatures, no restraints were applied to the ends of the test assembly. All the thermocouples were connected to the data logging system where the temperatures were recorded for the whole duration of the test. Once the beam assembly was ready for testing, it was heated in accordance with the standard fire curve, ISO-834 [7] for a period of 90 mins after which the heating was discontinued.

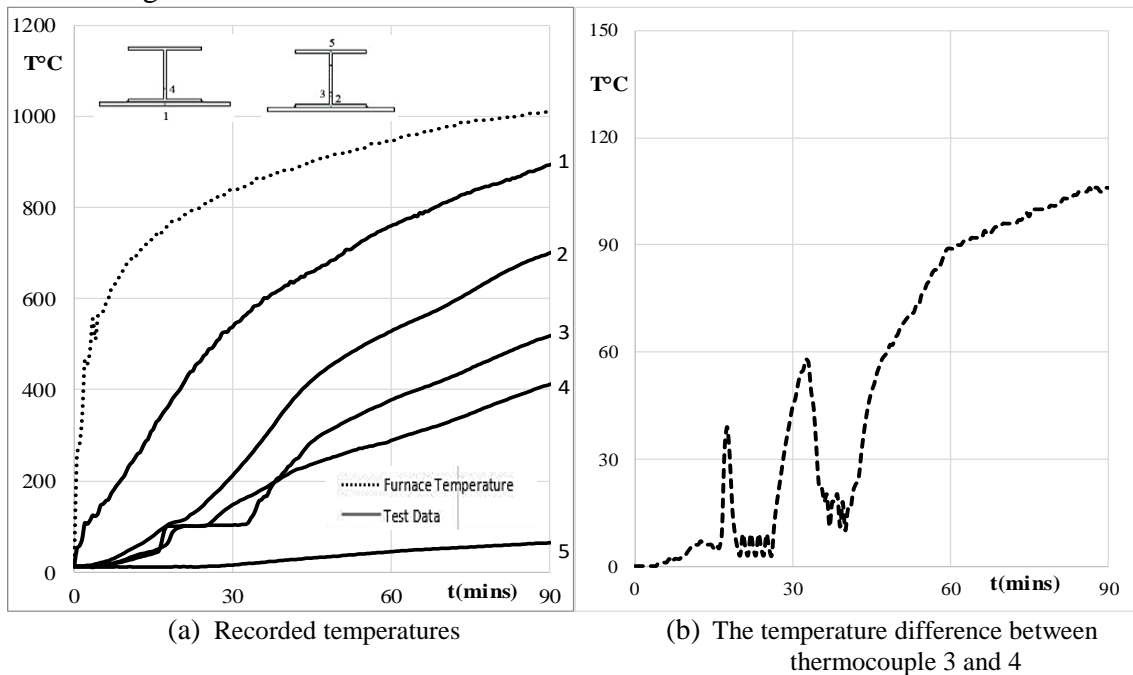


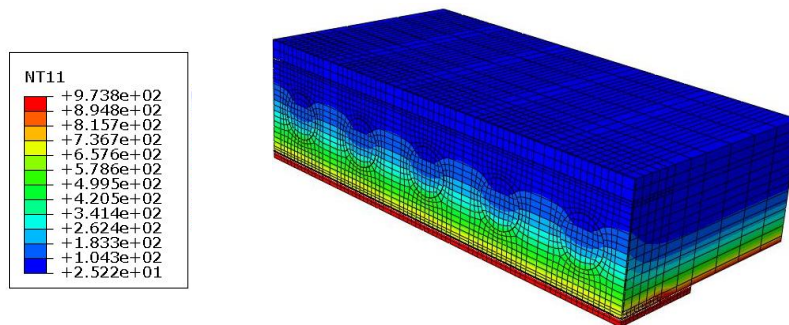
Fig 2: Recorded test data for the slim floor beam assembly with web openings

Data acquired during the fire test in terms of the temperatures is presented in Fig 2. The numbers corresponding to temperatures in Fig 2(a) represent the thermocouple positions shown earlier in Fig 1(d) and Fig 1(e). Alike other slim floor beams, there is a high thermal gradient across the section with the exposed lower parts being at higher temperatures in comparison to the unexposed upper parts. It is also seen that there is a significant temperature difference between thermocouples 3 and 4 positioned at the same distance from the inner edge of the bottom flange. Temperatures recorded on the web below the opening, thermocouple 3, are higher compared to those recorded at the adjacent location on the web-post, thermocouple 4. This temperature difference is presented in Fig 2 (b), which shows a temperature difference of 90°C and 107°C after a fire exposure of 60 mins and 90 mins respectively. The resulting temperature difference is due to discontinuity of the steel in the web. The steel in the web opening is replaced by the concrete with a low thermal conductivity which restricts the efficient flow of heat across the steel section. As a result, temperatures on the web under the opening are comparatively higher as compared to those on the adjacent web-post. The recorded test data suggests that the web openings in slim floor beams have a considerable influence on their thermal behaviour in fire conditions.

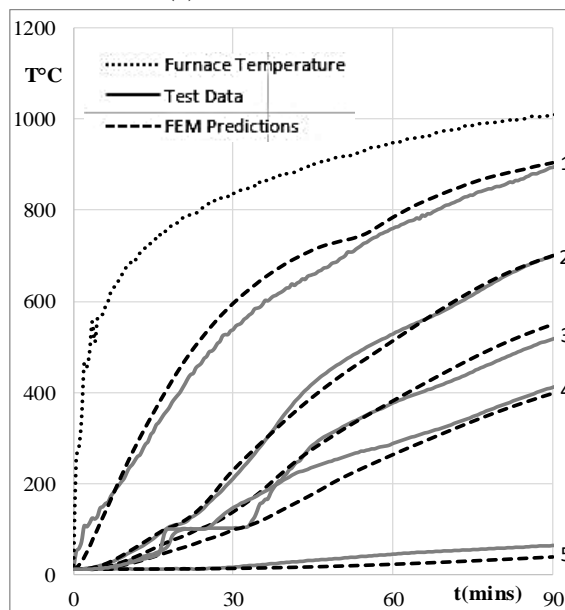
3 FINITE ELEMENT MODELING

Finite element modelling (FEM) for the test assembly is conducted using ABAQUS [8]. Though several studies have been conducted to analyse the behaviour of shallow floor systems in fire, these

previous studies address the slim floor beams with no web openings [9] [10]. During the current study, FEM is first conducted for the validation of the fire test. During the validation process, a quarter of the test assembly is modelled and heated using the recorded furnace temperatures. All the boundary conditions are kept alike the test. Non-linear material properties, including the thermal conductivity, specific heat, and the density are taken from the codes [11] while 8-node hexahedral solid linear heat transfer elements (DC3D8) are used to model both steel and concrete. Heat transfer through the surfaces of the test assembly is modelled via convection and radiation. The convection coefficients for exposed and unexposed surfaces are taken as $25\text{W/m}^2\text{K}$ and $9\text{W/m}^2\text{K}$ respectively following the code recommendations [12]. Any heat transfer through radiation from the unexposed surfaces is ignored while the same for the exposed surfaces and for the cavity between the welded plate and bottom flange, is modelled using an emissivity of 0.7 following the recommendation of codes, [13] [14]. Perfect thermal contact is modelled between the steel and the concrete allowing efficient and full heat transfer following the methods presented in similar studies conducted previously on other types of shallow floor systems [9] [10].



(a) Thermal contours, FEM



(b) Test vs FEM, the thermal predictions

Fig 3: FEM results and the model verification

The results obtained from FEM are presented in Fig 3. The thermal contours in Fig 3(a) show the influence of web openings on the heat transfer across the section and along the span of the slim floor beam. Alike the test, temperatures on the web below the opening are higher as compared to those predicted for the adjacent locations on the web-post. It can also be seen that the temperatures on the web above the opening are lesser than those predicted on the adjacent web-post at the same levels. The predicted temperatures from the FEM are plotted against the recorded test data in Fig 3(b) and are in good agreement for all thermocouple locations. Hence, the FEM method used in this

study can predict the thermal response of slim floor beams having web openings with good accuracy and can be used to conduct sensitivity studies.

4 SENSITIVITY ANALYSIS

A sensitivity analysis was conducted to analyse the influence of the spacing and the size of the web openings on thermal behaviour of slim floor beams in fire. During this part of the research, the verified FEM method, discussed in section 3, was used. Different spacings of the web openings result in variable web-post widths as shown in *Fig 4*. Three investigations were conducted to analyse the effect of spacings of web openings. During these investigations, the size of the openings was kept 100 mm in diameter while the opening spacings were 200 mm, 150 mm and 300 mm. The minimum width of the web-post resulting from the variable opening spacings was 100 mm, 50 mm and 200 mm respectively, *Fig 4*. To investigate the effect of the opening size, FEM was conducted on a slim floor beam assembly having web openings of 130 mm diameter (equivalent to 70% of web depth) at 230 mm centres. Such an arrangement of the web openings results in a stem width of 100 mm, *Fig 4(d)*. The stem width for case (a) and (d) in *Fig 4* is same while the size of the opening in both cases is different. The dimensions of the slim floor beam assembly used during the sensitivity analysis are same as the one used during the model verification discussed in section 3.

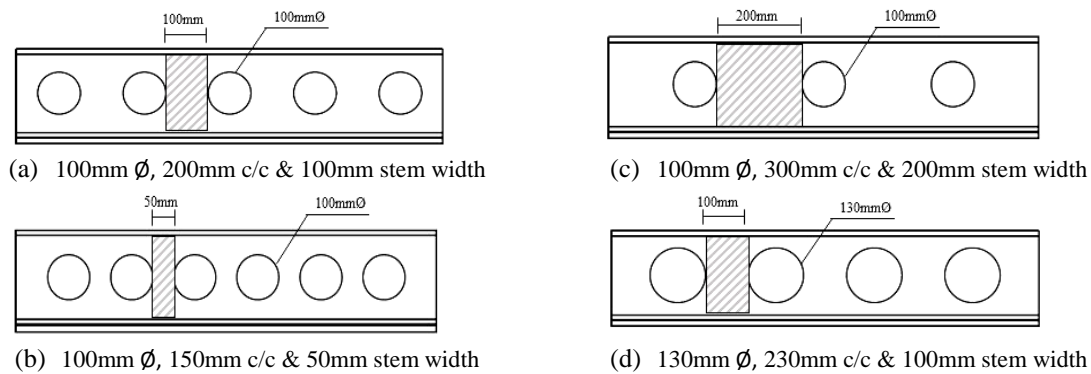


Fig 4: Sensitivity study, the effect of the spacing and size of openings

4.1 Effect of the spacing or the stem width

Results obtained from FEM on the effect of opening spacings are presented in *Fig 5(a), (b) & (c)*. It is seen in *Fig 5(a)* that the temperature differences between the parts of web below the opening and the adjacent web-posts are lesser for smaller opening spacings as compared to those predicted for larger spacings. This means that for smaller web-post widths and closely spaced openings, temperatures on the web under the opening as well as on the web-post are higher in comparison to those for slim floor beams with larger web-post widths. Hence, smaller opening spacings produce more severe temperatures in slim floor beams. The temperatures differences on the upper parts of the web are less severe as compared to those for the lower parts. Temperatures predicted for the web above the opening are lesser than those predicted for the adjacent web-post, *Fig 5(b)*. These temperature differences are higher for smaller web-post widths as compared to larger widths, *Fig 5(b)*. It is interesting to note that the predicted temperatures in the middle of the stem for all cases with same opening sizes are same irrespective of their spacings, *Fig 5(c)*.

4.2 Effect of the web opening size

The results from FEM show that the increase in the size of the opening also influences the thermal behaviour of slim floor beams. This increase in the size of openings induces higher temperature difference between parts of the web under the opening and on the adjacent web-post, *Fig 5(d)*. The effect of the opening size is less significant for parts of the web above the opening, *Fig 5(d)*.

These results show that the spacing of the openings and their size has an influence on the thermal response of slim floor beams with web openings in fire. Closely spaced openings and their larger sizes have more severe effects on the thermal behaviour of slim floor beams in fire.

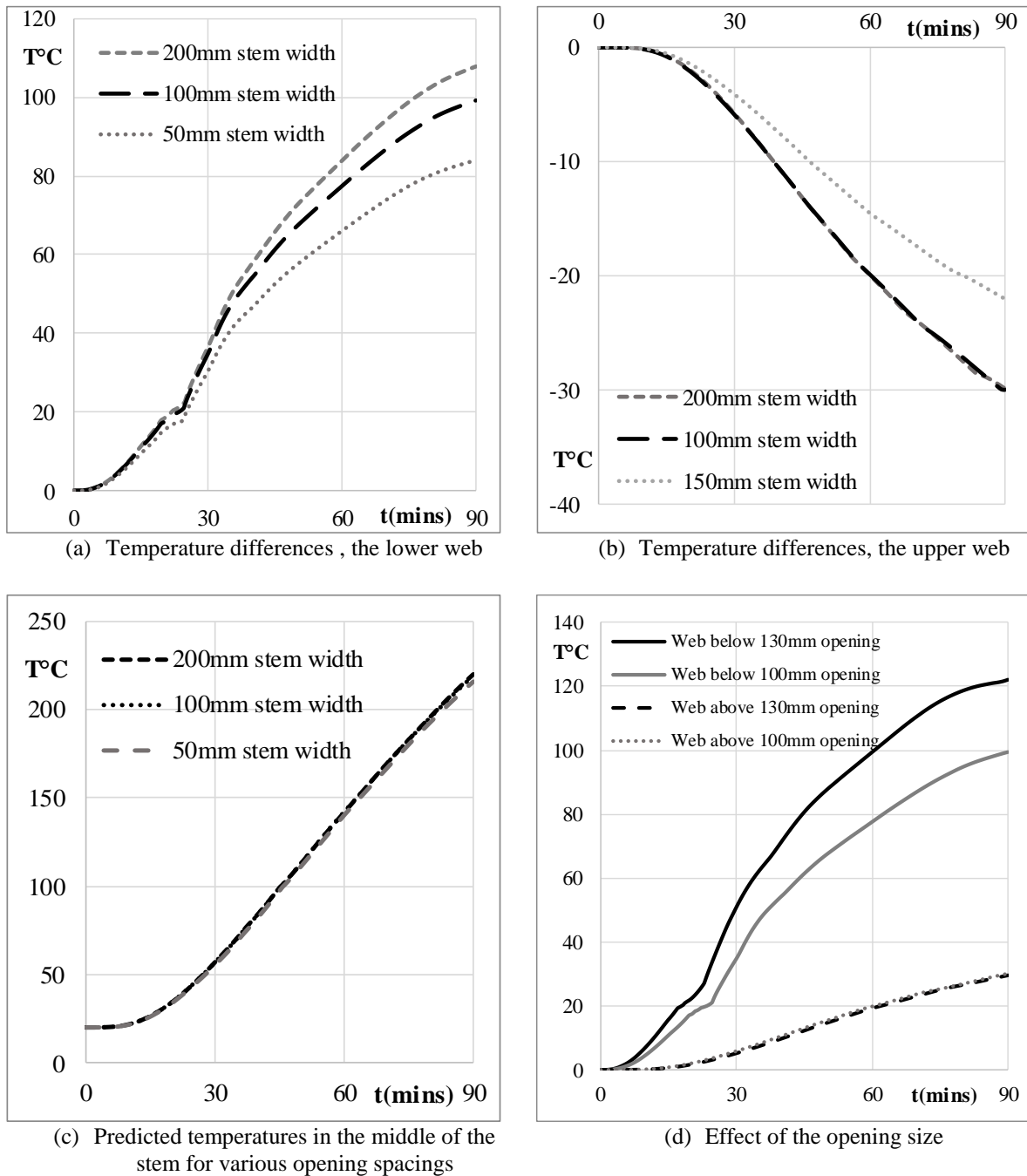


Fig 5: Influence of the opening spacings and sizes on thermal behaviour of slim floor beams

5 CONCLUSIONS

This research presents the findings of an experimental and an analytical investigation conducted to study the influence of the web openings on thermal behaviour of slim floor beams in fire. During the experimental investigation, it was found that the presence of web openings has a considerable influence on their thermal behaviour in fire. It was observed that the presence of the web openings results in higher temperatures on the parts of web below the openings as compared to those on the adjacent web-post. During the sensitivity study, it was observed that the smaller spacing of

openings results in more severe temperature distributions, producing higher temperatures on the web below the opening as well as on the web-post. Temperatures on the centre of the web-post were found to be unaffected by the variations in spacing of the openings. Investigations on the influence of the opening sizes show that the temperature differences on the bottom part of the steel web, under the opening and on the adjacent web-post, are more severe for larger opening sizes as compared to those for smaller openings. Hence, smaller spacing of openings and larger opening sizes have a severe influence on the thermal behaviour of slim floor beams in fire.

REFERENCES

1. De Nardin, S. & El Debs, A.L.H.C., 2009. *Study of partially encased composite beams with innovative position of stud bolts*. Journal of Constructional Steel Research, 65(2), pp.342–350. <http://dx.doi.org/10.1016/j.jcsr.2008.03.021>.
2. D. L. Mullet, (1998), *Composite Floor Systems*, The Steel Construction Institute, 1st edition London.
3. Newman, G.M., (1995), *Fire resistance of slim floor beams*. Journal of Constructional Steel Research, 33(1-2), pp.87–100. [http://dx.doi.org/10.1016/0143-974x\(94\)00016-b](http://dx.doi.org/10.1016/0143-974x(94)00016-b).
4. Tsavdaridis, K.D., D’Mello, C. & Huo, B.Y., 2013. *Experimental and computational study of the vertical shear behaviour of partially encased perforated steel beams*. Engineering Structures, 56, pp.805–822. <http://dx.doi.org/10.1016/j.engstruct.2013.04.025>.
5. Tsavdaridis, K.D. & D’Mello, C., 2012. *Vierendeel Bending Study of Perforated Steel Beams with Various Novel Web Opening Shapes through Nonlinear Finite-Element Analyses*. Journal of Structural Engineering, 138(10), pp.1214–1230. [http://dx.doi.org/10.1061/\(asce\)st.1943-541x.0000562](http://dx.doi.org/10.1061/(asce)st.1943-541x.0000562).
6. Huo, B.Y. & D’Mello, C.A., 2013. *Push-out tests and analytical study of shear transfer mechanisms in composite shallow cellular floor beams*. Journal of Constructional Steel Research, 88, pp.191–205. <http://dx.doi.org/10.1016/j.jcsr.2013.05.007>
7. International Standards Organization. (1999). *ISO 834-1, Fire Resistance Tests- Elements of Building Construction. Part 1: General Requirements*. International Standards Organization.
8. ABAQUS, (2016), *Finite Element Modelling Programme and Standard User’s Manual*, Version 6.14. SIMULIA.
9. Alam, N., Nadjai, A., Ali, F., Nadjai, W., (2018). *Structural response of unprotected and protected slim floors in fire*. Journal of Constructional Steel Research, 142, pp.44–54. <http://dx.doi.org/10.1016/j.jcsr.2017.12.009>.
10. Maraveas, C., Swailes, T. & Wang, Y., (2012), *A detailed methodology for the finite element analysis of asymmetric slim floor beams in fire*. Steel Construction, 5(3), pp.191–198. <http://dx.doi.org/10.1002/stco.201210024>.
11. European Committee for Standardization, (2014), *BS EN 1994-1-2: Eurocode 4: Design of composite steel and concrete structures - General rules — Structural fire design*, European Committee for Standardization, Vol. 3.
12. European Committee for Standardization, (2008), *BS EN 1992-1-2 Eurocode 2: Design of concrete structures part 1-2 General rules – Structural fire design*, European Committee for Standardization.
13. European Committee for Standardization (2009), *BS EN 1993-1-2 Eurocode 3: Design of steel structures, Part 1-2, General rules – Structural fire design*, European Committee for Standardization.
14. European Committee for Standardization (2009), *EN1991-1-2, Eurocode 1 – Actions on structures – Part 1-2: General Rules –Structural Fire Design*, European Committee for Standardization.

FIRE PERFORMANCE OF STEEL REINFORCED ULTRA HIGH TOUGHNESS CEMENTITIOUS COMPOSITES BEAM

Chao-Jie Sun¹, Qing-Hua Li², Jun-Feng Lu³, Shi-Lang Xu⁴

ABSTRACT

Fire performance of steel reinforced ultra high toughness cementitious composites (UHTCC) (SRU) beam is investigated in this paper. Four-point bending tests on the SRU beam and the steel reinforced concrete (SRC) beam exposed to the ISO-834 standard fire were carried out. The failure modes, temperature distributions and structural responses of the SRU beam were described and compared with that of the SRC beam. Huge performance differences were found between the two kinds of beams. Better fire performances of the SRU beam were exhibited compared to the SRC beam. The internal temperatures of the SRU beam were evidently lower than that of the SRC beam after being heated for the same time. The fire resistance of the SRU beam was longer than that of the SRC beam under the same load ratio.

Keywords: Fire performance, steel reinforced, ultra high toughness cementitious composites, concrete, beam

1 INTRODUCTION

Steel reinforced concrete structures have been widely used all over the world in recent decades. Due to the low thermal conductivity and high thermal capacity of concrete, the steel embedded in the concrete is nearly free from the influence of high temperatures in fire case. However, explosive spalling tends to occur on concrete at high temperatures [1, 2] and the internal steel will be exposed to fire in which the bearing capacity of structures will be seriously reduced.

UHTCC, also called engineered cementitious composites (ECC) or strain hardening cementitious composites (SHCC) has been developed in recent decades as a kind of high performance concrete or ultra high performance concrete owing to its strain hardening performance at ambient temperatures [3-5]. Researches have done much work on the basic properties of UHTCC [3-12], including compression properties, tensile properties, flexural properties, fatigue behaviour, bonding properties to steel, durability, etc. UHTCC had been used in structures in previous literatures and it is found UHTCC keeps good bond condition with reinforced bars [11-12].

The mechanical and thermal properties of these high performance composite materials at elevated temperatures or after exposure to high temperatures were researched these years [13-16]. Test results of Sahmaran et al. revealed that no significant changes in the mechanical properties for tested ECC specimens exposed to temperatures up to 400°C and no explosive spalling occurred in any tested ECC specimens during the fire tests [13]. Yu et al. investigated the residual mechanical

¹ PhD Candidate. Institute of Advanced Engineering Structures and Materials, Zhejiang University, Hangzhou, China.
e-mail: sunchaojie@zju.edu.cn

² Professor. Institute of Advanced Engineering Structures and Materials, Zhejiang University, Hangzhou, China.
e-mail: liqinghua@zju.edu.cn

³ Assistant Engineer. China Southwest Architecture Design and Research Institute Corp.Ltd, Chengdu, China.
e-mail: lvjunfeng1991@gmail.com

⁴ Professor. Institute of Advanced Engineering Structures and Materials, Zhejiang University, Hangzhou, China.
e-mail: slxu@zju.edu.cn

performance of high volume fly ash ECC (HVFA-ECC) after sub-elevated temperatures. It was found that HVFA-ECC can resist a sub-elevated temperature (no more than 200°C) exposure, and a moderate temperature treatment (no more than 100°C) may actually enhance ECC's tensile properties [14]. Bhat et al. studied the elevated temperature effect on tensile strength and strain capacity, compressive strength, failure mode, moisture loss and spalling behaviour of ECC. The results showed that no reduction in ECC compressive strength even after 6 hours of exposure to 600°C, and no spalling was observed in both ECC tensile and compressive specimens even after 6 hours of exposure to 600°C [15]. Li et al. investigated the microstructure and mechanical properties of hybrid fibre UHTCC after exposure to elevated temperatures from 20°C to 800°C. The results indicated that the residual compressive strength of UHTCC performed much better when the temperature was not higher than 600°C and explosive spalling of UHTCC was not observed in any situation in the tests [16]. The thermal conductivity of UHTCC have been studied by several researchers [17-19]. It was found that the thermal conductivity of UHTCC is lower than that of normal concrete [17, 20].

Considering the superior fire performances of UHTCC, including low thermal conductivity and explosive spalling resistance, UHTCC is promising to substitute concrete for composite structures considering the threat of fire. This experimental research aims to investigate the fire performance of the SRU beam using hybrid fibre UHTCC and compare with that of the SRC beam. The comparisons included the failure modes, spalling patterns, temperature distributions and the mid-span deflections of the two kinds of beams. This research is one part of a systematic study on development of high performance composite structures.

2 EXPERIMENTAL PROGRAM

2.1 Specimen preparation

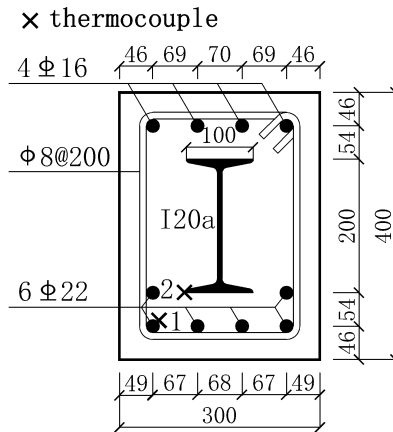


Fig. 1. Cross section configuration (unit: mm)

The UHTCC matrix was made by mixing P·O 52.5 ordinary Portland cement, I grade fly ash, silica-based fine sand, Nano-SiO₂, water, steel fibre and PVA fibre. The mass content of Nano-SiO₂ to the binder (cement and fly ash) was 3.2%. The volume content of steel fibre and PVA fibre were 1.4% and 2.5%, respectively. Polycarboxylate superplasticizer was used to reduce the water consumption. The water cement ratio was 0.31. The average compression cube strength at the testing day was 47.22 MPa with the cube size of 100 mm in length.

Commercial concrete with the water cement ratio 0.32 was used for the SRC beam. The aggregate used was siliceous. The average compression cube strength at the testing day was 53.07 MPa. The cube length was 150 mm.

The commercial I-shaped hot rolled section steel was adopted in the beam with the type of 20a according to Chinese standard GB/T 706-2016 [21]. The cross section height and width of the

section steel were 200 mm and 100 mm, respectively. The measured average yield strength of the shaped steel was 432 MPa. The measured average yield strength of longitudinal bars ($\Phi 16$ and $\Phi 22$) were 470 MPa and 446 MPa, respectively. The stirrup spacing was 200 mm with the bar diameter of 8 mm. The standard value of yield strength of stirrup was 335 MPa according to Chinese standard GB 50010-2010 [22].

Two composite beam specimens were cast for tests, in which one was SRU beam and the other was SRC beam. In the SRU beam, UHTCC was used to replace all of the concrete. The beam specimens were 5,000 mm long with the cross-sectional dimension of 300 mm \times 400 mm. The test was carried out when the beams were cast for 112 days. Two thermocouples were mounted at the mid-span of the beam to measure the temperatures inside the specimen. The detail dimensions of beams and locations of the two thermocouples are depicted in *Fig. 1*.

2.2 Test apparatus and procedures

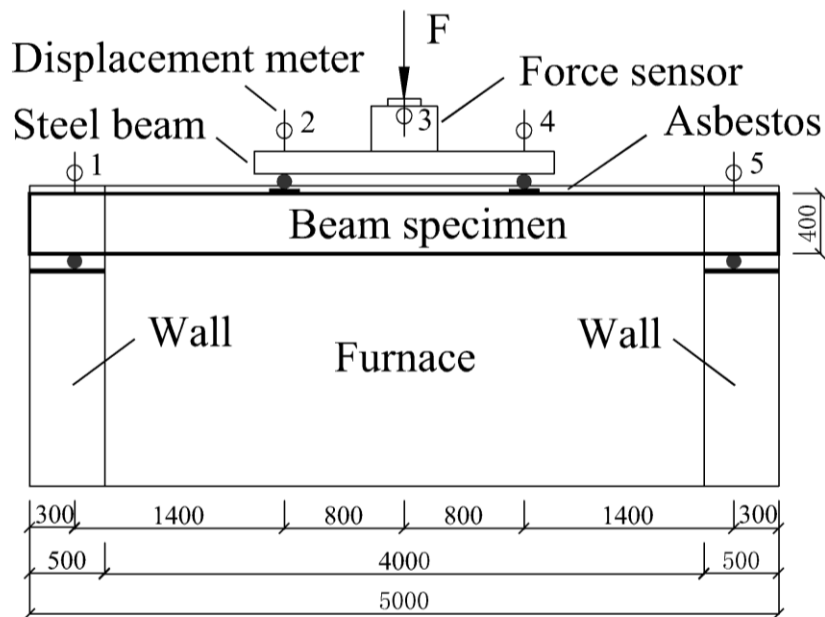


Fig. 2. The mounted state of specimen (unit: mm)

During the test, the beam specimens were exposed to standard fire and constant load simultaneously in a furnace built for horizontal specimens. The specimen mounted state is shown in *Fig. 2*. The heating temperature-time curve followed the ISO-834 [23] standard fire curve and the length of beam exposed in fire was 4,000 mm. The two side surfaces and the bottom surface of the beam were exposed to fire while the top surface wrapped with asbestos. Simple support boundary condition at both ends was applied on the beam specimen.

Four-point bending test was adopted in which the load ratio was set as 0.7. The load ratio was defined as the ratio of applied load (F) to ultimate bearing capacity (N_u). N_u was measured by ultimate bearing capacity test on the same beam specimens at ambient temperature. In the fire tests, applied loads of the SRC beam and the SRU beam were 434 kN and 462 kN, respectively, while the N_u were 620 kN and 660 kN, respectively.

The mid-span deflection of the beam specimen was recorded by displacement meters mounted on the top surface of the specimen and the loading device. The internal temperatures of the furnace and beams were measured by thermocouples.

At the beginning of the fire test, the designed load, F , was applied on the test specimen level by level with every step load of 30 kN and then kept constant. When the mid-span deflection was stable, the furnace temperature was raised following the ISO-834 [23] standard fire curve until the beam specimen failed. In this paper, the specific performance criteria in ISO-834-1 [24] was

adopted to judge whether the beam specimen was damaged or not and to get the fire resistance of the beam specimen.

3 EXPERIMENTAL RESULTS AND DISCUSSIONS

3.1 Failure modes



Fig. 3. Failure mode of the SRU beam



Fig. 4. Failure mode of the SRC beam

After fire exposure for 107 min, the applied load could not be maintained and the SRU beam failed. The failed SRU beam specimen kept intact except only slight spalling as shown in *Fig. 3*. At the bottom surface of the SRU specimen, several longitudinal cracks were observed. Reticulate cracks were observed on the two side surfaces of the SRU beam. On the top surface of the SRU specimen, cracks were roughly distributed along the transverse. The crack spacing was from 200 mm to 300 mm. And two black strips can be found on the side surface of the SRU beam. This may be attributed to the fact that PVA fibre melted when the temperature was raised higher than 230°C, the melting point of PVA fibre. On the whole, the ductile failure occurred to the SRU beam. The failure mode of the SRU beam could be regarded as bending failure.

On the other hand, bending failure occurred to the SRC beam too as depicted in *Fig. 4* and the fire resistance of the SRC beam was 97 min. However, the crack forms were different to that of the SRU specimen. Obvious transverse cracks were found on the bottom and the two side surfaces while the crack spacing was similar to the stirrup spacing. This may be attributed to the thermal expansion of stirrups. On the compression area of the SRC beam, concrete explosive spalling were severe and the steel bars were exposed to the outside.

3.2 Spalling patterns

From *Fig. 3*, it can be found that only slight spalling of UHTCC occurred to the SRU beam. Only several small and thin UHTCC slices spalled on the two side surfaces of the SRU beam. And the spalling depth was within 8 mm. During the heating process, the pungent odor produced by the PVA fibre melting can be smelled. Channels can be formed in the UHTCC matrix after the PVA fibre melting and the water vapour overflowed through the channel. Therefore, the vapor pressure in the UHTCC matrix was not very high and spalling of UHTCC was slight.

As for the SRC beam, concrete explosive spalling was severe as depicted in *Fig. 4*. The spalling was concentrated on the side compression area of the SRC beam while the spalling depth can even reached 50 mm. On the process of heating, vibration can be felt on the surface of the cover of the furnace. The concrete explosive spalling occurred after 12 min exposure to fire and ended after being heated for 48 min. Water vapour could not overflow from the concrete matrix due to the fact that concrete was compact. When the pressure of water vapour exceeded a certain value, the concrete explosive spalling occurred.

3.3 Temperature distributions

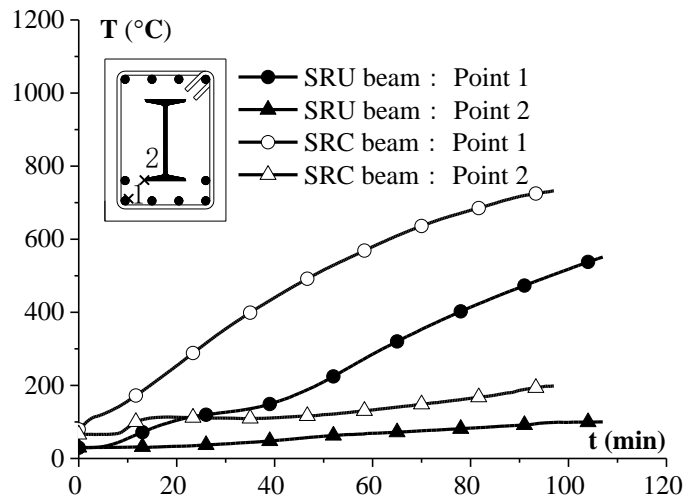


Fig. 5. Temperature distributions

The measured temperatures of the SRU beam and the SRC beam are shown in Fig. 5. Point 1 was set at the longitudinal reinforcement while point 2 was attached to the flange of the shaped steel. It can be found that:

When the temperature of shallow layer concrete was high, the temperature of internal section steel still kept very low whether it was the SRU beam or the SRC beam. For example, the temperatures of point 1 of the SRU beam and the SRC beam after fire exposure for 97 min were 503°C and 732°C, respectively, while the corresponding temperatures of point 2 were 99°C and 199°C, respectively. The differences were 404°C and 533°C, respectively. That is because both UHTCC and concrete possess the low thermal conductivity and high thermal capacity which delay the heat transferring to the interior of specimens.

The heating rate of points 1 and 2 in both beam specimens decreased at around 100°C. This may be attributed to the thermally induced migration of the moisture toward the centre of the beam specimen [25]. The farther the distance away from the surface exposed to fire was, the more obvious this phenomenon was.

The temperatures of the SRC beam were much higher than that of the SRU beam at the same depth of beam specimens after the same time of fire exposure. The temperature differences were 229°C and 100°C for point 1 and point 2, respectively, after heating for 97min. This may be attributed two reasons. Firstly, the thermal conductivity of UHTCC at ambient temperature, 0.492 W/(m·K) [17], is smaller than that of concrete, 1.355 W/(m·K) [25]. Secondly, the cross section of the SRC beam was reduced due to severe concrete explosive spalling and heat was more easily transferred to the interior of the beam specimen.

3.4 Structural responses

The fire resistances of the SRU beam and the SRC beam were 107 min and 97 min respectively with the load ratio as 0.7. The mid-span deformation (Δ) versus time (t) curve of the SRU beam is gentle and smooth while it is steep for SRC beam shown in Fig. 6. The mid-span deflection was calculated by the five displacement meters. Actually, the calculated value was the displacement at the loading point which was slightly smaller than the actual mid-span deflection, but this did not affect the qualitative analysis. The mid-span deformation of the SRC beam was larger than that of the SRU beam during the whole heating process while the elastic modulus at ambient temperature of concrete was far greater than that of UHTCC used in the tests. This may be attributed that internal temperatures of the SRU beam were lower than that of the SRC beam resulting in less strength and stiffness degradation of UHTCC. This shows that the SRU beam has a better anti-deformability at elevated temperatures which is beneficial to the structure safety.

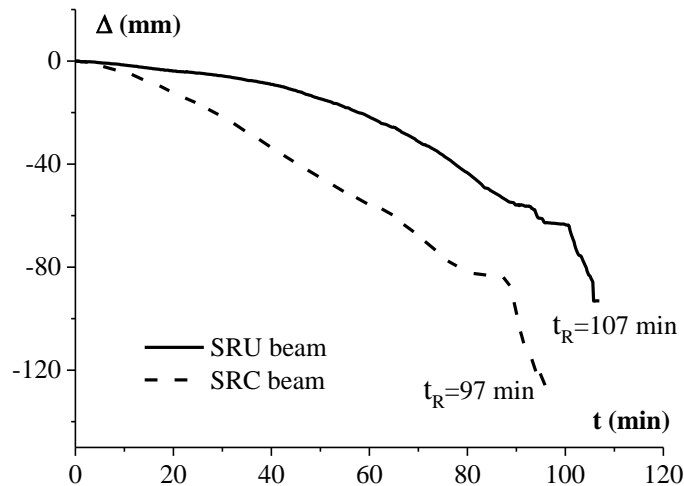


Fig. 6. Mid-span deflection versus time curves

4 CONCLUSIONS

Based on the experimental results in this study, the conclusions can be summarized as follows:

- The SRU beam can prevent explosive spalling effectively and maintain complete in fire condition while concrete explosive spalling could happen to the SRC beam.
- Both UHTCC and concrete delay the raise of internal temperatures of composite beam due to low thermal conductivity and high thermal capacity and protect the internal reinforcement and steel from fire damage. The fire protective effect of UHTCC on internal steel is better than that of concrete.
- The SRU beam has longer fire resistance and smaller deformation than the SRC beam at the same load ratio. It is beneficial to improve the fire resistance of the structure using UHTCC.

ACKNOWLEDGMENT

This research was supported by National Natural Science Foundation of China with Grant No. 51622811 and National Key Technology Research and Development Program of the Ministry of Science and Technology of China with Grant No. 2012BAJ13B04. The financial support is highly appreciated.

REFERENCES

1. V. K. R. Kodur, Fu-Ping Cheng, Tien-Chih Wang, M.A. Sultan (2003). *Effect of strength and fiber reinforcement on fire resistance of high-strength concrete columns*. Journal of Structural Engineering, 129(2), pp 253-259.
2. Tian-Yi Song, Lin-Hai Han, Zhong Tao (2015). *Structural behavior of src beam-to-column joints subjected to simulated fire including cooling phase*. Journal of Structural Engineering, 141(9), pp 04014234.
3. Victor C. Li (1993). *From micromechanics to structural engineering-the design of cementitious composites for civil engineering applications*. Proceedings of the Japan Society of Civil Engineers, 10(471), 1-12.
4. Victor C. Li, Toshiyuki Hashida (1993). *Engineering ductile fracture in brittle-matrix composites*. Journal of Materials Science Letters, 12(12), pp 898-901.
5. He-Dong Li, Shi-Lang Xu, C. K. Y. Leung (2009). *Tensile and flexural properties of ultra high toughness cementitious composite*. Journal of Wuhan University of Technology, 24(4), pp 677-683.

6. Shi-Lang Xu, Xiang-Rong Cai (2010). *Experimental study and theoretical models on compressive properties of ultra high toughness cementitious composites*. Journal of Materials in Civil Engineering, 22(10), pp 1067-1077.
7. Jia-Jia Zhou, Jin-Long Pan, C. K. Y. Leung (2015). *Mechanical behavior of fiber-reinforced engineered cementitious composites in uniaxial compression*. Journal of Materials in Civil Engineering, 27(1), 04014111.
8. Victor C. Li, Shu-Xin Wang, Cynthia Wu (2001). *Tensile strain-hardening behavior of polyvinyl alcohol engineered cementitious composite (PVA-ECC)*. ACI Materials Journal, 98(6), pp 483-492.
9. Bo-Tao Huang, Qing-Hua Li, Shi-Lang Xu, Bao-Min Zhou (2017). *Frequency effect on the compressive fatigue behavior of ultrahigh toughness cementitious composites: experimental study and probabilistic analysis*. Journal of Structural Engineering, 143(8), 04017073.
10. Qing-Hua Li, Shi-Lang Xu (2009). *Performance and application of ultra high toughness cementitious composite: a review*. Engineering Mechanics, 26(Suppl. 2), pp 23-67 (in Chinese).
11. Yun-Yong Kim, Gregor Fischer, Victor C. Li (2004). *Performance of bridge deck link slabs designed with ductile engineered cementitious composite*. ACI Structural Journal, 101(6), pp 792-801.
12. Parra-Montesinos Gustavo, James K. Wight (2000). *Seismic response of exterior RC column-to-steel beam connections*. Journal of structural engineering, 126(10), pp 1113-1121.
13. Mustafa Sahmaran, Mohamed Lachemi, Victor C. Li (2010). *Assessing mechanical properties and microstructure of fire-damaged engineered cementitious composites*. ACI Materials Journal, 107(3), pp 297-304.
14. Jiang-Tao Yu, Jian-Hui Lin, Zhi-Gang Zhang, Victor C. Li (2015). *Mechanical performance of ecc with high-volume fly ash after sub-elevated temperatures*. Construction & Building Materials, 99, pp 82-89.
15. Prakash S. Bhat, Vivian Chang, Mo Li (2014). *Effect of elevated temperature on strain-hardening engineered cementitious composites*. Construction & Building Materials, 69, pp 370-380.
16. Qing-Hua Li, Xiang Gao, Shi-Lang Xu, Yu Peng, Ye Fu (2016). *Microstructure and mechanical properties of high-toughness fiber-reinforced cementitious composites after exposure to elevated temperatures*. Journal of Materials in Civil Engineering, 28(11), 04016132.
17. Qing-Hua Li, Xiang Gao, Shi-Lang Xu, Xin Zhao (2015). *Permanent formwork of ultra high toughness cementitious composites added with nano-SiO₂*. China Civil Engineering Journal, 48(6), pp 9-16 (in Chinese).
18. Xiao-Yan Huang, Ravi Ranade, Qian Zhang, Wen Ni, Victor C. Li (2013). *Mechanical and thermal properties of green lightweight engineered cementitious composites*. Construction & Building Materials, 48(19), pp 954-960.
19. Xiu-Ling Li, Yi Bao, Lele Wu, Qing-Xi Yan, Hong-Yan Ma, Genda Chen, Hui-Ning Zhang (2017). *Thermal and mechanical properties of high-performance fiber-reinforced cementitious composites after exposure to high temperatures*. Construction and Building Materials, 157, pp 829-838.
20. T. T. Lie, V. K. R. Kodur (1996). *Thermal and mechanical properties of steel-fibre-reinforced concrete at elevated temperatures*. Canadian Journal of Civil Engineering, 23(2), pp 511-517.
21. GB/T 706-2016 (2016). *Hot rolled section steel*. Chinese Standard, Beijing.
22. GB 50010-2010 (2010). *Code for design of concrete structures*. Chinese Standard, Beijing.
23. ISO-834 (1975). *Fire resistance tests-elements of building construction*. International Standard, Geneva.
24. ISO-834-1 (1999). *Fire-resistance tests-elements of building construction —Part 1: General requirements*. International Standard, Geneva.
25. T. T. Lie (1994). *Fire Resistance of Circular Steel Columns Filled with Bar-Reinforced Concrete*. Journal of Structural Engineering, 120(5), pp 1489-1509.

Composite Structures

NUMERICAL AND EXPERIMENTAL INVESTIGATION OF THE STRUCTURAL BEHAVIOR OF PERFORATED BEAMS EXPOSED TO HYDROCARBON FIRES IN OFFSHORE PLATFORMS

Hooman Atefi¹, Ali Nadjai², Faris Ali³

ABSTRACT

The current regulations for design of steel elements in offshore platforms use a single limiting temperature for any section utilisations. This paper presents a numerical and structural investigation conducted to compare the limiting temperature of three different composite perforated beams which are exposed to ISO-834 fire and hydrocarbon fire with the same section utilisation of 30%.

A finite element model is developed based on the experiment conducted on three different composite perforated beams exposed to the standard fire. The numerical simulation entails a heat transfer analysis to predict the temperature profile of beams and structural analysis to determine the performance of the beams under applied loads. The experimental and numerical results show that the limiting temperature of the perforated composite beams exposed to the standard fire is about 730°C. The validated numerical model for simulation of the beams at ISO fire is developed to simulate the performance of beams against the hydrocarbon fire. The results show that the limiting temperature of beams for hydrocarbon fire is about 740°C.

The comparison between the performance of the beams under the hydrocarbon and cellulose fires shows that the limiting temperature is almost identical for both fire conditions. More importantly this temperature considerably higher the existing limiting temperature in offshore regulations.

Keywords: Offshore accommodation platforms, finite element modelling, hydrocarbon fires, perforated beams.

1 INTRODUCTION

A clear gap exists in codes regarding the structural performance of perforated beams exposed to hydrocarbon fires. Hydrocarbon fires may occur onshore and in residential, industrial or commercial buildings such as car parks, aircraft warehouses, industrial buildings with fuel storage vessels, train stations, coach stations, ports, etc. However, they mostly occur in the oil and gas industry and particularly the offshore sector. The high risk of hydrocarbon fire is the offshore sector is due to the existence of high temperature and high-pressure crude oil and gas pipes and vessels and the dense distribution of instruments in limited space of platforms in highly curvilinear environment. In terms of the specification of limiting temperatures, offshore standards tend to refer to a single limiting temperature for all members. ISO 13702 [1] clearly suggests 400°C as the limiting temperature of structural steelwork for offshore facilities. It does not provide a table for different load ratios or different type of members similar to Table 8 of BS 5950-8 [2]. API standards do not categorise limiting temperatures as per load ratios. For instance API 2218 [3] for refineries, uses a failure temperature of 1000°F (538°C) as per the standard fire test (UL 1709) [4].

¹ Chartered Engineer. Special Service Division, Mott MacDonald, Croydon, UK.

e-mail: Hooman.Atefi@mottmac.com

² Professor and Director of Fire Safety Engineering Research Technology Centre, Ulster University, Belfast, UK.

e-mail: a.nadjai@ulster.ac.uk

³ Professor. Belfast School of Architecture and the Built Environment, Ulster University, Belfast, UK.

e-mail: f.ali@ulster.ac.uk

The Health and Safety Executive (HSE) [5] also set the limiting temperature of steel elements for accommodation area and helideck structure of offshore facilities to 400°C. DNV-OS-D301[6] gives a limiting temperature of 400°C to 450°C for steel members. Having a single limiting temperature for different members with different load ratios leads to overdesign steel members and using extra fire protections. The overdesign of members and fire insulations lead to the increased cost of construction and weight of offshore platform, which is a crucial parameter in the design of platform topsides. This paper explores the influence of hydrocarbon fires on the structural performance of perforated beams and aims to provide a strategy and guidelines which narrow this particular gap in the standards.

2 GENERAL

The research procedure in this paper comprises three stages as follows:

1. Experimental investigation of the thermal and structural behaviour of composite perforated beams [CCBs] which are exposed to ISO-834 fire [7].
2. Create numerical models based on conducted tests with standard ISO fire to understand the behaviour of CCBs exposed to the cellulose fire.
3. Develop the validated numerical models of beams exposed to standard ISO fire (step 2) to predict the behaviour of beams against the hydrocarbon fire.

3 EXPERIMENTAL WORK

3.1 General arrangement of beams

Three full-scale cellular composite beams protected by intumescent coating are examined. The length of the beams is 5 m and they are fabricated from standard sections with a steel grade of S355. The beams are loaded gradually with one or two point loads. Figure 1 demonstrates the configuration of the 3 beams. Their corresponding geometries are shown in Table 1.



Figure 1. Configurations of cellular steel beams as they are being prepared for the tests

Table 1. The geometry of the beams used for FEA simulations

Geometry	Beam 1 (mm)	Beam 2 (mm)	Beam 3 (mm)
Span	4500	4500	4500
Top flange width	172	190	172
Top flange thickness	13	14.5	13
Top tee depth	255	275	255
Bottom flange width	307	190	190
Bottom flange thickness	23.6	14.5	14.5
Bottom tee depth	300	275	300
Web thickness - top	8	9	8
Web thickness - bottom	14	9	9
Overall depth	555	550	555
Cell diameter	375	335	375
Cell spacing	600	600	600

Concrete slabs are made from normal-weight concrete with a grade of 35 N/mm². The overall thickness of the concrete slab is 150 mm and the width of the slab is 1100 mm.

3.2 Loading

The cellular beams are subjected to concentrated loads, which are symmetric about the mid-spans of the beams. The loads applied to beams 1, 2 and 3 are 200 kN, 150 kN and 150 kN, respectively (see Figure 2). The loading is approximately 30% of the ultimate load found from the pre-design at cold conditions and by accounting for previous tests conducted at the University of Ulster [8, 9].

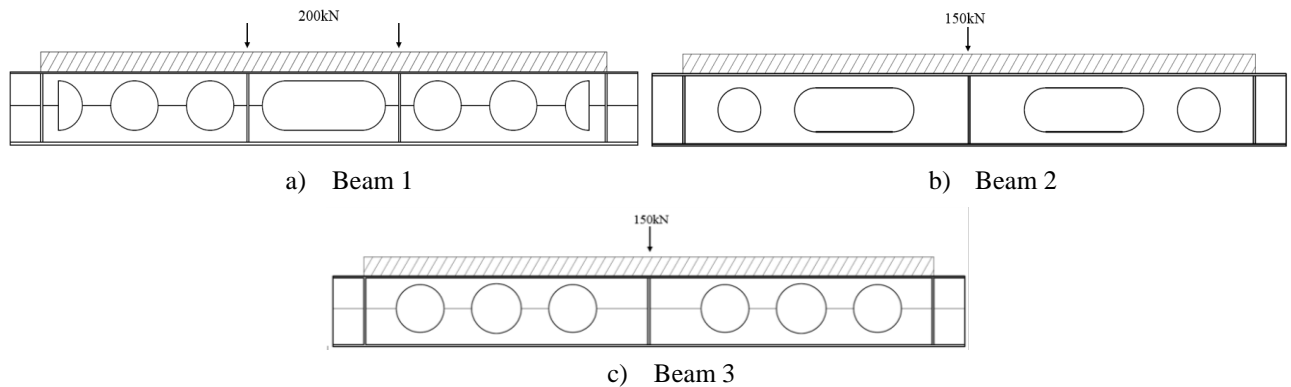


Figure 2 Location of applied loads on beams

The burners are turned on after the beams are fully loaded by a hydraulic jack. In order to take temperature readings during the tests, thermocouples are attached to the beams at various locations.

4 NUMERICAL MODELING

The 3D simulations are designed to establish a numerical model for the simulation of heat transfer within the intumescent material and steel beams and the deformation of the beams due to the applied loads. In the pre-processing stage of the simulation, the initial and boundary conditions, material properties and geometry of the model are defined.

4.1 Material properties

The thermal conductivity of the intumescent coatings is estimated using the results of the experiments conducted on four short un-loaded beams. The conductivity is calculated in accordance with BS EN 13381-8:2013 [10]. Correction factors are calculated based on Annex D BS EN 13381-8:2013 to calibrate the conductivity of the coating for the three loaded beams. The details of experiments and conductivity calculations are provided in Atefi.H [11].

The specific heat of the intumescent coating is set to 1000 J/kg°C in accordance with Equation E.7 in BS EN 13381-8:2013 [10, 12, 13]. The density of the intumescent coating is set to 100 kg/m³ [12, 13]. Steel and concrete properties and material temperature degradation are defined in accordance with BS EN 5950-8-2003 [14].

4.2 Processing

Two sets of analyses are conducted to simulate the loaded composite beams in a furnace. The first analysis is a heat transfer analysis in which the thermal load and interactions are applied to the beams. The temperature history of each node in the models is saved in an output file for use in a second type of analysis, which has two stages. The first stage is a static analysis in which the mechanical load and the boundary conditions are applied to the beam. During this stage, the temperature of the beams is set to the lab ambient temperature and the beams deform under the applied load. Essentially, this stage simulates the behaviour of the beam prior to the furnace burners being turned on during the experiment. A static analysis is chosen for the second stage, which starts at the end of the first stage. Temperature dependent material properties are defined for the model.

The initial geometry of the model in this stage is the deformed shape of the beam obtained at the end of the first stage. The applied load remains steady and is equal to the load at the end of the first stage. The temperature history of all the nodes from the first set of the analyses (heat transfer analysis) is assigned to the nodes in the second stage. By increasing the temperature of the nodes in the second stage, the CCBs begin losing their strength and stiffness and consequently the beams become more deflected under the applied load from the first stage. An artificial damping is introduced into the general static method to enable the model to simulate the local failure of the web-post. The ratio of the dissipated energy due to damping to the total strain energy is limited to 2.5%.

A shell element is used for the modelling of the concrete slab and a solid element is used for the rest of the beam. The steel deck and reinforcement bars are defined as composite layers within the shell composite section. For the heat transfer analysis, 4-node heat transfer quadrilateral shell elements and 8-node linear heat transfer bricks are used for the concrete slab and coated beams, respectively. For the static analysis, 4-node doubly curved thin or thick shell elements and 8-node linear brick elements are used for the concrete slab and the steel beam, respectively (see Figure 3).

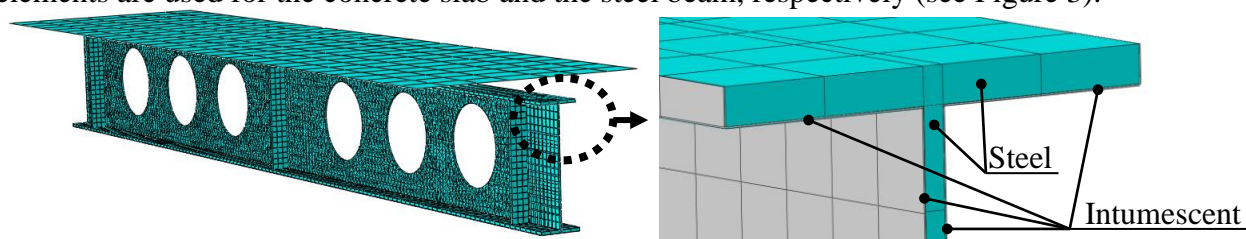


Figure 3 Beam 3 computational mesh

4.3 Boundary condition and thermal interactions

Convection and radiation interactions are defined between the furnace and the intumescent coating and between the furnace and the bottom surface of the concrete slab (steel deck), and between the top surface of the concrete slab and the lab ambient. For the beams exposed to the ISO fire, the recorded temperatures of furnace during the experiment are used to define transient ambient temperatures around the protected beam and under the concrete slab. However, for the beams exposed to the hydrocarbon fire, the recorded ambient temperature is changed to the hydrocarbon fire curve. Convection and radiation interactions are defined for the top surface of the slab and the ambient temperature for the top surface is set to 20° C.

The convection coefficient for the standard and hydrocarbon fires are assumed to be 25 W/m² k and 50 W/m² k, respectively [15-18]. The emissivity of the intumescent coating in different publications is reported to be between 0.7 and 0.95 [13, 19, 20]. This research work sets the emissivity to 0.9 as recommended by the intumescent material provider. The emissivity of the steel deck is set to 0.4 [21]. It is assumed that there are no air pockets between the beam and the coating after the coating activation and consequently all the heat is transferred between the coating and the steel beams. Therefore, fully thermal restrained interactions are defined between the intumescent and the steel beams.

Simply supported boundary conditions are assigned to the beams ends. Due to the high distribution density of shear studs, it can be assumed that the concrete slabs and steel beams are bonded. Therefore, for simplification of the models, steel studs are not modelled and instead of the studs a fully constrained interaction is defined between steel and concrete. This means that no relative motion occurs between the bottom surface of the slabs and the top surface of the upper flanges.

5 RESULTS

Figure 4 shows the deformation of mid beams exposed to hydrocarbon and cellulose fire curves. The numerical model is developed in a way can simulate the post failure behaviour of beams. Vertical lines in Figure 4 show the time at which the rate of beams deformation increases and consequently leads to beams failure. The full results of the heat transfer analysis and the temperatures recorded during the experiments can be found in Atefi.H [22].

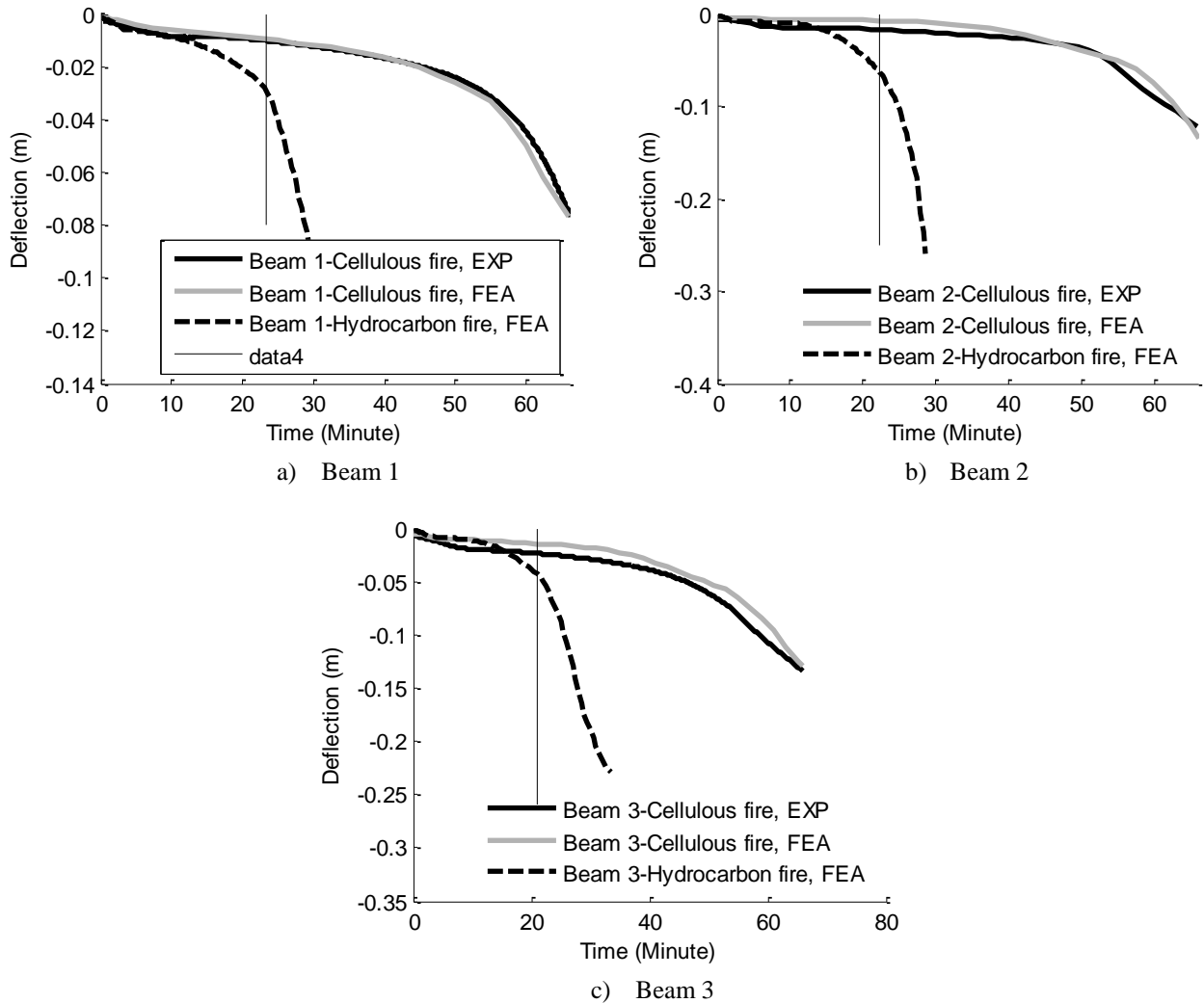
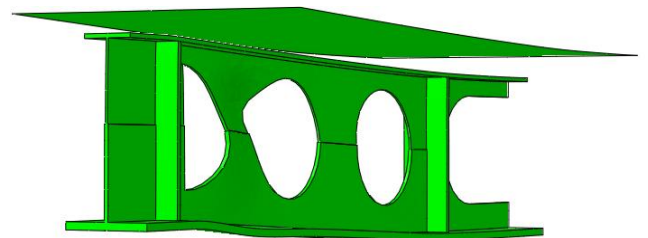


Figure 4 deformation of mid spans – experimental (EXP) and numerical (FEA) results



a) Beam A – experiment



b) Beam A failure – numerical model

Numerical and Experimental Investigation of the Structural Behavior of Perforated Beams Exposed to Hydrocarbon Fires in Offshore Platforms

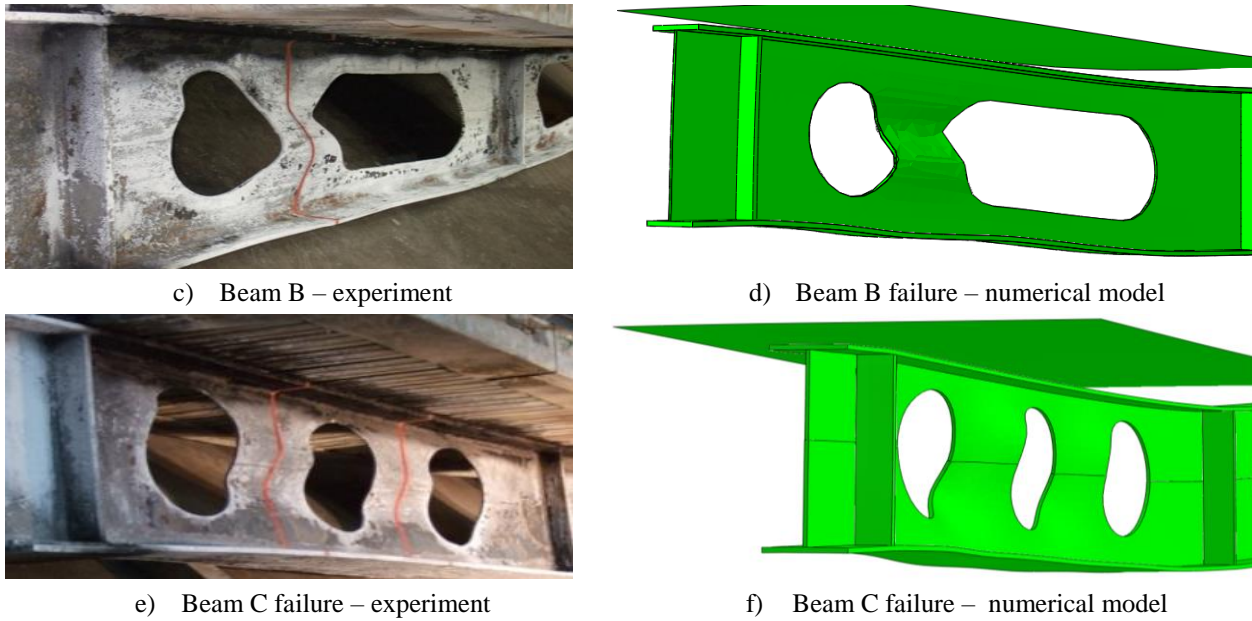
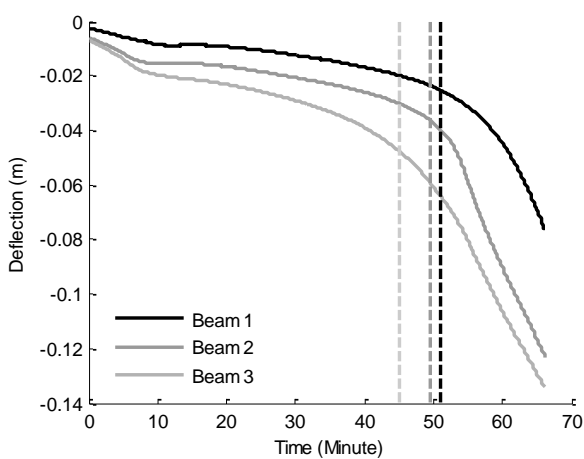


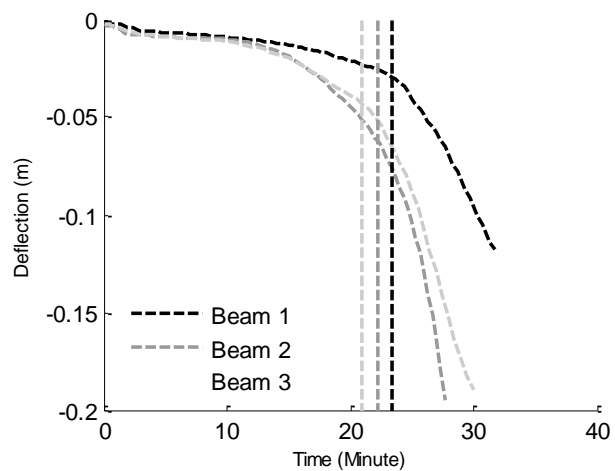
Figure 5 Failure mode of beams

Figure 5 shows the deformed shape of the three beams at the point of failure. The numerically estimated temperature profile and deformation of the beams are in good agreement with the experimental outcomes.

Figure 6a shows that for beams 1, 2 and 3 which were exposed to the standard fire the rate of beam deflection increases after approximately 51, 49 and 45 minutes, respectively. Figure 6b demonstrates that for beams 1, 2 and 3 which were exposed to the hydrocarbon fire, the rate of beam deflection for each beam increases after approximately 23, 22 and 21 minutes, respectively. The maximum temperature at web-posts are approximately 730°C for the standard fire (see Figure 6c, e and g) and 740°C for the hydrocarbon fire (see Figure 6d, f and h) at the times where the rate of deformation was increased. The deflection at these times can be regarded as critical deflection points.



a) Deformation of beams, cellulose fire



b) Deformation of beams, hydrocarbon fire

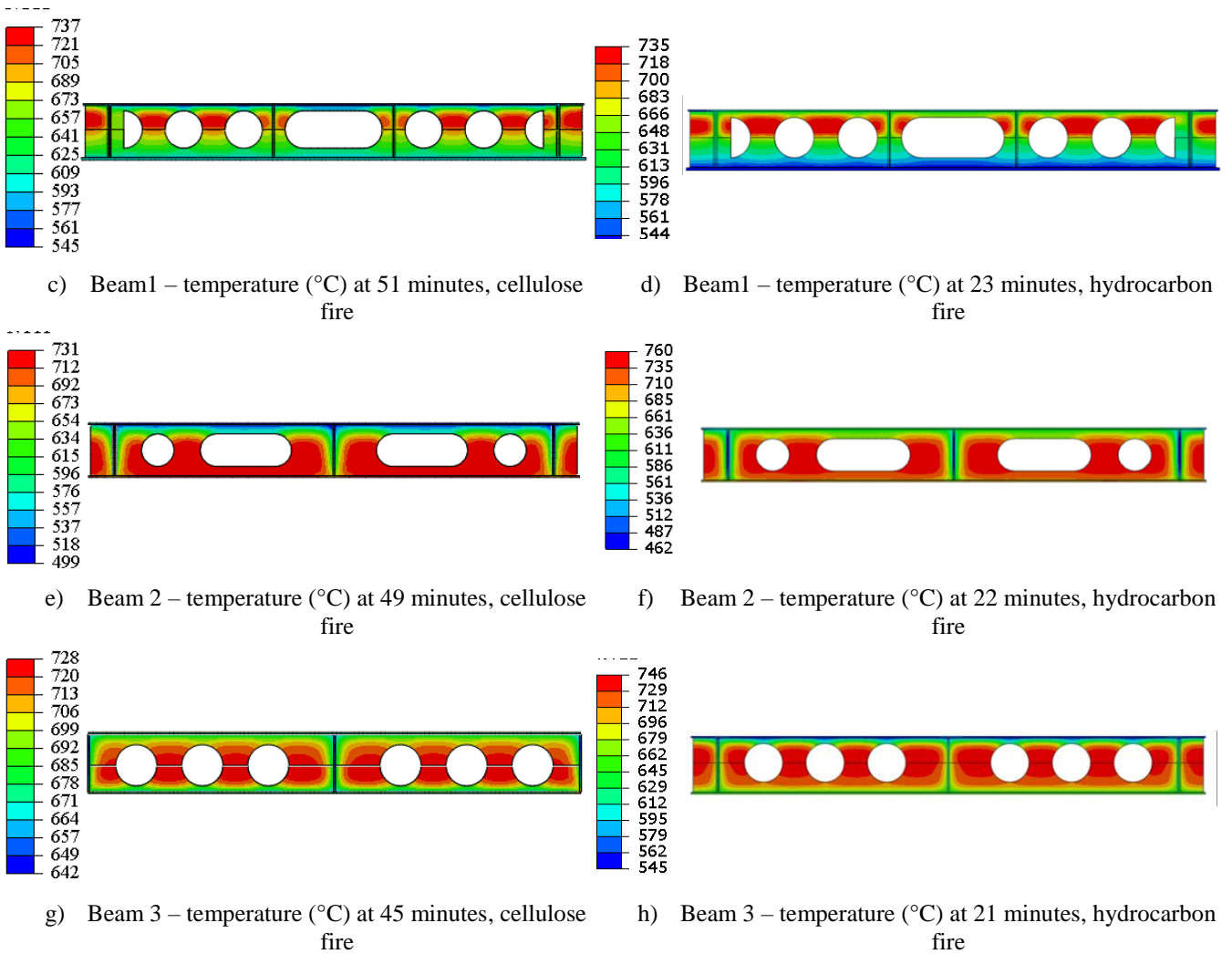


Figure 6 Critical deformation and temperature – cellulose and hydrocarbon fire

6 CONCLUSIONS

This paper describes an experimental and numerical study of the thermal and structural performance of loaded perforated beams protected with intumescent coating, exposed to ISO standard and hydrocarbon fire, and compares the critical temperature of cellulose and hydrocarbon fire. The paper concludes that:

- The beams fail due to web failure between openings with high shear forces.
- The numerical and experimental results show that the web temperature between the openings of a perforated beam is higher than the rest of beams. For the beams which were exposed to ISO standard fire, the results show that when the temperature of web-posts reach around 730°C, the beams deflect at a faster rate. This is followed by web-post failure.
- For the beams, which were exposed to the hydrocarbon fire, the web-post reaches its maximum (failure) temperature of around 740°C after 20 minutes. The beam fails 50 minutes earlier than they do in standard fire and the limiting temperature is around 10°C higher than that of standard fire.
- In summary, the limiting temperature of the perforated composite beams with different geometries, opening configurations, and loading conditions for the load ratio of 30% is 730°C and 740°C for beams exposed to standard ISO and hydrocarbon fire, respectively.
- Currently, in the offshore industry, the limiting temperature is set to a single value which is about 400°C for all steel members. However, the findings in this research show that the limiting temperature of perforated beams is considerably higher for hydrocarbon fire and

almost is same the standard ISO fire. This means that the size of the steel section and the thickness of the protection for hydrocarbon fire can be reduced due to increases in the limiting temperature. This can reduce the weight of offshore structures, which is a crucial parameter. It also reduces steel and insulation cost, and CO₂ emission.

REFERENCES

1. ISO, *ISO 13702: Petroleum and natural gas industries, in Control and mitigation of fires and explosions on offshore production installations -- Requirements and guidelines*. 2015.
2. BSI, *BS 5950-8:2003 Structural use of steelwork in building, in Part 8: Code of practice for fire resistant design*. 2003.
3. API, *RP I 2218: Fireproofing Practises In Petroleum and Petrochemical Processing Plants*. 2013.
4. UL, *UL 1709: Standard for Rapid Rise Fire Tests of Protection Materials for Structural Steel*. 2011.
5. HSE, *Fire and explosion structural integrity assessment, in Appendix 2 - Technical background note*. 2017.
6. DNV, *DNV-OS-D301, Fire Protection*. 2013.
7. ISO, *ISO 834-1:1999: Fire resistance tests- elements of building construction. Part 1: General requirements*. 1999.
8. Nadjai, A., et al., *Performance of unprotected and protected cellular beams in fire conditions*. *Construction and Building Materials*, 2016. **105**: p. 579-588.
9. Naili, E., et al. *Experimental and Numerical Modelling of Cellular Beams with Elongations Openings at Elevated Temperature*. in *Structures in Fire: Proceeding of the 6th International Conference*. 2010. DES tech Publications, Inc.
10. BSI, *BS EN 13381-8, Test Methods for Determining the Contribution to the Fire Resistance of Structural Members, in Part 8: Applied reactive protection to steel members*. 2010, BSI: London.
11. Atefi, H., A. Nadjai, and F. Ali, *Numerical and experimental investigation of thermal behavior of coated cellular beams with intumescent coating, in IFireSS 2017 – 2nd International Fire Safety Symposium*. 2017: Italy.
12. Dai, X., Y. Wang, and C. Bailey, *A Simple Method to Predict Temperatures in Steel Joints with Partial Intumescent Coating Fire Protection*. *Fire Technology*, 2009. **46**(1): p. 19-35.
13. Wang, Y., et al. *A model for prediction of temperature in steel structure protected by intumescent coating, based on tests in the Cone Calorimeter*. in *IAFSS 8th Symposium on Fire Safety Science*. 2005. IAFSS.
14. BSI, *BS 5950-8: 2003 Structural use of steelwork in building, in Part 8: Code of practice for fire resistant design*. 2003.
15. Drysdale, D., *An introduction to fire dynamics*. 2011: John Wiley & Sons.
16. Lawson, R. and G. Newman, *Fire Resistant Design of Steel Structures: A Handbook to BS 5950*. 1990: Steel Construction Institute.
17. Milke, J.A., *Analytical methods for determining fire resistance of steel members, in SFPE handbook of fire protection engineering*. 1995, Springer. p. 1909-1948.
18. BSI, *BS EN 1992-1-2: 2004 Eurocode 2: Design of concrete structures, in Part 1-2: General rules — Structural fire design*. 2008. p. 1992-2.
19. Bartholmai, M., R. Schriever, and B. Schartel, *Influence of external heat flux and coating thickness on the thermal insulation properties of two different intumescent coatings using cone calorimeter and numerical analysis*. *Fire and materials*, 2003. **27**(4): p. 151-162.
20. Henderson, J.B., J. Wiebelt, and M. Tant, *A model for the thermal response of polymer composite materials with experimental verification*. *Journal of Composite Materials*, 1985. **19**(6): p. 579-595.
21. SCI, *Structural applications of ferritic stainless steels (SAFSS), in WP 3.5 Heat Trnsfer characteristic of ferric stainless steel decking*. 2012.
22. Atefi, H., *Numerical and Experimental Investigation of Perforated Beam at Elevated Temperature, in Fire Safety Engineering Research Technology Centre*. 2017, University of Ulster.

EXPERIMENTAL STUDY OF A STEEL-CONCRETE COMPOSITE BRIDGE UNDER FIRE

Jose Alos-Moya¹, Ignacio Paya-Zaforteza², Antonio Hospitaler³

ABSTRACT

Bridges are a critical component of the infrastructure whose damage can result in major losses. However, current codes and recommendations do not guide on how to protect bridges from fire, which has motivated a lot of research. This research has been mainly based on the use of numerical models. These models need experimental validation but experimental work on bridge fires is very scarce and complex due to the magnitude of the fire loads involved and the dimensions of bridge components.

Within this context this paper details the main results and findings of the Valencia bridge fire tests, a battery of eight fire tests carried out under a composite bridge built at the Universitat Politècnica de València in Spain. The bridge had a RC deck supported on two I-girders and its span was 6 m. The results presented enable the calibration of the numerical models used to study bridge fires and show that: (a) gas temperatures vary significantly along the longitudinal axis of the bridge and therefore it cannot be assumed that these temperatures are uniform and (b) the most important factors affecting the response of the bridge are the position and the magnitude of the fire load.

Keywords: Valencia bridge fire tests, composite bridge, open-air fire test, bridge resilience

1 INTRODUCTION

Bridges are a critical component of the transportation system which have suffered severe damage due to fires as proved e.g. by Garlock et al [1] and by a bridge failure survey carried out in 2011 and cited in [1] which collected data related to 1746 bridge failures from the departments of transportation of 18 US states. This survey showed that fire had caused more bridge collapses than earthquakes and that fire had been the fifth cause of bridge collapses.

However, and despite its importance, bridge fires have got very little attention in the past, especially considering that bridge fires are different to building or tunnel fires and deserve a particular approach (see [2] for more details). The particular features of bridge fires together with the lack of guidelines on how to deal with them has motivated a lot of recent research in recent years related, among other topics, to risk analysis methodologies (see e.g. [3, 4]) and the fire response of girder bridges, trusses and cable supported bridges (see e.g. [5-13]). The aforementioned works used both simplified (e.g. [5]) and advanced methodologies (e.g. [6-13]) but these models require experimental validation. Within this context, this paper summarizes the main results and

¹ Researcher. ICITECH, Universitat Politècnica de València, Spain.

e-mail: joalmol1@cam.upv.es

² Associate Professor. Department of Construction Engineering and Civil Engineering Projects, ICITECH, Universitat Politècnica de València, Spain.

e-mail: igpaza@cst.upv.es

³ Professor. Department of Construction Engineering and Civil Engineering Projects, ICITECH, Universitat Politècnica de València, Spain.

e-mail: ahospitaler@cst.upv.es

conclusions of the Valencia bridge fire tests, an experimental campaign carried out at the campus of the Universitat Politècnica de València in València, Spain, with a steel-concrete composite bridge. The goal of this study was to obtain a set of experimental results that: (a) enable the calibration of the numerical models used in bridge fire engineering and (b) provide qualitative information on the main features of bridge fires. A more comprehensive description of the tests and their results can be found in Alos-Moya et al. [2]. A validation of simplified and advanced methodologies that can be used to model the tests can be found in Alos-Moya et al. [14].

2 DESCRIPTION OF THE BRIDGE

Figure 1 shows the experimental bridge built. It consisted of:

1. Two reinforced concrete abutments.
2. A composite steel-concrete deck spanning 6 m resting on the abutments by means of elastomeric bearings. The deck had a concrete slab 0.15 m thick and 2 m wide which was connected with shear studs to two IPE-160 steel girders. The transverse separation between the axes of the two girders was 1 m.
3. Two auxiliary steel frames used to fix the LVDT sensors that recorded the vertical deflections of the deck during the tests.

It must be noted that a composite deck with I-girders was chosen because: (1) this structural system is very common for short and medium span highway bridges, (2) according to the study by Peris-Sayol et al. [2], this structural system was the most common among the bridges that had collapsed or suffered severe damage in fire events.

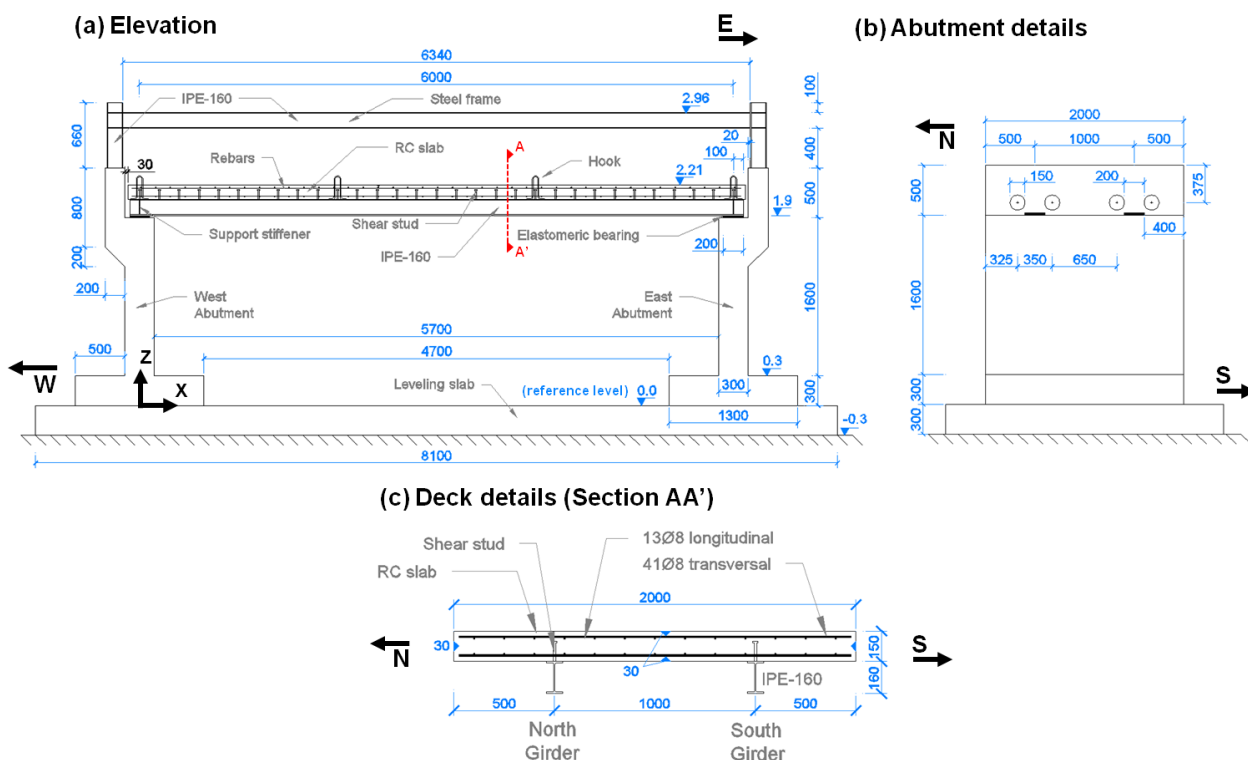


Figure 1. Description of the experimental bridge. All the dimensions are expressed in mm. All the levels (z coordinates) are expressed in m.

Table 1. Mechanical properties of the bridge materials

Material	Mechanical properties	Notes
Concrete	$f_c=33$ MPa $E=33.8$ GPa	Mean values obtained with four cylindrical specimens
Structural steel	Elastic limit = 360.5 MPa Yield strength =488.5 MPa	Mean values obtained with eight specimens
Reinforcing steel	Elastic limit = 541.5 MPa Yield strength =634 MPa	Mean values obtained with seven specimens

3 EXPERIMENTAL CAMPAIGN

3.1 Fire scenarios

Before the experimental bridge was built, a series of preliminary tests were carried out with the main goals of characterise the fire loads and establish a protocol to perform the tests with the actual bridge safely (see Alos et al [2] for more details). Then a total of eight fire tests corresponding to four different fire scenarios under the bridge deck were carried out. These scenarios involved different magnitudes of the fire load and fire load positions (see Table 2 and Fig. 2). The choice of placing the fire load under the bridge was motivated by the fact that the statistical analysis of bridge fires by Peris-Sayol et al. [2] shows that this type of fire scenarios are the most harmful for girder bridges. A fire protection board with a length of 1.65 m was located between the girders and adjacent to the East abutment in Tests 5 and 6.

Table 2. Fire scenarios in the Valencia bridge fire tests. “x” and “z” coordinates are defined in Fig. 1. “z” coordinate is related to the base of the pan.

Fire scenario	Pan side (m)	Fire location	HRR (kW)	Test	Distance to East Abutment (m)	Center pan location	
						x (m)	z (m)
Fire 1	0.5	Mid-span	415	1	-	3	0.2
				2	-		
Fire 2	0.75	Mid-span	1131	3	-	3	0.2
				4	-		
Fire 3	0.5	Lateral	415	5	0.33	5.27	0.5
				6	0.01		
				7	0.01		
Fire 4	0.75	Mid-span	1131	8	-	3	0.8

Fire load magnitude was defined by the Heat Release Rate (HRR). HRR was obtained as explained by Drysdale [15] and considering that the Valencia bridge fire tests involved gasoline in two square pans, one with a side of 0.5 m and the other one with a side of 0.75 m. It must be noted that the fire loads used are smaller than those present in tanker truck fires, but the difference is not important if the following circumstances are considered:

- The research goals of the experimental campaign required several tests with the fire under the bridge but without the bridge suffering any major damage.
- The temperatures in the steel girders in Test 8 were similar to those of real fire events.

Experimental study of a steel-concrete composite bridge under fire

- The fire load in the tests was high enough to make the flames impinge on the deck, as usually happens in tanker truck fires under bridges.
- Due to economic, environmental and safety reasons it was impossible to use fire loads similar to those involved in a typical tanker truck accident.

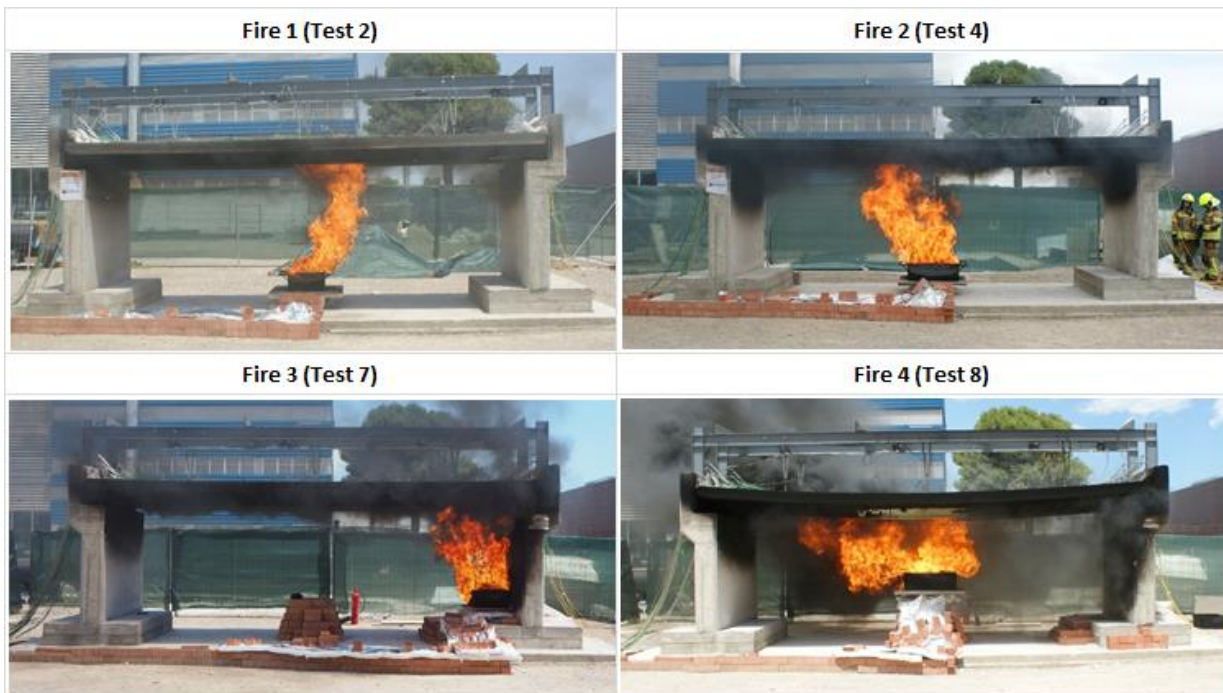


Figure 3. Valencia bridge fire tests. Images illustrating the fire scenarios considered.

3.2 Test monitoring.

The following variables were continuously monitored during the tests:

- Weight of fuel, which was used to obtain the HRR during the tests. This was measured using a scale.
- Temperatures in the gas surrounding the deck and deck temperatures. These variables were measured using type K thermocouples (TCs).
- Vertical deflections at various points of the deck. Deflections were measured by means of a weight scale.

A total of 72 TCs and 22 LVDTs were installed. In addition, 17 high temperature fiber optic sensors developed by the authors (see Rinaudo et al. [16, 17]) were also placed to check their behaviour under realistic fire scenarios. Some of the monitoring systems can be found in Fig. 4. A detailed description of the monitoring systems and their location can be found in Alos-Moya et al. [2]

Composite structures

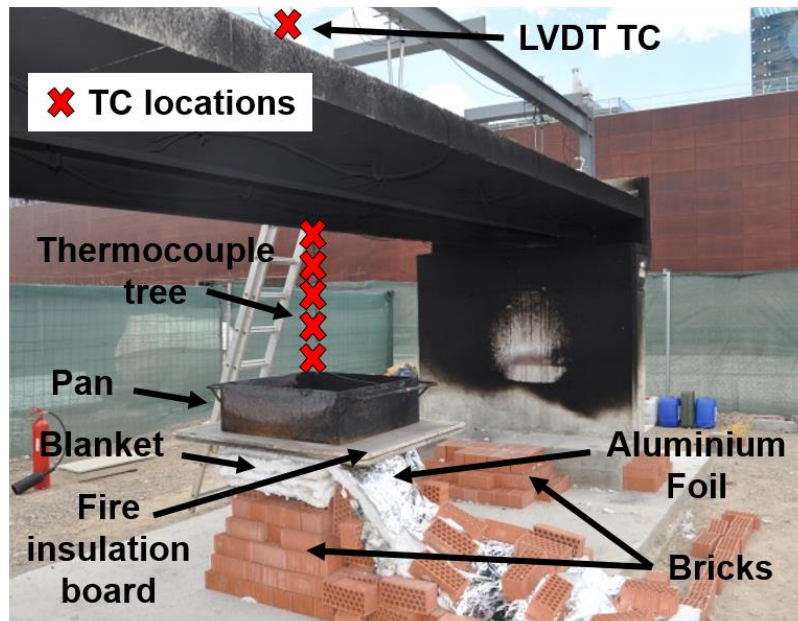


Figure 4. Some of the monitoring systems used.

3.3 Gas temperatures

Gas temperatures reached maximum values in the central area between the two girders and varied between 320°C (Fire 1 scenario) and 920°C (Fire 4 scenario). Figure 5 shows the temperatures recorded during the tests 7 and 8 at the central area between two bridge girders at two significant cross sections of the bridge. This gradient was 350°C/m for the Fire 4 scenario and 220°C/m for Fire 3 scenario.

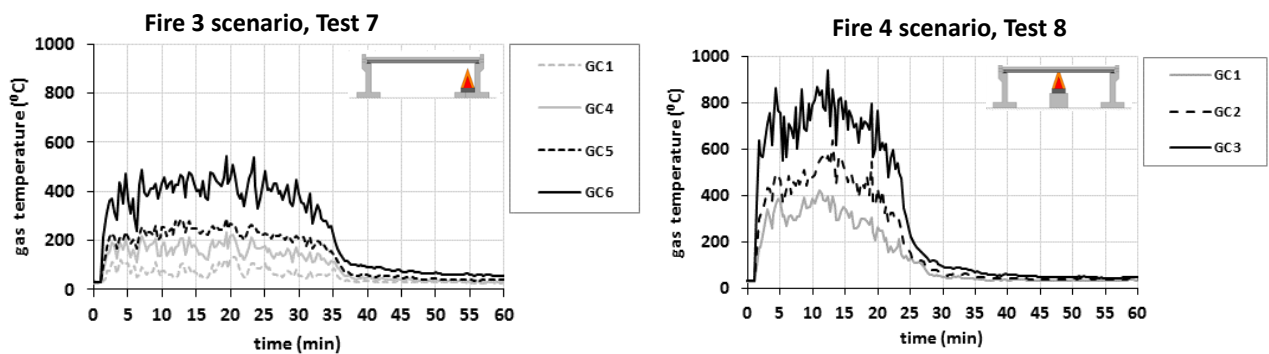


Figure 5. Temperatures recorded in the central region between two bridge girders. Left:(a) Fire 3 scenario, Test 7; Right: Fire 4 scenario, Test 8. GC1, GC 2, GC 3, GC4 and GC 6 are the names of the six TCs used to measure gas temperatures in the central region. They were located at the sections with the “x” coordinates 0.5 m, 1.5 m, 2.5 m, 3.5 m, 4.5 m and 5.5 m respectively.

3.4 Steel temperatures

Maximum steel temperatures varied during the tests and reached values of 226°C, 512 °C, 469°C and 749°C for the scenarios Fire 1, Fire 2, Fire 3 and Fire 4 respectively. Steel temperatures also experienced important variations along the longitudinal axis of the bridge (see Fig. 6) and the values of the thermal gradients were 250°C/m for Fire 4 scenario, 200 °C/m in Fire scenarios 2 and 3, and 60 °C/m in the Fire 1 scenario. Therefore, it is not realistic to assume, when doing the fire analysis of a bridge, a uniform heating of the bridge along its longitudinal axis.

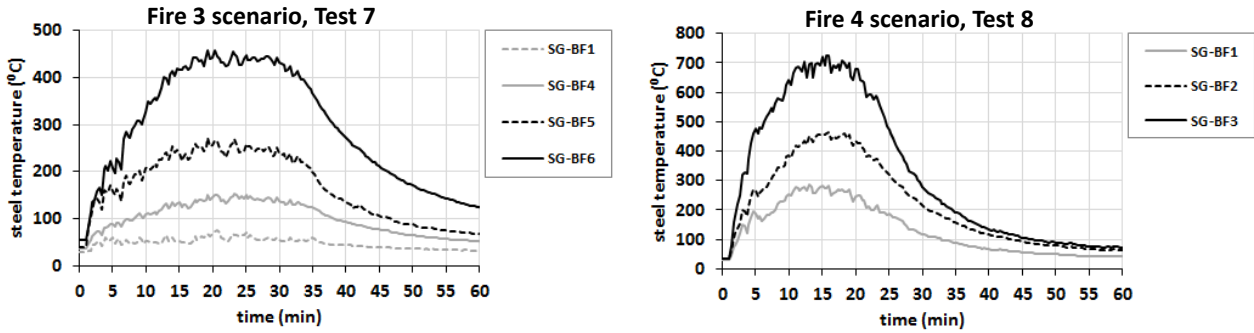


Figure 6. Temperatures recorded in the bottom flange of the South Girder. Left: (a) Fire 3 scenario, Test 7; Right: Fire 4 scenario, Test 8. SG-BF1, SG-BF2, SG-BF3, SG-BF4, SG-BF5 and SG-BF6 are the names of the six TCs used to measure gas temperatures in the bottom flange of the South Girder. Additional TCs were located They were located at the sections with the “x” coordinates 0.5 m, 1.5 m, 2.5 m, 3.5 m, 4.5 m and 5.5 m respectively.

Another important observation in the tests was that bottom flange temperatures were very similar to web temperatures and higher than top flange temperatures. This can be observed in Fig. 7a which shows the maximum temperatures at different elements of the bridge girders. Top flange temperatures were significantly smaller due to the protection of the top flange by the reinforced concrete slab. Finally, the analysis of the results of the experiments points out that the power of the fire and the vertical distance from the fire to the bridge deck are factors that have a major influence on the response of the bridge.

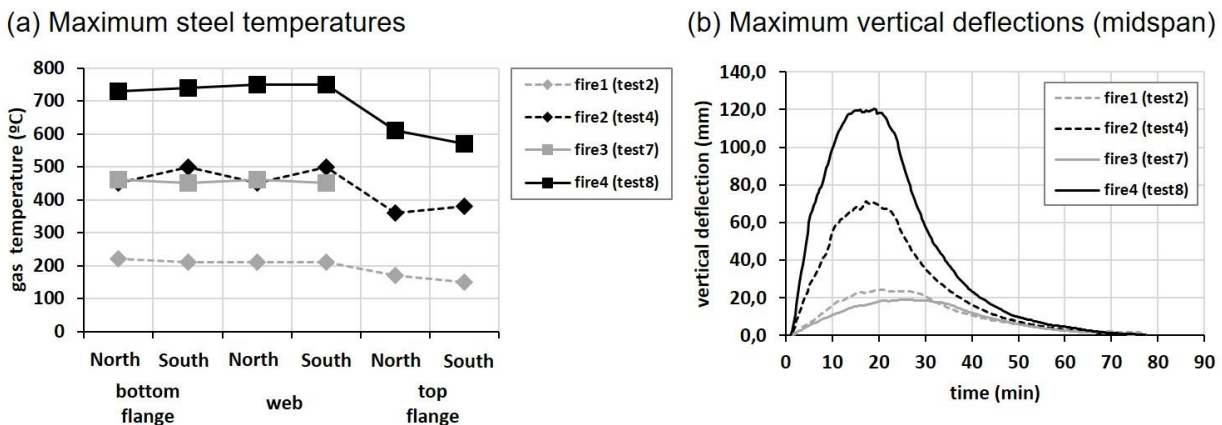


Figure 7. (a) maximum steel temperatures per region, (b) maximum vertical deflection at mid-span at North Girder in mid-span.

3.5 Deck deflections

Fig. 7b shows the evolution of the mid-span deflections at the North Girder in four of the tests carried out (similar results were obtained for the South girder. Maximum deflection was 0.12 m and was reached in Test 8 during six minutes. During this time, the distance between the fire load and the steel girders was only 0.98 m due to the deck deflection of 0.12 m. The girders did not suffer any plastic damage because no residual deflection was measured when the test ended.

4 CONCLUSIONS

This paper describes a set of tests carried out at the Universitat Politècnica de València in Valencia, Spain to improve current knowledge on the response of bridges to fires. A total of eight tests

involving different fire load magnitudes and positions were carried out under a 6 m long I-girder composite bridge. The tests enabled to obtain the following conclusions:

- Gas temperatures reach maximum values in the central area between the two girders. These temperatures experimented important variations along the longitudinal axis of the bridge. For example, the average longitudinal thermal gradient is 350°C/m for the Fire 4 scenario and 220°C/m for Fire 3.
- Steel temperatures also varied significantly along the longitudinal axis of the bridge and prove the existence of an important thermal gradient (250°C/m for Fire 4 scenario, 200 °C/m in Fire scenarios 2 and 3, and 60 °C/m in the Fire 1 scenario). Therefore, and even for short span bridges, it is not realistic to assume a uniform heating of the girders.
- Maximum web and bottom flange girder temperatures are very similar. Top flange temperatures are significantly smaller due to the protection of the top flange by the reinforced concrete slab.
- The experiments point out that the power of the fire and the vertical distance from the fire to the bridge deck are factors that have a major influence on the response of the bridge. This influence had been foreseen in the analysis of a typical steel I-girder bridge carried out by Peris-Sayol et al. [2], but the experiments described here have verified it experimentally for the first time.

The results of the tests are of major importance because they provide qualitative and quantitative information for the validation of the numerical models used in bridge fire engineering and to improve bridge resilience against fire hazards.

ACKNOWLEDGEMENTS

Funding for this research was provided by the Spanish Ministry of Science and Innovation (Research Project BIA 2011–27104). The authors are grateful to the Infrastructure and Safety departments of the Universitat Politècnica de València and the City of Valencia Fire Department (Cuerpo de Bomberos de Valencia), which provided crucial support in conducting the tests. Finally, the authors would like to thank Dr. Luke Bisby from the University of Edinburgh, and Dr. Juan Hidalgo and Dr. Cristian Maluk from the University of Queensland for their advice and support during the early stages of planning the fire tests.

REFERENCES

1. M.E. Garlock, I. Paya-Zaforteza, V. Kodur, L. Gu (2012). *Fire hazard in bridges: review, assessment and repair strategies*. Engineering Structures 2012; 35. pp 89-98.
<https://doi.org/10.1016/j.engstruct.2011.11.002>
2. J. Alos-Moya, I. Paya-Zaforteza, A. Hospitaler, P. Rinaudo (2017). Valencia bridge fire tests: Experimental study of a composite bridge under fire. Journal of Constructional Steel Research, 138 pp 538-558.
<https://doi.org/10.1016/j.jcsr.2017.08.008>
3. H. Gil, S. Seo, C. Park (2015). Fire Risk Management for Highway Bridges in Korea. *IABSE Conference Structural Engineering: Providing Solutions to Global Challenges* Geneva (Switzerland) pp 890-896.
4. G. Peris-Sayol G, I. Paya-Zaforteza, S. Balasch-Parisi, J. Alos-Moya (2017). *Detailed Analysis of the Causes of Bridge Fires and Their Associated Damage Levels*. Journal of Performance of Constructed Facilities 31(3).
[https://doi.org/10.1061/\(ASCE\)CF.1943-5509](https://doi.org/10.1061/(ASCE)CF.1943-5509)
5. S.E. Quiel, T. Yokoyama, L.S. Bregman, K.A. Mueller, S.M. Marjanishvili (2015). *A streamlined framework for calculating the response of steel-supported bridges to open-air tanker truck fires*. Fire Safety Journal, 73 pp. 63-65.

<https://doi.org/10.1016/j.firesaf.2015.03.004>

6. I. Payá-Zaforteza and MEM Garlock (2012). *A numerical investigation on the fire response of a steel girder bridge*. Journal of Constructional Steel Research 75:93–103, 2012.
<https://doi.org/10.1016/j.jcsr.2012.03.012>
7. W. Wright, B. Lattimer, M. Woodworth, M. Nahid, and E. Sotelino (2013). *Highway bridge fire assessment draft final report*. NCHRP Program Transportation Research Board of the National Academies. Virginia Polytechnic Institute and State University. Blacksburg, VA; 2013.
8. J Alos-Moya, I Paya-Zaforteza, MEM Garlock, E Loma-Ossorio, D Schiffner, A Hospitaler (2014). *Analysis of a bridge failure due to fire using computational fluid dynamics and finite element models*. Engineering Structures, 68 pp. 96-110. <https://doi.org/10.1016/j.engstruct.2014.02.022>
9. G Peris-Sayol, J Alós-Moya, I Payá-Zaforteza, A Hospitaler-Pérez (2014). *A parametric study on the thermo-mechanical response of a multi-girder steel bridge submitted to real fires (Estudio paramétrico de la respuesta termo-estructural de un puente metálico multijácena sometido a incendios reales)*. Informes de la Construcción, 66 (Nº Extra-1) pp. 1-11.
<http://dx.doi.org/10.3989/ic.13.077>
10. X. Gong, AK Agrawal (2015). *Numerical Simulation of Fire Damage to a Long-Span Truss Bridge*. Journal Bridge Engineering, 20(10).
[https://doi.org/10.1061/\(ASCE\)BE.1943-5592.0000707](https://doi.org/10.1061/(ASCE)BE.1943-5592.0000707)
11. G. Peris-Sayol, I. Paya-Zaforteza, J. Alos-Moya, A. Hospitaler (2015). *Analysis of the influence of geometric, modeling and environmental parameters on the fire response of steel bridges subjected to realistic fire scenarios*. Computers and Structures, 158 pp. 333-345.
<http://dx.doi.org/10.1016/j.compstruc.2015.06.003>
12. X. Gong, AK Agrawal (2016). *Safety of Cable-Supported Bridges during Fire Hazards*. Journal of Bridge Engineering, 21(4).
[https://doi.org/10.1061/\(ASCE\)BE.1943-5592.0000870](https://doi.org/10.1061/(ASCE)BE.1943-5592.0000870)
13. J. Glassman, MEM Garlock, E. Aziz and V. Kodur. *Modeling parameters for predicting the postbuckling shear strength of steel plate girders*. Journal of Constructional Steel Research, 121 pp. 136-143.
<https://doi.org/10.1016/j.jcsr.2016.01.004>.
14. J Alos-Moya, I Paya-Zaforteza, A Hospitaler, E Loma-Ossorio. *Valencia bridge fire tests: Validation of simplified and advanced numerical approaches to model bridge fire scenarios*. Paper submitted to Engineering Structures.
15. D. Drysdale (2011). *An Introduction to Fire Dynamics*. John Wiley and Sons. United Kingdom.
16. P. Rinaudo, B. Torres, I. Paya-Zaforteza, PA Calderón, S Sales (2015). *Evaluation of new regenerated fiber Bragg grating high-temperature sensors in an ISO 834 fire test*. Fire Safety Journal, 71 pp. 332-339
<https://doi.org/doi:10.1016/j.firesaf.2014.11.024>
17. P. Rinaudo, I. Paya-Zaforteza, P. Calderón, S. Sales. (2016). *Experimental and analytical evaluation of the response time of high temperature fiber optic sensors*. Sensors and Actuators, A: Physical, 243 pp. 167-174
<https://doi.org/10.1016/j.sna.2016.03.022>

EXPERIMENTAL INVESTIGATION OF POST-TENSIONED CONCRETE BRIDGE BEAMS EXPOSED TO HYDROCARBON FIRE

XI QIANG WU¹, FRANCIS TAT KWONG AU², JING LI³

ABSTRACT

This paper presents the fire tests of six scaled post-tensioned bonded concrete bridge beams, which simulate the action of hydrocarbon fire. The test variables considered include beam section type, fire exposure time and loading level. The phenomena observed during testing, including water evaporation, smoke, flame, noise, etc. were recorded. The temperatures and displacements at critical locations were measured. The measurements of displacement and loading after fire exposure were utilized to evaluate the post-fire load-carrying capacity. Results showed that the box girders under lower loading sustained for around 3 hours before collapse, while those under higher loading sustained for around 2.5 hours. Results also showed that about 12% of load-carrying capacity at ambient temperature was lost after exposure to simulated hydrocarbon fire for around 1.5 hours. Post-fire evaluation showed that the specimens experienced severe spalling during fire exposure.

Keywords: Concrete bridge, hydrocarbon curve, limited fire exposure, loading level, fire tests

1 INTRODUCTION

Bridge fire is often described as a kind of ‘Low-possibility but high-consequence’ event, indicating that, while it rarely happens, it may cause a significant hazard once it occurs. Reports showed that about 17% of the total bridge failures caused by fire are concrete bridges [1]. Regarding its consequence, literature shows that the fire of the MacArthur Maze costs around \$90 million [2]. Most of the investigation into the influence of fire on bridge focuses on composite bridges [3-5]. Owing to the enormous expenses needed in a fire test of real bridge members and the difficulty to monitor the responses of a bridge during fire, there has been relatively little experimental or field data on the response of a bridge exposed to fire.

Fire tests on prestressed building component or structures have been carried out. For example, tests on prestressed concrete beams of tee section exposed to ASTM E119 standard fire curve were conducted by Gustafarro et al. [6]. The response of continuous prestressed concrete beams of rectangular section under ISO 834 standard fire was investigated to study the influence of several critical variables [7]. While these tests provide us better understanding of their performance during fire, these experimental data cannot be directly applied to predict the response of a bridge girder exposed to fire because of the different section types generally adopted in bridge design and the more severe fire conditions that bridges may encounter.

To investigate the response of a post-tensioned concrete bridge girder exposed to simulated hydrocarbon fire, tests on six scaled specimens were conducted to study the effect of section type,

¹ PhD student. Department of Civil Engineering, The University of Hong Kong, Hong Kong, China.
e-mail: wuxiqiang1988@gmail.com

² Professor and Head. Department of Civil Engineering, The University of Hong Kong, Hong Kong, China.
e-mail: francis.au@hku.hk

³ Associate professor. School of Civil Engineering and Transportation, South China University of Technology, Guangzhou, China
e-mail: cvjingli@scut.edu.cn

fire exposure time and loading level on the fire resistance of post-tensioned concrete beams and to provide guidance for the prediction of behaviour of bridges exposed to fire.

2 FIRE EXPERIMENT

Six bridge beams labelled as S1 and F1 to F5 were fabricated. Among them, Specimen S1 and F1-F3 were of box sections, while Specimens F4 and F5 were of tee sections. Specimen S1 was tested at the ambient temperature to provide information on the reference load-carrying capacity. Specimen F1 was exposed to fire until collapse and hence could be taken as another reference case. Specimen F2 was loaded after cooling down from a 1.5-hour fire exposure. F3 was loaded to a higher level of loading and then exposed to fire until collapse. Specimens F4 and F5 of tee sections were similar to Specimens F1 and F2 respectively. Details of the test parameters are shown in *Table 1*.

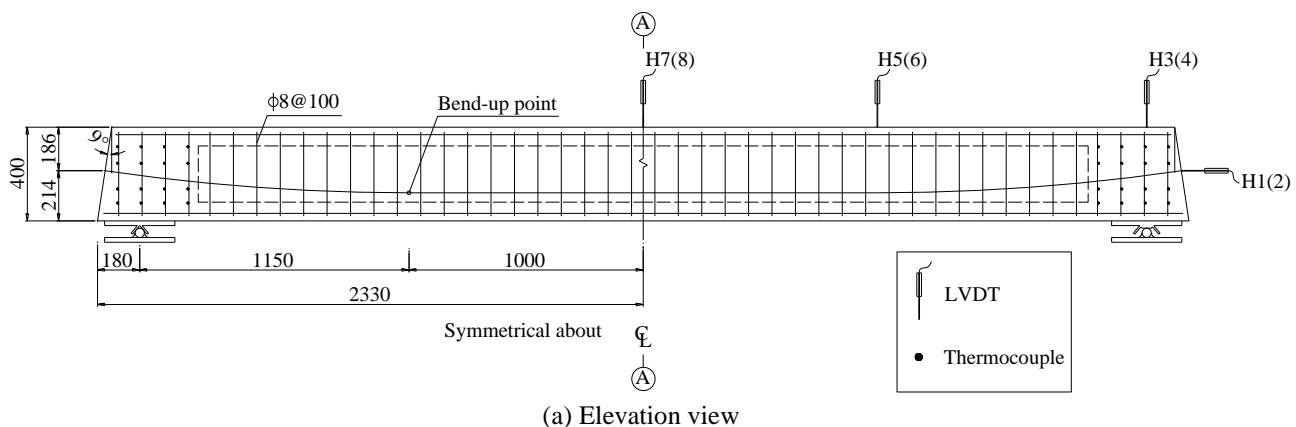
Table 1. Key parameters and test results

Specimens	Section type	Loading level (kN)	Exposure time (min)	Load-carrying capacity (kN)	Extent of spalling
S1	Box	410	0	400	--
F1	Box	160	184	--	severe
F2	Box	160	60	355	moderate
F3	Box	240	147	--	severe
F4	Tee	60	105	--	severe
F5	Tee	60	60	115	severe

2.1 Test specimens

Two commonly used types of bridge girder, i.e. box section and tee section, were simplified and adopted in the specimens. All specimens were designed as fully prestressed concrete beams. The span of the specimen was limited by the internal dimensions of the furnace. The depth of specimen was determined based on a span-depth ratio of 10. All specimens were 4600 mm in length and 400 mm in depth. The concrete cover to reinforcement was 20 mm. The detailed dimensions of the specimens are shown in *Fig. 1*.

Ready-mixed self-consolidating concrete of grade C50 was used in the fabrication of specimens. Concrete cores were taken from the specimens to measure the moisture content. Grade 335 deformed reinforcing bars 8 mm in diameter were used. High-strength steel strands of nominal diameters 15.2 mm and 12.7 mm were used in specimens of box section and tee section respectively. The design effective stress of prestressing strand was 60% of its ultimate strength of 1860 MPa. After post-tensioning, cement grout of water-cement ratio in weight of 0.45 was injected into the ducts.



Composite structures

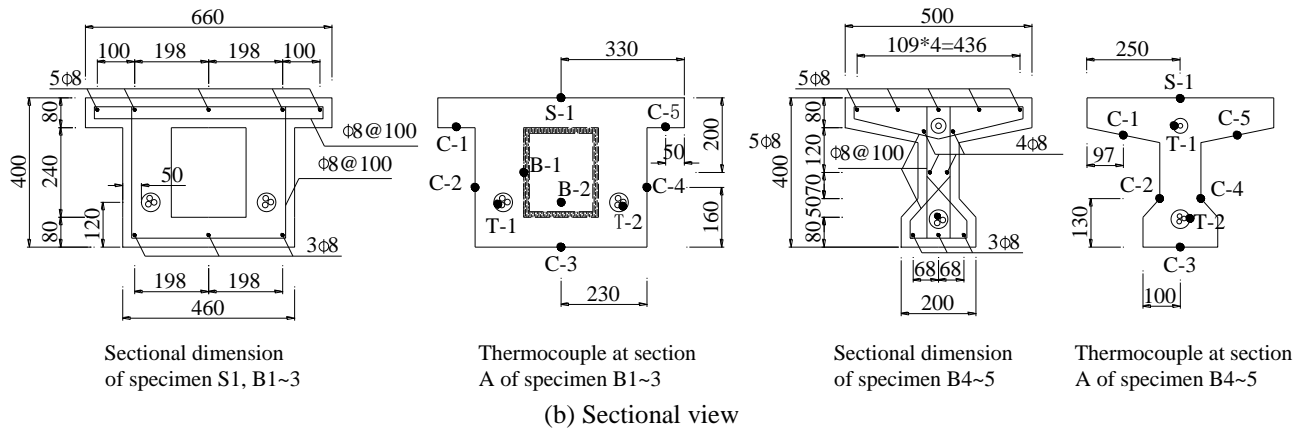


Fig. 1. Dimensions of specimen (unit: mm) and layout of LVDTs and thermocouples

2.2 Testing instrumentation

The furnace shown in Fig. 2 allowed the simultaneous or sequential application of loading and heating. The loading system comprised a steel loading frame and a 500 kN hydraulic jack. The internal space of furnace was 1.8 m in height, 3.0 m in width and 4.0 m in length. Twelve natural gas burners were mounted within the furnace for heating. In this study, specimens were exposed to heating according to the hydrocarbon curve [8] to simulate the fire caused by a petroleum tanker truck [9].

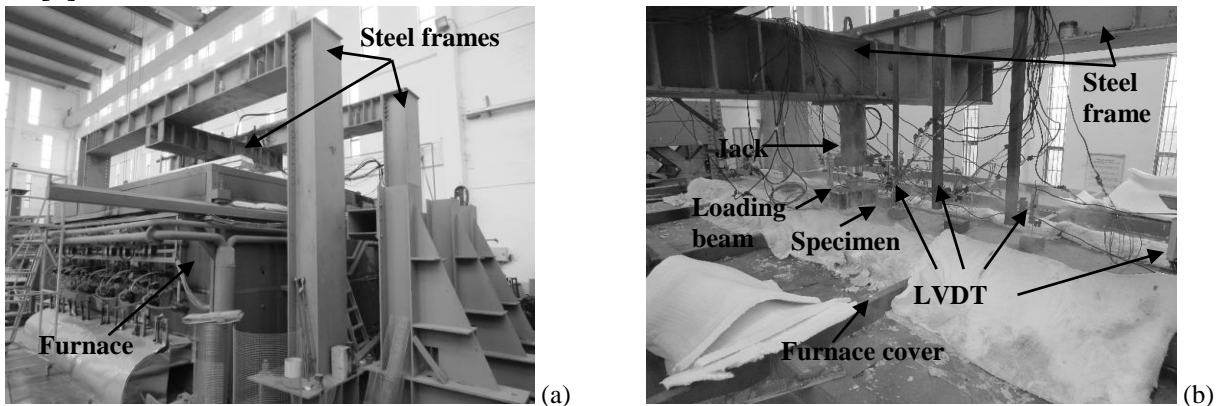


Fig. 2. Setup of experiment. (a) Testing furnace; (b) Loading system and instrumentation

Strain gauges were provided at the soffit of specimen to monitor the local strain development. Linear variable differential transformers (LVDTs) and thermocouples were used to record the deflections of specimen and the temperatures inside the specimen respectively at selected locations. The arrangement of instrumentation is shown in Fig. 1.

2.3 Testing procedure

To simulate the stress state of fully prestressed concrete bridges under service load, no cracking should have been formed before the specimens were exposed to fire. Results of static loading test shown in Fig. 3 indicate that the cracking load is about 180 kN for specimens of box section, which agrees well with results of manual calculation based on BS EN1992-1-1 [10]. The cracking load of tee sectional specimens was evaluated by the same method to be 78 kN. The applied loads were chosen to be slightly smaller than the calculated cracking loads, with those for Specimens F1 and F2 for box section and Specimens F4 and F5 taken to be 160 kN and 60 kN respectively. According to the strains shown in Fig. 3, these specimens were uncracked before exposure to fire. Specimen F3 was purposely loaded to a higher value of 240 kN to simulate the response of a bridge under heavy vehicle loading causing initial cracking and then exposed to fire.

All the specimens were simply supported and loaded at mid-span. The load was applied 15 minutes prior to the start of fire and was maintained constant throughout the subsequent fire test. For the tests on Specimens F2 and F5, fire was terminated after a 1.5-hour fire exposure and afterwards the specimens were left to cool down naturally to ambient temperature. An increasing load was subsequently applied on these specimens to investigate the residual load-carrying capacity.

For the tests on Specimens F1, F3 and F4, fire was ceased when the ratio of deflection (unit mm/min) exceeds $L^2/9000 d$, where L is the span length and d is distance from the extreme fibre of the design compression zone to the extreme fibre of the design tensile zone of the structural section [11]. LVDTs were set zero before ignition. The temperatures and deflections at various locations were continuously measured during the fire test.

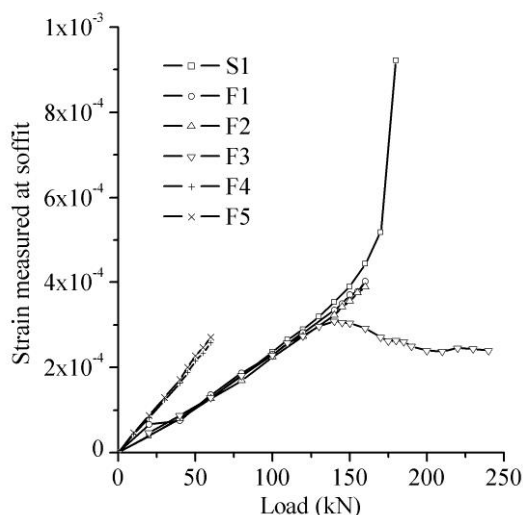


Fig. 3. Strains at soffit prior to fire exposure

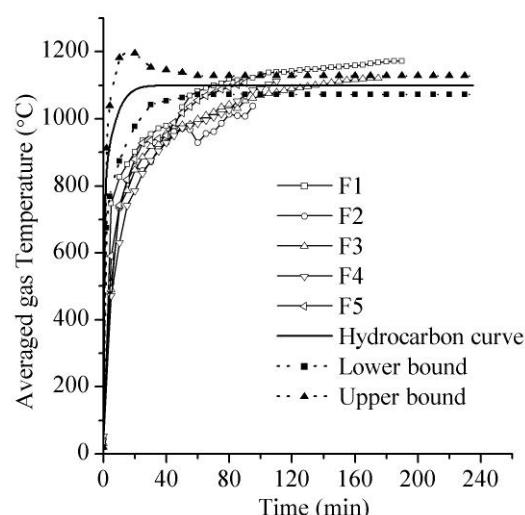


Fig. 4. Variations of average gas temperature with time

3 TEST RESULTS AND DISCUSSION

3.1 Observations

Emissions of noise and water vapour were observed during the fire tests. These phenomena occurred to almost all the fire tests at the similar time after ignition. Gentle noise was continuously heard from the beginning of each fire test. This sound might have come from concrete spalling at the soffit. The phenomenon of water evaporation was similar to that in the previous tests conducted by other researchers [7]. Water vapour was observed to be emitted from the gap between the specimen and furnace cover about 3 to 5 minutes after ignition. With further heating, the free water in concrete either vaporized or escaped from the heated surface to the inner layer. After 40 minutes, no further emission of water vapour was observed. Liquid water oozed out from the anchorage 17 minutes after ignition, which could be attributed to water evaporation in the prestressing duct.

3.2 Thermal responses

The gas temperature inside the furnace was programmed to follow the hydrocarbon curve. Fig. 4 shows the average temperature measured by thermocouples mounted on the wall of the furnace. Owing to various limitations of the furnace, the real temperatures were slightly lower than those specified until 100 minutes after ignition. The measured temperatures of concrete near the soffit of both top and bottom flanges and the outside surface of web are shown in Fig. 5. The temperatures at these locations were lower than the corresponding gas temperatures shown in Fig. 4 because the thermocouples were embedded in concrete 2 mm from the surface. Fig. 5 shows the results of Specimens F1-F3, in which the temperature curves can be divided into three groups: the highest temperatures at the soffit of bottom flange, the moderate temperatures at the outside surface of web and the lowest temperatures at the soffit of top flange. Those faces with lower temperatures were

limited because of indirect heating through radiation and convection. The temperature at the soffit of bottom flange of Specimen F1 was much higher than the rest because of severe concrete spalling at the location.

The temperatures of prestressing strand are plotted in *Fig. 6*. The temperature curves for different locations of strand in duct of the same specimen are almost the same as each other. There is an apparent plateau at about 100-140 °C. This was apparently caused by water evaporation in the grout and the high thermal inertia of concrete, which slowed down the heat transfer to the inner part of concrete.

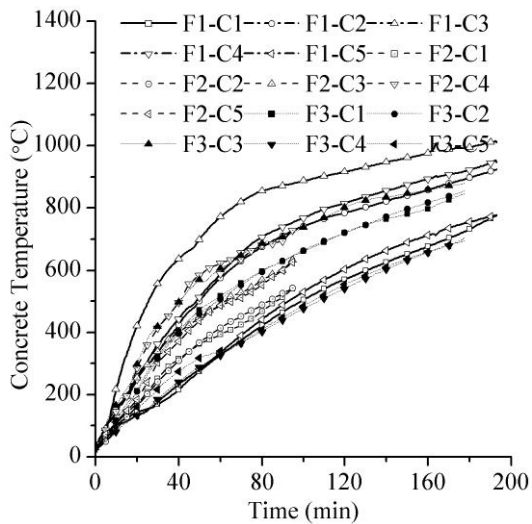


Fig. 5. Temperatures of concrete of Specimens F1-F3

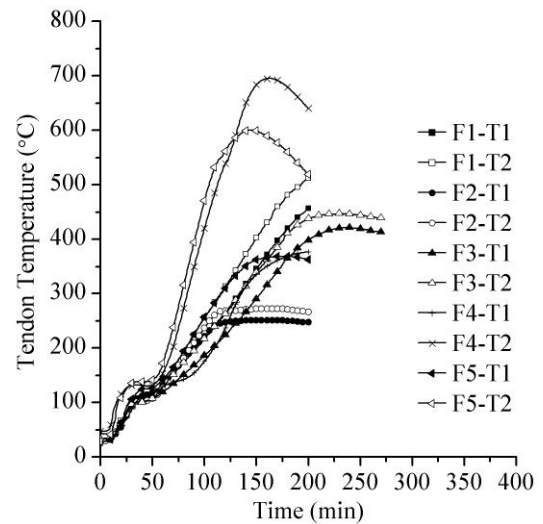


Fig. 6. Temperatures of strands

3.3 Structural responses

The structural responses during fire can be illustrated by the measured mid-span deflections. Fire tests on Specimens F1 and F4 were conducted to study the fire resistance. Most of the mid-span deflection curves illustrated in *Fig. 8* show three distinct phases: initial rapid increase, gradual increase and accelerating increase. A rapidly developed downward deflection (around 15mm) was observed around 30 minutes after ignition, primarily because of the high thermal gradient and the resulting differential thermal expansion across the section depth of a specimen [7, 12]. With the further increase of fire exposure time, the ratio of deflection gradually decreased, which can be principally attributed to the combined effects of multiple factors [13]. Then prior to the failure of specimen, the deflection showed a distinct increase again when the temperature of strand approached 350 °C. The loss of prestress and mechanical degradation could have dominated this phase. Specimens F1 and F4 finally failed 184 minutes and 105 minutes after ignition respectively. While the deflection curves of Specimens F1 and F3 have almost the same trend, their values of deflection and fire resistance period differ, which is mainly due to the prior cracking of Specimen F3 under heavier loading before exposure to fire. The cracks not only lowered the integral stiffness of the beam, but also accelerated the heat penetration to the interior concrete and prestressing strands. Specimen F3 failed 147 minutes after ignition.

The effect of fire exposure time on the structural response can be explained by reviewing the deflections of Specimens F2 and S1 shown in *Fig. 9*. Heating of specimen was terminated after exposure to fire for 1.5 hours. Specimen F2 was then left to cool down naturally to the ambient temperature, during which period the loads on the specimen were kept almost constant. Reloading of specimen F2 showed that even though the stiffness was not affected much, 12% of the load-carrying capacity had lost.

Specimen F5 was also exposed to fire for 1.5 hours, but it did not rebound after termination of fire test. Instead, the deflection continued to increase, and finally it almost failed. The deflection curve of Specimen F5 largely coincides with that of Specimen F4. This can be explained by the continual increase of temperature in prestressing strand. As shown in *Fig. 6*, the temperature curve of the lower strand of Specimen F5 almost matches with that of Specimen F4 even after termination of fire test of Specimen F5. After attaining a high temperature, the lower strand of Specimen F5 yielded, resulting in the crushing of concrete at the top and bringing it close to collapse. Load was applied on Specimen F5 after cooling down. As shown in *Fig. 9*, 20% of load-carrying capacity at the ambient temperature (143kN as calculated) was lost due to fire exposure.

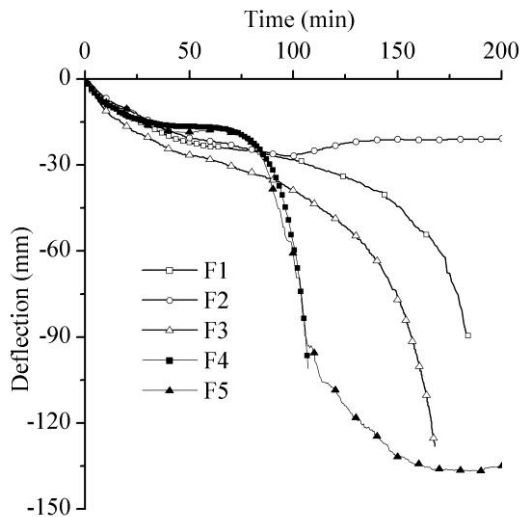


Fig. 8. Mid-span deflections during test

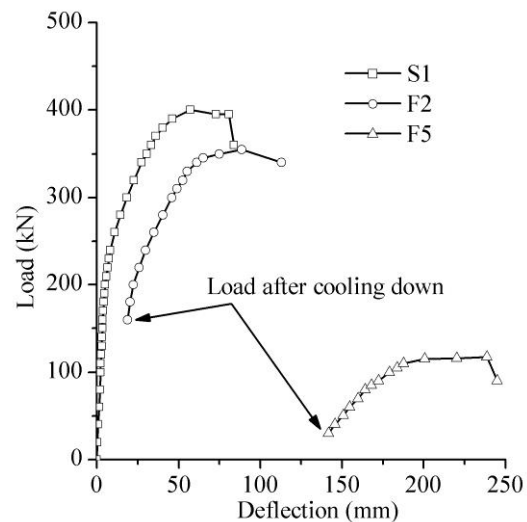


Fig. 9. Load-deflection curves

3.4 Post-fire evaluation

Post-fire evaluation was conducted mainly focusing on the occurrence of cracking, failure mode and spalling pattern. *Fig. 10* shows the typical vertical flexural cracks near the mid-span in the test of Specimen F1. These cracks originated from the bottom flange and extended to the top flange. Immediately after a loud noise possibly indicating the fracture of strand, the concrete adjacent to loading beam was crushed and the specimen failed. Thermal contraction cracks appeared on the side surfaces upon cooling down (*Fig. 11*) and they were distributed along the beam and aligned with the stirrups. This is mainly attributed to that at temperature 200-650 °C, the thermal expansion coefficient of concrete is larger than that of steel [14], and this disparity leads to the accumulation of tensile stress in concrete surrounding the transverse reinforcement during the cooling stage.

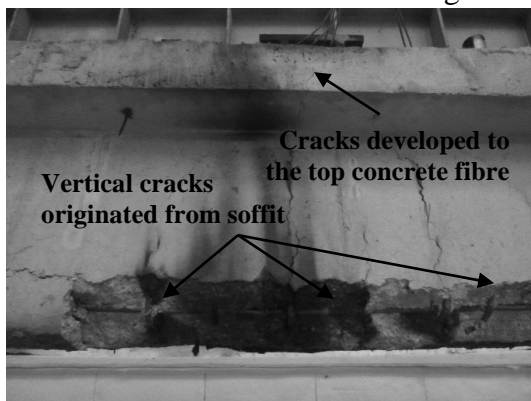


Fig. 10. Flexural cracks near mid-span

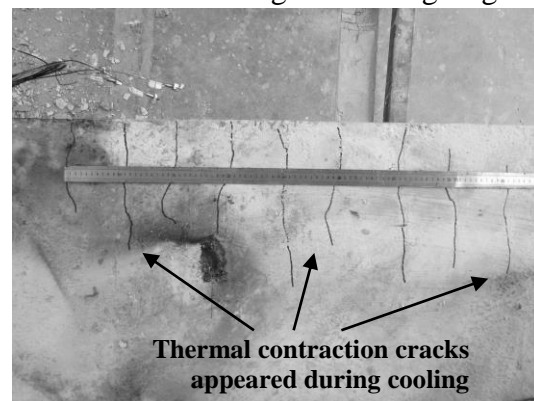


Fig. 11. Thermal contraction cracks

Concrete spalling is often observed in fire tests, but up to date no simple model is capable of predicting the extent of spalling accurately due to the complexity of this phenomenon [15]. It is

generally accepted that spalling can be induced by pore pressure or thermal dilation. The spalling phenomena observed in the tests appeared to be consistent.

As shown in *Fig. 12(a)*, severe spalling occurred to Specimen F1. Most areas of the soffit and corners of bottom flange were spalled. The severe spalling can be attributed to the high moisture content of 4.0%. Large area of spalling reached the outermost layer of reinforcement [16]. The most severe spalling happened to the region nearing the support, where the thickest layer of spalling could be 60 mm. The spalling pattern of Specimens F4 and F5 as shown in *Fig. 12(d)* are similar to that of Specimen F1. The spalling in certain area at the top flange was due to the flame coming out from the furnace through gaps between covers.

Severe spalling of Specimen F2 as shown in *Fig. 12(b)* was also observed throughout the region within 1.5 m from the support, while only small chunks of concrete spalled in the region near the mid-span. The spalling pattern of Specimen F3 as shown in *Fig. 12(c)* is similar to that of Specimen F2. For Specimen F3, owing to the high loading, the concrete at the soffit near the mid-span had cracked before being exposed to fire. These cracks not only reduced the compressive stresses resulting from thermal dilation, but also relieved the pore pressure through emission of steam.

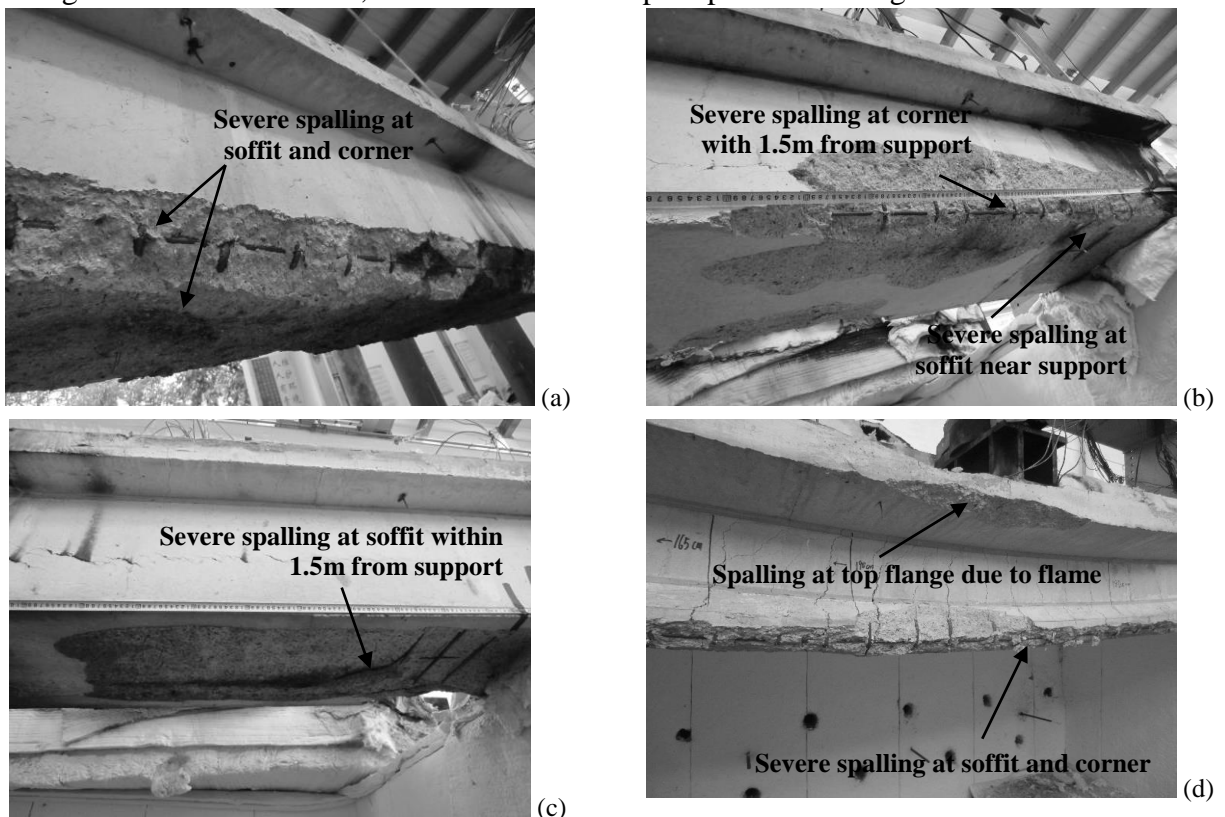


Fig. 12. Spalling pattern of specimen. (a) F1; (b) F2; (c) F3; (d) F4 and F5.

4 CONCLUSIONS

Fire tests were carried out in this study to evaluate the possible effects of heating according to the hydrocarbon curve on the response of prestressed concrete bridge beams. Based on the experimental results, the following conclusions can be drawn:

- Prestressed concrete box beam with tendons with concrete cover of 75 mm can sustain for about three hours in hydrocarbon fire.
- The effect of loading level is significant in respect of both fire resistance period and structural response. Higher loading leads to not only a reduction of fire resistance period but also larger deflections during fire.

- After a limited fire exposure period, the integral stiffness of structural member may not be affected too much, but a certain amount of load-carrying capacity may be lost.
- Heating still continues to penetrate to the interior of a structural member after the fire is put out, which may elevate the temperature of strands and may reduce the safety margin.
- Severe spalling will be induced in a prestressed concrete member having a high moisture content when exposed to a drastic fire. However, cracking caused by higher level of loading can relieve the pore pressure and compression due to thermal dilation, which may lessen the degree of spalling.

REFERENCES

1. Wardhana Kumalasari and Fabian C Hadipriono (2003). *Analysis of recent bridge failures in the United States*. Journal of Performance of Constructed Facilities, 17(3): pp. 144-150.
2. Giuliani Luisa, C Crosti and F Gentili (2012). Vulnerability of bridges to fire. *Proceedings of the 6th International Conference on Bridge Maintenance, Safety and Management*, 2012: pp. 8-12.
3. Choi Joonho, Rami Haj-Ali and Hee Sun Kim (2012). *Integrated fire dynamic and thermomechanical modeling of a bridge under fire*. Structural Engineering and Mechanics, 42(6): pp. 815-829.
4. Jose Alos-Moya, Ignacio Paya-Zaforteza, Maria Garlock, Eduardo Loma-Ossorio, et al. (2014). *Analysis of a bridge failure due to fire using computational fluid dynamics and finite element models*. Engineering Structures, 68: pp. 96-110.
5. Gong Xu and Anil K. Agrawal (2014). *Numerical Simulation of Fire Damage to a Long-Span Truss Bridge*. Journal of Bridge Engineering: pp. 04014109.
6. Gustaferro Armand H, Melvin S Abrams and EA Salse (1971). *Fire resistance of prestressed concrete beams-study C: structural behavior during fire tests*. Portland Cement Association R & D Lab Bulletin.
7. Xiaomeng Hou, Venkatesh Kodur and Wenzhong Zheng (2015). *Factors governing the fire response of bonded prestressed concrete continuous beams*. Materials and Structures, 48(9): pp. 2885-2900.
8. BS EN 1991-1-2, *Eurocode 1: Actions on structures - Part 1-2: General Actions — Actions on structures exposed to fire*. British Standard Institution, London, UK, 2002.
9. Garlock Maria, Ignacio Paya-Zaforteza, Venkatesh Kodur and Li Gu (2012). *Fire hazard in bridges: Review, assessment and repair strategies*. Engineering Structures, 35: pp. 89-98.
10. BS EN 1992-1-1, *Eurocode 2: Design of concrete structures - Part 1-1: General rules and rules for buildings*. British Standard Institution, London, UK, 2004.
11. International Standard ISO 834-1-1999(E) (1999). *Fire-resistance tests - Elements of building construction - Part 1: general requirement*.
12. Monther Dwaikat and Venkatesh Kodur (2009). *Response of Restrained Concrete Beams under Design Fire Exposure*. Journal of Structural Engineering - ASCE, 135(11): pp. 1408-1417.
13. Gales John, Kathleen Hartin and Luke Bisby, *Structural fire performance of contemporary post-tensioned concrete construction*. 2015: Springer.
14. BS EN 1992-1-2, *Eurocode 2: Design of concrete structures - Part 1-2: General rules - Structural fire design*. British Standard Institution, London, UK, 2004.
15. Venkatesh Kodur. Spalling in high strength concrete exposed to fire: concerns, causes, critical parameters and cures. *Advanced Technology in Structural Engineering*. 2000. pp. 1-9.
16. Venkatesh Kodur and Monther Dwaikat (2007). *Performance-based fire safety design of reinforced concrete beams*. Journal of Fire Protection Engineering, 17(4): pp. 293-320.

FIRE BEHAVIOUR OF STEEL REINFORCED CONCRETE FILLED STAINLESS STEEL TUBULAR (SRCFSST) COLUMNS WITH SQUARE HOLLOW SECTION

Qinghua Tan¹, Leroy Gardner², Bin Chen³, Linhai Han⁴, Yaoyuan Zhang⁵

ABSTRACT

Steel reinforced concrete filled stainless steel tubular (SRCFSST) columns is an effective way to decrease the amount of stainless steel and in the meantime improve the fire resistance and ductility of concrete-filled stainless steel tubular (CFSST) columns by splitting the same total cross-sectional area of steel into two parts, i.e., the outer stainless steel tube and the embedded inner carbon steel profile. Although SRCFSST columns with circular hollow section have better confinement than those with square hollow section, the latter have more convenient joint details and decoration. Fire behaviour of SRCFSST columns with square hollow section has yet to be investigated. The behaviour of SRCFSST columns under the ISO 843-1 standard fire is investigated by finite element (FE) analysis in this paper. On the basis of the validated FE models, the working mechanisms of a full-scale SRCFSST column with square hollow section under fire are illustrated by analysis of the temperature field, failure modes, axial deformation versus time response and internal forces redistribution and in the mean time the excellent fire performance of SRCFSST columns is examined in comparison with a CFST column with equivalent sectional load-bearing capacity at ambient temperature and a CFSST column with the same total cross-sectional area of steel. It is found that for the studied SRCFSST column, the outer stainless steel tube and the contact conductance of the interface delays the process of the heat transfer to the concrete and the inner steel profile, and the encased profile plays an important part in improving the fire resistance of the SRCFSST columns.

Keywords: Steel reinforced concrete filled stainless steel tubular (SRCFSST) column, fire resistance, finite element (FE) models, fire safety engineering

1 INTRODUCTION

Concrete-filled stainless steel tubular (CFSST) columns combine the advantages of concrete-filled steel tubular (CFST) columns and stainless steel, which have greater corrosion resistance, enhanced ductility and improved fire resistance [1-3]. However, as a result of the high initial cost of stainless steel, the initial cost of CFSST columns is higher than that of CFST columns for a given load-

¹ Lecturer. Department of Material Science and Engineering, National University of Defense Technology, P.R. China.
e-mail: tanqinghua@nudt.edu.cn

² Professor. Department of Civil and Environmental Engineering, Imperial College London, UK.
e-mail: leroy.gardner@imperial.ac.uk

³ Professor. Department of Applied Mechanics, National University of Defense Technology, P.R. China.
e-mail: chenbin_gfkd@sina.com

⁴ Professor. Department of Civil Engineering, Tsinghua University, P.R. China.
e-mail: lhhan@tsinghua.edu.cn

⁵ Master Degree Candidate. Department of Civil and Environmental Engineering, Imperial College London, UK.
e-mail: yyzhang16@imperial.ac.uk

bearing capacity which limits its wide application in engineering structures. One of the way to solve the problem is that splitting the same total cross-sectional area of steel into two parts, i.e. the outer stainless steel tube and the embedded inner carbon steel profile. The composite column is called as steel reinforced concrete filled stainless steel tubular (SRCFSST) column, which combines the advantages of CFSST columns and steel reinforced concrete (SRC) columns. Compared with CFSST column, SRCFSST column has fewer amounts of stainless steel and better integrity, ductility and fire performance as a result of the encased profile.

Fire is regarded as a significant hazard during life-cycle of a structure, and it is a regulatory requirement of any building design to maintain structural integrity during fire attack. Recently, some research has been devoted to focusing on the fire resistance of CFSST columns. Han et al. [2] tested five axially-loaded CFSST columns at elevated temperature, and an finite element (FE) model was then validated against the test results. The parametric analysis shows that the section type, section size, slenderness ratio and load level are critical parameters. Tao and Ghannam [4] employed FE modelling to determine the temperature field in CFST and CFSST columns. Tao et al. [3] conducted an experimental and analytical investigation of 12 CFSST columns in fire and after fire exposure. An FE model was also established and shown to be able to replicate the experimental results with reasonable accuracy. Overall, CFSST columns have been showed to offer fire performance over CFST columns due to the greater ductility and favourable thermal characteristics of stainless steel.

Similarly, SRCFSST columns are expected to show excellent ductility and fire performance. Tan et al. [5] established a finite element (FE) model to explore the performance of SRCFSST columns at elevated temperature. The results show that the encased profile plays an important role in enhancing the fire resistance of SRCFSST column and the outer tube and inner steel profile of SRCFSST columns need to be carefully chosen to find the optimal balance between room temperature and fire performance. However, the results conducted by Tan et al. [5] focused on the working mechanism of SRCFSST columns with circular hollow section at elevated temperature. Although SRCFSST columns with circular hollow section have better confinement than those with square hollow section, the latter have more convenient joint details and decoration. Fire behaviour of SRCFSST columns with square hollow section has yet to be investigated.

In this paper, the performance of SRCFSST columns with square hollow section at elevated temperature is studied by FE analysis. On basis of the validated FE models in [5], the behavioural mechanisms of SRCFSST columns with square hollow section under fire are explained and compared with a CFST column with equivalent sectional load-bearing capacity at ambient temperature and a CFSST column with the same total cross-sectional area of steel. The temperature field, failure modes, axial deformation versus time response and internal forces redistribution of the three kinds of composite columns are analysed.

2 BRIEF INTRODUCTION OF FE MODELS AND ANALYSIS CONDITIONS

On the basis of the finite element package ABAQUS [6], FE models for SRCFSST columns under fire are developed and validated comprehensively by Tan et al. [5]. In this paper, the FE modelling reported in [5], including the material properties, interfaces, meshing, boundary conditions and initial imperfection, is employed to perform mechanical analysis of SRCFSST columns with square hollow section under fire conditions. Meshing and boundary conditions of the FE models for SRCFSST column with square hollow section are shown in *Fig. 1*.

In order to evaluate the fire performance of SRCFSST columns as well as to quantify the advantages of SRCFSST columns over CFSST and CFST columns, the structural behaviour and failure mechanism of SRCFSST columns at elevated temperatures were examined by comparisons with a CFSST column with the same total cross-sectional area of steel and a CFST column with the same axial load-bearing capacity at room temperature. As the SRCFSST and CFSST columns have not been used in the practical engineering, an initial CFST column with square section of 800 mm ×

16.0 mm (marked as CFST-16), used in a practical engineering application in China reported by Han [7], was chosen as a reference section. The SRCFSST column has the same axial load-bearing capacity at room temperature of the CFST column with a square stainless tube (788 mm×10 mm), and an embedded carbon steel profile (600 mm × 300 mm × 29.6 mm × 29.6 mm), marked as SRCFSST-LC-10. The CFSST column has the same total cross-sectional area of steel of the reference CFST column with a square stainless steel tube (800 mm×16 mm), marked as CFSST-16.

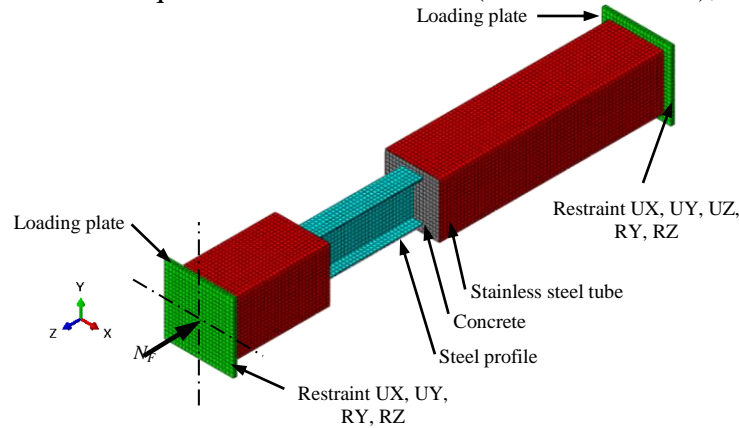


Fig. 1. Meshing and boundary conditions of the FE models

The cube compressive strength and elastic modulus of the in-filled concrete are 60 MPa and 3.6×10^4 N/mm², respectively. The outer tube is formed from Grade S304 austenitic stainless steel, which is specified in CECS 410: 2015 [8] to have a 0.2% proof strength ($\sigma_{0.2}$) and ultimate strength (σ_u) of 205 MPa and 515 MPa, respectively. The yield stress and elastic modulus of the embedded H-shaped carbon steel profile, and the outer tube for the CFST sections, are 345 MPa and 2.05×10^5 N/mm², respectively.

For comparison purposes, all the columns have a height (H) of 6400 mm with pinned-pinned boundary conditions at the two ends. All the load ratio applied on the three kinds of the composite columns are 0.4, calculated as $n = N_F/N_u$, where N_F and N_u are the axial load applied to the columns and the bearing capacity of the composite columns at ambient temperature, respectively. N_u can be determined according to EN 1994-1-1: 2004 [9]. The composite columns with square hollow section are heated on the outer four surfaces of steel tube along the whole length and the temperature of heated air evenly follows the ISO 834-1 standard fire [10].

3 WORKING MECHANISM ANALYSIS

In this section, the temperature field, failure modes, axial deformation versus time response and internal forces of the three kinds of composite columns are analyzed and compared.

3.1 Temperature history

Temperature (T) versus time (t) curves for the modelled specimens are shown in Fig. 2. The following points are monitored: two interfacial points (point 1 at the inner surface of the tube, and point 2 at the surface of the in-filled concrete), two points for in-filled concrete (point 3 at the quarter of width and point 4 at the centroid of the in-filled concrete), and two points on the embedded steel profile (point 5 at the midpoint of web and point 6 at the edge of the flange).

For the interfacial temperature at points 1 and 2, it can be found that the temperature of point 1 at the inner surface of the tube is higher than that at point 2 at the surface of the in-filled concrete, with a maximum difference of up to 150 °C for the CFST column, 214 °C for the CFSST column and 249 °C for the SRCFSST column, and point 1 at the inner surface of the stainless steel tube is higher than that of the carbon steel tube. This is because the heat conductance of the interface is included in the FE models and the heat conductance between carbon steel and concrete is higher than that of stainless steel [2, 3]; and the thermal conductivity of stainless steel is lower than that of

carbon steel below 800 °C, therefore more heat is used to warm the stainless steel tube under the same conditions.

For the temperature of in-filled concrete, the temperatures at the points 3 and 4 nearly keep the same as the ambient temperature during the whole heating process as a results of the protection of the outer concrete layer. For the profile temperatures at points 5 and 6 shown in *Fig. 2(c)*, the temperatures of the embedded profile are less than 125 °C due to the protection of the stainless steel tube and the in-filled concrete, which means that the steel profile maintains almost its full strength and bears more load, transferred from the degraded concrete and stainless steel tube at elevated temperatures. Additionally, the predicted curves for points 2, 3 and 4 in the concrete appear to have a platform at 100~200 °C. The results shows that the increase in the specific heat of the concrete between 100 °C and 200 °C can capture the characteristic of the water in the concrete evaporating at approximately 100 °C.

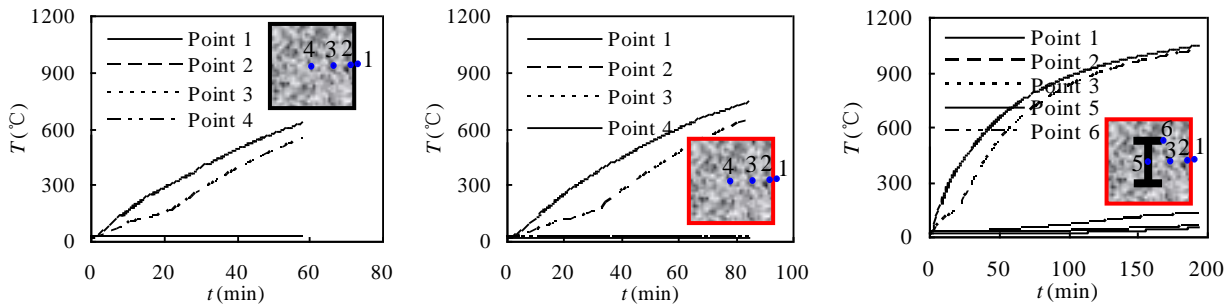


Fig. 2. Temperature (T) versus time (t) curves of the composite columns: a) CFST-16; b) CFSST-SR-16; c) SRCFSST-LC-10

3.2 Failure modes

All the three kinds of steel–concrete composite columns fail with global lateral bending since the column is susceptible to global buckling (slenderness $\lambda=27.7$) with an initial imperfection of amplitude $H/2000$. The failure mode of the studied composite columns under fire is shown in *Fig. 3*.

Local buckling of steel tube along the whole length is also observed for all the three kinds of steel–concrete composite columns. The space and severity of local buckling for the CFST column is less than that for the CFSST column as the yield strength of stainless steel is lower than that of carbon steel and in the meantime the temperature of the stainless steel tube is higher than that of carbon steel. For the SRCFSST column, even local buckling is also observed along the whole length of the tube and the space is less than that of the CFSST column as the thickness of stainless tube for the former is less than that of the latter. Significant global lateral bending is also observed in the steel profile without obvious local buckling due to the restraint from the in-filled concrete.

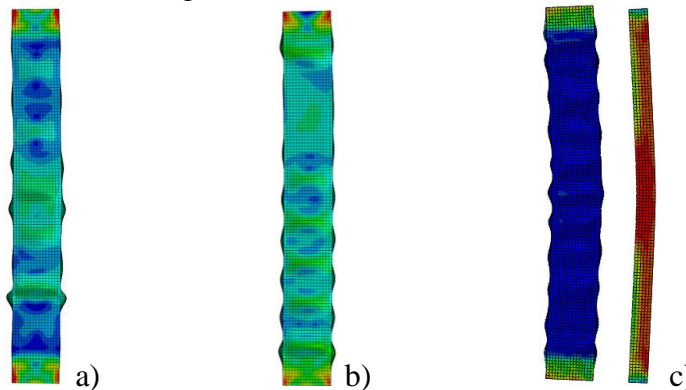


Fig. 3. Typical failure modes of the composite columns: a) CFST-16; b) CFSST-SR-16; c) SRCFSST-LC-10

It is concluded that the possible failure mode of SRCFSST columns with square hollow section at elevated temperature are similar to those of CFSST columns reported in Han et al. [2] and Tao et al. [3]. The fire resistance of the SRCFSST column is as high as 194 mins, which is 3.4 and 2.3 times as those of the CFST column and the CFSST column, respectively.

3.3 Axial deformation versus time curves

Fig. 4 shows the axial displacement (Δ) versus time (t) curve of the three kinds of steel–concrete composite columns at elevated temperature. The typical Δ – t curves of the composite columns can be divided into four characteristic stages, i.e.

1. Ambient loading stage (O-A). During this stage, the loads applied to the composite columns are increased linearly to the design load.
2. Expansion stage (A-B). During this stage, the loads on the composite columns remain constant, and the environmental temperature increases following the ISO 834-1 standard fire curve [10]. The materials of components expand and deteriorate simultaneously with the increasing of temperature. Generally, in this stage, the axial deformation related to thermal expansion is dominant over that due to material deterioration. Therefore, all the three kinds of the composite columns expand until the effects of materials expansion and degradation are balanced. The balance point is marked as point B in *Fig. 4* where the expansion displacement reaches its peak value and the expansion stage ends.

However, the magnitude of peak value is different for the three composite columns: those of the CFST and SRCFSST columns are the maximum and minimum ones, respectively, while that of the CFSST column lies between them. The expansion deformation of the composite columns is mainly caused by the outer tube as the increment of temperature for the outer tube is higher than that of the in-filled concrete as shown in *Fig. 2*. Therefore, the above difference can be explained by the different properties of stainless steel and carbon steel and proportions of the applied load carried by the outer tube of the composite columns: (a) temperature of the stainless steel tube for the CFSST and SRCFSST columns are greater than that of the carbon steel tube for the CFST column under the same fire condition as shown in *Fig. 2*; (b) yielding strength of stainless steel degrades remarkably compared with that of carbon steel below 600 °C; (c) proportion of the applied load carried by the outer carbon steel tube of the CFST column increase from 35.4% to 80.4%, from 34.1% to 46.4% for the outer stainless steel tube of the CFSST column and from 19.2% to 22.8% for the outer stainless steel tube of the SRCFSST column as shown in *Fig. 5*.

3. Softening stage (B-C). During this stage, the applied load is still kept constant and the temperature is increased further following the ISO 834-1 standard fire curve [10]. As the material temperature increases, the contractive deformation due to the material degradation under high temperature becomes dominant. The total axial deformation of the column changes from expansion to contraction. The contraction increases gradually as the material is heated and deteriorates further, while the lateral deflection of the column also starts to rise. The softening stage ends at point C. In this stage, the slope of contraction for the three composite columns shows different trends: contraction of the CFST column increases sharply and that of the SRCFSST column increases slowly, while that of the CFSST column lies between them. The above difference can be explained as follows: (a) yielding strength of carbon steel degrades remarkably compared with that of stainless steel above 600 °C; (b) the profile of the SRCFSST column plays a significant part in load-carrying as described in Section 3.4.
4. Accelerated failure stage (C-D). In this stage, the second-order effect induced by the axial force and the lateral deformation becomes dominant; as a result, the axial deformation of the three composite columns increase sharply and the columns fail when the maximum axial contraction or the rate of contraction reach the failure criteria specified in ISO-834-1 [10].

When the load ratio of the column exceeds 0.4, the axial expansion becomes very small, even non-existent in the composite columns because the contractive deformation induced by the axial load and material degradation dominate over the effect of thermal expansion. In this case, the Δ - t curve only contains three stages, i.e. the ambient loading stage, the softening stage and the accelerated failure stage.

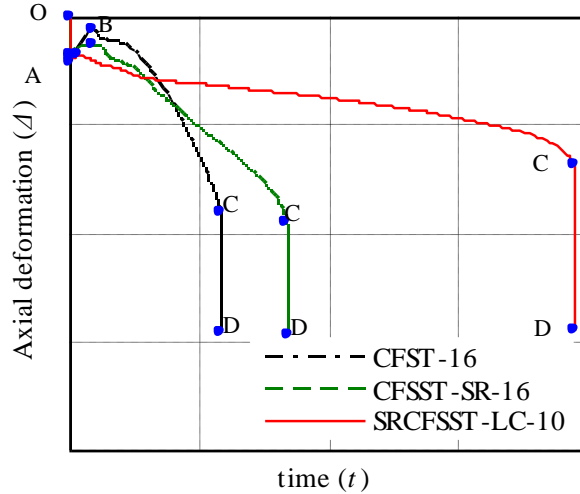


Fig. 4. Typical axial deformation (Δ) versus time (t) curves of the composite columns

3.4 Internal forces redistribution at the mid-span section

The three composite columns are composed of the outer stainless steel (carbon steel) tube, the in-filled concrete and the embedded carbon steel profile, and the external load is borne by the two or three components. At ambient temperature, the loads are borne by the two or three components according to their axial stiffness. However, in fire, the properties of the constituent material degrade as the temperature rises, and the relative axial stiffness of the constituent components change. Therefore, for a constant external load, the section internal forces of an column redistribute among the two or three components as the environment temperature increases. To examine the internal force redistribution in the three composite columns during the ambient temperature and heating phases, the proportions of the applied load carried by the stainless steel (carbon steel) tube (p_t), the in-filled concrete (p_c) and the carbon steel profile (p_p) are extracted from the FE analysis, and the proportion versus time curves are shown in Fig. 5, in which points O, A, B, C and D correspond to the key points in Fig. 4. Positive and negative values of the proportion represent the specified part being in compression and tension, respectively. It can be seen from Fig. 5 that:

1. Ambient loading stage (O-A). The two or three components of the three composite columns are in compression at the end of the ambient temperature phase (point A), in which, $p_t=35.4\%$ and $p_c=64.6\%$ for the CFST column; $p_t=35.1\%$ and $p_c=64.9\%$ for the CFSST column; $p_t=19.2\%$, $p_c=59.1\%$ and $p_p=21.7\%$ for the SRCFSST column.
2. Expansive stage (A-B). At the beginning of the heating phase, the stainless steel and the outer layer of concrete are heated and their properties degrade; the thermal expansion deformation of steel tube is greater than that of in-filled concrete, and the longitudinal slip between steel tube and concrete results in a gap between the loading plate and in-filled concrete. Therefore, p_t increases with the increasing expansion deformation while the p_c and p_p decrease. At the end of expansion stage, p_t increases up to 80.4% for the CFST column, 46.4% for the CFSST column and 22.8% for the SRCFSST column.
3. Softening stage (B-C). As the material temperature increases, the contractive deformation due to the material degradation under high temperature becomes dominant. The stainless steel (carbon steel) and the outer layer of concrete are heated and their properties degrade dramatically; the corresponding loss of axial stiffness causes load to be transferred to the interior layer of

concrete and the embedded steel profile. Therefore, p_t decreases with the increasing contractive deformation while the p_c and p_p increase. It is shown in *Fig. 5* that at the end of softening stage, p_t decreases up to 16.3% for the CFST column and 15.7% for the CFSST column while p_c increases up to 83.7% for the CFST column and 84.3% for the CFSST column. For the SRCFSSST column, as the heating time increases, the temperature of the inner material layers including the concrete and the embedded steel profile increases, and the proportion of the load borne by the steel profile p_p increases from 20.6% to 61.5%, while the proportion of the load borne by the outer tube p_t decreases further from 22.8% to 1.0%.

4. Accelerated failure stage (C-D). As the temperature increases further, the proportion of the load borne by the outer tube reduces from 16.3% to 16.0% for the CFST column, from 15.7% to 15.1% for the CFSST column and from 1.0% to 0.4% for the SRCFSSST column, and the corresponding value of p_p increases from 61.5% to 68.4% for the SRCFSSST column.

In general, the proportion of the load borne by the outer tube p_t firstly increases as its thermal expansion deformation increases and then decreases as the strength and elastic modulus degrade for the three composite columns. When the composite columns fail with global lateral bending as shown in *Fig. 3*, the proportions of the load borne by the outer tube p_t are still around 1/6 for the CFST and CFSST columns, while p_t is nearly 0 for the SRCFSSST column. The corresponding loss of axial stiffness of the outer tube causes load to be transferred to the interior layer of concrete and the embedded steel profile. The embedded steel profile, which is thermally protected by the concrete, plays an important role in bearing the applied load with the proportion varying between 20.6% and 68.4%. Therefore, the SRCFSSST columns survive longer than the CFST and CFSST columns under the same fire conditions.

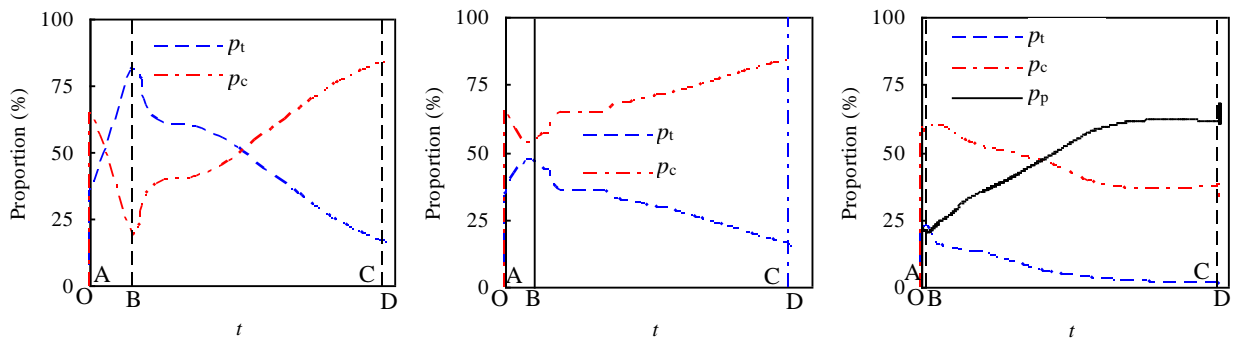


Fig. 5. Proportion of load borne by each component of the composite columns: a) CFST-16; b) CFSST-SR-16; c) SRCFSSST-LC-10

4 CONCLUSIONS

On the basis of the validated FE models, the working mechanisms of a full-scale SRCFSSST column with square hollow section under the ISO 834 standard fire curve was simulated and analysed by comparison with a CFST column with the same total cross-sectional area of steel and a CFSST column with equivalent sectional load-bearing capacity at ambient temperature. It was found that for the studied SRCFSSST column, the outer stainless steel tube and the contact conductance of the interface delays the process of the heat transfer to the concrete and the inner steel profile, and the encased profile plays an important part in improving the fire resistance of the SRCFSSST columns.

ACKNOWLEDGMENT

The research reported in the paper is part of the Project 51308539 supported by the National Natural Science Foundation of China. The financial support is highly appreciated.

REFERENCES

1. Gardner L (2005). *The use of stainless steel in structures*. Progress in Structural Engineering and Materials, 7. pp 45-55.
2. Han L H, Chen F, Liao F Y, Tao Z, Uy B (2013). *Fire performance of concrete filled stainless steel tubular columns*. Engineering Structures, 56. pp 165-181.
3. Tao Z, Mohamed G, Song T Y, Han L H (2016). *Experimental and numerical investigation of concrete-filled stainless steel columns exposed to fire*. Journal of Constructional Steel Research, 118. pp 120-134.
4. Tao Z, Mohamed G (2013). *Heat transfer in concrete-filled carbon and stainless steel tubes exposed to fire*. Fire Safety Journal, 161. pp 1-11.
5. Tan QH, Gardner L, Han LH (2017). *Performance of steel reinforced concrete filled stainless steel tubular columns at elevated temperature*. International Journal of Structural Stability and Dynamics, under review.
6. ABAQUS. (2014). *ABAQUS/Standard Version 6.14 User's Manual: Volumes I-III*. Dassault Systèmes Simulia Corp, Rhode Island, USA.
7. Han L H (2016). *Concrete filled steel tubular structures-theory and practice*. Science Press, Beijing, China. (in Chinese)
8. CECS 410: 2015. (2015). *Technical specification for stainless steel structures*. Beijing: China Planning Press. (In Chinese)
9. EN 1994-1-1: 2004. (2004). *Design of composite steel and concrete structures—Part 1-1: General rules and rules for buildings*. European committee for standardization, Brussels.
10. ISO 834-1 (1999). *Fire-resistance tests - elements of building construction - Part 1: General requirements*. International Standard ISO 834, Geneva.

BEHAVIOR OF CIRCULAR CONCRETE-FILLED DOUBLE-SKIN, DOUBLE-TUBE AND INNER CONCRETE RING TUBULAR COLUMNS SUBJECTED TO FIRE

Aline L. Camargo¹, João Paulo C. Rodrigues², Ricardo H. Fakury³, Tiago A. C. Pires⁴

ABSTRACT

The use of concrete filled hollow columns has increased in the last decades. This type of columns has several advantages, such as the exemption of formworks, high load bearing capacity and possibility of using smaller cross sections. Although it has a good behavior in fire, the use of slender columns and the increasing number of tall building's structures makes necessary to find solutions to ensure their fire resistance. In this sense, this paper presents a comparative experimental study on the behavior of circular concrete filled double-skin and double-tube and inner concrete ring hollow columns subjected to fire. The fire resistance tests were carried out in the Laboratory of Testing Materials and Structures of University of Coimbra, in Portugal. Several parameters that might have influence on the column's behavior have been investigated, such as the stiffness of the surrounding structure, the load level and the type of concrete filling. The paper presents the results of fire resistances, restraining forces, temperatures and critical times of the tested columns. As a main conclusion of this research an increasing of the stiffness of the surrounding structure leads to an increasing of the restraining forces and a reduction of the axial deformation of the columns, although this did not influence the critical times. The columns with inner concrete ring showed not to be a good construction solution since the concrete ring prematurely collapsed during the fire.

Keywords: double-skin, double-tube, inner concrete ring, composite columns, fire tests

1 INTRODUCTION

The use of concrete filled hollow columns is increasing due to several advantages, among them, the exemption of using formworks and its higher load bearing capacity. This fact allows using smaller cross sections, increasing the free space in the building and reducing the maintenance costs. In this type of columns, each material works optimally, while the steel tube has excellent structural properties and provides confinement to the concrete; the concrete core may increase the load bearing capacity and mitigates local buckling of the steel tube. It is also observed a higher fire resistance without using external fire protection and with this providing a cleaner and more pleasant aesthetic view of the column. Therefore, a concrete filled hollow column when well-designed leads to a good economic, constructive and architectural solution.

There are several researches on the behavior of concrete filled hollow columns in case of fire. The National Research Council of Canada (NRCC) in conjunction with the American Institute of Iron

¹PhD Student. Department of Structural Engineering, Federal University of Minas Gerais, Brazil.

e-mail: alinecamargo@dees.ufmg.br

²Professor. LAETA. Department of Civil Engineering, University of Coimbra, Portugal.

e-mail: jpaulocr@dec.uc.pt

³Professor. Department of Structural Engineering, Federal University of Minas Gerais, Brazil.

e-mail: fakury@dees.ufmg.br

⁴Professor. Department of Civil Engineering, Federal University of Pernambuco, Brazil.

e-mail: tacpires@yahoo.com.br

and Steel (AISI) carried out in the early 90's a series of tests in which investigated the influence of the cross-section type and dimensions, steel tube wall's thickness, concrete strength, aggregate type and load level on the fire resistance of this type of columns [1]. Also noteworthy are the tests performed by Han et al. (2003) [2] on protected and unprotected columns, where were tested the influence of parameters such as the cross-sectional dimensions, steel tube wall's thickness and load eccentricity on the column's behavior in fire. Moreover, the studies presented by Romero et al. (2011) [3], related to slender columns with the variation of the load level and type of concrete filling were also good pieces of work. In addition, they are also numerical researches, such as those presented by Hong and Varma (2009) [4] and Espinós et al. (2010) [5].

In general, the main conclusions of these studies are that parameters as the loading level, cross-sectional dimensions, buckling length, slenderness of the column and type of concrete filling have a significant influence on the fire resistance. Other parameters, such as the concrete and steel strength, aggregate type and load eccentricity, have a moderate influence. On the other hand, the percentage of steel reinforcement, the thickness of the steel tube and the position of the reinforcing bars, in relation to the inner surface of the steel tube, have little influence on its fire resistance [6].

Considering the influence of the restraining to thermal elongation on the behavior of the columns in fire it should be highlighted the experimental and numerical works of Pires et al [6, 7]. The restraining to thermal elongation caused by the surrounding structure of the building plays in certain cases a key role on the column's stability in case of fire, since it induces different forms of interaction between the heated column and the adjacent cold structure. The thermal restraining of the underlying structure increases not only the axial but also the rotational restraining. While the axial restraining may reduce the fire resistance (critical time) the rotational restraining may increase it. However, if the axial is much higher than the rotational restraining the fire resistance may be reduced, resulting in the reduction of the critical time and also the critical temperature of the columns [8, 9].

This research consists in comparing part of a set of 40 fire resistance tests carried out at the Laboratory of Testing Materials and Structures of University of Coimbra, in Portugal. The parameters tested included the slenderness, cross-sectional diameter, load level, stiffness of the surrounding structure, percentage of steel reinforcement and degree of concrete filling inside the steel tube. Recently a new set of tests was carried out at the same laboratory, but with new cross section configurations. Ten double-skin and double-tube columns with different types of concrete filling were tested in a fire situation. The results of these testes are still under analyses but this paper presents now some of them. In this sense, this work presents a comparative study on the fire resistance of concrete filled hollow columns with double-tube, double-skin and inner ring with plain and reinforced concrete. The double-tube columns are composed of two steel tubes, one external and one internal, the internal approximately half the diameter of the outer tube, both filled with concrete. Therefore, the concrete core and inner tube, because they are at lower temperatures under fire, can keep their capacity resilient. The double-skin are similar to the double-tube columns but the internal tube is void [10].

2 EXPERIMENTAL PROGRAM

2.1 Test set-up

The experimental set-up is capable of testing columns with restrained thermal elongation in case of fire (*Fig. 1a*). The test set-up, in addition to other parts, consists of a spatial restraining frame with variable stiffness k . This restraining frame has the function of simulating the stiffness of the surrounding structure to the column in case of fire. It allows to simulate not only the axial but also the rotational stiffness on the thermal elongation of the column. It consists of two upper and lower crossed beams connected by four columns, all orthogonally arranged. The beams and columns were made with HEB300 profiles of S355 steel class connected by M24 class 8.8 steel bolts.

Different positions of the holes in the flanges of the beams of the spatial restraining frame allowed mounting the columns in several positions resulting with this different stiffness of the surrounding structure to the thermal elongation of the column (*Fig.1b*). During the tests, a constant axial compression load was applied to simulate the serviceability load. For this, a ENERPAC hydraulic jack, with a maximum capacity of 3 MN, controlled by a W+B servo-hydraulic central unit, was used. The load applied was continuously measured by a load cell placed between the top flange of the upper beam of the spatial restraining frame and the head of the hydraulic jack's piston. The hydraulic jack was hanging in a plane reaction frame composed of two HEB500 columns and a HEB600 beam, S355 steel class, fitted with M24 class 8.8 bolts.

The thermal action was applied by a modular electric furnace composed of two modules of 1,5 m x 1,5 m x 1,0 m and a module of 1,5 m x 1,5 m x 0,5 m, placed on the top of each other, forming a chamber of 2.5 m height around the column. This furnace is capable to run heating curves as demanding as to the ISO 834.

A special device was used to measure the restraining forces generated on the column during the fire resistance tests (*Fig.1c*). It consists on a hollow high strength steel cylinder, rigidly connected to the upper beams of the spatial restraining frame, on which a massif steel cylinder, rigidly connected to the head of the testing column, entered. The side surface of the massif steel cylinder was Teflon (PTFE) lined for preventing the friction between the two steel cylinders. The restraining forces were measured by a 3MN load cell, placed inside the hollow steel cylinder, which was compressed by the massif steel cylinder due to the thermal elongation of the testing column during test. Further details on the configuration of the test-set up can be found in references [6-9].

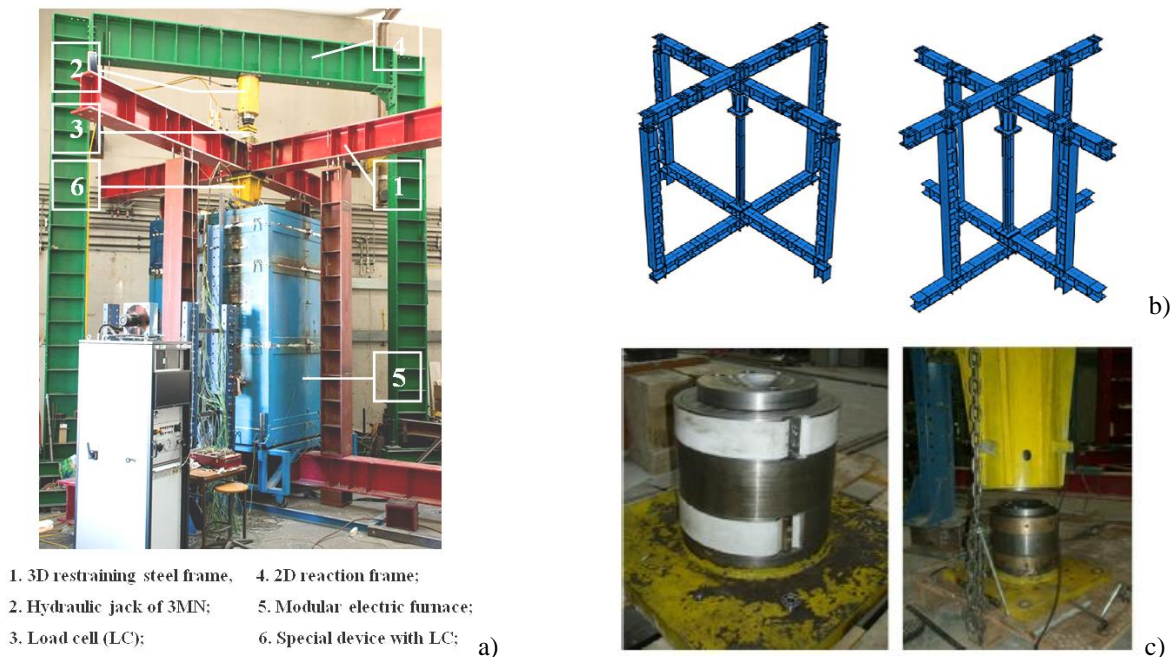


Fig. 1. a) General view of the experimental set-up; b) Stiffness of the surrounding structure arrangements [8]; c) Special device for measuring the restraining forces [9].

2.2 Specimens

Among the tested columns, twelve columns with six different cross sections were compared (*Fig. 2*): two PCR - plain concrete ring, two RCR - reinforced concrete ring, two DSC - Double-skin columns, two PCC - plain concrete columns, two RCC - reinforced concrete columns and two DTC - double-tube columns. All the tested columns were made from circular hollow steel sections, steel grade S355, with external diameter of 219.1 mm and a wall thickness of 6 mm for the PCR,

RCR, PCC and RCC and 8 mm for the DSC and DTC columns. In the DSC and DTC, the inner tube had a diameter of 101.6 mm and a wall thickness of 6 mm. All columns were 3 m high, but only 2.5 m of the height were exposed directly to the heating.

The columns were filled with calcareous concrete of C25/30 S3XC2 (P) D16.C10.4 class. The concrete ring in the PCR and RCR had 50 mm thickness. The columns with reinforced concrete had 6 ϕ 12 mm rebars and ϕ 6 mm diameter stirrups spaced 200 mm, both A500 class. The distance of the central axis of the longitudinal rebar to the inner surface of the column's wall was 30 mm.

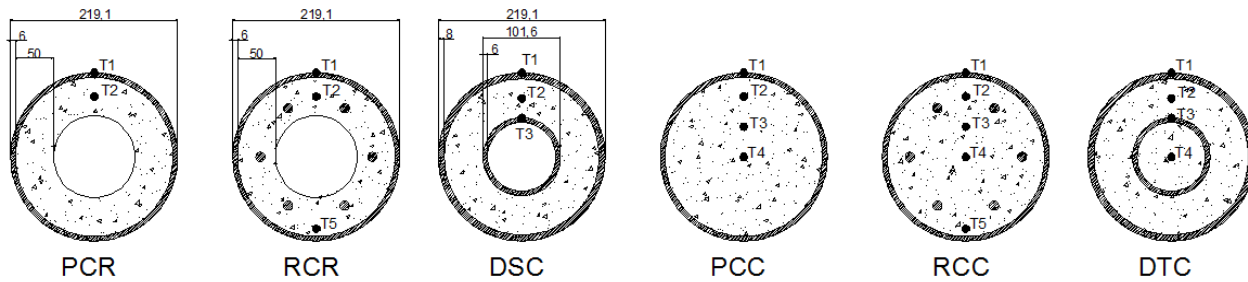


Fig. 2. Schematic representation of the tested cross sections

2.3 Test Plan

The values of the serviceability loads applied to the columns were 30% of the design value of the buckling load at ambient temperature ($N_{b,Rd}$) calculated according to EN1994-1-1 [11]. The load level in composite concrete filled hollow columns, in actual structures, is usually between 30% and 50% of the design value of the buckling load at ambient temperature [12]. Columns PCR, RCR, PCC and RCC are part of a major research previously carried out by Pires (2013) [7].

In these tests, two values of stiffness of the surrounding structure were used, corresponding to an axial stiffness of 13 kN/mm and rotational stiffness of 4091 and 1992 kN m/rad in the directions X1 and X2, respectively (stiffness $k1$) and 128 kN/mm of axial stiffness and 5079 and 2536 kN m/rad of rotational stiffness in the directions X1 and X2, respectively (stiffness $k2$).

The heating curve adopted was ISO 834 [13].

Table 1 shows the parameters of the tested columns.

Table 1. Test plan

Column reference	D_{out} (mm)	t_{out} (mm)	D_{int} (mm)	t_{int} (mm)	Rebars	Stiffness (kN/mm)	Serviceability load (kN)
PCR1	219.1	6	-	-	-	13	532
PCR2	219.1	6	-	-	-	128	532
RCR1	219.1	6	-	-	6 ϕ 12mm	13	584
RCR2	219.1	6	-	-	6 ϕ 12mm	128	584
DSC1	219.1	8	101.6	6	-	30	716
DSC2	219.1	8	101.6	6	-	110	716
PCC1	219.1	6	-	-	-	13	583
PCC2	219.1	6	-	-	-	128	583
RCC1	219.1	6	-	-	6 ϕ 12mm	13	633
RCC2	219.1	6	-	-	6 ϕ 12mm	128	633
DTC1	219.1	8	101.6	6	-	30	732
DTC2	219.1	8	101.6	6	-	110	732

3 COMPARISON BETWEEN THE TESTED COLUMNS

3.1 Temperatures

The average temperature in the furnace was similar in all cases. Comparing the evolution of this temperature with the ISO834 fire curve (Figs 3-5), there was a small delay in the first 8 min of the test due to the thermal inertia of the furnace. This phenomenon is common in electric furnaces.

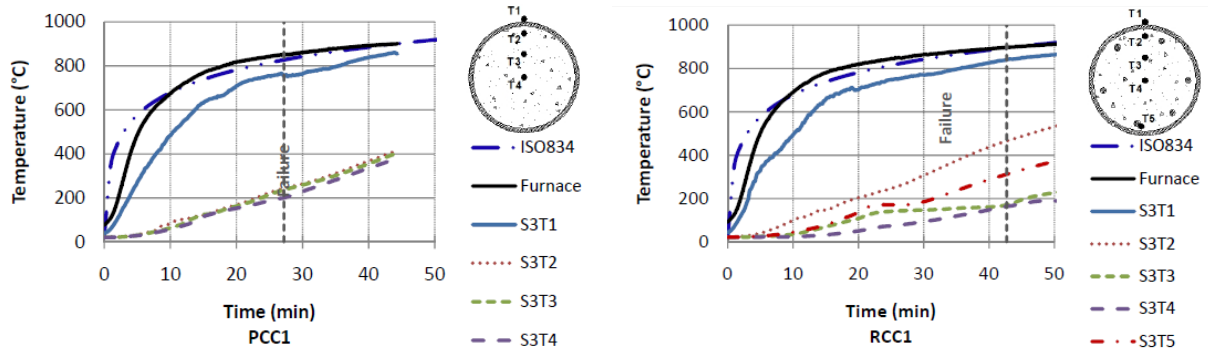


Fig. 3. Temperatures in the PCC1 and RCC1 columns

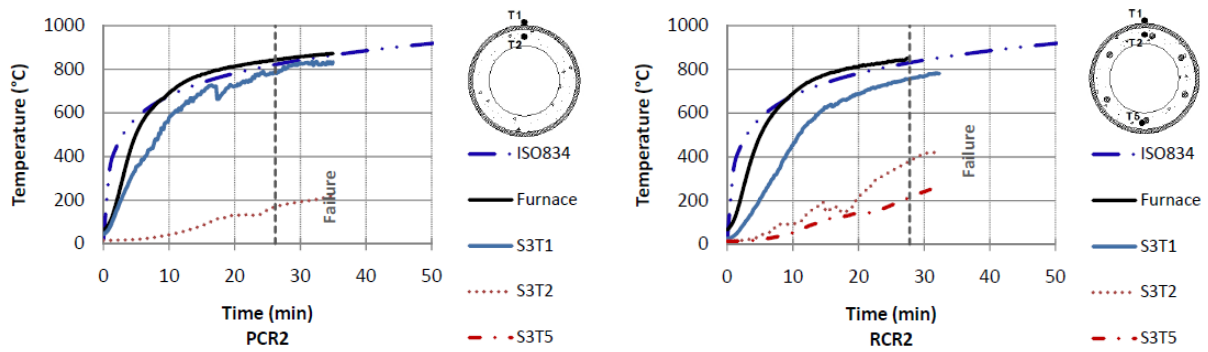


Fig. 4. Temperatures in the PCR2 and RCR2 columns

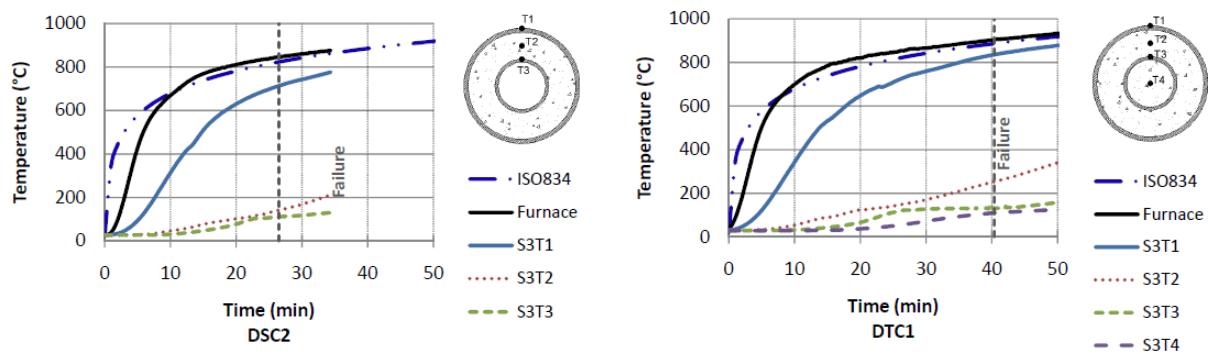


Fig. 5. Temperatures in the DSC2 and DTC1 columns

Comparing the temperature evolution in section S3, corresponding to the cross section at middle height of the column, it can be observed that in all the tests the temperature in the outer steel tube (T1) increased much faster than in the concrete and tends to reach the furnace temperatures (Figs 3-5). For the PCC, RCC and DTC it can be also observed that the temperature in the concrete at the center of the column (T4) reached a maximum temperature of 200°C at the instant of collapse, which means that the concrete has maintained its properties up to that instant.

In the reinforced concrete columns, RCC and RCR, the temperature in the rebars (T5) did not reach 400°C, therefore, the steel maintained its resistance even after 40 minutes of test (Fig. 3b). For the DTC and DSC columns, the temperatures in the inner tube (T3) remained close to 100°C, thus preserving all the properties of the steel, even with 30 or 50 minutes of testing (Fig. 5).

3.2 Restraining Forces

The restraining forces as function of time are presented in a non-dimension way in Fig. 6 by dividing its absolute value by the initial applied load (P/P_0). Until the critical time, all tested columns had similar behaviour. The relative restraining forces increase to a maximum and then decrease returning to the initial applied load due to the degradation of the mechanical properties of the materials (steel and concrete). Higher values for the relative restraining forces were observed for higher stiffness on the restraining frame for columns of the same cross section. The relative restraining forces were between 20% and 30%, for the columns subjected to the lower stiffness (Fig. 6-a). They reached up to 100% of the initial applied load for the higher stiffness (Fig. 6-b). The behavior of the reinforced concrete filled hollow columns (RCC) was very similar to the one of the double-skin and double-tube composite columns (DSC and DTC), especially for the lower stiffness (Fig. 6-a), because after the relative restraining forces returned to its initial value they remained at this level for a considerable time (up to 30 minutes). The plain concrete filled hollow columns (PCC), and the concrete ring (PCR and RCR) hollow columns presented a more pronounced decrease of the restraining forces after reaching the maximum values.

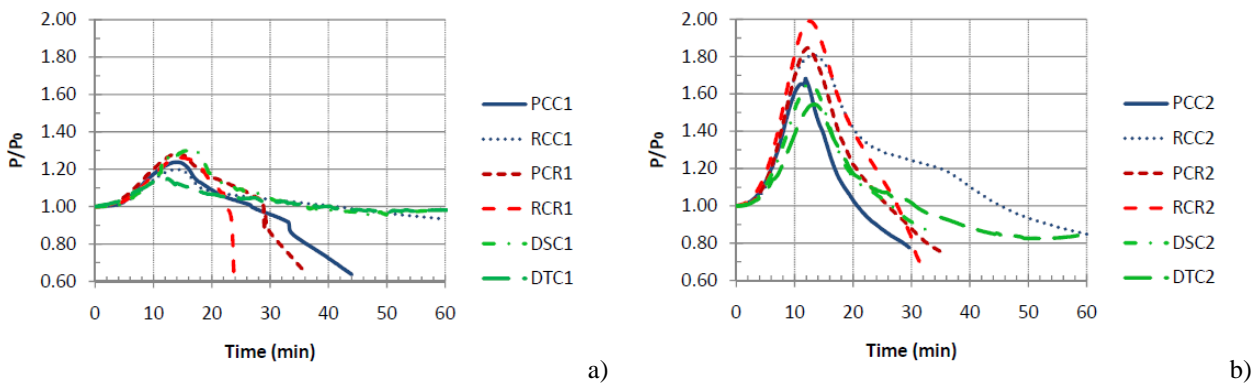


Fig. 6. Restraining forces: a) stiffness k1; b) stiffness k2

3.3 Critical Times

The tests conducted in this research were not standard fire resistance tests, therefore it was more appropriate to use the concept of critical time instead of fire resistance [14]. Critical time is here defined as the instant when the restraining forces return again to the value of the initial applied load, after increasing up to a maximum due to the column's restraining thermal elongation and then decreasing due to degradation of the material's mechanical properties in function of the temperature.

The critical times obtained in these tests are presented in Table 2. The results show that changing the stiffness of the surrounding structure did not lead to great changes in the critical times of the columns. This phenomenon may occur because usually associated with an increasing on axial stiffness is an increasing on rotational stiffness. As it is known an increasing on axial stiffness leads to a reduction on the critical time while an increasing on the rotational stiffness has the opposite effect [8, 9]. The double-tube columns (DTC) and the reinforced concrete filled hollow columns (RCC) presented the highest critical times.

Table 2. Test plan

Column reference	Stiffness (kN/mm)	Critical Time (min)	Failure mode
PCR1	13	29	Global buckling
PCR2	128	26	Global buckling
RCR1	13	23	Global + local buckling
RCR2	128	28	Global buckling
DSC1	30	36	Global buckling
DSC2	110	26	Global buckling
PCC1	13	27	Global buckling
PCC2	128	21	Global buckling
RCC1	13	43	Global buckling
RCC2	128	46	Global buckling
DTC1	30	41	Global buckling
DTC2	110	31	Global buckling

3.4 Failure modes

The failure in these columns were mainly by global buckling (*Fig. 7* and *Table 2*). The columns with inner concrete ring presented in some cases also local buckling (RCR1). The column DTC1 presented a higher curvature, but probably due to longer fire exposure, than the others. It should be here highlighted that these are failure modes after test because as the furnace is completely closed it was not possible to observe the deformed shapes of the columns during the different phases of the tests.

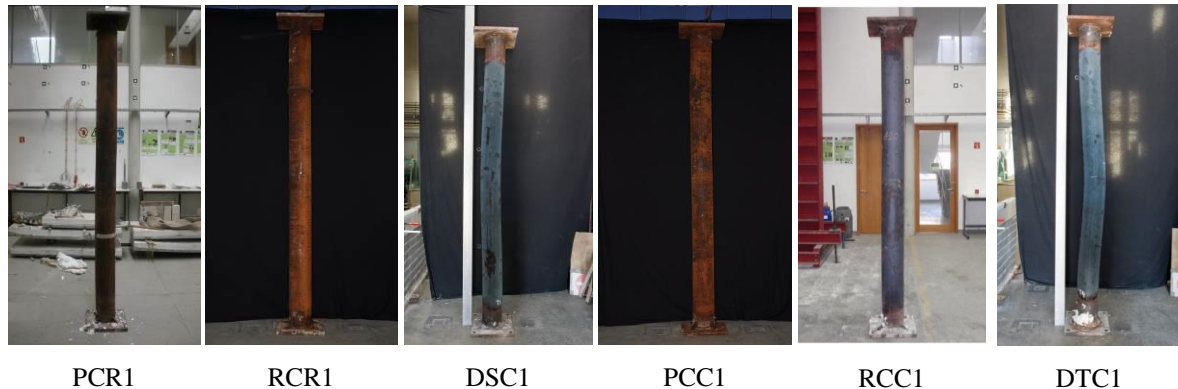


Fig. 7. Deformed shape of columns subjected to lower stiffness after test

4 CONCLUSIONS

The following conclusions may be drawn from the results of this research:

- The temperatures in the plain concrete (PCC) in inner ring columns (PCR and RCR) rose quicker than the others.
- Increasing the axial stiffness of the surrounding structure did not lead to major changes in the critical times of the columns because associated with an increasing of this stiffness is an increasing on the rotational stiffness that has an opposite effect to the first.
- Increasing the axial stiffness of the surrounding structure leads to an increasing in the restraining forces of the columns although this did not influence the critical time.

- The columns presented in general global buckling however in some cases of inner concrete ring local buckling also occurred. This surely resulted from the fact that the inner concrete ring collapsed inside the tube by degradation with increasing temperature.
- As a main conclusion of this paper it can be stated that the double-skin columns are a better construction solution for fire case than the inner concrete ring ones. The columns with inner concrete ring can be a good solution on anti-seismic construction of buildings due to weight reduction but are bad in fire case because the inner concrete ring collapses easily inside the tube with temperature increase. The behaviour and critical time of the double-tube columns and the reinforced concrete filled hollow columns are very similar.

ACKNOWLEDGMENTS

The authors gratefully acknowledge the European Union (EU), Research Fund for Coal and Steel (RFCS), for the support under the research project FRISCC (RFSR-CT-2012-00025) and the Brazilian Federal Agency for Support and Evaluation of Graduate Education within the Ministry of Education of Brazil (CAPES) for the scholarship given to the first author.

REFERENCES

1. V K R Kodur (1999). *Performance-based fire resistance design of concrete-filled steel columns*. Journal of Constructional Steel Research, 51, pp 975-981.
2. L H Han, Y F Yang, & L Xu (2003). *An experimental study and calculation on the fire resistance of concrete-filled SHS and RHS columns*. Journal of Constructional Steel Research, 59, pp 427-452.
3. M L Romero, V Moliner, C Ibañez, A Espinós, A Hospitalier & A Pascual-Pastor (2011). *Test of fire resistance of slender CFT columns*. EUROSTEEL 2011, Budapest, Hungary. pp. 1557-1562.
4. S Hong & A H Varma (2009). *Analytical modeling of standard fire behavior of loaded CFT columns*. Journal of Constructional Steel Research, 65, pp 54-69.
5. A Espinos, M L Romero, & A Hospitalier (2010). *Advanced model for predicting the fire response of concrete filled tubular columns*. Journal of Constructional Steel Research, 66, pp 1030-1046.
6. T A Pires, J P C Rodrigues & J J Silva (2012). *Fire Resistance of Concrete Filled Steel Circular Hollow Columns with Restrained Thermal Elongation*. J. of Const. Steel Research, 77, pp 82-94.
7. T A Pires (2013). *Fire Resistance of Concrete Filled Steel Circular Hollow Columns with Restrained Thermal Elongation*. PhD thesis, Dept. of Civil Engineering, Faculty of Sciences and Technology of the University of Coimbra, 2013, pp 207.
8. A J P M Correia, J P C Rodrigues, & F C T Gomes (2013). *A simplified calculation method for fire design of steel columns with restraining thermal elongation*. Computers and Struct., 116, pp 20-41.
9. A J P M Correia & J P C Rodrigues (2012). *Fire resistance of steel columns with restrained thermal elongation*. Fire Safety Journal, Vol. 50, pp 1-11.
10. M L Romero, A Espinós, J M Portolés, A Hospitalier & C Ibañez (2014). *Concrete filled circular double-tube steel columns subjected to fire*. Proceeding of the 8th International Conference on Structures in Fire, Shanghai, China, pp 769-776.
11. EN 1994-1-1. Design of composite steel and concrete structures - Part 1-1: general rules and rules for buildings. CEN - European Committee for Standardization; 2004.
12. V K R Kodur and Rustin Fike (2009). *Response of Concrete-Filled HSS Columns in Real Fires*. Engineering Journal, Fourth Quarter, pp 243-256.
13. EN 1991-1-2. Actions on structures - Part 1-2: general actions - actions on structures exposed to fire. CEN - European Committee for Standardization; 2002.
14. EN 1994-1-2. Design of composite steel and concrete structures. Part 1-2: general rules – structural fire design. CEN - European Committee for Standardization; 2005.

NUMERICAL AND EXPERIMENTAL TESTS ON CONCRETE FILLED SQUARE AND RECTANGULAR HOLLOW COLUMNS SUBJECTED TO FIRE

Luís Laím¹, João Paulo C. Rodrigues^{2,*}, Venkatesh K.R. Kodur³

¹ ISISE, Department of Civil Engineering, University of Coimbra, Portugal.

² LAETA, Department of Civil Engineering, University of Coimbra, Portugal.

³ Department of Civil and Environmental Engineering, Michigan State University, East Lansing, USA

* Author for contact. Tel.: +351 239 797 237; Fax: +351 239 797 123; E-mail: jpaulocr@dec.uc.pt

ABSTRACT

Concrete filled steel tubular columns are increasingly selected for structural applications in construction on the basis of their high load bearing capacity, seismic resistance, slenderness and reduction on both time and construction costs. Despite the existence of a large number of research studies related to the structural fire resistance of such columns, the analysis undertaken and knowledge developed up to date is still incomplete. The lack of results is even more pronounced if the study considers the effects of axial and rotational restraint to the element, a situation likely to occur when the column is part of a building. This paper presents the results of experimental tests and a calibrated numerical model on concrete filled hollow columns subjected to fire. Some parameters such as slenderness, type of section geometry and axial and rotational restraint level imposed by the surrounding structure to the column were tested in order to evaluate their influence on the fire resistance of such columns. Finally, the results showed that the stiffness of the restraining structure does not assume a major influence on critical time of the columns, especially on the rotationally restrained ones.

Keywords: fire, composite, hollow column, square and rectangular cross-section, thermal restraint.

1 INTRODUCTION

Concrete filled steel tubular (CFST) columns are increasingly assuming a greater role in civil construction. This is due to the combination of some of the best features that each material has to offer, making it structurally advantageous and an efficient solution [1, 2]. Concrete filling offers an attractive practical solution for providing fire protection to steel hollow columns without any external protection. The fire resistance of concrete-filled steel square hollow section (SHS) columns may be between 50 and 100 minutes, depending on the type of concrete filling (plain concrete, bar-reinforced concrete or steel fibre-reinforced concrete) [3], whereas the fire resistance of common steel tube columns is less than 30 minutes [4]. This increase is also due to the composite action between concrete core and steel tube [5]. At first, the steel tube expands more than the concrete core, due to the higher temperature and thermal expansion coefficient of the steel, which sustains the serviceability load applied to the column. In the latter stages the steel tube starts to buckle locally which transfers the load to the concrete core. Finally, when the concrete core loses its strength, the column buckles [6]. The existing studies on columns made of concrete-filled steel hollow sections at high temperatures addressed the effect of the depth-to-thickness ratio [7], the column slenderness [8], the initial applied load level, the load eccentricity [9] and the local buckling in the concrete-filled steel tube on their fire resistance. These studies proved that both the simple calculation model in clause 4.3.5.1 and the method in Annex H of EN 1994-1-2:2005 [10] lead to unsafe predictions for both axially and eccentrically loaded columns [11]. However, most studies

did not take into account the interaction between the column and the surrounding building structure. The response of these columns when inserted in a building structure is different than when isolated. Restraints to the thermal elongation of the column plays an important role on column's stability, since it induces different forms of interaction between the heated column and the cold adjacent structure. Whereas the axial restraint to thermal elongation of the columns may have a detrimental effect, the rotational restraint may have a beneficial effect on the fire resistance [12, 13].

Therefore, with the main purpose of obtaining, by the authors in the near future, analytical formulae for simplified design or verification of the fire resistance of innovative and slender concrete filled tubular composite columns, it is intended to describe in detail in this paper all parameters, considerations and assumptions took into account in a three-dimensional nonlinear finite element model to predict the behaviour of CFST slender columns in fire. Several fire tests were firstly carried out in order to assess mainly the fire resistance and the buckling failures of the respective columns [14]. These ones make it possible to calibrate the developed finite element model and consequently to obtain reliable numerical results outside the bounds of the original experimental tests.

2 EXPERIMENTAL INVESTIGATION

2.1 Tested columns

The specimens consisted of columns made of hollow steel profiles completely filled with reinforced concrete (fig. 1). All reinforcing bars used in the test specimens were made of B500 structural steel and all specimens presented a similar concrete composition with calcareous aggregate and C25/30 class, according to EN 1992-1-1:2004 [15]. In addition, all steel profiles were 3.15 m tall and were made of S355 structural steel (with a nominal yield strength of 355 MPa and a tensile strength of 510 MPa), according to EN 1993-1-1:2004 [16]. Another important point to note is that three-five days after concrete casting, the moisture content of the concrete was about 4.5%, according to the procedure described in EN 1097-5:2009 [17]. This parameter was measured as soon as possible because the water loss from the concrete inside the steel tubes is too limited.

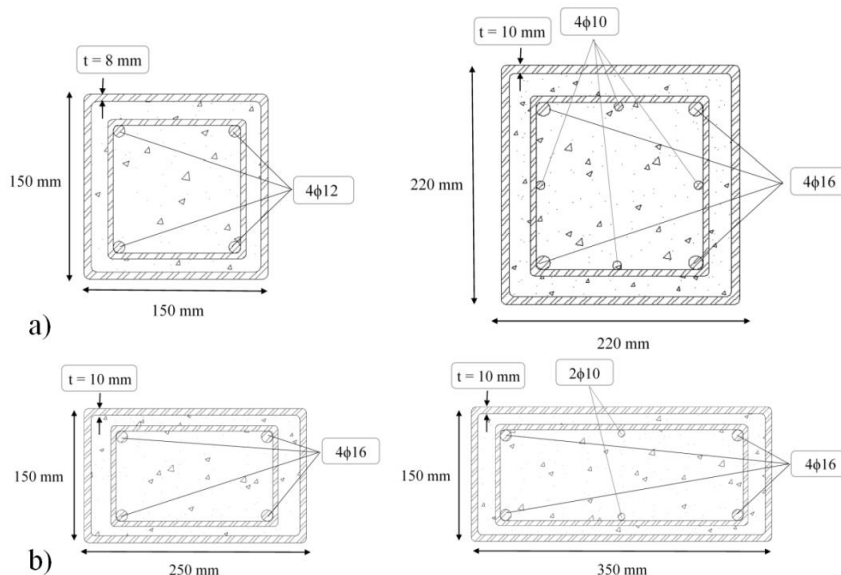


Fig. 1. Scheme of the cross-sections of the tested columns: (a) square columns; (b) rectangular columns

Square and rectangular columns were selected for this study. For each specimen the transversal reinforcement was performed by 8 mm diameter stirrups with a spacing of 150 mm until about 800 mm from the supports, and with a spacing of 200 mm in the central part. The concrete covering related to the rebars for all tested columns was about 25 mm. For each type of column, two different cross-sections were tested. Therefore, the square hollow steel sections were 150 mm and 220 mm wide, and the rectangular ones were 250mm and 350 mm height and 150 mm wide. The largest

square column had eight longitudinal rebars, four of which were 16 mm in diameter ($4\phi 16$) and the others were 10 mm ($4\phi 10$), and the steel tube had a 10 mm wall thickness; whereas the narrowest column had four longitudinal rebars of 12 mm in diameter ($4\phi 12$) and a steel tube had 8 mm wall's thickness. On the other hand, the largest rectangular column had six longitudinal rebars, four of which of 16 mm in diameter ($4\phi 16$) and the others of 10 mm ($2\phi 10$), whereas the narrowest rectangular column had four longitudinal rebars of 16 mm in diameter ($4\phi 16$). Both rectangular steel tubes had a 10 mm wall's thickness. Note that these longitudinal rebars were chosen for this study in order to have similar longitudinal reinforcement ratios between columns with the same geometric shape. As well as that the widest rebars were placed at the corners of the cross-sections and the others in the middle, as shown in Figure 1.

2.2 Test facility

A general view of the experimental system used in these tests is illustrated in Figures 2. The system comprises a two-dimensional reaction steel frame (1) and a three-dimensional restraining steel frame of variable stiffness (2) with the function of simulating the restraint that a surrounding structure imposes on the CFST columns under fire conditions. The actual axial restraint, k_a , imposed by the surrounding structure on the CFST columns were 30 and 110 kN/mm. A hydraulic jack of 3MN capacity in compression (3) was hung on the 2D reaction frame (1) and controlled by a servo hydraulic central unit (4).

The test columns (5) were placed in the centre of the 3D restraining frame and properly fitted to it (at each end plate) with four M24 steel grade 8.8 bolts, simulating semi-rigid ended support conditions. Additionally, above the specimen a 3MN compression load cell (6) was mounted to monitor the axial restraining forces generated in the CFST columns during the whole test. The thermal action was applied by a vertical modular electric furnace (7) programmed to reproduce the ISO 834 standard fire curve [18].

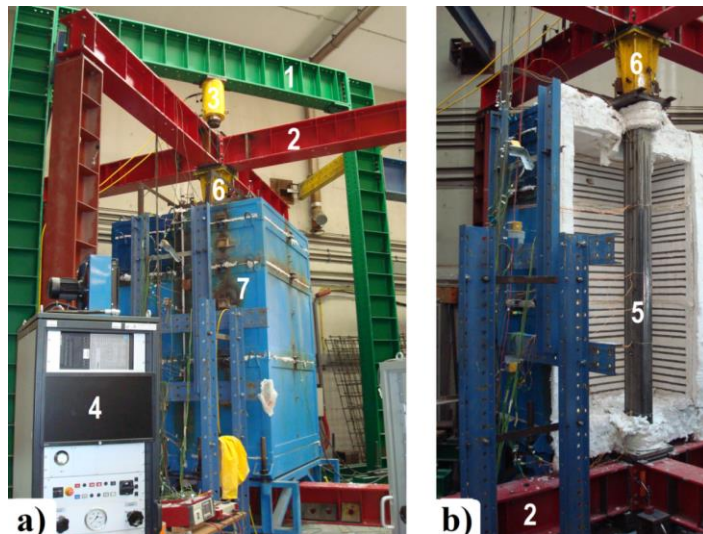


Fig. 2. General view of the experimental set-up (a) and the test column (b)

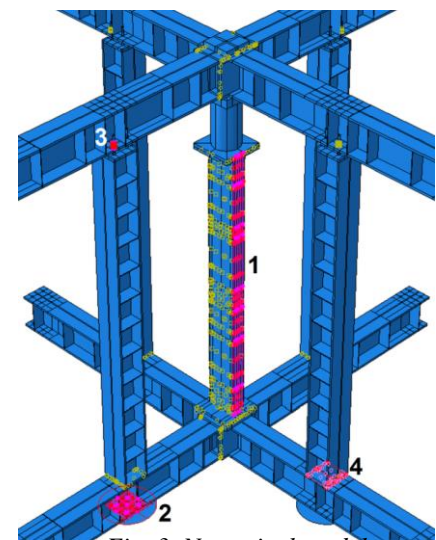


Fig. 3. Numerical model

2.3 Test procedure

Briefly, the test procedure first involved the positioning of the CFST test column in the centre of the 3D restraining frame, followed by applying the serviceability load. The load level applied on the columns, P_0 , was 30% of the design value of the buckling load of the columns at ambient temperature, calculated in accordance with the methods proposed in EN 1994-1-1:2004 [19] (i.e., based on characteristic material properties). Note that, during the load application, the upper beams of the 3D restraining frame were not connected to the respective columns in such a way that these beams could move freely downward as a rigid body, ensuring that the target load was directly applied to the test specimen. Once the predefined load level was reached, the vertical rigid body

movement of the upper beams of the three dimensional restraining frame was blocked (the connections between the upper beams and the peripheral columns of the restraining frame were fastened with locking nuts, washers and threaded rods) in order to activate the restraint imposed by the restraining frame on the CFST column. Finally, the electric furnace was turned on and the specimen was uniformly exposed to the ISO 834 standard fire curve [18]. During the heating period, the load was kept constant until the specimen buckled. The failure criterion adopted in this study was based on the ultimate load bearing capacity of the column (column strength); in other words, a column was considered to have failed when it could no longer support the initial applied load (serviceability load), and not when its buckling load was reached (maximum compressive strength of column).

3 NUMERICAL INVESTIGATION

3.1 Finite element type and mesh

The program Abaqus/Standard version 6.14-1 [20] was used extensively by the authors to develop a finite element model which aimed to simulate properly the behaviour and strength of composite steel-concrete columns under compressive loading conditions and fire. All CFST columns were modelled by using solid elements (C3D8R - a three-dimensional, continuum, hexahedral and an eight-node brick element with reduced integration, hourglass control, first-order interpolation and three degrees of freedom per node, corresponding to translations in the three spatial and orthogonal directions) for both the steel tube and the concrete core. The longitudinal rebars were modelled as embedded elements in the concrete core of the column with truss elements (T3D2), as assumed by other researchers in this field [11].

3.2 Material modelling

Material non-linearity in the specimens was modelled using the “Plastic-plasticity” model for the steel and “Concrete damaged plasticity” model for the concrete, from the Abaqus program library [24]. Both reduction factors for the yield strength and Young’s modulus of these materials at elevated temperatures, as well as their stress-strain relationships were obtained from EN 1994-1-2 (2005) [10]. All other components were modelled as elastic, i.e. the Young’s modulus was equal to 210 GPa for the steel and 31 GPa for the concrete, and the Poisson’s ratio was equal to 0.3 for the steel and 0.2 for the concrete, both at ambient temperature. However, this last parameter was assumed to remain unchanged with increasing temperature as well as the parameters which define the plastic behaviour of the concrete, including the dilation angle, the eccentricity, the ratio of initial equibiaxial compressive yield stress to initial uniaxial compressive yield stress, the K and the viscosity parameter. The dilation angle was taken as 15° whereas the other ones as 0.1, 1.16, 0.667 and 0, respectively, in other words, the default values given in the Abaqus program library [20]. Residual stresses were neglected in these analyses. Finally, the thermal properties of the respective materials at elevated temperatures considered in the model (mass density, thermal conductivity and specific heat) were also those established in EN 1994-1-2 (2005) [10]. It is still important to stress that the lower limit of thermal conductivity defined in this Standard and just 80% of the thermal expansion for the steel were employed in the developed numerical models.

3.3 Boundary, loading and contact conditions

A three-dimensional numerical model was used to describe all buckling modes observed in the experimental tests. Such as observed in the real test set-up (fig. 2), a three-dimensional frame was performed for the calibration of the finite element model to take into account not only the axial stiffness but also the rotational stiffness of the surrounding structure on the test column (fig. 3). It is worth remembering that different values of stiffness were provided by positioning the peripheral columns of the restraining frame at different positions.

Regarding the boundary conditions, all degrees of freedom of the nodes located on the bottom flange of the bottom beam of the restraining frame, right below the test column, were fixed. As well

as that, analytical rigid surfaces were also used below the peripheral columns and the bottom beams of the restraining frame (no. 2 in fig. 3) to model the slab floor of the laboratory where the experimental tests were carried out. All six degrees of freedom of their reference node were fixed. Note that the three-dimensional restraining steel frame was just laid down on the floor.

The axial load was applied to a rigid plate attached to the centre of upper beams of the restraining frame so as to distribute possible concentrated forces on them (preventing excessive deformation of the upper beams) and, in the end, to transmit load to both the concrete core and the steel tube (no. 1 in fig. 3). The thermal action was applied on the testing column, at different heights, because it was observed in the experimental tests a significant temperature gradient along the vertical direction, in the gas inside the furnace. So, to reproduce as faithful as possible the test conditions, the column was partitioned into different parts. The fire action was defined in Abaqus program by two types of surface, namely “film condition” and “radiation to ambient”, corresponding respectively to heat transfer by convection and radiation. Hence, the radiative heat flux was calculated using a steel emissivity value of 0.8 (as suggested by Correia *et al.* [21]) and 1.0 for fire (as recommended by EN 1991-1-2:2002 [22]), and the Stefan-Boltzmann constant was $5.67 \times 10^{-8} \text{ W/m}^2\text{K}^4$. On the other hand, convection was considered with heat transfer coefficient equal to $20 \text{ W/(m}^2\text{K)}$. The thermal resistance at the boundary between the steel tube and the concrete core was taken into account through a gap conductance value of $200 \text{ W/m}^2\text{K}$, as adopted in other investigations [6, 11]. Lastly, the initial temperature of all nodes of the numerical model was taken as 20°C . Note that the emissivity coefficients, the heat transfer coefficients and the thermal contact conductance coefficients remained unchanged with increasing temperature.

It was assumed a tangential friction coefficient of 0.2 for the contact behaviour in tangential direction and a hard contact (full transmission of compressive forces and no transmission of tensile forces) for the contact behaviour in normal direction, between the steel profile and the concrete (no. 1 in fig. 3). The same steel–concrete mechanical interaction was employed to take into account the contact between the bottom beams of the restraining frame and the analytical rigid surfaces (no. 2 in fig. 3) as well as between the upper beams and the threaded rods (no. 3 in fig. 3), during the load application in order to ensure that the axial load was directly applied to the test specimen. However, a rough and hard contact between these last elements was adopted during the heating period, with the purpose of mobilizing the restraint imposed by the restraining frame on the test column. Lastly, relative displacement between all other connections of the restraining frame (no. 4 in fig. 3) was prevented by means of the *TIE Constraints option in Abaqus. This method combines the two parts in all degrees of freedom at the connected region. Such simplification significantly reduces additional contact configuration and converging challenges.

4 CALIBRATION, RESULTS AND DISCUSSION

4.1 Structural failure analysis

Comparisons of the experimental and numerical results are given to demonstrate the confidence in using Abaqus to model the fire resistance and behaviour of this type of columns outside the bounds of the original experimental tests. Figure 4 shows, for example, the comparison of the relative axial restraining force (P/P_0) - time curves of the axially and rotationally restrained CFST columns obtained from the experimental tests (Exp.) and finite element analysis (FEA) used for the calibration of the model. When a composite column with restrained thermal elongation is subjected to fire, it is expected that the axial compression force increases during an initial phase (because the column is not free to elongate), but eventually it starts to decrease up to the initial axial compression force applied to the column (service load, P_0), firstly due to bowing of column, local buckling of steel tube and/or steel compressive strength loss and secondly, but less significantly, due to the deterioration of the concrete's mechanical properties near the steel-concrete interface, i.e. concrete between the steel tube and rebars. It is observed that the fire resistance of the columns was around 30 minutes for a 30% load level and it seems that the fire resistance of identical columns

may be not significantly affected by the stiffness of the surrounding structure. All curves from FEA (dashed red lines) fit well with the experimental curves (continuous blue line). In fact, the mean differences between these experimental and numerical results were around 5 % in terms of fire resistance of the columns.

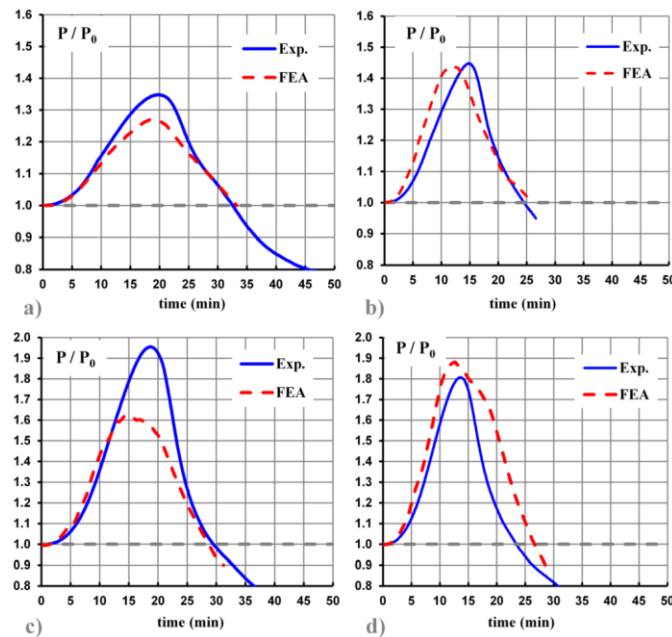


Fig. 4. Comparison of the FEA and experimental axial restraining forces results for the RC250-30ka (a), SC150-30ka (b), RC250-110ka (c), and SC150-110ka (d) columns

4.2 Failure mode analysis

Figure 5 illustrates the FEA failure modes of the rectangular columns under fire conditions (figs. 5b, c and d) as well as its final experimental deformed configuration (fig. 5a).

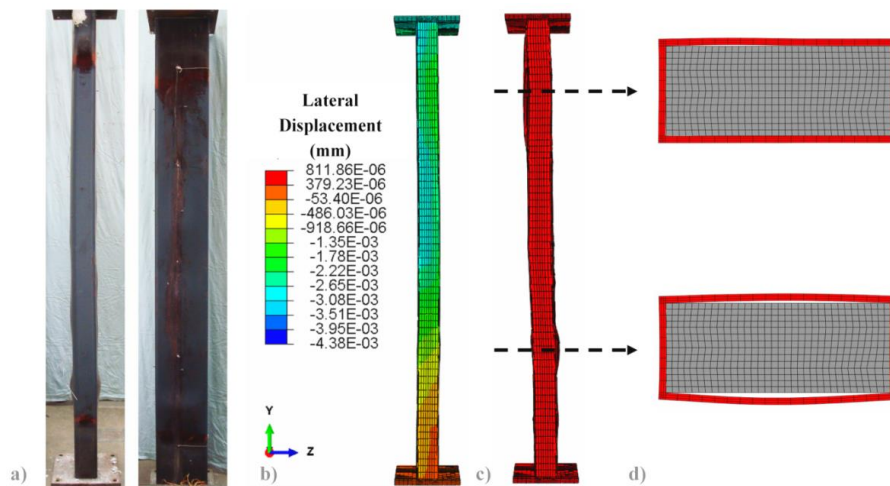


Fig. 5. Experimental (a) and numerical (b, c, d) configuration of the RC250-30ka column after fire test: general (b) and local (c, d) view

Both pictures show that the combined global and local buckling was the main failure mode responsible for the collapse of the rectangular columns with 350 mm of cross-section's depth, which is not expected at all for low cross-sectional slenderness values (in accordance with clause 6.7.1(9) of EN 1994-1-1:2004 [19]). It is worth mentioning that local buckling plays an important role in the failure of the rectangular cross-section columns. Multiple local buckling half-waves along the column length occurred on these semi-rigid ended columns. Global flexural buckling was the main failure mode responsible for the collapse of the all other columns. This good agreement

and accuracy between the experimental and numerical data may then ensure reliability of results obtained from parametric studies.

4.3 Effect of axial restraining forces

A preliminary parametric study was performed to enhance the understanding of the influence of the restraint to thermal elongation on the fire resistance of CFST columns. Hence, different axial restraint ratios ($k_a/k_{a,c} = 0, 2, 4, 16, 64$ and 128%) were selected for this parametric study. In order to reduce the amount of assembling and CPU time, a linear spring model was used during the parametric study (instead of the 3D restraining steel frame) for modelling the axial and rotational restraining system to the test column. It is interesting to observe that the higher the axial restraint (k_a) is, the higher the maximum axial restraining force becomes and the sooner the buckling load occurs, as can be seen in Figure 6a. However, it seems that the fire resistance of columns was not significantly affected by the stiffness of the surrounding structure, especially for fixed-ended columns. Actually, their fire resistance was not affected at all for axial restraint ratios ($k_a/k_{a,c}$) higher than 40% (fig. 6b). For example, when the axial restraint ratio increased from 0 to 40%, the fire resistance of the rectangular column RC_350_150_10 under a 30% load level decreased by 10.7% (from 28 to 25min) for fixed-ended support conditions and 16.0% (from 20.2 to 17min) for pin-ended support conditions. It is also clear that the rotational restraint had a beneficial effect on the fire resistance of such column. When this column was completely rotationally restrained, its fire resistance increased around 43%.

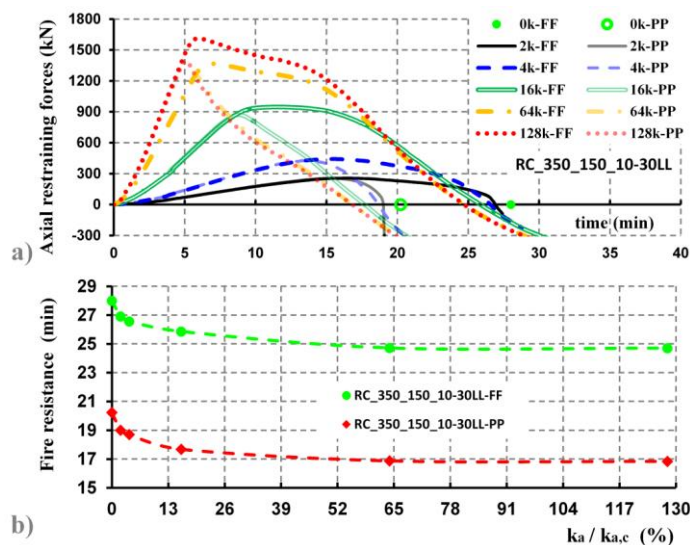


Fig. 6. Evolution of axial restraining forces and fire resistance of restrained rectangular columns

5 CONCLUSIONS

This paper has described a finite element model developed to simulate the fire response and behaviour of concrete filled steel tubular columns with square and rectangular cross-sections. It was first observed that the model was found to be accurate in predicting the structural behaviour of such columns in fire situation, especially their fire resistances, with an average difference of not more than 5% when compared with the results obtained from several experimental tests previously performed by the authors [14]. Despite this, the main conclusion of this investigation was that the axial restraint to the thermal elongation of such columns may slightly affect their fire resistance (around 15% in the maximum) and beyond certain values of axial restraint ratio ($k_a/k_{a,c} \approx 40\%$) the surrounding structure to the CFST columns has no further influence on their fire resistance. On the other hand, it is recommended that the local buckling effect should be still considered in the contribution of the steel component in the structural fire behaviour of concrete-filled hollow sections for relative depth-to-thickness ratios higher than 35.

REFERENCES

1. W. Qiu, F. McCann, A. Espinos, M.L. Romero, L. Gardner (2017). *Numerical analysis and design of slender concrete-filled elliptical hollow section columns and beam-columns*. Engineering Structures 131. pp 90–100.
2. Fang Yuan, Mengcheng Chen, Hong Huang, Li Xie, Chao Wang (2018). *Circular concrete filled steel tubular (CFST) columns under cyclic load and acid rain at-tack: Test simulation*. Thin-Walled Structures 122. pp 90–101.
3. Venkatesh K.R. Kodur (1999). *Performance-based fire resistance design of concrete-filled steel columns*. Journal of Constructional Steel Research 51. pp 21-36.
4. Tom Scullion, Faris Ali, Ali Nadjai (2011). *Effect of axial restraint on the performance of Elliptical Hollow Section steel columns, in hydrocarbon fire*. Engineering Structures 33. pp 3155–3161.
5. Yuyin Wang, Peng Chen, Changyong Liu, Ying Zhang (2017). *Size effect of circular concrete-filled steel tubular short columns subjected to axial compression*. Thin-Walled Structures 120. pp 397–407.
6. Ana Espinos, Manuel L. Romero, Dennis Lam (2016). *Fire performance of innovative steel-concrete composite columns using high strength steels*. Thin-Walled Structures 106. pp 113–128.
7. A. Espinos, M.L. Romero, E. Serra, A. Hospitaler (2015). *Experimental investigation on the fire behaviour of rectangular and elliptical slender concrete-filled tubular columns*. Thin-Walled Structures 93. pp 137-148.
8. Nandor Mago, Stephen J. Hicks (2016). *Fire behaviour of slender, highly utilized, eccentrically loaded concrete filled tubular columns*. Journal of Constructional Steel Research 119. pp 123–132.
9. YaoYao, Hao Li, Hongcun Guo, Kanghai Tan (2016). *Fire resistance of eccentrically loaded slender concrete-filled steel tubular columns*. Thin-Walled Structures 106. pp 102-112.
10. EN 1994-1-2 (2005). Eurocode 4 - Design of composite steel and concrete structures, Part 1-2: General rules - Structural fire design. European Committee for Standardization. Brussels, Belgium.
11. V. Albero, A. Espinos, M.L. Romero, A. Hospitaler, G. Bihina, C. Renaud (2016). *Proposal of a new method in EN1994-1-2 for the fire design of concrete filled steel tubular columns*. Engineering Structures 128. pp 237–255.
12. Carmen Ibañez, Manuel L. Romero, Antonio Hospitaler (2016). *Effects of axial and rotational restraints on concrete-filled tubular columns under fire*. Jour. Constr. Steel Research 125. pp 114–127.
13. João P.C. Rodrigues, Luís Laím (2017a). *Fire response of restrained composite columns made with concrete filled hollow sections under different end-support conditions*. Eng Structures 141. pp 83-96.
14. João P.C. Rodrigues, Luís Laím (2017b). *Fire resistance of restrained composite columns made of concrete filled hollow sections*. Journal of Constructional Steel Research 133. pp 65-76.
15. EN 1992-1-1 (2004). Eurocode 2 - Design of concrete structures - Part 1-1: General rules and rules for buildings. European Committee for Standardization. Brussels, Belgium.
16. EN 1993-1.1 (2004). Design of steel structures. General rules and rules for buildings. European Committee for Standardization. Brussels, Belgium.
17. EN 1097-5 (2009). Test for mechanical and physical properties of aggregates – Part 5: Determination of the water content by drying in a ventilated oven. European Committee for Standardization. Brussels, Belgium.
18. ISO 834-1 (1999) Fire resistance tests – elements of building construction, Part 1: general requirements, International Organization for Standardization, Geneva, Switzerland.
19. EN 1994-1-1 (2004). Eurocode 4 - Design of composite steel and concrete structures - Part 1-1: General rules and rules for buildings. European Committee for Standardization. Brussels, Belgium.
20. Abaqus/CAE Standard User's Manual, version 6.14-1, Dassault systems, Simulia Corp., USA, 2014.
21. António J.P.M. Correia, João P.C. Rodrigues, Fernando C.T. Gomes (2013). *A simplified calculation method for fire design of steel columns with restrained thermal elongation*. Computers and Structures 116. pp 20-34.
22. EN 1991-1-2 (2002). Actions on structures, Part 1-2: General actions – Actions on structures exposed to fire. European Committee for Standardisation, Brussels, Belgium.

INVESTIGATION OF PARTIAL CONNECTION THEORY ON COMPOSITE BEAMS UNDER FIRE EXPOSURE

Sven Brunkhorst¹, Samuel Pfenning², Jochen Zehfuß³, Martin Mensinger⁴

ABSTRACT

Under ambient conditions, it is state of the art [1] to use the partial connection theory for composite beams, in which the minimum degree of shear connection is considered. However, this reduction of the number of shear connectors is not directly applicable when designing for fire resistance. This is due to the different behaviour of the steel and concrete components at elevated temperature, resulting in high residual stresses and deformation of the composite girder.

This paper presents the results of extensive experimental and numerical investigations on the shear connection of fire exposed composite beams. In the experimental investigation, large-scale fire tests were conducted to analyse the influence of the degree of shear connection and different heating rates on the deformation behaviour of unprotected composite girders. In the numerical analysis a simplified finite element model was developed for a parameter study on the slip of the composite joint under elevated temperatures. The discussed parameters are the stiffness of the shear connection, the ratio of the tensile strength of the concrete chord to shear strength, as well as the relation between the plastic moment resistance and the inner lever arm of the composite section.

Keywords: Composite beam, partial connection theory, degree of shear connection, large-scale fire tests

1 INTRODUCTION

Composite construction using steel and concrete members is a modern and widely used construction method. Using this design, the positive strength properties of both composite partners are used in a very efficient way. To ensure the composite loadbearing effect, shear connectors with sufficient load-bearing and deformation capacity have to be used. By the application of the partial connection theory according to Eurocode 4 Part 1-1 [1] the number of shear connectors can be reduced. The minimum degree of shear connection depends on the maximum allowable slip between the two composite partners [1].

For composite structures with requirements for fire resistance the variation of longitudinal shear forces due to thermal strains according to Eurocode 4 Part 1-2 [2] need to be considered when using the partial connection theory. Design rules to calculate the changes in the longitudinal shear forces in fire are not included in [2] or [3]. Due to that, composite beams with requirements for fire resistance are mostly produced with full shear connection, which presents an economic disadvantage.

¹ PhD Candidate. Institute of Building Materials, Concrete Construction and Fire Safety, Division of Fire Safety, Technische Universität Braunschweig, GERMANY.

e-mail: s.brunkhorst@ibmb.tu-bs.de.

² PhD Candidate. Chair of Metal Structures, Technical University of Munich, GERMANY.

e-mail: s.pfenning@tum.de.

³ Professor. Institute of Building Materials, Concrete Construction and Fire Safety, Division of Fire Safety, Technische Universität Braunschweig, GERMANY.

e-mail: j.zehfuss@ibmb.tu-bs.de

⁴ Professor. Chair of Metal Structures, Technical University of Munich, GERMANY.

e-mail: m.mensinger@tum.de

2 EXPERIMENTAL INVESTIGATION

2.1 Large-scale fire tests

In accordance to EN 1363 Part 1 and EN 1365 Part 3, four large-scale fire tests were conducted to investigate the influence of the degree of shear connection and different heating rates on the deformation behaviour as well as the maximum slip in the composite joint. Furthermore, the test results serve as validation for a developed complex finite element model.

The test specimens with a length of 9.0 meters consist of an unprotected steel section and a concrete chord with a cross-section of 100 x 15 cm² and grade C45/55 according to EN 206. In *Fig 1* a picture of a large-scale fire test is shown. Two specimens are tested simultaneously in one fire test as single-span beams loaded with three single loads.



Fig. 1. Photograph of a large-scale fire test

Table 1. Test programme

Test series	Number of the girder	Profile section	Steel grade	Production process	Degree of shear connection	Fire load
A	1	IPE 300	S460	Propped structure - the weight of concrete elements is applied to the steel elements which are supported in the span	40 %	ISO 834
	2	IPE 300	S460		60 %	
B	3	HEB 300	S355		40 %	ISO 834
	4	HEB 300	S355		60 %	
C	5	IPE 300	S355	Un-propped structure - the weight of concrete elements is applied to steel elements which are unsupported in the span	40 %	ISO 834
	6	HEB 300	S355		40 %	
D	7	IPE 300	S355		40 %	Natural fire curve
	8	HEB 300	S355		40 %	

Four test series (A-D) on composite girders were carried out. *Table 1* presents an overview of the test program. The degree of shear connection is determined at ambient conditions. Test series A, B and C are exposed to ISO 834 fire and test series D had a fire load according to a determined natural fire curve [4]. As it can be seen, two different steel grades in accordance with EN 10025 Part 2 are used, as well as strength values controlled by tensile testing. The shear connection consist of welded headed studs (class: SD1) in accordance to EN ISO 13918 with 22 mm diameter and 125 mm length.

The test sequence occurs in accordance to EN 1365 Part 3. Firstly a mechanical load is applied for test sequence A as a constant load and for test sequences B, C and D as a cyclic load to overcome the adhesive bond in the composite joint. When starting the fire exposure, the specimens are loaded with a constant load of 110 kN per girder, except test series B. Here the constant load was 288 kN per girder. A gradually load increase of 0.5 kN/s takes place after reaching a steel temperature of 600 °C at the steel section. A vertical deflection limitation at mid-span of 44 cm required the fire test to be stopped to prevent possible damage on the test setup or bearing brackets.

Further details regarding the test setup, the bearing conditions and the specimen are published in [5] and [6] and will be presented in [7].

It should be noted that these fire tests were conducted only to analyse the composite loadbearing effect and the behaviour inside the composite joint of unprotected composite girders. The fire tests were not meant to test the fire resistance duration. The presented test results do not enable a derivation to a fire-resistance class.

2.2 Test results

2.2.1 Fire exposure

The influence of different heating rates is investigated by comparing the test results of the vertical deflection at mid-span for test series C and D. The temperature-time curves of this comparison is presented in *Fig. 2*. The presumed design fire, the simulation model used, as well as further boundary conditions to calculate the natural fire curve are published in [4].

In *Fig. 3* the influence of the different fire exposure is shown for the mid-span vertical deflection. The initial displacement is due to the cyclic mechanical load needed to overcome the adhesive bond in the composite joint before the start of the fire exposure. It can be seen, that a lower heating rate only leads to a time shift in the progress of the deflection curve. This is due to the strong correlation of the decrease of the steel stiffness with rising temperatures in the unprotected steel section and the deformation behaviour. Therefore, it can be noted that different heating rates only have an impact on the test duration, i.e. when the chosen abort criterion is reached, but not on the ultimate limit state of a composite beam in fire.

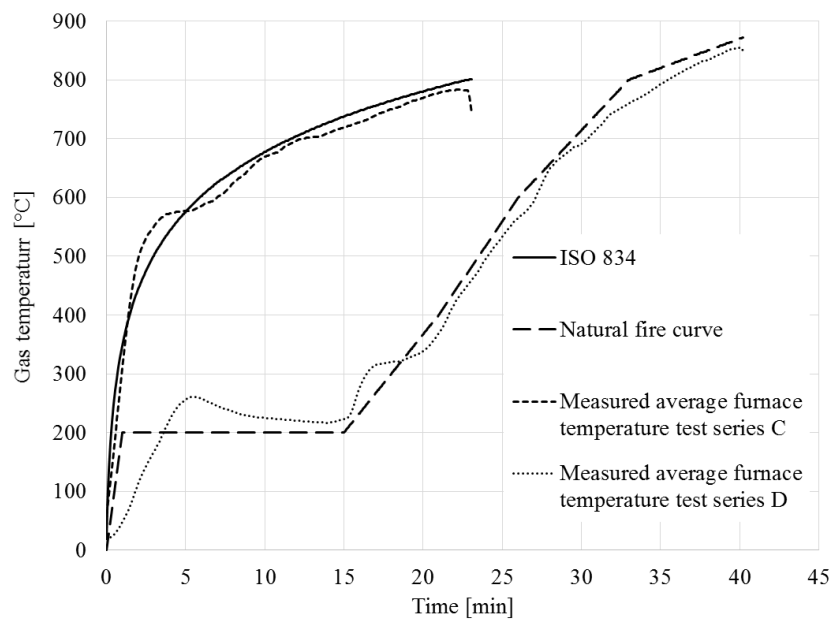


Fig. 2. Comparison of the different fire loads of test series C and D

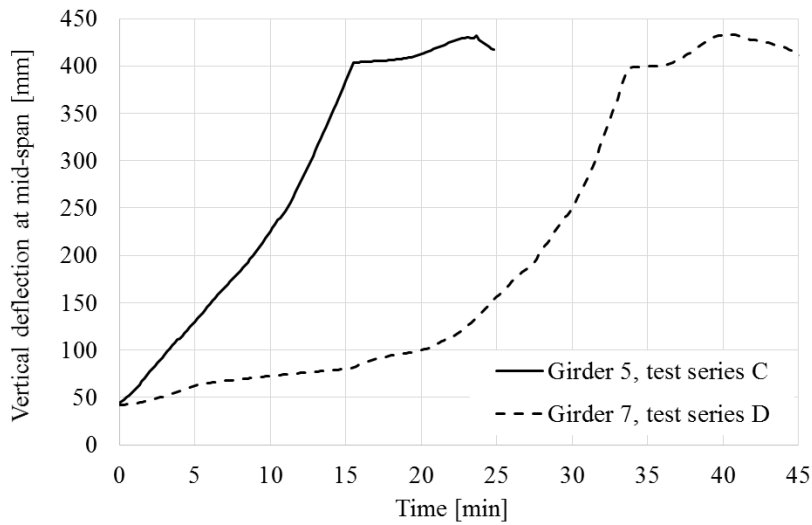


Fig. 3. Comparison of the vertical deflection at mid-span in terms of different heating rates

2.2.2 Degree of shear connection

For investigating the influence of the degree of shear connection on the deformation behaviour, girder 1 and 3 are constructed with 60 % degree of shear connection, whereas girder 2 and 4 are constructed with 40 % degree of shear connection. Fig. 4 shows the comparison of the vertical deflection at mid-span of test series A and B. Even though the initial stiffness of beams with different degrees of shear connection is different, the ultimate limit state for the tested degrees of shear connection is similar. This can be seen in both test series A and B, whereas there is a growing difference of vertical deflection in the first part of the test, this difference stays constant in the second part of the fire test. This leads to the approach that the degree of shear connection has no significantly influences on the deformation behaviour of the composite beam at elevated temperatures in this test configuration. Under fire exposure the deformation behaviour depends strongly on the heating of the steel section or rather the reduction of the stiffness caused by the temperature rise.

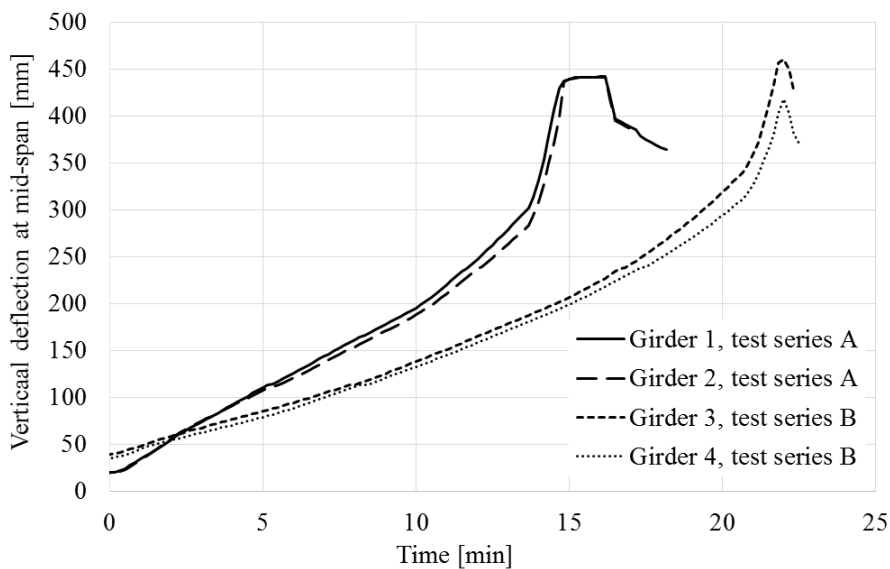


Fig. 4. Comparison of the vertical deflection at mid-span in terms of a different degree of shear connections

3 PARAMETER STUDY

To ensure the composite action of a composite beam in fire, the maximum slip between the concrete chord and the steel section needs to be limited to the maximum deformation capacity of the used shear connectors. When using headed stud shear connectors according to [1] the ductility of these shear connectors is limited to a maximum interface slip of 6 mm. Therefore the command variable of the parameter study is the maximum slip between concrete chord and steel section as illustrated in *Fig. 5*.

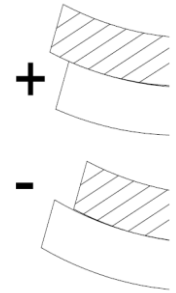


Fig. 5. Interface slip between concrete and steel section

3.1 Setup and load assumptions

An important assumption for the parametric study are the mechanical loads on the composite section. As elaborated in [8], the degree of shear connection does not influence the ultimate load carrying capacity of a composite beam in fire. In fact, the ruling case for a composite beam in fire is the unloaded case, when the slip due to thermal elongation of the steel section (effect I) is only recovered by the slip due to the high thermal gradient in the composite beam resulting in thermal curvature (effect II) and not due to bending of the steel section with mechanical loads (effect III) [4]. Therefore, the entire parametric study is done without additional mechanical loads, only self-weight and thermal loads. In the presented parametric study, a wide range of different composite beams in case of fire are calculated, always evaluating the maximum and minimum slip of the beam within the first 30 minutes of fire exposure according to ISO 834. In the following *Table 2* all investigated parameters are listed. In total 854 setups have been calculated.

Table 2: Parameters of the parametric study

Steel grade	Section length	Profile section	Section height	Degree of shear connection	Height of concrete chord
S235	6 m	IPE	300 mm	20 %	140 mm
S355	8 m	HEA	600 mm	40 %	170 mm
S460	10 m	HEM	500 mm	70 %	200 mm
			900 mm	100 %	

3.2 Finite element model

For the parametric study a precise and complex FE-model was developed and verified against the test results, details are published in [6]. The complex and large model was then simplified for faster calculation, this way the calculation time was reduced from four hours to just over one hour. An important modelling assumption is the nonlinear behaviour of the headed stud shear connectors. Whereas a multi-linear load-slip curve is set for the loading of the headed studs, unloading is assumed to be linear, as it is presented in *Fig. 6*.

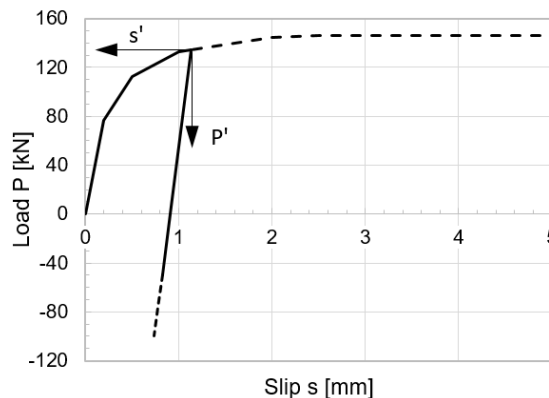


Fig. 6. Exemplary Load-Slip curve of a headed stud

3.3 Simulation results

The results of the calculation show three tendencies:

1. The stiffness of the shear connection highly influences the maximum slip.
2. When the tensile strength of the concrete chord is lower than the shear strength of the composite connection, moderate maximum slip can be expected.
3. The relation between the plastic moment of resistance of the composite section $M_{pl,Rk}$ and the inner lever of the composite section e has a large influence on the maximum slip.

3.3.1 Stiffness of the shear connection

The stiffness of the shear connection has a significant influence on the maximum slip. This stiffness is not only influenced by the degree of shear connection of the composite beam, but also by the steel grade of the steel section as well as the shear connectors itself. Both, a high degree of shear connection and a high steel grade, lead to a high number of needed shear connectors. A higher number of shear connectors leads to a stiffer shear connection. The highest interface slip generally occurs just before effect II, slip due to thermal curvature, becomes dominant. At this point the maximum stress in the steel section is still well below the respective yield stress, therefore the higher allowable strain of steel with a higher steel grade does not affect the maximum slip. The following Fig. 7 displays the maximum slip of all 854 setups over the stiffness of the composite joint.

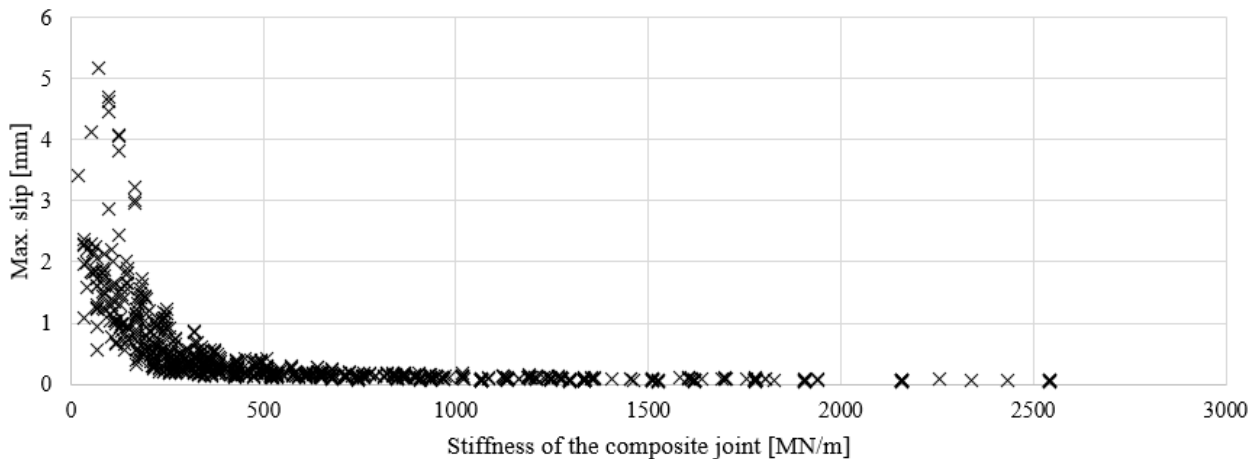


Fig. 7. Maximum slip of composite beams at 30 minutes fire exposure according to ISO 834 in relation to the stiffness of the composite joint

3.3.2 Tensile strength of concrete chord to shear strength relation

With rising temperatures the thermal elongation of the steel section, and therefore the positive slip, becomes more and more dominant. As large parts of the concrete chord stay at ambient temperature during heating, there is a compressive force in the steel section, as well as a tensile force in the concrete chord. When the load carrying capacity of the shear connection (V_{comp}) is higher than the tensile capacity of the concrete chord (F_{ct}), cracking of the concrete is very likely to occur, which then leads to a moderate maximum slip under fire exposure.

In the parameter study all beams with an F_{ct}/V_{comp} ratio equal or lower than one have a maximum slip of less than 3 mm. For beams with an F_{ct}/V_{comp} ratio higher than one the results are quite manifold, there are many configurations with a maximum slip of less than 3 mm, but also some configurations with a max. slip of over 5 mm. In the following Fig. 8 the maximum slip can be seen in relation to the described F_{ct}/V_{comp} ratio.

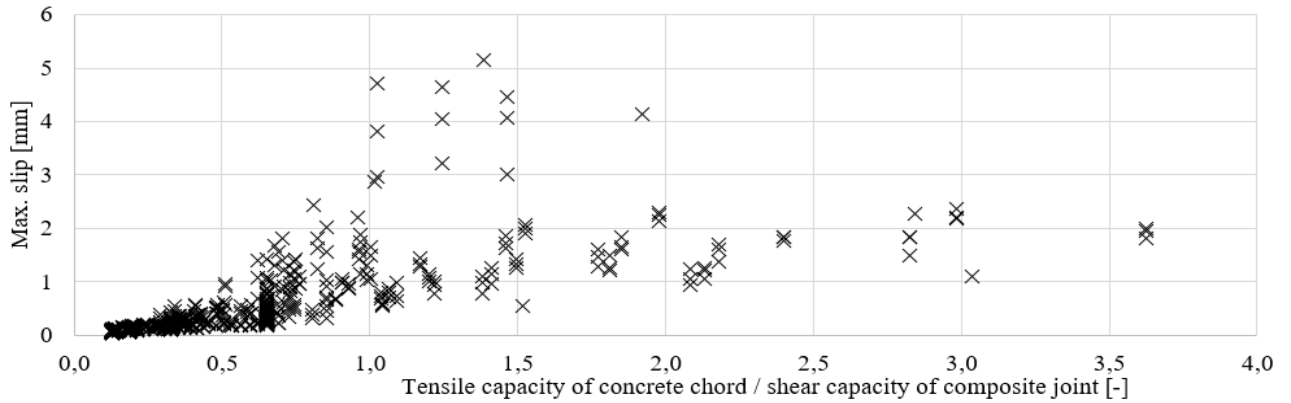


Fig. 8. Maximum slip of composite beams at 30 minutes fire exposure according to ISO 834 in relation to the F_{ct} / V_{comp} ratio

3.3.3 Plastic moment to inner lever relation

Supposing concrete cracking occurs as described in paragraph 3.3.2, another significant influence on the maximum slip of a composite beam in fire is the ratio between the plastic resistance moment of the composite section ($M_{pl,Rk}$) and the inner lever arm between concrete and steel section (e), which is shown in Fig. 10. This is due to the interaction of effect I, thermal elongation of the steel section, and effect II, bedding of the steel section due to the thermal curvature of the composite section. As slip due to effect I is growing proportionately to rising temperatures in the steel section, slip due to effect II is primarily caused by reaction force due to the different elongation of the composite components. Whereas the reaction force is dependent on the inner lever arm (e), the crosssection of the steel and the temperatur difference, the bending of the structure is dependent on the bending mold of the cross section (see Fig. 9). Therefore the relation between the acting moment, influenced by the inner lever arm e and the resistance to it, $M_{pl,R,k}$, define the magnitude of effect II and therefore also of the magnitude of the maximum slip.

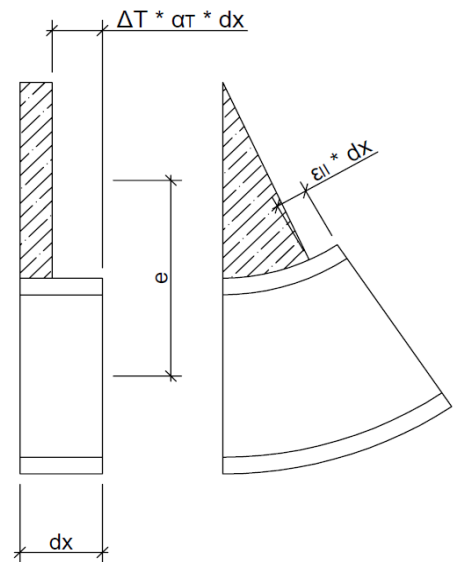


Fig. 9. Deformation due to thermal elongation of the steel section, left side: free deformation, right side: curvature due to bending

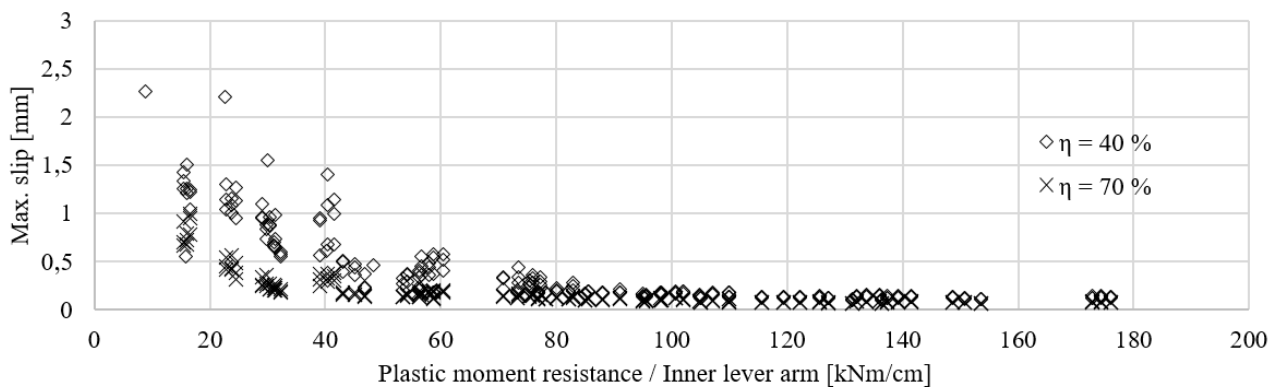


Fig. 10. Maximum slip of composite beams in 30 minutes fire according to ISO 834 in relation to the $M_{pl,rk} / e$ ratio for 40 % and 70 % degree of shear connection

4 CONCLUSION

A fire exposure on a composite beam has a significant influence on the composite shear connection. Experimental and numerical research is conducted to determine the application range of partial connection theory under fire exposure. The experimental research shows that the heating rate of a composite beam in fire does not influence the vertical deflection behaviour, there is only a time shift observed for the lower heating rate. Furthermore, the experimental results imply that the degree of shear connection does not affect the ultimate limit state, but only the initial stiffness of a composite beam in fire. A parameter study with 854 samples was conducted, with parameters representing large parts of construction practice. The parameter study focuses on the maximum slip of a composite beam without additional mechanical loads in the first 30 min of fire exposure according to ISO 834. Three major influences on the maximum slip are detected: the stiffness of the shear connection, the ratio of the tensile strength of the concrete chord to the shear strength of the composite connection and the ratio between the plastic moment resistance of the composite beam to the inner lever arm between concrete chord and steel section.

ACKNOWLEDGMENT

This research project (IGF project No. 19105 N) of Research Association for Steel Application (FOSTA) is funded by the German Federation of Industrial Research Associations (AiF) in the framework program of the Industrial Research Community (IGF) by a resolution of the Federal Ministry of Economics and Technology (BMWi). The authors gratefully thank the FOSTA for financial and organizational support enabling a development in the field of application research.

REFERENCES

1. EN 1994-1-1: Eurocode 4: Design of composite steel and concrete structures –Part 1-1: General rules and rules for buildings; German version, December 2010.
2. EN 1994-1-2: Eurocode 4: Design of composite steel and concrete structures –Part 1-2: General rules – Structural fire design; German version, December 2010.
3. EN 1994-1-2/NA: National Annex – Nationally determined parameters – Eurocode 4: Design of composite steel and concrete structures – Part 1-2: General rules – Structural fire design; Germany, December 2010.
4. Samuel Pfenning, Sven Brunkhorst, Martin Mensinger, Jochen Zehfuß (2017). Investigation of the effects on the shear connection of composite beams under various fire exposure. *2nd International Fire Safety Symposium*. Napoli, Italy, June 7–9, IFireSS, 2017. pp 211–218.
5. Sven Brunkhorst, Samuel Pfenning, Jochen Zehfuß, Martin Mensinger. (2017) Experimentelle und Numerische Untersuchungen zur Mindestverdübelung von Verbundträgern unter Brandbeanspruchung. *4th Symposium Structural Fire Engineering*. Braunschweig, Germany. pp. 12–27.
6. Samuel Pfenning, Sven Brunkhorst, Martin Mensinger, Jochen Zehfuß. (2017) Mindestverdübelung von Verbundträgern im Brand – Betrachtung der Auswirkung von erhöhten Temperaturen auf die Verbundfuge. *Münchener Stahlbautage 2017*. Munich, Germany. pp. 1–27.
7. Sven Brunkhorst, Samuel Pfenning, Jochen Zehfuß, Martin Mensinger (2018). *Influence of elevated temperatures on the composite joint of a composite beam in fire*. In: Fire Technology - Special Issue - Fire Experiments and Buildings (In review progress)
8. Samuel Pfenning, Jürgen Tresch, Luca Pennisi, Sven Brunkhorst, Martin Mensinger. (2017) Influence of the degree of shear connection on the load carrying capacity of a composite beam in fire. XI Congresso de construação metálica e mista. Coimbra, Portugal

KEY GOVERNING FACTORS THAT DEFINE THE FIRE PERFORMANCE OF STRUCTURAL INSULATED PANELS USED IN FLOOR SYSTEMS

Aaron Bolanos¹, Cristian Maluk², Jose L. Torero³

ABSTRACT

Structural Insulated Panels (SIPs) made from two Magnesium Oxide Boards (MGO) and Expanded Polystyrene (EPS) as insulated core are becoming widely introduced into the built environment. The study presented here focuses on the analysis of a specific type of SIP used in floor systems. Four-point bending experiments were carried to determine the failure mechanism that govern the performance of SIPs at ambient temperature conditions; found to be driven by tensile strength capacity of the bottom MGO. This article shows the results from an analytical stress-strain model for a SIP in bending. The expression accurately approximates the relation between stress and deflection in the elastic region when compared with experimental data. Fire experiments using a Heat-Transfer Rate Inducing System (H-TRIS) method were performed to assess the effect of temperature for the integrity of SIPs. These experiments evidenced that the EPS core degrades and contracts at around 100°C. The reduction of load-carrying capacity for MGO was investigated by performing residual tensile stress strength and tensile elastic modulus. MGO test samples were heated up to a steady state conditions at temperatures ranging from ambient to 350°C. Test temperatures were purposely kept below the ignition temperature of EPS to focus on structural issues and not flammability. Experimental results show that the tensile stress strength and tensile elastic modulus of MGO reduces to half of its value at ambient temperature at around 250°C.

Keywords: structural insulated panels, magnesium oxide board, structural fire performance

1 INTRODUCTION

Structural Insulated Panels (SIPs) are a specific kind of sandwich panel. For the purpose of this research, it consists of an Expanded Polystyrene (EPS) insulation core bonded between two Magnesium Oxide (MGO)-based composite boards. *Figure 1* shows a cross section of the standard panel. SIPs can act as load bearing elements, external claddings or as internal partitioning within a structure. When assembled properly, SIPs are usually known for offering good thermal insulation, air tightness and sound proofing; and as a modular system, they reduce construction time and costs, diminish waste onsite and enhance safe working conditions [1]. Engineering companies in the Australian construction market currently commercialize SIPs as a primary load-bearing component of one or two-story structures.

The research work presented here studies the structural fire performance of SIPs by identifying first the relevant failure modes of the panels at ambient temperature conditions, the integrity of EPS during fire, and the load-carrying capacity of MGO during and after fire.

¹ PhD Candidate. School of Civil Engineering, The University of Queensland, Brisbane, Australia.

e-mail: a.bolanoscuevas@uq.edu.au

² Lecturer. School of Civil Engineering, The University of Queensland, Brisbane, Australia.

e-mail: c.maluk@uq.edu.au

³ Director. Center for Disaster Resilience, A. James Clark School of Engineering, The University of Maryland, USA.

e-mail: jltorero@umd.edu

Key governing factors that define the fire performance of structural insulated panels used in floor systems

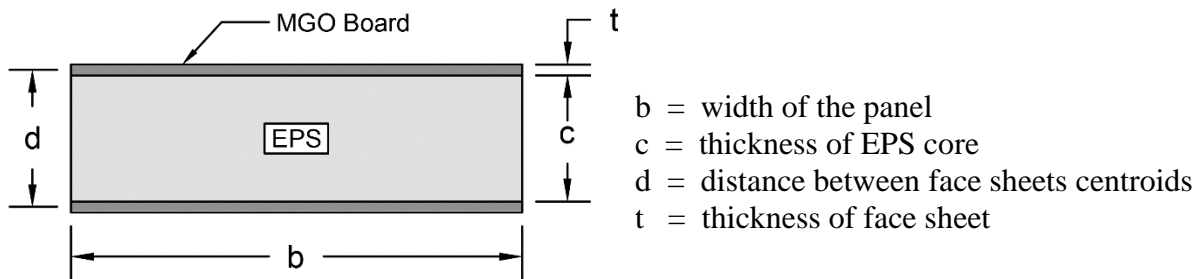


Fig. 1. Panel cross-section

1.1 Background of the study

Structural behaviour of SIPs at ambient temperature conditions has been studied extensively [2-3] and an incipient acceptance in the construction market has been achieved. On the other hand, several authors have indeed studied fire performance of SIPs. While discussing the relevance of proper installation, Cooke [4] provided a force and deflection calculation method for horizontal panels exposed to fire. Birman et al [5] presented an analytical study of the bending mechanics of panels exposed to fire and calculated the maximum deflection and shear stresses, among other important variables as a function of temperature. Rusthi et al [6] presented their experimental results from full scale tests on MGO board lined LSF wall systems and reported bending and cracking of the material as a key failure criterion.

To date, studies have addressed structural behaviour and fire performance in a separate manner. Fire performance has been generally studied as a flammability problem. A thorough understanding of how the temperature-related processes reduce structural strength and modify the failure mechanisms is yet to be achieved. The work described herein describes a method of analysis in which the failure mechanism under four-point bending and ambient conditions are determined before assessing the shift in material properties after being exposed to elevated temperatures, allowing to establish which variables inherent of the comprising materials become critical in a fire scenario.

2 BEHAVIOUR AT AMBIENT CONDITIONS – FOUR POINT BENDING TEST

2.1 Determination of failure mode

A 1 MN experimental loading apparatus was used to set up a four-point bending test on a set of 2500 mm long samples of SIPs, each with a cross section as described in *Figure 1*. The force-applying mechanism was centred longitudinally on top of the panel, with the distance between loading points ' b ' being 800 mm, the span between supports being 2000 mm and 250mm free portions on each end denoted by ' e ' in *Figure 2*. The distance ' a ' from the loading point to the roller/pin support point was 600 mm.

Load was applied at a rate of 2 mm/min up to failure of the sample which occurred at around 8.8 KN. A high definition camera was used to locate the initial cracking of the tested SIPs. It was determined from there that the failure mode of the sample is defined by overcoming of tensile strength on the lower MGO board face sheet. A crack then appears and immediately travels upwards through the EPS core and lastly reaches the upper face sheet, resulting in the collapse of the sample. Throughout these experiments, deflection was measured at mid span between supports using two high precision Linear Variable Differential Transformers. A plot of applied force vs deflection was then obtained from the results of this test and is included in *Figure 3*.

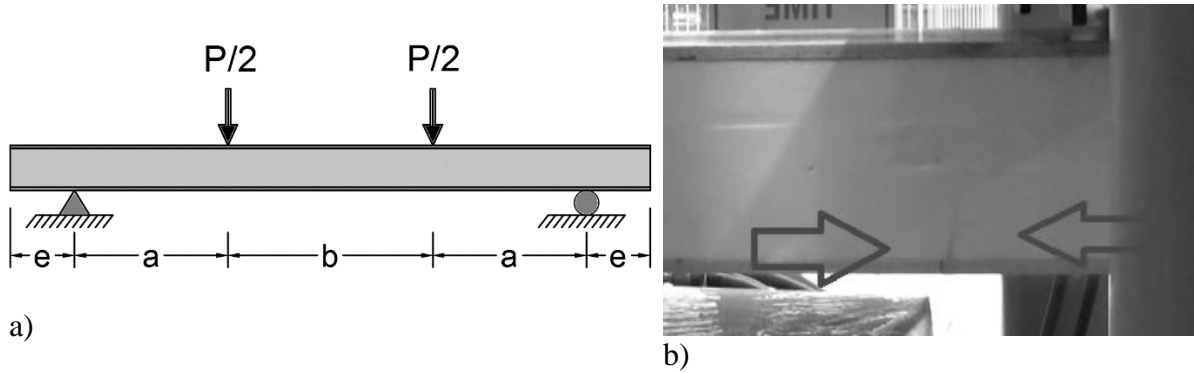


Fig. 2. a) Loading setup of the four-point bending test; b) crack in tension forming from the lower face sheet

2.2 Quantitative solution of bending conditions

This section shows the analytical expression used for describing the stress-strain model of the SIP in bending. The out-of-plane deflection in any x position (where the x -axis is aligned lengthwise with the panel) can be expressed by the sum of the deflections (δ) due to pure bending and the deflections derived from shear stresses [7].

$$\delta_{total} = \delta_{bending} + \delta_{shear} \quad (1)$$

Furthermore, if the ratio c/t is equal or higher than 5.35, the panel face sheets can be classified as “thin”. Therefore, the face sheets determine the bending strength of the panel and the EPS core does not contribute to the flexural rigidity (D) of the system [8]. By simple calculations this criteria can be demonstrated and *Eq. 2* defines this parameter.

$$D = EI = \frac{E_{face} t d^2 b}{2} \quad (2)$$

where E_{face} is the modulus of elasticity of the MGO board.

Visualizing the setup as a simply supported beam, at mid span between the supports stress on the face sheets σ_{face} and deflection due to bending can be defined as follows:

$$\sigma_{face} = \frac{P a}{2 b d t} \quad (3)$$

$$\delta_{bending} = \frac{Pa}{48EI} (3L^2 - 4a^2) \quad (4)$$

where P is the total load applied onto the system and L is the span between supports.

The model herein assumes that the modulus of elasticity in planes parallel with the surface of the SIP is zero but the shear modulus in planes perpendicular to the face sheets is finite [9]. Making use of this concept, bending stresses in core may be neglected and *Eq. 5* defines the deflections due to shear for the simply supported setup.

$$\delta_{shear} = \frac{P a c}{2 G b d^2} \quad (5)$$

where G is the shear modulus of EPS core.

By substituting *Eqs. 2-5* into *Eq. 1*, an expression that correlates deflection of the SIP to bending stress can be obtained.

$$\delta_{total} = \frac{\sigma_{face} t}{d} \left(\frac{3L^2 - 4a^2}{12 E_{face} t} + \frac{c}{G} \right) \quad (6)$$

Using the geometrical parameters already described and mechanical properties obtained from experiments described in Section 3.2 herein, a stress-deflection plot allowing to compare the analytical results with the experimental observations was generated (see *Figure 3*). *Table 1* summarizes the values gathered for these calculations.

Table 1. Data used for analytical model verification

Parameter	Value
a (mm)	600
c (mm)	140
d (mm)	152
L (mm)	2000
t (mm)	12
E_{face} (MPa)	3829 [2]
G (MPa)	2.52

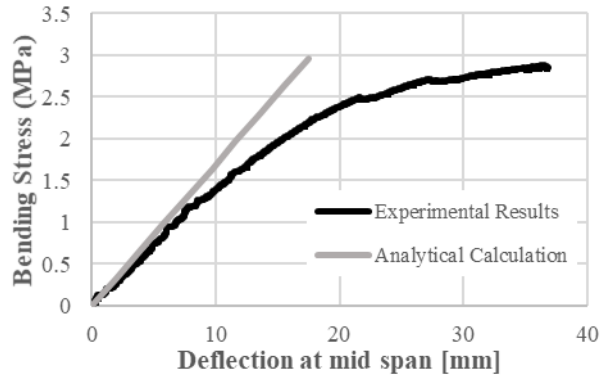


Fig. 3. Stress-deflection plot of 4-point bending test

3 BEHAVIOUR AT ELEVATED TEMPERATURES

3.1 SIP integrity

Thermal behaviour of SIPs without the imposition of mechanical loads was studied using a Heat-Transfer Rate Inducing System (H-TRIS) method. Constant incident radiant heat flux in the order of 15 – 20 kW/m² were imposed. One side exposure was performed, and samples were carefully instrumented for in-depth temperature measurement. For this purpose, 24 thermocouples were placed on three different axes in the panel's cross section. Temperatures were measured at the back of the heat-exposed MGO face sheet, on both sides of the unexposed face and evenly distributed throughout the core. *Figure 4* shows the results of these measurements, where a plateau indicating a degradation process in the EPS can be identified at a temperature near 100°C. However, it is not clear whether the cause of this behaviour is the actual shrinking and loss of structure of the EPS, or merely a process of a water front migrating from the MgO into the EPS

In any case, it was demonstrated by visual inspection of the sample at the end of the test that EPS did lose its structure and experienced shrinking. *Figure 4c* shows the final condition of the EPS core in the area behind the exposed MgO face.

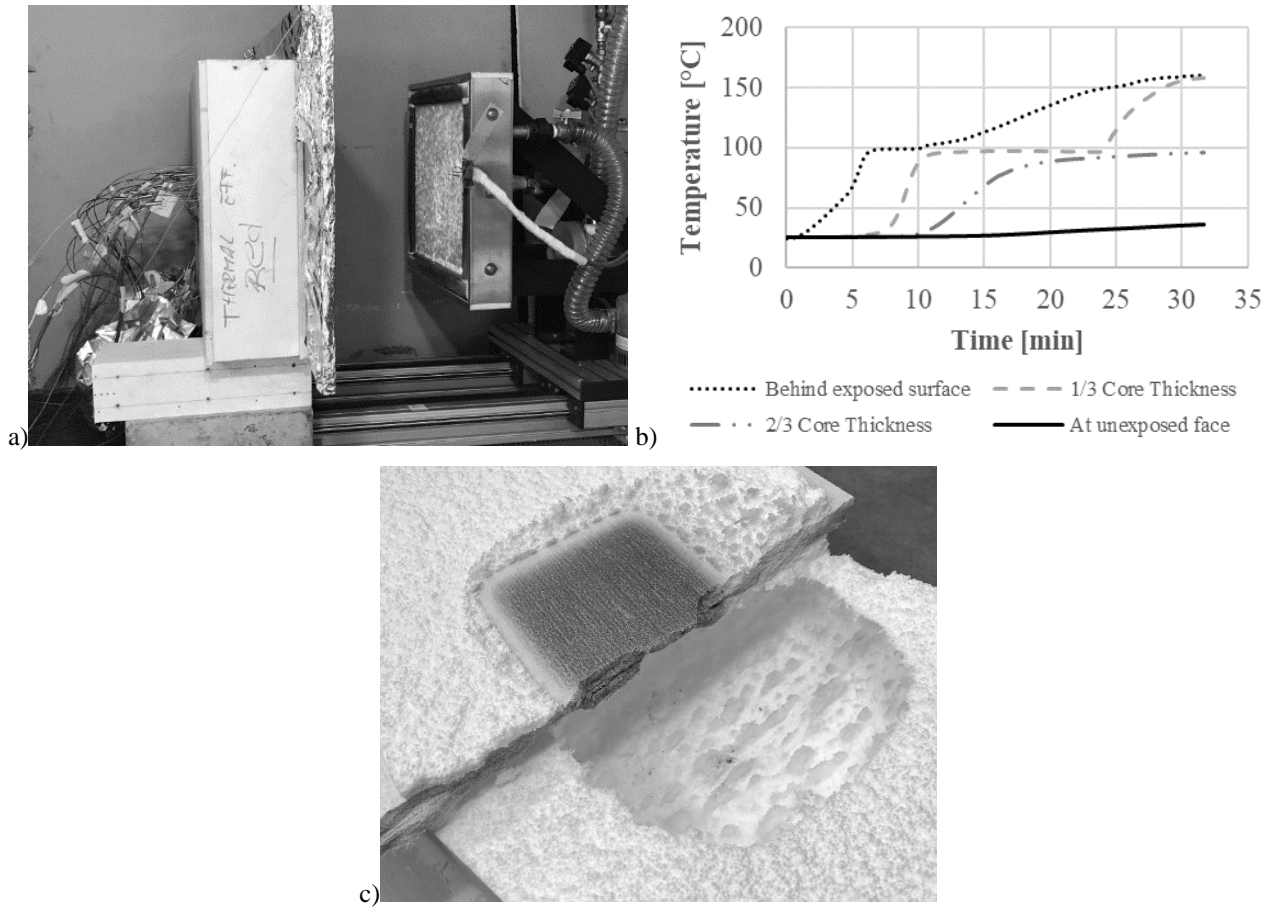


Fig. 4. a) H-TRIS and thermocouples-in-depth setup; b) Temperature evolution at different locations within the core; c) Final condition of the sample after testing.

Regarding the MGO, a maximum temperature of 160°C was measured at the unexposed face of the face sheet directly exposed to the heat source. While the test was running, a clear obscuration in the colour of the board was noticed, but no flaming or smoke was generated. Nevertheless, minutes after the test was over and the heat source was removed, cracks started to appear in the previously exposed area of the MGO facing.

3.2 Residual Tensile Strength of MGO face sheets

In order to assess the response of MGO boards to high temperatures in terms of its ability to maintain its strength, tensile strength tests were performed using a 250 KN loading testing apparatus. Bone-shaped coupons 60 mm wide and 300 mm long were cut from a 12 mm thick MGO board and exposed inside a furnace to temperatures of 100, 200, 250, 300, and 350°C. After heating, and reaching the target temperature, samples were allowed to cool down for a period of 24 hours.

Samples were then tensile tested at a rate of 2 mm per minute while strain was measured on both faces of the board using strain gages. Experimental results were used to obtain residual tensile strength and residual tensile elastic modulus for MGO after a heating regime reaching a target temperature (see *Figure 5*).

Key governing factors that define the fire performance of structural insulated panels used in floor systems

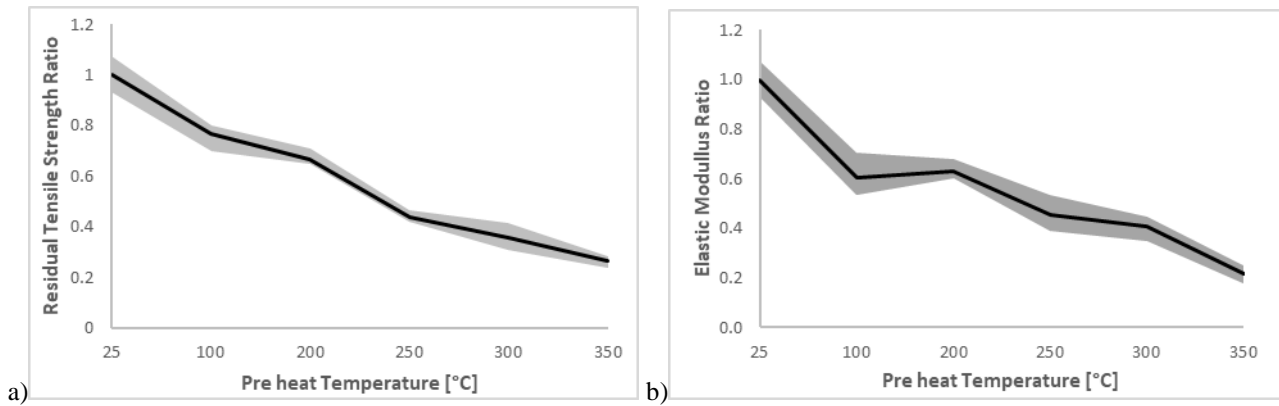


Fig. 5. Reduction of a) residual tensile strength b) residual tensile elastic at elevated temperatures.

4 DISCUSSION

Efficient performance of a sandwich panel is heavily dependent on its ability to maintain integrity allowing for complete composite action between layers. Each component of the structure has a specific function; it has been demonstrated that the face sheets (MGO in this case) take the load and that the core (EPS in this case) can be considered as another ply with negligible stiffness and strength properties. Therefore, design of panelling systems is driven by the failure mechanism that may take place in each of its components [10]. At ambient conditions, material properties, layer dimensions and loading conditions define these failure mechanisms.

In this study, a bending moment applied to the system resulted in initial failure of the lower MGO board due to the build-up of tensile stresses higher in magnitude than its tensile strength. At that point, the core layer and upper MGO board combined bending strength was significantly reduced, and failure of the SIP as a result. Prior to failure, no wrinkling in the upper MGO board was observed. Since no debonding between MGO and EPS was noticed either, it is concluded that the bond between the facings and the core was not breached throughout the loading process and that the core performed its stress distribution role efficiently up to the point of failure.

Under the premises of a) no loss of bonding between MGO and EPS and b) isotropic EPS behaviour, the stress-strain analysis described in Section 2.2 provides a reasonable approximation of the relation between bending stress and deflection at mid span of the panel. Agreement between analytical and experimental results is best at early stages of loading, but drift apart at higher loads. This seems natural as bending of the panel is never a fully elastic process. Hence, the analysis described herein is mainly valid for loading states below a third of the bending capacity.

Fire scenario conditions (i.e. imposition of a heat flux and raise of temperature) provokes degradation of the MGO board and EPS core as described in Section 3.1. At low heat fluxes such as the ones described, which can be easily reached in a household fire, it was demonstrated that even with the face sheet acting as a thermal barrier, the EPS degrades quickly. If this is the case, the core's ability to distribute stresses is lost and the MGO face sheets no longer work in unison. Therefore, the whole performance of the panel narrows down to the facings ability to a) adequately encapsulate the core, and b) maintain its tensile strength at elevated temperatures. Degradation of MGO is therefore a critical aspect.

The starting point of the study was set under the premise that this process is not reversible and therefore the reduction of material strength is a consequence of the maximum temperature reached. Based on this principle it can be concluded (conservatively at least) that at 100°C, there is a

reduction of 20% to 30% in tensile strength and of 30% to 45% in the tensile strength modulus of elasticity of MGO. At this point, it is possible to calculate new deformations of the SIP when exposed to a heating regime, by using the analytical model described herein. Nonetheless, this model needs to be corroborated by performing simultaneous heating and loading tests on structural elements in bending. In this sense, the fact that MGO boards cracked shortly after the heat source was removed (as described in Section 3.1) becomes relevant as the phenomenon observed might be caused by the steep thermal gradient resulted from a sudden cooling process. Although this condition was avoided in the heating procedure described in Section 3.2, the behaviour and its possible consequences (additional loss of tensile strength) needs further analysis.

5 CONCLUSIONS

The following can be concluded based on findings described herein:

- SIPs made from MGO boards as face sheets and EPS as core subject to bending conditions exhibited tensile fracture of the bottom sheet due to failure of the MGO tensile strength capacity. No wrinkling or debonding was observed during the loading period;
- An analytical model that describes the bending stress-strain state of the SIP shows an acceptable approximation to experimental results, particularly for the early stages of the stress – deflection plot, where elastic behaviour still applies;
- When exposed to incident heat fluxes of 15 – 20 kW/m² on one of the face sheets, the core EPS exhibited a degradation front triggered at temperatures close to 100°C. No flaming was observed in either material at any stage of the test
- Residual tensile strength and residual tensile modulus of elasticity was determined for MGO heated at 100, 200, 250, 300 ,and 350°C;
- MGO shows a reduction of 0.76 for tensile strength for samples heated up to a target temperature of 100°C and a reduction of 0.26 for samples heated up to 350°C;
- MGO shows a reduction of 0.61 for tensile modulus of elasticity for samples heated up to a target temperature of 100°C and a reduction of 0.22 for samples heated up to 350°C.

ACKNOWLEDGEMENTS

The authors wish to thank the Australian Research Council (ARC) for the initial funding provided for this research and Vision Developments Australia for providing the samples used for testing.

REFERENCES

1. Mark Lawson, Ray Ogden, Chris Goodier (2014), *Design in Modular Construction*. CRC Press.
2. Lukasz Smakosz and J Tejchman (2014). *Evaluation of strength, deformability and failure mode of composite structural insulated panels*. *Materials & Design* (1980-2015), 54. pp 1068-1082.
3. A. Vaidya, N. Uddin and U. Vaidya, (2010). *Structural Characterization of Composite Structural Insulated Panels for Exterior Wall Applications*. *Journal of Composites for Construction*, 14(4). pp 464-469.
4. Gordon M. Cooke (2004). *Stability of lightweight structural sandwich panels exposed to fire*. *Fire and Materials*, 28(2-4). pp 299-308.

Key governing factors that define the fire performance of structural insulated panels used in floor systems

5. Victor Birman, George A. Kardomateas, George J. Simitzes, Renfu Li (2006). Response of a sandwich panel subject to fire or elevated temperature on one of the surfaces. *Composites Part A: Applied Science and Manufacturing*, 37(7). pp 981-988.
6. Mohamed Rusthi, Anthony Ariyanayagam, Mahen Mahendran, Poologanathan Keerthan (2017). *Fire tests of Magnesium Oxide board lined light gauge steel frame wall systems*. *Fire Safety Journal*, 90(Supplement C). pp 15-27.
7. Mohammed Mousa, Nasim Uddin (2011). *Flexural Behavior of Full-Scale Composite Structural Insulated Floor Panels*. *Advanced Composite Materials*, 20(6). pp 547-567.
8. Leif A. Carlsson, George A. Kardomateas (2011). *Structural and Failure Mechanics of Sandwich Composites* (Vol. 121). Dordrecht: Springer Netherlands, Dordrecht.
9. Howard G. Allen (1969). *Analysis and design of structural sandwich panels*. Oxford: New York, Pergamon Press.
10. Christos Kassapoglou (2013). *Design and analysis of composite structures: with applications to aerospace structures*. John Wiley & Sons.

EXPERIMENTAL AND NUMERICAL INVESTIGATIONS ON THE LOAD-BEARING BEHAVIOUR OF AN INNOVATIVE PRESTRESSED COMPOSITE SLAB SYSTEM UNDER A NATURAL FIRE SCENARIO

P. Schaumann¹, P. Meyer¹, M. Mensinger², S. K. Koh²

ABSTRACT

In Germany, regulations for hollow spaces in slab systems require a 30-minutes standard fire resistance of the load-bearing steel construction. Within a current national research project, a natural fire scenario for the hollow space is developed based on realistic fire loads and ventilation conditions in the hollow space. Assuming this realistic fire scenario in the hollow space, two large-scale tests on an innovative composite slab system are performed to evaluate the influence on the load-bearing behaviour of a composite slab system.

In this paper, experimental and numerical investigations regarding the heating and load-bearing behaviour of an innovative composite slab system under the natural fire scenario of hollow spaces are presented. The objective is to evaluate the influence of a newly developed natural fire scenario for hollow spaces on the load-bearing behaviour of the slab system based on the performed large-scale fire tests. Furthermore, a three-dimensional numerical Abaqus model, which is validated against test data, will be used for an enhanced understanding of the load-bearing behaviour.

Keywords: Innovative slab system, natural fire scenario, experimental and numerical investigations

1 INTRODUCTION

At the present time, the importance of a resource-saving and sustainable construction comprises a significant part in the design stage of a structure because of regulations for climate protection. Therefore, an integrated and sustainable composite slab system was developed in several research projects [1, 2], considering a high flexibility and adaptability of the usage over the entire lifecycle of the building without affecting the load-bearing structure. This integrated and sustainable composite slab system (so-called *InaDeck*) consists of a prestressed concrete slab, an unprotected, bisected hot rolled I-profile with composite dowels either in puzzle or clothoidal shape, and removable floor panels on the top of the I-profile (see Fig. 1). This slab system was developed as a precast system for systems length up to 16 m and a live load of 5 kN/m². The standard fire resistance R90 for the fire scenario below the slab system has already been proven successfully [1, 3].

In addition to the national requirements for the fire scenario below the slab system, regulations exist for hollow spaces concerning the fire resistance of the load-bearing structure of slab systems. The national regulations [4] require a 30-minutes standard fire resistance of the load-bearing steel construction of the composite slab system. Thus, until today fire protection is required for the steel construction of the composite beam to achieve 30 minutes standard fire resistance (R30). This requirement is limiting the competitiveness of composite beams in comparison to other slab systems. However, it is in doubt that fire loads and ventilation conditions in the hollow space are suitable to reach temperature levels comparable to the ISO standard fire curve. Therefore, in a current national research project, a natural fire scenario for the hollow space is developed based on realistic fire

¹ Institute for Steel Construction, Leibniz Universität Hannover, Hannover, Germany. Professor P. Schaumann (e-mail: schaumann@stahl.uni-hannover.de); PhD Candidate P. Meyer (e-mail: meyer@stahl.uni-hannover.de)

² Chair of Metal Structures, Technische Universität München, München, Germany. Professor M. Mensinger (e-mail: mensinger@tum.de); PhD Candidate S. K. Koh (e-mail: sk.koh@tum.de)

loads and ventilation conditions in the hollow space [1, 5]. Assuming this realistic fire scenario in the hollow space, two large-scale tests were performed on the slab system *InaDeck*.

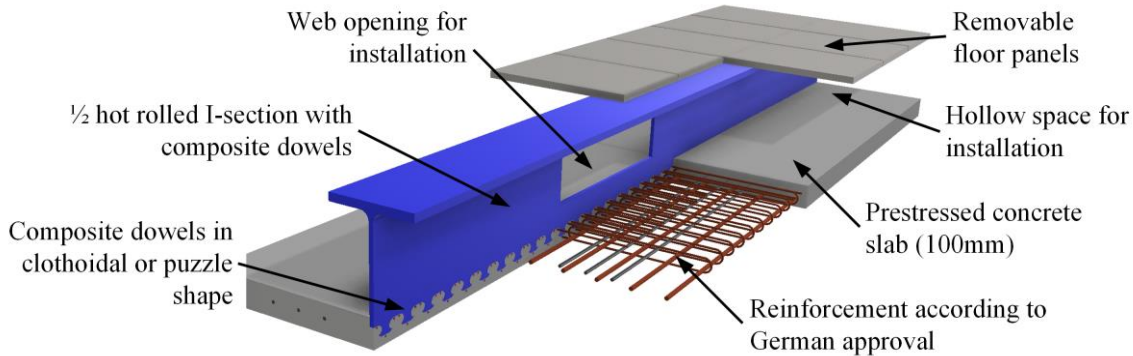


Fig. 1. Overview of the innovative composite slab system *InaDeck*.

In this paper, the experimental investigations on *InaDeck* will be presented. Throughout the heating phase, the specimens are subjected at first to the fire scenario for the hollow space and later to the ISO standard fire curve. Besides the load-bearing behaviour of the slab system, the influence of the web opening on the load-bearing behaviour will be discussed. Furthermore, a numerical three-dimensional Abaqus model, which is validated against the test data, will be presented and used for an enhanced comprehension of the load-bearing behaviour.

2 EXPERIMENTAL INVESTIGATIONS

2.1 Natural fire scenario “hollow space”

As aforementioned, the regulations for the unprotected load-bearing steel construction of composite slab system in the hollow space require a 30-minutes standard fire resistance. Actually, the fire loads and ventilation conditions are not sufficient to reach a comparable fire scenario according to the ISO standard fire curve. For this reason, small-scale tests were performed based on the real fire loads and ventilation conditions to verify and develop a realistic fire scenario for the hollow space of slab systems [5]. A simplified curve for the hollow space of a slab system was derived based on the 95%-fractile value of the small-scale tests (see Fig. 2). This natural fire scenario, named *hollow space* in the following, is characterised by three parts. First, the fire scenario is a linear increase of the temperature up to 500 °C within 5 minutes, followed by a constant temperature level of 500 °C for 10 minutes. Afterwards, the temperature decreases exponentially until reaching room temperature again.

In the fire test, the descending branch of the fire scenario was approximated with a linear decrease. After the fire scenario *hollow space*, the specimens are subjected to the ISO standard fire curve until the failure of the slab system (see Fig. 2). The ISO standard fire curve is started in the cooling phase of the natural fire scenario after 25 minutes.

2.2 Specimens of experimental investigations

In the large-scale fire tests, the load-bearing behaviour was investigated for two specimens of the slab system *InaDeck*, each with a length of 7.8 m. The second specimen has a web opening with the dimensions of 750 x 250 mm. The web opening is typically positioned at the side of the slab system with a distance of 1.025 m from the edge of the specimen. The specimens consist of a bisected

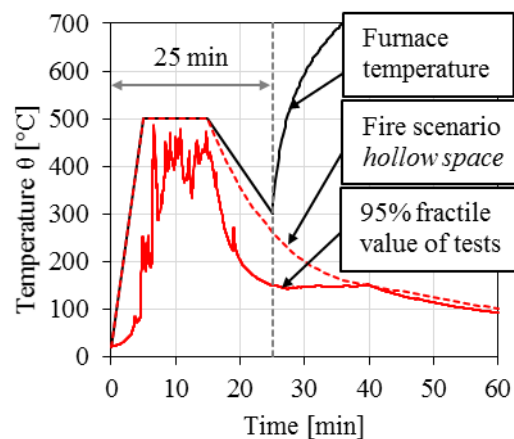


Fig. 2. Temperatures versus time curves of fire scenario for hollow spaces and the furnace temperature.

HE800A with composite dowels in clothoidal shape with a longitudinal distance e_x of 100 mm according to the German approval [2] and a prestressed concrete slab (four prestressing steels) with a width of 1.25 m and a thickness of 100 mm (see Fig. 3). The properties of the used materials are listed in Table 1.

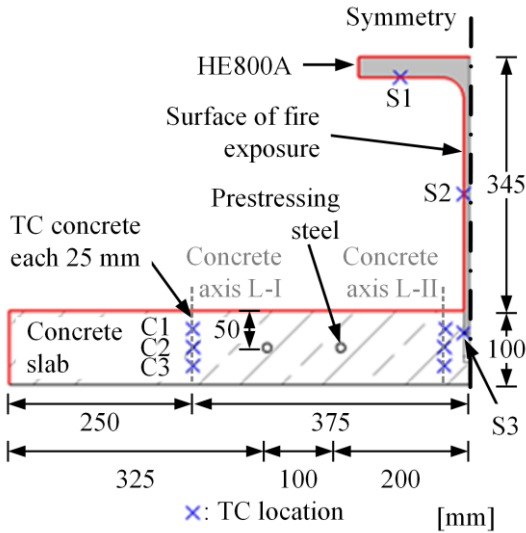


Fig. 3. Cross-section of the specimens with the positions of thermocouples (TC).

Table 1. Material properties of the different parts of the specimens.

Material	Measured values
Steel S355	$f_{a,y} = 446 \text{ N/mm}^2$ $f_{a,u} = 546 \text{ N/mm}^2$ $E_a = 210,000 \text{ N/mm}^2$
Concrete C50/60	$f_{c,cube,m} (28 \text{ d}) = 75.5 \text{ N/mm}^2$ * $f_{c,cube,m} (113 \text{ d}) = 77.4 \text{ N/mm}^2$ ** $f_{c,cyl,m} (28 \text{ d}) = 70.4 \text{ N/mm}^2$ * $E (28 \text{ d}) = 45,500 \text{ N/mm}^2$ *
Reinforcement BSt500 (Ø8, Ø16)	$f_{s,0,2,k,m} = 551 \text{ N/mm}^2$ * $f_{s,t,m} = 648 \text{ N/mm}^2$ * $E_{s,m} = 202,412 \text{ N/mm}^2$ *
Prestressing steel St1660/1860 (Ø12.5)	$f_{p,0,2,k} = 1660 \text{ N/mm}^2$ *** $f_{p,t} = 1860 \text{ N/mm}^2$ *** $E_p = 196,000 \text{ N/mm}^2$ ***

* Mean value of three specimens

** Determination on date of fire test

*** Nominal values

The prestress value of each prestressing steels amounts to $\sigma_{pmo} 1075 \text{ N/mm}^2$. This value is based on the previous project [1], in which the specimens were prestressed according to the self-weight g_k (including the removable floor panels) and the live load of 2.5 kN/m^2 . The arrangement of the reinforcement of the composite dowels corresponds to the German approval [6]. Based on the design at room temperature of the slab system, the diameter of the longitudinal reinforcement was determined to be 16 mm, and the diameter of the upper reinforcement and concrete reinforcement of the composite dowels were determined to be 8 mm.

The temperature during the fire tests are measured with thermocouples (TC) of type K and are assembled at the I-profile and in the concrete slab of the slab system. The temperature of the bisected HE800A was measured at the flange (S1), in the middle of the web (S2), and at the beginning of the composite dowel (S3) (see Fig. 3). To evaluate the influence on the heating behaviour of the web opening, two additional TC at the web opening were applied; one TC above and one beneath the web opening. Besides the temperature distribution through the height, the temperature field in longitudinal and transversal direction was recorded. Also, the displacement of the specimens were measured in the load introduction axis (axis I, axis IV) and in the middle of the specimens (between axis II and axis III) (see Fig. 4 a)). Within the next section of this paper, the reasons for this set-up of the measurement of the displacement will be explained.

2.3 Test set-up for natural fire scenario hollow space

Usually, *InaDeck* is assembled with the concrete slab in the tension zone of the cross-section (see Fig. 1; Fig. 4 b)). To enable the fire scenario *hollow space* within the test facilities (furnace) and to perform a four-point bending test, a special test set-up was invented. In this special test set-up, the specimens are rotated along the longitudinal axis so that the concrete slab is at the top of the cross-section (see Fig. 4 a); Fig. 4 b)). To realise the same stress distribution in the specimens with the concrete slab at the top of the cross-section, the specimens are fixed in the third points (axis II and III) and loaded at both ends (axis I and IV). In doing so, the same stress distribution in the specimens is realised as in the assembly situation of the slab system *InaDeck* (see Fig. 5 b)). The thermal expansion of the specimen is not impeded by this static system of the test set-up. The fixed boundary conditions of axis II and III are realised with welded plates to the web of the bisected I-

profile. These plates are established through the concrete slab and connected to the suspension of the fire test consisting of HE180B profiles (see Fig.5 a)).

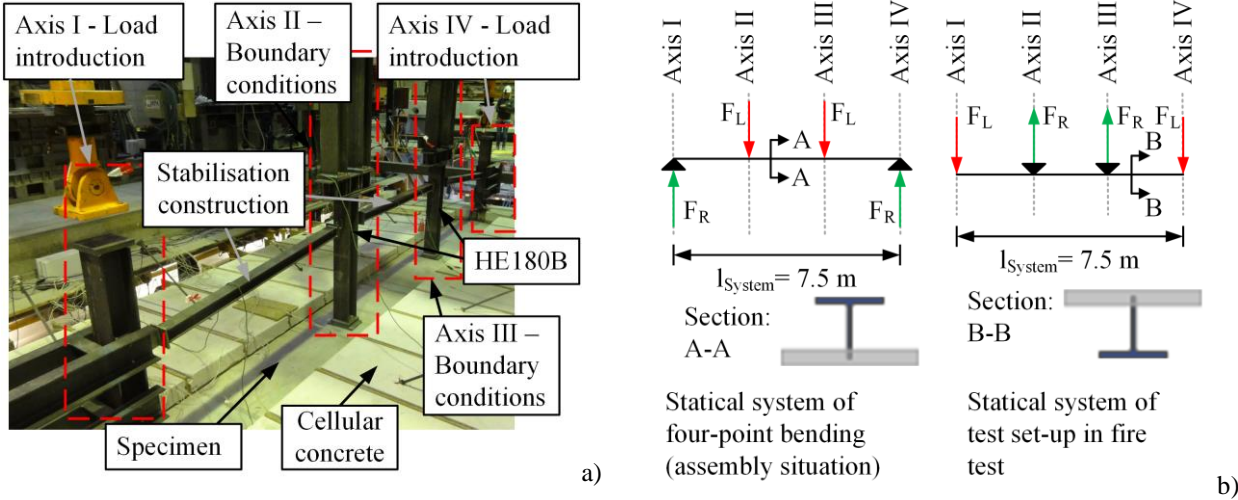


Fig. 4. a) Innovative test set-up of fire test; b) Comparison of different static systems of the test set-up of the fire tests. The utilisation factor in fire of the slab system *InaDeck* with a length of 16 m (η_{16m}) amounts to 29.5 %. In the fire test each specimen has a span width of 7.5 m. To compare and transfer the results of the fire to the assembly situation with a length of 16 m, the utilisation factor ($\eta_{7.5m}$) in the fire test is equal to the utilisation factor of the slab system *InaDeck* with a length of 16 m. The utilisation factor within the fire test is based on the design values of the materials of the specimens which corresponds to a test load of 85 kN in each load introduction axis. Moreover, the self-weight of the cellular concrete is considered within the utilisation factor $\eta_{7.5m}$. Within the fire test the acting load on the specimens are kept constant over the time. The specimens in the fire test are subjected to the fire scenario as given in Sect. 2.1. A more detailed description of the test set-up is given in [7].

3 RESULTS OF EXPERIMENTAL INVESTIGATIONS

Within the fire tests, the temperature evaluation of the steel profile and the concrete slab are measured. The temporal temperature development of all measurement points of both specimens is shown in Fig. 5 and Fig. 6.

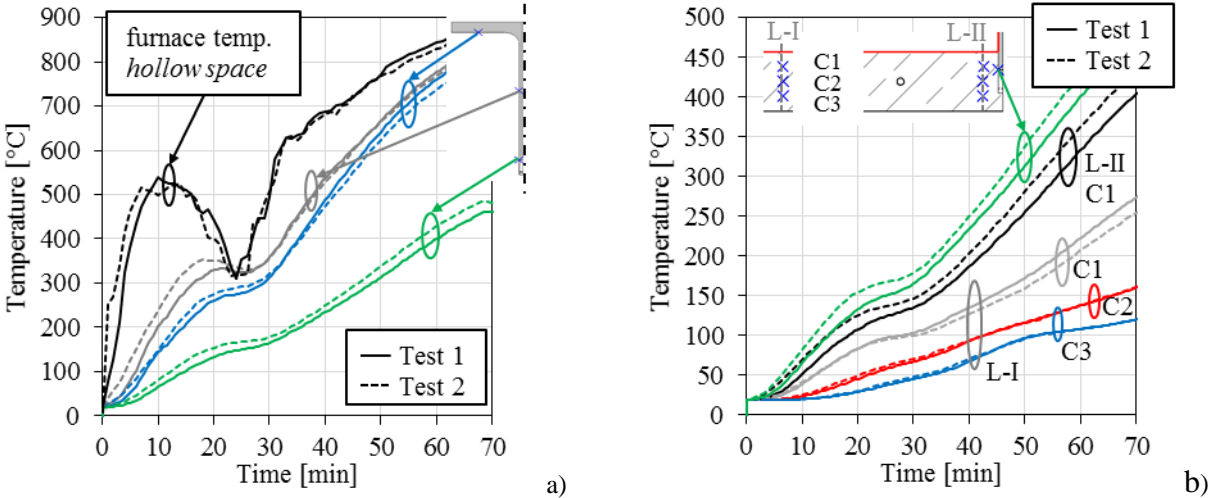


Fig. 5. Average temperature versus time curves; a) Temperature evaluation of the bisected I-profile; b) Temperature evaluation in the concrete slab.

The temperature development of the both specimens in the parts of the cross-section without a web opening are nearly identical. The temperatures of the I-profile are presented in Fig. 5 a) and as well

the measured furnace temperatures. Before the cross-section is subjected to the ISO standard fire curve, the temperatures of the steel section reach a maximum value of approximately 350 °C. Within the cooling phase of the fire scenario *hollow space*, the temperatures of the steel section are decreasing whereas the temperatures in the concrete slab are remaining nearly constant. The temperatures of the unprotected steel section reach approximately 800 °C, and the composite dowels have a maximum temperature of approximately 475 °C (see Fig. 5 a)). Due to the heat transfer from the steel section into the concrete slab (axis L-II) around the composite dowels, the concrete slab has locally higher temperatures. After the fire impact a difference of approximately 150 °C appears between the axis L-I and L-II in the concrete slab. Furthermore, the temperature evaluation of the steel and concrete section at the web opening are measured (see Fig. 6).

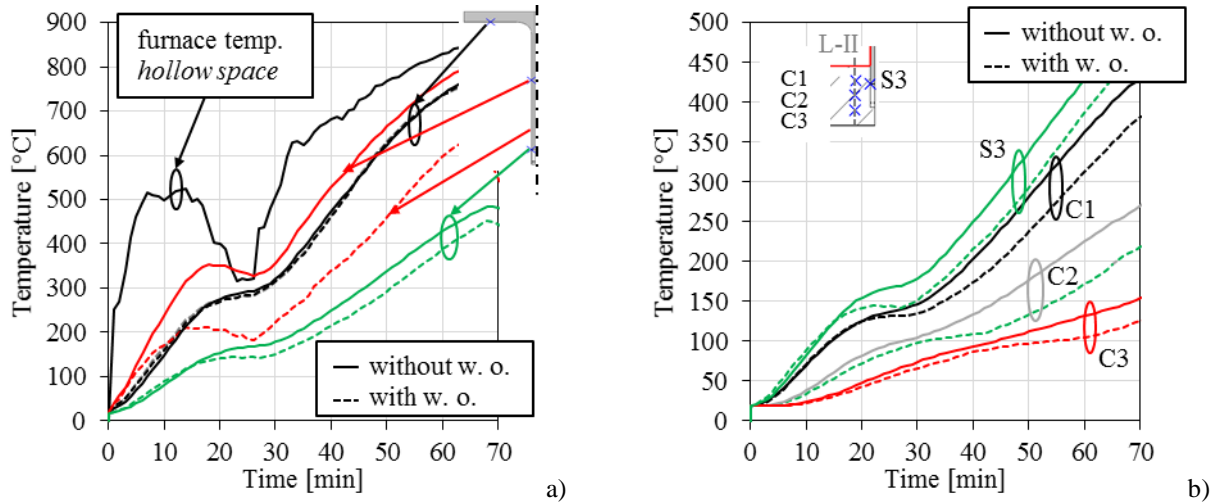


Fig. 6. Comparison of the temperature versus time curves of the section with and without web opening of specimen 2; a) Temperature time curves in the bisected I-profile; b) Temperature time curves in the concrete slab (only axis L-II).

An influence on the temperature development in the concrete slab (axis L-II) and at the composite dowel is noticeable. The difference between the section without and with a web opening (w. o.) are similar at the end of the fire impact. Within the impact through the natural fire scenario, a significant difference in the temperatures is not observed.

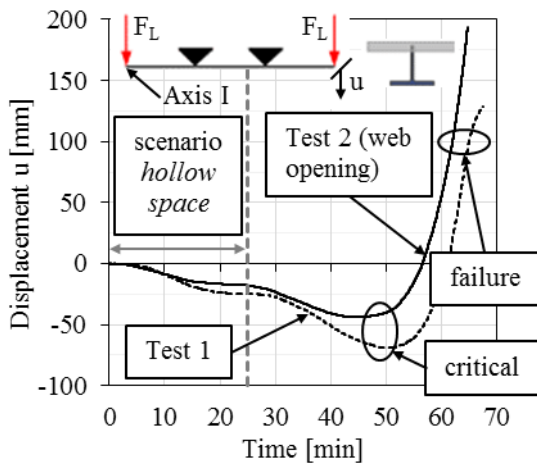


Fig. 7. Displacement behaviour of the specimens with and without web opening.

Table 2. Displacements and appropriate temperatures of significant points throughout the displacement behaviour of the slab system.

	Specimen 1	Specimen 2 (web opening)
$\theta_{critical, flange}$	635 °C	534 °C
$\theta_{failure, flange}$ ($u = 100$ mm)	801 °C	755 °C
$t_{critical}$	~ 50 min	~ 44 min
$t_{failure}$ ($u = 100$ mm)	~ 65 min	~ 62 min
$u_{max, critical}$	- 68.8 mm	- 43.9 mm

The displacement behaviour of the natural fire scenario is significantly different from the behaviour of a slab system with a fire impact below the concrete slab. The unprotected steel profile is directly exposed to the fire impact and heats up significantly faster than the concrete slab. As a consequence of this, a thermal gradient occurs within the cross-section (see Fig. 5). Consequently, the steel profile expands more than the concrete slab. Hence, a thermal induced bending of the cross-section occurs towards the concrete slab. The thermal induced bending of the cross-section results in a

movement of the specimens against the loading of the specimens until the critical temperature of the steel profile is reached (see Fig. 7).

Once the critical temperature (maximum displacement against the load) of the steel profile of the cross-section is reached, the displacement in the direction of the loading is increasing until bending failure of the specimens. The failure times and temperatures are given in Table 2. The fire tests prove that the natural fire scenario *hollow space* is not critical for the load-bearing behaviour of this slab system. Moreover, even a fire resistance R30 is achieved within the performed fire test of the unprotected steel beam of the composite slab system *InaDeck*.

4 NUMERICAL INVESTIGATIONS

4.1 Numerical model

For an enhanced understanding of the load-bearing behaviour of *InaDeck* under this natural fire scenario, a three-dimensional numerical Abaqus model (see Fig. 8) is validated against the test data. Volume elements are used for the steel profile and the concrete slab (8-node elements). The reinforcement and the prestressing steel is modelled with truss elements (2-node elements) which are embedded in the concrete slab. In the thermal analysis, the composite dowels are modelled explicitly for the validation of the thermal material properties. The composite dowels in the mechanical analysis are modelled with connector elements (CONN3D2). These connector elements contain an elastic stiffness and a non-linear branch which is derived on the load-slip capacity of experimental investigations of the composite dowels [1]. In tangential direction, friction with a coefficient of 0.3 and in normal direction “hard contact” are used as contact formulations for the contact between the concrete and the web of I-profile.

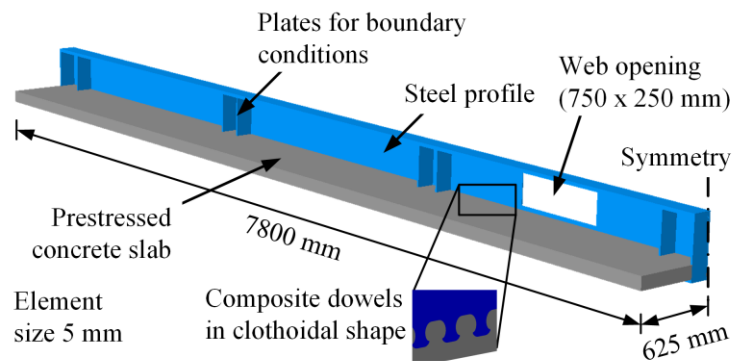


Fig. 8. Numerical model of the specimens

4.2 Properties of materials

Thermal and mechanical material properties for steel, reinforcement, and prestressing steel according to EN 1992-1-2 and EN 1994-1-2 are used within the numerical model. The isotropic elastic-plastic model is applied as constitutive law for these materials.

For the temperature-dependent material properties of concrete the data of EN 1994-1-2 are applied. The upper limit of the conductivity and the specific heat with a moisture content of 7 % are used to describe the thermal properties of concrete. The formulations of EN 1992-1-2 with a linear softening behaviour are used for the stress-strain relation of the concrete in the compression area. The tensile stress-strain relation is approximated with a bi-linear behaviour.

The thermal conductance between the composite dowels and the concrete slab is considered as perfect within the thermal analysis.

4.3 Thermal validation of simulation

Initially, a thermal simulation of the specimens is performed to validate the thermal model before the mechanical analysis. By applying the aforementioned temperature-dependent material properties of steel and concrete, the temperature field within the cross-section is approximated accurately (see Fig. 9). In the thermal simulation of the specimens, shadow effects are considered at the flange and at the web of the I-profile. These shadow effects have a significant influence on the temperature evaluation in the steel section of the specimens and are caused by turbulences in the furnace.

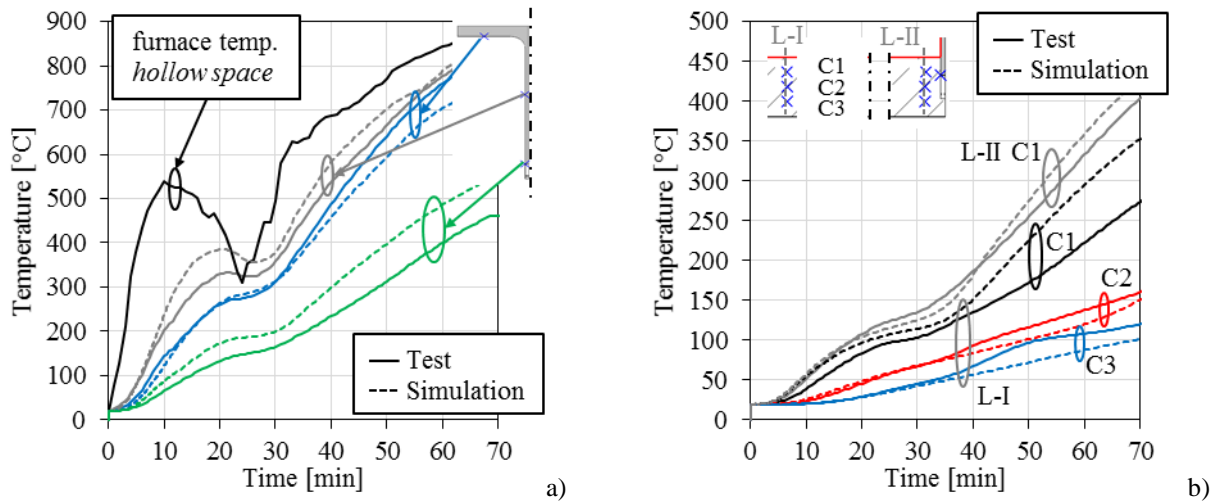


Fig. 9. Comparison of temperature versus time curves of specimen 1; a) temperature evaluation of I-profile; b) temperature evaluation in the concrete slab.

4.4 Mechanical validation of simulation

Based on the validated thermal model of the specimens, the load-bearing behaviour is investigated in the simulation. Within the fire test, a thermal gradient in the cross-section occurs (after 10 minutes of ~ 175 °C). Therefore the steel profile experiences a significantly greater expansion than the concrete slab. Hence a bending towards the concrete slab occurs as well as a thermal elongation in the longitudinal direction of the specimens. Based on the higher thermal expansion of the steel profile, the thermal expansion of the steel profile causes a tensile stress distribution in the concrete slab of the cross-section. The tensile stress distribution in the concrete slab is increasing with increasing time and temperature gradient until reaching the ultimate tensile strength of the concrete. The maximum tensile strength of the concrete is reached after approximately 10 minutes of the fire impact.

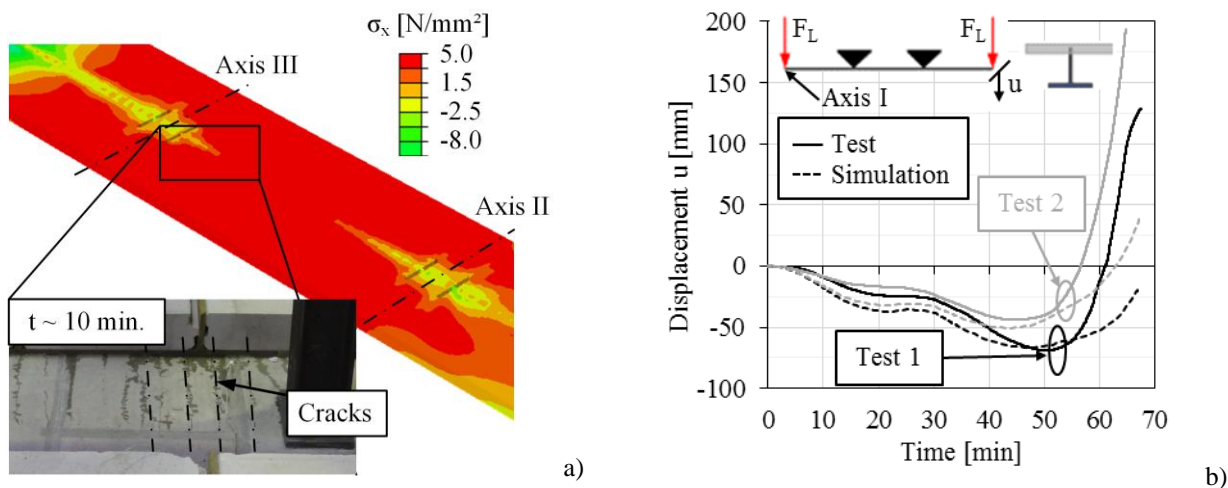


Fig. 10. a) Tensile stress distribution within the concrete slab and crack pattern during the fire test after approximately 10 minutes; b) Comparison of the displacement behaviour of the experiment and simulation.

Cracks are observed in the fire tests at the same time and position in the concrete slabs as in the simulation on the concrete slab (see Fig. 10 a)). The simulation fails since Abaqus is not able to simulate the cracks explicitly when the maximum value of the tensile strength of the concrete is reached. If a temperature-independent tensile strength for the concrete is considered the displacement behaviour can be simulated with the numerical model (see Fig. 10 b)). The displacement behaviour of the composite beam with a temperature-independent tensile strength of the concrete is approximated well with the numerical model. The maximum displacement is approximated accurately with the simulation. The displacement within the first 30 minutes is overestimated because

the temperatures of the steel profile are overestimated (see Fig. 9). The failure time of approximately 67 minutes for the numerical model of specimen 2 coincides with the failure time of the fire tests. Due to the temperature-independent tensile strength, the displacement behaviour is overestimated after reaching the critical point. Within the evaluation of the experimental investigations, a regular crack pattern (distance between each transversal crack: approximately 100 mm) was observed on the top of the concrete slab. This crack pattern results from the thermal expansion of the steel profile which causes a tensile stress distribution in the concrete slab.

5 CONCLUSIONS

In Germany, regulations for hollow spaces require a 30-minutes standard fire resistance of the load-bearing steel construction of a composite slab system. Real fire loads and ventilation conditions in the hollow space of a slab system are less severe in comparison to the ISO standard fire curve. Within this paper, experimental and numerical investigation on the heating behaviour and load-bearing of the innovative composite slab system *InaDeck* are presented under a newly-developed natural fire scenario for the hollow space. In consideration of this fire scenario, two large-scale fire tests are performed to prove, whether the natural fire scenario is critical for the load-bearing capacity of the slab system *InaDeck*. The fire tests demonstrated that the natural fire scenario is not critical for the load-bearing capacity of the slab system. Nevertheless, R30 is reached within the fire tests. A three-dimensional numerical Abaqus model is presented and validated against the test data. The simulation showed that the thermal expansion of the steel section has a significant influence on the tensile stress distribution in the concrete slab and hence on the displacement behaviour.

ACKNOWLEDGMENT

This IGF project (IGF-Nr. 18894N) of the FOSTA is supported via AiF within the programme for promoting the Industrial Collective Research (IGF) of the German Ministry of Economic Affairs and Energy (BMWi), based on a resolution of the German Parliament.

REFERENCES

1. Josef Hegger, Markus Feldmann, Peter Schaumann, et. al (2016). *Integrated and Sustainable Floor Slab Systems in Steel and Composite Structure*. Research Project P 879, FOSTA.
2. Martin Mensinger, Suet Kwan Koh, Peter Schaumann, et. al (2017). *Rise of temperature in hollow spaces of suspended ceilings, in hollow space floors and access floors and its effects on the load-bearing capacity of inner steel elements*. Research Project P 1139, FOSTA (current national research project).
3. Josef Hegger, Markus Feldmann, Peter Schaumann, et al. (2014). *Multifunctional composite slab system with integrated building services - Studies on the load bearing and fire behavior, thermal efficiency and sustainability of a novel composite floor system*. Stahlbau 83 (7), pp. 452–460.
4. Fachkommission Bauaufsicht der ARGEBAU, *Muster-Richtlinie über brandschutztechnische Anforderungen an Systemböden (Muster-Systembödenrichtlinie (MSysBöR))*, Fassung September 2005. (in German)
5. Suet Kwan Koh, Martin Mensinger, Peter Schaumann, et. al (2017). *Fire in hollow spaces: Short circuit as ignition source and the role of ventilation*. 2nd International Fire Safety Symposium (IFireSS), Naples, Italy, 7th - 9th June, 2017. pp. 781-788.
6. Allgemeine bauaufsichtliche Zulassung Nr. Z-26.4-56, Verbunddübelleisten, Deutsches Institut für Bautechnik, 2013. (in German)
7. Peter Schaumann, Patrick Meyer, Martin Mensinger, et. al (2018). *Experimental investigations on the load-bearing behaviour of an innovative prestressed composite floor system in fire*. 12th International Conference on Advances in Steel-Concrete Composite Construction (ASCCS 2018), Valencia, Spain, 27th - 29th June, 2018. (Paper accepted)

LOAD-BEARING FIRE TESTS OF UNPROTECTED COMPOSITE BEAMS PINNED WITH STEEL GIRDERS

R. Dwiputra¹, N. Yotsumoto², T. Hirashima³, F. Ozaki⁴, Y. Murakami⁵, K. Kimura⁶

ABSTRACT

In order to accurately examine the fire resistance of this synthetic floor system, it is necessary to determine not only the behavior of the floor slab accompanying the membrane effect under fire, but also the behavior of the beam itself as the composite beam without fire protection. In this study, load-bearing fire tests on 3 large scale specimens, (1) simply supported beam, (2) protected web-pin-joined beam and (3) unprotected web-pin-joined beam, were conducted to clarify the behavior of unprotected composite beams which are web-pin-joined with girders in case of the standard fire. As the result, the under-fire behavior of simply supported beam and web-pin-joined beam were compared, and the restraint on rotation of the beam end occurred by the web bolt joint was examined. In addition, a thermal stress analysis, which takes into consideration the behavior of high-strength bolted friction joints, was also conducted and showed that the analysis method integrating the model of beam end web pin-joint could approximated this experimental behavior.

Keywords: Fire resistance, Fully composite beam, Pin joint, Unprotected steel beam, Load-bearing fire test, Deflection behavior

1 INTRODUCTION

A fire safety design method by examining fire resistance as a synthetic floor system integrating steel beams and a floor slab with attention paid to the strength increment due to the membrane action of the floor slab system under fire condition has been proposed [1]. Since today in Japanese fire safety design method each element of a steel structure is examined separately, applying this method could make a possibility that the fire protection of the beam can be omitted. In order to accurately examine the fire resistance of this synthetic floor system, it is necessary to determine not only the behavior of the floor slab accompanying the membrane effect under fire, but also the behavior of the beam itself as the composite beam without fire protection. In some previous studies that examined the fire resistance of composite beams, experiments on load-bearing fire tests of simply supported beams [2] or both end fixed beams [3] assuming girder beams have been reported. But there is no experimental study studied in the actual beam web bolt-joint type.

¹ Nihon Sekkei Inc., Tokyo, Japan

e-mail: r-dwiputra@nihonsekkei.co.jp

² General Building Research Corporation of Japan, Osaka, Japan

e-mail: yotsumoto@gbrc.or.jp

³ Professor. Graduate School of Engineering, Chiba University, Chiba, Japan

e-mail: hirashima@faculty.chiba-u.jp

⁴ Associate Professor. Graduate School of Environmental Studies, Nagoya University, Nagoya, Japan

e-mail: ozaki@dali.nuac.nagoya-u.ac.jp

⁵ JFE Steel Corporation, Tokyo, Japan

e-mail: yu-murakami@jfe-steel.co.jp

⁶ Nippon Steel & Sumitomo Metal Corporation, Tokyo, Japan

e-mail: kimura.ze8.kei@jp.nssmc.com

In this study, a load-bearing fire test was conducted to clarify the behavior of unprotected composite beams which are web-pin-joined with girders in case of the standard fire. In addition, a thermal stress analysis, which takes into consideration the behavior of high-strength bolted friction joints [4, 5], was conducted for these experiments in order to clarify the transition of the stress distribution in the composite beam in fire condition, which could not be determined by the experiment.

2 LOAD-BEARING FIRE TESTS OF UNPROTECTED COMPOSITE BEAMS

2.1 Specimens and Experiment Method

In this study, as shown in *Table 1* experiments on 3 large scale specimens, (1) simply supported beam, (2) protected web-pin-joined (3 bolts) beam and (3) unprotected web-pin-joined (6 bolts) beam, were conducted. The experiment on simply supported beam is to clarify the sagging bending strength at the central part of the unprotected composite beam and the fundamental deflection behavior under fire. And, experiments using web-pin-join are experiments to clarify the influence due to the constraint of the end of the beam in case of fire.

The specimen size is shown in *Fig.1*. The composite beam is a fully composite beam (H-300×150×6.5×9, SN400B), stud-bonded with a reinforced concrete (RC) floor slab using flat deck (width 950 mm, thickness 120 mm, Fc 24). The joint of specimen no.2 was designed as a joint using the common number of bolts with fire protection. On the other hand, the joint of specimen no.3 was specified not to be fire-protected but the number of bolts was increased, as shown in *Fig.2* and *Photo 1*.

The loading method was a two-point loading at a position 600 mm on both sides from the mid-span of the composite beam, and the loading load was 1/2 of the load at which the long-term allowable stress of the simply supported composite beam occurs. Considering the weight of the floor slab itself, the load at the loading point is 25.7 kN at each point. For the displacement, the vertical displacement of the composite beam and the horizontal displacement at the end were measured. Before heating, load was applied up to the target load, held for 15 minutes, and then heated under constant load under ISO standard heating temperature curve. The temperature was measured at the central part (18 points×3 specimens) · Fire-protected joint part (12 points×2 sides) · Unprotected joint part (12 places x 2 side).

2.2 The Condition of Each Test Specimen after the Experiment

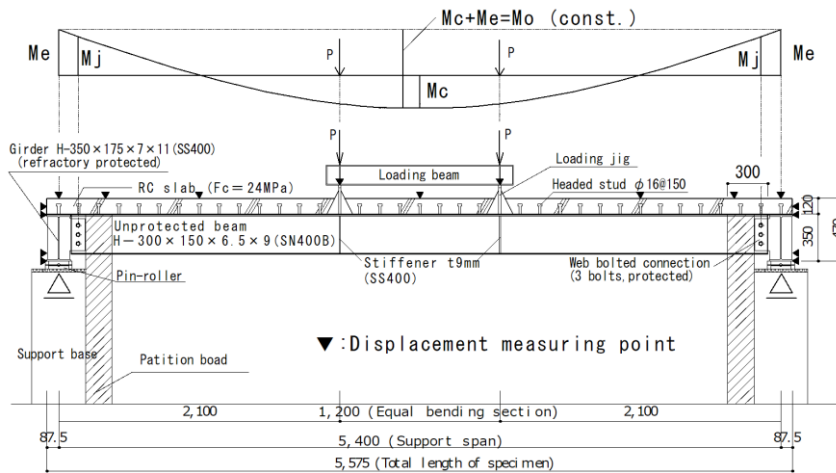
The condition of each test specimen after the experiment is shown in *Photo 2* (a) - (d).

In simply supported beam specimen No. 1, large bending deformation occurred as shown in *Photo 2* (a), and a bending failure was confirmed at the upper end of the concrete slab near the loading point. On the other hand, as shown in *Photo 2* (b), in No.2 and No.3, unlike the deformation situation of No.1, beam end rotation constraint was observed. Bending cracks from the lower end of the slab occurred in the section of about 1700 mm from the center of the span on both sides, and as shown in *Photo 2* (c), bending cracks occurred from the upper end of the concrete slab in the section of about 1000 mm from the beam end. This indicates that the rebar inside the slab was resisting to the hogging bending moment due to the beam end. The section in which cracks from the upper end of the slab occurred in No.3 was a section closer to the beam end than No.2. This is because in No.3, the pin-joint was unprotected so that the rotation restraint at the joint part was reduced.

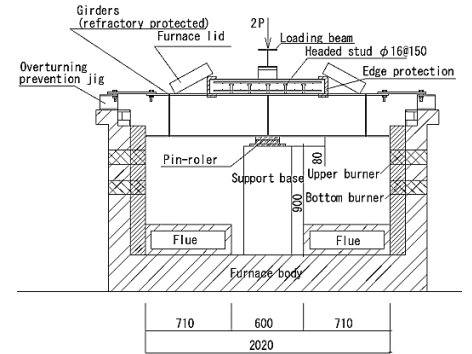
As shown in *Photo 2* (d), both the shear buckling of the web and the local buckling of the lower flange were confirmed at both positions near the joint. In the cooling process, even the predetermined load was kept applied, neither the joint failure nor a large deformation was observed in both cases. It is considered that the headed stud and rebars in the slab on the orthogonal beam contributed to the rotation restraint of the beam end.

Table 1. Test parameters

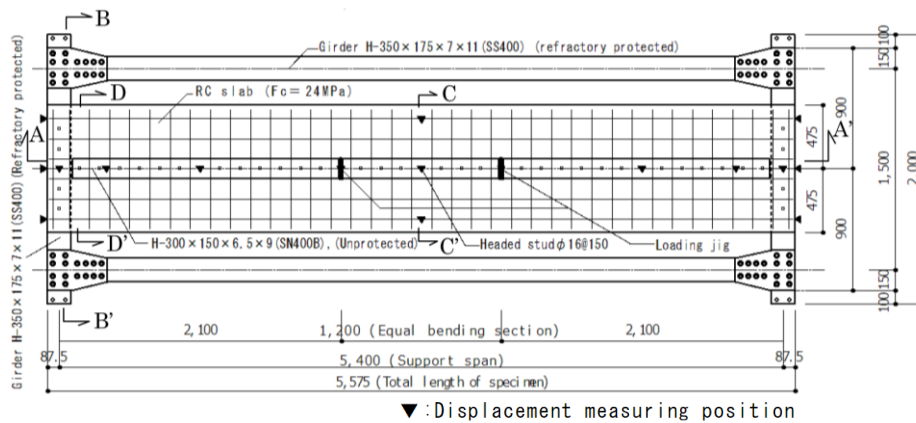
Specimen number	Boundary Condition of the ends	Number of bolts	Fire protection		
			steel beam	pin joints	steel girders
No.1	Simply supported				
No.2	Web bolted to steel girders	3 bolts(3 bolts×1 row)	unprotected	protected	protected
No.3		6 bolts(3 bolts×2 rows)		unprotected	



(a) A-A' section

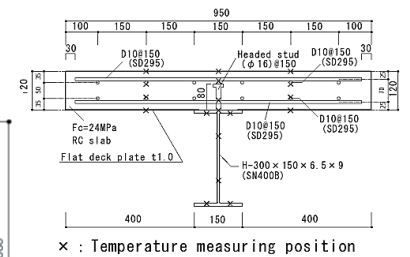


(b) B-B' section



(c) C-C' section (mid-span)

(e) Plan view



(d) D-D' section (pin joint)

Fig 1. Specimen No.2 drawing (No.1 and No.3 are same)

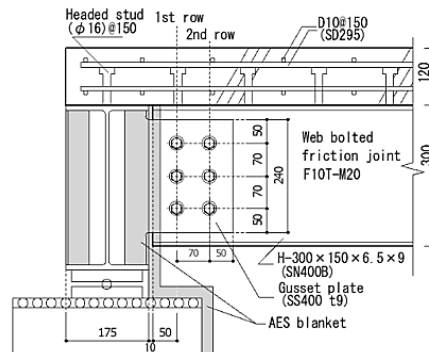
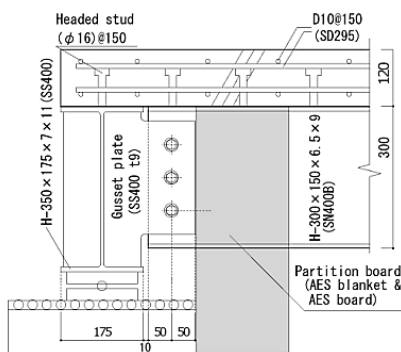
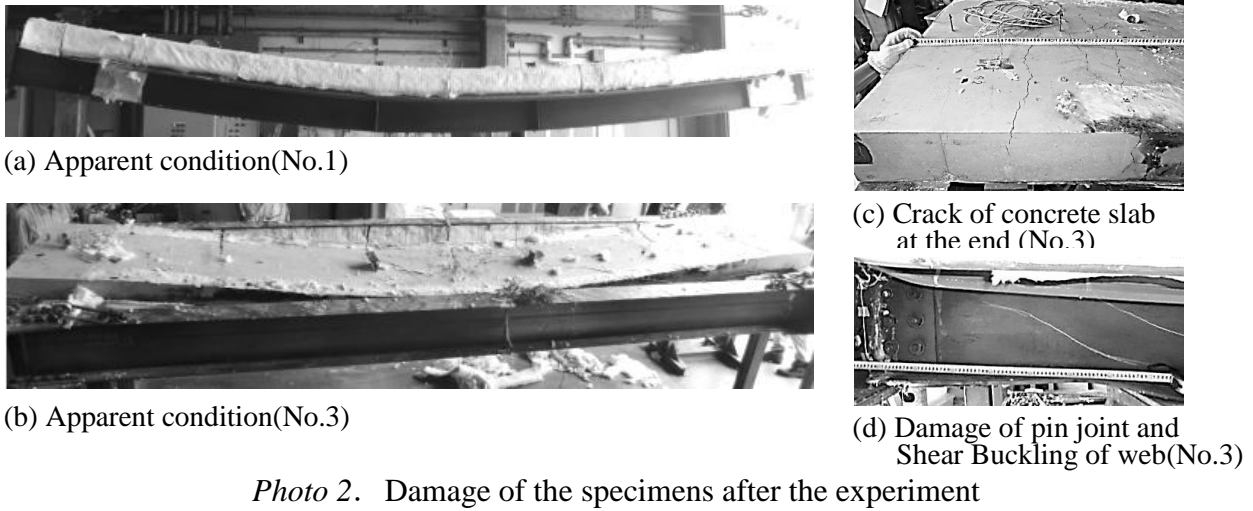


Fig. 2. Detail of the pin joint (left : No.2, right : No.3) Photo 1. Protect condition of thermocouples at joint



2.3 Temperature Measurement Result

Fig. 3 (a) shows the temperature measurement result of the center part of the beam, with sample No.2 as a representative. The results in the central part of the beam were similar for all three specimens. However, heating ended at 30 minutes for No.1, 62 minutes for No.2, and 58 minutes for No.3. Around 30 minutes after heating, the steel temperature of the lower flange at the center part and the unprotected web was difference from the ISO standard heating by 50°C. The temperature of the lower flange itself was about 800°C at 30 minutes and about 930°C at 60

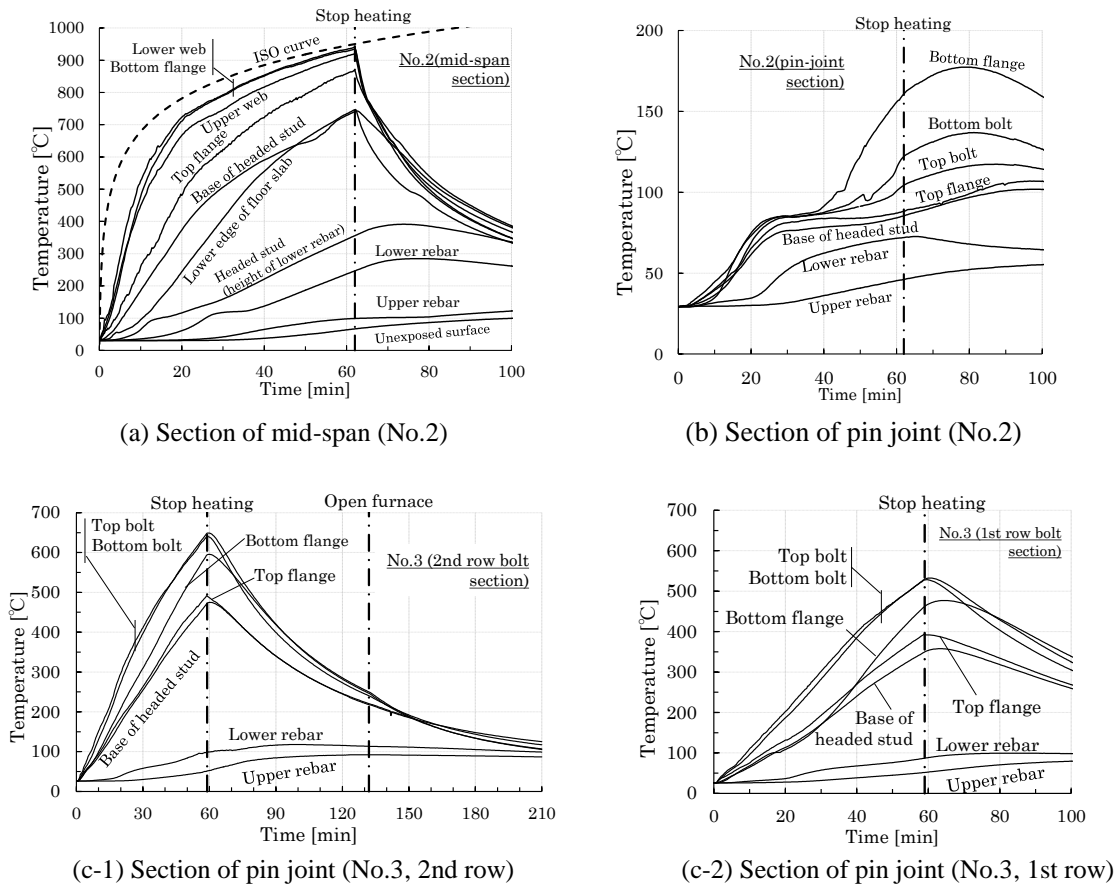


Fig.3. Measurement results of temperature

minutes. About 30 minutes at the end of heating, the temperature of the root part of the stud attached at the top of the steel beam (hereinafter referred to as the stud part) was influenced by heat transfer from the steel beam, and got higher than the lower slab side (hereinafter referred to as "lower slab (side)"). The temperature of the lower rebar in the RC slab was also influenced by the heat transfer from the unprotected steel beam part, but for the upper rebar and the non-heating surface, the temperature was about the same at the center part and the side part of the beam.

Fig. 3 (b) shows the temperature-time relationship of No.2 fire-resistant junction. The temperature of the high-strength bolt was increased by heat transfer from the unprotected part of the small beam even after the heating was finished, and the steel temperature was the highest at about 18 minutes after the heating stopped, which was about 120°C. The temperature of the reinforcing bars of the RC slab was 100°C or less. It is considered that the strength decrement at the joint part of No.2 was small. The reason for the rapid temperature rise at the lower slab (side) at 20 minutes is considered to be due to the separation of the RC slab and the deck plate at that time. Similar behaviors were also observed immediately after the removal of the furnace.

In No.3, as shown in *Fig. 2*, the temperature measurement was performed in the first row of bolts and the second row of bolts (70 mm away from the first row in the center direction of the span), respectively, as shown in *Fig. 3 (c-1)* and *(c-2)*. Since the joint was unprotected, the temperature of the high-strength bolt arranged on the web exceeded 600°C in the second row on the center side and exceeded 500°C even in the first row on the end side. The difference between the temperatures of the steel materials in the first row and the second row was about 150°C. The temperature of the stud part was about 500°C or less. On the other hand, the temperature of the reinforcing bars in the RC slab at the joint was about 200°C even in the lower rebar. In the lower slab (side), similarly to the specimen No.2, a sharp rise in temperature occurred at 20 minutes and thereafter a tendency became constant at 100°C.

2.4 Deflection Behavior

The time-center deflection relationship and the time-center deflection speed relationship of No.1 to 3 are shown in *Figs 4* and *5*. In the figures, the limit deflection and limit deflection speed of ISO 834 obtained by equations (1) and (2) are also described.

$$\text{Limit deflection, } D = L^2 / (400 d) \quad [\text{mm}] \quad (1)$$

$$\text{Limit deflection speed, } dD / dt = L^2 / (9000 d) \quad [\text{mm/min}] \quad (2)$$

Here, d: small beam thickness (300 mm)

(Limiting deflection speed regulation is not applied until deflection reaches L/30)

As for No. 1, the deflection sharply increased due to the temperature difference within the cross section of the unprotected beam at the initial stage of heating, but as the change of the temperature difference of the upper and lower flanges became smaller, as shown in *Fig. 3 (a)*, after 7 minutes the deflection speed calmed down. After that, the deflection speed again increased after 10 minutes, exceeded the limit deflection speed regulation at 20 minutes, reached ISO limit deflection at 24 minutes. The deflection speed further increased with that, and the measuring device reached the limit at the time of 30.5 minutes, the load heating was ended.

No. 2 and No. 3 exhibited almost the same deflection behavior as both of them. Until ten minutes the deflection behavior was similar to that of No. 1, but after that the deflection speed decreased and the deflection speed became minimal in about 30 minutes. After 30 minutes gradually the deflection speed increased, at No. 2 at 61 minutes, No. 3 at 57.5 minutes it reached the ISO limit deflection, so heating was terminated, while the loading still continued.

In both No. 2 and 3, the deflection sharply increased temporarily immediately after the end of heating, and the same phenomenon in which the ISO limit deflection speed was exceeded was also

observed. It is considered that this is due to the fact that strong tensile force is generated in the concrete slab near the edge of the beam as a result of the quenching contraction of the beam and the temporary bending temporarily increases due to the occurrence of the splitting split by the reinforcing bars at the end of the slab. Immediately after the end of the heating, there was such a phenomenon of rapidly increasing the deflection, but the deflection was gradually reduced without losing the load supporting ability in the subsequent cooling process.

In addition, in order to examine the whole beam deflection behavior of simply supported beam and web-pin-joined beam, the deflection distribution behaviour of specimen No. 1 and specimen No. 2 at several stages of time shown in Fig. 6 (a) and (b). No. 2 and No. 3 exhibited almost the same deflection behavior as both of them.

At the minutes 15, the deflection distribution behavior of No. 2 was similar to that of No. 1, but after that, as shown in Fig. 6 (b), it seems that the beam end rotation restraining effect at the pin-joint began to be demonstrated at the specimen No.2. From Fig. 6 (a), during the fire, for specimen No.1, the deflection at the point close to the end of the beam increased almost monotonously. On the other hand, for the specimen No. 2, the point close to the end of the beam – where the pin-joint located – did not show any increment in deflection but showed increment in rotation. It is considered that in reaching the ISO limit deflection, in No. 1, the deflection behavior due to positive bending occupies the majority of the deflection component, whether in Nos. 2 and 3, the positive bending rigidity of the unprotected composite beam and the shear buckling of the beam end web are the main factors.

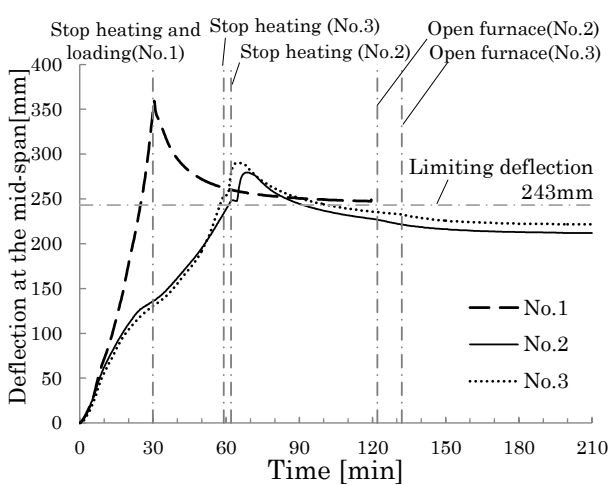


Fig.4. Time-center deflection relationship

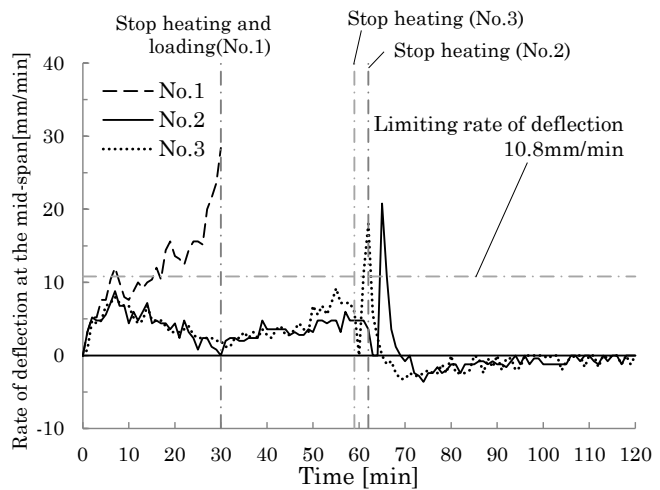
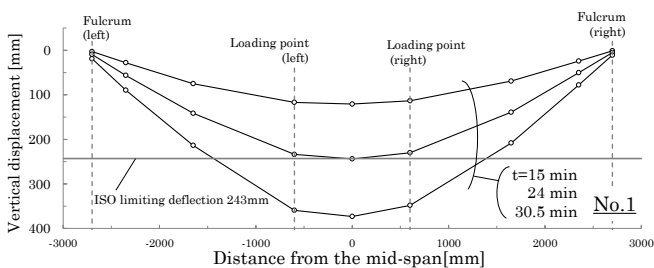
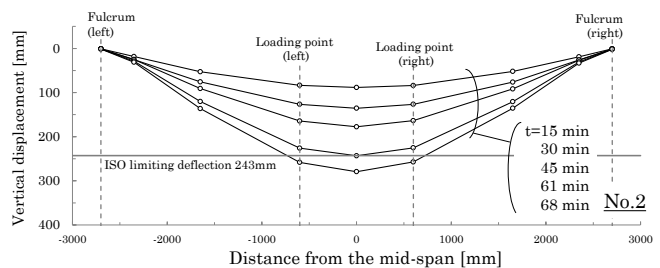


Fig.5. Time-center deflection speed relationship



(a) simply supported beam (No. 1)



(b) web-pin-joined beam (No. 2)

Fig.6. Deflection distribution behavior

3 THERMAL-STRESS ANALYSIS INTEGRATING COMPONENT BASED MODEL

In this analytical study, the analytical model of No. 2 composite beam with a beam end pin joint is shown in Fig. 7. The analytical model was half of the test specimen, considering the symmetry and configured as a subdivided wire rod model. Regarding the boundary conditions of No. 2 and No. 3, the rotation of the beam end was fixed and the displacement in the horizontal direction was free. The component based model proposed in the previous research [4, 5] was used for the joint as shown in Fig. 8. The high-temperature characteristics of steel, rebar, and high strength bolt used in this analysis were formulated from the stress-strain relation obtained by the high temperature tensile test of the material used in this experiment. The temperature measurement result obtained by the experiment was used as the temperature input value.

Fig. 9 shows comparison of the mid-span deflection-time relationship between the experimental results and the analysis results. As for specimen No. 2, as shown in Fig. 9 (b), this analysis result roughly agreed with the experimental results up to about 10 minutes, but the subsequent deflection exceeded the experimental result. In this joint model, the end rotation restraint by the RC slab is not taken into consideration, so it is considered that the joint of only three bolts could not exhibit sufficient rotation restraint. On the other hand, in the specimen No. 3, as shown in Fig. 9 (c), since the number of bolts is twice as compared with No. 2, even in the analytical model considers only the web-bolted-joint, the rotation constraint is appropriately evaluated, and it was agreed with experiment results. However, since slab elements are not taken into consideration, the strength of the steel beam joint part greatly decreased due to high temperature from 45 minutes of heating, and the deflection slightly exceeded the experimental result.

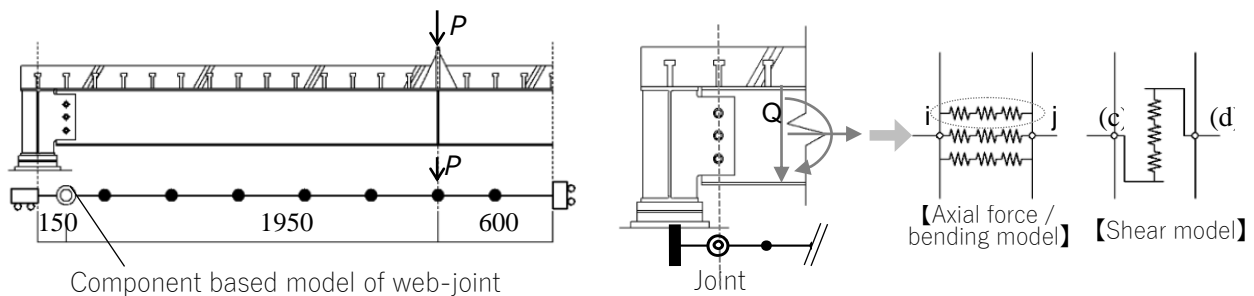


Fig 7. Thermal-stress analytical model (No.2) Fig 8. Component based model of web bolted joint

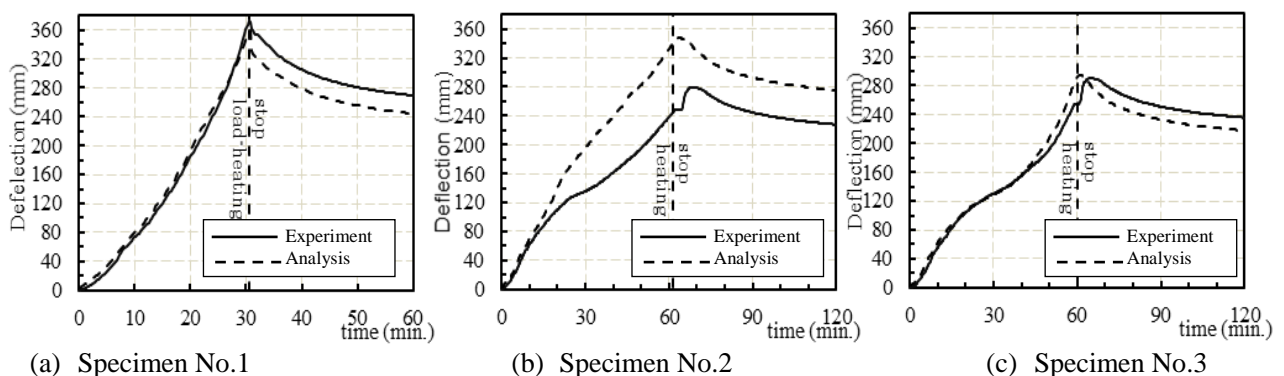


Fig 9. Comparison of the mid-span deflection-time relationship between the experimental results and the analysis results

4 CONCLUSIONS

In this study, load-bearing fire tests on simply supported unprotected composite beam and unprotected composite beam pin-jointed to steel girders were conducted. The main conclusions from the test results were as follows:

- 1) In fire condition, the center deflection of the unprotected composite beams web-bolted pinned with the steel girders was largely suppressed by the restraining effect against rotation at the pin joint. This restraining effect was exerted because the rebar worked effectively by tying the steel girder and the concrete slab with the headed stud. As a result, the time to reach ISO limit deflection was 24 min for No. 1 of the simply supported beam, whereas it was 61 min for No.2 of the web-pinned beam and 57.5 min for No. 3 of the web-pinned beam, the fire performance has been greatly improved by restraining effect at the pin joints.
- 2) In this experiment, bending collapse mechanism (3 hinge state) was not observed for the web-pinned beams. On the other hand, shear buckling of the web and local buckling of the lower flange occurred at the ends of the beam, but it is inferred that the load-bearing capacity was not lost immediately after the shear yield of the web.
- 3) No significant damage (such as bolt failure and plate tear-out failure) and deformation (such as shear deformation of the bolt and bearing deformation of plate) at the pin joints were observed during heating and cooling process.
- 4) The analysis method integrating the model of beam end web pin-joint could approximate this experimental behavior.

ACKNOWLEDGMENT

This research was undertaken with the aid of the Japan Iron and Steel Federation Steel Structure Research and Education Promotion Project (Objective Research). The deck plate used for the specimen was provided by JFE Metal Products & Engineering Inc. We got a lot of cooperation to the people of TOA-RIKA Co., Ltd. in the test specimens fabrication. The author expressly acknowledges it.

REFERENCES

1. C. G. Bailey, D. B. Moore: *The structural behaviour of steel frames with composite floorslabs subject to fire (1. Theory)*, 2000.
2. S. Yasuda, S. Michikoshi, Y. Tagawa: *EXPERIMENTAL STUDY ON ULTIMATE FLEXURAL STRENGTH OF COMPOSITE BEAM IN FIRE*, J. Struct. Constr. Eng. No.634, pp2271-2278, 2008.12 (In Japanese).
3. S. Yasuda, S. Michikoshi, Y. Tagawa: *STUDY ON ULTIMATE STRENGTH OF COMPOSITE BEAM WITH ENDS RESTRAINED AGAINST ROTATION IN FIRE*, J. Struct. Constr. Eng. Vol. 74 No.643, pp1691-1698,2009.9 (In Japanese)
4. Marwan Sarraj: *The Behaviour of Steel Fin Plate Connections in Fire*, PhD thesis, The University of Sheffield, 2007
5. R. Dwiputra, S. Ando, T. Hirashima: *NUMERICAL ANALYSIS MODELING OF FRICTION TYPE HIGH STRENGTH BOLTED SPLICE CONNECTION EXPOSED TO FIRE*, Journal of Structural and Construction Engineering (Transactions of AIJ) Vol. 82 No.733, p. 493-501, 2017.3 (In Japanese).

FIRE BEHAVIOUR OF SLENDER CONCRETE-FILLED STEEL TUBULAR COLUMNS UNDER BIAXIAL BENDING

Ana Espinós¹, Vicente Albero¹, Manuel L. Romero¹, Maximilian Mund², Patrick Meyer², Peter Schaumann², Inka Kleiboemer³

ABSTRACT

The fire performance of concrete-filled steel tubular (CFST) columns has been profusely investigated in recent years, through both numerical and experimental studies. Extensive fire testing on slender CFST columns has been performed in the framework of the European Project FRISCC (Fire Resistance of Innovative Slender Concrete-filled Columns). The results of recent investigations have led to the development of new design rules that allow for the calculation of the buckling load of slender columns in the fire situation, under axial compression as well as combined compression and uniaxial bending. The current design guidelines have been revised and extended by the Project Team SC4.T4 to build up the new method that will replace the current Annex H in EN 1994-1-2. However, the situation of columns subjected to biaxial bending has not been investigated and no fire tests on CFST columns under biaxial bending have been carried out so far. Hence, the extension of the design rules to biaxial bending can only be based on numerical simulations. To ensure the applicability of the model, both tests under biaxial bending at room temperature and tests under uniaxial bending in case of fire can serve for validation. In this paper, a numerical model is presented for simulating the fire behaviour of slender CFST columns subjected to eccentric load in the two sectional axes, which is subsequently used to compare the results with the new design rules for uniaxially loaded columns.

Keywords: Concrete-filled steel tubular columns, fire, numerical modelling, biaxial bending, simplified method

1 INTRODUCTION

In recent years, the usage of concrete-filled steel tubular (CFST) columns has increased due to several advantages obtained by combining both materials: high strength, high ductility and a high fire resistance without additional protection [1]. The behaviour of these composite columns under axial compression as well as combined compression and uniaxial bending has been well studied at elevated temperatures through experimental and numerical investigations. However, the performance of CFST columns subjected to biaxial bending and especially in case of fire has been scarcely investigated. Only few tests at room temperature can be found in literature for this load situation.

In this paper, a numerical model is presented for studies on the behaviour of CFST columns with a rectangular cross-section subjected to biaxial bending in case of fire. Due to the lack of experimental investigations on biaxially loaded columns at elevated temperatures, the numerical model is validated with experimental tests for uniaxial as well as biaxial bending at room temperature, while for the fire situation it is validated with tests on columns subjected to uniaxial bending. Based on this numerical

¹ Concrete Science and Technology Institute (ICITECH), Universitat Politècnica de València, Valencia, Spain.

A. Espinós (e-mail: aespinos@mes.upv.es); V. Albero (e-mail: valbero@mes.upv.es); M. Romero (e-mail: mrromero@mes.upv.es)

² Institute for Steel Construction, Leibniz Universität Hannover, Hannover, Germany.

M. Mund (e-mail: mund@stahl.uni-hannover.de); P. Meyer (e-mail: meyer@stahl.uni-hannover.de);

P. Schaumann (email: schaumann@stahl.uni-hannover.de)

³ Hagen Ingenieurgesellschaft für Brandschutz mbH, Hannover, Germany.

I. Kleiboemer (e-mail: inka.kleiboemer@hagen-ingenieure.de)

model, a parametric study is carried out to assess the validity of the proposed method of the Project Team SC4.T4 [2], which is limited to uniaxial bending. Comparing the fire resistances of the numerical simulations and the simplified method, it is investigated whether it is possible to extend the proposal to the new load situation.

2 NUMERICAL MODEL

A three-dimensional finite element model is developed by using the program ABAQUS [3]. With the numerical model, the temperature field is calculated in a separate heat transfer analysis and the shape of the initial imperfection in a previous eigenmode analysis. The numerical model is composed of the following parts: steel tube, concrete core, reinforcing bars and a loading plate at each end of the column to apply the load and the boundary conditions (see *Fig. 1*). A detailed description of the numerical model is given in the following subsections.

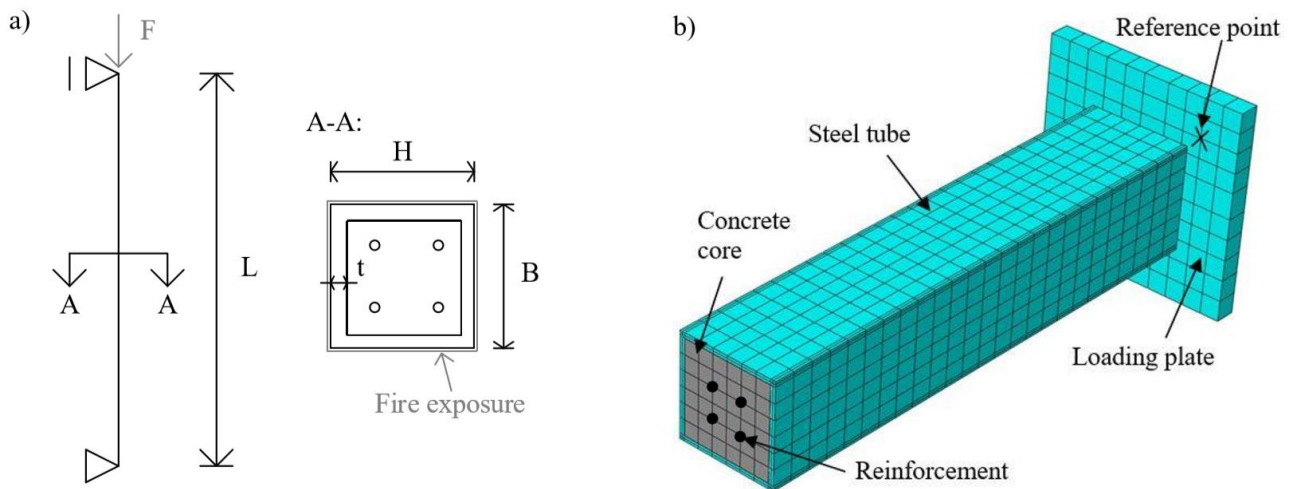


Fig. 1. a) Statical system and cross-section; b) Numerical model in ABAQUS

2.1 Finite element mesh

In the numerical model, the element size in lateral as well as in longitudinal direction of 2 cm is selected as a result of a mesh sensitivity study. In the lateral direction of the steel tube, two elements are defined. For the concrete core, the steel tube as well as the loading plates, linear eight-noded solid elements with a reduced integration (C3D8R) are used. Furthermore, the reinforcement is modelled with three-dimensional two-noded truss elements (T3D2) [4].

2.2 Boundary conditions

At both ends, loading plates are modelled to apply the boundary conditions (see *Fig. 1b*). These plates are defined as rigid bodies, which means that the movement of all nodes is the same as that of the coupled reference point. Depending on the load eccentricity and the end moment ratio from the cases used for validation, the position of this point differs. The top end reference point can move freely in axial direction, whereas at the bottom end all the translational degrees of freedom are restricted. In terms of rotation, all movements are allowed. Furthermore, the load is applied at the top end reference point.

2.3 Initial imperfection

The initial imperfection is taken into account to initiate the global buckling of the column. For the case of biaxial bending, only the first mode is used, corresponding to a half-sine wave around the weak axis, according to the proposal of the EN1994-1-1[5] at room temperature. The absolute value of the amplitude of the initial imperfection is defined to be $L/1000$ as proposed by other authors [4, 6].

2.4 Thermal properties

The separate heat transfer analysis is based on the material properties given in EN 1992-1-2 [7] and EN 1993-1-2 [8], respectively. The conductivity, density and specific heat of steel are taken from EN 1992-1-2 [7]. For concrete, the upper limit of the conductivity and a constant density are defined. Furthermore, a moisture content of 4% is assumed as recommended in EN 1994-1-2 [10]. Between the steel tube and the concrete core, a thermal gap conductance of $k = 200 \text{ W/m}^2\text{K}$ is defined as recommended by other authors [4]. The ISO 834 standard fire curve is applied in the parametric study. Required parameters for the convective and radiative transfer are also obtained from EN 1991-1-2 [12], with the coefficient of convective heat transfer at the exposed surface being $25 \text{ W/m}^2\text{K}$ and the emissivity of the steel tube 0.7.

2.5 Contact formulations

The contact between the steel tube and the concrete core as well as between the concrete core and the loading plates has to be defined. The contact in normal direction is defined as “Hard Contact” with the Augmented Lagrange method. In tangential direction, the Coulomb friction model with a constant friction coefficient of $\mu = 0.3$ is employed. Moreover, the steel tube is directly tied at the plates because of the welded connection [4].

2.6 Constitutive material models

For steel, the isotropic elastic-plastic model based on the temperature-dependent data of EN 1993-1-2 [8] is used. To define the elastic behaviour of steel, two parameters are needed: the temperature-dependent Young’s modulus of elasticity E and the Poisson’s ratio ν . The plastic behaviour is described by defining the yield stress and the corresponding plastic strain in ABAQUS. The temperature-dependency is incorporated by using the reduction coefficients of EN 1994-1-2 [10].

The elastic behaviour of concrete is also defined with the secant modulus of elasticity and the Poisson’s ratio, which is adjusted at elevated temperatures by using the reduction coefficients of Bahr et al. [9]. The temperature-dependent stress-strain relation in terms of compression is adopted from EN1994-1-2 with a linear decreasing branch (see Fig. 2) [10]. The tensile behaviour is also defined with the maximum strength from the EN 1992-1-2 [7] and a bilinear decreasing branch as recommended in the Model Code CEB-FiB 2010 [11].

For the description of the three-dimensional plastic behaviour the Concrete Damaged Plasticity (CDP) Model is used in ABAQUS. The input parameters are the following: dilation angle 30° , eccentricity parameter of the plastic potential surface 0.5, ratio of the initial biaxial to initial uniaxial compressive yield stress $f_{b0}/f_{t0} = 1.16$, parameter related to the shape of yield surface in the deviatoric plane $\kappa = 2/3$ and viscosity parameter is equal to 0 [4].

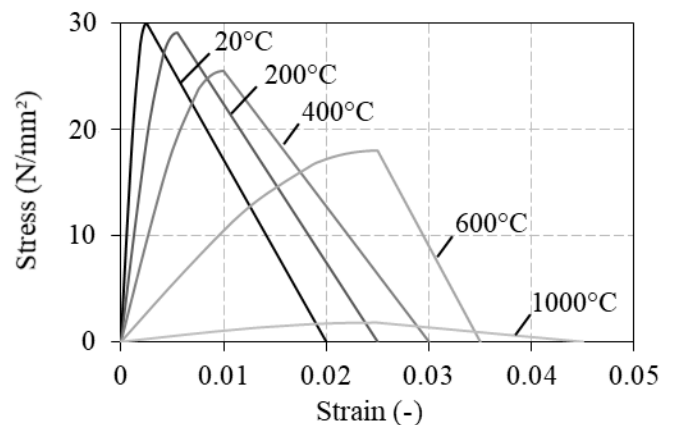


Fig. 2. Stress-strain relation of concrete at elevated temperatures in terms of compression

3 VALIDATION OF THE NUMERICAL MODEL

Due to the lack of experimental tests on CFST columns subjected to biaxial bending in case of fire, the numerical model is firstly validated with tests on eccentrically loaded columns at room temperature (uniaxial and biaxial bending) and on a second stage for the case of uniaxial bending at elevated temperatures. Thereby it is expected that the model is reliable for predicting the response of those columns under biaxial bending.

3.1 Uniaxial bending at room temperature

The validation of the numerical model for columns subjected to uniaxial bending at room temperature was carried out with experimental tests from Hernández-Figueirido et al. [13] and Patel et al. [14]. The properties of the numerical model conform to the experimental data. The investigations of Hernández-Figueirido et al. [13] include nine tests on eccentrically loaded CFST-columns. The specimens were made of normal strength concrete (C30/37) and cold-formed steel tubes of steel grade S275JR. A representative result of the validation is shown in Fig. 3. It can be seen that the behaviour of the square column is well predicted. The differing stiffness in the range of the ultimate force emerges because the residual stress from the cold-formed fabrication of the steel tube is not included in the numerical model.

3.2 Biaxial bending at room temperature

The numerical model was further validated with tests from Wang [15] for columns subjected to biaxial bending. The experimental investigations include four tests of with different rectangular CFST columns, in which the position of the eccentric load causes biaxial bending. Differences exist in the value of the eccentricity and the applied end moment ratios. As a representative result, in Fig. 4 the validation for one test is shown. In this case, the load is only applied at the top end, so that the corresponding distribution of the bending moment over the length of the column is triangular. The ultimate load and the behaviour of the column in both axes is in a good agreement with the test. The relative slenderness is 1.1 and 1.56 in major and minor axis, respectively. For the concrete core, a cylinder strength of 50 N/mm² was used and the tube was fabricated of steel with a yield stress of 370 N/mm². All the column specimens were unreinforced.

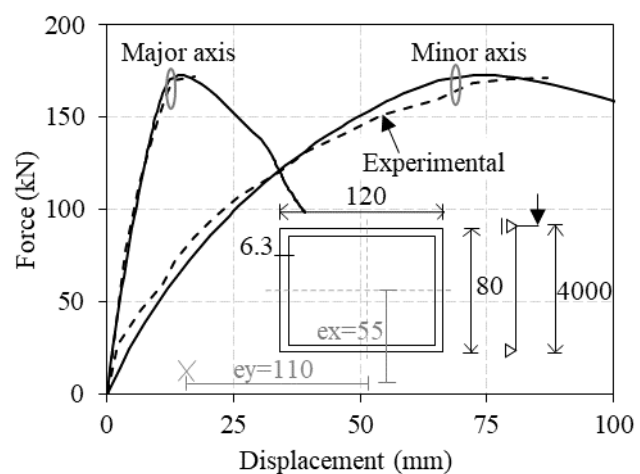
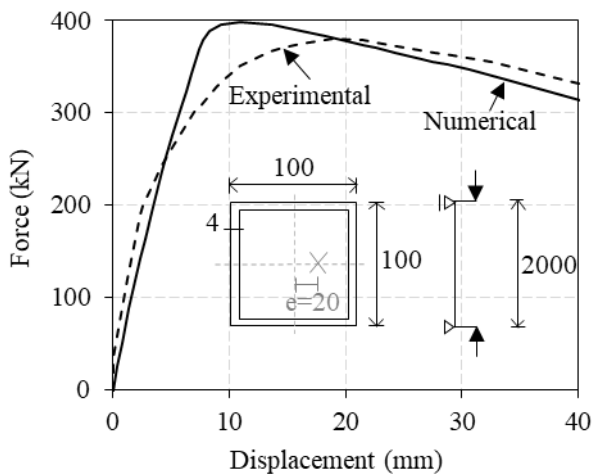


Fig. 3. Validation of the numerical model for uniaxial bending at room temperature

Fig. 4. Validation of the numerical model for biaxial bending at room temperature

3.3 Uniaxial bending at elevated temperature

The last part of the validation of the numerical model corresponds to rectangular CFST columns subjected to uniaxial bending in case of fire, comparing with experimental tests from Espinós et al. [16]. The experimental program includes seven tests with normal strength concrete and steel tubes of grade S355. In these tests, a 20% of the ultimate load at room temperature was applied before the direct fire exposure inside a gas furnace following the standard ISO 834 fire curve. The temperature field obtained by a previous heat transfer analysis as well as the mechanical response during the fire exposure are validated. This can be seen in Fig. 5, where the temperature at the thermocouple positions (a) as well as the axial displacement measured at the top end of the column (b) versus the time is plotted. For the sake of clarity, the temperature development is only plotted in one plane, which is situated L/4 above the bottom end. Different positions of the thermocouples are highlighted

with different grey tones. The eccentricity of this case is applied at 30 mm in the strong axis direction, causing buckling about the weak axis.

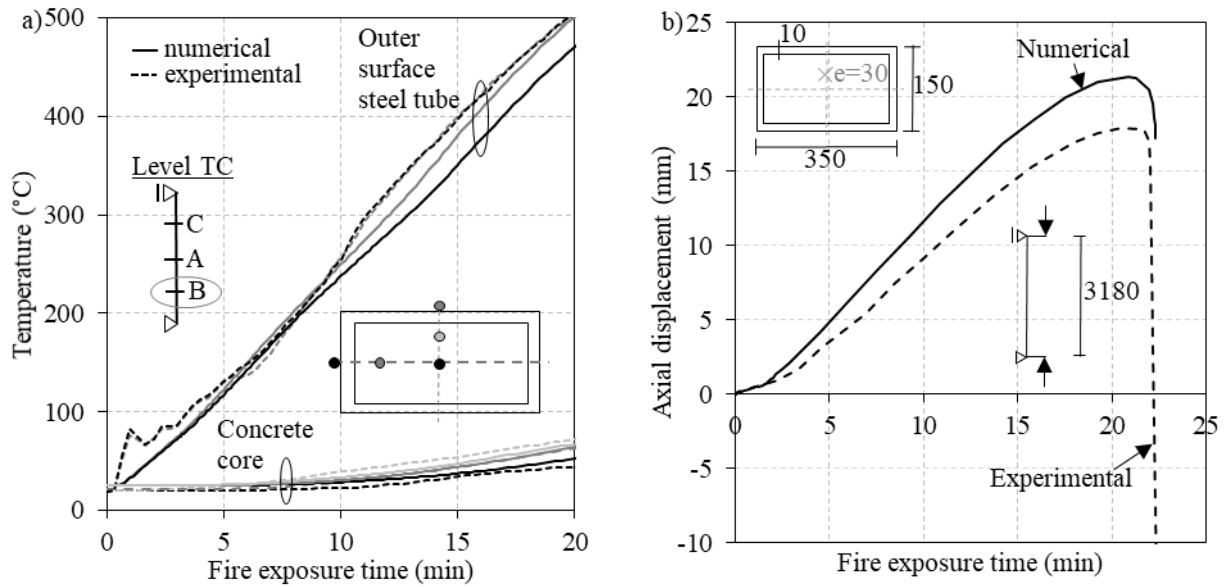


Fig. 5. Validation for uniaxial bending in case of fire: a) temperature field b) mechanical response

3.4 Parametric study on CFST columns subjected to biaxial bending in case of fire

Using the validated numerical model, a parametric study on CFST columns was carried out. In Table 1, the range of parameters investigated are listed. The steel grade used is S355, the concrete strength class C30/37 and the reinforcement is made of BSt500. The rotation of the columns at both ends is free in all directions (pinned-pinned). Different load and eccentricity ratios are applied, but the bending moment distribution is constant over the length in all cases. The load ratio relates to the ultimate load at room temperature, which is obtained from a previous numerical analysis.

Table 1: Scope of the parametric study on columns subjected to biaxial bending in case of fire

H x B x t [mm]	L [mm]	Reinforcement	Load ratio μ [%]	$e/B = e/H$ [-]	e^{bottom}/e^{top} [-]
100 x 100 x 5	500	4 \varnothing 8 mm	15	0.25	1
			30	0.5	
	1000		60	0.75	
				1.0	

In Fig. 6 the results of the numerical analysis for the CFST columns with a length of 500 mm are shown. The typical behaviour of CFST columns at elevated temperatures is observed. At first, the steel tube expands faster than the concrete core in longitudinal direction (here negative sign). A transfer of the load from the steel tube to the concrete core is not possible in these cases and the columns fail due to global buckling. The numerical failure times are obtained by applying the failure criteria of EN 1363-1 [17], in which a maximum value for the vertical contraction as well as a value for the maximum rate of the vertical contraction is given.

4 ASSESSMENT OF THE PROPOSED SIMPLIFIED METHOD FROM EN1994-1-2 ANNEX H

Previous investigations pointed out that the current method of Annex H of EN 1994-1-2 leads to unsafe results for slender columns [16]. Therefore, the Project Team SC4.T4 developed a revised simplified method for CFST columns based on experimental and numerical investigations. The range of the application of the proposed method includes square, circular, rectangular and elliptical cross-sections and uniaxially loaded columns.

In this section, this new simplified method, which will be incorporated in the Annex H of EN 1994-1-2 [9] in the next generation of the Eurocodes, is applied to the cases of the parametric study. Although it is limited to CFST columns subjected to uniaxial bending because an interaction between the axes is not employed yet, it is used in this paper for assessing its application to biaxially loaded cases. To determine the fire resistance of these columns, the temperature field of the cross-section is calculated on a simplified way by using the proposed equivalent temperatures for each member. The material strengths are reduced and the elevated temperatures are incorporated in the method. The effective flexural stiffness is modified with an additional factor to consider the effects caused by fire. These two parts are not dependent on the load situation but only on the cross-section dimensions and the fire exposure time, therefore they can be applied to the cases of this parametric study. The effective flexural stiffness is calculated with Eq. 1. Due to the different second moments of area about each axis in case of biaxial bending, it is necessary to calculate the effective flexural stiffness for both axes.

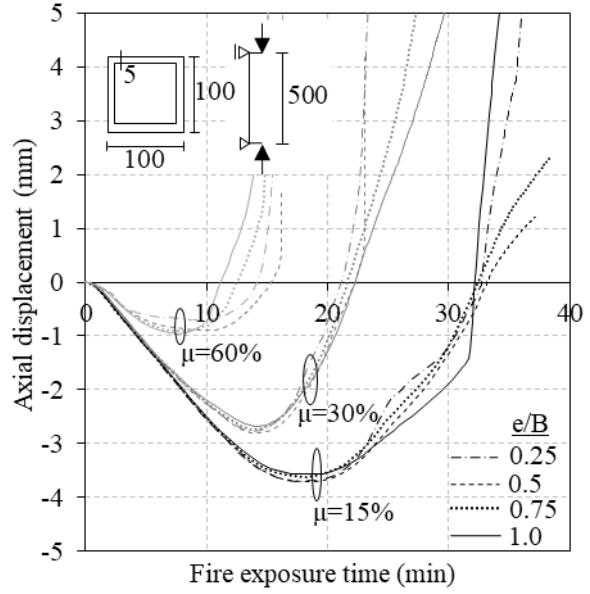


Fig. 6. Numerical results from the parametric study

$$(EI)_{fi,eff,II} = K_{\theta} * K_0 * [\varphi_{a,\theta} * E_{a,\theta} * I_a + K_{e,II} * \varphi_{c,\theta} * E_{c,\theta} * I_c + \varphi_{s,\theta} * E_{s,\theta} * I_s] \quad (1)$$

where K_{θ} Correction factor for the fire situation
 K_0 Calibration factor from Clause 6.7.3.4 of EN 1994-1-1 [5]
 $K_{e,II}$ Correction factor from Clause 6.7.3.4 of EN 1994-1-1 [5]
 $\varphi_{i,\theta}$ Reduction coefficients depending on the effect of thermal stress in the fire situation
 $E_{i,\theta}$ Modulus of elasticity of each section component at elevated temperature
 I_i Second moment of area of each section

In the next step, the method refers to design guidelines of EN 1994-1-1 [5] at room temperature. In case of biaxial bending, the M-N interaction diagram is calculated for both axes using the simplified approach though four points to obtain the interaction coefficients μ_{di} , which combine the load situation of axial compression and bending moment. The stability check of Clause 6.7.3.7 of EN 1994-1-1 [5] is carried out (see Eq. 2).

$$\frac{M_{y,Ed}}{\mu_{dy} * M_{pl,y,Rd}} + \frac{M_{z,Ed}}{\mu_{dz} * M_{pl,z,Rd}} \leq 1.0 \quad (2)$$

where $M_{i,Ed}$ Design bending moment
 μ_{di} Factor related to the plane of bending
 $M_{pl,i,Rd}$ Design value of the plastic resistance moment

The plastic resistance moments are calculated under the consideration of the reduced strengths at elevated temperatures. The applied bending moment of the weak axis is obtained by the addition of the part produced by the eccentricity of the parabolic initial imperfection ($L/1000$) and the constant bending moment of the applied load eccentricity (see Eq. 3).

$$M_{i,Ed} = N_{Ed} * e_{load} * k + N_{Ed} * e_{imp} * k_{imp} \quad (3)$$

where N_{Ed} Design value of the compressive normal force
 e_{load}, e_{imp} Eccentricity of loading and the initial imperfection
 k, k_{imp} Amplification factors for second-order effects

The factor of the initial imperfection is not applied for the bending moment about the strong axis because the imperfection is considered only in the weak axis according to Clause 6.7.3.7 (1) of EN 1994-1-1 [5] at room temperature.

In Fig. 7 the comparison of the fire resistances obtained by means of the numerical simulations and the proposed method of Annex H for the CFST columns with a square cross-section of 100 mm x 100 mm is plotted. It is evident that there are also cases which lay on the unsafe side. Furthermore, it can be seen that the results scatter. The average value of the ratio between the numerical fire resistance time and the analytic one is 1.05, showing good accuracy and a conservative trend, although with a number of unsafe results. Nevertheless, it is necessary to extend the scope of investigated cases to build a wider basis for the adjustment of the method to CFST columns subjected to biaxial bending. An interaction between the weak and the strong axis is not considered in the method. Owing to this, it can be a possibility to modify the equation of the effective flexural stiffness with an additional parameter for the different load situations as the Project Team SC4.T4 did for incorporating the effects of high temperatures. The approach for calculating an equivalent temperature for each member of the cross-section is independent of the load situation and can be adopted for columns subjected to biaxial bending. After obtaining the effective flexural stiffness, the method refers to EN 1994-1-1 [5] at room temperature. This should be kept for this modification, too.

5 CONCLUSIONS

In this paper, a numerical model is presented to analyse the behaviour of CFST columns subjected to uniaxial bending exposed to fire. On the basis of the numerical results from a parametric study, the proposed method of Annex H of EN 1994-1-2 is assessed, which is limited to uniaxial bending and will be incorporated in the future generation of the Eurocodes. It was found that it is not possible to extend the method to biaxial bending without modifications, because the obtained ratio of the fire resistances shows a significant scattering. It is recommended for future researches to extend the scope of the numerical investigations on CFST columns subjected to biaxial bending and check the possibility to define an additional parameter for the effective flexural stiffness, which considers different load situations.

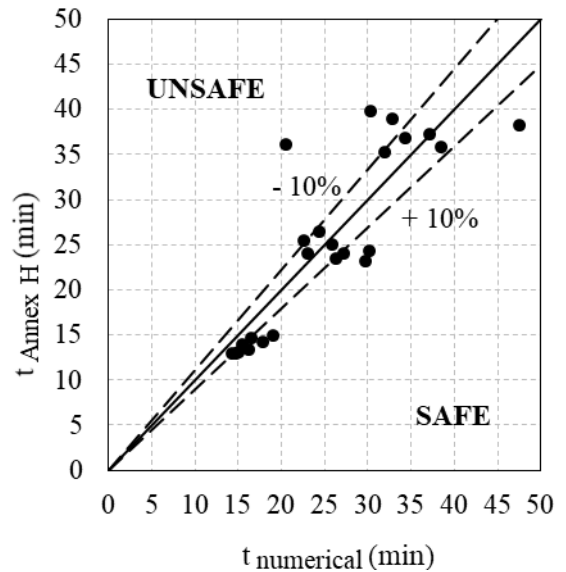


Fig. 7. Comparison between the fire resistances from the numerical simulations and the proposed Annex H method

ACKNOWLEDGMENTS

The authors would like to express their sincere gratitude to the “Conselleria d’Educació, Investigació, Cultura i Esport” of the Valencian Community (Spain) for the help provided through the project GV/2017/026. Most of the work has been carried out within the Master thesis of Maximilian Mund under the joint supervision of Leibniz Universitaet Hannover and Universitat Politècnica de València.

REFERENCES

1. Lin-Hai Han, Wei Li, Reidar Bjorhovde (2014). *Developments and advanced applications of concrete-filled steel tubular (CFST) structures: members*. Journal of Constructional Steel Research 100. pp 211-228.
2. CEN/TC250/SC4 N1836. *SC4.T4 Final Draft Annex H. Simple calculation model for concrete filled hollow sections exposed to fire all around the column according to the standard temperature-time curve*.
3. ABAQUS. *ABAQUS/ standard version 6.14 user’s manuel*. Dassault Systèmes, USA.
4. Ana Espinós, Manuel L. Romero, Antonio Hospitaler (2010). *Advanced model for predicting the fire response of concrete filled tubular columns*. Journal of Constructional Steel Research 66. pp 1030-1046.
5. EN 1994-1-1. *Eurocode 4. Design of composite steel and concrete structures. Part 1-1: General rules and rules for buildings*. Brussels (Belgium); Comité Européen de Normalisation (CEN); 2004.
6. Vipulkumar Ishvarbhai Patel, Qing Quan Liang, Muhammad N.S. Hadi (2017). *Nonlinear analysis of biaxially loaded rectangular concrete-filled stainless steel tubular slender beam-columns*. Engineering Structures 140. pp 120-133.
7. EN 1992-1-2. *Eurocode 2. Design of concrete structures. Part 1-2: General rules – Structural fire design*. Brussels (Belgium); Comité Européen de Normalisation (CEN); 2010.
8. EN 1993-1-2. *Eurocode 3. Design of steel structures. Part 1-2: General rules – Structural fire design*. Brussels (Belgium); Comité Européen de Normalisation (CEN); 2010.
9. Oliver Bahr, Peter Schaumann, Bart Bollen, Joris Bracke (2013). *Young’s modulus and Poisson’s ratio of concrete at high temperatures: Experimental investigations*. Materials and Design 45. pp 421-429.
10. EN 1994-1-2. *Eurocode 4. Design of composite steel and concrete structures. Part 1-2: General rules – Structural fire design*. Brussels (Belgium); Comité Européen de Normalisation (CEN); 2010.
11. FIB. *Model Code 2010 (Volume 1)*. Lausanne, Switzerland.
12. EN 1991-1-2. *Eurocode 1. Actions on structures Part 1-2: General actions – Actions on structures exposed to fire*. Brussels (Belgium); Comité Européen de Normalisation (CEN); 2010.
13. David Hernández-Figueirido, Manuel L. Romero, José L. Bonet, José M. Montalvá (2012). *Ultimate capacity of rectangular concrete-filled steel tubular columns under unequal load eccentricities*. Journal of Constructional Steel Research 68. pp 107-117.
14. Vipulkumar Ishvarbhai Patel, Qing Quan Liang, Muhammad N.S. Hadi (2012). *High strength thin-walled rectangular concrete-filled steel tubular slender beam-columns, Part II: Behavior*. Journal of Constructional Steel Research 70. pp 368-376.
15. Yong C. Wang (1999). *Tests on slender composite columns*. Journal of Constructional Steel Research 49. pp 25-41.
16. Ana Espinós, Manuel L. Romero, Enrique Serra, Antonio Hospitaler (2015). *Experimental investigation on the fire behaviour of rectangular and elliptical slender concrete-filled tubular columns*. Thin-Walled Structures 93. pp 137-148.
17. EN 1363-1. *Fire resistance tests. Part 1: General Requirements*. Brussels (Belgium); Comité Européen de Normalisation (CEN); 2012

NUMERICAL ANALYSIS OF THE THERMAL BEHAVIOUR OF STEEL-TIMBER HYBRID BEAMS IN FIRE SITUATION

Antoine Béreyziat¹, Maxime Audebert², Abdelhamid Bouchaïr³, Sébastien Durif⁴

ABSTRACT

Numerical simulations are used to evaluate the thermal behaviour of steel-timber hybrid beams in fire situation. The studied beams are either partially encased or totally encased with timber. The steel sections are made of "I" or "T" shaped steel members. The combination of these materials allows to design some configurations with improved mechanical and thermal performances. Steel shows high performances in normal situation and it is non-combustible. However, its mechanical properties decrease dramatically at elevated temperatures. Timber is a combustible material but presents good fire resistance when appropriate thickness is used. The aim of this study is to evaluate the possibility of using wood as fire protection material for steel. Indeed, the fire insulation performances of wood can be mobilised to reduce the heating of steel.

Moreover, the combustion of wood causes the migration of a portion of its water toward the internal steel plate that behaves as a hydric barrier. This phenomenon is modelled by varying the thermo-physical properties of wood as a function of temperature and depending on the location in the section. A comparative analysis is done on the basis of fire exposure time leading to a given steel temperature considered as a critical. The time required to reach this critical temperature is significantly increased by the use of timber as fire protection. It depends also on the steel flanges exposed to fire that influences the average temperature in the steel section.

Keywords: Steel-timber beam, fire resistance, thermo-hydric behaviour, numerical model.

1 INTRODUCTION

In civil engineering, several examples of combination of steel and timber exist at different scales and applications. For example, there are mixed structural systems [1], such as truss consisting in a combination of timber members and steel members (*Figure 1*). On a smaller scale, wood and steel can be combined within the same member to obtain hybrid elementary component (*Figure 2*). The combination of steel and timber can be used for various applications: connection of a wooden frame to a steel frame, mechanical reinforcement of existing or new structural element, fire protection, optimization of the cross-section dimensions compared to an equivalent one made of wood only, reinforcement of steel beams against local or global buckling effects, aesthetic aspects...

¹ Engineering student. University of Lyon, Ecole National d'Ingénieurs de Saint-Etienne, France.
e-mail: antoine.bereyziat@enise.fr

² Associate-Professor. University of Lyon, Ecole National d'Ingénieurs de Saint-Etienne, France.
e-mail: maxime.audebert@enise.fr

³ Professor. Université Clermont Auvergne, CNRS, Clermont-Ferrand, France.
e-mail: abdelhamid.bouchair@uca.fr

⁴ Associate-Professor. Université Clermont Auvergne, CNRS, Clermont-Ferrand, France.
e-mail: sebastien.durif@uca.fr



Fig. 1: Steel-timber hybrid structural system (truss) [2]



Fig. 2: Steel-timber hybrid elementary component [3]

Several solutions exist for the design of timber-steel hybrid elements, one of the oldest applications is the flitch-beam [4]. It is a beam composed of two timber elements assembled on both sides of a metal plate. There are also flitch beams with two metal plates and three pieces of wood. Steel is used to strengthen and stiffen the timber elements while wood provides lateral stability to the metal plate, increasing its resistance against buckling effects. Timber and steel elements share the load, at elastic stage, proportionally to their relative stiffness. The connection is usually made of bolts or nails and these hybrid elements are mainly used for the construction of light frame structures [5].

Another way of combination of steel and wood is to insert metal reinforcements into a wooden element using epoxy resin as connection. This principle is used both to repair damaged wooden elements and to produce prefabricated steel-wood beams made of glued laminated timber and steel rods [1]. These beams are characterized by greater stiffness and strength compared to a normal glued laminated timber element of the same section. Another advantage is that these beams exhibit a more ductile behaviour up to failure [1]. Alam *et al.* [4] pointed out that steel is further optimized when it is positioned at the location of maximum bending stresses, thus, timber beams using steel rebars appeared more efficient than flitch beams using steel plates regarding material weight. It is nevertheless interesting to hide the steel inside the wooden member for aesthetic reasons and in order to improve the fire resistance by avoiding steel exposure to fire.

Winter *et al.* [6] worked on the numerous benefits that steel-wood hybrid elements could offer for high rise construction. Their attention was mainly focused on cold-formed metal profiles, assembled in "I" shape and encapsulated in wooden elements. These ones were made of glued laminated timber or cross laminated timber. The first one showed the best mechanical performances when associated to steel. The authors also showed that such elements could be effective on the following points: cost, ease of assembly, section dimensions, earthquake resistance, creep and fire safety.

The first attempts to exploit a thermal interaction between wood and steel were carried out between 1999 and 2004 by the Building Research Institute in Japan. Sakamoto *et al.* [7], experimentally studied the thermomechanical behaviour of a steel profile, inserted into wooden member. The steel was completely encased in wood and insulated from fire with a 60 millimetres wood thickness. These elements were subjected to a heating phase for a period of one hour, then to a cooling period lasting three hours, while bearing mechanical load. The beams showed a 1-hour fire resistance, followed by self-extinguishing behaviour during the cooling phase and the ability to withstand applied loads even after the fire exposure, without risk of re-ignition, char progression or temperature rising after the test. So, the designed timber-steel hybrid beam was confirmed to be one-hour fire proof, even using wood which is a combustible material.

Jurkiewicz *et al.* [8] carried out three-point bending tests on 3 meters span steel-timber beams, consisting of either an IPE 160 or a "T" metal profile, assembled with lateral wooden elements. Those were assembled on both sides of the web of the metal profiles using bolts passing through it

and screws passing through the flanges. This study shows that the number of these fasteners has no significant influence on the behaviour of the beams in the elastic domain. The elastic bending stiffness of the tested hybrid beams is mainly influenced by the steel beam with a low contribution of the wood, regarding the dimensions of the connected elements. It was also observed that the combination of wood and steel can delay the lateral buckling and the local buckling of the steel profile. The present study aims to complete the work of Jurkiewicz et al. by modelling the thermal behaviour of steel beams "I" or "T" shaped, associated with timber members (*figure 3*) starting from the geometries tested mechanically.

2 MODELLING

Firstly, a simplified analysis was led to define some interesting configurations for the thermal modelling and for further experimental fire exposure tests. This approach is based on an analytical method proposed by EN 1993-1-2 [9]. It allows to calculate the heating of steel plates protected by wood members considered with constant thickness. Even if this method contains some serious limitations about the geometry and the consideration of wood combustion, it is used to evaluate the performances of some configurations.

One steel element alone is analysed with three hybrid cross-sections, based on IPE 300 steel profile (*figure 3*). The first geometry consists in an IPE 300 without fire protection. The second is a hybrid configuration which consists in a "I" shaped steel profile "partially encased" in wood. The third is similar to the second but uses a "T" shaped steel profile instead of "I" profile. The last consists in a "I" shaped steel profile "fully encased" in wood.

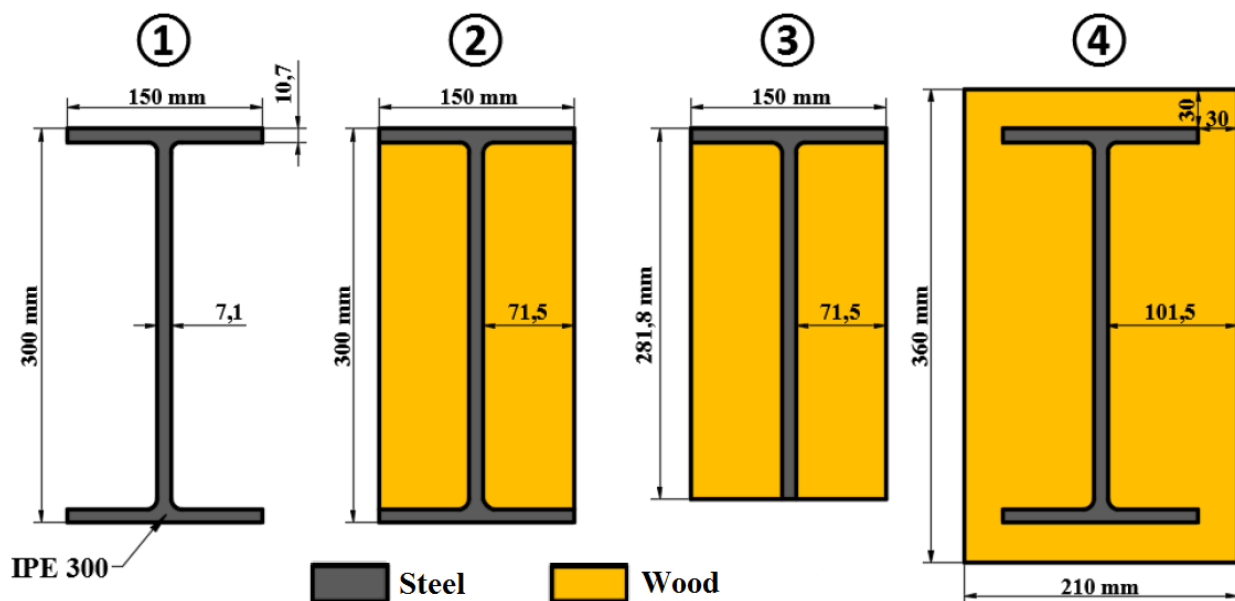


Fig. 3: Modelled geometries

The thermal behaviour of these configurations was analysed with a numerical model using the finite element method, carried out with the MSC Marc software [10]. The thermo-physical properties selected for the modelling of steel are those given in EN 1993-1-2 [9]. The modelling of the wood material is based on properties derived from the literature [11] considering the hydric transfers that occur into wood during fire exposure. Indeed, the combustion of wood induces the evaporation of the contained water. Part of this water vapour escapes while the rest migrates inside the section to condensate in cold zone [12]. For timber-to-steel connections [11], it has been observed that this migration leads to an accumulation of water against the steel plate that acts as a barrier. Thus, the

steel plate is cooled until the evaporation of the all water. These mass transfers are not easy to model, that is why this phenomenon is simulated numerically considering only its final state, after the complete migration of the water that has not escaped and its accumulation against the steel plate surface. To represent the thermal influence of this water, the wood adjacent to the steel, over a 3 millimetres thickness, is characterized by a high 100°C volumetric heat capacity peak as proposed by Audebert et al. [11]. Indeed, when a given volume of wood reaches 100°C , the amount of energy needed to raise its temperature is very important when it contains a lot of water to evaporate. This characteristic allows the simulation of the delay in the increase of the steel temperature induced by the water contained in the adjacent wood. Conversely, wood distant from steel by more than 3 millimetres is characterized by a low 100°C volumetric heat capacity peak, since it is assumed that the water is just passing through it, which implies that the amount of energy needed to evaporate the small quantity of contained water is low. The values of these volumetric heat capacity peak are calibrated for steel-to-timber connections, made of glued laminated timber members and steel plates with dimensions comparable to those of the configurations modelled in this study [11]. Thus, two variants of wood material are used in the modelling, one to represent the thermo-hydric behaviour of wood distant from steel and the second to model the behaviour close to the steel plate (in a wood thickness of 3mm). *Figure 4* presents the evolutions of volumetric heat capacity for the two variants of wood material modelled.

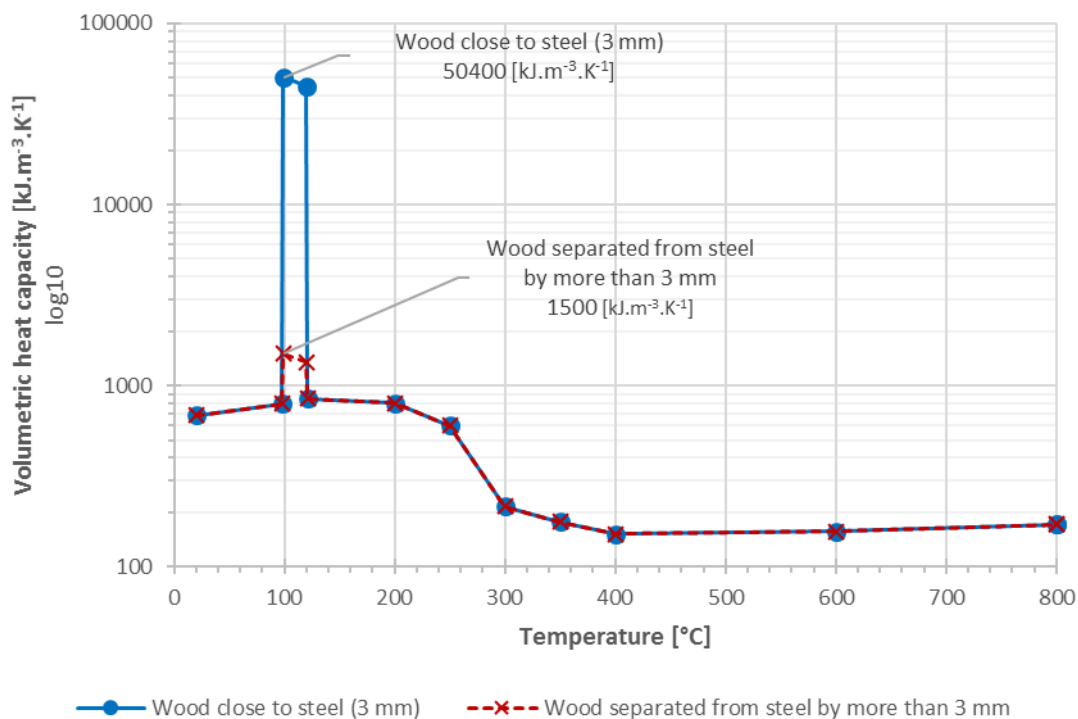


Fig. 4: Evolution of the volumetric heat capacity for the two variants of wood material modelled

In the numerical analysis, the different configurations are exposed during 60 minutes to ISO 834 fire recommended by EN 1991-1-2 [13]. The numerical analysis was used to evaluate the influence of several factors, such as geometry, number of sides exposed to fire, and the way to model the materials and the hydric transfers.

3 RESULTS

3.1 Results considering three sides exposed to fire

Figure 4 presents the evolutions of the average temperature on the whole steel cross-section of the studied configurations (1), (2), (3) and (4) illustrated in *figure 3*. It has been considered that only

the lower face and the side faces are exposed to fire. This hypothesis may correspond to the reality of a beam supporting a floor which would protect the upper face of the beam against fire. The results take into account wood material model presented previously. The properties of the materials are the same for all configurations (steel according to EN 1993-1-2 [9] and wood according to literature reference [11]).

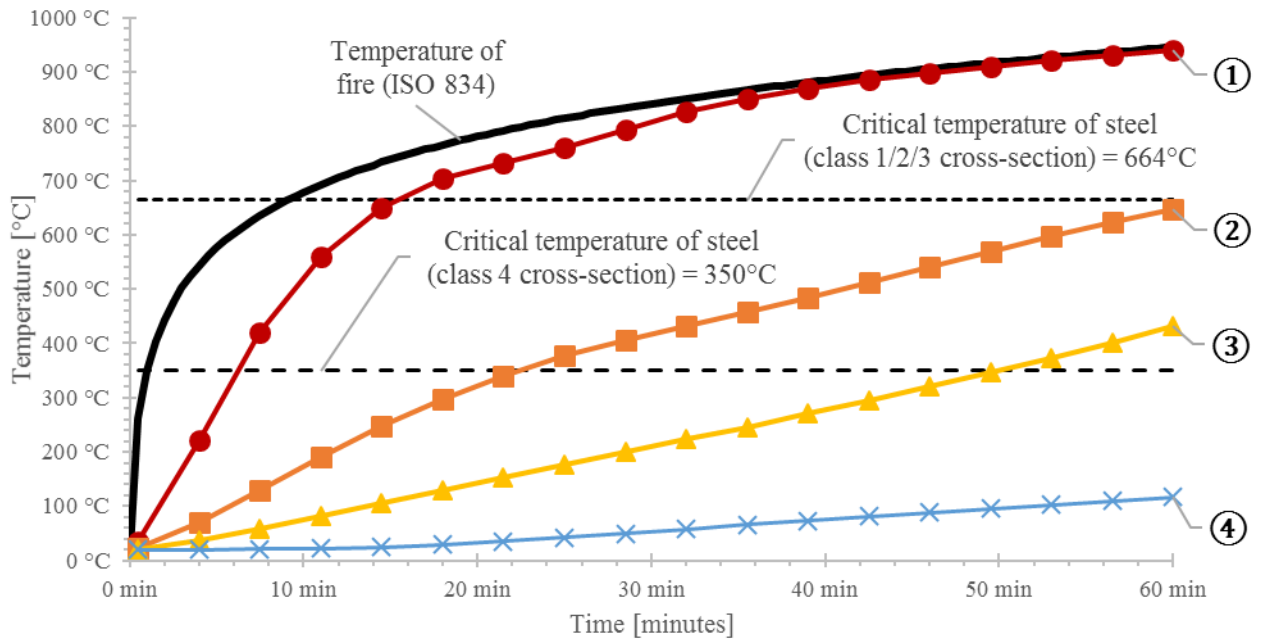


Fig. 5: Evolution of the average temperature of steel cross-sections for the 4 configurations with 3 sides exposed to fire

The results presented in *figure 5* concern only three faces exposed to fire (the bottom and the lateral ones). They show that a hybrid profile based on IPE 300 fully encased in wood (configuration (4)) has an excellent thermal behaviour in case of fire, even if the thickness of wood is low (30 mm). In fact, the steel of the configuration (4) reaches an average temperature of 115 °C after one hour of exposure, which is low in comparison with 941 °C reached for the unprotected "I" profile of the configuration (1). The partially encased profiles (configurations (2) & (3)) are less efficient but can limit the steel heating. Indeed, after one hour, an unprotected "I" profile (configuration (1)) and the same profile partially encased in wood (configuration (2)) show a difference of temperature equal to 293 °C. Finally, the "T" shaped profile (configuration (3)) shows a better thermal behaviour than the "I" shaped one since it has a smaller unprotected steel surface. After one hour, a difference of steel temperature equal to 215 °C is observed between the configurations (2) and (3).

EN 1993-1-2 presents the concept of "critical temperature" which is defined as follows: "For a given load level, the temperature at which failure is expected to occur in a structural steel element for a uniform temperature distribution" [7]. For class 4 steel cross-sections, this critical temperature is 350 °C. For the other classes of cross-sections, it is 664 °C, considering a 30% loading rate in case of fire. *Figure 6* presents the time required to reach these critical temperatures, as a criterion to quantify the thermal performance of the configurations (1), (2), (3) and (4) illustrated in *figure 3*. These values correspond to the average of calculated temperatures on the whole cross-section of the steel profile.

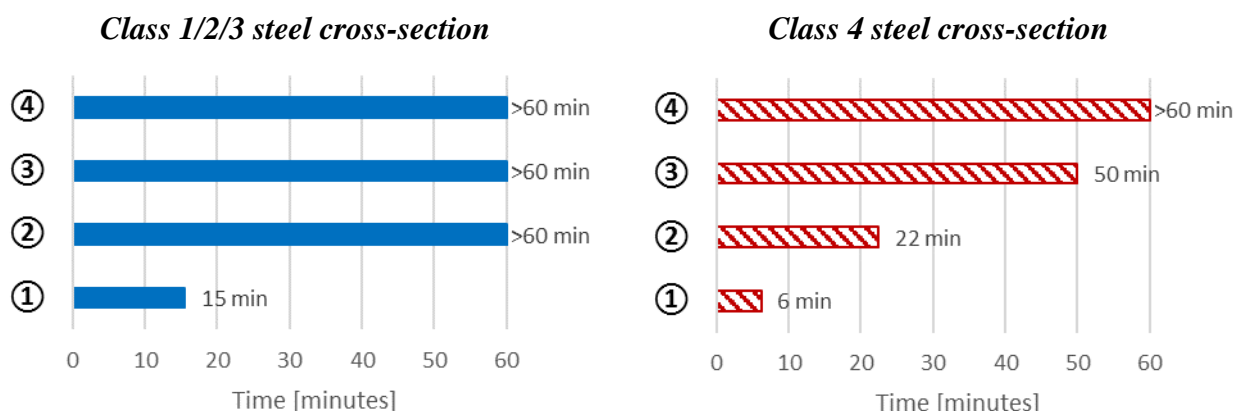


Fig. 6: Time to reach critical temperature of steel cross-sections (configurations with 3 sides exposed to fire)

It can be seen in *figure 6* that all protection configurations allow reaching important fire resistance compared to the unprotected profile. Both configurations (3) and (4) have greater performances compared to the partially encased “I” beam. The comparison of the configurations (2) and (3) points out the impact of the lower flange exposure on the elevation of temperature of the configurations (1). Numerical simulation has shown that there may be a large temperature difference (up to 200 ° C) between the flanges and the web for partially encased "I" steel cross-sections. Indeed, in this configuration, the lower flange is directly exposed to fire while the web benefits from the thermo-hydric protection of wood. So, the results shown in *figure 6* can be observed as “partial” because the concept of critical temperature defined by EN 1993-1-2 is based on the hypothesis considering that the temperature is uniform in the steel cross-section. However, even considering a small critical temperature as 350°C (given for class 4 steel sections [7]), which is the most severe, it is found that all the steel-wood hybrid profiles studied have interesting thermal behaviour, when compared to an unprotected steel profile. In addition, as wood provides a lateral support to steel plates against local and global buckling, a reclassification of class 4 steel sections to higher steel sections classes is possible, which allows to consider a higher critical temperature of steel and improved thermal behaviour.

3.2 Results considering four sides exposed to fire

The numerical simulation has also been carried out considering a fire exposure on four sides. This simulation considers the same material properties of wood and steel as before: water accumulation at the steel-wood interface, steel characteristics according to EN 1993-1-2 [9] and wood according to literature reference [11]. *Figure. 7* presents the evolutions of the average temperature on the whole steel cross-section of the studied configurations illustrated in *figure 3*. These configurations, exposed on four sides, are called (1b), (2b), (3b) and (4b) to distinguish from those exposed on three sides.

It can be seen in *figure. 7* that even with a fire exposure on four sides, the fully encased configuration (4b), still presents an excellent thermal behaviour in case of fire as the average temperature of steel reaches 160°C after one hour of exposure, instead of 115°C observed for the exposure on three sides (configuration (4)). Besides, the configurations with partially encased steel profiles ((2b) and (3b)), present a thermal behaviour that decreases dramatically due to the increase of exposed steel surface. Indeed, the average temperature of the partially encased “I” shaped steel profile (2b) is only 92°C lower than that of the unprotected “I” steel profile (1b). In the same way the difference between the steel average temperature for the “T” shaped profile (3b) and the partially encased “I” profile (2b) is equal to 90°C instead of 215°C observed for the configurations with three sides exposed to fire. This means that the steel surface exposed is a determining factor for the fire resistance of the hybrid elements.

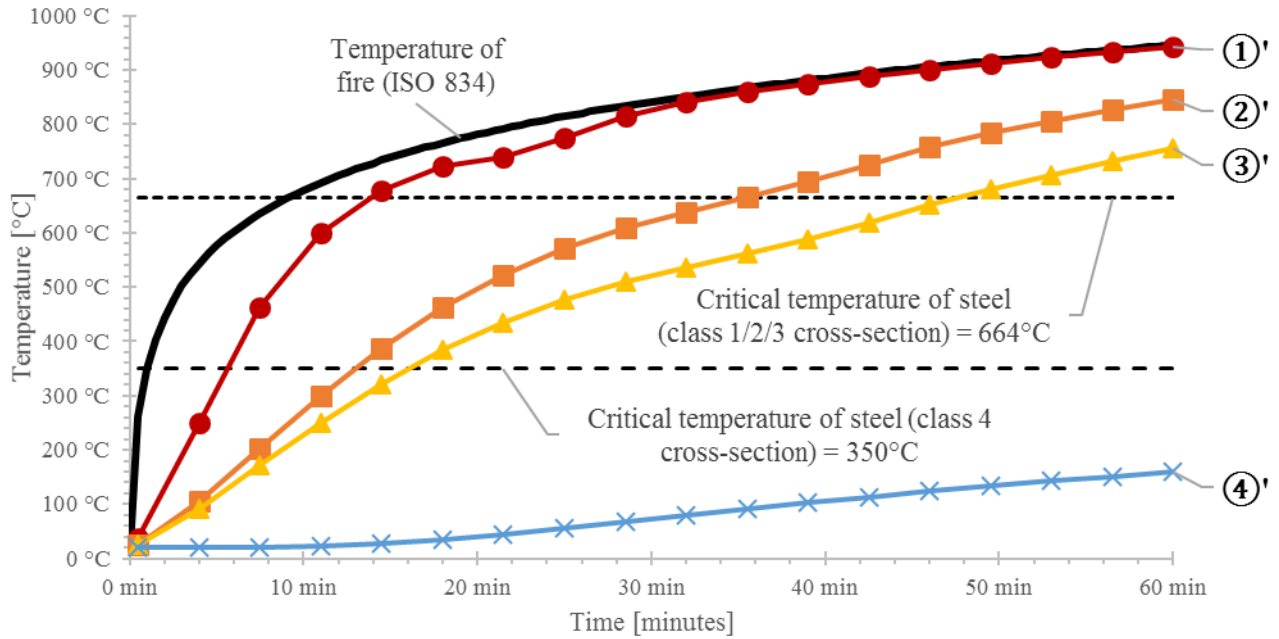


Fig. 7: Evolution of the average temperature of steel cross-sections for the 4 configurations with 4 sides exposed to fire

The same critical temperatures, as for the three faces exposures, have been used to evaluate the thermal performance of the configurations with four faces exposed to fire. *Figure. 8* presents the time required to reach the critical temperatures of 350°C and 664°C. It shows that the fully encased profile (4b) keeps its high thermal performance as the critical temperature of steel profile is not reached after one-hour of fire exposure. However, the average steel temperature of the other configurations reaches the critical values more quickly compared to the three-sided exposure (less than 16 minutes for 350°C). This means that the exposure of both flanges to fire can be very critical and reduce significantly the efficiency of the wood fire protection.

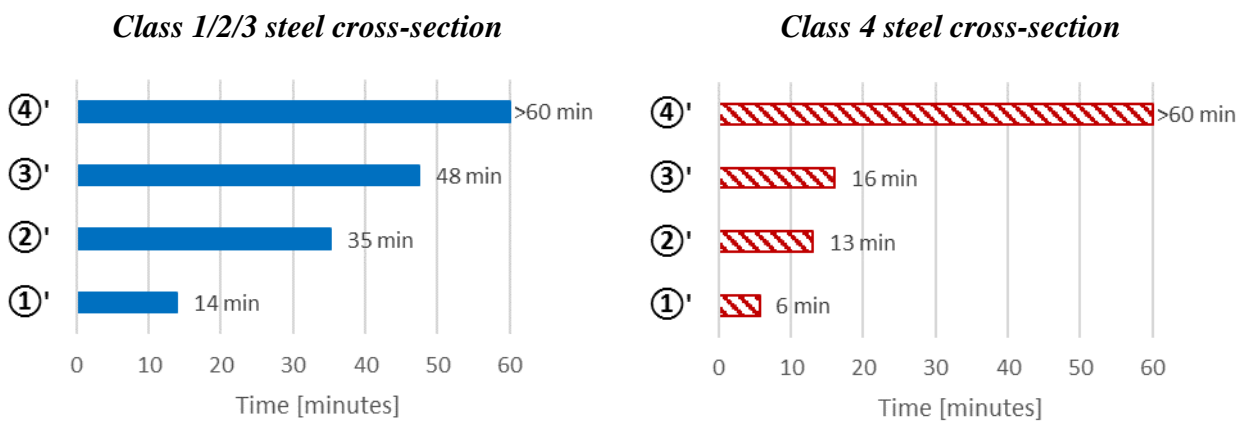


Fig. 8: Time to reach critical temperature of steel cross-sections (configurations with 4 sides exposed to fire)

4 CONCLUSION

The numerical analysis proposed in this study showed good performances for the thermal behaviour of steel-wood hybrid beams in a fire situation. It also exhibits the potential of some configurations of these hybrid beams in terms of fire resistance. Indeed, although wood is a combustible material, a sufficient thickness of wood (30 mm) can be enough to obtain one-hour protection of steel beams according to the numerical simulation. Partial timber protection can also slow down the heating of a steel profile exposed to fire, but steel-timber hybrid elements are more effective when the steel

profile is fully encased in timber elements or at least when the design allows considering a fire exposure on three sides only. Furthermore, the advantage of wood, compared to other fire protection materials, is its ability to provide mechanical support to steel against buckling effects, while its light weight does not significantly increase the weight of the beam. This aspect will be evaluated in further works through thermo-mechanical modelling of those hybrid beams. Finally, this work is used to prepare an experimental test program to validate and complete the thermal numerical simulation proposed in this study.

ACKNOWLEDGMENT

The authors thank the Tremplin Carnot MECD for the financial support (MiBAPro Project).

REFERENCES

1. Cecobois. *Aréna et pavillon de services de l'Université du Québec à Chicoutimi (UQAC)*. Available at: <https://cecobois.com/fr/projets/arena-et-pavillon-de-services-uqac?search=0> (Accessed: 23 March 2018).
2. SurreySteel Structures. *Surrey Steels - connection types*. Available at: <http://surreysteels.com/offer/connection-types> (Accessed: 27 September 2017).
3. Maurizio Piazza (2016). Optimization Process in the Use of Wood and Wood-Based Materials in Hybrid and Composite Structures. *World Conference on Timber Engineering WCTE 2016*, Vienna, Austria, August 22–25. 10 pages.
4. Parvez Alam, Martin Ansell, Dave Smedley (2012). *Effects of reinforcement geometry on strength and stiffness in adhesively bonded steel-timber flexural beams*. *Buildings* 2(4). pp 231-244.
5. Jim De Stefano (2007). *Flitch plate beams: Design guide*. *Structure*, June 2007. pp 56-57.
6. Wolfgang Winter, Kamyar Tavoussi, Felipe Riola Parada, Andrew Bradley (2016). Timber-Steel Hybrid Beams for Multi-Storey Buildings : Final Report. *World Conference on Timber Engineering WCTE 2016*, Vienna, Austria, August 22–25. 10 pages.
7. Isao Sakamoto, Naohito Kawai, Hisashi Okada, Shuitsu Yusa (2003). *Final report of a research and development project on timber-based hybrid building structures*. The University of Tokyo. 6 pages. http://support.sbcindustry.com/Archive/2004/jun/Paper_076.pdf
8. Bruno Jurkiewicz, Sébastien Durif, Abdelhamid Bouchaïr (2017). Behaviour of steel-timber beam in bending. *Eurosteel 2017*, Copenhagen, Denmark, September 13-15. 9 pages.
9. European Committee for Standardization (2005). EN 1993-1-2, *Eurocode 3 - Design of steel structures - Part 1-2: General rules - Structural fire design*. Brussels.
10. MSC Software Corporation (2014) *User's manual - Volume A : Theory and User Information*.
11. Maxime Audebert, Dhionis Dhima, Mustapha Taazount, Abdelhamid Bouchaïr (2012). *Numerical investigations on the thermo-mechanical behavior of steel-to-timber joints exposed to fire*. *Engineering Structures*, 39. pp. 116–125.
12. Abdoulaye Samake (2016). *Etude de l'influence des transferts thermo-hydriques sur les composants d'assemblages bois sous incendie*. Doctoral thesis, Université Blaise Pascal - Clermont II.
13. European Committee for Standardization (2003). EN 1991-1-2, *Eurocode 1 - Actions on structures - Part 1-2: General actions - Actions on structures exposed to fire*. Brussels.

STUDY ON THE USE OF ULTRA-LIGHTWEIGHT CEMENT COMPOSITE FOR ENHANCING FIRE PERFORMANCE OF CONCRETE-FILLED TUBULAR COLUMNS

Wojciech Szymkuc¹, Piotr Toklowicz², Adam Glema³, Helder Craveiro⁴

ABSTRACT

This paper investigates potential advantages of using cenosphere-based ultra-lightweight cement composite (ULCC) in structural fire design, namely as a filling in concrete-filled tubular (CFT) columns exposed to fire. Results of an initial experimental campaign regarding residual strength of cement composites modified with cenospheres are presented. Specimens are heated up to 100°C, 400°C, 600°C, 700°C, 800°C and 1000°C at a constant rate of 6°C/min. Residual compressive strength is tested one day after heating. It is significantly higher than values reported for typical concretes, while mean strength of reference prism specimens is higher than 50 MPa. Other advantages are low thermal conductivity (0.6 W/(m·K)), low density (1400 kg/m³) and high specific heat. The abovementioned properties are used to perform a study on potential use of ULCC for enhancing fire performance of CFT columns. Results of a numerical study show that their fire resistance time (FRT) can be significantly higher when compared to columns filled with typical concrete.

Keywords: Concrete-filled tubular columns; High temperature properties; Cenosphere; Lightweight concrete; Fire resistance; Finite element analysis

1 INTRODUCTION

In this paper use of cenosphere is studied, not only for reducing the weight of construction, but also to increase the fire resistance. Cenosphere (or microsphere) is hollow silica and alumina sphere with a diameter less than 0.5 mm. Microsphere is produced as a by-product of coal combustion in thermal power plants. The most important characteristics of microspheres are low bulk density (about 400 kg/m³), high compressive strength, low thermal conductivity 0.1 W/(m·K) at room temperature [1] and high melting temperature, which is above 1200°C. Cenospheres are used in production of paints, fire proofing layers and insulating materials.

One of the causes of damage of concrete at high temperatures is microcracking due to thermal incompatibility between the aggregate and cement paste. Arizmendi-Morquecho [1] studied high temperature behaviour of thermal barrier coatings based on cenospheres and reported low thermal expansion coefficient of cenospheres ($6.13 \cdot 10^{-6}$ 1/°C). Since thermal expansion of cenosphere is less than a half of expansion of concrete (acc. to Eurocode), we expected better compatibility between cenospheres and cement paste. The favourable effect of using cenospheres as lightweight

¹ Research assistant. Insitute of Structural Engineering, Poznan University of Technology, Poznan, Poland.
e-mail: wojciech.szymkuc@put.poznan.pl

² Alumnus. Insitute of Structural Engineering, Poznan University of Technology, Poznan, Poland.
e-mail: piotr.toklowicz@gmail.com

³ Professor. Deputy Director of Insitute of Structural Engineering, Poznan University of Technology, Poznan, Poland.
e-mail: adam.glema@put.poznan.pl

⁴ Assistant Professor. Insitute for Sustainability and Innovation in Structural Engineering, University of Coimbra, Coimbra, Portugal.
e-mail: heldercraveiro.eng@uc.pt

fillers is confirmed in microstructure analysis presented later in this paper. Cenosphere based composites are investigated by some researchers, mainly at room temperature [2, 3]. Recently [4] performed a study where it is found that cenosphere based cement composites have similar residual compressive strength when compared to typical concretes.

2 MATERIALS AND METHODS

Ultra lightweight cement composite (ULCC) studied in this paper is made of cement CEM I 42.5 R, silica fume (SF), cenospheres, water and polymeric superplasticizer. The mix design is presented in Table 1.

Tab. 1. Mix proportions of ULCC

Water	Cement	Silica fume	Cenospheres	SP	(w+SP)/(c+SF)
0.30	0.92	0.08	0.42	2.5 % cm	0.30

Specimens are prepared in the Laboratory of Institute of Structural Engineering (PUT) using standard mixer (EN 196-1). Since there is no coarse aggregate in the mix, prism specimens 4x4x16 cm are made. Flow is determined using flow table (EN 1015-3). The specimens are demoulded 24h after casting and kept in water for 28 days. Basic properties measured on samples without exposure to high temperatures are presented in Table 2.

Tab. 2. Experimental results at 20°C.

Compressive strength (MPa)	Density (kg/m ³)	Oven-dried density (kg/m ³)	Thermal conductivity without drying (W/(m·K))	Flow (mm)
52.5	1443	1282	0.60	125

Specimens are tested about 6 months after casting, taking into account recommendations of RILEM [5]. Prior to exposure to high temperatures, samples are dried in an oven at 105°C. This is due to initial mix design without polypropylene fibres, dense structure and high water content. Constant mass is reached after 7 days. Evaporated water to dry mass of concrete is 12.5 %. After drying, specimens are heated up to 105°C, 400°C, 600°C, 700°C, 800°C and 1000°C at a constant rate of 6°C/min. Samples are kept at target temperature until they reach steady-state. Then the furnace is shut down to allow natural cooling. Specimens are tested one day after heating. Their residual strength (%) related to strength at room temperature is measured. Each result after exposure to high temperature is an average of at least four compressive strength tests.

3 RESULTS AND DISCUSSION

3.1 Compressive strength and density

Residual strength of cenosphere-based ULCC is presented in Fig. 1 and Table 3. It is remarkably higher than values reported for “hot” normal strength concrete (NSC), as shown in Fig. 1. After exposure to 105°C, there is a strength gain of 11%. Heating to 400 and 600°C has a minor effect on residual strength. Up to 700°C the strength loss is not severe, while it becomes more distinct at temperatures above 700°C, reaching 23 and 42 % at 800 and 1000°C, respectively.

Toric et al. [6] shows that specimens exhibit further deterioration when tested after 24, 48 and 72 hours after heating. To evaluate the influence of time of testing, additional specimens heated to 700°C are also tested 14 days after exposure. The relative residual compressive strength after 14 days is 82 %, compared to 89 % one day after heating. Visual examination of samples 6 months after heating shows no visible signs of further sample deterioration.

Mechanical performance of ULCC after heating can be compared to High Alumina Cement (HAC) [7] or geopolymer concretes [8]. However, ULCC excels at its light weight and low thermal conductivity, which might make it a suitable filling for CFT columns that are required to maintain their load-bearing capacity during severe fire conditions or a long time.

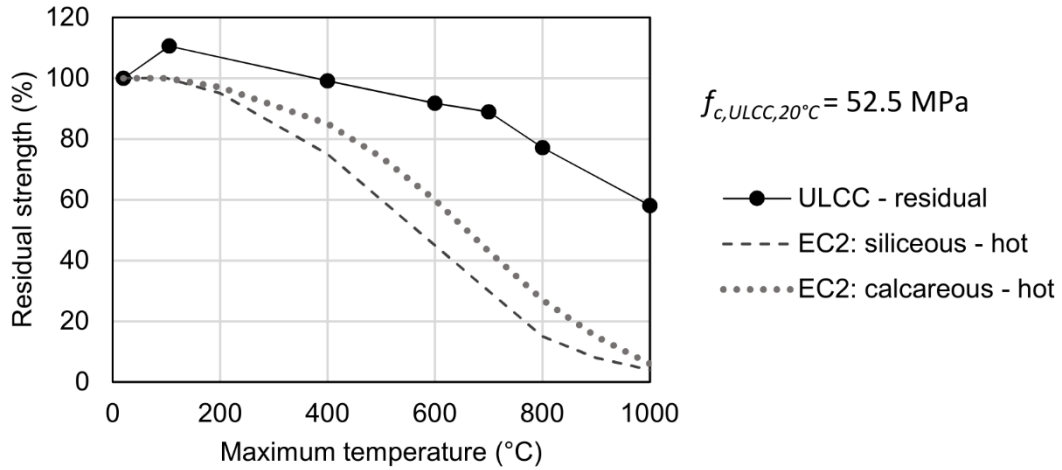


Fig. 1. Residual compressive strength of ULCC (own tests) and hot strength of concrete (Eurocode).

Tab. 3. Residual compressive strength after exposure to elevated temperatures.

Temperature (°C)	20	105	400	600	700	800	1000
Residual strength (MPa)	52.5	58.1	52.1	48.2	46.7	40.5	30.5
Residual strength (%)	100	111	99	92	89	77	58
Density (%)	100	89	85	85	83	81	80

3.2 Thermal properties

Thermal conductivity at room temperature is measured using Transient Plane Source (TPS) technique at the University of Coimbra. Mean value of thermal conductivity is 0.60 W/(m·K), without pre-drying in an oven. Other researchers [9, 10] report values 0.35-0.40 W/(m·K) for similar mixes that are oven-dried at 105°C and then tested at room temperature. There is no data for thermal conductivity at higher temperatures. For numerical simulations that are presented in this paper, thermal conductivity is assumed to be 0.60 W/(m·K) at temperatures in range from 20 to 100°C and 0.35 W/(m·K) above 110°C. It is a safe assumption since thermal conductivity is expected to be even lower at higher temperatures.

Specific heat is measured using two techniques: TPS and Differential Scanning Calorimetry (DSC). We used TPS at University of Coimbra to measure it at room temperature. The result is 1462 kJ/(m³·K), which is 1013 J/(kg·K).

DSC is used to measure specific heat up to 500°C. The results are presented in Fig. 2. It can be seen that specific heat at room temperature is 1180 J/(kg·K). There is a notable peak at 120°C (3470 J/(kg·K)). Afterwards it falls to about 1500 J/(kg·K) at 500°C. Nevertheless, it is higher than values reported for typical concrete in the Eurocode.

Specific heat peak is 3470 J/(kg·K), while for usual concrete with water content of 3 and 10 % it would be 2020 and 5600 J/(kg·K), respectively, according to Eurocode. This can probably be explained in terms of sample preparation. Sample for DSC is taken from prism that was previously

tested for flexural strength. About 100 mg of concrete is scratched from the inner surface. Scratching is done several days after bending, so the surface is exposed to air and probably it dries. This does not explain why measurement at room temperature with TPS gives lower specific heat than DSC, especially since sample tested using TPS technique has its “natural” water content of about 12 % (see Fig. 3). This might be result of different technique being used [10].

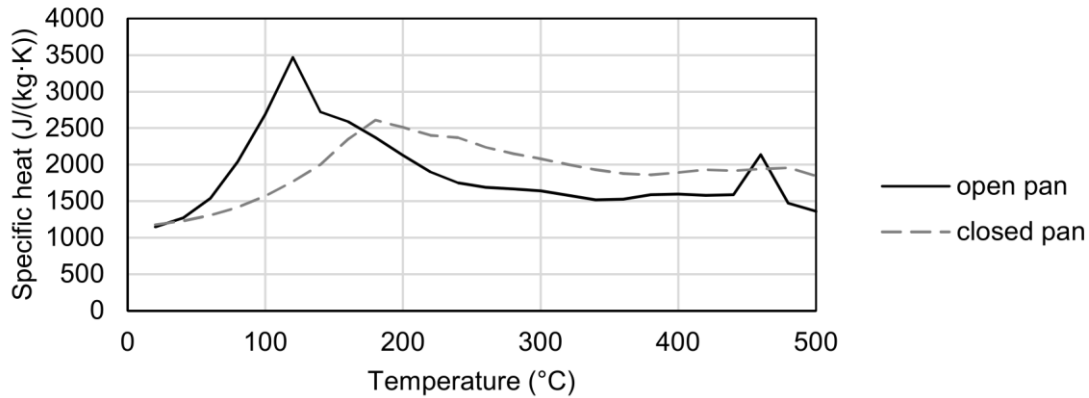


Fig. 2. Specific heat obtained using DSC with open and closed pan.

Since concrete inside a steel column might be considered as sealed, second DSC analysis is run with closed pan, results are presented in Fig. 2.

3.3 Analysis of the microstructure

The analysis of the microstructure is conducted using SEM technique at Poznan University of Technology. Two samples are analysed, one after exposure up to 600°C and reference specimen. Two SEM images are presented in Fig. 3. Hollow spheres can be seen, occupying between one third and a half of the images. Most of the cenospheres are broken in half, and their inside can be seen along with the thickness of their porous outer layer. There are no visible cracks. The interface transition zone between cenosphere and cement paste seems to be unaffected by exposure to 600°C.

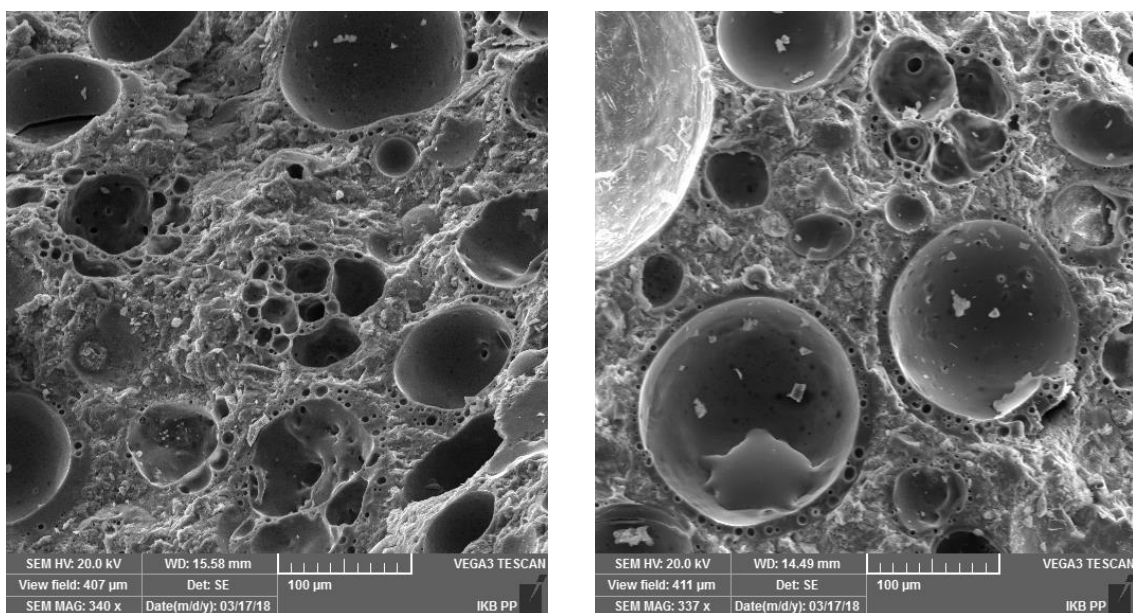


Fig. 3. SEM image of samples before and after heating to 600°C.

4 IMPACT ON THE FIRE RESISTANCE

4.1 Concrete Filled Tubular Columns

Numerical model in Abaqus developed in [11] is used to calculate fire resistance times (FRT) of circular CFT full-scale columns. All simulations are performed assuming emissivity of steel surface ε and the convective heat transfer coefficient h_c equal to 0.7 and 25 W/(m²·K), respectively. Pressure-dependent Drucker-Prager yield criterion is chosen for concrete. Friction and dilation angles are assumed as $\beta=36^\circ$ and $\psi=36^\circ$, respectively. Linear elastic stress-strain relationship is assumed up to $0.4f_{c,\theta}$ with further hardening up to temperature dependent compressive strength $f_{c,\theta}$. Initial geometrical imperfection of columns is L/1000, while mesh size is approximately 20x20x40 mm inside concrete core. Thermal contact conductance (gap conductance) between steel tube and concrete core is assumed to be 100 W/(m²·K). Other material properties, such as stress-strain relationships, thermal properties and thermal expansion are taken from Eurocodes. Increasing the number of equilibrium iterations before the check for increasing residuals is found to be beneficial. The default convergence criterion for the ratio of largest solution correction to the largest corresponding incremental value is increased to overcome problems with premature convergence problems.

Three types of columns filled with ULCC are investigated: without reinforcement (Fig. 4), bar-reinforced and double-skin (Section 4.2). Due to lack of data regarding stress-strain relationship of cenosphere-based ULCC at elevated temperatures, relationship given by Eurocode 2 is used.

Results of numerical simulations for 58 columns filled with plain ULCC are presented in Fig. 2 and compared with results with NSC filling. All columns are originally filled with plain NSC and are reported in the literature. The model validation based on these columns is presented in [11].

Change of FRT in Fig. 4 is related to the result of a numerical analysis of the specific column. For example, the first column presented in Fig. 4 a) is taken from [12]. Its measured fire resistance time, reported in [12] is 56 minutes, while calculated FRT is 48 minutes (86 %). When favourable compressive strength reduction factors presented in Fig. 1 are assumed along with original strength of concrete reported in [12], the resulting calculated FRT is 85 minutes (77 % more than 48 minutes calculated for NSC). Additional study is run (Fig. 4 b), where only thermal properties of lightweight composite are considered, resulting in FRT of 62.5 minutes (30 % more) for this column.

That average increase of FRT is 78 % due to favourable materials properties of ULCC at elevated temperatures (Fig. 4). For some of the investigated columns FRT decreases. This can be explained, since in these cases concrete core does not contribute to FRT mechanically – it only acts as a heat sink. Lower thermal conductivity of ULCC causes increased temperature of external steel tube and its faster failure, which in these cases coincide with failure of entire column. When only columns with an increase of FRT are considered, an average increase of FRT is 101 %.

Additional study is performed, investigating only effect of favourable thermal properties: specific heat, thermal conductivity and density, while strength is assumed to be the same as reported in the literature and Eurocodes. In this case, an average increase of FRT is 17% (23 minutes). When taking into account only columns with an increase of FRT, it is 26 % (31 minutes).

Another study concerns the possibility of lowering the external dimensions of a column. It is found that columns that would be filled with ULCC could on average be 20 % smaller in diameter, resulting in less material consumption and even less weight, when compared to standard solutions. Cost of one tonne of cenosphere is about 700 €, but the potential savings in terms of space, material use and increase of fire resistance time may balance additional expenses.

Study on the use of ultra-lightweight cement composite for enhancing fire performance of concrete filled tubular columns

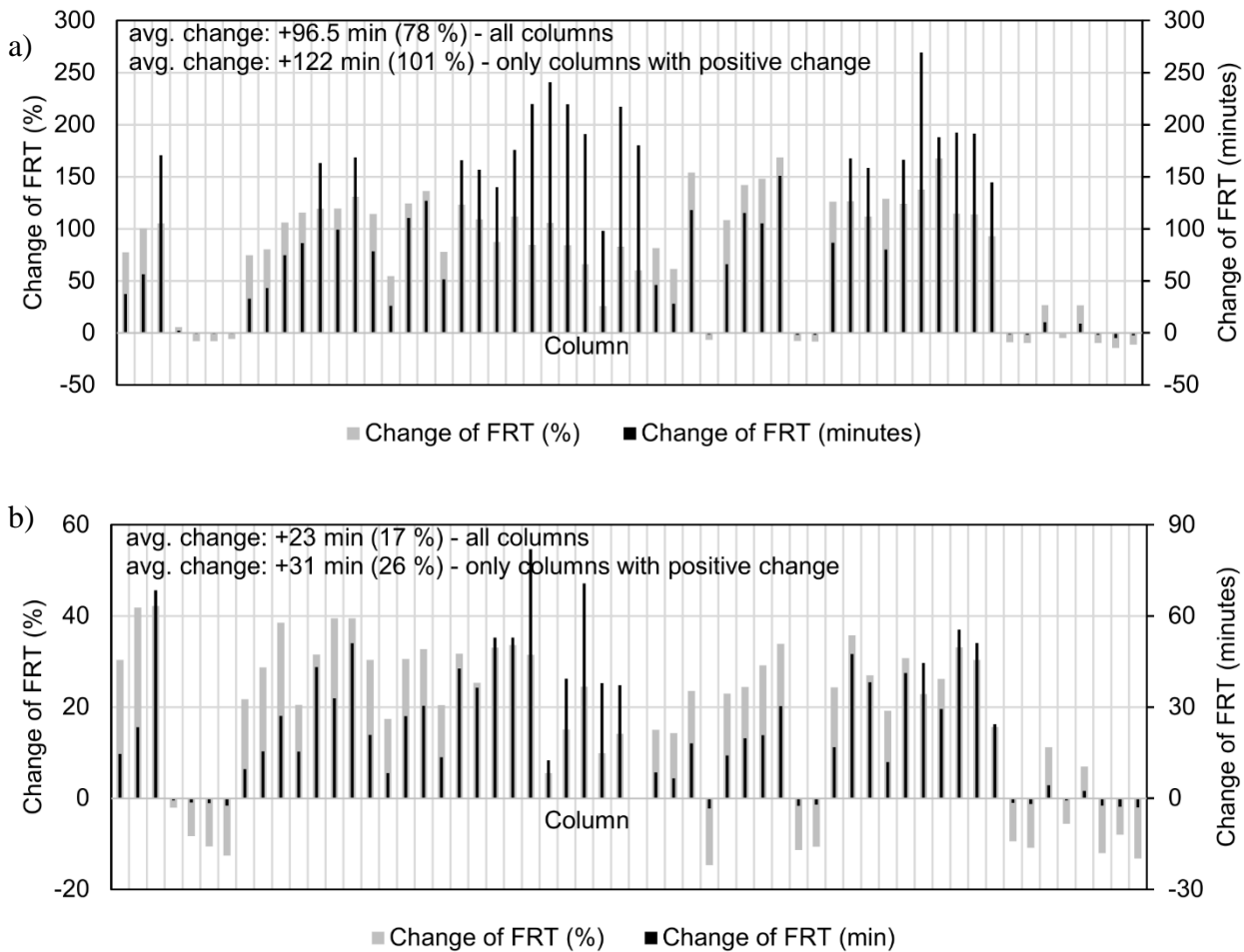


Fig. 4. Change of fire resistance time (FRT) in minutes and % for 58 analysed columns. Change is caused by using ULCC instead of NSC filling. a) results are calculated using original initial strength (reported by researchers) but assuming strength reduction factors from own experiments on ULCC (Fig. 1); b) only thermal properties are used in calculations, while reduction factors of compressive strength follow relationships presented in Eurocode.

4.2 Reinforced and Double Skin Composite Columns

ULCC could possibly be used as a filling of Double Skin columns. It is expected that the most cost-effective combination of concretes would be cenosphere-based composite poured between two tubes (with favourable mechanical and insulating properties) and concrete with relatively high thermal conductivity inside the inner tube (standard NSC). Concrete inside inner tube would serve a purpose of a heat sink – lowering the temperature of inner tube. For a range of typically used Double Skin columns, temperature of the inner tube could be lowered by up to 300°C, when compared to pure NSC infill. Using ULCC as an infill of reinforced CFT columns results in temperatures that are lower by 100-250°C, when compared to pure NSC infill.

An example is made for Double Skin column with outer tube 219.1x5 mm and inner tube 159x5 mm. Hence, the distance between two tubes is only 25 mm. Temperatures presented here are calculated after one hour of ISO fire exposure. If lower Eurocode limit of thermal conductivity is assumed, temperatures of outer and inner tubes would be 901 and 405°, respectively. If ULCC is used as an infill between tubes, while inner tube is filled with typical concrete, temperatures of outer and inner tubes would be 914 and 233°C, respectively. This combination of materials makes temperature of inner tube 172°C lower. This way, cost-effectiveness might be achieved, since

ULCC would constitute to only 45% of total volume of concrete if it was poured only between tubes of the described cross-section.

Tab. 4. Temperatures of Double Skin column consisting of two tubes: 219.1x5 mm and 159x6 mm after 1 hour of the ISO fire.

Type of filling		Temperature (°C)		
Inside	Between tubes	Inner tube	Outside tube	Core center
NSC	NSC	405	901	126
NSC	ULCC	233	914	87
NSC*	ULCC	221	914	106
ULCC	NSC	454	905	60
ULCC	ULCC	275	915	47
*in this single case upper limit of thermal conductivity is assumed				

5 CONCLUSIONS

Using novel, lightweight cement composites with low thermal conductivity and high residual strength might be a promising direction for enhancing fire performance of structures. The developed composite offers good insulating properties and remarkable residual compressive strength. Further investigation should be made to test its properties at elevated temperatures, including thermal conductivity, compressive strength and full stress-strain relationships. CFT columns filled with ULCC might be significantly less sensitive to fire, due to favourable insulating and mechanical properties of a developed lightweight composite. It is shown that for some columns fire resistance times might be more than 3 times longer when using ULCC instead of typical concretes. The developed composite material could be used in Double-Skin columns to lower temperature of the inner tube.

ACKNOWLEDGMENT

We would like to thank Maria Ratajczak (Institute of Structural Engineering, PUT) for providing SEM images.

REFERENCES

1. Arizmendi-Morquecho, A., Chávez-Valdez, A., Alvarez-Quintana, J., (2012). *High temperature thermal barrier coatings from recycled fly ash cenospheres*, Applied Thermal Engineering, Vol. 48(2012), pp. 117-121.
2. Chia, K.S. Liu, X. Liew, J.Y.R., Zhang, M.H. (2014). *Experimental study on creep and shrinkage of high-performance ultra lightweight cement composite of 60MPa*, Structural Engineering and Mechanics Vol. 50, Issue 5, pp. 635-652.
3. Rheinheimer, V., Wu, Y., Wu, T., Celik, K., Wang, J., De Lorenzis, L., Wriggers, P., Zhang, M-H., Monteiro, P.J.M. (2017). *Multi-Scale Study of High-Strength Low-Thermal-Conductivity Cement Composites Containing Cenospheres*, Cement and Concrete Composites 80(2017), pp. 91-103.
4. Huang, Z., Padmaja, K., Li, S., Liew, J.Y.R. (2018). *Mechanical properties and microstructure of ultra-lightweight cement composites with fly ash cenospheres after exposure to high temperatures*, Construction and Building Materials 164 (2018), pp. 760–774.
5. RILEM TC 129-MHT (1995) *Test methods for mechanical properties of concrete at high temperatures: Compressive strength for service and accident conditions*. Materials and Structures, vol. 28, no. 181, pp.410–414.

6. Torić, N. Boko, I. Juradin, S., Baloević, G. (2016). *Mechanical properties of lightweight concrete after fire exposure*, Structural Concrete 17 (2016), No. 6, pp. 1071-1081.
7. Vejmelková, E., Koňáková, D., Scheinherrová, L., Doleželová, M., Keppert, M., Černý, R. (2018) *High temperature durability of fiber reinforced high alumina cement composites*, Construction and Building Materials 162, pp. 881-891.
8. Kong, D.L.Y., Sanjayan, J.G. (2010). *Effect of elevated temperatures on geopolymer paste, mortar and concrete*, Cement and Concrete Research 40, pp. 334-339.
9. Hanif, A., Diao, S., Lu, Z., Fan, T., Li, Z., (2016). *Green lightweight cementitious composite incorporating aerogels and fly ash cenospheres – Mechanical and thermal insulating properties*, Construction and Building Materials 116 (2016), pp. 422-430.
10. Khoury, G.A., Anderberg, Y., Both, K., Fellingner, J, Høj, N.P., Majorana, C. (2007). *fib Bulletin No. 38: Fire design of concrete structures - materials, structures and modelling*, International Federation for Structural Concrete (fib)
11. Szymkuć, W., Glema, A., Malendowski, M. (2015). Fire performance of steel tubular columns filled with normal strength concrete, *Proceedings of 5th International Workshop on Performance, Protection & Strengthening of Structures under Extreme Loading (PROTECT 2015)*, Michigan State University, East Lansing, USA, DEStech Publications Inc., pp. 865-872
12. Wainman, D.E., Toner, R.P. (1992). “*BS476: Part 21 Fire Resistance Tests. The Construction and Testing of Three Loaded CHS Columns Filled with Concrete*”, British Steel Report No. SL/HED/R/S2139/1/92/D

METHODS TO ASSESS THE BEARING CAPACITY OF CONCRETE-FILLED HOLLOW SECTION COLUMNS IN FIRE

Alberto Compagnone¹, Antonio Bilotta², Emidio Nigro³

ABSTRACT

Steel-concrete composite columns such as concrete-filled hollow section columns behave excellent strength and stability both at ambient temperature and in fire. Indeed the concrete provides both good restraint to local and global buckling and natural protection against temperature growth in steel. The Eurocode 4 (EN1994-1-2) suggests simplified methods for design and verification of some types of composite columns in fire. National and European sub-committees for codes update, which include some authors of this paper, have conducted activities in order to update these simplified methods. In this framework, the paper summarizes also some activities of the Project Team SC4.T4 devoted to the composite columns with concrete-filled hollow sections. The bearing capacity of the composite columns is calculated by means of simplified and accurate calculation methods suggested in literature. Comparisons between the results obtained applying the methods and the experimental results collected in literature suggest possible further improvements.

Keywords: Code, simplified method, numerical analyses, fire resistance, buckling.

1 INTRODUCTION

Composite steel-concrete columns are characterised by excellent strength and stability both at ambient and in fire situation. In fire, the concrete protects the steel against heating. Nevertheless, fire safety checks of the columns in fire are yet an open issue, for both accurate and simplified methods. In the framework of the activities by national and international committees to update the simplified methods suggested in the Eurocode 4 Part 1-2 [2], the paper treats the concrete filled steel columns, which are the main object of study of the Project Team SC4.T4. The following sections summarize the main steps of a general and a simplified method for safety checks of columns. The simplified method, suggested in the Annex H of EN1994-1-2, has been modified according to the suggestions provided by the SC4.T4. Test results collected in literature are finally used for benchmark.

2 ACCURATE METHOD

The accurate method is based on a finite element analysis of the section for the calculations of both temperatures and capacity under combined bending and axial force. The II-order effects and buckling are taken into account through the well-known analytical approach named “Model column”, which is based on the definition of the moment-curvature diagram of the cross-section.

¹ PhD Student, Department of Structures for Engineering and Architecture, University of Naples Federico II, Napoli, Italy.
e-mail: alberto.compagnone@unina.it

² Assistant Professor, Department of Structures for Engineering and Architecture, University of Naples Federico II, Napoli, Italy.
e-mail: antonio.bilotta@unina.it

³ Full Professor, Department of Structures for Engineering and Architecture, University of Naples Federico II, Napoli, Italy.
e-mail: emidio.nigro@unina.it

High temperatures cause the variation of the mechanical properties of structural materials and the thermal expansion of elements. These phenomena influence the magnitude of internal forces, the displacements and the resistances of the column. As concerns the thermal and mechanical properties of steel and concrete depending on temperature, we refer to the relationships defined in the EN1994-1-2 ([2]) valid both in tension and in compression.

The temperature in concrete structural members is not uniform due to the low thermal conductivity of concrete. Therefore, structural analysis is performed by using fibre models in which different temperatures – and then the related constitutive laws – apply to different fibres. The temperature in the cross section has been evaluated through a finite element approach, by using the software SAFIR ([4]) with the thermal properties of materials defined according to Eurocode 4 1994-1-2. The FEM analysis allows obtaining the temperatures during the fire exposure (see Fig. 1) to characterise each point of the section with its own constitutive law and then proceed with the mechanical analysis, which allows to evaluate the plastic capacity of the section.

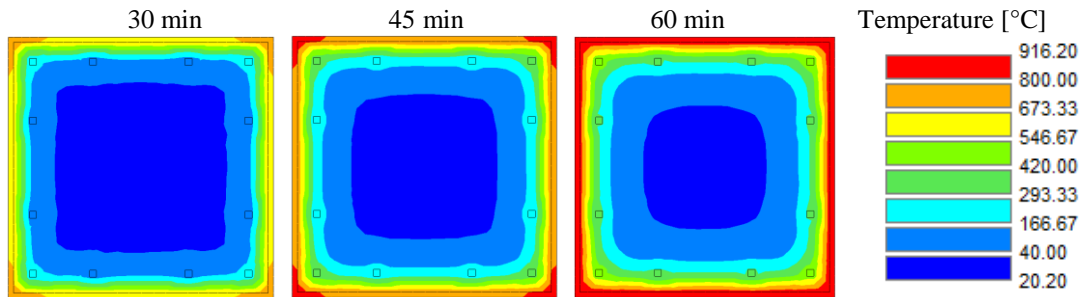


Fig. 1. Temperature in a concrete-filled hollow section exposed to standard fire curve

The behaviour of structural members under combined bending and axial force can be studied through diagrams that describe the relationship between bending moment and curvature of the section. This relationship, which is a function of the temperature for a given time t of exposure to fire, is based on equilibrium and compatibility conditions of the deformed shape for each analysis step. The analysis based on the moment-curvature relationship is suitable for single structural members but can be used also when dealing with complex structures. For members that exhibit phenomena of geometric non-linearity, such as slender columns, second-order effects can be easily included. The behaviour of the section has been studied by means of the software Morvat Fire [3] which calculate both moment-curvature relationship and M-N interaction domains for composite sections (up to three different materials) subject to fire. The temperature field within the section can be determined by using an external FE code to solve the thermal problem (for instance, SAFIR [4] or Fires-T3 [5]). The fundamental hypothesis is that cross-sections remain plane during the exposure to fire. The strains of materials at high temperatures are generally defined by assuming that the total strain ε_{tot} is given by the sum of mechanical and thermal strains ([8]):

$$\varepsilon_{tot} = \varepsilon_{\sigma}(\sigma, \theta) + \varepsilon_T(\theta) \quad (1)$$

The sets of $(M ; \chi)$ couples represent the moment-curvature diagram of the section. Fig. 2 shows bending moment versus curvature laws obtained for different normalized axial forces $v = N/N_{pl}$ (Fig. 2a) and at different time of fire exposure (Fig. 2b). To assess the global deflection of a structural member the thermal strains need to be introduced. Fig. 3a shows M-N interaction domains obtained by considering or neglecting the effect of thermal expansion. Thermal expansion cause internal redistributions of stresses among the various fibres of the section, whose magnitude is higher in case of high thermal gradients; however, their effect on the interaction domain seems to be relatively limited, except for high values of axial force. Finally, Fig. 3b shows that the maximum normal forces, N_{pl} , is attained with the concrete core in softening. Note that the constitutive law for each material doesn't respect the Drucker's material stability postulate, thus the M-N diagram may be not convex.

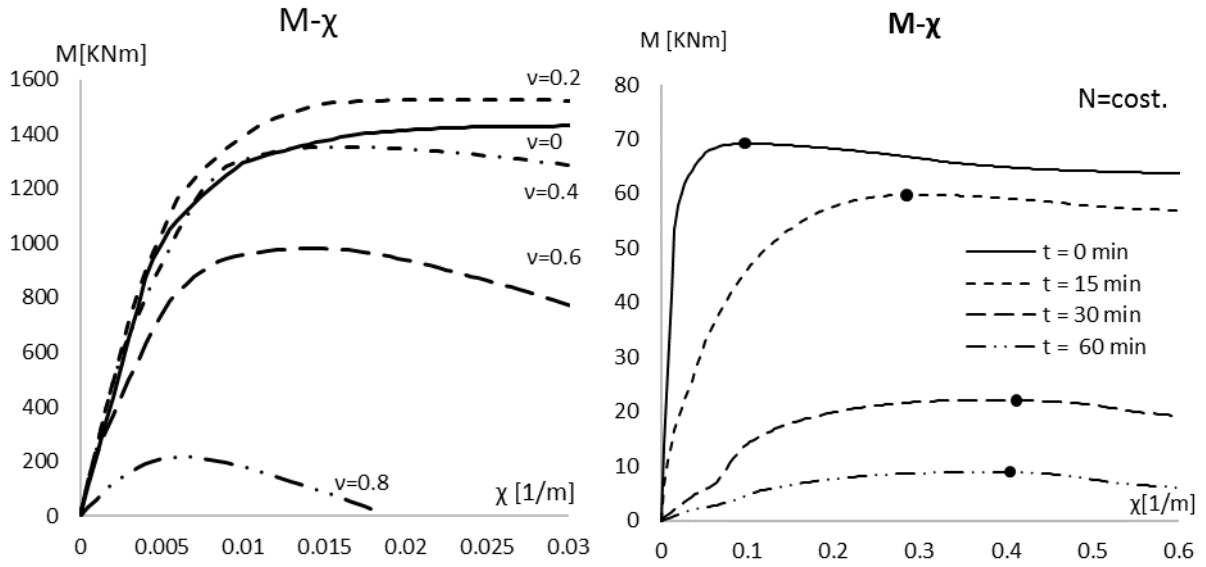


Fig. 2. M- χ diagrams by varying (a) normal force and (b) time of fire exposure

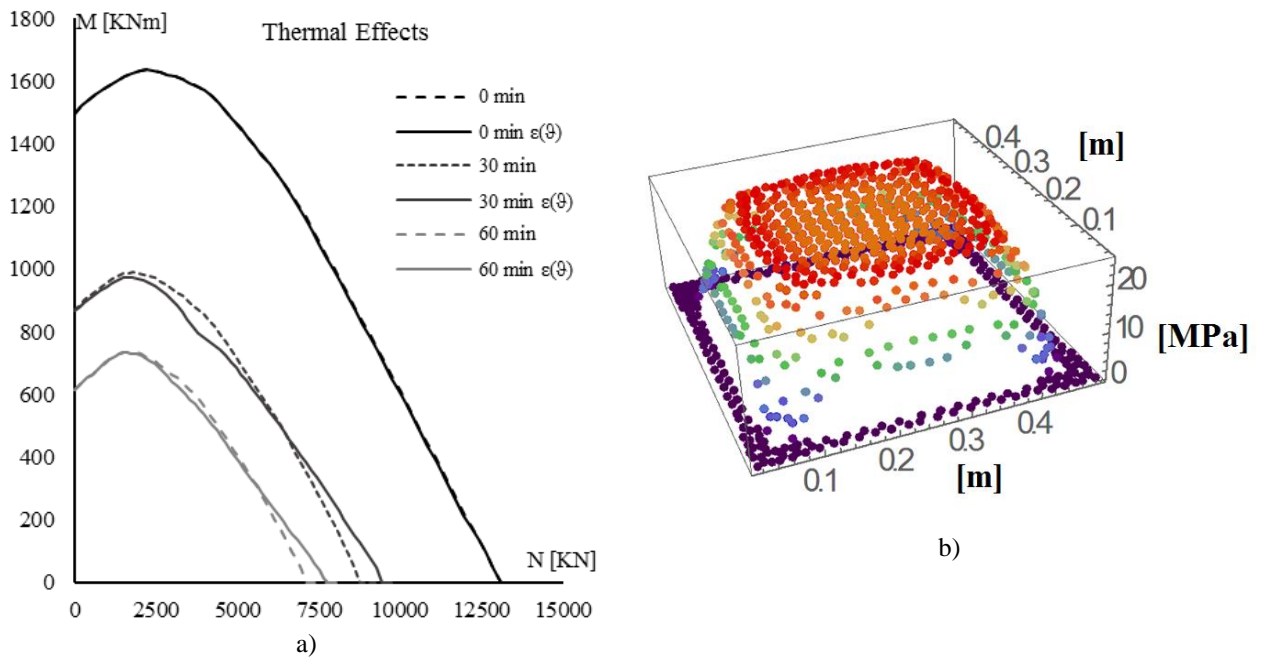


Fig.3. a) thermal effects on M-N domains; b) softening in the concrete core at N_{pl}

Thermal distortions and the related self-equilibrating stresses are significant for the evaluation of deflections and deformation in structural members, which play a role in buckling and second-order effects [8]. These aspects are modelled by means of the model column's method [9] with the introduction of an equivalent member imperfection. The model column's method allows to consider the aforementioned effects and is based on the definition of the moment-curvature diagrams of the section, where the highest values of internal forces are acting for different values of axial force and time of fire exposure. Based on the moment-curvature diagram, the maximum value of resistant bending moment can be determined by subtracting from the resistant bending moment the bending moment due to second-order effects, which can be evaluated through the simple equation:

$$M_{II} = N \cdot \frac{L_o^2}{\pi^2} \cdot \chi \tag{2}$$

This procedure is implemented by constructing the moment-curvature diagrams for several time of fire exposure. To consider geometrical and mechanical imperfections an equivalent member imperfection $e_0 = L/200$ is assumed. Therefore, the interaction domain of the slender columns, taking into account the II-order effects, can be obtained by reducing the resistant bending moment values of the plastic M-N domain, according to the following equation:

$$M_{u,rid} = M_{u,tot} - M_{II} - N \cdot e_0 \quad (3)$$

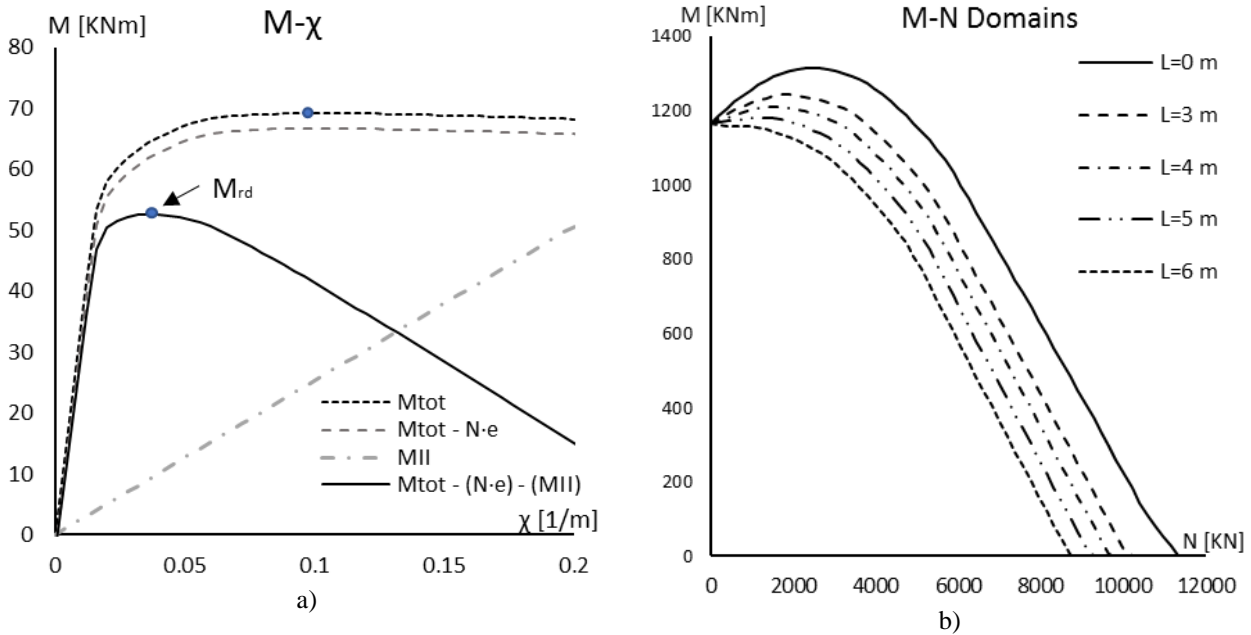


Fig. 4. (a) M_{rd} calculated with the model column's method and (b) related M-N domains for different columns length

3 SIMPLIFIED METHOD

The simplest constitutive law used for hand calculations under normal temperature conditions is rigid-plastic. According to this model, changes of stress in the material are not dependent on changes of strain. This simplified model does not reflect the reality but is easy to use because it respects the Drucker stability postulate. To extend this model to structure in fire, the strength of the materials is generally reduced by a coefficient, k_θ , specific of each material and depending on temperature.

The simple methods suggested by Eurocode 4 Part 1-2 are based on the assumption of reduced rigid-plastic laws for the materials in fire. In this context is framed the method proposed by Project Team SC4.T4 ([6],[11]), which now is in its final revision. To simplify the thermal analysis of the concrete filled composite sections, some formulas are suggested, providing a uniform temperature for each material with reference to the standard fire curve ISO834. These formulations have been calibrated in order to obtain a decrease of strength in the whole section equivalent to that obtained by using a FE analysis (see [10],[12]). The expressions (4) depend only on the fire exposure time, t_R , the section factor, A_m/V , and the concrete cover, c :

$$\theta_{c,eq} = f(t_R, A_m/V) \quad \theta_{a,eq} = f(t_R, A_m/V) \quad \theta_{s,eq} = f(t_R, c) \quad (4)$$

Therefore, to simplify the analytical formulas, the effective position of the reinforcing bars and the dimensions of the cross-section are not considered. Note that these aspects could have some influence on the actual temperature field within the cross section.

Safety checks for composite columns at ambient can be performed by verifying that the applied forces N_{Ed} and M_{Ed} are inside the interaction domain. From an analytical point of view, this condition can be written with the relationship (7), suggested in EN1994-1-1 ([7]):

$$M_{Ed} \leq \alpha_M M_{pl,Rd}(N_{Ed}) \quad (5)$$

where M_{Ed} is the acting bending moment; $M_{pl,Rd}(N_{Ed})$ is the resistant plastic bending moment depending on the axial force; α_M is a coefficient that takes into account the approximations induced by the assumption of the plastic domain in the simplified method ($\alpha_M = 0.9$ for steel S235 and S355, $\alpha_M = 0.8$ for steel S420 and S460). The buckling of columns, with II-order effects, is introduced through the stability curve method and a corrective factor [7].

The above mentioned simplified method provides two procedures for checks in fire situation, depending on the load conditions of the column.

For columns concentrically loaded, the effective flexural stiffness in fire is evaluated according to the equation:

$$(EI)_{fi,eff} = \varphi_{a,\theta} E_a(\theta_{a,eq}) I_a + \varphi_{c,\theta} E_c(\theta_{c,eq}) I_c + \varphi_{s,\theta} E_s(\theta_{s,eq}) I_s \quad (6)$$

where:

I_i is the second moment of area of the part i of the cross-section;

$E_c(\theta_{c,eq})$, $E_a(\theta_{a,eq})$ and $E_s(\theta_{s,eq})$ are the elastic modules of the materials at the relevant temperatures;

$\varphi_{a,\theta} = f(A_m/V)$ reduces the stiffness of the steel tube, depending on the section factor;

$\varphi_{s,\theta} = f(t_R)$ reduces the stiffness of the reinforcing bars, depending on the fire duration;

$\varphi_{c,\theta}$ reduces the stiffness of the concrete (0.8 or 1.2 if tangent or secant modulus are used).

Hence, the slenderness ratio can be evaluated through the classical formula:

$$\bar{\lambda}_\theta = \sqrt{\frac{N_{fi,pl,R}}{N_{fi,cr}}} = \sqrt{\frac{b_c h_c f_{c,\theta}(\theta_{c,eq}) + A_a f_{y,\theta}(\theta_{a,eq}) + A_s f_{s,\theta}(\theta_{s,eq})}{\pi^2 (EI)_{fi,eff} / L_0^2}} \quad (7)$$

Buckling curves are used to evaluate the buckling factor, χ , to calculate the buckling axial force

$$N_{b,Rd} = \chi N_{pl} \quad (8)$$

For eccentrically loaded composite columns, the flexural stiffness in fire is evaluated by means of some coefficients which adjust the formula suggested in EN1994-1-1 for check at ambient. Thus, the stiffness is estimated through the Equation (9):

$$(EI)_{eff} = K_\theta K_0 [\varphi_{a,\theta} E_a(\theta_{a,eq}) I_a + K_{e,II} \varphi_{c,\theta} E_c(\theta_{c,eq}) I_c + \varphi_{s,\theta} E_s(\theta_{s,eq}) I_s] \quad (9)$$

with $K_\theta = 0.67$, $K_0 = 0.9$ e $K_{e,II} = 0.5$.

The II-order effects are introduced through an amplification factor $1/[1-(N_{Ed}/N_{fi,cr})]$. The term $N \cdot e_0$ is added to the bending moment to take in account the equivalent member imperfection e_0 . Therefore, the safety check of eccentrically loaded columns in fire becomes:

$$\frac{M_{Ed} + N_{Ed} \cdot e_0}{(1 - N_{Ed}/N_{fi,cr})} \leq \alpha_M M_{fi,Rd}(N_{Ed}) \quad (10)$$

This equation impose that the plastic resistance of the column must be higher than the demand bending moment amplified by the II-order effects. Rearranging the Eq. (10), the bending resistance can be written as:

$$M_{rid,Rd} = \left[\alpha_M M_{Rd}(N_{Ed}) \cdot \left(1 - \frac{N}{N_{cr}} \right) \right] - N \cdot e_0 \quad (11)$$

4 BENCHMARK

In this section, we compare the test results collected in literature [13-19] with the numerical results obtained by the application of both simplified and accurate method. Among the tests only CHS (Circular Hollow Section) columns are selected for benchmark, obtaining a database of 76 tests (extended database). The extended database was reduced considering only tests which satisfy the scope of the simplified method on the length of the column exposed to fire over the diameter of the column L_0/D , the section factor A_m/V , the diameter to thickness of steel tube ratio D/t and resistance time, $t_R \geq 30$ min. The reduced database consists of 41 tests. The restraint condition are generally well defined by the researchers, but in some cases it is difficult to provide a perfect hinge restraint. In some cases, the boundary conditions do not depend only on the pin at the end of members, but also on the stiffness of the columns due to the non-uniform heating during the test. The most particular case is [19], in which the base of the column is fixed, while the other end is constrained with a bolted joint, whose stiffness is proportional to the bending stiffness of the load frame. Therefore, for these tests [19] the buckling length was conservatively assumed to be equal to 70% of the column's length for all tests which end before 30 minutes. However, there are 4 tests which collapsed after 30 minutes and for these ones the buckling length was assumed as fixed at both ends because in fire situation it is highly probable that the columns can be considered fixed-fixed due to stiffness degradation. A more accurate stiffness evaluation could provide greater precision in the buckling length estimation. Fig. 5 shows the ratio between the axial load recorded at failure during the test (NT) and the axial load calculated (NC) respectively with the simplified method (Fig. 5a for the reduced database, and Fig.5c for the extended database) and with the accurate method (Fig. 5b for the reduced database, and Fig.5d for the external database). Both methods (simplified and accurate) are conservative on the reduced database, with average of 1.81 and 1.67 respectively, and both 16th fractiles greater than one. Furthermore, the accurate method provides an estimation better than the simplified, with standard deviations lower than 20% (0.57 accurate vs 0.68 simplified). As regard the extended database, the simplified method becomes slightly less conservative (1.62 vs 1.81) with a higher standard deviation (0.81 vs 0.68), namely a greater coefficient of variation (50% vs. 38%), as a consequence of the simplified nature of the method. In this regards, the accurate method, which is more flexible, provides similar standard deviation on both the extended and the reduced database (0.61 vs 0.57) and in any case lower than those of the simplified method (0.68 and 0.81, respectively on the reduced and extended database). On the extended database, the 16th fractiles of the two methods are similar, but the lower standard deviation show that the accurate method is more reliable. Results are summarize in Table 1.

Table 1. Statistics of the Reduced and Extended Database

	Reduced Database (41 tests)		Extended Database (76 tests)	
	Simplified	Accurate	Simplified	Accurate
Mean	1.81	1.67	1.62	1.37
St. Dev.	0.68	0.57	0.81	0.61
CoV	38%	34%	50%	44%

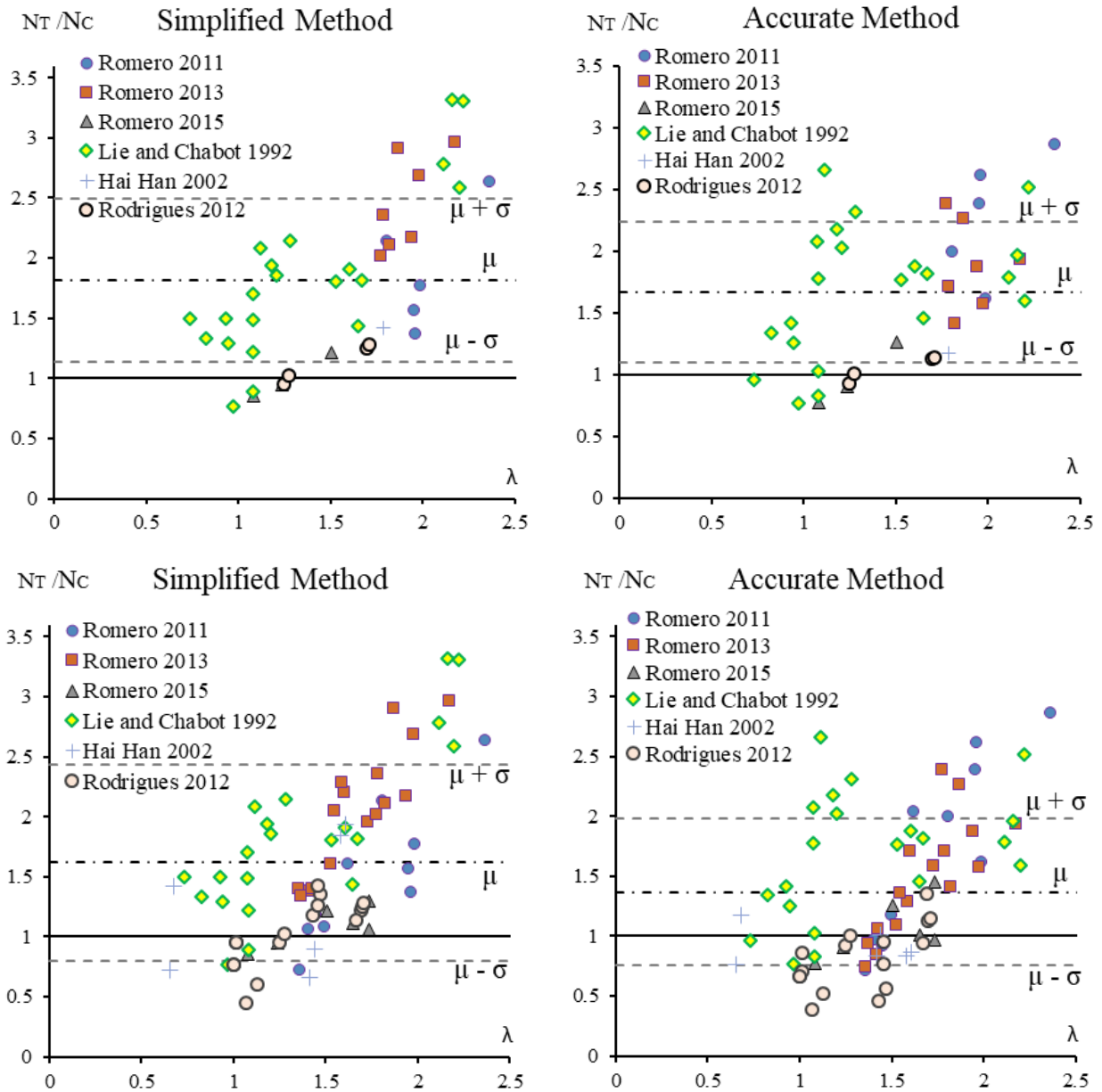


Fig. 1. N_T/N_c ratios for simplified and accurate methods - Reduced Database (a,b) and Extended Database (c,d)

5 CONCLUSIONS

This paper shows the applications of (i) a simplified method proposed by the Project Team SC4.T4 and (ii) an accurate method based on the FEM thermal analysis of the section and II-order analysis through the “model column” method. Some experimental results have been used for a benchmark of both methods, allowing to conclude that:

- the simplified method is safe and reliable in most cases;
- the benchmark highlights high scatter for both simplified method (CoV = 38÷50%) and accurate method (CoV = 34÷44%), which is partially due to an high experimental scatter;
- a backwards calibration of equivalent eccentricity in the accurate method could provide more reliable results;
- accurate method allows to take in account the non-uniform heating of members due to the various exposure conditions. Furthermore the accurate method application removes the discontinuity provided by the simplified method due the two different formulations which permit to evaluate the axial load with and without bending moment stress.

Despite of the good results, further experimental investigation with indepth analyses of the boundary conditions (thermal and mechanical) should be performed to improve reliability of both simplified and accurate method.

6 REFERENCES

- [1] G. A. Khoury, B. N. Grainger, P.J.E. Sullivan (1975). Transient thermal strain of concrete: literature review, conditions within specimen and behaviour of individual constituents. Magazine of concrete research. pp. 131-144.
- [2] UNI EN1994-1-2 Eurocode 4 (2005). Design of composite steel and concrete structures – Part 1-2: Structural fire design
- [3] Compagnone A. (2016). Analisi termomeccaniche con modelli di incendio avanzati. Structural and Geotechnical Engineering Master Degree Thesis, Università di Napoli Federico II.
- [4] J.M. Franssen , V.K.R. Kondor, J. Mason (2000). SAFIR User Manual. University of Liege, Belgium.
- [5] R. Iding, B. Bresler, Z. Nizamuddin, (1977). Fires–T3 a computer program for the fire response of structures. National Institute of Standards and Technology. USA.
- [6] SC4.T4. (2017). Simplified design method for evaluating the fire resistance of concrete-filled steel tubular columns
- [7] UNI EN1994 -1-1 Eurocode 4 (2005). Design of composite steel and concrete structures – Part 1-1: General rules.
- [8] Y. Wang, I. Burgess, F. Wald, M. Gillie (2013). Performance-Based Fire Engineering of Structures. 1st Edition. CRC Press.
- [9] T. T. Lie, D. C. Stringer. (1994). Calculation of the fire resistance of steel hollow structural section columns filled with plain concrete. Canadian journal of civil Engineering. pp 382-385.
- [10] Research Programme of the Research Fund for Coal and Steel, (2005). F.R.I.S.C.C. Fire resistance of innovative and slender concrete filled tubular composite columns. Bruxelles.
- [11] SC4.T4. (2016). Review of existing fire design methods of concrete-filled tubular columns.
- [12] Espinòs A., Romero M. L., Mercé E. S., Hospitaler A. (2015) Circular and square Slender Concrete-Filled tubular columns under large eccentricities and fire. Journal of Constructional Steel Research
- [13] TT Lie, M. Chabot (1992) Experimental studies on the fire resistance of hollow steel columns filled with plain concrete, internal report No. 611, Ottawa (Canada): Institute for Research in Construction, NRC of Canada
- [14] Romero M. L., V. Moliner, A. Espinos, C. Ibanez, A. Hospitaler, Fire behavior of axially loaded slender high strength concrete – filled tubular columns, Journal of Constructional Steel Research, Vol. 67, pp 1953-1965
- [15] Romero M. L., V. Moliner, A. Espinos, A. Hospitaler, (2013) Fire behavior of eccentrically loaded slender high strength concrete – filled tubular columns, Journal of Constructional Steel Research, Vol. 83, pp 137-146
- [16] Romero M. L., E. Serra, A. Espinos, A. Hospitaler, (2015) Circular and square slender concrete – filled tubular columns under large eccentricities and fire, Journal of Constructional Steel Research, Vol. 110, pp 90-100
- [17] Lin-Hai Han, Xiao-Ling Zhao, You-Fu Yang, Jiu-Bin Feng (2002), Experimental Study and Calculation of Fire Resistance of Concrete-Filled Hollow Steel Columns, Journal of Structural Engineering, Vol. 129, pp 346-356
- [18] V. K. R. Kodur (1998), Performance-based fire resistance design of concrete-filled steel columns, Journal of Constructional Steel Research, Vol. 51, pp 21-36
- [19] Pires T.A.C., João Paulo C. Rodrigues, José J. Rêgo Silva (2012), Fire resistance of concrete filled circular hollow columns with restrained thermal elongation, Journal of Constructional Steel Research, Vol.77, pp 82-94

FIRE PERFORMANCE OF LONG-SPAN COMPOSITE BEAMS WITH GRAVITY CONNECTIONS

Lisa Choe¹, Selvarajah Ramesh², Mina Seif³, Matthew S. Hoehler⁴, William Grosshandler⁵,
John Gross⁶, Matthew Bundy⁷

ABSTRACT

Prescriptive fire-resistance ratings for structural components provide limited insight into the system-level performance of steel-concrete composite structures in fire. Specifically, long-span composite beam assemblies exposed to fire have vulnerabilities resulting from thermal restraint conditions that can be vastly different from those in short-span assemblies. This paper presents an overview of recent experiments on 12.8 m composite beams with various end support conditions, exposed to combined structural and fire loading. This paper focuses on the results for the specimens with double-angle beam-to-column connections, with and without slab continuity. The experiments showed that the specimens experienced similar thermal and displacement behaviour during the first 40 minutes after ignition regardless of the presence of slab continuity. The specimens exhibited local buckling of the beam near the connection, at the average bottom flange temperature of 400 °C. A thermal gradient in the specimen was observed during the heating and cooling phase. For the specimen with slab continuity, forces in the continuity bars increased when this local buckling occurred but decreased due to concrete fracture. This specimen did not collapse during the fire until its vertical displacement exceeded 1/20 span length. The collapse failure was observed during the cooling phase, which was resulted from weld fracture of the beam end connection due to contraction of the heated beam as it cooled down.

Keywords: Composite beams, double-angle connections, compartment fires, fire tests

1 INTRODUCTION

The span length of composite steel-concrete floor assemblies has increased over the years due to the availability of higher-strength materials, as well as architectural trends. The detailing of the member connections to withstand gravity loads (e.g., bolt hole and gap clearances), however, has

¹ Research Structural Engineer, National Institute of Standards and Technology, Gaithersburg, MD, USA.
e-mail: lisa.choe@nist.gov

² Guest Researcher, National Institute of Standards and Technology, Gaithersburg, MD, USA.
e-mail: selvarajah.ramesh@nist.gov

³ Research Structural Engineer, National Institute of Standards and Technology, Gaithersburg, MD, USA.
e-mail: mina.seif@nist.gov

⁴ Research Structural Engineer, National Institute of Standards and Technology, Gaithersburg, MD, USA.
e-mail: matthew.hoehler@nist.gov

⁵ Guest Researcher, National Institute of Standards and Technology, Gaithersburg, MD, USA.
e-mail: william.grosshandler@nist.gov

⁶ Guest Researcher, National Institute of Standards and Technology, Gaithersburg, MD, USA.
e-mail: john.gross@nist.gov

⁷ Supervisory Mechanical Engineer, National Institute of Standards and Technology, Gaithersburg, MD, USA.
e-mail: matthew.bundy@nist.gov

remained largely unchanged. Fire not only leads to degradation of material strength and stiffness, but also introduces additional forces into the assembly as thermal elongation is restrained by the adjoining structure. Since the magnitude of thermal strains is proportional to the heated length, the effect of thermal restraint is more significant on longer beams than shorter ones. These forces can potentially alter the sequence of failures in beam assemblies which are often only designed for limit states relevant to gravity loads at ambient temperature.

A series of 12.8 m composite beams exposed to combined structural and fire loading was recently conducted at the National Fire Research Laboratory [1]. This paper presents an overview of the test program, and the results for the specimens with double-angle connections. The goal of this work is to provide data to help advance performance-based fire design approach for steel frame buildings with composite floor systems.

2 TEST PROGRAM

2.1 Test Matrix and Specimen Design

Table 1 shows the test matrix. Test variables included the type of beam-end connections (double angles versus single plate) and the slab continuity conditions. Test 1 was an ambient-temperature test in which the ultimate moment capacity and the sequence of failure were studied [2]. The remaining specimens were subjected to flexural loading and fire. The applied flexural load was 45 % of the ultimate moment capacity (M_{max}) measured from Test 1. The fire was generated using three natural gas burners with a maximum total heat release rate of 4 MW.

The specimens were designed in accordance with current U.S. codes and standards [3, 4]. Details are presented in [5] and summarized here. *Fig. 1a* shows a cross-section of the specimens, which consisted of a 1.8 m wide by 12.8 m long concrete slab cast on trapezoidal metal decking, and a W18×35 floor beam. The slab was partially-composite with the steel beam via 19 mm headed shear studs spaced at 305 mm (design composite effectiveness 82 %). Welded wire fabric (0.06 mm²/mm in orthogonal directions) was placed at the mid height of 83 mm thick concrete topping. The bottom flange of the beams with double-angle connections was coped at both ends. The steel beam was protected with Sprayed Fire Resistive Materials (SFRM) to achieve a 2 hour fire rating along the member and a 3 hour fire rating at the connections. *Fig. 1b* shows the specimen with the double-angle connections and slab continuity. The 9.5 mm thick angles were bolted to the beam web using three 19 mm high-strength structural bolts (with the minimum tensile strength of 830 MPa) and welded to a sacrificial plate on the flange of the column. The specimens for Test 3 and Test 5 included four no. 4 reinforcing bars (with the minimum tensile strength of 415 MPa) in the hogging moment region for crack control. Slab continuity was achieved by anchoring the reinforcement to a hollow steel section attached to the support column.

The steel beams and angles were made with hot-rolled steel with the minimum yield strength of 345 MPa and 250 MPa, respectively. The slab was cast using lightweight aggregate concrete with a design compressive cylinder strength of 28 MPa. The concrete mix included polypropylene microfibers to minimize spalling during heating. The measured ambient-temperature mechanical properties of all the structural components are reported in [5].

Table 1. Test Matrix

Test	Connection type	Slab continuity	Flexural load	Fire load
1	Double angle	No	M_{max}	
2	Double angle	No	$0.45M_{max}$	4 MW
3	Double angle	Yes	$0.45M_{max}$	4 MW
4	Single plate	No	$0.45M_{max}$	4 MW
5	Single plate	Yes	$0.45M_{max}$	4 MW

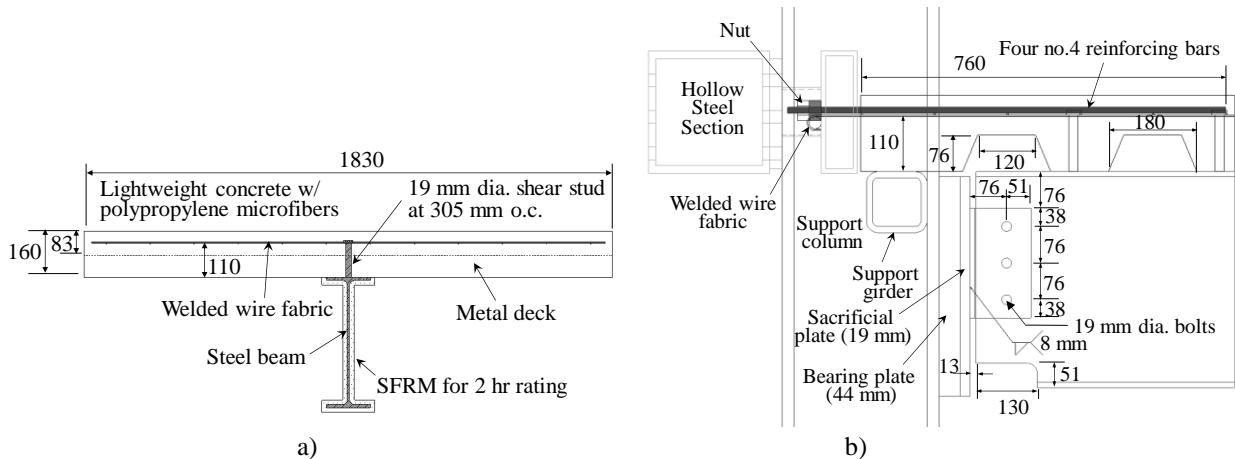


Fig. 1. a) Cross section of the specimen; b) Connections of specimen with double-angles and continuity (units: mm)

2.2 Test Setup, Fire Load, and Instrumentation

The test setup is shown in *Figs. 2a* and *2b*. The composite beam specimen was supported by W12×106 columns with bracing modules, using the connections listed in *Table 1*. The distance from the center bolt of the beam connection to the strong floor was 3.6 m. The measured average lateral stiffness of the braced column at this height (i.e. the axial stiffness provided at the beam ends) was 220 kN/mm. The beam specimen was loaded by six equally distributed point loads (*Fig. 2a*). Three loading beams running transverse to the specimen were loaded using an actuator at each of the six ends. The vertical force of each loading beam was transferred to the beam specimen via triangular trusses. The slab was laterally braced at the locations of the three loading beams. The vertical displacements and end rotations of the specimen were measured using four linear position transducers and two inclinometers mounted on the top of the slab, respectively. The thermally-induced axial restraint force at the beam support was measured using the strain gauges attached on the diagonal brace members of the bracing modules. Washer load cells were used to measure the forces in the no. 4 reinforcing bars in Tests 3 and Test 5.

Three natural gas burners (each 1 m wide × 1.5 m long) distributed along the center of the compartment floor were used to heat the specimen. The fire was designed to achieve an upper layer temperature of around 1000 °C, and avoid combustion outside of the compartment. Peak heat release rate per unit volume was 40 kW/m³, which corresponds to a range of total fuel loads between 550 MJ/m² and 1100 MJ/m² for fire durations between one and two hours. To confine the fire below the specimen, enclosure walls (with a total surface area of 110 m²) were constructed using cold-formed steel framing and sheet steel as shown in *Fig. 2b*. The total ventilation opening area was about 5 m². The fire-exposed wall surfaces were protected with a 50 mm thick layer of ceramic blankets. *Fig. 2c* shows the predicted spatially-averaged temperatures in the upper gas layer and along the lower flange of the steel beam underneath the SFRM layer, using the Fire Dynamic Simulator (FDS) [6] prior to conducting the test series. The heat release rate increases linearly to a maximum of 4 MW during the first 15 minutes and remains steady up to 70 minutes, followed by a linear decrease to zero at 112 minutes.

Fig. 3 show the thermocouple layout. Four Inconel shielded thermocouples (K-type, 24 gauge) were used to measure the average bottom flange temperature. Glass-sheathed thermocouples were mounted at various locations of the steel beam and the connection elements. However, there was considerable difficulty in getting reliable temperatures of the steel beam beyond the first fifteen minutes of the heating. Glass shielding of thermocouples burned off and made secondary junctions when exposed to hot gas temperatures. In some cases, contact between the thermocouple beads and the steel surface could not be maintained as the beam heated and deformed. In other cases, fissures in the insulation layer permitted hot gas to penetrate to the thermocouple on steel surface. All these effects could lead to higher temperature readings during heating. *Table 2* summarizes the estimated total expanded measurement uncertainties with a coverage factor of 2 as defined in [7].

Fire performance of long-span composite beams with gravity connections

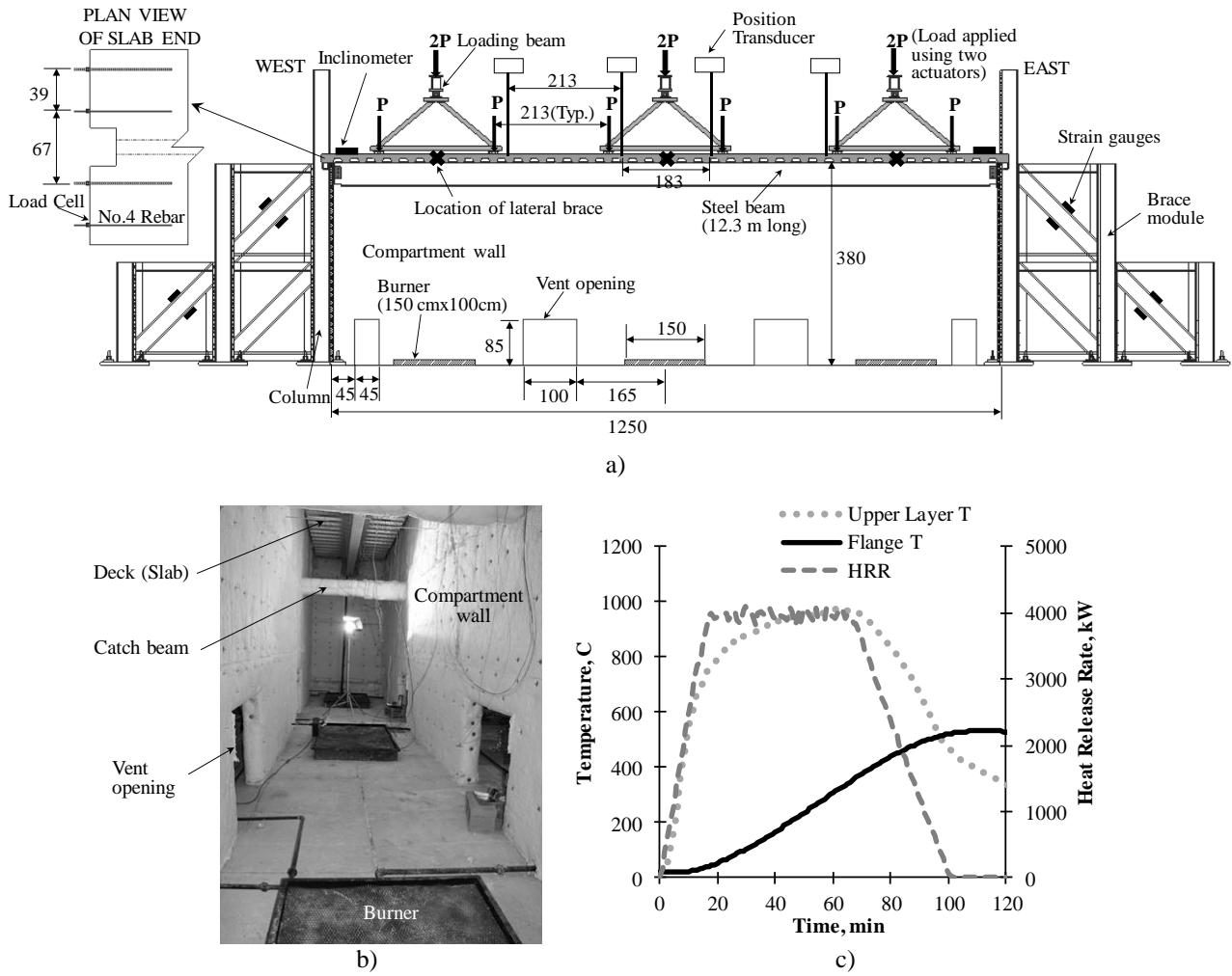


Fig. 2. a) Longitudinal section of the setup (units: cm); b) Photograph of inside the compartment; c) Temperature predictions using the FDS

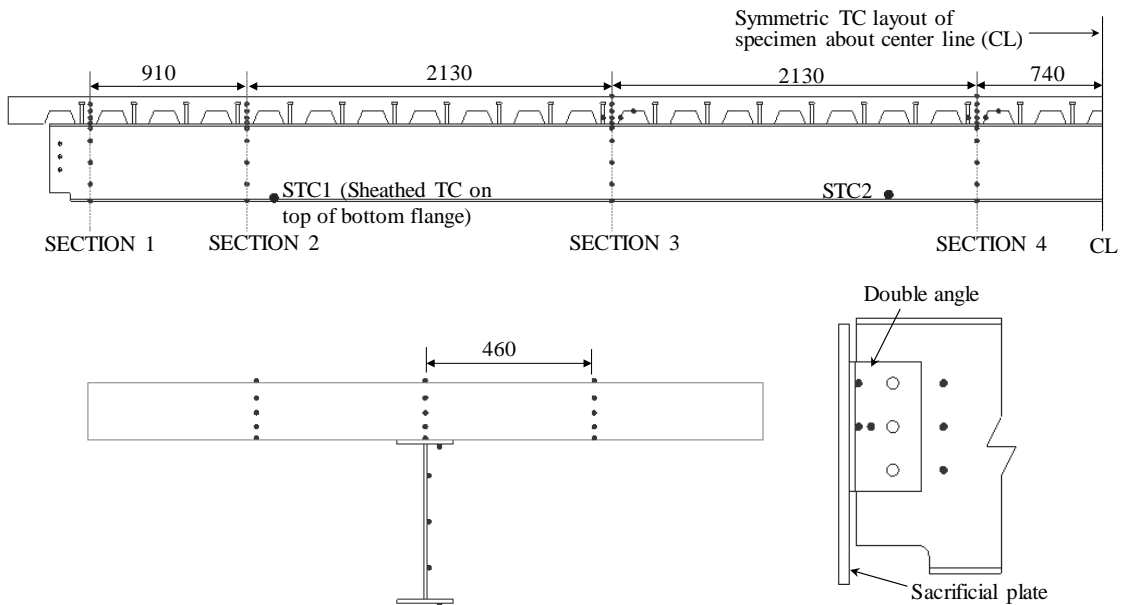


Fig. 3. Location of thermocouples along the beam length, in the beam cross section and connection region (units: mm)

Table 2. Measurement Uncertainty

Measurand	Range (max)	Total expanded uncertainty (coverage factor of 2)
Mechanical load (Actuators)	220 kN	±10 %
Displacement	760 mm	±15 %
Strain	50,000 $\mu\epsilon$	±6 %
Heat release rate	4 MW	±7 %
Steel Temperature (Inconel sheathed thermocouples)	1200 °C	±25 %

3 RESULTS AND DISCUSSION

Tests 2 (T2) and Test 3 (T3) studied the behaviour of the composite beam with the double-angle connection subjected to combined flexural loading and compartment fire described above. The experiments were conducted as follows: i) A total mechanical load of 106 kN was applied and held constant at ambient temperature, ii) the heat release rate was increased to 4 MW over a period of 15 minutes and held constant until the mechanical load was eliminated, and iii) the cooling phase was initiated by linearly decreasing the heat release rate over 30 minutes.

Fig. 4a shows plots of the total mechanical load and the burner heat release rate. *Fig. 4b* shows the average gas temperature measured using thermocouple probes located 810 mm below the slab and the heat release rate measured with the calorimeter. Elimination of the mechanical loads was triggered by the pre-set limit of actuators. In Test 2, the actuators were depressurized when the total mechanical load dropped below 90 kN (about 85 % of its original value applied at ambient temperature) around 30 minutes, when the beam web near the angle connection buckled.

For Test 3, the pre-set load limit was removed and a displacement limit was implemented instead. The mechanical load was removed around 65 minutes after ignition when the vertical displacement of the specimen reached 620 mm. The heat release rates and resulting gas temperatures were comparable until 40 minutes (*Fig. 4b*). The gas temperature reached 900 °C at 15 minutes after ignition. Peak average temperatures exceeded 1000 °C around 40 minutes. The maximum measured temperatures were as much as 100 °C above the values predicted by FDS model (*Fig. 2c*).

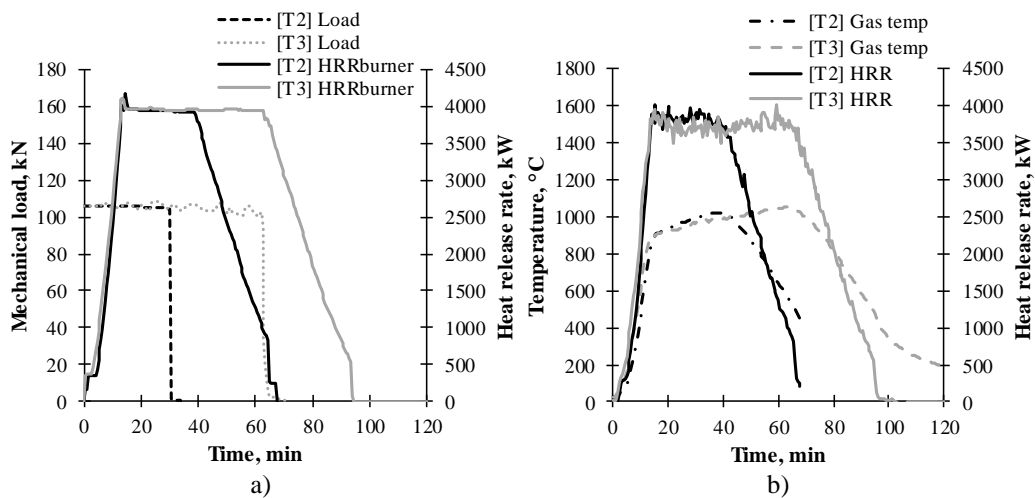


Fig. 4. a) Heat release rate based on fuel flow and total mechanical load applied using actuators; b) Heat release rate measured using the calorimeter and gas temperature inside the compartment

3.1 Thermal Response

Fig. 5 shows the range of a) the average steel temperatures at various locations, including the bottom flange of the steel beam in the middle of compartment and the connection region, and b) the slab temperatures near midspan. Since similar fire conditions were maintained in Tests 2 and 3 up to 40 minutes (Fig. 4), the thermal response of the specimens for these tests was comparable.

Although the upper layer gas temperature was approximately constant with an average standard deviation of 30 °C, a thermal gradient still existed in the specimen along the beam length and across the section. The metal deck rapidly heated with increasing gas temperatures, exceeding 700 °C in 1 hour after ignition. The temperature increase in the connection region with thicker SFRM and inside the slab above the steel beam was slower. In Test 3, the measured peak average temperature of the beam web next to the edges of the angle and the angle itself were around 400 °C and 200 °C, respectively. The temperatures in the slab above the steel beam remained below 300 °C.

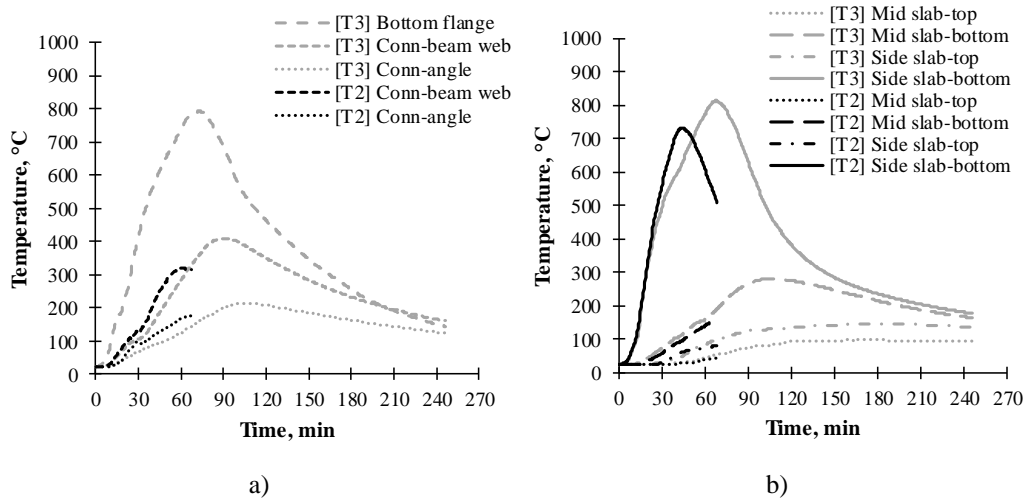


Fig. 5. a) Steel temperatures; b) Concrete temperatures measured in Test 2 and 3

3.2 Structural Response and Failure

The specimens with the double-angle connections exhibited diverse behaviours during the heating and cooling. Fig. 6 shows the vertical displacement of the specimen measured 1.1 m from midspan and the average axial restraints induced at the beam ends as a function of the beam lower flange temperature. The positive values of displacements indicate downward displacements; the negative values of axial restraints represent compressive axial force in the specimen.

As shown in Fig. 6a, for both Tests 2 and 3, the specimen deflected downward after ignition. The beam web near the angle connection buckled around 30 minutes, at the corresponding bottom flange temperature of 400 °C. The peak axial restraint of 370 kN was observed around this temperature (Fig. 6b). From this point through the cooling phase, there was no further failure observed in Test 2 since the mechanical load was removed. During the 30-minute period at which the heat release rate linearly decreased, the vertical displacement continued to increase due to the weight of the specimen and loading fixtures. For Test 3, in which this pre-set load limit was eliminated, the loaded specimen continuously bent down with increasing temperatures following buckling of the beam web around 400 °C. The mechanical load was removed at the vertical displacement of 620 mm (1/20 span length), at the bottom flange temperature of 760 °C. The heated specimen continued to deflect downward while the heat release rate was decreased. The measured peak vertical displacement was 690 mm (1/18 span length). The vertical displacement decreased after the burner was shut off. Figs 6c-d show photographs of the specimens after cool-down.

Composite Structures

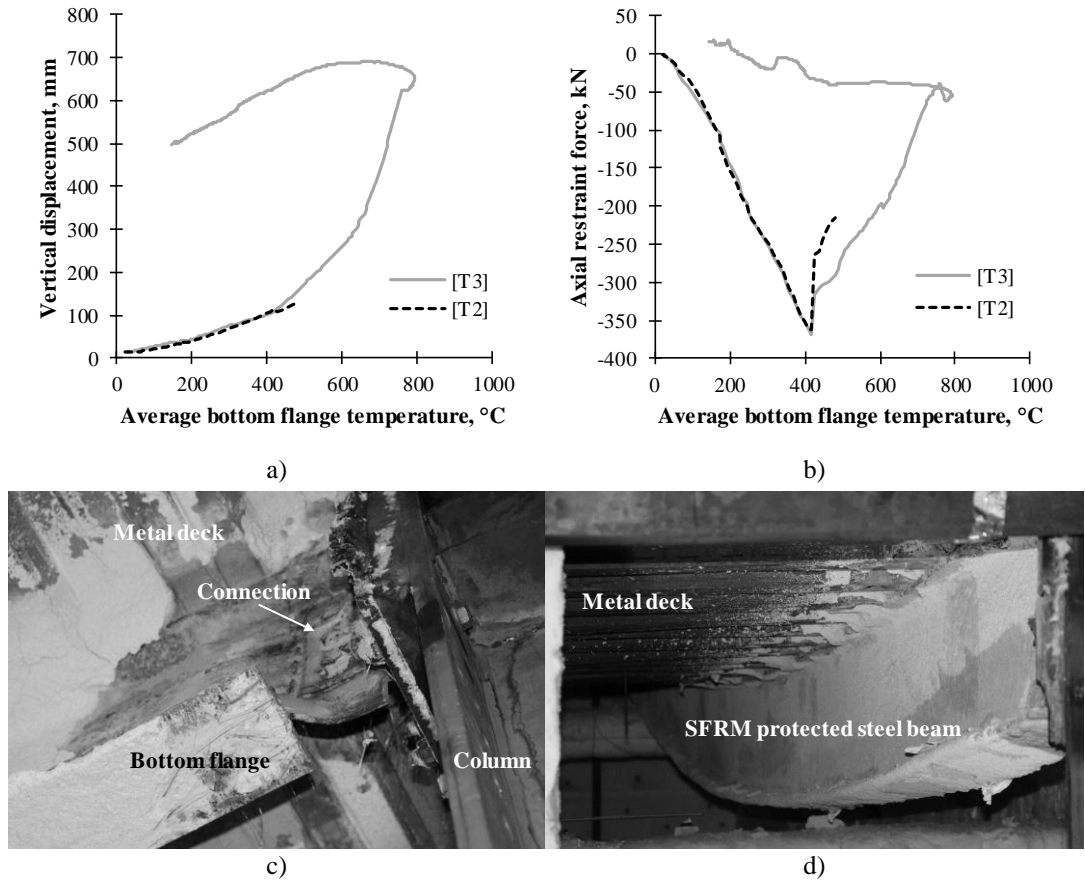


Fig. 6. a) Vertical displacement; b) Axial restraint force as a function of average bottom flange temperature; c-d) Photograph of buckled beam web (Test 2) and deformed specimen (Test 3) after cool-down

The concrete slab in Test 3 had no. 4 reinforcing bars anchored at slab ends (Fig. 1). Fig. 7a shows a comparison of the tensile forces developed in the bars, located at 335 mm from the longitudinal centreline of the slab (Fig. 2a), along with the range of the vertical displacement of the specimen. Fig. 7b shows a photograph of fracture after the test. The tensile forces in the rebars significantly increased after buckling of the beam web occurred around 30 minutes. The magnitude of tensile forces became larger as the vertical displacements increased from 200 mm to 350 mm, followed by a rapid drop indicating the development of concrete failure near the reinforcement. The triangular shape of concrete fracture was observed after cool-down, as shown in Fig. 7b.

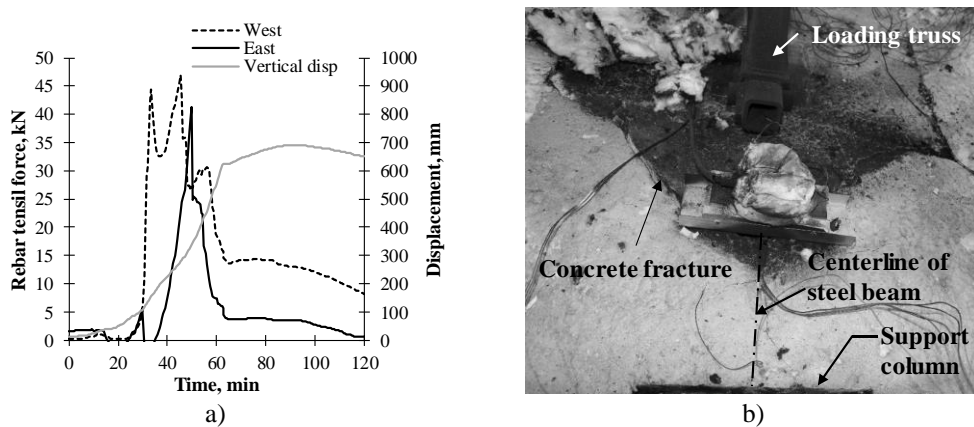


Fig. 7. a) Forces in the continuity bars; b) Slab at west end after cool-down

This specimen did not collapse during the fire. Around five hours after the fire was extinguished, however, the specimen collapsed by weld fracture of the east angle connection. The angles at both ends pried due to contraction of the specimen during cool-down, but there was neither weld failure of the west angle connection nor failure of shear studs.

4 CONCLUSIONS

The fire experiments on the loaded steel-concrete composite beam specimens with double-angle connections (Tests 2 and 3) showed:

- Similar thermal and structural responses during the first 40 minutes after ignition;
- A thermal gradient along the beam length and across the section during the heating and cooling phase in Test 3;
- Local buckling of the beam near the connection and increase of tensile forces in the continuity bars around 30 minutes after ignition, at the average bottom flange temperature of 400 °C;
- Vertical displacements exceeding 1/20 times the span length during the fire in Test 3; and
- Collapse failure by weld fracture of the double angle connection at east end during the cooling phase in Test 3.

ACKNOWLEDGMENTS

The authors would like to acknowledge the great support of NIST colleagues for their hard work to safely complete the experiments. They would also like to thank the expert panel members including William Baker, Glenn Bell, Craig Beyler, Luke Bisby, Ian Burgess, Charlie Carter, Charles Clifton, Michael Engelhardt, Graeme Flint, Nestor Iwankiw, Kevin LaMalva, Roberto Leon, Jose Torero, and Amit Varma for their support throughout this project.

REFERENCES

1. Bundy, M., Hamins, A., Gross, J., Grosshandler, W., and Choe, L. (2016). *Structural fire experimental capabilities at the NIST National Fire Research Laboratory*. Fire Technology, 52(4), 959-966.
2. Choe, L., Ramesh, S., Hoehler, M., Gross, J. (2018). Experimental Study on Long-Span Composite Floor Beams Subject to Fire: Baseline Data at Ambient Temperature. *Proc. of Structures Congress 2018*, Fort Worth, Texas, April 19-21, 2018.
3. ANSI/AISC-360 (2016). *Specification for Structural Steel Buildings*. American Institute of Steel Construction, Chicago, Illinois.
4. ASCE/SEI 7 (2016). *Minimum Design Loads for Buildings and Other Structures*. American Society of Civil Engineers, Reston, Virginia.
5. Ramesh, S., Choe, L., Hoehler, M., Grosshandler, W., Gross, J. (2018). Design and Construction of Long-Span Composite Beam Specimens for Large Structural-Fire Tests. *Proc. of Structures Congress 2018*, Fort Worth, Texas, April 19-21, 2018.
6. McGrattan, K., Hostikka, S., McDermott, R., Floyd, J., Weinschenk, C., and Overholt, K. (2013). *Fire Dynamics Simulator, Technical Reference Guide*, National Institute of Standards and Technology, Gaithersburg, Maryland, USA, and VTT Technical Research Centre of Finland, Espoo, Finland, sixth edition, September 2013.
7. Taylor, B. N., and Kuyatt, C. E. (1994). *Guidelines for Evaluating and Expressing the Uncertainty of NIST Measurement Results*. National Institute of Standards and Technology, NIST Technical Note TN-1297, Gaithersburg, Maryland.

STEEL STRUCTURES

Steel Structures

PERFORMANCE OF BEAM-COLUMN SUBASSEMBLAGES WITH CONTINUOUS H SHAPED COLUMNS IN SEVERE FIRES

Chia Mohammadjani¹, Charles Clifton², Anthony Abu³

1 INTRODUCTION

Standard Fire tests on columns involve heating the column over the full length in a furnace under a constant level of imposed axial load. Failure is typically by member buckling, although local buckling can occur in stocky columns with cross sections comprising slender elements. These buckling modes have also been observed in real building fires [1] and are the dominant failure modes for steel columns in fire. Wang et al. showed [2] that the buckling resistance of steel H shape columns in severe fire is especially affected by the extent of axial restraint as the temperature increases. Jiang, et al. investigated [3] the influence of both axial and rotational restraints on individual lengths of columns heated by severe fire. They found out that the performance of columns could be quasi-static up to the buckling point and then dynamic effects may occur depending on strength of restraint, load amount and column slenderness. With low level of rotational and axial springs and higher imposed loads, the column buckling mode is dynamic, with a rapid increase in downwards deflection. Kodur [4] has been investigating the behaviour of linked beam column sub-assemblages, linked by structural beam elements in finite element studies and subjected to natural fire conditions. His study has shown the importance of increased axial restraints which leads to enhanced compressive forces resulting in lateral buckling and to the importance of high temperature creep on response of restrained beams. However, this still leaves a significant void in understanding the behaviour of beam-column sub-assemblages with continuous columns, when the column is strongly heated one storey at a time by severe fire and is subjected to rotational demands from the connected beams. The objective of this study is to determine this behaviour, using columns designed for structural continuity in earthquake in accordance to the New Zealand design provisions and investigating the effect of the beam actions. This also includes determining the influence of column splices on the heated floor (columns are typically spliced every third level). This study is in its early stage and the timeframe has been significantly slowed by funding constraints. Further funding is being sought to enable the full scope of work envisaged to be completed.

2 STRUCTURE GEOMETRY

2.1 The subassembly including splices

The subassembly including splices comprises 2 universal columns connected by a splice joint and one beam with fixed end connection to the column's strong axis. The beam's section is UB 356×171×67 and columns are UC 305×305×118 as the bottom column and the UC 254×253×73 as the top column (*Fig. 1*). The continuous column, the splice and the beam lie within the middle floor which is the fire floor. The half column above and below the fire floor are included in the model, with the half height being modelled as a point of contraflexure. The top and bottom floor beams and the beam running into the column's weak axis on the fire floor have not been modelled but instead replaced by appropriate boundary conditions. The columns and the beam have been designed base

¹PhD Candidate, Department of Civil and Environmental Engineering, University of Auckland, Auckland, New Zealand.
Email: chia.mohammadjani@auckland.ac.nz

²Associate Professor, Department of Civil and Environmental Engineering, University of Auckland, Auckland, New Zealand.
Email: c.clifton@auckland.ac.nz

³Senior Lecturer, Civil & Natural Resources Engineering, University of Canterbury, Christ Church, New Zealand.
Email: anthony.abu@canterbury.ac.nz

on Eurocode 1 [5] for gravity loads and on Eurocode 3 part 2 [6] for structural fire design. This has been done to enable the model to be developed, but the sub-assemblage will be replaced by one designed to the developing New Zealand fire engineering design provisions contained in [7]. The beam to column connection has been considered in this initial model as rigid and a distributed load of 8 kN/m has been applied to the beam.

2.2 Continuous column splice

The continuous column system in this study is comprised of two universal columns given in [8]. The column splice design procedure was based on the joints design process presented by SCI P358 publication [9] which is in accordance with BS EN 1993-1-8 [10]. The column splice connects the universal column 254×253×73 at top to the universal column 305×305×118 at bottom using a bolted cover plate splice for I sections. The splice is bearing type which is constructed without any gaps between two columns, therefore, allowing the loads to be transferred directly from top column to the division plate and from division plate to the bottom column. Splice details are presented in the **Error! Reference source not found.** and *Table 1*. The splice was designed for the permanent action $N_{Ed,G} = 760$ kN , total action $N_{Ed} = 1630$ kN , $M_{y,Ed} = 110$ kNm and $V_{Ed} = 60$ kN. The splice is designed in a way that two columns stay in line after applying the gravity loads to the system and do not oscillate due to the shear forces. Eurocode 3 part 8 [10] suggests two methods of design procedures for bolted cover plate splices based on bolts preloading condition.

3 FINITE ELEMENT MODEL

The analyses are being carried out in accordance with a Sequentially Coupled Thermal-Stress Analysis procedure using ABAQUS [11]. In the first step, the uncoupled thermal heat transfer analysis is undertaken, where the temperature field does not depend on the stress field. This uses the fire input temperature time conditions determined as described in section 3.1 and which generates the structural element time temperature conditions. In the second step, first the design vertical loading associated with the fire emergency condition is applied, followed by the element temperature time history. The structural response is obtained from this second step.

This method is realistic, provided the structural changes don't have a significant effect on the thermal characteristics, which is the case with bare steel columns and composite beams but is not so accurate for concrete filled hollow steel section columns.

3.1 Thermal analysis

As this initial analysis is based on a bare steel column and bare steel beam subassemblage, the aim has been to generate a fire time temperature history associated with a structural fire severity of 20 minutes, which can be resisted by the unprotected steel members in accordance with [7]. A design time of exposure to the ISO Standard Fire of 20 minutes was chosen; this is termed the structural fire severity. Then, using the time equivalent concept of matching the temperature at 20 minutes of Standard Fire Exposure generated in an insulated UC 254×253×73 column member with profile protection 10mm of sprayed mineral fibre fire protection to the maximum temperature reached in the same cross section exposed to the Modified Eurocode fire (section D5 of [7]) the parametric fire conditions shown in *Fig.3* were generated. This corresponded to a Fire Load Energy Density of 220 MJ/m² floor area applied to an enclosure with normal weight concrete ceiling and floors.

At this initial stage, the intention was to generate fire time-temperature conditions associated with temperatures for which bare steel members would be appropriate. The fire is representative of what

¹PhD Candidate, Department of Civil and Environmental Engineering, University of Auckland, Auckland, New Zealand.
Email: chia.mohammadjani@auckland.ac.nz

²Associate Professor, Department of Civil and Environmental Engineering, University of Auckland, Auckland, New Zealand.
Email: c.clifton@auckland.ac.nz

³Senior Lecturer, Civil & Natural Resources Engineering, University of Canterbury, Christ Church, New Zealand.
Email: anthony.abu@canterbury.ac.nz

might occur in a hotel or motel room, involving rapid growth to nearly 800 °C after 8 minutes, followed by a slower cooling period dropping to 500 °C 22 minutes after the fire start.

The heat transfer data including the temperature dependent steel properties for the transient heat transfer analysis were obtained using Eurocode 3 Part 2 [6] which are illustrated in *Table 2*. The finite element model for the thermal analysis was built using two types of elements available in the ABAQUS mesh module. The elements locate at the splice zone including the bolts were solid DC3D8 solid 8-node linear heat transfer elements and for the rest of structural members shell DS4, 4-node heat transfer quadrilateral shell elements (*Fig. 4*) were assigned.

3.2 Structural analysis

The simulation was established based on dynamic coupled thermal-stress analysis using the explicit integration. The splice zone was modelled using solid C3D8R 8-node linear brick, reduced integration, hourglass control elements (*Fig. 4*). The splice zone is made by 600 mm of top and bottom columns and the splice plates and bolts as presented in *Table 1*. The rest of the sub-assembly is modelled using S4R 4-node doubly curved reduced integration hourglass control shell elements [11].

3.2.1 Temperature dependent mechanical properties

The ambient temperature properties used for the G300 steel from [12] were determined from mechanical testing for a previous project. *Fig. 5* shows the stress-strain curves for the coupon test (dashed line) and calculated stress-strain relations for higher temperatures from Eurocode 3 Part-2 [6]. These properties were assigned to all structural members except bolts. The elasticity was set to 210 GPa at 20 °C and then reduced following the reduction factors presented in *Table 3.1* of Eurocode 3 Part-2, which are presented in equation form as equations 4.2 from [7]. The mechanical properties of the M20 Property Class 8.8 bolts were taken from tensile testing by Clifton [13] on a previous project. These give ambient temperature yield stress and tensile strength as 726 MPa and 977 MPa respectively. The variation of properties with elevated temperature were determined from *Figure 7.3.2.5* of AS/NZS 2327 [14].

3.2.2 Loading and boundary conditions

Because the level of imposed vertical load from G, Q on the column prior to the start the fire has significant impact on the column behaviour [1], it was important that this loading not be underestimated. Therefore, the load combination used in this research was the maximum gravity load combination offered by the Eurocode [5] which is referred here as *Eq (1)* where G is the dead load and Q is the live load on the structure. The applied gravity loads need to be in a value that the *Eq (2)* satisfies where the N^* stands for applied axial load, which is 760 kN, and the Φ the N_n are the strength reduction factor and the nominal axial load capacity respectively.

The bolts pretension load was set to 40 kN for each M20 bolt. The bolts were made of a single solid part and C3D8R nodes were assigned to them. At the top of the column, vertical axial springs with stiffness equal to 0.1 x and 1 x of top column axial stiffness were used to account for upper floors element resistance to expansion. At this point the column was prevented from U_x and U_z and U_{Ry} (*Fig. 4*). The bottom of the column and the end of the beam were restrained against all degrees of freedoms. Axially restrained columns fire performance has been investigated by many researchers. Huang et.al. [15] has proposed an analytical approach to calculate column's yield load at elevated temperature with considering the creep effects. Kodur, from other hand assesses beam-column assemblies fire performance by defining axial springs with varied coefficients [4]. The axial springs at top of the column in this paper are based on the classical axial stiffness formula (*Eq (3)*) where α is varying from 0.1 to 1. At this early stage in the project, the beam was modelled as rigidly fixed to the column and so axial and rotational springs were not used at the end of the beam. The top flange

of the beam has been restrained against UX, UZ and URY to approximately account for composite slab interaction.

4 FINITE ELEMENT RESULTS

Only preliminary results are available at the time of completing this paper. These results show that the column splice capacity is sufficient to resist the natural fire condition associated with R20 structural fire severity. Splice members, including the bolts and the critical bolt hole zones, did not undergo deformation (*Fig.6&7*). Most of bolts axial and shear stresses were below the determined f_y when they were experiencing the highest temperature and during the cooling face. Therefore, it is concluded that for the bare steel assembly with the column-column splice designed based on Eurocode guidelines, the failure will not be initiated from the splice zone. At 700 C° the top column experienced considerable deformation, especially at the bottom of beam -column interaction (*Fig. 6*). The local buckling of the column inside flange below the beam is initiated by the moment coming in from the beam, putting additional compression into that flange from bending. In contrast the inside column flange above the beam is stable due to the tension induced by the incoming beam bending moment. The column buckling mode is similar to that observed for columns in the 1991 Broadgate fire [16] The stress was higher than 170 MPa this time which lies into the failure zone based on stress strain relation already illustrated (*Fig. 5*). Therefore, it can be concluded that the column will eventually fail at around 700 C° just below the beam-column connection zone.

As already mentioned, two types of axial springs have been used to date in this research. The axial spring has significant influence on column's response to the increased axial load due to expansion and contraction. The column with axial spring of 0.1x was able to push the spring 4 mm up while the column with equal axial spring was not able to push the spring up at all (*Fig.8*). Contrastingly, for the column with weaker spring very high deflection was recorded during the cooling face because of axial spring's lack of ability to hold the column. Based on the above observations it should be concluded that a column which comes with a stronger axial spring is more prone to the failure during the heating and the column with the weaker axial spring is more prone to the failure during the cooling. However, this will be modified when the axial springs are modified to better represent the different stiffnesses in each direction (in tension the spring stiffness represents load sharing between columns and is much lower than in compression).

5 CONCLUSIONS AND SCOPE OF FUTURE STUDIES

This research project is just commencing, looking at the performance of beam-column sub-assemblies with continuous H shaped column in severe fires. The present paper is a summary of developed simulations techniques which are going to be calibrated against the future planned experimental tests. Several important criteria are known to be effective on a steel subassembly performance during a sever fire propagation. The sections dimensions and the insulation material properties as a factor of structural fire severity are among those. As other influential parameters could refer to the connection types at the beam-column or column-column joints and to the axial and rotational stiffness of the surrounding members. In this research the influence of the above floor members axial stiffness and the presence of a splice at the bottom column – top column connection were investigated. Although, the splice had not undergone a serious damage, still failure propagation could occur at this region for different splice geometries and column cross-sections. The situation at the beam-column connection could be worse because of higher shear force expectancies there. Funding permitting, this study will be looking at the influence of the following parameters:

1. The effects of low, medium and high structural fire severity

2. The influence of column top axial and rotational restraint
3. The influence of column splices versus continuous columns
4. Beam to column connections with different rotational stiffnesses
5. The influence of slab reinforcement on the beam to column connection.
6. The effect of fire spread over successive floors

It is planned that the scope of the experimental testing will be expanded through a parametric study using ABAQUS on the above criteria in order to develop a clear understanding of a full scale subassembly's performance in a fully developed fire.

TABLES

Table 1. Splice members dimensions

Section Description	Dimintions (mm)	Thickness (mm)	Diameter (mm)	Number	Geometric View
Flange Cover Plate	525×250	12	–	2	
Flange Pack	250×240	30	–	2	
Division Plate	310×265	25	–	1	
Web Cleat	82×82×150	8	–	4	
Preloaded M20 Bolts	–	–	21	24	

Table 2. Input parameters used for the heat transfer analysis

Fire input parameters	Fire load energy density (FLED) Mj/m^2	$q_{f,d}$	220
	Thermal inertia		1700
	Initial temperature ($^{\circ}\text{C}$)		20
	Duration of ISO curve (min)		180
	Decay rate ($^{\circ}\text{C}/\text{min}$)		20
	Stephan Boltzman constant ($\text{W}/\text{m}^2\text{k}^4$)	σ	5.67×10^{-8}
Encluser geometry	Width (m)	W	10
	Length (m)	L	10
	Height (m)	h	3.2
	Area of vertical opening (m^2)		20
	Height of vertical opening (m)		2
Steel heat properties in ambient temperature	Density (kg/m^3)	ρ	7850
	Thermal Conductivity (W/mk)	λ	53.33
	Specific heat $\text{J}/\text{kg.k}$	C_p	440
	Convection coefficient ($\text{W}/\text{m}^2\text{k}$)	α_c	25
	Surface Emissivity		0.7

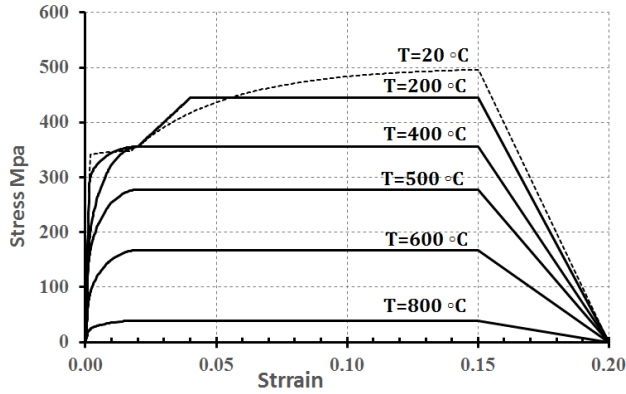


Fig. 5. Carbon Steel stress-strain curves

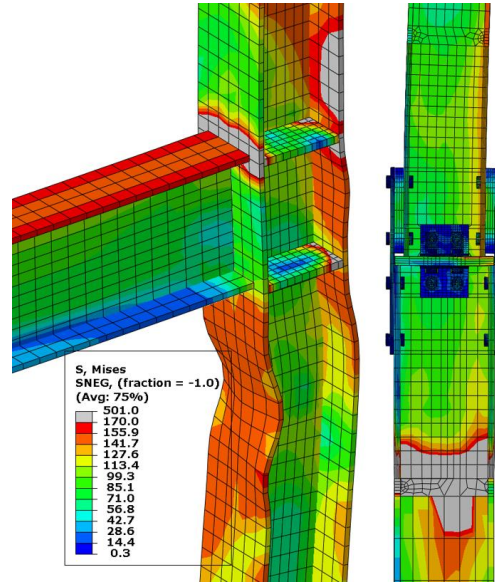


Fig. 6: Beam-Column and column splice zone stress contour

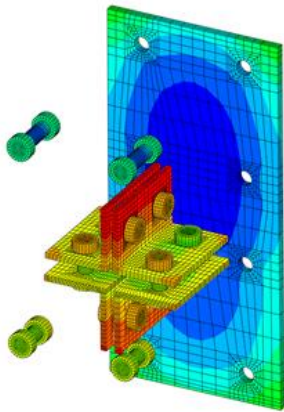


Fig. 7: Splice members condition in high temperature

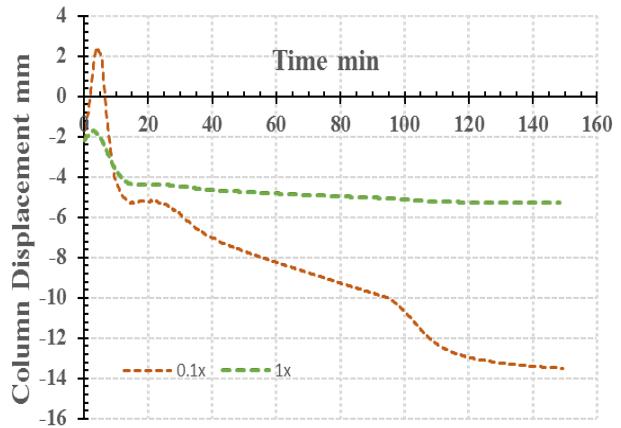


Fig. 8: Vertical displacement at the top of the column

EQUATIONS

$$1.35G+1.5Q \quad (1)$$

$$N^* \leq \Phi N_n \quad (2)$$

$$K = \alpha \left(\frac{EA}{L} \right)_{column} \quad (3)$$

ABSTRACT

This research project focuses on the performance of the entire sub-assembly of multi-story steel framing systems designed to current earthquake requirements, which have continuous columns with connections to incoming beams which are designed for dependable ductile response. The nature of the fire exposure will be that applying to a well-designed and detailed multi-story building, where the floors function as effective fire separations, delaying fire spread from one level to the level above by a period of time. The principal tool used to determine the sub-assembly response is advanced finite element modelling. The outputs from this research includes a review of current sub-assembly-based design procedures for sub-assemblies with bare steel continuous columns and incoming beams and proposing changes required to these procedures.

REFERENCES

1. Andrew H. Buchanan, A.K.A., *Structural Design for Fire Safety*-Wiley 2017. **Second Edition**.
2. Wang, W., et al., *Experimental study on local buckling of axially compressed steel stub columns at elevated temperatures*. Thin-Walled Structures, 2014. **82**: p. 33-45.
3. Jiang, B., G.-Q. Li, and B.A. Izzuddin, *Dynamic performance of axially and rotationally restrained steel columns under fire*. Journal of Constructional Steel Research, 2016. **122**: p. 308-315.
4. Kodur, V.K.R. and M.M.S. Dwaikat, *Response of steel beam–columns exposed to fire*. Engineering Structures, 2009. **31**(2): p. 369-379.
5. EN1991-1-1, *Eurocode 1: Actions on Structures in Part 1-1: General actions - Densities, self-weight, imposed loads for buildings*. 2009, European Committee for Standardization.
6. EN1993-1-2, *Eurocode 3: Design of steel structures, in Part 1-2: General rules — Structural fire design*. 2009, European Committee for Standardization.
7. Abu, A.K. and G.C. Clifton, *Fire Engineering Design of Multi-storey Steel and Composite Steel/Concrete Structures; Demand/Capacity Document; Recommendations and Questions Version 2.16 November 2017*. 2017, Univeristy of Auckland Auckland.
8. ASI, *Design Capacity Tables for Structural Steel, Volume 1: Open Sections Third Edition*, A.S. Institute, Editor. 1999, Australian Steel Institute: Sydney, Australia.
9. SCI, *SCI P358, in Joints in Steel Construction Simple Joints to Eurocode 3*. 2014, The Steel Construction Institute: London.
10. EN1993-1-8, *Eurocode 3: Design of steel structures, in Part 1-8: Design of joints*. 2009, European Committee for Standardization.
11. SIMULIA. *Abaqus Manual 2017*. 2017; Available from: http://help.3ds.com/2017/English/DSSIMULIA_Established/SIMULIA_Established_Front_matterMap/DSDocAbaqus.htm?ContextScope=all&id=06bd125b77f8472aa38e1f33fd8ecf1a#Pg0&ProductType=DS&ProductName=DSSIMULIA_Established.
12. NZS3404, *Steel structures standard, incorporating Amendments 1 and 2*. 1997/2001/2007, Wellington, NZ: Standards New Zealand.
13. Clifton, G., *Semi-Rigid Joints for Moment-Resisting Steel Framed Seismic-Resisting Systems*, in *Civil and Environmental Engineering*. 2005, University of Auckland: Auckland. p. 417 pages.
14. AS/NZS2327, *Composite structures - Composite steel-concrete construction in buildings*. 2017, Standards Australia/Standards New Zealand: Wellington, New Zealand.
15. Z. F. Huang, K.H.T., *Analytical Fire Resistance of Axially Restrained Steel Columns*. Journal of Structural Engineering, 2003. **129**, No. **11**.
16. Lawson, R.M., *Structural Fire Engineering: Investigation of the Broadgate Phase 8 Fire*. 1991, Steel Construction Institute: Ascot, England.

EXPERIMENTAL ANALYSIS OF THE INFLUENCE OF CREEP ON FIRE-EXPOSED STEEL AND ALUMINIUM COLUMNS

Neno Torić¹, Ivica Boko², Vladimir Divić³, Ian W. Burgess⁴, Marko Goreta⁵

ABSTRACT

The paper presents test results of a study aiming to explore the influence of creep strain on reduction of the load-bearing capacity of fire-exposed steel and aluminium columns. The research focuses on the behaviour of columns made of steel grade S275JR and aluminium grade EN6082AW T6. Two types of high-temperature column tests were conducted in the study: constant-temperature capacity and creep tests. The temperature ranges for both capacity and creep tests are between 400-600°C for steel and 160-300°C for aluminium. The test results have shown that creep can reduce a steel column's load-bearing capacity, even at 400°C. The influence of creep on load-bearing capacity, without prolonged exposure to high-temperature, can be observed when the axial compressive load is above 87% of the steel column's axial load capacity. In the case of aluminium, creep starts to develop at approximately 160°C, at which the reduction in load bearing capacity is observed at loads above 88% of the column's axial load capacity.

Keywords: Steel, aluminium, fire, creep, column, S275JR, EN6082AWT6

1 INTRODUCTION

Experimental studies regarding the creep behaviour of steel and aluminium members in general are very scarce, due to the complexity of the experiments, which is necessary in order to properly capture the effects of creep in reducing load-bearing capacity. The influence of creep strain on the load capacity of metallic structures is a topic which has started to receive attention from scientists and researchers over the past decade. A major reason for the lack of previous research effort in this area is the fact that creep strain has long been considered as irrelevant to the response of metallic structures exposed to high temperature. Furthermore, the bulk of the fire tests performed by the scientific community have been conducted using standardized heating regimes that impose very rapid heating rates, generally above 20-25°C/min [1, 2], on a tested member; this ultimately leads to rapid member failure. With the introduction of natural fire curves into structural fire analysis for performance-based design it has become clear that it is not unusual for structures to be exposed to heating rates below 20°C/min, especially if the structure is exposed to slow-burning long-lived fires, or if it is covered with fire-protection material. Another possible reason for the paucity of

¹ Assistant Professor. University of Split, Faculty of Civil Engineering, Architecture and Geodesy, Croatia.
e-mail: neno.toric@gradst.hr

² Professor. University of Split, Faculty of Civil Engineering, Architecture and Geodesy, Croatia.
e-mail: ivica.boko@gradst.hr

³ Assistant Professor. University of Split, Faculty of Civil Engineering, Architecture and Geodesy, Croatia.
e-mail: vladimir.divic@gradst.hr

⁴ Professor. University of Sheffield, Department of Civil and Structural Engineering, UK.
e-mail: ian.burgess@sheffield.ac.uk

⁵ PhD Candidate. University of Split, Faculty of Civil Engineering, Architecture and Geodesy, Croatia.
e-mail: marko.goreta@gradst.hr

creep-related research is the availability of implicit-creep stress-strain models, which are provided to practising engineers in codes of practice for various applications. The implicit-creep material model within the Eurocodes [3] for metallic structures are widely used, even beyond Europe. Several experimental studies conducted on steel beams [4, 5] have shown that the Eurocode 3 model has limitations in predicting deflection in cases where heating rates are lower than 10°C/min. The lack of detailed experimental data regarding creep development in contemporary European steel and aluminium grades, and very scarce member test studies, have resulted in the development of a research programme [6, 7] aiming to explore the influence of the time of high-temperature exposure on the overall load-bearing capacity of columns. The behaviour of columns in fire conditions is necessary [8, 9] since they represent the most vulnerable parts of a structure in terms of actual collapse. This study is part of a joint research programme (Croatian Science Foundation project no. UIP-2014-09-5711) conducted by the Universities of Split and Sheffield. Its three phases are: development of explicit creep models for alloys S275JR and EN6082AW T6 with the help of coupon stationary-creep tests, experimental tests on columns using constant-temperature tests, and the corresponding verification of these creep models. S275JR steel is widely used as a construction material in civil engineering across Europe, and the Aluminium alloy EN6082AW T6 is a structural alloy with minimum proof strength of 260 MPa, which is comparable to grade S275 steel.

2 METHODOLOGY AND TEST RESULTS

2.1 The heating and loading equipment

The column tests have been conducted at the University of Split. The heating arrangement used in this test study is based on induction heating. The induction equipment, which generates up to 35 kW of power, produces fields of high-frequency electrical currents in ferromagnetic metals located within its electric field, which cause them to heat rapidly. In the test setup used, these fields are generated in a cylindrical steel jacket surrounded by induction cables, as shown on Figure 1. The test setup and the steel/aluminium column specimens (HE140B and the section 220/170/15/9) are shown in this figure. A specimen placed inside the jacket is heated predominantly by radiation from the inner surface of the jacket, but also partially by the electrical currents which pass through the specimen (this is particularly true for steel specimens, which are ferromagnetic). With this kind of induction heating equipment it is possible to achieve very uniform heating in the column cross-sections, inducing negligible temperature variations between the columns' upper and lower flanges.



Fig. 1. a) Test setup for aluminium columns; b) steel column; c) aluminium column

There are some temperature variations over the column length, especially at their ends where slightly lower temperatures are generated. The two types of high-temperature column tests conducted in the study are constant-temperature capacity and creep tests. The temperature ranges for both test types were planned to be between 400-600°C for steel and 160-300°C for aluminium.

These were based on previous coupon test results, which suggested that within these temperature ranges both metals exhibit very rapid strength reduction. Therefore, it was impractical to conduct tests beyond 600°C for steel [6] or 300°C for aluminium [7], since above these temperature thresholds more than 70% of the materials' strengths are lost, according to these coupon studies.

The loading equipment comprised two hydraulic rams capable of applying axial force up to 1500 kN (horizontal ram) and 300 kN (vertical ram). Measurement of axial end-displacements and transverse mid-span displacement was conducted using LVDTs in the appropriate positions. As can be seen from Figure 1, the column is transversally loaded with a relatively small force about its weak axis.

2.2 Capacity tests

Capacity tests were conducted in order to determine a column's axial load capacity at a prescribed constant temperature with a constant transverse force. The column was heated to the prescribed temperature, loaded with the constant lateral force, and subsequently loaded with a controlled increasing axial compressive force until column failure. Capacity tests were conducted at temperature levels of 400-500-600°C for steel and at 160-220-260°C for aluminium.

2.3 Creep tests

The creep tests were conducted by firstly heating the column to a prescribed temperature, and then loading it with the constant lateral force. The final step was then to add a constant axial compressive force, defined as a fraction of the axial load capacity at the prescribed temperature level. The column was then maintained at the prescribed temperature and load level until a gradual column failure due to creep occurred. These constant-temperature creep tests were also performed at temperature levels of 400-500-600°C for steel and 160-220-260°C for aluminium.

2.4 Temperature measurements

Temperature measurements were conducted at thirteen different points, with a total of five cross-sections containing either two or three discrete measuring points. This unusually large number of measuring points is necessary in order to properly record the temperature fields during the experiment. The heating rate of the induction equipment was monitored using two thermocouples, one placed on the inner surface of the jacket and the second placed on the web of the specimen at mid-span. Figure 2 shows the temperature measuring points on the steel specimen. The distribution of the measuring points for temperature in case of aluminium columns is identical to that for steel columns. Figure 3 presents the temperature measurements at various points for the steel column experiments conducted at 400°C.

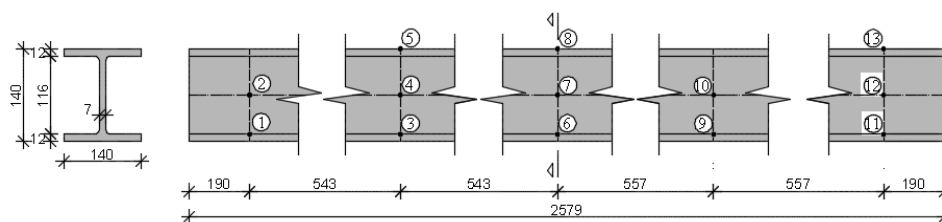


Fig. 2. Measuring points for temperature – steel columns

It can be seen from Figure 3 that the column ends are heated to slightly lower temperatures than those at mid-span. This difference varies with the level of the target temperature, and can be higher for the 500°C and 600°C target temperatures than that for 400°C. In both capacity and creep tests thermal expansion of the column was left unrestrained before the application of the external load.

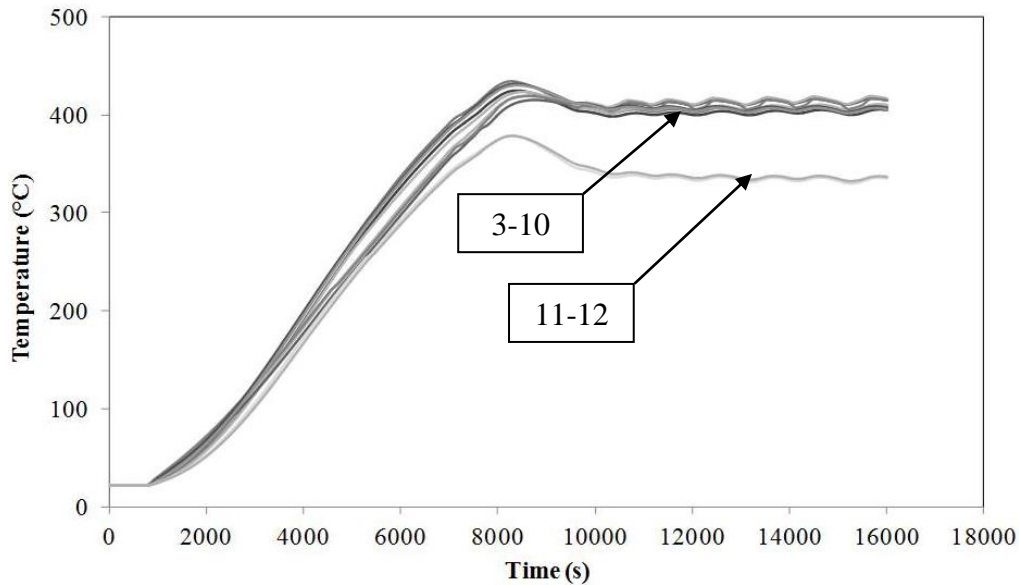


Fig. 3. Temperature measurements – steel creep test at 400°C

2.5 The influence of friction

It is well known that, during column compressive tests, the influence of friction can be substantial on the measured load-bearing capacity [9]. Therefore, it is necessary to give specific consideration to reducing this unavoidable effect. In the research presented here the friction is reduced by using two strategies. The first is general, and includes lubrication of the pins as well as the supporting plates. The second is the use of a lubricated cylindrical thin steel shim between the pin and its bearing, which effectively increases the lubricated surface. Column tests at normal temperature with and without the applied lubrication strategy have shown that the reduction of the friction effect where the column’s critical force is about 44%, indicating that this lubrication strategy is effective.

2.6 Test results

The test study presented in this paper will eventually include tests on a total of 17 steel and 36 aluminium columns. Tables 1 and 2 present the test parameters of the capacity tests conducted so far. Tables 3 and 4 present the test parameters of the creep tests at 400°C (steel) and 160°C (aluminium).

Table 1. Capacity test results for steel

Temperature (°C)	Axial load (kN)	Vertical load (kN)
20	478.0	46.0
400	560.0	37.0
500	530.0	30.0
600	376.0	16.0

Table 2. Capacity test results for aluminium

Temperature (°C)	Axial load (kN)	Vertical load (kN)
20	656.0	60.0
160	488.0	48.0
210	624.0	37.7
260	402.0	26.0

Steel structures

Table 3. Results of steel creep tests – 400°C

Test No.	Axial load (kN)	Vertical load (kN)	Failure time (min)	Load ratio (%)
1	488.0	37.0	37.8	87
2	518.0	37.0	7.5	93
3	535.0	37.0	6.1	96

Table 4. Results of aluminium creep tests – 160°C

Test No.	Axial load (kN)	Vertical load (kN)	Failure time (min)	Load ratio (%)
1	427.0	48.0	151.7	88
2	457.5	48.0	25.9	94
3	475.8	48.0	3.6	98

Figure 4 presents creep test results for axial force and displacement of aluminium columns at 160°C (Tests No. 2&3). The capacity and creep tests are generally terminated when the axial displacement begins to indicate run-away behaviour.

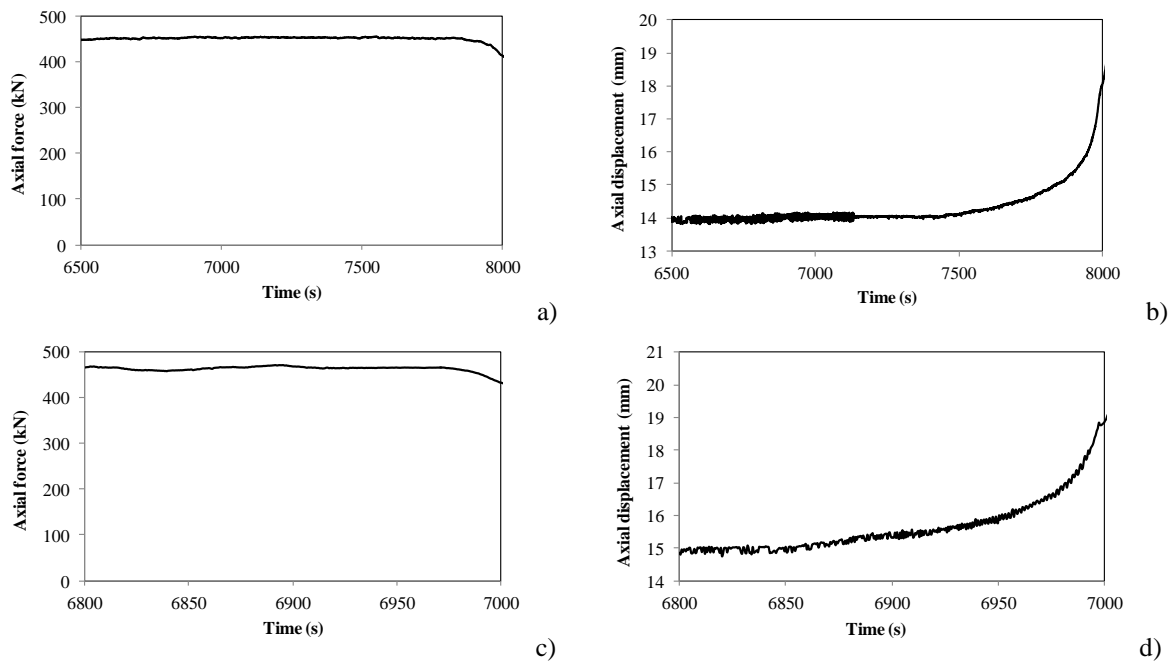


Fig. 4. Creep test results of aluminium at 160°C: a)-b) - Test No.2 ; c)-d) – Test No. 3

3 DISCUSSION OF THE RESULTS

It can be seen from the creep tests for steel that at 400°C columns have very low short-term creep resistance for axial loads higher than 90% of the column's axial load capacity. However, for load ratios below 90% the column's creep resistance starts to increase rapidly. A similar observation can be made for the presented aluminium creep tests. This suggests that, at any discrete temperature level, a range of load ratio exists within which creep rapidly reduces the column's axial load capacity. This short-term creep resistance could be a problem for high-rise structures where lower-storey columns are predominately loaded by axial compressive force. It is important to note that even at 400°C (for steel) and 160°C (for aluminium) the results have shown that the columns are sensitive to prolonged high-temperature exposure, indicating that these temperature levels should be treated with care in structural design procedures. For steel, 400°C is not generally considered as a

critical temperature, since at this temperature level there is a negligible reduction in yield strength for European low-carbon steels. However, when considering the period of time within which steel is exposed to high temperature, it is obvious that a reduction of a column's load-bearing capacity is possible, even at 400°C. This suggests that a new way of thinking on the ultimate load bearing capacity of columns in fire conditions is necessary, including the period of time for which they are exposed to high temperatures. This may need consideration in the future development of building codes.

4 CONCLUSIONS

The column tests conducted so far suggest that there is a connection between the critical temperature interval for creep development, obtained in previous coupon studies, and the results from this column study, in terms of failure due to creep. Very low short-term creep resistance can be observed for the columns under loads which are higher than approximately 90% of their axial load capacity at 400°C (steel) and 160°C (aluminium). Further studies will include analysis of the column creep behaviour at temperature levels up to 600°C in the case of steel and 300°C in case of aluminium. The experimental study will be supported by numerical analysis of the tests in order to appropriately track the reduction of load capacity due to creep.

ACKNOWLEDGMENT

This work has been fully supported by Croatian Science Foundation under the project *Influence of creep strain on the load capacity of steel and aluminium columns exposed to fire* (UIP-2014-09-5711). Any opinions, findings, and conclusions or recommendations expressed in this material are those of the authors and do not necessarily reflect the views of Croatian Science Foundation.

REFERENCES

1. ISO 834, Fire Resistance Tests – Elements of Building Construction, International Organization for Standardization, Switzerland, 1975.
2. ASTM, Standard Methods of Fire Tests of Building Construction and Materials (ASTM Standard E119-05), American Society for Testing and Materials, West Conshohocken, PA., 2005.
3. EN 1993-1-2:2005, “Eurocode 3 – Design of steel structures – Part 1-2: General Rules – Structural fire design”, European Committee for Standardization, Brussels, 2005.
4. Neno Torić, Alen Harapin, Ivica Boko (2013). *Experimental Verification of a Newly Developed Implicit Creep Model for Steel Structures Exposed to Fire*. Engineering Structures 57 pp 116-124.
5. Neno Torić, Alen Harapin, Ivica Boko (2015). *Modelling of the Influence of Creep Strains on the Fire Response of Stationary Heated Steel Members*. Journal of Structural Fire Engineering 6(3) pp 155-176.
6. Neno Torić, Josip Brnić, Ivica Boko, Marino Brčić, Ian W. Burgess, Ivana Uzelac Glavinić (2017). *Development of a High Temperature Material Model for Grade S275JR*. Journal of Constructional Steel Research 137. pp 161-168.
7. Neno Torić, Josip Brnić, Ivica Boko, Marino Brčić, Ian W. Burgess, Ivana Uzelac Glavinić (2017). *Experimental Analysis of the Behaviour of Aluminium Alloy EN6082 AW T6 at High Temperature*. Metals, 7, 126.
8. Mohammed A. Morovat, Michael D. Engelhardt, Todd A. Helwig, Eric M. Taleff (2014). *High-Temperature Creep Buckling Phenomenon of Steel Columns Subjected to Fire*, Journal of Structural Fire Engineering 5(3). pp 189-202.
9. Kang-Hai Tan, Wee-Siang Toh, Zhan-Fei Huang, Guan-Hwee Phng (2007). *Structural Responses of Restrained Steel Columns at Elevated Temperatures Part 1: Experiments*, Engineering Structures 29(8). pp 1641–1652.

INFLUENCE OF FIRE ON THE SHEAR CAPACITY OF STEEL-SHEATHED COLD-FORMED STEEL FRAMED SHEAR WALLS

Matthew S. Hoehler¹, Blanca Andres²

ABSTRACT

This paper discusses an experimental investigation of the influence of fire on the lateral load-carrying behaviour of steel-sheathed cold-formed steel framed shear walls. The completed Phase 1 tests showed an important example of structure-fire interaction and highlighted the relevance of the gypsum boards for both the thermal and mechanical behaviour of these systems. A second phase of the study is underway and is outlined in this paper with focus on the test program, specimen design and fire exposure development.

Keywords: cold-formed steel, fire, shear wall, steel-gypsum composite board

1 INTRODUCTION

Lightweight construction using cold-formed steel (CFS) studs represents roughly 20 % of the multi-story nonresidential building market in the United States [1]. These buildings rely on their lateral force-resisting systems (LFRS) to resist horizontal loads; e.g. from wind or earthquakes. While information exists about the structural performance and fire resistance of cold-formed steel construction; see for example [2–5], there is limited knowledge about the performance of CFS-LFRS under combined hazards. This information is needed to inform: (i) fire compartmentation design when significant lateral deformation of a building is anticipated, (ii) post-fire assessment of a structure, and (iii) first responder decisions to enter a building when earthquake aftershocks are likely.

In 2016, a series of experiments (Phase 1) was performed at the National Fire Research Laboratory at the National Institute of Standards and Technology (NIST) to investigate the performance of earthquake-damaged steel-sheathed cold-formed steel shear walls under fire load [6]. A second phase of the project currently underway (Phase 2) extends the study to two additional levels of fire severity and two additional types of CFS-LFRS. In this paper, the authors summarize key findings from Phase 1 and present the test program and setup for Phase 2; with focus on the steel-gypsum composite board assemblies. The Phase 2 experiments are being conducted at the time of writing this paper.

2 PHASE 1

The Phase 1 experiments were performed in conjunction with the project *Earthquake and Post-Earthquake Fire Performance of Mid-Rise Light-Gauge Cold-Formed Steel Framed Buildings* conducted at the University of California, San Diego (UCSD), which investigated the earthquake and fire performance of a six-story, cold-formed steel framed test building [7]. The NIST tests were conducted immediately prior to the six-story building tests to experimentally determine the influence

¹ Reserach Strucutral Engineer, National Institute of Standards and Technology, Gaithersburg, USA.

e-mail: matthew.hoehler@nist.gov

² PhD Student, Danish Institute of Fire and Security Technology, Hvidovre, Denmark.

e-mail: bav@dbi-net.dk

of the planned fires on the lateral load-resistance of the building to help inform the selection of the earthquake motion intensities used in the UCSD tests before and after the fires.

2.1 Test program and specimens

Table 1 shows the Phase 1 test matrix. Six identical 2.74 m by 3.66 m shear wall specimens were fabricated consisting of 150 mm wide CFS framing sheathed on one side with sheet steel adhered to 15.9 mm thick Type X (per [8]) gypsum board (Sure-Board 200³) and on the opposite side with 15.9 mm thick Type X gypsum board (Fig. 1). Fabrication details are provided in [6]. The specimens were subjected sequentially to varied combinations of mechanical (shear) deformation and thermal (fire) loading. Specimen 1 (CFS01) was used to establish the monotonic ‘pushover’ load-displacement response of the wall system. Specimen 2 (CFS02) was loaded by symmetric-amplitude reverse-cyclic shear deformation to destruction to establish the cyclic load-displacement response. Specimen 3 and 4 (CFS03 and CFS04) were cycled to deformations just before and after the peak load was achieved, respectively, burned for 13 min and 20 s and then cycling was continued until destruction of the wall. For Specimen 5 (CFS05), an undamaged wall was exposed to fire for 13 min and 20 s and then cycled to destruction. Specimen 6 (CFS06) was tested similarly to Specimen 3, however, the burn duration was doubled.

Table 1. Test matrix for Phase 1

Wall Type	Specimen Name	Loading		
		Before Fire	Fire	After Fire
Sure-Board	CFS01	Monotonic pushover	-	-
	CFS02	Cycle to failure	-	-
	CFS03	Cycle to 1 % drift	13 min 20 s burn	Cycle to failure
	CFS04	Cycle to 1.8 % drift	13 min 20 s burn	Cycle to failure
	CFS05	-	13 min 20 s burn	Cycle to failure
	CFS06	Cycle to 1 % drift	26 min 40 s burn	Cycle to failure

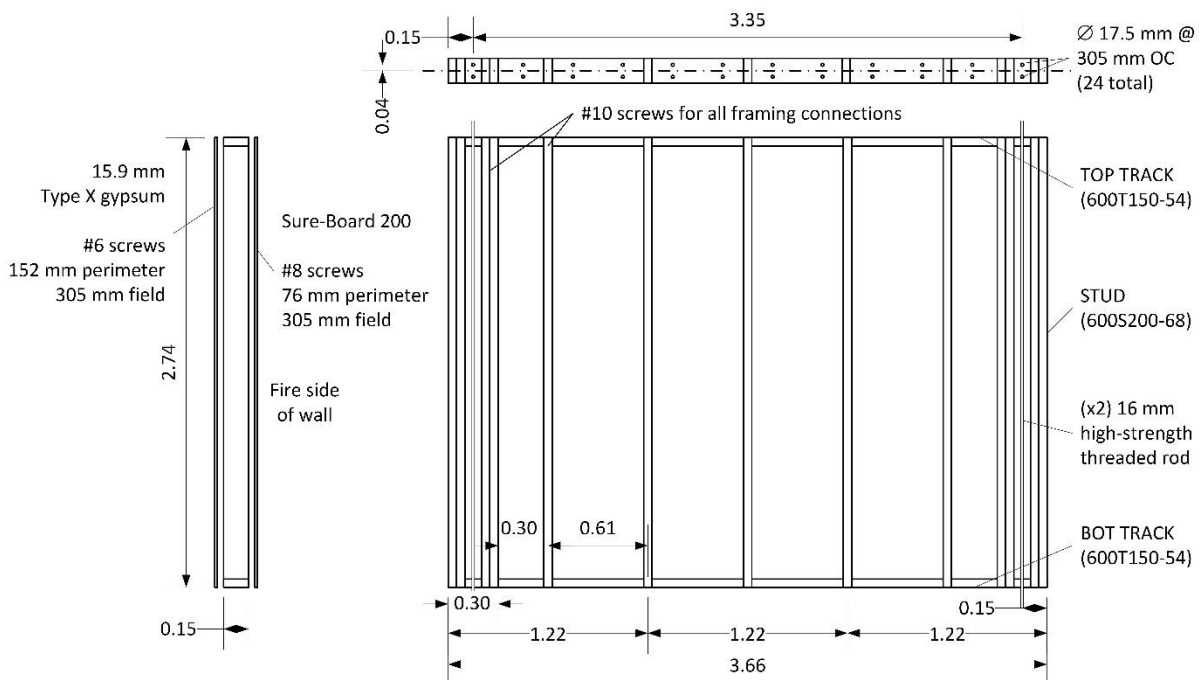


Fig. 1. Phase 1 specimen geometry (units in meters unless noted)

³ Certain commercial products are identified in this paper to specify the materials used and the procedures employed. In no case does such identification imply endorsement or recommendation by the National Institute of Standards and Technology, nor does it indicate that the products are necessarily the best available for the purpose.

2.2 Test setup and procedure

The test setup was informed by ASTM E2126-11 [9] but deviated slightly to accommodate a burn compartment on a rolling platform. Details are provided in [6].

The test specimens were loaded mechanically by holding the base of the wall fixed and applying a prescribed in-plane deformation to the top of the wall as shown in *Fig. 2a*. Out-of-plane movement of the wall was limited by four structural steel guide frames. Mechanical load was applied using a servo-hydraulically controlled actuator with a load capacity of 240 kN in tension and 365 kN in compression. Axial loading to the wall was limited to the self-weight of the specimen, actuator and top loading beam. ASTM E2126-11 Method C (CUREE Basic Loading Protocol) was used with a reference deformation based on the expected deformation at peak load under monotonic loading. This protocol is widely used in the United States to characterize the seismic horizontal load resistance of vertical elements intended to form the lateral force resisting system in buildings. The loading procedure involved displacement cycles grouped in phases at incrementally increasing displacement levels. The rate of displacement was selected to be 1.52 mm/s to minimize inertial influences.

The fire load was provided by a natural gas diffusion burner in a compartment (interior dimensions: 2.9 m high \times 3.5 m long \times 1.2 m deep; see *Fig. 2b*) designed to approximate a portion of the corridor in the six-story building tested at UCSD. The open side of the compartment mated with the test specimen on the steel-gypsum composite board side of the shear wall. The openings at the ends of the compartment were 1.7 m high by 1.2 m wide. The mass flow rate of the natural gas was controlled to approximate the predicted time-temperature curves for upper gas layer temperatures in the 2nd floor corridor of the six-story building at UCSD during the fire tests. This was achieved by rapidly increasing (rise time less than 60 s) the Heat Release Rate (HRR) of the burner to 1900 kW and holding it constant for 800 s (13 min 20 s); for specimen CFS06 the burn duration was doubled. While the compartment temperatures rose more rapidly than for the standard fire curve in American Society of Testing and Materials (ASTM) standard E119 [10] (or International Organization for Standardization (ISO) standard ISO 834 [11]), they were representative of conditions present in residential fires in modern buildings [12]. The burn duration for the UCSD tests that the NIST tests were intended to simulate, was limited to about 15 minutes by the fire authorities in San Diego.

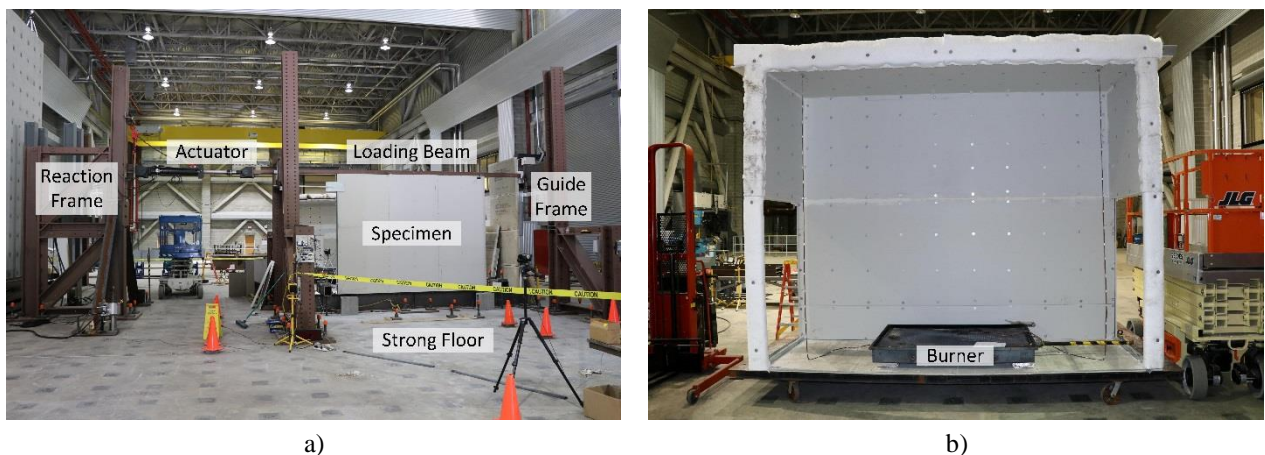


Fig. 2. Photograph of test setups: a) Mechanical loading; b) Fire loading

2.3 Phase 1 results

The Phase 1 results are discussed in detail in [6,13] and data and videos can be downloaded at [14]. The uncertainties associated with all Phase 1 measurements are provided in [6]. The total expanded

uncertainties (using a coverage factor of 2) associated with the forces and displacements reported in this paper are 1.6 kN and 2.3 mm, respectively.

Specimen 3 represents a typical loading case in Phase 1. The specimen was first cycled to a prescribed drift, subjected to fire load, and then, after the wall cooled, mechanical cycling was continued until the wall failed (defined as approximately 70 % reduction of post-peak load capacity). The resulting load-displacement curve is shown in *Fig. 3a*. The local maxima (load) for each step in the loading pattern are indicated for compression (circles) and tension (squares) excursions. The curves defined by these maxima show an abrupt reduction of force after the specimen was subjected to the fire.

The enveloping curves ('backbone') defined by the local maxima of applied force versus drift for the five cyclic tests are compared in *Fig. 3b*. Displacements (drifts) measured at the top of the specimens are converted to drift ratios by dividing by the specimen height (2.74 m). The portions of the curves indicated by dashed lines represent the mechanical response in the post-fire test. Test CFS02 represents the stiffness and capacity of the wall under ambient conditions. Test CFS05 represents the stiffness and capacity of the specimen after the steel-sheathed side has been subjected to the investigated fire load for 13 min 20 s. The reduction in peak load capacity was 35 % and the response was roughly symmetric for tension and compression cycles. The reduction in the peak load was accompanied by a shift in failure mode of the specimens from local buckling of the sheet steel (*Fig. 4a*) to global buckling of the sheet steel (*Fig. 4b*) for the unburned (CFS02) and burned (CFS05) walls, respectively. The fire severely damaged the gypsum on the burn side reducing the stiffness of the shear panels out-of-plane and creating a 15.9 mm standoff between the screw heads and the sheet steel; i.e. the thickness of the lost gypsum. This, in effect, transformed the specimen to a plain sheet steel shear wall with reduced constraint around the panel boundaries. Pre-damaging the specimen by reversed shear cycling to 1 % (CFS03) or 1.8 % (CFS04) drift ratio prior to the fire loading had no noticeable influence on the residual load bearing capacity of the wall. Doubling the burn time to 26 min 40 s (CFS06) caused additional reduction (approximately 15 %) of the post-fire lateral load bearing capacity due to the damage to the nonstructural gypsum board on the back side (cold side) of the wall during the longer burn; which was not present in the shorter tests.

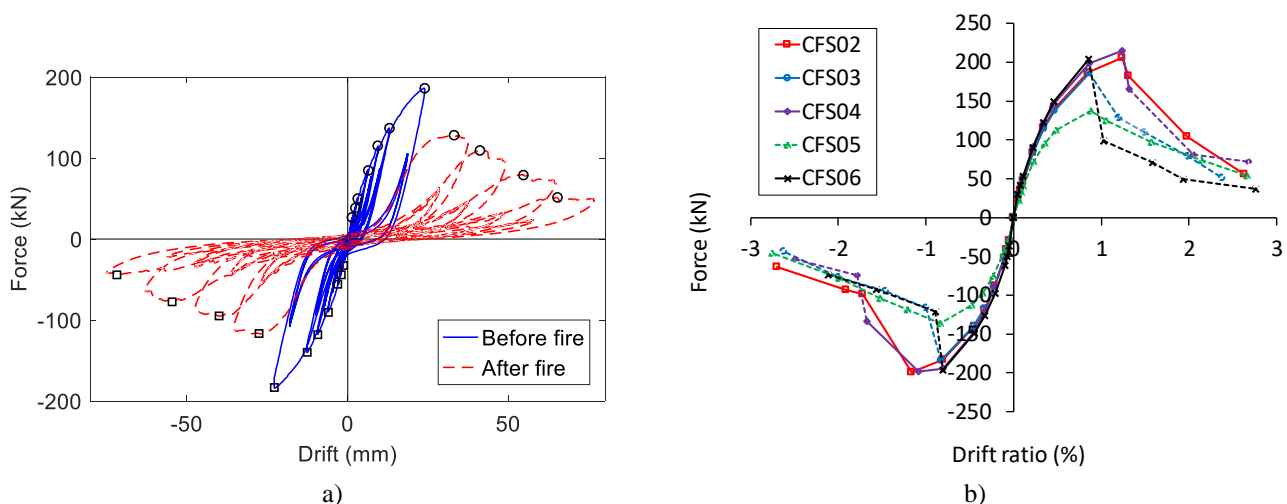


Fig. 3. a) Lateral load versus drift for Specimen 3 (CFS03); b) Envelope force versus drift ratio curves for all cyclic tests (CFS02 to CFS06)



Fig. 4. Photograph of back of sheathed side of wall with the nonstructural gypsum removed after mechanical loading to failure: a) Unburned wall after cycling (local buckling); b) Cycling after burning (global buckling)

3 PHASE 2

The Phase 1 experiments showed a clear example of structure-fire interaction (the shift in failure modes for the relatively short-duration fire) and highlighted the relevance of the gypsum for both the thermal and mechanical behaviour of these systems. Moreover, it appeared that this behaviour was predictable. This motivated the Phase 2 tests which include two additional types of CFS-LFRS, two additional levels of fire exposure, and locates the fire on the non-egress side of the shear wall.

3.1 Test program

Table 2 provides the test matrix for Phase 2. In addition to retesting the sheet steel adhered to Type X gypsum board (Sure-Board 200), Oriented Strand Board (OSB), and strap braced walls will be investigated. As in Phase 1, the walls are subjected to sequences of mechanical and fire loading. The test setup and mechanical loading procedure are the same as in Phase 1, however, the fire loadings differ as discussed below.

Table 2. Test matrix for Phase 2

Wall Type	Specimen Name	Loading		
		Before Fire	Fire	After Fire
Sure-Board	SB01	Cycle to failure	-	-
	SB02	-	ASTM E119 (1-hour)	Cycle to failure
	SB03	-	Severe Parametric	Cycle to failure
	SB04	-	Mild Parametric	Cycle to failure
OSB	OSB01	Cycle to failure	-	-
	OSB02	-	ASTM E119 (1-hour)	Cycle to failure
	OSB03	-	Severe Parametric	Cycle to failure
	OSB04	-	Mild Parametric	Cycle to failure
	OSB05	Drift Level 3	Severe Parametric	Cycle to failure
	OSB06	Drift Level 2	Severe Parametric	Cycle to failure
	OSB07	Drift Level 1	Severe Parametric	Cycle to failure
Strap braced	S01	Cycle to failure	-	-
	S02	-	ASTM E119 (1-hour)	Cycle to failure
	S03	-	Severe Parametric	Cycle to failure
	S04	-	Mild Parametric	Cycle to failure
	S05	Drift Level 3	Severe Parametric	Cycle to failure
	S06	Drift Level 2	Severe Parametric	Cycle to failure
	S07	Drift Level 1	Severe Parametric	Cycle to failure

Drift Level 1 = 0.5 %; Drift Level 2 = 1.0 %; Drift Level 3 = to be determined based on SB01, OSB01, and S01

3.2 Test specimen

The dimensioning of the walls is similar to Phase 1, however, the CFS framing design and tension holddowns are modified to be more representative of typical U.S. practice; the Phase 1 detailing focused on buildings with more than five storeys. The walls are designed using Allowable Stress Design (ASD) nominally following American Iron and Steel Institute (AISI) standards S400-15/S1-16 [15] and AISI S100-16 [16] assuming the walls are located on the interior of the building. The details for the gypsum and sheet-steel sheathed (Sure-Board 200) walls are shown in Fig. 5.

The walls are designed to achieve a 1-hour fire-resistance rating per ASTM E119 [10]. The design for fire-resistance of the steel-gypsum composite board walls is based on [17]. The walls use 15.9 mm thick Type X gypsum board with the joints taped and joints and fastener heads covered with one coat of joint compound on the fire side of the wall. The influence of insulation material in the wall cavity is not investigated.

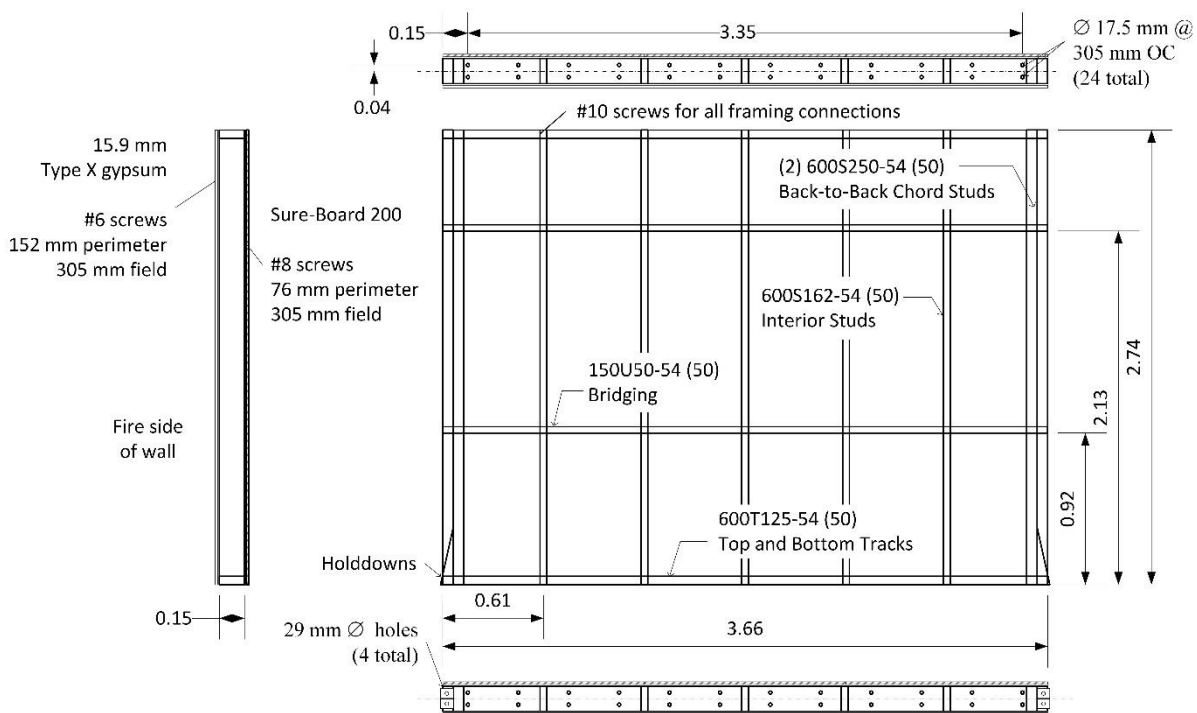


Fig. 5. Phase 2 steel-gypsum composite board specimen geometry (units in meters unless noted)

3.3 Fire load

The target fire exposures are selected to represent various levels of fire severity. Three exposures are considered in Phase 2: (1) a 1-hour standard ASTM E119 fire curve (comparable to ISO 834), (2) a ‘severe’ fire exposure, and (3) a ‘mild’ fire exposure. The severe and mild fires represent realistic post-flashover compartment fire conditions with heating, fully-developed and decay phases. Fig. 6 plots the target temperature-time curves along with a typical upper layer gas temperature measured during Phase 1.

The severity of the fire is defined in terms of exposure time and peak temperature. These values are informed by a statistical fit of data from compartment fire tests reported by Hunt [18]. A peak temperature of 1100 °C represents 95 % of the reported peak temperatures and 900 °C represents 50 % assuming a normal distribution. These values were selected as the maximum temperatures for the ‘severe’ and ‘mild’ fires, respectively. Likewise, assuming a normal distribution of the duration of the fire, 70 minutes and 50 minutes represent 70 % and 50 % of the reported data, respectively.

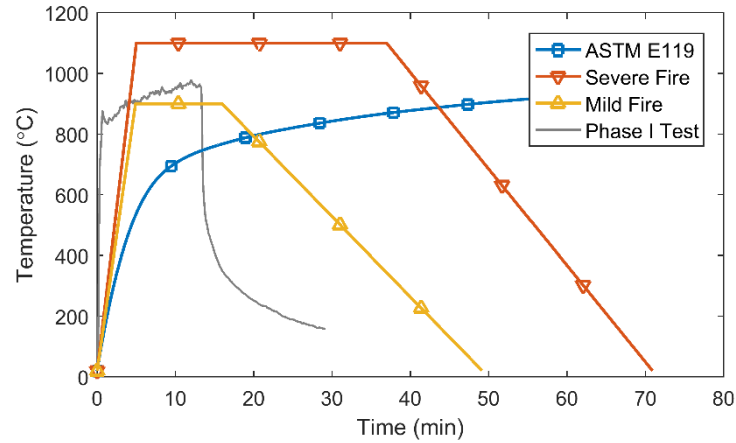


Fig. 6. Target temperature-time curves for Phase 2

The length of the plateau is calculated using the time-to-burnout for the enclosure fire (τ_b) per [18] and as given in Eq. (1).

$$\tau_b = \frac{E \cdot A_f}{90A_o\sqrt{H_o}} \text{ (minutes)} \quad (1)$$

where E is the fuel (energy) load per unit floor area of the enclosure (MJ/m²),
 A_f is the floor area of the enclosure over which combustibles are present (m²),
 A_o is the opening area (m²), and
 H_o is the opening height (m).

In multi-unit residential buildings, shear walls are commonly located along corridors adjacent to a kitchen. Assuming a kitchen compartment and taking the mean values of floor area and fuel load density reported by the National Research Council Canada [19] for multi-family dwellings (9.8 m² floor area with 805 MJ/m²), opening factors⁴ of 0.04 m^{1/2} and 0.09 m^{1/2} provide a time-to-burnout of 37 minutes and 16 minutes, respectively. These times defined the temperature plateaus for the ‘severe’ and ‘mild’ fires.

For comparison, the area under the target curve for the ‘severe’ fire represents a 20 % higher energy than ASTM E119 and the ‘mild’ fire corresponds to 40 % lower energy. The ‘mild’ fire is similar to the average upper gas layer time-temperature curves achieved in the Phase 1 tests.

4 SUMMARY

The results from Phase 1 indicate that a relatively short-duration (13 min 20 s) fire representative of modern furnished residential spaces acting directly on the shear panels caused a shift in the failure mode of the investigated steel-sheathed and gypsum shear walls under lateral loading from local to global buckling of the sheet steel with an accompanying reduction of the load capacity. The shear walls maintained a predictable, but reduced, lateral load capacity compared to ambient conditions. These observations prompted a second phase (Phase 2) of investigation described in this paper to extend the study to two additional shear wall systems and two additional fire loading exposures.

⁴ Opening factor is defined as $\frac{A_o\sqrt{H_o}}{A_t}$, where A_o is the opening area (m²), H_o is the opening height (m), and A_t is the area total enclosure (m²).

ACKNOWLEDGEMENT

We thank Sure-Board, CEMCO, Marino/WARE, Panel Systems, Inc., Larry Williams, Benjamin Schafer, Rob Madsen, and the National Fire Research Laboratory staff for their expertise and support.

REFERENCES

- [1] Steel Framing Industry Association, Market Share and Comparative Report: Cold-formed Steel Framing and Project Specification Trends, 2016.
- [2] M.A. Sultan, A Model for Predicting Heat Transfer through Noninsulated Unloaded Steel-Stud Gypsum Board Wall Assemblies Exposed to Fire, *Fire Technol.* 32 (1996) 239–257.
- [3] P. Keerthan, M. Mahendran, Numerical modelling of non-load-bearing light gauge cold-formed steel frame walls under fire conditions, *J. Fire Sci.* 30 (2012) 375–403. doi:10.1177/0734904112440688.
- [4] H. Takeda, A model to predict fire resistance of non-load bearing wood-stud walls, *Fire Mater.* 27 (2003) 19–39. doi:10.1002/fam.816.
- [5] X. Wang, E. Pantoli, T.C. Hutchinson, J.I. Restrepo, R.L. Wood, M.S. Hoehler, P. Grzesik, F.H. Sesma, Seismic Performance of Cold-Formed Steel Wall Systems in a Full-Scale Building, *J. Struct. Eng.* (United States). 141 (2015). doi:10.1061/(ASCE)ST.1943-541X.0001245.
- [6] M.S. Hoehler, C.M. Smith, Influence of fire on the lateral load capacity of steel-sheathed cold-formed steel shear walls - report of test, Gaithersburg, MD, 2016. doi:10.6028/NIST.IR.8160.
- [7] X. Wang, T.C. Hutchinson, G. Hegemier, S. Gunisetty, P. Kamath, B. Meacham, Earthquake and fire performance of a mid-rise cold-formed steel framed building – test program and test results: rapid release (preliminary) report (SSRP-2016/07), San Diego, CA, 2016.
- [8] ASTM C1396-17 Standard Specification for Gypsum Board, ASTM International, West Conshohocken, PA, 2015. doi:10.1520/C1396.
- [9] ASTM E2126-11 Standard Test Methods for Cyclic (Reversed) Load Test for Shear Resistance of Vertical Elements of the Lateral Force Resisting Systems for Buildings, ASTM International, West Conshohocken, PA, 2011. doi:10.1520/E2126-11.
- [10] ASTM E119-16a Standard Test Methods for Fire Tests of Building Construction and Materials, ASTM International, West Conshohocken, PA, 2016. doi:10.1520/E0119.
- [11] ISO 834-1 Fire Resistance Tests - Elements of Building Construction - Part 1: General Requirements, International Organization for Standardization, Genève, Switzerland, 1999.
- [12] S. Kerber, Analysis of Changing Residential Fire Dynamics and Its Implications on Firefighter Operational Timeframes, *Fire Technol.* 48 (2012) 865–891. doi:10.1007/s10694-011-0249-2.
- [13] M.S. Hoehler, C.M. Smith, T.C. Hutchinson, X. Wang, B.J. Meacham, P. Kamath, Behavior of steel-sheathed shear walls subjected to seismic and fire loads, *Fire Saf. J.* 91 (2017) 524–531. doi:10.1016/j.firesaf.2017.03.021.
- [14] M.S. Hoehler, C.M. Smith, Dataset from Influence of Fire on the Lateral Resistance of Cold-Formed Steel Shear Walls - Phase I, (2018). doi:https://doi.org/10.18434/T4/1422515.
- [15] AISI S400-15 w/S1-16, North American Standard for Seismic Design of Cold-Formed Steel Structural Systems (with Supplement 1), American Iron and Steel Institute (AISI), Washington, DC, 2016.
- [16] AISI S100-16 North American Specification for the Design of Cold-Formed Steel Structural Members, American Iron and Steel Institute (AISI), Washington, DC, 2016.
- [17] IAPMO-ER-1261 Sure-Board Series 200, 200W, and 200B Structural Panels Installed on Cold-Formed Steel or Wood Framed Shear Walls, International Association of Plumbing and Mechanical Officials (IAPMO), 2018.
- [18] S.P. Hunt, J. Cutonilli, M. Hurley, Evaluation of Enclosure Temperature Empirical Models, Society of Fire Protection Engineers (SFPE), 2010.
- [19] A.C. Bwalya, G.D. Loughheed, A. Kashef, H.H. Saber, Survey Results of Combustible Contents and Floor Areas in Multi-Family Dwellings, National Research Council Canada, 2008.

BEHAVIOUR OF STEEL FRAME STRUCTURES UNDER LOCALISED FIRE INCLUDING PROGRESSIVE COLLAPSE DURING COOLING

Thomas Gernay¹, Antonio Gamba²

ABSTRACT

Accounting for the effects of non-standard fire exposures on structures is a key component of performance-based structural fire engineering. Under natural fire (including cooling), steel and concrete members may fail during or after the cooling phase; yet research so far has focused mainly on isolated beams and columns, therefore disregarding the effects of thermally-induced restraint forces in assemblies. To investigate these effects, this paper analyses the mechanisms of load redistribution in structural systems comprising one steel column subject to localised fire, with a focus on the effects of the cooling phase. Numerical simulations show that significant tensile forces can build up in a fire-exposed column part of a framed structure when the temperatures are reduced back to ambient due to reversed thermal expansion and recovery of the properties. These tensile forces overload the adjacent vertical members, possibly leading to failure of members not directly affected by the fire. Therefore steel-framed structures subjected to localised fire attacking one column are vulnerable to progressive collapse occurring during or after the cooling phase. This suggests that the effects of thermally-induced forces associated with a fire event should be taken into account when designing with alternative load path method under column loss.

Keywords: Progressive collapse; Thermal loads; Localised Fire; Steel frame; Robustness

1 INTRODUCTION

Structural fire engineering has long relied on a prescriptive approach based on isolated member behaviour under continuously heating standard fire. By definition, this approach does not allow comprehending the effects of interaction between members of a complete structure nor the effects of real fire exposure. Yet, such effects can have a significant influence on the response of real buildings to fire [1]. For instance, the cooling phase that inevitably occurs in real fires generates effects that may endanger a structure stability; this has been attested by real structural collapses and poses a specific threat to firefighters.

Understanding the behaviour of structural assemblies under realistic fire exposure, including the interaction between members and the effects of heating-cooling sequences, is of paramount importance for developing performance-based structural fire design. Computational modelling (by non-linear finite element method) provides an efficient and powerful method to investigate this behaviour. Previous works have notably established that failure of isolated structural members may occur during or even after the cooling phase of natural fires [2-3]. Recent research has also looked at the effects of sophisticated fire scenarios on structural assemblies, such as traveling fires on buildings [4] or tanker truck fires on bridges [5]. Yet, the specific effects of non-uniform and

¹ Assistant Professor. Department of Civil Engineering, Johns Hopkins University, Baltimore, MD, United States.

e-mail: tgernay@jhu.edu

² PhD Candidate. Department of Architecture, Geology, Environment & Constructions (ArGENCo), University of Liège, Belgium.

e-mail: antonio.gamba@uliege.be

heating-cooling thermal exposures on structural assemblies still remain to be understood. In particular, the question arises whether thermally-induced forces in a structure during the cooling phase of a localised fire may produce load redistributions which threaten the stability and trigger a progressive collapse.

Progressive collapse events of multi-story buildings have underlined the need to prevent, in case of a local failure of a structural element, the failure spreading from element to element resulting in a collapse disproportionate to the original cause. For engineers, the alternative load path method is a common design approach to verify that a structure has enough redundancy for developing new load paths toward a different static equilibrium in case of loss of a member [6]. The alternative load path method is generally regarded as a threat-independent method, meaning that the event triggering the local failure needs not be explicitly considered. As this event is generally assumed as dynamic (blast, impact), simplified methods have been developed to account for the dynamic effects in non-linear static analyses; typically the loads are amplified by a dynamic increase factor [7]. However, no method exists to account for the specific thermal effects that can arise in case of a fire-induced loss of a member.

This paper starts by analysing a simple system composed of a column and a linear spring, where the column is subject to a heating-cooling sequence. This allows identifying the main parameters governing the load redistributions between a fire-exposed column and the surrounding structure. Then, numerical simulations are performed on reduced-scale steel frames for which experimental data are available. Parametric analyses are performed to investigate the cases where the development of tensile forces in the heated-cooled column lead to collapse of adjacent columns, hence triggering a progressive collapse mechanism due to thermal forces. Finally, an application on a twenty-story steel moment frame is analysed under localised fire attacking one ground level column, to investigate the possibility of the highlighted mechanisms to develop in real designs.

2 RESTRAINED COLUMN SUBJECTED TO HEATING AND COOLING

A system made of a S355 steel HEA 300 column in series with a linear spring is studied (*Fig. 1*). The spring represents the structure surrounding the fire-exposed column. The stiffness of the spring, K_s , is adjusted to model different levels of restraint on the column. The column is initially loaded in compression at 50% of its axial (plastic) capacity $F_{y,20^\circ\text{C}}$. The force F , maintained constant during the fire, is distributed between the spring (F_s) and the column (F_c). The temperature distribution in the column section is uniform. Temperature creates thermal elongation of the column and a variation of its mechanical properties. Buckling is prevented. Steel strength is partly irrecoverable: a loss of 0.3 MPa/K is assumed when steel has been heated beyond 600°C.

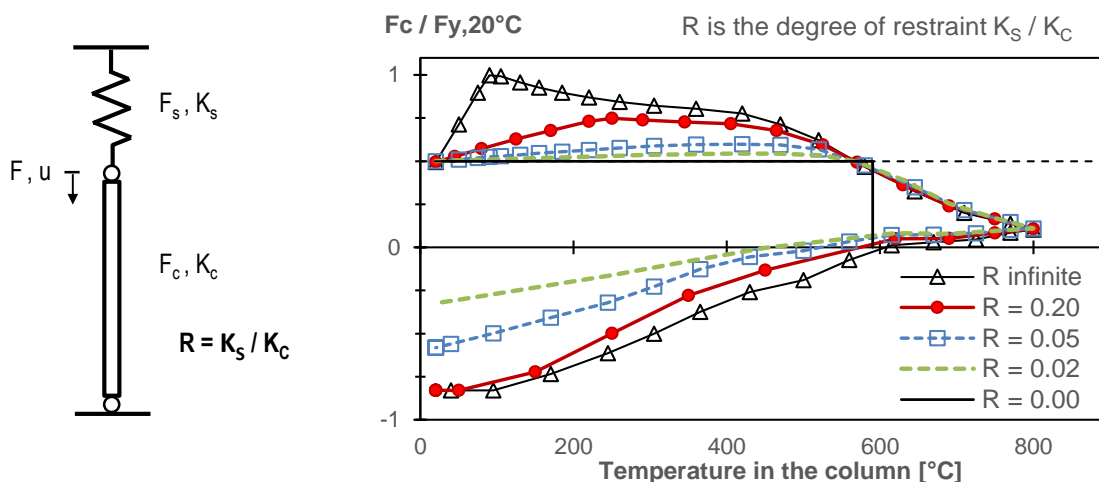


Fig. 1. Evolution of axial load in a restrained column heated to 800°C then cooled down.

Fig. 1 plots the evolution of the column axial load when heated to 800°C then cooled down, as a function of the degree of axial restraint $R (=K_s/K_c)$ obtained by adjusting the spring stiffness. When the spring provides no stiffness ($R=0$), the column is an isolated member subject to constant applied load and it fails at a critical temperature of 590°C (corresponding to a strength loss of 50%). In all other cases, the column is restrained and can transfer forces. In the heating phase, the compressive axial force in the column increases progressively, reaches a peak, and then decreases. But the most interesting outcome is the behaviour during cooling. The column develops tension because it has experienced significant yielding during heating and thermal strain is recovered. Tension building up in the fire-exposed column implies that the force transferred to the rest of the structure exceeds the initial axial force in the column. The amount of force that is transferred at the end of the fire increases with the maximum reached temperature and the degree of restraint. The maximum amount of tension that can possibly develop equals the residual plastic capacity of the section at ambient temperature, which is a very large amount of load to be absorbed by the surrounding structure.

3 STEEL FRAME UNDER LOCALISED FIRE

3.1 Numerical simulation of the experimental tests

Numerical simulations are performed on steel moment frames for which experimental data are available and used for validation. Steel moment frames subject to a localised fire scenario have recently been tested at Tongji University [8]. In these tests, the frames contained four bays and two stories, and the ground floor middle column was heated using a specific electric furnace (*Fig. 2*). The two central bays span 2.2 m each while the two side bays span 2.0 m each. The height of the first and second story are 1.3 m and 1.2 m, respectively. The steel members have rectangular tubular sections. For Frame 1, the section dimensions (in mm) were equal to 50x30x3 for the columns, 60x40x3.5 for the side bay beams, and 150x50x5 for the middle bay beams. The frame was loaded prior to the application of the fire, with an initial load in the heated column equal to 9.8 kN (i.e. 6% of the plastic capacity of the section). The structural response was measured during the full course of the fire including in the column post-buckling stage and in the cooling phase.

The test on Frame 1 is modelled using the non-linear finite element software SAFIR [9]. A thermal analysis of the column section is first conducted using the furnace temperature as boundary condition on the four faces of the column. The Eurocode steel model for thermal analysis is adopted. The temperature evolution predicted by SAFIR matches very well the test results (*Fig. 3*). The temperature is almost perfectly uniform across the section due to the small thickness of the profile and the applied boundary conditions.

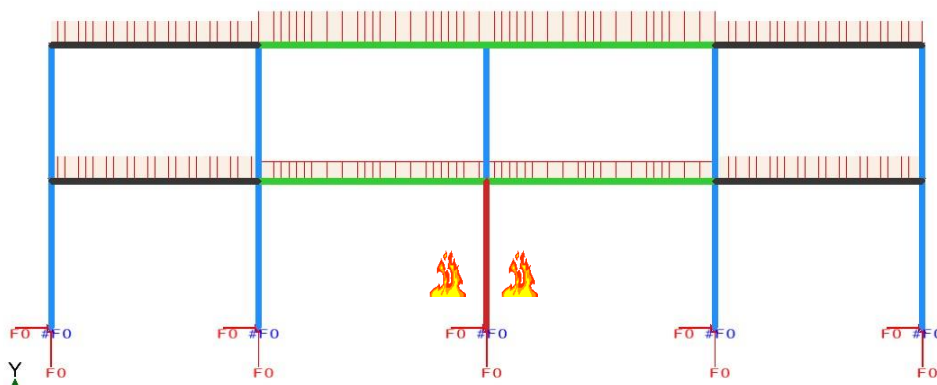


Fig. 2 SAFIR model of tested frame no 1.

Then, a 2D structural analysis is performed using 550 beam FE for modelling the frame. The material properties reported in [8] were used in the simulation (steel yield strength at ambient

temperature equal to 310.8 MPa for the 150x50x5 beam, 290.0 MPa for the 60x40x3.5 beam, and 360.8 MPa for the columns) and reduced with temperature according to Eurocode. The evolution of the vertical displacement at the top of the central column is plotted in *Fig. 3*. During the cooling phase, the frame top displacement continues to move downward. As a result, further load redistribution occurs from the fire-exposed column to the adjacent columns during this phase. The fire-exposed column is eventually in tension. These results validate the ability of the numerical model to reproduce the experimental behaviour during the different stages of the fire.

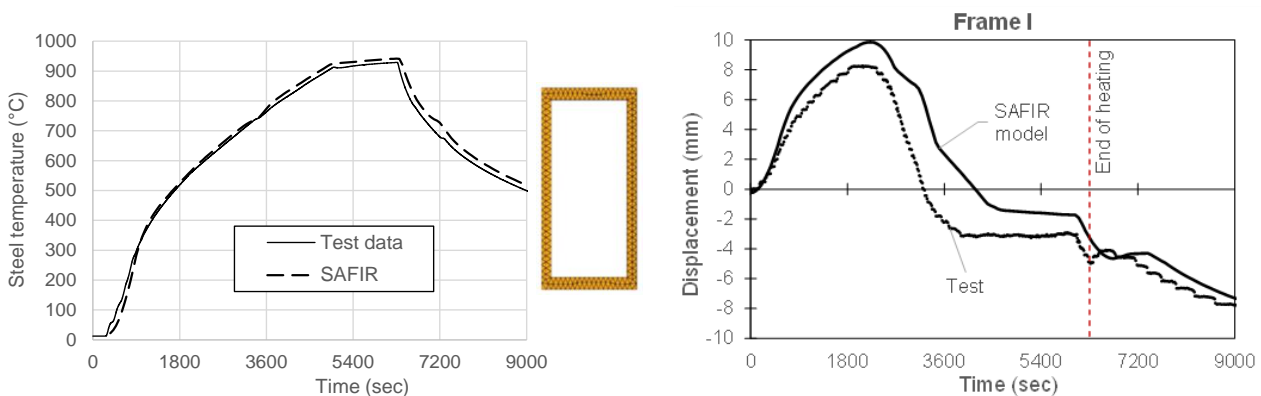


Fig. 3. Results of the thermal analysis (left) giving the temperature evolution in the heated column; and structural analysis (right) giving the vertical deflection at the top of the heated column.

3.2 Parametric analysis on the steel frame

A parametric analysis is then conducted on the steel frame under localised fire. The objective is to investigate the possibility of global collapse of the frame triggered by the load redistributions during cooling. In the test modelled in Section 3.1, the heated-cooled column developed tension, but the tensile force was not significant enough for overloading the adjacent columns up to failure. From the results of Section 2, it is known that the main parameters affecting the amount of transferred loads are the maximum reached temperature in the heated column and the degree of axial restraint. Therefore, different configurations are numerically studied where varying maximum temperature and degree of restraint (through different beam sections) are used. Furthermore, the initial gravity loading applied on the frame is also varied to investigate cases where the initial utilisation ratio of the columns is higher. Finally, different fire curves are used.

Fig. 4 shows the results obtained for a steel frame such as the one of Section 3.1 except that:

- The middle bay beam profiles are upgraded to 250x100x5 (mm). This leads to a degree of axial restraint for the heated column, R , of 0.16.
- The applied gravity loads are increased to reach an initial load in the heated column equal to 67 kN. This corresponds to 42% of the room temperature plastic capacity of the heated column.
- The applied fire curve is the Eurocode parametric fire with $\Gamma=1$ (i.e. the heating curve approximates the standard ISO fire) and a duration of heating phase (DHP) of 15 min [3].

For this frame, a global collapse is observed when the (cold) column on the right of the fire-exposed column buckles (*Fig. 4*). This collapse occurs after the end of the localised fire, 16 minutes after the gas temperatures are back to ambient. At that time, the fire-exposed column has developed large tensile forces (of the same order of magnitude of the compressive forces initially carried) and thus pulls down the rest of the structure. This eventually triggers a global failure when the column adjacent to the right buckles due to overloading.

In the mechanism highlighted numerically here, it is important to note that the progressive collapse that is triggered is not simply due to one column losing its capacity. Indeed, *Fig. 4c* shows that, at

one stage during the localised fire, the heated column does not carry any compressive load, yet the frame remains stable. The problem arises when, later on, the fire-exposed column cools down and develops tensile forces. At the onset of collapse (*Fig. 4d*), the middle column is subjected to a tension of 60 kN. As a result, the compressive force in the adjacent columns has increased from 63 kN (before the fire, *Fig. 4a*) to 152 kN. This leads to buckling of the adjacent column (*Fig. 4e*) and therefore global collapse of the frame.

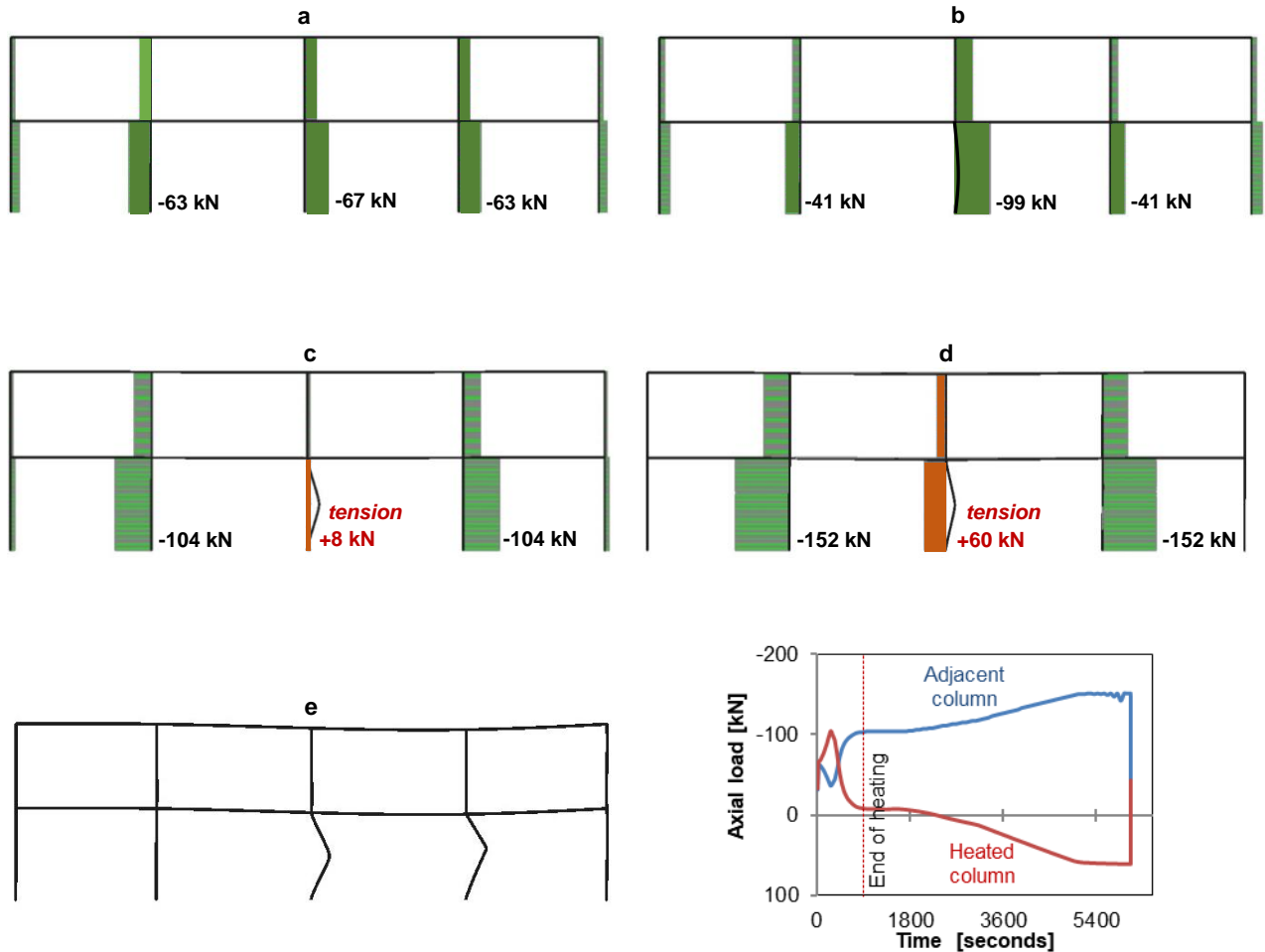


Fig. 4. Failure mechanism of a steel frame under localised fire due to load redistributions from the heated-cooled middle column to the adjacent columns. (a) Pre-fire load distribution. (b) Beginning of heating with restrained axial expansion of the middle column. (c) Further heating resulting in loss of stiffness and strength of the middle column. (d) Cooling and development of tension in the column. (e) Frame collapse due to buckling of the adjacent right column. (f) Plot of the evolution of the axial load in the columns; the global failure occurs after the end of the fire.

4 FINITE ELEMENT ANALYSIS OF A 20-STORY STEEL MOMENT FRAME

Finally, the behaviour of a twenty-story steel moment resisting frame is analysed under localised fire attacking one ground level column. The objective is to confirm whether the discussed mechanisms can occur in a real design, and potentially lead to progressive collapse.

The frame is designed according to the U.S. standards. The total height of the building is 80.76 m, divided between a first floor of 5.486 m high and the 19 other floors of 3.962 m high. There are five bays of 6.096 m length each. The column section at ground level is W36x485. The girders are W33x141. Steel yield strength is 345 MPa. The column bases are considered as fixed. It is assumed that pile foundations are used which can withstand tension.

The focus of the analysis is on the effects, for a structural system, of a thermal exposure that is spatially non-uniform and includes the heating-cooling sequence. Therefore, the specificities of the fire scenario producing such an exposure are not the focus of the analysis. It is sufficient to recognize that such thermal exposure could happen, for instance resulting from a terrorist attack, or from an accidental localised fire occurring in the vicinity of the column; hence there is a need to study what the effects would be on a structure. In this study, one column part of the frame is heated uniformly up to 800°C and then cooled down back to ambient temperature. Efforts towards quantifying the thermal exposure associated with specific scenarios are of course also of importance, but they are out of the scope of this study. In this sense, the approach here centres on the structural behaviour in a similar philosophy as is done when adopting event-independent alternative load paths methodologies for assessing progressive collapse of structures under blast or impact loading. Follow-up analyses are looking at the effect of thermal gradients on perimeter columns, as these lead to specific effects not addressed in this study.

The structural analysis is performed using the software SAFIR and 2200 beam finite elements. Geometrical and material non-linearities, including large deflections and buckling, are taken into account. The effects of initial geometric imperfections are introduced in the model through equivalent horizontal forces (according to Eurocode 3). Continuous columns are considered with rigid beam-column connections, where the connections are not explicitly modelled. The slab contribution is neglected. The fire-exposed column has a degree of axial restraint R equal to 0.12. Application of the load factors for the fire situation leads to an initial axial force of 1805 kN in the column, merely 6% of the axial capacity at ambient temperature (note that the column is part of a moment resisting frame with the design governed by wind loads).

The structure is loaded with the distributed loads, then the fire-exposed column is heated up to 800°C and subsequently cooled down. *Fig. 5* shows the evolution of the axial force (relative to capacity at ambient temperature) in the fire-exposed column and in the adjacent right column. Starting at 6% for both columns, the force increases in the heated column due to restrained thermal expansion, up to a maximum value of 42% (or 13370 kN) when the steel temperature reaches 502°C. Then, the axial force in the fire-exposed column drops, first due to a reduction of the properties in heating and then due to the recovery of thermal strains in cooling. At the end of the cooling phase, when the steel temperature is back to 20°C, the fire-exposed column is in tension with a tensile force equals 43% of the maximum capacity at ambient temperature. By equilibrium, the difference is supported by the surrounding columns; indeed the axial force in the adjacent right column has increased from 6% to 26% after the fire event, i.e. an increase of 6342 kN. This mechanism of amplification of the load transfer from the column affected by the hazard to adjacent members, with pulling due to thermal effects, is specific to fire scenarios.

For the studied frame, the load redistribution did not trigger a progressive collapse. This is due mainly to the low initial level of applied gravity loads. Yet, the analysis shows that a fire can lead to overload of an adjacent column by a value (here, +20% of $F_{y,20^\circ\text{C}}$) that is significantly larger than the load initially supported by the fire-exposed column (6% of $F_{y,20^\circ\text{C}}$). This raises potential concerns about other configurations in which a combination exists of high applied gravity loads and high restraint for the heated members.

Fig. 6 illustrates how forces are redistributed due to a localised fire, and compares the outcome of the structural fire analysis with the situation evaluated using the classical alternative load path method. In the latter, a notional column removal approach is used with a non-linear static analysis using a dynamic increase factor of 2 (which is the upper threshold value). Before the loss of the column, the initial compressive force in the adjacent right column is 1805 kN. After the fire, the compressive force in the adjacent column has increased to 8147 kN (value predicted by a non-linear transient thermal-mechanical analysis in SAFIR). However, the common alternative load path method predicts a maximum compressive force of 4003 kN after the loss of the column (value predicted by a non-linear static analysis at ambient temperature with dynamic increase factor in

SAFIR). Therefore, it appears clearly that the thermal effects may lead to load redistributions much more severe than the ones considered by a typical scenario of notional column removal.

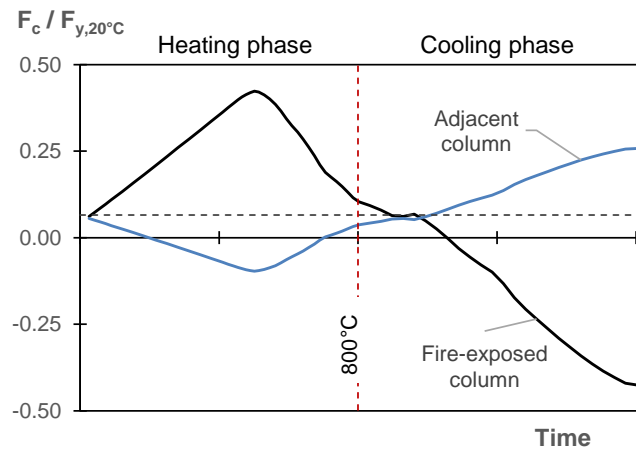


Fig. 5. Evolution of axial force in the fire-exposed column and the adjacent column (compression is positive).

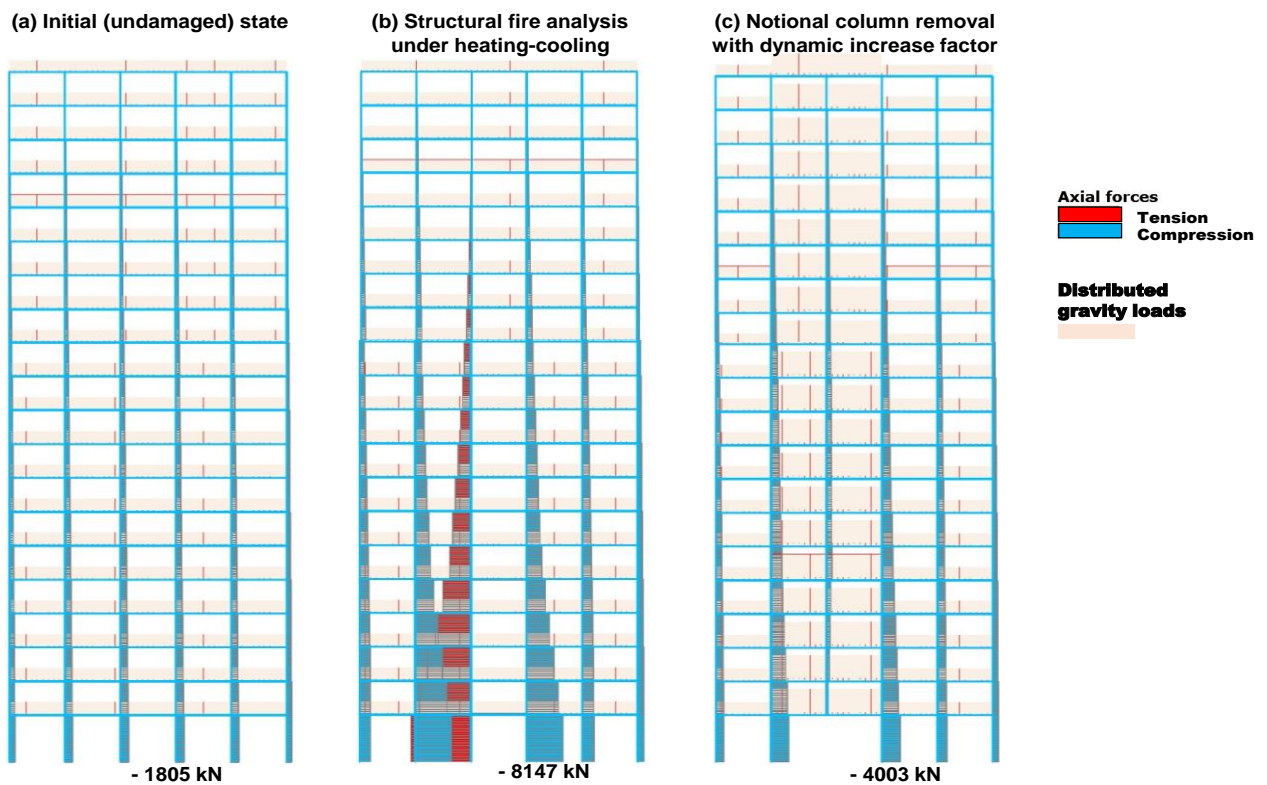


Fig. 6. Axial forces in the columns of the 20-story moment frame under: (a) initial gravity loading in undamaged state; (b) fire-induced collapse of a ground floor column as analysed by a nonlinear thermo-mechanical analysis; (c) alternative load path method with notional column removal using a dynamic increase factor of 2 for gravity loads. The thermo-mechanical analysis predicts much larger compressive loads in the column adjacent to the fire-exposed column because of the effects of thermal forces.

5 CONCLUSIONS

This paper has described load redistribution mechanisms that occur when a localised fire affects a column that is part of a structural frame. The mechanisms result in tension building up in the fire-

exposed column and overloading the adjacent columns in compression, which could lead to failure of members not directly affected by the fire and trigger a progressive collapse. This suggests that (localised) fire scenarios potentially lead to specific detrimental effects that are not observed with other exceptional events causing local damage in structures. These results have two important implications:

- The results highlight the possibility to have failure of structural assemblies during the cooling phase of localised fires. Besides the factors promoting delayed failure of isolated members (such as heat transfer and additional damage processes in the materials), load redistributions are identified as a key factor playing a role at the structural system level.
- The results question the validity of adopting an event-independent alternative load path method for assessing the effect of fire-induced column loss on progressive collapse. While such methods can consider dynamic effects (associated with blast or impact scenarios) in a simplified manner, they currently do not account for thermal forces effects (associated with fire scenarios). Since this paper shows that the load transferred from a fire-attacked column to the surrounding structure can exceed significantly the load initially carried by the column, specific provisions should be introduced in event-independent alternative load path methods if one wants to account for potential fire scenarios through such methods.

Future works will look at the effects of thermal gradients and more sophisticated localised fire exposures on the described mechanisms. The role of connections, and possible failure of these components, also needs further investigation.

REFERENCES

1. Martin Gillie, Asif Usmani, JM Rotter (2001). *A structural analysis of the first Cardington test*. Journal of Constructional Steel Research 57(6). pp 581-601.
2. Thomas Gernay, Mohamed Salah Dimia (2013). *Structural Behaviour of Concrete Columns under Natural Fires*. Engineering Computations 30(6). pp 854 – 872.
3. Thomas Gernay, Jean-Marc Franssen (2015). *A performance indicator for structures under natural fire*. Engineering Structures 100. pp 94-103.
4. Behrouz Behnam (2016). *On the effect of travelling fire on the stability of seismic-damaged large reinforced concrete structures*. International Journal of Civil Engineering 14(8). pp 535-545.
5. Guillermo Peris-Sayol, Ignacio Paya-Zaforteza, Jose Alós-Moya, Antonio Hospitaler (2015). *Analysis of the influence of geometric, modeling and environmental parameters on the fire response of steel bridges subjected to realistic fire scenarios*. Computers & Structures 158. pp 333-345.
6. Sherif El-Tawil, Honghao Li, Sashi Kunnath (2013). *Computational simulation of gravity-induced progressive collapse of steel-frame buildings: Current trends and future research needs*. Journal of Structural Engineering 140(8), A2513001.
7. DoD (2009). Department of Defense. Unified Facilities Criteria (UFC): Design of buildings to resist progressive collapse, 4-023-03, Washington, D.C.
8. Binhui Jiang, Guo-Qiang Li, Liulian Li, B.A. Izzuddin (2018). *Experimental studies on progressive collapse resistance of Steel Moment Frames under Localized Furnace Loading*, Journal of Structural Engineering 144(2): 04017190.
9. Jean-Marc Franssen, Thomas Gernay (2017). *Modeling structures in fire with SAFIR®: Theoretical background and capabilities*, Journal of Structural Fire Engineering, 8(3). pp 300-323.

FIRE TESTS OF LOAD BEARING DOUBLE STUD LSF WALLS

Harikrishnan Magarabooshanam¹, Anthony Deloge Ariyanayagam², Mahen Mahendran³

ABSTRACT

Single stud LSF walls are commonly used as load bearing and non-load bearing structures in the residential sector. But in situations such as partition walls, town houses, places where acoustic insulation and load carrying capacities required are higher, double stud LSF walls are used. Extensive research has been conducted on the fire performance of single stud LSF walls under various load ratios and the data is readily available. It included the effects of different layers of plasterboard, joint arrangements, various steel grades and thicknesses of lipped channel section studs under standard and realistic design fire curves. However, there is inadequate research data on the fire performance of double stud wall systems. This research therefore investigated the fire and structural performance of double stud walls using full scale ISO834-1 standard fire tests of two 3m x 3m LSF walls made of 90mm lipped channel studs. The fire test results of the double stud LSF wall systems are then compared with the fire test results of single stud LSF walls with varying stud depth. This paper presents the results of this investigation and the results.

Keywords: Double stud wall, Single stud wall, time-temperature curve, LSF.

1 INTRODUCTION

The usage of Light Gauge Steel Frame walls commonly known as LSF walls is rapidly increasing in the residential and commercial sectors of the construction industry. The most common wall system used is the single stud LSF wall where single row of studs is sandwiched between one or more layers of plasterboards. Double stud walls are those with two parallel rows of lipped channel section (LCS) studs with studs arranged directly opposite to each other separated by an air gap as shown in *Fig. 1*. Many factors are involved in the structural and thermal performance of these LSF walls exposed to fire conditions. Apart from the structural loads such as dead/live loads, seismic and wind loads acting on the building, thermal loads due to the outbreak of fire in a building can also be a vital cause for the failure of the walls. The structural performance of LSF walls is generally governed by the behaviour of cold-formed steel studs within the wall due to the applied loads at elevated temperatures. Thermal performance of LSF walls is mainly contributed both by the plasterboards and steel studs as both these entities contribute to the heat transfer. The geometric configuration of the studs within LSF walls significantly governs the thermal performance of LSF walls and thus also the structural performance of load bearing LSF walls. But to date the majority of research has been carried out only for wall systems with single row of studs under different fire curves [1, 2]. Researchers have also attempted to study the fire performance of complex LSF walls but no clear research data is available for the same [3]. Attempts were also made to study the heat transfer in partition walls by numerical studies, but detailed temperature data or the structural behaviour of the double stud wall system is not

¹ PhD Researcher. Civil Engineering and Built Environment, Queensland University of Technology, Australia.
e-mail: h.magarabooshanam@qut.edu.au

² Research Fellow. Civil Engineering and Built Environment, Queensland University of Technology, Australia.
e-mail: a.ariyanayagam@qut.edu.au

³ Professor. Civil Engineering and Built Environment, Queensland University of Technology, Australia.
e-mail: m.mahendran@qut.edu.au

available [4]. In single stud LSF walls the major mode of heat transfer from fire side to the ambient side is by conduction through plasterboards from fire side followed by convection and radiation within the cavity [5]. Likewise, for double stud walls there is no research data available on the thermal performance of double stud LSF walls. Therefore, it becomes a necessity to investigate the fire performance of load bearing double stud LSF walls.

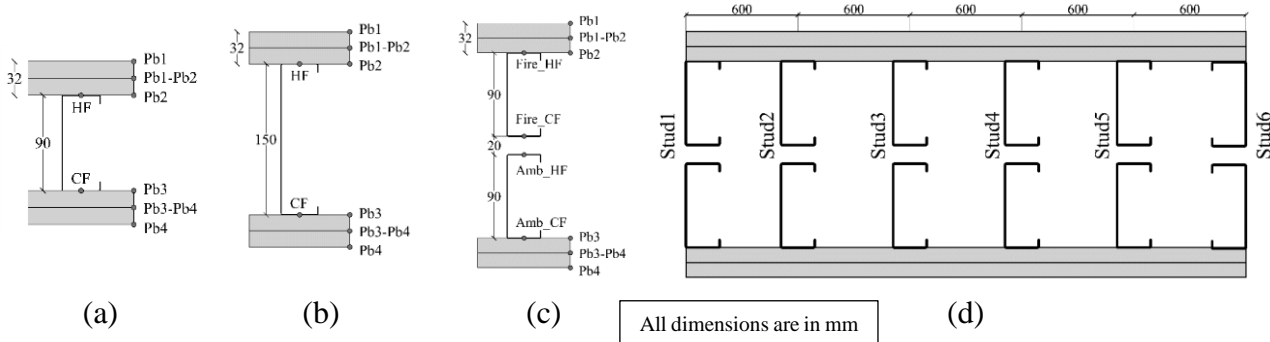


Fig. 1. a) Single stud wall - 90 mm; b) Single stud wall - 150 mm; c) Double stud wall - 90 mm; d) Plan view of double stud wall for full-scale fire test.

2 HEAT TRANSFER IN LSF WALLS

In LSF walls the plasterboard provides lateral restraints to both flanges of the stud and protects the steel studs during fire depending on the number of layers of plasterboard lining. During fire exposure the plasterboard on the fire side calcinates and the heat from plasterboard transfers to the stud hot flange. Due to the calcination of plasterboard on one side only the temperature distribution on the stud will be non-uniform causing thermal bowing. This also leads to non-uniform mechanical properties of steel, resulting in neutral axis shift for the load bearing studs. These actions caused by fire exposure on one side induce the thin-walled studs to be subjected to a bending moment in addition to the applied axial compression load [6].

Normally, in a single stud wall with double plasterboard lining the fire exposed plasterboard transfers the heat to the next plasterboard and then to the stud hot flange through conduction. Conduction is the major form of heat transfer in the wall system until it reaches the hot flange of the stud. But within the cavity, the heat transfer from the fire side cavity to the ambient side cavity surface occurs through both convection and radiation. The air within the cavity offers certain resistance to the heat transfer depending upon the depth and volume of the air cavity. There is also a certain amount of heat transfer through the conduction of air within the air cavity. But the conductivity of air is low when compared with plasterboard at higher temperatures. There is a significant amount of radiation into the cavity and conduction through the studs in single stud wall systems.

In a double stud walls, the heat transfer mechanism from fire side to ambient side is unknown. There exists a 20 mm air gap between the two rows of stud which eliminates the heat transfer by conduction through the studs to the ambient side plasterboard. Due to this wall arrangement the heat transfer from the fire side to the ambient side may result in lower temperature on the ambient side plasterboard. This reduced heat transfer in the wall may result in uniform temperature distribution in the studs, resulting in reduced thermal bowing and neutral axis shift. But no research data is available to understand these effects that generally occur in double stud walls. Therefore, this research investigated the structural fire performance of two load bearing double stud LSF walls using full scale ISO834-1 standard fire tests. The stud depth was kept constant at 90 mm for both fire tests while the thickness of the stud was varied from 0.75 mm to 0.95 mm. Finally, the full-scale fire test results from double stud walls are compared with available full-scale fire test results of 90 and 150 mm single stud walls [7]. This paper presents the details of this investigation and the results.

3 EXPERIMENTAL STUDIES ON DOUBLE STUD WALLS

The LSF wall panels were constructed with frame dimensions of 3 m x 3 m. Single stud walls were constructed using single row of 90 mm (Test T1) and 150 mm (Test T2) Lipped Channel Section (LCS) studs whereas for double stud walls two rows of 90 mm (Grade 550) LCS studs were used. Fire Tests T1 and T2 were previously conducted at the Wind and Fire Engineering Lab of QUT whereas the Fire Tests T3 and T4 were conducted in this study. Studs were positioned at 600 mm centre to centre spacing. The steel studs used had 1.15 mm thickness in Tests T1 and T2 while 0.75 mm thick studs were used in Test T3 and 0.95 mm thick studs in Test T4 as shown in *Table 1*. Commercially used BlueScope steel stud sections were used in the fire tests. A 20 mm gap was maintained between the two rows of steel frames by using 50 x 200 mm spacer plates for Tests T3 and T4. Two layers of 16 mm Boral Firestop gypsum plasterboards were used as lining on both sides of the wall panel. Each layer of the plasterboard had two horizontal and vertical joints on the fire exposed and ambient sides of the wall. Basecoat 60 was used as the joint compound with 50 mm wide cellulose based joint tape. Sixty four thermocouples were used to measure the temperatures across the width and depth of the wall at various locations. Ten Linear Variable Displacement Transducers (LVDTs) were used to measure the axial shortening and lateral deflection of the wall. The fire tests were conducted using standard ISO834 fire curve at a Load Ratio (LR) of 0.4.

Table 1. Fire test configurations

	Test - T1	Test - T2	Test - T3	Test - T4
Rows of stud	Single		Double	
Test wall dimensions	3 m x 3 m			
Stud sizes	90 x 35 x 8 mm	150 x 35 x 8 mm	90 x 35 x 8 mm	
Stud thickness	1.15 mm		0.75 mm	0.95 mm
Plasterboard	2 x 16 mm USG Boral Firestop			
Load Ratio (LR)	0.4			
Failure time (min)	124	164	132	176

Fire tests T1 and T2 were conducted for 124 and 164 min. Fire test T3 was conducted for 132 min. The failure mode was due to structural adequacy in all the fire tests. Local compressive failure was observed on studs 3 and 4 in Test T3 as shown in *Fig. 2*. The maximum lateral deflection and axial displacement was 17 mm and 7.5 mm on Stud 3 as shown in *Fig. 3 (a)*. Significant plasterboard fall-off was observed near studs 3 and 4 post fire test, possibly leading to earlier failure.

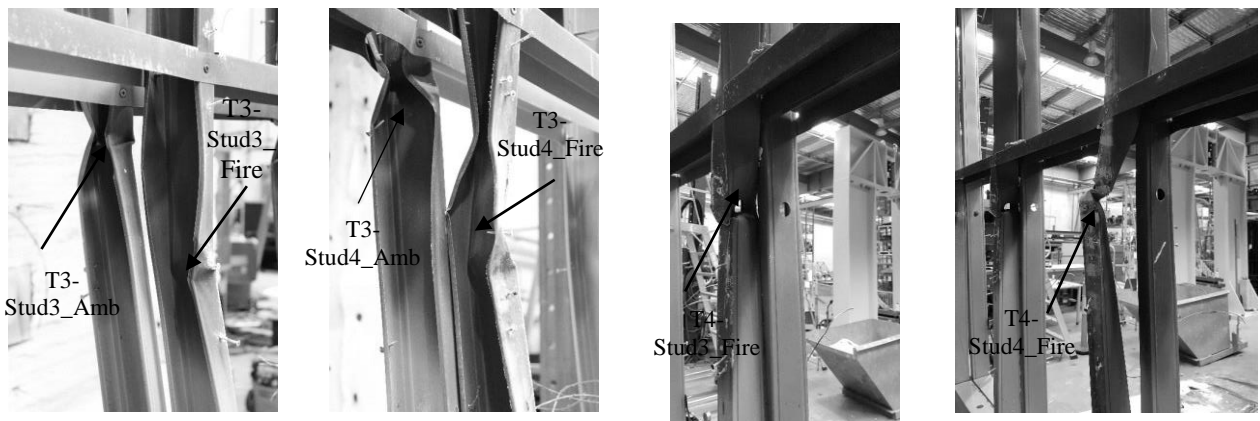


Fig. 2. Local compressive failure in studs of double stud walls

Fire Tests of Load Bearing Double Stud LSF Walls

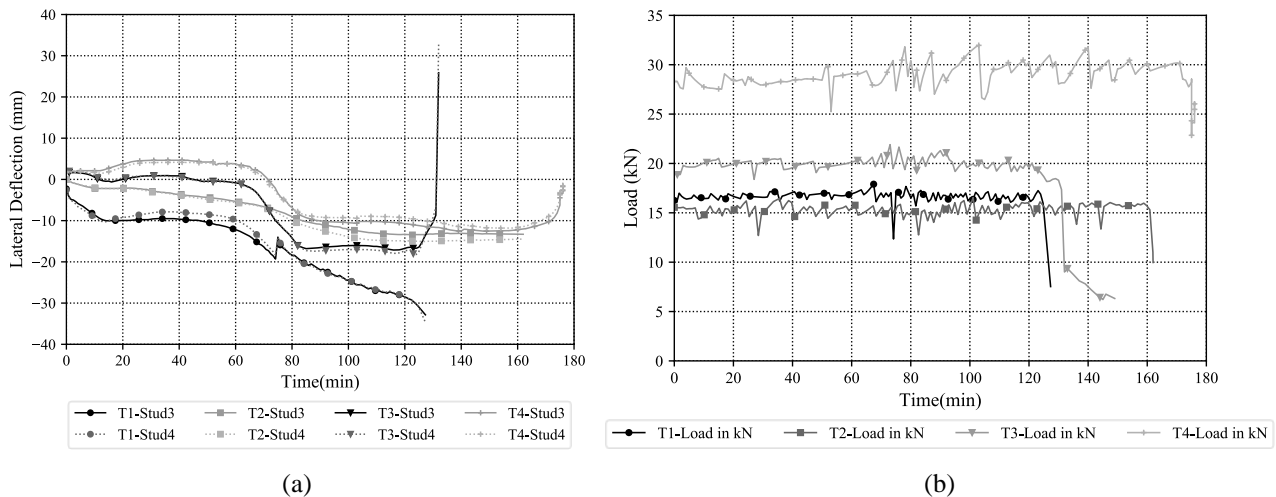


Fig. 3. Results from fire test T1 to T4 a) Lateral deflection versus time b) Applied load in kN versus time curves

Fire Test T4 was conducted for 176 min and the failure was due to structural inadequacy as shown in Fig. 3 (b). No significant plasterboard fall-off was observed in Test T4 compared to Test 3. The maximum lateral deflection and axial displacement were 14 mm and 8 mm, respectively. It is to be noted that the lateral deflection suddenly increased from 2 mm to 17 mm between 60 to 80 min of fire exposure and was constant at 17 mm till 132 min in Test T3 whereas in Test T4 the increase in deflection was gradual from 3 mm to 14 mm during 60 to 80 min of fire exposure.

4 FIRE PERFORMANCE COMPARISON OF SINGLE AND DOUBLE STUD WALLS

The time-temperature curves of the plasterboard and studs for Test T3 are shown in Fig. 4. For comparison the time-temperature curves from 90 mm (Test T1) and 150 mm (Test T2) stud wall fire tests are plotted against fire test results from Test T3. Similarly, the time-temperature curves from Test T4 are plotted against Tests T1 and T2 in Fig. 5. The fire side and the ambient side plasterboards are referred to as Pb1 and Pb4. Fire side and ambient side plasterboard cavity surfaces are referred to as Pb2 and Pb3. The interface between the two plasterboard layers on the fire side is referred to as Pb1-Pb2 while the interface between the ambient side plasterboards is referred to as Pb3-Pb4. The hot and cold flanges of single stud walls are referred as HF and CF. In double stud walls with two rows of stud, the hot and cold flanges of studs on the fire expose side are referred to as Fire_HF and Fire_CF whereas for those on the unexposed side is referred as Amb_HF and Amb_CF.

4.1 COMPARISON OF PLASTERBOARD TIME-TEMPERATURE CURVES

The time-temperature curves of Pb1 from Tests T1 to T4 exhibited similar behaviour and agreed well with the standard fire curve. The time-temperature curve for Pb1-Pb2 interface on the fire side of the double stud wall was flat from 80 to 110 min of fire exposure for Tests T3 and T4 as shown in Fig. 4 and 5. This behaviour is due to the presence of the larger cavity when compared to the 90 mm (T1) and 150 mm (T2) single stud LSF walls. This can be confirmed by comparing the temperatures at the Pb1 and Pb2 interface (Pb1-Pb2) in Tests T1 to T4. It can be inferred that larger the cavity the curve becomes flatter. Test T2 also exhibits a similar behaviour in Pb1-Pb2 as shown in Fig. 4 (b). But this behaviour was not noticed in Test T1. The curve was flatter in T4 when compared to T3 as shown in Fig. 5 because there was a significant plasterboard fall off in Test T3, which did not happen in Test T4. The plasterboard fall-off on the fire side contributed to the sudden rise in the Pb1-Pb2 time temperature curve in Test T3 at 110 min. The temperature at 80 min for Pb1-Pb2 in Tests T3 and T4 were 666 °C and 655 °C. It can also be noted that the time-temperature curves for Tests T2, T3 and T4 flatten after 80 min of fire exposure till 110 min. This is because Pb1 has completely calcinated at this point and the heat had to be taken up by the Pb2. But as the immediate surface next to the Pb2 is the large air cavity, the heat is transferred to the large air cavity, resulting in the time-temperature

curve becoming flat in this region. But in Test T1 with the smaller 90 mm cavity this phenomenon did not occur. The temperature at 80 min for Pb2 in Tests T3 and T4 were 320 °C and 240 °C while at 110 min they were 346 °C and 276 °C. The temperature rises were only 26 °C and 36°C.

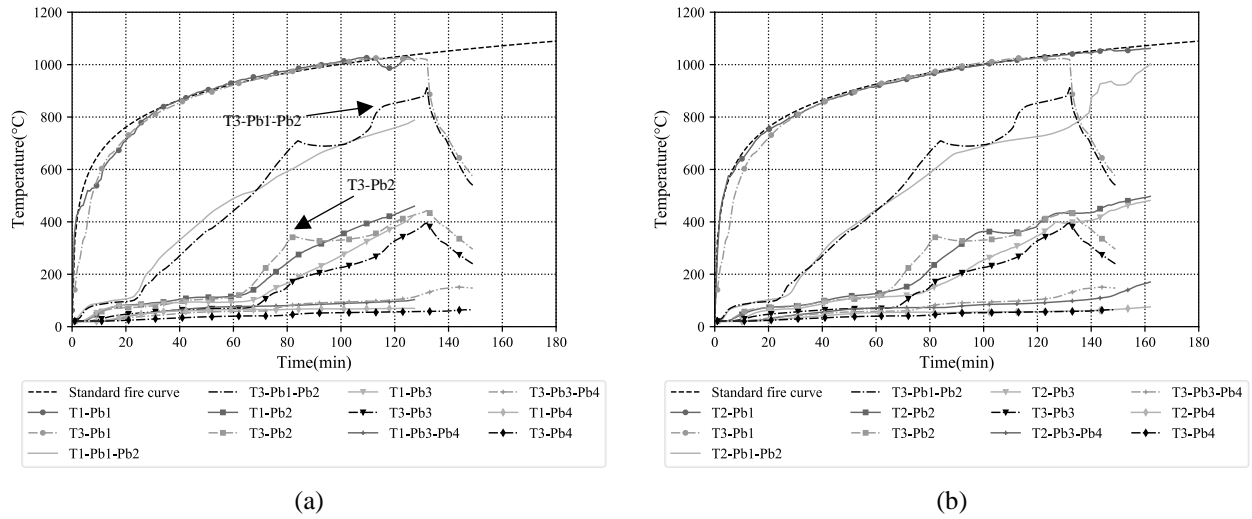


Fig. 4. Plasterboard time-temperature curves of 90 mm, 150mm single stud wall and double stud wall 0.75 mm thick a) T1 vs T3 and b) T2 vs T3

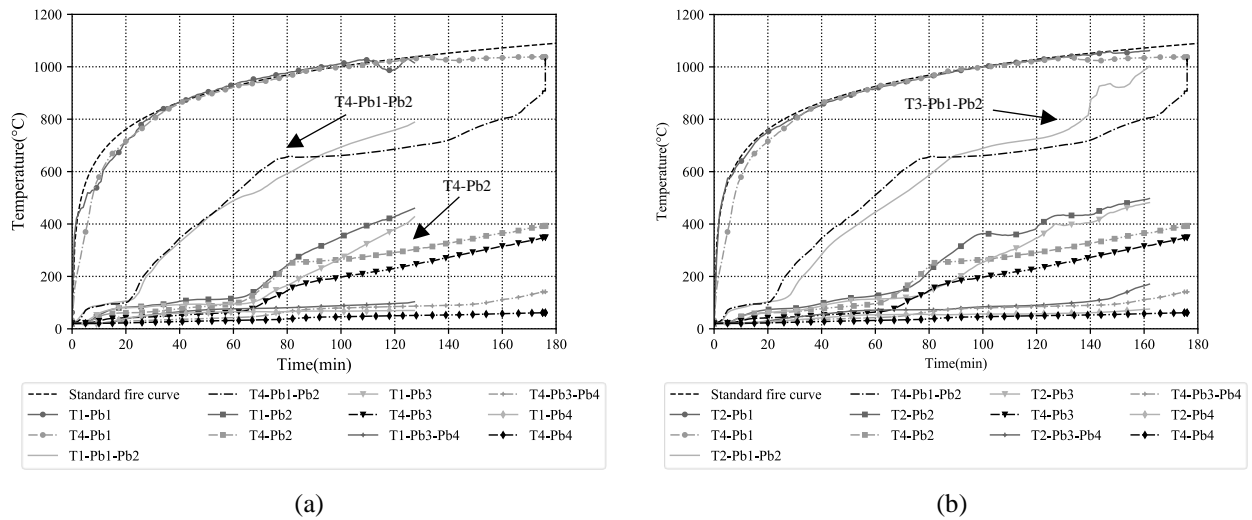


Fig. 5. Plasterboard time-temperature curves of 90 mm, 150mm single stud wall and double stud wall 0.95 mm thick a) T1 vs T4 and b) T2 vs T4

This infers that for 30 min the heat energy from Pb2 was transferred by convection into the air cavity as the temperature rise in Pb3 is very low in Tests T3 and T4. The time-temperature curves on the ambient side cavity surface of Tests T3 and T4 were well below those of T1 and T2. This effect is because of the influence of air movement causing natural convection within the cavity due to larger cavity depth. It can be noted that the two rows of studs in the double stud wall panel are not in contact with each other, and thus eliminating the heat transfer by pure conduction through the studs to the ambient plasterboard (Pb3). The radiation method of heat transfer is dominant only if there exists a large temperature gradient between two surfaces. Therefore, the radiation mode of heat transfer was dominant only during the initial 70 min of fire test in the double stud walls (T3 and T4). From then, due to the lesser temperature gradient between the source (which is the fire side plasterboard cavity surface: Pb2) and the destination (Pb3) the radiation mode of heat transfer is not predominant. Once the air within the cavity reaches equilibrium the time-temperature curve starts to rise till the end of testing in T3 and T4. This unique behaviour of heat transfer is not predominant in test T1 due to the small cavity size. The time-temperature curves of Pb1-Pb2 or Pb2 in Test T1 do not exhibit any flat

region after 20 min of the test. But in Test T2 there is a flat region in the time-temperature curve Pb1-Pb2. This infers that the depth of cavity has considerable influence in the case of single stud LSF walls and the discontinuity in studs is a key factor for the flat region in the time-temperature curves. This phenomenon is more evident in the stud time-temperature curves.

4.2 STUD TIME-TEMPERATURE COMPARISON

The critical central studs 3 and 4 are considered for comparison. The time-temperature curves of Stud3-HF and Stud4-HF in Test T1 and T2 showed a steep increase in temperature after 50 min of fire exposure as shown in Fig. 6. Similar behaviour was also exhibited by Stud3_Fire-HF and Stud4_Fire-HF in Tests T3 and T4 as shown in Fig. 6 and 7 up to 50 min of fire exposure. In Tests T3 and T4 the time-temperature curve shows a steep rise after 55 min. In Test T3 Stud4_Fire-HF reaches the first peak of 470°C at 97 min of fire exposure whereas in Test T4 Stud3_Fire-HF reaches the first peak of 390°C at 103 min of fire exposure. There is a flat region in Stud3 and Stud4_Fire HF curves but the duration of the flat region in the time-temperature curve is short when compared to Test T4. This is because of the plasterboard fall-off on the fire side resulting in sudden increase in temperature at 110 min thereby reaching the final peak at 444 °C at 132 min in Stud3_Fire-HF and 592 °C in Stud4_Fire-HF at 132 min. There was a sudden drop in the applied load and the fire test was stopped at this stage. Similar time-temperature behaviour was observed in the fire and ambient side cold flanges of the stud in Tests T3 and T4. Hot flanges in both tests T3 and T4 recorded almost similar time-temperature curves for the initial 80 min. The flat region in the time-temperature curve was observed only in Tests T3 and T4 whereas no such unique behaviour was observed in Tests T1 and T2. Although the time-temperature curve of plasterboard in Test T2 had a flat region it was not reflected in the stud time-temperature curve. This is because the heat transfer through the stud is by pure conduction in Tests T1 and T2 whereas there is a 20 mm gap in the in Tests T3 and T4. This phenomenon is evident from the fire side cold flange time-temperature curves in Tests T3 and T4.

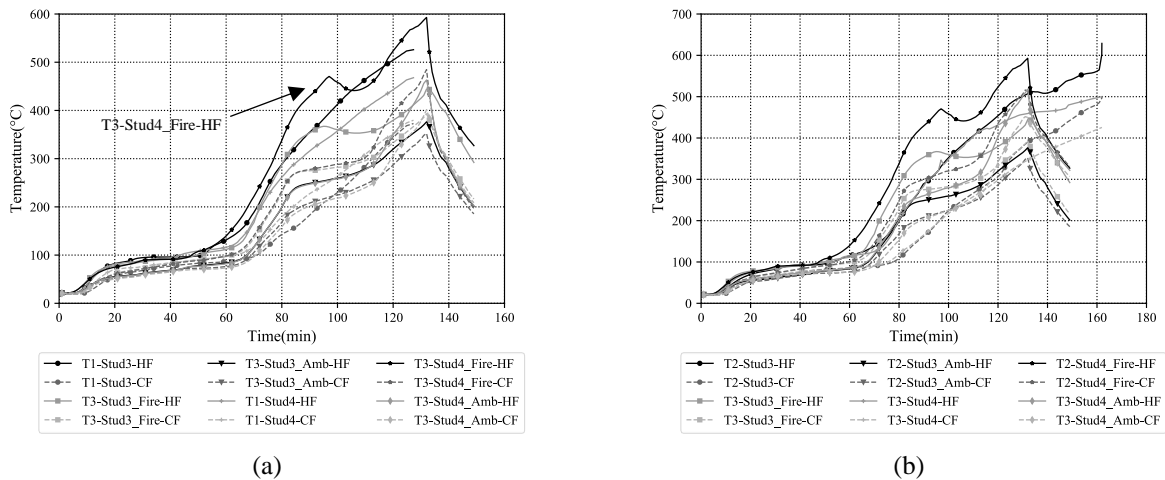


Fig. 6. Stud time-temperature curves of 90 mm, 150mm single stud wall and double stud wall 0.75 mm thick a) T1 vs T3 and b) T2 vs T3

It is to be noted that the plasterboards provide lateral restraints to the stud flanges during fire events. In tests T1 and T2 the plasterboards were screwed at 300 mm intervals on the hot and cold flanges of the stud. But in tests T3 and T4 the plasterboard restraints were provided only the fire side hot flange (Fire_HF) and ambient side cold flange (Amb_CF). The fire side cold flange (Fire_CF) and the ambient side hot flange (Amb_HF) had restraints only through intermittent noggings provided at 1 m along the height. The lateral deflections in tests T1 and T2 were 24 mm and 15 mm. The lateral deflections in tests T3 and T4 were 17 mm and 14 mm. It is to be noted that the studs used in tests T1 and T2 were 1.15 mm thick whereas the studs used in tests T3 and T4 were 0.75 and 0.95 mm thick. The Fire Resistance Level (FRL) of tests T1 and T2 were 124 and 162 min while for tests T3 and T4 gave an FRL of 132 and 176 min. Even though thicker studs were used in test T1 and the studs had full restraints in both flanges, test T3 resulted in 9% higher FRL under same load ratio (0.4). But

when the test T3 is compared with test T2 and T4 the FRL was 19% and 8% lower. This is because of the higher slenderness of the 0.75 mm thick studs in comparison with 0.95 and 1.15 mm thick studs. But test T4 with lower stud thickness (0.95 mm) resulted in 41% higher FRL when compared to test T2 with higher stud thickness (1.15 mm).

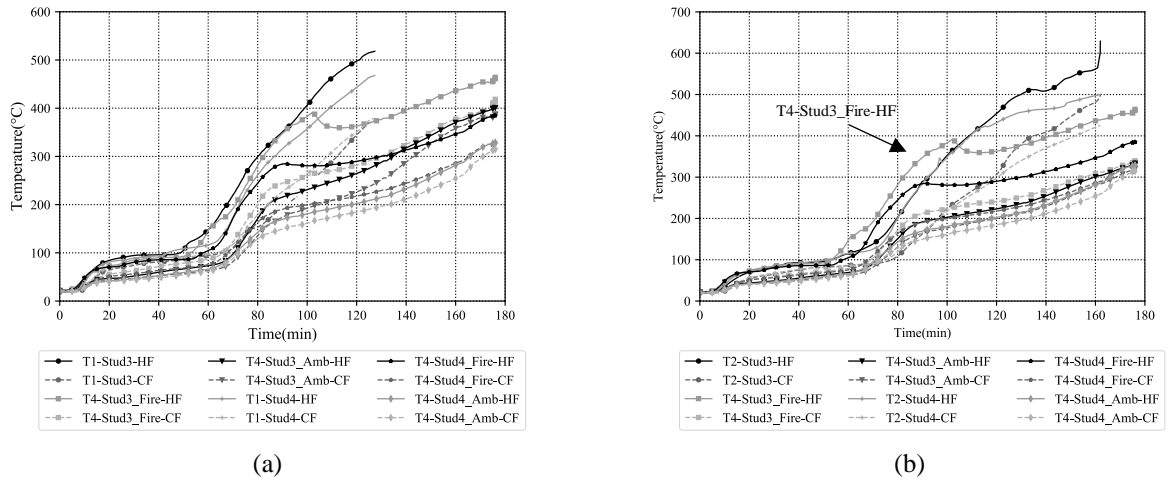


Fig. 7. Stud Time-Temperature Curves of 90 mm, 150mm single stud wall and double stud wall 0.95 mm thick a) T1 vs T4 and b) T2 vs T4

5 EFFECT OF STUD DEPTH ON THE THERMAL PERFORMANCE OF SINGLE STUD WALLS

To understand the temperature distribution across single stud walls with different cavity depth, the results from Test T1 with cavity depth 90 mm and Test T2 with cavity depth 150 mm are compared. Both fire tests were conducted at 0.4 load ratio with 1.15 mm stud thickness under ISO standard fire curve. The time-temperature curve Pb1 agrees well with the ISO standard fire curve. But there is a flat region in the Pb1-Pb2 surface as observed in Tests T3 and T4 from 80 to 110 min (see Fig. 8). This flat region is not present in Pb2 or Pb3 unlike Tests T3 and T4. This reflects in the time-temperature curve of the studs. The flat region which was a common phenomenon in the hot flanges of studs in Tests T3 and T4 is very unlikely in Test T1. But there is a flat region in Stud3_HF and Stud4_CF in Test T2 from 100 to 110 min of fire exposure as shown in Fig. 8 (b).

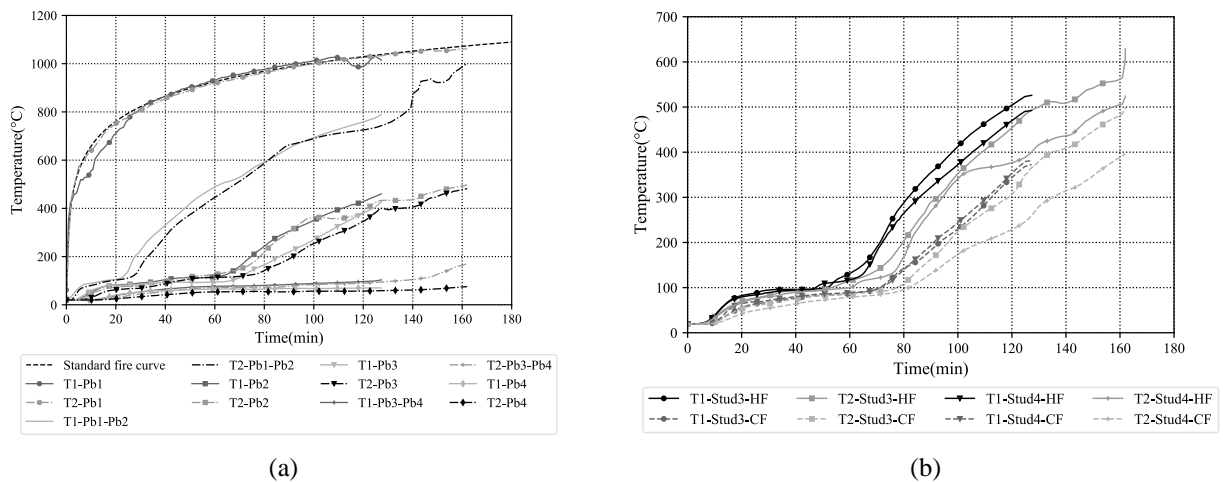


Fig. 8. Time-Temperature Curves of 90 mm (T1) and 150 mm (T2) single stud walls a) Plasterboard and b) Stud. This is because of the contribution from Pb2 as the time-temperature curve is flat during 100 to 110 min as shown in Fig. 8 (a). By this it can be inferred that the cavity depth has a significant effect on the temperature distribution in single stud LSF walls. Due to reduced temperature distribution on the

studs, Test T2 results in higher FRL (164 min) when compared to Test T1 (124 min). Since there is no change in the lateral restraints provided to the plasterboard on both sides unlike in the double stud wall there is no significant effect on the lateral deflection in single stud walls. Therefore, the thermal bowing is higher in single stud LSF walls when compared to double stud LSF walls.

6 CONCLUSIONS

This paper has summarised the fire test results of two load bearing double stud LSF walls. A comparative study with single stud LSF walls is made to understand the superior fire performance of double stud LSF walls. The heat transfer mechanism observed within the double stud LSF wall is clearly identified as the reason for the differences in the fire behaviour of double and single stud LSF walls. The experimental results show that the FRL of the double stud LSF wall with 90 mm studs of 0.95 mm thickness increased by 41% when compared with a similar single stud LSF wall under the same load ratio. But when 90 mm double stud LSF wall of 0.95 mm thickness is compared with 150 mm single stud LSF wall the increase in FRL is only 8%. Likewise, the FRL of double stud LSF wall with 90 mm studs of 0.75 mm thickness increased by 9% when compared with 90 mm single stud LSF wall, but it decreased by 19% when compared with 150 mm single stud LSF wall. Future work is being undertaken at the Wind and Fire Engineering Lab of QUT to investigate the effect of insulation on the FRL of double stud LSF walls.

ACKNOWLEDGMENT

The authors would like to thank QUT, National Association of Steel Framed Housing and Stoddart Group for providing financial support and test materials for this study and Senior Technicians Barry Hume and Glenn Atlee for their assistance with the fire tests.

REFERENCES

1. Chen, W., J. Ye, Y. Bai, and X.-L. Zhao (2013), *Improved fire resistant performance of load bearing cold-formed steel interior and exterior wall systems*. *Thin-Walled Structures*. 73. pp. 145-157.
2. Ariyanayagam, A. and M. Mahendran (2014), *Experimental Study of Load-Bearing Cold-Formed Steel Walls Exposed to Realistic Design Fires*. *Journal of Structural Fire Engineering*. 5(4). pp. 291-330.
3. Kodur, V.K.R. and M.A. Sultan, *Factors Influencing Fire Resistance of Load-bearing Steel Stud Walls*, in *Fire Technology*. 2006, Springer Science & Business Media: Norwell. pp. 5-26.
4. Lázaro, D., E. Puente, M. Lázaro, P.G. Lázaro, and J. Peña (2016), *Thermal modelling of gypsum plasterboard assemblies exposed to standard fire tests*. *Fire and Materials*. 40(4). pp. 568-585.
5. Kontogeorgos, D., K. Ghazi Wakili, E. Hugi, and M. Founti (2012), *Heat and moisture transfer through a steel stud gypsum board assembly exposed to fire*. *Construction and Building Materials*. 26(1). pp. 746-754.
6. Gunalan, S., P. Kolarkar, and M. Mahendran (2013), *Experimental study of load bearing cold-formed steel wall systems under fire conditions*. *Thin-Walled Structures*. 65. pp. 72-92.
7. Ariyanayagam, A.D. and M. Mahendran (2018), *Fire performance of load bearing LSF wall systems made of low strength steel studs*. *Thin-Walled Structures* (under review).

PERFORMANCE OF INTUMESCENT FIRE PROTECTION COATINGS ON STEEL TENSION ROD SYSTEMS

Mai Häßler¹, Dustin Häßler², Sascha Hothan³, Simone Krüger⁴

ABSTRACT

Steel tension rod systems consist of tension rods, fork connectors and associated intersection or connecting plates. They are used for truss systems, bracings or suspensions owing to slender design and increased economic efficiency. In case of fire, beside the tension rods themselves, the connection parts require appropriate fire protection. The use of intumescent fire protection coatings prevents a rapid heating of the steel and helps to ensure the load-carrying capacity of the structures. Because the connection components of the tension rod systems feature surface curvature as well as a complex geometry, high demand is placed on the intumescence and thermal protection effectiveness of the reactive fire protection coatings. Experimental studies were carried out to investigate the performance of intumescent coatings applied to the components of tension rod systems. The examined aspects include the foaming and cracking behaviour of the intumescent coatings, the influence of different dry film thicknesses (DFT), the heating rate of the steel connecting parts in comparison to the tension rods, as well as the mounting orientation of the tension rods together with their associated fork connectors. The results show that a decrease in the surface curvature and/or an increase in the mass concentration of the steel components lead to a lower heating rate of the steel. Moreover, the performance of the intumescent coating on tension rod systems is influenced by the mounting orientation of the steel components.

Keywords: Steel, tension rod system, intumescent fire protection coating, reactive fire protection system, real-scale fire test

1 INTRODUCTION

Steel tension rod systems are used for truss systems, bracings or suspensions. They consist of tension rods, fork connectors and associated intersection or connecting plates. To ensure the load-carrying capacity and prevent a rapid heating of the steel tension rod system in case of fire, appropriate fire protective measures are required. Intumescent fire protection coatings, which belong to the group of reactive fire protection systems (RFPS), offer an advantageous fire resistance measure that preserves the architectural appearance of slender constructions taking advantage of profile-following application and low coating thickness requirement.

The performance of intumescent coatings on steel tension members with circular solid section (CSS) has been previously investigated [1-3]. The results show that the application of intumescent coatings on steel tension members with circular solid section is possible. Nevertheless, due to

¹ Formerly postdoctoral researcher at Division 7.3 “Fire Engineering”, Bundesanstalt für Materialforschung und -prüfung (BAM), Berlin, Germany. e-mail: mai.haessler@gmx.de

² Postdoctoral researcher at Division 7.3 “Fire Engineering”, Bundesanstalt für Materialforschung und -prüfung (BAM), Berlin, Germany. e-mail: dustin.haessler@bam.de (corresponding author)

³ Head of Division 7.3 “Fire Engineering”, Bundesanstalt für Materialforschung und -prüfung (BAM), Berlin, Germany. e-mail: sascha.hothan@bam.de

⁴ Senior researcher at Division 7.5 “Technical Properties of Polymeric Materials”, Bundesanstalt für Materialforschung und -prüfung (BAM), Berlin, Germany. e-mail: simone.krueger@bam.de

slender cross-sections typically used for steel tension rods and the high surface curvature of these profiles, high requirements are placed particularly on the performance of the intumescent coatings applied to tension rods.

In addition to tension rods themselves, the connection parts must be protected against rapid heating in case of fire to ensure the structure's fire resistance. In practice, the same dry film thickness of the intumescent coating is applied to the connection parts as for the tension rods. However, these connection components, e.g. fork connectors, possess not only high surface curvature but also a complex geometry, which place high demand on the intumescence and thermal protection effectiveness of the reactive fire protection coating. So far, the performance of intumescent coatings applied to the connection components as part of the tension rod systems has not been analysed. Currently, there is a lack of scientific studies on this topic. To overcome the shortcomings, the present work aims to examine experimentally the behaviour of intumescent coatings applied to tension rod systems, in particular the connection components. The focused aspects include the foaming and cracking behaviour of intumescent coatings, the influence of different dry film thickness, the heating rate of the steel connecting parts in comparison to the tension rods, as well as the mounting orientation of the tension rods together with their associated fork connectors.

The experimental study is first described, including specifications of the specimens, experimental setup and performance of the fire tests. After that, the results of the fire tests are presented. Finally, the conclusions and outlook of the work are given.

2 EXPERIMENTAL STUDY

2.1 Specimens

The behaviour of the intumescent coating was analysed by case studies on the tension rod system Type 860 [4] with a rod-diameter of 20 mm (M20). The specimens consist of circular solid cross-sectional tension rods with a length of 700 mm, fork connectors, lock nuts and intersection or connecting plates. The tension rods are made of structural steel S460N, the fork connectors of nodular iron and the intersection or connecting plates of structural steel S355. The intersection plate with a connection angle of 90° and the connection plates have a thickness of 15 mm.

For the measurement of the steel temperatures, mineral-insulated stainless steel sheathed thermocouples (TC) were attached to the specimens before the application of the intumescent coating. The method developed in [2] was applied for attaching the thermocouples at the surface of steel members. The cross-sections of the steel members were kept undamaged with the application of the thermocouples. In addition, a tight-fitting thin wire was welded over a length of approximately 30 mm along each thermocouple cable to serve as a strain relief and fix the thermocouples. Three thermocouples were welded in a row along the longitudinal axis of each rod. The distance between the first, second and third thermocouples is 150 mm (see Fig. 1).

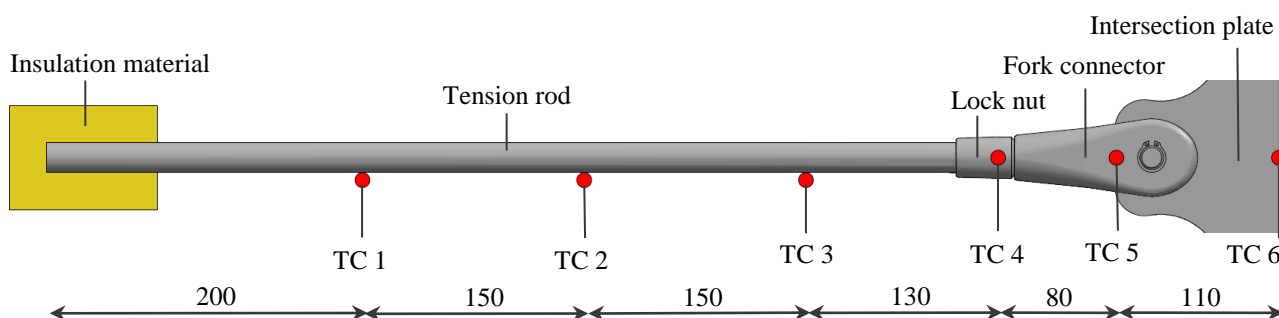


Fig. 1. Position of the thermocouples (TC) at the horizontal oriented tension rod system of Setup 2 [mm]

To minimize a possible influence on the formation of longitudinal cracks on the top of the rods, the thermocouples were attached generally at the bottom of the rods. Moreover, two thermocouples

were welded to both sides of each fork connector as well as one thermocouple to each of the four selected locknuts, those were connected to the horizontally and vertically oriented rods.

According to the manufacturer's technical recommendation, all steel components were sandblasted (SA 2½ in accordance with [5]) before applying the intumescent coating. The intumescent fire protection coating is a water-based conventional product with a valid European Technical Assessment [6] and a national approval for the application on steel tension members with circular solid and hollow sections [7]. The components were tested with dry film thickness of 2.5 mm and 3.5 mm.

2.2 Setup of the fire tests

The experiments were performed for two types of connection setup. In the first type, Setup 1, three rods are connected to a joint in different orientation, i.e. horizontal, 45° inclined and vertical orientation. The joint is composed of two perpendicularly welded steel plates as well as three welded connection plates that represent the condition in a frame corner or gusset plate connection to a beam. The second type, Setup 2, consists of four rods and an intersection plate. Two rods are oriented horizontally, one rod is 45° inclined and another rod is vertically oriented. For comparison purposes, one of the horizontal oriented rods and its lock nut in Setup 2 were not coated. Apart from that, all components of the tension rod systems were protected with the intumescent coating. The experimental setups are presented in *Fig. 2*.

The vertical furnace offers sufficient space with a test chamber of 4.50 m × 3.50 m × 1.50 m to test the two setups together. Six oil burners were used to heat the furnace; three were located on the east side of the furnace and three on the west side. To prevent a direct impingement to the specimens, appropriate flame deviating wedges made of vermiculite were arranged in the furnace in front of the two bottom burner openings on both sides of the specimens. To avoid shadowing effects, a minimum distance to the furnace wall and the flame deviating wedges of approximately 300 mm was maintained on all sides of the specimens.

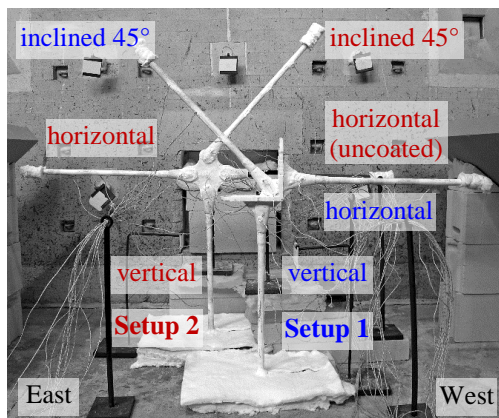


Fig. 2. Experimental setup before the fire tests

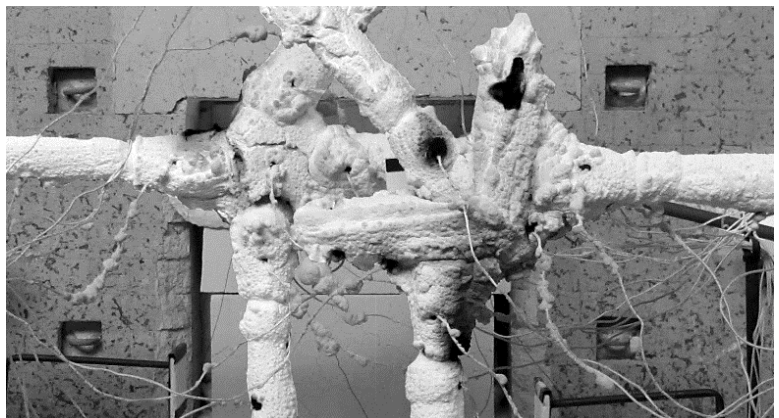


Fig. 3. Specimens after the fire test (DFT 3.5 mm)

2.3 Performance of the fire tests

The fire tests were carried out at the vertical furnace of Division 7.3 Fire Engineering, Bundesanstalt für Materialforschung und -prüfung (BAM). To save the experimental effort, the real-scale fire tests were carried out without mechanical loading. The fire tests were performed with reference to DIN EN 1361-1 [8] using the standard temperature/time curve. Four plate-thermocouples were used to measure the gas-temperatures; two were positioned parallel to the

intersection and connection plates at a height of approximately 800 mm from the furnace ground, while the other two were placed alongside the vertically oriented rods at a height of about 600 mm. All plate-thermocouples were arranged at approximately 100 mm from the specimens.

The fire tests were conducted until a maximum steel temperature on the specimens of about 700 °C was reached. After exceeding the temperature of 700 °C, the strength of the steel becomes very low and the members most likely lose their static function in the structure. Throughout the fire tests, the foaming of the intumescent coating was observed. After the fire tests, the height of the foamed intumescent coating was measured.

3 RESULTS

During the fire tests, the intumescent fire protection coating formed a thermal protective layer around the steel components of the tension rod systems. Similar to the observations regarding the steel rods [1-3], due to the volume expansion of the intumescent coating, cracks occurred in the foam in longitudinal direction of the steel rods. Generally, the fork connectors and the lock nuts showed no cracks in the foam (see *Fig. 3*). However, at the joint area between the rods and the fork connectors, small cracks appeared in the foam in circumferential direction. Nevertheless, almost all cracks were completely closed by the foaming process of the intumescent coating. Despite the curved and complex surface of the connecting components, particularly at the fork connectors, no sliding-down of the foam occurred during and after the fire tests.

The setups with a dry film thickness of 2.5 mm and 3.5 mm showed no significant visual differences of the foamed intumescent coating. But generally, the increase of the dry film thickness resulted in higher foam thicknesses and the heating of the steel was slowed down. The foam thicknesses of the intumescent fire protection coating at the components of Setup 1 and Setup 2 with a dry film thickness of 2.5 mm are given in *Table 1*. The 45° inclined tension rods as well as the associated fork connectors and lock nuts showed in general a lower foam thickness of the intumescent coating compared to the horizontally or vertically oriented rods and components. The lower foam thickness caused a reduction of the thermal protection effectiveness and higher steel temperatures. However, the influence of the component orientation on the foam thickness and the steel temperature decreases as the dry film thickness is increased from 2.5 mm to 3.5 mm. Furthermore, the specimens showed usually lower foam thicknesses at the side facing the furnace wall compared to the side facing the centre of the furnace. This is due to the position of the burner axis, which runs between the specimens of Setup 1 and Setup 2. Thus, the gas temperature was slightly higher in the centre of the furnace and decreased towards the furnace wall.

Regarding the steel temperature, with decreasing surface curvature or increasing mass concentration of the steel components, a lower heating rate of the steel occurred (see *Fig. 4*). Therefore, the slender tension rods with their high surface curvature heated up the fastest. The intersection plate with its plain surface curvature showed the slowest heating. Considering the mounting orientation of the structural components, the steel temperature of differently oriented tension rods and fork connectors is influenced by the component orientation, as presented in *Fig. 5*. To avoid an influence from local differences in the combustion gas temperatures and thus to ensure comparability between the horizontally and vertically oriented as well as 45° inclined tension rods, the measuring point nearest to the fork connector was selected. The 45° inclined tension rods and their associated fork connectors heated up the fastest, while the vertically oriented components heated up the slowest. Taking into consideration the foam thickness of the intumescent coating that was measured after the fire tests (see *Table 1*), the increase of the dry film thickness from 2.5 mm to 3.5 mm generally decreased the influence of the component orientation. The different design of the connection area of Setup 1 and Setup 2 did not cause a significant difference in the measured steel temperatures of the fork connectors. Thus, shadowing effects resulting from the different arrangements of the intersection or connection plates were not detected.

Table 1. Foam thicknesses of the intumescent coating at the steel components of Setup 1 and Setup 2 (DFT 2.5 mm)

		Foam thickness [mm]					
		Setup 1			Setup 2		
Component	Orientation	0°	45°	90°	0°	45°	90°
Tension rod	Average value	19	17	19	23	21	19
	Maximum value	24	22	26	30	25	27
Fork connector	Average value	18	17	19	20	19	27
	Maximum value	25	21	28	28	30	41
Lock nut	Average value	18	17	22	19	17	19
	Maximum value	23	20	34	30	21	22

0° = horizontally oriented; 45° = inclined; 90° = vertically oriented; the foam thickness was measured near the thermocouple position.

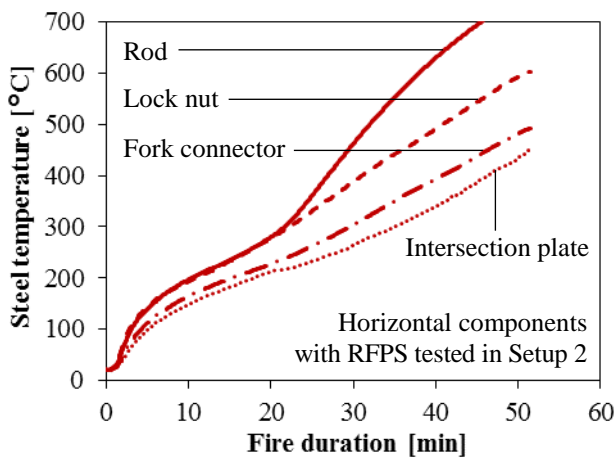


Fig. 4. Comparison of steel temperatures between different components of the tension rod system (DFT 3.5 mm)

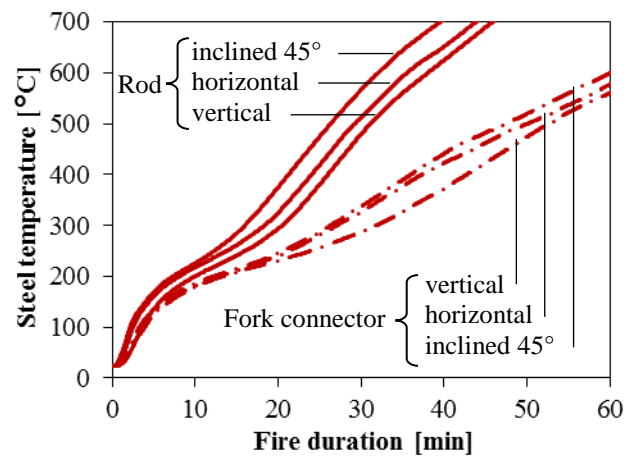


Fig. 5. Influence of the component orientation on the steel temperature (DFT 2.5 mm)

4 CONCLUSIONS AND OUTLOOK

The performance of the intumescent fire protection coating applied to tension rod systems, particularly the connection components, was assessed based on two unloaded real-scale fire tests. For all specimens including the fork connectors with their curved and complex geometry, the intumescent coating formed stable foams with only few cracks. Higher foam thicknesses of the intumescent coating were achieved with an increase of the dry film thickness, which also led to a slower heating rate of the steel. With the same dry film thickness, the slender tension rods heated up faster than the components of the connection area, i.e. lock nuts, fork connectors and intersection or connection plates. This results from a decrease in the surface curvature and/or an increase in the mass concentration of the steel components causing a lower heating rate of the steel.

The slower heating of the connection components compared to the tension rod can possibly be used to activate load-bearing capacity reserves in case of fire. The reason is that for the structural design at ambient temperature, usually the threaded section of the tension rod is decisive for the load-bearing capacity of the entire tension rod system. If the steel temperatures at the connection area are lower than that of the tension rod, the full cross-section of the tension rod may be used for the load-bearing capacity in case of fire. The decisive factor for the load-bearing capacity in case of fire is the steel temperature and the corresponding reduction factor of the steel strength. The assessment of the fire resistance and identification of the relevant failure location of the tension rod system in case of fire requires mechanically loaded fire tests. Apart from that, there is also the possibility to reduce

the required dry film thickness at the connection area to save the effort and costs for the on-site application of the intumescent coating.

The experimental-based investigation provides insights into the influence of the mounting orientation on the performance of the intumescent coating on steel rods and their associated connecting components. Since the component orientation influences the performance of the intumescent coating and can decrease the thermal protection effectiveness, it is essential to adequately consider this effect in the assessment. To address this matter, appropriate fire tests should be carried out. Based on these tests, an adjustment factor considering the component orientation of structural members can be developed. Without experimental tests, it is not recommended generally to transfer temperature results from a tested component with a certain orientation to any other orientation.

The presented fire tests for the tension rod systems are part of a research work [9] to examine the performance of intumescent coatings on steel components with curved and complex geometry. Other investigated systems, which are not part of this paper, are torispherical and hemispherical heads. Further results of the research work will be subsequently published. Recommendations for the testing and assessment of the intumescent fire protection coatings applied to steel components with curved and complex geometry will be given.

ACKNOWLEDGEMENT

The authors would like to acknowledge the supply of the tension rod system specimens by PFEIFER Seil- und Hebeteknik GmbH and the application of the intumescent coating on the test specimens by Rudolf Hensel GmbH.

REFERENCES

1. Sascha Hothan, Dustin Häbeler (2015). *Numerische und versuchstechnische Untersuchungen zur Anwendung von reaktiven Brandschutzsystemen auf Zuggliedern aus Stahl*. Final report, Project number 7539, Bundesanstalt für Materialforschung und -prüfung (BAM), Berlin.
<https://www.baufachinformation.de/forschungsbericht/243409>
2. Dustin Häbeler (2016). *Verhalten reaktiver Brandschutzsysteme auf kreisrunden Zuggliedern aus Blank- und Baustahl*. Dissertation, Leibniz University Hannover.
<http://nbn-resolving.org/urn:nbn:de:kobv:b43-371495>
3. Dustin Häbeler, Sascha Hothan (2016). *Fire tests of reactive fire protection systems applied to steel tension members with solid circular section*. 9th International Conference on Structures in Fire, Princeton, USA, June 8-10, pp. 1099-1106.
4. ETA-04/0039 (2013). *European Technical Approval for prefabricated tension rod system "Pfeifer Zugstabsystem 860"*. Deutsches Institut für Bautechnik (DIBt), Berlin.
5. DIN EN ISO 8501-1 (2007). *Preparation of steel substrates before application of paints and related products – Visual assessment of surface cleanliness – Part 1: Rust grades and preparation grades of uncoated steel substrates and of steel substrates after overall removal of previous coatings*. Beuth, Berlin.
6. ETA-12/0050 (2013): *European Technical Assessment for the reactive fire protection system "HENSOTHERM® 420 KS"*. Warrington Certification Limited, Warrington.
7. AbZ Nr. Z-19.11-2194 (2015). *Allgemeine bauaufsichtliche Zulassung für das reaktive Brandschutzsystem "Hensotherm 420 KS" zur Anwendung auf Stahlzuggliedern*. Deutsches Institut für Bautechnik (DIBt), Berlin.
8. DIN EN 1363-1 (2012). *Fire resistance tests – Part 1: General Requirements*. Beuth, Berlin.
9. Bundesanstalt für Materialforschung und -prüfung (BAM) (2015-2018). *Research project "Novel Tasks - Fire Stability Tomorrow"*. Berlin.

PRELIMINARY STUDY ON QUANTITATIVE DETERMINATION OF COLLAPSE PROCESS OF STEEL PORTAL FRAMES IN FIRE

Guobiao Lou¹, Chenghao Wang², Jian Jiang³, Guo-Qiang Li⁴

ABSTRACT

This paper quantitatively evaluates the collapse behavior of steel portal frames exposed to standard fires. The complete collapse process is divided into safe, alert, dangerous and collapse stages based on the key displacements of the fire exposed columns and beams. These correspond to warnings for firefighters to make timely reactions to stay, ready to evacuate, or must evacuate, respectively. Numerical models are established and validated against fire tests on a full-scale steel portal frame. It is found that one should be ready to evacuate when the heated rafter shows large deflections, and must evacuate when the heated column moves back to its initial position. Unprotected steel portal frames have a collapse resistance of 30~40 mins, and it is suggested to evacuate within 30 mins after the fire ignition. The 1h, 2h, 3h fire rating of protected steel portal frames can be used to estimate the ready-evacuate, must-evacuate and collapse warning time, respectively. The findings from this preliminary study aim to provide references for firefighters to make wise decisions to evacuate timely and safety from the fire scene.

Keywords: Quantitative evaluation, progressive collapse process, portal frame, warning time, fire rating, evacuation

1 INTRODUCTION

The progressive collapse of structures in fire will most likely endanger the life safety of firefighters since few occupants are still present in the building after hours' development of fire before collapse. Statistic data show that an average of 20 firefighters sacrificed each year in China [1], and construction collapse is deemed to be one of the most primary reasons. A total of 15 firefighters sacrificed at fire scenes in the United States in 2016 [2], among which 7 deaths were in fires involving steel portal frames such as dwellings and stores. The NFPA report [2] also mentioned that fires in non-residential structures such as manufacturing and storage properties are more hazardous to firefighters than residential structure fires. In UK, the annually average number of firefighter deaths was at least 4 for the last 30 years [3]. *Table 1* lists a survey on the deadliest firefighter events over the past twenty years. All fatalities were due to the collapse of the fire exposed buildings. The multi-storey buildings (No. 3, 4, 6) and portal frames (No. 5 and No. 8) exposed to fire are more prone to collapse, accounting for the largest shares of firefighter fatalities. To ensure life safety of firefighters, it is necessary to quantitatively determine the collapse process of these buildings in fire,

¹ PhD. State Key Laboratory for Disaster Reduction in Civil Engineering, Tongji University, Shanghai 200092, China
e-mail: gblou@tongji.edu.cn

² Master candidate. College of Civil Engineering, Tongji University, Shanghai 200092, China.
e-mail: mzmxwch@163.com

³ PhD. College of Civil Engineering, Tongji University, Shanghai 200092, China.
e-mail: jiangjian_0131@163.com

⁴ Professor. State Key Laboratory for Disaster Reduction in Civil Engineering, Tongji University, Shanghai 200092, China
e-mail: gqli@tongji.edu.cn

and thus to make timely warning for them to evacuate the fire scene. The objective of this study is to quantitatively determine the collapse process.

The collapse time is a key parameter to warn firefighters to evacuate the fire site in time. However, most previous research focuses on evaluating whether the structure collapses as well as how it collapses [4-8], rather than estimating the collapse time. The findings from these studies apply to multi-storey and tall buildings, but their application to long-span structures is questionable. Compared to multi-storey buildings, long-span structures have lower level of redundancy and higher level of fire loads which make them more prone to collapse in case of fire [9]. A number of recent fires in industrial structures have drawn attention to a current lack of understanding about the progressive collapse of steel portal frames under fire conditions. Efforts have been taken to investigate the fire-induced behaviour of steel portal frames [10-14]. However, all these studies focus on numerical modeling, while experimental studies are lacking. The existing experiments are based on either small-scale portal frames [15] or cold-formed frames [16] where limited information on the thermal and structural responses of the frames is available. Therefore, it is necessary to conduct full-scale fire tests on hot-rolled steel portal frames (the most common form) to investigate its fire-induced progressive collapse behavior, and to provide validation references for numerical modeling, which is another objective of this study.

This paper quantitatively investigated the collapse behavior of single-storey steel portal frames exposed to fire. Based on the key displacements of fire exposed columns and beams, a four-stage collapse process was proposed including safe, ready-evacuate, must-evacuate and collapse stages. Numerical models were established and validated against fire tests on a full-scale steel portal frame. The key warning times for these four stages were numerically determined.

Table 1. List of deadliest firefighter disasters in the past two decades

No.	Building	Place	Year	No. of storey	Fire duration before collapse	Deaths of firefighters
1	World Trade Center	USA	2001	110	60min	343
2	Store building	Iran	2017	17	Several hours	30
3	Hengyang building	China	2003	8	4h	20
4	Sofa super store	USA	2007	6	40min	9
5	Bowling house	Taiwan	2015	2	60min	6
6	Storage/warehouse	USA	1999	6	-	6
7	Supermarket	China	2015	11	9h	5
8	Warehouse	UK	2007	1	-	4

2 CONCEPT OF FOUR-STAGE COLLAPSE PROCESS

A typical deformation process of steel portal frames is shown in *Fig.1*. The four stages shown in *Table 2* can be used to determine the collapse process of steel portal frames. The heated column will move outwards at the early stage of heating due to thermal expansion of the heated rafter (*Fig. 1a*). The large deflection of the rafter and degraded material properties at elevated temperatures will drive the column back to its initial position (*Fig. 1b*), which can be defined as the ready-evacuate stage. The frame will collapse inward (*Fig. 1c*) driven by the tensile forces in the rafter at large deflections. The horizontal displacements of columns and vertical displacements of rafters can be used to determine the four stages. If the frame collapses towards one side without occurrence of returning back of the column, the rate of displacement of the column can be adopted to quantify the collapse process. For practical application, the lateral displacement of the heated columns is the

most visible parameter to judge and the easiest parameter to measure. It can be used for a quick evaluation of the safety level of buildings exposed to fire.

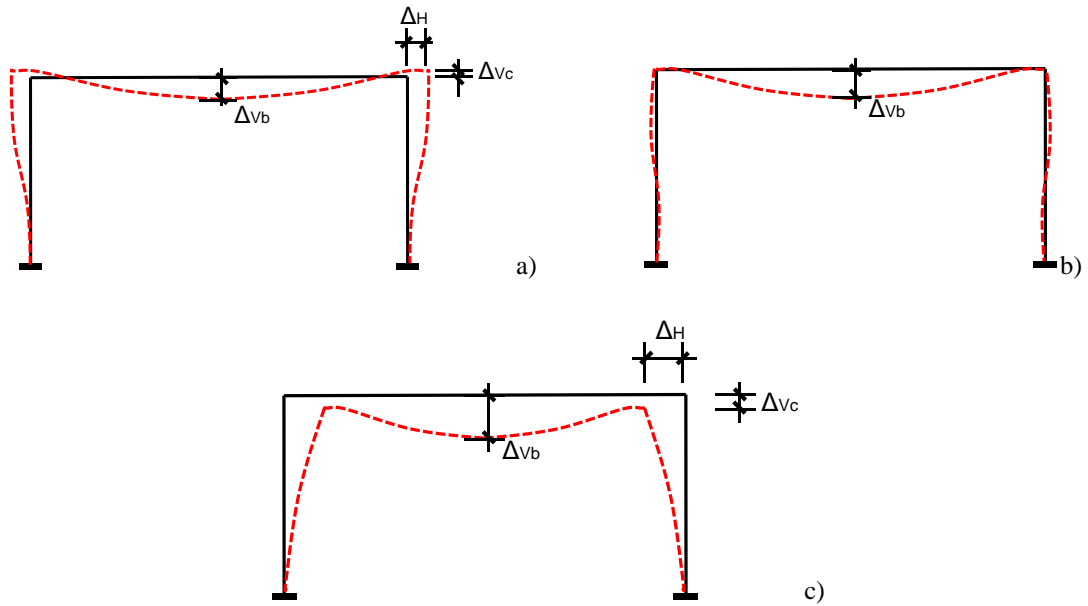


Fig. 1. Typical deformation process of steel portal frames: a) safe stage; b) ready-evacuate stage; c) must-evacuate stage and collapse stage

Table 2. Failure process of steel columns exposed to fire

Stage	Time	Displacement	Rate of displacement	Target reaction
Safe	t_1	Maximum upward movement of column Δ_{vc}	$d\Delta/dt < 0$	1 st warning
Alert	t_2	Large deflection of rafter Δ_{vb}	$d\Delta/dt > 0$	2 nd warning (ready to evacuate)
Dangerous	t_3	Returning back of column $\Delta_H = 0$	$d\Delta/dt > 0$	3 rd warning (must evacuate)
Collapse	t_u	Large downward movement of column Δ_{vc}	$d\Delta/dt \gg 0$	Collapse

3 NUMERICAL MODEL AND VALIDATION

Numerical analysis was conducted in finite element software LS-DYNA. The three-dimensional Hughes Liu beam element was used to model the steel members [8]. The numerical model was validated against a natural fire test recently conducted by the authors on a full-scale 36m×12m steel portal frame (Fig. 2). A comparison of observed and predicted collapse mode of the tested frame is shown in Fig. 3. A reasonable agreement of the key displacements of the heated columns and rafters was achieved (Fig. 4). The details of the modelling and comparison between measured and predicted results can be found in the reference [17]. The test data of thermal and structural responses can be used for calibration numerical models.

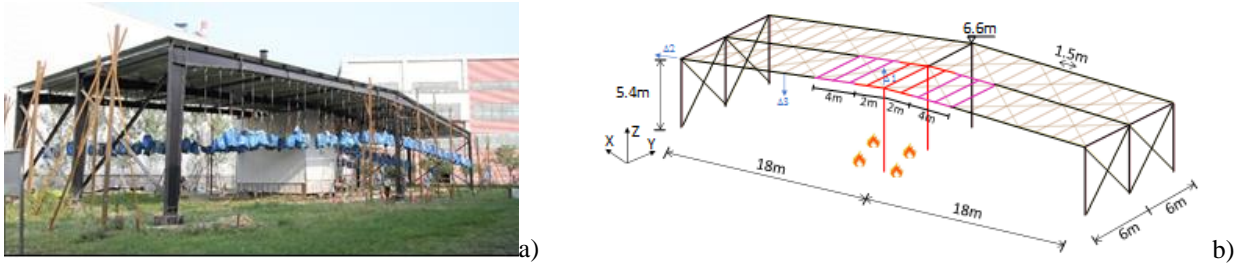


Fig. 2. Fire test on a full-scale steel portal frame: a) on-site portal frame; b) numerical model

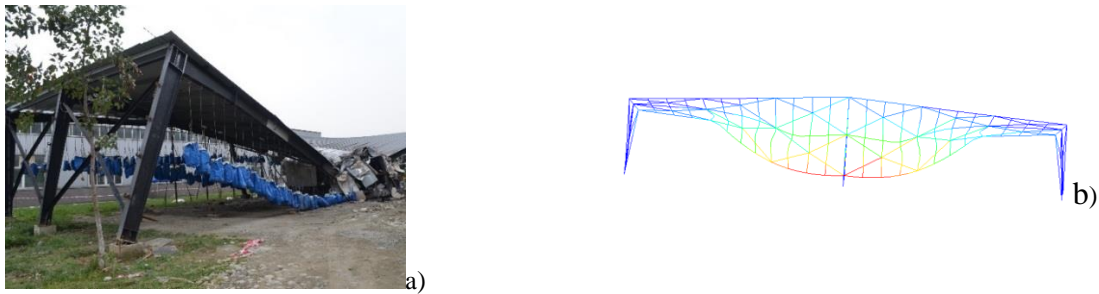


Fig. 3. Comparison of observed and predicted collapse mode of the tested frame: a) observed mode; b) predicted mode

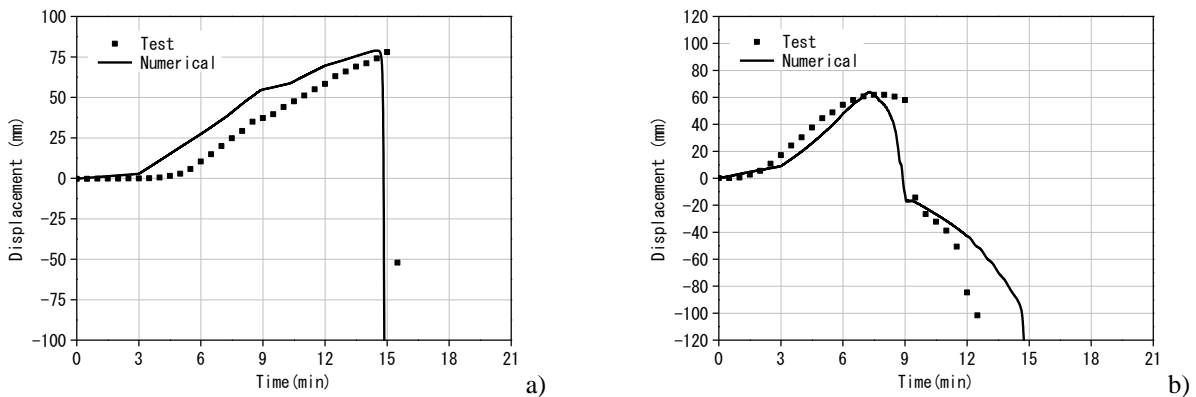


Fig. 4. Comparison of measured and predicted displacements of the frame: a) axial displacement of the heated column; b) mid-span deflection of the heated rafter

4 EXAMPLES OF COLLAPSE OF STEEL PORTAL FRAMES

A three-dimensional steel portal frames with a span of 30m were modelled (Fig. 5a). It had 11 bays of portal frames. The eaves height was 8.4m, and column spacing was 7.5m. The column, rafter and purlin had a section of H1018×250×8×10, H979×220×6×10, and H250×125×4.5×6, respectively. The design dead and live loads were taken as 0.25kN/m² and 0.45kN/m². Endwall columns (H350×175×4.5×6) were arranged at the two ends of the frames. The column bracing and roof bracing (Φ25×5) were arranged at the end bays and middle bay of the frames. The yield strength of the columns, rafters, column bracing was 345MPa, while that of other members such as roof bracing and purlin was 235MPa. The MAT_202 (MAT_Steel_EC3) was used for steel. A severest fire scenario was considered where it was assumed that the whole frame was uniformly heated following the ISO standard fire.

An explicit dynamic analysis was carried out in this study. To save the computing cost of explicit analyses, the hour's real fire time was scaled down to seconds' computing time without causing oscillation. Sensitivity analyses were conducted to determine the appropriate time scale, and the results showed that it was possible to run an 8-second explicit analysis instead of 1-hour heating in a standard fire [8].

The effect of fire protections on the collapse time of the portal frame was considered. Four levels of fire protection were considered: unprotected, low level (1h-fire rating for columns, 1h-fire rating for rafters), medium level (2h-fire rating for columns, 1.5h-fire rating for beams) and high level (3h-fire rating for columns, 2h-fire rating for beams). Two collapse modes of the steel portal frames were found as shown in *Fig. 6*. The unprotected frame collapsed downward and towards the inside of the frame, which was triggered by the buckling of frame columns. While for the protected frame, the columns were protected and had higher strength at elevated temperature, and thus the rafters experienced large deflections which led to significant lateral drift of columns. The protected frame showed a lateral drift collapse mode.

A typical variation of displacements of the frame is shown in *Fig. 5b* where the warning times were determined according to the key displacements. The warning times for the four stages of frames with different levels of fire protections are shown in *Table 3*. It can be found that: (1) Unprotected steel portal frames have a collapse resistance of 30~40 mins, and it is suggested to evacuate within 30 mins after the fire ignition; (2) For steel portal frames with 1h fire rating, the 2nd warning time t_2 can be estimated as equal to the fire rating, i.e. $t_2=60$ min. The 3rd warning time is 10 mins delay; (3) For steel portal frames with 2h fire rating, the 3rd warning time can be predicted as the fire rating, i.e. $t_3=120$ min. The ready-evacuate time t_2 can be calculated 10 mins early; (4) Steel portal frames with 3h fire rating will collapse after 3h fire exposure, i.e. $t_u=180$ min. The ready-evacuate and must-evacuate time can be estimated by 30 mins and 15 mins in advance, i.e. $t_2=150$ min and $t_3=165$ min.

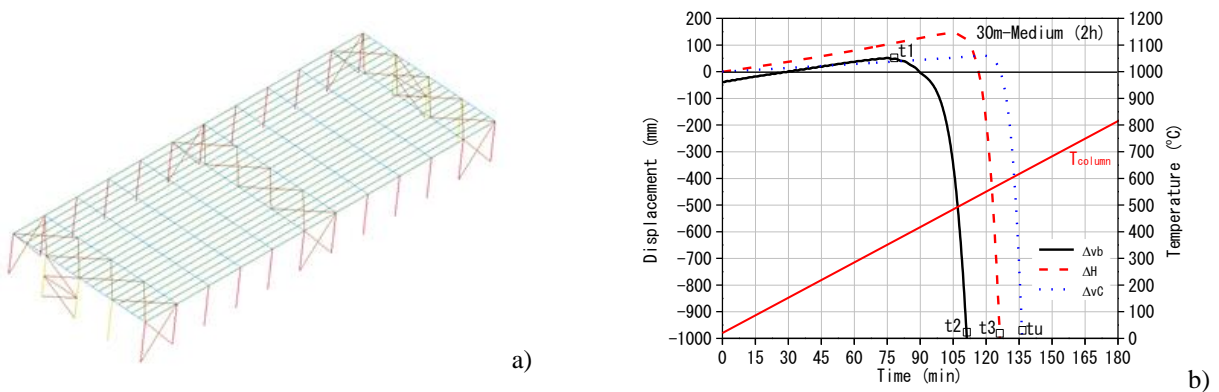


Fig. 5. Collapse process of a 30m-span steel portal frame in fire: a) numerical model; b) displacement-time curve

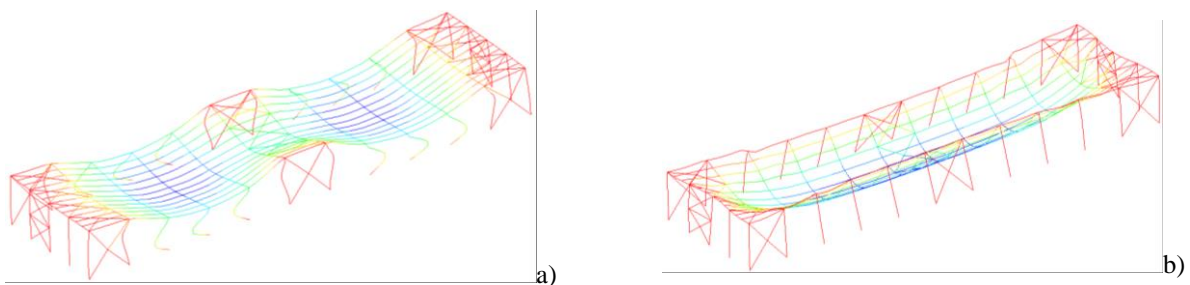


Fig. 6. Collapse mode of steel portal frames in fire: a) unprotected portal frame; b) protected portal frame

Table 3. Quantitative evaluation of collapse process of the 30m-span frame exposed to fire

Target reaction	Warning time (min)	Level of fire protection of columns			
		Unprotected	Low (1h)	Medium (2h)	High (3h)
1 st warning	t_1	21	50	75	101
2 nd warning (ready to evacuate)	t_2	33	72	111	145
3 rd warning (must evacuate)	t_3	40	81	126	167
Collapse	t_u	40	84	136	185

5 CONCLUSIONS

This paper presented quantitative evaluation of the collapse process of steel portal frames exposed to standard fires. The whole collapse process was divided by four warning times representing the safe, ready-evacuate, must-evacuate and collapse stages, respectively. It was found that the warning times can be evaluated based on the key displacements of the fire exposed columns and rafters. One should be ready to evacuate for the occurrence of large deflection in the heated rafter, and must evacuate when the heated column moves horizontally back to its initial position. Unprotected steel portal frames have a collapse resistance of 30~40 mins, and it is suggested to evacuate within 30 mins after the fire ignition. For steel portal frames with 1h fire rating, the ready-evacuate warning time t_2 can be estimated as equal to the fire rating, i.e. $t_2=60\text{min}$. For steel portal frames with 2h fire rating, the must-evacuate warning time t_3 can be predicted as the fire rating, i.e. $t_3=120\text{min}$. Steel portal frames with 3h fire rating will collapse after 3h fire exposure, i.e. $t_u=180\text{min}$. The ready-evacuate and must-evacuate time can be estimated by 30 mins and 15 mins in advance, i.e. $t_2=150\text{min}$ and $t_3=165\text{min}$.

These quantitative conclusions were drawn from one example of a 30m-span portal frame. In order to draw generalized conclusions applying to steel portal frames, further parametric studies are necessary, depending on various frame dimensions and fire scenarios.

ACKNOWLEDGMENT

The work presented in this paper was supported by the National Natural Science Foundation of China with grant 51578420, and Key project of Fire Department of Ministry of public security with grant 2015XFGG06.

REFERENCES

1. L.R. Jiang, Q.L. Zhang, J.X. Shi, Y. Li (2012). *Statistic study on sacrifices of firefighters in China*. Procedia Engineering 45. pp 700-704.
2. NFPA. (2017) *Firefighter fatalities in the United States-2016*, Report No. FFD10, National Fire Protection Association (NFPA).
3. LRD. *Firefighter deaths in the UK since 1978*. Report by the Labour Research Department (LRD) for the Fire Bridges Union, 2008.
4. D. Lange, C. Roben, A.S. Usmani (2012). *Tall Building Collapse Mechanisms Initiated by Fire: Mechanisms and Design Methodology*. Engineering Structures 36. pp 90-103.
5. J. Jiang, G.Q. Li, A.S. Usmani (2014). *Progressive collapse mechanisms of steel frames exposed to fire*. Advances in Structural Engineering 17(3). p 381-398.
6. G.L.F. Porcari, E. Zalok, W. Mekky (2015). *Fire induced disproportional collapse of steel building structures: A review of the mechanisms*. Engineering Structures 82. pp 261-267.
7. J. Jiang, G.Q. Li (2017). *Disproportional Collapse of 3D Steel-framed Structures Exposed to Various Compartment Fires*. Journal of Constructional Steel Research 138. pp 594-607.

8. J. Jiang, G.Q. Li (2017). *Progressive collapse analysis of 3D steel frames with concrete slabs exposed to localized fire*. Engineering Structures 149. pp 21-34.
9. SCI. (2002) *Single Storey Steel Framed Buildings in Fire Boundary Conditions*. Steel Construction Institute (SCI), Publication P313, Berkshire, UK, 2002.
10. H.M. Ali, P.E. Senseny, R.L. Alpert (2004). *Lateral displacement and collapse of single-story steel frames in uncontrolled fires*. Engineering Structures 26. pp 593-607.
11. Y. Song, Z. Huang, I.W. Burgess (2007). The design of pitched-roof steel portal frames against fire. *5th International Conference on Advances in Steel Structures*, Singapore, 2007. pp 728-733.
12. M.W. Bong, A.H. Buchanan, R.P. Dhakal, P.J Moss (2007). Fire performance of steel portal frame buildings. *Pacific Structural Steel Conference 2007*, Wairakei, New Zealand, 2007.
13. P.J. Moss, R.P. Dhakal, M.W. Bong, A.H. Buchanan (2009). *Design of steel portal frame buildings for fire safety*. Journal of Constructional Steel Research 65. pp 1216-1224.
14. H. Garcia, M.V. Biezma, J. Cuadrado, M. Zubizarreta (2016). *Dual-steel portal frame design to withstand a fire exposure to 45 minutes*. International Journal of Steel Structures 16(3). pp 705-717.
15. S.Y. Wong (2001). *The Structural Response of Industrial Portal Frame Structures in Fire*, PhD Thesis, University of Sheffield, UK, 2001.
16. L. Pyl, L. Schueremans, W. Dierckx, I. Georgieva (2012). *Fire safety analysis of a 3D frame structure based on a full-scale fire test*. Thin-Walled Structures 61. pp 204-212.
17. G.B. Lou, C.H. Wang, J. Jiang, Y.Q. Jiang, L.W. Wang, G.Q. Li (2018). *Fire tests on full-scale steel portal frames against progressive collapse*. Journal of Constructional Steel Research. (in press)

STEADY-STATE AND TRANSIENT-STATE TESTS ON S355 TO S500 STEEL GRADES

François Hanus¹, Nicolas Caillet², Sylvain Gaillard³, Olivier Vassart⁴

ABSTRACT

Two experimental programmes launched on thermo-mechanical steel grades ranging from S355 to S500 in 2011 and 2015 are presented in this paper. Both steady-state (constant temperature, as defined in testing standards) and transient-state (constant mechanical loading, closer to real conditions of structures subjected to fire) testing procedures have been applied for these characterisation tests. For steady-state tests, the former EN 10002-5 [1] and the current ISO 6892-2 [2] test procedures have been applied. For transient tests, no standardized procedure exists and 5 K/min and 10 K/min heating rates were used. Tests results have been compared to the reduction factors defined in the EN 1993-1-2 standard [3], currently limited to S460 grade, to assess if the scope of application of reduction factors defined by Eurocode 3 could be enlarged to S500.

Keywords: High-strength steel, thermo-mechanical properties, steady-state tests, transient-state tests

1 REASON FOR EXPERIMENTAL PROGRAMMES

The current version of EN 1993-1-2 [3] provides a stress-strain diagram for carbon steel at elevated temperatures for grades S235 to S460. This stress-strain diagram includes an elliptic branch between a proportional limit and the yield limit to consider implicitly creep effects and avoid complex material models accounting explicitly for creep [4]. In reality, creep is strongly depending on the loading-heating sequence, level of loading and heating rate [5] but this elliptic branch of EN 1993-1-2 was calibrated on experimental coupon and large-scale tests on mild steels for heating rates from 2 K/min to 30 K/min [6].

During the last decade, many research programmes have been dedicated to the mechanical properties of high-strength and very high-strength carbon steels. Some of these investigations led to the conclusion that the application of Eurocode 3 reduction factors could be unsafe [7, 8, 9] where others conclude that Eurocode 3 material law correlates well, even for S690/S700 grades [10, 11]. However, it should be mentioned that the researches leading to safe results are often performed under steady-state conditions.

ArcelorMittal, with the support of LIST, launched two experimental programmes to investigate the behaviour of S460M and S500M steel grades developed for hot-rolled sections. The first research

¹ Senior Research Engineer, ArcelorMittal Global R&D, Luxembourg.

e-mail: Francois.Hanus@arcelormittal.com

² Head of Laboratories and Metallurgical process Department,

e-mail: Nicolas.Caillet@arcelormittal.com

³ Lead Engineer, Luxembourg Institute of Science and Technology (LIST), Luxembourg

e-mail: sylvain.gaillard@list.lu

⁴ Head of ArcelorMittal Global R&D Long Carbon.

e-mail: olivier.vassart@arcelormittal.com

programme was focused on a comparison between S355 and S460 grades, following the EN 10002-5 testing procedure, where the second experimental programme was focused on the recently developed S500M steel grade and comprised:

- Steady-state tests according ISO 6892-2 testing procedure
- Transient-state tests under 5 K/min and 10 K/min heating rates
- Large-scale tests on beams under ISO fire and 10 K/min heating rate

The large-scale tests, performed at the University of Liège, have been successfully reproduced numerically by use of EN 1993-1-2 material law and are not described in the present paper as they have already been published [12].

2 TESTING PROCEDURE AND TEST PROGRAMME

2.1 Description of the set-up

The tests have been performed on proportional samples ($k=5,65$) with circular cross-section areas, in compliance with the test standard (EN 10002-5 or ISO 6892-2). Two different geometries of samples have been used and are drawn in

Fig. 1.

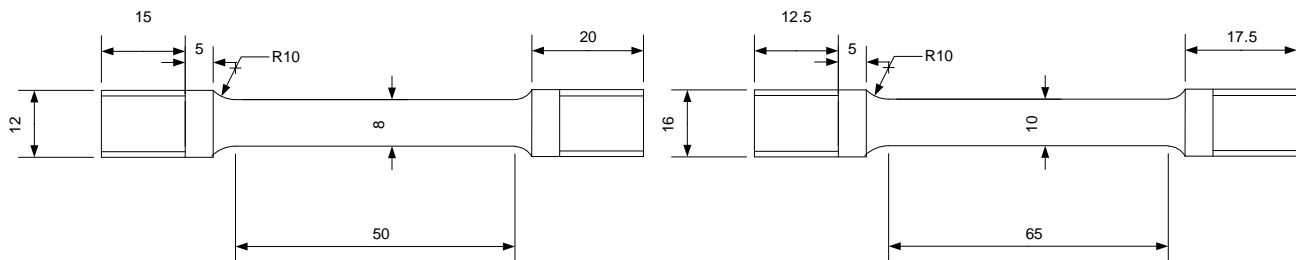


Fig. 1. Geometry of samples used for the first programme (left) and the second programme (right)

An MTS oven (type 653.04) was set up in the test machine in order to heat the sample at the required temperature. The temperature is regulated by a Eurotherm controller (type 2216e) and is based on the measurements of three thermocouples (type N), which are directly fixed on the calibrated length of the sample.

Depending on the programme and on the kind of tests, several test machines have been used (see *Fig 2*):

- 200kN Instron testing machine, type: 1251 (steady-state tests for programme 1);
- 100kN MTS tensile testing machine: type 810 (steady-state tests for programme 2 and transient-state tests with a rate of 10 K/min);
- 500kN Zwick testing machine, type HB500 (transient-state tests with a rate of 5 K/min).

Loads and displacements are measured by the test machines.

Elongations have been measured with a MTS extensometer (type BT2-EXUD63213.MT02).

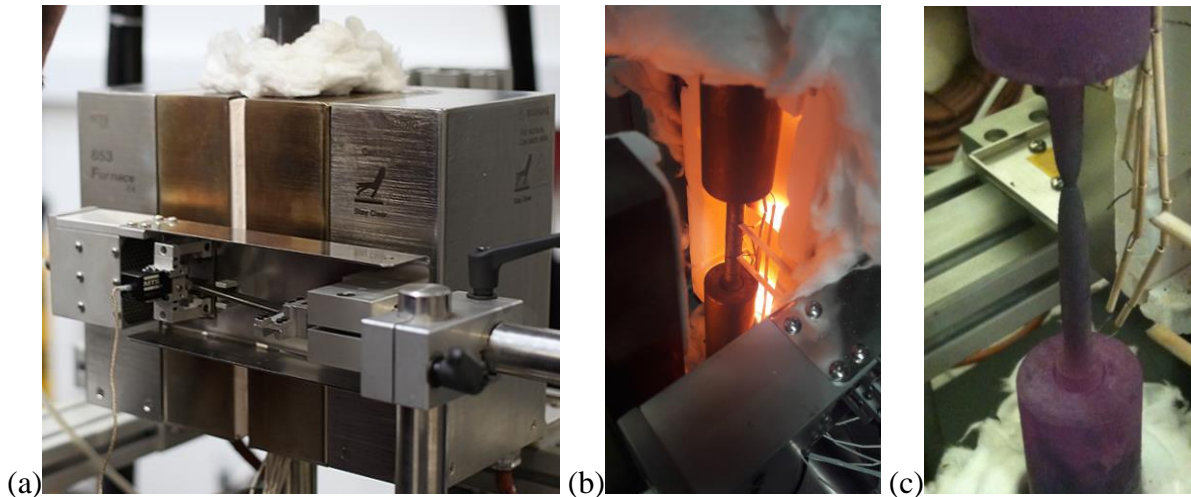


Fig. 2. Photos of the testing device: (a) overall view of the testing device; (b) view of the oven during heating phase (artificially open for the picture); (c) sample after fracture

Steady-state tests

The test procedure consists in heating the sample in a first step until the required test temperature, with a heating rate of 10 K/min, and keeping temperature constant for ten minutes. Then the tensile test starts, with a given strain rate until fracture, while the test temperature remains controlled. The strain rate control is based on the test machine displacement, reported to the calibrated length of the sample.

In the first test programme, the strain rate was 0.004 min^{-1} until $R_{p0,2}$ and then increased to 0.1 min^{-1} until the fracture, allowing the determination of R_{t2} . Only a few additional tests have been performed with a unique 0.004 min^{-1} heating rate until R_{t2} until the end of the test.

In the second programme, the strain rate remained constant at 0.0042 min^{-1} until the determination of R_{t2} , according to ISO 6892-2 [2], but a few additional tests were also performed on samples extracted from the same beam, with an increase of the strain rate to 0.084 min^{-1} after $R_{p0,2}$, allowing a quantification of the influence of test procedure on results.

Transient-state tests

The transient-state test procedure consists in applying, at room temperature, the required stress on the sample and keeping it constant during the whole test. After, the heating phase starts. Two values of heating rate have been used: 10 K/min and 5 K/min. The elongation of the sample is measured by the extensometer until the fracture or until the limit of displacement of the extensometer.

2.2 Description of the test programme

All the steady-state and transient-state tested are respectively listed in *Table 1* and *Table 2*. Two S355 grades have been analysed (the first one with a 0.19% content of carbon and the second one, micro-alloyed, with a 0.1% content of carbon). For S460M, the thicker profile was produced with a quenching and self-tempering process.

All the tests have been performed on samples extracted from the flanges. At ambient temperature, the yield strength is defined as the stress where the initial elastic branch offset at 0.2% strain intersects the stress-strain curve ($R_{p,0.2}$). Often, a yield plateau with cyclic variations is observed at ambient temperature. In these cases, according to ISO 6892-1 [13], the yield strength is always defined as the

maximum value on this plateau ($R_{e,H}$). The consideration of $R_{e,H}$ will be slightly safe-sided, as this tends to reduce the reduction factor deduced from tests.

It should be noted that the nominal yield strength depends on the grade and the product thickness, according to EN 10025-4 [14].

Table 1. List of tests under steady-state conditions

Programme	Ref.	Section	Grade	$R_{e,H}$ (or $R_{p,0.2}$)	$f_{y,nom}$	Temp. Range
(-)	(-)	(-)	(-)	(MPa)	(MPa)	(°C)
1	TC2	HD 320x300	S355J0	382	335	20 - 900
	TC3	HEM 650	S355K2	371	345	20 - 900
	TC4	WF 14x16	S460M	488	440	20 - 900
	TC5	IPE A 500	S460M	462	460	20 - 900
2	NC 1327	HEB 300	S500M	524	500	20 - 900

As mentioned earlier, steady-state tests have been performed according to the norm in application. For transient tests, two heating rates were chosen: 10 K/min, commonly used for this type of tests and 5 K/min, corresponding to a protected steel element satisfying to R120 fire requirement.

Table 2. List of tests under transient-state conditions

Ref.	Beam	Grade	$R_{e,H}$ (or $R_{p,0.2}$)	$f_{y,nom}$	Heating rate
(-)	(-)	(-)	(MPa)	(MPa)	
NC 1327	HEB 300	S500M	524	500	10 K/min
NC 1327	HEB 300	S500M	524	500	5 K/min

3 RESULTS

At elevated temperatures, the effective yield strength is the stress level leading to a total 2% strain. This value was also considered for the determination of the critical temperature in transient-state tests. However, for transient-state tests, thermal dilatation must be deduced from total measured strains.

Fig. 3 and Fig. 4 show comparisons between experimental reduction factors to EN 1993-1-2 obtained from the first experimental programme. The correlation is good and only a few unsafe results are obtained: except for S355J0, slightly unsafe results are obtained around 400°C, corresponding to the end of the plateau with $k_y = 1$.

These tests also demonstrate that thermomechanical S460 steels obtained by thermomechanical rolling with QST (TC4) or without QST (TC5) lead to comparable results.

Fig. 5 and Fig. 6 show similar ratios $R_{t2}/R_{e,H,20^\circ\text{C}}$ for S355K2 and S500 steel grades when the strain rate has been changed before or after the determination of R_{t2} . The effect of strain rate was already highlighted by [15]. Results are much closer to the Eurocode 3 curve when no acceleration is applied after reaching $R_{p,0.2}$ and results are much on the safe side when acceleration is applied. At 600°C, the difference between the two testing methods is around 20% and this difference rises to 30% at 700°C and 800°C.

Steel Structures

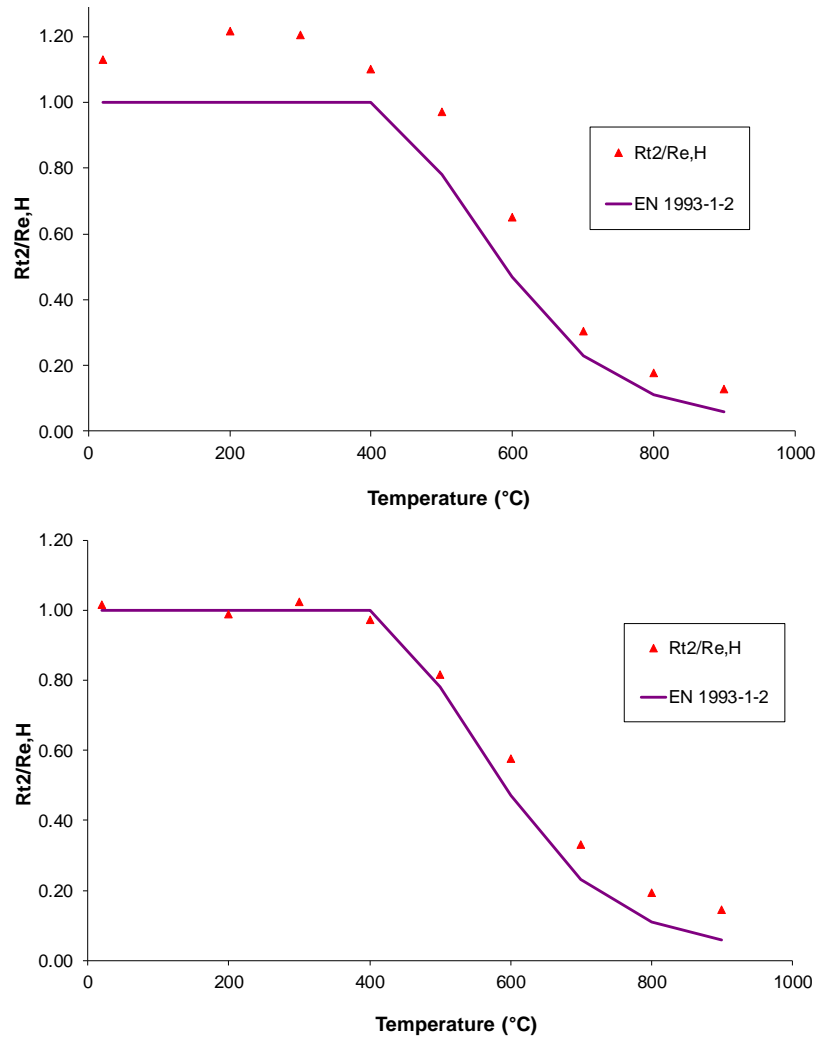


Fig. 3. Comparison between experimental and EN 1993-1-2 reduction factors for S355J0 (above) and S355K2 (below)

Steady-state and transient-state tests on S355 to S500 steel grades

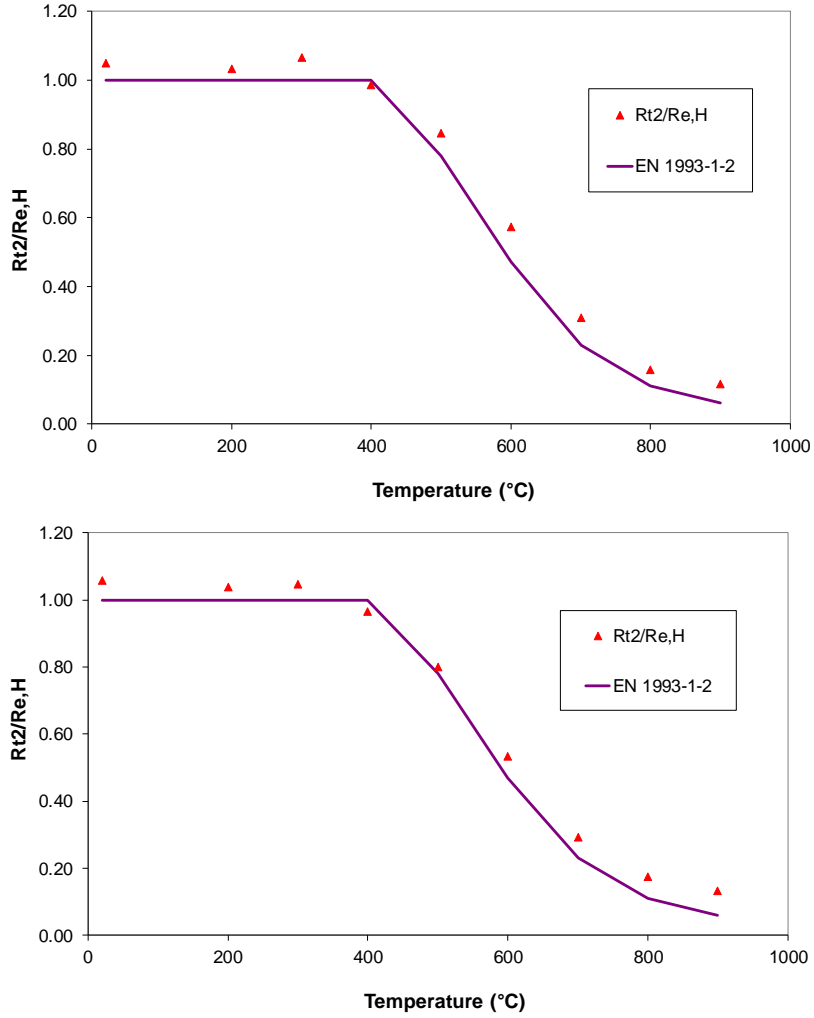


Fig. 4. Comparison between experimental and EN 1993-1-2 reduction factors for S460M (with QST, above and without QST, below)

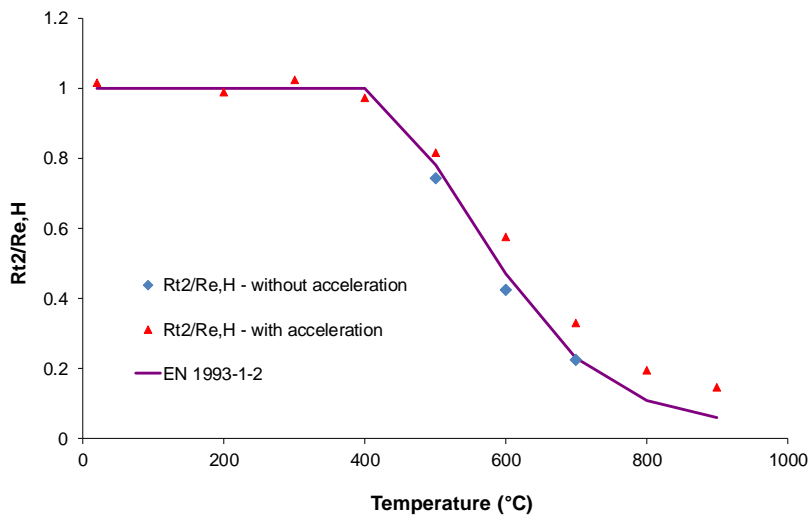


Fig. 5. Comparison between experimental and EN 1993-1-2 reduction factors for S355K2 with and without acceleration

Steel Structures

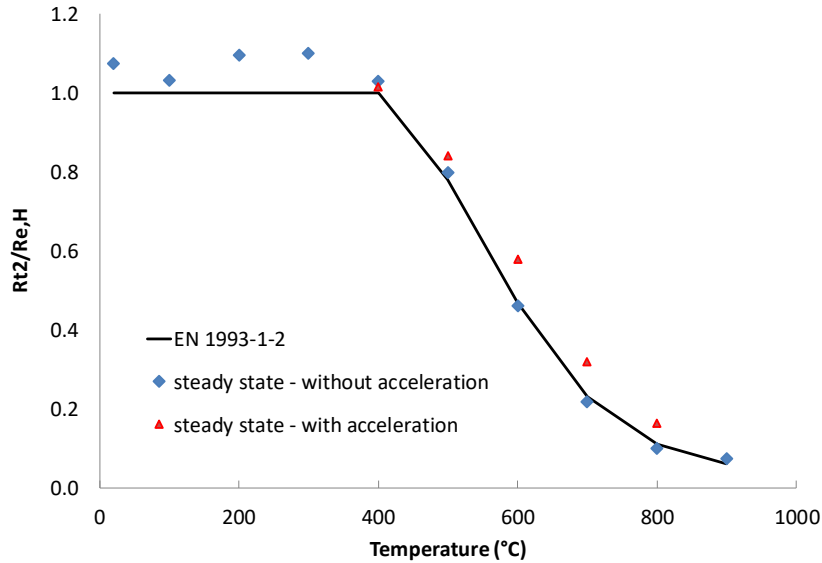


Fig. 6. Comparison between experimental and EN 1993-1-2 reduction factors for S500M with and without acceleration

Finally, results obtained from transient-state tests are plotted on Fig. 7. Experimental results are again really close to EN 1993-1-2 and a large majority of these results are safe-sided. By extrapolation, the comparison between results obtained close to 550°C under 5 K/min and 10 K/min leads to a difference of 15%.

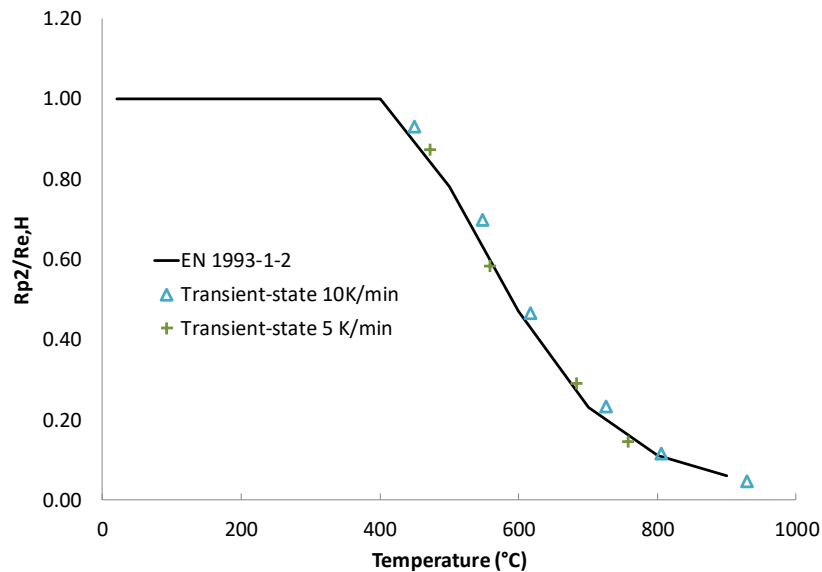


Fig. 7. Comparison between experimental and EN 1993-1-2 reduction factors for S500M

4 CONCLUSIONS

Two experimental programmes were launched on steel grades ranging from S355 to S500 in 2011 and 2015. The results of these steady-state and transient-state tests correlate well with the reduction factors defined in the EN 1993-1-2 standard, currently limited to S460 grade. On the basis of this study, the scope of EN 1993-1-2 could be extended to S500 grades. For steady-state tests, the testing procedure (with and without acceleration after $R_{p0.2}$) led to noticeable differences. Transient-state tests, that are not standardized up to now, have been performed considering 5 K/min and 10 K/min constant heating rates. As expected, the slowest rate leads to lower strengths as creep effects are more significant. However, all the results are in line with EN 1993-1-2 material law.

5 REFERENCES

1. EN 10002-5 (1991). *Metallic materials – Tensile testing – Part 5: Method of testing at elevated temperature*. CEN, Brussels.
2. EN ISO 6892-2 (2011). *Metallic materials – Tensile testing – Part 2: Method of test at elevated temperature*. ISO, Switzerland.
3. EN 1993-1-2 (2005). *Eurocode 3: Design of steel structures – Part 1-2: General rules – Structural fire design*. CEN, Brussels.
4. Neno Toric, Ian W. Burgess (2016). *A unified rheological model for modelling steel behavior in fire conditions*. Journal of Constructional Steel Research, 127. pp 221-230.
5. Venkatesh K. Kodur, Esam M. Aziz (2014). *Effect of temperature on creep in ASTM A572 high-strength low-alloy steels*. Materials and Structures. DOI 10.1617/s11527-014-0262-2.
6. Achim Rubert, Peter Schaumann (1986). *Structural Steel and Plane Frame Assemblies under Fire Action*. Fire Safety Journal, 10. pp 173-184.
7. Regine Schneider (2011). *Untersuchungen zum zeitabhängigen mechanischen Materialverhalten von S460 im Brandfall*. Thesis, TU Darmstadt.
8. Xuhong Qiang, Frans S.K. Bijlaard, Henk Kolstein (2013). *Elevated-temperature mechanical properties of high strength structural steel S460N: Experimental study and recommendations for fire-resistance design*. Fire Safety Journal, 55. pp 15-21.
9. Markus Feldmann, Nicole Schillo et al. (2016). *RUOSTE – Rules on high-strength steel – Final Report RFSR-CT-2012-00036*. ISSN 1831-9424.
10. Dorothy Winful, Katherine A. Cashell et al. (2017). *Elevated temperature material behavior of high-strength steel*. ICE Journal Structures and Buildings, Special Issue on High Strength Steel Structures.
11. Weiyong Wang, Linbo Zhang (2017). *Mechanical properties of high strength Q690 steel at elevated temperatures*. Eurosteel 2017, Copenhagen, Denmark.
12. François Hanus, Olivier Vassart, Nicolas, Jean-Marc Franssen (2017). *High temperature full-scale tests performed on S500M steel grade beams*. Journal of Constructional Steel Research, 133. pp 448-458.
13. EN ISO 6892-1 (2016). *Metallic materials – Tensile testing – Part 1: Method of test at room temperature*. ISO, Switzerland.
14. EN 10025-4 (2004). *Hot rolled products of structural steels – Part 4: Technical delivery conditions for thermomechanical rolled weldable fine grain structural steels*. CEN, Brussels.
15. Markus Knobloch, Jacqueline Pauli, Mario Fontana (2013). *Influence of the strain-rate on the mechanical properties of mild carbon steel at elevated temperatures*. Materials and Design, 49. pp 553-565.

ESTIMATION OF CHARPY IMPACT VALUES FOR STEEL WELDED CONNECTIONS AT HIGH TEMPERATURE AND AFTER HEATING AND COOLING PROCESSES

KAI YE¹ and Fuminobu OZAKI²

ABSTRACT

Charpy impact tests for steel welded connections under high temperatures and the ambient temperature after heating and cooling processes are respectively conducted, to verify a possibility of the brittle fracture at fire. The high temperature tests focus on verification of the brittle fracture under blue brittleness temperature region (100-300 °C). V-notch specimens respectively quarried from steel base metal, weld metal and heat affect zone parts in the welded connection are heated and offered to the Charpy impact tests. On the other hand, for the ambient temperature tests after the heating and cooling processes, the heated specimens are treated with air cooling in a furnace and quenching, respectively. According to the test results, it is clarified that the Charpy impact values hardly decrease in the blue brittleness temperature regions between 100 and 300 °C and the quenched welded connection possess the low Charpy impact values because of the occurrence of martensite transformation.

1 INTRODUCTION

It is well known that many steel welded connections in buildings exhibited brittle fracture as a starting point by ductile cracks at the past severe earthquake (Kobe earthquake, 1995). On the other hand, it has been considered that the brittle fracture hardly occurs under building fire because the fracture toughness generally increases with the member temperature increase. However, in accordance with the past experimental research on the steel welded connection at the elevated temperature, it has been reported that the brittle fracture in the heat affect zone occurred at 400 °C [1]. It is, furthermore, known that the steel under temperatures between 100 and 300 °C exhibits "a blue brittleness phenomenon" and the total elongation under the temperature regions becomes smaller in comparison with the ambient temperature [2]. For the above reason, we must verify a possibility that the steel member under early fire stages including the blue brittleness temperatures brittlely fractures. Additionally, when considering reuse of the steel structure subjected to the fire, there is the possibility that the fracture toughness after the fire is changed by heated temperature and cooling processes [3, 4]. The main purpose of this study is to investigate Charpy impact values for the steel welded connections under the high temperatures and the ambient temperature after the heating and cooling processes.

2 OVERVIEW OF CHARPY IMPACT TESTS

2.1 Specimens

JIS SN400B and YGW11 are respectively used for the steel and welding material of the welded connection specimens. The chemical components based on the mill sheets are shown in Table 1. Both steels are usually used for the building structures in Japan, and SN400B steel is standardized

¹Grad. student, Graduate School of Environmental Studies, Nagoya University, Nagoya, JAPAN

e-mail: yelaokai122@gmail.com

² Assoc. Prof., Grad. S. Envi. Studies, Nagoya University, Nagoya, JAPAN

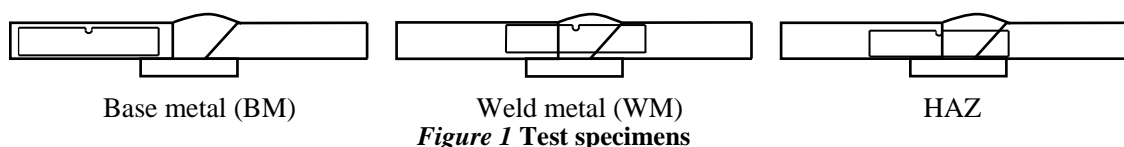
e-mail: ozaki@dali.nuac.nagoya-u.ac.jp

to satisfy that a yield point and tensile strength at the ambient temperature are larger than 235 and 400 MPa, respectively. YGW11 is the conventional welding material using for SN400B.

Table 1 Chemical components

Steel	Chemical (mass %)								
	C	Si	Mn	P	S	Ni	Mo	Cu	Ti+Zr
SN400B	0.12	0.2	0.64	0.011	0.004	0.02	0.01		
YGW11	0.06	0.77	1.6	0.014	0.011			0.3	0.24

We prepared the V-notch specimens (the size: 10 mm×10 mm×55 mm) respectively quarried from steel base metal (BM), weld metal zone(WM) and heat affect zone (HAZ) parts in the welded connection (Figure 1.).



2.2 Test method

2.2.1 High temperature experiments

For the high temperature experiments focusing on the Charpy impact values under the blue brittleness temperatures, the test temperatures were given by 0, 100, 200, 300, 400, 500 and 600 °C . Furthermore, the tests at -20, -40 and -70 °C were conducted to verify a brittleness-ductility transition temperature. The specimens for the target test temperatures over 100 °C is heated by an electric furnace. Three specimens for each test at the same temperature are used and an average Charpy impact value for three specimens was estimated.

In order to conduct the accurate Charpy impact tests at the high temperature, two dummy specimens respectively attached a thermocouple were prepared, for measuring the specimen temperature in an electric furnace and that at the impact test in progress (Figure 2). The temperature of the heated specimens in the furnace was checked by the former one with the thermocouple. The specimens were taken out of the furnace and set to a Charpy impact test machine at the ambient temperature. Since the temperature of the heated specimen taken out of the furnace rapidly decreases, the temperature change from the ejection to setting the machine was measured by the latter one with the thermocouple. The measured temperature and elapsed time relationships up to run time of the Charpy impact test (the time when striking the specimen by a hammer of the machine) are shown in Figure 3. The specimen at the ejection from the furnace had a little higher temperature than the target test temperature. The elapsed times for the specimens above 300 °C were measured and it was confirmed that they were within the limit elapsed time of each target test temperature. On the other hand, in the case of 100 and 200 °C tests, the elapsed times have not been measured because the temperature reduction is very slow as shown in Figure 3.

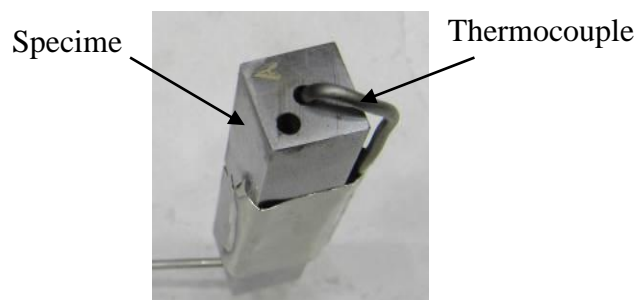


Figure 2 A specimen for measuring temperature

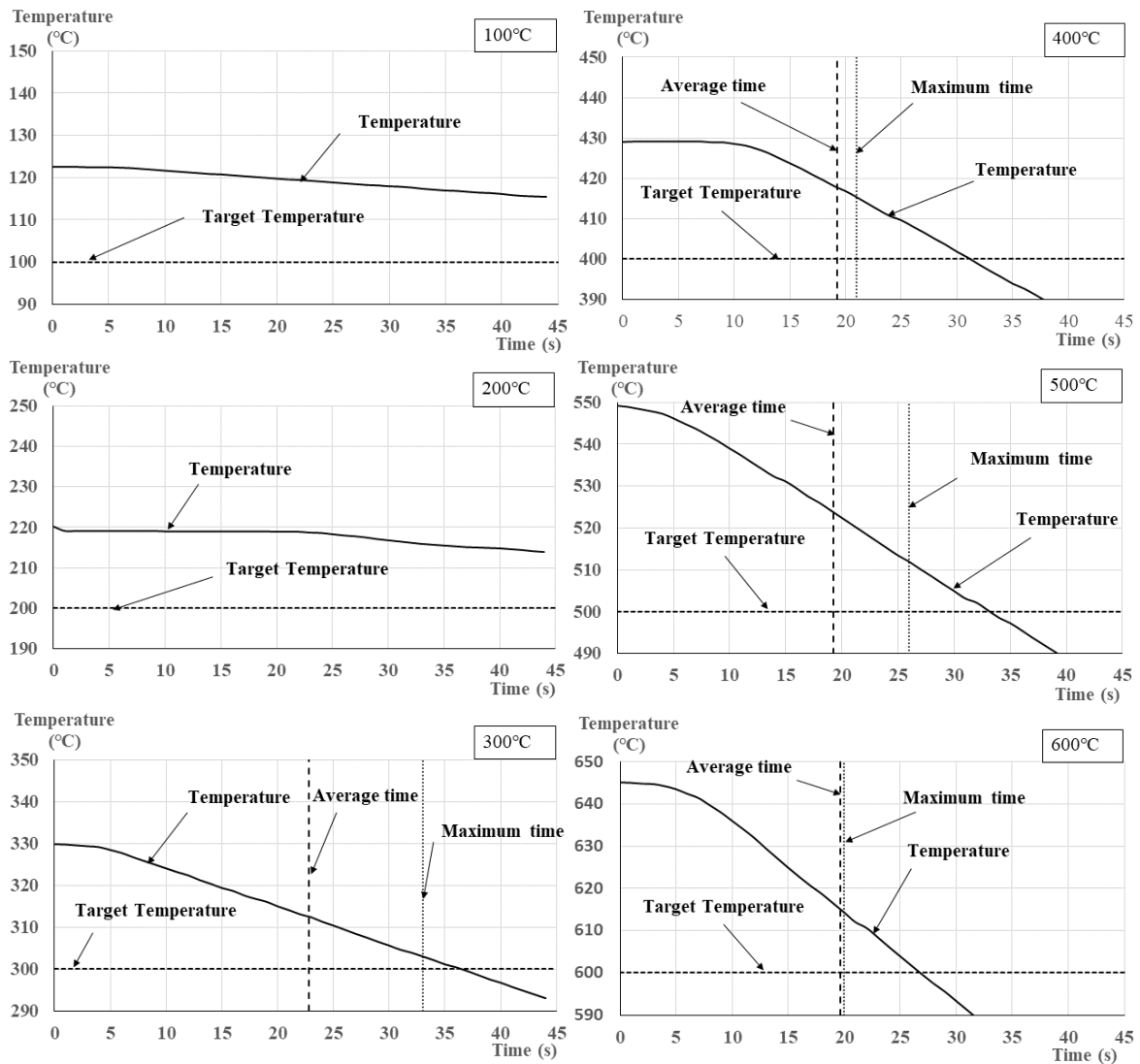


Figure 3 Temperature-elapsed time relationships up to run time of the impact tests

2.2.2 Ambient temperature experiments after heating and cooling processes

For the ambient temperature experiments after the heating and cooling processes, the specimens are heated up to 600, 700, 800, 900 °C by the electric furnace and cooled with water (hereinafter, described as water-cooling) and leaving in the furnace whose temperature is lowered (hereinafter, described as furnace-cooling). The water-cooling process assumes fire extinguishing situation using the water. The Charpy impact tests are conducted at 0, furthermore, -40 °C and -20 °C tests are conducted to consider the situation of the steel structures in a cold region. The number of the specimens under the same temperature test is three expect for -20 °C test. At the latter test, two specimens were offered to the Charpy impact test, because of lacking the specimens prepared in advance.

2.3 Coupon Tests for Steel Base Metal at High Temperatures

We conducted coupon tests at the elevated temperatures for the steel base metal (JIS SN400B). The stress-strain relationships are shown in Figure 4. Figure 5 shows the relationships between the breaking elongation and the test temperature. As shown Figure 4 and 5, the tensile strength/breaking elongation between 100 and 300 °C is larger/smaller than the ambient temperature results, because of the blue brittleness phenomenon.

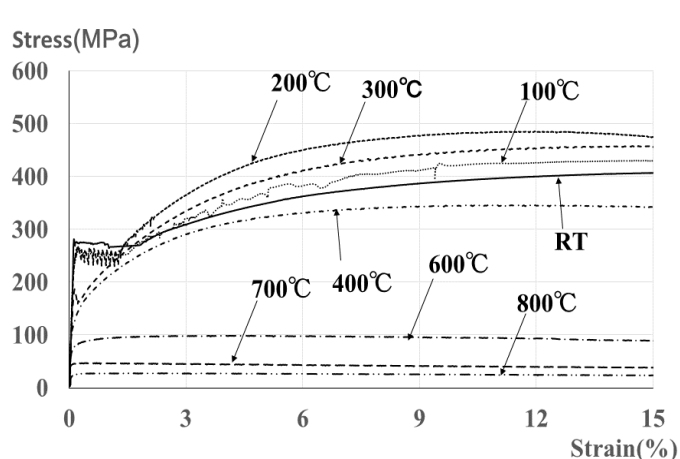


Figure 4 Stress-strain relationships (SN400B)

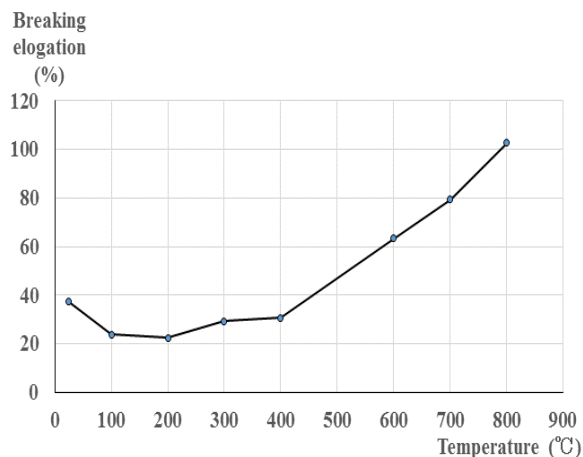


Figure 5 Breaking elongation at high temperature (SN400B)

3 EXPERIMENTAL RESULTS AT HIGH TEMPERATURES

Figure 6 shows the temperature and the Charpy impact value relationships for the base metal (BM), weld metal (WM) and HAZ specimens. The Charpy impact value at each test temperature is given by the average value of three specimens and those values are shown in Table 2. Table 3 shows an energy transition temperature [4] calculated from the test results. It was assumed that the test results at 0 and -70 °C were respectively used for the upper and lower shelf energy temperatures for the BM and HAZ specimens. On the other hand, both shelf energies for the WM specimen were assumed by 100 and 0 °C, respectively.

Table 2 Average Charpy impact values

Temperature	°C	-70	-40	-20	0	100	200	300	400	500	600
BM	J	14.9	136	173.8	234.8	171.5	267.2	247.2	167.8	116.7	152.3
WM	J	11.4	13.3	18.3	66.1	208.9	287.3	278.8	155.4	114.3	112.2
HAZ	J	15.8	163.3	205.9	223.2	229.1	293.4	261.7	175.1	126.2	175.3

Table 3 Transition Temperatures

Specimens	Ductile fracture energy		Transition Energy	Transition temperature
	°C	J	J	°C
BM	0	234.8	124.8	-42.8
WM	100	208.9	111.1	31.5
HAZ	0	223.2	119.5	-48.9

As shown in Figure 6, lower shelf energy of the specimen was observed at -70°C. The brittle fracture appearance for the fracture surface was observed (Figure 7). Both BM and HAZ specimens possess the large impact values which exceed 200 J at the ambient temperature (0°C), on the other hand, the test result of the weld metal specimen is smaller than those values. However, the WM specimen at 100 °C possesses the large impact value which exceeds 200 J. As shown in Figure 5, the breaking elongation of the base metal from 100 to 300 °C is smaller than that at the ambient temperature because of an effect on the blue brittleness, however, the Charpy impact values in the blue brittleness temperatures hardly decrease, except in the base metal specimen at 100 °C. At the

high temperatures above 300 °C, the impact values gradually decrease, because the steel strength of the coupon test result decreases. At the temperature above 100 °C, it was observed that the fracture surfaces of the specimens were ductile fracture appearance (Figure 7). According to the test results, we can conclude that there is the small possibility that the welded connections subjected to the fire exhibits the brittle fracture, in comparison with the ambient temperature.

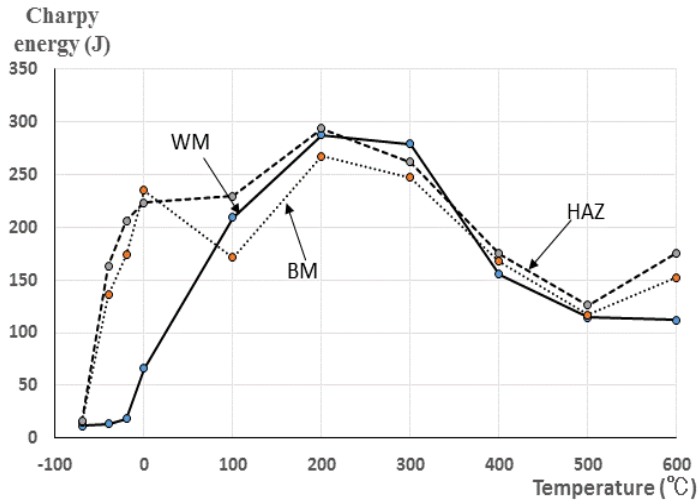


Figure 6 Experimental results of the Charpy impact test at high temperature

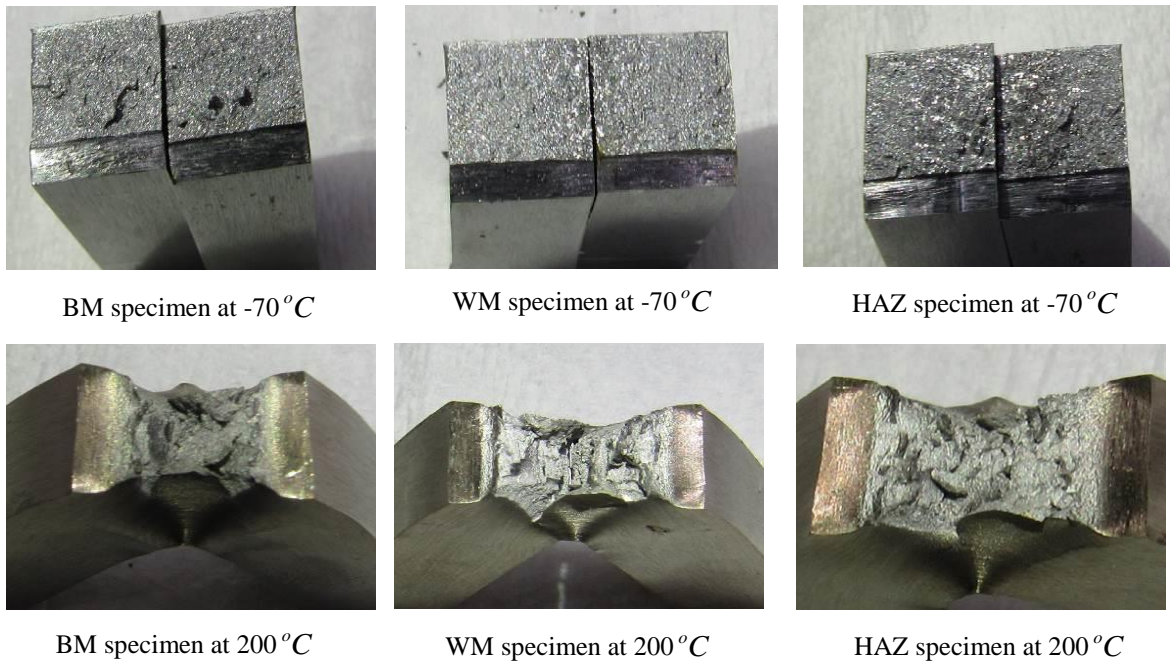


Figure 7 Fracture surface of specimens

4 EXPERIMENTAL RESULTS AFTER HEATING AND COOLING PROCESSES

Figure 8 shows the test results (average values) for the BM, WM and HAZ specimens after the heating and cooling processes. Table 4 shows those average Charpy impact values at 0, -20 and -40 °C. In Table 4, the results at the test temperatures (-40, -20 and 0 °C) without the heating and cooling processes, which are the tests results shown in Table 2, are shown. The horizontal axis of Figure 8 means heated temperatures from 600 to 900 °C. The left end values on the horizontal axis of Figure 8 are the test results without the heating and cooling processes. As shown in Figure 8, the

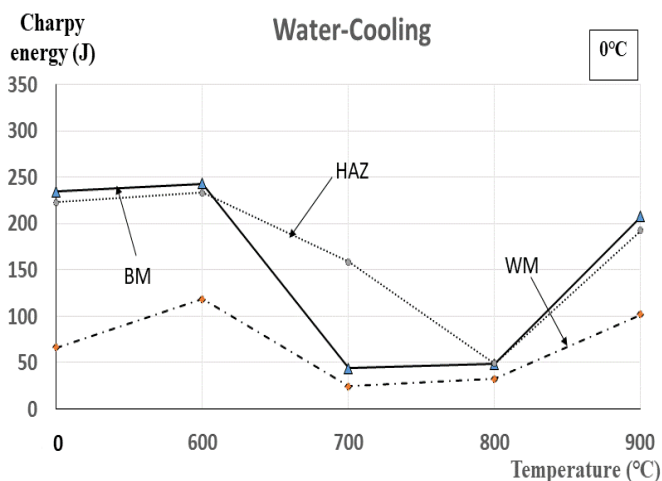
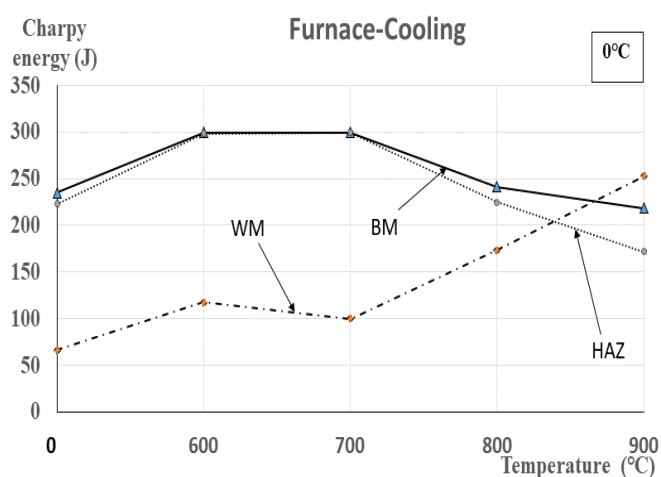
Charpy impact values in the case of the water-cooling when the heated temperatures are 700 and 800 °C remarkably reduce, because martensite transformation occurs by the water-cooling. On the other hand, for the test results when the heated temperature is 900 °C, the Charpy impact values are recovered in many cases. This reason is currently under consideration.

Table 4 Charpy impact values after heating and cooling processes

Impact Temperature	0 °C					
	Furnace-Cooling			Water-Cooling		
Heated Temperature	B(J)	W(J)	H(J)	B(J)	W(J)	H(J)
0 °C	234.8	66.1	223.2	234.8	66.1	223.2
600 °C	299.6	117.7	298.3	243.4	118.7	233.3
700 °C	299.6	99.7	299.6	43.8	24.2	158.6
800 °C	241.1	173.3	224.9	48.7	32.8	49.1
900 °C	218.6	253.0	172.0	207.8	101.9	192.6

Impact Temperature	-20 °C					
	Furnace-Cooling			Water-Cooling		
heating temperature	B(J)	W(J)	H(J)	B(J)	W(J)	H(J)
-20 °C	173.8	18.3	166.6	173.8	18.3	166.6
600 °C	299.8	62.6	270.1	190.2	18.7	226.4
700 °C	299.7	19.1	206.4	13.2	13.4	33.4
800 °C	208.1	22.7	195.9	20.4	27.3	23.1
900 °C	208.4	172.4	148.3	241.8	77.5	180.0

Impact Temperature	-40 °C					
	Furnace-Cooling			Water-Cooling		
heating temperature	B(J)	W(J)	H(J)	B(J)	W(J)	H(J)
-40 °C	136.1	13.3	163.4	136.1	13.3	163.4
600 °C	144.2	9.0	159.6	143.0	10.0	188.1
700 °C	21.1	13.1	195.0	11.6	11.3	13.2
800 °C	40.8	48.0	79.2	14.4	16.4	17.4
900 °C	29.9	100.6	16.5	194.0	48.6	139.2



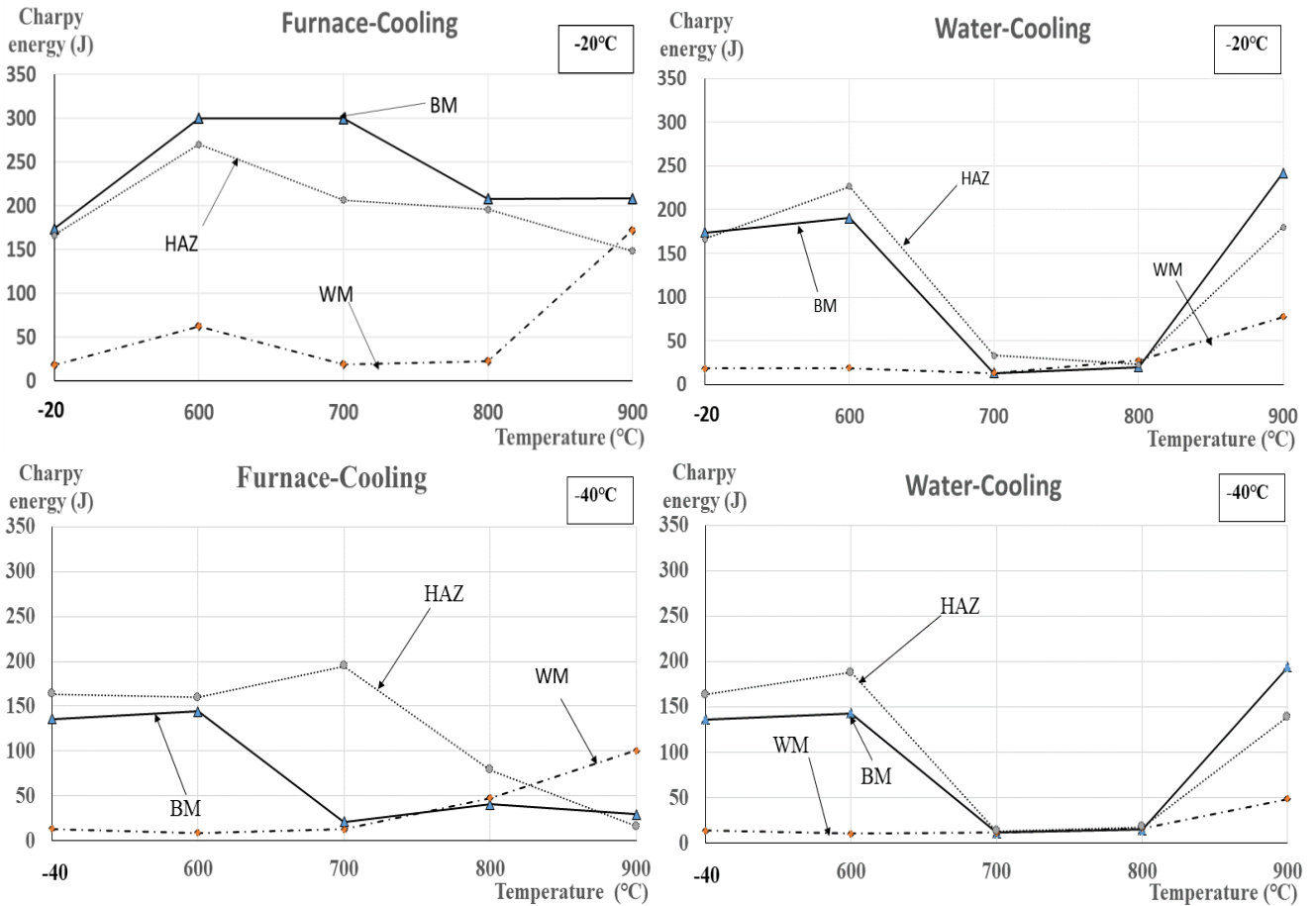


Figure 8 Experimental results of the Charpy impact test after heating and cooling processes

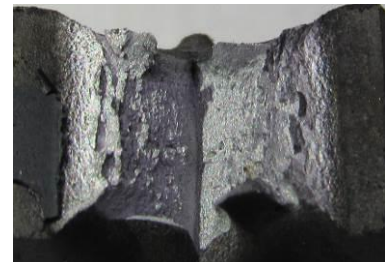
Figure 9 shows the fracture surface images of the BM, WM and HAZ specimens subjected to the water-cooling (the Charpy test temperature is 0 °C). The left end pictures show the fracture surface of the specimens without the heating and cooling processes. As shown in Figure 9, the ductile and brittle fracture appearance are observed for the specimens without the heating and cooling processes, and with the 700°C heating and water-cooling, respectively. On the other hand, the specimens with the 900°C heating and the water-cooling exhibit the ductile fractures, and those Charpy impact values increase in comparison with the other water-cooling specimens (Figure 8 and Table 4).



BM specimen without heating



BM specimen subjected to 700°C heating



BM specimen subjected to 900°C heating

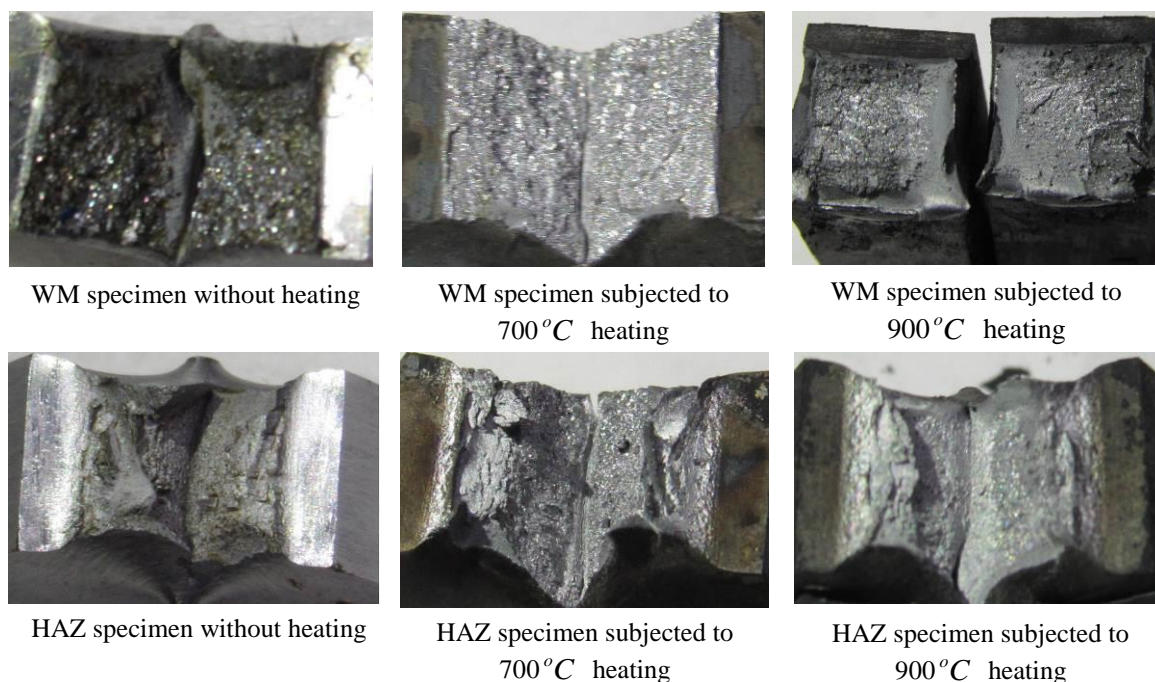


Figure 9 Fracture surface of water-cooling specimens at 0 °C impact tests

5 CONCLUSIONS

The Charpy impact values for the base metal (JIS SN400B), weld metal (JIS YGW-11) and HAZ parts in the steel welded connections at the high temperature and the ambient temperature after the heating and cooling processes were investigated. According to the high temperature experimental results, it was confirmed that the Charpy impact values hardly decrease in the blue brittleness temperature regions between 100 and 300 °C. It is, for the reason, considered that there is the small possibility that the welded connections subjected to the fire exhibits the brittle fracture, in comparison with the ambient temperature in the case of a combination of JIS SN400B and YGW-11. Furthermore, according to the ambient temperature experimental results after the heating and cooling processes, it was clarified that the specimens subjected to the water-cooling possess the low Charpy impact values because of the occurrence of martensite transformation. That is, for instance, in the case when the unprotected steel member is exposed to flame of the fire and quenched by the fire extinguishment, it is necessary to be careful when reusing it as the seismic resistance member after the fire.

REFERENCES

1. Minh-Phuong Nguyen, Kang-Hai Tai, Tat-Ching Fung and Thu-Mai Le (2014). *STRUCTURAL BEHAVIOUR OF WELDED FLANGE BOLTED WEB BEAM-TO-COLUMN COMPOSITE JOINTS IN FIRE CONDITIONS*, Proceedings of the 8th International Conference on Structures in Fire, Vol.1, pp.803-810
2. The Society of Materials Science, Japan (2007). Engineering Materials (in Japanese)
3. Mikihiro HIROHATA, Kaito NEZU, Taishi NAKAYAMA, Shigeyuki MATSUSUI (2018). *Effect of heating and cooling processes simulating fire damage on mechanical properties of steels used in aged bridges*. Steel Construction Engineering Vol.24, No.95, pp.49-57 (in Japanese)
4. Murakami KOUFU, Katsuo MIKA Itou FUYUKI (2017). *A Study on Steel Mechanical Property Considering Heating History Temperature and Cooling Method Part V Effect of Steel Type on Impact properties*. Summaries of Technical Papers of Annual Meeting Architectural Institute of Japan, Fire Safety, pp.171-172 (in Japanese)

STUDY ON TEMPERATURE DISTRIBUTION OF WELDED TUBULAR SQUARE JOINTS

Jolanta Bączkiewicz¹, Mikko Malaska², Sami Pajunen³, Markku Heinisuo⁴

ABSTRACT

The paper presents experimental and numerical research on steel square hollow section (SHS) joints under fire conditions. The focus of the paper is on the definition of the joint area heat distribution under standard fire exposure and its effect on the joint resistance and failure modes. The experimental programme included three fire tests in which six different joint configurations, T-, Y-, K-, and KT-joints were carried out. Subsequently, the finite element commercial software Abaqus/CAE was used to simulate the results of the experimental test. The finite element (FE) model was first validated against the test data and then applied to parameter study. The parameter study took under consideration different parameters that may influence the temperature distribution within the joint, such as joint type, β parameter and τ parameter.

Keywords: steel joint, hollow section, fire test, parametric study, component method, temperature distribution.

1 INTRODUCTION

Due to their light weight and easy fabrication, tubular steel trusses are widely used in onshore and offshore structures. Connections are important components of steel trusses, as they transfer internal forces between surrounding structural components. The failure of a connection can cause the collapse of the whole truss, and the collapse may also lead to the progressive collapse of a much larger area of the building structure. Therefore, it is of significant importance that the connections are designed reliably both at the ambient and elevated temperatures. The current design approach for welded tubular joints at elevated temperatures is described in EN 1993-1-2 [1] and EN 1993-1-8 [2]. The procedure is limited to basic beam elements. Even though forces, to which the connections are subject to in fire conditions, are different from those at ambient temperature, the assessment of joint forces are typically not included in the fire design approach. Little attention is paid to the different temperature distribution between the connection members and to the effects of different temperatures on the failure modes. Missing the critical failure mode may lead to the failure of attached truss members and potentially trigger the progressive collapse of the whole structure.

The experimental research and data available on the actual steel hollow section joint temperatures are very limited. A preliminary study of temperature distribution within SHS joints has been reported by Bączkiewicz et al. [3] including KT-joints of three different configurations. Another experimental study has been conducted by Yang et al. [4], who measured the displacements of axially loaded SHS

¹ PhD Candidate. Laboratory of Civil Engineering, Tampere University of Technology, Tampere, Finland.

e-mail: jolanta.baczkiewicz@tut.fi

² Professor. Laboratory of Civil Engineering, Tampere University of Technology, Tampere, Finland.

e-mail: mikko.malaska@tut.fi

³ Professor. Laboratory of Civil Engineering, Tampere University of Technology, Tampere, Finland.

e-mail: sami.pajunen@tut.fi

⁴ Professor. Laboratory of Civil Engineering, Tampere University of Technology, Tampere, Finland.

e-mail: markku.heinisuo@tut.fi

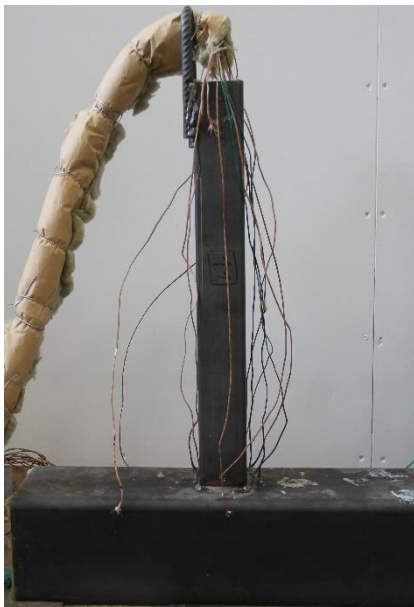
T-joints exposed to fire conditions. The aim of the research was to obtain the resistance and failure mode of the joints. A numerical research has been carried out by Ozyurt et al. [5] to simulate the behaviour of CHS and SHS joints under compression and tension loading and to estimate the limit loads for the joints. The main conclusion from the abovementioned studies is that the technical data about SHS section joints is very limited. More research is needed concerning the joint performance at elevated temperatures, which would be beneficial for improving the fire design approach of welded tubular joints.

Tampere University of Technology has carried out experimental full-scale tests and numerical simulations on brace-to-chord joints of tubular steel trusses to better understand the temperature distributions in the vicinity of SHS joints and at each individual component of the joint. The aim of the research is to develop experimental and calculation methods to determine joint temperatures and to transfer this information into the joint design approach. Based on the results of the experimental research by Bączkiewicz et al. [6] a finite element (FE) model was developed and validated. A parametric study has then been carried out using the numerical model to study the effects of different joint configurations and parameters on the temperatures and temperature distribution within joints. This paper introduces the experimental and numerical research and the main observations related to the temperatures and the numerical results.

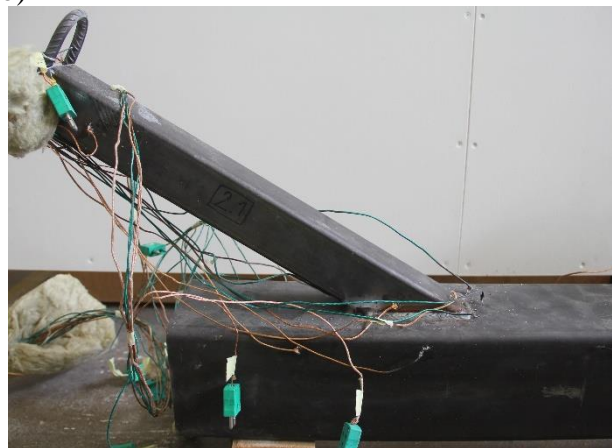
2 EXPERIMENTAL STUDY

The experimental study included six unprotected SHS joint specimens of four different joint configurations (T-, Y-, K- and KT-joint) tested in a full-scale test furnace. *Figure 1* presents specimens tested for 60 minutes in standard ISO-834 fire exposure. Every specimen was equipped with 33-49 thermocouples and the results provided very detailed information about the SHS joint temperatures under standard fire conditions. The details of the tested specimen are provided in *Table 1*.

a)



b)



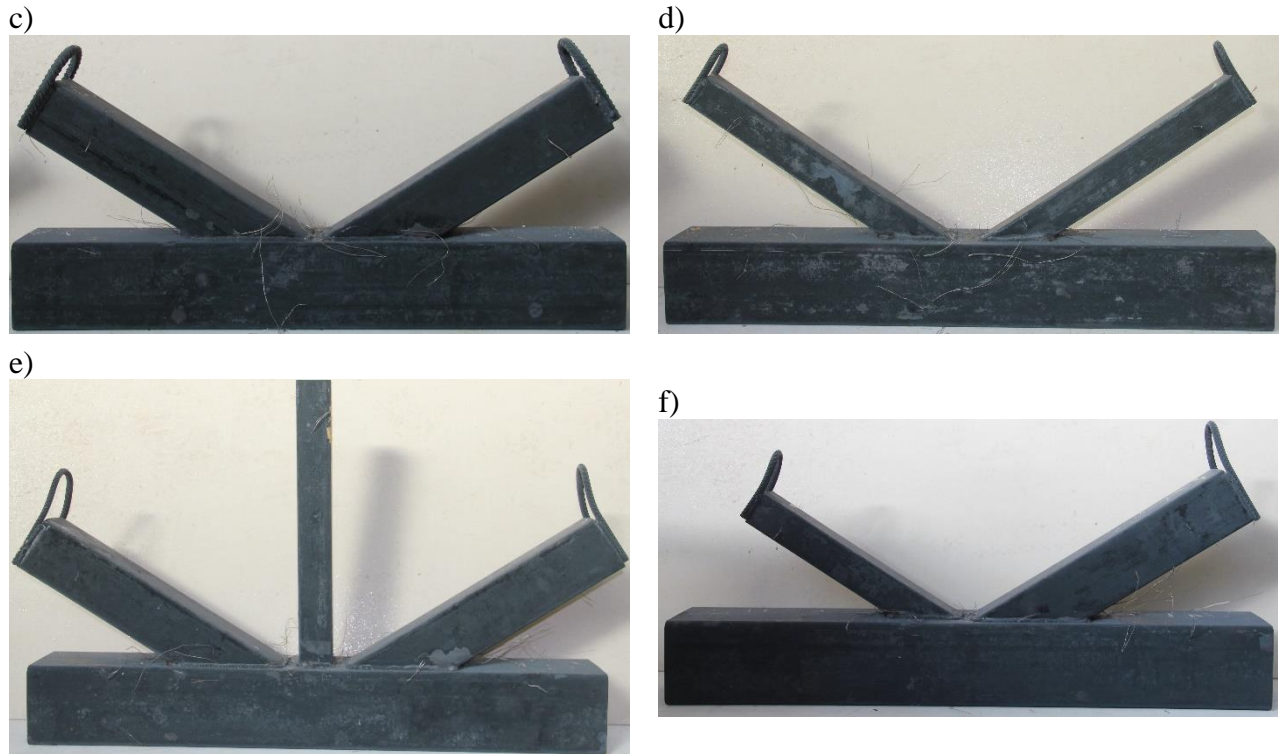


Fig. 1. Test specimens: a) K1; b) K2; c) K3; d) K4; e) K5; f) K6

Table 1. Geometric properties of the specimens [6]

Specimen	Joint type	Chord (mm)		Brace 1 (mm)		Brace 2 (mm)		Brace 3 (mm)	
		Width	Thickness	Width	Thickness	Width	Thickness	Width	Thickness
K1	T-	140.1	6.1	60.1	3.0	100.1	4.1	-	-
K2	Y-	140.2	5.9	60.2	3.0	100.2	4.0	-	-
K3	K-	140.0	6.1	100.0	4.0	100.0	4.0	-	-
K4	K-	140.1	6.1	60.0	3.0	60.0	3.0	-	-
K5	KT-	140.2	6.0	100.1	4.0	60.0	2.9	100.1	4.0
K6	K-	140.0	6.0	100.0	4.0	60.0	3.0	-	-

The selected test results include data about one specimen to provide an example of the behaviour of the SHS joint. *Figure 2 a)* and *b)* illustrate the recorded temperatures of brace and chord of K-joint, respectively. The measured values were also compared with temperatures calculated based on EN 1993-1-2 [1] for beam element with a cross-section thickness of 3 mm for brace and 6 mm for chord. The location of the measured points is shown in the *Figure 2*. It can be seen in *Figure 2 a)* that the measured temperatures at the bottom of the brace (point 59, 62) provided similar values. The temperatures measured in the point 72, which is located far from the brace-chord connection followed the temperatures calculated according to EN 1993-1-2[1]. However, the non-uniformity of temperatures became remarkable when compared the values obtained by points 62 and 72. When the temperature of point 72 reaches 500°C, the temperature of point 62 is lower by 140°C.

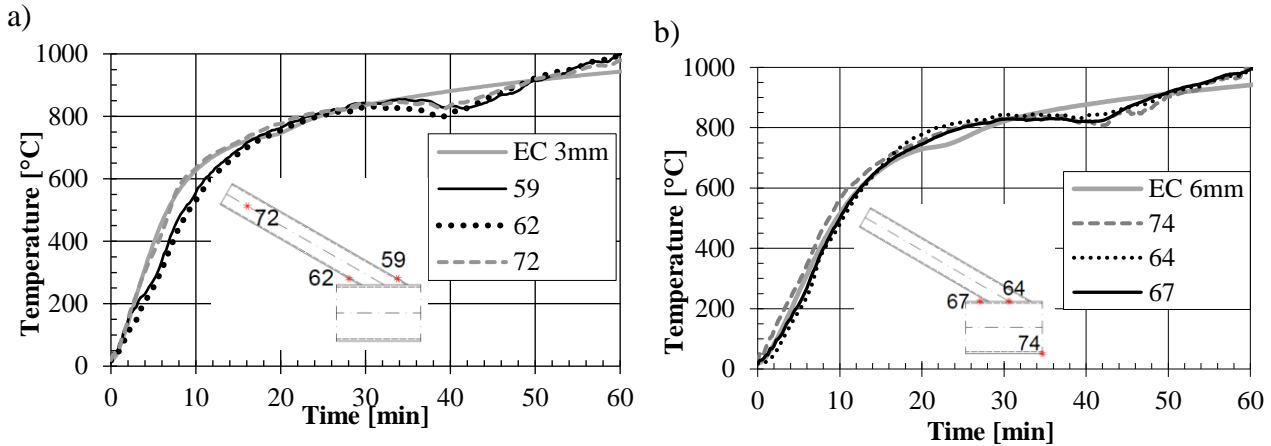


Fig. 2. Temperature distribution of K-joint measured temperature a) in brace; b) in chord [6].

The measured temperatures in the chord cross-section are presented in Figure 2 b). All temperatures are similar with slightly lower values at point 64. Point 64 was located in the chord top wall, inside the brace element. The maximum recorded temperature difference between point 64 and 74 at the bottom of the chord was 80°C at the sixth minute of the test.

In steel designing the most important factor characterizing steel is the strength of the steel element. At elevated temperature the steel strength is reduced by reduction factor for effective yield strength. The relation of reduction factor to the temperature of the steel element is described in EN 1993-1-2 [1]. The comparison of reduction factors for the temperatures for point from Figure 2 is presented in Figure 3, for brace and chord separately. For the brace element, the difference between point 62 and 72 was 140°C, which provides a difference in yield strength of 164 MPa. For the chord element, the differences in temperature were relatively small but when compared reduction factors for effective yield strength the non-uniformities become more visible. The difference in steel strength between points 74 and 64 reaches 140 MPa obtained for the temperature of 500°C for point 74.

In general, the same phenomenon can be noticed as for temperature comparison; points more distant from brace-chord connection reached reduction factor values close to results of Eurocode EN 1993-1-2 [1]. As an example, point 72 reached the reduction factor of 0.47 (value for 600°C) four minutes earlier than points close to brace-chord connection (points 59 and 62).

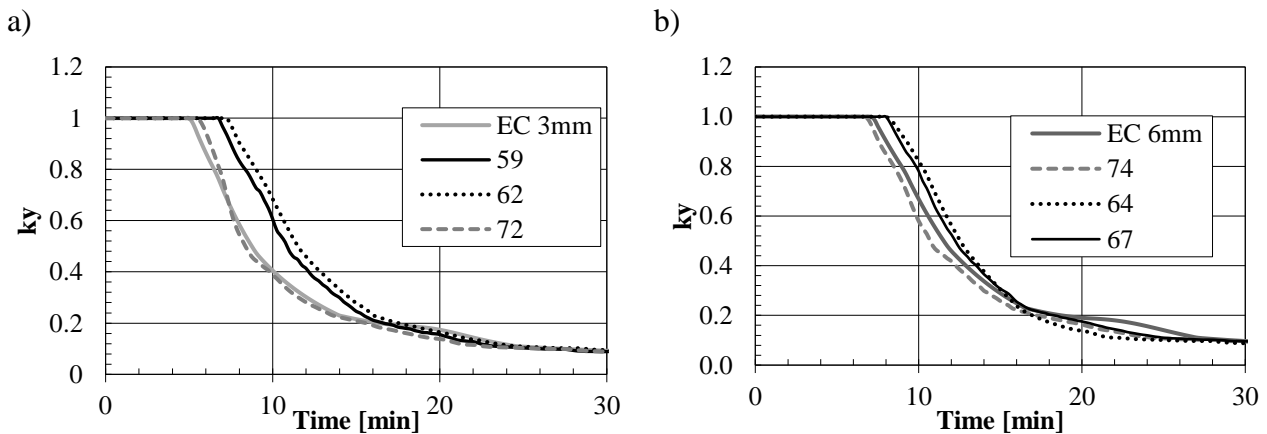


Fig. 3. The comparison of reduction factors for effective yield strength of K-joint a) in brace; b) in chord [6].

The main observation from the obtained data was that the measured temperatures within the joints are significantly non-uniform. In general, the temperatures close to the brace-to-chord connections were lower than the temperatures at the free ends of the brace and chord members. The maximum temperature differences measured within the joints were as high as 140°C. The experimental results

were also compared against the temperatures calculated using the method of EN-1993-1-2 [1]. The results demonstrate that the calculation method lead to temperatures higher than the measured values. Based on the above observations, the temperature differences within the joint area are so high that the non-uniform distribution may affect the resistance of the joint and should, therefore, be taken into account in the joint design approach.

3 NUMERICAL STUDY

The experimental research was complemented by numerical analysis in finite element software ABAQUS CAE [7]. The model was built from three-dimensional solid diffusive elements with second order (parabolic) interpolation (DC3D20). The boundary conditions and the material properties were applied in accordance with EN 1991-1-2 [8] and EN 1993-1-2 [1], respectively. An extensive verification and validation with experimental results was conducted for the FE model to achieve an accurate simulation of the heat transfer phenomenon. *Figure 4* presents the comparison of temperature measured in experimental test and simulated in numerical analysis. It can be seen that in the area close to the brace-chord connection a satisfactory correlation of temperatures was obtained.

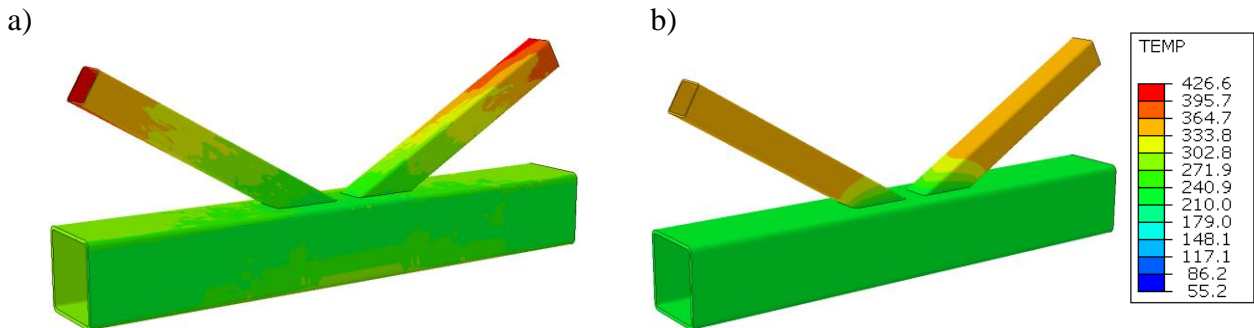


Fig. 4. K-joint heat distribution at 5th minute obtained from: a) experimental tests; b) numerical analysis [6].

3.1 Parametric study

Parameter study was carried out to investigate the influence of geometric parameters and different joint configurations on thermal distribution within the joint. For all analysis the mean temperature of the point located on the top wall of the chord, close to the brace/chord intersection was used.

First, the influence of different joint configuration was taken under investigation. *Figure 5* presents the comparison of the temperature of the chord for different joint types. ‘FEM/EC’ is the ratio of the numerically analysed chord temperature to the temperature calculated in accordance with EN 1993-1-2 [1]. β parameter for the compared cases was equal to 0.71. For T- and Y-joints the temperature ratio followed the same curve. The minimal reached value was 0.82, which corresponds the simulated temperature of 82% of the predicted temperature by Eurocode [1]. For K-joint the values of temperature ratio have in general lower values than result of T- and Y-joint. The minimum value reaches even 0.76 at the beginning of the analysis.

The influence of cross-sectional parameter β on the temperature distribution was analysed for each joint configuration separately. The results of chord temperatures of K-joints with different β parameter are shown in *Figure 6*. The temperatures were simulated for cross-sections with the same wall thickness. It can be seen that the obtained values are very similar for all β parameter values.

In all analysed cases, β parameter had only a marginal effect on the increase of temperature. The numerical results demonstrated that the temperature distributions of different joint configurations depend mainly on the level of the mass concentration in the joint. A K-joint has a bigger mass concentration than a Y-joint and, therefore, the measured and calculated temperatures in the K-joint were lower than in the Y-joint.

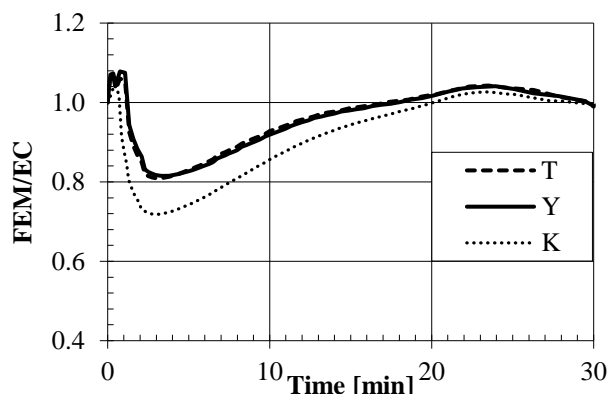


Fig. 5. Effects of joint type on the thermal distribution of the chord for $\beta=0.71$.

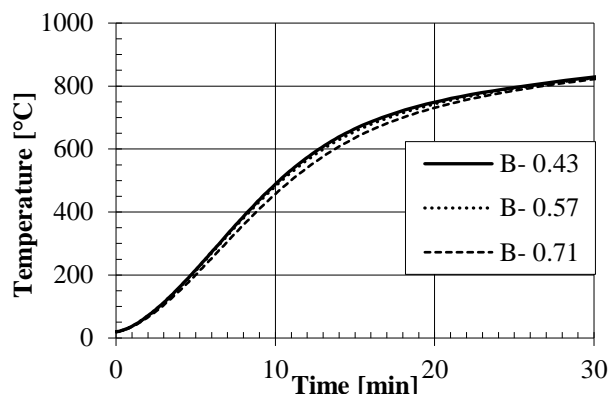


Fig. 6. Effects of β parameter on the thermal distribution of the chord for K-joints.

4 CONCLUSIONS

In this study the temperatures of SHS joints exposed to standard fire are investigated experimentally and numerically. The aim of the study was to define the level of the non-uniformity of temperatures within the joint area and to determine the influence of different joint configurations and geometrical parameters on the temperatures and temperature distribution. The following conclusions can be drawn:

1. The joint configuration has a significant influence on the temperature distribution within the joint. Different brace-to-chord angle causes changes in the air free flow around the brace member. Moreover, different joint configurations are characterized by different values of mass concentration within the joint. The highest value of mass concentration occurs in K-joint due to two braces welded to the chord. The mass concentration is also influenced by the brace-to-chord angle, smaller angle leads to bigger mass concentration and analogically causes slower temperature development.
2. The comparison of β parameter showed that only slightly lower temperatures were observed for sections with higher parameter values. For joints with relatively small β parameter no influence on the temperature distribution was observed. The influence of β parameter can be neglected in further analysis. More significant parameter that should be taken into account is the thickness of the wall of the cross-sections, which directly influence the temperature distribution in steel element.
3. The effective yield strength of steel is dependent on the steel temperature. When the temperature distribution within a joint is non-uniform, different joint components are in different temperature. When the temperature differences are high, the strength of different components varies. This will affect the resistance and failure mode of the joint. More accurate information about the joint temperatures would lead to more realistic joint analysis and design, and allow for better optimisation of the joint properties and truss designs.
4. The experimental tests and numerical study results proved that EN 1993-1-2 [1] provides a safe approximation of temperatures of SHS joints under standard fire conditions. However, at the beginning of the analysis, for relatively low temperatures, the standardize method recommends conservative results.

REFERENCES

1. EN 1993-1-2: Eurocode 3: Design of steel structures. Part 1-2: General rules – Structural fire design, European Committee for Standardization (CEN), Brussels, 2005.
2. EN 1993-1-8: Eurocode 3: Design of steel structures. Part 1-8: Design of joints, European Committee for Standardization (CEN), Brussels, 2005.

Steel structures

3. Jolanta Bączkiewicz, Mikko Malaska, Sami Pajunen, Markku Heinisuo (2017). *Fire design of rectangular hollow section joints*. Proceedings of conference Eurosteel 2017 1(2). pp. 2601-2609.
4. Yang J., Shao Y.B., Chen C (2014). *Experimental study on fire resistance of square hollow section (SHS) tubular T-joint under axial compression*. Advanced Steel Construction 10. pp 72-84.
5. Ozyurt E., Wang Y.C., Tan K.H (2014). *Elevated temperature resistance of welded tubular joints under axial load in the brace member*. Engineering Structures 59. pp 574-586.
6. Jolanta Bączkiewicz, Mikko Malaska, Sami Pajunen, Markku Heinisuo (2018). *Experimental and numerical study on temperature distribution of welded square hollow section joints*. Journal of Constructional Steel Research 142. pp 31-43.
7. ABAQUS 6.13/CAE User's Manual Dassault Systemes, (2013).
8. EN 1991-1-2: Eurocode 1: Actions on structures. Part 1-2: General actions – Actions on structures exposed to fire, European Committee for Standardization (CEN), Brussels, 2005.

PROGRESSIVE COLLAPSE OF BRACED STEEL FRAMED STRUCTURES EXPOSED TO FIRE

Jian Jiang¹, Guo-Qiang Li²

ABSTRACT

This paper investigates the influence of bracing systems on the progressive collapse resistance of steel framed buildings exposed to compartment fires. This includes the influence of type, number and location of bracing systems on the local and global collapse behaviour of 3D structures. The results show that the presence of braces can significantly enhance the fire-induced collapse resistance of unprotected buildings to a level of 60 mins. This is achieved by uniformly redistributing loads, limiting lateral drift of columns, and restraining deflection of slabs. It is found that the collapse of frames can be prevented by using either horizontal or vertical braces. A combination of hat braces at perimeter and vertical braces at interior is recommended. The presence of vertical braces at interior bays is essential to prevent collapse. For fires at corner is more dangerous than those at interior, it is suggested to conduct fire partition at corner of buildings to ensure that the fire is confined in one compartment without spread to adjacent compartments. This fire partition is beneficial to reducing the amount of bracing systems and also fire protection demands.

Keywords: Progressive collapse, compartment fire, 3D model, horizontal bracing, vertical bracing

1 INTRODUCTION

Previous studies focus on the robustness of structures against progressive collapse and collapse modes [1-6]. Among them most are conducted based on two-dimensional buildings. Although capable of capturing some key issues of fire-induced collapse mechanisms of structures, they fail to fully consider the load redistribution path in a realistic structure [6], and especially the effect of tensile membrane action of floors [7]. Agarwal and Varma [8] studied the progressive collapse behavior of a 3D 10-storey steel building exposed to fire. It was found that the interior gravity columns played a key role in the overall stability of the building. The collapse behaviour of a 3D 8-storey steel frame with concrete slabs was studied by Jiang and Li [4,6]. It was found that the fire protection of steel members had a significant influence on the resistance of structures against fire-induced collapse. A protected frame did not collapse immediately after the local failure but experienced a relatively long withstanding period of at least 60 min [4]. Generally, the collapse will be triggered by the buckling of the heated columns followed by lateral drift of adjacent columns at ambient temperatures, which is driven by the catenary action of the heated beams or tensile membrane action of the heated floors.

The FEMA report [9] proposed a call to determine “whether there are feasible design and construction features that would permit such buildings to arrest or limit a collapse, once it began”. Preventing the spread of local failure is the key to ensure the resistance to progressive collapse.

¹ PhD. College of Civil Engineering, Tongji University, Shanghai 200092, China.

e-mail: jiangjian_0131@163.com

² Professor. State Key Laboratory for Disaster Reduction in Civil Engineering, Tongji University, Shanghai 200092, China

e-mail: gqli@tongji.edu.cn

Increasing structural redundancy is an effective way for this purpose to enhance the robustness of structures against collapse. Some attempts have been made to answer the FEMA call by using bracing systems to enhance redundancy of structures at ambient temperatures [10,11]. In the case of fire, the application of bracing systems to improve progressive collapse resistance of steel frames is not well established in the literature. Most previous studies are based on 2D models [12,13], and their validity and generalization in practice is questionable when it comes to 3D structures.

This paper presents an attempt by using bracing systems to enhance redundancy of 3D steel framed structures, and thus to prevent or delay the collapse. The influence of horizontal and vertical bracing systems on the collapse resistance of buildings was investigated. Recommendations for the selection of bracing systems were proposed to provide a guide for fire-resistant design of steel frames against progressive collapse.

2 MODELING OF PROTOTYPE BUILDING

2.1 Layout of building model

An 8-storey moment resisting steel framed building was modelled as a prototype structure in LS-DYNA, as shown in *Fig. 1a*. Details of the frame configuration are presented in the reference [6]. An explicit dynamic analysis was carried out instead of implicit analysis to overcome its convergence problems. To save the computing cost of explicit analysis, an 8-second explicit analysis instead of 1-hour heating in a standard fire was run without causing oscillation.

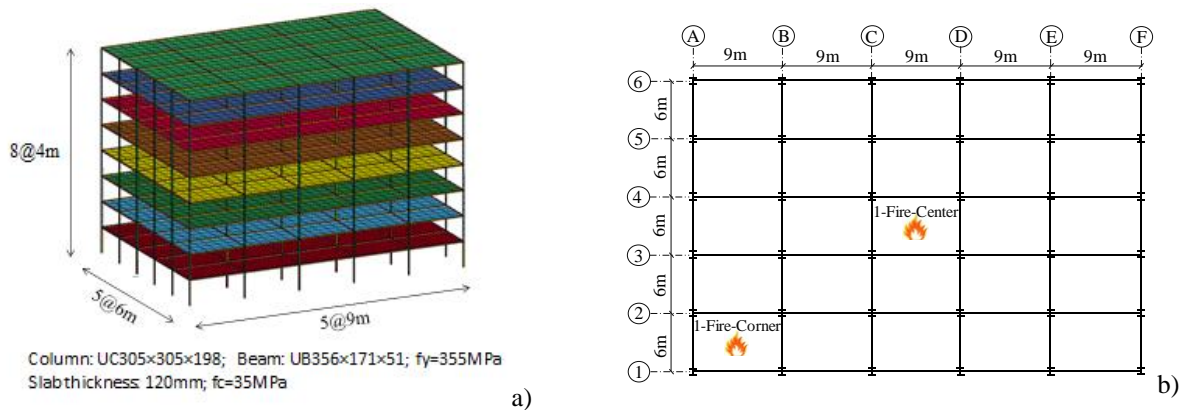


Fig. 1. Model of a 3D moment-resisting building: a) numerical model; b) collapse mode of unbraced frame

2.2 Layout of compartment fires

The ISO 834 standard fire was used, and it was assumed that the slabs, columns, beams and braces in the fire compartment were uniformly heated up to 4 hours. The cooling phase was not considered. A single-compartment fire at the center (1-Fire-Center) and at corner (1-Fire-Corner) of the ground floor, respectively, was considered in this study as shown in *Fig. 1b*. This is always adopted in the analysis of structures in fire, assuming that the fire is confined in the source compartment by fire doors or walls.

2.3 Layout of bracing systems

Inverted V-bracing systems with a square hollow structural section (HSS) were used which was designed according to AISC 341 [14]. The bracing section of HSS 203x203x13 was used for the first two storey, HSS 178x178x13 for the 3-6 storey, and HSS 152x152x10 for the upper two storey. Different bracing layouts were considered, including horizontal arrangements on the top storey (hat bracing, *Fig. 2*) and/or on the middle height (belt bracing, *Fig. 3*), as well as vertical arrangements. Three locations of vertical bracing systems were considered: one braced bay at midspan (Vertical-midspan, *Fig. 4*), two braced bays at interior (Vertical-interior, *Fig. 5*), two braced bays at ends (Vertical-end, *Fig. 6*).

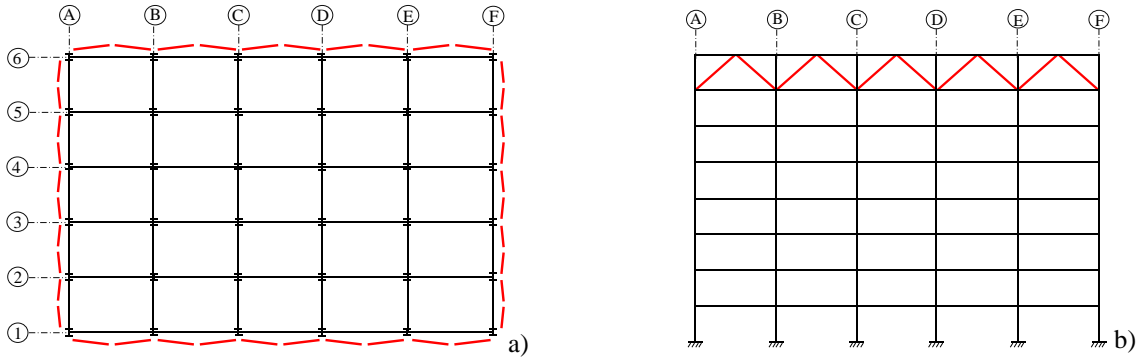


Fig. 2. Layout of hat bracing systems (Hat-perimeter): a) plan view; b) elevation view

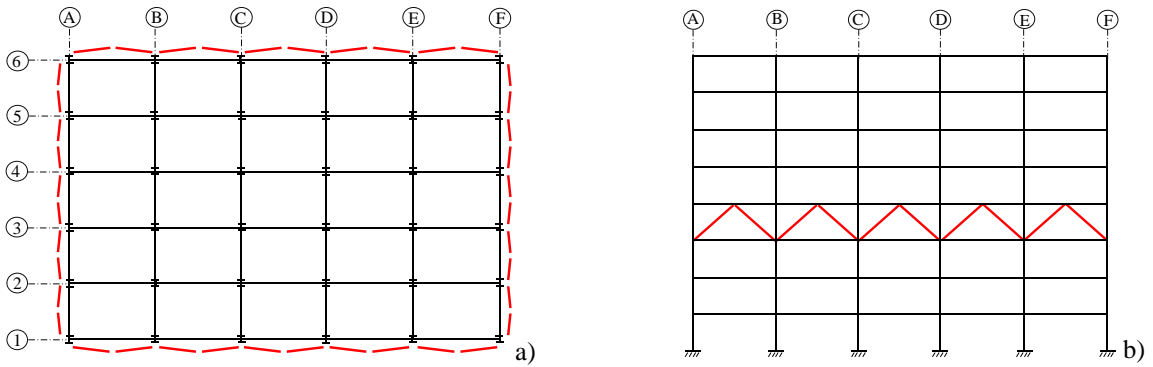


Fig. 3. Layout of belt bracing systems (Belt-middle): a) plan view; b) elevation view

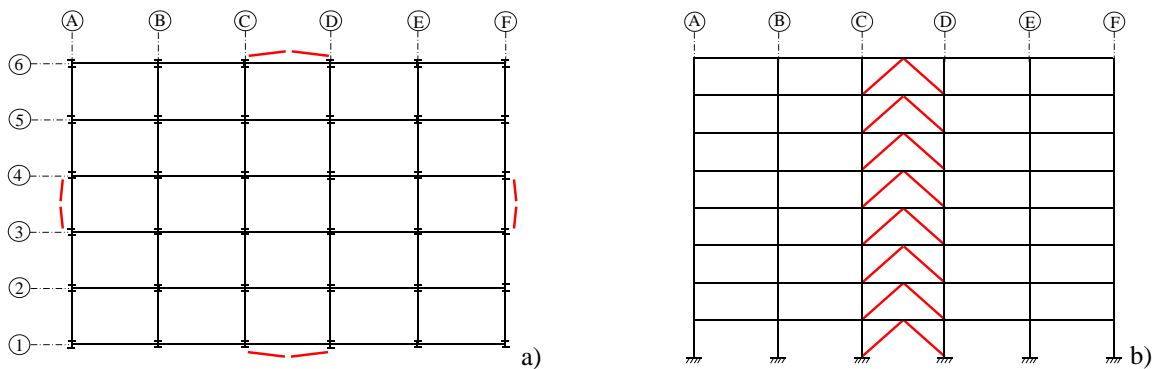


Fig. 4. Layout of vertical bracing systems at midspan (Vertical-midspan): a) plan view; b) elevation view

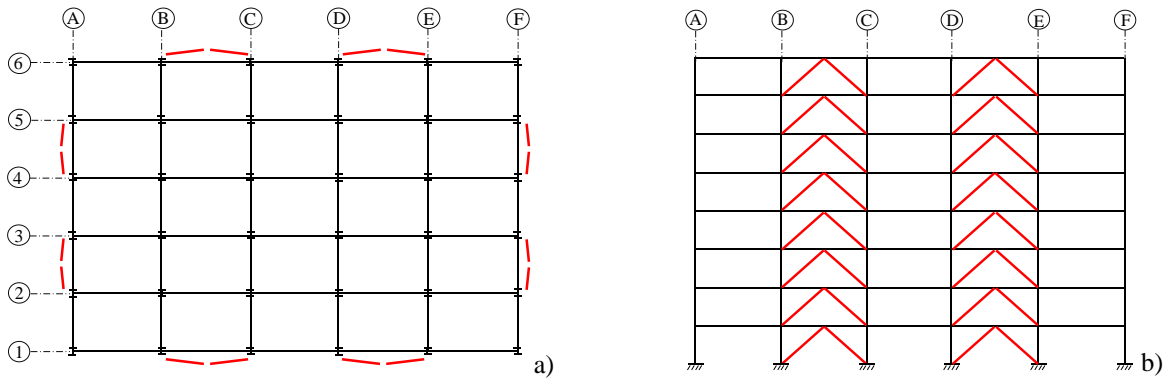


Fig. 5. Layout of vertical bracing systems at interior (Vertical-interior): a) plan view; b) elevation view

Progressive collapse of braced steel framed structures exposed to fire

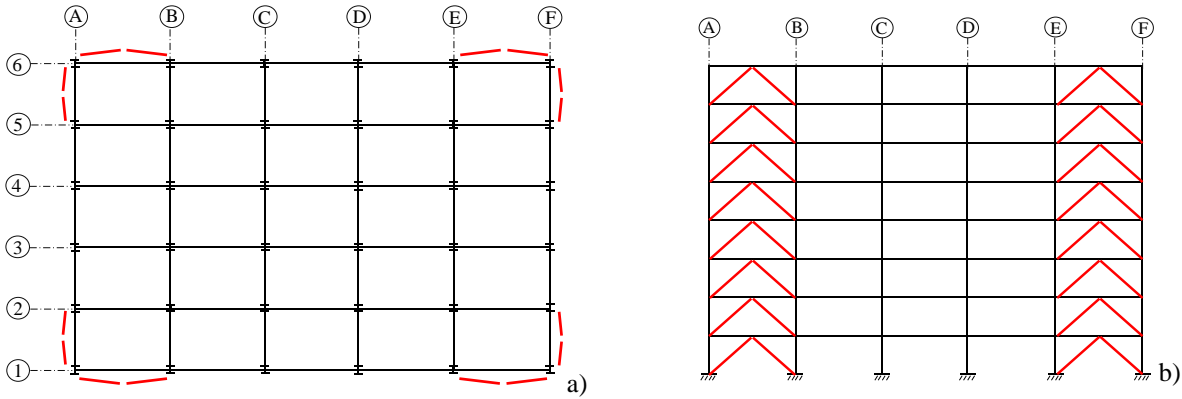


Fig. 6. Layout of vertical bracing systems at ends (Vertical-end): a) plan view; b) elevation view

3 BEHAVIOR OF BRACED FRAMES IN FIRE

The unbraced frame collapsed globally under the center and corner fire, respectively (Fig. 7). The collapse was represented by the sequential buckling of columns from the fire compartment to the adjacent compartments, as well as lateral drift of columns. The lateral drift was more significant in the center fire due to catenary action in the heated beams and tensile membrane action in the heated slab.

Therefore, the key to mitigate the collapse of a frame is to uniformly redistribute loads to adjacent columns, and to limit the lateral drift of adjacent columns. The former can be achieved by using horizontal bracing, while the latter by vertical bracing. This feasibility for single-compartment fire was first investigated in the following section.

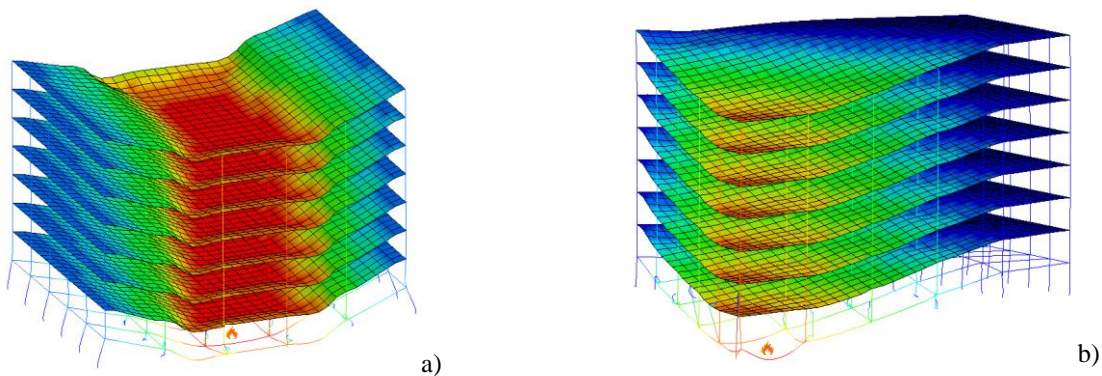


Fig. 7. Collapse modes of unbraced frames subjected to: a) 1-Fire-Center; b) 1-Fire-Corner

3.1 Horizontal bracing system

No global collapse occurred for the frames with horizontal braces. For the center fire, no adjacent columns at ambient temperatures (C2, C5, D2, D5) failed for the frames with hat braces, in addition to the buckling of the heated columns. In contrast, the adjacent columns buckled for the frame with belt braces. No buckling of braces occurred for the center fire. For the corner fire, the belt bracing had a better collapse resistance for the corner fire than a center fire. This is because the presence of belt braces had a significant effect on the axial displacement of adjacent columns. The belt braces placed in the middle height storey experience larger compressive forces than the hat braces, and thus become the weakness of horizontal bracing system. It was found that the frame with belt bracing alone would collapse under a corner fire if a smaller cross section of belt braces was taken (i.e. the same as the hat braces), as shown in Fig. 8. The collapse was due to the sequential buckling

of the belt braces in compression. While the frame with belt braces in a smaller section withstood the center fire.

The above results showed that hat bracing and belt bracing had a good performance for the center fire and corner fire, respectively. A combined hat and belt bracing is recommended in view of the uncertainty of fire locations. Special attention should be paid to the strength of the belt braces to prevent the global collapse of frames.

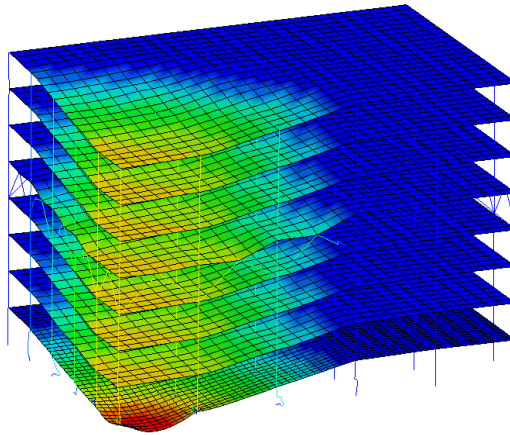


Fig. 8. Collapse mode of the frame with belt bracing in a smaller section

3.2 Vertical bracing system

For the center fire, the frame with Vertical-end bracing collapsed (*Fig. 9*), while the other frames withstood. The failure of adjacent columns in the frame with end braces was because of their large lateral displacements since the presence of braces at ends had limited effect on the lateral resistance of columns at interior. The large lateral displacement caused large $P-\Delta$ effect in the columns, resulting in their buckling. The collapse of the frame with end braces alone indicates the importance to apply vertical braces at the interior bays. The frames with midspan and interior bracing showed a similar behavior.

No frame with vertical bracing collapsed under the corner fire. The Vertical-interior bracing had the best collapse resistance since it led to the smallest axial displacement (170 mm) of the heated columns, compared to more than 800 mm for the other two layouts.

It showed that the frame with two braced bays at interior had a good performance under both center and corner fire. The presence of vertical braces at interior is important to enhance the collapse resistance.

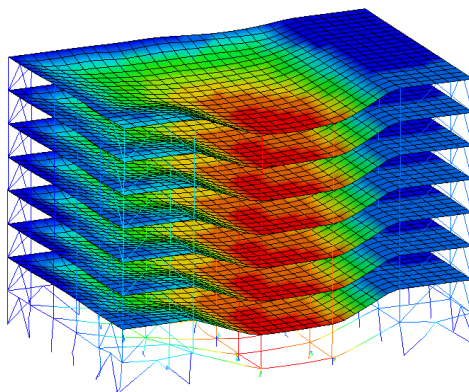


Fig. 9. Collapse mode of the frame with Vertical-end bracing under 1-Fire-Center

3.3 Combined horizontal and vertical system

In practice, the vertical braces are always used in a combination of horizontal braces, and the behavior of frames with combined horizontal-vertical bracing systems was studied in this section. The frame with Hat&Vertical-end bracing under the center fire collapsed, while the other frames withstood both the center and corner fire. Compared to the buckling of braces in the frame with Hat-perimeter bracing under a corner fire, the presence of vertical braces at interior prevented the buckling of hat braces. The application of horizontal braces in the vertically braced frame helps to enhance the collapse resistance by reducing the axial displacements of columns.

Therefore, from the perspective of efficiency and cost effectiveness, the optimal layout of bracing systems to resist single-compartment fires is the combination of hat braces at perimeters and vertical braces at interior. The frame with this combined bracing showed good collapse resistance and reduced dynamic effect for both center and corner fires.

4 CONCLUSIONS

This paper investigated the effect of bracing systems on the collapse resistance of 3D steel frames subjected to single-compartment fires on the ground floor. The horizontal and vertical bracing systems as well as their combination were considered. The results showed that it is feasible to use bracing systems to enhance the collapse resistance of steel framed buildings. The presence of braces was beneficial for uniformly redistributing loads, limiting lateral drift of columns, and restraining deflection of slabs. The collapse of braced frames can be delayed by 60 mins compared to unbraced frames. The collapse of frames under a single-compartment fire can be prevented by using either horizontal or vertical braces. A combination of hat braces at perimeter and vertical braces at interior is recommended since it showed a better performance for both interior and corner fires. It was found that the presence of vertical braces at interior bays of a frame was essential to prevent its collapse. A corner fire may cause the buckling of horizontal braces in compression. A combination of hat and belt braces or combination of vertical braces at interior can prevent the buckling of braces.

For practical design, it indicates that if fire doors (or fire walls) are used for the compartmentation of a building, the amount of bracing systems can be reduced to the extent that only applying hat braces around the perimeter or vertical braces at the midspan bay. For fires at corner is more dangerous than those at interior, it is suggested to conduct fire partition at corner of buildings to ensure that the fire is confined in one compartment without spread to adjacent compartments. This fire partition is beneficial to reducing the amount of bracing systems and also fire protection demands.

Further work is underway to investigate the influence of connection type (all connections were assumed rigid in this study) and cooling phase (a structure may collapse during cooling) on the collapse behaviour of structures.

ACKNOWLEDGMENT

The work presented in this paper was supported by the National Natural Science Foundation of China with grant 51408418, and Research project of State Key Laboratory for Disaster Reduction in Civil Engineering with grant SLDRCE14-A-05.

REFERENCES

1. D. Lange, C. Roben, A.S. Usmani (2012). *Tall Building Collapse Mechanisms Initiated by Fire: Mechanisms and Design Methodology*. Engineering Structures, 36. pp 90-103.
2. G.L.F. Porcari, E. Zalok, W. Mekky (2015). *Fire induced progressive collapse of steel building structures: A review of the mechanisms*. Engineering Structures, 82. pp 261-267.
3. J. Jiang, G.Q. Li, A.S. Usmani (2014). *Progressive collapse mechanisms of steel frames exposed to fire*. Advances in Structural Engineering, 17(3). p 381-398.

4. J. Jiang, G.Q. Li (2017). *Disproportional Collapse of 3D Steel-framed Structures Exposed to Various Compartment Fires*. Journal of Constructional Steel Research, 138. pp 594-607.
5. R.R. Sun, Z.H. Huang, I. Burgess (2012). *Progressive Collapse Analysis of Steel Structures under Fire Conditions*. Engineering Structures, 34. pp 400-413.
6. J. Jiang, G.Q. Li (2017). *Progressive collapse analysis of 3D steel frames with concrete slabs exposed to localized fire*. Engineering Structures, 149. pp 21-34.
7. X.D. Pham, K.H. Tan (2013). *Membrane actions of RC slabs in mitigating progressive collapse of building structures*. Engineering Structures, 55. pp 107-115.
8. A. Agarwal, A.H. Varma (2014). *Fire induced progressive collapse of steel building structures: The role of interior gravity columns*. Engineering Structures, 58. pp 129-140.
9. FEMA (2002) World Trade Center building performance study. Report 403, Federal Emergency Management Agency, Washington D.C., 2002.
10. K. Khandelwal, S. El-Tawil, F. Sadek (2009). *Progressive collapse analysis of seismically designed steel braced frames*. Journal of Constructional Steel Research, 65. pp 699-708.
11. J. Kim, Y. Lee, H. Choi (2011). *Progressive collapse resisting capacity of braced frames*. The Structural Design of Tall and Special Buildings, 20. pp 257-270.
12. J. Jiang, G.Q. Li, A.S. Usmani (2015). *Effect of bracing systems on the fire-induced progressive collapse of steel structures*. Fire Technology, 51. pp 1249-1273.
13. R.R. Sun, Z.H. Huang, I. Burgess (2012). *The collapse behaviour of braced steel frames exposed to fire*. Journal of Constructional Steel Research, 72. pp 130-142.
14. AISC 341. *Seismic Provisions for Structural Steel Buildings*, American Institute of Steel Construction (AISC), Inc., 2005

NUMERICAL PARAMETRIC STUDY OF COLD-FORMED STEEL C-SHAPED COLUMNS EXPOSED TO FIRE

Luís Laím¹, João Paulo C. Rodrigues^{2,*}, Leroy Gardner³

¹ ISISE – Institute Sustainability and Innovation on Structural Engineering, University of Coimbra, Portugal.

² Department of Civil Engineering, University of Coimbra, Portugal.

³ Department of Civil and Environmental Engineering, Imperial College London, UK

* Author for contact. Tel.: +351 239 797 237; Fax: +351 239 797 123; E-mail: jpaulocr@dec.uc.pt

ABSTRACT

A numerical investigation into the structural behaviour of cold formed steel C-shaped columns commonly used in warehouses and industrial buildings subjected to fire is presented in this paper. The structural performance of cold-formed steel columns under fire conditions has been examined in a number of recent studies. However, the great majority of them have assumed that the internal forces and moments at the supports of the members remain unchanged throughout the fire exposure. Hence, a detailed parametric numerical investigation into the response of axially and rotationally restrained cold-formed steel C-shaped columns in fire has been addressed in this paper. In the first phase of this research, a finite element model was developed and calibrated against experimental fire tests. A parametric analysis was then undertaken using the calibrated finite element model with the purpose of investigating numerically the effect of some key parameters such as initial applied load on the column, slenderness and the influence of restraint to thermal elongation of such columns. A further objective of this research was to compare the numerical results with the predictions from available design rules (Eurocode 3). The results of this research showed that the critical temperature of cold-formed C-section columns with elastically restrained thermal elongation may drop significantly in comparison to the unrestrained scenario.

Keywords: Cold-formed, steel, columns, fire, thermal restraint, finite element analysis, buckling, design rules.

1 INTRODUCTION

The structural performance of cold-formed steel (CFS) members under fire conditions has increasingly been studied in recent years. Existing research shows that fire resistance for unprotected columns and beams is generally less than 30 minutes [1] and between 30 and 120 minutes depending on the load ratio when protected by plasterboards [2]. The features, such as low thickness, open cross-sections and significant flexural rigidity differences about the two cross-sectional axes, lead to buckling being the key phenomenon in the failure of CFS members. CFS columns are susceptible to three main buckling modes, i) local, ii) global (flexural or flexural-torsional) and iii) distortional buckling [3]. Short columns mostly fail by local and distortional buckling while long columns commonly fail by flexural and flexural-torsional buckling. Most of the studies into flexural-torsional buckling of CFS columns at elevated temperatures (up to 700 °C) were carried out using the steady-state method [4]. For the successful use of cold-formed steel members in buildings without any fire damage, they should be protected or designed based on reliable fire design rules. Elevated temperature design standards mainly focus on hot-rolled steel members and recommend the same guidelines for the design of cold-formed steel members with some limitations, despite the fact that the behaviour of cold-formed steel members is different from

that of hot-rolled steel members. This is why, currently, the structural fire behaviour of light gauge steel structures has become an important area of research in order to improve their fire safety [5]. The fire code Eurocode 3 Part 1.2 [6] recommends the use of the ambient temperature effective area to account for local and distortional buckling. This may result in too conservative predictions at elevated temperatures, which may lead to uneconomical designs for CFS structures. Hence it has been recommended that ambient temperature design guidelines but with elevated temperature mechanical properties should be used to predict the local buckling capacities of CFS members in fire [7].

The great majority of these previous studies have been performed on individual/independent members i.e. neglecting the stiffness of the surrounding members/structure [8] and assuming that the internal forces and moments at the supports of the members remain unchanged throughout the fire exposure [9]. However, in reality, the connection between the investigated member and the other elements of a structure leads to axial restraint against thermal elongation and also rotational restraint at the member ends. This restraint may have an important influence on the behaviour of the members under fire conditions, and therefore their critical temperature and fire resistance. The imposed axial restraint can generate substantial unforeseen forces in the members during fire leading potentially to premature structural failure, while the rotational restraint will typically have a positive influence [10]. Note that this subject has only been studied on hot-rolled steel members (class 1 or 2 cross-sections) [11, 12]. Most of the conclusions from these works state that the fire resistance of compression members may be not significantly affected by the stiffness of the surrounding structure, due to the beneficial effect of the rotational restraint at their ends [11, 12].

In this paper, a numerical parametric study into the structural behaviour of restrained cold-formed galvanized steel C-shaped columns under fire conditions (using the transient state method) is presented. A suitable finite element model was first developed to compare with experimental results [1]. After calibrating the developed finite element model against the experimental results, a parametric study was performed outside the bounds of the original experimental tests, concentrating particularly on variation in slenderness of the columns (by changing the section size and end-support conditions), level of initial applied load on the columns and stiffness of the surrounding structure. The aim was to investigate the extent to which the axial and rotational restraint at the column supports can affect the structural performance of the columns in fire. The numerical results were also compared with the predictions from available design rules (Eurocode 3) [6].

2 EXPERIMENTAL INVESTIGATION

2.1 Tested columns

Extensive experimental research work on CFS columns in fire has been carried out over the past few years at University of Coimbra, in Portugal [1, 13]. The aim was to produce accurate data for the use in and calibration of different numerical analyses. Four different cross-sections were selected for these studies, including C, U, lipped I, R and 2R sections (fig. 1). All these cross-sections were 2.5 mm thick and 43 mm wide. The internal bend radius and the length of the edge stiffeners of the C profiles were 2 and 15 mm, respectively. The C sections were 150 mm tall, whereas the U sections were 155 mm tall, so that the C profiles could be placed between the flanges of the U profiles (R column), as illustrated in Figure 1. The built-up I columns consisted of two C's connected in the web, whereas the built-up R columns consisted of one C profile and one U profile connected in the flanges. The built-up 2R columns were made of two R columns connected together by the C profiles' web. These connections were materialized by means of carbon steel self-drilling screws in S235 structural steel. The CFS test sections were manufactured from S280GD+Z275 structural steel sheets pre-galvanized with a standard zinc coating thickness of 0.04 mm (275 g/m²) by cold rolling. The columns length was 2950 mm for all specimens and the distance between the screws along the column length was around 625 mm (L/4.75).

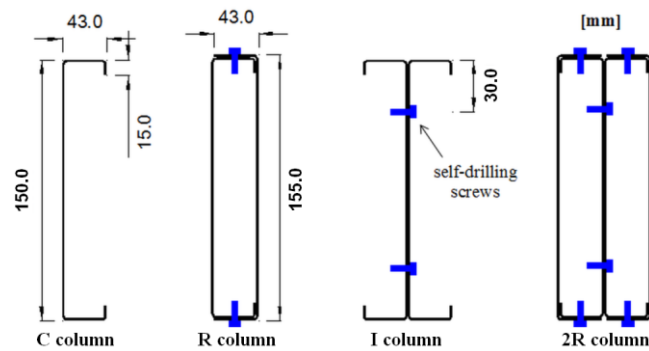


Fig. 1. Scheme of the cross-sections of the tested columns

2.2 Test facility

Figure 2 illustrates a view of the experimental system used in the fire resistance tests of CFS columns in which all the components are labelled. The experimental set-up comprised a two dimensional (2D) reaction steel frame (1) and a three dimensional (3D) restraining steel frame (2) in order to simulate the restraint imposed by a surrounding structure on the CFS column under fire conditions. Note that several holes distributed along the flanges of the beams of the restraining frame (2) allowed the assembly of the corresponding peripheral columns at different positions, leading to different spans of the beams which corresponded to different values of stiffness of the surrounding structure. The stiffness could be then modified when the column or beam cross-section was changed. A hydraulic jack (3) was hung on the 2D reaction frame (1) and controlled by a servo hydraulic central unit and; beneath this, a load cell (4) was mounted in order to monitor the applied load during all tests. The test columns (5) were placed in the centre of the 3D restraining frame (2) and properly fitted to it by means of two end-support devices, with the purpose of simulating both semi-rigid ended and pin-ended support conditions. The pin-ended support about the minor axis was obtained using a Teflon-lined steel pin as a hinge. The Teflon lining was used to reduce friction. The semi-rigid end-support was obtained by blocking the hinge of the pin-ended supports with a set of steel plates. Additionally, above the specimen (5) a special device (6) that consisted in a massive steel cylinder that entered in a high stiffness hollow steel cylinder was mounted. Inside the hollow steel cylinder existed a load cell to monitor the axial restraining forces generated in the CFS columns during the whole test. Regarding the thermal action, the test specimens were heated by means of a vertical modular electric furnace (7) which was programmed to reproduce the standard fire curve ISO 834 [14].

2.3 Test procedure

The fire tests on the CFS columns were conducted under transient state temperature conditions, involving two stages: the loading and heating stages. The specimens were first concentrically loaded up to the target force under load control at a rate of 0.1 kN/s. The load level applied to the columns, P_0 , was a percentage of the design value of the buckling load of the columns at ambient temperature, calculated in accordance with the methods given in EN 1993-1.1:2004 [15], EN 1993-1.3:2004 [16] and EN 1993-1.5:2006 [17]. In the second stage (when the load reached the desired level), the column was exposed on all four sides to high temperatures in such a way that the average temperature in the furnace followed as closely as possible the ISO 834 standard fire curve [14]. Note that, the load was kept constant until the specimen failed. The failure criterion adopted in this study was based on the ultimate bearing capacity of the column (column strength); in other words, a column was considered to have failed when it could no longer support the initial applied load (serviceability load), and not when its buckling load was reached (maximum compressive strength of column). This approach is the same as that established in other research works which were focused on the fire behaviour of structural members with restrained thermal elongation [10-12].

3 NUMERICAL INVESTIGATION

3.1 Numerical model

A three-dimensional numerical model, developed in the advanced finite element program ABAQUS/CAE 6.14-1 [18] (fig. 3), was used to describe all buckling modes observed in the experimental tests [1, 19]. Note that this paper reports and discusses the results of a numerical investigation into the structural behaviour of CFS C-shaped cross-section columns under combined fire and compressive loading conditions. Axial compression tests on semi-rigid ended and pin-ended CFS columns were simulated, i.e., the applied load was equally distributed along the perimeter of the cross-section by means of the *Coupling Constraints option in ABAQUS [18]. To simulate the pin-ended support conditions all degrees of freedom of translation in the column supports were constrained, except for the top support of the columns where the vertical translation was free. On the other hand, a linear spring model was used for the modelling of the axial and rotational restraining system (including the semi-rigid ended support conditions). Finally, the rotation at each support about the longitudinal direction of the column was constrained in order to prevent torsion at the column supports. All C-shaped columns were modelled using shell elements (S4R) [18].

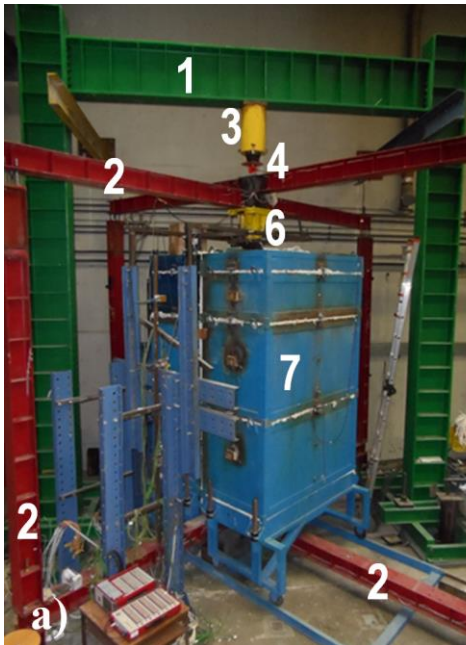


Fig. 2. General view of the experimental set-up (a) and the test column (b)

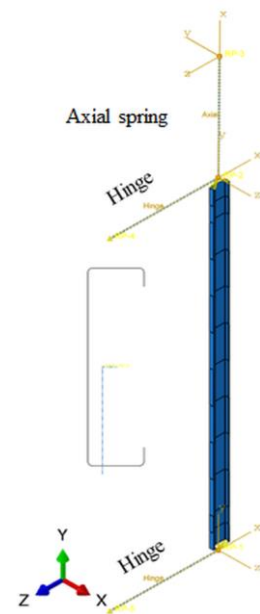


Fig. 3. Numerical model

Material non-linearity in the specimens was modelled with the von Mises yield criteria and isotropic hardening. The stress-strain relationship of the CFS profiles was described by a gradual yielding behaviour followed by a considerable period of strain hardening. The material modelling was based on the mechanical and thermal properties of the S280GD+Z steel previously determined by the authors [20]. The yield strength, elastic modulus and the stress-strain curves were determined at both ambient temperature and elevated temperatures up to 800°C. The stress-strain curves used as input were converted to true stress and logarithmic plastic strain. Thermal properties were also determined experimentally using the Transient Plane Source Technique [20]. Residual stresses and cold-work of forming (where the apparent yield stress in the corners is increased) were ignored in these analyses; in other words, the mechanical properties of the steel were assumed to be uniform across the cross-section, as assumed by other researchers in this field [21].

The numerical analysis was conducted in three sequential steps: elastic buckling analysis, heat transfer analysis and nonlinear static structural analysis. Elastic buckling analysis was performed to establish the buckling modes which were observed in those experimental tests [1], which were then used as imperfections. It was observed that a suitable maximum value for global imperfections was

approximately $L/1000$, for distortional imperfections t and for local imperfections $h/200$ [22]. A heat transfer analysis was used to develop temperature profiles through the cross-section for the duration of the fire. The fire action was defined in Abaqus through two types of surface, namely “film condition” and “radiation to ambient”, corresponding respectively to heat transfer by convection and radiation. The columns were heated according to the standard fire curve ISO 834 [14]. Finally, a nonlinear static structural analysis was undertaken. A serviceability load was first applied on the columns as mentioned above and afterwards the temperature profiles calculated in the heat transfer analysis were used as a result of the fire action. During this heating phase, the load was kept constant until the specimen buckled.

3.2 Calibration of numerical model

Comparisons of the experimental and numerical results are given to demonstrate the authors’ confidence in using Abaqus to model the fire resistance and behaviour of this type of column outside the bounds of the original experimental tests. Figure 4 shows, for example, the comparison of the relative axial restraining force-temperature ($P/P_0 - \bar{\theta}_C$) curves of the axially and rotationally restrained C columns obtained from the experimental tests and finite element analysis (FEA) used for the calibration of the model.

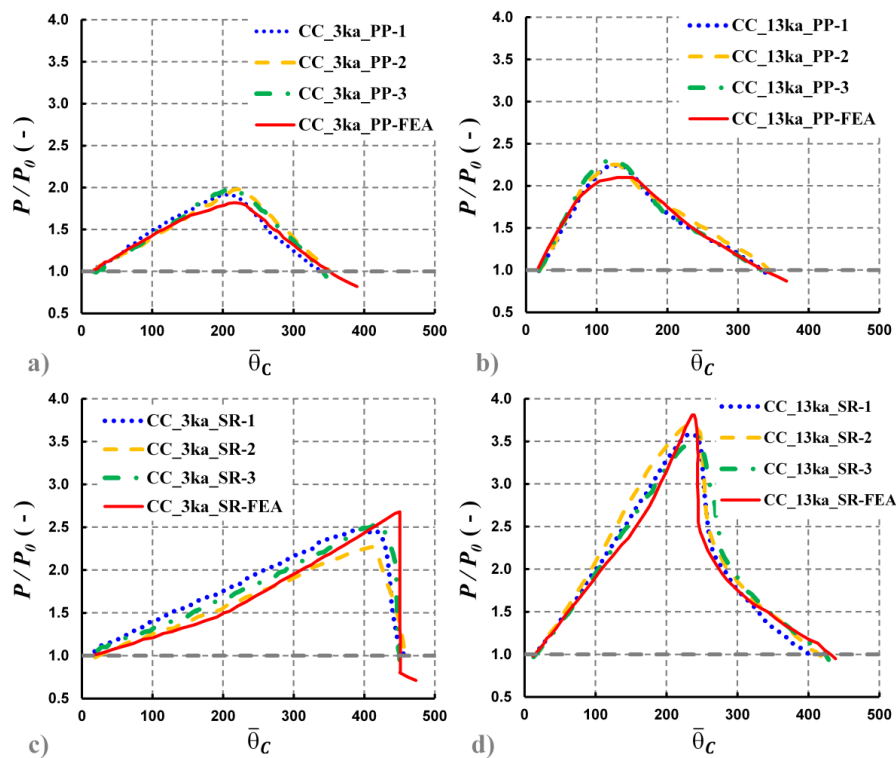


Fig. 4. Comparison of the FEA and experimental axial restraining forces generated in the pin-ended (a, b) and semi-rigid end (c, d) C columns with 3 (a, c) and 13 (b, d) kN/mm restrained thermal elongation and under a 50% load level

When a steel column with restrained thermal elongation is subjected to fire, it is expected that the axial compression force increases during an initial phase (because the column is not free to elongate), but eventually it starts to decrease up to the initial axial compression force applied to the column (service load, P_0), due to bowing and/or warping of the heated column and to the degradation of the material’s mechanical properties. It is observed that the buckling temperature (when the maximum compressive strength of column is reached) was higher in the semi-rigid ended columns than in the pin-ended columns (i.e., higher capacity for plasticity), but the post-buckling range is shorter in the semi-rigid ended columns than in the pin-ended columns due to the higher compressive state along such columns. All curves from FEA (continuous red line) fit closely with the experimental curves. Actually, the mean differences between these experimental and numerical results were around 5 % in terms of critical temperature of the columns. Note that the average of the

measured critical temperature was 346°C for the pin-ended C columns under a 50% load level and a 3 kN/mm restrained thermal elongation (fig. 4a), 339°C for the pin-ended C columns under a 50% load level and a 13 kN/mm restrained thermal elongation (fig. 4b), 454°C for the semi-rigid ended C columns under a 50% load level and a 3 kN/mm restrained thermal elongation (fig. 4c) and 415°C for the semi-rigid ended C columns under a 50% load level and a 13 kN/mm restrained thermal elongation, whereas the estimated critical temperature was respectively 369°C, 343°C, 450°C and 433°C. This good agreement and accuracy between the experimental and numerical results may ensure reliability of results obtained from parametric studies.

4 PARAMETRIC STUDY

4.1 Effect of axial restraint

An extensive parametric study was performed to enhance the understanding of the complicated structural behaviour of restrained C columns and supply sufficient data on this type of section to evaluate current design rules. The FEA specimens had different thicknesses (1.5, 2.5mm), heights (150, 250mm) and lengths (1000, 1500, 2000, 2500, 3000mm) so that most columns used in CFS structures were evaluated. Additionally, different initial applied load levels (LL) on the columns (30, 50, 70% of the design value of the buckling load of the columns at ambient temperature), boundary conditions (pin-ended and semi-rigid ended supports) and axial restraint ratios ($k_a/k_{a,c} = 0, 2.5, 5, 10, 15, 20, 25, 50, 100, 1000\%$) were still selected in the parametric study, thus covering most serviceability loads and restraining conditions commonly established in this type of building.

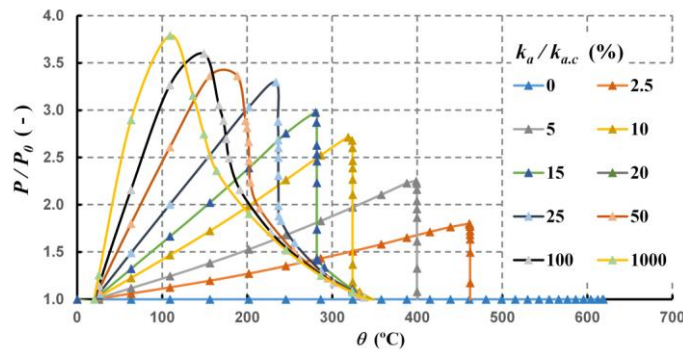


Fig. 5. Evolution of axial restraining forces in axially restrained C150_1.5_3000 column with semi-rigid ended support conditions and under a 70% load level as a function of its mean temperature

It is interesting to observe that the higher the axial restraint (k_a) is, the higher the maximum axial restraining force becomes and the sooner it occurs (i.e., the lower the buckling temperature is as can be seen in Figure 5), but the value of the critical temperature of the columns remains constant beyond a certain level of axial restraint (fig. 6).

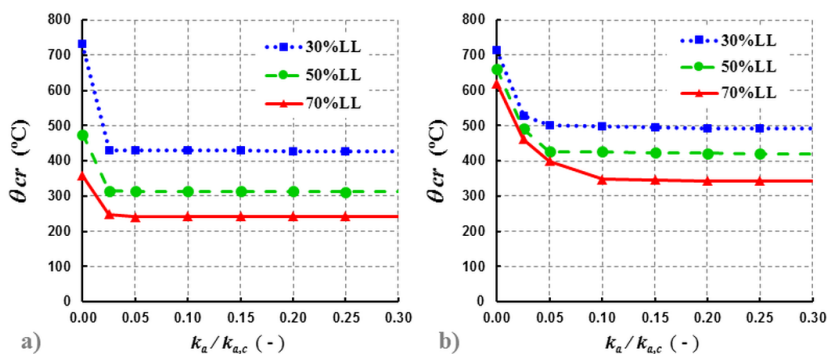


Fig. 6. Effect of axial restraint on the critical temperature of C150_1.5_3000 column with pin-ended (a) and semi-rigid ended (b) support conditions

It seems that the critical temperature of axially CFS columns remains almost unchanged for ratios between the axial restraint and the axial stiffness of the column ($k_a/k_{a,c}$) higher than 0.025 for pin-ended columns and 0.05 for semi-rigid ended columns under a 30% load level; and 0.05 and 0.10

for columns under a 70% load level, respectively. However, this amount of axial restraint may decrease the critical temperature by 65%. This means that such columns under fire conditions are sensitive to axial restraint for small values, with the pin-ended columns being slightly more affected than the semi-rigid ended columns.

4.2 Accuracy of design methods

Figure 7 displays the comparison of the FEA results obtained for different slenderness of C columns with pin-ended support conditions, fire and different restraining conditions (including no restraints and partial axial restraint to the thermal elongation of the column) with the design curves obtained from the fire design code, EN 1993-1.2:2005 [6]. It can be seen that code predictions may be slightly unsafe (for pin-ended columns with no axial restraints) and over non-conservative (for pin-ended columns with a 0.20 axial restraint ratio) whatever the load level and the column slenderness. For example, when the methods established in EN 1993-1.2:2005 [6] are used for CFS C columns under a 50% load level the estimated critical temperatures may have an average non-conservative error equal to 8% (with a maximum error equal to 14%) for non-restrained columns and an average non-conservative error equal to 80% for columns with a 0.20 axial restraint ratio.

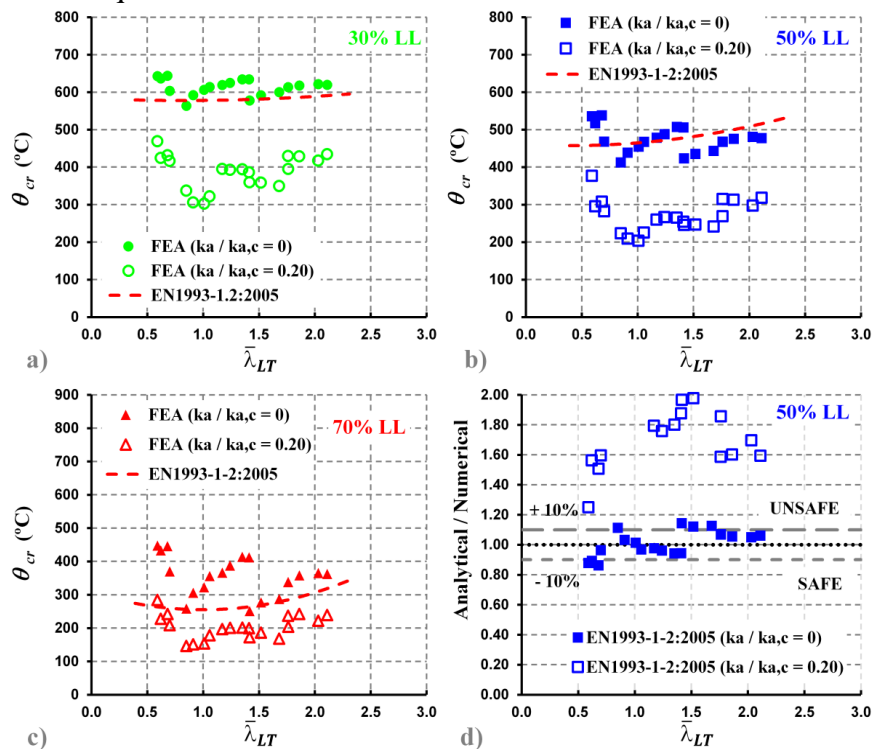


Fig. 7. Comparison of FEA results with EN 1993-1.2:2005 [6] for C columns under different load levels: 30% (a), 50% (b, d) and 70% (c)

5 CONCLUSIONS

This paper has described a finite element model developed to simulate the fire response and behaviour of cold-formed steel C-shaped columns. It was first observed that the model was found to be accurate in predicting the structural behaviour of such columns in the fire situation, especially their critical temperatures, with an average difference of not more than 10% when compared with the results obtained from several experimental tests previously performed by the authors [1]. Despite this, the main conclusion of this investigation was that the design rules given in EN 1993-1.2:2005 [6] are not suitable for designing cold-formed steel compression members subjected to fire. The design predictions give too non-conservative results for axial restrained columns. Adding axial restraint to the thermal elongation of columns may significantly affect their critical temperature (reaching differences around 60%) and beyond certain values of the axial restraint ratio

($k_a/k_{a,c} \approx 10\%$) from the surrounding structure to the CFS columns, the restraint has no further influence on their fire resistance and behaviour. It is therefore recommended that in the near future the current simple calculation model in EN 1993-1.2:2005 [6] should be revised and improved for CFS columns on the basis of these findings.

REFERENCES

1. Helder D. Craveiro, João P.C. Rodrigues, Luís Laím (2014). *Cold-formed steel columns made with open cross-sections subjected to fire*. Thin-Walled Structures 85. pp 1-14.
2. Shanmuganathan Gunalan, Mahen Mahendran (2014). Fire performance of cold-formed steel wall panels and prediction of their fire resistance rating. Fire Safety Journal 64. pp. 61–80.
3. Anthony D. Ariyanayagam, Mahen Mahendran (2018). *Residual capacity of fire exposed light gauge steel frame walls*. Thin-Walled Structures 124. pp. 107–120.
4. Shanshan Cheng, Long-yuan Li, Boksun Kim (2015). *Buckling analysis of partially protected cold-formed steel channel-section columns at elevated temperatures*. Fire Safety Journal 72. pp. 7–15.
5. Muhammad F. Javed, Nor Hafizah, Shazim A. Memon, Mohammad Jameel, Muhammad Aslam (2017). *Recent research on cold-formed steel beams and columns subjected to elevated temperature: A review*. Construction and Building Materials 144. pp. 686–701.
6. EN 1993-1.2 (2005). Design of steel structures. General rules. Structural fire design. European Committee for Standardization, Brussels, Belgium.
7. Shanmuganathan Gunalan, Yasintha B. Heva, Mahen Mahendran (2015). *Local buckling studies of cold-formed steel compression members at elevated temperatures*. Journal of Constructional Steel Research 108. pp. 31–45.
8. Shanshan Cheng, Long-yuan Li, Boksun Kim (2015). *Buckling analysis of cold-formed steel channel-section beams at elevated temperatures*. Journal of Constr. Steel Research 104. pp 74-80.
9. Ju Chen, Ben Young (2007). *Cold-formed steel lipped channel columns at elevated temperatures*. Engineering Structures 29. pp 2445-2456.
10. Faris Ali, David O'Connor (2001). *Structural performance of rotationally restrained steel columns in fire*. Fire Safety Journal 36. pp 679-691.
11. João Paulo C. Rodrigues, Luís Laim (2017). *Fire response of restrained composite columns made with concrete filled hollow sections under different end-support conditions*. Eng. Struct. 141. pp 83–96.
12. Jean-Marc Franssen (2000). *Failure temperature of a system comprising a restrained column submitted to fire*. Fire Safety Journal 34. pp 191-207.
13. Helder David da Silva Craveiro (2015). *Fire resistance of cold-formed steel columns*. Thesis for the degree of Doctor of Philosophy (Ph.D.) in Fire Safety Engineering, Department of Civil Engineering, Faculty of Sciences and Technology, University of Coimbra, Portugal.
14. ISO 834-1 (1999) Fire resistance tests – elements of building construction, Part 1: general requirements, International Organization for Standardization, Geneva, Switzerland.
15. EN 1993-1.1 (2004). Design of steel structures. General rules and rules for buildings. European Committee for Standardization. Brussels, Belgium.
16. EN 1993-1.3 (2004). Design of steel structures. General rules. Supplementary rules for cold-formed members and sheeting. European Committee for Standardization. Brussels, Belgium.
17. EN 1993-1.5 (2006). Design of steel structures, Part 1-5: Plated structural elements, European Committee for Standardization, Brussels, Belgium.
18. Abaqus/CAE Standard User's Manual, version 6.14-1, Dassault systèmes, Simulia Corp., USA, 2014.
19. Helder D. Craveiro, João P.C. Rodrigues, Luís Laím (2017). *Cold-formed steel columns at both ambient and fire conditions*. Journal of Structural Fire Engineering, 14 p.
20. Helder D. Craveiro, João P.C. Rodrigues, Aldina Santiago, Luís Laím (2016). *Review of the high temperature mechanical and thermal properties of the steels used in cold formed steel structures – The case of the S280GD+Z steel*. Thin-Walled Structures 98. pp. 154-168.
21. J.-H Zhang, B. Young (2015). *Numerical investigation and design of cold-formed steel built-up open section columns with longitudinal stiffeners*. Thin-Walled Structures 89. pp. 178-191.
22. Duarte Nuno Ferreira de Oliveira (2016). *Numerical Analysis of Compressed Cold Formed Steel Elements subjected to Ambient and High Temperatures*. MSc Thesis in Civil Engineering, Faculty of Sciences and Technology, University of Coimbra, Portugal (in Portuguese).

AN EQUIVALENT STRESS METHOD FOR CONSIDERING LOCAL BUCKLING IN BEAM FINITE ELEMENTS IN THE FIRE SITUATION

Chrysanthos Maraveas¹, Thomas Gernay², Jean-Marc Franssen³

ABSTRACT

The use of slender steel sections has increased in recent years because they provide excellent strength to weight ratio. Yet, a major issue with slender sections is local buckling in compression zones. Several researchers have proposed design methods at elevated temperatures based on the effective width approach to calculate the capacity of the plates that compose these steel members, but this approach is not easily compatible with the implementation and use in Bernoulli beam elements. Another approach is the development of a stress based model, i.e. an “effective” constitutive law of steel. This approach was proposed previously by Liege University researchers for slender steel members exposed to high temperatures, and implemented within the framework of fiber type Bernoulli beam elements; however it was giving overly conservative results. This paper presents an improved temperature-dependent constitutive model for steel that accounts for local instabilities using the stress based method. The improved model is derived from refined plate analysis methodology and implemented in the SAFIR finite element analysis software. Validation shows good agreement against experimental and shell element analysis results.

Keywords: Local buckling, slender cross-sections, fire, beam finite elements, stress based method

1 INTRODUCTION

The use of slender steel sections has increased in recent years because they provide excellent strength to weight ratio; this trend has also been favoured by the development of higher steel grades. Yet, a major issue with slender sections is local buckling that may occur in compression zones: in the flange under compression for elements in bending and essentially in the web for elements in compression. In very deep sections, shear can also trigger local buckling in the web if it is too slender. Local buckling can also have a significant influence on the behaviour of steel members in the fire situation. Detailed information regarding the local buckling of steel members exposed to fire is presented in [1].

Furthermore, past fire accidents have demonstrated local buckling failures in structural members with slender cross sections, like in WTC 5 [2] and Broadgate fire [3].

To take local instabilities into account, several design methods have been proposed by researchers relying on the effective width approach and based on numerical models of isolated plates [4], [5], [6] or analytical methods [7], but this approach is not easily compatible with the implementation and use in Bernoulli beam elements. Beyond the complexities associated with estimating the effective width (which formally depends on the stress distribution), the development of thermal strains in the fire situation may lead to reversal from tension to compression, and vice versa, in

¹ Post-Doctoral Research Fellow, Department of Architecture, Geology, Environment & Constructions (ArGEnCo), Liège University, Belgium. e-mail: c.maraveas@maraveas.gr

² Assistant Professor. Department of Civil Engineering, Johns Hopkins University, USA.
e-mail: tgernay@jhu.edu

³ Professor. Department of Architecture, Geology, Environment & Constructions (ArGEnCo), Liège University, Belgium.
e-mail: jm.franssen@ulg.ac.be

different parts of the cross section, rendering the effective width approach particularly difficult to implement. Therefore another approach was proposed by Liege University researchers as the development of a stress based model, i.e. an “effective” constitutive law of steel [8]. This effective stress based approach for slender steel members exposed to high temperatures was implemented within the framework of fiber type Bernoulli beam finite elements. However the implemented model was giving overly conservative results.

This paper presents an improved temperature-dependent constitutive model for steel that accounts for local instabilities using the stress based method. Based on a refined methodology and revisited assumptions [9], [10], [11], improved buckling reduction factor vs plate slenderness relationships have been derived and, based on these relationships, a novel equivalent stress-strain-temperature relationship has been derived. The model is intended to be used in nonlinear numerical analysis with fiber type beam finite elements aiming at calculation of the fire resistance of thin-walled steel elements. The model can be easily implemented into any finite element software which include this type of FE.

2 PROPOSED MODEL

2.1 Model development

The effective law is derived with the same objective as the effective width: the compressive capacity obtained with the effective law in the full section should be equal to the capacity of the slender plate with the real material under local buckling. Because local buckling develops only in compression, the real stress-strain relationship needs to be modified only in compression and remains untouched in tension. It thus leads to an effective law that is non-symmetrical with respect to compression-tension. The tangent modulus at the origin of the law is not modified (because low compression stresses do not produce local instabilities), but the development of local instabilities is reflected by a reduction of the limit of proportionality and of the effective yield strength. The effective stress-strain relationship in compression depends on the slenderness, on the boundary conditions of the plates and on the temperature.

The model development is based on parametric finite element analyses of isolated plates in pure compression. Steady-state compression tests are performed on the plates at different (constant) high temperatures. The analyses are performed for three sides simply supported (flange equivalent) and four sides simply supported plates (web equivalent), for steel grades from S235 and up to S460 and for temperatures from 20°C to 900°C. The following assumptions are adopted: imperfection amplitude equal to 1/200 of the plate width b [9]; sinusoidal shape of imperfections with m half-waves ($m = 1$ for webs and $m = 1$ and 4 for flanges) [10], [11], and plate length ratio a/b equal to 1 for web and 5 for flange [10]. The software SAFIR[®] [12] is used for the finite element analyses. Typical analysis results are presented in *Fig. 1* that presents the critical stress, defined as the critical buckling load divided by the cross section area, as a function of the slenderness ratio for different temperatures.

The results can be rewritten in terms of buckling reduction factor, defined as the critical stress divided with the yield stress, as a function of the non-dimensional plate slenderness. The non-dimensional plate slenderness is defined according to *Eq. 1* which is taken from EN 1993-1-5 [13]:

$$\lambda_{p,\theta} = \frac{b/t}{28.4\epsilon\sqrt{k_\sigma}} \quad (1)$$

where k_σ is a factor considering the applied boundary conditions defined in EN 1993-1-5 [13] and ϵ has been taken for elevated temperatures from the equation:

$$\epsilon = \sqrt{\frac{k_{E,\theta}}{k_{y,\theta}}} \sqrt{\frac{235}{f_y}} \quad (2)$$

where $k_{E,\theta}$ and $k_{y,\theta}$ are the reduction factors of Young’s modulus and yield strength respectively for temperature θ [14].

The results are plotted in Fig. 2. As it can be seen, all analysis results are lying within a narrow band except for the curves at temperatures of 20 °C and 200°C. Therefore, it seems reasonable to adopt a single buckling reduction factor curve for the temperatures in the range of 300°C to 900°C.

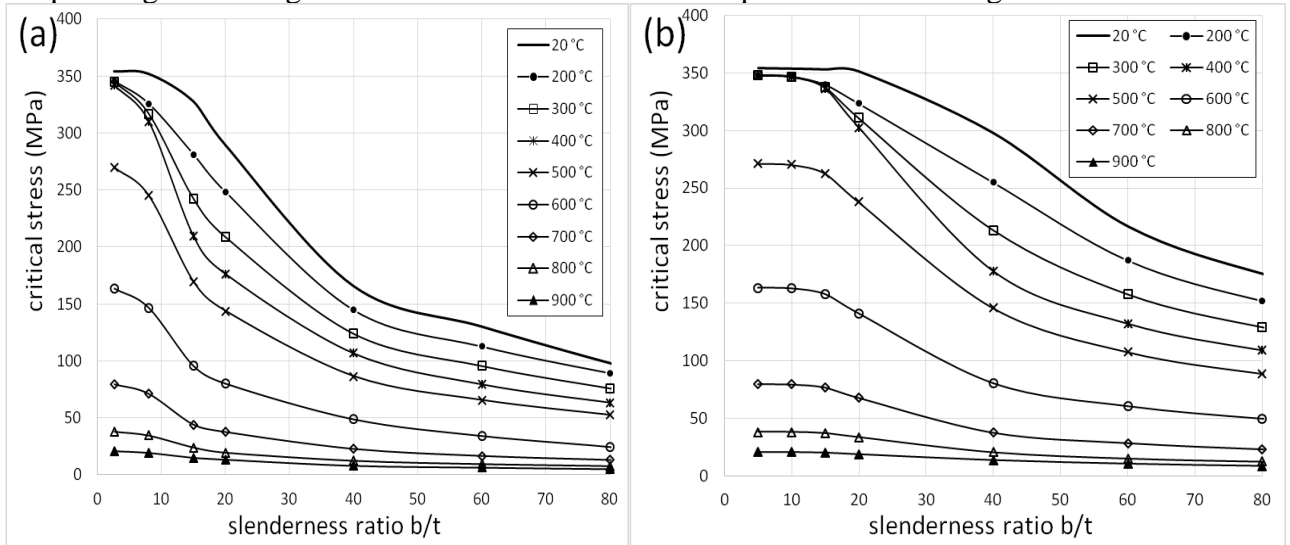


Fig. 1. Isolate plate (S355) analysis results (a) three sides simply supported (flange equivalent); (b) four sides simply supported (web equivalent)

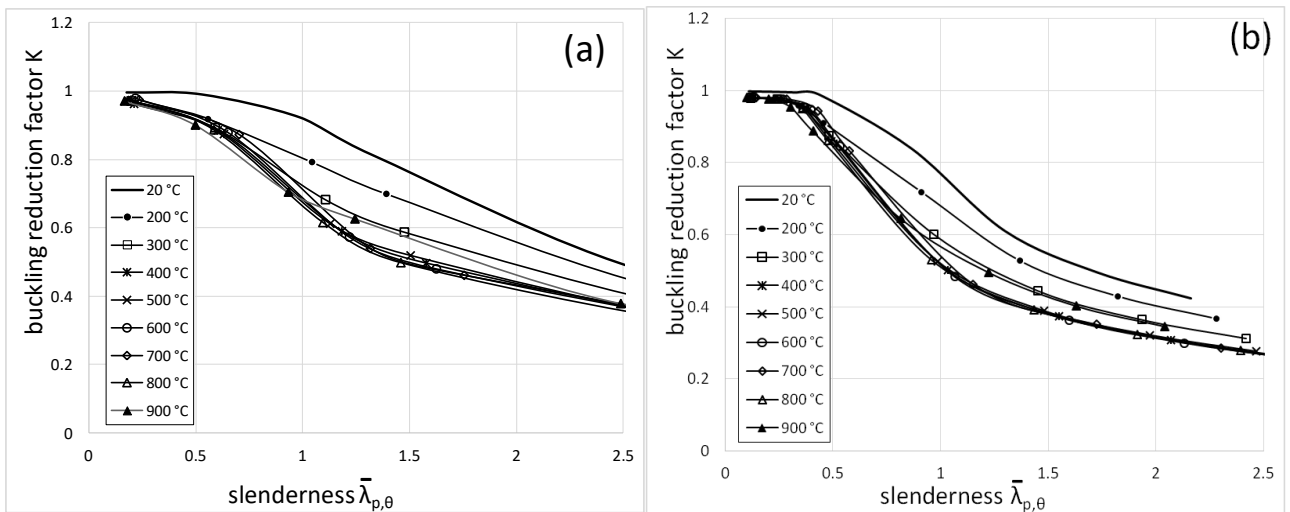


Fig. 2. Buckling reduction factor vs slenderness for S355 plates (a) three sides simply supported (flange equivalent); (b) four sides simply supported (web equivalent)

2.2 Proposed plate buckling model

Eq. 3 is proposed to model the buckling curves of Fig. 2:

$$k_{\theta} = \frac{1}{\alpha \cdot \lambda_{p,\theta}^2 + \beta \cdot \lambda_{p,\theta} + \gamma} \quad (3)$$

where k_{θ} is the buckling reduction factor at temperature θ and α , β and γ are model parameters. A statistical analysis based on the least square method is conducted on the results of the isolated plate analyses to establish the model parameters (see Fig. 3). The obtained values are presented in Table 1 for the parameters α , β and γ , estimated at 20°C, 200°C, and 300°C-900°C, for flange and web plates (six sets of parameters). It was chosen to keep the proposed model for buckling reduction factor as a function of plate slenderness independent of the steel grade to reduce the number of parameters and hence simplify its application; this approximation has only a slight influence on the model accuracy.

Table 1. Proposed model parameters

Type of plate	Temperature (°C)	α	β	γ
Flange	20	-0.19800	1.375	-0.0368
	200	-0.10000	1.000	0.6350
	300 and higher	-0.05500	1.130	0.6200
Web	20	-0.00066	0.446	0.9000
	200	0.04860	0.723	0.7400
	300 and higher	-0.03100	1.347	0.5300

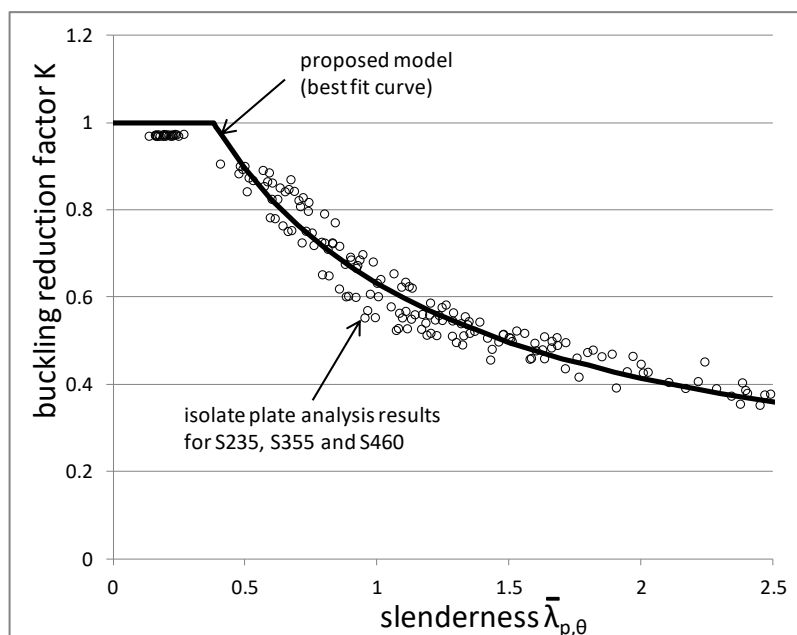


Fig. 3. FEA results and proposed model curve for the isolated four sides simply supported plate for grades S235, S355 and S460 and temperatures equal or higher than 300°C.

2.3 Stress-strain-temperature relationship

A modified stress-strain-temperature relationship for steel is derived based on EN1993-1-2 [14] and the proposed plate buckling model. The tension part of the EN1993-1-2 material law remains unchanged. In compression, the proportional limit and the yield strength are reduced by the factor k_θ (Eq. 3). The strain corresponding to the compressive yield strength is also reduced by the factor k_θ . As a result, the proposed material law is asymmetric in tension and compression, and a different law is used for the flanges and for the web as different factors k_θ apply (Fig. 4).

The proposed model was implemented in the software SAFIR [12] where it is used in every point of integration in the beam elements. This means that, for example, the strain varies in the web of a section under bending and, as a consequence, also the factor k_θ .

3 VALIDATION OF PROPOSED MODEL

3.1 Validation against fire test results

In order to validate the proposed model, experimental results collated from two different sources [15], [16] were used. The fire tests No 3 and No 5 from [15] were simulated with beam finite elements. These tests performed in Liege University Fire Labs during FIDESC4 Research Program. The fire test No 3 specimen had cross section 150x5(flanges) and 450x4(web) and length 2.7 m. The applied load was 122.4 kN. Load eccentricity of 4 mm applied in the weak direction to avoid global buckling failure due to global imperfection. The amplitude of local imperfections was 2.6 mm at the web and 4.9 mm at the flange. The fire test No 5 specimen had cross section 150x5(flanges) and 360x4(web) and length 2.7 m. The applied load was 231 kN. Load eccentricity of 71 mm applied in the strong direction at the bottom and at the top. The amplitude of local

imperfections was 6.8 mm at the web and 2.3 mm at the flange. The load eccentricity of test No 5 has not been considered for the simulation for the reason explained in Section 4. The comparison between experimental results and beam element analysis results is presented in Fig. 5 and shows good agreement with the tests. A clear improvement from the original model proposed in [8] is also visible.

The simulation of the tests from [16] considered only the heated part of the column and the comparison between experimental results and beam element analysis results is presented in Table 2, showing good agreement.

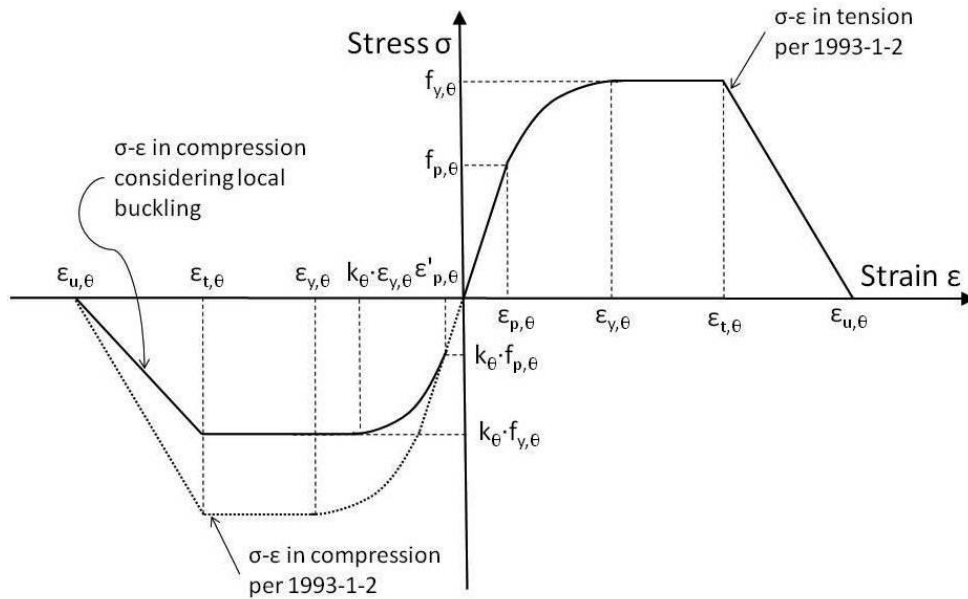


Fig. 4. Stress-strain relationship per EN1993-1-2[14] compared with the proposed modified relationship.

Table 2. Validation against experimental results form [17]

Cross section (mm)	Ambient temperature yield stress (MPa)	Temperature (°C)	Buckling resistance (kN)[17]	Buckling resistance (kN) Beam element - proposed model
250x250x6x8	306.4(flange), 321.9(web)	450	800	791
316x200x6x8	306.4(flange), 321.9(web)	450	750	785
250x220x8x8	538.1	450	1500	1378
336x160x8x8	538.1	450	1400	1383
250x250x6x8	306.4(flange), 321.9(web)	650	240	269
316x200x6x8	306.4(flange), 321.9(web)	650	265	292
250x220x8x8	538.1	650	400	426
336x160x8x8	538.1	650	360	388

3.2 Validation against shell element numerical analysis results

In order to validate the proposed model against shell element analysis results, SAFIR was used to model columns under pure compression and beams under pure bending (laterally restrained to avoid lateral torsional buckling). The shell element analysis results compared with the proposed model beam element analysis results are presented in Fig. 6 and show good agreement.

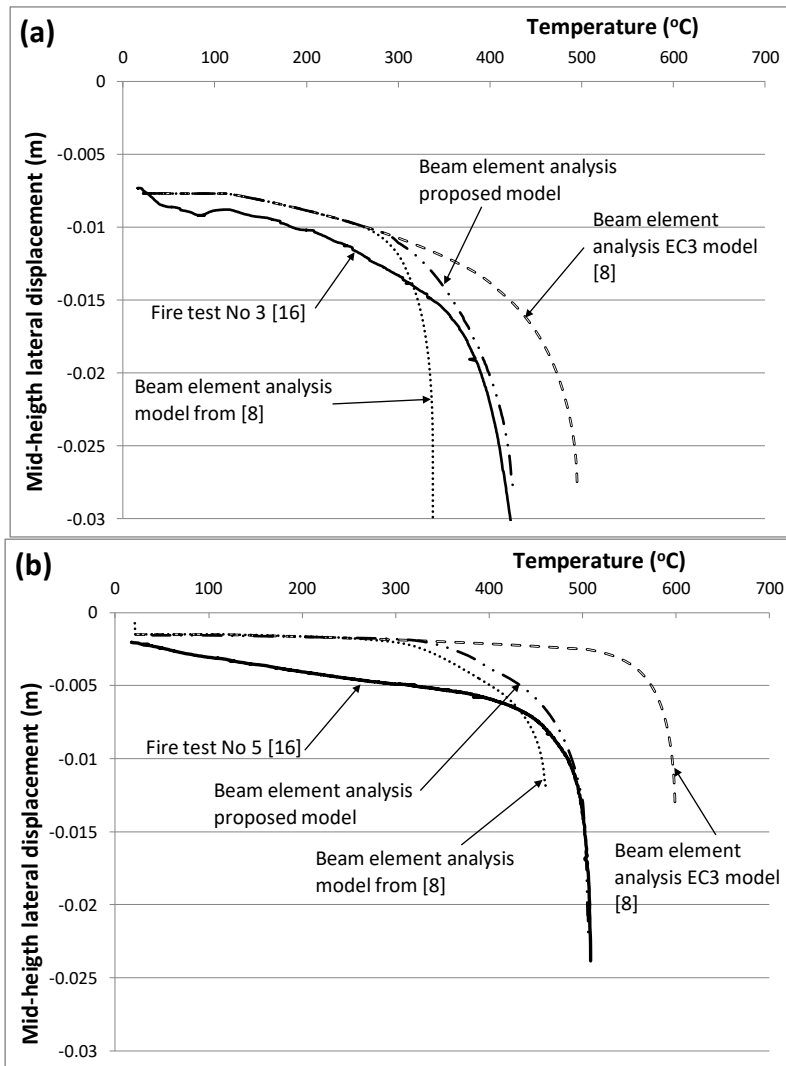


Fig. 5. Model validation against fire test results a) Test No 3[16]; b) Test No 5[16]

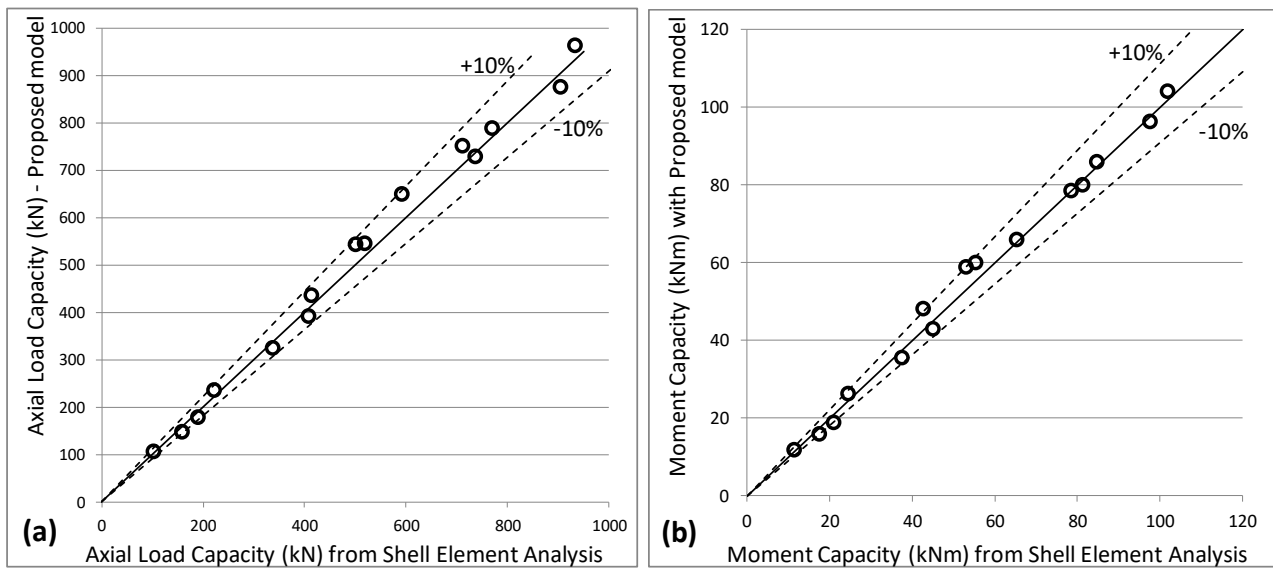


Fig. 6 Beam element analysis (proposed model) vs shell element analysis results for 150x5(flange) and 380x4(web) and temperatures from 300 °C and up to 700 °C for S235, S355 and S460 (a) Pure compression and (b) Moment capacity.

4 LIMITATIONS AND FURTHER DEVELOPMENT

The proposed model has been developed based on the assumption that a uniform displacement applies on the plate's edge [9], [10], [11]. This is accurate for columns in pure compression and it is giving good results in pure bending because of the limited bending capacity of the web. When the eccentricity is large ($\psi \ll 1$ in *Fig. 7*) the uniform displacement assumption is conservative, as it limits the compressive stress capacity to the critical uniform stress. Ongoing research aims at incorporating this effect to enhance the proposed model by considering the ψ factor. The enhanced model will be validated against fire tests which are under final preparation at the fire lab of Liège University and which will be designed to include large eccentricities to inform the model development.

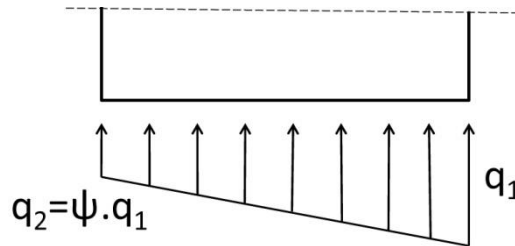


Fig. 7. Non-uniform stress distribution and definition of the parameter ψ

5 CONCLUSIONS

A model based on an equivalent stress method has been proposed as an efficient way to consider local buckling in steel members exposed to fire. The proposed stress-strain-temperature relationship is asymmetric and is modified in compression only, by reducing the proportional limit, the yield stress and the strain at yield stress. The reduction of these parameters depends on the plate's boundary conditions, slenderness and temperature.

The proposed stress-strain-temperature relationship has been implemented in the software SAFIR and validated against experimental and shell element analysis results, showing good agreement over a range of profile dimensions, temperatures and steel grades.

The proposed model is suitable for use with fibre type beam finite elements. Such a model can save enormous computational time compared with traditional shell models for thin-plate members. For example, a typical column modelled with the equivalent stress method and beam FE may have 300 degrees of freedom and a computational time shorter than 72 seconds for 350 time steps (with use of a Core i5 computer), whereas the same column modelled with shell elements would have 47750 degrees of freedom and a computational time of 847 seconds for the same time steps. It must be noted that the computational time is increased enormously when the analysis considers a larger number of structural elements.

The model is still giving conservative results for large compressive load eccentricities. For this reason an enhanced model is under development. Further extension of the proposed equivalent stress method is its modification for high and very high strength steel grades.

ACKNOWLEDGMENT

This research was supported by the University of Liege and the EU in the context of the FP7-PEOPLE-COFUND-BeIPD project.

REFERENCES

1. Chrysanthos Maraveas, Jean-Marc Franssen (2018). *Local buckling of steel members under fire conditions: A review*, Fire Technology (under review)
2. Therese McAllister, (2008). Federal building and fire safety investigation of the World Trade Center disaster: structural fire response and probable collapse sequence of World Trade Center building 7. Gaithersburg, MD, National Institute of Standards and Technology [NIST NCSTAR 1-9].
3. Yong Wang, (2002). *Steel and composite structures: behaviour and design for fire safety*, CRC Press, London.
4. Carlos Couto, C., Paulo Vila Real, Nuno Lopes, Bin Zhao (2014). *Effective width method to account for the local buckling of steel thin plates at elevated temperatures*, Thin-Walled Structures, 84, p. 134-149.
5. Carlos Couto, C., Paulo Vila Real, Nuno Lopes, Bin Zhao (2015). *Resistance of steel cross-sections with local buckling at elevated temperatures*, Constructional Steel Research, 109, p. 101-104.
6. Spencer E. Quiel, Maria E.M. Garlock, (2010). *Calculating the buckling strength of steel plates exposed to fire*, Thin-Walled Structures, 48, p. 684-695.
7. Markus Knobloch, Mario Fontana, (2006). *Strain-based approach to local buckling of steel sections subjected to fire*. Constructional Steel Research, 62, p. 44-67.
8. Jean-Marc Franssen, Baptiste Cowez, Thomas Gernay (2014). *Effective stress method to be used in beam finite elements to take local instabilities into account*. Fire Safety Science 11, 544-557. 10.3801/IAFSS.FSS.11-544.
9. Chrysanthos Maraveas, Thomas Gernay, Jean-Marc Franssen (2017) *Amplitude of local imperfections for the analysis of thin-walled steel members at elevated temperatures*, Applications of Structural Fire Engineering (ASFE'17), Manchester, UK.
10. Chrysanthos Maraveas, Thomas Gernay, Jean-Marc Franssen (2017) *Buckling of steel plates at elevated temperatures: Theory of perfect plates vs Finite Element Analysis*, 2nd International Conference on Structural Safety Under Fire and Blast Loading – CONFAB, London, UK.
11. Chrysanthos Maraveas, Thomas Gernay, Jean-Marc Franssen (2017) *Thin-walled steel members at elevated temperatures considering local imperfections: numerical simulation of isolated plates*, 9th National Conference of Steel Structures, Larisa, Greece.
12. Jean-Marc Franssen, Thomas Gernay (2017). *Modeling structures in fire with SAFIR®: Theoretical background and capabilities*, Journal of Structural Fire Engineering, 8(3):300-323. 10.1108/JSFE-07-2016-0010.
13. EN 1993-1-5 (2006). *Eurocode 3 — design of steel structures — part 1-5: plated structural elements*. Brussels: European Committee for Standardisation.
14. EN 1993-1-2 (2005). *Eurocode 3: design of steel structures — part 1-2: general rules — structural fire design*. Brussels: European Committee for Standardisation.
15. FIDESC4 (2015), *Fire design of steel members with welded or hot-rolled class 4 cross-sections*, Final report, Research program of the Research Fund for Coal and Steel.
16. Weiyong Wang, Venkatesh Kodur, Xingcai Yang, Guoqiang Li (2014) *Experimental study on local buckling of axially compressed steel stub columns at elevated temperatures*, Thin-Walled Structures, 82, 33-45.

BEHAVIOR OF BOLTED CONNECTIONS COMPONENT UNDER ELEVATED TEMPERATURES

Ioan Both¹, Florea Dinu², Calin Neagu³, Ioan Marginean⁴, Raul Zaharia⁵

ABSTRACT

The capacity of multi-storey steel frame buildings to resist extreme loading depends on the performance of the beam-to-column joints to allow for the development of alternate loads paths. In case of an extreme scenario such as a column loss under fire, dynamic effects should be considered when evaluating the resistance and ductility of the connection. End plate bolted connections are widely used in the steel framed constructions. The simple macro-component through which the response of such a connection is assessed, consists in the T-stub model included in EN1993-1-8. The paper presents experimental results on T-stubs subjected to normal and elevated temperatures, in both quasi-static and high strain rate conditions, and emphasizes the failure mechanism change caused by temperature and loading conditions.

Keywords: bolted connections, T-stubs, elevated temperatures, strain rate

1 INTRODUCTION

The simple macro-component through which the response of a steel joint is assessed, consists in the T-stub model presented by EN1993-1-8 [1]. Extensive studies on the influence of rate of strain and temperature on yield stresses of mild steel were performed since 1944 [2-4], but few literature is dedicated to the response of T-stubs subjected to actions related to robust design of structures [5]. The paper presents the experimental results obtained on a set of T-stub configurations that were designed according to EN1993-1-8 to fail in two modes, i.e. complete yielding of the flange (Mode 1) and bolt failure with yielding of the flange (Mode 2). The tests were performed at normal and elevated temperatures, under quasi-static and high strain rate loading. The T-stubs were tested in the laboratory of Steel Structures and Structural Mechanics of the Politehnica University of Timisoara. The specimens were introduced in an environmental chamber and subjected to elevated temperature of 542°C. This temperature corresponds to a reduction factor for the design load level in fire situation of 0.65 (as suggested by EN1993-1-2 [6] in a simplified manner). Each test was performed by connecting two identical T-stubs using two M16 bolts.

¹ Lecturer. Department of Steel Structures and Structural Mechanics, Politehnica University of Timisoara, Timisoara, RO.
e-mail: ioan.both@upt.ro

² Professor. Department of Steel Structures and Structural Mechanics, Politehnica University of Timisoara, Timisoara, RO.
e-mail: florea.dinu@upt.ro

³ Lecturer. Department of Steel Structures and Structural Mechanics, Politehnica University of Timisoara, Timisoara, RO.
e-mail: calin.neagu@upt.ro

⁴ Assistant Professor. Department of Steel Structures and Structural Mechanics, Politehnica University of Timisoara, Timisoara, RO.
e-mail: ioan.marginean@upt.ro

⁵ Professor. Department of Steel Structures and Structural Mechanics, Politehnica University of Timisoara, Timisoara, RO.
e-mail: raul.zaharia@upt.ro

2 EXPERIMENTAL PROGRAM

Previous tests on T-stubs using M16 grade 10.9 bolts and flange thicknesses of 10 and 12 mm, for which the resistance was dictated by the flange failure (Mode 1) were performed by the authors [7, 8]. In order to reach both flange plastic deformation and bolt failure (Mode 2), another set of T-stubs was tested, with higher flange thicknesses of 15 mm and M16 grade 8.8 bolts.

The nominal and real dimensions of the specimens are presented in Table 1, according to the notations in Figure 1.

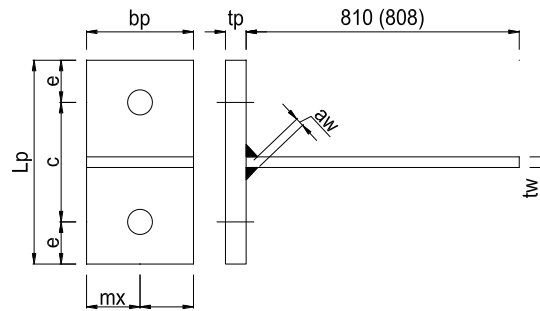


Fig. 1. Specimen geometry

Table 1. Dimensions of the specimens

Specimen	Nominal						Measured								
	t_p	b_p	L_p	c	e	m_x	t_p	b_p	L_p	c	e	m_x	a_w	t_w	
T-15-16-100C	15	90	160	100	30	45	15.8	88.65	159	100.7	20.2	44.0	7	10	
							15.8	89.1	160	101.5	20.05	46.5	7	10	
T-15-16-100CS	15	90	160	100	30	45	15.8	88.4	159	101.2	19.8	44.1	7	10	
							15.7	89	160	102.1	20.05	42.4	7	10	
T-15-16-100T	15	90	160	100	30	45	15.8	88.85	159	100.3	20.35	46.3	7	10	
							15.7	88.9	159	100.1	20.3	47.3	7	10	
T-15-16-100TS	15	90	160	100	30	45	15.7	88.85	159	103.1	19.45	45.8	7	10	
							15.6	87.5	159	99.9	19.7	44.8	7	10	
T-15-16-120C	15	90	180	120	30	45	15.8	89.15	179	120.7	20.9	45.2	7	10	
							15.8	88.75	178.5	120.2	20.7	44.5	7	10	
T-15-16-120CS	15	90	180	120	30	45	16.2	89.05	179	121.0	22.2	44.9	7	10	
							15.9	88.75	179	120.3	21.1	43.9	7	10	
T-15-16-120T	15	90	180	120	30	45	15.8	88.9	179	120.3	19.7	44.3	7	10	
							14.8	89.05	179	120.1	20.4	44.1	7	10	
T-15-16-120TS	15	90	180	120	30	45	15.8	89	179	120.3	21.8	44.9	7	10	
							15.7	90.45	179	122.2	19.7	40.2	7	10	
T-15-16-140C	15	90	200	140	30	45	15.85	89.35	199	140.6	21.1	45.7	7	10	
							16.3	88.9	198	139.8	20.4	44.4	7	10	
T-15-16-140CS	15	90	200	140	30	45	15.6	88.7	199	141.7	21.2	45.1	7	10	
							16.2	88.9	198	140.5	19.75	44.1	7	10	
T-15-16-140T	15	90	200	140	30	45	15.8	88.85	198	141.4	21.5	44.4	7	10	
							15.8	88.75	198	141.1	19.8	45.1	7	10	
T-15-16-140TS	15	90	200	140	30	45	15.9	88.7	198	139.9	19.7	43.2	7	10	
							15.7	88.65	199	141.1	19	44.5	7	10	

As presented in Table 1, the new specimens are T-15-16-100 C (CS, T, TS), T-15-16-120 C (CS, T, TS), T-15-16-140 C (CS, T, TS), T-18-16-120 C (CS, T, TS), T-18-16-140 C (CS, T, TS). The name of the specimens is related to the flange thickness of 15mm, the bolt diameter of 16 mm, the distance between the bolts (100, 120 or 140 mm), the testing temperature (C for normal temperature or T for the elevated temperature) and the strain rate (S for the high strain rate). As in the previous tests, the testing temperatures were the normal temperature of 20 °C (C) and the elevated temperature of 542 °C (T), while the mechanical load was applied with 0.05 mm/s (C, T) or high strain rate of 10 mm/s (CS, TS).

The mechanical properties of the base material of the T-stub supplied specimens (S235 and S355), are presented in Table 2.

Table 2. Average characteristic values for the steel plates and bolts

Element	f_y [N/mm ²]	f_u [N/mm ²]	A_{gt} [%]	A_t [%]
T-stub web, t = 10 mm	390	569	18.7	26.5
T-stub flange, t = 15 mm	275	400	21.6	34.4

Note: A_{gt} - total elongation at maximum force; A_t - total elongation at fracture

While the mechanical load was applied by the Instron dynamic universal testing machine of 1000 kN, an environmental chamber was used to reach the testing temperature. The specimen temperature was monitored by four K-type thermocouples, welded on each flange. After reaching the 542 °C at an approximate rate of 6 °C/min, the temperature was kept constant for almost an hour, to ensure the uniform distribution of temperature within the specimen.

3 TEST RESULTS

3.1 Normal temperature

The plastic deformations of the T-stubs after failure, depicted in Fig. 2, demonstrate Mode 2 failure mechanism (as designed according to EN1993-1-8), with the plasticisation of the flange and ultimately the failure of the bolts, for both quasi-static and high rate strain loading conditions.

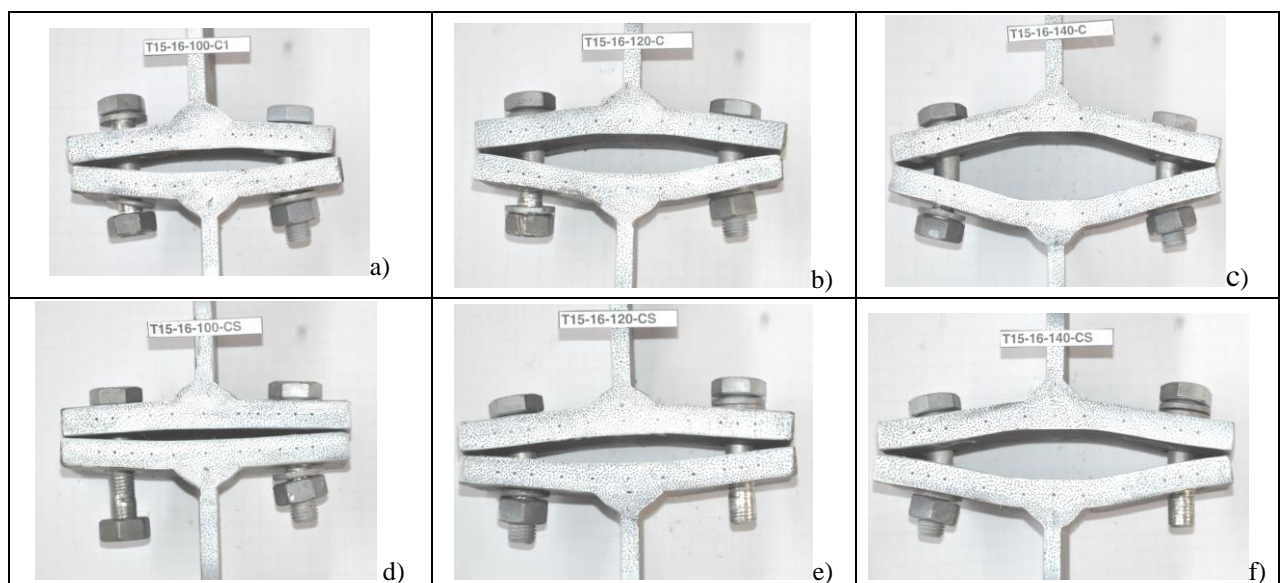


Fig.2 . T-stubs after failure at normal temperature a) T-15-16-100C; b) T-15-16-120C; c) T-15-16-140C; d) T-15-16-100CS; e) T-15-16-120CS; f) T-15-16-140CS

As shown in Figure 3, high strain rate loading produced only a small increase (maximum of 7 %) in the resistance of the T-stubs with 15mm flanges and M16 grade 8.8 bolts, under normal temperature conditions. From this point of view, this new set of T-stubs, for which Mode 2 failure was obtained, performed similarly to the previous sets of 10 and 12mm, using M16 grade 10.9 bolts for which Mode 1 failure was presented [7,8].

In terms of deformations, the increase of the distance between the bolts increases the deformability of the T-stub but, compared to the ultimate deformations presented in [7,8], the deformations are significantly reduced.

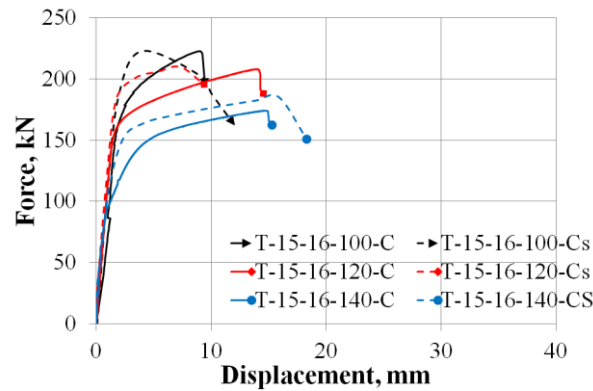


Fig. 3. Force-displacement curves for normal temperature tests of T-stub with 15mm flanges

3.2 Elevated temperature

The plastic deformations of the T-stubs tested under elevated temperature, depicted in Fig. 4, demonstrate a clear Mode 2 failure mechanism for high strain rate loading conditions, while for the quasi-static tests the failure mode is closer to Mode 3.

The failure mode change may be explained by the fact that the ratio of the resistances of bolts/flanges is different at elevated temperatures. According to EN1993-1-2 [6], at 542 °C, the steel resistance in the flanges is reduced to 65%, while the resistance of the bolts suffers a stronger reduction, to 41%. Therefore, the relative resistance of the bolt in the T-stub assembly is smaller at elevated temperatures and the failure of the bolt is produced in the quasi-static tests before the flanges may develop important plastic deformations. On the other hand, the over-strength of the bolts due to the high strain rate loading (T-stubs resistance higher by around 50%, as shown in Fig. 5 and 6a), allow the flanges to develop plastic deformations and to obtain Mode 2 failure (as designed for normal temperature and load conditions).

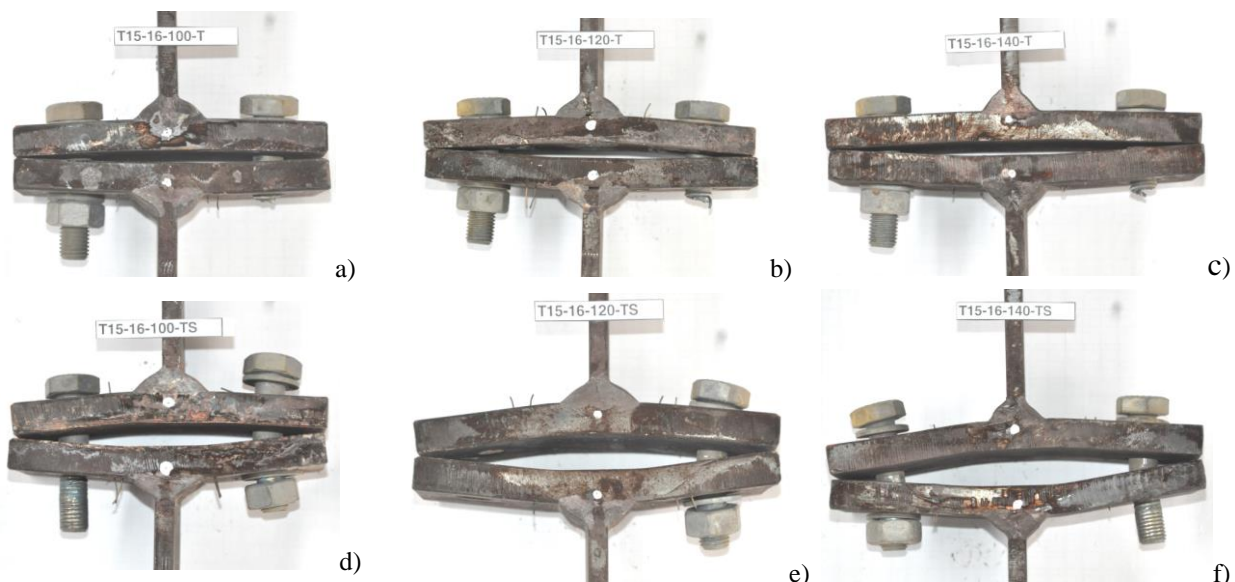


Fig. 4. T-stubs after failure at elevated temperature: a) T-15-16-100T; b) T-15-16-120T; c) T-15-16-140T; d) T-15-16-100TS; e) T-15-16-120TS; f) T-15-16-140TS

This behaviour is similar to the one observed for the previously tested specimens of 10-12mm with M16 grade 10.9 bolts [7,8]. For these specimens, at normal temperature, only failure Mode 1 was obtained under both quasi-static and high strain rate loading. At elevated temperature, clear Mode 1 failure for all specimens was exhibited only under high strain rate, while under quasi-static loading failure modes closer to Mode 2 were obtained.

As expected, the T-stub resistance under elevated temperature is smaller than the normal temperature resistance although the deformability resulted from the quasi-static and high strain rate tests is grouped in two distinct ranges for each testing conditions.

Consistent with the previous tested specimens of 10 and 12 mm, the high strain rate tests for the set of 15mm flanges and 8.8 grade bolts exhibit a much higher resistance compared to the quasi-static tests in elevated temperature conditions, as shown in Fig. 5.

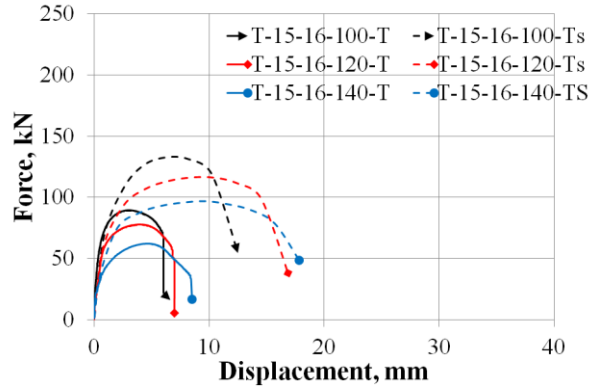


Fig. 5. Force-displacement curves for elevated temperature tests of T-stub with 15mm flanges

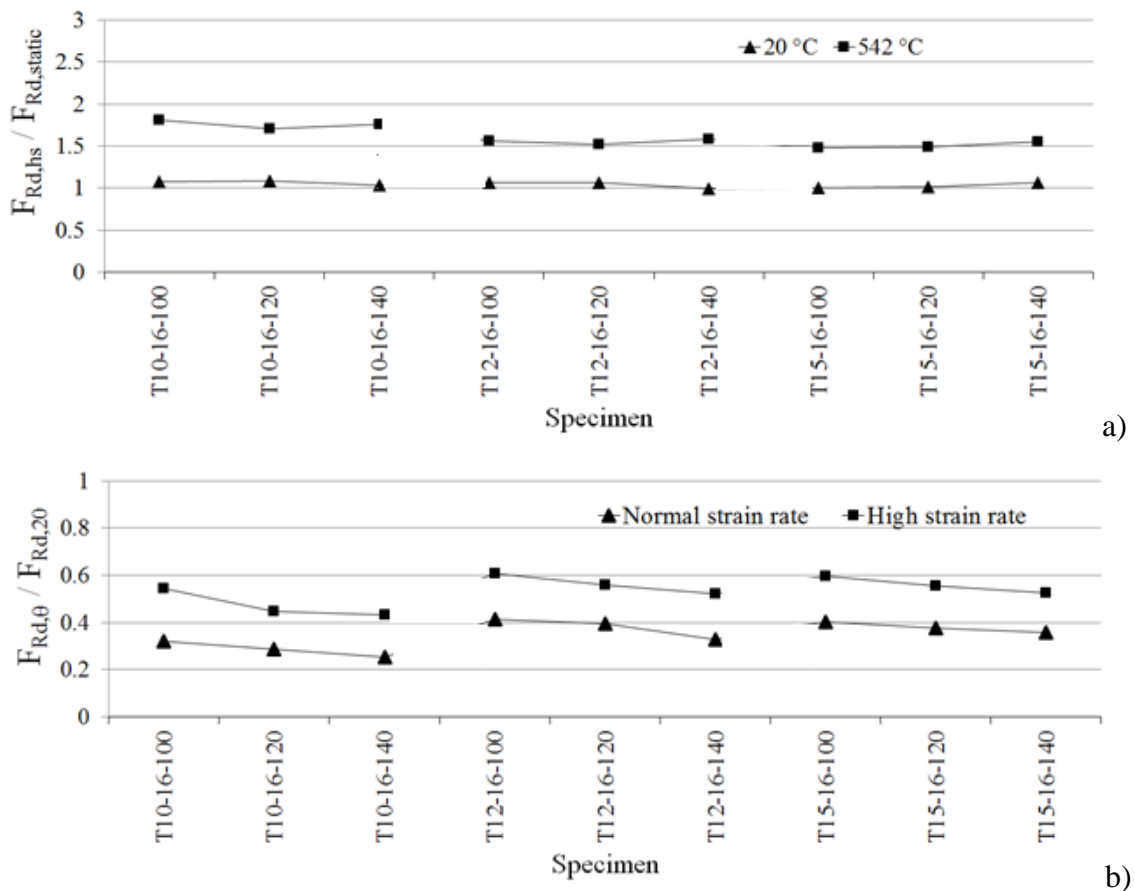


Fig. 6. a) high strain rate resistance to normal strain rate resistance ratio, b) elevated temperature resistance to normal temperature resistance ratio

The ratio between the high strain rate / quasi-static resistance of the tested specimens, for both normal and elevated temperature conditions, is shown in Figure 6a. The trend observed for 10-12 mm M16 grade 10.9 bolts is continued for the current tested specimens with 15mm and M16 grade 8.8 bolts. Also, the elevated temperature resistance to normal temperature resistance ratios for

normal and high strain rate, remain similar to the ratios obtained for 12 mm flange thickness, see Fig. 6b.

4 CONCLUSIONS

An experimental program performed on T-stub elements designed to exhibit failure Mode 1, under quasi-static and high strain rate loading and elevated temperature was continued with specimens designed for failure Mode 2. All specimens presented a significant increase of both resistance and ductility under elevated temperatures when subjected to high strain rate loading, in comparison with the quasi-static loading.

The deformations obtained under elevated temperatures at high strain rate are similar with the ones obtained in the tests at normal temperature. While at normal temperature there are small differences in terms of deformations between normal and high strain rates, in the case of elevated temperatures the deformations recorded at normal strain rate are smaller.

A change of the failure mode was recorded at elevated temperature for the T-stubs subjected to quasi-static loading. The specimens designed to exhibit failure Mode 1 presented in these conditions failure modes closer to Mode 2, while the specimens designed to exhibit failure Mode 2 presented failure modes closer to Mode 3.

This is due to the fact that the relative resistance of the bolt in the T-stub assembly is smaller at elevated temperatures and the failure of the bolt is produced in the quasi-static tests before the flanges may develop important plastic deformations.

ACKNOWLEDGMENT

This work was partly supported by a grant of the Romanian National Authority for Scientific Research and Innovation, CNCS/CCCDI - UEFISCDI, project number PN-III-P2-2.1-PED-2016-0962, within PNCDI III: "Experimental validation of the response of a full-scale frame building subjected to blast load" - FRAMEBLAST (2017-2018).

REFERENCES

1. C.E.N.(2005) *Eurocode 3: Design of steel structures - Part 1-8: Design of joints*, Brussels 2005
2. Manjoine, M.J. (1944). Influence of rate of strain and temperature on yield stresses of mild steel. *Trans. ASME*, 66, 1944
3. Johnson, G., Cook, W.H. (1983). A constitutive model and data for metals subjected to large strains, high strain rates and high temperatures. *In Proceeding of the 7th International Symposium on Ballistics*. Hague, 1983
4. Kaneko H., Influence of strain-rate on yield ratio, *Kobe Earthquake Damage to Steel Moment Connections and Suggested Improvement*. JSSC Technical Report No.39, 1997
5. Ribeiro J., Santiago A., Riguiero C. (2014). Assesment of the T-stub component subject to high strain-rate. *Proceedings of the 9th International Conference on Structural Dynamics*, Porto, Portugal, EUROLYN 2014
6. C.E.N. (2005). *Eurocode 3: Design of steel structures - Part 1-2: General rules - Structural fire design*. Brussels.
7. Both, I., Marginean, I., Neagu, C., Dinu, F., Dubina, D., Zaharia, R., (2017). Experimental Research on T-Stubs Under Elevated Temperatures, in: Wald, F., Burgess, I., Jelcic, R.M., Bjegovic, D., Horova, K. (Eds.), *Applications of Structural Fire Engineering*. CVUT Prague, pp 153-158.
8. Both I., Zaharia R., Mărginean I., Neagu C., Dinu F., Dubina D. (2016). T-stubs response to extreme loading. *Proceedings of the International Colloquium on Stability and Ductility of Steel Structures SDSS2016*, Timisoara, Romania, 30 May – 01 June 2016, pp. 673-680

BEHAVIOUR OF FULL HIGH STRENGTH STEEL EXTENDED ENDPLATE CONNECTIONS AFTER FIRE

Xuhong Qiang¹, Huan Chen², Xu Jiang³, Frans S.K. Bijlaard⁴

ABSTRACT

In order to reveal more information and better understanding on the behavior and failure mechanisms of full high strength steel extended endplate connections after fire, an experimental and numerical study has been conducted. The current provisions of Eurocode 3 are verified with the test results. The validations of the numerical simulations against all experimental results on failure mode and moment-rotation curves of high strength steel endplate connections at ambient temperature and after fire show good agreements exist. It is found that the current provisions of EC3 can justifiably predict failure mode and plastic flexural resistance of full HSS extended endplate connections both at ambient temperature and after fire, but it is not the case for their initial rotational stiffness and rotation capacity. What is more, after cooling down from 550 °C, HSS endplate connections can regain more than 90% of its original load-bearing capacity and more than 80% of its original initial rotational stiffness.

Keywords: high strength steel, extended endplate connections, after fire

1 INTRODUCTION

Since 9.11 Tragedy, structural fire safety has been a worldwide key consideration in the design of building structures. Provided that collapse does not occur when a steel structure is exposed to fire, the steel members will begin to cool once the fire starts to decay and the air temperature begins to decrease. Residual forces and deformations redevelop in steel structures during the cooling phase due to the shrinkage of the steel members, which might be more dangerous conditions than in fire. Whether the structures exposed to fire should be demolished, repaired or reused directly, a reliable assessment is needed.

In Europe, endplate connections are typical beam-to-column connections for steel structures produced by welding at workshops and erected by bolting in situ. Rules for prediction of strength, stiffness and deformation capacity of endplate connections at ambient temperature have been included in current leading design standards, such as Eurocode 3 Part 1-8 [1]. According to Eurocode 3, for structural steels up to S460, plastic design of connections may be used. However, for steel grades higher than S460 up to S700 only elastic design of connections can be employed, which is very uneconomical for steel structures. This is due to the lack of experimental and theoretical evidence that these high strength steel (HSS) connections have sufficient deformation capacities. Girao Coelho and Bijlaard et al. [2-4] have found that HSS S690 endplate connections

¹ Assistant Professor. College of Civil Engineering, Tongji University, China; Department of Structural Engineering, Faculty of Civil Engineering, Delft University of Technology, the Netherlands.

e-mail: qiangxuhong@tongji.edu.cn; x.qiang@tudelft.nl

² Graduate Student. College of Civil Engineering, Tongji University, China.

e-mail: 812759913@qq.com

³ Assistant Professor. College of Civil Engineering, Tongji University, China; Department of Structural Engineering, Faculty of Civil Engineering, Delft University of Technology, the Netherlands.

e-mail: jiangxu@tongji.edu.cn; xu.jiang@tudelft.nl

⁴ Professor. Department of Structural Engineering, Faculty of Civil Engineering, Delft University of Technology, the Netherlands.

e-mail: F.S.K.Bijlaard@tudelft.nl

satisfy the European design provisions for resistance and achieve reasonable rotation demands at ambient temperature. Qiang and Bijlaard et al. [5-8] have revealed that a proper thinner high strength steel endplate can enhance the rotation capacity of flush endplate connection both at ambient temperature, in fire and after fire (which guarantees the safety of an entire structure), and simultaneously achieve almost the same moment resistance with a mild steel endplate connection. However, research results on fire performance of full HSS extended endplate connections are not available in literature.

In this paper, an experimental and numerical study on full high strength steel extended endplate connections at ambient temperature and after fire is investigated, where all components including the endplate, column and beam are all made of HSS. The aim of this research is to reveal more information and understanding on post-fire behaviour of full high strength steel extended endplate connections, which serves for exploring an optimization design method.

2 EXPERIMENTAL STUDY

2.1 Test Specimen

In the experimental study at ambient temperature, there are two endplate connections JD1 and JD2 designed according to Eurocode 3 Part: 1-8 [1]. In the HSS endplate connections, the beams, columns and endplates are made of HSS Q690. The beam and column sections used in this experimental study are $300 \times 180 \times 10 \times 12$ and $340 \times 200 \times 10 \times 12$ respectively, while the dimension of endplate is $500 \times 200 \times 12$. The welds between endplate and beam are continuous 45° -fillet welds, which were executed at workshop in a down-hand position. The endplate was connected to column using hand-tightened full-threaded M27 grade 10.9 bolts. Since the failure is expected to occur on the endplate and bolts, stiffeners were welded on the column shear web panel and the beam web for loading. The details and dimensions of the test specimens are shown in *Fig. 1*. The location and numbering of bolts can be seen in *Fig. 1 (b)*. In order to evaluate the residual performance of HSS endplate connections after cooling down from elevated temperature 550°C , this paper presents an experimental study on two endplate connections JD1P and JD2P after fire as well, whose materials, dimensions and details are identical to JD1 and JD2.

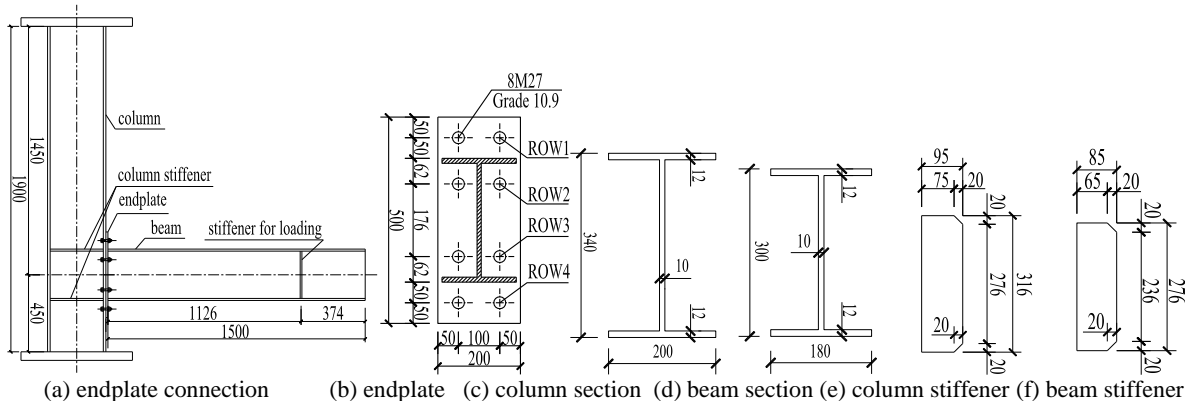


Fig. 1 Specimen of endplate connection

2.2 Test set-up and procedures

For the experiment at ambient temperature, the main features of the test set-up are illustrated in *Fig.2*. Before tests, all the equipment was examined by trial loading. During trial loading, the displacement gauges and the applied force were checked. In the actual loading, displacement control was employed via controlling the displacement of the hydraulic actuator's piston at 10 mm/min.

For the experiment after fire, the heating process was conducted in a gas furnace ($4.5 \text{ m} \times 3.0 \text{ m} \times 1.7 \text{ m}$). The specimen was firstly heated to 550°C at a constant heating rate of $10^\circ\text{C}/\text{min}$ which corresponds to the normally protected steel members in fire. After the temperature of connection

components achieving 550 °C, approximately 15 min holding time was required. Then the heating was stopped and the specimen began to cool down to ambient temperature. After cooling down, the post-fire connection specimen was loaded at ambient temperature until failure. The loading process and test set-up are same with that of the experiment at ambient temperature.

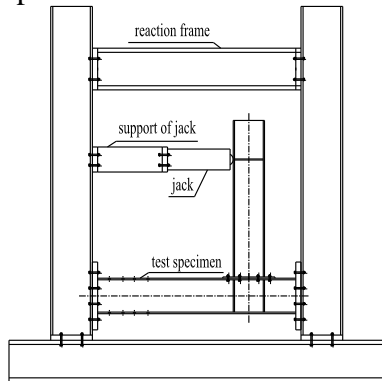


Fig. 2 Test set-up

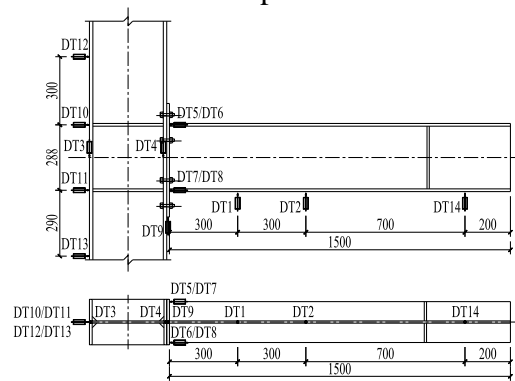


Fig.3 Location of displacement sensors

2.3 Displacement measurements

The location of displacement sensors were displayed in Fig. 3. In this experimental study, 3 vertical displacement sensors (DT1, DT2 and DT14) were used to obtain the vertical displacement of the beam. In order to record the displacement of column, 2 vertical displacement sensors (DT3 and DT4) and 4 horizontal displacement sensors (DT10-DT13) were arranged. In order to measure the displacement of endplate, 1 vertical displacement sensor (DT9) and 4 horizontal displacement sensors (DT5-DT8) were placed. Based on the displacements of the aforementioned components, the rotation of endplate connection in tests can be obtained.

3 TEST RESULTS AND DISCUSSIONS

3.1 Deformation at the end of tests and failure modes

An overall description on components of all connections is given in Table 1. The failure modes of the endplate connections obtained according to the component method proposed in Eurocode 3 Part: 1-8 [1] are compared with those from experimental study, see Table 2. It can be observed that good agreements exist between theoretical analysis and experimental study. Thus the component method proposed in Eurocode 3 Part: 1-8 can justifiably predict the failure mode of HSS connections both at ambient temperature and after fire.

Table 1. Description of components at the end of tests

Condition	Test ID	Endplate yielding	Fracture of bolts in ROW 2	Nuts in top tensile zone stripped off	Weld failure in heat affected zone	Bolts in compression almost straight
Ambient temperature	JD1	Yes	Yes	No	No	Yes
	JD2	Yes	Yes	No	No	Yes
After fire	JD1P	Yes	Yes	No	No	Yes
	JD2P	Yes	Yes	No	No	Yes

Table 2. Failure modes of endplate connections

Condition	Test ID	EC3	Test
Ambient temperature	JD1	Failure mode 2	Failure mode 2
	JD2		Failure mode 2
After fire	JD1P	Failure mode 2	Failure mode 2
	JD2P		Failure mode 2

3.2 Moment- rotation relationship of endplate connections

The $M-\theta$ curves of all connections can be seen in Fig.4. From $M-\theta$ curves of the connections, a series of connections characteristics can be determined, such as plastic flexural resistance M_y , rotation corresponding to plastic flexural resistance θ_y , maximum bending moment M_{max} , rotation

corresponding to maximum bending moment θ_{\max} , maximum rotation Φ_c , initial rotational stiffness K_{ini} , post-yield rotational stiffness K_p and so on.

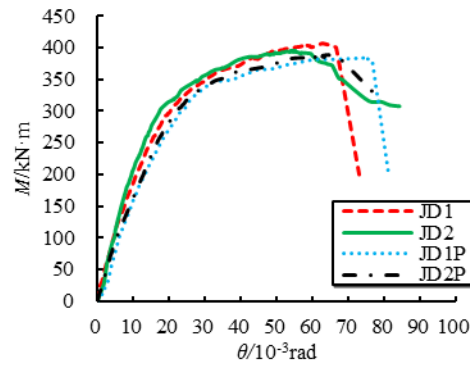


Fig.4 M- θ curves

3.3 Plastic flexural resistance

The $M_{y,\text{test}}$, $M_{y,\text{EC3}}$ of all endplate connections and the residual factor of $M_{y,\text{test}}$, which is the ratio between average value of $M_{y,\text{test}}$ of JD1, JD2 and the average value of $M_{y,\text{test}}$ of JD1P, JD2P are listed in Table 3. It can be observed that good agreement exists between the theoretical prediction and the experimental results. This validates that the accuracy of component method in Eurocode 3 is acceptable when used to predict the plastic flexural resistance of HSS endplate connections no matter at ambient temperature or after fire. It can also be found that full HSS extended endplate connections can regain more than 90% of its original load bearing capacity after cooling down from fire temperature 550 °C, which is similar with the post-fire behavior of HSS flush endplate connection where endplate is made of HSS while beam and column are made of mild steels [7].

Table 3. Plastic flexural resistance of endplate connections

Condition	Test ID	$M_y(\text{kN}\cdot\text{m})$		Ratio= $M_{y,\text{test}}/M_{y,\text{EC3}}$	Average value of $M_{y,\text{test}}$ (kN·m)	Residual factor of $M_{y,\text{test}}$
		Experimental value $M_{y,\text{test}}$	Theoretical value $M_{y,\text{EC3}}$			
Ambient temperature	JD1	298.86	292.03	1.02	301.40	0.96
	JD2	303.93				
After fire	JD1P	287.30	263.67	1.09	289.84	
	JD2P	292.37		1.11		

3.4 Initial rotational stiffness

Table 4. Initial rotational stiffness of endplate connections

Condition	Test ID	$K_{\text{ini}}(\text{kN}\cdot\text{m}\cdot\text{rad}^{-1})$		Ratio= $K_{\text{ini},\text{test}}/K_{\text{ini},\text{EC3}}$	Average value of $K_{\text{ini},\text{test}}$ (kN·m·rad ⁻¹)	Residual factor of $K_{\text{ini},\text{test}}$
		Experimental value $K_{\text{ini},\text{test}}$	Theoretical value $K_{\text{ini},\text{EC3}}$			
Ambient temperature	JD1	20439	34271	0.60	21291	0.85
	JD2	22142				
After fire	JD1P	17484	34253	0.52	18058	
	JD2P	18632		0.54		

The test values of K_{ini} which is named $K_{\text{ini},\text{test}}$ of all endplate connections and the residual factor of $K_{\text{ini},\text{test}}$ are listed in Table 4. It can be found that the component method adopted in Eurocode 3 Part: 1-8 overestimates initial rotational stiffness of full HSS extended endplate connections, especially after cooling down from fire temperature 550 °C. Thus the component method of Eurocode 3 Part: 1-8 for predicting the initial rotational stiffness of HSS connections needs further verification or modification. It can also be found that full HSS endplate extended connections can regain more than 80% of its original initial rotational stiffness after cooling down from fire temperature 550 °C.

3.5 Rotation capacity

Based on the $M-\theta$ curves, Φ_c of all HSS extended endplate connections can be determined and are listed in *Table 5*. θ_p of all HSS extended endplate connections are calculated according to Eurocode 3 are also presented in *Table 5*. It can be found that Φ_c and θ_p of all specimens, no matter at ambient temperature or after fire, are much higher than $40\sim 50\times 10^{-3}$ rad and 30×10^{-3} rad respectively, which ensures “sufficient rotation capacity” of a bolted joint in a partial strength scenario [9]. Thus it can be concluded that full HSS extended endplate connections have sufficient rotation capacity no matter at ambient temperature or after fire. It is identical to previous study on partial HSS flush endplate connections [7], where the endplate is made of HSS while the column and beam are made of mild steels.

Eurocode 3 Part: 1-8 [1] states that a bolted endplate joint would have sufficient rotation capacity for plastic analysis, if both of the following conditions could be satisfied: (i) the moment resistance of the joint should be governed by the resistance of either the column flange in bending or the endplate in bending, and (ii) the thickness, t , of either the column flange or the endplate (not necessarily the same basic component as in (i)) should satisfy *Eq. (1)*.

$$t \leq 0.36d \sqrt{f_{u,b} / f_y} \quad (1)$$

It can be found that the first condition is guaranteed for all specimens (the moment resistance of connection is always governed by the resistance of the endplate in bending), while the second condition is not satisfied for all specimens (According to *Eq. (1)*, the endplate thickness should not be larger than 11.93 mm at ambient temperature and 10.83 mm after fire). Therefore, the relevant provisions of Eurocode 3 Part: 1-8 seem to be conservative on the rotation capacity of HSS endplate connections no matter at ambient temperature or after fire. In addition, the current provisions on rotation capacity of endplate connections in EC3 are mainly obtained from endplate connections made of mild steels, which need to be verified and modified when applied to connections made of HSS.

4 NUMERICAL STUDY

4.1 Finite Element Model

The geometric details of all connections' components modelled in FEM are same as the test specimens. Because the geometric details, load, temperature distribution and boundary conditions of the endplate connection are symmetric, half of the endplate connection was modelled to reduce computer costs and shorten computing time. There are 4 surface-to-surface contact interactions and 4 tie interactions in this FE model, and the materials are endowed with non-linear properties. The whole connection was modelled using C3D8R element.

4.2 Contact interaction and Failure criterion

The contact pairs in this numerical model comprise the column flange-to-endplate, bolts-to-endplate, nuts-to-column flange and bolts-to-bolt holes. The tie constrains in this numerical model comprise the bolts-to-nuts, beam-to endplate, column stiffeners-to-column and beam stiffener-to-beam. Surface-to-surface contact, with a small sliding option, was employed for all contact surfaces to fully transfer load. The penalty friction was employed in the contact interaction property. The failure criterion employed herein is based on deformation by assuming that cracking occurs when the ultimate strain ϵ_u of the material (either endplate or bolt) is reached, as proposed by Girao Coelho et al. [9].

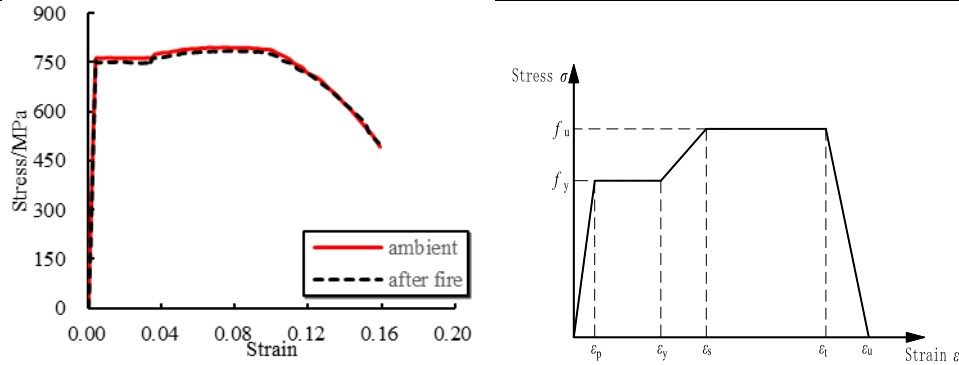
4.3 Material properties

In this FE modelling, the material properties of all the components are listed in *Table 5*. The engineering stress–strain curves of Q690 at ambient temperature and after fire are presented in *Fig.5(a)*. The engineering stress–strain curves of bolts at ambient temperature and after fire are

determined according to Eurocode 3 Part: 1-2 [10] as presented in Fig.5(b). The input mechanical properties of various materials in this FE modelling are true plastic strain and true stress.

Table 5. Mechanical properties of materials

Test condition	Steel grade	Yield strength (MPa)	Ultimate strength (MPa)	Elastic modulus (MPa)
Ambient temperature	Q690	763	796	198501
	Bolts 10.9	1130	1152	201000
After fire	Q690	751	787	201562
	Bolts 10.9	897	933	166860

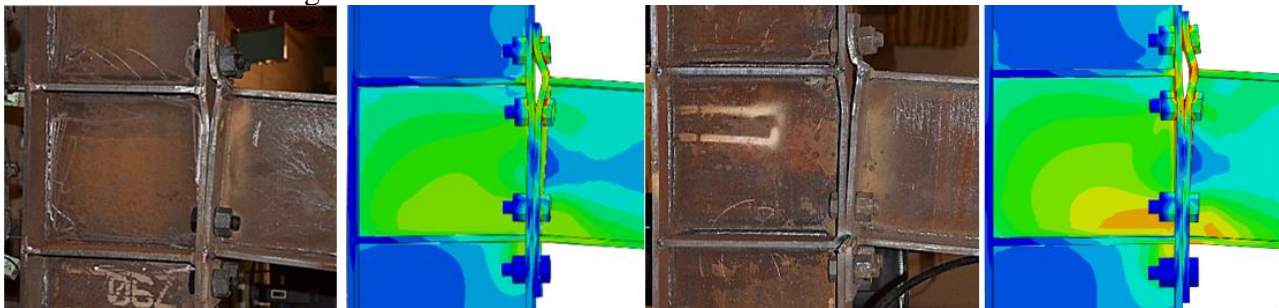


(a) engineering stress-strain curves of Q690 (b) engineering stress-strain curves of bolts
 Fig. 5 Engineering stress-strain curves of the involved materials

5 VALIDATION OF NUMERICAL MODEL AGAINST EXPERIMENTAL RESULTS

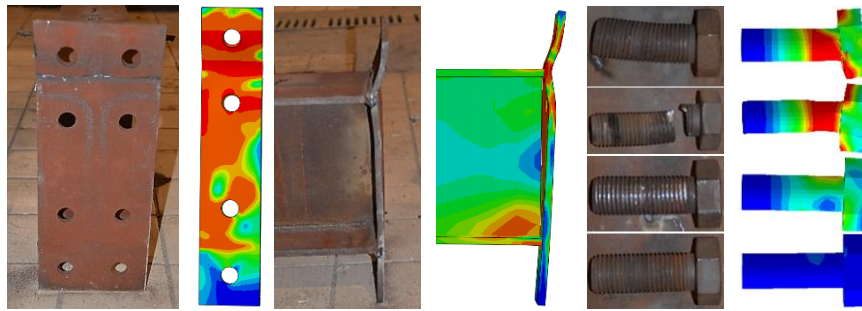
5.1 Deformation at the end of test

Because the final deformation states of JD1 and JD2, JD1P and JD2P were identical respectively, only the numerically simulated final deformation states of JD1 and JD1P were compared with those obtained from the experimental study. Fig.6 presents the comparisons on the final deformation states of JD1 and JD1P. Figs.7 show the comparisons on the final deformation states of the components of JD1P after failure. From Figs.6-7, it can be seen that good agreements exist on the final deformation of JD1 and JD1P. Although the current numerical model cannot simulate the fracture of the bolts, it is able to reveal the location where the fracture initiates, as shown in Fig.7. In the numerical model, the equivalent plastic strain (PEEQ, as simplified by ABAQUS) indicates whether the material is currently yielding or not. The contour plots of equivalent plastic strain (PEEQ) obtained from the numerical models of JD1 and JD1P after failure are compared with their experimental final deformations in Fig.8, where good agreements between the experimental results and numerical modelling exist.

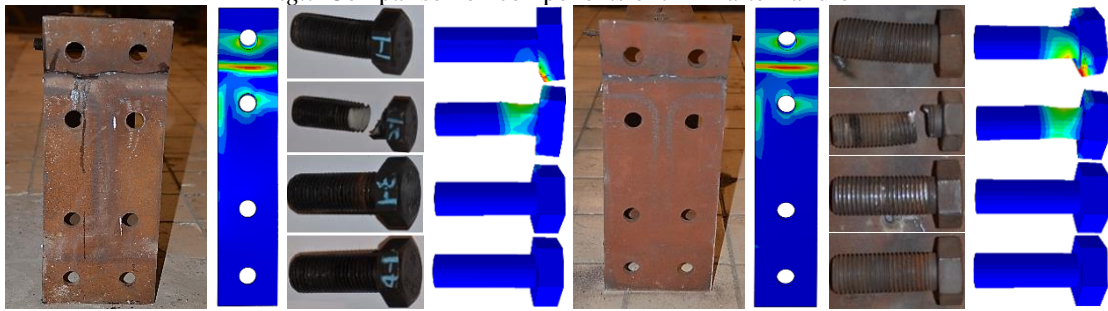


(a) JD1 (b) JD1P

Fig.6 Comparison on final deformation states of JD1 and JD1P



(a) front view of endplate (b) side view of endplate (c) bolts
 Fig.7 Comparison on components of JD1P after failure

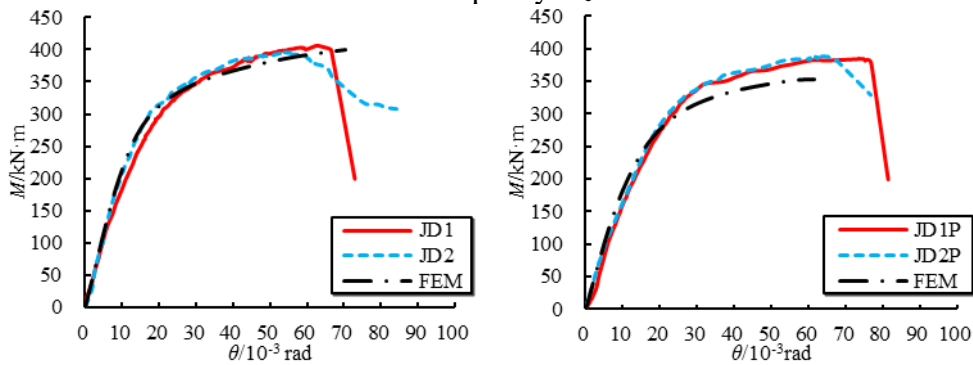


(a) endplate of JD1 (b) bolts of JD1 (c) endplate of JD1P (d) bolts of JD1P

Fig.8 Comparison of final deformation and numerically predicted PEEQ of connection JD1 and JD1P

5.2 Moment-rotation curves

The comparisons between numerical model and experimental study on the $M-\theta$ relationships of all endplate connections are shown in Fig.9. It can be seen that the numerically simulated $M-\theta$ relationships agree well with that from experimental results on initial rotational stiffness, load bearing capacity and connection rotation at the maximum load level θ_{max} . However, this current FE model cannot simulate the descending stage of the $M-\theta$ curves obtained in tests; hence it is not able to simulate the maximum connection rotation capacity Φ_c .



(a) JD1 (b) JD1P

Fig.9 Moment-rotation comparison of JD1 and JD1P

The peak loads of various endplate connections obtained from numerical model and experimental study are listed in Table 6. It can be found that for the experiments at ambient temperature, the maximum deviation of the peak load between numerical model and experimental result is 1.74%. But for the experiments after fire, the deviation is up to 9.64%. The deviation between numerical model and post-fire experimental study might attribute to the deviations of material properties of structural steels and temperature field distribution in various components of connection specimens when they are exposed to fire in full-scale tests.

Based on the above validations, it has been demonstrated that this finite element model gives reasonable accuracy compared with the experimental results, providing an efficient, economical, and accurate tool to study the performance of high strength steel endplate connections both at ambient temperature and after fire.

Table 6. Validation of numerical study against experimental study on peak moment

Condition	Test ID	Peak moment (kN·m)		Deviation (%)
		Tests	FEM	
Ambient temperature	JD1	406.32	399.36	1.74
	JD2	394.98		1.10
After fire	JD1P	385.10	353.50	8.94
	JD2P	387.56		9.64

6 CONCLUSIONS

Based on the experimental and numerical study, the following conclusions can be drawn:

- (1) The component method employed in EC3 can justifiably predict the failure mode of full HSS extended endplate connections both at ambient temperature and after fire. However, the component method overestimates initial rotational stiffness of full HSS extended endplate connections, especially their initial rotational stiffness after fire.
- (2) The accuracy of EC3 for predicting the plastic flexural resistance of HSS endplate connections is acceptable no matter at ambient temperature or after fire. However, the provisions of EC3 on the rotation capacity of connections seem rather conservative for HSS endplate connections.
- (3) The rotation capacity of HSS endplate connections is considered to be sufficient, no matter at ambient temperature or after fire, which guarantees the ductility of steel structures with endplate connections made of HSS.
- (4) After cooling down from 550 °C, HSS endplate connections can regain more than 90% of its original load-bearing capacity and more than 80% of its original initial rotational stiffness.

REFERENCES

1. CEN. Eurocode3: Design of steel structures, Part 1–8: design of joints. Brussels; 2005.
2. Coelho AMG, Bijlaard FSK. Experimental behaviour of high strength steel endplate connections. *J Constr Steel Res* 2007;63:1228–40.
3. Coelho AMG, da Silva LS, Bijlaard FSK. Experimental assessment of the ductility of extended end plate connections. *Eng Struct* 2004; 26:1185-1206.
4. Coelho AMG, da Silva LS, Bijlaard FSK. Ductility analysis of bolted extended end plate beam-to-column connections in the framework of the component method. *Steel Compos Struct* 2006;6:33–53.
5. Qiang X, Bijlaard FSK, Kolstein MH, Jiang X. Behaviour of beam-to-column high strength steel endplate connections under fire conditions – Part 1: Experimental study. *Eng Struct* 2014; 64:23–38.
6. Qiang X, Bijlaard FSK, Kolstein MH, Jiang X. Behaviour of beam-to-column high strength steel endplate connections under fire conditions – Part 2: Numerical study [J]. *Eng Struct* 2014; 64:39–51..
7. Qiang X, Bijlaard FSK, Kolstein MH. Post-fire behaviour of high strength steel endplate connections - part 1: experimental study. *J Constr Steel Res* 2015;108:82–93.
8. Qiang X, Bijlaard FSK, Kolstein MH. Post-fire behaviour of high strength steel endplate connections - part 2: numerical study. *J Constr Steel Res* 2015;108:94–102.
9. Coelho AMG. Characterization of the ductility of bolted end plate beam-to column steel connections, PhD thesis. Coimbra, Portugal: University of Coimbra; 2004.
10. CEN. Eurocode3: Design of steel structures, Part 1–2: General rules – structural fire design. Brussels; 2005

DIRECT METHOD FOR CRITICAL TEMPERATURE OF A STEEL MEMBER SUSCEPTIBLE TO STABILITY LOSS

Teemu Tiainen¹, Jolanta Baczkiewicz², Timo Jokinen³, Mikko Salminen⁴

ABSTRACT

Steel structures typically require some protection against elevated temperatures present in the case of fire. The typical protection methods are sheetings and intumescent paints. The concept of critical temperature is widely used when considering dimensioning the protection thickness. However, to obtain the critical temperature of members susceptible to stability loss according to EN 1993-1-2 standard requires an iterative calculation. To authors knowledge, only few contributions are available on the topic in the literature. To fill this gap, the authors propose a new relatively simple direct calculation method for finding the critical temperature of a steel member susceptible to stability loss. It is validated against calculations with the iterative approach of EN 1993-1-2 and some numerical calculations performed with software "SAFIR". The method is based on the design procedure found in EN 1993-1-2. However, it might be modified for use with other standards and codes as well.

1 INTRODUCTION

In addition to resistance in room temperature, structures in buildings need typically to be designed to resist loads at elevated temperatures such as fire. The typical design practice uses the concept of "critical temperature of a steel member", which is the highest temperature that member can sustain under a certain loading without a failure. The critical temperatures of members are given to a fire protection designer as an acceptance criteria for the thermal analysis of the fire protected structure. Because member strength depends only on material's yield limit, whereas member stability depends on both yield limit and elastic modulus, critical temperature is easier to calculate if stability phenomena can be ignored. Such method is presented in the existing European design standards [1]. When stability is taken into account, calculation procedure becomes iterative (example of the iteration shown in [2]). The main focus of steel designers tends to be in ultimate limit state design according to [3]. The fire design according to [1] is considered as a secondary action in which any extra work connected to iterative calculation is unwanted.

The authors, however, are aware of only few contributions in the literature considering direct method for calculating the critical temperature of a member where stability is taken into account. According to reference [4], in Japanese code, there is a design formula for critical temperature of steel columns which takes into account the slenderness. However, the maximum slenderness when using this design method is $\lambda = 1$. Moreover, it was noticed that this method

¹ PhD Candidate, Tampere university of technology, Finland.
email: teemu.tiainen@tut.fi

² PhD Candidate, Tampere university of technology, Finland.
email: jolanta.baczkiewicz@tut.fi

³ Fire design engineer, Fire Engineering and Fire Safety Design Consultants Markku Kauriala Ltd, Finland.
email: timo.jokinen@kauriala.fi

⁴ Senior Technical Advisor, Finnish Constructional Steelwork Association, Finland.
email: mikko.salminen@rakennusteollisuus.fi

gives in many cases critical temperatures that are clearly on the safe side compared to the iterative method of EN 1993-1-2. The ECCS guide [5] presents dimensionless buckling curves for steel columns at elevated temperatures, from where the critical temperatures can be determined graphically. However, analytical formulas are not given.

Therefore, in this paper, a non-iterative or direct method to obtain the critical temperature of a member susceptible to stability loss is presented. The proposed method involves two parameters, namely slenderness and utilization ratio. In the following sections the method is presented in detail and its behaviour is compared to results given by EN 1993-1-2 iterative procedure and a numerical analysis software.

2 NON-ITERATIVE METHOD FOR MEMBERS SUSCEPTIBLE TO STABILITY LOSS

The approach finding out critical temperature on members not susceptible to stability loss is given in the EN 1993-1-2. The utilization ratio defined by

$$\mu_0 = \frac{E_{fi,d}}{R_{fi,d,0}} \quad (1)$$

is used in

$$\theta_{cr,y}(\mu_0) = 39.19 \ln \left(\frac{1}{0.9674 \mu_0^{3.833}} - 1 \right) + 482 \quad (2)$$

to calculate the critical temperature.

If a member with tensile axial force is considered, the utilization ratio is calculated as

$$\mu_0 = \frac{E_{fi,d}}{R_{fi,d,0}} = \frac{N_{fi,Ed}}{A f_{y,0}} \quad (3)$$

Non-iterative method is based on observation that both material yield strength and Young's modulus are reduced due to elevated temperature. If member is not susceptible to stability loss (stocky member, or member in tension) the critical temperature can be calculated from inverse function of $k_{y,\theta}(\theta)$ (Figure 1). When considering pure stability loss similarly critical temperature is obtained from inverse of $k_{E,\theta}(\theta)$.

The function $k_{y,\theta}(\theta)$ is defined partwise linear in EN 1993-1-2. However, the formula in Eq. (2) can be considered continuous approximation of the inverse $\theta(f_{y,\theta}) = \theta(\mu_0)$.

Approximation for the function $\theta_{cr,E}(\mu_0)$ can be written as

$$\theta_{cr,E}(\mu_0) = 785 - 150\mu_0 - 250 \tan^{-1}(20\mu_0 - 0.9) - 30 \tan^{-1}(30\mu_0 - 19.5) - 120 \tan^{-1}(10\mu_0 - 8.65) \quad (4)$$

These curves are visualized in Figure 2 .

Idea of the proposed method is to linearly combine these effects as

$$\theta_{cr} = \alpha \theta_E + (1 - \alpha) \theta_y \quad (5)$$

where α is a factor depending on slenderness λ and initial state utilization factor μ_0 as

$$\alpha = \begin{cases} k_1 \lambda^3 + k_2 \lambda^2 + k_3 & \text{if } \lambda \leq 2 \\ k_4 & \text{if } \lambda > 2 \end{cases} \quad (6)$$

Steel Structures

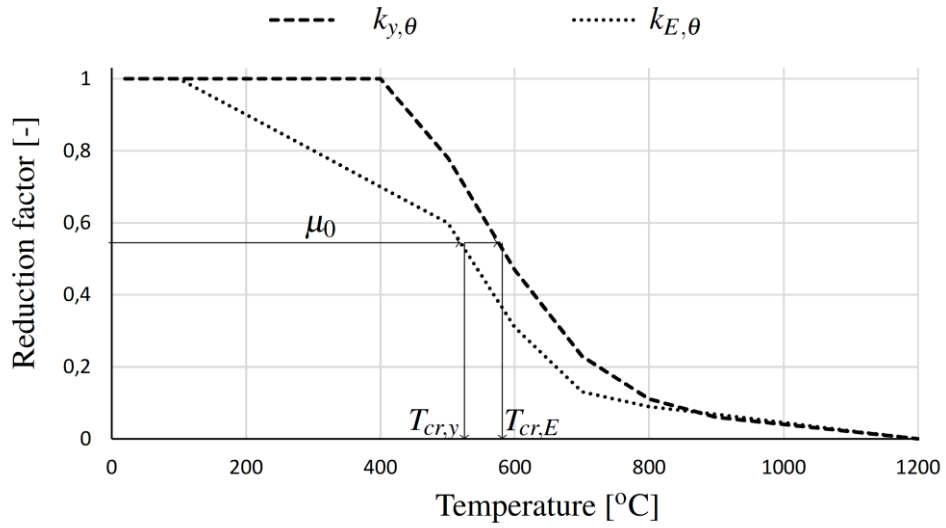


Figure 1: Idea of finding critical temperature with both effective yield stress and Young's modulus degradation. With shown μ_0 value, critical temperature based on yield degradation ($T_{cr,y}$) is approximately 50 degrees higher than value based on Young's modulus degradation ($T_{cr,E}$).

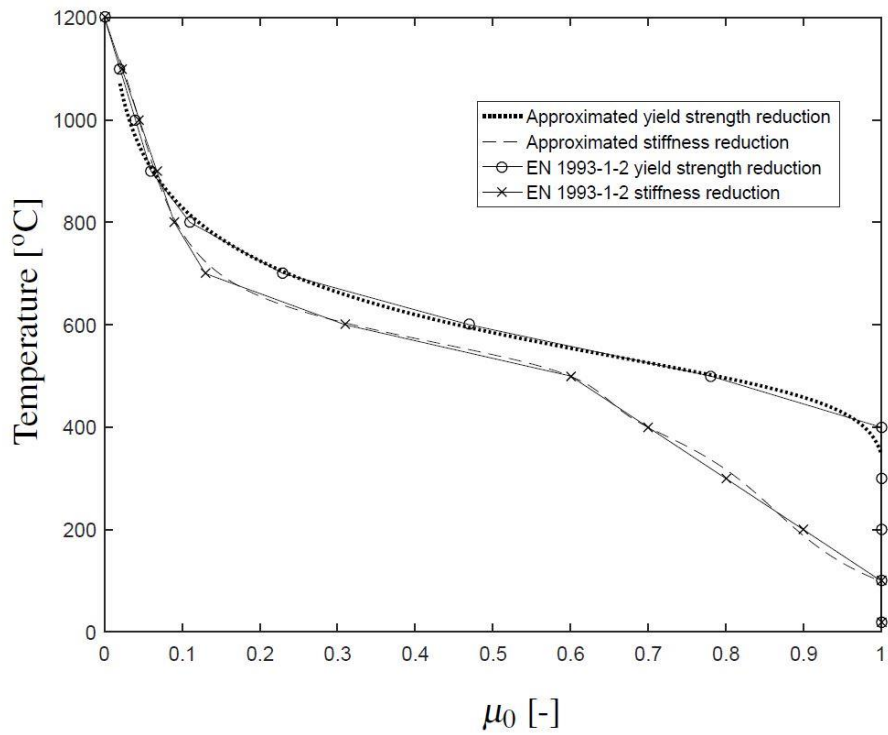


Figure 2: The continuous approximations of the curves against the partwise linear strength and stiffness reduction from EN 1993-1-2.

where λ is the non-dimensional slenderness in ambient temperature (see [3]) defined as

$$\lambda = \sqrt{\frac{f_y A}{N_{cr}}} \quad (7)$$

and

$$k_4 = a_1 \mu_0^2 + b_1 \mu_0 + c_1 \quad (8)$$

$$k_3 = a_2 \mu_0^2 + b_2 \mu_0 + c_2 \quad (9)$$

$$k_1 = \frac{k_3 - k_4}{4} \quad (10)$$

$$k_2 = \frac{3(k_4 - k_3)}{4} \quad (11)$$

where a_i , b_i and c_i are constant coefficients. The values found suitable by the authors for normal structural steel are seen in Table 1 .

Table 1: Values of a_i , b_i and c_i for structural steel.

i	a	b	c
1	-1	1.2	0.7
2	0.8	-0.7	0.3

The procedure is general and if the temperature curves for stiffness and strength are known, it can be applied to other steels as well if appropriate coefficient values in Eq. (6) and Table 1 are found. For more accurate results, the expressions for k_3 and k_4 can be replaced with 3rd order polynomials resulting in 8 adjustable parameters.

3 NUMERICAL VERIFICATION

The behaviour of the method is verified against the iterative procedure from EN 1993-1-2 and compared to numerical results obtained with SAFIR software.

3.1 EN 1993-1-2

To verify the proposed method, number of "exact" critical temperatures are calculated using the EN 1993-1-2 formulas for a compressed member:

$$N_{b,fi,t,Rd} = \frac{\chi_{fi} A k_{y,\theta} f_y}{\gamma_{M,fi}} \quad (12)$$

$$\chi_{fi} = \min \left\{ \frac{1}{\phi_\theta + \sqrt{\phi_\theta^2 - \lambda_\theta^2}}, 1 \right\} \quad (13)$$

$$\phi_\theta = \frac{1}{2} (1 + \alpha \lambda_\theta + \lambda_\theta^2) \quad (14)$$

$$\alpha = 0.65 \sqrt{\frac{235}{f_y}} \quad (15)$$

$$\lambda_{\theta} = \lambda \sqrt{\frac{k_{y,\theta}}{k_{E,\theta}}} \quad (16)$$

The following non-linear group of equations is solved numerically.

The verification was done for slenderness values $\lambda = \{0, 0.5, 1, \dots, 4.5, 5\}$, force values $\mu_0 = \{0.1, 0.2, 0.3, \dots, 0.8, 0.9\}$ and yield strength values $f_y = \{235, 355, 460, 700\}$ MPa. In total there are $11 \cdot 9 \cdot 4 = 396$ verification points. The resulting points are shown in Figure 3. It seems that compared with the EN 1993-1-2, the proposed approach gives very similar results with the differences noted mainly on safe side. The material yield strength does not seem to have significant effect on the behaviour of the method.

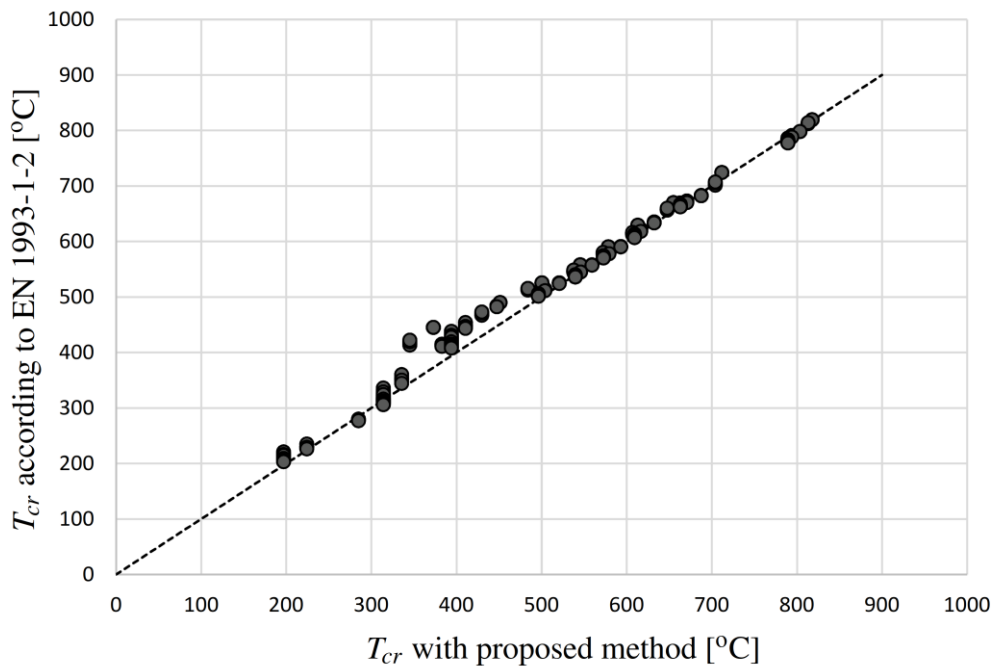


Figure 3: EN 1993-1-2 iterative vs. proposed direct approach.

3.2 Comparison to SAFIR results

The resistance evaluation at elevated temperatures was based on EN 1993-1-2 which can also a simplified method for hand calculations. In this subsection proposed approach is compared to critical temperature values obtained with a numerical analysis software "SAFIR" which has been thoroughly validated in numerous references [6, 7, 8, 9, 10].

In SAFIR analysis, a constant loading is applied to single column under uniformly distributed increasing temperature. In the ambient temperature two values of initial imperfection are applied ($L/1000$ based on EN 1993-1-2 4.3.3 (7) and $L/200$ based on EN 1993-1-1 Table 5.1) and 20 beam elements are used to model the column.

Three profiles are considered:

- Square hollow section with thick wall 100x10
- Square hollow section with thin wall 120x4
- Open section HEB220

The dimensions of profiles of thick-walled hollow section was chosen to meet requirement for cross-section class 1 and the thin-walled section cross-section class 2, both in room temperature and fire. The steel yield strength f_y is 355 MPa.

The models of the sections used in SAFIR (Figure 4) have 229 (HEB 220) and 192 (SHS profiles) elements. The comparison was done in total of 48 points with values $\lambda = \{0.5, 1, 1.5, 2\}$ and $\mu_0 = \{0.1, 0.3, 0.5, 0.7\}$.

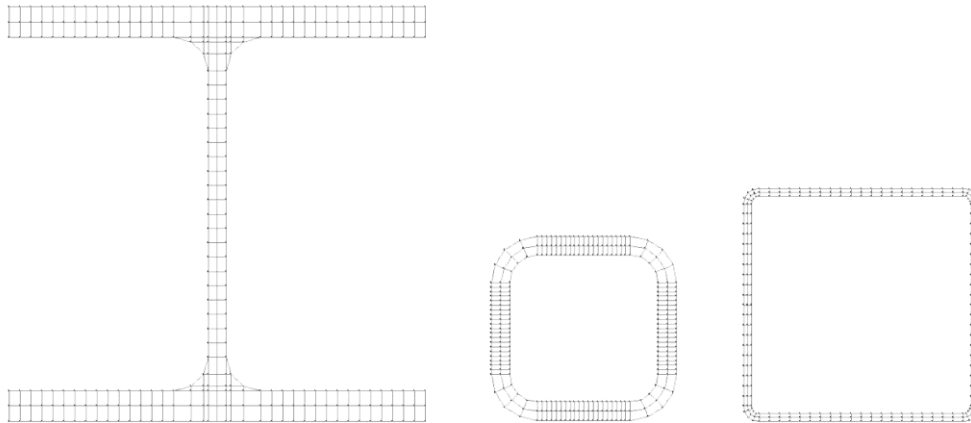


Figure 4: The discretization of sections used in SAFIR models. Left HEB 220, center 100x10 square hollow section, right 120x4 square hollow section.

The amplitude of initial imperfection seems to have significant effect on the critical temperature (Figure 5). When comparing the results with initial imperfection value $L/1000$ with the proposed method good agreement is obtained. Using the larger initial imperfection value $L/200$ seems to result in considerably lower critical temperatures. The effect is largest in cases with $\lambda \geq 1$ and $\mu_0 = 0.7$ the difference in critical temperature being on average around 150 °C. It seems that this value of initial imperfection implies a significant bending moment to the profile.

The mid-point deflection for the case with $\lambda \geq 1$, $\mu_0 = 0.7$ and square hollow section profile 120x4 is seen Figure 6 . The rest of the cases give temperature difference of 44 degrees on average.

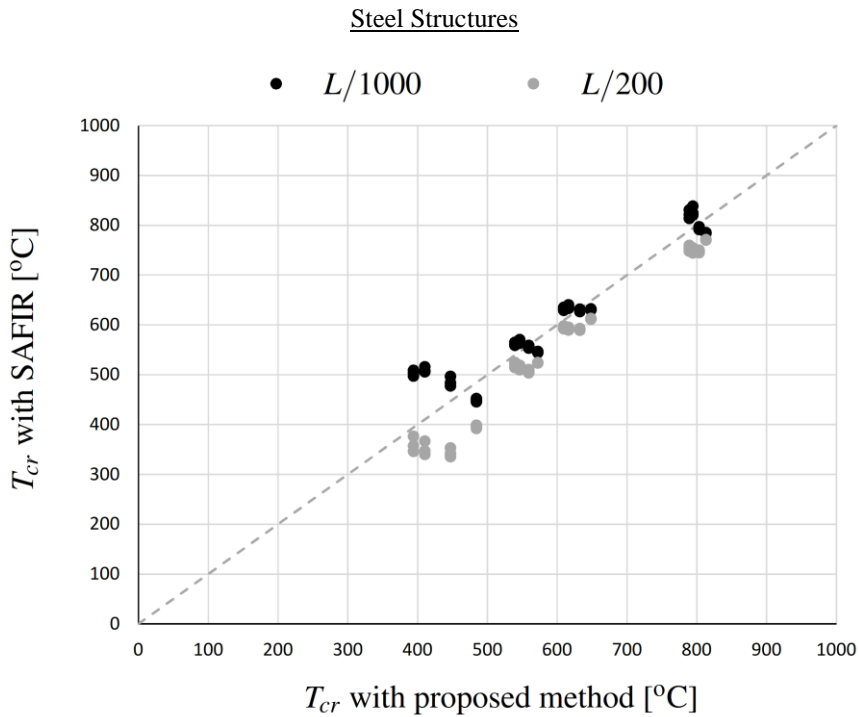


Figure 5: Critical temperatures obtained with SAFIR and proposed method.

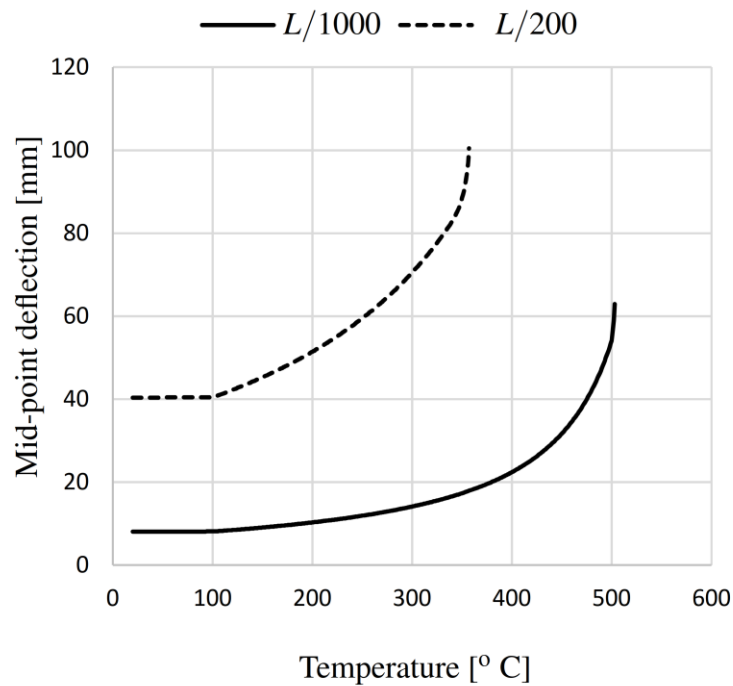


Figure 6: The effect of initial imperfection in mid-point deflection as function temperature. Profile SHS 120x4, $\mu_0 = 0.7$, $\lambda = 2.0$.

4 CONCLUSIONS

This paper shows a relatively simple non-iterative method for calculating the critical temperature of steel member subjected to stability loss. The method performs consistently throughout the area where most of the interest is in practical design work. The check can be considered valid for stability loss due to buckling, lateral torsion buckling or shear buckling as

similar buckling curves and equations are to be applied. However, the numerical behaviour was in this paper tested only for flexural buckling. The combined actions, such as the combined bending and axial force resistance evaluation remain as open question for future research.

ACKNOWLEDGEMENTS

The financial support of Finnish Cultural Foundation, Pirkanmaa Regional fund is gratefully acknowledged.

REFERENCES

- [1] EN 1993-1-2. *EN-1993-1-2. Eurocode 3: Design of steel structures. Part 1-2: General rules – structural fire design*. CEN, 2006.
- [2] J. M. Franssen and P. Vila Real. *Fire Design of Steel Structures. ECCS Eurocode Design Manuals*. ECCS, 2010.
- [3] EN 1993-1-1. *EN-1993-1-1. Eurocode 3: Design of steel structures. Part 1-1: General rules and rules for buildings*. CEN, 2006.
- [4] K. Harada, Y. Ohmiya, A. Nanbu, and A. Nakamichi. Technical basis on structural fire resistance design in building standards law of japan. In *Second International Workshop: Structures in Fire*, Christchurch, March 2002.
- [5] European Convention for Constructional Steelwork, Technical Committee 3. *European Recommendations for the Fire Safety of Steel Structures*. Elsevier, 1983.
- [6] J.-M. Franssen, J.-B. Schleich, L.-G. Cajot, D. Talamona, B. Zhao, L. Twilt, and K. Both. A comparison between five structural fire codes applied to steel elements. In *Fourth International Symposium on Fire Safety Science*, Ottawa, 2012.
- [7] D. Pintea and J.-M. Franssen. Evaluation of the thermal part of the code safir by comparison with the code tasef. In *Proceedings of the 8th International Conference on Steel Structures, Vol. 2*, Timisoara, 1997.
- [8] J. M. Franssen and J. Unanua. *Appui a la normalisation – Volet II. Partie 2: Validation de Programmes Numeriques Modelisant lers Structures en cas d’incendie*. Research Report. University of Liege., 2000.
- [9] R. Zaharia and T. Gernay. Validation of the advanced calculation model safir through din en 1991-1-2 procedure. In *Proceedings of the 10th International Conference ASCCS 2012.*, National University of Singapore., 2012.
- [10] T. Gernay and J. M. Franssen. Modeling structures in fire with safir®: Theoretical background and capabilities. *Journal of Structural Fire Engineering*, 8:300–323, 2017.

ANALYTICAL DETERMINATION OF TEMPERATURE DISTRIBUTION IN STEEL CABLES CONSIDERING CAVITY RADIATION EFFECT

Yong Du¹, Liang Li², Jian Jiang³, Guo-Qiang Li⁴

ABSTRACT

This paper investigated the temperature distribution of steel cables, both theoretically and numerically. A simple model of heat transfer among wires has been developed to capture the cavity radiation and conduction by a parallel thermal resistance to determine the total thermal resistance of wires. A simple formula has been derived from the lump capacitance equilibrium to capture the temperature history in the center of steel cables considering of cavity radiation. Meanwhile, numerical model has been established by using ABAQUS software to conduct the 2D heat transfer analyses on a series of realistic cable section under ISO834 fire. The results from parametric studies show that the cavity radiation accelerated the heating rate of steel cables compared to round steel bar model. This indicates that it is not safe to directly use the equivalent steel bar model to determine the temperature history of steel cables in the previous studies. The results from parametric studies show the non-uniform temperature history of steel cables. Higher center temperatures of steel cables are achieved due to the cavity radiation effect compared to that of round steel bars.

Keywords: steel cable; temperature distribution; cavity radiation; calculation method; thermal resistance

1 INTRODUCTION

Pre-tensioned steel cables have been increasingly used in large-span buildings and bridges, and their fire safety issues have received growing attention [1-2]. The behaviour of steel cables, as one of the important load-bearing components of pre-tensioned steel structures, significantly affects the global structural performance. However, at elevated temperatures, steel cables experience degraded mechanical properties [3] and thermal expansion which may affect its load bearing capacity and tensile force in them [4]. An accurate prediction of temperature of steel cables is essential to determine the fire-induced mechanical responses of cable-supported structures. Previous studies focus on the prediction of temperature distribution in traditional steel members or steel-concrete composite members. The effect of contact thermal resistance on the temperature distribution of concrete-filled steel tubes in fire was investigated by previous studies [5]. Mao and Kodur [6] investigated the temperature distribution of protected steel columns with concrete under three-side and four-side fire exposure. Wang and Xia [7] proposed a theoretical method for predicting temperature rise in steel columns protected by fireproof boards. The effect of cavity radiation due to the gap between steel member and board was considered. Recently, Bennetts et al. [8] numerically studied the temperature field of steel cables which were simulated by round steel bar models.

However, the heat transfer theories in previous approaches are based on continuous medium. A steel cable is composed of multiple wires (or strands), and there is gap between wires filled by air. The cavity radiation effect due to the gap may significantly affect the temperature distribution in the cable, leading to a different temperature configuration compared to steel cylinders [9]. Therefore, it is

¹ College of Civil Engineering, Nanjing Tech University, Nanjing 211816, China..

e-mail: yongdu_mail@njut.edu.cn

² College of Civil Engineering, Nanjing Tech University, Nanjing 211816, China.

e-mail: liangli_Mail@163.com

³ Engineering Laboratory, National Institute of Standards and Technology (NIST), Gaithersburg 20899, MD.

e-mail: jian.jiang@nist.gov

⁴ State Key Laboratory for Disaster Reduction in Civil Engineering, Shanghai 200092, China.

e-mail: gqli@tongji.edu.cn

necessary to investigate the effect of heat transfer by cavity radiation on the temperature distribution of steel cables, which is the objective of this study.

2 THEORETICAL STUDY ON TEMPERATURE DISTRIBUTION OF STEEL CABLES

2.1 Heat transfer by cavity radiation

The heat transfer by radiation between the two gray surfaces constituting the cavity can be written as:

$$q_{cavity} = \varepsilon_s \cdot X_{i,j} \cdot A_i \cdot (E_{bi} - E_{bj}) = \varepsilon_s \cdot X_{j,i} \cdot A_i \cdot (E_{bi} - E_{bj}) \quad (1)$$

in which

$$\varepsilon_s = \frac{1}{1 + X_{i,j} \left(\frac{1}{\varepsilon_i} - 1 \right) + X_{j,i} \left(\frac{1}{\varepsilon_i} - 1 \right)} \quad (2)$$

$$E_{bi} = \sigma \cdot (T_i + 273)^4 \quad (3)$$

$$E_{bj} = \sigma \cdot (T_j + 273)^4 \quad (4)$$

where q_{cavity} is the heat flux by radiation from the gray surface i to the gray surface j , in W;

A_i, A_j are the area of the surfaces i and j , respectively, in m^2 ;

E_{bi}, E_{bj} are the heat released from the surfaces i and j per unit time and area, respectively, in W/m^2 ;

$X_{i,j}$ is the configuration factor from the surface i to surface j ;

ε_s is the emissivity of the system;

For a concentric cylinder, the configuration factors $X_{i,j}$ and $X_{j,i}$ are taken as 1.0;

$\varepsilon_i, \varepsilon_j$ are the emissivity of the gray surfaces i and j , respectively;

For steel, the emissivity is taken as $\varepsilon_i = \varepsilon_j = 0.8$ [10];

T_i, T_j are the temperature of the surfaces i and j , respectively, in $^{\circ}C$.

Substituting Eqs. (2)-(4) into Eq. (1) yields:

$$q_{cavity} = h_{cavity} \cdot A_i \cdot (T_i - T_j) \quad (5)$$

where h_{cavity} is defined as:

$$h_{cavity} = \varepsilon_s \cdot X_{i,j} \cdot \sigma \cdot [(T_i + 273) + (T_j + 273)] \cdot [(T_i + 273)^2 + (T_j + 273)^2]$$

2.2 Calculation of thermal resistance

Similar to Ohm' law (resistance=potential difference/current), the thermal resistance represents the relationship between the heat energy and temperature difference during the heat transfer process.

The thermal resistance $R_{t,conv}$ of heat transfer by convection between the plane wall and surrounding is defined as:

$$R_{t,conv} = \frac{T_f - T_b}{q_c} = \frac{1}{\alpha_c A} \quad (6)$$

By defining the coefficient of heat transfer by radiation:

$$h_r = \varphi \cdot \varepsilon \cdot \sigma \cdot [(T_f + 273) + (T_b + 273)] \cdot [(T_f + 273)^2 + (T_b + 273)^2] \cdot (T_f - T_b) \quad (7)$$

where q_c is the net heat flux per area from convection, in W;

α_c is the convective heat transfer coefficient, $\alpha_c=25 W/(m^2 \cdot ^{\circ}C)$.

The net heat flux q_r by radiation between the hot smoke and external surface of a steel cable can be determined by:

$$q_r = h_r \cdot A \cdot (T_f - T_b) \quad (8)$$

where q_r is the net heat flux per area from radiation, in W;

A is the surface area of the member perpendicular to the heat flow direction, in m^2 ;

ε is the resultant emissivity, $\varepsilon = \varepsilon_f \varepsilon_m$ where ε_f is the emissivity of fire, usually taken as equal to 1.0, and ε_m is the emissivity of the surface material, for steel $\varepsilon_m = 0.8$;

T_b is the surface temperature, in $^{\circ}C$;

T_f is the temperature of the gas adjacent to the surface, in °C;
 $\sigma = 5.67 \times 10^{-8} \text{ W/(m}^2\cdot\text{K}^4)$ is the Stephan-Boltzmann constant.
 ϕ is the configuration factor (or view factor) which should be taken as 1.0 for a surface surrounded by hot smoke;

According to Eq. (8), the thermal resistance of heat transfer by radiation between the plane wall and surrounding is determined by:

$$R_{t,rad} = \frac{T_f - T_b}{q_r} = \frac{1}{h_r A} \quad (9)$$

According to Eq. (5), the thermal resistance of heat transfer by radiation of the cavity between two different objects with different temperatures is determined by:

$$R_{cavity} = \frac{T_i - T_j}{q_{cavity}} = \frac{1}{h_{cavity} A_i} \quad (10)$$

According to Fourier's law, the thermal conduction resistance of the plane wall is determined by:

$$R_{t,cond} = \frac{T_{s1} - T_{s2}}{q_x} = \frac{d}{\lambda A} \quad (11)$$

where d is the thickness of the plane wall, in m; T_{s1}, T_{s2} are the temperature of two sides of the walls, in W/m·°C.
 λ is the thermal conductivity of plane walls, in W/m·°C.

The thermal conduction resistance in the radial direction of cross section of the cylinder is determined by:

$$R'_{t,cond} = \frac{\ln(r_{i+1}/r_i)}{2\pi L \lambda_i} \quad (12)$$

where r_{i+1}, r_i are the diameter of adjacent cylinders in Fig. 1, respectively, in m;
 λ_i is the thermal conductivity of the layer i , in W/m·°C;
 L is the length of the member, in m.

2.3 Calculation of temperature of steel cables with cavity

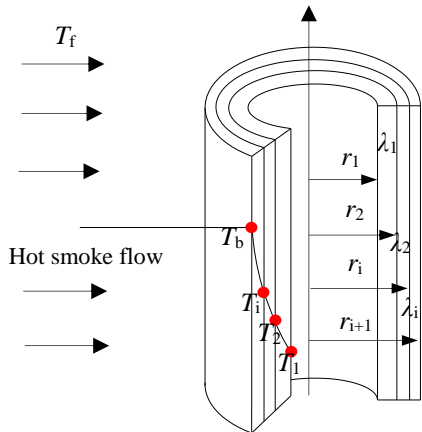


Fig. 1 Model for calculating thermal conductivity of multilayer cylinders

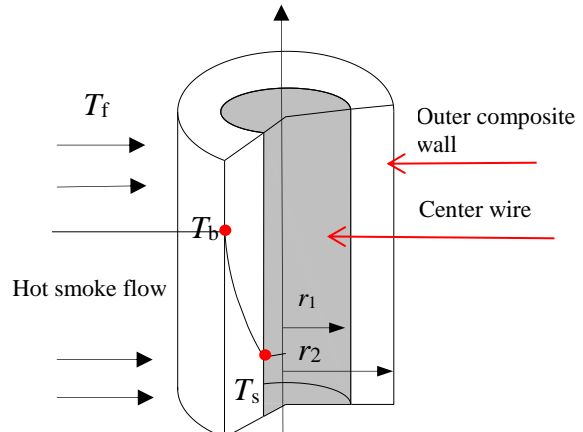


Fig. 2 Model for calculating temperature history of steel cylinders

The thermal resistance of a multilayer cylinder is calculated as series resistance, as shown in Fig. 1. A steel cylinder (e.g. concrete-filled steel tubes) can be classified as a multilayer cylinder, as shown in Fig. 2. The thermal resistance of its outer component (e.g. steel tube) can be determined by Eq. (12). For a steel cable, its cross section is equivalent to a composite cylinder consisting of external wires and cavity which have different thermal properties in Fig. 3. The thermal resistance of the outer component (include external wire and cavity) can be treated as parallel resistance. Both the steel cylinder and steel cable can be equivalent to a protected steel member in Fig. 4 where their outer components are equivalent to the protection layer and their central member is equivalent to the steel member. The thermal resistance of the protection layer (i.e. the outer component of protected steel member) can be determined by Eq. (11).

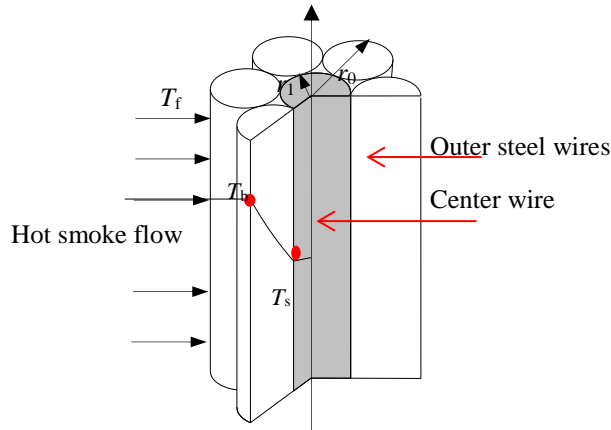


Fig. 3 Model for calculating temperature history of steel cables

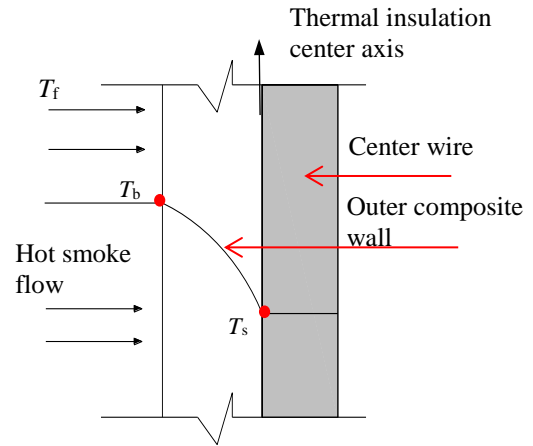


Fig. 4 Model for calculating temperature history of fire protected steel members

It was assumed that the central member in Fig. 2 and central wire in Fig. 3 had a uniform temperature distribution. Its temperature can thus be determined by the lumped heat capacity method. The outer members of steel cylinders and steel cables are equivalent to the protection layer. Therefore, the thermal conduction resistance of the protection layer can be used for the outer member in Figs. 2-3. According to [11], the temperature of the central member considering thermal conduction resistance in the radial direction of cylinder and thermal resistance of cavity can be determined by:

$$T_s(t + \Delta t) = \frac{1}{\rho_s c_s V (R_{c,r} + R)} \cdot \frac{1}{1 + \mu / 2} \cdot [T_f(t) - T_s(t)] \cdot \Delta t + T_s(t) \quad (13)$$

in which $\mu = \frac{Q_i}{Q_s} = \frac{\rho_i c_i F_i d_i}{\rho_s c_s V}$

where Δt is the time interval, in s;
 $T_s(t)$ is the temperature of central member, in °C;
 $T_f(t)$ is the temperature of heat flow medium, in °C;
 $R_{c,r}$ is the total thermal resistance of heat transfer between surface of outer member and environment, determined by Eq. (14);
 d_i is the thickness of the protection, in m;
 R is the total thermal conduction resistance of outer member, determined by Eqs. (15)-(16), respectively, for the steel cylinder and steel cable;

ρ_s, ρ_i are the density of the central member and outer member, respectively, in kg/m³;
 c_s, c_i are the specific heat of the central member and outer member, respectively, in J/°C · kg; V is the volume of the central member per unit length, in m³/m;
 F_i is the interior surface area of the protection per unit length, in m²/m;
 Q_i is the thermal capacity of the outer member per unit length, in J/°C · m;
 Q_s is the thermal capacity of the central member per unit length, in J/°C · m.

2.4 Modified calculation of temperature of steel cables with cavity

The total thermal resistance $R_{c,r}$ of heat transfer between environment and outer surface of members exposed to fire is in a form of parallel thermal resistance of heat transfer by radiation and convection:

$$R_{c,r} = \frac{1}{\frac{1}{R_{t,rad}} + \frac{1}{R_{t,conv}}} = \frac{1}{Ah_r + A\alpha_c} \quad (14)$$

As shown in Fig. 2, the total thermal resistance of outer member of steel cylinders can be determined by Eq. (12) without considering cavity radiation effect:

$$R = R'_{t,cond} = \frac{\ln(r_2 / r_1)}{2\pi L \lambda} \quad (15)$$

where λ is the thermal conductivity of steel, in $W/(m \cdot ^\circ C)$.

In the case of steel cables, there is a composite cylindrical wall outside the central wire which is composed of outer steel wires and cavity in the radial direction of section. The total thermal resistance of steel cables is a parallel resistance of thermal conduction resistance of cylinder in the radial direction of section and thermal resistance of heat transfer by cavity radiation. The total thermal resistance of outer component of steel cables can then be determined as:

$$R = R'_{t, \text{cavity}} = \frac{1}{\frac{1}{R'_{t, \text{cond}}} + \frac{1}{R_{\text{cavity}}}}, \text{ and } R'_{t, \text{cond}} = \frac{\ln(r_j/r_i)}{2\pi L\lambda} \quad (16)$$

Substituting Eq. (14) and Eq. (16) into Eq. (13) yields the temperature history of central steel wire of steel cables in Fig. 3 as:

$$\begin{aligned} T_s(t + \Delta t) &= \frac{1}{\rho_s c_s V(R_{c, r} + R)} \cdot \frac{1}{1 + \mu/2} \cdot [T_f(t) - T_s(t)] \cdot \Delta t + T_s(t) \\ &= \frac{1}{\rho_s c_s V \left(\frac{1}{Ah_r + A\alpha_c} + \frac{1}{\frac{1}{R'_{t, \text{cond}}} + \frac{1}{R_{\text{cavity}}}} \right)} \cdot \frac{1}{1 + \frac{\rho_i c_i F_i d_i}{2\rho_s c_s V}} \cdot [T_f(t) - T_s(t)] \cdot \Delta t + T_s(t) \end{aligned} \quad (17)$$

in which $R'_{t, \text{cond}} = \frac{\ln(r_3/r_2')}{2\pi L\lambda}$; $R_{\text{cavity}} = \frac{1}{h_{\text{cavity}} A_i} = \frac{1}{2\pi r_2' h_{\text{cavity}}}$;

To be on the safe side, the surface temperature T_b of members in contact with heat flow medium and temperature of gray surface T_i, T_j were taken as $T_b=T_f$ and $T_i=T_j=T_f$.

By substituting Eqs. (14)-(15) into Eq. (13), the temperature history of central member of steel cylinders in Fig. 2 can be determined as:

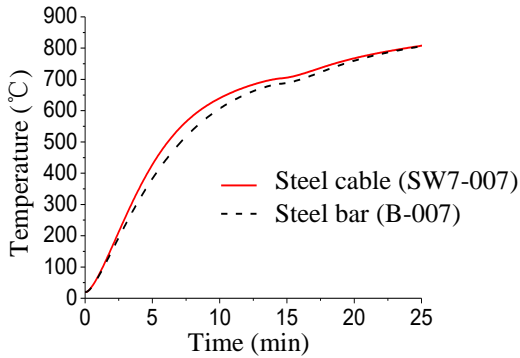


Fig. 5 Comparison of temperature history of steel cables and round steel bars

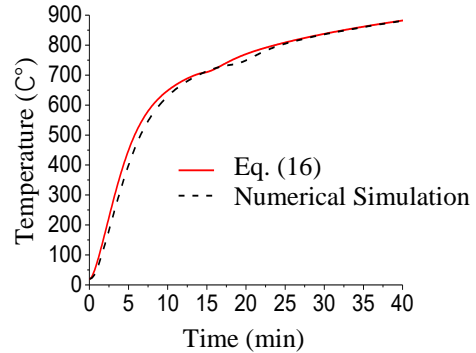


Fig. 6 Comparison of theoretical and numerical predictions of temperature of steel cables

$$\begin{aligned} T_s(t + \Delta t) &= \frac{1}{\rho_s c_s V(R_{c, r} + R'_{t, \text{cond}})} \cdot \frac{1}{1 + \mu/2} \cdot [T_f(t) - T_s(t)] \cdot \Delta t + T_s(t) \\ &= \frac{1}{\rho_s c_s V \left(\frac{1}{Ah_r + A\alpha_c} + \frac{\ln(r_2/r_1)}{2\pi L\lambda} \right)} \cdot \frac{1}{1 + \frac{\rho_s c_s F_i d_i}{2\rho_s c_s V}} \cdot [T_f(t) - T_s(t)] \cdot \Delta t + T_s(t) \end{aligned} \quad (18)$$

The temperature history of steel cables and round steel bars were determined by Eqs. (17)-(18), respectively, as shown in Fig. 5. The temperature of steel cables was higher than that from equivalent steel cylinder model by Eq. (18). This is because the surface area of steel cables perpendicular to the direction of heat flow is larger than that of steel bars. In addition, the combined density of outer component of steel cables is smaller than that of steel bars.

3 NUMERICAL STUDY ON TEMPERATURE DISTRIBUTION OF STEEL CABLES

A steel cable with 61 wires in a diameter of 7mm was modelled in finite element software ABAQUS. An equivalent steel bar in a diameter of 63mm was also modelled. The temperature-dependent specific heat and thermal conductivity of steel are given by EC2. The ISO834 standard fire curve was used. According to [12], the coefficient of heat transfer by convection and radiation emissivity were taken as $25\text{W}/(\text{m}^2\cdot\text{K})$ and 0.8, respectively.

The pressure in cavity was assumed as a standard atmospheric pressure. The cavity radiation model in ABAQUS was used to simulate the heat transfer by cavity radiation. The emissivity of the surface was taken as 0.8. The quadrilateral DC2D4 element given by ABAQUS software was used for the two-dimensional heat conduction of steel cables.

Fig. 6 shows the comparison of numerical and theoretical results of temperature history of steel cables. A good agreement was achieved, indicating that Eq. (17) as well as the numerical model can accurately predicate the temperature history of steel cables.

4 PARAMETRIC STUDY

In this section, the effect of cable dimension and cavity radiation on the temperature history of steel cables was numerically investigated. A series of steel cables with different diameters and numbers of wires were used, as listed in Table 1. The round steel bars with the same diameter to the steel cable (15mm-63mm) were also simulated. The temperature measurement points are shown in Fig. 7.



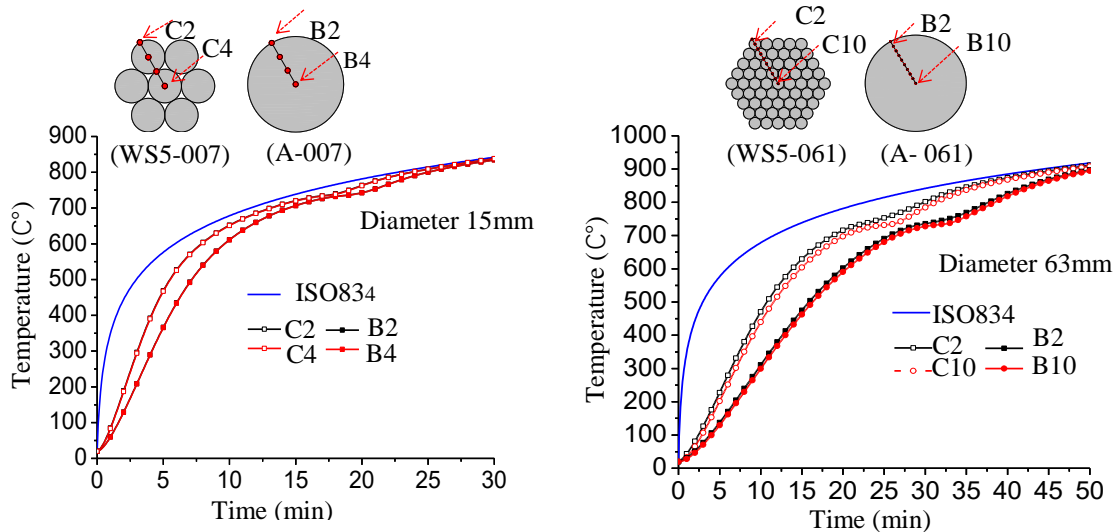
Fig. 7 Layout of temperature measurement points of steel cables and steel bars

Table. 1 List of cross-section dimension of steel cables and round steel bars

Steel cable				Round steel bar		
Diameter of wires	Type	No. of wires	Measurement points	Type	Diameter of bars	Measurement points
5mm	WS5-007	7	C1-C4	A-007	15	B1-B4
	WS5-019	19	C1-C6	A-019	25	B1-B6
	WS5-037	37	C1-C8	A-037	35	B1-B8
	WS5-061	61	C1-C10	A-061	45	B1-B10
7mm	WS7-007	7	C1-C4	B-007	21	B1-B4
	WS7-019	19	C1-C6	B-019	35	B1-B6
	WS7-037	37	C1-C8	B-037	49	B1-B8
	WS7-061	61	C1-C10	B-061	63	B1-B10

4.1 Effect of sectional dimension of cables on cavity radiation

The temperature history at the center of the external wire and central wire of WS5-007 and WS5-061 are shown in Fig. 8. These results were also compared to those from the equivalent steel bars A-007 and B-061. The temperature rise of steel cables lagged behind the gas temperature following the ISO 834 heating curve. The temperature of steel cables including cavity radiation effect was higher than that of round steel bars. The temperature distribution within the cross section of steel cables became more inhomogeneous as the sectional dimension increased.



a) Comparison between WS5-007 and A-007 b) Comparison between WS5-061 and B-061

Fig. 8 Comparison of temperature history of steel cables and round steel bars

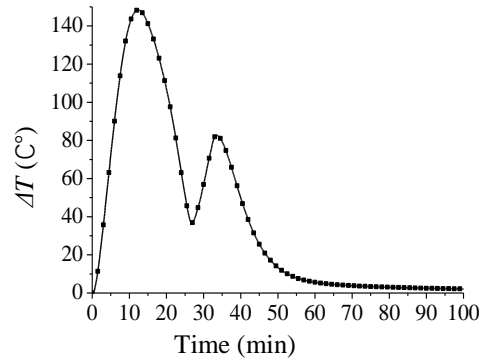
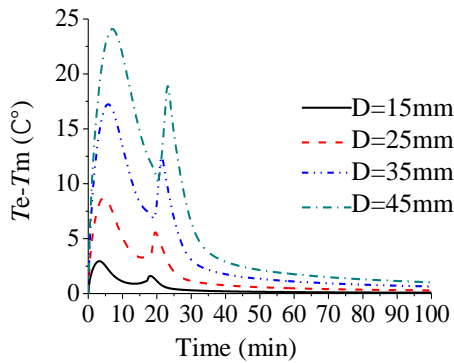


Fig. 9 Comparison of temperature differences of steel cables PES5 Fig. 10 Comparison of center temperature difference of PES7-061 and B-061

Fig. 9 shows the time history of temperature differences between the external wire and central wire of steel cables. The temperature rise of the center wire lagged behind that of the external wire. As the temperature of steel cables approached the gas temperature, the temperature difference decayed again and asymptotically approached zero. Fig. 9 also shows that the occurrence of peak temperature difference delayed with the increase of cross-section dimension of steel cables. The maximum temperature difference was within 35°C. Note that T_e is the temperature at the center of the outer layer wires, and T_m is the temperature of the center wire.

4.2 Effect of cavity radiation on temperature of steel cables

A comparison of temperature difference between the central wire of steel cables and center of round steel bars is shown in Fig. 10. The heating rate of steel cables was larger than that of steel bars, and thus the temperature difference increased and decayed with the increase of time. With a higher heating rate, the central temperature of steel cables was higher than that of steel bars when considering cavity radiation, and the maximum temperature difference reached about 148°C. The heating rate of steel cables considering cavity radiation effect was faster than that of steel bars. Therefore, it is not safe to directly use the equivalent steel cylinder model to determine the temperature of steel cables.

5 CONCLUSIONS

This paper theoretically and numerically investigated the temperature distribution in steel cables. The effect of cavity radiation was taken into account. The following conclusions can be drawn:

- A calculation method was proposed to determine the temperature history of steel cables by

considering the effect of cavity radiation.

- The accuracy of the proposed method was verified against numerical results. It was found that the cavity radiation accelerated the heating rate of steel cables compared to equivalent steel cylinder model. This indicates that it is not safe to directly use the equivalent steel cylinder model to determine the temperature of steel cables.
- The results from parametric studies showed that the temperature distribution of steel cables became more nonuniform with the increase of cross sectional dimension. The trend of non-uniform results during the heating process was not monotonic. A higher center temperature of steel cables was achieved due to the cavity radiation effect compared to that of round steel bars.

ACKNOWLEDGMENT

The authors gratefully acknowledge the financial support of the Civil Engineering Disaster Prevention National Key Laboratory in China, and the International Structural Fire Research Laboratory (ISFRL) in Nanjing Tech University, China.

REFERENCES

1. Sanghyun Joo, Seulgi Kim, Yongjae Kim, Cheolwoo Park, (2017). Fire Risk Evaluation of Bridge underneath Conditions based on Field Investigation. *6th International Workshop on Performance, Protection & Strengthening of Structures under Extreme Loading*, China.
2. Heungbae Gil, Jong-Chil Park, Sang-Sup Ahn and Kyoungbong Han (2017). Repair of a fire damaged cable stayed bridge. *9th International Symposium on Steel Structures*, Jeju, Korea.
3. EN 1992-1-2 (2013). *Eurocode 2 : General Actions- Actions on Structures Exposed to Fire*. The European Union.
4. F. Cheng, Y. Du, H.M. Sheng (2016). Analytical Method of Mechanical Behaviors for Beam String Structure Exposed to Localized Fires. *Proceedings of the 8th International Conference on Steel and Aluminium Structures*, Hong Kong
5. Ghojel J. (2004). *Experimental and analytical technique for estimating interface thermal conductance in composite structural elements under simulated fire conditions*. Experimental Thermal and Fluid Science, Vol. 28(4): 347-354.
6. X.Y. Mao, Kodur V K R. (2011). *Fire resistance of concrete encased steel columns under 3-and-4-side standard heating*. Journal of constructional steel research, Vol. 67(3):270-280.
7. Wang Pei-jun, Xia Jin-huan. (2015). *An approach for predicting cross-section temperature of four-side fire exposed steel columns protected by insulation bord*. Progress in Steel Building Structures, Vol. 17(2):44-51. (in Chinese)
8. Bennetts, I. Moinuddin, K. (2009). *Evaluation of the impact of potential fire scenarios on structural elements of a cable-stayed bridge*. Journal of fire protection engineering, Vol. 19(2), 85-106.
9. Atalioti, G. Rein, P. Kotsovinos. (2017). *Computational study of the 2D thermal response of high-strength structural steel cables under various heating regimes*. Applications of Fire Engineering. Manchester, UK, 2017; 235-245.
10. Frank. P. Incropera, David.P. dewitt. (2002). *Fundamentals of Heat and Mass Transfer fifth edition*. John Wiley and Sons.
11. CECS 200 (2006). *Technical code for fire safety of steel structure in building*. Beijing: China Planning Press. (in Chinese).
12. EN 1993-1-2 (2013). *Eurocode 3: Design of Steel Structures-Part 1.2: General Rules-Structural Fire Design*. London: British Standard Institution.

RESEARCH ON POST-FIRE LOAD-BEARING CAPACITY ASSESSMENT OF AXIAL RESTRAINED HIGH-STRENGTH STEEL COLUMNS

Guo-Qiang Li ¹, Jia-Rong Miao ²

ABSTRACT

The strength of high-strength steel degrades more significantly than conventional mild carbon steel after fire exposure. Therefore, it is more important to evaluate if high-strength steel components after fire exposure has enough remained load-bearing capacity to ensure the safety of the structure including the fire-affected components. In practice, the steel columns in a building are restrained by other components of the structure, and the restraint influences the residual bending deformation and residual stress in the fire exposed steel columns, which have further significant effect on the residual capacities of the columns. Thus, in this paper, corresponding finite-element numerical models are established in ABAQUS to investigate the post-fire load-bearing capacity of axial restrained high-strength steel columns. It is observed that the residual capacities of the columns are affected obviously by load ratio, axial rigidity ratio of the restraint to the column and the maximum temperature of the restrained steel column under fire.

Keywords: post-fire, finite-element numerical model, load-bearing capacity, high-strength steel column, axial restrained

1 INTRODUCTION

The application of high-strength steel in structural engineering can effectively decrease the steel consumption and the cost of manufacturing and installation for construction of buildings and bridges. However, the strength of steel, especially high-strength steel, will be evidently reduced at and after high temperatures over 500°C due to, for instance, fire. The studies [1, 2] show that the reduction coefficients of yield strength of Q235 steel, Q460 steel, Q550 steel and Q690 steel after cooling in the air are respectively equal to 0.85, 0.8, 0.61 and 0.59, when the fire temperature is 800 °C. So, the post-fire load-bearing capacity assessment of high-strength steel elements is a very important issue for the evaluating safety of continuing use of the steel structures after fire.

For the post-fire load-bearing capacity of steel columns, Chen et al. [3] investigated the post-fire load-bearing capacity of non-restrained Q235 steel columns with H-shaped section, considering the reduction of mechanical properties of steel and the eccentric effect caused by the uneven temperature of the section under fire. Liu [4] proposed a simplified calculation method of the post-fire axial load-bearing capacity of non-restrained Q460 steel columns with H-shaped and box-shaped section by parameter analysis, considering the change of the residual stress and mechanical properties of steel under different cooling modes during fire. Bailey [5] and Zhou et al. [6] studied the influence of the heating and cooling process on the restrained steel columns. The studies show that the steel columns in frame structure will have obvious deflection and residual stress after fire, and the properties of constraint have great influence on the deflection.

¹ Professor. State Key Laboratory for Disaster Reduction in Civil Engineering, Tongji University, Shanghai, China.
e-mail: gqli@tongji.edu.cn

² M.S. Candidate. College of Civil Engineering, Tongji University, Shanghai, China.
e-mail: jiarongmiao@tongji.edu.cn

In the above studies, the research on the post-fire load-bearing capacity of steel components has been mainly conducted on mild steel with yielding strength below 400MPa. Few studies have been made on the post-fire load-bearing capacity of high-strength steel columns and the effects of restraints have not been considered. Actually, the steel columns in a building are restrained by other components of the structure for the building in practice. The restraint will induce additional permanent deflection and stress in the columns after fire, which will further reduce the post-fire load-bearing capacity of steel columns. Therefore, load-bearing capacity of axial restrained high-strength steel columns after fire is investigated in this paper.

2 NUMERICAL MODEL

A finite-element numerical model is built in ABAQUS to investigate the post-fire load-bearing capacity of axial restrained high-strength steel columns. The finite-element model will then be verified against experimental test.

2.1 Geometrical details

The steel column is 2 meters long and the cross section is H 130×6×120×10 (slenderness ratio is 65). The initial deflection of the column is considered as 1/1000 bar length in the analysis, and the residual stress is introduced according to the residual stress model of high-strength H-shaped steel component proposed by Ban [7].

2.2 Material properties

The material properties used in the model are based on Q690 steel and the ideal elastic-plastic model is used in the analysis. At ambient temperature, the measured yield strength of Q690 steel is 771N/mm², the elastic modulus is 1.96×10⁵ N/mm². The yield strength and elastic modulus of steel are calculated according to formulas (1) and (2) for those under fire [8] and formulas (3) and (4) for those after fire [2].

$$\frac{f_{y,T}}{f_{y,20}} = 0.02186 + (1 - 0.02186) \exp \left[-\frac{1}{2} \left(\frac{T - 20}{3.233 \times 10^4} \right)^{0.4352} - \frac{1}{2} \left(\frac{T - 20}{540.1} \right)^{6.259} \right] \quad 20^\circ\text{C} \leq T \leq 800^\circ\text{C} \quad (1)$$

$$\frac{E_T}{E_{20}} = \exp \left[-\frac{1}{2} \left(\frac{T - 20}{655.8} \right)^{8.308} - \frac{1}{2} \left(\frac{T - 20}{1035} \right)^{2.684} \right] \quad 20^\circ\text{C} \leq T \leq 800^\circ\text{C} \quad (2)$$

$$\frac{f_{y,T}}{f_{y,20}} = \begin{cases} 1 & 20^\circ\text{C} \leq T \leq 500^\circ\text{C} \\ 1.69 \times 10^{-6} T^2 - 0.00369T + 2.42 & 500^\circ\text{C} < T \leq 900^\circ\text{C} \end{cases} \quad (3)$$

$$E_T = E_{20} \quad 20^\circ\text{C} \leq T \leq 900^\circ\text{C} \quad (4)$$

where $f_{y,20}$ and E_{20} are the yield strength and elastic modulus of Q690 steel at ambient temperature.

2.3 Element type and grid partition

Shell elements (S4R) are assigned to the restrained steel column, and the column is divided into 60 units in the length direction, while the web is divided into 20 grids and the two sides of the flange are divided into 10 grids respectively, as shown in *Fig.1*. The boundary conditions of the column are set as hinge, and a spring element (SPRING2) is set on the top of the column to simulate the axial restraint. Four analysis steps are set up to simulate the process of dead load, fire heating, cooling, and static load (to get post-fire ultimate bearing capacity of the steel columns).

2.4 Validation of numerical results

A finite-element numerical model is established in accordance with the paper [9] using the method above. And the numerical results are compared with the experimental results to validate the model.

The comparisons of axial force-temperature curve between numerical and experimental results are presented in Fig.2 (a, b, c). As it can be seen, the axial force-temperature curves obtained from the numerical results agree well with that obtained from the test during the heating process. The comparisons of critical buckling temperature between numerical and experimental results are presented in Fig.2 (d), and the average difference between simulation and test values is 4.7% which is within the allowable range of error.

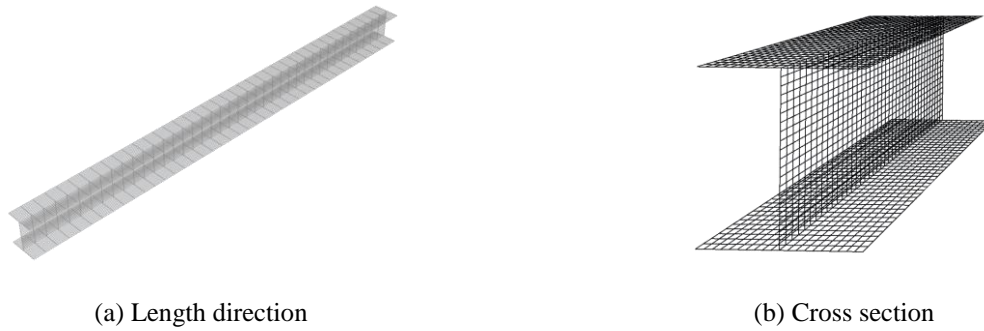


Fig.1. Grid partition

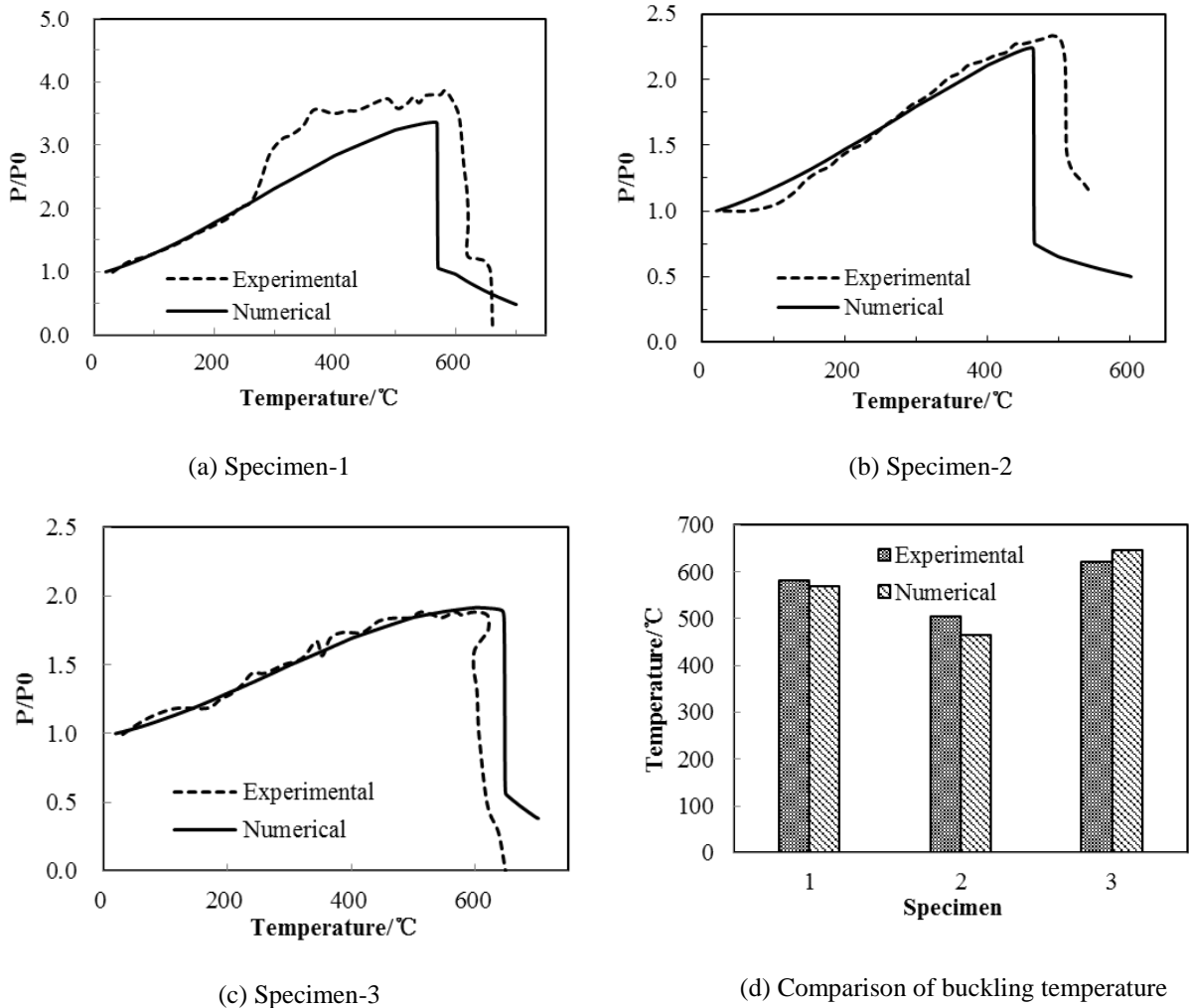


Fig.2. Validation of the numerical model

3 PARAMETERS ANALYSIS

Based on the validated numerical models presented in the previous section, a series of parametric analysis are conducted to investigate how the post-fire load-bearing capacity of axial restrained high-strength steel columns are affected by the parameters as following: (1) the maximum temperature of the restrained steel column under fire (T); (2) the axial load ratio (ρ); and (3) the axial rigidity ratio of the restraint to the column (β).

The following notation are used for the parametric studies: (1) the critical buckling temperature of the restrained steel column is defined as T_{bu} ; (2) during the heating process, the critical temperature of the restrained steel column is defined as T_{cr} when its axial force is restored to the initial state after buckling [10]; (3) the ratio of the column's load-bearing capacity after fire to the load-bearing capacity before fire is defined as α ; and (4) The relative temperature is defined as $\eta = (T - T_{bu}) / (T_{cr} - T_{bu})$.

3.1 Influence of T

As depicted in Fig.3 ($\beta = 0.3$), when $\eta < 0$ ($T < T_{bu}$), the ratio of the column's load-bearing capacity after fire to the load-bearing capacity before fire (α) is equal to 1. Because the temperature of the restrained steel column during fire is lower than the buckling temperature, the steel column deforms only elastically but not plastically, so that the deformation of the steel column can fully recover after fire. In addition, the buckling temperature of the restrained column is lower than 500°C in general, so that the temperature (T) lower than the buckling temperature does not affect the yield strength and elastic modulus of steel after fire. Therefore, the load-bearing capacity of the restrained column after fire is equal to that of before fire.

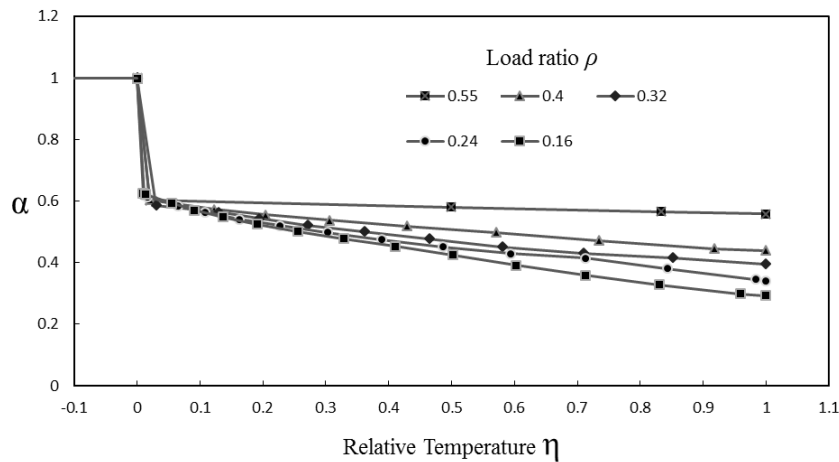


Fig.3. $\alpha - \eta$ relationship

When $\eta = 0$ ($T = T_{bu}$), the ratio of the column's load-bearing capacity after fire to the load-bearing capacity before fire (α) is reduced rapidly ($\alpha = \alpha_{bu}$ is defined). The reason is that the restrained steel column just buckled as the temperature rise to T_{bu} during fire, while plastic bending deformation of the column is rapidly developed. As the deformation of the steel column cannot fully recover after fire, the load-bearing capacity of the restrained column after fire is reduced rapidly.

When $0 \leq \eta \leq 1$ ($T_{bu} \leq T \leq T_{cr}$), the ratio of the column's load-bearing capacity after fire to the load-bearing capacity before fire (α) has an approximately negative linear correlation with the relative temperature (η). The reason is that the flexural and plastic deformation induced by the thermal expansion and axial force of the column increases with the maximum temperature of the restrained

steel column under fire (T). As a result, a higher η leads to a more remarkable residual bending deformation after fire, which further reduces the post-fire load-bearing capacity of the column. When $\eta = 1$ ($T = T_{cr}$), $\alpha = \alpha_{cr}$ is defined. Considering the restrained steel column is in a state of critical destruction under fire, T_{cr} is the maximum temperature considered in this study. As there is a linear relationship between α and η ($0 \leq \eta \leq 1$), $\alpha - \eta$ curves can be determined by α_{bu} and α_{cr} in any cases, so the following analysis will focus on analysing the influence of axial load ratio (ρ) and axial rigidity ratio (β) on α_{bu} and α_{cr} .

3.2 Influence of ρ

As it can be seen in Fig.4, the axial load ratio (ρ) has less effect on α_{bu} in any axial rigidity ratio (β), but it has significant effect on α_{cr} which has an approximately positive linear correlation with load ratio (ρ). Because α_{cr} corresponds to the state in which the axial force of the restrained steel column is restored to the initial load under fire, the bigger the initial load is, the less deflection and lower temperature are required in that state, so that the post-fire load-bearing capacity is higher.

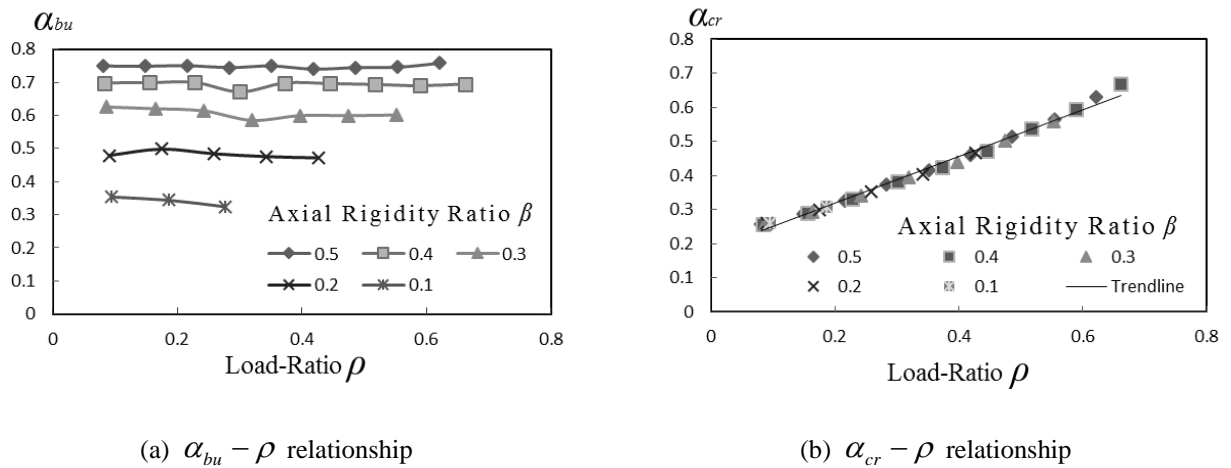


Fig.4. The influence of ρ

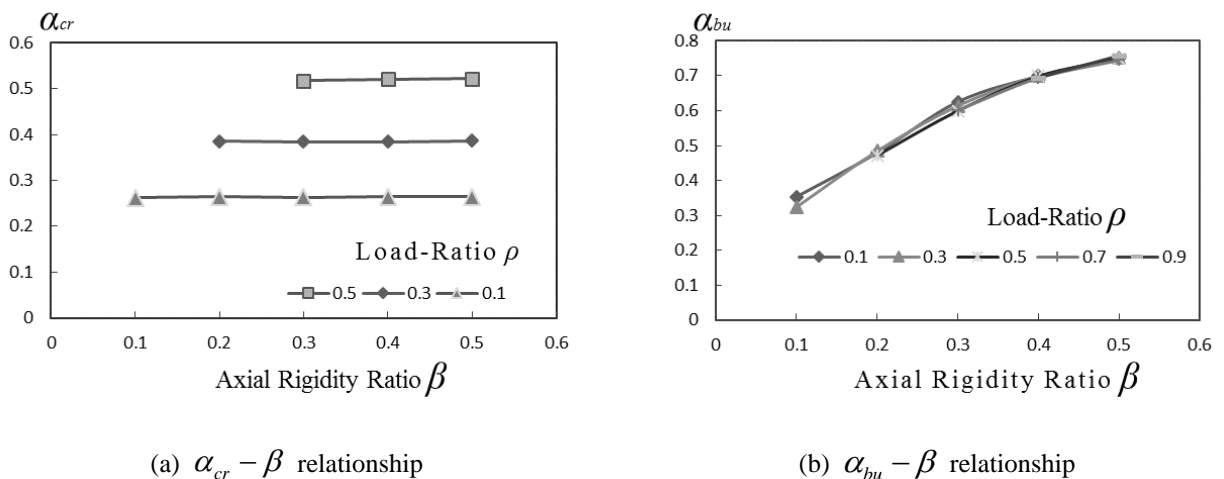


Fig.5. The influence of β

3.3 Influence of β

As it can be seen in Fig.5, the axial rigidity ratio (β) has less effect on α_{cr} in any load ratio(ρ), but it has significant effect on α_{bu} . While the rigidity of the axial restraint increases, α_{bu} also increases. One possible explanation is that the buckling temperature gets lower while the rigidity of

the axial restraint increases, furthermore, the length increment of the column induced by thermal expansion during fire gets less. As a consequence, the plastic bending deformation of the column during the process from pre-buckling state to post-buckling state decreases. Therefore, the residual deflection of the column decreases after fire, and the post-fire load bearing capacity of the column increases.

4 CONCLUSION

In this paper, post-fire load-bearing capacity of the axial restrained high-strength steel column is investigated by means of parameters analysis based on the validated finite-element numerical model. The results obtained can be summarized as follows:

- When $20^{\circ}\text{C} \leq T < T_{bu}$, the fire process does not affect the load-bearing capacity of the restrained steel column.
- When $T = T_{bu}$, the restrained steel column buckles during the heating process, and the post-fire load-bearing capacity will be significantly reduced. At this moment, $\alpha = \alpha_{bu}$ is defined. While the rigidity of the axial restraint increases, α_{bu} also increase. And the axial load ratio has less effect on α_{bu} .
- When $T_{bu} < T < T_{cr}$, the post-fire load-bearing capacity of the restrained steel column has an approximately negative linear correlation with the maximum temperature of the restrained steel column under the fire.
- When $T = T_{cr}$, $\alpha = \alpha_{cr}$ is defined. While the axial load ratio increases, α_{cr} also increases. And the rigidity of the axial restraint has no effect on α_{cr} .

REFERENCES

1. Li G., Lyu H., Zhang C. (2016). *Post-fire mechanical properties of high strength Q550 structural steel*. Proceedings of the 11th Pacific Structural Steel Conference, 2016. pp 1410-1416.
2. Li G., Lyu H., Zhang C. (2017). *Post-fire mechanical properties of high strength Q690 structural steel*. Journal of Constructional Steel Research, 38(5). pp 109-116.
3. Chen J., Zhou T., Sun B. (2013). *Study on stability bearing capacity of steel column under axial compression after fire*. Journal of Water Resources and Water Engineering, 4. pp 71-73.
4. Liu T. (2015). *Study on Post-fire Mechanical Behaviour of High Strength Q460 Steel Columns* (Master Degree thesis). Chongqing University, Chongqing.
5. Bailey C. (1996). *Analyses of the effects of cooling and fire spread on steel-framed buildings*. Fire Safety Journal, 26(4). pp 273-293.
6. Zhou M., Wang X., Zheng X. (2012). *Experimental research on post-fire mechanical behaviour of H-steel columns with different restraint*. Industrial Construction, 42(6). pp 153-157.
7. Ban H. (2012). *Research on the overall buckling behavior and design method of high strength steel columns under axial compression* (Ph.D. thesis). Tsinghua University, Beijing.
8. Huang L. (2017). *Research on mechanical properties of domestic high strength structural steel at elevated temperature* (Master Degree thesis). Tongji University, Shanghai.
9. Wang W., Ge Y. (2015). *Experimental study on fire resistance of axially restrained high strength Q460 steel columns*. Journal of Building Structures, 8. pp 116-122.
10. Simms W. I., O' Connor D. J., Ali F., et al. (1995). *An experimental investigation on the structural performance of steel columns subjected to elevated temperature*. Journal of Applied Fire Science, 5(4). pp 269-281.

EFFECTS OF TOPCOAT ON INSULATION OF INTUMESCENT COATING FOR FIRE PROTECTION OF STEEL STRUCTURES

Qing Xu¹, Guo-Qiang Li², Xiao Zhao³, Xing-Yuan Zhao⁴

ABSTRACT

An investigation of the effect of topcoat on the fire protection of intumescent coatings by conducting standard fire tests on steel elements protected by intumescent coatings with and without topcoats is presented in this paper. There are 82 steel elements in total, including plate, I-section and C-section. The specimens were tested to study the influence of different intumescent coating type and thickness, number of topcoat layers and the steel section factor. Temperatures of steel specimens and expansion ratios of the intumescent coatings with and without topcoat were compared. Then the effective constant thermal conductivity is calculated to quantitatively assess the fire performance of intumescent coatings. The test results show that topcoat has noticeable detrimental effects on solvent-based intumescent coatings, causing expansion reduction and thermal conductivity increase. The effective constant thermal conductivities of solvent-based intumescent coatings with topcoat increased by about 20% on average than those without topcoat. Topcoat has little influence on the insulation of waterborne intumescent coatings. The effect of topcoat increases when intumescent coatings are thinner and section factors are smaller.

Keywords: intumescent coating; topcoat; insulation; furnace fire test; effective constant thermal conductivity

1 INTRODUCTION

Intumescent coatings are the main passive fire protective materials for steel structures because of their advantages such as attractive appearance. They are thermally reactive material and can swell up to 100 times of its initial thickness to form a porous char layer with low thermal conductivity under high temperature. Topcoats are applied above the surface of intumescent coatings for protection against aging and for better appearance. They are considered necessary for the long-term fire resistance of steel structures, particularly outdoor ones. Topcoats are commonly believed to affect the expansion of the intumescent coatings, resulting in lower expansion ratios and therefore worse insulation. However, few research on the influence of topcoat on the fire insulative performance of intumescent coating were carried out. This can cause problems if the topcoat arrangement of fire tests in the laboratory researches is not consistent with that in applications.

Till now, the researches investigating the effect of topcoats on insulation of intumescent coatings were limited. Wang [1] found that the fire resistance time of waterborne intumescent coatings with topcoat were slightly reduced because of coating expansion reduction. The effect was minimal

¹ PhD Candidate. College of Civil Engineering, Tongji University, Shanghai, China.
e-mail: xuqing36@tongji.edu.cn

² Professor. State Key Laboratory for Disaster Reduction in Civil Engineering, Tongji University, Shanghai, China.
e-mail: gqli@tongji.edu.cn

³ Master's student. College of Civil Engineering, Tongji University, Shanghai, China.
e-mail: zhaoxiao@tongji.edu.cn

⁴ Master's student. College of Civil Engineering, Tongji University, Shanghai, China.
e-mail: 1732469@tongji.edu.cn

when the topcoat and the intumescent coating used were compatible. Jimenez et al. [2] conducted some small-scale hydrocarbon fire tests of epoxy-based intumescent coatings coated with four types of topcoat. The result show that the porous structure changed for intumescent coatings with topcoat and different types of topcoats have different effect on the insulation of the intumescent coating tested. Han [3] found that topcoat may greatly reduce the fire insulation of solvent-based intumescent coatings. The different conclusions of such investigations highlight the necessity to carry out a further comprehensive study to research the effect of topcoat on the insulation of intumescent coatings.

The concept of effective thermal conductivity is commonly adopted in practice. The effective thermal conductivity is calculated by the inverse equation of the protected steel temperature calculation equation in codes, with fire and steel temperatures from fire tests as the input data. However, the temperature-dependent variable thermal conductivity of intumescent coatings is inconvenient to use in steel temperature calculations. To solve this problem, effective constant thermal conductivity method was proposed by Li et al. [4]. The effective constant thermal conductivity is defined as the temperature-averaged effective thermal conductivity within the temperature range of 400 °C-600 °C in steel. The accurate prediction of the temperature rises of steel structures protected by intumescent coatings without topcoat under various fire conditions verified the feasibility of this method [4,5]. The effective constant thermal conductivity was adopted in this paper to quantitatively assess the insulation of intumescent coatings.

This paper presents a set of experimental results on steel members to investigate how the effective constant thermal conductivity varies between steel elements protected by intumescent coatings with and without topcoat, under various conditions, including intumescent coating type (waterborne or solvent-based) and the thickness, number of topcoat layers and steel section factor.

2 EXPERIMENTAL INVESTIGATIONS

2.1 Test specimens

Eighty-two specimens were tested in total, including 58 steel plate, 12 steel I-section and 12 steel C-section specimens. *Figure 1* presents the dimensions of the three types of steel specimens. The section factors are 142.4m^{-1} for the steel plates, 177.9m^{-1} for I-sections and 228.6 for C-sections.

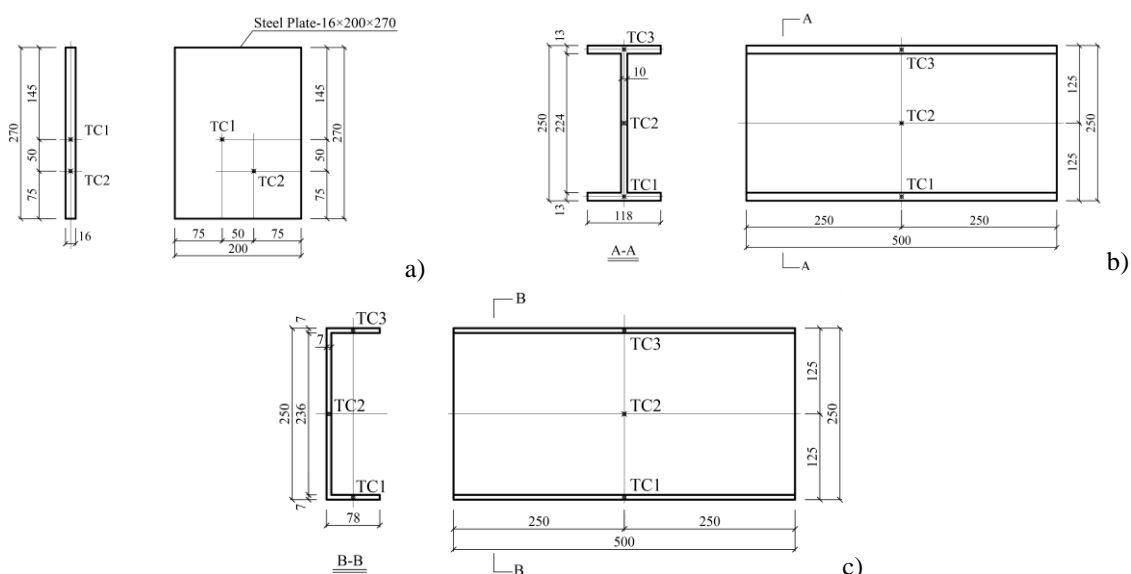


Fig. 1. Dimensions of test specimens and arrangement of thermocouples. a) steel plate. b) I-section. c) C-section.

Two thermocouples were equipped for the steel plate specimens, and three for the I- sections and C- sections to measure the temperature of bottom flange, web and top flange, as shown in *Fig.1* with locations represented by TC1, TC2, TC3.

2.2 Fire protection

Two types of intumescent coatings were used as fire protection, denoted as “Type A” and “Type B”, respectively. Type A is a waterborne intumescent coating, and Type B is a solvent-based intumescent coating. For Type A coating, three target dry film thicknesses (DFT) of 0.6, 1.4, and 2.2mm were used, and for Type B coating the DFTs were 0.6, 1.2 and 2.0mm. All the I-section and C-section specimens were protected by Type A coating, while for the steel plate specimens both Type A and B coatings were used.

The polyurethane topcoat used was provided by the same manufacturer with the intumescent coating and is suitable for the both types of intumescent coating tested. The effect of the number of layers of topcoat was investigated in this research by applying none, one, three, and five layers of topcoat within each group. The DFT of each layer of topcoat was about 35 μ m.

2.3 Fire setup

The furnace at Tongji University were used for the fire tests, as shown in *Fig. 2*. *Fig. 3* shows the internal dimensions of the furnace, being 1m \times 1m \times 1.2m. The furnace temperature was controlled according to the ISO834 standard fire [6] in all tests. The measured furnace temperature by two thermocouples was very close to the standard fire curves.



Fig. 2. Test furnace of Tongji University

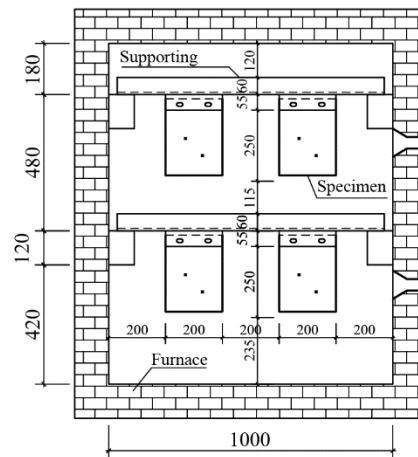


Fig. 3. Cross-section dimensions of the furnace and the arrangement of specimens

3 TEST RESULTS

3.1 Appearance and expansion of intumescent coatings

The intumescent coatings without and with topcoat after test for typical steel specimens were compared in *Fig.4*. Bubbles are generally formed on the coating surface in expansion process. Uniform small bubbles were shown on the surface of the coatings without topcoat (*Fig. 4a*). While hard char with big bubbles and cracks appeared on the surface of the coatings when topcoat was used, and that hard surface was the remains of the topcoat after fire. Moreover, the bubble surface of the topcoat was fragile and it may fell off the coating during fire test, for thick topcoats in particular, as shown in *Fig. 4b*.

Table 1 presents the post-fire thicknesses and the expansion ratios for some typical test specimens. Generally, the waterborne intumescent coatings showed similar expansion ratios after fire tests when section factor and DFT were the same, no matter with or without topcoat. Specimens with the

solvent-based coatings showed lower expansion ratios when topcoat was applied. However, coatings with different layers of topcoat showed similar expansion ratios.



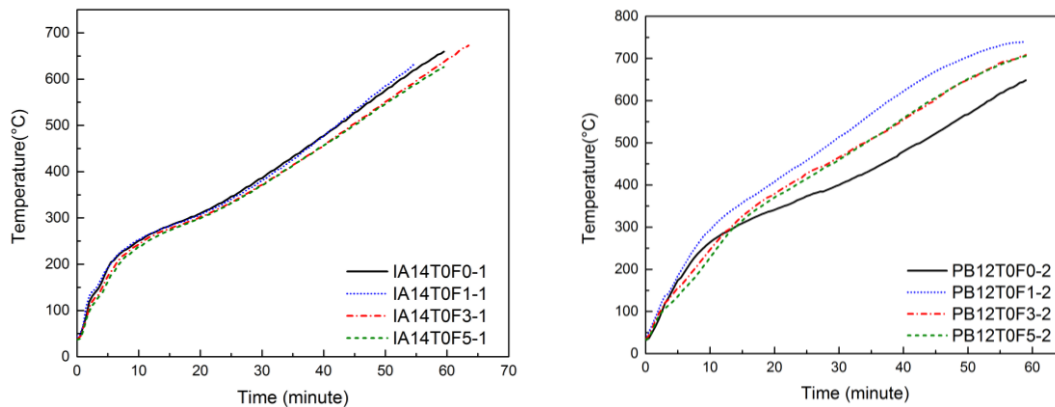
a) specimen without topcoat

b) specimen with topcoat

Fig. 4. Intumescent coatings without and with topcoat on steel specimens after fire tests

3.2 Steel temperatures

Figure 5 shows measured temperatures of typical steel specimens protected by the two types of intumescent coating with none, 1,3,5 layers of topcoat. It can be clearly seen that in Fig. 5a, the steel temperatures curves for different topcoat layer condition were very close and it indicates that topcoat had little influence on the steel temperature of the test specimens with waterborne intumescent coatings. On the other hand, the steel temperature was significantly higher with topcoat for the specimens coated with solvent-based intumescent coatings. The above results are consistent with the results for expansion previously presented.



a) Specimens with waterborne coatings

b) Specimens with solvent-based coatings

Fig. 5. Measured steel temperatures of specimens with various layers of topcoat

3.3 Effective constant thermal conductivity

Chinese code CECS 200:2006 [7] gives the following mathematical fitting equation as a simplified method with satisfied precision to calculate the temperature of protected steel under ISO834 standard fires:

$$T_s = \left(\sqrt{5 \times 10^{-5} \times \frac{1}{R_i} \cdot \frac{F_i}{V} + 0.044 - 0.2} \right) t + 20 \quad (1)$$

Where F_i/V is the section factor for the steel member insulated by fire protection material;
 F_i is the area of fire protection material per unit length of the steel member [m^2/m];
 V is the volume of the steel member per unit length [m^3/m];
 t is the fire duration [s];
 T_s is the steel temperature[K];
 R_i is the thermal resistance of fire protection material [$m^2/W K$];

The inverse solution to Eq. (2) gives the equivalent thermal resistance and the effective thermal conductivity, as shown below.

$$R_i = \frac{5 \times 10^{-5}}{\left(\frac{T_s - 20}{t} + 0.2\right)^2 - 0.044} \cdot \frac{F_i}{V} \quad (2)$$

$$\lambda(T_s) = \frac{d_p}{R_i} \quad (3)$$

where d_p is the initial thickness of the intumescent coating [m];
 λ is the thermal conductivity of the fire protection material [W/m K];

The effective constant thermal conductivity λ_e is defined as the temperature-averaged effective thermal conductivity within steel temperatures range of 400 °C to 600 °C [4], calculated as follows:

$$\lambda_e = \frac{1}{200} \cdot \int_{T_s=400}^{T_s=600} \lambda(T_s) dT_s \quad (4)$$

The effective constant thermal conductivities were then obtained by Eq. (4) to quantitatively assess the insulation of intumescent coating. These values were then used to predict the steel temperature. The close result between the predicted and measured steel temperature in the range of 400°C -600°C verified the applicability of this method for steel specimens with and without topcoat. Table 1 lists the effective constant thermal conductivity of typical specimens with 0.6DFT.

Table 1. Effective constant thermal conductivities and expansions of steel plates with 0.6DFT for waterborne and solvent-based coating

Coating type	Topcoat Layers	Effective Constant Thermal Conductivity	Thickness after expansion	Expansion ratio	Average expansion ratio
A	0	0.01599	18	32.5	32.5
	1	0.01199	25	34.9	34.9
	3	0.01259	25.4	30.6	30.6
	5	0.01613	24.6	34.2	34.2
B	0	0.01462	15.1	23.5	23.5
	1	0.01750	10.9	17.3	19.1
	3	0.02033	16.2	25.5	24.3
	5	0.01785	9.1	14.8	15.5

4 DISCUSSIONS

4.1 Effect of topcoat for different types of coating

The results for effective constant thermal conductivities of the waterborne coating and of the solvent-based coating are presented in Table 2 and Table 3 respectively. The results in Table 2 are

similar with slight difference with that without topcoat for all the parameters studied, including numbers of topcoat layers, coating thicknesses and section factors. The average variations from the value without topcoat are little, at 0.90%, 3.29% and 0.97% for one, three and five layers of topcoat respectively. The differences are within 10% in most cases tested. The largest positive difference is -24%, and the largest negative one is 14%. Large differences like that are uncommon. Therefore, the influence of topcoat can be neglected for waterborne intumescent coatings under standard fire. Compared with *Table 2*, the values in *Table 3* show that topcoat has noticeable detrimental impact upon the insulation of solvent-based intumescent coatings. The effective constant thermal conductivities for test specimens with topcoat increase approximately 20%-25% on average and up to 40% compared with those without topcoat. However, the number of topcoat layers make little difference. Therefore, for solvent-based intumescent coatings under standard fire, a modification factor of 1.25 should be considered for topcoat.

Table 2. Difference in effective constant thermal conductivity between waterborne intumescent coatings with topcoat and that without topcoat

Number of topcoat layers	Section type	Nominal dry film thickness (mm)			Average difference
		0.6	1.4	2.2	
1	Plate	-23.11%	5.02%	13.15%	0.90%
	I-section	-2.18%	2.95%	4.74%	
	C-section	-1.94%	9.58%	-0.09%	
3	Plate	-2.26%	-2.70%	7.93%	3.29%
	I-section	6.90%	2.46%	8.32%	
	C-section	-2.11%	-0.46%	11.52%	
5	Plate	-24.70%	-6.82%	14.29%	0.67%
	I-section	10.18%	-5.03%	11.38%	
	C-section	6.09%	-6.81%	7.43%	

Table 3. Difference in effective constant thermal conductivity between solvent-based intumescent coatings with topcoat and that without topcoat

Number of Topcoat layers	0.6 DFT	1.2 DFT	2.0 DFT	Average difference
1	29.36%	28.87%	14.32%	24.18%
3	19.18%	35.49%	7.67%	20.78%
5	44.18%	18.14%	11.83%	24.72%

4.2 Effect of topcoat for solvent-based intumescent coatings with different coating thicknesses

Figure 6 shows that the influence of topcoat decreases with the increase of intumescent coating thickness. One possible reason is that only the intumescent coating layer adjacent to topcoat would be affected and the expansion of this layer would be restrained by the topcoat. The influence to the remaining intumescent coating would be insignificant. Therefore, a proportionally larger amount of intumescent coatings would be affected by the topcoat for those with lower DFT.

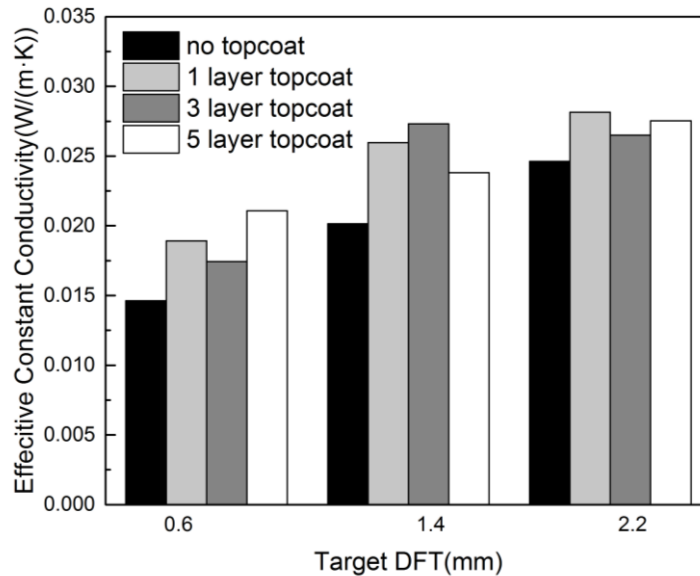


Fig. 6. Effect of topcoat for solvent-based intumescent coatings with different thicknesses

5 CONCLUSIONS

The main conclusions may be drawn as follows:

- It is feasible to use effective constant thermal conductivity to assess the insulation of intumescent coatings with topcoats.
- The topcoat had little influence on the insulation of waterborne intumescent coatings: similar expansion ratios and close steel temperatures were shown for the intumescent coatings with and without topcoat, and their average difference in effective constant thermal conductivity were within 5% for various steel section factors and DFTs.
- The topcoat had significant negative effects on solvent-based intumescent coatings: the specimens with topcoat experienced expansion reduction of the intumescent coating, steel temperature rise, and an increase of about 25% on average in the effective thermal conductivity compared with those without topcoat. The influence of topcoat decreases with the increase of DFT.

ACKNOWLEDGMENTS

This research was supported by the Ministry of Science and Technology of China (SLDRCE14-A-05). The authors would like to thank Professor Yong C. Wang and Dr Jun Han for all suggestions and helpful discussion about this work. They are also grateful to the collaborating manufacturer for supplying intumescent coatings free of charge.

REFERENCES

1. J. Han (2017). *Study on the performance of intumescent coating under large space fires (Ph.D thesis)*. Tongji University, Shanghai.
2. J. Wang (2016). *The protective effects and aging process of the topcoat of intumescent fire-retardant coatings applied to steel structures*. Journal of Coating Technology Research, 13(1). pp 143-157.
3. M. Jimenez, S. Duquesne, S. Bourbigot (2016). *Characterization of the performance of an intumescent fire protective coating*. Surface and Coatings Technology, 201(3-4). pp 979-987.
4. G. Q. Li, J. Han, G. B. Lou, et al (2016). *Predicting intumescent coating protected steel temperature in fire using constant thermal conductivity*. Thin-Walled Structures, 98. pp 177-184.

5. G. Q. Li, J. Han, Y. C. Wang (2017). *Constant effective thermal conductivity of intumescent coatings: analysis of experimental results*. Journal of Fire Sciences, 35(2). pp 132-155.
6. ISO/CD 834-11: 2014, MOD. *Fire Resistance Tests- Elements of Building Construction, Specific requirements for the assessment of fire protection to structural steel elements*. International Organization for Standardization.
7. CECS 200:2006 (2006). *Technical code for fire safety of steel structure in buildings*. China Planning Press, Beijing.

DEVELOPMENT OF AN ANALYTICAL METHOD FOR THE FIRE RESISTANCE CALCULATION OF ANGELINA BEAMS

Jérôme Randaxhe¹, François Hanus², Olivier Vassart³

ABSTRACT

Angelina beam is a patented type of beam with large sinusoidal openings. Such a geometry allows to let important section pipes and other HVAC systems through its web. The sinusoidal shape of its openings brings an aesthetic aspect to structures and it requires only one cut in the web which permits an economic fabrication process. Web post buckling is usually not critical as the web width is much larger than for beams with circular openings. With those advantages Angelina beams is desired in the construction sector and to facilitate its design, an analytical method for the mechanical resistance calculation was developed in the 2000's, by CTICM and ArcelorMittal Global R&D [1] and [2].

This paper presents how the analytical method developed at ambient temperature can be used to calculate the critical temperature considering the different failure modes of an Angelina beam submitted to a uniform loading. Through the modification of different parameters, the existing model is calibrated on results obtained from a series of FE calculations to account for the more pronounced effects of Tee instabilities on Vierendeel mechanism at elevated temperatures.

Keywords: Steel structures, cellular beam, fire resistance, sinusoidal openings, Vierendeel effect.

1 INTRODUCTION

Angelina beam has been invented as an improvement of common steel cellular beams making them lighter and allowing increased spans. The important depth of the beam offers a high resistance to bending moment but the large opening in the web make it more subject to combination of bending and shear, leading to *Vierendeel* mechanism *Fig. 1*. The existing analytical model already developed at ambient temperature was based on experimental observations and numerical simulations which confirmed this mechanism and validated calculation tests.

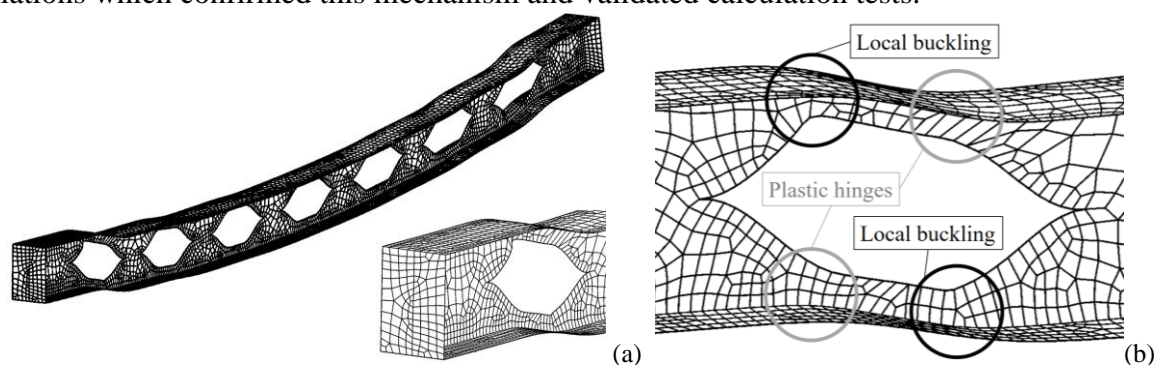


Fig. 1. (a) Vierendeel Mechanism; (b) Local buckling and plastic hinges

¹ Researcher in ArcelorMittal Global R&D, Structural Long Products, Luxembourg. (PhD student, University of Trento, Italy)
e-mail: jerome.randaxhe@arcelormittal.com

² Senior Research Engineer in ArcelorMittal Global R&D, Structural Long Products, Luxembourg
e-mail: francois.hanus@arcelormittal.com

³ Professor. Head of ArcelorMittal Global R&D Long Carbon. Department of Research & Development, Luxembourg.
e-mail: olivier.vassart@arcelormittal.com

The failure Vierendeel mechanism occurs due to the local buckling from two compressed T cross-sections surrounding an opening. This causes an internal force redistribution in the opening leading the two tensioned T cross-sections to their plastic resistance. This mechanism generates four hinges around an opening as illustrated on the Fig. 1 (b). [3].

2 SCOPE OF THE RESEARCH

2.1 Parameters of Angelina beam

The main parameters defining the geometry of an Angelina beam are illustrated on Fig. 2 and defined in the Table 1. The important criteria to be fulfilled in the scope of the method developed in this paper are stated in the Table 2.

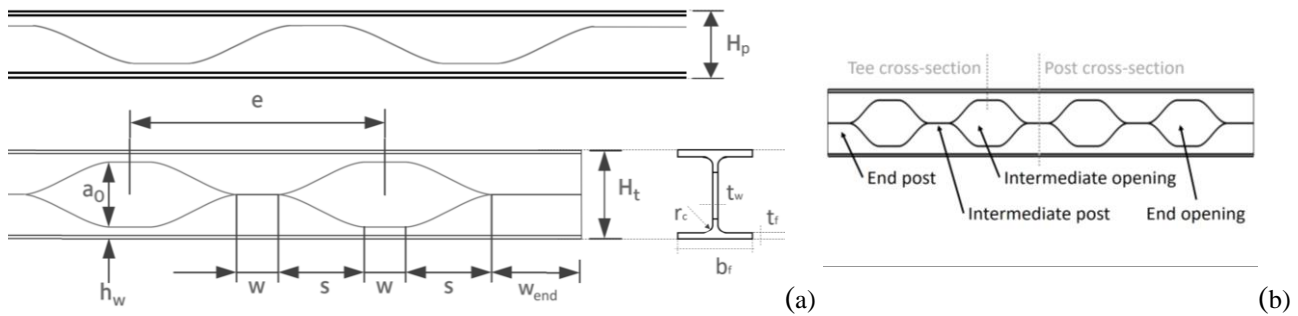


Fig. 2. (a) Main Parameters; (b) Terminology for the posts, openings and cross-sections

Table 1. Parameters definition

Parameters	Symbols	Parameters	Symbols
Height of the basic profile	h_p	Height of the opening	a_o
Width of the profile	b_f	Width of the sinusoidal part	s
Web thickness	t_w	Width of the post / flat part of the opening	w
Flange thickness	t_f	Width of the end post	w_{end}
Radius	r_c	Height of the Angelina beam	H_t
		Height of the T cross-section (at the opening center)	$h_{T,0} = (H_t - a_o)/2$

Table 2. Criteria to be fulfilled for the applicability of the method

Minimum depth of the initial profile:	$h_p \geq 140 \text{ mm}$
Steel grades:	S235 to S460 including HISTAR
Minimum width of the intermediate posts:	$w \geq 150 \text{ mm}$
Minimum width of the end posts:	$w_{end} \geq 100 \text{ mm}$
Slenderness of the openings:	$(2s+w) / a_o \leq 5$
Slenderness of the web:	$h_w / t_w \leq 124\epsilon$ with $\epsilon = (235 / f_y)^{1/2}$
Minimum number of openings:	$n \geq 4$

2.2 The 38 configurations analysed

The study conducted through this paper is focused on 38 Angelina beams made from IPE and HEA profiles (more appropriate to be used as beam) and presenting different geometrical configurations. Simultaneously, the beams are subjected to a uniformly distributed mechanical loading while temperature increases until the failure of the beam. The following Table 3 defines the different Angelina beam configurations tested.

Table 3. The 38 Angelina beam configurations

Profile	Beam N°	Profile	Steel Grade	Span [m]	Openings characteristics			Load q_{Ed} [kN/m]	Beam N°	Steel Grade	Load q_{Ed} [kN/m]
					a_0 [mm]	s [mm]	w [mm]				
IPE	1	IPE270	S355	6	285	285	200	16.9	2	S460	19.4
	3	IPE300		6	315	315	200	15.4	4		23.4
	5	IPE300		8	315	315	200	12.9	6		12.9
	7	IPE300		10	315	315	200	10.9	8		12.4
	9	IPE330		10	345	345	200	14.5	10		16.5
	11	IPE360		14	375	375	250	10.1	12		11.6
	13	IPE400		8	415	415	250	22.6	14		22.6
	15	IPE450		18	465	465	250	10.3	16		10.3
	17	IPE500		14	515	515	250	20.9	18		20.9
	19	IPE600		14	615	615	250	29.2	20		30.2
	21	IPE750x173		24	765	765	250	21.3	22	26.3	
HEA	23	HEA300		8	305	305	200	26.4	24	30.9	
	25	HEA300		10	305	305	200	21.4	26	25.4	
	27	HEA340		18	345	345	200	11.0	28	13.0	
	29	HEA400		10	405	405	250	32.7	30	43.7	
	31	HEA500		18	500	500	250	19.0	32	26.0	
	33	HEA600		28	600	600	250	12.8	34	15.3	
	35	HEA700		20	755	755	250	31.5	36	34.5	
	37	HEA900		24	900	900	250	32.5	38	40.0	

3 ANALYTICAL MODEL FOR THE COLD RESISTANCE CALCULATION

For given geometry and load configurations, the existing analytical model [1] and [2] permits to state if the Angelina beam will fail or stand.

3.1 Classification of the cross-sections

The Table 4. summarizes the classification of the web for post- and T cross-sections according to the rule provided by the EN1993-1-1 [4].

Table 4. Classification of the webs

Class of the web for post cross-section		Class of the web for T cross-section	
if $h_w/t_w \leq 72\epsilon$ then	$C_{wp} = 1$	if $h_{wT}/t_w \leq 9\epsilon$ then	$C_{wT} = 1$
if $h_w/t_w \leq 83\epsilon$ then	$C_{wp} = 2$	if $h_{wT}/t_w \leq 10\epsilon$ then	$C_{wT} = 2$
if $83\epsilon \leq h_w/t_w \leq 124\epsilon$ then	$C_{wp} = 3$	if $10\epsilon \leq h_{wT}/t_w \leq 14\epsilon$ then	$C_{wT} = 3$
if $h_w/t_w \geq 124\epsilon$ then	$C_{wp} = 4$	if $h_{wT}/t_w \geq 14\epsilon$ then	$C_{wT} = 4$
with $h_w = H_T - 2(t_f + r_c)$		with $h_{wT} = (h_w - a_0)/2$	

3.2 Resistance of T cross-sections

To ensure the resistance of the T cross-sections in the four quarters around an opening [Fig. 2 (a)], the three following criteria in the Eq. (1), (2) and (3) must be calculated for every section i.

$$\Gamma_{Vi} = \frac{V_{i,Ed}}{V_{i,Rd}} \quad (1) \quad \Gamma_{MNi} = \frac{M_{i,Ed}}{M_{i,Rd}} + \left(\frac{N_{i,Ed}}{N_{i,Rd}} \right)^\alpha \quad (2) \quad \Gamma_{MNVi} = \frac{M_{i,Ed}}{M_{V,pl,i,Rd}} + \left(\frac{N_{i,Ed}}{N_{V,pl,i,Rd}} \right)^\alpha \quad (3)$$

The parameter α vary between 1 and 2 depending on the flexural rigidity of the ends posts. The more rigid the post is, the higher α is.

The internal forces $V_{i,Ed}$, $N_{i,Ed}$ and $M_{i,Ed}$ are represented in the Fig.3 (a) and (b) and defined in Table 5.

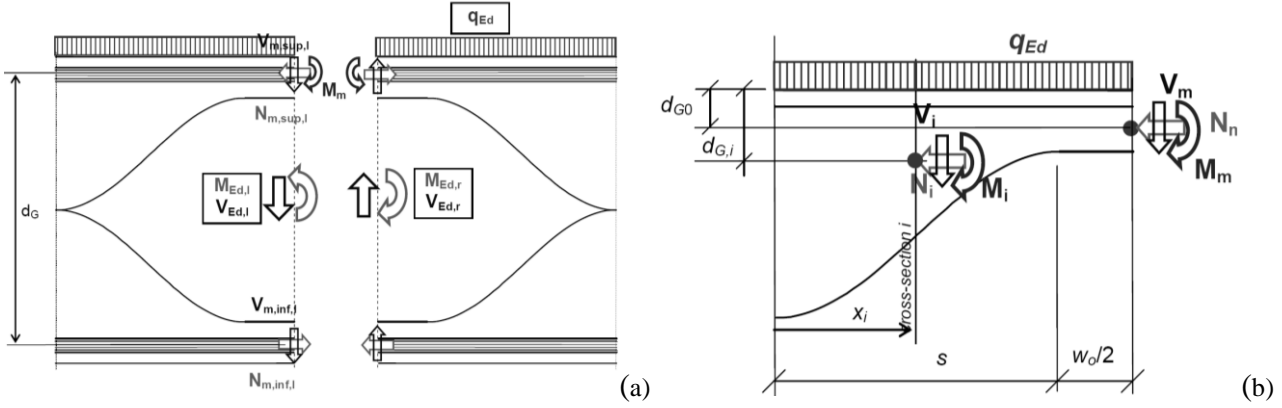


Fig. 3. (a) Internal forces and moments in an opening cross-section; (b) Internal forces and moments in one quarter

Table 5. Internal forces $V_{i,Ed}$, $N_{i,Ed}$ and $M_{i,Ed}$

Forces at the center of an opening				Internal forces in the T cross-sections
Quarter	Normal force N_m	Shear force V_m	Bending moment M_m	$N_{i,Ed} = N_m$
Sup. left	$M_{Ed,l} / d_G$	$V_{Ed,l} / 2$	$-k_M q_{Ed} l_{op}^2 / 24$	$V_{i,Ed} = V_m + q_{Ed} (l_{op}/2 - x_i)$
Inf. left	$-M_{Ed,l} / d_G$	$-V_{Ed,l} / 2$	0	$M_{i,Ed} = M_m + V_m (l_{op}/2 - x_i) - N_m (d_{Gi} - d_{G0}) + q_{Ed}/2 (l_{op}/2 - x_i)^2$
Sup. right	$M_{Ed,r} / d_G$	$-V_{Ed,r} / 2$	$-k_M q_{Ed} l_{op}^2 / 24$	
Inf. right	$-M_{Ed,r} / d_G$	$V_{Ed,r} / 2$	0	

where $q_{Ed} = 0$ for inferior quarters, l_{op} is the width of an opening ($2s+w$)

d_{Gi} is the centroid of the T cross-section i and d_{G0} is the centroid of the one at the center.

k_M is a factor varying between 1 and 2 depending on the flexural rigidity of the ends posts, the upper chords is considered fixed at its end ($k_M = 1$) or simply supported ($k_M = 2$).

The resistant forces $V_{i,Rd}$, $N_{i,Rd}$ and $M_{i,Rd}$ are defined by the Eq. (4), (5) and (6).

$$V_{i,Rd} = \frac{A_{v,i} f_y}{\sqrt{3} \gamma_{M0}} \quad (4) \quad N_{i,Rd} = \frac{A_i f_y}{\gamma_{M0}} \quad (5) \quad M_{i,Rd} = \frac{W_{pl,i} f_y}{\gamma_{M0}} \quad (6)$$

The expressions $N_{V,pl,i,Rd}$ and $M_{V,pl,i,Rd}$ are identical to (5) and (6) with a yield limit f_y reduced by the presence of shear force. if $\Gamma_{Vi} > 0.5$ then $f_y = (1 - (2\Gamma_{Vi} - 1)^2) f_y$.

$A_{v,i}$ and A_i are the shear area and area of the T cross-section i . considering the effective dimensions. The effective height $h_{eff,T,i}$ is function of the class and the effective width of the profile $b_{f,eff}$ is reduced under compression.

if the web class $C_{wT} = 1, 2$ or 3 then $h_{eff,T,i} = h_{T,i}$

if the web class $C_{wT} = 4$ then $h_{eff,T,i} = \rho \cdot h_{T,i}$

with ρ a reduction factor defined the Eurocode 3 [3] in the Eq. (7): $\rho = h_{TCL3} / h_{T,0}$ (7)

where $h_{TCL3} = t_f + r_c + 14 \epsilon t_w$ is the maximum height of a T cross-section to remain in class 3.

$W_{pl,i}$ is the plastic modulus of the T cross-section considering its effective dimensions.

Finally, the following resistance criteria [Eq. (8), (9) and (10)] must be verified:

$$\Gamma_{Vo} \leq 1 \quad (8) \quad \Gamma_{MNo} = \sqrt{\frac{\Gamma_{MN,top}^2 + \Gamma_{MN,bot}^2}{2}} \leq 1 \quad (9) \quad \Gamma_{MNVo} = \sqrt{\frac{\Gamma_{MNV,top}^2 + \Gamma_{MNV,bot}^2}{2}} \leq 1 \quad (10)$$

Where Γ_{Vo} , $\Gamma_{MN,top}$, $\Gamma_{MN,bot}$, $\Gamma_{MNV,top}$ and $\Gamma_{MNV,bot}$ are the greatest criteria Γ_{Vi} , Γ_{MNi} and Γ_{MNVi} respectively observed in the top and bottom quarters of the opening for every T cross-sections all along the beam.

3.3 Resistance of posts to horizontal shear force

To ensure the resistance of the post cross-sections, the following criteria expressed in the Eq. (11) must be verified for every post.

$$\Gamma_{Vh} = \frac{|V_{h,Ed}|}{V_{h,Rd}} \leq 1 \quad (11) \quad \text{with } V_{h,Rd} \text{ defined in the Eq. (12): } V_{h,Rd} = \eta w t_w f_y / \sqrt{3} \gamma_{M0} \quad (12)$$

The resistance factor η is used to consider that the yielding of a post does not lead to the failure of the beam but to a plastic forces redistribution. The value of η has been calibrated between 1.2 and 1.3. The horizontal shear force acting in an intermediate post is the difference between the normal forces N_m in the two openings surrounding the post as it is written in the Eq. (13) and (14).

$$V_{h,Ed} = N_{m,inf,r,o1} - N_{m,inf,l,o2} \quad (13)$$

$$\text{For end post: } V_{h,Ed,end} = N_{m,inf,l,o1} \quad (14)$$

3.4 Failures modes

In the Fig. 4 are illustrated the main failure modes of Angelina beams.

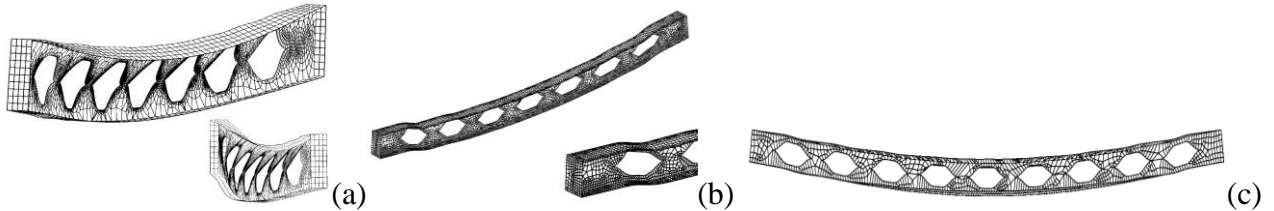


Fig. 4. Failure modes: (a) Post buckling; (b) Vierendeel Effect; (c) Yielding of the central T section

3.5 Use of the analytical model to determine the critical temperature for a given load.

Considering a defined Angelina beams geometry and a given temperature, the corresponding critical temperature can be determined by applying the reduction coefficient $k_{y,\theta}$ on the yield limit f_y . This reduction coefficient $k_{y,\theta}$ is decreasing with the temperature increasing according to the diagram of the Fig. 5 given the EN1993-1-2 [5]. The effect of the reduced Young's modulus is implicitly considered by use of correction factors described hereafter in the section 5.

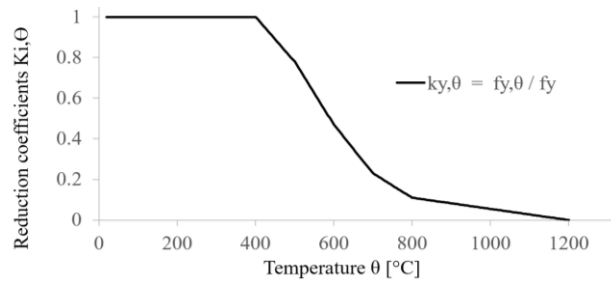


Fig. 5. Reduction coefficients $k_{y,\theta}$ for the yield limit f_y

Resistance criteria (1), (2), (3) and (11) are function of the distributed load q_{Ed} and the yield limit and they can be written with the following Eq. (15), (16), (17) and (18).

$$\Gamma_{Vi} = \frac{q_{Ed}}{k_{y,\theta} f_y} a_1 \quad (15) \quad \Gamma_{MNi} = \frac{q_{Ed}}{k_{y,\theta} f_y} a_2 + \left(\frac{q_{Ed}}{k_{y,\theta} f_y} a_3 \right)^\alpha \quad (16)$$

$$\Gamma_{MNVi} = \frac{q_{Ed}}{k_{y,\theta} f_y} a_4 + \left(\frac{q_{Ed}}{k_{y,\theta} f_y} a_5 \right)^\alpha \quad (17) \quad \Gamma_{Vh} = \frac{q_{Ed}}{\eta k_{y,\theta} f_y} a_6 \quad (18)$$

Where a_1, a_2, a_3, a_4, a_5 and a_6 are constant values for each cross-section i geometry.

The critical value of $k_{y,\theta}$ making one of the four criteria equal to 1 can be determined and then the corresponding critical temperature $T_{cr,ana}$ is directly deductible from the diagram of the Fig. 5. The critical temperature has been determined with this manner for the 38 Angelina beams studied.

4 NUMERICAL SIMULATIONS

4.1 Approach adopted

A SAFIR® finite elements model was created [6] for the calibration of the existing method explained here above at elevated temperatures. This model reproduces the steel profiles with shell elements presenting different thicknesses for the web or the flanges. The beam is simply-supported at both ends and the lateral torsional buckling is continuously prevented all along the upper flange. This FE model has been used for this analytical method adaptation. The steel beam is heated gradually (1 [°C/s]) and the mechanical loading, applied on the top flange, is kept constant. Using this procedure, the failure time indicates the critical temperature. For the 38 Angelina beams studied, the critical temperatures $T_{cr,SAFIR}$ have been numerically computed and they constitute the numerical baseline data which allows the adaptation of the model in the section 5. They are compared with the analytical results on the diagram in the Fig. 6.

4.2 Comparison of the analytical and numerical results

Fig. 6 plots the ratio $T_{cr,analyt} / T_{cr,SAFIR}$ of the critical temperatures obtained respectively using analytical and numerical models. It can be observed that most of them are above 1 which is unsafe. This comparison demonstrates that the existing analytical model, if used without any adaptations, provides unsafe results in case of fire and needs to be calibrated.

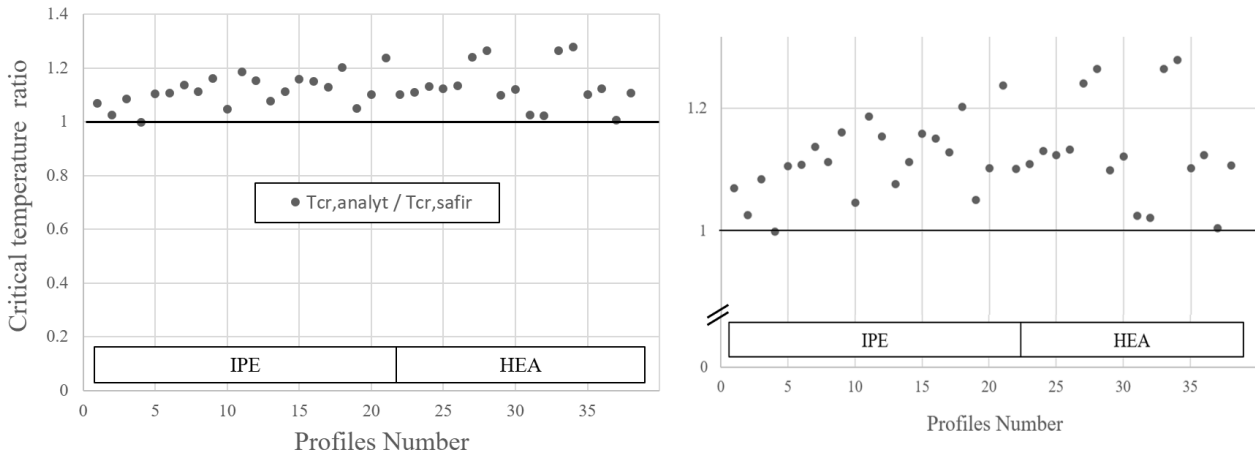


Fig. 6. Critical temperatures ratio for the 38 configurations analysed with the existing model

5 ADAPTATION OF THE ANALYTICAL MODEL

In this section, the analytical method described in the section 3 is modified through the calibration of parameters summarized in the Table 6. This calibration takes into account the Vierendeel mechanism study and the young's modulus decreasing faster than the yield strength making the T cross-sections more prone to instabilities and local buckling in case of fire. Here below in the subsections are successively explained the impacts of the different parameters and their modification effect is illustrated on the diagram in the Fig. 7.

5.1 Calibration of the proper parameters

Table 6. Summary of the different parameters calibration in the existing method.

Steel Grade	$\alpha = 1$ and $\eta = 1$		
	$A_w/A_f \leq 0.8$	$A_w/A_f > 0.8$	
	Class 1, 2, 3 and 4	Class1	Class 2, 3 or 4
S235	$0.8 \leq \rho \leq 1$	$\rho=1$	$\rho=1$
S355			$0.9 \leq \rho \leq 1$
S460			$0.8 \leq \rho \leq 1$

5.1.1 Modification of the coefficient α and η

The coefficient α appears in the resistance criteria (2) and (3) to take into consideration the flexural rigidity of the post. The resistance factor η is used in the equation (12) to consider the resistance offered due to plastic redistribution of forces around a failing post.

Considering important temperatures, this flexural rigidity is highly reduced, and this plastic redistribution is not considered anymore. For this reason, the coefficient α and the resistance factor η are set to 1 for fire cases: $\alpha=1$ and $\eta=1$

The Eq. (16), (17) and (18) can be written as the Eq. (19), (20) and (21).

$$\Gamma_{MNi} = \frac{q_{Ed}}{k_{y,\theta} f_y} (a_2 + a_3) \quad (19) \quad \Gamma_{MNVi} = \frac{q_{Ed}}{k_{y,\theta} f_y} (a_4 + a_5) \quad (20) \quad \Gamma_{Vh} = \frac{q_{Ed}}{k_{y,\theta} f_y} a_6 \quad (21)$$

5.1.2 Consideration of the steel grade

At elevated temperatures, structural elements are more prone to instabilities as the young's modulus decreases faster than the yield strength. This effect is still more significant for high grades as their yield strength is higher. To consider this phenomenon, different thresholds are applied on the reduction coefficient ρ depending on the steel grade and the cross-section classification as summarized in the Table 6.

5.1.3 Modification of the effective section

For high temperatures the EN1993-1-2 [5] defines a more severe coefficient ε used in the cross-section classification, as follow, Eq. (22): $\varepsilon = 0.85 (235/f_y)^{0.5}$ (22)

For fire case a safe modification of the effective cross-sections is imposed for the class 2, 3 and 4.

The coefficient ρ defined in the Eq. (7) is reduced as follow in the Eq. (23): $\rho = h_{TCL1}/h_{T,i}$ (23)

with $h_{TCL1} = t_f + r_c + 9 \varepsilon t_w$ is the maximum height of a T cross-section to remain in class 1.

$h_{T,0}$ becomes $h_{T,i}$ to properly reduce the coefficient ρ by considering the correct height for each T cross-section i. As this height $h_{T,i}$ can be very high near the posts the value of the coefficient ρ is limited between 0.9 and 1 for S355 and 0.8 and 1 for S460.

5.1.4 Consideration of the beam section geometry

The ratio A_w/A_f of a profile (web section on flange section) has an impact on the method precision. This ratio is defined by the Eq. (24): $A_w/A_f = (H_T - 2t_f) t_w / (b_f \cdot t_f)$ (24)

Profiles as HEA presenting a small ratio A_w/A_f provide unsafe results compared to the F.E. results.

For beams presenting a ratio A_w/A_f below 0.8 the values of the coefficient ρ is limited between 0.8 and 1 for every sections classes.

5.2 Comparaison of the results

On the diagram here below in the Fig. 7, the initial and final critical temperatures ratio are represented to illustrate the safe adaptation of the model.

Initial critical temperatures ratio: $T_{cr,analyt} / T_{cr,SAFIR}$

Final critical temperatures ratio: $T_{cr,analyt,modif} / T_{cr,SAFIR}$

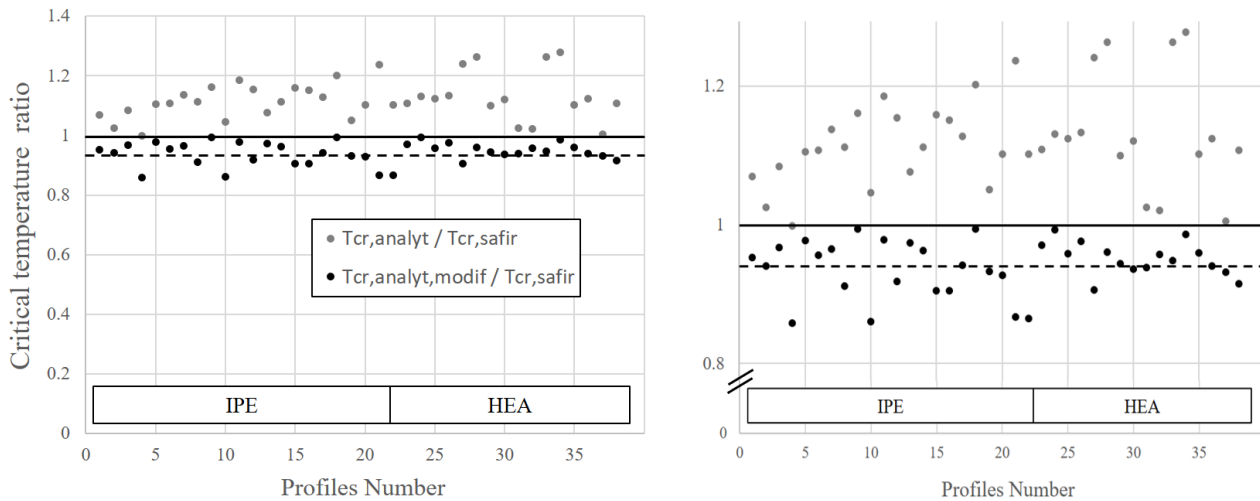


Fig. 7. Critical temperatures ratio for the 38 configurations analysed before and after the models' modifications

6 CONCLUSION

As it can be observed on the *Fig. 7*, the existing analytical model developed for cold situation does not provide satisfying critical temperatures for the beam resistance study in case of fire. This is due to the T cross-sections more subjected to local buckling since the yield strength decreases with temperature while the Young modulus reduction remains unconsidered.

The model has been adapted through four main modifications to take this phenomenon into account and to provide improved critical temperatures. Every ratio $T_{cr,analyt,modif} / T_{cr,SAFIR}$ obtained after the modifications are inferior to 1 (solid line) and their average is 0.94 (dashed line). It proves the validity of the calibrated method. The existing model can be now used in fire case as long as the modifications summarized in the *Table 6* are respected.

REFERENCES

- [1] Martin P.-O., Couchaux M., Vassart O., Bureau A. (2017) An analytical method for the resistance of cellular beams with sinusoidal openings, CTICM, France and ArcelorMittal Global R&D, Luxembourg.
- [2] Cajot L.-G., (2012) FICEB Project - Fire resistance of long span cellular beam made of rolled profiles, ArcelorMittal Global R&D, Luxembourg.
- [3] Durif S., Bouchair A. Analytical model to predict the resistance of cellular beams with sinusoidal openings, *J. Constr. Steel Res.* 121 2016 80-96
- [4] EN 1993-1-1: Eurocode 3 – Design of steel structures – Part 1-1 General rules and rules for buildings. 2010
- [5] EN 1993-1-2: Eurocode 3 – Design of steel structures – Part 1-2 General rules - Structural fire design. 2005
- [6] Franssen J.-M., (2003) SAFIR, A thermal/structural Program Modelling Structures under Fire, Proc. NASCC, AISC Inc., April 2-4 2003, Baltimore, MA, USA.

TESTS ON CREEP BUCKLING OF HIGH STRENGTH STEEL COLUMNS AT ELEVATED TEMPERATURES

Weiyong Wang¹, Linbo Zhang², Hongyang Zhou³, Venkatesh Kodur⁴

ABSTRACT

To investigate the creep buckling phenomenon, a comprehensive test program on the creep buckling of high strength steel columns at elevated temperature was carried out. The test specimens comprised of 12 H-shaped welded steel columns with length of 2700mm. Six of these columns are made from Q460 steel, with nominal yield strength of 460MPa, and the other 6 columns are made from Q690 steel, with nominal yield strength of 690MPa. In order to investigate the critical factors governing creep buckling time of the columns, for each type steel columns, 2 slenderness ratios, 2 target temperatures and 2 load levels were considered. In the test, the pinned columns are heated to the predetermined target temperature and when the temperature in the steel columns is uniform, a compression load was applied step by step until it reaches the designed load level. The creep buckling time of the columns when creep buckling happens were obtained based on axial displacement and deflection evolutions of the columns subjected to constant temperature and load. The test results showed that the creep deformations of steel columns are quite significant when the temperature exceeding 600°C. All the specimens experienced creep buckling within 27 hours, and the creep buckling time decreases with the increases of slenderness ratio and load level, and the failure time of creep buckling is highly dependent on temperature level.

Keywords: High strength steel columns, creep buckling, elevated temperature

1 INTRODUCTION

The yield strength of steel being above 460MPa is often classified as high strength steel. High strength steels are widely used in building structures, especially in high-rise and long-span structures because of higher yield strength and good ductility, such as, the National Stadium of China, where the opening ceremony of 2008 Olympic Games was held. In fire condition, steel structures exhibit relatively lower fire resistance due to faster loss of strength and stiffness properties of steel with temperature and also due to rapid rise in temperatures resulting from high thermal conductivity and low specific heat of steel. When exposed to elevated temperatures, steel structures undergo increasing permanent deformations with time even when the applied stress level is below that of yield stress and this time-dependent deformation is referred to as creep.

Recent years, some researchers carried out test on creep deformation in steel at elevated temperature. Such as, Morovat et al. [1] compared creep curve of ASTM A992M with Harmathy creep model and Fields and Fields creep model, and found steel types and temperature distribution

¹ Professor of School of Civil Engineering, Chongqing University, Chongqing, China
e-mail: wywang@cqu.edu.cn

² Graduate student of School of Civil Engineering, Chongqing University, Chongqing, China
e-mail: zhanglinbo@cqu.edu.cn

³ Graduate student of School of Civil Engineering, Chongqing University, Chongqing, China
e-mail: cquzhou@cqu.edu.cn

⁴ Professor of Department of Civil and Environmental Engineering, Michigan State University, East Lansing, MI, USA
e-mail: kodur@egr.msu.edu

can influence the creep response of steel. Kodur and Aziz [2] carried out test on creep of ASTM A572 steel at elevated temperature and the results clearly showed that the develop of creep is influenced by the chemical composition of steel and high dependent of grades of steel. Wang et al. [3-4] presented an experimental investigation into temperature induced creep in high strength Q460 and Q690 steels, and found that temperature had significant influence on the magnitude of creep deformations in high strength steels, especially when the temperature in steel exceeds 400 °C .Schneider and Lange [5] proposed a constitutive equations and empirical creep law of structural steel S460 at high temperatures based on test data of creep in steel S460. All the previous test presented a lot of useful creep data for establishing creep model.

Under fire conditions, steel columns can exhibit creep buckling, a phenomenon in which the critical buckling load for a column depends not only on slenderness and temperature, but also on the duration of applied load. There have been considerable experimental and numerical investigations carried out on the behavior of steel columns subjected to elevated temperature. Li et al. [6] investigated the behavior of axially restrained steel columns exposed to four different fire scenarios including two arbitrary fires and two post-flashover fires, and find creep has effect on the buckling temperature of axially restrained steel columns in real fires. Tondini et al. [7] conducted an experimental-numerical study on the behavior of high strength steel columns (yield strength of 820 MPa) at elevated temperature, both on circular hollow sections and on a concrete filled tube. Chen et al. [8] carried out a series of tests at elevated temperatures on specimens of high strength steel BISPLATE 80, which is comparable to EN10137-2 S690Q. Byeongnam et al. [9] investigate the creep buckling behavior of a stainless steel column (yield stress of 252MPa) under axial compressive loading at extremely high temperatures. Huang et al. [10] conducted a series of numerical studies conducted on thermally restrained steel columns subjected to predominantly axial loads, and discussed four parameters including column slenderness ratio, axial restraint ratio, rotational restraint ratio, and axial load utilization factor. Byeongnam et al. [11] measured buckling load for metallic plate columns from room temperature to 1200 °C by two test methods.

Although material creep and consequently the phenomenon of creep buckling can adversely impact the response of steel columns subjected to fire, high temperature creep phenomenon has received relatively little research attention, and are not currently explicitly considered in code-based design formula for columns at elevated temperatures, such as those in the Eurocode 3 [12] or in the AISC Specification [13]. The present work focuses on the creep bucking experimental campaign and the related analyses of Q460 and Q690 high strength steel(HSS) columns subjected to constant temperature and load. The furnace temperature, column temperature, axial displacement and lateral displacement were measured in this experiment, and three parameters including temperature, load ratio and slenderness ratio are discussed in this paper.

2 EXPERIMENTAL PROGRAM

A comprehensive test program was designed to undertake creep buckling tests on Q460 and Q690 steel columns. The creep tests were carried out at three temperatures; namely, 600, 700 and 800 °C and at various stress levels.

2.1 Material properties

Three steel coupons were extracted from the Q460 and Q690 steel plate respectively and tensile test was carried out to obtain the actual mechanical properties. The shape and size of tensile strength coupons are prepared in accordance with GB/T 228.1-2010 [14], and the test results of material properties are presented in *Table 1*. High strength steels have higher measured yield strength than nominal yield strength than that of mild steel.

2.2 Test specimens

To evaluate the influence of three factors, load ratio, temperature, slenderness, on creep buckling of steel column, 12 welding H-shaped columns with same length of 2700mm were fabricated using

Q460 and Q690 high strength steel plate. The measured dimension of specimens was tabulated in *Table 2*, where L is the length of column; B is the width of flange; t_f and t_w are the thickness of flange and web. respectively. Taking W690-800-0.3 for example to illustrate the specimen labelling, W denotes the wide section of column which means small slenderness ratio (N denotes narrow section); 800 is the temperature level ($^{\circ}\text{C}$); 0.3 is load ratio. The load ratio α was calculated by *Eq. (1)*.

$$\alpha = N / N_{cr,T} \quad (1)$$

where N is the applied load,

$N_{cr,T}$ is the bearing capacity of steel column at elevated temperature,

$N_{cr,T}$ is obtained by using calculation method specified in design code [15].

Table 1. Mechanical properties of high strength Q460 and Q690 steel

Steel type	Yield strength	Tensile strength	Elastic modulus	Elongation
	f_y/MPa	f_u/MPa	E/GPa	φ
Q460	587	628	199.4	18.4
Q690	821	840	187.2	16.0

Table 2. Measured dimensions of test specimens

Specimen No.	Nominal Dimensions	L	B	t_f	t_w	H	i	β
		mm	mm	mm	mm	mm	mm	mm
N690-800-0.3	H200×150×14×14	2731.50	151.8	13.81	13.9	200.5	0.47	1.58
N690-800-0.6	H200×150×14×14	2734.75	150.3	14.07	14.09	199.9	2.61	1.63
W690-800-0.3	H200×200×14×14	2732.50	199.7	13.84	13.95	200.2	2.55	1.56
W690-800-0.6	H200×200×14×14	2732.00	199.9	13.91	14.15	200.4	2.23	1.07
N690-700-0.3	H200×150×14×14	2731.70	200.4	14.01	14.1	199.6	3.61	1.44
W690-700-0.6	H200×200×14×14	2731.15	200.2	14.22	14.17	200.8	3.00	1.92
N460-800-0.08	H200×150×14×14	2735.45	150.76	13.89	13.89	200.43	2.83	1.35
N460-800-0.10	H200×150×14×14	2727.80	150.76	13.63	13.60	200.26	2.20	1.16
W460-800-0.07	H200×200×14×14	2735.45	200.62	13.69	13.63	199.88	1.38	0.99
W460-800-0.10	H200×200×14×14	2730.25	200.36	13.77	13.81	199.98	1.74	0.91
N460-600-0.11	H200×150×14×14	2728.43	151.04	13.75	13.68	200.59	2.18	1.42
W460-600-0.11	H200×200×14×14	2728.98	200.89	13.65	13.61	200.97	1.39	1.89

The measured mechanical properties of high strength steel at high temperature obtained by Wang [4, 15] was utilized to get reduction factors of yield strength and elastic modulus of high strength Q460 and Q690 steel in this paper.

The imperfections of steel column were measured, and the results are tabulated in *Table 2*. The i shows the global geometric imperfections of column at mid-height the column length, and β is local geometric imperfection of the flange due to welding deformation. It should be noted that the height of hinge supports (274mm in total) was accounted for when using effective length of column to calculate its slenderness ratio.

2.3 Test set-up

A special set-up was designed to investigate the creep buckling of Q460 and Q690 steel column under constant load and elevated temperature. As shown in *Fig.1a*, a cylinder-shaped furnace is installed in a high stiffness self-reaction frame with an overall dimension of 5.85m (height) × 2m (width). The transfer girder acted as a restriction on horizontal movement of hinge support and fixed load cell. The hinge supports were installed at each end of column to ensure that the column had no rotational restraint. The connection of hinge supports, and the ends of transfer girder were lubricated to minimize the influence of friction. The ends of steel columns and adjacent support were protected with fire insulation and furnace was closed. The electric furnace, which is 2700mm height and consisted of 6 segments, were lifted using a base table to keep the similar height with steel column.

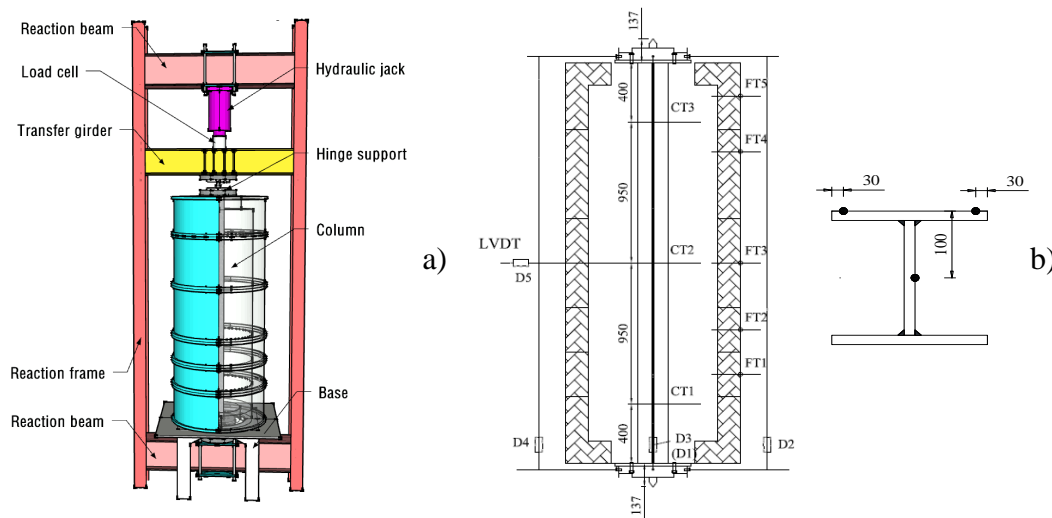


Fig.1. a) Test set-up, b) Locations of LVDTs and thermocouples on column

2.4 Instrumentation detail

Nine thermal couples were mounted on each column to monitor the temperature variations in three sections (*Fig.2b*). The temperatures of furnace were also measured by five thermocouples. The axial displacement was recorded in four locations using four LVDTs, which were fitted to the braces between two support hinges. As to lateral deflection, a nickel-chromium alloy wire was employed to link the lateral LVDT and the centre of web through a hole on the furnace. This alloy wire is not sensitive to fire due to its low thermal expansion coefficient of $1.8 \times 10^{-5}/^{\circ}\text{C}$.

2.5 Test procedure

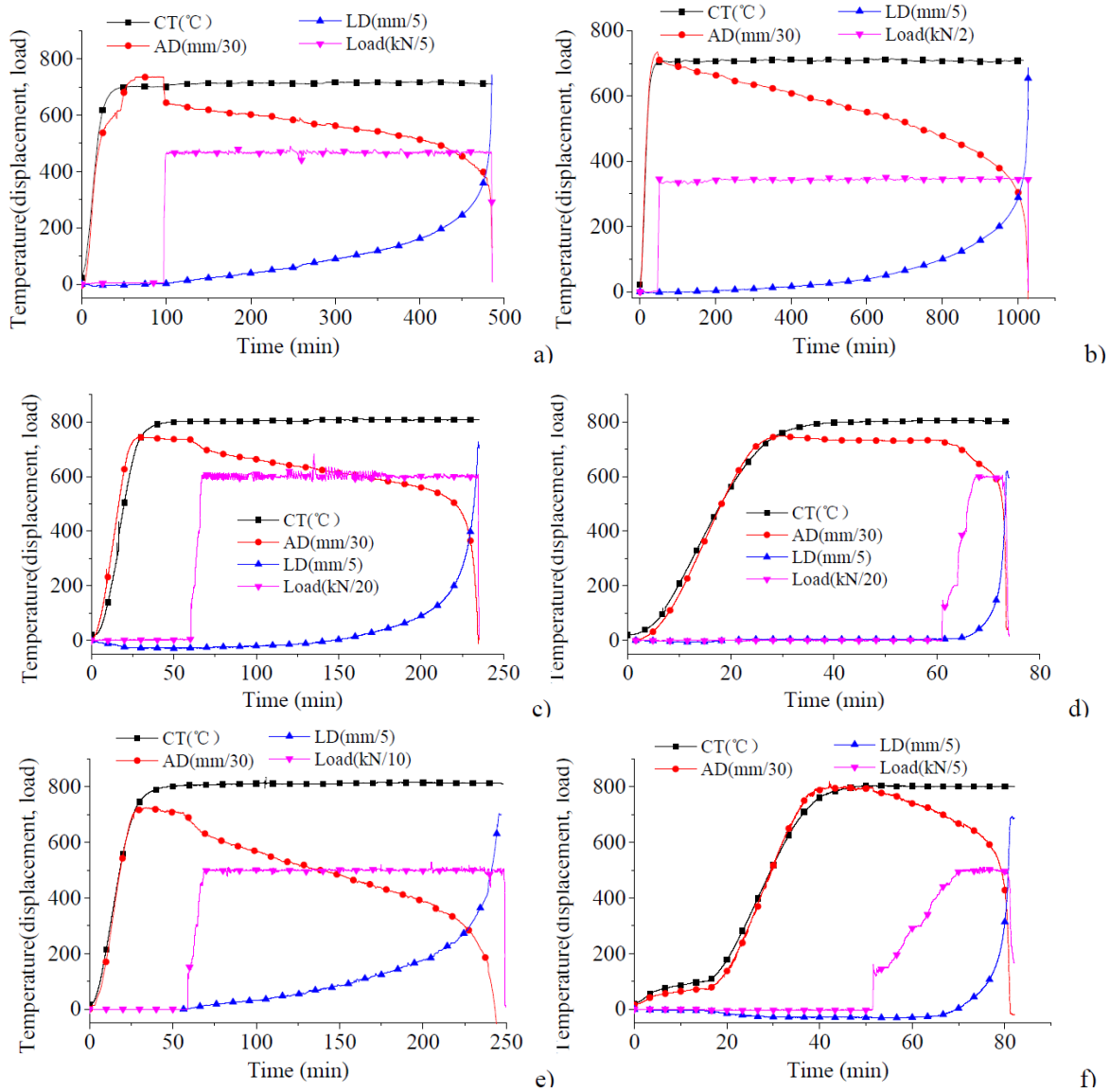
Each test procedure mainly includes the following steps: (1) The steel column was installed into the furnace and corresponding measurement instruments, including thermocouples and displacement meters were connected, then the furnace was closed. (2) The hydraulic jack was started, and the axial load was increased to 10% of ultimate bearing capacity. After two minutes, the load was released. This preloading procedure was carried out to examine the reliability of all the instruments. (3) After setting the intended target temperature, the furnace was turned on and the temperature increased with maximum power of the furnace. (4) When all the temperatures of steel column reached to target temperature, the load was increased to designed level and then it was kept constant to observe the creep deformation. (5) Once the lateral deflection of test column reaches a predetermined limit, namely $L/20$, where L is the length of the column, the hydraulic jack was stopped, and the furnace was turned off. (6) All the data recorded in the test, including temperature and displacement were saved.

3 TEST RESULTS AND DISCUSSION

3.1 Thermal and structural response

The response of the test specimen, including temperature evolution, load variation and displacement recorded, are plotted in Fig.3, where CT, AD and LD means the average temperature of the nine thermocouples arranged in three sections, axial displacement and lateral deflection of steel column, respectively. The discrepancies between measured and target temperature of columns are no more than 20°C. Due to mechanical problem of the electronic furnace, the temperature of specimen W690-800-0.6 shows an unusual heating phase. Some load curves present slight fluctuation, because the hydraulic jack is manual controlled, and the axial displacement of column increases throughout the loading phase. It is difficult to maintain the load constant.

During the heating phase, the axial displacement increases with the elevated temperature due to the thermal expansion and then drops with increasing applied load. In the next stage when load and temperature are kept constant, the axial displacement of each column accumulates slowly due to creep effect.



Test on creep buckling of high strength steel columns at elevated temperatures

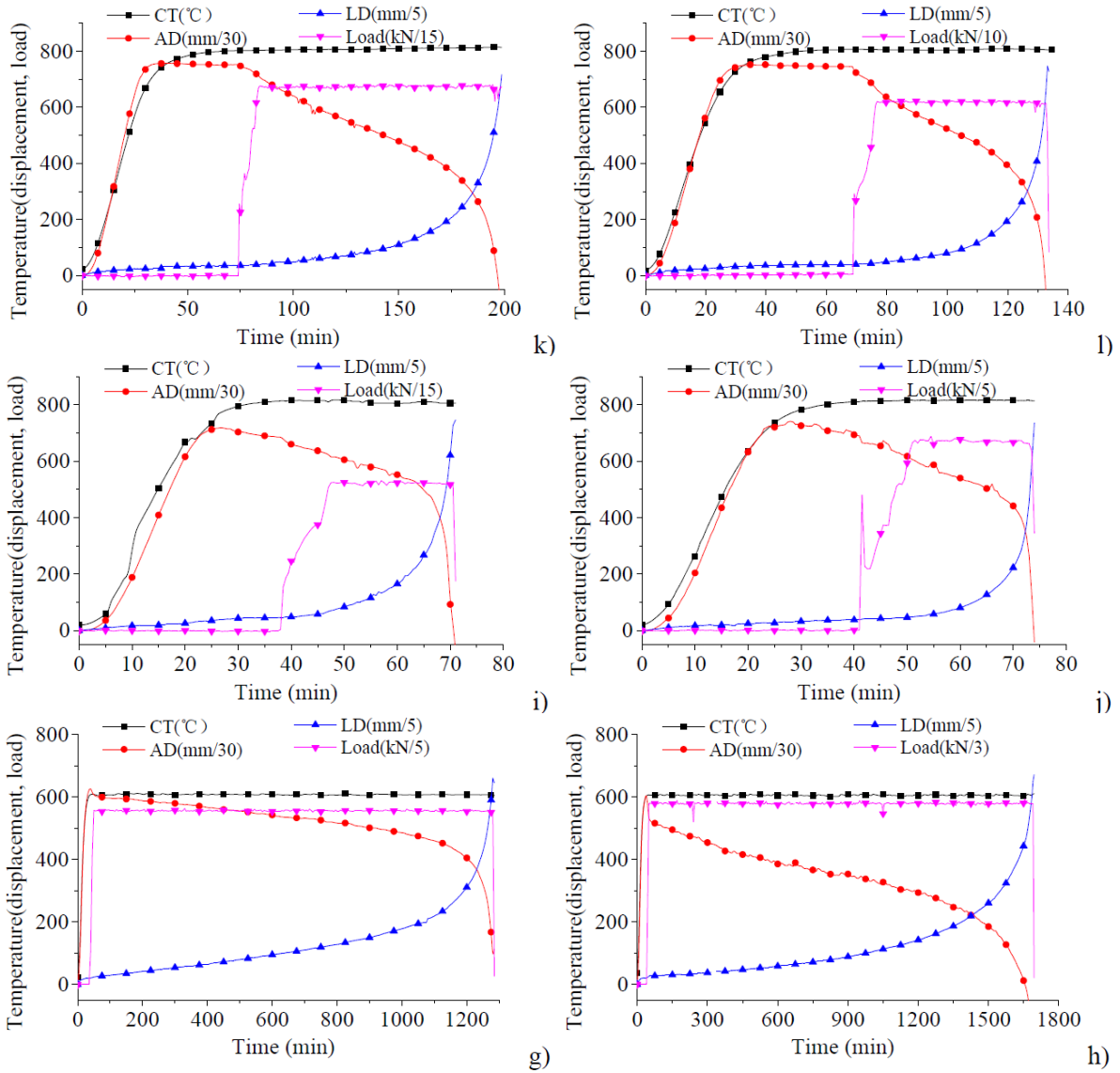


Fig.3. Thermal and structural response of high strength steel columns: a) N690-700-0.6, b) W690-700-0.6, c) N690-800-0.3, d) N690-800-0.6, e) N690-800-0.3, f) N690-800-0.6, g) N460-600-0.11, h) W460-600-0.11, i) N460-800-0.08, j) N460-800-0.10, k) W460-800-0.07, l) W460-800-0.10

In the last stage, the axial displacement increases rapidly when approaching a critical value, and the acceleration is relevant low for steel columns with small slenderness. The lateral deflection of column rises slightly with increasing temperature and load. After that, consist with the trend of axial displacement, lateral deflection of column increases gradually when the temperature and applied load maintain steady, and then accelerate to failure.

3.2 Creep buckling failure time

The term creep buckling failure time, used in this paper, refers to the duration from the time when applied load reaches to the target level to the time when column failures. The evolutions of axial and lateral displacements of columns in constant loading phase are plotted in Fig.4. Since the buckling time of each columns varies from 6 min to 1648 min, the natural logarithm of time is adopted as X axis scale and the creep buckling failure times of each column were also shown in Fig.4. At same load ratio and temperature level, the buckling time of steel column with larger slenderness is relevant short. The difference induced by slenderness ratio is not obvious between N690-800-0.3 and W690-800-0.3 (168 min and 177 min), which can be attributed that the smaller crookedness exists in N690-800-0.3 (0.47mm) compared to that in W690-800-0.3 (2.55mm). Besides, the evolution curves of axial displacement indicate that the steel columns with smaller

slenderness ratio can maintain stability when experiencing larger deformation compared to that of bigger slenderness ratio. The load ratio has considerable influence on fire duration of column that buckling time decreases with increasing load level under similar conditions. The buckling times at 800°C are much shorter than that at lower temperature, that is, the creep buckling failure times of Q460 and Q690 steel columns vary greatly at different temperatures.

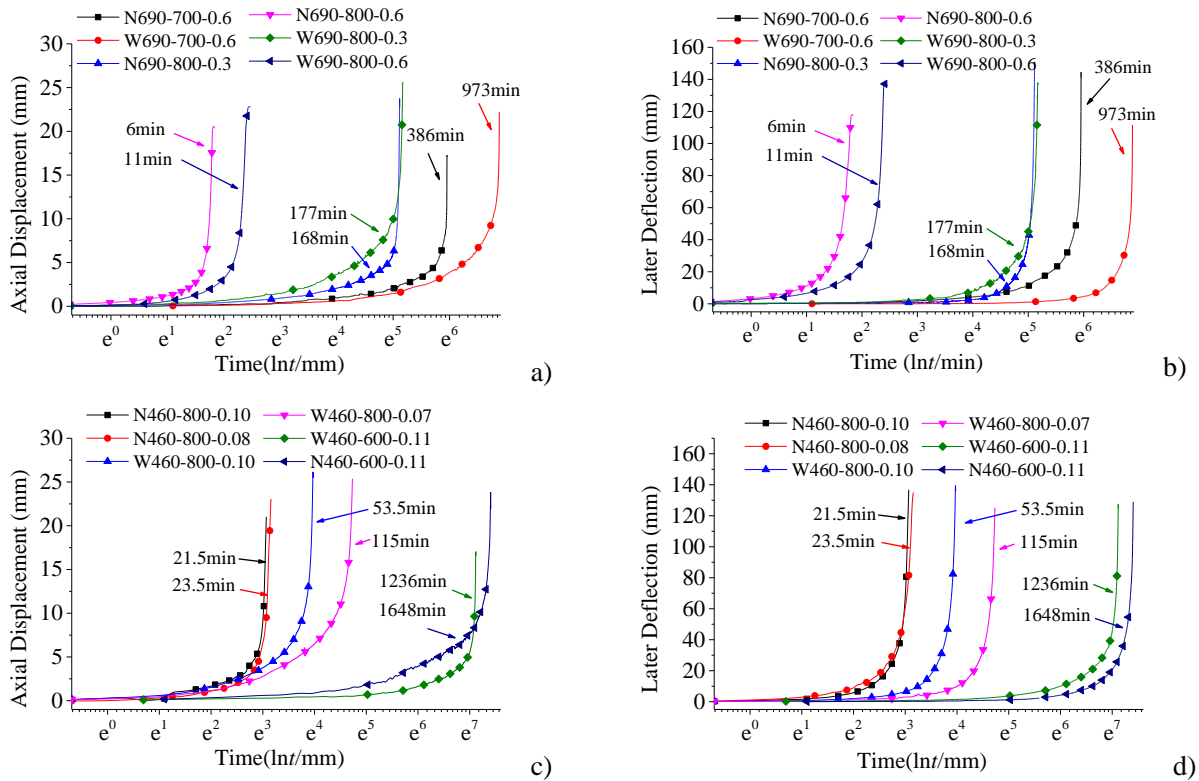


Fig.4. Comparison of creep buckling failure time of steel columns



Fig.5. Specimens of Q690 columns after failure: a) N690-700-0.6, b) W690-700-0.6, c) N690-800-0.3, d) N690-800-0.6, e) W690-800-0.3, f) W690-800-0.6, g) N460-600-0.11, h) W460-600-0.11, i) N460-800-0.08, j) N460-800-0.10, k) W460-800-0.07, l) W460-600-0.11

3.3 Failure patterns

All the high strength Q460 and Q690 steel columns exhibit global flexural buckling about the weak axis, as shown in Fig.5. The maximum deflection of the columns located at the mid-height and the failure mode has no relation with load ratio, temperature and steel type.

4 CONCLUSIONS

The creep buckling behaviour of 12 H-shaped section columns made of high strength Q460 and Q690 steel were investigated in this experimental program. During each test, temperature and load were kept constant when they reached a certain level. Generally, two load ratios, two slenderness ratios and two temperatures were considered. When exposed to constant elevated temperature and subjected to constant load level, the axial and lateral displacements of steel columns increase slowly with time at early stage and then soar until column collapses. All the specimens were tested to failure between 6min to 1648min, indicating that creep effect could not be neglected in fire safety design of high strength steel column. The considered factors in the test have considerable influence on creep buckling of steel columns, that is, the failure time decreases with increasing load level, temperature or slenderness. All the failure modes of tested specimens are global flexural buckling about the weak axis.

5 ACKNOWLEDGEMENTS

The authors wish to acknowledge the support of the Natural Science Foundation of China (51678090) on the work presented in this paper.

6 REFERENCES

1. Mohammed Morovat, Michael Engelhardt, Todd Helwig, Eric Taleff (2014). *High-temperature creep buckling phenomenon of steel columns subjected to fire*. Journal of Structural Fire Engineering, 5(3). pp 189-202.
2. Venkatesh Kodur, Esam M. Aziz (2015). *Effect of temperature on creep in ASTM A572 high-strength low-alloy steels*. Materials and Structures, 48(6). pp 1669–1677.
3. Weiyong Wang, Shouhai Yan (2017). *Studies on temperature induced creep in high strength Q460 steel*. Materials and Structures. pp 50-68.
4. Weiyong Wang, Kang Wang, Venkatesh Kodur, Bing Wang (2018). Mechanical properties of high strength Q690 steel at elevated temperature. Journal of Materials in Civil Engineering, 30(5). pp 04018062.
5. Regine Schneider, Jörg Lange (2011) *Constitutive equations and empirical creep law of structural steel S460 at high temperatures*. Journal of Structural Fire Engineering, 2(3). pp 217-229.
6. Guoqiang Li, Chao Zhang (2012). *Creep effect on buckling of axially restrained steel columns in real fires*. Journal of Constructional Steel Research, 71. pp 182-188.
7. Tondini N, Hoang VL, Demonceau JF, Franssen JM (2013). *Experimental and numerical investigation of high-strength steel circular columns subjected to fire*. Journal of Constructional Steel Research, 80. pp 57-81.
8. Ju Chen, Ben Young (2008). *Design of high strength steel columns at elevated temperatures*. Journal of Constructional Steel Research, 64. pp 689-703.
9. Byeongnam Jo, Koji Okamoto (2017). *Experimental investigation into creep buckling of a stainless steel plate column under axial compression at extremely high temperatures*. Journal of Pressure Vessel Technology, 139.
10. Zhanfei Huang, Kanghai Tan, Sengkiong Ting (2006). *Heating rate and boundary restraint effects on fire resistance of steel columns with creep*. Engineering Structures, 28. pp 805-817
11. Byeongnam Jo, Wataru Sagawa, Koji Okamoto (2014). *Measurement of buckling load for metallic plate columns in severe accident conditions*. Nuclear Engineering and Design, 274, pp 118-128
12. EC3 (2005). *Eurocode 3: Design of steel structures–part 1.2: general rules–structural fire design*. European committee for standardization, BS EN 1993–1–2:2005 CEN, Brussels.
13. ANSI/AISC 360-10 (2010). *Specification for Structural Steel Buildings*. American Institute of Steel Construction, Chicago.
14. GB/T 228.1-2010 (2010). *Standardization Administration of the People's Republic of China (SAC) Metallic materials-tensile testing-Part 1: method of test at room temperature.*, China Standard Press, Beijing.
15. Weiyong Wang, Bing Liu, Venkatesh Kodur (2013). *Effect of temperature on strength and elastic modulus of high-strength steel*. Journal of Materials in Civil Engineering, 25 (2). pp 174-182.

DEVELOPING FRAGILITY CURVES & ESTIMATING FAILURE PROBABILITIES FOR PROTECTED STEEL STRUCTURAL ELEMENTS SUBJECT TO FULLY DEVELOPED FIRES

Danny Hopkin¹ Ruben Van Coile² & Ian Fu³

ABSTRACT

Reliability methods are at the core of ambient Eurocode design. Realising exceptional / complex buildings necessitates that an adequate level of safety be demonstrated. Rationally demonstrating adequate safety can only be achieved through the application of probabilistic risk assessment (PRA). This paper presents a novel application of PRA in a structural fire engineering context. It first proposes a generalised limit state for protected steel members undergoing failure modes dictated by yielding. Subsequently, fragility curves describing failure likelihood in function of protection specification and mean fire load are presented for a 1,000 m² compartment, subject to fully developed fires (parametric and travelling fires). The presented fragility curves have subsequently proven to be of value for further life-time-cost-optimisation applications, with the intent of arriving at explicit safety targets.

1 INTRODUCTION

Realising exceptional buildings necessitates that an adequate level of fire safety be explicitly demonstrated. This requires an evaluation of all foreseeable consequences, and the probability of their manifestation [1]. Unlike ambient temperature evaluations of structural reliability, further sources of uncertainty exist at high temperature that relate to: the characterisation of fires, their implications for structural element temperatures, the degradation of material properties, permanent and imposed loading at the time of the fire, and further (potential) model uncertainties. Previous studies by Hopkin, et. al. [2], have evaluated failure probabilities for protected steel elements with different protection specifications (i.e. 30, 60, 90 and 120 minutes) by comparing the probability density functions (PDFs) for maximum temperatures attained during fire to a deterministic limiting temperature. Uncertainties regarding the structural loading, degradation of material properties at elevated temperatures and model uncertainties were, however, not considered. This paper builds upon the work by Hopkin, et al. [2] by introducing these additional uncertainties noted above, resulting in a more complete estimation of failure probabilities for isolated protected steel elements.

2 OVERVIEW OF THE PROBABILISTIC STUDY

2.1 Probabilistic factors leading to a fire induced structural failure

The events that lead-up to a potential structural failure in case of fire all have a probability of occurring. In the first instance a fire must develop, subsequently there must be a compound failure

¹ Associate Director, Olsson Fire and Risk. Visiting Professor, University of Sheffield, UK.
e-mail: Danny.Hopkin@OlssonFire.com and D.J.Hopkin@Sheffield.ac.uk

² Assistant Professor, University of Ghent, Belgium.
e-mail: Ruben.VanCoile@UGent.be

³ Graduate Fire Engineer, Olsson Fire and Risk, UK.
e-mail: Ian.Fu@OlssonFire.com

of early intervention by the occupants, active measures and the fire brigade. From this point, the fire may become fully developed (or ‘significant’). Allied to this, the structure must be sufficiently affected by the fully developed fire such that it undergoes damage and, potentially, fails. Broadly, within this series of events, two domains can be identified – (i) the event instigation domain, and (ii) the response domain. This differentiation allows benchmarking of performance against two safety targets – (a) an overall reliability index β which includes the likelihood of the fire event, and (b) a reliability index given a significant fire (β_{fi}). Discussion on the meaning of β in fire can be found elsewhere [3]. While β refers to the (annual) probability of fire-induced failure and can be compared with failure rates due to other unforeseen events, the conditional reliability index β_{fi} relates to the robustness of the structure in the unlikely event of a fully developed fire.

2.2 The event instigation domain

The event instigation domain simply describes the ignition likelihood, and consequently the occurrence rate of structurally significant fires, i.e. those that have the potential to undermine structural integrity. Studies, such as those in the Natural Fire Safety Concept Valorisation Project [4], provide means for estimating the structurally significant fire occurrence rate in function of e.g. compartment size, occupancy and various system and management based intervention possibilities.

2.3 The response domain

The response domain is the principal focus of this paper, and in the specific application of protected steel structures. Evaluating the stochastic response of a structural element subject to a significant fire occurrence necessitates that: (a) the probabilistic manifestations of potential significant fire scenarios be evaluated, and (b) subsequently, subject to a given fire manifestation, an evaluation is made of structural response. (a) requires appropriate fire models, with corresponding stochastic inputs for relevant parameters describing a fire’s development. (b) needs an evaluation of both the: (stochastic) applied action at the time of the fire (cognisant of the variability in the permanent and variable components), and the available resistance of the structure or structural component (impacted by uncertainty in fundamental material properties, how they degrade with temperature, etc.). Common to (a) and (b) are further (potential) model uncertainties.

3 STOCHASTIC FIRE MANIFESTATION

The procedure for arriving at probability density functions for the maximum temperature attained by a protected steel element subject to a fully developed fire is subject to wider discussion in Hopkin, et. al. [2] and is summarised herein. First, there must be an idealisation of the fire’s development (i.e. a fire model), and second, the stochastic inputs for that model are assigned distributions through a combination of measurements or judgement. Two fire models are adopted, in recognition of two likely outcomes should a significant fire occur. The first is the Eurocode parametric fire for cases where flashover can reasonably be expected to occur. The second, is a travelling fire model proposed by Hopkin [5]. The decision as to whether to adopt a post-flashover fire vs. a travelling fire is informed by: (a) spread rates, and (b) the ventilation conditions. That is, flashover is only considered viable if: (i) the fire has spread to the far end of the compartment before the origin starts to decay; and (ii) the ventilation conditions lead to an opening factor, as defined in BS EN 1991-1-2, of between 0.02 and 0.2 m^{0.5}. The above conditions naturally lead to more post-flashover fires in smaller, relative to larger compartments. Albeit, conditions to support flashover can occur in moderate sized compartments, where the spread rate is rapid. Subject to a thus defined fire time-temperature curve and protection specification, the maximum temperature of a protected element is simply derived from the bulk-capacitance methodology given in EN 1993-1-2 [6]. The stochastic variables required to describe fire development are discussed in Section 6.2.

4 PROTECTION SPECIFICATIONS FOR PROTECTED ELEMENTS

For the steel section and insulation properties specified further in *Table 4*, the insulation thickness required based on current deterministic design procedures is given in *Fig. 1* (left) in function of the fire utilisation u_{fi} , for different ISO 834 standard fire exposures. The fire utilisation u_{fi} is given by *Eq. (1)*, where the global resistance factor γ_R equals unity when $\gamma_s = 1$. η_{fi} is the reduction factor of the design load for the fire situation as specified in the Eurocodes (e.g. EN 1993-1-2 [6]), given by *Eq. (2)* for the EQU limit state in normal design conditions. ψ_{fi} is the imposed load combination factor for the fire design and χ the load ratio defined by *Eq. (3)*. *Fig. 1* (right) visualizes *Eq. (2)* for different ψ_{fi} and load ratio χ .

$$u_{fi} = \frac{E_{fi,d}}{R_{fi,d}(t=0)} = \frac{\eta_{fi}E_d}{\gamma_R R_d} = \frac{\eta_{fi}u}{\gamma_R} \quad (1)$$

$$\eta_{fi} = \frac{1 + \psi_{fi} \frac{\chi}{1 - \chi}}{\gamma_G + \gamma_Q \frac{\chi}{1 - \chi}} = \frac{1 + \psi_{fi} \frac{\chi}{1 - \chi}}{\phi} \quad (2)$$

$$\chi = \frac{Q_k}{Q_k + G_k} = \frac{M_{Qk}}{M_{Qk} + M_{Gk}} \quad (3)$$

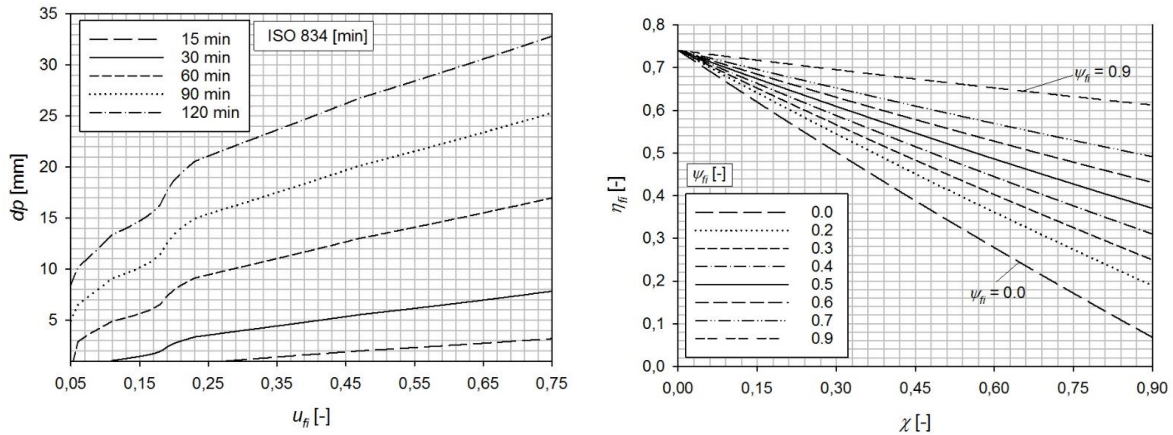


Fig. 1. (left) Required insulation thickness in function of utilisation u_{fi} and fire resistance period, (right) Fire design load reduction factor in function of the load ratio χ , for different ψ_{fi} , considering the EQU limit state in normal design.

5 A GENERALISED LIMIT STATE FOR STEEL ELEMENTS UNDER YIELDING

5.1 Basis – a specific limit state for a bending element

In the case of beams subjected to pure bending, the limit state defining failure is given by *Eq. (4)*, with parameters as listed further in *Table 1*. For elements subjected to pure tension, an equivalent limit state can be formulated. The beam is assumed to have a utilization ratio $u \leq 1$ in normal design conditions, in accordance with the ultimate limit state (ULS) design requirements of EN 1990 [7], i.e. *Eq. (5)*, with M_{Ed} the design value of the bending moment induced by the load effect and M_{Rd} the design value of the bending moment capacity.

$$Z = K_R M_R - K_E (M_G + M_Q) \quad (4)$$

$$M_{Ed} = u M_{Rd} \quad (5)$$

Considering a uniform temperature of the steel beam in case of fire exposure (as obtained through the bulk-capacitance model of EN 1993-1-2 [6]), the bending moment capacity M_R is given by Eq. (6), with k_{fy} the temperature dependent reduction factor for the steel yield strength. Consequently, the general limit state of Eq. (4) can be rewritten as Eq. (7), where all temperature-dependent and temperature-independent variables have been grouped.

$$M_R = W_{pl} k_{fy} f_y \quad (6)$$

$$Z_{fi} = k_{fy} - \frac{K_E (M_G + M_Q)}{K_R W_{pl} f_y} = k_{fy} - k_{fy,req} \quad (7)$$

As indicated by the right-hand equation in (7), the temperature-independent variables define the (minimum) required value for k_{fy} , Eq. (8). This allows the splitting of the reliability analysis in a fire-dependent evaluation of k_{fy} and a generally applicable, fire-independent evaluation of $k_{fy,req}$.

$$k_{fy,req} = \frac{K_E (M_G + M_Q)}{K_R W_{pl} f_y} \quad (8)$$

5.2 A generalised limit state – required residual yield strength

Starting from Eq. (8) and analytically combining both lognormal model uncertainties in a single total model uncertainty K_T , Eq. (8) is rewritten as Eq. (9) by introducing scaled variables $X^* = X / c$, with c a constant factor. The scaled variables applied in Eq. (9) are listed in Table 2.

$$k_{fy,req} = \frac{K_E (M_G + M_Q)}{K_R W_{pl} f_y} = \frac{\mu_{KT} M_{Gk}}{W_{pl} f_{yk}} K_T^* \frac{(G^* + Q^*)}{f_y^*} = \frac{\mu_{KT} u}{\gamma_s \phi} K_T^* \frac{(G^* + Q^*)}{f_y^*} \quad (9)$$

Simplifying Eq. (9), $k_{fy,req}$ is found to be independent of the beam properties (W_{pl} , f_{yk}). The formulation can be further generalized by introducing $nk_{fy,req}$ in Eq. (10), allowing a stochastic representation of the minimum required strength factor independent of the utilization u and the choice of μ_{KT} (as this parameter is not clearly defined for fire applications). For a given utilization and μ_{KT} , $nk_{fy,req}$ can be scaled directly to $k_{fy,req}$. Monte Carlo results for $nk_{fy,req}$ are visualized in Fig. 2, indicating that $nk_{fy,req}$ can be approximated by a lognormal distribution.

$$nk_{fy,req} = \frac{\gamma_s k_{fy,req}}{\mu_{KT} u} = \frac{K_T^* (G^* + Q^*)}{\phi f_y^*} \quad (10)$$

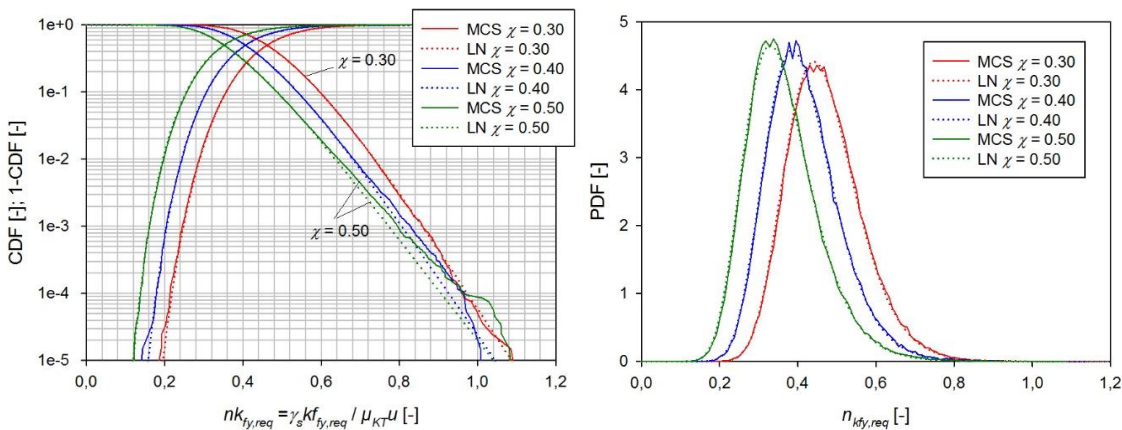


Fig. 2. (left) CDF and cCDF for $nk_{fy,req}$, (right) PDF for $nk_{fy,req}$. Monte Carlo simulations and lognormal approximation.

6 STOCHASTIC PARAMETERS

6.1 Parameters describing the bending limit state

The distributions in *Table 1* describing the stochastic variables are based on the literature review by Holicky and Sykora [8] and the JCSS Probabilistic Model Code [9]. A 5-year reference period is considered for the imposed load effect to take into account the imposed load present at the time of fire exposure. For normal design conditions, lognormal model uncertainties K_R and K_E apply. Appropriate model uncertainties for the fire condition are currently not clearly defined. In the following it is assumed that also in case of fire, the model uncertainties can reasonably be described by a lognormal distribution. To account for increased uncertainty and reduced redundancy during fire, the parameters for K_R have been modified relative to the (bracketed) normal design situation.

Table 1. Parameters for the bending limit state

Symbol	Name	Dimension	Distribution	Mean (μ)	COV (V)
K_R	Model uncertainty for the resistance effect	-	Lognormal (LN)	1.10 (1.15)	0.10 (0.05)
M_R	Bending moment capacity	kNm	TBD		
K_E	Model uncertainty for the load effect	-	Lognormal (LN)	1.00	0.10
M_G	Bending moment induced by the permanent load effect	kNm	Normal (N)	M_{Gk}	0.10
M_Q	Bending moment induced by the imposed load effect	kNm	Gumbel (G)	$0.2 M_{Qk}$ (5-year reference)	1.1 (5-year reference)

Table 2. Original and scaled variables. Distributions given as distribution type (mean value, coefficient of variation)

Original variable	Original distribution	Constant	Scaled variable	Scaled distribution
K_T	LN ($\mu_{KT}; V_{KT}$)	μ_{KT}	K_T^*	LN (1; V_{KT})
M_G	N ($M_{Gk}; 0.1$)	M_{Gk}	G^*	N (1; 0.1)
M_Q	$G\left(0.2 \frac{\chi}{1-\chi} M_{Gk}; 1.1\right)$	M_{Gk}	Q^*	$G\left(0.2 \frac{\chi}{1-\chi}; 1.1\right)$
f_y	$LN\left(\frac{f_{yk}}{1-2V_{fy}}; V_{fy}\right)$	f_{yk}	f_y^*	$LN\left(\frac{1}{1-2V_{fy}}; V_{fy}\right)$

6.2 Fire development parameters

Fire development inputs vary according to the fire dynamics model adopted, i.e. post-flashover parametric fires or travelling fires. Input distributions are provided for e.g. fire load density, percentage glazing failure and combustion efficiency. *Table 3* summarizes the input distributions for all fire development metrics. These are generally adopted from the research literature, e.g. [4]. However, in instances, it has been necessary to apply judgement, and simply present an upper and lower bound, assuming a uniform distribution in-between (indicated via a min and max).

6.3 Yield strength retention parameters

Khorasani [10] proposed probabilistic models for the steel yield stress retention (reduction) factor at elevated temperatures. In the following, the ‘no base’ logistic model is applied, as given by *Eq. (11)*, with ε a standard normally distributed error term. Note that also at 20°C there is considerable variability of k_{fy} in this model. This is because part of the uncertainty regarding f_y (*Table 2*) is also considered in the k_{fy} model, thus the reliability at low temperatures will be underestimated. Further research is underway to further evaluate its impact. At elevated temperatures this effect disappears.

$$k_{fy}(\theta) = 1.2 \frac{\exp(1.61 - 1.68 \cdot 10^{-3} \theta - 3.36 \cdot 10^{-6} \theta^2 + 0.35 \varepsilon)}{\exp(1.61 - 1.68 \cdot 10^{-3} \theta - 3.36 \cdot 10^{-6} \theta^2 + 0.35 \varepsilon) + 1} \quad (11)$$

Table 3. Fire development parameters

Symbol	Name	Dim	Distribution	Mean (μ)	COV (V)
q_F	Fire load density	MJ/m ²	Gumbel	$q_{F,nom}$	0.3
t_{lim}	Limit time fuel controlled fire (EN 1991-1-2)	min	Deterministic	20	-
HRR_pua	Heat release rate per unit area	MW/m ²	Deterministic	0.25	-
φ_w	Fraction of glazing failure	-	Uniform	min: 0.1250	max: 0.9999
φ_b	Beam position relative to compartment length	-	Uniform	min: 0.6	max: 0.9
φ_c	Combustion efficiency	-	Uniform	min: 0.75	max: 0.999
sr	Spread rate	m/s	Uniform	min: 0.0035	max: 0.0193
T_{nf}	Near field fire temperature	°C	Normal	1050	$\mu_{T_{nf}} \cdot (1.939 - 0.266 \cdot \ln(\mu_{T_{nf}}))$

7 PILOT STUDY – GENERATING FRAGILITY CURVES IN FUNCTION OF DP

7.1 Overview

Obtaining fragility curves for protected steel elements in function of insulation thickness and fire characteristics necessitates three prerequisites: (1) the generation of maximum temperature PDFs, i.e. as reported by Hopkin, et. al. [2], (2) the translation of the maximum temperature PDFs into corresponding CDFs for achieved yield strength retention (k_{fy} in Eq. (7)), and (3) benchmarking of the achieved yield strength retention factors against $k_{fy,req}$, with failure corresponding with a condition whereby the right-hand side of equation (7) is negative. Core deterministic parameters for the pilot study are given in Table 4. Probabilistic variables are as discussed previously in Section 6.

Table 4. Deterministic parameters for pilot study

Symbol	Name	Dim	Metric	Symbol	Name	Dim	Metric
w	Room width	m	22.36	k_p	Insulation thermal conductivity	W/mK	0.2
l	Room depth	m	44.72	c_p	Insulation specific heat	J/kgK	1700
h	Room height	m	3.40	ρ_p	Insulation density	kg/m ³	800
v_w	Total window width	m	129.45	H_p	Heated perimeter	m	2.14
h_w	Window height	m	3.06	A_p	Cross-section area	m ²	0.017
d_p	Insulation thickness	mm	$d_{p,nom}$	Δt	Time step temperature calculation	s	15

7.2 Maximum temperature PDF

Considering the parameters listed in Table 4, the complementary CDF describing the probability of the steel section exceeding a specified maximum temperature is given in Fig. 3 (left) for different nominal (mean) fire load density q_F (insulation thickness $d_p = 5.7$ mm) and in Fig. 3 (right) for different nominal insulation thickness d_p ($q_F = 400$ MJ/m²). These results were obtained through 10,000 Latin Hypercube Simulations (LHS).

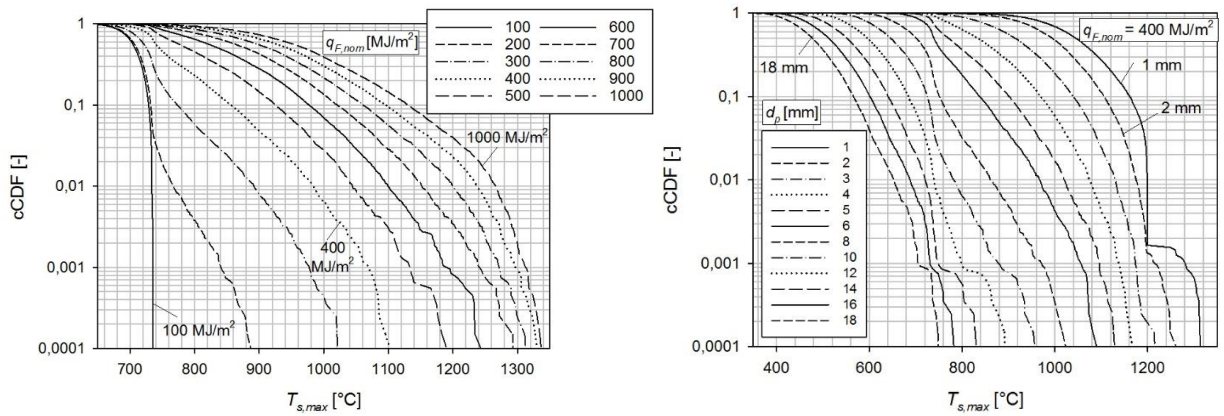


Fig. 3. (left) cCDF of $T_{s,max}$ for different $q_{F,nom}$ ($d_p = 5.7\text{mm}$); and (right) of $T_{s,max}$ for different d_p ($q_{F,nom} = 400\text{ MJ/m}^2$)

7.3 Yield strength retention CDF in function of fire characteristics

The steel yield strength retention factor (i.e. minimum residual strength) is visualized in Fig. 4 taking into account the distribution of the maximum steel temperature $T_{s,max}$ as observed in Fig. 3, and the stochastic model for k_{fy} as discussed in Section 6.3.

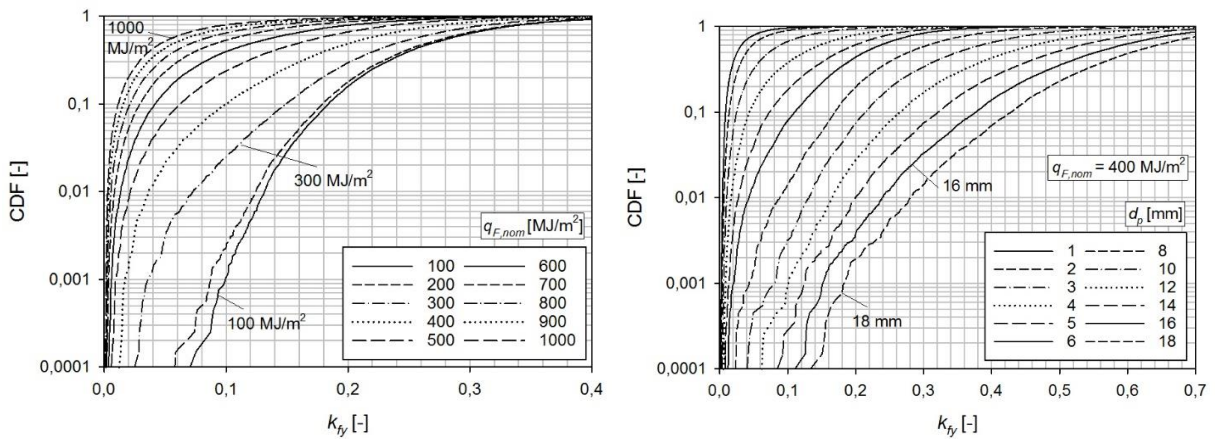


Fig. 4. (left) CDF of $k_{fy,ach}$ for different $q_{F,nom}$ ($d_p = 5.7\text{mm}$), (right) CDF of $k_{fy,ach}$ for different d_p ($q_{F,nom} = 400\text{ MJ/m}^2$)

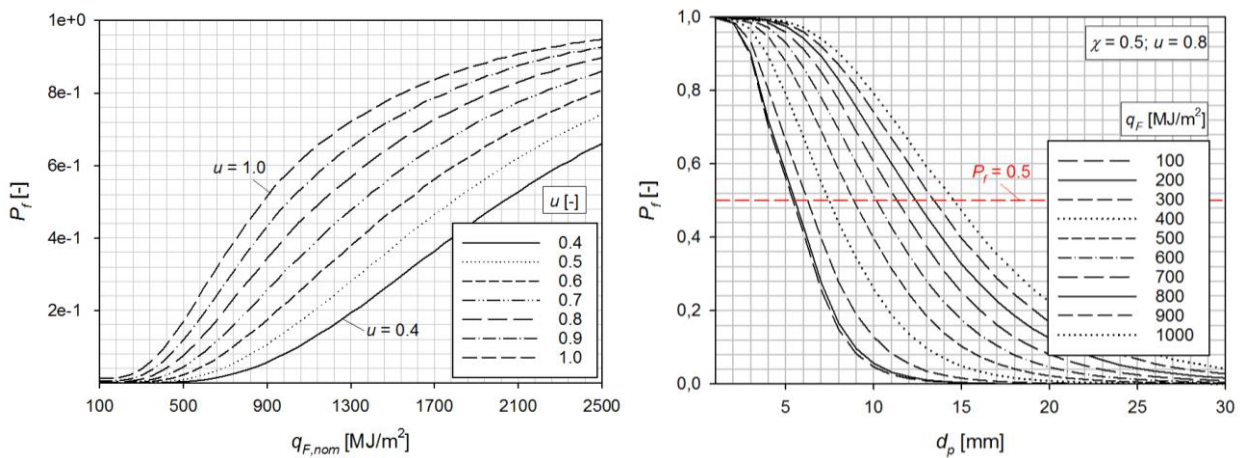


Fig. 5. (left) Fragility curve in function of $q_{F,nom}$, for $d_p = 16\text{ mm}$, $\chi = 0.50$, and different ambient utilization u , and (right) Fragility curve in function of the insulation thickness d_p , for $u = 0.8$, $\chi = 0.50$, and different $q_{F,nom}$.

7.4 Fragility curves for protected elements

Resulting fragility curves visualizing the parameter-dependency of the probability of failure are given in Fig. 5, with $\mu_{KT} = 0.92$ and $\gamma_R = 1$. Fig. 5 (left) visualises the probability of failure in function of the nominal fire load $q_{F,nom}$. Fig. 5 (right) visualises fragilities for given nominal fire load density q_F , in function of the insulation thickness d_p using logarithmic axes. For failure probabilities below 0.5, this visualization of the fragility curve is approximately linear. This is of particular interest for cost-optimization calculations, as presented in follow up research [11].

8 DISCUSSION & CONCLUSIONS

Currently no simplified reliability-based methods exist for structural fire design, as is the case for ambient design following the Eurocodes. In order to demonstrate adequate structural fire safety, risk-based methodologies should be applied, requiring an assessment of the reliability of structural systems exposed to fire. To this end, a step-wise approach to evaluate the failure probability of insulated steel elements has been presented, taking into account uncertainties with respect to both the fire exposure, and thermal and mechanical properties, with due consideration of the wide range of possible fire behaviours (travelling fires vs. post-flashover fires). The methodology has been applied to derive fragility curves for protected steel beams in function of the insulation thickness, nominal fire load density and ambient utilisation ratio. The results emphasize the strong effect of the nominal fire load density and the insulation thickness on the failure probability, providing input for rationally differentiating investments in structural fire protection between buildings. The presented results have been applied as a basis for cost-optimization in follow-up research, resulting in an assessment of optimum (target) reliability levels for structural fire design of protected steel structural elements.

REFERENCES

1. Hopkin, D., Van Coile, R., Lange, D. (2017). *Certain Uncertainty – Demonstrating safety in fire engineering and the need for safety targets*. SFPE Europe, 07.
2. Hopkin, D., Anastasov, S., Swinburne, K., Rush, D., & Van Coile, R. (2017). Applicability of ambient temperature reliability targets for appraising structures exposed to fire. In *2nd International Conference on Structural Safety under Fire and Blast Loading*, London, UK, September 10-12.
3. Van Coile, R., Hopkin, D., Bisby, L., & Caspeele, R. (2017). *The meaning of Beta: background and applicability of the target reliability index for normal conditions to structural fire engineering*. Procedia Engineering, 210, 528-536.
4. EC. (2002). Competitive steel buildings through natural fire safety concepts. *Office for Official Publications of the European Union*.
5. Hopkin, D. J. (2013). Testing the single zone structural fire design hypothesis. In *Interflam 2013, Proceedings of the 13th International Conference*, London, UK, June 24-26, 139-150.
6. CEN. (2005). Eurocode 3: design of steel structures – Part 1–2: General rules – structural fire design. EN 1993-1-2. *European Standard*.
7. CEN. (2002). EN 1990: Eurocode 0: Basis of structural design. *European Standard*.
8. Holický, M., Sýkora, M. (2010), Stochastic models in analysis of structural reliability. In *Proceedings of the international symposium on stochastic models in reliability engineering, life sciences and operation management*, Beer Sheva, Israel, February 08-11/02.
9. JCSS. (2015). *Probabilistic Model Code*. The Joint Committee on Structural Safety.
10. Khorasani, N.E. (2015). A probabilistic framework for multi-hazard evaluations of buildings and communities subject to fire and earthquake scenarios. *Doctoral dissertation*. Princeton University.
11. Van Coile, R., Hopkin, D. (2018). Target safety levels for insulated steel beams exposed to fire, based on Lifetime Cost Optimisation. In *Proceedings of IALCCE 2018*, Ghent, Belgium, October 28-31, in press.

STABILITY CHECK OF TAPERED STEEL BEAMS IN FIRE

Carlos Couto¹, Élio Maia², Paulo Vila Real³, Nuno Lopes⁴

ABSTRACT

Non-uniform (tapered) steel members are widely used in steel construction due to their structural efficiency as material savings can be achieved. EN1993-1-2 [1] provides several approaches to the stability verification of steel members but no fire design rules are provided for the case of tapered steel members. On that regard, current proposals/design methodologies at normal temperature (General Method [2], DIN 18800-2 [3] and Marques *et al.*'s proposal [4]) were adapted to fire situation in the scope of this work and the results were evaluated by means of a parametric study and GMNIA analyses. The proposal in [4] was deemed unsafe at elevated temperatures, which is understandable considering that it was fine-tuned to closely fit numerical data at normal temperature. DIN 18800-2's methodology was seen as unreliable in fire given the high scatter of the data points. Out of the three approaches, the modified General Method is recommended for the safety-check of a tapered member in fire, although several results are overconservative.

This work reinforces the need of deeper investigation on the stability of tapered beams at elevated temperatures as evidence points towards the adaptation to fire of existing methods at normal temperature not being enough to produce accurate predictions of resistance by themselves.

Keywords: Tapered, beams, lateral-torsional buckling, finite element method

1 INTRODUCTION

The simple fire design methods of Part 1-2 of Eurocode 3 (EC3) [1] are limited to uniform members and no rules are provided for non-uniform members. At room temperature, the out-of-plane stability check of non-uniform members should be performed using the General Method given in clause 6.3.4 of EN1993-1-1 [2]. This method is not widely validated at room temperature and is omitted in EN1993-1-2.

Preliminary investigation on the adaptation of General Method for fire design of tapered beams [5] and beam-columns [6], demonstrated safe results but, in those references, only one bending diagram was considered. In the scope of the project TaperSteel [7], some of the limitations/inconsistencies of tapered member design were addressed by Marques *et al.* [4], leading to the proposal of a new thorough design methodology for the stability of tapered beams at normal temperature. The German norm DIN 18800-2 [3] also treats the out-of-plane stability of tapered beams but some inconsistencies were pointed out by Braham *et al.* [8]. As such, given the scarcity of normative methodologies, this paper discusses and evaluates the adaptation of Marques *et al.*'s [4] proposal, the General Method [2] and DIN 18800-2's [3] methodology for the out-of-plane stability of web-tapered beams to fire situation. The ultimate capacity of members in fire is obtained numerically using shell finite elements for a materially non-linear analysis with imperfections (GMNIA) in SAFIR [9] and compared to those from the abovementioned design approaches. Finally, the main conclusions are drawn based on the results from a parametric study.

¹ Post-doc researcher. RISCO, Civil Engineering Department, University of Aveiro, Portugal.

² PhD student. RISCO, Civil Engineering Department, University of Aveiro, Portugal.

³ Full Professor. RISCO, Civil Engineering Department, University of Aveiro, Portugal.

⁴ Assistant Professor. RISCO, Civil Engineering Department, University of Aveiro, Portugal.

e-mail: ccouto@ua.pt

e-mail: eliomaia@ua.pt

e-mail: pvreal@ua.pt

e-mail: nuno.lopes@ua.pt

2 STABILITY CHECK OF TAPERED BEAMS

2.1 General Method

2.1.1 Normal temperature

The stability of uniform beams in EC3-1-1 [2] is checked by the application of clause 6.3.2. Regarding the stability of a non-uniform member, this clause is not applicable as the evaluation of the buckling resistance of such members lies outside the range of application of the interaction formulae. For those cases, verification should be performed using clause 6.3.4 (denoted as General Method or GM).

The out-of-plane stability of members is verified by ensuring that condition (1) is verified.

$$\frac{\chi_{op} \cdot \alpha_{ult,k}}{\gamma_{M1}} \geq 1 \quad (1)$$

where χ_{op} is the reduction factor for the non-dimensional slenderness $\bar{\lambda}_{op}$, obtained in (3), and analytically describes the reduction in resistance due to out-of-plane (“op”) instability phenomena, $\alpha_{ult,k}$ is the minimum load amplifier of the design loads in order to reach the characteristic resistance of the most critical cross-section of the structural component considering only the in-plane behaviour of the member, for a beam it can be obtained with Eq. (2).

$$\alpha_{ult,k} = \frac{M_{y,Rk}}{M_{y,Ed}} \quad (2)$$

$$\bar{\lambda}_{op} = \sqrt{\frac{\alpha_{ult,k}}{\alpha_{cr,op}}} \quad (3)$$

where $\alpha_{cr,op}$ is the minimum amplifier for the in-plane design loads to reach the elastic critical resistance of the structural component in regard to the lateral/lateral-torsional buckling.

2.1.2 Adaptation to fire situation

The adaptation of this methodology to fire is done by accounting for the reduction in steel material properties with the temperature, namely the yield strength $f_{y,\theta}$ and Young’s Modulus $E_{a,\theta}$ with the reduction factors $k_{y,\theta}$ and $k_{E,\theta}$, respectively. Then, given the direct proportionality of the load amplifier to the yield strength and of the critical amplifier to the Young’s Modulus, the following expressions can be deduced:

$$\bar{\lambda}_{op,\theta} = \sqrt{\frac{\alpha_{ult,\theta,k}}{\alpha_{cr,\theta,op}}} = \sqrt{\frac{k_{y,\theta} \cdot \alpha_{ult,k}}{k_{E,\theta} \cdot \alpha_{cr,op}}} = \bar{\lambda}_{op} \cdot \sqrt{\frac{k_{y,\theta}}{k_{E,\theta}}} \quad (4)$$

The load amplifier of the in-plane design loads – for the fire situation – to reach the characteristic resistance in fire situation may be determined with Eq. (5).

$$\alpha_{ult,\theta,k} = \frac{M_{y,\theta,Rk}}{M_{y,fi,Ed}} \quad (5)$$

The final condition to be fulfilled in fire situation for the General Method is thus,

$$\frac{\chi_{op,fi} \cdot \alpha_{ult,\theta,k}}{\gamma_{M,fi}} \geq 1 \quad (6)$$

The reduction factor $\chi_{op,fi}$, for the particular case of lateral-torsional buckling (LTB) in fire situation can be calculated with Eq. (7) following the principles of the EN 1993-1-2 [1], and taking $\bar{\lambda}_{LT,\theta} = \bar{\lambda}_{op,\theta}$, as

$$\chi_{op,fi} = \chi_{LT,fi} = \frac{1}{\phi_{LT,\theta} + \sqrt{\phi_{LT,\theta}^2 - \bar{\lambda}_{LT,\theta}^2}} \quad (7)$$

2.2 DIN 18800-2

2.2.1 Normal temperature

The German norm DIN 18800-2 [3] treats the out-of-plane stability of prismatic beams in clause 3.3.4. According to this clause, the stability of beams is checked as long as condition (8) is verified. Linearly web-tapered beams are covered in the formulae via factor n .

$$\frac{M_y}{k_M \cdot M_{pl,y,d}} \leq 1 \quad (8)$$

The reduction factor for LTB k_M (analogous to χ_{LT} in EC3) is obtained with Eq. (9).

$$k_M = \begin{cases} 1 & , \bar{\lambda}_M \leq 0.4 \\ \left(\frac{1}{1 + \bar{\lambda}_M^{2n}} \right)^{1/n} & , \bar{\lambda}_M > 0.4 \end{cases} \quad (9)$$

where $\bar{\lambda}_M$ (similar to $\bar{\lambda}_{LT}$ in EC3) is the non-dimensional in-plane slenderness, calculated

$$\bar{\lambda}_M = \sqrt{\frac{M_{pl,y}}{M_{Ki,y}}} \quad (10)$$

where $M_{Ki,y}$ is the elastic critical bending moment (the M_{cr} in EC3 notation), n is given by

$$n = 0.7 + 1.8 \frac{h_{\min}}{h_{\max}}, \frac{h_{\min}}{h_{\max}} \geq 0.25 \quad (11)$$

and h_{\min} and h_{\max} are the height of the smaller and bigger cross-sections respectively. In case the flanges are welded to the web, factor n must be multiplied by 0.8. However, following the recommendations in [8], this factor is taken as 1. Also, if bending moments with $\psi > 0.5$ are present, factor n is to be multiplied by a coefficient k_n , present in the norm;

2.2.2 Adaptation to fire situation

Similarly to what was done with the General Method, the non-dimensional slenderness and the reduction factor for LTB are adapted to elevated temperatures – $\bar{\lambda}_{M,\theta}$ and $k_{M,fi}$ – and calculated as

$$\bar{\lambda}_{M,\theta} = \sqrt{\frac{M_{pl,\theta,y}}{M_{Ki,\theta,y}}} \quad (12)$$

$$k_{M,fi} = \begin{cases} 1 & , \bar{\lambda}_{M,\theta} \leq 0.4 \\ \left(\frac{1}{1 + \bar{\lambda}_{M,\theta}^{2n}} \right)^{1/n} & , \bar{\lambda}_{M,\theta} > 0.4 \end{cases} \quad (13)$$

Finally, the out-of-plane stability of the member is checked if condition (14) is verified.

$$\frac{M_y}{k_{M,fi} \cdot M_{pl,\theta,y}} \leq 1 \quad (14)$$

2.3 Marques *et al.* (2013) [4]

2.3.1 Normal temperature

A design model for the out-of-plane stability of tapered beams was proposed in Marques *et al.* [4] and validated against numerical data. This proposal includes a calibrated “over-strength” factor as well as the determination of the second order failure cross-section location $x_{c,lim}^{II}$. The verification procedure for the LTB resistance of web-tapered beams for taper ratios $y_h \leq 4$, (ratio between the section heights) and $\gamma_w \leq 6.5$ (ratio between the section modulus) is described below.

The first step of the procedure is finding the first order failure location $x_{c,M}^I$. This corresponds to the location in which the value of Eq. (15) is maximum.

$$\varepsilon(x) = M_{y,Ed}(x)/M_{y,Rk}(x) \quad (15)$$

Similar to the General Method, the load multiplier $\alpha_{ult,k}(x_{c,M}^I)$ is calculated in Eq. (16) and the elastic critical multiplier α_{cr} can be obtained from a Linear Buckling Analysis.

$$\alpha_{ult,k}(x_{c,M}^I) = M_{y,Rk}(x_{c,M}^I)/M_{y,Ed}(x_{c,M}^I) \quad (16)$$

Stability is verified with Eq. (17) where $\chi_{LT}(x_{c,M}^I)$ is obtained from Eq. (18).

$$\chi_{LT}(x_{c,M}^I) \cdot \alpha_{ult,k}(x_{c,M}^I) = \alpha_b \geq 1 \quad (17)$$

$$\chi_{LT}(x_{c,M}^I) = \frac{\phi_{LT}}{\phi_{LT} + \sqrt{\phi_{LT}^2 - \phi_{LM} \cdot \bar{\lambda}_{LT}^2(x_{c,M}^I)}} \leq 1 \quad (18)$$

$$\phi_{LT} = 0.5 \cdot \left(1 + \phi_{LT} \cdot \eta_{LT} \cdot \frac{\bar{\lambda}_{LT}^2(x_{c,M}^I)}{\bar{\lambda}_z^2(x_{c,lim}^I)} + \phi_{LT} \cdot \bar{\lambda}_{LT}^2(x_{c,M}^I) \right) \quad (19)$$

$$\bar{\lambda}_{LT}(x_c^I) = \sqrt{\alpha_{ult,k}(x_{c,M}^I)/\alpha_{cr}} \quad (20)$$

$$\phi_{LT} = \begin{cases} A \cdot \psi^2 + B \cdot \psi + C \geq 1 & , \text{if } -1 \leq \psi \leq 1 \\ -0.0025a_\gamma^2 + 0.015a_\gamma + 1.05 & , \text{if UDL} \end{cases} \quad (21)$$

where η_{LT} is the generalized imperfection factor obtained by (22), α_{LT} is obtained by (23) and $\bar{\lambda}_z(x_{c,lim}^I)$ is calculated with (24) and is the non-dimensional slenderness for weak-axis flexural buckling calculated at the second-order cross-section failure position – $x_{c,lim}^I$ – determined from (25a)-(25d), A, B, C, a_γ are auxiliary parameters (refer to [4] for more details).

$$\eta_{LT} = \alpha_{LT} \cdot (\bar{\lambda}_z(x_{c,lim}^I) - 0.2)$$

$$\eta_{LT} \leq \sqrt{\frac{w_{y,el}(x_{c,lim}^I)^{y,el}}{w_{z,el}(x_{c,lim}^I)^{z,el}}} \cdot (0.12\psi^2 - 0.23\psi + 0.35) \quad (\text{only for welded}) \quad (22)$$

$$\alpha_{LT} = \begin{cases} 0.16 \cdot \sqrt{\frac{w_{y,el}(x_{c,lim}^I)^{y,el}}{w_{z,el}(x_{c,lim}^I)^{z,el}}} \leq 0.49 & , \text{hot rolled} \\ 0.21 \cdot \sqrt{\frac{w_{y,el}(x_{c,lim}^I)^{y,el}}{w_{z,el}(x_{c,lim}^I)^{z,el}}} \leq 0.64 & , \text{welded} \end{cases} \quad (23)$$

$$\bar{\lambda}_z(x_{c,lim}^I) = \sqrt{N_{Rk}(x_{c,lim}^I)/N_{cr}(x_{c,lim}^I)} \quad (24)$$

where $N_{Rk}(x_{c,lim}^I)$ and $N_{cr}(x_{c,lim}^I)$ are the cross-sectional resistance and Euler load, respectively, for a cross-section with the geometry at $x_{c,lim}^I$.

$$x_{c,lim}^I/L = 0.12 - 0.03(\gamma_h - 1) \quad (25a)$$

$$x_{c,lim}^I/L = (0.75 - 0.18\psi - 0.07\psi^2) + (0.025\psi^2 - 0.006\psi - 0.06) \cdot (\gamma_h - 1) \geq 0 \quad (25b)$$

$$\alpha = |\psi| \cdot \gamma_w \quad (25c)$$

$$\alpha_{lim} = 1 + 1.214(\gamma_h - 1) \quad (25d)$$

2.3.2 Adaptation to fire situation

The adaptation of this approach to fire situation is done for Eq. (20) and Eq. (24) as was done for the General Method in section 2.2.2. From it, the non-dimensional slenderness $\bar{\lambda}_{LT,\theta}$ and the non-dimensional slenderness about the minor axis $\bar{\lambda}_{z,\theta}(x_{c,lim}^I)$ in fire situation are deduced. As noticed, the calculation of the second-order failure position $x_{c,lim}^I$ uses the original values calibrated in [4] for the room temperature design situation.

3 NUMERICAL MODEL

The Geometrically and Material Non-Linear Analyses with Imperfections (GMNIA) were performed using the finite element software SAFIR [9]. The numerical model (*Fig. 1*) had a mesh with 12 elements in the flange, 18 in the web and 100 along the length. The loads were applied to the model using nodal forces and “Fork-support” conditions were modelled by restraining the vertical displacements of the bottom flange and the out-of-the plane displacements of the web. The present numerical model was previously validated by the authors [12] and later used in [13].

The geometric imperfections have been introduced in the model by changing the nodal coordinates to represent the worst scenario for the assessment of member resistance. This has been considered as the shape given by the modes of a linear buckling analysis (LBA) calculated with the software Cast3M [14]. In addition, the recommendations given in the Annex C of EN1993-1-5 [16] were followed: *i*) a combination of local and global modes were considered by taking the lowest mode as the leading imperfection and the other one reduced to 70%, *ii*) the amplitude of the imperfections was chosen as 80% of the fabrication tolerances given in the EN1090-2 [17], accordingly, an amplitude of 80% of $L/750$ for the global mode and 80% of $b/100$ for the local mode was used, where L is the member span and b is the flange width or web height, depending on which the maximum displacement occurs in the corresponding buckling mode. For the material imperfections, the pattern of residual stresses of welded cross-sections was included in the numerical simulations (see [18]).

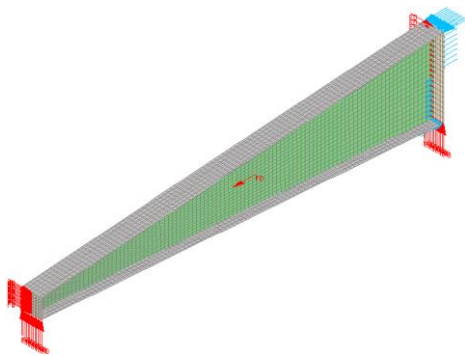


Fig. 1. Shell finite element numerical model.

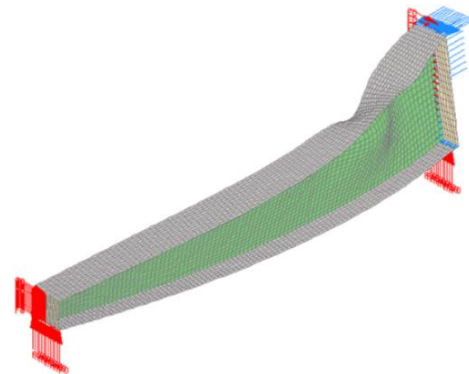


Fig. 2. Collapse shape for $\psi = 0$ at 550°C.

Examples of collapse shapes are given in *Fig. 2* and *Fig. 3* compares the numerical data at 20°C and the calibrated analytical formulae of [4], described in 2.4.

4 NUMERICAL STUDY

4.1 Parametric analysis

Table 1 specifies the parameters considered in the numerical study performed in the scope of this work, which were chosen based on the study done in [4]. As in [4], steel grade S235 was selected.

Table 1. Parameters considered in the analyses.

Reference cross-section	Height-taper ratio	Bending diagrams	Temperature	Member length				$\bar{\lambda}_{LT}(x'_c)$
-	-	-	(°C)	(m)				-
IPE 200 HEB 300	$\gamma_h = 1$	$\psi = -1$	350	0.5	3.5	6.5	10.0	[0;4]
	$\gamma_h = 2$		450	1.0	4.5	7.0	12.0	
	$\gamma_h = 3$	$\psi = 1$	550	2.5	5.0	8.0	13.0	
	$\gamma_h = 4$		700	3.0	6.0	9.0	14.0	

The accuracy of the design methodologies is assessed by comparing the reduction factors for lateral-torsional buckling χ_{Method} , obtained in *Eqs. (7), (13) and (18)* for each methodology, against their numerically obtained counterpart χ_{FEM} . When appropriate, the cross-sectional resistance is obtained according to the procedure proposed in [11] for class 3 and 4 cross-sections. The numerical simulations presenting collapse due to shear failure were not considered.

Fig. 3 shows the comparison between FEM results, denoted χ_{FEM} , and the different methodologies.

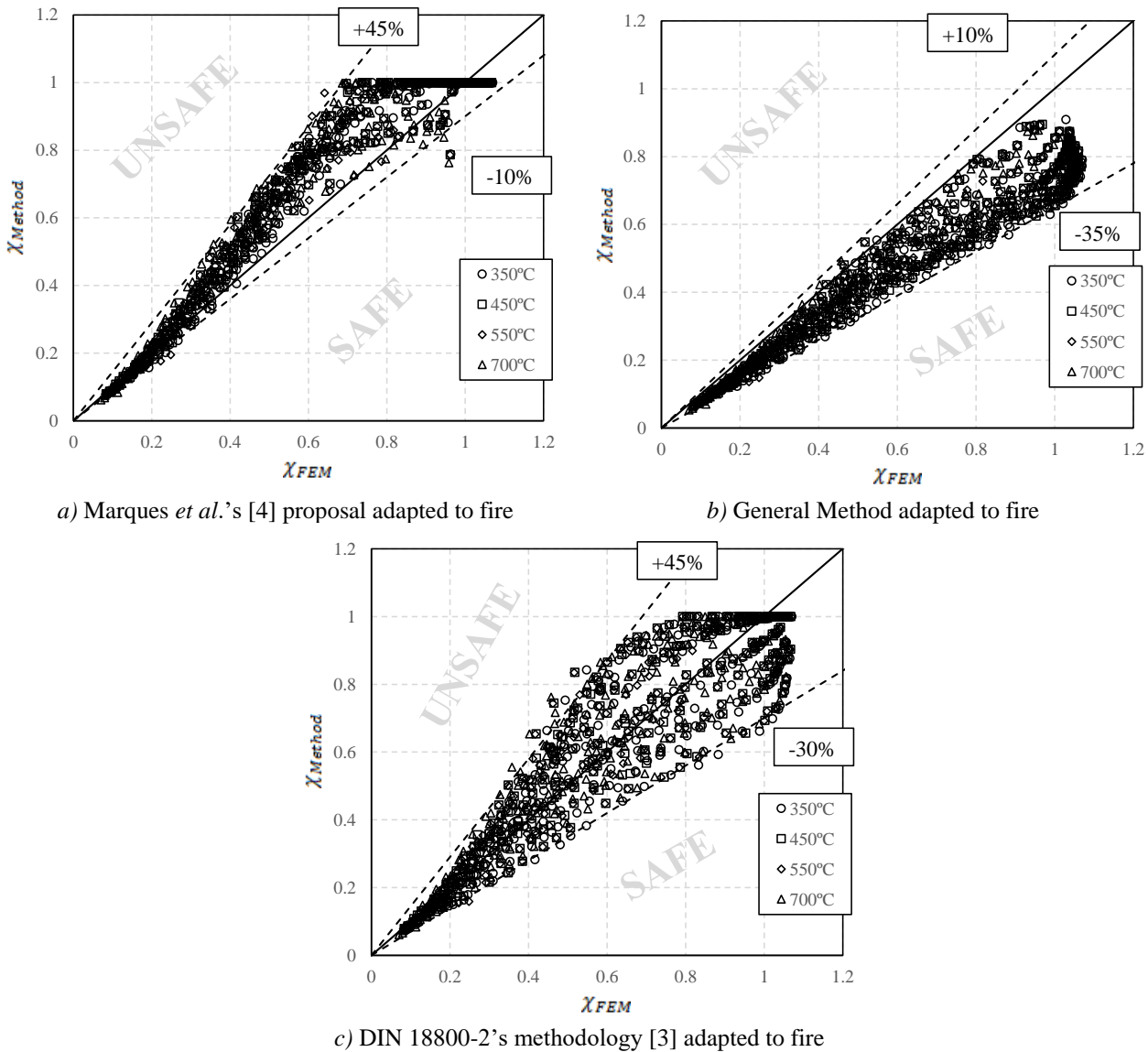


Fig. 3. Comparison of different methodologies and FEM simulations.

From the results, three overall interpretations can be made from the adapted methodologies: the General Method is conservative (in line with previous conclusions by the authors in a smaller-scale study [5]) while adaptation of Marques *et al.*'s proposal to fire is not accurate and should be further improved. DIN 18800-2 seems to produce a very wide array of data points ranging from 30% safe to 40-50% unsafe values. Additionally, at first glance, all temperatures are scattered inside the cloud of data points and no clear patterns are evident. The statistical study presented in section 5 helps shed some light on this matter. Specifically regarding the adaptation of [4] (see Fig. 3a), since this methodology was fine-tuned to closely fit numerical data at normal temperature, it is understandable that a basic analytical manipulation of the formulae may not be enough to accurately predict the safety of a tapered member at elevated temperatures. For instance, possible assumptions made during the conception of the formulae may be valid exclusively for 20°C, such as the polynomial regression of the auxiliary parameters in Eq. (21). Regarding DIN 18800-2, the adapted methodology produces an undesirable scatter of safe/unsafe data points thus it is not suitable for the stability check at elevated temperatures. Finally, despite providing very conservative results, the

modified General Method to fire is the recommended approach to predict the fire resistance of a tapered member, until improved methods are developed.

4.2 Statistical analysis

In order to better understand the significance and the variability of the numerical results in comparison to the abovementioned methodologies, some statistical parameters are presented and organized in *Table 2*, where the ratio χ_{Method}/χ_{FEM} is dissected. For the three cases, a ratio lower than 1.00 represents a safe result for the approach, in comparison to FEM results.

Table 2. Statistical evaluation of the ratio χ_{Method}/χ_{FEM} – analysis by sub-sets.

Sub-set/case	N. of cases	Mean	St. Dev.	Coef. Var.	Min.	Max.	%Unsafe	%(>1.05)	
General Method	All	1204	0.79	0.084	10.6%	0.60	1.08	0.8%	0.2%
	350°C	293	0.77	0.080	10.4%	0.64	1.01	0.3%	0.0%
	450°C	298	0.79	0.083	10.4%	0.66	1.06	1.0%	0.3%
	550°C	303	0.80	0.083	10.4%	0.60	1.06	1.0%	0.3%
	700°C	310	0.81	0.086	10.6%	0.63	1.08	1.0%	0.3%
DIN 18800-2	All	1204	1.02	0.188	18.4%	0.64	1.66	46.6%	37.1%
	350°C	293	0.99	0.175	17.7%	0.67	1.54	41.0%	31.1%
	450°C	298	1.02	0.189	18.5%	0.69	1.61	47.0%	37.6%
	550°C	303	1.03	0.188	18.3%	0.64	1.62	47.5%	39.6%
	700°C	310	1.04	0.193	18.6%	0.69	1.66	50.6%	40.0%
Marques et al. 2013	All	1204	1.12	0.148	13.2%	0.74	1.51	69.9%	59.5%
	350°C	293	1.08	0.129	11.9%	0.81	1.40	65.2%	53.9%
	450°C	298	1.12	0.147	13.1%	0.82	1.44	70.8%	59.4%
	550°C	303	1.12	0.150	13.4%	0.79	1.51	71.6%	61.1%
	700°C	310	1.14	0.158	13.9%	0.74	1.48	71.9%	63.2%

As initially pointed out, the modified General Method emerges as the most suitable method of the three given the low percentages of unsafe values (“%Unsafe” column). DIN 18800-2 produces the higher scatter among the three, given the highest standard deviation and coefficient of variance, as well as the lowest minimum and the highest maximum values. The highest percentage of unsafe values belongs to Marques *et al.*’s adapted proposal with close to 60% of data points above an arbitrary 5% safety margin (“%(>1.05)” column). *Table 2* shows a slight increase in the mean value (“Mean” column) for higher temperatures in all three approaches. This observation points towards the modifications producing increasingly unsafe predictions of stability for higher temperatures.

5 CONCLUSIONS

This work describes a numerical and parametric study on the adaptation to fire of existing approaches for the out-of-plane stability of web-tapered steel beams. Given the scarcity of normative guidelines, analytical modifications to fire of three approaches developed for normal temperature (General Method [2], DIN 18800-2 [3] and Marques *et al.* [4]) are analysed.

The adaptation of the abovementioned methodologies to fire is done by accounting for the reduction with the temperature in yield strength and stiffness of steel with the respective reduction factors for the yield strength $k_{y,\theta}$ and for the Young’s Modulus $k_{E,\theta}$.

The majority of data points from Marques *et al.*’s proposal were deemed unsafe, which is understandable since it was fine-tuned to closely fit numerical data at normal temperature. Regarding DIN 18800-2’s methodology, considering the high scatter of results (ranging from 30% safe to 40-50% unsafe values), it is seen as unreliable for the out-of-plane stability check of tapered beams in fire. Finally, despite providing very conservative results, out of the three approaches, it is recommended the use of the modified General Method for the safety-check of a tapered member in fire.

To conclude, this work reinforces the need of deeper investigation on the stability of tapered beams at elevated temperatures and evidence points towards the adaptation to fire of existing methods at

normal temperature not being enough to account for all the nuances of the structural behaviour of steel at elevated temperatures and to produce accurate predictions of resistance by themselves.

ACKNOWLEDGEMENTS

This research work was partially funded by the Portuguese Government through the FCT (Foundation for Science and Technology) under the Post-doc grant SFRH/BPD/114816/2016, awarded to the first author and the PhD grant SFRH/BD/114838/2016 awarded to the second author.

BIBLIOGRAPHY

1. EN1993-1-2: Design of steel structures – Part 1-2 General rules - Structural fire design. 2005.
2. EN1993-1-1: Design of steel structures – Part 1-1 General rules and rules for buildings. 2005.
3. DIN 18800-2, Steel structures - Part 2: Stability - Buckling of bars and skeletal structures.2008.
4. Marques L, Simões da Silva L, Greiner R, Rebelo C, Taras A. Development of a consistent design procedure for lateral-torsional buckling of tapered beams. *J Constr Steel Res* 2013;89:213–35.
5. Couto C, Vila Real P, Ferreira J, Lopes N. Numerical validation of the General Method for structural fire design of web tapered beams. Eurosteel 2014, 2014.
6. Couto C, Duarte P, Vila Real P, Lopes N. Verification of web tapered beam-columns in case of fire using the general method of Eurocode 3. *IFireSS 2015*, Coimbra: 2015, p. 79–86.
7. TaperSteel, Stability design of non-uniform steel members PTDC/ECM-EST/1970/2012.
8. Braham M, Hanikenne D. Lateral buckling of web tapered beams: an original design method confronted with a computer simulation. *J Constr Steel Res* 1993;27:23–36.
9. Franssen, J., Gernay, T. Modeling structures in fire with SAFIR ® : Theoretical background and capabilities. *Journal of Structural Fire Engineering* 2017;8:300-23.
10. Couto C, Vila Real P, Lopes N, Zhao B. Resistance of steel cross-sections with local buckling at elevated temperatures. *J Constr Steel Res* 2015;109:101-14.
11. Couto C, Vila Real P, Lopes N, Zhao B. Effective width method to account for the local buckling of steel thin plates at elevated temperatures. *Thin-Walled Struct* 2014;84:134–49.
12. Prachar M, Hricak J, Jandera M, Wald F, Zhao B. Experiments of Class 4 open section beams at elevated temperature. *Thin-Walled Struct* 2016;98:2-18.
13. Couto C, Vila Real P, Lopes N, Zhao B. Numerical investigation of the lateral torsional buckling of beams with slender cross-sections for the case of fire. *Eng Struct* 2016;106:410–21.
14. CEA. CAST 3M is a research FEM environment; its development is sponsored by the French Atomic Energy Commission <<http://www-cast3m.cea.fr/>>. 2015.
15. Couto C, Vila Real P, Lopes N. RUBY - an interface software for running a buckling analysis of SAFIR models using Cast3M 2013.
16. CEN. EN 1993-1-5, Eurocode 3: Design of steel structures - Part 1-5: General rules - Plated structural elements. 2006.
17. CEN. EN 1090-2: Execution of steel structures and aluminium structures - Part 2 : Technical requirements for steel structures. 2008.
18. Maia É, Couto C, Vila Real P, Lopes N. Critical temperatures of class 4 cross-sections. *J Constr Steel Res* 2016;121:370–82.

SHEAR ANALYSIS OF CLIPPED WEBS IN FIRE AND AMBIENT CONDITIONS

Veronica A. Boyce¹, Maria E. Moreyra Garlock²

ABSTRACT

The webs of deep steel beams (plate girders) are subject to a large amount of shear loading near the supports. Understanding how these plates buckle and yield under this shear load is critical for safe and efficient design, both at ambient and elevated temperatures. Further, deep steel girder bridges have exhibited shear buckling behaviour in recent fire events on bridges. The objective of this paper is to examine web plate modifications to enhance shear performance at ambient and elevated temperatures. In particular, “clipping” the corners on the compression field diagonal is examined. Finite element models, which have been validated with experimental data, are used to examine the behaviour of plates with various clipped web designs. The following parameters are studied: (1) temperature – ambient and 700°C, (2) varying thicknesses to maintain constant volume given the clips, and (3) two depths of clipping. Observations are based on elastic shear buckling strength (V_{cr}), ultimate shear postbuckling strength (V_u), and Von Mises stresses at V_u . Results reveal that clipping the corners of the compression field increases V_{cr} significantly, but V_u less significantly. Further, clipping the web plate corners had a larger effect on the 700°C plates than on the ambient temperature plates.

Keywords: Structures, fire, bridge, finite element modelling, web shear buckling, postbuckling

1 INTRODUCTION

Many bridges and buildings are designed with deep steel beams (e.g. plate girders) that have deep and thin webs, and are susceptible to buckling under shear load. It has been demonstrated in the past that web plates that elastically buckle due to shear load (V_{cr}) often still possess a significant amount of postbuckling shear strength (V_u). This phenomenon is currently considered in the design of plate girders, though the design equations are based on the tensile response of the plate (tension field action, TFA). However, recent research has shown that the fundamental assumptions upon which TFA are based do not represent the true mechanics behind web shear buckling [1, 2]. This buckling is a concern both at ambient and elevated temperatures, as it has been shown in recent years that a primary cause of steel bridge failure during fire events is shear buckling. *Fig. 1* shows a picture from the 2007 MacArthur Maze fire, where the shear buckling occurring in the girders is clearly visible. Due to the importance of this phenomenon, more studies and analyses of deep steel beams and their behaviour under buckling are required.

¹ Master of Science Candidate. Department of Civil and Environmental Engineering, Princeton University, USA.
e-mail: vboyce@princeton.edu

² Professor. Department of Civil and Environmental Engineering, Princeton University, USA.
e-mail: mgarlock@princeton.edu



Fig. 1. MacArthur Maze Fire [3]

Previous research has been conducted on thin web plates subjected to shear. Ambient temperature shear studies have been conducted for some time, and much of that research has been incorporated into design codes, but elevated studies are less abundant and more recent. Recent publications related to web shear buckling at elevated temperatures have focused on varying topics. Some have created computational and numerical models which predict shear strength at elevated temperatures [4, 5, 6, 7], while others have addressed the mechanisms behind buckling [8], and some have conducted physical experiments [9, 10, 11]. In addition, component-based methods have been used to better understand both web and flange buckling [12, 13], and fire hazard and thermal analysis have been used to predict the reduction in the critical buckling stress during fire [14]. This paper is unique because the focus is on understanding how the shape of the plate affects the shear capacity of these deep steel beams at both ambient and elevated temperatures; additionally, the paper aims to provide potential solutions for improving the design of these plates in fire scenarios.

Fig. 2(a) represents a plate under pure shear loading conditions, where a typical web plate experiences a tension field running parallel to corners 1-3 and a compression field running parallel to corners 2-4 during the elastic phase of loading. Tension field action assumes that after buckling, the main source of postbuckling shear strength is the development of tensile stresses in the tension field diagonal. However, previous studies by the 2nd author have found that after buckling, the compression field diagonal continues to increase in magnitude, which is contrary to current design equation assumptions [2, 15, 16]. In addition, the same studies found that at ambient temperature, cutting the corners of the compression field resulted in a significant increase in critical elastic shear buckling strength.

The objective of this paper is to examine the behaviour and mechanics of steel plates, with ‘clipped webs’, under shear loading. Clipped webs are defined as shown in Fig. 2(b). This paper expands the study of [17] by examining the effects of more parameters. The study uses finite element studies, with models that have been validated by experimental results of full plates.

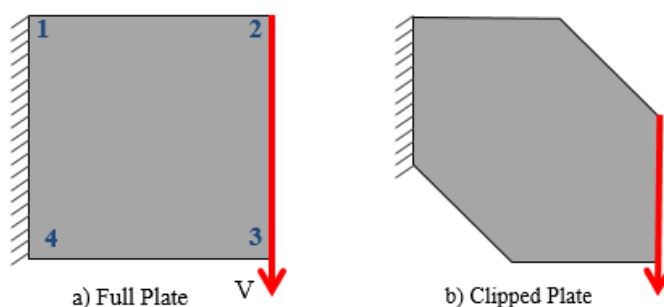


Fig. 2. Typical plate configuration

2 FINITE ELEMENT MODEL

The finite element modelling software used in this analysis is ABAQUS. A validation study was performed by the 2nd author by comparison of ABAQUS predictions of critical elastic shear buckling (henceforth referred to as elastic shear buckling, V_{cr}) and ultimate shear postbuckling, V_u , for several plate designs at varying temperatures, to experimental data from previously published papers [4]. The study found that the results from the ABAQUS modelling matched well with the experimental results, and that this analytical approach was an accurate way to predict shear strength.

The current study modelled a plate as an S4 shell element (doubly curved, general-purpose, finite membrane strains). The plate dimensions are based on a typical steel girder with a 27.4-meter span (90-foot). The plate depth, D , is 1.473 m and the thickness, t , is 11 mm, resulting in a slenderness ratio (D/t) equal to 134. The a/D ratio of the plate was assumed to equal 1.0. The boundary conditions were simply supported and were based on the optimal boundary conditions found in the validation study. The steel material was assumed to have a nominal yield stress of 345 MPa (50 ksi). Eurocode temperature dependent models were used in order to determine the material characteristics at each temperature (reduction factors for yield stress, proportional limit stress, and Young's modulus), and strain hardening was permitted for temperatures under 400°C [18].

A shear load was applied along one side of the plate, and the elastic shear buckling strength was determined using eigenvalue analysis. Then, a Riks solver was implemented, which increased the shear load incrementally to obtain the ultimate shear postbuckling strength of the plate, defined as the peak in the load-deformation plot. A schematic of the model and boundary conditions used are shown in *Fig. 3*.

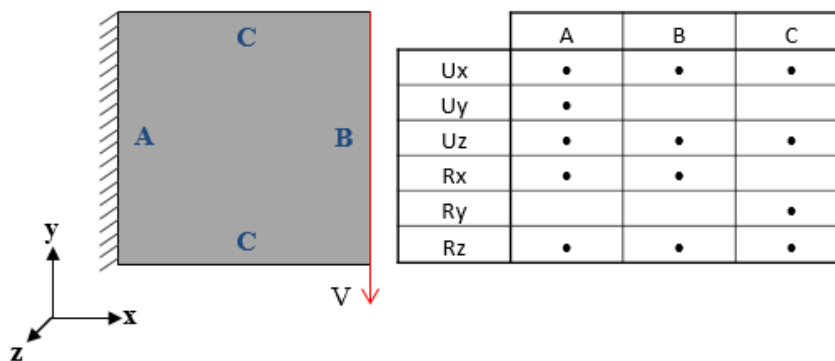


Fig. 3. Loading and boundary conditions on typical plate

3 PARAMETERS OF STUDY AND ANALYSIS RESULTS

3.1 Parameters

Three parameters were varied throughout this study: temperature, cut depth, and plate thickness. *Table 1* presents a matrix of nomenclature and model runs completed, with explanations of each parameter following.

Table 1. Model Nomenclature

Temperature (°C)	Cut Depth	Thickness (mm)	Model Name
20	0	11.0	A-0
	24	11.0 11.7	A-24 A-24-t
	40	11.0 13.2	A-40 A-40-t
700	0	11.0	T-0
	24	11.0 11.7	T-24 T-24-t
	40	11.0 13.2	T-40 T-40-t

3.1.1 Ambient vs. Elevated

As explained in the introduction, web shear buckling is an important phenomenon at both ambient and elevated temperatures. Therefore, each analysis was conducted at two temperatures: ambient (“A”), equal to 20°C, and elevated (“T”), which was set at 700°C. This value of 700°C was based on [19], where it was determined that 700°C was close to the maximum average for steel girders in fire based on experiments and CFD modelling. Examining these plates at both ambient and elevated temperatures permits an understanding of how these deep steel beams behave under different temperature conditions, and therefore the results could be useful for general design, but also for fire engineering.

3.1.2 Clipped Web Depth

Three different versions of the plate geometry are examined, as shown in *Fig. 4*, each with a different cut depth “C” representing a percentage of the full depth “D”. The numbers 24 and 40 represent C-values equal to 0.24D and 0.40D, respectively. These values were chosen as it was previously determined that the 40D plate resulted in high increases in elastic shear strength [17], and examining another plate cut in-between the full plate and 40D plate assists in understanding how the change in strength progresses with increasing cuts.

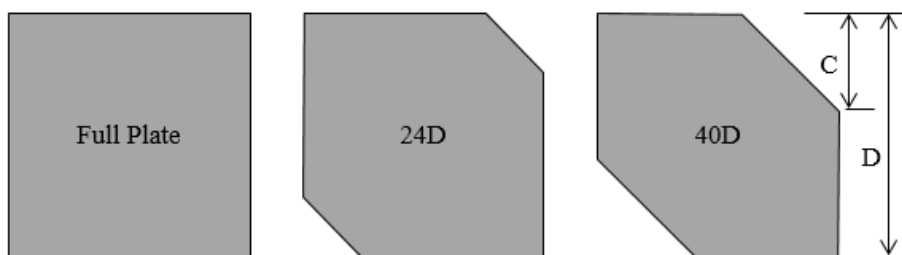


Fig. 4. Clipped web depth parameters studied

3.1.3 Constant Volume

Another parameter studied was based on keeping the volume of steel in the clipped designs equal to the full plate volume; thus the plate thickness was increased to examine potential increase in strength. The full plate remained at 11 mm thickness, while the thickness for the 24D plate increased to 11.7 mm and the 40D plate to 13.2 mm. This parameter allowed for a comparison between constant thickness and constant volume designs.

3.2 Results

The finite element modelling results are presented in *Table 2*. The left-most column of the table lists the cut depth, which varies between the full plate (0) and the 40D plate (40). Then, the results for the ambient models are presented, first with the constant thickness of 11 mm, and then with the constant volume. Within each of these are the elastic shear buckling strength (V_{cr}) and the ultimate shear postbuckling strength (V_u). The same data is then presented for the elevated models. A discussion of these results is presented in the next section.

Table 2. Elastic (V_{cr}) and Ultimate (V_u) Shear Buckling Results

Cut	Ambient				700°C			
	Thickness = 11 mm		Constant Volume		Thickness = 11 mm		Constant Volume	
	V_{cr} (kN)	V_u (kN)	V_{cr} (kN)	V_u (kN)	V_{cr} (kN)	V_u (kN)	V_{cr} (kN)	V_u (kN)
0	1532	2641	1532	2641	119	490	119	490
24	2212	2542	2661	2762	287	495	346	534
40	3734	2563	6445	3248	485	466	838	579

Note: strikethrough represents $V_{cr} > V_u$

In addition to the values for elastic shear buckling and ultimate shear postbuckling strength, the stress distribution within the plate is of interest. *Fig. 5* presents the Von Mises stresses at V_u on the front and back of the plate for each of the ambient models with constant thickness. The contour scale goes from 0 to 3.449 MPa, with the darker colour representing the highest stress, and the colourless (white) areas representing locations where the plate has reached the yield surface. The elevated temperature models are not presented, as the entire plate surface (both top and bottom) reached yield for all cases. The black dashed lines show where the 40D cut is made, so that there can be a more direct comparison of the stress contours. These results are discussed in the next section.

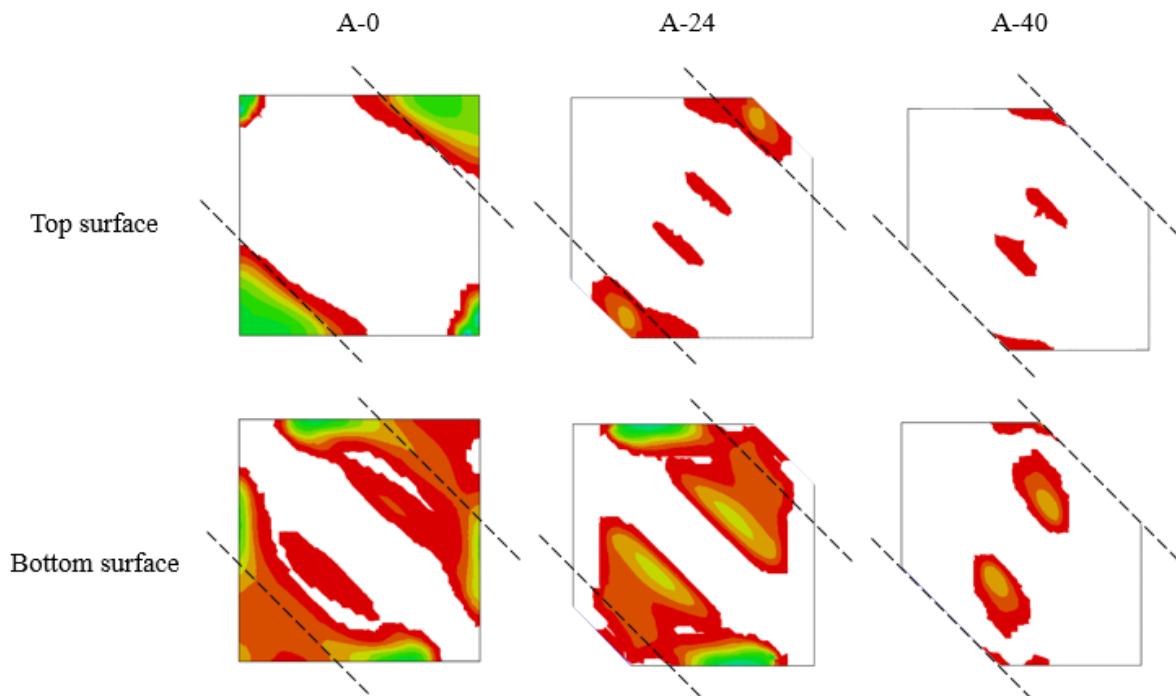


Fig. 5. Von Mises Stresses at top and bottom face of plate at ambient temperature. Dashed lines represent the 40% cut line.

4 DISCUSSION OF RESULTS

4.1 Effect of Temperature

As can be seen in *Table 2*, the elastic shear buckling, V_{cr} , and ultimate shear postbuckling, V_u , values for the ambient model are much higher than the results obtained for the elevated model. This is to be expected, as the strength of steel decreases significantly as temperature increases. Using values from *Table 2*, *Table 3* provides the ratios of V_{cr} and V_u of each plate normalized by the strength of the full plate (A-0 or T-0), thus indicating whether the cut increased or decreased the shear strength of the plate, and by what percentage.

As can be seen in *Table 3*, both the ambient and 700°C models experience an increase in V_{cr} with the cuts, but there is a much larger percentage increase for the 700°C model. This increase may be due to the fact that the 700°C model has little strength to begin with, so cuts have a larger effect percentage-wise. While there was a large increase in V_{cr} as the plates were cut, V_u was not as affected, either at ambient or 700°C temperatures. It will be shown in Sect. 4.3 that the increase in V_u at constant volume is mainly due to the increase in plate thickness.

Table 3. Elastic and Ultimate Shear Result Comparison

Cut	Ambient				700°C			
	Thickness = 11 mm		Constant Volume		Thickness = 11 mm		Constant Volume	
	V_{cr} / V_{cr}^*	V_u / V_u^*						
0*	1.00	1.00	1.00	1.00	1.00	1.00	1.00	1.00
24	1.44	0.96	1.74	1.05	2.41	1.01	2.90	1.09
40	2.44	0.97	4.21	1.23	4.07	0.95	7.03	1.18

Note: strikethrough represents $V_{cr} > V_u$;
* = baseline = A-0 or T-0 model

4.2 Effect of Clipped Web

The elastic shear buckling strength, V_{cr} , increased with increasing cuts in the compression field (see *Table 3*). The ambient model shows an increase of 1.44 for the 24D model and 2.44 for the 40D model. This is a bit misleading, however, as the 40D model will not buckle since it will fail by yielding first. The 700°C temperature model shows an even higher increase in elastic shear buckling strength, as explained in Section 4.1. Again, the 40D model is going to reach yield failure before it elastically buckles.

The clipping of the web had less of an effect on V_u than it did on V_{cr} . As can be seen in *Table 3*, the ratios of V_u increase as the cut increases for the constant volume models, but decreases slightly for most of the $t = 11$ mm models. *Fig. 5* shows that the areas that were eliminated through the plate cuts do not reach yield in the full plate model. This could be a clue as to why V_u remains mostly unchanged. Understanding this failure mechanism is an area of future study.

4.3 Effect of Volume

The effect of increasing the thickness to ensure a plate of constant volume is evaluated by comparing V_{cr} and V_u for constant thickness ($t = 11$ mm) to constant volume models that have larger thickness. *Table 4* presents a comparison of these two thickness models. The first two columns present the change in thickness, which was determined by dividing the new plate thickness by 11 mm. The other columns present the increase in V_{cr} and V_u normalized by the relevant constant thickness model (i.e., the relevant model with $t = 11$ mm). For example, $[V_{cr}(A-24-t)]/[V_{cr}(A-24)] = 346/287$ (from *Table 2*) = 1.2.

As can be seen in the *Table 4*, there is a consistent increase in V_{cr} and V_u when the thickness of the plate is increased. It is seen that percentage increases in V_u , at both ambient and 700°C temperatures, are similar to percentage increases in thickness. These results suggest that increases in V_u are proportionally related to the thickness of the plate, thus indicating that plate yielding is playing an important role for reaching V_u .

Table 4. Comparison of constant thickness and constant volume

Cut	t increase (mm)	t increase / t _{11 mm}	Ambient		700°C	
			V_{cr} / V_{cr}^{**}	V_u / V_u^{**}	V_{cr} / V_{cr}^{**}	V_u / V_u^{**}
24	11.7	1.06	1.20	1.09	1.20	1.08
40	13.2	1.20	1.73	1.27	1.73	1.24

Note: ** = baseline = relevant model with $t = 11$ mm.
E.g., $V_{cr}(A-24-t)/V_{cr}(A-24)$, $V_u(T-40-t)/V_u(T-40)$, etc.

5 CONCLUSIONS

Understanding the mechanics of web shear buckling is critical for deep steel beams at both ambient and 700°C temperatures. This paper examined modifications to the web in an effort to enhance its shear performance – in particular, the web corners on the compression field diagonal were “clipped” in an attempt to delay critical elastic shear buckling (V_{cr}) and increase ultimate shear postbuckling capacity (V_u). Both V_{cr} and V_u were examined for the parameters studied: (1) temperature – ambient and 700°C, (2) varying thicknesses to maintain constant volume given the clips, and (3) two depths of clipping. The results and conclusions of this study are summarized as follows:

- Clipping the web plate corners had a larger effect on the 700°C plates than on the ambient temperature plates.
- There was a large increase in V_{cr} as the plate corners were clipped, however V_u was not as affected (if at all).
- V_{cr} increased with increasing cut depths, however when the cut was 40% of the plate depth, the plate reached yield failure before it elastically buckled.
- Von Mises stress distributions on the full plate (no clipped corners) showed that the areas in the corners of the compression field (areas that were cut in the clipped models) do not reach yield. This observation may explain the ineffectiveness of clipping corners on V_u .
- For the plates with increased thickness, percentage increases in V_u , at both ambient and 700°C temperatures, are similar to percentage increases in thickness. These results suggest that increases in V_u are proportionally related to the thickness of the plate, thus indicating that plate yielding is playing an important role for reaching V_u .

Overall, this study shows that adjusting the plate geometry of a typical deep steel beam can have a significant effect on V_{cr} ; however, V_u is less affected. Future work by the authors will focus on understanding the failure mechanism of these plates, examining more cut parameters, and determining the relationship between the plate and flange in deep steel beams.

ACKNOWLEDGEMENTS

The authors acknowledge the contributions of Dr. Jonathan Glassman and Mr. José Alós-Moya, whose work with web shear buckling formed the foundation of this work.

REFERENCES

1. Yoo, C. H. and Lee, S. C. (2006). "Mechanics of Web Panel Postbuckling Behavior in Shear," *Journal of Structural Engineering*, vol. 132, no. 10, pp. 1580-1589.
2. Glassman, J. and Garlock, M.E.M. (2016). "A Compression Model for Ultimate Postbuckling Shear Strength," *Thin-Walled Structures*, vol. 102, pp. 258–272.
3. *Amazing: The Rebuilding of the MacArthur Maze*. (2008). [DVD] Directed by D. Brown. Brisbane, California: David L. Brown Productions.
4. Garlock, M. and Glassman, J. (2014). "Elevated temperature evaluation of an existing steel web shear buckling analytical model," *Journal of Constructional Steel Research*, vol. 101, pp.395-406.
5. Vimonsatit, V., Tan, K.H., and Ting, S.K. (2007). "Shear strength of plate girder web panel at elevated temperature," *Journal of Constructional Steel Research*, vol. 63, pp. 1442-1451.
6. Glassman, J.D., and Garlock, M.E.M. (2016). "Modeling parameters for predicting the postbuckling shear strength of steel plate girders," *Journal of Constructional Steel Research*, vol. 121, pp. 136-143.
7. Reis, A., Lopes, N., Vila Real, P., and Real, E. (2017). "Stainless steel plate girders subjected to shear buckling at normal and elevated temperatures," *Fire Technology*, vol. 53, no. 2, pp. 815-843.
8. Glassman, J.D., Garlock, M.E.M. (2013). "Shear buckling behavior of steel plate girders at elevated temperatures," *Proceedings of the Structures Congress 2013*, Pittsburgh, Pennsylvania, May 2-4.
9. Aziz, E.M. (2015). *Response of fire exposed steel bridge girders*. PhD. Michigan State University.
10. Aziz, E.M., Kodur, V.K., Glassman, J.D., and Garlock, M.E.M. (2015). "Behavior of steel bridge girders under fire conditions," *Journal of Constructional Steel Research*, vol. 106, pp. 11-22.
11. Vimonsatit, V., Tan, K.H., and Qian, Z.H. (2007). "Testing of plate girder web panel loaded in shear at elevated temperature," *Journal of Structural Engineering*, vol. 133, no. 6, pp. 815-824.
12. Guan, Q., Huang, S., and Burgess, I. (2017). "The behaviour and effects of beam-end buckling in fire using a component-based method," *Engineering Structures*, vol. 139, pp. 15-30.
13. Guan, Q., Huang, S., and Burgess, I. (2016). "Component-based model of buckling panels of steel beams at elevated temperatures," *Journal of Constructional Steel Research*, vol. 118, pp. 91-104.
14. Wang, Y., and Liu, Muyu. (2016). "Buckling Instability Behavior of Steel Bridge under Fire Hazard," *Mathematical Problems in Engineering*, vol. 2016, pp. 11.
15. Garlock, M.E.M, Quiel, S.E., Alós-Moya, J., Wang, P., Glassman, J. (2017). "Postbuckling Mechanics of a Square Slender Steel Plate in Pure Shear," Submitted to AISCs *Engineering Journal*.
16. Garlock, M.E.M., Quiel, S.E, Alós-Moya, J., Glassman, J. (2017). "Postbuckling mechanics of square slender steel plates in pure shear: Examining the role of second order effects", *Proceedings of the Annual Stability Conference - Structural Stability Research Council*, San Antonio, Texas, March 21-24
17. Garlock, M.E.M., Alós-Moya, J., Paya Zaforteza, I. (2017). "Alternative designs to improve behavior of thin steel plates in pure shear under fire," *Proceedings of the 2nd International Fire Safety Symposium (IFireSS)*, Naples, Italy, June 7-9.
18. European Committee for Standardization (CEN), "Eurocode 1: Actions on Structures - Part 1-2: General Actions - Actions on Structures Exposed to Fire," CEN, Brussels, 2002.
19. Wang, P., Garlock, M.E.M. (2017). "Effects of Composite Slab on Shear Strength of Steel Plate Girders," *Proceeding of the 8th International Conference on Composite Construction in Steel and Concrete*, Jackson, Wyoming, July 30-August 2.

EFFECTIVENESS OF STIFFENERS ON THE SHEAR CAPACITY OF STEEL WEB PLATES AT AMBIENT AND ELEVATED TEMPERATURES

Veronica A. Boyce¹, Jonathan Glassman², Maria E. Moreyra Garlock³

ABSTRACT

The webs of deep steel beams tend to be slender plates, which are highly susceptible to buckling under shear load; thus, transverse stiffeners are used to add stability. Tension field action (TFA) theory is the basis for the design of these slender web plates for shear load, but the assumptions behind TFA theory have been questioned in recent years. As a result, an understanding of the role stiffeners play in resisting shear load for thin plates is required. The objective of this paper is to examine the effectiveness of stiffeners for enhancing the shear capacity of slender plates, at both ambient and elevated temperatures. Finite element models, which have been validated with experimental data, are used to examine four plate designs: no stiffener (NS), vertical stiffener (VS), diagonal stiffener in the tension path (DT), and diagonal stiffener in the compression path (DC). Observations are based on critical elastic shear buckling strength, ultimate shear postbuckling strength, and axial force in the stiffeners. Results reveal that the use of stiffeners, particularly DC stiffeners, could be valuable for increasing shear resistance at ambient, but are unlikely to be effective at elevated temperatures. Axial force in each model was a small portion of the shear load applied, leading to the conclusion that the main role of the stiffener is to provide lateral restraint, and not to carry the vertical load as assumed in TFA.

Keywords: Plate girder, web shear buckling, stiffener, elevated temperature, postbuckling

1 INTRODUCTION & BACKGROUND

Deep steel girders, such as those found in bridges, typically have webs composed of thin steel plates. The slenderness of these plates (i.e., depth-to-thickness ratio) is typically large, and therefore the plates are highly susceptible to buckling. This is particularly true at elevated temperatures, which occur during a bridge fire. Under pure shear loading conditions, before elastic buckling, a typical web plate experiences a tension field at a 45 degree angle from the vertical load, and a compression field running perpendicular to the tension field. Transverse stiffeners are currently used to increase the stability of these plates. After the plate reaches the critical elastic shear buckling load, V_{cr} , it continues to carry load until it reaches the ultimate shear postbuckling load, V_u . Tension field action (TFA), which is the basis of many design equations used to predict V_u , assumes that these vertical stiffeners act like a post of a Pratt truss in order to satisfy equilibrium. However, recent and prior research has begun to question the role that these stiffeners play in TFA, both at ambient and elevated temperatures [1, 2, 3, 4]. While the current US design specification for steel buildings recognizes that the vertical stiffener does not carry the full vertical component of the tension field force, it is still not known how much force the vertical stiffener

¹ Master of Science Candidate. Department of Civil and Environmental Engineering, Princeton University, Princeton, NJ, USA.
e-mail: boyce.veronica@gmail.com

² Senior Engineer. Exponent, Inc., California, USA.
e-mail: glassman.jonathan@gmail.com

³ Professor. Department of Civil and Environmental Engineering, Princeton University, Princeton, NJ, USA.
e-mail: mgarlock@princeton.edu

carries, if any. It is also not known how the forces in the tension field are resolved, if it is not the vertical stiffener that contributes to equilibrium.

The objective of this paper is to examine the effectiveness of stiffeners for enhancing the shear capacity of slender plates, both at ambient and elevated temperatures. Specific focus is on (1) examining different stiffener modifications to increase the shear capacity of the plate, (2) determining the ability of the stiffener to provide lateral restraint, and (3) examining how the stiffener contributes to TFA and V_u .

Recent research has included an extensive literature review of the proposed models for the shear resistance of transversely stiffened I-girders at *ambient* temperature, which provides valuable information about the most promising models for understanding stiffeners [5]. Additionally, previous researchers have investigated diagonal stiffeners in the context of bridges [6] and buildings [7]. However, a conclusive opinion of the contribution of stiffeners to shear strength has not been made, and studies regarding the varying stiffener designs have not been completed in the context of fire, nor with a close examination of the stresses in the web and stiffener.

2 FINITE ELEMENT MODELS

This study proposes four different stiffener configurations in order to explore the effectiveness of stiffeners for resisting shear in thin steel plates. The plate designs are shown in *Fig. 1* and are as follows: (a) **no stiffener (NS)**, (b) **vertical stiffener (VS)**, (c) **diagonal stiffener along the tension path (DT)**, and (d) **diagonal stiffener along the compression path (DC)**. The dimensions of these web plates were based on a design example from the National Steel Bridge Alliance (NBSA) for a three-span continuous straight composite I-girder [8]. The only variation in geometry is the plate thickness, which was modelled at both 10 mm and 14 mm. This was done in order to better understand the relationship between the plate thickness and the stiffener's contribution to shear strength.

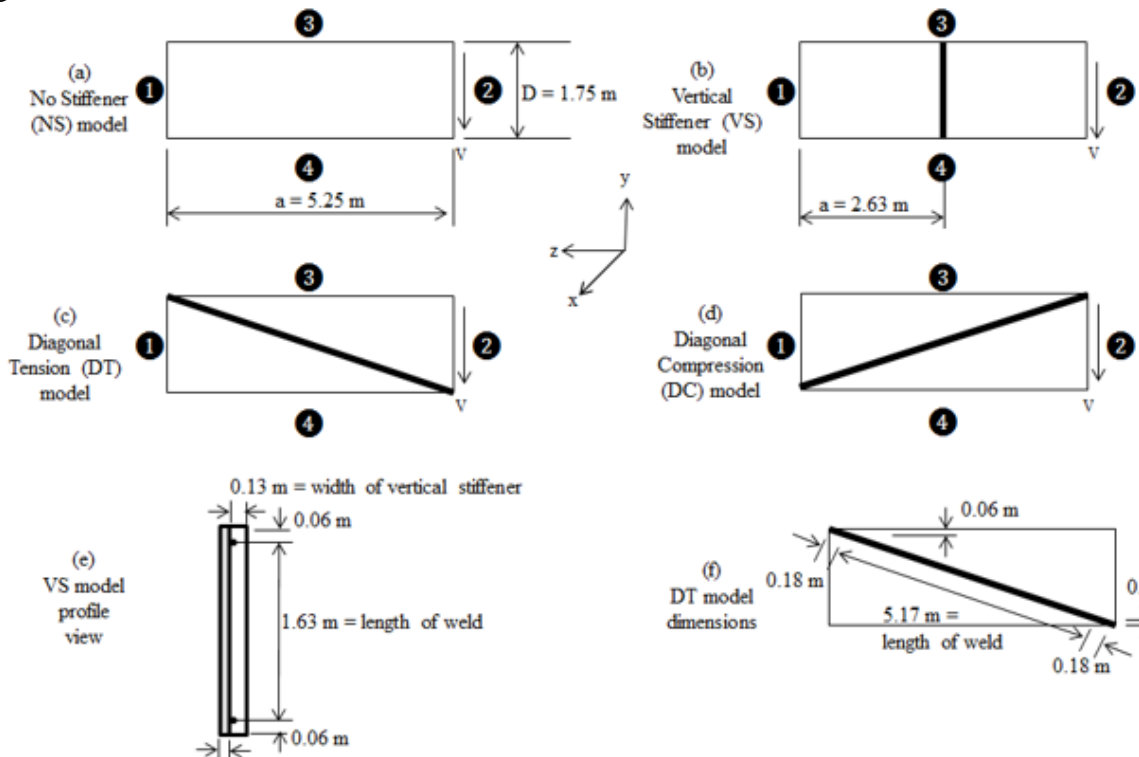


Fig. 1. Geometry of the simply supported web plates studied in this paper. Refer to table 2 for boundary conditions [9].

The proposed designs were modelled using the finite element software ABAQUS. A validation study was completed by the 2nd and 3rd authors by comparison of ABAQUS predictions of critical elastic shear buckling (V_{cr}) and ultimate shear postbuckling (V_u) to experimental data from previously published papers [8]. The study found that the results from the ABAQUS modelling matched the experimental results, and so validated the use of these analytical models.

The four proposed models each used the same boundary conditions in order to achieve pure shear behaviour, as presented in *Table 1*. Vertical transverse stiffeners are assumed to be at sides ① and ② and are idealized as simple supports based on previous research [11, 12, 13]. Sides ③ and ④ are located at the web-flange juncture and have also been idealized as simply supported, as this paper presents a relative study between stiffener configurations. These boundary conditions still allow for postbuckling behaviour to be observed [14].

Table 1. Simply supported boundary conditions corresponding to the web plates in Fig. 1. A “●” indicates a restrained degree of freedom [1].

Side	Translation			Rotation		
	U_x	U_y	U_z	UR_x	UR_y	UR_z
①	●	●	●	●		●
②	●		●	●		●
③	●		●	●	●	
④	●		●	●	●	
Stiffener	●		●	●	●	

In addition, to examine the stiffener’s role in providing out-of-plane lateral restraint, the VS, DT, and DC models were also created without a physical stiffener. Instead, boundary conditions were placed along the location where the stiffener would be placed, which are modelled by restraining only U_x for each model. These three model types were called the **BC** (boundary condition) models, and are henceforth referred to as VS-BC, DT-BC, and DC-BC, respectively.

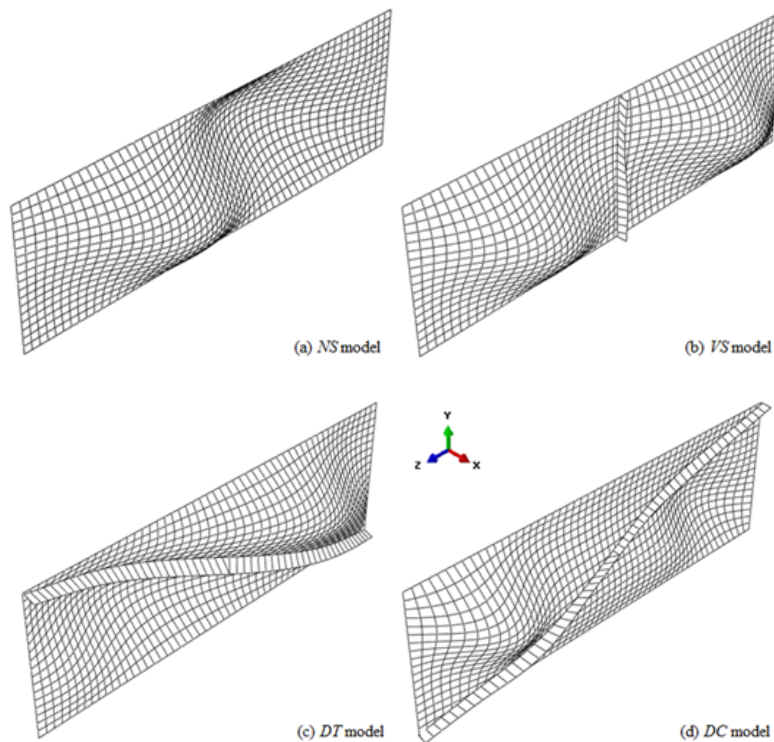


Fig. 2. Mesh densities lowest buckling mode shapes at 20°C for (a) NS, (b) VS, (c) DT, and (d) DC models.

The ambient temperature (20°C) material properties were based on the same NSBA design example [8]. Young’s modulus, E , and yield stress, σ_y , were $2e11 \text{ N/m}^2$ and 345 MPa, respectively. The Eurocode elevated temperature material model was assumed, which employs temperature-dependent reduction factors to compute E and σ_y for temperatures exceeding 20°C [15]. Strain hardening was permitted for temperatures less than 400°C [15].

A mesh convergence study was conducted using an eigenvalue extraction analysis at 20°C. Fig. 2 shows the selected mesh densities and lowest buckling mode shapes (eigenmodes) for the four FE models at 20°C. The mesh densities for all four models were based on a mesh convergence study for the NS model since the remaining models were created by adding stiffeners to the NS model.

3 BUCKLING LOADS

The critical elastic shear buckling load, V_{cr} , and the ultimate shear postbuckling load, V_u , are presented in Table 2. The critical elastic shear buckling load is obtained through eigenvalue analysis, where the lowest positive eigenvalue is determined to be V_{cr} . The ultimate shear postbuckling load is determined through Riks analysis, where V_u is the peak in the load-deformation plot. Both the elastic buckling shear load and ultimate postbuckling shear load are presented for the two temperatures and two thicknesses examined. Each model presents the load for the model with the stiffener explicitly modelled (VS, DT, DC), the load for the model which uses boundary conditions to represent a stiffener (VS-BC, DT-BC, DC-BC), and a ratio which compares the two values. This ratio was found by dividing the BC models by the stiffener models.

Table 2. Elastic shear buckling (V_{cr}) and ultimate shear postbuckling (V_u) results in kN. Comparison of BC stiffener models (lateral restraint only) to models with stiffener explicitly modelled.

	Temp.	t_w (mm)	Vertical Stiffener			Tension Diag. Stiffener			Compression Diag. Stiffener		
			VS	VS-BC	Ratio: VS-BC/VS	DT	DT-BC	Ratio: DT-BC/DT	DC	DC-BC	Ratio: DC-BC/DC
V_{cr}	20°C	10	758	756	1.00	1047	1195	1.14	1459	1616	1.11
		14	2074	2073	1.00	2532	3236	1.28	3714	4356	1.17
	700°C	10	98	98	1.00	136	155	1.14	190	210	1.11
		14	270	270	1.00	329	421	1.28	483	566	1.17
V_u	20°C	10	2191	2184	1.00	1735	1971	1.14	2556	2968	1.16
		14	3479	3479	1.00	3022	3688	1.22	4211	4566	1.08
	700°C	10	445	456	1.02	345	394	1.14	336	478	1.42
		14	593	692	1.17	536	414	0.77	480	767	1.60

3.1 Effect of Thickness and Temperature on V_{cr} and V_u

As expected, the models with a higher thickness, 14 mm, have larger shear capacities than the thinner 10 mm models. Temperature has a similar effect, where the 20°C models exhibit higher strength than the 700°C model, due to the decrease in Young’s modulus and yield stress values at elevated temperatures. For the V_{cr} values, the decrease in strength for the 700°C models is directly due to the decrease in E . The value of E for the 700°C model is provided by the Eurocode model, and is 0.13 times the ambient model. It is seen in Table 2 that this same value of 0.13 could be applied to the 20°C results and the 700°C results would be obtained (e.g. VS at 20°C for 14 mm is 2074. $2074 \cdot 0.13 = 270$, which is the result for VS at 700°C for 14 mm). The value for V_u is subject to both geometric and material nonlinearities and is thus not only dependent on E . Therefore, the same trend for V_{cr} is not seen for V_u .

3.2 Critical Elastic Shear Buckling Strength, V_{cr}

The data presented in *Table 2* shows a clear trend for V_{cr} . The VS model has the lowest V_{cr} for both thicknesses and temperatures. The DT model is the next strongest in each case, with the DC model exhibiting a significantly higher capacity for shear load in each scenario. The V_{cr} values for the DC model ranged from 1.79 to 1.93 times greater than those of the VS model. This large increase is logical, as the DC model is stiffening the plate along the diagonal compression field, and therefore is directly stiffening the portion of the plate at highest risk of buckling. The V_{cr} values for the DT model ranged from 1.22 to 1.39 times greater than those of the VS model. Again, this increase is logical as this stiffener is affecting a much larger portion of the plate than the VS model stiffener. However, since it is along the tension diagonal, it won't have as large an effect as the DC model, which has a stiffener across the part of the plate under compression and thus most susceptible to buckling.

For the VS model, the BC model provided exactly the same values as the stiffener model for the elastic shear buckling strength and the ambient ultimate postbuckling shear strength, resulting in ratios of 1.0. This means that the stiffener is providing complete lateral restraint, and also means that it is likely that the stiffener is not carrying any significant axial load. If it were, then the values for the stiffener model would be higher than the BC model. The DT and DC models show that, for V_{cr} , the increase in capacity due to the BCs is consistent for models of the same plate thickness, regardless of temperature. This implies that the stiffener has the same impact, regardless of material properties, but that these stiffeners are not as effective at providing lateral restraint. Additionally, the DT models have higher ratios than the DC models, thus indicating that stiffener in the DC models is better at providing lateral restraint than the DT models. Finally, the thinner plates have values closer to one, meaning that the stiffener is more effective for thinner plates than for thicker plates.

3.3 Ultimate Shear Postbuckling Strength, V_u

Examining V_u in *Table 2*, it is seen that at 20°C, both the 10 mm and 14 mm models show that the DC model is strongest in shear, followed by the VS model, and then the DT model. This is likely because providing lateral stiffness and restraint along the portion of the plate in tension is not going to have as large an effect as providing lateral stiffness and restraint along the the compression field (i.e., the DC model). At 700°C, however, the DC model is weakest in each case, with the VS model providing the most shear capacity, followed by the DT model. Unlike in the ambient model, though, each model does provide similar values, with the VS model at 700°C only larger on the order of 100 kN compared to the DT and DC models. Such a difference is negligible considering that at ambient the capacity is on the order of thousands of kN. Since the stiffener is also at 700°C, it loses stiffness with increasing temperature; thus, the stiffener has less of an effect as temperature increases, regardless of orientation. These results are clearly seen in *Fig. 3*, which plots V_u versus temperature for the various stiffener designs (and 10mm thickness plate).

For the ultimate shear postbuckling strength, the VS-BC model offered a larger capacity for the 700°C model, whereas the ambient model continued to have ratios of 1.0. This means that, at ambient, the stiffener is still fully effective in providing lateral restraint and does not carry significant load. At 700°C, however, the stiffener likely begins to lose strength due to the material properties at elevated temperatures, resulting in less lateral restraint.

For V_u , the results of DT and DC have more variation. At ambient, the DT model shows a similar increase in ratio as for V_{cr} , implying that the stiffener is still less stiff than the BC models. The DC model, however, shows an increase in ratio for both thicknesses, but sees a larger value for the thinner plate. This implies that, at V_u , the stiffener is more effective in the thick plate, contrary to the other models. At elevated temperature, the 10 mm DT plate has the same increase in ratio as the

other 10 mm DT models, while the 14 mm plate experiences a decrease in ratio for the BC model. This could be due to this stiffener playing a larger role than lateral restraint, and the elimination of this stiffener results in significantly less strength. For the elevated-temperatures DC model at V_u , it is seen that the stiffeners are once again back to being more effective for the thinner plate. In addition, the elevated-temperature DC models show a much higher ratio than all other models, implying that these stiffeners are providing the least lateral restraint and may be contributing the most to carrying shear load.

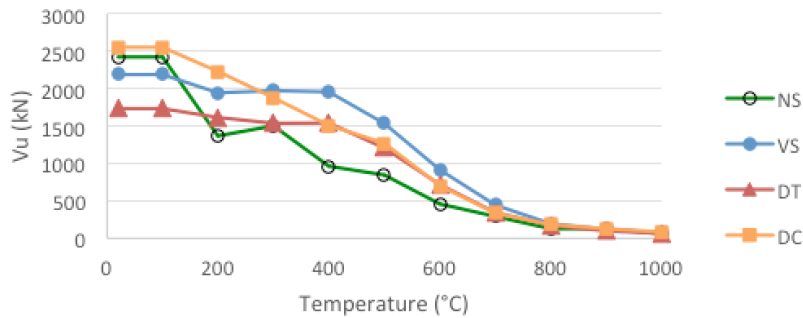


Fig. 3. V_u versus temperature for the 10mm thickness plate.

4 AXIAL LOAD IN STIFFENER

The axial force in the stiffeners is determined for each model, and the results are used to make a comparison between the stiffener configurations, as well as to better understand the contribution of the stiffeners to carrying shear load. The axial load was determined by extracting the axial stresses in the finite element model, and then multiplying the stress by the cross-sectional area of the stiffener.

The axial load in the stiffener for each model at 20°C and 700°C was determined, and the results are presented in Fig. 4, which plots the maximum axial force in the stiffener at V_u (referred to as P_{max}) normalized by V_u , versus temperature for all three stiffener designs. At 20°C, the percentage of V_u carried by the stiffener is between 4% and 14% for all cases. This is consistent with the previous findings, where it was determined that at ambient, the stiffeners were contributing very little to the shear strength of the plate. There is a clear trend at ambient, where DT has the smallest percentage of shear carried by the stiffener, followed by VS, and then DC with the highest percentage. It can also be seen that, in general, the percentage carried by the stiffener is higher for the thinner plate, which also matches the previous observations. At 700°C, the data varies more, with the percentage of shear load carried in the stiffener ranging from 12% to 38%. For the thinner 10 mm plate, the stiffener carries more of the load for the DT and DC models, when compared with the 14 mm plate. The opposite is true for the VS plate, however. Comparing Fig. 4(a) to 4(b) it is seen that the stiffener carries a larger percentage of V_u at 700°C compared to ambient. Fig. 4(c) shows that the percentage of V_u carried by the stiffener is small at lower temperatures, increases significantly between approximately 300°C and 800°C for the VS and DT models, and then decreases again after 800°C.

Steel Structures

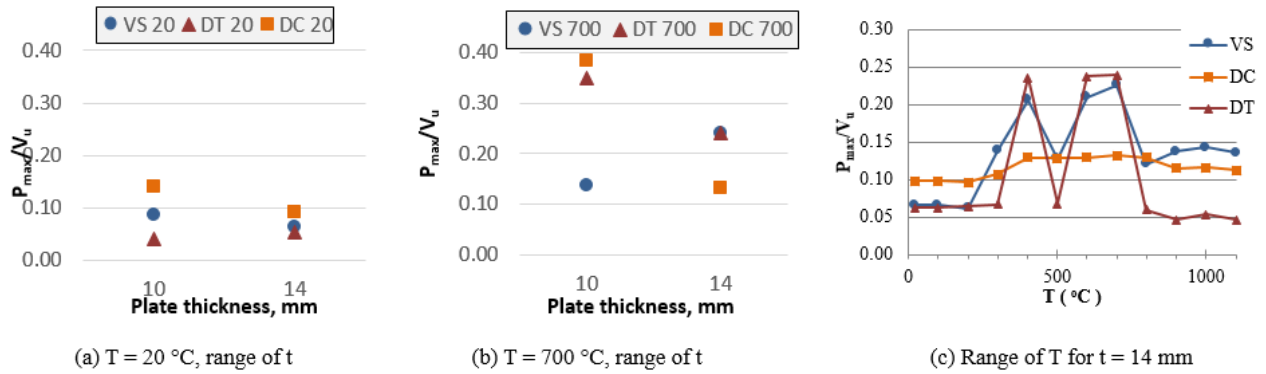


Fig. 3. Maximum axial force in stiffener normalized by V_u .

5 SUMMARY AND CONCLUSIONS

A thin plate subject to increasing shear reaches the critical elastic shear buckling load, V_{cr} , first, then it continues to carry load until it reaches the ultimate shear postbuckling load, V_u . The objectives of this research, as presented in the Introduction, were to (1) examine different stiffener modifications to increase the shear capacity, (2) determine the ability of the stiffener to provide lateral restraint, and (3) examine how the stiffener contributes to V_u . The results of each goal are summarized below.

- (1) It was observed that V_{cr} is largest for the diagonal stiffener in the compressive direction (DC) models, followed by diagonal stiffener in the tensile direction (DT) models, and then vertical stiffeners (VS) models. This is logical as buckling is due to compressive forces, so strengthening the compressive field has the largest effect on elastic buckling. The DC model remains most effective for V_u at ambient temperature, but at higher temperatures, the stiffener loses so much stiffness that the stiffener design and orientation become negligible.
- (2) The vertical stiffener is fully effective at providing lateral restraint for V_{cr} , at both ambient and elevated temperature. The DC model is more effective than the DT model, but neither provide full lateral restraint at V_{cr} . The VS stiffener is fully effective for V_u at ambient temperature, but less so at elevated temperatures. Neither DC nor DT are fully effective at lateral restraint for V_u .
- (3) At ambient temperature, less than 15% of V_u is carried by the stiffeners. At elevated temperature, a larger percent of V_u is carried by the stiffener in comparison to ambient.

Overall, the results of this research indicate that the main role of the stiffener is to provide lateral restraint, not to carry the vertical load resultant of the TFA as in a Pratt truss. Such is true at both ambient and elevated temperatures, though the stiffener typically carries a higher percentage of the load at increased temperatures. At lower temperatures, the diagonal compression stiffener is most effective at stiffening the plate. At higher temperatures, the stiffener loses so much stiffness that the stiffener design and orientation become negligible, though the vertical stiffener offers slightly more capacity than the diagonal designs. A more in-depth presentation of this topic can be found in [16, 17].

ACKNOWLEDGEMENTS

This research was made with Government support under and awarded by DoD, Air Force Office of Scientific Research, National Defense Science and Engineering Graduate (NDSEG) Fellowship, 32 CFR 168a, provided to Dr. Glassman. This research was also sponsored by the National Science Foundation (NSF) under grant CMMI-1068252. All opinions, findings, and conclusions expressed in this paper are of the authors and do not necessarily reflect the policies and views of the sponsors.

REFERENCES

1. Glassman, J., and Garlock, M. (2017). "A compression model for ultimate postbuckling shear strength at elevated temperatures", *Journal of Structural Engineering*, Volume 143 Issue 6 - June.
2. Glassman, J., and Garlock, M. (2016). "A Compression Model for Ultimate Postbuckling Shear Strength". *Thin Walled Structures*, Elsevier, Volume 102, pages 258–272.
3. Rahal, K. and Harding, J. (1990). Transversely Stiffened Girder Webs Subjected to Shear Loading – Part 1: behaviour. *Proceedings of the Institution of Civil Engineers*, 89(1), pp.47-65.
4. Rahal, K. and Harding, J. (1990). Transversely Stiffened Girder Webs Subjected to Shear Loading – Part 2: stiffener design. *Proceedings of the Institution of Civil Engineers*, 89(1), pp.67-87.
5. White, D. and Barker, M. (2008). Shear Resistance of Transversely Stiffened Steel I-Girders. *Journal of Structural Engineering*, 134(9), pp.1425-1436.
6. H. Yonezawa, I. Mikami, M. Dogaki and H. Uno, "Shear Strength of Plate Girders with Diagonally Stiffened Webs," *Proceedings of Japanese Society of Civil Engineers*, vol. 269, pp. 17-27, 1978.
7. F. Nateghi and E. Alavi, "Non-linear behavior and shear strength of diagonally stiffened steel plate shear walls," *International Journal of Engineering Transactions B*, vol. 22, no. 4, pp. 343-356, 2009.
8. American Institute of Steel Construction, "Steel Bridge Design Handbook," 2012. [Online]. Available: <http://www.aisc.org/contentNSBA.aspx?id=20244>. [Accessed 21 December 2012].
9. J. D. Glassman and M. E. M. Garlock, "High temperatures and bridges: transverse stiffeners in steel girder fire performance," in *7th New York City Bridge Conference*, New York, 2013.
10. Garlock, M. and Glassman, J. (2014). "Elevated temperature evaluation of an existing steel web shear buckling analytical model," *Journal of Constructional Steel Research*, vol. 101, pp.395-406.
11. R. D. Ziemian, *Guide to Stability Design Criteria for Metal Structures*, 6th ed., Hoboken: John Wiley & Sons, 2010.
12. S. Lee, J. Davidson and C. Yoo, "Shear Buckling Coefficients of Plate Girder Web Panels," *Computers and Structures*, vol. 59, no. 5, pp. 789-795, 1996.
13. S. C. Lee and C. H. Yoo, "Strength of Plate Girder Web Panels Under Pure Shear," *Journal of Structural Engineering*, vol. 124, no. 2, pp. 184-194, 1998.
14. C. H. Yoo and S. C. Lee, "Mechanics of Web Panel Postbuckling Behavior in Shear," *Journal of Structural Engineering*, vol. 132, no. 1, pp. 1580-1589, 2006.
15. European Committee for Standardization (CEN), "Eurocode 1: Actions on Structures - Part 1-2: General Actions - Actions on Structures Exposed to Fire," CEN, Brussels, 2002.
16. Boyce, V. (2018). *Enhancing the Fire Performance of Steel Plate Girders Subject to Shear Loads*. Master of Science. Princeton University.
17. Glassman, J., Boyce, V., Garlock, M. (2018). "Effectiveness of stiffeners on steel plate shear buckling at ambient and elevated temperatures" in preparation for submission to *Jnl of Constructional Steel Research*.

FAILURE MECHANISM OF STEEL FRAMES SUBJECTED TO POST-EARTHQUAKE FIRES

Gabriel-Victor Risco¹, Luisa Giuliani², Varvara Zania³

ABSTRACT

Despite building fires may occur as a consequence of a previous earthquake, current regulations do not require fire verifications on a structure previously or concurrently solicited by a seismic action, thus implicitly considering fire and earthquake as a statistically independent accidental actions.

On the other side, modern seismic design relies on the structural ductility, meaning that a post-earthquake fire will act on a weakened and deformed structure, which could potentially possess a lower fire resistance than expected by the design performed on an integer structure.

This paper aims at investigating the post-earthquake fire resistance of steel buildings, looking in particular at the structural response of two uninsulated steel moment resisting frames of different height (a 5-storey and a 10-storey frame). Each frame was subjected to two different earthquakes, selected among 9 different accelerograms, and then several different fire scenarios were considered, where the elements involved in the fire were assigned a temperature history calculated from a standard fire exposure. Times of local element failure and global collapse in case of post-earthquake fire are reported and compared with the case of fire acting on the integer structure. The results show that the fire resistance of both frames is not strongly affected by a previous earthquake, but the collapse mechanism can in some cases change in a detrimental way for firefighting operations.

Keywords: Post-earthquake fire, steel structures, moment resisting frame, parametric study

1 INTRODUCTION

Current structural fire design methods are based on the structural verification of the elements heated by a design fire (typically a standard fire curve [1]) and loaded according to an accidental design combination [2], where permanent and especially live loads are strongly reduced with respect to the ultimate limit state value, in reason of the rare fire occurrence. Generally, only the primary live load is present, as the combination factor for concomitant live loads are zero (although this may vary from country to country). As a result, the fire resistance of a structure is mostly dependent on the permanent vertical loads and do not consider possible effects of horizontal solicitations. Furthermore, one accidental action at a time is to be considered in the accidental design situation. If this assumption seems reasonable for statistically independent actions such as e.g. earthquakes and malevolent explosions or arsons, it is though less convincing for concurrent events such as earthquakes and fires. It is well known that fires are often a consequence of the damages induced by the earthquake in a building (such as e.g. of rupture of gas lines, arcing of electrical wires, leaking of flammable liquids stored in the house, or tipping of stoves, lamps, candles, etc.) and several are the examples of severe post-earthquake fires, which throughout history have caused greater damage rather than the earthquake itself [3], [4]: the Great Lisbon Earthquake in 1755 was followed by fires that lasted 5 days [5]; the 1906 San Francisco earthquake and the 1923 Kanto earthquake in Tokyo

¹ Graduate Fire Engineer, Trenton Fire Ltd, London, United Kingdom.

e-mail: gabriel.risco@trentonfire.co.uk

² Associate Professor. Department of Civil Engineering, Technical University of Denmark, Kongens Lyngby, Denmark.

e-mail: lugi@byg.dtu.dk

³ Associate Professor. Department of Civil Engineering, Technical University of Denmark, Kongens Lyngby, Denmark.

e-mail: vaza@byg.dtu.dk

are considered the largest fires occurring during peace-time history [6]; more recently, numerous fires developed into large urban conflagrations during Kobe earthquake in 1995, few years later the 1999 Marmara earthquake, Turkey, caused the fire of a petroleum refinery, which burnt for several days [6]; the detrimental effects of post-earthquake fire on industrial facilities have gained the attention of the media some years later, when the Tohoku earthquake and tsunami resulted in the Fukushima nuclear accident. These examples clearly show the need of investigating the structural response to earthquake and concurrent or following fires and check whether the fire resistance of the structure can be reduced by the damages caused by the earthquake.

Della Corte et al. [8] distinguished the earthquake damage in a geometrical damage, due to residual deformations that modify the initial geometry of the building after the earthquake, and a mechanical damage, due to the permanent degradation of the mechanical properties at the locations where repeated plastic deformations occur during the earthquake. The first type of damage is the one mostly investigated in literature and also considered in this study. The reason is twofolded: on one side, as noted by the aforementioned authors, the plastic damage is expected to be negligible on buildings adequately designed for earthquakes; on the other side, the geometrical damage could be significant, due to the ductile design used to dissipate energy. A very ductile steel frame may undergo large deformations without rupturing, but the strain increment in the member will cause a stress redistribution on adjacent elements and induce second order effects from the vertical loads acting on the building.

On these grounds, several studies on post-earthquake fires have been carried out on both insulated and uninsulated steel structures. The aforementioned authors [8] investigated two multi-storey uninsulated steel frames, one designed for ultimate-limit-state and a second designed for both ULS and SLS by means of a parametric study. The frames tended to undergo lateral sway collapse in the post-earthquake fire scenarios, unlike the direct fire where the buildings collapsed in on themselves. The reduction in fire resistance was negligible for properly designed frames (under 10%), whilst a significant reduction is observed for very rare earthquakes or frames designed only to ULS. Pintea et al. [9] performed a similar study on uninsulated steel MRF by applying temperature increase by means of a parametric or a standard fire curve. It was concluded that frames designed to resist strong earthquakes possess an additional reserve of fire resistance. However, frames which sustained permanent damage experienced a small decrease of the resistance, which may be disregarded. Other investigations were performed by Jelinek et al. [10] on an identical frame subjected to several earthquake accelerograms and a standard fire curve. It was observed that properly designed frames conforming to current codes, do not suffer a significant decrease of the fire resistance. A methodology for assessing the fire performance of buildings after an earthquake was developed by Faggiano and Mazzolani [11], by defining several performance levels, which correlate the degree of damage to the seismic intensity. It was concluded that the fire resistance is affected only by significant damage. Memari et al. [12] arrived at a similar outcome, by researching the response of reduced beam sections during fire on frames of different height, observing that the post-earthquake fire (PEF) action had no significant impact on the time of global collapse.

This study aims at further investigating the problem, by comparing the PEF resistance of two frames of different heights, thus highlighting possible enhanced nonlinear effects on the fire resistance of tall buildings raised by the geometrical damage induced by the earthquake. A numerical model has been implemented in a commercial finite element (FE) software, where the collapse mechanism developing in two steel frames of different heights is investigated, in case of two different earthquakes and a number of different fire scenarios. The response of the two frames is discussed and compared in terms of local failure (failure of a single element) and collapse (progressive failure of part of, or the entire structure). The post-earthquake times of fire resistance are also compared with the corresponding fire resistance in case of a fire directly acting on the integer structure (direct fire).

2 NUMERICAL MODEL

2.1 Building design

Two frames are designed according to current Eurocode standards [13, 14] for ultimate-limit-state and serviceability-limit-state using the commercial FEM software SAP2000 [15], as shown in *Fig. 1*. Frame A was selected from literature [9], which was redesigned in accordance with up-to-date standards using the strong-columns weak-beams concept. This implies that plastic hinges are desired to develop at the ends of the beams, instead of the columns. Frame B was modelled using the same principles, with similar horizontal dimensions, while being double in height. Both are assumed to be of high ductility class (DCH), as they are designed to a peak ground acceleration (PGA) of $a_g=0.36g$.

The frames are considered to be internal to the building; hence it was assumed proper to model the frames as 2-dimensional using Euler-Bernoulli beam elements for both the beams and the columns. Queil et al. [16] investigated high-rise steel frames under fire by comparing the structural response of 3-D frame models with 2-D plane frame models. It was concluded that it is sufficient to simplify the problem to 2-D with reasonable accuracy, whereas a model of the full 3-D structure would require a longer run time and very high computational capacity.

The two buildings were first designed against vertical loads and earthquake. The details of the design and the main numerical modelling aspects (material parameters, methodology, earthquake loading, fire definition and scenarios) are presented hereafter.

2.2 Material properties

The properties of steel are introduced by defining a nonlinear thermo-plastic material model based on a degradation of the steel strength and stiffness proposed by Hertz [17]. The selected steel grade is S235 and an elastic-perfectly plastic material with no damage effects due to cyclic loading is considered at ambient temperature. At high temperatures, carbon steel does not have a clear yielding point but a strain hardening that stretches from the elastic strain to ca. 2% strain, where the maximum yield strength is achieved at all temperatures. This is represented in the numerical model by defining a multi-linear stress-strain at high temperatures. The diagram is defined by a linear branch up to the 0.2% proof stress (i.e. the stress corresponding to a 0.2% residual stress after unloading), a bilinear branch describing the yielding curve up to 2% deformation, when the maximum yielding strength of 235 MPa is achieved, and a perfectly plastic branch afterwards.

2.3 Methodology

The numerical study has been carried out in the FE software Abaqus [18]. A model analysis and a response spectrum analysis were preliminary carried out in order to calibrate the models by determining the seismic design parameters. Then the main analysis procedure comprised the following steps:

- Vertical loading – This step is represented by the dead and live loads acting on the frame (2 kN/m² and 4 kN/m² for intermediate floors, respectively 3.5 kN/m² and 1.5 kN/m² for roof);
- Earthquake action – Using a dynamic analysis with implicit time integration, the seismic motion is applied according to the chosen accelerograms. The step was extended by 20 seconds in order for the structure to become still, prior to initiation of the following step.
- Fire action – In a further implicit dynamic step, temperature-time histories calculated from standard fire exposure are applied to the elements involved in each considered fire scenario.

In order to evaluate the impact of a post-earthquake fire, the same fire scenarios were also considered on the undamaged frames (direct fire).

2.4 Earthquake simulation

In order to assess the structural response, 9 earthquake accelerograms have been applied, selected from the PEER Ground Motion Database and European Strong-Motion Database. The strong motions were scaled to the aforementioned design peak ground acceleration (PGA), which was

chosen as the 70% fractile of the maximum European value. An extension of 20 seconds is applied to the recordings to ensure that the vibrations are dissipated or reduced sufficiently not to affect the thermal analysis. From all applied earthquakes, the two most critical are selected for further investigation based on the highest strains, inter-storey drift ratios (IDR) and largest load utilisation factor within the frame. The earthquake selection is represented in *Table 1*.

Table 1. The earthquakes considered in the numerical study

Name	Location	Year	Magnitude M_w
Artificial	n/a	n/a	n/a
Hollister	Hollister, USA	1961	6.9
Friuli	Friuli, Italy	1976	6.5
Montenegro	Ulcinj, Montenegro	1979	6.9
Loma Prieta	Loma Prieta, USA	1989	6.9
Racha	Racha, Georgia	1991	7.0
Northridge	Northridge, USA	1994	6.7
Turkey	Izmit, Turkey	1999	7.6
Luoli	L'Aquila, Italy	2009	6.3

2.5 Fire scenarios

A total number of 21 scenarios were investigated, 10 on the low frame and 11 on the tall frame, which are all shown in *Fig. 2*. The selection of these scenarios is based on the seismic response, mainly on the location of the largest IDR and largest residual strain, recorded during the seismic simulation.

In particular, it was assumed that each bay of the frame would correspond to a separate fire compartment and 7 different compartment fire scenarios were investigated on both the low and tall frames. These scenarios are identified by a letter A or B indicating the investigated frame, a number from 1 to 10 indicating the floor, and another letter indicating the position of the bay within the floor (L for left, R for right and C for centre). In addition to these compartment fire scenarios, a loss of compartmentalization along a whole floor (indicated by the final letter F) and along two floors in two bays (A23RC, B45RC) is assumed and a few larger fire scenarios are considered on both frames.

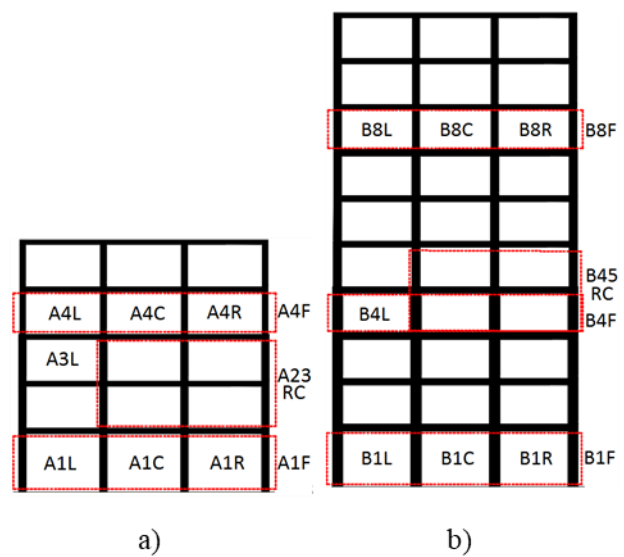
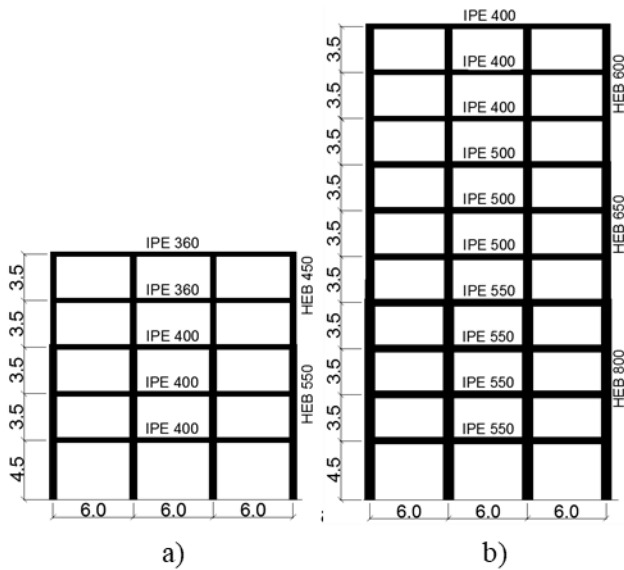


Fig. 1. Investigated frames; Frame A (a) and Frame B (b)

Fig. 2. Fire scenarios for Frame A (a) and Frame B (b)

The fire is assumed to ignite and reach flashover after the end of the earthquake, meaning that the dynamic effects of the earthquake are dissipated and the structure is at rest. All beams and columns

of the bays included in the fire scenarios are assumed to be uninsulated and exposed to a standard fire curve ISO-834. Although not representative of a realistic fire, this curve is mostly used for design purpose and fire rating of the elements, as it has the advantage of not being dependent on the combustible, thermal and geometrical properties of the compartment, as parametric fires. For this reason, this curve is also used in this study, in order to obtain results that are solely dependent on the structural design of the buildings. The section factors of the elements are calculated on the assumption that columns are exposed on all sides, whilst the beams are protected on the top side by the deck system. The element heating is then calculated from the section factor, according to the heating formula presented by Pettersson et al. [19].

3 RESULTS

Results are presented and discussed for both frames in terms of post-earthquake response to fire and direct fire response.

3.1 Seismic response

A total of 9 earthquakes were applied on both frames to assess their seismic response. Although all earthquakes are scaled at the same PGA, different results are obtained, based on the most affected mode of vibration of the frame. The maximum IDRs for each applied motion are depicted in *Fig. 3*. Two earthquakes with the most significant impact are selected for further investigation: the Montenegro earthquake and the Artificial earthquake. The different IDRs for the Montenegro motion are reported in *Fig. 4*, along with the Eurocode IDR limitations. It can be observed that this limit is exceeded at different levels during the earthquake and a permanent displacement at the top is observed as the vibrations are dissipated.

No degradation of the material properties due to damage is accounted for (such as a result of cyclic loading); however it is highlighted whether the stress redistribution due to the formation of plastic hinges will affect the fire resistance. The stress redistribution can be observed in the bending moment – curvature diagram presented in *Fig. 5* for a beam support.

Following the earthquake, a different moment distribution is noticed along the beam span. The supports seem to be unloaded, while an increase of the moment magnitude occurs on the beam mid-span. Therefore, some columns experience a decrease of the bending moment, while for others an increase is noticed.

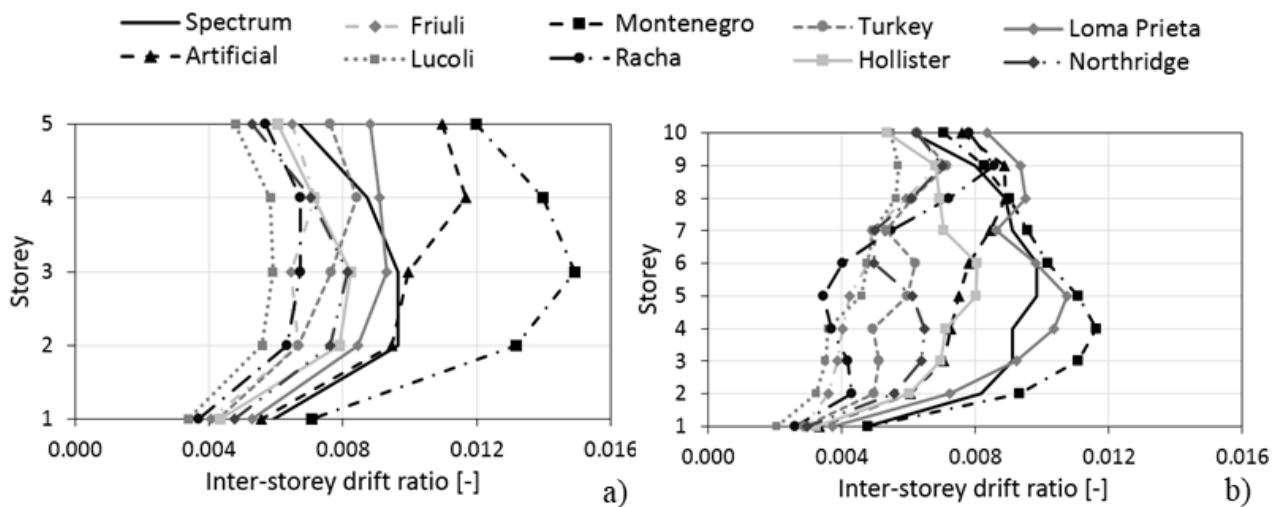


Fig. 3. Maximum IDR for Frame A (a) and Frame B (b)

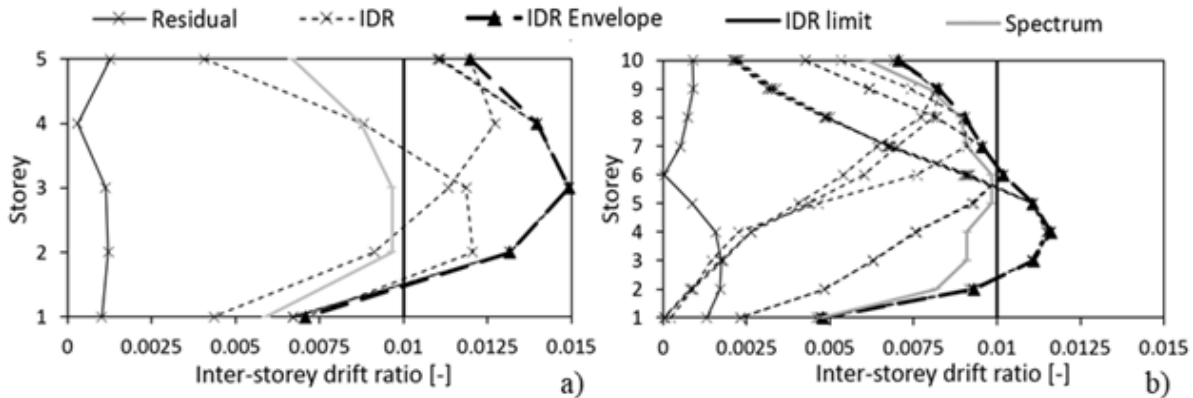


Fig. 4. Residual IDR for Montenegro earthquakes; Frame A (a) and Frame B (b)

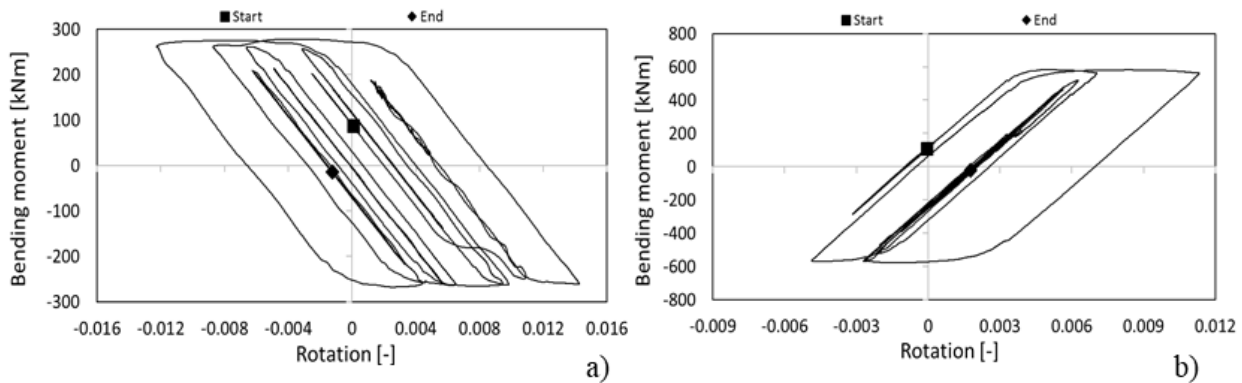


Fig. 5. Hysteresis loops for a beam support for Frame A (a) and Frame B (b)

3.2 Post-earthquake fire response

The steel heating curves calculated from the standard fire are applied on the elements involved in the fire scenarios of both frames as either direct fire (DF) or post-earthquake fire (PEF). The results in terms of fire resistance with respect to element and global failure are reported in *Fig. 6* for all scenarios. In the following, the collapse mechanisms of the building in case of scenario A1C is also reported, as most representative one among the different scenarios:

- All heated elements undergo thermal expansion and enter the elastic-plastic range of the material; then two perfect plastic hinges form on the beam-ends.
- A third plastic hinge forms on the beam mid-span and the beam becomes a mechanism.
- A small catenary effect occurs in the beams, as the vertical displacement becomes significant and pulls the beam ends inwards.
- Three plastic hinges form in the first columns, which fails, followed shortly by the second column as well.
- The frame cannot sustain the loss of two columns and collapses under the acting loads.

Despite this collapse mechanism being quite similar for the majority of the fire scenarios, a difference was noted in the scenarios affecting the ground floor level of the frames. The collapse of Frame A followed the same progression described above, where the failure of the beams acted as a warning. In case of Frame B, the columns fail before the beam. This kind of collapse is abrupt and can potentially affect fire rescue intervention. An explanation of the different collapse mechanism may be the fact that the cross-section of the beams of frame B was determined by the IDR

limitations imposed by the Eurocode rather than strength requirement, thus leading to a lower load-to-resistance ratio of the beams, which, in turn, results in a longer fire resistance of the beams.

The results of all investigated scenarios are represented in *Fig. 6* for both global collapse of the frame (left) and first element failure (right). A normalization of the results obtained in PEF scenarios is done with respect to the time until failure recorded in case of DF for all scenarios. The resistance has been grouped for all fires acting on the same floor level (e.g. A1R, A1C) under the same line ($x=1$). Similarly, scenarios affecting two storeys simultaneously are represented in-between the floor numbers. The reduction of time until local failure is mainly interesting in terms of occurrence of a warning sign, while the time until global collapse is a central parameter for the stability of the structure.

The results do not show any clear trend for local failure, while the time of global collapse is relatively constant with respect to the fire scenarios, building height, and occurrence or not occurrence of an earthquake prior the fire.

Surprisingly, in some scenarios a slight increase of the time until failure was noted. Similar results were also noted in a previous study on uninsulated steel frames [10] and it is believed to be a consequence of the stress redistribution, which has a favourable effect on the overall fire resistance of the frame. At the end of the seismic motion, a smaller magnitude of the bending moment is observed in the supports of the beams, contrary to the increase of moment in the mid-span. Consequently, the reduced moments are transmitted to the columns which tend to experience a delay of the failure. However, this phenomenon was noted only for some scenarios, being highly dependent on the residual deformed shape of the structure.

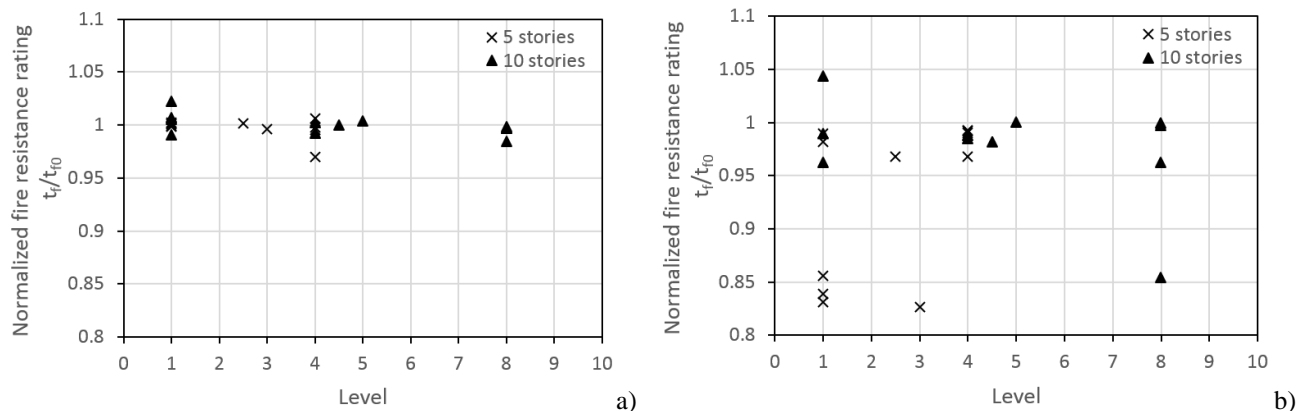


Fig. 6. Normalized fire resistance rating; a) Global collapse; b) Local collapse

4 CONCLUSION

The main goal of this study was to determine if the residual stresses developed during an earthquake affect the fire resistance of steel structures, implying a need of more stringent design criteria for seismic areas. Further on, different collapse mechanisms were analysed on steel frames with two different heights and their post-earthquake fire resistance times were compared.

A comparison of the frames shows that the effect of non-linear geometries is not more significant for the tall structure as expected since the reduction percentage is similar for both; nonetheless, differences can be noted in the development of the collapse. For the small frame, the failure mode was symmetrical and it tended to collapse in on itself. Taller frames over 5 storeys high undergo sway due to higher displacements at the top. This should be treated with care as it may endanger neighbouring structures or pose a threat to people located in close proximity.

The same progression of collapse was noted in almost all cases, with the only difference between the DF and PEF scenarios being a variation in the failure of the columns: some undergo compressive failure of the cross-section, while others tend to develop three plastic hinges.

In terms of fire resistance, it can be concluded that the permanent deformations or residual stresses alone do not have a significant influence on the fire response of the frame. Further on, in some cases the stress redistribution seemed to have an unexpected effect, of slightly increasing the time until collapse. Generally, the results are in accordance with other similar investigations [8], [9] and [10].

REFERENCES

1. ISO834-1, *Fire resistance tests - Elements of building construction - Part 1: General requirements for fire resistance testing*, Switzerland: International Organization for Standardization (ISO), 1999.
2. EN1990, *Eurocode 0 - Basis of structural design*. European Committee for Standardization, 2002.
3. A. Buchanan. *Structural Design for Fire Safety*, John Wiley and Sons, 2001.
4. H. Yassin, F. Iqbal, A. Bagchi and V.K.R. Kodur. Assessment of post-earthquake fire performance of steel-frame buildings. Beijing, China: *The 14th World Conference on Earthquake Engineering*, 2008.
5. B. Faggiano. Urban habitat construction under catastrophic events: Fire after earthquake. *In the WG1 Meeting*, Praha, Czech Republic, 2017.
6. C. Scawthorn, J.M. Edinger, A.J. Schiff. *Fire Following Earthquake*. American Society of Civil Engineers Publications, 2005.
7. D. Todd, N. Carino, R.M. Chung, H.S. Lew, A.W. Taylor and W.D. Walton. *1994 Northridge earthquake: Performance of structures, lifelines and fire protection systems*. Technical report, National Institute of Standards and Technology, Gaithersburg, 1994.
8. G. Della Corte, R. Landolfo, and F.M. Mazzolani. Post-earthquake fire resistance of moment resisting steel frames. *Fire Safety Journal*, 38(7):593-612, November 2003.
9. R. Zaharia and D. Pintea. Fire after earthquake analysis of steel moment resisting frames. *International Journal of Steel Structures*, 9(4):275-284, December 2009.
10. T. Jelinek, V. Zania, L. Giuliani, Post-earthquake fire resistance of steel buildings, *Journal of Constructional Steel Research* 138 (2017) 774-782.
11. B. Faggiano, M. Esposito, and F.M. Mazzolani. Risk assessment of steel structures under fire. *In The 14th World Conference on Earthquake Engineering*, Beijing, China, 2008.
12. M. Memari, H. Mahmoud, and B. Ellingwood. Post-earthquake fire performance of moment resisting frames with reduced beam section connections. *Journal of Constructional Steel Research*, 103:215-229, September 2014.
13. EN1993-1-1. *Eurocode 3: Design of Steel Structures - Part 1-1: General Rules and Rules for Buildings*. Standard, European Committee for Standardization, Brussels, December 2005.
14. EN1998-1-2. *Eurocode 8: Design of Structures for Earthquake Resistance -Part 1: General rules, Seismic Actions and Rules for Buildings*. Standard, European Committee for Standardization, Brussels, July 2009.
15. SAP2000. Linear and nonlinear static and dynamic analysis and design of three-dimensional structures. Computers and structures, Inc., August 2004.
16. S. E. Quiel, M. E. Garlock. Modelling high-rise steel framed buildings under fire. *ASCE Structures Congress. Crossing Borders*; 2008.
17. K. Hertz, "Reinforcement Data for Fire Safety Design," *Magazine of Concrete Research*, vol. 56, no. 8, pp. 453-459, 2004.
18. Abaqus 6.10 online documentation, Dassault Systèmes, 2010.
19. O. Pettersson, S.E. Magnusson, T. Joergen. Fire Engineering Design of Steel Structures. *Bulletin 52*, Lund Institute of Technology, 1976.

CHARACTERISING THE THERMOMECHANICAL RESPONSE OF STEEL COLUMNS SUBJECT TO LOCALISED FIRES

Yavor Panev¹, Teodor Sofroniev², Luke Bisby³, Panos Kotsovinos⁴, Graeme Flint⁵

1 INTRODUCTION

In large compartments like open plan offices, atriums and stadia, occurrence a localised or traveling fire is more likely than a post-flashover fire. Sources of fuel, like rubbish bins, furniture and exhibition boards, are usually concentrated in localised packs around structural columns. Addressing the structural response of columns subject to localised fire conditions is therefore necessary for performance based design. Current structural design guidelines such as Eurocode 1 are typically based on the assumption that the whole element is subjected to the same temperature along its cross section, as is widely assumed for post-flashover conditions.

This assumption may not be justified in all fire scenarios. Wiesner (2017) reported non-uniform temperature distributions in steel columns subjected to heating from adjacent bin fires. Hamins et al. (2005) reported that non-uniform gas temperatures and asymmetrical heating were common in developed enclosure fires investigated in large fire tests at NIST. A high temperature gradient was observed in external steel column subjected to heat fluxes from a compartment fire window (Pultar et al., 2010). Higginson (2012) confirmed highly localised heating and subsequent two-directional thermal gradient in an I-beam above a localised pool fire. Localised heating has also been reported for damaged fire protection (Wang et al., 2008).

Additionally, previous research has highlighted that asymmetric thermal gradients across the column section could lead to unanticipated mechanical responses. Both Wiesner (2017) and Sjoström et al. (2012) reported large deflections due to thermal bowing which can be potentially harmful due to consequent second order actions. Wiesner (2017) also observed significant localised swelling of the column surface at places where the flame impinged for prolonged periods of time.

The aim of this paper is to characterise the thermomechanical response of a steel column subjected to concentric and eccentric loads and asymmetric thermal gradients which are typical of localised fires. A series of load tests on representative steel columns subjected to asymmetric fire actions were conducted. A finite element model was developed and compared with the experimental data. The validated model was then used to further study and characterise the mechanical response, failure mechanisms, and post-failure behaviour of the investigated columns. A comparison of the numerical and experimental findings against structural capacity predictions from Eurocode 1 is also provided.

¹ Arup, UK. Corresponding author:

yavor.panev@arup.com

² Cundall, Manchester, UK

³ University of Edinburgh, Edinburgh, UK.

⁴ Arup, UK

⁵ Arup, UK

Characterising the thermomechanical response of steel columns subject to localised fires

In the majority of previous research the mechanical load has been applied after the section has reached thermal equilibrium; this is not representative of what happens in true fire scenario where the static load is present before and during heating. Eccentric static loads were not specifically addressed in previous research. This is evident given that axial-flexural (M-N) interactions form the basis of current design equations for columns. There is also noticeable absence of studies focused on locally applied thermal gradients, while all surveyed reports on real fires indicate strong thermal gradients both across the column length and through the element's section.

As a result the experiments in the current study were specifically designed to address the effects of eccentrically applied static loads and asymmetric local heating applied whilst the column was subjected to the sustained applied loads.

2 EXPERIMENTAL STUDY

1500 mm long standard steel columns UKC 152x152x23-s355 with slenderness ratios of 39 were axially loaded to a 0.57 utilisation at the Fire Limit State (FLS), as defined in BS EN 1991-2, using hydraulic jack system. The utilisation at FLS was derived assuming the columns were utilised to 0.9 at the ultimate limit state. The loading and slenderness of the tested specimens were deemed representative of columns in real buildings.

Two columns (Test 1 and Test 2) were loaded concentrically and with 50 mm eccentricity, respectively. This eccentricity value was chosen to engage the column equally in both bending and compression. After loading the columns were heated at mid-height via radiant panels to an average heat flux of 45KW/m². This is considered representative for heat fluxes achieved from real localised fires as reported by Wiesner (2017).

The temperature distribution was measured by 48 thermocouples located both across the section and across the length. Lateral deformations along the length of the column were measured by linear potentiometers. The test was continued until failure, which was defined as loss of strength capacity, run-on deflection, or deformation exceeding $h/10$ limit. A schematic of the adopted testing setup is illustrated in Figure 1.

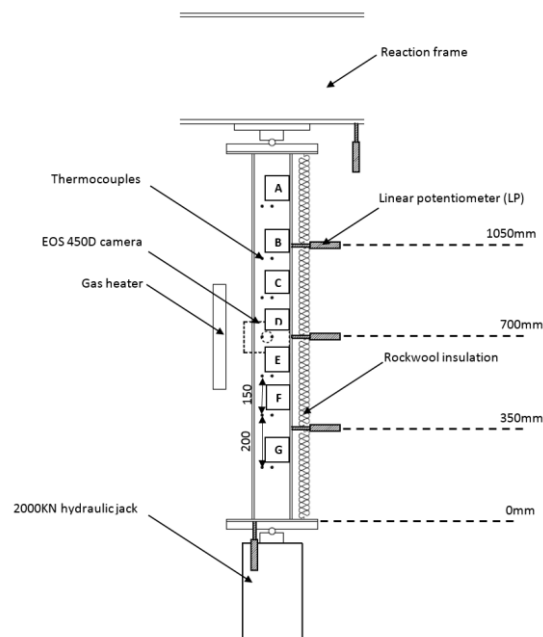


Figure 1 Experimental apparatus

3 EXPERIMENTAL RESULTS

3.1 Thermal response

The columns from the two tests demonstrated similar thermal responses. A non-uniform thermal gradient was observed, and the magnitudes were similar to those reported by Wiesner (2017) in his study on thermal response of steelwork to localised fires.

Figure 2 illustrates the average temperature evolution in the front and back flange for Level A (top), Level D (centre), and Level G (bottom). Unsurprisingly, the temperatures in the central portion of the column were almost twice higher compared to the significant localised exposure to high heat flux. The temperature distribution was also not symmetrical around the mid-height. Both the average front and back flange temperatures at the top of the column (Level A) were almost twice higher than the corresponding temperatures at the bottom (Level G). This was due significant convective heating.

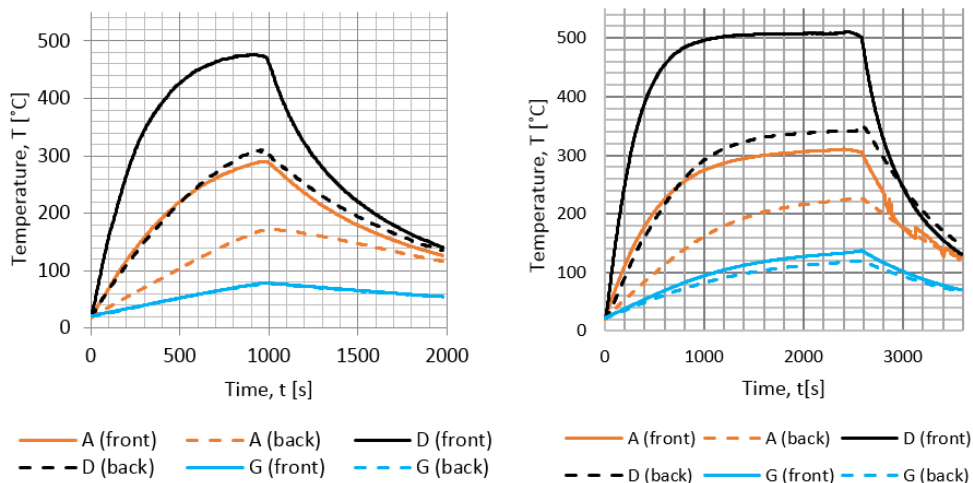


Figure 2 Temperature distributions for Test 1 (left) and Test 2 (right)

3.2 Mechanical response

Upon heating both tested columns started to bow towards the heater from the moment the flange steel temperature began to increase. This was accompanied by an increase of axial load due to partially restrained thermal expansion. From measurements of the vertical deformation of the tested frame, the relative stiffness of the connection (stiffness of column/stiffness of supporting frame) was estimated to be 0.4. This is slightly above 0.3, which is the relative stiffness expected in a typical steel frame structure as reported by Ali et al. (1998).

As the axial load increased, an increasing bending moment was induced in the opposite direction which reduced the thermal bowing. For the concentric case the reduction was up to 8% due to the secondary P-Delta moment. For the eccentric test, however, the reduction was up to 32% due to the increase in the static moment caused by the eccentric axial load.

In both tests, the horizontal thermal bowing reached a peak followed by sharp reverse of deflection direction succeeded by run-on deflection with minimal recorded increase of axial load (Figure 3).

Characterising the thermomechanical response of steel columns subject to localised fires

The maximum attained temperature at failure was 450°C while the average section temperature was only 232°C. Initiation of flange buckling was at mid-height, the hottest part of the column.



Figure 3 Load-deflection response (left) and post-failure buckling response (right) for Test 3 (concentric loading)

4 DISCUSSION OF FAILURE MECHANISM

A series of numerical finite element models were developed in Abaqus, which were validated against the experimental study and allowed investigating the sensitivity to various parameters. The specimen geometry, boundary conditions, and static loading were modelled according to the experimental procedure. The thermal loading input was based on interpolating the collected experimental results from the 49 installed thermocouples.

Due to time constraints for the experimental work, coupon tests of the used steel were not performed. Therefore, the exact material properties remain unknown. From the analysis of the ambient test results it was concluded that the steel yield strength was in the range of 352 MPa. The ultimate strength was in the range of 440 MPa, calculated 25% higher than the yield strength, as per Eurocode guidance. Two temperature dependant material models were used.

Model 1, Proportional limit, assumes the proportional limit for steel corresponds with the yield strength at ambient conditions (Figure 4). The steel hardens linearly to the ultimate stress at 0.04 strain. At elevated temperatures the proportional limit drops following the Eurocode predictions for yield strength degradation. Model 2, called No limit, disregards the effect of proportional limit; i.e. a bi-linear representation is assumed as shown (Figure 4). Both models incorporate degradation of Young's modulus, as per Eurocode 3 reduction curves.

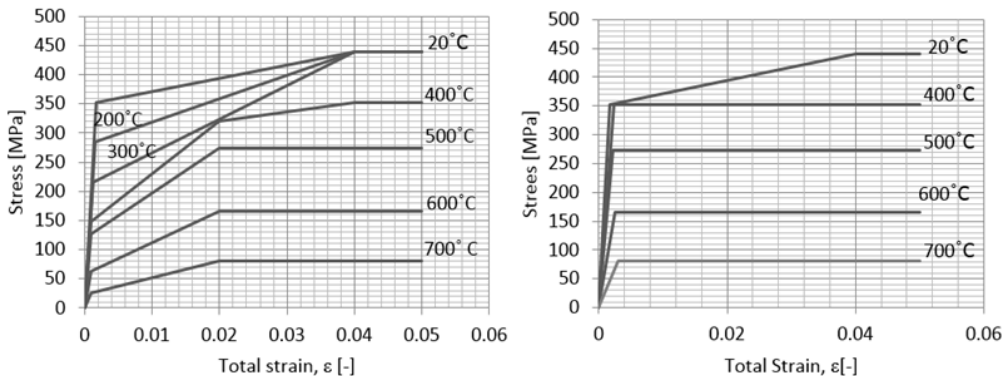


Figure 4 Proportional limit material model (left) and No limit model (right)

The results of the numerical models during the heating stage are compared to the experimental results. The plots on Figure 5 show the axial load and horizontal deflection against real time during the experiment.

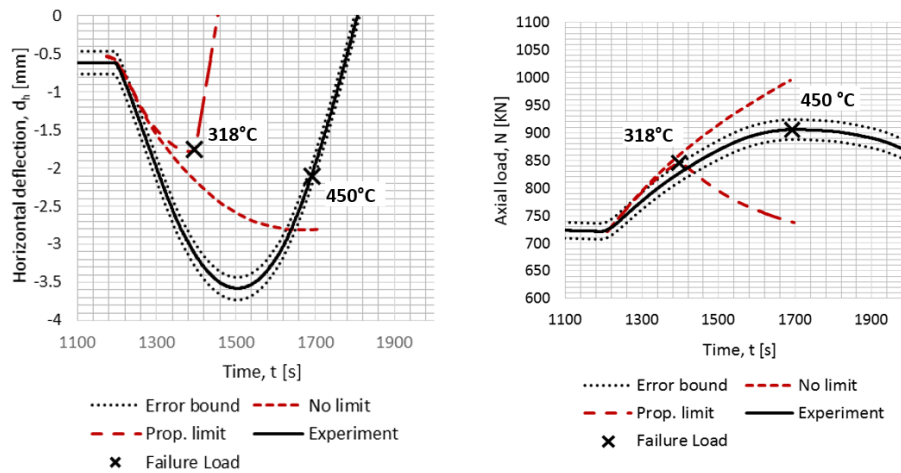


Figure 5 Thermal bowing and axial load comparison with numerical model for Test 1 (conc.)

There is considerable divergence between both models' results and the experimental data after the first 150 seconds of the heating phase. The Proportional limit model indicated a sharp reverse of horizontal deflection, followed by decrease run-on deformation and decrease of axial reaction force. The maximum temperature in the specimen temperature is, on average, 130°C less than the experimental failure temperature in both cases.

The No limit model does not show any loss of axial reaction in both tests, nor reversal of horizontal direction during the full duration of the simulation. However, analysis of the state of stress, at the time when the experiment failure temperature is reached, shows the column is close to its yield capacity and there are few locations undergoing plastic deformations.

The observed experimental failure remains bounded between the predictions of the two models. This clearly demonstrates that the mechanical response of the model is sensitive to the location of the proportional limit and its degradation with temperature.

Detailed analysis of the thermal and plastic strains through the column, as predicted by the numerical models, provides further insight into this dependence. Initially, the column bowed toward the heater as the thermal expansion induced tensile thermal strains in the heated parts of the exposed flange (Figure 6). Due to the restrained expansion of the column the mechanical compressive stresses increased. At the same time the proportional limit degraded due to the elevated temperatures. Once the local state of stress was larger than the proportional limit, the column accommodated the elevated mechanical stress via compressive plastic strains, whose magnitude increased at a faster rate than the thermal strains. Consequently, the column reversed the bowing direction as the local plastic compressive strains exceeded the local tensile thermal strains. The plastic strains propagated further into the sections to accommodate the continuing increase of axial force, finally leading to formation of a plastic hinge.

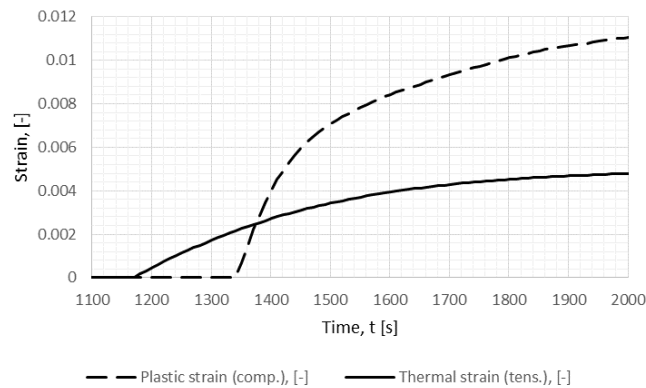


Figure 6 Thermal and plastic strains evolution for centre point at the exposed flange

5 COMPARISON TO CURRENT DESIGN PRACTICES

The results of the conducted experiments are benchmarked against the structural resistance prediction following the BS EN 1991-1-2 procedure, and are presented in Table 1.

Table 1 Comparison to Eurocode assessment

Test	Experimental [KN]	Predicted - BS EN 1993-1-2:2005 [kN]	Difference [%]
Test 1 (conc.)	906±18	812	12
Test 2 (ecc.)	550±11	458	20

The Eurocode method appears conservative in predicting the resistance of the column at the failure experimental temperature distribution. This was expected as the method is based on material degradation and plastic yielding which was the governing principle behind the failure mechanism discussed above. However, the Eurocode assessment does not consider the 30% increase of load demand due to the thermal restraints observed in the experimental and numerical studies. Failing to do so might lead to unconservative design despite the fact that the structural resistance is calculated conservatively. Accurate assessment of the load demand is also critically important for the member connections to be designed with the proper allowance to accommodate thermal expansion effects.

6 CONCLUSIONS

This study has investigated the thermomechanical performance of steel H-section columns subjected to asymmetric thermal gradients. It includes an experimental stage where steel columns were loaded and then centrally heated to simulate localised fires. A finite element model was then developed and partially validated against the experimental results, to provide further insight into the failure mechanism of the studied columns.

During the heating process the axial load increased by up to 30% due to restrained thermal expansion by the end supports. All experimental columns failed by excessive plastic deformations at the heated regions leading to localised flange buckling. The maximum failure temperature was 450°C and the maximum average temperature was just 212°C. This confirms that estimating limiting temperature using a lumped capacitance model is not an adequate technique for assessing the structural resistance of steel columns subjected to localised heating.

Steel Structures

Investigation of the observed failure mechanisms by FE models indicates that the failure point is highly sensitive to the degradation of the proportional limit of steel as this is the point where plastic deformations are initiated. The degradation of proportional limit with temperature should therefore be explicitly taken in consideration when assessing the structural resistance under localised fire scenarios.

Eurocode 3 design equations for structural fire resistance of steelwork based on the assumption of uniform maximum temperature proved conservative for the assessed columns. However, it should be noted that the calculation relied on a predefined knowledge of the temperature distribution in the steel section – this cannot be determined by lumped capacity calculation approach. Additionally, EN1993-1-2 does not account for the 30% increase in load demand that was observed. This could potentially lead to an overall non-conservative structural fire

REFERENCES

- Agarwal, A., Choe, L., Varma, A.H., 2014. Fire design of steel columns: Effects of thermal gradients. *Journal of Constructional Steel Research* 93, 107–118. doi:10.1016/j.jcsr.2013.10.023
- BS EN 1991-1-2, 2002. *Actions on Structures — Part 1-2: General actions — Actions on structures exposed to fire.*
- Garlock, M., Quiel, S., 2007. Mechanics of wide-flanged steel sections that develop thermal gradients due to fire exposure. *International journal of steel structures* 7, 153–162.
- Hamins, A. et al., 2005. *Experiments and Modeling of Unprotected Structural Steel Elements Exposed to a Fire.* Gaithersburg, National Institute of Standards and Technology.
- Higginson, S., 2012. *Heat Transfer to a Steel Beam: Testing the Theories [MEng Thesis] University of Edinburgh.*
- Lange, D., Sjöström, J., 2014. Mechanical response of a partially restrained column exposed to localised fires. *Fire Safety Journal* 67, 82–95. doi:10.1016/j.firesaf.2014.05.013
- Pultar, M., Sokol, Z. & Wald, F., 2010. *Temperature of External Column during Fire Test.* s.l., DEStech Publications, Inc.
- Quiel, S., Garlock, M., 2010. Closed-Form Prediction of the Thermal and Structural Response of a Perimeter Column in a Fire. *The Open Construction and Building Technology Journal* 4, 64–78. doi:10.2174/1874836801004010064
- Wang, W.-Y., Li, G.-Q., 2008. Fire-resistance study of restrained steel columns with partial damage to fire protection. *Fire Safety Journal* 44, 1088–1094. doi:10.1016/j.firesaf.2009.08.002
- Wiesner, F., Peters, G., Bisby, L., Hadden, R. (2017). *Structural Steel Columns Subjected To Localised Fires*, International Fire Safety Symposium (IFireSS), Naples, Italy.

CROSS-SECTION RESISTANCE OF SLENDER STAINLESS STEEL I PROFILES IN CASE OF FIRE

Nuno Lopes¹, Carlos Couto¹, Jorge Azevedo¹, Paulo Vila Real¹

ABSTRACT

This paper presents a numerical study on the cross-section resistance of I-shape stainless steel members subjected to compression or bending at elevated temperatures, addressing with special focus the performance of thin walled profiles. The behaviour of isolated plates, corresponded to the web and flanges of those I sections, is analysed, comparing the numerically obtained ultimate load bearing capacities with simplified calculation formulae for the application of the effective width method. Following the better understanding of the behaviour of those internal and outstand elements, finite element modelling is applied for the determination of the ultimate axial and bending resistance capacities of the complete I shape composition. Being the obtained results compared with Eurocode 3 prescriptions and with a recent proposal for carbon steel Class 4 sections in fire, concluding that these simplified design methodologies are generally conservative for stainless steel sections.

Keywords: Cross-section resistance, stainless steel, numerical analysis

1 INTRODUCTION

The application of stainless steel as a structural material has been increasing, due to a number of desirable qualities such as its durability, resistance to corrosion and aesthetic appearance [1,2]. Despite having a high initial cost, stainless steel can be a competitive material if life cycle cost analysis is considered, due to its low maintenance needs. Moreover, it has a higher fire resistance when compared to carbon steel [3] allowing in some cases the absence of thermal protection.

In order to have a comprehensive understanding of the overall member resistance, it is important to first analyse the cross-section resistance, which is directly affected by local instabilities occurrence.

For structural design purposes, Eurocode 3 (EC3) [4] considers that the walls slenderness determine the cross-section classification (from Class 1 - stocky sections to Class 4 - slender sections). Subsequently, the cross-section resistance is calculated considering plastic section properties for Classes 1 and 2 sections, elastic section properties for Class 3 sections and effective section properties, applying the effective width method, for Class 4 sections. In addition, for cross-section of Classes 1, 2 and 3 at elevated temperatures the strength at 2% total strain should be considered as the yield strength and for Class 4 cross-sections it should be applied the 0.2% proof strength [3].

Although the subject of local buckling at elevated temperatures has been studied by different authors [5-10], the mentioned research works only address carbon steel elements and research of the local buckling effect on stainless steel sections at elevated temperatures is scarce and mostly focus on the member behaviour.

According to Part 1-2 of EC3 [3] design rules, stainless steel stress-strain relationships at elevated temperatures are characterized by having always a non-linear behaviour with an extensive hardening phase, when compared with carbon steel constitutive law. As existing fire design guidelines for stainless steel, such as in EN 1993-1-2 [3], are based on the formulations developed

¹ RISCO, Civil Engineering Department, University of Aveiro, Portugal.
Corresponding author e-mail: nuno.lopez@ua.pt

for carbon steel members [11,12], in spite of their different material behaviour, it is still necessary to develop knowledge on stainless steel structural behaviour at elevated temperatures.

This research work has the main objective of analysing the accuracy of EC3 calculation proposals for stainless steel I cross-sections in case of fire, subjected to compression or bending, by means of Geometrical and Material Non-linear Analysis with Imperfections applying the Finite Element software SAFIR [13]. Plates behaviour at elevated temperatures is analysed considering compression or bending and different boundary conditions for modelling isolated outstand elements (flanges) and internal elements (webs), following the methodology used for the development of carbon steel design approaches [5,7,12]. And finally, the resistance of cross-sections of different Classes, in restrained axially compressed members and laterally restrained beams, is analysed as recently was also performed for carbon steel cross-sections [6] (study on the scope of the research project FIDESC4 [7]).

Comparisons between the obtained numerical results, the EC3 design methods and a recent proposal for Class 4 carbon steel sections [6], are made, being concluded that new design expressions should be developed for the effective with method application on stainless steel I-sections subjected to fire.

2 SIMPLIFIED CALCULATION FORMULAE

2.1 Eurocode 3 design rules

According to EN 1993-1-2 [3], the section resistance of a stainless steel member in case of fire is calculated in the same way as for carbon steel, changing only the mechanical properties of the material to consider uniform elevated temperatures in the section.

Regarding the cross-section classification, *Eq. (1)* was used to determine the factor ε , a parameter necessary for the determination of the EC3 classification limits [14]

$$\varepsilon_{\theta} = 0.85 \left[\frac{235}{f_y} \frac{E}{210000} \right]^{0.5} \quad (1)$$

The design resistance value of axially compressed members of Class 1, 2 or 3 cross-sections with a uniform temperature θ_a shall be determined from *Eq. (2)*.

$$N_{fi,t,Rd} = A f_{y,\theta} / \gamma_{M,fi} \quad (2)$$

For Class 4 sections, according to Annex E of EN 1993-1-2, the effective area (A_{eff}), obtained from EN 1993-1-5 [12], should be considered instead of the gross cross-section area A .

In a fire situation higher strains are acceptable when compared to normal temperature design, therefore, instead of 0.2% proof strength usually considered at normal temperature, for cross-section of classes 1, 2 and 3 at elevated temperatures the stress corresponding to 2% of total strain should be adopted as the yield strength [3].

$$f_{y,\theta} = f_{2\%,\theta} = k_{2\%,\theta} f_y \quad (3)$$

However, for Class 4 cross-sections, according to Annex E of EN 1993-1-2, the proof strength at 0.2% strain should be used, thus

$$f_{y,\theta} = f_{0.2p,\theta} = k_{0.2p,\theta} f_y \quad (4)$$

In beams, the design value of the bending moment resistance of a cross-section with a uniform temperature θ_a shall be determined from:

$$M_{fi,\theta,Rd} = k_{y,\theta} [\gamma_{M,0} / \gamma_{M,fi}] M_{c,Rd} \quad (5)$$

Being $M_{c,Rd}$ for Classes 1 and 2 the plastic bending moment capacity, for Class 3 the elastic bending moment capacity, and for Class 4 sections the effective bending moment capacity, at normal temperature, determined with the effective section properties obtained from EN 1993-1-5.

The effective area and effective section modulus ($W_{eff,y}$) are determined through the application of the effective width method, considering the reduction of resistance due to local buckling effects [12]. On this regard, the EN 1993-1-4 [4] provides specific equations for the determination of the plate reduction factors (ρ) to the width of elements composing the stainless steel sections, as presented in Eq. (6) and Table 1.

$$b_{eff} = \rho \cdot b \quad (6)$$

Table 1. Reduction factor for stainless steel sections elements.

Cross-section elements	Reduction factor
Welded outstand elements	$\rho = \frac{1}{\bar{\lambda}_p} - \frac{0.242}{\bar{\lambda}_p^2} \leq 1$
Welded internal elements	$\rho = \frac{0.772}{\bar{\lambda}_p} - \frac{0.125}{\bar{\lambda}_p^2} \leq 1$

The plate slenderness – $\bar{\lambda}_p$ – value is determined with Eq. (7).

$$\bar{\lambda}_p = \sqrt{\frac{f_y}{\sigma_{cr}}} = \frac{\bar{b}/t}{28.4 \varepsilon \sqrt{k_\sigma}} \quad (7)$$

2.2 Proposal for Class 4 carbon steel sections at elevated temperatures

As mentioned before, recent research works [6,8] proposed the use of the stress corresponding to 2% of total strain as the steel yield strength also for Class 4 cross-sections at elevated temperatures, as it is done for the remaining sections, providing the plate reduction factors would be calculated as presented in Table 2. The accuracy of the application of this proposal for stainless steel sections is tested in this paper.

Table 2. Reduction factor proposed for carbon steel sections elements in case of fire [5].

Cross-section elements	Reduction factor
Outstand elements	$\rho = \frac{(\bar{\lambda}_p + 1.1 - \frac{0.52}{\varepsilon})^{1.2} - 0.188}{(\bar{\lambda}_p + 1.1 - \frac{0.52}{\varepsilon})^{2.4}} \leq 1.0$
Internal elements	$\rho = \frac{(\bar{\lambda}_p + 0.9 - \frac{0.26}{\varepsilon})^{1.5} - 0.055(3 + \psi)}{(\bar{\lambda}_p + 0.9 - \frac{0.26}{\varepsilon})^3} \leq 1.0$

3 PLATE BEHAVIOUR

3.1 Numerical modelling

Members composed of I-shape sections subjected to compression have both flanges and web in compression, whereas when the members are subjected to bending in the strong axis, a flange is in compression while the web is subjected to bending.

To determine the ultimate load of rectangular plates the program SAFIR was used. Each shell element has four nodes and six degrees of freedom (three translations and three rotations). Simply

supported conditions were applied to the plates by restraining the vertical displacements and additionally the rotations at the edges of the plate were also restrained to simulate the web-flange continuity. For the outstand elements, the vertical displacements were restrained on three sides while for the internal elements the vertical displacements were restrained in all four sides, this methodology follows the same principles as in [5]. *Fig. 1* presents the obtained deformed shapes of an outstand element subjected to compression, an internal element subjected to compression and an internal element subjected to bending.

Geometric imperfections were introduced into the numerical model by changing the nodal coordinates affine to the buckling mode shapes obtained with the program CAST3M [15] and applying the interface RUBY [16]. For the amplitude of the imperfections, it was considered 80% of $b/50$ for outstand elements and 80% of $b/100$ for internal elements, following the recommendations of EN 1090-2 [17]. Plates of the stainless steel grade 1.4301 [4] subjected to four temperatures were considered (350°C, 450°C, 550°C and 650°C).

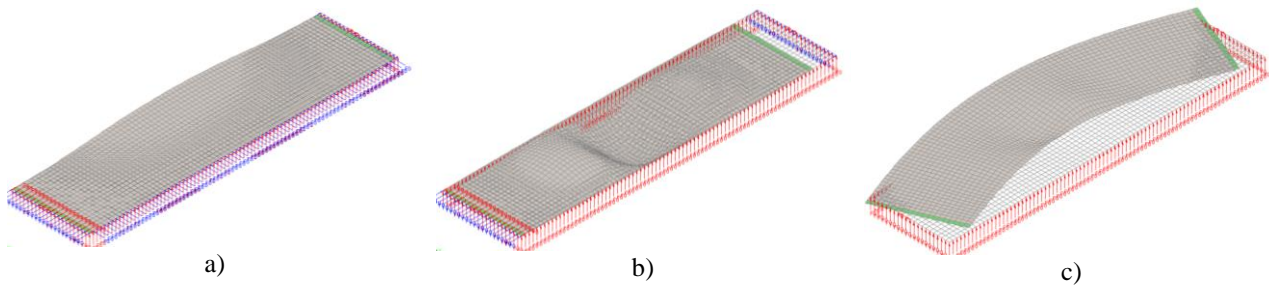


Fig. 1. Deformed shapes (x5): a) outstand element subjected to compression; b) internal element subjected to compression; c) internal element subjected to bending.

3.2 Plates subjected to compression

The results obtained for outstand and internal plate elements subjected to compression are presented in this section. At elevated temperatures, the equation to determine the reduction factor has to be adapted due to the transition that occurs from Class 3 to Class 4 section because of the change on the limit strength, leading to a discontinuity in the curve, as presented in *Eq. (8)*.

$$\rho_{\theta} = \frac{N_{c,Rd}}{N_{Rd}} = \rho \frac{f_{y,\theta}}{f_{z,\theta}} \quad (8)$$

Fig. 2 presents comparisons between the ultimate load bearing capacities, for outstand and internal plate elements subjected to compression, obtained with EC3 (named “EN 1993-1-4” in the graph), the new proposal for Class 4 carbon steel elements (named “CS new proposal” in the graph) and SAFIR.

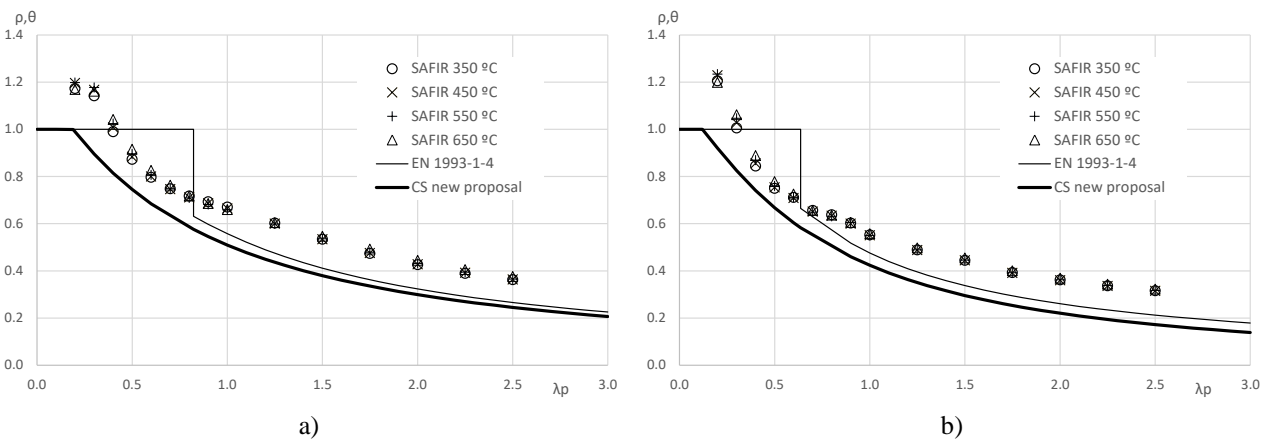


Fig. 2. Results for: a) outstand elements subjected to compression; internal elements subjected to compression.

For both outstand and internal elements subjected to compression, the proposal for carbon steel Class 4 sections [5] eliminates the un-conservative nature given by the plateau of EC3. It is also

observed that results are almost insensitive to the temperature value on the cross-section. Nonetheless, the results highlight the need of improved design equations specifically developed for stainless steel plates subjected to compression at elevated temperatures.

3.3 Plates subjected to bending

The obtained results for internal plate elements subjected to bending are presented in *Fig. 3*. The ultimate bending moments obtained in each plate for all methods were divided by the plastic bending moments. The different plateaus, in this figure, observed in Eurocode procedure of EN 1993-1-4 correspond to the transitions between Class 2 and Class 3 sections (from plastic to elastic resistance) and from Class 3 to Class 4 where at elevated temperatures the yield strength changes, as mentioned before. The curves from both proposals are over conservative when compared with the numerical results, which leads to conclude that specific formulae for stainless steel plates should be developed.

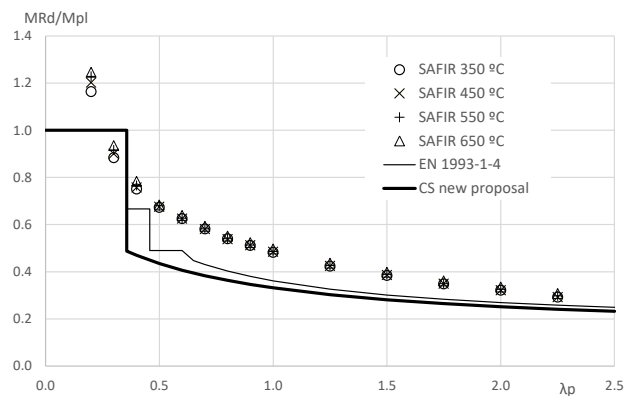


Fig. 3. Results for internal elements subjected to bending.

4 CROSS-SECTION RESISTANCE

4.1 Numerical modelling and case study

A parametric study was developed based on finite element analysis using the software SAFIR to determine and compare the ultimate bearing capacity of different I-shape cross-sections subjected to compression or bending. The results determined with EC3 formulae and with the new proposal for carbon steel sections [6] are compared to the numerical ultimate cross-sectional capacity.

The I-shape sections considered in this study are presented in *Table 3* and *4* for the elements submitted to compression or major-axis bending, respectively. The dimensions were chosen in order to have the flanges and webs covering a wide range of plate slenderness values.

Table 3. Cross-sections chosen for the compression study.

h_w [mm]	t_w [mm]	Web Class	b [mm]	t_f [mm]	Flange Class	Section Class	$(h_w/t_w)(2t_f/b)$
120	5	C3	145	8	C3	C3	2.65
150	5	C4	135	8	C2	C4	3.56
140	5	C4	145	8	C3	C4	3.09
165	5	C4	165	8	C4	C4	3.20
250	6	C4	200	8	C4	C4	3.33

Table 4. Cross-sections chosen for the major-axis bending study.

h_w [mm]	t_w [mm]	Web Class	b [mm]	t_f [mm]	Flange Class	Section Class	$(h_w/t_w)(2t_f/b)$
416	8	C3	150	8	C3	C3	5.55

Cross-section resistance of slender stainless steel I sections in case of fire

416	5	C4	135	8	C2	C4	9.86
336	5	C4	150	8	C3	C4	7.17
416	5	C4	200	8	C4	C4	6.66
516	5	C4	255	8	C4	C4	6.48

The tested profiles were of the stainless steel grade 1.4301 at temperatures 350°C, 450°C, 550°C and 650°C.

Following the recommendations from Part 1-5 of EC3, geometric imperfections were introduced into the model by applying the first buckling mode shape, obtained from the program CAST3M [15] and applying the interface RUBY [16], with corresponding amplitude of 80% of the geometric manufacturing tolerance given by EN 1090-2 [17]. Consequently, the amplitude was considered equal to $b/100$, where b is the height of the web or the width of the flange, depending on the location of the most displaced node. For both models, residual stresses were not considered as their effects may be negligible on determination of ultimate strength of cross-sections at elevated temperatures [6].

Fig. 4 shows the obtained deformed shape of restrained members subjected to compression and bending with Class 4 sections at 350 °C. It can be observed the occurrence of local instabilities in the profiles due to the thinner walls from which they are composed of.

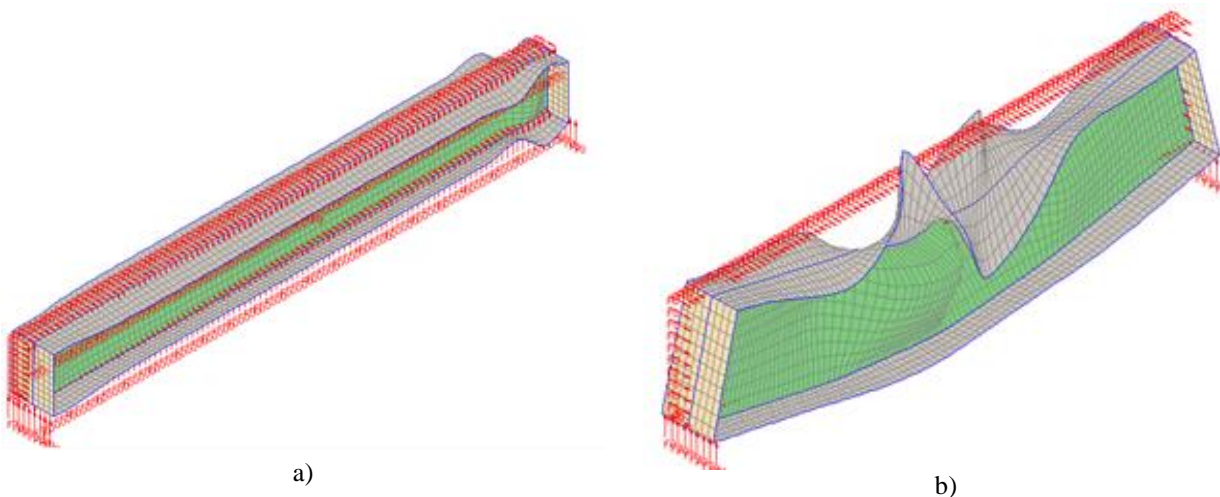


Fig. 4. Deformed shape (x5) of: a) restrained compressed Class 4 member; b) laterally restrained Class 4 beam.

4.2 Restrained axially compressed members

Fig. 5 presents the comparison between the results for restrained compressed members obtained using SAFIR and the simplified calculation methods. The ratios between the resistance obtained by SAFIR (denoted “NSAFIR”) and the method of EN1993-1-2 [3] (denoted “NEN1993-1-2”) and the new proposal for carbon steel [6] (named “NCSproposal”) are shown. Results below 1.0 are on the safe side and over 1.0 are unsafe.

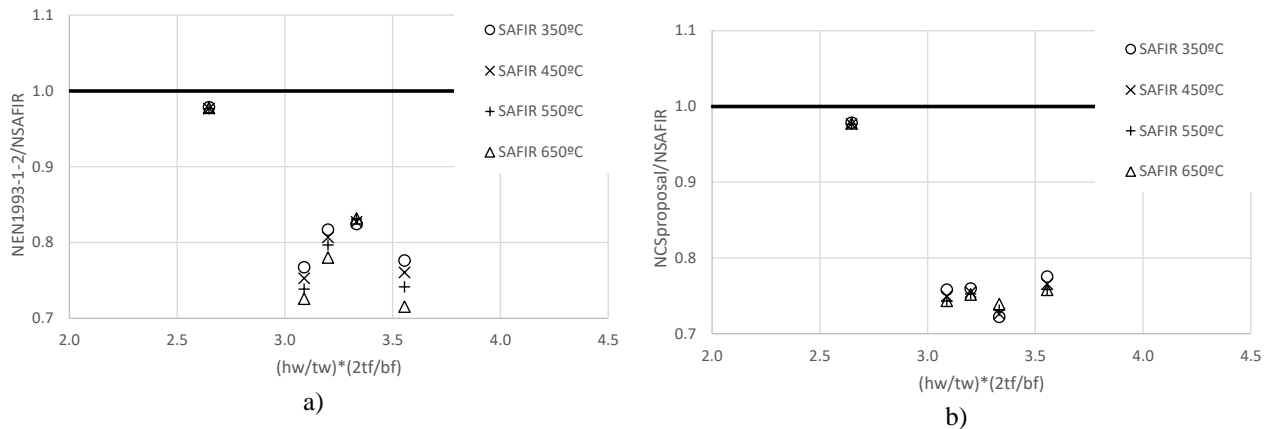


Fig. 5. Comparisons between simplified calculation proposals and numerical predictions of stainless steel I sections subjected to compression: a) comparison with EC3; b) comparison with proposal for carbon steel [6].

Results show that the design proposals are generally too conservative when compared to the numerical results.

4.3 Laterally restrained beams

As in the previous section, Fig. 6 presents the comparison between the results for laterally restrained beams obtained using SAFIR and the simplified calculation methods. The ratios between the resistance obtained by SAFIR (denoted “MSAFIR”) and the method of EN1993-1-2 (labelled “MEN1993-1-2”) and the new proposal for carbon steel [6] (identified as “MCSproposal”) are shown.

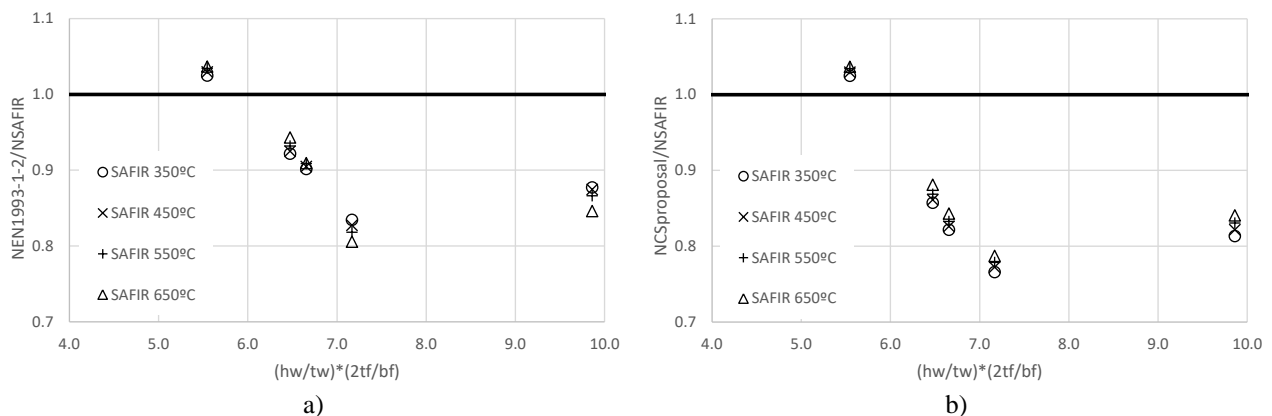


Fig. 6. Comparisons between simplified calculation proposals and numerical predictions of stainless steel I sections subjected to bending: a) comparison with EC3; b) comparison with proposal for carbon steel [6].

Again, the design proposals are generally too conservative. The spread in the results also highlights the need of improved design methodologies for ascertaining the cross-sectional capacity of I-shape sections submitted to bending about the major-axis.

5 CONCLUSIONS

This work presented a numerical study regarding the behaviour and the cross-sectional capacity of restrained axially compressed members and laterally restrained beams, of different cross-section classes, in stainless steel 1.4301, with I-shape profiles in fire situation.

In order to better understand the behaviour of these stainless steel I sections, thin plates at elevated temperatures were analysed. This study, on compressed outstand elements, compressed internal elements and internal elements subjected to bending, concluded that EC3 does not provide accurate and safe approximations to their numerically obtained counterparts regarding the ultimate load bearing capacities. Following this conclusion, a recent proposal for carbon steel plates [5] was also

investigated. It was observed that using this proposal allowed to overcome the unsafety that was previously observed for Class 3 sections, but results remained too conservative for Class 4 sections. In what regards the numerical study on the cross-section resistance of stainless steel members at elevated temperatures, it was possible to conclude that, for axially compressed members, both EC3 simplified calculation rules and the recently proposed formulation for Class 4 carbon steel sections [6], which suggests the use of the stress corresponding to 2% strain as yield strength for Class 4 sections, are too conservative. Regarding laterally restrained beams, the formulations yield too conservative approximations.

In summary, the prediction of cross-section resistance of stainless steel members for the case of fire is still not completely understood, thus motivating and justifying the development of more studies with the objective to achieve more precise and safe formulations for these members.

REFERENCES

1. Leroy Gardner (2005). *The use of stainless steel in structures*. Progress in Structural Engineering and Materials, vol 7, pp 45-55.
2. Euro Inox, SCI, Steel Construction Institute (2006). *Design Manual for Structural Stainless Steel*. 3rd edition.
3. CEN European Committee for Standardisation (2005). *EN 1993-1-2, Eurocode 3, Design of Steel Structures – Part 1-2: General rules – Structural fire design*. Belgium.
4. CEN European Committee for Standardisation (2006). *EN 1993-1-4, Eurocode 3: Design of steel Structures – Part 1-4: General rules – Supplementary Rules for Stainless steels*. Belgium.
5. Carlos Couto, Paulo Vila Real, Nuno Lopes, Bin Zhao (2014). *Effective width method to account for the local buckling of steel thin plates at elevated temperatures*. Thin Walled Structures, 84, 134–149.
6. Carlos Couto, Paulo Vila Real, Nuno Lopes, Bin Zhao (2015). *Resistance of steel cross-sections with local buckling at elevated temperatures*. Journal of Constructional Steel Research, 109, pp. 101–114.
7. FIDESC4 (2014) *Fire Design of Steel Members with Welded or Hot-Rolled Class 4 Cross-Section*. RFCS-CT-2011-2014, Technical Report No. 5”.
8. Knobloch, M., & Fontana, M. (2006). *Strain-based approach to local buckling of steel sections subjected to fire*. Journal of Constructional Steel Research, 62(1–2), 44–67.
9. Quiel, S. E., & Garlock, M. E. M. (2010). *Calculating the buckling strength of steel plates exposed to fire*. Thin-Walled Structures, 48(9), 684–695.
10. Chrysanthos Maraveas, Thomas Gernay, Jean-Marc Franssen (2017) *Amplitude of local imperfections for the analysis of thin-walled steel members at elevated temperatures*, Applications of Structural Fire Engineering (ASFE’17), Manchester, UK.
11. CEN European Committee for Standardisation (2005). *EN 1993-1-1, Eurocode 3: Design of steel Structures – Part 1-1: General rules and rules for buildings*. Belgium.
12. CEN European Committee for Standardisation (2006). *EN 1993-1-5, Eurocode 3: Design of steel Structures – Part 1-5: Plated structural elements*. Belgium.
13. Jean-Marc Franssen, Thomas Gernay (2017). *Modelling structures in fire with SAFIR®: theoretical background and capabilities*. Journal of Structural Fire Engineering.
14. Jean-Marc Franssen, Paulo Vila Real (2015) *Fire Design of Steel Structures*. ECCS; Ernst & Sohn, a Wiley Company, 2nd edition.
15. CEA (2012). *CAST 3M research FEM environment*. development sponsored by the French Atomic Energy Commission <<http://www-cast3m.cea.fr/>>.
16. Carlos Couto, Paulo Vila Real, Nuno Lopes (2013). *RUBY an interface software for running a buckling analysis of SAFIR models using Cast3M*. University of Aveiro.
17. CEN European Committee for Standardisation (2011). *EN 1090-2, Technical requirements for the execution of steel structures*. Belgium.

IMPLICATION OF THE END CONNECTION TYPE OF STEEL BEAMS ON THE CRITICAL/LIMITING TEMPERATURE EQUATIONS

Jashnav Pancheti¹, Arul S Jayachandran²

ABSTRACT

EN 1993-1-2: 2005 and AS 4100 -1998/NZS 3404 codes provide two strength-based design methods for steel beams subjected to fire – temperature domain method and moment capacity method. The temperature domain method gives equations to find the critical temperature in the Eurocode and the limiting temperatures in the latter two codes. The EN 1993-1-2: 2005 equation is back calculated from equating the moment resistance to demand. The AS 4100 equation is developed based on limited experiments performed on simply supported beams as mentioned in the Handbook of BS 5950 Part 8 (Lawson and Newman 1990). The fire behavior of steel beams – mid-span deflections, rotations at the ends and the failure are highly dependent on the beam end connection types. During the fire, they prolong the run-away failure by the virtue of stress distribution in the member and by providing axial and rotational restraint to thermal expansion and rotations during the catenary action respectively. Once the boundary condition changes both of the equations are not useful and iterative procedure has to be followed for the combined loading of moments and axial forces that develop due to thermal expansion. The study proposes to slightly modify these equations in the codes so as to incorporate the effect of end connection types in the equations.

Keywords: Steel beams, end connection type, limiting temperature, critical temperature

1 INTRODUCTION

Codes along with the strength method for fire design also provide temperature domain method. These equations from the two codes EN 1993-1-2: 2005 and AS 4100 -1998 are presented below. EN 1993-1-2 (2005) gives an equation to find the critical temperatures of tension members and beams with Class 1,2 and 3 classifications laterally supported which depends on the degree of utilization of the member μ_o , presented in Eq. (1).

$$\theta_{a,cr} = 39.19 \ln \left[\frac{1}{0.9674 \mu_o^{3.833}} - 1 \right] + 482 \quad (1)$$

On the other hand, AS4100 gives a simpler equation for the limiting temperature which also depends only on the load ratio r_f . The equation is presented in Eq. (2).

$$T_l = 905 - 690r_f \quad (2)$$

The former equation is applicable for only beams with bending and no axial forces and the equation is developed from the beam bending capacity equation. When axially restrained beams have to be designed for fire, an iterative procedure have to be followed. Which is complicated and may

¹ Project Associate, Structural Engineering Laboratory, Department of Civil Eng., Indian Institute of Technology Madras, India.
e-mail: panchetijashnav@gmail.com

² Associate Professor, Structural Engineering Laboratory, Department of Civil Eng., Indian Institute of Technology Madras, India.
e-mail: aruls@iitm.ac.in

consume more time. The latter equation is developed based on limited experiments conducted on simply supported beams which are not axially not restrained. Fire behavior of steel beams when axially/rotationally restrained the behavior completely changes and the limiting/critical temperatures may vary from the equation. In reality, all the beams are beam-columns in case of fire because of a significant amount of axial forces that are developed in the member due to thermal expansion. The authors with the help of numerical studies slightly modify the above-mentioned equations so as to account for the axial and rotational restraint provided by the supports and the adjacent structure. Both the equations are plotted and presented in the *Fig. 1*.

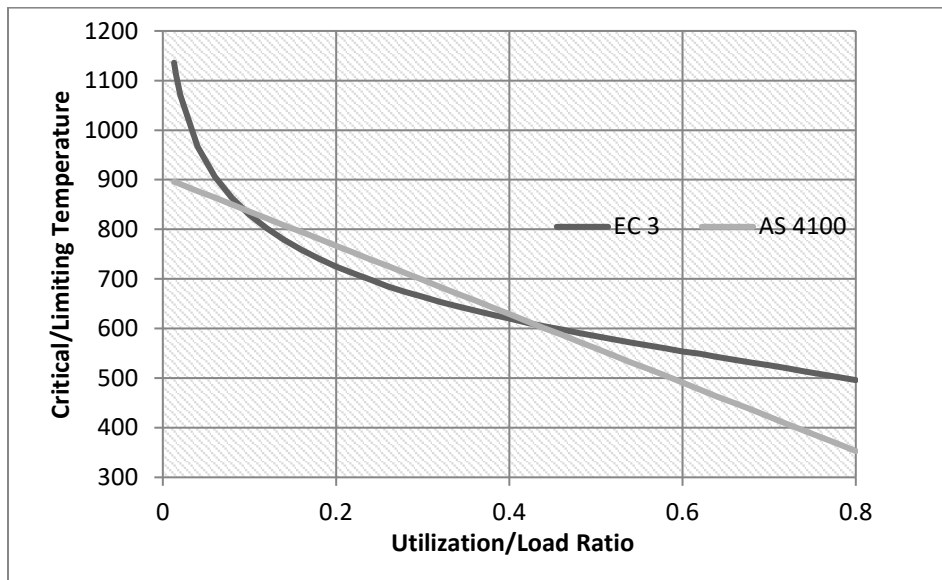


Fig. 1. EC3 and AS4100 equations are plotted

This study focuses only on the laterally restrained beams. A small sample is taken and analyzed numerically to find the temperatures and mid-span deflections. Based on this sample connection factors named 'k' are proposed for the two codes. There have been studies similar to this but with a different approach. [1] presented equations to analytically calculate axial stiffness and then modify the limiting temperature equations. As the present study is based on numerical finite element analysis the effect of axial loads developed and axial restraint provided by the supports is automatically incorporated. [2] compared the fire behavior of fixed-fixed and simply supported beam. They conclude that based on limiting temperature the fixed-fixed beam reaches yield first but when the simply supported beam fails in run-away action the fixed-fixed beam was still able to stand which is the main intent of structural fire safety. This study shows that limiting temperature gives very uneconomical results. During a fire accident, the first yielding plays a very little role. And also research shows that after the fire the steel regains it 80 to 90 % strength back. On the other hand, the critical temperature is the temperature at which the resistance equals demand. During a fire accident, this temperature does not play any crucial role, since the behavior of restrained beams during a fire is dependent on the catenary action. Hence we authors feel economical design can be achieved by considering the deflection limit of span/20 and the corresponding temperature called failure temperature hereafter instead of critical/limiting temperature.

This is not the first time studies are being done on steel beams with respect to different boundary conditions. [3] performed numerical studies with various boundary conditions. There have been several experiments as well with different types of connections. But none of the studies tried to modify the equation present for simply supported beams so that the effect due to end condition is incorporated and the iterative procedure can be avoided.

2 NUMERICAL STUDIES

2.1 Validation

This study is based on the numerical analysis performed using ABAQUS. Hence the model & procedure used for the studies have to be validated with either experiments or studies validated with experiments. [3] consists of a numerical analysis of steel beams with different end connections. The validation of the model is done with experiments in [4] of the same authors. As this study focuses on the catenary action of steel beams, [3] is used for validating the model used by authors, an indirect method to validate with experiments. An 8 m long UB 454 x 152 x 60 beams with pinned ends subjected to UDL with 0.4 and 0.7 load ratios have been presented. The same beam is modeled in ABAQUS. Though shell elements have been used in [3] we authors used solid elements to take the contribution of temperature difference over the thickness of the elements. The effect is negligible in this study. The results are presented in *Fig 2.1* and *Fig 2.2*

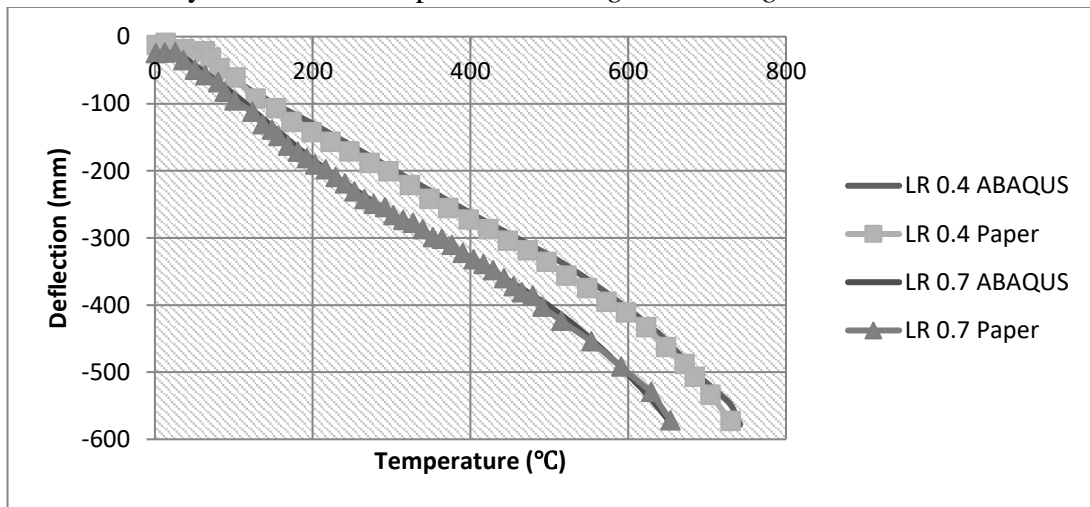


Fig 2.1. Midspan deflection

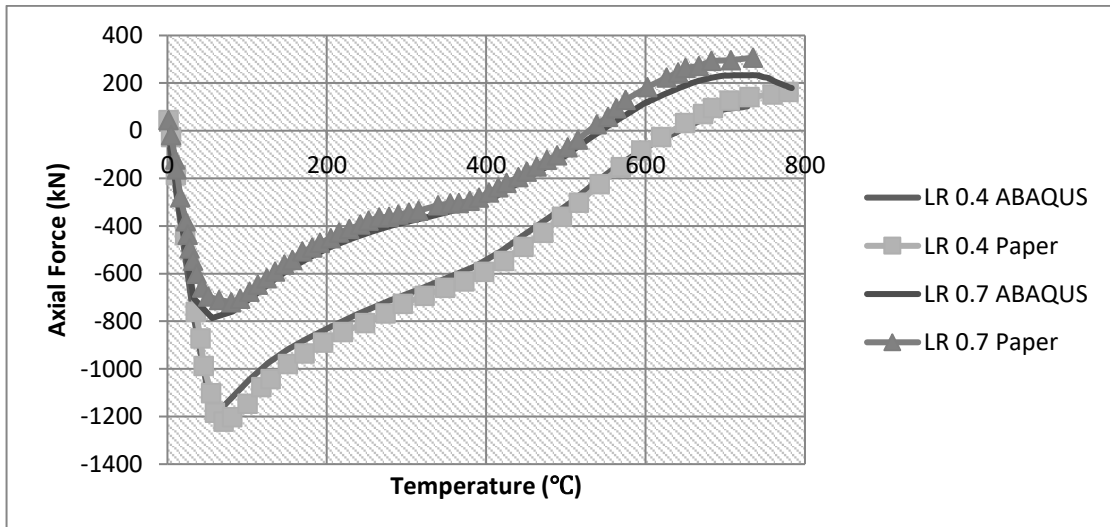


Fig 2.2. Axial force developed at the support

The results of the current model match with (publication) result. Hence the model is used for further studies. The support conditions and other parameters like length load ration were studied to find the failure temperature.

2.2 Parametric Studies (Part 1)

The first part of the parametric studies consists of a numerical analysis of a steel beam with different end conditions by keeping all other parameters constant. UB 305 × 127 × 48 beam is chosen with 5m length and 0.4 load ratio. The load is applied as UDL. The material properties are based on EN 1993-1-2 code. The beams were subjected to ISO 834 fire curve to study the deflections. The load ratio is calculated according to a maximum bending moment in the beam with respect to the end conditions divided by the plastic capacity of the beam as presented in Eq (3).

$$\text{load ratio } (r/\mu_o) = M_{\text{max corresponding}}/M_{\text{capacity}} \quad (3)$$

As discussed in the introduction failure temperature defined as the temperature at which the mid-span deflection of the beam cross span/20 limit is used to present the results in Fig 2.3.

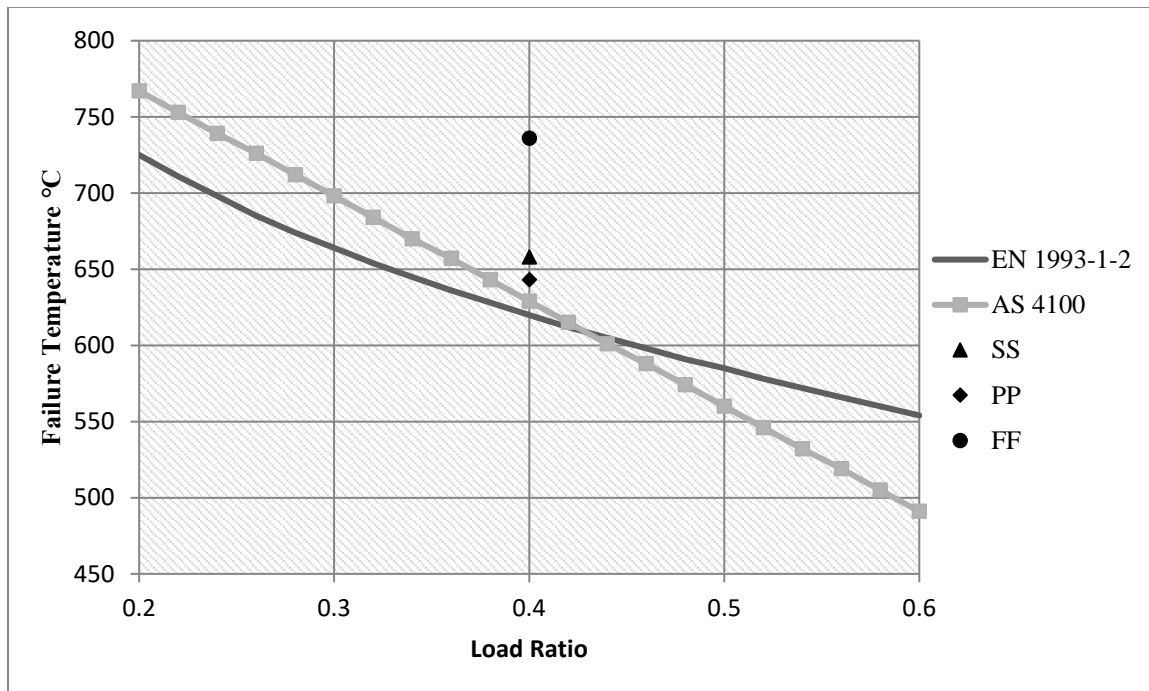


Fig 2.3 Results from the parametric study (Part 1)

From the results, it can be seen that the failure temperature of the simply supported beam with no axial rigidity is almost equal to the critical temperature/limiting temperature with respect to that load ratio. The introduction of pinned ends that is axial rigidity did not improve the performance of the beam and the failure temperature is same as the simply supported case. But when the rotation rigidity is brought in the performance of the beam has increased considerably. The failure temperature increased almost 13% compared to the PP case and 18% and 27% with respect to EN and AS code equations respectively. More stress distribution taking place in the fixed-fixed beam is the reason for improved performance compared to the simply supported and pinned-pinned beams. As the numerical studies have excelled quite far from the past the equations for simply supported beams can be slightly modified to account for the end conditions to avoid the iterative procedure. The effect of length and load ratio on the failure is studied in the next section.

2.3 Parametric Studies (Part 2)

The previous section considered only the change of end conditions and it was observed that the rotation restraint at the end condition increases the failure temperature. The second part of parametric studies focuses on the effect of load ratio and length of the beam on the conclusions made in the parametric studies (Part1). The behavior is studied with three different lengths of 3m, 4m, and 5m. Then numerical studies were carried out at three different load ratios 0.2, 0.4 and 0.6.

The same beam used in parametric studies (part 1) is used in this study as well. *Table 1* presents the failure temperatures of beams with different lengths and load ratios.

Table 1. Parametric studies (Part 2) results

Length (m)	Load ratio	Failure temperature (°C)		
		Simply Supported	Pinned-Pinned	Fixed-Fixed
5	0.6	594	580	672
	0.4	658	643	736
	0.2	754.5	728	840.5
4	0.6	596	605	670
	0.4	660	667	735
	0.2	756	760	836
3	0.6	603	612	672
	0.4	662.5	675	734
	0.2	759	774	830

The results show that the parameters load ratio and beam length did not change the expected behavior and the conclusions speculated in parametric studies (part 1). Beams with higher length (5m) the failure temperature of pinned-pinned beams was lesser than the simply supported beams may due to the P- δ second order effect that are developed due to huge mid-span deflections. Though the failure temperature of pinned-pinned beams is very close to simply supported beams, the beams were able to sustain longer compared to the simply supported beams. The runaway failure changes to a gradually increasing deflection in the latter two cases.

3 RESULTS

The results obtained from both the parametric studies are presented in *Table 2*. The aim of the study was to retain the already present equations and modify them slightly to incorporate the end condition influence. Hence, rather than bring out new equation a factor is proposed which can be multiplied directly by the limiting or critical temperature based on the end conditions.

Table 2. Failure temperatures vs Critical temperatures of EN 1993-1-2

Length (m)	Load ratio	θ_{cr} (°C)	Failure temperature (°C)					
			SS	% Diff	PP	% Diff	FF	%Diff
5	0.6	554	594	7.22	580	4.69	672	21.30
	0.4	620	658	6.13	643	3.71	736	18.71
	0.2	725	754.5	4.07	728	0.41	840.5	15.93
4	0.6	554	596	7.58	605	9.21	670	20.94
	0.4	620	660	6.45	667	7.58	735	18.55
	0.2	725	756	4.28	760	4.83	836	15.31
3	0.6	554	603	8.84	612	10.47	672	21.30
	0.4	620	662.5	6.85	675	8.87	733	18.23
	0.2	725	759	4.68	774	6.76	830	14.48

The fixed-fixed beam has a considerable increase in the failure temperatures compared with the pinned-pinned beam. The length of the beam did not play much role in the failure temperatures. But higher the load ratio higher was the influence of end conditions on the failure temperatures.

Implication of the end connection type of steel beams on the critical/limiting temperature equations

The connection factor is calculated using the lower bound theory that is the from the parametric studies performed, the least improvement or the greatest decrease in the temperature due to these end conditions is taken into account. The percentage increase or decrease with respect to code formulas are compared for the all the beams and load ratio ratios. Based these values the factor is decided later. The correction factor ‘k’ for En 1993-1-2 are presented in *Table 3*.

Table 3. Connection factors ‘k’ for EN 1993-1-2

Load ratio	Connection factor k		
	SS	PP	FF
0.6	1	1	1.2
0.4	1	1	1.18
0.2	1	1	1.14

‘k’ values for pinned-pinned beams are taken as 1 because the failure temperatures were very close to equations with only 10% or lesser difference. There was also high variation in the failure temperatures of pinned-pinned beams with respect to both length and load ratios making it difficult to fit in one single factor.

Results compared with the limiting temperatures of AS 4100 are presented in *Table 4*.

Table 4. Failure temperatures vs limiting temperatures of AS 4100

Length (m)	Load ratio	θ_{lim} (°C)	Failure temperature (°C)				%Diff	
			SS	% Diff	PP	% Diff		
5	0.6	491	594	20.98	580	18.13	672	36.86
	0.4	629	658	4.61	643	2.23	736	17.01
	0.2	767	754.5	-1.63	728	-5.08	840.5	9.58
4	0.6	491	596	21.38	605	23.22	670	36.46
	0.4	629	660	4.93	667	6.04	735	16.85
	0.2	767	756	-1.43	760	-0.91	836	9.00
3	0.6	491	603	22.81	612	24.64	672	36.86
	0.4	629	662.5	5.33	675	7.31	733	16.53
	0.2	767	759	-1.04	774	0.91	830	8.21

The qualitative behavior remains the same in this case as well. There is a slight increase in the failure temperature of fixed-fixed beams with load ratio 0.6. The connection factors for the As 4100 code are presented in *Table 5*.

Table 5. Connection factors ‘k’ for AS 4100

Load ratio	Connection factor 'k'		
	SS	PP	FF
0.6	1	1	1.36
0.4	1	1	1.16
0.2	1	1	1.08

These connection factors are to be multiplied by the critical/limiting temperature equations. The load ratio is calculated by dividing plastic moment capacity of the beam with a corresponding maximum moment in the beam with different boundary conditions.

4 CONCLUSIONS

Codes mention simple equations to find limiting/critical temperatures for bending alone and tension members. When there is axial and rotational restraint coming into the picture a lengthy and complex iterative procedure should be followed. There are several studies in the literature on the behavior of steel beams with different boundary conditions. The failure temperatures used in this study were also mentioned in some the publications. But none of the publications tried to use the studies to simplify this procedure. This study takes a small sample of a single beam shape with different lengths and load ratios. Based on the results produced a connection factor to be multiplied by the critical/limiting temperatures are presented. This results in saving huge computation and design time. The simpler the design procedure the more it is used in the design instead of neglecting. As the simple procedure is introduced more accurately failure temperatures will be used to calculate the projected thickness resulting in an economical design. With the introduction of rotational fixity at the ends resulted in an increase of the failure temperatures ranging from 1.14 times to 1.36 times with respect to the load ratio. Keeping this study as a basis more sophisticated studies can be performed with a large number of samples and considering other factors like size effect, bigger range of spans semi-rigid connections and load ratios. Hence this study:

- kindles and idea to use the numerical studies to simplify the design procedure
- presents a factor called connection factor to be multiplied by the critical/limiting temperature calculated with proposed load ratio
- an iterative procedure can be avoided with the further improvisation of this method to calculate failure temperatures in beams with combined loading

REFERENCES

1. M.B.Wong (2005) *Modelling of axial restraints for limiting temperature calculation of steel members in fire*. Journal of Constructional Steel Research, 61. Pp 675-687.
<https://doi:10.1016/j.jcsr.2004.10.003>
2. Marlena Kucz, Katarzyna Rzeszut, Polus Łukasz, Michał Malendowski (2013). *Influence of Boundary Conditions on the Thermal Response of Selected Steel Members*. Procedia Engineering, 57. pp 977 – 985.
<https://doi.org/10.1016/j.proeng.2013.04.124>
3. Y.Z. Yin, Y.C. Wang (2005) *Analysis of catenary action in steel beams using a simplified hand calculation method, Part 1: theory and validation for uniform temperature distribution*. Journal of Constructional Steel Research, 61. Pp 183–21.
<https://doi:10.1016/j.jcsr.2004.07.002>
4. Y.Z. Yin, Y.C. Wang (2004) *A numerical study of large deflection behaviour of restrained steel beams at elevated temperatures*. Journal of Constructional Steel Research, 60. pp 1029–1047.
<https://doi:10.1016/j.jcsr.2003.09.005>

DIRECT STRENGTH METHOD FOR CALCULATING DISTORTIONAL BUCKLING RESISTANCE OF COLD-FORMED THIN-WALLED STEEL BEAMS WITH NON-UNIFORM ELEVATED TEMPERATURES

Mutiu Adeoye Alabi-Bello¹, Yong Chang Wang²

ABSTRACT

This paper presents a preliminary finite element simulation based assessment of thin-walled steel beams prone to distortional buckling failure under non-uniform elevated temperatures. Numerical heat transfer analyses were performed to compare temperature distributions in thin-walled steel beams exposed to fire from one side to those reported in experimental tests. Based on heat transfer analyses, it was found that the temperature distributions in the cross-section of these beams are non-uniform and non-linear. The possibility of using a simplified temperature distribution in the cross-section was established and confirmed. Upon validation of the numerical model against existing tests on beams at non-uniform elevated temperatures, a parametric study using sequentially coupled structural-thermal non-linear analysis in ABAQUS was used to determine the bending resistance of beams at elevated temperatures in distortional buckling failure mode. The assessment was performed by comparing Direct Strength Method (DSM) structural strength predictions with those determined from finite element simulations. The results show that based on the use of plastic and critical buckling moments at elevated temperatures, the existing DSM method overestimates the design strength. A set of modified DSM equations have been proposed.

Keywords: Thin-walled steel beams, cold-formed channel sections, direct strength method, distortional buckling, finite element model, non-uniform elevated temperatures.

1 INTRODUCTION

The use of cold-formed, thin-walled construction continues to grow owing to their many advantages including high strength to weight ratio, flexibility of manufacture, fast and easy construction as well as low handling and transportation costs [1].

The high width to thickness ratios of these thin-walled structural members make them easily susceptible to different buckling modes; local, distortional, global and their combinations. This makes their behaviour complicated and the task of developing simple analytical methods for design purpose challenging. To overcome these design challenges, Direct Strength Method (DSM) has been developed [2-4].

DSM equations for these members under bending at ambient temperature are well established. The method is based on elastic buckling stability analysis using the yield strength and critical elastic buckling loads of members to determine the ultimate flexural capacity of cold-formed steel beam sections [3]. The method has now been incorporated into a number of design codes such as American Standard code of practice [5] and Australian code AS/NZS 4600 [6].

Previous studies on thin-walled steel beams at elevated temperatures have been carried out by [7-16]. The recent studies on distortional buckling failure of beams at elevated temperatures include: [12]- reporting an experimental investigation of different profile sections at elevated temperatures

¹ PhD Candidate. School of Mechanical, Aerospace and Civil Engineering, University of Manchester, Manchester, UK.
e-mail: mutiu.alabi-bello@manchester.ac.uk

² Professor. School of Mechanical, Aerospace and Civil Engineering, University of Manchester, Manchester, UK.
e-mail: yong.wang@manchester.ac.uk

and design evaluation based on the recommendations of [17]; [15]- numerical investigation of distortional failure and DSM design of beams under uniform elevated temperatures. [12] noticed that the presence of axial restraints greatly affects the critical temperatures of beams when subjected to fire conditions while [15] showed that the existing DSM could not accurately predict strengths for beams at elevated temperatures especially in the low-to-moderate slenderness range.

These previous studies have shown that the use of DSM for the design of beams at elevated temperatures has not been established, particularly under non-uniform temperature distribution. In order to develop DSM for the design of these members under non-uniform temperature distribution, numerical non-linear analyses are being carried out and the preliminary results are presented herein. In this paper, finite element model (FEM) was validated against experimental tests of [9] and was used in coupled non-linear structural-thermal simulations to determine failure loads of beam at non-uniform elevated temperatures under distortional buckling.

Since mechanical properties in the thin walled steel cross-sections are non-uniformly distributed due to non-uniform heating, it would be much easier to use the plastic resistance, rather than the first yield resistance, of the cross-section, when using DSM. The estimated DSM results were subsequently compared with FEM simulation results.

2 NUMERICAL HEAT TRANSFER VALIDATION

[9] carried out experimental fire tests on cold-formed steel beams; open channel sections. The joist arrangements are shown in *Fig. 1*. The steel beams are arranged at 600 mm centre to centre and 150 mm to the edges.

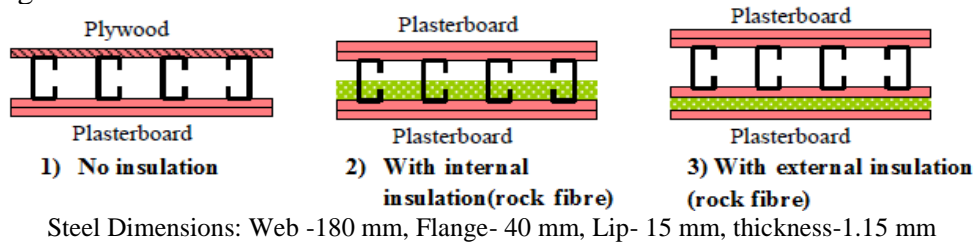


Fig. 1. Floor joist arrangement using lipped channel sections [9]

For validation, 2D numerical heat transfer analyses were carried out in ABAQUS [18] to obtain temperature distributions in the steel sections which are compared with test results.

To correctly model the fire performance of these assemblies, correct thermal properties of the components must be used. Thermal properties and density of steel as given in [19] were used. For plasterboard, propositions of [20], [21] and [22] were adopted for specific heat capacity, density and thermal conductivity respectively. Thermal properties proposed by [20] and those of [22] were adopted for rock fibre insulation and plywood respectively. Other key parameters in the numerical heat transfer analysis are:

- Emissivity(ϵ) of 0.9 proposed by [20] for both ambient (topmost part in configurations) and fire (bottom part in configurations) sides; Cavity radiation ($\epsilon=0.6$) used for the voids between steel sections and between steel beams and open cavity at the edges;
- Convective heat coefficients $25 \text{ W/m}^2\text{K}$ and $10 \text{ W/m}^2\text{K}$ for fire and ambient sides respectively;
- Standard fire temperature-time curve;
- Element DC2D4: two elements each in the thickness direction for the steel beams and 6 elements in thickness direction for the 16 mm thick plasterboard and plywood;
- TIE constraint to represent heat transfer by conduction between components.

Fig. 2 presents the average mid-flange temperatures of the beams as a representative example. It shows good agreement between test and numerical results for test 3 of [9]. Similar accuracy was also noticed for the other tests.

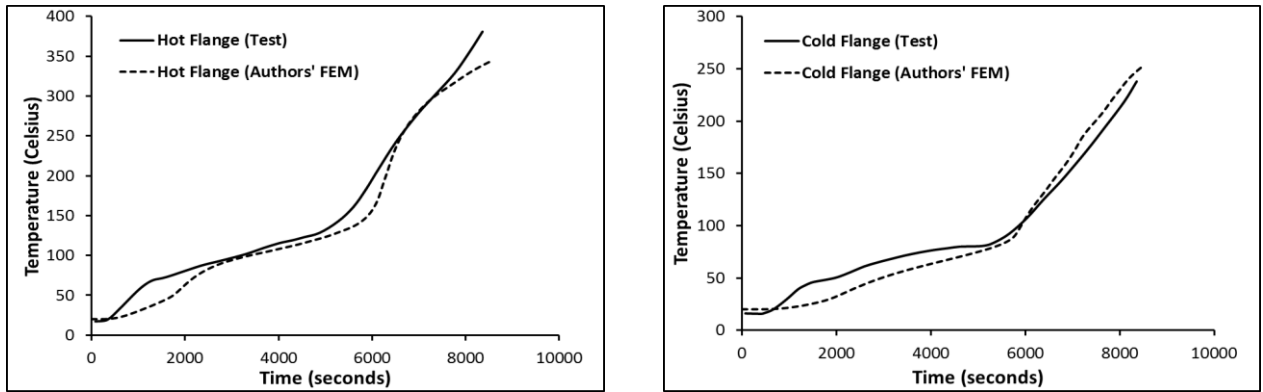


Fig. 2. Comparison between test (3) results of [9] and numerical heat transfer results of the authors

3 VALIDATION OF MODELLING AT AMBIENT TEMPERATURE

The bending tests of [9] were used to validate the ABAQUS finite element modelling. Shell elements S4R with 4, 8, 20 elements in the lips, flanges and web respectively with 10 mm size in the longitudinal direction were used for modelling. The simply supported beams span 2.4 m and are restrained at the compression and tension flanges laterally to represent screw locations in experimental tests, as well as prevent global lateral torsional buckling. A total pressure load was applied on the compression flange of the beams. Fig. 3(a) shows a finite element configuration.

The stress-strain curve was assumed to be elastic-perfectly plastic, with yield strength (σ_y) of 612 MPa, Young's modulus (E) of 210 GPa and Poisson's ratio (μ) is 0.3 based on the test data.

[23] recommended that the effects of residual stress and cold-working may be ignored based on the assumption that they offset each other. Therefore, in this research, neither of these two effects was included in the simulation model.

The maximum initial imperfection for the first local buckling mode was assumed to be $0.34t$ (where t is section thickness), which corresponds to the 50% CDF value as recommended by [24]. The buckling mode was determined via elastic buckling analysis in ABAQUS [18].

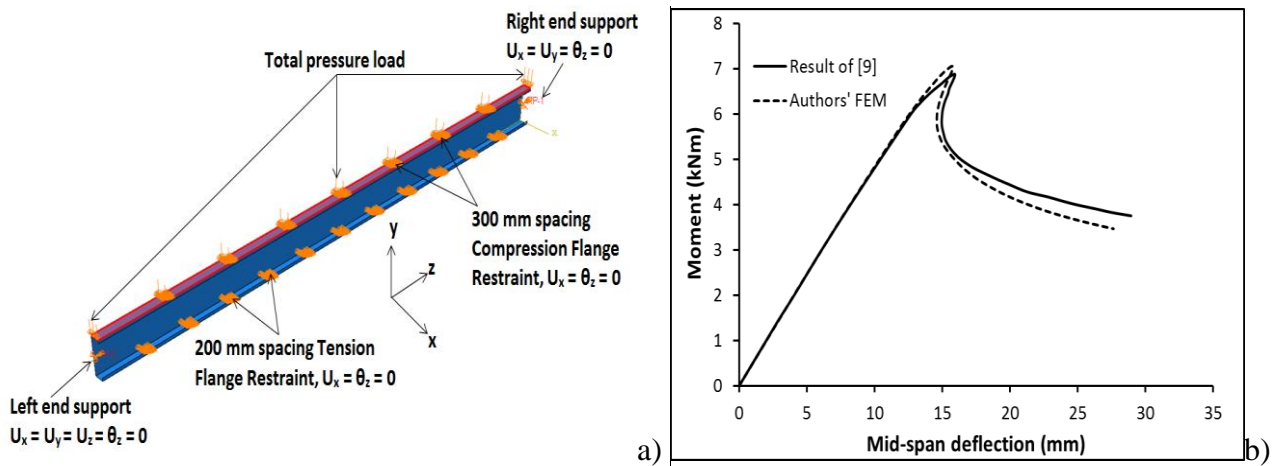


Fig. 3. a) Finite element model; b) Load-deflection curves

Fig. 3(b) compares the load-deflection curves and demonstrates excellent agreement between the authors' FEM result and the result of [9].

4 SIMPLIFIED TEMPERATURE DISTRIBUTION ASSUMPTION

The temperature distribution in the cross-section of steel beams exposed to fire from one side is non-uniform and non-linear. Including the exact non-uniform temperature distribution in subsequent structural modelling is time consuming. This research examined whether it would be possible to use a simplified temperature distribution in the cross-section. In the simplified temperature distribution, it is assumed that the hot flange/lip have the same temperature (magnitude equal of that of midflange), the cold flange/lip have the same temperature and the temperature distribution in the web is bilinear with the end temperatures equaling to the hot flange/lip and cold flange/lip temperatures, intersected at the position of the interior insulation for arrangements with internal insulation. For arrangements without insulation, the web temperature distribution is assumed to be linear. In addition, uniform temperature along the member length was also assumed. Transient state analysis in the form of sequentially coupled structural-thermal analysis was carried out in ABAQUS using the validated model in section 3. In the analysis, the beam was incrementally loaded up to a target mechanical load value (a percentage of the ambient temperature failure load) and then subsequently heated up until failure. The ambient temperature failure load and temperature distributions were based on the results in sections 3 and 2. The elevated temperature mechanical properties (strength, σ_y and Stiffness, E) were according to those proposed by [25] and the linear coefficient of expansion of [26] was used. Fig. 4(a) shows the stress-strain of [9]. Fig. 4(b) shows a typical example of comparison between the simulated beam displacement-time relationships between using the actual non-uniform temperature distribution and the simplified temperature distribution, confirming that the simplified temperature distribution is acceptable.

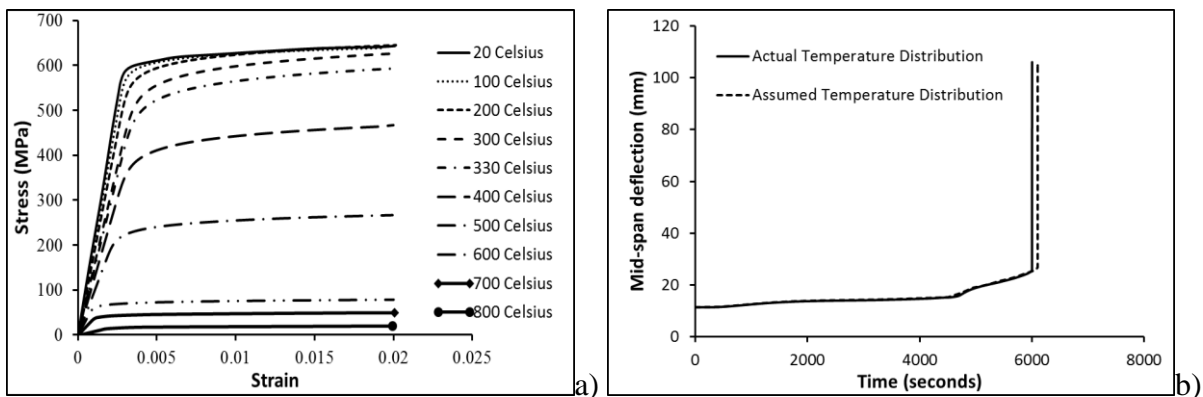


Fig. 4. a) Stress-strain curves; b) Comparison of displacement-time curves

5 VALIDATION AT ELEVATED TEMPERATURE

The fire tests of [9] were used. The applied load was 40% of the ambient temperature failure load. Fig. 5 compares the results for tests 1 and 2 of [9].

Good agreement is achieved, in particular when compared with the simulation results of [9], confirming accuracy of the authors' simulation model. Some differences were observed in failure times, which may be attributed to presence of flange restraints throughout the heating period in the numerical models. In contrast, as reported in the fire tests, there were some plasterboard fall-off prior to failure of the steel beams, which implies that the restraint was not present throughout the heating period. However, this effect could not be quantified and was neglected in the authors' simulation model as well as the simulation model of [9].

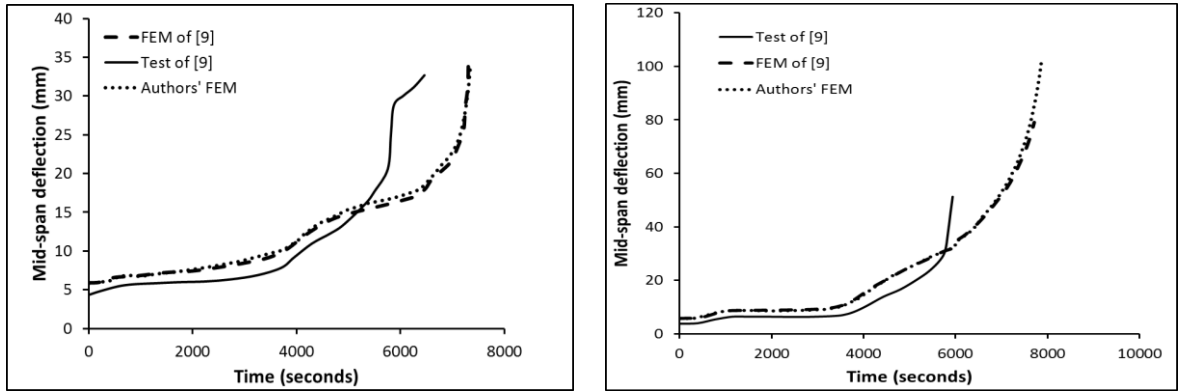


Fig. 5. Comparison between the authors' simulation, tests and simulation displacement-time curves of [9]

6 NUMERICAL PARAMETRIC STUDY AND ASSESSMENT OF DSM

Using the validated numerical simulation models for sequential structural-heat transfer modelling and the simplified cross-section temperature distribution, a parametric study has been carried out to determine bending resistance of thin-walled steel beams at non-uniform elevated temperatures in the distortional buckling failure mode. To enforce distortional buckling and retaining centreline dimensions, the section thickness of the tests of [9] was increased to 2.5 mm and 3 mm. Fig. 6 displays typical critical elastic distortional buckling mode.

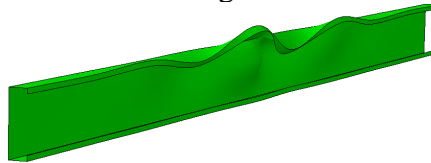


Fig. 6. Distortional buckling mode

Fig. 7 shows the flange and web temperatures for the 2.5 mm section using numerical heat transfer analyses in ABAQUS [18].

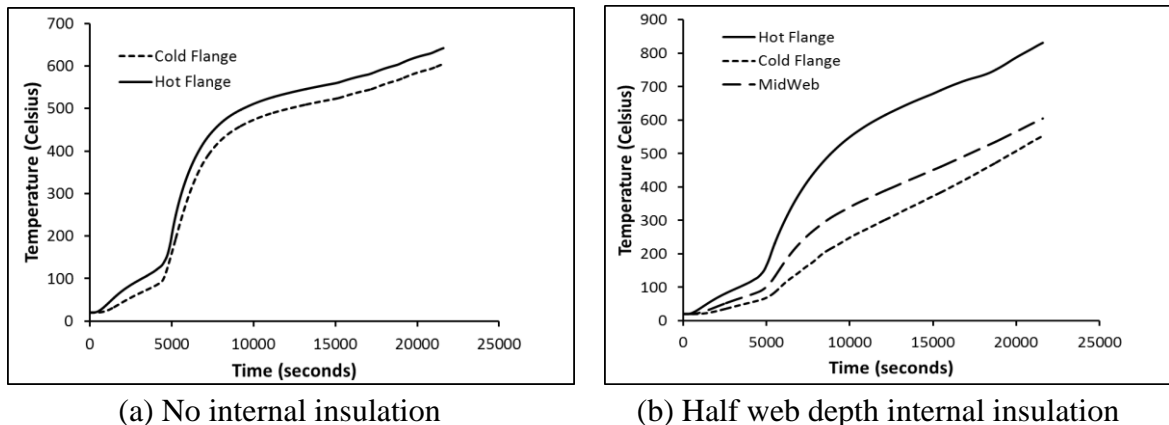


Fig. 7. Temperature distribution profiles in 181.35 x 41.35 x 15.68 x 2.5 mm channel section

6.1 Assessment of DSM for distortional buckling at ambient temperature

To establish the accuracy of base DSM at ambient temperature, some finite element simulations were run and the failure loads compared with DSM predictions. The maximum initial imperfection was 0.94t corresponding to the first distortional buckling mode with 50% CDF [24]. In addition, different steel yield strengths (275 MPa, 355 MPa, 435 MPa and 612 MPa) were used. Table 1 shows the results of this assessment.

The DSM equations for calculating the distortional buckling resistance (M_{nd}) are:

$$\text{for } \lambda_d \leq 0.673, \quad M_{nd} = M_y \quad (1)$$

$$\text{for } \lambda_d > 0.673, \quad M_{nd} = \left[1 - 0.22 \left(\frac{M_{crd}}{M_y} \right)^{0.5} \right] \left(\frac{M_{crd}}{M_y} \right)^{0.5} M_y \quad (2)$$

where λ_d is the distortional buckling slenderness given by $\lambda_d = \sqrt{\frac{M_y}{M_{crd}}}$,
 M_{crd} is the critical elastic distortional buckling moment,
 M_y is the yield moment.

Table 1. Assessment of DSM at ambient temperature

Section Thickness (mm)	M_{crd} (kNm)	M_y (kNm)	M_{nd} (kNm) DSM	M_{FEM} (kNm)	M_{nd}/M_{FEM}
2.50	34.62	9.95	9.95	9.90	1.004
2.50	34.62	12.84	12.84	12.30	1.043
2.50	34.62	15.73	15.72	14.49	1.085
2.50	34.62	22.13	20.06	18.79	1.068
3.00	52.60	11.94	11.94	12.29	0.971
3.00	52.60	15.41	15.41	15.36	1.003
3.00	52.60	18.88	18.88	18.21	1.037
3.00	52.60	26.56	25.81	23.88	1.081
Average					1.037
Standard Deviation					0.041

Table 1 shows very good agreement between FEM and DSM results, confirming accuracy of the base DSM equations at ambient temperature.

6.2 Assessment of DSM for distortional buckling at elevated temperatures

The elevated temperature assessment was performed based on the beams in the previous section (6.1) with different percentages (10-90) of some of the ambient temperature failure loads in Table 1. After applying the mechanical load, the simplified temperature distributions, based on the numerical heat transfer results were applied until beam failure.

To obtain beam resistance using DSM, the elastic critical load (M_{crd}) of the beam (obtained using ABAQUS [18]) and the cross-section plastic moment (M_p) was determined at the same temperatures of the beam as at the end of the sequential heat transfer-structural behaviour modelling. Fig. 8 compares the beam resistance – slenderness relationships. It is important to notice that the simulation results all group around one single curve, indicating that it is feasible to propose one DSM equation. However, it should be pointed out that the base DSM curve at ambient temperature is based using the first yield resistance of the cross-section. When using the original DSM equations with the plastic resistance of the cross-section, the beam resistances are overestimated compared to the simulation results. However, for conveniently dealing with non-uniform temperature distributions, this research proposes using the plastic resistance of the cross-section in DSM. To improve the accuracy of DSM predictions, this research proposes a set of modified DSM equations as follows:

$$\text{for } \lambda_d \leq 0.48, \quad M_{nd} = M_p \quad (3)$$

$$\text{for } \lambda_d > 0.48, \quad M_{nd} = \left[0.90 - 0.20 \left(\frac{M_{crd}}{M_p} \right)^{0.48} \right] \left(\frac{M_{crd}}{M_p} \right)^{0.48} M_p \quad (4)$$

where M_{nd} is beam bending resistance for distortional buckling

Results using the proposed revised DSM equations are in very good agreement with the simulation results, giving an average value of DSM calculation to simulation result ratio of 0.985 and a standard deviation of 0.033.

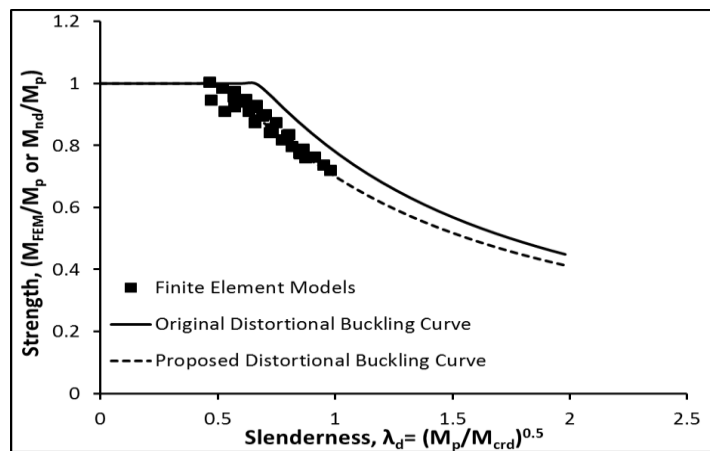


Fig. 8. Comparison between numerical simulation results with DSM for distortional buckling

7 CONCLUSIONS

This paper has presented the results of a preliminary numerical simulation study to develop a direct strength method for distortional buckling of thin-walled steel beams under non-uniform elevated temperatures. The assessment was based on simulation results generated using an ABAQUS model that was validated against the test results of [9]. The following main conclusions can be drawn:

- Numerical heat transfer analysis using correct temperature-dependent material properties gave temperature distribution profiles in good agreement with fire test results;
- The non-linear, non-uniform temperature distribution in thin-walled steel beams exposed to fire from one side can be simplified by assumed uniform temperature distributions in the exposed and unexposed flanges and lips with temperatures equal those of the mid-flange, and a bilinear web temperature distribution with intersection at the position of interior insulation;
- The ABAQUS simulation model was able to accurately predict distortional buckling behaviour at ambient and elevated temperatures;
- The base DSM equations at ambient temperature are sufficiently accurate for distortional buckling;
- DSM can be applied to thin-walled steel beams with non-uniform temperature distribution under distortional buckling. However, due to using the plastic resistance, instead of the first yield resistance of the cross-section, the ambient temperature DSM equations overestimate the beam resistance at elevated temperatures. A set of revised DSM equations for non-uniform, elevated temperature applications have been proposed;
- The proposed DSM equations gave very good agreement with numerical simulation results.

ACKNOWLEDGEMENT

This research is sponsored by Petroleum Technology Development Fund, Nigeria.

REFERENCES

1. Hancock, G.J., Murray, T.M., Ellifritt, D.S. (2001). *Cold-formed steel structures to the AISC Specification* Marcel Dekker Incorporation.
2. Hancock, G.J., Y.B. Kwon, E.S. Bernard, (1994). "Strength design curves for thin-walled sections undergoing distortional buckling." *Journal of Constructional Steel Research*, 31 (2-3) 169-186.

3. Schafer, B. W. & Pekoz, T. 1998a. Direct strength prediction of cold-formed steel members using numerical elastic buckling solutions. *Fourteenth International Specialty Conference on Cold-Formed Steel Structures* St. Louis, Missouri.
4. Schafer, B. W. 2002. Progress on the Direct Strength Method. *Sixteenth International Specialty Conference on Cold-Formed Steel Structures*. Orlando, Florida USA.
5. American Iron and Steel Institute (AISI) (2004). North American Specification for the design of cold-formed steel structural members, Washington, USA.
6. Standards Australia (SA) (2005). Cold-formed steel structures, AS/NZS 4600, Sydney.
7. Alfawakhiri, F. 2001. *Behaviour of cold-formed-steel-framed walls and floors in standard fire resistance tests* PhD, Carleton University, Ottawa, Ontario, Canada.
8. Kaitila, O. (2002). Finite element modelling of cold-formed steel members at high temperatures. Licentiate thesis, Helsinki University of Technology, Helsinki, Finland.
9. Baleshan, B. 2012. *Numerical and experimental studies of cold-formed steel floor systems under standard fire conditions*. PhD, Queensland University of Technology, Australia.
10. Kankanamge, N. D. 2010. *Structural behaviour and design of cold-formed steel beams at elevated temperatures*. PhD, Queensland University of Technology.
11. Kankanamge, N. & Mahendran, M. 2012. Behaviour and design of cold-formed steel beams subject to lateral-torsional buckling at elevated temperatures. *Thin-Walled Structures*, 61, 213-228.
12. Laím, L., Rodrigues, J. P. C. & Silva, L. S. D. 2013. Experimental and numerical analysis on the structural behaviour of cold-formed steel beams. *Thin-Walled Structures*, 72, 1-13.
13. Laím, L., Rodrigues, J. P. C. & DA Silva, L. S. 2014. Experimental analysis on cold-formed steel beams subjected to fire. *Thin-Walled Structures*, 74, 104-117.
14. Cheng, S., Li, L.-Y. & Kim, B. 2015. Buckling analysis of cold-formed steel channel-section beams at elevated temperatures. *Journal of Constructional Steel Research*, 104, 74-80.
15. Landesmann, A. & Camotim, D. 2016. Distortional failure and DSM design of cold-formed steel lipped channel beams under elevated temperatures. *Thin-Walled Structures*, 98, 75-93.
16. Jatheeshan, V. & Mahendran, M. 2015. Experimental study of cold-formed steel floors made of hollow flange channel section joists under fire conditions. *Journal of Structural Engineering American Society of Civil Engineers*, 14.
17. EN1993-1.1: Design of steel structures. General rules and rules for buildings. European Committee for Standardization. Brussels, Belgium; June 2004.
18. Abaqus (2014), Abaqus Unified FEA v6.14-3 Documentation, Dassault Systèmes Simulia Corp.
19. EN1993-1.2. Design of steel structures. General rules. Structural fire design. European Committee for Standardization, Brussels, Belgium; June 2004.
20. Keerthan, P. & Mahendran, M. 2012. Numerical studies of gypsum plasterboard panels under standard fire conditions. *Fire Safety Journal*, 53, 105-119.
21. Rahmanian, I. & Wang, Y. C. 2012. A combined experimental and numerical method for extracting temperature-dependent thermal conductivity of gypsum boards. *Construction and Building Materials*, 26, 707-722.
22. Jatheeshan, V. & Mahendran, M. 2016. Thermal performance of LSF floors made of hollow flange channel section joists under fire conditions. *Fire Safety Journal*, 84, 25-39.
23. Schafer, B. W., Li, Z. & Moen, C. D. 2010. Computational modelling of cold-formed steel. *Thin-Walled Structures*, 48, 752-762.
24. Schafer, B. W. & Pekoz, T. 1998b. Computational modelling of cold-formed steel: characterizing geometric imperfections and residual stresses. *Journal of Constructional Steel Research*, 47, 193-210.
25. Kankanamge, N. & Mahendran, M. 2010. Mechanical properties of cold-formed steels at elevated temperatures. *Thin-Walled Structures*, 49 (1), 26-44.
26. Lie, T. T. (Ed.), *Structural Fire Protection*, American Society of Civil Engineers, New York, 1992.

THERMO-MECHANICAL BEHAVIOUR OF STRUCTURAL STAINLESS STEEL FRAMES IN FIRE

Mian Zhou¹, Rui Cardoso², Hamid Bahai³, Aisf Usmani⁴

ABSTRACT

The accuracy of finite element (FE) models is strongly dependent on the constitutive relation adopted for the material model, which is an important prerequisite of a finite element analysis (FEA). Using newly developed material models in OpenSees for stainless and carbon steels, the thermo-mechanical behaviour of stainless steel in fire is investigated using the FEA approach, highlighting its difference in behaviour from carbon steel structures.

1 INTRODUCTION

Stainless steel has been of interest to researchers and industry since early 1960s. In Europe, the First edition of the “Design Manual for Structural Stainless Steel (DMSSS)” was published in 1994. Several European research projects have since been carried out to analyse the performance of structural stainless steel, with the latest 4th edition of the Manual [1] published in 2017 as a result. Testing the behaviour of steel subassemblies and frame structures in a fire is extremely expensive and any one test only provides limited data. So far experiments of stainless steel structures in fire have been limited to individual structural components. Meanwhile, large scale fire tests of carbon steel structures, such as Cardington tests have revealed significant difference between global structural behaviour in fire and an individual structural component tested in a furnace.

The current research gap in understanding stainless steel structural systems in fire can be approached economically and efficiently using FEA; by taking advantage of existing experimental observations and experiences using FEA on large carbon steel structures in fire. This paper reports the findings of stainless steel structural system behaviour in fire based on the analysis results using the finite element software – OpenSees, with a focus on the comparisons in behaviour between carbon steel and stainless steel structures. In particular the importance of highly nonlinear material characteristics of stainless steel in structural behaviour in fire is highlighted, the impact of higher thermal expansion of stainless steel is discussed. In cases where little testing data of stainless steel structures is available, the FE models used in this paper are validated against existing testing data of carbon steel structures in fire.

2 STAINLESS STEEL MATERIAL BEHAVIOUR AT ELEVATED TEMPERATURES

A sound understanding of material behaviour is the foundation of a FEA based study of structural behaviour. For thermo-mechanical analysis of building structures in fire, the primary concerns at the material level are its reductions in strength and stiffness, thermal expansion and thermal properties associated with temperature development within the structure. A comparison between these properties for stainless and carbon steel is discussed in this section.

¹ PhD Candidate. Department of Civil , Environmental Engineering, Brunel University, London, UK..
e-mail: mian.zhou@brunel.ac.uk

² Senior Lecturer. Department of Mechanical, Aerospace Engineering, Brunel University London, UK
e-mail: rui.cardoso@brunel.ac.uk

³ Professor. Head of Department of Mechanical, Aerospace Engineering, Brunel University London, UK
e-mail: hamid.bahai@brunel.ac.uk

⁴ Professor. Head of Department of Mechanical, Aerospace Engineering, Hongkong Polytechnic University, Hong Kong
e-mail: asif.usmani@polyu.edu.hk

2.1 Material nonlinearity

The accuracy of FE models is strongly dependent on the constitutive relation adopted for the material model. Unlike carbon steel, stainless steel exhibits a rounded stress-strain relationship with no pronounced yield point at room temperature. Figure 1 plots the nominal stress strain curves for Carbon steel based on EC 3 [2] and Austenitic group III grades based on DMSSS [1]. When temperature exceeds 100°C, the perfectly elastic-plastic Carbon steel starts showing non-linear hardening of a saturation type, approaching the asymptotic value of the 2% proof strength. On the other hand, the stress strain curves of stainless steel are best fitted using a power law.

2.2 Strength and stiffness retention

The primary motivation behind exploring stainless steels behaviour in fire conditions comes from observations of its superior stiffness and strength retention at elevated temperatures in material tests. Figure 2 presents retention factors of initial Elastic Modulus provided by EC 3[2] for carbon steel and DMSSS [1] for stainless steel, which shows stainless steel offers better stiffness retention capability at temperatures higher than 250 °C. Figure 3 shows the strength retention factor $k_{0.2p, \theta}$ for Carbon steel, Austenitic and Duplex groups of stainless steel. Below around 200°C, carbon steel exhibits better proof strength ($f_{0.2}$) retention than all of the stainless steel groups except for Austenitic III. Austenitic III offers the best $f_{0.2}$ retention capability among all stainless groups, yet its superiority to carbon steel only starts when temperatures are above 200°C.

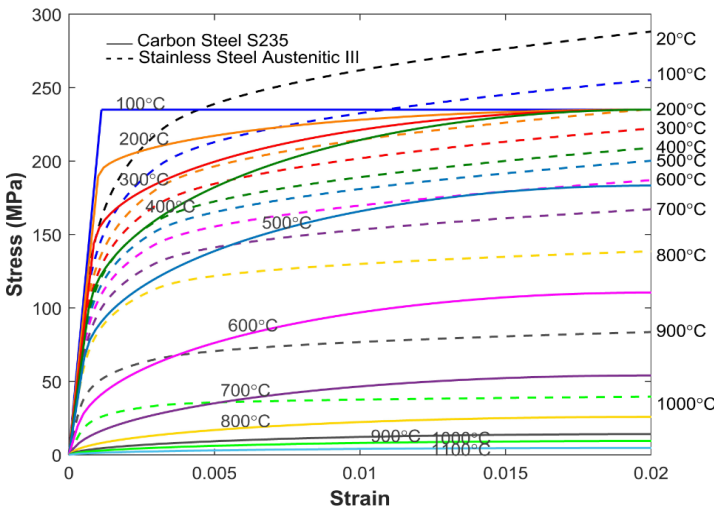


Fig 1: Stress strain curves at elevated temperatures

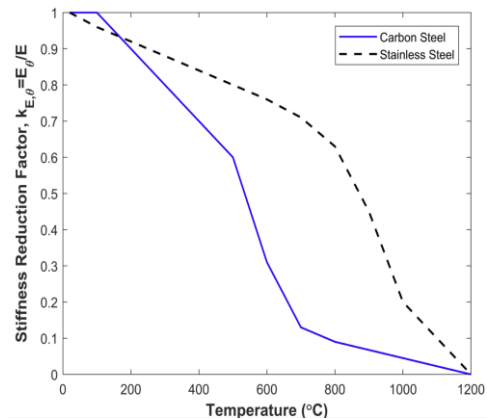


Fig 2: Stiffness retention factors

2.3 Thermal expansion

The mean thermal expansion coefficients of typical types of stainless steel specified in DMSSS [1] are plotted in Figure 4 in the form of thermal elongation, in conjunction with that of carbon steel specified in EC 3[2]. In short, stainless steels exhibit higher thermal expansion than carbon steel with Austenitic grades being the highest.

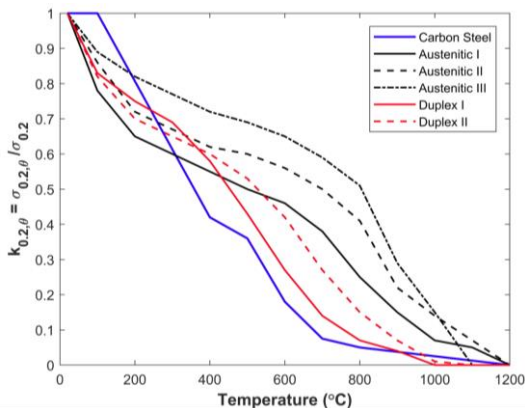


Fig 3: 0.2% Proof strength retention factors

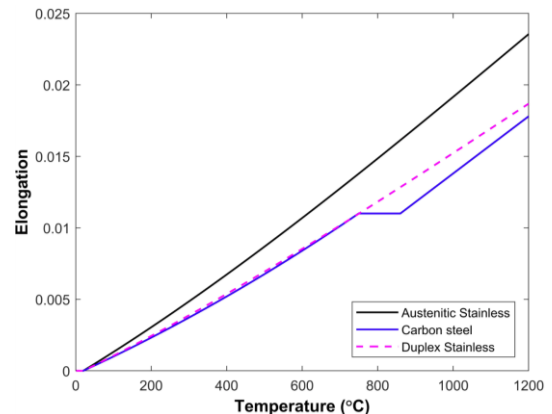


Fig 4: Thermal elongation comparison

2.4 Thermal properties

Stainless steel possesses different thermal conductivity and specific heat than carbon steel. However, it is believed that their influence on the temperature development within structural I sections is limited in a radiation dominated building fire. The most significant difference is stainless steel shows a lower emissivity of 0.4 than the 0.7 of carbon steel due to its polished surface.

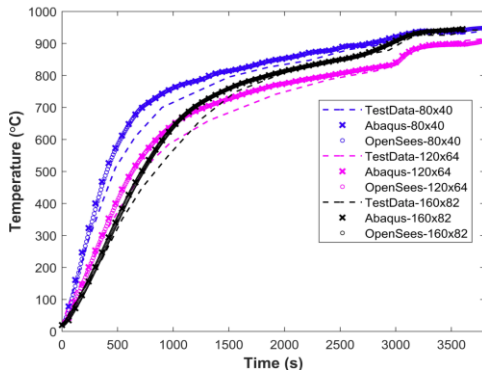


Fig 5: Temperature development within sections

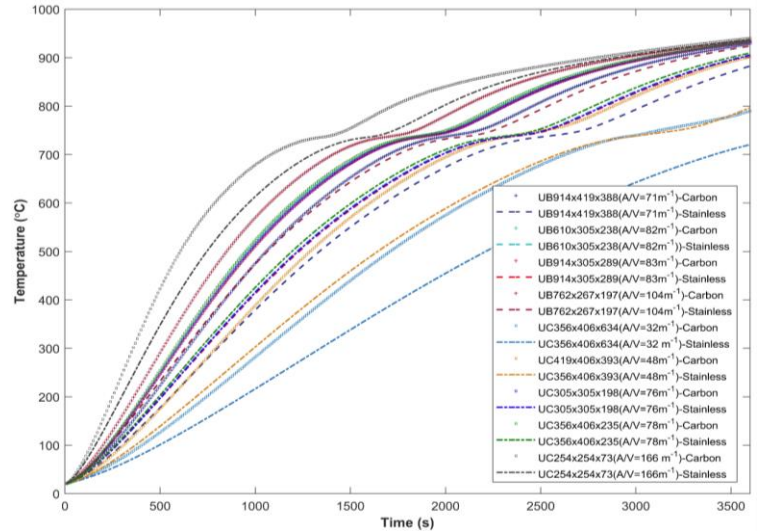


Fig 6: Temperature development in bottom flange, 4 sides heating

3 MATERIAL MODEL DEVELOPMENT

3.1 Stainless steel heat transfer model validation and verification

The heat transfer models are validated by comparing the OpenSees heat transfer results with the testing data obtained by Gardner and Ng [3] which are 3 stainless steel I sections, all sides exposed, subjected to standard fire in furnace. Further verification is conducted by comparing the results with that produced by finite element software Abaqus. The comparison results are presented in Figure 5, where a good agreement is shown.

3.2 Thermo-mechanical steel material model development

3.2.1 Material plasticity algorithm implementation in thermo-mechanical analysis

The existing material model for thermo-mechanical analysis of carbon steel structures using nonlinear EC3 [2] stress strain relationships in fire in OpenSees cannot accommodate strain reversals in fire. Khorasani et al. [4] recently added a material class based on studies by Franssen [5] to accommodate strain reversals at elevated temperature, however the constitutive stress strain curves were simplified into a trilinear relationship.

A new material class is added into OpenSees, which is developed based on EC3 [2] stress strain relationship of carbon steel with algorithm for classical rate-independence plasticity implemented. The nonlinear behaviour of carbon steel at elevated temperatures is captured using nonlinear strain hardening law – Voce equation:

$$\frac{\sigma}{Y} = 1 - a * \exp^{-b * \epsilon^p} \quad (1)$$

where Y is the 2% proof strength, ϵ^p is the accumulated plastic strain, Coefficients a , b are obtained by least square curve fitting of EC stress strain curves of carbon steel.

Similarly, two more material class are added for Austenitic III and Duplex II Stainless steel grade groups respectively. The nonlinear behaviour of stainless steel, based on the nominal stress strain relationships at elevated temperature specified by DMSSS [1], is captured using Modified Ludwick isotropic hardening formula:

$$\frac{\sigma}{Y} = 1 + a * (\epsilon^p + c)^b \quad (2)$$

where Y is the initial yield stress, ϵ^p is the accumulated plastic strain. Coefficients a, b and c are material constants obtained by least square curve fitting of nominal stress strain curves.

The yield condition at elevated temperature can be generally expressed in terms of the stress σ_{ij} , plastic strain ϵ_{ij}^p and temperature T

$$F = F(\sigma_{ij}, \epsilon_{ij}^p, T) = 0 \quad (3)$$

where ϵ_{ij}^p is the accumulated plastic strain tensor. Thermal expansion only causes volumetric change in the material consequently ϵ_{ij}^p is not affected by temperature changes.

Von Mises yield criterion has been adopted in this work. It has shown that steel yield surface shrinks in the stress space at elevated temperature. However for most steels where Von Mises criterion is appropriate, the yield surfaces are always circles in deviatoric stress space, expanding steadily during continued loading [6]. The elastic constants are assumed to retain the same values provided they are defined with respect to the current shape of the element. Moreover, it is supposed that the yield surface recovers its original shape when reloaded along the same path to the initial state of stress, and there is no hysteresis loop.

Figures 7 and 8 demonstrate the classic Elastic Predictor/Return Mapping algorithm implemented in 1D material model for thermo-mechanical analysis in OpenSees, illustrating the stress strain computing procedures at increasing temperatures. The same procedure is also applicable for analysing structural behaviour during cooling.

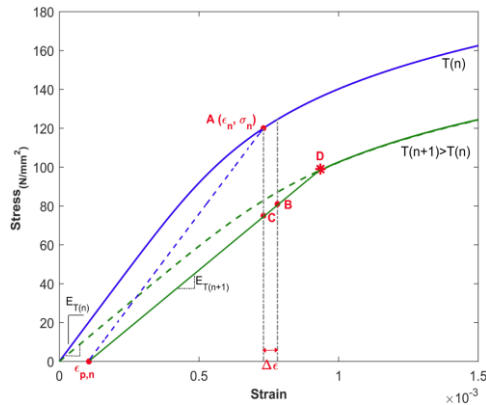


Fig 7: Constitutive material model

1D Material Model for Thermo-mechanical Analysis, Strain Based

1. Previously converged point A (ϵ_n, σ_n) at Temperature T(n), accumulated plastic strain ϵ^p
2. Compute current yield stress at temperature T(n+1) using hardening law, Point D
 $\sigma_{y,T(n+1)} = H_{T(n+1)}(\epsilon^p)$
 $H_{T(n+1)}$: Hardening law at T(n+1), ϵ^p : accumulated plastic strain
3. Associative Flow rule
 $\dot{\epsilon}^p = \gamma \cdot \dot{\sigma}$, γ : plastic consistency parameter
4. Compute stress of equivalent point C at T(n+1) to point A at T(n)
 $\sigma_C = E_{T(n+1)} * (\epsilon_n - \epsilon_{p,n})$
5. Elastic predictor
 $\Delta\sigma^{trial} = E_{T(n+1)} * \Delta\epsilon$, $\sigma^{trial} = \sigma_C + \Delta\sigma^{trial}$, $\Delta\epsilon$: mechanical strain increment
6. Yield condition
 $f(\sigma, \epsilon^p) = |\sigma^{trial}| - \sigma_{y,T(n+1)} \leq 0$
7. Kuhn-Tucker complementarity conditions
 $\dot{\gamma} \geq 0 \quad \dot{\gamma} f = 0 \quad f \leq 0$
 If $f \leq 0$, then $\sigma_{n+1} = \sigma^{trial}, \epsilon_{n+1} = \epsilon_n + \Delta\epsilon$
 Exit to Step 9
8. Compute γ based on plastic consistency condition using Return Mapping
 $\dot{\gamma} f = 0$
 Newton-Raphson iteration method is employed to solve γ for nonlinear material
9. Update stress, accumulated plastic strain
10. Newly converged Point B at T(n+1)

Fig 8: 1D material model analysis procedures

3.2.2 Verification studies

The verification studies of the implemented material classes are carried out by comparing the OpenSees results with results obtained from Abaqus.

In the first study, the material class added for carbon steel (SteelEC02Thermal) was tested using a column model of length = 500mm, cross section 80mmx80mm, bottom end fully fixed and top end free. At the first step, an axial compression $P=5e^5$ N was applied at the top, representing a common column design in building structure. At step 2, thermal loading is applied where the column was uniformly heated along the length. A cross sectional thermal gradient, 600 – 300°C was applied. Large deflection was observed during this step. At step 3, an axial tension $T=1e^6$ N was applied at

top, which represents the unloading stage of a column within a global structure. A larger value of the reversal force was used to model the cooling phase in addition to the unloading phase.

Figure 9 shows the comparison of horizontal and vertical displacements at the top of column between Abaqus and OpenSees. Good agreement is observed. Figure 10 shows the development of mechanical stress and strain at bottom, middle and top of the column respectively, throughout the three steps. As shown, mechanical strains initially increase in the compressive direction due to the ramp-up axial compression, followed by a gradual increase caused by the reduced material stiffness and strength during heating. A linear strain recovery caused by the applied tension is observed. Moreover, the unrecoverable plastic strains developed during the heating are clearly captured. The comparison between Abaqus and OpenSees show a good agreement.

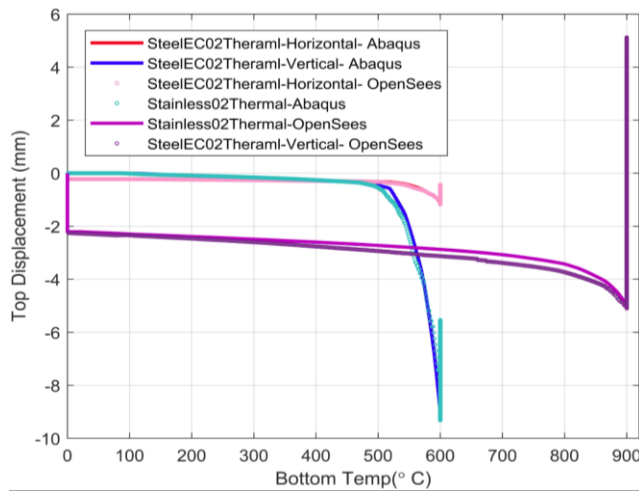


Fig 9: Deflection development

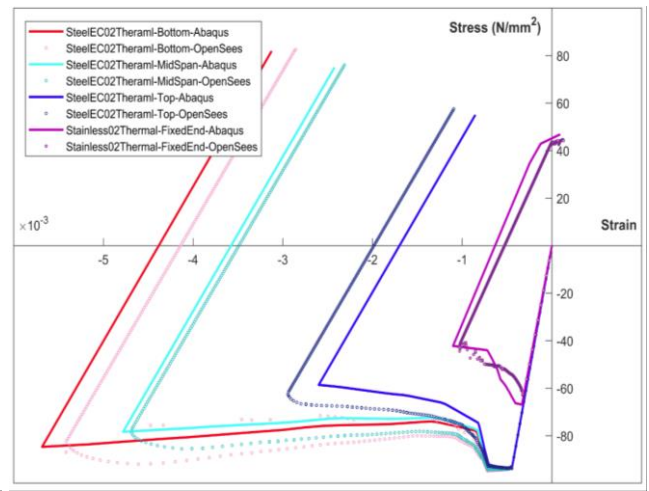


Fig 10: Stress strain development

In the second study the material class added for stainless steel (Stainless02Thermal) was verified using a cantilever of a length=1000mm, cross section 80mmx80mm. At first a uniformly distributed line load, UDL=-12N/mm (downward) was applied, then the bottom of the beam was heated to 900°C while the top was heated to 800°C. Finally, at the free-end of the cantilever a point load $T=1e^4$ N (upward) was applied. Figure 9 shows the deflection of free end with temperature. During heating, the deflection increases downwards as a result of reduced stiffness and thermal gradient (between top and bottom flanges). After heating, the free end deflects upwards due to point load T. Figure 10 shows the stress and strain development at the fixed end of the cantilever throughout the 3 stages. Abaqus and OpenSees demonstrate good agreement and both predict the hysteresis loop. Therefore, it is concluded the classical flow rule has been successfully implemented.

4 STAINLESS STEEL STRUCTURES IN FIRE

4.1 Temperature development within I Sections

Temperature development within stainless steel I sections is studied using heat transfer model in Open Sees. For steel structural members subjected to high temperature, particularly I sections, radiation is the predominant heat transfer mode and conduction within the cross section is almost instantaneous due to high thermal conductivity. Comparison study of temperature development within carbon steel and stainless steel I sections were carried out for 9 typical steel I sections, results shown in Figure 6. Section factor (A/V) is defined as the heated perimeter of the exposed cross section divided by the total cross section area. The results suggest that the larger A/V is, the smaller difference in the temperature development between carbon steel and stainless steel. The maximum temperature difference observed could reach around 100°C. The slower temperature increase experienced in stainless steel is believed mainly attributed to its lower emissivity.

4.2 Simply supported beams in uniform heating

Nonlinear analysis taking account of both material nonlinearity and geometric nonlinearity of simply supported beams (one end pinned the other roller restraint) is performed in OpenSees.

Rubert and Schaumann [7] conducted a series of experiments where the simply supported beams (IPE80, St37) under constant load were subjected to uniform heating, with the applied load varying from 0.2 to 0.85 of the beam's ultimate load bearing capacity. The FE models were validated by comparing the OpenSees results of the middle span deflection with the reported test data. The comparison results shown in Figure 11 suggest the FE model is capable of capturing the behaviour of simply supported beams at elevated temperatures to a satisfactory accuracy. A comparison study was subsequently carried out using the established structural FE model.

For all the comparison analyses conducted in this paper, Carbon steel S235, Austenitic 1.4571 (group III) and Duplex 1.4162 (group II) are adopted because, as discussed in section 2.2, Austenitic III shows the most promising stiffness and strength retention, Duplex II shows overall better stiffness and strength retention than Duplex I. Besides the lean duplex grade (Duplex 1.4162) is the most popular of all stainless steel grades in onshore building construction. For S235, Young's Modulus (E) = 2.1 GPa, $f_{0.2}$ = 235 MPa; for Austenitic 1.4571, E = 2.0 GPa, $f_{0.2}$ = 220 MPa; for Duplex 1.4162, E = 2.0 GPa, $f_{0.2}$ = 450 MPa. The nominal stress strain relationships of Austenitic 1.4571 and Duplex 1.4162 grade at elevated temperature in DMSSS 4 are adopted whereas the Eurocode 3 stress strain curves of Carbon steel are used. Four series of comparison analyses were performed, in each series the applied load was kept constant for each beam, to attain comparable deflection values at the start of the fire. The utilisation load ratio ($LR = M_{\text{applied}}/M_{\text{pl}}$) was lower in Duplex beam because of its higher yield strength.

The middle span deflection results of the comparison analyses are shown in Figure 12. In the 1st series the deflection of carbon steel beam starts to increase noticeably at around 500°C and develops into the run-away mechanism at about 600°C. Identical deflection development until near run-away point at around 800°C is observed in Austenitic and Duplex grades because of their identical stiffness retention factors and the material primarily remaining elastic in both grades at the start of the fire. Figure 13(a) shows the mechanical stress strain developments in which carbon steel beam behaves entirely elastically whereas noticeable plastic strains have developed in stainless steel beams because of material nonlinearity, noted that thermal strain does not contribute to the material yielding in simply supported beams. In the 2nd series, Figure 12 shows the run-away initiates in carbon steel when temperature is around 420°C. The deflection of Austenitic grades develops faster than that of Duplex grade because the material approaches nonlinear region faster with a higher LR. As shown in Figure 13(b), substantial amount of strain hardening is experienced in stainless steels. In the 3rd series Austenitic grade beam falls quickly into large deflection mode because material tangent modulus rapidly reduces from its initial value due to its high LR = 0.75. The run-away occurs at around 450°C in Carbon steel beam and around 600°C in Duplex. Figure 13(c) shows Duplex grade possesses higher strain hardening. In the 4th series, only Carbon steel beam (LR = 0.85) and Duplex beam (LR = 0.44) are compared. Carbon steel beams starts to run-away at around 400 °C, about 150°C lower than Duplex grade beam. However, Figure 13(d) shows substantial plastic strain developed in duplex beam albeit its LR is about half of that of carbon steel.

The comparison results suggest that the initiation of run-away mechanism of simply supported beams in fire is primarily determined by the material's stiffness degradation and initial load ratio. At the lowest LR, the run-away mechanism occurs when the stiffness retention factor of the material starts to deteriorate rapidly—around 500°C for carbon steel and 800°C for stainless steel. With the same starting deflection, the Duplex grade beams show the best behaviour in fire as a result of its high yield strength and strain hardening potential. It should be noted that, the effect of stainless steel material nonlinearity is clearly observed in the development of plastic strain within the beams, which is distinctive from carbon steel.

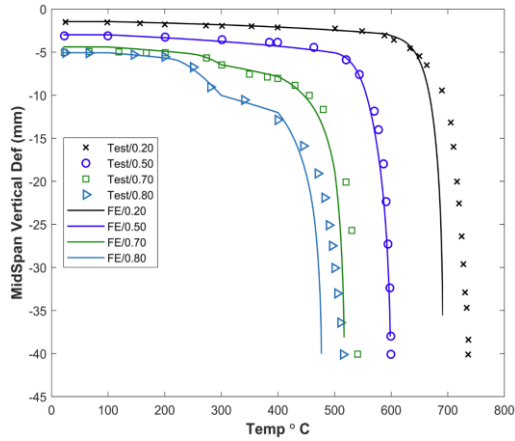


Fig 11: Simply supported beam deflection

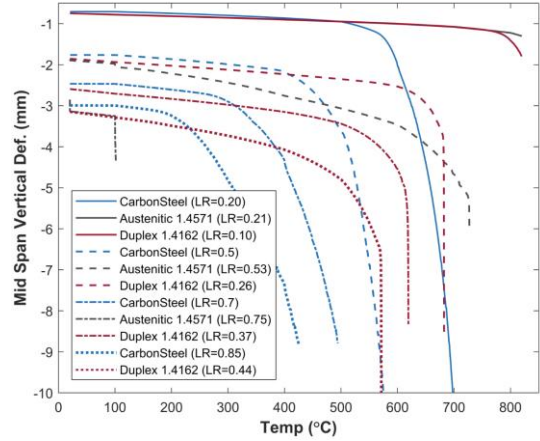


Fig 12: Deflection comparison

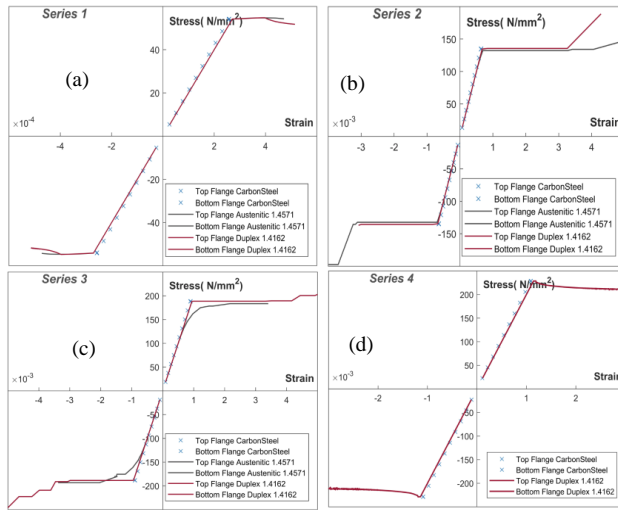


Fig 13: Stress strain development - SS beams

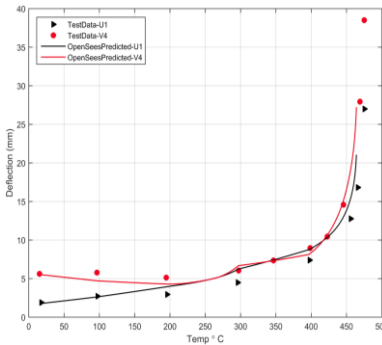


Fig 14: Deflection development - EHR3

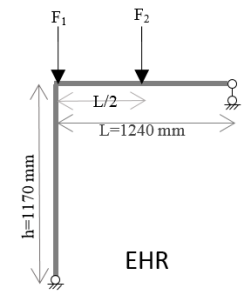


Fig 15: EHR frame

4.3 Plane frames in fire

Unlike simply supported beams, in real structures where there are end constraints provided by the surrounding structure, thermal expansion induced compression dominates the beam's behaviour. Consequently, the real life performance of stainless steel frame structures in fire will be determined by two competing factors – superior stiffness retention and higher thermal expansion. Study of stainless steel frames was carried out in OpenSees with the FE model validated against the testing data of the EHR carbon steel frame tests performed by Rubert and Schaumann [7], configuration shown in Figure 15. All the members were uniformly heated during the test. The temperature dependant material properties used in the tests [7] are used for validation. Comparisons of the temperature-deformation history were carried out for validation based on available test data, results shown as in Figure 14.

For frame EHR, frame beam was pinned at right end while column pinned at bottom, consequently, during heating the thermal expansion could only go upwards in column and towards left in beam, which exerted a clockwise rotational moment at the beam-column joint. Figure 16 shows the middle span deflection of the frame beam and column at varying LR. The deflection comparison results suggest Austenitic 1.4571 beams exhibit the best behaviour during heating while comparable LR is applied. In cases of columns of comparable LR, slower deflection development was observed in carbon steel frame column whereas large deflection mode showed the latest in Austenitic 1.4571 columns. When both started with the same deflection, Duplex 1.4162 frame beam shows better behaviour in fire than Carbon S235, however, the advantage of Duplex 1.4162 quickly diminished as the LR increased. When experiencing comparable LR, Duplex beam/column fall into large deflection mode sooner than the other two materials.

Figure 17 shows the stress strain development in the columns at the beam-column joint during heating for the lowest LR case. Initially, the joint was in negative bending moment due to applied F_2 . As getting heated uniformly, thermal expansion in beam and column started exerting clockwise rotation at the joint, giving rise to negative bending moment. As the column continued reducing in stiffness, the compressive stress became dominating the column, resulting in reduction in the tensile stress and strain at the top flange, yet the top flange remained in tension due to the P-delta effect of the column. The strain reversals observed are caused by thermal unloading. Austenitic 1.4571 accumulated the highest strain energy in this case.

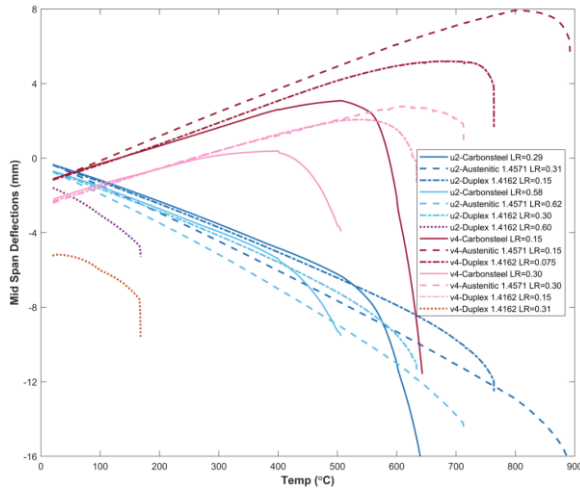


Fig 16: Deflection development, EHR frames

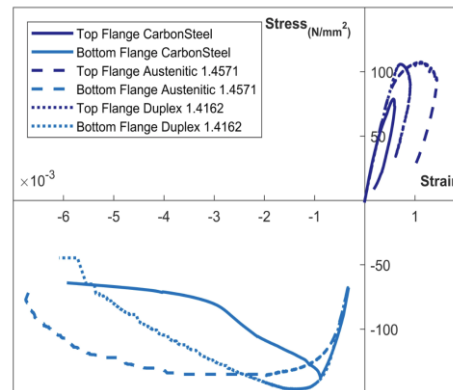


Fig 17: Stress strain development - Column top

5 CONCLUSIONS

Strain reversals can occur in frame structures subjected to fire due to load redistribution, thermal unloading and cooling. Three new materials models representing nonlinear steel material behaviour at elevated temperature and accommodating strain reversals have been implemented in OpenSees. Larger deflections were observed in stainless steel structures due to their higher thermal expansion. Initial load ratio presents a greater impact on stainless steel structural performance in fire because the tangent stiffness modulus quickly reduces to about 50% of material's initial value when loading approaches 50% of the strength capacity. Furthermore, stainless steel structures accumulate higher plastic strain energy during heating due to material nonlinearity.

REFERENCES

1. *Design Manual for Structural Stainless Steel, 4th Edition, 2017.*
2. *Eurocode 3: Design of steel structures - Part 1-2: General rules -Structural fire design, 2005.*
3. L.Gardner, K.T.Ng (2006). *Full-scale Temperature development in structural stainless steel sections exposed to fire.* Fire Safety Journal 41(3). pp 185-203.
4. Negar Elhami Khorasani, Maria E.M. Garlock, Spencer E. Quiel (2015). *Modelling steel structures in OpenSees: Enhancements for fire and multi-hazard probabilistic analysis.* Computers and Structures (157). pp 218-23.
5. J-M Franssen (1990). *The unloading of building materials submitted to fire.* Fire Safety Journal (16). pp 213-217.
6. R.Hill (1950). *The mathematical theory of plasticity.* Oxford university press.
7. Achim Rubert, Peter Schaumann (1986). *Structural steel and plane frame assemblies under fire action.* Fire Safety Journal 10(3). pp 173-184.

EXPERIMENTAL RESEARCH AND ANY OTHER

Experimental Research and any Other

PERFORMANCE ASSESSMENT OF A STRUCTURE SUBJECTED TO FIRE THROUGH HYBRID (NUMERICAL-EXPERIMENTAL) SIMULATION

Xuguang Wang¹, Robin E. Kim², Oh-Sung Kwon³, Inwhan Yeo⁴, Jaekwon Ahn⁵

ABSTRACT

The application of hybrid (numerical-experimental) simulation method can facilitate the structural fire design by allowing assessment of the performance of a structural system subjected to fire. In the hybrid simulation method, a structural member that is directly exposed to fire is physically modelled in a fire testing equipment while the rest of the structure is modelled numerically. The displacement compatibility and the force equilibrium at the interface between the numerical and physical models are satisfied by solving a nonlinear system equation in the numerical model. To accurately control the deformation of the specimen, the elastic deformation of the loading frame needs to be considered at each simulation time step. In this paper, the hybrid fire simulation methods using UT-SIM framework, the compensation scheme to consider the elastic deformation of the loading frame, and potential stability issues during a hybrid fire simulation are discussed. The paper provides a short summary of two hybrid simulation results on a steel moment resisting frame.

Keywords: hybrid fire simulation, steel moment resisting frame

1 INTRODUCTION

In the performance-based design approach for structures subject to fire, it is necessary to evaluate the fire performance of a structural system. In the conventional fire testing method, the fire resistance of each structural element is evaluated by imposing a constant load and increasing the temperature of the furnace following a standard fire curve. This approach is effective in understanding the element level behaviour, but difficult to consider the interaction between the tested elements with the rest of the structural system. Numerical modelling of a structural element subjected to fire load is also very challenging due to highly nonlinear and complex characteristics of structural elements at high temperature. The fire performance of a structural system can be experimentally evaluated through a fire testing of a full-scale specimen. However, the full-scale test is very expensive and limited by the capacity of a testing facility. Furthermore, it is neither feasible nor necessary to test a large structural system, such as a high-rise building, where only a compartment fire scenario needs to be considered.

To overcome these limitations, a hybrid (numerical-experimental) simulation method has been developed. The hybrid simulation method allows the integration of experimentally tested element(s) with a numerical model of a structural system. In this method, the most critical element(s), that is difficult to model numerically, are realistically modelled as physical specimens. The rest of the structural system is modelled numerically. Several research papers present hybrid fire simulation method [1-5]. Among these studies, Mostafeid (2013)[4] tested a large-scale concrete column in furnace while the rest of the structural system was modelled numerically in SAFIR [6]. The hybrid

¹ Graduate Research Assistant, Department of Civil Engineering, University of Toronto, Toronto, Canada.

e-mail: xuguang.wang@mail.utoronto.ca

² Research Specialist, Multi Disaster Countermeasure Organization, Korea Institute of Civil Engineering and Building Technology.

e-mail: robineunjukim@kict.re.kr

³ Associate Professor, Department of Civil Engineering, University of Toronto, Toronto, Canada.

e-mail: os.kwon@utoronto.ca

⁴ Research Fellow, Multi Disaster Countermeasure Organization, Korea Institute of Civil Engineering and Building Technology.

e-mail: yeo@kict.re.kr

⁵ Senior Researcher, Fire Research Institute, Korea Institute of Civil Engineering and Building Technology.

e-mail: jaekwonahn@kict.re.kr

simulation was carried out manually by controlling the force applied to the experimental specimen and by imposing measured deformation to the numerical model. Recently, Wang et al. [7] developed a general framework for hybrid fire simulation where a numerical model in ABAQUS is tightly integrated with a specimen in a column testing furnace. In the latest study, Wang et al. [8] implemented real-time continuous hybrid fire simulation method with full characterization of stability issue in a hybrid fire simulation. This paper presents high-level overview of the hybrid fire simulation method that has been developed by the authors. For more details on the implementation of the hybrid fire simulation method, references are made to [7,8].

2 HYBRID FIRE SIMULATION USING UT-SIM FRAMEWORK

2.1 UT-SIM framework

The developed hybrid fire simulation employs the UT-SIM framework [9], an open framework for integrated multi-platform simulations which can be used to integrate various numerical and experimental substructures. The substructures in the framework communicate with each other using a standardized data exchange format and network communication protocol. A general purpose actuator controller can be integrated into the hybrid simulation via the network interface for controllers, NICON [10]. In a hybrid simulation, the numerical model calculates displacement increment to resolve the unbalanced force, and send the displacement to NICON. Then, NICON converts the received displacement to an analog signal, which is fed into an actuator controller. After the actuator imposes the displacement on the specimen, then the force is measured which is fed back to NICON as analog signals. NICON also controls the data exchange rate between the numerical model and the experimental specimen such that the temperature in the furnace and the numerical model can be fully synchronized. The architecture of the hybrid simulation method is presented in Figure 1.

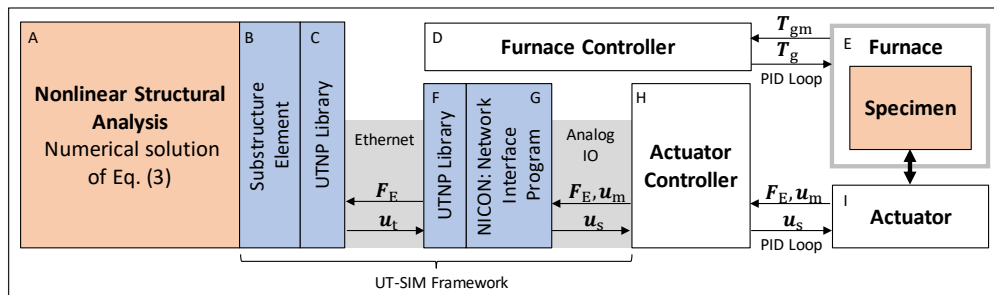


Figure 1. The architecture of the hybrid fire simulation

2.2 The hybrid fire simulation methods

In a fire event, large internal force is developed due to the thermal expansion of an element subjected to the temperature load. In addition, the material properties of the structural element change as temperature increases, while the gravity load on the structure remains constant. Thus, the restoring force vector of the structural system, F , should be constant throughout the fire event and equals to the applied external force, f . The governing system equation is:

$$F(u, T) = f \quad (1)$$

where u and T are the displacement and the temperature at each degree of freedom. The structure is divided into a numerical substructure and an experimental substructure in the hybrid fire simulation. The sum of the force vector from the numerical substructure, F_N , and the measured force vector from the experimental substructure, F_E , equals to the total restoring force, F . Thus, Eq. (1) can be rewritten as:

$$F_N(u, T) + F_E(u, T) = f \quad (2)$$

The displacement increment at each step, Δu , is calculated as:

$$\Delta u = -k^{-1}(F_N(u, T) + F_E(u, T) - f) \quad (3)$$

where \mathbf{k} is a stiffness matrix representing the linear relationship between the displacement and the force vectors. The other terms in the parentheses of right-hand side of Eq. (3) is the unbalanced force vector. In each time step of hybrid simulation, \mathbf{F}_E is measured from an experimental substructure and fed back to the numerical substructure to solve Eq. (3) as illustrated in Figure 1.

A hybrid fire simulation can be carried out in a ramp and hold manner [7] or in a continuous manner [8]. Those methods are illustrated in Figure 2. In the ramp-hold method, each analysis time step, Δt , consists of several ramp (δt_{ramp}) and hold (δt_{hold}) substeps, which is followed by an idle period. NICON receives the displacement command from the numerical substructure at the beginning of each analysis time step and send the corresponding analogue signal to the actuator controller by generating a ramp. Because of the elastic deformation of the loading frame, the deformation of the specimen does not reach the target displacement. Thus, several iterations are necessary to achieve the target displacement with sufficient accuracy. Once the target displacement is achieved, NICON sends the measured force back to the numerical substructure for calculating the next displacement command. NICON idles until the total time from the beginning of the step becomes Δt . During this idling period, the numerical model solves Eq. (3). The time step of analysis, Δt , in the ramp-hold method has to be long enough for the numerical substructure to complete the calculation during the idling period.

The ramp-hold method is an efficient way to perform a hybrid fire simulation and relatively straightforward to implement. However, because the temperature in a furnace is not controlled in a discrete manner, the specimen continues to develop thermal strain during the ramp and hold periods. Thus, at the end of imposing the target displacement, the measured force not only includes the restoring force resulting from the imposed displacement but also the force resulting from the thermal expansion during the analysis time step (Δt). While the increased unbalanced force can be reduced in the subsequent time steps, the unbalanced force may not be fully resolved, or even accumulate depending on the analysis time step (Δt), the initial stiffness (\mathbf{k}) used to solve Eq. (3), and rate of thermal expansion. When a numerical substructure includes numerous finite elements, then the analysis time step, Δt , needs to be large enough such that Eq. (3) can be solved within the analysis time step. In addition, the structural material may develop relaxation during the hold period.

To overcome these limitations, the continuous hybrid simulation method was implemented by the authors based on the continuous hybrid simulation method for structures subjected to earthquake excitation which was originally proposed in [11]. In the continuous hybrid simulation method, the displacement command from the numerical substructure is updated at each time step, Δt , and the command sent to the actuator controller from NICON is updated at higher refreshing rate, δt . At the beginning of each analysis step, the numerical substructure calculates the displacement ($\mathbf{u}_{s,n+1}$) of each degree of freedom for the next step ($n + 1$) by solving Eq. (3). While the numerical substructure runs the calculation, NICON continues to generate displacement commands by extrapolating the displacement commands from previous analysis steps (i.e. $\mathbf{u}_{s,n-3}$, $\mathbf{u}_{s,n-2}$, $\mathbf{u}_{s,n-1}$, $\mathbf{u}_{s,n}$). When the numerical substructure completes the calculation of $\mathbf{u}_{s,n+1}$, NICON receives the displacement command from the numerical substructure and starts updating the command by interpolating the command (i.e. $\mathbf{u}_{s,n-2}$, $\mathbf{u}_{s,n-1}$, $\mathbf{u}_{s,n}$, $\mathbf{u}_{s,n+1}$). Once the target displacement is achieved at time $(n + 1)\Delta t$, then the measured force from the experimental substructure is sent back to the numerical substructure for calculating the next displacement command. The equation for the extrapolation process is:

$$u_{s,n+1}^j = \sum_{i=0}^3 a_i^j u_{t,n-i} \quad (4)$$

where $u_{s,n+1}^j$ is the extrapolated displacement by NICON at j^{th} δt of time step $n+1$, $u_{t,n-i}$ is the displacement command at the end of analysis step $n - i$ calculated by the numerical substructure, and a_i^j are:

$$a_0^j = \frac{1}{6} \left(\frac{j\delta t}{\Delta t} + 1 \right) \left(\frac{j\delta t}{\Delta t} + 2 \right) \left(\frac{j\delta t}{\Delta t} + 3 \right), \quad a_1^j = -\frac{1}{2} \left(\frac{j\delta t}{\Delta t} \right) \left(\frac{j\delta t}{\Delta t} + 2 \right) \left(\frac{j\delta t}{\Delta t} + 3 \right),$$

frame ($k_{f,a}$), and $\beta_s (= k_s/k_{f,a})$, a ratio between the stiffness of the specimen and the actual stiffness of the loading frame. To achieve a stable response, the following condition should be satisfied, which is presented in detail in [8].

$$\beta_f > 1 - \frac{1}{1 + 2\beta_s} \quad (7)$$

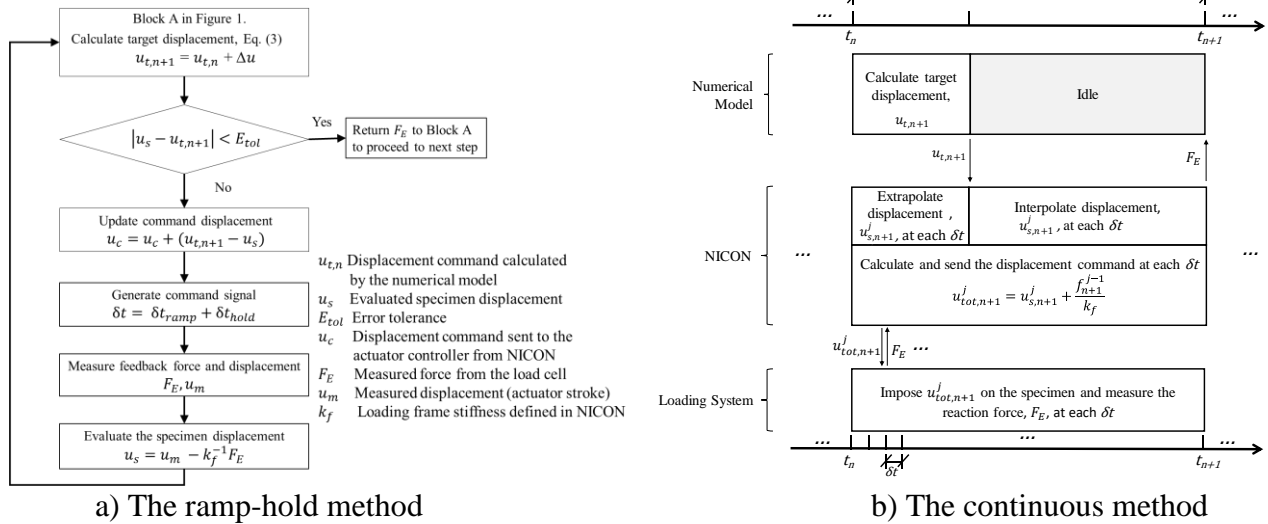
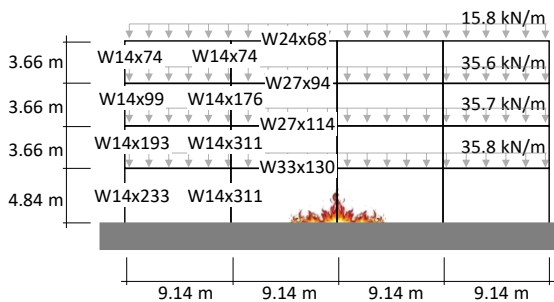


Figure 3. The loading frame elastic deformation compensation schemes

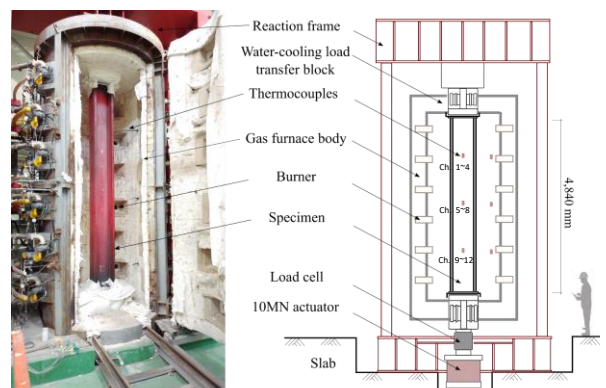
3 VALIDATION TESTS

3.1 Reference structure and experiment setup

Both the ramp-hold method and the continuous method are validated with a 4-story 4-bay steel moment resisting frame designed by Jin and El-tawil [12] as shown in Figure 4 a). In the simulation, the middle column on the first floor was represented with a physical specimen in a column testing furnace while the rest of the structural system was modeled numerically. The setup of the experimental substructure is illustrated in Figure 4 b). The numerical substructure in the validation test for the ramp-hold method was modelled in ABAQUS with 2D frame elements. In the validation test for the continuous method, the numerical substructure is represented with a multi-resolution model (i.e. continuum elements and frame elements) in ABAQUS. The beam-column connection adjacent to the tested column is modeled with 3D brick elements and the other structural members are modeled by 3D frame element.



a) The reference moment frame



b) Setup of the experimental substructure

Figure 4. The reference structure and experimental substructure

3.2 Testing procedure

Two specimens (Specimen #1 and Specimen #2) were tested using the ramp-hold method and the continuous method, respectively. Preliminary tests are required before a hybrid fire simulation: One of the required preliminary tests is the heat transfer analysis. For both validation tests, the ISO834

standard fire curve was applied as the thermal load. The column that was represented by the experimental substructure was subjected to fire curve directly while the temperature of the members that were represented by the numerical substructure changed only through conduction. Thus, the specimen was first heated with the fire curve to obtain the temperature history. During the heating, no gravity load was applied to the specimen and allowed for the free expansion. The obtained thermal history was applied to the numerical substructure as the thermal boundary condition at the interface of the numerical and experimental substructures to run heat transfer analysis. The result of the numerical heat transfer analysis was used as the thermal boundary condition of the numerical substructure in the later hybrid fire test. The specimens for both validation tests were heated to 740°C in 44 mins. The specimens were cooled down by opening the furnace gate at the end of the heating phase.

The other required preliminary test is to evaluate the loading frame stiffness. In the validation tests, the specimen was loaded within the elastic range at the ambient temperature. The measured force and actuator stroke were recorded for each load increment. The deformation of the specimen was calculated by the measured force and theoretical axial stiffness based on the section properties. The loading frame deformation was calculated by subtracting the specimen deformation at each load increment from the recorded actuator stroke. Then, the loading frame stiffness was estimated as the ratio between the measured force and the loading frame deformation. Ideally, the loading frame stiffness should be a constant. The test results, however, showed that the loading frame developed nonlinear elastic hysteresis at the beginning of loading, and linear elastic after developing full contact with the specimen. It is expected that the nonlinear elastic behaviour of the loading frame was due to the development of contact between the specimen and the loading frame. The upper bound of the loading frame stiffness was 450 kN/mm for the test conducted on Specimen #1 and 460 kN/mm for the test conducted on Specimen #2.

The loading frame stiffness evaluated from the preliminary test was used in NICON for conducting the hybrid fire simulation. As mentioned in Section 2.3, to ensure the stability, loading frame stiffness of 500 kN/mm was defined for the validation test for the continuous method. In the ramp-hold method, however, the stiffness of the loading frame of 450 kN/mm was used. The gravity load was applied to the numerical and experimental substructures at the ambient temperature. After applying the initial load, the gravity load was kept constant throughout the test. The ISO834 fire curve was applied in the heating phase for 44 min. Then, the heating stopped and the furnace gated was opened to start the cooling. During the heating and cooling phases, the numerical substructure and the experimental substructure exchanged data at the specified time interval. The time step for the ramp-hold method was 6 sec. In each time step, four iterations were performed for the error compensation. The ramp and hold duration for each iteration was 0.1 sec and 0.4 sec respectively. In the continuous method, the time step was 10 sec and NICON extrapolate or interpolate displacement at every 0.01 sec.

3.3 Test results and discussion

The test results of the ramp-hold method and the continuous method, along with the numerical analysis result are presented in Figure 5. As shown in the figure, the measured force in column test with the ramp-hold method fluctuated during the heating phase before yielding occurred. It is speculated that the fluctuation is caused by the unresolved force generated in each time step due to the large strain rate. When the yielding occurred, the force increment in each step was much smaller and the fluctuation was mitigated as shown in Figure 5 b). The other possible reason for the fluctuation is the defined loading frame stiffness (450 kN/mm) was slightly smaller than the actual loading frame stiffness and the specimen stiffness at ambient temperature was much larger than the loading frame stiffness. So that, the relationship described by Eq. 7 in section 2.3 was not satisfied at the beginning of the heating phase. While the temperature increase, the right-hand-side of Eq.7 getting smaller. When the equation is satisfied, the fluctuation was mitigated. In the cooling phase, Eq. 7 was violated

again when the specimen gain strength while the temperature decrease. However, due to a much milder strain rate compare to the heating phase, the fluctuation shown in the end of the cooling phase was not as significant as it was in the heating phase. In average, the measured force from the ramp-hold method is in between of the other two sets of results. As shown in Figure 5 b), the measured force in the test with continuous method in the heating phase before yielding is very close to the upper boundary of the test result using ramp-hold method while the result from the numerical model follows the lower boundary. Thus, in Figure 5 a), it can be seen that the column tested with the continuous method developed smallest peak deformation in the positive direction compared to the ramp-hold method and the numerical analysis due to larger compressive force. The result from the continuous methods shows the largest nonlinearity while the result from the numerical analysis shows least nonlinearity among the three sets of the results. The nonlinearity at high temperature caused by material degradation is better captured in the continuous method. Consequently, the plastic deformation that developed under high temperature was better pronounced from the continuous method.

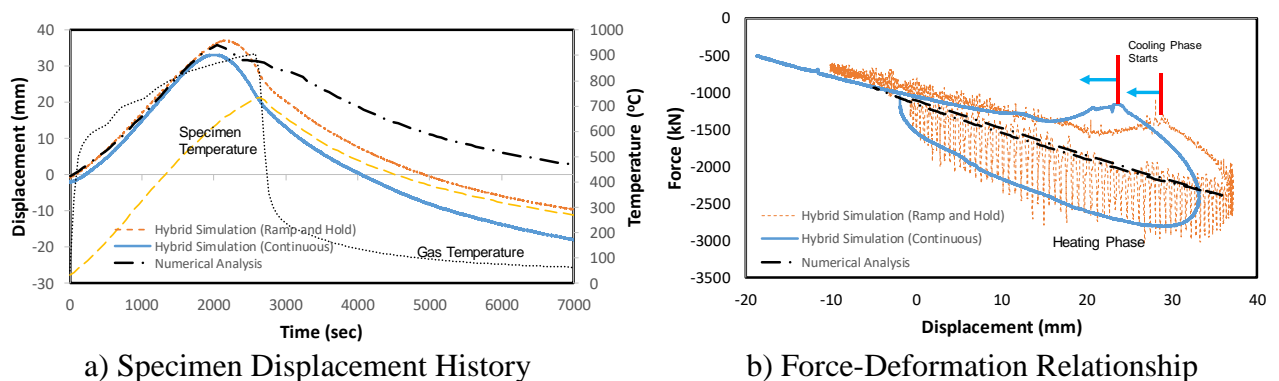


Figure 5. Hybrid Fire Simulation Results

4 CONCLUSION

Two hybrid fire simulation methods, ramp-hold and continuous methods, have been developed to allow system level performance assessment when a structure is subjected to fire. The validation tests were carried out with a steel moment resisting frame where one column on the first floor was represented as a physical specimen while the rest of the system was modelled numerically. The column was subjected to ISO834 fire curve. The findings are summarized as follows.

- The ramp-hold method works well while the stiffness of the loading frame used in the error compensation scheme satisfies Eq. (7). The ramp-hold method can be inaccurate due to continuous change of temperature and relaxation of material during the hold period.
- The continuous hybrid fire simulation method can resolve the unbalanced force caused by the thermal expansion in each simulation step by moving the actuator continuously. It allows longer time step and more detailed numerical model compared to the ramp-hold hybrid fire simulation method.
- The stiffness evaluation test for the loading frame stiffness has to be carried out carefully. The defined loading frame stiffness influence accuracy and stability of the simulation.
- The developed methods are robust and reliable. The structural members that are difficult to modeled numerically, such as concert columns and beams, can be assessed using the developed methods.

Further research is in progress to apply the hybrid fire simulation method to a horizontal member (e.g. beams) where catenary action can be fully taken into account.

ACKNOWLEDGEMENT S

This work was supported by the National Research Council of Science & Technology (NST) grant by the Korea government (MSIP) (No. CRC-16-02-KICT) and the Ministry of Trade, Industry and Energy (Grant No. 10063448).

REFERENCES

1. Kiel, M. (1989). Entwicklung einer intelligenten Prüfmaschine für brandbeanspruchte Gesamttragwerke. *Proc. of the Braunschweiger Brandschutztag*, Braunschweig, Germany.
2. Korzen, M., Magonette, G., Buchet, P. (1999). Mechanical Loading of Columns in Fire Tests by Means of the Substructuring Method. *Zeitschrift für Angewandte Mathematik und Mechanik*, 79, S617–S618.
3. Robert, F., Rimlinger, S., Collignon, C. (2010). Structure fire resistance: a joint approach between modelling and full scale testing (substructuring system). *Proc. of 3rd International fib Congress*, Washington, DC, USA.
4. Mostafaei, H. (2013). *Hybrid fire testing for assessing performance of structures in fire - Methodology*. *Fire Safety Journal*, 58, pp 170–179.
5. Whyte, C. A., Mackie, K. R., and Stojadinovic, B. (2016). *Hybrid Simulation of Thermomechanical Structural Response*. *Journal of Structural Engineering* 142(2), 4015107.
6. Nwosu, D. I., Kodur, V.R., Franssen, J., Hum, J.K. (1999). *User Manual for SAFIR: A Computer Program for Analysis of Structures at Elevated Temperature Conditions*. National Research Council Canada, Internal Report. 782. 10.4224/20331287.
7. Wang, X., Kim, R., Kwon, O., and Yeo, I. (2018). *Hybrid Simulation Method for a Structure Subjected to Fire and its Application to a Steel Frame*. *ASCE Journal of Structural Engineering* (accepted).
8. Wang, X., Kim, R., Kwon, O., Yeo, I., and Ahn, J. (2018). *Continuous Real-Time Hybrid Simulation Method for Structures Subject to Fire*. *ASCE Journal of Structural Engineering* (in review).
9. Huang, X., and Kwon, O. (2018). *A Generalized Numerical/Experimental Distributed Simulation Framework*. *Journal of Earthquake Engineering*, 1–22. DOI: 10.1080/13632469.2018.1423585.
10. Zhan, H., and Kwon, O. (2015). Actuator controller interface program for pseudo- dynamic hybrid simulation. *2015 World Congress on Advances in Structural Engineering and Mechanics*, Songdo, Korea, Aug. pp 25-29.
11. Nakashima, M., and Masaoka, N. (1999). *Real-time on-line test for MDOF systems*. *Earthquake Engineering and Structural Dynamics* 28(4). pp 393–420.
12. Jin, J., and El-tawil, S. (2005). *Seismic performance of steel frames with reduced beam section connections*. *Journal of Constructional Steel Research* 61(4). pp 453–471. DOI: 10.1016/j.jcsr.2004.10.006.

A PI-CONTROLLER FOR HYBRID FIRE TESTING IN A NON-LINEAR ENVIRONMENT

Elke Mergny¹, Guillaume Drion², Thomas Gernay³, Jean-Marc Franssen⁴

ABSTRACT

Hybrid Fire Testing (HFT) is an innovative testing methodology: it improves the existing experimental method by updating continuously the boundary conditions at the ends of a tested specimen. However, HFT methodologies are still in their infancy and, despite several previous applications, a rigorous framework for formulating the general problem is still lacking. To address this need, this paper proposes a new framework based on linear control system theory. Adoption of this robust theory to HFT allows deriving the general state equations and stability conditions of the problem. It is shown that the use of a P-controller leads to a stable process and that the conditions of stability can be formally expressed. However, the P-controller presents a major drawback, namely an inability to adapt to changes of stiffness in the system. A PI-controller is developed to overcome these limitations, and the corresponding state equations are established. A virtual HFT (using FEM) is performed on a 2D steel frame to compare the two different controllers. The results show that a PI-controller is more efficient in reproducing the global behaviour of the frame. The proposed methodology is versatile and can be used when the surrounding structure is non-linear, including when it is also subjected to fire.

Keywords: Hybrid Fire Testing, Linear Control System, P-Controller, PI-Controller, Steel Frame

1 INTRODUCTION

Hybrid Fire Testing (HFT) is a promising testing approach coupling fire tests and numerical simulations. The approach consists in continuously updating the boundary conditions at the extremities of a specimen during a fire test, using the response of a so-called numerical substructure, obtained from a model (for instance a finite element model), to determine these boundary conditions. The first HFT was performed by Korzen *et al.* in 1999 [1]. A steel column was tested in a furnace. The axial force in the specimen was adjusted as a function of the elastic response of the numerical substructure to the displacement of the heated column. Since then, a few other tests have been performed, notably on a concrete slab with several degrees of freedom [2], on a concrete column with the axial force being controlled and the numerical substructure being modelled in SAFIR[®] [3], and on small-scale elements with one degree of freedom [4]. All these investigations made a step forward in the design of experimental set-up intended for HFT. However, these tests remained either simple in their control process (for instance, modifying manually the conditions at the interface every few

¹ PhD Candidate, Department of Architecture, Geology, Environment & Constructions (ArGEnCo), Liège University, Belgium.
e-mail: elke.mergny@uliege.be

² Professor, Department of Electrical Engineering and Computer Science, Liège University, Belgium.
e-mail: gdrion@ulg.ac.be

³ Assistant Professor, Department of Civil Engineering, Johns Hopkins University, Baltimore, USA.
e-mail: tgernay@jhu.edu

⁴ Professor, Department of Architecture, Geology, Environment & Constructions (ArGEnCo), Liège University, Belgium.
e-mail: jm.franssen@ulg.ac.be

minutes), or encountered some stability issues, because they were conducted for demonstration purpose but without a clear theoretical framework supporting the control process.

The main methodological contributions for HFT include the development of a static partition solver based on the FETI algorithm [5], which requires knowing the stiffness of the physical substructure to stabilize the loading control process, as well as the works by Sauca *et al.* [6] which addressed the conditions leading to stability and equilibrium in HFT in case of a one degree-of-freedom system. The latter works lead to a new methodology for a displacement control procedure and a linear environment, which was validated numerically. Yet, this notable contribution did not allow to establish formally the stability conditions for multi-degrees-of-freedom systems. A rigorous framework linking the input parameters, especially the substructures stiffness and sample time, to the stability and convergence rate, remains to be developed. Finally, the previous research did not address the case of non-linear heated numerical substructures.

This paper proposes to reformulate the problem of HFT in the framework of linear control system theory. Control theory proved its worth in many domains such as electronics, climate modelling and neural network and HFT is a process like any other that can take advantage of this rigorous and advanced field. The objective of this research is to develop a control model (called state equation) for controlling a system (HFT) using a control action (P-controller and PI-controller) in an optimum way (without overshoot) and ensuring stability. The developed theory is finally applied to a virtual hybrid test (i.e. a test where both substructures are numerically modelled) on a 2D steel frame.

2 BACKGROUND

2.1 State-space representation

A state-space representation is a mathematical model of a physical system. In discrete time, the state difference system is given by *Eq. 1* [7]:

$$\begin{aligned} \mathbf{x}[n + 1] &= \mathbf{A} \mathbf{x}[n] + \mathbf{B} \mathbf{w}[n] \\ \mathbf{y}[n] &= \mathbf{C} \mathbf{x}[n] + \mathbf{D} \mathbf{w}[n] \end{aligned} \quad (1)$$

$\mathbf{x}[n]$ is the state variable at time n . It is the smallest subset of system variables that defines the entire state of the system at any given time. The size of $\mathbf{x}[n]$ is the dimension of the system. $\mathbf{w}[n]$ is called the input vector and $\mathbf{y}[n]$ the output vector. \mathbf{A} refers to the dynamics matrix, \mathbf{B} the input matrix, \mathbf{C} the output matrix and \mathbf{D} the feedthrough matrix. A linear discrete-time system described by *Eq. 1* is asymptotically stable if and only if all eigenvalues of \mathbf{A} have a module smaller than one. These eigenvalues are called the “poles” of the system.

2.2 Time step response

The time step response is the time behaviour of the output of a system when its inputs change from zero to one in a very short time. It can be described by the following parameters:

- Rise time T_r : time for the system to go from 10% to 90% of its final value;
- Settling time T_s : time required for the oscillations to stay within some specified small percentage of the final value (the values most commonly used are 1%, 2% and 5%).
- Overshoot M_p : maximum deviation of system output from its final value.

The poles determine the values of these parameters and thus the behaviour of the system dynamics. The “pole placement design” is the procedure through which the matrix \mathbf{A} is defined to obtain the desired system behaviour [7]. The following hypothesis is admitted: it exists a design of the system (i.e. the HFT) such that the system poles are all real with one of the poles having a module significantly higher than the others (the “dominant pole”). This hypothesis implies that the only relevant parameter is the rise time T_r given by *Eq. 2*, which is a measure of the system reactivity.

$$T_r = \frac{T_{sa} \exp(-1)}{|\ln(p)|} \quad (2)$$

T_{sa} is the sample time. For HFT, it corresponds to the time step for updating the boundary conditions (chosen by the user, considering the constraints such as CPU time to run the model of the numerical

substructure, response time of the actuators, etc.). T_r is directly proportional to this time step, but also depends on p , the dominant pole. For p varying between 0 and 1, T_r decreases if p decreases. If p tends to 0, T_r is null, meaning that the reactivity of the system is instantaneous. If p tends to 1, T_r tends to infinity, meaning that the system never reaches the target value. In practice, this means that the matrix \mathbf{A} of the state-space representation of the HFT system must be chosen wisely, because its eigenvalues directly influence the time needed by the system to reach the target value when the boundary conditions are updated (through T_r).

3 STATE-SPACE REPRESENTATION OF HYBRID FIRE TESTING

HFT can be expressed as a closed-loop system formalized by the block diagram in *Fig. 1*. The system comprises two subsystems: one for the Physical Substructure (PS) and one for the Numerical Substructure (NS). The aim of the following developments is to establish the state equation of the HFT system. One will consider that the PS and NS have the same number of controlled degrees of freedom (DOF) d and that geometrical transformations are not necessary. If this is not the case, additional transformations must be considered, but it will not change the outcomes. If the subsystems are non-linear, the developments are still valid provided one uses the tangent stiffness of the PS and NS.

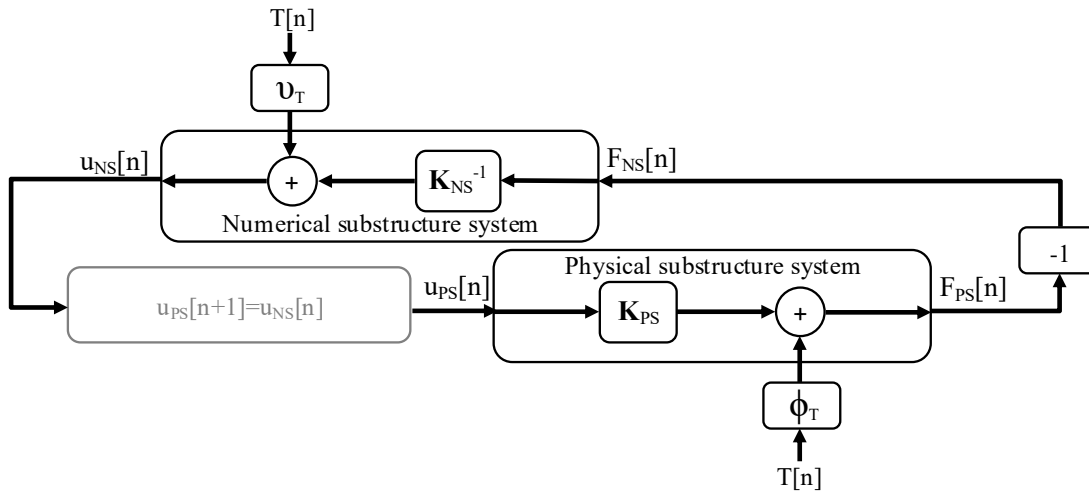


Fig. 1 - Simplified block diagram of hybrid fire testing

3.1 PS Subsystem

The input \mathbf{u}_{PS} of the PS subsystem at step n is the output \mathbf{u}_{NS} of the NS subsystem at step $n-1$:

$$\mathbf{u}_{PS}[n] = \mathbf{u}_{NS}[n-1] \quad (3)$$

$\mathbf{u}_{PS}[n]$ [$d \times 1$] is the displacement of the PS and $\mathbf{u}_{NS}[n]$ [$d \times 1$] is the displacement of the NS. The PS is affected by a disturbance, the variation of temperature.

The output is the force $\mathbf{F}_{PS}[n]$ [$d \times 1$] given by:

$$\mathbf{F}_{PS}[n] = \mathbf{K}_{PS}\mathbf{u}_{PS}[n] + \Phi_T\mathbf{T}[n] \quad (4)$$

$\mathbf{T}[n]$ [$d \times 1$] is the vector of temperature differences. \mathbf{K}_{PS} [$d \times d$] is the stiffness of the PS.

Φ_T [$d \times d$] contains the thermal forces generated by a temperature difference of 1 Kelvin.

3.2 NS Subsystem

The input is the force $\mathbf{F}_{NS}[n]$ [$d \times 1$]:

$$\mathbf{F}_{NS}[n] = -\mathbf{F}_{PS}[n] \quad (5)$$

In the most general case, the NS is affected by the temperature as well. The output is the displacement.

$$\mathbf{u}_{NS}[n] = \mathbf{K}_{NS}^{-1}\mathbf{F}_{NS}[n] + \mathbf{v}_T\mathbf{T}[n] \quad (6)$$

\mathbf{K}_{NS} [$d \times d$] is the stiffness of the NS. \mathbf{v}_T [$d \times d$] contains the displacements generated by a temperature difference of 1 Kelvin.

3.3 State equation

Using Eq. 3-6, the discrete state equation of the closed-loop system can be written as:

$$\mathbf{u}_{PS}[n+1] = -\mathbf{K}_{NS}^{-1}\mathbf{K}_{PS}\mathbf{u}_{PS}[n] + [-\mathbf{K}_{NS}^{-1}\boldsymbol{\Phi}_T + \mathbf{v}_T]\mathbf{T}[n] \quad (7)$$

By identification of Eq. 7 with Eq. 1, it results that the dynamics matrix $\mathbf{A} = -\mathbf{K}_{NS}^{-1}\mathbf{K}_{PS}$. The system is stable if the modules of the eigenvalues of the matrix \mathbf{A} are lower than 1. For a one DOF system, the matrix \mathbf{A} simplifies into $-\mathbf{K}_{PS} / \mathbf{K}_{NS}$, i.e. the ratio between the stiffness of the PS and NS. This result is similar to [6], and the same limitations can now be rigorously explained through the theory of poles. Using Eq. 7, the poles of \mathbf{A} only depend on the stiffness of the PS and NS, which is a design constraint specific to each problem; hence the HFT system characteristics of stability and rise time are constraints resulting from the structure and cannot be improved. This also implies that no HFT could be performed (or, would be stable) on structural configurations such that the stiffness of the PS and NS yield a matrix \mathbf{A} that has at least one eigenvalue with module higher than one. As it will be shown next, these limitations can be overcome by using a controller.

4 PROPORTIONAL CONTROL

Here, the displacement applied on the PS is corrected using a proportional controller. This means that the correction applied to the controlled variable \mathbf{u}_{PS} (the displacement at the interface of the physical specimen) is proportional to the difference between the reference value $\mathbf{u}_{NS}[n]$ (the displacement calculated from the numerical substructure) and the measured value $\mathbf{u}_{PS}[n]$ (the displacement applied on the specimen at the previous time step). Fig. 2 shows a block diagram of HFT with a P-controller.

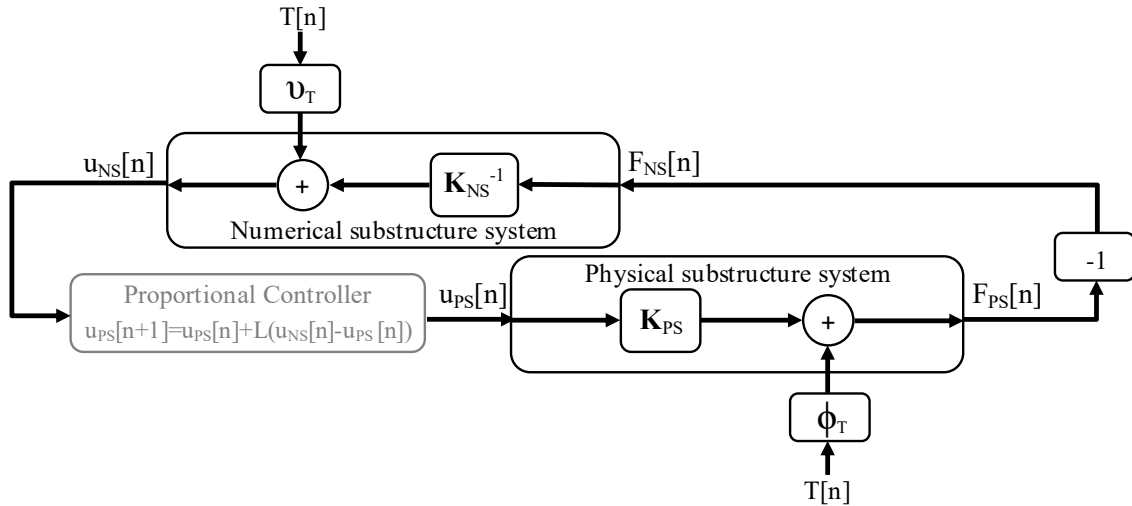


Fig. 2 – Simplified block diagram of hybrid fire testing with a proportional controller

For d DOF, the basic state equation is:

$$\mathbf{u}_{PS}[n+1] = \mathbf{u}_{PS}[n] + \mathbf{L}(\mathbf{u}_{NS}[n] - \mathbf{u}_{PS}[n]) \quad (8)$$

\mathbf{L} [$d \times d$] is the gain matrix. Using Eq. 3-6, a new state equation is established:

$$\mathbf{u}_{PS}[n+1] = [\mathbf{I} - \mathbf{L}\mathbf{K}_{NS}^{-1}\mathbf{K}_{PS} - \mathbf{L}]\mathbf{u}_{PS}[n] + [-\mathbf{L}\mathbf{K}_{NS}^{-1}\boldsymbol{\Phi}_T + \mathbf{L}\mathbf{v}_T]\mathbf{T}[n] \quad (9)$$

Identification with Eq. 1 yields $\mathbf{A} = [\mathbf{I} - \mathbf{L}\mathbf{K}_{NS}^{-1}\mathbf{K}_{PS} - \mathbf{L}]$. Owing to the incorporation of the controller, the characteristics of the system can now be tuned through \mathbf{L} ; the elements of the gain matrix \mathbf{L} must be chosen to allow stability and ensure that the system has appropriate rise time. The optimal case is for the eigenvalues of \mathbf{A} being equal to zero (see Eq. 2), i.e. for \mathbf{A} being the zero matrix. It yields: $\mathbf{L}\mathbf{K}_{NS}^{-1}\mathbf{K}_{PS} + \mathbf{L} = \mathbf{I}$. So, \mathbf{L} must be defined as:

$$\mathbf{L} = (\mathbf{K}_{NS}^{-1}\mathbf{K}_{PS}^* + \mathbf{I})^{-1} \quad (10)$$

where a \mathbf{K}_{PS}^* has been used instead of \mathbf{K}_{PS} to indicate the fact that \mathbf{K}_{PS} is, generally, unknown by the user. Hence an estimation \mathbf{K}_{PS}^* must be used within \mathbf{L} (e.g. the tangent stiffness). It gives Eq. 9:

$$\mathbf{u}_{PS}[n+1] = [\mathbf{I} - (\mathbf{K}_{PS}^* + \mathbf{K}_{NS})^{-1}(\mathbf{K}_{PS} + \mathbf{K}_{NS})]\mathbf{u}_{PS}[n] + [-\mathbf{K}_{NS}^{-1}\boldsymbol{\Phi}_T + \mathbf{v}_T]\mathbf{T}[n] \quad (11)$$

The stability and rise time of the system depend on the estimator \mathbf{K}_{PS}^* . An accurate estimation of \mathbf{K}_{PS} gives poles equal to zero and the lowest rise time. Eq. 11 is in fact equivalent to the developments of Sauca *et al.* [6], but the formulation used here highlights an important limitation of this methodology. Even if \mathbf{L} is well designed initially ($\mathbf{K}_{PS}^* = \mathbf{K}_{PS}$), the eigenvalues of \mathbf{A} change as the stiffness of the PS and NS are affected by the fire. The time properties (rise time, overshoot, and settling time) will unavoidably deteriorate during the test because the stiffness of the specimen will reduce and hence the poles will start diverging from zero. There are two possible solutions to mitigate this limitation: adapt \mathbf{L} during the HFT by continuously estimating \mathbf{K}_{PS} and \mathbf{K}_{NS} or use a proportional integral controller which will handle the adaptation automatically. The first solution is hard to implement and potentially hazardous because the behaviour of the tested element is unknown and could vary quickly. The second is the most appropriate: adding an integral term accelerates the movement of the process and allow to adapt to the variations of the stiffness of both substructures.

5 PROPORTIONAL INTEGRAL CONTROL

While the proportional term considers the current magnitude of the error at the time of the calculation, the integral term of a PI-controller consists in considering the history of the error (*Fig. 3*).

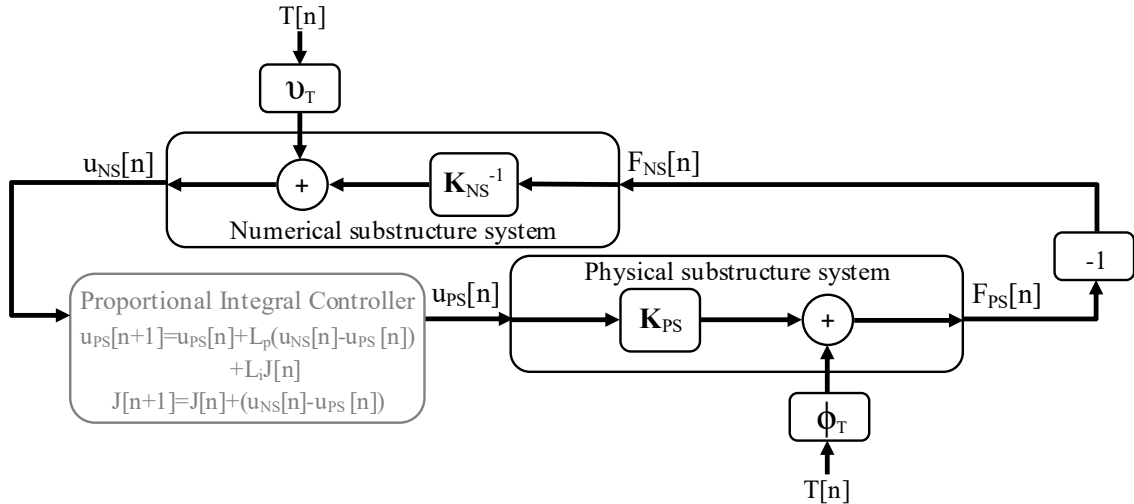


Fig. 3 – Simplified block diagram of hybrid fire testing with a proportional integral controller

For d DOF, Eq. 12 gives the basic state equation:

$$\begin{aligned} \mathbf{u}_{PS}[n+1] &= \mathbf{u}_{PS}[n] + \mathbf{L}_p(\mathbf{u}_{NS}[n] - \mathbf{u}_{PS}[n]) + \mathbf{L}_i \mathbf{J}[n] \\ \mathbf{J}[n+1] &= \mathbf{J}[n] + (\mathbf{u}_{NS}[n] - \mathbf{u}_{PS}[n]) \end{aligned} \quad (12)$$

$\mathbf{L}_p [d \times d]$ is the gain matrix of the proportional term and $\mathbf{L}_i [d \times d]$ is the gain matrix of the integral term $\mathbf{J}[n] [d \times 1]$. It is assumed that both matrices are diagonal. Each diagonal term i corresponds to a gain of the i^{th} DOF. Using Eq. 3-6 yields:

$$\begin{bmatrix} \mathbf{u}_{PS}[n+1] \\ \mathbf{J}[n+1] \end{bmatrix} = \begin{bmatrix} \mathbf{I} - \mathbf{L}_p \mathbf{K}_{NS}^{-1} \mathbf{K}_{PS} - \mathbf{L}_p & \mathbf{L}_i \\ -\mathbf{K}_{NS}^{-1} \mathbf{K}_{PS} - \mathbf{I} & \mathbf{I} \end{bmatrix} \begin{bmatrix} \mathbf{u}_{PS}[n] \\ \mathbf{J}[n] \end{bmatrix} + \begin{bmatrix} -\mathbf{L}_p \mathbf{K}_{NS}^{-1} \boldsymbol{\Phi}_T + \mathbf{L}_p \mathbf{v}_T \\ -\mathbf{K}_{NS}^{-1} \boldsymbol{\Phi}_T + \mathbf{v}_T \end{bmatrix} \mathbf{T}[n] \quad (13)$$

The design of a PI-controller consists in determining the diagonal elements of the gain matrices to obtain appropriate poles. The optimal case arises when the poles are real positive with values lower than 1 and as close as possible to 0.

6 APPLICATION

6.1 Virtual Hybrid Fire Testing

The reference structure (Fig. 4 a) is an office building with 4 longitudinal bays. It is composed of steel beams (IPE300, S355) and columns (HEB200, S355), supporting a 150 mm thick concrete floor slab. Live loads are taken from EN 1991-1. A complete compartment is subjected to the ISO-834 standard fire.

A “virtual” HFT (VHFT) is performed (see Fig. 5). The NS is a FE model (in SAFIR® [8]) which allows accounting for its nonlinear response and the fact that it is partly heated. Until now, most previous applications of HFT (except [3]) had considered an elastic response of the NS. The PS is also modelled, separately, in SAFIR®.

To perform a VHFT with PS and NS modelled in SAFIR®, the HFT methodology is implemented as an automatic procedure in SAFIR. An intermediate software was also developed to ensure the connections between PS and NS by transmitting forces or displacements at the right nodes located at the interface of both subsystems.

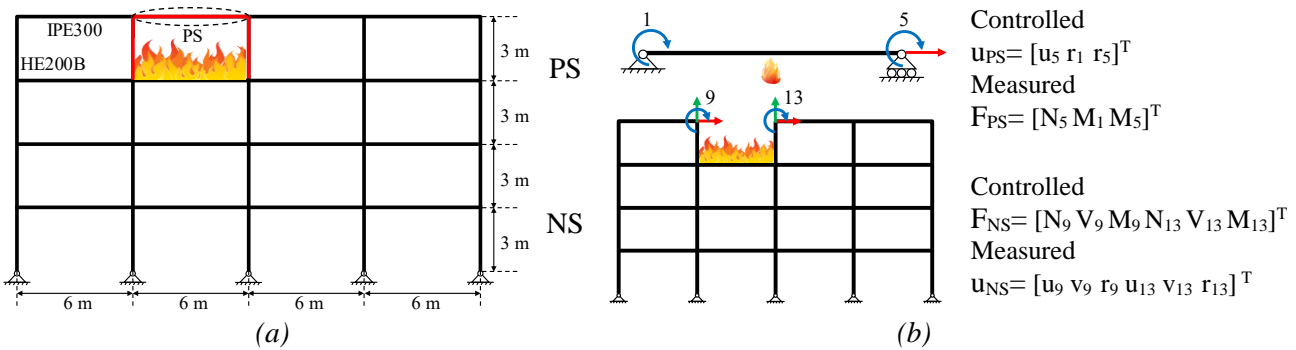


Fig. 4 – Structure elevation (a) – DOF of the PS and NS (b)

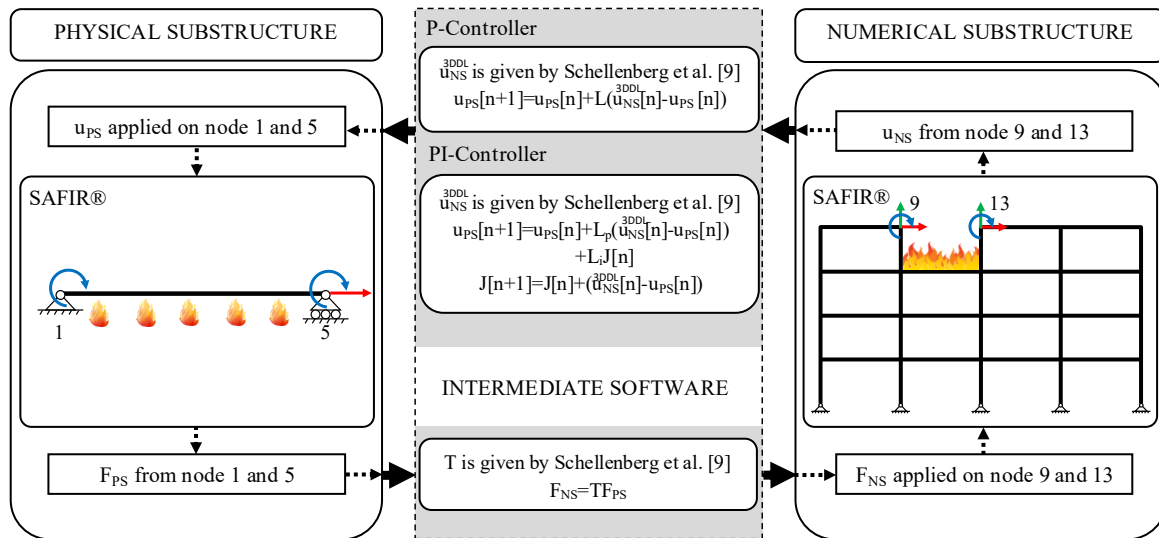


Fig. 5 - Virtual Hybrid testing

The PS (Fig. 4 b) is a protected IPE300 beam situated on the last floor. The fire is applied on three faces. Three DOF are controlled for the PS: the axial displacement u_5 and two rotations r_1 and r_5 . The NS is the remaining structure. Two columns are heated. Six reactions are controlled in the NS, $F_{NS} = [N_9 \ V_9 \ M_9 \ N_{13} \ V_{13} \ M_{13}]^T$. As the number of DOF is not the same in the PS and NS, the necessary transformations are performed [9].

At each time step Δt_H , the boundary conditions are updated. Δt_H is variable and is composed of the time response of the actuators Δt_{ACT} needed to apply the new displacements (fixed, set here to 5s) and the CPU time Δt_{NUM} needed to run the model of the numerical substructure (variable).

For the P-controller, L is calculated using *Eq. 10*. For the PI-controller, the three diagonal terms of each matrix L_p and L_i are determined for a dominant pole equal to 0.4 (lowest value possible). An estimation of the stiffness of the PS is necessary to determine L , L_p and L_i .

6.2 Results

Results are shown in *Fig. 6*. Displacements/forces are given according to the mean temperature of the PS (it is possible to present the evolution of the results as a function of time). The curve “Reference” refers to a numerical simulation in SAFIR® of the complete frame, i.e. the response that the HFT aims at reproducing.

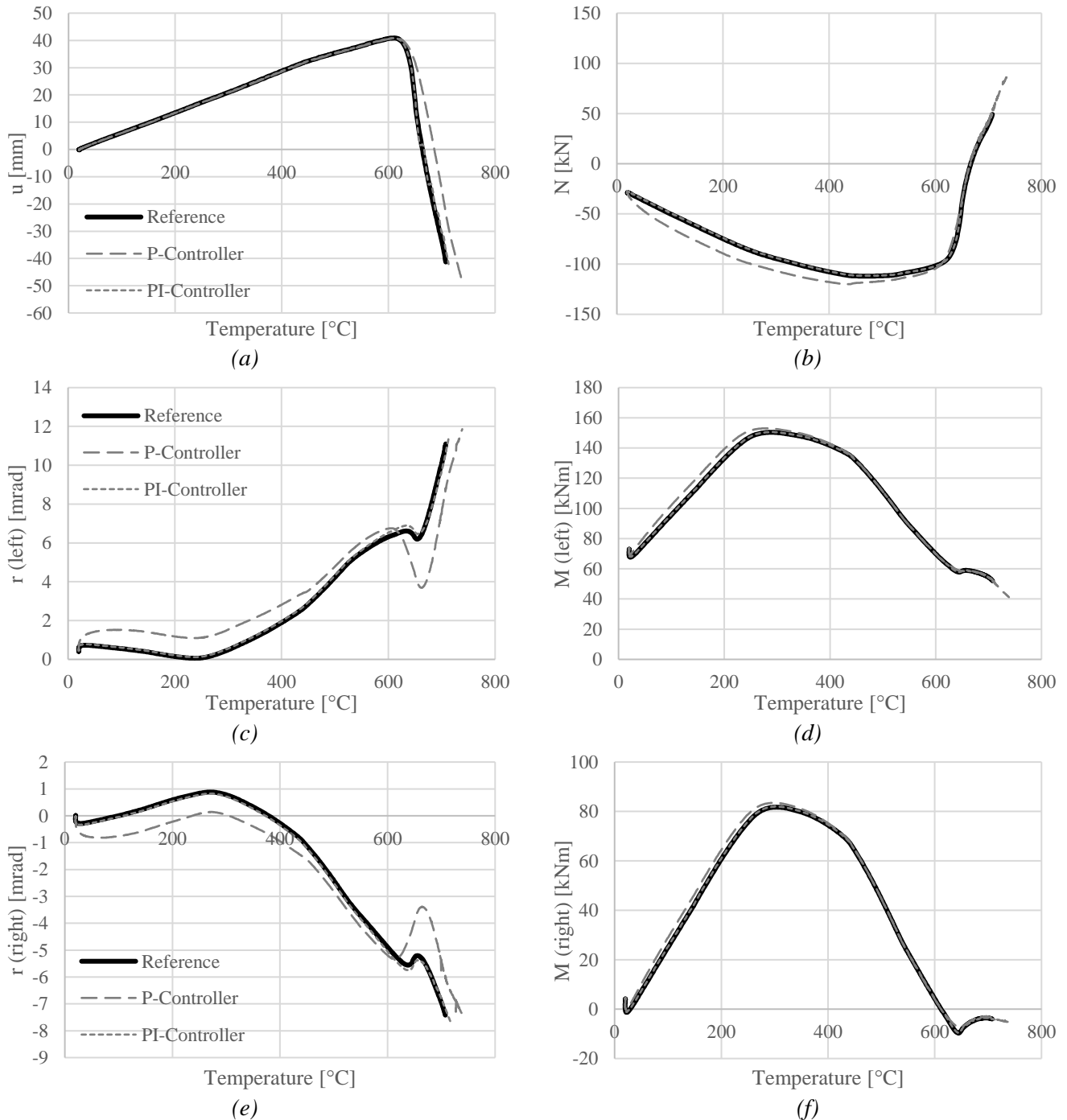


Fig. 6 – Axial displacement (a) – Normal force (b) – Rotations (c,e) – Bending moments (d,f)

For the P-controller, the solution of the axial displacement (a) is well captured except for temperature higher than 620 °C, temperature for which the beam fails under combined bending and compression

and the behaviour changes to tensile action. However, the curve of the axial force (b) exhibits a certain lag from the beginning. It indicates that even if it is very low, an error is left out between the axial displacement and the reference. The curves in (c) and (e) begin also to diverge highly from the beginning. In transient state (e. g. changes of temperature), the P-controller is often too slow to follow correctly the reference. That drawback is inherent to a P-controller that is more appropriate when the state variables do not vary too much. Moreover, the gain matrix \mathbf{L} was designed for the initial situation and becomes less optimal as the stiffness of both substructures is affected by fire.

For the PI-controller, the reference solution is well reproduced in each graph with very small divergence at the end (the curves can hardly be distinguished from the reference curve on the figures) although the behaviour of the PS changes dramatically in the last moments of the test. This demonstrates the advantage of using a PI-controller to automatically adapt to the variations of stiffness that inevitably occur during a HFT.

7 CONCLUSION

The application of linear system control theory to HFT allows establishing the stability condition and time properties in a rigorous framework that was lacking in previous research.

As the system stability depends on the stiffness of both substructures, a controller is necessary. A proportional controller is a simple method that allows ensuring initial stability and does not increase the dimension of the problem. However, P-controller is subject to a sensitivity to changes in stiffness of the substructures. A proportional integral controller allows overcoming these issues and yields superior results compared to a P-controller. The efficiency of a PI-controller has been demonstrated in a virtual HFT on a multi-story building where both the physical substructure and the numerical substructure were heated and acting non-linearly. Nevertheless, further improvements of the method can be done; notably this paper relied on the hypothesis that the poles of the system were real and positive. In case of PI-controller, an extension of the design to complex poles will be conducted in further research.

REFERENCES

1. M Korzen, G Magonette, P Buchet (1999). *Mechanical Loading of columns in Fire Tests by Means of the Substructuring Method*. Zeitschrift für Angewandte Math. und Mech., Vol. 79, pp S617-S618.
2. F Robert, S Rimlinger, C Collignon (2010). *Structure fire resistance: a joint approach between modelling and full-scale testing (substructuring system)*, 3rd fib International Congress.
3. H Mostafaei (2013). *Hybrid fire testing for assessing performance of structures in fire –Application*, Fire Safety Journal, 56, pp 30–38.
4. C A Whyte, K R Mackie, B Stojadinovici (2016). *Hybrid Simulation of Thermomechanical Structural Response*, Journal of Structural Engineering, pp 142(2).
5. N Tondini, G Abbiati, L Possidente, B Stojadinovic. (2016). *A Static Partitioned Solver for Hybrid Fire Testing*, 9th International Conference on Structures in Fire, DEstech Publications inc.
6. A Sauca, T Gernay, F Robert, N Tondini, J M Franssen (2018). Hybrid fire testing: Discussion on stability and implementation of a new method in a virtual environment, *Journal of Structural Fire Engineering*. doi: 10.1108/JSFE-01-2017-0017.
7. J Åström, R Murray (2016). *Feedback Systems: An Introduction for Scientists and Engineers*, Princeton University Press, 2nd edition, November 2016.
8. J M Franssen, T Gernay (2017), *Modeling structures in fire with SAFIR®: Theoretical background and capabilities*, Journal of Structural Fire Engineering, 8(3):300-323.
9. A H Schellenberg, S A Mahin, G L Fenves (2009). *Advanced implementation of Hybrid Simulation*, PEER Report 2009/104, University of California, Berkeley

EFFECT OF COMBINED POLYPROPYLENE AND STEEL FIBRES ON PORE-PRESSURE DEVELOPMENT IN ULTRA-HIGH-PERFORMANCE CONCRETE IN FIRE

Ye Li¹, Pierre Pimienta², Nicolas PINOTEAU³, Kang Hai Tan⁴

ABSTRACT

This paper investigates the individual and combined effect of polypropylene (PP) fibres and steel fibres on spalling behaviour and pore pressure build-up of ultra-high-performance concrete (UHPC) exposed to elevated temperature. Simultaneous measurements of pore pressure and temperature were conducted at different depths in UHPC specimens under one-sided heating. Compressive, tensile and permeability tests were performed. Addition of PP fibres effectively prevented spalling and they increase permeability compared to steel fibres. The combined use of PP and steel fibres showed strong synergistic effect on reducing pore pressure. Two plateaus were observed from the temperature history due to vaporisation of liquid water (between 115 and 125 °C) and release of water vapour (started from 180 °C), respectively. The second plateau was identified as functional temperature of PP fibres. Maximum measured pore pressures in spalled specimens were much lower than their tensile strengths.

Keywords: Explosive spalling, ultra-high-performance concrete, pore pressure, PP fibre, steel fibre

1 INTRODUCTION

Fire is one of the most serious risks for tunnels, high-rise buildings and underground structures [1]. Explosive spalling of concrete at elevated temperature is a complicated phenomenon that causes concrete to crack, to spall and steel reinforcements to expose to fire. This leads to a reduction of load-carrying capacity of affected members [2-4].

Ultra-high-performance concrete (UHPC) has high strength ($f_c > 150$ MPa), high ductility and enhanced durability [5, 6]. It has been increasingly utilized in improving structural resistance of buildings and bridges [7-9]. However, it is particularly vulnerable to explosive spalling under fire condition due to its densely packed microstructure and very low permeability compared to normal strength concrete [10, 11].

Addition of polypropylene (PP) fibres is the most widely accepted method to mitigate explosive spalling [12-14]. Inclusion of steel fibres has shown to reduce explosive spalling and enhance fire endurance of HSC columns [3, 14]. However, their effect on spalling of UHPC has been controversial [15, 16]. The combined use of PP and steel fibres to prevent spalling of fibre-reinforced self-consolidating concrete (FRSCC) and HSC was investigated [12, 13], but their contribution and mechanism is not clear yet.

Pore pressure is a critical factor leading to spalling because it can generate large tensile stresses, which may exceed tensile strength of concrete [17]. However, quantitative analysis of pore pressure

¹ Ph.D. candidate of School of Civil and Environmental Engineering, Nanyang Technological University, Singapore.
e-mail: liye0006@e.ntu.edu.sg

² Professor. Université Paris Est, CSTB, Centre Scientifique et Technique du Bâtiment, Marne la Vallée, France.
e-mail: pierre.pimienta@cstb.fr

³ CSTB, Centre Scientifique et Technique du Bâtiment, Marne la Vallée, France.
e-mail: Nicolas.PINOTEAU@cstb.fr

⁴ Professor School of Civil and Environmental Engineering, Nanyang Technological University, Singapore.
e-mail: ckhtan@ntu.edu.sg

is one of the greatest difficulties in more spalling studies. Monitoring of pore pressure in UHPC specimens during fire exposure is even limited. This paper studies the individual and combined effects of PP fibres and steel fibres on explosive spalling and pore pressure build-up of UHPC at elevated temperature. UHPC specimens were prepared to be subjected to unidirectional heat source. Compressive strength, tensile strength and residual permeability were measured to analyse spalling and pore pressures.

2 EXPERIMENTAL PROGRAM

2.1 Mix proportions and specimen preparation

Portland cement (ASIA[®] CEM I 52.5 N), fine aggregate (natural river sands sieved to 0.6 mm), micro silica sand (median particle size of 130 μm), highly reactive silica fume (Grade 940 from Elkem Microsilica[®]), 3rd generation polycarboxylate-based superplasticizer (Sika[®] ViscoCrete[®]-2044), steel fibres with a length of 13 mm and a diameter of 0.22 mm, and monofilament cylindrical PP fibres with a length of 12 mm and a diameter of 30 μm were used to prepare the UHPC mixes. Water-to-binder ratio was 0.22 to achieve dense packing in concrete specimens.

Four mix proportions were prepared as shown in *Table 1*. A plain UHPC mix was used as a control mix denoted by C. PP fibres and steel fibres were variables to be investigated. PP contains 3.0 kg/m^3 of PP fibres, ST has 196.3 kg/m^3 (2.5% by volume) of steel fibres, while PPST contains combined PP and steel fibres.

Table 1. Mixture proportion of the specimens

Mix Design	PP fibre (kg/m^3)	Steel fibre (kg/m^3)	Relative weight ratio to cement					
			C	AG	SF	SS	SP	W/B
C	0.00	0.00	1.00	1.1	0.25	0.25	0.04	0.22
PP	3.00	0.00	1.00	1.1	0.25	0.25	0.04	0.22
ST	0.00	196.3	1.00	1.1	0.25	0.25	0.04	0.22
PPST	3.00	196.3	1.00	1.1	0.25	0.25	0.04	0.22

C: cement, AG: aggregates, SF: silica fume, SS: silica sand, SP: superplasticizer, W/B: water-to-binder ratio.

Binders (cement and silica fume) and fillers (silica sand and sieved river sand) were dry-mixed in a Hobart[®] planetary mixer for 2-3 min to ensure good dispersion. Thereafter, premixed water and superplasticizer were added and mixed for another 3 to 5 minutes until the fresh mortar is homogenous and consistent. Fibres were then added and mixed for another 2 min. The fresh UHPC mixtures were then cast into cubical (50×50×50 mm^3), dog-bone shaped (36×18 mm^2 cross section), cylindrical ($\text{\O}150 \text{ mm} \times 48 \text{ mm}$) and cuboid (300×300×120 mm^3) moulds for compressive strength, uniaxial tensile, permeability and spalling tests, respectively. Pore pressure gauges and thermocouples were inserted into the specimens.

2.2 Experimental setup and heating procedure

The experimental device for measuring pore pressure and temperature was developed by Kalifa et al. [18] and modified by the authors. Fig. 1 shows the schematic experimental setup. The specimens were placed at the opening of the electric furnace. Five pore pressure gauges were placed at the central area of the specimens at 5, 10, 20, 30 and 50 mm depth from the heated surface, respectively. A tube without a metal cup was located at 2 mm from the heated surface for measuring temperature only. The tubes of the pore pressure gauges emerged from the rear face of the specimens and were connected to piezoelectric pressure transducers by connectors. Thermocouples were inserted from the second exit of the connectors down to the head of the

pressure gauges. Thermal load was applied on the face (300×300 mm²) of the UHPC specimens a heating rate of 2 °C/min. The target temperature was 600 °C.

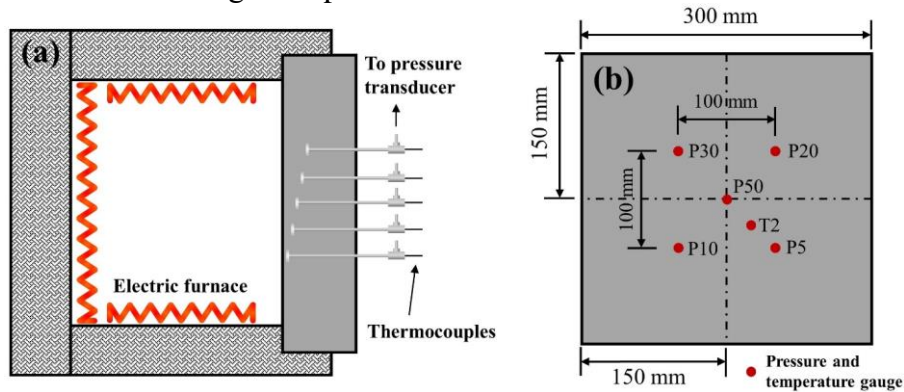


Fig. 1. (a) schematic experimental setup; (b) locations of gauges.

2.3 Compressive strength, tensile strength and permeability measurements

Compressive strength measurements were conducted at ambient temperature following ASTM C109/C109M-11 [19]. The hydraulic compression machine had a capacity of 3,000 kN. A constant loading rate of 100 kN/min was adopted and the maximum force was recorded automatically. Uniaxial tensile strength tests were carried out by means of an electro-mechanical testing machine with a tensile capacity of 30 kN. A personal computer was connected to the testing machine to acquire the test data. The tests were displacement-controlled at a rate of 0.2 mm/min.

Apparent gas permeability was determined by means of RILEM-CEMBUREAU method [20] based on Darcy’s law which was later modified by the Hagen-Poiseuille relationship [21]. Intrinsic gas permeability was adopted because it is independent from the inlet pressure to correct the apparent gas permeability [22]. Permeability tests were performed at residual state and at ambient temperature, after the specimens were heated to 200 °C.

3 RESULTS AND DISCUSSIONS

3.1 Mechanical properties and permeability of UHPC

The results shown in Table 2 are average values of three samples of each UHPC mix. The C mix had a compressive strength of 149.6 MPa and a tensile strength of 8.85 MPa. Adding PP fibres did not change compressive strength and tensile strength significantly. Addition of steel fibres significantly increased compressive strength by 15% and tensile strength by 40.6%. Combined PP and steel fibres also increased both compressive and tensile strengths of UHPC.

Table 2. Mechanical properties and permeability of UHPCs

Mix Design	f_c (MPa)	f_t (MPa)	Permeability (10^{-18} m ²)
C	149.6±4.8	8.85±0.67	0.73±0.49
PP	159.7±5.7	8.53±0.69	13.83±7.0
ST	172.1±3.7	12.44±0.34	0.15±0.06
PPST	154.8±2.3	11.1±0.53	758.04±173.2

f_c : Compressive strength; f_t : Uniaxial tensile strength.

For permeability, sole addition of 3 kg/m³ PP fibres significantly increased permeability of UHPC from 0.73×10^{-18} to 13.83×10^{-18} m² (almost 19-fold increase). The addition of steel fibres alone slightly reduced intrinsic permeability. Combined use of PP and steel fibres showed synergistic effect and significantly increased permeability by 3 orders of magnitude with respect to the Control

mix, which is attributed to enhanced connectivity of PP fibre tunnels by multiple microcracks generated from thermal incompatibility between the steel fibres and the UHPC matrix.

3.2 Spalling behaviour

Fig. 2 shows the heated faces of UHPC specimens after the spalling tests. PP fibres showed clear effect on preventing spalling, since C and ST specimens with very low permeability (Table 2) spalled severely, while PP and PPST specimens did not spall at all. Steel fibres alone helped to improve mechanical properties of UHPC, but spalling could not be prevented. For C, intermittent loud explosive sounds of spalling were heard during the tests accompanied with intermittent lower popcorn-cooking like sounds, which inferred progressive spalling. For ST samples, only several loud sounds were noticed. The spalled areas were non-uniform, due to non-homogeneous distribution and orientation of steel fibres in the concrete.

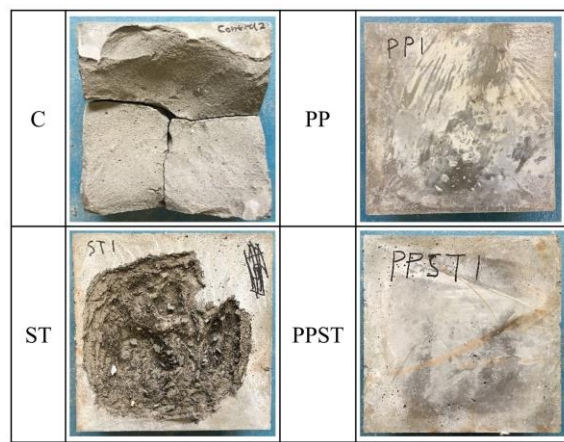


Fig. 2. Spalling behaviour of UHPC specimens.

3.3 Results of temperature and pore pressure measurements

Fig. 3 presents temperature and pore pressure evolution of UHPC mix designs. From the temperature history, plateaus between 115 °C and 125 °C can be observed in all the UHPC mixes due to phase change of liquid water as vaporisation of water is endothermic. The higher vaporisation temperature than 100 °C is due to the presence of high capillary forces at the interface between liquid water, gas phase (vapour and dry air) and concrete matrix [1]. For PP and PPST, second plateau between 180 °C and 220 °C can be observed (as marked in Fig. 3 PPST), which is due to release of water vapour caused by melting of PP fibres and formation of microcracks. For C and ST, on the other hand, sharp drops of temperature due to a sudden release of compressed water vapour indicating spalling had taken place. For C, the average first spalling time was 218 min. However, due to the enhanced mechanical properties, ST specimens resisted higher temperature and spalling took place at 234 min.

From evolution of pore pressure, after reaching the maximum pore pressure, the pressure of the spalled specimens C and ST dropped directly down to 0 MPa due to severe concrete spalling and exposure of pressure gauges. On the other hand, pore pressures of un-spalled specimens PP and PPST followed a bell-shape curve with smooth transitions between the ascending and the descending parts.

By comparing C and PPST in terms of temperature and pore pressure history as a function of time, at the first plateaus on the temperature curve, liquid water vaporised but trapped in the pores. Thus, the pore pressures kept increasing. With increasing of temperature, when spalling occurred in C specimen, pore pressure dropped down to 0 MPa, accompanied with sharp drops of temperature due to full release of water vapour. For PPST without spalling, second temperature plateau started with

gradually reduced rate of pore pressure and accompanied with peaks of pore pressure as marked in Fig. 3 PPST. When the rate of vapour release (due to vapour flow towards the exposed surface) exceeded the rate of vapour supplying (due to dehydration and moisture transport), pore pressure started to drop [1, 11]. The difference between C and PPST highlights that release of water is responsible for build-up of pore pressure and explosive spalling.

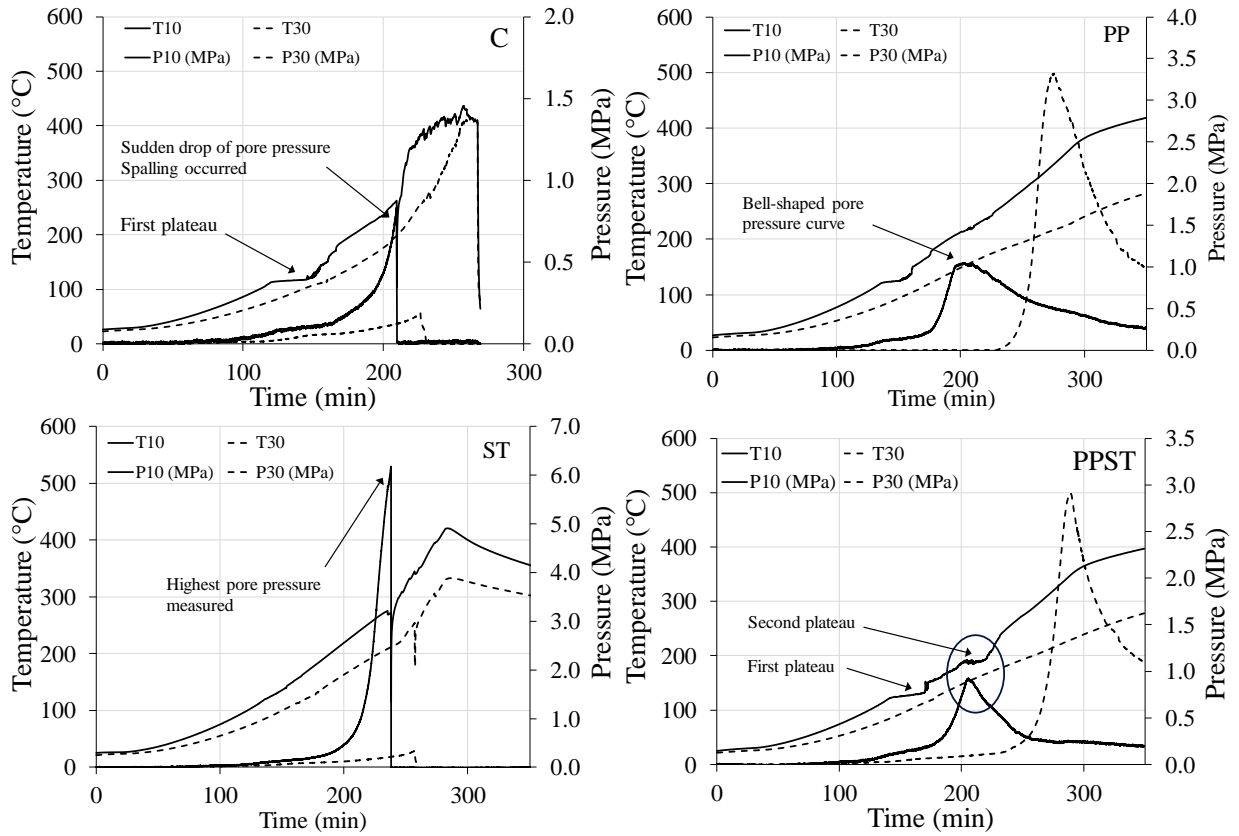


Fig. 3. Temperature and pore pressure profile evolve with time.

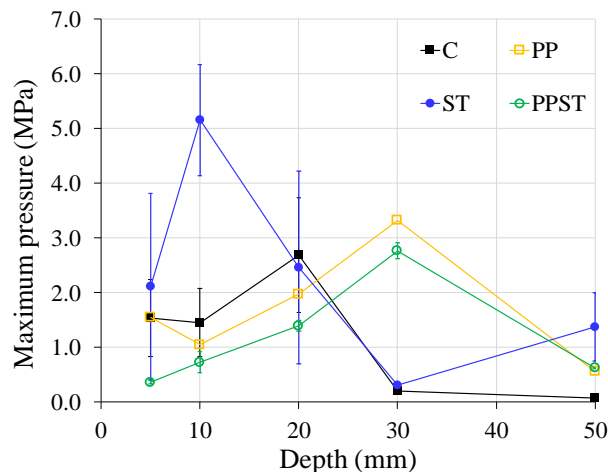


Fig. 4. Maximum pore pressure of UHPC mix designs at different depths.

Fig. 4 summarises the average maximum pore pressure of each UHPC mix at different locations. The maximum pore pressures of C and ST appeared in shallower regions (less than 20 mm from the heated face) because very dense microstructure hindered water vapour from migrating into deeper regions of the specimens. Spalling occurred and created a new free surface, which helped to release

large amount of water vapour. A maximum pore pressure of 5.2 MPa was observed in the ST specimen at 10 mm from the heated surface due to the inclusion of steel fibres. The maximum pore pressures of PP and PPST took place in deeper regions (30 mm from the heated surface) due to migration of moisture into the cooler regions of the specimens. The maximum pore pressure of PPST was lower than that of PP (2.8 MPa for PPST vs. 3.3 MPa for PP) due to microcracks caused by expansion of steel fibres helped to increase permeability of UHPC and facilitate the release water vapour. This highlights the effect of permeability on thermo-hydral behaviour, in particular, on the build-up of pore pressure. Moreover, more fibres introduced more discrete air bubbles during the mixing process, which can act as discontinuous reservoirs for pressure relief [13].

3.4 Discussion on pore pressure and temperature results

Fig. 5 presents the evolution of pore pressure as a function of temperature. Pore pressure profiles are compared to saturated vapour pressure (P_{vsat}). For C and ST, the measured pressures were lower than the P_{vsat} curve due to low initial moisture content of UHPC compared to that of ordinary concrete and HSC. Moisture clogs might have been formed in the shallower regions of the specimens, but the dense microstructure of C and ST hindered the moisture from reaching the pressure gauges. On the other hand, the PP fibres created an interconnected microcrack network, so that water vapour can be transferred to the pore pressure gauges. Therefore, the pore pressure of PP and PPST at 20 mm depth increased and followed the P_{vsat} curve in the upper part of the ascending branch as marked in Fig. 5. Moreover, the measured pressures even exceeded the P_{vsat} at 30 mm, which is possibly attributed to that at high degree of saturation, the free volume available for dry air to expand is lower. As a consequence, the partial pressure of the dry air enclosed in the specimens contributed to the total pressure [18].

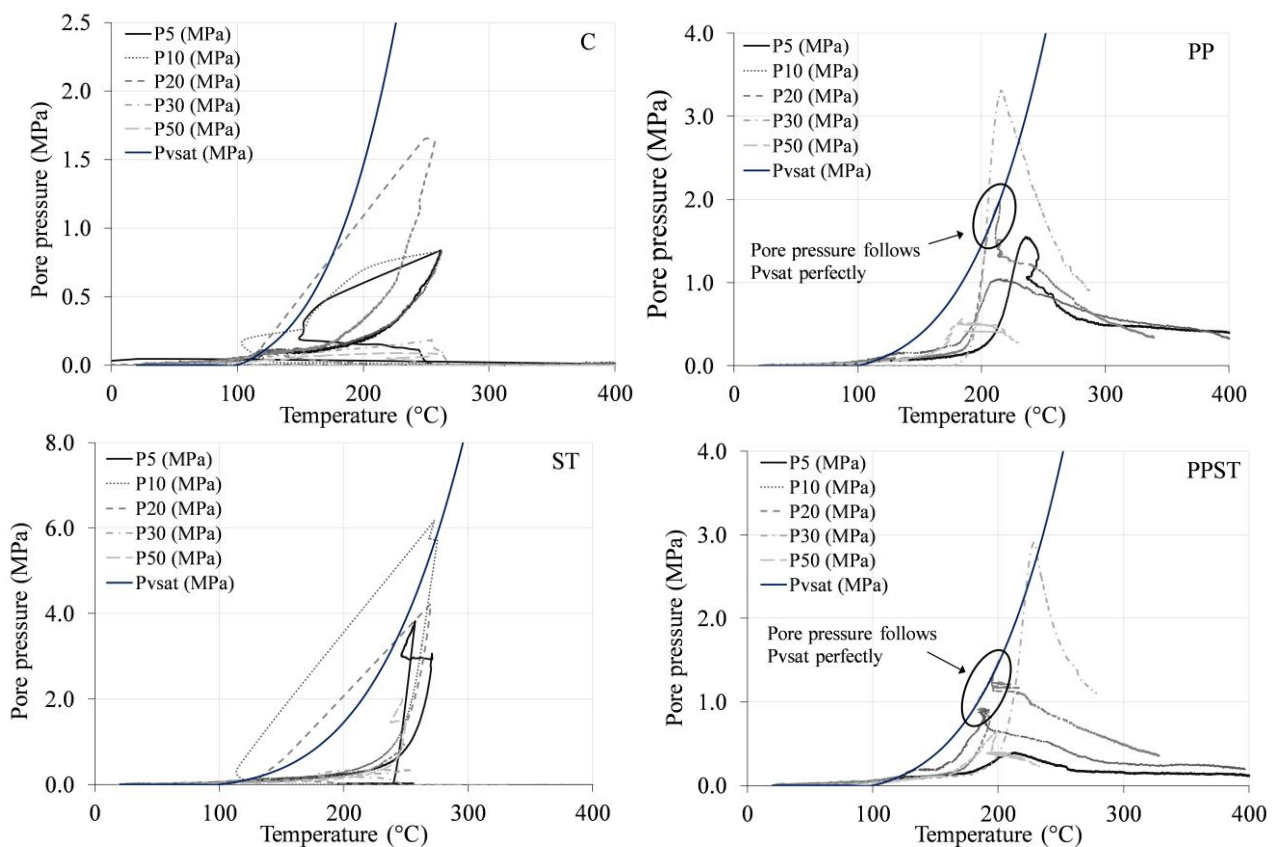


Fig. 5. Pressures as a function of temperature plotted with the saturated vapour pressure curve.

By comparing the maximum pressure and the tensile strength in Table 2, it is obvious that the pore pressure was far lower than the tensile strength of the samples. In Felicetti's research, high pore

pressure during heating only reduced apparent tensile strength of HPC with a rate of 0.24 due to the less interconnected porosity of high grade concrete [23]. Therefore, pore pressure can only contribute to spalling to a limited extent and it may not be the only factor leading to spalling since thermal stress cannot be neglected. One possible explanation is that the locations of measurements were not those that experienced the maximum pressure. Also, the diameter of the pressure probes has a bearing on the magnitude. To obtain more accurate pore pressure measurements more advanced methods should be studied. On the other hand, in the region of moisture clog, discrepancy between thermal expansion of pore fluid and concrete matrix can lead to very high build-up of hydraulic pressure and cause spalling [24]. The walls between closed pores with super-heated water and open pores with lower pressure can be destroyed by the pressure difference, which can lead to progressive breakdown of microstructure [25, 26].

4 CONCLUSIONS

Individual and combined effects of polypropylene (PP) fibres and steel fibres on development of pore pressure and temperature in UHPC during heating were investigated. Mechanical properties and permeability of UHPC mixes were measured. Results showed that plain UHPC and UHPC with steel fibres alone had very low permeability and suffered severe explosive spalling. Addition of PP fibres suppressed explosive spalling. Combined use of PP and steel fibres synergistically prevented explosive spalling. Vaporisation of liquid water caused plateaus in temperature curves in all the UHPC mixes between 115 °C and 125 °C. Melting of PP fibres and formation of microcracks functioned between 180 and 220 °C to release water vapour and result in another plateau in the temperature curve, which was accompanied with peaks of pore pressures. The maximum pore pressure of the spalled specimens was much lower than the P_{vsat} curve and the measured pore pressure was much lower than the tensile strength of the corresponding UHPC mix designs. This could be due to the limitation of the pressure gauges used.

ACKNOWLEDGMENT

This material is based on research/work supported by the Land and Liveability National Innovation Challenge under L2 NIC Award No. L2NICCFP1-2013-4. The authors thankfully acknowledge the support received from Dr. Jihad MIAH, Dr. MEGE Romain and Mr. Pierre-Jean DEGIOVANNI during the experiments at CSTB, France.

REFERENCES

1. Jean-Christophe Mindeguia, Pierre Pimienta, Albert Noumowé, and Mulumba Kanema (2010). *Temperature, pore pressure and mass variation of concrete subjected to high temperature — Experimental and numerical discussion on spalling risk*. Cement and Concrete Research. 40(3). pp. 477-487.
2. Eike Wolfram Heinrich Klingsch, *EXPLOSIVE SPALLING OF CONCRETE IN FIRE*. 2014, ETH: Zurich.
3. VKR Kodur and L Phan (2007). *Critical factors governing the fire performance of high strength concrete systems*. Fire Safety Journal. 42(6). pp. 482-488.
4. D. Gawin, C. Alonso, C. Andrade, C. E. Majorana, and F. Pesavento (2005). *Effect of damage on permeability and hygro-thermal behaviour of HPCs at elevated temperatures: Part I. Experimental results*. Computers and Concrete. 2(3). pp. 189-202.
5. Dehui Wang, Caijun Shi, Zemei Wu, Jianfan Xiao, Zhengyu Huang, and Zhi Fang (2015). *A review on ultra high performance concrete: Part II. Hydration, microstructure and properties*. Construction and Building Materials. 96. pp. 368-377.
6. Caijun Shi, Zemei Wu, Jianfan Xiao, Dehui Wang, Zhengyu Huang, and Zhi Fang (2015). *A review on ultra high performance concrete: Part I. Raw materials and mixture design*. Construction and Building Materials. 101. pp. 741-751.

7. SL Yang, SG Millard, MN Soutsos, SJ Barnett, and TT Le (2009). *Influence of aggregate and curing regime on the mechanical properties of ultra-high performance fibre reinforced concrete (UHPRFC)*. Construction and Building Materials. 23(6). pp. 2291-2298.
8. Michael Schmidt and Ekkehard Fehling (2005). *Ultra-high-performance concrete: research, development and application in Europe*. ACI Special publication. 228. pp. 51-78.
9. Jacques Resplendino (2004). First recommendations for ultra-high-performance concretes and examples of application. *International Symposium on Ultra High Performance Concrete*, 2004. pp. 79-90
10. VKR Kodur (2000). Spalling in high strength concrete exposed to fire—concerns, causes, critical parameters and cures. *Proceedings, ASCE Structures Congress*, Philadelphia, PA, 2000. pp. 1-8
11. Mugume Rodgers Bangi and Takashi Horiguchi (2011). *Pore pressure development in hybrid fibre-reinforced high strength concrete at elevated temperatures*. Cement and Concrete Research. 41(11). pp. 1150-1156.
12. Yining Ding, Cong Zhang, Mingli Cao, Yulin Zhang, and Cecília Azevedo (2016). *Influence of different fibers on the change of pore pressure of self-consolidating concrete exposed to fire*. Construction and Building Materials. 113. pp. 456-469.
13. Mugume Rodgers Bangi and Takashi Horiguchi (2012). *Effect of fibre type and geometry on maximum pore pressures in fibre-reinforced high strength concrete at elevated temperatures*. Cement and Concrete Research. 42(2). pp. 459-466.
14. VKR Kodur, Fu-Ping Cheng, Tien-Chih Wang, and MA Sultan (2003). *Effect of strength and fiber reinforcement on fire resistance of high-strength concrete columns*. Journal of Structural Engineering. 129(2). pp. 253-259.
15. K Hertz, *Heat-induced explosion of dense concretes*. 1984.
16. Kristian Dahl Hertz (1992). *Danish investigations on silica fume concretes at elevated temperatures*. ACI Materials journal. 89(4).
17. G. A. Houry, C. E. Majorana, F. Pesavento, and B. A. Schrefler (2002). *Modelling of heated concrete*. Magazine of Concrete Research. 54(2). pp. 77-101.
18. Pierre Kalifa, Francois-Dominique Menneteau, and Daniel Quenard (2000). *Spalling and pore pressure in HPC at high temperatures*. Cement and concrete research. 30(12). pp. 1915-1927.
19. Am. Soc. Test. Mater., *ASTM C 109/C 109 M-11, Standard Test Method for Compressive Strength of Hydraulic Cement Mortars (Using 2-in. or 50-mm Cube Specimens)*. 2011.
20. JJ Kollek (1989). *The determination of the permeability of concrete to oxygen by the Cembureau method—a recommendation*. Materials and structures. 22(3). pp. 225-230.
21. C Gallé and J Sercombe (2001). *Permeability and pore structure evolution of silicocalcareous and hematite high-strength concretes submitted to high temperatures*. Materials and Structures. 34(10). pp. 619-628.
22. LJ Klinkenberg (1941). The permeability of porous media to liquids and gases. *Drilling and production practice*, 1941. American Petroleum Institute
23. Roberto Felicetti, Francesco Lo Monte, and Pierre Pimienta (2017). *A new test method to study the influence of pore pressure on fracture behaviour of concrete during heating*. Cement and Concrete Research. 94. pp. 13-23.
24. Siavash Ghabezloo, Jean Sulem, and Jérémie Saint-Marc (2009). *The effect of undrained heating on a fluid-saturated hardened cement paste*. Cement and Concrete Research. 39(1). pp. 54-64.
25. VG Petrov-Denisov, LA Maslennikov, and AM Pitckob (1972). *Heat-and moisture transport during drying and first heating of heat resistant concrete*. Concrete and Reinforced Concrete. 2. pp. 17-8.
26. Kristian Dahl Hertz (2003). *Limits of spalling of fire-exposed concrete*. Fire safety journal. 38(2). pp. 103-116.

SCALING APPROACH FOR STUDYING FIRE RESPONSE OF STEEL BEAMS

Mahmood Yahyai¹, Abbas Rezaeian², Peter C. Chang³

ABSTRACT

Testing of scaled structural models is effective and economical for the investigation of the static and dynamic behavior of structures. The aim of the current study is to evaluate the ability of a scaled model in predicting the thermal and mechanical responses of steel structures in fire conditions. An analytical method is presented to adjust the scaled model for the purpose of properly scaling the effects of conduction, convection, radiation, stress, and deformation. The similarity relations for temperature history and the structural responses including temperature-deflection of a steel beam in moment resisting frames are discussed. Experimental fire tests on two steel beams in different scales (full- and half-scale) were carried out to validate the scaling approach. It was found that the presented simplified scaling approach can be applied, without sacrificing the accuracy of the results, to predict full-scale structural behavior of steel beams in fire conditions.

Keywords: steel beam, fire test, scaled model, elevated temperature.

1 INTRODUCTION

Full-scale fire experiments are essential for a comprehensive understanding of a structure's behavior in fire conditions. The size and expenses involved in such experiments make them prohibitively time-consuming and costly. Since fire-resistance designs rely on testing the structural components subjected to standard temperature curves [1, 2] (such as ASTM E119 [3] and ISO 834 [4]), few full-scale fire tests on structural components have been carried out by a limited number of researchers [5-10]. This approach can ensure the adequate strength of structural components for design purposes at elevated temperatures.

Scaled models have been utilized by engineers and researchers to predict the behavior of the prototype in many areas of engineering such as wind and earthquake engineering. Scaled experiment can be employed as an economical option instead of a full-scale fire experiment. Some researchers suggested scaling rules for the structural fire testing design [11-15]. A testing procedure has been proposed by Issen [16] and O'Connor et al. [17] for the evaluation of fire resistance of concrete structural components at reduced scales. The time scale applied by them was not appropriate for a test in a compartment fire, where the gravity or buoyancy forces are the cause of heat flow. In such a condition, Quintiere [12] showed that the time scale should be, $t \sim s^{0.5}$, where $s = L_m/L_p$, represents the physical scale of the model. However, other effects such as stress, acceleration, conduction, radiation, and convection follow different scaling laws [12].

This paper presents a method of adjusting the scaled model to properly simulate the combined effects of thermal and mechanical loadings in a steel beam. An experimental study on steel beams was also carried out and showed that the obtained results compare well to a full-scale experiment at elevated temperatures.

¹ Professor, Civil Engineering Department, K.N. Toosi University of Technology, Tehran, Iran.
e-mail: yahyai@kntu.ac.ir

² Assistant Professor, Civil Engineering Department, Shahid Chamran University of Ahvaz, Ahvaz, Iran.
e-mail: rezaeian_a@scu.ac.ir

³ Associate Professor, Department of Civil and Environmental Engineering, University of Maryland, Maryland, USA.
e-mail: pchang@umd.edu

2 METHODOLOGY OF SCALING IN FIRE

A method is presented for testing the scaled models of steel structures in fire. This approach is challenging because the effects of acceleration, conduction, convection, and radiation are not scaled in the same way. The procedure of applying a scaled model to predict the failure of a structure under fire conditions is schematically represented in *Fig. 1*. Scale modeling in fire is divided into the following steps: (1) prototype conditions assessment, (2) compartment fire scaling, and (3) structural scaling. During a fire, ventilation can vary over time, which must be considered in the scaled model. It is essential to define the mechanical loading on a structure based on the real loading condition in a fire disaster.

3 SCALING OF STEEL FRAMES

The temperature of hot gas in the compartment depends on the difference between the heat generation rate from the fire, \dot{Q} , and the heat loss rate through the compartment boundaries, \dot{q} . Assuming that the properties within the compartment are uniform, this relation is expressed in the form of energy conservation equation as follows [12]:

$$\rho_{\infty} c V \frac{dT}{dt} + \dot{m} c (T - T_{\infty}) \sim \dot{Q} - \dot{q} \quad (1)$$

In a furnace heated by natural fire, the natural convection is caused by the buoyancy force resulting from the density variation of hot gas. The scaled model of scale s with equivalent convection heat requires the time that be scaled to $s^{0.5}$, and the dimensionless Zukoski number, Π_f , should be preserved [18]. Assuming that the fire is proportional to the model scale (s), ρ_{∞} , c , and T_{∞} of the scaled model are the same as those in the prototype [19]:

$$\Pi_f = \frac{\dot{Q}}{\rho_{\infty} c T_{\infty} \sqrt{g} s^{5/2}} \rightarrow \dot{Q} \sim s^{5/2} \quad (2)$$

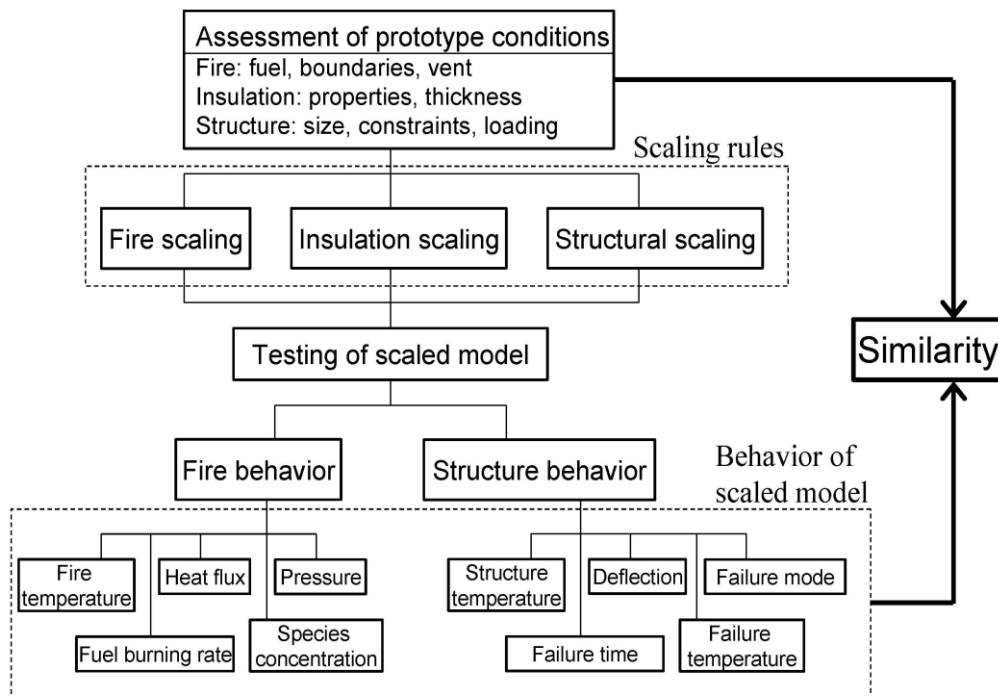


Fig. 1. Schema of scaling methodology in fire.

Heat transfer of a non-insulated sample is primarily through convection and radiation. Therefore, the ration of the convection and radiation heat transfer to the enthalpy flow should be preserved.

$$\Pi_c = \frac{\dot{q}_c}{\rho_\infty c T_\infty \sqrt{g} s^{5/2}} \sim \frac{h_c T_\infty A_m}{\rho_\infty c T_\infty \sqrt{g} s^{5/2}} \quad (3)$$

$$\Pi_r = \frac{\dot{q}_r}{\rho_\infty c T_\infty \sqrt{g} s^{5/2}} \sim \frac{\sigma \epsilon T_\infty^4 A_m}{\rho_\infty c T_\infty \sqrt{g} s^{5/2}} \quad (4)$$

Since the ambient temperature, T_∞ , and the convection coefficient, h_c , of the model and the prototype are the same, Eq. (3) shows that matching the effect of convection requires the surface area of the model to be $A_m = s^{5/2} A_p$. If the temperature in the furnace of the scaled model is the same as that of the prototype, then $(\sigma \epsilon T_\infty^3)_p = (\sigma \epsilon T_\infty^3)_m$. Therefore, matching the effects of radiation also require that $A_m = s^{5/2} A_p$. The length of the scaled members is $L_m = s L_p$. This implies that matching the effects of convection and radiation requires the scaled model to have the width and height of $w_m = s^{1.5} w_p$ and $h_m = s^{1.5} h_p$, respectively.

Mechanical loads in the prototype and scaled beam fire tests are concentrated gravity loads (P), as shown in Fig. 2. Therefore the maximum stresses in the prototype (σ_p) and scaled model (σ_m) should be equal. Hence, the load on the scaled model is scaled to produce the same stress; i.e. $\sigma_p = \sigma_m$. Equating these stresses gives the load scaling factor as;

$$\alpha = \frac{I_m}{I_p} \left(\frac{1}{s^{2.5}} \right) \quad (5)$$

The deflection ratio of the scaled model compared to that of the prototype is:

$$\frac{\delta_m}{\delta_p} = \alpha s^3 \left(\frac{I_p}{I_m} \right) = s^{0.5} \quad (6)$$

The bolts in the top and bottom flanges resist the force $F = M/h$. The ratio of this force in the scaled model to that in the prototype is

$$\frac{F_m}{F_p} = \frac{M_m/h_m}{M_p/h_p} = \frac{\alpha}{s^{0.5}} \quad (7)$$

Hence, the diameter of bolts in flange splice of the scaled model, which transfer bending moment, is scaled by

$$\left(\frac{d_m}{d_p} \right)_{flange} = \frac{\sqrt{\alpha}}{s^{0.25}} \quad (8)$$

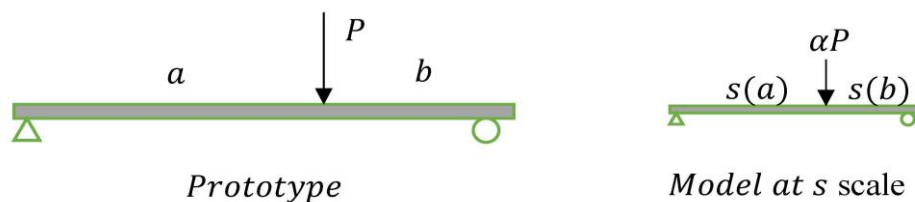


Fig. 2. Prototype and scaled beam.

Similarly, the bolts in the web splice connection resist the shear force. The ratio of this shear force in the scaled model to that in the prototype is:

$$\frac{V_m}{V_p} = \alpha \quad (9)$$

Hence, the diameter of bolts in web splice in the scaled model is scaled by

$$\left(\frac{d_m}{d_p} \right)_{web} = \sqrt{\alpha} \quad (10)$$

The thicknesses of the flange and the web, t_f and t_w respectively, do not need to be scaled. The effect of the thicker model is accounted for by scaling the load, and the small thicknesses of the model may be difficult to be produced and welded. Instead, reasonable thicknesses of $t_f = 4 \text{ mm}$ and $t_w = 3 \text{ mm}$ can be used without affecting the similitude of the scaled model. Following these procedures, the scaling factors for the furnace test on steel beam under concentrated gravity loads, are summarized in *Table 1*.

4 EXPERIMENTAL STUDY

Two fire tests were carried out to evaluate the ability of scaled specimen to accurately predict the behavior of the full-scale fire test in moment resisting frame. The behavior of splice connections and beam under fire loading in full-scale and half-scale steel beams in moment resisting frames were studied.

As shown in *Fig. 3*, two stub beams were strictly welded to the columns in both specimens, and then a link beam was mechanically fastened to the ends of stub beams by means of flange and web splice plates. A ceramic fiber blanket was used to protect the supporting frame (the columns and bottom girder) as well as the lateral restraint system against the fire. The lateral displacement of the specimen was prevented at 1/5 of the beam span away from both ends and the mid-span point. Two concentrated loads were applied on the beam at the same distance away from either side of the beam mid-span. *Table 2* summarizes the details and the geometry of specimens.

The full-scale specimen with $L_p = 4000 \text{ mm}$, using an IPE 200 European profile, was subjected to ISO 834 standard fire exposure and two concentrated loads of $P=20.6 \text{ kN}$, as shown in *Fig. 3*. The half-scale model was a custom-made one. Gravity loads for the half-scale model was scaled by α as shown in *Eq. (9)* and *Table 1*. The temperature profiles for the experiments were scaled based on $t_m = t_p \sqrt{s}$, because the furnace operated under natural convection, without any forced air.

Table 1. Scaling factors for furnace tests

Physical	Scaling factor
Time (t)	$s^{0.5}$
Beam length (L)	s
Flange width (b)	$s^{1.5}$
Web height (h)	$s^{1.5}$
Gravitational load (P)	$\alpha = \frac{I_m}{I_p} \left(\frac{1}{s^{2.5}} \right)$
Flange thickness (t_f)	-
Web thickness (t_w)	-
Moment of inertia (I)	$f(t_f, t_w)$
Flange bolt diameter (d)	$\frac{\sqrt{\alpha}}{s^{0.25}}$
Web bolt diameter (d)	$\sqrt{\alpha}$
Deflection (δ)	$s^{0.5}$

Table 2. Prototype and half-scale model dimensions

	Prototype	Half-scale model
Beam length (L)	4000 mm	2000 mm
Flange width (b_f)	100 mm	35 mm
Web height (h_w)	200 mm	71 mm
Gravitational load (P)	20.60 kN	2.27 kN
Flange thickness (t_f)	8.5 mm	4 mm
Web thickness (t_w)	5.6 mm	3 mm
Moment of inertia (I)	1940 cm ⁴	38 cm ⁴
Flange splice bolt diameter (d)	12 mm	6 mm
Web splice bolt diameter (d)	12 mm	6 mm
Deflection (δ)	δ_p	$\delta_p \times 0.707$

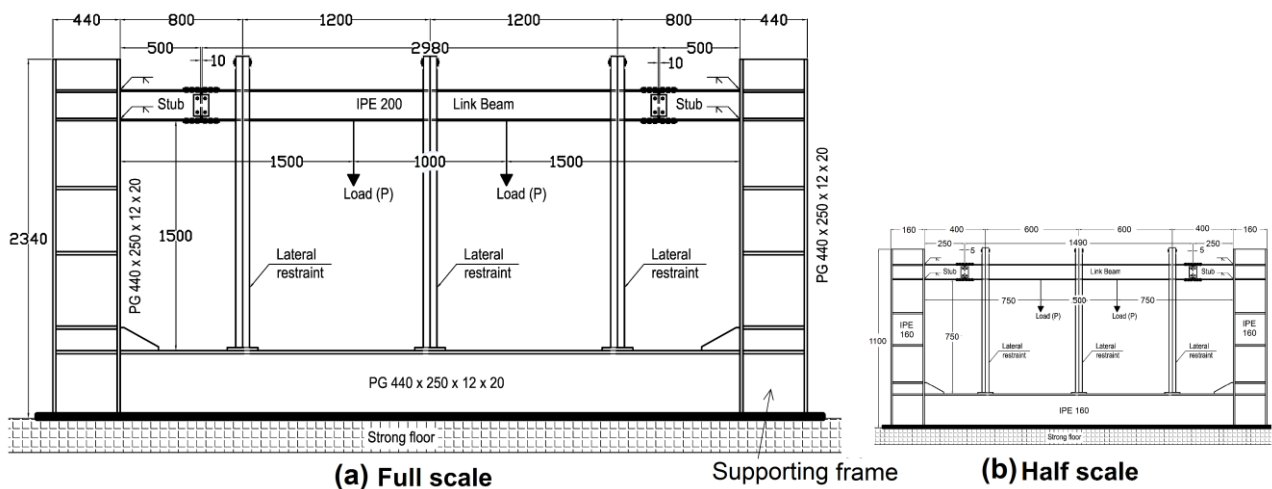


Fig. 3. Schematic view of the setup for testing steel beams: a) full-scale test, b) half-scale.

The linear variable displacement transducers (LVDT) were used on both sides of the splice zones and mid-span of the beam. All displacement transducers were positioned outside the furnace, and coated ceramic rods inserted through the fiber lining of the furnace were used to measure displacements. The supporting frame, beam, bolts, and splice plates were equipped with several K-type thermocouples in order to capture the history and distribution of temperature in the specimen.

Standard tensile coupon tests were used to measure the mechanical properties of steel members of both specimens at room temperature, and cross-sectional dimensions were recorded before the test in the furnace. The beams and splice plates were made of S235 carbon steel, and the bolts were grade 8.8 high-strength steel bolts [20].

The testing methodology applied in the study was composed of two sequential steps. The mechanical load, followed by heating, was applied to reach a predefined level. Whereas the thermal load was increased according to ISO 834 standard time-temperature curve, the mechanical load was kept constant until the connection failed.

5 EXPERIMENTAL RESULTS AND DISCUSSION

5.1 Temperature distribution

Temperature histories of the furnace and specimens were captured. The temperature was measured in the cross section of the mid-span of the beam on the web and flanges during the tests. Fig. Fig. 4 shows the time-temperature curves of the full-scale and half-scale experiments. The half-scale test was conducted at time $t_m = \sqrt{s} t_p = 0.707 t_p$. Hence, comparing the full-scale and half-scale

experimental results requires the time of half-scale experiment to be scaled by $t = 1.414 t_m$. Therefore, the results are plotted in the full-scale time for clear comparison. As shown in Fig. 4, the temperatures of the scaled specimen match those measured in the full-scale experiment to within 10% throughout the experiment and in all the measured points.

5.2 Beam deflection and deformation

Represented in Fig. 5, are the temperature-deflection curves of the beam at the mid-span. Recording of the measurements was carried on until the beam splice failed. Since the deflection of the half-scale specimen is $0.707 \delta_p$, the deflections of half-scale specimen are scaled by $1.414 \delta_m$ in comparison to that of the full-scale specimen. Comparison of mid-span deflections in the full-scale and half-scale experiments reveals that the scaled furnace test could successfully predict the behavior of the full-scale test throughout the temperature loading. The temperature and deflection measures gained in the scaled furnace test were within 10% of curves obtained in the full-scale experiment. The deformed shapes of beam in full- and half-scale specimens after tests are shown in Fig. 6. It can be seen that the deformed shapes of the specimens were similar, and both beams experienced large deflections before the end of the test.

6 CONCLUSIONS

The following conclusions are drawn based on the studies presented in this paper:

1. An analytical technique for simulating fire testing on a steel beam and its connections was explored using small-scale tests, and scaling rules for designing the scaled test specimen were developed.
2. Experimental fire tests on steel moment resisting frames in two scales (full-scale and half-scale) show that steel beams reached the deflection failure criterion during the fire in both scales. The failure temperatures and failure time of specimens in the half-scale test compared favorably with those of the full-scale test, with relative differences within 5% and 3%, respectively, which can be attributed to the difference in the fire temperature profiles of two compartment fires.
3. The presented simplified scaling approach can be applied without significantly sacrificing the accuracy of the results. Employing scaled models is possible for predicting full-scale structural behavior of a steel beam in fire.

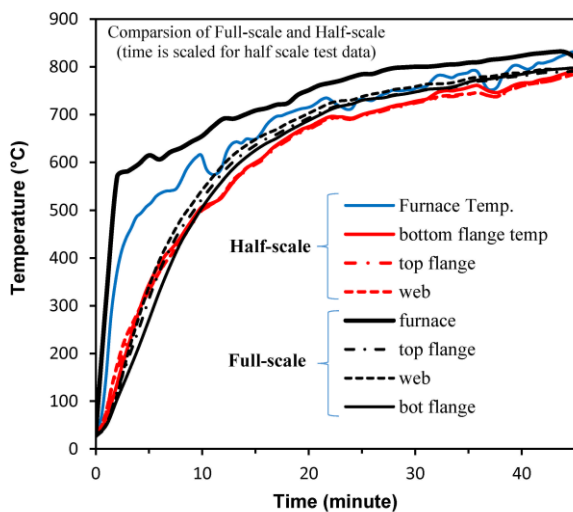


Fig. 4. Temperature of steel in full- and half-scale specimens and furnace temperature history.

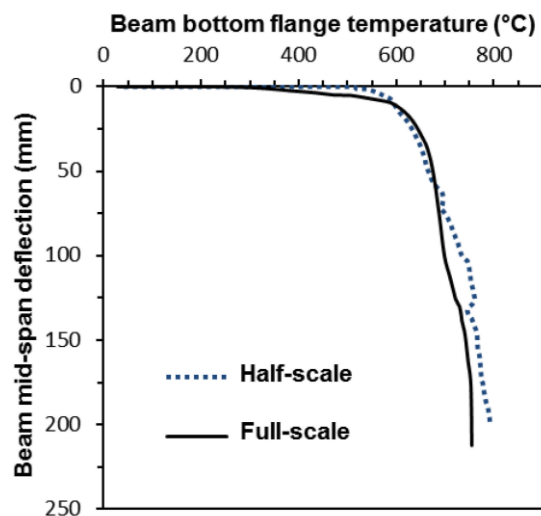


Fig. 5. Beam mid-span temperature-deflection of the full- and half-scale specimens.

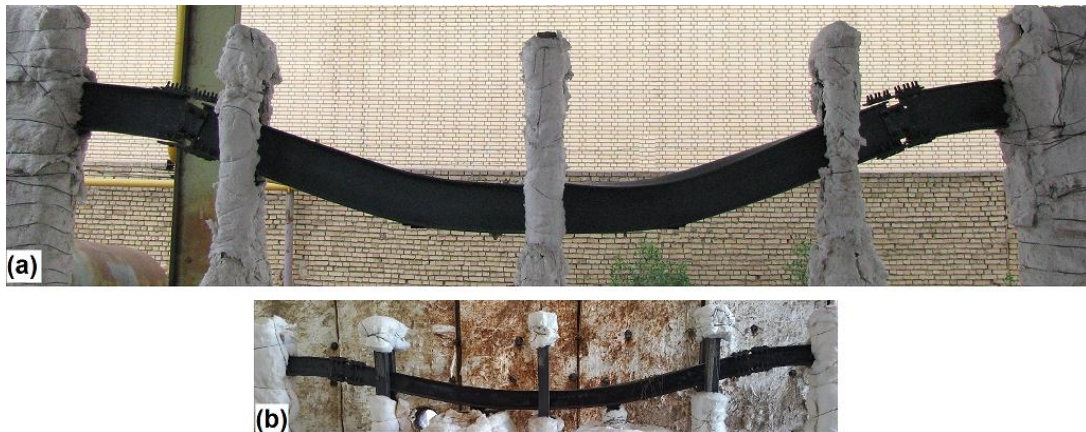


Fig. 6. Deformed beam after the furnace test: a) full-scale, b) half-scale.

NOTATION

The following symbols are used in this paper:

A = area

A_m = cross sectional area of scaled model

A_p = cross sectional area of prototype

I_m = moment of inertia of scaled model

I_p = moment of inertia of scaled model

L = length of beam

L_m = length of scaled model

L_p = length of prototype

M = bending moment

P = gravitational load

\dot{Q} = heat generation rate

T = temperature

T_∞ = ambient temperature

V = volume

b_f = flange width of beam

c = specific heat of steel

d_m = diameter of bolt in scaled model

d_p = diameter of bolt in prototype

g = gravitational acceleration

h_c = convection coefficient

h_m = web height in scaled model

h_p = web height in prototype

\dot{m} = mass flow rate

\dot{q} = heat loss rate

s = geometric length scale

t = time

t_f = thickness of flange

t_w = thickness of web

t_m = model time

t_p = prototype time

w_m = width of scaled model

w_p = width of prototype

α = load scaling factor

δ_m = deflection of scaled model

δ_p = deflection of prototype

ε = strain

ρ_∞ = density of air at ambient temperature

σ_m = stress in scaled model

σ_p = stress in prototype

REFERENCES

1. AISC (2003). *Fire resistance of structural steel framing*. American Institute of Steel Construction Inc.: Chicago.
2. UL (2003). *Fire tests of building construction and materials*, thirteenth edition, Standard No. UL 263. Underwriters Laboratories Inc.: Northbrook.
3. ASTM (2014). *Standard test methods for fire tests of building construction and materials E119*. American Society for Testing and Materials: West Conshohocken, PA.
4. ISO (1999). *ISO 834: Fire resistance test-elements of building construction*. International Organization for Standardization: Geneva.
5. A Santiago, L Simoes da Silva, G Vaz, P Vila Real, A Gameiro Lopes (2008). *Experimental investigation of the behaviour of a steel sub-frame under a natural fire*. *Steel and Composite Structures*, 8, pp 243-264.

6. YC Wang, XH Dai, CG Bailey (2011). *An experimental study of relative structural fire behaviour and robustness of different types of steel joint in restrained steel frames*. Journal of Constructional Steel Research, 67. pp1149-1163.
7. EI Wellman, AH Varma, R Fike, VK Kodur (2011). *Experimental evaluation of thin composite floor assemblies under fire loading*. ASCE Journal of Structural Engineering, 137(9).
8. A Rezaeian, M Yahyai (2015). *Fire response of steel column-tree moment resisting frames*. Materials and Structures, 48. pp 1771-1784.
9. M Yahyai, A Rezaeian (2015). *Behavior of beams in bolted column-tree frames at elevated temperature*. Fire and Materials, 40. pp 482-497.
10. EM Aziz, VK Kodur, JD Glassman, MEM Garlock (2015). *Behavior of steel bridge girders under fire conditions*. Journal of Constructional Steel Research, 106. pp 11-22.
11. JG Quintiere (1989). *Scaling application in fire research*. Fire Safety Journal, 15. pp 3-29.
12. JG Quintiere, PC Chang (2003). *How to use a scale model to simulate fire and structural failure*. *Proceeding of Designing Structures for Fire*, Baltimore.
13. JA Perricone (2005). *Scale modeling of the transient behavior of wood crib fires in enclosures*. MS thesis, University of Maryland.
14. M Wang, PC Chang, JG Quintiere (2006). *Scale modeling of insulated steel framed structural testing in fire*. *Proceeding of the 4th International Workshop of Structures in Fire (SiF'06)*, Aveiro.
15. J Perricone, M Wang, JG Quintiere (2008). *Scale modeling of the transient thermal response of insulated structural frames exposed to fire*. Fire Technology, 44 (2). pp 113-136.
16. L Issen (1966). *Scaled models in fire research on concrete structures*. Portland cement association. Research and development laboratories journal, 8(3). pp 10-26.
17. DJ O'Connor, GWH Silcock, B Morris (1996). *Furnace heat transfer processes applied to a strategy for the fire testing of reduced scale structural models*. Fire Safety Journal, 27. pp 1-22.
18. EE Zukoski (1986). *Fluid dynamic aspects of room fires*. *Proceeding of first international symposium, fire safety science*.
19. JG Quintiere (2006). *Fundamentals of fire phenomena*. John Wiley & Sons, Inc.,.
20. V Kodur, M Yahyai, A Rezaeian, M Eslami, A Poormohamadi (2017). *Residual mechanical properties of high strength steel bolts subjected to heating-cooling cycle*. Journal of Constructional Steel Research, 131. pp 122-131.

RADIATIVE FLUX AFFECTING VERTICAL STEEL MEMBER AWAY FROM THE FIRE – SIMPLIFIED METHOD LOCAFI

Camille Sautot¹, François Hanus², Christophe Thauvoye³, Giacomo Erez⁴, Aurélien Thiry⁵

ABSTRACT

Whether for questions of fire safety engineering or research, the characterization of fire and smoke behaviour are two essential themes. This cannot be done without resorting to experiment, but data on scenarios or atypical configurations as large volumes are rare. Medium and large-scale fire experiments were carried out by the LCPP in a large volume hangar. The realization of these full-scale tests aims at acquiring experimental data about large localized fires in such a volume. The radiative fluxes measured are used for the final validation of a simplified method developed in the European research project LOCAFI. It is an analytical method allowing the calculation of fluxes received by vertical steel members situated outside the fire. The comparison between measures and LOCAFI results shows that the simple design method gives a great approximation of the fluxes while providing a reasonable safety margin.

Keywords: Fire tests, localized fire, simple design method, radiative fluxes

1 INTRODUCTION

Fire is one of the most difficult hazards to address for steel structures. Moreover, for building typologies where a generalised fire cannot develop, localised fires are an important issue. Zone models are not considering the effects of localised fires on structures. The main challenge for this is the calculation of the thermal profiles in the structural members as a function of the fire location and its development. In the last few years, this subject has been investigated [1]. In the European research project LOCAFI [2], a method was developed to address this issue. It was developed and validated on the basis of experimental data with maximum Heat Release Rate (HRR) ranging from 500 kW up to 4 MW and on numerical simulations.

Many data are available for small scale tests (an office or a residential room), but few data are available for large compartments (museum, hall...). Medium and large-scale fire experiments carried out in 2017 by LCPP (*Laboratoire Central de la Préfecture de Police de Paris*) in the HN6 hangar hall, situated in Orly, before demolition, give valuable data. Tests were focused on smoke and fire developments, including temperatures and radiation measurements for fires in the huge

¹ Research Engineer. Fire Research Division, CTICM, Saint Aubin, France.
e-mail: csautot@cticm.com

² Senior Research Engineer. Long Products Research & Development, ArcelorMittal Global R&D, Esch/Alzette, Luxembourg.
e-mail: francois.hanus@arcelormittal.com

³ Research Engineer. Fire Research Division, CTICM, Saint Aubin, France.
e-mail: cthauvoye@cticm.com

⁴ PhD Candidate. Fire Engineering Department, Central Police Laboratory, Paris, France.
e-mail: giacomo.erez@interieur.gouv.fr

⁵ Section Head. Fire Engineering Department, Central Police Laboratory, Paris, France.
e-mail: aurelien.thiry@interieur.gouv.fr

compartment. CTICM participated in the test campaign with radiative flux measurements in order to complete the LOCAFI validation for large-scale fires.

2 EXPERIMENTAL SETUP

The test campaign was carried out in the hall of the hangar HN6 situated in Orly. In this building, owned by ADP (*Aéroport de Paris*) and made available to the LCPP and its partners, the maximum ceiling height is 17 m, for an area of approximately 300 m × 50 m (see Figure 1). The volume is equipped with 5 quartering screens (2 m high), and the roof has 8 smoke vents of 24 m² each.



Figure 1: The hangar HN6

The test campaign includes several phases using different fuels. The first phase uses stacks of standard wood pallets (Figure 2) while the second phase involves pool fires. Each time, there is an upscaling: from 20 pallets up to 110 pallets and from 20 l up to 300 l of kerosene. In this paper, only the first phase is analysed, and the second phase will be analysed in a further article. Tests are repeated twice in order to study the variability.

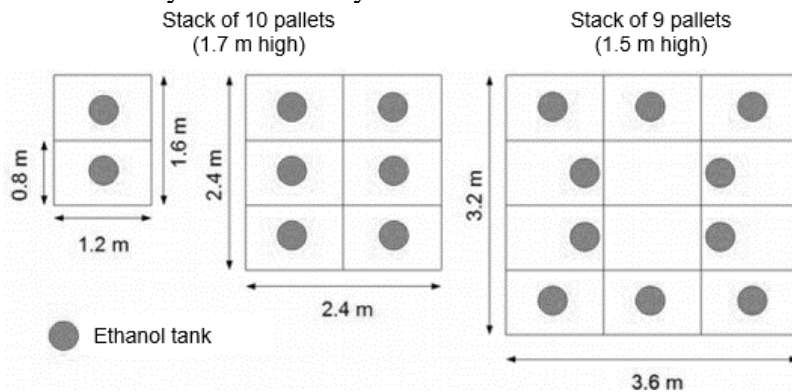


Figure 2: Size of the fireplaces

The measurement devices include (see Figure 3 and Figure 4):

- 85 thermocouples on 8 trees (Tc A to Tc H), located from 2 m height up to 16 m,
- 10 gauge heat flux sensors, some of which equipped with a cooling system and covering a radiative flux range up to 50 kW/m². Uncooled flux sensors cover a flux range up to 10 kW/m²,
- A spectrometer,
- A flame opacimetry measurement device,
- IR and visible cameras.

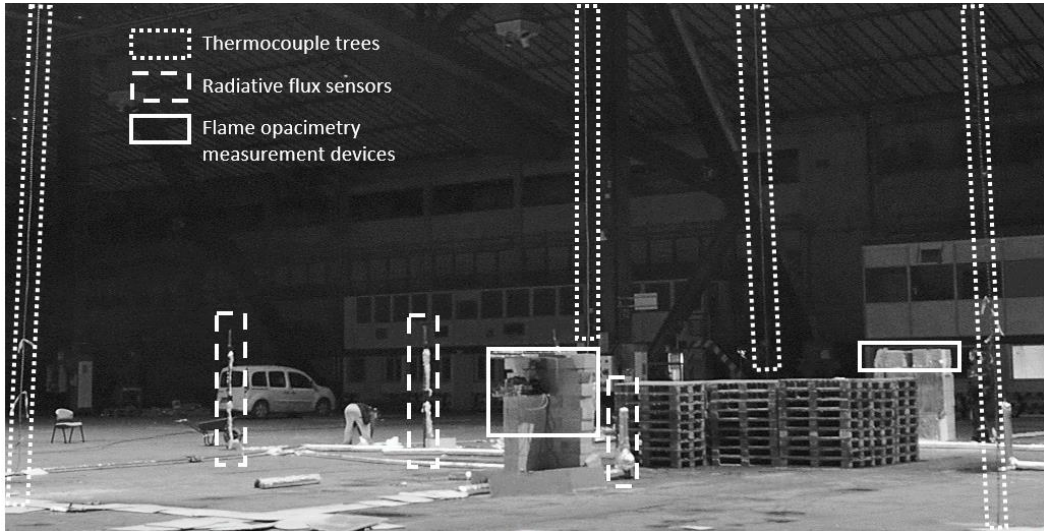


Figure 3: Experimental setup

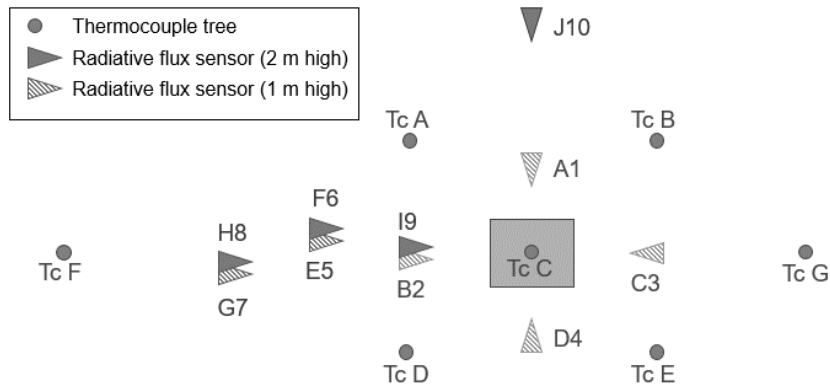


Figure 4: Flux sensors and thermocouples set-up

In practice, radiative heat fluxes vary with position, thus gauges were placed at several distances from the fire center and also at two heights as indicated in Table 1 and Table 2. Gauges A1 to D4 were placed at the same distance from the fire center in order to detect flame tilting. Others gauges were used to measure the heat flux decay. The gauge J10 is next to the spectrometer located farther.

Gauge	Small test	Medium test	Large test
A1, B2, C3, D4	2 m	3 m	4 m
E5	4 m	6 m	8 m
G7	6 m	9 m	12 m

Table 1: Distance to fire center for gauge at 1 m height

Gauge	Small test	Medium test	Large test
I9	2 m	3 m	4 m
F6	4 m	6 m	8 m
H8	6 m	9 m	12 m

Table 2: Distance to fire center for gauge at 2 m height

As the gauges have a specific measurement range depending on their type, their position was determined, prior to the tests, using the LOCAFI method. A short description of the method is

provided in part 3. The main input is the heat release rate (HRR). The HRR of each fire was calculated using the formula of the SFPE Handbook [3]:

$$\text{HRR} = 919 S (1 + 2.14h_p) (1 - 0.03M) \text{ [kW]} \quad (1)$$

where h_p is the stack height (either 1.5 m or 1.7 m), S the ground area of pallets, and M is moisture (10 %).

For the small fire (20 pallets), the estimated HRR is 6 MW, for the medium test (60 pallets), the estimated HRR is 17 MW while for the larger test (108 pallets) the estimated HRR is 31 MW. Distances were targeted to give a gauge heat flux close to 30 kW/m² for the closest sensors, close to 10 kW/m² for the intermediate sensors and close to 5 kW/m² for the farthest sensors.

After ignition, flame spread slowly inside the pallets (no heat fluxes are detected). Then it grows very fast as flames spread over all pallets in 3-4 minutes. At this stage, a steady-state occurs and the heat fluxes are maximum. The last stage happens with the collapse of pallets when boards are totally burned. The heat fluxes decrease to a constant low value for a long period (several hours if the fire is not extinguished) corresponding to the burning of the remaining thick blocks of wood composing the pallets. Most of the pallets collapse on each other but in some tests, a few pallets fall outwards. This explains the peak measured by gauges (e.g. D4 on the large fire) followed by a loss of the signal (cables were burned by the collapsed pallets).

During the tests, no strong flame tilting was observed and measured heat fluxes were in the targeted range. Temperature measurements on the flame axis decrease very fast and they does not exceed 250°C in the smoke layer under the ceiling (at 16 m) for the largest test.



Figure 5: Flames for each fire tests

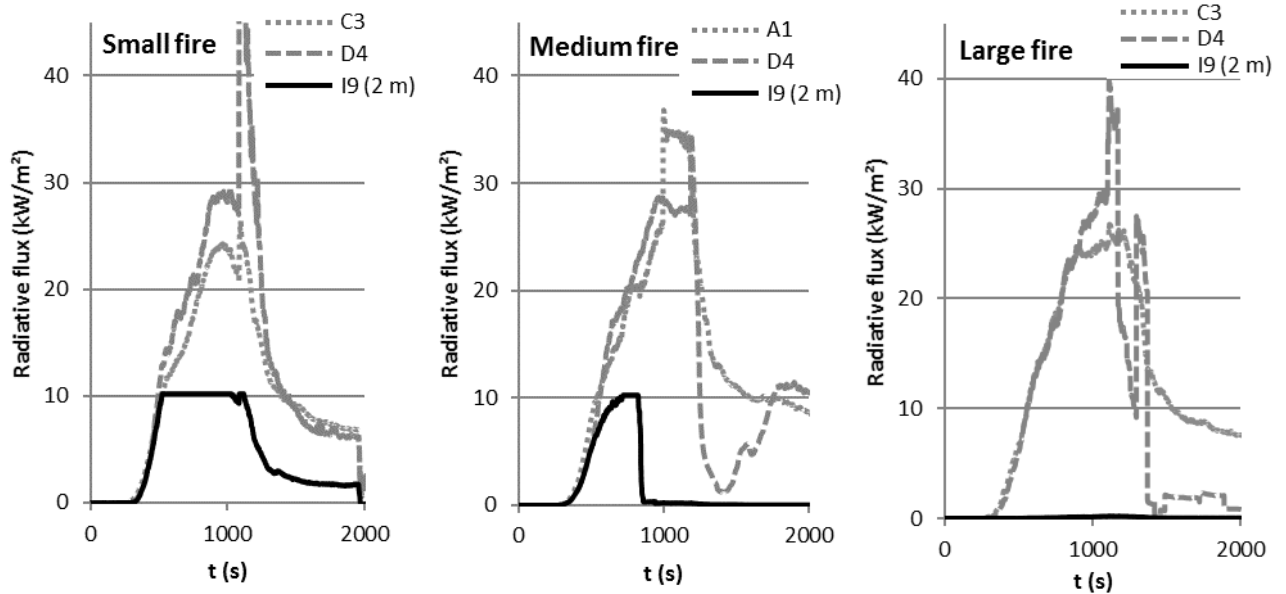


Figure 6: Radiative fluxes measurement for the closest sensors

3 VIRTUAL SOLID FLAME MODEL

The LOCAFI project led to the development of an analytical model based on the innovative concept of virtual solid flame. It assumes that the flame is a radiating surface with a conical shape which radiative properties are computed according to equations available in Eurocode 1991-1-2 [4]. The virtual solid flame is meshed into finite radiating bands and finite faces. Then, the total radiative heat flux received by the member are calculated using the concept of configuration factor. Its application is focused on vertical members situated outside the fire source. A complete description is available in [2] and [5].

4 RESULTS AND DISCUSSION

One of the most important data in the Virtual Solid Flame calculation is the heat released during the combustion. Relying only on a correlation may not give accurate results. A specific analysis is performed to evaluate the HRR. Radiative heat fluxes are proportional to the power radiated and the power radiated is proportional to the heat released by the fire. This means that the HRR curve has the same shape as the radiate heat flux curves. For the shape of the HRR curve, the mean of radiative heat fluxes measured by gauges A1 to D4 is used.

Then, this curve is normalized so that the area under the curve is equal to the energy released. The energy released during the fire is deduced using the mass of pallets (mean mass of 25 kg per pallet), a standard heat of combustion of 17 MJ/kg and a combustion efficiency of 80%. The normalization is not based on the total mass of wood pallets because tests were stopped before their complete burning. As indicated previously, several stages are observed during the tests. The boards of pallets burn in first while the remaining thick pieces of wood take a longer time to burn. These block burn after the collapsing of the pallets. The boards represent 70% of the mass of a pallet. It is that mass and the related energy that are considered for the normalisation process.

This process leads to the curves of Figure 7 which show that the HRR estimated through correlation (1) is reliable.

Radiative flux affecting vertical steel member away from the fire – simplified method LOCAFI

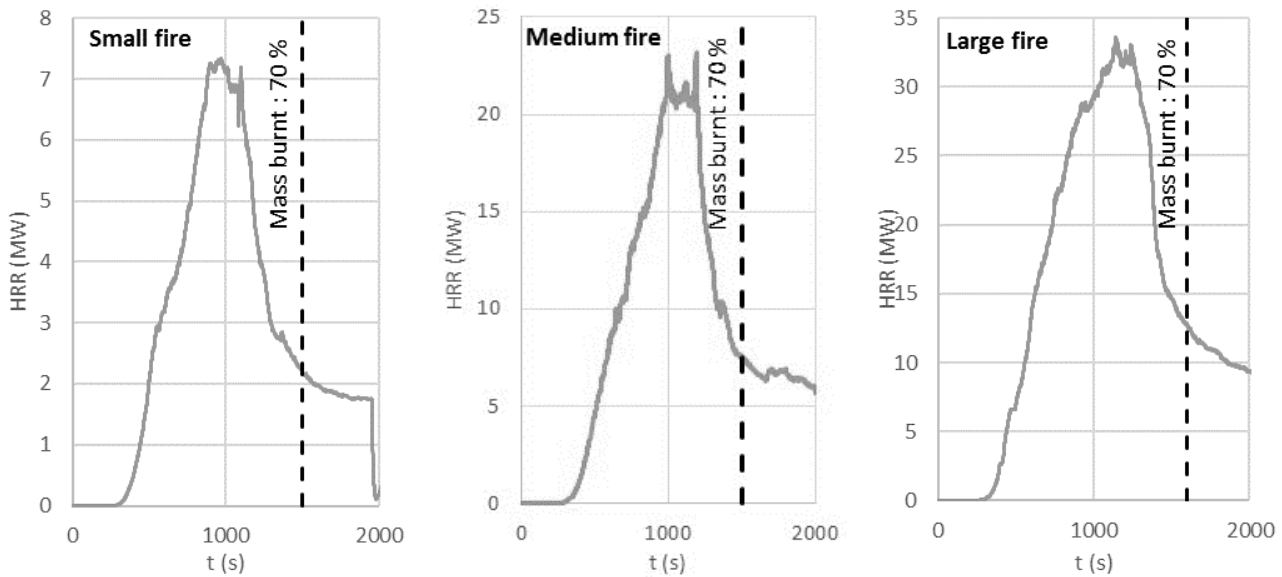


Figure 7: Computed heat release rate

With the aim to validate the Virtual Solid Flame model for large-scale fires, results given by simple design model are compared with experimental measurements for the three fire sizes. The heat release rate used for the modelling is calculated with formula (1) and depends on the number of pallets. For each test, the measured fluxes are averaged as the mean value of the flux received by the sensor during the steady phase of fire, and compared with the flux calculated using the Virtual Solid Flame model.

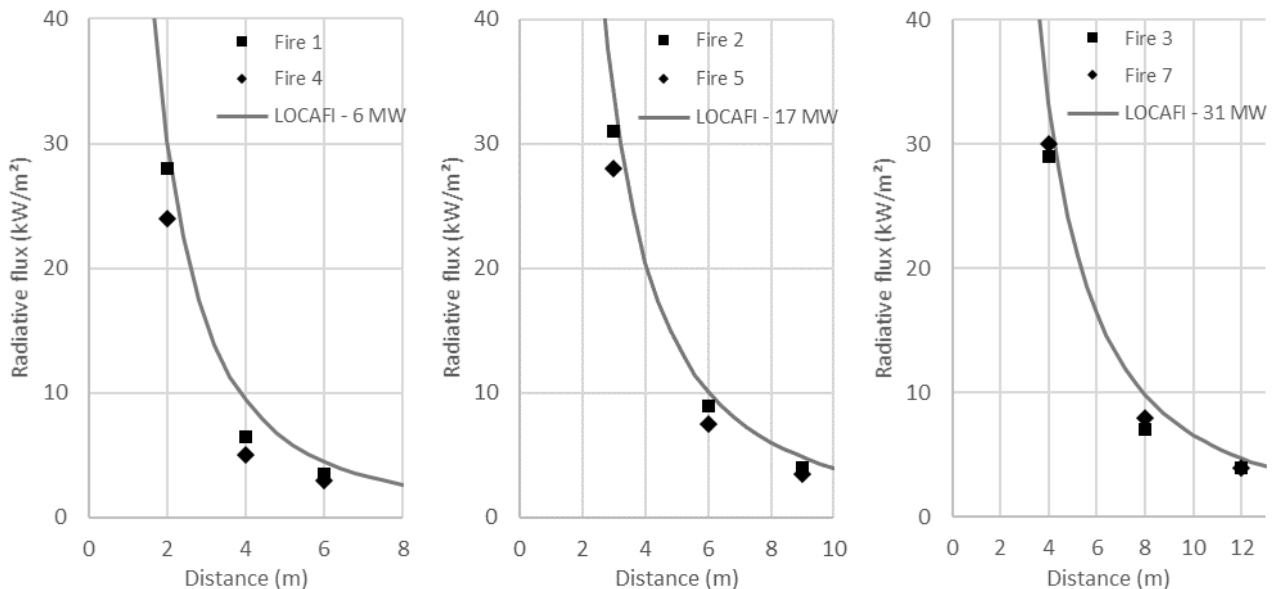


Figure 8: Comparison between experiment heat flux and calculation results

The Virtual Solid Flame model gives a reasonably good correlation between calculation results and experimental measurements. In all cases, the simple design method overestimates heat flux of the fire which is conservative. The decrease of the flux with distance to fire is also well represented.

One last parameter is investigated: the moisture content, a higher value leading to lower HRR. Thus, a last analysis is conducted increasing the moisture from 10% to 16% (typical range for moisture content of wood in buildings is 8 % - 15 % [6]). In that case, the heat release rate per ground unit area

decreases to 2 MW/m² while in the previous calculations, the heat release rate per ground unit area is close to 3 MW/m². Then, the HRR is 4 MW for small fire, 12 MW for medium fire and 23 MW for large fire. With these values, the method gives very close results but the latter are always slightly higher than measured heat fluxes.

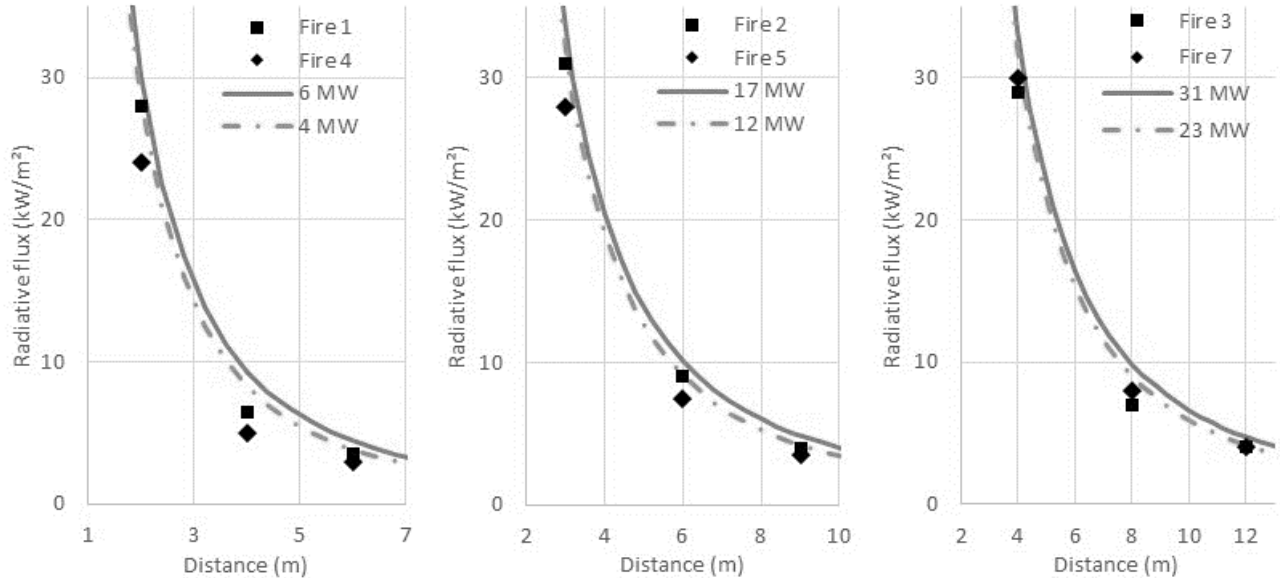


Figure 9: Calculation with lower HRR

5 CONCLUSIONS

The experiments realised by LCPP in the hangar HN6 provided many measurements about fire, including radiative fluxes. These measures were used for the validation of the Virtual Solid Flame model for large volume fires, the model having already been validated on many tests ranging from small scale (500 kW) to intermediate scale (4 MW). The model was therefore compared with measurements made during the test campaign. The comparison showed that the Virtual Solid Flame model provides slightly safe-sided predictions of radiative heat fluxes received by a member located outside the flames and at a distance from the fire. A specific analysis was carried out on the heat release rate which is a significant parameter in this method. All analyses show that the method remains safe sided even in case the HRR was underestimated. In order to investigate behaviour related to polyurethane foam blocks and to complete data set concerning kerosene fires, new series of tests will be carried out.

ACKNOWLEDGMENTS

The access to the hangar HN6 was provided under courtesy of Aéroports de Paris and the project was led by the Laboratoire Central de la Préfecture de Police (French laboratory). This work was carried out in collaboration with the Brigade de sapeurs-pompiers de Paris (French firemen), the Laboratoire Energies et Mécanique Théorique et Appliquée (French University of Lorraine), the Büro für Brandschutz.

REFERENCES

1. A. Byström, J. Sjöström, U. Wickström, D. Lange, M. Veljkovic (2014), Large scale test on a steel column exposed to localized fire, *Journal of Structural Fire Engineering*, vol. 5(2), pp147-159.
2. LOCAFI (2016), Temperature assessment of a vertical steel member subjected to localised fire, Final Report, Contract RFSR-CT-2012-00023.
3. The SPFE Handbook of Fire Protection Engineering, 4th Edition, National Fire Protection Association, Quincy, MA, USA.
4. EN 1991-1-2 (2002) Eurocode 1: Actions on structures, Part 1-2: General actions – Actions on structures exposed to fire, CEN, Brussels.
5. C. Thauvoye, F. Hanus, O. Vassart, B. Zhao (2016), Temperature assessment of a vertical steel member subjected to localised fire, *Interflam*.
6. A. Frangi, M. Fontana (2003), Charring rates and temperature profiles of wood sections, *Fire and Materials*, vol 27(2), pp91-102.

EVALUATING UNCERTAINTY IN STEEL-COMPOSITE STRUCTURE RESPONSE UNDER FIRE – APPLICATION OF THE ME-MDRM

Ruben Van Coile¹, Thomas Gernay², Negar Elhami Khorasani³ & Danny Hopkin⁴

ABSTRACT

Probabilistic applications of structural fire engineering will be central to the realisation of complex buildings, where reliance on precedent / experience is insufficient, and an adequate level of safety must be explicitly demonstrated. The practical application of probabilistic methods in structural fire safety has, to date, been limited to simplistic structural systems due to a lack of an efficient, unbiased calculation methodology. Herein, two examples are presented whereby the Maximum Entropy Multiplicative Dimensional Reduction Method, ME-MDRM for short, is applied to estimate the probability density function of performance metrics output from finite element analyses. Given a limited number of model realisations (order of 10^1), it is shown that the ME-MDRM can give valuable insight into the distribution of failure time, and maximum supported load under ISO fire conditions for a composite column, and composite slab panel, respectively. The former is benchmarked against Monte Carlo Simulations, with excellent agreement. Finally, limitations in the stochastic data and in the application of the ME-MDRM itself are discussed, with future research needs identified.

1 INTRODUCTION

The rise of Performance Based Design (PBD) methodologies for fire safety engineering has increased the interest of the fire safety community in the concepts of risk and reliability. Practical applications have, however, been severely hampered by the lack of an efficient unbiased calculation methodology. This is because on the one hand, the distribution types of model output variables in fire safety engineering are not known and traditional distribution types such as, for example, the normal and lognormal distribution may result in unreliable approximations. Therefore, unbiased methods must be applied which make no (implicit) assumptions on the probability density function (PDF) type, e.g. Monte Carlo simulations. However, Monte Carlo simulations require many model evaluations and are, therefore, too computationally expensive when large and nonlinear calculation models are applied, as is common in structural fire engineering (e.g. finite element models).

2 AN UNBIASED METHOD FOR ESTIMATING PDFs – ME-MDRM

A computationally very efficient method to make an unbiased estimate of the mathematical function f_Y describing the probability density function (PDF) of a scalar model output Y has been developed by Zhang [1]. The method is known as the Maximum Entropy Multiplicative Dimensional Reduction Method, ME-MDRM for short, and has been tweaked for ease-of-use and applied to fire

¹ Assistant Professor, Department of Structural Engineering, Ghent University, Belgium.

e-mail: Ruben.VanCoile@UGent.be

² Assistant Professor, Department of Civil Engineering, Johns Hopkins University, Baltimore, MD, U.S.A.

e-mail: tgernay@jhu.edu

³ Assistant Professor, Department of Civil, Structural and Environmental Engineering, University at Buffalo, Buffalo, NY, U.S.A.

e-mail: negarkho@buffalo.edu

⁴ Associate Director, Olsson Fire & Risk, Oxford, UK. Visiting Professor, University of Sheffield, Sheffield, UK.

e-mail: Danny.Hopkin@OlssonFire.com

safety engineering problems in [2]. The unbiased nature of the method is important to emphasize, as it means that no assumptions are made with respect to the shape of the PDF (e.g. normal, lognormal). When considering n stochastic variables, the ME-MDRM requires only $4n+1$ model evaluations. The subsequent estimation of the PDF for a model output of interest is based on a semi-numerical mathematical optimization which can require a couple of hours of calculation by itself (on a single core). For computationally expensive numerical models with only a limited number of parameters governing the variability of the model output, the ME-MDRM provides, thus, a realistic opportunity for assessing the full range of model outcomes. This is commonly the case in structural fire safety engineering where advanced model evaluations are computationally expensive (and may need manual checking), where a limited number of input variables are often determinative in the model output (e.g. fire load density, steel yield stress), and where a single scalar model output (e.g. fire resistance time, or load bearing capacity) is of interest. Furthermore, in structural fire safety, limited statistical data exists justifying prior assumptions on the distribution type (shape) of output variables.

2.1 Summary introduction to the ME-MDRM calculation procedure

In [2], the ME-MDRM is introduced in detail starting from mathematical derivations. In the following the same calculation procedure is directly introduced step-wise, focussing on procedural clarity in the calculation steps:

1. A deterministic model is developed describing the structural effect of interest. For example, a model capable of calculating the fire resistance time for a given set of input values;
2. Input variables with important uncertainty associated with their value, and which have (or are considered to have) a significant influence on the model output are identified and their stochastic distributions determined. The symbol n denotes the total number of stochastic variables;
3. For each stochastic variable X_l , 5 realizations $x_{l,j}$ are calculated through Eq. (1), with the 5 ‘Gauss points’ z_j given in Table 1;
4. For each realization $x_{l,j}$, the model is evaluated using this realization for the variable X_l , and using the median value (i.e. $x_{k,3}$) for all other stochastic variables X_k , resulting in the model realization $y_{l,j}$. This implies 5 model realizations per stochastic variable, but as the model with all stochastic variables equal to their median value has to be evaluated only once (model realization y_0), the total number of model realizations is $4n+1$;
5. The minimization of Eq. (2) is performed, with $M_Y^{\alpha_i}$ the α_i^{th} moment of Y evaluated from the $4n+1$ model evaluations through Eq. (4), thus determining the parameters λ_i and α_i , with λ_0 a normalization constant calculated with Eq. (5). The parameter m is the estimation order and can for practical purposes be set equal to 4 [2]. The evaluation of Eq. (2) is easily programmed, but the minimization result may depend on the starting solution. Therefore, the optimization is done in a step-wise approach:
 - a. A large number of input values (i.e. Latin Hypercube samples) for α_i are generated. Without loss of generality, α_i can be chosen in the range $[-2;2]$.
 - b. For each set of α_i , the minimization of Eq. (2) is readily performed, resulting in corresponding values for λ_i .
 - c. Across all realisations for α_i with associated minimizing values for λ_i , the set with the lowest function evaluation of Eq. (2) is maintained.
6. The estimated mathematical formulation for the PDF describing the model output Y is given by Eq. (3). This mathematical formulation gives direct insight in the (estimated) shape of the PDF. Eq. (3) results from application of the Maximum Entropy principle (i.e. an acknowledgement of uncertainty with respect to the distribution shape). The mathematical basis underlying this equation and the minimization in Step 5 above are clarified in [3].

$$x_{l,j} = F_{x_l}^{-1}(\Phi(z_j)) \quad \& \quad \text{Minimize: } \lambda_0 + \sum_{i=1}^m \lambda_i M_Y^{\alpha_i} \quad (1 - 2)$$

where $F_{x_i}^{-1}(\cdot)$ is the inverse cumulative distribution function for variable X_i

$\Phi(\cdot)$ is the standard normal cumulative distribution function

$M_Y^{\alpha_i}$ is the α_i^{th} sample moment, calculated with Eq. (4)

λ_0 is a normalization constant calculated with Eq. (5)

$$f_Y(y) = \exp\left(-\lambda_0 - \sum_{i=1}^m \lambda_i y^{\alpha_i}\right) \quad \& \quad M_Y^{\alpha_i} \approx \left[y_0^{1-n}\right]^{\alpha_i} \prod_{l=1}^n \sum_{j=1}^L w_j y_{j,l}^{\alpha_i} \quad (3 - 4)$$

where w_j is the Gauss weight associated with z_j (see Table 1)

$$\lambda_0 = \ln \left[\int_Y \exp\left(-\sum_{i=1}^m \lambda_i y^{\alpha_i}\right) dy \right] \quad (5)$$

Table 1. Gauss points z_j and associated Gauss weights w_j

	1	2	3	4	5
z_j	-2.857	-1.356	0	1.356	2.857
w_j	0.011257	0.222076	0.533333	0.222076	0.011257

2.2 Objective of the ME-MDRM application

So far, the ME-MDRM has not yet been applied together with advanced and validated finite element models for structural fire response. To build confidence in the application of the ME-MDRM, the method will be applied in the following using the dedicated simulation software SAFIR [4], considering an ISO 834 standard fire exposure.

3 SOURCES OF UNCERTAINTY IN STRUCTURAL FIRE SAFETY

This study includes two application examples that will be described in Sections 4 and 5, for which a number of stochastic variables are introduced. In both examples, these include material strength at ambient and elevated temperatures, namely yield strength of (rebar or rolled shape) steel at 20°C and elevated temperatures ($f_{s,20}$ or $f_{y,20}$ and $f_{s,T}$ or $f_{y,T}$), and concrete compressive strength at 20°C and elevated temperatures ($f_{c,20}$ and $f_{c,T}$). The uncertainty for material strength at ambient temperature is modelled based upon recommendations by Holicky and Sykora [5], as described in Table 2, where the type of distribution, mean, and coefficient of variation (COV) or standard deviation are listed. The stochastic models for material strength at elevated temperatures are based on logistic functions, see background in [6]. Table 2 provides the logistic functions for strength reduction factors of both steel $k_{y,T}$ or $k_{s,T}$ and concrete $k_{c,T}$, where T is temperature in Celsius and ε is a realization of standard normal distribution. The reduction factor for steel is a function of the Eurocode [7] strength reduction factor $k_{y,EN}$. In case of the first application example, the applied load and the sinusoidal geometrical imperfection are taken as additional random variables. Uncertainty quantification for the applied load includes both permanent and 5-year imposed loads, as described in Table 2 based on [5], as well as the modelling uncertainty for the load and resistance effects. For modelling purposes, the total load is combined with the total model uncertainty into a single lognormal load variable. The uncertainty in sinusoidal geometrical imperfection is assumed to follow a normal distribution. For the second example, thermal conductivity k_p of insulation is taken as an additional random variable, implemented as in [6], with the model provided in Table 2 (where T is temperature in Celsius and ε is a realization of standard normal distribution).

Table 2. List of stochastic variables and assumed distributions

Parameter	Description
$f_{y,20}$ rolled shape [MPa]	Lognormal with mean= $f_{yk,20} + 2\sigma$ and COV=0.07
$f_{s,20}$ rebar [MPa]	Lognormal with mean= $f_{sk,20} + 2\sigma$ and $\sigma = 30$ [MPa]
$f_{c,20}$ [MPa]	Lognormal with mean= $f_{ck,20} + 2\sigma$ and COV=0.15
$k_{y,T}$ or $k_{s,T}$	$k_{y,T} = \frac{1.7 \times \exp[r_{logit} + 0.412 - 0.81 \times 10^{-3} \times T + 0.58 \times 10^{-6} \times T^{1.9} + 0.43 \times \varepsilon]}{1 + \exp[r_{logit} + 0.412 - 0.81 \times 10^{-3} \times T + 0.58 \times 10^{-6} \times T^{1.9} + 0.43 \times \varepsilon]}$ with $r_{logit} = \ln \frac{(k_{y,EN} + 10^{-6})/1.7}{1 - (k_{y,EN} + 10^{-6})/1.7}$
$k_{c,T}$	$k_{c,T} = \frac{1.3 \times \exp[1.145 + 1.86 \times 10^{-3} \times T - 6.37 \times 10^{-6} \times T^2 + 0.48 \times \varepsilon]}{1 + \exp[1.145 + 1.86 \times 10^{-3} \times T - 6.37 \times 10^{-6} \times T^2 + 0.48 \times \varepsilon]}$
Applied load P [kN]	Permanent load G : Normal with G_{mean} and COV=0.1 Imposed (5 yr) Q : Gumbel distribution with $0.2Q_k$ and COV=1.1 Total model uncertainty K_T : Lognormal distribution, mean of 1.02 and COV = 0.16
Geometric imperfection	Normal with mean = 0 and St.dev.= $H/1000$ where H is column height
k_p [W/mK]	$k_p = \exp(-2.72 + 1.89 \times 10^{-3}T - 0.195 \times 10^{-6}T^2 + 0.209 \times \varepsilon)$

4 APPLICATION A – A COMPOSITE COLUMN

4.1 The application and inputs

The first application is adopted from the German DIN National Annex CC of EN 1992-1-2, Example no 11 [8]. It is a composite column with a steel section partially encased in concrete. The column is 4 m long. The square cross section has a width $b = h = 300$ mm. The steel profile is a HEB 300 in S235. The section is reinforced with 4 $\Phi 28$ rebars in hot-rolled B500 steel, with an axis cover of 50 mm. The concrete is a C25/30 with 3% humidity per mass. The column is axially loaded with a compressive load of 1700 kN in the fire situation. Both ends are fixed in rotation. The column is subjected to ISO standard fire exposure on four sides. The thermal-mechanical response of the column under applied gravity loading and fire exposure is simulated in the non-linear finite element software SAFIR [4]. For the thermal analysis, the cross-section is modelled with 2,686 triangular finite elements. For the structural analysis, the column is modelled in 2D, with strong axis orientation, using 10 BEAM elements of equal sizes.

First, a deterministic analysis is conducted as a reference case. The deterministic analysis uses the characteristic values for the material properties ($f_{ck} = 25$ MPa, $f_{sk,20} = 500$ MPa, $f_{yk,20} = 235$ MPa). The material models SILCON_ETC [9], STEELEC2EN and STEELEC3EN are used in SAFIR with the temperature-dependent reduction factors from Eurocodes. The applied load is 1,700 kN and the maximum amplitude of the geometric imperfection is 4 mm. This deterministic analysis predicts a failure time of 93 min based on the last converged step of the simulation, for which a runaway failure is observed. This is in very good agreement with the value of 92 min given in the DIN [8].

Secondly, probabilistic analyses are performed with the objective of establishing the PDF for failure time of the column under ISO fire. Stochastic variables are as defined in Section 3. The mean values of the material strengths at ambient temperature are evaluated from the characteristic values given above and as discussed in Table 2. This yields $f_{c,mean} = 35.7$ MPa, $f_{s,mean} = 560.0$ MPa, and $f_{y,mean} = 273.3$ MPa. At high temperature, reduction factors $k_{y,T}$, $k_{s,T}$, and $k_{c,T}$ are applied to the material strengths using models discussed in Table 2. The mean value of the applied load in the fire situation is estimated as 1,390.6 kN with $G_{mean} = 1,275$ kN and $Q_{mean} = 85$ kN ($Q_k = 425$ kN). Note: that the nominal case (obtained using the mean values for the random parameters) differs from the deterministic case. In the nominal case, the fire resistance time obtained with SAFIR is 136 min.

4.2 ME-MDRM Results and Monte Carlo validation

The variability of the fire resistance time t_R is evaluated probabilistically, using on the one hand 1,500 Monte Carlo simulations (MCS), and on the other hand the ME-MDRM procedure of Section 2. With 8 stochastic variables, the ME-MDRM procedure requires only 33 model evaluations. Furthermore, the feasibility of using a lognormal distribution (LN) for describing t_R is evaluated, using on the one hand the 1,500 MCS to estimate the parameters of the LN, and on the other hand estimating the parameters by estimating the moments of the lognormal distribution through Eq. (4), i.e. applying the ME-MDRM procedure of Section 2 from step 1 to step 4, followed by application of Eq. (4) and assuming the LN distribution. This last methodology has been named the MDRM-G in [2]. Results are visualized in Fig. 1, demonstrating:

- i) The excellent performance of the ME-MDRM in approximating the histogram and observed cumulative frequency of the fire resistance time. Special emphasis is placed on the excellent match of the CDF estimate for low quantiles of t_R . The (seeming) upper bound for t_R in the MCS at about 200 minutes is not captured by the ME-MDRM, but low probability upper bounds to t_R are of minor practical relevance relative to lower bounds.
- ii) The reasonableness of the lognormal approximation for this specific case, matching both the histogram shape and the ME-MDRM estimated curve. Furthermore, the LN with parameters estimated through the reduced methodology of the MDRM-G (33 model evaluations) quasi-perfectly matches the LN approximated using the 1,500 MCS.
- iii) The feasibility of using the ME-MDRM to extrapolate to low occurrence frequencies, e.g. a lower bound fire resistance time with a probability of only 10^{-4} of being exceeded.

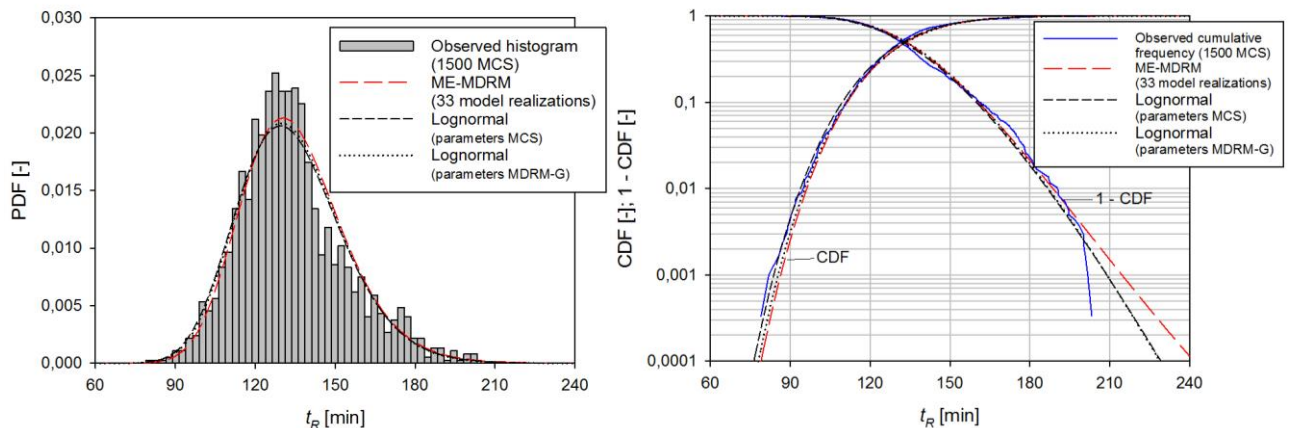


Fig. 1 Fire resistance time t_R for composite column. Comparison of 1500 MCS with ME-MDRM (33 simulations) and lognormal approximations. (a) PDF; (b) CDF and complementary CDF.

5 APPLICATION B – A SLAB PANEL

5.1 The application and inputs

The second application is a partially protected steel-composite slab panel undergoing tensile membrane action (TMA) (Fig. 2). The typology is inspired by a FEMA reference archetype structure, on which a performance-based SFE design has been performed [10]. The ambient temperature design is according to ASCE 7-10 and the AISC Steel Construction Manual. The panel is 9.14 m by 9.14 m in plan. The floor slab is a steel deck of 38.1 mm topped by a concrete slab of 63.5 mm (Fig. 2a). The girders are W21x44, while the boundary beams and central beams are W18x35 (Fig. 2b). The slab contains a single layer of reinforcing mesh with $503 \text{ mm}^2/\text{m}$ in each of the two orthogonal directions. The rebars are cold-worked class B steel, $f_{sk,20} = 416 \text{ MPa}$, and located at mid-height of the slab. The steel beams have a yield strength $f_{yk,20}$ of 345 MPa, whereas the concrete compressive strength $f_{ck,20}$ is 28 MPa. The uniformly distributed load is 5.4 kN/m^2 in the fire situation. The girders and boundary beams are protected with 2.06 and 2.22 cm of Spray-

Applied Fire Resistive Material (SFRM), a dry mix CAFCO Blaze-Shield II from Isolatak, for a 2 h fire resistance rating. The fire resistive performance of the entire floor system, on the other hand, is based on the consideration of the structural fire behavior and the development of TMA.

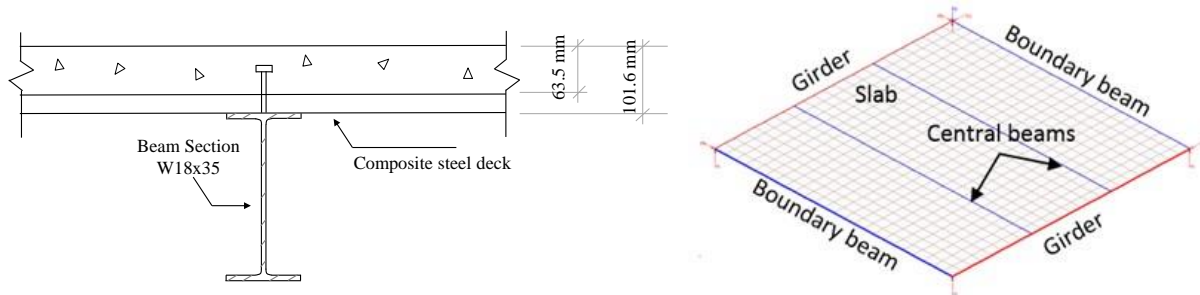


Fig. 2 Steel-concrete floor: (1) cross section; (2) 3D view of the SAFIR numerical model.

The thermal-mechanical response under applied gravity loading and ISO fire exposure is simulated in SAFIR. For the structural analysis, 576 shell elements are used for the slab, while 24 elements are used for each beam and girder. First, a deterministic analysis is conducted as a reference case. For the thermal analysis, a key parameter are the properties of the SFRM. The following properties are assumed as a reference (constant with temperature): conductivity 0.12 W/m.K, specific heat 1,100 J/kgK, dry specific mass 240 kg/m³, water content 16.5 kg/m³, coefficient of heat transfer by convection 25 W/m²K (hot) and 4 W/m²K (cold), and emissivity 0.8. The deterministic analysis uses the characteristic values for the material properties ($f_{ck,20} = 28$ MPa, $f_{sk,20} = 416$ MPa, $f_{yk,20} = 345$ MPa). The material models SILCOETC2D [9], STEELEC2EN and STEELEC3 are used in SAFIR with the temperature-dependent reduction factors from Eurocodes. With an applied load of 5.4 kN/m², the deterministic analysis predicts a failure time of 108 min based on the last converged step of the simulation; at that time failure occurs by yielding of a boundary beam. Secondly, probabilistic analyses are performed. In contrast to the composite column application earlier, Monte Carlo simulations are too computationally expensive to allow for a direct assessment of the histogram. 7 stochastic variables are introduced, comprising the materials strengths at ambient and elevated temperature and the thermal conductivity k_p of the protection layer. The material strengths are treated in a similar way as for the first application. For the SFRM conductivity, the model listed in Table 2 is used where the mean value is 0.07 W/mK at 20°C but the conductivity increases significantly with temperature. In the nominal case (using mean values for all random parameters), the fire resistance time obtained with SAFIR is 75 min; this time is shorter than in the deterministic case because the SFRM conductivity increases with temperature. The ME-MDRM is used to establish the PDF of the failure load for a 90 minutes of standard fire exposure, giving insight into the distribution of the maximum load level which can be sustained for a given fire severity.

5.2 ME-MDRM Results

To assess the PDF of maximum supportable load after 90 minutes of standard fire exposure, the ME-MDRM procedure of Section 2 is applied. Considering 7 stochastic variables, only 29 model evaluations are required. (Note: that finding the distributed load resulting in structural failure after a given time, through a transient finite element analysis, is an iterative process - for any given set of values of the stochastic variables a number of simulations are needed varying the load until failure occurs at 90 minutes). Results are visualized in Fig. 3. Comparing the unbiased ME-MDRM results with a lognormal approximation based on the MDRM-G methodology discussed earlier, it is clear that a lognormal distribution can be used to model the load bearing capacity of the fire exposed slab system, taking into account tensile membrane action. For this case, the performance of the ME-MDRM cannot reasonably be validated in this case using MCS, but the stand-alone application is exactly the intended use for the ME-MDRM. As illustrated in Fig. 3, potentially valuable information on the lower bound of the load bearing capacity is obtained through the applied methodology, while requiring only limited model evaluations. Notably, Fig. 3 (b) indicates there is

approximately a 1.5% probability that the load bearing capacity at 90 min ISO 834 exposure is lower than 2 kN/m².

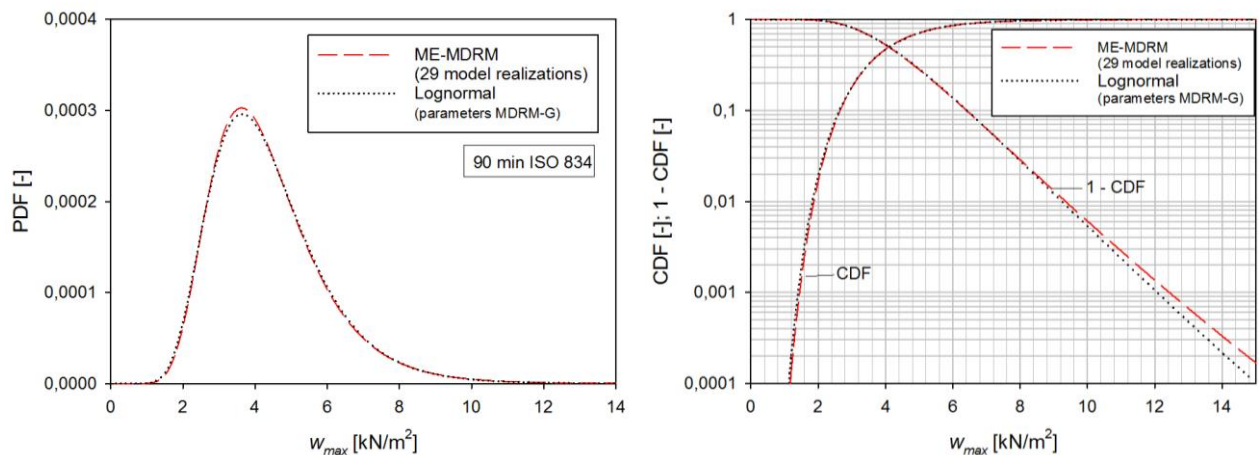


Fig. 3 Uniformly distributed load resulting in structural failure for 90 minutes ISO 834 exposure. Comparison of ME-MDRM (29 simulations) and LN approximation (MDRM-G). (a) PDF; (b) CDF and complementary CDF.

6 DISCUSSION AND CONCLUSIONS

6.1 Discussion of inputs

Previous sensitivity analyses confirm the importance of the random variables that are included in this study and their effect on fire safety [12]. However, there is no well-established set of models to quantify uncertainty in parameters at elevated temperatures. This section discusses the assumptions that are made in the adapted probabilistic models discussed in Section 3. When developing a probabilistic model for material strength, it is preferable to adapt a model that is compatible with normal structural reliability calculations at ambient temperatures, while capturing the variation in temperature dependent material properties at elevated temperatures. In this paper, the random variables for yield strength of steel and concrete compressive strength are first generated based on their characteristic values and variance at the ambient temperature. The logistic functions, as discussed in Section 3, are then used to capture variance at elevated temperatures. However, it should be noted that the logistic functions are derived by a Bayesian-based fit to a set of experimental data that include points at ambient temperature. Therefore, the extent to which the approach taken in capturing uncertainty at ambient temperature is redundant requires further investigation. In addition, the adapted model for yield strength of steel is based on EC3 [7], which provides reduction factors for 2% strain, rather than the convention of 0.2% offset at room-temperature. In quantifying uncertainty in the applied gravity load, the part that is characterized as imposed is time-dependent. In this study, a 5-year reference period has been assumed, thus implicitly modelling the load as an intermittent wave process with a 5-year return period. The implications of this also warrants further investigation.

6.2 Discussion on the effectiveness of the ME-MDRM and limitations

For the example cases presented, a lognormal approximation was found to give a very accurate approximation of the ME-MDRM output. In this situation, the unbiased nature of the ME-MDRM may seem superfluous, but it must be emphasized that the distribution shape of a given parameter in structural fire engineering problems is not known beforehand in general. Examples of calculations resulting in non-traditional distribution shapes, for example considering the bending moment capacity for fire exposed concrete slabs have been described in [2]. The ME-MDRM, however, also has its limitations. Considering Eq. (1) and the Gauss integration applied in Eq. (4), non-traditional distribution types for the input variables can be expected to result in difficulties for the ME-MDRM evaluation. This is especially the case for truncated, non-continuous and multimodal distributions. Further limitations relate to the scalar nature of the output variable. However, when applied with

care, the ME-MDRM can provide valuable support to probabilistic structural fire engineering. Importantly, the examples elaborated in the current paper demonstrate the feasibility of combining the ME-MDRM with highly regarded dedicated structural fire engineering software that is commonly used to support performance based designs.

6.3 SFE & PRA – Conclusions & a forward look

Realising exceptional buildings necessitates that an adequate level of fire safety be explicitly demonstrated. This requires an evaluation of all foreseeable consequences, and the probability of their manifestation. This is only readily achievable through PRA methods [13]. To date, the application of PRA in structural fire engineering has been limited to single element or simple assembly applications. That is, the full realisation of PRA in SFE has been hindered by the lack of an efficient unbiased calculation methodology. Herein, two finite element applications have been presented applying the ME-MDRM to provide an estimation of the PDFs of failure time and load, under standard fire conditions. Both were achieved with a limited number of SAFIR model realisations – 33 and 29 model realisations, respectively. This contrasts with MCS alternatives, where the required number of model realisations are of the order of $10^3 - 10^5$. It has been concluded that identifying a robust suite of probabilistic material properties is central to realising the full benefits of the ME-MDRM. This will be subject to future research.

REFERENCES

1. Zhang, X. (2013). Efficient Computational Methods for Structural Reliability and Global Sensitivity Analyses. *Doctoral dissertation*. University of Waterloo, Waterloo, Canada
2. Van Coile, R., Balomenos, G. P., Pandey, M. D., & Caspeele, R. (2017). An Unbiased Method for Probabilistic Fire Safety Engineering, Requiring a Limited Number of Model Evaluations. *Fire Technology*, 53(5), 1705-1744.
3. Novi Inverardi, P.L., Tagliani, A. (2003). Maximum Entropy Density Estimation from Fractional Moments. *Communications in Statistics – Theory and Methods*, 32, 327-345.
4. Jean-Marc Franssen, Thomas Gernay (2017). *Modeling structures in fire with SAFIR®: Theoretical background and capabilities*, Journal of Structural Fire Engineering, 8(3). pp 300-323.
5. Milan Holický, Miroslav Sýkora (2010), Stochastic models in analysis of structural reliability. In *Proceedings of the international symposium on stochastic models in reliability engineering, life sciences and operation management*, Beer Sheva, 08-11/02, Israel.
6. Negar Elhami Khorasani, Paolo Gardoni, Maria Garlock. (2015). Probabilistic fire analysis: evaluation of steel structural members. *Journal of Structural Engineering*, 141(12).
7. EC3. (2005). Eurocode 3: design of steel structures – Part 1–2: General rules – structural fire design. EN 1993-1-2. *European Standard*.
8. DIN EN 1991-1-2/NA (2010), *National Annex - Eurocode 1: Actions on structures - Part 1-2: General actions - Actions on structures exposed to fire*, Deutsche Norm.
9. Thomas Gernay, Jean-Marc Franssen (2012). *A formulation of the Eurocode 2 concrete model at elevated temperature that includes an explicit term for transient creep*, Fire Safety J, 51. pp 1-9.
10. Negar Elhami Khorasani, Chenyang Fang, Thomas Gernay (2017), Performance-based fire design and the U.S. prescriptive guidelines: A comparative study. *39th IABSE Symposium – Engineering the Future (Proc. of 39th IABSE)* (pp. 3377-3383). Vancouver, Canada, Sep 21-23.
11. Thomas Gernay, Alain Millard, Jean-Marc Franssen (2013). *A multiaxial constitutive model for concrete in the fire situation: Theoretical formulation*, International Journal of Solids and Structures, 50(22-23). pp 3659-3673.
12. Gernay, T., Elhami Khorasani, N., Garlock, M. (2017). Fire risk assessment of multi-story buildings based on fragility analysis. *Proceedings of the 2nd Int. Fire Safety Symposium - IFireSS*. Naples, Italy, June 7-9.
13. Hopkin, D., Van Coile, R., & Lange, D. (2017). Certain Uncertainty. *SFPE Europe – Issue 7*.

EXPERIMENTAL INVESTIGATION OF LIQUID POOL FIRES AND EXTERNALLY VENTING FLAMES IN CORRIDOR-LIKE ENCLOSURES

Kostantinos Chotzoglou¹, Eleni Asimakopoulou², Jianping Zhang³, Michael Delichatsios⁴

ABSTRACT

Understanding of the physics and mechanisms of fire development and externally venting flames (EVF) in corridor-like enclosures is fundamental to studying fire spread to adjacent floors in high-rise buildings. This work aims to investigate the burning behaviour of a liquid fuel pool fire in a corridor-like enclosure and to identify the key factors influencing EVF characteristics and its impact on façades. A series of experiments is conducted in a medium-scale corridor-facade configuration using ethanol pool fires. A new fuel supply system has been developed to keep the fuel level constant to minimize lip effects. The influence of fuel surface area and ventilation factor on the fire development is also investigated. Experimental measurements consist of mass loss, heat release rate, temperatures and heat fluxes inside the corridor and the facade. Three distinct burning regions are observed and their characteristics as well as the ones of the subsequent EVF depend on the pan size and ventilation factor. A power dependence of EVF height in relation to excess heat release rate has been found. The impact of EVF on the façade has been investigated by means of heat flux at the façade using thin steel plate probes measurements. EVF characteristics strongly depend on opening characteristics; for large opening widths EVF tend to emerge from the opening as two separate fire plumes.

Keywords: liquid pool fire, corridor-like enclosure, façade fire, flame height, heat flux

1 INTRODUCTION

Understanding of the physics and mechanisms of fire development in enclosures and flames emerging through openings is fundamental to studying fire spread to adjacent floors and subsequent evaluation of the integrity of structural elements. Recent high-rise building fires around the world highlight the importance of understanding the mechanisms of fire spread not only at the interior of buildings but also due to Externally Venting Flames (EVF) [1,2]. Consequences of these EVF induced fire events include loss of life and injuries, health impact through smoke exposure, property and infrastructure loss, business interruption, ecosystem degradation, soil erosion and huge firefighting costs [1,3]. Though substantial research has been conducted on fire characteristics of EVF in typical cubic-like compartments [4,5,6], there is still limited data in other geometries (e.g. long corridors, tunnels etc). For the few studies in corridor-like enclosures [7], gaseous fuels were used. As the mass flow rate (thus heat release rate) of gaseous fuels must be pre-defined, it does not consider the interaction

¹ PhD Candidate. Belfast School of Architecture and the Built Environment, Ulster University, Belfast, UK and Effectis, UK/Ireland.
e-mail: chotzoglou-k@ulster.ac.uk

² Research Associate. Belfast School of Architecture and the Built Environment, Ulster University, Belfast, UK
e-mail: e.asimakopoulou@ulster.ac.uk

³ Reader. Belfast School of Architecture and the Built Environment, Ulster University, Belfast, UK
e-mail: j.zhang@ulster.ac.uk

⁴ Northeastern University, Boston, USA and University of Science and Technology of China (USTC), Hefei, China
e-mail: madelicha@aol.com

between the flame, hot gas layer and the pyrolysis rate of the fuel, which is of fundamental importance in growth and development of real fires. This work investigates the burning behaviour of a liquid fuel pool fire in a corridor-like enclosure and the heat impact of the subsequent EVF on the façade. The effects of the size and location of the pool fire and the dimensions of the opening on the burning characteristics of the EVF are examined. Experimental measurements consist of gas temperature inside the enclosure, mass burning rate, heat release rate, heat fluxes on the enclosure floor and on the façade and production of CO and smoke. The experiments were video recorded, based on which the flame height of the EVF is deduced using an in-house image processing software. The deduced flame height is correlated with the external heat release rate and compared to previous studies using gaseous fuels.

2 EXPERIMENTAL DETAILS

2.1 Corridor-like enclosure and façade configuration

The experiments were conducted in a medium-scale corridor-façade configuration having internal dimensions 3 m x 0.5 m x 0.5 m and a 1.8 m x 1 m façade was attached to the front box. A schematic of the experimental facility, illustrating the locations of the employed measuring devices, is given in Fig. 1.

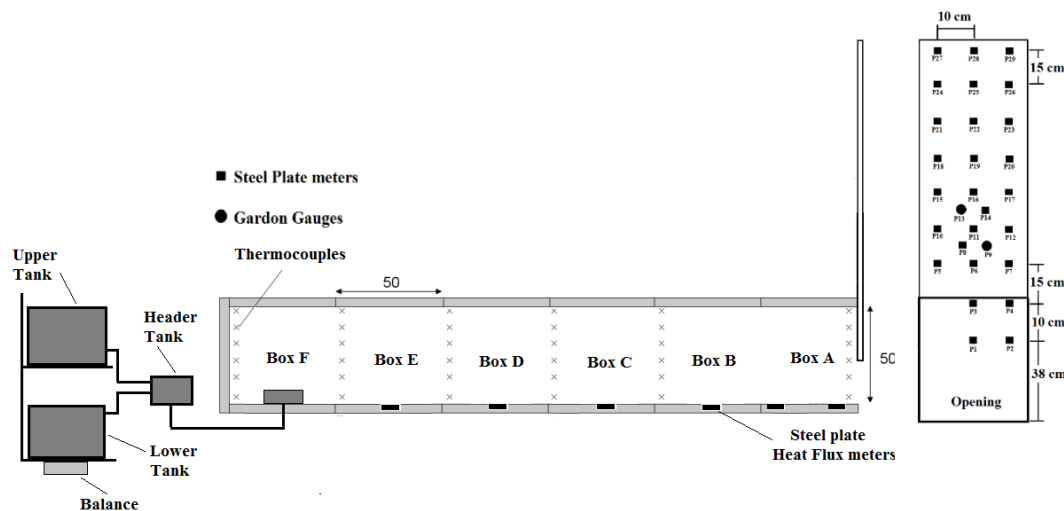


Fig. 1. Fire test configuration and experimental setup.

A new liquid fuel supply system was developed to keep the fuel level constant to minimize lip effects; ethanol was used in a circular sandbox burner positioned either in the geometrical centre of Box A or F. The fuel surface area and ventilation factor (opening size) were varied to examine their effects on the fire development. In total, more than 60 experiments were conducted, and the effect of ventilation is investigated by altering the dimensions of the door-like opening. A summary of the main operational parameters, i.e., burner position, opening size (opening width W_o and opening height H_o), ventilation factor ($A_o H_o^{1/2}$ where A_o corresponds to the opening area), Global Equivalence Ratio (GER), ventilation regime (i.e., under-ventilated or over-ventilated), and the characteristic length scale ($l_f = (A_o H_o^{1/2})^{2/5}$) [6] is shown in Table 1 for the test cases where EVF was observed.

2.2 Sensors and data acquisition system

A total of thirty-six K-type 1.5 mm diameter thermocouples were used to monitor gas temperatures inside the enclosure every 6 s [7,8], with six thermocouple trees located in each of the boxes and 5 cm from the side wall. The six thermocouples are located at 2, 10, 20, 30, 40 and 48 cm height from the floor. Both steel plates (square shape) and Gardon gauges (round shape) have been used to monitor

the heat flux at the façade as shown in *Fig. 1*. The experimental set-up was placed under a 3 x 3 m² 1 MW hood to measure the experimental heat release rate, \dot{Q}_{exp} , production of CO, CO₂ and smoke. Videos were recorded by a CCD camera facing the façade, based on which an in-house developed image processing tool is used to evaluate the geometric characteristics of the façade fires by calculating the average flame probability (intermittency) [9]. Each frame was converted into a binary image using a set of rules, employing appropriate threshold limits for Red, Green and Blue colour levels and luminosity, based on the prevailing lighting conditions in each test case. The threshold limits were acquired through an extended statistical analysis of the flame at *Region III*.

Table 1. Summary of main operational parameters for all the test cases with EVF.

a/a	Test	Burner position	Pan diam.	Opening size	$A_o H_o^{1/2}$	Ventilation regime	GER	l_i
		Box	m	m x m	m ^{5/2}		-	-
1	FR20W20xH20	A	0.2	0.20x0.20	0.0179	O	0.64	0.20
2	FR20W25xH25	A	0.2	0.25x0.25	0.0313	O	0.59	0.25
3	FR30W10xH25	A	0.3	0.10x0.25	0.0125	U	1.37	0.17
4	FR30W20xH20	A	0.3	0.20x0.20	0.0179	O	0.83	0.20
5	FR30W25xH25	A	0.3	0.25x0.25	0.0313	O	0.91	0.25
6	FR30W30xH30	A	0.3	0.30x0.30	0.0493	U	1.02	0.30
7	FR30W50xH25	A	0.3	0.50x0.25	0.0625	U	1.09	0.33
8	FR30W50xH50	A	0.3	0.50x0.50	0.1768	O	0.34	0.50
9	BC20W25xH25	F	0.2	0.25x0.25	0.0313	U	1.35	0.25
10	BC20W30xH30	F	0.2	0.30x0.30	0.0493	U	1.36	0.30
11	BC20W50xH25	F	0.2	0.50x0.25	0.0625	U	1.16	0.33
12	BC30W25xH25	F	0.3	0.25x0.25	0.0313	U	1.38	0.25
13	BC30W30xH30	F	0.3	0.30x0.30	0.0493	U	1.50	0.30
14	BC30W50xH25	F	0.3	0.50x0.25	0.0625	U	1.29	0.33
15	BC30W50xH50	F	0.3	0.50x0.50	0.1768	O	0.57	0.50

3 RESULTS AND DISCUSSION

3.1 Heat release rate inside the enclosure

A parametric analysis was performed to identify the main parameters influencing the burning behaviour and subsequent EVF namely pan size, pan location and ventilation factor. To demonstrate the main characteristic stages regarding the fire growth, the temporal evolution of measured HRR, \dot{Q}_{exp} , and theoretical HRR, \dot{Q}_{th} , are plotted in *Fig. 2* for two characteristic under-ventilated test cases, namely for BC20W30H30 and BC30W30H30. The theoretical HRR, \dot{Q}_{th} , is calculated by multiplying the fuel mass loss rate by the heat of combustion of ethanol, 26.78 MJ/kg. The maximum HRR in stoichiometric conditions inside an enclosure, $\dot{Q}_{st,in}$, can be calculated by multiplying the air inflow rate by the heat released by complete combustion of 1 kg oxygen, which for most fuels is found to be approximately equal to 3000 kJ/kg [3].

A general description of the fire temporal evolution is presented based on visual observations and *HRR*. For all under-ventilated fires with the pan located in Box F, as indicatively shown in *Fig. 2*, the fire behaviour is characterized by three distinct phases namely *Regions I, II* and *III* appearing in succession. *Region I* corresponds to the fuel-controlled period (growth period), where the combustion efficiency is close to unity and thus \dot{Q}_{exp} and \dot{Q}_{th} are almost equal. During *Region II*, fire gradually

becomes ventilation-controlled; \dot{Q}_{exp} reaches a plateau until flames ejects through the opening and \dot{Q}_{exp} does not reach the maximum heat released inside the enclosure approaching $1500A_oH_o^{1/2}$ value according to relevant research concerning compartment fires [5]. This value is decreased, calculated at approximately $1100A_oH_o^{1/2}$, as the amount of air inflow in long corridors is less than in rectangular enclosures with the same opening geometry [10]. GER is used to describe the fire in during *Region II* as fuel- or ventilation-controlled [11] by calculating the ratio of the fuel mass flux, \dot{m}_T , to the oxygen mass flux entering the enclosure, \dot{m}_{O_2} , divided by the fuel-to-oxygen stoichiometric ratio of the fuel, S [3]. Relevant results of GER for each test case are presented in Table 1.

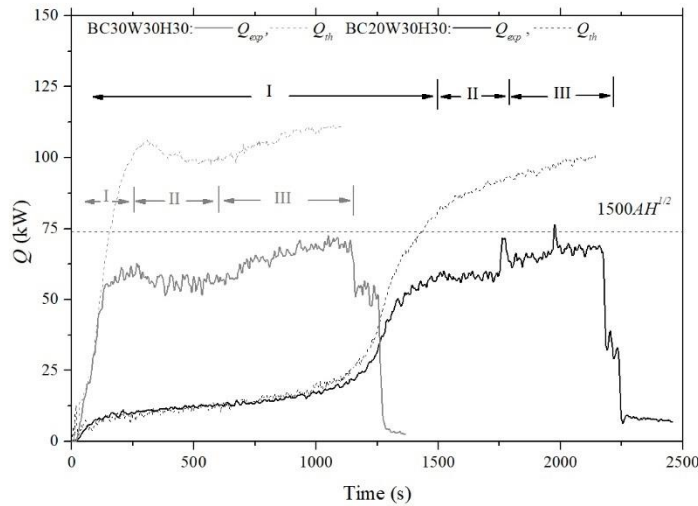


Fig. 2. Temporal evolution of \dot{Q}_{exp} and \dot{Q}_{th} for test cases BC30W30H30 and BC20W30H30.

Flames ejection, often associated with a sudden increase in the \dot{Q}_{exp} indicates the beginning of *Region III*, where sustained external burning is observed until a plateau is formed indicating that steady state conditions are established. As depicted in Fig. 2, not all the excess fuel burns at the exterior of the corridor as the combustion is incomplete and the combustion efficiency in *Region III* is calculated at approximately 0.74 for both cases. As demonstrated in Fig. 3, pan size has a significant effect on the time to reaching steady burning, as in test cases using smaller pans it takes longer for the walls to be heated. For under-ventilated cases with the fuel pan located at the rear of the corridor and larger pan sizes, EVF appeared shortly after ignition and the duration of *Regions I* and *II* becomes considerably reduced as the increasing rate of the mass loss rate/heat release rate is significantly increased. The start of *Region II* corresponds to a transition from fuel controlled to ventilation- controlled conditions where combustion efficiency is decreased due to insufficient O_2 availability thus resulting in an increase production of intermediate products, e.g. CO . During *Region III*, the concentration of intermediate combustion products, e.g. CO , exiting through the opening is decreased due to external burning. In order to determine the external heat release, \dot{Q}_{ex} , it is assumed that the burning inside the corridor remains the same and thus \dot{Q}_{ex} can be found from the difference between the steady heat release rate in *Region III* and that at the end of *Region II* and the relevant values are shown in Table 2, along with the flame height, which will be further discussed in Section 3.3.

Table 2. Summary of main operational parameters for the examined test cases.

a/a	1	2	3	4	5	6	7	8	9	10	11	12	13	14	15
\dot{Q}_{exp} (kW)	12.1	21.5	22.2	17.0	31.0	56.1	75.1	69.5	39.0	68.5	74.0	39.5	70.0	77.0	105.0
\dot{Q}_{ex} (kW)	-	-	-	-	-	-	-	-	2.5	11.1	9.0	2.9	14.0	9.0	-
Z_f (m)	0.11	0.21	0.22	0.13	0.34	0.49	0.48	0.33	0.22	0.51	0.37	0.19	0.58	0.64	0.30

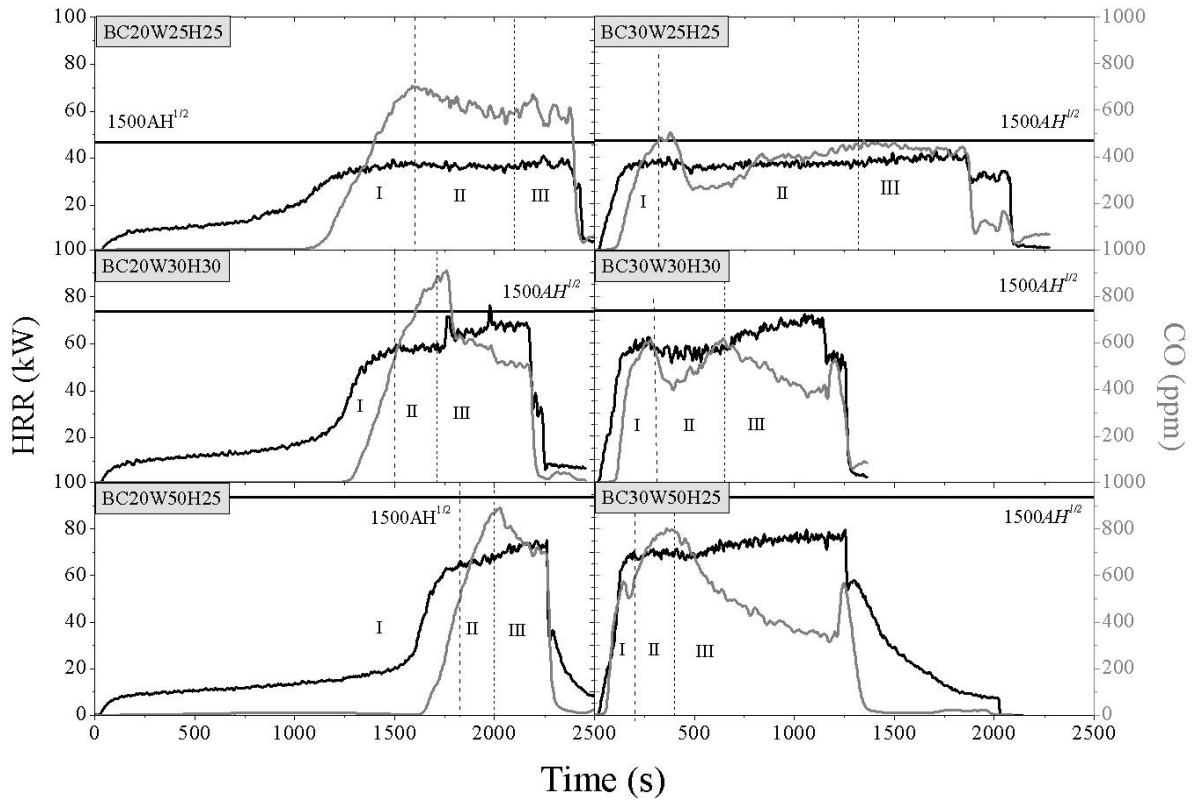


Fig. 3. Temporal evolution of Q_{exp} and CO volume concentrations measured at the hood for test cases B20W25H25, B20W30H30, B20W50H25 (left) and B30W25H25, B30W30H30, B30W50H25 (right).

3.2 Gas temperature inside the enclosure

The present analysis focuses on under-ventilated cases in which EVF occur. The gaseous temperature inside the corridor at three characteristic time frames representing the three Regions discussed in previous section for test cases BC30W30H30 and FR30W30H30 is depicted in Fig. 4.

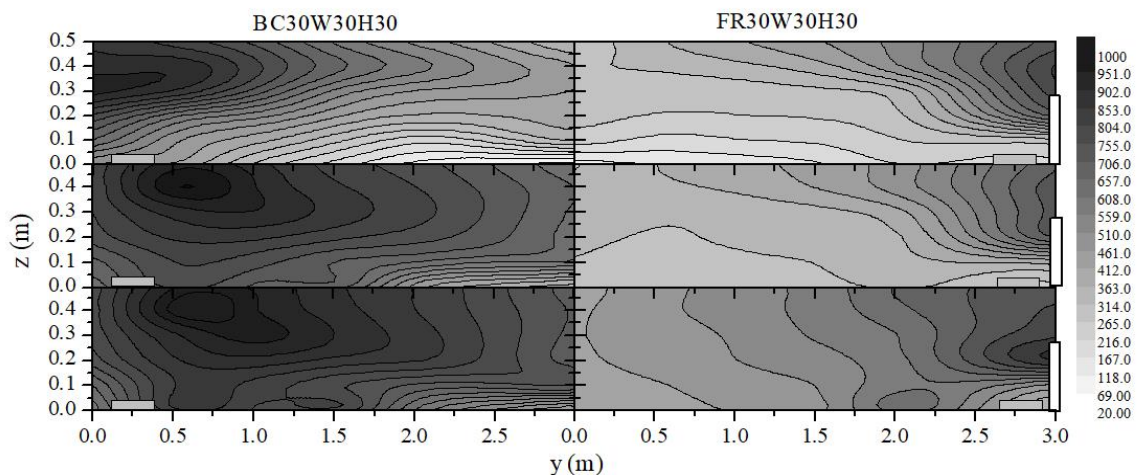


Fig. 4. Spatial visualization of gaseous temperature at the interior of the corridor for test cases F30W30H30 (left) and B30W30H30 (right) for 120, 400 and 900s

During *Region I*, low gas temperatures are observed in the lower layer as fresh air enters the enclosure through the opening that is located at the right side of the corridor. In BC30W30H30 test case, during

Region II, highest temperatures are observed at the vicinity of Boxes E and D indicating that combustion mainly takes place in those regions and flames gradually propagate towards the opening seeking for available oxygen [7, 8]. During *Region III*, the difference of gas temperatures between the upper and the lower layer decreases towards the closed end of the corridor, but still, they cannot be assumed uniform inside the corridor. In *Region III*, flames fill the upper layer of the corridor extending towards the opening and eventually emerges from the opening when the HRR becomes sufficiently large. In test case FR30W30H30, temperature stratification in the interior of the corridor is less evident as EVF emerge more quickly from the opening resulting in lower temperature profiles at Boxes C to F.

3.3 EVF height

Figure 5 plots dimensional flame height, Z_f/l_1 , against dimensionless external heat release rate, \dot{Q}_{ex}^* , using experimental data from gas burner experiments in rectangular geometries [8], corridors [7] and liquid pool fires in corridors (current study). It is demonstrated that for small flame heights and larger openings the power dependence on the \dot{Q}_{ex}^* , calculated in accordance to established methodology [7], is 2/3 in accordance the physical mechanism corresponding to “wall fire”, flame attached to the façade wall and “half axisymmetric fire”, flame detached from the façade wall, regimes [8, 11, 12]. For $\dot{Q}_{ex}^* > 1$ and subsequent larger flame heights, gas burner experimental results from both rectangular and corridor geometries corroborate a 2/5 dependence on the \dot{Q}_{ex}^* [8,11,13].

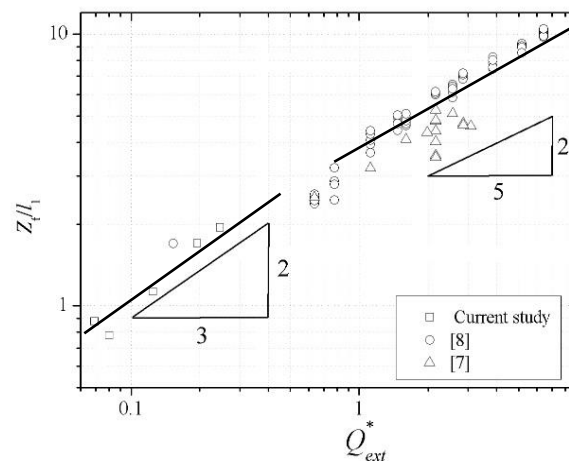


Fig. 5. Flame height correlation for gas burner experiments in rectangular geometries [8] corridors [7] and liquid pool fires in corridors (current study).

3.4 Heat fluxes

Heat fluxes on the façade were measured using thin steel plate probes [8,14], the results of which have been verified by comparison with the Gardon gauge results [15]. Fig. 6 depicts the vertical distribution of the heat flux measurements at the centreline of the façade for all test cases. Measured heat fluxes decrease with increasing height as expected. The highest heat flux is always found along the centreline above the opening except for test cases with the widest opening, i.e., BC30H50W50 and FR30H50W50. As it can be seen from their intermittency contours in Fig. 7, the resulted EVF for these two cases tend to emerge as two separate fire plumes from the opening and as a result the maximum heat flux values are off the centreline in contrast to other cases. This finding highlights the importance of the width of the opening in addition to the ventilation factor. For the same opening and pan size, higher heat flux values are found when the fuel pan is positioned in Box A, near the opening.

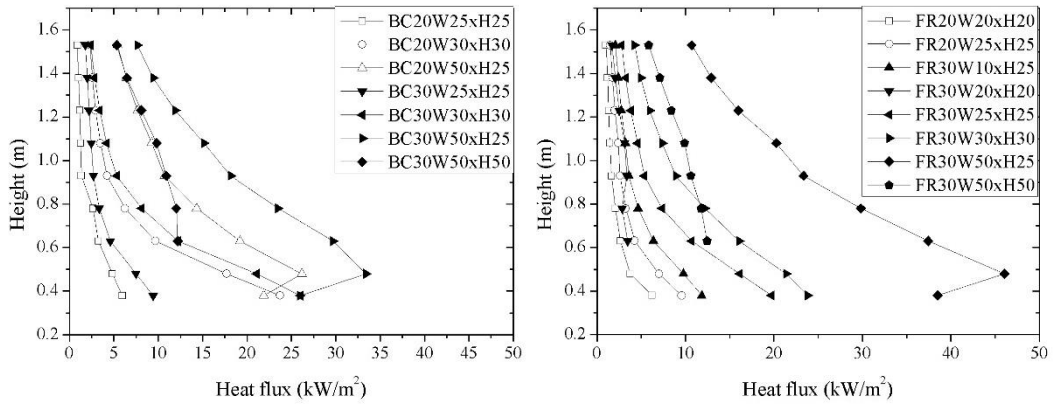


Fig. 6. Vertical distribution of heat flux at the centreline of the façade for the BC (left) and FR (right) cases.

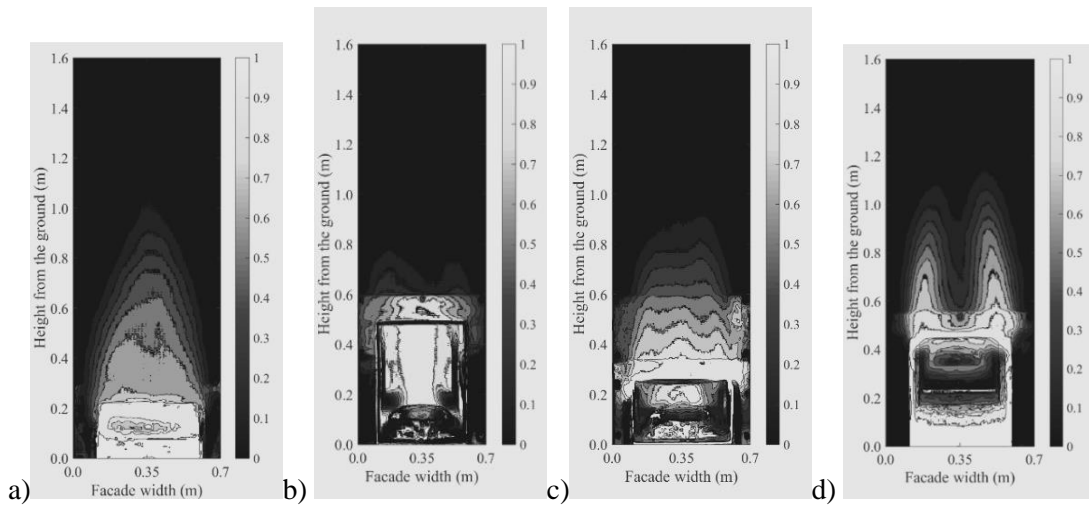


Fig. 7. Intermittency contours for (a)BC30H25W50, (b)BC30H50W50, (c)FR30H25W50, (d)FR30H50W50.

4 CONCLUSIONS

We presented an experimental study on burning characteristics of a liquid pool fire in a reduced-scale corridor-like enclosure and the resulting externally venting flames (EVF) and their impact on the façade. The size and location of the pool fire and opening size were systematically varied. The main conclusions of this work are:

1. Three distinct burning regions (*Region I, II* and *III*) were observed based on \dot{Q}_{exp} corresponding respectively to fuel-controlled, ventilation-controlled and steady-state burning.
2. The location and size of the fuel pan has a strong impact on HRR and subsequent EVF characteristics.
3. For the cases with small flame heights and larger openings, the power dependence of the flame height of the EVF on the dimensionless external heat release rate \dot{Q}_{ex}^* is $2/3$, compared to $2/5$ for larger \dot{Q}_{ex}^* values found for gaseous fuels in previous studies [7,8].
4. The heat flux measurements using thin steel plate probes are consistent with those measured using Gardon gauges. Centreline heat fluxes are nearly constant just above the opening where the consistent flame region is and subsequently decreases with height. The heat fluxes measurements are consistent with those of heat release rate and flame height.
5. EVF for openings with the largest width (same as that of the enclosure) exhibit different characteristics and tend to emerge from the opening as two separate fire plumes resulting in lower heat flux values at the façade centreline.

6. The obtained extensive set of experimental data derived for the interior and exterior of the corridor-like enclosure, can be used to validate CFD models or to evaluate the accuracy of available fire design correlations.

ACKNOWLEDGMENT

Present work has been financially supported by “ELISSA: Energy Efficient Lightweight-Sustainable-Safe-Steel Construction” project (FP7-2013-NMP-ENV-EeB). Technical assistance of Mr. M. McKee, Mr. B. Veighy and Mr. K. Kowalski is gratefully acknowledged.

REFERENCE

1. Nathan White, Michael Delichatsios “Fire hazards of exterior wall assemblies containing combustible components”, 1st ed., SpringerBriefs in Fire, Springer, New York, U.S.A., 2014.
2. Eleni K. Asimakopoulou, Dionysios K. Kolaitis, Maria A. Founti (2017). *Thermal characteristics of externally venting flames and their effect on the exposed façade surface*. Fire Safety Journal 91 pp 451-460. <https://doi.org/10.1016/j.firesaf.2017.03.075>
3. Daniel J. O’Connor “The Building Envelope: Fire Spread, Construction Features and Loss Examples”, SFPE Handbook of Fire Protection Engineering (5th ed.) Hurley M.J., National Fire Protection Association, Quincy, MA 02269, 2016, p 3242/3512.
4. Kunio Kawagoe, Fire Behaviour in Rooms, Report 27, Building Research Institute, Tokyo, 1958.
5. Michael A. Delichatsios, Gordon W.H. Silcock, Xijuan Liu, Mary Delichatsios, Yee-Ping Lee (2004). *Mass pyrolysis rates and excess pyrolysate in Fully Developed Enclosure Fires*. Fire Safety Journal 39 pp 1– 21. <https://doi.org/10.1016/j.firesaf.2003.07.006>
6. Eleni K. Asimakopoulou, Konstantinos Chotzoglou, Dionysios K. Kolaitis, Maria A. Founti (2016). *Characteristics of externally venting flames and their effects on the façade: a detailed experimental study*. Fire Technology 52 pp 2043-2069. <https://doi.org/10.1007/s10694-016-0575-5>
7. Tarek Beji, Sebastian Ukleja, Jianping Zhang, Michael A. Delichatsios (2012). *Fire behaviour and external flames in corridor and tunnel-like enclosures*, Fire and Materials 36 pp 636-647. <https://doi.org/10.1002/fam.1124>
8. Yee-Ping Lee, Michael A. Delichatsios, GWH Silcock (2007). *Heat fluxes and flame heights in facades from fires in enclosures of varying geometry*. Proceedings of the Combustion Institute 31 pp 2521-2528. <https://doi.org/10.1016/j.proci.2006.08.033>
9. Eleni K. Asimakopoulou, Dionysios Kolaitis, Maria A. Founti (2016). *Geometrical characteristics of externally venting flames: Assessment of fire engineering design correlations using medium-scale compartment-façade fire tests*. Journal of Loss Prevention in the Process Industries 44 pp 780-790. <http://dx.doi.org/10.1016/j.jlp.2016.09.006>
10. Ee Yii, Charles Fleischmann, Andrew Buchanan (2007). *Vent flows in fire compartments with large openings*. Journal of Fire Protection Engineering 17 pp 221-237. <http://dx.doi.org/10.1177/1042391507069634>
11. Sizuo Yokoi (1960). *Study on the prevention of fire spread caused by hot upward current*, Japanese Ministry of Construction, Building Research Institute Report 34, 1960.
12. James Quintiere, Margaret Harkleroad, Yuji Hasemi (1986) *Wall Flames and Implications for Upward Flame Spread*. Combustion Science and Technology 48 pp 191–222. <https://doi.org/10.1080/00102208608923893>
13. K.H. Lu, L. H. Hu, F. Tang, L.H. He, X.C. Zhang, Z.W. Qiu (2014). *Heat flux profile upon building facade with side walls due to window ejected fire plume: An experimental investigation and global correlation*. Fire Safety Journal 70 pp 14-22. <http://dx.doi.org/10.1016/j.firesaf.2014.08.001>
14. Jianping Zhang, Michael A. Delichatsios (2009). *Determination of the convective heat transfer coefficient in three-dimensional inverse heat conduction problems*. Fire Safety Journal 44 pp 681-690. <https://doi.org/10.1016/j.firesaf.2009.01.004>
15. Piotr Tofilo, Michael A. Delichatsios., Gordon W.H. Silcock, Jim Shields (2004). *Wall Heat Fluxes in Enclosure Fires, 6th Asia-Oceania Symposium on Fire Science & Technology*, Daegu Korea, March 17, AOSFST, 2004. pp 108-119.

SEISMIC PERFORMANCE OF REINFORCED CONCRETE FRAMES AFTER FIRE

Ling-zhi Li ¹, Xin Liu ^{2*}, Zhou-dao Lu³, Kai Wei ⁴

ABSTRACT

To investigate the seismic behaviour of post-fire reinforced concrete (RC) frames with different beam-column sectional sizes, four specimens were fabricated, which include a strong-beam-weak-column frame and a strong-column-weak-beam frame under room temperature, as well as another two frames with the same sectional sizes as those under room temperature but being exposed to fire. The fire test was conducted in a furnace chamber followed the ISO834 temperature curve, and then a quasi-static test was carried out for all the specimens under a low-frequency cyclic load. In the loading process, the crack patterns, the hysteretic loops, the plastic hinges, and the failure modes were observed. Two factors were considered in this study, one is the fire and another is the beam-column sectional-size relationship, and their influence on the mechanical performance were analysed and compared. The experimental results show that the ultimate bearing capacity and stiffness of the RC frames decreased after fire. Furthermore, the failure modes of the strong-column-weak-beam frame that failed in the form of beam-end plastic hinges at room temperature changed into the column failure mode after being exposed to fire.

Keywords: Reinforced concrete frame, quasi-static test, seismic performance, high temperature

1 INTRODUCTION

Existing reinforced concrete (RC) frame structures that were constructed before the 1980s usually do not meet current seismic standard in China. For instance, the stirrup ratios in the joint zone may be too small to resist the shear force, which will lead to the harmful brittle joint shear failure. Another situation is that the beam-to-column linear rotational restraint ratio i is too large, which will result in a strong-beam-weak-column frame and cause joint shear failures such as column hinging. Besides, fire is the most frequent disaster in the world that can damage the buildings and decrease the structure's mechanical performance to a large extent. Therefore, there is a very slim chance that these seismically deficient RC frames will survive an earthquake after being exposed to a fire.

Although the evaluation of the post-fire performance of the substandard RC frames is of great importance, most researches in literature mainly focused on the material and component aspects rather than the structural aspect. Researchers ^[1-4] found that the mechanical properties of concrete could be affected largely by elevated temperatures, such as the compressive strength and elasticity modulus. Similarly, the influence of fire to the yield strength, ultimate strength and the

¹ Associate Professor. College of Civil Engineering, Tongji University, Shanghai, China.
e-mail: lilingzhi@tongji.edu.cn

² PhD Candidate. College of Civil Engineering, Tongji University, Shanghai, China.
e-mail: lx900314@126.com

³ Professor. College of Civil Engineering, Tongji University, Shanghai, China.
e-mail: lzd@tongji.edu.cn

⁴ MPhil Candidate. College of Civil Engineering, Tongji University, Shanghai, China.
e-mail: m13660469974@163.com

deformability of steel bars were also studied [5-7]. While on the aspect of RC components, the post-fire performance of RC beams has been experimentally investigated by Jiang [8], and a series of experiments have been conducted by researchers on the behaviour of RC columns and slabs after fire.

On the other hand, researchers [9-10] have found that the structural response of a statically indeterminate structure in fire is much more complicated than those of single members. Thus, many researchers have investigated the mechanical behaviour of RC frames under fire [11]. Researchers studied the post-fire seismic behaviour of RC frames, the test results indicated that the damage pattern of post-fire RC frames can transform from a ductile strong-column-weak-beam failure into a brittle strong-beam-weak-column one [12]. Furthermore, existing studies of high temperature experiment on RC frames usually ignore the impact of the slabs and cross beams, which resulted in a considerable discrepancy between the experimental specimens and actual buildings. Set against this background, an experimental study on the seismic behaviour of RC frames after being exposed to fire was presented in this paper. The test parameters include the beam-to-column cross-sectional size relationship and whether or not to be subjected to fire.

2 EXPERIMENTAL PROGRAM

2.1 Design of Specimens

The experimental program consisted of reversed cyclic loading of four half scale RC frame specimens that had identical column dimensions. Two units (C1 and C2) were tested as control frames, and two units (FC1 and FC2) were exposed to fire prior to quasi-static testing. Specimen C1 represented a seismic RC frame designed to meet the requirements of current seismic design code in China, whereas specimen C2 had a relative strong beam and represented a non-seismic RC frame. FC1 and FC2 represented the post-fire specimens corresponding to the control specimens C1 and C2. The design parameters are shown in Table 1.

The column height was 1800 mm with a cross section of 250 mm×250 mm, and the clear beam length between the two column side faces was 2350 mm, with a cross section of 120 mm×250 mm for C1 and FC1, and 120 mm×250 mm for C2 and FC2. The longitudinal reinforcement used in the column was 8D16, corresponding to a 2% reinforcement ratio. The top and bottom longitudinal reinforcements of the RC beams in C1 and FC1 were 2D14, corresponding to a 1.03 % reinforcement ratio. While those of the RC beams in C2 and FC2 were 3D16 corresponding to a 1.15 % reinforcement ratio. The transverse reinforcements of the columns and beams were R6-150 mm. The sectional size, the top and bottom longitudinal reinforcements, and the transverse reinforcement of the base beam were 300 mm×250 mm, 3D20, and R6-100 respectively. The thickness of the concrete cover was 15 mm with half of the figures compared to full-scale specimens. The notations 'D' and 'R' denote the high-yield deformed steel bars and the mild steel round bars. The common details of dimensions and reinforcement are shown in Fig. 1.

Table 1 Design parameters of specimens

specimen	Beam cross sectional dimension b×h (mm)	Column cross-sectional dimension b×h (mm)	Type	Temperature
C1	120×250	250×250	Strong-Column-Weak-Beam	Unheated
C2	150×350	250×250	Strong-Beam-Weak-Column	Unheated
FC1	120×250	250×250	Strong-Column-Weak-Beam	Heated
FC2	150×350	250×250	Strong-Beam-Weak-Column	Heated

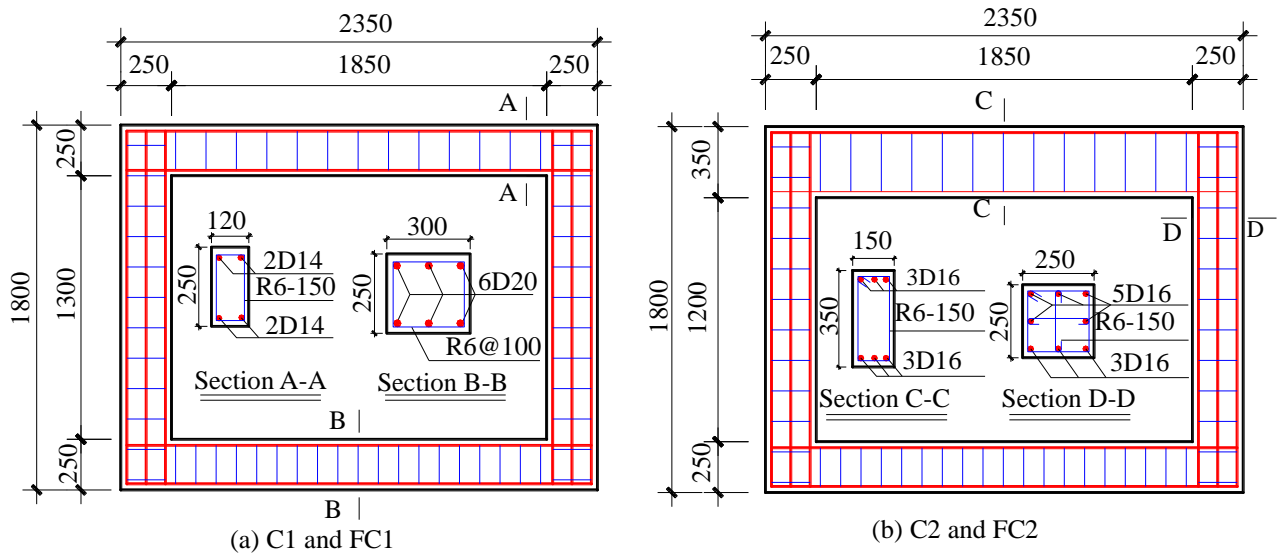


Fig. 1 Dimensions and reinforcement details (dimensions in mm)

2.2 Material properties

Ready-mixed concrete was used with a 28d compressive strength of 43.9 MPa. Three steel bar samples were tested under room temperature to obtain the yield strength and ultimate strength. The properties of longitudinal and transverse reinforcements are shown in Table 2.

Table 2 Mechanical properties of reinforcement

Sample	Diameter (mm)	Yield strength (MPa)	Ultimate strength (MPa)
R6	6	413.4	510.2
D14	14	589.9	701.7
D16	16	484.0	597.3
D20	20	446.5	582.3

2.3 Test setup

This experimental study was composed of two parts: a fire test and a quasi -static test. As shown in Fig. 2, a furnace of 4 m × 3 m × 1.8 m was used to conduct the fire test, and the temperatures in the furnace followed the ISO 834 heating curve. The starting temperatures of the fire test were about 38°C. The specimens FC1 and FC2 were heated on all side faces for column, both the tensile soffit and the two side faces for beam. Besides, due to the concrete slab was used as the furnace top cover, thus only the bottom face of slab was heated. The heating time was 140 minutes.



Fig. 2 General view of specimens under fire exposure

After the fire test, a reversed cyclic loading test was conducted for all specimens, as shown in Fig 3. Lateral cyclic loading with increasing amplitudes was statically applied to the top of the column in two opposite directions, parallel to the longitudinal axis of the beam, by a hydraulic actuator with a ± 500 kN loading capacity and a ± 500 mm displacement range, and two vertical 500 kN capacity hydraulic jacks were used to apply constant axial load to the columns by a rigid distribution beam to simulate gravity loads. For each specimen a total of nine strain gauges were attached to longitudinal and transverse reinforcements at critical locations to record the strains that developed at different loading phases, and five linear variable displacement transducers (LVDTs) were used to record the horizontal displacements at various locations.



Fig. 3 Overview of reversed cyclic loading test setup

3 RESULTS AND DISCUSSION

3.1 Experimental Phenomena Under Fire

At the beginning of the fire test, a small amount of water stains appeared at the top surface of the slab due to the evaporation of free water inside concrete (see Fig 4(a)), which has absorbed amount of the heat input from the fire and delayed the temperature increasing. As the temperature rising, the area of the water stains becomes larger and more water evaporation can be easily seen. Finally, the water stains disappeared and lots of cracks appeared on the slab top surface. After flameout, the specimens were cooled naturally, there were tons of cracks appeared at the surface of the beams and columns. Furthermore, the concrete of slab bottom surface spalling seriously that lead to the exposure of reinforcements, as shown in Fig 4(b).



(a)



(b)

Fig. 4 Experimental phenomena after fire

3.2 Failure Modes

During the loading process, diagonal cracks were emerged and gradually developed into X-shaped cracks on the beams and columns as well as the joint zones. The reference frame C1 failed in the form of beam-end plastic hinging, as shown in Fig 5(a), illustrating that C1 failed by flexural yielding in the beam with moderately ductile performance. While the control specimen C2 was observed with the column shear failure due to the larger cross section of beams than that of columns. The typical shear-bond failure was observed for the post-fire specimen FC1 and FC2 due to the serious peeling between concrete and reinforcements, as shown in Fig. 5(b) & (d). Moreover, it should be noted that the failure mode of FC1 was changed from strong-column-weak-beam to strong-beam-weak-column, which demonstrated that the fire function could transferred a ductile damage pattern of RC frame into a brittle one.

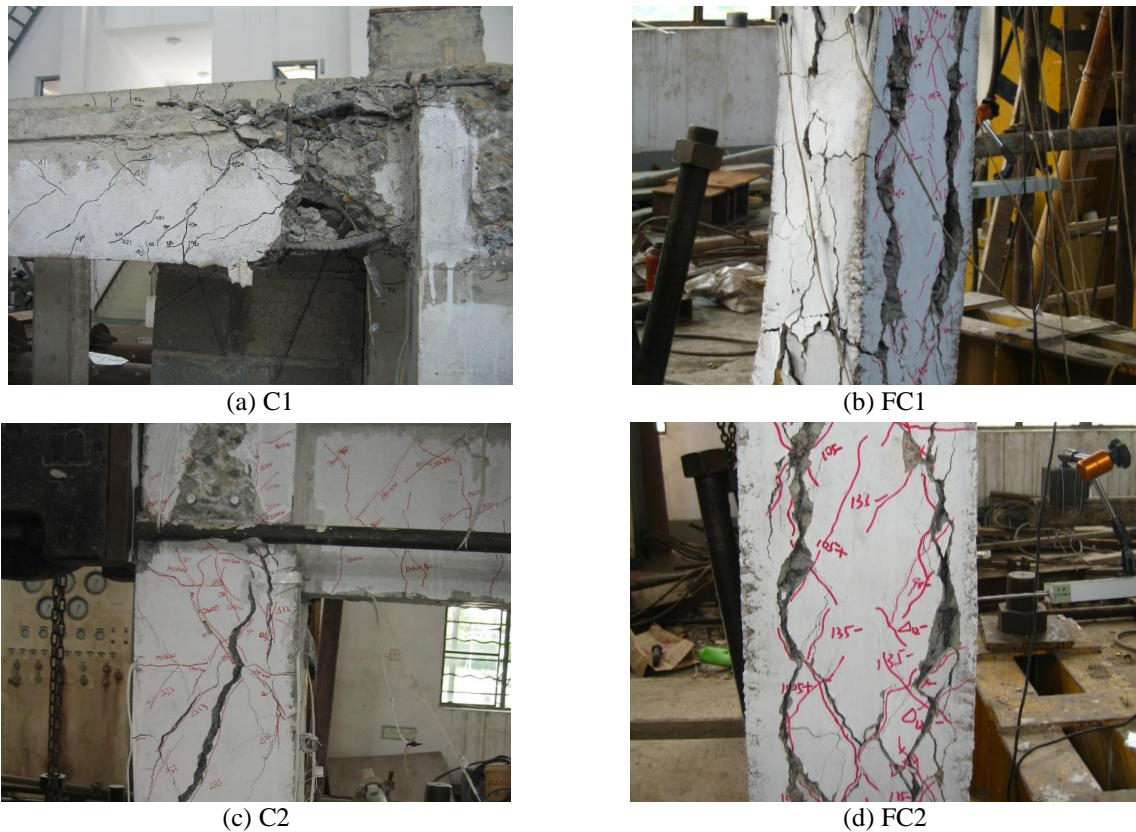


Fig. 5 Failure modes of the specimens

3.3 Load-deflection Responses

The load-deflection hysteretic curves are shown in Fig 6, where the X-axis represents the displacements while the Y-axis represents the load. As shown in Fig 6(a) & (b), there is no noticeable pinching in the hysteretic loops of C1 due to the ductile failure mode of beam-end hinging, the ultimate load and stiffness are obviously larger than those of the post-fire specimen FC1. As for C2 and FC2 (see Fig 6(c) & (d)), there was a substantial difference not only in the ultimate loads and displacements, but also in the energy dissipation capacity. Compared with C2, the post-fire specimen FC2 exhibited a lower load under the same displacement, and the hysteretic loops show remarkable pinching, stiffness and strength degradation with the increasing lateral loads. The largest difference is in the area of hysteretic loops per cycle, where the specimens after fire have been witnessed a dramatic fall. In conclusion, all these results indicate that the fire decreased the seismic performance of RC frames to a certain degree.

Seismic performance of reinforced concrete frames after fire

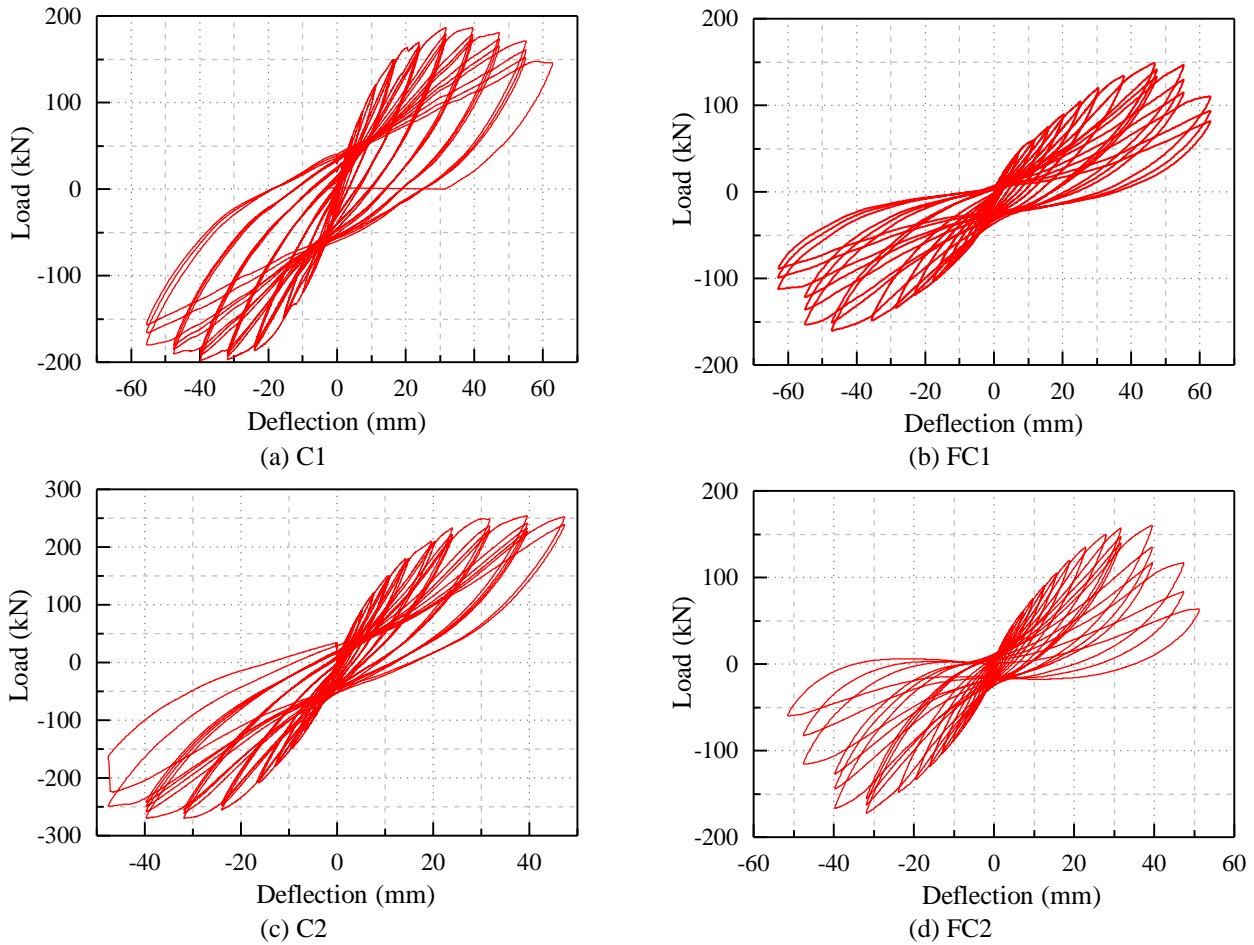


Fig. 6 Hysteresis curves of the four RC frames

3.4 Back-bone load-deflection curves

Fig 7 shows the back-bone load-deflection curves of all the four specimens obtained connecting the peak loads for each first cycle at a given drift amplitude. Significant force decays and stiffness degradation were found on the post-fire specimens FC1 and FC2 when compared to their corresponding control specimens C1 and C2. The ultimate loads of specimens C1 and FC1 were about 185 kN and 150 kN in the positive quadrant, and 200 kN and 160 kN in the negative quadrant, respectively. Similarly, the maximum load of C2 was about 250 kN at a displacement of 32 mm in the positive quadrant, while for FC2, the maximum loads was around 160 kN corresponding to a deflection of 40 mm. In addition, although the load capacity of C1 was lower than C2 under the same deflection, it shows a relative better ductility. But the ductility performance of FC1 and FC2 have little difference due to the same failure mode of column shear-bond. Overall, the test results indicate that the fire damaged the bearing capacity and stiffness of RC frames to a large extent, and the non-seismic specimen in the form of strong-beam-weak-column exhibits a larger strength loss and a smaller ductility after being exposed to fire than the strong-column-weak-beam specimen.

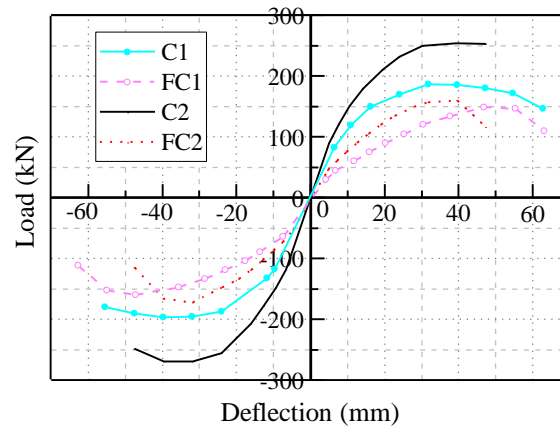


Fig. 7 Comparison of the back-bone curves

4 CONCLUSIONS

The key findings of the experimental program are as following:

(1) Three damage patterns were observed in the test: (a) the beam-end plastic hinging occurred in C1 due to the yielding of reinforcements, (b) the column shear failure occurred in C2 due to the larger beam-to-column linear rotational restraint ratio, and (c) the column shear-bond failure caused by the strength degradation and the peeling of concrete for the post-fire specimens FC1 and FC2.

(2) The seismically and non-seismically detailed post-fire specimens showed a high rate of strength and stiffness degradation when compared to the corresponding control specimens. After fire, the difference in stiffness degradation between beam and column can possibly transform a strong-column-weak-beam frame into a strong-beam-weak-column one that performs poorly under reversed cyclic loadings.

(3) The average maximum peak loads for the positive and negative loading directions for the post-fire specimens was decreased by 17% and 36% for FC1 and FC2 with respect to the corresponding control specimens, which indicates that the non-seismic specimen exhibited a larger strength loss.

(4) The post-fire specimens showed a significantly pinching in the load–deflection hysteretic curves, which indicates that the seismic performance of the specimens decreased after.

(5) Although the yield displacements of the fire-damaged specimens increased, their ultimate displacements decreased.

ACKNOWLEDGMENT

The research described here received financial support from the National Natural Science Foundation of China (Project No. 51778496 and No. 51778497).

REFERENCES

1. Cruz C. R (1900). *Elastic properties of concrete at high temperatures*. Portland Cement Assoc R & D Lab Bull. 8(1)
2. Arioiz Omer (2007). *Effects of elevated temperatures on properties of concrete*. Fire Safety Journal. 42(8). pp 516-522
3. Kodur Venkatesh (2014). *Properties of Concrete at Elevated Temperatures*. Isrn Civil Engineering. pp 1-15
4. Yu Kequan, Yu Jiangtao, Lu Zhoudao (2014). *Determination of residual fracture parameters of post-fire normal strength concrete Up to 600°C using an energy approach*. Construction & Building Materials. 73. pp 610-617
5. Ünlüoğlu Eşref, Topçu İlker Bekir, Yalaman Burçak (2007). *Concrete cover effect on reinforced*

Seismic performance of reinforced concrete frames after fire

- concrete bars exposed to high temperatures*. Construction & Building Materials. 21(6). pp1155-1160
6. Felicetti Roberto, Gambarova Pietro G., Meda Alberto (2009). *Residual behavior of steel rebars and R/C sections after a fire*. Construction & Building Materials. 23(12). pp 3546-3555
 7. U Lker Bekir Top, Karakurt Cenk (2015). *Properties of Reinforced Concrete Steel Rebars Exposed to High Temperatures*. Advances in Materials Science & Engineering. 2008(208). 4
 8. Jiang Chang Jiu, Lu Zhou Dao, Li Ling Zhi (2017). *Shear Performance of Fire-Damaged Reinforced Concrete Beams Repaired by a Bolted Side-Plating Technique*. Journal of Structural Engineering. 143(5). pp 4017007
 9. Becker James M., Bresler Boris (1977). *REINFORCED CONCRETE FRAMES IN FIRE ENVIRONMENTS*. American Society of Civil Engineers. 103(1). pp 211-224
 10. Vecchio Frank J., Sato James A. *Thermal gradient effects in reinforced concrete frame structures*. Aci Structural Journal. (1990). 87(3). pp 262-275
 11. Raouffard Mohammad Mahdi, Nishiyama Minehiro (2015). *Fire Resistance of Reinforced Concrete Frames Subjected to Service Load: Part 1. Experimental Study*. Journal of Advanced Concrete Technology. Vol. 13(No. 12). pp 554-563
 12. Xiao J. Z., Li Jie, Huang Z. F (2008). *Fire response of high-performance concrete frames and their post-fire seismic performance*. Aci Structural Journal. 105(5). pp 531-540

MONITORING SPALLING OF HEATED CONCRETE USING LASER DISTANCE METRE

Jin-Cheng Liu¹, Kang Hai Tan²

ABSTRACT

Monitoring spalling of concrete under heating is an important but challenging task. This paper adopted an innovative method – laser measurement technology to measure progressive spalling of concrete under heating in real time. Laser distance metre was shown to be an effective tool to record spalling history of concrete during heating. This experiment also measured temperature and pore pressure in concrete specimens at different locations. Discussion on the relationship between temperature, pore pressure, and spalling was provided.

Keywords: high temperature, progressive spalling, concrete, laser distance metre

1 INTRODUCTION

Explosive spalling of concrete under fire is an unfavorable phenomenon leading to premature failure of concrete elements and structures. So far, there have been a large number of studies on spalling mechanism of concrete exposed to fire [1-4]. However, only a limited number of work is conducted on quantification of spalling of concrete, i.e., when and where spalling occurs in concrete under fire. Quantification of spalling provides new insights into spalling behaviour of concrete. It is important information to determine fire behaviour and fire resistance of concrete members when explosive spalling occurs. It also provides valuable data for validating numerical spalling models. Mass loss is frequently used to measure the degree of spalling in concrete [5-7]. It is often measured in residual state, and it does not exclude the mass loss due to water loss. Most importantly, it does not provide when and where spalling occurs, which can affect fire resistance of concrete members significantly. Alternatively, acoustic emission has been used to measure the time of spalling [8]. But the locations of spalling are unknown, and sometimes it is difficult to separate spalling from cracking. Ultrasonic Pulse-Echo (UPE) technique has been used to measure the time of spalling and to obtain corresponding spalling depth through extrapolation [9]. This method is an indirect way to measure spalling depth and still requires further validation. This paper proposes a straightforward method to measure time and location of spalling through laser distance metres.

2 TEST PROGRAM

To simplify the test, 1-D heating scheme was adopted for applying laser measurement technology. For 1-D heating tests, two 200mm×200mm×150mm panel specimens were used. Two types of concrete mixes were used in this study. The mix proportions of these two concrete mixes (M1 and M2) are given in *Table 1*. The properties of PVA fibre and steel fibre can be found in [10]. The 1D

¹ Research Associate. School of Civil and Environmental Engineering, Nanyang Technological University, Singapore.

e-mail: liujc@ntu.edu.sg

² Professor. School of Civil and Environmental Engineering, Nanyang Technological University, Singapore.

e-mail: ckhtan@ntu.edu.sg

heating test setup is shown in Fig. 1. Both moisture transfer and heat transfer were confined in the thickness direction of the specimen block. To ensure 1D moisture transfer through the block, high-temperature silicone was applied on four lateral faces. To ensure 1D heat transfer, the specimen was wrapped with ceramic blankets on four faces. The specimen was then placed on one vertical opening of the furnace with the interior face exposed to heating and the exterior face to ambient environment. In front of the other vertical opening of the furnace, a set of three laser distance metres was installed on a tripod to monitor spalling process in the heating direction as shown in Fig. 1.

Table 1. Mix Proportions of concrete (kg/m³)

Mix name	Cement	Fly ash	Sand	Water	PVA fibre	Steel fibre	Superplasticizer
M1	537	645	537	333	19.5	39	5.5
M2	537	645	537	333	-	-	5.5

The specimens were instrumented with thermocouples and pressure gauges to obtain temperature and pore pressure simultaneously at the same location (Fig. 2). These gauges consisted of a sintered stainless steel porous disk (12 mm diameter and 2 mm thick) encapsulated into a stainless steel cup that was welded to a stainless steel tube (Fig. 2). Prior to testing, all gauges were filled with silicone oil to transfer the measured pressure. The free end of the tube was connected to a pressure transducer. Four pairs of gauges were deposited at 10, 20, 30, and 40 mm from the heated face. The arrangement of temperature and pressure gauges is shown in Fig. 3. Three remote target points were for spalling detection in the direction of specimen thickness and they were tagged respectively with ‘L’ (left), ‘C’ (centre), and ‘R’ (right).

Heating in the furnace followed a curve shown in Fig. 1. The temperature rose to 600 °C in 10 minutes and was held constant for a period of 2 hours. However, during heating of the M2 specimen severe spalling occurred. To prevent unexpected accident and damage to the furnace, heating was stopped ahead of time.

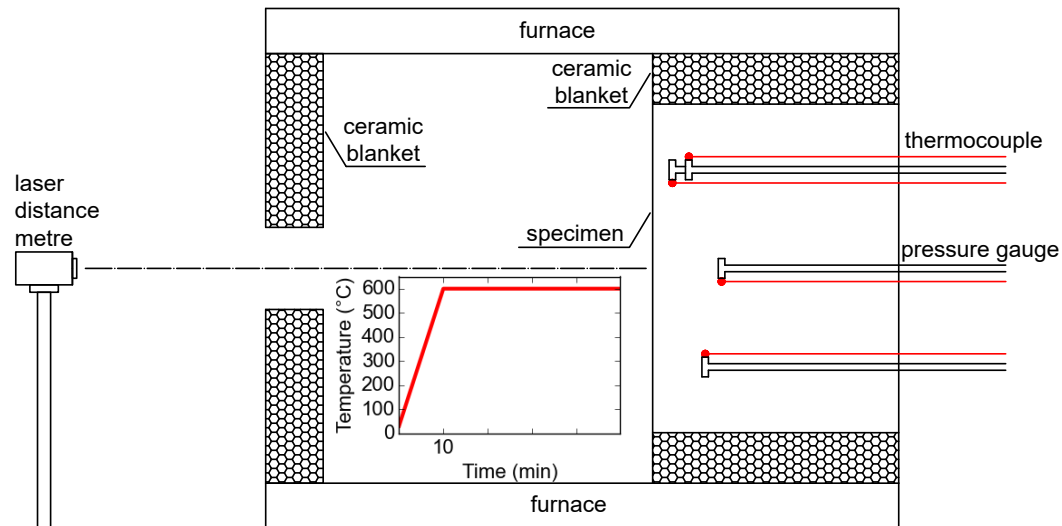


Fig. 1. Experimental setup for 1D heating test

After fabrication, the specimens were stored in a sealed bag for the first 7 days, and then in laboratory room conditions for at least 180 days so that they achieved an equilibrium moisture state. The moisture content was measured using 50 mm cube specimens stored in the same condition, by

drying the specimens at 105 °C until they achieved a constant mass (0.02% / day). Moisture contents of M1 and M2 samples were respectively 0.9% and 1.1%, which were far below the threshold moisture content (3%) to initiate explosive spalling according to [11].



Fig. 2. Placement of thermocouples and pressure gauges

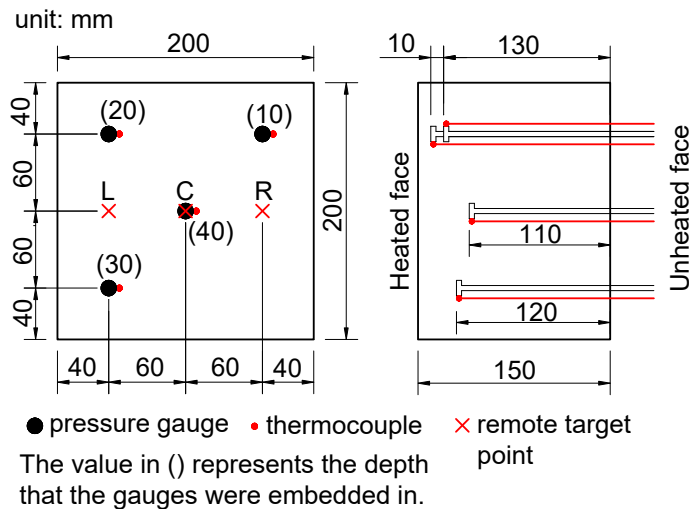


Fig. 3. Schematic of thermocouple, pressure gauge, and remote spalling detection point locations in the specimen

3 RESULTS AND DISCUSSION

Explosive spalling typically occurs in a consecutive manner under fast, severe heating. Consequently, boundary conditions for heat and moisture transfer will be changed from time to time. By recording the spalling history, effect of spalling on temperature and pore pressure may be studied. Also, approximate spalling temperature and moisture state at spalling locations can be deduced based on recorded temperature, pressure, and spalling history.

During the 1D heating tests, no spalling occurred in concrete M1, while severe spalling occurred in concrete M2, as evidenced in M1 and M2 specimens after heating (Fig. 4). In fact, small spalled-off M2 concrete pieces were observed to eject through the furnace opening opposite to the specimen at a high speed during heating. The trajectory of the spalled-off piece could be simplified to a horizontal parabola. From the farthest landing spot of spalled-off concrete pieces, the maximum velocity of the spalled-off concrete piece was calculated to be about 13.2 m/s. There were also continuous loud popping sounds accompanying ejection of spalled-off concrete pieces. Therefore, progressive spalling process was accompanied by the release of a large amount of internal energy originally stored in free water inside the specimen.

In Fig. 5 and Fig. 6, the temperature history and pore pressure history at different locations of concrete M1 and M2 are plotted. M1 and M2 specimens had a similar thermal behaviour at each depth at the early stage of heating before 10 min as shown in Fig. 5. As heating continued, the temperature in concrete M2 suddenly rose faster than concrete M1 for each depth due to successive spalling. At the end of heating of M2 specimen, the temperature differences at 10, 20, 30 and 40 mm between M2 and M1 specimens reached approximately 200 °C.

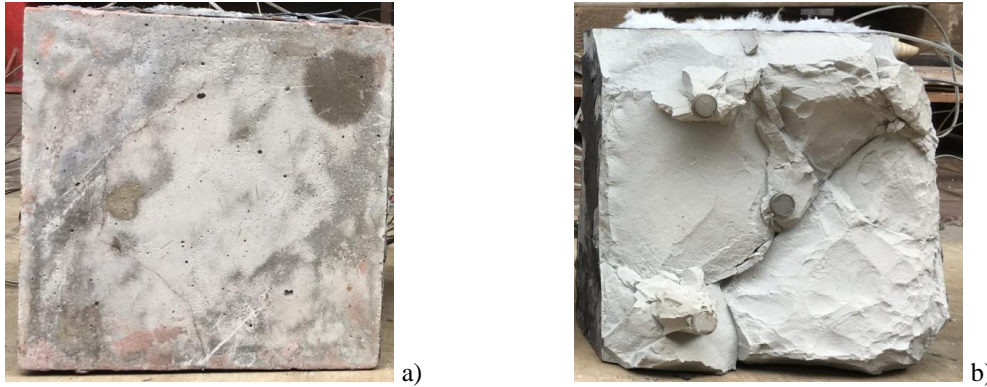


Fig. 4. Concrete a) M1 and b) M2 specimen after heating

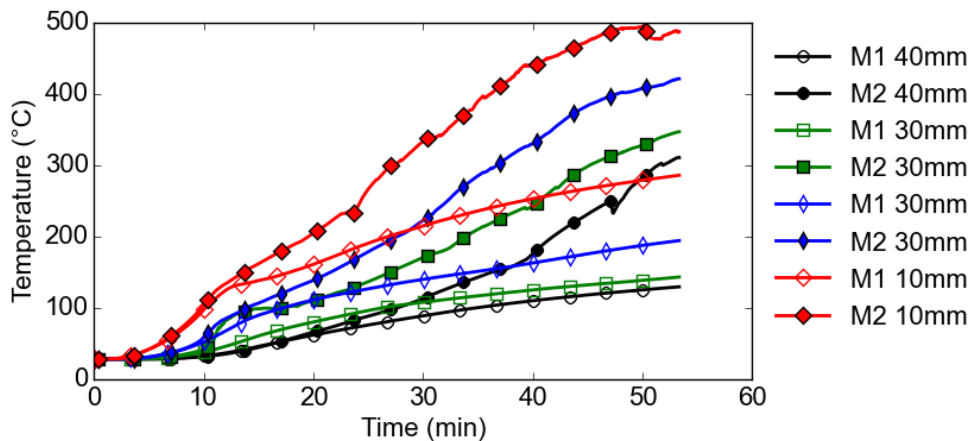


Fig. 5. Evolution of temperature at various depths of concrete M1 and M2 with time

Fig. 7 shows the spalling depth of M1 specimen at monitored points L, C, and R (Fig. 3) as a function of heating time. It was noted that there was negligible change (± 1 mm) in the reading from the laser distance metre before spalling started to occur. This confirmed effectiveness of the laser measuring system in a hot environment (600 °C). The laser distance metres had to be activated every 150s manually. Monitoring was stopped after 33 min to avoid potential injury to personnel due to more violent ejections of spalled-off concrete pieces. The monitored point C and the thermocouple embedded at a depth of 40 mm were along the centre axis of the M1 specimen. There was a direct correlation between spalling history at point C and temperature history at the depth of 40 mm.

Fig. 8 plots the spalling history of M1 specimen at point C and temperature histories of M1 and M2 at 40mm from the heated surface. When the first spalling occurred at point C, temperature of M2 started to separate from temperature of M1. With occurrences of second and third spalling, the rate of increase in temperature of M2 increased slightly. The correlation between spalling and change in temperature was clearly shown in Fig. 8, demonstrating the applicability of the laser distance metre to measure spalling history of concrete.

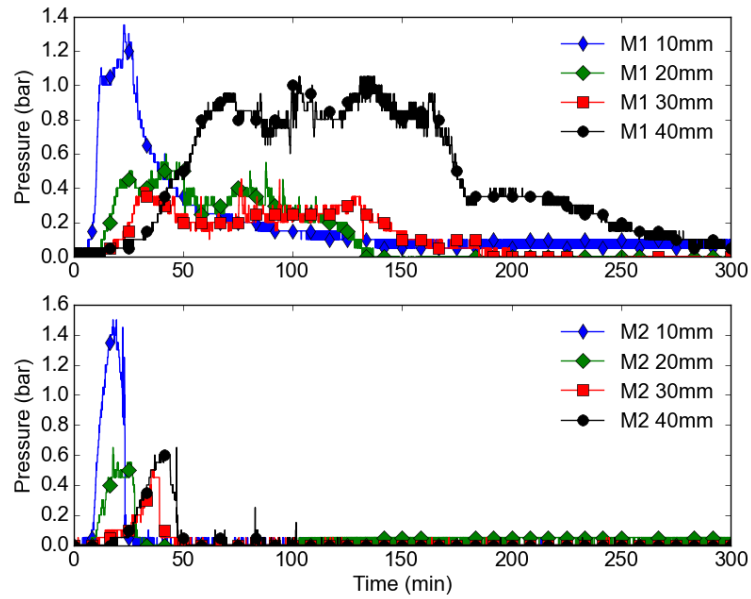


Fig. 6. Evolution of pore pressure at various depths of concrete M1 and M2 with time

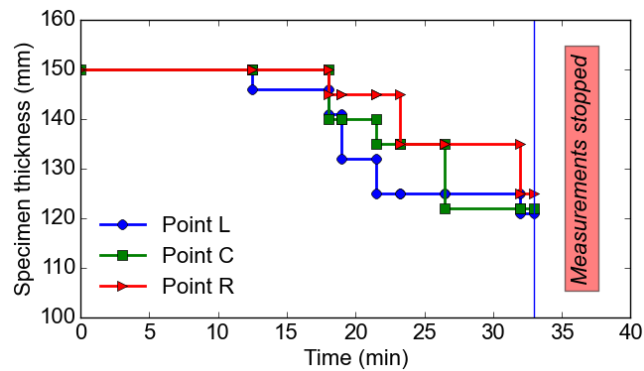


Fig. 7. Spalling depth at point L, C, and R as a function of heating time for concrete M2

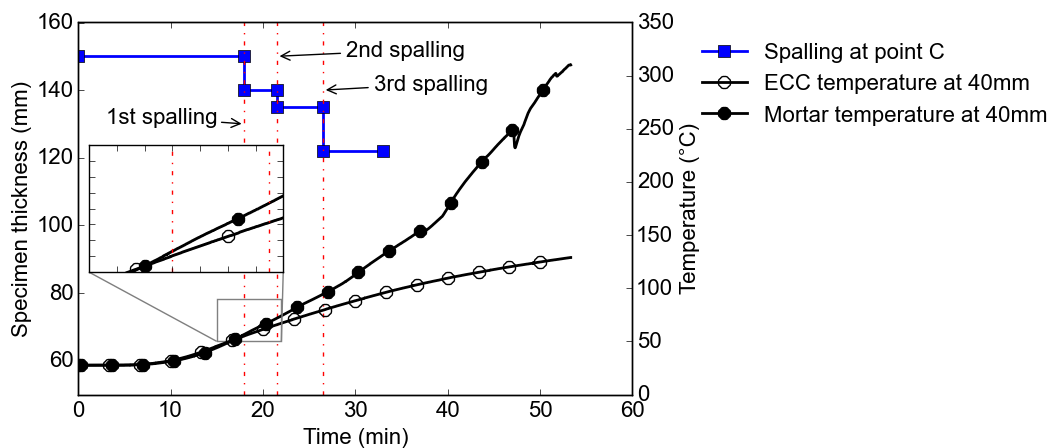


Fig. 8. Correlation between spalling and temperature of concrete M2 at 40 mm

The evolutions of pressure with time at 10, 20, 30, and 40 mm of M1 and M2, shown in Fig. 6, seemed to be less predictable. There is still some useful information that can be gleaned from the curves. For M1, the pore pressure at each depth decreased gradually after reaching the peak value. But for M2, the pore pressure at each depth dropped suddenly after arriving at the peak. The

difference was caused by spalling of concrete M2. This was expected since spalling not only changed the boundary conditions for heat transfer, but also for moisture transfer.

Fig. 9 plots the spalling history at point C and pore pressure histories in M1 and M2 at 40mm. After the third spalling, pore pressure in M2 surged up at around 26 min. It was noted that there was a sudden drop in pore pressure in M2 at 43 min and 47 min. At 43 min, the pore pressure did not drop to zero, while the pore pressure diminished to zero at 47 min. This is believed to be caused by spalling right at the central location, which changed the moisture state and consequently the pore pressure at a depth of 40 mm. It indicated that the accumulated spalling thickness had not reached 40 mm at 43 min, but at 47 min, the accumulated spalling thickness had reached or exceeded 40 mm.

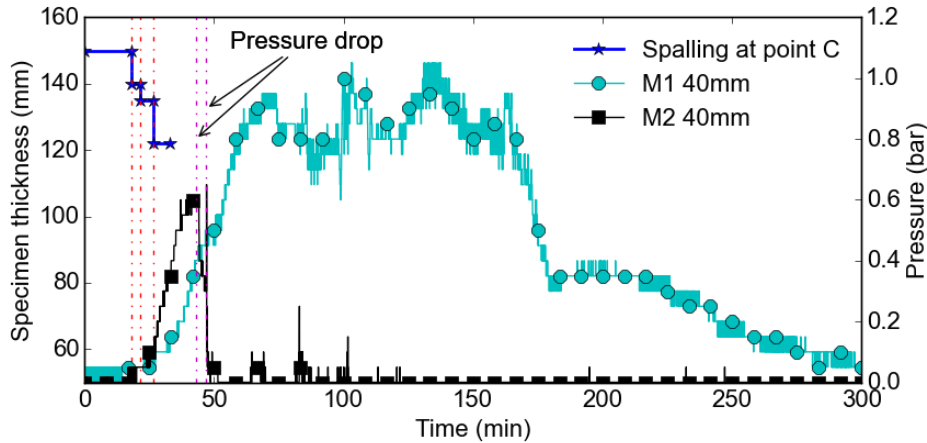


Fig. 9. Correlation between spalling and pressure in concrete M2 at 40 mm

From the spalling histories at the three target points shown in Fig. 7, it was observed that spalling occurred in concrete M2 at an early stage of heating. The first spalling time for point L, C, R was 12.5, 18, and 18 min, respectively. The time interval between successive spalling at each location was small, ranging from 1 min to 10.5 min. The successive spalling thickness at each location ranged from 4 to 13 mm, consistent with small spalled-off pieces observed after cooling down.

Based on the temperature history and spalling history, an estimate can be made of the temperature of concrete M2 at the time of spalling. The first spalling depth of M2 right at the centre (point C) was around 10 mm (Fig. 7). Therefore, the main focus was to know the temperature at 10 mm. Unfortunately, although a thermocouple was embedded at 10 mm away from the heated face as shown in Fig. 3, the first spalling in that location occurred earlier than that in the centre location as shown in Fig. 10. In view of this, the temperature of concrete M1 at 10 mm was assumed to be the same as that of concrete M2 before any spalling occurred, since both of them had similar thermal properties as evidenced by their temperature histories (Fig. 5) up until about 10 min.

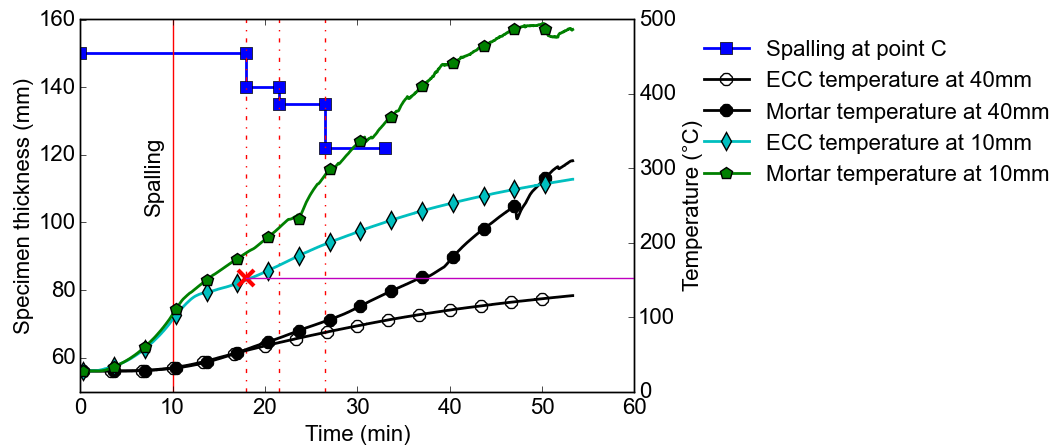


Fig. 10. Inference of spalling temperature

4 CONCLUSIONS

Based on the test results and analyses, the following conclusions can be drawn:

- (1) Explosive spalling of concrete M2 occurred in a progressive manner at a spalling temperature of about 150 °C. Although the size of the spalled-off concrete pieces was small, the ejection velocity of spalled-off debris could be as high as 13.2m/s.
- (2) Laser distance metre is an effective tool to measure spalling depth and corresponding spalling time of 1-D heated samples. The recorded spalling history offers valuable data for validating numerical models to predict progressive spalling scenario, which involves changing boundary conditions for heat and moisture transfer. In future, this tool can be explored to record spalling history of loaded concrete.

ACKNOWLEDGMENT

This material is based on research/work supported by the Land and Liveability National Innovation Challenge (L2NIC) Award No. L2NICCFP1-2013-4.

DISCLAIMER

Any opinions, findings, and conclusions or recommendations expressed in this material are those of the author(s) and do not necessarily reflect the views of the L2 NIC.

REFERENCES

1. G. Van der Heijden, L. Pel, O. Adan (2012). *Fire spalling of concrete, as studied by NMR*. Cem Concr Res 42(2). pp 265-271.
2. J.-C. Mindeguia, P. Pimienta, A. Noumowé, M. Kanema (2010). *Temperature, pore pressure and mass variation of concrete subjected to high temperature—experimental and numerical discussion on spalling risk*. Cem Concr Res 40(3). pp 477-487.
3. N. Toropovs, F.L. Monte, M. Wyrzykowski, B. Weber, G. Sahmenko, P. Vontobel, R. Felicetti, P. Lura (2015). *Real-time measurements of temperature, pressure and moisture profiles in High-Performance Concrete exposed to high temperatures during neutron radiography imaging*. Cem Concr Res 68. pp 166-173.
4. V. Kodur, Spalling in high strength concrete exposed to fire: concerns, causes, critical parameters and cures, ASCE Structures Congress, Philadelphia, Pennsylvania, United States, 2000, pp. 1-9.
5. Y.-S. Heo, J.G. Sanjayan, C.-G. Han, M.-C. Han (2010). *Synergistic effect of combined fibers for spalling protection of concrete in fire*. Cem Concr Res 40(10). pp 1547-1554.
6. F. Ali, A. Nadjai, G. Silcock, A. Abu-Tair (2004). *Outcomes of a major research on fire resistance of concrete columns*. Fire Safety J 39(6). pp 433-445.

7. İ. Yüksel, R. Siddique, Ö. Özkan (2011). *Influence of high temperature on the properties of concretes made with industrial by-products as fine aggregate replacement*. Constr Build Mater 25(2). pp 967-972.
8. M. Ozawa, S. Uchida, T. Kamada, H. Morimoto (2012). *Study of mechanisms of explosive spalling in high-strength concrete at high temperatures using acoustic emission*. Constr Build Mater 37. pp 621-628.
9. F. Roberto, M. Francesco Lo (2016). Pulse-Echo monitoring of concrete damage and spalling during fire. *9th International Conference on Structures in Fire*, Princeton USA, 2016. pp 851-858.
10. J.-C. Liu, K.H. Tan, D. Zhang (2017). *Multi-response optimization of post-fire performance of strain hardening cementitious composite*. Cem Concr Compos 80. pp 80-90.
11. K.D. Hertz (2003). *Limits of spalling of fire-exposed concrete*. Fire Safety J 38(2). pp 103-116.

EXPERIMENTAL STUDIES ON EARLY WARNING APPROACHES OF THE COLLAPSE OF STEEL PORTAL FRAME STRUCTURES IN FIRE

Ya-Qiang Jiang¹, Bo Zhong², Guo-biao Lou³, Jun-jun Liu⁴, Guo-jian Lu⁵, Jian-zhong Rong⁶

ABSTRACT

Sudden collapse of structures in fire poses great safety threat to both occupants and fire fighters stranded in building. Predicting a potential structural collapse is one of the most challenging tasks for fire commander and for the whole structural fire community. It is proposed by the authors that real-time monitoring on the global displacements of critical structural members could provide significant information to predict structural collapse in fire. For this purpose, three types of remote monitoring systems were developed by researchers at the Sichuan Fire Research Institute (SCFRI). Two full scale fire tests using steel portal frames were carried out by SCFRI and Tongji University, where the critical collapse criteria and the performances of different monitoring systems were investigated. Results show that among other systems the Radar Interferometry Monitoring System (RIMS) demonstrated the most versatile performance for real-time non-contact monitoring of structures in fire. It was also suggested that a combination of axial deformation and deformation rate of columns adjacent to fire could be used as reliable collapse criteria for the purpose of early warning. According to test results, this approach is able to predict structural collapse up to 7 mins in advance that is of great importance to fire fighters during their emergency operations.

Keywords: steel structure, structural collapse, early warning capability, non-contact remote monitoring

1 INTRODUCTION

Recent fire accidents that involved sudden structural collapse have drawn great attention to fire brigades and structural fire engineers around the world^[1]. Without accurate information of the structural status, fire fighters may be confused on when to break into or retreat from a burning building. Based a wide range of survey of fire fighters in China, decisions are usually made based on empirical judgments, such as cracks on the wall, sudden change of smoke or flame color, acoustic behaviours from structure, etc. However, due to lack of full understanding of the physics behind, it is not possible for firefighters to make sound decisions based on these empirical phenomena for all types of structures. After the collapse of WTC towers, researchers at the National Institute of Standards and Technology (NIST) investigated several potential tools and techniques

¹ Research Associate, Sichuan Fire Research Institute of Ministry of Public Security, Chengdu 610036, China.
e-mail: jiang.yaqiang@scfri.cn

² Research Associate, Sichuan Fire Research Institute of Ministry of Public Security, Chengdu 610036, China.
e-mail: zhongbo_scfri@163.com

³ Associate Professor, College of Civil Engineering, Tongji University, Shanghai, China
e-mail: gblou@tongji.edu.cn

⁴ Deputy Head of Institute, Sichuan Fire Research Institute of Ministry of Public Security, Chengdu 610036, China.
e-mail: junjunliu@scfri.cn

⁵ Deputy Head of Institute, Sichuan Fire Research Institute of Ministry of Public Security, Chengdu 610036, China.
e-mail: guojianlu@scfri.cn

⁶ Research Associate, Sichuan Fire Research Institute of Ministry of Public Security, Chengdu 610036, China.
e-mail: jianzhongrong@scfri.cn

for predicting structural collapse, including thermal image capturing, laser range finding, motion sensing, and acoustic monitoring^[2]. It is suggested that acceleration data obtained from buildings have shown the best potential for providing information concerning building stability and collapse. However, acquisition of acceleration data of a building requires pre-deployed or manually deployed sensors, which may be damaged in fire situations. In addition, it is also lack of reliable collapse criteria based on acceleration data. This paper investigates the possibility of using failure criteria of structural members as collapse criteria for the structural assembly or the whole structure. It also presents a novel approach that gives early warning of building collapse by remotely monitoring primary structural parameters (column axial deformation, deformation rate) of critical structural members. This approach was validated by full scale fire tests using steel portal frame structures, which suggest 3.5~7 mins early warning time ahead of the actual collapses.

2 EXPERIMENTAL DESIGN AND INSTRUMENTATION

2.1 Theoretical consideration

For any collapse warning techniques, it is important to use appropriate and reliable criteria in order to trigger a warning signal. The approach presented in this paper is based on the hypothesis that no matter how complex a building is, the failure criteria for its structural members like steel columns do not differ significantly from those in isolated situations like in furnace tests. Therefore, simple and robust failure criteria such as those present in ref^[3] for columns are adopted here. This provides great convenience for fire fighters who need only to focus on the deformation information of columns directly subjected to fire.

$$C = \frac{h}{100} \quad \text{in mm} \quad (1)$$

$$\frac{dC}{dt} = \frac{3h}{1000} \quad \text{in mm/min} \quad (2)$$

Where C represents the axial deformation of column, h is the height of column, with units both in mm.

2.2 Fire and structural design

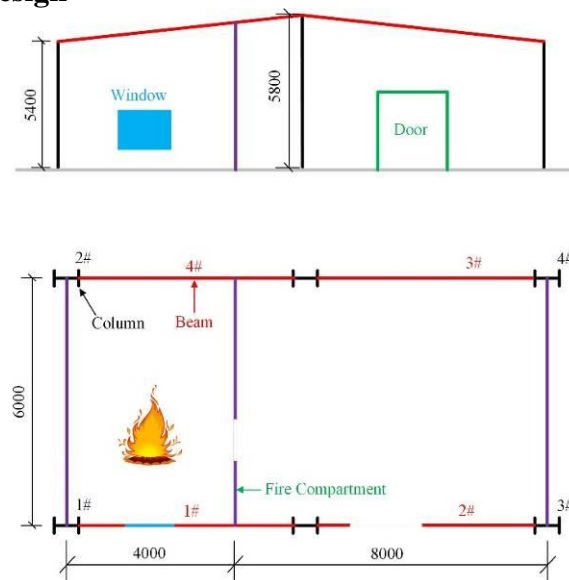


Fig. 1. Plan and elevation views of the structure in Test 1

Two full scale steel portal frame structures to simulate industrial buildings were built by SCFRI. The first structure is a one-story, two-bay steel portal frame with a 4m×6m fire compartment. Stone wool sandwich panels are used for the walls and roofs of the compartment. An inner separation wall with 3h fire resistance level was built to prevent fire propagation. The second

structure is also a one-story portal frame but with longer spans. The plan and elevation views of the two tests are shown in *Fig.1* and *Fig. 2*.

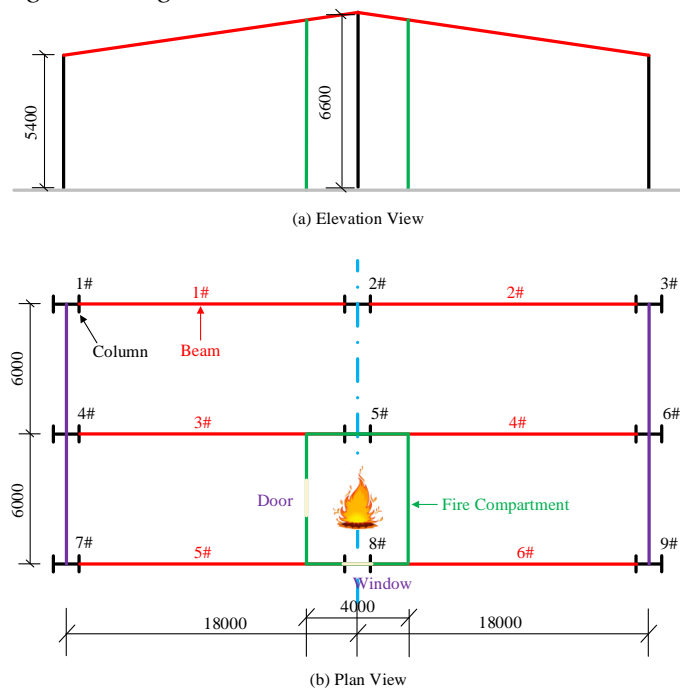


Fig.2. Plan and elevation views of the structure in Test 2

Sand bags were uniformly distributed on each of the steel beams to simulate the vertical load of 1100 kg, and the lateral wind load was also added on the columns located at the left end of the two structures.

The sizes of the fire compartments are identical in the two structures. Wood cribs were used to simulate post-flahover fires with peak heat release rates around 20 MW and 32 MW respectively in the two tests. Fire load densities are 3412.5MJ/m² and 5118.75MJ/m² respectively in the two tests, which are designed according to the levels of storage places of wooden furniture^[4].

2.3 Experimental instrumentation

The tested structures were heavily instrumented with conventional thermocouples and linear variable differential transducers (LVDT) to measure temperatures and deformations of critical regions and members, as shown in *Fig.3*. The LVDT values were used as benchmark data against the measurements from other remote monitoring devices.



Fig.3. Mounting of LVDT on the structure

Three kinds of remote monitoring systems are newly developed by the authors, including the Radar Interferometry Monitoring System (RIMS), the Laser Array Monitoring System (LAMS), and the Electronic Distance Measuring System (EDMS) that is developed based on commercially available total stations. These systems were used to measure the structural deformation at multiple critical positions, and their accuracy and performance in hash environment with smoke and flame will be compared against the LVDTs values. RIMS are used to monitor the deformation of column and the

displacement of beam at locations adjacent fire compartment, while other remote devices are used for locations that are less affected by fire smoke. The accuracy and performance of these systems in harsh environment with smoke and flames will be compared against the LVDTs values.

3 EXPERIMENTAL RESULTS

3.1 Visual observation

In both the two tests, the steel structures were not fire protected, which gradually deformed within the first 10 minutes as fire was developing. Local collapses of the two structures were observed at 19 min and 14 min respectively from ignition, as shown in *Fig.4* and *Fig.5*. It should be noted that it took longer time for the first structure towards collapse due to the presence of a 3h fire partition wall, which could share some of the loading from the beams and roof. It was also observed that the structural deformation began to accelerate just before their collapses. It is difficult to predict the time to collapse just by visual observation of the structures as the initial deformation took place at a millimetre scale, and for the fire fighters there may be no enough reaction time to the sudden arrival of collapse.



Fig.4. Structural collapse in Test 1



Fig.5. Structural collapse in Test 2

3.2 Collapse Criteria

Preliminary numerical investigations from the authors showed that, for a long span portal frame structure, the top of perimeter columns would firstly move outward due to thermal expansion of the beams, and then move inward as large displacements took place for the beams that produces load redistribution of the whole structure. This was visually observed in the Test 2 with the aid of LAMS which was not deployed in Test 1. As shown in *Fig.6*, LAMS was used to produce ten parallel laser beams with equal distance of 10cm, and four of them were just spotted on the top of the column. As the laser array was kept in a fixed status, the whole mechanism is like using a ruler to measure the relative displacement of a slowly moving object. It can be seen from the figure that the top of the column was moving outward during the first 11 mins 51secs, and then gradually started to move inward. If the moment at which the outward movement just begins to transfer into inward is defined as the critical point of collapse warning, then a valuable 2 mins 9secs would be obtained for arranging emergency evacuation on-site firefighters. An interesting phenomenon was observed from the video footage that the structure demonstrated intense shaking in the last 2 mins before collapse, which may be used as additional reference information for the judgment of collapse. Although the LAMS technique is visually easy to follow, it is acknowledged that this approach is

still a crude method due to an accuracy of 10cm that is unable to capture the whole deformation process.

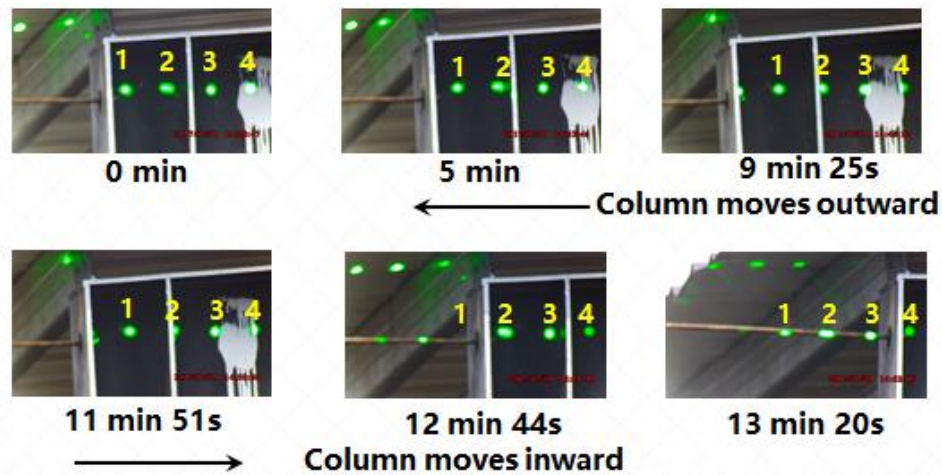


Fig.6. Monitoring column movement with LAMS

Results from Test 1 showed that the axial deformation of the steel column (column 1#) in the fire compartment started at around 7mins after ignition, as given in Fig. 7. Then the column seemed to gradually deform faster and it reached critical deformation rate at 14mins while it reached critical deformation value at 16mins. This suggests that Eq.(1) may be a more conservative collapse criteria that gave 2 mins more time for early warning in this case. Analyses of the column deformation in Test 2 also produces similar results that critical deformation rate was found at 10 mins, while critical deformation was found at 10.5 mins, as given in Table 1. This is able to give 3.5~4 mins early warning time prior to final collapse at 14 mins. Thus it could be concluded that by monitoring the column deformation in real-time it is possible to release collapse signal for early warning based on empirical formula as given Eq.(1)-(2).

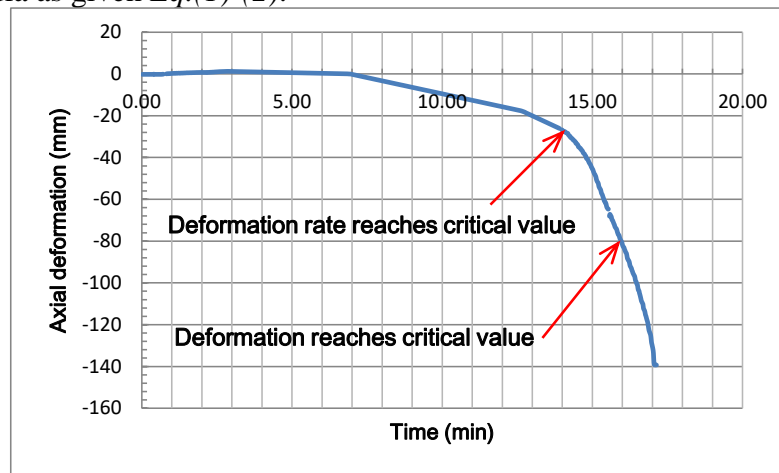


Fig.7. Axial deformation of steel column subjected to fire in Test 1

Table 1 Early warning time from different collapse criteria for Test 2

Collapse criteria (column)	Warning Point(min)	Warning time available(min)
Axial deformation: $h/100$ (mm)	10.5 (column 8#, LVDTs)	3.5
Axial deformation rate : $3h/1000$ (mm/min)	10 (column 8#, LVDTs)	4

3.3 Performance of different remote monitoring systems

By comparing the measured values from those remote monitoring systems and LVDT system, it is found that data from RIMS agreed well with the LVDT measurements, while the EDMS

measurements seemed very sensitive to hot smoke that presented large fluctuations. *Fig. 8* shows the temporal vertical displacement at the mid-span of the 6# beam, from which we can see that measurements from LVDT and RIMS were very close in the first 10 mins and some degree of variations were observed in the following 2 mins. But generally speaking, the RIMS seems to be a reliable remote monitoring approach in view of its accuracy and the ability against the interference of flame and hot smoke.

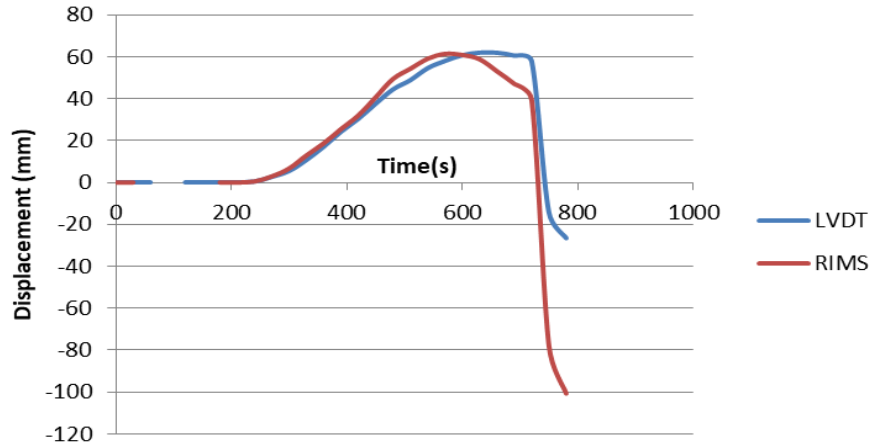


Fig.8. Displacement at the mid-span of the 6# beam

Displacement was also recorded at the mid-span of the 5# beam using both LVDT and EDMS. *Fig.9* shows the comparison of results from the two approaches, which suggests that the EDMS measures were much lower than the LVDT results prior to 12 mins that may be strongly affected by hot smoke escaped from the fire compartment.

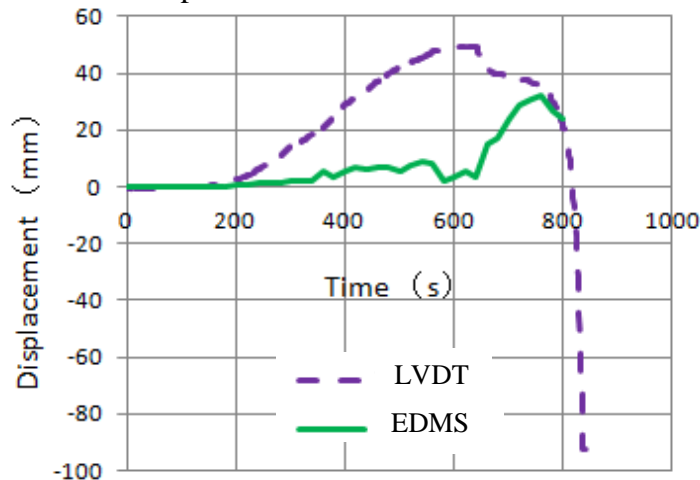


Fig.9. Displacement at the mid-span of the 5# beam

The commercially available video-based displacement measurement technique was also used in the two tests, however it was found that this kind of device seemed to be most affected by smoke and flames. As discussed in Section 3.2, the LAMS was useful for on-site visual observation of the movement of critical structural members.

4 DISCUSSION AND CONCLUSIONS

It seems reasonable to use structural deformation or deflection as the key parameter to establish the early-warning methodology concerning collapse in fire, as it directly reflects the status of a structural member. Using the currently available failure criteria of column as structural collapse criteria is able to give several valuable minutes before the final collapse that were tested against two full scale steel portal frame structures, although more validations should be performed against other types of structures. Remote monitoring system designed based on this idea should be resilient to

challenging interference including hot smoke, daylight difference, all-weather conditions etc. Results from full scale tests suggest that, among other remote monitoring devices, the Radar Interferometry Monitoring System (RIMS) that was validated against full scale tests, seems to be the most promising approach with regard to that aspect.

This paper presented the tests results in terms of early warning capability of structural collapse that is particularly important for firefighters. Discussions on the results in perspective of structural fire design will be presented in a separate paper submitted to SiF2018.

Acknowledgments

This research is funded by the National Key R&D Program of China under Grant No. 2016YFC0800604, the Key Program of the Fire Department of the Ministry of Public Security of China under Grant No. 2015XFGG06, and the SCFRI Grant with No. 20188806Z.

REFERENCES

1. Buchanan, A(2008). *The Challenges of Predicting Structural Performance in Fires*. Fire Safety Science 9, pp 79-90.
2. Stroup D.W., Bryner N.P.(2007). *Structural Collapse Research at NIST*. In Proceedings of the 11th International Interflam Conference, 2007:593-604, London.
3. Fire-resistance tests-Elements of building construction-Part 1: General requirements. ISO 834-1:1999.
4. Morgan J. Hurley (Editor-in-Chief,2016). *SFPE Handbook of Fire Protection Engineering*(5th ed).Springer:New York

Experimental Research and any Other

INSTANTANEOUS STIFFNESS CORRECTION FOR HYBRID FIRE TESTING

Ramla Qureshi¹ and Negar Elhami-Khorasani²

ABSTRACT

Standard fire resistance tests do not capture the continuity and restraining effects between different structural members of a building during a fire event. By providing actuators at the specimen boundaries, contributions of adjacent structural elements can be replicated in real time in the form of a varying force-displacement response. This method, termed as Hybrid Fire Testing, relies on the concept of substructuring, but the constantly degrading stiffness of the burning physical specimen induces instabilities within the actuator control, leading to loss of equilibrium at the interface of the numerical and physical substructures. This paper presents a compensation scheme that calculates the instantaneous secant stiffness of the physical substructure, by applying a Broyden update of the stiffness matrix to various formulations for actuator control. The fire-performance response history of the specimen is taken into account to provide a reasonable value of the instantaneous stiffness for each time step within the hybrid process. The presented method was validated in a virtual environment for both modes of actuator control formulation, i.e., displacement and force-based. Additionally, the applicability towards variations in initial stiffness ratio between the specimen and surrounding structure was also confirmed.

1 INTRODUCTION

A structurally significant fire event, if not controlled, might have globalized detrimental effects to a structure. Unfortunately, limited full-scale experimental data exists that could help engineers fully understand realistic structural response under fire. While full-scale building tests are possible, these are highly expensive and time-consuming, and require specialized laboratory environment and full-scale models. Conversely, simpler tests of individual building members in a standard furnace (i.e., standard fire resistance tests) do not capture the global stiffness, load redistribution, and redundancy of the boundary structure. These tests provide only member-level, *passive* end conditions that do not reflect the true performance of a burning building as a whole. Research is now being conducted to provide *active* boundary conditions when testing for fire, where behaviour of the structure surrounding an element is simulated in real time in order to continuously update the applied boundary effects. This technique of hybrid simulation is borrowed from the field of earthquake engineering, and has been termed here as Hybrid Fire Testing, or HFT. In this method, a structure is divided into two substructures: (a) a physical substructure “PS”, that can be a configuration of individual members being tested in the laboratory; and (b) a numerical substructure “NS”, which is a computer simulation of the remaining building. The interaction of the physical and numerical substructures is communicated within the hybrid framework in the form of a varying force-displacement response via actuators in feedback control. *Fig. 1a* presents a schematic for a typical real-time hybrid simulation with due compensations.

¹ PhD Candidate, Department of Civil and Environmental Engineering, University at Buffalo, USA.
e-mail: ramlakar@buffalo.edu

² Assistant Professor, Department of Civil and Environmental Engineering, University at Buffalo, USA.
e-mail: negarkho@buffalo.edu

Initial applications of HFT involved testing for changes in column axial load due to increase in temperature. By assuming an effective stiffness for the rest of the building, Korzen [1] measured and adjusted the thermally induced axial forces within the numerical simulation model by assigning a single thermal degree of freedom, and applied the calculated resulting displacements on a column through an actuator in displacement control. Over a decade later, in 2013, Mostafaei [2], [3] tested a column subjected to axial and elevated thermal loading in a furnace chamber. The remaining building was analysed numerically with the help of a numerical model simulated using the finite element software SAFIR [4]. A 5-minute time step allowed for the user to manually record the axial deformations observed for the physical specimen to the computational portion of the test, which in turn calculated resulting loads. These loads were then once again manually fed to the physical specimen by means of actuators and the hybrid loops were repeated. However, the above mentioned procedure is only conditionally stable. As intrinsically stiff systems, actuators are good in position control [5], however a force control setup leads to a much more stable test in case of stiffer structures [6]. Previous research shows both force control and position control procedures may experience instabilities during HFT even within a virtual environment [7], [9]. Sauca et al. [7] observed that formulations where solution of nodal interactions between the two substructures was solely dependent on characteristics of the NS were sensitive to the initial stiffness ratio between the NS and PS. To solve the instability issues, Tondini et al. [8] applied Lagrangean optimization in position control to ensure numerical continuity at the interface of the two substructures. However, this was done without updating stiffness of the simulated physical substructure at each time step. Whyte et al. [9] tested a physical steel coupon in displacement control, but instabilities were identified similar to those ascertained by Sauca et al. Temperature was increased only up to 200 °C for this test, and updating modulus of elasticity or yield strength of steel was disregarded throughout the test. As there was no estimate of an expected threshold value for the convergence of updating displacement, this test gave unrealistic intermittent force/displacements results. In an actual fire, the stiffness of the PS will degrade due to heat effect, and assuming a constant stiffness may lead to instabilities. Therefore, there is need to provide a compensation scheme that takes into account the changes in structural stiffness throughout the duration of the test.

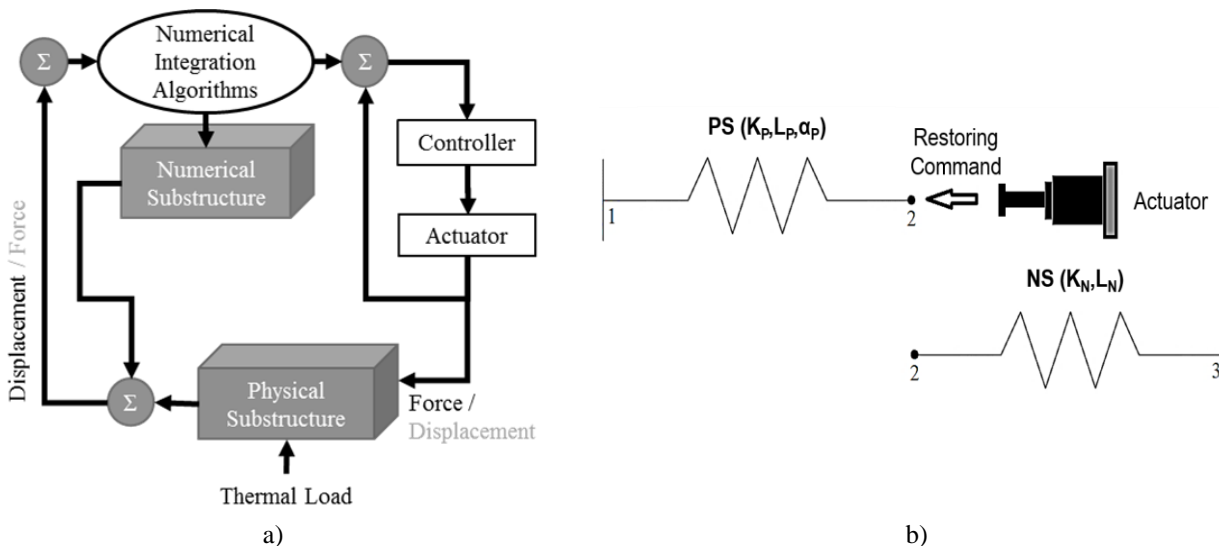


Fig. 1. a) Schematic for a typical real-time hybrid simulation; b) Two-spring model for virtually conducted HFT

2 SUBSTRUCTURING APPROACH FOR FEEDBACK FORMULATION

Partitioning of the equation of motion for a hybrid problem is led either by displacement- or force-based formulation for actuator control. Consider for example, the simple, two-member truss system with a singular interfacing degree of freedom, at node 2 as shown in Fig. 1b. Both the numerical

substructure (NS) and physical substructure (PS) are structural steel members that are modelled within a MATLAB [10] environment. For the purpose of this research, a lumped mass is assumed. The NS is taken as cold throughout duration of the HFT simulation, and therefore has constant stiffness throughout the duration of fire. For the sake of simplicity, a constant temperature is assumed throughout the cross-section of the PS at any given time step, and therefore no moments are considered. Heat flow is not considered. Thermal coupling is not taken within the scope of this paper, and the HFT is taken to be running in real time. No initial external load is applied to the structure. Disregarding inertial effects, at least for the beginning of the fire event, the direct stiffness method can be used to write total equilibrium conditions as:

$$\begin{bmatrix} K_{PS} & -K_{PS} & 0 \\ -K_{PS} & K_{PS}+K_{NS} & -K_{NS} \\ 0 & -K_{NS} & K_{NS} \end{bmatrix} \times \begin{bmatrix} \Delta_1 \\ \Delta_2 \\ \Delta_3 \end{bmatrix} = \begin{bmatrix} f_{M1} \\ f_{M2} \\ f_{M3} \end{bmatrix} - \begin{bmatrix} f_{TP1} \\ f_{TP2} \\ 0 \end{bmatrix} \quad (1)$$

where K_{PS} is the stiffness of the physical substructure,

K_{NS} is the stiffness of the numerical substructure,

Δ_i are the mechanical displacements at nodes $i = 1$ to 3 , where values of Δ_1 and Δ_3 should be zero.

f_{Mi} are the mechanical forces for nodes $i = 1$ to 3 , where value of f_{M2} should be zero.

f_{TPi} are the temperature loads for nodes $i = 1$ to 2 , as only the PS is hot.

If Eq. (1) is substructured for a displacement-based formulation, thermal elongation is restrained, generating an axial force internally. At each time step, the actuator measures this constraining force generated within the NS. In this study, the constraining force is numerically simulated as a function of the thermal elongation of the PS times the available stiffness. Loss of compatibility happens when, during the hybrid loop, due to the continuously increasing thermal elongation and time lag in the process, the force in the actuator, $F_{Actuator}$ no longer matches the actual mechanical force, f_{MNS2} required at node 2. The incremental actuator mechanical displacement command at time step t , $\Delta_{MPS2(t)}$ can then be calculated as:

$$\Delta_{MPS2(t)} = \Delta_{MPS2(t-1)} + \left(\frac{Error(t)}{K_{NS} + K_{PS}^*} \right) \quad (2)$$

where $Error$ is the quantification of compatibility loss, and is equal to $F_{Actuator} - f_{MNS2}$

K_{PS}^* is the continuously varying stiffness of the physical specimen.

On the other hand, for a force-based formulation, the mechanical displacement at node 2 due to heating, Δ_{MPS2} is measured. Here, this displacement is simulated as a function of the addition of the mechanical force in the previous time step, $f_{MNS2(t-1)}$ and the force caused by thermal elongation, $f_{TP2(t)}$ divided by the available stiffness of the PS at the same time step, $K_{PS(t)}^*$. The position of the actuator, replicating the NS, is a function of NS stiffness and force, $\Delta_{NS2} = F_{Actuator(t-1)} / K_{NS}$. Compatibility at node 2 is disturbed when Δ_{NS2} is not at Δ_{MPS2} , where it mechanically should be. However, this can be resolved by correctly predicting and updating the force in the actuator. The mechanical interface force for each time step can then be computed as:

$$f_{MNS2(t)} = f_{MNS2(t-1)} - Error(t) \left(\frac{K_{NS} \times K_{PS}^*}{K_{NS} + K_{PS}^*} \right) \quad (3)$$

where $Error$ is equal to $\Delta_{NS2} - \Delta_{MPS2(t)}$ in this formulation.

In both formulations, the updated command equation depends on the constantly decreasing stiffness of the physical substructure, which poses a risk of gradual numerical instability, and therefore loss of actuator equilibrium. A few cases are discussed in the following section.

3 INSTABILITIES

One option applied by previous researchers [7], [8] was to estimate an initial value of stiffness for the physical substructure, and keep it constant throughout the entire fire time history. This is problematic, as an overestimate of the stiffness value could lead to unusually high actuator command outputs, and the actuator can lose compatibility and become unstable. For displacement control formulation, only while the NS is assumed to remain cold, and especially for cases like testing a singular beam in a building structure, where mostly $K_{PS}^* \ll K_{NS}$, the displacement update might not be much effected by the decrease in value of K_{PS}^* . This is because, for displacement formulation, the ambient stiffness of the NS would have a much more significant consequence on the results from Eq. (2) as compared to that of the PS. In all other cases, and especially for force control (which serves the cause of HFT better due to the expectation of very small thermal elongations, at least at the start), as soon as the PS stiffness reduces, incorrect estimation can induce large instability within the HFT process, and can even lead to specimen or actuator attrition.

To explain; consider the simple, two spring model from Fig. 1b. Adapted from Sauca et al. [7], both the NS and PS are taken as steel bars with initial Young's modulus $E_{PS} = E_{NS} = 210000 \text{ N/mm}^2$, $\alpha_{PS} = \alpha_{NS} = 0.000012 \text{ /}^\circ\text{C}$, and effective yield strength, $f_y = 355 \text{ MPa}$; all at ambient temperature. However, it should be noted that for this research, all these values have been modelled to gradually change according to the progression of heat in the PS as per the Eurocode reduction factors for carbon steel at elevated temperatures [11]. Cross-sectional area is taken as $A_{PS} = A_{NS} = 20100 \text{ mm}^2$ for both bars. Therefore, stiffness is only varied here based on the length of either substructure. Here, for the case of PS stiffness smaller than that of NS, i.e., $K_{PS} < K_{NS}$, PS is taken to be $L_{PS} = 3.0 \text{ m}$ long, while length of NS is taken as $L_{NS} = 1.5\text{m}$. Alternatively, for $K_{NS} < K_{PS}$ the values of length are taken vice versa. Heat is applied to the physical substructure at a constant rate of $1 \text{ }^\circ\text{C/s}$. Here, once again, the NS is taken as cold for the sake of simplicity.

Formulation detailed in the previous section and material data mentioned above were used to conduct a virtual HFT in the MATLAB environment. Fig. 2 shows results from the force-based formulation for a case of $K_{PS} < K_{NS}$, and compares them with a target curve obtained from SAFIR for a similar but non-substructured test. It can be observed that the HFT system first oscillates near the target value, and then becomes completely unstable, giving extremely large, abnormal values of force. Therefore, it was decided to apply an iterative update process that provides an incremental convergence for the actuator response command.

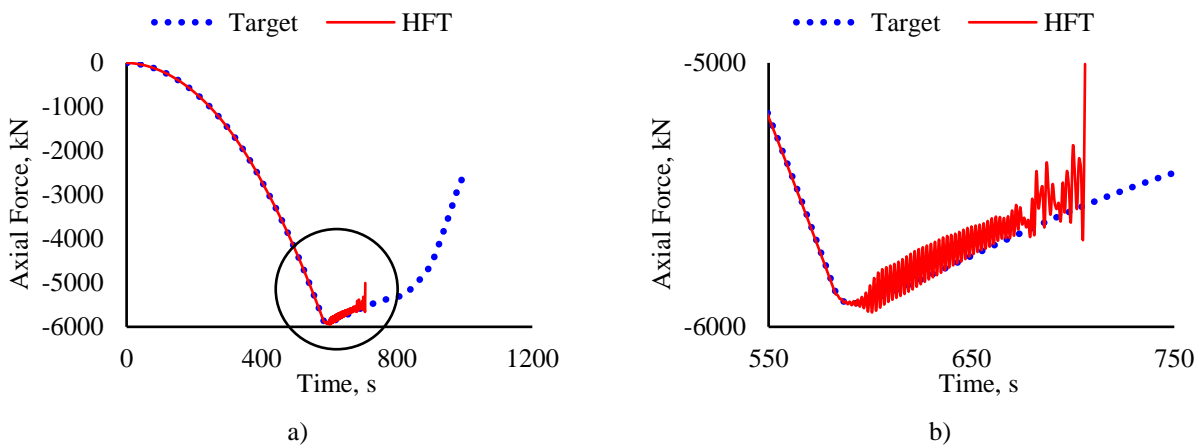


Fig. 2. a) Instability with the force-based HFT process; b) encircled part in (a) zoomed-in for better visual inspection

4 SECANT STIFFNESS UPDATE

In this section, the loss of equilibrium in the hybrid process is corrected by updating the actuator command, which depends on stiffness of the PS. Borrowing knowledge from the field of earthquake engineering, this paper adapts the method of Broyden update of the Jacobian for stiffness matrix of the physical substructure, as presented by Nakata et al. [12], and investigates its application to HFT by determining the instantaneous secant stiffness based on the previous history of the physical substructure performance.

A compensation scheme is presented for mitigating instabilities previously experienced in calculating the structural stiffness of a steel member, as it progressively degrades during fire. If the HFT process is conducted in n time steps, the initial (ambient) value of stiffness of the PS is only used when the incremental temperature, $\Delta T = 0$. As the temperature gradually increases, an instantaneous secant stiffness update is calculated for each time step, Δt taking into account the recent history of structural response as:

$$K_{PS(t)}^* = \left\| \left\| K_{PS(t-1)}^* + \frac{\overline{\Delta f}_{MNS2} - K_{PS(t-1)}^* \times \overline{\Delta}_{MPS2}}{\overline{\Delta}_{MPS2}} \right\| \right\| \quad (4)$$

where $\overline{\Delta f}_{MNS2}$ is the variation in value of force calculated from previous time steps, and is equal to

$$\begin{aligned} & f_{MNS2(t)} - f_{MNS2(t-1)} \text{ for displacement-based, and} \\ & f_{MNS2(t-1)} - f_{MNS2(t-2)} \text{ for force-based formulation;} \end{aligned}$$

$$\begin{aligned} & \overline{\Delta}_{MPS2} \text{ is the variation in displacement calculated from previous time steps, and is equal to} \\ & \Delta_{MPS2(t-1)} - \Delta_{MPS2(t-2)} \text{ for displacement-based, and} \\ & \Delta_{MPS2(t)} - \Delta_{MPS2(t-1)} \text{ for force-based formulation;} \end{aligned}$$

and $K_{PS(t)}^*$ is an updated PS stiffness at the t -th time step.

Applying the updated stiffness from Eq. (4), the actuator command can now be calculated using either of Eq. (2) or Eq. (3), based on the choice of HFT formulation. This is an explicit integration scheme that aims to control the command exerted on the specimen in comparison to a desired target. As the stiffness is now updated incrementally, the hybrid procedure does not fall apart owing to abrupt material or geometric nonlinearity. An additional tolerance limit sets the convergence control and prevents instability due to the predictor-corrector nature of the update. This stiffness update is also computationally fast and helps speed up the HFT process.

5 APPLICATION TO VIRTUAL HFT CASE STUDY

The instantaneous stiffness update method presented in this paper was applied to a virtual HFT to validate its applicability for various HFT methods. Continuing from formulation described for the two-spring example presented previously, duration of the hybrid test is discretized for the time increment, $\Delta t = 1$ s. Within MATLAB environment, the previously mentioned temperature load is applied to the PS steel bar, and material degradation is virtually modelled according to the temperature dependent stress-strain relations from Eurocode. Therefore, at each time step, the stiffness of the physical specimen had to be re-estimated. Both cases of initial stiffness ratio variations, i.e., $K_{PS} < K_{NS}$ and $K_{PS} > K_{NS}$ were modelled to confirm that the method is not selectively stable. Additionally, both displacement and force based formulations were created for comparison purposes. It should be noted here that actuator delays, equipment noise, and other environmental factors can also cause instabilities, but were not considered as within the scope of

this paper. All HFT results were plotted together with the target curve obtained from SAFIR for a non-hybrid structural analysis for the same structure, but with a lumped mass and uniform cross-sectional temperature, and are presented in *Figs. 3* and *4*.

Figs. 3a and *b* present results obtained for actuator in displacement control for both cases of variation of initial stiffness ratio. It can be observed that the HFT provisional results are in good agreement with the target curve. Similarly, *Figs. 4a* and *b* display results obtained for a force-based formulation. For the case of *Fig. 4a*, where $K_{PS} < K_{NS}$ some slight instability is still present at the tail-end of the HFT response. This can be reduced by changing the convergence tolerance value for the stiffness formulation, based on how the actuator has been tuned.

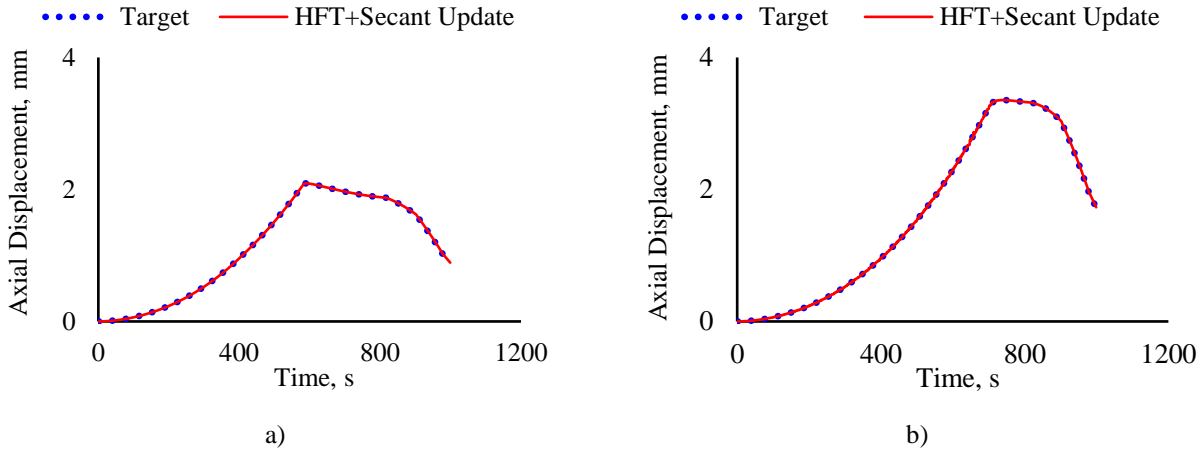


Fig. 3. Axial displacement obtained from displ. based formulation for a) $K_{PS} < K_{NS}$; and b) $K_{PS} > K_{NS}$

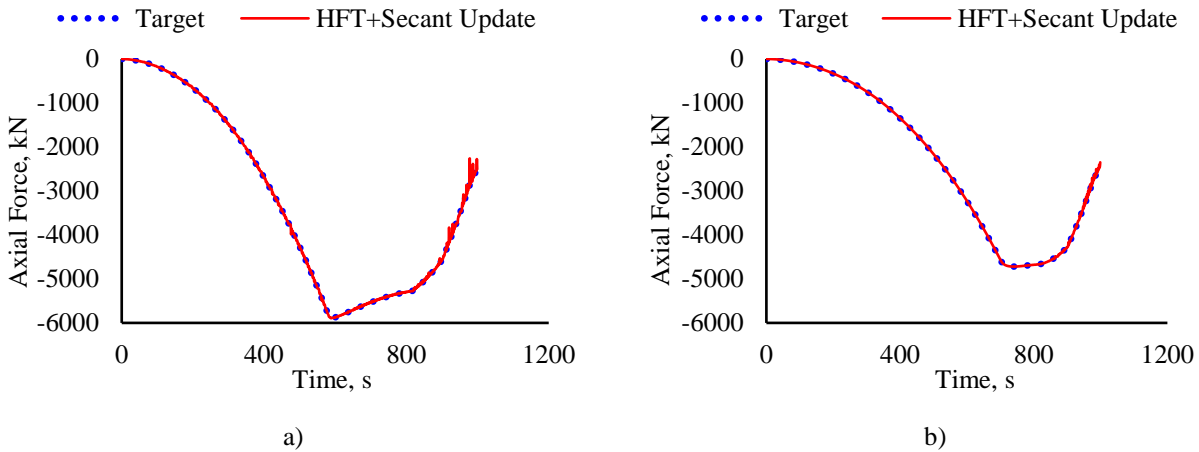


Fig. 4. Axial force obtained from force based formulation for a) $K_{PS} < K_{NS}$; and b) $K_{PS} > K_{NS}$

6 CONCLUSIONS

The concept of a substructured hybrid simulation was applied to provide *active* boundary conditions to a conventional structural fire test, in order to incorporate the real time, *active* contribution of the boundary structure. Combining knowledge from both earthquake and fire engineering, this paper presents a novel contribution to account for the continuously changing stiffness of the heated physical substructure. Both force and displacement formulations were modelled in a virtual MATLAB environment. Real time, temperature dependent material degradation was considered for the physical substructure. A predictor-corrector compensation scheme in the form of an instantaneous secant stiffness update was applied for mitigating instabilities within the process, and

to provide a plausible threshold value of actuator command. The implemented methodology is tested for two cases with different initial stiffness ratios between the NS and PS. Future work includes experimental validation for the presented methodology for an actual, real time hybrid fire test.

REFERENCES

1. Manfred Korzen., G. Magonette, and P. Buchet (1999). *Mechanical loading of columns in fire tests by means of the substructuring method*.
2. Hossein Mostafaei (2013). *Hybrid fire testing for assessing performance of structures in fire—Methodology*. Fire Safety Journal. 58: p. 170-179.
3. Hossein Mostafaei (2013). *Hybrid fire testing for assessing performance of structures in fire—Application*. Fire safety journal. 56: p. 30-38.
4. Jean-Marc Franssen (2005). *SAFIR: A thermal/structural program for modeling structures under fire*. Engineering Journal-American Institute of Steel Construction Inc. 42(3): p. 143-158.
5. Mettupalayam V. Sivaselvan, Andrei M Reinhorn, Xiaoyun Shao, and Scot Weinreber (2008). *Dynamic force control with hydraulic actuators using added compliance and displacement compensation*. Earthquake Engineering & Structural Dynamics. 37(15): p. 1785-1800.
6. Stathis N. Bousias (2014). *Seismic Hybrid Simulation of Stiff Structures: Overview and Current Advances*. Journal of Structures, 2014.
7. Ana Sauca, Thomas Gernay, Fabienne Robert, Nicola Tondini, and Jean-Marc Franssen (2016). *Stability in hybrid fire testing*. in *Structures in Fire (Proceedings of the Ninth International Conference)*. DEStech Publications, Inc.
8. Nicola Tondini, Giuseppe Abbiati, Luca Possidente, and Bozidar Stojadinovic (2016). *Hybrid simulation applied to fire testing: a newly conceived numerical framework*. in *Proceedings of the 6th European Conference of Structural Control and Health Monitoring*. EACS.
9. Catherine A Whyte, Kevin R Mackie, Bozidar Stojadinovic (2015). *Hybrid simulation of thermomechanical structural response*. Journal of Structural Engineering. 142(2): p. 04015107.
10. Matlab Users Guide (1998). *The mathworks*. Inc., Natick, MA. 5: p. 333.
11. British Standard (2006). *Eurocode 3—Design of steel structures—*. BS EN 1993-1. 1: p. 2005.
12. Narutoshi Nakata, B. Spencer, and Amr S. Elnashai (2006). *Mixed load/displacement control strategy for hybrid simulation*. in *Proceedings, 4th International Conference on Earthquake Engineering*.

Experimental Research and any Other

EXPERIMENTAL INVESTIGATION OF THERMOMECHANICAL BEHAVIOUR OF THE CARBON TEXTILE REINFORCED CONCRETE COMPOSITE: EFFICIENCY COEFFICIENT OF CARBON TEXTILE AT ELEVATED TEMPERATURE

Manh Tien Tran¹, Xuan Hong Vu², Emmanuel Ferrier³

ABSTRACT

The carbon textile reinforced concrete (carbon TRC) can be used for the reparation and the reinforcement of civil engineering works thanks to its advantages as good supported load capacities, high strength and Young's modulus to traction, etc. This paper presents the experiment results on carbon TRC and carbon textile specimens in the range of temperatures from 25°C to 600°C. The evolution of some characteristics of TRC (the ultimate stress, different characteristic stresses, the initial stiffness, the stiffness of the post cracked composite) and mechanical properties of carbon textile (the ultimate strength, Young's modulus) was experimentally identified. In comparison between both results of the TRC and carbon textile, this study shows that the efficiency coefficient of carbon textile varies as a function of the temperature.

Keywords: Textile reinforced concrete (TRC), carbon textile, elevated temperature, thermo-mechanical behaviour, stress-strain curve

1 INTRODUCTION

Carbon textile reinforced concrete (carbon TRC) has been increasingly and widely used for the strengthening or reinforcement of the civil engineering structures thanks to its advantages as good supported load capacities, high strength and Young's modulus to traction, etc. In carbon TRC, carbon textile plays a very important role in the carrying capacity and stiffness. So, carbon textile is manufactured as commercial products for application in TRC to strengthen or reinforce civil engineering structures (slab, beam, column, etc.). Even if civil engineering structure strengthened by carbon TRC is simultaneously subjected to mechanical loading and elevated temperatures of fire, carbon TRC can maintain its resistance thanks to the elevated temperature working capacity of carbon textile. In the literature, there were few studies on the behaviour of fibre textiles and TRC under the mechanical load and temperature actions. There were direct tensile tests to characterize the residual or thermomechanical behaviour of fibre textiles and TRC at different temperatures. In their recent work, Rambo et al [1-3] carried out the tests on samples of basalt textile and basalt TRC in residual and hot conditions with different temperature levels. Colombo et al [4] carried out tensile tests on the TRC specimens based on the alkali-resistant (AR) glass fibres reinforced Portland cement matrix at different temperatures. Nguyen et al [5] realized the direct tensile tests at elevated temperatures on the TRC based on the sulfo-aluminous matrix reinforced with AR glass fibres for the characterization of TRC thermomechanical behaviour. TLAIJI et al [6] recently studied experimentally and comparatively thermomechanical and residual behaviours of AR glass TRC subjected to elevated temperature loading. To the best of our knowledge, no results are

¹ PhD Candidate, Université de LYON, Université Claude Bernard LYON 1; Laboratoire des Matériaux Composites pour la Construction LMC2; Hanoi Univ. of Mining & Geology, Dept. of Mining, Hanoi, Vietnam; e-mail: manh-tien.tran@etu.univ-lyon1.fr

² Associated Professor, Université de LYON, Université Claude Bernard LYON 1; Laboratoire des Matériaux Composites pour la Construction LMC2, France; e-mail: Xuan-Hong.Vu@univ-lyon1.fr

³ Professor and Director, Université de LYON, Université Claude Bernard LYON 1; Laboratoire des Matériaux Composites pour la Construction LMC2; e-mail: Emmanuel.ferrier@univ-lyon1.fr

available concerning experimental tests with simultaneous mechanical and elevated temperature loadings carried out on carbon textile and carbon TRC. There are also not yet results regarding the efficiency coefficient of carbon textile at elevated temperatures. This paper presents an experimental study on the direct tensile behaviour of carbon textile and carbon TRC subjected to simultaneous actions of mechanical loading and elevated temperatures. By using the thermomechanical machine (TM20kN-1200C), direct tensile tests on the test specimens were carried out at temperatures from 25°C to 600°C. The purpose of this paper is to characterize the thermomechanical behaviours of carbon textiles and of carbon TRC at elevated temperature in order to find the efficiency coefficient of carbon textile in its TRC at elevated temperatures.

2 EXPERIMENTAL WORK

This section presents the equipment used, the TRC and specimens, the summary of specimens and tests and the test procedure.

2.1 Equipment used

The experimental study of carbon textile test specimens was carried out by using a universal traction machine (TM20kN-1200C) at the LMC2 laboratory, France. This machine has a mechanical capacity of 20kN and is equipped with a cylindrical furnace that can generate temperature loadings around of specimen potentially up to 1200°C. The maximum heating rate of this furnace is 30°C/min. The temperatures in the furnace are controlled by integrated thermocouples. This experimental device makes it possible to apply simultaneous tensile mechanical and elevated temperature loadings on sample. The laser sensor equipped on the machine is used to measure the longitudinal deformation of test specimens at elevated temperatures (non-contact measurement method). This equipment allowed to characterize thermomechanical behaviours of glass TRCs [5,6] and carbon fibre reinforced polymer [9].

2.2 Carbon TRC and specimens

The concrete matrix used in this study was designed following the compressible packing model routine [7,8] as in the works of Rambo et al [1-3], and then adapted to the laboratory condition to produce carbon TRC specimens. This matrix consists of a silico-aluminous-calcium synthetic aggregates obtained by melting (containing about 40% of alumina), and a cement essentially composed of calcium aluminates making a binder for refractory applications. For a small thickness of application, the maximum aggregate diameter had to be less than 1.25 mm, and a small amount of superplasticizer and viscosity modifier agent (see table 1) was added in the component of the concrete. The water/ cement ratio of this concrete was 0.35. Table 1 gives the composition of the concrete matrix. The continuous carbon textile used (GC2 carbon textile) in this experiment is an industrial product that was manufactured in factory. The GC2 carbon textile was made of bi-directional, high-strength carbon fibre mesh for low-thickness structural reinforcements. The geometry of the grid in the longitudinal and transverse directions is 17 mm x 17 mm, the warp and the weft are formed by about 3200 monofilaments (longitudinal direction: 2 x 1600 tex/ strand and transverse direction: 1 x 3200 tex /strand). The properties of the GC2 carbon textile are summarized in Table 2. The test specimens in this study were prepared by hand in the laboratory. For GC2 carbon textile specimens, a longitudinal yarn (the warp) of the textile was cut to obtain GC2 carbon textile samples of 750 mm in length. For carbon TRC (called F.GC2 in this study), rectangular plates measuring 740 mm x 515 mm x 11.5 mm (length x width x thickness) were produced using a lamination technique. In this study, a single layer of carbon textile (volume fraction: 1.79%) was used as reinforcement in the F.GC2. After 28 days in a room condition, the rectangular plates were cut, resulting in 9 specimens of 740 mm x 51.5 mm x 11.5 mm (length x width x thickness). To prepare the specimen for the test, four aluminium plates were glued to the ends of each specimen using an epoxy adhesive (Eponal 380) to ensure transfer efficiency of the mechanical load and to

prevent failure in the clamps. The cross-sectional area was determined by the average of three measurements (width and thickness) at three different points of each F.GC2 sample.

Composition	
Aggregate (kg/m ³)	1390.50
Cement (kg/m ³)	554.90
Superplasticizer (kg/m ³)	3.60
Viscosity modifier agent – VMA (kg/m ³)	0.42
Water (kg/m ³)	194.24
Water/cement ratio	0.35

Table 1. Mixture composition of the TRC matrix

Properties	GC2
Density (g/cm ³)	1.79
Grid geometry (longitudinal x transverse spacing)	17x17 (mm)
Type of coating	Amorphous silica
Individual strand cross-sectional area	1.795 mm ²

Table 2. Properties of the studied carbon textile

2.3 Summary of specimens and tests

Table 3 shows the list of the specimens and the tests carried out. There are 28 tests carried out on the specimens of carbon textile and carbon TRC at temperature levels varying from 25°C to 600°C.

Table 3. List of tests carried on the specimens of carbon textile and carbon TRC

Designation of the specimens	Dimensions of the specimens [cross section, S (mm ²); length, l (mm)]	Temperature (°C)	Exposure duration	Number of tests
GC2-25-a,b,c	S = 1.795 (mm ²) ; l = 750 (mm)	25	-	3
GC2-200-a,b,c		200	1h	3
GC2-400-a,b,c		400	1h	3
GC2-500-a,b,c		500	1h	3
GC2-600-a,b		600	1h	2
F.GC2-25-a,b,c	S=11.5 x 51.5 (mm ²); l=740 (mm)	25	-	3
F.GC2-200-a,b,c		200	1h	3
F.GC2-400-a,b,c		400	1h	3
F.GC2-500-a,b,c		500	1h	3
F.GC2-600-a,b		600	1h	2
Total of tests				28

2.4. Test procedure

The loading application chosen for the tests carried out on carbon textile and TRC specimens consists of the following three phases as in [5-6, 9]: the first test phase consists of increasing temperature around sample to the desired temperature level; the second test phase consists of maintaining the desired temperature level for a period of one hour in order to homogenize the temperature around carbon textile specimens or TRC ones; the third test phase consists of applying monotonical quasi-static mechanical load to specimen until its rupture.

3 RESULTS

This section shows results of tests carried out on carbon textile specimens and TRC ones.

3.1 Results of carbon textile specimens

Figure 1 shows the "stress - strain" relationships of the thermomechanical behaviour of GC2 carbon textile for temperatures ranging from 25°C to 500°C. From Figure 1, it can be seen that the GC2 carbon textile typically gives a quasi-linear behaviour up to the failure. Table 4 shows the experimental results on all of GC2 textile samples.

3.2 Results of carbon TRC specimens

Figure 2 shows the "stress - strain" curves of the thermomechanical behaviour of F.GC2 composite for temperature levels ranging from 25°C to 600°C. Similar to the GC2 carbon textile specimens tested in thermomechanical condition, a reduction in tensile strength is clearly observed from the stress-strain curves of all TRC specimens. From Figure 2, it can be observed that the F.GC2 composite typically gives a hardening behaviour with three distinguishable phases up to the failure (as in the literature) for temperature levels ranging from 25°C to 200°C. At 400°C, this TRC

provides a hardening behaviour with two phases (specimen is broken in the cracking phase). At temperature above 400°C, thermomechanical behaviour of carbon TRC specimens was quasi-linear up to their failure. Evaluation results of all curves, shown in Figure 2, are given in Table 5 below.

4 DISCUSSION

This section presents the evolution of the thermomechanical properties of the GC2 carbon textile and the F.GC2 composite as a function of the temperature.

4.1 Evolution of the properties of the GC2 carbon textile as a function of the temperature

Figures 3a,b show the mechanical property evolution of the GC2 carbon textile as a function of the temperature. The normalized mechanical properties (normalized ultimate stress and Young's modulus) are defined as the ratio between the mechanical property at a temperature (T) and that at room temperature. The GC2 carbon textile gives almost linear reduction of the normalized ultimate stress values when the temperature increases from 25 °C to 600 °C. At 200 °C, the ultimate stress of the GC2 carbon textile remains 87.9% of its ultimate stress at room temperature. The normalized ultimate stress of the GC2 textile is 54% at 400 °C and 22% at 500 °C.

Figure 3a shows the evolution of the normalized ultimate stress of the GC2 carbon textile as a function of the temperature compared with the other experimental results on the carbon fibre reinforced polymer (CFRP) obtained by Bisby et al. 2005 [10], by Yu et al. 2014 [11] and PL. Nguyen et al. 2018 [9]. Figure 3b shows the normalized Young's modulus of the GC2 carbon

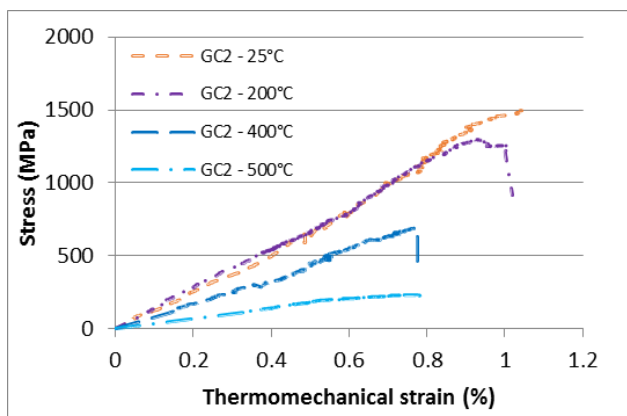


Fig. 1. Thermomechanical behaviour of the GC2 carbon textile: stress – strain relationship at different temperatures (25°C, 200°C, 400°C, 500°C)

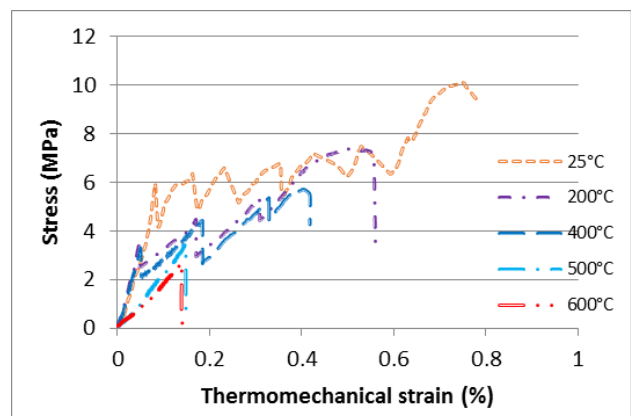
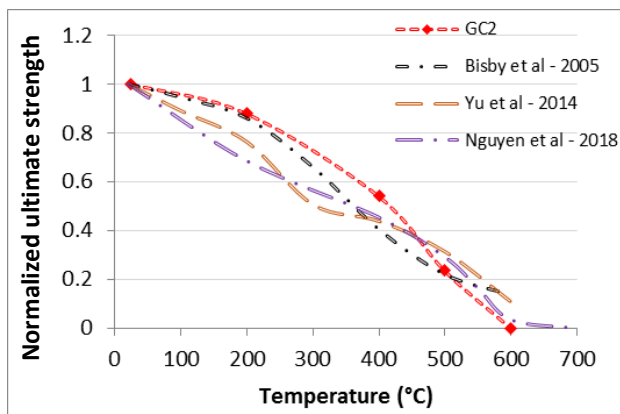
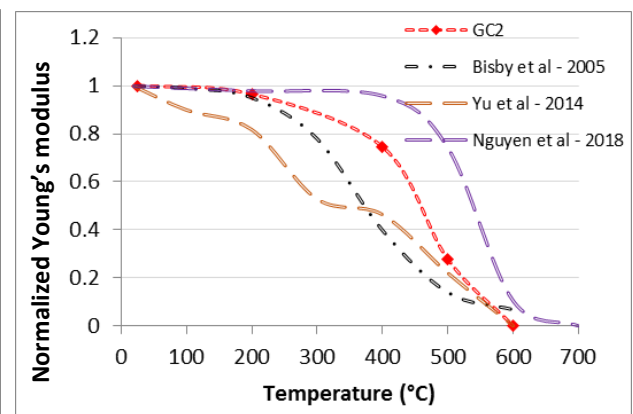


Fig. 2. Thermomechanical behaviour of the F.GC2 composite: stress – strain relationship at different temperatures (25°C, 200°C, 400°C, 500°C, 600°C)



a) Normalized ultimate strength



b) Normalized Young's modulus

Fig. 3. Evolution of normalized thermomechanical properties obtained for the GC2 carbon textile compared with experimental results on the CFRP obtained by Bisby et al. 2005 [10]; Yu et al. 2014 [11]; Nguyen et al. 2018 [9]

textile as a function of the temperature. It can be found that the influence of temperature on Young's modulus of the GC2 carbon textile could be divided into two temperature intervals. The first interval, from 25 °C to 400 °C, is described by a slight reduction of Young's modulus. The normalized Young's modulus values are 96.4% at 200 °C, 74.4% at 400 °C. In the second interval, from 400 °C to 600 °C, the normalized Young's modulus greatly decreases and is almost negligible at 600 °C. At 500°C, the normalized Young's modulus value of this carbon textile is 23.8%.

Table 4. Results of the direct tensile tests performed on GC2 carbon textile specimens

Results	T°C	Ultimate stress (MPa)	Average stress (MPa)	Standard deviation (MPa)	Young modulus (GPa)	Average modulus (GPa)	Standard deviation (GPa)
GC2 – 25°C - a	25	1211.36	1311.52	158.26	150.40	143.83	7.22
GC2 – 25°C - b		1493.97			136.10		
GC2 – 25°C - c		1229.22			145.00		
GC2 – 200°C - a	200	1296.51	1152.54	204.89	130.42	138.61	14.01
GC2 – 200°C - b		917.97			154.79		
GC2 – 200°C - c		1243.14			130.62		
GC2 – 400°C - a	400	689.92	708.78	71.81	87.15	107.07	18.62
GC2 – 400°C - b		788.12			124.03		
GC2 – 400°C - b		648.23			110.40		
GC2 – 500°C - a	500	235.43	308.12	67.78	34.53	39.73	9.53
GC2 – 500°C - b		319.33			33.93		
GC2 – 500°C - c		367.59			50.73		

Table 5. Results of the direct tensile tests performed on F.GC2 specimens at different temperatures; P_I , σ_I , ϵ_I : force, stress, strain corresponding to the beginning of the macro-cracking; E_I : initial stiffness; σ_{II} , ϵ_{II} : stress, strain corresponding to the end of the macro-cracking; E_{II} : stiffness of the stress-strain curve second phase; P_{UTS} , σ_{UTS} , ϵ_{UTS} : force, stress, strain corresponding to composite failure; E_{III} : post-cracked composite stiffness

Results	T (°C)	Parameters identified with the first phase of the strain-stress curve				Parameters identified with the second phase of the strain-stress curve			Parameters identified with the third phase of the strain-stress curve			
		P_I (kN)	σ_I (MPa)	ϵ_I (%)	E_I (GPa)	σ_{II} (MPa)	ϵ_{II} (%)	E_{II} (GPa)	P_{UTS} (kN)	σ_{UTS} (MPa)	ϵ_{UTS} (%)	E_{III} (GPa)
F.GC2 – 25°C	25	3.91 (+0.13)	6.38 (+0.54)	0.083 (+0.004)	11.33 (+0.63)	7.51 (+0.46)	0.671 (+0.074)	0.33 (+0.14)	6.34 (+0.46)	10.30 (+0.41)	0.813 (+0.071)	2.50 (+0.43)
F.GC2 – 200°C	200	2.24 (+0.27)	3.59 (+0.60)	0.045 (+0.008)	8.48 (+0.37)	4.93 (+0.54)	0.304 (+0.007)	0.85 (+0.10)	4.35 (+0.17)	6.95 (+0.35)	0.497 (+0.059)	2.13 (+0.08)
F.GC2 – 400°C	400	2.23 (+0.43)	3.63 (+0.53)	0.055 (+0.006)	7.13 (+0.73)		-	-	3.75 (+0.40)	6.11 (+0.41)	0.359 (+0.045)	1.15 (+0.30)
F.GC2 – 500°C	500	1.98 (+0.24)	3.39 (+0.43)	0.139 (+0.026)	3.75 (+0.34)							
F.GC2 – 600°C	600	1.42 (+0.31)	2.40 (+0.39)	0.148 (+0.012)	2.14 (+0.02)							

4.2 Evolution of the properties of the F.GC2 composite as a function of the temperature

From Figure 4, it can be observed the mechanical property evolution of F.GC2 composite as a function of the temperature. The normalized mechanical properties (normalized thermomechanical ultimate strength, normalized initial stiffness) are defined like that for results of GC2 carbon textile. In Figure 4a, it can be seen that the normalized ultimate strength values of the F.GC2 composite linearly decreases with the increase of the temperature from 25 °C to 600 °C. Figure 4a shows the evolution of the normalized ultimate strength of carbon TRC as a function of the temperature compared with the experimental results on the basalt TRC obtained by Rambo et al. [1-3], glass TRC obtained by Tlajji et al. [6] and with characteristic tensile strength reduction of steel and

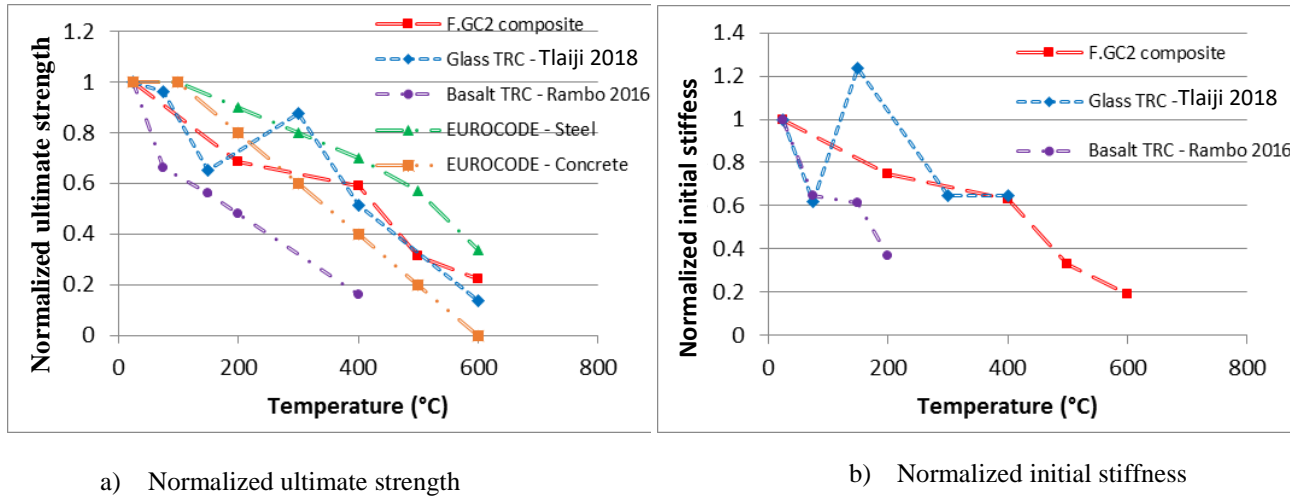


Fig. 4. Evolution of the normalized thermomechanical ultimate strength (a) and of the normalized initial stiffness obtained for F.GC2 composite compared with the experimental results on the basalt TRC obtained by Rambo et al. [1-3], glass TRC obtained by Tlajji et al. [6] and on concrete, steel in Eurocode [12]

concrete presented in EUROCODE 2 - Design of concrete structures [12]. As regards to evolution of thermomechanical properties of TRC in first phase, the decrease of cracking stress (σ_c) in comparison with that at room temperature is 49.5%, 43.0%, 46.8% and 62.3% for temperatures of 200°C, 400°C, 500°C and 600°C (see Table 5), respectively, while its initial stiffness (E_i) remains 74.9%, 62.9%, 33.1% and 18.8% of that at room temperature, respectively for the same level of temperature (see Table 5). Figure 4b shows the evolution of the normalized initial stiffness in first phase of carbon TRC as a function of the temperature compared with the experimental results in the literature.

4.3. Efficiency coefficient of carbon textile in TRC at elevated temperatures

The efficiency coefficient of reinforcement textile in TRC is normally defined by the ratio between TRC ultimate force and that of reinforcement textile. However, under elevated temperature action, this coefficient can be determined by several ways depending on the temperature. In this work, for the carbon TRC (F.GC2) (having 3 warps of GC2 textile), the efficiency coefficient of carbon textile varies with temperature level. Figure 5 shows the evolution of the ultimate force of the carbon TRC (F.GC2) as function of the temperature by comparing with that of one and three warps of carbon textile. From Figure 5, it can be observed that, at temperature below 400°C, the contribution of carbon textile is important on the loading capacity of TRC, and it strongly influences on the TRC ultimate force. So, the efficiency coefficient of carbon textile can be calculated by the ratio between the ultimate force of TRC and that of carbon textile. At room temperature, the efficiency coefficient value of carbon textile is 0.87, whereas this value is 0.68 at 200°C. At temperature above 400°C, F.GC2 composite specimens are broken when there is a damage of carbon textile and concrete matrix at the same time. So, the efficiency coefficient of carbon textile can be calculated by the Eq. (1) below:

$$\sigma_c(T) = \eta_f(T) \cdot \sigma_f(T) \cdot V_f + \eta_m(T) \cdot \sigma_m(T) \cdot (1 - V_f) \quad (1)$$

Where: $\sigma_c(T)$ is ultimate strength of TRC at temperature T; $\eta_f(T), \eta_m(T)$ are the efficiency coefficients of carbon textile and concrete matrix at temperature T; $\sigma_f(T), \sigma_m(T)$ are the tensile stresses of carbon textile and concrete matrix; V_f is the reinforcement ratio in TRC (in the tensile loading direction, 0.81%).

At elevated temperature, it can be supposed that the efficiency coefficients of carbon textile and concrete matrix are equal. So, the efficiency coefficient of both constituent materials can be calculated by the following Eq (2):

$$\eta_f(T) = \frac{\sigma_c(T)}{\sigma_f(T) \cdot V_f + \sigma_m(T) \cdot (1 - V_f)} \quad (2)$$

At 600°C, the carbon textile specimens are broken in 2nd phase of test procedure (see 2.4), so carbon textile contribution in mechanical resistance of carbon TRC can be considered as negligible. All values of efficiency coefficient of carbon textile are presented in Table 6. Figure 6 shows the influence of the temperature on efficiency coefficient of carbon textile used in carbon TRC. Figure 6 shows that the mentioned coefficient progressively decreases when the temperature increases from 25°C to 600°C.

Table 6: Efficiency coefficient of carbon textile used in TRC composite at different temperature [$V_f = 0.81\%$: reinforcement carbon textile ratio in the F.GC2 composite (in the tensile loading direction)]

Temperature	25°C	200°C	400°C	500°C	600°C
$\sigma_c(T)$	10.30	6.95	6.11	3.39	2.40
$\sigma_f(T)$	1311.5	1152.5	708.8	308.1	-
$\sigma_m(T)$	0	0	3.63	3.39	2.4
$\eta_f(T)$	0.97	0.74	0.65	0.58	0

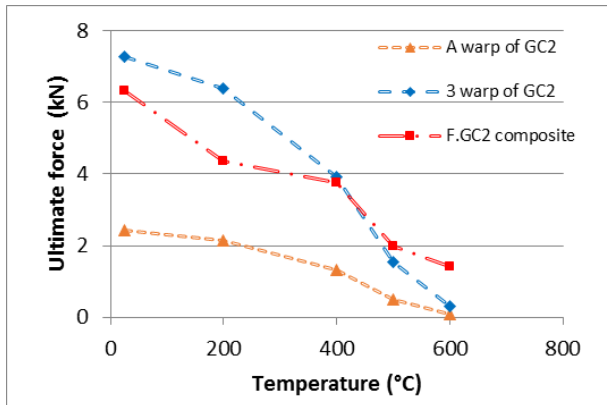


Fig. 5. Evolution of ultimate force of the F.GC2 (having 3 warps of GC2) as function of the temperature by comparing with that of one and three warps of GC2 textile

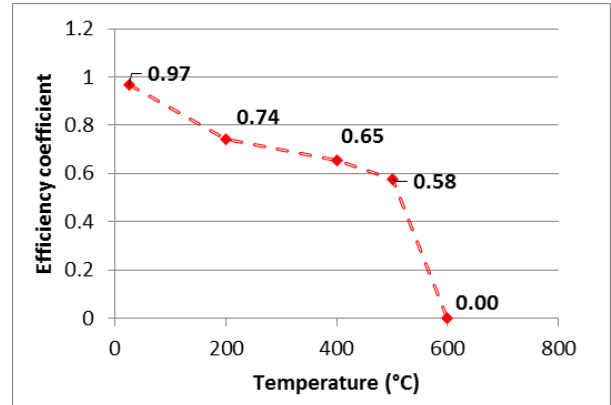


Fig. 6. Efficiency coefficient of carbon textile used in carbon TRC (F.GC2) at different temperatures

5 CONCLUSION

The objective of this work is to identify the thermomechanical behaviour of carbon textile and carbon TRC subjected to mechanical and thermal loadings. The GC2 carbon textile and the F.GC2 composite specimens were tested under thermomechanical loading at five temperature levels (25 °C, 200 °C, 400 °C, 500 °C, and 600 °C). All thermomechanical properties (characteristic strengths and stiffnesses) at different phases of carbon TRC of carbon textile were identified and presented. At elevated temperatures, the GC2 carbon textile typically gives a quasi-linear thermomechanical behaviour up to the failure. Whereas the F.GC2 composite provides hardening behaviour with different phases depending on the temperature level. Regarding the evolution of mechanical properties of the GC2 carbon textile and the F.GC2 composite as a function of the temperature, an almost linear reduction can be found for ultimate strength of both materials (GC2 and F.GC2) and for the initial stiffness of the first phase of the F.GC2 composite, whereas the initial stiffness of the first phase of the GC2 textile reduces with two steps: the first step with a slight reduction (approximately 20%) in the temperature range from 25 °C to 400 °C, and the second step with a very large decrease to a negligible value at 600 °C. Other finding presented in this paper is the

evolution of the efficiency coefficient of the GC2 carbon textile in the F.GC2 composite at different temperatures. The ultimate strength of the F.GC2 composite strongly depends on carbon textile loading capacity in the temperature ranging from 25°C to 400°C, whereas the refractory concrete matrix contributes and plays a very important role in the carrying capacity and stiffness of the F.GC2 composite at the temperature above 400°C.

ACKNOWLEDGMENT

This research has been performed with the financial support of LMC2 (thanks to its industrial projects) for the experimental works and with the financial support of a doctoral scholarship from the Ministry of Education and Training of Vietnam to the first author. We would like to thank the society Kerneos Aluminate Technologies, France for the supply of the materials (cement, aggregates, superplasticizer) and the society BASF (France) for the supply of the viscosity modifier agent used in this study. We would like to thank the technicians (Mr. E. JANIN, Mr. N. COTTET) from the Civil Engineering department of IUT Lyon 1 and LMC2, University of Lyon 1 for their technical support.

REFERENCES

1. D.A.S. Rambo., F.A. Silva, R.D.T. Filho, O.F.M. Gomes (2015). *Effect of elevated temperatures on the mechanical behavior of basalt textile reinforced refractory concrete*. Mater. & Design,65,24-33.
2. D. A. S. Rambo, F. A. Silva, R. D. T. Filho, N. Ukrainczyk, E. Koenders (2016). *Tensile strength of a calcium-aluminate cementitious composite reinforced with basalt textile in a high-temperature environment*. Cement and Concrete Composite, 70, pp 183-193.
3. D. A. S. Rambo, T. Filho, B. Mobasher (2017). *Experimental investigation and modelling of the temperature effects on the tensile behavior of textile reinforced refractory concretes*. Cement and Concrete Composites, 75, pp 51-61.
4. I. Colombo, M. Colombo, A. Magri, G. Zani, M. di Prisco (2011). *Textile reinforced mortar at high temperatures*. Applied Mechanics and Materials, 82, pp 202-207.
5. T. H. Nguyen, X. H. Vu, A. Si Larbi, E. Ferrier (2016). *Experimental study of the effect of simultaneous mechanical and high-temperature loadings on the behaviour of textile-reinforced concrete (TRC)*. Construction and Building Materials, 125, pp 253-270.
6. Tala Talaiji, Xuan Hong Vu, Emmanuel Ferrier, Amir Si Larbi (2018). *Thermomechanical behaviour and residual properties of textile reinforced concrete (TRC) subjected to elevated and high temperature loading: Experimental and comparative study*. Composites Part B, 144, pp 99-110.
7. F. De Larrard (1999). *Concrete mixture Proportioning: a Scientific Approach*. E&FN SPON, London, 1999 [in French].
8. T. Sedran (1999). *Rhéologie et rhéométrie des bétons: application aux bétons autonivelants*. Doctoral dissertation, Ecole Nationale des Ponts et Chaussées, pp 484 [in French].
9. Phi Long Nguyen, Xuan Hong Vu, Emmanuel Ferrier (2018). *Characterization of pultruded carbon fibre reinforced polymer (P-CFRP) under two elevated temperature-mechanical load cases: Residual and thermo-mechanical regimes*. Construction and Building Materials, 165, pp 395-412.
10. L.A. Bisby, B. K. Williams, V.K. R. Kodur, M. F. Green, E. Chowdhury (2005). *Fire performance of FRP systems for infrastructure: A state-of-the art report*. NRC-CNRC, Res. Report 179, Canada.
11. B. Yu, V. Kodur (2014). *Effect of temperature on strength and stiffness properties of near-surface mounted FRP reinforcement*. Composites: Part B, 58, pp 510-517.
12. Eurocode 2: Design of concrete structures - Part 1-2: General rules - Structural fire design 2004.

AN EXPERIMENTAL APPROACH FOR EVALUATING RESIDUAL CAPACITY OF FIRE DAMAGED CONCRETE MEMBERS

Ankit Agrawal¹, Venkatesh Kodur²

ABSTRACT

This paper presents a three-stage experimental approach to develop rational methodologies for evaluating residual capacity of fire damaged concrete members. The residual capacity of fire exposed concrete members is evaluated in three sequential stages, namely, during pre-fire exposure conditions; during fire exposure comprising of heating and cooling phases of fire, followed by complete cooldown of the member to ambient temperatures; and the finally during post-fire exposure conditions. Key response parameters including deflections, temperatures, cracking propagation patterns, spalling, and post-fire residual deformations are monitored to evaluate performance of the member during each stage of testing. The applicability of the proposed approach is demonstrated by testing two concrete beams for residual capacity after subjecting them to fire exposure. Data generated in these tests is utilized to highlight importance of each stage of testing in evaluating realistic residual capacity of fire damaged concrete members.

Keywords: Reinforced concrete members, fire damage, cooling phase, residual capacity

1 INTRODUCTION

Structural members in buildings have to satisfy code specified fire resistance requirements as fire safety is one of the key considerations in building design [1]. However, complete collapse of a structural system due to fire, especially in case of concrete structures, is rare owing to inherent fire resistance properties of concrete [2]. Therefore, it is reasonable to assume that concrete structures will regain significant residual capacity, after most fire incidents, and can be opened to re-occupancy with adequate repair and retrofitting [3].

Nonetheless, extent of fire induced damage in concrete structures is highly variable. In case of exposure to a severe fire, concrete structural members might experience significant loss in structural capacity and relatively larger permanent (residual) deformations. Alternatively, exposure to a moderate fire may result in non-noticeable residual deformations, and minimal loss of structural capacity. Thus, it is necessary to assess if sufficient residual capacity exists in concrete members prior to re-occupancy after the fire incident.

At present, residual response of fire damaged concrete members is not well established. In particular, there are no standardized experimental approaches to evaluate residual capacity of fire damaged concrete members. Majority of previous approaches rely on testing material cores taken from fire damaged members, with few studies carried out at the structural level. In previous laboratory tests, service conditions present in the member prior to fire exposure, and their effect on residual capacity was not considered explicitly. Moreover, approaches used in previous studies [4–6] did not monitor conditions present during extended cooling phase of the member, as well as resulting of post-fire residual deformations, which impact post-fire residual response. In addition,

¹ PhD Candidate. Department of Civil and Environmental Engineering, Michigan State University, East Lansing, Michigan, USA.
e-mail: agrawa36@msu.edu

² University Distinguished Professor and Chairperson, Department of Civil and Environmental Engineering, Michigan State University, East Lansing, Michigan, USA.
e-mail: kodur@egr.msu.edu

residual response was evaluated using a load controlled technique in majority of previous studies, which may not capture nonlinear response of the fire damaged concrete member accurately. To address these knowledge gaps, a three-stage experimental approach is proposed to evaluate residual capacity of fire damaged concrete members. The complete response of the concrete member from pre-fire exposure conditions to complete cooldown of the member, and post-fire response are captured in the three sequential stages of testing. The proposed experimental approach is applied to evaluate residual capacity of two concrete beams, after subjecting them to different fire exposure scenarios. Data from these tests illustrates significance of each stage of testing, and highlights key parameters influencing residual capacity of fire damaged concrete members.

2 APPROACH FOR EVALUATING POST-FIRE RESIDUAL CAPACITY

The residual response of a fire damaged concrete members is strongly influenced by conditions existing just prior to the fire incident, as well as during complete fire exposure duration, including extended cooling phase when cross-sectional temperatures in the member reverts back to ambient conditions. Therefore, to capture the realistic residual capacity of the member a three stage evaluation approach is required. The three staged comprise of; Stage 1: evaluating the member response at room temperature during service (load) conditions as present prior to fire exposure; Stage 2: evaluating member response during heating and cooling phases as present in a fire incident, and during extended cooldown phase of the member to simulate conditions as occurring after fire is extinguished or burnout conditions are attained; and Stage 3: evaluating residual response of the fire damaged member following complete cooldown. A flowchart depicting these three distinct stages of testing is shown in *Fig. 1*.

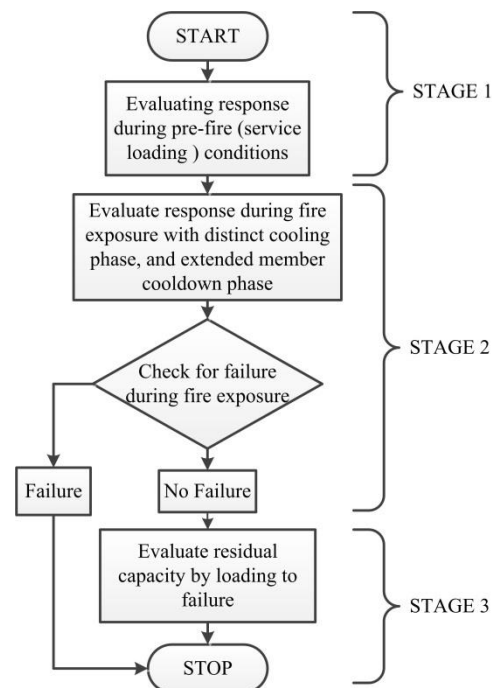


Fig. 1. Flow chart describing the three stages involved in residual capacity tests

Monitoring different response parameters during each stage of testing is crucial for capturing realistic residual response of fire damaged concrete members. Stage 1 of testing involves simulating service conditions in the member just prior to a fire incident. This is achieved by subjecting the member to load (stress) and boundary conditions, as present in the structural member under normal day-to-day conditions. Loads need to be applied in small increments to simulate quasi-static conditions, until service conditions are reached, and maintained constant using load controlled technique, for a sustained period (typically 1 to 2 hours) until deflections in the member stabilize.

During this stage of testing, the load-deflection response is to be monitored to establish initial (pre-fire exposure) stiffness of the structural member, as well as to ensure realistic level of cracking (damage) in the test specimen (beam) prior to fire exposure. Level of loading (stress) applied on the structural member during Stage 1 has a significant effect on its performance during fire exposure in Stage 2 of testing.

In Stage 2 of testing, extent of fire damage in the structural member, as occurring in a real fire incident, needs to be simulated. Thus, the loaded structural member is to be exposed to a realistic fire exposure scenario having a distinct cooling phase. It is also important to note that cross-sectional temperatures within the structural member may remain significantly high for prolonged time following burnout conditions or after fire is extinguished, owing to high thermal inertia of concrete. In fact, temperatures within the member may not cooldown to ambient conditions until 24 to 72 hours after fire has been extinguished, depending on size (thermal mass) of the member. Thus, loads on the member are maintained constant during complete duration of fire exposure, and until cross-sectional temperatures in the member revert back to ambient conditions. The load level maintained during this extended cooling phase of the member can also affect extent of recovery in the member. Thus, key parameters to be monitored during Stage 2 of testing include temperatures, deflections, spalling, cracking propagation patterns, and load level maintained during extended cooldown of the member. Once the member cools down to ambient conditions, the member is unloaded to record recovery in post-fire deformations, and measure extent of irrecoverable (plastic) residual deformations.

Following complete cooldown of the structural member to room temperature, and if there is no failure in Stage 2 of testing, residual response of the fire damaged member is traced in Stage 3 of testing. The post-fire residual response of the member is to be traced by incrementally loading the member to failure through a displacement controlled loading technique. This ensures that the nonlinear response of the tested member till actual failure to be captured accurately. During Stage 3 of testing, the load-deflection response, cracking propagation patterns, spalling, and modes of failure in the structural member are to be recorded.

3 RESIDUAL CAPACITY TESTS

The proposed three-stage experimental approach was applied to evaluate residual capacity of two reinforced concrete (RC) beams after exposure to different fire scenarios. The response of the beams was evaluated during pre-fire exposure conditions in Stage 1, and then during complete fire exposure and extended cooldown of the beams in Stage 2. Following complete cooldown, the fire damaged beams were loaded to failure to evaluate residual capacity in Stage 3 of testing.

3.1 Design and fabrication of beams

Two RC beams, of rectangular cross section (see *Fig. 2*), designated as beams B1 and B2, were designed as per ACI 318 specifications [7]. Beam B1 was fabricated using high strength concrete (HSC), while beam B2 was made of normal strength concrete (NSC). The average compressive cylinder strength of measured at 28 days and on test day was 93 MPa and 106 MPa for HSC and 49 MPa and 62 MPa for NSC respectively. The beams were cured in the laboratory for an extended period to ensure that these beams attained realistic moisture condition as observed in actual buildings. Both beams had identical reinforcement with the steel of the main reinforcing bars and stirrups having specified yield strength of 420 MPa and 280 MPa, respectively. *Fig. 2* shows the elevation and cross-sectional details of fabricated beams, together with the locations of the stirrups. The beams were instrumented with thermocouples during fabrication at three different cross-sections in each beam for measuring concrete and rebar temperatures, as shown in *Fig. 2*. During each stage of the test, the deflection of each beam was monitored by placing displacement transducers at mid-span, as well as at the location of one of the two point loads. Test parameters of these RC beams are summarized in *Table 1*.

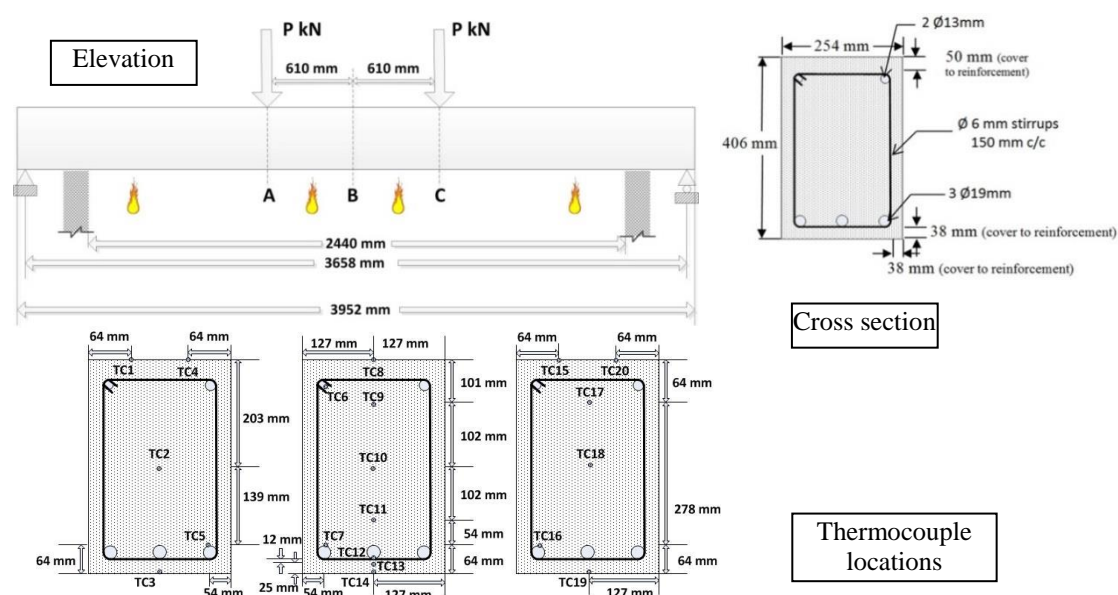


Fig. 2. Reinforcement, loading, and instrumentation details of tested RC beams

Table 1. Test parameters for RC beams

Beam designation	Fire exposure	Concrete type	Support conditions	Fire resistance (ACI 216): min	Applied load: kN (% of capacity)	Relative humidity %	Moisture content (% by weight)	Measured fire resistance (min)	Spalled volume ratio (%)
B1	LF	HSC	Simply supported	90 min	55(58%)	77.4	2.2	No Failure	1.5
B2	SF	NSC			50(54%)	91.8	2.6	No Failure	0.1

3.2 Test-setup and procedure

Each stage of testing was carried out in a specially designed test setup. The application of loads at room temperature (Stage 1), and subsequent fire exposure tests (Stage 2) on the two beams were carried out in the fire test furnace. Subsequently, upon complete cooldown of the member residual capacity tests were conducted in a specially designed displacement controlled flexural testing setup.

3.2.1 Testing prior to fire exposure

In Stage 1 of testing, the response of the two beams is traced under day-to-day service conditions as present prior to a real fire incident. Each of the beams were setup in the load-cum-heating furnace, and two point loads of magnitude 50 kN and 55 kN for beams B1 and B2 respectively, were applied incrementally on the top face at 1.4 m from support ends. The applied loading produced bending moment in beams B1 and B2 of about 58% and 54% of the beam (ultimate) capacity calculated according ACI 318 [7], similar to load (stress) level typically present during pre-fire exposure conditions. The load was maintained on the beams through a load controlled technique, till deflections stabilized, and then during Stage 2 of testing. During Stage 1, the load-deflection response and crack propagation in the beam were monitored.

3.2.2 Testing during fire exposure conditions

In Stage 2 of testing, the loaded beams were subjected to fire in a test furnace [1]. A constant load level was maintained throughout the duration of fire exposure in both beams. Only three sides (bottom and two sides), of the beam were exposed to fire (see Fig. 2) to simulate conditions encountered in practice where a concrete slab insulates the top surface of the beam. The fire exposure on the beams comprised of a heating phase followed by a distinct cooling phase, as shown in Fig. 3a. Beam B1 was subject to rapid heating for 120 minutes (refer LF in Fig. 3a), while beam

B2 was heated as per ASTM E119 standard fire [8] for 90 minutes (indicated as SF in Fig. 3a). Cooling phase of fire exposure in beam B1 followed a rapid non-linear decay (cooling) rate, while a linear decay rate of approximately -6°C per minute was adopted for beam B2. The fire exposure was assumed to have ended once furnace temperatures dropped below 200°C , and lasted for 210 minutes and 230 minutes for beams B1 and B2 respectively.

Following end of fire exposure, representing extinguishing of fire in a building, the recovery of cross-sectional temperatures and deflections was monitored 24 hours after fire exposure to gauge extent of recovery in the strength and stiffness properties of the beams during extended cooling phase. The effect of load level present during extended cooldown period on extent of recovery in the beams was also studied. In case of beam B1, applied loads were removed at approximately 300 minutes into Stage 2 of the test, once rebar temperatures dropped below 300°C and mid-span deflections began to recover. For beam B2 however, applied loads were kept constant until the beam cooled down completely to ambient conditions. Following cool down of the beams, post-fire inspection was carried out to record observations relating to fire induced spalling, and cracking propagation patterns in the tested beams.

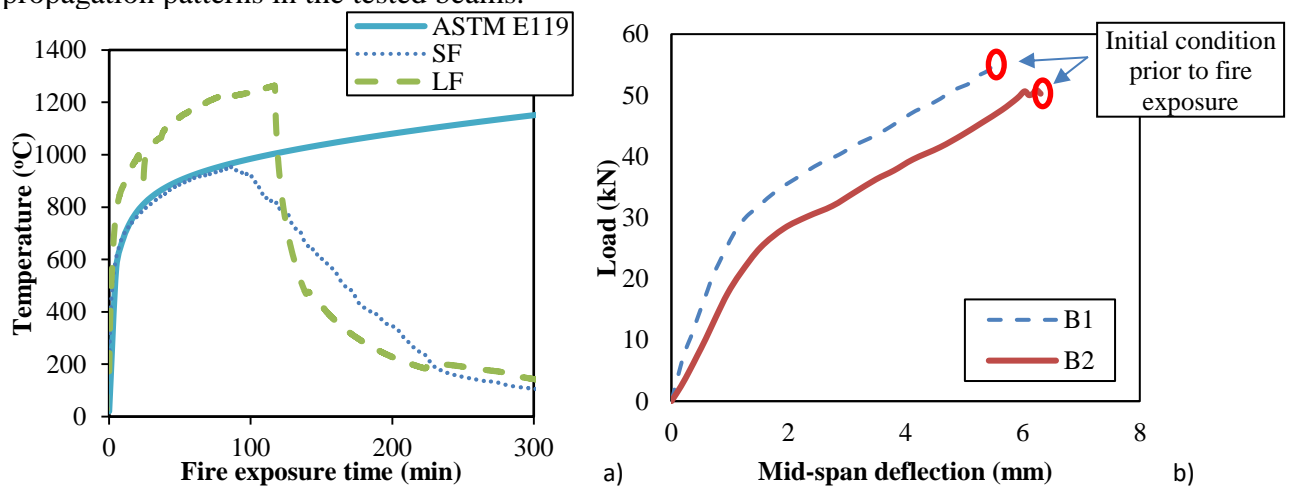


Fig. 3. a) Time–temperature curves for fire scenarios used in the fire tests; b) Response of RC beams during loading at room temperature (Stage 1)

3.2.3 Testing during post-fire residual conditions

Following complete cooldown of the beams, the residual response of the fire damaged beams was traced by subjecting them to incremental flexural loading. Similar to Stages 1 and 2, two point loads at 1.4 m from the supports were applied on the top face of the beam through a displacement controlled actuator. This ensured that a displacement controlled technique with a rate of 2 mm per minute was adopted for simulating quasi-static loading conditions and capturing nonlinear response of the beam, especially during the post-peak phase just prior to failure. During this stage of testing, load-deflection response, crack propagation patterns and failure modes of the beams were recorded.

4 RESULTS FROM RESIDUAL CAPACITY TESTS

Both beams did not fail during fire exposure; Stage 2 of testing; and hence were tested for residual capacity in Stage 3.

4.1 Response prior to fire exposure (Stage 1)

The measured mid-span deflection in Stage 1 is plotted as a function of applied load in Fig. 3b for both tested beams. As expected, deflection in both beams increases monotonically with increasing load. Furthermore, the response of both beams is almost linear until the onset of tensile cracking. This tensile cracking is primarily confined to the critical region between the two point loads, subject to a constant bending moment (flexural stresses). In addition, the response of beam B1 (made of

HSC) is relatively stiffer as compared to beam B2 (made of NSC) owing to higher strength and modulus properties of HSC (see *Fig. 3b*). The average (secant) stiffness of the beams at peak load for each beam were calculated to be about 10 kN/mm for beam B1 and 8 kN/mm for beam B2. Data generated in the form of initial stiffness and deflections in the beam is quite useful since this can be compared with corresponding post-fire response parameters (measured during Stage 3) so as to gauge the extent of fire damage induced during Stage 2 of testing.

Thus, pre-fire load (stress) conditions and tensile cracking, as expected in the critical section (mid-span) of the beams during day to day service conditions were simulated in Stage 1 of testing. Once deflections stabilized, the beams were prepared for fire testing in Stage 2.

4.2 Response during fire exposure conditions (Stage 2)

During Stage 2 of testing (fire exposure), thermal and structural response of the beams was evaluated not only till the end of fire exposure, but over an extending cooling period i.e. period covering between fire being extinguished to complete cooling down, which included time taken for entire cross-section of the structural member to revert back to room temperature. Response parameters monitored during this stage included cross-sectional temperatures, deflections, spalling, crack propagation patterns, and also post-fire residual deformation.

4.2.1 Thermal response

The thermal response of beams B1 and B2 during fire exposure is presented in *Fig. 4a-b* by plotting rebar and concrete temperatures at different locations along the cross section, as a function of fire exposure time. The duration of heating phase as well as peak fire exposure temperatures in case of beam B1 were greater as compared to beam B2. Nonetheless, peak cross-sectional temperatures attained in concrete at mid-depth and at the level of tensile rebar for both beams are comparable primarily due to the slower cooling rate adopted in the latter case, as well as greater reduction in thermal conductivity of HSC as compared to NSC during cooling phase [1,9]. Also, peak cross-sectional temperatures occur during cooling (decay) phase of fire exposure (depicted as phase 'II' in *Fig. 4a-b*) for both tested beams, owing to thermal inertia of concrete. While rebar temperatures begin to decay during cooling phase of fire exposure, temperatures at mid-depth of concrete decay after fire exposure has ended (see phase 'III' in *Fig. 4a-b*).

Peak temperatures at concrete mid-depth reach 325°C and 335°C at about 290 minutes and 330 minutes into fire exposure for beams B1 and B2 respectively. Similarly, beams B1 and B2 experience peak rebar temperatures of 521°C at 155 minutes and 592°C at 140 minutes into fire exposure respectively. It should also be noted that the duration of extended cooldown of the beams (marked as phase 'III' in *Fig. 4a-b*) is significantly greater than the duration of the fire exposure. For instance, in case of beam B1 subject to fire exposure lasting 3.5 hours, the cross-sectional temperatures reach ambient temperatures about 24 hours after fire has been extinguished.

4.2.2 Structural response

Measured mid-span deflection for the tested beams is plotted as a function of time is plotted in *Fig. 5a*. During early stages of fire exposure, deflection rise was mainly governed by thermal gradients. As fire exposure (time) progresses further, deflection is governed by temperature induced degradation in mechanical properties of rebar and concrete and increases with rebar temperature.

As rebar temperatures begin to decay, the mid-span deflections in the beam begin to revert back primarily due to the recovery in strength and modulus properties in reinforcing steel as rebar temperatures begin to cooldown. This rate of recovery is also influenced by the rate of cooling (phase) of fire exposure, as well as load level present during cooling phase of the member.

In case of beam B1, mid-span deflections reduce by almost 80% of their peak value during cooldown of the beam after fire exposure (marked as phase 'III' in *Fig. 5a*), due to removal of applied loads during extended cooldown of the member. On the other hand, mid-span deflections in beam B2 reduce by only 15% of their peak value due to slower rate of cooling and constant load

level during extended cooling phase. Thus, the extent of recovery in the beam is governed by not only cross-sectional temperatures but also extent of load level present during cooldown. Once the cross-sectional temperatures drop below 150°C during extended cooldown of the member (phase 'III' in Fig. 5a), the mid-span deflections attain a steady state value. Furthermore, beams B1 and B2 experience post-fire residual deformation of 12 mm and 14 mm respectively, even after applied loads are removed from the beams. As beams B1 and B2 did not fail during fire exposure [8], they were tested to for residual capacity after cool down to ambient conditions.

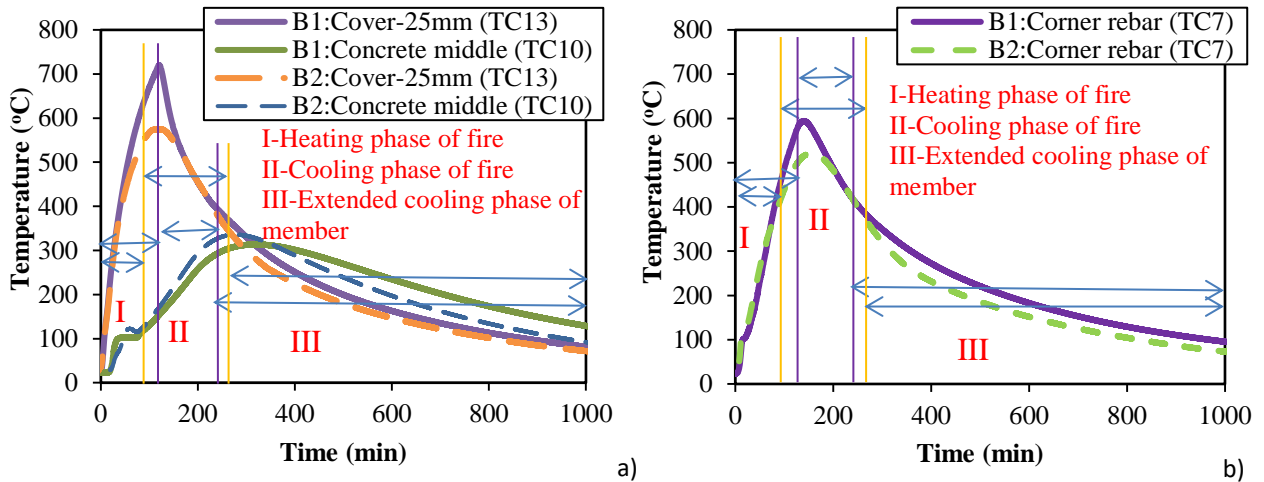


Fig. 4. Measured a) concrete; and b) rebar temperatures as a function of time

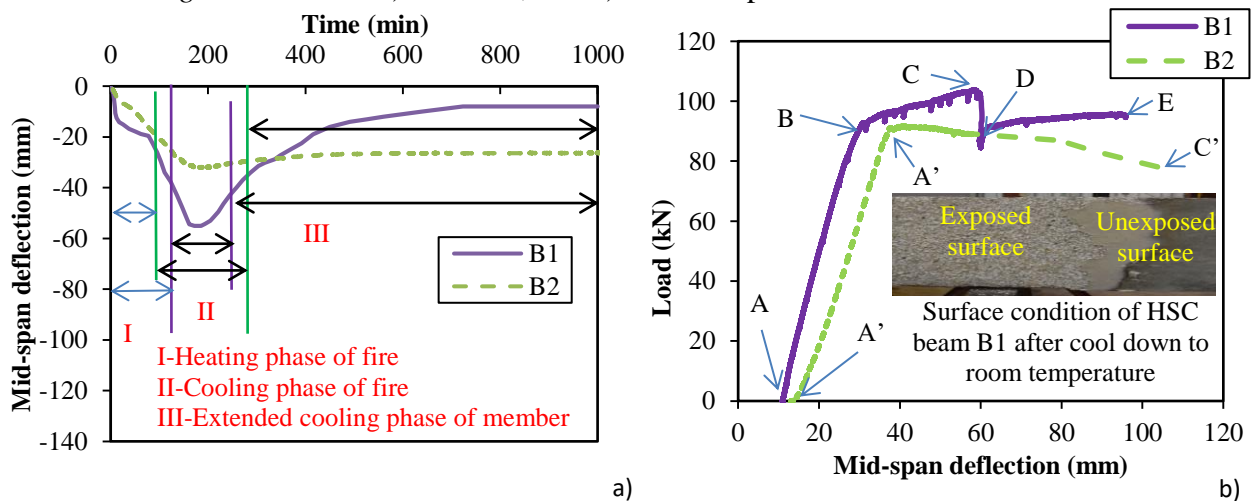


Fig. 5. a) Mid-span deflection of tested beams as a function of time (Stage 2); b) Load-deflection response of fire-damaged RC beams during residual strength test (Stage 3)

4.2.3 Temperature induced spalling and cracking

Observations from the fire tests in Stage 2 indicated that explosive spalling did not occur in both of beams during heating and cooling phases of fire exposure. Nonetheless, upon examination of beams, 24 hours after fire exposure, it was seen that the beams underwent spalling during extended cooling phase. The HSC beam B1, having lower water to cement ratio, underwent significant spalling confined to convex corners of the beam, along with significant surface pitting and peeling (see inset photo in Fig. 5b) as a result of decarbonation in calcareous aggregates [10]. On the contrary, no surface pitting and very limited corner spalling was seen in the NSC beam B2 due to higher moisture content present in the NSC mix, as well as presence of much higher free water in capillary pores as compared to that in HSC.

In addition to spalling, flexural cracks were seen in the fire exposure span of the beam resulting from applied loading, and temperature induced degradation in tensile strength of concrete during fire exposure. In addition to flexural cracks, tensile splitting cracks along the length of the

reinforcing bars were seen primarily in beams B1 made of HSC after it cooled down to room temperature.

4.3 Residual response during post-fire conditions (Stage 3)

Following complete cooldown, each of the beams was tested to evaluate residual capacity in Stage 3. For this purpose, each beam was loaded incrementally using a deflection controlled technique till failure occurred. The measured load-deflection response for beams B1 and B2 is plotted in *Fig. 5b*. Residual deformations (marked as A in beam B1; A' in beam B2) occur in both beams at zero load due to irrecoverable plastic strains in rebar and concrete during to fire exposure. As applied load (deflection) increases, both beams depict an almost linear response in the first phase of deformation progression (marked as A-B for beam B1, and A'-B' for beam B2 in *Fig. 5b*). The stiffness of beams B1 and B2 reduce by almost 40% and 55% respectively from their initial stiffness measured prior to fire exposure during Stage 1 of testing. While beam B2 is experiences lower peak rebar temperatures by almost 80°C as compared to beam B1, it undergoes a greater reduction in stiffness and experiences higher residual deformations. Thus, higher residual deformations are indicative of greater reduction in stiffness due to fire damage in concrete members.

The second phase of load-deflection response i.e., onset of yielding in tensile steel reinforcement (marked as B for beam B1, and B' for beam B2 in *Fig. 5b*), occurs at similar applied loads of 90 kN and 91 kN for beams B1 and B2 respectively, as they experience similar peak rebar temperatures. Once yielding occurs, beam B1 exhibits a strain hardening response and load carrying capacity increases (see B-C in *Fig. 5b*) by almost 12% in the third (plastic) phase. Upon reaching peak load carrying capacity, a sudden drop in load level occurs beam B1 accompanied with visible crushing of concrete at the extreme (top) fibre in the fourth phase (marked as D-E in *Fig. 5b*) of load-deflection response. On the contrary, beam B2 exhibits a strain softening response after yielding until failure (see B'-C' in *Fig. 5b*). Thus, it is better to load the beam through displacement controlled technique during Stage 3 of testing for capturing different post-peak response with sufficient accuracy.

Cracking propagation patterns seen at critical section (mid-span) of the beams indicate that both beams failed under flexure. The peak load-carrying capacity in beams B1 and B2 was measured to be 102 kN and 91 kN respectively, which is comparable to their respective design capacities of 92.7 kN and 94.5 kN, computed as per ACI 318 [7].

5 ONGOING STUDIES

A three-stage experimental approach is proposed for evaluating realistic residual capacity of fire damaged concrete members. The approach is capable in capturing response of the member during pre-fire conditions, during complete fire exposure conditions, and post-fire residual conditions This approach is currently being applied to undertake a series of residual capacity tests on reinforced concrete beams and columns at Michigan State University [11]. Data generated from these tests is being utilized to further validate a numerical model specifically developed to trace residual response of fire exposed concrete members [3,12]. The model will be applied to undertake a series of parametric studies, results of which will be utilized to develop rational approaches for evaluating residual capacity of fire damaged concrete members.

6 CONCLUSIONS

An experimental approach to evaluate residual capacity of fire damaged concrete members is proposed and validated thorough tests on concrete beams. Based on information presented in the paper, following conclusions can be drawn:

- A three-stage testing approach comprising of response evaluation prior to fire exposure, response during fire exposure including extended cooldown of the member, and post-fire exposure conditions for determining residual capacity of fire damaged concrete members.

- Extent of recovery observed in fire damaged concrete members is strongly influenced by rate of temperature decay during cooling phase of fire exposure, as well as level of load present on the member during extended cooldown, after fire exposure has ended.
- Irrecoverable residual deformations result when concrete members are exposed to fire. The level of deformations can give an indication on the extent of stiffness degradation in fire damaged concrete members.
- Concrete beams following fire exposure, recover much of their flexural capacity, provided rebar temperatures do not exceed 600°C, and there is no significant spalling in the beams, including during extended cooldown of the beam.

ACKNOWLEDGEMENT

The authors wish to acknowledge the support of United States Agency for International Development (through Pakistan-US Science and Technology Cooperative Program grant [PGA-2000003665](#)) and Michigan State University for undertaking this research. Any opinions, findings, conclusions, or recommendations expressed in this paper are those of the author and do not necessarily reflect the views of the institution.

REFERENCES

1. M. B. Dwaikat, V. K. R. Kodur (2009). *Response of restrained concrete beams under design fire exposure*. Journal of Structural Engineering, 135(11). pp 1408–1417.
2. J. J. Beitel, N. R. Iwankiw (2005). *Historical survey of multi-story building collapses due to fire*. Fire Protection Engineering, 3rd Quarter. pp 1-10.
3. V.K.R. Kodur, Ankit Agrawal (2016). *An approach for evaluating residual capacity of reinforced concrete beams exposed to fire*. Engineering Structures, 110. pp 293–306.
4. Moetaz M. El-Hawary, Ahmed M. Ragab, Ahmed Abd El-Azim, Shadia Elibiari (1996). *Effect of fire on flexural behaviour of RC beams*. Construction and Building Materials, 10(2). pp 147–150.
5. Yu Ye Xu, Bo Wu, Ming Jiang, Xin Huang (2012). *Experimental study on residual flexural behavior of reinforced concrete beams after exposure to fire*. Advanced Materials Research, 457. pp 183–187.
6. V. K. R. Kodur, M. B. Dwaikat, R. S. Fike (2010). *An approach for evaluating the residual strength of fire-exposed RC beams*. Magazine of Concrete Research, 62. pp 479–488.
7. ACI. *ACI 318-14: Building code requirements for reinforced concrete*. American Concrete Institute, Vol. 552, Detroit, MI; 2014.
8. ASTM. *ASTM E119-16: Standard methods of fire test of building construction and materials*. American Society of Testing Materials, West Conshohocken, PA; 2016.
9. Venkatesh Kodur, Wasim Khaliq (2011). *Effect of Temperature on Thermal Properties of Different Types of High-Strength Concrete*. Journal of Materials in Civil Engineering, 23. pp 793–801.
10. Zhi Xing, Ronan Hébert, Anne-Lise Beaucour, Béatrice Ledésert, Albert Noumowé (2013). *Influence of chemical and mineralogical composition of concrete aggregates on their behaviour at elevated temperature*. Materials and Structures, 47(11). pp 1921–40.
11. Venkatesh Kodur, Derek Hibner, Ankit Agrawal. *Residual response fo reinforced concrete columns exposed to design fires*. 6th International Workshop on Performance, Protection & Strengthening of Structures under Extreme Loading, Guangzhou (Canton), China, December 11-12, PROTECT2017, 2017. pp 574-581.
12. Venkatesh K. Kodur, Ankit Agrawal (2016). *Critical factors governing the residual response of reinforced concrete beams exposed to fire*. Fire Technology, 52(4). pp 967-993.

Experimental Research and any Other

EVALUATION METHOD OF THERMAL ELONGATION OF STEEL BEAMS DURING FIRE BASED ON ACTUAL SCALE TESTS

Tomohito Okazaki¹, Mamoru Kohno²

ABSTRACT

The effect of RC slabs to constrain thermal elongation of steel beams during fire in actual buildings was quantitatively grasped by our past researches. Furthermore, the evaluation method to calculate simply the thermal elongation of a steel beam in an actual building was proposed in the case when RC slabs were arranged on both sides to the heated beam [1]. Calculated values by the proposed method matched accurately test results. In this study, the evaluation method was improved based on the actual scale fire test of an RC slab arranged on only one side of the steel beam so that this method can also be applied to beams attached to the outer frame on the circumference of buildings. Moreover, the application of the improved evaluation method to the actual scale fire test bracing frame suggested that the thermal elongation of steel beams during fire can accurately be calculated by the proposed evaluation method.

Keywords: steel beam, thermal elongation, in-plane stiffness of RC slab, actual scale fire test

1 INTRODUCTION

In evaluating the structural stability of a steel structure building during fire, it is extremely important to consider the thermal deformation of structural frames. For example, it is assumed that the collapse of WTC7 was caused by the thermal elongation of the steel beam connected the column [2]. In Japan, the Fire Resistance Verification Method (FRVM) was introduced in Building Standard Law (BSL) in 2000, and since then the performance-based fire resistance design has generally been applied to the design of buildings. The BSL specifically shows the method of calculating the Fire Resistance Time (FRT) of structural members of a building. In other words, for the fire safety designers in Japan, it is important to evaluate the structural stability of a building during fire by a simple formula without the application of advanced numerical analysis such as the finite element method (FEM). The FRT evaluation method for structural members described in the FRVM has been constructed based on many fire test results of single members such as columns and beams conducted in the past. Therefore, from the viewpoint of the fire resistance of a single member, it is considered that this evaluation method accurately reflects actual phenomena. However, it is difficult to accurately reproduce boundary conditions of actual buildings in the fire test of a single member, and so in the FRVM in Japan, the evaluation method for predicting thermal deformation properties of structural frames such as thermal elongations of steel beams has not been established. In the general performance-based fire design in Japan, the thermal elongation of steel beams has been defined around 80% to 100% of the value that was calculated by multiplying three factors: temperature, heated length and thermal expansion coefficient of steel. On the other hand, it is considered that the thermal elongation of a steel beam in an actual building is suppressed by its adjacent structural members such as columns, transverse beams and RC slabs which are directly connected to the heated beams, as shown in Figure 1. Furthermore, the suppressive effect of

¹ Chief Researcher, Research and Development Institute, Takenaka Corporation, Chiba 270-1395, Japan.
e-mail: okazaki.tomohito@takenaka.co.jp

² Professor, Department of Architecture, Engineering, Tokyo University of Science, Tokyo 125-8585, Japan.
e-mail: kohno@rs.kagu.tus.ac.jp

adjacent members to thermal elongation of steel beams is expected to depend on the shape of the building and the structural system type.

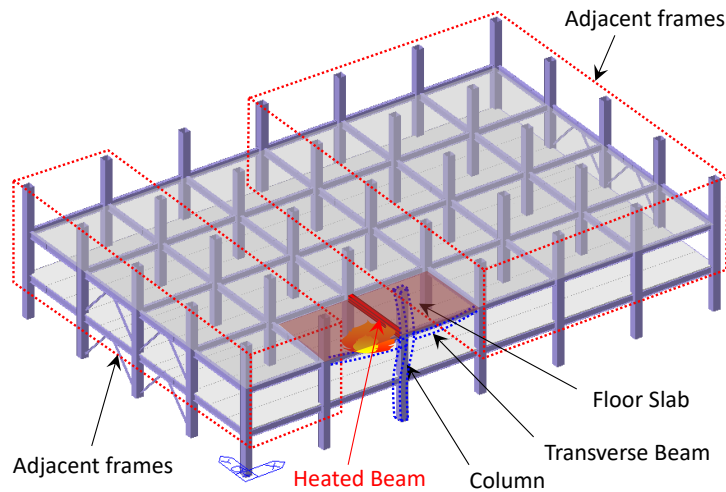


Figure 1. Schematic 3D structural model of a part of an actual building structure

From the above background, in our past study [3, 4], six types of large scale furnace tests were carried out to grasp the thermal elongation of steel beams which were connected to RC slabs. All specimens were composed of fire-protected steel beams and RC slabs. In order to simulate side steel beams in actual buildings, two of the specimens had RC slabs arranged on only one of their sides. In addition, in the case of test frames with RC slabs arranged on both sides of the heated steel beams, an evaluation method based on a simple formula to calculate the value of the thermal elongation of steel beams during fire in the actual building was suggested.

In this study, the previously suggested evaluation method of the thermal elongation of steel beams was improved for the case of beams of the outer frames on the circumference of buildings. Furthermore, the suggested evaluation method was applied to a test frame which was composed of a steel beam with braced lateral frames on both of its sides and an RC slab at its top, and the calculated value of the thermal elongation of the steel beam matched precisely the test results.

2 FIRE TESTS

In previous studies by the authors, six types of large scale furnace tests were carried out to grasp the thermal elongation of steel beams which were connected to RC slabs. In these studies [3, 4], ISO 834 standard fire curve was used to heat the test frames, and then evaluate the elongation of steel beams. This study took bases on these past experimental studies carried out by the authors. In addition, the furnace which was used in these past tests is the biggest one in Japan where actual scale fire tests can be carried out.

2.1 Test frame

All the six specimens were composed of fire-protected (with wrap type fireproofing materials made of rock wool) steel beams and RC slabs. However, in order to simulate side steel beams of actual buildings, two of the specimens had RC slabs arranged on only one of their sides (see Figure 2). Test parameters were the cross sectional size of the beam and grade of fire protection, as shown in Table 1. In the test phase where the temperature of the steel beams was the same, it was considered that the forces transmitted from the steel beams to RC slabs increase with the increase of the cross-section area of the steel beams. Due to the difference in the grade of fire protection, different temperatures could be obtained for each test frame at the same heated time. In other words, the

difference in the grade of fire protection meant the extent of the high temperature degradation of RC slabs at a certain temperature of the steel beam.



(a) With RC slabs on both sides

(b) With RC slab on one side

Figure 2. Overview of test frame

Table 1. Specimens' specifications and test parameters

Specimen	Size of beam	Grade of fire protection	Slab arrangement	Width (mm)	Length (mm)
H400-1	H-400×200× 8×13	1 hour	Both sides	4,880	3,565
H400-2		2 hour			
H600-1	H-600×200×11×17	1 hour			
H600-2		2 hour			
H400-2S	H-400×200× 8×13	2 hour	One side	2,440	3,565
H600-2S	H-600×200×11×17	2 hour			

2.2 Setting situation of test frame

Figure 3 shows the setting situation of the test frame to the furnace. By this setting situation, one of the ends of the heated steel beam was fixed and the other one end was free. Therefore, the steel beam was able to expand in the direction of its axis. Three sides of the RC slabs excluding the side on the expansion direction of the steel beam were completely restrained to the test furnace. The heating length of the steel beam was 6.0 m and the heating surface of the RC slab was 2.95×3.0 m (2.95×1.95 m in the case of the RC slab arranged on only one side of the beam). In addition, as these test focused on the thermal elongation of the steel beam, the vertical load was not applied to the test frames.

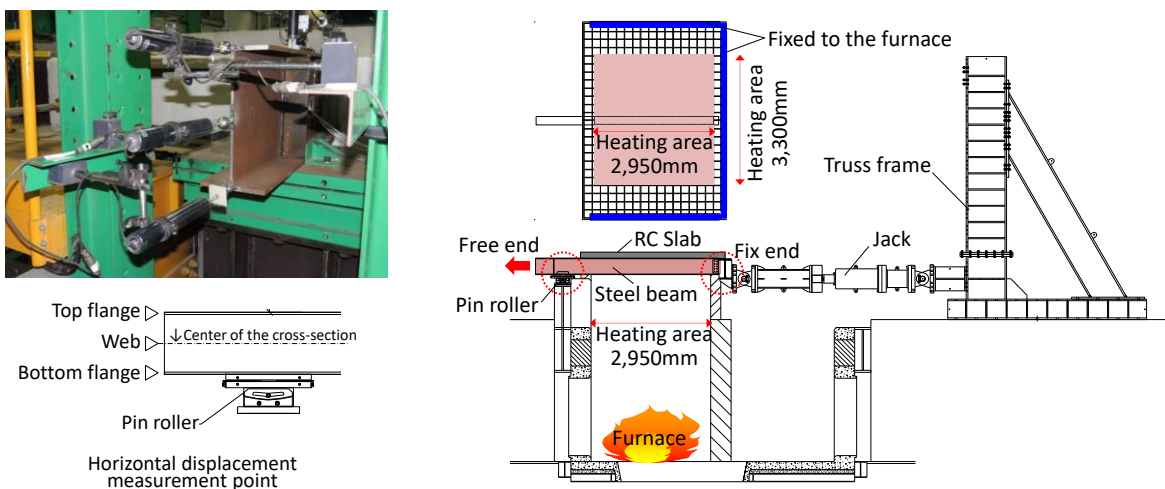


Figure 3. Schematic setting situation of the test frame to the furnace

Horizontal displacements of the heated beams at the free end were measured at the top flange, the web (centre of the cross-section) and the bottom flange (see Figure 3). Temperatures of the heated beams were measured at two locations on the heating length, using a couple of thermocouple each at the top flange, the web and the bottom flange. Therefore, in the studies carried out by the authors including this study, the average values of the measured temperatures of each couple of thermocouple were considered as the temperatures of each part.

2.3 Test result

Figure 4 shows the ratio of the test value of the thermal elongation of the steel beam to the free expansion value provided by Eurocode 4 [5]. Considering the ratio of the thermal elongation at the web position (centre of the cross-section), the thermal elongations of beams with RC slabs on both sides were around 80% to 90% of those of the free expansion. On the other hands, the thermal elongations of beams with RC slabs on one side were around 90% to 100 % of those of the free expansion.

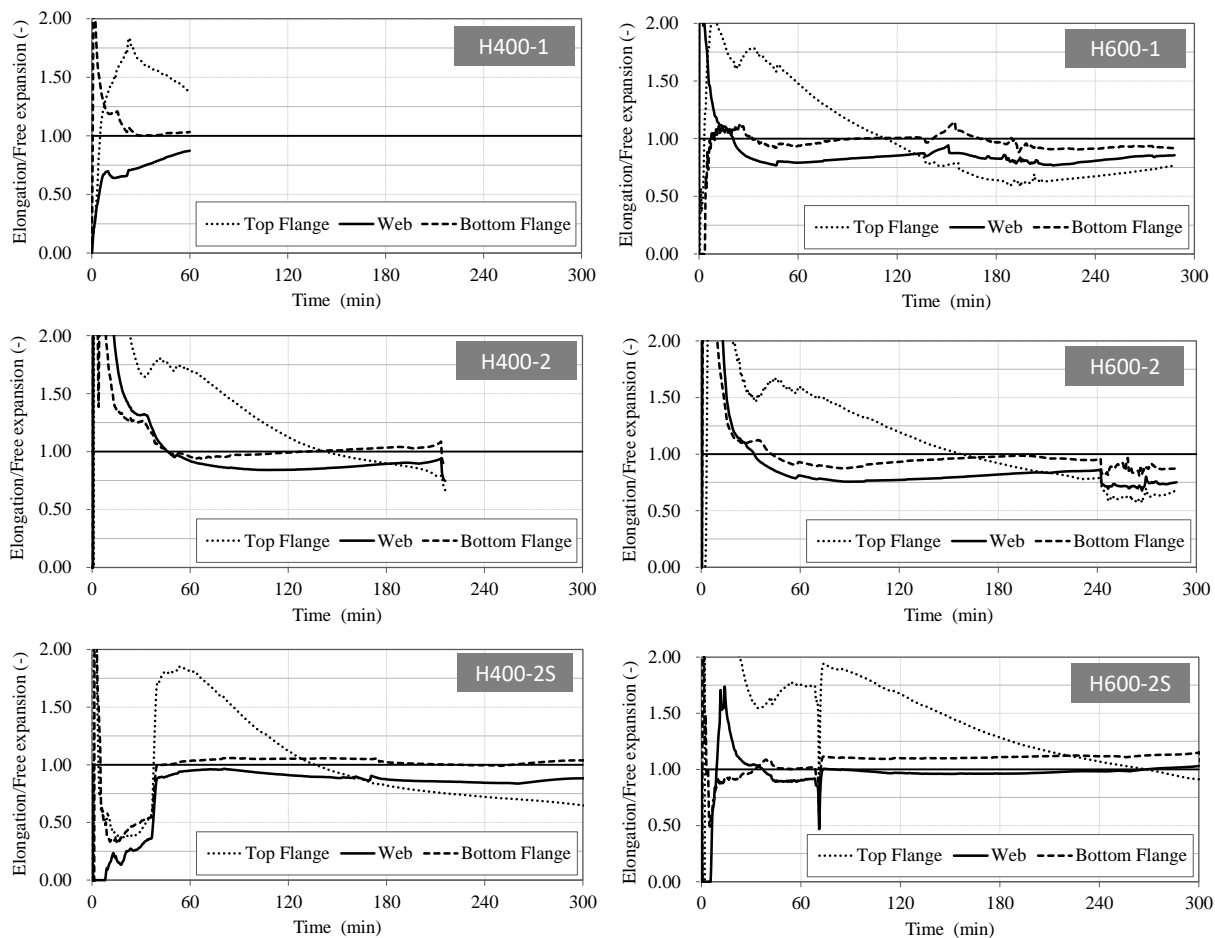


Figure 4. Ratio of the test thermal elongation to free expansion by Eurocode 4

3 EVALUATION METHOD

In this study, the aim was to calculate simply the thermal elongation of steel beams during fire in an actual building without using advanced analyses such as the FEM. To do so, the heated beam was considered as a wire rod element, and the evaluation point of the thermal elongation of the steel beam was defined as the centroid of its cross-section taking into consideration the reduction of Young's modulus due to temperature rise.

3.1 Theory of thermal elongation

The evaluation method of the thermal elongation of the steel beam in the present study was based on simple theories of thermal expansion and boundary conditions of steel beams assuming that the temperature of the cross-section is uniform. Figure 5 shows schematic diagram of the relationship of the thermal elongation boundary conditions of beams. When the ends of a beam are completely fixed, only thermal stresses develop. On the other hands, when an end of a beam is free, only thermal expansion occurs. Furthermore, when an end of a beam is restrained by springs both thermal stresses and expansion take place. In an actual building, it was considered that the thermal elongation of the heated steel beams was restrained by the bending rigidity of adjacent structural members such as columns and transverse beams. When the restraining effect of adjacent structural members could be considered as a spring at the end of the steel beam, it might be possible to evaluate the thermal elongation of the steel beam during fire by the simple theoretical formula given in [6].

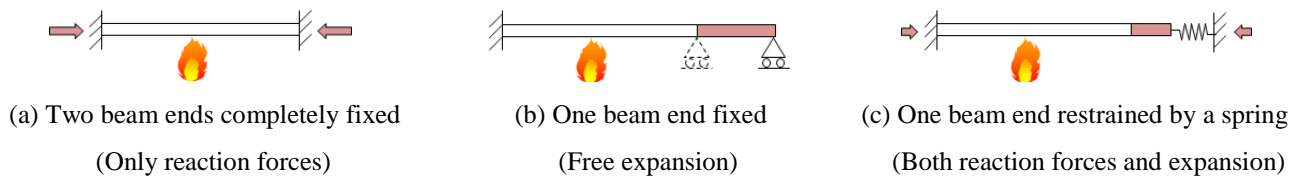


Figure 5. Schematic diagram of the relationship of the thermal elongation and the boundary condition

3.2 Evaluation point

Generally, since RC slabs are placed on the top of steel beams in actual buildings, top flanges of the heated beams during fire are not subjected to heat from the interface with the RC slab, and a temperature difference occurs in the cross-section. In case the steel beam could expand freely on its cross section, the thermal strain distribution would be considered non-linear as the temperature distribution. However, in practice, the thermal strain of steel beams was considered linearly distributed even if the temperature distribution in the cross-section of the heated beams was non-linear as shown in figure 6.

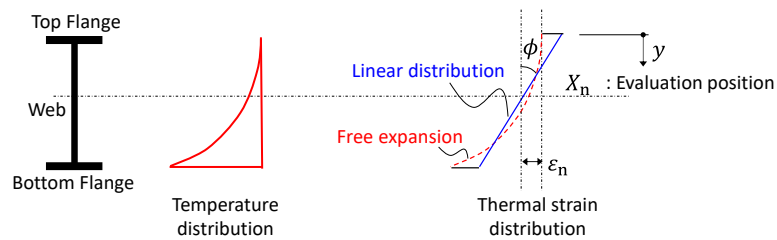


Figure 6. Schematic diagram of the evaluation position

The evaluation position of the thermal elongation of the steel beam in the present study was defined as the centroid of the cross-section taking consideration the reduction of Young's modulus due to temperature rise. The evaluation position (X_n) is given by:

$$X_n = \frac{\int sE(T) \cdot y \, dA}{\int sE(T) \, dA} \quad (1)$$

where $sE(T)$ is Young's modulus of steel considering high temperature, and the reduction ratio of the Young's modulus of steel at elevated temperature provided by Eurocode 4 is used.

3.3 In-plane stiffness of RC slab

In the past study [1], the restrain effect of the RC slab to the thermal elongation of the steel beam was presented by its in-plane bending stiffness. In addition, the ratio of the in-plane bending stiffness reduction due to cracks at elevated temperature was indicated by an exponential Equation.

(See Equation 2) However, Equation 2 was based on only tests in the case of the beam with RC slabs on their both sides.

$$\frac{K_{slab}(T)}{E K_{slab}(T)} = \beta \cdot \exp(-s T_{TF} \cdot A_{TF} \cdot 10^{-6}) \quad (2)$$

where $K_{slab}(T)$ is the bending stiffness of the RC slab considering the reduction due to the deterioration including cracks at elevated temperature, $E K_{slab}(T)$ is the elastic bending stiffness of the RC slab considering only the reduction of Young's modulus due to temperature rise, β is a constant depending on the beam height, $s T_{TF}$ is the top flange temperature of the beam and $s A_{TF}$ is the top flange area of the beam.

In this study, the evaluation formula (equation 2) proposed in the past study [1] was improved considering test results in the case of the beam with the RC slab arranged on only one side of its sides. Figure 7 shows the ratio of stiffness reduction of the tested RC slabs. The vertical axis illustrates the ratio of the bending stiffness reduction and the values on the horizontal axis are obtained by dividing the product of the top flange area and the top flange temperature by 1.5 times of the beam height. Only when the value on the horizontal axis was beyond 2.00×10^3 , the stiffness reduction ratio of RC slabs was approximately expressed by Equation 3 for all specimens, because before that range the thermal elongations of RC slabs in the early time of the heating were larger than the thermal elongations of the steel beams.

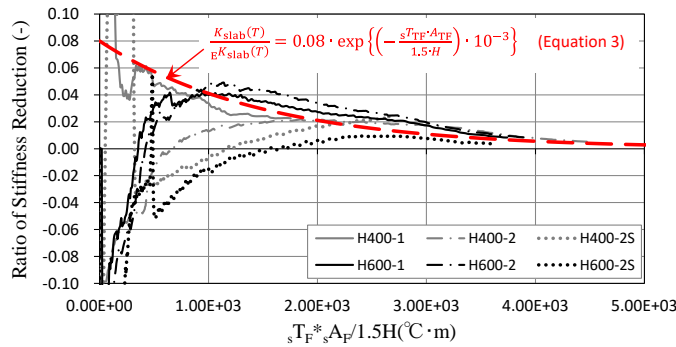


Figure 7. Ratio of the bending stiffness reduction of the RC slab

$$\frac{K_{slab}(T)}{E K_{slab}(T)} = 0.08 \cdot \exp\left(-\frac{s T_{TF} \cdot A_{TF}}{1.5 \cdot H} \cdot 10^{-3}\right) \quad (3)$$

3.4 Thermal elongation of steel beams during fire

In this study, the restrain effects of adjacent structural members and adjacent frames were cumulated at the end of the heated beam as in the past study [1]. The cumulated restrain effect was calculated by Equation 4 as combining springs at the end of the heated beam (cf. Figure 1).

$$K_{total} = K_{column}(T) + K_{tr_beam}(T) + \frac{1}{\frac{1}{K_{slab}(T)} + \frac{1}{K_{adjacent}}} \quad (4)$$

where K are the stiffnesses of the adjacent structural members or adjacent frames and subscript means names of members or frames.

Furthermore, the thermal elongation of the steel beam restrained by a spring at the end could be calculated by Equation 5 which was based on the simple theory of the thermal expansion and boundary conditions.

$$\Delta\ell(T_n) = \ell \cdot \int_0^{T_n} \alpha(T) \cdot T \cdot \left[1 - \frac{1}{1 + \frac{\int_0^T E(T) dA}{K_{total} \cdot \ell}} \right] \quad (5)$$

where ℓ is the heating length of the steel beam, $\int_0^{T_n} \alpha(T)$ is thermal expansion coefficient provided by Eurocode 4 and T_n is the beam temperature at the evaluation position.

4 APPLICATION OF EVALUATION METHOD

The improved evaluation method was applied to the actual scale fire test frame [7] simulating a part of an actual building. The test frame was composed of a steel beam connected to an RC slab which was supported by braced lateral frames at two sides. The braced frames simulated the adjacent frame located outside the fire compartment. The boundary conditions of the heated beam were the same as test frames mentioned above, so that the heated beam was able to expand in only one direction (see Figure 8).

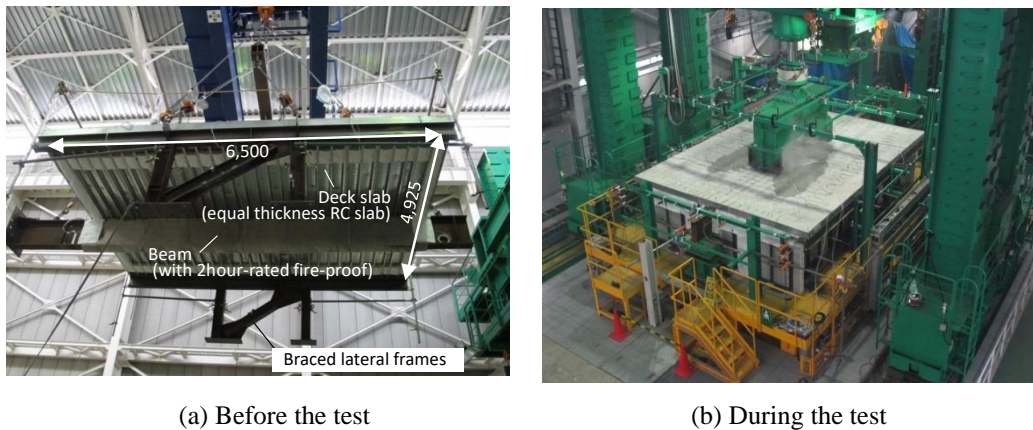


Figure 8. Overview of test frame with bracing

In case of this test, the restrain effects on the thermal elongation were the bending stiffness and the horizontal rigidity of adjacent frames. In other words, the total spring was composed with the bending stiffness of the RC slabs and the horizontal rigidity of adjacent frames. Figure 9 shows the relationship between the calculated value of the thermal elongation and the test result. (The free expansion provided by Eurocode 4 was also included as reference.) The calculated value by Equation 5 using K_{total} (given by equations 3 and 4) in the test frame with bracing was 28.7 mm and the test result was 26.3 mm at 120 minutes after the start of heating. By comparing the calculated value and the test result, both values were approximately similar until 120 minutes. However, beyond the 120 minutes, the calculated elongation became much larger than the test result. Figure 10 shows the local buckling that occurred at the beam bottom flange of the fixed end side. The steel beam was covered with 2hour-rated fire-proof covering. Therefore, it might be considered that the thermal elongation of the steel beam was absorbed by the out-of-plane deformation due to the local buckling which occurred in the beam after 120 minutes. From the above, it was suggested that the proposed evaluation method could easily and conservatively estimate the thermal elongation of the steel beam during fire in an actual building.

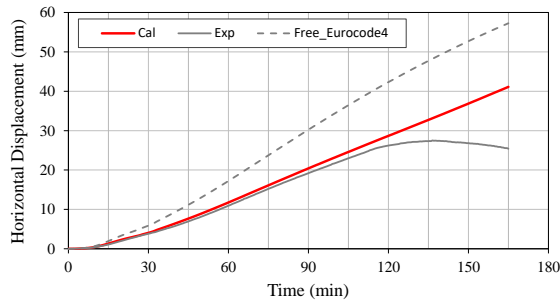


Figure 9. Comparison of the thermal elongations



Figure 10. Local buckling at the bottom flange

5 CONCLUSIONS

This study focused on the thermal elongation of the steel beams during fire in the actual buildings. In addition, the main purpose of this study was to propose a method for evaluating the thermal elongation of steel beams by simple theoretical formula without using advanced analyses such as the FEM.

In this study, the proposed evaluation method in the past study carried out by the authors [1] was improved based on the actual scale fire tests of RC slabs arranged on only one side of steel beams. Furthermore, by applying the improved evaluation method to the test frame which was composed of a steel beam with braced lateral frames on both of its sides and an RC slab at its top, it was found that the calculated values of the thermal elongation by the proposed evaluation method based on simple theoretical formula matched accurately test results.

ACKNOWLEDGEMENTS

This work was supported by JSPS KAKENHI Grant Number JP16H04456.

REFERENCES

1. Tomohito Okazaki, Mamoru Kohno (2016). *Evaluation method for thermal elongation of steel beams and in-plane stiffness reduction of RC slab during fire*. Journal of structural and construction engineering, AIJ. Vol. 81 No. 720, 369-376, Feb., 2016 (in Japanese)
2. NIST NCSTAR 1-9, Federal Building and Fire Safety Investigation of the World Trade Center Disaster: Structural Fire Response and Probable Collapse Sequence of World Trade Center Building 7, Vol. 1, Nov., 2008
3. Tomohito Okazaki, Mamoru Kohno (2015). *Experimental study on thermal elongation of steel beams connected to RC slab during fire*. Journal of structural and construction engineering, AIJ. Vol. 80 No. 718, 2011-2020, Dec., 2015 (in Japanese)
4. Tomohito Okazaki, Mamoru Kohno (2016). *Thermal elongation of side steel beams connected to RC slab during fire*. Journal of Technology and design, AIJ, 89-90, Aug., 2016 (in Japanese)
5. BS EN 1994-1-2: Eurocode 4 -Design of composite steel and concrete structure-, Part1-2: General rules -Structural fire design-. 2005
6. A.S. Usmani, J.M. Rotter, S. Lamont, A.M. Sanad, M. Gillie (2001). *Fundamental principles of structural behaviour under thermal effects*. Fire Safety Journal, Vol. 36 (8). 721-744, Nov., 2001
7. Tomohito Okazaki, Tsutomu Nagaoka, Mamoru Kohno (2013). *Experimental study on thermal elongation of steel beams in fire –Suppressive effect of adjacent frames connected by RC slab-*. Journal of structural engineering, AIJ. Vol. 59B, 232-238, Mar., 2013 (in Japanese)

EXPERIMENTAL INVESTIGATION OF STAINLESS STEEL BOLTS A2-70 DURING AND AFTER FIRE

Sheng Lin Tang¹, Ying Hu^{2*}, George Adomako Kumi³

ABSTRACT

The performance of any component of steel connections during and after fire is of great worth in the general analysis, assessment and design of fire resistant steel structures. In order to uncover more information and better understanding of the behaviour of stainless steel bolts during and after fire, a comprehensive experimental study was performed and has been presented in this study. A total of 72 M20 × 120 size of stainless steel bolts A2-70 were used in this experimental process. 52 of the stainless steel bolts were initially subjected to different high temperatures from ambient temperature to 900°C subsequently being allowed to cool down to ambient temperature with the aid of two cooling methods: natural air and water. The bolts were then processed into standardised coupon specimens before conducting tensile tests on them. On the other hand, the remaining 20 stainless steel bolts were directly processed into tensile coupon specimens and then heated to specified temperatures and consequently loaded at a constant temperature until failure occurred. Through the tensile tests, mechanical properties mainly: the 0.2% yield strength, ultimate strength, ultimate strain and elastic modulus were determined of stainless steel bolts A2-70 during and after fire. It is widely expected that this study will lead to a better understanding of the application and performance of austenitic stainless steel bolts A2-70 in structural applications.

Keywords: Stainless steel bolts, natural air cooling method, water cooling method, mechanical properties.

1 INTRODUCTION

Since, the global collapse of the Twin Towers of the World Trade Centre Building located in New York, due to the terrorists attack in September 2001, the focus of the engineering community has now been steered towards the understanding of the consequences of connection failure due to the outbreak of fire. In addition to the events of the September 11, 2001 terrorists' attacks, the Cardington Fire Experiments have also contributed to generating a widespread interest in the behaviour of steel connections. Connections are known to play a major role in the transfer of loads from one member to another. Hence, any failure in connections is likely to result in partial or total collapse of the structure.

Over the course of time, various research studies have been conducted globally concerning the behaviour of steel connections and its associated components mainly bolts during and after fire [1-5]. Unfortunately, the focus of these previous researches has been centred on high strength steel bolts whilst the knowledge of the performance of stainless steel bolts remains relatively unknown. Stainless steel materials have been adjudged by many researchers as a material that possesses

¹ Graduate Student. School of Civil Engineering, Chongqing University, Chongqing, China.
e-mail: 2279099024@qq.com

^{2*} Associate Professor. School of Civil Engineering, Chongqing University, Chongqing, China.
e-mail: y.hu@cqu.edu.cn

³ Graduate Student. School of Civil Engineering, Chongqing University, Chongqing, China
e-mail: gegekumi2@yahoo.com

improved fire resistance as compared to other conventional steels and structural steels. In view of this assertion, it is expected that stainless steel bolts will offer much of the same improved fire resistance when used in structural applications.

The dearth of available literature on the performance of stainless steel bolts during and after fire has prompted the exigent need for this research. This research study essentially reports on an experimental investigation carried out on austenitic stainless steel bolts A2-70 to evaluate both the mechanical properties at elevated temperatures and post-fire mechanical properties after cooling down to ambient temperature. Two cooling methods with different cooling rates were considered. Through data from the experimental investigation, an assessment of the various mechanical properties during and after the course of fire will be conducted as part of this study.

2 EXPERIMENT PROGRAMME

2.1 Test specimens

In this experimental process, commercially available fully threaded stainless steel bolts A2-70 of 20mm diameter and 120mm length were used for the tests as shown in Figure 1. The standardised A2-70 stainless bolts were ordered based on provisions stipulated in the GB/T 3098.6 [6] and the BS EN ISO 3506-1 [7]. According to the ISO 4954 [8], the stainless steel material for the manufacturing of this bolt is the austenitic stainless steel grade EN 1.4301. The chemical compositions of the stainless steel bolt A2-70 has been outlined in *Table 1*.

Table 1. Chemical composition of stainless steel bolt A2-70

A2-70	Chemical composition (%)									
	C	Si	Mn	P	S	Ni	Cr	Mo	Cu	N
Material report	0.032	0.40	0.62	0.044	0.004	8.04	18.33	0.08	0.83	0.051
ISO 3506-1	0.100	1.00	2.00	0.045	0.03	8.0-9.0	15.0-20.0	-	4.00	0.22

A total of 72 bolts were processed into standard coupon specimens as shown in Figure 2. 52 of the total processed coupon specimens were used for the post-fire tests whilst the remaining 20 were used for the high temperature tests. The geometry and dimensional details of the standard coupon specimens have been outlined in Figure 2 below. Prior to the conducting of the tensile tests, both ends of the coupon were threaded to enable a firm grip to be made whilst the lower end was allowed to expand freely.



Fig. 1. Stainless steel bolt

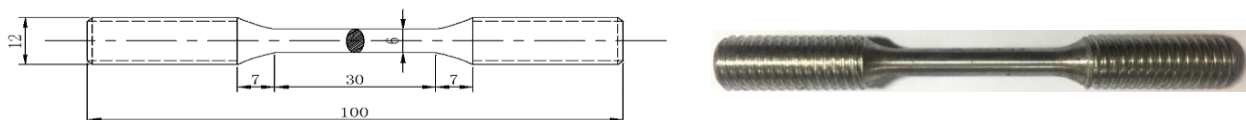


Fig. 2. Dimensions of standard tensile coupon specimens

2.2 Heating and Cooling

An electronically controlled automatic heating furnace which boasts of a maximum heating rate of 500W in addition to a maximum heating temperature of 950 degrees was used to heat the bolts. A total of 52 bolts were heated in the electric furnace. In order to measure the temperature of the bolts, one end of a thermocouple was fixed into a drilled hole located in the bolt head for accurate measurement of the temperature experienced within the bolts whilst the other end was connected to a computer through a data logger system for recording of the temperature experienced during the heating and subsequent cooling processes. The bolts were heated from room temperature up to pre-selected temperatures at a rate of 20°C/min. Upon reaching the targeted temperature, a soaking period of 25 minutes was allowed in order to ensure uniform temperature circulation within the

bolts. The margin of error allowed in the temperature tests was $\pm 5^{\circ}\text{C}$ degrees. Thirteen temperatures gradients ranging from 20°C , 100°C , 200°C , 300°C , 400°C , 500°C , 600°C , 650°C , 700°C , 750°C , 800°C , 850°C and 900°C were selected for the residual tests. For this experiment investigation, two cooling methods were used: natural air cooling and cooling under water. These two methods were chosen carefully to depict the two possible scenarios; one in which a fire is made to burn up naturally and the use of water to extinguish fire [9-10]. It should be noted that all specimens were free from loading during the heating and cooling. The temperature-time relationship for the tests has been illustrated in Figure 3.

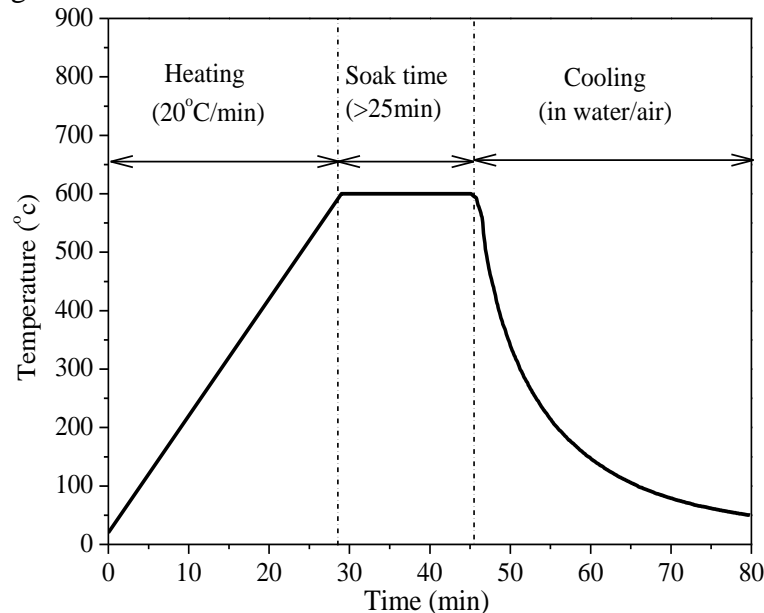


Fig. 3. Temperature-time relationship

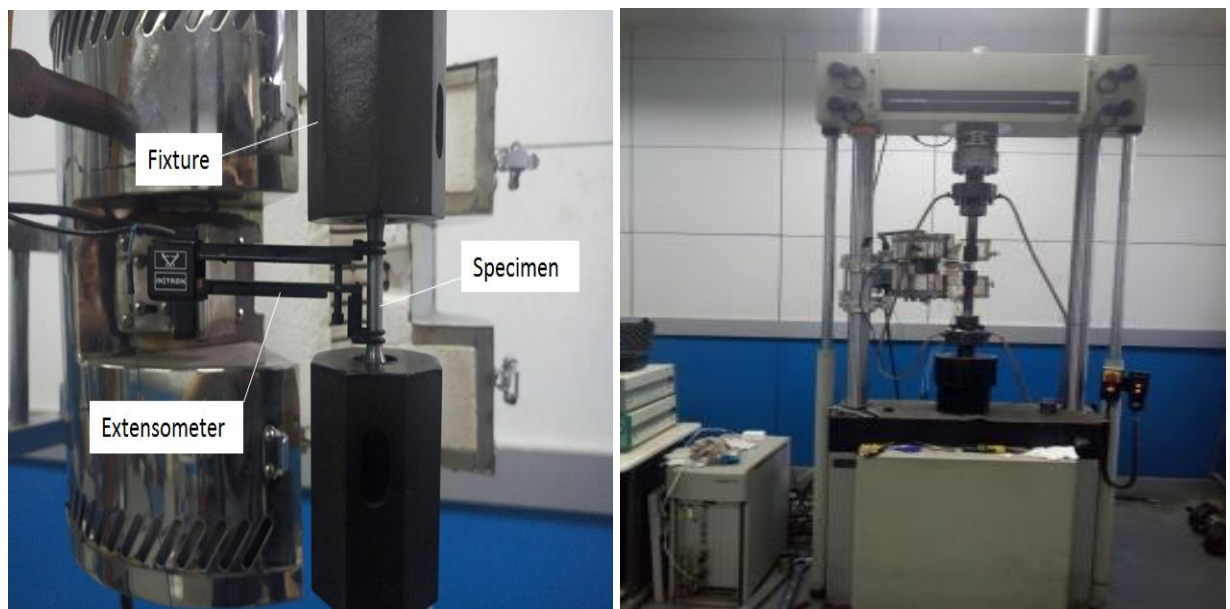


Fig. 4. Experimental setup arrangement

2.3 Testing

There are two kinds of tensile test, room temperature tensile test and high temperature tensile test. In accordance to the requirements of the ISO 6892-1: 2009 and ISO 783: 1999, 52 coupon specimens which had been earmarked for the post-fire tests were subjected to the room temperature tensile tests whereas 20 untreated coupon specimens which had been earmarked for the high

temperature tests of temperature gradients including 20°C, 100 °C,200 °C,300 °C,400 °C,500 °C,600 °C,700 °C,800 °C and 900 °C were subjected to the high temperature tensile tests. Each tensile test was initially performed at an estimated strain rate of 0.00025/s ($\dot{\epsilon}_{Lc}$) until the expected proof strength was reached after which the strain rate was increased further to 0.002 /s ($\dot{\epsilon}_{Lc}$) until fracture occurred. In order to measure the strain variations, a uniaxial strain gauge extensometer of lengths 25mm and 12.5mm was used for the room temperature and high temperature tensile tests respectively. Test equipment setup and arrangement can be seen in Figure 4. During the testing, the full-range stress-strain curve was recorded for the coupon specimens with critical material properties obtained e.g. 0.2% proof strength ($f_{0.2,T}$), ultimate tensile strength ($f_{u,T}$), Young’s Modulus ($E_{0,T}$) and ultimate strain ($\epsilon_{u,T}$). It is noteworthy that the subscript T indicates that the maximum temperature experienced of the post-fire bolts and also indicates that the temperature around the bolts during tensile for high-temperature tests. Without the subscript T, it means no post-fire treatment and room temperature experiment.

2.4 Experimental results

Both high temperature and post-fire mechanical properties of the austenitic stainless steel bolts are thoroughly discussed in this section. A summary of both the reduction factors (high temperature tests) and residual factors (post-fire tests) for the experimental tests conducted on the stainless steel bolt A2-70 have been shown in Table 2.

Table 2. Experimental results

T (°C)	$f_{0.2,T}/f_{0.2}$			$f_{u,T}/f_u$			$E_{0,T}/E_0$			$\epsilon_{u,T}/\epsilon_u$		
	HT	CA	CW	HT	CA	CW	HT	CA	CW	HT	A	W
20	1.00	1.00	1.00	1.00	1.00	1.00	1.00	1.00	1.00	1.00	1.00	1.00
100	0.94	1.00	0.99	0.81	1.00	1.00	0.96	1.05	1.08	0.80	1.02	1.02
200	0.86	1.07	1.00	0.72	1.01	0.99	0.83	1.11	1.12	0.37	1.06	1.06
300	0.83	1.13	1.12	0.66	1.01	1.01	0.81	1.08	1.07	0.34	1.03	1.07
400	0.85	1.18	1.13	0.70	1.04	1.00	0.98	1.13	1.01	0.32	1.01	1.05
500	0.76	1.14	1.12	0.61	1.02	0.99	0.87	1.09	1.13	0.39	1.05	1.06
600	0.68	1.12	1.06	0.53	1.02	1.01	0.86	1.20	1.10	0.28	1.03	1.10
650	-	1.02	0.98	-	1.02	0.99	-	1.15	1.09	-	1.06	1.10
700	0.51	0.99	0.91	0.36	1.01	0.99	0.69	1.19	1.05	0.09	1.06	1.09
750	-	0.93	0.90	-	1.01	1.00	-	1.20	1.12	-	1.05	1.08
800	0.32	0.91	0.85	0.22	1.00	0.99	0.56	1.09	1.08	0.04	1.05	1.02
850	-	0.88	0.84	-	1.00	0.99	-	1.18	1.06	-	1.12	1.14
900	0.11	0.84	0.84	0.10	0.97	0.99	0.43	1.19	1.16	0.38	1.19	0.93

Note: HT- High temperature, CA- Cooling in natural air and CW - Cooling in water

2.5 0.2% yield strength

The 0.2% yield strength was evaluated based on the yield strength which corresponds to the 0.2% strain on the stress-strain curve by adopting the intersection point of the stress-strain and the proportional offset line by the 0.2% strain [10]. In order to examine the rate of degradation, the results of the 0.2% yield strength for both the high temperature and post-fire temperature tests were utilised to derive reduction factors and residual factors. The reduction or residual factors were determined based on the ratio of the 0.2% yield strength measured at each designated temperature to the 0.2% yield strength measured at ambient temperature. A plot of the 0.2% yield strength reduction and residual factors for the A2-70 stainless steel bolt has been illustrated in Figure 5.

A review of the high temperature test results did indicate that the 0.2% yield strength of the A2-70 stainless steel bolts when subjected to temperatures exceeding 100°C starts to decrease similarly to the behaviour of other conventional steels. It was also observed that the reduction in 0.2% yield

strength that occurred in the A2-70 at elevated temperatures was gradual at temperatures lower than 600°C whilst a steep decrease was seen in temperatures higher than 600°C.

On the other hand, results of the post-fire tests showed that the residual yield strength at temperatures lower than 600°C suffered no significant degradation irrespective of the cooling method adopted. At extremely high temperatures of 900°C, the residual yield strength retained is about 84% of the 0.2% yield strength measured at room temperature for both cooling methods.

2.6 Ultimate strength

The resulting ultimate reduction and residual factors were also derived from the mean reduction and residual factors obtained from the test results. The results showed that the reduction in strength of the A2-70 gradually deteriorated as temperature increased. For the residual factors, no obvious difference was seen in the effects of both cooling methods on the residual ultimate strengths. It can also be stressed that the application of the two cooling methods allows the nominal ultimate strength to be recovered even after being heated up to 900°C. A graphical representation of the results has been shown in Figure 6.

2.7 Elastic modulus

The Elastic modulus was determined from the initial slope of the stress-strain curve. The trend of results of the elastic modulus reduction factors at high temperatures reveals a gradual loss from room temperature up to 900°C. Similarly, to that of the residual yield and ultimate strengths, there was no significant difference between the effects of the cooling methods on the residual elastic modulus. As far as both cooling methods were concerned, there was no loss in elastic modulus throughout the tested temperature range. This shows that the nominal stiffness of the A2-70 can be recovered when cooled down from 900°C to ambient temperature whilst using either natural air or water cooling methods as has been highlighted in Figure 7.

2.8 Ultimate strain

The ultimate strain is often termed as the strain corresponding to the ultimate strength. The reduction and residual factors of the ultimate strain at both high temperatures and post-fire temperatures have been plotted in Figure 8. For the high temperature tests, a sharp decrease in ultimate strain was experienced especially at temperatures below 800 °C whilst for the post-fire temperature conditions, no significant variations were witnessed at temperatures less than 800°C for both water and natural air cooling methods. However, it was seen that at temperatures above 800 °C, the residual ultimate strains increased in the case of air cooling whilst a significant reduction was experienced in the case of the water cooling methods.

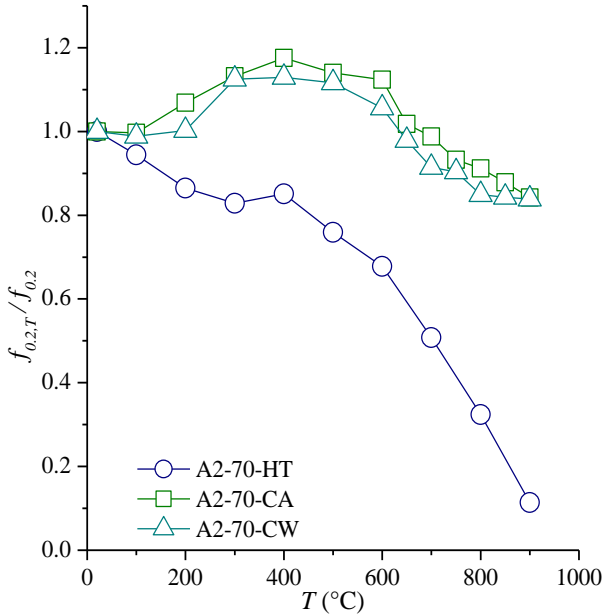


Fig. 5. 0.2% yield strength

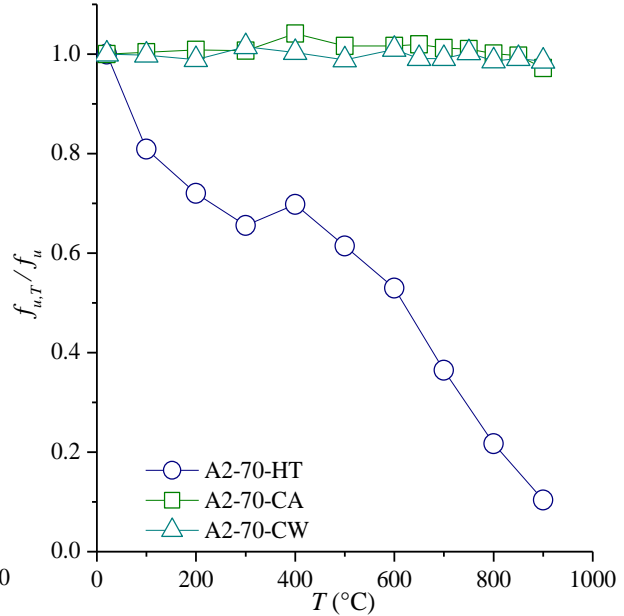


Fig. 6. Ultimate strength

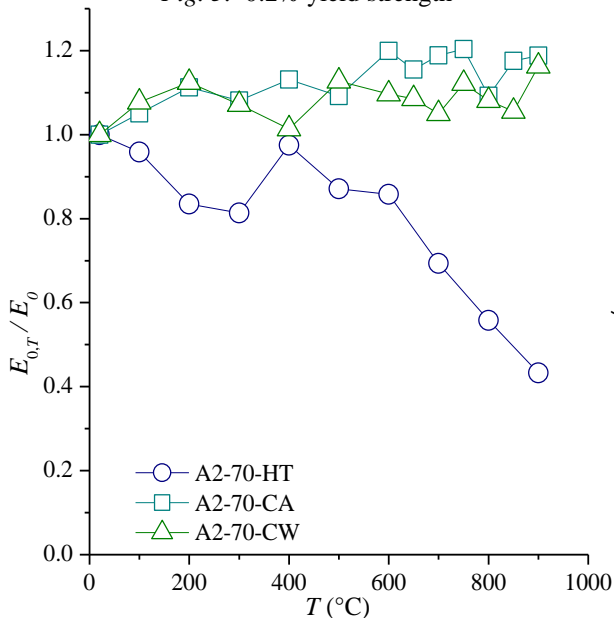


Fig. 7. Elastic modulus

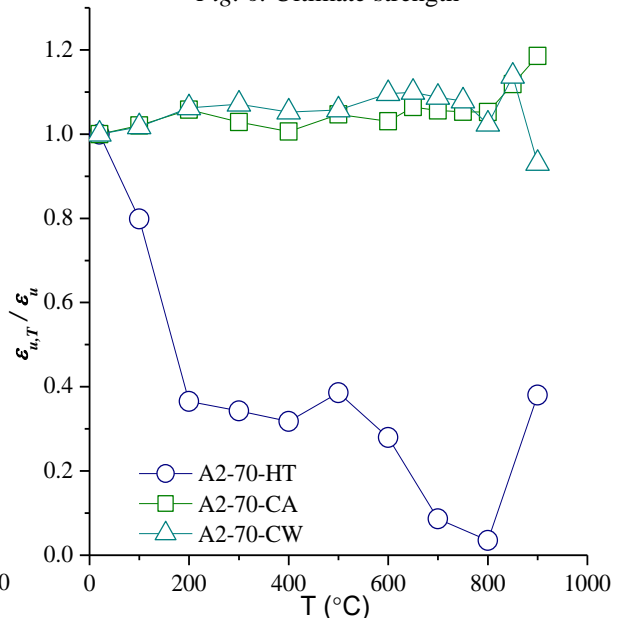


Fig. 8. Ultimate strain

3 CONCLUSIONS

In this research study, a series of experimental tests were conducted to determine both the mechanical properties of stainless steel bolts A2-70 during and after fire. The post-fire tests involved two cooling methods that have different cooling rates. Relevant mechanical properties such as the 0.2% proof strength ($f_{0.2,T}$), ultimate tensile strength ($f_{u,T}$), Young's Modulus ($E_{0,T}$) and ultimate strain ($\epsilon_{u,T}$) were determined. The experimental investigation revealed that at high temperatures, the A2-70 stainless steel bolts suffer a rapid deterioration in mechanical properties; on the contrary it can be well maintained without significant decrease for post-fire tests especially it has a little increase below 600 degrees for the 0.2% proof strength, and the initial elastic modulus with a gradual increase associated with a slight fluctuation can also be found. There is no obvious difference in the effect of the cooling method on the material properties of the A2-70 bolts after fire.

ACKNOWLEDGEMENTS

The research discussed in this paper is part of Project No. 51578092 funded by National Natural Science Foundation of China, Project No. 106112016CDJXY200006 funded by Central Government Educational Association, Project No. cstc2016jcyjA1097 funded by Chongqing Science and Technology for Fundamental Science and Leading Technology and Project No. cstc2015shmszx1227 funded by Chongqing Science & Technology Commission for Technology Innovation of Social Business and Insurance. These financial supports are gratefully acknowledged by the authors. The valuable comments and assistance of Mr. Wen, J.L. and Mr. Yao, G. from Shenyang National Laboratory for Materials Science of the Chinese Academy of Sciences are also appreciated.

REFERENCES

1. Venkatesh Kodur, Sonali Kand, Wassim Khaliq (2012). *Effect of temperature on thermal and mechanical properties of steel bolts*. Journal of Materials in Civil Engineering, 24(6).pp 765-774.
2. B.R. Kirby (1995). *The behaviour of high-strength grade 8.8 bolts in fire*. Journal of Constructional Steel Research, 33. pp 3-38.
3. Guo-Qiang Li, Shou-Chao Jiang, Ying-Zhi Yin, Kai Chen, Ming-Fei Li (2003). *Experimental studies on the properties of constructional steel at elevated temperatures*. Journal of Structural Engineering, 129(12). pp 1717-721.
4. Y. Sakumoto, T. Yamaguchi, M. Ohashi, H. Saito (1992). *High temperature properties of fire-resistant steel for buildings*. Journal of Structural Engineering, 118(2). pp 392-407.
5. Y. Theodorou (2001). *Mechanical properties of grade 8.80 bolts at elevated temperatures*. MSc Dissertation, University of Sheffield, UK.
6. GB/T 3098.6 (2014). *Mechanical properties of fasteners-Stainless steel bolts, screws and studs*. China Standard Press, Beijing. (In Chinese).
7. ISO 3506-1 (2009). *Material properties of corrosion resistant stainless steel fasteners- Part 1 Bolts, screws and studs*. ISO copyright office, Switzerland.
8. ISO 4954-2 (1993). *Steels for cold heating and cold extruding*. ISO copyright office, Switzerland.
9. Guo-Biao Lou, Shang Yu, Rui Wang, Guo-Qiang Li (2012). *Mechanical properties of high strength steel bolts after fire*. Structures and Buildings, 28(SB7).
10. Weiyong Wang, Tianzi Liu, Jiepeng Liu (2015). *Experimental study on post-fire mechanical properties of high strength Q460 steel*. Journal of Constructional Steel Research 114. pp 100-109.
11. Ju Chen, Ben Young (2006). *Stress-strain curves for stainless steel at elevated temperatures*. Engineering Structures, 28. pp 229-239.

Experimental Research and any Other

EXPERIMENTAL STUDY ON THERMAL AND STRUCTURAL RESPONSES OF A FULL-SCALE STEEL STRUCTURE UNDER NATURAL FIRE

Bo Zhong¹, Ya-Qiang Jiang², Guo-Biao Lou³

ABSTRACT

Steel structures can be severely damaged towards total collapse in fire, leading to great number of casualties. In this paper, a full-scale steel portal frame was constructed and was exposed to a natural fire using 6 m³ wood cribs. The temperature development, horizontal and vertical displacements of various structural members are examined from the beginning of ignition until the total collapse of the structure. Post-flashover fire was developed during the test and the characteristics of measured temperatures are discussed and compared with the standard fire curve. Meanwhile, the failure criterion of structural elements is investigated and compared with that in ISO 834-1. Results indicate that the temperature of upper space is higher than that of lower space in the compartment, thus the upper half of steel columns directly exposed to fire are buckling and almost lost their load-bearing capacity at 15 minutes after the ignition. Preliminary analyses show that the rate of column axial deformation seemed to be a reliable indicator representing structural failure. The corresponding formula suggested in ISO 834-1 was verified in this study, which could be potentially used to establish the basis of early warning techniques for firefighting actions.

Keywords: Steel structure, fire, structural collapse

1 INTRODUCTION

In recent years, some large fire incidents have alerted the engineering profession to the possibility of structural collapse under fire scenarios, posing a great threat to safety of people's life and property. For example, the collapse of World Trade Center Building 7 during "9/11" terrorist attacks, and the most recent collapse of the 17-story Plasco Building (Iran) following a huge fire, causing at least 50 firefighters lost their lives. Therefore, it is quite essential to have a deep insight into the behaviours of building structures subjected to fire loading.

In order to investigate the failure mechanisms of structural elements under fire conditions, quite a lot of research work was focused on both thermal and structural behaviours of isolated structural members under standard fire [1,2]. However, these tested results cannot reflect the interaction between structural members of a structural system. Moreover, the natural fire is characterized by three stages: pre-flashover, post-flashover and decay, which is quite different from the standard fire [3]. To address these issues and to improve the knowledge on behaviours of structural system under real fires, a total of seven large-scale fire tests were conducted at Cardington Laboratory [2,4], and the behaviours of structural components with real restraint under real fire are assessed. However, results of structural collapse are not generated since all the columns are fire protected.

¹ Research Assistant. Sichuan Fire Research Institute of Ministry of Public Security, Chengdu, China.
e-mail: zhongbo_scfri@163.com

² Research Assistant. Sichuan Fire Research Institute of Ministry of Public Security, Chengdu, China.
e-mail: yaqiang.jiang@foxmail.com

³ Professor. College of Civil Engineering, Tongji University, Shanghai, China.
e-mail: gblou@tongji.edu.cn

In this paper, a full-scale steel portal frame structure was constructed and was subjected to a natural fire resembling factory storage scenarios. The principle purpose of this study is to fully investigate the thermal and overall structural behaviours of steel structures as well as the initiation symptoms of structural collapse.

2 EXPERIMENTAL PROGRAM AND INSTRUMENTATION

The full-scale steel portal frame is constructed with a 4 m×6 m fire compartment, in which 6 m³ wood cribs are uniformly distributed. The plan and elevation views are shown in *Fig. 1*, and it has one-story and is two bays wide (2×6 m=12 m) by one bay deep (6 m) in plan. The roof and perimeter walls are constructed with stone wool sandwich panels, and the inner partition wall has a 3-hour fire resistance level to prevent fire propagation as shown in *Fig. 2. a*).

The test frame structure is heavily instrumented with thermocouples and linear variable differential transducers (LVDT) to measure temperatures and deformations of critical regions and members, respectively. It is necessary to impose some vertical load onto the structure so that a specific loading level could be achieved. As can be seen in *Fig. 2. b*), sand bags are hung onto the steel beams to represent the vertical loading system in this study.

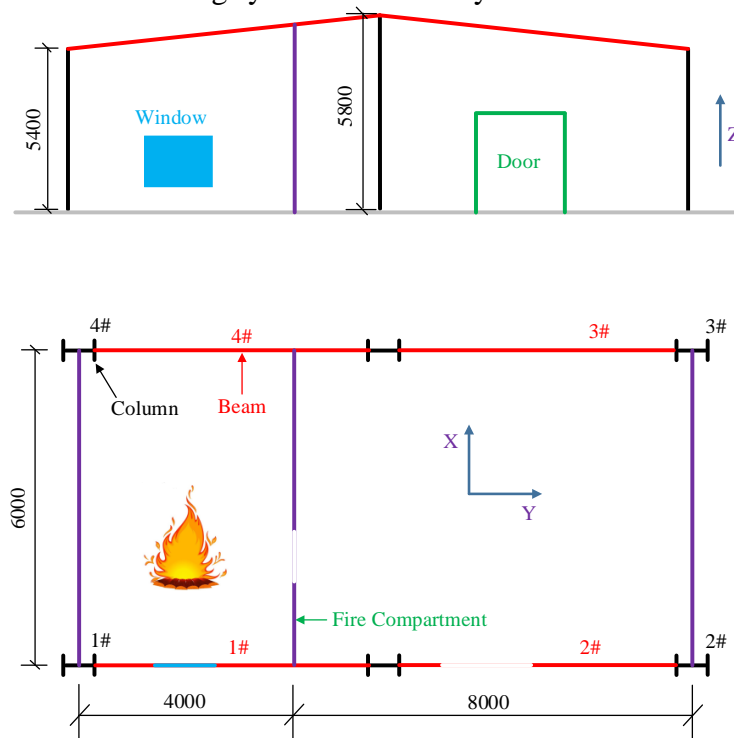


Fig. 1. Plan and elevation views of the steel structure



Fig. 2. a) The inner partition wall; b) The sand bags for vertical loading

3 EXPERIMENTAL RESULTS

3.1 Thermal response

All the beams and columns are unprotected in this test. And the thermocouples are settled in the 1/4, 2/4, 3/4 and 4/4 of the column height, as shown in *Fig. 3*. In addition, five different positions of the column section are equipped with thermocouples, which is also shown in this figure.

The measured time-temperature curves of column 1# (section n/4-3#) and the standard ISO-834 fire curve for structural fire design are compared in *Fig. 4*. As can be observed from this figure, after about 300 seconds of ignition, flashover occurred in the fire compartment with the window glass broken. Then, the temperature increases to over 1000 °C rapidly, at which temperature steel material almost loses its strength completely [5], leading to buckling of the upper half column. This is mainly because that the hot air and smoke rise to the roof due to the buoyancy caused by the fire plume, and it is consistent with the measured maximum temperatures of about 1100 °C, 1000 °C, 950 °C and 650 °C at 3/4, 4/4, 2/4 and 1/4 position of column height, respectively. In addition, in the pre-flashover stage, the heating release rate of the standard ISO-834 fire curve is remarkably higher than that of the natural fire in the experiment. However, in the post-flashover stage, the heating release rate of the standard ISO-834 fire curve is slow down, while the measured fire curves are rising rapidly, which indicates that the conventional structural fire design based on standard ISO-834 fire curve may be not reliable.

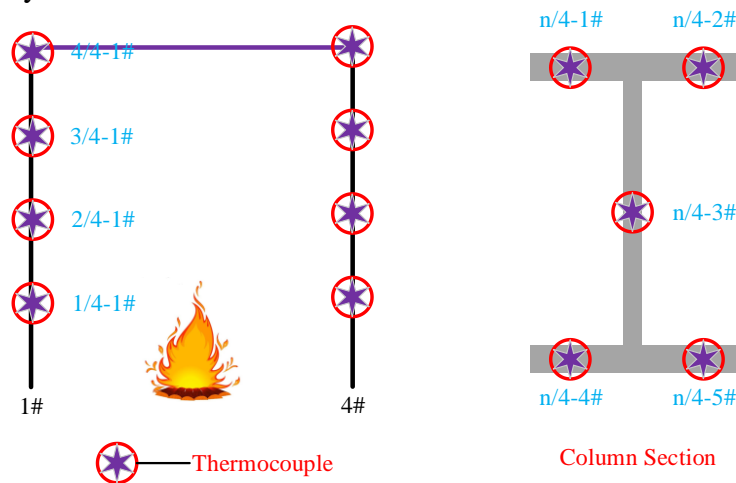


Fig. 3. Thermocouple distributions in the vertical direction and column section

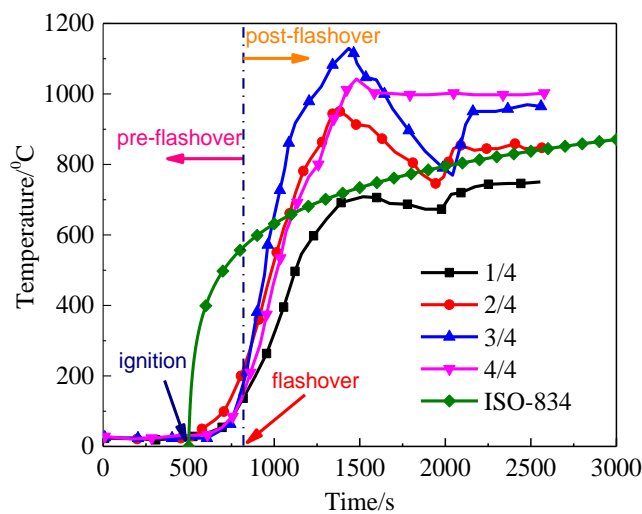


Fig. 4. Comparisons of the standard ISO-834 fire curve and the recorded temperatures in the test

3.2 Structural response

In this experiment, displacement time histories of critical locations on the columns are captured by the LVDTs mounted on the cantilever columns around the tested frame. Fig. 5. a) shows the vertical displacement time histories of column 1#, column 2# and column 3# at the top height. And Fig. 5. b) shows the vertical displacement time histories of column 1#, column 2# and column 3# at the middle height. As can be observed, the axial contraction of column 1# starts to increase at about 6 minutes after ignition, when flashover occurs, and the temperature reaches about 600 °C. Then, the axial contraction rate changes remarkably at about 15 minutes after ignition, while that at middle height does not change a lot, indicating that only upper half of column 1# fails in the fire.

Moreover, the failure points based on both deformation (failure point A) and deformation rate (failure point B) are marked in Fig. 5. a). It is obvious that the failure point calculated from the deformation rate criteria is earlier than that from the deformation criteria, indicating that the deformation rate is a better indicator for early warning of structural collapse in fire.

As shown in Fig. 6. a), the column top end moves outward initially until 15 minutes in the span direction, when it starts to move inward substantially. This is mainly because that expansion of the steel beams puts the columns outward, while the buckling of columns forces it inward. It can be seen from Fig. 6. b) that the bottom half of the column is put outward of about 110 mm permanently, indicating that the bottom half of column 1# and column 4# is still standing.

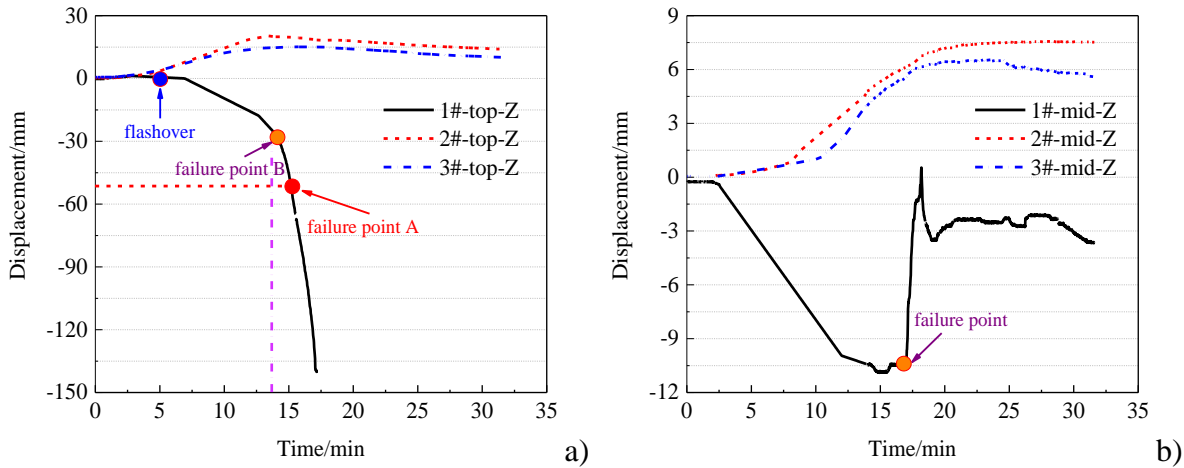


Fig. 5. a) Vertical displacement time histories of columns at the top height; b) Vertical displacement time histories of columns at the middle height

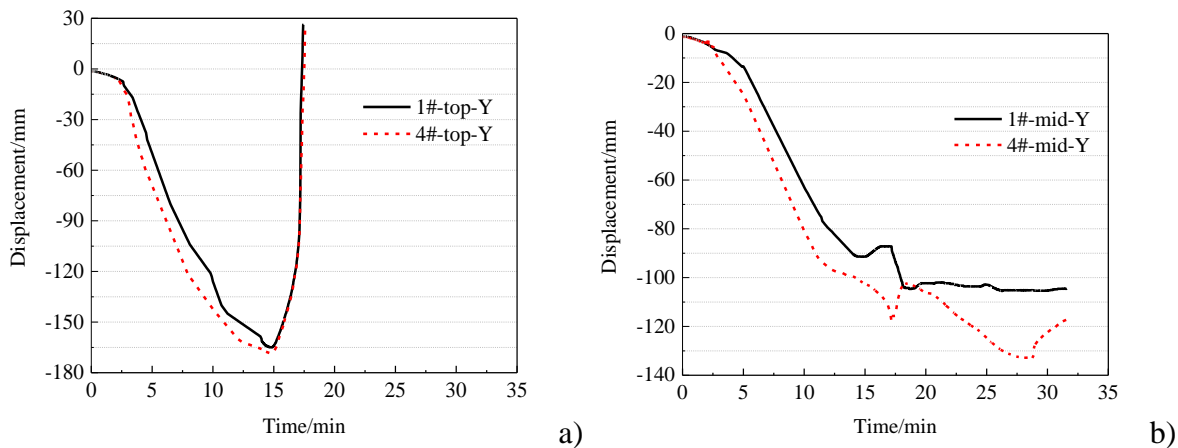


Fig. 6. a) Horizontal displacement time histories of columns at the top height; b) Horizontal displacement time histories of columns at the middle height

4 DISCUSSION ON STRUCTURAL FAILURE MECHANISM

It is essential to have a deep insight into the failure mechanisms of steel structures under fire loading for both structural safety in the design phase and the purpose of early warning of structural collapse. In this experiment, the axial deformations of column 1#, 2#, 3# at both top and middle positions are well compared in *Fig. 5*. As we all know, a natural fire typically has three periods, namely pre-flashover, post-flashover and decay. The flashover was developed at about 5 minutes after ignition with the window glass broken when the local fire spreads to all the wood cribs within the compartment as shown in *Fig. 7. a)*. It can be seen from *Fig. 7. b)* that the beam flanges on top of the partition wall buckled in the high temperature environment, while the right-hand side of the structure survived due to the fire partition wall. *Fig. 7. c)* shows the final state of the corner area of the fire compartment, as can be observed, the unprotected beams and columns are buckled in the fire with the connection teared out.

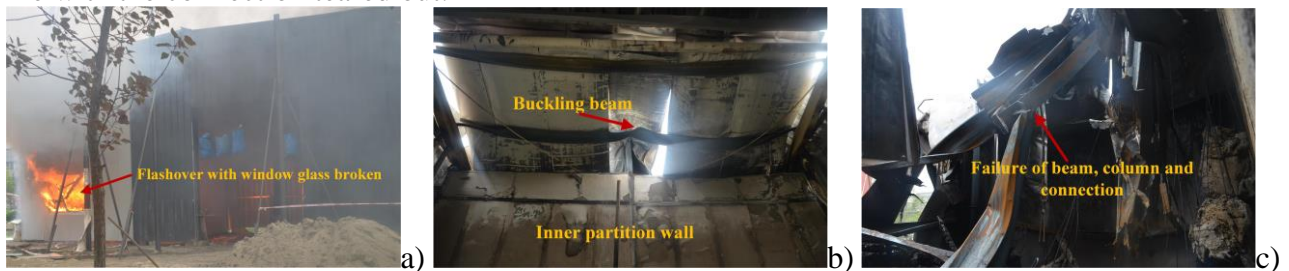


Fig. 7. a) Flashover of the compartment fire; *b)* Buckling of the beam; *c)* Failure of the beam, column and connection in the fire compartment

For axially loaded elements, the limiting axial contraction is $h/100$ mm, and the limiting rate of axial contraction is $3h/1000$ mm/min, where h is the initial height in millimetres [6]. In this experiment, the column height is about 5400 mm, and the calculated limiting axial contraction and limiting rate of axial contraction are 54 mm (failure point A in *Fig. 5. a)*, 16 minutes) and 16.2 mm/min (failure point B in *Fig. 5. b)*, 13.5 minutes), respectively. This indicates that the rate of axial contraction can be a very effective indicator for early warning of structural collapse under fire conditions.

The collapse process of the tested steel frame is shown in *Fig. 8*, as can be observed, the steel structure is severely damaged and suffered a partial collapse in the post-flashover stage with the two load-bearing columns (1# and 4#) buckled under the high temperature up to 1000 °C. However, the local collapse does not transfer to the right-hand side of the structure due to the 3-hour fire resistant partition wall.



Fig. 8. Collapse process of the steel structure

5 CONCLUSIONS

In this study, a full-scale steel portal frame is tested under a natural fire condition. Both temperatures and structural deformations are recorded from ignition until the final collapse state. Some main conclusions are as follow:

- (1) There is a large difference between the standard ISO-834 fire curve and the fire curve generated in a natural fire, which highlights the urgent need for revision of structural fire safety design standard;
- (2) It is very essential to do fireproof protection on load-bearing steel columns;
- (3) The partition wall of fire compartment is very effective to prevent fire propagation and total collapse of the structure;
- (4) The deformation rate can be a very effective indicator for early warning of structural collapse.

ACKNOWLEDGMENT

This research is funded by the National Key R&D Program of China under Grant No. 2016YFC0800604, the Key Program of Fire Department of Ministry of Public Security of China under Grant No. 2015XFGG06 and the funding from Sichuan Fire Research Institute under Grant No. 20188806Z.

REFERENCES

1. Franssen, J. M., Talamona, D., Kruppa, J., Cajot, L. G. (1998). *Stability of steel columns in case of fire: experimental evaluation*. Journal of structural engineering 124(2). pp 158-163.
2. Wald, F., da Silva, L. S., Moore, D. B., Lennon, T., Chladna, M., Santiago, A., Benes M., Borges, L. (2006). *Experimental behaviour of a steel structure under natural fire*. Fire Safety Journal 41(7). pp 509-522.
3. Song, Y. (2008). *Analysis of industrial steel portal frames under fire conditions*. University of Sheffield.
4. Foster, S., Chladná, M., Hsieh, C., Burgess, I., Plank, R. (2007). *Thermal and structural behaviour of a full-scale composite building subject to a severe compartment fire*. Fire Safety Journal 42(3). pp 183-199.
5. EN 1993-1-2 (2005), *Design of steel structures, Part 1.2: General Rules-Structural Fire Design*. European Committee for Standardization (CEN), Brussels.
6. ISO 834 (1999). *Fire resistance tests-elements of building construction*. International Organization for Standardization, Geneva, Switzerland.

FIRE RESISTANT GFRP FAÇADE SYSTEM

Kate Nguyen¹, Tuan Ngo² and Priyan Mendis³

ABSTRACT

With the current trend for sustainable construction, much focus is given on the energy efficiency of the façade. However, the important aspect of fire performance of such façade in fire is of less attention. Since the façade design, and its behaviour in fire changed significantly, it can be the most critical element of building fire spread, if it is not designed with adequate fire resistance. The Grenfell Tower fire has demonstrated how vulnerable modern facades may be to fires and how this vulnerability directly affects the safety of building occupants. In the recent past, more attention has been given to alternative “greener” materials like fibre reinforced polymer composites (FRPCs). This paper will present a comprehensive summary of the analytical, experimental and numerical investigations of fire performance of FRPC façades. Nanoclay is introduced in this study, as a novel flame retardant for FRPCs. This study covering types of thermosetting resins, types of nanoclay at different concentrations and methods to incorporate nanoclay is successfully conducted to predict the optimum combination. Resin and clay types are found to have significant effects on the ratio of peak of heat release rate to time to reach this peak as well as the total heat release responses of the composite. The proposed Component-layer model developed in this work addresses the aim to capture the fire growth index evolution with several case studies conducted.

Keywords: Façade, fire, glass fibre reinforced composites, nanoclay

1 INTRODUCTION

With the current trend for green building concepts to be adopted and sustainable construction, much focus is given on the energy efficiency of the façade. New energy efficient lightweight materials with better thermal insulation properties are being used to reduce the heat gain and loss through the façade. However, the important aspect that has been given less attention is the behaviour of such facades in case of a fire. Since the façade design, and thus its behaviour in fire changed significantly, it can be the most critical element of building fire spread, if it is not designed with adequate fire resistance. The Grenfell Tower fire has demonstrated how vulnerable modern facades may be to fires and how this vulnerability directly affects the safety of building occupants. An unprecedented opportunity exists to learn from the Grenfell Tower fire to avoid similar occurrences around the world. Similar events unveiled after the Lacrosse tower fire (2014) in Melbourne. A post-incident analysis has identified that the external wall was not non-combustible and did not satisfy the requirements of the Building Code of Australia (BCA) [1]. After the incident, Standards Australia has developed a new Australian Standard (AS 5113-2016) [2] on “Fire propagation testing and classification of external walls of buildings”, that provides procedures for the fire propagation

¹ Research Fellow and Leader of Innovative Fire Engineering Group, Department of Infrastructure Engineering, The University of Melbourne, Australia.

email: kate.nguyen@unimelb.edu.au

² Professor and Research Director of ARC Centre for Advanced Manufacturing of Prefabricated Housing, University of Melbourne, Australia.

email: dtngo@unimelb.edu.au

³ Professor and Director of ARC Centre for Advanced Manufacturing of Prefabricated Housing, University of Melbourne, Australia.

email: pamendis@unimelb.edu.au

testing and classification of external walls of buildings according to their tendency to limit the spread of fire via the external wall and between adjacent buildings.

Glass façades became preferable in contemporary architecture in last few decades due to its superiority in transmitting light and aesthetic appearance. In the recent past, more attention has been given to alternative “greener” materials like fibre reinforced polymer composites (FRPCs). Metallic materials require a high amount of energy owing to their manufacture at extremely high temperature. Lower weight and higher strength are two critical key properties that make FRPC “greener” than commonly used aluminium and steel. Fire retardancy is an issue as FRPC is sensitive to elevated temperatures and the failure of the composite structure should be studied comprehensively to ensure the safety of the occupants in fire incidents [3, 4]. Consequently, it was considered to be important to conduct a research project which focuses on the performance of FRPC as a member of facade systems to identify the potential risks, to provide basic guidelines for appropriate FRPC in building applications as well as to offer solutions for FRPC facades to meet the available standards for building materials.

This paper will present a comprehensive summary of the analytical, experimental and numerical investigations of fire performance of FRPC façades conducted at the University of Melbourne. Experimental testing was conducted to evaluate the performance of the material in accordance with safety codes and standards as well as to validate numerical simulation. Numerical simulation, in turn, accounts for evaluations where experimental testing is limited owing to cost and time commitment. The analytical study was conducted to provide the background theories required for the research and to design the experimental testing and support numerical simulation.

2 DEVELOPMENT OF FLAME RETARDANTS FOR FRPC

2.1 Effect of aluminium hydroxide

In this study the authors have focussed on investigating the performance of a sandwich panel composed of two E-glass/polyester composite facets and a polyurethane foam core. The choice of materials for this study is based on a number of factors including manufacturing effectiveness, cost, and the ability to achieve a high score on the Green Star rating system in Australia and other similar regulations in other regions. Unsaturated polyester resin used in this study is the most popular matrix for fibre reinforced composites as they possess many advantages related to simplicity in the fabrication process. The flame retardant aluminium hydroxide hydrate (ATH) obtained from Sigma Aldrich is mixed with the resin. The mixing ratio of ATH to resin is chosen to be 3:2 sufficiently to maintain adequate viscosity and resin curing time while maximising the fire-resistant content. The polyurethane foam core is used partially for the benefit of fire performance and weight.

The single burning item (SBI) test in accordance with EN 13823:2010 [5] was used to evaluate the fire performance of the GFRP composite panel. The fire behaviour of the specimen is assessed through the heat and smoke released from a specimen exposed to a propane gas burner of constant heat flux. The performance is evaluated over the first 20 minutes of exposure. Photos of the SBI experimental setup and the test in progress are given in *Fig. 1*, with arrowed lines indicating the wing's and the burner's locations.

Fig. 2 shows the time evolution of the calculated value of HRR_{av} of the GFRP composite specimen associated with the left-hand side vertical axis. Two grey horizontal straight lines are plotted to indicate the critical safety limits that materials subjected to fire need to comply with.

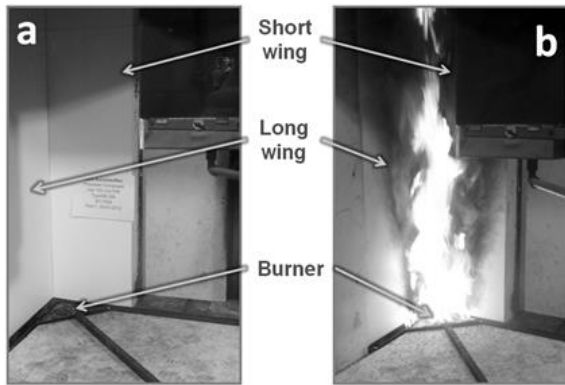


Fig. 1. Pictures of the single burning item test setup and the test in progress

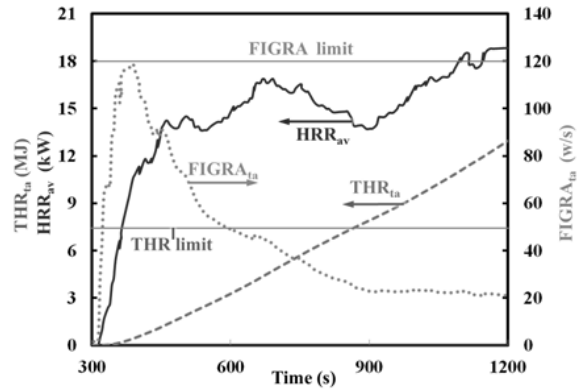


Fig. 2. Average heat release rate (HRR_{av}), total heat release (THR_{ta}), and fire growth rate ($FIGRA_{ta}$) curves obtained from the SBI of a composite panel.

It is clearly shown in this figure that both $FIGRA_{ta}$ and THR_{ta} curves stay below the limit lines, especially for the first 600 s (from the 300th s to the 900th s), which evidently proves that the tested composite structure has successfully met the requirements for construction materials in accordance with fire classification code EN 13501:2007 [6]. The first 100 s after material exposure to the propane burner, the development of combustion (HRR_{av} curve) to its half-peak at 12 kW was observed. The gel-coat as the outermost layer of the composite structure corresponds primarily for the combustion during this period of time. Two other peaks are achieved after around 450 s and 700 s, which correspond to the 750th s and 1000th s, respectively. While the main peak of 18.38 kW (HRR_{av} curve) is reached at the final stage of the SBI test, the first half-peak is associated with the highest peak of the $FIGRA_{ta}$ curve approaching the FIGRA limit. After reaching the peak value, FIGRA rapidly decreases and no longer poses an issue in terms of fire performance. From this study, it is important to note that one of the most critical periods of time is the first 200 s involving the burning of the coating and possibly the surface layer of the resin. While details of the physical burning process during this critical period of time is very important for the fire performance improvement of the sandwich structure, it is very challenging to capture the details of this process experimentally. It is therefore important to develop a numerical model to simulate the whole SBI experiment and provide insights and snapshots of the burning process.

2.2 Development of nanoclay to improve fire performance

Since the discovery of nanoclay by the Toyota research group in the 1990's, many researchers have investigated the influence of nanoclay on improving the properties of nanocomposites at low levels of replacement (3–5%). Most of them were interested in the mechanical, electrical and thermal properties [7-10]. Other studies [11-15] discovered the enhancing effect of nanoclay/organo-modified clay on the fire performance of thermoplastic-based composites. However, the constraints of large dimension, highly complex shape and manufacturing time make thermoplastic-based composites inapplicable in most façade panels.

The effect of nanoclay on the fire retardancy of thermosetting resin-based composites was also investigated. Liu et al. [16] dispersed organo-modified clay Nanocor I.30 into epoxy with different hardeners. The composites have been tested using a cone calorimeter at a heat flux of 50 kW/m². The sample of bisphenol A epoxy/diethyl toluene diamine (as the hardener) and 5% nanoclay gave a peak heat release rate (PHRR) 16.5% lower than that of the neat resin. However, the laminates with nanoclay showed more severe combustion properties. This could be attributed to the dispersing technique, as the nanoclay and the resin had been mixed mechanically for one hour. The performance of the nanocomposite has been known to depend greatly on the dispersion of the nanoparticles in the mixture.

In this study, the effects of organoclay quantity, mixing procedure, and resin type on the fire performance of FRPCs are investigated using Taguchi design of experiments (DoE) L₉ orthogonal array. Three types of thermosetting resin, namely unsaturated polyester, vinyl ester and epoxy have been tested. Montmorillonite modified by two different organic agents are used at three different levels (1% wt., 3% wt. and 5% wt.). The results of the L₉ orthogonal array are evaluated by the general linear model for analysis of variance (GLM ANOVA). The favourable combination has been predicted from this evaluation and validated with experimental trials. Two grades of organophilic clay, 682632 and 682640, from Sigma Aldrich Australia were used. Both of them are specially designed for flame retardant purposes. Three different procedures are proposed for the composite preparation with nanoclay in this work [17]. Fire retardancy of the composite was evaluated using cone calorimetry in accordance with ISO 5660-1. Samples were tested in a horizontal orientation. The samples were cut from post-cured panels to a size of 100 x 100 x 3 mm and were exposed to a 50 kW/m² radiant cone.

In order to understand the influences of material choices and fabrication processes on fire performance properties of composites, the Taguchi design of experiments (DoE) method was employed. Preferred combinations of factors to enhance the fire resistance of the composite were determined using a combination of the Taguchi DoE and general linear model (GLM) for analysis of variance (ANOVA) techniques.

In this study, four factors were selected, namely clay type, clay content, resin type and fabrication procedure. Each factor was composed of 1, 2 or 3 levels of design options, as shown in *Table 1*.

This setup results in a typical three-level, four factors L₉ Taguchi DoE layout with a set of nine experiments, instead of 54 full-factorial combinations to cover all possible cases. S/N ratio analysis is intended to evaluate the effect of each factor on the final characteristics.

Table 1. Factors and levels used in Taguchi DoE layout

Level	Factor			
	Resin	Clay type	Clay content	Procedure
1	Polyester	Type A	1% wt.	A
2	Vinyl ester	Type B	3% wt.	B
3	Epoxy		5% wt.	C

To determine the S/N ratio for each factor, the first step is to determine that of each experiment conducted. Minimising and maximising functions for S/N calculations are used, depending on the objectives of the optimisation. The former is for minimising the final characteristics, while the latter is for maximising. The S/N function is defined for each experiment as follows (*Eq. (1)* and *Eq. (2)*):

$$S/N_{\text{minimizing}}^j = -10 \log \left(\sum_{k=1}^{N_j} \frac{Y_k^2}{N_j} \right) \quad (1)$$

$$S/N_{\text{maximizing}}^j = -10 \log \left(\frac{1}{N_j} \sum_{k=1}^{N_j} \frac{1}{Y_k^2} \right), \quad (2)$$

where N_j is the number of trials for experiment j , and Y_k is the response's value at the k^{th} trial. The k^{th} trial is selected if the repose Y_k varies not more than $\pm 5\%$ from the average value. To ensure the reproduction of the experimental value, N_j is not less than 3 for each experiment j .

The S/N ratio of each factor and level is then calculated as an average from the S/N^j ratios for the experiments. The larger-the-better S/N range reflects the higher influence of the factor on the final characteristics.

To obtain the best fire resistance for the composites, it is necessary to perform analysis on the key response parameters to minimise the HRR. The HRR curves of the nine samples are shown graphically in *Fig. 3*. It is important to note that these curves are obtained from averaging the trial

results for each experiment. As shown in this figure, the polyester-based and vinyl ester-based laminates (C1–C6) have a quite similar profile, with PHRR values all below 400 kW/m²; whereas the epoxy-based composites (C7–C9) have PHRR values well above 500 kW/m². It is also clearly visible from this figure that among the epoxy-based samples, the C8 sample with the highest level nanoclay content of 5% has the lowest PHRR value. In fact, this PHRR value is 15% lower than those of samples with 1% (C7) and 3% (C9) nanoclay.

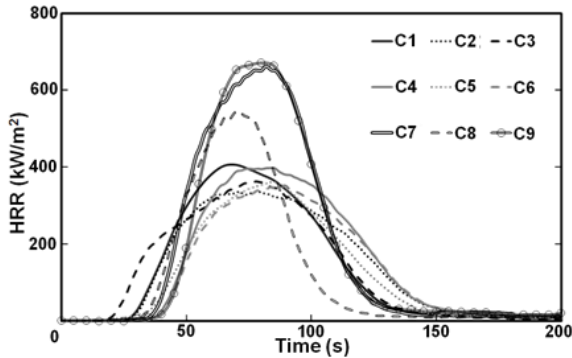


Fig. 3. Heat release rate (HRR) versus time of samples designed by Taguchi DoE and subjected to 50 kW/m² heat flux

Resin and clay types are found to have significant effects on the PHRR/TP and THR responses of the composite. The fabrication procedure using ultrasonic agitation seems to yield better fire performance due to the better nanoclay distributions. The addition of a heat treatment step to remove the residual solvent does not seem to enhance fire performance while requiring further processing time.

The combination of unsaturated polyester with 5% nanoclay type B, treated by procedure B has been identified as a desired fabrication configuration to produce best fire-resistance composite sample.

3 NUMERICAL SIMULATION OF FRPC FAÇADES

3.1 Thermal response models

The numerical framework of the Fire Dynamic Simulator (FDS), which is a computational fluid dynamics (CFD) model of fire-driven fluid flow, is employed in this work to simulate the combustion process during the Cone Calorimetry. The model solves numerically a form of the Navier-Stokes equations for low-speed, thermally-driven flow to capture the smoke and heat transport from fires [18]. The finite difference technique is utilized to solve a system of partial differential equations of mass, momentum and energy with specified boundary and initial conditions. Sample S0 (baseline sample without organoclay) is chosen as the test case for the numerical validation and mesh convergence studies. The samples are discretised into 3 mm-thick square cells with different sizes of 10 mm, 5 mm and 2.5 mm, respectively, corresponding to three different models for mesh convergence study. It is also important to recall that each sample has a dimension of 100x100x3 mm. The total heat release (THR) from experiments of sample S0 are validated with the numerical results from fire test simulation when using the different mesh discretisation. The final THR values achieved from the fire model are shown in Fig. 4. With an element size of 10 mm, the final THR value achieved from the fire model is 13% lower than that of the experimental one. The reductions of cell size to 5 mm and 2.5 mm help to obtain the final THR values of 30.5 and 29.8 MJ/m² respectively (Fig. 4), which are within ±5% of experimental results of 30.95 MJ/m².

With the introduction of organoclay in the composite, two different numerical models are developed to simulate the fire performance of the organoclay-composite samples. The first one is called composite model (CPS), in which the sample is modelled as a homogenized structure, and the second one is called component model (CPN), which takes into account individual effects of each constituent (resin & organoclay). The aim is to evaluate the accuracy of each model in modelling the thermal responses of the organoclay-composite. In the CPN model, TGA tests of the resin and organoclay are conducted separately. Kinetic parameters of these reactions are evaluated and then

used in the fire model to calculate the fire growth index (FGI) and total heat release (THR). In Fig. 5, the fire growth index and final total heat release of each case is calculated according to our previous work. The excellent agreement between numerical results and experimental data of samples S0-5 further confirms the ability of this model to simulate the burning process of composite laminates integrated with organoclay particles.

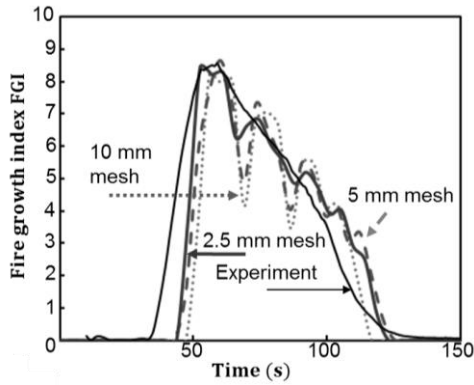


Fig. 4. Mesh sensitivity analysis

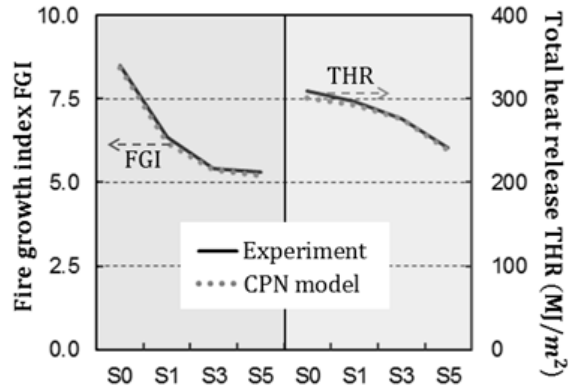


Fig. 5. Fire growth index (FGI) – left axis and total heat release (THR) – right axis of sample with 0% (S0), 1% (S1), 3% (S3) and 5% (S5) organoclay

3.2 Case study of Office Building

City Office is one of the world’s first buildings with a GFRP curtain wall. In this project, other conventional materials for curtain walls such as aluminium and steel do not meet the architectural requirements for this façade, while GFRP offers the possibility to construct this façade with a high aesthetic requirement.

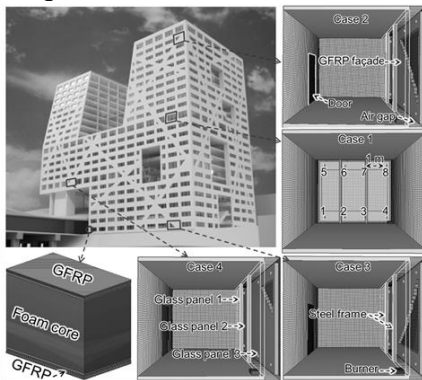


Fig. 6. City Office, Utrecht: four different façade configurations investigated

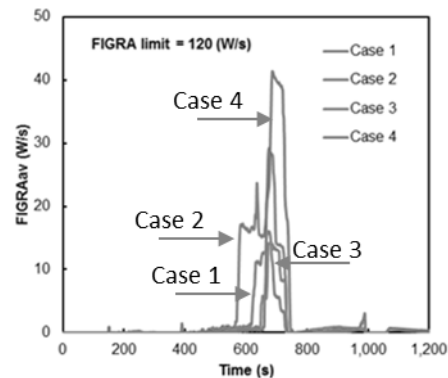


Fig. 7. $FIGRA_{av}$ versus time curves recorded in the four cases

The application of GFRP in this building raises the concern about fire safety, thus GFRP façade incorporated with nanoclay was simulated to predict the behaviour of this façade in fire scenarios. The façade of City Office is unique as the configurations vary at each floor level. The GFRP façade panel composes of the foam core sandwiched in two layers of GFRP on both surfaces. These GFRP layers also act as the final finishing surfaces. Four case configurations were chosen as illustrated in Fig. 6. Case 1 is the office surrounded by GFRP façade with a rectangular hole which represents most of the office configurations in City Office. Fig. 7 plots the time history of $FIGRA_{av}$ for Case 1 - 4. It was observed that in Case 2 and Case 4, fire develops more severe than Case 1 and Case 3. The result of Case 1 is as expected because the composite façade in case has the least coverage over the room, i.e. the least burning material taking part in the fire. Case 2 and Case 3 has the same

coverage area of FRPC façade however the triangle openings are located at different height and orientation. The triangle opening is located at the upper right corner in the former while in the latter this opening is at the lower right corner. $FIGRA_{av}$ in Case 2 peaks at 29.2 W s^{-1} which almost doubles that in Case 3. In all the four cases, Case 4 has the strongest burning process where $FIGRA_{av}$ reaches 41.4 W s^{-1} . For the application in buildings, $FIGRA_{av}$ must not exceed 120 W s^{-1} during the fire test according to EN 13501-1:2007 [6]. It is shown through Fig. 7 that $FIGRA_{av}$ stays well below this threshold level even in the worst scenario – Case 4.

4 CONCLUSIONS

- The SBI fire performance of the composite sandwich sample according to European testing standard EN 13823 [5] and fire classification EN 13501 [6] was tested. The results from the SBI experimental program and various thermogravimetric tests on individual materials were reported for the values of heat release rate, and associated parameters such as total heat release (THR) and fire growth rate (FIGRA). These THR and FIGRA values were compared with the fire safety requirements for heat release, confirming satisfaction.
- Taguchi DoE and GLM ANOVA were applied to maximise the fire performance of a set of designed composites for façade applications. The investigation of the influences of resin type, clay type, clay content, and procedure were conducted according to L_9 orthogonal array. The use of nanoclay in thermosetting glass fibre composites can be successfully optimised by the combination of Taguchi DoE and two-stage GLM ANOVA to meet the demand of improving FRPC façade fire performance. Further experimental and numerical analysis in accordance with safety codes and standards for particular façade applications is recommended.
- Numerical models were developed to simulate the thermal responses of organoclay-composite. While excellent agreements are achieved from three models for total heat release, the component models were able to capture very well the fire growth index evolution and the FGI peak value for organoclay-composites with organoclay placement from 0%-5%.
- In the case study of Utrecht City Office, nanoclay/GFRP façade was investigated with four different façade configurations. FIGRA and THR results in all the configurations were well below the threshold level requirement for building materials according to standard EN 13501-1:2007 [6].

ACKNOWLEDGMENT

This work is conducted with the financial support of ARC Linkage Grant LP110100429. The authors would also like to acknowledge the support of Permasteelisa Pty Ltd with the experimental program.

REFERENCES

1. The Australian Building Codes Board, *National construction code - 2016 Building code of Australia*. 2016.
2. Standards Australia, *AS 5113:2016 Fire propagation testing and classification of external walls of buildings*. 2016.
3. Ngo, T., et al., *Effect of nanoclay on thermomechanical properties of epoxy/glass fibre composites*. Arabian Journal for Science and Engineering, 2016. **41**(4): p. 1251-1261.
4. Ngo, T.D., Q.T. Nguyen, and P. Tran. *Heat release and flame propagation in prefabricated modular unit with GFRP composite facades*. in *Building Simulation*. 2016. Springer.

5. European Committee for Standardization, *EN 13823:2010 Reaction to fire tests for building products - Building products excluding floorings exposed to the thermal attack by a single burning item*. 2010.
6. European Committee for Standardization, *EN 13501-1:2007 Fire Classification Of Construction Products And Building Elements - Part 1: Classification Using Data From Reaction To Fire Tests*. 2007.
7. Gonzalez, L., et al., *Mechanical and thermal properties of polypropylene/montmorillonite nanocomposites using stearic acid as both an interface and a clay surface modifier*. Polymer Composites, 2014. **35**(1): p. 1-9.
8. Karimzadeh, M., A. Sabet, and M. Beheshty, *Effect of nanoclay particles on mold-filling performance in composites made via resin infusion process*. Polymer Composites, 2012. **33**(5): p. 745-752.
9. Poorabdollah, M., et al., *Cure kinetic study of organoclay-unsaturated polyester resin nanocomposites by using advanced isoconversional approach*. Polymer Composites, 2013. **34**(11): p. 1824-1831.
10. Thelakkadan, A., et al., *Effect of the nature of clay on the thermo-mechanodynamical and electrical properties of epoxy/clay nanocomposites*. Polymer Composites, 2011. **32**(10): p. 1499-1504.
11. Awad, W.H., et al., *Material properties of nanoclay PVC composites*. Polymer, 2009. **50**(8): p. 1857-1867.
12. Fina, A., F. Cuttica, and G. Camino, *Ignition of polypropylene/montmorillonite nanocomposites*. Polymer degradation and stability, 2012. **97**(12): p. 2619-2626.
13. Mohanty, S. and S.K. Nayak, *Effect of organo-modified layered silicates on the properties of poly (methyl methacrylate) nanocomposites*. Journal of Thermoplastic Composite Materials, 2010. **23**(5): p. 623-645.
14. Pavlidou, S. and C. Papaspyrides, *A review on polymer-layered silicate nanocomposites*. Progress in polymer science, 2008. **33**(12): p. 1119-1198.
15. Varley, R.J., A.M. Groth, and K. Leong, *The role of nanodispersion on the fire performance of organoclay-polyamide nanocomposites*. Composites science and technology, 2008. **68**(14): p. 2882-2891.
16. Liu, Y., et al., *An efficiently halogen-free flame-retardant long-glass-fiber-reinforced polypropylene system*. Polymer degradation and stability, 2011. **96**(3): p. 363-370.
17. Nguyen, Q.T., et al., *Influences of clay and manufacturing on fire resistance of organoclay/thermoset nanocomposites*. Composites Part A: Applied Science and Manufacturing, 2015. **74**: p. 26-37.
18. McGrattan, K., et al., *Fire dynamics simulator (version 5), technical reference guide*. NIST special publication, 2004. **1018**(5).

TIMBER AND THE FIRE RESISTANCE FURNACE – A COMPARATIVE STUDY OF THE CONDITIONS IN A FIRE RESISTANCE FURNACE WHEN TESTING COMBUSTIBLE AND NON-COMBUSTIBLE CONSTRUCTION

David Lange¹, Johan Sjöström², Joachim Schmid³, Daniel Brandon⁴

ABSTRACT

This paper reports on two experiments conducted in a fire resistance furnace to study the differences in the boundary conditions, the fire dynamics and the fuel required to run the furnace when a combustible timber specimen as opposed to a non-combustible concrete specimen is tested. In both experiments 17 non-control plate thermometers were distributed throughout the furnace; and O₂, CO₂ and CO gas measurements were taken at different distances from the specimen surface and in the furnace exhaust. One of the bricks comprising the furnace lining was instrumented with thermocouples at different depths from the exposed surface in order to estimate the relative energy absorbed by the furnace lining between the two tests. Mass loss of the combustible timber specimen was also measured. We conclude that; (1) the fire dynamics in a furnace are dependent on the specimen being tested; (2) that the test with the combustible specimen requires less fuel flow to the burners such that the control plate thermometers follow the ISO 834 temperature-time curve compared to the non-combustible specimen, however that this is not only a result of the combustibility of the specimen but is also a consequence of the different thermal inertia of the two materials; and (3) that the boundary condition for heat transfer to a test object in furnace tests is dependent on the properties of the specimen being tested.

Keywords: furnace testing, timber, fire resistance

1 INTRODUCTION

Life cycle cost, rapid and clean construction, and attractiveness is driving a rapid growth in the application of timber in building design around the world, such as Brock Commons in British Columbia [1]. The realisation of these designs however is limited in many countries by fire safety regulations, as evidenced by the issues surrounding 475 West 18th Street in New York [2], and the “Framework” building in Portland [3], winners of a national competition to design a high rise timber building on the east and the west coasts of the United States. Conceptual designs abound for even higher timber buildings, e.g. the HSB / Møller plans for a 34 storey timber high rise in Stockholm [4] and the 80-storey tall Oakwood Tower in London [5].

Fire safety regulations for structural elements are based on periods for which specimens have to resist exposure to a standard fire, defined by ISO 834 [6], in a fire resistance furnace. Durations of fire resistance incorporated in regulations can be traced all the way back to several series’ of compartment fire tests conducted in the 1920’s which were done in compartments comprising mainly non-combustible construction. An unbiased discussion of this work is given in [7,8].

¹ Senior lecturer in Structural Engineering, Engineering Architecture and Information Technology, the University of Queensland, Brisbane, Australia. e-mail: d.lange@uq.edu.au

² Senior researcher, Transport and Safety – Fire resistance, RISE, Borås, Sweden. e-mail: johan.sjostrom@ri.se

³ Research Assistant, PhD Candidate, ETH Zurich, Switzerland. e-mail: schmid@ibk.baug.ethz.ch

⁴ Senior researcher, Transport and Safety – Fire resistance, RISE, Borås, Sweden. e-mail: daniel.brandon@ri.se

Most modern fire resistance furnaces work by injecting fuel via burners, typically either oil or gas, into an enclosure with a test specimen either on top of or at the side of the furnace. The enclosure of a horizontal furnace is typically of the order of between 4 and 5 metres long, by 3 metres wide, and 3 metres in depth. The fuel is regulated such that the temperature of measurement devices follow the predefined temperature history of the standard fire, in Europe and in some other countries plate thermometers (PTs) are used, whereas elsewhere (typically in US / Canada) sheathed thermocouples are used. Where PTs are used then these face away from the test object and into the furnace. Repeated discussions in workshops and in the literature occur about the suitability of furnaces as a means of fire testing combustible elements and it is clear that more work is needed in this regard.

A letter recently published by SFPE Europe (The Society of Fire Protection Engineers) [9] highlights some of the items currently under discussion, specifically that: (a) the fire dynamics in a compartment are not independent of the construction material; (b) that due to the contribution of a combustible test object to the total fuel in a furnace test results from fire resistance tests are un-conservative since they do not represent the same fire as when non-combustible objects are tested. Open questions include: a) how the extra fuel comprised of pyrolysis gases emitted as the char forms contributes to the fire inside of the furnace; b) if the oxygen limitation of the fire in the furnace makes the additional fuel insignificant, (in comparison to a post-flashover fire, this fuel would burn outside the fire compartment in question and not contribute to the fuel consumed within the compartment); and finally c) if the temperature evolution controlled using PTs is a good measure of fire exposure of combustible elements.

This article reports on two horizontal fire resistance tests, one on a representative non-combustible specimen and one on a timber specimen in order to address the following questions:

- *What is the impact on the amount of 'fuel' needed in fire resistance testing as a result of including a combustible test specimen in the furnace as opposed to a non-combustible specimen? i.e. should furnace testing of timber elements include more fuel, implying a longer requirement for fire resistance, to represent the combustible items in compartment fires?*
- *How much of the fuel and the pyrolysisate from the timber is left unburnt during a furnace test of a combustible specimen and are burnt in the furnace exhausts?*
- *What is the oxygen concentration in a fire resistance furnace test of a combustible as opposed to a non-combustible construction?*
- *What is the spatial variation in the furnace of plate thermometer temperature and oxygen content during tests of combustible and non-combustible construction?*

2 EXPERIMENTAL SETUP

2.1 Furnace layout

The furnace used has 12 burners, 6 on either of the long sides of the furnace. The layout of the furnace including the control devices is shown in Figure 1. Both experiments, incorporating non-combustible and combustible construction, were conducted according to EN 1363-1 [10], Temperature control in the tests was based on 14 PTs inside the furnace. These control PTs were distributed 100 mm below the specimen facing down away from the test object. The temperature of the PTs is controlled to follow the ISO 834 standard temperature-time curve by controlling the flow of propane and air to these burners. In addition to these control PTs a number of additional PTs were installed in the furnace to help with characterisation of the distribution of temperature throughout the volume. These are installed adjacent to different walls facing both into and away from the walls as well as closer to the specimen and facing the specimen. Figure 1 shows only a

small number of the additional PT's which were present in the furnace. All PT's will be included and reported in a future publication related to these tests:

- *Thermocouples 2, 3, and 4 were positioned 100 mm to the east of control plate thermometers. TC 7 was west of one of the control PT's. All 4 of these were facing up towards the specimens surface, 100 mm away.*
- *Thermocouples 10, 11 and 12 were positioned adjacent to the north wall, with 10 facing the wall and 11 and 12 facing away from the wall. 10 and 11 were positioned approximately in the centre of the wall with a horizontal distance between them of 200 mm. 12 was positioned closer to the corner, 800 mm from the east wall. All three of TC 10, 11 and 12 were 100 mm away from the north wall.*
- *Thermocouples 16, 17 and 18 were positioned 100 mm from the floor of the furnace facing up.*

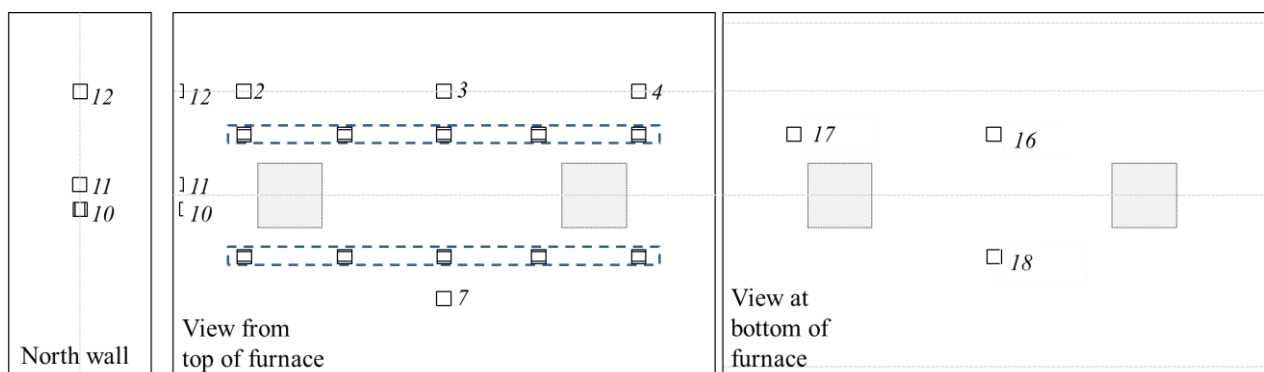


Fig. 1 furnace device layout

This distribution of PTs was intended to provide significant additional information about the temperature distribution throughout the furnace, and since it has been shown that PTs may be used as a robust kind of heat flux gauge [10,11] their response is also used in the discussion of results as a proxy for incident heat flux.

Concentrations of O₂, CO₂ and CO were also measured during the tests. Sampling points were positioned at 3 locations on a line in the very centre of the furnace, at 10 mm, 100 mm and 1200 mm from the exposed surface of the specimens. Gas concentrations were also measured in the exhaust ducts of the furnace: at the opening of one of the exhaust ducts, and at the junction of the two exhaust ducts below the centre of the furnace.

One of the bricks which comprised the furnace wall was instrumented with thermocouples at 5, 10, 20 and 30 mm from the exposed surface. This brick was located on the south east wall of the furnace.

2.2 Specimen preparation

Timber and concrete specimens were installed in a steel frame which was larger than the opening of the furnace so that it could be placed around the perimeter of the furnace. For the timber test, this frame was placed on load cells. This allowed the mass loss of the timber to be recorded throughout the test.

The timber test specimen's initially unprotected surface was about 5000 mm x 3000 mm. This was comprised of thirteen individual glulam timber elements of cross section 400 mm x 139 mm. The elements were oriented in the steel frame such that the lamellas of the beams were vertical to avoid any falling off of individual lamella creating freshly exposed timber during the fire test. This

resulted in a depth of timber on the furnace of 139 mm. The individual timber elements were bonded with Melamine Urea Formaldehyde adhesive (MUF). At delivery, all beams delivered had a mass of 1051 kg. Based on this, the bulk density was estimated to be 464 kg/m³. One spare beam was delivered. On the day of the test, the moisture content of the spare element was estimated to approximately 12% with an electrical-resistance meter. The total mass of the specimen assembled out of 13 elements was 975.9 kg.

3 POST TEST ANALYSIS

3.1 Temperature distribution

The measurement of the control PTs, i.e. those which are used to guide the throttle to the individual burners in the test is summarised to the left of Figure 2. Of particular interest is the fact that the variation in the temperature of the control PTs is lower in the timber test than it is in the concrete test (although both are still within the bounds dictated by the standard). The fluctuations in the temperature as the furnace is adjusted in response to the start of burning of the timber are also clear. As indicated above, for brevity we only report in this article a small number of the additional PT measurements. For clarity the PT measurements are shown relative to the ISO 834 temperature time curve. The right part of Figure 2 shows the difference between the ISO 834 temperature-time curve and PTs 2, 3, 4 and 7 facing up at 100 mm distance. Note that the PTs adjacent to these and facing down are the control PTs and follow closely the ISO 834 curve. The concrete surface is at a lower temperature than the rest of the furnace, whereas the timber surface is in fact very similar in temperature to the rest of the furnace.

Examples of PTs adjacent to the furnace walls and adjacent to the furnace floor are given in Figure 3. Again, here it can also be seen that the PTs in the test with the combustible timber material closely follow the ISO 834 curve, whereas the PT's in the concrete test generally measure a temperature higher than the ISO 834 curve. Given that the PTs with a very high view angle to the concrete were lower than the ISO 834 curve this indicates that either the gas temperature or the radiation temperature of the walls is higher than the ISO 834 curve in the concrete test.

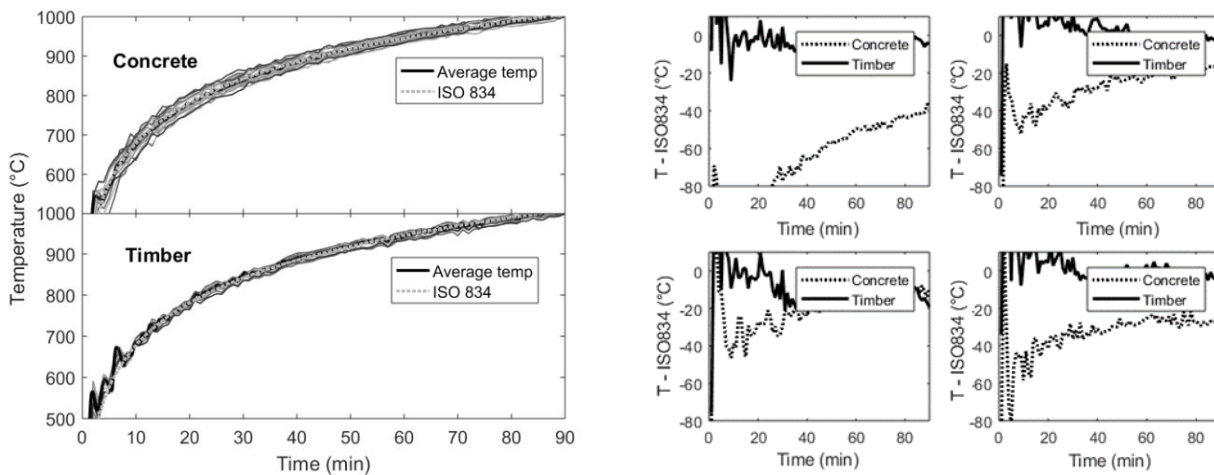


Fig. 2 PT temperature in the furnace: right, average temperature of control PT's; left, difference in temperature between PT's facing up 100 mm from the specimen surface and ISO 834.

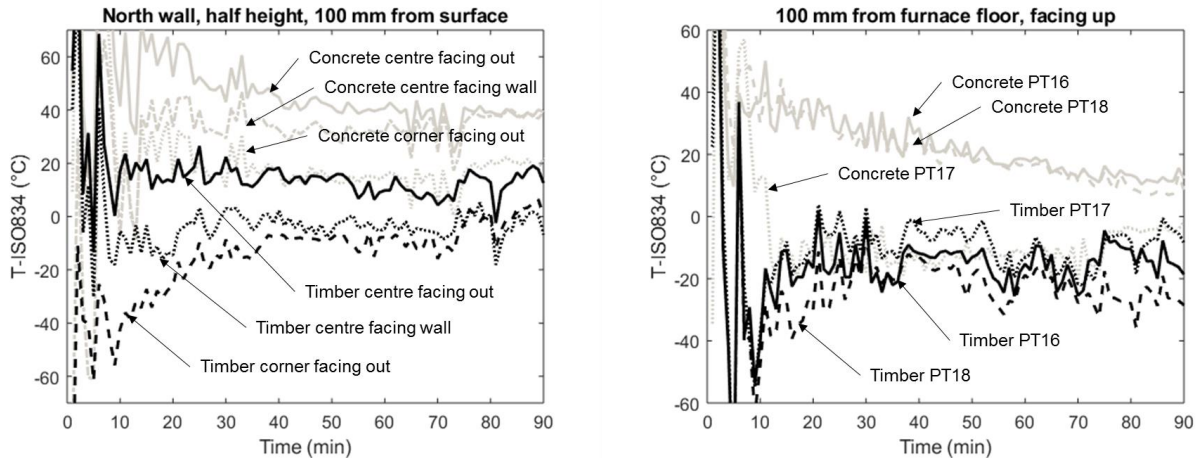


Fig. 3 temperature difference between PTs and ISO 834; right, PTs adj. the north wall; left, PTs adj. the floor.

3.2 Gas analysis

Concentrations of O₂, CO and CO₂ in the furnace in both tests are shown in Figure 4. These are the average concentrations for the period from 30 minutes into the tests until the end of the 90 minute tests. Over this period the concentrations were largely constant with time. Up until this period there was some variation, as concentrations approached this value from ambient levels.

The concentrations of gas in the concrete test indicate a very well mixed combustion process inside of the furnace. Conversely the concentrations of gas in the furnace when timber is being tested shows some dilution of the combustion products in the upper part of the furnace, indicated by the reduction in concentration of CO₂ and CO between the exposed surface and the exhaust outlet. The reaction in this region is lean, indicated by the lack of O₂, becoming richer towards the bottom of the furnace. The increase in concentration of O₂, corresponding with the decrease in concentration of CO indicates the presence of a flame front, with combustion process occurring above this front, somewhere between this region and the exposed surface.

CO concentration in the concrete test is uniformly very low, implying that the combustion process is efficient throughout the volume of the furnace, as would be expected given that the flow of oxygen to the furnace is dependent on the flow of fuel via the burners. In comparison, the CO concentration in the timber test is relatively high, as high as 10 %, at the surface of the timber, suggesting that the reaction with O₂ is incomplete. The CO concentration in the timber test at the horizontal centre of the furnace and in the flow of the furnace exhaust are very low, similar to the concentrations in the concrete test, again implying almost complete combustion by the time that the gases leave the furnace. The lack of increased concentration of CO₂ or decreased concentration of O₂ further into the exhaust indicates that there is very little further combustion in the furnace exhaust. Since there is both an availability of O₂ and very high heat here we conclude that most of the fuel has been used by this point. This could be further verified in the future by repeating this test with measurement of more gas species throughout.

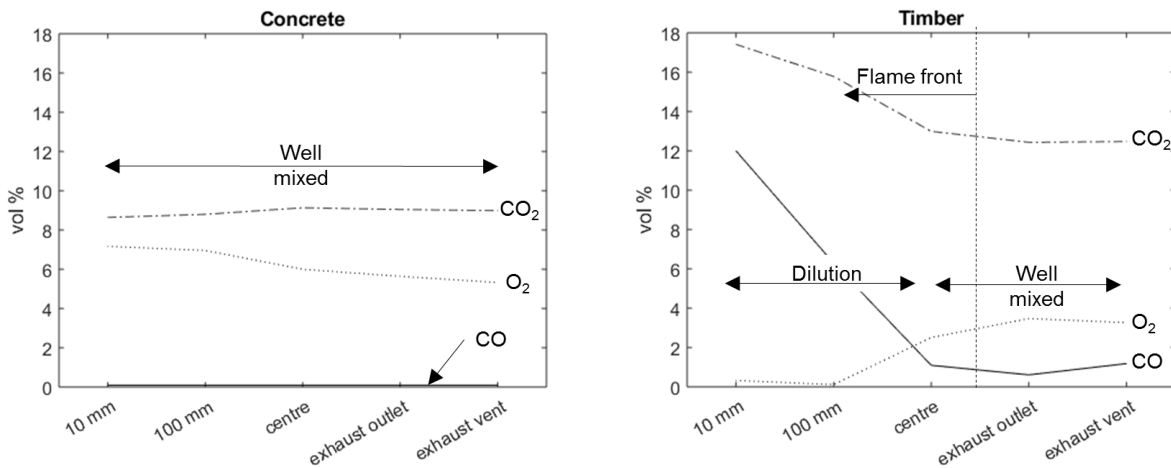


Fig. 4. Concentrations of CO, CO₂ and O₂ in the furnace during the concrete test (left) and the timber test (right)

3.3 Fuel consumption

The amount of fuel which is consumed by a furnace controlled to follow the standard temperature time curve using PTs is significantly different when timber is tested as opposed to concrete. Total mass of propane used in the timber test was 131 kg, whereas 338 kg was used in the concrete test. Assuming a heat of combustion of 31.2 MJ/kg and a 100 % efficiency of combustion, for a 90 minute test inside of the fire resistance furnace, the timber used only ca. 39 % of the fuel which was required to heat the furnace when concrete was being tested. Accounting for the mass of timber which is lost and assuming a heat of combustion of 20 MJ/kg and a 100 % combustion efficiency, a conservative estimate of the contribution of fuel to the fire test of the timber is 40 % of the total energy in the concrete test, or approximately the same as the energy introduced via the burners. This additional contribution of burning timber is largely consumed inside of the furnace enclosure, as suggested by the availability of both heat and oxygen in the lower part of the furnace and in the furnace exhaust as discussed above. However, this results in a difference in total fuel used in the two fire tests of ca. 21 %.

3.4 The instrumented brick

One brick of the furnace lining was instrumented with thermocouples at 5, 10, 20 and 30 mm from the exposed surface. The temperature response of this brick in both tests is shown in Figure 5. Temperatures towards the surface of the brick are higher in the concrete test than in the timber test. This is in line with the response of plate thermometers discussed above, where those in the concrete test, with the exception of those facing the specimen and 100 mm from its surface, are seen to have a temperature between 148 and 37 K lower than the ISO 834 curve at different times (see Figure 3), as opposed to in the timber test where all plate thermometers have a very small variation from the same.

The reason for the higher temperatures in the brick in the concrete test as opposed to the timber test is attributed to the relative thermal inertia of the two specimens which is in line with conclusions from other studies [14,15]. The thermal inertia of wood according to Eurocode 5 [12] varies between about 6.6 % and 24 % of concrete according to Eurocode 2 [13], depending on the state of the timber. This means that the concrete acts as more of a heat sink relative to the timber, drawing energy away from the exposed surface resulting in a cooler surface and therefore lower radiation from the exposed surface to the furnace linings. More energy is therefore required to be put into the furnace via the burners in order to heat up the linings which in turn contributes to heating, by radiation, the control PTs such that they follow the ISO 834 curve.

This also means that more of the total energy in the furnace is absorbed through the depth of the concrete at high temperatures. The resulting lower concrete surface temperature results in a need for hotter furnace walls in order to maintain the ISO 834 temperature at the control PTs, and accounts for some of the remaining 21 % of total external energy supplied by the fuel and required to heat the furnace according to the standard temperature time curve. As the plate thermometer temperatures near the relatively cold concrete surface are controlled to be equal to the ISO 834 curve, the remaining surfaces of the furnace need to be hotter than the ISO 834 curve. Achieving these higher temperatures required some of the additional 21% energy supplied in the test with the concrete specimen in comparison with the test with the timber specimen.

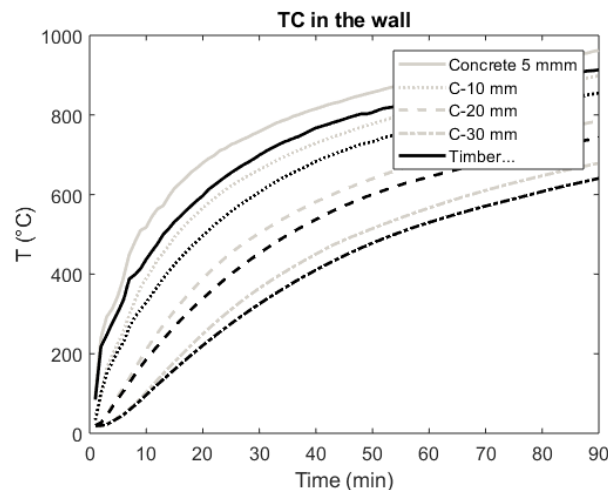


Fig. 5. Temperature distribution in the instrumented wall brick

The relative fuel consumptions are not very sensitive to the assumption of combustion efficiency, and in fact the combustion efficiency of timber is likely to be much lower than 100 %. This implies that the total additional fuel used to heat the furnace linings in the concrete test is much more than the 21 % suggested here, further implying that this effect may be as important if not more so than the combustibility of the specimen.

4 DISCUSSION AND CONCLUSIONS

The fire dynamics inside of a furnace are strongly dependent on the material being tested.

The inclusion of a combustible specimen as opposed to a non-combustible specimen results in the need for significantly less fuel to be added to the furnace via the burners than when a non-combustible specimen is tested. However, this is not the entire story and we find that the relative thermal inertia of the two materials also has a significant impact on the relative amount of fuel needed between the two tests.

Based on the gas measurements it seems as though only a small amount of either the pyrolisate from the timber or the externally added fuel in either test is left unburnt in the exhaust in the timber test. Oxygen concentration in a test of a non-combustible specimen is relatively uniform throughout the furnace volume, at just over 6 %. However, in a test of combustible construction it varies between nearly 0 % at the specimen surface and just above 4 % in the furnace exhaust.

The variation between the control and the additional PT temperatures varies between the two tests. The temperatures in the timber test are closer to the ISO 834 temperature time curve. This fact we attribute to the difference in thermal inertia between the two materials. The lower thermal inertia of

the timber means that less total energy is needed in the furnace test to be used to heat up the linings of the furnace such that the control PTs follow the standard temperature time curve.

Since we can use the temperature of the PTs as a proxy for heat flux gauges, there is very little variation in the heat flux to the PTs between the two tests. This however is not surprising since we control the fuel flow to the furnace such that the PTs follow the same temperature history irrespective of the test object. This means that the balance of heat flux coming from surface linings and from the gas in the furnace is such that the net heat flux to the control PTs are the same in both tests.

However, since the furnace linings are hotter when testing high thermal inertia materials the radiation temperature is different. In order to have the same PT temperature either the gas temperature has to be lower or the convective heat transfer coefficient has to be lower. Since it has been shown that the gas temperature, the radiation temperature and the surface temperature varies between the two specimens while the PT temperature does not, it can be concluded that the boundary condition for heat transfer varies between fire resistance tests of materials with different characteristics and the PT temperature may not always be a suitable substitute for the gas temperature and the radiation temperature.

5 REFERENCES

1. Brock Commons Tallwood House; <https://www.naturallywood.com/emerging-trends/tallwood/brock-commons-tallwood-house>, accessed 21st March 2018
2. Shoparc 475 West 18th; <http://www.shoparc.com/projects/475-west-18th/>, accessed 21st March 2018
3. Lever architecture, Framework; <https://leverarchitecture.com/projects/framework>, accessed 21st March 2018
4. C.F.Møller, Wooden Skyscraper, <http://www.cfmoller.com/r/Wooden-Skyscraper-i13265.html>, accessed 21st March 2018
5. PLP Architecture, Oakwood timber tower, <https://www.plparchitecture.com/oakwood-timber-tower.html>, accessed 21st March 2018
6. ISO – the International Organisation for Standardisation, ISO 834-1:1999 Fire-resistance tests -- Elements of building construction -- Part 1: General requirements, 1999
7. P.H. Thomas, "The Fire Resistance Required to Survive Burnout–Fire Research Note No. 901, Borehamwood, 1970.
8. Robertson, A.F.; Gross, D.; Fire load, fire severity, and fire endurance; Fire test performance, ASTM STP 464, American society for testing and materials, 1970, pp.3 – 29
9. Law, A.; Hadden, R.; Burnout means burnout; SFPE Europe Q1 2017 Issue 5
10. EN 1363-1; Fire resistance tests. General requirements
11. Ingason, H; Wickström, U (2007); Measuring incident radiant heat flux using the plate thermometer; Fire Safety Journal 42(2). Pp 161-166
12. Andreas Häggkvist, Johan Sjöström, Ulf Wickström (2013), Using plate thermometer measurements to calculate incident heat radiation, Journal of Fire Sciences 31(2), pp. 166-177.
13. European Committee for Standardisation, EN 1995-1-2: Design of timber structures - Part 1-2: General - Structural fire design.
14. European Committee for Standardisation, EN 1992-1-2: Design of concrete structures - Part 1-2: General - Structural fire design.
15. Schmid J, Brandon D, Werther N, Klippel M. Thermal exposure of wood in standard fire resistance tests. Fire Safety Journal, 2018.
16. Harmathy, T. Z. "Design of fire test furnaces." Fire Technology 5.2 (1969): 140-150

HYBRID FIRE TESTING OF A SINGLE DEGREE-OF-FREEDOM LINEAR SYSTEM

Ana Sauca¹, Chao Zhang², Artur Chernovsky³, Mina Seif⁴

ABSTRACT

As the structural engineering industry transitions towards performance based design methods, a better understanding of the performance of structures as full systems, especially under extreme loading conditions like fire, becomes a must. Full scale testing will provide such information, however, at an unrealistic cost. Hybrid Fire Testing (HFT) is inspired from sub-structuring method, which provides the insight through testing individual members exposed to elevated temperatures, while simultaneously accounting for the effect of the surrounding structure, which is numerically modelled aside. The tested member and the numerically represented surrounding must communicate during the entire test. This communication framework is a key component for a successful HFT. However, there is lack of availability of generic frameworks that enable the use of different software and hardware configurations. This paper presents the development of such generic communication framework. First, a validation of the communication framework was done in a virtual environment, where both the tested member and the surrounding are numerically modelled separately. Next, a hybrid fire test was performed on a single degree-of-freedom linear system.

Keywords: Hybrid fire testing, fire tests, substructures, communication framework

1 INTRODUCTION

There is a lack of understanding of how structures, as whole systems, perform under realistic, uncontrolled fires. A better understanding of the problem will support the development of performance-based standards and tools that explicitly consider realistic fire effects for both the design of new buildings and the assessment and retrofit of existing ones. The Hybrid Fire Testing (HFT) method, through sub-structuring, assumes testing individual members/components (referred to as physical substructure PS), while simultaneously accounting for the action of the surrounding structure (referred to as numerical substructure NS) which is computationally modelled aside. Thus, HFT allows, through testing individual members, the prediction of the global behaviour of whole structural systems. To date, only few HFT performed on full size structures are found in the literature [1-4]. Small scale HFT are presented in [5,6] and virtual hybrid fire tests VHFT (the PS and NS are represented numerically) are presented in [7,8] to validate new methods. These studies have been performed considering standard fire curves (e.g., [9]), while more researchers are currently focused on studying the behaviour of structures exposed to realistic fire scenarios [10-11].

¹ Guest Researcher, National Institute of Standards and Technology NIST, Gaithersburg, MD.
e-mail: ana.sauca@nist.gov

² Guest Researcher, National Institute of Standards and Technology NIST, Gaithersburg, MD.
e-mail: chao.zhang@nist.gov

³ Research Electric Engineer, National Institute of Standards and Technology NIST, Gaithersburg, MD.
e-mail: artur.chernovsky@nist.gov

⁴ Research Structural Engineer, National Institute of Standards and Technology NIST, Gaithersburg, MD.
e-mail: mina.seif@nist.gov

A recent study performed on a prototype building exposed to two simulated realistic fire scenarios [12] showed how much the simulation of individual members could be different than the simulation of the complete structural system in terms of behaviour. Analysis of individual members simulated individual member test behaviour while analysis of the full structure simulated the full-scale testing of the structure as a system. The study highlighted that in some cases, individual members survived the fire, while failure occurred when the complete structural system was modelled. Thus, difference between the individual member testing and full-scale testing can be crucial in terms of safety. HFT is a potential solution that insures the proper accounting of the surrounding system on the individual member behaviour.

To perform a successful HFT, several key components are crucial [13], one of them is the framework for the experimental setup and control. Most testing facilities develop their own framework, while open-source frameworks such as OpenFresco [14] and UI-Simcor [15] have been successfully used in the seismic field. To perform a HFT using frameworks as OpenFresco or UI-SimCor, some modifications need to be implemented, making them more generic, thus allowing them to integrate with certain finite element software that have the capability to solve structures loaded with both mechanical and fire loads (e.g., SAFIR[®] [16]). The main objective of this paper was to validate the HFT concept through developing a generic communication framework and using it to perform a HFT on a single degree-of-freedom (1-DoF) linear system. Some modifications were implemented so that OpenFresco can communicate with SAFIR. A virtual hybrid fire test VHFT was performed on a single degree-of-freedom (1-DoF) linear system in order to test these modifications. The communication proved to be successful and this framework can be used in future HFT where the NS is to be represented in SAFIR or other similar software packages. Following the VHFT, a HFT was performed on the 1-DoF linear structural system. National Instrument's LabView [17] is used to establish data exchange between the third-party frameworks OpenFresco (OpenSees) / Matlab / SAFIR. This simplified test setup helped validate the HFT methodology presented in [18], and the interface described above.

2 APLICABILITY OF HYBRID FIRE TESTING

It is important to study behaviour of structures exposed to fire conditions in the most similar conditions with reality. In real fires, it has been observed that the fire spreads from one compartment to another, and in order to understand the real behaviour of structures in these specific conditions, real-scale tests are required to validate the fire models and structural models.

Most of the fire tests are performed on individual structural members exposed to standard fires, based on the assumption that the predictions of these tests are overly conservative. A recent study [12] performed on a prototype 10-story moment resisting frame [19] when exposed to 2 design fire scenarios showed that the results from the simulation of the individual members are not conservative compared with the results of the complete structure simulation. The study highlighted that performing fire tests on individual members might not always be a conservatively safe solution. The beam situated in the fire compartment where the fire initiated was considered as a key element of the structure and it was studied in different possible configurations. The following boundary conditions are possible when testing the beam as a standalone member: f-f (fixed-fixed ends), f-th (fixed-fixed ends with free thermal expansions), f-h (fixed-hinged ends), f-r (fixed-rolling supports), s-s (simply supported beam), h-h (hinged-hinged ends).

Fig. 1 shows the evolution in time of the mid-span displacement of the beam when subjected to the mentioned boundary conditions. It is noted that these results come from finite element analysis and not from real tests. In most cases of the standalone member analysis (e.g., "f-f", "h-h" in *Fig. 1*), the mid-span displacements of the beam are higher than in the case when the full structure assembly was analysed ("full-scale S1 and "full-scale S2" represent the two different fire scenarios). Nevertheless, the standard testing simulation did not lead to the failure of the members, while in the case of the full-assembly simulation, the failure of the structural system occurred in both fire

scenario cases. The standalone member testing (analysis) does not capture the full effect of the surrounding members during the test. The surrounding assembly starts being exposed to fire since the fire spreads from one compartment to another. The capacity of the member is overestimated if the effect of the surrounding members is neglected. This is a clear example of HFT applicability, it is built on the concept of continually accounting for the whole assembly behaviour while realistically testing a member or sub-assembly.

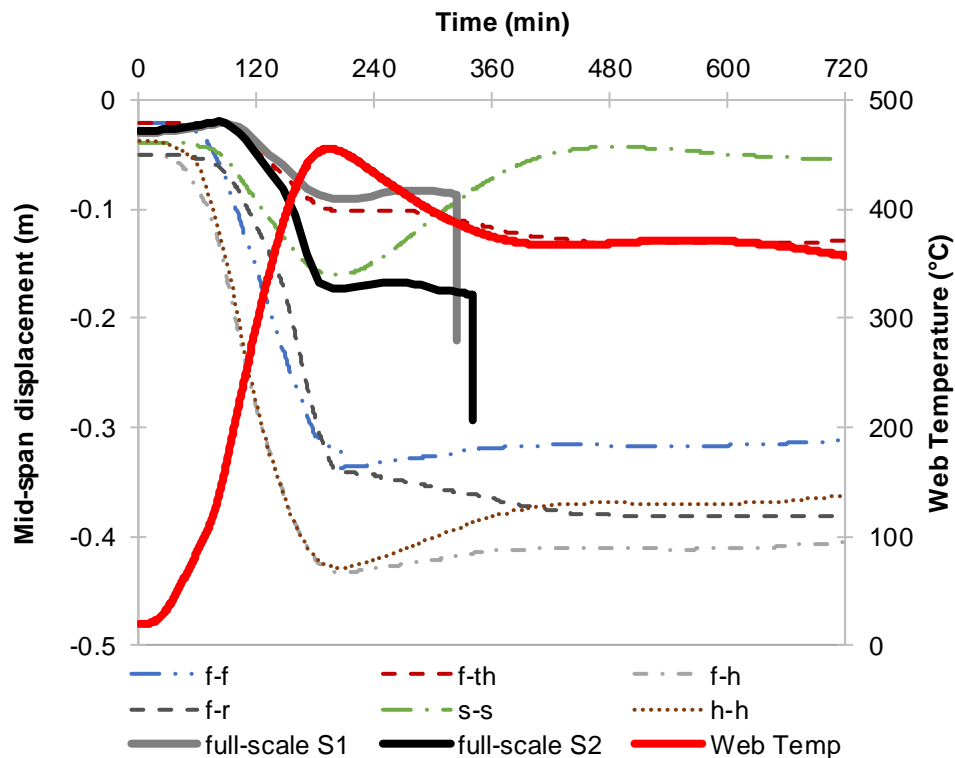


Fig. 1. Mid-span displacement of the beam in different testing configurations

3 HFT ON A SINGLE DEGREE-OF-FREEDOM SYSTEM

As presented in [13], one of the biggest challenges in performing HFT is to ensure a proper communication between the PS and NS. Frameworks for experimental setup and control such as OpenFresco and UI-SIMCOR have been successfully used in seismic hybrid simulations. These frameworks ensure the proper control of the PS, which communicate in real time with the NS during the entire test.

To perform a HFT using frameworks as OpenFresco or UI-SimCor, some modifications are due, making them more generic, thus allowing them to integrate with certain finite element software that have the capability to solve structures loaded with both mechanical and fire loads (e.g., such as SAFIR®).

To make the communication between SAFIR and OpenFresco possible, some modifications were implemented in SAFIR and a communication framework was developed in MATLAB. To test this communication interface, first a virtual hybrid fire test VHFT was performed, in which the PS and NS are both modelled numerically. Once the VHFT confirmed the successful continuous communication, a real HFT was performed. The main purpose of the test was to validate the hybrid fire testing methodology presented in [18] and the communication framework mentioned above. The 1-DoF linear system (Fig. 2) considered in this example was composed of 2 bars, defined by their stiffness. One of the bars was exposed to elevated temperature, and the thermal expansion induced changes at the interface node 2. For the sake of simplicity, the stiffness of the heated substructure was considered constant during the entire test.

Hybrid fire testing of a single degree-of-freedom linear system

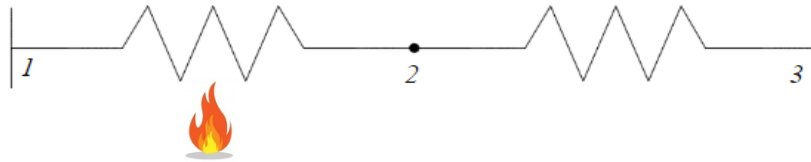


Fig. 2. One degree-of freedom linear system

The main characteristics of simplified 1-DoF linear system considered in this example are the following:

- The stiffness of the substructures: $K_P=11.30 \text{ N/mm}$ (PS) and $K_N=11.30 \text{ N/mm}$ (NS)
- The length of the substructures: $L_P=260 \text{ mm}$ (PS) and $L_N=260 \text{ mm}$ (NS)
- The thermal coefficient of the material is $\alpha=0.00012 \text{ 1/K}$
- The rate of temperature increase of the heated substructure is taken as $200 \text{ }^\circ\text{C/s}$ (the stiffness of the PS is considered constant).

Prior the real HFT, a VHFT was performed and the results are presented in the following section.

3.1 Virtual Hybrid Fire test (VHFT)

Performing a VHFT (PS and NS are both represented numerically, i.e., separately modelled) is generally useful for the purposes of: (i) testing the framework integrating the different analytical software, and (ii) preparing for the real HFT by helping select the proper time step for the simulation in cases for which no analytical formulations are available.

To make facilitate the communication between SAFIR and OpenFresco, a communication framework was developed in Matlab (see Fig. 3). In addition, modifications were done in SAFIR's code in order to allow such communication. The HFT methodology presented in [13] was used in this VHFT, and it was implemented inside the communication framework. The advantage of this particular framework is that it allows the communication between experimental setup and control frameworks with a wider range of software packages that have the capabilities to solve structures loaded with both mechanical and fire load (in this case SAFIR). Also, this communication framework is generic, and can be accessed and modified based on the needs of each case study.

In this VHFT example, the heated substructure was modelled in SAFIR, while the cold substructure was modelled in OpenSees [20]. OpenFresco was used to communicate between SAFIR and OpenSees. In a real HFT, OpenFresco will instead communicate between the tested PS and modelled NS in SAFIR.

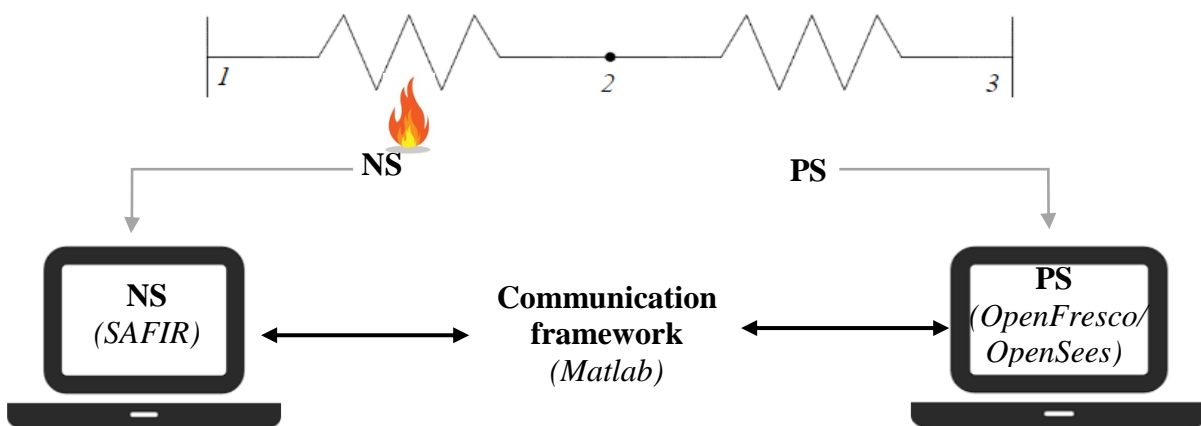


Fig. 3. Communication between OpenFresco / OpenSees and SAFIR during the VHFT

Fig. 4 presents the evolution of the interface force versus the interface displacement of the 1-DoF linear system, i.e., the interface force and displacement of the node 2 (see Fig. 3). Each of the graphs presents the solution of the global (whole system) analysis of the 1-DoF linear system (referred to as “Global”) along with the solution from the VHFT (“NS” is the interface solution of the NS analysed in SAFIR and “PS” is the interface solution of the PS analysed in OpenSees). The

VHFT solutions are presented for two different considered time steps Δt : $\Delta t=1\text{ s}$ and $\Delta t=10\text{ s}$. The time step refers to the time when the displacement is fixed to a constant value (since a displacement control procedure is used). Once the new solution is computed, it needs to be updated on the PS and NS before running the next step. For this example, 1 s is the time needed to update these values on the substructures.

This VHFT showed that the interface solution of the PS and NS were the same, meaning that the equilibrium and compatibility were both satisfied. Moreover, the global solution was reproduced successfully by VHFT (the lines on the plot align on top of each other). The heated substructure (NS) needs to expand but the displacement is constant during one-time step (displacement control procedure), therefore, the interface force is increasing. The force increase of the NS during one time step is obvious in this example for a time step equal to 10 s (*Fig. 4 b*). Once the interface displacement is updated, the reaction force of the NS (heated substructure) is in equilibrium with the reaction force of the PS.

The stiffness values of the PS and NS are required for the calculation process of the updated boundary conditions (displacement of the node 2). However, as the substructures are exposed to elevated temperatures, their mechanical and material properties (which are temperature-dependent) degrade, i.e., the stiffness varies with temperature. In a real HFT the stiffnesses of the PS and NS can be updated every time step or it can be kept constant. If the stiffness is kept constant, then several iterations are required to converge to the correct solution. For this simplified example, the hypothesis that the stiffness is not affected by the elevated temperatures was adopted. Therefore, the stiffness of the PS and NS were kept constant during this entire VHFT and once the displacement was updated at the interface, the correct solution was achieved along with the equilibrium and compatibility (no iterations were required).

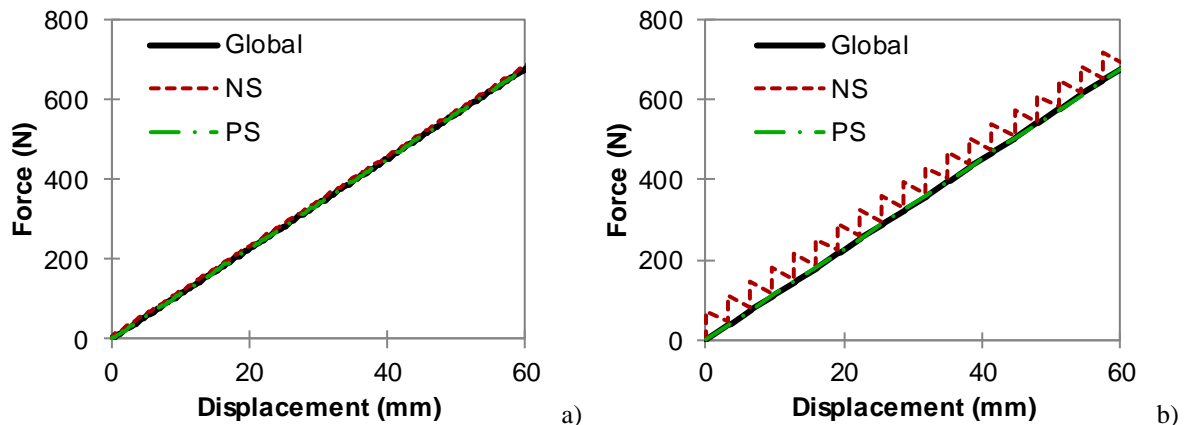


Fig. 4. Interface solution (force versus displacement) for the 1-DoF linear system: a) $\Delta t=1\text{ s}$; b) $\Delta t=10\text{ s}$

This VHFT’s communication framework successfully enabled the communication between SAFIR and OpenFresco / OpenSees. The following section shows how the developed communication framework was implemented in a real HFT performed on a 1-DoF linear system. In general, performing a VHFT prior to conducting a real HFT is beneficial for many reasons. It can be used to properly select the optimum value of the required time step. It can also be helpful in determining the influence of using constant stiffness values (versus updating them every time step) of the PS and NS on the results.

3.2 HFT of a 1-DoF linear system

Following the VHFT, a HFT was performed on the single degree-of-freedom (1-DoF) linear structural system shown in *Fig. 5*. In this setup, the PS and NS were represented by springs. Prior the HFT, the stiffness of the PS was measured and had a value of 11.30 N/mm . The stiffness of the NS was assumed to be equal to the stiffness of the PS. All the characteristics of the system are presented in section 3. Since the objective of this experiment was to test and validate the communication framework, and not necessary the specific structural response to the fire load, the

unheated substructure was physically tested (PS) while the heated substructure was modelled (NS) in SAFIR. National Instrument's LabView was used to establish the data exchange between the frameworks PS / OpenFresco / Matlab / SAFIR.

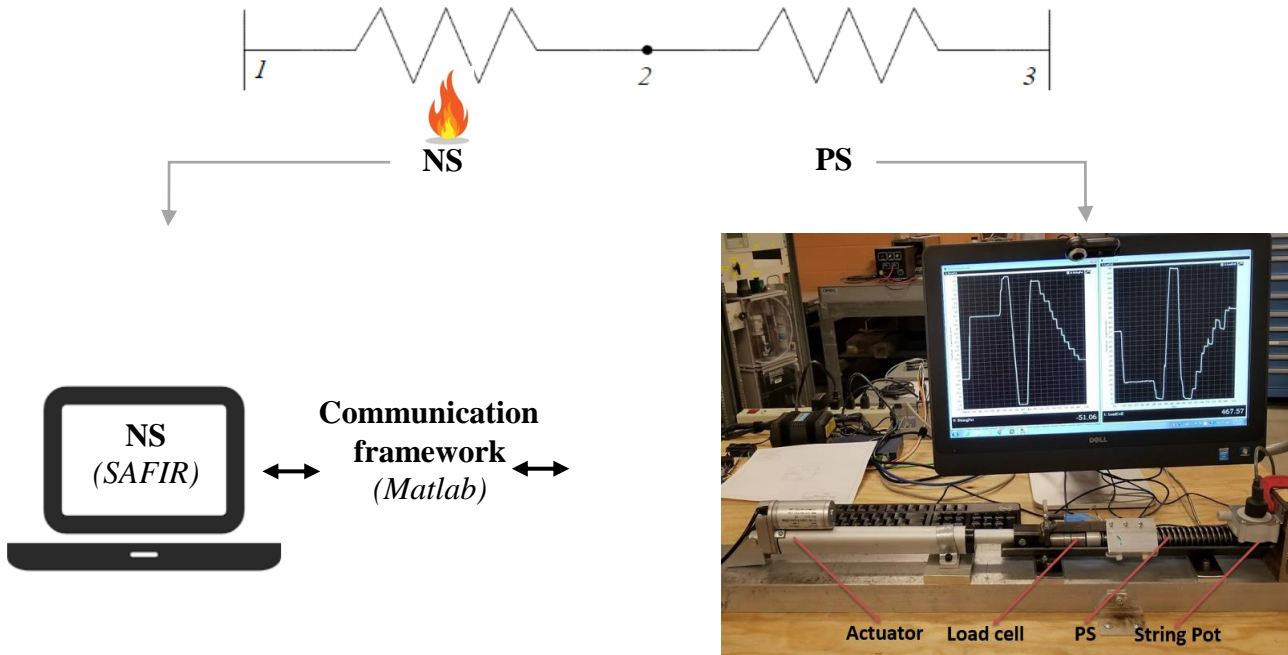


Fig. 5. HFT of the 1-DoF linear system

The test setup is presented in Fig. 5. The actuator is imposing the target displacement which is measured by the string pot. The force is measured by the load cell. The properties of the measurement instruments along with the uncertainty of measurements are presented towards the end of this section.

Fig. 6 presents force versus displacement at the interface, i.e., at node 2 (Fig. 5), during the HFT. The global solution results from the global numerical analysis of the 1-DoF linear system (referred to as “Global” on the plot) while the results from the HFT are “PS” (the interface solution of the PS) and “NS” (the interface solution of the NS). It is noted that this work is underway, and the results presented in the Fig. 6 are preliminary results. A time step of 10 s was used to update the interface displacement and the time to induce the target displacement was 1 s. During one-time step, the displacement is kept constant at the interface and this induces an increase of the reaction force of the heated substructure (NS in this case). Once the displacement is updated, the reaction force of the NS reduces and has the same value as the reaction force of the PS. This shows that the compatibility and the equilibrium are both satisfied in each time step. In order to reduce the spikes of the NS’s solution, a shorter time step can be used as presented in the VHFT (see Fig. 4 a)). A slight deviation of the HFT solution from the global analytical solution was observed toward the end of the test which could be due to the spring bowing out of plane once it gets compressed.

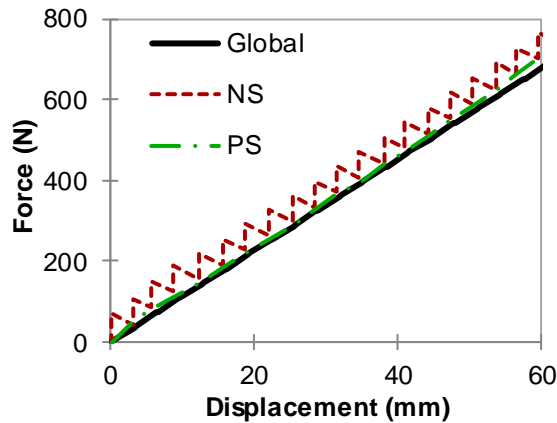


Fig. 6. Force-displacement during HFT of the 1-DoF linear system

This simplified HFT showed successful implementation of the developed communication framework. It is noted that this setup could be reversed where the fire load is applied to the PS instead of the NS. In real HFT applications, the fire would potentially be applied on the tested substructure (PS), as the unheated structure could be numerically modelled with less uncertainty than the heated sub-structure. This framework is also ready to be extended to more complicated systems with multiple DoF (requiring multiple actuators).

Although the work described herein is a proof of concept for the purpose of presenting the successful implementation of the developed communication framework, some details of the measurements are worth mentioning. It is noted that the string pot used was a Celesco SP2-50, with a 1270 mm maximum measuring length. Its combined uncertainty was $\pm 2\%$, and the total expanded uncertainty based on coverage factor of two (corresponding to a 95 % confidence interval) was 4 %. The load cell was an OMEGA LCWD-20K, with a 90 kN capacity. Its combined uncertainty was $\pm 10\%$, and the total expanded uncertainty was 20 %. The uncertainties for both measurements were calculated based on [21].

4 CONCLUSIONS

There is a lack of understanding of how structures, as whole systems, perform under realistic, uncontrolled fires. The Hybrid Fire Testing (HFT) method, through sub-structuring, and testing individual members/components, while simultaneously accounting for the action of the surrounding structure which is computationally modelled aside, has proven to have great potential for solving this problem. However, a main challenge in HFT is the continuous communication between the tested sub-structure and its numerically modelled surroundings. This paper presented the successful implementation of a newly developed communication framework for HFT. It was performed on a single degree-of-freedom linear system, both in a virtual and in a real setup.

DISCLAIMER

Certain commercial software or materials are identified to describe a procedure or concept adequately; such identification is not intended to imply recommendation, endorsement, or implication by the National Institute of Standards and Technology (NIST) that the software or materials are necessarily the best available for the purpose.

REFERENCES

1. Kiel, M. (1989). "Entwicklung einer intelligenten Prüfmaschine für brandbeanspruchte Gesamttragwerke." *Proceedings of the Braunschweiger Brandschutztag 1989*, Braunschweig, Germany.

2. Korzen, M., Magonette, G., Buchet, Ph. (1999). "Mechanical Loading of Columns in Fire Tests by Means of the Substructuring Method." *Zeitschrift für Angewandte Mathematik und Mechanik*, Vol. 79, pp. S617-S618.
3. Robert, F., Rimlinger, S., Collignon, C., (2009). "Promethee, Fire Resistance Facility Taking Into Account the Surrounding Structure." *1st international Workshop on Concrete Spalling due to Fire Exposure*, 2009, 3-5 sept.
4. Mostafei, H. (2013a). "Hybrid Fire Testing for Assessing Performance of Structures in Fire – Application." *Fire Safety Journal*, Vol. 56, pp. 30-38.
5. Whyte, C.A., Mackie, K.R. and Stojadinovici, B. (2016). "Hybrid Simulation of Thermomechanical Structural Response", *Journal of Structural Engineering*, 142(2): 04015107-1 – 04015107-11.
6. Schulthess, P., Neuenschwander, M., Knoblock, M. and Fontana, M. (2016). "Consolidated Fire Analysis – Coupled Thermo-Mechanical Modelling for Global Structural Fire Analysis", *9th International conference on Structures in Fire*, 8-10 June, pg. 819-826.
7. Tondini, N., Hoang, V. L., Demonceau, J.-F., & Franssen, J.-M. (2013). "Experimental and numerical investigation of high-strength steel circular columns subjected to fire." *Journal of Constructional Steel Research*, 80, 57-81.
8. Sauca, A., Mergny, E., Gernay, T., and Franssen, J.M. (2017a). "A method for Hybrid Fire Testing: Development, implementation and numerical application." *Proceedings of Applications of Structural Fire Engineering (ASFI'17)*, September 7-8.
9. ASTM E119-16a (2016). Standard test methods for fire tests of building construction and materials, 2016.
10. Rackauskaite, E., Kotsovinos, P., Jeffers, A., Rein, G. (2017b). "Structural analysis of multi-storey steel frame exposed to travelling fires and traditional design fires." *Engineering Structures*, 150, 271-287.
11. Choe, L., Ramesh, S, Hoehler, M., Seif, M., Gross, J., Zhang, C., and Bundy, M. (2018). "NIST Technical Note 1983. National Fire Research Laboratory Commissioning Project: Testing Steel Beams under Localized Fire Exposure."
12. Sauca, A., Zhang, C., Seif, M. (2018). "Stability of Steel Structures at Elevated Temperature: A Hybrid Fire Testing Approach" *Proceedings of the Annual Stability Conference*, April 10-13
13. Sauca, A., (2017). "Development and implementation of a methodology for hybrid fire testing applied to concrete structures with elastic boundary conditions." *Doctoral Thesis*, University of Liege, Liege, Belgium, 2017
14. OpenFresco 2016. "Open Framework for Experimental Setup and Control." UC Berkley
15. UI-SimCor, University of Illinois
16. Franssen, J.-M. (2005), "SAFIR, A Thermal/Structural Program Modelling Structures under Fire", *A.I.S.C. Engineering Journal*, 42 (3) 143–158.
17. Elliott, C., Vijayakumar, V., Zink, W., Hansen, R. (2007), "National Instruments LabVIEW: A Programming Environment for Laboratory Automation and Measurement" Cytokinetics, Inc., San Francisco, CA.
18. Sauca, A., Gernay, T., Robert, F., Tondini, N., & Franssen, J.-M. (2017b). "Hybrid Fire Testing: Discussion on Stability and Implementation of a New Method in a Virtual Environment." *Journal of Structural Fire Engineering* (in press).
19. Sadek, F., Main, J. A., Lew, H. S., Robert, S. D., Chiarito, V. P., and El-Tawil, S. (2010). "NIST Technical Note 1669. An Experimental and Computational Study of Steel Moment Connection under a Column Removal Scenario."
20. OpenSees. UC Berkley
21. Taylor, B., N., Kuyatt, C., E. (1994). "Guidelines for Evaluating and Expressing the Uncertainty of NIST Measurement Results." NIST Technical Note 1297

EXPERIMENTAL AND ANALYSIS OF LOCALIZED POOL FIRE TESTS ON STEEL COLUMNS WITH COMPARTMENT OPEN CEILING

Ali Nadjai¹, Sanghoon Han², Olivier Vassart³, Francois Hanus⁴

ABSTRACT

Elevated temperatures, above 400°C, starts altering the mechanical properties of steel and may lead to the collapse of a structure. Performance-based approaches allow designers to assess more precisely the elevation of temperature in a structure subjected to a compartment fire or under localised fire. This paper presents a part of a major research initiative funded by the European commission dealing with temperature assessment of a vertical steel members subjected to localised fires. Fire tests on a large-scale steel structure composed of different column sections has been carried out. The test measurements are focused on heat transfer in various steel column sections subjected to different fuel loads, kerosene, diesel and wood cribs. Temperature distributions have been recorded in the steel columns engulfed or situated outside the fire, using thermocouples and thermo-plates. Heat fluxes have also been measured at various locations. The evolution of the heat release rate generated by the fire has been obtained by use of a specifically instrumented calorimeter hood. The temperature along the vertical axis of the fire source has been compared to the temperatures predicted by the Annex C of EN-1992-1-2. The other measurements provide a large amount of data for the assessment of the heat received by a member situated outside the fire.

Keywords: Experimental, Localised Fire, Pool Fires, Column Analysis,

1 INTRODUCTION

In large compartments like atria, open car parks, railway stations, airports or commercial buildings, fire events often do not lead to fully-developed fires for several reasons: low level of fire load, non-uniform distribution of fire load, dimensions of the compartment, large ventilation, etc. In such cases, the fire is fuel-controlled and the gas temperature remains quite low in the compartment, except close to the fire source. Then, the application of performance-based approaches necessitates considering local fire scenarii to assess the evolution of temperature in the structural elements. The thermal impact of such localised fires depends not only on the flame temperature but also on the magnitude and dimensions of the flames as the major heat transfer is radiation. Hence, the exposure of the member will depend on the distance from the fire and the magnitude and dimensions of flames. Furthermore, only one part of the structural elements will be affected, where compartment fires implying a flashover represent a quite uniform thermal attack to the structure.

¹ Professor and Director of Fire Safety Engineering Research Technology Centre, Ulster University, Belfast, UK..
e-mail: a.nadjai@ulster.ac.uk

² Fire Safety Engineering Research Technology Centre, Ulster University, Belfast, UK..
e-mail: s.han@ulster.ac.uk

³ Head of ArcelorMittal Global R&D Long Carbon
e-mail: olivier.vassart@arcelormittal.com

⁴ Senior Research Engineer ArcelorMittal Long Products:
e-mail: francois.hanus@arcelormittal.com

On one hand, localised fire may allow a redistribution of internal forces to the less affected elements of a robust structure. On the other hand, the non-uniform action of the fire may cause thermal-induced bowing of the column and have an influence on the buckling resistance of the column. The consideration of such non-uniform distributions of temperature usually requires the use of finite element analyses.

For design purposes, data on localized fire can be determined by plume theories [1-3] which have been implemented in models of Eurocode 1 [4,5]. During the last decade, many researchers have investigated the thermal behaviour of steel columns subject to localised fire [6-10]. Experimental and numerical results have shown that temperatures in steel column are strongly influenced by the position of the localised fire (distance to the fire source, column adjacent to the fire, or column surrounded by the fire), the plume height (impacting or not impacting the ceiling), and the ventilation conditions. For columns exposed to fires not impacting the ceiling, the maximum temperatures are reached in the lower parts of the column (Ferraz, 2014). For columns surrounded by the fire, the failure condition is often similar to that of columns subject to post-flashover fires (Zhang et al., 2014). For columns, which are adjacent to a localised fire, the buckling temperature of the column may be much lower than that for columns subject to uniform heating conditions (Zhang et al., 2014). However, very limited experimental data from full-scale fire tests on columns is available in literature. This work summarises full-scale experiments on steel columns with different cross-sections exposed to pool fires using three different fuels: kerosene, diesel and wood cribs.

Overall objective of this research is to provide designers with scientific evidence database, put in design models and, in the future, in the regulations that will allow them to design steel (and other types of) columns subjected to localised fires such as those which may arise, for example, in car parks. In fact, at the time being, such evidence, models and regulations exist for beams located under the ceiling, but nothing is available for columns, and this may lead to unnecessary and excessive thermal insulation that jeopardizes the competitiveness of steel and composite structures

2 EXPERIMENTAL TEST PROGRAMME

2.1 Steel Structure

A 7m by 7m steel unprotected structure with 9 columns (IPE, CHS and HE sections) and 12 beams without ceiling was built under the large hood of 20 MW capacity inside the laboratory of FireSERT as shown in *Fig. 1*. The temperature measurements in the columns were measured under different combinations of fuel type, pool diameter and fire positions. The distance between two consecutive columns is 3.5 m and all the columns are 5 m high. The beams are situated 3.5m above ground floor.

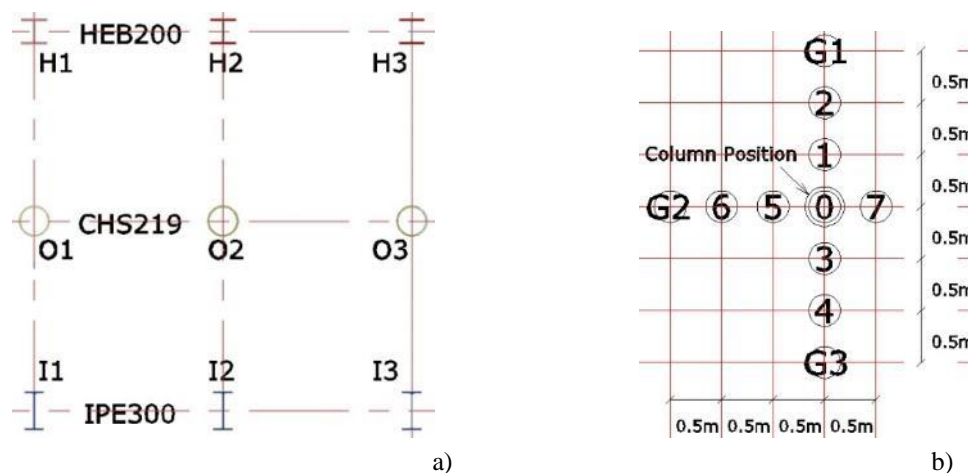


Fig. 1. Steel frame structure with fire pan load locations, a) View plan, b) Gardon gauges locations



Fig. 2. Preparation of tests with liquid fuel pans or wood cribs around the circular column

Thirty-seven experiments on steel columns exposed to localised fire were conducted at Ulster University. Details of fourteen selected tests are given in Table 1. These localised fire tests are focused on heat transfer to steel columns by fires implying various fuel types (kerosene, diesel and wood cribs). Temperature distributions in the surrounding steel structure were recorded using thermocouples, thermo-plates and heat flux measurements at different locations along the height of the columns.

Table 1. Fourteen selected tests are presented with no ceiling near different columns

Specimen	Test Number	Pan Diameter/ Position	Fuel/ Amount	Gordon Gage Position
Column O2	O1	0.7m / (1)	Kerosene/ 15L	G1
	O2	0.7m / (2)	Kerosene/ 15L	G1
	O3	0.7m / (1)	Diesel/ 15L	G1
	O4	0.7m / (2)	Diesel/ 15L	G1
	O8	1.6m/ (0)	Kerosene/ 60L	G1
	O9	0.7m / (1)(3)(5)(7)	Kerosene/ 60L	G1
	O10	1.6m / (0)	Diesel/ 60L	G1
	O12	1.6m/ (0)	Kerosene/ 20L	G1
	O14	Cribs/ (1)(3)(5)(7)	Wood/ 0.5x0.5x0.5m	G1
Column I2	I9	1.6m/ (0)	Kerosene/ 60L	G1, G2
	I10	1.6m/ (0)	Kerosene/ 20L	G1, G2
	I11	0.7m / (1)(5)(7)	Kerosene/ 45L	G1, G2
Column H2	H4	0.7m/ (6)	Kerosene/ 15L	G2, G3
	H7	1.6m/ (0)	Kerosene/ 20L	G2, G3

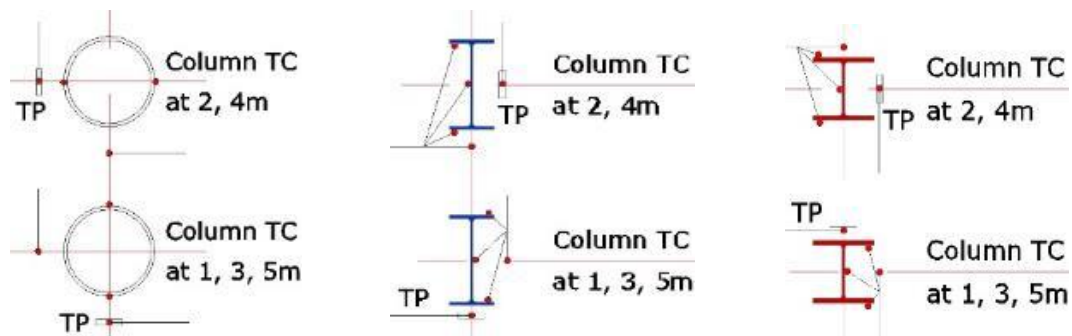
2.2 Fire loads

Three types of fuels (diesel, kerosene and crib woods) were used to create fire conditions during this investigation. The selection of fire fuel was based on the difference in density and flame speed reaction. All columns were exposed to different circular steel pool of fire placed at different locations around the columns as shown in *Figs 2 and 3*. A single pan with a diameter of 1.6m or multiple pans with 0.70m diameter (providing max diameter equal to 2.2 m) and having a typical depth of 0.20m, were used for the experiments as shown in *Fig. 4*.

2.3 Measurement and instrumentation

Thermocouples (K-type) and thermo-plates were installed to measure temperature profiles on the column and gas temperature near the columns. Heat flux was also measured to determine the heat

generated by different fuels through Gardon gauges. These gauges were placed at 1m and 2m height and at a distance of 1.5 m from the column centre in two directions. Heat release rate was calculated using a calorimeter and recorded by modern data logging system available at the facility.



CHS219(t : 10mm,
 $A_m/V=100m^{-1}$)

IPE300(t_w : 7.1mm, t_f : 10.7mm,
 $A_m/V=216m^{-1}$)

HEB200(t_w : 9mm, t_f : 15mm,
 $A_m/V=147m^{-1}$)

Fig. 5.

Typical thermocouple and plates arrangement around column

Figure 5 illustrates typical thermal couple locations and their arrangement at different columns cross-sections and along their height. Plate thermocouples were used to measure the adiabatic surface temperatures which can be used to calculate heat transfer when limited information is available. Free standing thermocouples were positioned adjacent to the column on the unexposed side at heights 1.0m, 2.0m, 3.0m, 4.0m and 5.0m above floor level.

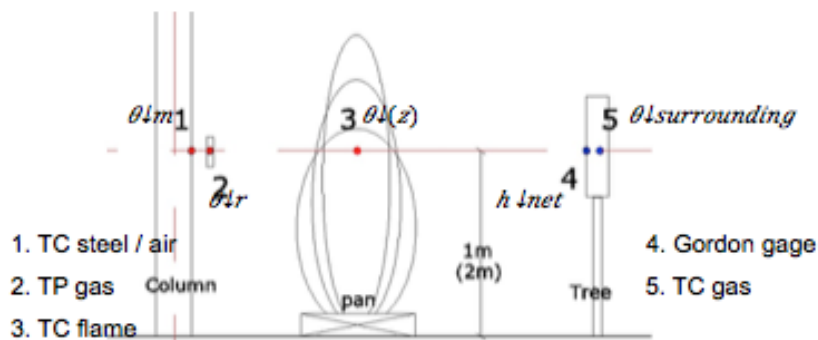


Fig.6. Typical heat flux measurements on steel column adjacent to localized fire

Fig. 6 shows typical heat flux measurements on steel column adjacent to localized fire sources from prospective of an application to the structural fire safety design of steel construction.

Experiments were conducted under the 20MW calorimeter whose dimensions on the ground are 9m by 9m with a height of 9m above the floor. The Heat Release Rate (Q) was measured in kilowatts (kW) which shows the importance of fire and its damage potential. The heat release rate value is directly related to flame height, which indicated the significance of flame height. Furthermore, the heat release rate is directly connected to the radiant heat flux surrounding the fire and potential for fire growth and flashover.

3 RESULTS OF THE FIRE TESTS

As the compartment is not enclosed and resulting variations in the behaviour of the flame can be seen, mostly resulting from a cross wind in the fire hall which had a maximum speed of 0.7m/s. Because of this natural air flow in the fire hall, the flames were tilted away from the steel column in some experiments. This tilting may also result in the variation of thermo-plate temperature

recordings. Logically, at higher locations on the column, the effects of this tilting are more prominent as compared to that on the lower locations. Fig. 7 shows the steel temperatures distribution along the height of the columns with different shapes (CHS, HE, IPE) subjected to different fires and fuel quantity. It can be observed that the IPE-section web temperature is higher than the one of CHS and HE column sections. This results due to lower thickness of web of the I-section. The shadow effect caused the temperature at 1 m H-column height is not the same as that for the CHS column cross section. It can be seen that the steel temperatures of all column sections tested with different fuel exceed the 300°C at 1m and 2m heights and reaches the range in which steel mechanical properties are reduced

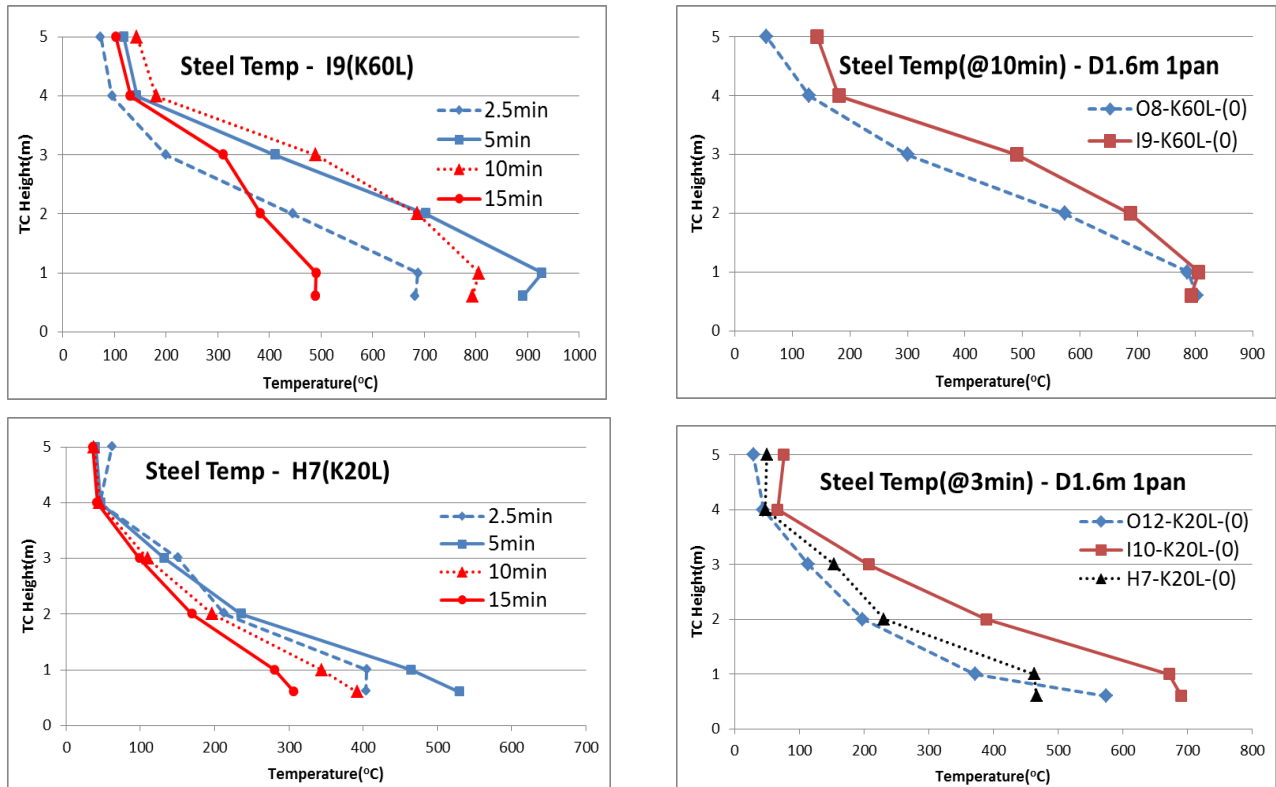


Fig. 7. Steel Temperature comparison between the different cross sections

3.1 Heat Flux

Fig. 8 illustrates the experimental heat flux recorded and compared with equation 6 when gain and loss heat fluxes are considered taking into consideration the experimental results or data. It can be seen that the calculated Heat flux is in good agreement when compared with the experimental tests using:

- **Heat flux Gain**

$$h_{net} = \alpha_c (\theta_g - \theta_m) + \Phi \cdot \varepsilon_m \cdot \varepsilon_f \cdot \sigma \cdot [(\theta_r + 273)^4 - (\theta_m + 273)^4]$$

- **Heat flux Loss**

$$h_{net,loss} = (1 - \Phi) \cdot \varepsilon_{fus} \cdot \sigma [(\theta_{m2} + 273)^4 - (20 + 273)^4] + \alpha_c (\theta_m - 20)$$

Experimental and analysis of localised pool fire tests on steel columns with compartment open ceiling

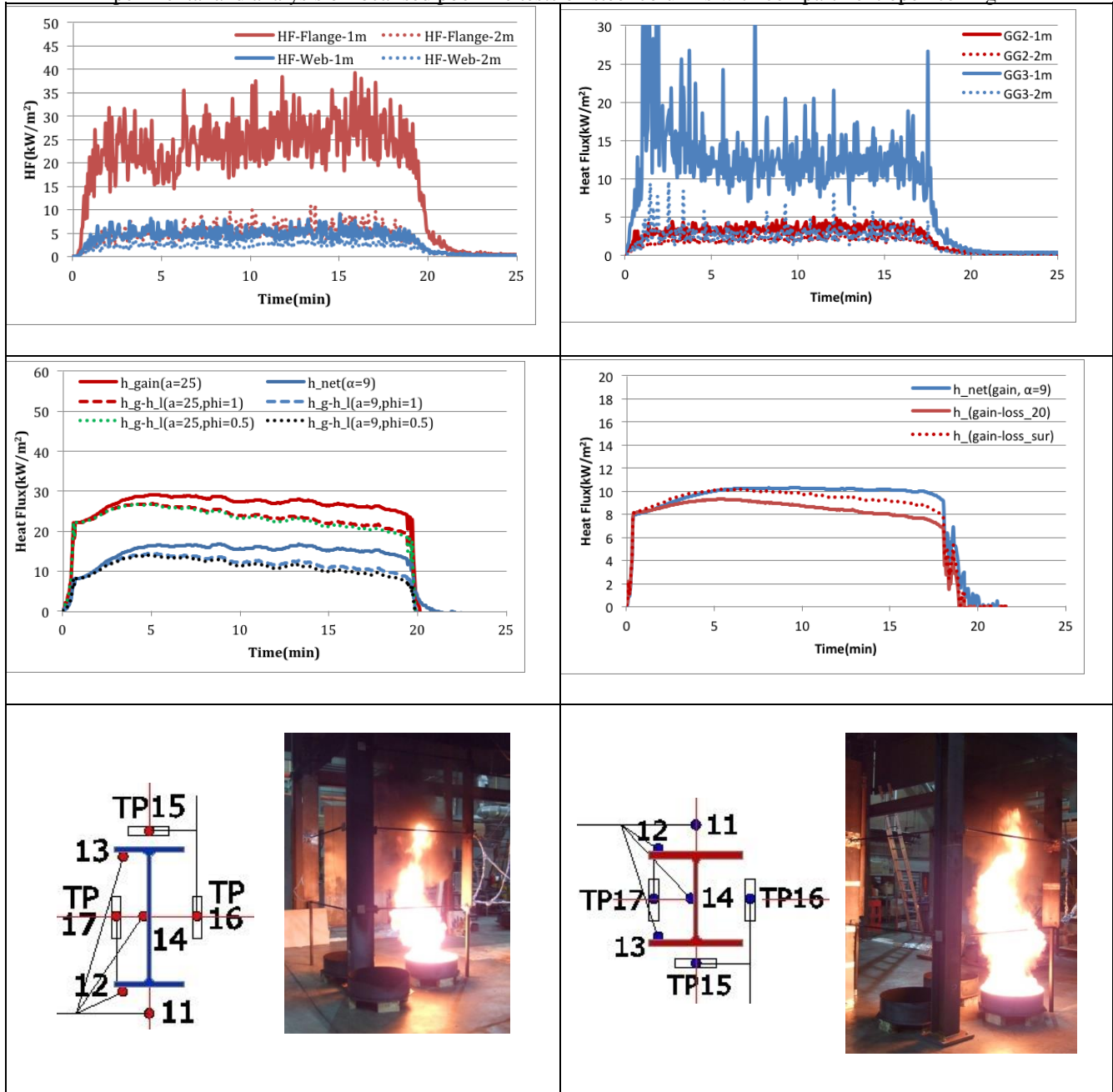


Fig. 8. Heat flux calculation using the experimental results data of tests I9 and H7

One of the most important prerequisites for application of the general expression of net heat flux is the configuration factor Φ ; in EN 1991-1-2 (2002) which presents a method to calculate the configuration factor in columns exposed to external fires. Similar studies should be conducted to estimate the configuration factor in localised fire scenarios.

3.2 Flame Temperature compared with Annex C (EN 1991-1-2)

In case of localized fire, the height of flames depends on burning source size D and HRR

$$L_f = -1.02 \cdot D + 0.0148 \cdot Q^{2/3} \quad (1)$$

Where; D : flame diameter [m] and Q : Rate of Heat Release [W]

When the flame is not effected by the ceiling of a compartment, the temperature $\theta_{(z)}$ in the plume along the symmetrical vertical flame axis is given by:

$$\theta_{(z)} = 20 + 0.25 \cdot Q_c^{2/3} \cdot (z - z_0)^{-5/3} \leq 900 \quad (2)$$

$$z_0 = -1.02 \cdot D + 0.00524 \cdot Q^{2/3} \quad (3)$$

Q_c is the convective part of the HRR[W], considered as equal to $0.8Q$

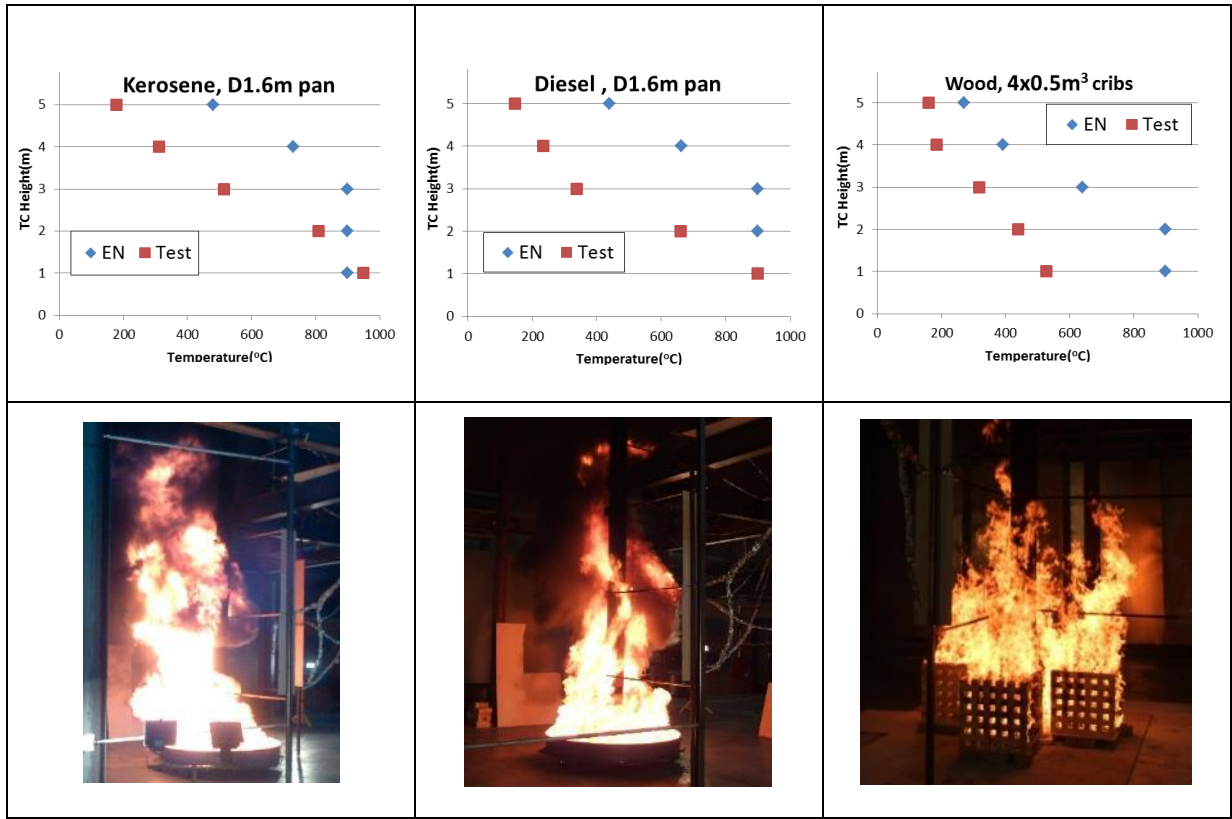


Fig. 9. * TC are located on steel column, middle of 4 wood cribs. (Test No. O14)

3.3 Steel Temperature Development (EN 1993-1-2)

Assuming a uniform temperature distribution in the cross-section, the increase of temperature $\Delta\theta_{a,t}$ in an unprotected steel member during a time interval Δt should be determined from:

$$\Delta\theta_{a,t} = k_{st} \frac{A_m/V}{c_a \rho_a} \dot{h}_{net,t} \Delta t \quad (4)$$

On exposed fire surfaces, the net heat flux $\dot{h}_{net,t}$ should be determined considering heat transfer by convection and radiation as;

$$\dot{h}_{net,t} = \dot{h}_{net,t,c} + \dot{h}_{net,t,r} \quad (5)$$

where

$$\dot{h}_{net,t,c} = \alpha_c \cdot (\theta_g - \theta_{s,n}) \quad (6)$$

$$\dot{h}_{net,t,r} = \Phi \cdot \varepsilon_m \cdot \varepsilon_f \cdot \sigma \cdot [(\theta_r + 273)^4 - (\theta_m + 273)^4] \quad (7)$$

Using a time step of five seconds, a simple spreadsheet-based calculation procedure was used to calculate the relationship (see Table 3) and compared with the recorded data during the tests.

Table 3. Comparison of steel temperature predicted by Heskestad method and measured during the tests (experimental data from TC on steel 5 min after ignition)

HEIGHT	TEST NO. O8 (KEROSENE, D1.6M)		TEST NO. O10 (DIESEL, D1.6M)		TEST NO. I9 (KEROSENE, D1.6M)	
	EN	EXP.	EN	EXP.	EN	EXP.
1M	678	545	678	550	828	790
2M	678	313	678	230	828	627
3M	678	156	678	113	828	342
4M	438	62	356	48	584	128
5M	181	60	153	45	227	100

4 CONCLUSIONS

From this study, we may conclude that Eurocode recommendations overestimate the thermal exposures as steel temperatures of members subjected to localised fire may be over-estimated by several hundred degrees. By example, the assumption of the flame emissivity equal to 1 in the Eurocodes appears to be a very safe assumption.

This study also provides a large amount of experimental data for the development and calibration of CFD models. Analytical investigations could also lead to the development of new methods for the assessment of vertical members subjected to localised fires.

The tests have shown that, even for tests performed inside a laboratory, the flame tilting was influencing quite significantly the measurements.

ACKNOWLEDGMENT

To the Research Fund for Coal and Steel for the project funding (RFSR-CT-2012-00023).

REFERENCES

1. Le Pense P., "Les parkings aériens en structure acier: développements récents / Multi-storey car parks in steel structure: last developments", La Revue de Métallurgie-CIT, p. 867-874, Octobre 2002.
2. Hasemi, Y., Thermal Modeling Of Upward Wall Flame Spread. Fire Safety Science 1, pp. 87-96, 1986
3. Heskestad, G. "Fire plumes", The SFPE Handbook of Fire Protection Engineering, Quincy, Mass.: National Fire Protection Association, pp. 2-9, 1995.
4. Eurocode 1: Actions on structures – Part 1-2: General actions – Actions on structures exposed to fire", European committee for standardization, November 2002, 59p.
5. EN 1991-1-1, 2009. Eurocode 1 - Design of steel structures – Part 1-1: General actions, Densities, self-weight, imposed loads for buildings. Brussels: CEN.
6. Kamikawa, D., Hasemi, Y., Wakamatsu, T. & Kagiya, K., Experimental Flame Heat Transfer Correlations For A Steel Column Adjacent To And Surrounded By A Pool Fire. Fire Safety Science 7, pp. 989-1000, 2003.
7. Wald F., Chlouba J., Uhl.r A., Kallerov. P., Stujberov. M. "Temperatures during fire tests on structure and its prediction according to Eurocodes". Fire Safety Journal, p. 135–146, 2009.
8. Zhang C., Gross J. L., Choe L., "Behavior of steel components subjected to localized fire", 8th International Conference on Structures in Fire, Shanghai, China, June 11-13, pp.171-178, 2014.
9. Bystrom, A., Sj.str.m, J., Wickstr.m, U., Lange D., Veljkovic, M. "Large scale test on a steel column exposed to localized fire", Journal of Structural Fire Engineering, Vol.5, n.2, 2014.
10. Zhang C., Gross J. L., Choe L., "Behavior of steel components subjected to localized fire", 8th International Conference on Structures in Fire, Shanghai, China, June 11-13, pp.171-178,

AUTHOR INDEX

A

Abdalla J, p107
Abu A, p611
Achenbach M, p101
Agarwal A p157, p139, p949
Ahn J, p853
Alabi-Bello M A, p835
Alam N, p473
Albero V, p569
Ali F, p147, p473, p489
Al-Nuaimi N, p107
Alos-Moya J, p497
Alston J, p217
Andres B, p625
Anvari A T, p265
Ariyanayagam A D, p641, p193
Asimakopoulou E, p901
Atefi H, p489
Au F T K, p505
Audebert M, p375, p577
Azevedo J, p819

B

Bączkiewicz J, p679, p725
Baertschi R, p77
Bahai H, p843
Bamonte P, p139
Barber D, p209, p217
Battini J-M, p325
Benýšek M, p391
Béreyziat A, p577
Bhatt P, p107
Bijlaard F, p717
Bilotta A, p593
Bisby L, p811
Blesák L, p391
Boko I, p619
Bolanos A, p545
Both I, p711
Bouchaïr A, p577
Boyce V, p795, p797
Brandon D, p241, p249, p299, p989
Brunkhorst S, p537
Bundy M, p249, p601
Burgess I, p619

C

Cábová K, p391
Cai W, p359
Caillet N, p663
Camargo A, p521

Cardoso R, p843
Carlo T, p69
Carvel R, p3
Cashell K, p349
Chang P, p877
Charlier M, p341
Chaudhary R K, p431
Chen B, p513
Chen H, p717
Chen L, p61
Chernovsky A, p997
Chinthapalli H K, p157
Choe L, p601
Chotzoglou K, p901
Clark T, p117
Clifton C, p611
Compagnone A, p593
Couto C, p779, p819
Craveiro H, p585

D

Dahli R, p275
Dai X, p3, p341, p455
Daryan A S, p33
Dasari A, p85, p201
Delichatsios M, p901
Dinu F, p711
Divić V, p619
Dixon R, p217
Dolinar U, p133
Douk N, p375
Drion G, p861
Du Y, p733
Durif S, p577
Dwiputra R, p561

E

Eichhorn-Gruber M, p383
Elhami-Khorasani N, p933
Engelhardt M, p33, p359
Erez G, p885
Espinós A, p569

F

Fahrni R, p257
Fakury R, p521
Ferreira J D R, p317
Ferrier E, p367, p941
Fischer E, p25
Flint G, p11, p811
Fontana M, p77
Frangi A, p183, p241, p257, p283

Franssen J-M, p317, p341, p703, p861
Fu I, p771

G

Gaillard S, p663
Gales J, p173, p275
Gamba A, p341, p633
Gardner L, p513, p695
Gernay T, p101, p317, p633, p703, p861, p893
Gillie M, p275
Giuliani L, p803
Glassman J, p795
Glema A, p407, p585
Gnanachelvam S, p193
Goreta M, p619
Green M, p41
Gross J, p601
Grosshandler W, p601
Guo Q, p17

H

Hajiloo H, p41
Han C, p61
Han L, p513
Han S, p1005
Hanus F, p473, p663, p755, p885, p1005
Häßler D, p649
Häßler M, p649
Haweeleh R, p107
Heinisuo M, p679
Hirashima T, p291, p561
Hochenauer C, p383
Hoehler M, p249, p299, p601, p625
Hofmann J, p165, p439
Hopkin D, p771, p893
Hospitaler A, p415, p497
Hospitaler T, p415
Hothan S, p649
Hozjan T, p133
Hu J, p3
Hu Y, p967
Hussain S, p93

I

Ichikawa M, p291
Ishii S, p291

J

Jayachandran A, p827

Jeanneret C, p173
Jeffers A, p463
Jiang J, p399, p655, p687,
p733
Jiang L, p41, p349
Jiang X, p717
Jiang Y-Q, p925, p975
Jokinen T, p725
Just A, p233, p283

K

Kalaba N, p139
Kahanji C, p147
Katakura Y, p291
Keerthan P, p193
Ketabdari H, p33
Khan M A, p349
Khorasani N E, p893
Kim R, p853
Kimball A, p249, p299
Kimura K, p561
Kleiboemer I, p569
Klippel M, p241, p257
Kodur V, p107, p139, p529,
p763, p949
Koh S K, p553
Kohno M, p959
Kotsovinos P, p11, p173,
p811
Krüger S, p649
Kumi G A, p967
Kwon O-S, p853

L

Lafrance P-S, p249
Laím L, p529, p695
Lakhani H, p165, p439
Lange D, p241, p989
Li G-Q, p655, p687, p733,
p741, p747
Li J, p505
Li L, p733
Li L-Z, p909
Li Q-H, p481
Li X, p61
Li Y, p869
Liu J-C, p917
Liu J-J, p925
Liu W, p333
Liu X, p909
Lopes N, p779, p819
Lou G-B, p655, p 925, p975
Lu F, p77
Lu G-J, p925
Lu J-F, p481
Lu Z-D, p909

M

Ma T, p309
Magarabooshanam H, p641
Mäger K N, p283
Mahamid M, p265
Mahendran M, p193, p641
Maia E, p779
Main J, p399
Malaska M, p679
Malendowski M, p407, p423
Maluk C, p117, p545
Maraveas C, p703
Marginean I, p711
Martinez J, p463
Matsagar V, p431
Mayrhofer M, p383
Mendis P, p125, p981
Mensingher M, p537, p553
Mergny E, p861
Meyer P, p553, p569
Miao J-R, p741
Mielcarek A, p407
Mohammadjani C, p611
Molkens T, p447
Moreyra Garlock M, p787,
p795
Morgenthal G, p101
Morovat M, p33, p359
Mund M, p569
Murakami Y, p561

N

Nadjai A, p147, p473, p489,
p1005
Naito C, p17
Neagu C, p711
Ng Y H, p201
Ngo T, p125, p981
Nguyen H, p51
Nguyen K, p125, p981
Nguyen P L, p367
Nigro E, p593

O

Okazaki T, p959
Östman B, p249, p299
Ozaki F, p561, p671

P

Pagán-Martínez J, p415
Pajunen S, p679
Palma P, p183
Pancheti J, p827
Panev Y, p11, p811
Payá-Zaforteza I, p415, p497
Pfenning S, p537
Pimienta P, p869

Pinoteau N, p869
Pires T, p521
Possidente L, p325
Poteralski A, p407
Prieler R, p383

Q

Qiang X, p717
Quiel S, p17
Qureshi R, p933

R

Ramesh S, p601
Randaxhe J, p755
Rein G, p173
Rezaeian A, p877
Ridout A, p9117
Risco G-V, p803
Rodrigues J P, p69, p521,
p529, p695
Romero M L, p569
Rong, J-Z, p925
Root K, p17
Roy T, p431

S

Sadek F, p399
Salminen M, p725
Sander L, p225
Sauca A, p997
Sautot C, p885
Schaumann P, p225, p553,
p569
Schmid J, p241, p257, p299,
p989
Schwabegger G, p383
Seif M, p601, p997
Sharma U K, p93
Si Larbi A, p375
Sieverts L, p217
Sjöström J, p241, p989
Smardz P, p407
Sofroniev T, p811
Su J, p249, p299
Sun C-J, p481
Szymkuć W, p407, p585

T

Tan K H, p51, p85, p201,
p869, p917
Tan Q, p513
Tang S L, p967
Thauvoye C, p885
Thiry A, p885
Tiainen T, p725
Tiso M, p233
Tofilo P, p423

Tokłowicz P, p585
Tondini N, p325
Torero J, p545
Torić N, p619
Torra-Bilal I, p265
Tran M T, p941
Trtnik G, 133

U

Usmani A, p3, p41, p349,
p455, p843

V

Van Coile R, p771, p893
van der Merwe J E, p77
Varma A, p25
Vassart O, p341, p473,
p663, p755, p1005
Vial Real P, p779, p819
Vu X H, p367, p375, p941

W

Wald F, p391
Wang C, p655
Wang L, p333
Wang W, p763
Wang X, p853
Wang Y C, p61, p835
Weerasinghe P, p125
Węgrzyński W, p423
Wei K, p909
Weigand J, p399
Weisheim W, p225
Welch S, p341, p455
Woodburn P, p11
Wu X Q, p505

X

Xu L, p309
Xu Q, p61
Xu Q, p747
Xu S-L, p481
Xue W, p61

Y

Yahyai M, p33, p877
Yarlagadda T, p41
Ye K, p671
Yeo I, p853
Yotsumoto N, p561

Z

Zaharia R, p711
Zania V, p803
Zehfuß J, p225, p537
Zeman F, p391
Zhang C, p997

Zhang D, p85
Zhang J, p901
Zhang L, p333
Zhang L, p763
Zhang Y, p513
Zhang Y, p61
Zhao X, p747
Zhao X-Y, p747
Zhong B, p925
Zhong B, p975
Zhou H, p763
Zhou M, p843

